

New Manual of Seismological Observatory Practice - NMSOP

New Manual of Seismological Observatory Practice (2002), revised version, electronically published 2009

[Search fulltext and list articles.](#)

[Preface](#)

[Editorial remarks](#)

[Authors \(their contributions to the NMSOP and addresses\)](#)

Chapters

[CHAPTER 1: Aim and Scope of the IASPEI New Manual of Seismological Observatory Practice](#)

(P. Bormann)

[PDF.](#) - DOI: [10.2312/GFZ.NMSOP_r1_ch1](https://doi.org/10.2312/GFZ.NMSOP_r1_ch1)

[CHAPTER 2: Seismic Wave Propagation and Earth Models](#) (P. Bormann, E. R. Engdahl and R. Kind)

[PDF.](#) - DOI: [10.2312/GFZ.NMSOP_r1_ch2](https://doi.org/10.2312/GFZ.NMSOP_r1_ch2)

[CHAPTER 3: Seismic Sources and Source Parameters](#) (P. Bormann, M. Baumbach, G. Bock, H. Grosse, G. L. Choy and J. Boatwright)

[PDF.](#) - DOI: [10.2312/GFZ.NMSOP_r1_ch3](https://doi.org/10.2312/GFZ.NMSOP_r1_ch3)

[CHAPTER 4: Seismic Signals and Noise](#) (P. Bormann)

[PDF.](#) - DOI: [10.2312/GFZ.NMSOP_r1_ch4](https://doi.org/10.2312/GFZ.NMSOP_r1_ch4)

[CHAPTER 5: Seismic Sensors and their Calibration](#) (E. Wielandt)

[PDF.](#) - DOI: [10.2312/GFZ.NMSOP_r1_ch5](https://doi.org/10.2312/GFZ.NMSOP_r1_ch5)

[CHAPTER 6: Seismic Recording Systems](#) (G. Asch)

[PDF.](#) - DOI: [10.2312/GFZ.NMSOP_r1_ch6](https://doi.org/10.2312/GFZ.NMSOP_r1_ch6)

[CHAPTER 7: Site Selection, Preparation and Installation of Seismic Stations](#) (A. Trnkoczy, P. Bormann, W. Hanka, L. G. Holcomb and R. L. Nigbor)

[PDF.](#) - DOI: [10.2312/GFZ.NMSOP_r1_ch7](https://doi.org/10.2312/GFZ.NMSOP_r1_ch7)

[CHAPTER 8: Seismic Networks](#) (A. Trnkoczy, J. Havskov and L. Ottemöller)

[PDF.](#) - DOI: [10.2312/GFZ.NMSOP_r1_ch8](https://doi.org/10.2312/GFZ.NMSOP_r1_ch8)

[CHAPTER 9: Seismic Arrays](#) (J. Schweitzer, J. Fyen, S. Mykkeltveit and T. Kvaerna)

[PDF.](#) - DOI: [10.2312/GFZ.NMSOP_r1_ch9](https://doi.org/10.2312/GFZ.NMSOP_r1_ch9)

[CHAPTER 10: Seismic Data Formats, Archival and Exchange](#) (B. Dost, J. Zednik, J. Havskov, R. J. Willemann and P. Bormann)

[PDF.](#) - DOI: [10.2312/GFZ.NMSOP_r1_ch10](https://doi.org/10.2312/GFZ.NMSOP_r1_ch10)

[CHAPTER 11: Data Analysis and Seismogram Interpretation](#) (P. Bormann, K. Klinge and S. Wendt)

[PDF](#). - DOI: [10.2312/GFZ.NMSOP_r1_ch11](https://doi.org/10.2312/GFZ.NMSOP_r1_ch11)

[CHAPTER 12: Intensity and Intensity Scales](#) (R. M. W. Musson)

[PDF](#). - DOI: [10.2312/GFZ.NMSOP_r1_ch12](https://doi.org/10.2312/GFZ.NMSOP_r1_ch12)

[CHAPTER 13: Volcano Seismology](#) (J. Wassermann)

[PDF](#). - DOI: [10.2312/GFZ.NMSOP_r1_ch13](https://doi.org/10.2312/GFZ.NMSOP_r1_ch13)

Datasheets

[DS 2.1: Global 1-D Earth Models](#) (P. Bormann)

[PDF](#). - DOI: [10.2312/GFZ.NMSOP_r1_DS_2.1](https://doi.org/10.2312/GFZ.NMSOP_r1_DS_2.1)

[DS 3.1: Magnitude calibration functions and complementary data](#) (P. Bormann)

[PDF](#). - DOI: [10.2312/GFZ.NMSOP_r1_DS_3.1](https://doi.org/10.2312/GFZ.NMSOP_r1_DS_3.1)

[DS 5.1: Common seismic sensors](#) (E. Wielandt)

[PDF](#). - DOI: [10.2312/GFZ.NMSOP_r1_DS_5.1](https://doi.org/10.2312/GFZ.NMSOP_r1_DS_5.1)

[DS 11.1: Additional local and regional seismogram examples](#) (K. Klinge)

[PDF](#). - DOI: [10.2312/GFZ.NMSOP_r1_DS_11.1](https://doi.org/10.2312/GFZ.NMSOP_r1_DS_11.1)

[DS 11.2: Additional seismogram examples in the distance range 13°-100°](#) (K. Klinge)

[PDF](#). - DOI: [10.2312/GFZ.NMSOP_r1_DS_11.2](https://doi.org/10.2312/GFZ.NMSOP_r1_DS_11.2)

[DS 11.3: Additional seismogram examples at distances beyond 100°](#) (K. Klinge, S. Wendt, P. Bormann)

[PDF](#). - DOI: [10.2312/GFZ.NMSOP_r1_DS_11.3](https://doi.org/10.2312/GFZ.NMSOP_r1_DS_11.3)

[DS 11.4: Record examples of underground nuclear explosions](#) (K. Klinge, J. Schweitzer, P. Bormann)

[PDF](#). - DOI: [10.2312/GFZ.NMSOP_r1_DS_11.4](https://doi.org/10.2312/GFZ.NMSOP_r1_DS_11.4)

Exercises

[EX 3.1: Magnitude determinations](#) (P. Bormann)

[PDF](#). - DOI: [10.2312/GFZ.NMSOP_r1_EX_3.1](https://doi.org/10.2312/GFZ.NMSOP_r1_EX_3.1)

[EX 3.2: Determination of fault plane solutions](#) (M. Baumbach, P. Bormann)

[PDF](#). - DOI: [10.2312/GFZ.NMSOP_r1_EX_3.2](https://doi.org/10.2312/GFZ.NMSOP_r1_EX_3.2)

[EX 3.3: Take-off angle calculations for fault plane solutions and reconstruction of nodal planes from the parameters of fault-plane solutions](#) (P. Bormann)

[PDF](#). - DOI: [10.2312/GFZ.NMSOP_r1_EX_3.3](https://doi.org/10.2312/GFZ.NMSOP_r1_EX_3.3)

[EX 3.4: Determination of source parameters from seismic spectra](#) (M. Baumbach, P. Bormann)

[PDF](#). - DOI: [10.2312/GFZ.NMSOP_r1_EX_3.4](https://doi.org/10.2312/GFZ.NMSOP_r1_EX_3.4)

[EX 3.5: Moment-tensor determination and decomposition](#) (F. Krüger, G. Bock)

[PDF](#). - DOI: [10.2312/GFZ.NMSOP_r1_EX_3.5](https://doi.org/10.2312/GFZ.NMSOP_r1_EX_3.5)

[EX 4.1: Bandwidth-dependent transformation of noise data from frequency into time domain and vice versa](#) (P. Bormann, E. Wielandt)

[PDF](#). - DOI: [10.2312/GFZ.NMSOP_r1_EX_4.1](https://doi.org/10.2312/GFZ.NMSOP_r1_EX_4.1)

[EX 5.1: Plotting seismograph response \(BODE-diagram\)](#) (J. Bribach)

[PDF](#). - DOI: [10.2312/GFZ.NMSOP_r1_EX_5.1](https://doi.org/10.2312/GFZ.NMSOP_r1_EX_5.1)

[EX 5.2: Estimating seismometer parameters by step function \(STEP\)](#) (J. Bribach)

[PDF](#). - DOI: [10.2312/GFZ.NMSOP_r1_EX_5.2](https://doi.org/10.2312/GFZ.NMSOP_r1_EX_5.2)

[EX 5.3: Seismometer calibration by harmonic drive](#) (J. Bribach)

[PDF](#). - DOI: [10.2312/GFZ.NMSOP_r1_EX_5.3](https://doi.org/10.2312/GFZ.NMSOP_r1_EX_5.3)

[EX 5.4: Seismometer calibration with program CALEX](#) (E. Wielandt)

[PDF](#). - DOI: [10.2312/GFZ.NMSOP_r1_EX_5.4](https://doi.org/10.2312/GFZ.NMSOP_r1_EX_5.4)

[EX 5.5: Determination of seismograph response from poles and zeros](#) (E. Wielandt)

[PDF](#). - DOI: [10.2312/GFZ.NMSOP_r1_EX_5.5](https://doi.org/10.2312/GFZ.NMSOP_r1_EX_5.5)

[EX 11.1: Estimating the epicenters of local and regional seismic sources by hand, using the circle and chord method](#) (P. Bormann, K. Wylegalla)

[PDF](#). - DOI: [10.2312/GFZ.NMSOP_r1_EX_11.1](https://doi.org/10.2312/GFZ.NMSOP_r1_EX_11.1)

[EX 11.2: Earthquake location at teleseismic distances by hand from 3-component records](#) (P. Bormann, K. Wylegalla)

[PDF](#). - DOI: [10.2312/GFZ.NMSOP_r1_EX_11.2](https://doi.org/10.2312/GFZ.NMSOP_r1_EX_11.2)

[EX 11.3: Identification and analysis of short-period core phases](#) (S. Wendt, P. Bormann)

[PDF](#). - DOI: [10.2312/GFZ.NMSOP_r1_EX_11.3](https://doi.org/10.2312/GFZ.NMSOP_r1_EX_11.3)

Information Sheets

[IS 2.1: Standard nomenclature of seismic phases](#) (D. A. Storchak, P. Bormann, J. Schweitzer)

[IS 3.1: Theoretical source representation](#) (H. Grosser, P. Bormann, A. Udias)

[IS 3.2: Proposal for unique magnitude nomenclature](#) (P. Bormann)

[IS 5.1: Strainmeters](#) (W. Zürn)

[IS 5.2: Constructing response curves: Introduction to the BODE-diagram](#) (J. Bribach)

[IS 7.1: What to prepare and provide if seismic site selection is purchased?](#) (A. Trnkoczy)

[IS 7.2: Using existing communication tower sites as seismic sites](#) (A. Trnkoczy)

[IS 7.3: Recommended minimal distances of seismic sites from sources of seismic noise](#) (A. Trnkoczy)

[IS 7.4: Detectability and earthquake location accuracy modeling of seismic networks](#) (M. Živčić, J. Ravnik)

[IS 8.1: Understanding and parameter setting of STA/LTA trigger algorithm](#) (A. Trnkoczy)

[IS 8.2: Seismic data transmission links used in seismology in brief](#) (A. Trnkoczy)

[IS 8.3: Retrieving data from IRIS/USGS stations](#) (C. Peterson)

[IS 10.1: Data-Type Bulletin IMS1.0: Short](#) (R. J. Willemann)

[IS 10.2: Example of station parameter reports grouped according IMS1.0 with ISF1.0 extensions](#) (R. J. Willemann)

[IS 10.3: Access to the CMR seismic/hydroacoustic/infrasonic data](#) (X. Yang, R. North)
[IS 11.1: Earthquake location](#) (J. Havskov, P. Bormann, J. Schweitzer)
[IS 11.2: Reports and bulletins](#) (G. Hartmann)
[IS 11.3: Animation of seismic ray propagation and seismogram formation](#) (S. Wendt, U. Starke, P. Bormann)

Program Descriptions

[PD 4.1: NOISECON](#) (E. Wielandt)
[PD 5.1: CALIBRAT](#) (J. Bribach)
[PD 5.2: CALEX](#) (E. Wielandt)
[PD 5.3: DISPCAL](#) (E. Wielandt)
[PD 5.4: DISPCAL1](#) (E. Wielandt)
[PD 5.5: TILTCAL](#) (E. Wielandt)
[PD 5.6: SINFIT](#) (E. Wielandt)
[PD 5.7: UNICROSP](#) (E. Wielandt)
[PD 5.8: POL_ZERO](#) (E. Wielandt)
[PD 5.9: WINPLOT](#) (E. Wielandt)
[PD 11.1: HYPOSAT/HYPOMOD](#) (J. Schweitzer)
[PD 11.2: LAUFZE/LAUFPS](#) (J. Schweitzer)

Miscellaneous

[Acronyms](#)
[Glossary](#)
[References](#)
[Index](#)

Created: 01.07.2009

[to top](#)

Eine gemeinsame Bibliothek [Impressum](#) des [Deutschen GeoForschungsZentrums - GFZ](#),
des [Potsdam-Instituts für Klimafolgenforschung](#),
des [Alfred-Wegener-Instituts für Polar- und Meeresforschung](#), Forschungsstelle Potsdam

1

Aim and Scope of the IASPEI New Manual of Seismological Observatory Practice (NMSOP)

Peter Bormann

1.1 History of the Manual

Most of what we know today about the internal structure and physical properties of the Earth, and thus about the internal forces which drive plate motions and produce major geological features, has been derived from seismological data. Seismology continues to be a fundamental tool for investigating the kinematics and dynamics of geological processes at all scales. With continued advances in seismological methods we hope to better understand, predict and use our geological environment and its driving processes with their diverse benefits as well as hazards to human society.

Geological processes neither know nor care about human boundaries. Accordingly, both the resources and the hazards can be investigated and assessed effectively only when the causative phenomena are monitored not only on a local scale, but also on a regional and global scale. Moreover, geological phenomena typically must be recorded with great precision and reliability over long time-spans corresponding to geological time-scales. Such data, which are collected in different countries by different research groups, have to be compatible in subtle ways and need to be widely exchanged and jointly analyzed in order to have any global and lasting value. This necessitates global co-operation and agreement on standards for operational procedures and data formats. Therefore, it is not surprising that the international seismological community saw the need many decades ago to develop a Manual of Seismological Observatory Practice (MSOP). This matter was taken up by the scientific establishments of many nations, finally resulting, in the early 1960s, in a resolution of the United Nations Economic and Social Council (ECOSOC). In response, the Committee for the Standardization of Seismographs and Seismograms of the International Association of Seismology and Physics of the Earth's Interior (IASPEI) specified in 1963 the general requirements of such a Manual as follows:

- act as a guide for governments in setting up or running seismological networks;
- contain all necessary information on instrumentation and procedure so as to enable stations to fulfil normal international and local functions; and
- not to contain any extensive account of the aims or methods of utilizing the seismic data, as these were in the province of existing textbooks.

The first edition of the Manual of Seismological Observatory Practice was published in 1970 by the International Seismological Centre (ISC) with the financial assistance of the United

1. Aim and Scope of the New IASPEI Manual of Seismological Observ. Practice

Nations Educational, Scientific and Cultural Organization (UNESCO). A sustained demand for copies and suggestions for new material prompted the Commission on Practice of IASPEI in 1975 to prepare a second edition. The authors worked to achieve balance between western and Soviet traditions of seismological practice. This resulted in the 1979 version of the Manual, edited by P. L. Willmore, in which the basic duties of seismological observatories were envisaged as follows:

- maintain equipment in continuous operation, with instruments calibrated and adjusted to conform with agreed-upon standards;
- produce records which conform with necessary standards for internal use and international exchange; and
- undertake preliminary readings needed to meet the immediate requirements of data reporting.

The "final" interpretation of seismic records was considered to be an optional activity for which the Manual should provide some background material, but not attempt a full presentation. On the other hand, the Manual did provide more detailed guidance for observatory personnel when they are occasionally (but most importantly) required to collect and classify macroseismic observations. In general the international team of authors "... sought to extract the most general principles from a wide range of world practice, and to outline a course of action which will be consistent with those principles."

Even as the 1979 Edition of the Manual was published, it was obvious that there existed significant regional differences in practice and that the subject as a whole was rapidly advancing. Since this implied the need for continuous development it was decided to produce the book in loose-leaf form and to identify chapters with descriptive code names so as to allow for easy reassembling, updating and insertion of new chapters. This useful concept was not achieved, however, and no updating or addition of new chapters happened after the 1979 edition. Nevertheless, the old MSOP is still a valuable reference for many seismologists, especially those who still operate classical analog stations, and for those in developing countries where the MSOP is a valuable text for basic seismological training.

The general aims of the MSOP are still quite valid, although the scope of modern practice has broadened significantly and old analog stations are now being rapidly replaced by digital ones. Fortunately, in conjunction with the preparations for the IASPEI Centennial publications such as the International Handbook on Earthquake and Engineering Seismology (2002), the complete 1979 edition of the MSOP has now been made available as a pdf-file (images of each page) on CD-ROM and on the Internet. It can be viewed and retrieved from the website <http://www.216.103.65.234/iaspei.html> via the links "Supplementary Volumes on CDs", "Literature in Seismology" and then "MSOP"). Major parts of the 1979 Edition of the Manual are also available at the website http://www.seismo.com/msop/msop_intro.html in which the Manual has been converted to text by optical character recognition, so that the text is searchable and can be cut and pasted.

Since the last edition of the MSOP, seismology has undergone a technological revolution. This was driven by cheap computer power, the development of a new generation of seismometers and digital recording systems with very broad bandwidth and high dynamic range, and the advent of the Internet as an effective vehicle for rapid, large-scale data exchange. As the seismological community switches from analog to digital technology, more and more sections of the 1979 Manual have become obsolete or irrelevant, and the old MSOP

provides no guidance in many new areas which have become of critical importance for modern seismology.

In a workshop meeting organized in late 1993 by the International Seismological Observing Period (ISOP) in Golden, Colorado, entitled "Measurement Protocols for Routine Analysis of Digital Data", it was acknowledged that existing documents and publications are clearly inadequate to guide routine practice in the 1990s at seismological observatories acquiring digital data. It was concluded that a new edition of MSOP is needed as well as tutorials showing examples of measuring important seismological parameters (Bergman and Sipkin, 1994). This recommendation prompted the IASPEI Commission on Practice (CoP) at its meeting in Wellington, New Zealand, January 1994, to establish an international MSOP Working Group (WG) entrusted with the elaboration of an IASPEI New Manual of Seismological Observatory Practice (NMSOP). Peter Bormann was asked to assemble and chair the working group and to elaborate a concept on the aims, scope and approach for a new Manual.

The first concept for the NMSOP was put forward at the XXIV General Assembly of the European Seismological Commission (ESC) in Athens, September 19-24, 1994 (Bormann, 1994) and at the meeting of the IASPEI CoP on the occasion of the XXI General Assembly of the International Union of Geodesy and Geophysics (IUGG) in Boulder, Colorado. The concept was approved and both an IASPEI and an ESC Manual WG were formed. Most of the members met regularly at ESC and IASPEI Assemblies (ESC: 1996 in Reykjavík, 1998 in Tel Aviv and 2000 in Lisboa; IASPEI: 1997 in Thessaloniki, 1999 in Birmingham and 2001 in Hanoi) while others corresponded with the group and contributed to its work via the Internet. At these assemblies the Manual WG organized special workshop sessions, open to a broader public and well attended, with oral and poster presentations complemented by Internet demonstrations of the Manual web site under development. With a summary poster session at the IASPEI/IAGA meeting in Hanoi, 2001, the work of the IASPEI Manual WG was formally terminated and the WG chairman was entrusted with the final editorial work and the preparations for the publication of the Manual. IASPEI offered to attach a pre-publication CD-ROM version of the NMSOP to volume II of the International Handbook of Earthquake and Engineering Seismology and provided some financial support for a printed Manual version. The latter is scheduled for publication by the end of 2002. Part of the material contained in the NMSOP has already been made available piecewise since 1996 on the website of Global Seismological Services (<http://www.seismo.com>). Some of the contributions are still in a pre-review stage. The NMSOP website will be updated and completed (in a "first edition" sense) during 2002 and 2003.

1.2 Scope of the NMSOP

1.2.1 Historical and general conceptual background

Emil Wiechert (1861-1928), professor of geophysics in Göttingen, Germany, and designer of the famous early mechanical seismographs named after him, had the following motto carved over the entrance to the seismometer house in Göttingen: "Ferne Kunde bringt Dir der schwankende Boden - deute die Zeichen." ("The trembling rock bears tidings from afar – read the signs!"). He also considered it as the supreme goal of seismology to "understand each wiggle" in a seismic record. Indeed, only then would we understand or at least have developed a reasonable model to explain the complicated system and "information chain" of

1. Aim and Scope of the IASPEI New Manual of Seismological Observ. Practice

seismology with its many interrelated sub-systems such as the seismic source, wave propagation through the Earth, the masking and distortion of "useful signals" by noise, as well as the influence of the seismic sensors, recorders and processing techniques on the seismogram (see Fig. 1.1).

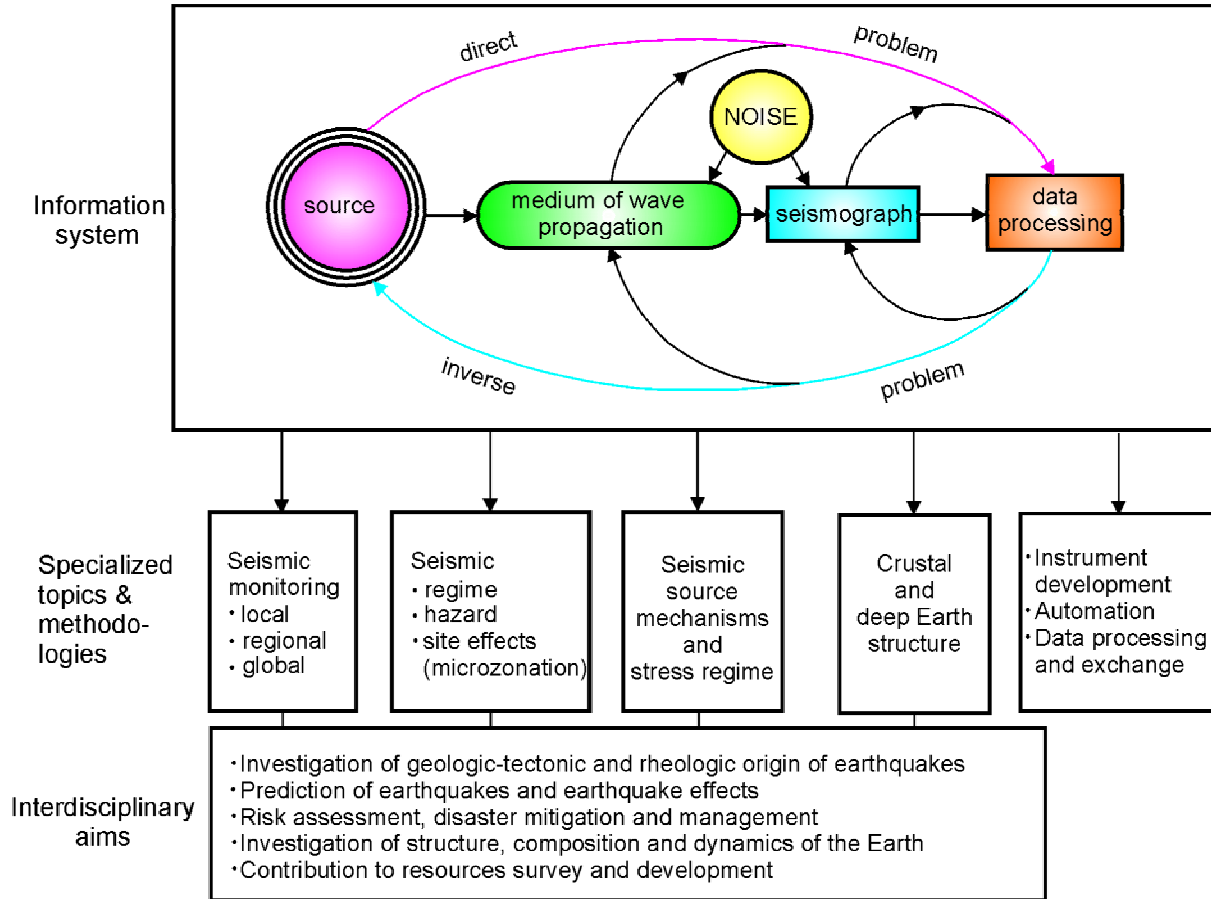


Fig. 1.1 Diagram illustrating seismology as the analysis of a complex information system linked to a diversity of specialized and interdisciplinary task of research and applications.

Despite the tremendous progress made since Wiechert in understanding the most prominent features in seismic records, long-period ones in particular, we are still well short of reaching the goal he set. In fact, most operators and analysts at seismological observatories, even those who work with the most modern equipment, have not advanced much beyond the mid 20th century with respect to their capability to "understand each wiggle" in a seismic record. There are several reasons for this lack of progress in the deeper understanding of seismogram analysis by station operators. Early seismic stations were mostly operated or supervised by broadly educated scientists who pioneered both the technical and scientific development of these observatories. They took an immediate interest in the analysis of the data themselves and had the necessary background knowledge to do it. After World War II the installation of new seismic stations boomed and rapid technological advance required an increasing specialization. Station operators became more and more technically oriented, focusing on equipment maintenance and raw data production with a minimum of effort and interest in routine data analysis. Thus, they have tended to become separated from the more comprehensive scientific and application-oriented use of their data products in society. Also

the seismological research community has become increasingly specialized, e.g., in conjunction with the monitoring and identification of underground nuclear tests. This trend has often caused changes in priorities and narrowed the view with respect to the kind of data and routine analysis required to better serve current scientific as well as public interest in earthquake seismology, improved hazard assessment and risk mitigation.

Hwang and Clayton (1991) published a revealing analysis of the phase reports to the International Seismological Centre (ISC) by all the affiliated seismological stations of the global seismic network. Most of them, even those equipped with both short- and long-period or broadband seismographs, reported only the first P-wave onset even though later energy arrivals in teleseismic records of strong events are clearly discernable. Even secondary phases with much larger amplitudes than P (e.g., Figs. 1.2 and 1.4, Fig. 2.23 in Chapter 2 and Figure 10c in DS 11.2) are usually not analyzed.

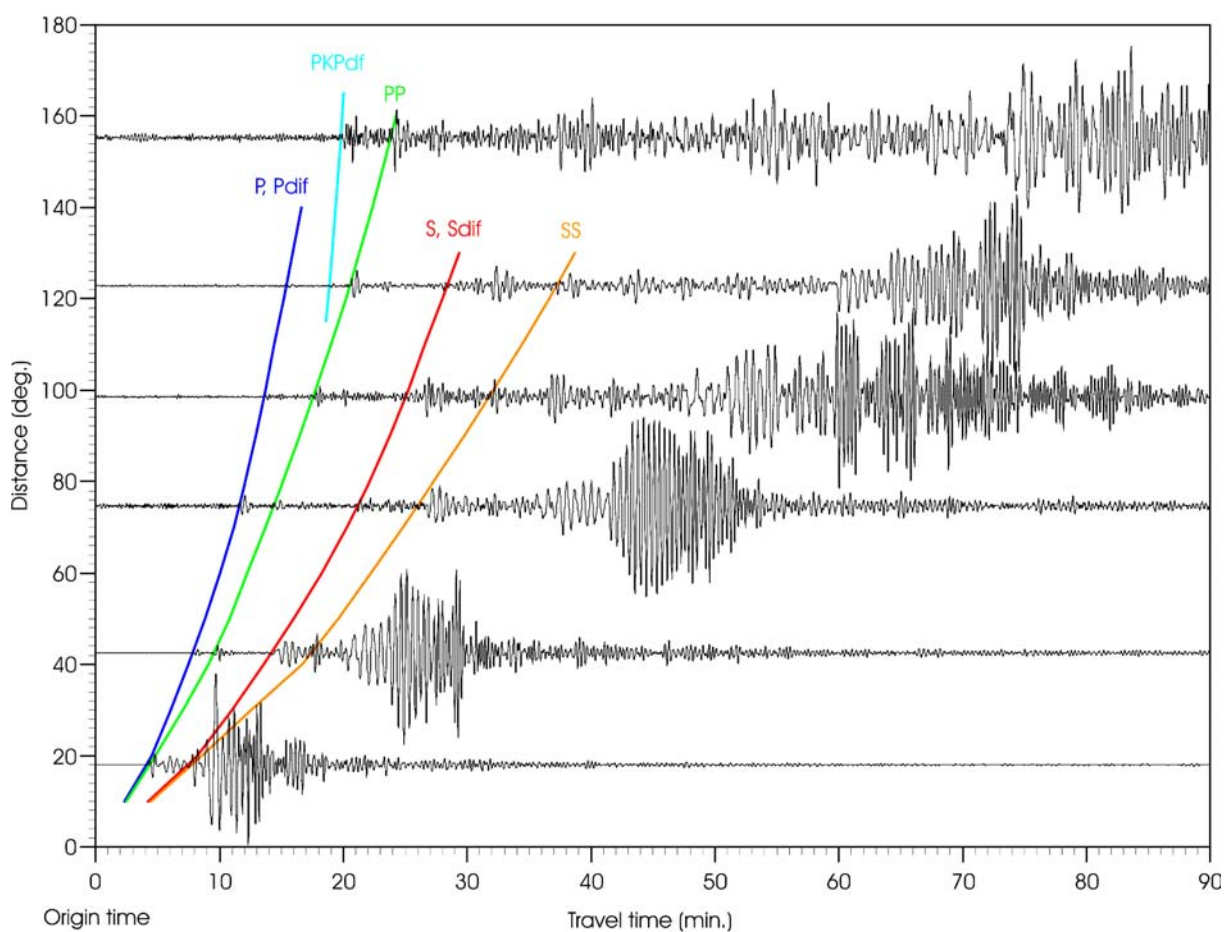


Fig. 1.2 Long-period filtered vertical-component broadband records of station CLL, Germany, of shallow earthquakes in the distance range 18° to 157° . Note the strong later longitudinal (PP) and transverse energy arrivals (S, SS) that are recognizable in the whole distance range, and the dispersed surface wave trains with large amplitudes. The record duration increases with distance (courtesy of S. Wendt, 2002).

Between 1974 and 1984, the first S-wave arrivals were reported on average to the ISC about twenty times less frequently than P, and other secondary phases are reported hundreds to thousands of times less often (Bergman, 1991). These differences reflect operations practice

1. Aim and Scope of the IASPEI New Manual of Seismological Observ. Practice

at least as much as the observability of secondary phases. For example, U.S. stations reported very few S phases in this period because the USGS National Earthquake Information Center (NEIC) did not normally use them in its routine processing and station operators knew that such readings would be "wasted". Conversely, a heavy proportion of all S readings came from European stations, especially those in former Soviet Bloc countries, where standards of practice included an emphasis on complete reading of seismograms.

The "classical" seismological observatory, for example, Moxa (MOX) in former East Germany, is now an endangered species. They depended on a social and political system that was prepared to devote relatively large numbers of personnel and other resources to station operation and analysis, with the goal of extracting the maximum amount of information out of a limited number of recordings. One can think of this as the "observatory-centered" model for observational seismology. Beginning in the 1960s, seismology in the west favored deployment of global networks (e.g., the WWSSN - World-wide Standard Seismograph Network) with relatively less attention given to individual stations or records, making up in quantity what they gave away in quality. This "network model" of observational seismology now dominates global seismology, but some balance between quantity and quality must still be found. This Manual is explicitly intended to support the side of quality in the acquisition, processing, and analysis of seismic data.

The accelerating advancement of computer capabilities during the last few decades is a strong incentive to automate more and more of the traditional tasks that need to be performed at seismological observatories. Despite significant progress made in this direction, automated phase identification and parameter determination is still inferior to the results achievable by a well-trained analyst. For this reason, and because this is more an area of research than of operational considerations, automated procedures are not considered in the Manual. Of course it will be easy to add such material to the web-based Manual whenever it is appropriate. The Manual focuses on providing guidance and advice to station operators and seismologists with less experience and to countries which lack specialists in the fields that should be covered by observatory personnel and application-oriented seismologists.

In designing the Manual for a global audience, we have tried to take into account the widely varying circumstances of observatory operators worldwide. While in developing countries proper education and full use of trained manpower for self-reliant development has (or should have) priority, highly advanced countries often push for the opposite, namely the advancement of automatic data acquisition and analysis. The main reasons for the latter tendency, besides the desire to limit personnel costs in high-wage countries, are:

- special requirements to assure most rapid and objective data processing and reporting by the primary (mostly array) stations of the International Monitoring System (IMS) in the framework of the Comprehensive Nuclear-Test-Ban Treaty Organization (CTBTO) (see 8.6.9.1) or
- coping with the huge data rates at dense digital seismic networks and arrays in areas of high seismicity.

Seismologists in highly industrialized countries can usually address their special concerns with national resources. They typically need no guidance with respect to high-tech developments from a Manual like this. Even so, specialists in program development and automation algorithms in these countries often lack the required background knowledge in seismology and/or the practical experience of operational applications in routine practice. A

similar argument applies to young scientists, beginning careers in seismological research, who often remain ignorant of the long history of operational seismology that produces the data available for their research. A typical graduate program in seismology gives scant attention to the historical development of measurement standards, which can lead either to neglect of valuable older data, or its misuse. In this sense, the NMSOP also aims at addressing the educational needs of this advanced user community with a view to broaden both their historical perspective and their ability to contribute to interdisciplinary research.

1.2.2 Creation of awareness

The subject of standards of practice at seismological observatories normally stays well below the active consciousness of most seismologists, yet it sometimes plays a central role in important research and policy debates.

1.2.2.1 The magnitude issue

Earthquake magnitude is one of the most widely used parameters in seismological practice, and one that is particularly subject to misunderstanding, even by seismologists. Examples of the way in which changing operational procedures have contaminated a valuable data set have recently been put forward and discussed in the *Seismological Research Letters*. After re-examining the earthquake catalogue for southern California between 1932 and 1990, Hutton and Jones (1993) concluded:

- ML magnitudes (in the following termed MI with l for “local”) had not been consistently determined over that period;
- amplitudes of ground velocities recorded on Wood-Anderson instruments and thus MI were systematically overestimated prior to 1944 compared to present reading procedures;
- in addition, changes from human to computerized estimation of MI led to slightly lower magnitude estimates after 1975;
- these changes contributed to an *apparently higher rate of seismicity* in the 1930’s and 1940’s and a later decrease in seismicity rate which has been interpreted as being related to the subsequent 1952 Kern County ($M_w = 7.5$) earthquake;
- variations in the rate of seismic activity have often been related to precursory activity prior to major earthquakes and therefore been considered suitable for earthquake prediction;
- the re-determination of ML in the catalogue for southern California, however, *does not confirm any changes in seismicity* rate above the level of 90% significance for the time interval considered.

Similar experiences with other local and global catalogues led Habermann (1995) to state: "... the heterogeneity of these catalogues makes characterizing the long-term behavior of seismic regions extremely difficult and interpreting time-dependent changes in those regions hazardous at best. ... Several proposed precursory seismicity behaviors (activation and quiescence) can be caused by simple errors in the catalogues used to identify them. ... Such mistakes have the potential to undermine the relationship between the seismological community and the public we serve. They are, therefore, a serious threat to the well-being of our community."

1. Aim and Scope of the IASPEI New Manual of Seismological Observ. Practice

Another striking example of the consequences of neglecting changes in observatory practice (and mixing in some political priorities as well) is the following: Classical seismology was based on the recordings of medium-period instruments of relatively wide bandwidth such as Wiechert, Golizyn, Mainka, and Press-Ewing seismographs. Gutenberg's (1945 b and c) and Gutenberg and Richter's (1956 a-c) work on earthquake body-wave magnitude scales for teleseismic event scaling and energy determination was mainly based on records of such seismographs. Then, with the introduction of the WWSSN short-period instruments, body-wave magnitudes were determined routinely in the United States only from amplitude-measurements of these short-period narrowband records, which have better detection performance for weaker events than medium- and long-period seismographs and yield a better discrimination between earthquakes and underground nuclear explosions on the basis of the mb-Ms criterion (see 11.2.5.2). However, American seismologists calibrated their amplitude measurements with the Gutenberg-Richter Q-functions for medium-period body waves. This resulted in a systematic underestimation of the P-wave magnitudes (termed mb). In contrast, at Soviet "basic" stations, the standard instrument was the medium-period broadband Kirnos seismometer (displacement proportional between about 0.1 s to 10(20)s). Accordingly, Russian medium-period body-wave magnitudes mB are more properly scaled to Gutenberg-Richters mB-Ms and logEs-Ms relations. It happens that the corresponding global magnitude-frequency relationship $\log N\text{-mB}$ yields a smaller number of annual $m = 4$ events than the U.S. WWSSN-based mb data (Riznichenko, 1960). Accordingly, in the late 1950s at the Geneva talks to negotiate a nuclear test ban treaty, the US delegation assumed a much more frequent occurrence of non-discriminated seismic events when only teleseismic records were available. This prompted them to demand some 200 to 600 unmanned stations on Soviet territory at local and regional distances as well as on-site inspections in case of uncertain events (Gilpin, 1962). Thus, a biased magnitude-frequency assessment played a significant role in the failure of these early negotiations aimed at achieving a Comprehensive Nuclear-Test-Ban Treaty (CTBT); underground testing continued for several more decades.

In 1996 the CTBT was finally agreed upon, and signed by 71 States as of 2002. The United Nations CTBT Organization in Vienna runs an International Data Centre (IDC) which also determines body-wave magnitudes from records of the International Monitoring System (IMS). However, in the interest of best possible discrimination between natural earthquakes and underground explosions by means of the body-wave/surface-wave magnitude ratio mb/Ms, they measure P-wave amplitudes after filtering the broadband records with a displacement frequency-response peaked around 5 Hz instead of around 1 Hz or 0.1 Hz. However, they calibrate their amplitude readings with a calibration function developed for 1 Hz data. Finally, they measure the maximum amplitudes for mb determination not, as recommended by IASPEI in the 1970s, within the whole P-wave train but within the first 5 seconds after the P-wave onset. These differences in practice result in systematically smaller mb(IDC) values as compared to the mb(NEIC). Although this difference is negligible for explosions it is significant for earthquakes. The discrepancy grows with magnitude and may reach 0.5 to 1.5 magnitude units. Nonetheless, the IDC magnitudes are given the same name mb, although they sample different properties of the P-wave signal. Users who are not aware of the underlying causes and tricky procedural problems behind magnitude determination, may not realize this incompatibility of data and come to completely different conclusions when using, e.g., the mb data of different data centers for seismic hazard assessment. In order to throw light onto the fuzzy practice of magnitude determinations and to push for standardization of procedures of magnitude estimation and unique magnitude names, the new Manual goes into great detail on this crucial issue. As a consequence, the magnitude sub-chapter 3.2 covers more pages than two of the smaller main Chapters.

1.2.2.2 Consequences of recent technical developments

When assembling the NMSOP we took into account that:

- modern seismic sensors, in conjunction with advanced digital data acquisition, allow recording of seismic waves in a very broad frequency band with extremely high resolution and within a much larger dynamic range than was possible in the days of analog seismology (see Fig. 1.3 below and Fig. 7.48);
- modern computer hardware and versatile analysis software tremendously ease the task of comprehensive and accurate seismogram analysis. This allows one to determine routinely parameters which were far beyond the scope of seismogram analysis a few decades ago;
- precise time-keeping and reading is much less of a problem than it was in the pre-GPS (Global Positioning System) and pre-computer era;
- the rapid global spread of high-speed communications links largely eliminates any technical barrier to widespread data exchange of full waveform data in near real time.

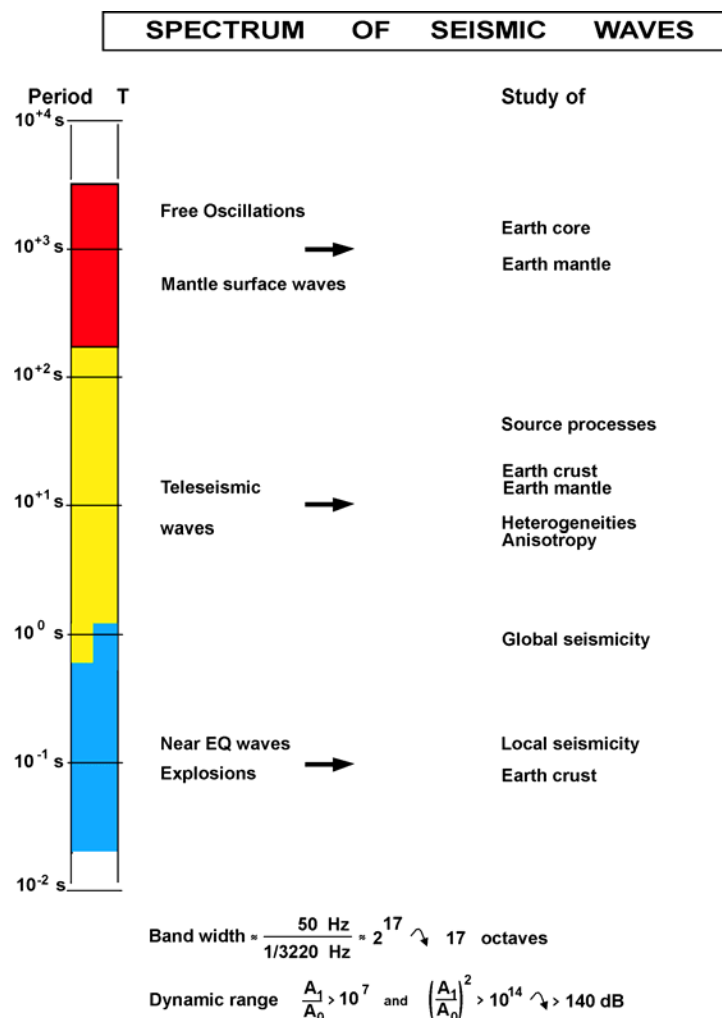


Fig. 1.3 Frequency range, bandwidth and dynamic range of modern seismology and related objects of research. The related wavelength of seismic waves vary, depending on their propagation velocity, between several meter (m) and more than 10,000 kilometer (km). The amplitudes to be recorded range from nanometer (nm) to decimeter (dm).

1. Aim and Scope of the IASPEI New Manual of Seismological Observ. Practice

At the same time, these new possibilities carry new risks:

- analysts who only use ready-made computer programs for solving a diversity of tasks, by feeding in the data and pressing the button, tend to lose a deeper understanding of the underlying model assumptions, inherent limitations and possible sources of error so that the quality of the results may be judged by the attractiveness of the graphic user interface;
- readily calculated and displayed standard deviations for all conceivable solutions often seem to indicate a reliability of the results which is far from the truth. Therefore, an understanding of the difference between internal, computational and also model-dependent *precision* on the one hand, and *accuracy* of the solutions with reference to reality on the other hand, has to be encouraged;
- specialist are increasingly required to operate and properly maintain modern seismic equipment and software. They usually lack a broader geoscientific background and thus an active interest in the use of the data which could result in declining concern for long-term data continuity and reliability, which is the backbone for any geoscientific observatory practice.

In consideration of these factors, the authors took as prime aims of the new Manual the creation of:

- interdisciplinary problem understanding; and
- motivation of observatory personnel to overcome boring routines by developing curiosity and an active interest in the use of the data they produce both in science and society.

1.2.2.3 The need for secondary phase readings

The currently dominant practice of reporting mainly first-arriving seismic phases, together with the inhomogeneous distribution of seismic sources and receivers over the globe, results in a very incomplete and inhomogeneous sampling of the structural features and properties of the Earth's interior. The consequences are not only ill-constrained Earth models of inferior resolution but also earthquake locations of insufficient accuracy to understand their seismotectonic origin and to identify the most likely places of their future occurrence. In the late 1980s, this prompted seismologists (e.g., Doornbos et al., 1991) to conceive a plan for an International Seismological Observing Period (ISOP) aimed at:

- maximum reporting of secondary phases from routine record readings aimed at improved source location and sampling of the Earth (see, e.g., Fig. 1.4);
- taking best advantage, in the routine analysis, of the increasing availability of digital broadband records and easy-to-use data preprocessing and analysis software;
- improved training of station operators and analysts;
- improved communication, co-ordination and co-operation between the stations of the global and regional seismic networks.

Ultimately, the ISOP plan for an international observational experiment focused on expanded reporting of secondary body wave phases collapsed in the face of entropy and inertia, but the issues raised in the ISOP project have remained important to many seismologists. The need for the NMSOP grew out of discussions within the ISOP project, and many seismologists who were active in ISOP went on to contribute to the NMSOP which has been developed in the spirit of ISOP. It is largely based on training material and practical exercises used in international training courses for station operators and analysts (see Bormann, 2000).

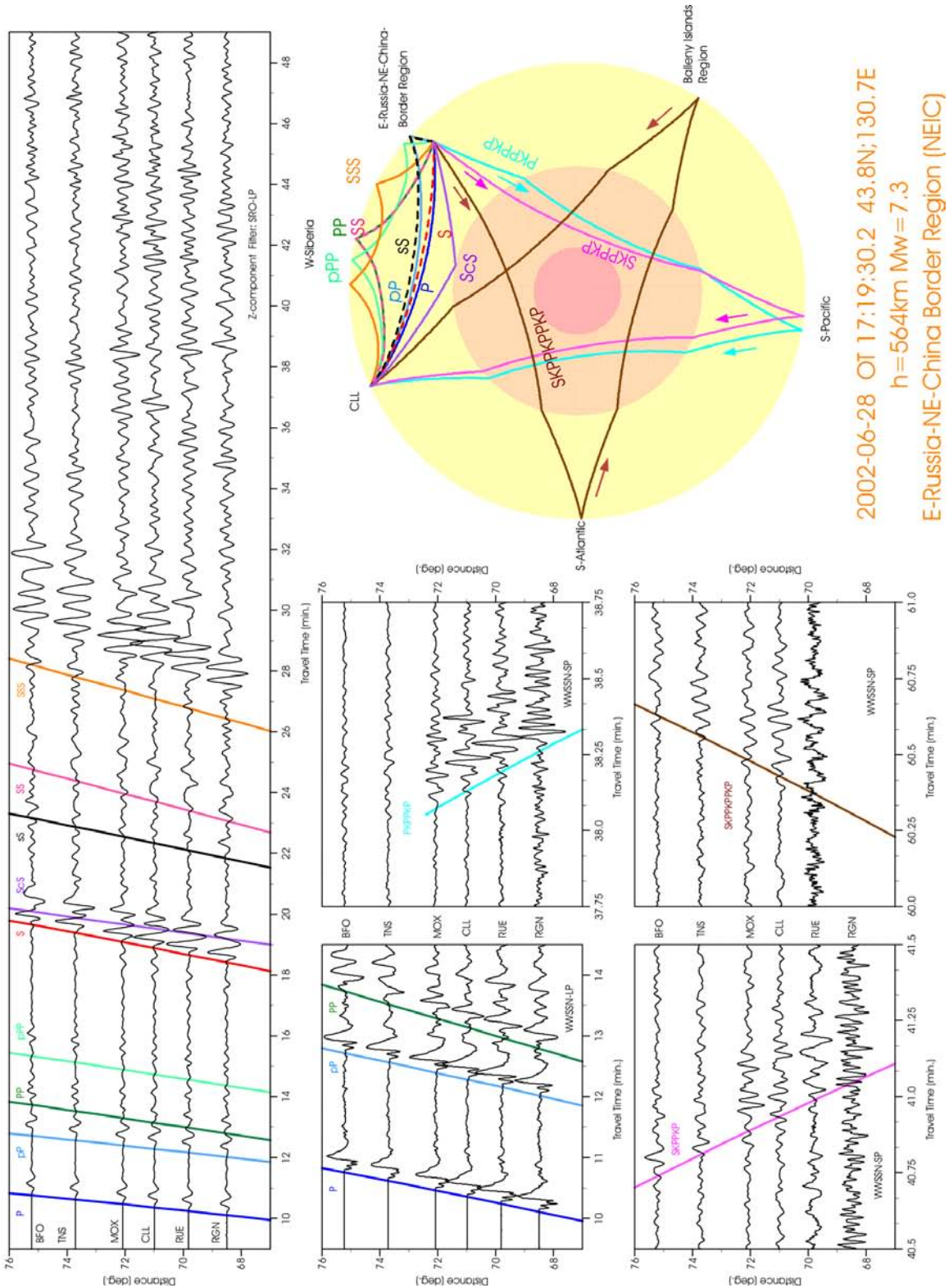


Fig. 1.4 Detailed interpretation of long-period (LP) and short-period (SP) filtered broadband records of the stations of the German Regional Seismic Network (GRSN). Note the clearly recognizable depth phases pP, pPP and sS, which are extremely important for more accurate depth determination of the event, and the rare but well developed multiple core phases PKPPKP, SKPPKP and SKPPKPPKP which sample very different parts of the deep Earth's interior than the direct mantle phases (courtesy of S. Wendt).

1. Aim and Scope of the IASPEI New Manual of Seismological Observ. Practice

Accordingly, Chapter 11 on Data Analysis and Seismogram Interpretation (101 pages) is, together with its extended annexes with seismogram examples (79 pages), event location and related software (45 pages), and several exercises on magnitude determination, event location and phase identification (40 pages) the most extensive part of the NMSOP.

1.2.2.4 New seismic sensors and sensor calibration

Modern broadband seismographs record ground motions with a minimum of distortion and it is possible to restore true ground motion computationally with high accuracy. Seismic waveforms carry much more information about the seismic source and wave-propagation process than simple parameter readings of onset times, amplitudes and prevailing periods of seismic phases. Therefore, waveform modeling and fitting has now become a major tool both of advanced seismic research and increasingly also of routine processing and analysis. Seismic waveforms and amplitudes, however, strongly depend on the transfer function and gain of the seismograph, which must be known with high accuracy if the full potential of waveform analysis is to be exploited. Also reliable amplitude-based magnitude estimates, most of them determined from band-limited recordings, require accurate knowledge of the recording system's frequency-dependent magnification. Consequently, instrument parameters that control the instrument response must be known and kept stable with an accuracy of better than a few percent. Unfortunately, at many seismic stations the seismographs have never been carefully calibrated, the actual gain and response shape is not precisely known and their stability with time is not regularly controlled. Some station operators rely on the parameters given in the data sheets of the manufacturers or those determined (possibly) by the primary installer of the stations. However, these parameters, instrumental gain in particular, are often not accurate enough. Therefore, station operators themselves should be able to carry out an independent, complete calibration of their instruments.

Long-period seismographs are strongly influenced by changes in ambient temperature and ground stability. However, for modern feedback-controlled broadband seismographs the basic parameters, eigenperiod and gain, are rather stable, provided that the seismometer mass is kept in the zero position. This should be regularly controlled, more frequently (e.g., every few weeks) in temporary installations and every few months in more stable permanent installations.

Although short-period instruments are generally considered to be much more robust and stable in their parameters, experience has shown that their eigenperiod and attenuation may change with time up to several tens percent, especially when these instruments are repeatedly deployed in temporary installations. Parameter changes of this order are not tolerable for quantitative analysis of waveform parameters. Therefore, more frequent control and absolute determination of these critical sensor parameters are strongly recommended after each re-installation.

Therefore, the NMSOP presents a rather extensive chapter on the basic theory of seismometry and the practice of instrument calibration and parameter determination, which is complemented by exercises and introductions to freely available software for parameter determination and response calculations. Additionally, in other chapters, the effects of different seismograph responses, post-record filtering or computational signal restitution on the appearance of seismograms and the reliability and reproducibility of parameter readings is demonstrated with many examples.

1.2.2.5 What has to be considered when installing new seismic networks

More and more countries now realize the importance of seismic monitoring of their territories for improved seismic hazard assessment and the development of appropriate risk-mitigation strategies. Installation and long-term operation of a self-reliant modern seismic network is quite a demanding and costly undertaking. Cost-efficiency largely depends on proper project definition, instrument and site selection based on a good knowledge of the actual seismotectonic and geographic-climatic situation, the availability of trained manpower and required infrastructure, and many other factors. Project-related funds are often available only within a limited time-window. Therefore, they are often spent quickly on high-tech hardware and turn-key installations by foreign manufacturers without careful site selection and proper allocation of funds for training and follow-up operation. If local people are not involved in these initial efforts and capable of using and maintaining these new facilities and data according to their potential, then the whole project might turn out to be a major investment with little or no meaningful return. These crucial practical and financial aspects are usually not discussed in any of the textbooks in seismology that mostly serve general academic education or research. Therefore, the NMSOP dedicates its largest chapter (108 pages) to just these problems.

What can be achieved with modern seismological networks, both physical and virtual ones, and how they relate with respect to aperture, data processing and results to specialized seismic arrays, is extensively dealt with in complementary chapters of the NMSOP.

1.3 Philosophy of the NMSOP

The concept for the NMSOP was developed with consideration of the benefits and drawbacks of the old Manual, taking into account the technological developments and opportunities which have appeared during the last 20 years, as well as the existing in-equalities in scientific-technical conditions and availability of trained manpower world-wide (Bormann, 1994).

Seismological stations and observatories are currently operated by a great variety of agencies, staffed by seismologists and technicians whose training and interests vary widely, or they are not staffed at all and operated remotely from a seismological data or analysis center. They are equipped with hardware and software ranging from very traditional analog technology to highly versatile and sophisticated digital technology. While in industrialized countries the observatory personnel normally have easy access to up-to-date technologies, spare parts, infrastructure, know-how, consultancy and maintenance services, those working in developing countries are often required to do a reliable job with very modest means, without much outside assistance and usually lacking textbooks on the fundamentals of seismology or information about standard observatory procedures.

To ensure that data from observatories can be properly processed and interpreted under these diverse conditions, it is necessary to establish protocols for all aspects of observatory operation that may affect the seismological data itself. In addition, competent guidance is often required in the stages of planning, bidding, procurement, site-selection, and installation of new seismic observatories and networks so that they will later meet basic international standards for data exchange and processing in a cost-effective and efficient manner.

1. Aim and Scope of the IASPEI New Manual of Seismological Observ. Practice

One drawback of the old Manual appeared to us to be that its chapters were organized purely according to components or tasks of observatory practice, namely:

- Organization of station networks;
- Instruments;
- Station operation;
- Record content;
- The determination of earthquake parameters;
- Reporting output;
- Macroseismic observations;
- International services.

A consequence of this structuring was that the seismological fundamentals required to understand the relevance and particulars of the various observatory tasks were sometimes referred to in various chapters and dealt with in a fragmented manner. This approach makes it difficult for observatory personnel to comprehend the interdisciplinary problems and aims behind observatory practice and to appreciate the related, often stringent requirements with respect to data quality, completeness, consistency of procedures etc. Further, this approach puts together in the same chapters basic scientific information, which is rather static, with technical aspects which evolve quickly. This makes it difficult to keep the Manual up-to-date without frequent rewriting of entire chapters.

The IASPEI WG on MSOP agreed, therefore, to structure the new Manual differently:

- the body of the Manual should have long-term character, outlining the scope, terms of reference, philosophy, basic procedures as well as the scientific-technical and social background of observatory practice. It should aim at creating the necessary awareness and sense of responsibility to meet the required standards in observatory work in the best interests of scientific progress and social service.
- this main body or backbone of the NMSOP (Volume 1) should be structured in a didactically systematic way, introducing first the scientific-technical fundamentals underlying each of the main components in the "information chain" (see Fig. 1.1) before going on to major tasks of observatory work.
- the core Manual should be complemented by annexes of complementary information (Volume 2) which can stand alone. Some of these topics are too bulky or specific to be included in the body of the Manual while others may require more frequent updating than the thematic Manual chapters. Therefore, they should be kept separate and individualized. Some annexes give more detailed descriptions of special problems (e.g., event location or theory of source representation); others provide data about commonly-used Earth models, shareware for problem solving, seismic record examples, calibration functions for magnitude determination, widely-used sensors and their key parameters, or job-related exercises with solutions for specific observatory tasks such as phase identification, event location, magnitude estimation, fault-plane determination, etc.

With this structure it is hoped to produce a new Manual which is a sufficiently complete, self-explanatory reference source ("cook and recipe book") with an aim to provide awareness of complex problems, basic background information, and specific instructions for the self-reliant execution of all common "routine" or "pre-research" jobs by the technical and scientific staff at seismological stations, observatories, and network centers. This includes system planning, site investigation and preparation, instrument calibration, installation, shielding, data

acquisition, processing and analysis, documentation and reporting to relevant national and international agencies, data centers or the public, and occasionally, also assessing and classifying earthquake damage.

The NMSOP will not cover the often highly automated procedures now in use at many international seismological data centers. These normally neither record nor analyze seismic records themselves but rather use the parameters or waveforms reported to them by stations, networks or arrays. Such centers usually have the expertise and the scientific-technical environment and international connections needed to carry out their duties effectively. Rather, the NMSOP should mainly serve the needs of the majority of less experienced or too narrowly specialized operators and analysts in both developing and industrialized countries, so as to assure that all necessary tasks within the scope and required standards for national and international data acquisition and exchange can be properly performed. Worldwide there is no formal university education or professional training available for seismic station operators and data analysts. Observatory personnel usually acquire their training through “learning by doing”. The formal educational background of observatory personnel may be very different: Physicists, geologists, electronic or computer engineers, rarely geophysicists. Accordingly, the NMSOP tries to be comprehensible for people with different backgrounds, to stimulate their interest in interdisciplinary problems and to guide the development of the required practical skills. The method of instruction is mainly descriptive. Higher mathematics is only used where it is indispensable, e.g., in the seismometry chapter.

The NMSOP should, however, also be a contribution, at least in part, to public, high school and university education in the field of geosciences. It is hoped that many components, practical exercises in particular, will be useful for students of geophysics. The NMSOP will therefore be made available in different forms:

- as a loose-leaf collection of printed chapters and annexes, which can easily be updated and complemented in accordance with changing job requirements and new developments without the need to re-edit and re-print the whole Manual. Also, these updates and complements can be disseminated to Manual owners as E-mail attachments and some Manual users may order only those parts which are relevant for them.;
- on a website with hyperlinks for convenient searches, linking external complementary resources, and easy extraction of problem-tailored educational modules (see 1.4.2);
- as a CD-ROM which will be affordable for everybody.

1.4 Contents of the NMSOP

1.4.1 The printed Manual

The IASPEI and ESC Working Groups for the NMSOP agreed on the following topical Manual chapters (for details see List of Contents):

- Chapter 1: Aim and scope of the IASPEI New Manual of Seismological Observatory Practice (NMSOP)
- Chapter 2: Seismic Wave Propagation and Earth Models
- Chapter 3: Seismic Sources and Source Parameters
- Chapter 4: Seismic Signals and Noise

1. Aim and Scope of the IASPEI New Manual of Seismological Observ. Practice

Chapter 5:	Seismic Sensors and their Calibration
Chapter 6:	Seismic Recording Systems
Chapter 7:	Site Selection, Preparation and Installation of Seismic Stations
Chapter 8:	Seismic Networks
Chapter 9:	Seismic Arrays
Chapter 10:	Data Formats, Storage, and Exchange
Chapter 11:	Data Analysis and Seismogram Interpretation
Chapter 12:	Intensity and Intensity Scales
Chapter 13:	Volcano Seismology

These chapters form Volume 1 of the printed NMSOP and cover either the fundamental aspects of the main sub-systems of the "Information Chain of Seismology" as presented schematically in Fig. 1.1, or related specific tasks, technologies or methodologies of data acquisition, formatting, processing and application.

Volume I is complemented by Volume 2. The latter contains annexes in the following categories:

- **Datasheets (DS):** Lists of sensor parameters; record examples, travel-time curves, Earth models, calibration functions, etc.;
- **Information Sheets (IS):** They contain more detailed treatments of special topics or condensed summaries of special instructions/recommendations for quick orientation, present the standard nomenclature of seismic phase and magnitude names, give examples for parameter reports and bulletins, etc.;
- **Exercises (EX):** Practical exercises with solutions on basic observatory tasks such as event location, magnitude estimation, determination of fault-plane solutions and other source parameters, instrument calibration and response construction. For educational purposes, most of these exercises are carried out Manually with very modest technical and computational means, however links are given to related software tools;
- **Program Descriptions (PD):** Short descriptions of essential features of freely available software for observatory practice and how to access it;
- **Miscellaneous:** Contains a list of acronyms, an extensive index, the list of authors with complete addresses and the list of references for Volume 1. Other items may be added later.

1.4.2 The NMSOP website

Very early in the discussions about a New Manual of Seismological Observatory Practice, it was decided that the usefulness and longevity of the project could be maximized by adapting it to the World Wide Web, which was only then becoming widely appreciated as a medium for exchanging information among scientists. Working scientists, especially older ones, are more oriented to the discipline of paper publication, with near-total control and permanence. The flexibility and unpredictability of the hyperlinked experience of a large technical document such as the NMSOP would require a different attitude on the part of the author, the editor, and the reader. The web-based Manual should be experienced more like a conversation than a prepared lecture; the reader must always evaluate the material for self-consistency and use common sense to evaluate apparent discrepancies as in electronic (e-)learning tools.

Compared to the printed version, the main advantages of a web-based Manual should be the ease with which it can be updated and expanded, navigation via hyperlinks (both within the Manual and to external data and information resources), and the ease with which the user may copy portions of the Manual for use in other computer-based documents, lecture notes, etc.

Regrettably, this ambitious original concept for the NMSOP could not yet be achieved because no person or institution has been found so far which felt able to produce, maintain and permanently update in the long run such has hyperlinked web-based Manual. Therefore, as an alternative, the GeoForschungsZentrum Potsdam, which had financed the printing of the hard-copy version of the first edition of the NMSOP, has agreed to put corrected and gradually updated and complemented pdf-versions of the Manual, after approval by the editor and/or the Commission on Seismic Observation and Interpretation (CoSOI) of IASPEI, on its website. The GFZ is willing to maintain and propagate the availability of this NMSOP website for the foreseeable future and strive to modernize it, as resources and upcoming new technologies will permit, into a tool of e-learning according to the original concept.

1.5 Outreach of the NMSOP

The authors and the webmaster of the NMSOP will strive to keep both the printed Manual and the NMSOP home page in tune with the most recent developments and needs. It is intended that the maintenance and regular updating of the NMSOP be a permanent obligation of the IASPEI Commission on Seismological Observation and Interpretation (CoSOI) and its relevant Working Groups. Production of an inexpensive printed loose-leaf collection of the Manual, complemented by a CD-ROM, will assure general availability of the Manual at every manned seismological station, network center, seismological institution or geoscience department at universities all over the world.

It is expected, therefore, that the user community of the NMSOP will not be limited to observatory personal. Many chapters and sections will be of general interest to lecturers and students in seismology, geophysics or geosciences in general. They will find both suitable lecture and exercise material. With the NMSOP on the Internet, special training institutions in the field of applied seismology may make use of this resource. They can retrieve self-tailored training modules from it according to their specific requirements, provided that the data source and the individual authors of the related Manual contribution are properly cited. The copyright rests with IASPEI (see Editorial remarks). We hope that the NMSOP will be of long-term and far-reaching benefit to a rather diverse user community.

Acknowledgments

Our thanks go to all members of the IASPEI Manual Working Group who have actively contributed to the development of the Manual concept and the currently available drafts. We also acknowledge the valuable comments and suggestions received on the draft of Chapter 1 from B. L. N. Kennett and S. A. Sipkin. Special thanks go to Ms. Margaret Adams (UK/USA) who took the trouble to do the final English proof-reading of the whole Manual and its Annexes. We also acknowledge with thanks the efforts by Ms. Ute Borchert and Ms. Regina Stromeyer (now Milkereit) of the GeoForschungsZentrum Potsdam who produced many of the figures contained in the Manual.

Recommended overview readings (see References under Miscellaneous in Volume 2)

Aki and Richards (2002)
Båth (1979)
Bolt (1982, 1993, 1999)
Havskov and Alguacil (2004)
Kennett (2001 and 2002)
Kulhánek (1990)
Lay and Wallace (1995)
Lilie (1998)
Scherbaum (2001)
Shearer (1999)
Udias (1999)
Willmore (1979)

2

Seismic Wave Propagation and Earth models

Peter Bormann, Bob Engdahl and Rainer Kind

2.1 Introduction

The key data to be recorded by means of *seismic sensors* (Chapter 5) and *recorders* (Chapter 6) at seismological observatories (*stations* – Chapter 7, *networks* – Chapter 8, *arrays* – Chapter 9) are *seismic waves*, radiated by *seismic sources* (Chapter 3). Weak signals may be masked or significantly distorted by *seismic noise* (Chapter 4), which is usually considered disturbing and unwanted. Only in some special engineering-seismological applications is seismic noise also appreciated as a useful signal, from which some information on the structure, velocity and fundamental resonance frequency of the uppermost sedimentary layers can be derived (e.g. Bard, 1999). But most of what we know today of the structure and physical properties of our planet Earth, from its uppermost crust down to its center, results from the analysis of seismic waves generated by more or less localized natural or man-made sources such as earthquakes or explosions (Figs. 3.1 to 3.4). Either (repeatedly) solving the so-called forward (direct) or the inverse problem of data analysis (Fig. 1.1) achieves this.

It is not the task of the New Manual of Seismological Observatory Practice (NMSOP), to provide an in-depth understanding of the theoretical tools for this kind of analysis. There exist quite a number of good introductory (Lillie, 1999; Shearer, 1999) and more advanced textbooks (e.g., Aki and Richards, 1980 and 2002; Ben-Menahem and Singh, 1981; Bullen and Bolt, 1985; Dahlen and Tromp, 1998; Lay and Wallace, 1995; Kennett, 2001), and a variety of special papers and monographs related to specific methods (e.g. Fuchs and Müller, 1971; Červený et al., 1977; Kennett, 1983; Müller, 1985; Červený, 2001), types of seismic waves (e.g., Malischewsky, 1987; Lapwood and Usami, 1981) or applications (e.g., Gilbert and Dziewonski, 1975; Sherif and Geldart, 1995). Rather, we will take here a more phenomenological approach and refer to related fundamentals in physics and mathematical theory only as far as they are indispensable for understanding the most essential features of seismic waves and their appearance in seismic records and as far as they are required for:

- identifying and discriminating the various types of seismic waves;
- understanding how the onset-times of these phases, as observed at different distances from the source, form so-called travel-time curves;
- understanding how these curves and some of their characteristic features are related to the velocity-structure of the Earth and to the observed (relative) amplitudes of these phases in seismic records;
- using travel-time and amplitude-distance curves for seismic source location and magnitude estimation;
- understanding how much these source-parameter estimates depend on the precision and accuracy of the commonly used 1-D Earth models (see IS 11.1);

2. Seismic Wave Propagation and Earth models

- appreciating how these source parameter estimates can be improved by using more realistic (2-D, 3-D) Earth models as well as later (secondary) phase onsets in the processing routines; and
- being aware of the common assumptions and simplifications used in synthetic seismogram calculations that are increasingly used nowadays in seismological routine practice (see 2.5.4.4, 2.8, 3.5.3).

2.2 Elastic moduli and body waves

2.2.1 Elastic moduli

Seismic waves are elastic waves. Earth material must behave elastically to transmit them. The degree of elasticity determines how well they are transmitted. By the pressure front expanding from an underground explosion, or by an earthquake shear rupture, the surrounding Earth material is subjected to *stress* (compression, tension and/or shearing). As a consequence, it undergoes *strain*, i.e., it changes volume and/or distorts shape. In an inelastic (plastic, ductile) material this deformation remains while elastic behavior means that the material returns to its original volume and shape when the stress load is over.

The degree of elasticity/plasticity of real Earth material depends mainly on the *strain rate*, i.e., on the length of time it takes to achieve a certain amount of distortion. At very low strain rates, such as movements in the order of mm or cm/year, it may behave ductilely. Examples are the formation of geologic folds or the slow plastic convective currents of the hot material in the Earth's mantle with velocity on the order of several cm per year. On the other hand, the Earth reacts elastically to the small but rapid deformations caused by a transient seismic source pulse. Only for very large amplitude seismic deformations in soft soil (e.g., from earthquake strong-motions in the order of 40% or more of the gravity acceleration of the Earth) or for extremely long-period free-oscillation modes (see 2.4) does the inelastic behavior of seismic waves have to be taken into account.

Within its elastic range the behavior of the Earth material can be described by *Hooke's Law* that states that the amount of strain is linearly proportional to the amount of stress. Beyond its elastic limit the material may either respond with brittle fracturing (e.g., earthquake faulting, see Chapter 3) or ductile behavior/plastic flow (Fig. 2.1).

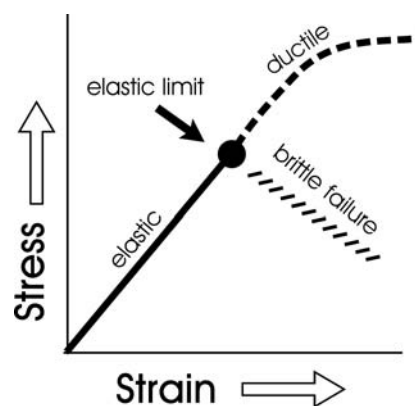


Fig. 2.1 Schematic presentation of the relationship between stress and strain.

Elastic material resists differently to stress depending on the type of deformation. It can be quantified by various elastic moduli:

- the *bulk modulus* κ is defined as the ratio of the hydrostatic (homogeneous all-sides) pressure change to the resulting relative volume change, i.e., $\kappa = \Delta P / (\Delta V/V)$, which is a measure of the *incompressibility* of the material (see Fig. 2.2 top);
- the *shear modulus* μ (or “rigidity”) is a measure of the resistance of the material to shearing, i.e., to changing the shape and not the volume of the material. Its value is given by half of the ratio between the applied shear stress τ_{xy} (or tangential force ΔF divided by the area A over which the force is applied) and the resulting shear strain e_{xy} (or the shear displacement ΔL divided by the length L of the area acted upon by ΔF), that is $\mu = \tau_{xy}/2 e_{xy}$ or $\mu = (\Delta F/A) / (\Delta L/L)$ (Fig. 2.2 middle). For fluids $\mu = 0$, and for material of very strong resistance (i.e. $\Delta L \rightarrow 0$) $\mu \rightarrow \infty$;
- the *Young’s modulus* E (or “stretch modulus”) describes the behavior of a cylinder of length L that is pulled on both ends. Its value is given by the ratio between the extensional stress to the resulting extensional strain of the cylinder, i.e., $E = (F/A) / (\Delta L/L)$ (Fig. 2.2 bottom);
- the *Poisson’s ratio* σ is the ratio between the lateral contraction (relative change of width W) of a cylinder being pulled on its ends to its relative longitudinal extension, i.e., $\sigma = (\Delta W/W) / (\Delta L/L)$ (Fig. 2.2 bottom).

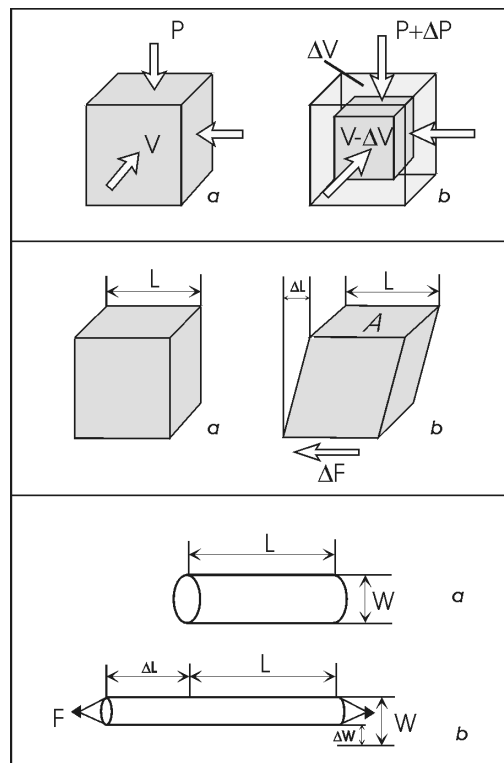


Fig. 2.2 Deformation of material samples for determining elastic moduli. Top: bulk modulus κ ; middle: shear modulus μ ; bottom: Young’s modulus E and Poisson’s ratio σ . a – original shape of the volume to be deformed; b – volume and/or shape after adding pressure ΔP to the volume V (top), shear force ΔF over the area A (middle) or stretching force F in the direction of the long axis of the bar (bottom).

2. Seismic Wave Propagation and Earth models

Young's modulus, the bulk modulus and the shear modulus all have the same physical units as pressure and stress, namely (in international standard (SI) units):

$$1 \text{ Pa} = 1 \text{ N m}^{-2} = 1 \text{ kg m}^{-1} \text{ s}^{-2} \quad (\text{with } 1 \text{ N} = 1 \text{ Newton} = 1 \text{ kg m s}^{-2}). \quad (2.1)$$

2.2.2 Stress-strain relationship

The most general linear relationship between stress and strain of an elastic medium is governed in the generalized *Hook's law* (see Equation (10) in the IS 3.1) by a fourth order parameter tensor. It contains 21 independent moduli. The properties of such a solid may vary with direction. Then the medium is called *anisotropic*. Otherwise, if the properties are the same in all directions, a medium is termed *isotropic*. Although in some parts of the Earth's interior anisotropy on the order of a few percent exists, isotropy has proven to be a reasonable first-order approximation for the Earth as a whole. The most common models, on which data processing in routine observatory practice is based, assume isotropy and changes of properties only with depth.

In the case of isotropy the number of independent parameters in the elastic tensor reduces to just two. They are called after the French physicist *Lamé* (1795-1870) the *Lamé parameters* λ and μ . The latter is identical with the *shear* modulus. λ does not have a straightforward physical explanation but it can be expressed in terms of the above mentioned elastic moduli and Poisson's ratio, namely

$$\lambda = \kappa - 2\mu/3 = \frac{\sigma E}{(1 + \sigma)(1 - 2\sigma)}. \quad (2.2)$$

The other elastic parameters can also be expressed as functions of μ , λ and/or κ :

$$E = \frac{(3\lambda + 2\mu)\mu}{(\lambda + \mu)} \quad (2.3)$$

and

$$\sigma = \frac{\lambda}{2(\lambda + \mu)} = \frac{3\kappa - 2\mu}{2(3\kappa + \mu)}. \quad (2.4)$$

For a *Poisson solid* $\lambda = \mu$ and thus, according to (2.4), $\sigma = 0.25$. Most crustal rocks have a Poisson's ratio between about 0.2 and 0.3. But σ may reach values of almost 0.5, e.g., for unconsolidated, water-saturated sediments, and even negative values of σ are possible (see Tab. 2.1).

The elastic parameters govern the velocity with which seismic waves propagate. The *equation of motion* for a continuum can be written as

$$\rho \frac{\partial^2 u_i}{\partial t^2} = \partial_j \tau_{ij} + \mathbf{f}_i, \quad (2.5)$$

with ρ - density of the material, u_i – displacement, τ_{ij} – stress tensor and f_i – the body force term that generally consists of a *gravity term* and a *source term*. The gravity term is important at low frequencies in *normal mode seismology* (see 2.4), but it can be neglected for calculations of body- and surface-wave propagation at typically observed wavelengths. Solutions of Eq. (2.5) which predict the ground motion at locations some distance away from the source are called *synthetic seismograms* (see Figs. 2.54 and 2.55).

In the case of an inhomogeneous medium, which involves gradients in the Lamé parameters, Eq. (2.5) takes a rather complicated form that is difficult to solve efficiently. Also, in case of strong inhomogeneities, transverse and longitudinal waves (see below) are not decoupled. This results in complicated particle motions. Therefore, most methods for synthetic seismogram computations ignore gradient terms of λ and μ in the equation of motion by modeling the material either as a series of homogeneous layers (which also allows to approximate gradient zones; see *reflectivity method* by Fuchs and Müller, 1971; Kennett, 1983; Müller, 1985) or by assuming that variations in the Lamé parameters are negligible over a wavelength Λ and thus these terms tend to zero at high frequencies (*ray theoretical approach*; e.g., Červený et al., 1977; Červený, 2001). In homogeneous media and for small deformations the *equation of motion* for seismic waves outside the source region (i.e., without the source term f_s and neglecting the gravity term f_g) takes the following simple form:

$$\rho \ddot{\mathbf{u}} = (\lambda + 2\mu)\nabla\nabla\cdot\mathbf{u} - \mu\nabla\times\nabla\times\mathbf{u} \quad (2.6)$$

where \mathbf{u} is the displacement vector and $\ddot{\mathbf{u}}$ its second time derivative. Eq. (2.6) provides the basis for most body-wave, synthetic seismogram calculations. Although it describes rather well most basic features in a seismic record we have to be aware that it is an approximation only for an isotropic homogeneous linearly elastic medium.

2.2.3 P- and S-wave velocities, waveforms and polarization

The first term on the right side of Eq. (2.6) contains the scalar product $\nabla\cdot\mathbf{u} = \text{div } \mathbf{u}$. It describes a volume change (compression and dilatation), which always contains some (rotation free!) shearing too, unless the medium is compressed hydrostatically (as in Fig. 2.2 top). The second term is a vector product ($\text{rot } \mathbf{u} = \nabla\times\mathbf{u}$) corresponding to a curl (rotation) and describes a change of shape without volume change (pure shearing). Generally, every vector field, such as the displacement field \mathbf{u} , can be decomposed into a rotation-free (\mathbf{u}^r) and a divergence-free (\mathbf{u}^d) part, i.e., we can write $\mathbf{u} = \mathbf{u}^r + \mathbf{u}^d$. Since the divergence of a curl and the rotation of a divergence are zero, we get accordingly two independent solutions for Eq. (2.6) when forming its scalar product $\nabla\cdot\mathbf{u}$ and vector product $\nabla\times\mathbf{u}$, respectively:

$$\frac{\partial^2(\nabla\cdot\mathbf{u})}{\partial^2 t} = \frac{\lambda + 2\mu}{\rho} \nabla^2(\nabla\cdot\mathbf{u}^r) \quad (2.7)$$

and

$$\frac{\partial^2(\nabla\times\mathbf{u})}{\partial^2 t} = \frac{\mu}{\rho} \nabla^2(\nabla\times\mathbf{u}^d). \quad (2.8)$$

2. Seismic Wave Propagation and Earth models

Eqs. (2.7) and (2.8) are solutions of the wave equation for the propagation of two independent types of seismic *body waves*, namely *longitudinal (compressional - dilatational) P waves* and *transverse (shear) S waves*. Their velocities are

$$v_p = \sqrt{\frac{\lambda + 2\mu}{\rho}} = \sqrt{\frac{\kappa + 4\mu/3}{\rho}} \quad (2.9)$$

and

$$v_s = \sqrt{\frac{\mu}{\rho}}. \quad (2.10)$$

Accordingly, for a Poisson solid with $\lambda = \mu$ $v_p/v_s = \sqrt{3}$. This comes close to the v_p/v_s ratio of consolidated sedimentary and igneous rocks in the Earth's crust (see Tab. 2.1). Eqs. (2.9) and 2.10) also mean that P (*primary*) waves travel significantly faster than S (*secondary*) waves and thus arrive ahead of S in a seismic record (see Fig. 2.3). The Poisson's ratio is often used as a measure of the v_p/v_s ratio, namely

$$\sigma = (v_p^2/v_s^2 - 2)/2(v_p^2/v_s^2 - 1) \quad (2.11)$$

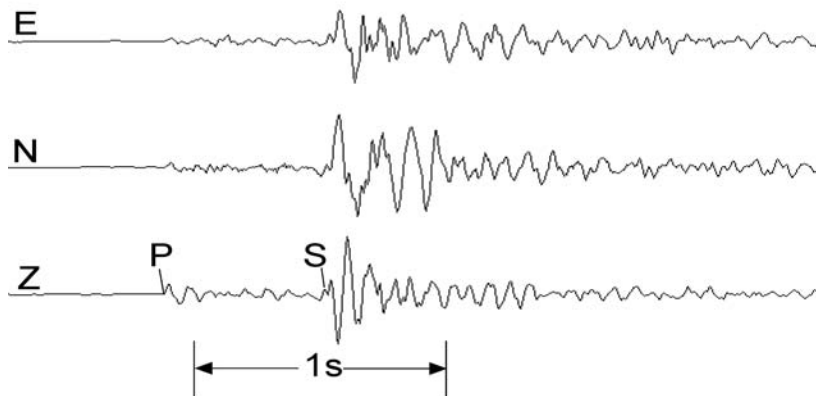


Fig. 2.3 The three components of ground-velocity proportional digital records of the P and S waves from a local event, an aftershock of the Killari-Latur earthquake, India (18.10.1993), at a hypocentral distance of about 5.3 km.

Note the simple *transient waveform (wavelet)* of P in the Z-component of Fig. 2.3. The waveform and duration of the primary body wave is related to the shape and duration of the source-time function. It is for an earthquake shear rupture usually a more or less complex displacement step (see Figs. 2.4 and 3.4) which can be described by the moment-release function $M(t)$ (see 3.5). In the *far-field*, i.e., at distances larger than the source dimension and several wavelengths of the considered signal, the related displacement $u(t)$ looks, in the idealized case, bell-shaped and identical with the moment-rate $\dot{M}(t)$ (or velocity source-time) function (see Fig. 2.4 middle). The base-width of this *far-field displacement source pulse* $u(t)$ corresponds to the duration of displacement at the source (for examples see Fig. 3.7). However, usually broadband seismometers record ground velocity $\dot{u}(t)$ instead of ground displacement. The recorded waveform then looks similar to the ones seen in Fig. 2.3 and Fig.

2.4 bottom. The period of the wavelet $\dot{u}(t)$ corresponds to the duration of the displacement of the source, τ_s . This waveform of primary body waves will be slightly changed due to frequency-dependent attenuation and other wave-propagation effects, e.g., those that cause phase shifts. But the duration of the body-wave ground-motion wavelet (or wave-group) will remain essentially that of the source process, independent of the observational distance, unless it is significantly prolonged and distorted by narrowband seismic recordings (see 4.2). We have made this point in order to better appreciate one of the principal differences in the appearance in seismic records of transient body waves on the one hand and of dispersed surface waves (see 2.3 and, e.g., Figs. 2.14 and 2.23) on the other hand.

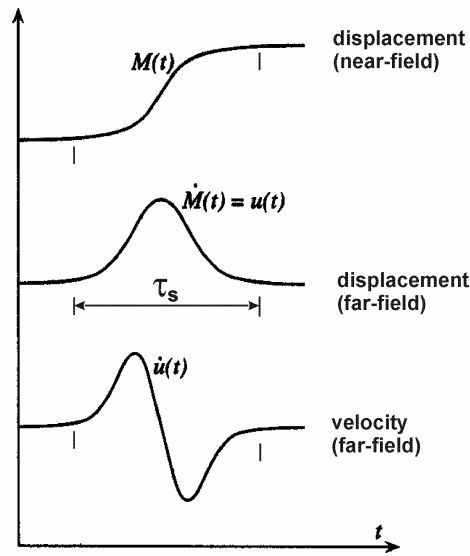


Fig. 2.4 Relationship between near-field displacement, far-field displacement and velocity from isotropic or double-couple source earthquake shear sources (modified from Shearer, Introduction to Seismology, 1999; with permission from Cambridge University Press).

Tab. 2.1 gives some approximate average values for the elastic moduli κ and μ , the density ρ and the seismic velocities v_p and v_s for air, water, ice and some selected Earth materials. The following general conclusions can be drawn from it:

- For the same material, shear waves travel always slower than compressional waves;
- The higher the rigidity of the material, the higher the P- and S-wave velocities;
- The rigidity usually increases with density ρ , but more rapidly than ρ . This explains why denser rocks have normally faster wave propagation velocities although $v^2 \sim 1/\rho$;
- Fluids (liquids or gasses) have no shear strength ($\mu = 0$) and thus do not propagate shear waves;
- For the same material, compressional waves travel slower through its liquid state than through its solid state (e.g., water and ice, or, in the Earth's core, through the liquid outer and solid inner iron core, respectively).

Seismic energy is usually radiated from localized sources with linear dimensions much smaller than the distance of observation. Therefore, seismic “wavefronts” from such “point sources,” i.e., the surfaces along which the propagating waves are oscillating *in phase*, are generally curved and the “seismic rays,” perpendicular to the wavefronts, are oriented in the

2. Seismic Wave Propagation and Earth models

radial directions of wave propagation. However, when the distance is large enough, the curvature of the wavefronts becomes so small that we can approximate them locally (e.g., within the aperture of a local seismic network or an array; see Chapters 8 and 9) by *plane waves* with parallel seismic rays.

Tab. 2.1 Typical values (averages and/or approximate ranges) of elastic constants, density, Poisson's ratio and seismic wave velocities for some selected materials, unconsolidated sediments, sedimentary rocks of different geologic age and igneous/plutonic rocks. Values for granite relate to 200 MPa confining pressure, corresponding to about 8 km depth, for basalt to 600 MPa (about 20 km depth), and for Peridotite, Dunite and Pyroxenite to 1000 MPa (about 30 km depth) (compiled from Hellwege, 1982; Lillie, 1999; and other sources).

Material or Geologic Formation	Bulk Modulus in 10^9 Pa	Shear Modulus in 10^9 Pa	Density in kg m^{-3}	Poisson Ratio	v_p in km s^{-1}	v_s in km s^{-1}	v_p/v_s
Air	0.0001	0	1.0	0.5	0.32	0	∞
Water	2.2	0	1000	0.5	1.5	0	∞
Ice	3.0	4.9	920	-0.034	3.2	2.3	1.39
Clastic sedimentary rocks					(1.4-5.3)		
Sandstone	24	17	2500	0.21	4.3	2.6	1.65
Salt	24	18	2200	0.17	4.6 (3.8-5.2)	2.9	1.59
Limestone	38	22	2700	0.19	4.7 (2.9-5.6)	2.9	1.62
Granite	56 (47-69)	34 (30-37)	2610 (2340-2670)	0.25 (0.20-0.31)	6.2 (5.8-6.4)	3.6 (3.4-3.7)	1.73 (1.65-1.91)
Basalt	71 (64-80)	38 (33-41)	2940 (2850-3050)	0.28 (0.26-0.29)	6.4 (6.1-6.7)	3.6 (3.4-3.7)	1.80 (1.76-1.82)
Peridotite, Dunit, Pyroxenite	128 (113-141)	63 (52-72)	3300 (3190-3365)	0.29 (0.26-0.29)	8.0 (7.5-8.4)	4.4 (4.0-4.7)	1.8 (1.76-1.91)
Metamorphic & igneous rocks					(3.8-6.4)		
Ultramafic rocks					(7.2-8.7)		
Cenozoic			1500-2100	0.38-<0.5	(0.2-1.9)		2.3 - 8
Cenozoic water saturated			1950	0.48	1.7	0.34	5
Cretaceous & Jurassic			2400-2500	0.28-0.43			1.8 - 2.8
Triassic			2500-2700	0.28-0.40			1.8 - 2.5
Upper Permian			2000-2900	0.23-0.31			1.7 - 1.9
Carboniferous				0.31-0.35			1.9 - 2.1

Fig. 2.5 depicts (exaggerated) the kind of displacements occurring from harmonic plane P and S waves. One clearly recognizes that P waves involve both a volume change and shearing (change in shape) while S-wave propagation is pure shear with no volume change. The P-wave particle motion is back and forth in the radial (R) direction of wave propagation

(*longitudinal polarization*) but that of the S wave is perpendicular (*transverse*) to it, in the given case oscillating up and down in the vertical plane (SV-wave). However, S waves may also oscillate purely in the horizontal plane (SH waves) or at any angle between vertical and horizontal, depending on the source mechanism (Chapter 3), the wave propagation history, and the incidence angle i_0 at the seismic station (see Fig. 2.27).

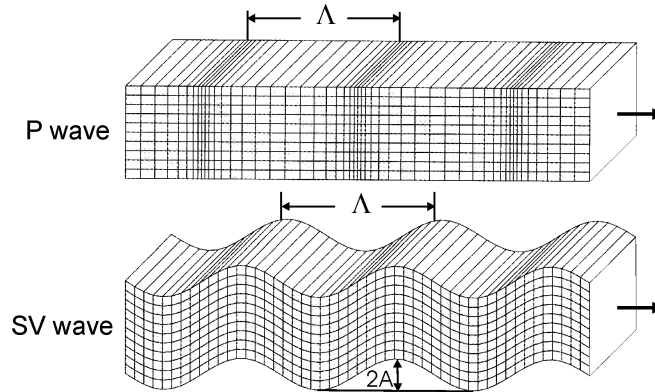


Fig. 2.5 Displacements from a harmonic plane P wave (top) and SV wave (bottom) propagating in a homogeneous isotropic medium. Λ is the wavelength. $2A$ means double amplitude. The white surface on the right is a segment of the propagating plane wavefront where all particles undergo the same motion at a given instant in time, i.e., they oscillate *in phase*. The arrows indicate the seismic rays, defined as the *normal* to the wavefront, which points in the direction of propagation (modified according to Shearer, Introduction to Seismology, 1999; with permission from Cambridge University Press).

The wavelength Λ is defined by the distance (in km) between neighboring wave peaks or troughs or volumes of maximum compression or dilatation (see Fig. 2.5). The wave period T is the duration of one oscillation (in s) and the frequency f is the number of oscillations per second (unit [Hz] = [s⁻¹]). The wavelength is the product of wave velocity v and period T while the wavenumber is the ratio $2\pi/\Lambda$. Tab. 2.2 summarizes all these various *harmonic wave parameters* and their mutual relationship.

Tab. 2.2 Harmonic wave parameters and their mutual relationship.

Name	Symbol	Relationships
Period	T	$T = 1/f = 2\pi/\omega = \Lambda/v$
Frequency	f	$f = 1/T = \omega/2\pi = v/\Lambda$
Angular frequency	ω	$\omega = 2\pi f = 2\pi/T = v \cdot k$
Velocity	v	$v = \Lambda/T = f \cdot \Lambda = \omega/k$
Wavelength	Λ	$\Lambda = v/f = v \cdot T = 2\pi/k$
Wavenumber	k	$k = \omega/v = 2\pi/\Lambda = 2\pi f/v$

In any case, the polarization of both P and S waves, when propagating in a homogenous and isotropic medium, is linear. This is confirmed rather well by particle motion analysis of real seismic recordings, if they are broadband (or long period). But higher frequencies, which are more strongly affected by local inhomogeneities in the Earth, show a more elliptical or irregular particle motion. Fig. 2.6 shows an example. While the rectilinearity of P is almost 1

2. Seismic Wave Propagation and Earth models

(0.95) in the BB record it is significantly less (0.82 as an average over 5 oscillations and down to 0.68 for some single oscillations) for the short-period filtered record.

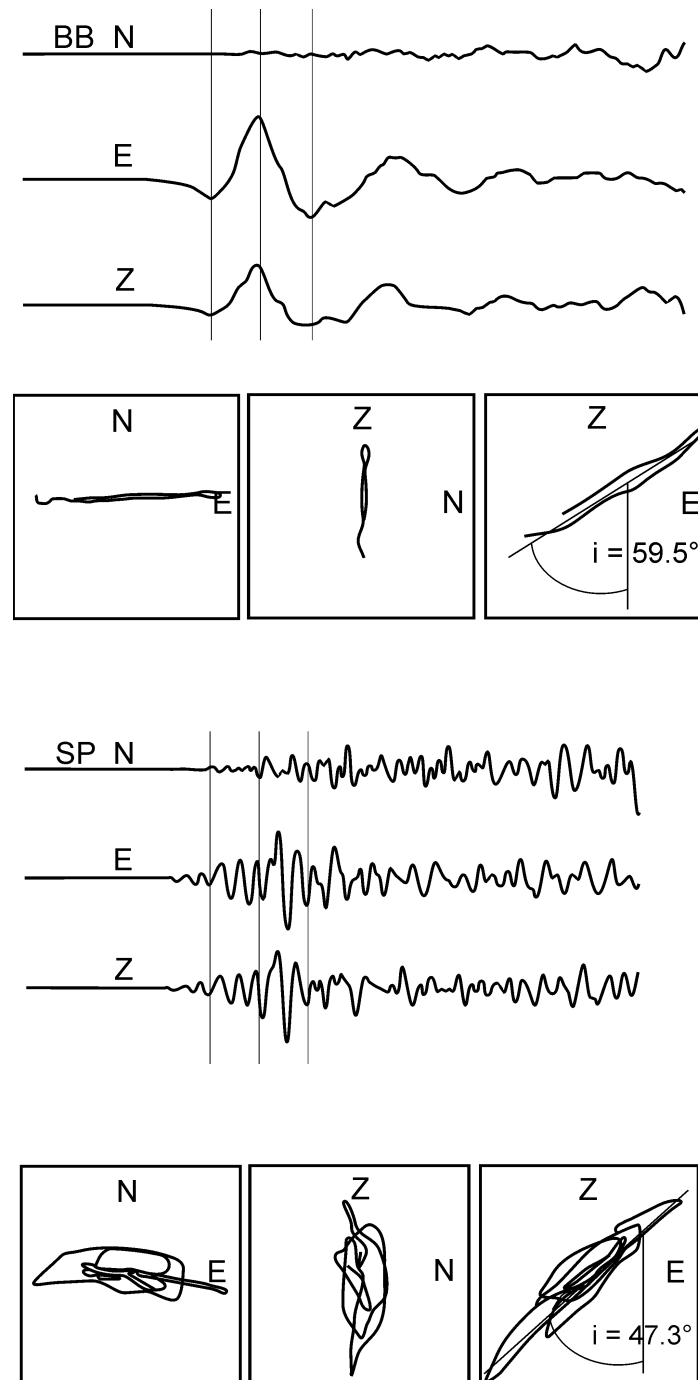


Fig. 2.6 3-component records at station MOX (top traces) and related plots of particle motion in the horizontal (N-E) plane and two vertical planes (Z-N and Z-E, respectively) of the P-wave onset from a local seismic event (mining collapse) in Germany (13.03.1989; $M_I = 5.5$; epicentral distance $D = 112$ km, backazimuth $BAZ = 273^\circ$). Upper part: broadband recording (0.1-5 Hz); lower part: filtered short-period recording (1- 5 Hz). **Note:** The incidence angle is 59.5° for the long-period P-wave oscillation and 47.3° for the high-frequency P-wave group.

S waves are also linearly polarized when propagating in homogeneous isotropic medium. However, in the presence of anisotropy, they split into a fast and slow component. These split waves propagate with different velocity that causes some time delay and related phase shift. Accordingly, the two split S-wave components superimpose to an elliptical polarization (Fig. 2.7). The orientation of the main axis and the degree of ellipticity are controlled by the fast and slow velocity directions of the medium with respect to the direction of wave propagation and the degree of anisotropy. Therefore, shear-wave splitting is often used to study S-wave velocity anisotropy in the Earth.

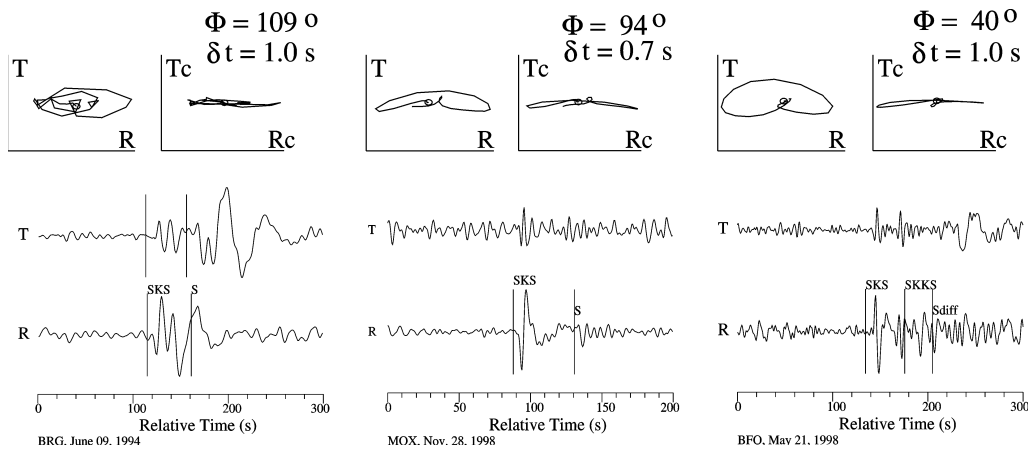


Fig. 2.7 Examples of SKS and SKKS recordings and plots of particle motion at three stations of the German Regional Seismograph Network. The horizontal radial (R) and transverse (T) components are shown. They were derived by rotation of the N-S and E-W horizontal components with the backazimuth angle. The T component at BFO has the same scale as the R component, while T is magnified two-fold relative to R at BRG and MOX. The top panels show the polarization in the R-T plane. Anisotropy is manifested in all three cases by the elliptical polarization. Linear polarization is obtained by correcting the R-T seismograms for the anisotropy effect using an anisotropy model where the direction of the fast shear wave is sub-horizontal and given by the angle Φ measured clockwise from north, and the delay time (in seconds) between the slow and the fast shear wave is given by δt (courtesy of G. Bock).

2.3 Surface waves

2.3.1 Origin

So far we have considered only body-wave solutions of the seismic wave equation. They exist in the elastic full space. However, in the presence of a free surface, as in the case of the Earth, other solutions are possible. They are called *surface waves*. There exist two types of surface waves, *Love waves* and *Rayleigh waves*. While Rayleigh (LR or R) waves exist at any free surface, Love (LQ or G) waves require some kind of a *wave guide* formed by a velocity increase with depth (gradient- or layer-wise). Both conditions are fulfilled in the real Earth.

SH waves are totally reflected at the free surface. Love waves are formed through constructive interference of repeated reflections of teleseismic SH at the free-surface (i.e., S3, S4, S5, etc.; see Fig. 2.42 and overlay to Figs. 2.48 and 2.49). They can also result from constructive interference between SH waves, which are *postcritically reflected* (see 2.5.3.5) within a homogeneous layer (or a set of i layers with increasing v_{si}) overlaying a half-space

2. Seismic Wave Propagation and Earth models

with higher velocity. The latter is the case of crustal layers, overlaying the upper mantle with a significant velocity increase at the base of the crust, called the “Mohorovičić-discontinuity” or *Moho* for short. The Moho marks the transition between the usually more mafic (often termed “basaltic”) lower crust and the peridotitic uppermost mantle (for related velocities see Tab. 2.1) and may, together with other pronounced intra-crustal velocity discontinuities give rise to the formation of complex guided crustal waves (see 2.3.3).

Generally, destructive interference of the upgoing and downgoing reflected SH waves will occur, except at certain discrete frequencies ω and n multiples of it (with n as an integer). The values of ω given for $n = 0$ are termed the *fundamental modes* while larger values of n define the *higher modes* or *overtones*. Fig. 2.8 (top) shows the horizontal (SH type) of displacement and linear polarization of the fundamental Love-wave mode as well as the exponential decay of its amplitudes with depth.

When a P (or SV) wave arrives at the surface the reflected wave energy contains (because of *mode conversion*, see 2.5.3.4) both P and SV waves. Lord Rayleigh showed more than 100 years ago that in this case a solution of the wave equation exists for two coupled inhomogeneous P and SV waves that propagate along the surface of a half-space. While Rayleigh waves show no dispersion in a homogeneous half-space, they are always dispersed in media with layering and/or velocity gradients such as in the real Earth. Rayleigh waves travel - for a Poisson solid - with a phase velocity $c = \sqrt{2 - 2/\sqrt{3}} v_s \approx 0.92 v_s$, i.e., they are slightly slower than Love waves. Therefore, they appear somewhat later in seismic records. The exact value of c depends on v_p and v_s . Since Rayleigh waves originate from coupled P and SV waves they are polarized in the vertical (SV) plane of propagation and due to the phase shift between P and SV the sense of their *particle motion* at the surface is *elliptical* and *retrograde* (counter clockwise). Fig. 2.8 (bottom) shows schematically the displacements for the fundamental mode of Rayleigh waves. They also decay exponentially with depth. The short-period fundamental mode of Rayleigh type in continental areas is termed Rg.

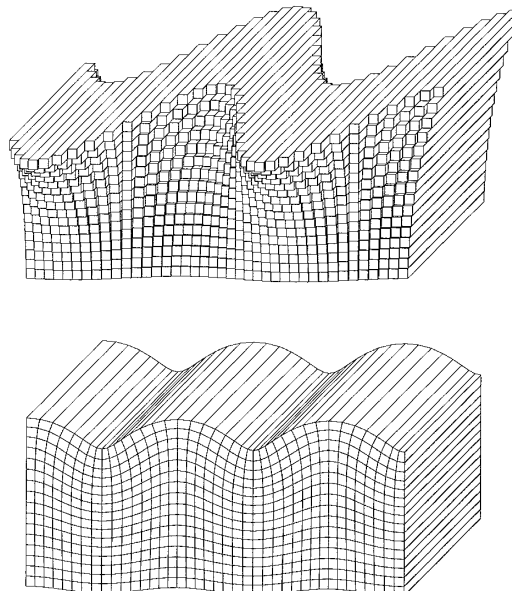


Fig. 2.8 Displacements caused by horizontally propagating fundamental Love (top) and Rayleigh waves (bottom). In both cases the wave amplitudes decay strongly with depth (from Shearer, Introduction to Seismology, 1999; with permission from Cambridge University Press).

2.3.2 Dispersion and polarization

The *penetration depth* below the surface increases with Λ . This is comparable with the frequency-dependent *skin effect* of electromagnetic waves propagating in a conducting medium with a free surface. Since the types of rocks, their rigidity and bulk modulus change (usually increase) with depth, the velocities of surface waves change accordingly since the longer waves “sense” deeper parts of the Earth. This results in a frequency dependence of their horizontal propagation velocity, called *dispersion*. Accordingly, while body-wave arrivals with no or negligibly small dispersion only (due to intrinsic attenuation) appear in seismic records as rather impulsive onsets or short transient wavelets (with the shape and duration depending on the bandwidth of the seismograph; see Chapter 4.2), the dispersion of surface waves forms long oscillating wave trains. Their duration increases with distance.

Usually, the more long-period surface waves arrive first (normal dispersion). But in some regions of the Earth low-velocity layers exist (e.g., the *asthenosphere* in the upper mantle; see the PREM model in 2.7, Fig. 2.53, in the depth range between about 80 and 220 km). This general trend may then be reversed for parts of the surface wave spectrum. Presentations of the propagation velocity of surface waves as a function of the period T or the frequency f are called *dispersion curves*. They differ for Love and Rayleigh waves and also depend on the velocity-depth structure of the Earth along the considered segment of the travel path (Fig. 2.9). Thus, from the inversion of surface wave dispersion data, information on the shear-wave velocity structure of the crust, and, when using periods up to about 500 s (mantle surface waves), even of the upper mantle and transition zone can be derived.

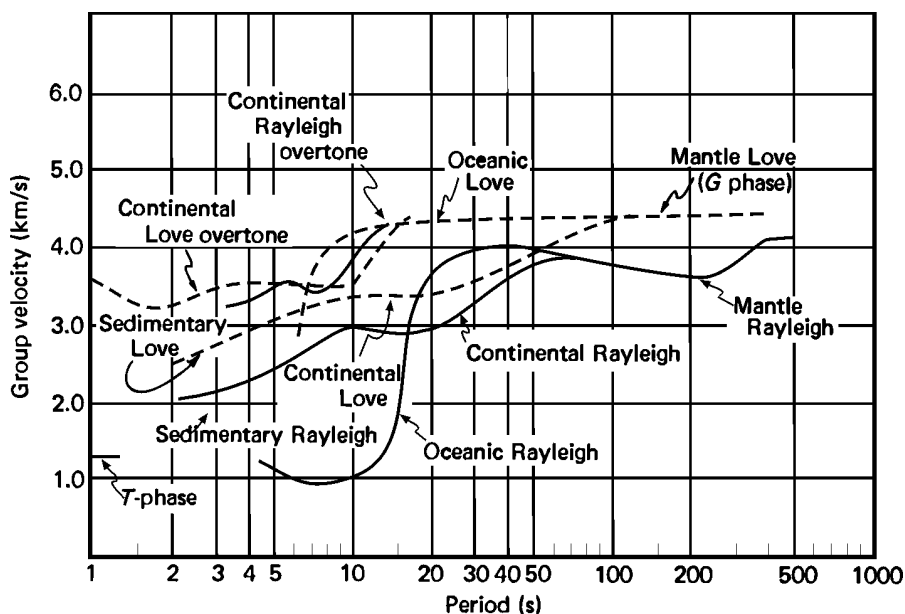


Fig. 2.9 Group-velocity dispersion curves as a function of period for Love and Rayleigh waves (fundamental modes and overtones) (from Bullen and Bolt, *An Introduction to the Theory of Seismology*, 1985; with permission from Cambridge University Press).

The large differences in crustal thickness, composition and velocities between oceanic and continental areas (Fig. 2.10) result in significant differences between their related average group-velocity dispersion curves (Fig. 2.9). They are particularly pronounced for Rayleigh

2. Seismic Wave Propagation and Earth models

waves. While the velocities for continental Rayleigh waves vary in the period range from about 15 and 30 s only from 2.9 to 3.3 km/s, they vary much more in oceanic areas (from about 1.5 to 4.0 km/s within the same period range). Consequently, LR wave trains from travel paths over continental areas are shorter and look more clearly dispersed because the various periods follow each other at shorter time differences (e.g., Figures 1d and 5a in DS 11.2). In contrast, LR wave trains with dominantly oceanic travel paths are much longer with almost monochromatic oscillations over many minutes (Fig. 2.11). Actually, the discovery of different surface-wave velocities along continental and oceanic paths were in the 1920s the first indication of the principle structural difference between oceanic and continental crust.

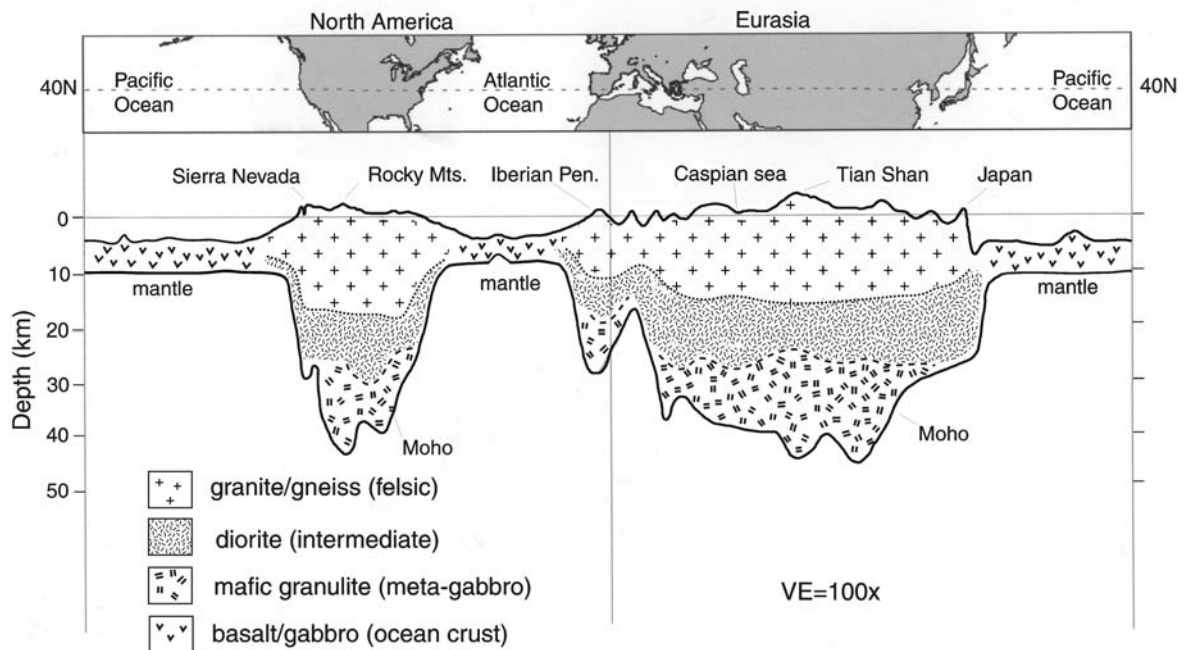


Fig. 2.10 Cross-section through the crust along 40° northern latitude. Note the different signatures for the upper (granitic), intermediate (dioritic) and lower (mafic) continental crust and the basaltic oceanic crust. The crustal base is termed “Moho” (according to its discoverer, the Croatian seismologist Andrija Mohorovičić). The P-wave velocity increases at the Moho from about 6.5-6.8 km/s to 7.8-8.2 km/s. The continental crust is about 25 to 45 km thick (average about 35 km) and has “roots” under young high mountain ranges which may reach down to nearly 70 km. The oceanic crust is rather thin (about 8 to 12 km) with a negligible upper crust (courtesy of Mooney and Detweiler, 2002).

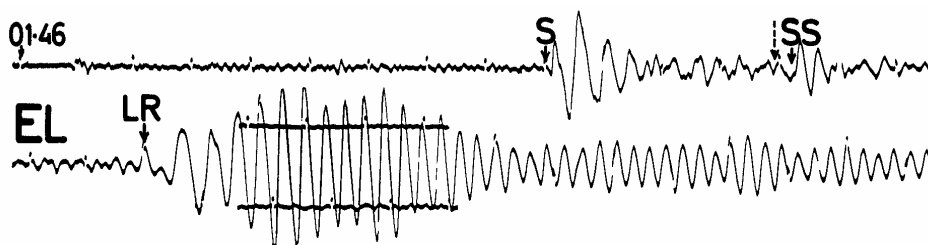


Fig. 2.11 Record of Rayleigh waves in the long-period vertical component at the station Toledo, Spain, from an earthquake in the Dominican Republic ($D = 6,622$ km; travel-path through the Atlantic Ocean) (courtesy of G. Payo, 1986).

Strictly speaking, when dealing with dispersive waves, one has to discriminate between the *group velocity* $U(T)$, with which the energy of the wave group moves and the *phase velocity* $c(T)$, with which the wave peaks and troughs at a given frequency travel along the surface. As seen from Fig. 2.12, $c(T)$ is always larger than $U(T)$. When comparing Figs. 2.9 and 2.12 the significant differences between dispersion curves calculated for a global 1-D Earth model like PREM (see 2.7, Fig. 2.53 and DS 2.1) and averaged measured curves for different types of crust or mantle models become obvious.

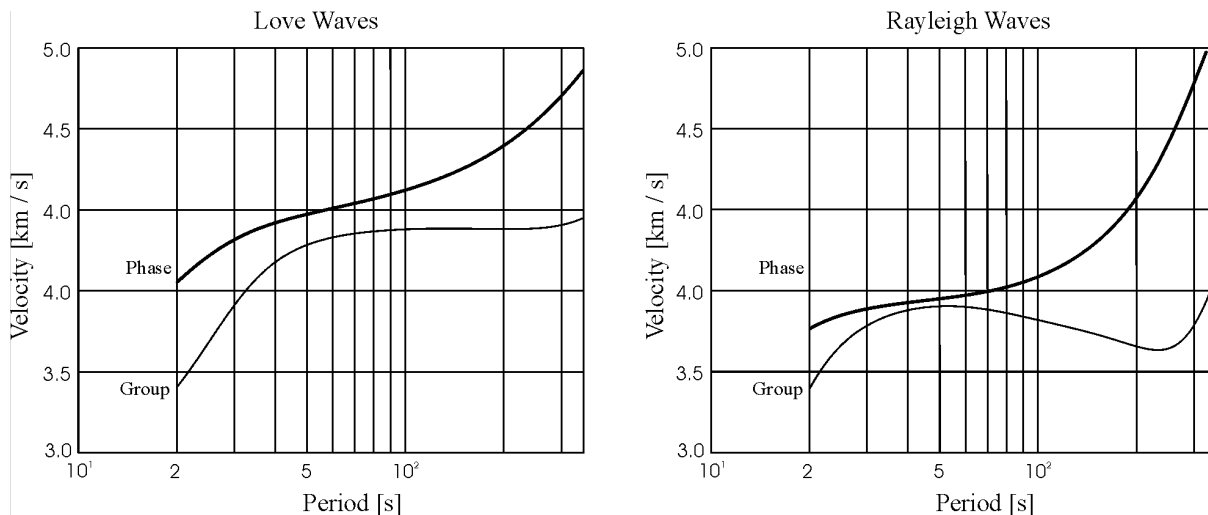


Fig. 2.12 Fundamental mode Love- and Rayleigh-wave dispersion curves computed for the PREM model with anisotropy (courtesy of Gabi Laske).

As shown in Fig. 2.13, the horizontal component of the fundamental Rayleigh wave mode will vanish in a uniform half-space at a depth of about $\Lambda/5$ and thus the particle motion becomes vertical linear. At larger depth the particle trajectories will be elliptical again, but with a *prograde* (clockwise) sense of motion. The amplitudes decay rapidly with depth. At a depth of $\Lambda/2$, the horizontal particle motion is about 10% of that at the surface while the vertical particle motion at the surface is reduced to about 30%.

Because of the strong decay of surface wave amplitudes with depth, earthquakes deeper than the recorded wavelengths will produce significantly reduced or no surface waves. The amplitude ratio between body and surface waves in broadband records is thus a reliable quick discriminator between shallow and deep earthquakes. For shallow teleseismic earthquakes the surface wave group has generally by far the largest amplitudes in broadband and long-period records (see Fig. 2.23). This is because of their 2-D propagation along the surface of the Earth and energy decay $\sim 1/r$ as compared to the 3-D propagation of body-waves and energy decay $\sim 1/r^2$. Also, the local maxima and minima in the group-velocity curves (Figs. 2.9 and 2.12) imply that surface wave energy in a wider period range around these extremes will travel with nearly the same velocity and arrive at a seismic station at about the same time, thus superimposing to large amplitudes. These amplitude maxima in the dispersive surface wave train are called *Airy phases*. For continental travel paths a pronounced Rayleigh wave Airy phase with periods around 20 s occurs which is rather stable and used for estimating the standard surface wave magnitude M_s (see 3.2.5.1). An example is given in Fig. 2.23. Long-period mantle Rayleigh waves have an Airy phase around $T \approx 220$ s (see Fig. 2.9).

2. Seismic Wave Propagation and Earth models

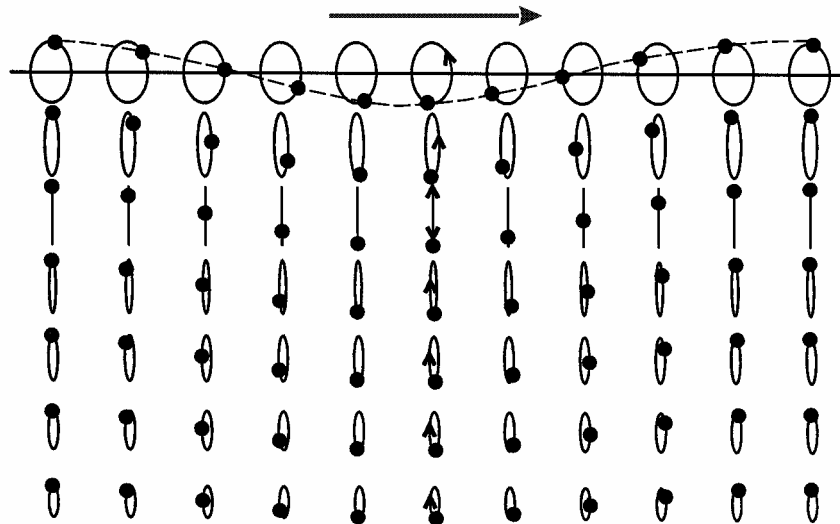


Fig. 2.13 Particle motion for the fundamental Rayleigh mode in a uniform half-space. Shown is one horizontal wavelength. At the surface the vertical motion is about 1.5 times larger than the horizontal motion. Note the change from retrograde to prograde sense of elliptical particle motion at a depth larger about $\Lambda/5$. The wave propagates from left to right. The dots show the position of the same particle at a fixed distance with time increasing from the right to the left (modified from Shearer, Introduction into Seismology, 1999; with permission from Cambridge University Press).

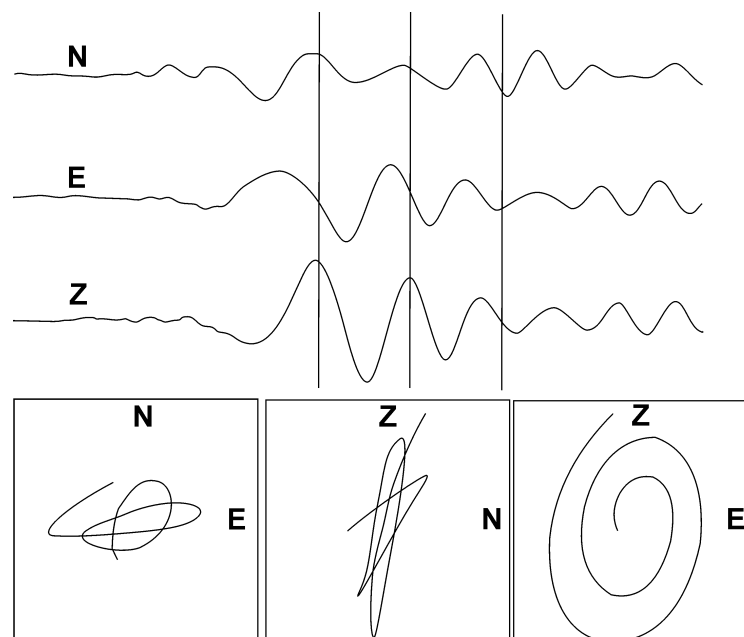


Fig. 2.14 3-component broadband records (top traces) and related plots of particle motion in the horizontal (N-E) plane and two vertical planes (Z-N and Z-E, respectively) of the surface-wave group of the same event as in Fig. 2.6 ($D = 112$ km; backazimuth $BAZ = 273^\circ$).

Fig. 2.14 above shows, for the event in Fig. 2.6, the 3-component broadband record of the Rayleigh-wave group and the related particle motion trajectories in three perpendicular planes. There exists indeed a strikingly clear retrograde elliptical motion in the vertical-east

(Z-E) plane, which is in this case almost identical with the vertical plane of wave propagation (backazimuth 273°). Also the amplitude ratio vertical/horizontal component is 1.5, as theoretically expected. In the horizontal N-E plane, however, there is also some transverse energy present in this wave group. It is due to some SH energy present in the N-S component. Generally, one should be aware that the theoretically expected complete separation of LQ and LR waves in a homogeneous isotropic (horizontally layered) half-space is not absolutely true in the real Earth because of heterogeneity and anisotropy. This may cause the coupling of some Rayleigh-wave energy into Love waves and vice versa (see e.g., Malischewsky (1987) and Meier et al. (1997)), similar to S-wave splitting in the presence of anisotropy (see Fig. 2.7).

Higher mode surface waves have a different depth dependence than fundamental modes and sample deeper structure than that probed by fundamental modes of the same period.

2.3.3 Crustal surface waves and guided waves

Because of the broad maximum of the group velocity of Love-wave continental overtones with values around 3.5 km/s between about 3 and 10 s (see Fig. 2.9) they may appear in seismic records as an onset-like Lg-wave group with almost no dispersion, sometimes even in pairs (Lg1, Lg2) because of the nearby local minimum in the dispersion curve. Since the group velocity of Lg-waves is higher than that of continental fundamental modes with $T < 30$ s (see Fig. 2.9), they may appear in broadband records with an upper corner period around 20 s as clear forerunners to the surface wave group. The Lg-wave group, however, is not a pure continental Love wave but rather a complex *guided crustal* wave. It is caused by superposition of multiple S-wave reverberations between the surface and the Moho and SV to P and/or P to SV conversions as well as by scattering of these waves at lateral heterogeneities in the crust. Accordingly, Lg waves are also recorded on vertical components (see Fig. 2.15). Beyond epicentral distances of about 3° their amplitude maximum is usually well-separated from the earlier onset of Sg. Lg usually dominates seismic records of local and regional events and may propagate rather effectively along continental paths, in shield regions in particular, over a few thousand kilometers (see Fig. 2.15). Because of the stability of Lg amplitude-distance relationships in continental areas this phase is well suited for reliable magnitude estimates of regional events (see 3.2.6.6). The propagation of Lg may be barred by lateral changes in the velocity structure such as sedimentary basins, Moho topography, the transition between oceanic and continental crust or the boundaries between different tectonic units.

Near-surface seismic events such as industrial or underground nuclear explosions, rock-bursts etc. also generate short-period fundamental-mode Rayleigh waves, termed Rg. Rg waves show normal dispersion and have relatively large amplitudes on vertical components (see Fig. 2.16.). They are not excited by seismic events deeper than about one wavelength and thus a good discriminator between often man-made seismic sources near the surface and most natural earthquakes with depths most likely between 5 and 25 km (crustal earthquakes) or even deeper (intermediate or deep earthquakes in subduction zones). Rg is more strongly attenuated than the guided wave Lg. Its range of propagation is limited to less than about 600 km. However, up to about 200 km distance Rg may dominate the recorded wave train from local near-surface seismic events.

2. Seismic Wave Propagation and Earth models

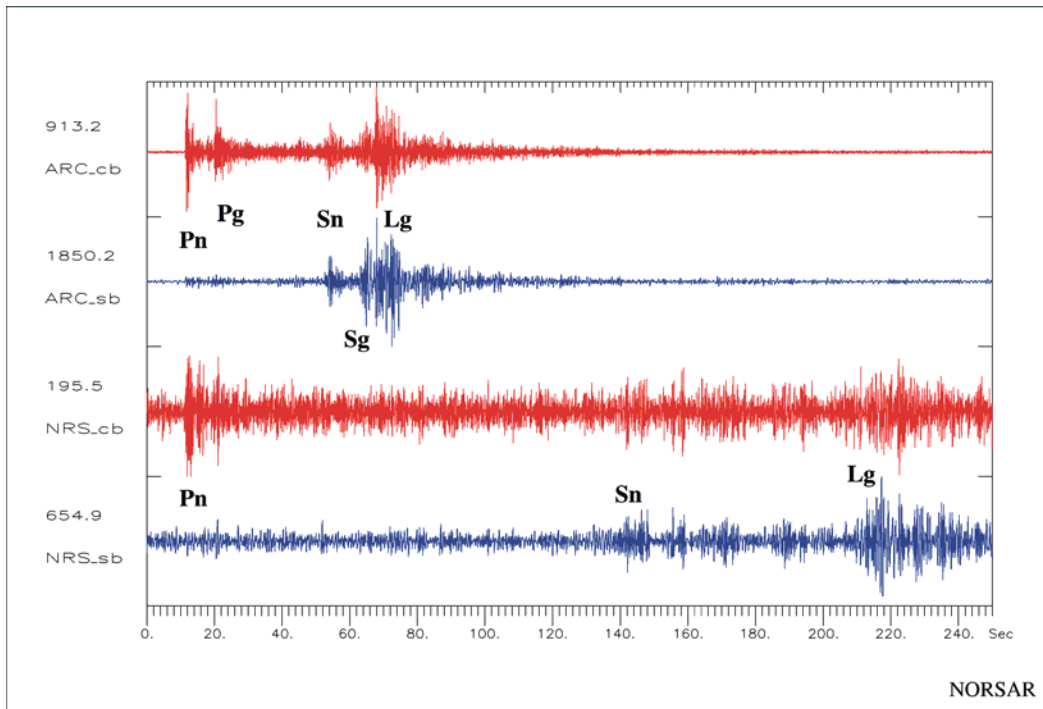


Fig. 2.15 Records of Lg, together with other crustal phases, in records of a Kola peninsula mining blast ($M_l = 2.4$) at the Norwegian array stations ARCES (distance $D = 391$ km; upper two traces) and NORES ($D = 1309$ km, bottom traces). cb and sb – P- and S-wave beams (see Chapter 9) of the vertical elements of the array, filtered with 2-8 Hz and 1-4 Hz, respectively (courtesy of J. Schweitzer).

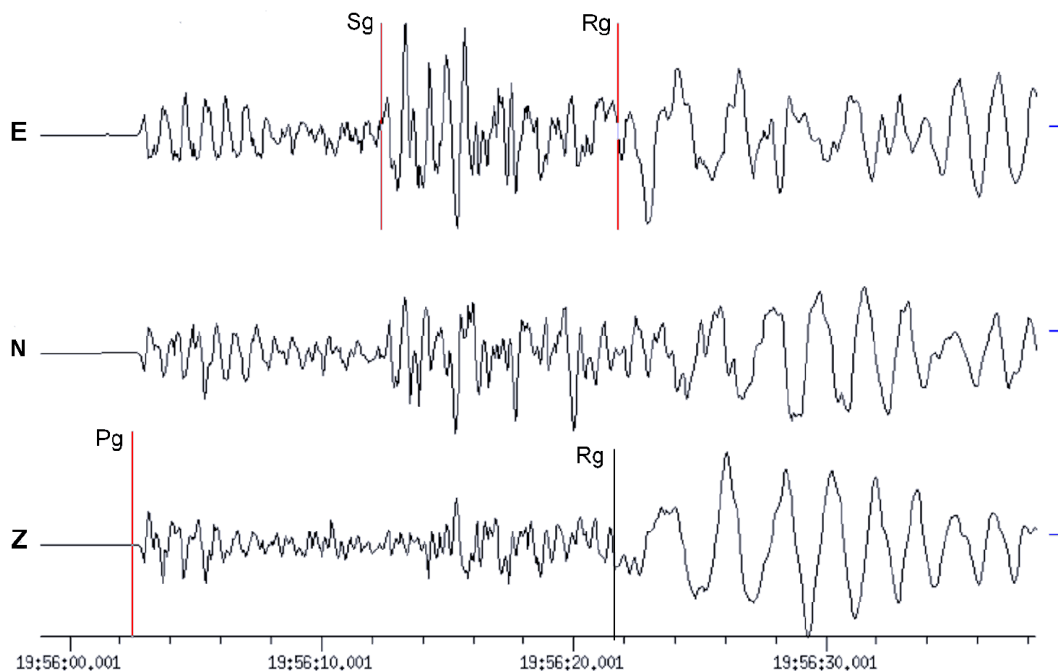


Fig. 2.16 Mining induced rock burst south of Saarbrücken, Germany, recorded at station WLF in Luxemburg ($D = 80$ km, $h = 1$ km, $M_l = 3.7$). Note the strong dispersive Rg phase.

2.3.4 Mantle surface waves

Love and Rayleigh waves travel along great circle paths around the globe. Surface waves from strong earthquakes may travel several times around the Earth. They are termed *global surface waves*. The first surface wave group arriving at a seismic station at the epicentral distance Δ° will have taken the shorter great circle while the later arrival has traveled the major arc path over $360^\circ - \Delta^\circ$ (Fig. 2.17).

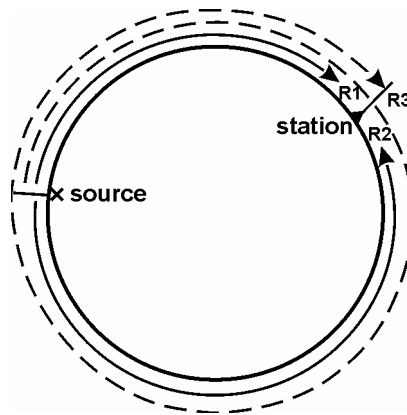


Fig. 2.17 Great circle paths for the first three arrivals of global Rayleigh waves.

These arrival groups are called R1, R2, R3, R4 etc. for Rayleigh waves and G1, G2, G3, G4 etc. for Love waves, respectively. R3 (or G3) have traveled over $360^\circ + \Delta^\circ$ and R4 over $720^\circ - \Delta^\circ$ etc. Fig. 2.18 gives an example for long-period records of P, SV, SH, R1, R2, G1 and G2 in the vertical (Z) and the two rotated horizontal components (radial R and transverse T). As expected, P appears only on Z and R while S has both SV and SH energy. The Love wave groups G1 and G2 are strongest in T and arrive ahead of R1 in R2, which are visible only on the R and Z components. But Fig. 2.18 is also a good example for inverse (negative) dispersion in the Rayleigh-wave groups. Their periods range from about 60 s to almost 200 s, with the longest periods arriving at the end of the R1 and R2 groups. This is just the period range of inverse dispersion according to Fig. 2.9 for both continental and oceanic mantle Rayleigh waves. This inverse dispersion is not seen in records of classical WWSSN long-period seismographs with a peak magnification around 15 s because the corresponding periods are filtered out by the system response of these seismographs.

Further, one should note in Fig. 2.18 that these surface waves originate from an earthquake in the Tonga trench subduction zone at a depth of $h = 230$ km. This seems to contradict the above statement, that no or only weak surface waves can be observed from deep earthquakes. However, there is no contradiction. As discussed above, the depth of penetration (and thus constructive interference) of surface waves increases with their wavelength. For the periods considered in Fig. 2.18 Λ ranges between about 230 and 880 km, i.e., it is comparable or larger than the source depth. Therefore, we still can expect significant surface wave energy in that period range for the largest amplitudes in Fig. 2.18. However, no periods below 50 s, as recorded in classical narrow-band long-period records, are recognizable in these surface-wave trains.

2. Seismic Wave Propagation and Earth models

With modern very broadband (VBB) recording systems of high dynamic range (see Chapter 5) it is possible to record such long-period global mantle surface waves up to about R7, riding on oscillations of solid Earth's tides of even longer period (more than 12 hours). Fig. 2.19 shows a striking example. The successive groups of R reveal an exponential decay of amplitudes. This allows the determination of the intrinsic frequency-dependent attenuation in the crust and mantle (see 2.5.4.2).

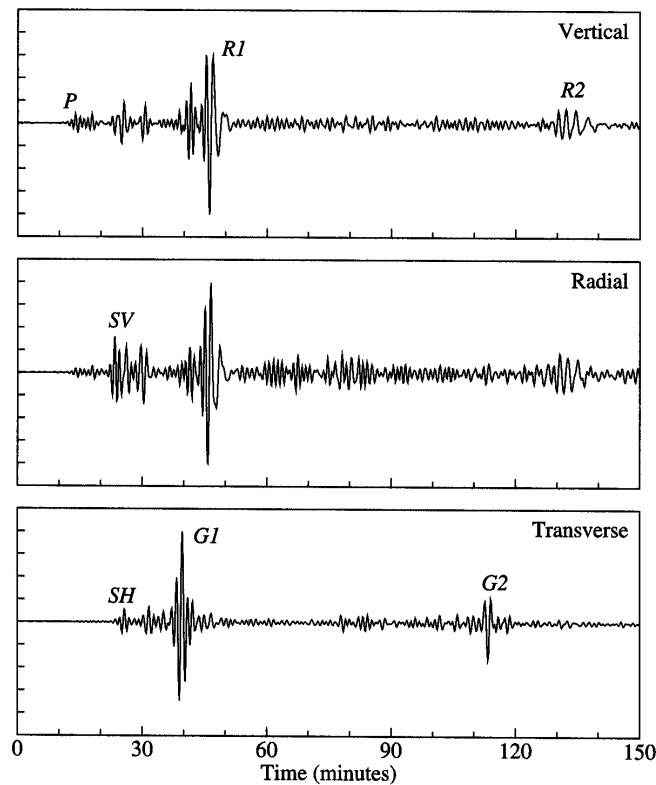


Fig. 2.18 Records of the March 11, 1989 Tonga trench earthquake ($h = 235$ km) in the Z, R and T components of the IRIS/IDA station NNA in Peru ($D = 93.7^\circ$) (from Shearer, Introduction to Seismology, 1999; with permission from Cambridge University Press).

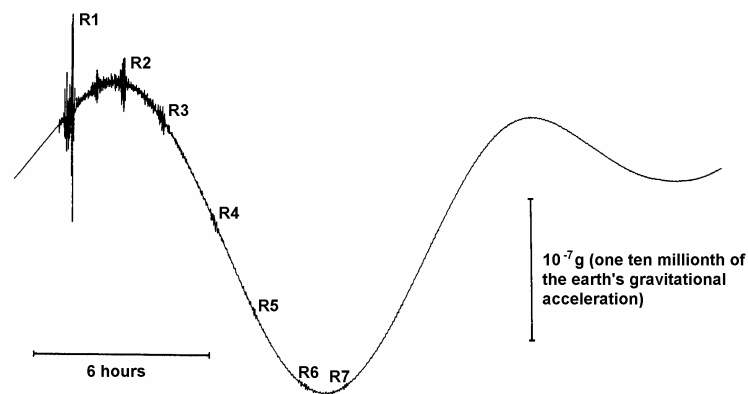


Fig. 2.19 Example of a very broadband (VBB) record with high dynamic range by the STS1 seismograph operated by the Nagoya University, Japan. The seismic wave groups from a magnitude 8.2 earthquake in the Kermadec Islands (October 20, 1986) are superimposed to solid Earth's tides (modified from a pamphlet of the Japanese Global Seismology Subcommittee for the POSEIDON project).

2.4 Normal modes

Since the Earth is not an infinite half-space but a finite body, all wave motions must be confined too. Body waves are reflected back from the surface into the Earth, surface waves orbit along great circle paths. Thus, there will be a multitude of different seismic phases arriving at a given point on the surface. Depending on their timing and periods they will interfere with each other, either in a more destructive or more constructive manner. The latter will be the case at certain resonant frequencies only. They are termed the Earth's *normal modes* and provide another alternative way of representing wave propagation. An analogy is the standing wave modes of a vibrating string fixed at both ends (Fig. 2.20). The lowest frequency is called the fundamental mode; the higher modes are the overtones. This can be treated as an eigenvalue problem: the resonant frequencies are called *eigenfrequencies*; the related displacements are termed the *eigenfunctions*.

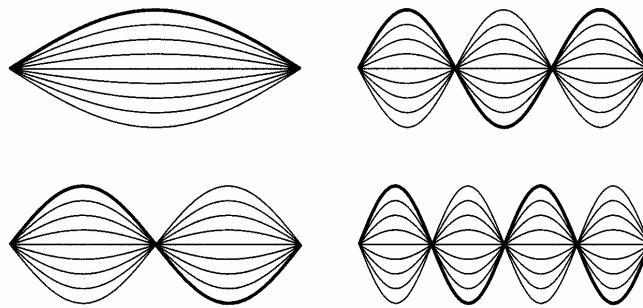


Fig. 2.20 The first four modes of vibration of a string between fixed endpoints (from Shearer, *Introduction to Seismology*, 1999; with permission from Cambridge University Press).

One should be aware of the following points about normal modes in observatory practice:

- any wave motion within the Earth may be expressed as a sum of normal modes with different excitation factors;
- there exist, in analogy to P/SV (Rayleigh) and SH (Love) -wave motion, *spheroidal modes* and *toroidal modes*, respectively;
- toroidal modes involve no radial motion and are only sensitive to the shear velocity;
- spheroidal modes have both radial and horizontal motion. They are sensitive to both compressional and shear velocities;
- long-period spheroidal modes are sensitive to gravity and thus provide information about the density structure of the Earth that may not be obtained in any other way;
- the ellipticity of the Earth, its rotation as well as its 3-D velocity variations will cause a splitting of the eigenfrequency spectral lines. Thus the investigation of normal mode splitting allows to constrain 3-D structures of the Earth;
- normal modes do (besides PKPdf amplitudes) provide information about the shear-wave velocity of the *inner core*;
- the decay of mode amplitudes with time has provided important information about the attenuation properties of the Earth at very long periods;
- normal modes provide a complete set of basis functions for the computation of synthetic seismograms for surface-wave and long-period body-wave seismology.

2. Seismic Wave Propagation and Earth models

Therefore, the collection of high-quality broadband data that also allow retrieval of normal modes is an important function of high-tech seismological broadband observatories. This requires very stable installation conditions, for horizontal seismometers in particular, e.g., in boreholes (see 7.4.5) or deep non-producing underground mines in order to reduce near surface tilt noise caused by barometric pressure variations. The latter may also be filtered out by correlating parallel recordings of seismometers and micro-barometers (e.g., Warburton and Goodkind, 1977; Beauduin et al., 1996; see Fig. 2.21).

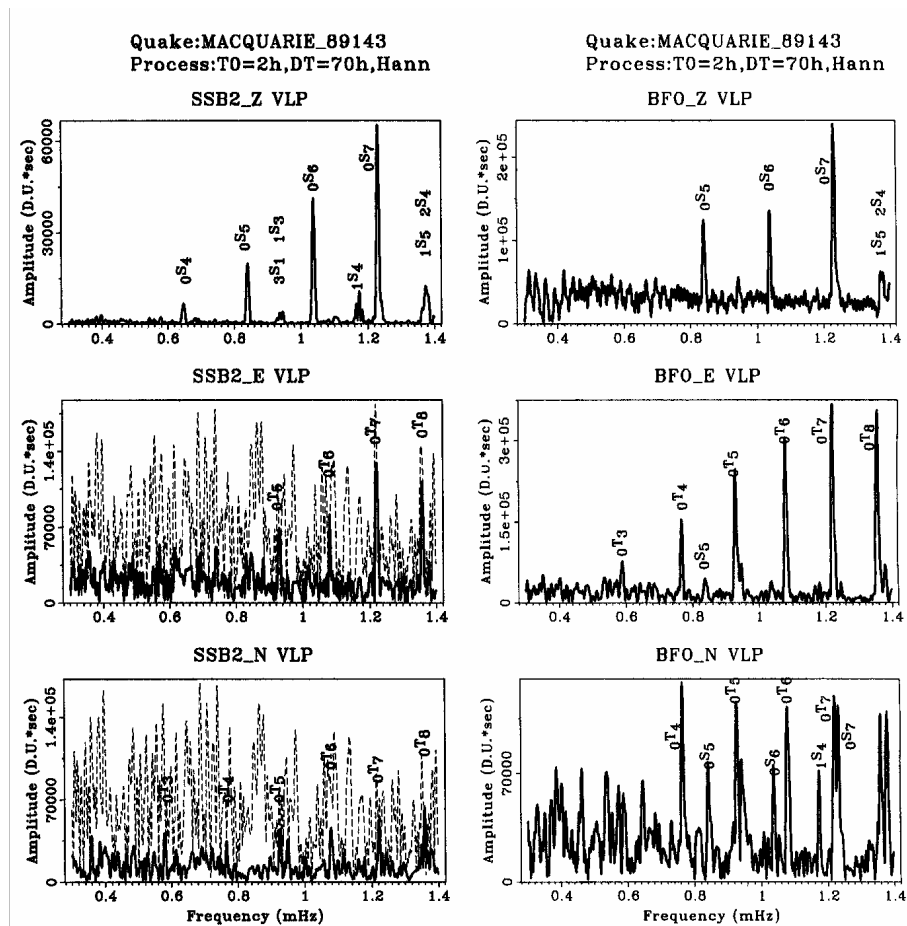


Fig. 2.21 Normal mode spectra excited by an $M_s = 8.2$ earthquake in the Macquarie Island region and recorded with STS1 at the stations SSB2 in France and BFO in Germany. BFO is located in an old silver mine and has very low tilt noise. The latter is high at SSB2 (broken lines) but could be filtered out (solid lines) by correlation with micro-barometric recordings (reproduced from Beauduin et al., *The Effects of the Atmospheric Pressure Changes on Seismic Signals ...*, Bull. Seism. Soc. Am., Vol. 86, No. 6, Fig. 8, page 1768, 1996; © Seismological Society of America).

In fact, normal mode analysis in the *spectral domain* (see Chapter 4.1) is the only practical way to examine seismic records at very long periods (> 500 s) and thus with wavelengths of 2000 and more kilometers. But normal mode studies themselves are beyond the scope of routine data analysis at seismological observatories and will not be considered in this Manual. (For further readings see Gilbert and Dziewonski, 1975; Aki and Richards, 1980 and 2002; Lapwood and Usami, 1981; Lay and Wallace, 1995; Dahlen and Tromp, 1998; Kennett, 2001).

First observations of some normal modes were made in conjunction with the strongest earthquake of the 20th century (Chile, 1960). Since then, further progress in seismometry and data analysis have permitted the identification of over a thousand modes and on that basis, to significantly refine velocity, density and attenuation models of the Earth (see 2.7; PREM model). Fig. 2.22 shows the patterns of surface and radial motions related to some of the spheroidal and toroidal modes. Their general nomenclature is ${}_nS_l$ and ${}_nT_l$. n is the number of zero crossings of amplitudes with depth while l is the number of zero (nodal) lines on the surface of the sphere.

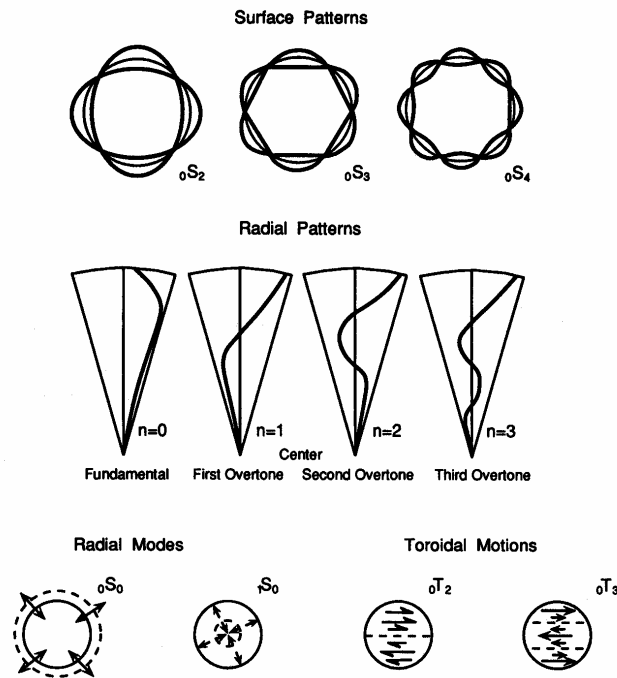


Fig. 2.22 Top: Surface and radial patterns of motions of spheroidal modes. Bottom: Purely radial modes involve no nodal pattern on the surface but have nodal surfaces at depth. Toroidal modes involve purely horizontal twisting of the Earth. For explanation of mode nomenclature see text (after Bolt, 1982; from Lay and Wallace, 1995, Fig. 4.24, p. 160; with permission of Elsevier Science (USA)).

Accordingly, the fundamental spheroidal “breathing” mode of the Earth is ${}_0S_0$ because it represents a simple expansion and contraction of the Earth. It has a period of about 20 min. ${}_0S_2$ has the longest period (≈ 54 min) and describes an oscillation between an ellipsoid of horizontal and vertical orientation, sometimes termed “rugby” mode. The toroidal mode ${}_0T_2$ corresponds to a purely horizontal twisting motion between the northern and southern hemisphere and has a period of about 44 min. Overtones ${}_iS$ and ${}_iT$ with $i = 1, 2, 3, \dots$ have one, two, three or more nodal surfaces at constant radii from the center of the Earth across which the sense of radial or twisting motions reverses.

In summary, strong earthquakes can make the planet Earth ring like a bell. Seismologists may be compared with experienced bell-makers who are able to infer from the complex sound spectra of a bell not only its size and general shape but also the composition of the alloy of which it is made.

2.5 Seismic rays, travel times, amplitudes and phases

2.5.1 Introduction

So far we have introduced seismic body and surface waves. We have learned why these different wave types travel with different velocities through and consequently appear in the seismogram at different times. We have seen that body waves form short transient wavelets (see Figs. 2.3 and 3.7), in contrast to the prolonged and dispersed wave trains of surface waves (e.g., Figs. 2.11 and 2.23). Fig. 2.23 shows a seismic record of an earthquake 73° away. Besides the discussed primary body and surface waves (P, S, LQ, and LR), several additional arrivals are marked in the seismogram and their symbols are given. These energy pulses are mainly caused by reflection or mode conversion of primary P or S waves either at the free surface of the Earth or at velocity-density discontinuities inside the Earth.

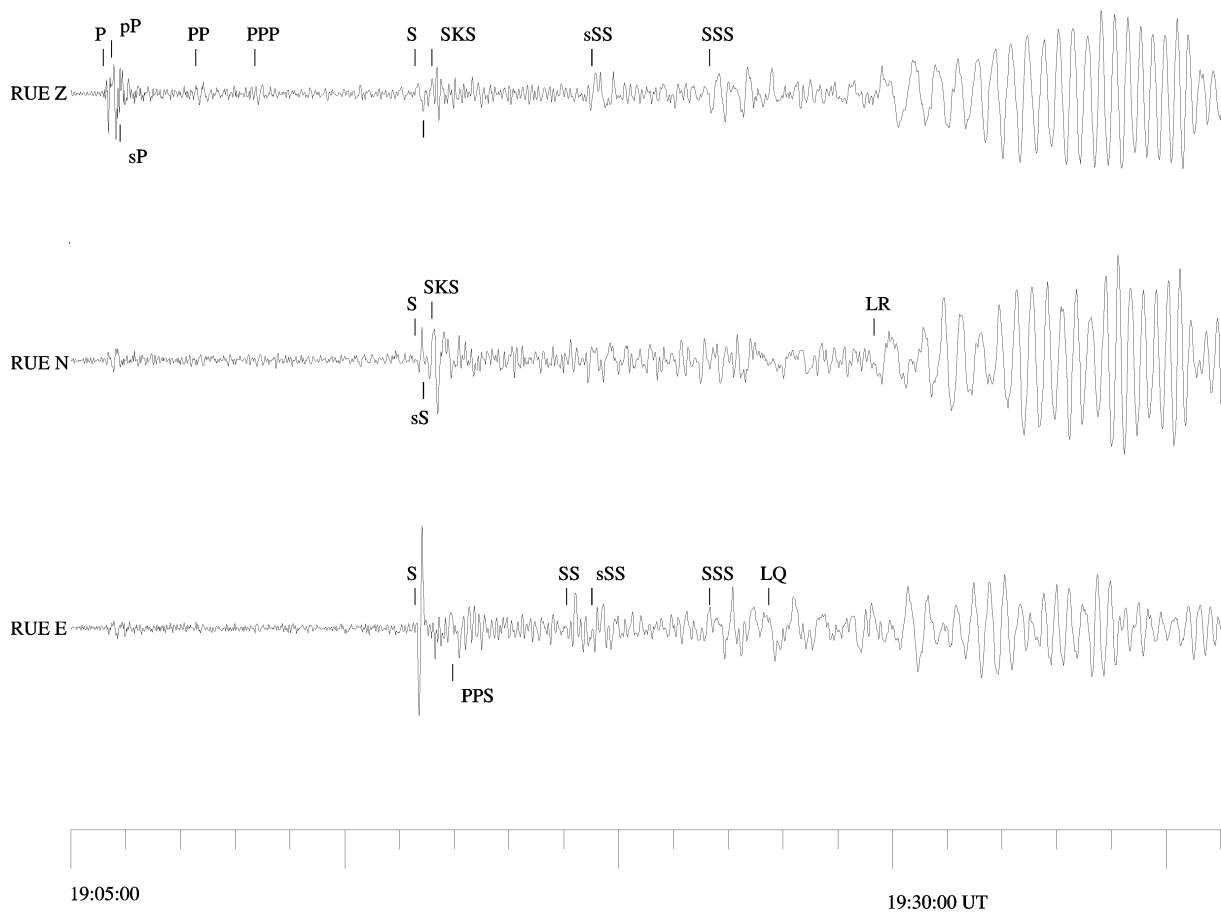


Fig. 2.23 Digital broadband record of the Seattle $M_w = 6,8$ earthquake on 28 February 2001 at the station Rüdersdorf (RUE), Germany (epicentral distance $D = 73^\circ$). Note the detailed interpretation of secondary phase onsets.

A proper understanding of these arrivals is essential for a correct phase identification that in turn is of great importance for event location (see IS 11.1) and magnitude determination (see 3.2 and EX 3.1) but also for later determination of seismic velocities inside the Earth. We will

introduce and use the concept of seismic rays to understand and illustrate the formation and propagation of these different wave arrivals.

Seismic ray theory is a very convenient and intuitive way to model the propagation of seismic energy and in particular of body waves. It is generally used to locate earthquakes and to determine focal mechanisms and velocity structure from body wave arrivals. Seismic ray theory is essentially analogous to optical ray theory, including phenomena like ray-bending, focusing and defocusing.

Using ray theory, it is important to keep in mind that it is an approximation that does not include all aspects of wave propagation. Ray theory is based on the so-called *high-frequency approximation* which states that fractional changes in velocity gradient over one seismic wavelength are small compared to the velocity. In other words, we may use ray theory only if the dimensions of structures to be considered are larger than the seismic wavelengths used.

These conditions are valid for most parts of the Earth (see global model in Fig. 2.53) and for the wavelengths that are usually recorded and analyzed in seismological observatory practice. The problem of relatively sharp boundaries, as for example the crust-mantle interface (Moho - discontinuity), discontinuities in the upper mantle, and the core-mantle boundary (CMB) or the inner-core boundary (ICB) can be tackled by matching the boundary conditions between neighboring regions in which the ray solutions are valid.

2.5.2 Huygen's and Fermat's Principle and Snell's Law

In classical optics, *Huygen's Principle* governs the geometry of a wave surface. It states that every point on a propagating wavefront can be considered the source of a small secondary wavefront that travels outward at the wave velocity in the medium at that point. The position of the wavefront at a later time is given by the tangent surface of the expanding secondary wavefronts. Since portions of the primary wave front, which are located in relatively high-velocity material, produce secondary wavefronts that travel faster than those produced by points in relatively low-velocity material, this results in temporal changes of the shape of the wavefront when propagating in an inhomogeneous medium. Since rays are defined as the normals to the wavefront, they will change accordingly. Rays are a convenient means for tracking an expanding wavefront. Fig. 2.24 depicts the change of direction of a plane wavefront and associated ray when traveling through a discontinuity which separates two homogeneous media with different but constant wave propagation velocity.

Fermat's Principle governs the geometry of the raypath. It states that the energy (or ray) will follow a *minimum time path*, i.e., it takes that path d between two points, which takes an extreme travel-time t (i.e., the shortest or the longest possible travel time, with $\partial t / \partial d = 0$). Such a path is called *stationary*. In case of a stationary time path there exist three possibilities, depending on the value (sign) of the higher derivatives of $\partial t / \partial d$:

for	$\partial^2 t / \partial d^2 > 0$	the ray follows a true <i>minimum time path</i> ,
for	$\partial^2 t / \partial d^2 < 0$	the ray follows a <i>maximum time path</i> and
for	$\partial^2 t / \partial d^2 = 0$	i.e., in case of an inflection point of the travel-time curve, the ray follows a <i>minimax time path</i> .

2. Seismic Wave Propagation and Earth models

Different kinds of seismic waves follow different time paths, e.g., the reflected waves pP (see Fig. 2.43) a true minimum path, the PP or the SKKS reflection (Fig. 2.42) a minimax path and the reflected wave P'P' (PKPPKP) (Fig. 2.44) a true maximum path. Note that the character of the stationary path influences the character (phase shift) of the reflected waveform. Whenever a seismic ray travels in some parts of its raypath as a maximum time ray, it touches a *caustic*. This caustic can be a focusing point (see 2.5.3.3 or 2.5.3.4) or a surface along which seismic rays superimpose each other (see 2.5.4.3). In any case prominent phase distortion can be observed and has to be taken into account during the analysis of seismograms.

2.5.2.1 Snell's Law for a flat Earth

From *Fermat's Principle* follows, with some simple geometry and mathematics, *Snell's Law* of wave refraction (e.g., Aki and Richards 1980 and 2002; Lay and Wallace, 1995; Shearer, 1999; Červený, 2001; Kennett, 2001):

$$\sin i/v = s \sin i = s_x = 1/v_{\text{app}} \equiv p = \text{constant} \quad (2.12)$$

where i is the angle of incidence, measured between the ray and the vertical (see Fig. 2.24), v is the velocity of wave propagation in the medium, $s = 1/v$ is called slowness, and p is the so-called ray parameter, $v/\sin i = v_{\text{app}}$ is the apparent horizontal wave propagation velocity in x -direction with $v_{\text{app}} = \infty$ for $i = 0$ (vertical incidence of the ray) and $s_x = 1/v_{\text{app}}$ is the horizontal component of the slowness vector s . Note, however, that p is constant for laterally homogeneous media only. In Fig. 2.24 the refraction of a seismic wavefront and of a related seismic ray across the interface of two half spaces with different but constant seismic velocities v_1 and v_2 is sketched. Such an instantaneous velocity jump is called first-order discontinuity. Because the ray parameter must remain constant across the interface, the ray angle has to change:

$$\sin i_1/v_1 = \sin i_2/v_2 = s_1 \sin i_1 = s_2 \sin i_2. \quad (2.13)$$

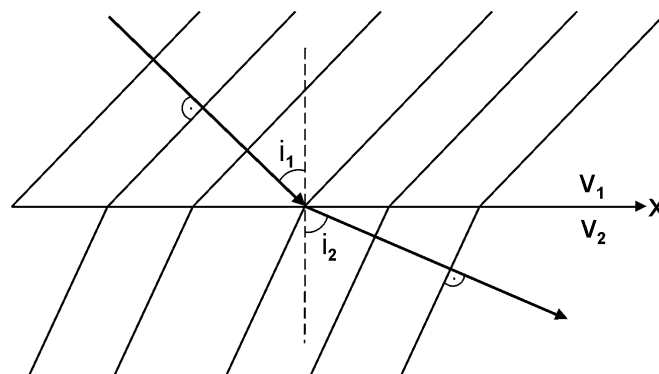


Fig. 2.24 A plane wavefront with the associated ray crossing a medium boundary with $v_2 > v_1$. The ray in medium two is refracted away from the vertical, i.e., $i_2 > i_1$.

2.5.2.2 Snell's Law for the spherical Earth

Above, a flat-layered case was considered. Yet the Earth is a sphere and curvature has to be taken into account at distances greater than about 12° . In this case the ray parameter has to be

modified. In Fig. 2.25 a ray is sketched in a sphere composed of two concentric shells 1 and 2 of different but constant velocity v_1 and v_2 or slowness $s_1 = 1/v_1$ and $s_2 = 1/v_2$, respectively. At the first interface between medium 1 and 2, Snell's Law must be satisfied locally, i.e.,:

$$s_1 \sin i_1(r_1) = s_2 \sin i_2(r_2) \quad (2.14)$$

for $r_1 = r_2$. Inside shell 2, however, despite $v_2 = \text{const.}$, the incidence angle changes as the ray progresses, namely, $i_1(r_1) \neq i'_2(r'_2)$. If we project the ray in medium 2 further to its turning point where $r = r_{\min}$ we see from the set of right triangles that the following relationship holds:

$$s_1 r_1 \sin i_1 = s_2 r'_2 \sin i'_2.$$

This is true along the entire ray path and we can generalize

$$s r \sin i = r \sin i/v \equiv p, \quad (2.15)$$

which is the modified Snell's Law for a spherical Earth.

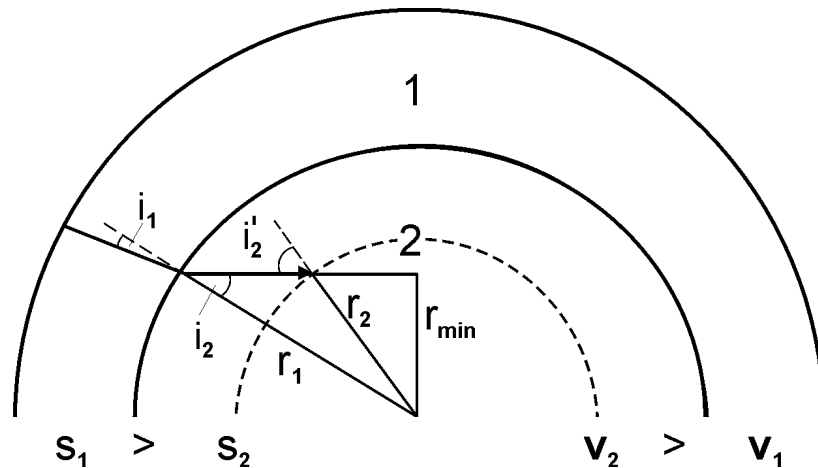


Fig. 2.25 Ray geometry for an Earth model consisting of two spherical shells of constant but different velocity v_1 and v_2 .

2.5.3 Rays and travel times in laterally homogeneous (1-D) media

2.5.3.1 Velocity gradient

It is true for most parts of the Earth that the seismic velocity increases with depth due to compaction of the material. Consider a ray travelling downwards through a stack of layers with constant velocities $v_i = 1/s_i$ each, however, increasing layer velocities with depth (Fig. 2.26). Applying Snell's law

$$p = s_1 \sin i_1 = s_2 \sin i_2 = s_3 \sin i_3 \dots \quad (2.16)$$

we can derive the incidence angle i , that is continuously increasing with depth, and finally approaching 90° . At $i = 90^\circ$ the ray is at its *turning point* tp .

2. Seismic Wave Propagation and Earth models

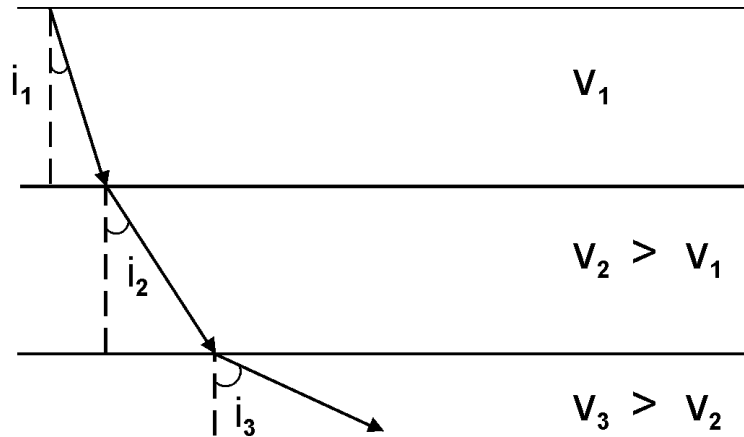


Fig. 2.26 Ray through a multi-layered model with constant velocity within the layers but increasing velocity with depth of the layers. The ray angle i increases accordingly with depth.

This can be generalized by modeling a velocity gradient with depth as a stack of many thin layers with constant velocity. Rays and travel times for this case are sketched in Fig. 2.27. The plot of arrival times t versus distance x is generally called the *travel-time curve*. The tangent dt_i/dx_i on the travel-time curve at any distance x_i corresponds to the inverse of the horizontal wave propagation velocity $1/v_{appi}$ and thus to the ray parameter p_i of that ray which comes back to the surface at x_i . Because of $\sin i = \sin 90^\circ = 1$ at the turning point of the ray, we can determine the velocity v_{tp} at the turning point of the ray either from the gradient of the travel-time curve at x_i via $p_i = dt_i/dx_i = 1/v_{tp}$ or by knowing the sub-surface velocity v_{oi} at station x_i and measuring the incidence angle i_{oi} at that station ($v_{tp} = v_{oi}/\sin i_{oi}$).

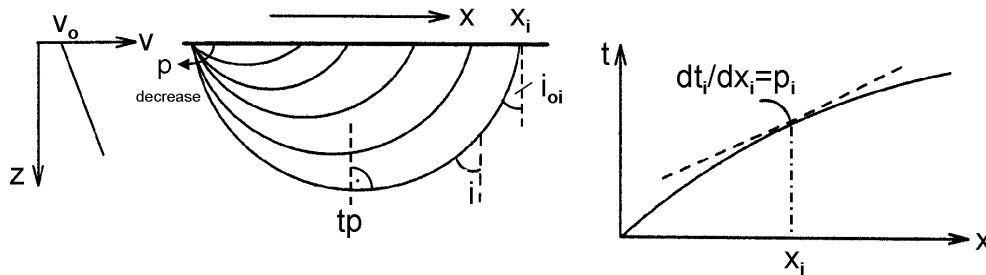


Fig. 2.27 Raypaths (middle) and travel-time curve (right) for a model with velocity v gradually increasing with depth z (left). The incidence angle i increases continuously until it reaches 90° at the turning point tp , then the rays turn up again to reach the surface at x_i . On the travel-time curve each point comes from a different ray with a different slowness and ray parameter p . The gradient of the tangent on the travel time curve at x_i is the ray parameter $p_i = dt_i/dx_i$. In the considered case of modest velocity increase with depth the distance x increases with decreasing p . The related travel-time curve is termed *prograde*.

2.5.3.2 Effect of a sharp velocity increase

Next we consider the effect of a sharp velocity increase, which may be an increase in gradient (second-order discontinuity) or an instantaneous velocity jump (first-order discontinuity). Fig.

2.28a shows on the left side a hypothetical velocity-depth model in the upper crust of the Earth together with the related seismic rays and on the right the corresponding travel-time curves in the reduced-time presentation $t_{\text{red}} = t - (x/v_{\text{red}})$. Usually travel-time increases with distance. Consequently, presenting absolute travel-time curves for large epicentral distances would require very long time-scales. Also, small changes in dt/dx are then not so well recognizable. Therefore, in order to reduce the time scale and to increase the resolution of changes in slowness, travel-time curves are often represented as *reduced travel-time curves*, in which $t_{\text{red}} = t - x/v_{\text{red}}$ is plotted (for some constant v_{red}) as a function of x . The reduction velocity v_{red} is usually chosen so as to be close to the mean velocity in the considered depth range or of the considered seismic phase. Its reduced travel-time is then constant and positive or negative slowness deviations are clearly recognizable.

In the ray diagram of Fig. 2.28a one recognizes that at certain distances x , rays with different incidence angles may emerge. Modest velocity gradients in the upper and lower part of the velocity profile result in rays which return to the surface with increasing distance x for decreasing ray parameter p . This produces prograde travel-time branches (yellow and green branches in the $t_{\text{red}}-x$ plot). In contrast, a strong velocity gradient leads to decreasing x with decreasing p and thus to a receding (retrograde) travel-time branch (red). Thus, a strong gradient zone between two weak gradient zones results in a *triplication* of the travel-time curve. The endpoints of the triplication are called *caustics*. At the caustics (positions x_1 and x_2) rays, which have left the source under different take-off angles, arrive at the surface at the same time. This causes a focusing of energy, large amplitudes and a waveform distortion (see 2.5.4.3). Fig. 2.28b shows qualitatively, with the same color coding as in Fig. 2.28a, the changes in the ray parameter p with distance x for the prograde and retrograde travel-time branch(es) of a triplication.

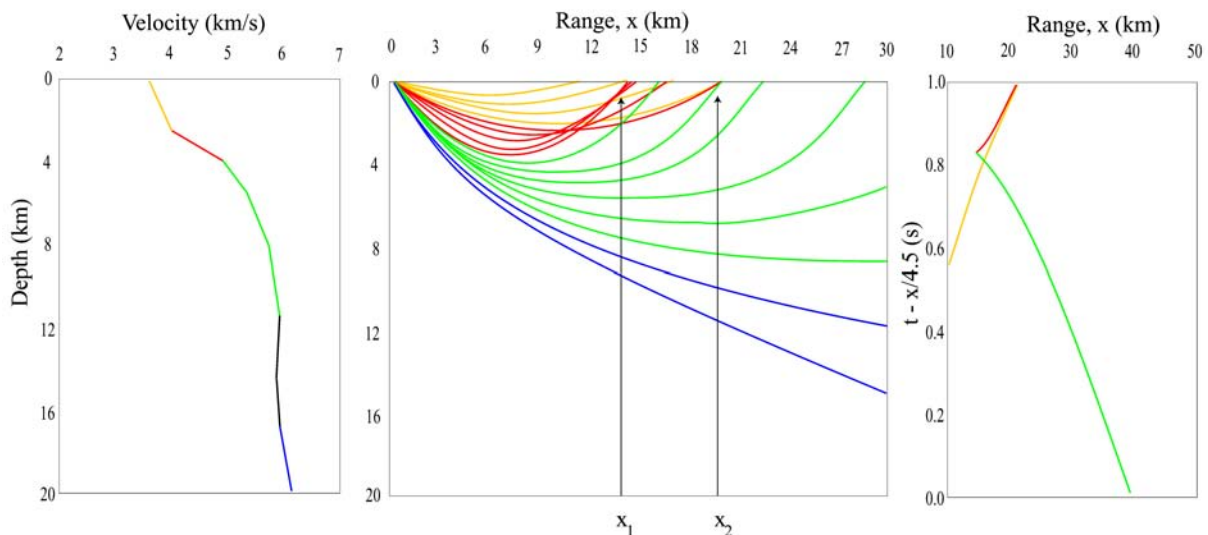


Fig. 2.28a **Left:** Velocity-depth profile in a model of the upper crust with a strong velocity gradient between about 2.5 and 6 km depth and related seismic rays from a surface source. **Right:** ray diagram and $t_{\text{red}}-x$ relation for the given model; $v_{\text{red}} = 4.5$ km/s. Note the differently colored segments of the velocity-depth distribution and of the travel-time branches that relate to the seismic rays given in the same color. Yellow and green: prograde travel-time curves, red: retrograde travel-time curve. Note the two lowermost blue rays that have already been affected by a low-velocity zone below 10 km depth (courtesy of P. Richards.)

2. Seismic Wave Propagation and Earth models

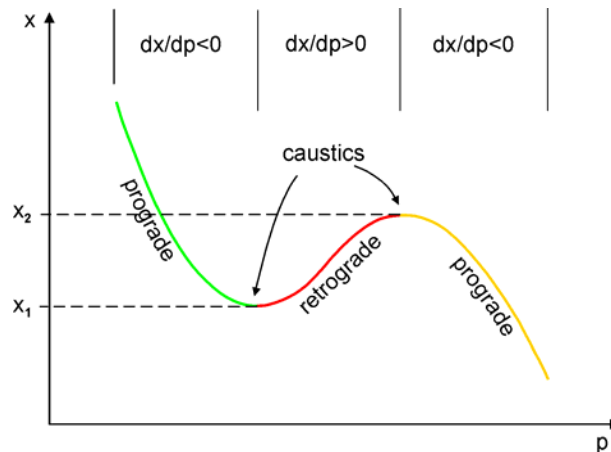


Fig. 2.28b Distance x as a function of ray parameter p for triplications. Note that the colors in this diagram correspond to the colors of the related rays and velocity segments in Fig. 2.28a.

The gradient of the retrograde travel-time branch and the position x_1 and x_2 of the caustics are controlled by the thickness and the velocity-gradient in this strong-gradient zone. Similar triplications develop in the presence of first-order discontinuities with positive velocity jump. In this case the retrograde branch relates to the postcritical reflections from such a discontinuity (see 2.5.3.6 and Fig. 2.32). The identification and quantification of such first- and second-order discontinuities is of greatest importance for the understanding of related changes in physical and/or compositional properties in the Earth. This necessitates, however, that not only first arrivals of seismic waves but also later, secondary arrivals are identified and their amplitudes measured. Since the latter may follow rather closely to the former, their proper identification and onset-time measurement may be difficult in very narrow-band filtered recordings because of their strong signal distortion (see figures in 4.2).

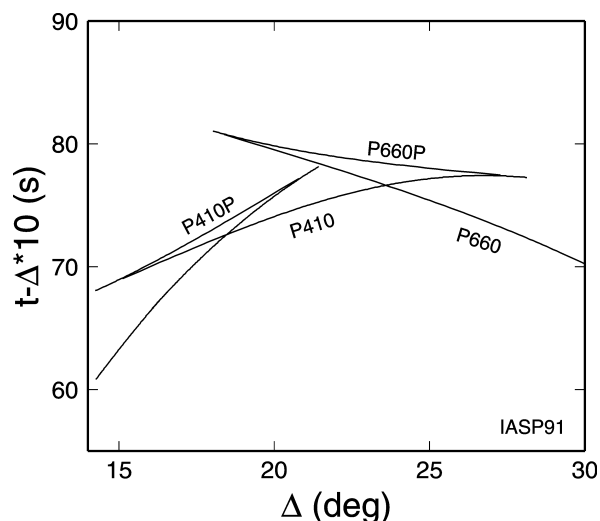


Fig. 2.29 Triplications of the P-wave travel-time curve (here in reduced presentation) due to the 410 km and 660 km upper mantle/transition zone discontinuities, calculated according to the IASP91 velocity model (Kennett and Engdahl, 1991) (see 2.7, Fig. 2.51). The P waves diving directly below the 410 km (660 km) are called P410 (P660); the phases P410P and P660P are the overcritical reflections from the outer side of these discontinuities, respectively.

Two of the most pronounced velocity and density increases occur at about 410 and 660 km below the surface (see 2.7, Figs. 2.51 and 2.53). They mark the lower boundary of the upper mantle and of the transition zone from the upper mantle to the lower mantle, respectively. Both are caused by phase transitions of the mantle material into states of higher density at critical pressure-temperature (P-T) conditions. These two pronounced discontinuities result in triplications of the P-wave travel-time curves in the distance range between about 14° and 28° (see Fig. 2.29) associated with a strong increase of P-wave amplitudes around 20° (so-called 20° discontinuity; see also Fig. 3.13).

2.5.3.3 Effect of a low-velocity zone

Velocity generally increases with depth due to compaction, however, lithologic changes or the presence of water or melts may result in low-velocity zones (LVZ). Fig. 2.30 shows the effects of an LVZ on seismic rays and the travel-time curve. The latter becomes discontinuous, forming a shadow zone within which no rays emerge back to the surface. Beyond the shadow zone the travel-time curve continues with a time off-set (delay) from a caustic with two branches: one retrograde branch (blue) beginning with the same apparent horizontal velocity as just before the beginning of the shadow zone and another prograde branch with higher apparent velocity (smaller dt/dx). This is shown in Fig. 2.30 which is in fact a continuation of the model shown in Fig. 2.28a towards greater depth. One recognizes a low-velocity zone between 12 and 18 km depth. The related ray diagram clearly shows how the rays that are affected by the LVZ jump from an arrival at distance 79 km to 170 km, and then go back to a caustic at 110 km before moving forward again. The related prograde travel-time branches and rays have been color-coded with green, blue and violet. The corresponding t_{red} - x plot on the right side of Fig. 2.30 shows nicely the travel-time offset and caustic beyond the shadow zone with two branches: a) retrograde (blue) and b) prograde (violet).

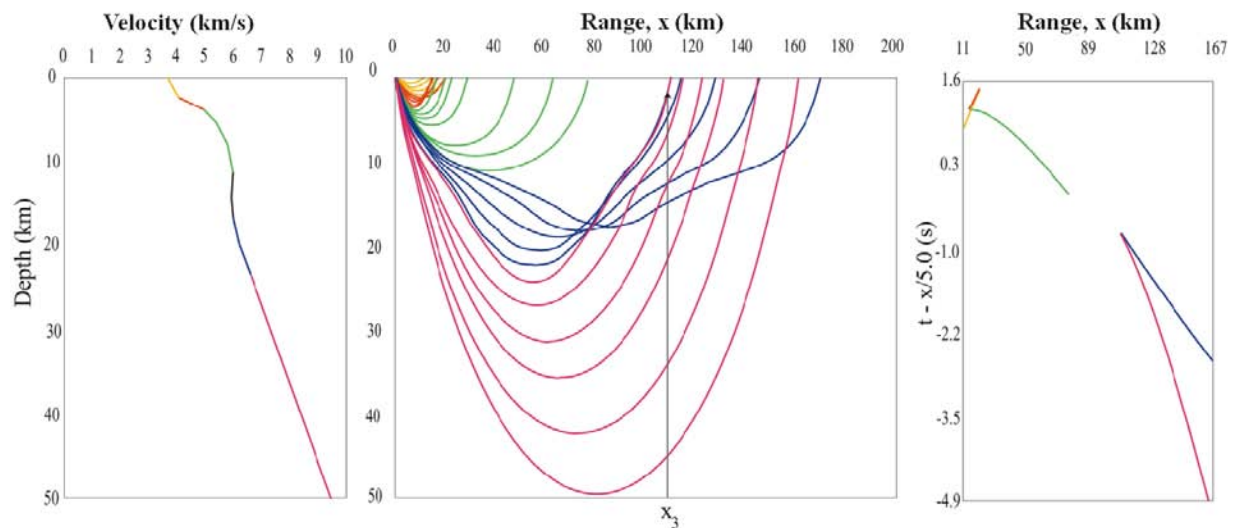


Fig. 2.30 **Left:** Velocity-depth profile and seismic rays in the crust with a low-velocity zone between $12 \text{ km} < h < 18 \text{ km}$ depth. The black segment in the velocity-depth curve produces the shadow zone. **Right:** ray diagram and t_{red} - x relation for the considered model. The reduction velocity is $v_{red} = 5.0 \text{ km/s}$. Note the additional colored travel-time branches which relate to the seismic rays given in the same color. Green and violet: prograde travel-time curves, blue and red: retrograde travel-time curves. There is a caustic at distance x_3 . Therefore, the end of the shadow has strong amplitudes (courtesy of P. Richards).

2. Seismic Wave Propagation and Earth models

An outstanding example for an LVZ, which shows these feature very clearly, is the outer core. At the core-mantle boundary the P-wave velocity drops from about 13.7 km/s in the lowermost mantle to about 8 km/s in the liquid outer core. This causes a shadow zone for short-period direct P waves between around 100° and 144° , however slightly “illuminated” by reflected arrivals from the inner-core boundary (PKiKP) and by rays that have been refracted backward to shorter distances (retrograde travel-time branch) due to the strong velocity increase in the inner core (phase PKPdf = PKIKP) (see Fig. 11.59). The travel-time branch PKPab corresponds qualitatively to the blue branch and the branch PKPdf beyond the caustic to the violet branch in Fig. 2.30 (compare with overlay to Fig. 2.47). There may exist, however, also LVZ's in the crust and in the upper mantle (asthenosphere; see PREM model in Fig. 2.53). Low-velocity zones are often more pronounced in S-wave velocity than in P-wave velocity because material weakening due to (partial) melting reduces more strongly the shear modulus μ than the bulk modulus κ (see Eqs. (2.9) and (2.10)).

2.5.3.4 Refraction, reflection, and conversion of waves at a boundary

So far we have only considered transmission of seismic waves at a boundary. However, generally not all energy is transmitted; parts are reflected or converted. If a P wave hits a boundary between different seismic velocities, four different waves may be generated: a transmitted P wave; a converted transmitted S wave purely polarized in the vertical plane of propagation (SV-wave); a reflected P wave; and a reflected converted SV wave (Fig. 2.31). The geometry of these waves is also governed by Snell's Law:

$$\sin i/v_{p1} = \sin j/v_{s1} = \sin i'/v_{p2} = \sin j'/v_{s2}. \quad (2.17)$$

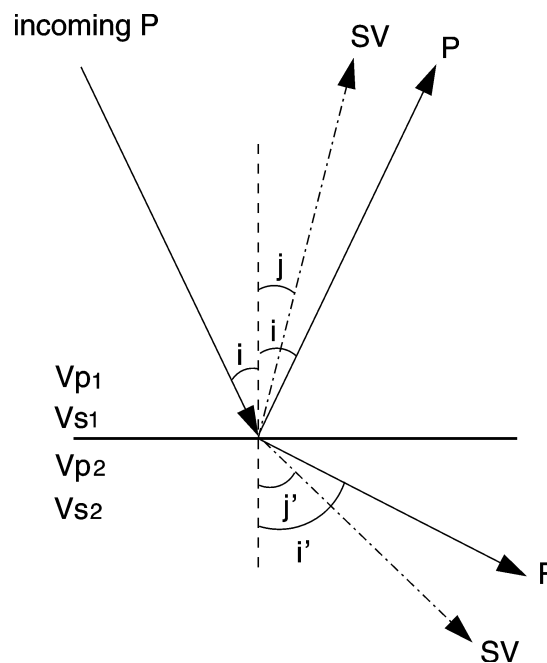


Fig. 2.31 An incident P wave at a solid-solid boundary (shown is the case $v_1 < v_2$) generates a reflected and a transmitted P wave and a reflected and transmitted SV wave. Snell's Law governs the angular relationship between the rays of the resultant waves.

In the case of an SH wave hitting the boundary, which is purely polarized in the horizontal plane, there is only a transmitted and a reflected SH wave, but no conversion into P or SV possible. If a single incident wave is split into multiple scattered waves, energy must be partitioned between these waves. Coefficients governing the partitioning between transmitted, reflected, and converted energy will generally depend on the incidence angle of the incoming wave and the *impedance contrast* at the boundary. Impedance is the product of wave velocity and density of the medium. Derivation of the expressions for reflection, transmission, and conversion coefficients is beyond the scope of this book. We refer, e.g., to the classic textbook of Aki and Richards (1980 and 2002) for a complete treatment and to Müller (1985) or Shearer (1999) for a condensed overview. The same applies to the following considerations below on seismic energy, amplitudes and phases.

2.5.3.5 Seismic rays and travel times in homogeneous models with horizontal and tilted layers

Below we consider a horizontal two-layer model above a half-space. Within the layers and in the half space the wave velocities are constant with $v_1 < v_2 < v_3$. The discontinuities between them are of first order, i.e., with instantaneous velocity jumps (see Fig. 2.32). For an incidence angle $i_1 = i_{cr}^1$, with $\sin i_{cr}^1 = v_1/v_2$ and $v_2 > v_1$, no wave energy can penetrate into the layer 2, because $\sin i_2 = 1$ and thus $i_2 = 90^\circ$. The angle i_{cr} is called the *critical angle* because for $i > i_{cr}$ all energy incident at a first-order discontinuity is totally reflected back into the overlaying layer. However, part of it may be converted. The point in the travel-time curve at which a critically reflected ray (reflection coefficient 1) comes back to the surface is termed the *critical point* x_{cr} . The travel-time curve has a caustic there. Reflected rays arriving with $i < i_{cr}$ are termed *precritical* (or steep angle) reflections (with reflection coefficients < 1), those with $i > i_{cr}$ as *postcritical*, *supercritical* or *wide-angle reflections* (with a reflection coefficient = 1) (see Fig. 2.32). However, in this case the reflection coefficient becomes a complex number which results in the above discussed phase distortion of overcritical reflections. Note that the travel-time hyperbola of the reflected waves from the bottom of the first layer (red curve) merges asymptotically at larger distances with the travel-time curve of the direct wave in this layer (yellow curve).

Seismic rays incident with $i_n = i_{cr}^n$ on the lower boundary of layer n are refracted with $i_{n+1} = 90^\circ$ into the boundary between the two layers n and $n+1$. They form so-called seismic head waves (green and blue rays and travel-time curves, respectively, in Fig. 2.32). Head waves are inhomogeneous boundary waves that travel along the discontinuity with the velocity of layer $n+1$ and radiate upward wave energy under the angle i_{cr}^n . The full description of this kind of wave is not possible in terms of ray theory but requires a wave-theoretical treatment. In the real Earth, with non-ideal first-order layer boundaries, true *head waves* will hardly exist but rather so-called *diving waves* which slightly penetrate - through the high-gradient zone between the two media - into the underlying high-velocity medium. There they travel sub-parallel to the discontinuity and are refracted back towards the surface under an angle $\approx i_{cr}$. In terms of travel time there is practically no difference between a diving wave and a pure head-wave along a first-order velocity discontinuity; diving waves, however, have usually larger amplitudes.

2. Seismic Wave Propagation and Earth models

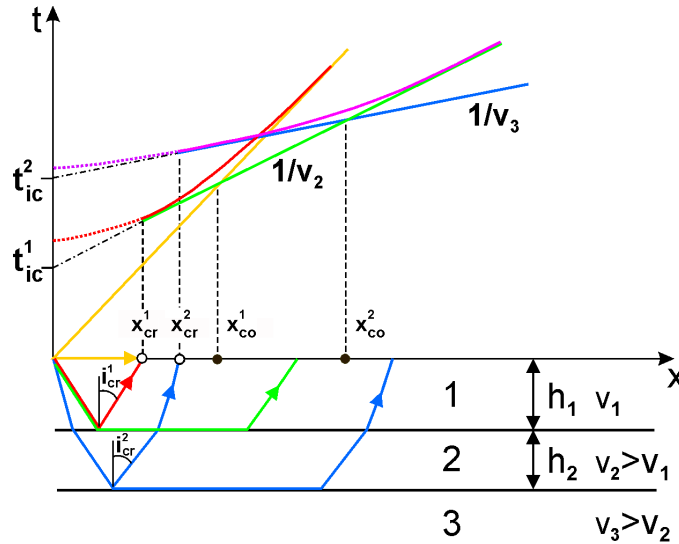


Fig. 2.32 Schematic local travel-time curves (time t over distance x from the source) for a horizontal two-layer model with constant layer velocities v_1 and v_2 , layer thickness h_1 and h_2 over a half-space with velocity v_3 . Other abbreviations stand for: t_{ic}^1 and t_{ic}^2 – intercept times at $x = 0$ of the extrapolated travel-time curves for the “head-waves”, which travel with v_2 along the intermediate discontinuity between the layers 1 and 2 and with v_3 along the discontinuity between layer 2 and the half-space, respectively. x_{cr}^1 and x_{cr}^2 mark the distances from the source at which the critically reflected rays from the bottom of the first and the second layer, respectively, return to the surface. Beyond x_{co}^1 and x_{co}^2 the head-waves from the bottom of the first and the second layer, respectively, become the first arriving waves (x_{co} - crossover distance). Rays and their corresponding travel-time curves are shown in the same color. The full red (violet) travel-time curve relates to the supercritical reflections ($i > i_{cr}$) from the intermediate (lower) discontinuity while the dotted red (violet) travel-time curve refers to the respective pre-critical ($i < i_{cr}$) steep angle reflections.

In the case of horizontal layering as in Fig. 2.32 the layer and half-space velocities can be determined from the gradients dt/dx of the yellow, green and blue travel-time curves which correspond to the inverse of the respective layer velocities. When determining additionally the related intercept times t_{ic}^1 and t_{ic}^2 by extrapolating the green and blue curves, or with help of the crossover distances x_{co}^1 and x_{co}^2 , then one can also determine the layer thickness h_1 and h_2 from the following relationships:

$$h_1 = 0.5 x_{co}^1 \sqrt{\frac{v_1 + v_2}{v_1 + v_2}} = 0.5 t_{ic}^1 \frac{v_1 \cdot v_2}{\sqrt{v_2^2 - v_1^2}} \quad \text{and} \quad h_2 = \frac{t_{ic}^2 - 2h_1 \sqrt{v_3^2 - v_1^2} (v_1 \cdot v_2)^{-1}}{2\sqrt{v_3^2 - v_2^2} \cdot (v_2 \cdot v_3)^{-1}}. \quad (2.18)$$

For the calculation of crossover distances for a simple one-layer model as a function of layer thickness and velocities see Equation (6) in IS 11.1.

In the case where the layer discontinuities are tilted, the observation of travel-times in only one direction away from the seismic source will allow neither the determination of the proper sub-layer velocity nor the differences in layer thickness. As can be seen from Fig. 2.33, the intercept times, the cross-over distances and the apparent horizontal velocities for the critically refracted head-waves differ when observed down-dip or up-dip from the source although their total travel times to a given distance from the source remain constant.

Therefore, especially in controlled-source seismology, *countershot* profiles are deliberately designed so as to identify changes in layer dip and thickness.

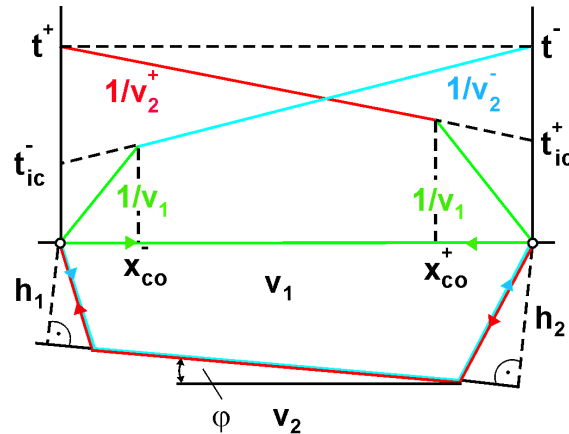


Fig. 2.33 Schematic travel-time curves for direct waves and head waves in a single-layer model with inclined lower boundary towards the half-space. Note the difference between up-dip and down-dip observations (“countershot profile”). t_{ic}^- and v_2^- are the intercept time and related apparent velocity of the down-dip head wave, t_{ic}^+ and v_2^+ the respective values for the up-dip travel-time curve.

For the considered simple one-layer case in Fig. 2.33 the dip angle ϕ and the orthogonal distance h_1 to the layer boundary underneath the seismic source on the left can be determined from the following relations:

$$\phi = \frac{1}{2} [\sin^{-1} (v_1/v_2^-) - \sin^{-1} (v_1/v_2^+)] \quad (2.19)$$

and

$$h_1 = \frac{1}{2} t_{ic}^- [v_1 v_2 / \sqrt{(v_2^2 - v_1^2)}]. \quad (2.20)$$

2.5.3.6 Wiechert-Herglotz inversion

In the case of velocity $v = f(z)$ increasing monotonously with depth z , as in Fig. 2.27, a continuous travel-time curve is observed because all rays return back to the surface. The epicentral distance $x = D$ of their return increases with decreasing p , i.e. $dx/dp < 0$. The related travel-time curve, with $dt/dx > 0$ is termed *prograde*. In this case an exact analytical solution of the inverse problem exists, i.e., when knowing the apparent horizontal velocity $c_x(D) = v_0/\sin i_0 = dD/dt$ at any point D , we know the velocity v_{tp} at the turning point of the ray that returns to the surface at D . Thus we can calculate the depth $z(p) = z_{tp}$ of its turning point. The following relations were given by Wiechert and Herglotz in 1910 for the return distance $D(p)$ and the depth of the turning point $z(p)$ of a given ray:

$$D(p) = 2 \int_0^{z(p)} \frac{p v(z)}{\sqrt{1 - p^2 v(z)^2}} dz \quad (2.21)$$

and

$$z(p) = \frac{1}{\pi} \int_0^D \cosh^{-1} \frac{c_x(D)}{c_x(x)} dx \quad (2.22)$$

2. Seismic Wave Propagation and Earth models

Note, however, that the velocity $v_{tp}(p)$ determined from dx/dt at distance $x = D$ does always relate to the respective depth half way between source and station! Nevertheless, practically all one-dimensional Earth models have been derived this way assuming that lateral variations of velocity are negligible as compared to the vertical velocity variations.

2.5.4 Amplitudes and phases

2.5.4.1 Energy of seismic waves

The energy density E contained in a seismic wave may be expressed as the sum of kinetic (E_{kin}) and potential (E_{pot}) energy densities :

$$E = E_{kin} + E_{pot} . \quad (2.23)$$

The potential energy results from the distortion of the material (strain; see. Figs. 2.2 and 2.5) working against the elastic restoring force (stress) while the kinetic energy density is

$$E_{kin} = \frac{1}{2} \rho a_v^2 , \quad (2.24)$$

where ρ is the density of the material, $a_v = A \omega \cos(\omega t - kx)$ is the ground-motion particle velocity, with A - wave amplitude, ω - angular frequency $2\pi f$ and k - wavenumber. Since the mean value of \cos^2 is $\frac{1}{2}$ it follows for the average kinetic energy density $\bar{E}_{kin} = \frac{1}{4} \rho A^2 \omega^2$, and with $E_{kin} = E_{pot}$ in case of an isotropic stress-strain relationship in a non-dispersive (closed) system for the average energy density

$$\bar{E} = \frac{1}{2} \rho A^2 \omega^2 . \quad (2.25)$$

The energy-flux density per unit of time in the direction of wave propagation with velocity v is then

$$E_{flux} = \frac{1}{2} v \rho A^2 \omega^2 \quad (2.26)$$

and the total energy-flux density \mathbf{E}_{flux} through a small surface area dS of the wavefront bounded by neighboring rays which form a *ray tube*

$$\mathbf{E}_{flux} = \frac{1}{2} v \rho A^2 \omega^2 dS . \quad (2.27)$$

When considering only waves with wavelengths being small as compared to the inhomogeneities of the medium of wave propagation (high-frequency approximation), then we can assume that the seismic energy only travels along the rays. According to the energy conservation law, the energy flux within a considered ray tube must remain constant although the surface area dS of the wavefront related to this ray tube may vary along the propagation path due to focusing or defocusing of the seismic rays (compare Fig. 2.28). Considering at different times two surface patches of the propagating wavefront $dS_1 \neq dS_2$, which are bounded by the same ray tube, and assuming that v and ρ are the same at these two locations then

$$A_1/A_2 = (dS_2/dS_1)^{1/2} , \quad (2.28)$$

i.e., the amplitudes vary inversely as the square root of the surface area of the wavefront patch bounded by the ray tube. Thus amplitudes increase due to ray focusing, which is particularly strong at caustics (see 2.5.3.2) and decrease when the wavefront spreads out.

Also, for a spherical wavefront (e.g., body-wave propagation in a homogeneous isotropic medium) the surface area grows with r^2 and for a cylindrical wavefront (e.g., for surface waves) with distance r only. Accordingly, the wave-amplitude decay is in the former case $\sim r^{-1}$ and in the latter case $\sim r^{-1/2}$. This difference in *geometrical spreading* is the main reason for the domination of surface wave amplitudes in seismic records of shallow events (see Fig. 2.23 above and Fig. 3.13).

However, wave amplitudes will also change, even in the absence of geometrical spreading, when density ρ and velocity v vary at different locations along the ray path. We then get

$$A_1/A_2 = [(\rho_2 v_2)/(\rho_1 v_1)]^{1/2}. \quad (2.29)$$

The product ρv is termed the *impedance* of the material and $(\rho_2 v_2)/(\rho_1 v_1)$ is the *impedance contrast* between the two adjacent media m_1 and m_2 . The latter largely controls the reflection and transmission coefficients at the media discontinuity. From Eq. (2.29) it follows that seismic amplitudes will increase as waves propagate into media of lower density and wave propagation velocity. This has two important implications. On the one hand, seismic stations on hard bedrock tend to record smaller amplitudes and thus to slightly underestimate event magnitudes as compared to stations on average or soft-soil conditions. On the other hand, ground shaking from strong earthquakes is usually more intense on top of unconsolidated sediments as compared with nearby rock sites. Additionally, reverberations and resonance within the unconsolidated near-surface layers above the basement rocks may significantly amplify the amplitudes at soft-soil sites. This may increase significantly local seismic hazard.

2.5.4.2 Wave attenuation

Amplitudes of seismic waves are not only controlled by geometrical spreading or focusing and by the reflection and transmission coefficients that occur at discontinuities. Besides this, wave amplitudes may be reduced because of energy loss due to inelastic material behavior or internal friction during wave propagation. These effects are called *intrinsic attenuation*. Also, scattering of energy at small-scale heterogeneities along the travel paths may reduce amplitudes of seismic waves. In the case of such *scattering attenuation*, however, the integrated energy in the total wavefield remains constant, while *intrinsic attenuation* results in loss of mechanical wave energy, e.g., by transformation into heat. The wave attenuation is usually expressed in terms of the dimensionless *quality factor* Q

$$Q = 2\pi E/\Delta E \quad (2.30)$$

with ΔE the dissipated energy per cycle. Large energy loss means low Q and vice versa, i.e., Q is inversely proportional to the attenuation. In a simplified way we can write for the decay of source amplitude A_0 with distance x

2. Seismic Wave Propagation and Earth models

$$A = \frac{A_0}{x^n} e^{-\frac{\omega t}{2Q}} = \frac{A_0}{x^n} e^{-\frac{\pi x}{QTv}} = \frac{A_0}{x^n} e^{-\frac{\omega x}{2Qv}}, \quad (2.31)$$

with A_0/x^n – the geometrical spreading term, $\exp(-x t/2Q) = \exp(-\pi/Q T v)$ the attenuation term, ω - angular frequency $2\pi/T$, T – period of wave, t – travel time, v – propagation velocity of wave, and n – exponential factor controlled by the kind of geometric spreading. According to experimental data, n varies between about 0.3 and 3, depending also on the type of seismic wave and distance range considered.

In ray theoretical methods, attenuation may be modeled through the use of the parameter t^* that is defined as the integrated value of the travel time divided by $1/Q$

$$t^* = \int_{\text{path}} \frac{dt}{Q(\vec{r})}, \quad (2.32)$$

where \vec{r} is the position vector. We can then write Eq. (2.31) as

$$A(\omega) = A_0(\omega) e^{-\omega t^*/2}. \quad (2.33)$$

Note, that P-wave attenuation Q_α and S-wave attenuation Q_β differ. They are related to the shear attenuation Q_μ and the bulk attenuation Q_κ by the relationships

$$Q_\beta = Q_\mu \quad \text{and} \quad 1/Q_\alpha = 4(\beta/\alpha)^2/3Q_\mu + [1 - 4(\beta/\alpha)^2/3]/Q_\kappa. \quad (2.34)$$

with P-wave velocity $\alpha = v_p$ and S-wave velocity $\beta = v_s$. In the Earth shear attenuation is much stronger than bulk attenuation. While Q_μ is smallest (and thus shear attenuation strongest) in the upper mantle and the inner core, Q_κ is generally assumed to be infinite, except in the inner core. While the P- and S-wave velocities are rather well known and do not differ much between different Earth models, the various model assumptions with respect to Q_α and Q_β as a function of depth still differ significantly (see Fig. 2.53). According to the PREM model, Q_μ is 600 for less than 80 km depth. It then drops between 80 and 220 km to 80, increases to 143 from 220 to 670 km, and is 312 for the lower mantle below 670 km depth.

In practice, it is difficult to separate intrinsic attenuation and scattering Q . Particularly in local earthquake records, which are strongly affected by scattering on crustal inhomogeneities, scattering Q dominates. Scattering Q is usually determined from the decay of coda waves following Sg (SmS) onsets (e.g., Fig. 2.40) and is called accordingly Q_c . A full discussion on these topics can be found, e.g., in Aki and Richards (1980; pp. 170-182).

In this context it should be mentioned that amplitudes of S waves are generally about five times larger than those of P waves (see Fig. 2.3). This follows directly from Eq. (3.2) in Chapter 3 or from the far-field term of the Green's function when modeling earthquake shear sources (see Equation (24) in the IS 3.1) taking into account that $v_P \approx v_S \sqrt{3}$ (see this Chapter, Eq. (2.9)). Also, the periods of S waves are longer than those of P waves, again by at least a factor of $\sqrt{3}$, due to the differences in wave propagation velocity and the related differences in the corner frequencies of the P- and S-wave source spectrum. Additionally, S waves are much stronger attenuated than P waves (see following section), thus filtering out higher frequencies more strongly. It should also be noted that S waves do not propagate in the fluid outer core

because of vanishing shear modulus (see Fig. 2.53). Therefore, no direct S waves are observed beyond 100° epicentral distance.

The discussed differences in amplitude-distance relationships have to be compensated by wave-type dependent calibration functions in order to be able to derive comparable magnitude values for seismic events based on amplitude readings from different types of seismic waves (see 3.2).

2.5.4.3 Phase distortions and Hilbert transform

As shown in Fig. 2.27 seismic rays will curve in the case of a vertical velocity gradient and thus seismic wavefronts will no longer be planar. Nevertheless, locally, between adjacent rays defining a *ray tube*, the wavefront still can be considered as a plane wavefront. In the case of strong gradients, retrograde travel-time branches will develop because rays bend stronger, cross each other and the wavefront folds over itself at the turning point (Fig. 2.34). Accordingly, a local plane wavefront traveling through a strong vertical velocity gradient will experience a constant, frequency-independent $\pi/2$ phase advance at the turning point. The envelope of turning points of these crossing bended rays is termed an *internal caustic surface*. Because of the $-\pi/2$ phase shift the up-going plane wave is the *Hilbert transform* of the down-going wave. More generally, whenever a ray has a non-pure minimum raypath (see 2.5.2) it touches such a caustic. Consequently, its pulse shape is altered (see Fig. 2.35). Example: The Hilbert transform of a pure sine wave is a cosine wave. In the case of seismic waves this phase shift by $-\pi/2$ has to be applied to each single frequency represented in the seismic pulse. This results in the known pulse shape alterations.

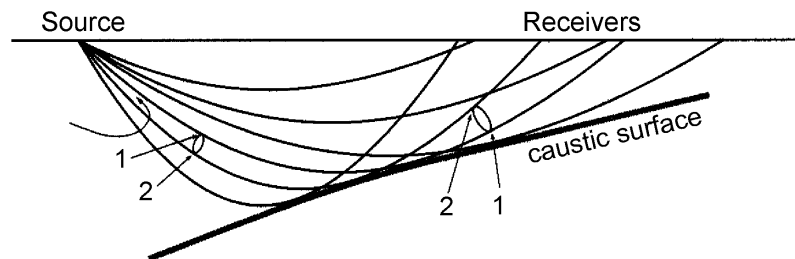


Fig. 2.34 In a medium with steep vertical velocity gradient, seismic rays with larger take-off angles from the source turn back towards the source thus forming a retrograde branch of a travel-time curve. The crossing of ray paths forms an internal caustic surface that produces a $-\pi/2$ phase shift in the waveforms (according to Choy and Richards, 1975; modified from Shearer, Introduction to Seismology, 1999; with permission from Cambridge University Press).

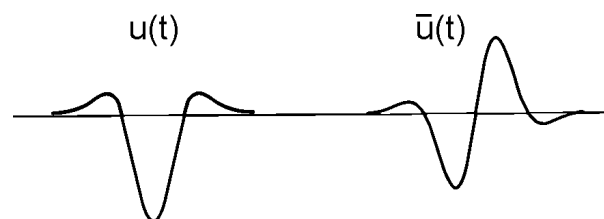


Fig. 2.35 Left: a typical seismic pulse; right: its Hilbert transform.

2. Seismic Wave Propagation and Earth models

Generally, in the case of a steep velocity gradient producing a retrograde travel-time branch, ray theory predicts that seismic wave arrivals along this branch are Hilbert transformed compared to the prograde branches. One should note, however, that also in case of relatively weak vertical velocity gradients, which do not produce a retrograde travel-time branch for the direct wave, the related reflected phase might nevertheless be Hilbert transformed (see Fig. 2.36 for PP waves). On the other hand, when the gradient becomes too steep, or in case of a first-order velocity step discontinuity, the postcritical reflection coefficients for such an interface involve a continuous change in phase with ray angle. The phase shift may then acquire any value other than a constant $-\pi/2$ phase shift.

Without exception, all the distorted waveforms bear little or no resemblance to the original waveforms. Accordingly, neither their onset times (first arrival of energy) nor the relative position of peaks and troughs of the distorted waveforms appear at the times that are theoretically predicted by ray theory. This biases onset-time picking, related travel-time determinations as well as waveform correlations between primary and Hilbert transformed phases. Therefore, modern digital data-analysis software can routinely apply the inverse Hilbert transform to phases distorted by internal caustics. The following major teleseismic body-wave phases are Hilbert transformed: PP, PS, SP, SS, PKPab, pPKPab, sPKPab, SKKSac, SKKSdf, PP', S'S'ac. For the nomenclature of these phases and their travel paths see Fig. 2.42 and IS 2.1). However, many phases pass caustics several times in the Earth and then the final pulse shapes are the sum of all internal caustic effects.

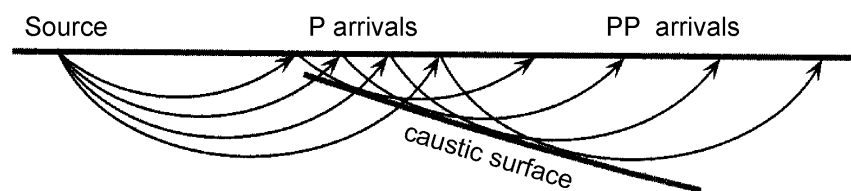


Fig. 2.36 Ray paths for the surface reflected phase PP. Note that the rays after the reflection points cross again and form an internal caustic. Accordingly, PP is Hilbert transformed relative to P and additionally has an opposite polarity (phase shift of π) due to the surface reflection (from Shearer, Introduction to Seismology, 1999; with permission from Cambridge University Press).

2.5.4.4 Effects not explained by ray theory

As mentioned above, ray theory is a high-frequency approximation that does not cover all aspects of wave propagation. Although detailed wave-theoretical considerations are beyond the scope of this Manual we will shortly mention three major phenomena that are of practical importance and not covered by ray theory.

Head waves

As mentioned in 2.5.4.1, seismic waves impinging at a discontinuity between the layers n and $n+1$ with $v_n < v_{n+1}$ under the critical incidence angle i_c with $\sin i_c = v_n/v_{n+1}$ are refracted into this discontinuity with the angle $i_{n+1} = 90^\circ$. There they travel along (or just below) this discontinuity with the velocity v_{n+1} of the lower faster medium. Such inhomogeneous waves

are usually referred to as *head waves*. They have the unique property to transmit energy back into the upper medium at exactly the critical angle i_c . However, the amplitudes of true head-wave are rather small as compared to direct, reflected or converted waves. The travel-time curve of a head wave is a straight line with the slope of $1/v_{n+1}$ (see Fig. 2.32). This provides a convenient and direct measure of the sub-discontinuity velocity. Head waves are of particular importance for crustal studies and in the analysis of seismic records from local and regional seismic events (see 2.6.1).

Seismic Diffraction

Diffraction, analog to optics, is the phenomenon of transmission of energy by non-geometric ray paths. In optics, the classic example is the diffraction of light “leaking” around the edge of an opaque screen. In seismology, diffraction occurs whenever the radius of curvature of a reflecting interface is less than a few wavelengths of the propagating wave. Seismic diffraction is important for example in steep-angle reflection data in the presence of sharp boundaries. But there are also long-period diffracted waves such as Pdif and Sdif which are “bended” around the core-mantle boundary into the core shadow zone beyond about 100° epicentral distance. Only little short-period P- and S-wave energy is observed in this shadow zone. In fact, the edge of a discontinuity/impedance contrast acts like a secondary source according to Huygen’s principle and radiates energy forward in all directions.

Diffractions can also be understood from the standpoint of *Fresnel zones*. This concept states that waves are not only reflected at a considered point of the discontinuity (like a seismic ray) but also from a larger surrounding area. The radius of the so-called first Fresnel zone is about $\frac{1}{2}$ wavelength around a considered ray arriving at a station, i.e., the range within which reflected energy might interfere constructively. The wavelength-dependent width of this Fresnel zone also determines the geometrical resolution of objects/impedance contrasts that can be at best achieved by seismic (or optical) methods.

Since the real Earth may significantly deviate from simplified global one-dimensional models, scattering and diffraction effects render not only amplitudes but also travel times of more low-frequency waves sensitive to the 3-D structure off the seismic rays. This has to be taken into account when making use of recent developments of automated travel-time measurement techniques which use cross-correlation of observed body wave phases in digital broadband records with the corresponding synthetic phases possible in spherical Earth. Marquering et al. (1999) showed that for an SS wave observed at an epicentral distance of 80° , near-surface heterogeneities situated more than 15° from the bounce point at 40° can exert a significant influence upon the travel time of an SS wave. They conclude that geometrical ray theory, which has been a cornerstone of seismology for about a century and proven useful in most practical applications, including earthquake location and tomography, is, however, valid only if the scale length of the 3-D heterogeneities is much greater than the seismic wavelengths. In other words, the validity of ray theory is based on a high-frequency (short-period) approximation. However, intermediate-period and long-period seismic waves, with wavelength of the order of 100 – 1000 km, already have comparable scale lengths with 3-D anomalies in current global tomographic models. When investigating smaller 3-D structures and applying new methods of waveform correlation, these wave-theoretical considerations gain growing importance, probably even in future observatory routines.

Scattering of seismic waves

Often the primary arrivals are followed by a multitude of later arrivals that can not be explained by simple 1-D models (Fig. 2.37). The complex wave train following the primary

2. Seismic Wave Propagation and Earth models

arrival is called coda. Coda arrivals are produced by scattering, that is, the wavefield's interaction with small-scale heterogeneities. Heterogeneity at different length scales is present almost universally inside the Earth. Seismic coda waves can be used to infer stochastic properties of the medium, i.e., scale amplitude of the average heterogeneities and to estimate coda Q_c which is particularly needed for correcting source spectra prior to deriving spectral source parameters from records of local events (see exercise EX 3.4).

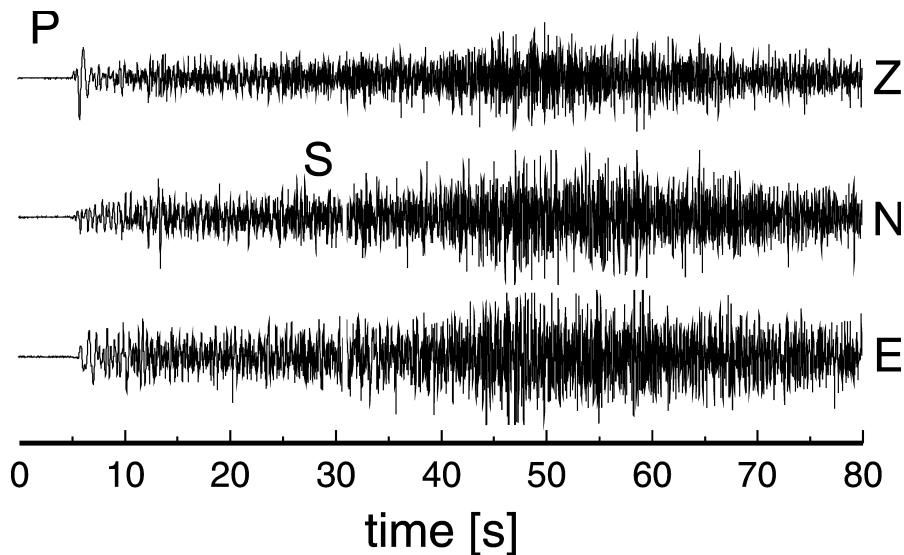


Fig. 2.37 Three-component seismogram of a local, 100 km deep earthquake recorded at a portable station on the active volcano Lascar in northern Chile. The P-wave arrival is followed by coda waves produced by heterogeneous structure in the vicinity of the volcano (courtesy of B. Schurr, 2001).

2.6 Seismic phases and travel times in the real Earth

The basic types of horizontally propagating seismic surface waves (Rayleigh waves, Love waves, and their higher modes; see 2.3) remain more or less unchanged with growing distance. Surface waves, however, do not form seismic phases (wavelets) with well-defined onsets and duration but rather dispersed wave trains. Due to the dispersion their duration increases with distance. Occasionally, surface wave trains of relatively high frequencies, as generated by shallow local events, may additionally be prolonged significantly due to lateral reverberations when propagating through strong lateral velocity contrasts in the crust (see Fig. 2.38). This phenomenon was used by Meier et al. (1997) to establish a tomography with reflected surface waves.

In contrast, seismic body waves, which propagate three-dimensionally, are more strongly affected than surface waves by refraction, reflection and mode conversion at the main impedance contrasts in the radial direction of the Earth. This gives rise, with growing distance, to the appearance of more and more secondary seismic body-wave phases following the direct P- and S-wave arrivals in seismic records. And since body waves show no dispersion in the considered frequency range below a few Hz these phases can usually be well observed and discriminated from each other as long as their travel-time curves do not overlap.

All of these secondary phases have a special story to tell about the geometrical and physical properties of the discontinuities which they encountered during their travel through the Earth's interior and which have shaped their waveforms and influenced their amplitude and frequency content. Therefore, the proper identification and parameter or waveform reporting about later phases in seismic records to relevant data centers is an important duty of seismological observatories. In addition, the complementary use of secondary phases significantly improves the precision and accuracy of seismic event locations, their source depth in particular (see Figure 7 in IS 11.1). In the following, we will introduce the main types of seismic body-wave phases that can generally be observed at local, regional and teleseismic distance ranges. They should be recognized and reported by the personnel at seismic observatories or data analysis centers. Basic features of their travel-time curves, polarization and frequency range of observation, which can guide their identification, will be presented.

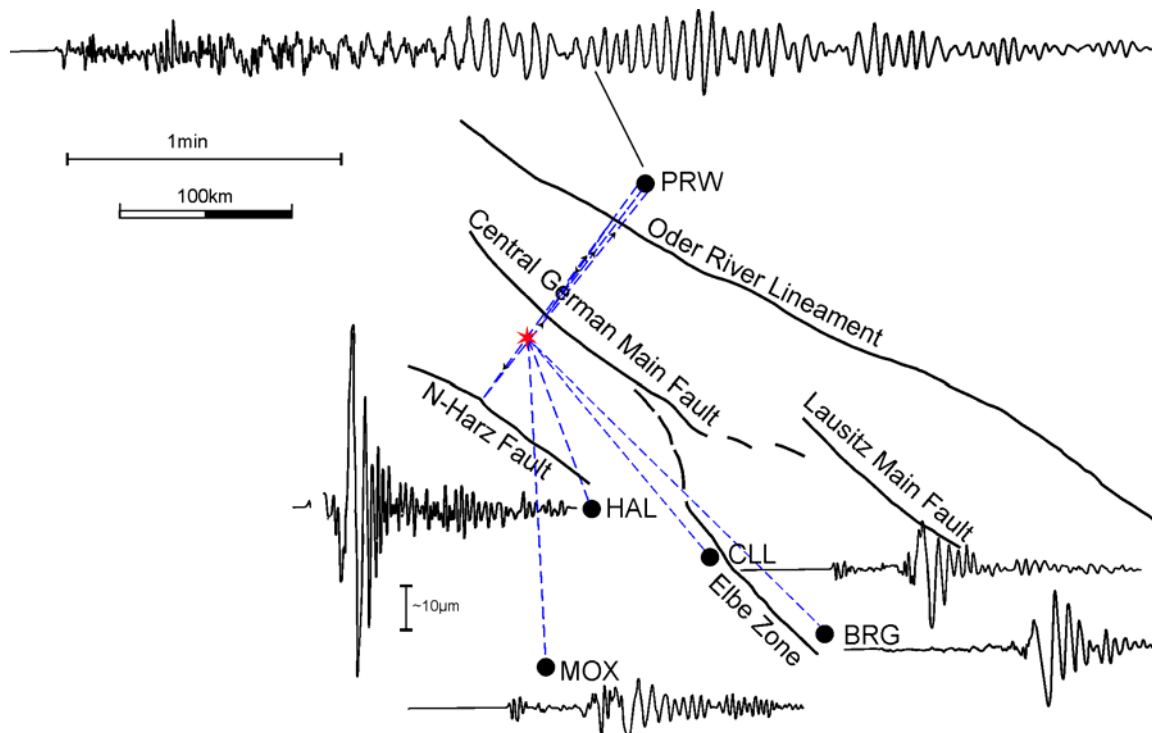


Fig. 2.38 Ray paths of surface waves (broken lines) from a mining collapse (star) to several seismic stations in the eastern part of Germany. Note: Records at stations along travel paths that have not or only once crossed some of the main tectonic faults in the area, are rather short. They have only one surface-wave maximum. In contrast, at station PRW, which is at the same epicentral distance as HAL, the seismic record is about four times longer and shows four surface-wave groups due to multiple reflections at several pronounced fault systems (compiled from data provided by H. Neunhöfer (1985; and personal communication)).

2.6.1 Seismic phases and travel times from local and regional seismic events

Seismic waves arriving at stations at local distances of up to about 150 km or regional distances of up to about 15° ($1^\circ = 111.2$ km) from the seismic source have traveled exclusively or dominantly through the crust or the sub-crustal uppermost mantle. The crust varies strongly in its thickness (see Fig. 2.10), petrologic composition and internal structure

2. Seismic Wave Propagation and Earth models

due to folding and faulting processes in the past. The resulting strong heterogeneities in its physical properties at scale length of several decameters to several km cause intensive scattering of P and S waves in the typical frequency range for the recording of near seismic events (about 0.5 to 50 Hz). Therefore, primary wave onsets are usually followed by signal-generated noise or coda waves that make it difficult to identify later seismic phases reflected or refracted from weaker intra-crustal discontinuities. It is usually only the significant velocity increase of about 20% at the base of the crust towards the upper mantle (*Mohorovičić discontinuity*, or *Moho* for short), which produces first or later wave onsets besides the direct P and S waves that are strong enough to be recognizable above the ambient or signal-generated noise level. Only in some continental regions may an intermediate discontinuity, named the *Conrad discontinuity* after its discoverer, produce recognizable critically refracted ($P_b = P^*$; $S_g = S^*$) or reflected waves (see Fig. 2.39). Accordingly, for purposes of routine seismological observatory practice, it is usually sufficient to represent the crust as a horizontal one-layer model above the half-space (upper mantle).

The currently most common global 1-D Earth model IASP91 (Kennett and Engdahl, 1991; see 2.7) assumes a homogeneous 35 km thick two-layer crust with the intermediate crustal discontinuity at 20 km depth. The respective average velocities for the upper and lower crust and the upper mantle are for P waves 5.8 km/s, 6.5 km/s and 8.04 km/s, and for S waves 3.36 km/s, 3.75 km/s and 4.47 km/s, respectively. The impedance contrast at the Conrad discontinuity and the Moho is about 1.3. Fig. 2.39 is a simplified depiction of such a two-layer crust and of the seismic rays of the main crustal/upper mantle phases to be expected. These are: P_g , S_g , P_b , S_b , P_n , S_n , P_mP and S_mS . For a detailed definition of the named phases see IS 2.1.

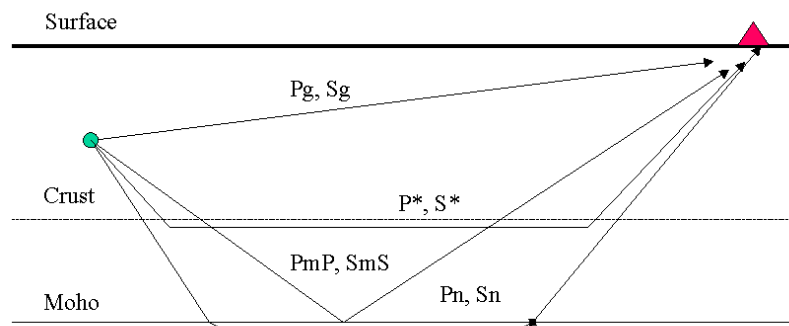


Fig. 2. 39 A simplified model of the crust showing the ray traces of the main “crustal phases” observed for near (local and regional) earthquakes. Note: $P^* = P_b$ and $S^* = S_g$.

The apparent horizontal velocity of the reflected P_mP and S_mS waves varies with distance according to their changing incidence angle on the surface. Their travel-time branches form hyperbolae that approach asymptotically the travel-time curves for P_g and S_g (or P_b and S_b) with increasing distance (see Fig. 2.40). Note that P_n and head waves have usually smaller amplitudes than P_g and S_g , at least for distances up to about 300 km. P_n can be usually identified above the noise level only when it becomes the P-wave first arrival. At larger distances, because of the stronger attenuation of upper crustal P_g and S_g and with P_n and S_n being less attenuated upper mantle diving phases, P_n and S_n may become clear P and S first arrivals (see Fig. 2.15). Beyond the critical point (at about 70-80 km distance for an average

crust) the supercritically reflected waves PmP and SmS have generally the largest amplitudes, however, arriving always closely after Pg and Sg, their onset times can usually not be picked reliably enough as to be of value for earthquake location. Therefore, these phases are usually not explicitly reported in routine observatory practice. However, reporting of Pg, Sg, Pn and Sn, if recognizable, is a must. This also applies to the reporting of the maximum amplitudes in records of near seismic events for the determination of local magnitudes M_l (see 3.2.4). Depending on source depth too, this amplitude maximum may be related to Sg/SmS, Lg, or Rg (see Figs. 2.15, 2.16 and 2.40).

Travel-time curves for the phases Pn, Pg, Sn, Sg and Lg for distances up to 400 km are given in Figure 4 of Exercise EX 11.1. These curves relate to an average single-layer crust for Central Europe. From the global Earth model IASP91, given in Datasheet DS 2.1, one may calculate respective travel-time curves for a two-layer crustal model. However, such global crustal travel-time curves may not be representative at all for certain regions and may serve as a starting model only to work with. It is one of the main tasks of operators of local and regional seismic networks to derive from their own carefully analyzed data of near events not only local/regional magnitude calibration functions (see 3.2.4) but also average local/regional travel-time curves. The latter will not only allow significantly improved seismic event locations but may later serve also as starting models for 3-D tomographic studies of crustal heterogeneities.

Fig. 2.40 shows real short-period seismic network records of two local earthquakes in Switzerland in the distance range between about 10 km and 180 km along different profiles together with the modeling of their reduced travel-time curves and inferred structural profiles. While one event was at a depth of only 5 km, the other event was about 30 km deep. The first one was observed by stations situated up-dip while the latter event was observed down-dip. One sees striking differences in the shape and gradient of the travel-time curves and in the crossover distance between Pg and Pn, in particular. In the case of the deeper event near to the Moho, Pn becomes the first arrival beyond 70 km distance, whereas for the shallower event Pn outruns Pg only at more than 130 km epicentral distance. In both cases Pg (Sg) and/or PmP (SmS) are the prominent P and S arrivals. The Pn first arrivals are relatively small. No Pb, Sb or reflected waves from a mid-crustal discontinuity are recognizable in Fig. 2.40. Note, however, that depending on the orientation of the earthquake rupture and thus of the related radiation characteristic of the source, it may happen that a maximum of energy is radiated in the direction of the Pn ray and a minimum in the direction of the Pg ray. Then the usual relationship $A_{Pn} < A_{Pg}$ may be reversed (examples are given in 11.5.1).

Misinterpretation of Pn as Pg or vice versa may result in large errors of event location. Therefore, one should have at least a rough idea at which distance in the region under study, depending on the average crustal thickness and velocity, one may expect Pn to become the first arrival. A “rule-of-thumb” for calculating the crossover distance x_{co} is given in Equation (6) of IS 11.1. For an average single-layer crust and a surface source, $x_{co} \approx 5 z_m$ with z_m – Moho depth. However, as demonstrated with Fig. 2.40, x_{co} is only about half as large for near Moho earthquakes and also the dip of the Moho and the direction of observation (up- or down-dip) does play a role. Yet, lower crustal earthquakes are rare in a continental (intraplate) environment. Mostly they occur in the upper crust.

Rules-of-thumb for calculating the source distance from the travel-time differences Sg-Pg and Sn-Pn are given in Eqs. (11.1) and (11.2).

2. Seismic Wave Propagation and Earth models

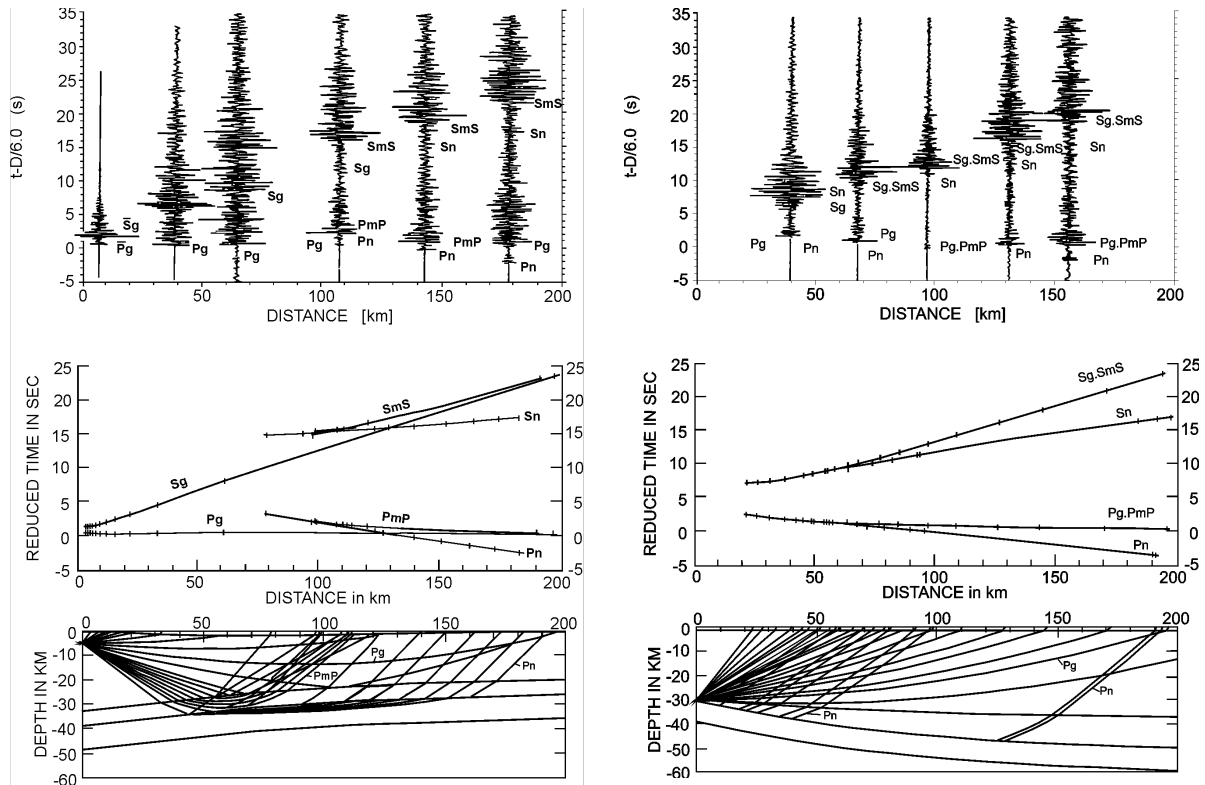


Fig. 2.40 Records (above) of two regional earthquakes of Oct. 9, 1986 at Sierre (left) and of July 7, 1985 at Langenthal, Switzerland together with the calculated reduced travel-time curves (middle) and ray-tracing crustal models which best fit the observations (below), redrawn and complemented from *Anatomy of Seismograms*, Kulhánek, plate 4, pp. 83-84, © 1990 (with permission from Elsevier Science).

Sometimes, very strong onsets after Pg, well before Sn or Sg can be expected, may be related to depth phases (e.g., sPmP; Bock et al., 1996). This may complicate proper interpretation of the local phases as well and can usually not be solved in routine analysis. Also be aware that in the case of sub-crustal earthquakes, which are common in subduction zones, none of the crustal phases discussed above exist. In this case, the first arriving longitudinal and shear wave onsets are termed P and S, respectively, as for teleseismic events (see Fig. 2.41).

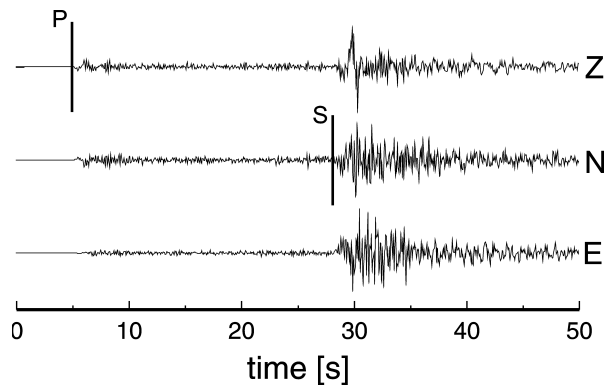


Fig. 2.41 P- and S-wave onsets from a local earthquake in northern Chile at a depth of 110 km and a hypocentral distance of about 240 km (courtesy of B. Schnurr, 2001).

2.6.2 Seismic phases and travel times at teleseismic distances

Seismic waves arriving at distances beyond 10° up to about 30° have mainly traveled through the upper mantle (from Moho to about 410 km depth) and the transition zone to the lower mantle (between about 410 km and 660 km depth). The strong discontinuities which mark the upper and lower boundary of the transition zone are associated with strong increases in seismic impedance (i.e., of both velocity and density; see Fig. 2.53). This results in two remarkable triplications of the travel-time curve for P waves (see Fig. 2.30) and S waves, which give rise to complicated short-period waveforms of P and S with rather long duration (up to about 10 and more seconds) and consisting of a sequence of successive onsets with different amplitudes.

For epicentral distances $D > 30^\circ$ P and S waves are followed by an increasing number of secondary waves, mainly phases, which have been reflected or converted at the surface of the Earth or at the core-mantle boundary. Fig. 2.42 depicts a typical collection of possible primary and secondary ray paths together with a three-component seismic record at a distance of $D = 112.5^\circ$ that relates to the suit of seismic rays shown in red in the upper part of the cross section through the Earth. The phase names are standardized and in detail explained in IS 2.1

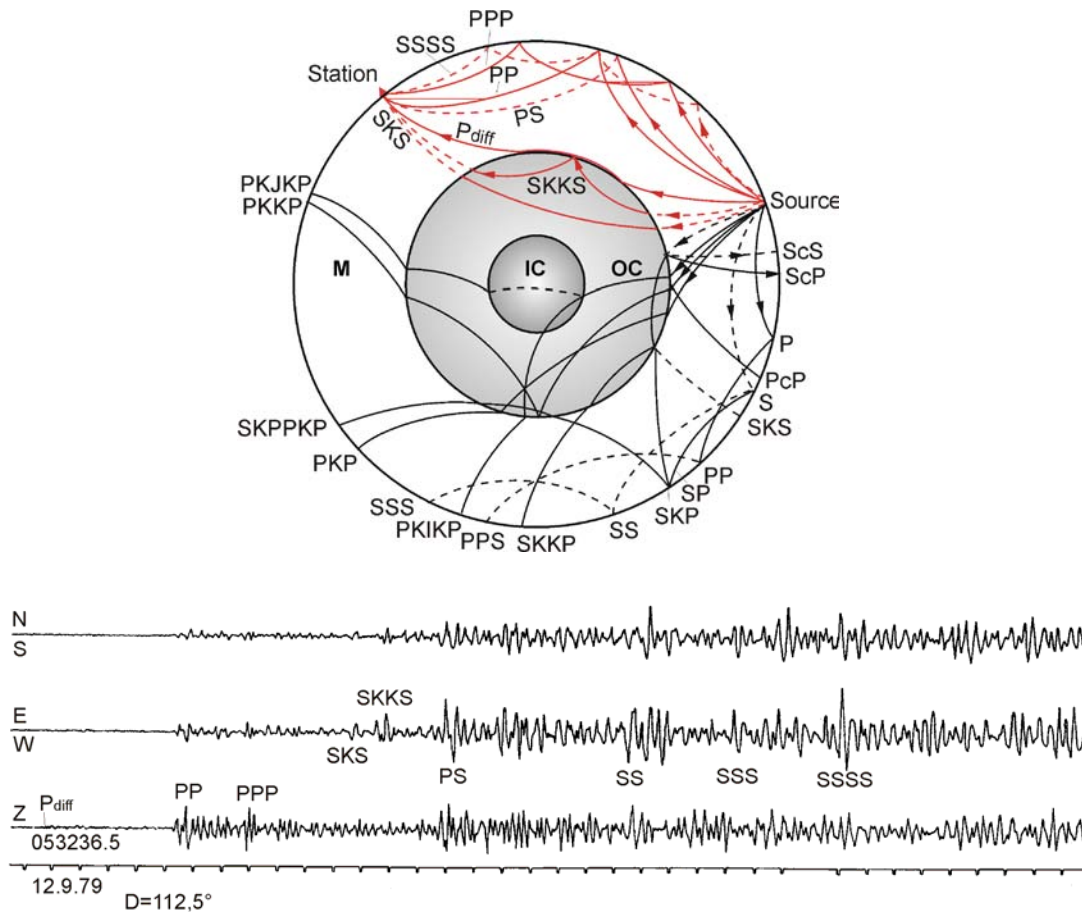


Fig. 2.42 Top: Seismic ray paths through the mantle (M), outer core (OC) and inner core (IC) of the Earth (above) with the respective phase symbols according to the international nomenclature (see IS 2.1, also for detailed ray tracing). Full lines: P rays; broken lines: S rays. Related travel-time curves are given in Fig. 2.46 and the transparency to Fig. 2.48. Red rays relate to the 3-component Kirnos SKD broadband seismograms recorded at station MOX, Germany (bottom) of body-waves from an earthquake at an epicentral distance of 112.5° .

2. Seismic Wave Propagation and Earth models

In the case of deep earthquakes the direct P wave that leaves the source downward will arrive at a teleseismic station first. It will be followed, depending on the source depth, up to about 4.5 min later by other phases that has left the source upward. These phases, reflected and eventually converted at the free surface of the Earth or an ocean bottom (e.g., pP, sP, pPP, sPP, pPKP, etc.), at the free surface of the ocean (e.g., pwP) or from the inner side of the Moho (e.g., pmP) are the so-called depth phases. Their proper identification, onset-time picking and reporting is of crucial importance for reliable determination of source depth (see 6.1 and Figure 7 in Information Sheet 11.1). Differential travel-time tables pP-P and sP-P are given in the Exercise EX 11.2. For the definition of these phases see also IS 2.1.

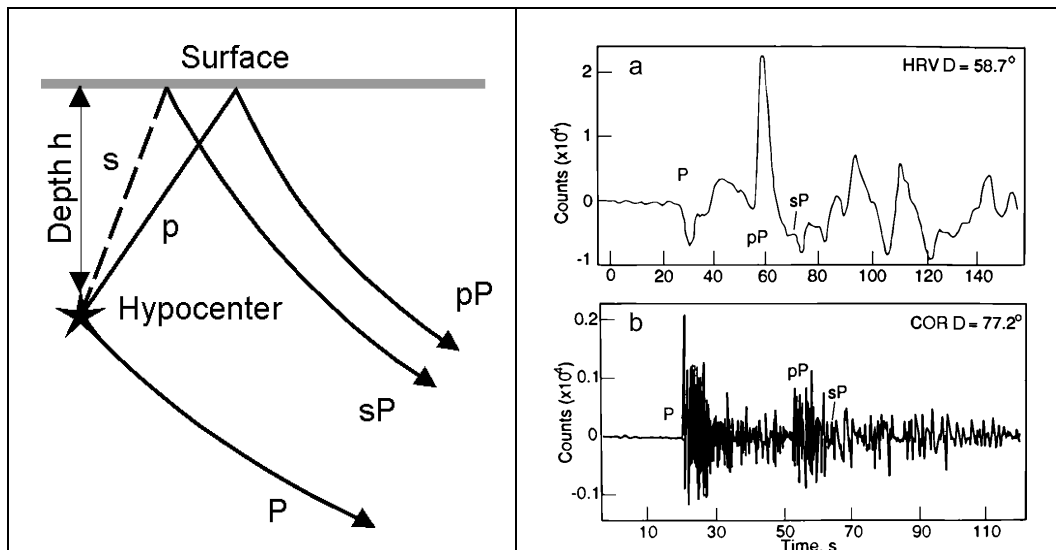


Fig. 2.43 Left: Different ray paths of a direct teleseismic P wave and of its depth phases. Right: Records of depth phases of the May 24, 1991 Peru earthquake (hypocentral depth $h = 127$ km); a) broadband record and b) simulated short-period recording (the right figure is a corrected cutout of Fig. 6.4 of Lay and Wallace, *Modern Global Seismology*, p. 205, © 1995; with permission of Elsevier Science (USA)).

However, the identification of depth phases is rather difficult for shallow crustal earthquakes because their onsets follow rather close to the direct phase, thus superposing with their wavelets. They may, however, be discriminated by waveform modeling with variable source depth (see subchapter 2.8, Fig. 2. 56).

Between about 30° and 100° epicentral distance P and S have traveled through the lower mantle, which is characterized by a rather smooth positive velocity and density gradient (see Fig. 2.53). In this distance range, seismograms are relatively clearly structured with P and S (or beyond 80° with SKS) being the first, prominent longitudinal and transverse wave arrivals, respectively, followed by multiple surface and core-mantle boundary (CMB) reflections or conversions of P and S such as PP, PS, SS and PcP, ScP etc. (see Fig. 2.42 and 2.48 with overlay). Within about 15 to 35 min after the first P arrival multiple reflections of PKP from the inner side of the CMB (PKKP; P3KP) or from the surface (PKPPK = P'P') may be recognizable in short-period seismic records. Their ray traces are shown in Fig. 2.44 and many more, with record examples, in 11.5.3.

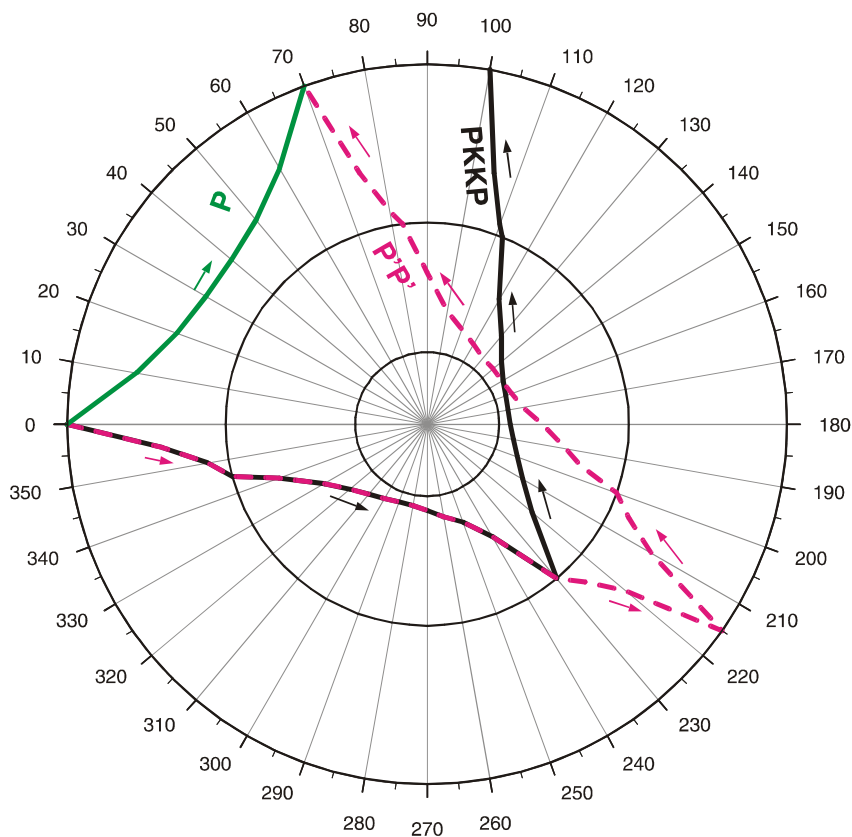


Fig. 2.44 Ray paths of PKKP and P'P' (= PKPPKP) with respect to the direct P phase (courtesy of S. Wendt, 2001).

Beyond 100° , only P-wave rays, which entered the outer core after strong downward refraction, will reach the surface. This is due to the dramatic reduction of the P-wave velocity at the CMB from about 13.7 km/s in the lowermost mantle to 8.0 km/s in the upper outer core. Thus, P waves form a *core shadow*. However, long-period P-wave energy is diffracted around the CMB into this shadow zone. According to the new IASPEI nomenclature of phase names (see IS 2.1) the diffracted P wave is termed Pdif, however the old phase symbol Pdiff is still widely used.

The amplitudes of Pdif are comparably small thus making PP the strongest longitudinal arrival up to nearly 144° (see Figs. 2.42, 2.55, 11.60 and 11.61). PKP has a caustic at 145° causing strong amplitudes comparable with those of P at much shorter distances around 50° (see Fig. 3.13) and separates into different branches beyond the caustic (see Figs. 2.45, 11.62 and 11.63).

In more detail, the types of seismic phases appearing in the various distance ranges and their peculiarities are discussed in Chapter 11 where many record examples are given both in the main text and in complementary Datasheets (DS 11.1 to 11.3).

2. Seismic Wave Propagation and Earth models

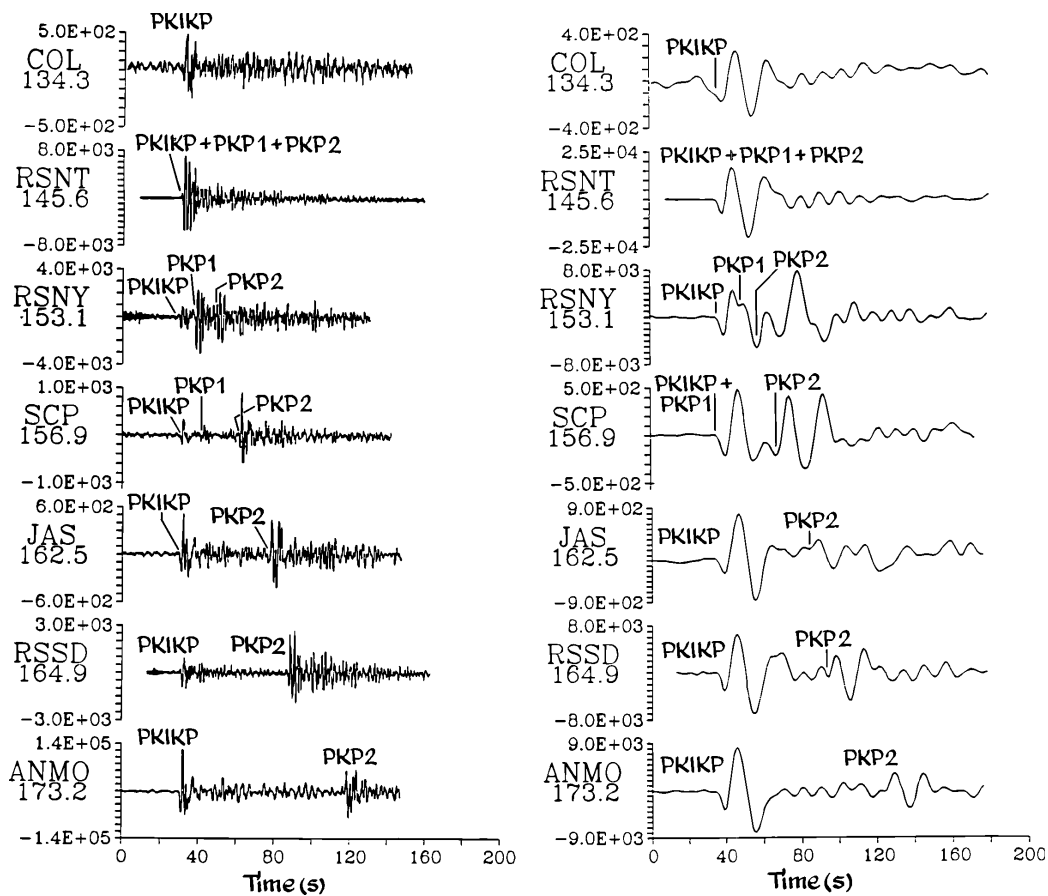


Fig. 2.45 Short-period (left) and long-period (right) seismograms for the Mid-Indian Rise earthquake on May 16, 1985 ($M = 6.0$, $h = 10$ km) in the range $D = 145.6^\circ$ to 173.2° . (From Kulháněk, *Anatomy of Seismograms*, plate 55, pp. 165-166, ©1990; with permission from Elsevier Science). Note: The figure above gives still the old names of the core phases. According to the new IASPEI phase names PKP2 should be replaced by PKPab, PKP1 by PKPbc and PKIKP by PKPdf (see IS 2.1, also for the detailed ray tracing of these phases).

The first discernable motion of a seismic phase in the record is called the *arrival time* and the measurement of it is termed *picking* of the arrival (see 11.2.2). Up to now, arrival time picking and reporting to international data centers is one of the major operations of data analysts at seismic stations or network centers. Plotting the time differences between reported arrival times and calculated origin times over the epicentral distance, seismologists were able to construct travel-time curves for the major phases and to use them to infer the average radial velocity structure of the Earth (see 2.7). In Fig. 2.46 (left) more than five million travel-time picks, archived by the International Seismological Centre (ISC) for the time 1964 to 1987, have been plotted. Most time picks align nicely to travel-time curves, which match well with the travel-time curves theoretically calculated for major seismic phases on the basis of the IASP91 model (Fig. 2.46 right).

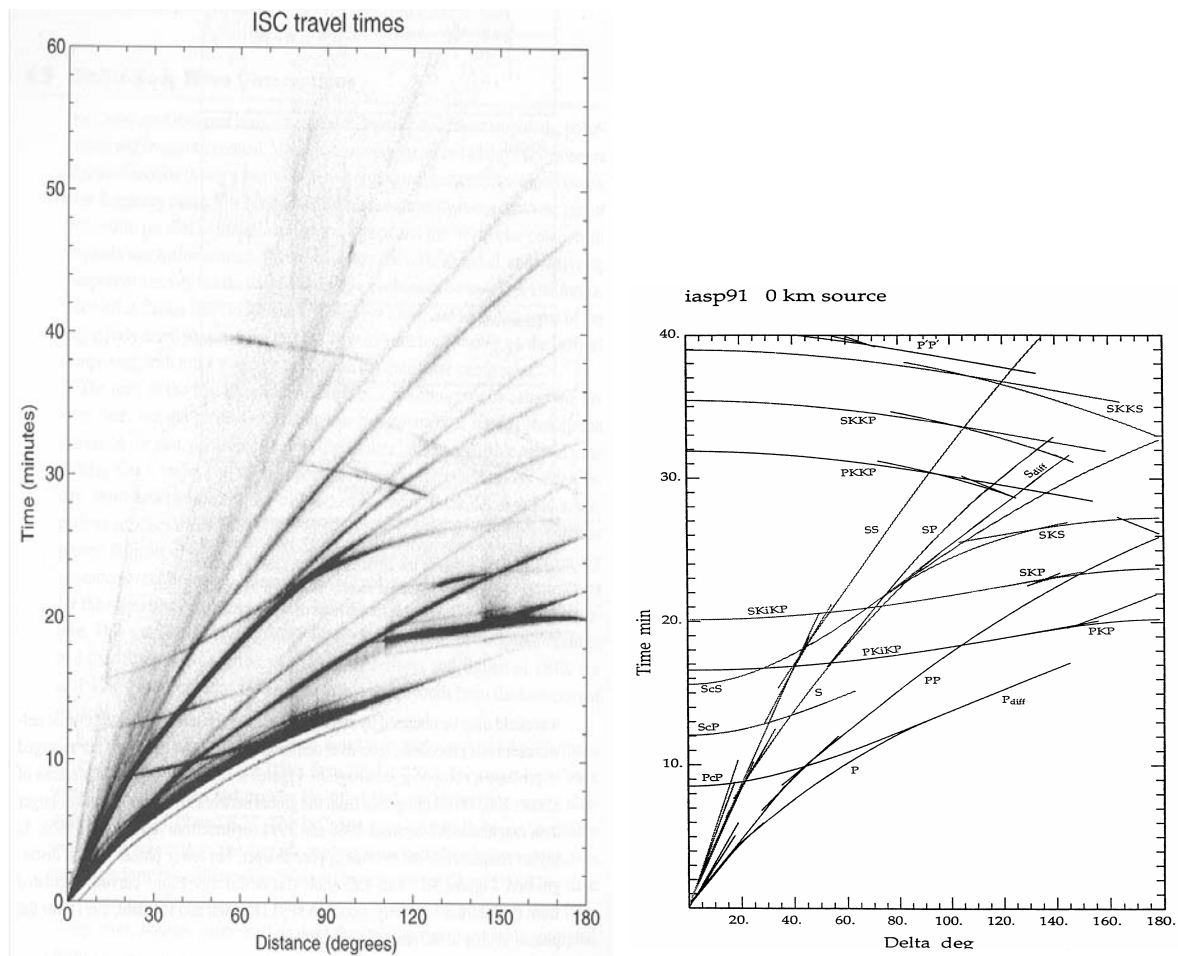


Fig. 2.46 Left: Travel-time picks collected by the ISC between 1964 and 1987 for events shallower than 50 km. (From Shearer, *Introduction to Seismology*, 1999; with permission from Cambridge University Press). Right: IASP91 travel-time curves for surface focus (from Kennett, 1991).

An even more complete picture of the entire seismic wavefield may nowadays be obtained by stacking data from modern digital seismic networks. For this, records at common source-receiver ranges are averaged to produce a composite seismogram. Stacks of almost 100,000 seismograms from the global digital networks are plotted in Fig. 2.47 (for short-period records with periods $T < 2\text{s}$) and Fig. 2.48 (for long-period records with $T > 10\text{s}$). Although the arrivals appear sharper at higher frequencies, much fewer later phases can be distinguished in short-period records. The late arriving reflected core phases P'P' (PKPPKP), PKKP, however, and higher multiples of them, are discernable in short-period records only. Note that the relative darkness with which the “curves” appear against the gray background is a measure of the relative frequency with which these phases can be observed above the noise level. The transparent overlays to the figures give the nomenclature for the visible phases in these stacks together with the more complete calculated travel-time curves according to the IASP91 velocity model (Kennett and Engdahl, 1991). They match very well.

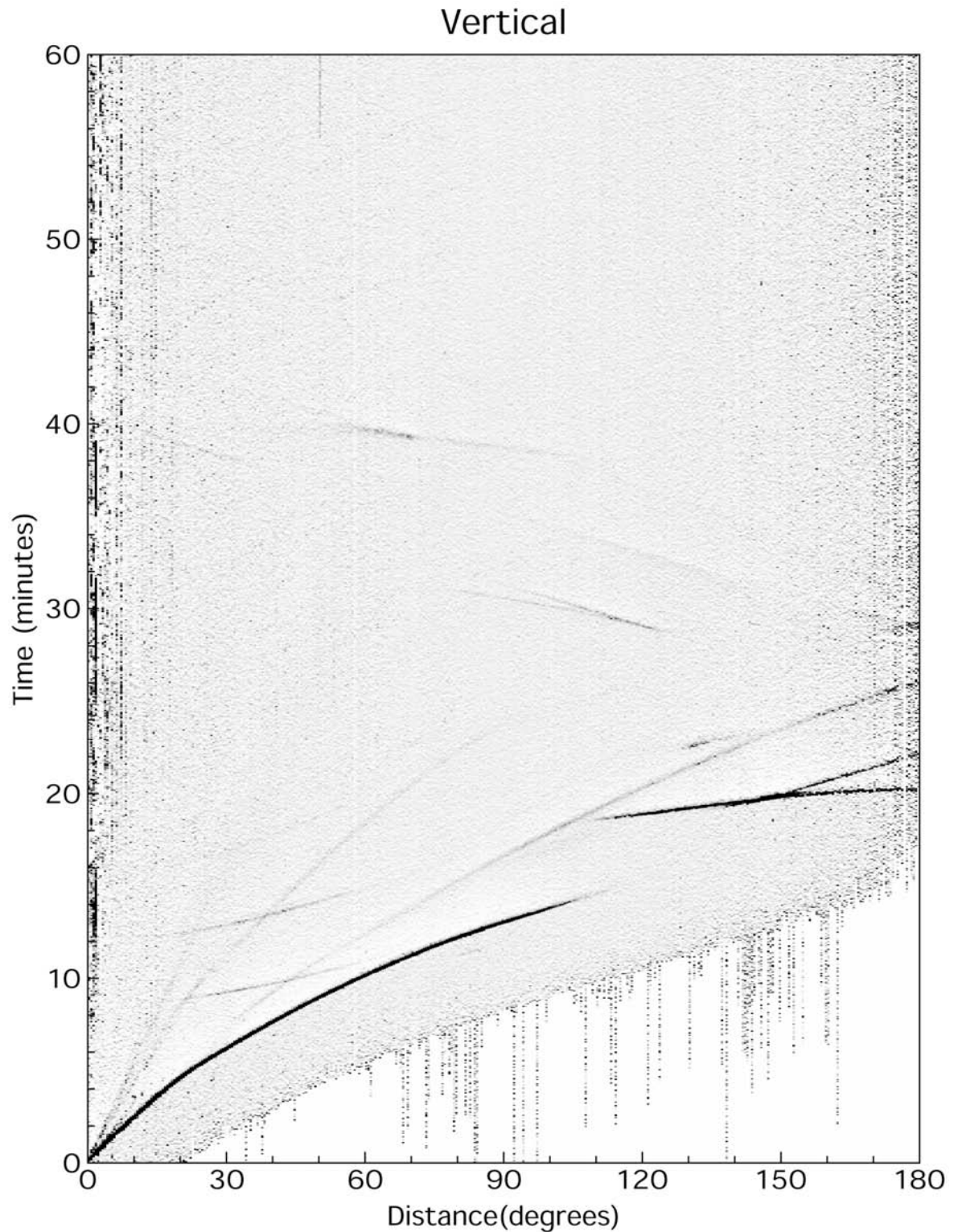
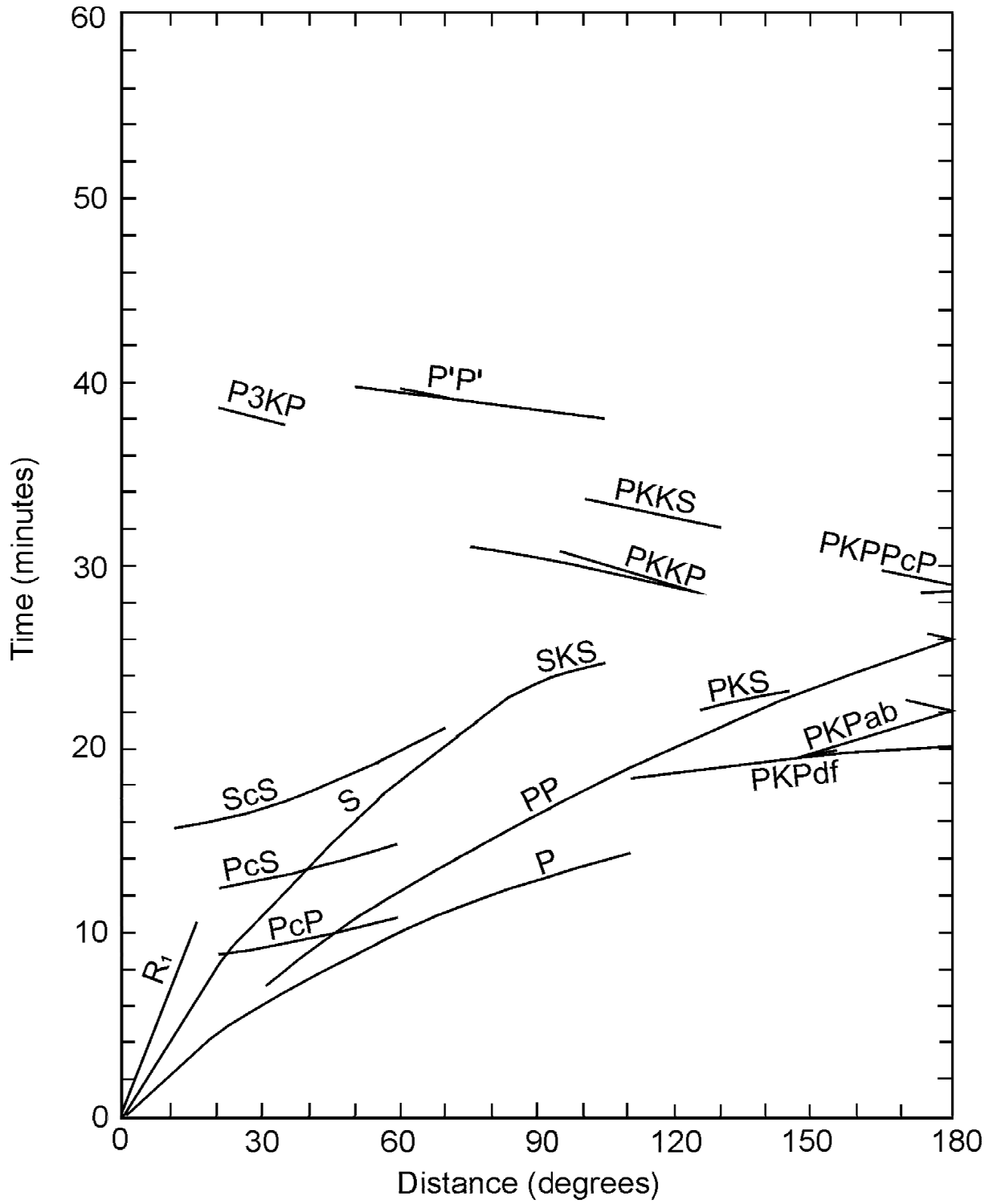
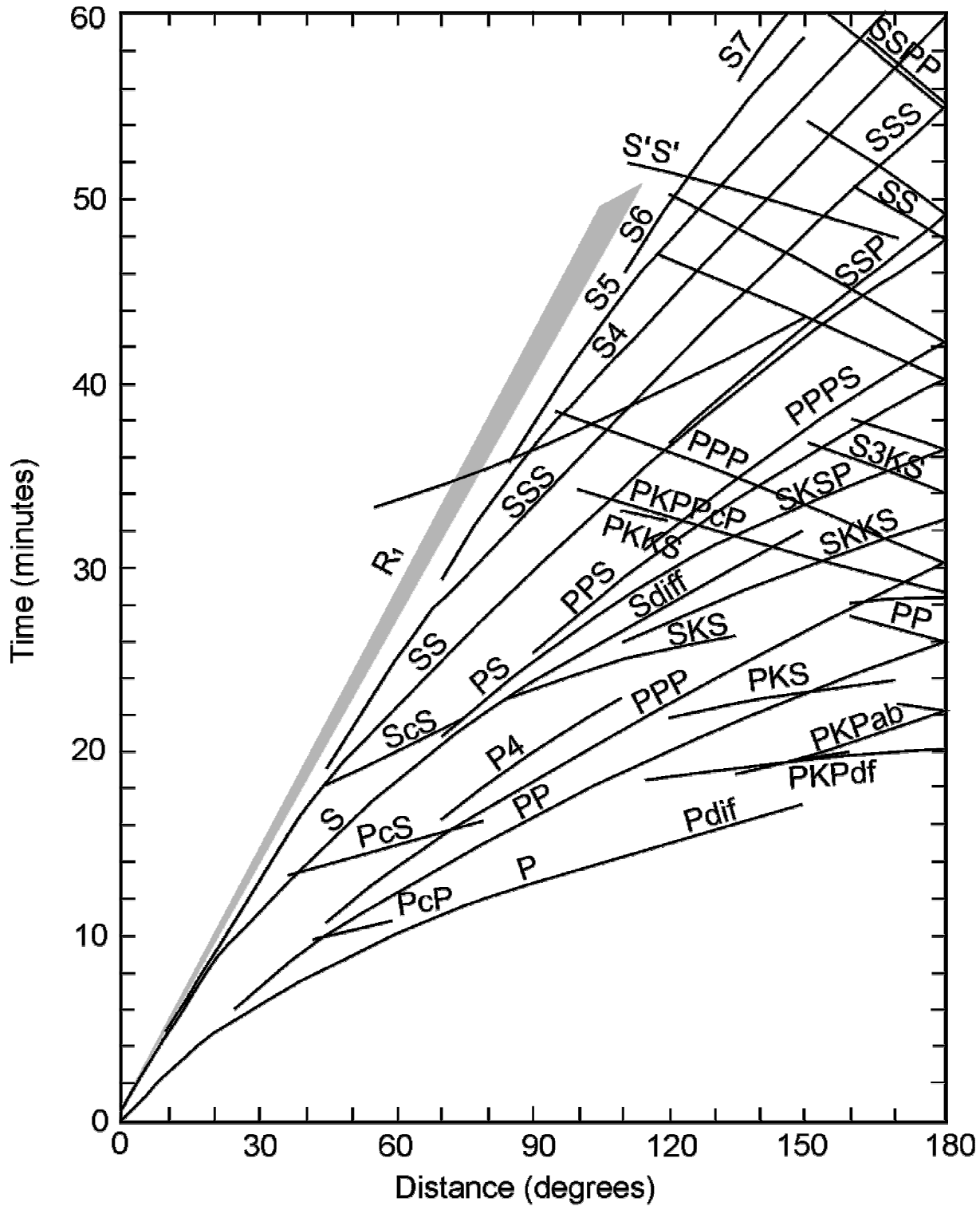


Fig. 2.47 A stack of short-period filtered (<2 s), vertical component data from the global networks between 1988 and 1994. See the overlay for the phase names and for the travel-time curves calculated using the IASP91 model (Kennett and Engdahl, 1991) (from Astiz et al., *Global Stacking of Broadband Seismograms*, *Seismological Research Letters*, Vol. 67, No. 4, p. 12, © 1996; with permission of Seismological Society of America).



Overlay to Fig. 2.47

2. Seismic Wave Propagation and Earth models



Overlay to Figs. 2.48 and 2.49

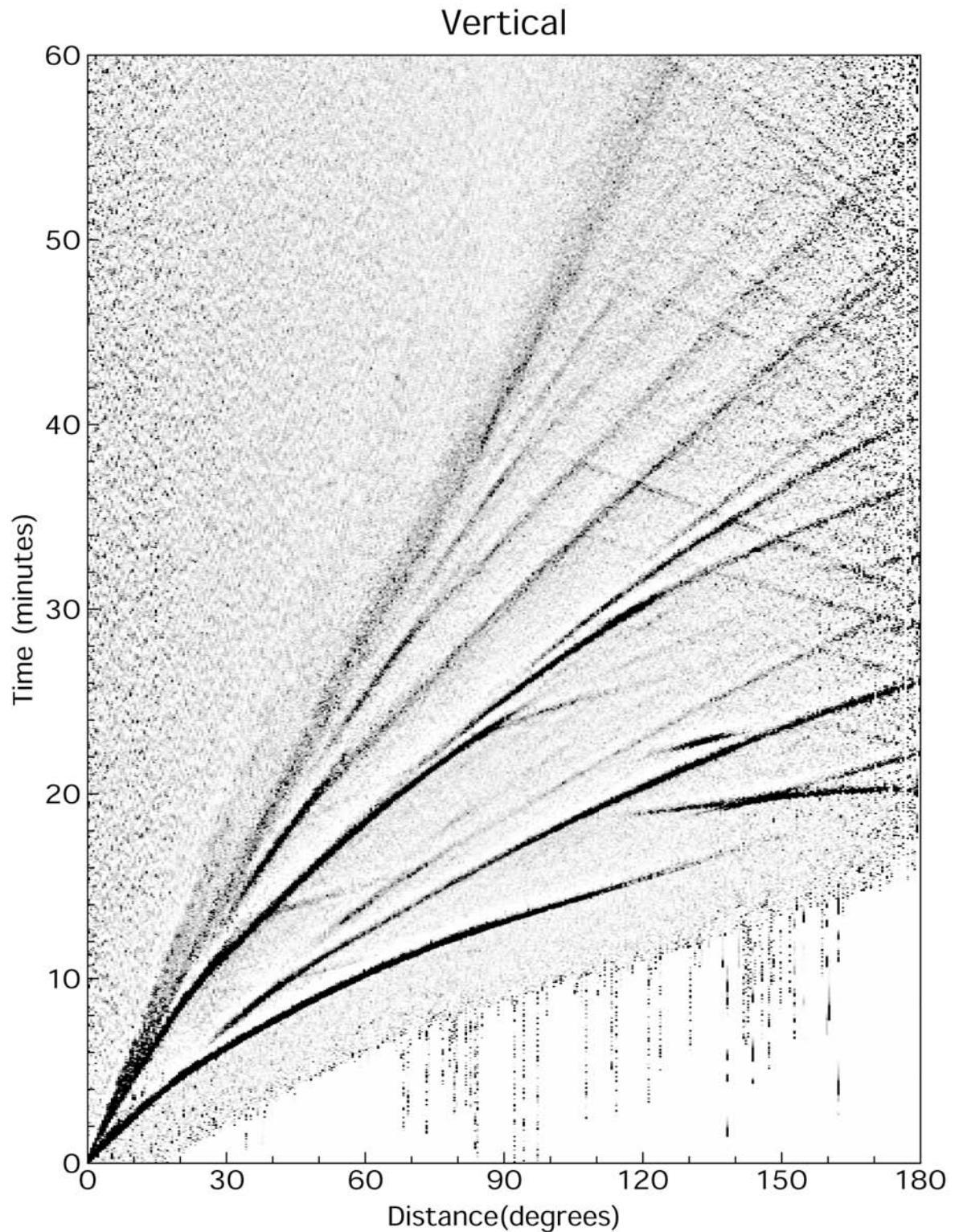


Fig. 2.48 A stack of long-period (> 10 s), vertical component data from the global networks between 1988 and 1994. See the overlay for the phase names and for the travel-time curves calculated for all types of phases (see also Fig. 2.49) using the IASP91 model (Kennett and Engdahl, 1991) (from Astiz et al., *Global Stacking of Broadband Seismograms*, *Seismological Research Letters*, Vol. 67, No. 4, p. 14, © 1996; with permission of Seismological Society of America).

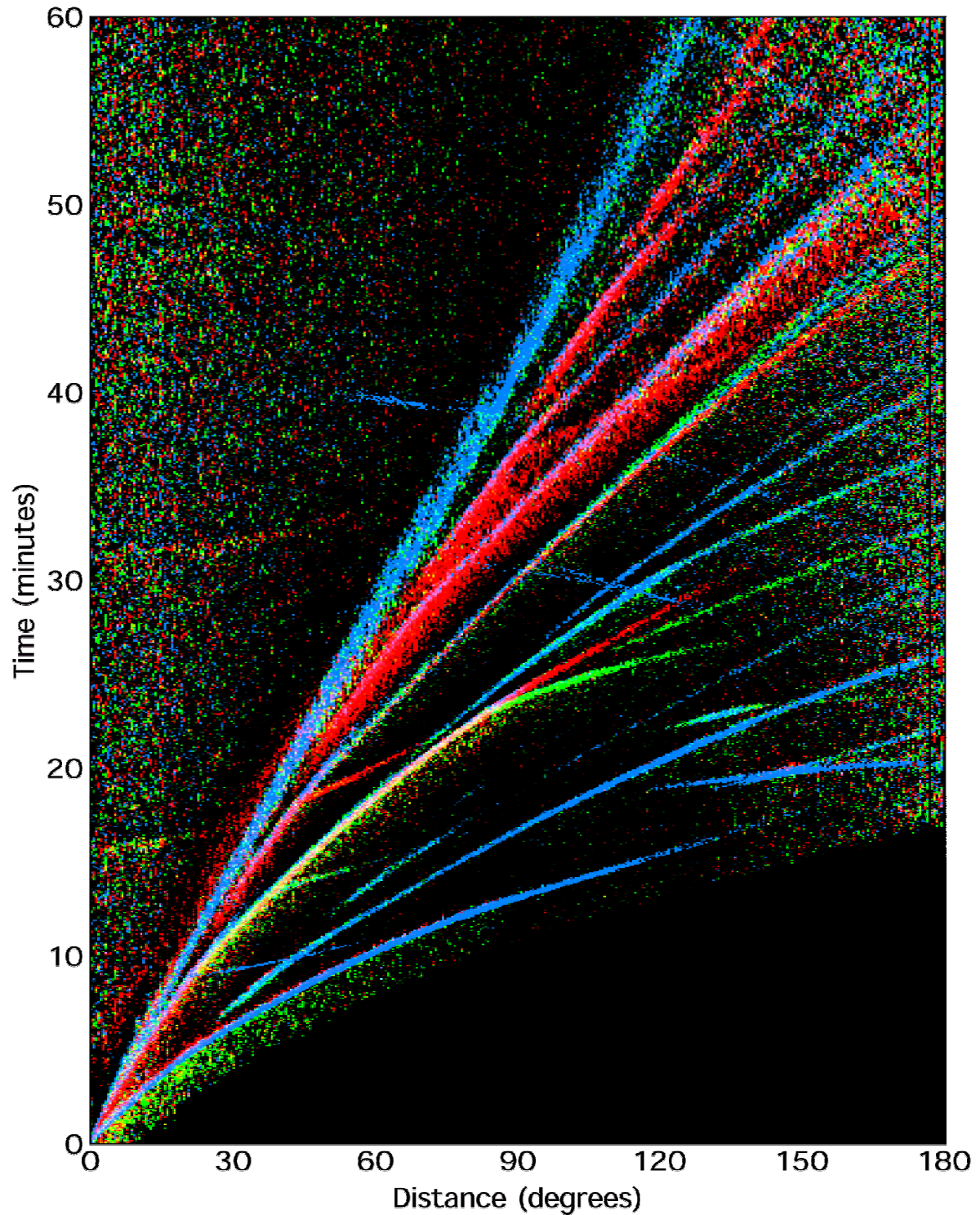


Fig. 2.49 Global travel-time curves for shallow earthquakes as produced by stacking broadband seismograms. Seismic phases are shown in different colors depending on their polarization (blue: vertical motion; green: radial-horizontal; and red: transverse-horizontal) (courtesy of L. Astiz).

Additionally, Fig. 2.49 reveals that the polarization of these various phases differs. While all primary longitudinal phases and all from P or K to S converted phases and vice versa appear

on vertical and radial-horizontal components only, multiple reflected S waves, which lose with each reflection more and more of their SV polarized energy due to conversion into P (or K at the CMB), become more and more transversely polarized. Primary S, however, has significant energy on both horizontal components that are oriented either parallel to the backazimuth to the source (radial) or perpendicular to it (transverse). Direct P waves, polarized in the direction of ray propagation, have in the teleseismic range dominating vertical components because of their steep incidence angle, which gets smaller and smaller with increasing distance (see e.g., PKP phases). PP, P3 and higher multiples may, however, have significant energy in the radial component too. These examples illustrate that the visibility and discrimination of body wave phases in seismic records depends on their relative amplitude, polarization and frequency content. All of these criteria have to be taken into account, besides the differences in travel-times, when analyzing seismic records.

2.7 Global Earth models

In the first part of the 20th century travel-time models for seismic phases, empirically derived from historical data, were rudimentary at best. One of the earliest travel-time model, the Zoeppritz tables (Zoeppritz, 1907) were applied by Herbert Hall Turner in a version as published by Galitzin (1914) to locate earthquakes for the ‘Bulletin of the British Association of the Advancement of Science, Seismology Committee’ for the years 1914 until 1917. During the 1920s, Turner gradually expanded these tables for newly discovered phases and better phase observations, often suggested and derived by Beno Gutenberg. These Zoeppritz-Turner tables were in use to locate earthquakes for the International Seismological Summary (ISS) from 1918 to 1929. This situation greatly improved with the introduction of the Jeffreys-Bullen (J-B) tables (Jeffreys and Bullen, 1940), which provided a complete, remarkably accurate representation of P, S and other later-arriving phases. Like the Gutenberg-Richter travel-time tables, the J-B tables were developed in the 1930s using reported arrival times of seismic phases from a sparse global network of stations, many of which often had poor time-keeping. Once the travel times of the main phases had been compiled, smoothed empirical representations of these travel times were inverted using the Herglotz-Wiechert method to generate a velocity model. The travel times for other phases were then determined directly from the velocity model. As a testament to the careful work that went into producing the J-B tables, they are still being used by the International Seismological Centre (ISC) and by the U. S. Geological Survey National Earthquake Information Center (NEIC) for routine earthquake location.

Although the limitations of the J-B tables were known for some time, it was not until the early 1980’s that a new generation of models was constructed in a completely different way. Instead of establishing smoothed, empirical representations of phase-travel times, inverse modeling was used to construct one-dimensional models for structure that fit phase travel times reported in the ISC Bulletin since 1964 and other parametric data. The Preliminary Reference Earth Model (PREM) of Dziewonski and Anderson (1981) was the most important member of this generation of new global 1-D models. However, PREM was constructed to fit both body-wave travel-time and normal-mode data, so it was not generally thought to be especially useful for earthquake location. In fact, soon afterwards Dziewonski and Anderson (1983) published a separate analysis of just P waves in an effort to produce an improved travel-time table.

2. Seismic Wave Propagation and Earth models

In 1987 the International Association of Seismology and Physics of the Earth's Interior (IASPEI) initiated a major international effort to construct new global travel-time tables for earthquake location and phase identification. As a result of this effort two models were developed: IASP91 (Kennett and Engdahl, 1991); and SP6 (Morelli and Dziewonski, 1992). Although differences in predicted travel times between these two models were small, some effort was still required to reconcile the travel times of some important, well-observed seismic phases before either of these models could be used by the ISC and NEIC for routine earthquake location. The upper mantle part of the IASP91 model was fitted to summary P and S wave travel times, binned in 1° intervals of epicentral distance, published by Dziewonski and Anderson (1981, 1983) (Fig. 2.50).

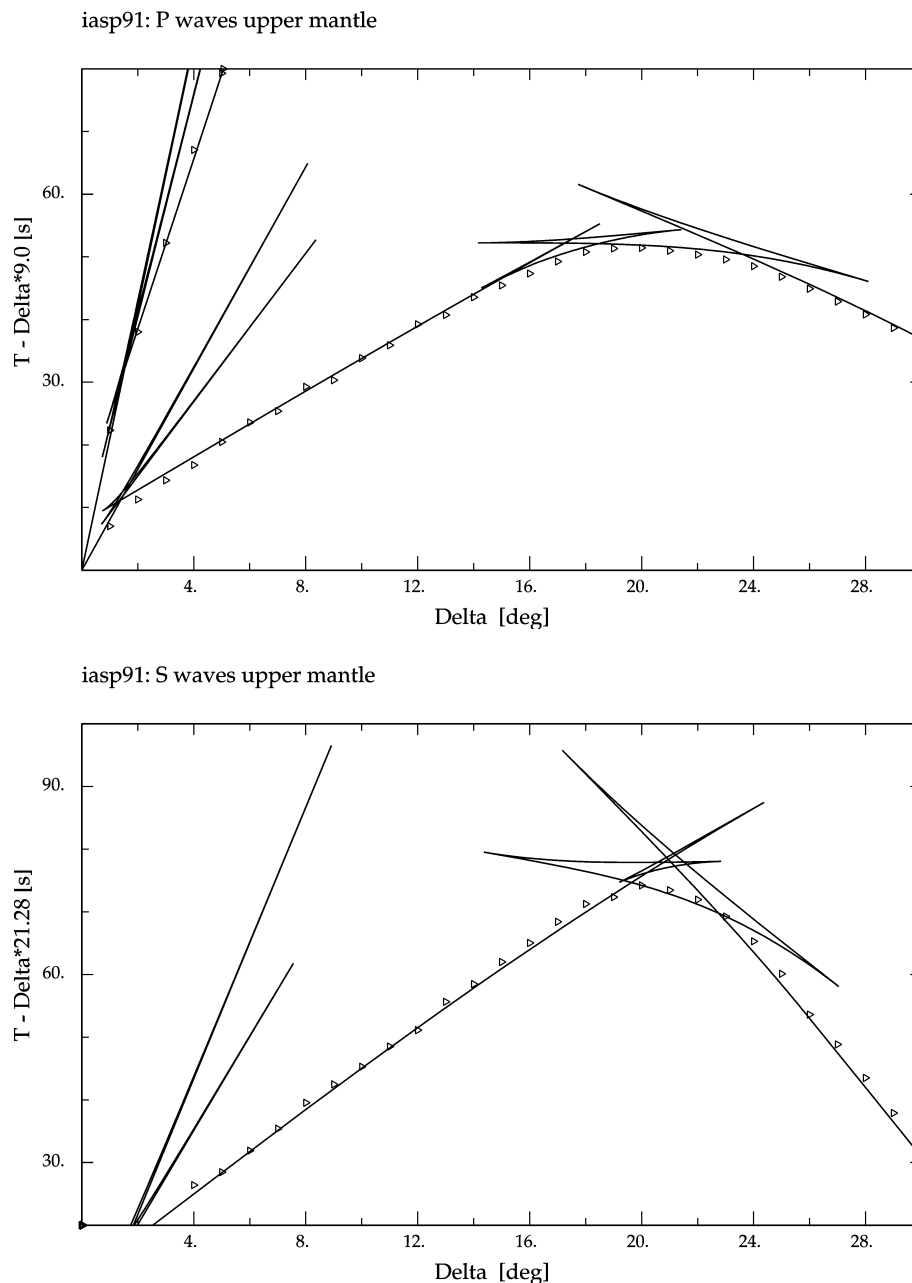


Fig. 2.50 Fitting of IASP91 upper mantle travel times as a function of epicentral distance to the summary first-arrival travel times of P (top) and S waves (bottom) according to Dziewonski and Anderson (1981, 1983) in time-reduced presentation (from Kennett and Engdahl, 1991).

As shown in Fig. 2.51, the IASP91 upper mantle differed substantially from PREM and, in particular, IASP91 had no mantle low-velocity zone for either P or S waves. Although this did run counter to the prevailing ideas about upper mantle structure, it did have a practical advantage for locating events because the upper mantle travel times in IASP91 were not discontinuous. Characteristics of the main upper mantle discontinuities were also different from previous models. In IASP91 the 210 km discontinuity was essentially absent. The 410 km and 660 km discontinuity velocity jumps in IASP91 were slightly greater in amplitude than in PREM. Path coverage was generally more uniform in the lower mantle, so these parts of the IASP91 P and S models were considered to be more representative of the average Earth. P structure was reasonably well constrained, except near the core-mantle boundary, but the complication of interfering phases put a practical limit on the amount and quality of data constraining S structure. Nevertheless, IASP91 seems to have done a reasonably good job of representing teleseismic travel times, as indicated by the analysis of arrival-time data from well-constrained explosions and earthquakes (Kennett and Engdahl, 1991).

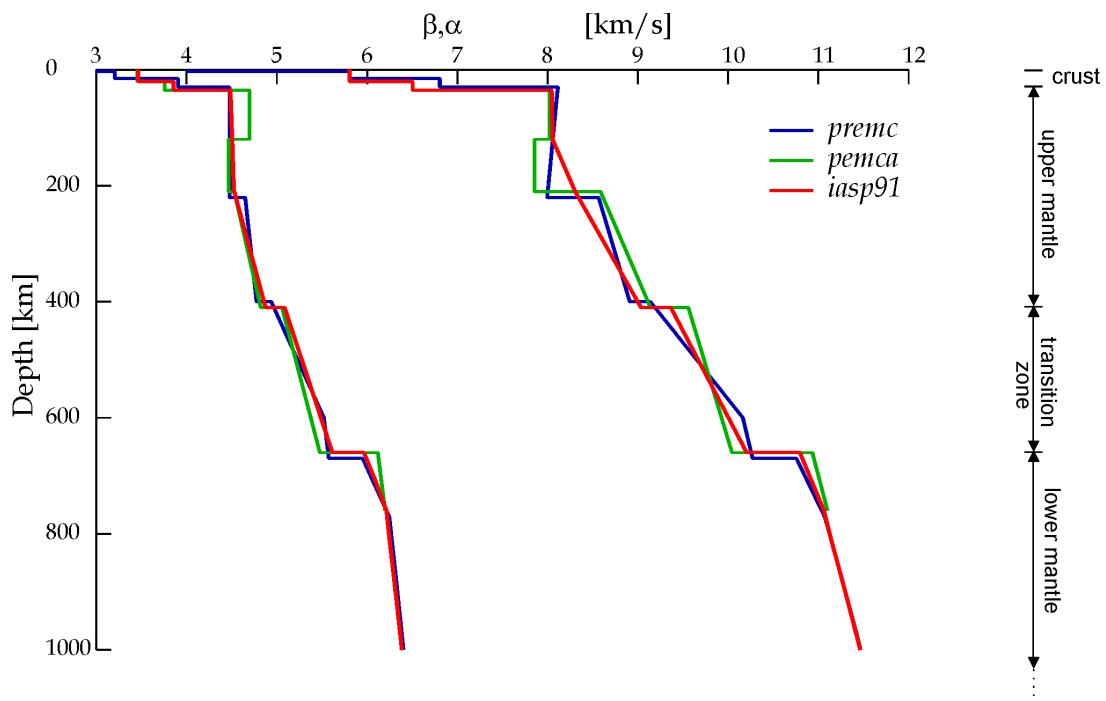


Fig. 2.51 Comparison of upper mantle velocity models for IASP91, PEMCA, and PREM (from Kennett and Engdahl, 1991;). Left: β - speed of S wave; right: α - speed of P wave.

Morelli and Dziewonski (1993) developed an alternative model (SP6) using the same model parameterization and upper mantle model as Kennett and Engdahl (1991). In their approach, they solved for multiple source-region station corrections averaged over 5° areas to account for lateral heterogeneity in an approximate manner. They then derived new sets of summary travel times for lower mantle and core P and S phases binned in 1° intervals of epicentral distance, and inverted those summary times for 1-D P and S velocity models. Although lower mantle P and S in the resulting model was generally comparable to IASP91, the models differed in that SP6 had slightly lower velocity gradients with depth and correspondingly higher velocity jumps at the 660-km discontinuity. Moreover, SP6 had incorporated a pronounced negative velocity gradient in the D'' region, a layer 100-150 km thick just above

2. Seismic Wave Propagation and Earth models

the core-mantle boundary. The SP6 model fitted the S data and all core-phase observations significantly better than IASP91. The differences in the seismic velocities between the models were significant for the core, owing to the addition of substantial core phase data in the construction of SP6.

The most significant differences between these new models and the older J-B travel-time model are in the upper mantle and core. The upper mantle is highly heterogeneous. Hence, velocities and major discontinuities in the upper mantle of recent models such as IASP91 and SP6 are set at values, which give an effective average representation of velocities for waves traveling out to 25° (see Kennett and Engdahl, 1991). The core models for IASP91 and SP6 predict more accurately than the J-B model the observed travel times of later-arriving core phases bottoming in the lowermost part of the outer core.

These models also resolve a long-standing problem in that the relocation of nuclear tests using the J-B travel-time model results in incorrect estimates of the origin times of nuclear explosions by about -1.8 sec. This error will propagate into all derived travel times and may affect the procedure of phase association. Kennett and Engdahl (1991) resolved this error in the absolute travel time (or "baseline" error) by fitting the IASP91 model to the mean teleseismic residual estimated from the origin times and hypocenters reported for explosions and well-constrained earthquakes by "test event" contributors. As a result, the times of teleseismic P and S waves for the IASP91 model now appear to be in better agreement with the travel time data than the times predicted by the J-B model. The IASP91 model has been adopted as the global reference model for the International Data Centre in Vienna established under the 1996 Comprehensive Nuclear-Test-Ban Treaty (CTBT).

Subsequently, Kennett et al. (1995) began with the best characteristics of the IASP91 and SP6 models and sought to enhance the data quality by improving the locations of a carefully selected set of geographically well-distributed events. The basic strategy was to use a location algorithm developed by Engdahl et al. (1998) with a IASP91 model modified to conform to the SP6 core to relocate events and improve phase identifications using only first arriving P phases and re-identified depth phases (pP, pwP and sP). The resulting set of smoothed empirical relations between travel time and epicentral distance for a wide range of re-identified seismic phases was then used to construct an improved reference model for the P and S radial velocity profile of the Earth (AK135). A composite residual plot (Fig. 2.52) shows that the model AK135 provides a very good fit to the empirical times of 18 seismic phases. The baseline and trend of S is well presented and most core phase times are quite well matched. Thus, for improved global earthquake location and phase association, there has been convergence on effective global, radially symmetric P- and S-velocity Earth models that provide a good average fit to smoothed empirical travel times of seismic phases.

The primary means of computing travel times from such models is based on a set of algorithms (Buland and Chapman, 1983) that provide rapid calculation of the travel times and derivatives of an arbitrary set of phases for a specified source depth and epicentral distance. In the mantle, AK135 differs from IASP91 only in the velocity gradient for the D" layer and in the baseline for S wave travel times (about -0.5 sec). Significant improvement in core velocities relative to earlier model fits was also realized. Inner core anisotropy, as discussed in the literature, is not yet accounted for in any of the newer 1-D Earth models. However there are so few reported arrivals of PKPdf at large distances along the spin axis of the Earth that the effects of this anisotropy in earthquake location are negligible.

The model AK135 has since been used for further reprocessing of the arrival time information (Engdahl et al., 1998). The reprocessed data set and the AK135 reference model have formed the basis of much recent work on high-resolution travel-time tomography to determine three-dimensional variations in seismic wave speed (e.g., Bijwaard et al., 1998). However, it is important to recognize that none of these models can properly account for the effect of lateral heterogeneities in the Earth on teleseismic earthquake location. Most deeper than normal earthquakes occur in or near subducted lithosphere where aspherical variations in seismic wave velocities are large (i.e., on the order of 5-10%). Such lateral variations in seismic velocity, the uneven spatial distribution of seismological stations, and the specific choice of seismic data used to determine the earthquake hypocenter can easily combine to produce bias in teleseismic earthquake locations of up to several tens of kilometers (Engdahl et al., 1998). For a review of recent advances in teleseismic event location, with the primary emphasis on applications using one-dimensional velocity models such as AK135, the reader is referred to Thurber and Engdahl (2000). The most accurate earthquake locations are best determined using a regional velocity model with phase arrival times from a dense local network, which may differ significantly (especially in focal depth) from the corresponding teleseismic locations.

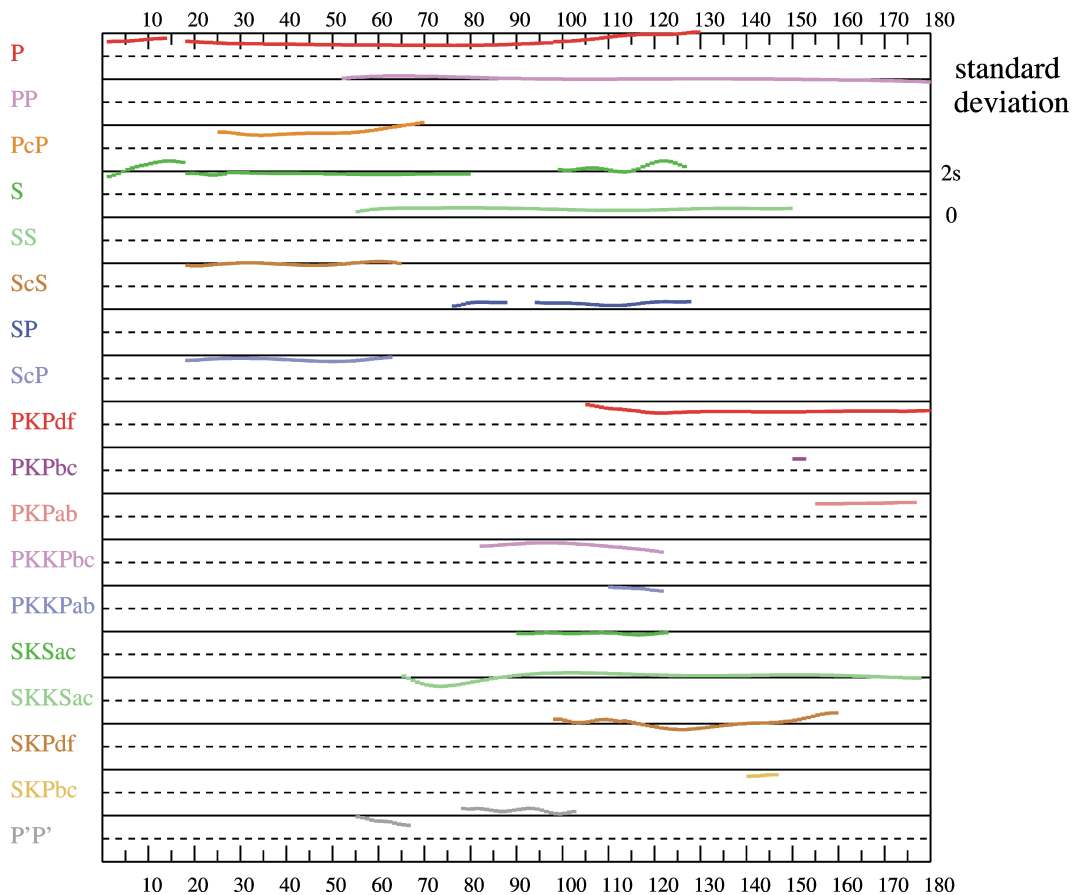


Fig. 2.52 Composite display of the estimates of standard deviations for the empirical travel times used in the construction of the AK135 velocity model (Kennett et al., 1995).

The AK135 wave speed reference model is shown in Fig. 2.53. However, though the P- and S-wave speeds are well constrained by high-frequency seismic phases, more information is needed to provide a full model for the structure of the Earth.

2. Seismic Wave Propagation and Earth models

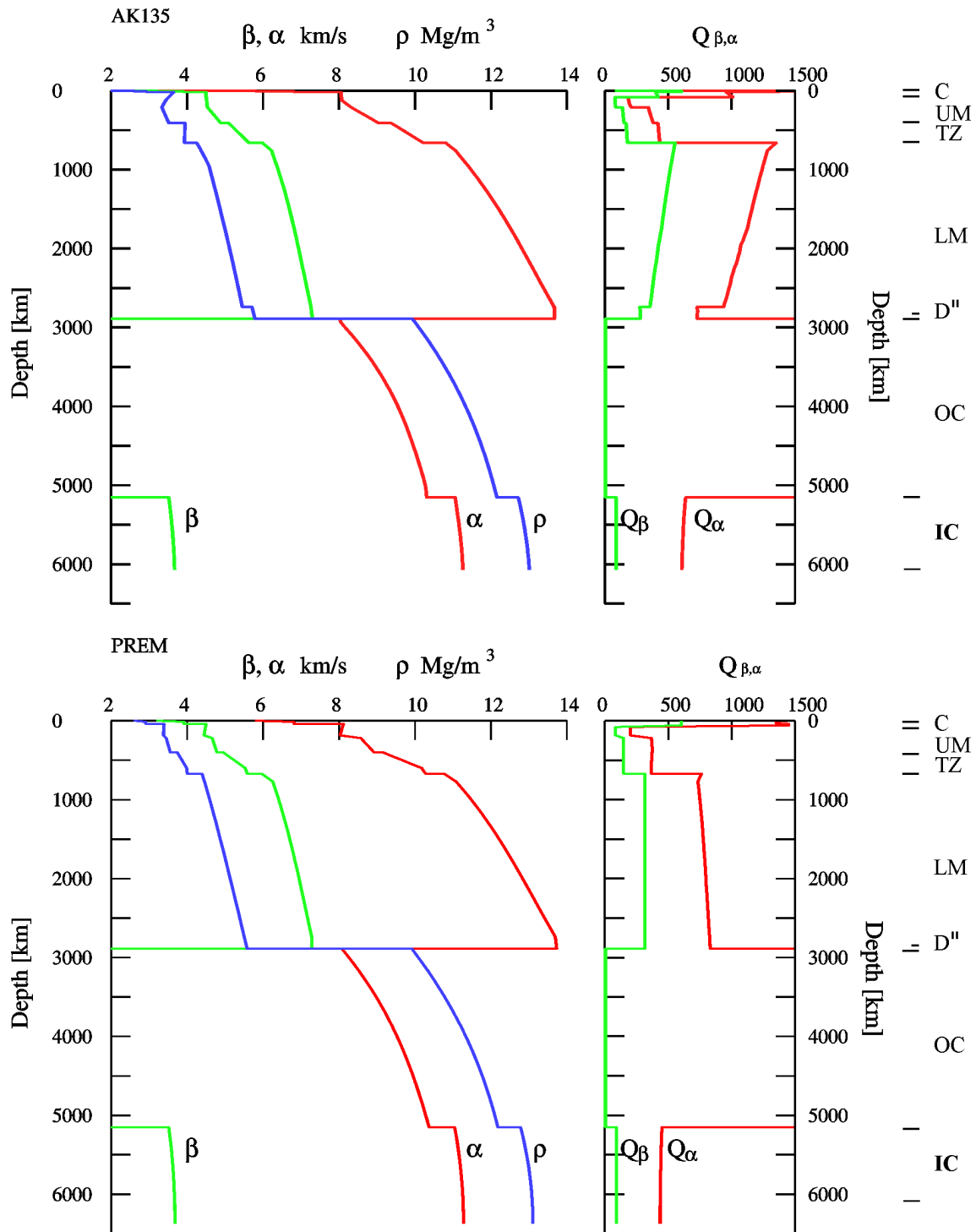


Fig. 2.53 Radial symmetric reference models of the Earth. Top: AK135 (seismic wave speeds according to Kennett et al. (1995), attenuation parameters and density according to Montagner and Kennett (1996); Bottom: PREM (Dziewonski and Anderson, 1981). α - and β : P- and S-wave velocity, respectively; ρ - density, Q_{α} and $Q_{\beta} = Q_{\mu}$ - “quality factor” Q for P and S waves. Note that wave attenuation is proportional to $1/Q$. The abbreviation on the outermost right stand, within the marked depth ranges, for: C – crust, UM – upper mantle, TZ – transition zone, LM – lower mantle, D''-layer, OC – outer core, IC – inner core.

In particular, any reference model should also include the density and inelastic attenuation distributions in the Earth. Work by Montagner and Kennett (1996) provided these parameters which, although known less precisely than the seismic velocities, are needed because it makes the model suitable for use as a reference to compute synthetic seismograms (see 2.8) without requiring additional assumptions. Nevertheless, the primary use of AK135 (and IASP91) remains earthquake location and phase identification. The PREM model of Dziewonski and Anderson (1981), also shown for comparison in Fig. 2.53, forms the basis for many current studies on global Earth's structure using quantitative exploitation of seismic waveforms at longer periods. It is the objective of the 'Working Group on Reference Earth models' in the 'IASPEI Commission on Earth Structure and Geodynamics' to retrieve a new 1-D reference Earth model for many depth-depending parameters which is also in agreement with observations of the Earth's normal modes.

The IASPEI 1991 Seismological Tables (Ed. Kennett, 1991) are now out of print. The more recent global P- and S-wave velocity and density model AK135, and the related body wave travel-time tables and plots are available via <http://rses.anu.edu.au/seismology/ak135/intro.html> and can be downloaded or printed in postscript. Additionally, software for travel-time routines and for corrections of the ellipticity of the Earth can be obtained via <http://rses.anu.edu.au/seismology/ttsoft.html>.

2.8 Synthetic seismograms and waveform modeling

A good measure of the advancement made by a scientific discipline is its ability to predict the phenomena with which it is dealing. One of the goals of seismology, as stated already over a hundred years ago by Emil Wiechert, is to understand every wiggle on the seismogram. This requires, as sketched in Fig. 1.1 of Chapter 1, an understanding and quantitative modeling of the contributions made to the seismic record (the output) by the various subsystems of the complex information chain: the source effects (input), the propagation effects (medium), the influence of the seismograph (sensor) and of the data processing. It is possible nowadays to model each of these effects quite well mathematically and thus to develop procedures for calculating *synthetic seismograms*. While the modeling of the seismometer response (see Chapter 5) and of the source effects (see 3.5 and IS 3.1) have been outlined in more detail in this Manual, it is beyond the scope of a handbook on observatory practice to go into the depth of wave propagation theory. Here we have to refer to pertinent textbooks such as Aki and Richards (1980 and 2002), Kennett (1983, 2001, 2002), Lay and Wallace (1995), Dahlen and Tromp (1998) or, for some condensed introduction, to Shearer (1999). Below we will only sketch some of the underlying principles, refer to some fundamental approaches, discuss their potential and shortcomings and give a few examples of synthetic seismogram calculation and waveform modeling for near and teleseismic events.

Based on advanced theoretical algorithms and the availability of powerful and fast computers the calculation of synthetic seismograms for realistic Earth models is becoming more and more a standard procedure both in research and in advanced observatory routines. Such calculations, based on certain model assumptions and parameter sets for the source, propagation path and sensor/recorder are sometimes referred to as the solution of the *direct* or *forward problem* whereas the other way around, namely, to draw inferences from the observed data itself on the effects and relevant parameters of propagation path and source is termed the *inverse problem* (see Fig. 1.1). With the exception of a few specialized cases of direct analytical solutions to the inverse problem (such as using the Wiechert-Herglotz

2. Seismic Wave Propagation and Earth models

inversion (Eqs. (2.21) and (2.22)) for calculating the velocity-depth distribution of the medium from the observed travel-time curves), most inverse problems are solved by comparing synthetic data with observed ones. The model parameters are then changed successively in an iterative process until the differences between the observed and the synthetic data reach a minimum. The procedure of comparing synthetic and observed seismograms is known as *waveform modeling*. It can be used in routine practice for better identification of seismic phases and more reliable onset-time picking in case of noisy data. Additionally, more and more advanced seismological data centers, such as NEIC, now make use of waveform fitting for fast seismic moment tensor and other source parameter solutions, such as source depth (see 3.5.6.1).

The underlying mathematical tool for constructing synthetic seismograms is the *linear filter theory*. The seismogram is thus treated as the output of a sequence of linear filters, each accounting for relevant aspects of the seismic source, propagation path and sensor/recorder. Accordingly, the seismogram $u(t)$ can be written as the result of convolution of three basic filters, namely:

$$u(t) = s(t) * g(t) * i(t), \quad (2.35)$$

where $s(t)$ is the signal from the seismic source, $g(t)$ is the propagation filter, and $i(t)$ is the overall instrument response. These basic filters can in fact be broken down into various sub-filters, each accounting for specific effects of the source (such as source radiation directivity, source-time function), the propagation medium (such as structure and attenuation) or the instrument (such as sensor and recorder). This makes it possible to study in detail the effects of a specific parameter or process on the character of the seismogram, e.g., the effects of the shape and bandwidth of the seismograph response on the recording (see 4.2) or of the source depth, rupture orientation or time-history of the rupture process on the signal shape (see pp. 400-412 in Lay and Wallace, 1995). With respect to the propagation term in Eq. (2.35) it may be modelled on the basis of a full wave-theoretical approach, solving Eq. (2.5) for 1-D media consisting of stacks of homogeneous horizontal layers. The complete response of such series of layers may be described by matrixes of their reflection and transmission coefficients and a so-called *propagator algorithm* (Thomson, 1950 and Haskell, 1953) or by generalized reflection and transmission coefficients for the entire stack as in the reflectivity method by Fuchs and Müller (1971), Kennett (1983), Müller (1985). Another, ray theoretical approach (e.g., Červený et al., 1977; Červený, 2001) is possible when assuming that variations in the elastic parameters of the media are negligible over a wavelength and thus these gradient terms tend to zero at high frequencies. While pure ray tracing allows one only to model travel-times, the assumption of so-called "*Gaussian beams*", i.e., "ray tubes" with a Gaussian bell-shaped energy distribution, permits the modeling of both travel-times and amplitudes and thus to calculate complete synthetic seismograms also for non-1-D structures. While a decade ago limited computer power allowed one to model realistically only relatively long-period teleseismic records, it is now possible to compute complete short-period seismograms of up to about 10 Hz or even higher frequencies. Several program packages (e.g. Fuchs and Müller, 1971; Kind, 1978; Kennett, 1983; Müller 1985; Sandmeier, 1990; Wang, 1999) permit one to compute routinely for given source parameters and, based on 1-D Earth models, synthetic seismograms for both near field and teleseismic events.

Two examples of synthetic seismogram sections in reduced travel-time presentation are shown below. Fig. 2.54 shows records for the local/regional distance range between 50 and 350 km with P, S and surface waves in the frequency range between about 0.5 and 2 Hz. Fig. 2.55 compiles synthetic records for longitudinal and some converted phases with frequencies between about 0.1 and 0.3 Hz in the teleseismic distance range between 32° and 172°. The

earth-flattening approximation of Müller (1977) is used to transform the flat layered model into a spherical model. This approximation does not permit calculation of phases travelling close to the center of the Earth. The theoretical record sections are noise-free and have simpler waveforms than most real seismograms, owing to the assumption of a simple source function. Fig. 2.54 does not show signal-generated codas of scattered waves that are so typical for short-period records of local events.

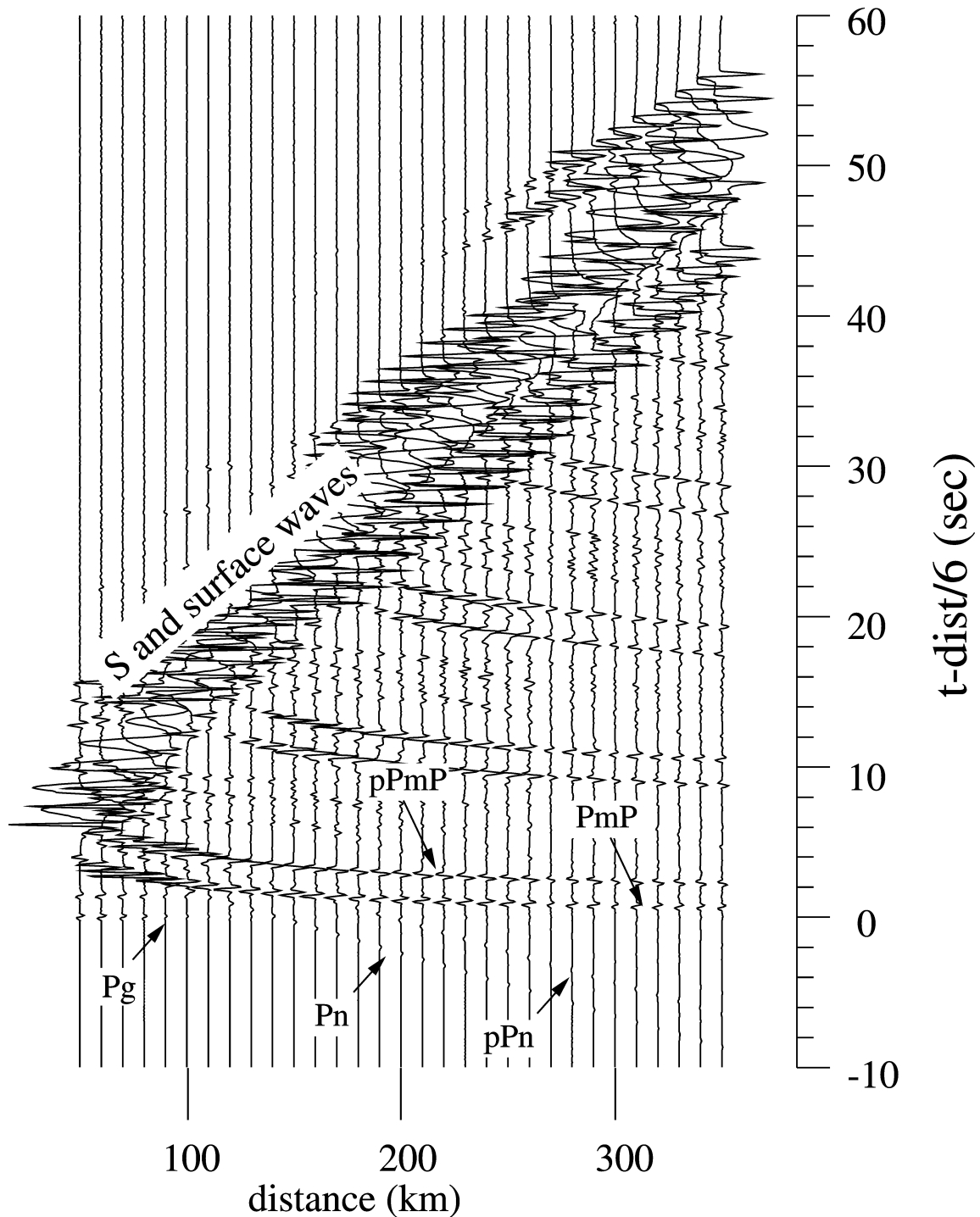


Fig. 2.54 Synthetic seismogram sections in the distance range 50-350 km, calculated for a hypothetical explosive source at 6 km depth in a homogenous single layer crustal model of 30 km thickness. For the calculation the program by Kind (1978) was used.

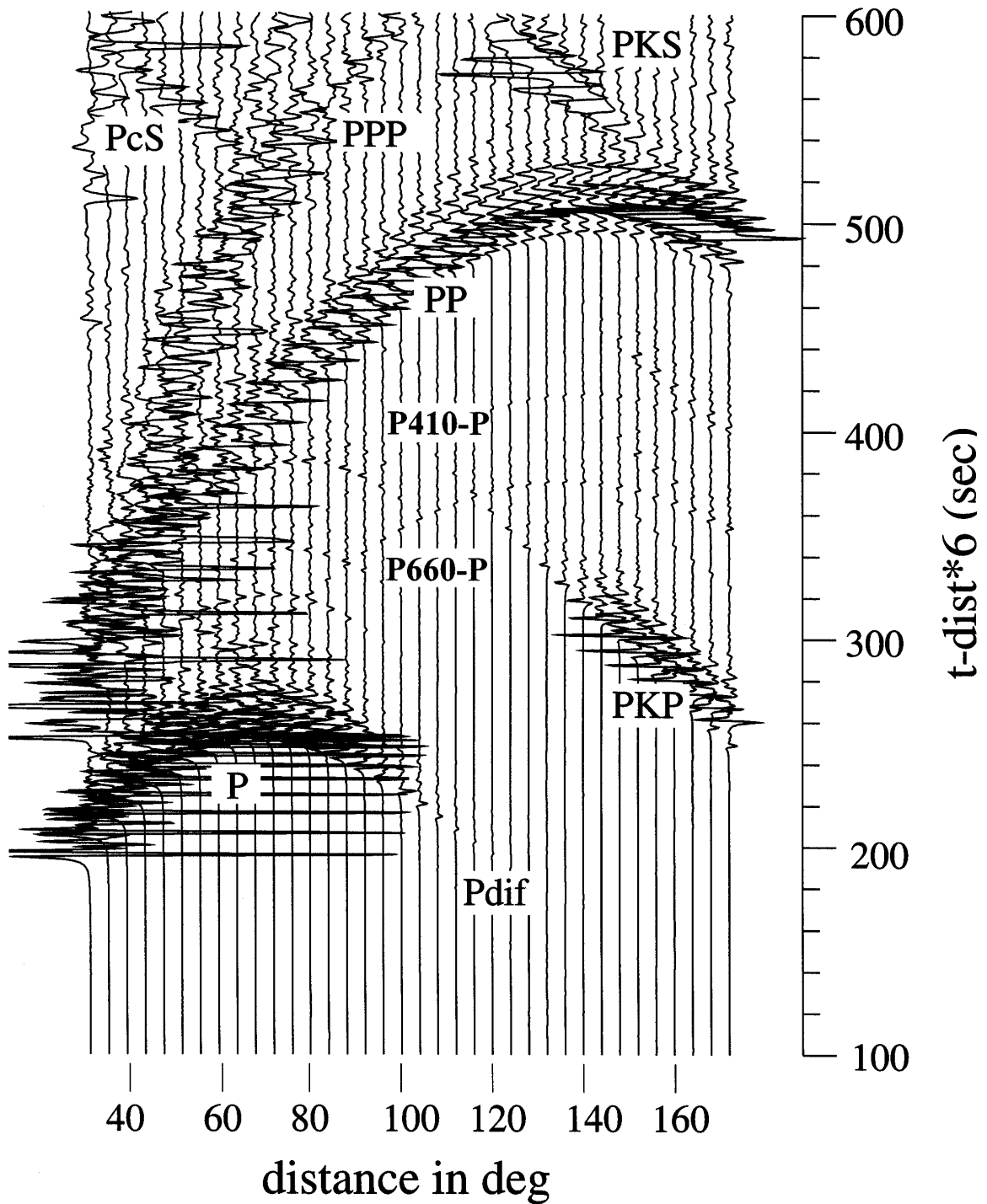


Fig. 2.55 Long-period synthetic seismic record section for the epicentral distance range 36°-166°, assuming a surface explosion and wave-propagation through the IASP91 model (Kennett and Engdahl, 1991). For the calculation the program by Kind (1978) was used.

2.8 Synthetic seismograms and waveform modeling

The synthetic record sections shown in Figs. 2.54 and 2.55 provide some general insights into basic features of seismograms in these two distance ranges such as:

- the overcritical Moho reflections PmP have the largest amplitudes in the P-wave part of near seismic recordings, with maximum amplitudes near the critical point around 70 km;
- Pg is the first arrival up to about 140 km (for a crustal thickness of 30 km) with amplitudes decaying rapidly with distance in this simple model example;
- since the travel-time curve of PmP approaches that of Pg asymptotically for larger distances, it may be difficult to separate Pg from Pm in real Earth for distances larger than about 100 km (see Fig. 2.40);
- Pn takes over as first arrival beyond about 140 km with generally rather weak amplitudes and higher apparent velocity;
- Sg (and in case of shallow events also surface waves, e.g., Rg) has (have) much larger amplitudes than the various types of direct, refracted or reflected P waves in records of local/regional events;
- the core shadow due to the strongly reduced P-wave velocities in the outer core is indeed clearly developed in epicentral distances between about 100° and 140°, however, long-period diffracted P waves may still be observable as relatively weak first arrivals up to 120° and more;
- PP is the first strong wave arrival in the core shadow range and, if Pdif or the weak inner-side reflections of P from the 660km or 410 km discontinuities (phase names P660-P and P440-P, respectively) are buried in the noise, PP can easily be misinterpreted as P-wave first arrival;
- the caustic of PKP around 145° produces very strong amplitudes comparable to those of P between about 50° to 70°;
- the branching of PKP into three travel-time branches beyond the caustic is well reproduced in the synthetic seismograms;
- converted core reflections (PcS) and converted core refractions (PKS) may be rather strong secondary later arrivals in the P-wave range between about 35°-55° and in the core-shadow range between about 120°-140°, respectively.

The following figures illustrate the potential of waveform modeling. Depth phases are not only very useful for determining the focal depth from teleseismic records, they are also frequently observed at regional distances and permit accurate depth determinations. Fig. 2.56 shows the ray paths for the phases Pn, pPn, sPn and sPP in a single layer crust from an event at depth h , as recorded in the distance range beyond 150 km, when Pn appears as the first arrival. Fig. 2.57 (left) shows the theoretical seismograms for all these phases at a distance of 210 km and as a function of source depth. It is easy to identify the depth phases. Fig. 2.57 (right) presents a compilation of the summation traces of all available vertical component records of the Gräfenberg array stations for the 1978 Swabian Jura (Germany) earthquake (September 3, 05:09 UT; $M_l = 6.0$) and for several of its aftershocks. All these events have been recorded at an epicentral distance of about 210 km. Depth phases sPn were observed in most records. From the correlation of sPn in neighboring traces it becomes obvious that the source depth migrated within 5 hours from the main shock at $h = 6.5$ km to a depth of only about 2-3 km for the aftershock at 10:03 UT.

2. Seismic Wave Propagation and Earth models

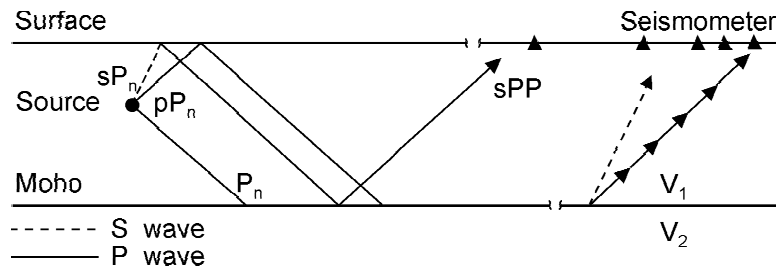


Fig. 2.56 Ray path of the sPn phases.

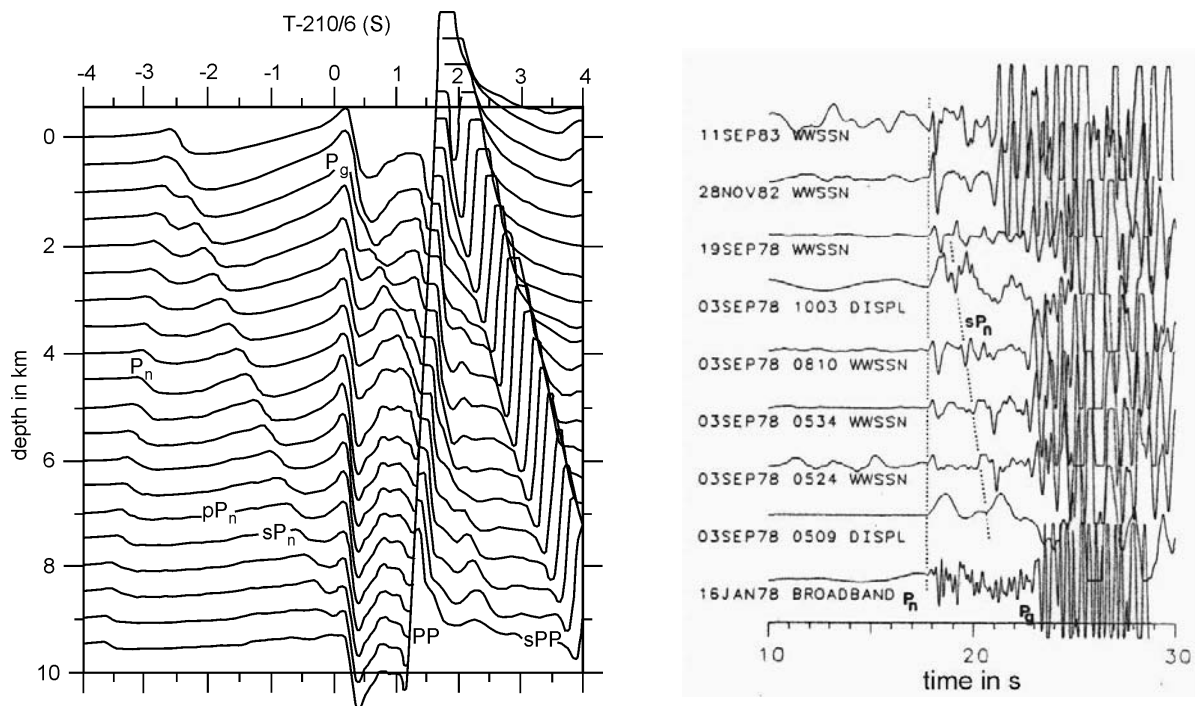


Fig. 2.57 **Left:** Theoretical seismograms in reduced travel-time presentation at 210 km epicentral distance as function of source depth for a single-layer crust (as in Fig. 2.56) of 30 km thickness. A clear depth phase sPn is recognizable between Pn and Pg; **right:** Gräfenberg records of Swabian Jura events in southern Germany. Epicentral distance is 210 km. Between the Pn and Pg arrival, a clear depth phase sPn can be observed. These observations indicate that after the main shock on September 3 at 05:09 the aftershocks migrated from 6.5 km depth to 2-3 km depth within 5 hours (from Kind, 1985).

Langston and HelMBERGER (1975) studied the influence of hypocenter depth h , type of source mechanism, source-time function and of stress drop on seismic waveforms. The superposition of P, pP and sP, which follow close one after another in the case of crustal earthquakes, make it difficult to separate these individual phases properly in more long-period teleseismic records and to pick the onset times of the depth phases reliably. However, because of the pronounced changes in the waveform of this P-wave group as a function of depth, one may be able to constrain also the source depth of distant earthquakes rather well by waveform modeling with an accuracy of about 5 km. On the other hand, one should be aware that there is a strong trade-off between source depth and the duration of the source-time function. A deeper source with source function of shorter duration may be similar to a shallower source

2.8 Synthetic seismograms and waveform modeling

with a longer source function. For simple sources, broadband data may help to overcome much of this trade-off. For complex source functions, however, these may trade-off with differences in source depth if only data from single stations are available. Using data from several stations instead could reduce this problem.

Generally, waveform modeling is much more powerful than first-motion focal mechanism determinations (see 3.4) in constraining fault orientation. Even with only a few stations and limited azimuthal coverage around the source superior results may be achieved. This is of particular importance for a fast determination of source parameters. Additionally, by comparing predicted and observed amplitudes of waveforms, the seismic moment can be determined rather reliably (see 3.5). Fig. 2.58 shows an example of waveform modeling in the teleseismic distance range for records of the 1989 Loma Prieta earthquake in different azimuth around the source. From the best fitting synthetics, the source-time function, fault strike ϕ , dip δ , rake λ and seismic moment M_0 were estimated. However, Kind and Basham (1987) could show that even with the broadband data from only one teleseismic station good estimates of fault depth, strike, dip and rake could be derived from waveform modeling.

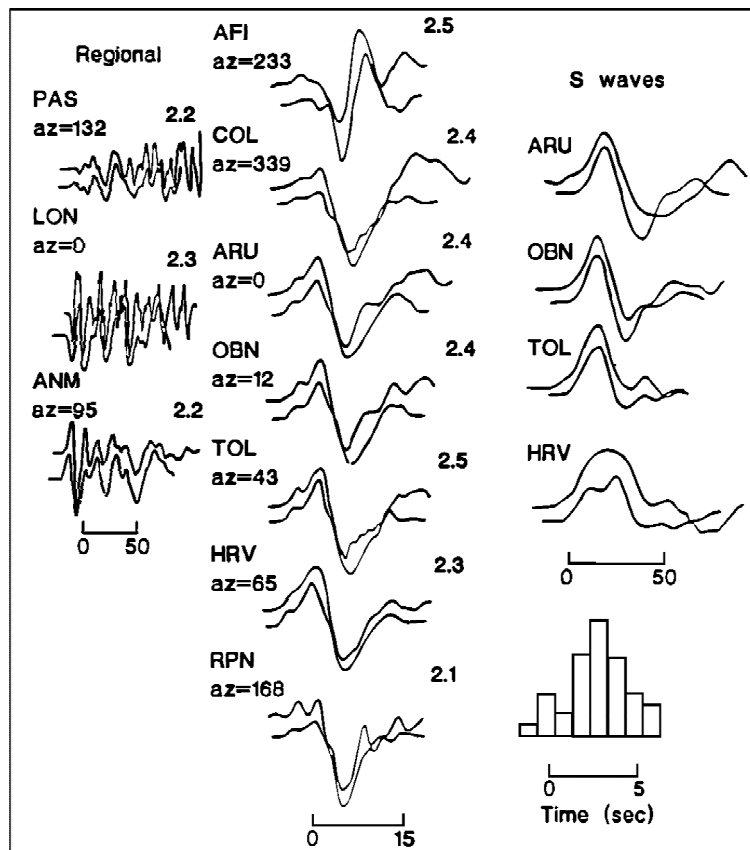


Fig. 2.58 Results of waveform modeling for the 1989 Loma Prieta earthquake. Depicted are the pairs of observed (top trace) and synthetic waveforms (bottom trace) for long-period Pn (left column), teleseismic P (middle column) and SH waves (right column). The time function used is shown at the lowermost right side. From the inversion of these data the following source parameters were determined: $\phi = 128^\circ \pm 3^\circ$, $\delta = 66^\circ \pm 4^\circ$, $\lambda = 133^\circ \pm 7^\circ$, and the moment $M_0 = 2.4 \times 10^{19}$ Nm (reproduced from Wallace et al., 1991, A broadband seismological investigation of the 1989 Loma Prieta, California, earthquake: Evidence for deep slow slip?, Bull. Seism. Soc. Am., Vol. 81, No. 5, Fig. 2, page 1627; 1991; © Seismological Society of America).

Acknowledgments

The authors thank P. Shearer, P. Malischewski and J. Schweitzer for careful proof-reading and many valuable suggestions. Thanks go also to M. Baumbach, B.L.N. Kennett, H. Neunhöfer, B. Schurr, J. Schweitzer and K. Wylegally for making some figures or related data for their production available.

Recommended overview readings (see References under Miscellaneous in Volume 2)

Aki and Richards (1980 and 2002)
Bullen and Bolt (1985)
Chapman (2002)
Kennett (2001 and 2002)
Lay and Wallace (1995)
Lognonne and Clevede (2002)
Sato et al. (2002)
Shearer (1999)

3

Seismic Sources and Source Parameters

Peter Bormann, Michael Baumbach, Günther Bock, Helmut Grosser,
George L. Choy and John Boatwright

3.1 Introduction to seismic sources and source parameters (P. Bormann)

3.1.1 Types and peculiarities of seismic source processes

Fig. 3.1 depicts the main kinds of sources which generate *seismic waves* (see Chapter 2). Seismic waves are oscillations due to elastic deformations which propagate through the Earth and can be recorded by *seismographic sensors* (see Chapter 5). The energy associated with these sources can have a tremendous range and, thus, can have a wide range of *intensities* (see Chapter 12) and *magnitudes* (see 3.2 below).

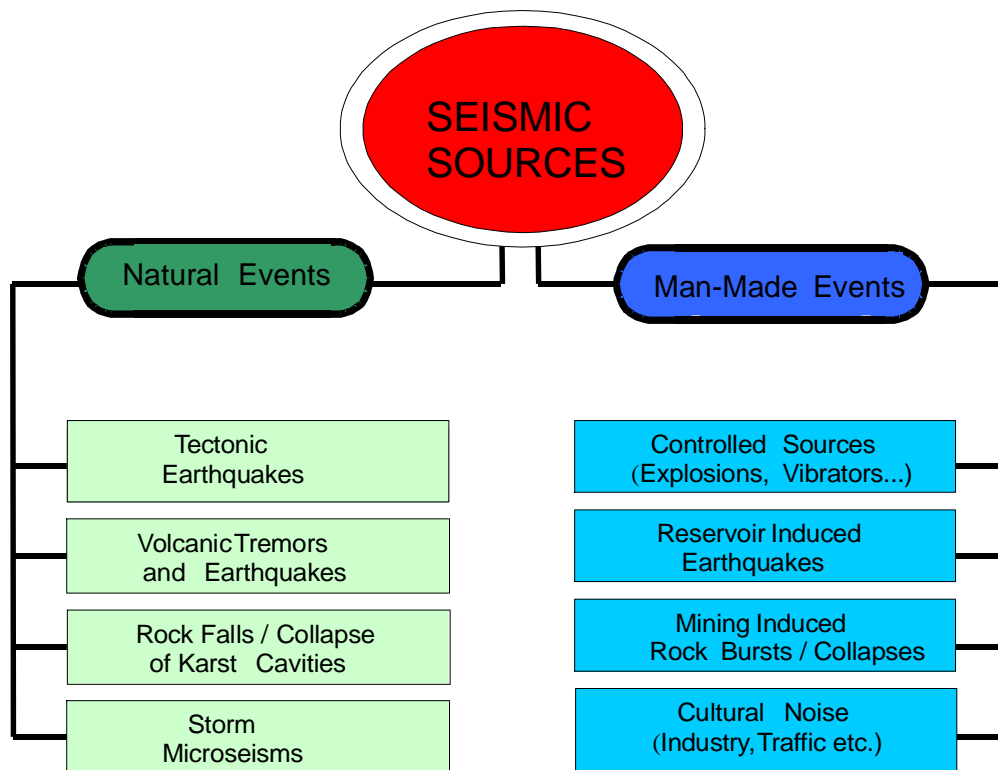


Fig. 3.1 Schematic classification of various kinds of events which generate seismic waves.

3. Seismic Sources and Source Parameters

3.1.1.1 Tectonic earthquakes

Tectonic earthquakes are caused when the brittle part of the Earth's crust is subjected to stress that exceeds its breaking strength. Sudden rupture will occur, mostly along pre-existing faults or sometimes along newly formed faults. Rocks on each side of the rupture "snap" into a new position. For very large earthquakes, the length of the ruptured zone may be as much as 1000 km and the slip along the fault can reach several meters.

Laboratory experiments show that homogeneous consolidated rocks under pressure and temperature conditions at the Earth's surface will fracture at a volume strain on the order of 10^{-2} - 10^{-3} (i.e., about 0.1 % to 1% volume change) depending upon their porosity. Rock strength is generally smaller under tension or shear than under compression. Shear strains on the order of about 10^{-4} or less may cause fracturing of solid brittle rock. Rock strength is further reduced if the rock is pre-fractured, which is usually the case in the crust. The strength of pre-fractured rock is much less than that of unbroken competent rock and is mainly controlled by the frictional resistance to motion of the two sides of the fault. Frictional resistance, which depends on the orientation of the faults with respect to the stress field and other conditions (see Scholz, 1990), can vary over a wide range. Accordingly, deformations on the order of only 10^{-5} to 10^{-7} , which correspond to bending of a lithospheric plate by about 0.1 mm to 1 cm over a distance of 1 km, may cause shear faulting along pre-existing zones of weakness. But the shear strength depends also on the composition and fabric (anisotropy) of rock, its temperature, the confining pressure, the rate of deformation, etc. as well as the total cumulative strain. More details on the physics of earthquake faulting and related geological and seismotectonic conditions in the real Earth can be found in Scholz (1990) and in section 3.1.3 on *Source representation*. Additional recommended overview articles on the rheology of the stratified lithosphere and its relation to crustal composition, age and heat flow were published by Meissner and Wever (1988), Ranalli and Murphy (1987) and Wever et al. (1987). They also explain the influence of these parameters on the thickness and maximum depth of the seismogenic zone in the crust, i.e., the zone within which brittle fracturing of the rocks is possible when the strains exceed the breaking strength or elastic limit of the rock (see Fig. 2.1).

The break-up of the lithosphere into plates due to deformation and stress loading is the main cause of tectonic earthquakes. The plates are driven, pushed and pulled by the slow motion of convection currents in the more plastic hot material of the mantle beneath the lithosphere. These relative motions are in the order of several cm per year. Fig. 3.2 shows the global pattern of earthquake belts and the major tectonic plates. There are also numerous small plates called sub- or micro-plates. Shallow earthquakes, within the upper part of the crust, take place mainly at plate boundaries but may also occur inside plates (interplate and intraplate earthquakes, respectively). Intermediate (down to about 300 km) and deep earthquakes (down to a maximum of 700 km depth) occur under ocean trenches and related subduction zones where the lithosphere plates are thrust or pulled down into the upper mantle. The major trenches are found around the Circum-Pacific earthquake and volcanic belt (see Fig. 3.2). However, intermediate and deep earthquakes may occur also in some other marine or continental collision zones (e.g., the Tyrrhenian and Aegean Sea or the Carpathians and Hindu Kush, respectively).

Most earthquakes occur along the main plate boundaries. These boundaries constitute either zones of extension (e.g., in the up-welling zones of the mid-oceanic ridges or intra-plate rifts), transcurrent shear zones (e.g., the San Andreas fault in the west coast of North America or the

3.1 Introduction to seismic sources and source parameters

North Anatolian fault in Turkey), or zones of plate collision (e.g., the Himalayan thrust front) or subduction (mostly along deep sea trenches). Accordingly, tectonic earthquakes may be associated with many different faulting types (strike-slip, normal, reverse, thrust faulting or mixed; see Figs. 3.32 and 3.33 in 3.4.2).

The largest strain rates are observed near active plate boundaries (about 10^{-8} to 3×10^{-10} per year). Strain rates are significantly less in active plate interiors (about 5×10^{-10} to 3×10^{-11} per year) or within stable continental platforms (about 5×10^{-11} to 10^{-12} per year) (personal communication by Giardini, 1994). Consequently, the critical cumulative strain for the pre-fractured/faulted seismogenic zone of lithosphere, which is on the order of about 10^{-6} to 10^{-7} , is reached roughly after some 100, 1000 to 10,000 or 10,000 to 100,000 years of loading, respectively. This agrees well with estimates of the mean return period of the largest possible events (seismic cycles) in different plate environments (Muir-Wood, 1993; Scholz, 1990).

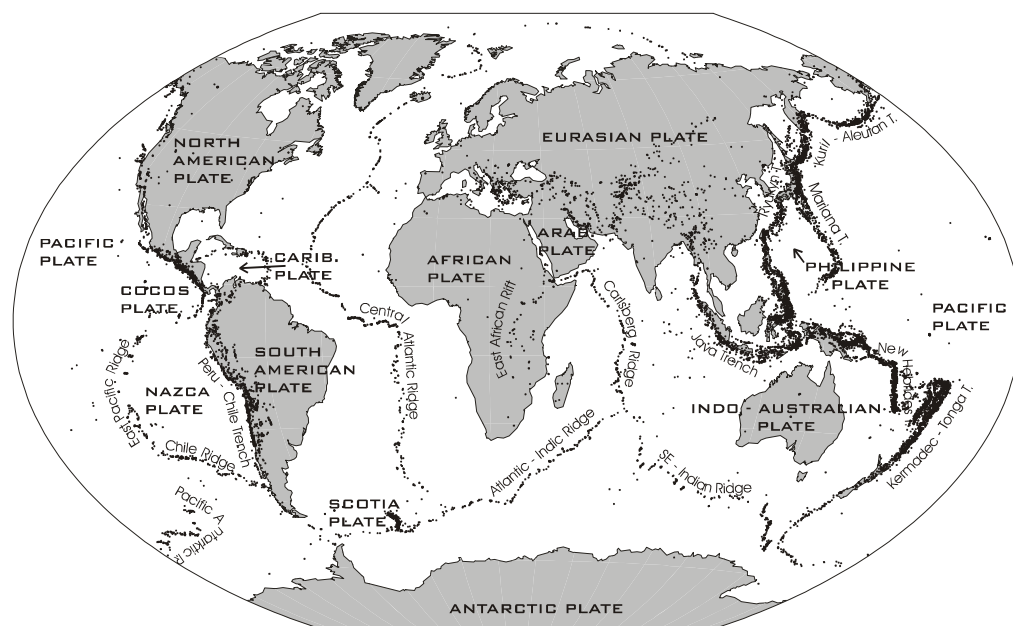


Fig. 3.2 Global distribution of earthquake epicenters according to the data catalog of the United States National Earthquake Information Center (NEIC), January 1977 to July 1997, and the related major lithosphere plates.

Although there are hundreds of thousands of weak tectonic earthquakes globally every year, most of them can only be recorded by sensitive nearby instruments. But in the long-term global statistical average about 100,000 earthquakes are strong enough ($M \geq 3$) to be potentially perceptible by humans in the near-source area. A few thousand are strong enough ($M \geq 5$) to cause slight damage and some 100 with magnitude $M > 6$ can cause heavy damage, if there are nearby settlements and built-up areas; while about 1 to 3 events every year (with $M \geq 8$) may result in wide-spread devastation and disaster. During the 20th century the 1995 Great Hanshin/Kobe earthquake caused the greatest economic loss (about 100 billion US\$), the 1976 Tangshan earthquake inflicted the most terrible human loss (about 243,000 people killed) while the Chile earthquake of 1960 released the largest amount of *seismic energy* E_S (see 3.1.2.2 below) of about $5 \cdot 10^{18}$ to 10^{19} Joule. The latter corresponds to about 25 to 100 years of the long-term annual average of global seismic energy release which is about $1 - 2 \times 10^{17}$ J (Lay and Wallace, 1995) and to about half a year of the total kinetic energy

3. Seismic Sources and Source Parameters

contained in the global lithosphere plate motion. The total *seismic moment* (see 3.1.2.3. below) of the Chile earthquake was about 3×10^{23} Nm. It ruptured about 800 - 1000 km of the subduction zone interface at the Peru-Chile trench in a width of about 200 km (Boore 1977; Scholz 1990). In summary: about 85 % of the total world-wide seismic moment release by earthquakes occurs in subduction zones and more than 95 % by shallow earthquakes along plate boundaries. The other 5 % are distributed between intraplate events and deep and intermediate focus earthquakes. The single 1960 Chile earthquake accounts for about 25 % of the total seismic moment release between 1904 and 1986.

It should be noted that most of the total energy release, E_T , is required to power the growth of the earthquake fracture and the production of heat. Only a small fraction of $E_T = E_S + E_f$ (with E_f - friction energy) goes into producing seismic waves. The seismic efficiency, i.e., the ratio of E_S/E_T , is perhaps only about 0.01 to 0.1. It depends both on the *stress drop* during the rupture as well as on the total stress in the source region (Spence, 1977; Scholz, 1990).

3.1.1.2 Volcanic earthquakes

Although the total energy released by the strongest historically known volcanic eruptions was even larger than E_T of the Chile earthquake, the seismic efficiency of volcanic eruptions is generally much smaller, due to their long duration. Nevertheless, in some cases, volcanic earthquakes may locally reach the shaking strength of destructive earthquakes (e.g., *magnitudes* of about 6; see 3.1.2.2). Most of the seismic oscillations produced in conjunction with sub-surface magma flows are of the tremor type, i.e., long-lasting and more or less monochromatic oscillations which come from a two- or three-phase (liquid- and/or gas-solid) source process which is not narrowly localized in space and time. They can not be analyzed in the traditional way of seismic recordings from tectonic earthquakes or explosions nor with traditional source parameters (see Chapter 13). Volcanic earthquakes contribute only an insignificant amount to the global seismic moment release (see Scholz 1990).

3.1.1.3 Explosions, implosions and other seismic events

Explosions are mostly anthropogenic, i.e., “man-made”, and controlled, i.e., with known location and source time. However, strong natural explosions in conjunction with volcanic eruptions or meteorite impacts, such as the Tunguska meteorite of 30 June 1908 in Siberia, may also occur. Explosions used in exploration seismology for the investigation of the crust have yields, Y , of a few kg to tons of TNT (Trinitrotoluol). This is sufficient to produce seismic waves which can be recorded from several km to hundreds of km distance. Underground nuclear explosions of kt up to Mt of equivalent TNT may be seismically recorded even world-wide (1 kt TNT = 4.2×10^{12} J). Nevertheless, even the strongest of all underground nuclear tests with an equivalent yield of about 5 Mt TNT produced body-waves of only magnitude $m_b \approx 7$. This corresponds to roughly 0.1% of the seismic energy released by the Chile earthquake of 1960. After 1974, underground tests with only $Y \leq 150$ kt were carried out. Only well contained underground chemical or nuclear explosions have a sufficiently good seismic coupling factor ϵ ($\epsilon \approx 10^{-2}$ to 10^{-3} , i.e., only 1 % to 0.1 % of the total released explosion energy is transformed into seismic energy). The coupling factor of explosions on the surface or in the atmosphere is much less ($\epsilon \approx 10^{-3}$ to 10^{-6} depending on the altitude).

Fig. 3.3 depicts schematically an idealized sub-surface explosion and tectonic earthquake (of pure strike-slip type) in a homogeneous medium.

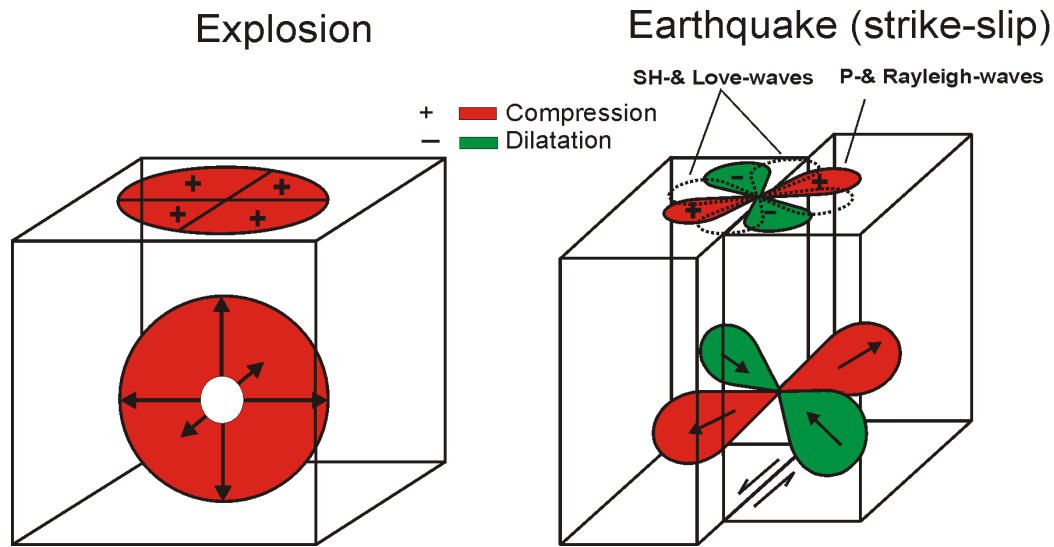


Fig. 3.3 Schematic sketches of an idealized underground explosion and of a strike-slip earthquake along a vertically dipping fault. The fault motion is "left-lateral", i.e., counter-clockwise. The arrows show the directions of compressional (outward, polarity +, red shaded) and dilatational (inward, polarity -, green shaded) motions. The patterns shown on the surface, termed amplitude or polarity patterns indicate the azimuthal variation of observed amplitudes or of the direction of first motions in seismic records, respectively. While point-like explosions in an isotropic medium should show no azimuth-dependent amplitudes and compressional first motions only, amplitudes and polarities vary for a tectonic earthquake. The dotted amplitude lobes in Fig. 3.3, right side, indicate qualitatively the different azimuth dependence of shear (S) waves as compared to longitudinal (P) waves (rotated by 45°) but their absolute values are much larger (about 5 times) than that of P waves.

It is obvious that the explosion produces a homogeneous outward directed compressional first motion in all directions while the tectonic earthquake produces first motions of different amplitude and polarity in different directions. These characteristics can be used to identify the type of source process (see 3.4) and to discriminate between explosions and tectonic earthquakes.

Compared to tectonic earthquakes, the *duration* of the source process of explosions and the *rise time* to the maximum level of displacement is much shorter (milliseconds as compared to seconds up to a few minutes) and more impulsive (Fig. 3.4). Accordingly, explosions of comparable body-wave magnitude excite more high-frequency oscillations (see Fig. 3.5). Rock falls may last for several minutes and cause seismic waves but generally with less distinct onsets and less separation of wave groups.

The collapse of karst caves, mining-induced rock bursts or collapses of mining galleries are generally of an *implosion* type. Accordingly, their first motion patterns should show dilatations in all azimuths if a secondary tectonic event has not been triggered by the collapse. The strongest events may reach magnitudes up to about $M = 5.5$ and be recorded world-wide (e.g., Bormann et al., 1992). *Reservoir induced* earthquakes have been frequently observed in

3. Seismic Sources and Source Parameters

conjunction with the impoundment of water or rapid water level changes behind large dams. Since these events are triggered along pre-existing and pre-stressed tectonic faults they show the typical polarity patterns of tectonic earthquakes (e.g., Fig. 3.3). The strongest events reported so far have reached magnitudes up to 6.5 (e.g., Koyna earthquake in 1967).

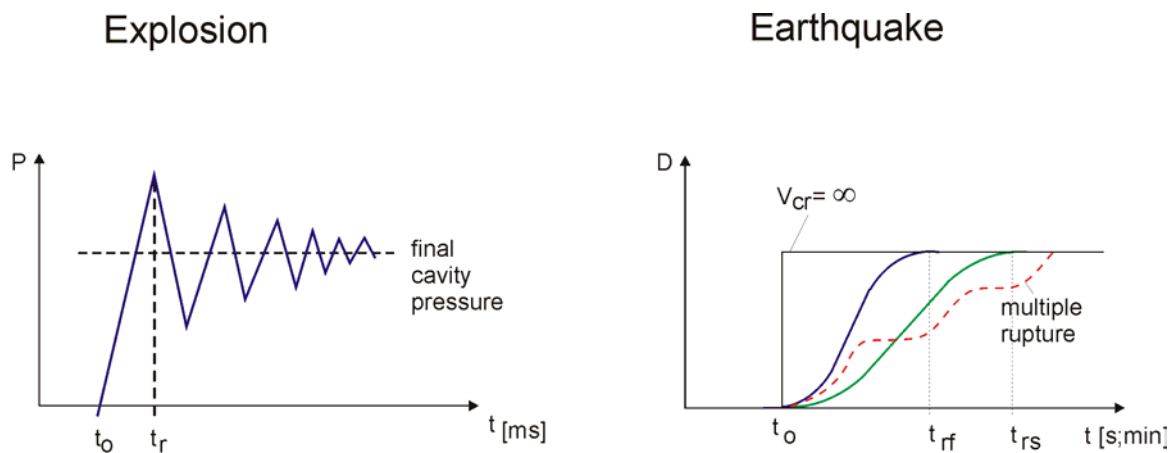


Fig. 3.4 Schematic diagrams of the different source functions of explosions (left) and earthquakes (right). P - pressure in the explosion cavity, D - fault displacement, t - time, t_0 - origin time of the event, t_r - rise time of P or D to its maximum values, t_{rf} - rise time of fast rupture, t_{rs} - rise time of slow rupture; the step function in the right diagram would correspond to an earthquake with infinite velocity of crack propagation v_{cr} . Current rupture models assume v_{cr} to be about 0.6 to 0.9 times of the velocity of shear-wave propagation, v_s .

3.1.1.4 Microseisms

Very different seismic signals are produced by storms over oceans or large water basins (seas, lakes, reservoirs) as well as by wind action on topography, vegetation or built-up surface cover. These seismic signals are called *microseisms*. Seismic signals due to human activities such as rotating or hammering machinery, traffic etc., are *cultural seismic noise*. Rushing waters or gas/steam (in rivers, water falls, dams, pipelines, geysers) may be additional sources of natural or anthropogenic *seismic noise*. They are not well localized in space nor fixed to a defined *origin time*. Accordingly, they produce more or less permanent on-going non-coherent interfering signals of more or less random amplitude fluctuations in a very wide frequency range of about 16 octaves (about 50 Hz to 1 mHz) which are often controlled in their intensity by the season (natural noise) or time of day (anthropogenic noise). Despite the large range of ambient noise displacement amplitudes (about 6 to 10 orders of magnitude; see Fig. 4.7) they are generally much smaller than those of earthquakes and not felt by people. The differences between signals from coherent seismic sources on the one hand and microseisms/seismic noise on the other hand are dealt with in more detail in Chapter 4.

3.1.2 Parameters which characterize size and strength of seismic sources

3.1.2.1 Macroseismic intensity

The effect of a seismic source may be characterized by its *macroseismic intensity*, **I**. Intensity describes the strength of shaking in terms of human perception, damage to buildings and other

structures, as well as changes in the surrounding environment. I depends on the distance from the source and the soil conditions and is mostly classified according to macroseismic scales of 12 degrees (e.g., Grünthal, 1998). From an analysis of the areal distribution of felt reports and damage one can estimate the epicentral intensity I_0 in the source area as well as the source depth, h . There exist empirical relationships between I_0 and other instrumentally determined measures of the earthquake size such as the *magnitude* and ground acceleration. For more details see Chapter 12.

3.1.2.2 Magnitude and seismic energy

Magnitude is a logarithmic measure of the size of an earthquake or explosion based on instrumental measurements. The magnitude concept was first proposed by Richter (1935). Magnitudes are derived from ground motion amplitudes and periods or from *signal duration* measured from instrumental records. There is no *a priori* scale limitation to magnitudes as exist for macroseismic intensity scales. Magnitudes are often misleadingly referred to in the press as "... according to the open-ended RICHTER scale...". In fact, the maximum size of tectonic earthquakes is limited by nature, i.e., by the maximum size of a brittle fracture in a finite and heterogeneous lithospheric plate. The largest moment magnitude, M_w , observed so far was that of the Chile earthquake in 1960 ($M_w \approx 9.5$; Kanamori 1977). On the other hand, the magnitude scale is open at the lower end. Nowadays, highly sensitive instrumentation close to the sources may record events with magnitude smaller than zero. According to Richter's original definition these magnitude values become negative. With empirical *energy-magnitude-relationships* the *seismic energy*, E_S radiated by the seismic source as seismic waves can be estimated. Common relationships are those given by Gutenberg and Richter (1954, 1956) between E_S and the surface-wave magnitude M_S and the body-wave magnitude m_B : $\log E_S = 11.8 + 1.5 M_S$ and $\log E_S = 5.8 + 2.4 m_B$, respectively (when E_S is given in erg; $1 \text{ erg} = 10^{-7} \text{ Joule}$). According to the first relationship, a change of M by two units corresponds to a change in E_S by a factor of 1000. Based on the analysis of digital recordings, there exist also direct procedures to estimate E_S (e.g., Purcaru and Berckhemer, 1978; Seidl and Berckhemer, 1982; Boatwright and Choy, 1986; Kanamori et al., 1993; Choy and Boatwright, 1995) and to define an "energy magnitude" M_e (see 3.3). Since most of the seismic energy is concentrated in the higher frequency part around the corner frequency of the spectrum, M_e is a more suitable measure of the earthquakes' potential for damage. In contrast, the seismic moment (see below) is related to the final static displacement after an earthquake and consequently, the moment magnitude, M_w , is more closely related to the tectonic effects of an earthquake.

3.1.2.3 Seismic source spectrum, seismic moment and size of the source area

Another quantitative measure of the size and strength of a seismic shear source is the scalar *seismic moment* M_0 (for its derivation see IS 3.1):

$$M_0 = \mu \bar{D} A \quad (3.1)$$

with μ - rigidity or shear modulus of the medium, \bar{D} - average final displacement after the rupture, A - the surface area of the rupture. M_0 is a measure of the irreversible inelastic deformation in the rupture area. This inelastic strain is described in (1) by the product $\bar{D} A$. On the basis of reasonable average assumptions about μ and the stress drop $\Delta\sigma$ (i.e., with

3. Seismic Sources and Source Parameters

$\Delta\sigma/\mu = \text{constant}$) Kanamori (1977) derives the relationship $E_S = 5 \times 10^{-5} M_0$ (in J). More information about the deformation in the source is described by the *seismic moment tensor* (IS 3.1). Its determination is now standard in the routine analysis of strong earthquakes by means of waveform inversion of long-period digital records (see 3.5).

In a homogeneous half-space M_0 can be determined from the spectra of seismic waves observed at the Earth's surface by using the relationship:

$$M_0 = 4\pi d \rho v_{p,s}^3 u_0 / R_{\theta,\phi}^{p,s} \quad (3.2)$$

with: d - hypocentral distance between the event and the seismic station; ρ - average density of the rock and $v_{p,s}$ - velocity of the P or S waves around the source; $R_{\theta,\phi}^{p,s}$ - a factor correcting the observed seismic amplitudes for the influence of the radiation pattern of the seismic source, which is different for P and S waves (see Figs. 3.3, 3.25 and 3.26), u_0 - the low-frequency amplitude level as derived from the seismic spectrum of P or S waves, corrected for the instrument response, wave attenuation and surface amplification. For details see EX 3.4.

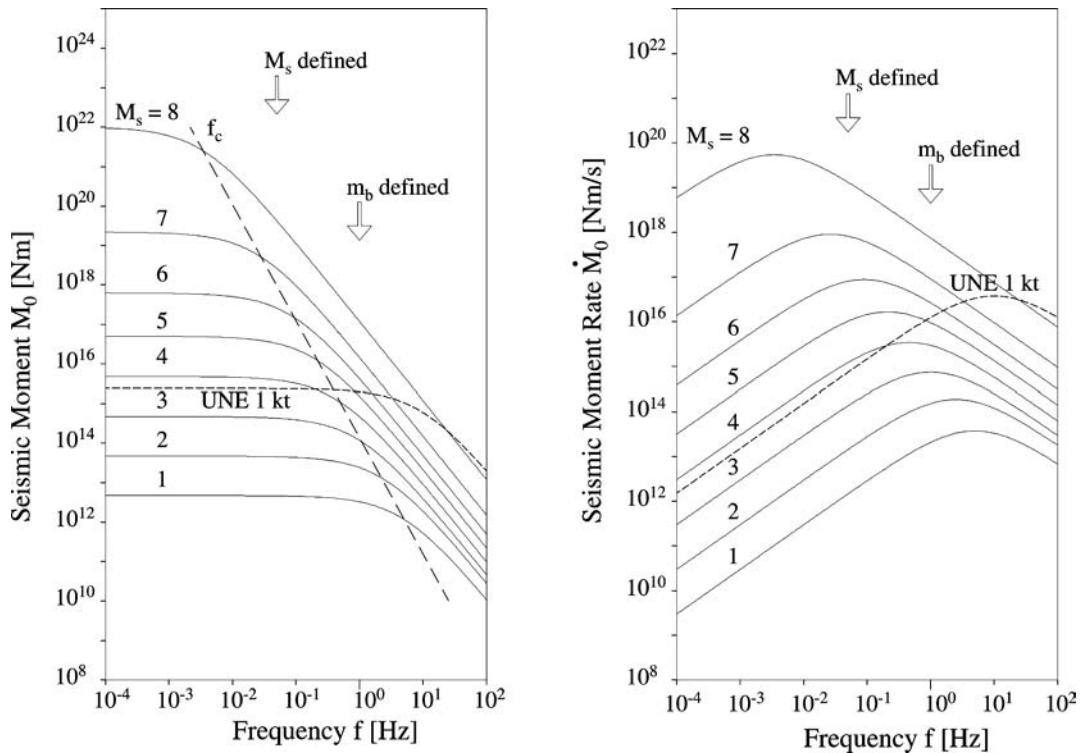


Fig. 3.5 "Source spectra" of ground displacement (left) and velocity (right) for a seismic shear source. "Source spectrum" means here the attenuation-corrected ground displacement $u(f)$ or ground velocity $\dot{u}(f)$ respectively, multiplied by the factor $4\pi d \rho v_{p,s}^3 / R_{\theta,\phi}^{p,s}$. The ordinates do not relate to the frequency-dependent spectra proper but rather to the low-frequency scalar seismic moments or moment rates that correspond to the depicted spectra. The broken line (long dashes) shows the increase of corner frequency f_c with decreasing seismic moment of the event, the short-dashed line gives the approximate "source spectrum" for a well contained underground nuclear explosion (UNE) of an equivalent yield of 1 kt TNT. Note the plateau ($u_0 = \text{const.}$) in the displacement spectrum towards low frequencies ($f < f_c$) and the high-frequency decay $\sim f^{-2}$ for frequencies $f > f_c$.

According to Aki (1967) a simple seismic shear source with linear rupture propagation shows in the far-field smooth displacement and velocity spectra. When corrected for the effects of geometrical spreading and attenuation we get "source spectra" similar to the generalized ones shown in Fig. 3.5. There the low-frequency values have been scaled to the scalar seismic moment M_0 (left) and moment rate dM_0/dt (right), respectively. The given magnitude values M_s correspond to a non-linear M_s -log M_0 relationship which is based on work published by Berckhemer (1962) and Purcaru and Berckhemer (1978). Note that the 1960 Chile earthquake had a seismic moment M_0 of about $3 \cdot 10^{23}$ Nm and a "saturated" magnitude (see discussion below) of $M_s = 8.5$. This corresponds well with Fig. 3.5. There exist also other, non-linear empirical M_s -log M_0 relationships (e.g., Geller, 1976).

The following general features are obvious from Fig. 3.5:

- "source spectra" are characterized by a "plateau" of constant displacement for frequencies smaller than the "corner frequency" f_c which is inversely proportional to the source dimension, i.e., $f_c \sim 1/L$;
- the decay of spectral displacement amplitude beyond $f > f_c$ is proportional to f^{-2} ;
- the plateau amplitude increases with seismic moment M_0 and magnitude, while at the same time f_c decreases proportional to M_0^{-3} (see Aki, 1967);
- the surface-wave magnitude, M_s , which is, according to the original definition by Gutenberg (1945), determined from displacement amplitudes with frequencies around 0.05 Hz, is not linearly scaled with M_0 for $M_s > 7$. While for larger events the amplitudes in the spectral plateau, i.e., for $f < f_c$, still increase proportional to M_0 there is no further (or only reduced) increase in spectral amplitudes at frequencies $f > f_c$. Accordingly, for $M_s > 7$ these magnitudes are systematically underestimated as compared to moment magnitudes M_w determined from M_0 (see 3.2.5.3). No $M_s > 8.5$ has ever been measured although moment magnitudes up to 9.5 to 10 have been observed. This effect is termed *magnitude saturation*;
- this saturation occurs much earlier for m_b , which is determined from amplitude measurements around 1 Hz. No $m_b > 7$ has been determined from narrowband short-period recordings, even for the largest events;
- since wave energy is proportional to the square of ground motion particle velocity, i.e., $E_S \sim (2\pi f u)^2 = (\omega u(\omega))^2$, its maximum occurs at f_c ;
- compared with an earthquake of the same seismic moment or magnitude, the corner frequency f_c of a well contained underground nuclear explosion (UNE) in hard rock is about ten times larger. Accordingly, an UNE produces relatively more high-frequency energy and thus has a larger E_S as compared with an earthquake of comparable magnitude m_b .

The main causes for this difference in E_S and high-frequency content between UNE and earthquakes are:

- the *duration* of the source process or *rise time*, t_r , to the final level of static displacement is much shorter for the case of explosions than for earthquakes (see Fig. 3.4);
- the shock-wave front of an explosion, which causes the deformation and fracturing of the surrounding rocks and thus the generation of seismic waves, propagates with approximately the P-wave velocity v_p while the velocity of crack propagation along

3. Seismic Sources and Source Parameters

- a shear fracture/fault is only about 0.5 to 0.9 of the S-wave velocity, i.e., about 0.3 to 0.5 times that of v_p ;
- the equivalent wave radiating surface area in the case of an explosion is a sphere $A = 4\pi r^2$ and not a plane $A = \pi r^2$. Accordingly, the equivalent source radius in the case of an explosion is smaller and thus the related corner frequency larger.

Note: Details of theoretical "source spectra" depend on the assumptions in the model of the rupture process, e.g., when the rupture is - more realistically - bilateral, the displacement spectrum of the source-time function is for $f \gg f_c$ proportional to f^{-2} , whereas this high-frequency decay is proportional to f^{-3} for an unilateral rupture. On the other hand, when the linear dimensions of the fault rupture differ in length and width then two corner frequencies will occur. Another factor is related to the details of the source time function. Whether the two or three corner frequencies are resolvable will depend on their separation. In the case of real spectra derived from data limited in both time and frequency domain, resolvability will depend on the signal-to-noise ratio. Normally, real data are too noisy to allow the discrimination between different types of rupture propagation and geometry.

The general shape of the seismic source spectra can be understood as follows: We know from optics that under a microscope no objects can be resolved which are smaller than the wavelength λ of the light with which it is observed. In this case the objects appear as a blurred point or dot. In order to resolve more details, electron microscopes are used which operate with much smaller wavelength. The same holds true in seismology. When observing a seismic source of radius r with wavelengths $\lambda \gg r$ at a great distance, one can not see any information about the details of the source process. One can only see the overall (integral) source process, i.e., one "sees" a point source. Accordingly, spectral amplitudes with these wavelengths are constant and form a spectral plateau (if the source duration can be neglected). On the other hand, wavelengths that have $\lambda \ll r$ can resolve internal details of the rupture process. In the case of an earthquake they correspond to smaller and smaller elements of the rupture processes or of the fault roughness (asperities and barriers). Therefore, their spectral amplitudes decay rapidly with higher frequencies. The corner frequency, f_c , marks a critical position in the spectrum which is obviously related to the size of the source. According to Brune (1970) and Madariaga (1976), both of whom modeled a circular fault, the corner frequency in the P- or S-wave spectrum, respectively, is $f_{c\ p/s} = c_m v_{p,s} / \pi r$. In contrast, assuming a rectangular fault, Haskell (1964) gives the relationship $f_{c\ p/s} = c_m v_{p,s} / (L \times W)^{1/2}$ with L the length and W the width of the fault. The values c_m are model dependent constants. Accordingly, the critical wavelength $\lambda_c = v / f_c$, beyond which the source can be realized as a point source only, is $\lambda_c = c_m \pi r$ or $\lambda_c = c_m (L \times W)^{1/2}$, respectively.

Thus, from both the source area (which, of course, is based on model assumptions of the shape of the rupture) and the seismic moment from seismic spectra, one can estimate from Eq. (3.1) the average total displacement, \bar{D} . Knowing \bar{D} , other parameters such as the *stress drop* in the source area can be inferred. Stress drop means the difference in acting stress at the source region before and after the earthquake. For more details see Figure 10 in IS 3.1 and for practical determination the exercise EX 3.4.

3.1.2.4 Orientation of the fault plane and the fault slip

Assuming that the earthquake rupture occurs along a planar fault surface the orientation of this plane in space can be described by three angles: *strike* ϕ (0° to 360° clockwise from

3.1 Introduction to seismic sources and source parameters

north), *dip* δ (0° to 90° against the horizontal) and the direction of slip on the fault by the *rake angle* λ (-180° to $+180^\circ$ against the horizontal). Fig. 3.30 and 3.31 in section 3.4.2 define these angles and show how to determine them from a stereographic (Wulff) net or equal area (Lambert-Schmidt) projection using observations of first motion polarities. It can be shown that a rupture along a plane perpendicular to the above mentioned fault plane with a slip vector perpendicular to the slip on the first plane causes an identical angular distribution of first motions. Therefore, on the basis of first motion analysis alone one can not decide which of the two planes is the true fault plane.

Note that in the case of a shear model the fault-plane solution (i.e., the information about the orientation of the fault plane and of the fault slip in space) forms, together with the information about the static seismic moment M_0 (see 3.1.2.3), the seismic moment tensor M_{ij} (see Equation (25) in IS 3.1). Its principal axes coincide with the direction of the pressure axis, P, and the tension axis, T, associated with fault-plane solutions. They should not be mistaken for the principal axes σ_1 , σ_2 and σ_3 (with $\sigma_1 > \sigma_2 > \sigma_3$) of the acting stress field in the Earth which is described by the stress tensor. Only in the case of a fresh crack in a homogeneous isotropic medium in a whole space with no pre-existing faults and vanishing internal friction is P in the direction of σ_1 while T has the opposite sense of σ_3 . P and T are perpendicular to each other and each one forms, under the above conditions, an angle of 45° with the two possible conjugate fault planes (*45°-hypothesis*) which are in this case perpendicular to each other (see Figs. 3.24 and 3.31 in 3.4). The orientation of P and T is also described by two angles each: the azimuth and the plunge. They can be determined by knowing the respective angles of the fault plane (see EX 3.2). If the above model assumptions hold true, one can, knowing the orientation of P and T in space, estimate the orientations of σ_1 and σ_3 . Most of the data used for compiling the global stress map (Zoback 1992) come from earthquake fault-plane solutions calculated under these assumptions.

In reality, the internal friction of rocks is not zero. For most rocks this results, according to Anderson's theory of faulting (1951), in the formation of conjugate pairs of faults which are oriented at about $\pm 30^\circ$ to σ_1 . In this case, the directions of P and T, as derived from fault-plane solutions, will not coincide with the principal stress directions. Near the surface of the Earth one of the principal stresses is almost always vertical. In the case of a horizontal compressive regime, the minimum stress σ_3 is vertical while σ_1 is horizontal. This results, when fresh faults are formed in unbroken rock, in thrust faults dipping about 30° and striking parallel or anti-parallel to σ_2 . In an extensional environment, σ_1 is vertical and the resulting dip of fresh normal faults is about 60° . When both σ_1 and σ_3 are horizontal, vertical strike-slip faults will develop, striking with $\pm 30^\circ$ to σ_1 . But most earthquakes are associated with the reactivation of pre-existing faults rather than occurring on fresh faults. Since the frictional strength of faults is generally less than that of unbroken rock, faults may be reactivated at angles between σ_1 and fault strike that are different from 30° . In a pre-faulted medium this tends to prevent failure on a new fault. Accordingly, there is no straightforward way to infer from the P and T directions determined for an individual earthquake the directions of the acting principal stress. On the other hand, it is possible to infer the regional stress based on the analysis of many earthquakes in that region since the possible suite of rupture mechanisms activated by a given stress regime is constrained. This method aims at finding an orientation for σ_1 and σ_3 which is consistent with as many as possible of the actually observed fault-plane solutions (e.g., Gephart and Forsyth, 1984; Reches, 1987; Rivera, 1989).

3.1.3 Mathematical source representation

It is beyond the scope of the NMSOP to dwell on the physical models of seismic sources and their mathematical representation. There exists quite a number of good text books on these issues (e.g., Aki and Richards, 1980 and 2002; Ben-Menahem and Singh, 1981; Das and Kostrov, 1988; Scholz, 1990; Lay and Wallace, 1995; Udías, 1999). However, most of these texts are rather elaborate and more research oriented. Therefore, we have appended a more concise introduction into the theory of source representation in IS 3.1. It outlines how the basic relationships used in practical applications of source parameter determinations have been derived, on what assumptions they are based and what their limitations are.

3.1.4 Detailed analysis of rupture kinematics and dynamics in space and time

Above we have considered earthquake models to derive suitable parameters for describing the size and behavior of faulting of earthquakes and to some extent also of explosions. In actuality, earthquakes do not rupture along perfect planes, nor are their rupture areas circular or rectangular. They do not occur in homogeneous rock, nor do they slip unilaterally or bilaterally. All these features are at best first order approximations or simplifications to the truth in order to make the problem mathematically and with limited data tractable. Real faults show jogs, steps, branching, splays, etc., both in their horizontal and vertical extent (Fig. 6). Such jogs and steps, depending on their severity, are impediments to smooth or ideal rupture, as are bumps or rough features along the contacting fault surfaces. More examples can be found in Scholz (1990). Since these features exist at all scales, which implies the self-similarity of fracture and faulting processes and their fractal nature, this will necessarily result in heterogeneous dynamic rupturing and finally also in rupture termination.

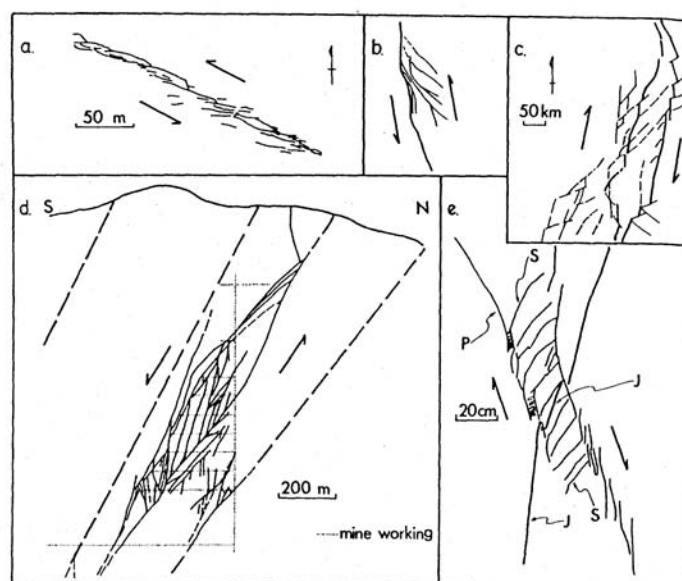


Fig. 3.6 Several fault zones mapped at different scales and viewed approximately normal to slip (from Scholz, *The mechanics of earthquakes and faulting*, 1990, Fig. 3.6, p. 106; with permission of Cambridge University Press).

3.1 Introduction to seismic sources and source parameters

As shown in Fig. 3.7 the complexity of the rupture process over time is a common feature of earthquakes, i.e., they often occur as multiple ruptures. This holds true for small earthquakes as well as very large earthquakes (Kikuchi and Ishida, 1993; Kikuchi and Fukao, 1987). And obviously, each event has its own "moment-rate fingerprint".

Only in a few lucky cases have dense strong-motion networks been fortuitously deployed in the very source region of a strong earthquake. Strong-motion records enable a detailed analysis of the rupture history in space and time using the moment-rate density. As an example, Fig. 3.8 depicts an inversion of data by Mendez and Anderson (1991) for the rupture process of the 1985 Michoacán, Mexico earthquake. Shown are snapshots, 4 s apart from each other, of the dip-slip velocity field. One recognizes two main clusters of maximum slip velocity being about 120 km and 30 s apart from each other. The related maximum cumulative displacement was more than 3 m in the first cluster and more than 4 m in the second cluster at about 55 km and 40 km depth, respectively. About 90 % of the total seismic moment was released within these two main clusters which had a rupture duration each of only 8 s while the total rupture lasted for about 56 s (Mendez and Anderson, 1991).

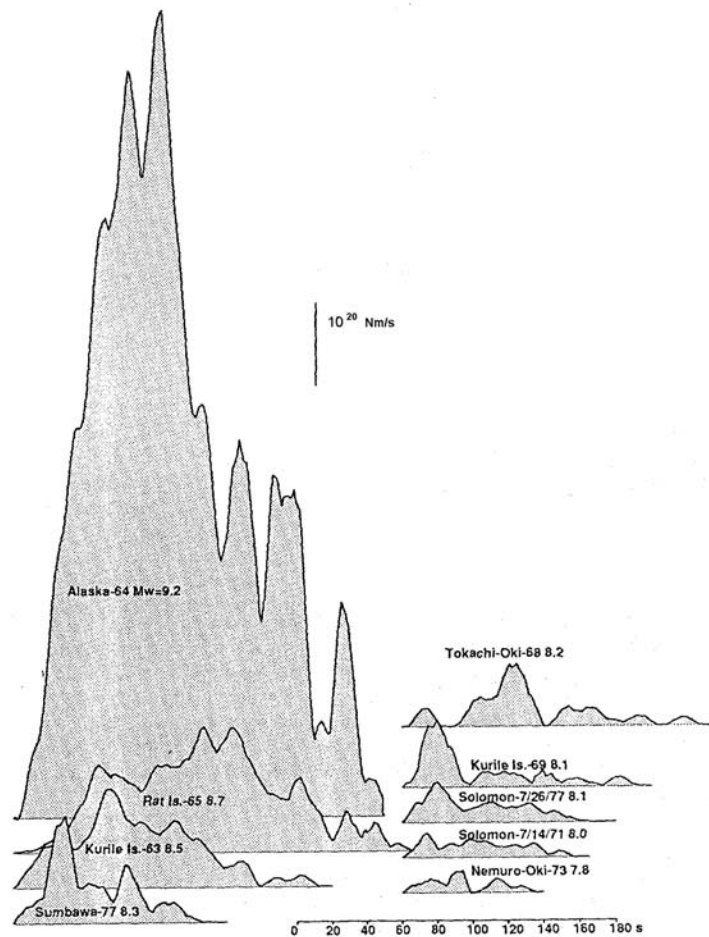


Fig. 3.7 Moment-rate (source time) functions for the largest earthquakes in the 1960s and 1970s as obtained by Kikuchi and Fukao (1987) (modified from Fig. 9 in Kikuchi and Ishida, Source retrieval for deep local earthquakes with broadband records, Bulletin Seismological Society of America, Vol. 83, No. 6, p. 1868, 1993, © Seismological Society of America.

3. Seismic Sources and Source Parameters

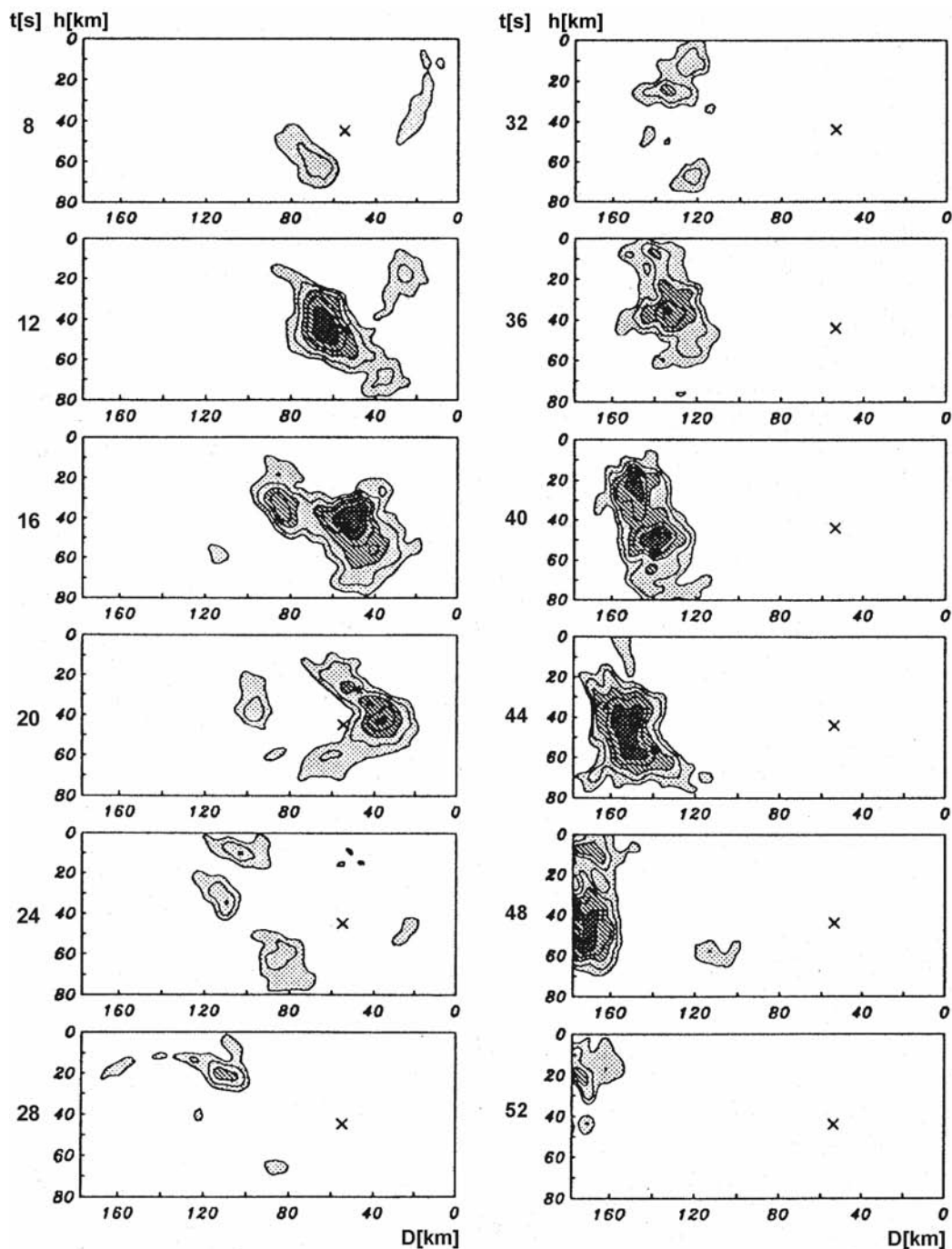


Fig. 3.8 Snapshots of the development in space and time of the inferred rupture process of the 1985 Michoacán, Mexico, earthquake. The contours represent dip-slip velocity at 5 cm/s interval, the cross denotes the NEIC hypocenter. Three consecutively darker shadings are used to depict areas with dip-slip velocities in the range: 12 to 22, 22 to 32, and greater than 32 cm/s, respectively. Abbreviations used: t - snapshot time after the origin time of the event, h - depth, D - distance in strike direction of the fault (redrawn and modified from Mendez and Anderson, The temporal and spatial evolution of the 19 September 1985 Michoacán earthquake as inferred from near-source ground-motion records, Bull. Seism. Soc. Am., Vol. 81, No. 3, Fig. 6, p. 857-858, 1991; © Seismological Society of America).

3.1 Introduction to seismic sources and source parameters

This rupturing of local asperities produces most of the high-frequency content of earthquakes. Accordingly, they contribute more to the cumulative seismic energy release than to the moment release. This is particularly important for engineering seismological assessments of expected earthquake effects. Damage to (predominately low-rise) structures is mainly due to frequencies > 2 Hz. They are grossly underestimated when analyzing strong earthquakes only on the basis of medium and long-period teleseismic records or when calculating model spectra assuming smooth rupturing along big faults of large earthquakes.

A detailed picture of the fracture process can be obtained only with dense strong-motion networks in source areas of potentially large earthquakes and by complementary field investigations and related modeling of the detailed rupture process in the case of clear surface expressions of the earthquake fault. Although this is beyond the scope of seismological observatory practice, observatory seismologists need to be aware of these problems and the limitations of their simplified standard procedures. Nevertheless, the value of these simplifications is that they allow a quick and rough first order analysis of the dominant type and orientation of earthquake faulting in a given region and their relationship to regional tectonics and stress field. The latter can also be inferred from other kinds of data such as overcoring experiments, geodetic data or field geological evidence. Their comparison with independent seismological data, which are mainly controlled by conditions at greater depth, may provide a deeper insight into the nature of the observed stress fields.

3.1.5 Summary and conclusions

The detailed understanding and quantification of the physical processes and geometry of seismic sources is one of the ultimate goals of seismology, be it in relation to understanding tectonics, improving assessment of seismic hazard or discriminating between natural and anthropogenic events. Earthquakes can be quantified with respect to various geometrical and physical parameters such as time and location of the (initial) rupture and orientation of the fault plane and slip, fault length, rupture area, amount of slip, magnitude, seismic moment, radiated energy, stress drop, duration and time-history (complexity) of faulting, particle velocity, acceleration of fault motion etc. It is impossible, to represent this complexity with just a single number or a few parameters.

There are different approaches to tackle the problem. One aims at the detailed analysis of a given event, both in the near- and far-field, analyzing waveforms and spectra of various kinds of seismic waves in a broad frequency range up to the static displacement field as well as looking into macroseismic data. Such a detailed and complex investigation requires a lot of time and effort. It is feasible only for selected important events. The second simplified approach describes the seismic source only by a limited number of parameters such as the origin time and (initial rupture) location, magnitude, intensity or acceleration of observed/measured ground shaking, and sometimes the fault-plane solution. These parameters can easily be obtained and have the advantage of rough but quick information being given to the public and concerned authorities. Furthermore, this approach provides standardized data for comprehensive earthquake catalogs which are fundamental for other kinds of research such as earthquake statistics and seismic hazard assessment. But we need to be aware that these simplified, often purely empirical parameters can not give a full description of the true nature and geometry, the time history nor the energy release of a seismic source. In the following we will describe only the most common procedures that can be used in routine seismological practice.

3.2 Magnitude of seismic events (P. Bormann)

3.2.1 History, scope and limitations of the magnitude concept

The concept of magnitude was introduced by Richter (1935) to provide an objective instrumental measure of the size of earthquakes. In contrast to seismic intensity I , which is based on the assessment and classification of shaking damage and human perceptions of shaking and thus depends on the distance from the source, the magnitude M uses instrumental measurements of the ground motion adjusted for epicentral distance and source depth. Standardized instrument characteristics were originally used to avoid instrumental effects on the magnitude estimates. Thus it was hoped that M could provide a single number to measure earthquake size which is related to the released seismic energy, E_S . However, as outlined in 3.1 above, such a simple empirical parameter is not directly related to any physical parameter of the source. Rather, the magnitude scale aims at providing a quickly determined simple " ... parameter which can be used for first-cut reconnaissance analysis of earthquake data (catalog) for various geophysical and engineering investigations; special precaution should be exercised in using the magnitude beyond the reconnaissance purpose" (Kanamori, 1983).

In the following we will use mainly the magnitude symbols, sometimes with slight modification, as they have historically developed and are still predominantly applied in common practice. However, as will be shown later, these "generic" magnitude symbols are often not explicit enough as to recognize on what type of records, components and phases these magnitudes are based. This requires more "specific" magnitude names where higher precision is required (see IS 3.2).

The original Richter magnitude, M_L or M_L , was based on maximum amplitudes measured in displacement-proportional records from the standardized short-period Wood-Anderson (WA) seismometer network in Southern California, which was suitable for the classification of local shocks in that region. In the following we will name it M_l (with "l" for "local") in order to avoid confusion with more specific names for magnitudes from surface waves where the phase symbol L stands for unspecified long-period surface waves. Gutenberg and Richter (1936) and Gutenberg (1945a, b and c) then extended the magnitude concept so as to be applicable to ground motion measurements from medium- and long-period seismographic recordings of both surface waves (M_s or M_s) and different types of body waves (m_B or m_B) in the teleseismic distance range. For the magnitude to be a better estimate of the seismic energy, they proposed to divide the measured displacement amplitudes by the associated periods to obtain ground velocities. Although they tried to scale the different magnitude scales together in order to match at certain magnitude values, it was realized that these scales are only imperfectly consistent with each other. Therefore, Gutenberg and Richter (1956a and b) provided correlation relations between various magnitude scales (see 3.2.7).

After the deployment of the World Wide Standardized Seismograph Network (WWSSN) in the 1960s it became customary to determine m_B on the basis of short-period narrow-band P-wave recordings only. This short-period body-wave magnitude is called m_b (or m_b). The introduction of m_b increased the inconsistency between the magnitude estimates from body and surface waves. The main reasons for this are:

- different magnitude scales use different periods and wave types which carry different information about the complex source process;

- the spectral amplitudes radiated from a seismic source increase linearly with its seismic moment for frequencies $f < f_c$ (f_c – corner frequency). This increase with moment, however, is reduced or completely saturated (zero) for $f > f_c$ (see Fig. 3.5). This changes the balance between high- and low-frequency content in the radiated source spectra as a function of event size;
- the maximum seismic energy is released around the corner frequency of the displacement spectrum because this relates to the maximum of the ground-velocity spectrum (see Fig. 3.5). Accordingly, M , which is supposed to be a measure of seismic energy released, strongly depends on the position of the corner frequency in the source spectrum with respect to the pass-band of the seismometer used for the magnitude determination;
- for a given level of long-period displacement amplitude, the corner frequency is controlled by the stress drop in the source. High stress drop results in the excitation of more high frequencies. Accordingly, seismic events with the same long-period magnitude estimates may have significantly different corner frequencies and thus ratios between short-period/long-period energy or m_b/M_s , respectively;
- seismographs with different transfer functions sample the ground motion in different frequency bands with different bandwidth. Therefore, no general agreement of the magnitudes determined on the basis of their records can be expected;
- additionally, band-pass recordings distort the recording amplitudes of transient seismic signals, the more so the narrower the bandwidth is. This can not be fully compensated by correcting only the frequency-dependent magnification of different seismographs based on their amplitude-frequency response. Although this is generally done in seismological practice in order to determine so-called "true ground motion" amplitudes for magnitude calculation, it is not fully correct. The reason is that the instrument magnification or amplitude-frequency response curves are valid only for steady-state oscillation conditions, i.e., after the decay of the seismograph's transient response to an input signal (see 4.2). True ground motion amplitudes can be determined only by taking into account the complex transfer function of the seismograph (see Chapter 5) and, in the case of short transient signals, by signal restitution in a very wide frequency band (Seidl, 1980; Seidl and Stammer, 1984; Seidl and Hellweg, 1988). Only recently a calibration function for very broadband P-wave recordings has been published (Nolet et al., 1998), however it has not yet been widely applied, tested and approved.

Efforts to unify or homogenize the results obtained by different methods of magnitude determination into a common measure of earthquake size or energy have generally been unsuccessful (e.g., Gutenberg and Richter, 1956a; Christoskov et al., 1985). Others, aware of the above mentioned reasons for systematic differences, have used these differences for better understanding the specifics of various seismic sources, e.g., for discriminating between tectonic earthquakes and underground nuclear explosions on the basis of the ratio m_b/M_s . Duda and Kaiser (1989) recommend the determination of different spectral magnitudes, based on measurements of the spectral amplitudes from one-octave bandpass- filtered digital broadband velocity records.

Another effort to provide a single measure of the earthquake size was made by Kanamori (1977). He developed the seismic moment magnitude M_w . It is tied to M_s but does not saturate for big events because it is based on seismic moment M_0 , which is made from the measurement of the (constant) level of low-frequency spectral displacement amplitudes for $f \ll f_c$. This level increases linearly with M_0 . According to Eq. (3.1), M_0 is proportional to the

3. Seismic Sources and Source Parameters

average static displacement and the area of the fault rupture and is so a good measure of the total deformation in the source region. On the other hand it is (see the above discussion on corner frequency and high-frequency content) neither a good measure of earthquake size in terms of seismic energy release nor a good measure of specifying seismic hazard since most earthquake damage is usually related to medium and low-rise structures with eigenfrequencies $f > 0.5$ Hz (i.e., lower than about 20 stories) and mainly caused by high-frequency strong ground motion. Consequently, there is no single number parameter available which could serve as a good estimate of earthquake "size" in all its different aspects. What is needed in practice are at least two parameters to characterize roughly both the size and related hazard of a seismic event, namely M_0 and f_c or M_w together with m_b or M_l (based on short-period measurements), respectively, or a comparison between the moment magnitude M_w and the energy magnitude M_e . The latter can today be determined from direct energy calculations based on the integration of digitally recorded waveforms of broadband velocity (Seidl and Berckhemer, 1982; Berckhemer and Lindenfeld, 1986; Boatwright and Choy 1986; Kanamori et al. 1993; Choy and Boatwright 1995) (see 3.3).

Despite their limitations, standard magnitude estimates have proved to be suitable also for getting, via empirical relationships, quick but rough estimates of other seismic source parameters such as the seismic moment M_0 , stress drop, amount of radiated seismic energy E_s , length L , radius r or area A of the fault rupture, as well as the intensity of ground shaking, I_0 , in the epicentral area and the probable extent of the area of felt shaking (see 3.6).

Magnitudes are also crucial for the quantitative classification and statistical treatment of seismic events aimed at assessing seismic activity and hazard, studying variations of seismic energy release in space and time, etc. Accordingly, they are also relevant in earthquake prediction research. All these studies have to be based on well-defined and stable long-term data. Therefore, magnitude values – notwithstanding the inherent systematic biases as discussed above - have to be determined over decades and even centuries by applying rigorously clear and well documented stable procedures and well calibrated instruments. Any changes in instrumentation, gain and filter characteristics have to be precisely documented in station log-books or event catalogs and data corrected accordingly. Otherwise, serious mistakes may result from research based on incompatible data.

Being aware now on the one hand of the inherent problems and limitations of the magnitude concept in general and specific magnitude estimates in particular and of the urgent need to strictly observe reproducible long-term standardized procedures of magnitude determination on the other hand we will review below the magnitude scales most commonly used in seismological practice. An older comprehensive review of the complex magnitude issue was given by Båth (1981), a more recent one by Duda (1989). Various special volumes with selected papers from symposia and workshops on the magnitude problem appeared in Tectonophysics (Vol. 93, No.3/4 (1983); Vol. 166, No. 1-3 (1989); Vol. 217, No. 3/4 (1993).

3.2.2. General assumptions and definition of magnitude

Magnitude scales are based on a few simple assumptions, e.g.:

- for a given source-receiver geometry "larger" events will produce wave arrivals of larger amplitudes at the seismic station. The logarithm of ground motion amplitudes A is used because of the enormous variability of earthquake displacements;

- magnitudes should be a measure of seismic energy released and thus be proportional to the velocity of ground motion, i.e., to A/T with T as the period of the considered wave;
- the decay of ground displacement amplitudes A with epicentral distance Δ and their dependence on source depth, h , i.e., the effects of geometric spreading and attenuation of the considered seismic waves is known at least empirically in a statistical sense. It can be compensated for by a calibration function $\sigma(\Delta, h)$. The latter is the log of the inverse of the reference amplitude $A_0(\Delta, h)$ of an event of zero magnitude, i.e., $\sigma(\Delta, h) = -\log A_0(\Delta, h)$;
- the maximum value $(A/T)_{\max}$ in a wave group for which $\sigma(\Delta, h)$ is known should provide the best and most stable estimate of the event magnitude;
- regionally variable preferred source directivity may be corrected by a regional source correction term, C_r , and the influence of local site effects on amplitudes (which depend on local crustal structure, near-surface rock type, soft soil cover and/or topography) may be accounted for by a station correction, C_s , which is not dependent on azimuth.

Accordingly, the general form of all magnitude scales based on measurements of ground displacement amplitudes A_d and periods T is:

$$M = \log(A_d/T)_{\max} + \sigma(\Delta, h) + C_r + C_s. \quad (3.3)$$

Note: Calibration functions used in common practice do not consider a frequency dependence of σ . This is a serious omission. Theoretical calculations by Duda and Janovskaya (1993) show that, e.g., the differences in $\sigma(\Delta, T)$ for P waves may become > 0.6 magnitude units for $T < 1$ s, however they are < 0.3 for $T > 4$ s and thus they are more or less negligible for magnitude determinations in the medium- and long-period range (see Fig. 3.15).

3.2.3 General rules and procedures for magnitude determination

Magnitudes can be determined on the basis of Eq. (1) by reading $(A/T)_{\max}$ for any body wave (e.g., P, S, Sg, PP) or surface waves (LQ or Lg, LR or Rg) for which calibration functions for either vertical (V) and/or horizontal (H) component records are available. If the period being measured is from a seismogram recorded by an instrument whose response is already proportional to velocity, then $(A_d/T)_{\max} = A_{v\max}/2\pi$, i.e., the measurement can be directly determined from the maximum trace amplitude of this wave or wave group with only a correction for the velocity magnification. In contrast, with displacement records one may not know with certainty where $(A/T)_{\max}$ is largest in the displacement waveform. Sometimes smaller amplitudes associated with smaller periods may yield larger $(A/T)_{\max}$. In the following we will always use A for A_d , if not otherwise explicitly specified.

In measuring A and T from seismograms for magnitude determinations and reporting them to national or international data centers, the following definitions and respective instructions given in the Manual of Seismological Observatory Practice (Willmore, 1979) as well as in the recommendations by the IASPEI Commission on Practice from its Canberra meeting in 1979 (slightly modified and amended below) should be observed:

- the trace amplitude B of a seismic signal on a record is defined as its largest peak (or trough) deflection from the base-line of the record trace;

3. Seismic Sources and Source Parameters

- for many phases, surface waves in particular, the recorded oscillations are more or less symmetrical about the zero line. B should then be measured either by direct measurement from the base-line or - preferably - by halving the peak-to-trough deflection (Figs. 3.9 a and c - e). For phases that are strongly asymmetrical (or clipped on one side) B should be measured as the maximum deflection from the base-line (Fig. 3.9 b);
- the corresponding period T is measured in seconds between those two neighboring peaks (or troughs) - or from (doubled!) trace crossings of the base-line - where the amplitude has been measured (Fig. 3.9);
- the trace amplitudes B measured on the record should be converted to ground displacement amplitudes A in nanometers (nm) or some other stated SI unit, using the A-T response (magnification) curve $\text{Mag}(T)$ of the given seismograph (see Fig.3.11); i.e., $A = B / \text{Mag}(T)$. (Note: In most computer programs for the analysis of digital seismograms, the measurement of period and amplitude is done automatically after marking the position on the record where A and T should be determined);
- amplitude and period measurements from the vertical component ($Z = V$) are most important. If horizontal components (N - north-south; E - east-west) are available, readings from both records should be made at the same time (and noted or reported separately) so that the amplitudes can be combined vectorially, i.e., $A_H = \sqrt{A_N^2 + A_E^2}$;
- when several instruments of different frequency response are available (or in the case of the analysis of digital broadband records filtered with different standard responses), A_{\max} and T measurements from each should be reported separately and the type of instrument used should be stated clearly (short-, medium- or long-period, broadband, Wood-Anderson, etc., or related abbreviations given for instrument classes with standardized response characteristics; see Fig. 3.11 and Tab. 3.1). For this, the classification given in the old Manual of Seismological Observatory Practice (Willmore 1979) may be used;
- broadband instruments are preferred for all measurements of amplitude and period;
- note that earthquakes are often complex multiple ruptures. Accordingly, the time, t_{\max} , at which a given seismic body wave phase has its maximum amplitude may be quite some time after its first onset. Accordingly, in the case of P and S waves the measurement should normally be taken within the first 25 s and 40-60 s, respectively, but in the case of very large earthquakes this interval may need to be extended to more than a minute. For subsequent earthquake studies it is also essential to report the time t_{\max} (see Fig. 3.9).
- for teleseismic ($\Delta > 20^\circ$) surface waves the procedures are basically the same as for body waves. However, $(A/T)_{\max}$ in the Airy phase of the dispersed surface wave train occurs much later and should normally be measured in the period range between 16 and 24 s although both shorter and longer periods may be associated with the maximum surface wave amplitudes (see 2.3).
- note that in displacement proportional records $(A/T)_{\max}$ may not coincide in time with B_{\max} . Sometimes, in dispersed surface wave records in particular, smaller amplitudes associated with significantly smaller periods may yield larger $(A/T)_{\max}$. In such cases also A_{\max} should be reported separately. In order to find $(A/T)_{\max}$ on horizontal component records it might be necessary to calculate A/T for several amplitudes on both record components and select the largest vectorially combined value. In records proportional to ground velocity, the maximum trace amplitude is always related to $(A/T)_{\max}$. Note, however, that as compared to the displacement amplitude A_d the velocity amplitude is $A_v = A_d 2\pi/T$.
- if mantle surface waves are observed, especially for large earthquakes (see 2.3), amplitudes and periods of the vertical and horizontal components with the periods in the neighborhood of 200 s should also be measured;

- on some types of short-period instruments (in particular analog) with insufficient resolutions it is not possible to measure the period of seismic waves recorded from nearby local events and thus to convert trace deflections properly to ground motion. In such cases magnitude scales should be used which depend on measurements of maximum trace amplitudes only;
- often local earthquakes will be clipped in (mostly analog) records of high-gain short-period seismographs with insufficient dynamic range. This makes amplitude readings impossible. In this case magnitude scales based on record duration (see 3.2.4.3) might be used instead, provided that they have been properly scaled with magnitudes based on amplitude measurements.

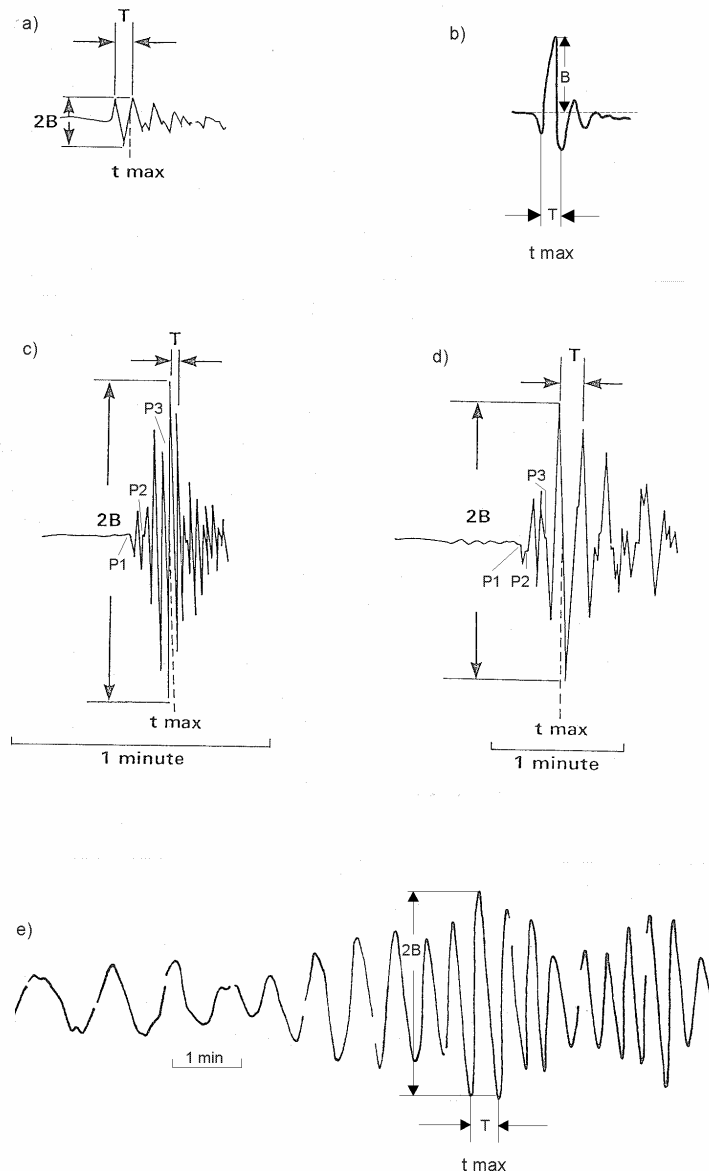


Fig. 3.9 Examples for measurements of trace amplitudes B and periods T in seismic records for magnitude determination: a) the case of a short wavelet with symmetric and b) with asymmetric deflections, c) and d) the case of a more complex P-wave group of longer duration (multiple rupture process) and e) the case of a dispersed surface wave train. Note: c) and d) are P-wave sections of the same event but recorded with different seismographs (classes A4 and C) while e) was recorded by a seismograph of class B3 (see Fig. 3.11).

3. Seismic Sources and Source Parameters

Tab. 3.1 Example from the former bulletin of station Moxa (MOX), Germany, based on the analysis of analog photographic recordings. The event occurred on January 1967. Note the clear annotation of the type of instruments used for the determination of onset times, amplitudes and periods. Multiple body wave onsets of distinctly different amplitudes, which are indicative of a multiple rupture process, have been separated. Seismographs of type A, B and C were nearly identical with the response characteristics A4, B3 and C in Fig. 3.11. V = Z - vertical component; H - vectorially combined horizontal components; Lm - maximum of the long-period surface wave train.

Day	Phase	Seismograph	h	m	s	Remarks
5.	+eiP1	A	00	24	15.5	<u>Mongolia</u> 48.08°N 102.80°E
	iP2	A		24	21.5	H = 00 14 40.4 h = normal MAG = 6.4
	iP3	A,C		24	28.0	$\Delta = 55.7^\circ$ Az = 309.6° (USCGS)
	Pmax	C		24	31	
	ePP2	C		26	27.5	PV1 A 1.2s 71.8nm MPV1(A)=5.6
	ePP3	C		26	34	PV2 A 1.8s 1120nm MPV2(A)=6.6
	eS2	C		32	04	PV3 A 1.6s 1575nm MPV3(A)=6.8
	i S3	C		32	11	PV3 C 8s 16.3 μ m MPV3(B)=7.1
	eiSS	B		35	56	SH3 C 18s 60 μ m MSH3(B)=7.3
	iSSS	B		36	44	LmV C 17s 610 μ m MLV(B)=7.8
	LmH	C		48.0		Note: P has a period of about 23s in the long-period seismograph of type B!

Note in Tab. 3.1 the distinct differences between individual magnitude determinations and the clear underestimation of short-period (type A) magnitudes. This early practice of specifying magnitude annotation has been officially recommended by the IASPEI Sub-Committee on Magnitudes in 1977 (see Willmore, 1979) but is not yet standard. However, current deliberations in IASPEI stress again the need for more specific magnitude measurements and reports to databases along these lines (see IS 3.2). When determining magnitudes according to more modern and physically based concepts such as radiated energy or seismic moment, special procedures have to be applied (see 3.3 and 3.5).

Global or regional data analysis centers calculate mean magnitudes on the basis of many A/T or M data reported by seismic stations from different distances and azimuths with respect to the source. This will more or less average out the influence of regional source and local station conditions. Therefore, A/T or M data reported by individual stations to such centers should not yet be corrected for C_r and C_s . These corrections can be determined best by network centers themselves when comparing the uncorrected data from many stations (e.g., Hutton and Boore, 1987). They may then use such corrections for reducing the scatter of individual readings and thus improve the average estimate.

When determining new calibration functions for the local magnitude M_l , station corrections have to be applied before the final data fit in order to reduce the influence of systematic biases on the data scatter. According to the procedure proposed by Richter (1958) these station corrections for M_l are sometimes determined independently for readings in the N-S and E-W components (e.g., Hutton and Boore, 1987). When calculating network magnitudes some centers prefer the median value of individual station reports of M_l as the best network estimate. As compared to the arithmetic mean it minimizes the influence of widely diverging individual station estimates due to outliers or wrong readings (Hutton and Jones, 1993).

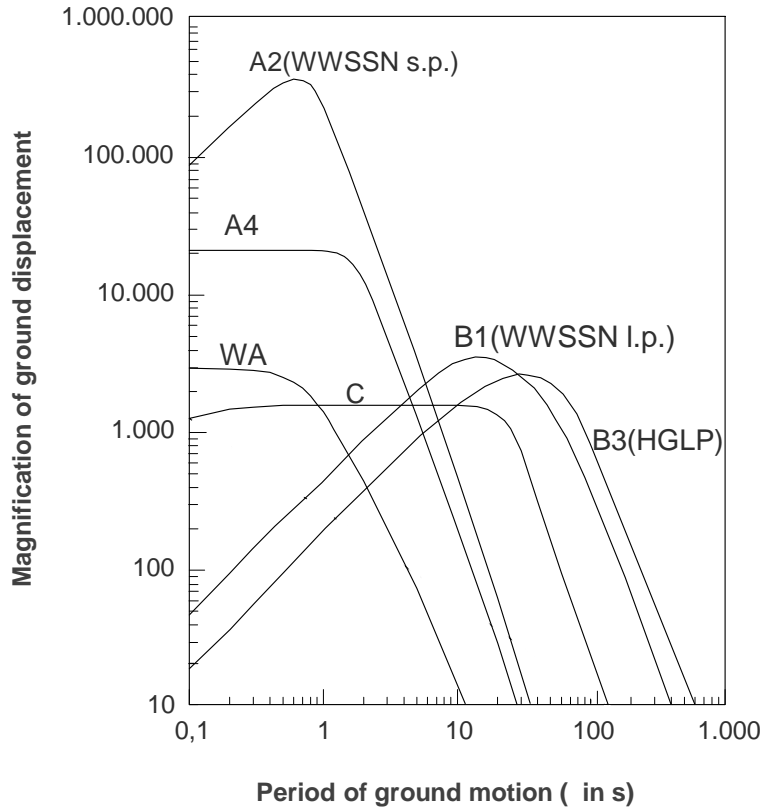


Fig. 3.11 Relative magnification curves for ground displacement for various classes of standardized analog recordings (partially redrawn from the old Manual of Seismological Observatory Practice, Willmore 1979 and amended). A4 and C are the magnification curves of the standard short-period and displacement broadband (Kirnos SKD) seismographs of the basic network of seismological stations in the former Soviet Union and Eastern European states while A2 and B1 are the standard characteristics for short- and long-period recordings at stations of the World Wide Standardized Seismograph Network (WWSSN) which was set up by the United States Geological Survey (USGS) in the 1960s and 1970s. The other magnification curves are: WA - Wood-Anderson torsion seismometer (see below), which was instrumental in the definition of the magnitude scale; HGLP - High Gain Long Period system.

In the following we will outline the origin, general features, formulae and specific differences of various magnitude scales currently in use. We will highlight which of these scales are at present accepted as world-wide standards and will also spell out related problems which still require consideration, clarifying discussion, recommendations or decisions by the IASPEI Commission on Seismological Observation and Interpretation. Data tables and diagrams on calibration functions used in actual magnitude determinations are given in Datasheet 3.1.

3.2.4 Magnitude scales for local events

The large variability of velocity and attenuation structure of the crust does in fact not permit the development of a unique, internationally standardized calibration function for local events. However, the original definition of magnitude by Richter (1935) did lead to the development of the local magnitude scale M_L (originally ML) for California. M_L scales for

3. Seismic Sources and Source Parameters

other areas are usually scaled to Richter's definition and also the procedure of measurement is more or less standardized.

3.2.4.1 The original Richter magnitude scale M_l

Following a recommendation by Wadati, Richter (1935) plotted the logarithm of maximum trace amplitudes, A_{\max} , measured from standard Wood-Anderson (WA) horizontal component torsion seismometer records as a function of epicentral distance Δ . The **WA seismometers** had the following parameters: natural period $T_S = 0.8$ s, damping factor $D_S = 0.8$, maximum **magnification** $V_{\max} = 2800$. Richter found that $\log A_{\max}$ decreased with distance along more or less parallel curves for earthquakes of different size. This led him to propose the following definition for the magnitude as a quantitative measure of earthquake size (Richter 1935, p. 7):
" The magnitude of any shock is taken as the logarithm of the maximum trace amplitude, expressed in microns, with which the standard short-period torsion seismometer ... would register that shock at an epicentral distance of 100 km".

Note 1: Uhrhammer and Collins (1990) found out that the magnification of 2800 of WA seismometers had been calculated on the basis of wrong assumptions on the suspension geometry. **A more correct value** (also in Fig. 3.11) is **2080 ± 60** (see also Uhrhammer et al., 1996). Accordingly, magnitude estimates based on synthesized WA records or amplification corrected amplitude readings assuming a WA magnification of 2800 systematically underestimate the size of the event by 0.13 magnitude units!

This local magnitude was later given the symbol M_l (Gutenberg and Richter, 1956b). In the following we use M_l (l = local). In order to calculate M_l also for other epicentral distances, Δ , between 30 and 600 km, Richter (1935) provided attenuation corrections. They were later complemented by attenuation corrections for $\Delta < 30$ km assuming a focal depth h of 18 km (Gutenberg and Richter, 1942; Hutton and Boore, 1987). Accordingly, one gets

$$M_l = \log A_{\max} - \log A_0 \quad (3.4)$$

with A_{\max} in mm of measured zero-to-peak trace amplitude in a Wood-Anderson seismogram. The respective corrections or calibration values $-\log A_0$ were published in tabulated form by Richter (1958) (see Table 1 in DS 3.1).

Note 2: In contrast to the general magnitude formula (3.3), Eq. (3.4) considers only the maximum displacement amplitudes but not their periods. Reason: WA instruments are short-period and their traditional analog recorders had a limited paper speed. Proper reading of the period of high-frequency waves from local events was rather difficult. It was assumed, therefore, that the maximum amplitude phase (which in the case of local events generally corresponds to S_g , L_g or R_g) always had roughly the same dominant period. Also, $-\log A_0$ does not consider the above discussed depth dependence of $\sigma(\Delta, h)$ since seismicity in southern California was believed to be always shallow (mostly less than 15 km). Eq. (3.4) also does not give regional or station correction terms since such correction terms were already taken into account when determining $-\log A_0$ for southern California.

Note 3: Richter's attenuation corrections are valid for southern California only. Their shape and level may be different in other regions of the world with different velocity and attenuation structure, crustal age and composition, heat-flow conditions and source depth. Accordingly, when determining M_l calibration functions for other regions, the amplitude attenuation law

has to be determined first and then this curve has to be scaled to the original definition of MI at 100 km epicentral distance (or even better at closer distance; see problem 1 below). Examples for other regional MI calibration functions are shown in Fig. 3.12).

Note 4: The smallest events recorded in local microearthquake studies have negative values of MI while the largest MI is about 7, i.e., the MI scale also suffers *saturation* (see Fig. 3.18). Despite these limitations, MI estimates of earthquake size are relevant for earthquake engineers and risk assessment since they are closely related to earthquake damage. The main reason is that many structures have natural periods close to that of the WA seismometer (0.8s) or are within the range of its pass-band (about 0.1 - 1 s).

A review of the development and use of the Richter scale for determining earthquake source parameters is given by Boore (1989).

Problems:

- 1) According to Hutton and Boore (1987) the *distance corrections developed by Richter for local earthquakes ($\Delta < 30$ km) are incorrect*. This leads to magnitude estimates from nearby stations that are smaller than those from more distant stations. Bakun and Joyner (1984) came to the same conclusion for weak events recorded in Central California at distances of less than 30 km.
- 2) In 3.2.3 it was said that, as a general rule, in the case of horizontal component recordings, A_{Hmax} is the maximum vector sum amplitude measured at t_{max} in both the N and E component. Deviating from this, Richter (1958) says: "*... In using ...both horizontal components it is correct to determine magnitude independently from each and to take the mean of the two determinations. This method is preferable to combining the components vectorially, for the maximum motion need not represent the same wave on the two seismograms, and it even may occur at different times.*" In most investigations aimed at deriving local MI scales $A_{Hmax} = (A_N + A_E)/2$ has been used instead to calculate MI although this is not fully identical with $MI = (MI_N + MI_E)/2$ and might give differences in magnitude of up to about 0.1 units.
- 3) The Richter MI from arithmetically averaged horizontal component amplitude readings will be smaller by at least 0.15 magnitude units as compared to MI from A_{Hmax} vector sum! In the case of significantly different amplitudes A_{Nmax} and A_{Emax} this difference might reach even several tenths of magnitude units. However, the method of combining vectorially the N and E component amplitudes, as generally practiced in other procedures for magnitude determination from horizontal component recordings, is hardly used for MI because of reasons of continuity in earthquake catalogs, even though it would be easy nowadays with digital data.

3.2.4.2 Other MI scales based on amplitude measurements

The problem of vector summing of amplitudes in horizontal component records or of arithmetic averaging of independent MI determinations in N and E components can be avoided by using A_{Vmax} from vertical component recordings instead, provided that the respective $-\log A_0$ curves are properly scaled to the original definition of Richter for $\Delta = 100$ km. Several new formulas for MI determinations based on readings of A_{Vmax} have been proposed for other regions (see Tab. 2 in DS 3.1). They mostly use Lg waves, sometimes well beyond the distance of 600 km for which $-\log A_0$ was defined by Richter (1958). Alsaker et

3. Seismic Sources and Source Parameters

al. (1991) and Greenhalgh and Singh (1986) showed that $A_{Z_{max}}$ is ≈ 1 to 1.2 times $A_{H_{max}} = 0.5 (A_{N_{max}} + A_{E_{max}})$ and thus yields practically the same magnitudes.

Since Richter's $\sigma(\Delta) = -\log A_0$ for southern California might not be correct for other regions, local calibration functions have been determined for other seismotectonic regions. Those for continental shield areas revealed significantly lower body-wave attenuation when compared with southern California. Despite scaling $-\log A_0(\Delta)$ for other regions to the value given by Richter for $\Delta = 100$ km, deviations from Richter's calibration function may become larger than one magnitude unit at several 100 km distances. Fig. 3.12 shows examples of MI scaling relations for other regions. Although cut in this figure for epicentral distances $\Delta > 600$ km some of the curves shown are defined for much larger distances (see Table 2 in DS 3.1).

Problem:

Hutton and Boore (1987) proposed that local magnitude scales be defined in the future such that $M_l = 3$ correspond to 10 mm of motion on a Wood-Anderson instrument at 17 km hypocentral distance rather than 1 mm of motion at 100 km. While being consistent with the original definition of magnitude in southern California this definition will allow more meaningful comparison of earthquakes in regions having very different wave attenuation within the first 100 km. This proposal has already been taken into consideration when developing a local magnitude scale for Tanzania, East Africa (Langston et al., 1998) and should be considered by IASPEI for assuring standardized procedures in the further development of local and regional M_l scales.

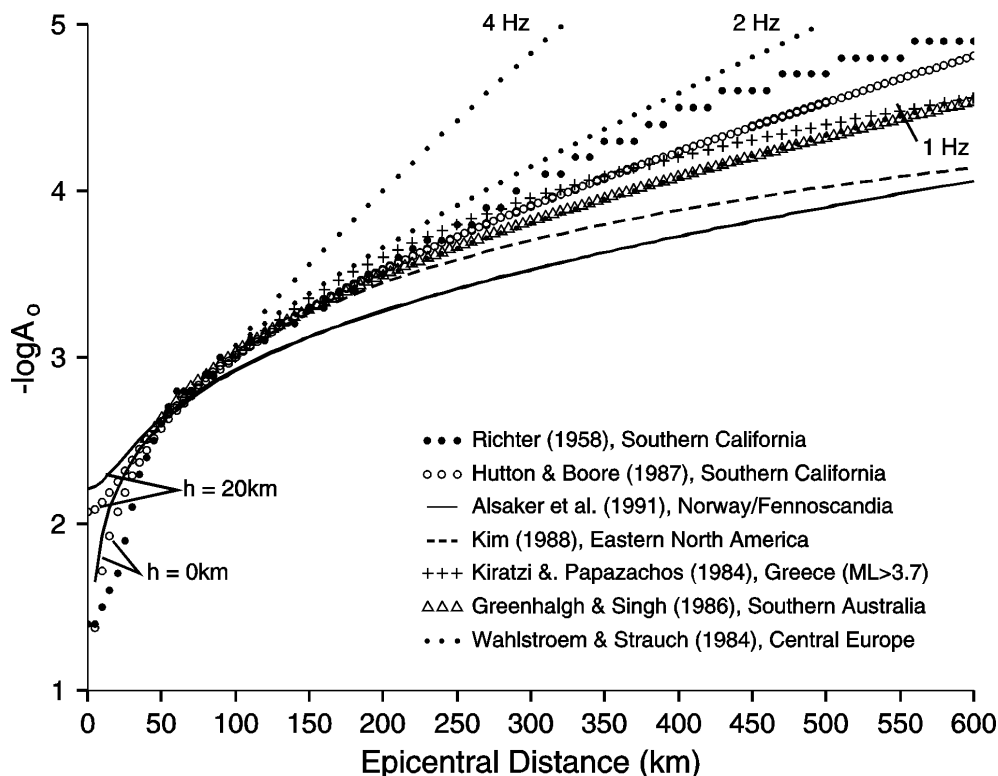


Fig. 3.12 Calibration functions for M_l determination for different regions. Note that the one for Central Europe is frequency dependent. The related M_l relationships and references are given in Table 2 of DS 3.1.

Some of the calibration functions shown in Fig. 3.12 for Lg waves extend in fact far beyond 600 km, e.g., that for Norway up to 1500 km distance. At this distance $-\log A_0$ differs by 1.7 magnitude units from the extrapolated calibration curve for southern California!

Note 1: Station corrections in some of these studies varied between -0.6 to $+0.3$ magnitude units (Bakun and Joyner, 1984; Greenhalgh and Singh, 1986; Hutton and Jones, 1993) and correlated broadly with regional geology. This points to the urgent need to determine both calibration functions and station corrections for MI on a regional basis.

Note 2: Since sources in other regions may be significantly deeper than in southern California, either $\sigma(\Delta, h)$ should be determined or at least the epicentral distance Δ should be replaced in the magnitude formulas by the "slant" or hypocentral distance $R = \sqrt{(\Delta^2 + h^2)}$. The latter is common practice now.

Procedures are currently available to synthesize precisely the response characteristic of Wood-Anderson seismographs from digital broadband recordings (e.g., Plešinger et al., 1996; see also 11.3.2). Therefore, WA seismographs are no longer required for carrying out MI determinations. Savage and Anderson (1995) and Uhrhammer, et al. (1996) demonstrated the ability to determine an unbiased measure of local magnitude from synthetic WA seismograms. Thus, a seamless catalog of MI could be maintained at Berkeley, California. In a first approximation (although not identical!) this can also be achieved by converting record amplitudes from another seismograph with a displacement frequency response $\text{Mag}(T_i)$ into respective WA trace amplitudes by multiplying them with the ratio $\text{Mag}_{\text{WA}}(T_i)/\text{Mag}(T_i)$ for the given period of A_{max} .

Sufficient time resolution of today's high-frequency digital records is likewise no longer a problem. There have been efforts to develop frequency-dependent calibration functions matched to the Richter scale at 100 km distance (e.g., Wahlström and Strauch, 1984; see Fig. 3.12) but this again breaks with the required continuity of procedures and complicates the calibration relationship for MI.

The increasing availability of strong-motion records and their advantage of not being clipped even by very strong nearby events have led to the development of (partially) frequency-dependent MI^{SM} scales for strong-motion data (Lee et al., 1990; Hatzidimitriou et al., 1993). The technique to calculate synthetic Wood-Anderson seismograph output from strong-motion accelerograms was first introduced by Kanamori and Jennings (1978).

3.2.4.3 Duration magnitude Md

Analog paper or film recordings have a very limited dynamic range of only about 40 dB and analog tape recordings of about 60 dB. For many years widely used digital recorders with 12 or 16 bit A-D converters enabled amplitude recordings with about 66 or 90 dB, respectively. Nevertheless, even these records were often clipped for strong local seismic events. This made magnitude determinations based on measurements of A_{max} impossible. Therefore, alternative magnitude scales such as Md were developed. They are based on the signal duration of an event. Nowadays with 24 bit A-D converters and ≈ 140 dB usable dynamic range, clipping is no longer a pressing problem. It is rare that an event is not considered for analysis.

3. Seismic Sources and Source Parameters

In the case of local seismic events the total signal duration, d , is primarily controlled by the length of the coda which follows the Sg onset. A theoretical description of the coda envelopes as an exponentially decaying function with time was presented by Herrmann (1975). He proposed a duration magnitude formula of the general form:

$$M_d = a_0 + a_1 \log d + a_2 \Delta \quad (3.5)$$

Different procedures have been proposed for determining signal or coda duration such as:

- duration from the P-wave onset to the end of the coda, i.e., where the signal disappears in the seismic noise of equal frequency;
- duration from the P-wave onset to that time when the coda amplitudes have decayed to a certain threshold level, given in terms of average signal-to-noise ratio or of absolute signal amplitudes or signal level;
- total elapsed time = coda threshold time minus origin time of the event.

An early formula for the determination of local magnitudes based on signal duration was developed for earthquakes in Kii Peninsula in Central Japan by Tsumura (1967) and scaled to the magnitudes M_{JMA} reported by the Japanese Meteorological Agency:

$$M_d = 2.85 \log (F - P) + 0.0014 \Delta - 2.53 \quad \text{for } 3 < M_{JMA} < 5 \quad (3.6)$$

with P as the onset time of the P wave and F as the end of the event record (i.e., where the signal has dropped down to be just above the noise level), $F - P$ in s and Δ in km.

Another duration magnitude equation of the same structure has been defined by Lee et al. (1972) for the Northern California Seismic Network (NCSN). The event duration, d (in s), is measured from the onset of the P wave to the point on the seismogram where the coda amplitude has diminished to 1 cm on the Develocorder film viewer screen with its 20 times magnification. With Δ in km these authors give:

$$M_d = 2.00 \log d + 0.0035 \Delta - 0.87 \quad \text{for } 0.5 < M_l < 5. \quad (3.7)$$

The location program HYPO71 (Lee and Lahr, 1975) employs Eq. (3.7) to compute duration magnitudes, called FMAG. But it was found that Eq. (3.7) yields seriously underestimated magnitudes of events $M_l > 3.5$. Therefore, several new duration magnitude formulae have been developed for the NCSN, all scaled to M_l . One of the latest versions by Eaton (1992) uses short-period vertical-component records, a normalization of instrument sensitivity, different distant correction terms for $\Delta < 40$ km, $40 \text{ km} \leq \Delta \leq 350$ km and $\Delta > 350$ km, as well as a depth correction for $h > 10$ km.

According to Aki and Chouet (1975) coda waves from local earthquakes are commonly interpreted as back-scattered waves from numerous heterogeneities uniformly distributed in the crust. Therefore, for a given local earthquake at epicentral distances shorter than 100 km the total duration of a seismogram is therefore almost independent of distance and azimuth and of structural details of the direct wave path from source to station. Also the shape of coda envelopes, which decay exponentially with time, remains practically unchanged. The dominating factor controlling the amplitude level of the coda envelope and signal duration is the earthquake size. This allows development of duration magnitude scales without a distance term, i.e.:

$$M_d = a_0 + a_1 \log d \quad (3.8)$$

Thus, quick magnitude estimates from local events are feasible even without knowing the exact distance of the stations to the source.

Note: Crustal structure, scattering and attenuation conditions vary from region to region. No general formulas can therefore be given. They must to be determined locally for any given station or network and be properly scaled to the best available amplitude-based MI scale. In addition, the resulting specific equation will depend on the chosen definition for d , the local noise conditions and the sensor sensitivity at the considered seismic station(s) of a network.

3.2.5 Common teleseismic magnitude scales

Wave propagation in deeper parts of the Earth is more regular than in the crust and can be described sufficiently well by 1-D velocity and attenuation models. This permits derivation of globally applicable teleseismic magnitude scales. Fig. 3.13 shows smoothed A - Δ relationships for short-period P and PKP waves as well as for long-period surface waves for teleseismic distances, normalized to a magnitude of 4.

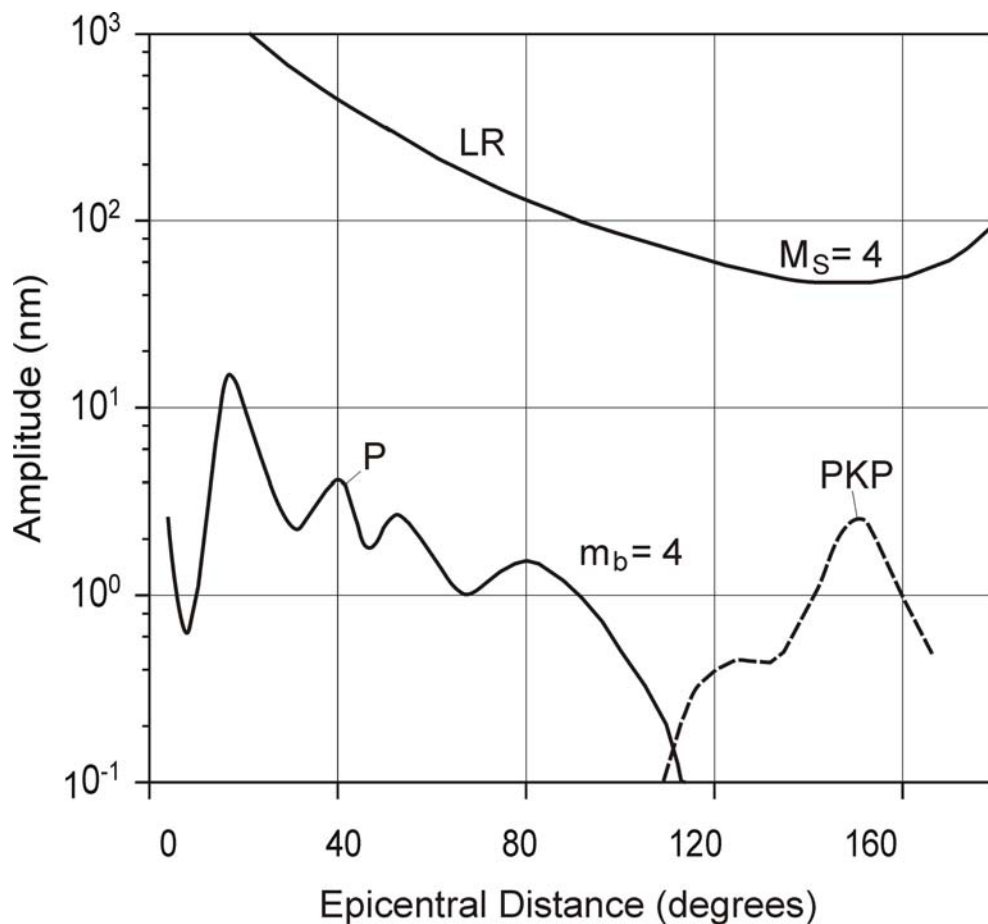


Fig. 3.13 Approximate smoothed amplitude-distance functions for P and PKP body waves (at about 1 Hz) and of long-period Rayleigh surface waves (LR, Airy phase, $T \approx 20$ s) for an event of magnitude 4.

3. Seismic Sources and Source Parameters

From Fig. 3.13 the following general conclusions can be drawn:

- surface waves and body waves have a different geometric spreading and attenuation. While the former propagate in two dimension only, the latter spread three-dimensionally. Accordingly, for shallow seismic events of the same magnitude, surface waves have generally larger amplitudes than body waves;
- surface wave amplitudes change smoothly with distance. They generally decay up to about 140° and increase again beyond about 150° - 160° . The latter is due to the increased geometric focusing towards the antipode of the spherical Earth's surface which then overwhelms the amplitude decay due to attenuation;
- in contrast to surface waves, the A- Δ relations for first arriving longitudinal waves (P and PKP) show significant amplitude variations. The latter are mainly caused by energy focusing and defocusing due to velocity discontinuities in deeper parts of the Earth. Thus the amplitude peaks at around 20° and 40° are related to discontinuities in the upper mantle at 410 km and 670 km depth, the rapid decay of short-period P-wave amplitudes beyond 90° is due to the strong velocity decrease at the core-mantle boundary ("core shadow"), and the amplitude peak for PKP near 145° is caused by the focusing effect of the outer core (see Fig. 11.59).

Other body wave candidates for magnitude determinations again behave differently, e.g. PP which is reflected at the Earth's surface half way between the source and receiver. PP does not have a core shadow problem and is well observed up to antipode distances. Furthermore, one has to consider that body waves are generated efficiently by both shallow and deep earthquakes. This is not the case for surface waves. Accordingly, the different A- Δ -h behavior of surface and body waves requires different calibration functions if one wants to use them for magnitude determination.

3.2.5.1 Surface-wave magnitude scale M_s

Gutenberg (1945a) developed the magnitude scale M_s for teleseismic surface waves:

$$M_s = \log A_{H_{\max}}(\Delta) + \sigma_S(\Delta). \quad (3.9)$$

It is based on measurements of the maximum horizontal "true" ground motion displacement amplitudes $A_{H_{\max}} = \sqrt{(A_N^2 + A_E^2)}$ of the surface wave train at periods $T = 20 \pm 2$ s. This maximum corresponds to the Airy phase, a local minimum in the group velocity dispersion curve of Rayleigh surface waves which arises from the existence of a low-velocity layer in the upper mantle (see 2.3). There was no corresponding formula given for using vertical component surface waves because no comparably sensitive and stable vertical component long-period seismographs were available at that time.

The calibration function $\sigma_S(\Delta)$ is the inverse of a semi-empirically determined A- Δ -relationship scaled to an event of $M_s = 0$, thus compensating for the decay of amplitude with distance. Richter (1958) gave tabulated values for $\sigma_S(\Delta)$ in the distance range $20^\circ \leq \Delta \leq 180^\circ$ (see Table 3 in DS 3.1).

This relationship was further developed by Eastern European scientists. Soloviev (1955) proposed the use of the maximum ground particle velocity $(A/T)_{\max}$ instead of the maximum

ground displacement A_{\max} since the former is more closely related to seismic energy. It also better accounts for the large variability of periods at the surface-wave amplitude maximum (Airy phase) depending on distance and crustal structure (see 2.3). For most continental Rayleigh waves the Airy phase periods are around 20 s and fall indeed within the narrow period window of 20 ± 2 s set by Gutenberg. However, periods as small as 7 s have been observed at 10° and of 16 s at 100° epicentral distances while the largest periods observed for continental paths may reach 28 s and be still somewhat higher for oceanic paths.

Collaboration between research teams in Prague, Moscow and Sofia resulted in the proposal of a new M_s scale and calibration function, termed Moscow-Prague formula, by Karnik et al. (1962):

$$M_s = \log (A/T)_{\max} + \sigma_S (\Delta) = \log (A/T)_{\max} + 1.66 \log \Delta + 3.3 \quad (3.10)$$

for epicentral distances $2^\circ < \Delta < 160^\circ$ and source depth $h < 50$ km. The IASPEI Committee on Magnitudes recommended at its Zürich meeting in 1967 the use of this formula as **standard for M_s determination for shallow seismic events ($h \leq 50$ km)**.

Another scale, said to be well calibrated with the Gutenberg and Richter M_s scale, however based on records from 5-s instruments, is used by the Japan Meteorological Agency for regional events only (Tsuboi, 1954):

$$M(\text{JMA}) = \log \sqrt{(A_N^2 + A_E^2)} + 1.73 \log \Delta - 0.83$$

with Δ in km and A ground amplitudes in μm .

Note 1: For 20 s surface waves of the same amplitudes Eq. (3.10) yields, on average, magnitudes which are about 0.2 units larger than the original Gutenberg-Richter M_s according to (3.9) and tabulated in Table 3 of DS 3.1. This has been confirmed by Abe (1981). He gave the following relationship between M_s determinations by NEIC using Eq. (3.10) and M_s according to Gutenberg-Richter:

$$M_s(\text{"Prague", NEIC}) = M_s(\text{Gutenberg-Richter}) + 0.18. \quad (3.11)$$

Note 2: Eq. (3.10) is defined only up to 160° . It does not account for the amplitude increase beyond 160° . However, the latter is obvious in the tabulated version of $\sigma(\Delta)_H$ issued by the Moscow-Prague-Sofia group (see Table 4 in DS 3.1).

Note 3: As shown in Fig. 3.5, surface-wave spectra from events with $M_s > 7$ and a seismic moment $M_0 > 10^{20}$ Nm will have their corner period at $T > 20$ s. Consequently, M_s scales based on $(A/T)_{\max}$ measurements for periods $T \approx 20$ s will systematically underestimate the size of larger events and saturate around $M_s = 8.5$ (see Fig. 3.18). Such was the case with the strongest earthquake of the 20th century in Chile 1960, which had a seismic moment $M_0 = 2\text{-}3 \times 10^{23}$ Nm for the main shock but an M_s of only 8.5 (see Lay and Wallace, 1995). Several efforts have therefore been made to develop a moment magnitude M_w (see 3.2.5.3) and other non-saturating magnitude scales (see 3.2.6.1 and 3.2.6.2).

Note 4: There may be significant regional biases due to surface-wave path effects. Lateral velocity variations in the crust and upper mantle as well as refraction at plate boundaries may result in significant focusing and de-focusing effects and related regional over- or underestimation of M_s (Lazareva and Yanovskaya, 1975). According to Abercrombie (1994)

3. Seismic Sources and Source Parameters

this seems to be the main cause for the anomalous high surface-wave magnitudes of continental earthquakes relative to their seismic moments rather than differences in the source process. Therefore, in order to obtain reliable, unbiased estimates of regional seismic strain rate and hazard, local/regional moment-magnitude relationships should be preferred to global ones.

The 1979 edition of MSOP (Willmore 1979) recommends the use of the standard formula Eq. (3.10) for both horizontal and vertical components. Bormann and Wylegalla (1975) and Bormann and Khalturin (1975) used a large global data set of long-period surface-wave magnitudes MLH and MLV determined at station MOX, Germany to show that this is justified. They used $(A/T)_{\max}$ surface-wave readings for the horizontal (H) and vertical (V) components of instruments of type C (see Fig. 3.11) in the magnitude range $3.7 < M_s < 8.2$ and adjusted them with the tabled calibration values (Table 4 in DS 3.1) corresponding to Eq. (3.10). They obtained the orthogonal regression relationship $MLV - 0.97 MLH = 0.19$ with a correlation coefficient 0.98 and a standard deviation of only ± 0.11 .

The NEIC adopted the vertical component as its standard in May 1975 (Willmore 1979), i.e., M_s is determined from the Rayleigh-wave maximum only. Table 5 in DS 3.1 may aid in finding the appropriate part of the record.

Today, both the ISC and NEIC use Eq. (3.10) for the determination of M_s from events with focal depth $h < 60$ km without specifying the type of waves or components considered. The ISC accepts both vertical or resultant horizontal amplitudes of surface waves with periods between 10 - 60 s from stations in the distance range $5^\circ - 160^\circ$ but calculates the representative average M_s only from observations between $20^\circ - 160^\circ$. In contrast, the NEIC calculates M_s only from vertical component readings of stations between $20^\circ \leq \Delta \leq 160^\circ$ and for reported periods of $18 \text{ s} \leq T \leq 22 \text{ s}$. This limitation in period range is not necessary and limits the possibility of M_s determinations from regional earthquakes.

Very recently Yacoub (1998) presented a method for accurate estimation of Rayleigh-wave spectral magnitudes M_R by velocity and frequency window analysis of digital records. He applied it to records of underground nuclear explosions in the distance range 5° to 110° and compared M_R with the classical time-window magnitude estimates, M_s , according to Eq. (3.10). While both agreed well, in general M_R had smaller standard deviations. Another advantage is that the procedure for M_R determination can easily be implemented for on-line automated magnitude measurements. (Note: According to proposed specific magnitude names M_R should be termed MLR; see IS 3.2).

Problems:

- 1) Herak and Herak (1993) found that $\sigma_S(\Delta)$ in the Moscow-Prague formula does not yield consistent magnitude estimates independent of Δ . They proposed instead the formula:

$$M_s = \log (A/T)_{\max} + 1.094 \log \Delta + 4.429. \quad (3.12)$$

This formula is based on USGS data, i.e., on amplitude readings in the period range 18 to 22 s. It provides distance-independent estimates of M_s over the whole distance range $4^\circ < \Delta < 180^\circ$. M_s values according to Eq. (3.12) are equal to those from Eq. (3.10) at $\Delta = 100^\circ$, larger by 0.39 magnitude units at $\Delta = 20^\circ$ and smaller by 0.12 units for $\Delta = 160^\circ$. Eq. (3.12) is practically equal to the magnitude formulae earlier proposed by von Seggern (1977) and similar to more recent results obtained by Rezapour and Pearce (1998).

- 2) The possible introduction of Eq. (3.12) as a new standard calibration function for M_s has not yet been discussed or recommended by the IASPEI Commission on Practice. The same applies to depth corrections for σ_s . Empirically derived corrections for intermediate and deep earthquakes were published by Båth (1985). They range between 0.1 and 0.5 magnitude units for focal depths of 50 - 100 km and between 0.5 and 0.7 units for depths of 100 - 700 km. But theoretical calculations by Panza et al. (1989) indicate that the depth correction may already exceed one magnitude unit even for shallow sources ($h \leq 60$ km). This is confirmed by an empirical formula used at seismic stations in Russia for determining the depth of shallow earthquakes ($h < 70$ km) from the ratio mB/M_s (Ochozinskaya, 1974): h (in km) = $54 mB - 34 M_s - 107$ (correlation coefficient 0.88).
- 3) Recently, there has been again a tendency to determine the surface-wave magnitude by specifying the type of the waves and/or components used, e.g., MLRH or MLRV from Rayleigh waves and MLQH from Love waves or simply MLH and MLV as was the practice in Eastern Germany in the 1960's (see Tab. 3.1) and recommended already in 1967 by the IASPEI Committee on Magnitude at Zürich. Since the newly proposed IASPEI Seismic Format (see 10.2.5) accepts such specifications in data reports to data centers, the IASPEI WG on Magnitude Measurements will elaborate recommendations for unambiguous standards and "specific" magnitude names (see IS 3.2).

3.2.5.2 Magnitude scales for teleseismic body waves

Gutenberg (1945b and c) developed a magnitude relationship for teleseismic body waves such as P, PP and S in the period range 0.5 s to 12 s. It is based on theoretical amplitude calculations corrected for geometric spreading and (only distance-dependent!) attenuation and then adjusted to empirical observations from shallow and deep-focus earthquakes, mostly in intermediate-period records:

$$mB = \log (A/T)_{\max} + Q(\Delta, h). \quad (3.13)$$

Gutenberg and Richter (1956a) published a table with $Q(\Delta)$ values for P-, PP- and S-wave observations in vertical ($V=Z$) and horizontal (H) components for shallow shocks (see Tab. 6 in DS 3.1), complemented by diagrams $Q(\Delta, h)$ for PV, PPV and SH (Figures. 1a-c in DS 3.1) which enable also magnitude determinations for intermediate and deep earthquakes. These calibration functions are correct when ground displacement amplitudes are measured in intermediate-period records and given in micrometers ($1 \mu\text{m} = 10^{-6}$ m).

Gutenberg and Richter (1956a) also proposed a *unified magnitude* m as a weighted average of the individual mB values determined for these different types of body waves. Because of their different propagation paths they also differ in their frequency spectra. In addition, these body waves leave the source at different take-off angles and have different radiation pattern coefficients. Using these body waves jointly for the computation of magnitude significantly reduces the effect of the source mechanism on the magnitude estimate. Gutenberg and Richter (1956a) also scaled m (and thus, in a first approximation, also individual mB) to the earlier magnitude scales M_l and M_s so as to match these scales at magnitudes between about 6 to 7. Since mB is based on amplitude measurements at shorter periods than those observed in the Airy phase of surface waves, the mB scale saturates somewhat earlier than M_s (see Fig. 3.18).

Later, with the introduction of the WWSSN short-period 1s-seismometers (see Fig. 3.11, type A2) it became common practice at the NEIC to use the calibration function $Q(\Delta, h)$ for short-period PV only. In addition, it was recommended that the largest amplitude be taken within

3. Seismic Sources and Source Parameters

the first few cycles (see Willmore, 1979) instead of measuring the maximum amplitude in the whole P-wave train. One should be aware that this practice was due to the focused interest on discriminating between earthquakes and underground nuclear explosions. The resulting short-period m_b values strongly underestimated the body-wave magnitudes for $m_B > 5$ (see Tab. 3.1) and, as a consequence, overestimated the annual frequency of small earthquakes in the magnitude range of kt-explosions. Also, m_b saturated much earlier than the original Gutenberg-Richter m_B for intermediate-period body waves or M_s for long-period surface waves (see Figs. 3.5 and 3.16). Therefore, the IASPEI Commission on Practice issued a revised recommendation in 1978 according to which the maximum P-wave amplitude for earthquakes of small to medium size should be measured within 20 s from the time of the first onset and for very large earthquakes even up to 60 s (see Willmore, 1979, p. 85). This somewhat reduced the discrepancy between m_B and m_b but in any event both are differently scaled to M_s and the short-period m_b necessarily saturates earlier than medium-period m_B (see Fig. 3.5). Interestingly, the effect of the source radiation pattern on the amplitudes used for m_b determination is relatively small (Schweitzer and Kväerna, 1999).

However, some of the national and international agencies have only much later or not even now changed their practice of measuring $(A/T)_{\max}$ for m_b determination in a very limited time-window, e.g., the International Data Centre for the monitoring of the CTBTO still uses a time window of only 6 s (5.5s after the P onset), regardless of the event size. In contrast with this and early practice at the NEIC of measuring A/T in P-wave records, the Soviet/Russian practice of analyzing short-period records was always to measure the true maximum on the entire record. These magnitudes were denoted as m_{PVA} (or m_{SKM} , using the abbreviation of the short-period Kirnos instrument type code) in order to differentiate them from m_b of NEIC derived from short-period Benioff instruments. Nevertheless, for the latter, similar magnitudes were determined for large earthquakes when using $(A/T)_{\max}$ in the whole P-wave train, e.g., by Koyama and Zeng (1985), denoted as m_b^* , and by Houston and Kanamori (1986), denoted \hat{m}_b . With respect to saturation, m_{SKM} , m_b^* and \hat{m}_b behave much like M_I , as could be expected from their common frequency band and considering that M_I is determined also from the maximum amplitude in the whole short-period record. M_I saturates around 7.5.

Problems:

- 1) Despite the strong recommendation of the Committee on Magnitudes at the IASPEI General Assembly in Zürich (1967) to report the magnitude for all waves for which calibration functions are available, both the ISC and NEIC continue to determine body-wave magnitudes only from vertical component short-period P wave readings of $T \leq 3$ s. No body-wave magnitudes from PP or S waves are determined despite their merits discussed above and the fact that digital broadband records, which now allow easy identification and parameter determination of these later phases, are more and more widely available.
- 2) Both NEIC and ISC still use for short-period m_b determination the Gutenberg and Richter (1956a) $Q(\Delta, h)_{PZ}$ functions although these were mainly derived from and used for intermediate-period data, as the Q-functions for PP and S too. However, in this context one has to consider that Gutenberg and Richter did not believe in the frequency-dependent attenuation model. The calibration curves were derived by assuming a linear model for attenuation proportional to $\exp(-0.00006 L)$, where L is the total length of the ray path from the station to the source. This seems to make the $Q(\Delta, h)$ functions equally applicable to 10 s data and 10 Hz data, which is not the case. Duda and Yanovskaya (1993) showed that theoretical spectral $\log A-D$ curves, calculated on the basis of the PREM model (see Fig. 2.53), differed in the teleseismic distance range between 20° and

100° for periods of 1 s and 10 s, respectively, by about 0.3 to 0.6 and, when calculated for the ABM attenuation model, by even 0.9 to 1.4 magnitude units (see Fig. 3.15). Between 1 Hz and 10 Hz these differences are even larger. When neglecting the frequency-dependent attenuation, amplitude readings at higher frequency systematically underestimate the magnitude when scaled with $Q(\Delta, h)_{PV}$. For medium-period waves, however, e.g., for periods between 4 and 16 s, these differences become < 0.3 magnitude units, independent of the attenuation model. This is another strong argument in favor of using preferably medium-period or even better broadband data for the determination of teleseismic body-wave magnitudes, thus also reducing or avoiding the saturation effect.

- 3) None of the more recent studies (see 3.2.6) has received world-wide consideration and endorsement for routine use, and the major international agencies are therefore continuing to apply the tables of Gutenberg and Richter (1956a) as recommended in 1967 by the Committee on Magnitudes.
- 4) No proper discrimination has been made yet at the international data centers between data readings from different kinds of instruments or filters although respective recommendations have already been made at the joint IASPEI/IAVCEI General Assembly in Durham, 1977 (see below).
- 5) Observations less than 21° or more than 100° are also ignored although good PP readings are available far beyond 100° and calibration functions $Q(\Delta, h)$ exist for PPH and PPV up to 170°. As shown by Bormann and Khalturin (1975), mB for P and PP waves are perfectly scaled (orthogonal regression $mB(PP) - mB(P) = 0.05$ with a standard deviation of only ± 0.15 magnitude units!). When using short-period amplitude readings for P and PP instead, the orthogonal relationship becomes magnitude-dependent ($mb(PP) = 1.25 mb(P) - 1.22$) and the standard deviation is much larger (± 0.26). This testifies the greater stability of body-wave magnitude determinations based on medium-period readings.
- 6) The suitability of PKP readings in the distance range of the core caustic around 145° and beyond has also been ignored so far (see 3.2.6.5).

Recommendations:

- 1) The IASPEI Commission on Seismological Observation and Interpretation with its WG on Magnitude Measurements must take the lead in recommending standards for magnitude-parameter readings. It should also propose a nomenclature that permits a more specific and unique reporting of measurements. For preliminary discussions along these lines see IS 3.2. They further develop earlier practices (as demonstrated with Tab. 3.1) and earlier recommendations at the joint General Assembly of the IASPEI/IAVCEI at Durham (1977). The latter are reproduced in the old MSOP (see Willmore, 1979, page 124) which is still accessible on the web site <http://216.103.65.234/iaspei.html> via the links “Supplementary Volumes on CDs”, “Literature in Seismology”, and then “MSOP”.
- 2) While these early recommendations for standard magnitude determinations were based on analog instrument classes as depicted in Fig. 3.11 and given in detail in Chapter INST 1.1 of the old MSOP, p. 41, broadband digital recordings are becoming more and more the standard. This requires to define the standard response characteristics required for standard magnitude determinations in terms of poles and zeros, with the range of tolerance for appropriate filters. These are required to synthesize these standard responses from original, usually velocity-proportional, digital broadband records (see 11.3.2).

3. Seismic Sources and Source Parameters

- 3) More recently developed magnitude scales for short-period and broadband P-wave readings, PKP and mantle surface waves etc. (see 3.2.6) should be rigorously tested and, in the case of their suitability and known relationship to other commonly used scales, be recommended for standardized routine practice.

3.2.5.3 Moment magnitude M_w

According to Eq. (3.2) and Fig. 3.5 the scalar seismic moment $M_0 = \mu \bar{D} A$ is determined from the asymptote of the displacement amplitude spectrum as frequency $f \rightarrow 0$ Hz and it does not saturate. Kanamori (1977) proposed, therefore, a moment magnitude, M_w , which is tied to M_s but which would not saturate. He reasoned as follows: According to Kostrov (1974) the radiated seismic strain energy is proportional to the stress drop $\Delta\sigma$, namely $E_s \approx \Delta\sigma \bar{D} A/2$. With Eq. (3.2) one can write $E_s \approx (\Delta\sigma/2\mu) M_0$. (For definition and determination of M_0 and $\Delta\sigma$ see IS 3.1 and EX 3.4). Assuming a reasonable value for the shear modulus μ in the crust and upper mantle (about $3\text{-}6 \times 10^4$ MPa) and assuming that, according to Kanamori and Anderson (1975) and Abe (1975), the stress drop of large earthquakes is remarkably constant (ranging between about 2 and 6 MPa; see Fig. 3.39), one gets as an average $E_s \approx M_0/2 \times 10^4$ (see Fig. 3.38). Inserting this into the relationship proposed by Gutenberg and Richter (1956c) between the released seismic strain energy E_s and M_s , namely

$$\log E_s = 4.8 + 1.5 M_s \text{ (in SI units Joule J = Newton meter Nm)} \quad (3.14)$$

it follows:

$$\log M_0 = 1.5 M_s + 9.1. \quad (3.15)$$

Solving (3.15) for the magnitude and replacing M_s with M_w one gets

$$M_w = 2/3 (\log M_0 - 9.1). \quad (3.16)$$

Note that M_w scales well with the logarithm of the rupture area (see Eq. (3.107)). The determination of M_0 on the basis of digital broadband records is becoming increasingly standard at modern observatories and network centers. This applies not only to very strong and teleseismic events but also to comparable scaling of moderate and weak events, both in the teleseismic and the local/regional range. The computed M_0 , however, depends on details of the individual inversion methodologies and thus related M_w may differ. A simple, fast and robust method of M_w determination from broadband P waveforms has been developed by Tsuboi et al. (1995) for rapid evaluation of the tsunami potential of large earthquakes.

3.2.6 Complementary magnitude scales

Below we describe several other complementary procedures for magnitude estimation. They are not (yet) based on internationally recommended standards but are also useful for applications in seismological practice.

3.2.6.1 Mantle magnitude M_m

Okal and Talandier (1989;1990) describe in detail the further development and use of a “mantle magnitude” which was earlier introduced by Brune and Engen (1969). Based on

observations of very long-period mantle surface waves (see 2.3), M_m was first developed for Rayleigh waves and later extended to Love waves. M_m is a magnitude scale which is also firmly related to the seismic moment M_0 and thus avoids saturation. On the other hand, it is closer to the original philosophy of a magnitude scale by allowing quick, even one-station automated measurements (Hyvernaud et al., 1993), that do not require the knowledge of either the earthquake's focal geometry or its exact depth. The latter parameters would be crucial for refining a moment estimate and require (global) network recordings. M_m is defined as $M_m = \log X(\omega) + C_S + C_D - 0.90$ with $X(\omega)$ as the spectral amplitude of a Rayleigh wave in $\mu\text{m}\cdot\text{s}$. C_S is a source correction, and C_D is a frequency-dependent distance correction. For details of the correction terms, see Okal and Talandier (1989 and 1990).

Applications of M_m to the reassessment of the moment of shallow, intermediate and deep historical earthquakes are extensively described by Okal (1992 a and b). M_m is an estimate of $(\log M_0 - 13)$ (when M_0 is given in Nm). For the Chile 1960 earthquake Okal (1992a) calculated values $M_m \approx 10$ to 10.3 and for $M_0 = 3.2 \cdot 10^{23}$ Nm. M_m determinations were extensively verified and are said to be accurate by about ± 0.2 magnitude units (Hyvernaud et al., 1993).

3.2.6.2 Energy magnitude M_e

According to Kanamori (1977) M_w agrees very well with M_s for many earthquakes with a rupture length of about 100 km. Furthermore, he suggested that Eq. (3.14) also gives a correct value of the seismic-wave energy for earthquakes up to rupture dimensions \leq about 100 km. Thus, he considered the M_w scale to be a natural continuation of the M_s scale for larger events. Inserting into the $\log E_S$ - M_s relationship the value of $M_w = 9.5$ for the Chile 1960 earthquake instead of the saturated value $M_s = 8.5$ one gets a seismic energy release that is 30 times larger!

When substituting in Eq. (3.14) the surface-wave magnitude M_s by an energy magnitude M_e , one gets

$$M_e = 2/3 (\log E_S - 4.8) \quad (3.17)$$

which reduces to $M_e = 2/3 (\log M_0 - 9.1) = M_w$ (see Eq. (3.16)) if Kanamori's condition $E_S/M_0 \approx 5 \cdot 10^{-5}$ holds. This result has been published earlier by Purcaru and Berckhemer (1978). But this is valid only for the average apparent stresses (and related stress drop) on which the Kanamori condition is based. As Choy and Boatwright (1995) showed, apparent stress, which is related to the ratio of E_S/M_0 , may vary even for shallow events over a wide range between about 0.03 and 20.7 MPa. They found systematic variations in apparent stress as a function of focal mechanism, tectonic environment and seismic setting. Oceanic intraplate and ridge-ridge transform earthquakes with strike-slip mechanisms tend to have higher stress drops than interplate thrust earthquakes. Accordingly, M_e for the former will often be significantly larger than M_w . The opposite will be true for the majority of thrust earthquakes: M_w will be larger than M_e . Riznichenko (1992) gave a correlation on the basis of data from various authors. It predicts (despite rather large scatter) an average increase of $\Delta\sigma$ with source depth h according to $\Delta\sigma = 1.7 + 0.2 h$, i.e., stress drops ranging over 100 MPa can be expected for very deep earthquakes. On the other hand, Kikuchi and Fukao (1988) found from analyzing 35 large earthquakes in all depth ranges that $E_S/M_0 \approx 5 \cdot 10^{-6}$, i.e., a ratio that is one order of magnitude less than the condition used by Kanamori for deriving M_w . Therefore, M_e is not uniquely determined by M_w . M_e and M_w can be considerably different.

3. Seismic Sources and Source Parameters

A striking example has been presented by G. Choy at the spring meeting 2002 of the American Geophysical Society (see Tab. 3.2 in 3.3.5). Nowadays, with digital broadband recordings and fast computer programs, it is feasible to determine directly the seismic energy, E_S , by integrating the radiated energy flux in velocity-squared seismograms over the duration of the source process and correcting it for the effects of geometric spreading, attenuation and radiation pattern. A method developed by Boatwright and Choy (1986) is now routinely applied at NEIC to compute radiated energies for shallow earthquakes of $m_b > 5.8$ (see 3.3) but its application is not so trivial and not for use with single stations. Using almost 400 events, Choy and Boatwright derived the relationship for E_S - M_s as

$$\log E_S = 1.5 M_s + 4.4 \quad (3.18)$$

It indicates that (3.14) slightly overestimates E_S . On the basis of these direct energy estimates these authors developed the non-saturating energy magnitude (see also 3.3.3)

$$M_e = 2/3 (\log E_S - 4.4) \quad (3.19)$$

which yields for earthquakes satisfying Kanamori's condition

$$M_e = 2/3 \log M_0 - 5.80 = M_w + 0.27 \quad (3.20)$$

i.e., an M_e that is somewhat larger than M_w and an M_e derived from the Gutenberg-Richter E_S/M_s relationship. M_e may become significantly larger for high stress drop earthquakes and much smaller than M_w for slow or "tsunami" earthquakes. The latter may generate a strong (namely long-period) tsunami but only weak short-period ground motion, which may cause no shaking-damage and might not even be felt by people such as the September 2, 1992 Nicaragua m_b 5.3 and M_w 7.6 earthquake (see also 3.2.6.9).

A strong argument to use M_e instead of M_w is that it follows more closely the original intent of the Gutenberg-Richter formula by relating magnitude to the velocity power spectrum and, thus, to energy. In contrast, M_w is related to the seismic moment M_0 that is derived from the low-frequency asymptote of the displacement spectrum. Consequently, M_e is more closely related to the seismic potential for damage while M_w is related to the final static displacement and the rupture area and thus related more to the tectonic consequences of an earthquake.

3.2.6.3 Broadband and spectral P-wave magnitude scales

A calibration function $Q_b(\Delta, h)$ based on broadband recordings of P waves (bandpass between 0.01 and 2 Hz) was derived recently by Nolet et al. (1998). It differs markedly from both $P(\Delta, h)_{SP}$ and $Q(\Delta, h)_{PZ}$.

Duda and Kaiser (1989) recommended instead the determination of spectral magnitudes based on measurements of spectral amplitudes from one-octave bandpass-filtered digital broadband records of P waves. As can be seen from Fig. 3.14, earthquakes of about the same magnitude m_b and recorded within about the same distance range may have, depending also on focal depth and the type of rupture mechanism, very different amplitudes in different spectral ranges. This is due to regional differences in ambient stress conditions and related stress drop. Duda and Yanovskaya (1993) also calculated theoretical spectral amplitude-distance curves based on the IASP91 velocity model (Kennett and Engdahl, 1991) and two different

attenuation models so as to allow the magnitude calibration of spectral amplitude measurements (see Fig. 3.15). This effort is a response to the problems discussed above. It also yields smoothed averaged estimates of the radiated seismic spectrum, its spectral plateau, corner frequency and high-frequency decay and thus of M_0 and stress drop of the given event. Thus one may draw inferences on systematic differences in the prevailing source processes (e.g., low, normal or high stress drop) and related ambient stress conditions in different source regions. However, this is not so much the concern of seismological routine practice, which is aimed at providing a simple one (or two) parameter size-scaling of seismic events for general earthquake statistics and hazard assessment. Rather, this is more a research issue, which can be best tackled, along with proper quantification of earthquake size, by determining both M_e and M_w or analyzing both M_0 and the shape of the overall source spectrum. On the other hand there is merit in determining the maximum spectral amplitude A_{vmax} of ground velocity directly from velocity broadband records by filtering them with constant bandwidth around the predominant period of the considered body-wave group and correcting it for the frequency-dependent attenuation. This should yield a saturation-free mB based on simple amplitude and period measurements at a single station, which comes closest to M_e and thus to the original intention of Gutenberg for the teleseismic body-wave magnitude. Preconditions are that the period of A_{vmax} is within the passband of the velocity response and the frequency-dependent attenuation is sufficiently well known. Such an mB, given together with the period of A_{vmax} , allows to assess the frequency content where the maximum seismic energy has been released. This is of great importance for assessing the damage potential of a given event.

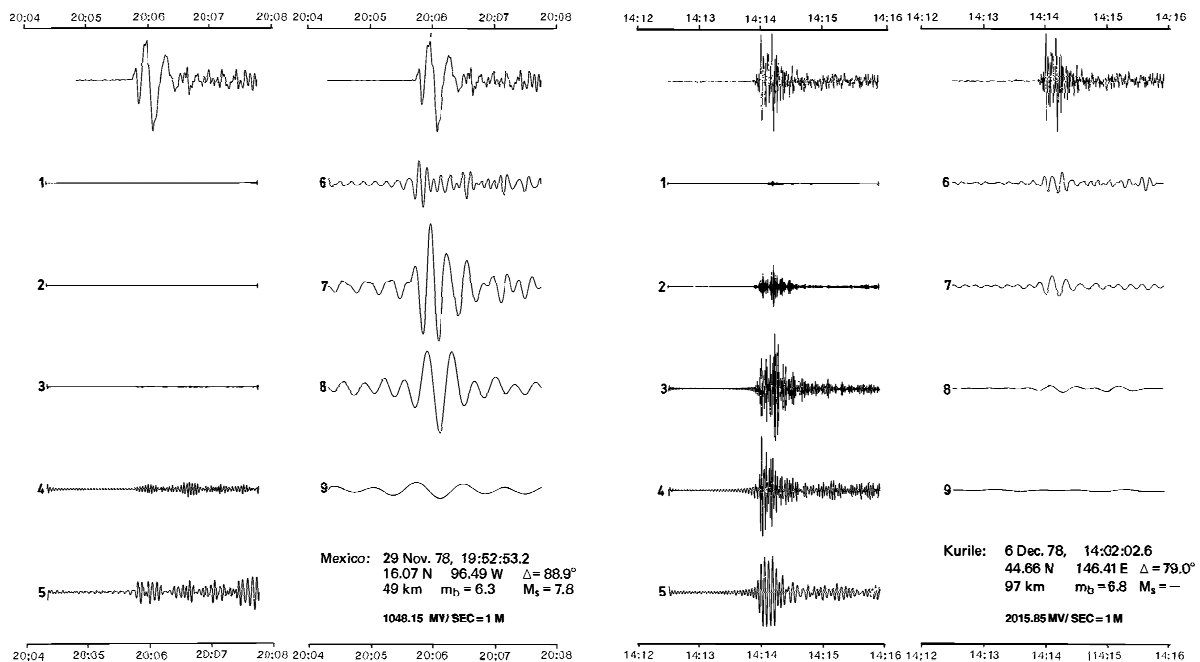


Fig. 3.14 Examples of broadband digital records proportional to ground velocity of the P-wave group from two earthquakes of similar magnitude m_b in different source regions (uppermost traces) and their one-octave bandpass-filtered outputs. The numbers 1 to 9 on the filtered traces relate to the different center periods between 0.25 s (1) and 64 s (9) in one-octave distance. Note that the event record on the left has its maximum ground velocity (or maximum A/T) at trace 7, which corresponds to a center period of 16 s while it is at 1 s in the case of the records from the Kuril earthquake (copied from Duda, 1986; with permission of the BGR Hannover).

3. Seismic Sources and Source Parameters

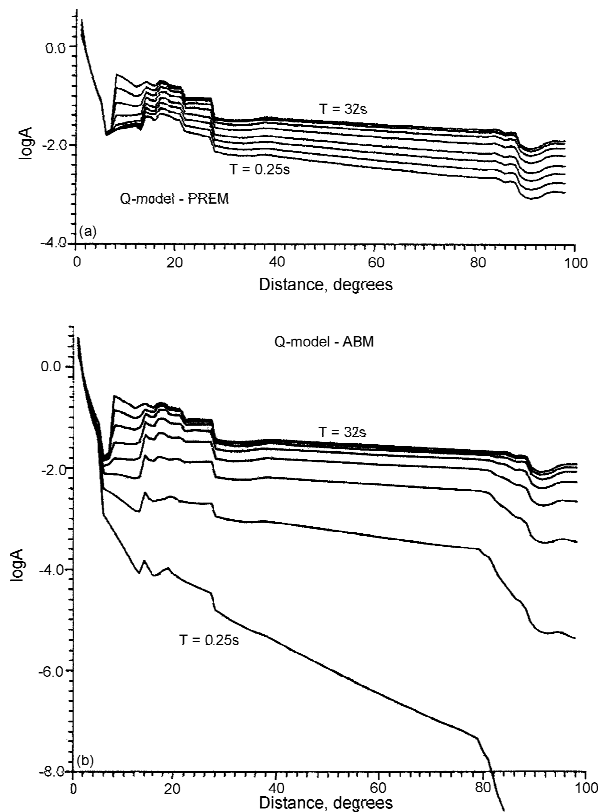


Fig. 3.15 Spectral amplitude-distance curves (in one-octave steps) as calculated for the IASP91 velocity model (Kennett and Engdahl, 1991) and two alternative Q-models according to Liu et al. (1976) as in the PREM model (upper diagram) and according to the ABM model of Anderson and Given (1982) (lower diagram) (modified from *Tectonophysics*, Vol. 217, Duda and Yanovskaya, 1993, Fig. 5, p. 263; with permission from Elsevier Science).

3.2.6.4 Short-period P-wave magnitude scale

Veith and Clawson (1972) developed a calibration function, $P(\Delta, h)_{SP}$, for short-period vertical-component P waves (Fig. 3.16) using data from underground nuclear explosions. It is consistent with observations and present-day concepts of attenuation. It looks much smoother than the curves $Q(\Delta, h)_{PZ}$ published by Gutenberg and Richter (1956a) and resembles an inverse $A-\Delta$ relationship for short-period P waves (see Fig. 3.13). For shallow events $mb(P)$ values agree well with $mb(Q)$ (average difference of - 0.03 magnitude units; Veith, 2001) but have less scatter. For deeper events, however, $mb(P)$ is systematically lower than $mb(Q)$ (up to about 0.4 magnitude units) due to a different attenuation law assumed in the upper mantle and transition zone (Veith, 2001). Deviating from the use of the Gutenberg-Richter Q functions, P values as given in Fig. 3.16 have to be used in conjunction with maximum P-wave peak-to-trough ($2A$) displacement amplitudes in units of nm (instead of μm). The Veith-Clawson calibration functions $P(\Delta, h)$ for short-period mb determination should be carefully considered by the IASPEI WG on Magnitude Measurements and existing discrepancies for deep earthquakes should be clarified. If $P(\Delta, h)$ in its present form or corrected for the currently best available attenuation model for short-period P waves promises to yield more reliable and stable mb values than $mb(Q)$ its introduction as a new standard may be considered. Some related discussion is given below.

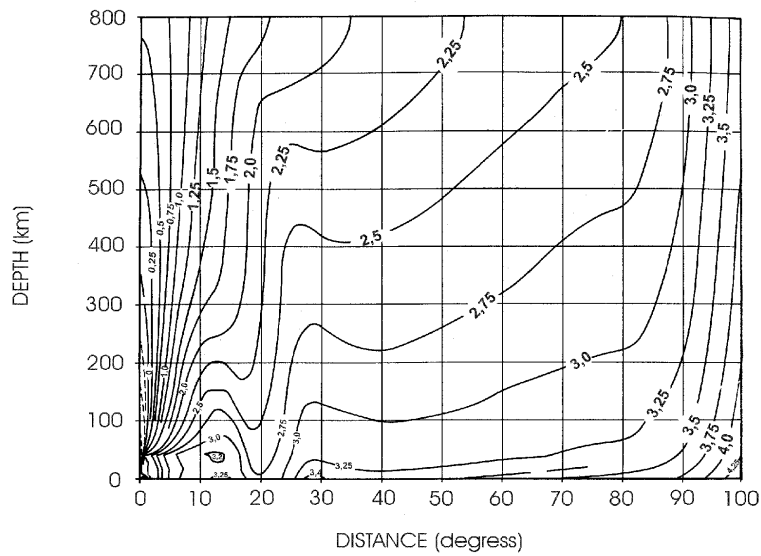


Fig. 3.16 Calibration functions $P(\Delta, h)$ for mb determination from narrow-band vertical-component short-period records with peak displacement magnification around 1 Hz (WWSSN-SP characteristic) according to Veith and Clawson (1972). **Note:** P values have to be used in conjunction with maximum P-wave peak-to-trough ($2A$!) amplitudes in units of nanometers ($1 \text{ nm} = 10^{-9} \text{ m}$). (Modified from Veith and Clawson, *Magnitude from short-period P-wave data*, BSSA, 62, 2, p. 446, © Seismological Society of America).

The Veith-Clawson magnitude calibration functions are officially used by the IDC in Vienna for mb determination although the IDC filter applied to the digital velocity-proportional broadband data prior to the amplitude measurements for mb results in a displacement response peaked around 4.5 Hz instead of around 1 Hz as required for the use of $P(\Delta, h)$. According to the spectral $\log A$ -D curves calculated by Duda and Yanovskaya (1993) for the PREM attenuation model, $\log A$ is, in the distance range between 10° and 100° , at 5 Hz at least 0.1 to 0.5 units smaller than at 1 Hz. The deviation may be even larger for other attenuation models (e.g., ABM; see Fig. 3.15). Thus, the use of $P(\Delta, h)$ in conjunction with the IDC filter response is physically not correct and tends to systematically underestimate mb. This is further aggravated by the fact that IDC determines A_{\max} within a time window of only 5 s after the P onset. This heuristic procedure, although very suitable for a best possible discrimination between earthquakes and underground explosions on the basis of the mb/Ms criterion (see 11.2.5.2), is not appropriate, however, for proper earthquake scaling, at least for larger events with corner frequencies $f_c < 1 \text{ Hz}$ and multiple rupture process longer than 5 s.

Granville et al. (2002) analyzed 10 medium-size earthquakes in the depth range $> 0 \text{ km}$ to 530 km and with magnitudes mb between 6.4 and 6.8 according to the PDE (Preliminary Determination of Epicenters) reports of the United States Geological Survey (USGS) and 13 underground nuclear tests (UNTs) with PDE magnitudes mb between 4.6 and 6.1. They compared these data, which were derived from simulated WWSSN-SP records, by using the traditional procedure of mb determination based on the Gutenberg-Richter Q-functions, with a) the mb for the same WWSSN-SP data but calibrated with the Veith-Clawson relationship and b) the body-wave magnitudes reported in the REB (Reviewed Event Bulletin) of the PIDC. From this study the following conclusions were drawn:

3. Seismic Sources and Source Parameters

- the agreement between $mb(Q)$ (Gutenberg-Richter) and $mb(P)$ (Veith-Clawson) based on WWSSN-SP data was reasonably good for the earthquakes (average difference $mb(Q)-mb(P) = 0.2$);
- for underground explosions (only shallow-depth events!) the agreement was even better (average $mb(P)-mb(Q) = 0.09$);
- the average discrepancy between $mb(P)$ and $mb(PIDC/REB)$ is much larger (0.5 magnitude units), although the latter are also scaled with the Veith-Clawson calibration functions. For 63% of the earthquake observations the difference was at least 0.4 mb units, and several of them had even an mb offset greater than 1 magnitude unit!;
- in contrast, the average discrepancy between $mb(P)$ and $mb(PIDC/REB)$ is 0.0 and 75% of the observations fall between -0.1 and $+0.1$;
- the PIDC (now IDC in Vienna) procedure is adequate for mb determination of underground nuclear explosions, but not for earthquakes.

3.2.6.5 Short-period PKP-wave magnitude

Calibration functions $Q(\Delta, h)_{PKP}$ for short-period amplitude and period readings from all three types of direct core phases (PKPab, PKPbc and PKPdc) have been developed by Wendt (see Bormann and Wendt, 1999; explanations and Figure 3 in DS 3.1). These phases appear in the distance range $\Delta = 145^\circ - 164^\circ$ (see Fig. 3.13, Figs. 11.62-63 and Figure 1 in EX 11.3) with amplitude levels comparable to those of P waves in the distance range $25^\circ < \Delta < 80^\circ$. Many earthquakes, especially in the Pacific (e.g., Tonga-Fiji-Kermadec Islands) occur in areas with no good local or regional seismic networks. Often these events, especially the weaker ones, are also not well recorded by more remote stations in the P-wave range but often excellently observed in the PKP distance range, e.g., in Central Europe. This also applies to several other event-station configurations. Available seismic information from PKP wave recordings could, therefore, improve magnitude estimates of events not well covered by P-wave observations.

3.2.6.6 Lg-wave magnitudes

Sg and Lg waves (see 2.3.3), recorded at local and regional distances and with periods $T < 3$ s, are often used for magnitude determination. Lg propagates well in continental platform areas and may be prominent up to about 30° . Lg magnitudes are calibrated either with respect to (or in a similar way as) MI or to teleseismic mb. In the latter case they are usually termed $mbLg$ or Mn (Ebel, 1982). Lg magnitudes allow rather stable magnitude estimates with small scatter. NEIC uses the original formulas derived by Nuttli (1973) for eastern North America:

$$mbLg = 3.75 + 0.90 \log\Delta + \log(A/T), \text{ for } 0.5^\circ \leq \Delta \leq 4^\circ \quad (3.21a)$$

$$mbLg = 3.30 + 1.66 \log\Delta + \log(A/T), \text{ for } 4^\circ \leq \Delta \leq 30^\circ. \quad (3.21b)$$

where A is the ground amplitude of the Lg trace maximum in μm and T its period in the range $0.6 \text{ s} \leq T \leq 1.4 \text{ s}$. Båth et al. (1976) developed a similar Lg scale for Sweden which is widely used in Scandinavia. Street (1976) recommended a unified $mbLg$ magnitude scale between central and northeastern North America. Herrmann and Nuttli (1982) showed (later also Kim, 1998) that $mbLg$ values are commonly similar to MI when based on amplitude readings with periods around 1 s. They also proposed to define regional attenuation relations so that $mbLg/Mn$ from different regions predict the same near source ground motions. Herrmann and

Kijko (1983) developed a frequency-dependent scales $mLg(f)$ in order to broaden the frequency domain within which $mbLg$ is applicable. Ebel (1994) proposed $mLg(f)$, calibrated to mb and computed with appropriate Lg spatial attenuation functions, to become the standard for regional seismic networks in northeastern North America. Ambraseys (1985) published calibration Q_g (for Sg and Lg) and Q_R (for crustal Rayleigh waves), respectively that are applicable for northwestern European earthquakes in the distance range $0.5^\circ < D < 11^\circ$.

Stable single-station estimates of magnitudes from Nevada test site underground nuclear explosions have been made by Mayeda (1993) using 1-Hz Lg -coda envelopes. As compared with Lg -magnitude estimates using third peak or RMS amplitudes, these coda magnitudes have generally a five times smaller scatter (0.03 to 0.04 magnitude units only). Rautian et al. (1981) had proposed earlier the use of coda amplitude, not duration, in the definition of coda-based magnitude. They designed two particular scales based on the records of short-period (SP) and medium-period (MP) instruments. A scale of this kind is used routinely by the Kamchatka seismic network (Lemzikov and Gusev, 1989). The main advantage of such magnitude scales is their unique intrinsic accuracy; even a single-station estimate has a root-mean-square (RMS) error of only 0.1 or even less.

3.2.6.7 Macroseismic magnitudes

Other efforts are directed at developing magnitude scales which are best suited for earthquake engineering assessment of potential damage and thus seismic risk. These efforts go in two directions: by relating M to macroseismic intensity I and/or shaking area A_I or by focusing on the high-frequency content of seismic records.

Macroseismic magnitudes, M_{ms} are particularly important for the analysis and statistical treatment of historical earthquakes. They were initially proposed by Kawasumi (1951) as the intensity at the 100 km distance, following Richter's definition of M_I as closely as possible. This approach is physically quite reasonable because for most earthquakes a distance of 100 km is already the far field and source finiteness can be ignored. This approach was further developed by Rautian et al. (1989). On the other hand, I_0 based definitions implicitly assume the point source model and must be often misleading. Of course, with historic catalogs, there is no other way. There are three main ways to compute macroseismic magnitudes:

- 1) M_{ms} is derived from the epicentral intensity I_0 (or the maximum reported intensity, I_{max}) assuming that the earthquake effects in the epicentral area are more or less representative of the strength of the event;
- 2) M_{ms} is derived from taking into consideration the whole macroseismic field, i.e., the size of the shaking is related to different degrees of intensity or the total area of perceptibility, A ;
- 3) M_{ms} is related to the product $P = I_0 \times A$ which is nearly independent of the focal depth, h , which is often not reliably known.

Accordingly, formulae for M_{ms} have the general form of

$$M_{ms} = a I_0 + b , \quad (3.22)$$

or, whenever the focal depth h (in km) is known

3. Seismic Sources and Source Parameters

$$M_{ms} = c I_0 + \log h + d, \quad (3.23)$$

or, when using the shaking area A_{fi} (in km^2) instead,

$$M_{ms} = e \log A_{fi} + f \quad (3.24)$$

with A_{fi} in km^2 shaken by intensities I_i with $i \geq \text{III}, \dots, \text{VIII}$, respectively. Sometimes the mean radius R_{fi} of the shaking area related to a given isoseismal intensity is used instead of the area A_i and (3.22) is then written (e.g., by Greenhalgh et al. 1989 and with M_{ms} scaled to M_L) as

$$M_{ms} = g \log R_{fi}^2 + h \log R_{fi} + j. \quad (3.25)$$

In these relationships a through j are different constants. They have to be determined independently for different regions. Most often M_{ms} is scaled to M_I which has proven to be best related to earthquake damage and engineering applications. Examples for regionally best fitting relationships according to equation (3.22) to (3.25) have been published for California and Western Nevada by Topozada (1975), for Italy by Tinti et al. (1987) and for Australia by Greenhalgh et al. (1989). For Europe, the relationship by Karnik (1969) yields the best results:

$$M_{ms} = 0.5 I_0 + \log h + 0.35. \quad (3.26)$$

Frankel (1994) compared felt area and moment magnitudes for California with its young mountain ranges with a global data set of earthquakes in stable continental regions (SCRs) such as central USA (Fig. 3.17). The main reason is that the average attenuation is at frequencies around 2-4 Hz, which is the range of best human perceptibility to ground shaking, is very different in these regions. After Frankel (1994), Q is about 490 and 1600, respectively.

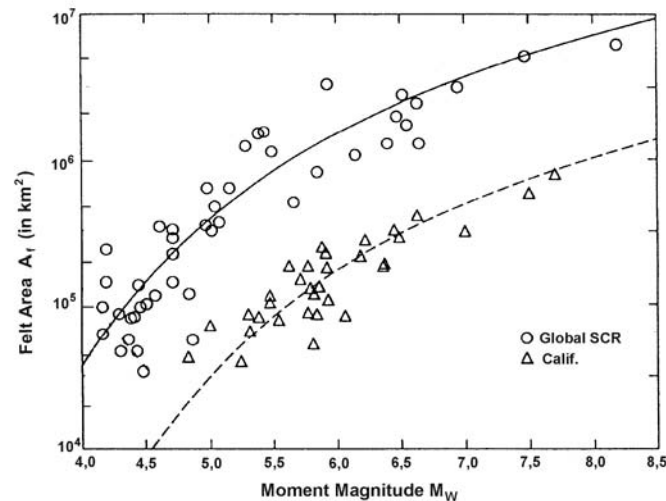


Fig. 3.17 Felt area A_f (in km^2) plotted against moment magnitude, M_w , for global data from stable continental regions (SCR) (open circles; from Johnston, 1993) and California data (triangles, from Hanks et al., 1975; Hanks and Johnston, 1992). Solid and dashed lines are fits according to an equation given by Frankel (1994) (modified from Frankel, Implications of felt area-magnitude relations for earthquake scaling and the average frequency of perceptible ground motion, Bull. Seism. Soc. Am., Vol. 84, No. 2, Fig. 1, p. 463, 1994; © Seismological Society of America).

Another M_{ms} scale based on $P = I_0 \times A$ (in km^2) had been published by Galanopoulos (1961):

$$M_{ms} = \log P + 0.2 (\log P - 6). \quad (3.27)$$

A macroseismic magnitude scaled to the body-wave magnitude of Central United States earthquakes in the range $2.7 \leq mb \leq 5.5$ was developed by Nuttli and Zollweg (1974):

$$mb = 2.65 + 0.098 \log A_f + 0.054 (\log A_f)^2. \quad (3.28)$$

It is applicable for magnitude estimates of central United States earthquakes with felt areas of shaking $A_f \leq 10^6 \text{ km}^2$ for which there are intensity maps but no instrumental data available.

A related problem is the determination of magnitudes of prehistoric and historic (pre-instrumental) earthquakes from dimensions (length L , width W and/or dislocation D) of observed seismo-dislocations (e.g., Khromovskikh, 1989; Wells and Coppersmith, 1994; Mason, 1996) based on correlation relationships between magnitudes and respective field data from recent events (see 3.6).

3.2.6.8 High-frequency moments and magnitudes

Koyama and Zheng (1985) developed a kind of short-period seismic moment M_1 which is related to the source excitation of short-period seismic waves and scaled to mb according to

$$\log M_1 = 1.24 mb + 10.9 \quad (\text{with } M_1 \text{ in } J = \text{Nm}). \quad (3.29)$$

They determined M_1 from WWSSN short-period analog recordings by applying an innovative approximation of spectral amplitudes

$$Y(f) = 1.07 A_{\max} (\tau/f_0)^{1/2} \quad (3.30)$$

with A_{\max} - maximum amplitude, f_0 - dominant frequency and τ - a characteristic duration of the complicated wave-packets. They analyzed more than 900 short-period recordings from 79 large earthquakes throughout the world in the moment range $7.5 \times 10^{17} \leq M_0 \leq 7.5 \times 10^{22} \text{ Nm}$. M_1 did not saturate in this range!

More recently, Atkinson and Hanks (1995) proposed a high-frequency magnitude scale

$$\mathbf{m} = 2 \log a_{\text{hf}} + 3 \quad (3.31)$$

with a_{hf} as the high-frequency level of the Fourier amplitude spectrum of acceleration in cm/s , i.e., for $f \gg f_c$. They use average or random horizontal component accelerometer amplitudes at a distance of 10 km from the hypocenter or from the closest fault segment. \mathbf{m} has been scaled to the moment magnitude $\mathbf{M} = M_w$ for events of average stress drop in eastern North America and California. When \mathbf{M} is known, \mathbf{m} is a measure of stress drop. For large pre-instrumental earthquakes \mathbf{m} can more reliably be estimated than \mathbf{M} from the felt area of earthquake shaking (see 3.2.6.7). When used together, \mathbf{m} and \mathbf{M} provide a good index of ground motion over the entire engineering frequency band, allow better estimates of response spectra and peak ground motions and thus of seismic hazard.

3. Seismic Sources and Source Parameters

3.2.6.9 Tsunami magnitudes

A different kind of magnitude is the tsunami magnitude scale M_t . According to Abe (1989)

$$M_t = \log H_{\max} + a \log \Delta + C \quad (3.32)$$

where H_{\max} is the maximum single (crest or trough) amplitude of tsunami waves in m as measured by tide-gage records and /or as derived from maximum inundation height, Δ - epicentral distance in km to the respective tide station and a and C - constants (a was found to be almost 1). In case of the long-wave approximation, i.e., with tsunami wavelengths being much larger than the bathymetric depths, the maximum tsunami height is strictly related to the maximum *vertical* deformation of the ocean bottom, $D_{\perp\max}$, and thus to the seismic moment M_0 . M_t was calibrated, therefore, with the average condition $M_t = M_w$ for the calibration data set. This resulted in:

$$M_t = \log H_{\max} + \log \Delta + 5.8. \quad (3.33)$$

(3.33) shows no saturation. For the Chile earthquake 1960 $M_t = 9.4$ while $M_w = 9.5$. Sometimes, very slow but large ruptures with a large seismic moment cause much stronger tsunami than would have been expected from their surface wave, energy or body-wave magnitudes M_s , M_e or m_b , respectively. Such events are called "tsunami earthquakes". A striking example is the April 1, 1946 Aleutian earthquake with $M_s = 7.3$ and $M_t = 9.3$. Such strong but very slow earthquakes may have negligibly small energy in the high-frequency range and cause no or only minor shaking damage (see paragraph below Eq. 3.20).

3.2.7 Relationships among magnitude scales

Gutenberg and Richter (1956a and b) provided correlation relations between various magnitude scales:

$$m = 2.5 + 0.63 M_s \quad (3.34)$$

$$m = 1.7 + 0.8 M_I - 0.01 M_I^2 \quad \text{and} \quad (3.35)$$

$$M_s = 1.27 (M_I - 1) - 0.016 M_I^2, \quad (3.36)$$

where m is the unified magnitude as the weighted mean of the body-wave magnitudes m_B determined from medium-period recordings. Practically the same relation as (3.34) was derived later by Abe and Kanamori (1980): $m_B = 2.5 + 0.65 M_s$, which is good up to $M_w = 8-8.5$; thereafter it shows saturation. Note, however, when using Eq. (3.34) and Eq. (3.84) in section 3.6.2 that the average difference between the Gutenberg-Richter M_s and the "Prague" M_s is about 0.2 magnitude units (see Eq. (3.11)).

Note that all these relations resulted from single random-variable parameter regression analysis assuming that the independent variable X (on the right side of the equation) is known and not afflicted with random errors and that the data scatter observed is due to random errors in the Y - (ordinate) direction only. Often they are wrongly applied, e.g., by solving Eq. (3.34) for M_s and calculating M_s for short-period m_b values as published by international data centers and finally calculating seismic energy E_s via E_s - M_s relationships (see 3.6). Note that Eq. (3.34) is an optimal estimator for m_B but not for M_s ! In fact, both m_B and M_s

determinations are afflicted with random errors and both account for the data scatter in an empirical mB-Ms diagram. Therefore, only a two random-variable parameter regression (so-called "orthogonal regression") analysis yields equations which can be used both ways for optimal parameter estimation (Bormann and Khalturin, 1975; Bormann and Wylegalla, 1975, Ambraseys, 1990). Equivalent to it are non-linear "maximum-likelihood" regressions as they have been systematically applied by Gusev (1991) to investigate the relationship between Mw and the magnitudes mb (with A_{\max} within first few seconds only), mSKM (with A_{\max} in the whole P-wave group), mB, m_b^* and \hat{m}_b , MI, Ms, and M(JMA) in both graphic and tabular form. Another paper comparing different magnitude scales was published by Utsu (1982).

When using medium-period readings of P and surface waves in displacement broadband records of type C (Kirnos SKD; see Fig. 3.11) and single random parameter regression, practically identical relationships to Eq. (3.34) were found both by Bune et al. (1970) on the basis of records of the former Soviet station network and by Bormann and Wylegalla (1975) for a single station in Germany (MOX; magnitude range 4.7 to 8.5). The latter is

$$\text{MPV} = 2.5 + 0.60 \text{ MLH}. \quad (3.37)$$

Note that the related orthogonal regression to Eq. (3.37), calculated for the same data set, is rather different:

$$\text{MPV} - 0.70 \text{ MLH} = 1.83 \quad (3.38)$$

and that the respective best fitting single random-parameter regression with respect to MLH is

$$\text{MLH} = - 1.54 + 1.25 \text{ MPV}. \quad (3.39)$$

The latter is clearly different from

$$\text{MLH} = - 4.17 + 1.67 \text{ MPV} \quad (3.40)$$

which one gets when resolving incorrectly Eq. (3.37) for MLH. As compared to Eq. (3.39), Eq. (3.40) results in an overestimation of MLH by about 1.2 magnitude units for mB = 8 and an underestimation of 0.8 units for mB = 5!

The single random-parameter regression relationship between short-period mb and Ms is very different from Eq. (3.34), namely, according to Gordon (1971),

$$\text{mb} = (0.47 \pm 0.02) \text{ Ms} + (2.79 \pm 0.09) \quad (3.41)$$

for a global station-earthquake data set. This agrees very well with the single-station average formula derived by Karnik (1972) for the Czech station Pruhonice (PRU):

$$\text{mb}(\text{sp, PRU}) = 0.47 \text{ MLH} + 2.95. \quad (3.42)$$

The orthogonal correlation between surface-wave magnitudes determined from vertical and horizontal component recordings using the so-called Prague-Moscow calibration function Eq. (3.10) is, according to Bormann and Wylegalla (1975), nearly ideal, namely:

$$\text{MLV} - 0.97 \text{ MLH} = 0.19 \quad (3.43)$$

3. Seismic Sources and Source Parameters

with a standard deviation of only 0.11 and a correlation coefficient of $r = 0.98$. This clearly justifies the use of this calibration function, which was originally derived from horizontal amplitude readings, for vertical component (Rayleigh wave) magnitude determinations, too.

When using medium-period broadband data only, the orthogonal regression relation between magnitude determinations from PV and PPV or SH waves, respectively, are almost ideal. Gutenberg and Richter (1956a) had published Q-functions for all three phases (see Figures 1a-c and Table 6 in DS 3.1). Bormann and Wylegalla (1975) found for a global earthquake data set recorded at station MOX the orthogonal fits:

$$M_{PPV} - M_{PV} = 0.05 \quad (3.44)$$

with a standard deviation of only ± 0.15 magnitude units and

$$M_{SH} - 1.1 M_{PV} = -0.64, \quad (3.45)$$

with a standard deviation of ± 0.19 and magnitude values for P and S waves, which differ in the whole range of $M_{PV}(=mB)$ between 4 and 8 less than 0.25 units from each other. This confirms the good mutual scaling of these original body-wave calibration functions with each other, provided that they are correctly applied to medium-period data only. Therefore, it is not understandable why the international data centers do not encourage data producers to report also amplitudes from PPV and SH waves for proper determination of mB.

Kanamori (1983) summarized the relationship between the various magnitude scales in graphical form (Fig. 3.18). It also gives the ranges of uncertainty for the various magnitude scales due to observational errors and intrinsic variations in source properties related to differences in stress drop, complexity, fault geometry and size, source depth etc. The range of periods for which these magnitudes are determined are for mb: ≈ 1 s; for M_L : $\approx 0.1 - 3$ s; for mB: $\approx 0.5 - 15$ s; for M_s : ≈ 20 s and for M_w : $\approx 10 \rightarrow \infty$ s. Accordingly, these different magnitude scales saturate differently: the shorter the dominating periods the earlier saturation occurs, i.e., for mb around 6.5, M_L around 7, mB at about 8 and M_s at about 8.5 while M_w does not saturate. This is in good agreement with the general conclusions drawn on the basis of seismic source spectra (see Fig. 3.5).

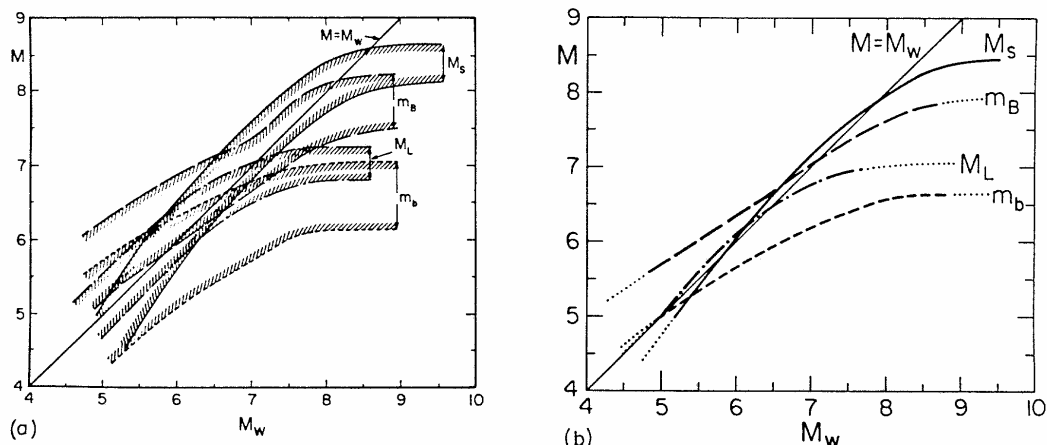


Fig. 3.18 Relations between magnitude scales (reprinted from *Tectonophysics*, 93, No. 3/4 Kanamori, *Magnitude scale and quantification of earthquakes*, 1983, Fig. 4, p. 193; with permission from Elsevier Science Publishers). Note the saturation of mb, mB, M_L and M_s .

Ambrasseys (1990), in an effort to arrive at uniform magnitudes for European earthquakes, re-evaluated magnitudes in the range $3 < M < 8$. He derived the following *orthogonal regression relationships* between the various common magnitude scales:

$$0.75 \text{ mb} - 0.66 \text{ mB} = 0.21 \quad (3.46)$$

$$0.77 \text{ mb} - 0.64 \text{ MI} = 0.73 \quad (3.47)$$

$$0.86 \text{ mb} - 0.49 \text{ Ms} = 1.94 \quad (3.48)$$

$$0.80 \text{ MI} - 0.60 \text{ Ms} = 1.04 \quad (3.49)$$

with mb being determined according to the ISC procedure from short-period P-wave recordings and mB using medium-period P-wave records. These relations can be solved for either one of the two variables. Other relationships have been published by Nuttli (1985) which allow estimating Ms for plate-margin earthquakes when mb is known. For $\text{mb} > 5$ their results differ less than 0.2 magnitude units from those of Eq. (3.48) when solved for Ms.

3.2.8 Summary remarks about magnitudes and their perspective

Magnitude was originally intended to be a measure of earthquake size in terms of the seismic energy E_S released by the source. E_S , which is proportional to the squared velocity of ground motion, can theoretically be obtained by integrating spectral energy density over all frequencies contained in the transient waveform, e.g., of the P-, S- or surface-wave train. This procedure could not be carried out efficiently with analog recordings. Therefore, Gutenberg (1945 a, b and c) assumed that the maximum amplitude observed in a wave group was a good measure of the total energy in that arrival. As classical seismographs were relatively broadband displacement sensors, he obtained a measure of ground motion velocity by dividing the measured maximum ground displacement by the associated period [see Eqs. (3.10) and (3.13) for surface- and body-wave magnitudes]. Note, however, that the related calibration functions did not account for frequency-dependent attenuation. Calibration functions are, therefore, usually applied only over rather limited frequency ranges, e.g., around 1 Hz and 0.05 Hz, respectively.

According to Fig. 3.5, magnitude can be a reasonable measure of E_S only if it samples the maximum amplitudes in the velocity spectrum which occur at the corner frequency f_c of the displacement "source spectrum"; f_c decreases with increasing seismic moment and, thus, with magnitude. Most classical band-limited seismic recordings sampled the ground motion over a bandwidth of not more than 0.3 to 0.9 decades (see Fig. 3.11). Hence, sampling of spectral amplitudes at frequencies smaller or larger than f_c of the wave spectrum underestimates the maximum ground velocity and, thus, E_S . This is the case for the body-wave magnitude mb, which is determined from narrow-band short-period recordings centered around 1 Hz, for magnitudes larger than about 5. Similarly, Ms, which is determined from surface waves with $T \approx 20$ s, underestimates maximum ground velocity and E_S for $M_s < 6$ and for $M_s > 7.5$.

One must also recognize that all band-limited magnitudes saturate, e.g., mb saturates for magnitudes > 6.5 and Ms saturates for magnitudes $>$ about 8.5. However, mB, determined from medium-period records saturates later than mb (see Fig. 3.18). To overcome this problem, magnitude determinations should be based on broadband digital recordings with a bandwidth of ideally about 4 decades or even more. Only then it can be assured that the peak of the ground-velocity spectrum as well as a fair part of higher and lower frequencies on both

3. Seismic Sources and Source Parameters

sides of the corner frequency are covered within the passband of the seismograph. This passband is sufficient to allow determination of both the scalar seismic moment M_0 (and the associated moment magnitude M_w) and the radiated energy E_S (and the associated energy magnitude M_e). Both M_w and M_e do not saturate. However, note that they express different aspects of the seismic source and may differ by more than one magnitude unit (see Tab. 3.2). Also, direct determination of E_S is not trivial and requires a good distribution of stations. Nevertheless, a single station, when equipped with a velocity-proportional digital broadband sensor, could easily determine a non-saturating mB (see 3.2.6.3) by sampling the maximum amplitudes of ground velocity. Such an mB might be a good preliminary estimate of M_e and the high-frequency energy released by the source. This needs to be tested with real data, however, the required frequency-dependent calibration functions are not yet well established. This should become a priority task of the IASPEI WG on magnitudes.

Despite the advantage of more physically based broadband magnitudes, the overwhelming majority of magnitude data is and will continue to be based for quite some more time on band-limited recordings using the classical formulas. In many earthquake-prone regions, particularly those lacking historical macroseismic data and strong-motion records, seismic hazard assessment rests on the availability of such data. Moreover, band-limited magnitudes sometimes have value for purposes other than energy or moment estimates. E.g., the mb/ M_s ratio is a very powerful teleseismic discriminator between earthquakes and underground nuclear explosions, and M_I is, at least up to medium-size earthquakes, well scaled with macroseismic intensity and, thus, damage. Therefore, magnitudes of different kinds will still be needed in the foreseeable future. Their proper use, however, requires an understanding of their potentials, limitations, original definitions and mutual relationships. Finally, one has to assure the long-term continuity and stability of magnitude values according to agreed standards of measurement by annotating different magnitudes in an unambiguous way (see IS 3.2), and by refraining from one-sided, internationally unrecognized and improperly documented changes in procedures which may cause baseline changes in earthquake catalogs. This section aimed at creating awareness and setting standards on this important issue.

3.3 Radiated seismic energy and energy magnitude (G. L. Choy and J. Boatwright)

3.3.1 Introduction

One of the most fundamental parameters for describing an earthquake is radiated seismic energy. In theory, its computation simply requires an integration of radiated energy flux in velocity-squared seismograms. In practice, energy has historically almost always been estimated with empirical formulas. The empirical approach dominated for two major reasons. First, until the 1980's most seismic data were analog, a format which was not amenable to spectral processing on a routine basis. Second, an accurate estimate of radiated energy requires the analysis of spectral information both above and below the corner frequency of an earthquake, about which energy density is most strongly peaked.

Prior to the worldwide deployment of broadband seismometers, which started in the 1970's, most seismograms were recorded by conventional seismographs with narrowly peaked instrument responses. The difficulties in processing analog data were thus compounded by the limitations in retrieving reliable spectral information over a broad bandwidth. Fortunately, theoretical and technological impediments to the direct computation of radiated energy have

been removed. The requisite spectral bandwidth is now recorded digitally by a number of seismograph networks and arrays with broadband capability, and frequency-dependent corrections for source mechanism and wave propagation are better understood now than at the time empirical formulas were first developed.

3.3.2 How is radiated seismic energy measured?

3.3.2.1 Method

The method described below for estimating the radiated seismic energy of teleseismic earthquakes is based on Boatwright and Choy (1986). Velocity-squared spectra of body waves are corrected for effects arising from source mechanism, depth phases, and propagation through the Earth.

For shallow earthquakes where the source functions of direct and surface-reflected body-wave arrivals may overlap in time, the radiated energy of a P -wave group (consisting of P , pP and sP) is related to the energy flux by

$$E_S^P = 4\pi \langle F^P \rangle^2 \left(\frac{R^P}{F^{gP}} \right)^2 \mathcal{E}_{gP}^* \quad (3.50)$$

where the P -wave energy flux, \mathcal{E}_{gP}^* , is the integral of the square of the ground velocity, taken over the duration of the body-wave arrival,

$$\mathcal{E}_{gP}^* = \rho\alpha \int_0^\infty \dot{u}(t)^2 dt \quad (3.51)$$

Here, \dot{u} is velocity, which must be corrected for frequency-dependent attenuation; ρ and α are density and velocity at the receiver, respectively; $\langle F^P \rangle^2$ is the mean-square radiation-pattern coefficient for P waves; R^P is the P -wave geometrical spreading factor; F^{gP} is the generalized radiation pattern coefficient for the P -wave group defined as

$$(F^{gP})^2 = (F^P)^2 + (\hat{P}P F^{pP})^2 + \frac{2\alpha q}{3\beta} (\hat{S}P F^{sP})^2 \quad (3.52)$$

where F^i are the radiation-pattern coefficients for $i = P, pP$, and sP ; $\hat{P}P$ and $\hat{S}P$ are plane-wave reflection coefficients of pP and sP at the free surface, respectively, corrected for free-surface amplification; and q is 15.6, the ratio of S -wave energy to P -wave energy (Boatwright and Fletcher, 1984). The correction factors explicitly take into account our knowledge that the earthquake is a double-couple, that measurements of the waveforms are affected by interference from depth phases, and that energy is partitioned between P and S waves. For teleseismically recorded earthquakes, energy is radiated predominantly in the bandwidth 0.01 to about 5.0 Hz. The wide bandwidth requires a frequency-dependent attenuation correction (Cormier, 1982). The correction is easily realized in the frequency domain by using Parseval's theorem to transform Eq. (3.51),

$$\mathcal{E}_{gP}^* = \frac{\rho\alpha}{\pi} \int_0^\infty \dot{u}(\omega)^2 e^{\omega t_\alpha^*} d\omega \quad (3.53)$$

where t_α^* is proportional to the integral over ray path of the imaginary part of complex slowness in an anelastic Earth. An appropriate operator, valid over the requisite broad

3. Seismic Sources and Source Parameters

bandwidth, is described by Choy and Cormier (1986) and shown in Fig. 3.19. The t_α^* of the P -wave operator ranges from 1.0 s at 0.1 Hz to 0.5 s at 2.0 Hz.

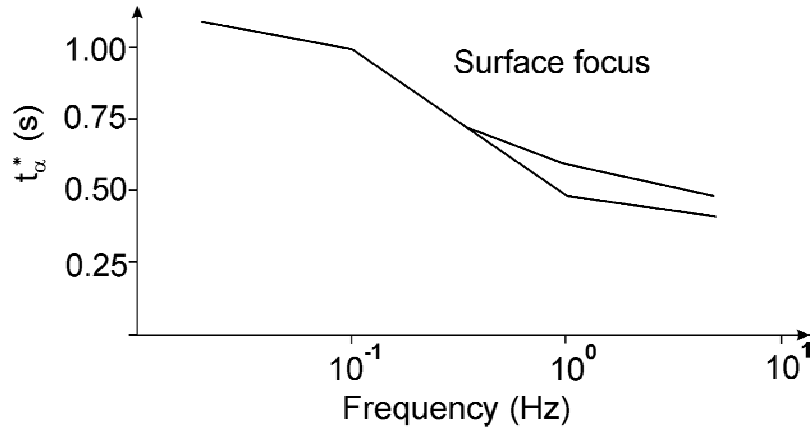


Fig. 3.19 Teleseismic t_α^* derived by Choy and Cormier (1986) plotted as a function of frequency for a surface-focus source and a surface receiver at a distance of 60° . The split in the curve at frequencies higher than 0.3 Hz indicates the variation in regional t_α^* expected for different receiver sites. In practice the mean of the two curves is used for the attenuation correction.

The numerical integration of Eq. (3.53) is limited to either the frequency at which signal falls below the noise level (typically at frequencies greater than 2.0-3.0 Hz) or to the Nyquist frequency. If this limiting or cutoff frequency, ω_c , is greater than the corner frequency, the remainder of the velocity spectrum is approximated by a curve that falls off by ω^{-1} . In practice, therefore, Eq. (3.53) consists of a numerical integral, N , truncated at ω_c , and a residual integral, R , which approximates the remainder of the integral out to infinite frequency,

$$\varepsilon_{gp}^* = \rho\alpha N + \rho\alpha R \quad (3.54)$$

where, as shown in Boatwright and Choy (1986),

$$R = \frac{\omega_c}{\pi} \left[\dot{u}_c(\omega_c) \right]^2 \quad (3.55)$$

in which \dot{u}_c is the attenuation-corrected value of velocity at ω_c .

Although teleseismic SH - and SV -wave groups from shallow earthquakes can be analyzed through a straightforward extension of Eq. (3.50) as described in Boatwright and Choy (1986), shear waves suffer substantially more attenuation in propagation through the Earth than the P waves. The loss of seismic signal due to shear attenuation usually precludes retrieving useful spectral information for frequencies higher than about 0.2-0.3 Hz for all but the largest earthquakes. Thus, for the routine estimation of energy, it is more practical and more accurate to use only the P -wave group (Eqs. (3.50) and (3.53)). The formula for computing the total radiated energy when using the P -wave group alone is

$$E_s = (1 + q) E_s^P. \quad (3.56)$$

3.3.2.2 Data

Data used in the direct measurement of energy must satisfy three requirements. First, the implementation of Eq. (3.53) requires that the velocity data contain spectral information about, above and below the corner frequency of an earthquake. Because the corner frequency can vary from earthquake to earthquake depending on source size and rupture complexity, the bandwidth of the data must be sufficiently wide so that it will always cover the requisite range of frequencies above and below the corner frequency. For body waves from teleseismically recorded earthquakes, a spectral response that is flat to ground velocity between 0.01 Hz through 5.0 Hz is usually sufficient. The second requirement is that the duration of the time window extracted from a seismogram should correspond to the time interval over which the fault is dynamically rupturing. As shown by the examples in Fig. 3.20, when broadband data are used, delimiting the time window is generally unequivocal regardless of the complexity of rupture or the size of the earthquake. The initial arrival of energy is obviously identified with the onset of the direct *P* wave. The radiation of energy becomes negligible when the amplitude of the velocity-squared signal decays to the level of the coda noise. The final requirement is that we use waveforms that are not complicated by triplications, diffractions or significant secondary phase arrivals. This restricts the usable distance range to stations within approximately 30°-90° of the epicenter. In addition, waveforms should not be used if the source duration of the *P*-wave group overlaps a significant secondary phase arrival. For example, this may occur when a very large earthquake generates a *P*-wave group with a duration of such length that it does not decay before the arrival of the *PP*-wave group.

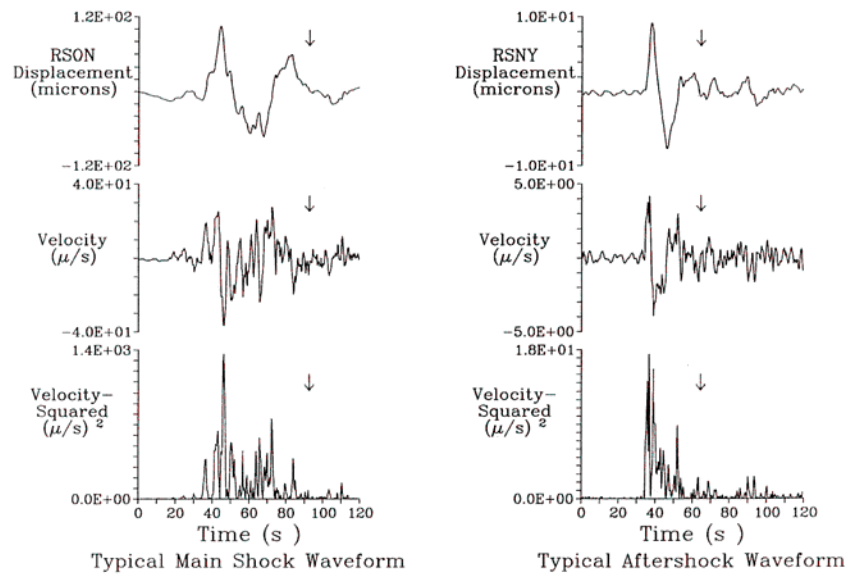


Fig. 3.20 (Left) Broadband displacement, velocity, and velocity-squared records for the large ($M_s = 7.8$, $M_e = 7.5$, $M_w = 7.7$) Chilean earthquake of 3 March 1985. Rupture complexity, in the form of a tiny precursor and a number of sub-events, is typical for large earthquakes. (Right) Broadband displacement, velocity and velocity-squared records for an aftershock ($m_b = 5.9$, $M_e = 6.2$, $M_w = 6.6$) to the Chilean earthquake that occurred 17 March 1985. The waveforms are less complex than those of the main shock. Despite the differences in rupture complexity, duration and amplitude, the time window over which energy arrives is unequivocal. In each part of the figure the arrows indicate when the velocity-squared amplitude has decreased to the level of the coda noise.

3.3.3 Development of an energy magnitude, M_e

In the Gutenberg-Richter formulation, an energy is constrained once magnitude is known through $\log E_S = a + b M$ where a and b are constants. For surface-wave magnitude, M_s , the Gutenberg-Richter formula takes the form

$$\log E_S = 4.8 + 1.5 M_s \quad (3.57)$$

where E_S is in units of Joules (J). In the normal usage of Eq. (3.57), an energy is derived after an M_s is computed. However, it is now recognized that for very large earthquakes or very deep earthquakes, the single frequency used to compute M_s is not necessarily representative of the dimensions of the earthquake and, therefore, might not be representative of the radiated energy. Since radiated energy can now be computed directly, it is an independent parameter from which a unique magnitude can be defined. In Fig. 3.21, the radiated energies for a set of 378 global shallow earthquakes from Choy and Boatwright (1995) are plotted against their magnitudes, M_s . The Gutenberg-Richter relationship is plotted as a dashed line in Fig. 3.21. Assuming a b -value of 1.5, the least-squares regression fit between the actual energies and magnitude is

$$\log E_S = 4.4 + 1.5 M_s \quad (3.58)$$

which is plotted as the solid line in Fig. 3.21. The a -value of 4.4 indicates that on average the original Gutenberg-Richter formula overestimates the radiated energy by a factor of two. To define energy magnitude, M_e , we replace M_s with M_e in Eq. (3.58)

$$\log E_S = 4.4 + 1.5 M_e \quad (3.59)$$

or

$$M_e = \frac{2}{3} \log E_S - 2.9. \quad (3.60)$$

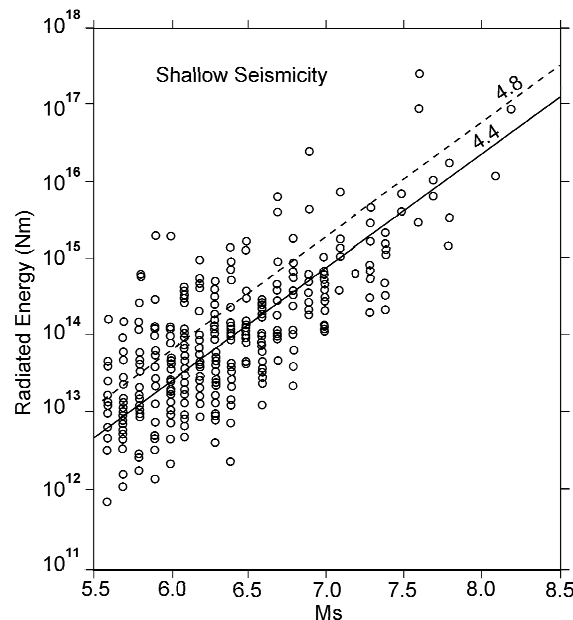


Fig. 3.21 Radiated energy (E_S) of global data as a function of surface-wave magnitude (M_s). The energy predicted by the Gutenberg-Richter formula, $\log E_S = 4.8 + 1.5 M_s$ (in units of Newton-meters), is shown by the dashed line. From a least-squares regression, the best-fitting line with the slope of 1.5 is $\log E_S = 4.4 + 1.5 M_s$ (according to Choy and Boatwright, 1995).

The usage of Eq. (3.60) is conceptually antithetical to that of Eq. (3.57). In Eq. (3.60) magnitude is derived explicitly from energy, whereas in Eq. (3.57) energy is dependent on the value of magnitude.

3.3.4 The relationship of radiated energy to moment and apparent stress

The energy and moment for a particular earthquake are related by apparent stress, σ_{app} (see Equation (59) in IS 3.1),

$$\sigma_{app} = \mu E_S / M_0 \quad (3.61)$$

where μ is the average rigidity at the source. When radiated energy, E_S , is plotted against seismic moment, M_0 , for global shallow earthquakes (Fig. 3.22), the best fit by least-squares regression of E_S on M_0 (solid line) yields

$$E_S = 1.6 \cdot 10^{-5} M_0. \quad (3.62)$$

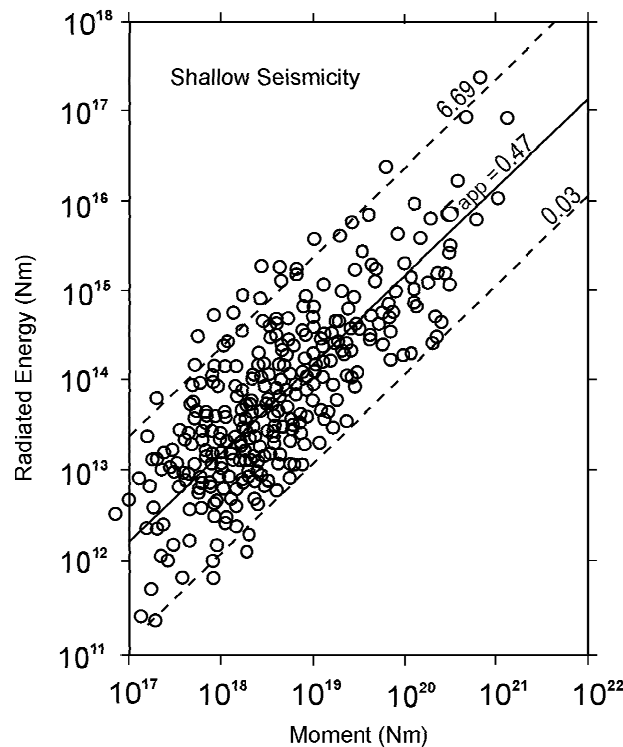


Fig. 3.22 Radiated energy, E_S , of 394 shallow-focus earthquakes as a function of seismic moment, M_0 . The slope of the least-squares log-normal regression (solid line) yields a global average apparent stress $\bar{\sigma}_{app}$ of about 0.5 MPa assuming a source rigidity of $0.3 \cdot 10^5$ MPa. The 95% spread (or width of distribution) about the regression line is indicated by the dashed lines (according to Choy and Boatwright, 1995).

Assuming an average rigidity for shallow earthquakes of $0.3 \cdot 10^5$ MPa, the slope of the regression line yields a worldwide average apparent stress, $\bar{\sigma}_{app}$ of about 0.47 MPa. The spread about the regression line is very large. In terms of apparent stress it is between 0.03 to 6.69 MPa. Empirical formulas, like those employing M_0 or M_s , ignore the spread and, thus,

3. Seismic Sources and Source Parameters

would be poor predictors of energy. Viewing the spread of E_s - M_0 values about the regression line in terms of apparent stress, rather than random scatter, may provide significant insight into the physics of earthquake occurrence. For example, the release of energy and apparent stress could vary systematically as a function of faulting type, lithospheric strength and tectonic region (Choy and Boatwright, 1995). As more statistics on the release of energy are accumulated, spatial and temporal variations in energy release and apparent stress might also be identified.

3.3.5 The relationship of M_e to M_w

Although M_e and M_w are magnitudes that describe the size of an earthquake, they are not equivalent. M_e , being derived from velocity power spectra, is a measure of the radiated energy in form of seismic waves and thus of the seismic potential for damage to anthropogenic structures. M_w , being derived from the low-frequency asymptote of displacement spectra, is physically related to the final static displacement of an earthquake. Because they measure different physical properties of an earthquake, there is no *a priori* reason that they should be numerically equal for any given seismic event. The usual definition of M_w is:

$$M_w = 2/3 \log M_0 - 6.0 \quad (\text{with } M_0 \text{ in Nm}). \quad (3.63)$$

The condition under which M_e is equal to M_w , found by equating Eq. (3.60) and Eq. (3.63), is $E_s/M_0 \sim 2.2 \cdot 10^{-5}$. From Eq. (3.61) this ratio is equivalent to $\sigma_{app} \sim 2.2 \cdot 10^{-5} \mu$. For shallow earthquakes, where $\mu \sim 0.3-0.6 \times 10^5$ MPa, this condition implies that M_e and M_w will be coincident only for earthquakes with apparent stresses in the range 0.66-1.32 MPa. As seen in Fig. 3.22, this range is but a tiny fraction of the spread of apparent stresses found for earthquakes. Therefore, the energy magnitude, M_e , is an essential complement to moment magnitude, M_w , for describing the size of an earthquake. How different these two magnitudes may be is illustrated in Tab. 3.2. Two earthquakes occurred in Chile within months of each other and their epicenters were less than 1° apart. Although their M_w 's and M_s 's were similar, their m_b 's and M_e 's differed by 1 to 1.4 magnitude units! Table 3.2 describes the macroseismic effects from the two earthquakes. The event with larger M_e caused significantly greater damage!

Tab. 3.2 (Reprinted from Choy et al., 2001.)

Date	LAT (°)	LON (E)	Depth (km)	M_e	M_w	m_b	M_s	σ_a (bars)	Faulting Type
6 JUL 1997 (1)	-30.06	-71.87	23.0	6.1	6.9	5.8	6.5	1	interplate-thrust
15 OCT 1997 (2)	-30.93	-71.22	58.0	7.5	7.1	6.8	6.8	44	intraslab-normal

(1) Felt (III) at Coquimbo, La Serena, Ovalle and Vicuna.
(2) Five people killed at Pueblo Nuevo, one person killed at Coquimbo, one person killed at La Chimba and another died of a heart attack at Punitaqui. More than 300 people injured, 5,000 houses destroyed, 5,700 houses severely damaged, another 10,000 houses slightly damaged, numerous power and telephone outages, landslides and rockslides in the epicentral region. Some damage (VII) at La Serena and (VI) at Ovalle. Felt (VI) at Alto del Carmen and Illapel; (V) at Copiapo, Huasco, San Antonio, Santiago and Vallenar; (IV) at Caldera, Chanaral, Rancagua and Tierra Amarilla; (III) at Talca; (II) at Concepcion and Taltal. Felt as far south as Valdivia. Felt (V) in Mendoza and San Juan Provinces, Argentina. Felt in Buenos Aires, Catamarca, Cordoba, Distrito Federal and La Rioja Provinces, Argentina. Also felt in parts of Bolivia and Peru.

3.3.6 Regional estimates of radiated seismic energy

Radiated energy from local and regional records can be computed in a fashion analogous to the teleseismic approach if suitable attenuation corrections, local site and receiver effects, and hypocentral information are available or can be derived. Boatwright and Fletcher (1984) demonstrated that integrated ground velocity from S waves could be used to estimate radiated energy in either the time or frequency domain by,

$$E_s = 4\pi C^2 r^2 \rho_r \beta_r \int_0^\infty \dot{u}_c(t)^2 dt \quad (3.64)$$

$$= 4\pi C^2 r^2 \rho_r \beta_r \int_0^\infty \dot{u}_c(\omega)^2 d\omega \quad (3.65)$$

where the ground velocity has been corrected for anelastic attenuation, C is a correction for radiation pattern coefficient and free-surface amplification, r is the source-receiver distance, and ρ_r and β_r are density and S-wave velocity at the receiver. The attenuation correction is usually of the type $\exp(\omega r/\beta Q)$, where Q is the whole-path attenuation. Similarly, Kanamori et al. (1993) use a time-domain method to estimate the S-wave energy radiated by large earthquakes in southern California,

$$E_\beta = 4\pi r^2 C_f^{-2} [r_0 q(r_0)/r q(r)]^2 \rho_0 \beta_0 \int_0^\infty \dot{u}^2(t) dt \quad (3.66)$$

where ρ_0 and β_0 are hypocentral density and S-wave velocity, C_f is the free-surface amplification factor, r is the source-receiver distance estimated from the epicentral distance Δ and a reference depth h of 8 km (such that $r^2 = \Delta^2 + h^2$). Attenuation is described by $q(r) = cr^{-n} \exp(-kr)$, which is the Richter (1935) attenuation curve as corrected by Jennings and Kanamori (1983). For southern California earthquakes, $c=0.49710$, $n=1.0322$, and $k=0.0035 \text{ km}^{-1}$.

3.3.7 Conclusions

Energy gives a physically different measure of earthquake size than moment. Energy is derived from the velocity power spectra, while moment is derived from the low-frequency asymptote of the displacement spectra. Thus, energy is a better measure of the severity of shaking and thus of the seismic potential for damage, while moment, being related to the final static displacement, is more related to the long-term tectonic effects of the earthquake process. Systematic variations in the release of energy and apparent stress as a function of faulting type and tectonic setting can now be identified that were previously undetectable because of the lack of reliable energy estimates. An energy magnitude, M_e , derived from an explicit computation of energy, can complement M_w and M_s in evaluating seismic and tsunamigenic potential.

3.4 Determination of fault-plane solutions (M. Baumbach, H. Grosser)

3.4.1 Introduction

The direction (polarity) and amplitude of motion of a seismic wave arriving at a distant station depends both on the wave type considered and the position of the station relative to the motion in the earthquake source. This is illustrated by Figs. 3.23a and b.

Fig. 3.23a represents a linear displacement of a point source S while Fig. 3.23b depicts a right lateral (dextral) shear dislocation along a fault plane F . Shear dislocations are the most common model to explain earthquake fault ruptures. Note that in the discussion below we consider the source to be a point source with rupture dimension much smaller than the distance to the stations and the wave length considered. First we look into the situation depicted in Fig. 3.23a. When S moves towards $\Delta 1$ then this station will observe a *compressional* (+) P-wave arrival (i.e., the first motion is *away* from S), $\Delta 4$ will record a P wave of opposite sign (-), a *dilatation* (i.e., first motion *towards* S), and station $\Delta 2$ will receive no P wave at all. On the other hand, S waves, which are polarized parallel to the displacement of S and perpendicular to the direction of wave propagation, will be recorded at $\Delta 2$ but not at $\Delta 1$ and $\Delta 4$ while station $\Delta 3$ will receive both P and S waves.

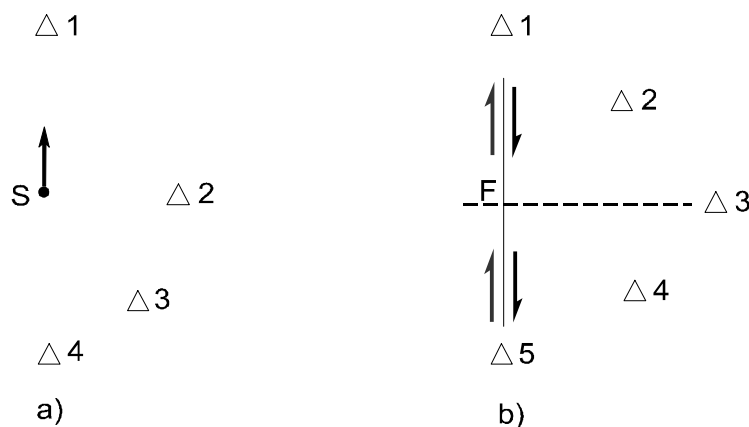


Fig. 3.23 Direction of source displacement with respect to seismic stations Δ_i for a) a single force at point S and b) a fault rupture F . Note that in the discussion below we consider the source to be a point source with a rupture dimension much smaller than the distance to the stations.

Somewhat different is the case of a fault rupture (Fig. 3.23b). At stations $\Delta 1$ and $\Delta 5$, which are positioned in the strike direction of the fault, the opposite signs of P motion on both side of the fault will cancel, i.e., no P waves will be observed. The latter also applies for station $\Delta 3$ which is sited perpendicular to the fault. On the other hand, stations $\Delta 2$ and $\Delta 4$, which are positioned at an angle of 45° with respect to the fault, will record the P-wave motions with maximum amplitudes but opposite sign. This becomes clear also from Fig. 3.25a. It shows the different polarities and the amplitude "lobes" in the four quadrants. The length of the displacement arrows is proportional to the P-wave amplitudes observed in different directions from the fault. Accordingly, by observing the sense of first motions of P waves at many stations at different azimuths with respect to the source it will be possible to deduce a "fault-

plane solution". But because of the symmetry of the first-motion patterns, two potential rupture planes, perpendicular to each other, can be constructed. Thus, on the basis of polarity data alone, an ambiguity will remain as to which one was the acting fault plane. This can only be decided by taking into account additional data on azimuthal amplitude and frequency or wave-form patterns, which are controlled by the Doppler effect of the moving source, and/or field data on the orientation and nature of seismotectonic faults.

In accordance with the above, the amplitude distribution of P waves for a point source with pure double-couple shear mechanism is described in a spherical co-ordinate system (θ , ϕ) (Aki and Richards, 1980; see Fig. 3.24) by

$$A_P(\theta, \phi) = \cos \phi \sin 2\theta. \quad (3.67)$$

This expression divides the focal sphere into four quadrants. The focal sphere for a seismic point source is conceived of as a sphere of arbitrarily small radius centered on the source. Within each quadrant the sign of the P-wave first motion (polarity) does not change but amplitudes are large in the center of the quadrant and small (or zero) near to (or at) the fault plane and the auxiliary plane. The nodal lines for P waves, on which $A_P(\theta, \phi) = \cos \phi \sin 2\theta = 0$, separate the quadrants. They coincide with the horizontal projection of the two orthogonal fault planes traces through the focal sphere. Opposite quadrants have the same polarity, neighboring quadrants different polarities. Note that *compression* is observed at stations falling in the *tension quadrant* (force directed away from the point source) while *dilatation* is observed at stations falling in the *compression quadrant* (force directed towards the point source).

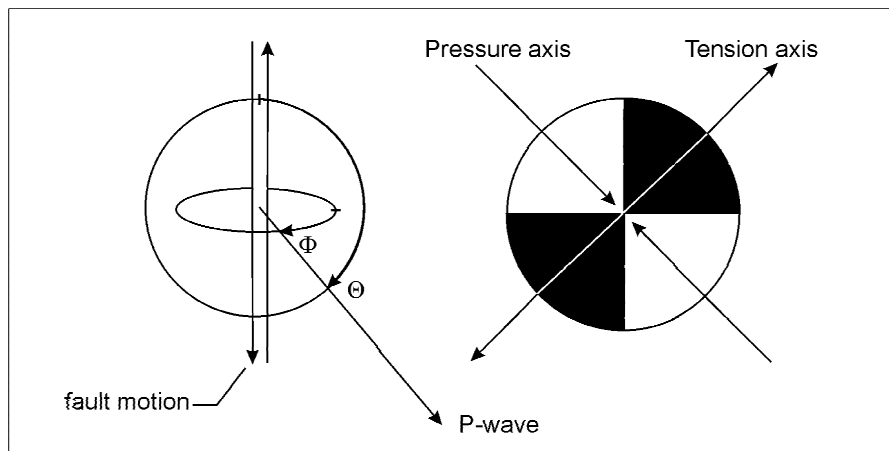


Fig. 3.24 Map view of P-wave radiation pattern for a shear fault. θ is the azimuth in the plane while ϕ is in fact three-dimensional. See also Fig. 3.23. Black areas: polarity +, white areas - .

The position of the quadrants on the focal sphere depends on the orientation of the active fault and of the slip direction in space. This is illustrated by Fig. 3.25, which shows the P-wave radiation pattern for a thrust event with some strike-slip component. Thus, the estimation of the P-wave first motion polarities and their back-projection onto the focal sphere allows us to identify the type of focal mechanism of a shear event (fault-plane solution). The only problem is, that the hypocenter and the seismic ray path from the source to the individual stations must be known. This may be difficult for a heterogeneous model with 2-D or 3-D velocity structure.

3. Seismic Sources and Source Parameters

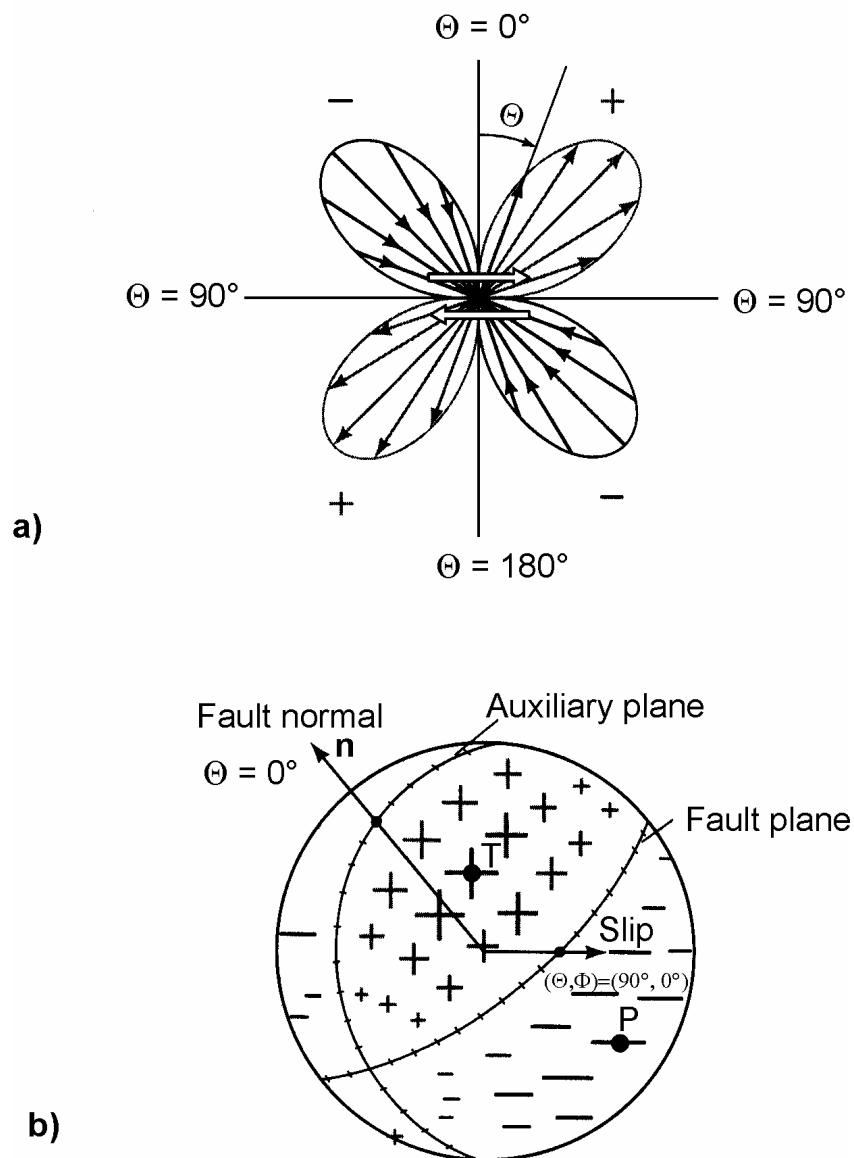


Fig. 3.25 Radiation pattern of the radial displacement component (P wave) due to a double-couple source: a) for a plane of constant azimuth (with lobe amplitudes proportional to $\sin 2\theta$) and b) over a sphere centered on the origin. Plus and minus signs of various sizes denote amplitude variation (with θ and ϕ) of outward and inward directed motions. The fault plane and auxiliary plane are nodal lines on which $\cos \phi \sin 2\theta = 0$. The pair of arrows in a) at the center denotes the shear dislocation. P and T mark the penetration points of the pressure and tension axes, respectively, through the focal sphere. Note the alternating quadrants of inward and outward directions of motion (compressional quadrant +; dilatational quadrant -) (modified from Aki and Richards 1980 ; with kind permission of the authors).

Fault-plane solutions based on P-wave first motion polarities will be better constrained if additionally the different radiation pattern of S waves displacement amplitudes is taken into account. An example is given in Fig. 3.26 for the same fault-plane solution as shown in Fig. 3.25 for P waves.

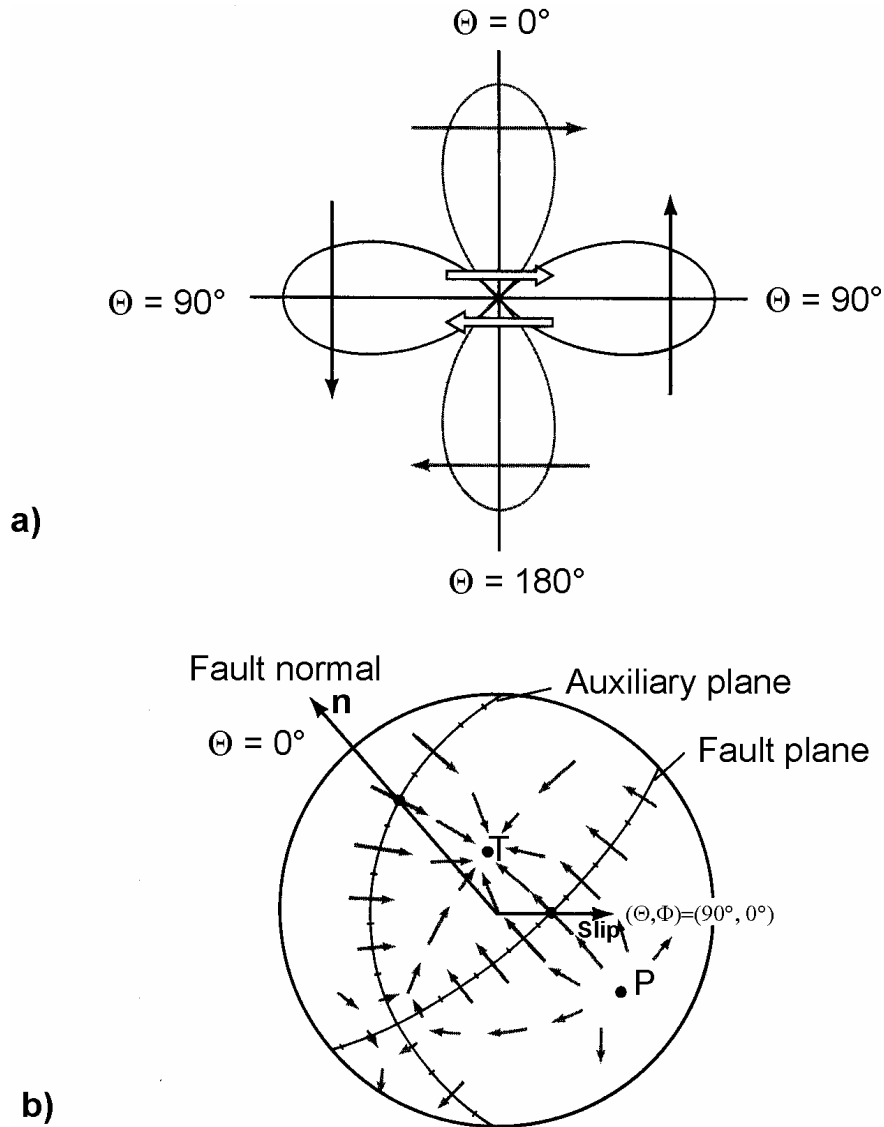


Fig. 3.26 Radiation pattern of the transverse displacement component (S wave) due to a double-couple source. a) in the plane $\{\phi = 0, \phi = \pi\}$ and b) over a sphere centered on the origin. Arrows imposed on each lobe in a) show the direction of particle displacement associated with the lobe while the arrows with varying size and direction in the spherical surface in b) indicate the variation of the transverse motions with θ and ϕ . P and T mark the penetration points of the pressure and tension axes, respectively, through the focal sphere. There are no nodal lines as in Fig. 3.25 but only nodal points where there is zero motion. The nodal point for transverse motion at $(\theta, \phi) = (45^\circ, 0^\circ)$ at T is a maximum in the pattern for longitudinal motion (see Fig.3.25) while the maximum transverse motion (e.g., at $\theta = 0$) occurs on a nodal line for the longitudinal motion. The pair of arrows in a) at the center denotes the shear dislocation (modified from Aki and Richards 1980; with kind permission of the authors).

In the case of a double-couple mechanism, according to Fig. 3.24, the S-wave amplitude pattern follows the relationship (see Aki and Richards, 1980)

3. Seismic Sources and Source Parameters

$$\mathbf{A}_S = \cos 2\theta \cos \phi \boldsymbol{\theta} - \cos \theta \sin \phi \boldsymbol{\phi} \quad (3.68)$$

with $\boldsymbol{\theta}$ and $\boldsymbol{\phi}$ - unit vectors in θ and ϕ direction, \mathbf{A}_S - shear-wave displacement vector.

3.4.2 Manual determination of fault-plane solutions

Manually determined fault-plane solutions are normally based on P-wave polarity readings only which are plotted on two kinds of projections, either the equal-angle Wulff net or the Lambert-Schmidt equal area projection (Figs. 3.27a and b; see also Aki and Richards, 1980, Vol. 1, p. 109-110). The latter provides a less cluttered plot of data with take-off angles less than 45° but in principle the procedure of constructing the fault planes is the same (see EX 3.2 and EX 3.3).

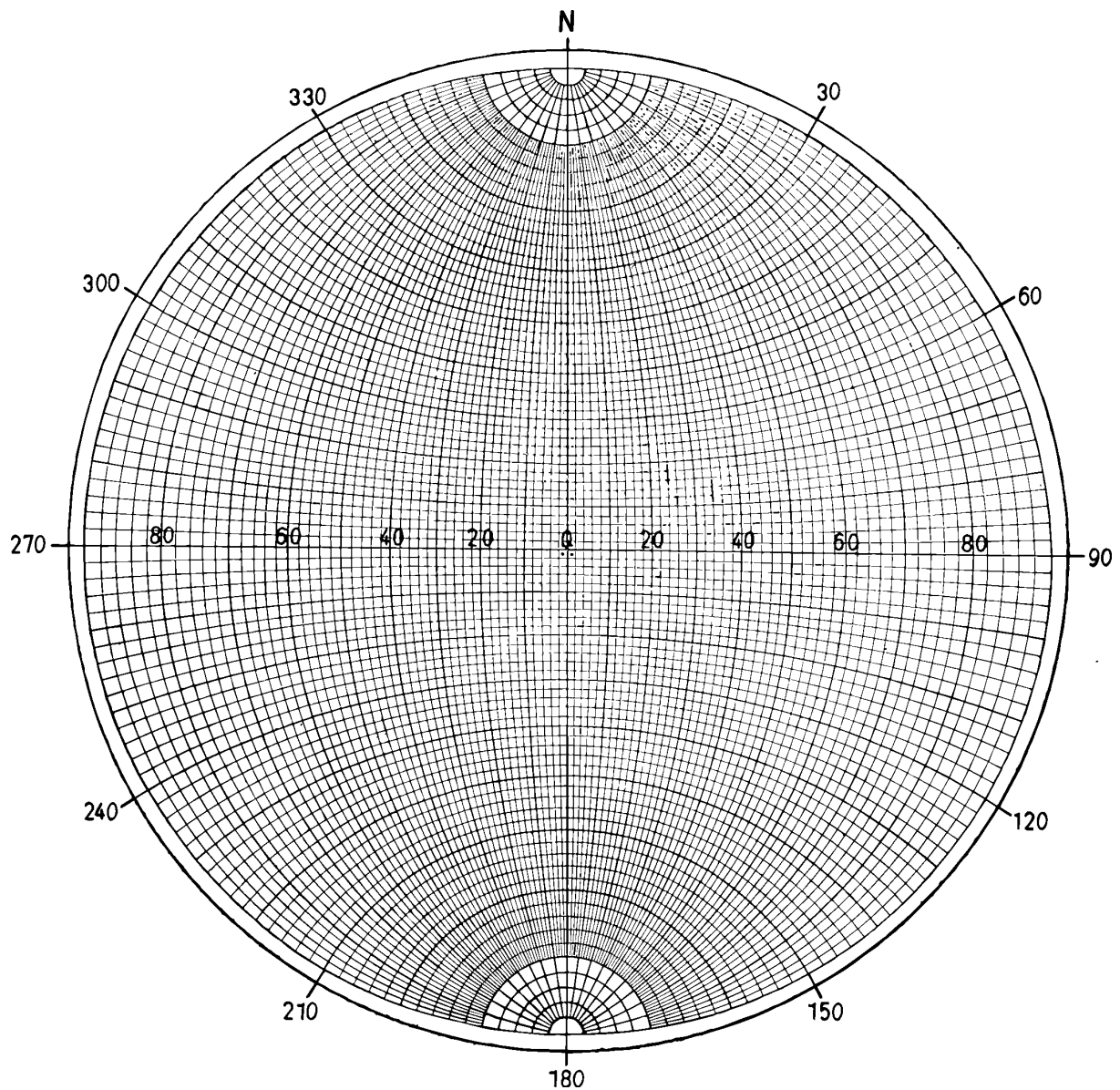


Fig. 3.27a The equal angle Wulff net. Note: Only the meridians are great circles!

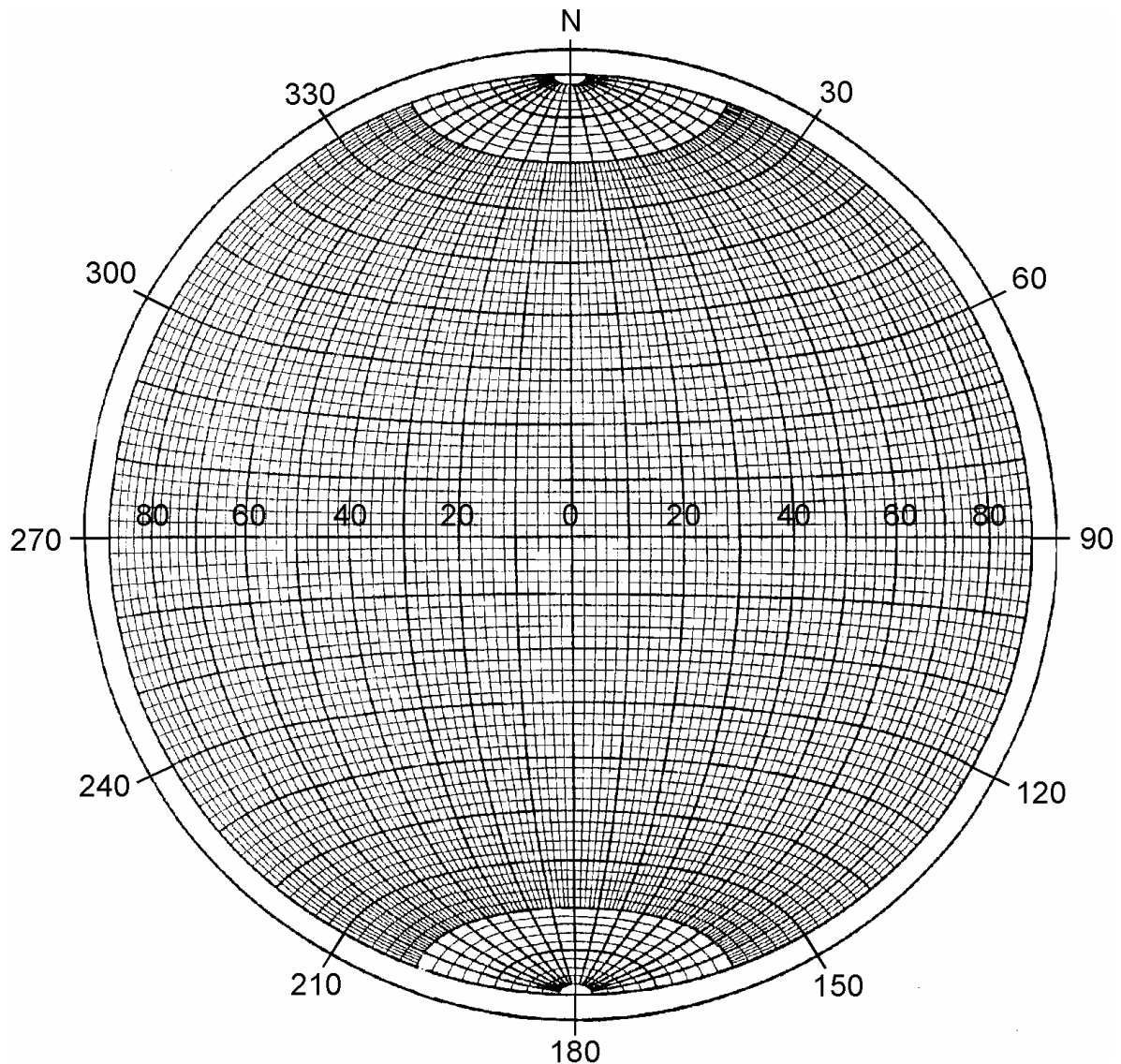


Fig. 3.27b The equal area Lambert-Schmidt net. Note: Only the meridians are great circles!

To obtain a fault-plane solution basically three steps are required:

- (1) Calculating the positions of the penetration points of the seismic rays through the focal sphere which are defined by the ray azimuth AZM and the take-off (incidence) angle AIN of the ray from the source.
- (2) Marking these penetration points through the upper or lower hemisphere in a horizontal projection of that sphere using different symbols for compressional and dilatational first arrivals. Usually, lower hemisphere projections are used. Rays which have left the upper hemisphere have to be transformed into their equivalent lower hemisphere ray. This is possible because of spherical symmetry of the radiation pattern (see Figs. 3.28 and 3.29).
- (3) Partitioning the projection of the lower focal sphere by two perpendicular great circles which separate all (or at least most) of the + and - arrivals in different quadrants.

3. Seismic Sources and Source Parameters

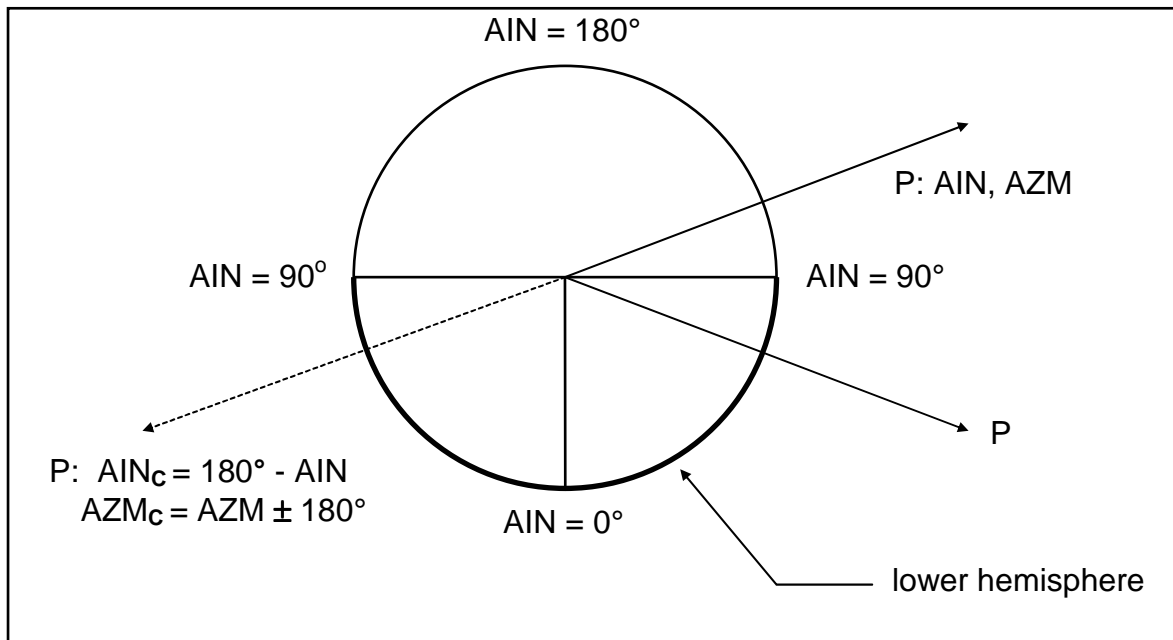


Fig. 3.28 Transformation of a ray leaving the focal sphere upwards with an incidence (take-off) angle A_{IN} into an equivalent downward ray with same polarity and changed incidence angle A_{IN_c} and azimuth AZM_c .

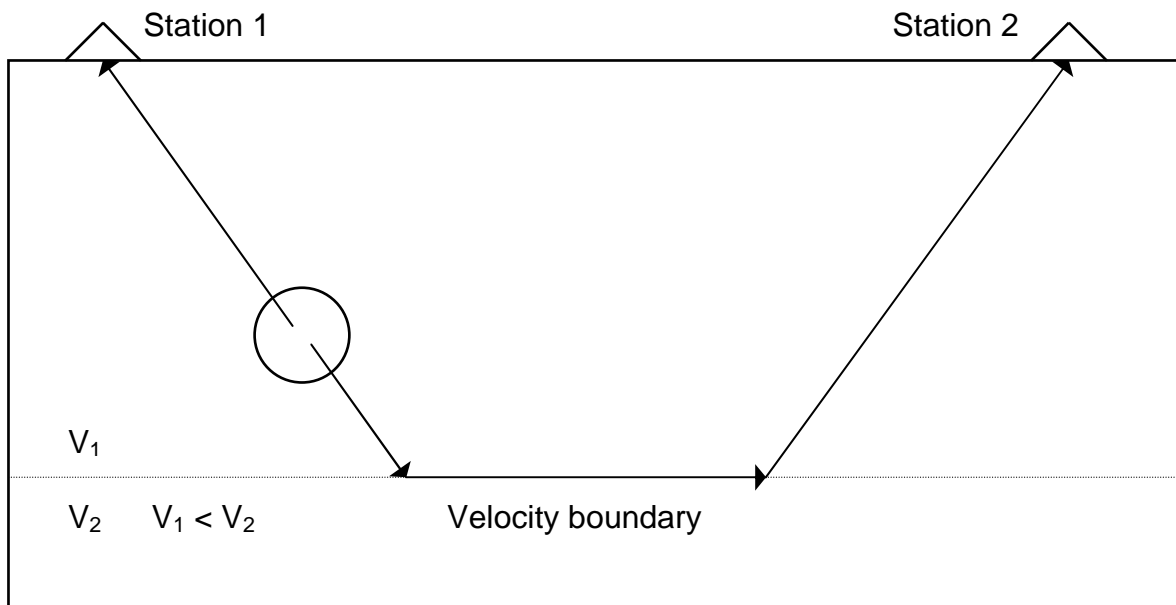


Fig. 3.29 Two rays, leaving the focal sphere in opposite directions, reach - because of the symmetry of radiation pattern - the stations 1 and 2 with the same polarity. The crossing point of the up-going ray with the focal sphere can, therefore, be remapped according to the formulas given in Fig. 3.28 into a crossing point with the lower hemisphere which coincides with the ray crossing-point for station 2.

3.4 Determination of fault plane solutions

Fig. 3.30 shows the angles which describe the orientation and motion of a fault plane and Fig. 3.31 shows their determination in the net projections. The **strike angle** ϕ is measured clockwise against North ($0^\circ \leq \phi \leq 360^\circ$). To resolve the 180° ambiguity, it is assumed that when looking into the strike direction the fault dips to the right hand side (i.e., its fault-trace projection is towards the right of the net center). The **dip angle** δ describes the inclination of the hanging wall against the horizontal ($0^\circ \leq \delta \leq 90^\circ$). The **rake angle** λ describes the displacement of the hanging wall relative to the foot wall ($-180^\circ \leq \lambda \leq 180^\circ$). $\lambda = 0$ corresponds to slip in strike direction, $\lambda > 0$ means upward motion of the hanging wall (i.e., *reverse or thrust faulting component*) and $\lambda < 0$ downward motion (i.e., *normal faulting component*).

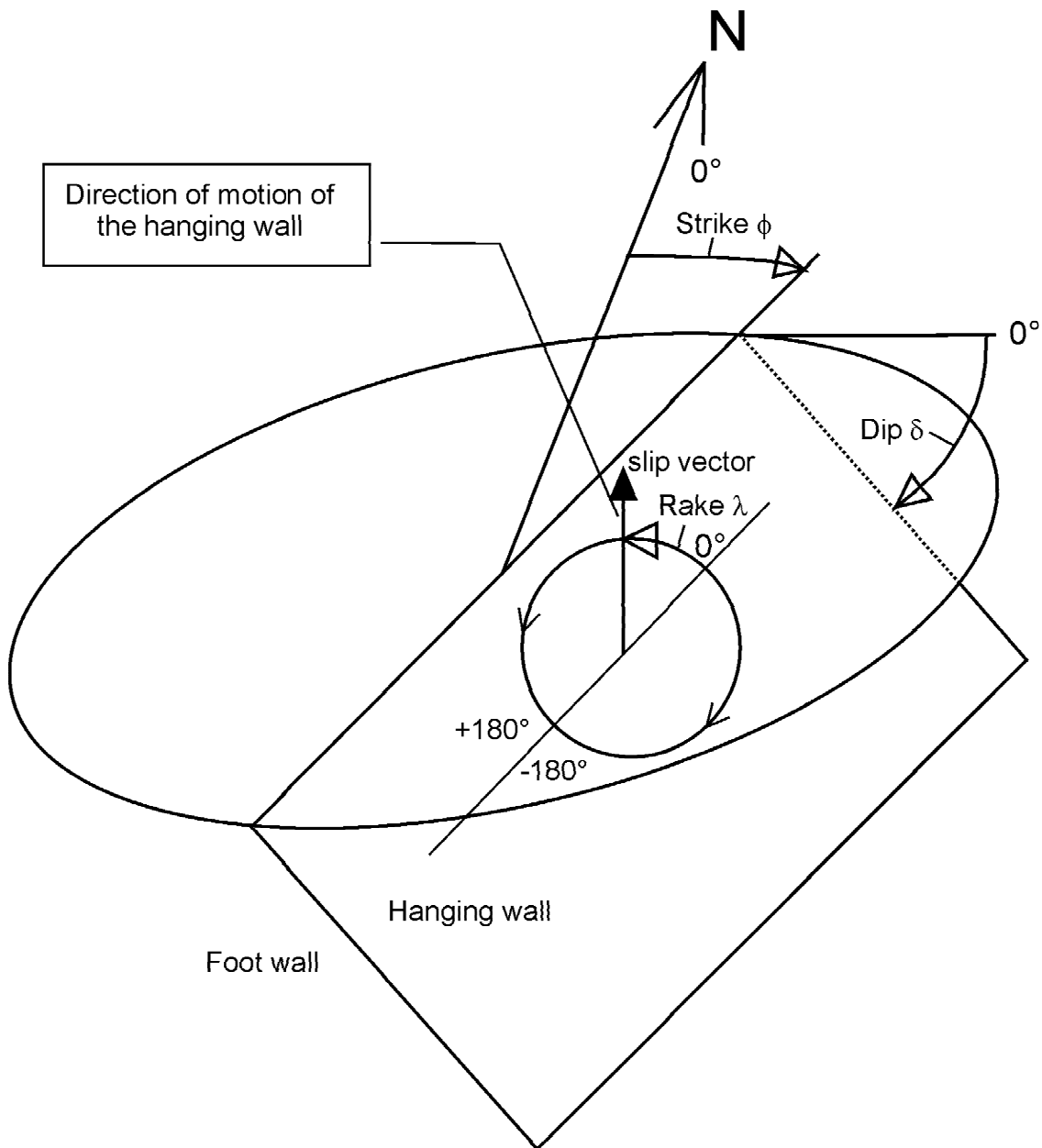


Fig. 3.30 Angles describing the orientation and motion of faults (see text).

3. Seismic Sources and Source Parameters

In Fig. 3.31 P1, P2 and P3 mark the positions of the poles of the planes FP1 (fault plane), FP2 (auxiliary plane) and EP (equatorial plane) in their net projections. From Fig. 3.30 it is obvious that all three planes are perpendicular to each other (i.e., 90° apart) and intersect in the poles of the respective third plane, i.e., FP1 and FP2 in P3, FP1 and EP in P2 etc. Note that on the basis of polarity readings alone it can not be decided whether FP1 or FP2 was the active fault. Discrimination from seismological data alone is still possible but requires additional study of the *directivity effects* such as azimuthal variation of frequency (*Doppler effect*), amplitudes and/or waveforms. For sufficiently large shocks these effects can more easily be studied in low-frequency teleseismic recordings while in the local distance range, high-frequency waveforms and amplitudes may be strongly influenced by resonance effects due to low-velocity near-surface layers. Seismotectonic considerations or field evidence from surface rupture in case of strong shallow earthquakes may allow us to resolve this ambiguity, too. Figs. 3.32 and 3.33 depict several basic types of earthquake faulting and their related fault-plane solutions in so-called "beach-ball" presentations of the net projections.

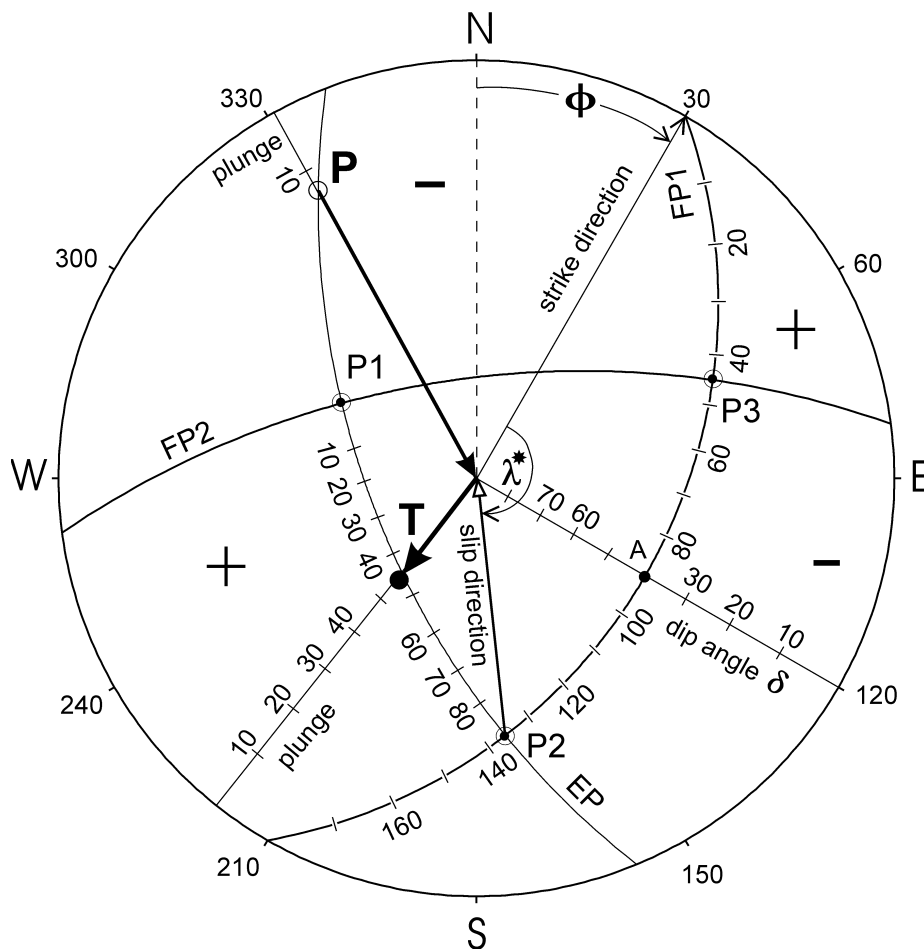
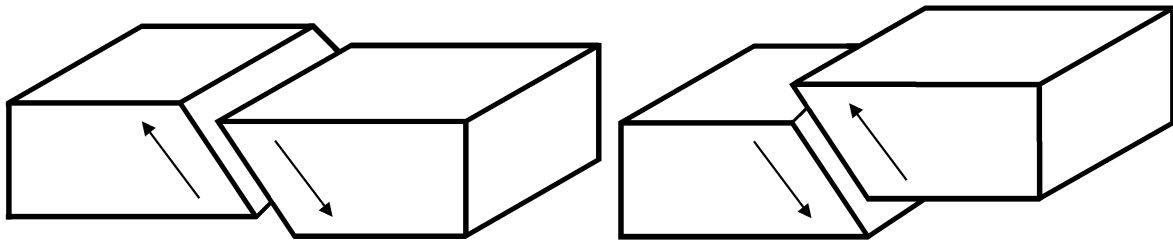


Fig. 3.31 Determination of the fault plane parameters ϕ , δ and λ in the net diagrams. The polarity distribution, slip direction and projection of FP1 shown qualitatively correspond to the faulting case depicted in Fig. 3.30. For abbreviations used see text. **Note:** $\lambda^* = 180^\circ - \lambda$ when the center of the net lies in the tension (+) quadrant (i.e., event with thrust component) or $\lambda^* = -\lambda$ when the center of the net lies in the pressure quadrant (i.e., event with normal faulting component). P1, P2 and P3 are the poles (i.e., 90° off) of FP1, FP2 and EP, respectively. P and T are the penetration points (poles) of the pressure and tension axes, respectively. + and - signs mark the quadrants with compressional and dilatational P-wave first motions.

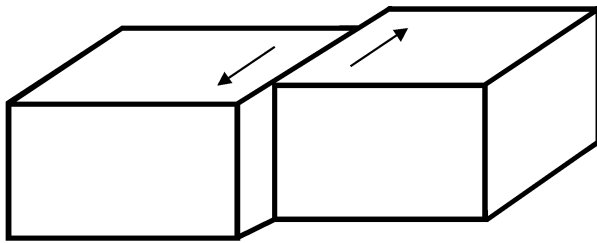


Pure normal faulting

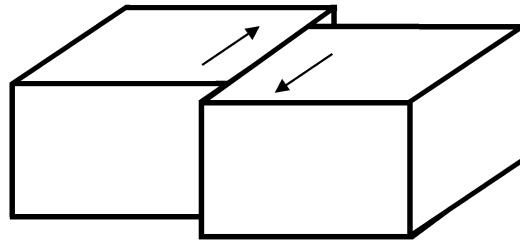
dip $0^\circ < \delta < 90^\circ$; rake = -90°

Pure thrust faulting

dip $0^\circ < \delta < 90^\circ$; rake = $+90^\circ$

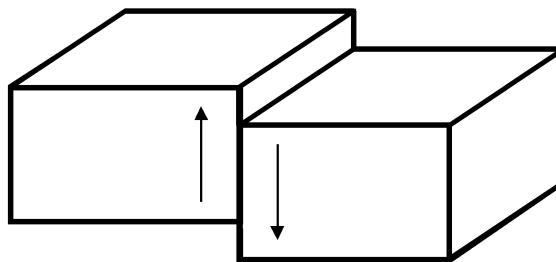


Pure strike slip
left lateral



Pure strike slip
right lateral

dip = 90° rake = 0° and 180° , respectively



Down slip

dip = 90° rake = $\pm 90^\circ$

Fig. 3.32 Basic types of earthquake faulting for some selected dip and rake angles. Note that mixed types of faulting occur when $\lambda \neq 0, 180^\circ$ or $\pm 90^\circ$, e.g., normal faulting with strike-slip component or strike-slip with thrust component. Also, dip angles may vary between $0^\circ < \delta \leq 90^\circ$. For fault plane traces and polarity distributions of these faulting types in their "beach-ball presentation" see Fig. 3.33.

3. Seismic Sources and Source Parameters

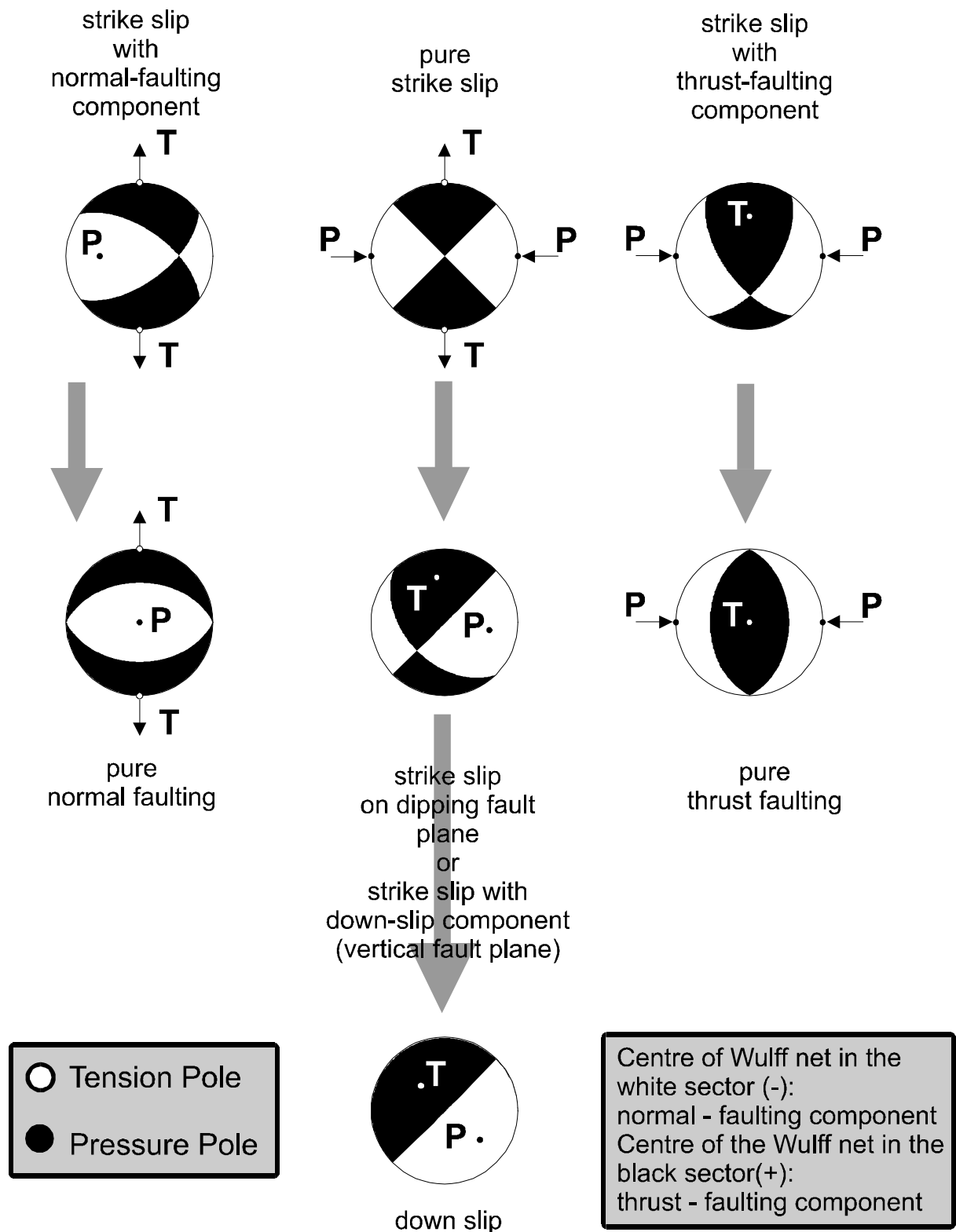


Fig. 3.33 “Beach-ball” presentation of the net projections of the fault plane cut-traces and of the penetration points (poles) of the P- and T-axes through the lower focal hemisphere for different faulting mechanisms. White sectors correspond to negative and black sectors to positive first-motion polarities.

3.4.3 Accuracy of fault-plane solutions

Fault planes determined by eye-fit to the polarity data may be uncertain by about $\pm 10^\circ$. This is acceptable. Even computer assisted best fits to the data will produce different acceptable solutions within about the same error range with only slightly different standard deviations (e.g., Figure 1 in EX 3.3, NEIC and HRVD solutions, respectively).

In addition, one has to be aware that different fitting algorithm or error-minimization procedures may produce different results within this range of uncertainty for the same data. A poor distribution of seismograph stations (resulting in insufficient polarity data for the net diagram), erroneous polarity readings and differences in model assumptions (e.g., in the velocity models used) may result in still larger deviations between the model solution and the actual fault planes. One should also be aware that the assumed constant angular (45°) relationship between the fault plane on the one hand and the pressure and tension axis on the other hand is true in fact only in the case of a fresh rupture in a homogeneous isotropic medium. It may not be correct in the stress environment of real tectonic situations (i.e., P and $T \neq \sigma_1$ and $-\sigma_3$, respectively; see discussion in 3.1.2.4).

3.4.4 Computer-assisted fault-plane solutions

There exist quite a number of computer programs for the determination of both single and joint fault-plane solutions from first-motion data (e.g., Brillinger et al., 1980; Buforn and Udías, 1984; Udías and Buforn, 1988, and others referred to below). In most applications for local earthquakes homogeneous flat-layered velocity models are acceptable, i.e., layers with constant velocities and velocity discontinuities at the boundaries. The majority of location programs (e.g., HYPO71 by Lee and Lahr, 1975; HYPOELLIPSE by Lahr, 1989; HYPOINVERS by Klein, 1985) are based on this type of velocity model. Additionally, HYPOINVERS and HYPOELLIPSE do accept layers with linear velocity gradients. Moreover, HYPOELLIPSE may locate local events with predefined travel-time tables, too. During the location procedure the ray paths to the stations are calculated. The azimuth AZM and the take-off angle AIN at which the P wave, arriving at a given station, leaves the focal sphere are listed in the output files. The remaining problem to be solved is to find the distribution of P-polarities on the focal sphere and to estimate the angles describing the focal mechanism.

The computer program FPFIT (Reasenberger and Oppenheimer, 1985) calculates double-couple fault-plane solutions based on P-wave polarity readings. It accepts as input the output files of the localization programs HYPO71, HYPOELLIPSE and HYPOINVERSE. The inversion is accomplished through a grid-search procedure that finds the source model by *minimizing a normalized weighted sum of first-motion polarity discrepancies*. Two weighting factors are incorporated in the minimization. One of them reflects the estimated variance of the data while the other one is based on the absolute value of the P-wave radiation amplitude. In addition to the minimum-misfit solution, FPFIT finds alternative solutions corresponding to significant relative misfit minima. The existence of several minima may be due to insufficient number of polarity readings, localization errors, polarity misreadings or an inadequate velocity model (e.g., not modeled refractions) resulting in an incorrect position of the P-wave first-motion polarities on the focal sphere. One has also to be aware that it sometimes may happen that the seismometer component outputs have been wrongly plugged at a given station, resulting in systematically wrong polarity reportings by such a station. In

3. Seismic Sources and Source Parameters

the case of models which perfectly fit the data, FPFIT applies an additional constraint. Its effect is to maximize the distance sum between the observation points and the nodal planes on the focal sphere. The display program FPLOT shows the final fault-plane solution and the estimated uncertainty in terms of the range of possible orientations of the pressure and tension axes which is consistent with the data.

While the above programs accept only the output files of the hypocenter localization programs for local events, another widely used program package for seismogram analysis, SEISAN (Havskov, 1996; version 1.2 now available as CD-ROM from the International Seismological Centre in Thatcham, UK) uses a modified version of the program HYPOCENTER (Lienert et al., 1988; Lienert, 1991; Lienert and Havskov, 1995). The main modifications are that it can also accept secondary phases and locate teleseismic events. The output files are used in conjunction with the FOCMEC program (Snoko et al., 1984) for the determination of the fault plane parameters but currently on the basis of polarity readings only. The implementation of the additional use of S-P amplitude ratios is intended.

In the case of sparse networks or weak events, the number of polarity data may be too small for reliable estimation of fault-plane solutions. In this case P-, SV- and SH-amplitudes can be used in addition to polarities in order to get more stable and better constrained, i.e., less ambiguous fault-plane solutions. This is due to the difference in P-wave (Fig. 3.25) and S-wave (Fig. 3.26) polarity and angular amplitude pattern for a given source mechanism.

The program FOCMEC (Snoko, 1984) allows us to calculate best fitting double-couple fault-plane solutions from P, SH and SV polarities and/or SV/P, SH/P or SV/SH amplitude ratios provided that the ratios are corrected to the focal sphere by taking into account geometrical spreading, attenuation and free-surface effects. For surface correction the program FREESURF, which is supplied together with FOCMEC, can be used. The applied Q-model has to be specified according to the regional attenuation conditions or related corrections. When adopting a constant V_P/V_S velocity ratio, the geometrical spreading is the same for P and S waves and absolute changes in amplitude cancel each other in the above amplitude ratios. Head waves and amplitude changes at velocity boundaries require special treatment. The solution is obtained by grid search over strike, dip and slip of the double-couple source. The program FOCPLT, also provided together with FOCMEC, allows us to plot upper or lower hemisphere projections of the focal sphere and to show the data, i.e., the fault planes together with the poles of the pressure (P) and tension (T) axes for SH and SV waves. Note that S-wave amplitudes are zero in the direction of P and T.

While the program HYPO71 is available as part of Vol.1 of the IASPEI software library (Lee, 1995) the programs FOCMEC, FPFIT, HYPOELLIPSE and HYPOINVERSE are freely available through the Internet under the following addresses:

FOCMEC: <http://www.iris.washington.edu> or as for FPFIT
FPFIT: <http://orfeus.knmi.nl/other.services/software.links.html#focalmech>
HYPOELLIPSE: <http://giseis.alaska.edu/pub/SOFTWARE/hypoel/>
HYPOINVERSE: <http://orfeus.knmi.nl/other.services/software.links.html#location>

3.5 Source parameters and moment-tensor solutions (G. Bock †)

3.5.1 Introduction

The concept of first order *moment tensor* provides a complete description of equivalent body forces of a general seismic point source (see Fig. 3.34 in section 3.5.2). A source can be considered a point source if both the distance D of the observer from the source and the wavelength λ of the data are much greater than the linear dimension of the source. Thus, moment-tensor solutions are generally derived from low-frequency data and they are representative of the gross properties of the rupture process averaged over tens of seconds or more. The double-couple source model describes the special case of shear dislocation along a planar fault. This model has proven to be very effective in explaining the amplitude and polarity pattern of P, S and surface waves radiated by tectonic earthquakes. In the following, we briefly outline the relevant relations (in a first order approximation) between the moment tensor of a seismic source and the observed seismogram. The latter may be either the complete seismogram, one of its main groups (P, S or surface waves), or specific features of seismograms such as peak-to-peak amplitudes of body waves, amplitude ratios or spectral amplitudes. Then we outline a linear inversion scheme for obtaining the moment tensor using waveform data in the time domain. Finally, we will give an overview of some useful programs for moment-tensor analysis. Applications of moment-tensor inversions to the rapid (i.e., generally within 24 hours after the event) determination of source parameters after significant earthquakes will also be described.

3.5.2 Basic relations

Following Jost and Herrmann (1989), the displacement d on the Earth's surface at a station can be expressed, in case of a point source, as a linear combination of time-dependent moment-tensor elements $M_{kj}(\xi, t)$ that are assumed to have the same time dependence convolved (indicated by the star symbol) with the derivative $G_{skj}(\mathbf{x}, \xi, t)$ of the Green's functions with regard to the spatial j -coordinate:

$$u_s(\mathbf{x}, t) = M_{kj}(\xi, t) * G_{skj}(\mathbf{x}, \xi, t). \quad (3.69)$$

$u_s(\mathbf{x}, t)$: s component of ground displacement at position \mathbf{x} and time t

$M_{kj}(\xi, t)$: components of 2nd order, symmetrical seismic moment tensor M

$G_{skj}(\mathbf{x}, \xi, t)$: derivative of the Green's function with regard to source coordinate ξ_j

\mathbf{x} : position vector of station with coordinates x_1, x_2, x_3 for north, east and down

ξ : position vector of point source with coordinates ξ_1, ξ_2, ξ_3 for north, east and down

Eq. (3.69) follows from the representation theorem in terms of the Green's function (see Equations (21) and (38) in IS 3.1). The Green's function represents the impulse response of the medium between source and receiver and thus contains the various wave propagation effects through the medium from source to receiver. These include energy losses through reflection and transmission at seismic discontinuities, anelastic absorption and geometrical spreading. The $M_{kj}(\xi, t)$ from Eq.(3.69) completely describes the forces acting in the source and their time dependence. The Einstein summation notation is applied in Eq. (3.69) and below, i.e., the repeated indices k and $j = 1, 2, 3$ imply summation over x_1, x_2 and x_3 . In Eq. (3.69) the higher order terms of the Taylor expansion around the source point of the Green's

3. Seismic Sources and Source Parameters

functions $G_{sk,j}(\mathbf{x}, \boldsymbol{\xi}, t)$ have been neglected. Note that the source-time history $s(t)$ (see 3.1, Figs. 3.4 and 3.7), which describes the time dependence of moment released at the source, is contained in c . If we assume that all the components of $M_{kj}(\boldsymbol{\xi}, t)$ have the same time dependence $s(t)$ the equation can be written as:

$$\mathbf{u}_s(\mathbf{x}, t) = M_{kj} [G_{sk,j}(\mathbf{x}, \boldsymbol{\xi}, t) * s(t)] \quad (3.70)$$

with $s(t)$: source time history.

When determining $M_{kj}(\boldsymbol{\xi}, t)$ from seismic records, $\mathbf{u}_s(\mathbf{x}, t)$ is calculated by convolution of the observed seismogram components $y_s(\mathbf{x}, t)$ with the inverse of the seismograph's displacement response function $i(t)$:

$$\mathbf{u}_s(\mathbf{x}, t) = y_s(\mathbf{x}, t) * \text{Inv}\{i(t)\}$$

In the frequency domain (see Eq. (14) in IS 3.1) convolution is replaced by multiplication:

$$D_s(\mathbf{x}, \omega) = Y_s(\mathbf{x}, \omega) I(\omega)^{-1}$$

where ω is circular frequency. The $D_s(\mathbf{x}, \omega)$, $Y_s(\mathbf{x}, \omega)$, and $I(\omega)^{-1}$ are the respective Fourier transforms of the time series $d_s(\mathbf{x}, t)$, $y_s(\mathbf{x}, t)$, and $i(t)^{-1}$ (see 5.2.7 where $I(\omega)^{-1}$ is denoted as $H_d(\omega)^{-1}$).

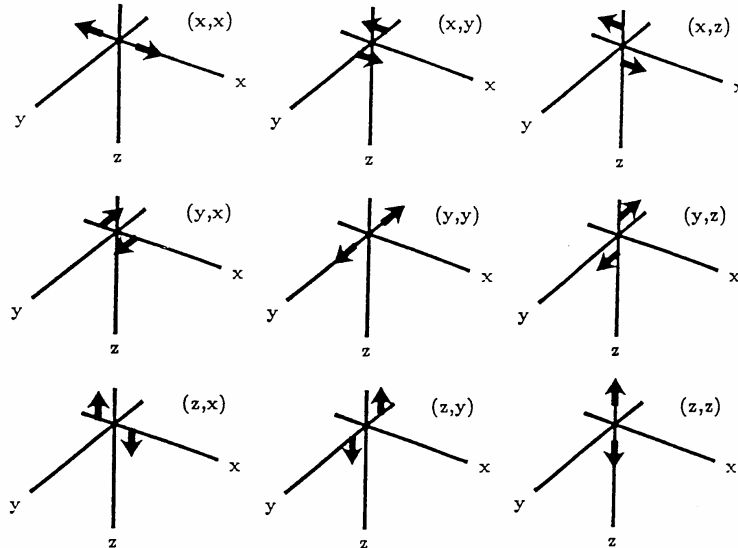


Fig. 3.34 The nine generalized couples representing $G_{sk,j}(\mathbf{x}, \boldsymbol{\xi}, t)$ in Eq. (3.69). Note that force couples acting on the y axis in x direction or vice versa (i.e., (x,y) or (y,x)) will cause shear faulting in the x and y direction, respectively. Superimposition of vector dipoles in x and y direction with opposite sign, e.g., $(x,x) + (-y,-y)$ will also cause shear faulting but 45° off the x and y direction, respectively. Both representations are equivalent (reproduced from Jost and Herrmann, A student's guide to and review of moment tensors. *Seismol. Res. Lett.*, **60**, 2, 1989, Fig. 2, p. 39; ©Seismological Society of America).

3.5 Source parameters and moment-tensor solutions

In the following we assume that the source-time function $s(t)$ is a delta function (i.e., a "needle" impulse). Then, $M_{kj}(\boldsymbol{\xi}, t) = M_{kj}(\boldsymbol{\xi}) \cdot \delta(t)$, and the right side of Eq.(3.70) simplifies to $M_{kj}(\boldsymbol{\xi}) \cdot G_{sk,j}(t)$. The seismogram recorded at x can be regarded as product of $G_{sk,j}$ and M_{kj} . (e.g., Aki and Richards, 1980, Lay and Wallace, 1995; Udias, 1999). Thus, the derivative of $G_{sk,j}$ with regard to the source coordinate ξ_i describes the response to a single couple with its lever arm pointing in the ξ_j direction (see Fig. 3.34). For $k = j$ we obtain a vector dipole; these are the couples (x,x), (y,y), and (z,z) in Fig. 3.34. A double-couple source is characterized by a moment tensor where one eigenvalue of the moment tensor vanishes (equivalent to the Null or B axis), and the sum of eigenvalues vanishes, i.e., the trace of the moment tensor is zero. Physically, this is a representation of a shear dislocation source without any volume changes.

Using the notation of Fig. 3.32, double-couple displacement fields are represented by the sum of two couples such as (x,y)+(y,x), (x,x)+(y,y), (y,y)+(z,z), (y,z)+(z,y) etc. An explosion source (corresponding to M_6 in Eq. (3.76) and Fig. 3.34) can be modeled by the sum of three vector dipoles (x,x) + (y,y) + (z,z). A compensated linear vector dipole (CLVD, see 3.5.4 below) can be represented by a vector dipole of strength 2 and two vector dipoles of unit strength but opposite sign in the two orthogonal directions.

The seismic moment tensor \mathbf{M} has, in general, six independent components which follows from the condition that the total angular momentum for the equivalent forces in the source must vanish. For vanishing trace, i.e., without volume change, we have five independent components that describe the deviatoric moment tensor. The double-couple source is a special case of the deviatoric moment tensor with the constraint that the determinant of \mathbf{M} is zero, i.e., that the stress field is two-dimensional.

In general, \mathbf{M} can be decomposed into an isotropic and a deviatoric part:

$$\mathbf{M} = \mathbf{M}^{\text{isotropic}} + \mathbf{M}^{\text{deviatoric}}. \quad (3.71)$$

The decomposition of \mathbf{M} is unique while further decomposition of $\mathbf{M}^{\text{deviatoric}}$ is not. Commonly, $\mathbf{M}^{\text{deviatoric}}$ is decomposed into a double couple and CLVD:

$$\mathbf{M}^{\text{deviatoric}} = \mathbf{M}^{\text{DC}} + \mathbf{M}^{\text{CLVD}}. \quad (3.72)$$

For a double-couple source, the Cartesian components of the moment tensor can be expressed in terms of strike ϕ , dip δ and rake λ of the shear dislocation source (fault plane), and the scalar seismic moment M_0 (Aki and Richards, 1980):

$$\begin{aligned} M_{xx} &= -M_0(\sin\delta \cos\lambda \sin 2\phi + \sin 2\delta \sin\lambda \sin^2\phi) \\ M_{xy} &= M_0(\sin\delta \cos\lambda \cos 2\phi + 0.5 \sin 2\delta \sin\lambda \sin 2\phi) \\ M_{xz} &= -M_0(\cos\delta \cos\lambda \cos\phi + \cos 2\delta \sin\lambda \sin\phi) \\ M_{yy} &= M_0(\sin\delta \cos\lambda \sin 2\phi - \sin 2\delta \sin\lambda \cos^2\phi) \\ M_{yz} &= -M_0(\cos\delta \cos\lambda \sin\phi - \cos 2\delta \sin\lambda \cos\phi) \\ M_{zz} &= M_0 \sin 2\delta \sin\lambda \end{aligned} \quad (3.73)$$

3. Seismic Sources and Source Parameters

As the tensor is always symmetric it can be rotated into a principal axis system such that all non-diagonal elements vanish and only the diagonal elements are non-zero. The diagonal elements are the *eigenvalues* (see Eq. (6) in Information Sheet 3.1) of \mathbf{M} ; the associated directions are the *eigenvectors* (i.e., the *principal axes*). A linear combination of the principal moment-tensor elements completely describes the radiation from a seismic source. In the case of a double-couple source, for example, the diagonal elements of \mathbf{M} in the principal axis system have two non-zero eigenvalues M_0 and $-M_0$ (with M_0 the scalar seismic moment) whose eigenvectors give the direction at the source of the tensional (positive) T axis and compressional (negative) P axis, respectively, while the zero eigenvalue is in the direction of the B (or Null) axis of the double couple (for definition and determination of M_0 see Exercise 3.4).

Eq. (3.70) describes the relation between seismic displacement and moment tensor in the time domain. If the source-time function is not known or the assumption of time-independent moment-tensor elements is dropped, e.g., for reasons of source complexity, the frequency-domain approach is chosen:

$$u_s(\mathbf{x}, f) = M_{kj}(f)G_{sk,j}(\mathbf{x}, \xi, f) \quad (3.74)$$

where f denotes frequency. Procedures for the linear moment-tensor inversion can be designed in both the time and frequency domain using Eq. (3.70) or (3.74). We can write (3.70) or (3.74) in matrix form:

$$\mathbf{u} = \mathbf{G} \bar{m}. \quad (3.75)$$

In the time domain, the \mathbf{u} is a vector containing n sampled values of observed ground displacement at various times, stations and sensor components, while \mathbf{G} is a $6 \times n$ matrix and the vector \bar{m} contains the six independent moment-tensor elements to be determined. In the frequency domain, \mathbf{u} contains k complex values of the displacement spectra determined for a given frequency f at various stations and sensor components. \mathbf{G} is a $6 \times k$ matrix and is generally complex like \bar{m} . For more details on the inversion problem in Eq. (3.75) the reader is referred to Chapter 6 in Lay and Wallace (1995), Chapter 12 in Aki and Richards (1980), or Chapter 19 of Udias (1999).

To invert Eq. (3.75) for the unknown \bar{m} , one has to calculate the derivatives of the Green's functions. The calculation of the Green's functions constitutes the most important part of any moment-tensor inversion scheme. A variety of methods exists to calculate synthetic seismograms (e.g., Müller, 1985; Doornbos, 1988; Kennett, 1988). Some of the synthetic seismogram codes allow calculations for the moment-tensor elements as input source while others allow input for double-couple and explosive point sources. The general moment tensor can be decomposed in various ways using moment-tensor elements of double-couple and explosive sources so that synthetic seismogram codes employing these source parameterizations can also be used in the inversion of (3.75).

3.5.3 An inversion scheme in the time domain

In this section, we will describe in short the moment-tensor inversion algorithm of Kikuchi and Kanamori(1991), where the moment tensor is decomposed into elementary double-couple sources and an explosive source. Adopting the notation used by Kikuchi and Kanamori(1991),

3.5 Source parameters and moment-tensor solutions

the moment tensor M_{kj} is represented by a linear combination of $N_e = 6$ elementary moment tensors M_n (Fig. 3.35):

$$M_{kj} = \sum_{n=1}^{N_e} a_n M_n \quad (3.76)$$

with

$$M_1: \begin{bmatrix} 0 & 1 & 0 \\ 1 & 0 & 0 \\ 0 & 0 & 0 \end{bmatrix}; \quad M_2: \begin{bmatrix} 1 & 0 & 0 \\ 0 & -1 & 0 \\ 0 & 0 & 0 \end{bmatrix}; \quad M_3: \begin{bmatrix} 0 & 0 & 0 \\ 0 & 0 & 1 \\ 0 & 1 & 0 \end{bmatrix}$$

$$M_4: \begin{bmatrix} 0 & 0 & 1 \\ 0 & 0 & 0 \\ 1 & 0 & 0 \end{bmatrix}; \quad M_5: \begin{bmatrix} -1 & 0 & 0 \\ 1 & 0 & 0 \\ 0 & 0 & 1 \end{bmatrix}; \quad M_6: \begin{bmatrix} 1 & 0 & 0 \\ 0 & 1 & 0 \\ 0 & 0 & 1 \end{bmatrix}$$

The M_1 and M_2 represent pure strike-slip faults; M_3 and M_4 represent dip-slip faults on vertical planes striking N-S and E-W, respectively, and M_5 represents a 45° dip-slip fault. The M_6 represents an isotropic source radiating energy equally into all directions (i.e., an explosion).

Elementary Moment Tensors

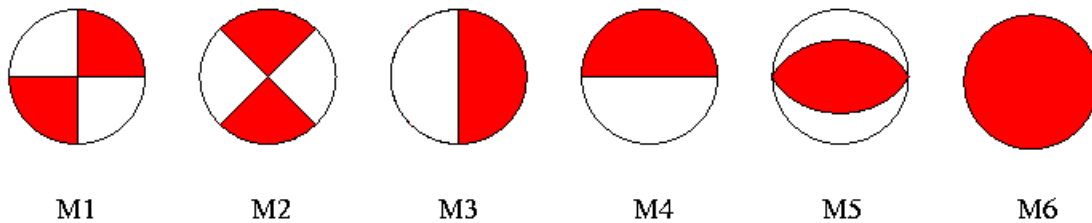


Fig. 3.35 Elementary moment tensors used in the inversion of the full moment tensor (after Kikuchi and Kanamori, 1991)

A pure deviatoric moment tensor ($\text{trace}(M_{kj}) = 0$) is entirely represented by the five elementary moment tensors M_1 to M_5 . The following brief description of the linear inversion for the moment tensor (Kikuchi and Kanamori, 1991) is an example of an inversion performed in the time domain. It can be easily adopted for an inversion in the frequency domain by replacing the time series by their spectra. Let $w_{sn}(t)$ denote the Green's function derivative at station s in response to the elementary moment tensor M_n , and let $x_s(t)$ be the observed ground displacement as function of time at station s . The best estimate for the coefficients a_n in Eq. (3.76) can be obtained from the condition that the difference between observed and synthetic displacement functions be zero:

3. Seismic Sources and Source Parameters

$$\begin{aligned}
 \Delta &= \sum_{s=1}^{N_s} \int \left[x_s(t) - \sum_{n=1}^{N_e} a_n w_{sn}(t) \right]^2 dt \\
 &= R_x - 2 \sum_{n=1}^{N_e} a_n G_n + \sum_{m=1}^{N_e} \sum_{n=1}^{N_e} R_{nm} a_n a_m \\
 &= \textit{Minimum} \tag{3.77}
 \end{aligned}$$

The N_e is the number of elementary moment tensors, and N_s is the number of displacement records used. The other terms in (3.77) are given by:

$$\begin{aligned}
 R_x &= \sum_{s=1}^{N_s} \int [x_s(t)]^2 dt \\
 R_{nm} &= \sum_{s=1}^{N_s} \int [w_{sn}(t) w_{sm}(t)] dt \\
 G_n &= \sum_{s=1}^{N_s} \int [w_{sn}(t) x_s(t)] dt
 \end{aligned}$$

Integration is carried out over selected portions of the waveforms. Evaluating $\partial\Delta/\partial a_n = 0$ for $n = 1, \dots, N_e$ yields the normal equations

$$\sum_{m=1}^{N_e} R_{nm} a_m = G_n \tag{3.78}$$

with n ranging from 1 to N_e . The solution for a_n is given by:

$$a_n = \sum_{m=1}^{N_e} R_{nm}^{-1} G_m \tag{3.79}$$

The inverse R_{nm}^{-1} of matrix R_{nm} can be obtained by the method of generalized least squares inversion (e.g., Pavlis, 1988). The resultant moment tensor is then given by

$$M_{kj} \begin{bmatrix} a_2 - a_5 + a_6 & a_1 & a_4 \\ a_1 & -a_2 + a_6 & a_3 \\ a_4 & a_3 & a_5 + a_6 \end{bmatrix} \tag{3.80}$$

The variance of the elements a_n can be calculated under the assumption that the data are statistically independent:

$$\text{var}(a_n) = \sum_{m=1}^{N_e} (R_{nm}^{-1})^2 \sigma_m^2$$

where σ_m^2 is the variance of the data G_n . In the case where the variance of the data is not known, $\sum_{m=1}^{N_e} (R_{nm}^{-1})^2$ can be used as relative measure for the uncertainty.

3.5.4 Decomposition of the moment tensor

Except for the volumetric and deviatoric components, the decomposition of the moment tensor is not unique. Useful computer programs for decomposition were written by Jost and distributed in Volume VIII of the Computer Programs in Seismology by Herrmann of Saint Louis University (<http://www.eas.slu.edu/People/RBHerrmann/ComputerPrograms.html> or e-mail to R. W. Herrmann: rbh@slueas.slu.edu). The first step in the decomposition is the calculation of eigenvalues and eigenvectors of the seismic moment tensor. For this the program *mteig* can be used. It performs rotation of the moment tensor \mathbf{M} into the principal axis system. The eigenvector of the largest eigenvalue gives the T (or tensional) axis; the eigenvector of the smallest eigenvalue gives the direction of the P (or compressional) axis, while the eigenvector associated with the intermediate eigenvalue gives the direction of the Null axis. The output of *mteig* is the diagonalized moment tensor

$$M = \begin{bmatrix} m_1 & 0 & 0 \\ 0 & m_2 & 0 \\ 0 & 0 & m_3 \end{bmatrix} \quad (3.81)$$

whose elements are input to another program, *mtdec*, which performs a moment-tensor decomposition. First, the moment tensor is decomposed into an isotropic and a deviatoric part (see Eq. 3.71):

$$M = \frac{1}{3} \begin{bmatrix} tr(M) & 0 & 0 \\ 0 & tr(M) & 0 \\ 0 & 0 & tr(M) \end{bmatrix} + \begin{bmatrix} m_1^1 & 0 & 0 \\ 0 & m_2^1 & 0 \\ 0 & 0 & m_3^1 \end{bmatrix} \quad (3.82)$$

with $tr(\mathbf{M}) = m_1 + m_2 + m_3$ being the trace of \mathbf{M} . The isotropic part of \mathbf{M} is important in quantifying volume changes of the source, but it is usually difficult to resolve so that isotropic parts of less than 10% are often not considered to be significant. The deviatoric part of the moment tensor can be further decomposed. Options include decompositions into three vector dipoles, into three double couples, into 3 CLVD sources, into a major and minor double couple, and into a best double couple and a CLVD having the same principal axis system. The source mechanisms reported by Harvard and USGS are based on the decomposition of the moment tensor into a best double couple and a CLVD. In addition to the best double couple they also provide the moment-tensor elements. To estimate the double-couple contribution to the deviatoric moment tensor, the parameter

3. Seismic Sources and Source Parameters

$$\varepsilon = \frac{|m_{\min}|}{|m_{\max}|}$$

is used (Dziewonski et al., 1981) where m_{\min} and m_{\max} are the smallest and largest eigenvalues of the deviatoric part of \mathbf{M} , respectively, both in absolute terms. For a pure double-couple source, $\varepsilon = 0$ because $m_{\min} = 0$; for a pure CLVD, $\varepsilon = 0.5$. The percentage double-couple contribution can be expressed as $(1-2\varepsilon)\times 100$. Significant CLVD components are often reported for large intermediate-depth and very deep earthquakes. In many cases, however, it can be shown that these are caused by superposition of several rupture events with different double-couple mechanisms (Kuge and Kawakatsu, 1990; Frohlich, 1995; Tibi et al., 1999).

Harvard and USGS publish the moment tensors using the notation of normal mode theory. It is based on spherical co-ordinates $(r; \Theta; \Phi)$ where r is the radial distance of the source from the center of the Earth, Θ is co-latitude, and Φ is longitude of the point source. The 6 independent moment-tensor elements in the $(x, y, z) = (\text{north, east, down})$ coordinate system are related to the components in $(r; \Theta; \Phi)$ by

$$M_{rr} = M_{zz}$$

$$M_{\Theta\Theta} = M_{xx}$$

$$M_{\Phi\Phi} = M_{yy}$$

$$M_{r\Theta} = M_{zx}$$

$$M_{r\Phi} = -M_{zy}$$

$$M_{\Theta\Phi} = -M_{xy}$$

3.5.5 Steps taken in moment-tensor inversion

Generally, the quality of moment-tensor inversion depends to a large extent on the number of data available and the azimuthal distribution of stations about the source. Dufumier (1996) gives a systematic overview for the effects caused by differences in the azimuthal coverage and the effects caused due to the use of only P waves, P plus SH waves or P and SH and SV waves for the inversion with body waves.

A systematic overview with respect to the effects caused by an erroneous velocity model for the Green function calculation and the effects due to wrong hypocenter coordinates can be found in Šílený et al. (1992), Šílený and Pšenčík (1995), Šílený et al. (1996) and Kravanja et al. (1999).

The following is a general outline of the various steps to be taken in a moment-tensor inversion using waveform data:

- 1) Data acquisition and pre-processing
 - good signal-to-noise ratio
 - unclipped signals

- good azimuthal coverage
 - removing mean value and linear trends
 - correcting for instrument response, converting seismograms to displacement
 - low-pass filtering to remove high-frequency noise and to satisfy the point source approximation
- 2) Calculation of synthetic Green's functions dependent on
 - Earth model
 - location of the source
 - receiver position
 - 3) Inversion
 - selection of waveforms, e.g., P, S H or full seismograms
 - taking care to match waveforms with corresponding synthetics
 - evaluation of Eqs. (3.76) and (3.77)
 - decomposition of moment tensor, e.g., into best double couple plus CLVD

The inversion may be done in the time domain or frequency domain. Care must be taken to match the synthetic and observed seismograms. Alignment of observed and synthetic waveforms is facilitated by cross-correlation techniques. In most moment-tensor inversion schemes, focal depth is assumed to be constant. The inversion is done for a range of focal depths and as best solution one takes that with the minimum variance of the estimate.

3.5.6 Some methods of moment-tensor inversion

3.5.6.1 NEIC fast moment tensors

This is an effort by the U.S. National Earthquake Information Center (NEIC) in co-operation with the IRIS Data Management Center to produce rapid estimates of the seismic moment tensor for earthquakes with body-wave magnitudes ≥ 5.8 . Digital waveform data are quickly retrieved from "open" IRIS stations and transmitted to NEIC by Internet. These data contain teleseismic P waveforms that are used to compute a seismic moment tensor using a technique based on optimal filter design (Sipkin, 1982). The solution is then disseminated by e-mail to a list of subscribers. To register send a request by e-mail to sipkin@usgs.gov. More information is available under http://gldss7.cr.usgs.gov/neis/FM/fast_moment.html.

3.5.6.2 Harvard CMT solutions

The Harvard group maintains an extensive catalog of centroid moment-tensor (CMT) solutions for strong (mainly $M > 5.5$) earthquakes over the period from 1976 till present. Their solutions, as well as quick CMT solutions of recent events, can be viewed at <http://www.seismology.harvard.edu/projects/CMT/>. The Harvard CMT method makes use of both very long-period ($T > 40$ s) body waves (from the P wave onset until the onset of the fundamental modes) and so-called mantle waves at $T > 135$ s that comprise the complete surface-wave train.

Besides the moment tensor the iterative inversion procedure seeks a solution for the best point source location of the earthquake. This is the point where the system of couples is located in the source model described by the moment tensor. It represents the integral of the moment density over the extended rupture area. This centroid location may, for very large earthquakes,

3. Seismic Sources and Source Parameters

significantly differ from the hypocenter location based on arrival times of the first P-wave onsets. The hypocenter location corresponds to the place where rupture started. Therefore, the offset of the centroid location relative to the hypocentral location gives a first indication on fault extent and rupture directivity. In case of the August 17, 1999 Izmit (Turkey) earthquake the centroid was located about 50 km east of the "P-wave" hypocenter. The centroid location coincided with the area where the maximum surface ruptures were observed.

3.5.6.3 EMSC rapid source parameter determinations

This is an initiative of the European-Mediterranean Seismological Center (Bruyeres-le-Chatel, France, <http://www.emsc-csem.org/>) and the GEOFON Programs at the GeoForschungs-Zentrum Potsdam (<http://www.gfz-potsdam.de/geofon/>). The EMSC method uses a grid search algorithm to derive the fault-plane solutions and seismic moments of earthquakes ($M > 5.5$) in the European- Mediterranean area. Solutions are derived within 24 hours after the occurrence of the event. The data used are P- and S-wave amplitudes and polarities. Fig. 3.36 shows an example of the kind of output data produced. More information can be obtained through <http://www.gfz-potsdam.de/pb2/pb24/emsc/emsc.html>.

3.5.6.4 Relative moment-tensor inversion

Especially for the inversion of local events so called relative moment-tensor inversion schemes have been developed (Onicescu, 1986; Dahm, 1996). If the sources are separated by not more than a wavelength, the Green's functions can be assumed to be equal with negligible error. In this case it is easy to construct a linear equation system that relates the moment-tensor components of a reference event to those of another nearby event. This avoids the calculation of high-frequency Green's functions necessary for small local events and all problems connected with that (especially the necessity of modeling site transfer functions in detail).

This is a very useful scheme for the analysis of aftershocks if a well determined moment tensor of the main shock is known. Moreover, if enough events with at least slightly different mechanisms and enough recordings are available, it is also possible to eliminate the reference mechanism from the equations (Dahm, 1996). This is interesting for volcanic areas where events are swarm-like and of similar magnitude, and where a reference moment tensor can not be provided (Dahm and Brandsdottir, 1997).

3.5.6.5 NEIC broadband depths and fault-plane solutions

Moment-tensor solutions, which are generally derived from low-frequency data, reflect the gross properties of the rupture process averaged over tens of seconds or more. These solutions may differ from solutions derived from high frequency data, which are more sensitive to the dynamic part of the rupture process during which most of the seismic energy is radiated. For this reason, beginning January 1996, the NEIC has determined, whenever possible, a fault plane solution and depth from broadband body waves for any earthquake having a magnitude greater than about 5.8 and it has published the source parameters in the Monthly Listings of the PDE. The broadband waveforms that are used have a flat displacement response over the frequency range 0.01-5.0 Hz. (This bandwidth, incidentally, is also commensurate with that

3.5 Source parameters and moment-tensor solutions

used by the NEIC to compute teleseismic E_S .) Initial constraints on focal mechanism are provided by polarities from P, pP and PKP waves, as well as by Hilbert-transformed body waves of certain secondary arrivals (e.g., PP), and from transversely polarized S waves. The fault-plane solution and depth are then refined by least-squares fitting of synthetic waveforms to teleseismically recorded P-wave groups (consisting of direct P, pP and sP). More information can be found under http://neic.usgs.gov/neis/nrg/bb_processing.html.

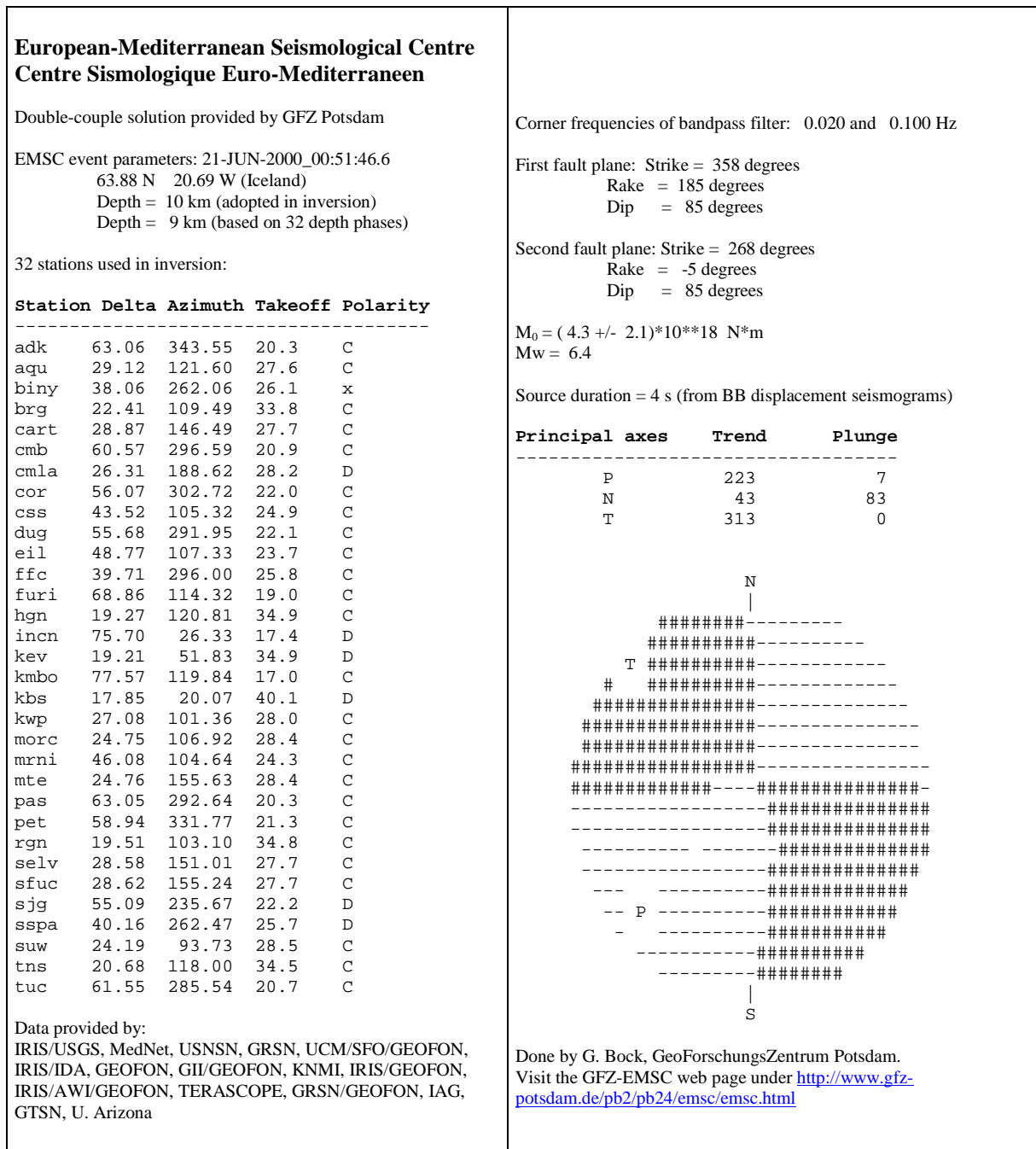


Fig. 3.36 Example of output data produced by the routine procedure for rapid EMSC source parameter determinations by the GEOFON group at the GFZ Potsdam.

3.6 Seismic scaling relations (P. Bormann)

3.6.1 Definition and use of seismic scaling relations

Empirical formulas relate one measured or calculated parameter to another. We have encountered such relationships in our discussions of seismic moment, energy and magnitude. Relations can also be found between other physical or geometrical parameters of earthquake size such as intensity, stress drop, duration of rupture, area or length of rupture, fault dislocation, area of felt shaking, etc. If any of these parameters appear to be related in a systematic and predictable manner over a wide range of earthquake size, scaling “laws” and similarity conditions may be inferred. These seismic scaling laws and similarity conditions allow the rough estimation of one parameter from another (e.g., E_S from M_0 or magnitude, or M_0 from field evidence such as surface rupture length and/or displacement). Therefore, the knowledge of theoretically well founded scaling laws or empirical scaling relationships is of crucial importance for both probabilistic and deterministic seismic hazard analyses. They aim at assessing the future earthquake potential of a region on the basis of data from past events, dating back as far as possible. Scaling laws are often the only way to estimate parameters of historical earthquakes which often lack instrumental measurements of magnitude, seismic energy or moment. Specifically, one often has to make reasonable estimates of the size of the largest earthquake that might have occurred at or could be generated by a particular fault or fault segment and of the kind of seismic spectrum it might (have) radiate(d). However, one has to be aware that seismic sources differ not only in their geometrical size and average slip. Ambient stress conditions, the dominant modes of faulting, ranges of stress drop and related seismic source spectra may also differ significantly from region to region. For instance, events of the same seismic moment may release seismic energies which differ by 2 to 3 orders. Therefore, the globally-derived scaling relations may not be appropriate for use for some areas. Regional scaling laws should be used, therefore, whenever available, particularly when inferences have to be drawn on regional seismic strain rates or on seismic hazard, the latter being mainly controlled by the frequency of occurrence and the potential of earthquakes to generate strong high-frequency motions.

3.6.2 Energy-magnitude-moment relations

Gutenberg and Richter (1956a) gave the following relationship between seismic energy E_S (in Joule ; $1 \text{ J} = 10^7 \text{ erg}$) and the so-called unified magnitude m which is related to m_B (see 3.2.5.2):

$$\log E_S = 2.4 m - 1.2. \quad (3.83)$$

Eq. (3.83) is supposed to have minimum of observation errors and yields, together with the relationship $m_B = 2.5 + 0.63 M_s$ in the same publication,

$$\log E_S = 1.5 M_s + 4.8. \quad (3.84)$$

After many revisions, Gutenberg and Richter (1956c) finally published Eq. (3.84) which is now most widely applied. It was also used by Kanamori (1977) in developing the seismic *moment magnitude* M_w (see 3.2.5.3). Recently, Choy and Boatwright (1995) found (see 3.3)

$$\log E_S = 1.5 M_s + 4.4. \quad (3.85)$$

From theoretical considerations Randall (1973) derived a relationship between E_S and the local magnitude M_l which was later confirmed empirically by Seidl and Berckhemer (1982) as well as by Berckhemer and Lindenfeld (1986). On the basis of direct energy calculations for earthquakes from the Friuli region, Italy, using digital broadband records of the Gräfenberg array in Germany, the latter obtained:

$$\log E_S \sim 2.0 M_l \quad (3.86)$$

This is close to the empirical findings by Gutenberg and Richter (1956a) ($\log E_S \sim 1.92 M_l$) for southern California and the more recent one by Kanamori et al. (1993). The latter got

$$\log E_S = 1.96 M_l + 2.05 \quad (3.87)$$

for the magnitude range $1.5 < M_l < 6.0$. For $M_l > 6.5$ M_l saturates.

For short-period body-wave magnitudes m_b Sadovsky et al. (1986) found the relationship

$$\log E_S = 1.7 m_b + 2.3 \quad (3.88)$$

which is applicable for both earthquakes and underground explosions. **Note:** According to the coefficient in the above equations one unit of magnitude increase in M_s , m_b , M_l and m_b , respectively, corresponds to an increase of E_S by a factor of about 32, 50, 100 and 250 times!

In this context one should mention that in the countries of the former USSR the energy scale after Rautian (1960), $K = \log E_S$ (with E_S in J), is widely used and given in the catalogs. It is based on the same elements as any other magnitude scale such as an empirical calibration function and a reference distance (here 10 km). K relates to magnitude M via

$$K = 1.8 M + 4. \quad (3.89)$$

Riznichenko (1992) summarized data and relationships published by many authors (see Fig. 3.37) between magnitude M and K on the one hand and $\log M_0$ on the other hand. Depending on the range of distance and size M stands here for M_l , m_b , m_b or M_s .

Kanamori (1983) published linear relationships between $\log E_S$ and $\log M_0$ for both shallow and intermediate to deep events (see Fig. 3.38). They are rather similar and correspond, on average, to the relationship $E_S/M_0 = 5 \times 10^{-5}$ which he used in the development of the moment magnitude scale M_w (Kanamori 1977).

However, as previously mentioned in the sub-sections 3.2.5.3 and 3.2.6.1 on moment and energy magnitudes, scaling laws must be used with caution. Later investigations have revealed sometimes significant deviations from this average E_S/M_0 - relationship (e.g., Kikuchi and Fukao, 1988; Choy and Boatwright, 1995). This is due to local and regional differences in source mechanism, stress drop, time history of the rupture process, etc. It makes global relationships of this type often unsuitable for drawing inferences on regional differences in tectonic deformation and stress accumulation rates. Furthermore, scaling laws for source parameters derived from low-frequency data may not be suitable for inferring seismic hazard, which is affected by the high frequencies that cause most earthquake damage and are more relevant for earthquake engineers.

3. Seismic Sources and Source Parameters

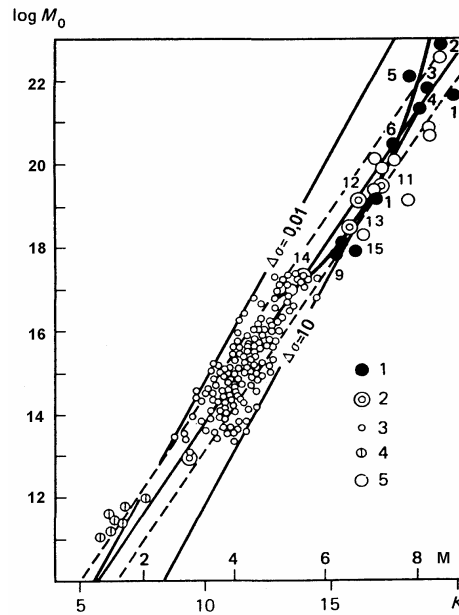


Fig. 3.37 Correlation between seismic moment M_0 (in $\text{Nm} = \text{J}$), magnitude M and Rautian's (1960) energetic class K according to a compilation of data from many authors. Related stress drop $\Delta\sigma$ has been given in MPa (full straight lines). Broken lines mark the 68% confidence interval. 1 - large global earthquakes; 2 - average values for individual regions; 3 - earthquakes in the western USA; 4 - micro-earthquakes in Nevada; 5 - M_0 determinations from field data; 6 to 15 - individual values from different regions (modified from Ryznichenko, 1992, Fig. 1; with permission from Springer-Verlag).

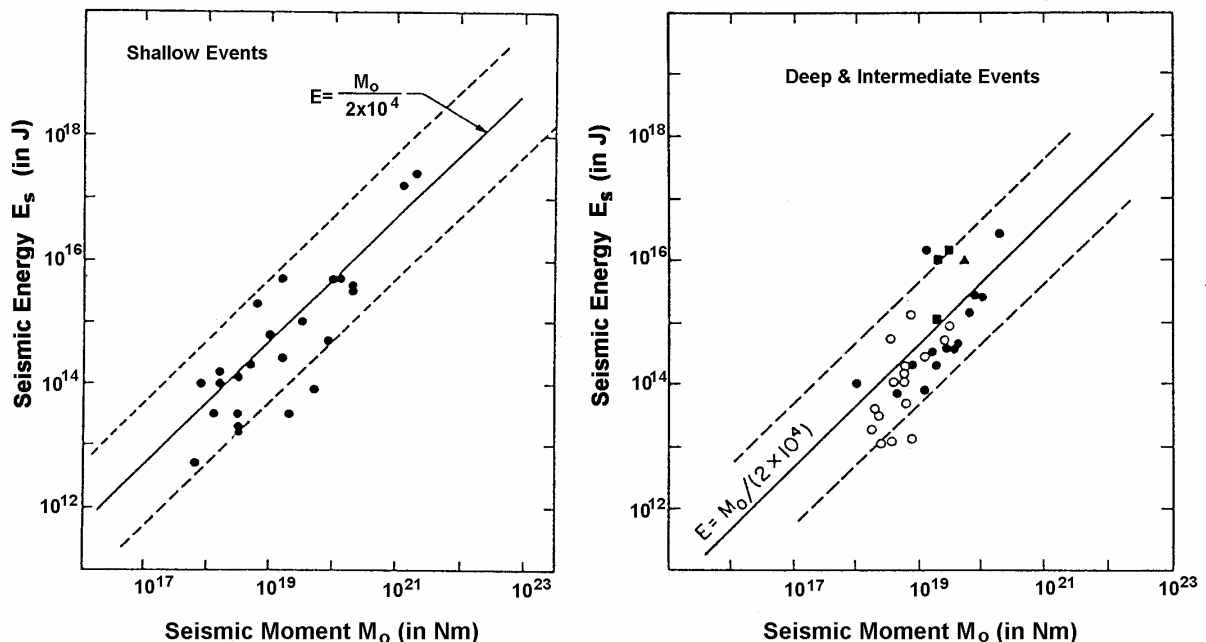


Fig. 3.38 Relations between seismic moment M_0 and energy E_s for shallow events (left) and intermediate to deep events (right) according to Vassiliou and Kanamori (1982). The solid line indicates the relation $E_s = M_0 / (2 \times 10^4)$ suggested by Kanamori (1977) on the basis of elastostatic considerations (modified from Kanamori, 1983 in *Tectonophysics*, Vol. 93, p. 191 and 192, with permission from Elsevier Science).

3.6.3 Moment-magnitude relations

Global relations between M_s and M_0 were derived by Ekström and Dziewonski (1988) from high quality determinations of M_0 from the Global Digital Seismic Network (GDSN). M_0 is given below in Nm ($1 \text{ Nm} = 1 \text{ J} = 10^7 \text{ dyn cm} = 10^7 \text{ ergs}$):

$$\log M_0 = M_s + 12.24 \quad \text{for} \quad M_s < 5.3, \quad (3.90)$$

$$\log M_0 = 23.20 - (92.45 - 11.40M_s)^{1/2} \quad \text{for} \quad 5.3 \leq M_s \leq 6.8, \quad (3.91)$$

$$\log M_0 = 1.5 M_s + 9.14 \quad \text{for} \quad M_s > 6.8. \quad (3.92)$$

Chen and Chen (1989) published detailed global relations between M_0 and M_s , as well as between m_b and M_l , based on data for about 800 earthquakes in the magnitude range $0 < M < 8.6$. These authors also showed that their empirical data are well fit by theoretical scaling relations derived from a modified Haskell model of a rectangular fault which produces displacement spectra with three corner frequencies. Similar global scaling relations had been derived earlier by Gellert (1976), also based on the Haskell (1964 and 1966) model. In both papers these relations show saturation for M_l at about 6.3, for m_b between about 6.0 and 6.5 and for M_s between about 8.2 and 8.5.

Other global relationships between M_0 and M_s were derived from Chen and Chen (1989) from a theoretical scaling law based on a modified Haskell source model. They fit well a set of global data with a standard deviation of individual values $\log M_0$ of about ± 0.4 and confirm the saturation of M_s at about 8.5:

$$\log M_0 = 1.0 M_s + 12.2 \quad \text{for} \quad M_s \leq 6.4, \quad (3.93)$$

$$\log M_0 = 1.5 M_s + 9.0 \quad \text{for} \quad 6.4 < M_s \leq 7.8, \quad (3.94)$$

$$\log M_0 = 3.0 M_s - 2.7 \quad \text{for} \quad 7.8 < M_s \leq 8.5, \text{ and} \quad (3.95)$$

$$M_s = 8.5 = \text{const. for } \log M_0 > 22.8 \text{ Nm.} \quad (3.96)$$

Also M_s - M_0 relations (and vice versa) show regional variability. According to Ambraseys (1990) the global relations (3.90) - (3.92) systematically underestimate M_s for events in the Alpine region of Europe and adjacent areas by 0.2 magnitude units on average. Abercrombie (1994) discussed possible reasons for the anomalous high surface-wave magnitudes of continental earthquakes relative to their seismic moment. This illustrates the need for regional scaling of moment-magnitude relationships even in the relatively long-period range.

For M_0 and body-wave magnitudes m_b (of 1s period) Chen and Chen (1989) give the following global scaling relations (with saturation at $m_b = 6.5$ for $\log M_0 > 20.7$):

$$\log M_0 = 1.5 m_b + 9.0 \quad \text{for} \quad 3.8 < m_b \leq 5.2, \quad (3.97)$$

3. Seismic Sources and Source Parameters

$$\log M_0 = 3 \text{ mb} + 1.2 \quad \text{for} \quad 5.2 < \text{mb} \leq 6.5, \quad (3.98)$$

and for M_0 and M_I for California (with saturation at $M_I = 6.3$ for $\log M_0 > 20.1$):

$$\log M_0 = M_I + 10.5 \quad \text{for} \quad M_I \leq 3.6, \quad (3.99)$$

$$\log M_0 = 1.5 M_I + 8.7 \quad \text{for} \quad 3.6 < M_I \leq 5.0, \quad (3.100)$$

$$\log M_0 = 3 M_I + 1.2 \quad \text{for} \quad 5.0 < M_I \leq 6.3. \quad (3.101)$$

Average scaling relations among mb , M_s and M_0 for plate-margin earthquakes have been derived by Nuttli (1985). They yield practically identical values as the equations (3.93)-(3.95) for M_0 when M_s is known while the deviations are not larger than about a factor of 2 when using mb and Eqs. (3.97) and (3.98).

The need for regional relationships between M_0 and magnitudes is particularly evident for M_I . When calculating M_0 according to Eqs. (3.98) and (3.100) for California and comparing them with the values calculated for a relationship given by Kim et al. (1989) for the Baltic Shield

$$\log M_0 = 1.01 M_I + 9.93 \quad \text{for} \quad 2.0 \leq M_I \leq 5.2 \quad (3.102)$$

we get for $M_I = 2.0, 4.0$ and 5.0 , respectively, values for M_0 which are 3.5, 5.4 and 16.6 times larger for California than for the Baltic Shield. Using instead an even more local relationship for travel paths within the Great Basin of California (Chávez and Priestley, 1985), namely

$$\log M_0 = 1.2 M_I + 10.49 \quad \text{for} \quad 1 \leq M_I \leq 6 \quad (3.103)$$

we get for the same magnitudes even 9, 21 and 32 times larger values for M_0 than for the Baltic Shield according to Eq. (3.102).

3.6.4 Scaling relations of M , M_0 and E_s with fault parameters

Scaling relations of magnitude, seismic moment and energy with fault parameters are used in two ways:

- 1) to get a rough estimate of relevant fault parameter when M , M_0 or E_s of the event are known from the evaluation of instrumental recordings; or
- 2) in order to get a magnitude, moment and/or energy estimates for historic or even prehistoric events for which no recordings are available but for which some fault parameters such as (maximum possible) length of surface rupture and/or amount of surface displacement can still be determined from field evidence.

The latter is particularly important for improved assessment of seismic hazard and for estimating the maximum possible earthquake, especially in areas with long mean recurrence times for strong seismic events. Of particular importance for hazard assessment are also relationships between macroseismic intensity, I , and magnitude, M , on the one hand (see Eqs. (3.22) to (3.28) in 3.2.6.7) and between ground acceleration and I or M , on the other hand. Unfortunately, the measured maximum accelerations for equal values of intensity I scatter in the whole range of $I = \text{III}$ to IX by about two orders of magnitude (Ambraseys, 1975). The

reason for this scatter is many-fold, e.g., human perception is strongest for frequencies around 3 Hz while acceleration and damage might be strongest for more high frequent ground motions. Also, damage depends not only on the peak value of acceleration but also depends on its frequency with respect to the natural period of the shaken structures and on the duration of strong ground shaking. For some structures damage is also more closely related to strong ground-motion displacement or velocity and not to acceleration.

Relationships between M_0 , M_s , and E_S with various fault parameters are mostly based on model assumptions on the fault geometry, rupture velocity and time history, ambient stress and stress drop etc. But sometimes these fault parameters can, at least partially, be confirmed or constrained by field evidence or by petrophysical laboratory experiments. As for other scaling relations discussed above, global relationships can give only a rough orientation since the scatter of data is considerable due to regional variability. Whenever possible, regional relationships should be developed.

Sadovsky et al. (1986) found that for both crustal earthquakes and underground explosions the following relationship holds between seismic energy E_S (in erg) and the seismic source volume V_s (in cm^3):

$$\log E_S = 3 + \log V_s \quad (3.104)$$

with V_s for earthquakes being estimated from the linear dimensions of the aftershock zone. This means that the critical energy density for both natural and artificial crustal seismic sources is about equal, roughly 10^3 erg/cm^3 or 100 J/m^3 . It does not depend on the energy released by the event. E_S increases only because of the volume increase of the source. Accordingly, it is not the type of seismic source but the properties of the medium that play the decisive role in the formation of the seismic wave field. However, local and regional differences in ambient stress and related stress drop $\Delta\sigma \approx 2\mu E_S/M_0$ may modify this conclusion (see 3.3).

Fig. 3.39 shows the relation between seismic moment M_0 and the area A_r of fault rupture as published by Kanamori and Anderson (1975). A_r is controlled by the stress drop $\Delta\sigma$; as $\Delta\sigma$ increases for a given rupture area, M_0 becomes larger. One recognizes that intraplate earthquakes have on average a higher stress drop (around 10 MPa = 100 bars) than interplate events (around 3 MPa). The data in Fig. 3.39 are also well fit by the average relationship suggested by Abe (1975), namely:

$$M_0 = 1.33 \times 10^{15} A_r^{3/2} \quad (3.105)$$

which is nearly identical with the relation by Purcaru and Berckhemer (1982):

$$\log M_0 = (1.5 \pm 0.02) \log A_r + (15.25 \pm 0.05) \quad (3.106)$$

with M_0 in Nm and A_r in km^2 . Eq. (3.106) corresponds to the theoretical scaling relation derived by Chen and Chen (1989) for a modified Haskell model with the assumption $L = 2W$ (L - length and W - width of fault rupture, $A_r = LW = 0.5 L^2$) and an average displacement $\bar{D} = 4.0 \times 10^{-5} L$. Note that experimental data indicate also other aspect ratios L/W up to about 30 (e.g., Purcaru and Berckhemer, 1982). Wells and Coppersmith (1994) gave another relation between moment magnitude and A_r :

3. Seismic Sources and Source Parameters

$$M_w = (0.98 \pm 0.03) \log A_r + (4.07 \pm 0.06) \quad (3.107)$$

derived from a very comprehensive data base of source parameters for historical shallow-focus earthquakes ($h < 40$ km) in continental interplate or intraplate environments.

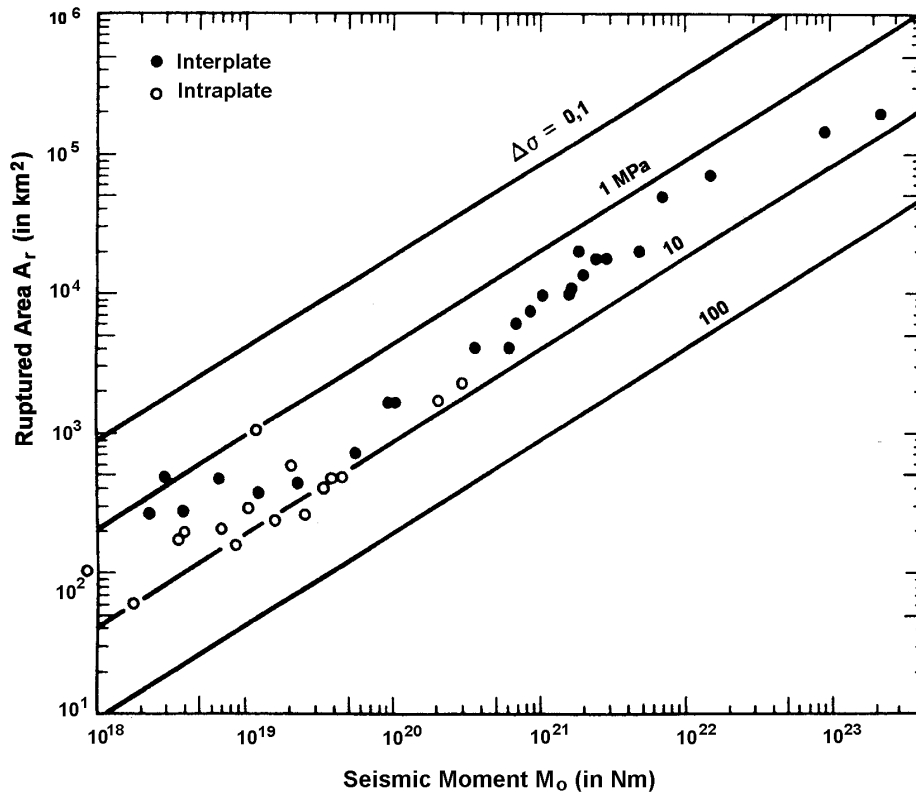


Fig. 3.39 Relation between area of fault rupture A_r and seismic moment M_0 for inter- and intraplate earthquakes. The solid lines give the respective relationships for different stress drop $\Delta\sigma$ (in MPa; $1 \text{ Pa} = 10^{-5}$ bars) (modified from Kanamori and Anderson, *Theoretical basis of some empirical relations in seismology*, Bull. Seism. Soc. Am., Vol. 65, p. 1077, Fig. 2, 1975; © Seismological Society of America).

There also exists a linear log-log relation between L and M_0 . Interestingly, for a given seismic moment L is on average about 6 times larger for interplate (strike-slip) events than for intraplate ones (see Fig. 3.40). The ratio α between average fault displacement (slip) \bar{D} and fault length L is according to Scholz et al. (1986) $\alpha \approx 1 \times 10^{-5}$ for interplate and $\alpha \approx 6 \times 10^{-5}$ for intraplate events. Since this result is independent of the type of fault mechanism, it implies that intraplate faults have a higher frictional strength (and thus stress drop) than plate boundary faults but smaller length for the same seismic moments.

The slope of the curves in Fig. 3.40 is 0.5. This corresponds to a relation $M_0 \sim L^2$ (Scholz 1982; Pegeler and Das, 1996) which is only valid for large earthquakes ($M >$ about 6.5 to 7). Then the width W of the fault is already saturated, i.e., equal to the thickness of the brittle fracturing zone in the lithosphere. Depending on heat flow and composition, the seismogenic zone in the crust is about 10 to 30 km thick. Accordingly, for large earthquakes, the growth of the fault area with increasing M_0 is in the length direction only.

Recently, there has been some serious debate on the scaling of large earthquakes and their ratio α (Scholz, 1994 and 1997; Romanowicz 1994; Romanowicz and Rundle, 1993 and 1994; Sornette and Sornette, 1994; Wang and Ou, 1998). Romanowicz (1992), who prefers to scale slip not with length but with width, even gives a relationship of $M_0 \sim L$ in case of very large earthquakes. In contrast, Hanks (1977) showed that earthquakes with rupture dimensions smaller than this seismogenic thickness scale according to $M_0 \sim L^3$ which is equivalent to Eq. (3.104).

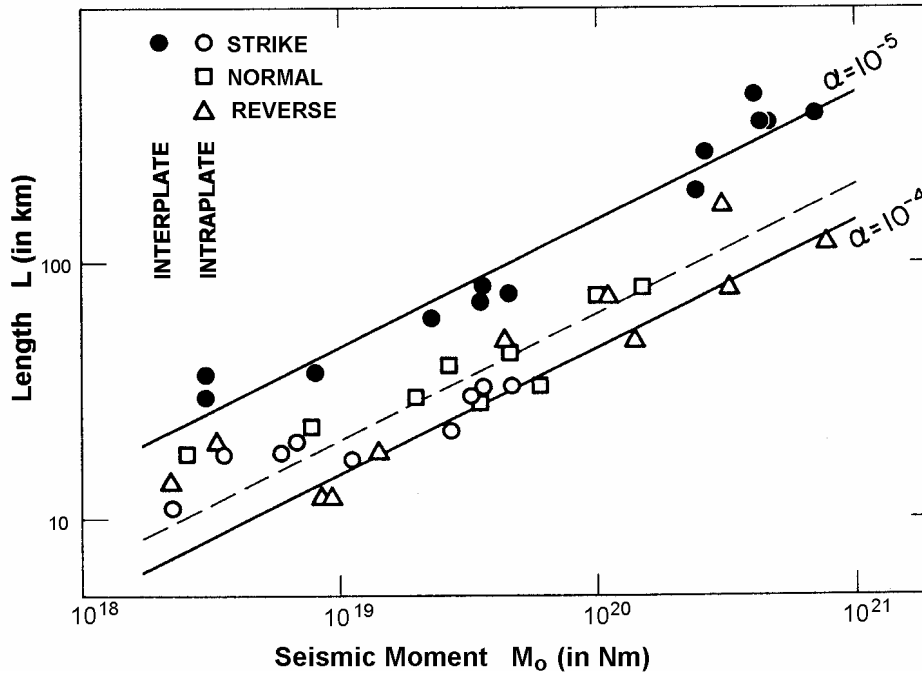


Fig. 3.40 Fault length L versus seismic moment M_0 for large inter- and intraplate earthquakes. The solid lines give the respective relationship for the ratio $\alpha = \bar{D}/L$ (modified from Scholz, Aviles, and Wesnousky, Scaling differences between large interplate and intraplate earthquakes, Bull. Seism. Soc. Am., Vol. 76, No. 1, p. 68, Fig. 1, 1986; © Seismological Society of America).

According to an older data compilation shown in Fig. 3.41 the correlation between source length L , magnitude M and energetic class K is not very good. Relations given by various authors for events in different environments often differ strongly.

Ambraseys (1988) published relationships derived from the dimensions of fault surface ruptures for Eastern Mediterranean and Middle Eastern earthquakes (with L - observed fault length in km, \bar{D} - relative fault displacement in cm, M_{SC} - predicted surface-wave magnitudes):

$$M_{SC} = 1.43 \log L + 4.63 \tag{3.108}$$

and

$$M_{SC} = 0.4 \log (L^{1.58} \bar{D}^2) + 1.1. \tag{3.109}$$

3. Seismic Sources and Source Parameters

They yield results which are in good agreement with those by Nowroozi (1985) for Iran but they differ significantly from the respective relations given by Tocher (1958) for Western USA and from Iida (1959) for Japan (see curves 1 and 2 in Fig. 3.41).

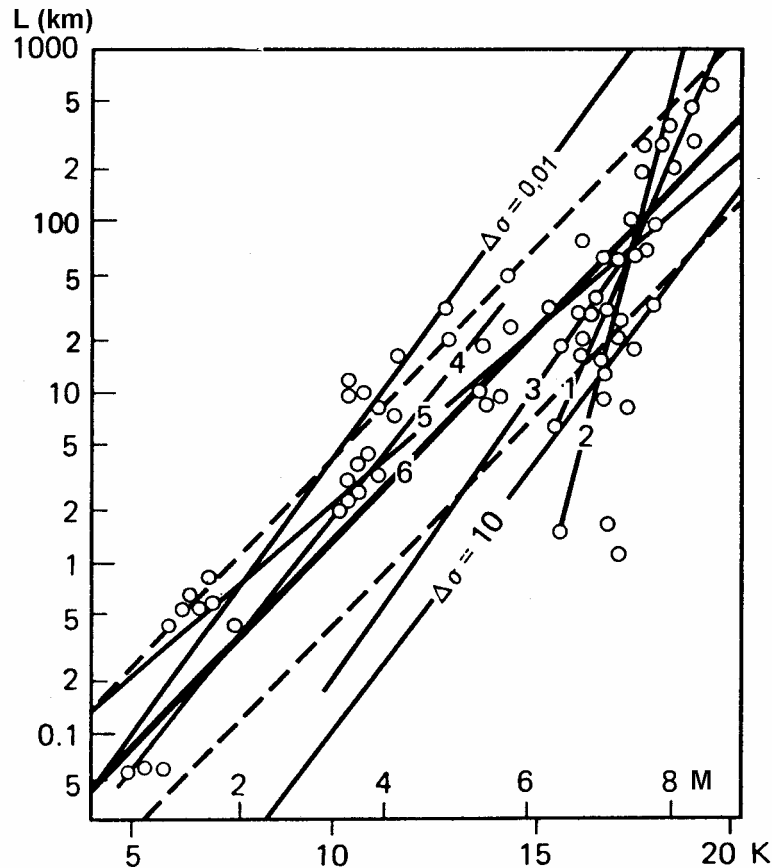


Fig. 3.41 Correlation of source length L with magnitude M and energetic class K according to data from various sources (e.g., curve 1 by Tocher, 1958, curve 2 by Iida, 1959; curve 6 average by Riznichenko, 1992). Thin straight lines: related stress drops $\Delta\sigma$ are given in MPa; broken lines mark the limits of the 68% confidence interval with respect to the average curve 6 (modified from Riznichenko, 1992, Fig. 3; with permission of Springer-Verlag).

Khromovskikh (1989) analyzed available data for more than 100 events of different faulting types from different seismotectonic regions of the Earth. He derived 7 different relationships between magnitude M and the length L of the rupture zone, amongst them those for the following regions:

a) the Circum-Pacific belt: $M = (0.96 \pm 0.25) \log L + (5.70 \pm 0.34)$ (3.110)

b) the Alpine fold belt: $M = (1.09 \pm 0.28) \log L + (5.39 \pm 0.42)$ (3.111)

c) rejuvenated platforms: $M = (1.25 \pm 0.19) \log L + (5.45 \pm 0.28)$ (3.112)

and compared them with respective relationships of other authors for similar areas.

Other relationships for estimating L (in km) when Ms is known were derived by Chen and Chen (1989) on the basis of their general scaling law based on the modified Haskell source model. These relationships clearly show the effect of width saturation:

$$\log L = Ms/3 - 0.873 \quad \text{for} \quad Ms \leq 6.4 \quad (3.113)$$

$$\log L = Ms/2 - 1.94 \quad \text{for} \quad 6.4 < Ms \leq 7.8 \quad (3.114)$$

$$\log L = Ms - 5.84 \quad \text{for} \quad 7.8 < Ms \leq 8.5. \quad (3.115)$$

The same authors also gave similar relations between the average dislocation \bar{D} (in m) and Ms, namely:

$$\log \bar{D} = Ms/3 - 2.271 \quad \text{for} \quad Ms \leq 6.4 \quad (3.116)$$

$$\log \bar{D} = Ms/2 - 3.34 \quad \text{for} \quad 6.4 < Ms \leq 7.8 \quad \text{and} \quad (3.117)$$

$$\log \bar{D} = Ms - 7.24 \quad \text{for} \quad 7.8 < Ms \leq 8.5 \quad (3.118)$$

while Chinnery (1969) derived from still sparse empirical data a linear relation between magnitude M and $\log \bar{D}$ (with \bar{D} in m) for the whole range $3 < M < 8.5$

$$M = 1.32 \log \bar{D} + 6.27 \quad (3.119)$$

which changes to

$$M = 1.04 \log \bar{D} + 6.96 \quad (3.120)$$

when only large magnitude events are considered.

Probably best established are the relations which Wells and Coppersmith (1994) have determined for shallow-focus (crustal) continental interplate or intraplate earthquakes on the basis of a rather comprehensive data base of historical events. Since most of these relations for strike-slip, reverse and normal faulting events were not statistically different (at a 95% level of significance) their average relations for all slip types are considered to be appropriate for most applications. Best established are the relationships between moment magnitude Mw and rupture area (see Eq. (3.107)), surface rupture length (SRL) and subsurface rupture length (RLD) (both in km). They have the strongest correlations ($r = 0.89$ to 0.95) and the least data scatter:

$$M_w = (1.16 \pm 0.07) \log (\text{SRL}) + (5.08 \pm 0.10) \quad (3.121)$$

$$M_w = (1.49 \pm 0.04) \log (\text{RLD}) + (4.38 \pm 0.06) \quad (3.122)$$

$$\log (\text{SLR}) = (0.69 \pm 0.04) M_w - (3.22 \pm 0.27) \quad (3.123)$$

$$\log (\text{RLD}) = (0.59 \pm 0.02) M_w - (2.44 \pm 0.11) \quad (3.124)$$

3. Seismic Sources and Source Parameters

Comparing Eqs. (3.123) and (3.124) it follows that in general the surface rupture length is only about 75% of the subsurface rupture length.

The correlations between M_w and \bar{D} as well as \bar{D} and SLR are somewhat smaller ($r = 0.71$ to 0.78):

$$M_w = (0.82 \pm 0.10) \log \bar{D} + (6.693 \pm 0.05) \quad (3.125)$$

$$\log \bar{D} = (0.69 \pm 0.08) M_w - (4.80 \pm 0.57) \quad (3.126)$$

$$\log \bar{D} = (0.88 \pm 0.11) \log (\text{SLR}) - (1.43 \pm 0.18) \quad (3.127)$$

$$\log (\text{SLR}) = (0.57 \pm 0.07) \log \bar{D} + (1.61 \pm 0.04). \quad (3.128)$$

Wells and Coppersmith (1994) reason that the weaker correlation may reflect the wide range of displacement values for a given rupture length (differences up to a factor 50 in their data set!). These authors also give relations between SLR and the maximum surface displacement which is, on average, twice the observed average surface displacement while the average subsurface slip ranges between the maximum and average surface displacement.

Chen and Chen (1989) also derived from their scaling law the following average values:

- rupture velocity $v_r = 2.65$ km/s;
- total rupture time T_r (in s) = 0.35 (s/km) \times L (km); (3.129)
- slip velocity $dD/dt = (2.87 - 11.43)$ m/s.

However, v_r and dD/dt usually vary along the fault during the fracture process. From teleseismic studies we can obtain only spatially and temporally averaged values of fault motion but the actual co-seismic slip is largely controlled by spatial heterogeneities along the fault rupture (see Fig. 3.8). Large slip velocities over 10 m/s suggest very high local stress drop of more than 10 MPa. (Yomogida and Nakata, 1994). On the other hand, sometimes very slow earthquakes may occur with very large seismic moment but low seismic energy radiation (e.g., "tsunami earthquakes"). This has special relevance when deriving scaling relations suitable for the prediction of strong ground motions (e.g., Fukushima, 1996).

Scaling relationships between fault parameters, especially between D and L , are also controlled by the fault growth history, by age and by whether the event can be considered to be single and rare or composite and frequent (e.g., Dawers et al., 1993; Tumarkin et al., 1994). There exist also scaling relations between fault length and recurrence interval which are of particular relevance for seismic hazard assessment (e.g., Marrett, 1994).

Using Eqs. (3.108), (3.110)-(3.112) and (3.121), one gets for a surface rupture length of 100 km magnitudes $M = 7.5, 7.7, 7.6, 7.95$ and 7.4 , respectively. Knowing the M_s or M_w and calculating L and \bar{D} according to Eqs. (3.114)-(3.118), (3.123) and (3.126), one gets for magnitude 7.0 $L = 36$ km and 41 km, $\bar{D} = 1.4$ m and 1.1 m and for magnitude 8.0 $L = 145$ km and 200 km, $\bar{D} = 3.8$ m and 5.2 m. The good agreement of the calculated values for magnitudes 7 and the stronger disagreement for magnitudes 8 are obviously due to the

growing difference between M_s (used in the relations by Chen and Chen, 1989) and M_w (used in the relations by Wells and Coppersmith, 1994) for $M_s > 7$ (saturation effect). For the rupture duration we get according to Eq. (3.129) for $M_s = 7$ and 8 approximately 13 s and 51 s, respectively.

3.6.5 Similarity conditions

Under certain assumptions there exist several conditions of static (geometric) and dynamic similarity. With the assumption of a constant stress drop one gets

$$W/L = k_1 \quad \text{i.e., a constant fault aspect ratio} \quad \text{and} \quad (3.130)$$

$$\bar{D}/L = k_2 \quad \text{i.e., constant strain } \alpha. \quad (3.131)$$

One can combine Eqs. (3.130) and (3.131) with the definition of the seismic moment $M_0 = \mu \bar{D} W L = \mu k_1 k_2 L^3$ and get $M_0 \sim L^3$ which is valid for source dimensions smaller than the thickness of the seismogenic layer. In addition there is a dynamic similarity, namely, the rise time t_r required for reaching the total displacement, i.e., the duration of the source-time function, is

$$t_r = k_3 \times L/v_{cr} \quad (3.132)$$

with v_{cr} the crack or rupture velocity (see Fig. 3.4). This is equivalent to the Eq. (3.131) of constant strain. Lay and Wallace (1995) showed that this results in period-dependent amplitudes of seismic waves which scale with the fault dimension. For periods $T \gg t_r$ the amplitude does not depend on fault length L . This corresponds to the plateau of the "source displacement spectrum". But if $T \ll t_r$ then the amplitudes scale as $1/L^2$ or f^{-2} (see Fig. 3.5). This explains the saturation effect when analyzing frequencies higher than the corner frequency of the source spectrum.

Acknowledgments

The authors acknowledge with thanks careful reviews by A. Udias and W. Brüstle. Their comments have helped to improve and streamline the first draft of this Chapter. The German authors are also much obliged to G. Choy who carefully proofread the English in their contributions to the whole manuscript. Special thanks go to the members of the IASPEI WG on Magnitude Measurements, particularly to J. Dewey, S. Gregersen, A. A. Gusev, R. A. Uhrhammer and K. Veith. Discussions with these members and complementary information provided by them enabled the Editor to complete the sub-chapter on magnitudes and the information sheet IS 3.2 on a common basis of understanding. This sets the stage for future standardization of magnitude measurements from digital data and for reaching agreement on a more precise and unique specific magnitude nomenclature. It is also acknowledged that S. Wendt of the Observatory Collmberg, University of Leipzig, provided Figure 3 of the Data Sheet 3.1 and that F. Krüger from the University of Potsdam contributed a short complementary paragraph to sub-chapter 3.5 and related references on relative moment-tensor inversion.

3. Seismic Sources and Source Parameters

Recommended overview readings (see References under Miscellaneous in Volume 2)

Richter (1958)

Aki and Richards (1980 and 2002)

Báth (1981)

Ben Menahem and Singh (1981)

Das and Kostrov (1988)

Duda (1989)

Scholz (1990)

Lay and Wallace (1995)

Udias (1999)

4

Seismic Signals and Noise

Peter Bormann

4.1 Nature and presentation of seismic signals and noise

As shown in Fig. 1.1, one of the key problems in seismology is to solve the inverse problem, i.e., to derive from the analysis of seismic records information about the structure and physical properties of the Earth medium through which the seismic waves propagate (see Chapter 2) as well as about the geometry, kinematics and dynamics of the seismic source process (see Chapter 3). This task is complicated by the fact that the seismic signals radiated by the source are weakened and distorted by geometric spreading and attenuation and, due to reflection, diffraction, mode conversion and interference during their travel through the Earth. They are also distorted by the *transfer function* of the seismograph. While the Earth acts as a low-pass filter by attenuating higher frequencies most effectively, a mechanical seismograph is a second order high-pass filter with a roll-off of -12 dB per octave for periods larger than its eigenperiod (see Chapter 5).

Additionally, seismic signals are superposed and, in the case of low *signal-to-noise ratio* (SNR), sometimes completely masked by seismic noise. Therefore, one of the main issues in applied seismology is to ensure high SNR or, where conditions are bad, to improve it by suitable ways of data acquisition and processing. The success of SNR improvement largely depends on our understanding of the ways in which seismic signals and noise differ.

4.1.1 Seismic signals

The signal radiated from a seismic source, be it an explosion or a shear rupture, is usually a more or less complicated displacement step function or velocity impulse of finite duration from milliseconds up to a few minutes at the most (see Figs. 2.4, 3.4 and 3.7). According to the *Fourier theorem* any arbitrary *transient function* $f(t)$ in the *time domain* can be represented by an equivalent function $F(\omega)$ in the *frequency domain*, the *Fourier transform* of $f(t)$. The following relations hold:

$$f(t) = (2\pi)^{-1} \int_{-\infty}^{\infty} F(\omega) \exp(i\omega t) d\omega \quad (4.1)$$

$$F(\omega) = \int_{-\infty}^{\infty} f(t) \exp(-i\omega t) dt = |F(\omega)| \exp(i\phi(\omega)) \quad (4.2)$$

(Note that other sign conventions are often used, e.g. $\exp(-i\omega t)$ in Eq. (4.1) and $\exp(i\omega t)$ in Eq. (4.2) in wave propagation studies in order to assure that the wave-number vector is positive in the direction of wave propagation).

4. Seismic Signals and Noise

$|F(\omega)| = A(\omega)$ is the *amplitude spectral density* with the unit m/Hz, $\omega = 2\pi f$ the angular frequency (with f - frequency in unit Hz) and $\phi(\omega)$ the *phase spectrum* with the units deg, rad or 2π rad. Fig. 4.1 gives an example. The integral in (4.1) is equivalent to a sum. Thus, the *Fourier theorem* states that an arbitrary finite time series, even an impulsive one, can be expressed as a sum of monochromatic periodic functions, i.e., $f(t) = 2\pi^{-1} \sum |F(\omega)| \exp(i[\omega t + \phi(\omega)])\Delta\omega$. Fig. 4.2 illustrates how a sum of harmonic terms can equal an arbitrary function.

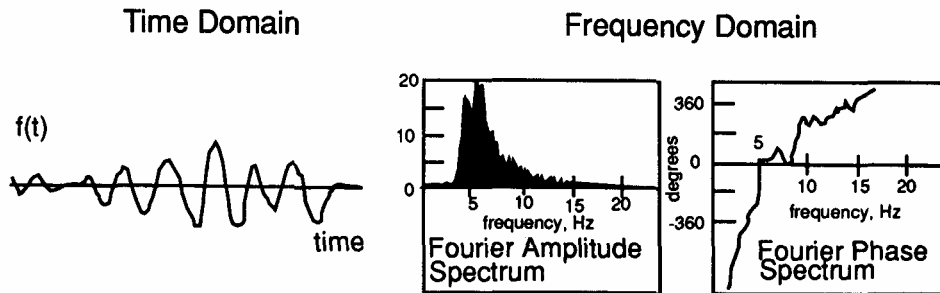


Fig. 4.1 A signal recorded as a function of time (left) can be represented equivalently in the frequency domain by its Fourier spectrum. The amplitude (middle) and phase spectrum (right) are both needed to provide the complete time series (reproduced from Lay and Wallace, 1995, Figure 5.B1.1, p. 176; with permission of Elsevier Science (USA)).

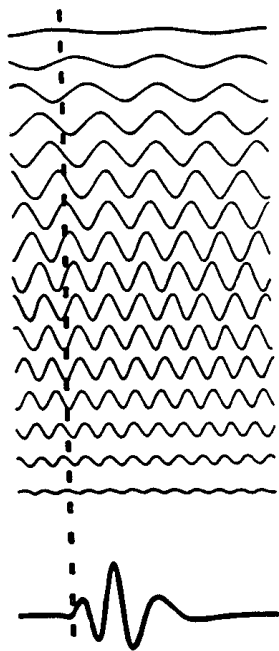


Fig. 4.2 The transient signal $f(t)$ is formed by summing up the infinite harmonic terms of a discretized version of Eq. (4.1). The amplitudes of each harmonic term vary, being prescribed by the amplitude spectrum. The shift of the phase of each harmonic term is given by the phase spectrum (reproduced from Lay and Wallace, 1995, Figure 5.B1.2, p. 177; with permission of Elsevier Science (USA)).

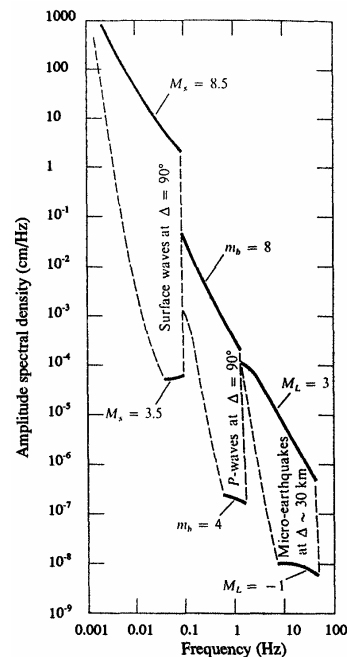


Fig. 4.3 Ranges of amplitude spectral densities for seismic waves. The lower bound is limited due to ambient seismic noise (according to Aki and Richards, 1980; with kind permission of the authors).

By high-, low- or band-pass filtering of an input signal, such as the one shown in Fig. 4.2, the amplitudes and phase relationships of its harmonic terms and thus the shape, amplitude and predominant period of the resulting output signal are changed. Examples will be given in 4.2.1 below. Therefore, magnitudes of seismic events determined from amplitude and period readings of seismic phases are comparable only when determined from analog seismic records with identical standard frequency responses or digital records filtered appropriately. Systematic differences between various magnitude scales as well as saturation effects are the consequence of filtering the input signals with different responses and in limited frequency ranges (see 3.2.7 and Fig. 3.18). Fig. 4.3 presents the range of amplitude spectral densities for seismic waves above the level of ambient seismic noise, depending on magnitude and distance.

4.1.2 Seismic noise

While the harmonic components of transient seismic signals radiated by localized sources of finite duration are coherent and their phase relationships defined by the phase spectrum, this is not the case for ambient seismic noise. The latter is caused by a diversity of different, spatially distributed, mostly unrelated and often continuous sources (see 4.3). Seismic noise (for records see 4.3) thus forms a more or less *stationary stochastic process* without a defined phase spectrum. The same applies to electronic instrumental self-noise and the Brownian (thermal) motion of the seismic mass (see 5.6). Early efforts in the years of analog seismology to get a quantitative measure of seismic noise as a function of frequency were based on drawing envelopes of peak amplitude readings in given time intervals for seismic noise at different times of the day and year. Such presentations are not commensurate when based on records or filtered time plots of different bandwidth and can not resolve spectral details (Fig. 4.4).

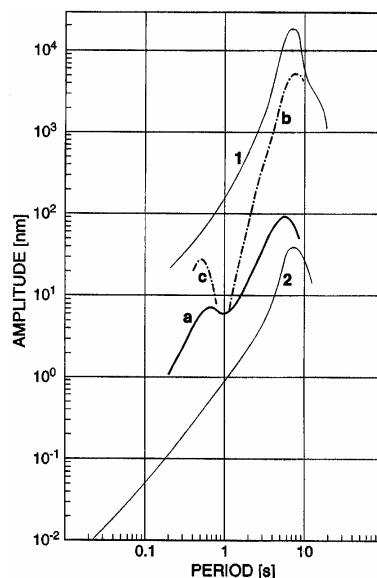


Fig. 4.4 Envelopes of maximum and minimum peak amplitudes for rural environments as determined from analog seismograph records of different type over a long time-span according to Brune and Oliver (1959) (curves 1 and 2: high- and very low-noise sites, respectively; bandwidth of recordings 1 to 2 octaves) together with envelope curves of peak noise amplitudes at station MOX, Germany, at times of minimum (a) and maximum noise (b and c; bandwidth of records 4 to 8 octaves) (reproduced from Journal of Seismology, 2, 1998, “Conversion and...”, P. Bormann, p. 38, Fig. 1; © Kluwer Academic Publishers, with permission of Kluwer Academic Publishers).

4. Seismic Signals and Noise

Instructions for reporting microseisms with periods $> 2s$ to be measured regularly at 00h, 06h, 12h and 18h daily, were given in the 1979 edition of MSOP (Willmore, 1979), Chapter on Reporting output. This is no longer practised in times of digital seismology and the possibility for computational spectral analysis. However, because of the stochastic nature of seismic noise, the integral in Eq. (4.2) does not converge. Consequently, *amplitude spectral density* and *phase spectrum* can not be calculated. Instead, we have to determine the *power spectral density* $P(\omega)$. It is the Fourier transform of the autocorrelation function $p(\tau) = \langle f(t) f(t + \tau) \rangle$, i.e.,

$$P(\omega) = \int_{-\infty}^{\infty} p(\tau) \exp(-i\omega\tau) d\tau. \quad (4.3)$$

The symbol $\langle \rangle$ indicates averaging over the time t . (For calculation see also Havskov and Alguacil (2002)). Depending on whether $f(t)$ is a displacement (d), velocity (v) or acceleration (a) record, $P(\omega)$ is given in units m^2/Hz , $(m/s)^2/Hz$ or $(m/s^2)^2/Hz$.

The oscillatory ground-motion $x(t)$ of seismic noise (but also of the harmonic terms of a transient signal) can be approximated by sine-waves $x(t) = a_d \sin\omega t$ with a_d as the displacement amplitude. Therefore, when converting displacements into the related velocities dx/dt or accelerations d^2x/dt^2 , we get as the respective velocity and acceleration amplitudes $a_v = a_d \omega$ and $a_a = a_d \omega^2$, respectively. Thus, knowing the displacement power spectral density value $P_d(\omega)$, one can calculate the respective values of the velocity (P_v) or acceleration power spectral density (P_a), i.e.,

$$P_v(\omega) = P_d \omega^2 = 4\pi^2 f^2 P_d \quad (4.4)$$

and

$$P_a(\omega) = P_d \omega^4 = 16\pi^4 f^4 P_d = 4\pi^2 f^2 P_v \quad (4.5)$$

or vice versa. Fig. 4.5 depicts the velocity power spectra of ambient noise at noisy and quiet conditions for a typical station on hard basement rock.

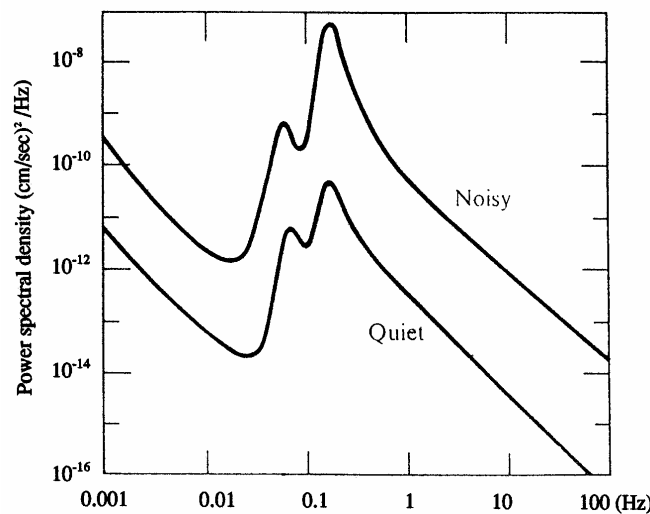


Fig. 4.5 Velocity power spectra of ambient seismic noise at noisy and quiet conditions for a typical station on hard basement rock (reproduced from Aki and Richards 1980; with kind permission of the authors).

An individual displacement power density spectrum as measured at a rather quiet site in NW Iran is depicted in Fig. 4.6.

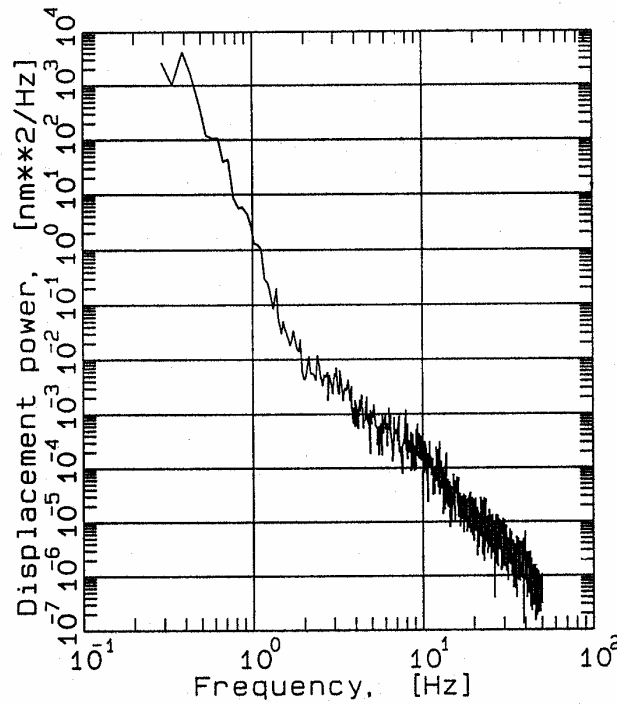


Fig. 4.6 Spectrum of displacement power spectral density calculated from 6 moving, 50% overlapping intervals of short-period noise records, 4096 samples long each, i.e., from a total record length of about 80 s at a rather quiet site in NW Iran.

As in acoustics, the relative seismic signal or noise power $(a_2/a_1)^2$ is often expressed in units of dB (= deciBel). The power difference in dB is $10 \log[(a_2/a_1)^2] = 20 \log(a_2/a_1)$. When expressing the power spectral density in units of dB referred to $1 \text{ (m/s}^2\text{)}^2/\text{Hz}$, (4.5) can be written as:

$$\mathbf{P_a[dB]} = 10 \log (\mathbf{P_a} / 1 \text{ (m/s}^2\text{)}^2/\text{Hz}). \quad (4.6)$$

Peterson (1993) has presented a new global noise model in these units. It represents the upper- and lower-bound envelopes of a cumulative compilation of representative ground acceleration power spectral densities determined for noisy and quiet periods at 75 digital stations world-wide. The models are commonly referred to as the New High Noise Model (NHNM) and New Low Noise Model (NLNM), respectively (Fig. 4.7) and they represent the currently accepted standard for expected limits of seismic noise. Exceptional cases may exceed these limits, of course.

By substituting the period $T = 1/f$ (in s) for the frequency f in (4.4) and (4.5), we get:

$$\mathbf{P_v[dB]} = \mathbf{P_a[dB]} + 20 \log (T/2\pi) \quad (4.7)$$

and

$$\mathbf{P_d[dB]} = \mathbf{P_a[dB]} + 40 \log (T/2\pi) = \mathbf{P_v[dB]} + 20 \log (T/2\pi). \quad (4.8)$$

4. Seismic Signals and Noise

Consequently, for the period $T = 2\pi = 6.28$ s $P_a = P_v = P_d$ (in numbers but not units of dB!). Also, $(P_d - P_a) = 2 \times (P_v - P_a) = \text{constant}$ for any given period, negative for $T < 2\pi$ and positive for $T > 2\pi$ (Fig. 4.7).

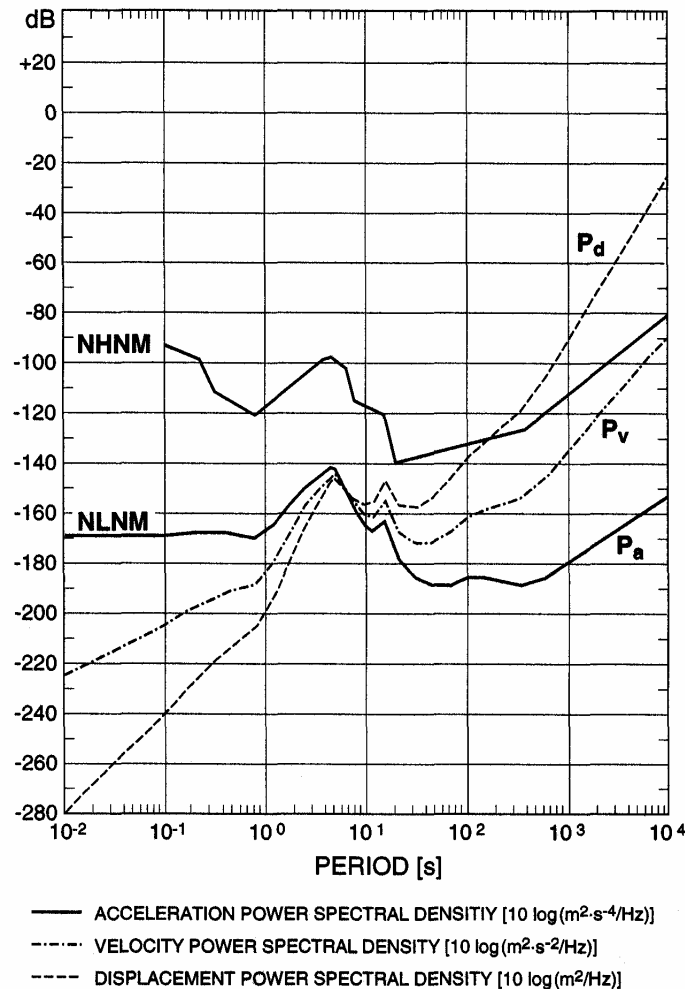


Fig. 4.7 Envelope curves of acceleration noise power spectral density P_a (in units of dB related to $1 \text{ (m/s}^2\text{)}^2/\text{Hz}$) as a function of noise period (according to Peterson, 1993). They define the new global high (NHNM) and low noise models (NLNM) which are currently the accepted standard curves for generally expected limits of seismic noise. Exceptional noise may exceed these limits. For the NLNM the related curves calculated for the displacement and velocity power spectral density P_d and P_v in units of dB with respect to $1 \text{ (m/s)}^2/\text{Hz}$ and $1 \text{ m}^2/\text{Hz}$ are given as well (reproduced from Journal of Seismology, 2, 1998, “Conversion and comparability of data presentations on seismic background noise”, P. Bormann, p. 39, Fig. 2; © Kluwer Academic Publishers, with permission of Kluwer Academic Publishers).

For periods which define the “corners” of the envelopes of the NLNM and NHNM, Tables 4.1 and 4.2 give the related displacement, velocity and acceleration power density values in their respective kinematic units as well as in dB.

The dynamic range of a seismic recording is also usually expressed in units of dB. According to Fig. 4.7 we would need a seismograph with a dynamic range of about 260 dB in order to cover the noise displacement amplitudes in the period range 10^{-2} to 10^4 s. This is more than the best

4.1 Nature and presentation of seismic signals and noise

currently available high-resolution broadband seismograph can achieve. When recording noise velocity or acceleration instead, the required dynamic range is reduced to about 140 dB and 110 dB, respectively. In the case of analog recordings on paper of about 30 cm width, the minimum double amplitude, which can be resolved visually on the record is about 1 mm and the maximum that can be recorded without clipping is 300 mm. Thus, the dynamic range is $10 \log (300/1)^2 = 20 \log (300)$, i.e., only 50 dB. In the case of digital recordings with an n-bit Analog-Digital-Converter (ADC; see Chapter 6) a dynamic range of $6 \times n$ in dB can be covered, i.e., 144 dB with a 24-bit ADC. This corresponds to an equivalent range on an analog recording of amplitudes between 1 mm and 16 km!

The dynamic range of digital seismographs is usually defined via the maximum recordable SNR above the level of ambient noise or instrumental self-noise, allowing for the resolution of noise by a few bits. But because of the differences (discussed above) between coherent transient seismic signals and the largely incoherent random seismic noise, this is not a straight-forward calculation. Below we show how signal and noise amplitudes can be expressed in a comparable way.

Tab. 4.1 Noise power spectral densities at selected periods and in different units which define the new global low-noise model (NLNM) as given by Peterson (1993). Peterson published values for \mathbf{P}_a [dB] only. The respective numbers for ground acceleration (\mathbf{P}_a), velocity (\mathbf{P}_v and \mathbf{P}_v) and displacement (\mathbf{P}_d and \mathbf{P}_d) have been calculated using Eqs. (4.4) to (4.8). Between the given periods the values are linearly interpolated in a PSD-logT diagram.

T [s]	\mathbf{P}_a [$\text{m}^2\text{s}^{-4}/\text{Hz}$]	\mathbf{P}_a [dB]	\mathbf{P}_v [$\text{m}^2\text{s}^{-2}/\text{Hz}$]	\mathbf{P}_v [dB]	\mathbf{P}_d [m^2/Hz]	\mathbf{P}_d [dB]
0.10	1.6×10^{-17}	- 168.0	4.1×10^{-21}	- 203.9	1.0×10^{-24}	- 239.9
0.17	2.1×10^{-17}	- 166.7	1.6×10^{-20}	- 198.1	1.1×10^{-23}	- 229.4
0.40	2.1×10^{-17}	- 166.7	8.7×10^{-20}	- 190.6	3.5×10^{-22}	- 214.6
0.80	1.2×10^{-17}	- 169.2	1.9×10^{-19}	- 187.1	3.2×10^{-21}	- 214.5
1.24	4.3×10^{-17}	- 163.7	1.7×10^{-18}	- 177.8	6.5×10^{-20}	- 191.9
2.40	1.4×10^{-15}	- 148.6	2.0×10^{-16}	- 157.0	3.0×10^{-17}	- 165.3
4.30	7.8×10^{-15}	- 141.1	3.6×10^{-15}	- 144.4	1.7×10^{-15}	- 147.7
5.00	7.8×10^{-15}	- 141.1	4.9×10^{-15}	- 143.1	3.1×10^{-15}	- 145.1
6.00	1.3×10^{-15}	- 149.0	1.1×10^{-15}	- 149.4	1.0×10^{-15}	- 149.8
10.00	4.2×10^{-17}	- 163.8	1.0×10^{-16}	- 159.7	2.7×10^{-16}	- 155.7
12.00	2.4×10^{-17}	- 166.2	8.7×10^{-17}	- 160.6	3.2×10^{-16}	- 155.0
15.60	6.2×10^{-17}	- 162.1	3.8×10^{-16}	- 154.2	2.3×10^{-15}	- 146.3
21.90	1.8×10^{-18}	- 177.5	2.2×10^{-17}	- 166.7	2.6×10^{-16}	- 155.8
31.60	3.2×10^{-19}	- 185.0	7.9×10^{-18}	- 171.0	2.0×10^{-16}	- 156.9
45.00	1.8×10^{-19}	- 187.5	9.1×10^{-18}	- 170.4	4.7×10^{-16}	- 153.3
70.00	1.8×10^{-19}	- 187.5	2.2×10^{-17}	- 166.6	2.8×10^{-15}	- 145.6
101.00	3.2×10^{-19}	- 185.0	9.7×10^{-17}	- 160.9	2.1×10^{-14}	- 136.8
154.00	3.2×10^{-19}	- 185.0	1.8×10^{-16}	- 157.2	1.1×10^{-13}	- 129.4
328.00	1.8×10^{-19}	- 187.5	4.9×10^{-16}	- 153.1	1.3×10^{-12}	- 118.7
600.00	3.5×10^{-19}	- 184.4	3.2×10^{-15}	- 144.8	3.0×10^{-11}	- 105.2
10^4	6.5×10^{-16}	- 151.9	3.5×10^{-14}	- 87.9	4.1×10^{-3}	- 23.8
10^5	4.9×10^{-11}	- 103.1	1.2×10^{-2}	- 19.1	2.6×10^6	+ 65.0

4. Seismic Signals and Noise

Tab. 4.2 Noise power spectral densities at selected periods and in different units which define the new global high-noise model (NHNM) as given by Peterson (1993). Peterson published values for \mathbf{P}_a [dB] only. The respective numbers for ground acceleration (\mathbf{P}_a), velocity (\mathbf{P}_v and \mathbf{P}_v) and displacement (\mathbf{P}_d and \mathbf{P}_d) have been calculated using Eqs. (4.4) to (4.8). Between the given periods the values are linearly interpolated in a PSD-logT diagram.

T [s]	\mathbf{P}_a [$\text{m}^2\text{s}^{-4}/\text{Hz}$]	\mathbf{P}_a [dB]	\mathbf{P}_v [$\text{m}^2\text{s}^{-2}/\text{Hz}$]	\mathbf{P}_v [dB]	\mathbf{P}_d [m^2/Hz]	\mathbf{P}_d [dB]
0.10	7.1×10^{-10}	- 91.5	1.8×10^{-13}	- 127.5	4.5×10^{-17}	- 163.4
0.22	1.8×10^{-10}	- 97.4	2.2×10^{-13}	- 126.5	2.7×10^{-16}	- 155.6
0.32	8.9×10^{-12}	- 110.5	2.3×10^{-14}	- 136.4	6.6×10^{-17}	- 162.2
0.80	1.0×10^{-12}	- 120.0	1.6×10^{-14}	- 137.9	2.6×10^{-16}	- 155.8
3.80	1.6×10^{-10}	- 98.0	5.8×10^{-11}	- 102.4	2.1×10^{-11}	- 106.7
4.60	2.2×10^{-10}	- 96.5	1.2×10^{-10}	- 99.2	6.4×10^{-11}	- 101.9
6.30	7.9×10^{-11}	- 101.0	8.0×10^{-11}	- 101.0	7.9×10^{-11}	- 101.0
7.90	4.5×10^{-12}	- 113.5	7.1×10^{-12}	- 111.5	1.4×10^{-11}	- 109.5
15.40	1.0×10^{-12}	- 120.0	6.0×10^{-12}	- 112.2	3.6×10^{-11}	- 104.4
20.00	1.4×10^{-14}	- 138.5	1.4×10^{-13}	- 128.4	1.4×10^{-12}	- 118.4
354.80	2.5×10^{-13}	- 126.0	8.0×10^{-10}	- 91.0	2.6×10^{-6}	- 55.9
10^4	9.7×10^{-9}	- 80.1	2.5×10^{-2}	- 16.1	6.2×10^4	+ 47.9
10^5	1.4×10^{-5}	- 48.5	3.6×10^3	+ 35.5	9.0×10^{11}	+ 119.6

4.1.3 Conversion of spectral amplitudes or power densities into recording amplitudes

According to Aki and Richards (1980) the *maximum* amplitude of a wavelet $f(t)$ near $t = 0$ can be *roughly approximated* by the product of the amplitude spectral density and bandwidth of the wavelet, i.e.,

$$f(t)_{t=0} = |F(\omega)| \sqrt{2(f_u - f_l)} \quad (4.9)$$

with f_u and f_l being the upper and lower corner frequencies of the band-passed signal. Likewise, if the power spectral density of noise is defined according to Eq. (4.3) for $-\infty < \omega < +\infty$ then we get for $P(\omega) = P = \text{const.}$ for $\omega_l < |\omega| < \omega_u$ and $P(\omega) = 0$ otherwise, the *mean square amplitude* of noise in the time domain is

$$\langle f^2(t) \rangle = 2P(f_u - f_l). \quad (4.10)$$

Thus, the power spectral density (PSD) must be integrated over the passband of a filter to obtain the power (or *mean square amplitude*) at the output of the filter. The square root of this power is then the *root mean square* (RMS) or effective filter amplitude

$$a_{\text{RMS}} = \{2P \times (f_u - f_l)\}^{1/2} \quad (4.11)$$

Therefore, specifying seismic noise by its RMS amplitudes is meaningless without definition of the bandwidth. If, however, the noise power P is not computed according to the

4.1 Nature and presentation of seismic signals and noise

mathematical approach based on complex notation but from positive frequencies only (so-called engineering approach; see Chapter 5 and explanations given to Eqs. (5.4) and (5.5)) then we obtain $P = 2P$ because of $P(-\omega) = P(+\omega)$, and accordingly

$$a_{\text{RMS}} = \{P \times (f_u - f_l)\}^{1/2}. \quad (4.12)$$

Note: The values given by **the NLNM and NHRM** in Fig. 4.7 and Tabs. 4.1 and 4.2, respectively, are in fact $P = 2P$, i.e., they **represent already the total power**. Calculating RMS amplitudes by inserting incorrectly P into Eq. (4.11) would yield values which are 3dB larger than those calculated by using (4.12). So one should make sure beforehand, which definition of power has been used to calculate the PSD. For consistency we will refer in the following only to (4.12).

From (4.12) it follows that the calculated a_{RMS} amplitudes increase with the absolute bandwidth. Therefore, signal and noise amplitudes can be made commensurate only when plotting them in a *constant relative bandwidth (RBW)* over the whole frequency range. The RBW can be expressed by a number or in terms of octaves or decades. Increasing the frequency of a signal by one octave means doubling its frequency, and by one decade multiplying it by ten. Accordingly, a band-passed signal (or filter) with n octaves or m decades has a corner frequency ratio

$$f_u / f_l = 2^n = 10^m \quad (4.13)$$

and a (not arithmetic but geometric!) *center frequency* f_o of

$$f_o = (f_u \times f_l)^{1/2} = f_l \times 2^{n/2} = f_l \times 10^{m/2}. \quad (4.14)$$

From this follows for the *relative bandwidth*

$$\mathbf{RBW} = (f_u - f_l) / f_o = (2^n - 1) / 2^{n/2} = (10^m - 1) / 10^{m/2} \quad (4.15)$$

and (4.12) can be written as

$$a_{\text{RMS}} = \{P \times (f_u - f_l)\}^{1/2} = (P \times f_o \times \mathbf{RBW})^{1/2} \quad (4.16)$$

Octaves n can be converted easily into decades m and vice versa by using the relation

$$m = \log(f_u/f_l) = n \log 2 \quad (4.17)$$

where $n = \log(f_u/f_l)/\log 2$. According to Eq. (4.15) the relative bandwidth for a 1 octave filter is 0.7071 and for a 2/3 octave filter 0.466. Aki and Richards (1980, vol.1, p. 498) converted PSD into ground motions by putting the bandwidth of the noise signal at half the considered (center) frequency, i.e., by assuming $f_u - f_l = 0.5 f_o$. This corresponds to an RBW of roughly 2/3 octave. By using the definition of power on which Eq. (4.11) is based they obtained $a_{\text{RMS}} = (P \times f_o)^{1/2}$.

Other authors (e.g., Fix, 1972; Melton, 1978) have used an integration bandwidth of 1/3 octave (a standard bandwidth in acoustics) for computing RMS amplitudes from PSD. Melton reasoned that this is nearly $\pm 10\%$ about the center period in width and thus close to the tolerance with which an analyst can measure the period on an analog seismogram. Therefore, using a 1/3 octave bandwidth seemed to him a reasonable convention for calculating RMS noise amplitudes from PSD. The differences, as compared to RMS values based on 1/4 or 1/2 octave bandwidths, are less than 20%. But 1/3 octave amplitudes will be only about 70% or 50% of the respective RMS

4. Seismic Signals and Noise

amplitudes calculated for 2/3 or 4/3 octave bandwidth, respectively. Typical response curves of short-period narrowband analog seismographs for recording of transient teleseismic body-wave onsets have bandwidths between about 1 and 2 octaves. Choosing a constant one-octave filter bandwidth for comparing amplitudes of noise and transient seismic signals seems to be rather appropriate therefore.

Fig. 4.8 depicts the a_{RMS} noise amplitudes of ground acceleration in a constant bandwidth of 1/6 decade corresponding to the NLNM shown in Fig. 4.7 while Fig. 7.49 in Chapter 7 gives the dynamic range of STS1 and STS2 (see DS 5.1) seismometers above their level of instrumental noise and in relation to the NLNM for RMS amplitudes calculated with 1/3 octave bandwidth. 1/6 decade bandwidth means between 82.5% and 121% of the central frequency f_0 . The corresponding values for 1/3 octave are between 89.1% and 112.4% of f_0 .

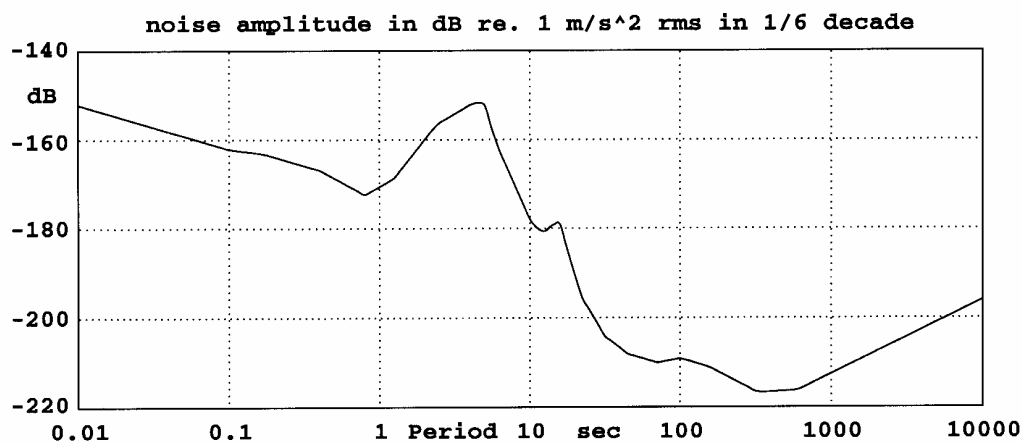


Fig. 4.8 The USGS New Low Noise Model, here expressed as RMS amplitudes of ground acceleration in a constant relative bandwidth of one-sixth decade (courtesy of E. Wieland).

For a_{RMS} determined according to (4.12) or (4.16) there is a 95% probability that the *instantaneous peak* amplitudes of a random wavelet with a Gaussian amplitude distribution will lie within a range of $2a_{\text{RMS}}$. Peterson (1993) showed that both broadband and long-period noise amplitudes follow closely a Gaussian probability distribution. In that case the absolute peak amplitudes of the narrowband filtered signal envelopes should follow a Rayleigh distribution. In the case of an ideal Rayleigh distribution the theoretical *average peak amplitudes* (APA) are $1.253 a_{\text{RMS}}$. From test samples of narrowband filtered VBB and LP noise records Peterson (1993) measured APA values between 1.194 and 1.275. Therefore, RMS amplitudes in 1/6-decade bandwidth correspond approximately to average peak amplitudes in 1/3 octave bandwidth. An example: According to Fig. 4.8 the minimum vertical ground noise between 10 and 20 s is at -180 dB relative to 1m/s^2 . This corresponds to average peak amplitudes of $10^{-180/20} \text{m/s}^2 = 1 \text{nm/s}^2$ in 1/3 octave bandwidth. Accordingly, the total average peak amplitude in this one octave band between 10 and 20 s is $\sqrt{3} \text{nm/s}^2$.

PD 4.1 in Volume 2 offers an interactive program NOISECON which converts noise specifications into all kinds of standard and non-standard units and compares them to the USGS NLNM, whereas EX 4.1 gives exercises for calculating RBWs and transforming PSDs into a_{RMS} for various kinematic units and bandwidths. It is complemented by several exercises combining eye-estimates and NOISECOM applications for interpreting and converting noise spectra.

4.2 Peculiarities of signal appearance in seismic records

4.2.1 Influence of the seismograph response: Empirical case studies

Fig. 4.9 shows recordings of a real earthquake P-wave onset in different short-period recordings with 1-Hz seismometers.

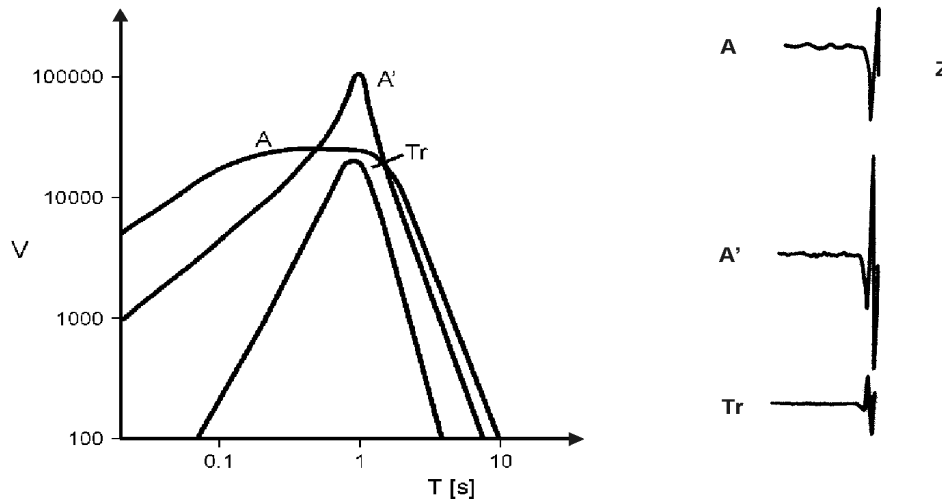


Fig. 4.9 Left: Displacement amplitude magnification curves of three types of short-period seismographs at seismic station MOX with 1/2 octave (type A'), one octave (Tr - trigger seismograph) and four octave bandwidth (type A), respectively; right: records with these seismographs of a P-wave onset of a deep earthquake at an epicentral distance of 72.3° and hypocentral depth of 544 km.

While in recordings of type A with 4 octave bandwidth, the first half cycle contains the largest amplitude, the maximum amplitude in records with 1/2 octave (type A') and one octave bandwidth (type Tr) is reached only at the third half-swing. Also, the first motion amplitude in the one octave record Tr is strongly reduced as compared to that in record A with four octave bandwidth, despite having nearly the same peak magnification. Accordingly, we have to consider that in narrowband records of high magnification (as with WWSSN short-period seismographs; bandwidth about 1.5 octaves) the reduced first motion amplitudes might get lost in the presence of noise. Since reliable first motion polarity readings are crucial for the determination of fault plane solutions and discriminating earthquakes from explosions, narrowband recordings might result in an unacceptable loss of primary information. Examples are given in Figs. 4.10 and 4.35. With broadband digital recording, this is now less of a problem.

Also note: The maximum amplitude of the P-wave onset in Tr of Fig. 4.9 is only about $\frac{1}{2}$ of that in record A although both have about the same peak magnification at 1 Hz for steady-state harmonic oscillations! And in record A' the maximum amplitude is only twice as large, even though the A' instrument has four times larger peak amplification than instrument A. This systematic underestimation of amplitudes of transient body-wave onsets of short duration in narrowband records - and thus of related magnitude estimates - has been a matter of considerable debate between the American and Russian delegations in the early Geneva

4. Seismic Signals and Noise

talks to achieve a Comprehensive Nuclear-Test-Ban Treaty (CTBT). In the Soviet Union standard seismographs with amplitude characteristics of type A (2 to 4 octaves) and broadband characteristics of type Kirnos with about 7 octaves bandwidth were used to determine body-wave magnitudes, while American-designed WWSSN stations determined body-wave magnitudes based only on their narrowband short-period standard records of 1.5 octaves bandwidth. A consequence of these differences in magnitude determination was that the American delegation reported a much larger number of weak, unidentified seismic events per year than the Soviet delegation and therefore felt that they required hundreds of U.S. unmanned stations on Soviet territory as well as the possibility for on-site inspections. This blocked, amongst other reasons, the agreement on a comprehensive test-ban treaty for two decades. Today these problems are more of historical interest since the analyst using digital broadband data can shape the filters any way desired. But it still remains a problem to exactly define what filter to use, and analysts should be aware therefore of the filter effects.

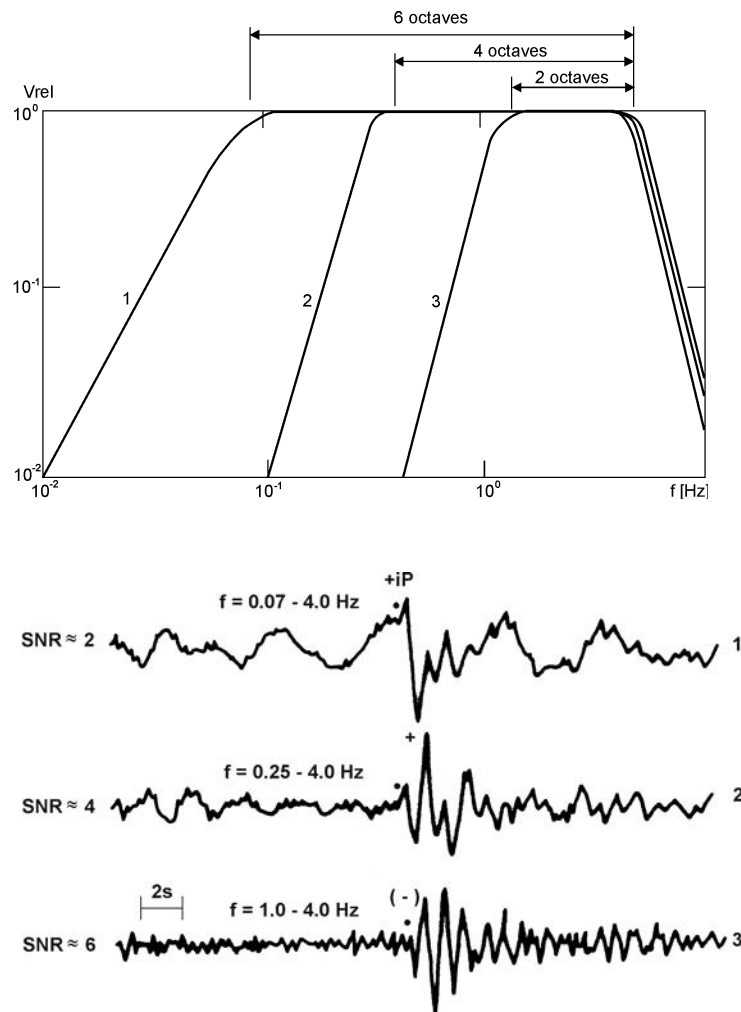


Fig. 4.10 A medium-period velocity-proportional digital broadband record (bandwidth almost 6 octaves between 0.07 – 4 Hz;) at station MOX of an underground nuclear explosion at the Nevada test site (record trace 1) has been filtered with a 4-octave and 2-octave bandpass filter (record traces 2 and 3). The positive first motion (to be expected from an explosion!) is clearly to be seen in the BB record despite of the low SNR, but it is buried in the noise of the 2 octave record despite the general SNR improvement due to narrowband filtering. Note that the different absolute amplitude levels in the three records have all been normalized to the same peak amplitude.

4.2 Peculiarities of signal appearance in seismic records

The narrower the record bandwidth is, the longer and more oscillating the recorded wavelet of a transient onset becomes. This makes it difficult to recognize, in narrowband records, secondary onsets following closely behind the first one, e.g., onset sequences due to a multiple earthquake rupture (Fig. 4.11), depth phases in the case of shallow earthquakes or branching/crossing of travel-time curves (see Chapter 2 and Fig. 4.12). But the identification and proper time picking of such closely spaced secondary arrivals is crucial for a better understanding of the rupture dynamics, for improved estimates of hypocenter depth or for studies of the fine structure of the Earth.

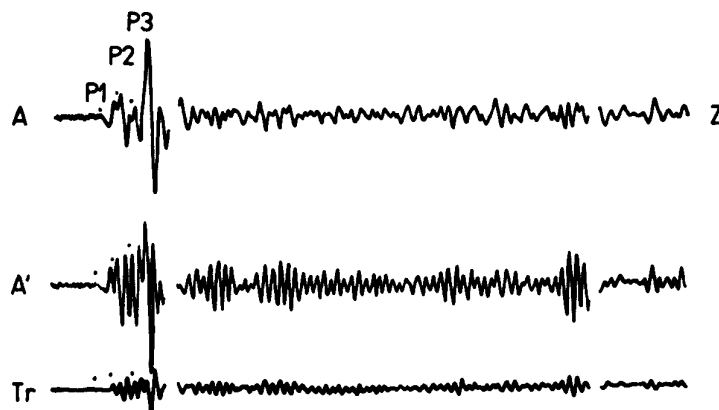


Fig. 4.11 Short-period records of station MOX of a multiple rupture event at Honshu ($D = 88.0^\circ$) with different amplitude response characteristics according to Fig. 4.9 left.

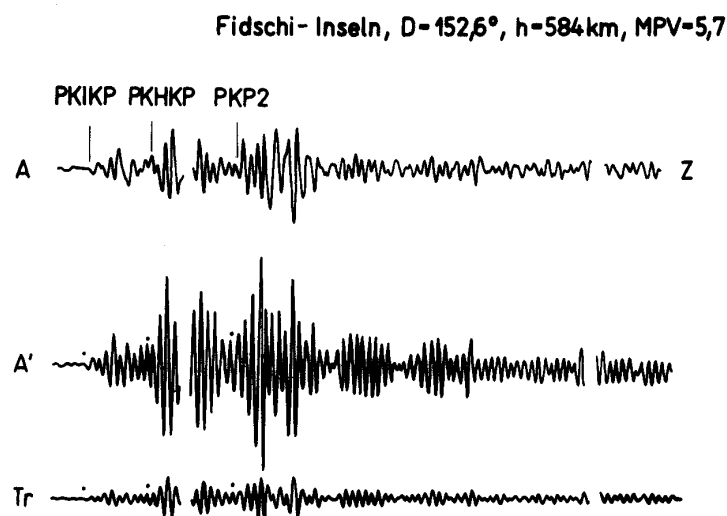


Fig. 4.12 Short-period records of station MOX of a sequence of core phases corresponding to the travel-time branches PKP_{df} (PKIKP), PKP_{bc} (PKHKP) and PKP_{ab} (PKP2) (see Chapter 11) with different amplitude response characteristics according to Fig. 4.9 left.

It is crucial, therefore, to record seismic signals with as large a bandwidth and with as high a linearity, resolution and dynamic range as possible, thus preserving the primary information with least distortion. Filtering should only be applied afterwards, as required for special purposes. With feedback-controlled broadband seismometers and digital data loggers with 24 bit ADCs being readily available, this is no longer a problem (see Chapters 5 and 6). In Fig.

4. Seismic Signals and Noise

4.13 it is clearly recognizable that in the displacement-proportional broadband record of about 10 octaves bandwidth the P-wave onset looks rather simple (negative impulse with only slight positive overswing of the second half-cycle). Its appearance resembles the expected source displacement pulse in the far field (see Fig. 2.4).

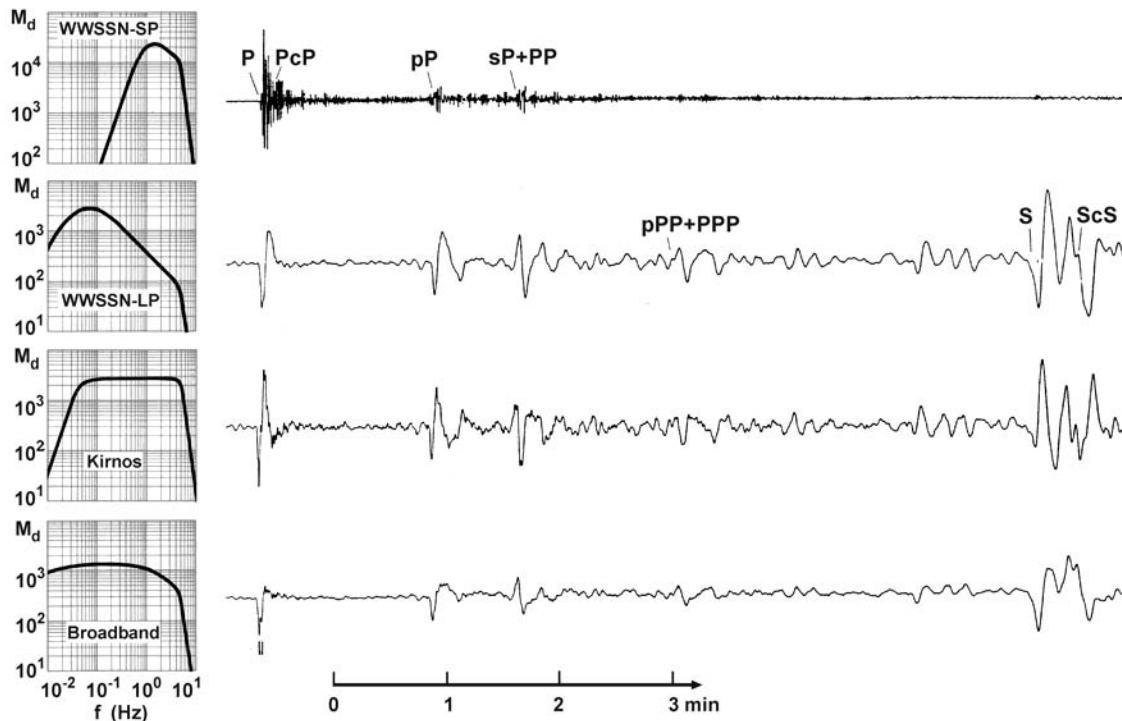


Fig. 4.13 Records of a deep earthquake ($h = 570$ km, $D = 75^\circ$) at the Gräfenberg Observatory, Germany. They have been derived by filtering a velocity-proportional digital broadband record (passband between 0.05 and 5 Hz) according to the response curves of some traditional standard characteristics (WWSSN_SP and LP, Kirnos) while the bottom trace shows the result of computational restitution of the (nearly real) true ground displacement by extending the lower corner period T_0 well beyond 100s (see text) (from Buttkus, 1986).

4.2.2 Theoretical considerations on signal distortion in seismic records

The basic theory of seismometry is outlined in Chapter 5. For a more comprehensive introduction to general filter theory and its applications in digital seismology (with exercises) see “Of Poles and Zeros: Fundamentals of Digital Seismology” by Scherbaum (second edition, 2001). The book is accompanied by a CD-ROM “Digital Seismology Tutor” by Schmidtke and Scherbaum (2001; <http://www.uni-potsdam.de/u/Geowissenschaft/Software/software.html>), which is a very versatile tutorial tool for demonstrating signal analysis and synthesis. Therefore, we will not dwell on it further, however, we will illustrate by way of example some of the essential effects of signal distortion by the transfer function of the seismograph. Signal distortion due to wave propagation effects in the Earth and ways how to eliminate at least some of them are discussed in Chapter 2.

The essence of Eq. (4.1) and Fig. 4.2 is the following: A Dirac (or needle) impulse (see section 5.2.4) in the time domain is equivalent to an infinite homogeneous (“white”) spectrum

4.2 Peculiarities of signal appearance in seismic records

in the frequency domain. Thus, if the far-field seismic source pulse comes close to a needle impulse of very short duration (e.g., an explosion) we would need in fact a seismograph with (nearly) an infinite bandwidth in order to be able to reproduce this impulse-like transient signal. On the other hand, an infinite monochromatic harmonic signal corresponds to just one spectral line in the frequency spectrum, or, the other way around, if the input signal is a needle impulse with an infinite spectrum but the bandwidth of the seismograph is extremely narrow ($\rightarrow 0$), then the record output would not be a needle impulse at all but rather (after the transient response is over) an (almost) un-attenuated infinite monochromatic record. Fig. 4.14 depicts these extreme cases and Fig. 4.15 sketches seismographic recordings of an impulse sequence with different response characteristics.

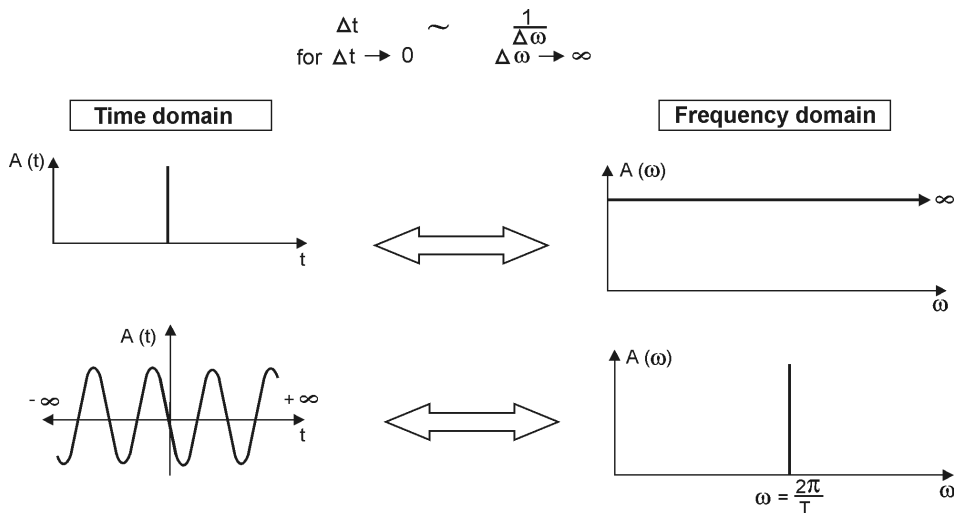


Fig. 4.14 Sketch of the equivalent representation of a needle impulse (above) and a stationary infinite monochromatic harmonic signal (below) in the time and frequency domain.

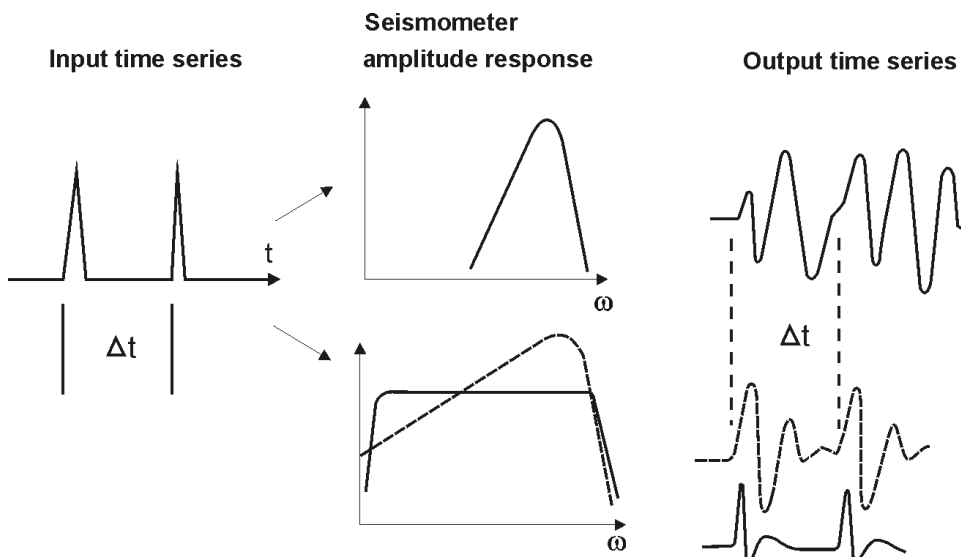


Fig. 4.15 Schematic illustration of the appearance of a sequence of seismic input impulses in record outputs of seismographs with narrow-band displacement response (uppermost trace) and broadband responses (below; broken line – velocity response, full line – displacement response).

4. Seismic Signals and Noise

According to theoretical considerations by Seidl and Hellweg (1988), the seismometer period T_0 has to be about 100 times larger than the duration τ_s of the source-time input function when the source signal shape and its “signal moment” (area under the impulse time curve) is to be reproduced with a relative error $< 8\%$. As a rule of thumb, these authors state that the relative error is less than about 10% if $T_0 > 20 \pi \tau_s$. This means that extreme long-period seismographs would be required to reproduce with sufficient accuracy the displacement impulse of strong seismic events. By “signal restoration” (i.e., instrument response correction or “deconvolution”) procedures (Seidl, 1980; Seidl and Stammer, 1984; Seidl and Hellweg, 1988; Ferber, 1989) the eigenperiod of long-period feedback seismometers such as STS1 ($T_0 = 360$ s) and STS2 ($T_0 = 125$ s) can be computationally extended - in the case of high signal-to-noise ratio - by a factor of about 3 to 10 times, and thus the very low-frequency content of the signals can be retrieved. Simulations of standard frequency responses from BB records are available in some of the software packages for signal pre-processing (e.g., PREPROC, Plešinger et al. 1996) or seismogram analysis (e.g., SEISAN, Havskov and Ottemöller, 1999 b; see <http://www.ifjf.uib.no/seismo/software/seisan.html/>; and Seismic Handler by K. Stammer; see <http://www.szgrf.bgr.de/sh-doc/index.html>).

Fig. 4.16 shows the very different response of three standard seismograph systems of different damping and bandwidth to a synthetic ground displacement input according to the Brune model of earthquake shear dislocation. The response has been simulated by using the PITSA seismological analysis software (Scherbaum and Johnson, 1992; and <http://www.uni-potsdam.de/u/Geowissenschaft/Software/software.html>). For the amplitude response of the seismographs of type Wood-Anderson (WA), Kirnos, WWSSN long-period (LP) and WWSSN short-period (SP) see Fig. 3.11.

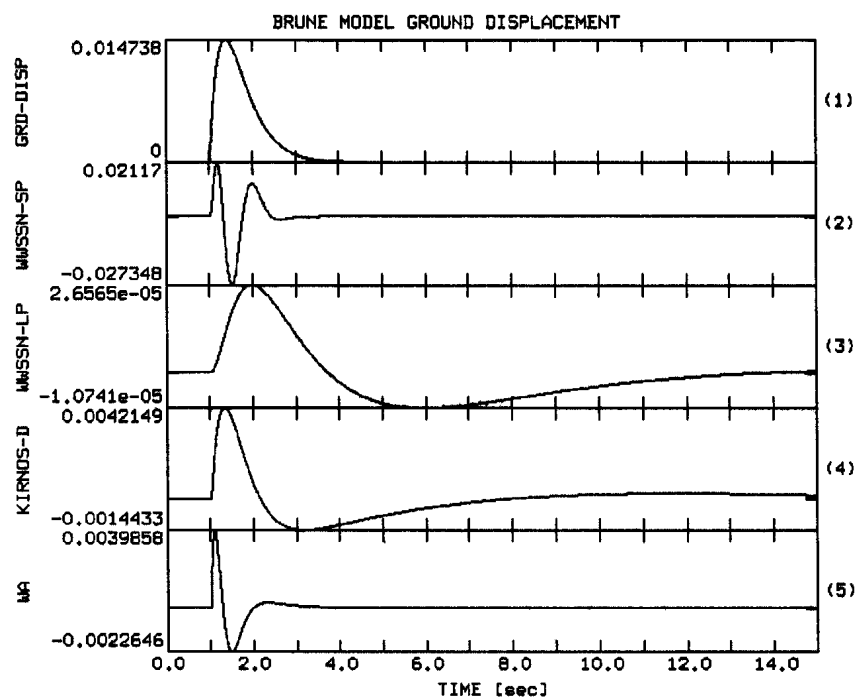


Fig. 4.16 Distortion of a synthetic ground displacement signal according to the Brune model of earthquake shear dislocation (top trace) by standard seismograph systems (for their response curves see Fig. 3.11) (from Scherbaum 2001, “Of Poles and Zeros”, Fig. 10.2, p. 167; © Kluwer Academic Publishers, with permission of Kluwer Academic Publishers).

4.2 Peculiarities of signal appearance in seismic records

The strong distortion in narrowband recordings after the transient onsets is due to their pronounced *transient response* (TR). It is due to the time required by the seismometer to achieve the values of frequency-dependent magnification and phase shift determined by its amplitude- and phase-frequency characteristics for steady-state harmonic oscillations (see 5.2, Fig. 5.6 and Figure 1a and b in IS 5.2). In Fig. 4.16, the effect of phase-shift adaptation during the time of transient response is clearly seen, especially in the records of the WWSSN and Wood-Anderson short-period instruments. Accordingly, the period of the first half cycle appears to be much shorter than that of the second and third half cycle. The transient response of the seismometer is $\sim \exp(-D_s T_s t)$ with D_s – damping and T_s – eigenperiod of the seismometer and t – time, i.e., $TR \rightarrow 0$ for $D_s T_s t \rightarrow \infty$. Thus, for a short-period seismometer with very low damping (narrow-band resonance characteristic!) it takes a long time before the transient response is over while for seismometers with overcritical damping and/or very large T_s (broadband!) the transient response is rather short and negligible.

Fig. 4.17 compares the response of the same seismographs and of the SRO-LP seismograph with the unfiltered velocity broadband record of the STS2 (see DS 5.1) from an earthquake in the Russia-China border region. The differences in record appearance depending on the response characteristic of the seismograph and the time resolution of the record are striking.

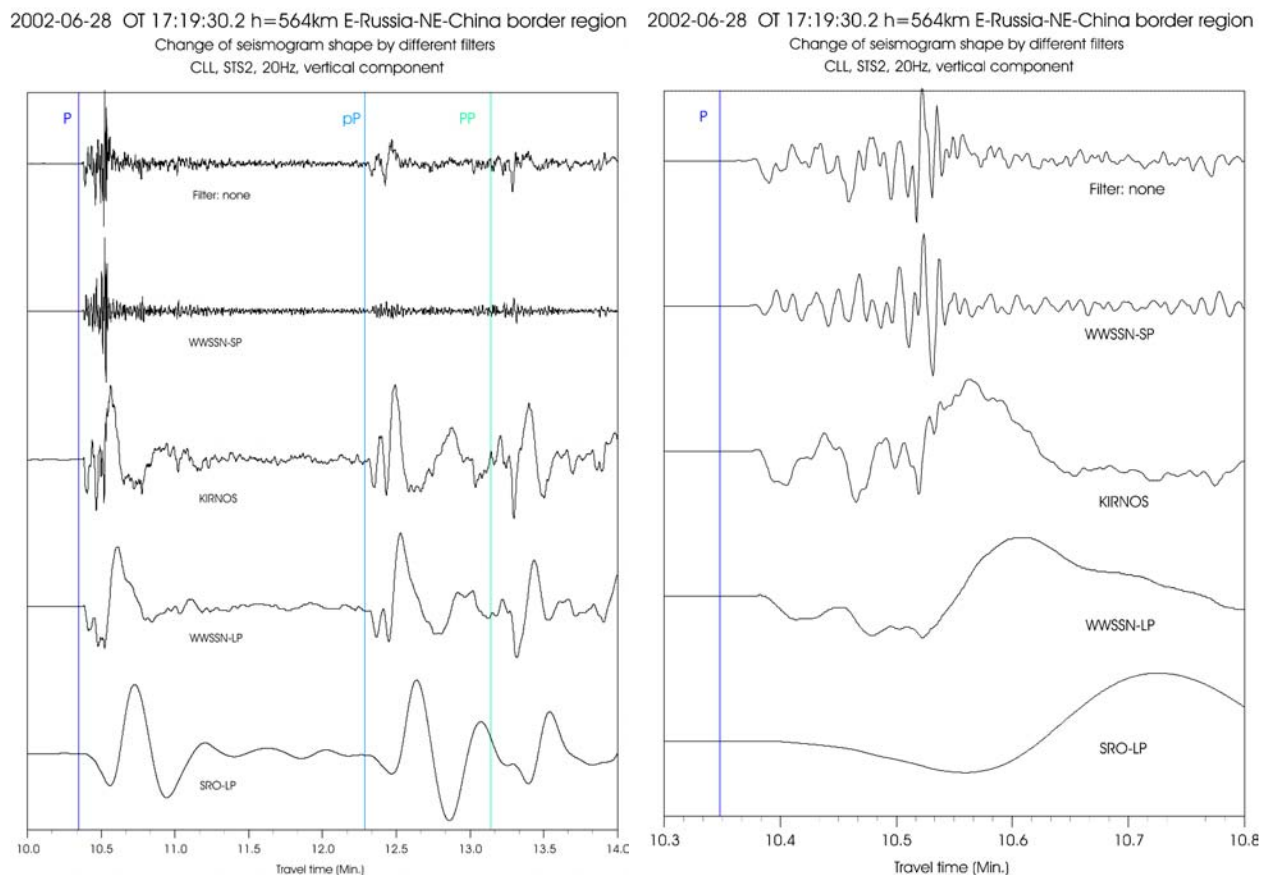


Fig. 4.17 Record segments from an earthquake at the Russia-China border of 4 min (left) and 30 s duration (right). Uppermost traces: unfiltered STS2 velocity broadband seismogram; other traces: filtered records which simulate the seismograms of standard recordings of type WWSSN-SP, Kirnos, WWSSN-LP and SRO-LP (courtesy of S. Wendt).

4. Seismic Signals and Noise

Fig. 4.18 gives an example from a simulation of seismometer response to a monochromatic harmonic ground motion $w(t)$ of frequency 1 Hz as input. It has been partly made from two different snapshots of an interactive web site demonstration of the Technical University of Clausthal, Germany (http://www.ifg-tu-clausthal.de/java/seis/seisdemo_d.html). Trace a) has been recorded with a seismometer of eigenperiod $T_s = 1$ Hz and damping $D_s = 0.2$ (i.e., resonance at 1 Hz!) while for trace b) $T_s = 20$ s and $D_s = 0.707$. In the first record the transient response takes about 3 s before the steady-state level of constant amplitudes corresponding to the amplitude response of the seismometer and the constant phase shift of about 110° have been reached (after the sixth record half cycle). In record b) the transient response takes less than half a second and the seismometer mass follows the ground motion with practically no phase shift.

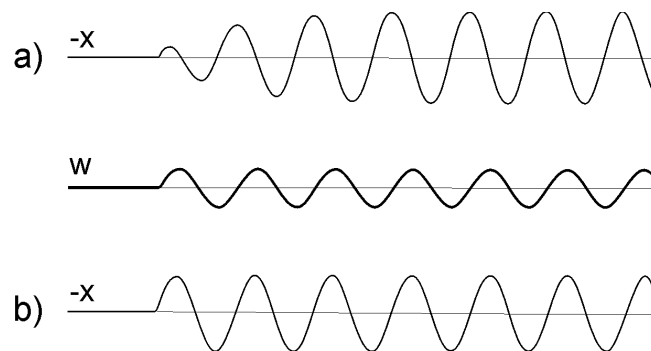


Fig. 4.18 Simulation of displacement signal output $x(t)$ (= relative displacement of the seismometer mass) of a spring-mass pendulum seismometer responding to a monochromatic harmonic ground motion $w(t)$ of period $T = 1$ s (thick line in the middle). a) Displacement output of a seismometer with low damping ($D_s = 0.2$) and eigenperiod $T_s = 1$ s (i.e., resonance); b) Displacement output of a long-period and normally damped seismometer ($T_s = 20$ s; $D_s = 0.707$). For discussion see text.

4.3 Causes and characteristics of ambient seismic noise

4.3.1 Ocean microseisms and ocean bottom noise

Most of the early 20th century seismographs by Wiechert, Mainka, Galizyn, Bosch-Omori, Milne-Shaw and others are medium-period broadband systems. The more sensitive ones with 100 to 500 times magnification of the ground motion were already able to record microseisms around the noise peak at about 6 ± 2 s (see Figs. 4.5 and 4.7). Such recordings were reported by Algue in 1900. Wiechert (1904) proposed at the second international seismological conference that these microseisms are caused by ocean waves on coasts. Later it was found that one must discriminate between: a) smaller primary ocean microseisms with periods around 14 ± 2 s and b) secondary ones related to the main noise peak around 6 s (see Fig. 4.5 and 4.7).

Primary ocean microseisms are generated only in shallow waters in coastal regions. Here the wave energy can be converted directly into seismic energy either through vertical pressure variations, or by the smashing surf on the shores, which have the same period as the water waves ($T \approx 10$ to 16 s) (Fig. 4.19a). Haubrich et al. (1963) compared the spectra of microseisms and of swell at the beaches and could demonstrate a close relationship between

4.3 Causes and characteristics of ambient seismic noise

the two data sets. Contrary to this, the secondary ocean microseisms could be explained by Longuet-Higgins (1950) as being generated by the superposition of ocean waves of equal period traveling in opposite directions, thus generating standing gravity waves of half the period. These standing waves cause non-linear pressure perturbations that propagate without attenuation to the ocean bottom. The area of interference X may be off-shore where the forward propagating waves generated by a low-pressure area L superpose with the waves traveling back after being reflected from the coast (Fig. 4.19b). But it may also be in the far deep ocean when the waves, excited earlier on the front side of the low-pressure zone, interfere later with the waves generated on the back-side of the propagating cyclone. Horizontal and vertical noise amplitudes of marine microseisms are similar. The particle motion is of Rayleigh-wave type, i.e., elliptical polarization of the particle motion in the vertical propagation plane. A more detailed discussion on sources and properties of primary and secondary microseisms can be found in Cessaro (1994) and Friedrich et al. (1998).

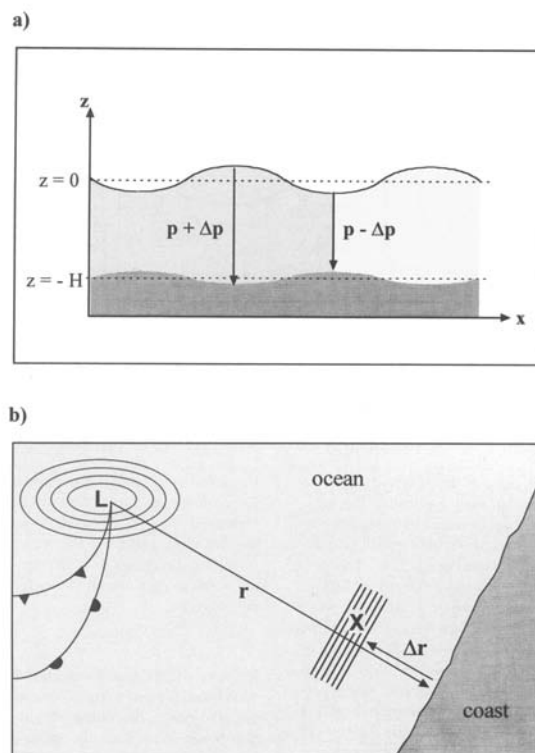


Fig. 4.19 Schemes for the generation of a) primary and b) secondary microseisms (for explanations see text). L – cyclone low-pressure area, X – area of interference where standing waves with half the period of ocean waves develop (reproduced from Journal of Seismology, 2, 1, 1998, “Ocean-generated microseismic noise located with the Gräfenberg array”; Friedrich, Krüger & Klinge, p. 62, Fig. 12; © Kluwer Academic Publishers, with permission of Kluwer Academic Publishers).

Note that the noise peak of secondary microseisms has a shorter period when generated in shallower inland seas or lakes ($T \approx 2$ to 4 s) instead of in deep oceans. Also, off-shore interference patterns largely depend on coastal geometries and the latter may allow the development of internal resonance phenomena in bays, fjords or channels (see Fig. 4.20 which affect the fine spectrum of microseisms. In fact, certain coastlines may be distinguished by unique “spectral fingerprints” of microseisms.

4. Seismic Signals and Noise

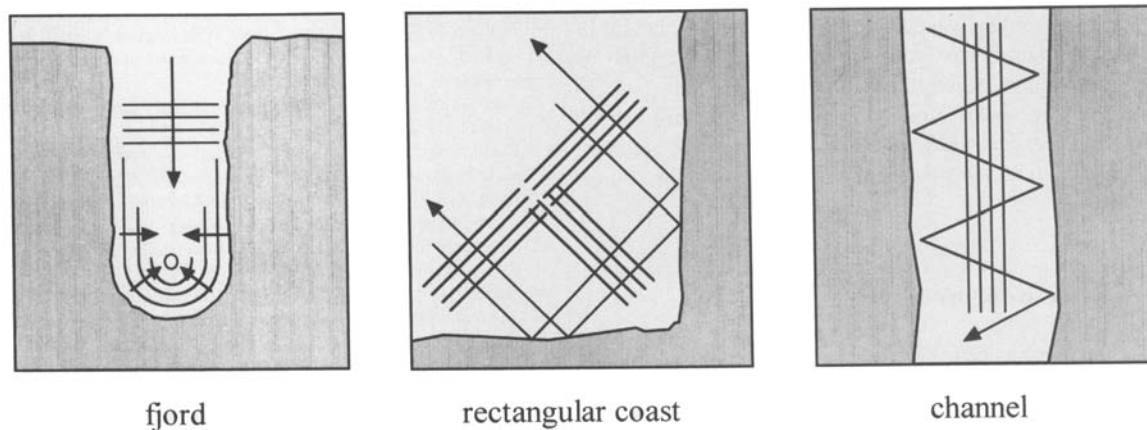


Fig. 4.20 Examples for coastline geometries that provide suitable interference conditions for the generation of secondary microseisms (reproduced from *Journal of Seismology*, 2, 1, 1998, “Ocean-generated microseismic noise located with the Gräfenberg array”; Friedrich, Krüger & Klinge, p. 63, Fig. 13; © Kluwer Academic Publishers, with permission of Kluwer Academic Publishers).

Medium-period ocean/sea microseisms experience low attenuation. They may therefore propagate hundreds of km inland. Since they are generated in relatively localized source areas, when looked at from afar they have - despite the inherent randomness of the source process - a rather well developed coherent portion, at least in the most energetic and prominent component. This allows one to locate the source areas and track their movement by means of seismic arrays (e.g., Cessaro, 1994; Friedrich et al., 1998; Fig. 4.21). This possibility has already been used decades ago by some countries, e.g., in India, for tracking approaching monsoons with seismic networks under the auspices of the Indian Meteorological Survey, although Cessaro (1994) showed that the primary and secondary microseism source locations do not follow the storm trajectories directly. While near-shore areas may be the source of both primary and secondary microseisms, the pelagic sources of secondary microseisms meander within the synoptic region of peak storm wave activity.

In recent years more and more ocean-bottom seismographs (OBS; see, e.g., Havskov and Alguacil) have been deployed in order to overcome the inhomogeneous distribution of land-based seismic stations. But permanent OBS installations are still rare. Generally, the noise level at the ocean bottom, even in deep seas, is higher than that on land (by about 10 to 30 dB) and increases with higher frequencies (e.g., Bradner and Dodds, 1964). On the ocean bottom, as on land, the secondary microseism noise peak between 0.1 and 1 Hz dominates. Background noise levels in this frequency range tend to be higher in the Pacific than in the Atlantic because of its larger size and its general weather conditions. While short-period body-wave arrivals around 1 Hz have been clearly recorded during calm-weather periods by OBSs in the North Atlantic, even at teleseismic distances, they are recognizable in OBS records in the Pacific only for very large events at distances of less than a few tens of degrees. On the other hand, long-period P, S and surface waves are consistently well recorded by OBSs in the noise minimum between about 0.03 and 0.08 Hz for magnitudes 6 ± 0.3 even at distances $D > 100^\circ$ (Blackman et al., 1995).

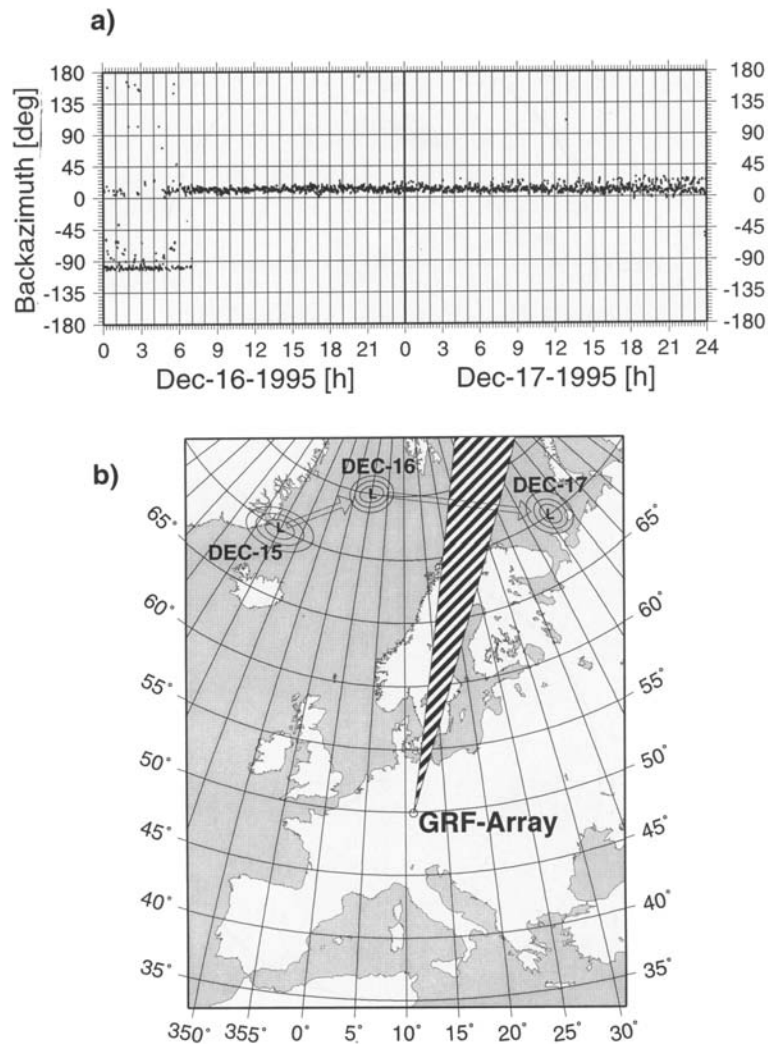


Fig. 4.21 An example of good coherence of medium-period secondary ocean microseisms at a longer distance from the source area which, in this case, allows rather reliable determinations of the backazimuth of the source area by f-k analysis with seismic arrays (see Chapter 9). Figure a) above shows how the backazimuth determination changed from one day to the next, while b) shows the location of the two storm areas and the seismic array. Observations by at least two arrays permit localization and tracking of the noise-generating low-pressure areas (reproduced from *Journal of Seismology*, 2, 1, 1998, “Ocean-generated microseismic noise located with the Gräfenberg array”; Friedrich, Krüger & Klinge, p. 55, Fig. 7; © Kluwer Academic Publishers, with permission of Kluwer Academic Publishers).

4.3.2 Short-period seismic noise

Short-period seismic noise may have natural causes such as wind (wind friction over rough terrain; trees and other vegetation or built-up objects swinging or vibrating in the wind), rushing waters (waterfalls or rapids in rivers and creeks) etc. Wind-generated noise is broadband, ranging from about 0.5 Hz up to about 15 to 60 Hz (Young et al., 1996). But the dominant sources of high-frequency noise are man-made (rotating or hammering machinery, road and rail traffic etc.; see Chapter 7.). Most of these sources are distributed, stationary or moving. Their contributions, coming from various directions, superpose to a rather complex,

4. Seismic Signals and Noise

more or less stationary random noise field. The particle motion of short-period noise is therefore more erratic than for long-period ocean noise. Nevertheless, polarization analysis, averaged over moving time-windows, sometimes reveals preferred azimuths of the main axis of horizontal particle motion hinting at localized noise sources. Also the vertical component is clearly developed and averaged particle motion in 3-component records indicates fundamental Rayleigh-wave type polarization. A rather popular and cost-effective microzonation method is based on this assumption. It derives information about the fundamental resonant frequency of the soft-soil cover and estimates local site amplification of ground motion from the peak in the horizontal to vertical component spectral noise ratio (*Nakamura method*, e.g., Nakamura, 1989; Bard, 1999).

Because of the surface-wave character of short- and medium-period noise, the horizontal propagation velocity of seismic noise is frequency dependent. It is close to the shear-wave velocity in the uppermost crustal layers (about 2.5 to 3.5 km/s for outcropping hard rock and about 300 to 650 m/s for unconsolidated sedimentary cover). This is rather different from the apparent horizontal propagation velocity of P waves and all other steeply emerging teleseismic body-wave onsets.

The surface-wave nature of seismic noise (including ocean noise) is also the reason for the exponential decay of noise amplitudes with depth, which is not the case for body waves (Fig. 4.22). Since the penetration depth of surface waves increases with wavelength, high frequency noise attenuates more rapidly with depth. In the case of Fig. 4.23, the noise power at 300 m depth in a borehole was reduced, as compared to the surface, by about 10 dB, at $f = 0.5$ Hz, 20 dB at 1 Hz and 35 dB at 10 Hz. Withers et al. (1996) found that for frequencies between 10 to 20 Hz, the SNR could be improved between 10 to 20 dB and for f between 23 and 55 Hz as much as 20 to 40 dB by deploying a short-period sensor at only 43 m below the surface. But both noise reduction as well as signal behavior with depth depend also on local geological conditions (see 4.4.5).

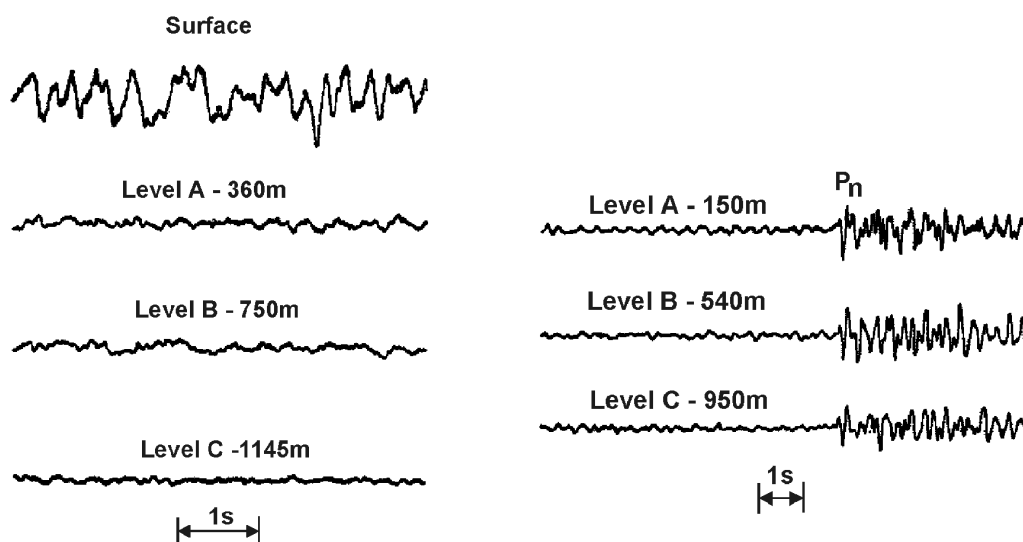


Fig. 4.22 Recording of short-period seismic noise (left) and signals (right) at the surface and at different depth levels of a borehole seismic array (modified from Broding et al., 1964).

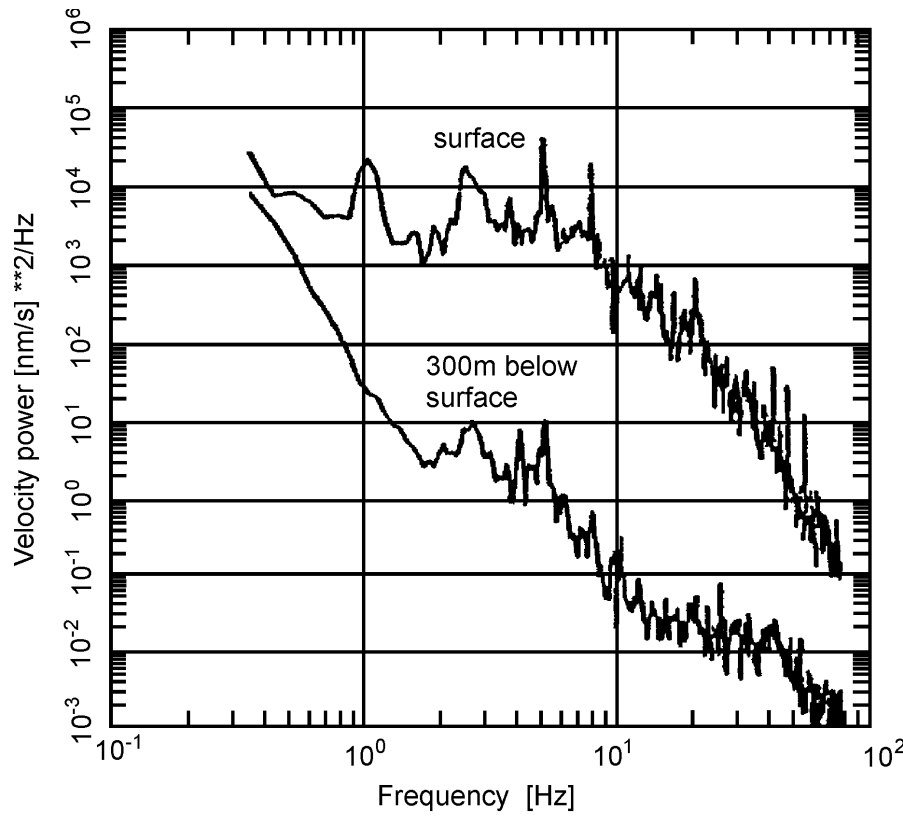


Fig. 4.23 Velocity power density spectra as obtained for noise records at the surface (top) and at 300 m depth in a borehole (below) near Gorleben, Germany (courtesy of M. Henger).

Signals which have small phase shifts and identical time dependence and polarization, so that they can interfere constructively, are termed coherent. This is usually the case for seismic signals generated and radiated by a common source process. The degree of coherence is defined by the ratio between the auto- and the cross-correlation of the time series. It may vary between 0 and 1. For seismic noise it shows a distinct frequency dependence. Coherence may be rather high for long-period ocean microseisms ($> 70\%$) while it drops usually below 30% for $f > 1$ Hz. Accordingly, the correlation radius, i.e., the longest distance between two seismographs for which the noise recorded in certain spectral ranges is still correlated, increases with the noise period. It may be several km for $f < 1$ Hz but drops to just a few tens of meters or even less for $f > 50$ Hz. For seismic noise, it is usually not larger than a few wavelengths.

Generally, there is a good correlation between increased noise levels and higher wind speeds. While for wind speeds below 3 to 4 m/s, one may observe omni-directional background noise coherent at frequencies below 15 Hz, this coherence is destroyed at higher wind speeds with increased air turbulence (Withers et al., 1996). Amplitudes of wind noise are apparently nonlinear. Wind noise increases dramatically at wind speeds greater than 3 to 4 m/s and may reach down to several hundred meters below the surface at wind speeds > 8 m/s (Young, 1996). But generally, the level and variability of wind noise is much higher at or near the surface and is reduced significantly with depth (Fig. 4.24).

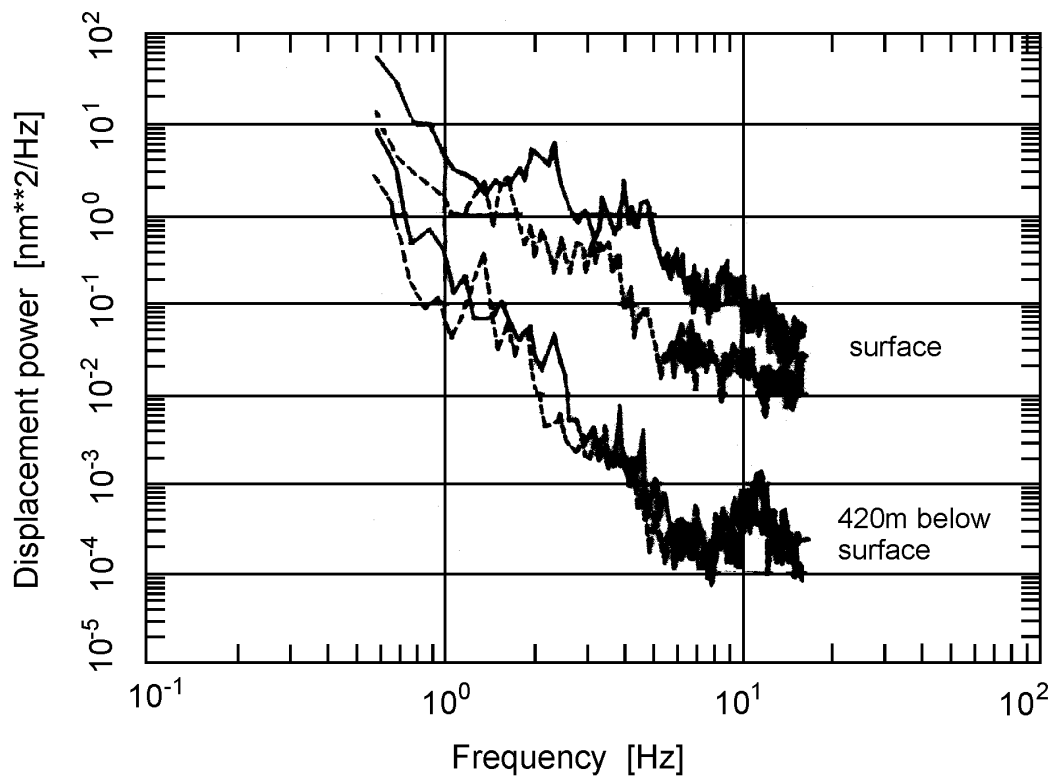


Fig. 4.24 Displacement power noise spectra measured at the surface (upper curves) and at 420 m below the surface in a disused salt mine at Morsleben, Germany (lower curves) on a very quiet day (hatched lines) and on a day with light wind on the surface (wind speed about 4 m/s; full lines).

Thus, differences in the frequency spectrum, horizontal wave-propagation velocity, degree of coherence and depth dependence between (short- and medium-period) seismic noise and seismic waves allows one to improve the signal-to-noise-ratio through appropriate data collection, processing or sensor installation at reasonable depth below the surface (see 4.4).

4.3.3 Long-period seismic noise

At long periods, horizontal noise power may be significantly larger than vertical noise power. The ratio increases with the period and may reach a factor of up to 300 (about 50 dB). A site can be considered as still favorable when the horizontal noise at 100 to 300 s is within 20 dB, as in Fig. 4.25. This is mainly due to tilt, which couples gravity into the horizontal components but not into the vertical (see 5.3.3 and Figs. 5.11 and 5.12). Tilt may be caused by traffic, wind or local fluctuations of barometric pressure. Recording the latter together with the seismic signals may allow correction for this long-period noise (e.g., Beauduin et al. 1996). Other reasons for increased long-period noise may be air circulation in the seismometer vault or underneath the sensor cover. Special care in seismometer *installation* and *shielding* is therefore required in order to reduce drifts and long-period environmental noise (see Chapters 5 and 7).

4.4 Measures for improving the signal-to-noise ratio (SNR)

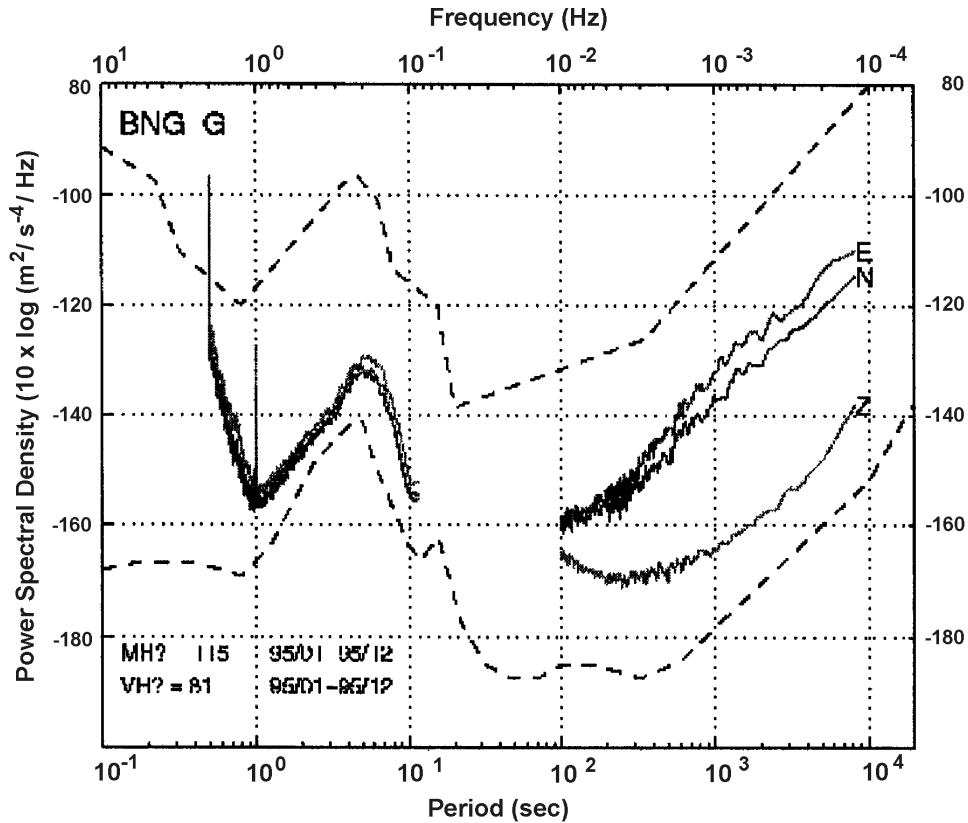


Fig. 4.25 Seismic noise at the station BNG (Bangui, Central Africa) as compared to the new global seismic noise model by Peterson (1963) (from the FDSN Station Book, http://www.fdsn.org/station_book/G/BNG/bng.g_allyr.gif).

4.4 Measures for improving the signal-to-noise ratio (SNR)

4.4.1 Frequency filtering

When the frequency spectrum of the seismic signal of interest differs significantly from that of the superposed seismic noise, band-pass filtering can help to improve the signal-to-noise ratio (SNR). Fig. 4.26 illustrates the principle and Figs. 4.27 and 4.28 show examples.

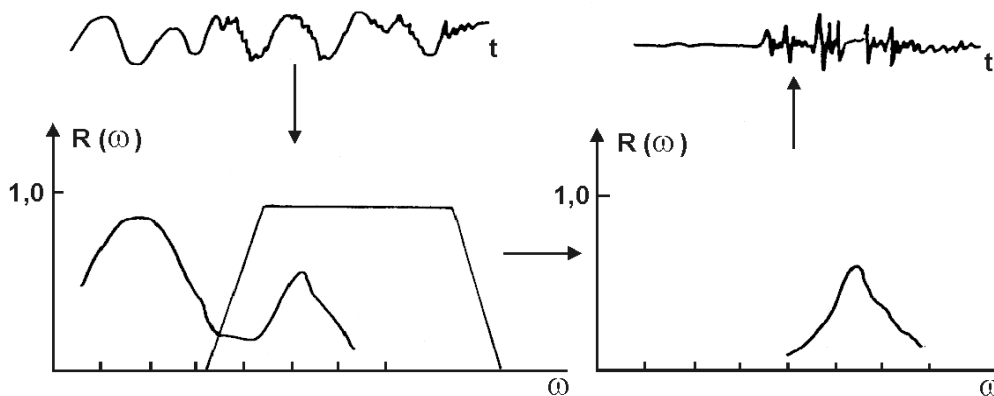


Fig. 4.26 Principle of FOURIER transform and bandpass filtering of a seismic record.

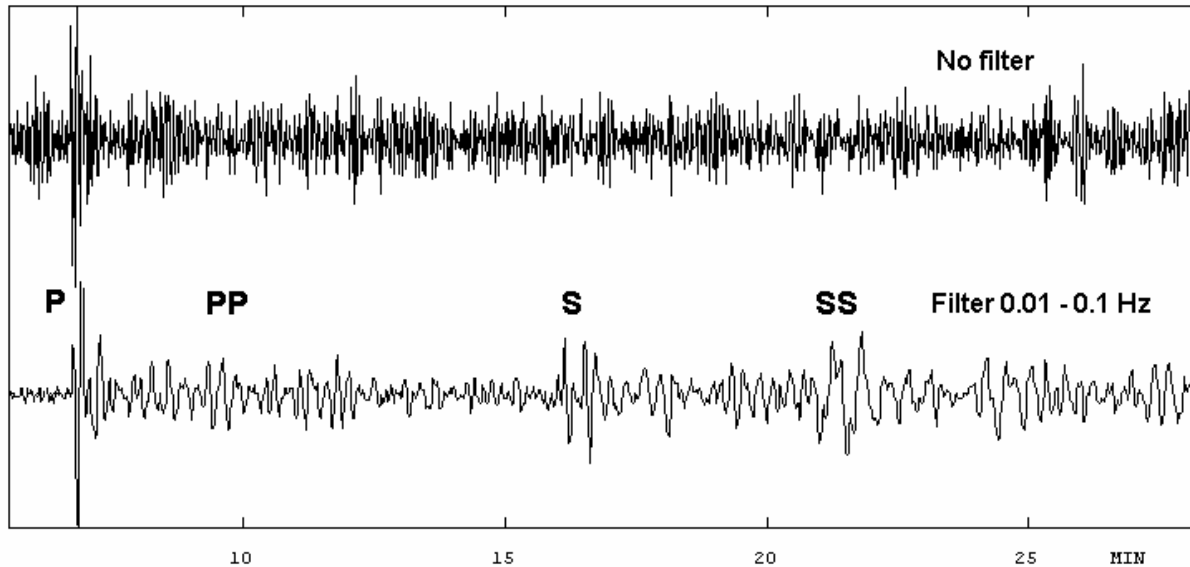


Fig. 4.27 Recording of a LP trace at a broadband station. The LP trace has a flat velocity response from 360 s to 0.5 s. On the unfiltered trace (top), only the P-phase might be identified, while on the filtered trace (bottom), the signal-to-noise ratio is much improved and several later phases are clearly recognizable since the microseisms have been removed by filtering (courtesy of J. Havskov, 2001).

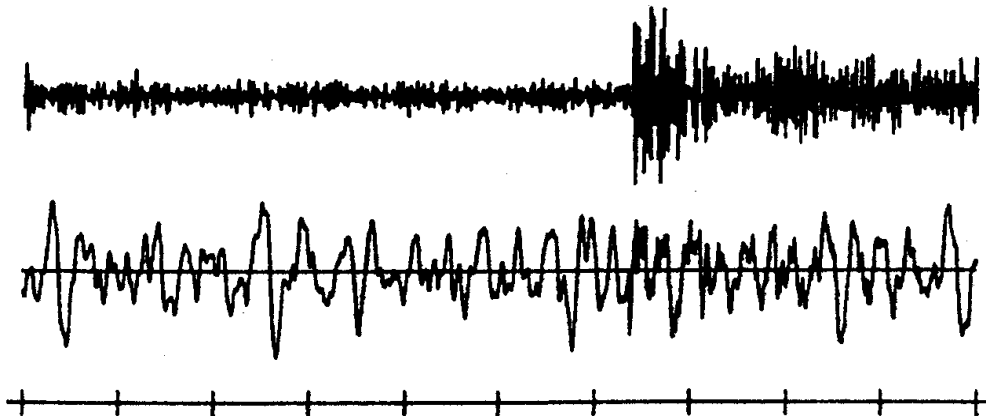


Fig. 4.28 Original (bottom) and frequency filtered record (top; $f = 2.0 - 4.0$ Hz) of an underground nuclear explosion at the Semipalatinsk test site, Eastern Kazakstan ($D = 38^\circ$) at station 01A00 of the NORSAR array. Time marks in seconds (from Tronrud, 1983b).

4.4.2 Velocity filtering and beamforming

Often the dominant signal frequencies may coincide with that of strong noise. Then frequency filtering does not improve the SNR. On the other hand, the horizontal propagation velocity of noise (see 4.3.2) is much lower than that of P waves and also lower than that of teleseismic S waves with a steep angle of incidence. This leads to frequency-wavenumber (f - k) filtering (see Chapter 9) as a way to improve SNR. To be able to determine the horizontal propagation direction and velocity of seismic signals by means of signal correlation, a group of seismic

4.4 Measures for improving the signal-to-noise ratio (SNR)

sensors must be deployed. If the aperture (diameter) of the sensor group is within the correlation radius of the signals it is called a seismic array (see Chapter 9); otherwise the group of sensors comprises a station network (see Chapter 8). Assuming that the noise within the array is random while the signal is coherent, even a simple direct summation of the n sensor outputs would already produce some modest SNR improvement. When the direction and velocity of travel of a signal through an array is known, one can compensate for the differences in arrival time at the individual sensors and then sum-up all the n record traces (beam forming). This increases the signal amplitude by a factor n while the random noise amplitudes increase in the beam trace only by \sqrt{n} , thus improving the SNR by \sqrt{n} . Fig. 4.29 compares the (normalized) individual records of 13 stations of the Gräfenberg array, Germany with the beam trace. A weak underground nuclear explosion at a distance of 143.6° , which is not recognizable in any of the single traces, is very evident in the beam trace.

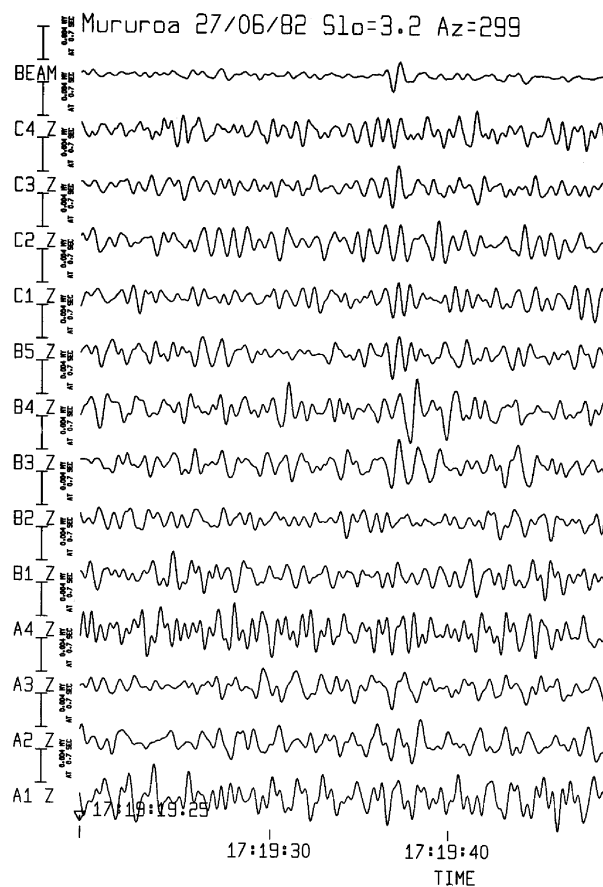


Fig. 4.29 Detection of a weak underground nuclear explosion in the 10 kt range at the Mururoa Atoll test site ($D = 145^\circ$) by beam forming (top trace). No signal is recognizable in any of the 13 individual record traces from stations of the Gräfenberg array, Germany (below) (from Buttkus, 1986).

4.4.3 Noise prediction-error filtering

In near real time, it is possible to use a moving time-window to determine the characteristics of a given noise field by means of cross- and auto-correlation of array sensor outputs. This then allows the prediction of the expected random noise in a subsequent time interval. Subtracting the predicted noise time series from the actual record results in a much reduced

4. Seismic Signals and Noise

noise level. Weak seismic signals, originally buried in the noise but not predicted by the noise “forecast” of the prediction-error filter (NPEF) may then stand out clearly. NPEFs have several advantages as compared to frequency filtering (compare with Fig. 4.30):

- no assumptions on the frequency spectrum of noise are required since actual noise properties are determined by the correlation of array sensor outputs;
- while frequency differences between signal and noise are lost in narrowband filtering, they are largely preserved in the case of the NPEF. This may aid signal identification and onset-time picking;
- signal first-motion polarity is preserved in the NPEF whereas it is no longer certain after zero-phase band-pass filtering (see section 4.2).

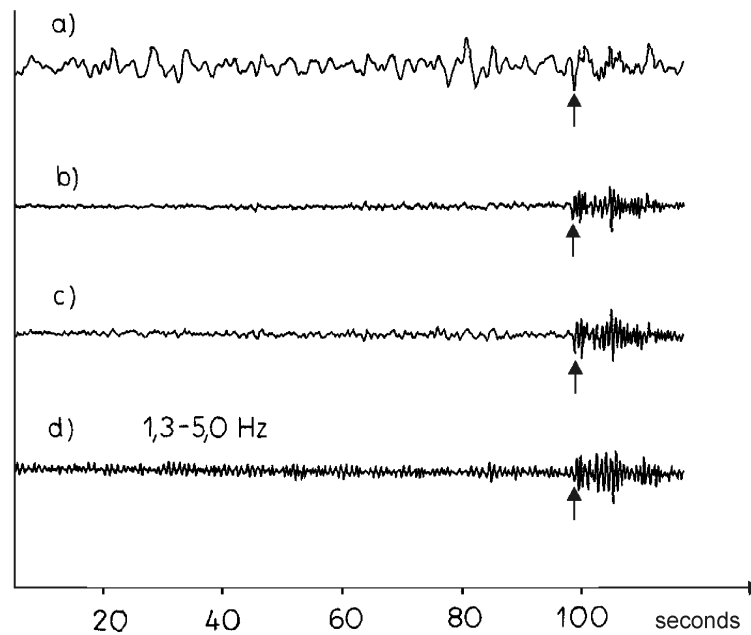


Fig. 4.30 Records of an underground nuclear explosion recorded at the Uinta Basin small aperture seismic array a) in the beam trace (sum of 10 seismometers), b) and c) after noise prediction error filtering with and without cross correlation (see 4.4.2) and d) after frequency band-pass filtering (1.3 – 5 Hz) (compiled by Bormann, 1966, from data published by Claerbout, 1964).

4.4.4 Noise polarization filtering

3-component recordings allow one to reconstruct the ground particle motion and to determine its polarization. Shimshoni and Smith (1964) investigated the cross product

$$M_j = \sum_{i=-n}^{+n} H_{i+j} \cdot V_{i+j} \quad (4.18)$$

in the time interval $j - n$ to $j + n$ with H and V as the horizontal and vertical component recordings, respectively. M is a measure of the total signal strength as well as of the degree of linear wave polarization. Eq. (4.18) vanishes for Rayleigh, Love and SH waves. On the other

hand, for linearly polarized P and SV waves, H and V are exactly in phase and the correlation function becomes $+1$ for P and -1 for SV waves. The longer the integration time, the better the suppression of randomly polarized noise (with a high LR component!). The optimal window length for good noise suppression, while still allowing good onset time picking, must be found by trial and error. Fig. 4.31 gives an example. One great advantage of polarization filtering is that it is independent of differences in the frequency and velocity spectrum of signal and noise and thus can be applied in concert with other procedures for SNR improvement.

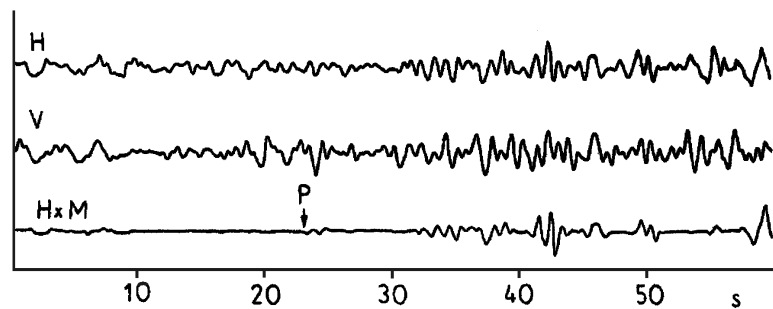


Fig. 4.31 Example of SNR improvement by polarization filtering according to Eq. (4.18) (bottom trace). H – horizontal component record, V – vertical component record (modified from Shimshoni and Smith, 1964).

4.4.5 SNR improvement by recordings in subsurface mines and boreholes

As shown in Figs. 4.23 and 4.24, short-period seismic noise is strongly reduced with the depth of sensor installation in boreholes or mines. However, when installing seismometers at depth, one must also consider effects on the signal. Generally, amplitudes of seismic body waves recorded at the free surface are systematically increased by as much as a factor of two, depending on the incidence angle and wavelength (see Exercise 3.4, Tab. 1). On the other hand, at a certain depth, destructive interference between incoming and surface-reflected waves may cause signal reduction. Therefore, because of the “free-surface effect”, peculiarities of the local noise field and geological conditions, the SNR does not necessarily increase steadily with depth. Fig. 4.32 compares two case studies of short-period signal and noise measurements in two deep boreholes in the USA.

While in a borehole in Texas the noise amplitudes decreased steadily (up to a factor of 30) down to 3000 m depth below surface, they decreased in another borehole in Oklahoma down to about 2000 m only and then increased again towards larger depth. At this greater depth a layer with 22% lower P-wave velocity was found by means of borehole seismic measurements (traveling noise in a low-velocity layer?). Also, the ratio of the noise in the borehole and at the surface, S_B/S_{OF} , differs in the two boreholes. Its mean value drops in the Texas borehole to $1/10^{\text{th}}$ at about 1500 m depth and increases again to $1/2$ of its surface value at 3000 m depth, while in the Oklahoma borehole it drops to about $1/3$ at about 1000 m depth and then remains roughly constant. Accordingly, we have no SNR improvement (on average) in the Texas borehole down to about 1000 m depth, but then the SNR increases to a factor of about 15 at 3000 m depth. Contrary to this, the SNR increases by a factor of 3 in the Oklahoma borehole within the first 800 m, but then remains roughly constant (ranging between 1 and 5) up to 3000 m depth.

4. Seismic Signals and Noise

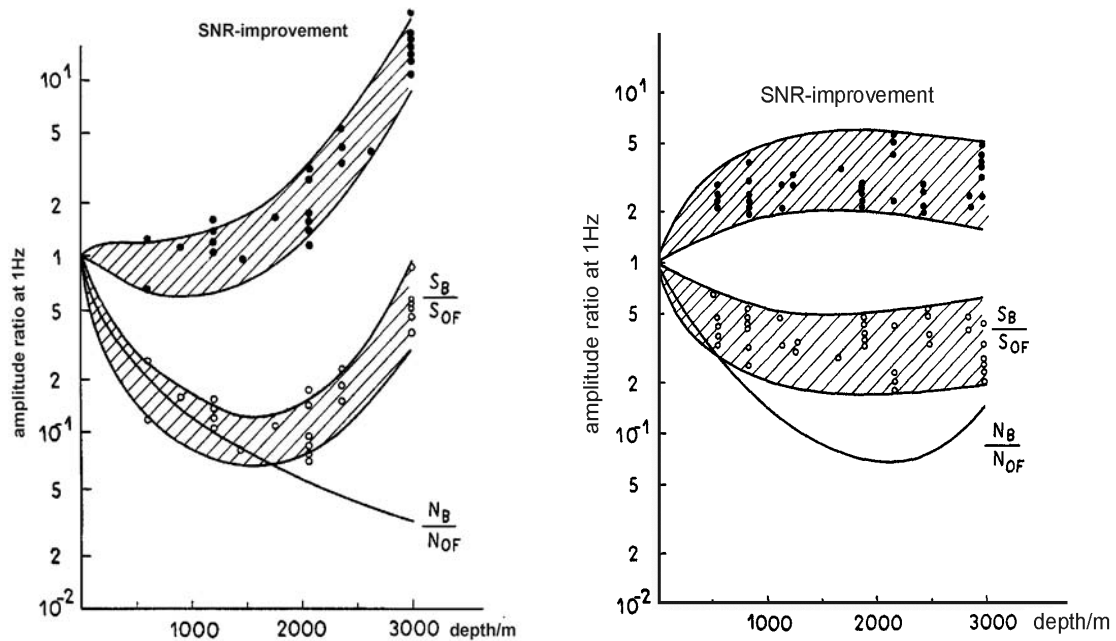


Fig. 4.32 Depth dependence of the signal-to-noise ratio (SNR). The top curve in both figures shows the improvement in SNR. The abbreviations are: S_B/S_{OF} : Ratio of signal in borehole and at the surface; N_B/N_{OF} : Ratio of noise in borehole and at the surface. SNR improvement in a borehole in Texas is shown left and in Oklahoma right (redrawn from Douze, 1964).

Therefore it follows that there is no straight-forward and continuous SNR improvement with depth. It may depend also on local geological and installation conditions. Nevertheless, we can generally expect a significant SNR improvement within the first few hundred meters depth. This applies particularly to borehole installations of long-period and broadband sensors which benefit greatly from the very stable temperature conditions and reduced tilt noise at depth. A depth of 100 m is generally sufficient to achieve most of the practicable reduction of long-period noise (-20 to -30 dB) (see 7.4.5). It should also be noted, that in records of deep borehole installation, the superposition of the first arriving waves with their respective surface reflection may cause irritating signal distortions although they can be filtered out by tuned signal processing (Fig. 4.33).

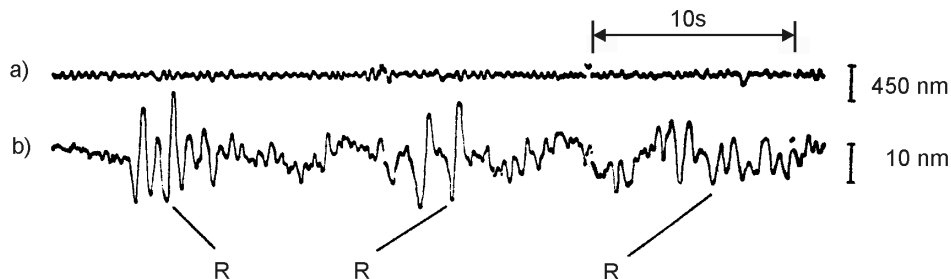


Fig. 4.33 Recording of a teleseismic event at $D = 80^\circ$ at a) the surface and b) at 3000 m depth in the Texas borehole (see Fig. 4.32 left). The SNR improved by a factor of about 10. Note that signal arrivals in the borehole record are followed by related arrivals of the surface reflections (R) about 3 s later (redrawn from Douze, 1964).

For installation depths less than 200 m the travel-time difference between direct and reflected waves is (in consolidated rock) less than 0.1 s and negligible. Since the cost of drilling and installation increases greatly with depth, no deeper permanent seismic borehole installations have yet been made. In any event, the borehole should be drilled through the soil or weathered rock cover and penetrate well into the compacted underlying rock formations.

4.4.6 Signal variations due to local site conditions

Compared to hard rock sites, both noise and signals may be amplified on soft soil cover. This signal amplification may partly or even fully outweigh the higher noise observed on such sites. Signal strength observed for a given event may vary strongly (up to a factor of about 10 to 30) within a given array or station network, even if its aperture is much smaller than the epicentral distance to the event ($< 10\text{-}20\%$), so that differences in backazimuth and amplitude-distance relationship are negligible (Fig. 4.34). Also, while one station of a network may record events rather weakly from a certain source area, the station may do as well as other stations (or even better) for events from another region, azimuth or distance (e.g., station GWS in Fig. 4.35 left and right, respectively).

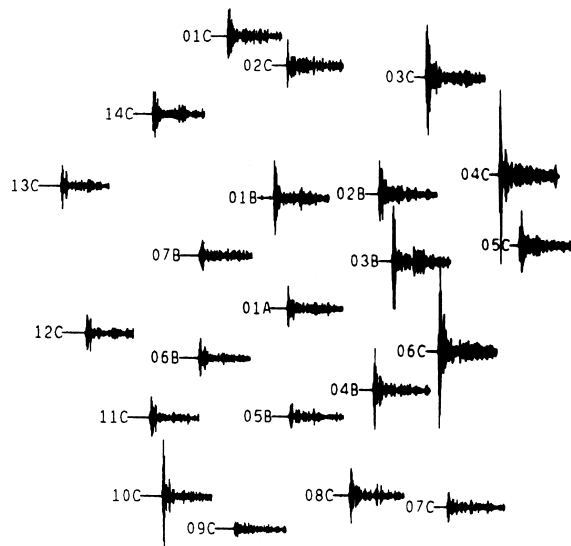


Fig. 4.34 Records of a Semipalatinsk event at stations of the NORSTAR seismic array (diameter about 90 km). The event is about $37\text{-}38^\circ$ away. Note the remarkable variations of signal amplitudes by a factor up to 10 (the standard deviation is about a factor of 2) (from Tronrud, 1983a).

Fig. 4.36 compares for regional and teleseismic events the short-period P-wave amplitude ratio (left) and SNR (right) of two stations of the German seismic network. In the same azimuth range, but at different epicentral distances, BRG may record both > 3 times larger as well as > 3 times smaller amplitudes than station MOX. This corresponds to magnitude differences up to one unit! The SNR ratio BGR/MOX also varies by a factor of 3 and more depending on azimuth and distance of events. Therefore, optimal site selection can not be made only on the basis of noise measurements. Also, the signal conditions at possible alternative sites should be compared. These differences in local signal conditions may become negligible in long-period recordings and thus play a lesser role in site selection for broadband networks and arrays.

4. Seismic Signals and Noise

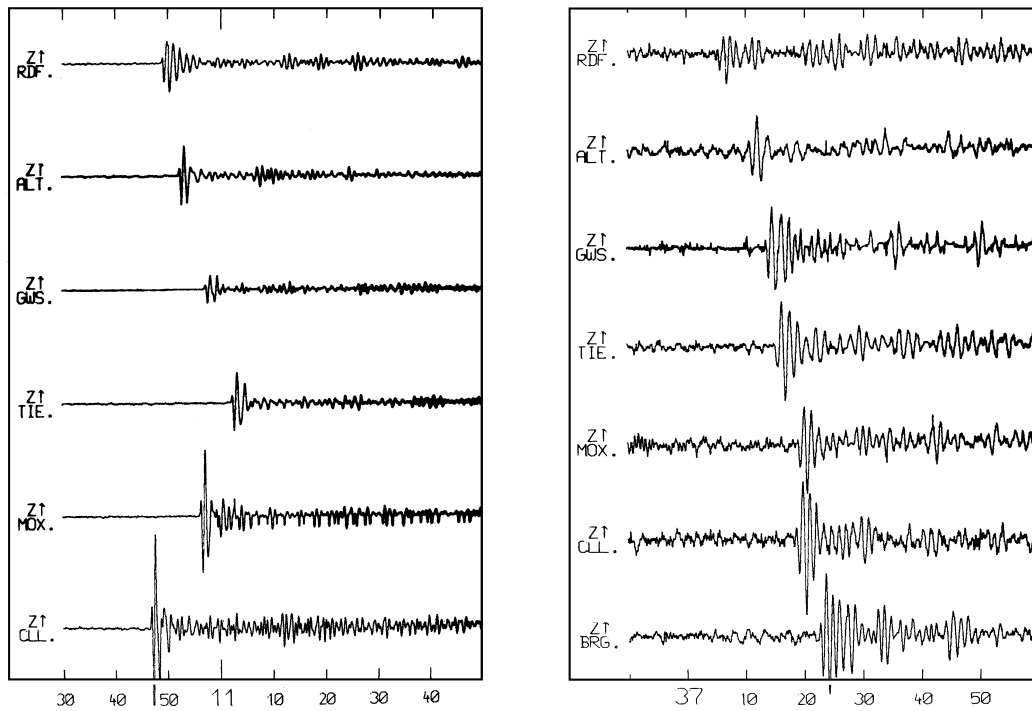


Fig. 4.35 Short-period records of underground nuclear explosions at the test sites of Semipalatinsk (left, D about $41^\circ \pm 1^\circ$) and Nevada (right; D about $81^\circ \pm 1^\circ$) at stations of the former East German seismic network. Note the differences in signal amplitudes both amongst the stations for a given event and for the same station pairs, when comparing events in different azimuth and distance. Also, at right, the compressive first motion is lost in the presence of noise due to the narrowband one-octave recording (see section 4.2.1). Small numbers on the x-axis are seconds, while big numbers are minutes.

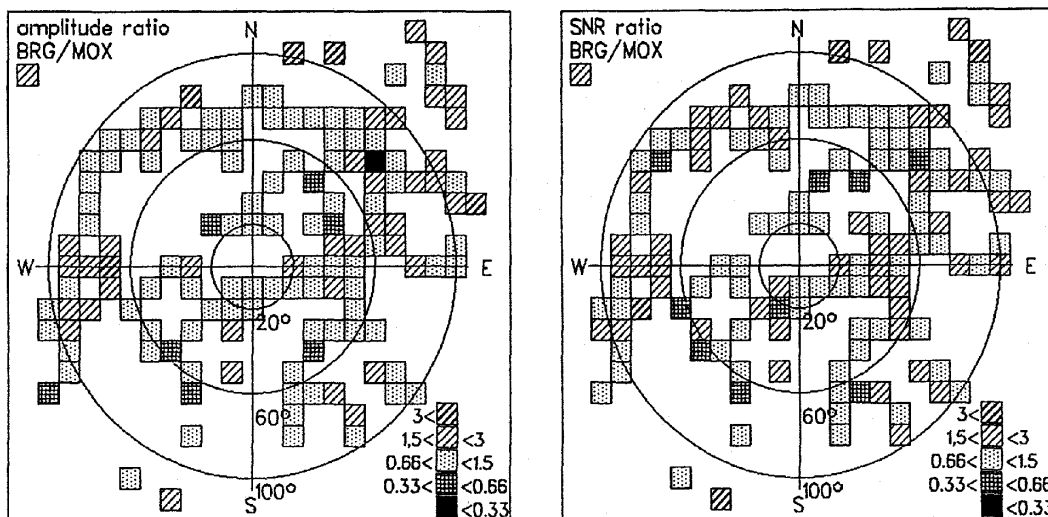


Fig. 4.36 Pattern of the relative short-period P-wave amplitudes at station BRG normalized to those of station MOX (170 km apart) in a distance-azimuth polar diagram (reproduced from *Physics of the Earth and Planetary Interiors*, 69; Bormann et al., “Potsdam seismological station network: ...”, p. 317, Fig. 7, © 1992; with permission of Elsevier Science).

Acknowledgments

The author thanks E. Bergman, J. Havskov and E. Hjortenberg for carefully reading the draft and for their valuable suggestions which helped to improve the text and a few figures.

Recommended overview readings (see References under Miscellaneous in Volume 2)

Havskov and Alguacil (2002)

Scherbaum (2001)

Tabulevich (1992)

Webb (2002)

5

Seismic Sensors and their Calibration

Erhard Wielandt

5.1 Overview

There are two basic types of seismic sensors: inertial seismometers which measure ground motion relative to an inertial reference (a suspended mass), and strainmeters or extensometers which measure the motion of one point of the ground relative to another. Since the motion of the ground relative to an inertial reference is in most cases much larger than the differential motion within a vault of reasonable dimensions, inertial seismometers are generally more sensitive to earthquake signals. However, at very low frequencies it becomes increasingly difficult to maintain an inertial reference, and for the observation of low-order free oscillations of the Earth, tidal motions, and quasi-static deformations, strainmeters may outperform inertial seismometers. Strainmeters are conceptually simpler than inertial seismometers although their technical realization and installation may be more difficult (see IS 5.1). This Chapter is concerned with inertial seismometers only. For a more comprehensive description of inertial seismometers, recorders and communication equipment see Havskov and Alguacil (2002).

An inertial seismometer converts ground motion into an electric signal but its properties can not be described by a single scale factor, such as output volts per millimeter of ground motion. The response of a seismometer to ground motion depends not only on the amplitude of the ground motion (how large it is) but also on its time scale (how sudden it is). This is because the seismic mass has to be kept in place by a mechanical or electromagnetic restoring force. When the ground motion is slow, the mass will move with the rest of the instrument, and the output signal for a given ground motion will therefore be smaller. The system is thus a high-pass filter for the ground displacement. This must be taken into account when the ground motion is reconstructed from the recorded signal, and is the reason why we have to go to some length in discussing the dynamic transfer properties of seismometers.

The dynamic behavior of a seismograph system within its linear range can, like that of any linear time-invariant (LTI) system, be described with the same degree of completeness in four different ways: by a linear differential equation, the Laplace transfer function (see 5.2.2), the complex frequency response (see 5.2.3), or the impulse response of the system (see 5.2.4). The first two are usually obtained by a mathematical analysis of the physical system (the hardware). The latter two are directly related to certain calibration procedures (see 5.7.4 and 5.7.5) and can therefore be determined from calibration experiments where the system is considered as a “black box” (this is sometimes called an identification procedure). However, since all four are mathematically equivalent, we can derive each of them either from a knowledge of the physical components of the system or from a calibration experiment. The mutual relations between the “time-domain” and “frequency-domain” representations are illustrated in Fig. 5.1. Practically, the mathematical description of a seismometer is limited to a certain bandwidth of frequencies that should at least include the bandwidth of seismic signals. Within this limit then any of the four representations describe the system's response to arbitrary input

5. Seismic Sensors and their Calibration

signals completely and unambiguously. The viewpoint from which they differ is how efficiently and accurately they can be implemented in different signal-processing procedures.

In digital signal processing, seismic sensors are often represented with other methods that are efficient and accurate but not mathematically exact, such as recursive (IIR) filters. Digital signal processing is however beyond the scope of this section. A wealth of textbooks is available both on analog and digital signal processing, for example Oppenheim and Willsky (1983) for analog processing, Oppenheim and Schaffer (1975) for digital processing, and Scherbaum (1996) for seismological applications.

The most commonly used description of a seismograph response in the classical observatory practice has been the “*magnification curve*”, i.e. the frequency-dependent magnification of the ground motion. Mathematically this is the modulus (absolute value) of the complex frequency response, usually called the *amplitude response*. It specifies the steady-state harmonic responsivity (amplification, magnification, conversion factor) of the seismograph as a function of frequency. However, for the correct interpretation of seismograms, also the phase response of the recording system must be known. It can in principle be calculated from the amplitude response, but is normally specified separately, or derived together with the amplitude response from the mathematically more elegant description of the system by its *complex transfer function* or its *complex frequency response*.

While for a purely electrical filter it is usually clear what the amplitude response is - a dimensionless factor by which the amplitude of a sinusoidal input signal must be multiplied to obtain the associated output signal - the situation is not always as clear for seismometers because different authors may prefer to measure the input signal (the ground motion) in different ways: as a displacement, a velocity, or an acceleration. Both the physical dimension and the mathematical form of the transfer function depend on the definition of the input signal, and one must sometimes guess from the physical dimension to what sort of input signal it applies. The output signal, traditionally a needle deflection, is now normally a voltage, a current, or a number of counts.

Calibrating a seismograph means measuring (and sometimes adjusting) its transfer properties and expressing them as a complex frequency response or one of its mathematical equivalents. For most applications the result must be available as parameters of a mathematical formula, not as raw data; so determining parameters by fitting a theoretical curve of known shape to the data is usually part of the procedure. Practically, seismometers are calibrated in two steps.

The first step is an electrical calibration (see 5.7) in which the seismic mass is excited with an electromagnetic force. Most seismometers have a built-in calibration coil that can be connected to an external signal generator for this purpose. Usually the response of the system to different sinusoidal signals at frequencies across the system's passband (steady-state method, 5.7.4), to impulses (transient method, 5.7.5), or to arbitrary broadband signals (random signal method, 5.7.6) is observed while the absolute magnification or gain remains unknown. For the exact calibration of sensors with a large dynamic range such as those employed in modern seismograph systems, the latter method is most appropriate.

The second step, the determination of the absolute gain, is more difficult because it requires mechanical test equipment in all but the simplest cases (see 5.8). The most direct method is to calibrate the seismometer on a shake table. The frequency at which the absolute

gain is measured must be chosen so as to minimize noise and systematic errors, and is often predetermined by these conditions within narrow limits. A calibration over a large bandwidth can not normally be done on a shake table. At the end of this Chapter we will propose some methods by which a seismometer can be absolutely calibrated without a shake table.

5.2 Basic theory

This section introduces some basic concepts of the theory of linear systems. For a more complete and rigorous treatment, the reader should consult a textbook such as by Oppenheim and Willsky (1983). Digital signal processing is based on the same concepts but the mathematical formulations are different for discrete (sampled) signals (see Oppenheim and Schaffer, 1975; Scherbaum, 1996; Plešinger et al., 1996). Readers who are familiar with the mathematics may proceed to section 5.2.7.

5.2.1 The complex notation

A fundamental mathematical property of linear time-invariant systems such as seismographs (as long as they are not driven out of their linear operating range) is that they do not change the waveform of sinewaves and of exponentially decaying or growing sinewaves. The mathematical reason for this fact is explained in the next section. An input signal of the form

$$f(t) = e^{\sigma t} (a_1 \cos \omega t + b_1 \sin \omega t) \quad (5.1)$$

will produce an output signal

$$g(t) = e^{\sigma t} (a_2 \cdot \cos \omega t + b_2 \cdot \sin \omega t) \quad (5.2)$$

with the same σ and ω , but possibly different a and b . Note that ω is the angular frequency, which is 2π times the common frequency. Using Euler's identity

$$e^{j\omega t} = \cos \omega t + j \sin \omega t \quad (5.3)$$

and the rules of complex algebra, we may write our input and output signals as

$$f(t) = \Re[c_1 \cdot e^{(\sigma+j\omega)t}] \quad \text{and} \quad g(t) = \Re[c_2 \cdot e^{(\sigma+j\omega)t}] \quad (5.4)$$

respectively, where $\Re[.]$ denotes the real part, and $c_1 = a_1 - jb_1$, $c_2 = a_2 - jb_2$. It can now be seen that the only difference between the input and output signal lies in the complex amplitude c , not in the waveform. The ratio c_2/c_1 is the complex gain of the system, and for $\sigma = 0$, it is the value of the complex frequency response at the angular frequency ω . What we have outlined here may be called the engineering approach to complex notation. The sign $\Re[.]$ for the real part is often omitted but always understood.

5. Seismic Sensors and their Calibration

The mathematical approach is slightly different in that real signals are not considered to be the real parts of complex signals but the sum of two complex-conjugate signals with positive and negative frequency:

$$f(t) = c_1 \cdot e^{(\sigma+j\omega)t} + c_1^* \cdot e^{(\sigma-j\omega)t} \quad (5.5)$$

where the asterisk * denotes the complex conjugate. The mathematical notation is slightly less concise, but since for real signals only the term with c_1 must be explicitly written down (the other one being its complex conjugate), the two notations become very similar. However, the c_1 term describes the whole signal in the engineering convention but only half of the signal in the mathematical notation! This may easily cause confusion, especially in the definition of power spectra. Power spectra computed after the engineer's method (such as the USGS Low Noise Model, see 5.5.1 and Chapter 4) attribute all power to positive frequencies and therefore have twice the power appearing in the mathematical notation.

5.2.2 The Laplace transformation

A signal that has a definite beginning in time (such as the seismic waves from an earthquake) can be decomposed into exponentially growing, stationary, or exponentially decaying sinusoidal signals with the *Laplace integral transformation*:

$$f(t) = \frac{1}{2\pi j} \int_{\sigma-j\infty}^{\sigma+j\infty} F(s) e^{st} ds, \quad F(s) = \int_0^{\infty} f(t) e^{-st} dt \quad (5.6)$$

The first integral defines the inverse transformation (the synthesis of the given signal) and the second integral the forward transformation (the analysis). It is assumed here that the signal begins at or after the time origin. s is a complex variable that may assume any value for which the second integral converges (depending on $f(t)$, it may not converge when s has a negative real part). The Laplace transform $F(s)$ is then said to “exist” for this value of s . The real parameter σ which defines the path of integration for the inverse transformation (the first integral) can be arbitrarily chosen as long as the path remains on the right side of all singularities of $F(s)$ in the complex s plane. This parameter decides whether $f(t)$ is synthesized from decaying ($\sigma < 0$), stationary ($\sigma = 0$) or growing ($\sigma > 0$) sinusoids (remember that the mathematical expression e^{st} with complex s represents a growing or decaying sinewave, and with imaginary s a pure sinewave).

The time derivative $\dot{f}(t)$ has the Laplace transform $s \cdot F(s)$, the second derivative $\ddot{f}(t)$ has $s^2 \cdot F(s)$, etc. Suppose now that an analog data-acquisition or data-processing system is characterized by the linear differential equation

$$c_2 \ddot{f}(t) + c_1 \dot{f}(t) + c_0 f(t) = d_2 \ddot{g}(t) + d_1 \dot{g}(t) + d_0 g(t) \quad (5.7)$$

where $f(t)$ is the input signal, $g(t)$ is the output signal, and the c_i and d_i are constants. We may then subject each term in the equation to a Laplace transformation and obtain

$$c_2s^2F(s) + c_1sF(s) + c_0F(s) = d_2s^2G(s) + d_1sG(s) + d_0G(s) \quad (5.8)$$

from which we get

$$G(s) = \frac{c_2s^2 + c_1s + c_0}{d_2s^2 + d_1s + d_0} F(s) \quad (5.9)$$

We have thus expressed the Laplace transform of the output signal by the Laplace transform of the input signal, multiplied by a known rational function of s . From this we obtain the output signal itself by an inverse Laplace transformation. This means, we can solve the differential equation by transforming it into an algebraic equation for the Laplace transforms. Of course, this is only practical if we are able to evaluate the integrals analytically, which is the case for a wide range of “mathematical” signals. Real signals must be approximated by suitable mathematical functions for a transformation. The method can obviously be applied to linear and time-invariant differential equations of any order. (Time-invariant means that the properties of the system, and hence the coefficients of the differential equation, do not depend on time.)

The rational function

$$H(s) = \frac{c_2s^2 + c_1s + c_0}{d_2s^2 + d_1s + d_0} \quad (5.10)$$

is the (Laplace) transfer function of the system described by the differential equation (5.7). It contains the same information on the system as the differential equation itself.

Generally, the transfer function $H(s)$ of an LTI system is the complex function for which

$$G(s) = H(s) \cdot F(s) \quad (5.11)$$

with $F(s)$ and $G(s)$ representing the Laplace transforms of the input and output signals.

A rational function like $H(s)$ in (5.10), and thus an LTU system, can be characterized up to a constant factor by its poles and zeros. This is discussed in section 5.2.6.

5.2.3 The Fourier transformation

Somewhat closer to intuitive understanding but mathematically less general than the Laplace transformation is the Fourier transformation

$$f(t) = \frac{1}{2\pi} \int_{-\infty}^{\infty} \tilde{F}(\omega) e^{j\omega t} d\omega, \quad \tilde{F}(\omega) = \int_{-\infty}^{\infty} f(t) e^{-j\omega t} dt \quad (5.12)$$

The signal is here assumed to have a finite energy so that the integrals converge. The condition that no signal is present at negative times can be dropped in this case. The Fourier trans-

5. Seismic Sensors and their Calibration

formation decomposes the signal into purely harmonic (sinusoidal) waves $e^{j\omega t}$. The direct and inverse Fourier transformation are also known as a harmonic analysis and synthesis.

Although the mathematical concepts behind the Fourier and Laplace transformations are different, we may consider the Fourier transformation as a special version of the Laplace transformation for real frequencies, i.e. for $s = j\omega$. In fact, by comparison with Eq. (5.6), we see that $\tilde{F}(\omega) = F(j\omega)$, i.e. the Fourier transform for real angular frequencies ω is identical to the Laplace transform for imaginary $s = j\omega$. For practical purposes the two transformations are thus nearly equivalent, and many of the relationships between time-signals and their transforms (such as the convolution theorem) are similar or the same for both. The function $\tilde{F}(\omega)$ is called the complex frequency response of the system. Some authors use the name “transfer function” for $\tilde{F}(\omega)$ as well; however, $\tilde{F}(\omega) = F(j\omega)$ is not the same function as $F(\omega)$, so different names are appropriate. The distinction between $\tilde{F}(\omega)$ and $F(s)$ is essential when systems are characterized by their poles and zeros. These are equivalent but not identical in the complex s and ω planes, and it is important to know whether the Laplace or Fourier transform is meant. Usually, poles and zeros are given for the Laplace transform. In case of doubt, one should check the symmetry of the poles and zeros in the complex plane: those of the Laplace transform are symmetric to the real axis as in Fig. 5.2 while those of the Fourier transform are symmetric to the imaginary axis.

The absolute value $|\tilde{F}(\omega)|$ is called the amplitude response, and the phase of $\tilde{F}(\omega)$ the phase response of the system. Note that amplitude and phase do not form a symmetric pair; however a certain mathematical symmetry (expressed by the Hilbert transformation) exists between the real and imaginary parts of a rational transfer function, and between the phase response and the natural logarithm of the amplitude response.

The definition of the Fourier transformation according to Eq. (5.12) applies to continuous transient signals. For other mathematical representations of signals, different definitions must be used:

$$f(t) = \sum_{v=-\infty}^{\infty} b_v e^{2\pi jvt/T}, \quad b_v = \frac{1}{T} \int_0^T f(t) e^{-2\pi jvt/T} dt \quad (5.13)$$

for periodic signals $f(t)$ with a period T , and

$$f_k = \frac{1}{M} \sum_{l=0}^{M-1} c_l e^{2\pi jkl/M}, \quad c_l = \sum_{k=0}^{M-1} f_k e^{-2\pi jkl/M} \quad (5.14)$$

for time series f_k consisting of M equidistant samples (such as digital seismic data). We have noted the inverse transform (the synthesis) first in each case.

The Fourier integral transformation (Eq. (5.12)) is mainly an analytical tool; the integrals are not normally evaluated numerically because the discrete Fourier transformation Eq. (5.14) permits more efficient computations. Eq. (5.13) is the Fourier series expansion of periodic functions, also mainly an analytical tool but also useful to represent periodic test signals. The

discrete Fourier transformation Eq. (5.13) is sometimes considered as being a discretized, approximate version of Eqs. (5.12) or (5.14) but is actually a mathematical tool in its own right: it is a mathematical identity that does not depend on any assumptions on the series f_k . Its relationship with the other two transformations, and especially the interpretation of the subscript l as representing a single frequency, do however depend on the properties of the original, continuous signal. The most important condition is that the bandwidth of the signal before sampling must be limited to less than half of the sampling rate f_s ; otherwise the sampled series will not contain the same information as the original. The bandwidth limit $f_n = f_s/2$ is called the *Nyquist frequency*. Whether we consider a signal as periodic or as having a finite duration (and thus a finite energy) is to some degree arbitrary since we can analyze real signals only for finite intervals of time, and it is then a matter of definition whether we assume the signal to have a periodic continuation outside the interval or not.

The Fast Fourier Transformation or FFT (see Cooley and Tukey, 1965) is a recursive algorithm to compute the sums in Eq. (5.14) efficiently, so it does not constitute a mathematically different definition of the discrete Fourier transformation.

5.2.4 The impulse response

A useful (although mathematically difficult) fiction is the Dirac “needle” pulse $\delta(t)$ (e.g. Oppenheim and Willsky, 1983), supposed to be an infinitely short, infinitely high, positive pulse at the time origin whose integral over time equals 1. It can not be realized, but its time-integral, the unit step function, can be approximated by switching a current on or off or by suddenly applying or removing a force. According to the definitions of the Laplace and Fourier transforms, both transforms of the Dirac pulse have the constant value 1. The amplitude spectrum of the Dirac pulse is “white”, this means, it contains all frequencies with equal amplitude. In this case Eq. (5.11) reduces to $G(s)=H(s)$, which means that the transfer function $H(s)$ is the Laplace transform of the impulse response $g(t)$. Likewise, the complex frequency response is the Fourier transform of the impulse response. All information contained in these complex functions is also contained in the impulse response of the system. The same is true for the step response, which is often used to test or calibrate seismic equipment.

Explicit expressions for the response of a linear system to impulses, steps, ramps and other simple waveforms can be obtained by evaluating the inverse Laplace transform over a suitable contour in the complex s plane, provided that the poles and zeros are known. The result, generally a sum of decaying complex exponential functions, can then be numerically evaluated with a computer or even a calculator. Although this is an elegant way of computing the response of a linear system to simple input signals with any desired precision, a warning is necessary: the numerical samples so obtained are not the same as the samples that would be obtained with an ideal digitizer. The digitizer must limit the bandwidth before sampling and therefore does not generate instantaneous samples but some sort of time-averages. For computing samples of band-limited signals, different mathematical concepts must be used (see Schuessler, 1981).

Specifying the impulse or step response of a system in place of its transfer function is not practical because the analytic expressions are cumbersome to write down and represent signals of infinite duration that can not be tabulated in full length.

5.2.5 The convolution theorem

Any signal may be understood as consisting of a sequence of pulses. This is obvious in the case of sampled signals, but can be generalized to continuous signals by representing the signal as a continuous sequence of Dirac pulses. We may construct the response of a linear system to an arbitrary input signal as a sum over suitably delayed and scaled impulse responses. This process is called a convolution:

$$g(t) = \int_0^\infty h(t') f(t-t') dt' = \int_0^\infty h(t-t') f(t') dt' \tag{5.15}$$

Here $f(t)$ is the input signal and $g(t)$ the output signal while $h(t)$ characterizes the system. We assume that the signals are causal (i.e. zero at negative time), otherwise the integration would have to start at $-\infty$. Taking $f(t) = \delta(t)$, i.e. using a single impulse as the input, we get $g(t) = \int h(t') \delta(t-t') dt' = h(t)$, so $h(t)$ is in fact the impulse response of the system.

The response of a linear system to an arbitrary input signal can thus be computed either by convolution of the input signal with the impulse response in time domain, or by multiplication of the Laplace-transformed input signal with the transfer function, or by multiplication of the Fourier-transformed input signal with the complex frequency response in frequency domain.

Since instrument responses are often specified as a function of frequency, the FFT algorithm has become a standard tool to compute output signals. The FFT method assumes, however, that all signals are periodic, and is therefore mathematically inaccurate when this is not the case. Signals must in general be tapered to avoid spurious results. Fig. 5.1 illustrates the interrelations between signal processing in the time and frequency domains.

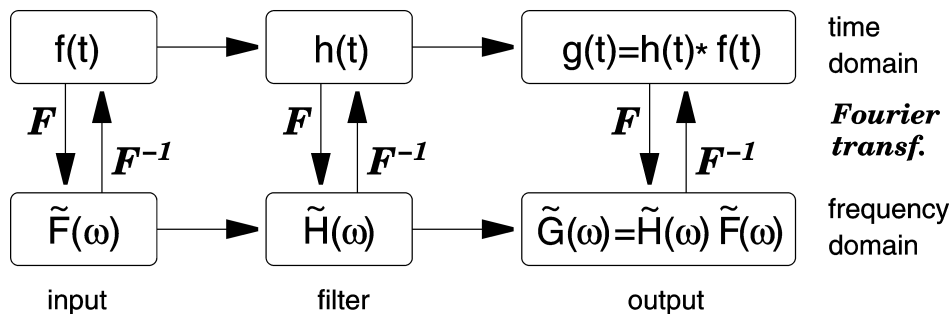


Fig. 5.1 Pathways of signal processing in the time and frequency domains. The asterisk between $f(t)$ and $g(t)$ indicates a convolution.

In digital processing, these methods translate into convolving discrete time series or transforming them with the FFT method and multiplying the transforms. For impulse responses with more than 100 samples, the FFT method is usually more efficient. The convolution method is also known as a FIR (finite impulse response) filtration. A third method, the recursive or IIR (infinite impulse response) filtration, is only applicable to digital signals; it is often preferred for its flexibility and efficiency although its accuracy requires special attention (see contribution by Scherbaum (1997) to the Manual web page under <http://www.seismo.com>).

5.2.6 Specifying a system

When $P(s)$ is a polynomial of s and $P(\alpha) = 0$, then $s = \alpha$ is called a zero, or a root, of the polynomial. A polynomial of order n has n complex zeros α_i , and can be factorized as $P(s) = p \cdot \prod (s - s_i)$. Thus, the zeros of a polynomial together with the factor p determine the polynomial completely. Since our transfer functions $H(s)$ are the ratio of two polynomials as in Eq. (5.10), they can be specified by their zeros (the zeros of the numerator $G(s)$), their poles (the zeros of the denominator $F(s)$), and a gain factor (or equivalently the total gain at a given frequency). The whole system, as long as it remains in its linear operating range and does not produce noise, can thus be described by a small number of discrete parameters.

Transfer functions are usually specified according to one of the following concepts:

1. The real coefficients of the polynomials in the numerator and denominator are listed.
2. The denominator polynomial is decomposed into normalized first-order and second-order factors with real coefficients (a total decomposition into first-order factors would require complex coefficients). The factors can in general be attributed to individual modules of the system. They are preferably given in a form from which corner periods and damping coefficients can be read, as in Eqs. (5.31) to (5.33). The numerator often reduces to a gain factor times a power of s .
3. The poles and zeros of the transfer function are listed together with a gain factor. Poles and zeros must either be real or symmetric to the real axis, as mentioned above. When the numerator polynomial is s^m , then $s = 0$ is an m -fold zero of the transfer function, and the system is a high-pass filter of order m . Depending on the order n of the denominator and accordingly on the number of poles, the response may be flat at high frequencies ($n = m$), or the system may act as a low-pass filter there ($n > m$). The case $n < m$ can occur only as an approximation in a limited bandwidth because no practical system can have an unlimited gain at high frequencies.

In the header of the widely-used SEED-format data (see 10.4), the gain factor is split up into a normalization factor bringing the gain to unity at some normalization frequency in the pass-band of the system, and a gain factor representing the actual gain at this frequency. EX 5.5 contains an exercise in determining the response from poles and zeros. A program POL_ZERO (in BASIC) is also available for this purpose (see 5.9).

5.2.7 The transfer function of a WWSSN-LP seismograph

The long-period seismographs of the now obsolete WWSSN (Worldwide Standardized Seismograph Network) consisted of a long-period electrodynamic seismometer normally tuned to a free period of 15 sec, and a long-period mirror-galvanometer with a free period around 90 sec. (In order to avoid confusion with the frequency variable $s = j\omega$ of the Laplace transformation, we use the non-standard abbreviation „sec“ for seconds in the present subsection.) The WWSSN seismograms were recorded on photographic paper rotating on a drum. We will now derive several equivalent forms of the transfer function for this system. In our example the damping constants are chosen as 0.6 for the seismometer and 0.9 for the galvanometer. Our

5. Seismic Sensors and their Calibration

treatment is slightly simplified. Actually, the free periods and damping constants are modified by coupling the seismometer and the galvanometer together; the above values are understood as being the modified ones.

As will be shown in section 5.2.9, Eq.(5.31), the transfer function of an electromagnetic seismometer (input: displacement, output: voltage) is

$$H_s(s) = Es^3 / (s^2 + 2s\omega_s h_s + \omega_s^2) \quad (5.16)$$

where $\omega_s = 2\pi/T_s$ is the angular eigenfrequency and h_s the numerical damping. (see EX 5.2 for a practical determination of these parameters.) The factor E is the generator constant of the electromagnetic transducer, for which we assume a value of 200 Vsec/m.

The galvanometer is a second-order low-pass filter and has the transfer function

$$H_g(s) = \gamma\omega_g^2 / (s^2 + 2s\omega_g h_g + \omega_g^2) \quad (5.17)$$

Here γ is the responsivity (in meters per volt) of the galvanometer with the given coupling network and optical path. We use a value of 393.5 m/V, which gives the desired overall magnification. The overall transfer function H_d of the seismograph is obtained in our simplified treatment as the product of the factors given in Eqs. (5.16) and (5.17):

$$H_d(s) = \frac{Cs^3}{(s^2 + 2s\omega_s h_s + \omega_s^2)(s^2 + 2s\omega_g h_g + \omega_g^2)} \quad (5.18)$$

The numerical values of the constants are $C = E\gamma\omega_g^2 = 383.6/\text{sec}$, $2\omega_s h_s = 0.5027/\text{sec}$, $\omega_s^2 = 0.1755/\text{sec}^2$, $2\omega_g h_g = 0.1257/\text{sec}$, and $\omega_g^2 = 0.00487/\text{sec}^2$.

As the input and output signals are displacements, the absolute value $|H_d(s)|$ of the transfer function is simply the frequency-dependent magnification of the seismograph. The gain factor C has the physical dimension sec^{-1} , so $H_d(s)$ is in fact a dimensionless quantity. C itself is however not the magnification of the seismograph. To obtain the magnification at the angular frequency ω we have to evaluate $M(\omega) = |H_d(j\omega)|$:

$$M(\omega) = \frac{C\omega^3}{\sqrt{(\omega_s^2 - \omega^2)^2 + 4\omega^2\omega_s^2 h_s^2} \sqrt{(\omega_g^2 - \omega^2)^2 + 4\omega^2\omega_g^2 h_g^2}} \quad (5.19)$$

Eq. (5.18) is a factorized form of the transfer function in which we still recognize the subunits of the system. We may of course insert the numerical constants and expand the denominator into a fourth-order polynomial

$$H_d(s) = 383.6s^3 / (s^4 + 0.6283s^3 + 0.2435s^2 + 0.0245s + 0.000855) \quad (5.20)$$

but the only advantage of this form would be its shortness.

The poles and zeros of the transfer function are most easily determined from Eq. (5.18). We read immediately that a triple zero is present at $s = 0$. Each factor $s^2 + 2s\omega_0 h + \omega_0^2$ in the denominator has the zeros

$$s_0 = \omega_0(-h \pm j\sqrt{1-h^2}) \quad \text{for } h < 1$$

$$s_0 = \omega_0(-h \pm \sqrt{h^2-1}) \quad \text{for } h \geq 1$$

so the poles of $H_d(s)$ in the complex s plane are (Fig. 5.2):

$$s_1 = \omega_s(-h_s + j\sqrt{1-h_s^2}) = -0.2513 + 0.3351j \quad [\text{sec}^{-1}]$$

$$s_2 = \omega_s(-h_s - j\sqrt{1-h_s^2}) = -0.2513 - 0.3351j \quad [\text{sec}^{-1}]$$

$$s_3 = \omega_g(-h_g + j\sqrt{1-h_g^2}) = -0.0628 + 0.0304j \quad [\text{sec}^{-1}]$$

$$s_4 = \omega_g(-h_g - j\sqrt{1-h_g^2}) = -0.0628 - 0.0304j \quad [\text{sec}^{-1}]$$

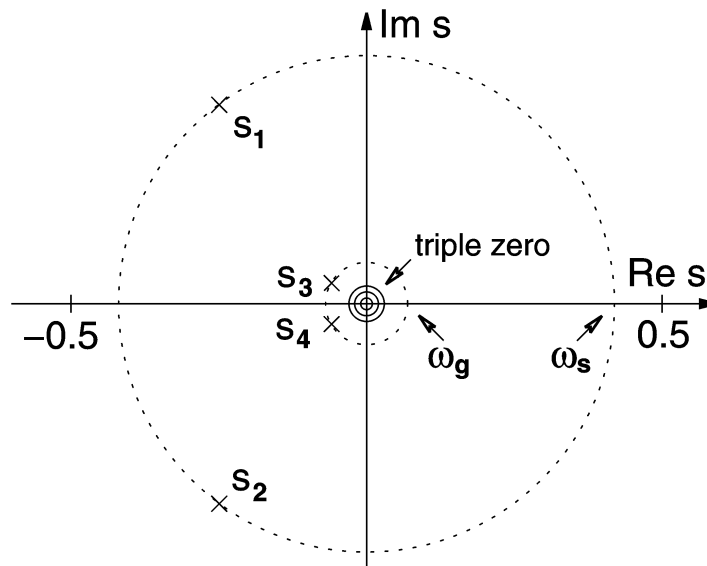


Fig. 5.2 Position of the poles of the WWSSN-LP system in the complex s plane.

In order to reconstruct $H_d(s)$ from its poles and zeros and the gain factor, we write

$$H_d(s) = \frac{Cs^3}{(s-s_1)(s-s_2)(s-s_3)(s-s_4)}. \quad (5.21)$$

It is now convenient to pairwise expand the factors of the denominator into second-order polynomials:

$$H_d(s) = \frac{Cs^3}{(s^2 - s(s_1 + s_2) + s_1s_2)(s^2 - s(s_3 + s_4) + s_3s_4)}. \quad (5.22)$$

5. Seismic Sensors and their Calibration

This makes all coefficients real because $s_2 = s_1^*$ and $s_4 = s_3^*$. Since $s_1 + s_2 = -2\omega_s h_s$, $s_1 s_2 = \omega_s^2$, $s_3 + s_4 = -2\omega_g h_g$, and $s_3 s_4 = \omega_g^2$, Eq. (5.22) is in fact the same as Eq. (5.18). We may of course also reconstruct $H_d(s)$ from the numerical values of the poles and zeros. Dropping the physical units, we obtain

$$H_d(s) = \frac{383.6s^3}{(s^2 + 0.5027s + 0.1755)(s^2 + 0.1257s + 0.00487)} \quad (5.23)$$

in agreement with Eq.(5.20).

Fig. 5.3 shows the corresponding amplitude response of the WWSSN seismograph as a function of frequency. The maximum magnification is 750 near a period of 15 sec. The slopes of the asymptotes are at each frequency determined by the dominant powers of s in the numerator and denominator of the transfer function. Generally, the low-frequency asymptote has the slope m (the number of zeros, here = 3) and the high-frequency asymptote has the slope $m-n$ (where n is the number of poles, here = 4). What happens in between depends on the position of the poles in the complex s plane. Generally, a pair of poles s_1, s_2 corresponds to a second-order corner of the amplitude response with $\omega_0^2 = s_1 s_2$ and $2\omega_0 h = -s_1 - s_2$. A single pole at s_0 is associated with a first-order corner with $\omega_0 = s_0$. The poles and zeros however do not indicate whether the respective subsystem is a low-pass, high-pass, or band-pass filter. This does not matter; the corners bend the amplitude response downward in each case. In the WWSSN-LP system, the low-frequency corner at 90 sec corresponding to the pole pair s_1, s_2 reduces the slope of the amplitude response from 3 to 1, and the corner at 15 sec corresponding to the pole pair s_3, s_4 reduces it further from 1 to -1.

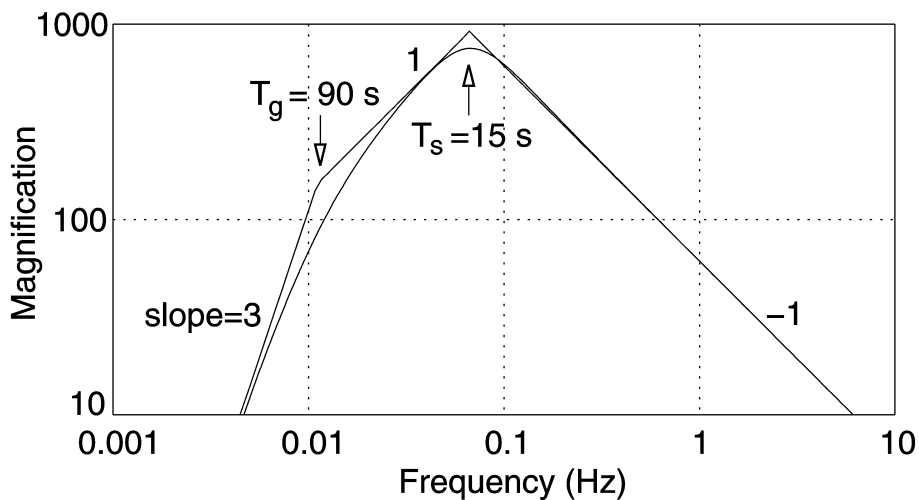


Fig. 5.3 Amplitude response of the WWSSN-LP system with asymptotes (Bode plot).

Looking at the transfer function H_s (Eq. (5.16)) of the electromagnetic seismometer alone, we see that the low-frequency asymptote has the slope 3 because of the triple zero in the numerator. The pole pair s_1, s_2 corresponds to a second-order corner in the amplitude response at ω_s which reduces the slope to 1. The resulting response is shown in a normalized form in the upper right panel of Fig. 5.6. As stated in section 5.2.6 under point 3, this case of $n < m$ can

only be an approximation in a limited bandwidth. In modern seismograph systems, the upper limit of the bandwidth is usually set by an analog or digital cut-off (anti-alias) filter.

As we will see in section 5.2.9, the classification of a subsystem as a high-pass, band-pass or low-pass filter may be a matter of definition rather than hardware; it depends on the type of ground motion (displacement, velocity, or acceleration) to which it relates. We also notice that interchanging ω_s, h_s with ω_g, h_g will change the gain factor C in the numerator of Eq. (5.19) from $E\gamma\omega_g^2$ to $E\gamma\omega_s^2$ and thus the gain, but will leave the denominator and therefore the shape of the response unchanged. While the transfer function is insensitive to arbitrary factorization, the hardware may be quite sensitive, and certain engineering rules must be observed when a given transfer function is realized in hardware. For example, it would have been difficult to realize a WWSSN seismograph with a 15 sec galvanometer and a 90 sec seismometer; the restoring force of a Lacoste-type suspension can not be made small enough without becoming unstable.

Fig. 5.4 illustrates the impulse responses of the seismometer, the galvanometer, and the whole WWSSN-LP system. We have chosen a pulse of acceleration (or of calibration current) as the input, so the figure does not refer to the transfer function H_d of Eq. (5.18) but to $H_a = s^{-2} H_d$. H_a has a single zero at $s = 0$ but the same poles as H_d . The pulse was slightly broadened for a better graphical display (the δ pulse is not plottable). The output signal (d) is the convolution of the input signal to the galvanometer (b) with the impulse response (c) of the galvanometer. (b) itself is the convolution of the broadband impulse (a) with the impulse response of the seismometer. (b) is then nearly the impulse response of the seismometer, and (d) is nearly the impulse response of the seismograph.

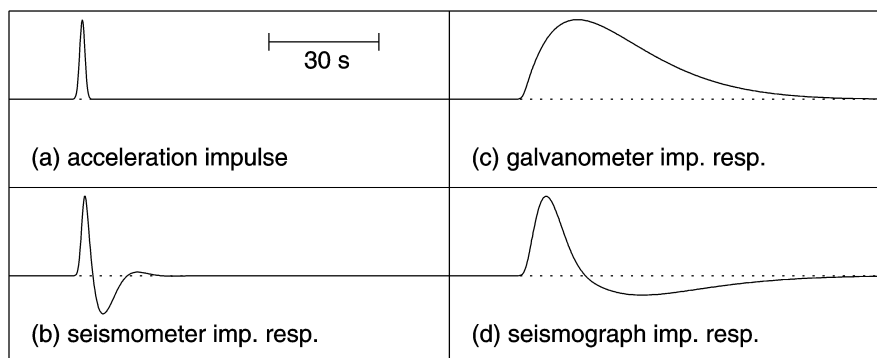


Fig. 5.4 WWSSN-LP system: Impulse responses of the seismometer, the galvanometer, and the seismograph. The input is an impulse of acceleration. The length of each trace is 2 minutes.

5.2.8 The mechanical pendulum

The simplest physical model for an inertial seismometer is a mass-and-spring system with viscous damping (Fig. 5.5).

We assume that the seismic mass is constrained to move along a straight line without rotation (i.e., it performs a pure translation). The mechanical elements are a mass of M kilograms, a spring with a stiffness S (measured in Newtons per meter), and a damping element with a constant of viscous friction R (in Newtons per meter per second). Let the time-dependent ground

5. Seismic Sensors and their Calibration

motion be $x(t)$, the absolute motion of the mass $y(t)$, and its motion relative to the ground $z(t) = y(t) - x(t)$. An acceleration $\ddot{y}(t)$ of the mass results from any external force $f(t)$ acting on the mass, and from the forces transmitted by the spring and the damper.

$$M \ddot{y}(t) = f(t) - S z(t) - R \dot{z}(t). \quad (5.24)$$

Since we are interested in the relationship between $z(t)$ and $x(t)$, we rearrange this into

$$M \ddot{z}(t) + R \dot{z}(t) + S z(t) = f(t) - M \ddot{x}(t). \quad (5.25)$$

We observe that an acceleration $\ddot{x}(t)$ of the ground has the same effect as an external force of magnitude $f(t) = -M \ddot{x}(t)$ acting on the mass in the absence of ground acceleration. We may thus simulate a ground motion $x(t)$ by applying a force $-M \ddot{x}(t)$ to the mass while the ground is not moving. The force is normally generated by sending a current through an electromagnetic transducer, but it may also be applied mechanically.

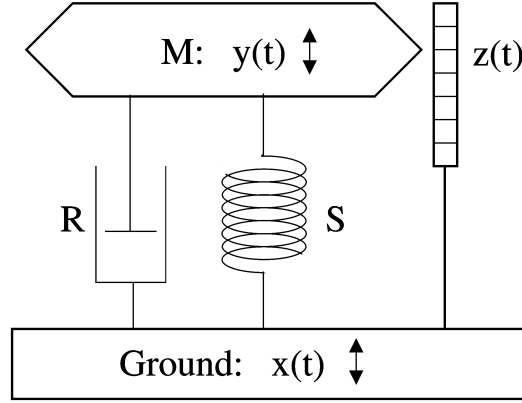


Fig. 5.5 Damped harmonic oscillator.

5.2.9 Transfer functions of pendulums and electromagnetic seismometers

According to Eqs.(5.7) and (5.8), Eq. (5.25) can be rewritten as

$$(s^2 M + s R + S) Z = F - s^2 M X \quad (5.26)$$

or

$$Z = (F / M - s^2 X) / (s^2 + s R / M + S / M). \quad (5.27)$$

From this we can obtain directly the transfer functions $T_f = Z/F$ for the external force F and $T_d = Z/X$ for the ground displacement X . We arrive at the same result, expressed by the Fourier-transformed quantities, by simply assuming a time-harmonic motion $x(t) = \tilde{X} e^{j\omega t} / 2\pi$ as well as a time-harmonic external force $f(t) = \tilde{F} e^{j\omega t} / 2\pi$, for which Eq. (5.25) reduces to

$$(-\omega^2 M + j\omega R + S) \tilde{Z} = \tilde{F} + \omega^2 M \tilde{X} \quad (5.28)$$

or

$$\tilde{Z} = (\tilde{F}/M + \omega^2 \tilde{X}) / (-\omega^2 + j\omega R/M + S/M). \quad (5.29)$$

While in mathematical derivations it is convenient to use the angular frequency $\omega = 2\pi f$ to characterize a sinusoidal signal of frequency f , and some authors omit the word „angular“ in this context, we reserve the term „frequency“ to the number of cycles per second.

By checking the behavior of $\tilde{Z}(\omega)$ in the limit of low and high frequencies, we find that the mass-and-spring system is a second-order high-pass filter for displacements and a second-order low-pass filter for accelerations and external forces (Fig. 5.6). Its corner frequency is $f_0 = \omega_0/2\pi$ with $\omega_0 = \sqrt{S/M}$. This is at the same time the „eigenfrequency“ or „natural frequency“ with which the mass oscillates when the damping is negligible. At the angular frequency ω_0 , the ground motion \tilde{X} is amplified by a factor $\omega_0 M/R$ and phase shifted by $\pi/2$. The imaginary term in the denominator is usually written as $2\omega\omega_0 h$ where $h = R/(2\omega_0 M)$ is the numerical damping, i.e., the ratio of the actual to the critical damping. Viscous friction will no longer appear explicitly in our formulas; the symbol R will later be used for electrical resistance.

In order to convert the motion of the mass into an electric signal, the mechanical pendulum in the simplest case is equipped with an electromagnetic velocity transducer (see 5.3.7) whose output voltage we denote with \tilde{U} . We then have an electromagnetic seismometer, also called a geophone when designed for seismic exploration. When the responsivity of the transducer is E (volts per meter per second; $\tilde{U} = -Ej\omega\tilde{Z}$) we get

$$\tilde{U} = -j\omega E(\tilde{F}/M + \omega^2 \tilde{X}) / (-\omega^2 + 2j\omega\omega_0 h + \omega_0^2) \quad (5.30)$$

from which, in the absence of an external force (i.e. $f(t) = 0, \tilde{F} = 0$), we obtain the frequency-dependent complex response functions

$$\tilde{H}_d(\omega) := \tilde{U} / \tilde{X} = -j\omega^3 E / (-\omega^2 + 2j\omega\omega_0 h + \omega_0^2) \quad (5.31)$$

for the displacement,

$$\tilde{H}_v(\omega) := \tilde{U} / (j\omega\tilde{X}) = -\omega^2 E / (-\omega^2 + 2j\omega\omega_0 h + \omega_0^2) \quad (5.32)$$

for the velocity, and

$$\tilde{H}_a(\omega) := \tilde{U} / (-\omega^2 \tilde{X}) = j\omega E / (-\omega^2 + 2j\omega\omega_0 h + \omega_0^2) \quad (5.33)$$

for the acceleration.

With respect to its frequency-dependent response, the electromagnetic seismometer is a second-order high-pass filter for the velocity, and a band-pass filter for the acceleration. Its response to displacement has no flat part and no concise name. These responses (or, more precisely speaking, the corresponding amplitude responses) are illustrated in Fig. 5.6. IS 5.2 shows response curves for different subsystems of analog seismographs in more detail and EX 5.1 illustrates the construction of the simplified response curve (Bode diagram) of a now historical electronic seismograph.

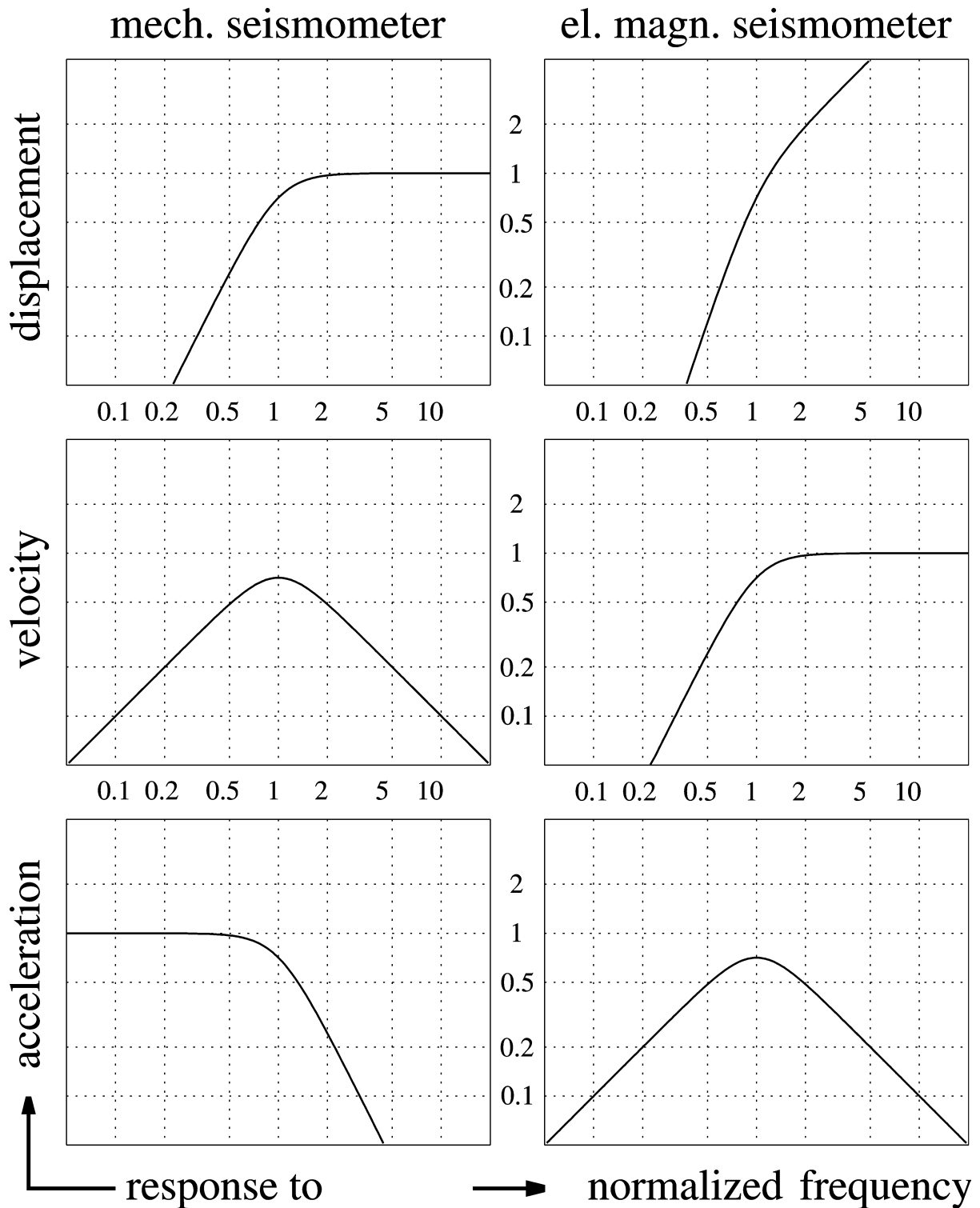


Fig. 5.6 Response curves of a mechanical seismometer (spring pendulum, left) and electrodynamic seismometer (geophone, right) with respect to different kinds of input signals (displacement, velocity and acceleration, respectively). The normalized frequency is the signal frequency divided by the eigenfrequency (corner frequency) of the seismometer. All of these response curves have a second-order corner at the normalized frequency 1. In analogy to it, Fig. 5.26 shows the normalized step responses of second-order high-pass, band-pass and low-pass filters.

5.3 Design of seismic sensors

Although the mass-and-spring system of Fig. 5.5 is a useful mathematical model for a seismometer, it is incomplete as a practical design. The suspension must suppress five out of the six degrees of freedom of the seismic mass (three translational and three rotational) but the mass must still move as freely as possible in the remaining direction. This section discusses some of the mechanical concepts by which this can be achieved. In principle it is also possible to let the mass move in all directions and observe its motion with three orthogonally arranged transducers, thus creating a three-component sensor with only one suspended mass. Indeed, some historical instruments have made use of this concept. It is, however, difficult to minimize the restoring force and to suppress parasitic rotations of the mass when its translational motion is unconstrained. Modern three-component seismometers therefore have separate mechanical sensors for the three axes of motion.

5.3.1 Pendulum-type seismometers

Most seismometers are of the pendulum type, i.e., they let the mass rotate around an axis rather than move along a straight line (Fig. 5.7 to Fig. 5.10). The point bearings in our figures are for illustration only; most seismometers have crossed flexural hinges. Pendulums are not only sensitive to translational but also to angular acceleration. Since the rotational component in seismic waves is normally small, there is not much practical difference between linear-motion and pendulum-type seismometers. However, they may behave differently in technical applications or on a shake table where it is not uncommon to have noticeable rotations.

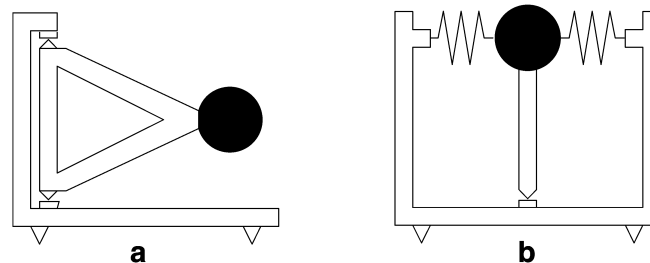


Fig. 5.7 (a) Garden-gate suspension; (b) Inverted pendulum.

For small translational ground motions the equation of motion of a pendulum is formally identical to Eq. (5.25) but z must then be interpreted as the angle of rotation. Since the rotational counterparts of the constants M , R , and S in Eq. (5.25) are of little interest in modern electronic seismometers, we will not discuss them further and refer the reader instead to the older literature, such as Berlage (1932) or Willmore (1979).

The simplest example of a pendulum is a mass suspended with a string or wire (like Foucault's pendulum). When the mass has small dimensions compared to the length ℓ of the string so that it can be idealized as a point mass, then the arrangement is called a mathematical pendulum. Its period of oscillation is $T = 2\pi\sqrt{\ell/g}$ where g is the gravitational acceleration. A mathematical pendulum of 1 m length has a period of nearly 2 seconds; for a period of 20 seconds the length has to be 100 m. Clearly, this is not a suitable design for a long-period seismometer.

5.3.2 Decreasing the restoring force

At low frequencies and in the absence of an external force, Eq. (5.25) can be simplified to $Sz = -M\ddot{x}$ and read as follows: a relative displacement of the seismic mass by $-\Delta z$ indicates a ground acceleration of magnitude

$$\ddot{x} = (S/M) \Delta z = \omega_0^2 \Delta z = (2\pi/T_0)^2 \Delta z \quad (5.34)$$

where ω_0 is the angular eigenfrequency of the pendulum, and T_0 its eigenperiod. If Δz is the smallest mechanical displacement that can be measured electronically, then the formula determines the smallest ground acceleration that can be observed at low frequencies. For a given transducer, it is inversely proportional to the square of the free period of the suspension. A sensitive long-period seismometer therefore requires either a pendulum with a low eigenfrequency or a very sensitive transducer. Since the eigenfrequency of an ordinary pendulum is essentially determined by its size, and seismometers must be reasonably small, astatic suspensions have been invented that combine small overall size with a long free period.

The simplest astatic suspension is the “garden-gate” pendulum used in horizontal seismometers (Fig. 5.7a). The mass moves in a nearly horizontal plane around a nearly vertical axis. Its free period is the same as that of a mass suspended from the point where the plumb line through the mass intersects the axis of rotation (Fig. 5.8a). The eigenperiod $T_0 = 2\pi\sqrt{\ell/g \sin \alpha}$ is infinite when the axis of rotation is vertical ($\alpha=0$), and is usually adjusted by tilting the whole instrument. This is one of the earliest designs for long-period horizontal seismometers.

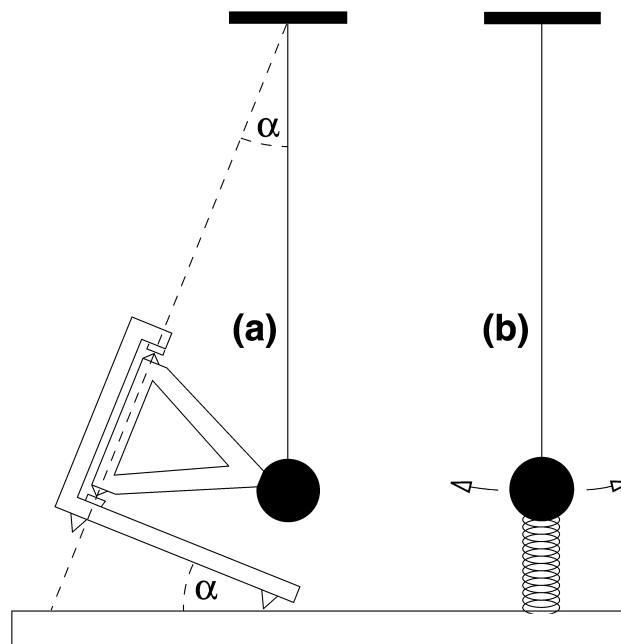


Fig. 5.8 Equivalence between a tilted “garden-gate” pendulum and a string pendulum. For a free period of 20 sec, the string pendulum must be 100 m long. The tilt angle α of a garden-gate pendulum with the same free period and a length of 30 cm is about 0.2° . The longer the period is made, the less stable it will be under the influence of small tilt changes. (b) Period-lengthening with an auxiliary compressed spring.

Another early design is the inverted pendulum held in stable equilibrium by springs or by a stiff hinge (Fig. 5.7b); a famous example is Wiechert's horizontal pendulum built around 1905.

An astatic spring geometry for vertical seismometers invented by LaCoste (1934) is shown in Fig. 5.9a. The mass is in neutral equilibrium and has therefore an infinite free period when three conditions are met: the spring is pre-stressed to zero length (i.e. the spring force is proportional to the total length of the spring), its end points are seen under a right angle from the hinge, and the mass is balanced in the horizontal position of the boom. A finite free period is obtained by making the angle of the spring slightly smaller than 90° , or by tilting the frame accordingly. By simply rotating the pendulum, astatic suspensions with a horizontal or oblique (Fig. 5.9b) axis of sensitivity can be constructed as well.

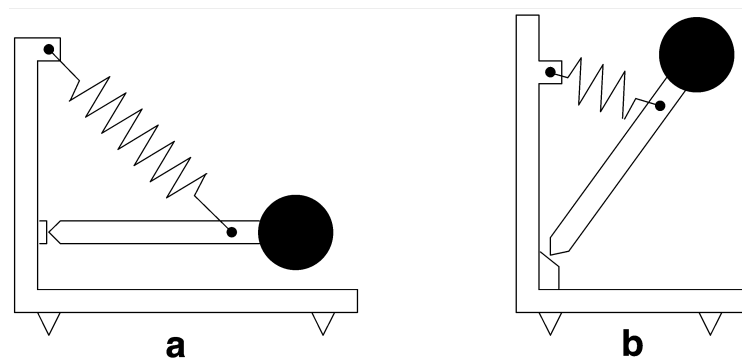


Fig. 5.9 LaCoste suspensions.

The astatic leaf-spring suspension (Fig. 5.10a, Wielandt, 1975), in a limited range around its equilibrium position, is comparable to a LaCoste suspension but is much simpler to manufacture. A similar spring geometry is also used in the triaxial seismometer Streckeisen STS2 (see Fig. 5.10b and DS 5.1). The delicate equilibrium of forces in astatic suspensions makes them susceptible to external disturbances such as changes in temperature; they are difficult to operate without a stabilizing feedback system.

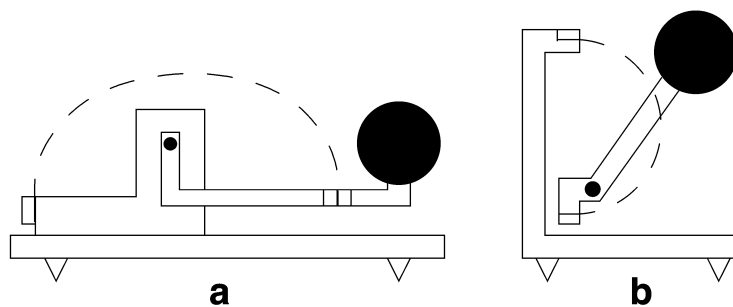


Fig. 5.10 Leaf-spring astatic suspensions.

Apart from genuinely astatic designs, almost any seismic suspension can be made astatic with an auxiliary spring acting normal to the line of motion of the mass and pushing the mass away from its equilibrium (Fig. 5.8b). The long-period performance of such suspensions, however, is quite limited. Neither the restoring force of the original suspension nor the destabilizing

5. Seismic Sensors and their Calibration

force of the auxiliary spring can be made perfectly linear (i.e. proportional to the displacement). While the linear components of the force may cancel, the nonlinear terms remain and cause the oscillation to become non-harmonic and even unstable at large amplitudes. Viscous and hysteretic behavior of the springs may also cause problems. The additional spring (which has to be soft) may introduce parasitic resonances. Modern seismometers do not use this concept and rely either on a genuinely astatic spring geometry or on the sensitivity of electronic transducers.

5.3.3 Sensitivity of horizontal seismometers to tilt

We have already seen (Eq. (5.25)) that a seismic acceleration of the ground has the same effect on the seismic mass as an external force. The largest such force is gravity. It is normally cancelled by the suspension, but when the seismometer is tilted, the projection of the vector of gravity onto the axis of sensitivity changes, producing a force that is in most cases undistinguishable from a seismic signal (Fig. 5.11). Undesired tilt at seismic frequencies may be caused by moving or variable surface loads such as cars, people, and atmospheric pressure. The resulting disturbances are a second-order effect in well-adjusted vertical seismometers but otherwise a first-order effect (see Rodgers, 1968; Rodgers, 1969). This explains why horizontal long-period seismic traces are always noisier than vertical ones. A short, impulsive tilt excursion is equivalent to a step-like change of ground velocity and therefore will cause a long-period transient in a horizontal broadband seismometer. For periodic signals, the apparent horizontal displacement associated with a given tilt increases with the square of the period (see also 5.8.1).

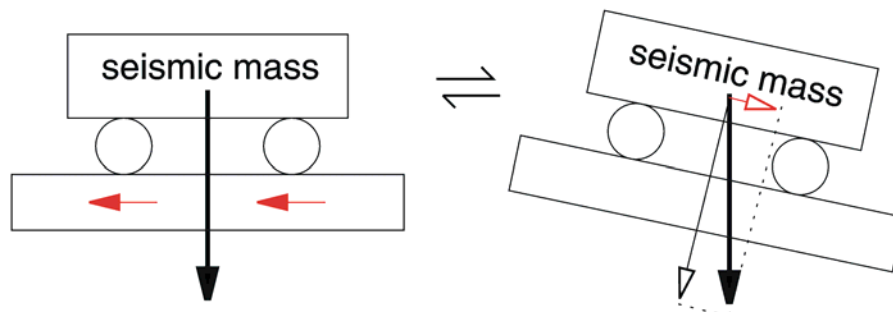


Fig. 5.11 The relative motion of the seismic mass is the same when the ground is accelerated to the left as when it is tilted to the right.

Fig. 5.12 illustrates the effect of barometrically induced ground tilt. Let us assume that the ground is vertically deformed by as little $\pm 1 \mu\text{m}$ over a distance of 3 km, and that this deformation oscillates with a period of 10 minutes. A simple calculation then shows that seismometers A and C see a vertical acceleration of $\pm 10^{-10} \text{ m/s}^2$ while B sees a horizontal acceleration of $\pm 10^{-8} \text{ m/s}^2$. The horizontal noise is thus 100 times larger than the vertical one. In absolute terms, even the vertical acceleration is by a factor of four above the minimum ground noise in one octave, as specified by the USGS Low Noise Model (see 5.5.1)

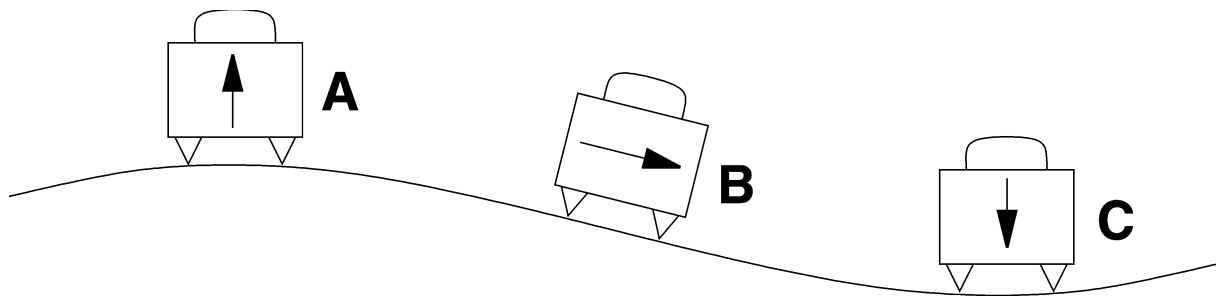


Fig. 5.12 Ground tilt caused by the atmospheric pressure is the main source of very-long-period noise on horizontal seismographs.

5.3.4 Direct effects of barometric pressure

Besides tilting the ground, the continuously fluctuating barometric pressure affects seismometers in at least three different ways: (1) when the seismometer is not enclosed in a hermetic housing, the mass will experience a variable buoyancy which can cause large disturbances in vertical sensors; (2) changes of pressure also produce adiabatic changes of temperature which affect the suspension (see the next subsection). Both effects can be greatly reduced by making the housing airtight or installing the sensor inside an external pressure jacket; however, then (3) the housing or jacket may be deformed by the pressure and these deformations may be transmitted to the seismic suspension as stress or tilt. While it is always worthwhile to protect vertical long-period seismometers from changes of the barometric pressure, it has often been found that horizontal long-period seismometers are less sensitive to barometric noise when they are not hermetically sealed. This, however, may cause other problems such as corrosion.

5.3.5 Effects of temperature

The equilibrium between gravity and the spring force in a vertical seismometer is disturbed when the temperature changes. Although thermally compensated alloys are available for springs, a self-compensated spring does not make a compensated seismometer. The geometry of the whole suspension changes with temperature; the seismometer must therefore be compensated as a whole. However, the different time constants involved prevent an efficient compensation at seismic frequencies. Short-term changes of temperature, therefore, must be suppressed by the combination of thermal insulation and thermal inertia. Special caution is required with seismometers where electronic components are enclosed with the mechanical sensor: these instruments heat themselves up when insulated and are then very sensitive to air drafts, so the insulation must at the same time suppress any possible air convection (see 5.5.3). Long-term (seasonal) changes of temperature do not interfere with the seismic signal (except when they cause convection in the vault) but may drive the seismic mass out of its operating range. Eq. (5.34) can be used to calculate the thermal drift of a vertical seismometer when the temperature coefficient of the spring force is formally assigned to the gravitational acceleration.

5.3.6 The homogeneous triaxial arrangement

In order to observe ground motion in all directions, a triple set of seismometers oriented towards North, East, and upward (Z) has been the standard for a century. However, horizontal and vertical seismometers differ in their construction, and it takes some effort to make their responses equal. An alternative way of manufacturing a three-component set is to use three sensors of identical construction whose sensitive axes are inclined against the vertical like the edges of a cube standing on its corner (Fig. 5.13), by an angle of $\arctan \sqrt{2}$, or 54.7 degrees.

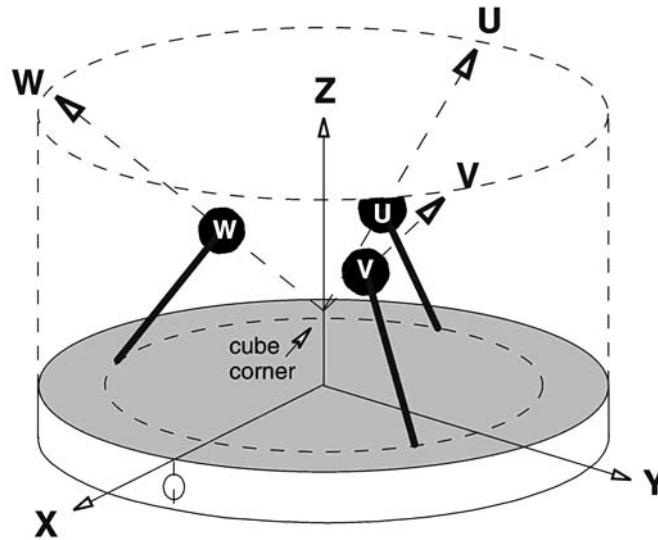


Fig. 5.13 The homogeneous triaxial geometry of the STS2 seismometer

At this time of writing, only one commercial seismometer, the Streckeisen STS2, makes use of this geometry, although it was not the first one to do so (see Gal'perin, 1955; Knothe, 1963; Melton and Kirkpatrick, 1970; Gal'perin, 1977). Since most seismologists want finally to see the conventional E, N and Z components of motion, the oblique components U, V, W of the STS2 are electrically recombined according to

$$\begin{pmatrix} X \\ Y \\ Z \end{pmatrix} = \frac{1}{\sqrt{6}} \begin{pmatrix} -2 & 1 & 1 \\ 0 & \sqrt{3} & -\sqrt{3} \\ \sqrt{2} & \sqrt{2} & \sqrt{2} \end{pmatrix} \begin{pmatrix} U \\ V \\ W \end{pmatrix} \quad (5.35)$$

The X axis of the STS2 seismometer is normally oriented towards East; the Y axis then points North. Noise originating in one of the sensors of a triaxial seismometer will appear on all three outputs (except for Y being independent of U). Its origin can be traced by transforming the X, Y and Z signals back to U, V and W with the inverse (transposed) matrix. Disturbances affecting only the horizontal outputs are unlikely to originate in the seismometer and are, in general, due to tilt. Disturbances of the vertical output only may be related to temperature, barometric pressure, or electrical problems affecting all three sensors in the same way as an unstable power supply.

5.3.7 Electromagnetic velocity sensing and damping

The simplest transducer both for sensing motions and for exerting forces is an electromagnetic (electrodynamics) device where a coil moves in the field of a permanent magnet, as in a loudspeaker (Fig. 5.14). The motion induces a voltage in the coil; a current flowing in the coil produces a force. From the conservation of energy it follows that the responsivity of the coil-magnet system as a force transducer, in Newtons per Ampere, and its responsivity as a velocity transducer, in Volts per meter per second, are identical. The units are in fact the same (remember that $1\text{Nm} = 1\text{Joule} = 1\text{VAs}$). When such a velocity transducer is loaded with a resistor, thus permitting a current to flow, then according to Lenz's law it generates a force, opposing the motion. This effect is used to damp the mechanical free oscillation of passive seismic sensors (geophones and electromagnetic seismometers).

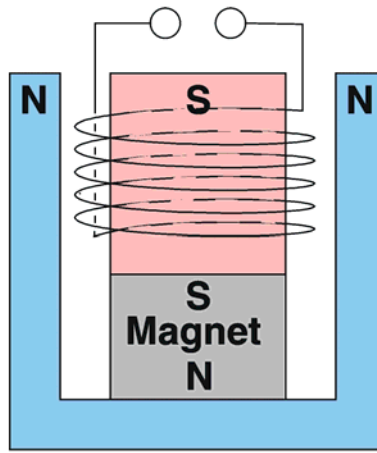


Fig. 5.14 Electromagnetic velocity and force transducer.

We have so far treated the damping of passive sensors as if it were a viscous effect in the mechanical receiver. Actually, only a small part h_m of the damping is due to mechanical causes. The main contribution normally comes from the electromagnetic transducer which is suitably shunted for this purpose. Its contribution is

$$h_{el} = E^2 / 2M\omega_0 R_d \quad (5.36)$$

where R_d is the total damping resistance (the sum of the resistances of the coil and of the external shunt). The total damping $h_m + h_{el}$ is preferably chosen as $1/\sqrt{2}$, a value that defines a second-order Butterworth filter characteristic, and gives a maximally flat response in the passband (such as the velocity-response of the electromagnetic seismometer in Fig. 5.6).

5.3.8 Electronic displacement sensing

At very low frequencies, the output signal of electromagnetic transducers becomes too small to be useful for seismic sensing. One then uses active electronic transducers where a carrier signal, usually in the audio frequency range, is modulated by the motion of the seismic mass. The basic modulating device is an inductive or capacitive half-bridge. Inductive half-bridges are detuned by a movable magnetic core. They require no electric connections to the moving

5. Seismic Sensors and their Calibration

part and are environmentally robust; however their sensitivity appears to be limited by the granular nature of magnetism. Capacitive half-bridges (Fig. 5.15) are realized as three-plate capacitors where either the central plate or the outer plates move with the seismic mass. Their sensitivity is limited by the ratio between the electrical noise of the demodulator and the electrical field strength; which is typically a hundred times better than that of the inductive type. The comprehensive paper by Jones and Richards (1973) on the design of capacitive transducers still represents state-of-the-art in all essential aspects.

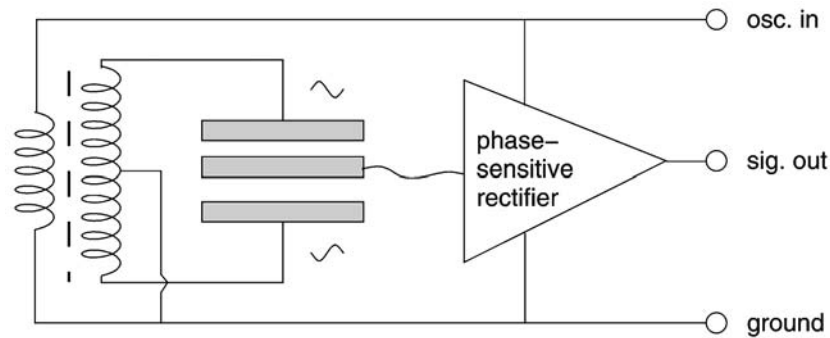


Fig. 5.15 Capacitive displacement *transducer* (Blumlein bridge).

5.4 Force-balance accelerometers and seismometers

5.4.1 The force-balance principle

In a conventional passive seismometer, the inertial force produced by a seismic ground motion deflects the mass from its equilibrium position, and the displacement or velocity of the mass is then converted into an electric signal. This principle of measurement is now used for short-period seismometers only. Long-period or broadband seismometers are built according to the force-balance principle. The inertial force is compensated (or 'balanced') with an electrically generated force so that the seismic mass moves as little as possible; of course some small motion is still required because otherwise the inertial force could not be observed. The feedback force is generated with an electromagnetic force transducer or 'forcer' (Fig. 5.14). The electronic circuit (Fig. 5.16) is a servo loop, as in an analog chart recorder.

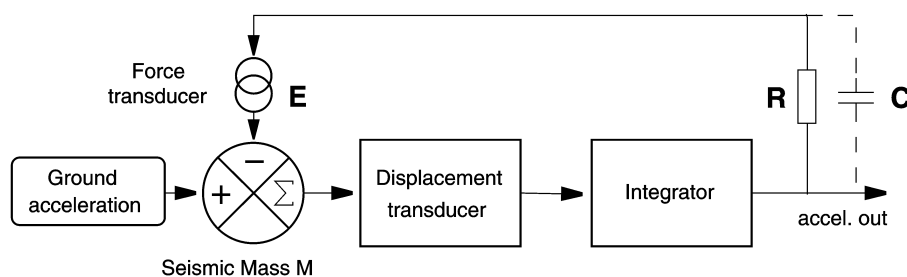


Fig. 5.16 Feedback circuit of a force-balance accelerometer (FBA). The motion of the mass is controlled by the sum of two forces: the inertial force due to ground acceleration, and the negative feedback force. The electronic circuit adjusts the feedback force so that the forces very nearly cancel each other.

A servo loop is most effective when it contains an integrator, in which case the offset of the mass is exactly nulled in the time average (in a chart recorder, the difference between the input signal and a voltage indicating the pen position, is nulled). Due to unavoidable delays in the feedback loop, force-balance systems have a limited bandwidth; however, at frequencies where they are effective, they force the mass to move with the ground by generating a feedback force strictly proportional to ground acceleration. When the force is proportional to the current in the transducer, then the current, the voltage across the feedback resistor R , and the output voltage are all proportional to ground acceleration. Thus we have converted the acceleration into an electric signal without depending on the precision of a mechanical suspension.

The response of a force-balance system is approximately inverse to the gain of the feedback path. It can be easily modified by giving the feedback path a frequency-dependent gain. For example, if we make the capacitor C large so that it determines the feedback current, then the gain of the feedback path increases linearly with frequency and we have a system whose responsivity to acceleration is inverse to frequency and thus flat to velocity over a certain pass-band. We will look more closely at this option in section 5.4.3.

5.4.2 Force-balance accelerometers

Fig. 5.16 without the capacitor C represents the circuit of a force-balance accelerometer (FBA), a device that is widely used for earthquake strong-motion recording, for measuring tilt, and for inertial navigation. By equating the inertial and the electromagnetic force, it is easily seen that the responsivity (the output voltage per ground acceleration) is

$$U_{out} / \ddot{x} = MR / E \quad (5.37)$$

where M is the seismic mass, R the total resistance of the feedback path, and E the responsivity of the forcer (in N/A). The conversion is determined by only three passive components of which the mass is error-free by definition (it defines the inertial reference), the resistor is a nearly ideal component, and the force transducer very precise because the motion is small. Some accelerometers do not have a built-in feedback resistor; the user can insert a resistor of his own choice and thus select the gain. The responsivity in terms of current per acceleration is simply $I_{out} / \ddot{x} = M / E$.

FBA's work down to zero frequency but the servo loop becomes ineffective at some upper corner frequency f_0 (usually a few hundred to a few thousand Hz), above which the arrangement acts like an ordinary inertial displacement sensor. The feedback loop behaves like an additional stiff spring; the response of the FBA sensor corresponds to that of a mechanical pendulum with the eigenfrequency f_0 , as is schematically represented in the left panels of Fig. 5.6.

5.4.3 Velocity broadband seismometers

For broadband seismic recording with high sensitivity, an output signal proportional to ground acceleration is unfavorable. At high frequencies, sensitive accelerometers are easily saturated by traffic noise or impulsive disturbances. At low frequencies, a system with a response flat to acceleration generates a permanent voltage at the output as soon as the suspen-

5. Seismic Sensors and their Calibration

sion is not completely balanced. The system would soon be saturated by the offset voltage resulting from thermal drift or tilt. What we need is a band-pass response in terms of acceleration, or equivalently a high-pass response in terms of ground velocity, like that of a normal electromagnetic seismometer (geophone, right panels in Fig. 5.6) but with a lower corner frequency.

The desired velocity broadband (VBB) response is obtained from the FBA circuit by adding paths for differential feedback and integral feedback (Fig. 5.17). A large capacitor C is chosen so that the differential feedback dominates throughout the desired passband. While the feedback current is still proportional to ground acceleration as before, the voltage across the capacitor C is a time integral of the current, and thus proportional to ground velocity. This voltage serves as the output signal. The output voltage per ground velocity, i.e. the apparent generator constant E_{app} of the feedback seismometer, is

$$E_{app} = V_{out} / \dot{x} = M / EC . \quad (5.38)$$

Again the response is essentially determined by three passive components. Although a capacitor with a solid dielectric is not quite as ideal a component as a good resistor, the response is still linear and very stable.

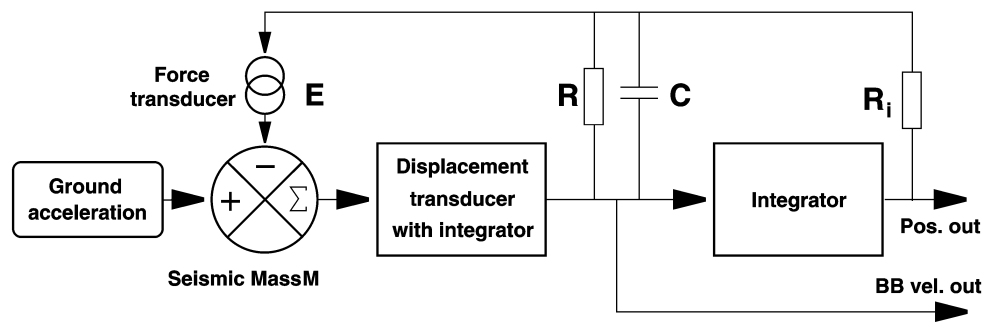


Fig. 5.17 Feedback circuit of a VBB (velocity-broadband) seismometer. As in Figure 5.16, the seismic mass is the summing point of the inertial force and the negative feedback force.

The output signal of the second integrator is normally accessible at the „mass position“ output. It does not indicate the actual position of the mass but indicates where the mass would go if the feedback were switched off. „Centering“ the mass of a feedback seismometer has the effect of discharging the integrator so that its full operating range is available for the seismic signal. The mass-position output is not normally used for seismic recording but is useful as a state-of-health diagnostic, and is used in some calibration procedures.

The relative strength of the integral feedback increases at lower frequencies while that of the differential feedback decreases. These two components of the feedback force are of opposite phase ($-\pi/2$ and $\pi/2$ relative to the output signal, respectively). At certain low frequency, the two contributions are of equal strength and cancel each other out. This is the lower corner frequency of the closed-loop system. Since the closed-loop response is inverse to that of the feedback path, one would expect to see a resonance in the closed-loop response at this frequency. However, the proportional feedback remains and damps the resonance; the resistor R acts as a damping resistor. At lower frequencies, the integral feedback dominates over the differential feedback, and the closed-loop response to ground velocity decreases with the

square of the frequency. As a result, the feedback system behaves like a conventional electromagnetic seismometer and can be described by the usual three parameters: free period, damping, and generator constant. In fact, electronic broadband seismometers, even if their actual electronic circuit is more complicated than presented here, follow the simple theoretical response of electromagnetic seismometers more closely than those ever did.

As far as the response is concerned, a force-balance circuit as described here may be seen as a means to convert a moderately stable short- to medium-period suspension into a stable electronic long-period or very-long-period seismometer. The corner period may be increased by a large factor, for example 24-fold (from 5 to 120 sec) in the STS2 seismometer or even 200-fold (from 0.6 to 120 sec) in a version of the CMG3. But this factor says little about the performance of the system. Feedback does not reduce the instrumental noise; a large extension of the bandwidth is useless when the system is noisy. According to Eq. (5.34), short-period suspensions must be combined with extremely sensitive transducers for a satisfactory sensitivity at long periods.

At some high frequency, the loop gain falls below unity. This is the upper corner frequency of the feedback system which marks the transition between a response flat to velocity and one flat to displacement. A well-defined and nearly ideal behavior of the seismometer, as at the lower corner frequency, should not be expected here both because the feedback becomes ineffective and because most suspensions have parasitic resonances slightly above the electrical corner frequency (otherwise they could have been designed for a larger bandwidth). The detailed response at the high-frequency corner, however, rarely matters since the upper corner frequency is usually outside the passband of the recorder. Its effect on the transfer function in most cases can be modeled as a small, constant delay (a few milliseconds) over the whole VBB passband.

5.4.4 Other methods of bandwidth extension

The force-balance principle permits the construction of high-performance, broadband seismic sensors but is not easily applicable to geophone-type sensors because fitting a displacement transducer to these is difficult. Sometimes it is desirable to broaden the response of an existing geophone without a mechanical redesign.

The simplest solution is to send the output signal of the geophone through a filter that removes its original response (this is called an inverse filtration) and replaces it by some other desired response, preferably that of a geophone with a lower eigenfrequency. The analog, electronic version of this process would only be used in connection with direct visible recording; for all other purposes, one would implement the filtration digitally as part of the data processing. Suitable filter algorithms are contained in seismic software packages, as listed in 5.9.

Alternatively, the bandwidth of a geophone may be enlarged by strong damping. This does not enhance the gain outside the passband but rather reduces it inside the passband; nevertheless, after appropriate amplification, the net effect is an extension of the bandwidth towards longer periods. Strong damping is obtained by connecting the coil to a preamplifier whose input impedance is negative. The total damping resistance, which is otherwise limited by the resistance of the coil (Eq. (5.36)), can then be made arbitrarily small. The response of the over-damped geophone is flat to acceleration around its free period. It can be made flat to

5. Seismic Sensors and their Calibration

velocity by an approximate (band-limited) integration. This technique is used in the Lennartz Le-1d and Le-3d seismometers (see DS 5.1) whose electronic corner period can be up to 40 times larger than the mechanical one. Although these are not strictly force-balance sensors, they take advantage of the fact that active damping (which is a form of negative feedback) greatly reduces the relative motion of the mass.

5.5 Seismic noise, site selection and installation

Electronic seismographs can be designed for any desired magnification of the ground motion. A practical limit, however, is imposed by the presence of undesired signals which must not be magnified so strongly as to obscure the record. Such signals are usually referred to as noise and may be of seismic, instrumental, or environmental origin. Seismic noise is treated in Chapter 4. Instrumental self-noise may have mechanical and electronic sources and will be discussed in the next section. Here we focus on those general aspects of site selection and of seismometer installation aimed at the reduction of environmental noise. For technical details on site selection as well as vault, tunnel and borehole installations see Chapter 7.

5.5.1 The USGS low-noise model

The USGS low-noise model (see Peterson, 1993, Fig. 5.18) is a graphical and numerical representation of the lowest vertical seismic noise levels observed worldwide, and is extremely useful as a reference for the quality of a site or of an instrument. Its origin and properties are discussed in Chapter 4.

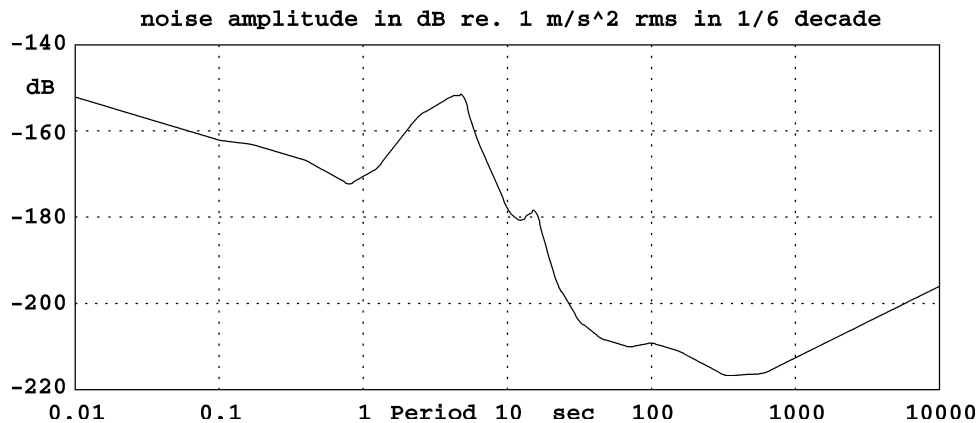


Fig. 5.18 The USGS New Low Noise Model (NLNM), here expressed as RMS amplitude of ground acceleration in a constant relative bandwidth of one-sixth decade.

5.5.2 Site selection

Site selection for a permanent station is always a compromise between two conflicting requirements: infrastructure and low seismic noise. The noise level depends on the geological situation and on the proximity of sources, some of which are usually associated with the infrastructure. A seismograph installed on solid basement rock can be expected to be fairly insensitive to local disturbances while one sitting on a thick layer of soft sediments will be noisy

even in the absence of identifiable sources. As a rule, the distance from potential sources of noise, such as roads and inhabited houses, should be very much larger than the thickness of the sediment layer. Broadband seismographs can be successfully operated in major cities when the geology is favourable; in unfavourable situations, such as in sedimentary basins, only deep mines (4.3.2 and 7.4.3) and boreholes (7.4.5) may offer acceptable noise levels.

Obviously, most sites have a noise level above the Low Noise Model, some of them by a large factor. This factor, however, is not uniform over time or over the seismic frequency band. At short periods (< 2 s), a noise level within a factor of 10 of the NLNM may be considered very good in most areas. Short-period noise at most sites is predominantly man-made and somewhat larger in the horizontal components than in the vertical. At intermediate periods (2 to 20 s), marine microseisms dominate. They have similar amplitudes in the horizontal and vertical directions and have large seasonal variations. In winter they may be 50 dB above the NLNM. At longer periods, the vertical ground noise is often within 10 or 20 dB of the NLNM even at otherwise noisy stations. The horizontal long-period noise may nevertheless be horrible at the same station due to tilt-gravity coupling (see 5.3.3). It may be larger than vertical noise by a factor of up to 300, the factor increasing with period. Therefore, a site can be considered as favourable when the horizontal noise at 100 to 300 sec is within 20 dB (i.e., a factor of 10 in amplitude) above the vertical noise. Tilt may be caused by traffic, wind, or local fluctuations of the barometric pressure. Large tilt noise is sometimes observed on concrete floors when an unventilated cavity exists underneath; the floor then acts like a membrane. Such noise can be identified by its linear polarization and its correlation with the barometric pressure. Even on an apparently solid foundation, the long-period noise often correlates with the barometric pressure (see Beauduin et al., 1996). If the situation can not be remedied otherwise, the barometric pressure should be recorded with the seismic signal and used for a correction. An example is shown in Fig. 2.21. For very-broadband seismographic stations, barometric recording is generally recommended.

Besides ground noise, environmental conditions must be considered. An aggressive atmosphere may cause corrosion, wind and short-term variations of temperature may induce noise, and seasonal variations of temperature may exceed the manufacturer's specifications for unattended operation. Seismometers must be protected against these conditions, sometimes by hermetic containers as described in the next subsection. As a precaution, cellars and vaults should be checked for signs of flooding.

5.5.3 Seismometer installation

We will briefly describe the installation of a portable broadband seismometer inside a building, vault, or cave. First, we mark the orientation of the sensor on the floor. This is best done with a geodetic gyroscope, but a magnetic compass will do in most cases. The magnetic declination must be taken into account. Since a compass may be deflected inside a building, the direction should be taken outside and transferred to the site of installation. A laser pointer may be useful for this purpose. When the magnetic declination is unknown or unpredictable (such as at high latitudes or in volcanic areas), the orientation should be determined with a sun compass.

To isolate the seismometer from stray currents, small glass or perspex plates should be cemented to the ground under its feet. Then the seismometer is installed, tested, and wrapped with a thick layer of thermally insulating material. The type of material does not matter very

5. Seismic Sensors and their Calibration

much; alternate layers of fibrous material and heat-reflecting blankets are probably most effective. The edges of the blankets should be taped to the floor around the seismometer.

Electronic seismometers produce heat and may induce convection in any open space inside the insulation; it is therefore important that the insulation has no gap and fits the seismometer tightly. Another method of insulation is to surround the seismometer with a large box which is then filled with fine styrofoam seeds. For a permanent installation under unfavourable environmental conditions, the seismometer should be enclosed in a hermetic container. A problem with such containers (as with all seismometer housings), however, is that they cause tilt noise when they are deformed by the barometric pressure. Essentially three precautions are possible: (1) either the base-plate is carefully cemented to the floor, or (2) it is made so massive that its deformation is negligible, or (3) a “warp-free” design is used, as described by Holcomb and Hutt (1992) for the STS1 seismometers (see DS 5.1). Also, some fresh desiccant (silicagel) should be placed inside the container, even into the vacuum bell of STS1 seismometers. Fig. 5.19 illustrates the shielding of the STS2 seismometers (see DS 5.1) in the German Regional Seismic Network (GRSN).

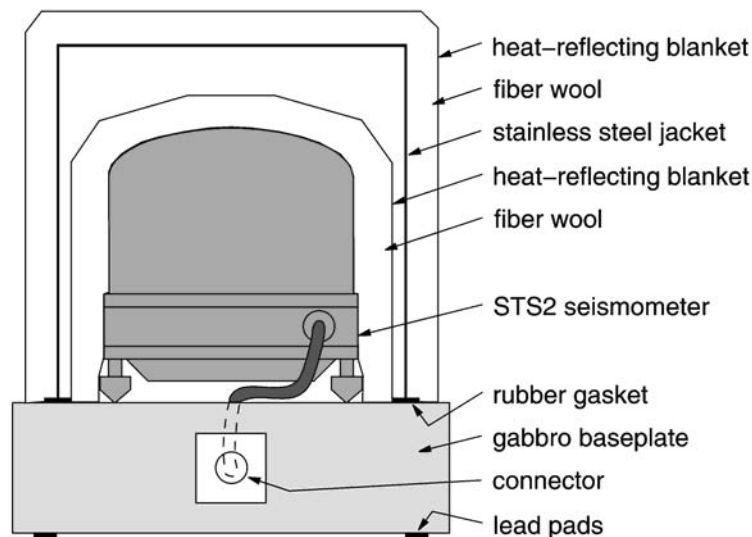


Fig. 5.19 The STS2 seismometer of the GRSN inside its shields.

Installation procedures for broadband seismometers are proposed in sub-Chapter 7.4 as well as on the web sites of the GeoForschungsZentrum Potsdam under <http://www.gfz-potsdam.de/geofon/index.html> (click on How to get a well-performing VBB Station?) and of the Seismological Lab, University of California at Berkeley: <http://www.seismo.berkeley.edu/seismo/bdsn/instrumentation/guidelines.html>.

5.5.4 Magnetic shielding

Broadband seismometers are to some degree sensitive to magnetic fields since all thermally compensated spring materials are slightly magnetic. This may be noticeable when the seismometers are operated in industrial areas or in the vicinity of dc-powered railway lines. Magnetic interferences are definitely suspect when the long-period noise follows a regular time table. Shields can be manufactured from permalloy (μ metal) but they are expensive and of

limited efficiency. An active compensation is often preferable. It may consist of a three-component fluxgate magnetometer that senses the field near the seismometer, an electronic driver circuit in which the signal is integrated with a short time constant (a few milliseconds), and a three-component set of Helmholtz coils which compensate changes of the magnetic field. The permanent geomagnetic field should not be compensated; the resulting offsets of the fluxgate outputs can be compensated electrically before the integration, or with a small permanent magnet mounted near the fluxgate.

5.6 Instrumental self-noise

All modern seismographs use semiconductor amplifiers which, like other active (power-dissipating) electronic components, produce continuous electronic noise whose origin is manifold but ultimately related to the quantisation of the electric charge. Electromagnetic transducers, such as those used in geophones, also produce thermal electronic noise (resistor noise). The contributions from semiconductor noise and resistor noise are often comparable, and together limit the sensitivity of the system. Another source of continuous noise, the Brownian (thermal) motion of the seismic mass, may be noticeable when the mass is very small (less than a few grams). Presently, however, manufactured seismometers have sufficient mass to make the Brownian noise negligible against electronic noise and we will therefore not discuss it here. Seismographs may also suffer from transient disturbances originating in slightly defective semiconductors or in the mechanical parts of the seismometer when subject to stresses. The present section is mainly concerned with identifying and measuring instrumental noise.

5.6.1 Electromagnetic short-period seismographs

Electromagnetic seismometers and geophones are passive sensors whose self-noise is of purely thermal origin and does not increase at low frequencies as it does in active (power-dissipating) devices. Their output signal level, however, is comparatively low, so a low-noise preamplifier must be inserted between the geophone and the recorder (Fig. 5.20). Unfortunately the noise of the preamplifier does increase at low frequencies and limits the overall sensitivity. We will call this combination an electromagnetic short-period seismograph or , EMS for short. It is now rarely used for long-period or broadband recording because of the superior performance of feedback instruments.

The sensitivity of an EMS is normally limited by amplifier noise (see Fig. 5.20). However, this noise does not depend on the amplifier alone but also on the impedance of the electromagnetic transducer (which can be chosen within wide limits). Up to a certain impedance the amplifier noise voltage is nearly constant, but then it increases linearly with the impedance, due to a noise current flowing out of the amplifier input. On the other hand, the signal voltage increases with the square root of the impedance. The best signal-to-noise ratio is therefore obtained with an optimum source impedance defined by the corner between voltage and current noise, which is different for each type of amplifier and also depends on frequency. Vice versa, when the transducer is given, the amplifier must be selected for low noise at the relevant impedance and frequency.

5. Seismic Sensors and their Calibration

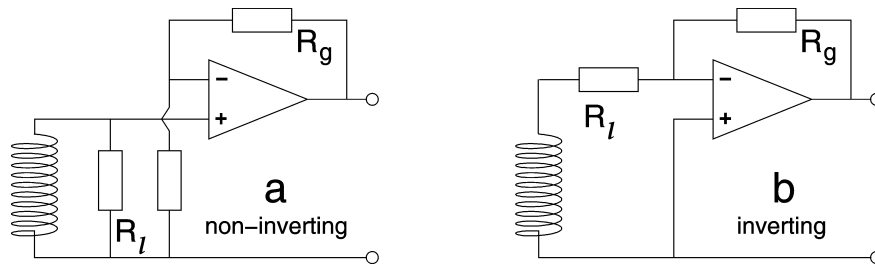


Fig. 5.20 Two alternative circuits for an EMS preamplifier with a low-noise op-amp. The non-inverting circuit is generally preferable when the damping resistor R_1 is much larger than the coil resistance and the inverting circuit when it is comparable or smaller. However, the relative performance also depends on the noise specifications of the op-amp. The gain is adjusted with R_g .

The electronic noise of an EMS can be predicted when the technical data of the sensor and the amplifier are known. Semiconductor noise increases at low frequencies; amplifier specifications must apply to seismic rather than audio frequencies. In combination with a given sensor, the noise can then be expressed as an equivalent seismic noise level and compared to real seismic signals or to the NLNM (Fig. 5.18). As an example, Fig. 5.21 shows the self-noise of one of the better seismometer-amplifier combinations. It resolves minimum ground noise between 0.1 and 10 s period. Discussions and more examples are found in Riedesel et al. (1990) and in Rodgers (1992, 1993 and 1994). The result is easily summarized:

Most well-designed seismometer-amplifier combinations resolve minimum ground noise up to 6 or 8 s period, that is, to the microseismic peak. A few of them may make it to about 15 s; they marginally resolve the secondary microseismic peak. To resolve minimum ground noise up to 30 s is hopeless, as is obvious from Fig. 5.21. Ground noise falls and electronic noise rises so rapidly beyond a period of 20 s that the cross-over point can not be substantially moved towards longer periods. Of course, at a reduced level of sensitivity, restoring long-period signals from short-period sensors may make sense, and the long-period surface waves of sufficiently large earthquakes may well be recorded with short-period electromagnetic seismometers.

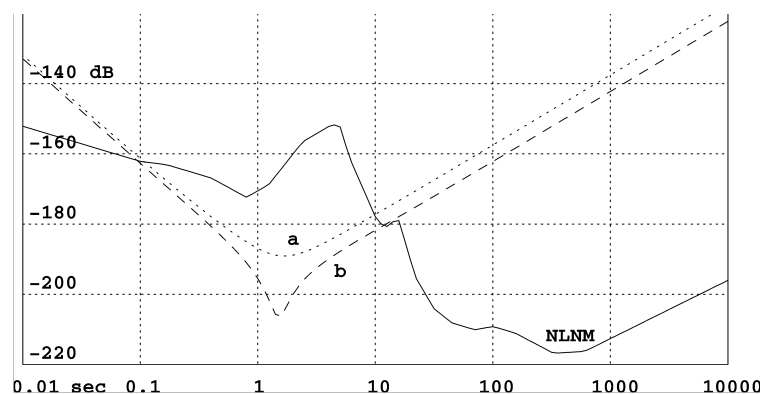


Fig. 5.21 Electronic self-noise of the input stage of a short-period seismograph. The EMS is a Sensonics Mk3 with two 8 kOhm coils in series and tuned to a free period of 1.5 s. The amplifier is the LT1012 op-amp. The curves a and b refer to the circuits of Fig. 5.20. NLNM is the USGS New Low Noise Model (Fig. 5.18). The ordinate gives rms noise amplitudes in dB relative to 1 m/s^2 in $1/6$ decade.

Amplifier noise can be observed by locking the sensor or tilting it until the mass is firmly at a stop, or by substituting it with an ohmic resistor that has the same resistance as the coil. If these manipulations do not significantly reduce the noise, then obviously the seismograph does not resolve seismic noise. However, this is only a test, not a way to precisely measure the electronic self-noise. A locked sensor or a resistor do not exactly represent the electric impedance of the unlocked sensor.

5.6.2 Force-balance seismometers

Force-balance sensors can not be tested for instrumental noise with the mass locked. Their self-noise can thus only be observed in the presence of seismic signals and seismic noise. Although seismic noise is generally a nuisance in this context, natural signals may also be useful as test signals. Marine microseisms should be visible on any sensitive seismograph whose seismometer has a free period of one second or longer; they normally form the strongest continuous signal on a broadband seismograph. However, their amplitude exhibits large seasonal and geographical variations.

For broadband seismographs at quiet sites, the tides of the solid Earth are a reliable and predictable test signal. They have a predominant period of slightly less than 12 hours and an amplitude in the order of 10^{-6} m/s². While normally invisible in the raw data, they may be extracted by low-pass filtration with a corner frequency of about 1 mHz. For this purpose it is helpful to have the original data available with a sampling rate of 1 per second or less. By comparison with the predicted tides, the gain and polarity of the seismograph may be checked. A seismic broadband station that records Earth's tides is likely to be up to international standards.

For a quantitative determination of the instrumental noise, two instruments must be operated side by side (see Holcomb, 1989; Holcomb, 1990). One can then determine the coherency between the two records and assume that coherent noise is seismic and incoherent noise is instrumental. This works well if the reference instrument is known to be a good one, but the method is not safe. The two instruments may respond coherently to environmental disturbances caused by barometric pressure, temperature, the supply voltage, magnetic fields, vibrations, or electromagnetic waves. Nonlinear behaviour (intermodulation) may produce coherent but spurious long-period signals. When no good reference instrument is available, the test should be done with two sensors of a different type, in the hope that they will not respond in the same way to non-seismic disturbances.

The analysis for coherency is somewhat tricky in detail. When the transfer functions of both instruments are precisely known, it is in fact theoretically possible to measure the seismic signal and the instrumental noise of each instrument separately as a function of frequency. Alternatively, one may assume that the transfer functions are not so well known but the reference instrument is noise-free; in this case the noise and the relative transfer function of the other instrument can be determined. As with all statistical methods, long time series are required for reliable results. We offer a computer program UNICROSP (see 5.9) for the analysis.

5.6.3 Transient disturbances

Most new seismometers produce spontaneous transient disturbances, i.e., quasi miniature earthquakes caused by stresses in the mechanical components. Although they do not necessarily originate in the spring, their waveform at the output seems to indicate a sudden and permanent (step-like) change in the spring force. Long-period seismic records are sometimes severely degraded by such disturbances. The transients often die out within months or years; if they do not, and especially when their frequency increases, corrosion must be suspected. Manufacturers try to mitigate the problem with a low-stress design and by aging the components or the finished seismometer (by extended storage, vibrations, or heating and cooling cycles). It is sometimes possible to virtually eliminate transient disturbances by hitting the pier around the seismometer with a hammer, a procedure that is recommended in each new installation.

5.7 Calibration

5.7.1 Electrical and mechanical calibration

The calibration of a seismograph establishes knowledge of the relationship between its input (the ground motion) and its output (an electric signal), and is a prerequisite for a reconstruction of the ground motion. Since precisely known ground motions are difficult to generate, one makes use of the equivalence between ground accelerations and external forces on the seismic mass (Eq. (5.25)), and calibrates seismometers with an electromagnetic force generated in a calibration coil. If the factor of proportionality between the current in the coil and the equivalent ground acceleration is known, then the calibration is a purely electrical measurement. Otherwise, the missing parameter - either the transducer constant of the calibration coil, or the responsivity of the sensor itself - must be determined from a mechanical experiment in which the seismometer is subject to a known mechanical motion or a tilt. This is called an absolute calibration. Since it is difficult to generate precise mechanical calibration signals over a large bandwidth, one does not attempt normally to determine the complete transfer function in this way.

The present section is mainly concerned with the electrical calibration although the same methods may also be used for the mechanical calibration on a shake table (see 5.8.1). Specific procedures for the mechanical calibration without a shake table are presented in 5.8.2 and 5.8.3.

5.7.2 General conditions

Calibration experiments are disturbed by seismic noise and tilt and should therefore be carried out in a basement room. However, the large operating range of modern seismometers permits a calibration with relatively large signal amplitudes, making background noise less of a problem than one might expect. Thermal drift is more serious because it interferes with the long-period response of broadband seismometers. For a calibration at long periods, seismometers must be protected from draft and allowed sufficient time to reach thermal equilibrium. Visible and digital recording in parallel is recommended. Recorders themselves must be absolutely calibrated before they can serve to calibrate seismometers. The input impedance of recorders

as well as the source impedance of sensors should be measured so that a correction can be applied for the loss of signal in the source impedance.

5.7.3 Calibration of geophones

Some simple electrodynamic seismometers (geophones) have no calibration coil. The calibration current must then be sent through the signal coil. There it produces an ohmic voltage in addition to the output signal generated by the motion of the mass. The undesired voltage can be compensated in a bridge circuit (see Willmore, 1959); the bridge is zeroed with the seismic mass locked or at a stop. When the calibration current and the output voltage are digitally recorded, it is more convenient to use only a half-bridge (Fig. 5.22) and to compensate the ohmic voltage numerically. The program CALEX (see 5.9.2) has provisions to do this automatically.

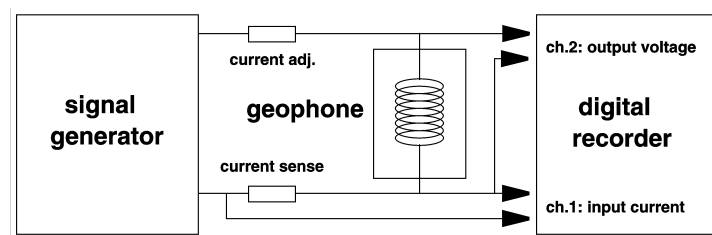


Fig. 5.22 Half-bridge circuit for calibrating electromagnetic seismometers

An alternative method has been proposed by Rodgers et al. (1995). A known direct current through the signal coil is interrupted and the resulting transient response of the seismometer recorded. The generator constant is then determined from the amplitude of the pulse.

Electrodynamic seismometers whose seismic mass moves along a straight line require no mechanical calibration when the size of the mass is known. The electromagnetic part of the numerical damping is inversely proportional to the total damping resistance (Eq.(5.36)); the factor of proportionality is $E^2 / 2M\omega_0$, so the generator constant E can be calculated from electrical calibrations with different resistive loads (Fig. 5.23).

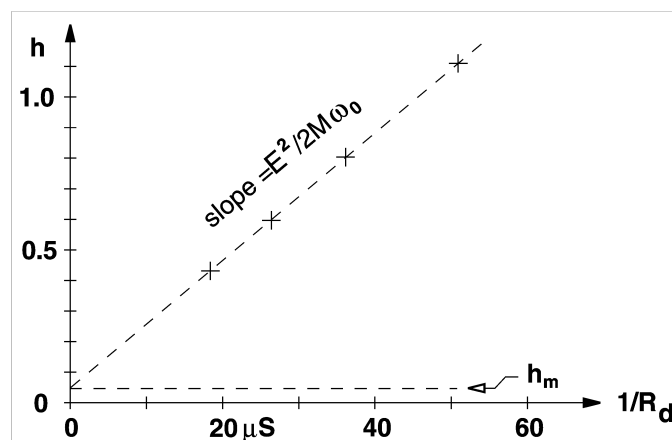


Fig. 5.23 Determining the generator constant from a plot of damping versus total damping resistance $R_d = R_{\text{coil}} + R_{\text{load}}$. The horizontal units are microsiemens (reciprocal Megohms).

5.7.4 Calibration with sinewaves

With a sinusoidal input, the output of a linear system is also sinusoidal, and the ratio of the two signal amplitudes is the absolute value of the transfer function. An experiment with sine-waves therefore permits an immediate check of the transfer function, without any a-priori knowledge of its mathematical form and without waveform modeling. This is often the first step in the identification of an unknown system (see EX 5.3 and 5.4). A computer program, however, would be required for deriving a parametric representation of the response from the measured values. A calibration with arbitrary signals, as described later, is more straightforward for this purpose.

When only analog equipment is available, the calibration coil or the shake table should be driven with a sinusoidal test signal and the input and output signals recorded with a chart recorder or an X-Y recorder. On the latter, the signals can be plotted as a Lissajous ellipse (Fig. 5.24) from which both the amplitude ratio and the phase can be read with good accuracy (see Mitronovas and Wielandt, 1975). For the calibration of high-frequency geophones, an oscilloscope may be used in place of an X-Y-recorder. The signal period should be measured with a counter or a stop watch because the frequency scale of sine-wave generators is often inaccurate.

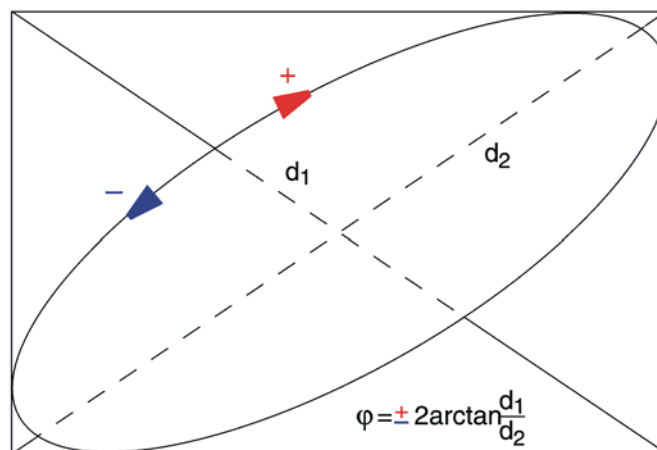


Fig. 5.24 Measuring the phase between two sine-waves with a Lissajous ellipse.

The accuracy of the graphic evaluation depends on the purity of the sine-wave. A better accuracy, of course, can be obtained with a numerical analysis of digitally recorded data. By fitting sine-waves to the signals, amplitudes and phases can be extracted for just one precisely known frequency at a time; distortions of the input signal don't matter. For best results, the frequency should be fitted as well, the fit should be computed for an integer number of cycles, and offsets should be removed from the data. A computer program „SINFIT" is offered for this purpose (see 5.9).

Eigenfrequency f_0 and damping h of electromagnetic and most other seismometers can be determined graphically with a set of standard resonance curves on double-logarithmic paper. (an empty sheet of such paper is contained in EX 5.1). The measured amplitude ratios are plotted as a function of frequency f on the same type of paper and overlain with the standard curves (Fig. 5.25). The desired quantities can be read directly. The method is simple but not very precise.

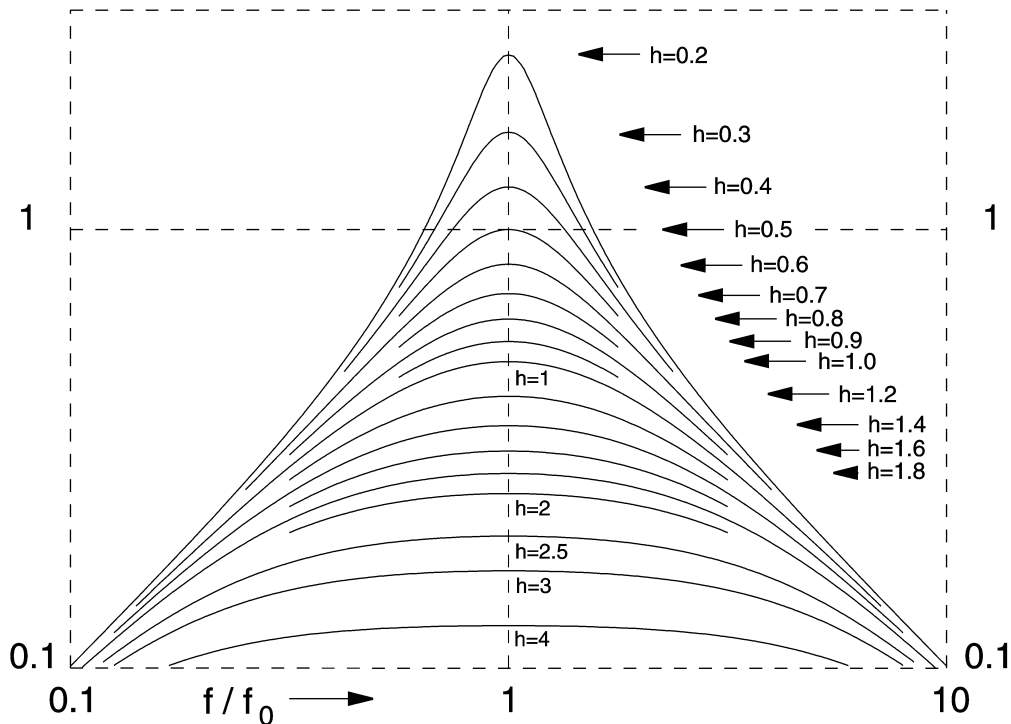


Fig. 5.25 Normalized resonance curves.

5.7.5 Step response and weight-lift test

The simplest, but only moderately accurate, calibration method is to observe the response of the system to a step input. It can be generated by switching on or off a current through the calibration coil, or by applying or removing a constant mechanical force on the seismic mass, usually by lifting a weight. Horizontal sensors used to be calibrated with a V-shaped thread attached to the mass at one end, to a fixed point at the other end, and to the test weight at half length. The thread was then burned off for a soft release.

The step-response experiment can be used both for a relative and an absolute calibration; when applicable, it is probably the simplest method for the latter. Using a known test weight w and knowing the seismic mass M , we also know the test signal: it is a step in acceleration whose magnitude is w/M times gravity (times a geometry factor when the force is applied through a thread). In case of a rotational pendulum, a correction factor must be applied when the force does not act at the center of gravity. The method has lost its former importance because the seismic mass of modern seismometers is not easily accessible, and the correction factor for rotational motion is rarely supplied by the manufacturers.

Interestingly, in the case of a simple electromagnetic seismometer with linear motion and a known mass, not even a calibration coil or the insertion of a test mass are required for an absolute calibration. A simple experiment where a step current is sent through the signal coil of the undamped sensor can supply all parameters of interest: the generator constant E , the free period, and the mechanical damping. The method is described in Chapter 4 of the old MSOP (see Willmore, 1979) and in EX 5.2. An alternative method is proposed in section 5.7.3.

5. Seismic Sensors and their Calibration

In the context of relative calibration, the step-response method is still useful as a quick and intuitive test, and has the advantage that it can be evaluated by hand. Software like PREPROC or CALEX covers the step response as well (see 5.9). Fig. 5.26 shows the characteristic step responses of second-order high-pass, band-pass, and low-pass filters with $1/\sqrt{2}$ of critical damping. The amplitude responses of these systems were shown in the left column of Fig. 5.6.

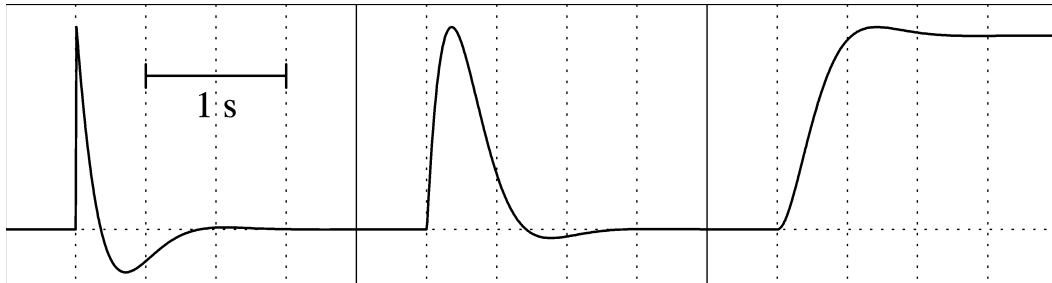


Fig. 5.26 Normalized step responses of second-order high-pass, band-pass and low-pass filters. The respective transfer functions are the same as in Fig. 5.6, left column. Compare also Fig. 5.4 which shows slightly smoothed impulse responses.

Each response is a strongly damped oscillation around its asymptotic value. With the specified damping, the systems are Butterworth filters, and the amplitude decays to $e^{-\pi}$ or 4.3% within one half-wave. The ratio of two subsequent amplitudes of opposite polarity is known as the overshoot ratio. It can be evaluated for the numerical damping h : when x_i and x_{i+n} are two (peak-to-peak) amplitudes n periods apart, with integer or half-integer n , then

$$\frac{1}{h^2} = 1 + \left(\frac{2\pi n}{\ln x_i - \ln x_{i+n}} \right)^2 \quad (5.39)$$

The free period, in principle, can also be determined from the impulse or step response of the damped system but should be measured preferably without electrical damping so that more oscillations can be observed. A system with the free period T_0 and damping h oscillates with the period $T_0/\sqrt{1-h^2}$ and the overshoot ratio $\exp(-\pi h/\sqrt{1-h^2})$. The determination of seismometer parameters from the step response is also explained in EX 5.2.

5.7.6 Calibration with arbitrary signals

In most cases, the purpose of calibration is to obtain the parameters of an analytic representation of the transfer function. Assuming that its mathematical form is known, the task is to determine its parameters from an experiment in which both the input and the output signals are known. Since only a signal that has been digitally recorded is known with some accuracy, both the input and the output signal should be recorded with a digital recorder. As compared to other methods where a predetermined input signal is used and only the output signal is recorded, recording both signals has the additional advantage of eliminating the transfer function of the recorder from the analysis.

Calibration is a classical inverse problem that can be solved with standard least-squares methods. The general solution is schematically depicted in Fig. 5.27. A computer algorithm (filter 1) is implemented that represents the seismometer as a filter and permits the computation of its response to an arbitrary input. An inversion scheme (3) is programmed around the filter algorithm in order to find best-fitting filter parameters for a given pair of input and output signals. The purpose of filter 2 is explained below. The sensor is then calibrated with a test signal (4) for which the response of the system is sensitive to the unknown parameters but which is otherwise arbitrary. When the system is linear, parameters determined from one test signal will also predict the response to any other signal.

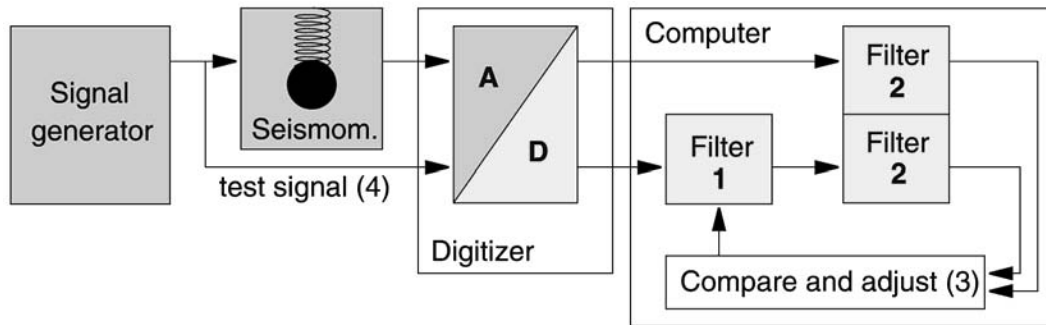


Fig. 5.27 Block diagram of the CALEX procedure. Storage and retrieval of the data are omitted from the figure.

When the transfer function has been correctly parameterized and the inversion has converged, then the residual error consists mainly of noise, drift, and nonlinear distortions. At a signal level of about one-third of the operating range, typical residuals are 0.03% to 0.05% rms for force-balance seismometers and $\geq 1\%$ for passive electrodynamic sensors.

The approximation of a rational transfer function with a discrete filtering algorithm is not trivial. For the program CALEX (see 5.9) we have chosen an impulse-invariant recursive filter (see Schuessler, 1981). This method formally requires that the seismometer has a negligible response at frequencies outside the Nyquist bandwidth (see 5.2.3) of the recorder, a condition that is severely violated by most digital seismographs; but this problem can be circumvented with an additional digital low-pass filtration (filter 2 in Fig. 5.27) that limits the bandwidth of the simulated system. Signals from a typical calibration experiment are shown in Fig. 5.28. A sweep as a test signal permits the residual error to be visualized as a function of time or frequency; since essentially only one frequency is present at a time, the time axis may as well be interpreted as a frequency axis. An exercise with the CALEX program is contained in EX 5.4.

With an appropriate choice of the test signal, other methods like the calibration with sine-waves step functions, random noise or random telegraph signals, can be duplicated and compared to each other. An advantage of the CALEX algorithm is that it makes no use of special properties of the test signal, such as being sinusoidal, periodic, step-like or random. Therefore, test signals can be short (a few times the free period of the seismometer) and can be generated with the most primitive means, even by hand (you may turn the dial of a sinewave generator by hand, or even produce the test signal with a battery and a potentiometer). A breakout box or a special cable, however, may be required for feeding the calibration signal into the digital recorder.

5. Seismic Sensors and their Calibration

Some other routines for seismograph calibration and system identification are contained in the PREPROC software package (see Plešinger et al., 1996). An overview of identification software which has also been made publicly available on the Internet is given by Plešinger (1998).

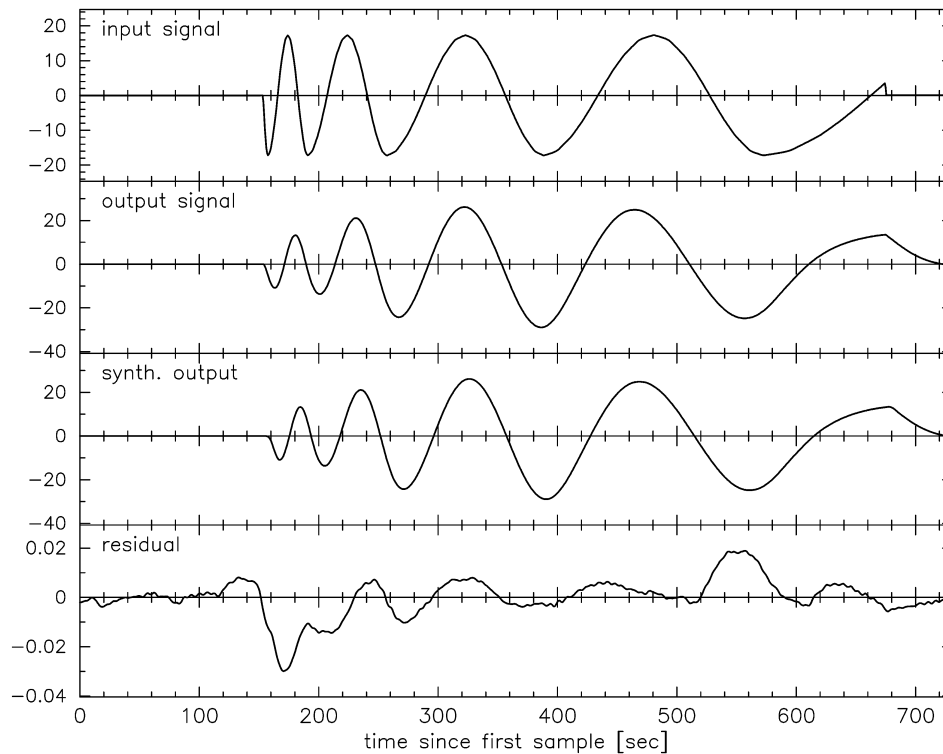


Fig. 5.28 Electrical calibration of an STS2 seismometer with CALEX. Traces from top to bottom: input signal (a sweep with a total duration of 10 min); observed output signal; modeled output signal; residual. The rms residual is 0.05 % of the rms output.

5.7.7 Calibration of triaxial seismometers

In a triaxial seismometer such as the Streckeisen STS2 (Fig. 5.13), transfer functions in a strict sense can only be attributed to the individual U,V,W sensors, not to the X,Y,Z outputs. Formally, the response of a triaxial seismometer to arbitrary ground motions is described by a nearly diagonal 3 x 3 matrix of transfer functions relating the X,Y,Z output signals to the X,Y,Z ground motions. (This is also true for conventional three-component sets if they are not perfectly aligned; only the composition of the matrix is slightly different.) If the U,V,W sensors are reasonably well matched, the effective transfer functions of the X,Y,Z channels have the traditional form and their parameters are weighted averages of those of the U,V,W sensors. The X,Y,Z outputs, therefore, can be calibrated as usual. For the simulation of horizontal and vertical ground accelerations via the calibration coils, each sensor must receive an appropriate portion of the calibration current. For the vertical component, this is approximately accomplished by connecting the three calibration coils in parallel. For the horizontal components and also for a more precise excitation of the vertical, the calibration current or voltage must be split into three individually adjustable and invertible U,V,W components. These are then adjusted so that the test signal appears only at the desired output of the seismometer.

It is also possible to calibrate the U, V, and W sensors separately - the Z output may be used for this purpose - and then to average the U, V, W transfer functions or parameters with a matrix whose elements are the squares of those of the matrix in Eq. (5.35):

$$\begin{pmatrix} T_x \\ T_y \\ T_z \end{pmatrix} = \frac{1}{6} \begin{pmatrix} 4 & 1 & 1 \\ 0 & 3 & 3 \\ 2 & 2 & 2 \end{pmatrix} \begin{pmatrix} T_u \\ T_v \\ T_w \end{pmatrix} \quad (5.40)$$

Eqs. (5.35) and (5.40) are only approximate since they assume the mechanical alignment to be perfect. Actually the resistor network that determines the matrix in Eq. (5.35) has been adjusted in each instrument so as to compensate for slight misalignments of the U, V and W sensors. The difference between the nominal and the actual matrix, however, can be ignored in the context of calibration.

5.7.8 Calibration against a reference sensor

Using ground noise or other seismic signals, an unknown sensor can be calibrated against a known one by operating the two sensors side by side (Pavlis and Vernon, 1994). As a method of relative (frequency-response) calibration, the method is limited to a frequency band where suitable seismic signals well above the instrumental noise level are present and spatially coherent between the two instruments. However, when the frequency response of the unknown sensor can be measured electrically, then its absolute gain may be determined quite accurately with this method. The two responses should be digitally equalized before the amplitudes are compared.

In a similar way, the orientation of a three-component borehole seismometer may be determined by comparison with a reference instrument at the surface.

5.8 Procedures for the mechanical calibration

5.8.1 Calibration on a shake table

Using a shake table is the most direct way of obtaining an absolute calibration. In practice, however, precision is usually poor outside a frequency band roughly from 0.5 to 5 Hz. At higher frequencies, a shake table loaded with a broadband seismometer may develop parasitic resonances, and inertial forces may cause undesired motions of the table. At low frequencies, the maximum displacement and thus the signal-to-noise ratio may be insufficient, and the motion may be non-uniform due to friction or roughness in the bearings. Still worse, most shake tables do not produce a purely translational motion but also some tilt. This has two undesired side-effects: the angular acceleration may be sensed by the seismometer, and gravity may be coupled into the seismic signal (see 5.3.3). Tilt can be catastrophic for the horizontal components at long periods since the error increases with the square of the signal period. One might think that a tilt of 10 μ rad per mm of linear motion should not matter; however, at a period of 30 s, such a tilt will induce seismic signals twice as large as those originating from the linear motion. At a period of 1 s, the effect of the same tilt would be negligible. Long-period measurements on a shake table, if possible at all, require extreme care.

5. Seismic Sensors and their Calibration

Although all calibration methods mentioned in the previous section are applicable on a shake table, the preferred method would be to record both the motion of the table (as measured with a displacement transducer) and the output signal of the seismometer, and to analyse these signals with CALEX or equivalent software (see 5.9). Depending on the definition of active and passive parameters, one might determine only the absolute gain (responsivity, generator constant) or any number of additional parameters of the frequency response.

5.8.2 Calibration by stepwise motion

The movable tables of machine tools like lathes and milling machines, and of mechanical balances, can replace a shake table for the absolute calibration of seismometers. The idea is to place the seismometer on the table, let it come to equilibrium, then move the table manually by a known amount and let it rest again. The apparent "ground" motion can then be calculated by inverse filtration of the output signal and compared with the known mechanical displacement. Since the calculation involves triple integrations, offset and drift must be carefully removed from the seismic trace. The main contribution to drift in the apparent horizontal „ground" velocity comes from tilt associated with the motion of the table. With the method subsequently described, it is possible to separate the contributions of displacement and tilt from each other so that the displacement can be reconstructed with good accuracy. This method of calibration is most convenient because it uses only normal workshop equipment; the inherent precision of machine tools and the use of relatively large displacements eliminate the problem of measuring small mechanical displacements. A FORTRAN program named DISPCAL is available for the evaluation (see 5.9).

The precision of the method depends on avoiding two main sources of error:

1 - The restitution of ground displacement from the seismic signal (a process of inverse filtration) is uncritical for broadband seismometers but requires a precise knowledge of the transfer function for short-period seismometers. Instruments with unstable parameters (such as electromagnetic seismometers) must be electrically calibrated while installed on the test table. However, once the response is known, the restitution of absolute ground motion is no problem even for a geophone with a free period of 0.1 s.

2 - The effect of tilt can only be removed from the displacement signal when the motion is sudden and short. The tilt is unknown during the motion, and is integrated twice in the calculation of the displacement. So the longer the interval of motion, the larger the effect the unknown tilt will be on the displacement signal. Practically, the motion may last about one second on a manually-operated machine tool, and about a quarter-second on a mechanical balance. It may be repeated at intervals of a few seconds.

Static tilt before and after the motion produces linear trends in the velocity which are easily removed. The effect of tilt during the motion, however, can be removed only approximately by interpolating the trends before and after the motion. The computational evaluation consists in the following major steps (Fig. 5.29):

- 1) the trace is deconvolved with the velocity transfer function of the seismometer;
- 2) the trace is piecewise detrended so that it is close to zero in the motion-free intervals; interpolated trends are removed from the interval of motion;

- 3) the trace is integrated;
- 4) The displacement steps are measured and compared to the actual motion.

In principle, a single step-like displacement is all that is needed. However, the experiment takes so little time that it is convenient to produce a dozen or more equal steps, average the results, and do some error statistics. On a milling machine or lathe, it is recommended to install some mechanical device that stops the motion after each full turn of the spindle. On a balance, the table is repeatedly moved from stop to stop. The displacement may be measured with a micrometer dial or determined from the motion of the beam (Fig. 5.30). From the mutual agreement between a number of different experiments, and from the comparison with shake-table calibrations, we estimate the absolute accuracy of the method to be better than 1%.

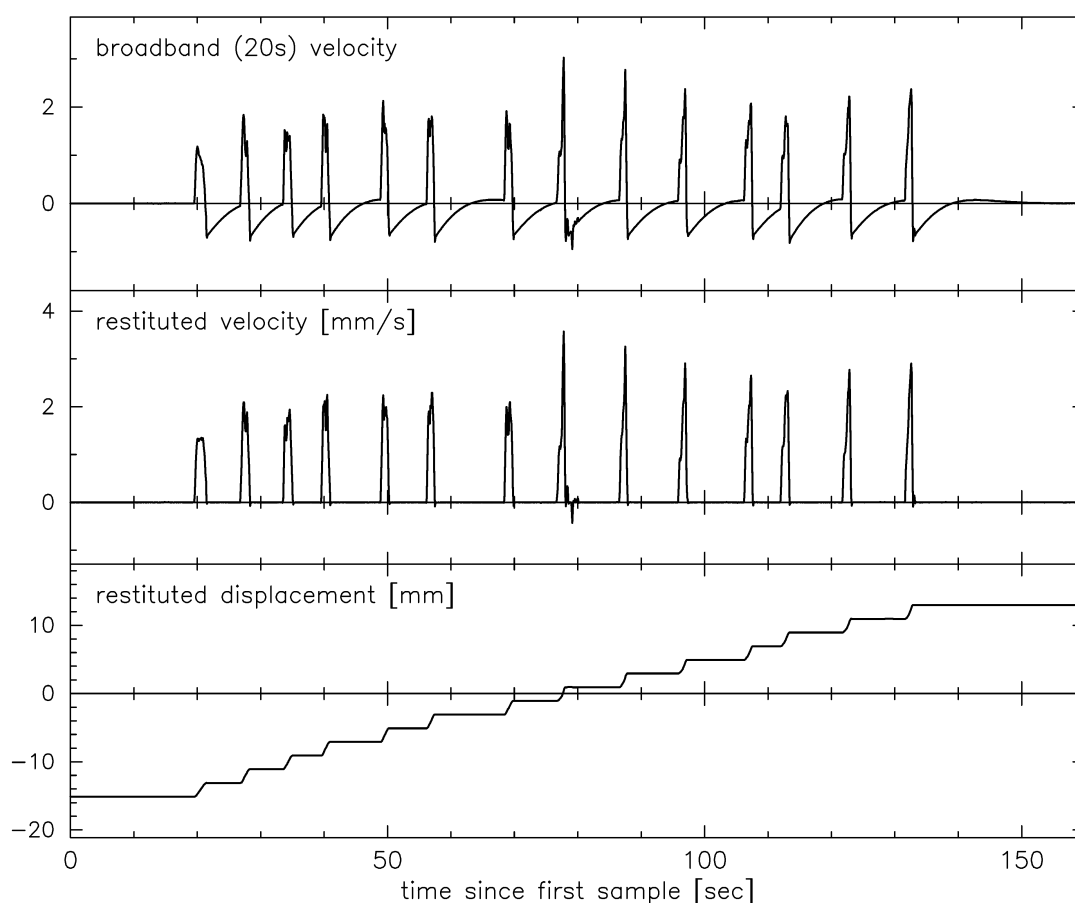


Fig. 5.29 Absolute mechanical calibration of an STS1-BB (20s) seismometer on the table of a milling machine, evaluated with DISPCAL. The table was manually moved in 14 steps of 2 mm each (one full turn of the dial at a time). Traces from top to bottom: recorded BB output signal; restored and de-trended velocity; restored displacement.

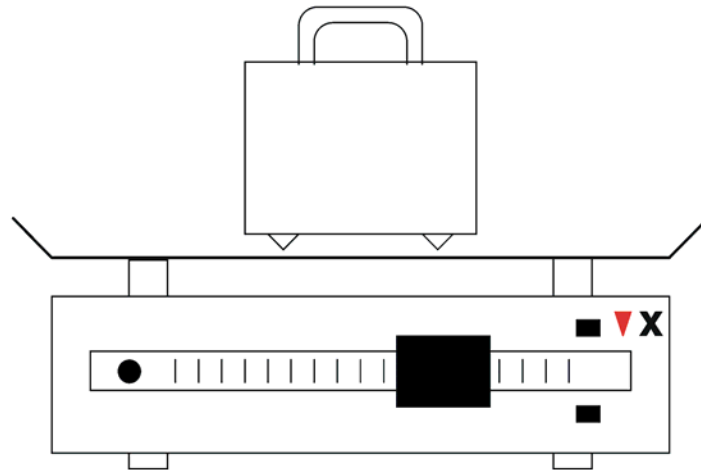


Fig. 5.30 Calibrating a vertical seismometer on a mechanical balance. When a mass of w_1 grams at some point X near the end of the beam is in balance with w_2 grams on the table or compensated with a corresponding shift of the sliding weight, then the motion of the table is by a factor w_1/w_2 smaller than the motion at X .

5.8.3 Calibration with tilt

Accelerometers can be statically calibrated on a tilt table. Starting from a horizontal position, the fraction of gravity coupled into the sensitive axis equals the sine of the tilt angle. (A tilt table is not required for accelerometers with an operating range exceeding $\pm 1g$; these are simply turned over.) Force-balance seismometers normally have a mass-position output which is a slowly responding acceleration output. With some patience, this output can likewise be calibrated on a tilt table; the small static tilt range of sensitive broadband seismometers, however, may be inconvenient. The transducer constant of the calibration coil is then obtained by sending a direct current through it and comparing its effect with the tilt calibration.

Finally, by exciting the coil with a sine-wave whose acceleration equivalent is now known, the absolute calibration of the broadband output is obtained. The method is not explained in more detail here because we propose a simpler method. Anyway, seismometers of the homogeneous-triaxial type can not be calibrated in this way because they do not have X,Y,Z mass-position signals.

The method which we propose (for horizontal components only; program TILTCAL) is similar to what was described under 5.8.2, but this time we excite the seismometer with a known step of tilt, and evaluate the recorded output signal for acceleration rather than displacement. This is simple: the difference between the drift rates of the de-convolved velocity trace before and after the step equals the tilt-induced acceleration; no baseline interpolation is involved. In order to produce repeatable steps of tilt, it is useful to prepare a small lever by which the tilt table or the seismometer can quickly be tilted back and forth by a known amount. The tilt may exceed the static operating range of the seismometer; then one has to watch the output signal and reverse the tilt before the seismometer comes to a stop.

5.9 Free software

Source codes of several computer programs mentioned in the text can be downloaded from the FTP sites given here (last update: August 2001). Some of these programs are used in IS 5.2 and EX 5.1 through EX 5.5. They are stand-alone programs for calibrating and testing seismometers and do not form a package for general seismic processing such as SAC, SEISMIC UNIX, PITSA, or PREPROC (see below). Wherever appropriate, test data, auxiliary files, and read.me files with detailed instructions are included. The Fortran programs do not produce graphic output but some of them generate data files in ASCII format from which the signals can be plotted.

5.9.1 Programs by J. Bribach in Turbo Pascal:

The CALIBRAT package consists of three programs:

- RESPONSE calculates the response function of a complete signal chain from seismometer/geophone via preamplifier and filter stages to analog or digital recorder. This response is represented as Amplitude/Phase Plot versus frequency (Bode Diagram) or as Poles and Zeros.
- CALISEIS calculates missing seismometer parameters by step response, and it designs the electronic scheme of the preamplifier stage as well as the calibration inputs to seismometer and preamplifier.
- SEISFILT designs single and complex electronic filter stages.

A short program description can be found in Volume 2 (see PD 5.1). The complete software can be downloaded from <ftp.gfz-potsdam.de/pub/home/dss/brib/calibrat> under the file names `calibrat.zip` (containing the programmes and sources) and `Calibrat.doc` (containing the complete program description).

5.9.2 Programs by E. Wielandt in Fortran:

- CALEX: Determines parameters of the transfer function of a seismometer from the response to an arbitrary input signal (both of which must have been digitally recorded). The transfer function is implemented in the time domain as an impulse-invariant recursive filter. Parameters represent the corner periods and damping constants of subsystems of first and second order.
- DISPCAL: Determines the generator constant of a horizontal or vertical seismometer from an experiment where the seismometer is moved stepwise on the table of a machine tool or a mechanical balance. Another, more automated version of the program is available as DISPCAL1.
- TILTCAL: Determines the generator constant of a horizontal seismometer from an experiment where the seismometer is stepwise tilted.

5. Seismic Sensors and their Calibration

- SINFIT: fits sine-waves to a pair of sinusoidal signals and determines their frequency and the relative amplitude and phase.
- UNICROSP: Estimates seismic and instrumental noise separately from the coherency of the output signals of two seismometers.
- NOISECON: converts noise specifications into all kind of standard and non standard units and compares them to the USGS New Low Noise model (see Peterson, 1993). Interactive program available in BASIC, FORTRAN, C and as a Windows 95 - Executable .

Program descriptions of the above are enclosed in Volume 2 as PD 5.2 through PD 5.7 and PD 4.1, respectively. (see the table of contents). The programs can be obtained from <ftp://ftp.geophys.uni-stuttgart.de/pub/ew> (141.58.73.149). Two auxiliary programs used in the exercises – WINPLOT and POL_ZERO – are also available from this site.

5.9.3 Free seismic software packages from other sources

- SAC: http://www.llnl.gov/sac/SAC_Info_Install/Availability.html
- SEISMIC UNIX: <http://www.cwp.mines.edu/cwpcodes/index.html>
- PITSA: http://www.uni-potsdam.de/u/Geowissenschaft/Software/haupt_software.html
- PREPROC: <ftp://orfeus.knmi.nl/pub/software/mirror/preproc/index.html>

If you can not find these websites, try

<http://www.seismolinks.com/Software/Seismological.htm>

<http://orfeus.knmi.nl/other.services/software.links.shtml>

Acknowledgments

Three careful reviews by the Editor of the NMSOP, Peter Bormann, and suggestions by Axel Plešinger and Jens Havskov have significantly improved the clarity and completeness of this text. A shorter version of this text, with some advanced topics added, has been submitted for publication in part A of the International Handbook of Earthquake and Engineering Seismology (Lee et al., 2002).

6

Seismic Recording Systems

Günter Asch

6.1 Introduction

During the last ten years, recording devices based on digital technology have completely replaced their old analog predecessors. The latter are costly, require specialized maintenance and consumables, and are incompatible with computer data processing and analysis. They are no longer produced although being still in operation at many older seismological stations and network centers. They are not dealt with in this chapter. Extensive reference to analog photographic and directly visual drum recording and processing of the records is given in the chapters Instruments and Station Operation in Willmore (1979) Manual of Seismological Observatory Practice.

The technological progress in digital signal processing, data storage techniques and highly integrated digital circuits has lead to several instruments being available on the market that all fulfill the basic requirements of a seismic recording instrument and offer several more advanced features as well.

In terms of this chapter, a recording device is an autonomous, self-contained equipment, designed to measure the output signal of a sensor, digitize the signal and record it. In seismological experiments, all three components of ground movement are of interest, whereas in reflection experiments, only the vertical component up to now has been taken into account. Specialized multi-channel recorders with more than 6 channels, preferred in exploration seismics, are not covered here.

Seismic experiments vary from reflection profiles with short recording windows and high sampling rates to the continuous recording of broadband sensors with high resolution at observatories. An instrument well suited for an observatory, may be a bad choice for a wide-angle experiment and vice versa.

This chapter is a short introduction to the principal concept of seismic recording systems and should help the non-technical users to decide which instrument is suitable for their specific requirements. Fig. 6.1 gives an overview of the principal units of a seismic recording system. Each unit will be discussed in detail in the following sections.

6. Seismic Recording Systems

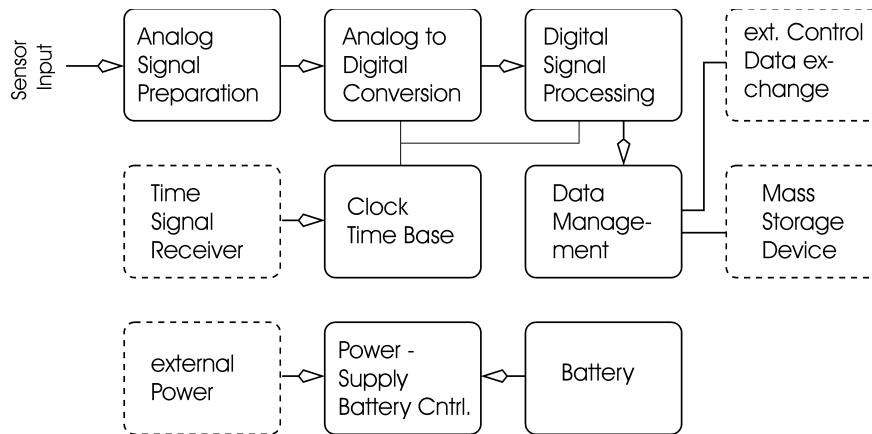


Fig. 6.1 Principal units of a seismic recording device. Dashed boxes relate to optional functions.

6.2 Analog signal preparation

6.2.1 The Analog Signal Preparation section

The seismic sensor is connected to the Analog Signal Preparation (ASP) section. This is not only a problem of correct wiring and polarity, but depends strongly on the type of transducer used. If a passive electrodynamic sensor is used, the impedance of the recording system influences the sensitivity and the frequency of the sensor itself. The sensor's response function (see 5.2.4 to 5.2.9 and Scherbaum, 1996) have to be corrected for the input impedance of the recording device. For this type of sensor, one has to think also about the resistivity and capacity of the cable, used to connect the sensor to the recording device, in case it exceeds several tens of meters. For active sensors, i.e., all broadband sensors, the effect of the input impedance can be neglected because it does not influence the sensor's characteristic, however long cables can introduce noise into the system. In general, short shielded cables, a single common analog ground and high quality connectors help to reduce this type of noise problems. The ASP section is also responsible for protecting the sensitive electronics of the recording system against high input electrostatic voltages.

The next step in ASP is the preamplifier which, together with the Analog to Digital Converter (ADC*), determines the resolution [counts/Volt] of the recording device. The preamplifier has to fulfill several demands, such as linearity with respect to amplitude and phase, low noise, quick recovery from overloading, i.e., no clamping, and in addition, low power consumption. In reality, there is a tradeoff between low noise and low power consumption, and the designer of the preamplifier stage has to find a compromise. In any case, the noise generated by the ASP should be distinctly lower than the least significant bit of the ADC stage. Other requirements are not as critical, but one has to take care in a system with more than one channel, that all the parts in the ASP are identical, so each channel has the same response and sampling is done simultaneously on all channels. The technical approach is explained in section 6.3.4.

* Terms typed in Arial letters are explained in more detail in 6.7: Glossary of technical terms and links.

6.2.2 Analog filters

Some recorders offer a high-pass filter to remove DC-offset and long-term drifts from the measured signal. These filters are intended to mask temperature and ageing problems, related to electronic components and to the system's specific design. Users should be able to decide whether they wish to activate these filters or not. As an example, the group delay of the optional high-pass filter from a PDAS recorder is given in Fig. 6.2. The high-pass filter is formed by a simple RC-element ($15\ \mu\text{F}||1\ \text{M}\Omega$) with a time constant of about 15 seconds. Signals with periods of about 3 seconds are delayed by approximately 1 sample, assuming a sampling rate of 100 Hz. For longer periods, the situation becomes worse and it is not acceptable to activate this high-pass filter to record signals from broadband sensors. From the scientific point of view, this filter makes no sense; it simply beautifies the signal and substitutes one problem for another.

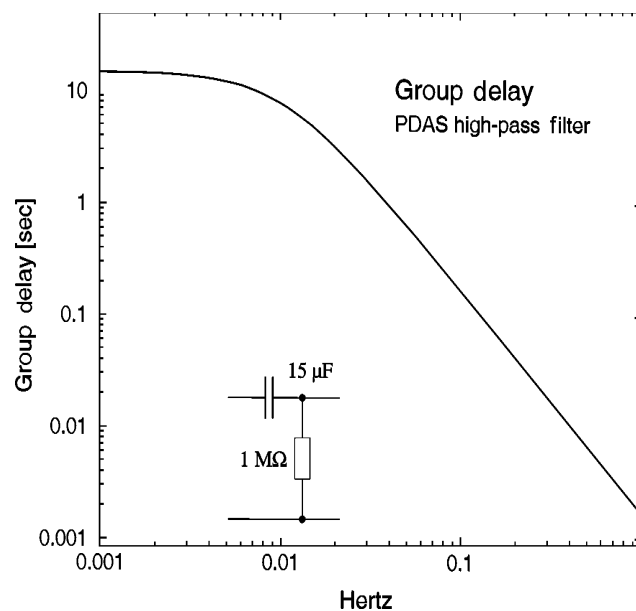


Fig. 6.2 Group delay of the optional PDAS high-pass filter.

Before converting the analog signal into counts, it has to pass a low-pass filter serving as an anti-alias filter. This limits the frequency content of the signal toward higher frequencies. The reason for this fundamental step is described in 6.3.1. In some cases, i.e., continuously integrating converters, this stage can be an integral part of the ADC itself.

6.3 Analog to digital conversion

Conversion of a continuous analog signal into a digital time series is based on quantization with respect to time and amplitude. Therefore it is necessary to understand the influences and limitations introduced by these two different operations. After filtering, the analog signal is sampled and converted into digital values. Since the digital domain consists only of finite length digital words, which have to represent a continuous signal, the conversion step introduces quantization errors.

6.3.1 Sampling theorem

The *sampling theorem* describes the effect of quantization at discrete times on an analog signal. It was first published by Shannon (1949). A simple model is given by a switch, closed periodically for a certain time. At first, this sounds quite simple but in fact, this simple device is a modulator, performing the multiplication of two signals. Fig. 6.3 shows that the output signal is the control signal of the switch, multiplied by the input signal. The control signal is a train of impulses, therefore it is periodic and can be expressed by a Fourier series:

$$P(t) = \sum_{n=-\infty}^{\infty} h \cdot \frac{\tau}{\Delta T} \cdot \frac{\sin(\pi n f_s \tau)}{\pi n f_s \tau} \cdot e^{i2\pi n f_s t}. \quad (6.1)$$

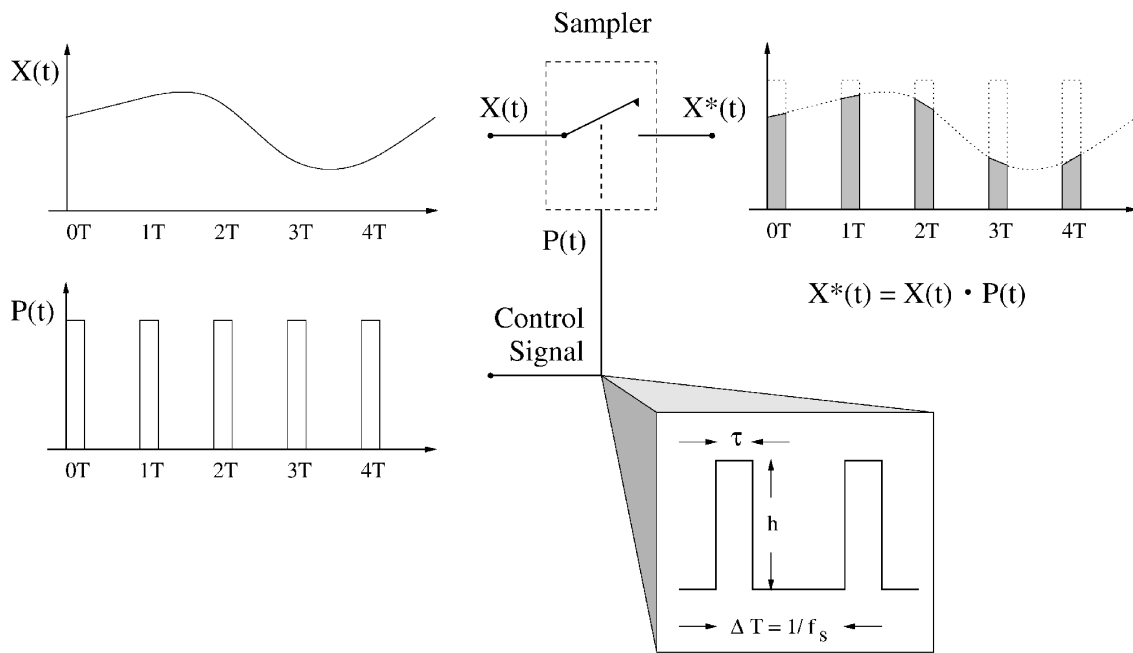


Fig. 6.3 Relation between input-, output- and control signal of a sample device.

The variables h , τ , ΔT , and f_s are explained in Fig. 6.3, and $\sin(\pi f_s \tau) / \pi f_s \tau$ is the Fourier transform of the n^{th} boxcar's impulse response. If we look at the sampler as an ideal device, τ approaches 0 and therefore $\lim_{\tau \rightarrow 0} \sin(\pi f_s \tau) / \pi f_s \tau = 1$, i.e., a so-called Dirac impulse. The energy of a single impulse is given by $A = h \cdot \tau$, so the output signal is described by

$$X^*(t) = X(t) \cdot \underbrace{\frac{A}{\Delta T} \sum_{n=-\infty}^{\infty} e^{i2\pi n f_s t}}_{P(t)} \quad (6.2)$$

Due to the periodic character of the control signal $P(t)$, we get an infinite number of impulse responses, separated from each other by $\Delta T = 1/f_s$ with f_s as the sampling frequency. This changes the frequency content of the measured signal, and the spectra of the input- and output signal are no longer identical. The Fourier transform of $X^*(t)$

$$X^*(f) = \frac{A}{\Delta T} \int_{-\infty}^{\infty} (X(t) \cdot \sum_{n=-\infty}^{\infty} e^{i2\pi n f_s t}) \cdot e^{-i2\pi f t} dt \quad (6.3)$$

results in

$$X^*(f) = \frac{A}{\Delta T} \sum_{n=-\infty}^{\infty} X(f - n f_s). \quad (6.4)$$

In other words, the spectrum of the input signal is transformed into a sequence of an infinite number of spectra. All these spectra, except the one of the order 0, are called the alias spectra of $X^*(f)$.

To illustrate this behavior, a concrete example is given in Fig. 6.4 which demonstrates the situation with the PDAS recording system. Sampling is done with a primary sampling rate of 1 kHz. The anti-alias filters are designed as Butterworth low-pass filter of an order of 6 (36 dB/octave). The corner frequency of this filter is set at 200 Hz. Its transfer function is given by

$$H(j\omega) = \frac{1}{\sqrt{1 + (j \frac{\omega}{\omega_0})^{2n}}} \quad (6.5)$$

with $\omega_0 = 2 \cdot \pi \cdot 200$ Hz and $n = 6$ is the order of the Butterworth filter.

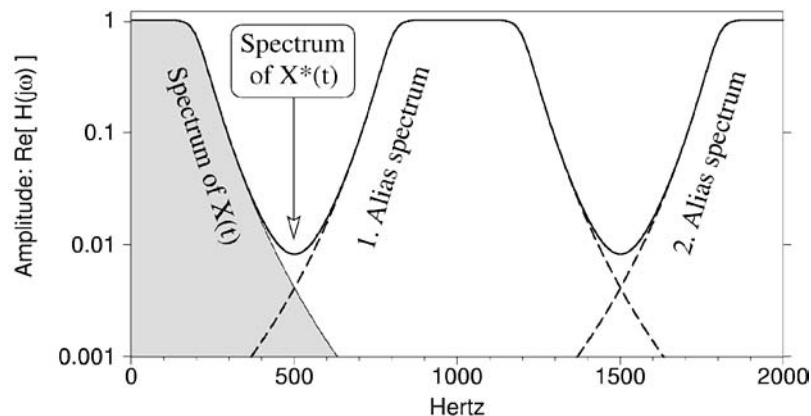


Fig. 6.4 Alias spectra in a PDAS recording system after sampling.

The consequence of aliasing in this example is that all signals with frequencies above the so-called Nyquist frequency $f_N = f_s / 2$ are mirrored into the spectrum of $X(t)$ (Eq. 6.2). A signal with a frequency of 600 Hz can not be distinguished from a 400 Hz signal, and a signal with 1 kHz is seen as DC with an amplitude, depending on its amplitude and the phase difference between the signal and control signal $P(t)$. That is why we have to assure, by applying an anti-alias low-pass filter to the analog input time series, that its high-frequency amplitudes are drastically reduced and thus do not mirror much energy into the alias spectra. Actually, the output of the sampler $X^*(t)$ is the summing curve of all spectra, as shown in Fig. 6.4. The spectra in Fig. 6.4 were calculated on the assumption that the PDAS recording system was fed with a white noise signal.

6. Seismic Recording Systems

In field seismology, very little data is collected with a sampling rate of 1 kHz. In local and regional experiments, 100 Hz sampling rate is sufficient, and for teleseismic studies even 20 Hz data are commonly used. Why does the PDAS sample at such a high frequency? One answer is that the first alias spectrum is shifted far away from the frequencies in which we are interested. A second answer is given in the next section.

6.3.2 Oversampling

There are several ways to describe how oversampling increases resolution. The following is adopted from a technical report published by Texas Instruments (1998). The maximum error of an ideal quantizer is ± 0.5 LSB (least significant bit). Since the input range of a n -bit ADC is divided into 2^n discrete levels, each represented by an n -bit binary word, the ADC input range and the word width n are a direct measure of the maximum absolute error. In addition, the quantization step can be analyzed in the frequency domain. The number of bits representing the digital value determines the signal-to-noise ratio (SNR). Therefore, by increasing the signal-to-noise ratio, the effective resolution of the conversion will be increased. Assuming the input signal is an ever-changing signal (always true in seismology), the error caused by quantization from an ideal ADC can be viewed as a white noise signal that spreads the energy uniformly across the whole bandwidth from DC to one half of the sampling rate. The RMS amplitude of the quantization error U_{neff} is given by Tietze and Schenk (1990)

$$U_{neff} = \frac{U_{LSB}}{\sqrt{12}} \quad (6.6)$$

For a full-scale sinewave signal, the RMS amplitude for an n -bit ADC is given by:

$$U_{seff} = \frac{1}{\sqrt{2}} \cdot \frac{1}{2} \cdot 2^n \cdot U_{LSB} \quad (6.7)$$

where the factor $1/2$ is caused by the signal having \pm maximum amplitude while the converter is from $0 - 2^n$. The $1/\sqrt{2}$ comes from conversion to RMS. On the basis of Eqs. (6.6) and (6.7) the signal-to-noise ratio can be calculated

$$\begin{aligned} SNR [dB] &= 20 \log_{10} \frac{U_{seff}}{U_{neff}} \\ &= 20 \log_{10} 2^n \cdot \frac{\sqrt{12}}{2 \cdot \sqrt{2}} \\ &\approx n \cdot 6 [dB] + 1.8 [dB] \end{aligned} \quad (6.8)$$

With an ideal ADC, the quantization noise power $P = U_{neff}^2$ is uniformly distributed across the spectrum between DC and half the sampling rate. This quantization noise power is independent of the sampling rate. If we use higher sampling rates, the noise power is spread over a wider range of frequencies. Therefore the effective noise power density at the band of interest is lower at higher sampling rates. Fig. 6.5 illustrates the effective noise power reduction in the frequency band of interest at a rate of oversampling of k and the resulting sampling rate of $k f_s$. One has to use digital low-pass filters to remove all frequencies above $f_s/2$. The effective resolution is determined by the quality of the digital filter. The remaining noise power beyond $f_s/2$ is a measure for the quantization noise and therefore responsible for a decrease in the signal-to-noise ratio.

In an oversampled system, the sampling rate is decimated - after or during filtering - by a factor of k . In such a case, an ideal low-pass filter and decimator will reduce the quantization noise also by the factor of k . Since the signal at the band is not affected by the filter, this leads to an enhancement of the signal-to-noise ratio. The formula for the improved signal-to-noise ratio is:

$$SNR [dB] = 20 \log_{10} \left(\frac{U_{seff}}{U_{neff}} \cdot \sqrt{k} \right) \tag{6.9}$$

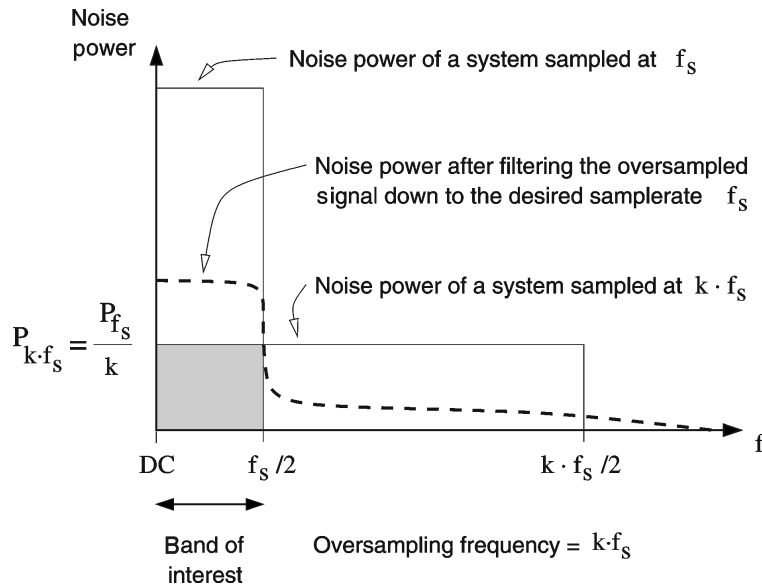


Fig. 6.5 Noise power reduction in an oversampled system.

The increase of the signal-to-noise ratio and the corresponding increase in the number of bits is shown in Fig. 6.6.

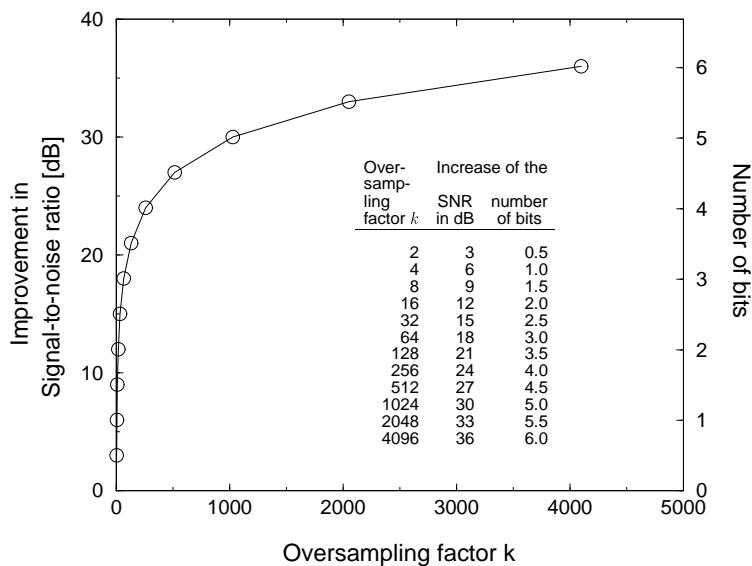


Fig. 6.6 Improvement of the signal-to-noise ratio with oversampling.

6.3.3 Digital filters

The concept of oversampling is strongly related to digital filters. In principal, there are two concepts available, filtering a digital data stream in the time domain. We distinguish between IIR and FIR filters. Both have their specific advantages and drawbacks and are discussed in detail by Buttkus (1991) and Scherbaum (1996). The IIR concept is adopted from analog filter design techniques and utilizes polynomial approximation to the desired transfer function. The name of this type of filter is given by the recursive design of the underlying algorithm. The FIR design is a non-causally approach, applying the time domain representation of the desired transfer function (Laplace transformation of the filter's impulse response; see 5.2.2) to the digital data stream. Both types have their specific benefits and disadvantages. On the one hand IIR filters are fast to compute, on the other hand they are not guaranteed to be stable with increasing order and, as their analog counterparts, introduce a phase shift depending on the frequency of the input signal. FIR filter are easy to implement, always stable and produce no phase shift (if expressed symmetrically). This results in a constant group delay and gives rise to small amplitude precursory artefacts at the output. A compromise getting the best from both approaches is the minimum-phase filter. A brief discussion about this problem and how to deal with is given by Scherbaum (see http://lbutler.geo.uni-potsdam.de/FIR/fir_daaf.htm).

All of the digital recorders available use FIR filters to decimate the digital data streams, and most of them are zero-phase filters. At the moment, only Earth Data and Kinematics (for the Quanterra records) offer minimum-phase decimation filters for their products.

6.3.4 Analog to Digital Converter (ADC)

The first generation of seismic recorders mainly utilized Successive Approximation Register ADCs (SAR). The concept is based on a DAC combined with a comparator and a shift register in a feedback loop.

It takes n steps to convert one sample with a binary resolution of n -bit. The right-hand part of Fig. 6.7 shows a block diagram of an SAR-ADC. In operation, the system enables the bits of the DAC one at a time, starting with the most significant bit (MSB). As each bit is enabled, the comparator gives an output signifying that the input signal is greater or less in amplitude than the output of the DAC. If the DAC output is greater than the input signal, the bit is reset, i.e., turned off. The system does this with the MSB first, then with the next most significant bit, etc. After n -steps, all the bits of the DAC have been tried, and the conversion cycle is completed. Fig. 6.7 shows the typical components and the signal flow for this type of ADC, as used for example, in the PDAS recorder. The anti-alias filter is followed by a Sample & Hold device. Using one common control signal $P(t)$ for all Sample & Hold devices results in sampling at the same time of all input channels. Thus only one ADC device is necessary for multiple analog input channels, reducing power consumption and cost.

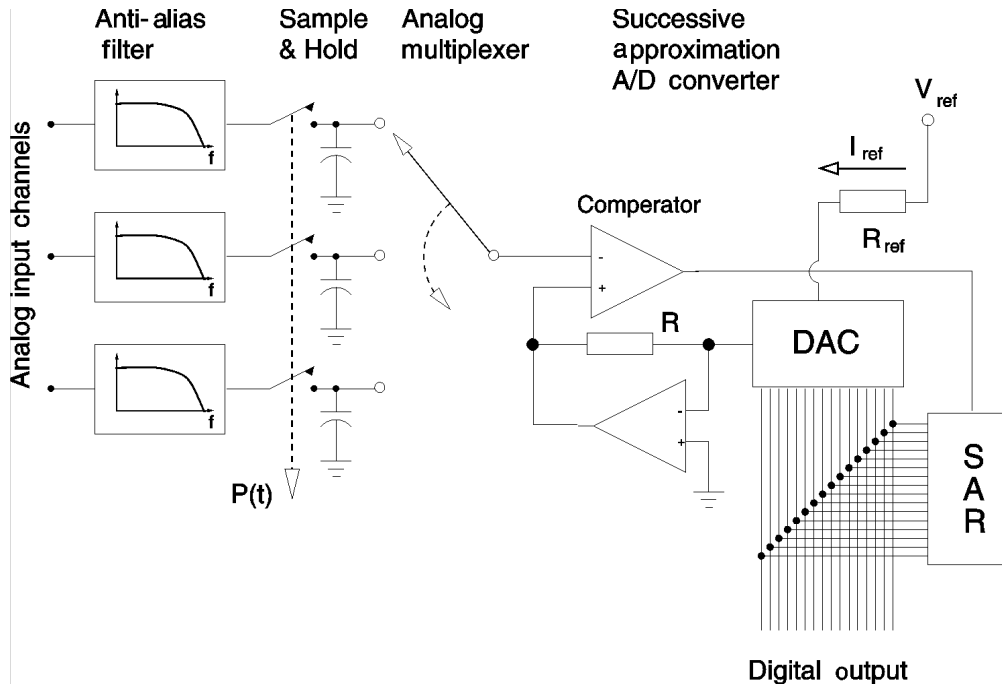


Fig. 6.7 ADC concept used in the first generation of digital recording systems with a 16 bit converter.

This concept, however, has some severe disadvantages. During the conversion cycle, the input voltage must be kept stable below the resolution of the ADC. For this, and the parallel sampling of all input channels, the Sample & Hold unit and the analog multiplexer are introduced. But there is no ideal sampler with $\lim_{\tau \rightarrow 0} \sin(\pi f_s \tau) / \pi f_s \tau = 1$ as required in Eq. (6.1). Also, the capacitor that holds the input voltage is not an ideal analog storage medium. All this together adds noise to the processed signal. But the most significant problem of this concept is the gap introduced between two Sample & Hold cycles, owing to the input signal being disconnected from the ADC.

Therefore small variations of the input signal are only taken into account if they are significant with respect to the resolution of the ADC stage. The noise reduction achieved by oversampling with this type of converter is proportional to the square root of the oversampling factor, as shown in Eq. (6.9) and Fig. 6.6.

In modern data acquisition systems, there is no clear separation any more of the **Analog to Digital Conversion** and the **Digital Signal Processing** stage, as shown in Fig. 6.1. The ADC itself does a lot of digital signal processing to achieve high resolution, high signal-to-noise ratio, and high dynamics. The used techniques are based on continuous integration and oversampling in combination with carefully designed digital low-pass filters. In most modern seismic recording systems, a Delta-Sigma-Modulator is used as ADC. A simplified block diagram of the signal flow is given in Fig. 6.8. The concept of continuously integrating the analog signal avoids gaps in the sampling process and takes into account variations of the input signal even below the resolution of the ADC. The drawback is that one has to have a separate unit for each input channel, but this is more than compensated for by having abolished the Sample & Hold- and multiplexer devices.

6. Seismic Recording Systems

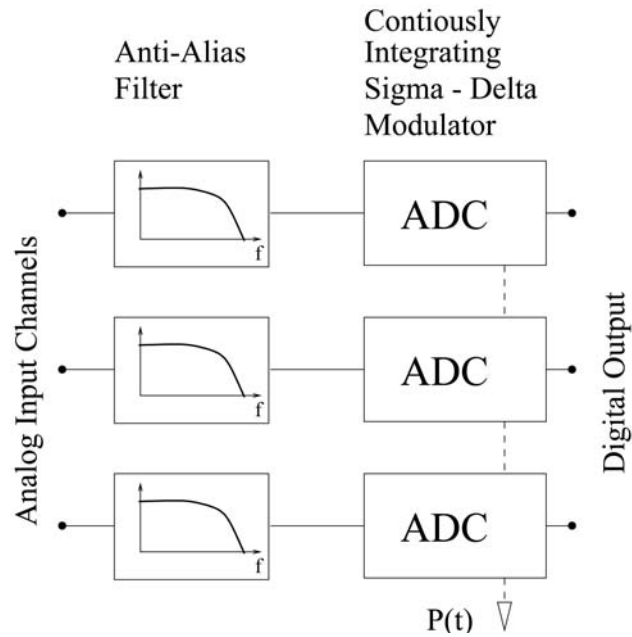


Fig. 6.8 ADC concept used in most modern digital recording systems.

The scheme of a Delta-Sigma-Modulator is given in Fig. 6.9. The negative feedback from the output along the 1-bit DAC and the sum amplifier at the input is performed at a high sampling rate, transferring the quantization noise into the stop band of the digital low-pass filter used for decimation.

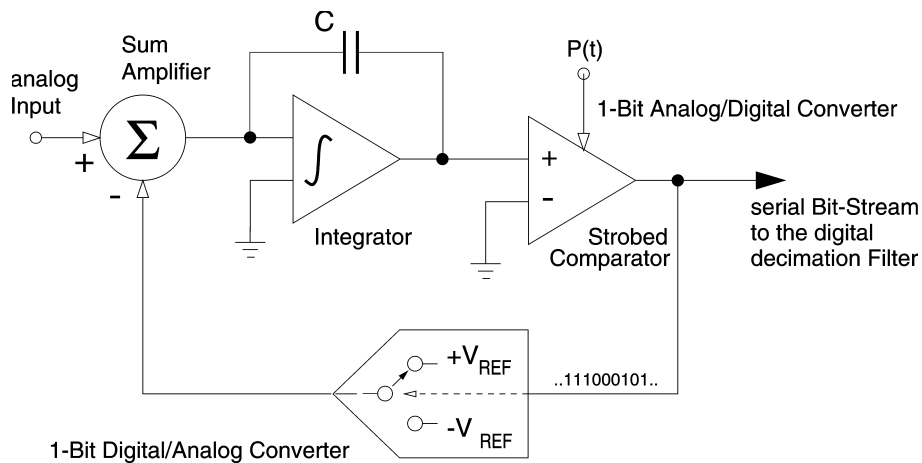


Fig. 6.9 First order Delta-Sigma Modulator.

The principal elements in the block diagram of the Delta-Sigma-ADC shown in Fig. 6.9 are :

- continuously sampling integrator;
- 1-Bit A/D converter (strobed comparator);
- 1-Bit D/A converter (feedback);
- sum amplifier;
- digital low-pass filter (not shown in Fig. 6.9);

In operation, the sampled analog signal is fed to the sum amplifier, along with the output of the 1-bit DAC. The integrated difference signal is fed to the strobed comparator, whose output samples the difference signal at a frequency (the actual sampling frequency) many times that of the analog signal frequency. The output of the comparator provides the digital input for the 1-bit DAC, so the system functions as a negative feedback loop which minimizes the difference signal by tracking the input. The integrator is continuously fed with the differential signal and there are no gaps in the analog input signal, as introduced by sample and hold devices. The digital information representing the analog input voltage is coded in the polarities of the pulse train appearing at the output of the comparator. It can be retrieved as a parallel binary data word applying a digital filter operator. In general Delta-Sigma ADCs are described by the order of the integrator, which is in fact an analog low-pass filter. Fig. 6.9 shows a simple first order integrator. In real world systems, an order of four is used. This reflects a compromise between oversampling factor and stability of the modulator limited only by the performance of the analog part of the Delta-Sigma-Modulator.

6.3.5 Noise test

The overall noise level of a recording system can be tested by shortening the input and recording for an adequate period of time. The variation of the measured values reflects the overall noise of the recording device. This test also helps to check temperature influences and find problems in the instruments design. Loading one channel with a defined signal and cross correlating with the others, gives a detailed insight into the system's real performance.

Fig. 6.10 gives an example measured with a PDAS recorder. Channel 1 was fed with a 50mV_{pp} sinusoidal signal with a period of one second. Channel 2 was shortened by a $2.5\text{k}\Omega$ resistor to simulate the output impedance of a standard passive geophone. All channels were recorded with 100 Hz sampling rate. The lower left section a) of Fig. 6.10 shows the measured signals on both channels with the left ordinate giving the μVolts of the input signal on channel 1 and the right ordinate the μVolts of the signal recorded on channel 2.

The two amplitude-spectra in Fig. 6.10 b) show a zoomed section between 0.5 to 5 Hz from a 2^{18} -point FFT, calculated from a 45 minute measured record. The signals at 2, 3, 4 and 5 Hz are overtones of the signal from the signal generator. They are the result of the non-ideal sinusoidal shape of the signal generator's output, used in this test. The mean level of the spectrum of channel 1 is about one decade above the spectrum of channel 2. This shift mainly reflects the difference in resolution in the gain-ranged mode, that we used in this example. In the record of channel 1, the resolution is 30 nV/count whereas channel 2 is resolved with 4 nV/count. But one can clearly see a peak at 1 Hz in the spectrum of channel 2. Its amplitude is about 6 decades below that of the input signal on channel 1. The cross correlation between the two channels over 500 samples is shown in Fig. 6.10 c). The peak-to-peak amplitude is 0.082 μVolts . From this, the cross coupling can be calculated as $20 \times \log(82\text{nV}/50\text{mV}) = -115 \text{ dB}$ for this specific instrument. This is a fairly good separation of the input channels for field installations if one keeps in mind that 3-component signals measured (not only) in seismology are highly correlated.

6. Seismic Recording Systems

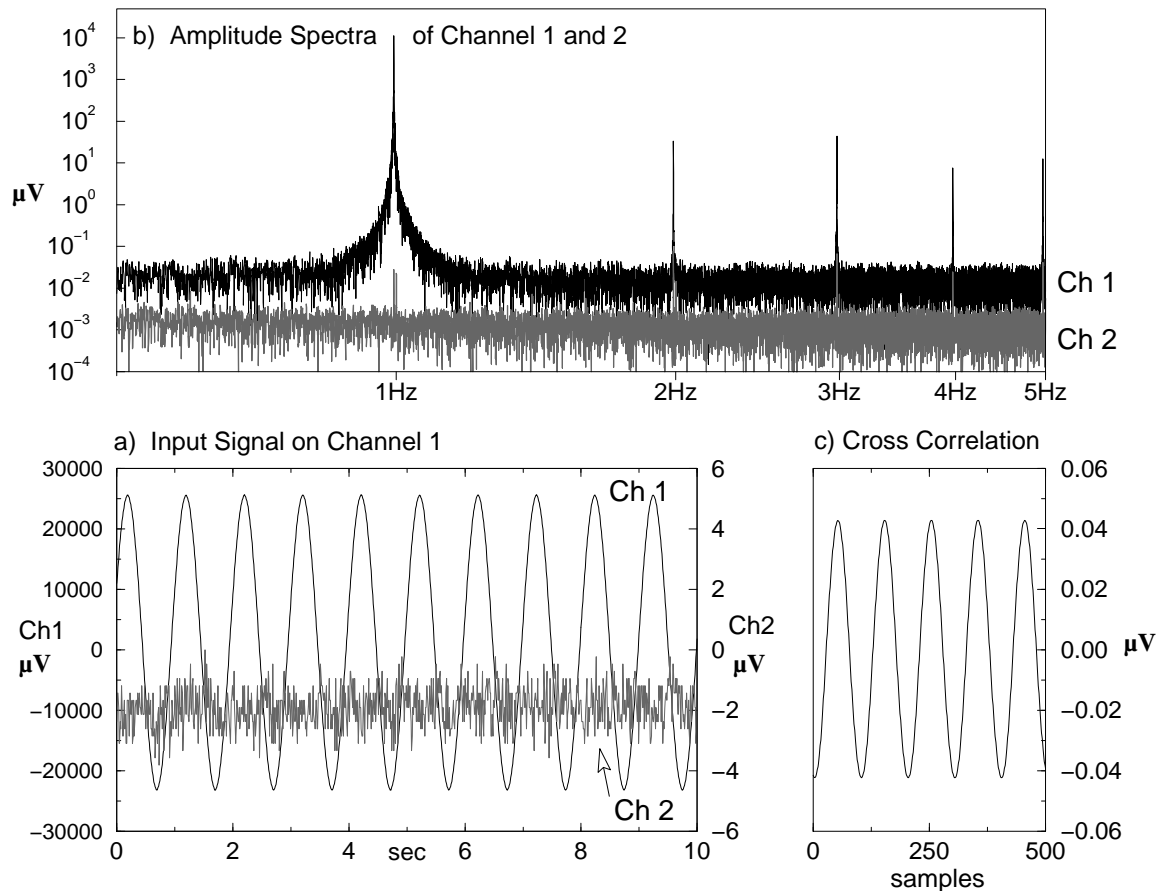


Fig. 6.10 Signal with 50 mV_{pp} amplitude and 1 Hz of channel 1 of a PDAS recorder and the cross coupled signal on channel 2. Shown are the a) measured signals, b) their amplitude-spectra and c) their cross correlation.

6.3.6 The Crystal chip set

Crystal's CS5321 analog modulator and the CS5322 digital filter function together as a high resolution ADC. Therefore they are widely used in geophysical applications. The Reftek and Güralp recording systems, as well as Nanometrics's Orion are based on this chip set. The CS5322/CS5321 combination performs sampling, A/D conversion and anti-alias filtering. The CS5321 utilizes a fourth order Delta-Sigma-Modulator architecture to produce highly accurate conversions at low power dissipation ($< 100 \text{ mW}$). It provides an oversampled serial bit stream at 128 kBit/second ($f_{in} = 512 \text{ kHz}$, 4th order oversampling architecture) to the CS5322 FIR decimation filter. From the manufacturer's data sheet, one can compile the characteristics of the CS5322/CS5321 modulator and filter combination as shown in Fig. 6.11.

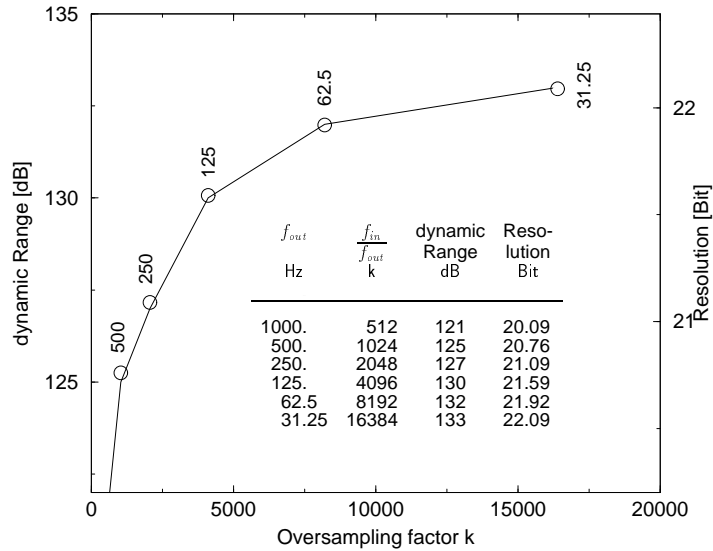


Fig. 6.11 Dynamic range of the CS5322/CS5321 chip set ($f_{in} = 512$ kHz).

The analog input is resolved between 20 and 22 bits, depending on the oversampling ratio k . The resolution in Fig. 6.11 is limited by the modulator, not by the filter. The CS5322 provides the digital decimation filter for the CS5321 modulator output. It is not a general purpose DSP but consists of a multi-stage FIR-filter. The decimation factor by which the oversampling frequency is reduced, is selectable from $64\times$ to $4096\times$. The data at the output of the digital filter is represented in a 24-bit serial format.

The -3 dB bandwidth of each decimation rate is approximately 82% of the Nyquist frequency. The filter achieves a minimum of 130 dB signal reduction at the Nyquist frequency for all filter selections. Tab. 6.1 gives an overview of the relation of the user selectable output sampling rate f_{out} with a Reftek data logger and the associated -3 dB bandwidth of the output spectra. Due to the zero-phase FIR design of the digital decimation filter CS5322, phase shift does not depend on frequency. This results in a constant factor for the group delay.

Tab.6.1 Selectable sampling rates, -3 dB bandwidth, and associated group delay in a Reftek system.

f_{out} Hz	f_{in} kHz	$\frac{f_{in}}{f_{out}}$ k	-3 dB Point Hz	Group Delay sec
1000	512.0	512	412.2	0.029
500	512.0	1024	206.0	0.058
250	512.0	2048	103.0	0.116
125	512.0	4096	51.5	0.232
200	409.6	2048	82.4	0.145
100	409.6	4096	41.2	0.290
50	409.6	8192	20.6	0.580
25	409.6	16384	10.3	1.160
40	327.68	8192	16.5	0.725
20	327.68	16384	8.2	1.450
10	81.92	8192	4.1	2.900
5	81.92	16384	2.1	5.800

6. Seismic Recording Systems

The CS5322 is realized as a cascade of three symmetrical FIR filters, which produce by design a constant delay of the output signal of $29/f_{out}$ (see the manufacturer's data sheet for details of the design). The resulting group delay is given in the last column of Tab. 6.1. The software of the recording system has to shift the time stamp of a sample at the output of the filter stage by this amount of time, which the DSP needs to calculate the filtered output sample. But one has to take into account that the filter settles to full accuracy only after all filter stages have been completely recalculated, i.e., after two times the group delay, according to 57 output words. A transient signal like a step appears at the output of the DSP 29 words later. But to settle to full accuracy it will take another 28 steps. This example demonstrates that the field of application for Delta-Sigma converters is to track slowly changing signals, but not to record transient signals like spikes and steps.

6.3.7 The Quanterra family

The main impact in modern broadband observation was the availability of the Wielandt/Streckeisen (1972) sensor, the presentation of the doctoral thesis of Steim (1986), and the cooperation of Wielandt and Steim (1986). Steim introduced a 24-bit digitizer (US Patent 4866442) which even today gives outstanding performance. It is the de-facto standard in leading broadband experiments such as IRIS GSN, TERRAScope and GEOFON, just to name a few. Steim's digitizer is a variant of the Delta-Sigma-Modulator described in section 6.3.4, but is built up from discrete electronic parts and circuits. The main difference with respect to Fig. 6.9 is the use of a 16-bit ADC instead of the strobed comparator. The digital decimation filter is fed with a 16 bit data stream at 20 kHz. The feedback loop within the Delta-Sigma-Modulator is realized as a 1-bit stream, similar to the design shown in Fig. 6.9.

The main drawback of the original Quanterra data loggers is their rather high electric power consumption. By no means is it a portable instrument; it is designed for the installation in an observatory. These days Kinematics offers an array of Quanterra products for different kinds of application, including portables.

6.4 Time base

The usual thing to say about timing on all recording devices is that they allow synchronizing the internal time base against an external clock signal. With the availability of relatively cheap GPS receivers, the timing problem has been solved in a global sense. This type of time signal receivers provides a stable clock reference in the order of μ seconds along with time, date and geographic position information, which allow synchronized data acquisition all over the world.

Moreover, the way a recording device synchronizes the internal data streams against the external clock signal differs, depending on the design goals. In active seismic field experiments, predefined time windows are recorded. The time slots vary from some tens of seconds in reflection - up to some tens of minutes in wide angle experiments. Also, in recent seismological experiments a triggered recording mode was mainly used due to limited storage capacities and computer facilities. In this mode, recording windows of several tens of minutes to hours are produced. Synchronizing a clock at the beginning of a recording window and keeping it running for several minutes up to hours will normally not produce significant drift errors. The situation becomes more complicated, if one has to synchronize a continuous

stream of data against an external clock signal. If the basic design is not done carefully, life can become a nightmare for people evaluating the data.

The standard procedure sounds quite simple. An internal clock signal is compared against an external time signal, normally the 1 pps (pulse per second) signal derived from a GPS receiver's output. From the difference in time, a control signal is derived and the internal clock is adjusted accordingly. Normally this is done by a phase locked loop in combination with a voltage controlled oscillator. All systems distinguish between two operation modes. If the difference is bigger than a selectable amount of time, the adjustment is done instantly. If everything works perfectly, the so-called jam set mode only occurs during the initializing phase of the system. While switching on the recorder, it updates the absolute time and date by reading the GPS input, and synchronizes the internal time base. During normal operation the time base advance and retard control provides the capability to adjust the internal oscillator without disturbing data acquisition. Adjustments in the order of μ seconds per millisecond of the time base are allowed to smoothly synchronize the internal timing clocks with an external source or to simply adjust the internal clocks for known drift rates.

There are important differences in the technical realization of the clock control, resulting in quite different behaviors of the data acquisition systems. Selecting the start time of a recording window for a PDAS, an Orion, or a Güralp, results in digital data streams, starting exactly at the full second of the selected time. A Reftek or a Quanterra will start somewhere in the vicinity of the desired start time. The difference in design is quite small, but of great consequence. In an experiment with more than one instrument of these two types, each recorder samples at the same sampling rate, but at different times. A sample, related to midnight, is randomly distributed over two days on different recorders. In the case of a Reftek or a Quanterra, the ADC/DSP timing signal is derived from an internal oscillator, only providing the clock signal for the ADC/DSP unit and not synchronized by the external clock. Synchronizing is done at the output of the digital decimation filter. The PDAS, Orion, and Güralp recorders are so-called mono-oscillator systems. All timing signals are derived from a master oscillator, providing a 1 pps signal, which controls the timing of the whole recording system. This internal 1 pps signal is adjusted to zero phase with respect to the synchronizing external 1 pps clock signal and forces synchronizing of the ADC, i.e., at the input of the decimation filter. With this timing concept, all instruments in an array or on a profile, take their samples at the same time, starting at full seconds. This simplifies data acquisition of continuous data streams to a great extent.

6.5 Data management

6.5.1 Storage media

In field experiments with continuously recording instruments, one collects about 30-50 MBytes of data per day at a 3-component station with 100 Hz sampling rate. During the last years, hard disks have overcome other mass storage technologies in field recording. They have become reliable, are quite cheap, robust if switched off, their power consumption is moderate, and access is much faster than on other mass storage media. The big advantage of hard disks against other magnetic- and opto-magnetic media is the fact that they are encapsulated and insensitive in rough and dusty environments. For connecting the hard disk to the recorder, many systems support SCSI. This bus system is an accepted and well defined

6. Seismic Recording Systems

industry standard, available on most platforms. Up to 7 devices can be connected in parallel on a 8-bit SCSI bus and the technical specification even allows hot pluggable devices, i.e., the operator can change the hard-disc without interrupting continuous recording. With an Orion or a Güralp system, it is possible to change the hard disk without interrupting the recording process. On a PDAS this will not only result in a corrupted file system, but one also has a good chance to kill the SCSI controller chip. The only problem with SCSI hard-discs is that they are developing more and more to the high performance server market. In this market segment, low-power (and low price) is not a basic design goal. All the hard-discs fulfilling the requirements for seismic recording systems, were designed for laptops, where IDE is the standard system interface. But to swap IDE devices in a running computer system for reading or writing, ranges from tricky to impossible. So we are still waiting for the manufacturer of seismological recording systems providing us with a hot pluggable mass storage device based on low-power IDE drives and equipped with a TCP/IP connection, which would allow access to a practically unlimited number of storage media at the same time, with all the benefits of a network connection.

6.5.2 Data formats, compression and metadata

Even a hard disk, designed for random access, can be used as a sequential block device, just like a tape drive. The data stream is subdivided into blocks of a fixed length, including the header which defines the type of data and holds the date and time stamp of the first sample. Besides the raw data streams, state of health and status information are generated. Additional channels containing information about internal voltages, temperatures, and information related to the synchronization against the external clock are recorded.

Each subsequent block of data is written to the hard disk. No file or directory structure is necessary and it is quite easy to implement compression algorithms or ring buffer structures. Steim (1986) introduced a widely used algorithm to compress integer time series without loss of information. Blocks of data are organized in frames with a fixed length. Only the difference with respect to the first sample in the frame is stored. An associated table, occupying a 2-bit/sample within the frame, holds the information about the significant word length of the stored differential value (8-, 16- or 32-bit). The compressional rate depends on the difference between two subsequent samples, or in terms of seismology, on the noise situation of the measured signal. In general the compression rate achieved with this so-called STEIM1 algorithm is in-between $1/3$ and $2/3$. Steim extended this scheme introducing 4 bit differences in the STEIM2 algorithm and gaining a compression rate up to 30% against STEIM1. The Quanterra, the Orion, and the Reftek compress their data with the STEIM1 algorithm, whereas Güralp has its own compression method, but there is no principal difference.

If the block header holds two additional pointers to its predecessor and successor, this is called a tagged file system. In fact, it allows only sequential access to the data of a specific stream. Some systems like the Orion reserve a certain amount of disk space for each raw data stream. This saves the two pointers and in addition, allows an easy implementation of ring buffers. After a ring buffer is filled, the oldest data are subsequently overwritten. This user selectable behavior utilizes continuous data acquisition with a fixed length of time history. If an event in which one is interested occurs, the length of the ring buffer gives the time in which one has to access the station and download the data. Sampling 3 channels at a rate of 100 Hz, a 4 GByte hard disc will provide recording capacity for about 80 days.

To read the data into a computer system, one has only to be able to access the physical raw data device and to know the logical structure of the data frames. The big disadvantage of the frame structure with compressed data is that there is no possibility to address an item directly as recorded at a specific time. One has to read all subsequent block headers from the beginning until finally accessing the data. This storage and compression concept in seismic recording systems is optimized with respect to disk space. This is the best solution for acquiring but a bad choice for processing the data. So the first step after reading the data into a computer system, is to convert and organize it within a file system. There are several different operating systems around, and each operates with several different versions or types of file systems. If a recording system relies on a specific file system, this can become a problem for the user, who has to organize the data on a different operating system.

File systems introduce an additional abstract layer to the data model and also have their specific limitations, starting with the number of characters in a file name, up to the maximum length of a single file. The PDAS is the only recorder mentioned here writing MS-DOSTM data files directly and organizing the data streams in a hierarchical directory structure. The Orion also utilizes the same file system. If the host system is able to mount an MS-DOSTM file system, the ring buffers are visible as ordinary files.

The conclusion of all the different data formats on different recording systems is that each one needs its special treatment. The only common level at the moment is the SCSI hardware, but even this will change in future. All systems have their own way to store the data logically. Even if Steim's compression algorithm is used to write the raw data, the block header structures may differ. But this is not the real annoyance. There is no common agreement on what type of additional information is or should be recorded by the system.

Each manufacturer has his own ideas, how to synchronize against the external clock signal and how to correct the drift of the time base, and of course, how to report this. So, from here on, no general recipe for converting raw data to the user's file system can be given. Also, no recipe is available on how to treat timing errors from different data loggers (there are systems around, even reporting *unknown error*).

The user's file system normally depends on the software being run to process the data. This is the scientific part of the game and may vary from project to project. To buy an instrument from a manufacturer who is supporting only one specific operating system and withholding information about the low-level data structures, may be a bad investment.

Unfortunately, the approach to unify the low level data formats for seismic recording systems, the SUDS-2 format initialized by Ward (1992), failed because of the complexity of the abstract data model and the non-agreement on a common platform for Unix and PC-based systems. Thus, the problem handling the metadata is still unsolved. All the data describing the instrumentation and the site location related to the stored waveform are called metadata. For archiving and exchange of waveform data, there are several data formats in use, mainly, the different variants of SEG-Y and GCF (pure ASCII code), which are independent of the hardware platform and even email-proof on 7-Bit mail servers. But the most complete and widely accepted standard is the SEED format and its MSEED variant. SEED is the only standard holding the most important metadata and the waveform data within one single file, a so-called SEED volume. MSEED is a subset of the SEED definition, holding the waveform-data only. Thanks to the excellent software library QLIB2, MSEED has become an easy-to-use and platform-independent data format.

6. Seismic Recording Systems

The software packages provided by the manufacturers are mainly reduced to set-up, quick lock, and quality check functions and are normally not intended for scientific evaluation of the data. The software should also provide converters to more common formats mentioned above. Here the GEOFON, the ORFEUS, and the PASSCAL home pages are ideal starting points to find all kinds of useful software and information.

6.6 Conclusions and final remarks

There is no "best" recording system available. It always depends on several aspects, which instrument to choose - and the weights are different from project to project. The requirements for a temporary installed, portable network are completely different from a permanent setup in an observatory, connected to the power supply system and the Internet. Beyond this, Delta-Sigma-Modulators with 130-140 dB and GPS-timing are state of the art, Web-hosted communication via Internet is coming up, and prices, hopefully, down. Within this chapter several products from various manufacturers are named. They are only used as examples to show specific differences in the technical realization of seismic recording systems. In fact, there are more products available but this chapter has no intention to give an overview of the market. If one particular product is not mentioned here, it is not an opinion in terms of its quality.

6.7 Glossary of technical terms and links

ADC : Analog to Digital Converter. A device that converts data from analog to digital form.

CS5321/CS5322 : A 24-bit word-length variable bandwidth ADC. The CS5321 is a Sigma-Delta-Modulator which functions together with the CS5322 digital filter as a high resolution ADC. The CS5322/CS5321 combination performs sampling, AD conversion, and anti-alias filtering. The circuits are manufactured by *Crystal* (<http://www.crystal.com/>).

DAC : Digital to Analog Converter. A device which takes a digital value and outputs a voltage which is proportional to the input value.

DSP : Digital Signal Processor. The *big four* programmable DSP chip manufacturers are Texas Instruments, with the TMS320 series of chips; Motorola, with the DSP56000, DSP56100, DSP56300, DSP56600, and DSP96000 series; Lucent Technologies (formerly AT&T), with the DSP1600 and DSP3200 series; and Analog Devices, with the ADSP2100 and ADSP21000 series. For further information have a look at www.bdti.com/pocket/dsp_guide.htm.

Earth Data : Earth Data Limited specializes in the research, design and manufacture of data acquisition, telemetry and 24-Bit portable recording systems (www.kenda.co.uk/edata) .

FIR : Finite Impulse Response filter, also named acausal- or, in their symmetrical realization, zero-phase-filters. For a brief description of digital filters (see Scherbaum,1996; and <http://lbutler.geo.uni-potsdam.de/service.htm>).

Gain-ranged Mode: A Gain Ranging Amplifier is scaling the input signal to fit the ADC's digitizing window based on signal level. This method increases the dynamic range, but not the resolution of a recording system. The resolution is limited to something less than

the number of bits available from the ADC, due to noise introduced by the uncertainties of the different gain steps. Gain-ranged mode was used in older 16-bit ADC based systems to achieve dynamic ranges up to 130 dB.

GEOFON : The GEOFON program of the GeoForschungsZentrum Potsdam presently operates, together with its partner organizations, 40 permanent and a varying number of longterm temporary broadband seismological stations. 30 permanent stations are located in Europe and the Mediterranean. Most of these stations are equipped with Streckeisen STS-2 very broad band seismometers and adequate Quanterra Q380 or Q4120 dataloggers (see www.gfz-potsdam.de/geofon/index.html).

GPS : **Global Positioning System**. There are a lot of good sites to start from, for example www.skydiversdepot.com/gps2.htm.

Güralp : Güralp Systems Ltd (GSL). Manufacturer of seismometers and data acquisition systems (www.guralp.demon.co.uk).

GSN : The IRIS Global Seismographic Network. The goal of the GSN is to deploy 128 permanent seismic recording stations uniformly over the Earth's surface. These stations continuously record seismic data from very broad band seismometers at 20 samples per second. It is also the goal of the GSN to record data with a dynamic range of 140 db (24 bit digitizers). (www.iris.washington.edu/GSN/index1.htm)

IDE : **Integrated Drive Electronics**. Originally called IDE, the ATA interface was invented by Compaq around 1986. Standardized by the ANSI group X3T10 (who named it *Advanced Technology Attachment* (ATA)). Ratification in November 1990.

IIR : **Infinite Impulse Response** filter, also named causal-filter. All analog filters are of this type. For brief discription of digital filters see Scherbaum (1996).

IRIS : **Incorporated Research Institutions for Seismology**. 1200 New York Ave. NW, Suite 800, Washington, DC 20005 (www.iris.edu).

Kinometrics : Kinometrics Inc. Manufacturer of seismic sensors and data acquisition systems. (see www.kinometrics.com).

Lennartz : Lennartz electronic GmbH. Manufacturer of seismic sensors and data acquisition systems (see www.lennartz-electronic.de).

MARSlite : The MARS recorders are an array of portable data loggers developed and manufactured by Lennartz electronic GmbH. Recent products are the MARSlite and M24 data loggers.

Nanometrics : Manufacturer of data acquisition systems. Nanometrics also offers complete network solutions based on satellite communication (see www.nanometrics.ca).

ORFEUS : **Observatories and Research Facilities for European Seismology**. ORFEUS is the European non-profit organization that aims at coordinating and promoting digital, broadband seismology in Europe (see orfeus.knmi.nl).

ORION : Digital recording system, manufactured by Nanometrics.

PASSCAL : **Program for the Array Seismic Studies of the Continental Lithosphere**. PASSCAL Instrument Center, New Mexico Tech, 100 East Road, Socorro, NM 87801, U.S.A (see www.passcal.nmt.edu/passcal/resources.htm).

6. Seismic Recording Systems

PDAS : Portable **D**ata **A**cquisition **S**ystem. Solid first generation digital recording system manufactured by Geotech/Teledyne, 3401 Shiloh Road, Garland, Texas 75041 (see www.geoinstr.com). This data-logger is no longer available on the market, but still widely used.

QLIB2 : Software library available as source code (C/Fortran) from Doug Neuhauser (doug@seismo.berkeley.edu) to read and write MSEED data files on different hardware platforms. Jewel found in the PASSCAL software distribution (Ver. 1.9) under contrib/mseed/qlib2. Unfortunately the PASSCAL routines do not profit from this library, because they used their own.

Quanterra : Advanced broad band remote data acquisition system. Developed by Steim (1986), it is the defacto standard in global broadband seismology. These days Kinemetrics is selling an array of Quanterra products with different specifications.

Reftek : Refraction Technology, Inc. 2626 Lombardy Lane, Suite 105, Dallas, TX 75220, U.S.A. (see www.reftek.com).

SAR-ADC : Successive Approximation Analog to Digital Converter.

SCSI : Small Computer System Interface. Bidirectional, parallel interface to connect up to 7 (15 with wide SCSI) external devices to a computer. ANSI-X-3T9.2 *American National Standards Institute* (see www.ieee.org/index.html).

TCP/IP : Transmission Control Protocol over Internet Protocol. The de facto standard Ethernet protocols. TCP/IP was developed by DARPA for internet working and encompasses both network layer and transport layer protocols. While TCP and refer to the entire DoD protocol suite based upon these, including telnet, FTP, UDP and RDP.

TERRAscope : is a very broadband seismographic network in Southern California. Each station consists of a Wielandt/Streckeisen seismograph, a strong-motion sensor, and a barograph. The data is recorded on-site using the 24-bit Quanterra datalogging system and collected by the Caltech Seismo Lab. (www.gps.caltech.edu/terrascope/TerraInfo.html).

Acknowledgments

Reviews and suggestions by P. Bormann, J. Bribach, J. Havskov and K.-H. Jäckel have been taken into account to complement the initial draft of this paper.

Recommended overview readings (see References under Miscellaneous in Volume 2)

Buttkus (1991)
Havskov and Alguacil (2004)
Scherbaum (1997)
Scherbaum (2001)
Shannon (1949)
Ward (1992).
Willmore (1979)

7

Site Selection, Preparation and Installation of Seismic Stations

Amadej Trnkoczy, Peter Bormann, Winfried Hanka,
L. Gary Holcomb and Robert L. Nigbor

7.1 Factors affecting seismic site quality and site selection procedure (A. Trnkoczy)

7.1.1 Introduction

Seismic site selection is not often given the amount of study it requires. The capacity of any new seismic network to detect earthquakes and to record representative event waveforms will be governed by the signal and noise characteristics of its sites, no matter how technologically advanced and expensive the equipment used. If seismic noise at the sites is too high, many of the benefits of modern, high dynamic-range equipment will be lost. If the noise contains excessive spikes or other transients, or if man-made seismic noise is present, high trigger thresholds will be needed and result in poor network detectability. If a station is situated on soft ground, very broadband (VBB) or even broadband (BB) recording can be useless and short-period (SP) signals may be unrepresentative due to local ground effects. If the network layout is inappropriate, the location of seismic events will be inaccurate, systematically biased, or even impossible. A professional site-selection procedure is therefore essential for the success of any new seismic station or network.

It is best to begin the process of site selection by choosing, generally, two to three times as many potential sites as will finally be used. One can then study each one and choose the sites that meet as many desired criteria as possible. One may even model the performance of a few most-likely network layouts and, by comparing the results, be able to make an informed decision about which layout will best record and locate seismic events.

All parameters relevant to the site selection process are discussed here and the process is demonstrated by seeking the best locations for a six-station network around a nuclear power plant. The main goals of this particular project (Trnkoczy and Živčić, 1992) were to monitor local seismicity with a high network detectability and the ability to accurately locate local events. Thus, the placement of short-period seismometers and of surface seismic vaults were mainly, but not solely, considered.

7. Site Selection, Preparation and Installation of Seismic Stations

7.1.2 Offsite studies

The site selection procedure includes off-site studies and fieldwork. Off-site, or "office" studies are relatively inexpensive. They should be performed first. One can study maps and gather information about the potential sites from local and regional authorities. Once we have gathered all this information, it is likely that many potential sites will be eliminated for one reason or another. This will minimize future fieldwork and its associated costs.

A list of parameters usually included in the off-site study includes:

- geographic region of interest
- seismo-geological conditions
- topographic conditions
- accessibility
- seismic noise sources in the region
- data transmission and power considerations
- land ownership and future land use issues
- climatic conditions

7.1.2.1 Definition of the geographic region of interest

The first step is defining the goals and the geographic region of interest taking both socio-economic and seismic information into account. If the main goal of the new seismic network is monitoring of the general seismicity in an entire country, this stage is greatly simplified. For other projects, one has to examine all the known major geologic faults from geological maps with a view to assess their neotectonic activity and potential, identify seismotectonic features from seismotectonic maps, if available, and compile all available information about the seismicity in the area. One has also to compile historical and instrumentally recorded events in the broader region from earthquake catalogs and other sources. The results of such a study are shown in the following figures for an area in Slovenia. Fig. 7.1 shows the broader region chosen for our example and the main geological faults within it.

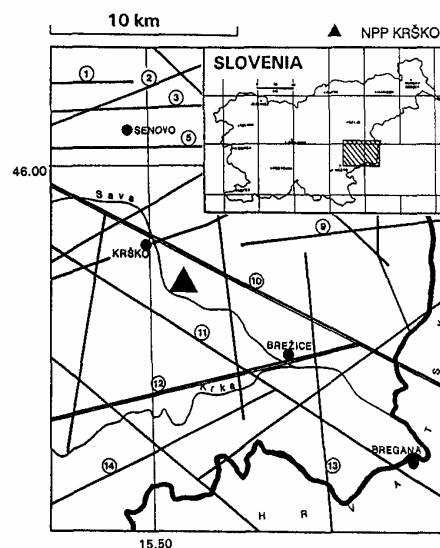


Fig. 7.1 The broader region chosen for the network in Slovenia and the main geological faults in this area (9 - Artice fault, 10 - Brestanica fault, 11 - Sava fault, 12 - Podbocje fault, 13 - Brežice fault, 14 - Orehovec fault).

7.1 Factors affecting seismic site quality and the site selection procedure

Fig. 7.2 shows the distribution of earthquake epicenters as taken from seismic catalogs while Fig. 7.3 depicts the isolines of seismic energy release during the time-span of the catalogs and the hatched area finally chosen for the detailed study.

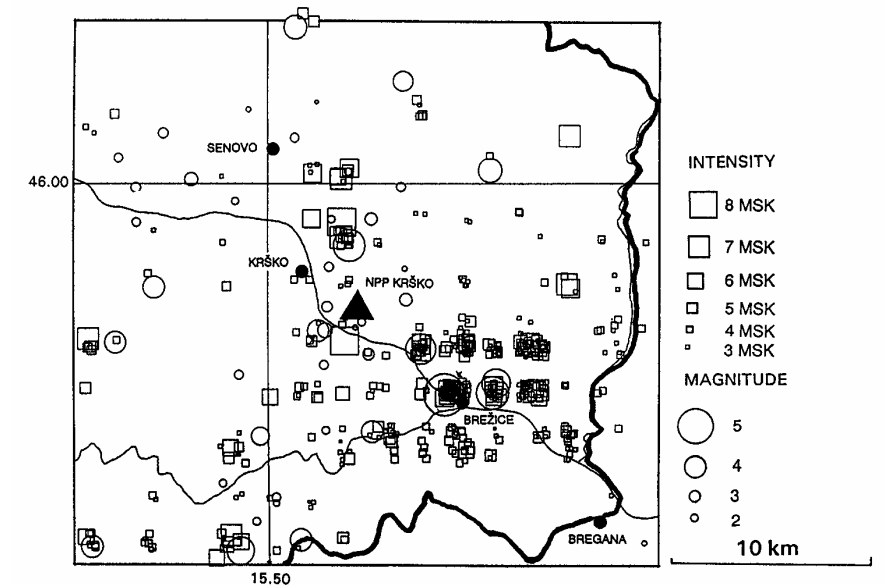


Fig. 7.2 Earthquakes in the wider region under investigation in Slovenia. The data were compiled from all available earthquake catalogs.

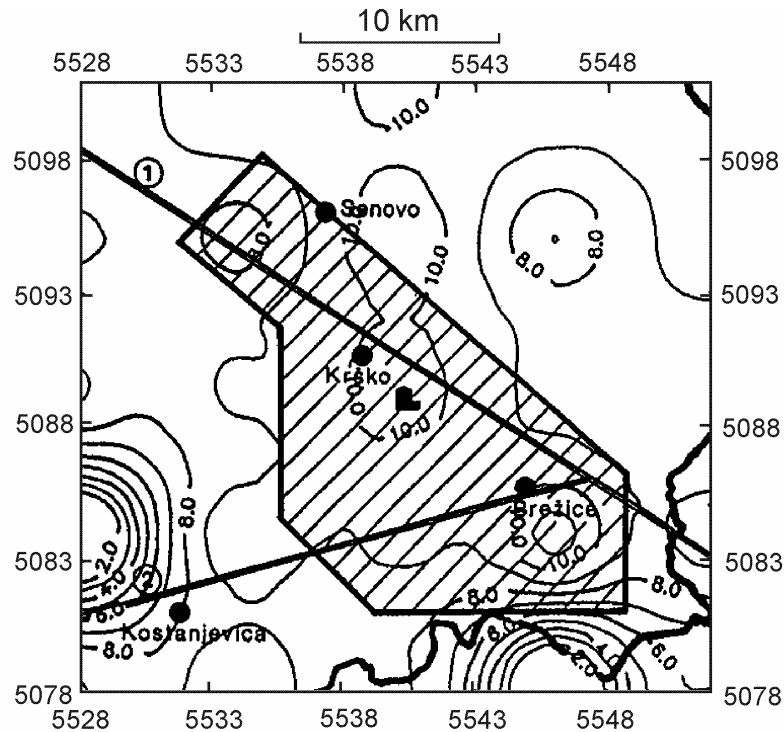


Fig. 7.3 Final choice of the area to be studied in detail by the seismic network (hatched area). Also shown are the isolines of released log-seismic energy during the time-span of the catalogs (in J/km^2).

7. Site Selection, Preparation and Installation of Seismic Stations

7.1.2.2 Seismo-geological considerations

The underground conditions at a station influence both the seismic signal and the noise conditions and thus have a significant bearing on the potential sensitivity of a seismic station. Usually, the higher the acoustic impedance of the bedrock, the smaller the seismic noise and the higher the maximum possible gain of a station. Therefore, for each new seismic network, one should at least prepare a map showing simplified seismo-geological conditions. One may then infer a related map in terms of acoustic impedance or bedrock quality grades with respect to their suitability for the installation of seismic recording sites. Fig. 7.4 shows an example for the region under study while Tab. 7.1 gives an example of how bedrock “quality” grades may be classified.

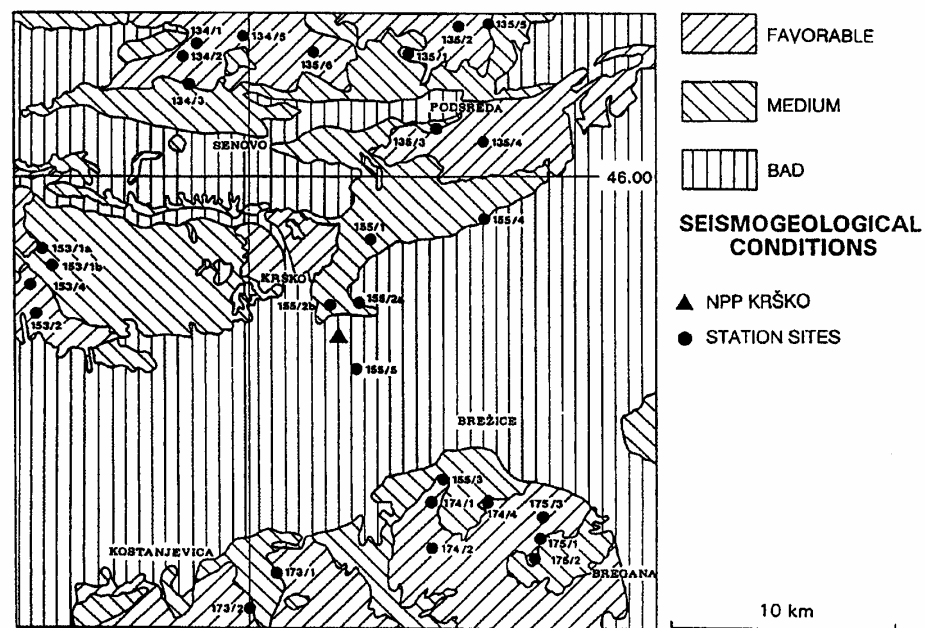


Fig. 7.4 Subdivision of the region shown in Fig. 7.2 into three grades of bedrock quality. The dots mark the positions of considered station sites.

Tab. 7.1 Classification of different types of outcropping geological formations in “quality” categories (according to R. Vidrih, personal communication 2001). Grade 5 is the best rock for seismic recordings and grade 1 is the worst.

Grade	Type of sediments/rocks	S-wave velocity
1	Unconsolidated (Alluvial) sediments (clays, sands, mud)	< 100 – 600 m/s
2	Consolidated clastic sediments (sandstone, marls); schist	500 – 2100 m/s
3	Less compact carbonatic rocks (limestone, dolomite) and less compact metamorphic rocks; conglomerates, breccia, ophiolite	1800 – 3800 m/s
4	Compact metamorphic rocks and carbonatic rocks	2100 – 3800 m/s
5	Magmatic rocks (granites, basalts) ; marble, quartzite	2500 - > 4000 m/s

Note: Shear-wave velocities given by engineers (e.g. Ambraseys et al., 1996) in relation to the category “bedrock” (> 750 m/s) are significantly smaller than for competent hard rock due to near surface weathering (see 7.1.3.3) and the consideration of very short wavelengths only.

7.1 Factors affecting seismic site quality and the site selection procedure

7.1.2.3 Topographical considerations

The topography in the vicinity of a potential site has to be considered. Extremely steep mountain slopes or deep valleys may unpredictably and unfavorably influence seismic waveforms and signal amplitudes. In addition, mountain peaks are usually much more susceptible to wind-generated seismic noise, lightning strikes, and perhaps icing of the communications equipment. Therefore it is wise to avoid such locations, if possible. Sites in moderately changing topography are preferable.

The topography also has to be considered for radio-frequency (RF) telemetry networks. Establishing RF links is much simpler if hill-top sites are selected, but it is important not to let this consideration compromise the seismological considerations. (See IS 7.2 Using existing communication tower sites as seismic sites.)

7.1.2.4 Station access considerations

Seismic stations are generally located in remote areas, as far as possible away from any human activity. This can often result in relatively difficult access. Public roads do not (or should not) reach most good seismic stations and walking a considerable distance, or the use of off-road vehicles, is more or less inevitable. Inexperience in site-selection often leads to too much compromise in this respect. One needs to find a reasonable trade-off between remoteness and ease of access. Stations which are too difficult to access are expensive to establish and maintain. In consequence, they often suffer from inadequate maintenance and long repair times.

Road maps and 1:25,000 scale topographic maps usually allow an approximate estimate of the difficulties and time needed to access any potential sites. In mountainous regions both the distance from the nearest road accessible by vehicle and the elevation difference between the site and the last point accessible by vehicle are important. One should allow between 15 and 30 min of cross-country walking time for each km of distance (25 to 50 min for each mile), depending on vegetation cover, and between 20 and 30 min for each 100 m (300 feet) of height difference. Stations which require more than half an hour of cross-country walking are rare. However, one has sometimes to accept longer walking distances, particularly if RF telemetry is involved.

Seismic stations are frequently set up at existing meteorological stations. This often happens in countries which are not experienced in seismometry and especially when meteorological institutions are appointed to maintain seismic installations. Such combination of stations or network operations are not advisable, since seismological and meteorological site selection criteria are very different.

7.1.2.5 Evaluation of seismic noise sources

An assessment of man-made and natural seismic noise sources in the region from maps is only the first stage of a proper seismic noise study. It should always be followed by field measurements of the noise. Nevertheless, road and railway traffic, heavy industry, mining and quarry activities, extensively exploited agricultural areas, and many other sources of man-made seismic noise around the potential sites, along with natural sources like ocean and lake

7. Site Selection, Preparation and Installation of Seismic Stations

shores, rivers or waterfalls can be evaluated in a qualitative manner from the maps and by inquiry of local authorities. Willmore (1979) gives valuable information about the recommended minimum distances between the site and these types of noise sources. Distances are given for three different sensitivities of a seismic station, two different geological conditions and both high and low seismic coupling between noise source and station site. The table is reproduced in IS 7.3 along with instructions for its use. An example for its application for the station Loma Palo Benito is given in Fig. 7.5. Nearly all the minimum distance requirements for recordings with a gain around 1 Hz of between 50,000 and 150,000 are fulfilled (the distance to the lake shore is an exception). Six criteria are not fulfilled for a gain of 200,000 or more (see shaded cells).

Note that the above guidelines were designed for 1960's technology (analog paper seismographs). They are most applicable for seismic signal frequencies above 0.1 Hz; i.e., for the medium- and high-frequency range of seismic signals. Seismic noise at lower frequencies is mainly influenced by seismo-geological and climatic conditions (see 7.1.2.8) at the recording site and much less by the seismic noise sources dealt with in the table.

STATION SITE NAME: Loma Palo Bonito COORDINATES: N 18° 46' 58.4" W 70° 13' 20.1"		SITE #:7			DATE OF VISIT: 02/14/1998			ACTUAL DISTANCE [km]	
		HARD ROCK GRANITE, ETC.			HARDPAN HARD CLAY, ETC.				
		RECOMMENDED MINIMAL DISTANCES [KM]							
		A	B	C	A	B	C		
1. Oceans, coastal mountains systems		300	50	1	300	50	1	75	
2. Large lakes		150	25	1	150	25	1	22	
3. Large dams, waterfalls	a	40	10	1	150	25	5	22	
	b	60	15	5	50	15	10		
4. Large oil pipelines	a	20	10	5	30	15	5		
	b	100	30	10	100	30	10		
5. Small lakes	a	20	10	1	20	10	1	20	
	b	50	15	1	50	15	1		
6. Heavy machinery, reciprocating machinery	a	15	3	1	20	5	2	25	
	b	25	5	2	40	15	3		
7. Low waterfalls, rapids of a large river, intermittent flow over large dams	a	5	2	0.1	15	5	1		
	b	15	3	1	25	8	2	6	
8. Railway, frequent operation	a	6	3	1	10	5	1	40	
	b	15	5	1	20	10	1		
9. Airport, air traffic		6	3	1	6	3	1		
10. Non-reciprocating machinery, balanced industrial machinery	a	2	0.5	0.1	10	4	1	25	
	b	4	1	0.2	15	6	1		
11. Busy highway, large farms		1	0.3	0.1	6	1	0.5	2.3	
12. Country roads, high buildings		0.3	0.2	0.05	2	1	0.5	2.0	
13. Low buildings, high trees and masts		0.1	0.03	0.01	0.1	0.1	0.05	0.03	
14. High fences, low trees, high bushes, large rocks		0.05	0.02	0.005	0.06	0.03	0.01	0.02	

Legend:

- A Seismic station with a gain of 200,000 or more at 1 Hz
- B Seismic station with a gain from 50,000 to 150,000 at 1 Hz
- C Seismic station with a gain of approximately 25,000 at 1 Hz
- a Source and seismometer on widely different formations or that mountain ranges or valleys intervene
- b Source and seismometer on the same formation and with no intervening alluvial valley or mountain ranges

Fig. 7.5 Minimum recommended noise-source-to-station-site distances according to Willmore (1979) and actual distances for the seismic station Loma Palo Benito, which is placed on hard granite rock. Shaded cells indicate that for these criteria the conditions for a class A site are not fulfilled.

7.1 Factors affecting seismic site quality and the site selection procedure

Nowadays, with the ready availability of seismic recorders with a large dynamic range, it would be preferable to express the seismometer gain classes A – C in terms of the achievable minimum resolution of ground displacement or velocity amplitudes above the noise level at about 1 Hz. These would be approximately < 5 nm or < 30 nm/s, respectively, for class A and about 2-4 times and > 8 times larger for classes B and C.

For each potential site in a network, one should determine, using maps, the actual distances of the site from relevant seismic noise sources (the extreme right column) and compare them with the recommended minimum distances. The sites which satisfy all or most of the recommendations are the best. Note, however, that local seismic noise sources like trees, buildings, fences, would require on-site evaluation. This information can be added to the table later during fieldwork.

Once we have gathered this information for all the potential sites in a network, we can draw a map, similar to that in Fig. 7.6, where all the potential sites and minimum recommended distances from known seismic noise sources are shown. The latter is achieved by drawing circles around point noise sources and bands of appropriate width along roads or railways. This gives a good overview of all the noise sources at once and helps us to see which ones and how many of them influence a particular potential seismic site.



Fig. 7.6 Map of the seismic network region with all potential station sites (full dots) and known seismic noise sources (roads, railway, cities, villages, industrial facilities, quarries, etc) with circles of minimum recommended distances drawn around them for the case of gain 25.000 for SP seismic stations at 1 Hz set on hard clay, hardpan and similar ground, i.e., case C b (i.e., source and seismometer on same formation and with no intervening alluvial valley or mountain range) according to Willmore (1979).

7. Site Selection, Preparation and Installation of Seismic Stations

7.1.2.6 Seismic data transmission and power considerations

For radio-telemetry networks we must consider the topography within the entire network in order to design the data transmission links. Topographic maps (1:50.000 or 1:25.000) are best for this purpose. We look for a topography which enables reliable direct radio frequency (RF) links from the remote stations to the central recording site, or the minimum number of RF repeaters if topography and/or distance do not allow direct connection. More information is given in section 7.3.

If telephone lines are used for seismic data transmission, we must first check for line availability and the distances over which new lines would have to be installed. This information can be obtained from local telephone companies. New phone lines are often a significant proportion of the total cost of site preparation.

The next question concerns the power supply. If mains power is not available on site, we need to calculate the distance over which new power lines would have to be laid and the likely costs. If this is not possible, or the cost is too great, the cost for solar panels has to be evaluated.

7.1.2.7 Land ownership and future land use

During planning of a new network it is very important to clarify the ownership of the land being considered for a station and any plans for its future use. It makes no sense to undertake extensive studies if one is actually unable to use certain sites because of property ownership issues or if it appears that future development will make the site unsuitable for a seismic station. This information should be gathered from local (land ownership) and regional (future land use) public offices and authorities.

If the land is privately owned, one should contact the owner as soon as possible and make every effort to agree on a renting or purchasing contract to the satisfaction of both parties. It is very important to have "friends" rather than "enemies" around the seismic stations. In many countries this may be very important for the security of the installed equipment.

7.1.2.8 Climatic considerations

Several climatic parameters can influence seismic site selection. Regional or national meteorological surveys can provide this information. It can also be found in yearly or longer-term bulletins, which are published by nearly every meteorological institution. In developing countries it is sometimes not easy to get complete information. However, we do not need precise values for these parameters and even rough estimates can help in site selection and design of seismic shelters.

The following climatic parameters are important:

- The minimum and maximum temperatures at a site determine how much thermal insulation will be needed for the seismic vault and instruments. Temperatures below zero degrees Celsius may cause icing of antennae. Special shielding is often required in high mountains and polar regions.

7.1 Factors affecting seismic site quality and the site selection procedure

- We need to know the frequency and maximum wind speeds at sites. Wind is a major source of seismic noise, so sites with less wind are preferable to sites placed on windy mountain ridges.
- Solar data is needed to determine the minimum size required for solar panels, if they are required to provide power. The number of sunny days in the worst month and/or the longest expected uninterrupted cloudy period in a year can serve as a measure.
- The frequency and amount of precipitation (total precipitation per year and maximum precipitation per hour) will determine protection measures required to keep the vaults dry.
- In colder climates, annual snowfall levels determine how accessible a station will be during the winter, the waterproofing measures required and – if used – the optimum installation angle and size for solar panels.
- Protection against lightning is very important and has significant financial consequences. One needs to decide on what protection equipment is necessary using information on the observed frequency of lightning. Alternatively, one has to calculate how much lightning damage is likely if protection measures are not implemented. The best method for this is to obtain isokeraunic isolines, which are related to the probability of a lightning strike. This data is rarely available and it is often easier to obtain less specific but more generally available meteorological parameters – such as the annual number of days with severe thunderstorms in the area. Lightning usually varies enormously from one region to another and also varies locally, depending on the topography. Serious consideration of these parameters and the knowledge of local people on these issues are definitely worthwhile.

7.1.3 Field studies

Field studies are the next step in the site selection process. Expect to make several visits to each potential site. A seismologist familiar with seismic noise measurements, a seismo-geologist, and a communications expert (if a telemetry network is considered) should all visit the sites. You should allow between one and three days per site to accomplish the fieldwork. This assumes that all pertinent maps and information are available in advance and the logistics are well organized. Much also depends on a country's infrastructure and the size of the network. If the network will use RF telemetry, add an extra 20% to the time for topographical profiling and RF link calculations.

If site selection is purchased as part of the services provided by an equipment manufacturer, see IS 7.1 for a summary of the information that should be provided to them.

In general, experts visiting the sites should:

- verify the ease (in any weather) of access to the site;
- search for very local man-made seismic noise sources which might influence the site, but may not be indicated on maps (see text to Fig. 7.7);
- perform seismic noise measurements;
- study the local seismo-geological conditions;
- investigate the local RF data transmission conditions (if applicable);
- verify availability of power and telephone lines.

7. Site Selection, Preparation and Installation of Seismic Stations

7.1.3.1 Station access verification

Station access should generally be possible throughout the year. However, a few days of inaccessibility due to snow or high water per year can normally be tolerated. This can be checked by talking to local people.

If non-public dirt roads are used to access the site, we need to ask about the future of these roads since roads built and owned by private, military, or forest authorities are sometimes abandoned. If there is no guarantee that such roads will be maintained in future, it is better to reposition the seismic site.

7.1.3.2 Local seismic noise sources and seismic noise measurements

During fieldwork, one should explore the vicinity of the potential site for local sources of seismic noise, usually man-made, which may not be resolvable from the available maps. A single small private "industrial" facility too close to the site may ruin its seismic noise performances completely. Local people are the best source of information.

Measuring seismic noise at the site is an important task. Seismic noise varies greatly depending on the season of the year, weather conditions, and innumerable daily occurrences. Seasonal variability of seismic noise has mainly natural causes and is clearly developed for periods, T , greater than 2 s. The variation may be as large as 20 dB at the spectral peak for ocean-storm microseisms close to $T = 7$ s. In contrast, high-frequency noise is mostly man-made (traffic, machinery), often with a pronounced diurnal variation of the order of 10 to 20 dB. In order to accurately record all these factors, it is best to take measurements at each site over a long period of time; long enough to record a number of earthquakes. These will allow a comparison of the sites based on signal-to-noise ratio, which is the main guiding parameter for the quality of a site.

Sufficiently long measurements are often not performed for financial reasons. In such cases, some measurements are much better than none at all. Short-term measurements can not provide complete information about the noise levels at a site, but they are still very useful to identify man-made noise sources and to assess the daily noise fluctuations in the important frequency range for small local and teleseismic events (i.e. from 0.5 Hz to 20 Hz). It is important that any short-term measurements (say of 15 min duration) are carried out during specific times when maximum and minimum noise conditions are expected.

To assess the potential influence of long-term natural seismic noise variation, we should also obtain noise data from existing seismic stations in the region. If there are none of these, we have to set up one or more temporal reference stations which are not moved from site to site. By comparing noise records taken at the same time at the reference station(s) and the potential new site locations we can, at least with respect to the long-period natural seismic noise, assess the representativeness of the noise data sampled at the potential sites by scaling it to the reference site(s). This assures that any variations in natural seismic noise levels over time will not affect the comparison of different potential sites.

Records of seismic noise are usually presented as noise spectra. These can reveal more information about the type and importance of various seismic noise sources around the site than the corresponding time-domain records alone. A typical noise spectrum is shown in Fig.

7.1 Factors affecting seismic site quality and the site selection procedure

7.7. We can easily see high levels of man-made seismic noise (frequencies around 15 Hz). Spectral spikes from 3 to 5 Hz shown in this spectrum originate from heavy machinery working in a quarry at 4 km distance.

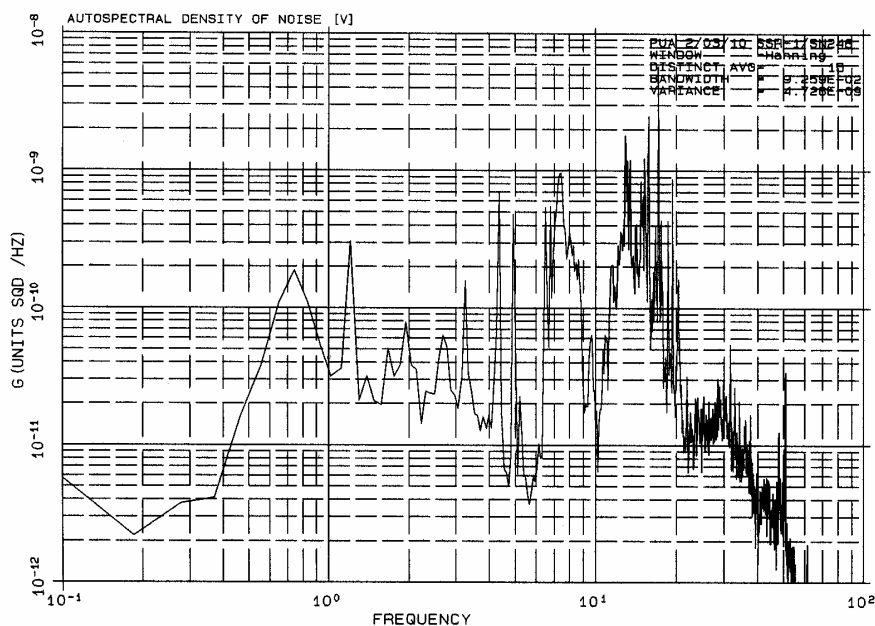


Fig. 7.7 Typical seismic noise spectrum (ground velocity power density in $\text{m}^2/\text{s}^2/\text{Hz}$) at a potential seismic station site showing man-made seismic noise generated by a nearby city and heavy machinery working in a 4 km distant quarry.

However, noise spectra should never be determined without prior inspection of the original time domain records which have to be cleaned of unrepresentative spurious or transient events. Also the analysis of noise conditions should never be made on the basis of the calculated spectra alone but always in conjunction with the related time-domain records. Examples are given in sub-Chapter 7.2.

The data requirements for noise analysis depend on the type of station to be installed. For short-period stations, use noise records that are at least two minutes long to allow calculation of stable seismic noise spectra in the frequency range from 0.1 to 50 Hz. For broadband stations, use noise records that are at least twenty minutes long for noise spectra calculations from 0.01 to 50 Hz. The sampling rate should be at least 100 Hz in both cases. In order to reduce any bias due to diurnal noise variations, the measurements at the various sites should be taken at about the same time of the day. Whenever possible, use identical equipment and processing methods at all potential sites and at the reference station(s). This greatly simplifies the normalization procedure. More information about seismic noise and its measurement is given in sub-Chapter 7.2

It should be mentioned here that the assessment of seismic noise for a Very-Broad-Band (VBB) seismic station requires much more effort. Days or even months of measurement are often required to get a full picture of the seismic noise conditions at the potential site (see Uhrhammer et al., 1998). A quiet short-period station site is not necessarily a good long-period noise site. Seismic noise may behave differently in the different frequency ranges.

7. Site Selection, Preparation and Installation of Seismic Stations

7.1.3.3 Field study of seismo-geological conditions

A seismo-geologist should study the geology to determine its local complexity. Uniform local underground conditions are preferred for seismic stations. The seismo-geologist should also verify the actual quality of bedrock as compared to that given in geologic maps and try to estimate the degree of weathering that local rocks have undergone. This can sometimes give a rough estimate of the depth required for the seismic vault to place the seismometers on unweathered bedrock. Unfortunately, it is often highly unreliable to judge the required vault depth in this way. At most sites only shallow seismic profiling, drilling, or actual digging of the vault can reliably reveal how deeply the rock is weathered and how deep the seismic vault must be. If shallow profiling is planned (see 7.1.3.5 below), the seismo-geologist should precisely determine the position of the profiles.

If there are local sources of high-frequency seismic noise around the site, a seismologist should carefully assess, both by inspection and measurement, to what extent they might affect recordings at the site. If the noise sources and the site are located on the same rock or soil formation, one can expect a high degree of seismic coupling between the noise source and the station. On the other hand, when the noise sources and the station are located on different geological formations with a significant impedance contrast between them, the seismic coupling is rather weak. In this case even nearby noise sources might not disturb seismic records much. The station BRG in Germany is a striking example. This is one of the best stations in the German Regional Seismograph Network (GRSN). The station is located in the middle of a busy resort town, next to a main road built on the aggraded bank of a rushing creek. The seismographs have been placed 150 m away from the road in an abandoned mining gallery which was driven horizontally from the road level into an outcropping Devonian hornschist rock cliff. Thus, the seismic sensors are well decoupled from the nearby-generated traffic noise. The site quality of BRG would correspond to B in Fig. 7.5.

7.1.3.4 Field survey of radio frequency (RF) conditions

A communications expert visiting the site should examine potential obstacles to radio-wave transmission. He or she should also examine the immediate topography surrounding the site because frequently it can not be resolved from 1:50,000 scale maps, normally used in RF topographical profiling. This study needs to define the minimum required antenna height for reliable data transmission. For more information see sub-Chapter 7.3.

7.1.3.5 Shallow seismic profiling

Shallow seismic profiling is usually the last step in the site selection process. It is probably the most expensive step and has usually to be contracted out to a seismic-engineering company. It should be done only at the most likely and most important sites. Shallow refraction profiles yield quantitative parameters on the rheological quality of the bedrock and enable determination of the depth of weathering. The results can determine the best position of the seismic vault as well as its required depth. One should use two approximately perpendicular profiles, each about 100 meters long, in order to determine the seismic wave velocity (for P and/or S waves, depending on the type of source used) down to a depth of 20 to 30 meters. This is enough even for the deepest seismic vaults considered. If the

7.1 Factors affecting seismic site quality and the site selection procedure

seismometer is to be installed in a borehole, seismic profiling needs to penetrate to depths of about 100m, the typical maximum borehole depth.

If seismic profiling is not included in the site evaluation, most likely for financial reasons, unexpected results may occur when digging the seismic vault. One should dig until reaching bedrock and that can sometimes be unexpectedly deep. One needs to anticipate that vaults will have to be repositioned and re-dug if weathered bedrock happens to be extremely thick. This often makes the relatively high cost of profiling a wise investment. The same argument applies to boreholes, although it is easier and less costly to deepen or move a borehole than it is for a vault.

7.1.4 Using computer models to determine network layout capabilities

Once we have decided on the final number of seismic stations and are very close to the final layout of the system, meaning that we have chosen two or three possible network layouts, the next useful step is to make a computer model of the network. The modeling should answer the question: Which particular network layout performs best for different aspects of network performances? One can then use these results to choose the best possible network layout for particular requirements. Among the parameters one may wish to study are:

- network detectability in terms of the spatial distribution of minimum magnitude of events which can still be recorded with a given signal-to-noise ratio (Fig. 7.8);
- precision (i.e., calculated accuracy) of event epicenter determinations in the region (Fig. 7.9);
- precision of event hypocenter determination in the region (Fig. 7.10);
- maximum magnitude of events that can be recorded without clipping (this requires an assumed gain and dynamic range of the recording equipment to be used in the network).

Note that optimal configurations for event location are often not optimal for source mechanism determination, tomographic studies or other tasks (Hardt and Scherbaum, 1994).

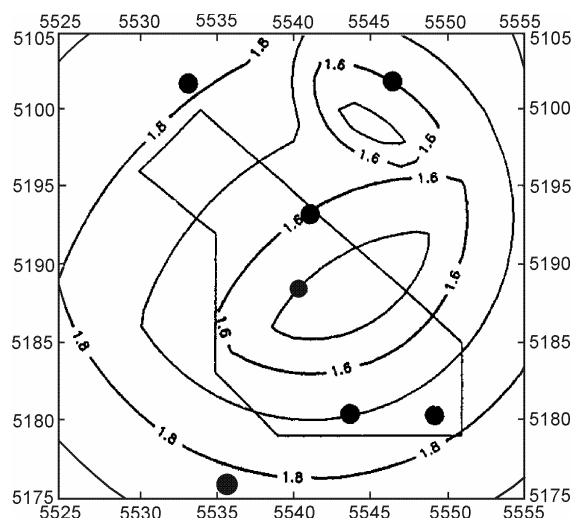


Fig. 7.8 An example of computer modeling of network capabilities. Isolines of minimum magnitude of events detected at 5 seismic stations (from six in the network) with a signal-to-noise-ratio >20 dB are shown for the best of the alternative network layouts.

7. Site Selection, Preparation and Installation of Seismic Stations

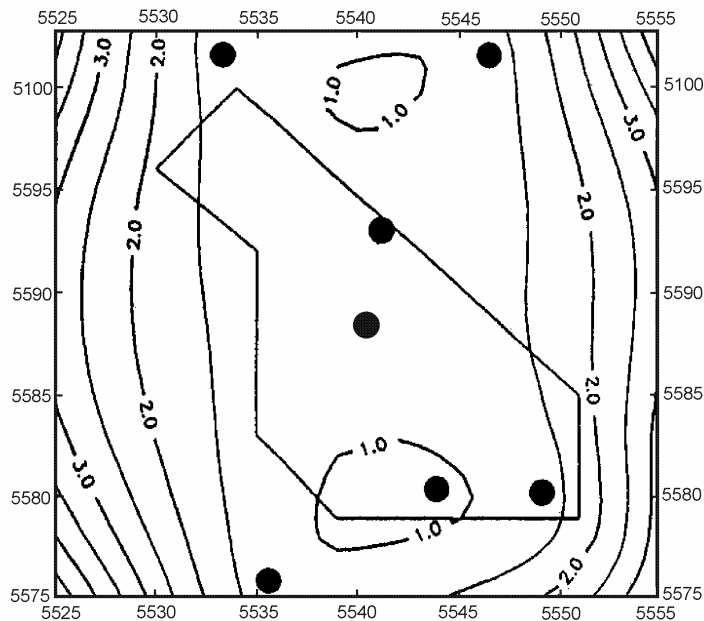


Fig. 7.9 An example of computer modeling of network capabilities. Isolines of uncertainty of epicenter determination in km (± 1 standard deviation) are shown for the best of the alternative network layouts.

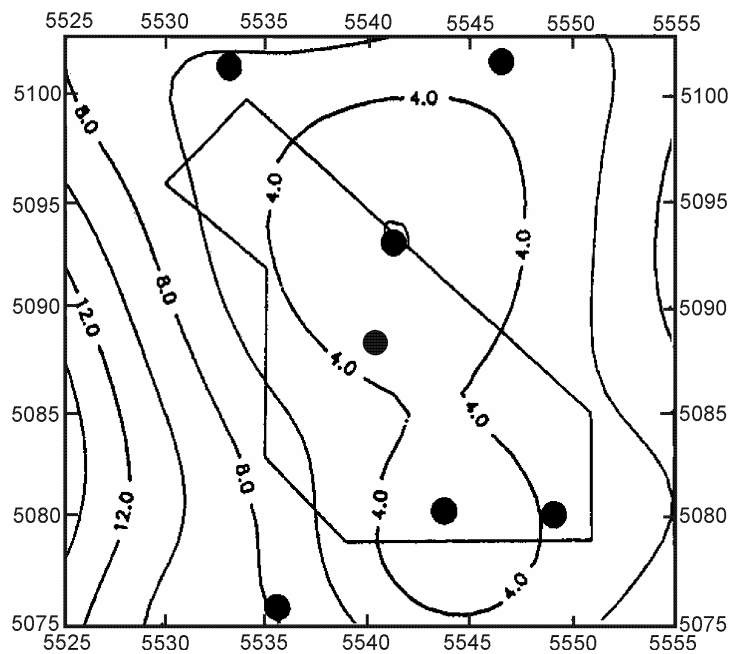


Fig. 7.10 An example of computer modeling of network capability. Isolines of uncertainty of hypocenter determination in km (± 1 standard deviation) are shown for the best of the alternative network layouts.

Several methods for direct computer calculation of optimal network configuration (layout) are described in the literature (e.g., Kijko, 1977; Rabinowitz and Steinberg, 1990; Steinberg et al., 1995). However, practical limiting conditions with respect to infrastructure, topography and accessibility usually outweigh such theoretical approaches. "Optimal" layouts calculated with these methods are rather sensitive to initial conditions such as the predicted gain of stations. This often renders results of questionable value. However, some of these programs may be of help in deciding whether to add or remove stations to an existing network (e.g., Trnkoczy and Živčić 1992; Hardt and Scherbaum 1994; Steinberg et al. 1995; Barta et al. 2000).

A more detailed discussion of these programs is beyond the scope of this Manual. Simple methods usually suffice for our purposes because we want to compare results for various layout options. Determination of network performances in an absolute sense requires a more sophisticated approach. One program which works rather well for relative performance and which can be made available on request is described in IS 7.4: "Detectability and earthquake location accuracy modeling of seismic networks". The program is based on a simplified and uniform attenuation law for seismic waves in a homogeneous half space or in a single- or double-layer ground model. The software uses estimated uncertainties in the P- and S- wave velocities in the model and in the P- and S-phase readings. The software requires as an input the predicted sensitivity of the seismic stations in the network based on measured seismic noise amplitudes at the sites.

No matter what modeling work is carried out, choosing a seismic network layout always involves making good, educated guesses based on experience.

7.2 Investigation of noise and signal conditions at potential sites (P. Bormann)

7.2.1 Introduction

The general factors affecting seismic site quality and suitable site selection procedures have been discussed above. This sub-Chapter discusses specifically the instrumental measurement of seismic noise and signals for optimal site selection, discusses specific features of noise records and spectra from different noise sources and gives recommendations for carrying out such measurements. In the following we discriminate between:

- reconnaissance noise studies prior to station site selection;
- comparison of noise and signal conditions at existing permanent stations;
- searching for alternative sites in a given network.

Examples for each case are based on data from noise surveys in Iran and Germany.

Many sites in a wide area usually have to be inspected and measured during reconnaissance noise studies, sometimes covering an entire country. Carrying out such a survey within a reasonable time and reasonable cost often dictates making measurements with short-period instruments. These are easily and quickly deployed, require less care than long-period or broadband sensors for thermal shielding and underground tilt stability, and yield stable records immediately after installation and useful high-frequency spectra from a few minutes of recording. Many potential sites can then be measured within a day and thus quickly give a

7. Site Selection, Preparation and Installation of Seismic Stations

good idea of their suitability depending on surface geology, topography, distance from potentially disturbing noise sources, etc.

However, short-term measurements using short-period seismographs do not allow judgement of the level of long-period noise ($T > 3$ s). They are also not very suitable for assessing seasonal or diurnal variation of seismic noise. Furthermore, it is highly unlikely that during the short time windows of measurements, any signals from real seismic events will be recorded which would allow comparison of signal-to-noise-ratios (SNR) at different sites. This is important because sites with the lowest noise are not necessarily the sites with the best signal-to-noise ratio. Signal amplitudes may vary by a factor of three or more, depending on local conditions (see Figs. 4.34 to 4.36).

Nevertheless, short-period and short-term noise measurements are sufficient to get an idea of the high-frequency ($f > 0.3$ Hz) background noise and to assess the potential influence of various types of man-made noise sources. It is also possible to assess the daily noise variability and to scale and compare measurements at the more remote sites by using a reference station at the nearest main source of man-made noise (town, factory, railway line, high way, etc.), which records throughout the investigation. In this way, we can get a reliable idea of the relative suitability of different potential sites for the frequency range of small local, regional and teleseismic events ($0.3 \text{ Hz} < f < 30 \text{ Hz}$).

Existing permanent recording sites with stable recording platforms and reasonable shielding against environmental influences allow long-term comparative measurements of both seismic noise and signals in a much broader frequency band. These will give a more reliable assessment of the suitability of sites for event detection and location and also for a variety of other seismological tasks, such as source mechanism studies, tomographic studies of the Earth's structure or the use of very long-period normal modes.

If some of the sites within a seismic network are significantly noisier than others, one should look for alternative sites. For a broadband network, the measurements at alternative sites must be made with the same type of broadband sensors and with every precautions for stable installation and appropriate shielding against wind, weather and direct sunshine. The recording time at each site should be long enough to ensure proper stabilization of the sensor after installation (a few hours to days). Additional days or weeks of recording are needed for assessing diurnal noise variability and relative SNRs for local and teleseismic events.

7.2.2 Reconnaissance noise studies prior to station site selection

7.2.2.1 Offsite assessment of expected noise levels and measurement of instrumental self-noise

Field measurements should always be preceded by offsite studies (see 7.1.2). They help locate the most promising sites and most likely noise sources, help speed up the measurements and reduce the risk of unwanted surprise in the field and final assessment.

When geologic, environmental, climatic, settlement and infrastructure conditions indicate that sites may have very low levels then only high-performance short-period seismographs with very low instrumental self-noise should be used for noise measurements (see 5.6). The level of self-noise should be measured before going into the field and compared with the global

7.2 Investigation of noise and signal conditions at potential sites

New Low Noise Model (NLNM) (see Fig. 5.21). The seismometer noise should be at least 6 dB below the minimum local seismic noise for the entire pass band of the sensor. The signal pre-amplification has to be set high enough to ensure that very low-level ambient noise is well resolved. The resolution of the data acquisition unit should be set at about 18 dB (3bits) below the minimum local seismic noise over the pass band of the seismograph. Clearly, the frequency response of the seismograph must be known or has to be determined beforehand (see 5.7 and 5.8 and well as the exercises EX 5.1 to 5.5).

Fig. 7.11 shows the combined frequency response of an SS-1 seismometer and an SSR-1 recorder used in field measurements for site selection in NW Iran.¹⁾ The sampling rate was 200 Hz using a 6th order low-pass filter with corner frequency $f_c = 50$ Hz in order to avoid spectral aliasing (see 6.3.1). The filter reduces the seismograph gain between f_c and the Nyquist frequency f_{Ny} (half of the sampling frequency) in such a way that very small seismic background noise signals no longer may be resolved above the least-count digitizer noise. Correcting the noise spectrum for the decrease in seismograph gain for $f > f_c$ results in an *apparent* increase of noise power between f_c and f_{Ny} . This is clearly to seen in Fig. 7.12. Here, therefore, we consider only noise spectra up to 1/4 or 1/2 of the sampling frequency.

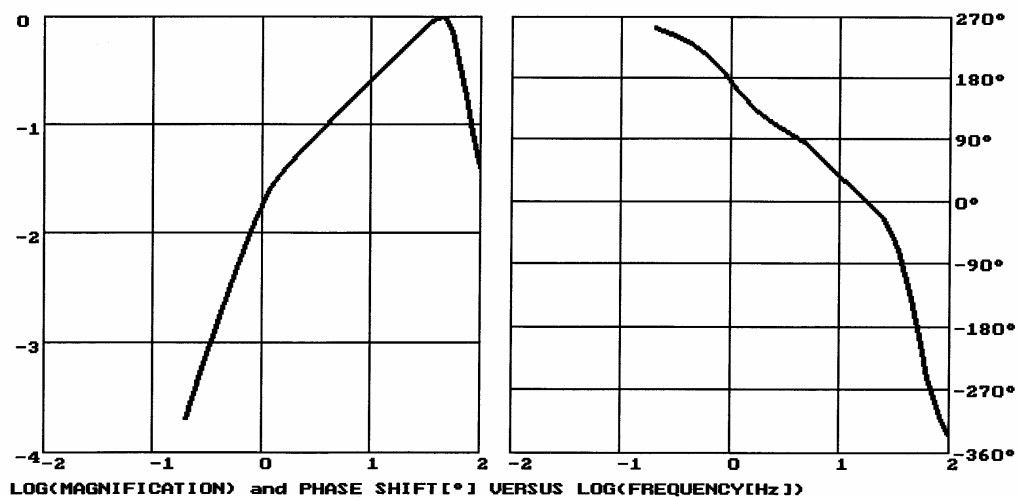


Fig. 7.11 Amplitude and phase response curves for the seismometer-recorder combination SS-1/SSR-1 as used in field measurements in NW Iran (see Figs. 7.12 to 7.21). The response is proportional to velocity between about 1 and 50 Hz.

¹⁾ The data in Iran have been collected as part of a joint project between the International Institute of Earthquake Engineering and Seismology (IIEES) and UNDP (Ref. No. IRA/90/009). The data relates to the seismic noise measurements at potential station sites for the Iranian National Seismic Network (INSN). The authors thank Prof. M. Ghafory-Ashtiany, President of IESSS, for the technical and staff support provided and for his kind permission to publish part of the data in this Manual.

7. Site Selection, Preparation and Installation of Seismic Stations

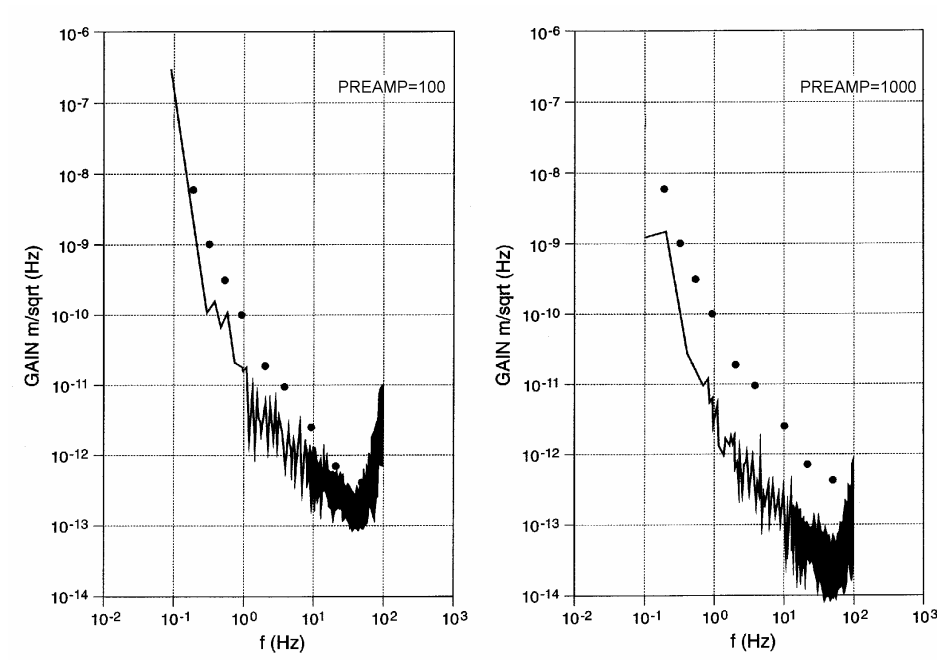


Fig. 7.12 Comparison of the average values (●) of the ground displacement spectrum of seismic noise recorded at the quietest site found during a noise survey in NW Iran with the equivalent displacement spectrum of the combined instrumental self-noise of the Kinematics SS-1 seismometer and SSR-1 data logger at a pre-amplification level of 100 times (left) and 1000 times (right). One order of magnitude difference in the amplitude spectra corresponds to 20 dB difference in the respective power spectra. Only the higher pre-amplification allows the resolution conditions to be met at the quietest sites in the area under investigation.

7.2.2.2 Sensor installation, measurements and logbook entries in the field

Potential measurement and reference sites should be pre-selected before going into the field, based on geologic and road maps and taking into account other significant aspects or findings from preceding offsite studies. The selections may be changed during the field inspection. Essential points to be considered in field studies have already been outlined in section 7.1.3. The following complementary rules should be observed:

- keep a log-book;
- note carefully all relevant features which characterize the measurement sites (local geology and topography, compact or weathered rock outcrop, soil type, vegetation cover, distance to settlements or industry, main roads, power lines);
- note the environmental conditions during measurement (weather, wind, rain, insolation) and the occurrence time of any transient events that might have influenced the noise record (e.g., wind gusts or cars, trains or people passing by at what distance);
- mark the position of any measurement site in your road and/or geological map;
- take representative photographs of each measurement site and sensor installation;
- whenever possible, position the seismometer directly on a flat outcropping rock surface and level it with its three adjustment screws. Unusually-long adjustment screws can be fitted to help level the sensor on rough rock surfaces (proper counter-locking of the screws ensures sensor stability);

7.2 Investigation of noise and signal conditions at potential sites

- in the case of well-binding (clayish) soil, screw long-leg tripod adjustments directly into the soil. Alternatively, position the seismometer on a thick solid rock plate placed firmly on the ground after removing any loose gravel or vegetation (Fig. 7.13). This may be the only reliable solution when making three-component noise measurements if three individual sensors are used requiring identical installation conditions. It may also work well on rough rock surfaces as long as a nearly horizontal stable three-point support of the plate can be found. A rock plate is not necessary if the three components are mounted in the same package, e.g. for Mark L4C-3D seismometers (see DS 5.1).

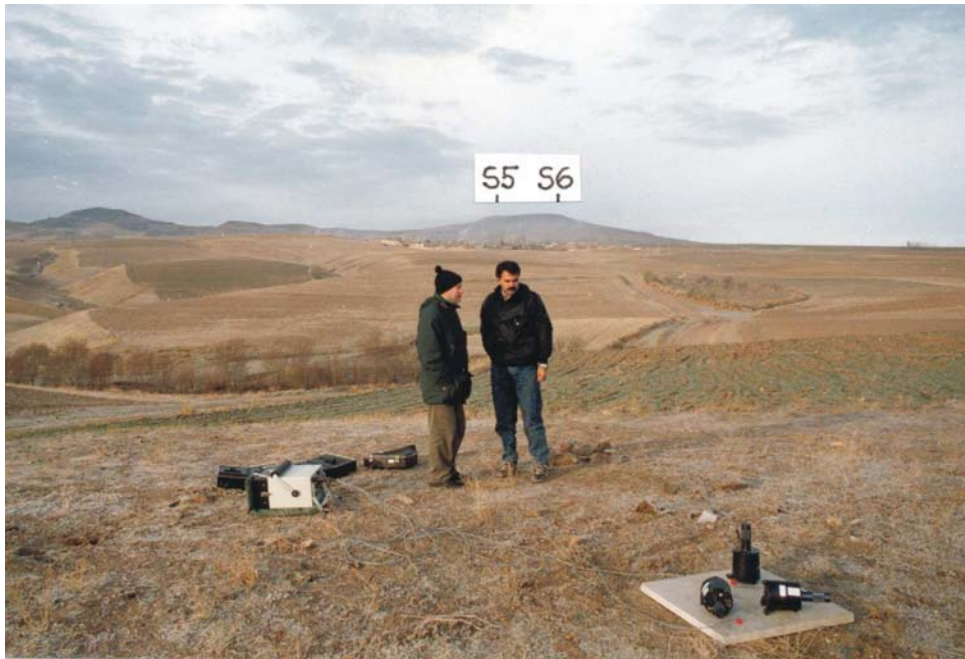


Fig.7.13 Temporary three-component reference installation in NW Iran on a leveled marble plate placed on unconsolidated ground. Two other measurement points on the horizon using outcropping hard rock are marked. The noise at the latter sites was close to the NLNM.

- in the case of wind, rain or snowfall, try to find shielding on the lee-side of a rock-face (Fig. 7.14) or bury the sensor in the ground and cover it with a tightened sheet or blanket or with a box;
- if test measurements show that noise levels are comparable for all three components in the area under investigation it is sufficient to continue the survey using only vertical component recordings. This is usually the case in isotropic noise fields, i.e. in the absence of distinct localized noise sources.
- set up at least one continuously-recording reference station in the study area in order to assess the influence of diurnal noise variations on the measurements made at different sites and at different times of the day. The reference station can be used to scale the noise records at the other sites (see Fig. 7.15).
- if, at low-noise sites, the ground displacements are of the order of nm (10^{-9} m), do not stand or walk close to the sensors during the recordings. Stay at least 10 m away, remain sitting down, and keep absolutely quiet (see Fig. 7.18).

7. Site Selection, Preparation and Installation of Seismic Stations



Fig. 7.14 Hiding with the noise recording equipment on a windy day with snowfall in a small cave on the lee-side of a rock cliff. Surface recordings under adverse weather conditions of the noise level at this site in NW Iran were close to the best sites in good weather.

- stay several hundreds of meters away from large power lines or transformer houses. Otherwise you may get strong induction currents in the seismometer's measurement coils or record 50 to 60 Hz vibrations that are typical of large transformers or heavily loaded power lines (see Fig. 7.19).
- take comparative measurements at different distances are recommended to assess the reduction of noise with distance from transient sources (such as nearby road or railway traffic). Measurements on different soil conditions may also be needed if the noise also depends on the lateral impedance contrast of adjacent rock formations (see Figs. 7.16 and 7.17).
- take daily synchronization of the internal clocks of the data loggers used in the field and at the reference site if they have no common time reference such as GPS-controlled clocks.

7.2.2.3 Case study of noise records in the frequency range $0.3 \text{ Hz} < f < 50 \text{ Hz}$

Fig. 7.15 shows the daily noise variation at a reference site in a town in NW Iran. The noise between night and day time varies by about 20 to 30 dB around 1 Hz and by about 50 dB around 10 Hz because of the site's proximity to a main road and poor underground conditions. Fig. 7.16 shows the large dependence of noise records and spectra on the geological underground conditions and remoteness from villages and traffic roads in the area around one of the reference stations in NW Iran .

Note that noise spectra should not be determined unless the related time domain records have been inspected and any non-representative spurious or transient events have been removed. The analysis and assessment of noise conditions should never be made on the basis of the calculated spectra alone but always in conjunction with the related time-domain records.

7.2 Investigation of noise and signal conditions at potential sites

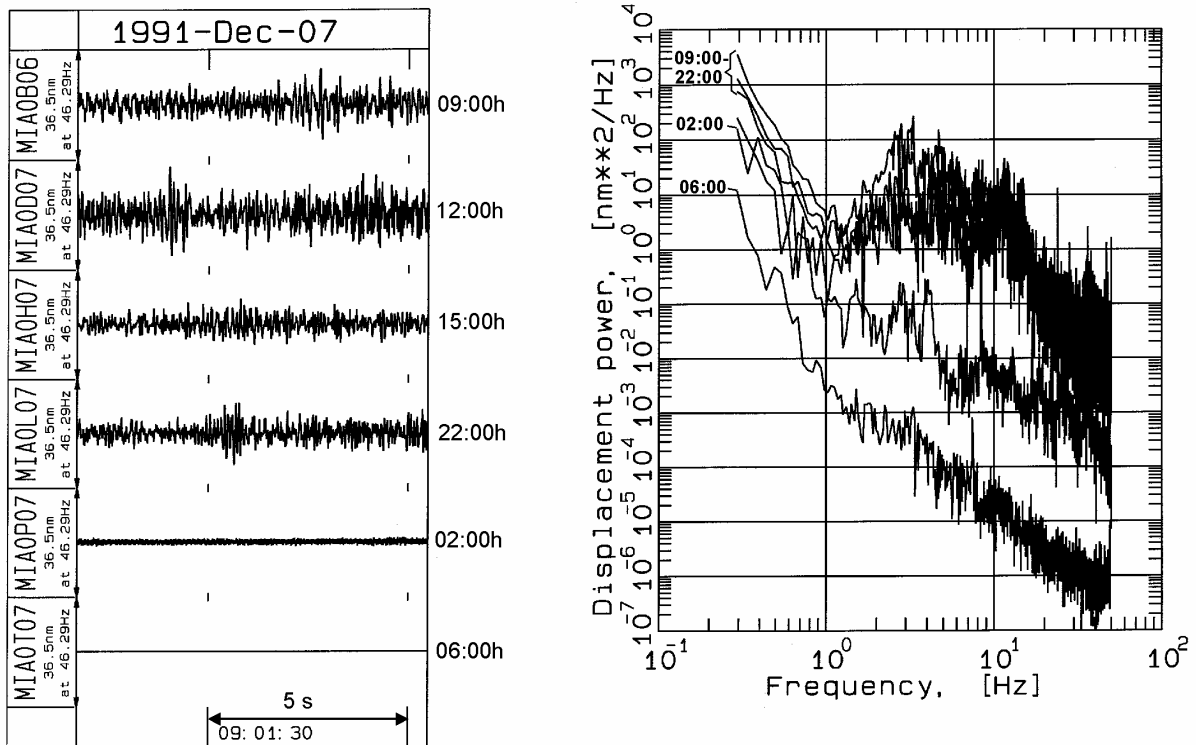


Fig. 7.15 Comparison of relatively quiet sections of vertical component noise records (left; without strong transients) and related power spectra (right) at a reference site in a town in NW Iran. The measurements were made at different times of the day.

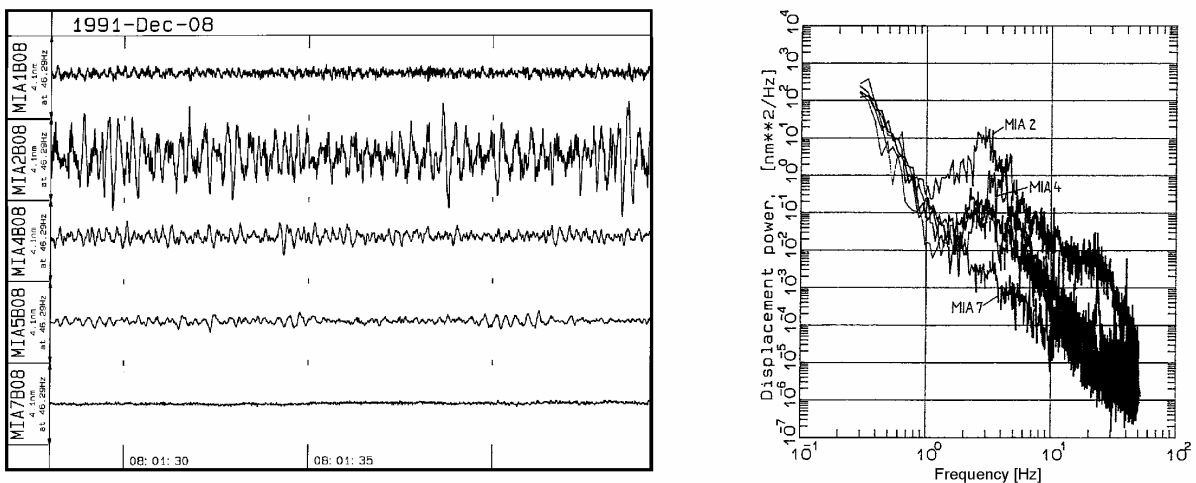


Fig. 7.16 Noise recordings (left) and related power spectra (right) at different sites in NW Iran. From top to bottom: 1) unconsolidated Miocene terrace, 2) unconsolidated Alluvial valley fill, about 2 km away from the main road, 3) as for 2) but some 5 km away from main road; 4) outcropping volcanic hard rock near the road in a valley (with no nearby traffic at the time of measurement, 5) volcanic hard rock surface near a mountain pass road. The noise at MIA 7 is around 1 Hz very close to the global New Low Noise Model (see 4.1) and at 10 Hz only about 14 dB above it.

7. Site Selection, Preparation and Installation of Seismic Stations

Fig. 7.17 shows a two minute noise record (left) and the related power spectra (right). The large amplitudes at the beginning are due to a truck and car passing by on the bumpy country road at some 100 to 400 m distance (documented by photograph and time check). Accordingly, for frequencies $f > 7$ Hz, the noise power of the first minute of the record is 10 to 20 dB higher than for the background noise after the transient is over.

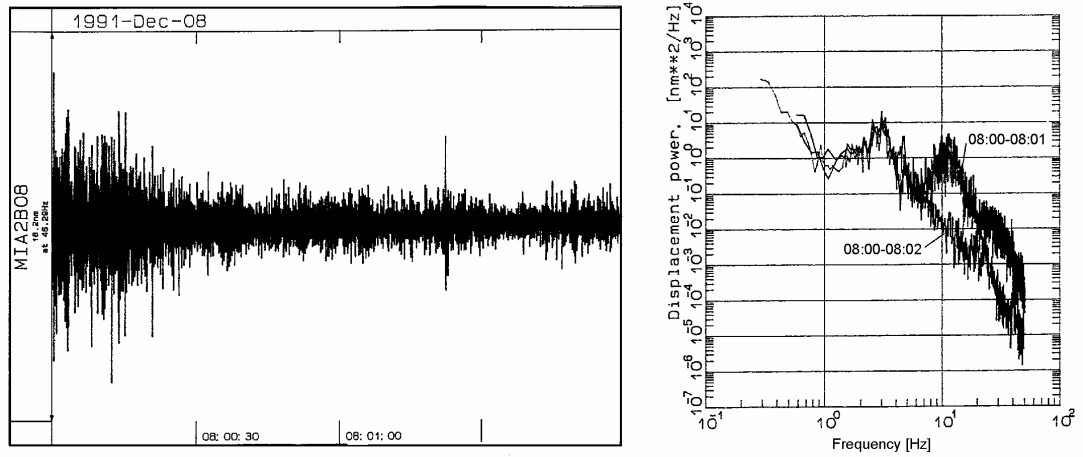


Fig.7.17 Noise record and related spectra for the first minute (transient) and second minute (background noise). The transient is due to a truck passing by at several 100 m distance from the recording site.

Fig. 7.18 shows a recording at a remote low-noise hard rock site. The first segments are very noisy because people were "stretching their legs" only a few meters away from the sensors. This man-made noise stopped abruptly at 13:06:15 hours when they were asked to sit down and not move. Comparing the related noise power spectra for these two different record segments shows amplitudes 20 to 30 dB lower for the unspoilt ambient noise. Therefore, all members of a noise measurement crew must be instructed to stay away from the sensors and keep very quiet during measurements.

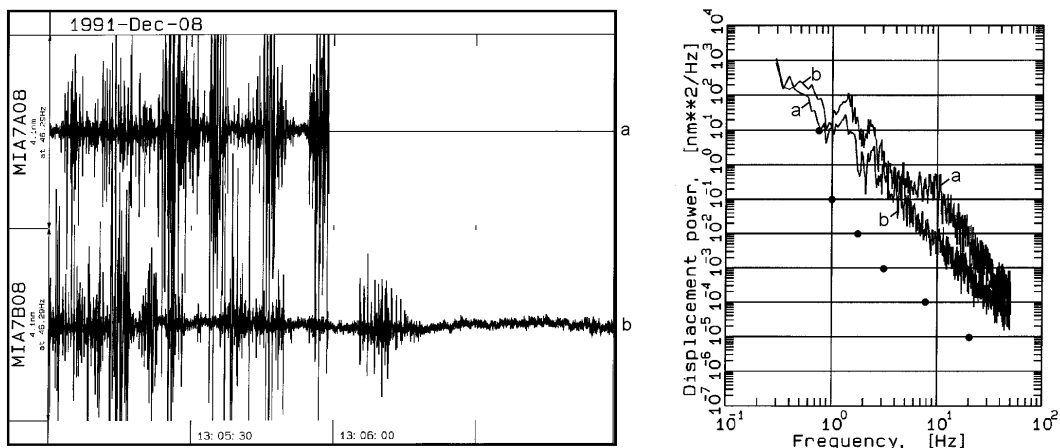


Fig. 7.18 Noise records (left) and related power spectra (right) at a remote low-noise hard rock site in NW Iran. The large, impulse-like amplitudes in the first part of the record are due to the movement of team members near to the sensors. Note the much lower noise (dots in the spectrum) after they were asked to "sit down and be quiet".

7.2 Investigation of noise and signal conditions at potential sites

Measurements near power lines and transformer houses likewise may significantly spoil the records. The recordings shown in Fig. 7.19 were made near a quiet countryside village. For frequencies below 13 Hz, the noise amplitudes are roughly the same in the vertical and horizontal components. At higher frequencies, surprisingly, the horizontal records are extremely noisy. The related power spectra show strong, almost monochromatic, noise peaks around 13, 30 and 50 Hz in the horizontal components. (Note that the spectral calculation stopped at the seismometer's upper corner frequency of 50 Hz; see Fig. 7.12). According to the notebook entry and site photograph the record was made only about 30 m away from a transformer house and power line. The strong monochromatic high-frequency noise peaks are probably due to strong electromagnetic induction in the horizontal measuring coils by the AC current frequency of 50 or 60 Hz and its lower harmonics (30 and 13 Hz). However, experience at other sites shows that large transformers and heavily loaded power lines may also vibrate at 50-60 Hz.

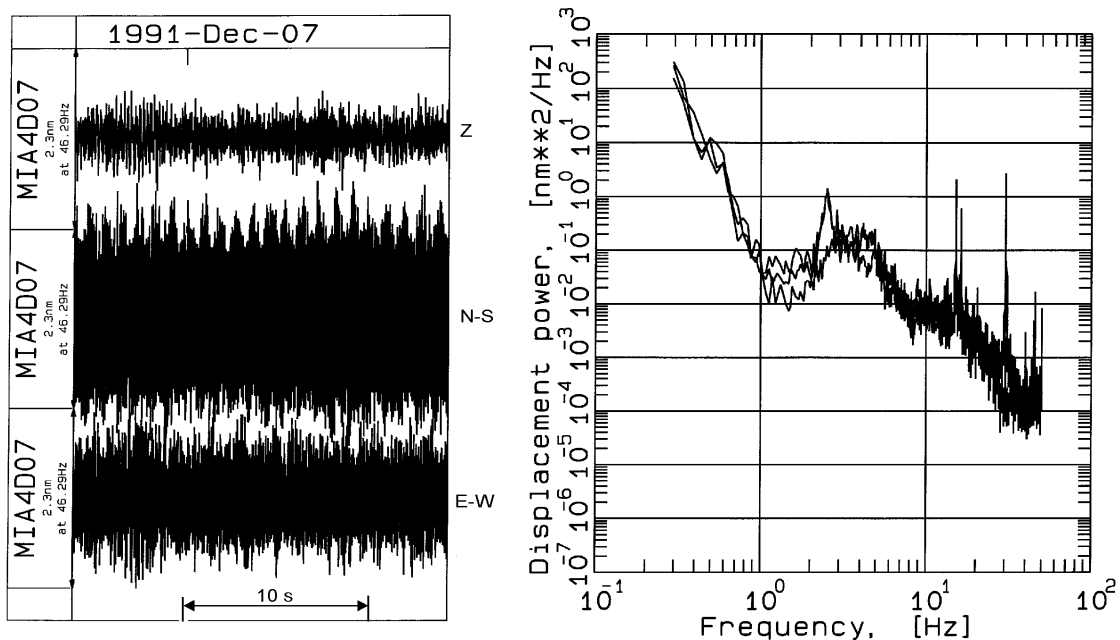


Fig. 7.19 Noise records and related power spectra near to a transformer house and power line. Note the monochromatic spectral lines around 13, 30 and 50-60 Hz, either induced by the AC current frequency and its lower harmonics and/or caused by the vibration of the transformer.

Another experiment demonstrates the attenuation of truck-traffic noise with distance from the road and the influence of the acoustic underground impedance on the recorded spectra. In two different cases, one sensor was placed at the foot of an asphalt-covered road embankment while the other one was installed about 1 km away from the main road in the countryside. In the first case, the underground consisted of wet alluvial coastal plane deposits; in the second case, outcropping competent Cretaceous tuffaceous sandstone, i.e. a rock with a much higher acoustic impedance. The recordings were made simultaneously and the time segments analyzed when a heavy truck was passing by on the main road. On the wet alluvium the vibrations caused by a truck were recorded on the road embankment with very strong amplitudes for almost 30 seconds. Frequencies between 0.3 Hz and 20 Hz were strongly excited. Although power spectral amplitudes at 1 km distant were generally 20 to 30 dB lower, high frequencies were still clearly visible in the record and the spectrum (Fig 7.20).

7. Site Selection, Preparation and Installation of Seismic Stations

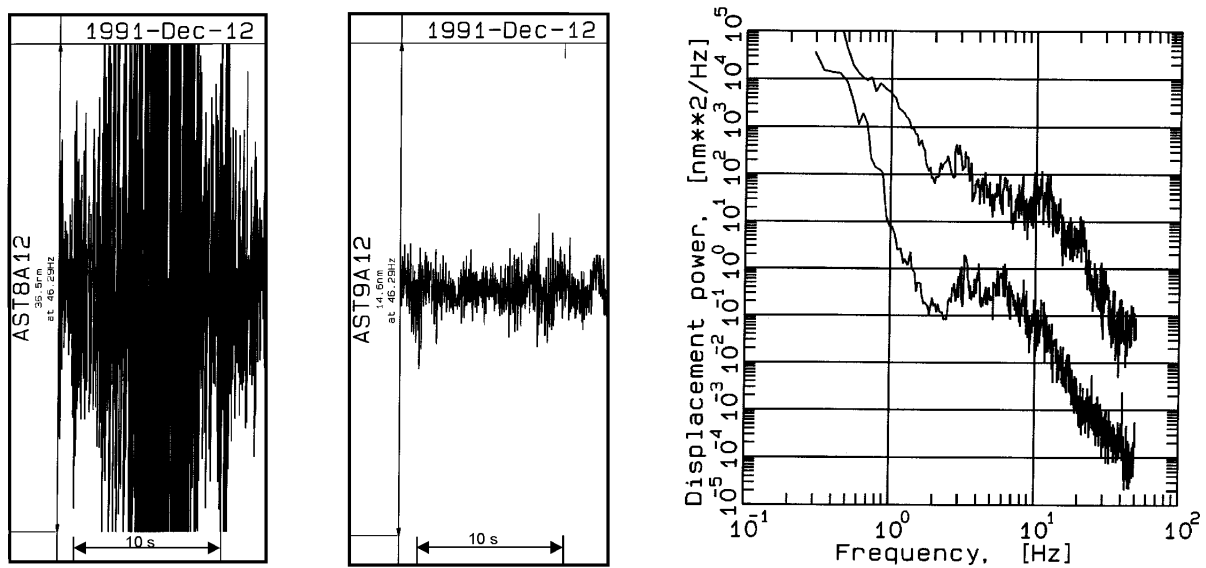


Fig. 7. 20 Comparison of seismic records and related noise spectra made at the time of passing of a heavy truck: Left: record near the road embankment; middle: record made about 1 km away from the road in the countryside (middle); right: noise power density spectra. Underground: wet Alluvial coastal plain deposits. (Note that the noise amplitudes in the left panel have been reproduced with only 40 % of the magnification in the central panel).

In contrast, Fig. 7.21 shows the records made at another section of the road embankment consisting of broken rock overlaying outcropping competent rock. A strong increase in noise amplitudes above the general background level was observed for about 5 s only, i.e., when the truck was close to the site. The general noise level, even at the time of the passing truck, was 20 to 30 dB lower than on the alluvial embankment. Also, at the broken/compact rock road embankment, spectral amplitudes for frequencies between 0.3 and 1.5 Hz were about the same as 1 km away in the side valley on the outcropping compact sandstone. On the other hand, high frequency amplitudes generated by the truck are no longer visible in the record at the hard rock site 1 km away from the main road and reduced by 20 to 30 dB in the power spectrum.

In summary, these examples show what one can expect for noise reduction with distance from main traffic roads or other sources of man-made noise, and their dependence on underground conditions. This may help guide reconnaissance field measurements for appropriate and accessible sites. The examples also illustrate the usefulness of comparing noise records in the time domain with the related power spectra in order to better identify the kind of noise sources and understand their appearance in the records.

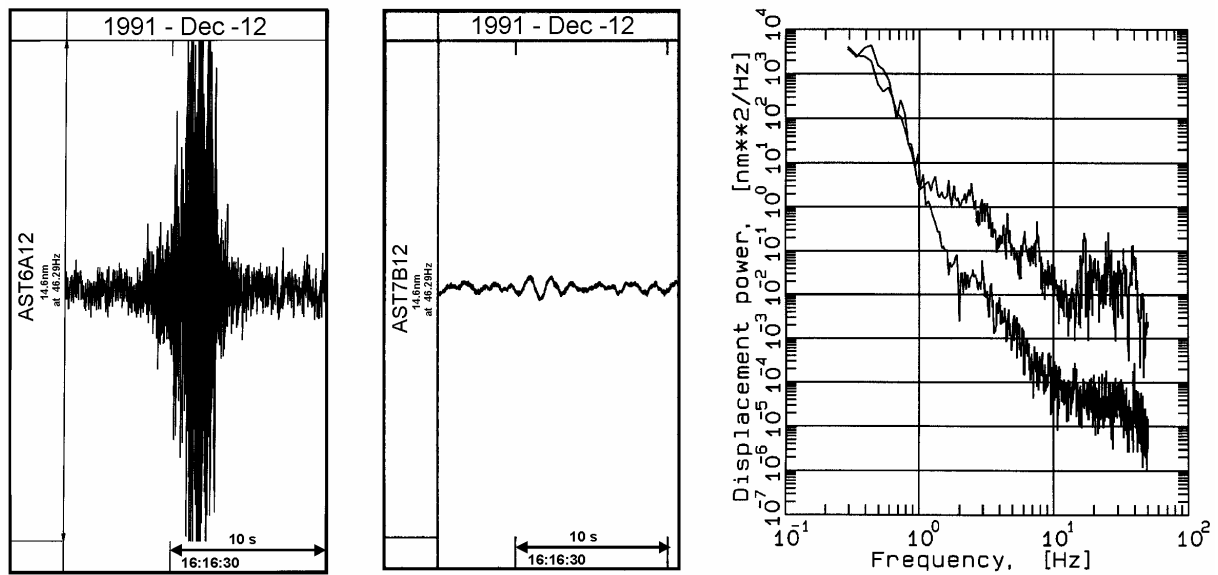


Fig. 7.21 As Fig. 7.20, except that records were made near a broken rock embankment of a main road and on outcropping compact tuffaceous sandstone, 1 km away in a side valley, respectively.

7.2.3 Comparison of noise and signals at permanent seismological stations

7.2.3.1 Introduction

Existing permanent seismological stations have historically been established by different institutions for different reasons and have often been installed under different underground and environmental conditions. The stations were usually operated independently, each reporting their own data readings to national or international data centers. Modern methods of data communication make it easy to link these stations, to merge them into virtual networks (see 8.4.3), to exchange waveform data in real time and to perform joint data analysis at local, national or regional data centers. The overall network performance and quality of results strongly depends on the local conditions at the individual stations. One crucial parameter is the detection threshold. This is mainly (but not exclusively) controlled by the noise conditions at the sites. High noise conditions at some stations reduces their contribution to event detection, discrimination and location accuracy of the network, may bias average network magnitude estimates and may result in inhomogeneous completeness and accuracy of earthquake catalogs. Therefore, when setting up new seismic networks or linking already existing stations into a network, a priority task should be to investigate and compare the signal-to-noise conditions at the various stations, and to find alternatives for inferior sites. Such decisions may have far-reaching consequences and involve significant cost and so should not be based on just a few short-term noise measurements in a limited frequency band. Noise measurements should be taken over at least several days, but preferably over weeks or even months, in order to get a clear understanding of the diurnal and seasonal variability of seismic noise in the full frequency band of interest for the operation of the network. Moreover, one should determine the signal-to-noise ratio (SNR) for events from different distance and azimuth ranges and compare this at existing and possible alternative sites. It is vital that all records should be made with equipment having an identical instrument response.

7. Site Selection, Preparation and Installation of Seismic Stations

This is demonstrated using data from the German Regional Seismic Network (GRSN) (see Fig. 8.15). Originally the GRSN consisted of 12 sites in western Germany. Several permanent stations in eastern Germany were subsequently added to the network. The GRSN now consists of 16 digital broadband stations equipped with STS2 seismometers (see DS 5.1), 24-bit data loggers and a seismological data center at the Gräfenberg BB array center (GRFO) in Erlangen. The network covers the whole territory of Germany with a station-spacing between 80 km and 240 km. The stations are located in very different environments: e.g., near the Baltic Sea coast (HAM and LID, now BSEG; RGN); up to distances of about 700 km away from the coast (FUR); within cities (BRNL, HAM) or up to about 10 km away from any major settlement, industry or busy roads. The underground varies from outcropping Paleozoic hard rocks in Hercynian mountain areas (BFO, BRG, CLL, CLZ, GERES, MOX, TNS, WET), sedimentary rocks in areas of Paleozoic (BUG, IBBN) or Mesozoic platform cover (GRFO, STU) to unconsolidated Pleistocene (glacial) deposits (BRNL, HAM, FUR, LID, RGN). The seismometers are installed either at surface level (CLL, CLZ, HAM, IBBN, RGN, WET), in shallow vaults just a few meters below the ground surface (BUG, FUR, GSH, TNS), in boreholes (GRFO, 116 m), or in bunkers, tunnels or abandoned mines between 20 and 162 m below surface (STU, MOX, BSEG, BRG, RUE, BFO). More details about these stations and their equipment can be found on the Internet at <http://www-seismo.hannover.bgr.de/grsn.html>.

Seismic background noise at GRSN stations varies in a wide range between the upper and lower bounds of the new global noise model (see Fig. 7.27). The noise conditions at the GRSN have been investigated in detail in the frequency range from 10^{-2} to 40 Hz by Bormann et al. (1997).

7.2.3.2 Data analysis

Continuous recordings at all stations were systematically screened at different times of the day (0, 6, 12 and 18 hrs UT) in order to reveal diurnal variations and their site dependence. Records were also monitored throughout the year in order to identify periods of minimum and maximum noise level and their seasonal variations. Respective record sections and related power spectral densities (PSD) were plotted together and checked for transient signals from seismic or other spurious events.

Data of the GRSN are acquired at a sampling rate of 80 Hz for most stations and 20 Hz at the more noisy stations. For most of the routine noise analysis, the 80 Hz data were re-sampled at 20 Hz. The Power Spectral Density (PSD) was calculated using a subroutine from the program SEIS89 (Baumbach 1999). It implements, in a somewhat modified form, an algorithm recommended as a standard for the calculation and presentation of noise spectra by the Ad Hoc Group of Scientific Experts (1991). The modification allows the use of segments of data larger than 512 samples, thus permitting the analysis of more long-period noise. The digital time series containing background noise are divided into a number of half-overlapping record segments, normally of 4096 samples. The power spectra are then calculated for each segment (after removing the mean and tapering the ends of each segment with a sine-cosine window) and then averaged over eight segments in order to reduce the variance of the PSD estimate. Accordingly, the presented power spectra are representative for noise records of about 15.4 min duration in case of 20 s.p.s. and of about 3.8 min duration for 80 s.p.s.. All spectra are corrected for the instrument response. The power spectra are presented in units of displacement power spectral density in nm^2/Hz . A lower frequency limit is imposed such that the longest period which can be analyzed using this procedure is one sixth of the segment length.

7.2 Investigation of noise and signal conditions at potential sites

According to Fig. 7.48 in section 7.4.4, STS2 seismographs have a self-noise which is below the global New Low-Noise Model between about 10^{-3} Hz and 10 Hz. According to Wielandt and Zürn (1991), they can resolve the noise at BFO, which is one of the quietest seismic stations in Germany, for frequencies below 30 Hz. Thus, instrumental and/or digitization noise can potentially affect the noise estimates at the best sites only at frequencies above and below this range.

Essential results of the analysis are presented below. Figs. 7.22 - 7.37 are reproduced from Journal of Seismology, Vol. 1, 1997, pp. 357-381, "Analysis of broadband seismic noise at the German Regional Seismic Network and search for improved alternative station sites" by P. Bormann, K. Wylegalla and K. Klinge, Figures 2, 4, 6-7, 9, 11-15, 17-20 and 22; © 1997 (with kind permission from Kluwer Academic Publishers).

7.2.3.3 Results

Fig. 7.22 shows an example of high-pass filtered short-period Z-component records of seismic background noise from 15 stations of the GRSN. Amplitudes differ by more than one order of magnitude. Noise amplitudes on vertical and horizontal recordings were about the same at any given station. Therefore, only spectra from Z-component records are considered. In long-period records, however, horizontal noise is sometimes significantly larger (e.g., for stations RGN and BSEG in Fig. 7.23), due to the high tilt sensitivity of long-period horizontal seismometers (see 5.3.3).

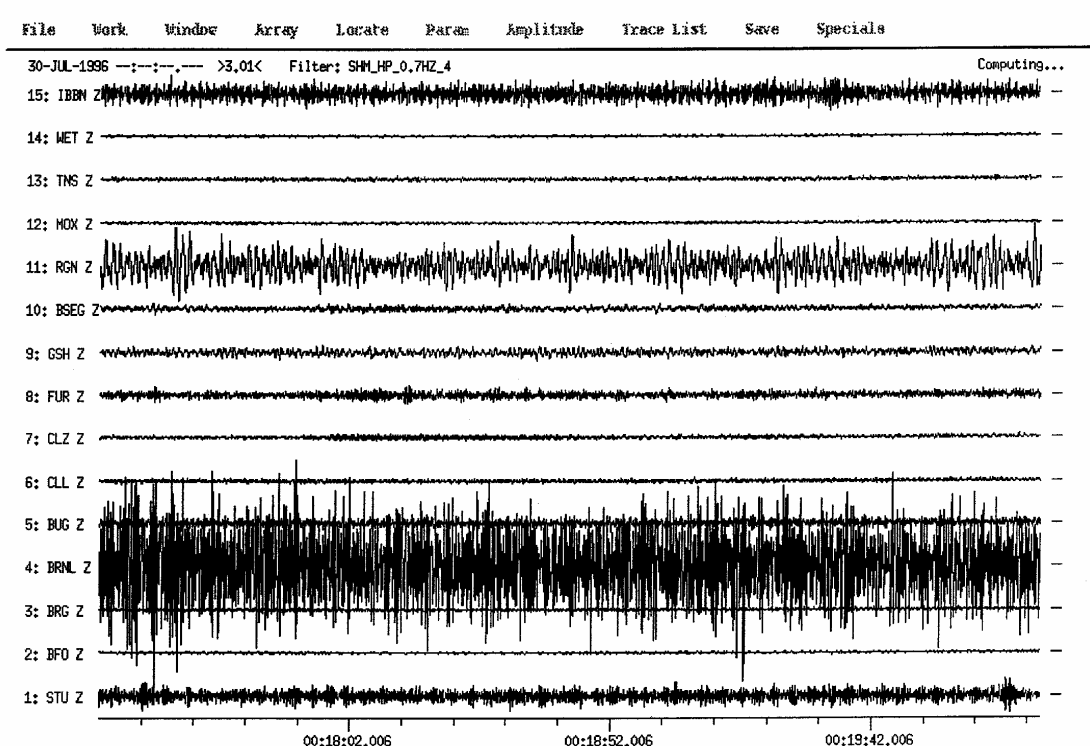


Fig. 7.22 High-pass filtered ($f_c = 0.7$ Hz) Z-component noise records of GRSN stations on July 30, 1996, at night time (from Bormann et al., 1997).

7. Site Selection, Preparation and Installation of Seismic Stations

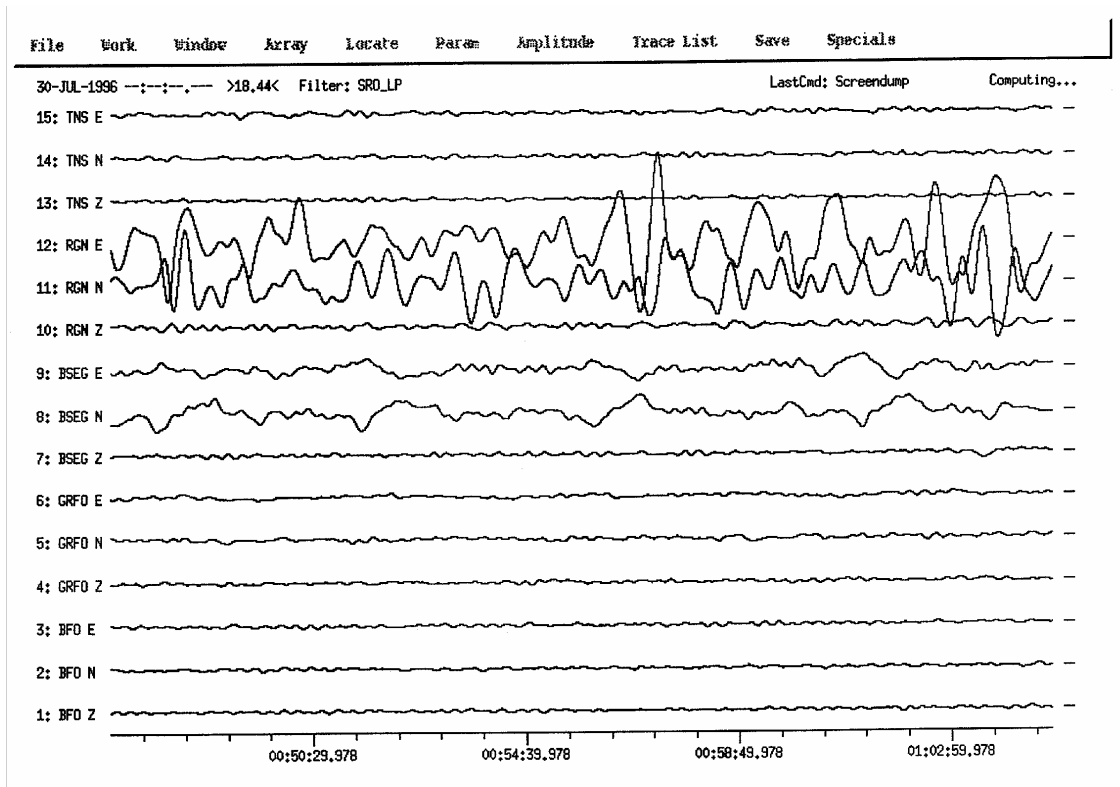


Fig. 7.23 Three-component recordings at five GRSN stations after applying a long-period SRO filter characteristic (from Bormann et al., 1997).

On very calm days at stations with very good environmental shielding (e.g., BFO, GRFO, TNS in Fig. 7.23), horizontal long-period noise might be equal to or only somewhat stronger than in vertical components. On stormy days with high wind pressure fluctuations and related tilts, however, the noise power in near-surface horizontal recordings might be 20 to 30 dB higher than in vertical ones. When the sensors are installed sufficiently deep in boreholes (as GRFO; 116 m below surface) or in mines (as BFO; 162 m below surface) this difference will be much less, even during stormy days.

Differences in the displacement PSD at the GRSN stations are most obvious for frequencies above 0.5 Hz. They may reach about 60 dB (Fig. 7.24) and are due to the varying proximity to man-made noise sources and differences in underground conditions. The stations BRNL (Berlin Lankwitz) and HAM (Hamburg) proved to be the worst sites. For longer periods ($T > 2$ s) the differences in noise level between the GRSN stations are much less pronounced; less than 10 dB in most cases. However, over a long period of time (Fig. 7.25) the noise power variability at individual stations of the GRSN proved to be smallest (and seasonally independent) around $f = 1$ Hz (about 5 to 10 dB variation only). It is larger between 2 to 10 Hz (up to about 20 dB) and largest for the secondary ocean-storm microseism peak around 7 s period (30 to 40 dB). Microseisms only occur episodically and with seasonally varying intensity (strongest at the time of winter storms). At periods around 20 s, the range of noise power variations still reaches 20 to 30 dB. This is equivalent to variations in the magnitude threshold for M_s determinations of up to 1.5 magnitude units.

7.2 Investigation of noise and signal conditions at potential sites

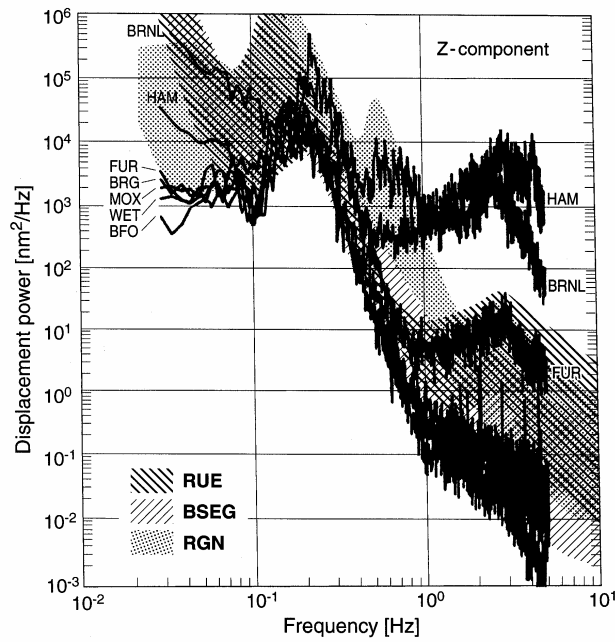


Fig. 7.24 Displacement power density spectra at selected GRSN stations determined from noise records on the morning of April 13, 1993. For comparison the ranges of noise power observed at the new sites BSEG, RGN and RUE are given as shaded areas (from Bormann et al., 1997).

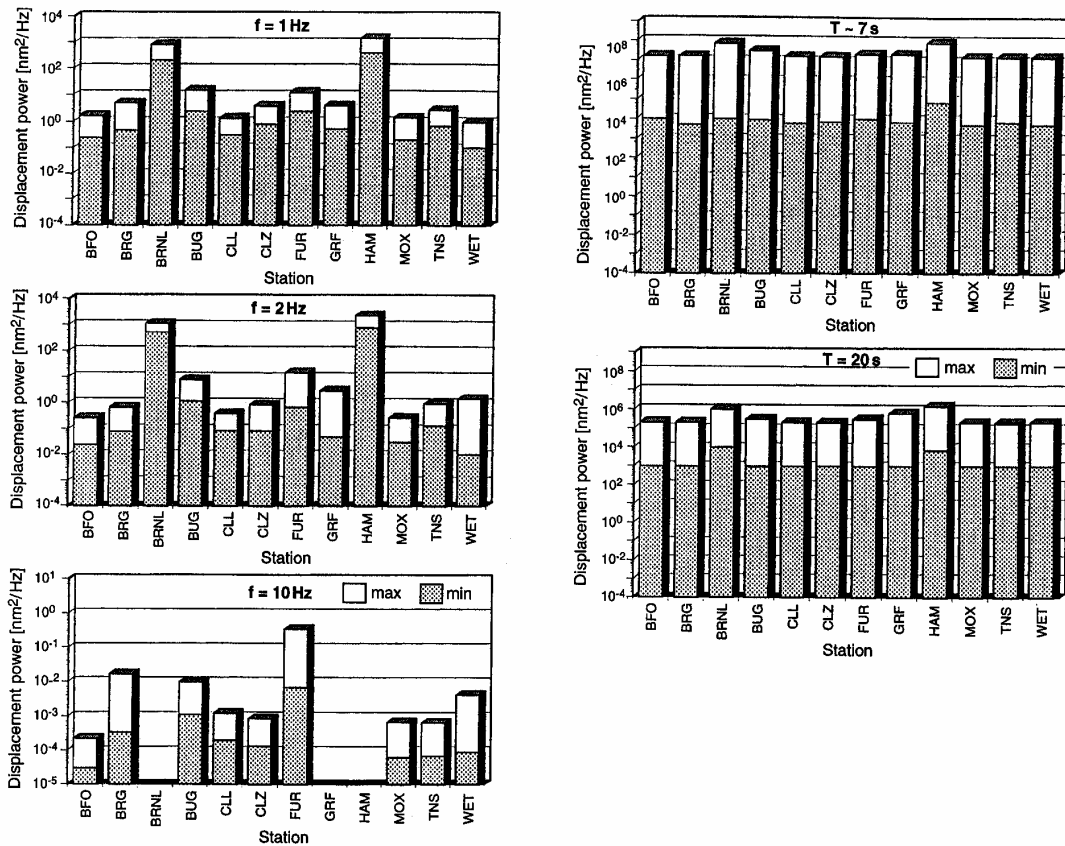


Fig. 7.25 Comparison of the minimum and maximum levels of short-period and long-period seismic noise power observed at GRSN stations (modified after Friedrich, 1996; from Bormann et al., 1997).

7. Site Selection, Preparation and Installation of Seismic Stations

Fig. 7.26 shows record sections of only 1 minute duration and with identical gain for one of the quietest and one of the noisiest days observed during a year at each of the stations MOX and HAM. The amplitudes of secondary ocean-storm microseisms with periods of about 6 to 7 s, on the noisy day, are at HAM only about twice as large as at MOX despite HAM being much closer to their origin along the European North Atlantic coastline. On the other hand, the high-frequency noise at HAM is always much larger than at MOX. The corresponding displacement power spectra for the quietest day at MOX (May 23) and the noisiest day at HAM (January 13) during 1993 are compared in Fig. 7.27 with the global New Low Noise Model (NLNM) and New High-noise Model (NHNM) according to Peterson (1993).

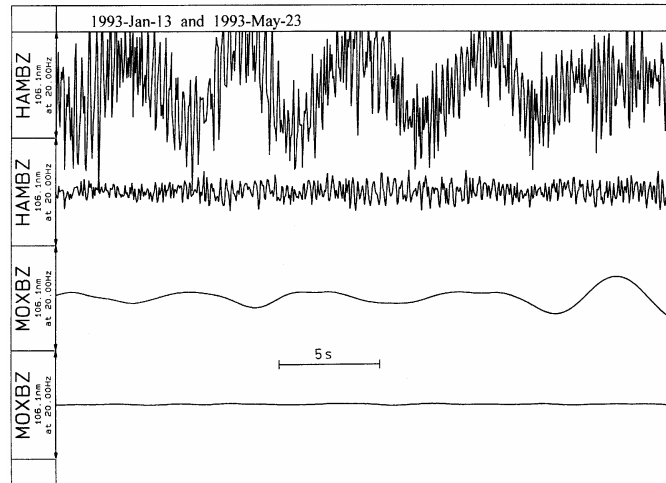


Fig. 7.26 Comparison of record segments with largest (13 January) and lowest seismic background noise (23 May) observed in 1993 at stations HAM (upper two traces) and MOX (lower two traces) (from Bormann et al., 1997).

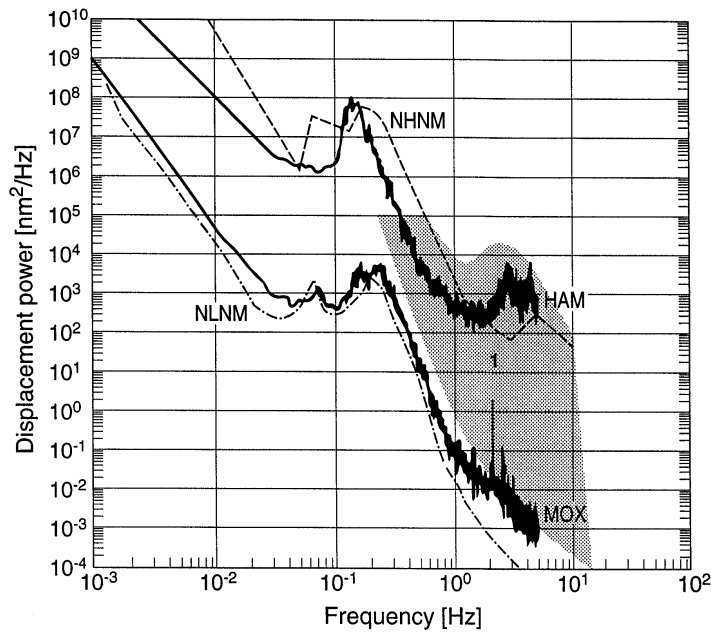


Fig. 7.27 Spectra for the noisiest day observed at HAM (January 13) and the quietest day at MOX (May 23) during 1993. The NHNM and NLNM according to Peterson (1993) are shown for comparison. The shaded area (1) covers the range of short-period noise power calculated by Henger (1995) for all GRSN stations on March 1, 1994 (modified from Bormann et al., 1997).

The diurnal variations of man-made noise have also been investigated at all stations of the GRSN. The variations are very distinct (20 to 30 dB) at the stations BRNL, BUG and FUR, i.e. at sites in densely populated areas and with thick unconsolidated subsoil. They are much less (< 5 to 10 dB) at stations on hard rock in smaller and less busy towns (such as BRG and CLZ) or even at several km distance to the nearest villages (CLL, MOX and TNS).

Due to the large differences in noise conditions at the GRSN stations, the capability to detect and locate events with at least 3 stations was rather inhomogeneous over German territory. The detection thresholds ranged between $MI = 1.5$ and 3. Since the network was supposed to detect and localize all local events with $MI \geq 2$, more suitable sites had to be found for some stations. This was particularly true for BRNL and HAM. The search for more appropriate alternative sites focused on areas not too far away from these stations in order to preserve the general configuration of the GRSN.

7.2.4 Searching for alternative sites in a given network

7.2.4.1 Geological and infrastructure considerations

We consider here two case studies for replacing the seismic stations BRNL and HAM.

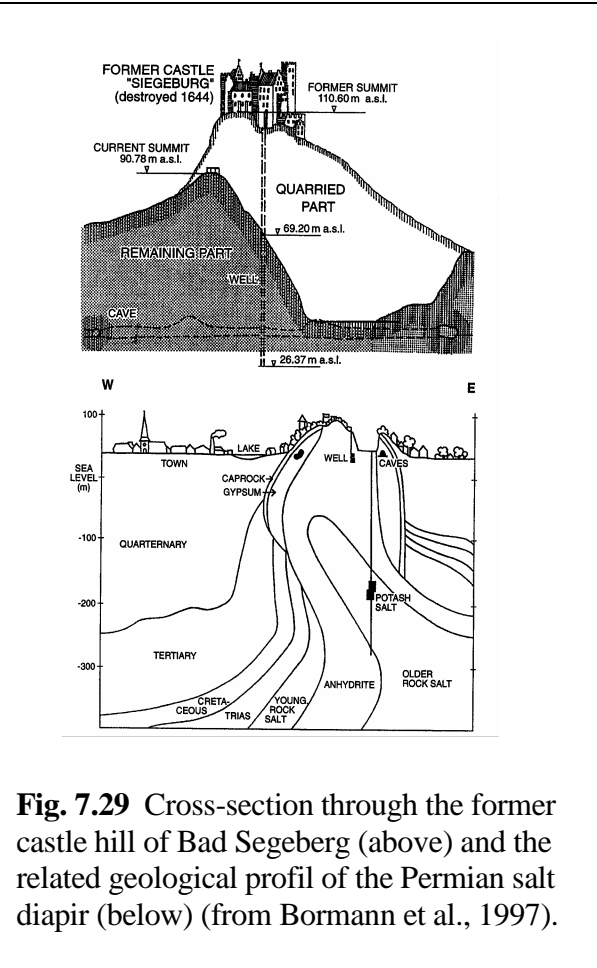
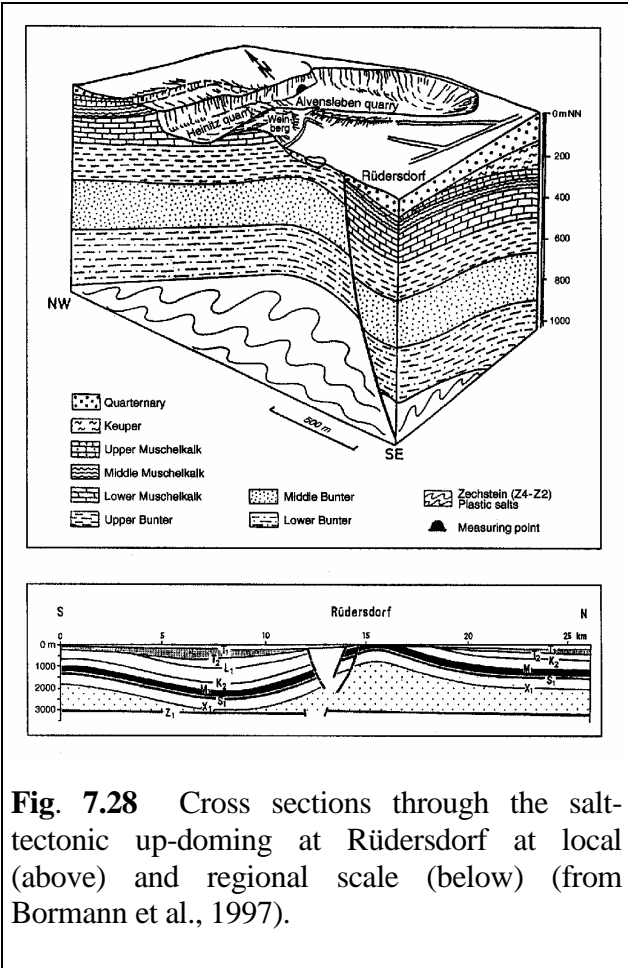
BRNL was located on the courtyard of the Geophysical Institute of the Free University of Berlin, about 12 km from the city center. The station underground consists of about 290 m unconsolidated Cenozoic sediments overlaying a thick sequence of Mesozoic sedimentary rocks. These unfavorable underground conditions, together with high population and nearby traffic density, made this station one of the noisiest in Germany. An alternative site had to be found in the wider surroundings of Berlin.

In the area of Berlin, the base of the Permian Zechstein subdivision is between about 2600 m and 4000 m below sea level. The pre-Permian basement is block-faulted with different vertical movements between adjacent blocks during post-Permian times. This mobilized the overlying plastic salt deposits of the Zechstein subdivision and resulted in the formation of dozens of salt-pillow structures, up-doming the Mesozoic sequences above. In a few cases, salt diapirs pierced through the post-Permian deposits to the present surface. The largest of these halokinetic structures exists beneath the small town of Rüdersdorf (Fig. 7.28) about 25 km east of the city center of Berlin. It was exposed by Pleistocene glacial erosion, thus forming the northernmost natural outcrop of Middle Tertiary limestones in Germany which has been mined for hundreds of years. Logistically, Rüdersdorf is easy to reach and has all the power and telecommunication connections needed for a GRSN station. The open-cast development stretches E-W and is about 0.5 to 4 km away from the eastern segment of the busy "Berliner Ring Autobahn" (motor highway). Despite the proximity to town and highway and the continuing surface mining in the quarries of Rüdersdorf, this area was considered to be the most promising alternative for the station BRNL both from a seismo-geological and logistical point of view. This was subsequently confirmed by measurements (see 7.2.4.3).

Hamburg is situated in the NW of the North German-Polish Depression. The regional geological conditions are similar to those around Berlin although the depression is much deeper here. The unconsolidated sediments above the basis of Tertiary are about 1.5 km thick beneath the station. HAM was situated about 12 km away from the city center but rather near (< 1 km) to different

7. Site Selection, Preparation and Installation of Seismic Stations

segments of the dense highway network. Accordingly, the noise conditions were the worst of all the seismic stations in Germany. The most promising alternative site was on an outcropping, partially mined, salt diapir in the town of Bad Segeberg, about 50 km NNE from the center of Hamburg, not too close to either the North Sea or Baltic Sea, easily accessible and with suitable infrastructure and communications facilities. There are Quarternary unconsolidated sediments, about 100 to 400 m thick, and Cretaceous and Triassic sedimentary rocks at a few hundred meters depth, adjacent to the diapir. Fig. 7.29 shows a schematic cross section through the former castle hill and the upper few hundred meters of the diapir of Bad Segeberg.



7.2.4.2 Recording conditions and data analysis of temporary noise measurements for alternative permanent broadband stations

Identical very broadband STS2 seismometers were used with PDAS digital data loggers for comparative measurements of seismic background noise at BRNL and with their potential alternative station sites RUE and BSEG. The data were sampled at 100 Hz. The seismometer at RUE was placed in a small tunnel in the quarry in order to reduce the influence of temperature variations and to enable stable broadband recordings. The tunnel was about 10 m long, with 55 m of limestone overburden, and the site was 2 to 3 km away from the highway and the village of Rüdersdorf. At BSEG, the STS2 was installed in a gypsum cave within the diapir caprock of Bad Segeberg, about 20 to 30 m below the surface. The cave is only a few hundred meters away from the town center of Bad Segeberg.

7.2 Investigation of noise and signal conditions at potential sites

In both cases the instruments were placed directly on a leveled hard rock surface. No additional thermal or pressure shielding was provided during the temporary measurements apart from the manufacturer's standard metallic sensor platform with cover hood. Therefore, in the data shown below, the long-period noise at RUE and BSEG is higher than it would be in a good permanent installation.

Note that in contrast to temporary noise measurements with short-period seismometers, broadband sensors require about one day to adapt to the environmental conditions and find a stable zero position. Meaningful data can only be acquired after this.

For several days, continuous noise and signal measurements were carried out at BSEG and RUE parallel to HAM and BRNL, respectively. Data sampled at 100 Hz. were used for the determination of displacement noise power between 0.1 and 50 Hz and re-sampled 20 Hz data were used for the range 0.03 to 5 Hz. The PSD subroutine described in 7.2.3.2 was used, with a basic record length of 4096 samples. The average power spectrum was determined using 25 consecutive segments with 50% overlap. Thus the spectra are representative for noise records of 8.87 min and 44.37 min length depending on whether they are based on data sampled at 100 or 20 Hz.

7.2.4.3 Results of noise and signal measurements at BRNL and RUE

Fig. 7.30 shows unfiltered 5-minute broadband segments of noise recordings at BRNL and RUE taken around noon and around midnight. Fig.7.31 shows the noise power at both sites in the frequency range 0.03 to 50 Hz.

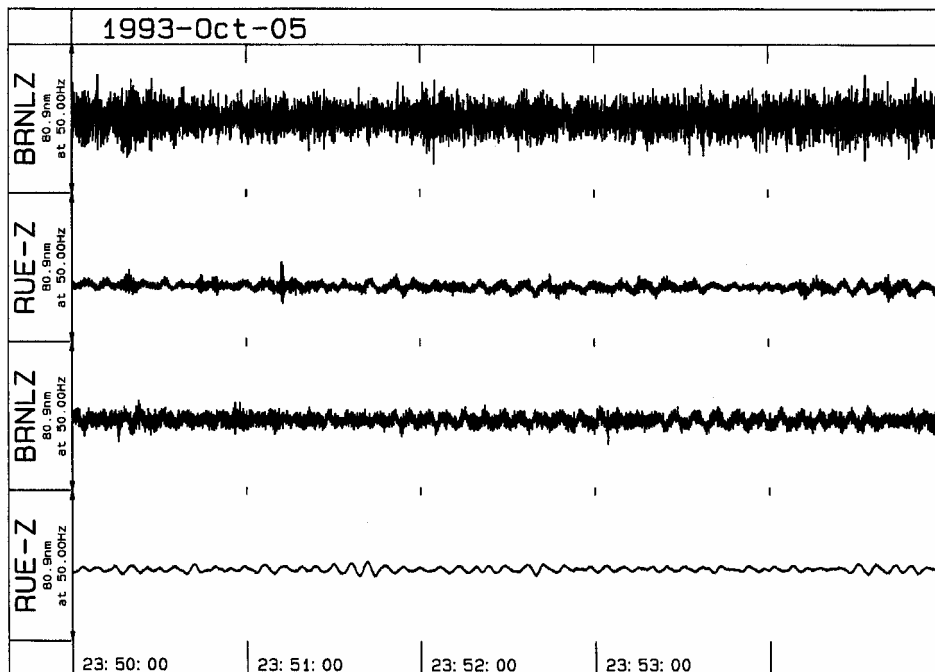


Fig. 7.30 Unfiltered Z-component broadband records of seismic noise with identical resolution at BRNL and RUE. Upper traces: 11:50 - 11:55 UT; lower traces: 23:50 to 23:55 UT (from Bormann et al., 1997).

7. Site Selection, Preparation and Installation of Seismic Stations

The comparison reveals that:

- the noise above 1 Hz at BRNL is some 15 to 25 dB higher than at RUE, both at day- and night-time;
- between 1 and 5 Hz the night-time noise is less than the day-time noise by about 10 dB at BRNL and by about 6 dB at RUE;
- below 0.5 Hz, BRNL has about the same noise power level as RUE with negligible diurnal variation at both sites;
- a range of different, spatially distributed random noise sources such as nearby traffic seem to dominate the short-period noise during day-time at both sites. This results in a rather high and "smooth" noise spectrum without any dominating spectral lines at BRNL and only a few sharp spectral lines at RUE (e.g. at $f = 8, 10, 16$ and 32 Hz);
- during night-time, when the traffic noise is reduced, several sharp spectral lines become dominant for $f > 5$ Hz at both BRNL and RUE. These are probably due to specific noise sources such as machinery rotating with constant frequency (and their lower and higher modes).

The last of these observations is clearly related to activity in the Rüdersdorfer quarry. Mining and stone crushing machinery are operating there throughout the day. Despite the generally lower noise level at RUE compared to BRNL, it is meaningful only to record at RUE low-pass filtered data ($f_c = 5$ Hz) sampled at 20 Hz. According to Fig. 7.24 the noise power at RUE is comparable with that at station Fürstenfeldbruck (FUR), a site of intermediate quality. A better result is not achievable with a near-surface installation in the surroundings of Berlin.

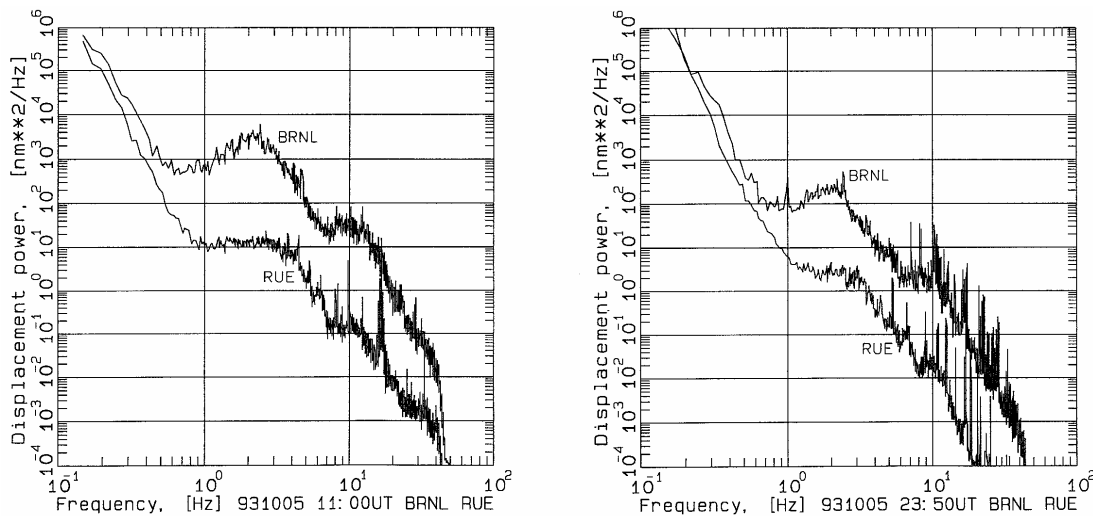


Fig. 7.31 Power spectra of seismic noise in Z-component broadband records at BRNL and RUE around noon (left) and midnight (right) (from Bormann et al., 1997).

Fig. 7.32 presents the broadband (top) and band-pass filtered (from 0.5 - 5 Hz, bottom) Z-component records at BRNL and RUE of a nearby event at approximately the same distance. In both cases the event is not visible at BRNL but is clearly recorded at RUE with several distinct wave groups. The spectral signal-to-noise ratio (SNR) of this event is ≤ 1 at BRNL and varies between 3 and 30 at RUE for $0.5 \text{ Hz} < f < 7 \text{ Hz}$. This is a significant improvement of recording conditions. As a consequence, station BRNL was closed and its equipment permanently moved to RUE.

7.2 Investigation of noise and signal conditions at potential sites

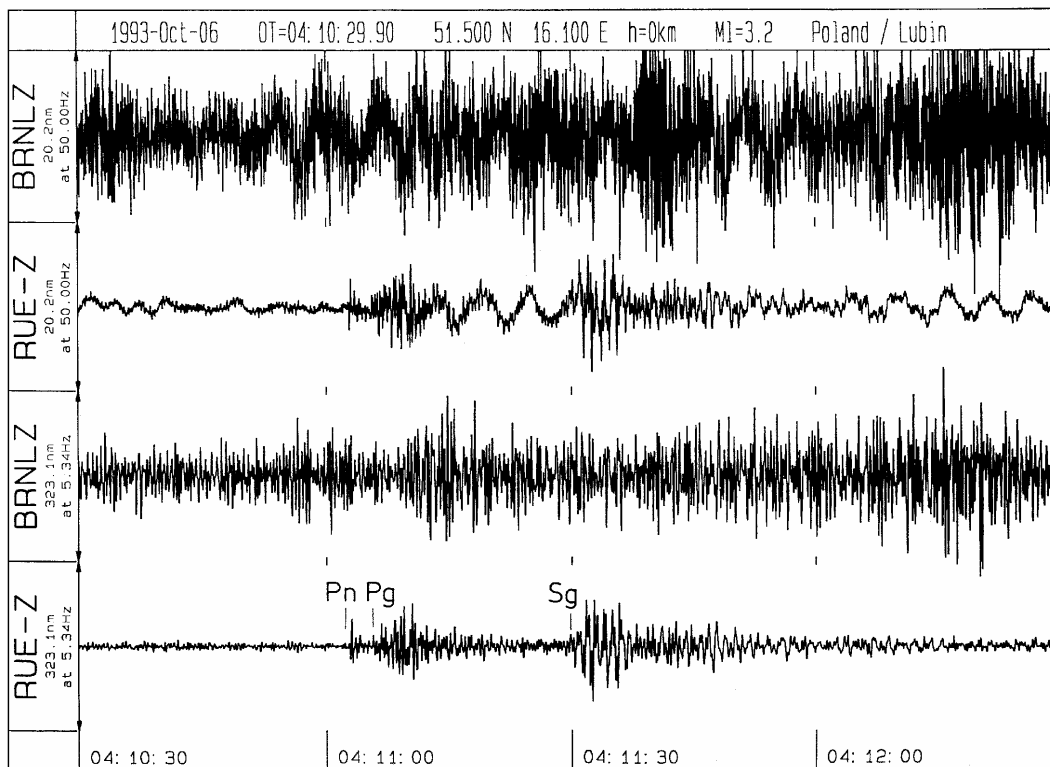


Fig. 7.32 Unfiltered broadband (upper two traces) and band-pass filtered ($f = 0.5 - 5$ Hz; lower two traces) Z-component records of a near seismic event in Poland at BRNL ($D = 214$ km) and RUE ($D = 191$ km) (from Bormann et al., 1997).

7.2.4.4 Results of noise and signal measurements at HAM and BSEG

Fig. 7.33 shows an example of day-time and night-time noise records at HAM and BSEG with identical resolution and Fig. 7.34 shows the related power spectra. The comparison, including that with spectra from other days and with Fig. 7.24, shows that:

- diurnal variations in seismic noise are remarkably small (≤ 10 dB) at HAM. The cause is very intense traffic and industrial activity in this busy large harbor town that does not vary much between day and night time.
- diurnal variations are significant (about 10 to 20 dB) at BSEG above 1.5 Hz but negligible below 1 Hz;
- between 0.5 and 40 Hz the noise power at BSEG is about 20 to 50 dB smaller than at HAM;
- for medium-period ocean storm microseisms (around 3 to 5 s period) the noise power is reduced by about 10 dB at BSEG;
- there is sometimes larger long-period noise at BSEG compared to HAM. This mainly non-seismic noise was significantly reduced after final installation and the level is now comparable with other good GRSN sites;
- noise conditions at BSEG above 1 Hz are only slightly inferior (≤ 10 dB) to good hard-rock sites of the GRSN.

7. Site Selection, Preparation and Installation of Seismic Stations

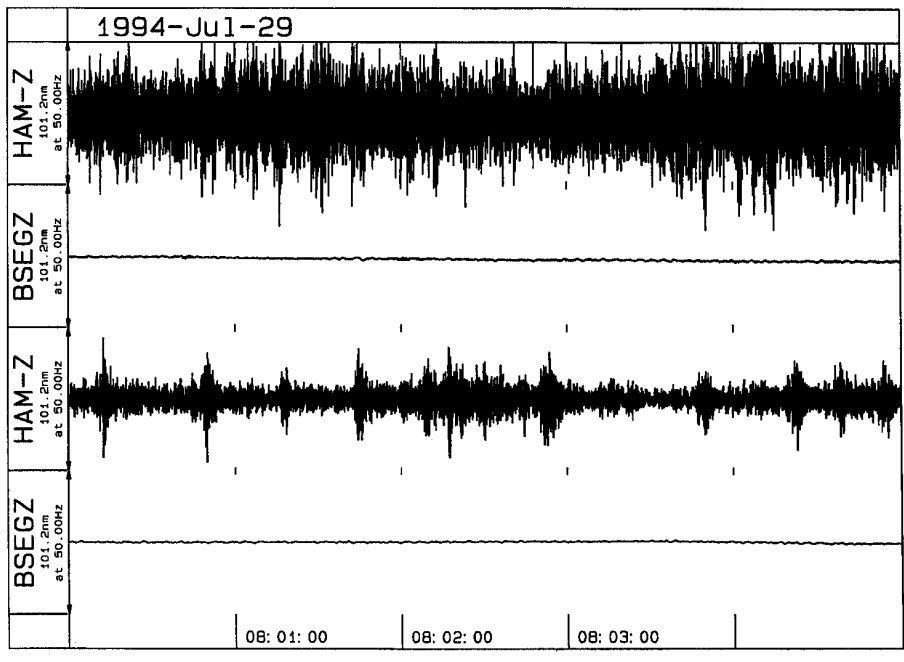


Fig. 7.33 Five minutes of unfiltered Z-component broadband records at HAM and BSEG on July 29, 1994 at 8:00 UT in the morning (upper two traces) and after midnight (lower two traces) (from Bormann et al., 1997).

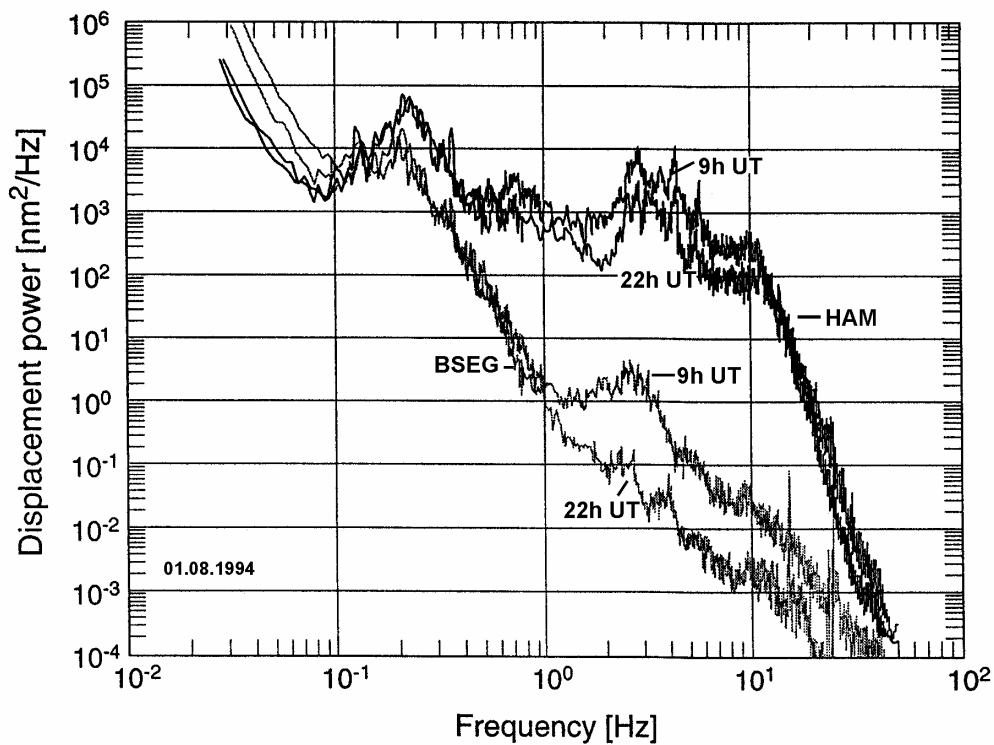


Fig. 7.34 Noise power spectra at HAM (upper two curves) and BSEG (lower two curves) determined from Z-component records on August 1, 1994, around 9 h UT and 22 h UT, respectively (from Bormann et al., 1997).

7.2 Investigation of noise and signal conditions at potential sites

Fig. 7.35 shows the Z-component broadband and short-period records at BSEG and HAM of a teleseismic event in Iran. The event was not recognizable at HAM but was recorded very well at BSEG. In contrast, the SNR for the P-wave onsets in long-period filtered records (Fig. 7.36) was comparable at HAM and BSEG since the P-wave wavelengths are > 50 km and therefore much larger than the size of the noise-reducing velocity anomaly of the diapir structure at Bad Segeberg.

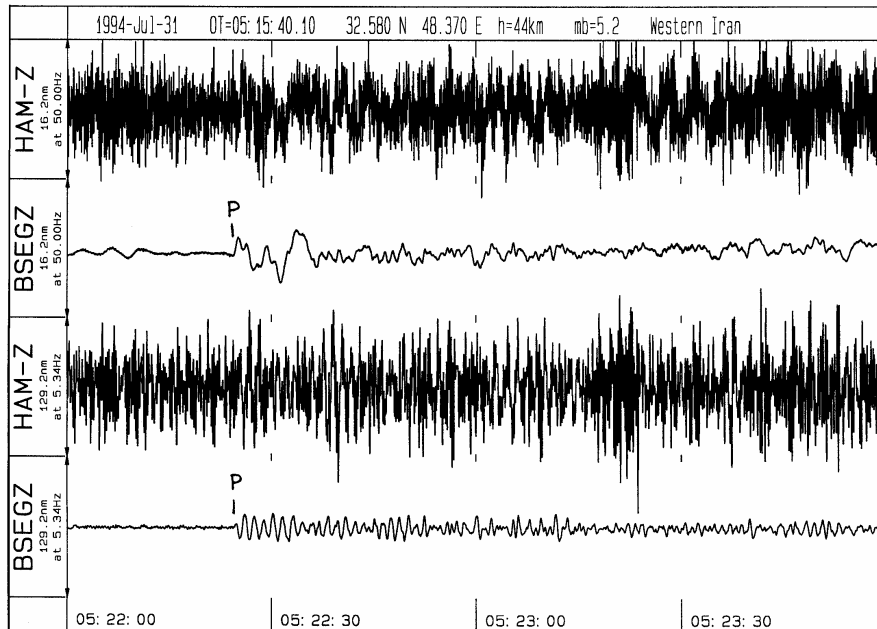


Fig. 7.35 Z-component records of an earthquake in Iran (distance about 3800 km) at HAM and BSEG. Upper two traces: unfiltered broadband records; lower two traces: band-pass filtered with $f = 0.5$ -5 Hz (from Bormann et al., 1997).

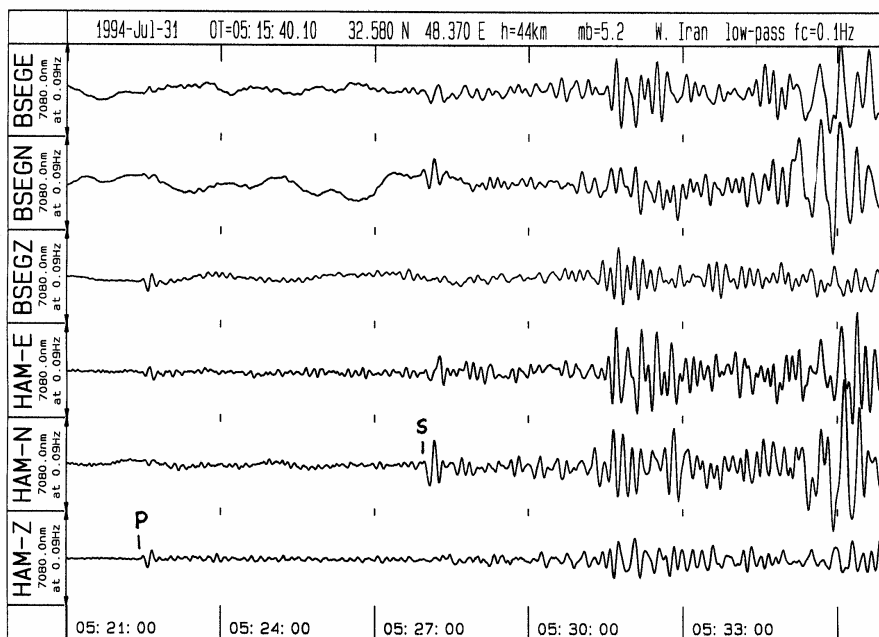


Fig. 7.36 Low-pass filtered ($f_c = 0.1$ Hz) long-period 3-component records at BSEG and HAM of the Iran earthquake (from Bormann et al., 1997).

7. Site Selection, Preparation and Installation of Seismic Stations

Two more examples of relatively weak ($m_b = 5$) earthquakes recorded at about 76° and 150° distance are shown in Fig. 7.37. Although the record traces for HAM have been reproduced at a resolution 10 times lower than the BSEG records the noise amplitudes are still much larger. The P and multiple PKP onsets (including depth phases) can be picked easily in the short-period filtered records of BSEG but not at HAM.

BSEG has now replaced HAM as a permanent GRSN station. Together with RUE, this has significantly improved the GRSN network detection and location performance for events in the northern part of Germany.

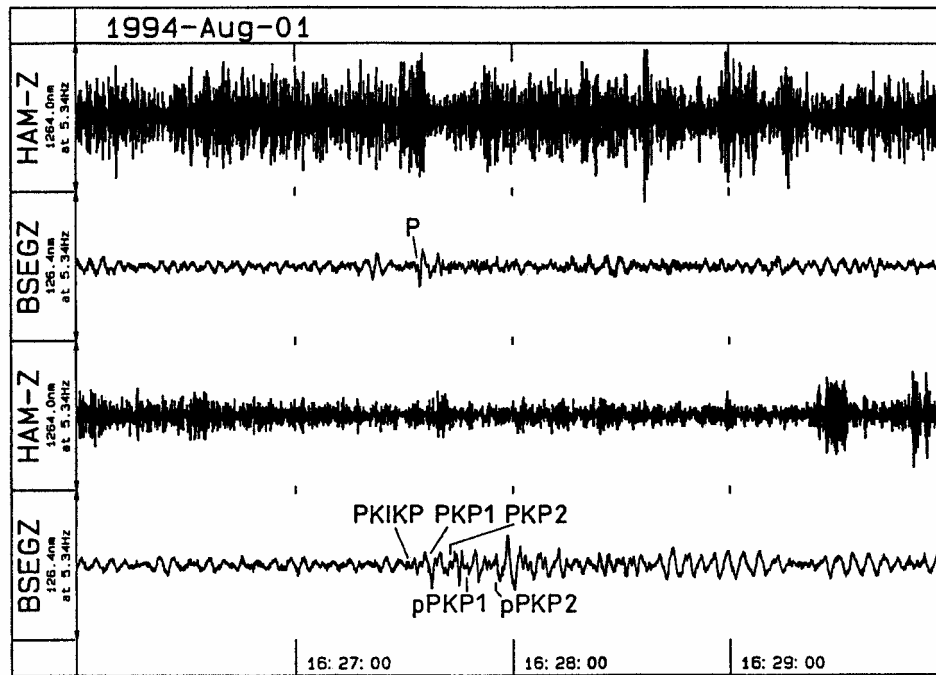


Fig. 7.37 Short-period band-pass filtered Z-component recordings ($f = 0.5 - 5\text{Hz}$) at HAM and BSEG. Upper two traces: P-wave onset of a Kurile Islands earthquake on 01.08.94 ($D = 76.2^\circ$ to HAM, $m_b = 5.0$); lower two traces: PKP-wave group from an earthquake in the Tonga Islands on 30.07.94 ($D = 150.1^\circ$ to HAM, $m_b = 5.0$) (from Bormann et al., 1997).

7.2.4.5 Causes of spectral noise reduction at RUE and BSEG and conclusions

Bormann et al. (1997) estimated quantitatively the reduction of noise amplitudes when traveling from a medium with a low acoustic impedance to a medium with higher acoustic impedance through a sharp impedance discontinuity. Taking into account the best available values for P- and S-wave velocities as well as the densities of the various rock and sedimentary formations in the area of BSEG and RUE, it was estimated that a noise power reduction of about 18.5 dB for BSEG and of 15.6 dB for RUE would be due to the lateral impedance contrast of the anomalous geological bodies at these two sites with respect to the surrounding unconsolidated Quaternary sediments. This would explain about half of the noise power reduction observed at BSEG with respect to HAM (some 30 to 40 dB between 1 and 15 Hz). The remaining reduction of about 10 to 20 dB at BSEG can be accounted for by the distance of BSEG (≈ 40 km) from the seismically noisy city of Hamburg.

For the noise power reduction observed at RUE with respect to BRNL (about 15 to 25 dB in the same frequency range), about 15 dB can be explained by the impedance contrast of the Rüdersdorf anticline. The change in distance to Berlin is less effective (RUE is about 20 km from the city center) because of the noise generated at a busy highway near RUE and ongoing production activity in the quarry.

Below 0.5 Hz, the effect of noise reduction due to these anomalous geological bodies is negligible because their near-surface diameter is then of the order of or smaller than the wavelength of the long-period noise. Large halokinetic, diapir or anticline structures do exist in many other parts of the world with dominating young soft sediment cover (e.g., around the Caspian Sea; west of the Zagros Mountains in Iran; in the USA). A systematic search and use of such structures (or of other anomalous local hardrock outcrops) as sites for permanent seismic recordings is recommended as a way to achieve significant short-period noise reduction. Otherwise, one has either to settle for rather bad noise conditions for near-surface installations or go for expensive borehole installations (see 7.4.5).

7.3 Data transmission by radio-link and RF survey (A. Trnkoczy)

7.3.1 Introduction

Radio links are often used for data transmission in a seismic network. Radio links offer seismic data transmission in real time, are continuous, independent, often robust to damaging earthquakes, and usually involve a reasonable cost (see also IS 8.2: Seismic data transmission links used in seismology in brief).

However, experience shows that the most frequent technical problems with radio frequency (RF) telemetry networks originate in the RF links themselves. This is often the result of a non-optimally designed RF system. Many seismic networks in the world experience unreliable and noisy data transmission. There are even reports of some complete failures. This Chapter gives some general advice on how to design a seismic telemetry system, covering VHF (usually 160 - 200 MHz for seismology) and UHF (usually around 450 MHz for seismology) frequency band FM modulated links, as well as spread spectrum (SS; around 900 MHz or 2.4 GHz) RF data transmission and satellite . The need for a professional RF survey will be explained.

The UHF and VHF frequency bands are still the most frequently used. Spread spectrum and satellite links are becoming more popular in seismology.

7.3.2 Types of RF data transmission used in seismology

Most of today's RF telemetry seismic networks use the VHF or UHF frequency band. Both bands can be used for frequency modulated (FM) analog signal transmission or digital data transmission with a variety of modulation schemes. Both usually use standard 3.5 kHz bandwidth "voice" channels. It is much easier to obtain permission for these than for special channels with a higher bandwidth. Direct connection distances of up to 150 km (100 miles) are possible with less than one Watt RF power transmitters, if topography permits.

7. Site Selection, Preparation and Installation of Seismic Stations

Unfortunately, the VHF band is almost completely occupied in most countries. It is therefore very difficult or even impossible to get permission to use this band. The band is also more susceptible to interference from other RF users and therefore is rarely used for new seismic networks.

Until very recently, the UHF band has been the most popular. But it is now becoming difficult to obtain permission for new frequencies within this band in many countries.

Spread spectrum RF telemetry is a new and increasingly popular alternative in seismology. These links operate at frequencies around 900 MHz or 2,4 GHz. Spread spectrum RF links do not use a single carrier frequency but instead use the entire frequency band dedicated for such links. Many users use the same frequency band so the corresponding transmitter and receiver must identify each other to discriminate from other users using special codes.

The practical advantages of spread spectrum links are that often no permission is needed for their operation and that they are very robust against RF interference (the technology was first developed for defense purposes for just this reason). There are limitations, however, because the maximum RF power of transmitters is defined by national regulations, varies greatly, and dictates the maximum practical connection distance between a transmitter and a receiver. This may impose severe limitations on the wider use of spread spectrum links for seismology. In Western European countries where the limit is 100 mW, connections are only possible up to 20 to 30 km. Direct connection distances around 100 km can be achieved using stronger transmitters (up to 4W) only in the countries that allow them.

Satellite links are becoming more popular in seismometry and undoubtedly represent the future for seismic data transmission. Costs are still a hindrance to the widespread implementation of this technology but these will surely come down.

Most of the commercially available satellite links are of the high throughput type. Usually they are purchased as 110 kHz bands in the GHz frequency range (e.g., Ku-band: 11 to 14 GHz). Frequently, the smallest available bandwidth (and consequently the baud rate) is much higher than usually required for a seismic station or even for a small seismic network. This makes satellite links relatively expensive for small networks. Prices for one 110 kHz band are currently around several hundred dollars per month (1998).

If the size of the network and the total bandwidth required is equal to or slightly smaller than any multiple of the available bandwidth increments, the cost of satellite data transmission may be more acceptable. This is easier to achieve in large national or regional seismic networks. The number of seismic data channels that can be transmitted in a 110 kHz frequency band depends on several parameters: the sampling rate; the number of bits per data sample (dynamic range); whether single direction (simplex) or bi-directional (duplex) links are used; the overhead bits required for error detection, forward error correction (FEC), and link management.

One of the important issues which varies from country to country relates to the central satellite recording site (the hub). In some countries, where the communication market is open, a seismic network owner may have its own 'private' hub directly at the central recording site. The cost of equipment for such a local hub varies from \$80,000 to about \$200,000 (in the year 2001). In countries with a more restricted communications market only a shared hub owned

by a communications company may be available. In this case, not only is the cost of satellite communications higher but there will be additional costs for the communication links from the shared hub to the seismological central recording site. These usually use leased lines and the costs can be significant, particularly if the distance involved is large. Cost analysis of different satellite systems is complex and the prices vary significantly from country to country. A very careful cost analysis is recommended before making any final decision about satellite links.

A practical problem with satellite links is the relatively high power consumption of the equipment installed at a seismic station. In most cases, we must consider at least 50W power consumption for the data transmission equipment at each site. This significantly exceeds the power consumption of RF equipment traditionally used in seismology, including spread spectrum transmitters. It creates the need for large arrays of solar panels at stations without mains power and for bigger back-up batteries for a given station autonomy.

Nonetheless, the costs of satellite communications are constantly decreasing thanks to increasing liberalization in the communications market which will encourage the use of satellite links. No other communication system has the potential of satellite links for high reliability at the most remote and distant seismic stations.

7.3.3 The need for a professional radio frequency (RF) survey

The design of VHF, UHF or spread spectrum RF telemetry links in a seismic network is a specialized professional technical matter. Practice shows that guesswork and an approach based on "common sense" usually lead to problems or even complete failure of a project. The following misunderstandings and oversimplifications are commonly encountered:

- the amount of data that must be transmitted in seismology is often underestimated. Seismology requires a much larger data flow (baud rate) than most other geophysical disciplines, for example several orders of magnitude more than meteorology;
- the required reliability for successful data transmission in seismology is also frequently underestimated. Missing data due to interruptions on the links, excessive noise, spikes, and data errors are particularly destructive for networks operating in triggered mode and/or having any kind of automatic processing. With old paper seismograms and analog technology, spikes, glitches, interruptions and other 'imperfections' are relatively easily "filtered out" by the seismologist's pattern recognition ability during the analysis. However, the same errors, if too frequent, can make the results of an automatic computer triggering and/or analysis totally unacceptable;
- a false comparison with voice RF channels is made frequently. People try to verify a seismological RF link between two points using walkie-talkies. If they can communicate, they expect that transmission of seismic data will also be successful. Note that voice channels allow a much lower signal-to-noise ratio while still being fully functional because human speech is highly redundant. Also, the RF equipment parameters in walkie-talkies and in seismic telemetry are very different, making such "testing" of RF links meaningless.

7. Site Selection, Preparation and Installation of Seismic Stations

- another wide-spread belief is that the "line of sight" between transmitter and receiver is a sufficient guarantee for a reliable RF link. This may or may not be true. It is only certain for very short links up to about 5 km length with absolutely no obstructions between the transmitter and the receiver (such links may occur in some small local seismic networks). Fading, i.e., the variation of the intensity or phase of an RF signal due to changes in the characteristics of the RF signal propagation path with time, becomes a major consideration on longer links. The real issues in link reliability calculations are the equipment's gains and losses, RF signal attenuation based on Fresnel ellipsoid obstruction, and the required fading margin. The resultant reliability of the link can then be expressed as a time availability (or probability of failure or time unavailability) as a percentage of time in the worst month of the year (or per year). During 'time unavailability', the signal-to-noise ratio at the output of the receiver is lower than required, or the bit error rate (BER) of digital data transmission link is higher than required. Many parameters are involved in the RF path analysis including transmitter power, frequency of operation, the various losses and gains from the transmitter outward through the medium, receiver antenna system to the input of the far end receiver and its characteristics. In link attenuation calculation, the curvature of the Earth, the regional gradient of air refractivity, the type of the link regarding topography, potential-wave diffraction and/or reflections, time dispersions of the RF carrier with digital links, processing gain and background noise level with spread spectrum links, etc. all play an important role.

We strongly recommend having a professional RF survey during the seismic network planning procedure. IS 7.1 provides the information on what preparation is needed if an RF survey is purchased as a service along with the seismic equipment.

7.3.4 Benefits of a professional RF survey

The benefits of a professional RF survey are:

- it ensures that the links will actually provide the desired reliability, which has to be decided beforehand. During the RF survey, the design parameters of the links in a network are varied until the probability of an outage in the worst month of a year drops below the desired value. This may require additional investment in equipment, but it will prevent unreliable operation or may save some money by loosening the requirements where appropriate;
- it guarantees the minimum number of RF repeaters in a network. This results in a direct benefit to the user in having less equipment, fewer spare parts, and in cheaper and easier maintenance. There will also be lower instrumental noise in the recorded signals for FM analog networks and a better BER performance for digital networks. Note that in most designs for analog FM telemetry, every additional repeater degrades data quality to some extent and always decreases the network reliability;
- It will determine the minimum number of licensed frequencies required in a network without sacrificing data transmission reliability. Note that the required number of different carrier frequencies in VHF and UHF telemetry can be significantly smaller than the total number of the links in the network. This prevents unnecessary pollution of RF space in the country. Use of fewer frequencies also benefits the user since they are easier to obtain and fewer different RF spare parts are required;

- the robustness of the entire seismic network to lightning threat is significantly increased by a proper RF layout, for example, one should always avoid repeaters which relay data from many seismic stations because any technical failure of the repeater will result in severe data loss;
- reduced power consumption can be achieved by calculating the minimum sufficient RF output of the transmitters. This results in less pollution of RF space in the country. The user also benefits from lower power consumption at remote stations;
- minimizing the heights of antenna masts and the minimum gains of the antennae has potential for cost saving.

7.3.5 Radio-frequency (RF) survey procedure

An RF survey usually considers the RF equipment to be used, a topographical profile from each transmitter site (remote seismic station) to each receiver site (central recording site or repeater), local RF path conditions, and the desired reliability of the link. It is based on decades of experience of transmission statistics from all over the world and computer modeling using specialized software. Field RF measurements are rarely performed because they are expensive and time-consuming and they are often less reliable than calculations. RF transmission conditions vary with time (diurnal, seasonal, weather dependent), vary unpredictably and within climatic zones. Theoretical calculations include the full statistics of these variations whereas practical one-time measurements suffer from unpredictable variations in fading. However, even if no measurements are planned, a communications expert still has to visit all potential seismic sites during the site selection procedures to assess local topography and to check for the existence of potential RF obstacles which may not be evident from topographic maps.

If the RF link calculation based on a given set of input parameters does not give the desired reliability, some of the input parameters must be changed. We can change topographical profile by either repositioning stations or by introducing a new RF repeater. We can change the antenna type and/or increase their gain. We can increase antenna mast height or increase transmitter output power (seldom effective) or we can change the RF equipment completely (significantly more powerful transmitters and/or more sensitive receivers).

Topographic profiles are usually taken from 1:50,000 scale topographical maps. In most cases, many more profiles than stations available in the network are taken and links calculated before we determine the final RF layout of a network. A great deal of this work can be done before fieldwork starts, but profiling is always needed during the fieldwork.

The result of an RF link calculation is shown in Fig. 7.38 with input parameters on the left and output parameters on the right. The figure intentionally shows an example where there is a "direct line of sight", but the profile doesn't guarantee acceptable link operation. Note the curved path of the first Fresnel ellipsoid where the RF energy actually travels from the transmitter to the receiver. This curvature is mostly due to the regional gradient of air refractivity. In the example, this ellipsoid hits the mountain ridge and causes a significant loss of energy or possibly link failure.

7. Site Selection, Preparation and Installation of Seismic Stations

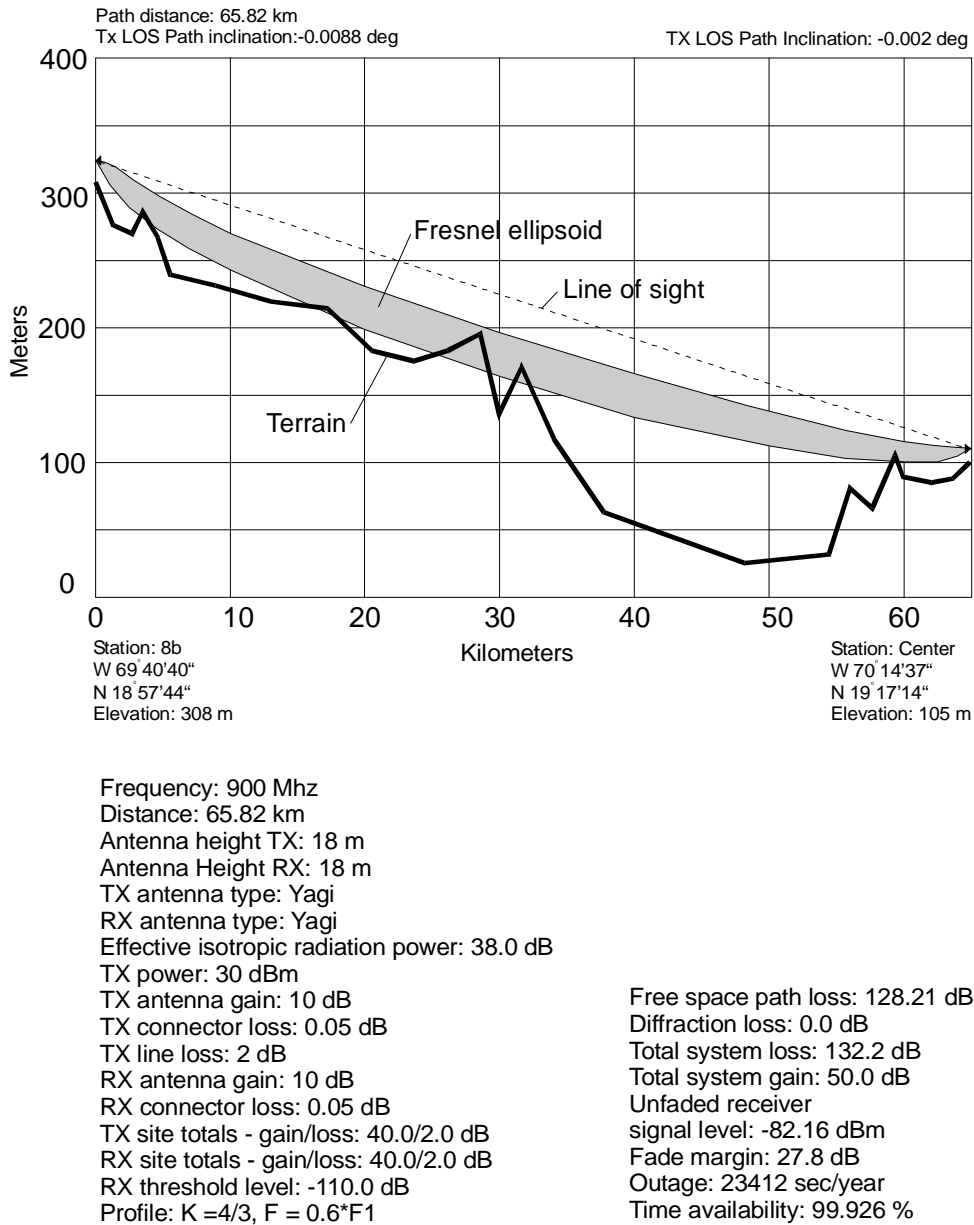


Fig. 7.38 Result of an RF link calculation with input parameters on the left and output parameters on the right.

For analog VHF or UHF telemetry it is usual to regard a time availability of about 99.95% (equivalent to about 15 minutes of outage of each link per month) in the worst month as being marginally acceptable and 99.99% as good. If we use an RF repeater between the seismic station and central recording site, we have to increase the required reliability of individual sections to give the required reliability for the entire link.

In digital data transmission, the bit error rate (BER) is used as a measure of data link reliability. BER strongly depends not only on physical reliability of the RF link but also on error detection and error correction methods used in the RF equipment (modems). For example, one-directional (simplex) links are generally far less reliable than bi-directional (duplex) links, even if the RF links themselves are of the same quality in terms of RF signal to noise. This is because duplex links allow repeated transmission of corrupted data blocks until

they are received without error whereas simplex links result in corrupted data, unless forward error correction (FEC) methods are used. Due to the complexity of the problem, a precise targeting of desired BER is usually beyond the scope of seismic network projects.

Something similar is the case for spread spectrum links where another factor complicates the situation. Spread spectrum receivers incorporate so-called "processing gain". These receivers are capable of resolving very weak RF signals, which may even be a few dB below the RF noise at the receiver site. However, the problem is that the amplitude of the RF noise at the receiver site is generally unknown. Note that every new spread spectrum transmitter increases the background noise in the band of operation of the spread spectrum system and since this band is open to the public, it is difficult to predict its actual noise. Consequently we will not know exactly the sensitivity of a receiver, resulting in a less reliable estimate of the link availability.

Specialized spread spectrum measuring equipment is extremely expensive. The algorithms which are used to resolve the sub-noise level RF signals in the receivers also present a problem. They are mostly proprietary and therefore not generally accessible. Both facts significantly reduce the practicality of measurements of the reliability of spread spectrum links for seismological purposes.

Fortunately, some spread spectrum equipment manufacturers provide special software which allows easy but approximate link reliability measurements for the transmitters and receivers to be used in the seismic system. Taking into account a safety margin due to temporal variation of RF transmission conditions, one can successfully use these measurements for an approximate estimate of link quality. However, it is difficult to relate these proprietary 'reliability scales' to standard parameters like probability of link outage or BER. Nevertheless, classical RF signal attenuation calculations still give valuable information about RF energy propagation over a given topographic profile. These results, combined with measurements using manufacturer's proprietary 'reliability scales' and practical experience, suffice in almost all seismometric projects.

The cost of a professional RF survey is generally around a few percent of the total investment in a new seismological network. Practice shows that its benefits are well worth the investment. An RF survey is a major step toward the reliable operation of any future telemetry seismic network.

7.3.6 The problem of radio-frequency interference

While spread spectrum links are fairly robust, radio-frequency interference between a VHF or UHF seismological system and other RF users is quite a common and difficult problem in many developing countries. In some countries, the lack of discipline in RF space causes unforeseen interference. In others, insufficient maintenance of high-power communication equipment results in strong radiation from the side-lobes of powerful transmitters that may also interfere with seismological links. Army facilities, particularly if they operate outside civil law, especially some types of radars, frequently interfere with seismological links. The risk of interference is very high if seismic stations are installed at sites which are also used for other high power RF communication equipment (see IS 7.2). Extensive use of walkie-talkies can also cause problems.

7. Site Selection, Preparation and Installation of Seismic Stations

In some developing countries, the use of RF spectrum analyzers, which can frequently reveal the origin of interfering signals, is prohibited for security reasons, particularly for foreigners. In any case, interfering RF sources may appear only very intermittently and so are difficult to detect.

Note that RF interference problems due to indiscipline in RF space are generally beyond the control of a seismic equipment manufacturer and/or foreign RF survey provider. They can only be solved, or at least mitigated, by involving local RF communication experts during the very early phases of network planning. These people are familiar with the real RF conditions in the country and can provide better advice than any foreign expert. If a new seismic network experiences interference problems, only very tedious and time consuming trial-and-error procedures (swapping frequencies of the links or even VHF/UHF bands, changing antenna orientation and polarization, or even re-positioning of stations or repeaters) may help. However, the results are unpredictable. One should also be aware that the allocation of frequencies may change in future and disturbances remedied today may reoccur later.

7.4 Seismic station site preparation, instrument installation and shielding

7.4.1 Introduction and general requirements (A. Trnkoczy)

When installing a seismometer inside a building, vault, or cave, the first task is to mark the orientation of the sensor on the floor. This is best done with a geodetic gyroscope although a magnetic compass will often suffice. The magnetic declination must be taken into account. A compass may be deflected, showing a false reading, when inside a building so the direction should be taken outside and transferred to the site of installation. A laser pointer may be useful for this purpose. When the magnetic declination is unknown or unpredictable (such as in high latitudes or volcanic areas), the orientation can be determined with a sun compass. Special requirements and tools for sensor orientation in boreholes are dealt with in 7.4.6.2.

To isolate the seismometer from stray electric currents, small glass or perspex plates should be cemented to the ground under its feet. The seismometer can then be installed and tested. Broadband seismometers should be wrapped with a thick layer of thermally insulating material. The exact type of material does not seem to matter; alternate layers of fibrous material and heat-reflecting blankets are probably the most effective. The edges of the blankets should be taped to the floor around the seismometer. Further information on suitable and proven thermal insulation for broadband seismometers, including illustrations, can be found in 7.4.2.1, 7.4.4.2 and 5.5.3. One has to be aware that electronic seismometers generate heat and so may induce convection in any open space inside the insulation. It is therefore important that the insulation fits the seismometer tightly.

For the permanent installation of broadband seismometers under unfavorable environmental conditions, they should be enclosed in a hermetic container. A problem with such containers (as with all seismometer housings) is that they cause tilt noise when they are deformed by barometric pressure. Essentially three precautions are possible: either the base-plate is carefully cemented to the floor, or it is made so massive that its deformation is negligible, or a "warp-free" design is used, as described by Holcomb and Hutt (1992) for the STS1 seismometer (see DS 5.1).

7.4 Seismic station site preparation, instrument installation and shielding

To prevent or reduce corrosion in humid climates, desiccant (silica gel) should be placed inside the container, including inside the vacuum bell, of an STS1 seismometer. Broadband seismometers may also require some magnetic shielding (see 5.5.4).

Civil engineering work at remote seismic stations should ensure that modern seismic instruments can be used to their fullest potential by sheltering them in an optimal working environment. Today's high dynamic range, high linearity seismic equipment is of such quality and sensitivity that seismic noise conditions at the site and the environment of the sensors have become much more important than in the past. Apart from site selection itself, the design of seismic shelters is the determining factor in the quality of seismic data acquisition.

Seismic vaults are currently the most common for new seismic stations (see 4.2). They are the least expensive but suffer more from seismic noise because of their near-surface installation. Alternatives include seismic installations in abandoned mines, in specially constructed tunnels (see 7.4.3) and in boreholes (see 7.4.5 and 7.4.6). These have the advantage of high temperature stability and significantly reduced surface and tilt noise because of the significant overburden. The low tilt noise is of particular importance for long-period and broadband seismometers because of their high tilt and temperature sensitivity (see 7.4.4, 5.3.3 and 5.3.5). A variety of factors must be considered before the optimal technical and financial solution for a seismic installation is found. These include the type of monitoring or research to be carried out, the kind of equipment to be installed, existing geological and climatic conditions, already existing potentially suitable structures and sites, available construction materials or alternative technical solutions, accessibility of and available infrastructure/power supply at the station.

Various solutions can be employed with equal success. Much depends on potential future upgrades of the instrumentation and site, what working conditions are desired for maintenance and service personnel, and, of course, on the funds available. Because of these diverse considerations, no firm design and civil engineering drawings are provided in this document. Instead, the general requirements that must be satisfied are described in detail so that, e.g., in the case of seismic vaults, any qualified civil engineer can design the shelter for optimal performance, taking into consideration local conditions in a given country and at a specific site.

7.4.2 Vault-type seismic stations (A. Trnkoczy)

This section describes the general conditions to be considered when constructing seismic vaults. A vault for seismic data acquisition and transmission equipment should satisfy the following general requirements:

- provide adequate environmental conditions for the equipment;
- ensure the proper mechanical contact of seismic sensors with bedrock;
- prevent seismic interaction between the seismic shelter and the surrounding ground;
- mitigate seismic noise generated by wind, people, animals, and by potential noise sources within the vault;
- ensure a suitable electric ground for sensitive electronic equipment;
- provide sufficient space for easy access and maintenance of the instruments.

7. Site Selection, Preparation and Installation of Seismic Stations

These requirements will be discussed in detail below. A design example of a seismic vault for a three-component short-period (SP) station together with its upgrade for broadband (BB) and potentially very broadband (VBB) seismic sensors will be given, complemented by some technical hints at the end of this section. Other examples of vault-type seismic shelters are given in 7.4.4.3 and even more can be consulted on the web page <http://www.gfz-potsdam.de/geofon/> via the link “How to get a well-performing VBB station?”. Alternative vault designs of typical ‘classic’ seismometer vaults are given in Figures 4.5b-e) of the old MSOP (<http://www.seismo.com/msop/msop79/sta/sta.html> via link “Examples of stations” or Willmore, 1979), while detailed installation guidelines for BB and VBB stations are given by Uhrhammer et al. (1998).

7.4.2.1 Controlling environmental conditions

Adequate shelter for seismic equipment should:

- prevent large temperature fluctuations in the equipment due to day/night temperature differences or because of weather changes;
- prevent large temperature fluctuations in the construction elements of the vault, resulting in seismometer tilt;
- ensure adequate lightning protection;
- mitigate electromagnetic interference (EMI);
- prevent water, dust and dirt from entering the shelter;
- prevent small animals from entering the shelter.

At very low seismic frequencies and in VBB seismometers, air pressure changes also influence seismometer output. Special installation measures and processing methods can be used to minimize the effect of air pressure. However this issue will not be treated here. For more information see Beauquin et al. (1996).

Mitigating temperature changes

In general, seismic equipment can operate in quite a broad temperature range. Most of the equipment on the market today is specified to function properly between -20 and $+50$ degrees Celcius. However, this is the operating temperature range – that is, guaranteeing only that the equipment functions at a given constant temperature within these limits.

Temperature changes with time, particularly diurnal changes, are far more important than the high or low average temperature itself. Many broadband seismometers require mass centering if the temperature “slips” more than a few degrees Celcius, although their operating range is much wider. Even small temperature changes can cause problems with mechanical and electronic drifts which may seriously deteriorate the quality of seismic data at very low frequencies. Unfortunately, the practical sensitivity of the equipment to temperature gradients is rarely provided by manufacturers. Very broadband (VBB) seismometers require extremely stable temperature conditions which are sometimes very difficult or impossible to assure in a vault-type shelter. VBB sensors usually require special installations (see Uhrhammer et al., 1998). Short-period (SP) seismometers, particularly passive ones, and accelerometers are much less sensitive to temperature changes.

7.4 Seismic station site preparation, instrument installation and shielding

In general, thermal drifts should be kept acceptably small by thermal insulation of the vault. However, the requirements differ significantly. Maximum ± 5 deg C short-term temperature changes can be considered a target for passive SP seismometers and force-feedback active accelerometers. To fully exploit the low-frequency characteristics of a typical 30-sec period BB seismometer, the temperature must be kept constant within less than one degree C. To fully exploit a several-hundred-seconds period VBB sensors only a few tens of millidegrees C per month are recommended.

Data loggers and digitizers can tolerate less stable temperatures, i.e., on average, the temperature change would be ten times greater than on a BB seismometer for the same change in output voltage. The best digitisers, for example, change their output voltage less than ± 3 counts in room temperature conditions. If daily temperature changes are less than 1 deg C, their output voltage changes less than ± 1 count (Quanterra, 1994).

Some elements such as some computer disk drives, diskette drives, and certain time-keeping equipment, may require narrower operating temperature tolerances. The most effective way to assure stable temperature conditions is an underground vault that is well insulated (see Fig. 7.39). Underground installations are also the best for a number of other reasons.

Thermal insulation of active seismic sensors is done in two places. First, the interior of the vault is insulated from external temperatures, and second, the sensors themselves are insulated from residual temperature changes in the vault. In the most critical installations, the seismic pier itself is insulated along with the sensors.

Underground vaults are usually insulated with a tight thermal cover made of styrofoam, foam rubber, polyisocyanuratic foam, or other similar, non-hygroscopic insulation material (Fig. 7.39, Figs. 7.41 and 7.42). Such materials are usually used in civil engineering for the thermal insulation of buildings. They come in various thicknesses, often with aluminum foil on one or both sides. This aluminum layer prevents heat exchange by blocking heat transfer through radiation. Thinner sheets can be glued together to make thicker ones. Casein-based glues are appropriate for styrofoam and expanding polyurethane resin is used to glue polyisocyanuratic foam sheets.

In continental climates, a 20 cm (8") layer is considered adequate but in extreme desert climates, up to 30 cm (12") of styrofoam is recommended. In equatorial climates a 10 cm (4") layer is considered sufficient.

There are two thermal cover design issues that are particularly important. Special care must be taken to assure a tight contact between the vault's walls and the thermal cover. If it is not tight, heat transfer due to convection through the gaps can easily be larger than the heat transfer through the thermal cover by conduction. This can undo the insulating effects of the cover. One way to achieve a tight thermal cover is shown in Fig. 7.43. A "rope" is tightly pressed into the gaps between the vault's walls and the thermal cover as well into the wedge-like gap between the cover halves seen in Fig. 7.41. This "rope" can be made of insulating fibers and is usually used for industrial hot water pipe insulation. It is available in different sizes and is inexpensive.

7. Site Selection, Preparation and Installation of Seismic Stations

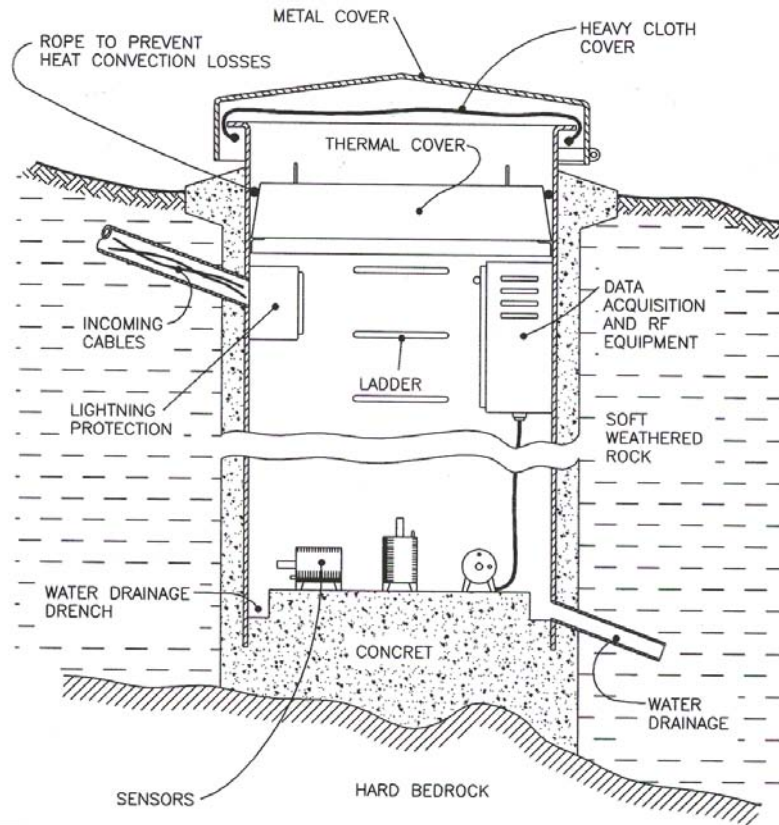


Fig. 7.39 Example of a vault for a short-period three-component seismic station made of a large-diameter metal pipe with thin concrete walls.



Fig. 7.40 Interior of a seismic vault made of welded metal sheets. The vault is big enough to accept weak- and strong-motion instrumentation together with data acquisition and transmission equipment.

7.4 Seismic station site preparation, instrument installation and shielding



Fig. 7.41 Thermal cover of a seismic vault in two pieces made of thick styrofoam. The gaps between the cover and the vault walls and between both pieces must be tightly sealed.

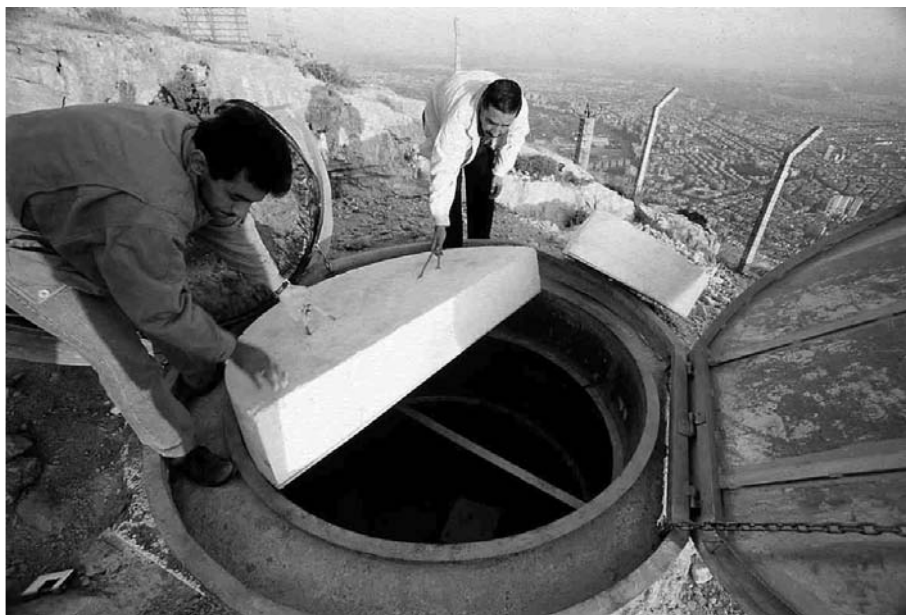


Fig. 7.42 Installing thermal cover in a seismic vault. In climates with large diurnal temperature changes the cover should be positioned lower in the vault where external ground temperature does not change significantly.

The cover should be placed at or below the depth at which the ground heats up during the day – not on the top of the vault. In desert areas, surface ground temperatures can exceed 80 deg C. At 30 cm (12") depth, temperatures of 50 deg C are not unusual. In such conditions, the thermal cover must be placed 40 - 50 cm (16" - 20") below ground level. A thermal cover of any thickness at the top of the vault, particularly if the vault's rim stands significantly above the surface, has almost no effect.

7. Site Selection, Preparation and Installation of Seismic Stations

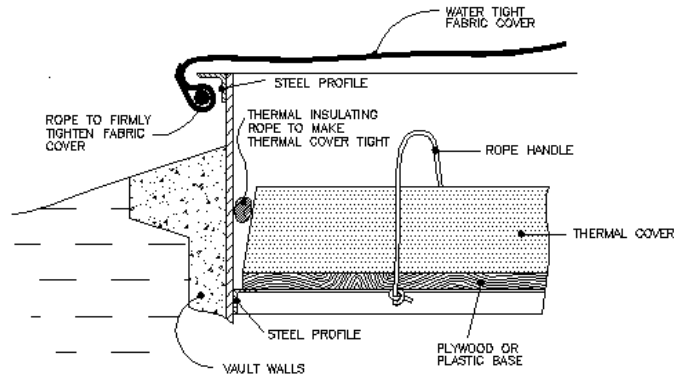


Fig. 7.43 Detail of making a thermal cover effective by filling up the gaps between the cover and vault walls with insulation material and making the vault tight against dust, dirt, and rain during windy periods with a fabric cover.

If vaults are used for BB or even VBB stations (see Wielandt, 1990), it is advisable to make a second inner thermal cover just above the sensor but below the floor where all other equipment is installed (see Fig. 7.44). Since most maintenance work relates to batteries, data recording, and data transmitting equipment, the thermal- and mechanical-sensitive BB/VBB sensors are not disturbed at all during service visits.

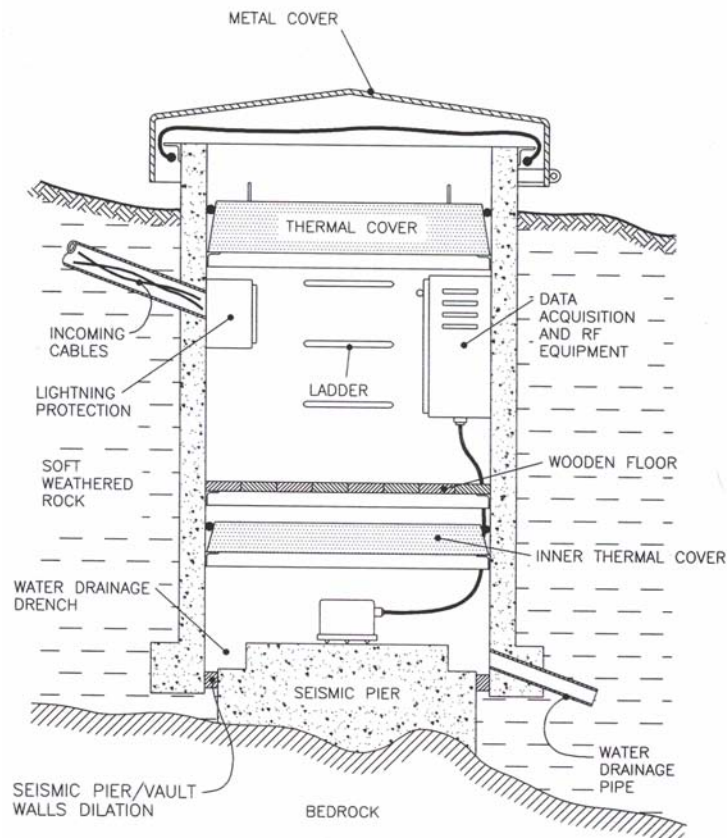


Fig. 7.44 Example of a BB or VBB seismic vault with a separate compartment for sensors and double thermal cover. Usually, the sensor itself is additionally isolated (see Fig. 7.50). A thermal isolation box is usually put around the sensors to additionally insulate them.

7.4 Seismic station site preparation, instrument installation and shielding

Thermal insulation of the seismic pier itself, together with the seismometer, is the best method of insulation (Fig. 7.45). This method keeps the heat transfer between seismometer and vault interior as low as possible, while at the same time assuring good thermal contact with the thermally very-stable ground. Thus, the thermal inertia of the system is very large, limiting the rate of temperature changes to a minimum.

A 10 – 20 cm (4" - 8") thick sheet of insulating material typically covers the seismometer box and the entire exposed seismic pier. The seams between the insulation sheets should be well filled with liquid foam. For details see Uhrhammer et al. (1998).

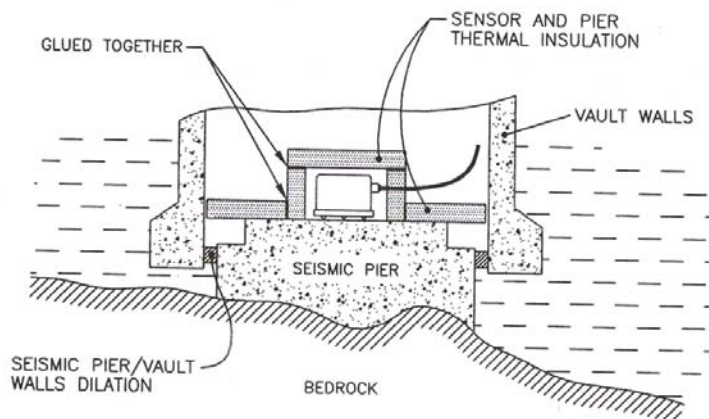


Fig. 7.45 Thermal isolation of a VBB sensor and surrounding seismic pier and mechanical separation of the pier from the vault walls for the most demanding applications.

Thermal tilt mitigation

Special measures are required to prevent thermal deformation and tilt of the seismic pier in a vault to allow the study of extremely low frequency signals with VBB seismometers. Modern VBB sensors, the horizontal components in particular, can detect tilts of a few nanoradians. A human hair placed under the corner of a level football field or an air pressure difference of only 0.1 mbar over a distance of several km would cause such a tilt. According to Wielandt (see section 5.3.3) a tilt of about 10^{-9} rad would result in a noise ground acceleration amplitude of 10^{-9} g in the horizontal components but only of 10^{-11} g in the vertical one.

Homogeneity of the seismic pier and surrounding soil, as well as civil engineering details of vault design are very important. Uhrhammer et al. (1998) recommend the physical separation of the seismometer pier and the vault walls (see Figs. 7.44 and 7.45). This separation assures that minute changes in the dimensions of the vault walls due to temperature change do not tilt the seismic pier. However, since such seismic vaults are not constructed "in one piece," one has to be particularly careful that the contact between the pier and vault walls is still watertight.

The seismic pier should be made of homogenous material and neither it nor the walls of the vault should use any steel reinforcement. Steel and concrete have different temperature expansion coefficients which cause stress and unwanted minute deformation of the structure of the vault if the temperature changes. Steel is unnecessary anyhow because structural strength is practically never an issue except in the very deepest of vaults. Sand aggregates

7. Site Selection, Preparation and Installation of Seismic Stations

used for concrete should be homogenous, fine-grain, and of uniform size rather than of varying size as in the usual concrete mixture. Uhrhammer et al. (1998) recommend sieved sand with 50% Portland cement. After the pier is poured, the concrete must be vibrated to remove any trapped air.

Lightning protection

Lightning causes most of the damage to seismic equipment around the world and lightning protection is probably the most important factor in preventing station failure. We know of several seismic networks that lost half or more of their equipment less than two years after installation because of inadequate lightning protection. Of course a direct hit by lightning will cause equipment damage despite the best protection. Fortunately, this rarely happens. Most lightning-related damage is caused by induction surges in cables, even when the source is some distance from the station.

Climatic and topographic conditions at a site vary greatly and determine the degree to which one should protect the system from lightning. Tropical countries and stations on top of mountains are the most vulnerable and therefore require the most lightning protection measures.

Lightning protection includes the following measures:

- proper cabling that minimizes voltage induction during lightning;
- proper use of special electronic devices to protect all cables entering the seismic vault from voltage surges;
- a good grounding system since no practical lightning protection measure works without grounding;
- enclose the equipment in a "Faraday cage" either by making a metal shielded seismic vault or a loose mesh of ground metal strips around the vault. This creates an equipotential electric field around the equipment, thus decreasing voltage drops on equipment and cables during lightning strikes.

If any one of these measures is not undertaken, the others become largely ineffective.

The best lightning protection is a metal seismic vault. The exterior of the vault should not be painted so that good electrical contact can be made with the surrounding soil, thereby lowering impedance. If the main cover or any other part of the vault is metal, it should be connected to the vault's walls using a thick flexible strained wire.

In any event it is necessary to protect all cables entering the seismic vault. Many high quality seismic instruments already have internal lightning protection circuitry, but these measures are sometimes not enough for high lightning threat regions. Lightning protection may include gas-discharge elements, transient voltage suppressors (transorbs), voltage dependant resistors, and similar protection components.

The lightning protection equipment of the cables must be installed at the point where they enter the vault. It must be grounded at the same point with a thick copper wire or strip that is as short as possible. The unprotected length of any cable within the vault must be kept to an absolute minimum.

7.4 Seismic station site preparation, instrument installation and shielding

All cables entering the vault must be protected. Voltage surges usually occur in all cables, and leaving a single long cable unprotected is virtually the same as leaving all the cables unprotected.

All metal equipment boxes should be grounded with a thick copper grounding wire or strip (> 25 mm² cross-section) to the same point where the lightning protection equipment of incoming cables is grounded. Use a tree-shaped scheme for grounding wires. All these wires should be as short as possible and without sharp turns. All the cables in a vault should be kept to a minimum length. No superfluous cables or even coiled lengths of excess cable are acceptable. These are true lightning catchers.

Telephone and power companies usually install lightning protection equipment for their lines. This should be required of them when arranging these services. Manufacturers of seismic equipment can also provide and install such equipment if asked.

Note that there is never a 100% safe lightning protection system. However, for high lightning risk regions and for expensive and delicate seismic equipment, long years of practice show that investing in an effective lightning-protection system pays off in the long run.

Electro-Magnetic Interference protection

The problem of electro-magnetic interference (EMI) is not normally a very important issue because seismic stations are generally situated in remote rural locations. However, in such regions the main power lines can frequently be of low quality. We recommend using mains power voltage stabilizing equipment in such cases. This equipment usually incorporates EMI filters and voltage surge protection, which further protects seismic equipment from failures and EMI-generated noise. In general, metal seismic vaults protect equipment from EMI very effectively.

Some passive seismometers with moving magnets and separate components generate EMI during mass motion. Since this may influence surrounding sensors, you should not install such seismometers too close together. A minimum distance of 0.5 m (1.5 feet) is recommended. A simple test can assure you that cross talk is insignificant. Disconnect and un-damp one component, move the seismometer mass by shaking it slightly and measure the output of both the other components. There should be no cross-talk.

In addition, seismometers should not be placed too close to the metal walls of a vault. This minimises potential changes in the static magnetic field, which may slightly influence the generator constant of some seismometers.

Data recording equipment with mains transformers should not be installed next to, or on the same pier as sensors. The transformer may cause noise in the seismometer signals either through its magnetic field or due to direct mechanical vibrations at 50 or 60 Hz. The same is true for magnetic voltage stabilizers, if used at the site. Place such equipment in a metal housing for additional magnetic shielding and install it on the wall of the vault.

Water protection

Water entering seismic vaults is probably the second most common cause of station failure. The most effective way to prevent water damage is vault drainage (Fig. 7.46). Use a hard

7. Site Selection, Preparation and Installation of Seismic Stations

plastic tube of about 3 cm (1") diameter, such as used for water pipelines. The drainage pipe must be continuous and have at least a 3% gradient, particularly in regions where the ground freezes during the winter. If drainage is impossible, as is often the case for deep vaults, water tightness of the vault is of the utmost importance. Note that a high ground water level and porous concrete vault walls more or less guarantee water intrusion.

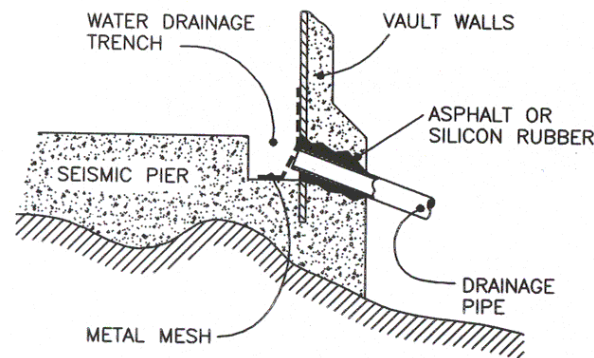


Fig. 7.46 Water drainage pipe and vault trench around the seismic pier.

Water tightness is easy to achieve if the walls of the vault are made of metal welded from plain or corrugated iron sheets or from large-diameter metal tubes, providing the welds are of good quality.

If the vault is made of concrete and has no water drainage, the concrete should be of a very good, uniform quality. Water-resistant chemicals should be added to the mix to help keep it water-tight. The concrete must be vibrated during construction to assure homogeneity of the walls.

The bottom of the seismic vault - the seismic pier - is always made of concrete. Once again, use good quality, uniform-aggregate concrete with water-resistant additives. The bottom should have a water drainage ditch (see Figs. 7.39 and 7.46) around the flat central pier on which the sensors are installed. For vaults with external water drainage, the ditch should be at least 5 cm (2") deep and 10 cm (4") wide. For the vaults without drainage, this ditch should be larger (at least 15-cm by 15-cm or 6"x 6") so it can collect more water.

Making the joint between the vault walls and floor requires special care. Use asphalt to seal any cracks by heating the concrete with a hot-air fan and then pouring hot asphalt into them. The cables entering the vault also require special care. They are normally installed in a plastic or metal tube that should fit snugly into the appropriate hole in the vault wall. Use silicon rubber or asphalt to seal any gaps.

In vaults designed for VBB seismometers whose seismic pier is mechanically separated from the walls, water tightness represents a special challenge. Once again use soft asphalt to make the gap between the walls and the pier watertight.

The upper rim of the vault must be at least 30 cm (1 foot) above the ground. At sites where a lot of snow is expected, this should be higher, up to 60 cm (2 feet). Slush is particularly troublesome with regard to keeping vaults watertight. Where possible, the surrounding terrain should descend radially from the top of the vault.

7.4 Seismic station site preparation, instrument installation and shielding

One practical measure is to create a small "overhang" at the top edge of the vault (see Fig. 7.43). This ledge should be about 5 cm (2") out from the vault wall. A thick, watertight fabric cover can be hooked over this metal edging. The cover is pulled tight to the vault by rope and prevents water from entering the vault during windy, rainy periods. It also protects against dust and dirt and provides some additional thermal insulation.

To minimize the danger of equipment flooding, install all equipment, apart from the sensors, on the wall of the vault or on a raised platform.

Protection from small animals

At first glance the issue of small animals may seem amusing. However, animals frequently use seismic vaults as dwellings. We have seen some very strange "seismic" records caused by ants, grasshoppers, lizards, and mice. Worse, such animals can cause severe damage to cables and other plastic parts of the equipment.

Tight metal (particularly effective), fabric or thermal vault covers usually prevent animals from entering the vault from above. Plastic tubes for cables and drainage should be protected by metal mesh. Placing metal, wool or glass shards in the free space in these tubes also helps. Insecticides can be used to drive away ants and other insects.

In extreme circumstances, animals may be deterred from chewing cables and other equipment by applying paints developed to prevent animal damage to trees.

7.4.2.2 Contact with bedrock

Good contact between seismic sensors and bedrock is a basic requirement. Soil and/or weathered rock layers between the sensor and the bedrock will modify seismic amplitudes and waveforms.

The depth of bedrock and the degree of weathering of layers beneath the surface can be determined by shallow seismic profiling of the site, by drilling (most often too expensive), or by actually digging the vault. Only rarely will a surface geological survey provide enough information about the required depth of the seismic vault (except where the bedrock is clearly outcropping).

If you choose not to carry out a shallow seismic profile, then expect surprises. You will need to dig until you reach bedrock, and that can sometimes be very deep; a vault may have to be repositioned and re-dug if weathered bedrock is extremely deep. These risks make the cost of shallow profiling a wise investment.

A definition of "good" bedrock is necessary when digging vaults without a seismic profile. Unfortunately, the definition is fairly vague, especially because some recent studies show that even a site with apparently hard, but cracked, rock may still have significant amplification compared to true solid bedrock. As a rule of thumb, "good" bedrock is rock hard enough to prevent any manual digging. If profiles are available, P-wave velocities should be higher than 2 km/s.

7. Site Selection, Preparation and Installation of Seismic Stations

Seismic vaults are on average 2 to 6 m (7 to 20 feet) deep. At sites where the solid, non-weathered bedrock is outcropping, the required depth is defined solely by the space required for the equipment. One meter (3 feet) or even less may be adequate if the requirements regarding temperature changes associated with the local climate allow. On some highly weathered rock sites, the required vault depth may exceed 10 m (30 feet). In some places a reasonably deep seismic vault can not reach bedrock at all and a borehole installation would ideally be required. Vaults are sometimes still used in such cases for financial reasons. More details on borehole installations are given in 7.4.5.

7.4.2.3 Seismic soil-structure interaction and wind-generated noise

The ideas behind the design and construction of seismic stations have greatly evolved in the last few decades. The increased sensitivity of seismometers and the complexity of seismic research, based more and more on waveforms, require very quiet sites and distortion free records. Sixty years ago, seismic stations were usually situated in houses and observatories. Sensors were installed on large, heavy concrete piers, mechanically isolated from structural elements of the buildings, sometimes well above the ground (see Figure 4.2 in the old MSOP; Willmore, 1979; or <http://www.seismo.com/msop/msop79/sta/sta.html> via link “Examples of stations”). Scientists increasingly observed that the interaction between surrounding soil and civil engineering structures in such installations substantially modified seismic signals during seismic events, particularly if the site was on relatively soft ground. Structures swinging in the wind also caused undesired seismic noise, and strong unilateral wind load or insolation on a building’s walls or the rock face of seismometer tunnel entries caused intolerable drifts in long-period or VBB records.

Further evidence arose (Bycroft, 1978; Luco et al., 1990) that every structure at a site modifies seismic waves to some extent. Therefore, today’s seismic stations are mostly ground vaults jutting only a few decimeters (about a foot) above ground level. All buildings, antennae and other masts are positioned well away from the vault to minimize the interaction.

In theory, there is no modification of the seismic signal by the soil-vault structure interaction if the vault's average density (taking into account the empty space in the vault) equals the density of the surrounding soil. However, seismic station design is never based on calculated average densities. The most important factors are that:

- the design is not too heavy, particularly if the surrounding soil is soft;
- all potential buildings and masts are placed away from the seismic vault;
- the vault rises above ground level as little as possible to minimize wind-generated seismic noise.

7.4.2.4 Other noise sources

We recommend that seismic stations are fenced, despite the fact that fences usually represent a significant expense. There are a few exceptions, such as stations in extremely remote desert or mountain sites. The fence minimizes seismic noise caused by human activities or by animals that graze too close to the vault. It also contributes to the security of the station.

The optimal size of the fence depends on several factors:

7.4 Seismic station site preparation, instrument installation and shielding

- density of population around the site and human activity close to the station;
- potential agricultural and other activities in the near vicinity;
- the probability of animal interference;
- general seismic noise amplitudes at the site (quiet stations require a bigger fenced area);
- seismic coupling between ground surface and bedrock. Non-consolidated surface ground and seismometers installed on good bedrock allow a smaller fence. A very deep vault has a similar effect.

The smallest recommended fenced area is 10 x 10 m (30 x 30 feet). In the worst case, a fence could be 100 x 100 m (300 x 300 feet). A height of about 2 m (6 - 7 feet) should be sufficient. Light construction with little wind resistance is preferable so that wind-generated seismic noise is minimized.

The equipment and the vault itself can also generate seismic noise. Equipment that includes mains transformers or rotating electromechanical elements like disk drives, diskette drives, cooling fans, etc. should be installed on the vault wall rather than on the seismic pier.

If the vault cover is not firmly fixed to the vault, it can swing and vibrate in strong winds, which can totally ruin seismic records. Be sure that the cover is very firmly fixed to the top of the vault, as its own weight may not be sufficient to prevent vibration in strong wind. When closed and strongly shaken by hand, there should be no play whatsoever between the vault and the cover. If there is, it will cause seismic noise during strong winds.

If a seismic station uses an antenna mast, place it well away from the vault to prevent seismic noise being generated by the antenna swinging in the wind. The required distance is usually between 5 and 50 m, depending on a number of factors such as:

- the maximum expected wind speed and the probability of windy weather at the site (the higher the speeds and the more often they appear, the greater the required distance);
- the antenna's height (the higher the antenna mast, the greater the required distance);
- the vault's depth (the deeper the vault, the smaller the distance);
- the degree of seismic coupling between sensors and antenna base (strong coupling requires larger distances); and
- general seismic noise at the site (very quiet sites require larger distances).

7.4.2.5 Electrical grounding

A grounding system is required for the proper functioning of electronic equipment. Grounding of equipment and cables keeps the instrument noise low. It is also a prerequisite for lightning-protection equipment and for interference-free RF telemetry. The grounding system design is usually a part of the RF link design in telemetry seismic systems.

A ground impedance below 1 ohm is usually desired. Generally, a radial star configured system, of five to six "legs" with 15 to 20 m (45 - 60 feet) length each, is required for a grounding system (see Fig. 7.47). The total length of the required grounding metal strips depends strongly on climate and local soil type and its humidity. The strips, made of zinc plated iron or copper, 3 x 30 mm (1/8" x 1.5") in cross-section, should be buried from 25 to

7. Site Selection, Preparation and Installation of Seismic Stations

35 cm (~1 foot) deep in the soil. In dry regions they should be deeper. The strips should be straight. No sharp turns (around rocks, for example) are allowed because this decreases lightning protection efficiency as a result of increased inductivity of the grounding system.

In arid regions, high deserts, or completely stony areas, longer and thicker strips are required. In these cases, a different approach to grounding and lightning protection is sometimes taken by trying to obtain an electric equipotential plane all around the station during lightning strikes. Grounding impedance is no longer the most important issue. High lightning threat regions and very dry or rocky ground usually require a specially-designed grounding system.

In seismic vaults without metal walls, bury a loose mesh made of grounding strips around the vault and connect them to the rest of the grounding system. The grid dimension of this mesh should be around 60 to 100 cm square (~2 to 3 feet square).

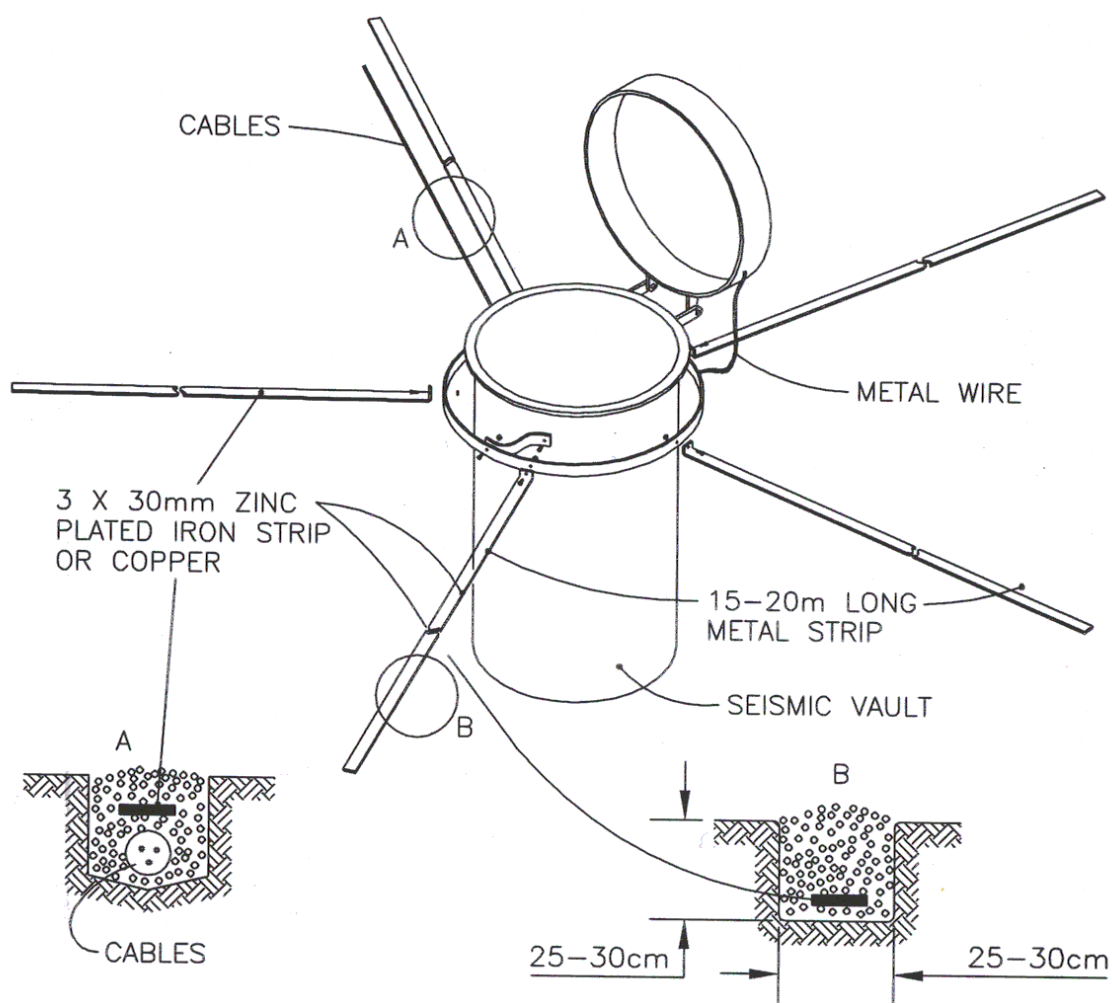


Fig. 7.47 An example of a seismic station grounding system. Note that its dimension depends on local soil humidity conditions.

At seismic stations with RF data transmission and antenna masts, the star-configured grounding system should be centered on the antenna mast, not on the seismic vault. The seismic vault should be included in one of the legs of the grounding system. One of the grounding strips must be laid exactly above the cables connecting the antenna mast and

7.4 Seismic station site preparation, instrument installation and shielding

seismic vault (see Fig. 7.47, detail A). This ensures a minimum voltage drop along the cables during lightning strikes and therefore a minimum induced voltage surge in the cables.

The antenna mast itself should be grounded and equipped with a lightning protection rod. Its highest point should be at least 1 m (3 feet) above the highest antenna or solar panel installed on the mast.

Note that any grounding system requires periodic service checks because contacts between the metal parts may slowly corrode. It is recommended that the grounding impedance of the system be checked once every two years. Regular maintenance visits should always include a check of the lightning protection system and equipment and replacement of any burnt-out elements.

7.4.2.6 Vault construction

Seismic vaults can be made with metal walls. Plain iron sheets or corrugated iron can be welded together, or pieces of large-diameter metal pipes can be used. We recommend zinc-plated metal for durability. It is not necessary to make metal vaults very strong and heavy. Water tightness is relatively easy with this design.

If the vaults are made from thin sheet metal (a few mm), then pour relatively thin, 15 - 20 cm (6 - 8") concrete walls around the metal to add strength. The quality and homogeneity of this concrete does not need to be high because water tightness is not a problem. Locally-available sand aggregates can be used in most cases. Such vaults, however, may cause problems if deformation and tilts of the vault due to external temperature changes are important.

The walls can also be made of only concrete – in which case it is easiest to make the vault rectangular. Note that the quality of the concrete must be good to make the vault watertight, as explained earlier. Apart from very deep vaults, strength is not a problem and therefore no steel reinforcement is needed.

At sites where accessibility allows, vaults can be made of the prefabricated concrete pipe sections used in sewerage systems. They are cheap and can be obtained in different diameters and lengths. In deeper vaults you can simply stack them to the required depth of the vault. Care must be taken to ensure that the joints between sections are watertight.

The bottom of the seismic vault – the seismic pier - is always made of high-quality, watertight concrete. Special requirements must be fulfilled for VBB sensors. More details are given in 7.4.2.1 above.

The depth of seismic vaults is determined by seismo-geological parameters. Apart from providing adequate space to put all the equipment, the diameter is primarily a matter of the desired ease of installation, maintenance and service.

For three-component stations with single component sensors, between 1 and 1.5 m² (10 to 15 square feet) of space on the seismic pier is required. Less space is needed for three-component seismometers, three-component accelerometers, or a single component sensor. If the vault contains (or will contain in future) three-component weak-motion and strong-motion sensors, about 1.5 - 2 m² (15 - 20 square feet) is required.

7. Site Selection, Preparation and Installation of Seismic Stations

We have found that a minimum vault diameter for installation and maintenance is 1.4 m (4.5 feet). If the vault is deeper, a 1.5 to 1.6 m (5 to 5.5 feet) diameter is recommended. Deep vaults (> 4 m (13 feet)) require a diameter of at least 1.6 to 1.7 m (5.5 to 6 feet). Vaults deeper than 1.2 m (4 feet) require a ladder.

7.4.2.7 Miscellaneous hints

Vault cover design

A seismic vault cover should have the following:

- at least 5% slope so that water drains quickly;
- vertical siding all around that extends at least 15 cm (6") below the upper rim of the vault to prevent rain from entering in windy conditions;
- a mechanism which firmly fixes the cover to the ground and a lock to mitigate vandalism;
- handles for easy opening and closing;
- be painted a light color, preferably white, that will reflect as much sun as possible, particularly in hot and dry desert regions.

The metal cover and thermal insulation cover of the vault should not be too heavy. They should be designed in such a way that a single person can open and close the vault smoothly and easily. Otherwise, maintenance visits will require two people in the field. For large vaults, the cover can be designed in two parts, or a simple pulley system may help.

Alternative materials

As material for a vault cover, metal is less appropriate in very hot and very cold climates as it becomes difficult to handle under extreme temperature conditions. UV light-resistant plastic or water-resistant plywood is a better alternative in dry regions. Plywood also has lower thermal conductivity, which improves thermal insulation, and less weight, making handling the cover easier.

Mitigating vandalism

Experience shows that, apart from political instability in a country, most vandalism of seismic stations is driven by people's curiosity. Therefore we believe that a large sign with a short and easy-to-understand explanation of the purpose of the station and posted at the entrance to the fenced area, may significantly mitigate vandalism.

Fixing seismometers to the ground

In regions where earthquakes with peak accelerations of 0.5 g or more can occur, seismometers must be firmly fixed to the seismic pier, a common practice with strong-motion sensors. Obviously, sensitive seismometers are clipped during very strong earthquakes. However, they should not shift or move during such events otherwise, the sensors will not be properly orientated for the recording of aftershocks .

7.4.3 Seismic installations in tunnels and mines (L. G. Holcomb)

Abandoned mines have been used for many years as ready-made quiet sites for installing seismic instrumentation. In some cases, active mine tunnels have proven to be successful, even though they may be somewhat noisy as a result of mining activity during the workday.

Existing tunnels in solid rock provide a low-cost, ready-made and accessible facility that often provides nearly ideal conditions for the installation and operation of high sensitivity seismic sensors. The bedrock in a mine tunnel is usually already exposed, providing an excellent firm foundation on which to install standard surface instruments. If unventilated, as is usually the case for abandoned mines, a mine tunnel provides an essentially constant-temperature environment that is ideal for seismic sensors. Depending on its thickness, the overburden above the mine tunnels provides isolation of the seismic sensors from the seismic noise that is always present at the surface of the Earth.

Obtaining permission to use an abandoned mine property may be difficult, even for non-working mines, because the operational organization or the property owners may quite understandably be reluctant to allow access because of legal liability. Access to working mines is usually even more difficult because the additional equipment and personnel involved in station activities tend to interfere with mining activities.

Mines are usually concentrated in mineralized zones. It is therefore unlikely that an existing mine will be found near the location of a proposed seismic installation. Tunnels are sometimes constructed solely for the purpose of the installation of seismic sensors. Digging tunnels in hard rock is a very expensive endeavor because tunneling on a small scale is highly labor-intensive.

In many respects, a tunnel installation is very similar to a surface vault installation. A poured concrete floor or pier is usually constructed on the rough bedrock floor of the tunnel to provide a flat and level surface on which to install the sensors. Despite the improved temperature stability found in a tunnel, it is still necessary to provide adequate thermal insulation around the sensors themselves in order to reduce thermally generated noise. Some type of air pressure variation reduction system is also necessary for long period sensors because the air pressure varies in underground tunnels. Usually, this is accomplished in the same manner as it is in a surface installation although sometimes an effort is made to seal off all or parts of the tunnel itself. Sealing a volume enclosed by natural rock walls is difficult because most tunnel walls are riddled with fractures.

However, there are significant differences between surface vault installations and tunnel sites. Rockfall is a real hazard in a tunnel installation. Both personnel and instrumentation must be protected at the actual location of the instruments and along access routes. Another hazard is the build up of harmful gasses (bad air) underground if the tunnel is not adequately ventilated.

The presence of water and high humidity levels in most underground passages is a common problem in tunnel installations. It is very difficult to keep instrumentation dry and the wet environment is frequently unpleasant to work in. The high humidity slowly corrodes the contacts in delicate electrical connectors, which frequently causes poor electrical contact and intermittent operation. The presence of moisture also slowly degrades the effectiveness of thermal insulation materials, and precautions must be taken to prevent moisture accumulation in the isolation system.

7. Site Selection, Preparation and Installation of Seismic Stations

Access to power and communication lines is usually more difficult in tunnel installations, depending, of course, on how far the equipment is placed in the tunnel. Frequently, power and or communication lines must be installed throughout the entire length of the tunnel. In the case of power, this can be quite expensive if long distances are involved; either large diameter cables or a high voltage line coupled with a step-down transformer must be installed to ensure that sufficient voltage is available at the site.

Determining the orientation of an underground sensor is considerably more difficult than in a surface installation. Usually, one must transfer an already known azimuth from outside the tunnel to the installation site using standard surveying techniques. Specially designed gyroscopic systems can be used to determine the orientation underground but they are relatively expensive.

It is more difficult to provide timing to a tunnel site than to a vault. This is particularly true for modern GPS based timing systems because the distance between the antenna (outside the tunnel) and the timing receiver is usually limited. Inline radio frequency amplifiers can be used for long antenna runs. It is preferable, however, to place the GPS receiver near the antenna, e.g., at the tunnel entrance. A serial connection can then be used between the receiver and the recorder either using RS422 (up to 1 km distance) or fiber optic cable. This approach has been used successfully in the Swiss digital seismic network.

7.4.4 Parameters which influence the very long-period performance of a seismological station: examples from the GEOFON Network (W. Hanka)

7.4.4.1 Introduction

The goal for a very broadband (VBB) station for the GEOFON network is to resolve the full seismic spectrum from high frequency (regional events) to very long period (VLP) (Earth's tides) with sufficient dynamic range. The overall instrument noise should remain below the New Low Noise Model (NLNM, Peterson 1993) throughout this frequency range. The GEOFON project (Hanka and Kind, 1994) aims to achieve this goal at minimum cost. This sets strict limits on costs for instrumentation, vault construction and remoteness of the sites.

It is relatively straightforward to get good station performance in the high frequency and medium-period band since the "only" measures to be taken are to get away from man-made noise sources and the sea shore and find a station site on as hard rock as possible. Good VLP performance is usually much more costly to achieve since adequate instrumentation and vaults with sufficient overburden or borehole installations are necessary. However, there are certain measures which can be taken to optimize the VLP station performance in shallow vaults. The parameters to be taken into account for good VLP performance are:

- Instrumentation
- Installation of instruments
- Vault construction
- Geology
- Depth of burial
- General climate

The influence of these different parameters will be demonstrated in the following case studies from the GEOFON network.

7.4.4.2 Comparison of instrumentation and installation

Which seismometer to choose?

The longer the period of ground motion to be recorded, the larger the potential influence of environmental disturbances, such as temperature and air pressure fluctuations and induced ground tilts on the seismic recording, and the larger the need for effective shielding against them. The instrument currently with the best VLP resolution is the Wielandt-Streckeisen STS1/VBB (Wielandt and Streckeisen, 1982; Wielandt and Steim, 1986). It is widely deployed in the IRIS GSN and GEOSCOPE global networks as well as in some regional networks (e.g., MedNet). The permanent GEOFON network uses mostly Wielandt-Streckeisen STS2 and a few STS1/VBB instruments (see DS 5.1) with comparably good results. Fig. 7.48 shows the resolution of the STS1/VBB and the STS2 in relation to the New Low Noise Model by Peterson (1993). The more compact, lighter and cheaper triaxial STS2 has a pass band with a slightly higher low-frequency corner (0.00833 Hz instead of 0.00278 Hz) and a significantly higher high-frequency corner (dashed lines in Fig. 7.48). Depending on the properties of the recording system, 50 Hz can easily be reached compared to the 10 Hz of the STS1. For nearly all sites on Earth, a properly installed STS2 seismometer will give nearly the same performance as a set of STS1/VBB seismometers. The maximum long-period resolution can only be achieved when the seismometers are properly shielded.

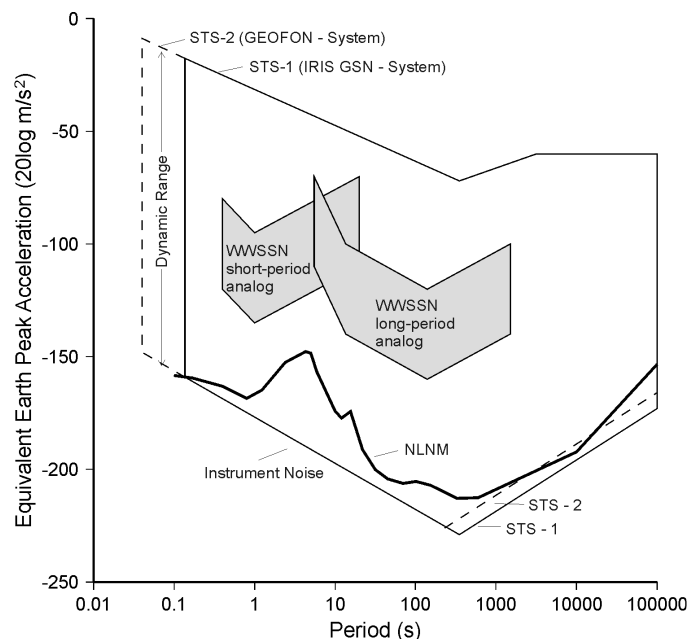


Fig. 7.48 A representation of the bandwidth and dynamic range of a conventional analog (WWSSN short- and long-period) and digital broadband seismographs (STS1/VBB and STS2 with GEOFON shielding, respectively). The depicted lower bound is determined by the instrumental self-noise. The scale is in decibels (dB) relative to 1 m/s². Noise is measured in a constant relative bandwidth of 1/3 octave and represented by "average peak" amplitudes equal to 1.253 times the RMS amplitude. NLNM is the global New Low Noise Model according to Peterson (1993).

7. Site Selection, Preparation and Installation of Seismic Stations

The GEOFON project exclusively uses Wielandt-Streckeisen seismometers. The discussion above and below reflects this fact and is not an endorsement of one make of seismometer over another. Potential instrument purchasers need to establish for themselves what instruments are best suited for their own purposes.

The discussion of the shielding efficiency at GEOFON stations in surface or shallow depth vaults or tunnels in the next Chapter is only based on the VLP channel plots (sampling frequency 0.1 Hz) of STS1 records (original or simulated from STS2 records by recursive filtering). The low self-noise of the STS2 allows us to effectively simulate STS1/VBB records down to tidal periods. Fig. 7.49 illustrates this using the recordings of a tidal wave recorded by an STS1/VBB and an STS2. It is difficult to tell the difference between them.

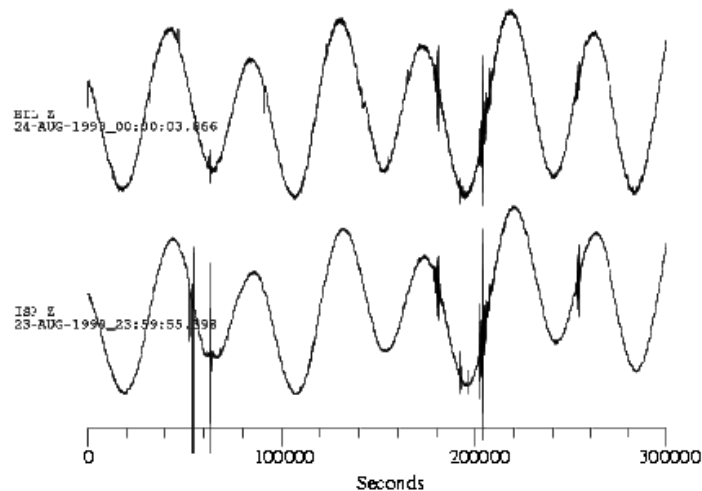


Fig. 7.49 Tidal recordings of STS1/VBB and STS2 do not differ very much when properly installed in a comparable environment. The two traces were recorded in the Eastern Mediterranean in buried vaults in limestone. At the station EIL (Eilat, Israel) an STS2 with additional GEOFON shielding and at ISP (Isparta, Turkey) a set of STS1/VBB are installed.

Installation of an STS1/VBB

Seismometers must be shielded against environmental influences, namely pressure and temperature variations as well as magnetic disturbances. The proper installation of an STS2 to achieve good VLP performance is discussed in detail in the next paragraph. Comments on installing the STS1/VBB are kept short here since this is a well known procedure and is described elsewhere (Wielandt and Streckeisen, 1982, Holcomb and Hutt, 1992).

The three separate STS1/VBB components are supplied with different shieldings: a permalloy helmet as magnetic shield (vertical only), an aluminum helmet and a glass bell jar for evacuation. The feedback electronics are placed in a separate container. There are two basic methods used for the installation of STS1/VBB seismometers. The "conventional" one, also suggested by the manufacturer, uses a plane glass plate which has to be cemented to a plane pier. The second method, introduced by Albuquerque Seismological Lab, uses a warp-free rigid stainless steel base plate (similar to the aluminum one used in the GEOFON STS2 shielding) on which the vacuum glass bells and the metal helmets are installed above the actual seismometer. The second method is faster and easier in practice and gives additional flexibility (see Holcomb and Hutt, 1992).

7.4 Seismic station site preparation, instrument installation and shielding

Installation of an STS2

The STS2 is not supplied with any shielding. All three components and the electronics are contained in a single casing. This casing provides magnetic and pressure shielding to some extent. Nevertheless, temperature shielding is still important in order to obtain longer period signals with a good signal/noise ratio. This is especially important because of thermal convection generated by heat from the electronics. A rather sophisticated shielding (see Fig. 7.50 a) was introduced by Wielandt (1990) for the first STS2 based network, the German Regional Seismograph Network (GRSN). The STS2 was installed on a 10-cm thick gabbro plate covered by an airtight aluminum helmet. Before being covered, the STS2 is insulated with a thermal blanket.

A simpler and more practical approach is used for GEOFON stations (see Fig. 7.50 b). This uses an aluminum casing consisting of a rigid thick base plate (3 cm) and a thinner aluminum helmet with a cylindrical foam rubber insert. As with the gabbro plate, the base plate can not be easily distorted by pressure variations and gives, together with the foam rubber insert, extra thermal stability. In addition, this shielding helps prevent corrosion and is separated from the pier or ground surface by adjustable tripod screws.

The GRSN shielding has extra internal cabling and a socket, whereas the GEOFON casing does not, and the casing is penetrated by the original STS2 cable through a special hole which is made tight with silicon. The GEOFON shielding potentially gives better electrical performance but has worse pressure integrity. The GEOFON shielding is portable and readily available which are problems with the GRSN shielding.

Even better thermal insulation than the one discussed above can be achieved for both installation methods when an additional styrofoam box, completely filled with styrofoam pieces, is used (as shown in Fig. 7.50 b). The box should be tightly glued to the pier or ground surface and the box lid glued to the box walls after filling with the styrofoam beads. Depending on the site conditions, this can give an additional order of magnitude in VLP noise reduction.

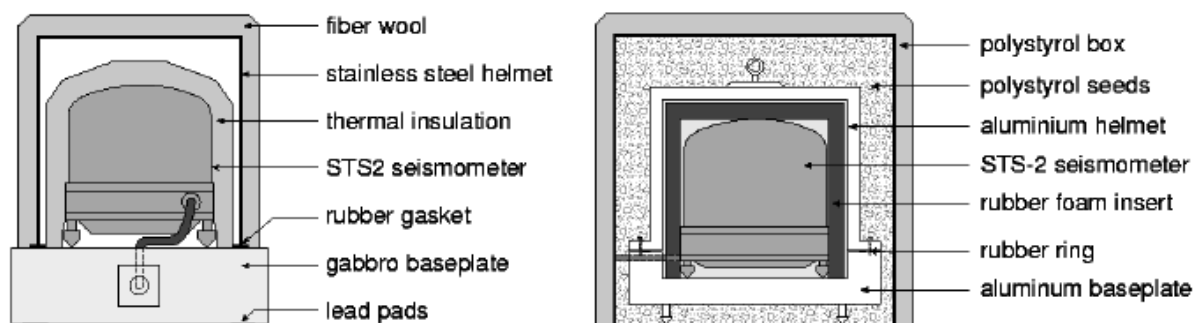


Fig. 7.50 GRSN (a) (after Wielandt, 2000) and GEOFON type (b) shielding for the STS2.

Fig. 7.51 shows the substantial LP and VLP noise reduction which can be achieved even by an incomplete GEOFON type shielding (aluminum casing only, no polystyrol box) in the period range from 30 to more than 10,000 seconds. A reduction of about two orders of magnitude in terms of spectral power (one order of magnitude in terms of amplitude) can clearly be seen between 100 and several thousands of seconds and again around 10,000 sec.

7. Site Selection, Preparation and Installation of Seismic Stations

The GRSN shielding gives exactly the same result in most cases. It is only in very rare situations - probably in connection with large air pressure variations – that the performance of Wielandt's approach is slightly better at periods of several hundreds of seconds.

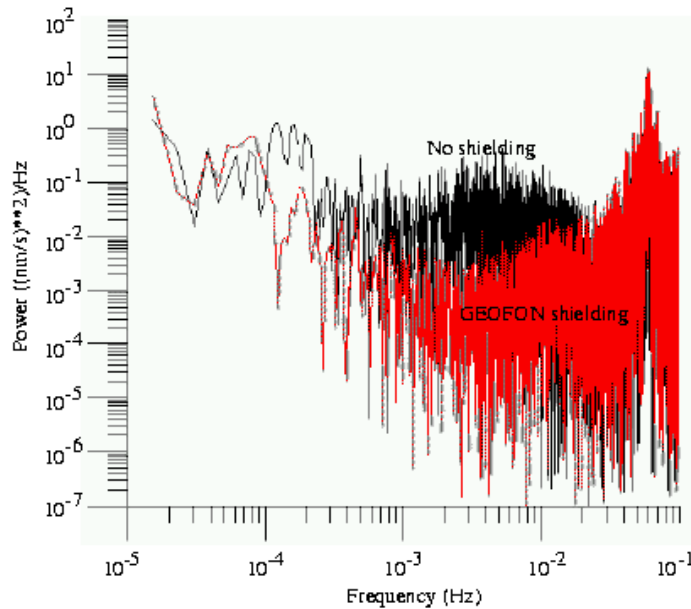


Fig. 7.51 VLP noise reduction achieved by using the simpler version of the GEOFON shielding method (no additional polystyrol box and beads). The relative noise power spectra of the vertical component of two STS2s positioned side-by-side are shown. No instrument correction has been applied. The black spectrum is from the unshielded STS2, the red spectrum from the shielded one.

7.4.4.3 Comparison of vault constructions, depth of burial, geology and climate

The harder the rock and the deeper the vault and the more stable the temperature and air pressure remain in the vault, the better is the VLP performance of a VBB station. In contrast, the shallower a vault is, the greater the influence of the general climate.

Tunnel vaults

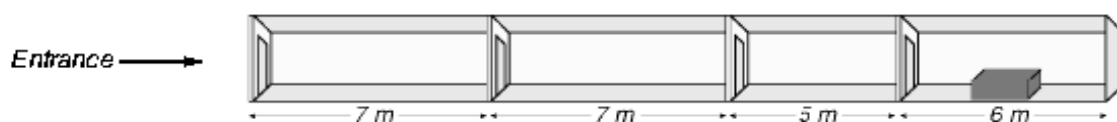


Fig. 7.52 Sketch of an artificial horizontal tunnel construction with different chambers to host a VBB seismological station. This type of construction is widely used within the IRIS/USGS part of the IRIS GSN network. The total length of the tunnel is approximately 25 m. The construction cost of such a vault can reach up to US\$ 100,000 depending on local conditions and infrastructure.

7.4 Seismic station site preparation, instrument installation and shielding

Fig. 7.52 shows the scheme of an artificial tunnel vault which is used at several IRIS/USGS installations in cases where no other existing underground facility can be used. The tunnel is about 25 m long and segmented using four doors (air locks). The last chamber contains the large seismometer pier. Since the tunnels are drilled into mountain slopes, depth of overburden is of the order of the tunnel length.

Although the vault construction is identical, the VLP performance at different sites is not. This is shown by the recordings Earth's tides in Fig. 7.53. The tunnel of the IRIS/GEOFON station LVC (Limon Verde, Chile) is built in hard basaltic rock and the traces show remarkably low VLP noise, while at KMBO (Kilima Mbogo, Kenya, also an IRIS/GEOFON site) a soft volcanic conglomerate drastically increases the noise, especially on the horizontal components. Another effect which can clearly be seen on the horizontal components is the large day-night noise variation. The general temperature increase and perhaps also the deformation of surface rocks caused by direct sunshine during the day, as well as stronger winds cause substantially larger VLP noise levels on the horizontals at both sites. This shows that even this kind of sophisticated and expensive tunnel vault construction gives no guarantee of seismic recordings free of environmental influences.

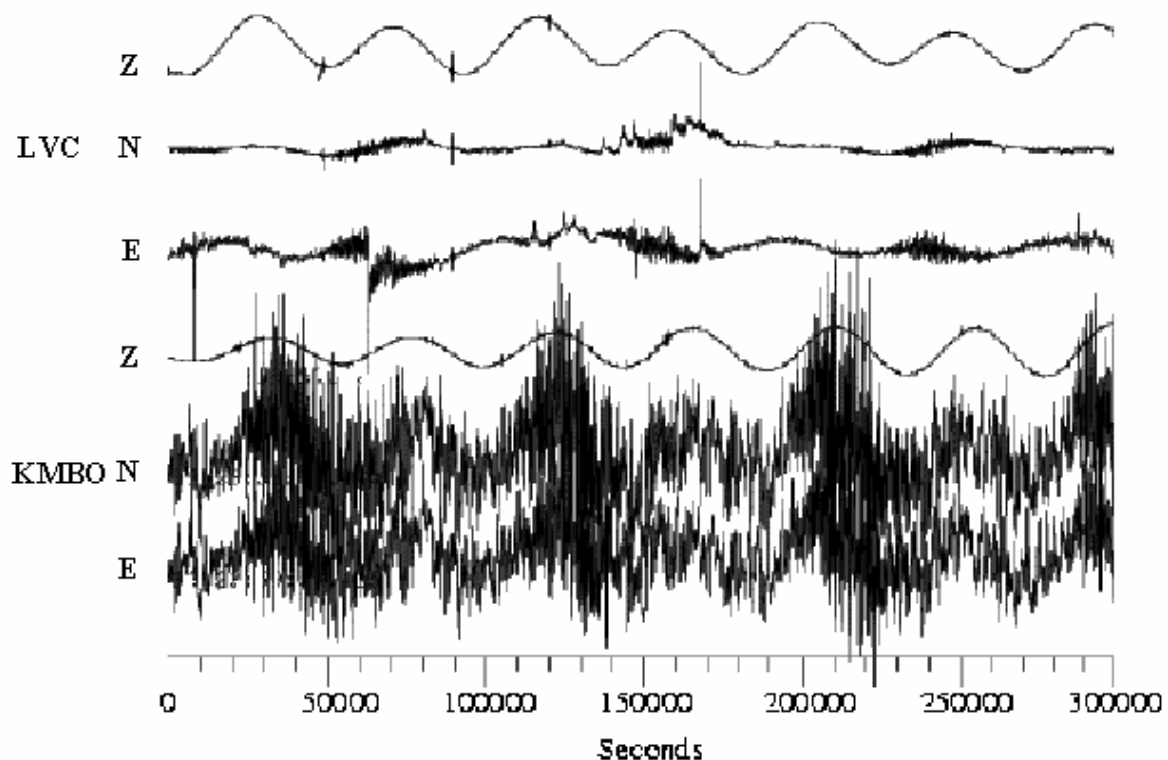


Fig. 7.53 Comparison of two 3-component STS1 VLP traces recorded in identical tunnel constructions but in different geological and climatological environments. LVC (Limon Verde, Chile) is built in hard basaltic rock in a full desert environment, KMBO (Kilima Mbogo, Kenya) is placed in rather soft volcanic conglomerate influenced mostly by a humid tropical environment. Day-to-night temperature gradients are high in both cases.

7. Site Selection, Preparation and Installation of Seismic Stations

Shallow vaults

If tunnel vaults are not affordable, other less expensive methods of getting the seismometers sufficiently buried have to be used. Several cases are discussed below.

Fig. 7.54 compares the recordings made at three different stations. The depth of burial is only about 4-5 m in all cases, which is very poor compared to tunnels. Nevertheless, the moderate climate at MORC (Moravsky Beroun, Czech Republic) and at ISP (Isparta, Turkey) gives a relatively good VLP performance. These vaults are build in hard rock and limestone, respectively. The spikes which can be seen mainly on the horizontal traces are due to human activity close to the site. In the arctic climate of KBS (Ny Alesund, Spitzbergen = Svalbard), the more drastic temperature changes cause increased VLP noise level on the horizontals. Here, there are also some spikes caused by local man-made disturbances.

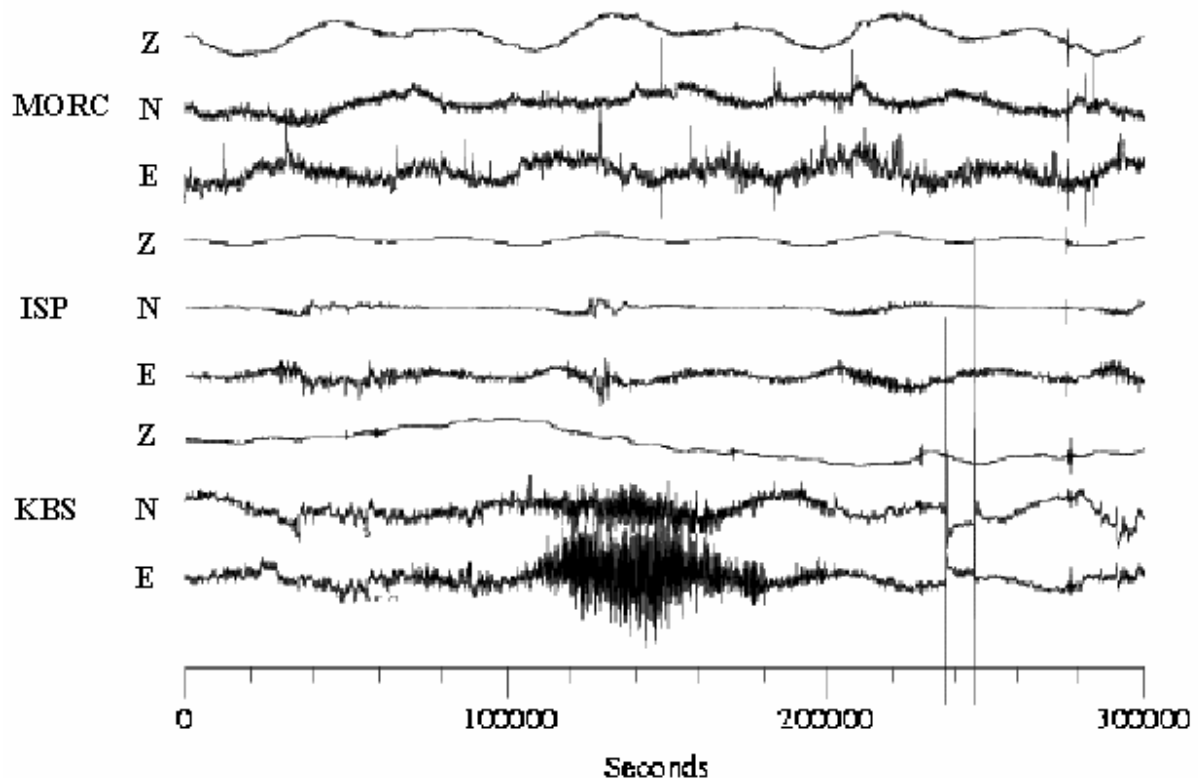


Fig. 7.54 Comparison of three 3-component VLP records in shallow vaults (4 - 5 m). At MORC (Moravsky Beroun, Czech Republic) an STS2 is installed in a 1 m wide borehole in hard rock; in ISP (Isparta, Turkey) and KBS (Ny Alesund, Spitsbergen) sets of STS1/VBB are installed in underground bunker vaults in limestone and weathered rock (permafrost), respectively.

The vaults at KBS and ISP are very similar: about 5 m deep large underground concrete bunkers with large concrete piers for the installation of the STS1/VBB seismometers (see Fig. 7.55 a). The geologies are different: weathered rock in permafrost (KBS) and limestone (ISP). The recording system at KBS is located elsewhere, while at ISP, recording is local in a house built above the vault. A very different construction is used at MORC: a very wide shallow vertical borehole has been drilled into hard rock and a one-meter wide steel tube placed into

7.4 Seismic station site preparation, instrument installation and shielding

it, with a concrete floor on the bottom. The STS2 in GEOFON shielding has been installed on this at about 5 m depth (see Fig. 7.55 b). Here and in the two other examples of construction schemes for STS2 stations (see Figs. 7.55 c and d), a recording room hosting all computer and communication equipment is located above the seismometer vault.

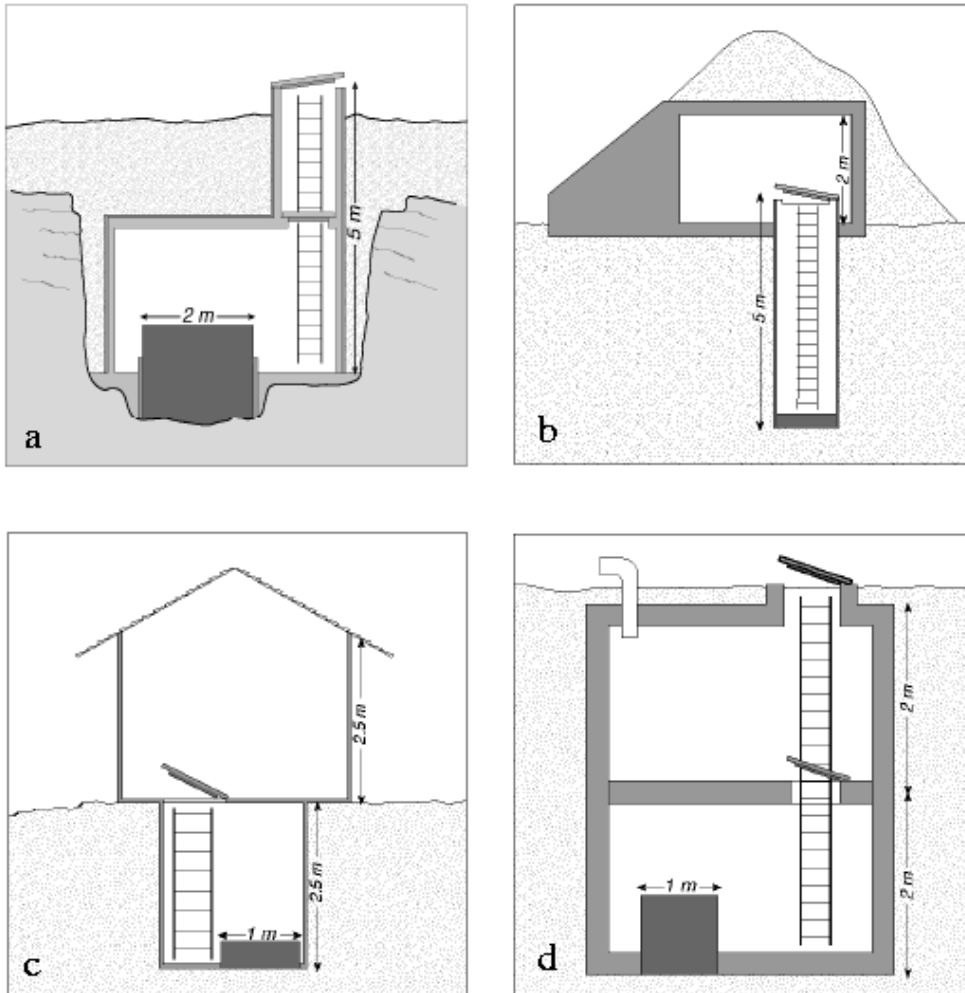


Fig. 7.55 a) Underground bunker vault construction for the installation of a set of STS1/VBB (remote recording); b) "wide & shallow borehole" vault construction for the installation of an STS2; c) and d) simple bunker vault construction schemes for an STS2. The vault constructions b - d allow onsite data recording thanks to the existence of a separate recording room.

Fig. 7.56 shows, again in comparison to MORC, the recordings at shallow vaults in locations near the equator. At PMG (Port Moresby, Papua New Guinea) a two-room underground vault hosts a set of STS1/VBB seismometers. The two-room construction is situated in a sedimentary layer above rock and is comparable in size with the one at KBS and ISP, but shallow (3 m) and with a horizontal entrance into the first (recording) room. UGM (University Gadjadara, Yogyakarta, Indonesia) uses a very simple, 2.5 meter deep bunker in limestone (construction after Fig. 7.55 c) with an STS2 and a small open recording hut above. Both show rather similar results to MORC, especially on the horizontals. The extreme large amplitudes at UGM during daytime are caused by human activity close to the station.

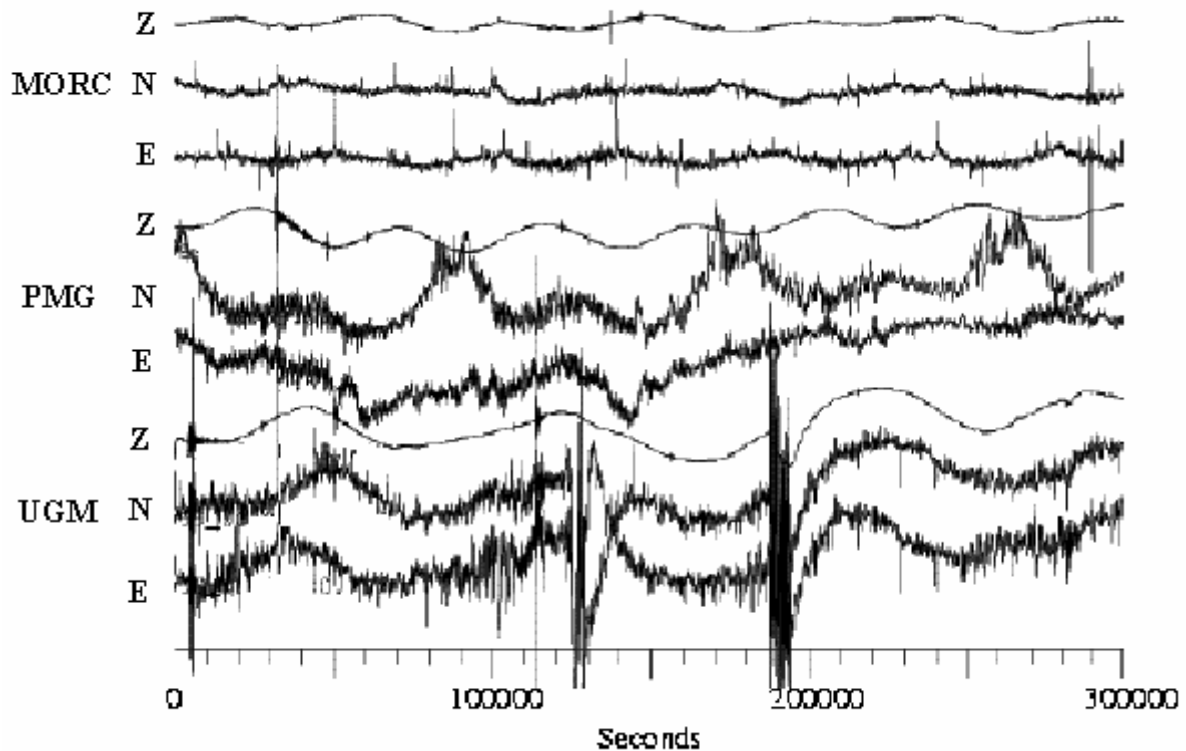


Fig. 7.56 Comparison of three 3-component VLP records from shallow vaults in rock in different climates. Data from two sites close to the equator (Port Moresby, Papua New Guinea, PMG, and Wanagama, Indonesia, UGM) are shown together with data from MORC (same station as in Fig. 7.54).

In principle, the VLP station performance is not so different at both equatorial sites, particularly the horizontal components which are not as good as at a site in a more moderate climate. The instrumentation and construction details do not play any significant role in determining the VLP noise performance.

Surface vaults in moderate climate

The STS2 records in Fig. 7.57 were obtained in a simple above-surface vault on rock (DSB) and a very shallow vault in soft sediments (RGN). Both sites are located in an area with a very moderate climate and close to the sea. Temperature shielding is a little better at RGN due to complete soil coverage on three sides and up to one meter on top. Therefore the general VLP performance - as seen on the vertical components - is better at RGN, but the horizontals show large additional distortions during daytime. These are most likely caused by temperature-induced swelling and related up-bending of the sand hill which is a very typical behavior for sediments (it can also be seen to some extent on the PMG records in Fig. 7.56). This is not the case with rock at DSB. It is remarkable that there is almost no day-night variation on the DSB records although the vault is completely above the surface. This is due to the maritime climate with very small day-night temperature changes.

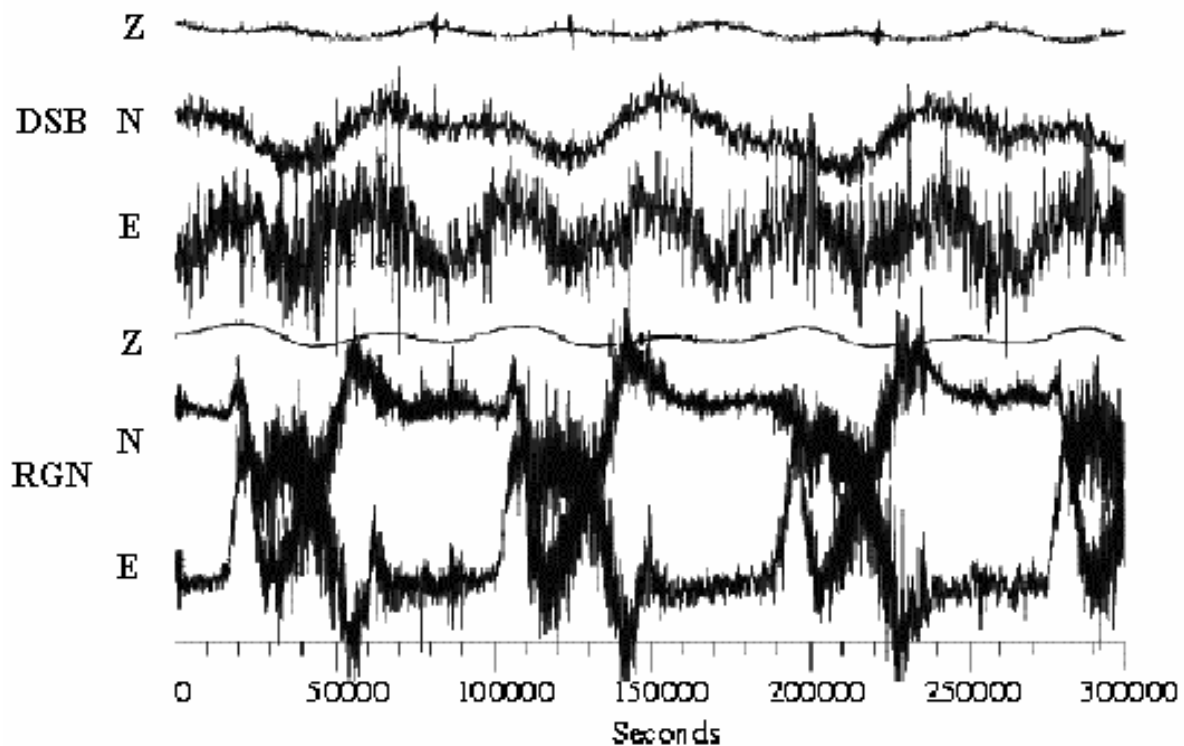


Fig. 7.57 Comparison of two surface vaults in moderate climate on rock and in sediments. At DSB (Dublin, Ireland), a small surface bunker was built in an old granite quarry. At RGN (Rügen Island, Germany), an old one-room military bunker with a thin (< 1m) soil cover on top is used. Both sites host STS2 seismometers with GEOFON shielding.

Surface vaults in arctic climate

The very poor VLP noise performance of surface stations in arctic climates can be seen in Fig. 7.58, where data from two stations in Greenland are shown. Both vaults are located in surface wooden huts built on weathered rock, more or less open to all kinds of atmospheric turbulence in terms of air pressure and temperature changes. The vaults are heated in winter. This results in about the worst conditions one can imagine for VLP noise performance. Earth's tides are no longer seen very clearly and the daily noise variations are large. However, there is no other choice in these regions. DAG is in one of the most remote places on Earth where it is almost impossible to build an underground vault.

7.4.4.4 Conclusions

The VLP performance of a VBB seismological station is directly dependent on several instrumental and environmental parameters. High quality VBB seismometers, a true 24-bit A/D converter and a continuous multi-stream data recording are essential. In the GEOFON network, only STS1/VBB and STS2 seismometers and Quanterra data loggers are used for this reason. With the appropriate shielding, the VLP performance of the STS2 is not much different from the STS1/VBB. Only in very rare cases at extremely quiet sites can the extra infrastructure, installation, maintenance and financial efforts related to the usage of STS1/VBB sensors be justified. The same is true for vault construction. The construction

7. Site Selection, Preparation and Installation of Seismic Stations

scheme itself has not much influence on the station performance as long as the depth of burial is deep enough and the environmental disturbances can be reduced to a minimum. With an adequate casing, a seismometer pier is not required to install an STS2 sensor properly underground. The geology plays a very important role. The harder the rock, the lower is the VLP noise at a certain depth since surface tilts caused by atmospheric influences do not penetrate as deep. Sediments show special tilting effects, which reduce drastically the daytime VLP performance of the horizontal components. The shallower a vault is, the more the influence of the general climate. In very moderate climates, e.g., close to the sea, even surface vaults can have a reasonable VLP noise level. In summary: Although the task of establishing a VBB station that is capable of recording with sufficient dynamic range the full seismic spectrum from high-frequency regional events up to the very long-period (VLP) Earth's tides seems to be a very difficult and costly effort, it can be achieved with rather simple means.

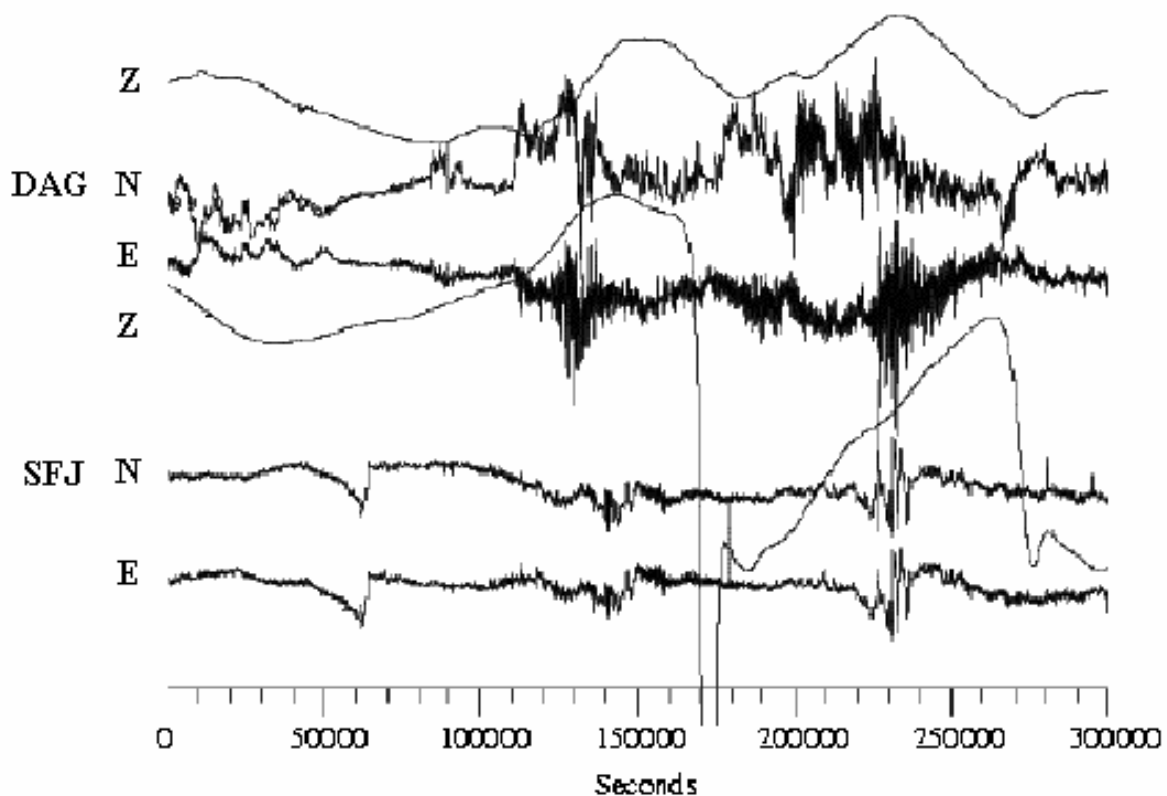


Fig. 7.58 VLP records obtained at two surface vaults on Greenland. At DAG (Danmarkshavn, NE Greenland) a STS2 in GEOFON shielding is installed in a wooden hut on weathered rock close to the sea shore. At SFJ (Sondre Stromfjord, SW Greenland) a set of STS1/VBB is located in a container-like building on top of a mountain. In both cases the geology is weathered rock in a permafrost environment.

More details on the installations made at various VBB stations and the comparison of noise data can be found on the web page <http://www.gfz-potsdam.de/geofon/>.

7.4.5 Broadband seismic installations in boreholes (L. G. Holcomb)

7.4.5.1 Introduction

Borehole seismology is a relatively new technology that has developed over the last 30 years or so. In the early years of seismology, installing a seismometer in a borehole was virtually impossible because of the relatively large physical size of instruments. As seismological technology matured, the instruments became smaller and it became more practical to consider borehole installations as alternatives to surface vaults or tunnels. There are several practical reasons for placing seismic instrumentation in boreholes; these include reduced noise levels, temperature stability and reduced pressure variability.

Experience gained over many years of installing both short- and long-period instruments has shown that sensor systems which are installed at depth are usually quieter than those installed at or near the surface of the Earth (see 4.4.). This is why abandoned underground mines are frequently used as sites for low-noise seismological stations. However, abandoned mines are not always found at the desired location of a seismic station. A borehole provides a practical solution to the need to install seismic sensors at depth almost anywhere.

A borehole is also a very stable operating environment in which to operate sensitive instruments because the temperature at depth is very stable and the pressure in a cased sealed borehole is very constant. Temperature changes and pressure variations at frequencies within the pass band of the sensor system are common sources of seismic noise (see 7.4.2.1). Systems installed on the surface or in shallow vaults require extensive thermal insulation systems in order to reduce the influences of temperature to acceptable levels. Similarly, elaborately designed pressure containers are required to eliminate pressure-induced noise particularly at long periods in vertical instruments. Both temperature and pressure considerations have become more important with the advent of broadband instruments because these instruments are sensitive to outside influences over a broader frequency range thereby making it more difficult to sufficiently isolate broadband instruments from extraneous influences. A sealed borehole of only moderate depth provides excellent temperature stability because of the tremendous thermal mass and inertia of the surrounding Earth. Furthermore, most seismic boreholes are cased with steel casing whose cylindrical walls are quite thick; this casing constitutes a quite rigid container, which greatly reduces atmospheric pressure variations within the borehole (assuming that both the top and bottom are sealed).

Boreholes are frequently considered to be expensive, but they sometimes represent the only practical alternative if an abandoned mine is not available. Excavating tunnels purely for seismological purposes into competent rock deep enough to provide sufficiently quiet seismic data is also a very expensive solution (see below). In many cases, a borehole may actually be the cheapest method for achieving an installation at depth unless the local manual labor costs are very low.

One advantage of a borehole installation over a vault is that there can be much less surface equipment on site, especially if no recording equipment is deployed on the site, say in a seismic array or small network. This can significantly save on costs and improve security. These advantages have led, in some cases, to the use of very shallow boreholes, or postholes, which are drilled to depths similar to vaults.

It is impossible to state exactly how much it would cost to construct either a borehole or a tunnel type vault because too many factors are involved. Precise costs will depend on the type

7. Site Selection, Preparation and Installation of Seismic Stations

of material in which the facility is constructed, raw material costs, local labor costs, etc.. However, here are some examples of approximate costs that have been encountered in constructing facilities for the IRIS program over the past 5 to 10 years. In Africa, IRIS has excavated three tunnel type seismic vaults that extended 25 to 40 meters horizontally into hillsides. The costs of these three projects ranged from approximately US\$ 150,000 to US\$ 250,000. For a typical borehole (100 meter deep), project costs range from approximately US\$ 25,000 to US\$ 200,000 at large landmass sites with boreholes in hard rock being significantly more costly than in soft soil. On the other hand, at small isolated Pacific Ocean island sites, borehole costs are in the US\$ 150,000 to US\$ 250,000 range.

7.4.5.2 Noise attenuation with depth

The main reason for installing broadband sensors in boreholes is to reduce the long-period tilt noise which plagues horizontal sensors installed on the surface. The question commonly asked by seismologists who are contemplating a borehole installation is how rapidly does the tilt noise decrease with depth and so how deep does the borehole need to be. There is no easy answer to this question because a borehole never eliminates all of the long-period tilt noise however deep it is. In general, the noise attenuation rate (db per unit depth) decreases as the depth increases; most of the noise reduction occurs in the upper parts of the borehole.

Fig. 7.59 illustrates the attenuation of long-period horizontal noise with depth. It shows the relative power spectral density (PSD) noise levels obtained from the simultaneous deployment of four broadband sensors located close to one another at the same site and installed at various depths. The first sensor was installed in a small vault on or near the surface. Three other three sensors were installed in boreholes at depths of 4.3, 89 and 152 m below the surface. The site consists of about 18 m of unconsolidated (soft/weathered) overburden overlying fractured Precambrian granite bedrock. In Fig. 7.59, noise attenuation data points in db relative to the noise level in the surface sensor are plotted for periods of 30, 100, and 1000 seconds. Note the very rapid decay in the noise level over the first few tens of meters followed by a much slower rate of decrease in noise levels at greater depths. Note that, in general, a depth of 100 m is sufficient to achieve most of the practicable reduction of long period noise.

The data in Fig. 7.59 should only be regarded as an example of noise attenuation with depth. Apparent surface noise levels at a particular site are frequently highly dependent on the methods used to install the instrumentation. This is particularly true of noise levels at many surface installations where faulty installation of broadband horizontal sensors causes excessive tilt noise at long periods.

Choosing the optimum depth for a borehole for a particular site involves comparing the cost of drilling the borehole to a given depth against the desired data quality, the anticipated surface noise levels (they are frequently determined by the anticipated wind speeds and wind persistence at the site), and the depth of the overburden at the site. Unfortunately, studies detailed enough to yield the precise relationships between the various factors have never been conducted. Therefore, choosing the depth of a borehole for a particular site usually involves non-quantitative consideration of the various factors involved. Many years of experience has demonstrated that 100 meter deep boreholes drilled at sites with a few tens of meters of overburden overlying relatively competent bedrock will provide a sufficiently quiet environment for installing a high quality borehole instrument. Most broadband IRIS borehole

7.4 Seismic station site preparation, instrument installation and shielding

instruments are installed at or near 100 meters depth. Boreholes at sites with more overburden and/or softer lower quality bedrock are sometimes deeper depending on construction costs and anticipated surface noise levels.

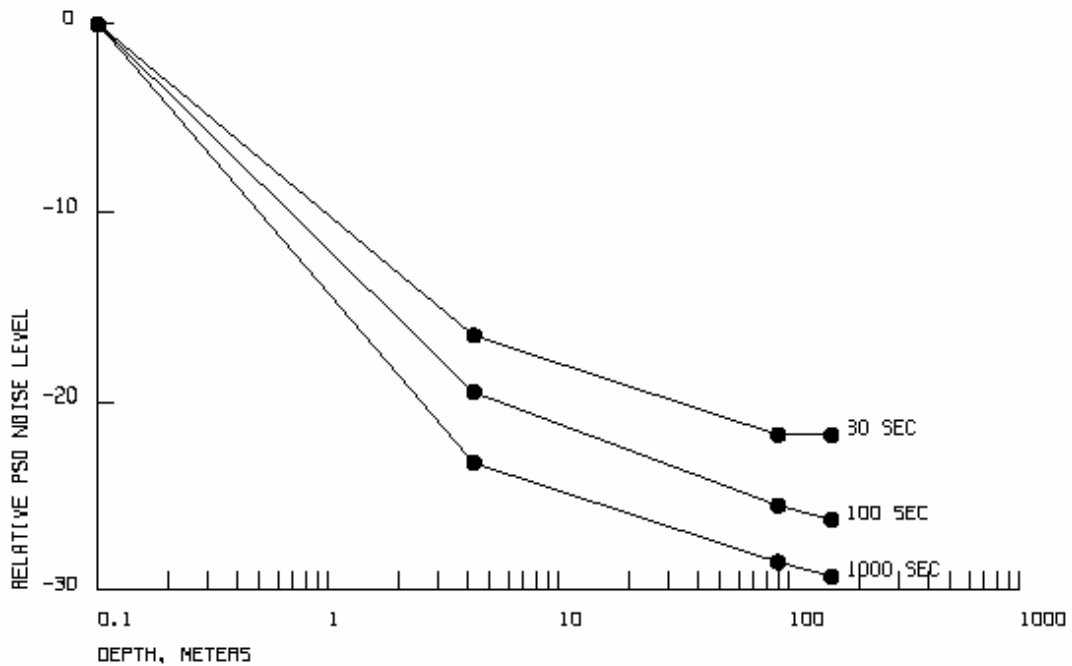


Fig. 7.59 Horizontal surface noise attenuation as a function of depth at three selected periods. The depths were 0, 4.3, 89, and 152 meters.

7.4.5.3 Site selection criteria

There are several criteria for selecting the site for a borehole installation. Ideally, one should select a site at which the surface background seismic noise over the band of interest is as low as possible. However, there are other factors such as accessibility, availability of power, improved network configuration, the presence of wide-spread thick alluvial fill, and/or the presence of cultural activity within the monitored area, which may force the choice of a site with higher background noise levels.

A good borehole should penetrate well into bedrock (70 to 100 meters) (see 7.4.2.2), so the site should have bedrock at or near the surface to minimize the need to drill through excessive overburden. If possible, the bedrock should be a relatively hard rock (see 7.1.2.2) such as granite or quartzite. Harder, more competent rock increases the rate of attenuation of surface noise with depth and also decreases the chances of borehole collapse during drilling. Soft rocks such as shale, mudstone, or low grade limestone should be avoided if possible.

Good bedrock is highly desirable for providing the best results from a borehole installation, but benefits are still there for boreholes in poorer rock. Note that the first data point in Fig.7.59 (only 4 meters down) was obtained in a very shallow borehole that was drilled entirely in loose alluvial fill. Therefore, the lack of shallow bedrock should not preclude the consideration of a borehole installation for a particular site.

7. Site Selection, Preparation and Installation of Seismic Stations

As with vault and tunnel installations, a reliable source of electricity will be necessary to power the site, a shelter will be needed to house the recording equipment, and some form of communication capability (telephone line, internet connection, or RF or satellite link) is frequently desirable (see IS 8.2). Accessibility for both the drilling equipment and maintenance personnel (see also 7.1.2.4) should also be considered during site selection activities.

Unfortunately, the need to be able to provide adequate security is also becoming a major factor in selecting station sites in many parts of the modern world. There is little point to investing in a good site if it can not be protected from vandalism. Adequate security has many different meanings depending on the particular situation. It may be as simple as a passive protective fence or as elaborate as alarmed fences and entry ways or even an on-site caretaker depending on the anticipated level of potential damage.

It should be noted that stations on very small islands (such as most coral atolls) do not benefit from borehole installations because the ground motion generated by ocean-wave loading of the beach penetrates rather deeply into the subsurface environment. For this reason, all borehole sites should be at an adequate distance (at least several km) from any coastline.

7.4.5.4 Contracting

Seismic boreholes are usually drilled by a local contractor using specifications supplied by the organization building the station. Hiring a local driller helps reduce mobilization and setup charges, which are frequently a significant portion of the cost of a seismic borehole. Specifications should be rigid and specific enough to ensure that the finished borehole will be suitable for seismology but flexible enough to prevent excessive costs. Most drilling contractors will have little or no experience of seismic boreholes and it is recommended that the contracting agency use an independent expert with extensive drilling and casing experience whose duties include on-site observation and supervision of all drilling and casing operations. This precaution is advisable to ensure that the drilling contractor performs all operations according to the specifications because departures from specifications are hard to detect, document, and prove after the project is finished. The contract should be specific about who is responsible for unexpected difficulties which might arise during the drilling and casing operations; courses of action should be specified if operations are delayed for any reason whatsoever. These include but should not necessarily be restricted to on-site down time which might be due to bad weather, shortage of drilling materials, crew availability, drill rig breakdowns, loss of circulation, injuries on the job, delays in subcontractor availability, holidays and unexpected changes which might be encountered in the quality of the subsurface rock.

7.4.5.5 Suggested borehole specifications

The drilling specifications for a seismic borehole should be written in such a way as to ensure that the completed borehole will be suitable for acquiring high quality seismic data. Parameters such as borehole verticality, depth, diameter, and casing type must be clearly specified. It is also important to specify how these parameters will be measured during construction or in the finished borehole.

7.4 Seismic station site preparation, instrument installation and shielding

Borehole verticality is the specification which drillers have most trouble meeting. Borehole verticality must be specified because all borehole seismometers have only a limited range of tilt over which their mechanical internal leveling mechanisms operate. Therefore, the sensor package must be aligned within a given tolerance from true vertical. This in turn requires that the borehole itself be aligned within a certain tolerance of true vertical. The required verticality specification will depend on which borehole seismometer is to be installed in the completed borehole because each seismometer has a unique mechanical leveling range (typical examples: CMG-3TB has a 3 degrees range, the KS-36000 has 3.5 degrees and the KS-54000 has 10 degrees). In general, the closer the verticality specification requirement is to vertical the higher the cost of the borehole.

The working depth of the borehole is usually specified as the depth of the open cylinder within the borehole confines after construction is complete. The driller is usually left with determining the depth of the hole to be drilled in the rock in order to achieve the desired working depth.

Most boreholes are cased with standard casing used in oil fields because it is readily available throughout the world. This casing is usually specified in terms of its outside diameter (OD) and its weight per unit length; the combination of these two parameters determines the wall thickness and in turn the inside diameter (ID) of the casing. The seismometer manufacturer usually recommends a range of casing in terms of the ID's of the casing in which his sensor will operate satisfactorily. These two methods for specifying borehole diameter must not be confused when writing specifications. As an example of typical hole diameters, a KS-54000 requires a casing with at least a 15.2 cm ID whereas, if equipped with proper hardware, a CMG-3TB (see DS 5.1) will fit into a slightly smaller casing. The specification usually permits the use of a range of OD's and weight specifications in order to facilitate acquiring the casing locally to decrease shipping costs. The individual threaded casing sections should be assembled together with a thread sealing compound and enough torque to ensure that each joint is properly sealed against leakage.

The bottom end of the casing is often equipped with a one way valve (called a float shoe) to seal the lower end against water entry and to facilitate cementing operations. This device allows the cementing mixture to be forced out of the bottom of the casing and prevents water from entering the borehole once the cementing operation is completed.

The casing must be firmly cemented to the surrounding rock walls of the borehole in order to ensure good mechanical coupling. The cementing operation usually consists of pumping a premixed cement mixture down the inside of the casing, out through the float shoe at the bottom, and forcing it back up to the surface between the casing and the bedrock. This operation ensures that all of the annular volume between the steel casing and the rock is filled with cement without voids containing air or liquid. When return cementing mix is observed in the annulus at the surface, a cleaning plunger is forced down the inside of the casing with water under high pressure. This expels the cement mix contained within the casing volume out of the bottom through the float shoe and finally sets (locks) the one way valve within the float shoe to prevent fluids from re-entering.

After the cement has set, it is advisable to require the driller to perform a leak test to ensure that the casing has been adequately sealed. Leak testing usually consists of first pressurizing the water-filled borehole to a specified pressure, sealing it off and leaving the pressurized

7. Site Selection, Preparation and Installation of Seismic Stations

borehole for a specified time period. The pressure within the borehole should not drop more than a pre-specified amount.

The upper end of the casing is normally terminated with a "packoff" device. This assembly is normally provided and installed by the contracting organization at the time of seismometer installation. The packoff unit seals the top of the borehole and provides a means of passing instrumentation cables into the borehole.

7.4.5.6 Instrument installation techniques

It is a relatively simple operation to install a borehole sensor but certain precautions are required. The sensors are usually fitted with two cables. The first cable is intended to provide sufficient strength to lift the weight of the sensor and any extra pulling force required to removing the sensor from the borehole. This is usually a steel cable or "wire rope". The second cable contains the electrical connections for power, control of the various mechanical operations within the sensor, and to transmit the seismic signals back up the borehole. For holes of significant depth, a small lightweight electrically driven winch and mast assembly can be used to lower the sensor into the hole and to retrieve it if necessary. Lowering and raising the sensor should be done fairly slowly because the sensor package sometimes catches on the casing pipe joints as it moves up or down the borehole. On the way down, this problem is usually temporary but usually results in a short free fall of the sensor and a sudden stop when the load-bearing cable becomes taut. If severe enough, the sudden stop can damage a sensitive instrument. If the sensor catches on a pipe joint on the way up, tension in the load bearing cable rapidly increases to dangerous levels if the winch is not stopped in time. If the sensor disengages from the pipe joint while the lifting cable is under high tension, the sensor will undergo possibly damaging levels of acceleration. If the sensor does not disengage and if the winch is powerful enough, the lifting cable may break and endanger personnel.

It is advisable to carry out a dummy run in the completed borehole using a metal cylinder with similar dimensions and weight to the seismometer package. This will help minimize the risk of damage to or losing the equipment during installation. Such a dummy run could be part of the acceptance procedures for the drilling contract.

Traditionally, borehole seismometers are rigidly clamped to the inside of the cased borehole with manufacturer-supplied mechanical hardware to ensure adequate coupling between the sensor and ground motion. The hardware usually includes a mechanically driven locking mechanism for clamping the sensor to the walls of the borehole. This device sometimes consists of a motor driven or spring loaded pawl that is extended on command from the side of the sensor package to contact the borehole wall opposite the sensor (GS-21, CMG-3TB). Sometimes this function is performed by a separate piece of hardware known as a "holelock" that is clamped into the borehole and on which the sensor package is subsequently placed (KS-36000, KS-54000, and earlier Guralp sensors). In the second case, additional hardware is sometimes required to stabilize the upper end of the sensor package (the centralizer assembly in KS instruments). Mechanical clamping mechanisms have been used successfully for many years and have produced satisfactory data from many installations.

However, many installations of this type produce more long-period noise in the horizontal components than in the vertical component. In some of these installations, the horizontals were orders of magnitude noisier at long periods than the vertical. The source of the excess

7.4 Seismic station site preparation, instrument installation and shielding

noise in the horizontal components has been difficult to isolate and eliminate. For many years, it was suspected that some of this noise was somehow generated by air motion in the vicinity of the sensor package. Conventionally designed horizontal components of long-period seismometers (this includes all sensors with garden-gate type of suspension such as the STS1, CMG-3 series, KS-36000 and KS-54000) are extremely sensitive to tilt because of their inability to separate the influences of pure horizontal acceleration input to the sensor frame (the desired input) from the signal that arises from the tilting of the sensor package (tilt noise). Therefore, fairly elaborate schemes for reducing the potential for air motion around the sensor within the borehole have been devised and utilized with varying success. Through trial and error, it has become customary to wrap the sensor package (KS-36000's and KS-54000's) with a thin layer of foam insulation in an attempt to somehow modify the flow of heat near the seismometer in the borehole. In addition, it has become common to place long plastic foam borehole plugs immediately above these sensor packages deep in the borehole and near the top of the borehole to block air motion in these sections of the borehole. Additional insulation, which is intended to further reduce air motion within the borehole, is sometimes utilized near the top of the sensor package.

Recently, a highly successful method for significantly reducing the long-period noise levels in borehole installed horizontal components has been developed at the Albuquerque Seismological Laboratory. It consists of simply filling the entire empty air space below and around the sensor package with sand. In this type of installation, none of the auxiliary installation hardware such as the borehole clamping mechanism or holelock, the azimuth ring, the pilot probe, the centralizer, the foam plugs and/or insulation are utilized to install the seismometer. The seismometer package is simply lowered onto a bed of sand at the bottom of the borehole - sometimes, a piece of hardware called a sand foot is installed on the bottom of the sensor. A volume of sand is then poured into the borehole to a depth extending to the top of the seismometer package. The volume required can be easily calculated from the dimensions of the package and the inner diameter of the borehole.

Experimental investigations have demonstrated that it is easy to remove the seismometer from the sand if necessary for maintenance purposes even when the sand is saturated. Normally, the sand left in the hole from a previous installation is not removed from the hole prior to the next installation. Only a fraction of a meter of borehole depth is lost per installation; if necessary, the sand can be removed from the borehole with a downhole vacuum cleaner that has been designed at ASL.

This method of installation is expected to reduce horizontal noise to levels approaching the noise level of the vertical component at any particular site. The horizontals should be expected to always be slightly noisier than the vertical component because remnant real ground tilt will always be present regardless of how deep the sensor is installed. To date, extensive testing at ASL utilizing both KS and CMG (see DS 5.1) instruments and several actual KS sand installations in the field have indicated that sand does indeed produce significantly reduced levels of horizontal noise. The sand installation method has been adopted for future installations by the IRIS GSN program.

One additional advantage of a sand installation is that the seismometer package costs considerably less than for a clamped installation.

One note of caution should be introduced at this point. Conventional hole-lock based installations produce very noisy horizontal data if the sensor package is immersed in water or

7. Site Selection, Preparation and Installation of Seismic Stations

another liquid such as motor oil. Therefore, every effort is normally made in the field to keep liquids out of the borehole. Although not thoroughly tested to date, sand installations are expected to provide quiet horizontal data even if the sensor is immersed in water as long as the water is not flowing.

Determining the orientation of the horizontal components of a seismometer installed in a deep borehole is not a simple matter because one can not physically get at the instrument once it is installed. One must resort to indirect methods for determining how the instrument is oriented. For the past 25 years, the KS series instrument installations have relied on a gyroscopic procedure to determine the seismometer orientation as follows. First, the hole-lock is installed in the borehole at the intended operating depth; then, a gyroscopic probe is lowered into the hole and mated with an alignment slot in the hole-lock. The gyro system determines the orientation of this alignment slot with respect to a known azimuth (usually north) on the surface. An adjustable azimuth ring located on the base of the KS sensor is then set to compensate for the alignment of the hole-lock slot to north. This ensures that when the seismometer is lowered into the borehole and the key on the alignment ring is mated with the alignment slot in the hole-lock, the sensor is in a north-south, east-west orientation.

This method was considered adequate to determine the azimuth of borehole installations for many years, but it had some serious shortcomings. The method was subject to errors due to mechanical assembly tolerances and was frequently plagued by nonlinear gyro drift. The major problem with the system was the fragile nature of the gyro probes themselves; they proved to be very susceptible to shipping damage and extremely expensive to repair. In addition, the manufacturer was not willing to warrant his expensive repair work in any way. Therefore, a much cheaper alternate method of orienting borehole seismometers has been developed and is currently replacing the gyro probe approach in programs with limited budgets.

The new method involves the installation of a horizontal reference seismometer on the surface near the borehole at a known orientation. The digitally recorded output of this surface sensor is then compared using the coherence and correlation functions with the digitally recorded outputs of the horizontal components of the sensor installed in the borehole to determine the relative azimuthal orientation of the borehole components with respect to the surface horizontal.

With the advent of sand installations, the horizontal components of newly installed seismometers are no longer being oriented in the conventional north-south east-west configuration. Instead, many borehole sensors are being installed at arbitrary azimuths with respect to north; the alignment of the horizontals with respect to north then becomes part of the data set. This approach has become feasible because modern computing power and digital data trivializes the task of rotating the data to any azimuth desired by the data user.

7.4.5.7 Typical borehole parameters

As the result of the SRO and IRIS programs, there are now many broadband borehole installations in use around the world. Most of these boreholes are geometrically quite similar because they were designed to accommodate the same seismic instruments. All of these boreholes are approximately 16.5 cm in diameter and most of them are drilled to a maximum

7.4 Seismic station site preparation, instrument installation and shielding

of 3.5 degrees departure from true vertical. They are all cased with standard oil field grade casing and most of them are watertight.

There is some variation in the depths of these boreholes. As mentioned above, the vast majority of seismic boreholes are approximately 100 meters deep. However, some of these boreholes are considerably deeper if they were drilled in areas with thick overburden or poor bedrock. For instance, the borehole sensor at DWPF (Florida) is installed at 162 meters depth because the overburden at DWPF is approximately 46 meters thick and the upper layers of bedrock consist of interleaved units of varying grades of soft limestone. The borehole at ANTO, which is drilled in competent rock for most of its depth, is the deepest and oldest IRIS borehole at 195 meters. This was the first field borehole that was drilled for the SRO program: as more experience was gained, it became apparent that boreholes that deep were not cost-effective. A few of the boreholes are shallower primarily because severe difficulties were encountered during the drilling operations that necessitated finishing the borehole at a shallower depth than originally desired. For example, the sensor at JOHN (Johnson Island) is at a depth of 39 meters because severe borehole collapses were encountered while attempting to drill deeper. The site is on a coral atoll and the surface layers are very poorly consolidated; true bedrock probably lies at very great depths. Drilling in volcanic regions often proves to be very difficult. The borehole at POHA on the island of Hawaii was terminated at 88 meters because the drillers experienced severe "loss of circulation" conditions throughout the drilling operation. The surface layers at POHA consist of badly fractured weathered basalt layers and basalt rubble separated by scoria rubble, ash flows, sand and other assorted debris produced by an active volcano. Drilling conditions in the volcanic deposits on Macquire Island proved to be so difficult that it was impossible to complete a borehole.

7.4.5.8 Commercial sources of borehole instruments

Currently, there are only two known commercial sources of high sensitivity broadband borehole seismometers. For many years, Teledyne Geotech in Dallas Texas, USA (now Geotech Instruments LLC; www.geoinstr.com) was the only source of high sensitivity instruments (KS-36000, KS-54000, GS-21, and 20171) designed specifically for borehole installation. Both the KS-36000 and the KS-54000 are three-component broadband, closed loop force feedback sensors that are designed for deep (up to 300 meters) borehole installation. The GS-21 is a conventionally designed short-period vertical deep borehole instrument intended for superior high frequency performance. The 20171 is a slightly noisier and slightly cheaper version of the GS-21. The KS-36000 is no longer manufactured but there are many of these instruments still in operation in boreholes around the world. Recently, Geotech has introduced a new sensor, the KS-2000, which is available both as a surface package and a 4-inch borehole package.

For the past few years, Guralp Systems Ltd. (www.guralp.demon.co.uk), Reading, UK, has been producing a borehole version of the CMG-3T (see DS 5.1; referred to by some as a CMG-3TB). This instrument is much smaller and much lighter than is a KS sensor; it is also considerably less expensive. This is a three component, broadband, closed loop, force feedback instrument that is very easy to install. Guralp Systems has recently introduced a new borehole sensor that has both a velocity and an acceleration output and is integrated with its own digitizer. In addition, they are willing to work with the customer to meet any specific requirements.

7. Site Selection, Preparation and Installation of Seismic Stations

A borehole version of the STS2 has been under development for several years. Currently, a basic prototype of the instrument exists but the instrument requires further development of the remote control functions and the final packaging design is yet to be determined. Streckeisen has not announced an availability date for the new instrument.

It is somewhat hazardous to quote sensor prices because they are continuously subject to change by the manufacturer and international currency exchange rates change daily, but here are some approximate current relative costs for borehole sensors in 1999 US dollars. These prices should be viewed as being approximate; potential buyers should consult the manufacturer for a current quote.

A basic Geotech KS-54000 was priced at nearly US\$ 65,000. Additional costs will be about US\$ 40,000 for a conventional installation or about US\$ 13,000 if installed in sand and if all the associated installation hardware has been purchased. However, this price may be reduced if the instruments are ordered in sufficient quantities (25 or more). A GS-21 was priced at about US\$ 8,000 and the 20171 was around US\$ 6,000 for the instruments themselves. The associated hardware (soft electrical cable, wire rope, winch etc.) is additional. Estimated delivery time for these instruments is 120 days or more after receipt of order depending on the availability of non-Geotech manufactured parts. The soon to be introduced KS-2000 sensor will be priced at below US\$ 10,000 for the surface system and the borehole version will probably be below US\$ 20,000.

A Guralp Systems CMG-3TB costs about \$28,000 if the instrument is to be installed in sand; and about \$39,000 for a hole-lock equipped version. Delivery is currently about 9 months but they are trying to decrease this to about 6 months.

7.4.5.9 Instrument noise

It is important to remember that the purpose of installing seismic instrumentation in boreholes is to obtain quiet seismic data. This will be foiled if the seismic sensor system itself is too noisy to resolve the lower levels of background noise of the Earth which are expected to be found at the bottom of the borehole. As delivered from the factory, sensor self-noise levels sometimes vary over a wide range and some instruments may be far too noisy to operate successfully in a quiet borehole. Therefore, it is recommended that the self-noise of all borehole instruments be measured before installation to ensure that they are quiet enough to be able to resolve the background noise levels anticipated at the bottom of the borehole. Self-noise measurements are usually made by installing two or more sensors physically close enough together to ensure that the ground motion input to all of the sensors is identical. The data produced by the sensors is then analyzed to determine the level of the incoherent power in each sensor's output; this incoherent power is usually interpreted as the sensor internal noise level (see 5.6). To achieve high fidelity recording of true ground motion, the seismometer system self-noise level should be well below the anticipated background Earth's motion levels across the band of interest at the site.

The low-noise models in Fig. 7.60 can serve as guidelines to the instrument noise levels that may be expected from the CMG-3TB and the KS-54000 sensor systems. In this figure, the CMG-3TB low-noise model (CMGLNM) is the thin solid line and the KS-54000 low noise model (KSLNM) is the thin dashed line. The solid heavy line in the figure is Peterson's (1993) new low-noise model (NLNM) for the background seismic noise at a quiet site. The

7.4 Seismic station site preparation, instrument installation and shielding

reader should recognize that there is no single known site in the world whose background power spectral density levels reach NLNM levels across the entire band. Instead, the NLNM is a composite of the lowest Earth's noise levels obtained from many sites. Similarly, the low-noise models for the instruments should not be regarded as being typical of all instruments because each seismic sensor has a distinct personality of its own. Instead, the low-noise models for the instruments should be regarded as lower limits of instrument noise just as is the case for the NLNM of ambient Earth's noise. In all probability, individual instruments will be noisier than the low-noise model for that instrument over at least portions of the spectrum.

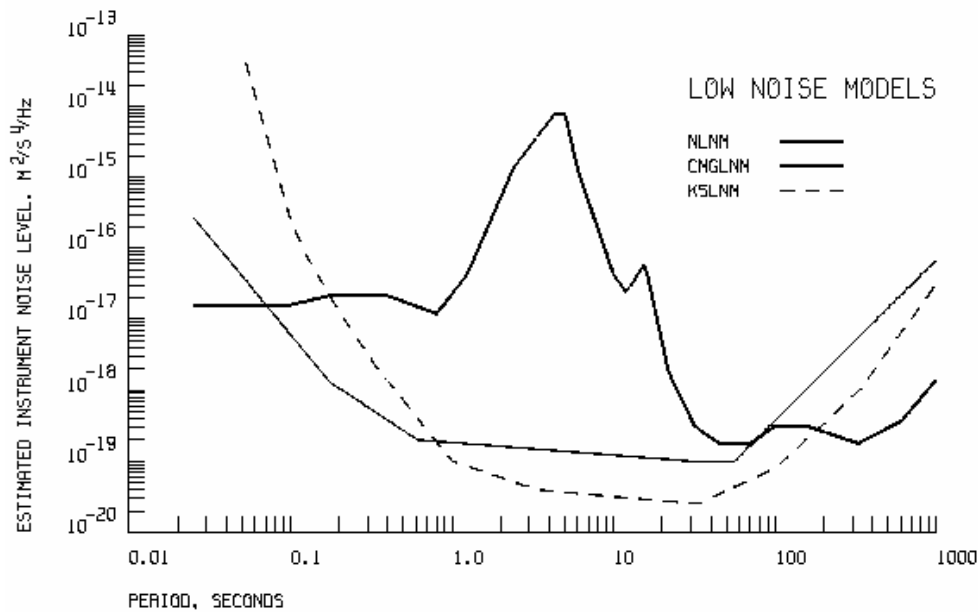


Fig. 7.60 Low-noise models for the KS-54000 (KSLNM) and the CMG-3TB (CMGLNM) sensor system self-noise relative to Peterson's (1993) new low-noise model (NLNM) for background Earth's motion.

The CMGLNM plot in Fig. 7.60 is based on a composite of experimental test data obtained at the Albuquerque Seismological Laboratory over a period of several years. The central portion (from about 0.6 to about 20 seconds) of the model was not actually measured because of numerical resolution limits of the data processing algorithms and this portion of the model is an estimate. As a general rule, many CMG-3TB instrument noise levels approach the CMGLNM at short periods (less than 0.6 seconds); fewer of these instruments achieve the indicated noise levels at long periods (greater than 20 seconds).

The KSLNM plot in Fig. 7.60 is a factory-derived theoretical instrument noise level. As such, it should be regarded as an optimistic estimate of the lower limits of the self-noise in the KS-54000. Most KS-54000 instruments are probably noisier than the levels indicated by the KSLNM curve.

7.4.5.10 Organizations with known noteworthy borehole experience

As an organization, Teledyne Geotech (Geotech Instruments – www.geoinstr.com) certainly has the longest history in seismic borehole technology. However, personnel turnover in the past few years has significantly depleted Geotech's direct hands-on experience in boreholes.

7. Site Selection, Preparation and Installation of Seismic Stations

Another organization with a long history of borehole experience is the United States Air Force Technical Applications Center (AFTAC – www.aftac.gov). Over the past 25 years they have deployed many KS instruments throughout the world. Most of these installations involve multiple sensor configurations deployed in arrays. Prior to the KS era, AFTAC used the older Geotech Triax instruments in boreholes at some of their arrays. As was the case with Teledyne Geotech, AFTAC does not have personnel with long-term borehole experience; US Air Force personnel tend to rotate in and out of their duty assignments every two years.

The Albuquerque Seismological Laboratory (<http://aslwww.cr.usgs.gov/>) has been deploying KS sensors in boreholes since 1974 at sites located all over the world and recently has begun installing Guralp CMG-3TB sensors at some sites. The Laboratory has borehole experience on all seven continents ranging from tropical jungle in Brazil to the permafrost of Antarctica. At ASL, the personnel situation has remained relatively stable and there are several personnel with many years of experience working with boreholes – some have been at it for over 25 years.

Southern Methodist University (Dr Eugene T. Herrin, e-mail: herrin@passion.isem.smu.edu) has been active in the borehole field off and on over the years. Recently they have been quite active in developing innovative economical methods for installing broadband borehole arrays.

As an organization, Sandia National Laboratories (www.sandia.gov) has considerable experience in borehole technology, most notably with their Remote Seismic Telemetered Network (RSTN) program. However, the lack of continuity in their seismic program has resulted in the loss of many of the personnel with real field experience in borehole technology.

During the past 10 years, the IDA group at the Scripps Institution of Oceanography at the University of California, San Diego (www-ida.ucsd.edu/public/home.nof.html) has become involved in land-based borehole seismology as a part of the IRIS GSN program. They now have experience in drilling boreholes and deploying instruments at several sites around the world.

In conjunction with personnel from the Woods Hole Oceanographic Institute, Scripps is also leading the US effort aimed at developing pioneering borehole seismology techniques for use on the ocean floor. Independent programs in ocean bottom borehole seismology are also currently conducted by groups in France and Japan. Installing seismic sensors in the deep ocean is developing rapidly and we will not attempt to summarize practices in this field.

7.4.6 Borehole strong-motion array installation (R. L. Nigbor)

7.4.6.1 Introduction

"An important factor in understanding and estimating local soil effects on ground motions and soil-structure interaction effects on structural response is the three dimensional nature of earthquake waves. ...For these purposes it is necessary to have available records of the motion at various points on the ground surface, along two mutually orthogonal directions, as well as at different depths."

7.4 Seismic station site preparation, instrument installation and shielding

These words, published in the proceedings of the 1981 U.S. National Workshop on Strong-Motion Earthquake Instrumentation in Santa Barbara, California, are echoed in every important meeting where policies and priorities have been set regarding strong-motion monitoring. Earthquake engineers and seismologists alike agree: borehole strong-motion data continue to be a priority for better understanding of site response and soil-structure interaction issues.

This section is somewhat of a departure from much of the New Manual of Seismological Observatory Practice, as borehole strong-motion observations are primarily focused on site response and not on the seismic source or wave propagation path. For engineering purposes, borehole data in shallow (< 100 m) soils are of primary importance; these data are used to study amplification of earthquake shaking in the soil layers. However, borehole data in rock, especially weathered rock in the upper 30 m, are also important for the understanding of strong ground shaking in earthquakes. Rock sites often show larger variability in measured ground motions than do soil sites. Examples of well-documented strong-motion borehole arrays are the EuroSeisTest Project (<http://daidalos.civil.auth.gr/euroseis>) and the Garner Valley Downhole Array (<http://www.crystal.ucsb.edu/observatories/gvda/>). The user of this Manual should consult these references for further information about the details of borehole arrays and the use of borehole strong-motion data.

As important as borehole data are, many practitioners experience difficulty designing and constructing such arrays. As with the more traditional seismological borehole systems (see 7.4.5), strong-motion borehole arrays present a variety of challenges. Fortunately, much has been learned about borehole strong-motion instrumentation and vertical strong-motion array construction. In the past, borehole systems rarely survived more than two years. However, today there are many successful, long-term three-dimensional strong-motion arrays throughout the world. This accomplishment can be traced to better design, to new instrumentation, to better understanding of the historical failures, and to improved installation procedures.

This section is intended to assist with planning and implementing a successful borehole strong-motion array. Details of the instrumentation are not directly discussed but are available from the manufacturers of borehole strong-motion systems such as Kinemetrics (<http://www.kmi.com>). The sections that follow discuss borehole array planning, borehole preparation, geotechnical/geophysical measurements, installation procedure, and costs.

Fig. 7.61 shows representative borehole array data from the Garner Valley Downhole Array, Fig. 7.62 is a sketch of a typical, simple borehole strong-motion installation and Fig. 7.63 shows an example of a borehole strong-motion array. These sketches are meant to show the various components and terminology that will be discussed in this section.

7. Site Selection, Preparation and Installation of Seismic Stations

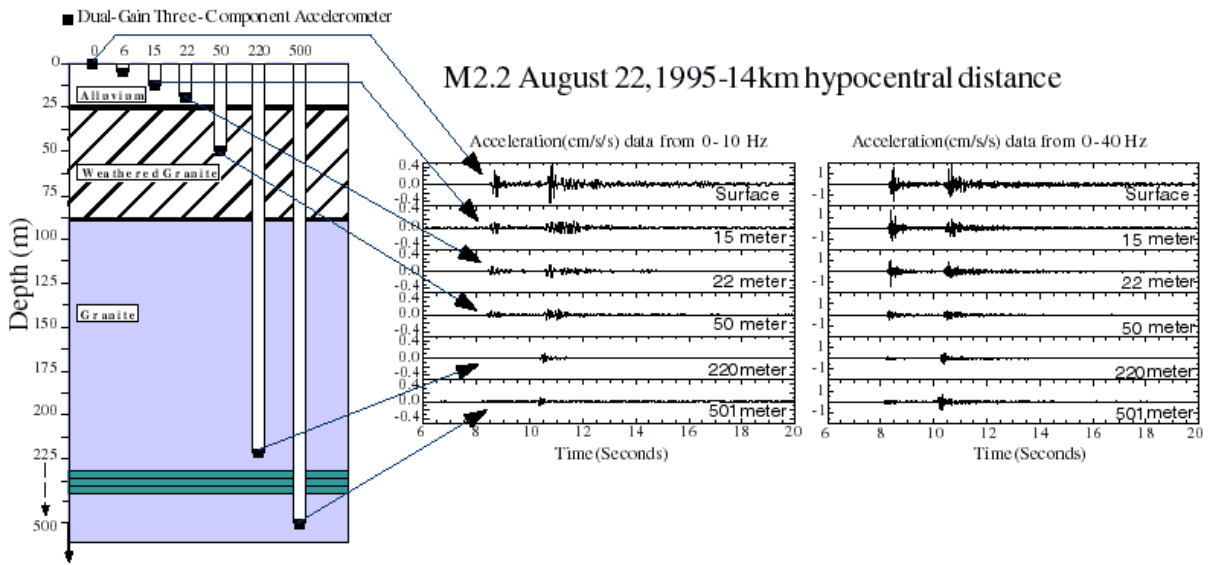


Fig. 7.61 Sample borehole strong-motion array data from Garner Valley downhole array, <http://www.crystal.ucsb.edu/observatories/gvda/>.

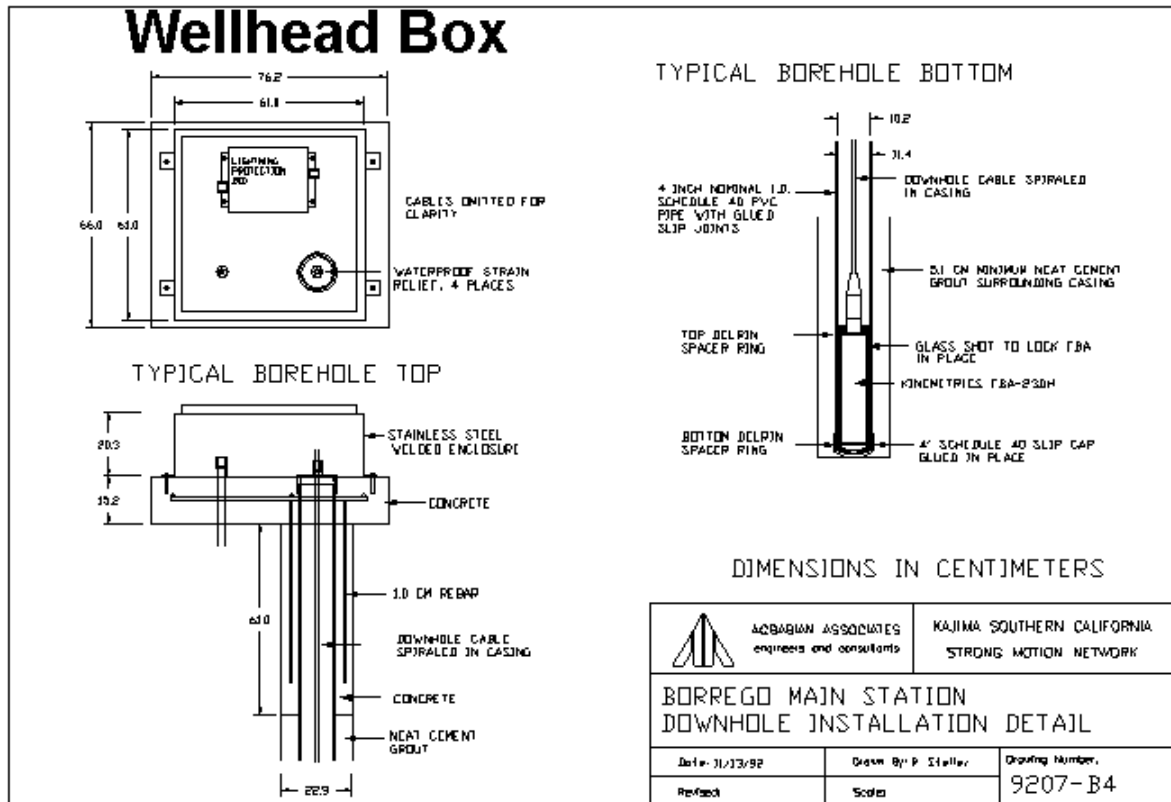


Fig.7.62 Sketch of borehole strong-motion accelerometer installation details.

7.4 Seismic station site preparation, instrument installation and shielding

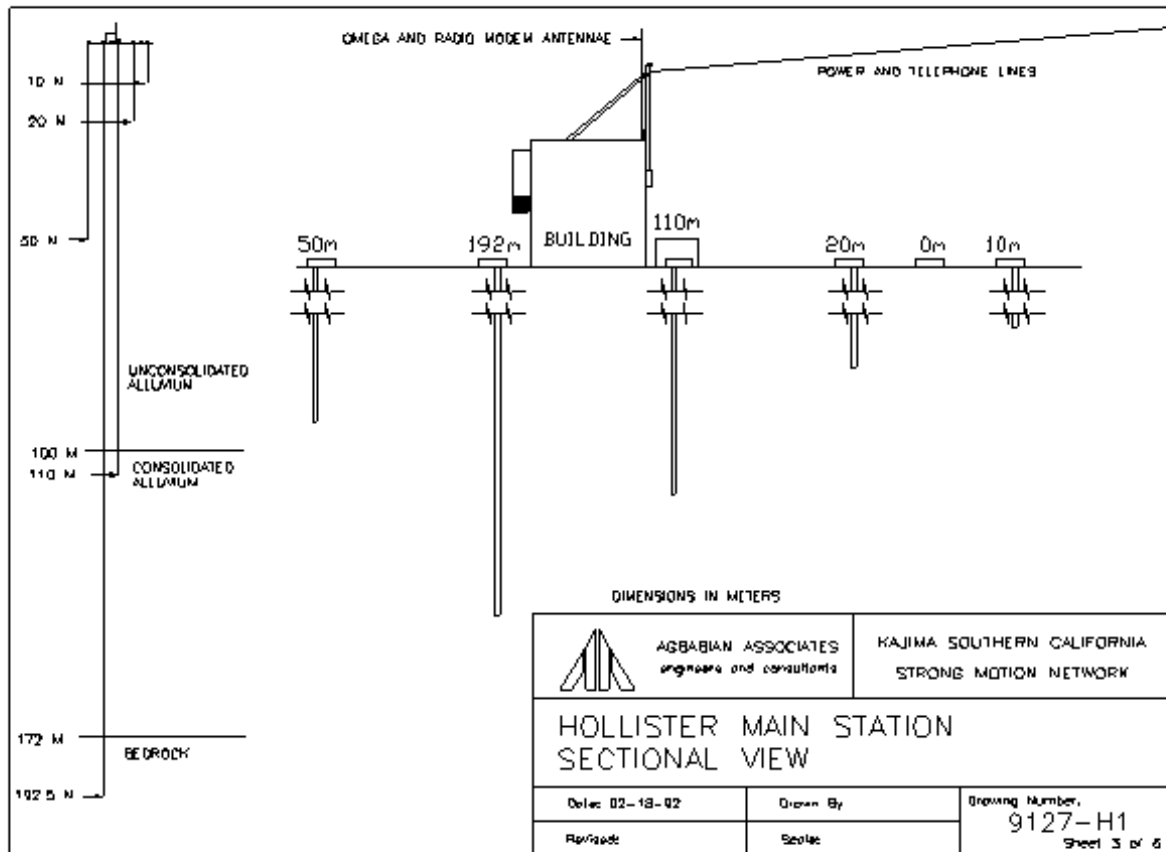


Fig. 7.63 Sketch of a borehole strong-motion array.

7.4.6.2 Borehole array planning

This section focuses on the planning issues related to borehole strong-motion array installation. The most important step in implementing a successful borehole accelerometer system is good planning. Done properly, by the time the borehole accelerometer package is actually lowered into the hole (as in Fig. 7.64 below), 95% of the effort will be complete. The following are important considerations:

- location;
- geologic implications;
- coupling and retrievability issues;
- sensor orientation;
- system issues.

Location

Borehole data are needed for source mechanism and wave propagation arrays, local site effects arrays, and as free field input to structural response arrays. The location of the borehole is principally dictated by the needs of the particular project and thus the required array configuration.

7. Site Selection, Preparation and Installation of Seismic Stations

Borehole location and depth will also depend on the soils and depth to bedrock. It is recommended that external advice or review be obtained for borehole location selection.



Fig. 7.64 Lowering a borehole accelerometer into the cased borehole.

Ground-borne noise is not the serious issue that it is with high-gain seismic systems, but it is still important to minimize non-earthquake vibrations in a borehole strong-motion installation. Few man-made signals will penetrate tens of meters of soil, so background noise will be reduced in a borehole sensor. However, some boreholes are shallow, and often the borehole accelerometer is collocated with a surface sensor. For this reason, the borehole should be located as far away from cultural (man-made) noise sources as possible. These include large, above ground structures, such as telephone poles, which can be driven by wind, vibration sources such as nearby rock quarries or industrial plants, and roadways bearing large vehicles.

The structure used for housing the recording station itself can be a source of coupled soil-structure vibration and must be designed carefully. The interaction of large structures with the soils can introduce noise into the ground motion. For this reason, the surface accelerometers should be located at least $1.5H$ distance away from the structure, where H is the height of the structure.

Within an array of borehole and surface sensors, one must optimize the layout with regard to physical concerns such as cabling and environmental protection. The lengths of surface cables should be minimized for several reasons. First, because of cost. Second, the longer the cable the greater the potential for damage or introduction of noise or induced voltage, even if the cable is shielded and in conduit, and even if there is lightning protection both at the wellhead box and at the recording station (as there should be). The recording station should be located near the wellhead boxes to minimize cable lengths.

7.4 Seismic station site preparation, instrument installation and shielding

Finally, it is best if the wellhead box is dry most of the time although it is assumed that the borehole itself is full of water and the wellhead box is designed to be waterproof. The top of the borehole should be positioned with regard to local water drainage and preferably not in a topographic low.

Geologic implications

Specific knowledge of the geology of a site is extremely useful during planning in order to meet project needs and accurately estimate the costs. The implications of local geology will depend upon the specific purpose of the borehole array. One should at least understand the surface geology, the depth to basement rock, and the local and regional tectonic structure. Fig. 7.65 shows a composite model of the EuroSeisTest site. This is an example of the kind of geologic understanding which should accompany a borehole strong-motion array installation.

The best information will come from both a thorough literature search to find existing information and then pre-installation geophysical studies. Once a site is selected, more detailed geophysical and geotechnical studies will be needed for ground motion and structural response modeling.

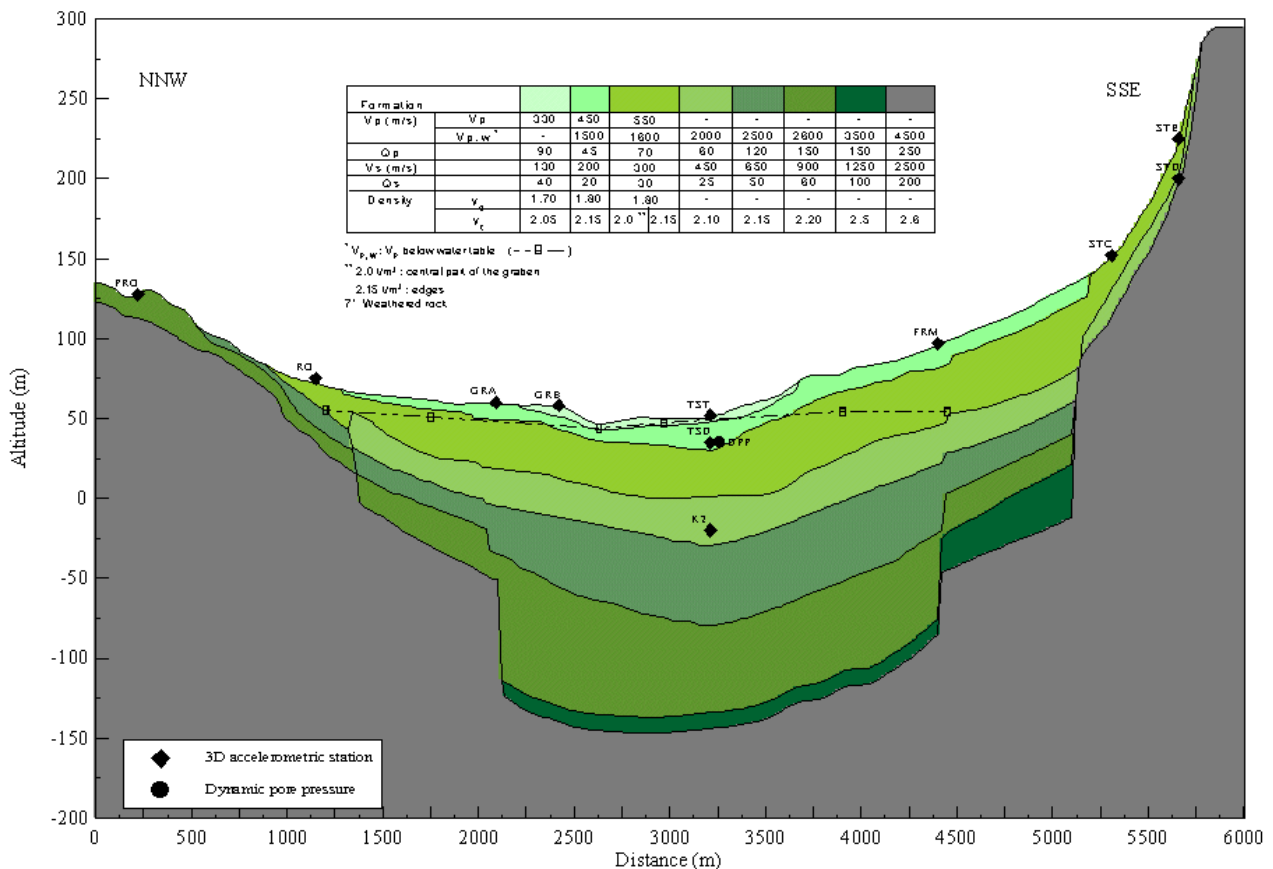


Fig. 7.65 Geologic model of EuroSeisTest showing array configuration (Ref.: The EUROSEISTEST Project, <http://daidalos.civil.auth.gr/euroseis/>).

7. Site Selection, Preparation and Installation of Seismic Stations

Coupling and retrievability issues

The coupling of the borehole sensor to the surrounding soil is a critical issue for borehole strong-motion systems. The goal of the measurement is to record the particle motion of the native soil or rock at depth. Care must be taken to ensure that the borehole installation minimizes the disturbance of the soil or rock column. The borehole itself, the casing, the grout used to seal the casing and couple it to the surrounding soils, the borehole accelerometer package, and the method used to couple the package to the wall of the casing, all can have some effect on the recorded motions, especially if the motions approach 1g. The issue of coupling is related to instrument retrievability, which is the ability to pull out a borehole sensor if repair is needed. For some borehole sensor installations, a permanent coupling solution (grouting or cementing the sensor in place) may be selected. This is not recommended as experience has shown that borehole sensor failure does occur. Failure of a borehole sensor that can not be retrieved not only entails the replacement of the sensor, but of the borehole as well, and the cost of the borehole often well exceeds that of the instrumentation.

If permanent coupling of the sensor is essential, using some sort of grout, it is advisable to design the borehole system to have a “weak point” above the sensor that will break cleanly when the cable is pulled and leave as little of the cable as is possible in the hole. If the sensor fails, it would be possible to abandon the sensor and cement in a replacement in the same borehole at a slightly shallower depth.

Removable coupling (locking) methods include backfilling the annular space around the package with some specified material, wedge-type locking systems, and pneumatic/hydraulic locking systems. Backfill materials used in the past have included sand, gravel, lead shot, and glass beads. Of these, water saturated sands can be expected to liquefy under vibrating conditions, and lead shot has been found to cold form over time, making retrieval difficult and even impossible. This leaves gravel or glass beads as successful alternatives. Kinemetrics recommends the use of a combination of 3mm and 5mm glass spheres as a coupling method; the company can be contacted for further details.

Several commercial wedge-type locking systems are available from borehole sensor manufacturers. Experience has shown that these will work well in shallower (<50m) installations, but may become unreliable in deeper installations. Some borehole installations, such as the 500m borehole sensor installation at the Garner Valley Downhole Array (<http://www.crystal.ucsb.edu/observatories/gvda/>), have used custom hydraulic locking systems. Some temporary borehole strong-motion sensor installations have used pneumatic (air-pressure) locking systems with success, but the air pressure must be maintained.

Sensor orientation

Another important issue in borehole strong-motion studies is the accurate orientation of the horizontal components of the borehole sensors. In the past, practitioners have most often relied on loading poles to manually orient the instrument package. Loading poles are generally square-section tubes which are rigidly attached to the accelerometer package. During installation, the loading poles are joined end-to-end with the painted side facing the same direction as the others, thereby permitting the package to be manually oriented from the top of the hole. This manual method can work well for shallow (< 20 m) borehole installations, but twisting of the poles can introduce large errors for deeper installations.

7.4 Seismic station site preparation, instrument installation and shielding

Fluxgate magnetometer sensors were first used with strong-motion borehole instrumentation in the late 1980's by a firm called Applied Geophysics of Los Angeles. At that time, the compass was used to determine the arbitrary orientation of a slotted end cap installed at the bottom of the PVC casing by the driller. The mating notch on a special borehole package was then rotated and fixed so that, once guided (by gravity) into position in the slot of the cap, the package was oriented as desired. This method was expensive because of the special construction and installation of the cap at the bottom of the hole, and the special packaging required to accommodate the orientation notch.

The current generation of commercial downhole accelerometers (for example, Kinometrics FBA-23DH) have provisions for an internal fluxgate magnetometer compass to make orientation simpler and much less expensive than either loading poles or borehole bottom devices. With this device, one simply observes the compass orientation via a notebook computer at the surface and rotates the sensor cable until the correct orientation is achieved. Accuracies of 2-3 degrees can be achieved with this method.

It is also possible to simply install a downhole accelerometer with random orientation and then to determine the orientation later by comparing the vector orientation of a surface sensor to that recorded from the borehole sensors. Orientation can be determined after installation by comparing surface and downhole data, either earthquake or microtremor. Note that anisotropy in the near surface soils can produce errors in this type of orientation unless the events are large regional events with significant long-period energy, i.e., with wavelengths much larger than the soil depths. Using a known source location, the orientations can be determined to $\pm 5^\circ$ by using linearity of 1st motions on radial and transverse components (see Aster and Shearer, 1991).

System issues

The borehole accelerometer package can not be installed properly without consideration of the overall system, and particularly the recording device. Usually, the recording system will have exceptional dynamic range to take advantage of the low noise qualities of the borehole installation and the accelerometer. Therefore, particular care must be taken to avoid system-related noise due to improper grounding and other common problems. Additional issues include system level lightning protection to protect circuitry against large voltage transients. Many of these system issues have been discussed in detail in 7.4.2.1.

7.4.6.3 Borehole preparation

A critical step in a successful borehole accelerometer installation is the preparation of the borehole itself. The borehole should be vertical, carefully drilled, with carefully installed casing grouted to ensure good coupling of ground motions at higher frequencies. Fig. 7.66 shows a typical drilling site. One can see that this can be a major construction effort.

Planning

Site selection for borehole accelerometers is often dictated by factors other than practicality for drilling operations. If there is room for adjustment of borehole location, try to meet or exceed the following minimum clearance requirements:

7. Site Selection, Preparation and Installation of Seismic Stations

- 2m from borehole to any obstructions such as fences, walls, or ditches;
- two 10m paths 4m wide on opposite sides of the borehole for drilling equipment;
- no overhead power lines

Access to the site should be able to support repeated trips with heavy trucks without damage. If a site is located in soft soils, consider the use of wood under the wheels of the drill rig and a four-wheel-drive water truck. Some sites may require the use of track-mounted drill rigs for access, or heavy earthmoving equipment to help position the drill rig on site. Fig. 7.67 below demonstrates why these are requirements for a drilling operation. Important steps in borehole preparation are planning, contractor selection, permitting, drilling, sampling, casing, and grouting. These issues are discussed below.



Fig. 7.66 Typical borehole drilling operation in an open area.



Fig. 7.67 Drilling operation in a confined area, showing size of drill rig.

7.4 Seismic station site preparation, instrument installation and shielding

Water availability is critical for drilling operations. A residential-type supply is adequate as long as an on-site water tank or truck is available to provide storage for peak demands. If all water is to be supplied by truck, a water supply capable of filling the truck quickly should be located within a 15 minute drive. Disposal of drill tailings and excess water is usually not a problem in remote sites where the tailings can be spread around the surrounding area to dry. In urban areas, fluids can be channeled sometimes down drains or ditches, but solid tailings must be removed. For shallow holes this can be done in drums and a pickup truck, if a nearby spot can be located to dispose of the tailings. In urban areas, a separation cone can be placed over a waterproof dumpster, and tailings collected in the dumpster, to be removed periodically by a liquid waste hauler with a vacuum-lift truck. In some areas, drill tailings are automatically classified as hazardous waste, which complicates disposal matters tremendously. Be sure to work these issues out before starting the project. In many developed areas, this can be a large cost item, easily as large as the drilling costs.

If multiple boreholes are to be drilled in one location, a separation of 6m between boreholes is generally adequate to prevent damage to a borehole during the drilling of subsequent boreholes. This should preclude the possibility of boreholes drifting laterally into each other during drilling. Shallow holes may be placed closer together by drilling in a line and backing the drill rig over the most-recently completed hole to protect it from damage.

The time of year chosen to begin a drilling project may significantly affect the schedule and cost of a project. Warmer weather is generally desirable, as are long periods of daylight and a lack of rain or snow.

Selection of drilling contractor

The selection of a drilling contractor must be based upon a number of factors; perhaps the least important of these is cost. If geotechnical sampling is to be performed, the contractor must have the equipment and crews familiar with geotechnical drilling practices. The key item in drilling is experience with the tasks to be performed and the equipment to be used. Drilling deeper (>50m) boreholes is not the place to have an inexperienced crew. The driller's reputation for completion of work and quality of work should be reviewed. It is strongly recommended that one obtain references for a drilling contractor.

When obtaining a bid, consider getting separate bids for a fixed price per meter and for actual time and materials used. For deep boreholes, fixed price per meter bids may appear more expensive but can save enormous amounts of money if a site is difficult. In addition, most companies will send out their best crews on fixed price bids, generally giving faster completion and fewer complications. In the long run, fixed price contracts often save money.

Permits

The drilling of boreholes near aquifers is carefully controlled in many countries to ensure that ground water sources are not contaminated. This control is generally exercised by local government, often through environmental health departments. Usually the responsible entity will require the submission of a permit application detailing depth, diameter, location, property lines, adjacent structures, wells and septic systems; well construction method, owner, and licensed driller to perform the work, and a fee of several hundred dollars per well. The application may require the signature of the land owner and the drilling contractor. In

7. Site Selection, Preparation and Installation of Seismic Stations

addition, some regions require copies of the driller's license and a performance bond before the driller is approved for work. In the US, typical permitting work is as follows:

- submission of permit application and fee;
- after permit application and payment of fee an inspector will usually visit the site before issuing approval of the permit;
- during construction, depending upon location, the inspector may visit the site several times, and may require notification 24 hours before grout is to be placed;
- in some municipalities, an inspector must be present during the grouting process;
- notifying the permitting agency of the completion of wells; usually this is in the form of a drill log which shows lithologic information and details of the well construction.

In other countries, and in rural or remote areas, permitting may not be needed. However, permission by the owner of the land will likely be required in all cases.

Drilling

There are several methods for shallow drilling in soils and rock. The book by Driscoll (1986) on Groundwater and Wells is a good reference for the various methods. Several ASTM (American Society for Testing and Materials) Standards describe drilling methods as well (see <http://www.astm.org>). A good start is ASTM D420-98 "Guide to Site Characterization for Engineering, Design, and Construction Purposes."

Direct rotary or "rotary mud" drilling is the drilling methodology best suited to most downhole accelerometer installation projects. One major advantage of this method is the support that the borehole wall receives from the drilling fluid that always fills the borehole. This method can be performed in both hard and soft formations, and can be done using fairly compact equipment. The drilling is performed by rotating a bit on the end of a heavy pipe or "drill string", which is driven down by its own weight, or by additional downward forces applied by hydraulic cylinders or chain pull-downs on the drill rig. The bit is lubricated, and drill cuttings are removed by drilling fluid or "mud" that is pumped down to the bit through the drill string. The fluid then returns to the surface through the annulus formed by the outer surface of the drill string and the borehole wall. This is possible because the borehole diameter is generally several inches larger in diameter than the drill string. As the fluid moves to the surface it carries with it the particulate debris produced by the cutting action of the bit. At the surface the fluid is directed into a holding area, either a box or dug pit, to let the cuttings settle out before the fluid is pumped down the drill string again.

Speed of completion is important in drilling due to the potential loss of a borehole by collapse. Some soil formations will remain open for long periods of time even if the fluid level drops significantly; other formations will cave in with the slightest provocation, even when filled with thick drilling fluid. In many instances, the premium paid to work around the clock is justified by the savings of not having to remove the drill string each evening, and the reduced risk of borehole collapse during the night.

Drilling is a messy business due to the large volume of water and mud involved. In a confined urban space such as an alley, a 100 m borehole might be drilled by a truck mounted rig only 8 m long, with an 8m tall tower, with only 1m of clearance on either side of the rig. Water and drill rod would be transported by a single 6m truck. All cuttings could be contained and

7.4 Seismic station site preparation, instrument installation and shielding

removed from the site in 200 liter drums or a larger container. This would be possible but is far from an ideal situation. In a rural or remote area, a 250 m borehole might use a rig 15 m long, with a tower of 10-15 m, a separate pumping rig 10 m long, a 12 m drill string trailer, a water storage tank, a mud pit 3 by 6 m, and an area several hundred m² to hold cuttings piles and miscellaneous support equipment. Fig. 7.67 shows such a setup.

Installation of a typical 100 mm (4 inch Schedule 40 or 80) PVC casing requires a minimum 200 mm (8 inch) diameter borehole. A larger diameter may be used when needed to maintain a clear hole, but this will increase drilling and grout costs and the potential of damage to the casing from grout cure heat, discussed further in the section on grouting. Most municipalities in the USA require a 50 mm (2 inch) annular seal around the casing, and this diameter meets this requirement. Depending upon the size of the drill rig used, this may be drilled in one pass, or a smaller pilot hole; usually 120 mm (4 7/8 inch) diameter will be drilled first, and all sampling and geophysical testing will be done in the pilot hole before drilling again to the final size.

There is a trade-off between speed of drilling and verticality of the borehole. Since verticality is an important issue for downhole sensor installations, it is important to make the driller aware of this, and stress that slow steady drill rates and perhaps collars attached to the drill string can help keep the borehole vertical. If you can get the driller to agree to a tolerance when doing a contract, this will also help keep the drill rig operator focused on this issue. Deviations of less than 5° from the vertical are acceptable. Larger deviations will affect the dynamic range of most sensors, unless the instrument has some type of auto-leveling device.

Geotechnical sampling

Generally, installation of a downhole accelerometer, or vertical array, is done to understand the effects of local site response on ground motion. Acquisition of soil or rock formation samples during drilling, as well as geophysical information, provide a great deal of information useful in site characterization studies. Not only can these samples provide clear indications of the formations beneath a site, but can also be used in laboratory studies to determine structural characteristics of the formation.

Soil sampling is described by Kenji Ishihara (1996) and by Driscoll (1986). Several ASTM standards also exist for sampling; two important references are ASTM D1586-99 “Standard Test Method for Penetration Test and Split-Barrel Sampling of Soils” and ASTM D1587-94 “Standard Practice for Thin-Walled Tube Geotechnical Sampling of Soils”, both from <http://www.astm.org>.

In general, one will use five major categories of sample types in borehole strong-motion array studies, as discussed below.

- **Bag samples** are simply a collection of drill cuttings carried to the surface by the drilling fluid and caught as they enter the mud box or pit. The accuracy of this sampling method is influenced by a number of factors including depth of the borehole, rate of circulation of drilling fluid, and size of cutting fragments produced by the drilling process. This method has limitations, due to the introduction of clays from the drilling fluid into the sample, as well as older material falling off the borehole wall. However, when used in conjunction with a detailed record of drilling rate, bag samples can provide extensive information about formation.

7. Site Selection, Preparation and Installation of Seismic Stations

- **Drive sampling** (“Split-Barrel Sampling” or “SPT” sampling) produces an intact but disturbed sample 2.5-5 cm (1-2 inch) in diameter by driving a sample tube into the formation at the bottom of the borehole. This is done by removing the drill string and lowering the sample tube, mounted on the bottom of a sliding hammer, to the bottom on a cable. The hammer is then actuated by lifting and dropping the cable until the sample tube has been advanced the desired distance. Often the number of blows to advance a given distance is recorded to provide blow count (SPT N-value), a measure of formation hardness. This procedure is time consuming because it requires the removal of the entire drill string from the borehole, but provides samples with excellent depth control. This method is useful only in soils. Fig. 7.68 shows typical drive samples.



Fig. 7.68 Drive samples being collected for later laboratory testing.

- **Pitcher samples** (“thin-walled tube” samples) produce an undisturbed sample 75 mm (3 inches) in diameter and up to 750 mm (30 inches) long. This technique is used when large high quality samples are required for laboratory tests, and where formations are too hard to yield results with a drive sampler. Pitcher sampling is performed by removing the drill string from the borehole and replacing the standard bit with a pitcher sample barrel. The barrel supports a thin wall steel tube on a spring loaded plunger. The plunger allows the tube to retract through the center of an annular carbide bit when it reaches the bottom of the borehole. Drilling then proceeds, cutting an annulus. The 75 mm (3 inch) center core is forced into the thin wall tube. When advancement is complete, the entire assembly is removed and the core shears off at the bottom of the thin wall core tube. The sample may then be stored and transported in the tube, or extruded at the drill site. The original bit is then replaced and lowered to the bottom of the borehole to resume drilling. This is a very time consuming procedure, as it requires removing and inserting the entire drill string twice, but it yields very good undisturbed soil samples. This method is not used in very stiff soils or rock. Fig. 7.69 shows some Pitcher samples in the field.



Fig. 7.69 Pitcher samples.

- **Diamond core samples** are taken in hard formations, usually rock. The procedure for diamond coring is identical to Pitcher sampling, except that a diamond core barrel is used. It also cuts an annulus while retaining the center core inside the core barrel. As with the Pitcher sample, this is a very time consuming procedure, as it requires removing and inserting the entire drill string twice, but is the only way to obtain samples in hard rock. Continuous coring provides a complete undisturbed record of the formations the borehole passes through. There are several ways of performing continuous coring; one method is referred to as “wireline” sampling. This, as well as most continuous methodologies, allow for the mounting of a variety of annular bits at the bottom of the drill string as well as for the exchange of the center portion of the bit from cutter to sample tube via a lightweight wireline cable through the center of the drill string. This permits the retrieval of cores without removing the drill string. This is a superior methodology for deep (>200m) boreholes where the larger drill rigs required to support it are justified.

Casing

A plastic (PVC, poly-vinyl-chloride) cased borehole is recommended for installations to 250 m depth. Medium-walled casing (“Schedule 40” in US standards) is acceptable to about 50 m depth; thick-walled (“Schedule 80”) should be used for installations between 50 and 250 m. Steel casing is recommended for deeper installations. As discussed elsewhere in this Manual, the Kinometrics FBA-23DH and its associated installation equipment are designed for use with Schedule 40 PVC casing. The bottom of the casing is closed with a slip cap. In the United States, this casing is typically supplied in 20 foot lengths with “bell-end” sockets molded at one end to receive the straight “spigot” end of the next casing section. Other sizes and forms of casing may be used but will require modification of associated installation items. Magnetic casing materials must not be used in conjunction with the flux-gate magnetometer compass option.

7. Site Selection, Preparation and Installation of Seismic Stations

Joining of PVC casing sections is done using a solvent glue. A primer is used to clean and etch the surfaces to be joined before the glue is applied. Low temperatures can significantly degrade the quality of a solvent joint, as can the presence of water on the joint surfaces. If temperatures are below 0 degrees C, a low temperature solvent glue should be used. More expensive screw-joint casing can be used as an alternative.

Installation of the casing, except in the shallowest holes, requires filling the casing with water, sometimes drilling fluid, to negate the buoyancy of the casing column thus allowing the casing to be pushed down into the fluid filled borehole, usually by hand. In addition, fluid inside the casing equalizes internal and external pressures, preventing the collapse of the casing due to external fluid pressure in deep boreholes (greater than 100 m).

Attempting to push empty casing into a fluid filled borehole with the weight of the drill rig causes casing to "snake" in the borehole, making accelerometer installation more difficult, as well as increasing the risk of damage to the top of the casing section being forced down or by telescoping an uncured glued joint.

Joining PVC casing by the use of screws in conjunction with gluing is not recommended, due to the potential for protrusion through the interior wall and subsequent damage to the cable during installation, as well as providing a path for leakage of water out of the casing following installation. If screws are used, only stainless steel screws set partially through the casing should be used. Pilot holes should be drilled in the casing after gluing to prevent fracturing of the casing during screw emplacement.

Grouting

Grouting the well casing involves filling the annular space between the casing and the borehole wall with a suitable slurry of cement or clay. For borehole accelerometer installations it is critical that this process is done with care, to ensure that the casing is well-coupled to the native soil or rock.

The grout is pumped into place through a small diameter pipe, usually a 25mm (1 inch) galvanized steel called a "tremie tube", lowered into the borehole between the casing and the borehole wall. When the end of the pipe reaches the bottom of the borehole, drilling fluid is circulated through the tremie tube to establish a clear path for the grout, and to clean the bottom of the borehole of any settled material. The grout is then pumped down to the bottom of the borehole, where it displaces drilling fluid out of the top of the borehole. The pumping may be done by the pump on the drill rig, or by a separate grout or concrete pump. When the drilling fluid is completely displaced and grout is flowing from the top of the borehole, the pump is stopped and the tremie tube withdrawn, disassembled and cleaned. Many U.S. municipalities require that the volume of grout placed be recorded and that it meet or exceed the volume calculated for the annulus. In some deep boreholes, grout will be placed in several separate loads or "lifts" to reduce the pressure exerted on the pipe by the liquid grout, as discussed later. This is usually scheduled as one lift per day.

Local codes usually require a sanitary seal of cement grout in the top 15m of a well, and seals between all aquifers penetrated by the well. The other areas may be filled with sand or gravel, but it is generally cheaper just to fill the entire annular space with cement grout. This will also make the eventual abandonment of the well (which can require another permit) much simpler.

7.4 Seismic station site preparation, instrument installation and shielding

Common grouting practices primarily center on the use of cement and water (“neat cement”), although the slurry may also contain sand, bentonite clay, or hydrated lime in certain situations. For downhole installations a mix of 400kg (20 U.S. sacks) of Portland cement type A or B per cubic meter of grout works well. Addition of 5kg of bentonite clay per cubic yard will ease the pumping of the grout into deep boreholes.

It is important to recognize that cement grouts exert greater collapse pressure on casing than water or drilling fluid. Installing grout 60m at a time for Schedule 40 PVC pipe provides a safety margin against casing collapse for the added effect of softening of the pipe by the heat of cure of the grout.

Other methods of placing grout, for example through a one-way valve in the bottom of the casing, are sometimes used but are generally considered to be less reliable. Be sure that the drilling contractor is completely comfortable with whatever method is to be used.

7.4.6.4 Geotechnical/Geophysical measurements

The primary motivation for installing downhole accelerometers is to increase understanding of the contribution of site response to the earthquake ground motion. Often the measurements of site response will be accompanied by analytical studies. Detailed understanding of the subsurface geology and soil/rock properties is necessary for such analytical studies. A good example of the kinds of site characterization data needed for strong-motion site response studies can be found in the ongoing project “Resolution of Site Response Issues in the Northridge Earthquake – ROSRINE” (see <http://geoinfo.usc.edu/rosrine>).

The basic site geology provides the primary description of the site. Information obtained during drilling (through observation and soil sample collection) will augment any prior geological knowledge of the general area. Normal laboratory testing of soil samples (disturbed or undisturbed) will confirm soil/rock types. Borehole and surface geophysical measurements can also assist in determination of site geology.

In addition to the site geology, dynamic soil and rock properties are needed for modeling of earthquake site response. The primary modeling properties are density, dynamic modulus, and damping (Q-value). The latter two properties are nonlinear functions of strain. These properties are obtained by laboratory testing of undisturbed samples and by one or more surface or borehole geophysical measurements of shear-wave velocity.

This Chapter gives a brief overview of the most common geological and geophysical measurements used in conjunction with borehole accelerometer installations to determine site geology and dynamic soil/rock properties.

Literature search

In most populated areas there will have been previous geological studies of the region and perhaps even local environmental, ground water, or planning studies. These can contain a wealth of information that will assist in site response studies. Planning for a borehole accelerometer installation should include a thorough literature search for such previous studies.

7. Site Selection, Preparation and Installation of Seismic Stations

Potential sources of information on a regional basis are government geological or natural resources agencies. An example is the U.S. Geological Survey. For local studies, sources of information are the local government planning agency, local universities, private water companies, and even local water well drilling companies. A literature search can be a very inexpensive source of information on site geology and even subsurface soil and rock properties.

Pre-installation geophysical studies

Before site selection and borehole drilling, geophysical methods can be used to obtain a more detailed understanding of the site geology and subsurface properties. A good review of methods for site characterization is found in ASTM Standard D420-98 “Guide to Site Characterization for Engineering, Design, and Construction Purposes” and in ASTM Standard D6429-99 “Standard Guide for Selecting Surface Geophysical Methods” (see <http://www.astm.org>). For borehole strong-motion array applications, common methods are:

- seismic reflection;
- seismic refraction;
- resistivity profiling;
- cone penetrometer.

Seismic reflection and refraction are two techniques for using surface measurements to determine the seismic wave velocity structure of the subsurface geology. Both use a surface source of energy (mechanical or explosive) and instrumentation for measuring travel times of seismic waves at various distances from the source. Inverse analysis of these travel times provides an estimate of the seismic wave velocities of soil and rock layers. These methods can provide a cost-effective determination of general soil/rock layer properties, bedrock depth, and water table depth over a wide area.

Resistivity profiling is another surface technique for measuring the electrical properties of the subsurface geology. The electrical field from a surface AC or DC current source is measured at several locations. Inverse analysis is then used to estimate the resistivity of the subsurface soil or rock. This method can assist in both shallow (< 100 m) or deep (> 100 m) geological studies of a site.

The previous methods have all been noninvasive surface techniques. Initial geological studies of a potential borehole accelerometer site can also include the invasive techniques of cone penetrometer studies. These allow detailed soil/rock type determination at a specific location. A cone penetrometer (a metal probe pushed into the soil) can also obtain information about shallow (< 30 m) soils. Exploratory drilling can also be used in these initial site characterization studies.

Lithology logging

An experienced geologist should be present during drilling to determine the soil and rock classification. This is done by observing the drill cuttings, the samples, and the action of the drill rig. A good procedure for such lithology logging exists in the ASTM Standard D5434-97 “Standard Guide for Field Logging of Subsurface Explorations of Soil and Rock” (see <http://www.astm.org>).

7.4 Seismic station site preparation, instrument installation and shielding

Laboratory testing of soil samples

Samples obtained during drilling are useful in determining the soil type and soil properties. Basic geotechnical soil properties can be determined by simple laboratory testing, including:

- moisture content;
- dry density;
- LL/PL; and
- void ratio (porosity).

These simple soil measurements can be performed by most commercial or university soil laboratories.

Dynamic laboratory testing, however, requires a much more skilled and specialized laboratory and very high quality undisturbed samples. Dynamic properties of primary interest for earthquake site response analysis are soil shear modulus and material damping ratio (in shear) and their variations with:

- shear strain;
- effective confining pressure;
- loading frequency;
- loading duration; and
- number of load cycles.

Dynamic testing should be performed using triaxial resonant column, simple shear, or torsional shear methods. Appropriate strain ranges for earthquake response studies are 0.0001% to 0.1%. Appropriate frequency ranges are <1Hz to 200Hz. Further details of dynamic testing can be found in the book *Soil Behaviour in Earthquake Geotechnics* by Ishihara (1996) and other textbooks on soil dynamics.

Borehole geophysical measurements

There are many geophysical measurements available for characterization of the soil and rock properties in a borehole. These can measure chemical, electrical, radiation, and mechanical properties. All require specialized instrumentation and a skilled, experienced field geophysicist.

The chemical, electrical, and radiation properties are generally not of interest in an earthquake site response study, except as they are useful in determining soil and rock types. Sometimes resistivity and natural gamma emission measurements in an uncased borehole (before installing PVC casing) can be useful in determining boundaries of clay, sand, and rock layers

Of particular interest to site response studies are the mechanical properties of the soil and rock, primarily the P-wave and S-wave velocities versus depth (velocity profile). Borehole methods for velocity profile measurement are:

- downhole (vertical seismic profiling);
- crosshole; and
- suspension.

7. Site Selection, Preparation and Installation of Seismic Stations

All three methods use a mechanical or electromechanical source to produce seismic waves, and one or more sensors (generally geophones) and a recording system to measure the induced ground motion. Details of these methods can be found in the book by Kenji Ishihara (1996).

For the downhole test, an impulsive energy source at the surface near the borehole top produces seismic waves which propagate radially. These can be either P waves or SH waves, depending upon source configuration. One or more sensors are installed in the borehole at known depths. The source and sensor signals are recorded, and the travel time of the first wave arrival is measured as a function of depth. The instantaneous slope of the travel time vs. depth curve is the reciprocal of the wave velocity at that depth.

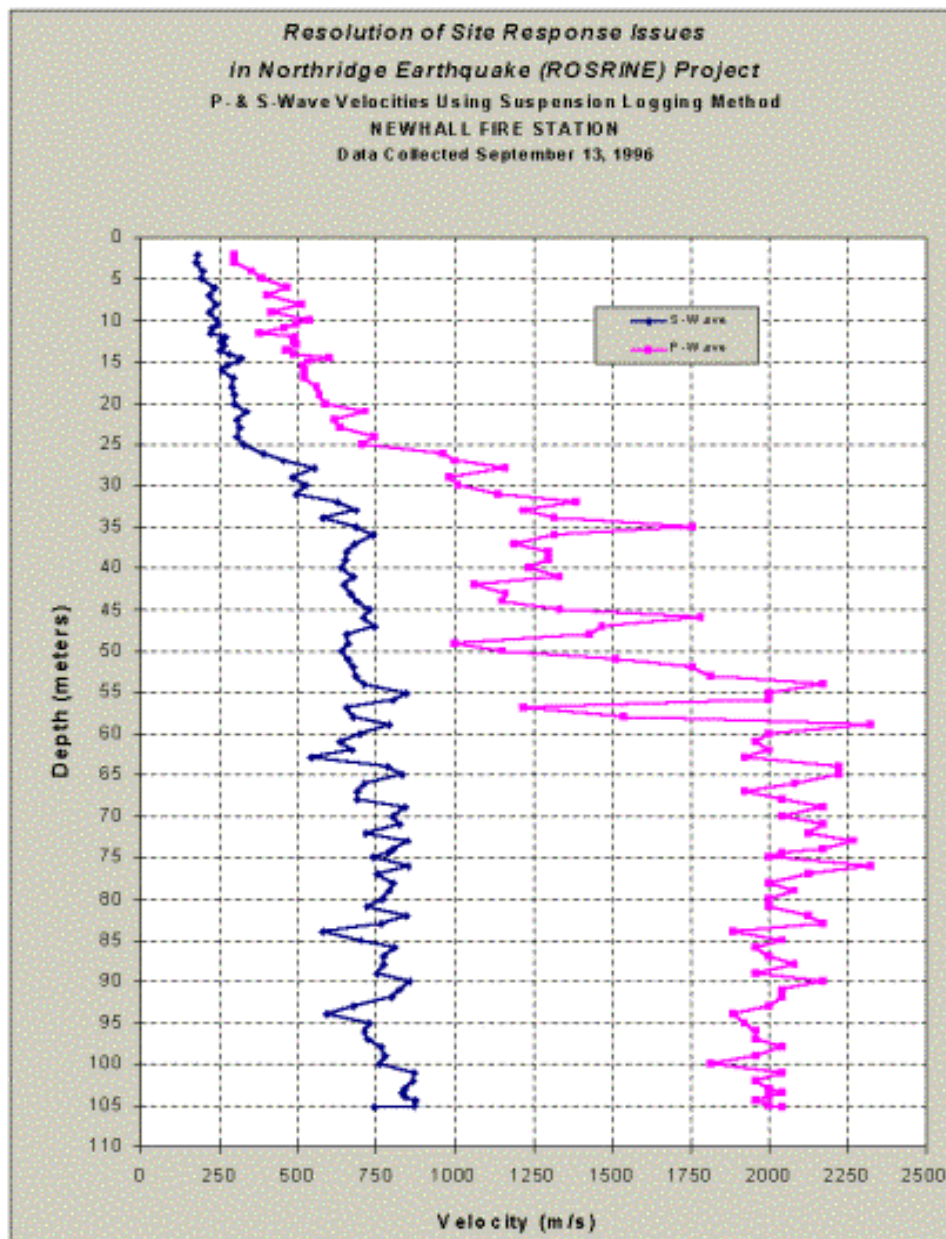


Fig.7.70 Velocity profiles for P waves (red curve) and S waves (blue curve) at a strong-motion site.

7.4 Seismic station site preparation, instrument installation and shielding

The crosshole test requires two or three adjacent boreholes separated by known distances. A source is installed in one borehole and receivers in the others, all at the same depth. The travel time of the generated seismic waves between boreholes is measured, and the velocity calculated by dividing the separation distance (at depth) by the travel time. This method requires careful control over the source and receiver depths, and detailed measurement of borehole separation versus depth. Both the downhole and crosshole methods are normally performed in cased boreholes. The suspension method, however, can be used in either cased or uncased boreholes. It consists of a single probe about 5 meters long, with an impulsive source at the bottom and two sensor sets ("receivers") near the top, separated by 1 meter. The source transmits energy through the borehole fluid to the borehole wall where it is transformed into both P and S waves. These are detected by both receivers, and the difference in arrival times is measured. Dividing the 1 meter separation by the travel time differences gives the P- and S-wave velocities for the 1 meter interval between sensors. Fig. 7.70 above is a plot of a velocity profile measured with the suspension method.

7.4.6.5 Installation procedure

This section describes the careful installation of a downhole strong-motion sensor. Accompanying this procedure will be a procedure for installation of the surface sensors, surface cabling, recording station, and other infrastructure; these are discussed in more detail in earlier sections of 7.4.

Discussed below are sensor installation, orientation, operational checkout, evaluation period, coupling/locking, and documentation/reporting.

Sensor installation

After completing functional tests of the sensor, the wellhead box, the cables and recorders, and calibrating the internal compass, the borehole package can be installed. The following procedure assumes a standard installation of a Kinometrics FBA-23DH sensor with glass beads or gravel, and the internal compass for orientation. Installation for other downhole strong-motion sensors will be similar.

If not already done, the borehole should be filled with clean water to within 6m of the top. Filling completely will make installation easier since the water gives the cable near- neutral buoyancy, allowing a single person to handle the weight. In any case, consideration must be given as to where the displaced excess water will go when the package and cable are lowered into the hole.

This is the main reason a drain should be provided for the wellhead box, even though it is sealed from weather, and also why sufficient slack surface cable should be provided in the wellhead box to allow the contents of the wellhead box to be temporarily moved out of the way. In a sealed system, it would be best if the drain were sealed off after performing this function, to prevent moisture from entering the wellhead box after installation is complete. If the borehole has already been checked, the package can be lowered smoothly using the cable, being careful not to allow the cable to slip away. Fig. 7.64 shows this procedure in action. It is good practice to have a second person feeding the cable to the person lowering the package.

7. Site Selection, Preparation and Installation of Seismic Stations

If the borehole has not been checked previously, care should be taken to "feel" for any constrictions in the casing which could signal trapping of the package. If such is felt, it is wise to move slowly, and then try coming back up every meter or so until the obstruction is passed. Check the total depth of installation by using the depth markers provided on the borehole cable (if available). Continue until the sensor is resting on the bottom of the borehole.

Orientation

This procedure assumes an internal compass in the sensor package. Once the sensor package has reached the bottom of the casing, apply power to the compass and rotate the package using the cable until the desired orientation is reached. Feed slack cable into the casing to help hold the sensor in position. Allow the package to rest on the bottom to get a steady reading, and measure the accelerometer offsets. Record the offsets carefully.

The acceptable DC offset depends on the final gains expected to be used with the system. If possible, it is desirable to keep the offsets to less than 25 millivolts. To accomplish this, compensating offsets will usually need to be applied to counteract the combination of residual factory offsets and vertical misalignment of the casing at the bottom of the borehole. In other words, if an offset of +150 millivolts is recorded for the horizontal sensor oriented east at the bottom of the hole, then when the package is removed to the top, the offset for the same sensor must be mechanically adjusted so that -150 millivolts is added to whatever the offset is before the adjustment. This must be done carefully so that the package orientation doesn't change from the beginning of the adjustment to the end. This is where some sort of test fixture is helpful to hold the package steady. This procedure may need to be repeated in order to get it right. In fact, expect to repeat this procedure once more after 30 or 60 days of operation before installing the backfill material, after the sensor has adjusted completely to the temperature at the bottom of the borehole. This requires opening the sensor package which can be difficult in field situations. Requiring the driller to produce a vertical borehole within a predetermined tolerance can often avoid this.

Operational checkout

Once the package has been installed and oriented with acceptable DC sensor offsets, one should connect the recording system and check for proper sensor operation. This operational checkout should follow manufacturer's procedures, and results of the system test should be compared with the factory reference test.

Evaluation period

It is recommended that the array be operated for at least 30 days and as much as 60 days prior to installation of the backfill material. This period is needed to eliminate any initial startup problems, and allow the sensors to achieve steady state temperature response. During this period, the sensor package will rest at the bottom of the borehole. While this is inadequate coupling for large earthquakes, it should prove adequate for small events.

Preamplifier gains in the recording system should be set 10 to 100 times higher than normal in order to record as many small events as possible during this initial test period. Data should be reviewed, and the sensor removed and checked if any problems or questions arise.

7.4 Seismic station site preparation, instrument installation and shielding

Coupling/Locking

Once the downhole accelerometer has functioned properly for a period of 30 to 60 days, it is time for installation of the coupling or locking device. If a permanent locking method (i.e., grout or cement) is to be used, one should carefully install the locking material without disturbing the sensor orientation. If a wedge-type, pneumatic, or hydraulic locking system is used, it should be tightened to final specifications. If sand, gravel, or glass bead backfill is used, proceed with backfilling. Resist the temptation to pull on the cable afterwards to confirm the security of the system. It is possible to shift the package enough to disturb the orientation, and not be able to get it right without pulling it out, or you could lose backfill material to the bottom of the borehole. It is better to trust the process, and assume the material is in position. The proof is in the results.

Documentation/Reporting

Excellent documentation is very important to preserve the details of construction and installation for better interpretation of the data. Most important is the proper organization and use of calibration data. It is suggested that a formal Commissioning Report be created to preserve this installation information. Photographic documentation is also important. All documentation should be preserved along with the data for use in future data analyses.

7.4.6.6 Costs

A borehole strong-motion array can be quite expensive when all the needed work is considered. Besides the cost of instrumentation, there are the planning, preparation, site studies and installation costs. One could omit some of the planning and site characterization costs (this is often done), but at a significant cost in understanding of the resulting strong-motion data.

Costs will vary considerably in different parts of the world. With this proviso, below is a commercial cost estimate for a representative borehole strong-motion array with one borehole at 100 m depth and one surface sensor. The year 2000 costs in US\$ in the U.S./California are:

- Instrumentation (one borehole accelerometer, one surface accelerometer, one 6-channel seismograph) - \$20,000;
- Downhole sensor cable - \$4,000;
- Array infrastructure (power, enclosures, communications, etc) - \$10,000 ;
- Planning and initial studies (includes one seismic refraction line) - \$10,000;
- Borehole preparation - \$15,000;
- Geotechnical/Geophysical Studies (includes lab testing of soils) - \$15,000;
- Array construction and installation - \$10,000;

TOTAL COST = \$84,000.

7. Site Selection, Preparation and Installation of Seismic Stations

Recommended overview readings (see References under Miscellaneous in Volume 2)

Havskov and Alguacil (2002)

Special References

Consortium of Strong Motion Observation Systems (COSMOS) <http://www.cosmos-eq.org>

Earthquake Engineering Field Investigation Team (EEFIT) (1993). EEFIT field investigations: Objectives and methods, leaflet.

Guide to Site Characterization for Engineering, Design, and Construction Purposes, ASTM D420-98, <http://www.astm.org>

Guidelines for Determining Design Basis Ground Motions, Report RP3302, March, 1993, Electric Power Research Institute, Palo Alto, CA.

Institute for Crustal Studies, University of California Santa Barbara, <http://www.crustal.ucsb.edu>

Lightning Protection Facts and Fallacies, Polyphaser Corporation, <http://www.polyphaser.com/download/PTD1021.pdf>

Resolution of Site Response Issues in the Northridge Earthquake (ROSRINE), Nigbor et al., <http://geoinfo.usc.edu/rosrine>

Standard Guide for Selecting Surface Geophysical Methods, ASTM D6429-99, <http://www.astm.org>

The EUROSEISTEST Project, <http://daidalos.civil.auth.gr/euroseis>

UCB, S. L., 1997. Guidelines for installing broadband seismic instrumentation. <http://www.seismo.berkeley.edu/seismo/bdsn/instrumentation/guidelines.html>.

Acknowledgments

The authors of Chapter 7 are thankful to Ahmed Elgamal, C. R. Hutt, Dieter Mayer-Rosa, Jamison Steidl, Rod Stewart and Peter Zweifel, for their reviews and suggestions which have helped to improve the original text. The non-native English-American contributors to this Chapter owe particular thanks to Rod Stewart for his careful English proof-reading of the whole text. W. Hanka, author of section 7.4.4, also thanks M. Brunner for many excellent ideas and carrying out the shielding experiments and K.-H. Jaeckel for very fruitful discussions around this topic.

8

Seismic Networks

Amadej Trnkoczy, Jens Havskov and Lars Ottemöller

8.1 Introduction

In this Chapter, a brief description of seismic systems will be given. It is intended to provide an overview on basic ideas in seismometry and describes the existing possibilities in the market (year 2000). For more thorough information about particular elements and concepts in seismometry and seismic recording systems see Chapters 5 and 6, respectively. Note that this Chapter shares most of the figures and some paragraphs with Havskov and Alguacil (2002). Since one of the authors is the same in both, no acknowledgments are given.

Before 1960, there were generally only individual seismic stations operating independently. Each station made its observations, which were usually sent to some central location. If several stations were operating in a country or region, it was possible to talk about networks. However the time lag between recording and manual processing were so long that such networks are not considered seismic networks in the modern sense. In the 1960s, 'real' seismic networks started operating. These were mainly networks made for microearthquake recording, and the distances between stations were a few kilometers to a couple of hundred kilometers. The key feature used to define them as networks was that the signals were transmitted in real time by wire or radio link to a central recording station where all data was recorded with central timing. This enabled very accurate relative timing between stations and therefore also made it possible to make more accurate locations of local earthquakes. Recording was initially analog and, over the years, it has evolved to be nearly exclusively digital. Lee and Stewart (1981) provide a good general description. With the evolution of communication capabilities to cover the whole world, seismic networks can now be local, regional or global. The distinction between networks is primarily no longer due to differences in data transfer, accuracy of timing, or time lag between data acquisition and analysis, but rather the scope of investigation, spatial resolution, and quality of data in terms of frequency content and dynamic range.

During the last two decades of the 20th century, numerous seismological projects have been undertaken in several countries. Unfortunately, when viewed from the latter half of the 1990s, one must acknowledge that many have not fulfilled their expectations. The main reason for this was probably a lack of knowledge about networks, instrumentation and data processing techniques. Yet such specialized knowledge is unquestionably required if one expects to establish and operate a truly beneficial seismic network. For that reason, in addition to the general description of networks, this document will also outline the basic steps to follow in order to establish a new seismic network.

8.2 Seismic network purpose

The three main purposes of seismic networks are for seismic alarm, or general or specific seismic monitoring, and research on the interior of the Earth. However, the very first and most basic goal is the determination of accurate earthquake locations. For that purpose we generally need at least three stations (Fig. 8.1).

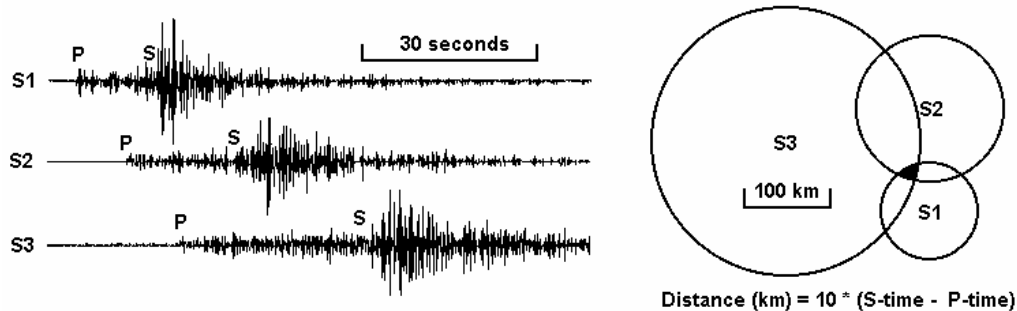


Fig. 8.1 Location by the circle (or arc) method. To the left is shown the seismograms at stations S1, S2 and S3 recording a local earthquake. Note that the amplitude scales are different. The stations are located at S1, S2 and S3 (right). The time separation between the P- and S-wave arrivals multiplied by the ratio $v_P v_S / (v_P - v_S)$ of the P- and S-wave velocities gives us the epicentral distance (distance from the station to the projection of the earthquake's focus at the surface). The epicenter is found within the black area where the circles cross. These circles will rarely cross at one point, which indicates errors in the observations, errors in the model, and/or a subsurface depth. With only two stations, we see that there are either two possible locations, or no possible location if the two circles do not intersect. With more than three stations, the uncertainty in location decreases. Note that the “rule-of-thumb” formula given for the distance calculation in the lower right of the figure is for Sn-Pn only.

The seismic alarm function, which requires an immediate response after strong earthquakes, serves civil defense purposes with the goal of mitigating the social and economic consequences of a damaging earthquake. Governments, which often finance new seismic networks, emphasize this goal.

Seismic monitoring aides in the long-term mitigation of seismic risk in a region or country as well as resolving the seismotectonics . Seismic hazard maps of the region may be made which enable the development and implementation of proper building codes. In the long term, building codes are very effective in mitigating seismic risk.

Some cases of seismic monitoring related to seismic risk caused by human activity are of special political concern. This includes monitoring for seismicity induced by large dams or around large mines. Monitoring of seismicity in a volcanic region (see Chapter 13) is also dedicated to volcanic risk mitigation through the prediction of eruptions. Another important function of seismic networks is for explosion monitoring, particularly underground nuclear explosions. Seismic networks are one of the most important tools used in monitoring the international nuclear test ban treaty.

Local, regional and global research into the Earth's interior is the oldest goal of seismology. Seismic networks are and will be probably forever the only tool that enables study of the detailed structure and physical properties of the deeper Earth's interior.

The purpose of a new seismic network largely defines the optimal technical design for it. Not every design serves equally well for different goals, and many fail completely for some particular goals. However, modern networks are more capable of dealing with several goals than older networks, which were more narrowly focused due to technical limitations.

8.3 Seismic sensors

8.3.1 General considerations

The choice of an appropriate sensor depends on the application, be it local, regional or global monitoring. The most important factors to consider for a particular application are:

- type of the sensor - accelerometer versus seismometer;
- number of sensor components per seismic station;
- sensor's sensitivity and dynamic range;
- sensor's frequency range of operation; and
- exactness of sensor's use (i.e., how demanding are its transportation, handling, installation, calibration, maintenance etc.).

8.3.2 Seismometers and/or accelerometers?

During most damaging earthquakes, weak-motion records recorded with seismometers installed close to the epicenter are clipped. Seismometers are very sensitive to small and distant events and are thus too sensitive for strong-motion signals. This was a very relevant aspect at the time of analog recordings. Traditionally, accelerometers have been considered for strong motion only and seismometers for weak motion. However, the latest generation accelerometers are nearly as sensitive as standard short-period (SP) seismometers and also have a large dynamic range (up to more than 110 dB; e.g., the Episensor ES-T in DS 5.1). Consequently, for most traditional SP networks, accelerometers would work just as well as 1-Hz SP seismometers although the latter are cheaper. In terms of signal processing, there is no difference in using a seismometer or an accelerometer.

In high seismic risk areas where the main goal of networks is future seismic risk mitigation, strong-motion recordings play an important role, and two sets of sensors will have to be installed so that the system never clips. Although there are significant differences in strong and weak-motion network designs, today both types of sensors are frequently integrated into a single system. Six-channel data loggers with three weak and three strong-motion channels are cost effective and are the current state-of-the-art. They are capable of covering the whole dynamic range of seismic events, from the lowest seismic noise to the largest damaging events. The relative merits of these systems, as well as specific technical details of strong-motion networks, are not addressed in this Manual. An exception is section 7.4.6 on borehole strong-motion array installations.

8.3.3 One- and three-component seismic stations

Historically, many seismic stations and networks used single-component sensors - usually vertical seismometers. Many of them still operate. This was the case because the equipment was analog and the record was often on paper. If three components had been used, three times the amount of equipment would have been required but the information generated would not have been three times more valuable. It was also very difficult, if not impossible, to generate a ground-motion vector from three separate paper seismograms.

Today, in the era of digital recording and processing of seismic data, the situation is different. The price/performance ratio is much more favorable for three-component stations. Most data recorders and data transmission links are capable of accepting at least three channels of seismic data. The cost of upgrading the central processing facilities to accommodate an increased number of channels is relatively small and ground-motion vectors may be generated easily with computer software.

Since ground motion is essentially a vector that contains all of the seismic information, and considering the fact that many modern seismological analyses require this vector as input information, one-component stations are no longer a desirable choice for new installations (not considering seismic arrays which are discussed in Chapter 9). On the other hand, one-component seismic stations are still a choice where communication capability and economy are limiting factors.

8.3.4 Sensitivity of seismic sensors

Strong-motion accelerometers are relatively insensitive since they are designed to record the strongest events at small hypocentral distances. Their maximum scale acceleration is usually expressed as a fraction of the Earth's gravity, g (9.81 m/s^2). Accelerometers with 0.25, 0.5, 1, 2, and 4 g full-scale sensitivity are available today. However, modern accelerometers have excellent dynamic range and good signal resolution. They will produce valuable records of smaller events within the close-in epicentral region as well, where seismometer records may still be clipped unless a high-dynamic range recording system is used. Of course, one should order full-scale sensitivity, fitting to the maximal expected acceleration at the sites of the new network. Ordering too sensitive accelerometers may result in clipped records of the strongest and most important events in the region. Accelerometers with too high full-scale range cause diminished sensitivity and needlessly reduce data acquisition resolution of all future records.

Weak-motion sensors - seismometers - are usually orders of magnitude more sensitive, however, they can not record as large of an amplitude as an accelerometer. They can record very weak and/or very distant events, which produce ground motion of comparable amplitudes to the background seismic noise. Some seismometers can measure ground motion smaller than the amplitudes of the lowest natural seismic noise found anywhere in the world. If one plans to purchase especially sensitive sensors, one must be willing and able to find appropriate, low seismic noise sites for their installation. Standard SP seismometers are in fact so sensitive that they will be able to resolve the ambient Earth's noise in nearly all networks where they are installed. If the sites are not appropriately chosen and/or have high seismic noise (natural and/or man made), a modern, highly sensitive seismometer is of little use, and a much cheaper sensor, like an accelerometer or a geophone, might be used. For many networks

with a moderate background noise, an 0.25g accelerometer would provide sufficient sensitivity and at the same time give a large dynamic range.

8.3.5 Frequency range of seismic sensors

Today's weak-motion sensors are roughly divided into three categories.

The short-period (SP) seismometers measure signals from approximately 0.1 to 100 Hz, with a corner frequency at 1 Hz. They have a flat response to ground velocity for frequencies greater than this corner frequency. Typical examples are the Kinometrics SS-1, the Geotech S13, and the Mark Products L-4C. The 4.5-Hz exploration-type geophone also belongs in this group. This sensor provides reasonably good signals down to about 0.3 Hz at a fraction of the cost of the 1.0-Hz sensor.

The broadband sensors (BB) have a flat response to ground velocity from approximately 0.01 to 50 Hz. Typical examples are the Guralp CMG40T seismometer with frequency range from 0.03 to 50 Hz, and the Wieland-Streckeisen seismometer STS2 with a frequency range from 0.008 to 40 Hz (see DS 5.1).

The very broadband seismometers (VBB) measure frequencies from below 0.001 Hz to approximately 10 Hz. Typical examples are the Wieland-Streckeisen STS1 seismometer with frequency range from 0.0028 to 10 Hz and the STS2; see 7.4.4. and DS 5.1) They are able to resolve Earth's tides.

On all these different seismometers more information is given in Volume 2, DS 5.1.

The frequency limits shown above are the corner frequencies of the sensors' frequency response function (FRF). This means that analysis below low-frequency corner and above high-frequency corner is sometimes still possible. How much we can extend this range depends on the sensor design and instrumental self-noise (see Chapter 6). The choice of the right sensor depends on its seismological application. In general, the flat portion of the frequency response function should cover the range of frequencies, which are generated by particular seismic events of interest or which are important in a particular phenomenon studied (see Fig. 5.6).

Strong-motion sensors (accelerometers) measure seismic signals between DC and 200 Hz (a typical example is the Kinometrics' EpiSensor; see DS 5.1). However, they differ from the weak-motion sensors in that their output voltage is proportional to ground acceleration and not to ground velocity as it is usual for seismometers. For this reason, they stress high frequencies and attenuate low frequencies as compared to seismometers. Some strong-motion sensors in the market have no DC response but a low-frequency, high-pass corner at around 0.1 Hz. These sensors have an important drawback: their records can not be used for residual displacement determination, either of the ground in the near field of very strong earthquakes, or of permanently damaged civil engineering structures after strong events. They are considered as less appropriate for seismic applications where low-frequency signals are important. The following table should help in the selection of appropriate sensors. It shows some typical seismological applications and their approximate frequency range of interest.

8. Seismic Networks

Tab. 8.1 Application description and approximate frequency range of interest.

Application	Frequency range (in Hz)
Seismic events associated with mining processes	5 - 2000
Very local and small earthquakes, dam induced seismicity	1 - 100
Local seismology	0.2 - 80
Strong-motion applications	0.0 - 100
General regional seismology	0.05 - 20
Frequency dependence of seismic-wave absorption	0.02 - 30
Energy calculations of distant earthquakes	0.01 - 10
Scattering and diffraction of seismic-waves on core boundary	0.02 - 2
Studies of dynamic processes in earthquake foci	0.005 - 100
Studies of crustal properties	0.02 - 1
Dispersion of surface waves	0.003 - 0.2
Free oscillations of the Earth, silent earthquakes	0.0005 - 0.01

8.3.6 Short-period (SP) seismometers

The SP sensors were historically developed as 'mechanical filters' for mitigating distracting natural seismic noise in the range 0.12 - 0.3 Hz. This noise heavily blurred small events on paper seismograms. However, with today's digital and high-resolution data recording and processing, this rigid 'hardware' filtering can easily be replaced by much more flexible computer processing. A need for sensors that filter seismic signals by themselves does not exist any more. In addition, when filtering the seismic signal with sensors, we irreversibly lose a portion of seismic information and introduce undesired signal phase distortion. Nevertheless, the SP seismometers, as well as the cheaper geophones, are still, and will remain in the future, a valid selection for several seismological applications, particularly for local seismology where low frequencies of seismic signal are not of major interest or do not exist at all.

Most SP seismometers are passive sensors with a flat response to velocity above the natural frequency. They are easy to install and operate and require no power, which allows use of smaller backup batteries for the rest of the equipment at remote station sites. They are relatively stable in a broad range of temperatures, which allows less exacting (and inexpensive) vault designs. The electronic drift and mass position instability usually associated with active sensors are typically not a problem. They are, in short, a very practical solution for all applications where seismic signals of interest are not expected to contain significant components below 0.1-0.3 Hz.

There now also exist active SP sensors in the market, which are either electronically extended 4.5-Hz geophones or accelerometers with electronically generated velocity output. These sensors are often cheaper and smaller. Their drawback is that they require power and are more complicated to repair. An example of such a seismometer is the Lennartz LE-1D (<http://www.lennartz-electronic.de/Pages/Seismology/Seismometers/Seismometers.html>).

8.3.7 Broadband (BB) seismometers

Today, the broadband sensors are a very popular choice. They provide complete seismic information from about 0.01 Hz to 50 Hz and therefore allow a much broader range of studies than the SP records. A single, high-performance BB seismic station can determine as much, if not more, information as several conventional SP seismometers measuring arrival time and first motion.

However, the BB seismometers are more expensive and demand more efforts for installation and operation than SP seismometers. The BB seismometers require a higher level of expertise with respect to instrumentation and analysis methods. They are active feedback sensors and require a stable single- or double-polarity power supply. They also require very careful site selection in a seismological-geological sense, a better-controlled environment in seismic vaults, and they are sometimes a bit tricky to install. Since they do not attenuate the 0.12 - 0.3 Hz natural seismic noise peak (see Fig. 4.7), their raw output signal contains much more seismic noise than signals from a SP seismometer. Consequently, useful seismic signals are often buried in seismic noise and can be resolved and analyzed only after filtering to remove the background noise. So, for all but the largest earthquakes, filtering is required even for making simple phase picks. BB sensors are often perceived as the 'best choice', however there are several examples of networks being installed with BB sensors where SP or strong-motion sensors could have served equally well the main task of the network, thereby avoiding costs in installation, maintenance and processing.

8.3.8 Very broadband (VBB) seismometers

The VBB sensors are utilized in global seismology studies. They are able to resolve the lowest frequencies resulting from Earth's tides and free oscillations of the Earth. Their primary purpose is the research of the deep interior of the Earth. Their only important advantage, however, as compared to BB seismometers, is their ability to record frequencies around and below 0.001 Hz. They are expensive, require very elaborate and expensive seismic shelters, and, as a rule, are tricky to install. They are ineffective for seismic risk mitigation purpose and some also lack frequency response high enough for local/regional seismology.

However, data from a VBB station is very useful to the international scientific seismological community. They are also excellent for educational purposes. For a large national project, installation of at least one VBB station is recommended and perhaps two to three in a very large country or region. Site selection and preparation for a VBB station requires extensive study and often expensive civil engineering work (e.g., Uhrhammer et al., 1998 and 7.4.4). The cost of preparation of a single good VBB site can exceed US\$ 100,000.

8.3.9 Long-period (LP) passive seismometers

The long-period passive sensors are not a suitable choice for new installations and are not sold anymore. These sensors have a corner frequency of 0.05 to 0.03 Hz and, in that respect, are inferior to most (but not all) BB sensors. Their dynamic range is in the order of 120 dB. An LP sensor with a 24-bit digitizer still makes an acceptable low-cost BB station provided the sensors and the vault are already available. However, nonlinear distortion of such an

installation may be problematic. Nevertheless, in the scope of new installations, long-period seismometers are of historical value only.

8.4 Seismic network configuration

8.4.1 Physical and virtual seismic networks

When the hardware connection among seismic stations is established, the next question is how the data are sent along the connection and what protocols are used for the units to communicate. This will define, to a large extent, the functionality of the seismic network.

In the days of only microearthquake networks and one-way data transmission (from stations to central-recording site), it was quite clear how a seismic network was defined. Today, the situation is more complex. Nowadays, more and more seismic stations are connected to the Internet or to the public phone system. Such stations usually have a local seismic signal recording capability and sometimes there is not any real-time data transmission to a central site. However, these stations still can be defined to be in a network since they are all connected to the global communication network. In principle, any networked computer can be used to collect data from a number of stations in what functionally is a seismic network. By defining a seismic network in this way, the distinction between local, regional, and global networks does not exist any more in terms of hardware, data transmission and acquisition, but is merely a question of how the data collection software is set up to handle communication, data collection and processing.

This means two types of seismic networks can be defined: physical and virtual.

A *physical seismic network* (usually local) consists of closely linked, remote seismic stations. The remote stations detect the ground motion and usually send data in real time to a central recording station for event detection and recording (see Fig. 8.2). This type of network covers both the old analog systems and the current digital systems.

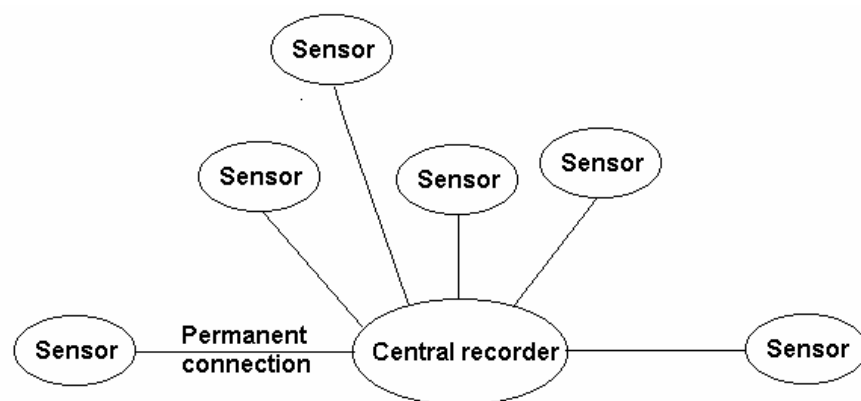


Fig. 8.2 Scheme of a physical seismic network. The sensors are connected to a central recorder through a permanent physical connection like a wire or radio link. The transmission may be analog with digitization taking place centrally, or an analog-to-digital converter (ADC) could also be placed at each sensor and the data transmitted digitally.

A *virtual seismic network* consists of seismic recorders connected to a global communication network or a public phone system (see Fig. 8.3). A recorder may be associated with a single seismic station or can be the central-recording site for a physical network. The remote recorders must be capable of local recording as the data are not sent to the central recording system in real time. The remote recorder must have a 2-way communication capability. The central recording station can manually or automatically connect to selected remote recorders and download triggered and/or continuous data and make intelligent evaluation of possible events.

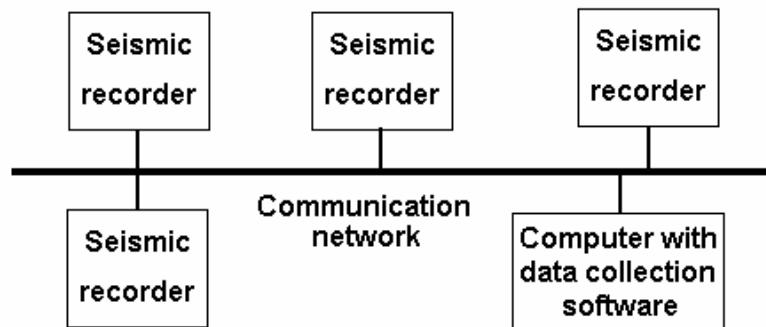


Fig. 8.3 Scheme of a virtual seismic network. The thick line is the communication network, which can have many physical implementations. The data collection computer collects data from some or all of the recorders connected to the network.

Both types of seismic networks might result in the same kind of output although the virtual network will deliver data with a larger time delay than most of the advanced physical networks.

8.4.2 Physical seismic networks

8.4.2.1 Stand-alone, central-recording, and network-based seismic systems

From the aspect of data transmission to the central-recording site, there are several basic concepts of the design of physical seismic networks.

In the simplest case, a seismic network is a group of stand-alone seismic stations with a local recording medium. Many of the older networks, particularly analog ones, are still of this type. The information is gathered in person, either by collecting paper seismograms or by downloading digital data from stations into a laptop computer. There exist no communication links from the remote stations to the data center. Data can be stored locally on a removable memory medium, like memory cards, DAT tapes, or removable hard or CD disk.

Such networks, of weak-motion type, are only suitable for low seismicity regions because of the small total amount of data acquired. However, they are used also often in strong-motion seismology where recordings are rare. Frequently, such networks are temporally established for aftershock studies or similar special research purposes, however, in these cases they require intensive human involvement to operate properly. As a permanent, national, or regional observatory seismic network, this design is rarely suitable.

8. Seismic Networks

The next level of network sophistication involves real time or near-real time data transfer from the remote stations to the central processing site. Data may be stored in 'event file' form or in the form of a continuous data stream. Networks in this group differ significantly in their capabilities, depending mainly on the trigger algorithm (if applicable) and communication links used. At present, these are the most frequent design.

The latest, most modern design concept of physical seismic networks is based on computer networks. Data transmission is done through public, governmental, or special users' wide area networks (WAN) or Internet. Event file seismic data as well as quasi-continuous data transfer is possible via the Internet today. These networks may work in an open architecture client/server environment. With such systems the 'central processing site' loses much of its meaning since data can be processed and/or archived at every authorized node of the WAN.

However, today, with computer-based seismic networks, the so-called 'last-mile' problem remains acute. The availability of the computer-network connection points and the indispensable remoteness of the seismic stations conflict with one another. The problem of transmitting seismic data to the nearest computer network node can be efficiently solved by short-distance spread spectrum RF links. Also, the time latency in such networks (data can be transmitted only in a near-real time manner with delays up to several tens of seconds) and their relative vulnerability to damaging events may represent a drawback if the emphasis is on seismic alarms.

Central recording and computer network-based physical seismic networks can use coincidence trigger algorithms in near real time (see 8.5.2) thus being very efficient in the detection of events. Virtual seismic networks depend on trigger algorithms that run at the remote seismic sites; so, a coincidence trigger on the central computer can only work after all trigger times have been received. Although this usually results in a significant number of false triggers on the field stations, the events detected by the virtual network will be the same as for the physical network, although delayed in time.

8.4.2.2 Proprietary versus standardized off-the-shelf hardware solutions

Another important issue with physical seismic networks is the hardware and software configuration. Most physical seismic networks today are made of proprietary hardware and software developed and manufactured by a few small companies specializing in seismology. Only recently have technical solutions utilizing little proprietary hardware and software become available. While the sensors and data loggers are still developed and manufactured by seismological equipment manufacturers, the remaining items are standard, commercially available products used in other fields and manufactured by much larger companies. Data transmission is done by commercially available and standardized software with the aid of off-the-shelf hardware components.

Using off-the-shelf hardware and software significantly reduces the cost of network ownership, increases reliability, and guarantees flexibility. The user is much less dependent on an individual manufacturer of the seismic system. Long-term maintenance and upgrading of the system is also much easier because proprietary electronic equipment is very hard to maintain and has an average 'life time' of only three or four years. Seismic equipment manufacturers try to support their users as much as possible, sometimes through expensive

'life time' buys of particular electronic components and parts. However, the life expectancy of modern electronic devices is shorter and shorter in spite of these efforts. Given this situation, the use of off-the-shelf standardized products, as opposed to proprietary products, is less costly because new products coming in the market are usually downward compatible. This is practically never the case with new designs from seismic equipment manufacturers.

8.4.3 Virtual seismic networks

8.4.3.1 General considerations

In the virtual network mode, network setup is dependent on the mode of communication. In general, all field stations are connected to the Internet and/or the public telephone system and there might not be any *a priori* defined network since public protocols are used. In the case of most commercial systems, the stations can only be reached by communication from a dedicated central computer using proprietary software. In both cases, the systems do not operate in real time. The network operation usually follows the same principles as for physical networks with some additional capabilities. A common scenario is:

The central computer copies detection lists and/or automatic phase picks from the remote stations (Fig. 8.4). Based on the detection lists and trigger parameters, events are declared. Here two options exist: either existing event waveforms are copied from the field stations to the central computer and no waveforms are copied from stations not triggered, or (assuming the field stations have ring buffers with continuous data), the same time interval of waveform data is extracted from all remote stations. In this way, waveform data from all stations in the network (as for the physical network) are gathered at the central station.

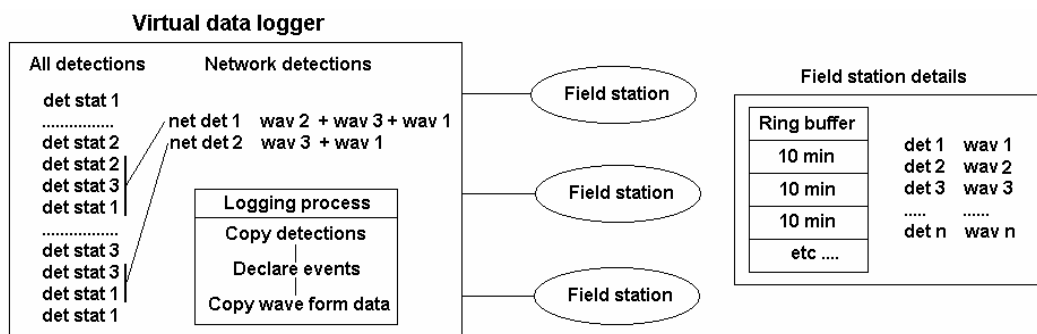


Fig. 8.4 Typical virtual data logger. The field station (right) has a ring buffer with files or segments 10 min long. It also has a list of detection times with associated parameters (det 1, det 2, etc.) and corresponding waveform files (wav 1, wav 2, etc.). The virtual data logger (left) has the following logging process: first, to get a time ordered copy of the detection times from all stations (det stat 1, det stat 2, etc, ... indicate a longer time window); second, based on these, a potential event is declared if at least two detections occur within a short-time window (net det 1 and net det 2); and third, in that case the waveform files are copied to the virtual data logger. In this example, the ring buffer is not used.

The speed of data collection depends on the communication system and the configuration of the data collection system. In a typical scenario, all data collection is controlled from the central computer and data is collected at the request of the central computer. Example: We

8. Seismic Networks

assume that, on average, 3 Mb of data per day is generated at each remote seismic station. This corresponds to selected events only with a record duration of 2500 s of uncompressed, 4-byte data at a sample rate of 100 Hz from three channels. Then, a network consisting of a central computer, 10 remote stations, and a single modem at the central-recording site, having 9600-baud data transfer, needs about 10 hours/day to transmit this data. This means that the maximum delay in getting the data will be 10 hours and the data transfer typically would be started once or twice a day. The same network connected to Internet, having a speed of 128 kb and a multi-line ISDN port would need less than 10 minutes for the same task. If the data collection software is set to operate more frequently, less data is transferred at once, and an even shorter time delay can be achieved. Thus, it can be said that the system operates in semi-real time.

The above systems are based on the traditional idea that the central computer controls the network. However, with some equipment it is also possible to set up the remote station to send parametric data to the central computer immediately after an event is detected. The central computer would then request waveform data if sufficient detections arrive within a given time window. In this way, events can be declared immediately after their occurrence. The problem with this solution is that it is not easy to develop reliable software to control the data flow in case the remote stations trigger wildly. This situation may, in the worst scenario, prevent any waveforms from being downloaded to the central computer. Currently, for most systems the central computer maintains control.

For virtual networks, the main challenge for the network operator is to obtain reliable software to link the stations into a network. Today, the main difficulty is lack of standards. There are many ways of accessing different types of seismic stations and many different formats for parameter and waveform data. When setting up a virtual network, the operators' selection of hardware may be limited by the available software.

8.4.3.2 Examples

Example 1: The IRIS/Global Seismic Network (GSN) is a typical example of a virtual seismic network. This global system consists of more than 100 broadband seismic stations, which can be reached by modem and/or Internet. At the IRIS data management center in Seattle, Washington, a public domain software system, SPYDER, automatically retrieves data from selected GSN stations based on preliminary determination of epicenters by the NEIC (National Earthquake Information Center) in Golden, Colorado. Thus event detection is not part of the SPYDER system. The SPYDER system has been installed in several places for local or global use. SPYDER, which runs under UNIX and LINUX, only works with GSN-type stations. Fig. 8.5 shows the GSN network and Fig. 8.11 the type of communications used.

Example 2: The public domain SEISNET system is another software enabling establishment of virtual seismic networks. SEISNET is similar to SPYDER, however, it operates other types of stations in addition to the GSN stations and also performs network detection and preliminary location (Ottemöller and Havskov, 1999). It was developed for the Norwegian National Seismic Network and is also used in several other places. SEISNET is very flexible and can be adopted for virtually any type of field station. Also SEISNET runs under UNIX and LINUX operation systems.

Example 3: Another widely used and publicly available software is EARTHWORM (runs on Solaris UNIX and Windows 2000/NT). It allows users to run virtual seismic networks of different purpose with emphasis on either real-time seismic data processing or data storage and user interaction. EARTHWORM was originally developed by the U.S. Geological Survey's (USGS) Northern California Seismic Network (NCSN), and currently consists of a world-wide community of installations that operate the system or its derivatives and contribute to its development. Coordination of this effort is now centered at the National Seismic Systems Project of the USGS in Golden, Colorado, which functions as the clearing house for development, distribution, documentation, and support (<http://gldbrick.cr.usgs.gov/ew-doc>). The great majority of US stations use this system, including the ~450-station NCSN, the ~150-station TRINET network in S. California, the ~100-station US National Seismic Network of BB stations, most other US regional networks as well as many other earthquake and volcano networks world-wide. EARTHWORM will also be used by the developing US Advanced National Seismic Network (ANSS; see <http://www.anss.org/>) that will combine national, regional and urban monitoring with stations that span the range from weak to strong motion.

Example 4: The proprietary ANTELOPE software is yet another virtual seismic network software package on the market. It supports a wide range of seismic stations as well as other environmental monitoring equipment. ANTELOPE's open-architecture, modular, UNIX-based, real-time acquisition, analysis, and network management software supports all telemetry using either standard duplex serial interfaces or standard TCP/IP protocol over multiple physical interfaces. In addition to data acquisition, the seismic network functionality includes real-time automated event detection, phase picking, seismic event association and location, archiving, system state-of-health monitoring, interactive control of remote stations, automated distribution of raw data and processed results, batch mode seismic array processing and a powerful development toolkit for system customizing. It can handle continuous and event file-based data and uses relational database management formalism and the CSS v. 3.0 scheme for information organization. It runs on Sun Microsystems' Solaris OS on SPARC and Intel architectures. It was developed by the BRRT Company and Kinematics and is currently used by IRIS networks, the US Air Force, many seismic networks in the U.S.A., and about eight national seismic networks in Asia and Europe.

GSN & FEDERATION OF DIGITAL BROADBAND SEISMIC NETWORKS (FDSN)

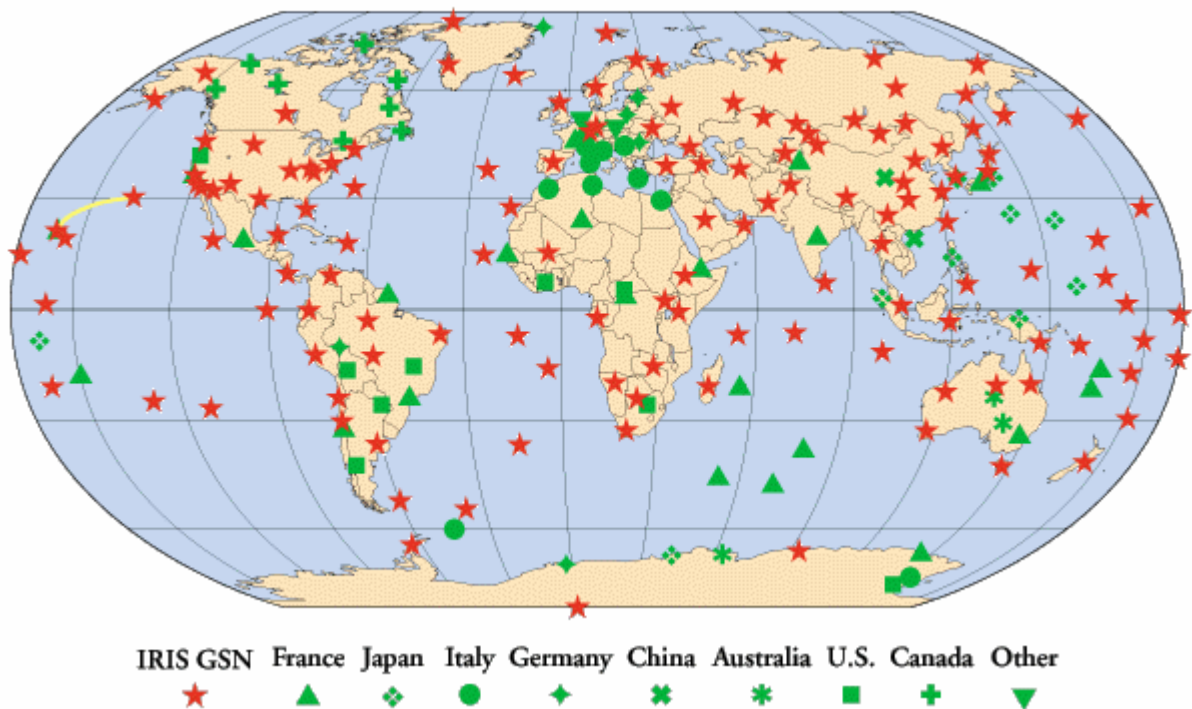


Fig. 8.5 The Global Seismic Network (GSN) and other global broadband stations that are members of the Federation of Digital Broad-Band Seismograph Networks (FDSN) (figure from IRIS home page <http://www.iris.edu>). For complementary information on the Global Seismograph Network (GSN) see Figure 1 in IS 8.3.

8.4.4 The choice between physical and virtual seismic systems

The decision on which type of network is optimal depends mainly on two factors: cost and the requirement for real-time data. For seismic networks with important alarm functionality, the main requirement is to locate events and determine magnitude as fast as possible. For this purpose one has to have raw data available in real time. This usually means that most of the virtual seismic networks are ruled out and a physical network must be used. Two exceptions exist: virtual seismic networks that can handle real-time data transfer via the Internet (like ANTELOPE) or networks in which each field station can provide accurate automatic event location and magnitude, and this information is immediately sent to the central station. Remote stations must initiate data transfer. The drawback is that remote automatic locations based on a single station data are less reliable and that the results can not be verified before the complete raw data arrives.

For seismic networks with the exclusive purpose of monitoring general seismicity and/or to serve research purposes, there is no need for real-time data. The two main factors in deciding which network is the most appropriate are cost of ownership and quality of data. For research purposes, flexibility is also a very important issue. If phone lines or coverage by a cellular phones system is available at seismically quiet sites, it may be less expensive to construct a

virtual network. For a large network, for which dedicated radio links are not an option, a virtual network will probably be the least expensive alternative.

Since communication costs are quickly decreasing and phone service is becoming universally available, it is likely that more and more networks will operate as virtual networks in the future.

8.5 Seismic data acquisition

8.5.1 Digital versus analog data acquisition

There exist three primary types of physical seismic networks with respect to the technology of data acquisition: analog, mixed, and digital.

8.5.1.1 Analog seismic systems

The analog seismic systems include sensors, which are always analog, analog signal conditioning, usually frequency modulated (FM) telemetry through radio (RF) or phone lines, analog demultiplexers, and analog drum or film recorders. Paper or film seismograms are the final result of a completely analog system. The two primary drawbacks of such systems are:

- 1) the low dynamic range and resolution of the acquired data (about 40-45 dB with single and about 60-65 dB with double, low and high-gain data transmission channels) lead to issues of incomplete data. On the one hand, many events have amplitudes that are too low to be resolved on paper or film records, while on the other hand, many records are clipped because their amplitude is too large for undistorted recording. In fact, only a very small portion of the full dynamic range of earthquakes that are of interest to seismologists are actually recorded distortion free on analog systems;
- 2) the incompatibility of paper and film records with computer analysis. This is a very serious drawback today because modern seismic analysis is almost entirely based on computer processing.

For these reasons such systems are no longer being built.

8.5.1.2 Mixed analog/digital systems

Mixed systems, frequently erroneously called digital, have analog sensors, analog signal conditioning, usually FM telemetry, and analog demultiplexers, but digital data acquisition at the central-recording site, digital processing, and digital data archiving.

8. Seismic Networks

Such systems also have a low dynamic range (usually FM data transmission links are the limiting factor) and therefore, they have the same disadvantage as the analog systems regarding data completeness and quality. However, they can accommodate off-line as well as automatic near-real time computer analysis. One can use most modern analysis methods, except those that require very high-resolution raw data. Such systems are still useful for some applications when the higher dynamic range of a fully digital system is not of prime importance and the purpose of the seismic network is limited to a specific goal. Advantages of these systems include low cost and low power consumption of the field equipment. Fig. 8.6 shows a typical setup.

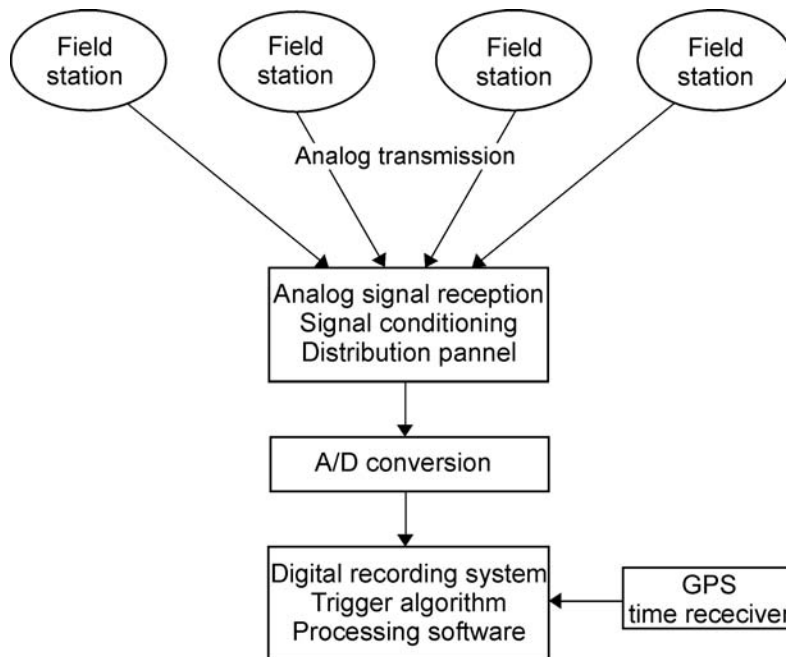


Fig. 8.6 Typical analog-digital network. The analog data is transmitted to the central site over fixed analog communication channels, usually FM modulated radio links or phone lines. At reception, the signals are put into a distribution panel where incoming signals are demodulated. Some filtering may take place before the data are digitized by a PC or similar recording system. Timing is done within the digital system. Today, very few alternatives to GPS exist.

8.5.1.3 Digital seismic systems

In digital systems, only the seismometers are analog. All other equipment are digital. The dynamic range and the resolution are much higher than that of analog and mixed type systems. These factors depend mainly, but not only, on the number of bits of the analog-to-digital (A/D) converter. 12- to 24-bit A/D converters are available today, which correspond to dynamic ranges of approximately 70 to 140 dB. In practice, however, the total dynamic range and the resolution of data acquisition is usually less than the number of bits an A/D converter would theoretically allow, since 24-bit converters rarely have a noise level as low as 1 bit.

There are two known design principles that can further increase the dynamic range and/or the resolution of seismic data recording.

The gain-ranging method automatically adjusts the analog gain of the system according to the amplitude of the seismic signal and thus prevents clipping of the strongest events. In this way, the dynamic range of data acquisition can be dramatically increased, however, the resolution remains roughly unchanged. Unfortunately, even modern electronics are imperfect and gain-ranging amplifiers introduce ‘gain-ranging errors’ in the data. Therefore, the resolution of gain-ranged recording is actually decreased. This decrease depends on the data itself, which makes these type of errors hard to detect. For this reason, many seismologists are reluctant to use the gain-ranging systems. They have been mostly replaced by straightforward, multi-bit A/D conversion, which nowadays allow nearly as wide a dynamic range.

The over-sampling principle (see 6.3.2) is another approach which helps improve the dynamic range and resolution of digital data acquisition. The data is sampled at a much higher rate than is required in seismology and then the value of each sample of the final (lower sampling rate) output data stream is calculated by a statistical model. The increase in the resolution is significant. However, the efficiency of over-sampling depends on the ratio between the over-sampling frequency and final sampling rate of actual seismic data. The higher the final sampling rate used, the less benefit is gained from over-sampling. Therefore, for example, in local seismology, which frequently requires 200-Hz sampled data, the benefit of over-sampling is quite modest with some data logger designs. Fig. 8.7 shows a typical setup.

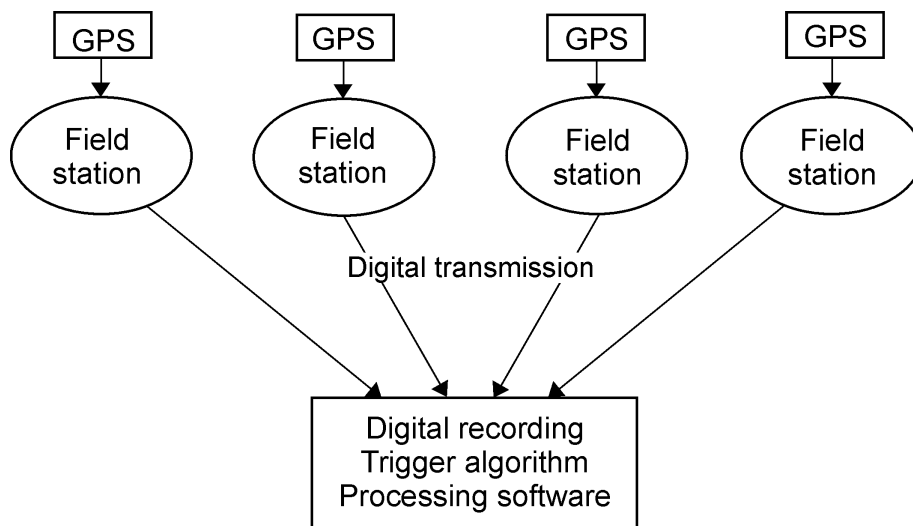


Fig. 8.7 Typical digital network. The digital data is transmitted to the central site over fixed digital communication channels. At reception, the signals enter the recorder directly. Timing normally takes place at the field stations, although some systems also time the signal on arrival.

Buyers of digital seismic networks sometimes ask for additional paper drum recorders because they wish to continuously monitor incoming signals and/or believe drum recorders will serve as an excellent educational tool. However, there are a number of problems with paper drum recorders in digital systems. One problem revolves around the requirement for additional electronic components, such as digital to analog converters. Being mechanical devices, drum recorders are and will continue to be expensive, often costing more than a multi-channel digital recorder. They require continuous and specialized maintenance and consumables. On the other hand, nearly all modern observatory seismic software packages

8. Seismic Networks

allow for the continuous, near-real-time observation of the incoming signals and some even simulate the traditional appearance of paper helicorder records. Our experience is that once a user becomes familiar with a digital system, expensive paper drum recorders soon prove to be of little use and are thus a poor investment.

8.5.2 Trigger algorithms and their implementation

8.5.2.1 Continuous versus triggered mode of data acquisition

Continuous, digitally-acquired seismic signals by their very nature provide a huge amount of data. A reasonably sized, digital, weak-motion seismic network operating in continuous mode will produce a volume of data so large that most networks would find it implausible to store for any length of time. Yet, only a small portion of that data are, in fact, useful earthquake information.

This storage problem has frequently led seismic network users to operate their systems on a "triggered" basis (particularly the local and regional seismic networks that require a high frequency of data sampling). Triggered systems still do continuous, real-time acquisition and processing of seismic signals, but only store signals associated with seismic events. Such systems do not store continuous time histories of seismic signals, but rather produce "event files".

A decision between a continuous and a triggered mode of operation usually means a decision between higher network event detectability versus reduced detectability. The difference is significant and can become drastic if man-made seismic noise at the remote station sites is high due to poorly selected sites or trigger parameters that are not adjusted optimally. In modern high-capacity recording systems, this decision is less important since these systems often provide for large temporary storage of continuous data in ring buffers (see below).

Note that the continuous seismic signal recording provides the most complete data, but storing and processing all of that data can be difficult, expensive, or even impossible. Obviously, systems in triggered mode will lose some weak events and produce a certain number of false triggers. The completeness of data inevitably is impaired because the efficiency of the trigger algorithms currently available is inferior to the pattern recognition ability of a trained seismologist's eye.

8.5.2.2 Trigger algorithm types

Triggered seismic systems can have various trigger algorithms.

The amplitude threshold trigger simply searches for any signal amplitude exceeding a preset threshold. Recording starts whenever this threshold is reached. This algorithm is normally used in strong-motion seismic instruments, which are systems that do not require high sensitivity. Consequently, man-made and natural seismic noise will only produce infrequent triggers.

The root-mean-square (RMS) threshold trigger is similar to the amplitude threshold algorithm, but the RMS value of the amplitude in a short time window is used instead of

'instant' signal amplitude. It is less sensitive to spike-like, man-made seismic noise, however it is rarely used in practice.

The ratio of the short-time average to the long-time average (STA/LTA) of the seismic signal is the basis of the most frequently used trigger algorithm in weak-motion seismology. It continuously calculates the average values of the absolute amplitude of the seismic signal in two consecutive moving time windows. The short-time window (STA) is 'sensitive' to seismic events, while the long-time window (LTA) provides information about the temporal amplitude variation of seismic noise at the site. When this ratio exceeds a preset value (usually set between 4 and 8), an event is 'declared' and data starts being recorded in a file. The STA/LTA trigger algorithm is well suited to cope with slow fluctuations of natural seismic noise. It is less effective in situations where man-made seismic noise of a bursting or spiky nature is present. At sites with high, irregular, man-made seismic noise, the STA/LTA trigger usually does not function well. For more details on STA/LTA algorithm and parameter setting see IS 8.1.

Several more sophisticated trigger algorithms are known from the literature. They are sometimes used in seismic networks but rarely in the seismic data loggers available on the market. In the hands of an expert they can significantly improve the event detections/false triggers ratio, particularly for a given type of seismic event. However, these triggers often require sophisticated parameter adjustments that can prove to be unwieldy and subject to error.

Every triggered seismic system must have an adjustable band-pass filter in front of the trigger algorithm. This is particularly important with BB and VBB seismometers where small earthquake signals are often buried in dominant 0.2-0.3 Hz seismic noise. The adjustable band-pass filter allows the trigger algorithm to be sensitive to the frequency band of one's interest. In this way such events may be resolved and acquired. Some recorders allow several trigger sets to be used simultaneously. This is needed if for example, a BB station has to trigger on microearthquakes, teleseismic P waves and surface waves which each require separate setting of filters, STA and LTA. The GSN Quanterra stations operate in this way.

8.5.2.3 Coincidence trigger principle

In seismic networks with standalone stations, each remote station has its own independent trigger. In such networks data are usually transferred to the central-recording site on request only or it is collected in person. These seismic networks have the lowest effectiveness of triggering and consequently, the smallest detection threshold and/or the highest rate of falsely-triggered records. The completeness of data is modest because not all stations in the network trigger simultaneously for each event. This approach requires a good deal of routine maintenance work in order to "clear" numerous false records from the local data memory if trigger thresholds are set low; if not, the network has a lower detection threshold. Remote stations may encounter 'memory full' situations due to having a limited local memory. Such networks absolutely require the careful selection of station sites with as low as possible man-made seismic noise. If low noise is not assured, an observatory quality network may be so insensitive as to be considered a serious project failure. However, such networks are frequently used as temporal seismic networks. They also function well where high sensitivity is not desired at all, for example, in most strong-motion networks.

8. Seismic Networks

Seismic networks that use the coincidence trigger algorithm are much better at detection thresholds and completeness of acquired data. In these systems, data are transmitted continuously from all remote stations to the central-recording site where a complex trigger algorithm discriminates between seismic events and seismic noise. The coincidence trigger takes into account not only signal amplitudes but also correlation in space and time of the activated stations within a given time window (the window allows for wave propagation). The trigger threshold level of such a robust algorithm can be significantly lowered, resulting in a more complete record of small events for the entire network. All stations in the network are recorded for every trigger, which greatly improves completeness of the recorded data. Virtual seismic networks can also request and store data from every station, however with some time delay.

8.5.2.4 Ring-buffer seismic systems

An even better solution is provided by systems that temporarily store continuous signals in memory (ring buffers, usually on disk) for a given period of time ranging from several hours to several days. After the specified time, these systems erase the old data, replacing them by the new incoming data. However, during the designated time, a seismologist can detect, associate, and analyze events far better than any automatic algorithm. While this method requires more or less prompt analysis of seismic signals, excellent completeness of data and detection threshold are obtained. In addition, for the most interesting periods, such as aftershock sequences or earthquake swarms, the data can be archived in a continuous manner, thus permanently keeping all information contained in the signals. Ring-buffered systems are also very useful if the seismic system is accessed by various institutions for different purposes. Every user can 'browse' for data according to their own interests.

Ring-buffer systems can still have an automatic trigger algorithm operating simultaneously, which enables automatic processing and a short reaction time following large events. Modern high capacity and very affordable hard disks enable the use of this approach, even by the relatively inexpensive systems. A ring-buffer system is presently the best compromise between a triggered and a fully continuous seismic system (see also 6.5.2).

8.6 Seismic data transmission and network examples

8.6.1 General considerations

While data transmission may not seem like an important technical issue for a seismic network, a poorly selected or designed data transmission system is one of the most frequent causes for disappointment and technical failures. The success of a seismic network operation rests largely on the reliability and the quality of data transmission.

Another very important but frequently overlooked factor is the cost of data transmission. In fact, these costs may largely determine the budget for a long-term seismic network operation. Many seismic networks all over the world have been forced to change to less expensive modes of transmission after some years of operation. The data transmission costs per year in a network established right after a damaging earthquake may seem completely acceptable at first, but may be viewed as excessive after just a few years of relative seismic quiescence.

There are three key technical parameters to consider in designing a physical data transmission system:

- the required information flow (channel bandwidth for analog links or data transfer rate with digital links);
- the distance to which data must be transmitted (becomes unimportant with computer-network-based seismic networks);
- the desired reliability (acceptable down-time of the links, that is, the maximum time period per year when the signal-to-noise ratio is lower than required (analog links) or bit error rate (BER) is higher than allowed (digital links)).

In virtual seismic networks two decisions are the most important:

- the physical network which will be used to establish a virtual seismic network (Internet, proprietary WANs (Wide Area Networks), analog public phone network, ISDN, etc.); and
- the protocol that will be used.

These parameters must fit the available data transmission infrastructure in the country or region, the available network operations budget, and the network's performances goals.

Technical considerations, reliability, initial price and operational costs of data transmission links vary widely from country to country. Local conditions in a particular country or region are a very important factor in the selection of an appropriate data transmission system. It is essential to get information about the availability, reliability and cost of different approaches from local communication experts. The manufacturers of seismic equipment are generally not familiar with the local conditions and may be unable to correctly advise the best solution for a particular country.

8.6.2 Types of physical data transmission links used in seismology

In seismometry there are several different kinds of physical data transmission links in use, from simple short-wire lines to satellite links on a global scale. They differ significantly with respect to data throughput, reliability of operation, maximum distance, robustness against damaging earthquakes, and cost of establishment and operation. A table in IS 8.2 enumerates the most common types, their major advantages and drawbacks, and their potential applications.

Note that strong-motion seismic networks generate far less data than weak-motion networks and therefore, their designs might differ significantly. Seismic data transmission links that are fully acceptable for strong-motion data may be inadequate for weak-motion data and data transmission links used in the weak-motion field may be an absolute overkill and too expensive for strong-motion networks.

8.6.3 Simplex versus duplex data transmission links

There are two basic types of digital data transmission links.

Simplex links transmit data only one-way - usually from remote stations to the center. These links are relatively error prone. Radio interference or fading may corrupt data during transmission and there is no way of recovering corrupted data, unless forward error-correction (FEC) methods are used (see 8.8.6.6). However, the FEC methods are rarely used except with satellite links. They require a significant bandwidth overhead, which is hard to provide using standard, low cost 3.5-kHz bandwidth RF channels. Simplex links usually use the type of error-checking that allows recognition of corrupted data but not its correction. The methods in common use range from a simple parity check or check-sum (CS) error detection to cyclic redundancy check (CRC) methods.

Duplex links allow data flow in both directions – from the remote station to the center and vice versa. Different types of error-checking methods are used, ranging from a simple parity check or CS error detection to CRC error detection. Once an error is detected, the data block is resent repeatedly until it is received correctly. In this way, a very significant increase of reliability of data transmission is achieved. However, these links require nearly double the amount of the RF equipment and are therefore expensive compared to the simplex links.

Another very important benefit of duplex links is that they allow remote access and modification of the data acquisition parameters of the remote seismic stations and the use of various diagnostic commands at the remote stations (see 8.8.6.3 below). This ability can significantly reduce the maintenance costs of such a seismic network.

8.6.4 Data transmission protocols and some examples of their use

Serial data communication and Ethernet are the most commonly used way to transmit digital seismic data.

Most seismic digitizers will send out a stream of data in serial format and all computers have hardware and software to communicate with serial data. A serial line requires at least 3 lines: One for sending data, one for receiving data, and ground. If data only is to be sent or received, two lines suffice. The serial lines use either RS-232 protocol or the RS-422 protocol. The former can run on up to 50 m long cables and the latter on cables up to 2 km long. Serial line communications may be used by modems, radio links, fixed telephone lines, cellular phone, and satellite links.

Below are some examples how serial data transmission is used in practice.

Example 1: One-way continuous communication (see Fig. 8.8). A remote station has a digitizer sending out RS-232 data, which enters a radio link to a PC, which reads the data and processes it. The communication is governed by the RS-232 protocols. The software on the PC can run a continuous- or triggered-mode data acquisition system.

8.6 Seismic data transmission and network examples

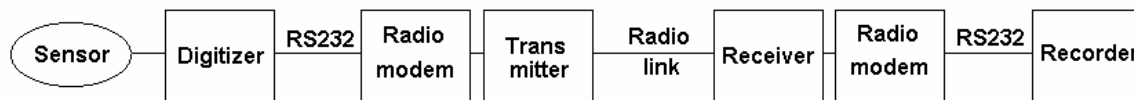


Fig. 8.8 One-way communication from a remotely installed digitizer via a digital radio link to a centrally located PC. The radio modem and transmitter /receiver might be one unit.

Example 2: Interactive communication with a remote seismic station (see Fig. 8.9). A user calls up a terminal emulator on his PC, connects to a modem with one of the PC's serial lines, dials the phone number of the modem connected to the remote station, and logs into the field station. Once logged in, several options are usually available. One is to browse a log file containing all triggered events in the local memory of the station. Another option is to initiate a download of event data. A very common way to do this over a serial line connection is to list the event file in ASCII form and then set up the terminal emulator at the local PC to capture the data. This is one way of getting data from a standard GSN seismic station. The advantage of this type of communication is that only very simple software is required and it is easy to access to many different seismic stations. This process can also be easily automated (see IS 8.3).

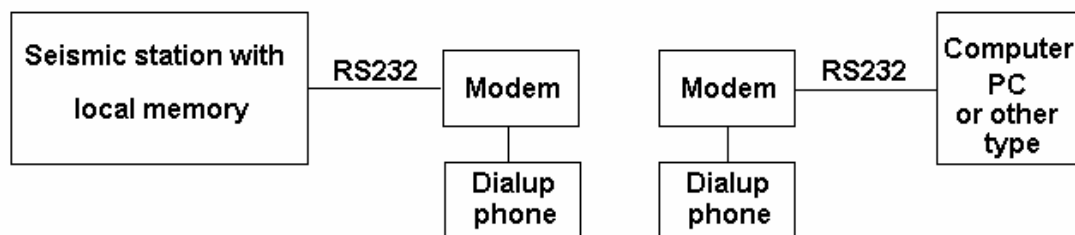


Fig. 8.9 Manual dial-up to a seismic station for data inspection and/or download. The dialing computer can be of any type as long as a terminal emulator program, such as Hyperterminal in MS Windows, is available.

Example 3: Interactive communication with a remote seismic station using proprietary software. The user starts up a manufacturer-supplied program on his local PC. The program handles all the communication to the field station purchased from this manufacturer. The user's connection with the field station will be as if sitting next door. Data download, acquisition parameter settings, system state-of-the-health verification, and diagnostic commands (if applicable) are managed through simple menus, and the event files may be automatically transferred to the user's local PC. The process can be run manually or in an automatic, unattended mode at specified times. With some systems, remote stations can initiate the transfer of triggered seismic events. The advantage with this setup is that communication with a particular remote station is very easy. Unfortunately, most of the software systems in the market work only with one type of seismic station.

In high-speed local area networks, Ethernet most commonly connects computers. This low-level protocol is not what the user sees directly, but rather a high-level communication protocol working on top of the Ethernet protocol. TCP/IP is the most widely used protocol for

8. Seismic Networks

file transfer and remote log-in. This is also the protocol used by the Internet although the low-level protocol used between the different Internet nodes might not be Ethernet. TCP/IP can also be used over serial lines and ISDN telephone lines.

The simplest seismic stations are usually not able to communicate via TCP/IP protocol, but as the computer power of remote stations is constantly increasing, more and more have TCP/IP and Ethernet built in. A remote seismic station, which can be reached by TCP/IP either through Internet, dial up ISDN, or regular phone lines, represents the most general purpose and flexible system available.

Fig. 8.10 shows the most common way of establishing TCP/IP connections to a central data collection system. Dashed lines between routers indicate that the connection is made to one station at a time. Large central routers that can communicate with many ISDN nodes at the same time are also available.

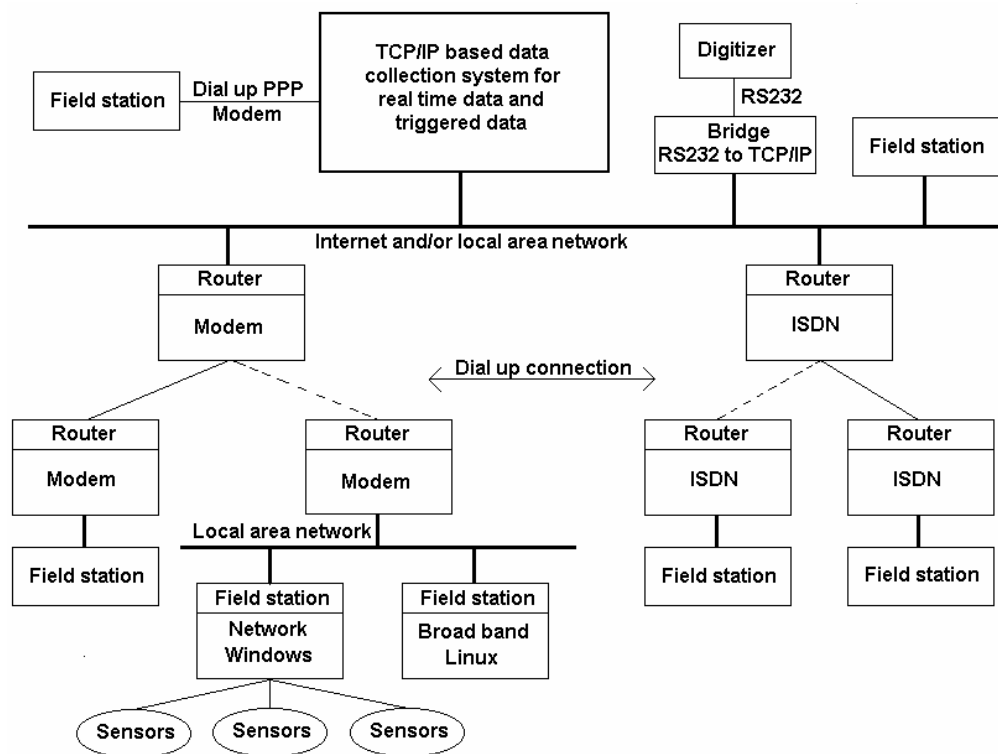


Fig. 8.10 Different ways of getting a TCP/IP connection to a central data collection system. The thick solid lines indicate permanent Ethernet connections.

Getting seismic data from a GSN station using Internet via a local computer is simple. The user uses the Telnet to login to the station. Once logged in, he can check available seismic data and use the FTP file transfer protocol to copy the data to the local computer. The process is easy to automate. Fig. 8.11 shows the communication links for the GSN network.

Many computers do not have direct access to the Internet but are able to send e-mail. Some seismic stations and centers, particularly in Europe, use a shared protocol for providing seismic waveform data semi-automatically by e-mail. This system is called AutoDRM (Automatic Data Request Manager; Kradolfer, U., 1996; <http://seismo.ethz.ch>). The user

sends an e-mail request for particular data and the remote system automatically ships back the data by E-mail.

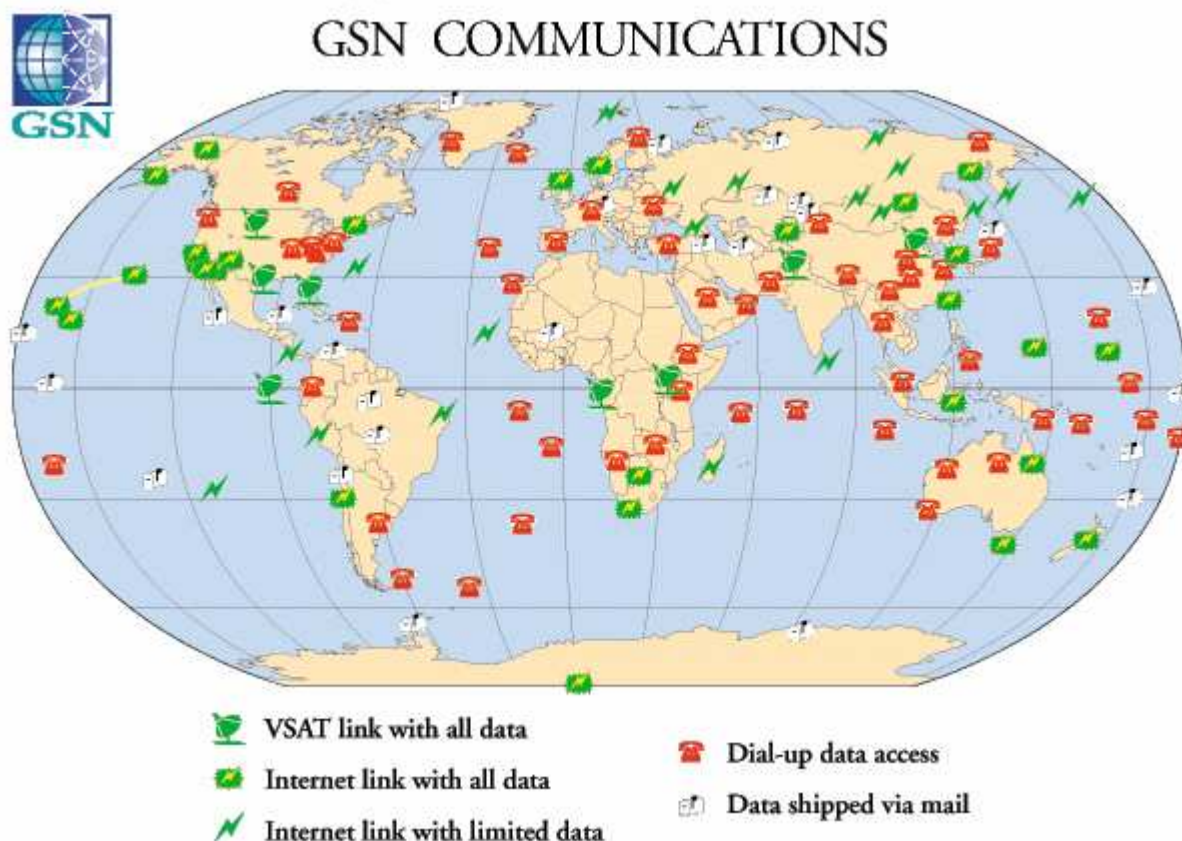


Fig. 8.11 Communication to GSN stations 2001. VSAT is a satellite connection. VSAT and Internet have real-time connections and potentially all data can be downloaded, while the dial up stations transmit a limited amount of data only (figure from IRIS home page <http://www.iris.edu>)

8.6.5 Compression of digital seismic data

Because of the high data rates from digital seismic stations and the throughput limitations of available data transmission links, data is often compressed before transmission. The compression generally can be expected to halve the quantity of seismic data. After transmission, data must be uncompressed unless it is stored directly without processing. There are several compression routines in use, some of which are in the public domain and others only in a particular type of equipment. Generally, public domain compression routines are used for data storage while proprietary algorithms are used only with specific equipment. If communication is by a telephone line with modem, the compression can take place in the modem with standard agreed protocols, and no compression software is needed at the seismic station.

With many compression algorithms, the degree of data compression depends on the amplitude of the seismic signal. Therefore the efficiency of the compression falls sharply during strong earthquakes. One should be sure that the local temporary memory and the link's throughput will suffice in case of large, long-duration events.

8.6.6 Error-correction methods used with seismic signals

All digital communications experience errors. In the transmission of seismograms this is particularly fatal since just one bit of error might result in a spike in the data with a value a million times larger than the true seismic signal. Obviously, this could wreak havoc in trigger systems, and one byte missing in an event file might corrupt the whole event file.

One of the principles of error correction is that data is sent in blocks, e.g., 1 s long, and along with the block of data there is some kind of 'check-sum'. If the check-sum does not tally with the received data, a request is sent to retransmit that particular block of data. Obviously this type of error correction requires duplex transmission lines and local data memory at the remote station. If only one-way transmission is available, the errors can not be corrected using the check-sum method but they can be detected and appropriate action taken at the receiving end. However, loss of data is inevitable.

Error correction can be utilized at different hardware and software levels and can be of various types.

Proprietary error correction is used in many systems on the market. In these cases, the system operates over dedicated links and all the responsibility for transmission and error correction lies with the system. An example would be a digital radio link to remote stations that uses a manufacture's protocol for error correction. The protocol in this case would be built into the commercial product.

Standardized hardware error correction is another possibility. The hardware unit, where the data enters the digital link and where it comes out, has its own error correction built in. From the user's standpoint, it is assumed that no errors occur between the input and output of this hardware. The most common example of such hardware error correction is a telephone modem that uses internal, industry-standard error correction.

Computer networks use their own error-correction methods. When computers are linked with common computer network protocols like TCP/IP or Kermit, error correction is built in from computer to computer. This is obviously the best solution, however it requires that the seismic remote stations operate quite sophisticated software. Most simple digital remote stations today can not benefit from this type of error correction, but the trend is to use more powerful processors in remote stations so this form of error correction might be more dominant in the future. Nevertheless, several seismic data loggers already on the market are capable of communication with higher-level protocols.

Satellite data transmission links usually use forward error-correction (FEC) methods. FEC works on simplex links and doesn't require any retransmission of data blocks to correct errors. FEC is similar to check-sum error detection. By comparing the transmitted check-sum and that of the received data, corrections can be made. One drawback, however, is an increased data channel bandwidth due to a significant data overhead dedicated to error correction.

One should carefully consider the interplay between the error-correction system built into a seismic system with that of the particular communication equipment to be used.

8.6.7 Seismic data transmission and timing

All digital data acquisition and transmission systems create a certain time delay. This delay depends on the digitizer, the digital protocol used for transmission and the computer receiving the data. For this reason, most digital field stations time stamp the data at the remote station and subsequent delays in the transmission have no effect on timing accuracy. However, there are also digital network designs where the timing takes place centrally. This can be done if the digital data arrives at the central site with a predictable or measurable time delay. The central computer must then time stamp the data when it arrives in real time and later correct it for the known transmission and digitizer delays. One advantage with this system is that only one clock is needed for timing the network. A further advantage is a simpler and less expensive remote station consisting only of a sensor and a digitizer. The disadvantage is that timing accuracy is not as good as with time stamping at the remote sites because time delays are known only with a limited precision and they may also vary in time. Also if the central clock or its synchronization with RF time signals fails, the whole network fails. Most networks are moving towards time stamping at the station because GPS clock prices are now a small fraction of total digitizer costs.

8.6.8 Notes on dial-up phone lines and selection of modems

Dial-up phone lines are very often proposed for seismic data transmission because they are readily available and apparently cheap. However, they have important limitations of which one must be aware. First, continuous seismic data transmission is not possible via dial-up lines. This makes coincidence triggers hardly applicable or at least very clumsy and slow. Second, their throughput is, in practice, frequently limited in spite of the high baud-rate capabilities of modern modems. Even the fastest modems do not help if the public phone system in a country is of low quality, unreliable, or overused. Especially in the developing countries, seismic network purchasers often overestimate public phone system reliability. This easily results in inefficient data transmission and tedious re-transmission of data files. A public phone system must be very reliable for reliable transmission of occasionally very big seismic event files.

In practice, dial-up weak-motion networks based on phone lines can not 'digest' earthquake swarms and the numerous aftershocks after strong events. In the worst case, the data will be lost, and in the best case, with large-capacity local recorders, the delay in receiving the data will be big. Therefore, they are an appropriate choice for low seismicity regions only. In addition, as they often do not function for several hours after strong events, due to either especially high usage of the public phone system or technical difficulties, they may not be the best choice for networks with the predominant purpose of giving seismic alarms. On the other hand, however, the USGS National Strong-Motion Program's dial-up network of about 200 stations (out of a total of 645 stations) (http://nsmp.wr.usgs.gov/near_real_time.html) has successfully contributed to local ShakeMaps (<http://quake.usgs.gov/research/strongmotion/effects/shake/about.html>) in California since 1999. The data typically are downloaded, processed, and exported automatically to clients within 3-5 minutes after strong-ground shaking begins. Also, the National Research Institute for Earth Science and Disaster Prevention (NIED) in Japan operates an event-triggered dial-up strong-motion network (K-net; see 8.6.9.4). It comprises more than 1000 strong-motion stations and their data are dialed-up to NIED in a couple of hours after the occurrence of strong earthquakes.

8. Seismic Networks

In many countries, public phone networks have specific properties and special 'tricks'. Therefore it is advisable to purchase modems locally. Obviously one has to choose a type of modem that has been officially approved in the country and that performs well under local circumstances. Modems react differently to each phone system's particular weak points. A modem, which works perfectly in one country, may not be the optimal solution for another country. We strongly recommend the purchase of modems only after consulting with local communication experts who have practical experience with digital data transmission over local phone lines in a particular country.

8.6.9 Some network examples

Along the lines described in the preceding section, some more examples are given of different types of seismic networks in operation, briefing both on their technical solutions and purpose.

8.6.9.1 International Monitoring System (IMS)

In recent years, a new global network, the International Monitoring System (IMS) has been set up aimed at monitoring the Comprehensive Nuclear-Test-Ban Treaty (CTBT) (see http://www.nemre.nn.doe.gov/nemre/introduction/ims_descript.html and Barrientos et al., 2001). The IMS consists of 50 stations designated as "primary", mostly arrays (see Chapter 9), with real-time data transmission to international data centers, including the IDC of the CTBTO in Vienna. In addition there are 120 "auxiliary" stations that provide data on request to the IDC. Many of the auxiliary stations are members of the Federation of Digital Broadband Seismograph Networks (FDSN; see Fig. 8.5 and <http://www.fdsn.org>). The IMS network (Fig. 8.12) is currently the largest and most modern physical real-time network in the world. However, when requesting data from auxiliary stations, it works like a virtual network where the real-time network makes the detections and preliminary locations and then requests additional information from remaining stations for improving these preliminary findings.

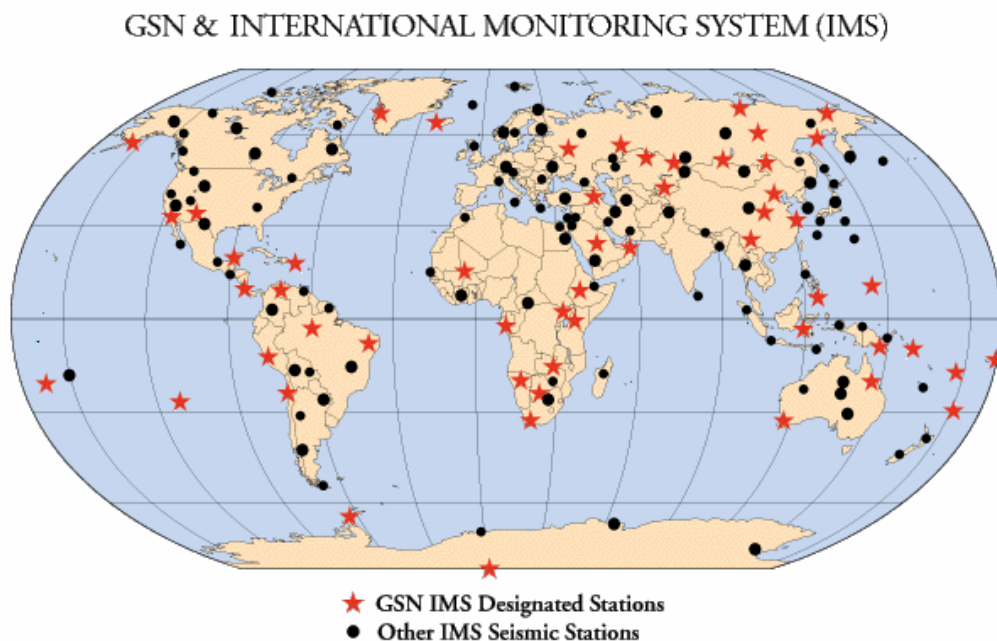


Fig. 8.12 Stations in the International Monitoring System (IMS).

8.6.9.2 Southern California Seismic Network (SCSN)

California probably has the world's largest density of seismologists and seismic stations and there are two large networks of more than 350 stations each in northern and southern California, respectively. The SCSN (Fig. 8. 13) is one of the largest and most automated regional networks in the world, consisting of a mixture of triggered and continuous systems using a large variety of equipment and communication means. Central recording takes place at CALTECH. This network and the NCSN have been early pioneers in setting up local networks (Lee and Stewart, 1981). The network can not be characterized as either physical or virtual since it is a complex mixture of both. It is interesting to note that despite the high technological level, there are still some simple robust analog stations in the network. This network is definitely NOT a turnkey network.

Digital and analog seismic stations in Southern California Seismic Network, January 1999

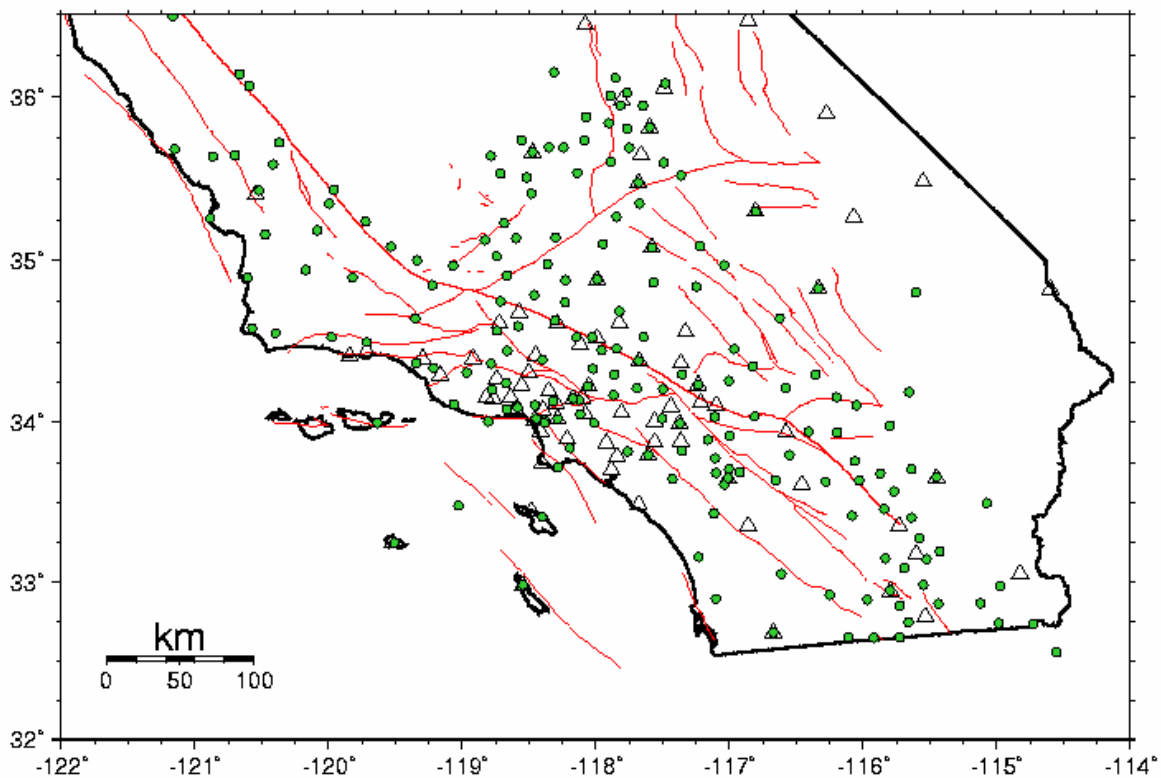


Fig. 8.13 The Southern California Seismic Network (SCSN). The system has several types of stations. Empty triangles are digital broadband stations; the filled-in triangles are other types of digital stations; and the round filled symbols are analog stations. The lines shown are faults (figure from the SCSN home page <http://www.trinet.org/scsn/scsn.html>).

8.6.9.3 Japanese Seismic Networks (Hi-net, F-net, and K-NET/KiK-net)

Three seismic networks (Fig. 8.14) are now operated by the National Research Institute for Earth Science and Disaster Prevention (NIED) in Japan. The first one is a high sensitivity seismograph network named the Hi-net. It comprises about 600 stations. At each Hi-net station a short-period seismograph is installed at the bottom of a borehole with a typical depth

8. Seismic Networks

of 100-200 m. The second network is a broadband seismograph network, named the F-net. It comprises about 70 stations. At each F-net station a broadband seismograph is installed, together with a strong-motion sensor with a velocity-proportional response, in a vault at a depth of about 50 m. Ground motion data collected by these networks are sampled with 100 Hz and recorded with a dynamic range of 144 db (24-bit words). The data are continuously transmitted to NIED via TCP/IP network. The third network is a strong-motion seismograph network named the K-NET, which comprises more than 1000 stations. At each K-NET station an accelerometer is installed on the ground surface. The event-triggered data are dialed-up to NIED in a couple of hours after the earthquake occurrence. Additionally, strong-motion accelerometers are installed at all Hi-net stations. This sub-net is named the KiK-net. At each KiK-net station accelerometers are installed both at the ground surface and at the bottom of a borehole, together with a Hi-net sensor. The data collection for the KiK-net is almost the same as that for the K-NET. Any user in the world has open access via the Internet to the data obtained from these networks (http://www.hinet.bosai.go.jp/jishin_portal/index_e.php).

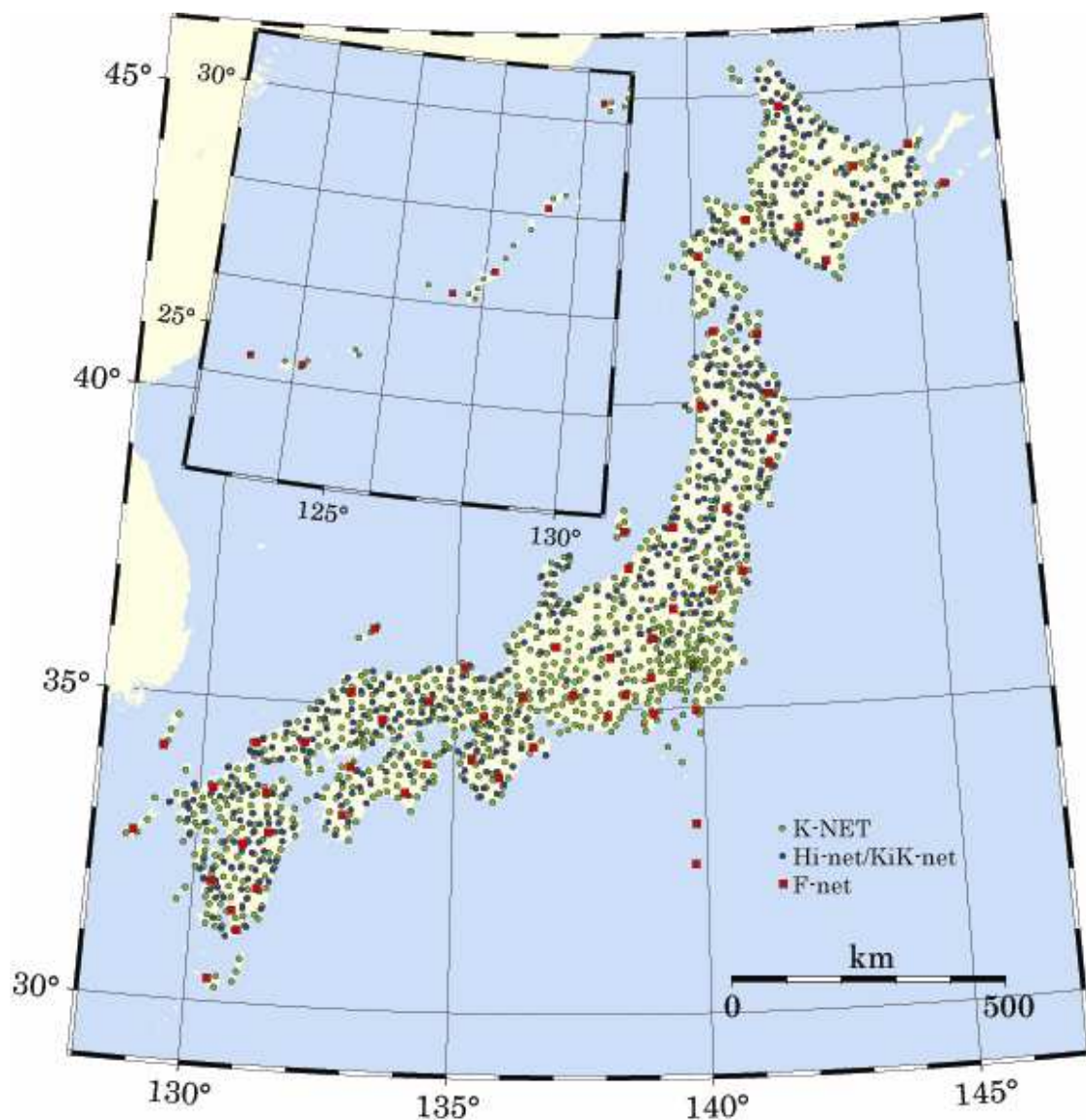


Fig. 8.14 Japanese Seismic Networks (Hi-net, F-net, and K-NET/KiK-net).

8.6.9.4 German Regional Seismic Network (GRSN)

The German Regional Seismic Network (GRSN) (see Fig. 8.15 and Senatskommission (2002)) is comprised of 16 STS2 digital broadband stations with a flat, velocity-proportional response characteristic in the frequency range 8.33 mHz to 40 Hz. Besides monitoring and collecting high-quality data from regional and global seismic events, it is specifically aimed at recording and locating all events with $M_l > 2$ on German territory. All stations are continuously recorded and, with one exception, connected via Internet with each other and with the network center at the Gräfenberg Observatory (GRFO) in Erlangen. The latter is also the center for the Gräfenberg broadband array (GRF). Five stations transmit their data to Erlangen in real time while the other networked stations automatically send data once a day at fixed times during the night or, in case of special events, on request by dialing-up. Thus, the GRSN is a mixture of a physical and a virtual network. For more details see the web site <http://www.szgrf.bgr.de/>.

GRSN/GRF stations

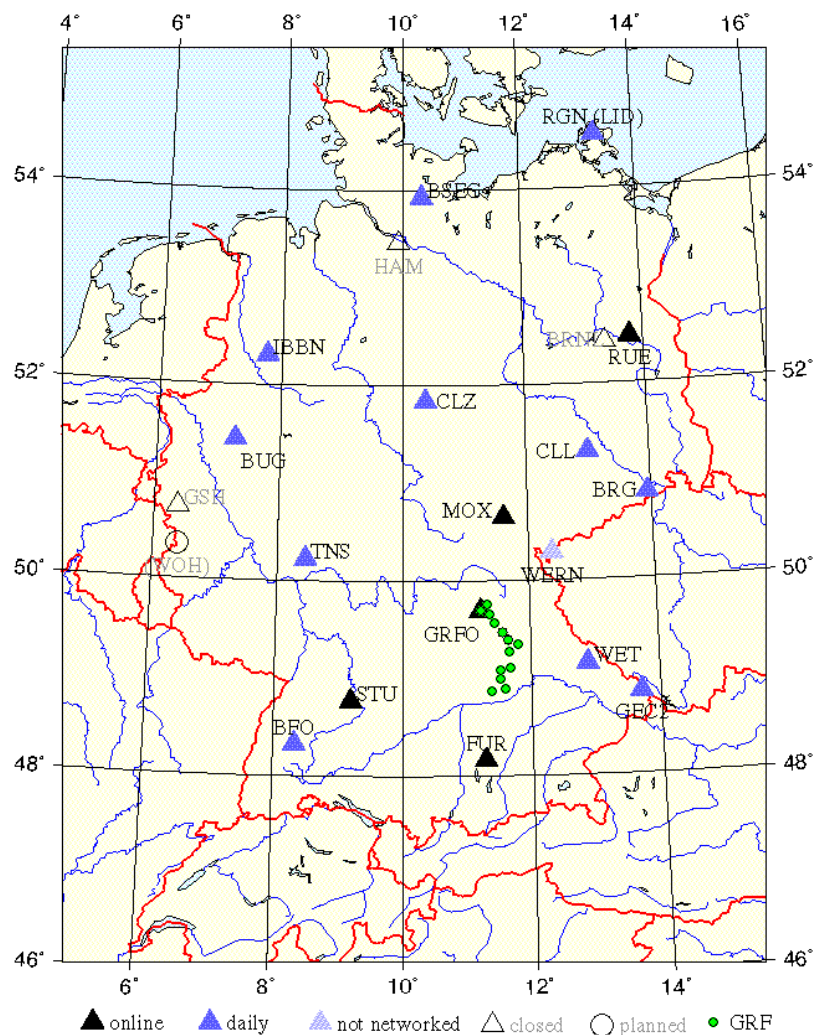


Fig. 8.15 Map of the station sites of the German Regional Seismic Network (GRSN).

8. Seismic Networks

8.6.9.5 Norwegian National Seismic Network

This network is a typical virtual network operated by the SEISNET data collection system. It consists of 22 stations of which six are connected to two analog sub-networks with analog transmission (see Fig. 8.16). Field stations are IRIS, GSN or SEISLOG types with Nanometrics digitizer, Earth data digitizer or multi-channel boards for the two analog networks.

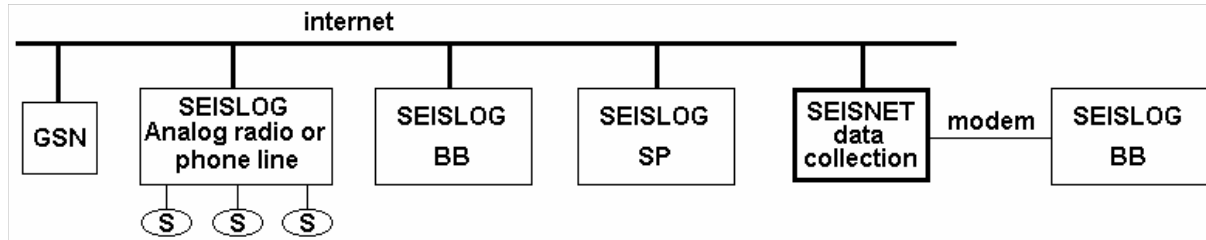


Fig. 8.16 Types of stations in the Norwegian National Seismic Network (NNSN). Nearly all stations are connected by Internet (fixed or ISDN dial up) with the rest connected by dial-up. Abbreviations are: S: seismic stations in a local network; and GSN: Quanterra type of GSN station.

The network covers a large area (see Fig. 8.17) and communication is by Internet (fixed or ISDN dial-up) or by a simple ASCII modem connection. For most stations only triggered data is used, while for three BB stations, continuous data is collected. Each station has its own trigger and, because of the large area, it is rare that an event is recorded at all stations.

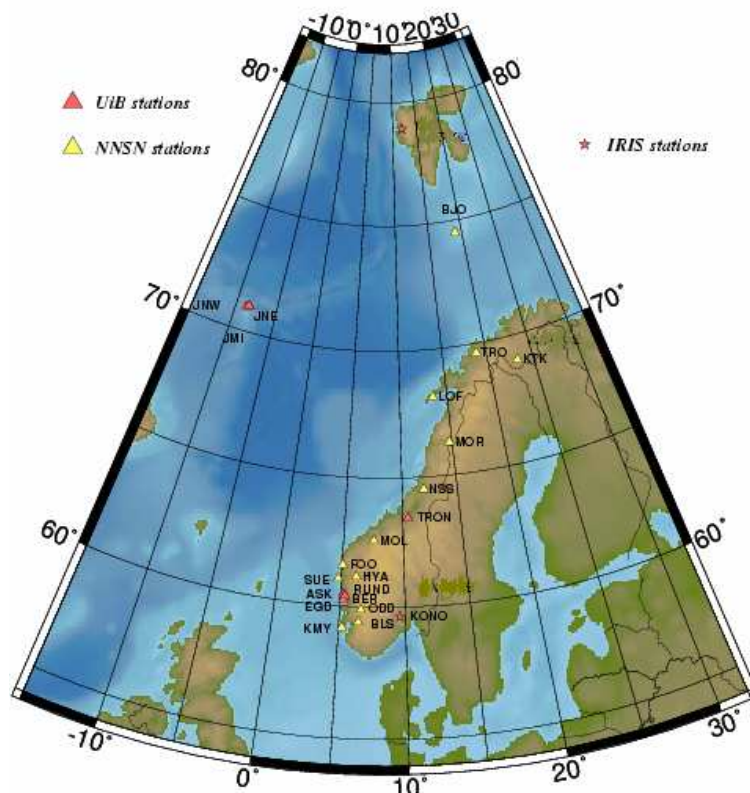


Fig. 8.17 Norwegian National Seismic Network (NNSN).

8.7 Seismic shelters

8.7.1 Purpose of seismic shelters and lightning protection

Civil engineering structures at seismic stations assure a good mechanical contact between seismic sensors and non-weathered, solid bedrock. They protect equipment from temperature, humidity, dust, dirt, lightning, and small animals. The shelter should also provide a good, low-resistance electric ground for sensitive electronic equipment and lightning protection, as well as easy and safe access for equipment maintenance and servicing. The well-engineered seismic shelter structure must also minimize distortion of seismic signals due to structure-soil interaction and man-made and wind generated seismic noise.

Seismic sensors require a stable thermal environment for operation, particularly BB and VBB sensors. With passive sensors, mass position may change too much and with active sensors, temperature changes result in an output voltage drift, which can not be resolved easily from low-frequency seismic signals. This can greatly reduce the signal-to-noise ratio at low frequencies or even clip the sensor completely. Also, many active sensors require mass centering if temperature slips below a few °C or the temporal temperature gradient is too large. Less than 0.5°C peak-to-peak temperature changes in a few days should be assured for good results when using broadband sensors. This is not a trivial requirement for a seismic shelter. Extremely demanding (usually non-vault type) VBB shelters can assure even better temperature stability. Peak-to-peak temperature changes as small as ~ 0.03°C in two months (Uhrhammer et al., 1998) are reported for the very best shelters. Passive SP seismometers and accelerometers are much less demanding than BB and VBB seismometers with respect to the thermal stability of sensor environment. Many will work well in an environment with many degrees of temperature fluctuation.

Two vital, however often overlooked issues with potentially fatal consequences, if neglected, are lightning protection and grounding system.

Lightning is the most frequent cause of seismic equipment failures. One needs to research the best lightning protection for each particular situation (lightning threat varies dramatically with station latitude, topography, and local climate) and then invest in its purchase, installation and maintenance. Several seismic networks have lost half or more of their equipment less than two years after installation because network operators simply neglected adequate lightning protection measures.

A good, low-impedance grounding system keeps instrument noise low, allowing proper grounding and shielding of equipment and cables. It is a prerequisite for a good lightning protection system and is also absolutely required for an interference free VHF or UHF RF telemetry.

In some areas a light fence may be required around the vault to minimize man- and animal-made seismic noise and to protect stations against vandalism. The area covered by the fence may range from 5 x 5 m to 100 x 100 m, depending on several factors, e.g.: what kind of activity goes on around the site; the population density in the vicinity; the ground quality; natural seismic noise levels; and the depth of the vault. Note that fencing often represents a significant portion of the site preparation costs.

8. Seismic Networks

Inadequate site preparation and seismometer placement can easily wipe out all the benefits of expensive, high-sensitivity, high-dynamic range seismic equipment. For example, thermal and wind effects on a shallow seismic vault located on unconsolidated alluvial deposits instead of bedrock can make broadband recording useless. It is pointless to invest money in expensive seismic equipment only to have its benefits wasted because of improper site conditions.

8.7.2 Types of seismic shelters

The three main types of seismic shelters are:

- surface vaults which are the least expensive and by far the most frequently used, however they suffer the greatest level of natural and man-made seismic noise (see 7.4.2);
- deep vaults placed in abandoned tunnels, old mines or natural caves which are usually the best locations with respect to the price/seismic-noise-performance ratio, however, they may not be available and sometimes require extensive cabling, which can increase their cost (see 7.4.3).
- borehole seismic stations with depths from 10 to 2000 m which are the best from the perspective of seismic noise. Improvement of the signal-to-noise ratio of up to 30 dB in ground velocity power density at about 0.01 Hz can be obtained by a 100-m deep hole. For high frequencies above 1 Hz the greatest gains in noise level reduction are realized within the first 100 m of hole depth. Wind-generated high frequency noise can be attenuated as well, however a complete shielding from it is possible only with a very deep borehole (Young et al. 1996). Boreholes are expensive. They may cost from US\$ 5,000 to US\$ 200,000 for the borehole itself, plus the cost of borehole type sensors, which are significantly more expensive than regular surface sensors. Boreholes are used principally in regions covered entirely by alluvial deposits where sites with good bedrock outcroppings are not available; or for the most demanding research work requiring low tilt-noise in horizontal component BB and VBB installations (see 7.4.5).

Shallow boreholes with a depth from a few meter to 15 m are sometimes used instead of surface vaults for pure economic reasons. A 15-m deep surface vault in a difficult terrain may cost more than a shallow borehole of the same depth. Seismic noise improvement in such shallow boreholes is negligible.

In terms of network cost, it might be cheaper to increase seismic station density to achieve a desired detection level rather than install a few borehole systems

8.7.3 Civil engineering works at vault seismic stations

Today, seismic stations are most often in the ground vault form. The massive, solid concrete "seismic piers", traditionally found in old seismic observatories, are no longer built. Above-ground buildings or shelters are not desired at all. In fact, above-ground structures are far less suitable than underground vaults because of potential structure-soil interaction problems as well as wind generated seismic noise caused by the above-surface structural elements. (Bycroft, 1978; Luco et al., 1990). Also, sufficient thermal stability of the environment is

much easier to achieve in an underground vault. If small buildings of any kind already exist at the selected location, make sure the seismometer vault is placed far enough away to minimize wind-generated noise, as recommended already in the old Manual of Seismological Observatory Practice (Willmore, 1979) (see IS 7.3). The structure of the vault should be light and above-ground parts kept to a minimum, creating as little wind resistance as possible.

Surface seismic vaults usually measure between 1 and 2 m in diameter, depending on their depth, the amount of installed equipment and the desired ease of maintenance. They are from 1 to 10 m deep, depending on the depth, quality, and weathering of bedrock at the site. Round or rectangular cross sections are equally suitable. Examples of their design are given in Figs. 7.39 and 7.40.

8.8 Establishing and running a new physical seismic network

8.8.1 Planning and feasibility study

8.8.1.1 Goal setting

The very first step toward establishing a new physical seismic network is understanding and setting the network's goals. These goals can differ significantly (see Tab. 8.1 in 8.3.5). The same applies to the seismic system requirements. Also, just as each country has unique seismicity, seismotectonics and geological formations, so every seismological project has unique contextual combinations that one must consider in order to find the optimal system design for that project.

Several issues must be addressed:

- the user's interests in ranked order: local seismology (epicentral distances < 150 km), regional seismology (epicentral distances between 150 and 2,000 km), and/or global seismology (epicentral distances > 2,000 km);
- the main purpose of setting up a network is usually either to monitor a region's general seismicity or to perform special studies (monitoring of special seismotectonic features, of important civil engineering structures, of engineering and/or nuclear explosions, of man-induced seismicity, etc.);
- the relative importance to the project's alarm function for civil defense purposes: Is the seismological research aimed at the long-term mitigation of the country's seismic risk or at the scientific research of the Earth's deep structure?

Many countries that have little or no seismic equipment should initially consider buying a system to monitor the region's general seismicity. They should expect the new system to help mitigate the region's seismic risk over a long period of time. Nevertheless, even for a project of such a well-defined scope, several questions must still be answered, including the country's needs as well as its financial, personal, and infrastructure capabilities:

- how big is the region to be monitored?

8. Seismic Networks

- what is the seismicity level in the region?
- what is the institution's existing level of seismometry knowledge, and what are its resources for improving that knowledge?
- what is available in terms of communication infrastructure?
- how much money is available to establish the system?
- how many resources are available, per year, to operate and maintain the system, and to support research work using the system's data?

Having realistically quantified the above facts, one can then begin shopping for a seismic system that meets those criteria. There is always a trade-off between desires and reality. This procedure ensures that the new network will perform successfully in the existing environment, if carried out realistically.

If there are few or even no seismology experts available in the country, definitely get help from consultants in the international academic world who are independent of commercial interests. In this early phase, focus on your country's specific socioeconomic needs and seismic awareness, and do not worry too much about specific equipment. Wait until the later phases of network design to contact sales and system engineers from seismic equipment manufacturers for help in defining the technical details of your system.

8.8.1.2 Financial reality

Often, newcomers to seismology do not know how to allocate their finances to obtain the optimal seismic network design. Too often they spend the majority of their network funds purely on purchasing equipment (boxes), even though an identically important expenditure is required for proper operation of this complex equipment. To make sure one has correctly prepared for the purchase of seismic network equipment, one's budget must include money for the following:

- a feasibility study that examines potential network layouts, site selection, and potential seismic systems;
- preparation of remote stations and a central-recording site;
- purchase of the network equipment;
- cost of manufacturer's services, such as installation, training, maintenance, and long-term support;
- cost of salaries and training for the new scientific and technical personnel usually required;
- network operation costs, including personnel, data transmission, data processing hardware and software, printing, backup storage, consumables, and spare parts;
- network servicing and maintenance cost.

The five figures on the following pages show examples of funding apportionment among several different established seismic network projects. The numbers in the figures show the amounts allocated to different tasks (normalized per single station), both in thousands of US dollars and as a percentage of the project's total cost.

8.8 Establishment and running a new physical seismic network

Fig. 8.18 shows an approximate cost distribution (per station) for establishing and operating the global seismic network (GSN) during five years, according to the IRIS plan 1990-1996. The IRIS consortium is composed of about 70 leading universities in USA with a research program in seismology. Not only did this network use the most demanding and expensive equipment available, expensive site preparation and worldwide maintenance were often required which increased the cost per station.

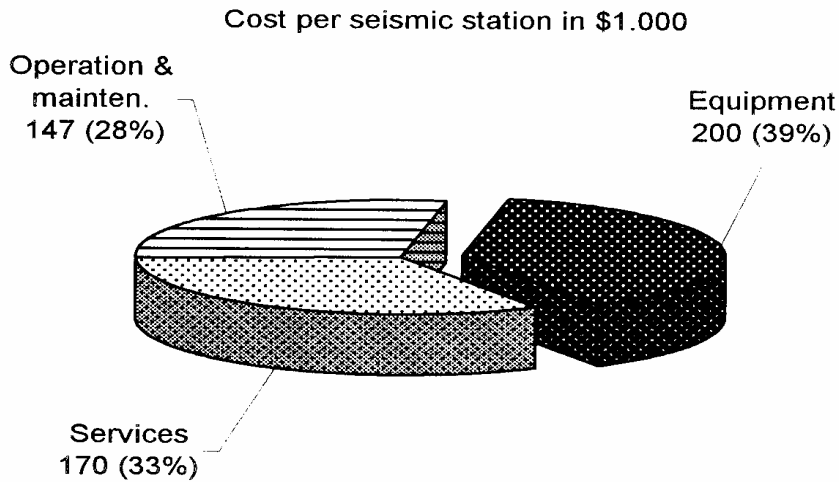


Fig. 8.18 Cost distribution of establishment and 5-year operation of a global seismic network (GSN) station. Number in () is percentage of the project's total cost.

Fig. 8.19 shows details of the IRIS GSN system's establishment costs (excluding all operations costs; again, costs are averaged per station). Surface vault seismic stations are considered only. IRIS constructed many of the sites of GSN network as deep, expensive borehole installations. Even if they are not taken into account in this figure, IRIS still allocated substantial funds for the vaults and to tasks other than equipment buying.

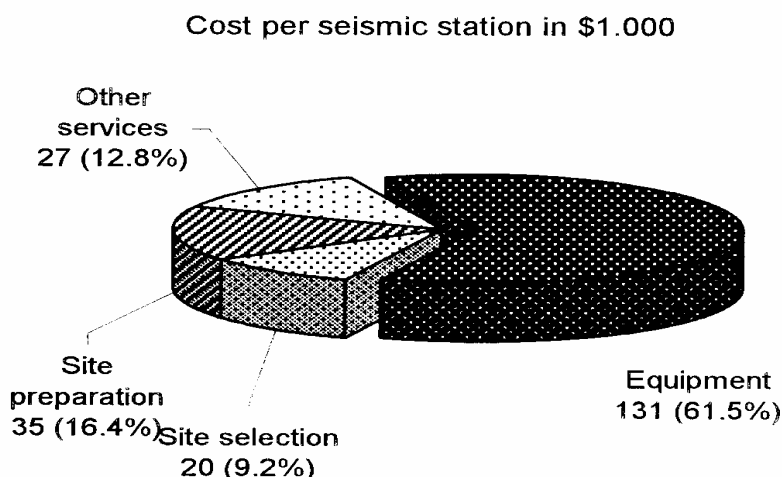


Fig. 8.19 Cost distribution of establishment of IRIS GSN surface vault seismic stations. In this and the following figures the number in () is percentage of the project's total cost.

8. Seismic Networks

Fig. 8.20 shows a distribution of the finances which a developing country spent to establish a reasonably large seismic network, using analog RF telemetry. The country's significant investment in services (21.6%) paid for training at the factory and during installation, as well as one year of the manufacturer's full-time engineer support. These expenditures were critical for the successful start-up and operation of this network.

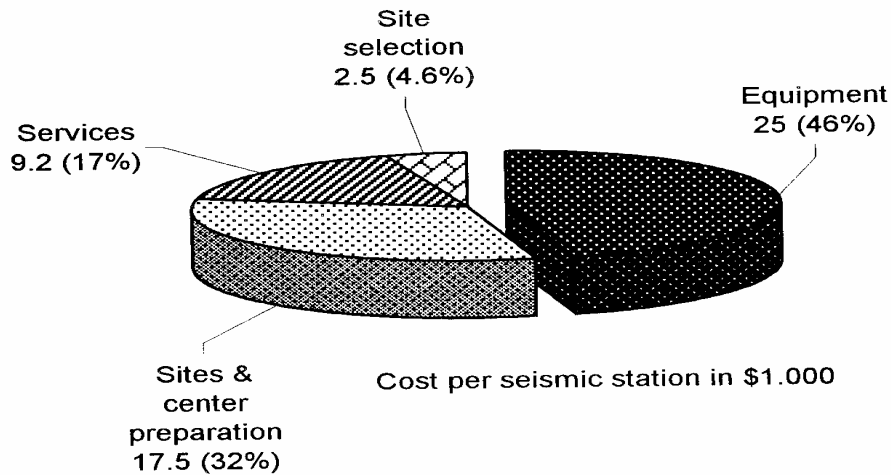


Fig. 8.20 Cost distribution of a relatively large national seismic network with 20 SP seismic stations, strong-motion instrumentation, and analog FM telemetry.

Fig. 8.21 shows a negative example of cost distribution, for a small, yet technologically demanding seismic network. Note the small amount invested in tasks other than equipment-purchases, particularly the site preparation works; 4.1% is surely not sufficient, making it difficult to believe that these sites could provide ample working conditions for such demanding sensors as very broadband (VBB) STS1 and STS2 seismometers. The relatively high amounts spent for services (9.3% for installation) came mostly because the purchasers desired a turnkey type of system. With no experiences in seismometry, the chances of efficiently using the installed equipment seem small.

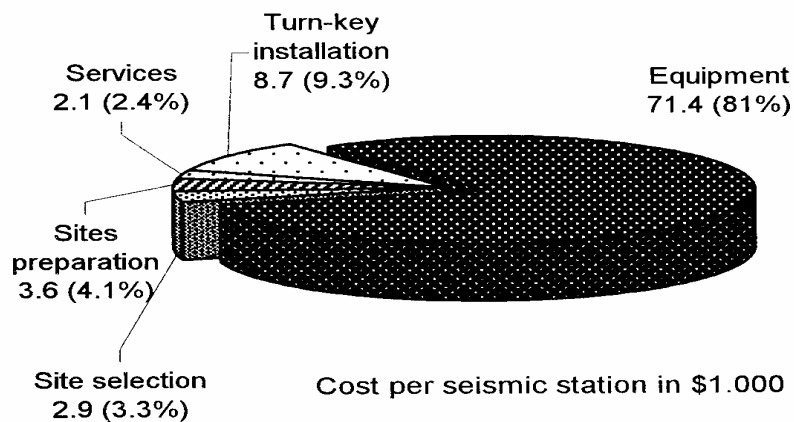


Fig. 8.21 Cost distribution of a small, technologically high-end seismic network with an inappropriate allocation of funds.

8.8 Establishment and running a new physical seismic network

Fig. 8.22 shows another example of a national seismic network installed in a large country and using high-end technology and duplex, digital telemetry system. But again, despite the network's size, the most modern equipment, and the central-recording equipment for two centers, the country only invested about 60 % of its total project funds in the equipment. The other half of the money was spent on follow-up services, including a great deal of training and two years of full-time engineer support provided by the equipment's manufacturer.

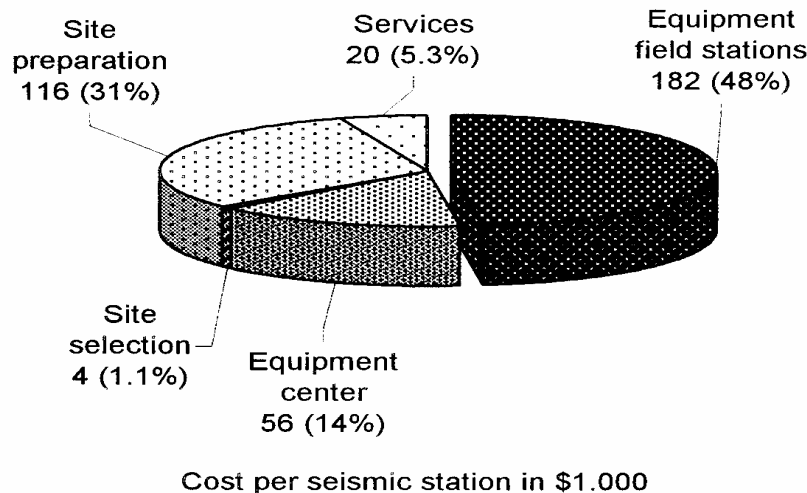


Fig. 8.22 Cost distribution of a very large national, high-end technology, duplex-digital RF and phone-line telemetry seismic network with two central-recording centers.

The funding distributions shown in Figs. 8.17 through 22 are approximate and for illustration purpose only. Generally, the prices of seismic equipment are somewhat lower today. Actual conditions (including the type of network, the level of existing local technical knowledge, local labor prices, and the type of seismic site preparation required) will change from country to country, thus significantly influencing dispersion of the funds. Regardless, the main message of these figures stays the same: one should not spend almost all the allocated funds on equipment. Despite deviations and the differences in absolute cost, these figures seem to indicate that the percentages of the total cost for each task remain nearly the same from network to network. As a rule, one should allocate at least one third of the money for a feasibility study, for establishing the proper working conditions, and for gaining the seismic expertise necessary to exploit the purchased equipment.

8.8.1.3 Basic system engineering parameters

Once the goals are clear and the funds properly allocated, one has to clarify the entire project's interrelated seismological and technological aspects. Attention should be paid to:

- the size and the layout of the proposed seismic network (this should affect the choice of the type of transmission links for transmission of seismic data from the remote stations to the center);

8. Seismic Networks

- the seismicity level to be monitored - in other words, the amount of data one will deal with (this should affect data transmission equipment, central processing site's real-time and offline capabilities, whether the system will need continuous or triggered data recording capabilities, if and what type of trigger algorithm it will use, the type of data archive system; this should also affect the partitioning between weak-motion and strong-motion equipment);
- how accurate and where one wants the network's central-recording site to be located (this will affect the number of stations and the network's layout);
- how wide a dynamic range and resolution are desired for the data acquired from the network (this should influence the choice of technology for data acquisition, as well as the sensor type and data logger designs);
- the importance of the new system having alarm capabilities for civil defense purposes and the desired alarm response time (this should influence which data transmission links will be chosen, as well as how much real-time processing power will be needed at the central-recording site);
- the amount of technical reliability one expects from the system (this should affect the choice of data transmission links, how much hardware system redundancy one can afford for mission critical applications, like auto-duplicating disk drives, tandem computers, etc., as well as decision between 'office-grade' and industrial-grade computers).; and
- the desired robustness of the system in terms of functioning throughout damaging earthquakes (this should influence the selection of data transmission links, of power backup utilities for the remote stations and the central-recording site, and last but not least, of seismic vulnerability of the building that houses the central processing site).

After reasonably assessing these aspects and making a decision for each unique situation, one can then create a rough system design and begin selecting equipment that best matches these goals. Obviously, certain tradeoffs will need to be made.

8.8.1.4 Determining the layout of a physical seismic network

Determining a layout for one's seismic network requires two steps: 1) determining the total number of stations required and their approximate locations, and 2) determining the final station locations.

Since the first stage closely relates to the goals of the network and available funds, the purchaser of the network should delineate how many stations he requires and can afford to set up, and where approximately they should be located.

Since the second stage typically requires knowledge of seismometry, seismo-geology, data transmission technology (if applicable), and seismic equipment capabilities and limitations, the customer may want to have it performed by the manufacturer of the network equipment.

8.8.1.5 Number of stations in a physical seismic network

The number of seismic stations should be based on the goals of the network, the size of the network, and, of course, on the available funding. For space reasons we will not go into details on the minimum number of stations that are technically required for a given seismological goal, but following there is a short overview.

For determination of an event location (based on phase readings), the theoretical minimum is four independent measurements, such as three P-arrival times and one S-arrival time. However, remember that such results, due to their uncertainty, usually have little value. For a more accurate determination of location, six stations acquiring good records of an event should provide scientifically credible evidence of an event's location, and ten to fifteen stations acquiring good quality records of an event should provide an acceptable basis for more sophisticated studies of the earthquake's source properties. Waveform analysis of digital, high dynamic range, three-component records leads to good results with fewer stations. In principle, one three-component station can determine the magnitude, epicenter and the origin time, however this requires a very well known model of the Earth.

Larger countries or regions will require a greater number of stations, unless, of course, their interest is only in the strongest earthquakes. Note that seismic researchers do not care much about the total number of stations in a network; what counts is the number of stations in the network that adequately record a given event ('adequately record' means that they triggered data acquisition and that the records have a high signal-to-noise ratio). For networks covering a large region, large epicentral distances often prevent the triggering of distant stations, or the earthquake signals get buried in the seismic noise. Thus the total information available for a given event, unless it is a strong one, typically comes from only a portion of the total network.

8.8.1.6 Laying out a new seismic network

Although the spatial distribution of the stations in a seismic network is very important for the network's capabilities of event determination, due to limited space we will only give a few, brief recommendations. For seismic arrays and their special location procedures and performance see Chapter 9.

On a map, subdivide the region to be monitored into a series of reasonably irregular triangles having approximately equal areas. Avoid very narrow, long triangles. Avoid thinking in rigid patterns, such as locating the stations into perfect triangles, circles or straight lines, because such rigidity may result in "blind spots" - that is regions with poor event location determination. The corners of these triangles are the approximate points where one will try to locate seismic stations. Take into account any existing seismic stations in neighboring countries or regions as well. If there are none, push some of seismic stations as close as possible to the borders of the region being monitored.

The geometry of the network will determine the accuracy of location in different directions, and a reasonably regular grid will give most uniform location accuracy. The worst configuration is a network with stations that are aligned (see Fig. 8.23 as an example).

8. Seismic Networks

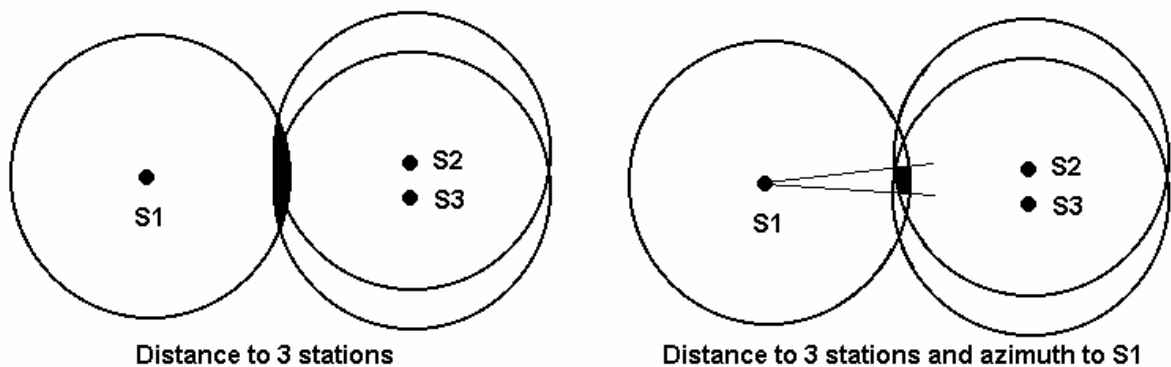


Fig. 8.23 Network geometry of aligned stations. The figure to the left shows three stations (S1, S2 and S3) almost aligned in the x-direction (left - right). The event has been located by using the distances to the three stations, and the shaded area in the middle gives an indication of the area within which the epicenter can be found. The figure to the right shows the same situation except that an azimuth determination has been made with three-component records at station S1. This limits the y-direction within which the epicenter can be located and thus reduces the epicenter error.

It is advisable to have realistic expectations concerning the earthquake depth determination based on phase readings. Previous studies (e.g., Francis et al., 1978; Uhrhammer, 1980; and McLaren and Frohlich, 1985) have shown that the accuracy of focal depths for shocks occurring in the vicinity of a seismic network is primarily a function of the geometry of the network, the number of the P- and S-phase arrivals read, and the adequacy of the assumed velocity model. Depths are generally more accurate for earthquakes where the distance from the epicenter to the closest station is less than the calculated focal depth for events located within the network or on its periphery. The accuracy of focal depths usually increases as the number of picked S-phase arrivals increases; however, systematic S-phase timing errors (due to mistaken identification of a converted phase as S) or "bad" S picks can degrade the focal depth estimation accuracy by several kilometers even when the azimuthal coverage is good (Gomberg et al., 1990). Estimate the depth of the shallowest events for which good depth control is desired then make sure that the average distance between stations in the seismic network does not exceed twice that depth. The latter is admittedly a tough requirement, especially in the large regions and in the regions where the events are typically shallow! Only a few small countries and practically none of the larger countries can afford such a dense network.

Yet, one can still temporarily afford to make the network denser in places. Buy a few portable seismic stations and then temporarily install them in any sub region of particular interest at the time. For example, such temporary networks are regularly established to perform aftershock studies in the epicentral region immediately after a strong event. At least for a time, this will drastically increase the seismic network's density in the region of interest, allowing the determination of much better locations, depths, and focal mechanisms. Such studies can be done with low-cost portable instruments since the main purpose is to get more phase readings.

Have realistic expectations also about the system's earthquake epicenter determinations. For events outside the seismic network, expect large errors in determining epicenters. Generally, do not expect reliable determination of events, unless the "seismic gap" (the largest of all angles among the lines connecting a potential epicenter with all the stations in the network that recorded the event) is less than 180 degrees. Thus, to increase the accuracy of epicenter determinations, especially for the events outside the seismic network, one needs to include data in the analysis from seismic stations in neighboring countries, as well as from any other available national or international sources. Acquiring this wider database is usually necessary for determining reliable event locations on the border or outside any seismic network. A virtual seismic network would typically be able to automatically collect such data.

8.8.2 Site selection

The matter of seismic site selection is too often not given sufficient depth of study and attention in spite of the fact that a weak-motion seismic network can only have a high detection threshold if the sites have satisfactory noise levels, no matter how technologically advanced and expensive equipment is. If seismic noise at the sites is high, all or a part of the benefits of modern equipment with large dynamic range are lost. If an excessive burst or spike-type, man-made seismic noise is present, high trigger thresholds and therefore poor event detectability will result. If stations are situated on soft ground, the VBB or even the BB recording can be useless and SP signals may be unrepresentative due to local ground effects. If the network layout is inappropriate, some event locations may be inaccurate or even impossible. For good results, many factors at the sites must be taken into consideration. A professional site selection procedure is therefore essential for success of any weak-motion seismic network.

Generally, it is best to begin the process of site selection by choosing two to three times as many potential sites as one actually plans to use. Then each site is studied to see which sites meet as many of the criteria as possible. Gradually, one will eliminate the poorest sites and get down to the number of sites required plus two or three. By comparing the results of computer modeling of a few of the most likely network layouts (see IS 7.4) one will be able to make an informed decision about the best network.

Note that one should not rely too much on algorithms designed to optimize seismic network configuration (e.g., Kijko, 1977; Rabinovitz and Steinberg, 1990). This is because the theoretical optimum configuration can hardly ever be realized nor their predicted theoretical potential information gain be exploited under real conditions. Stations often can not be installed at the recommended locations due to factors such as inaccessibility, poor ground conditions, proximity of strong noise sources, lack of required power, or unavailable communication link.

On the other hand, these programs may be of help selecting the best of a few realistic network configurations (e.g., Trnkoczy and Živčić, 1992; Hardt and Scherbaum, 1994; Steinberg et al., 1995; Bartalet al., 2000). For an existing network, they could help decide how best to improve the network by adding new stations or which stations, if removed, would cause least harm to the network. Keep in mind, however, that the best configuration for locating earthquakes may not be optimal for source mechanism determinations, tomographic studies or other tasks (Hardt and Scherbaum, 1994).

8. Seismic Networks

Only the basic steps of the site selection procedure will be presented here. More detailed information can be found in 7.1 and 7.2. The site selection procedure encompasses office and field studies.

Off-site, "office" studies are relatively inexpensive and are therefore the first to be performed. From an office, one can study maps and contact local authorities to gather information about potential sites. The first step is defining the geographical region of interest. The next step is to gather and examine existing geological faults, seismotectonic features, and all available information about seismicity in the area. If the main goal of the new network is monitoring general seismicity in an entire country, this stage is, of course, simpler. Then prepare a simplified map of regional seismo-geologic conditions showing the quality of bedrock. The rule is: the higher the acoustic impedance (acoustic impedance is the product of the density and the velocity) of the bedrock, the less the seismic noise and the higher the maximum possible gain of a seismic station. Next, study the topographical aspects of the possible locations. Moderately changing topography is desired. To study man-made and natural seismic noise sources in the region, one should evaluate road traffic, railway traffic, heavy industry, mining and quarry activities, agricultural development of the region, and any other sources of man-made seismic noise around the potential sites, along with the natural sources like oceans and lakes, rivers, waterfalls, animals, etc. (see IS 7.3). Much of the information we need can be found on maps or obtained by asking questions of local authorities.

If the new network is a radio frequency (RF) telemetry system, one has to correlate RF data transmission requirements with seismological requirements. Topographic profiling of RF paths based on topographical maps is performed. The next section "VHF, UHF and SS radio-link data transmission study" explains why this is highly recommended. If one plans the use of phone lines for data transmission, their availability and the length of new phone lines need to be checked. If one plans to use main power, the availability of main power lines and the distances to which new lines would have to be laid must be checked. The alternative is batteries, preferably charged by solar panels.

It is also very important to research land ownership, animal habitats, and future land use plans for the potential sites. It makes no sense to undertake extensive studies if one will be unable to use certain sites because of property ownership issues, endangered or protected animal species issues, or if it appears that future development will make the site unsuitable for seismic stations.

The climate at the sites also influences site selection and preparation. Temperatures, wind, precipitation, insulation data (for solar-panel powered stations), lightning threat, etc. may all influence site selection.

Once one has gathered all this information, it is likely that half or more of initially proposed sites will be eliminated for one reason or another.

Field studies are the next step in the site selection process. Expect to make several visits to each site. A seismologist familiar with seismic noise measurements, a seismo-geologist, and a communications expert (if we are considering a telemetry network) should all visit each site. They should verify the ease of access to the site, search for local man-made seismic noise sources, which may not be apparent from maps, perform seismic noise measurements, study the local seismo-geological conditions at the site, investigate the local RF data transmission conditions (if applicable), and on site verify power and phone line availability.

Local geology should be studied to determine its complexity and variations as well as seismic coupling between local seismic noise sources and the potential station site. To the extent possible, uniform local geology is preferred for seismic stations. The degree of weathering that local rocks have undergone is another important parameter, although it can give an unreliable estimate of the required depth of the seismic vault. The ideal approach for high-quality site selection is to make a shallow profile at each potential site to make sure the vault will reach hard bedrock. If this is too costly, then expect surprises when you begin digging seismic vaults. Many times it is a matter of almost pure chance what one might run into. Note that in some areas it will not be possible to reach bedrock.

After all these studies one ends up with two or three potential sets of the best suitable seismic stations. The resulting network layouts are then studied for the best network performance by computer modeling. By comparing the results, one will be able to make an informed decision about the final seismic network layout.

8.8.3 VHF, UHF and SS radio-link data transmission study

8.8.3.1 The need for a professional RF network design

The most frequent technical problems with radio-frequency (RF) telemetry seismic networks originate with inadequately designed data transmission links. Therefore we are discussing this topic separately. For more detailed description see 7.3.

The design of RF telemetry links in a seismic network is a specialized technical matter, therefore guessing and "common sense" approaches usually cause problems or even complete project failure. There are quite a few common misunderstandings and oversimplifications. The amount of data that must be transmitted and the degree of reliability required for successful transmission of seismological data are frequently underestimated. The significance of "open line of sight" between transmitters and receivers as a required and sufficient condition for reliable RF links is misunderstood. Frequently, over-simplified methods of link verification are practiced. However, the real issues in the RF link design and link reliability calculations are: the frequency of operation, Fresnel ellipsoid obstructions by topographic obstacles, the curvature of the Earth, the gradient of air reflectivity in the region, expected fading, potential-wave diffraction and/or reflections, time dispersions of the RF carrier with digital links, degradation of signal strength due to weather effects, etc. All these are specialized technical issues.

To prevent failures, a professional RF survey in planning a new seismic network is strongly recommended. It includes the calculation of RF links based on topographical data and occasional field measurements. A layout design based on a professional RF survey can significantly increase robustness of the radio network. The survey will:

- determine the minimum number of required links and RF repeaters in the network. Note that, in most designs, every RF repeater degrades data quality to some extent, (particularly for analog transmission), and obviously increases the probability of link-down time and the price of the system;
- determine the minimum number of licensed frequencies required;

8. Seismic Networks

- determine the optimal distribution of RF frequencies over the network, which minimizes the probability of RF interference problems;
- result in a less polluted RF space in the country;
- determine the minimum antennae sizes and mast heights, resulting in potential savings on antenna and antenna-mast cost.

The cost of a professional RF survey represents generally a few percent of the total investment. We believe that the combined benefits of an RF survey are well worth the investment, and are a major step toward the reliable operation of the seismic network.

8.8.3.2 Problems with RF interference

Radio frequency interference caused by other users of VHF or UHF RF space in many, particularly developing countries, is quite a common and difficult problem. There are several reasons for that. In some countries, there is confusion and a lack of discipline in matters of RF space: army, police, security authorities, and civil authorities may all operate under different (or no) rules and cause unforeseen interference. In other countries, poor maintenance of high-power communication equipment results in strong, stray radiation from the side lobes of powerful transmitters. This radiation can interfere with seismological radio links. Extensive, unauthorized use of walkie-talkies can also be the cause of problems.

The best, and more or less the only solution is to work closely with local RF experts during the design phase of a seismic network. They are practically the only source of information about true RF space conditions in a country. Note that RF interference problems are generally beyond control of seismic system manufacturers and seismological community. All RF equipment, no matter who manufactures it, are designed to be used in an RF space where everybody strictly obeys the rules.

Interference problems can be solved, or at least mitigated, only by employing local experts on the seismic network buyer's team while designing a network. One also has to, as much as possible, avoid other high-power RF space users (see IS 7.2).

8.8.3.3 Organization of RF data transmission network design

An RF layout design is always an integral part of a seismic site selection procedure. Theoretically the seismic system purchaser can perform it if he has adequate knowledge in this field. However, practice shows that this is rarely the case. Even if the RF survey is purchased from an independent company or from a seismic equipment manufacturer as a part of the services, the process still requires involvement of the seismic system buyer. For efficient office and fieldwork, the customer has to prepare beforehand an approximate initial seismic network layout, road and topographic maps, and climatic data. He has to make available knowledgeable staff members and well-informed local people acquainted with local conditions at the sites, who will join the site selection and RF survey field team. He should also assure efficient logistics during the fieldwork.

A detailed list of what to prepare is given in the IS 7.1.

8.8.4 Purchasing a physical seismic system

8.8.4.1 The bidding process

While sending out a Request for Proposal and asking for bids on a new seismic system may be a good way to get started, there are a number of important issues one must be aware of when requesting bids or proposals. First, certain technical requirements and business standards must be met in order to be able to compare "apples to apples" when it is time to analyze the system proposals received. Second, in order to find the most suitable system, one needs to invest a fair amount of additional time in research and investigation before sending out the bid specifications. Namely, some very important issues may be hard to define in the Request for Proposal. The proposals can easily give unclear information regarding the following crucial issues:

- actual reliability of the equipment;
- actual user friendliness of the system;
- availability of long-term support by the manufacturer including true availability of spare parts in the next years;
- financial stability of the manufacturer.

In the Request for Proposal, one should not forget to state clearly the goals of the new seismic network and to rate their relative importance. Too often what one wants to accomplish with the new system is not clearly described and the goals are not prioritized, resulting in vague instructions to manufacturers and hence, potentially disappointed customers.

In the Request for Proposal one should include all relevant basic technical information, so that the manufacturer can put together the corresponding technical solution. However, we recommend that the Request for Proposal does not contain an over-detailed technical description of the desired system (unless one already decided who should win the bidding process, which is illegal, but not so uncommon a practice). With too many technical details, one can end up limiting one's choices and even disqualifying the most suitable system just because a relatively unimportant technical detail can not be fulfilled.

We strongly recommend not pushing manufacturers to design a new system or add functionality to an existing system specifically for your needs. In spite of the fact that the majority of seismic equipment manufacturers are willing to design such 'custom made' systems, one should know that there is usually a high price for this commodity. Such systems will often be expensive, and as a 'prototype', obviously less tested than 'standard products' and more difficult to support in the long run.

Avoid buying brand new systems in the market unless you are really assured of excellent support from the manufacturer. Brand new systems frequently have more problems than older more tested systems. Their use will require a high level of knowledge and a really good working relationship with the manufacturer while solving these problems.

Some countries are required by law to accept the lowest bid. Unfortunately, crucial qualities like services, equipment reliability, user friendliness of the system, amount of factory testing,

8. Seismic Networks

setup and long-term support might be easily lost if one bases the choice solely on the lowest price for all of the stated (but practically never really sufficient) requirements of the bid. In a legitimate desire to keep the price as low as possible, manufacturers will most probably cut difficult 'to measure' qualities, particularly short- and long-term support, and services. This is a dangerous situation, particularly for less experienced customers. One way of avoiding this danger is spelling out explicitly all services required in the Request for Proposal. This is the place to be exact; specify services and support type, their goal, technical level expected, place and duration, parts and labor warranties; pricing structure after warranties expire, timeliness requirements, etc.

Manufacturers of seismic equipment often offer a turnkey system whereby they will purchase all of the necessary components not made by them. They will include their administrative labor costs for acquiring these components. Do not assume that they will be able to purchase every item at prices lower than you will be able to. Federal, state, and local governments and universities (typical operators of seismic networks) often have secured special pricing from vendors that can be substantially cheaper than what seismic equipment manufacturers can obtain.

8.8.4.2 Selecting a vendor

When evaluating the proposals, one should assess not only the technical qualities of the system, but also the quality of every manufacturer. What is their reputation? How long have they been in the seismological equipment business? Obviously, ask for references from users of the same or similar systems and learn about how well the company served them. As you get close to decision-making time, make a personal visit to the manufacturers whose offers you are considering seriously; meet their employees and tour their facilities. A company that serves you well before you have bought their product is more likely to continue to serve you well after you will have bought and paid for their product. Often, manufacturers will pay at least some of the expenses for new potential clients to visit their facilities and meet their staff.

Carefully select the people who will participate in these visits. In addition to a member fully responsible in financial issues, one member of the team should be the individual responsible for future operation of the network. Other members of the team should be those most knowledgeable and experienced in seismology, no matter what their position in the hierarchy or which institution they belong to.

Also take into consideration the size of the company. The relatively small ones may simply not have the "manpower" for long-term customer support of big projects, no matter how sincerely they want to support you. They may manufacture good, technically advanced equipment, but their ability to support large national projects, their longevity, and their system-testing capacities may cause problems later.

Generally, one would not expect the best results from companies that merely assemble systems but are not experts themselves in seismology. On one hand, the assembler of the system may be incapable of providing seismology-related technical support and, on the other hand, the actual manufacturer of the seismic equipment may not be willing to spend much time supporting a group that did not purchase the equipment directly. Experience shows that such projects rarely result in a happy end.

Ask for visits with manufacturer's sales or system engineers. Data sheets themselves seldom give enough technical information about a seismic system. Sales and system engineers can provide all the details of a particular technical solution. Such visits, however, are less appropriate during the early stage of the project when one's goals are not yet specifically set. It is understandable that sales representatives will be biased toward the equipment of the manufacturer they represent.

8.8.4.3 Equipment selection

As already mentioned, data sheets of seismic equipment alone seldom provide enough information. In addition, it is not easy to compare the data sheets of various manufacturers because each one, to some extent, uses a different system of specifications, measurement units, and definitions of technical parameters. For example, there are at least ten different ways of expressing intrinsic noise and dynamic range of seismic sensors or data. All of these factors must be well understood for a fair and accurate comparison. This can be best accomplished through in depth contact with the manufacturers and with the help of additional written information. Be sure to ask for all possible information about the system, including copies of the user Manuals (the customer can examine the quality of technical documentation provided with the system, which is also an important element) and the published results of independent testing.

Ideally, we recommend buying one piece of key equipment such as a sensor, a data logger, processing software with demo data or an RF link and testing the product yourself. In the case of large projects with adequate financing, manufacturers will often loan equipment for testing purposes free of charge. While it is ideal to get some firsthand experience before settling on which new system to purchase, this approach requires personnel who are knowledgeable about seismology and instrumentation. Be cautious about assembling products from different manufacturers in one system. It is not a simple or easy task to interface different products in terms of the dynamic range, the signal to noise ratio, the full-scale ranges, the baud rates, the processing power and the power supply sources. Stay with one manufacturer if possible, or, when that is not feasible, arrange to have one manufacturer be explicitly, contractually responsible for interface problems and the functioning of the system as a whole. Understand also that the time spent solving equipment-interfacing problems unique to a given customer also has its price.

Each technical system, or element in it, properly operates within a certain set of parameters, or "range". One should be familiar with these ranges and know where, within this range, the system will actually operate. If one or more of elements of the system are to operate at the extreme end of their operation range on a regular basis, most probably a different element or system should be selected. Note that there is always a price to pay for operating equipment under extremes. The results will often be disappointing if, for example, one plans on using the maximum possible number of channels in a FM radio-frequency link, or would like to acquire data with the maximum possible number of channels in a seismic system, or exploit the maximum number of channels in seismic data analysis software, or operate the hardware at extreme temperatures, etc. In such cases it is often better to find another system or system element, whose midrange parameters can accommodate one's needs. It is always best to have a safety margin in your system and do not expect it to operate continuously, efficiently, and reliably in extreme ranges.

8.8.4.4 The seismic equipment market is small

The global market for seismic systems and equipment is naturally quite limited. With very few exceptions, instruments are produced in small numbers. Inevitably, this sets a limit to the quantity and thoroughness of testing of the newly developed equipment. This is not a result of a lack of quality or commitment on the part of manufacturers in this field, but a simple, economic reality. Compared to industries with a far broader and more powerful economic base, like computer and electronic companies, seismic equipment moves into the field with relatively little testing, even by the most reputable manufacturers. In general, the equipment arrives with a higher than average number of bugs and technical imperfections that will need to be solved by the manufacturer and the user working in tandem.

The majority of seismic network manufactures have relatively little experience in seismic signal processing and as a general rule, do not have adequate software. It simply does not pay to develop this kind of software. On the other hand, there are public domain software packages available, which can solve these tasks and these are often offered by the manufactures. However, very little training is offered and a new network operator may end up with an expensive network but very primitive processing tools. Therefore, obtaining adequate processing software and training is an important and integral part of the planning of a new network. Unfortunately this is often not the case and the value of the network can be greatly reduced.

Currently, most seismic equipment and technical documentation is less user-friendly and complete than desired. Customers are rarely given comprehensive and easy-to-follow instructions on how to setup and use the system. Reputable manufacturers of seismic equipment compensate for this situation with committed and effective customer support services.

Due to the fact that, in many developing countries, there is often a lack of knowledgeable experts who can cope with the technical problems by themselves, it is truly necessary to maintain a long term working relationship with the provider of the seismic system. The manufacturer's support and a reliable, knowledgeable and friendly relationship thereafter is one of the most important and crucial issues for success of a seismic project in a country with little or no experience in seismometry.

8.8.5 System installation

8.8.5.1 Four ways of physical seismic system installation

Generally we can define four methods for the installation of a new seismic system.

- 1) The user installs the new system. Only 'boxes' are purchased. In this option, the customer is responsible for the proper functioning of the system as a whole and the manufacturer remains responsible for proper functioning of the elements, unless they are improperly used or installed. This approach gives the user great flexibility, but also the main responsibility. It is only an option if qualified staff can be appointed to this task and/or if local or international organizations can participate.

8.8 Establishment and running a new physical seismic network

- 2) The manufacturer demonstrates installation on a subsystem (a few stations, a sub-network). The user installs the rest. In this case, the manufacturer and the user, share responsibility for the system functioning. This approach is often successful. However, the customer must have a certain amount of experience with seismic, computer, and communication equipment for this method to work.
- 3) The manufacturer installs the whole system with a full assistance from local technical and seismological staff that will be responsible for running, maintaining, and servicing the network in the future. Responsibility for making sure the system functions lies with the manufacturer. The main benefit of this approach for the users is that they learn enormous amount during the hands-on installation and associated problem solving time. This is actually the most efficient method of training. The user should not expect savings and potential shortening of the installation time but rather some additional time and effort will be required from manufacturer. In our experience, this is the best way of installing a seismic network in a country where little or no experience with seismic equipment exists.
- 4) The manufacturer has the complete responsibility for installing a turnkey system and making sure it functions adequately without any assistance from the customer. In this case, the network will no doubt be successfully installed, but local staff members will not learn about its operation nor how to solve potential future problems. This approach is adequate only for the countries with a high level of seismological and technical knowledge.

Two technical details relating to system installation should also be mentioned here.

In the case that the system buyer will install the system or its parts, do not select the 'standard length' cables sometimes offered by seismic system manufacturers. The 'standard' cables rarely work well in the field. They are, according to Murphy's laws, always too short or too long. Do not loop or coil extra cable length because that will increase the threat of lightning damage, unnecessarily increase system noise, and in the end, you will be paying for the "extra" cable. Rather, ask for bulk cables with separate connectors or cables of a reasonable length margin and one-side mounted connectors only. During installation in the field they can then be cut to precisely the desired length. Note, however, that reliable, high quality soldering of connectors requires experience. Inexperienced technicians have little chance of performing the job correctly and poorly installed connectors are among the most frequent causes of problems at a seismic station.

Note also that, in case of purchased installation, the seismic station sites must be completely prepared before the manufacturer arrives to install the system. All construction works must be finished, logistics organized, and access permits prepared (if applicable). Time and time again, manufacturers are faced with unprepared sites when arriving for the installation. A significant loss of time results and often forces both parties to accept undesirable "last minute" technical improvisations and compromises during installation. This generally leads to less reliable functioning of the system. Note that services are usually paid by time, so an efficient use of this time is to customer's direct benefit.

8.8.5.2 Organization of civil engineering works

Whatever construction work is needed to prepare the sites, it is usually arranged and paid for by the customer of the new network rather than the manufacturer of the seismic equipment. Very large national projects may be an exception to this rule. Site construction will require a great deal of preparation and involvement by the system buyer. There are generally a number of good design alternatives from which to choose and we suggest hiring a local civil engineering contractor to design the best solution for a particular system and specific circumstances in the country. A seismo-geologist and a civil engineer should supervise the construction work. Their main responsibility is assuring that the enclosure is watertight and that the sensors have a good contact with solid bedrock. The system's manufacturer can usually provide sketches and suggestions for the procedure and may also supervise the work, but usually does not provide true structural engineering drawings for seismic shelters. Working in tandem with a local civil engineer is usually a better choice because the engineer will be familiar with all local circumstances that are unknown to the manufacturer of the seismic equipment. Local builders know best what materials and construction methods are available and workable in a particular country. Do not "over-engineer" the project; it is usually not necessary to have a big civil engineering firm design every detail, oversee all seismic site preparation, and then build the site.

8.8.6 Running a physical seismic network

8.8.6.1 Tuning of physical seismic networks

Before a seismic network can function with its full capacity, it must be tuned to local seismo-geological and system conditions. Tuning is especially important for networks that run in triggered mode. Unfortunately, many operators are not aware of the importance of fine-tuning.

The local and regional Earth's structure, the seismic network dimensions and layout, regional seismicity, seismic noise levels and spectra at station sites, seismic signal attenuation in the region, all play a role in these adjustments. One will not be able to correctly tune the system's recording and processing parameters until one has acquired sufficient experience with natural and man-made seismic noise and earthquake signals at all the sites in the network and until one fully understands the parameters that have to be tuned. Therefore, tuning a network takes normally months of systematic work. Because of the long time required to accomplish this task, the system's manufacturer simply can not do it. Only the network operator can correctly tune the network. Moreover, since seismic noise conditions at the sites may change with time, new stations may be added, the goals of the network may change, etc., re-tuning of the network will probably be required from time to time. In reality, tuning a seismic network is an ongoing task, which can not be done 'once and for all.'

Actual tuning procedures are manifold. We will just enumerate the most common hardware and real-time processing parameters that need to be adjusted in a physical seismic network. They are:

- seismic gain at individual stations;
- signal conditioning filter parameters;
- pre-trigger, band-pass filter parameters;

8.8 Establishment and running a new physical seismic network

- trigger algorithm parameters, which usually include:
 - trigger threshold values;
 - dettrigger threshold values;
 - trigger time windows' duration and other parameters;
 - weights of individual stations in coincident trigger algorithm;
 - grouping of stations into sub-regions for a coincidence-trigger algorithm;
- pre-event time duration;
- post-event time duration;
- minimum runtime and maximum runtime duration; and
- adjustment of the length of the propagation window.

Detailed discussion of individual parameters is beyond the scope of this text. Note that not all enumerated parameters exist in every seismic network and that some adjustments may be missing from this list. A thorough description and parameter adjustment procedure for the short-time-average/long-time-average (STA/LTA) seismic trigger algorithm is given in the annexed IS 8.1 on “Understanding and parameter setting of STA/LTA trigger algorithms”. Further guidelines for other network tuning procedures may be added later as complementary Information Sheets.

The following are some of the offline seismic analysis software issues that must be studied and prepared for efficient routine observatory work, and parameters that have to be adjusted for correct analysis of seismic records:

- files containing information about data acquisition parameters (data acquisition configuration file(s));
- files containing data about geometrical configuration of seismic stations (network configuration file(s));
- parameter files containing sensor calibration data;
- Earth model parameters of event location program(s) (layer thickness, seismic-wave velocity, seismic station weights, epicentral distance weighing function, and similar parameters depending on the program used);
- automatic phase-picker parameters;
- magnitude scale parameters;
- preparation of different macros and forms for routine, everyday analysis of seismic signals.

Some parameters, e.g., for the Earth model, are often insufficiently known at the time of network installation and require long term seismological research work, which results in gradual refinement of the model and increasingly better event locations.

No manufacturer can optimally pre-adjust all these parameters to the specific local conditions. Seismic networks usually come with a set of default values for all these parameters (factory pre-selected values based on 'world averages'). These values may work sufficiently well for the beginning of network operations, however, optimum seismic network performances requires reconsidering most of them.

8. Seismic Networks

8.8.6.2 Organizing routine operation tasks

Keeping one's network failure-free and in perfect working order while waiting to record earthquakes year after year requires hard and responsible work and a lot of discipline. Well-defined personal responsibility with respect to altering network operation parameters and strict obedience to the established procedures is an absolute must.

This goal is generally not simple to achieve. Seismic observatory staff will have to operate in a highly professional and reliable manner with:

- clearly defined personal responsibility for each task associated with the routine operation of the network and for other everyday analysis and archiving activities;
- regular maintenance of hardware and software;
- continuous verification of all tasks and hardware operations;
- maintenance of precise records of all relevant activities that effects data parameters, availability, continuity, and quality, such as changes to network operational parameters, processing procedures, data archiving, equipment maintenance and repair.

Regular processing of seismic data requires that all details of how data is processed and stored is well planned and that personnel are adequately trained.

Network recording parameters should be changed only if there is an important and well thought through reason. Because any change to the recording parameters will affect the network's ability to detect earthquakes, these changes should be avoided as much as possible. From the point of view of monitoring seismicity, ideally, there should be no changes for years after the network is fully adjusted. Nevertheless, those changes that are inevitably required from time to time should be kept to a minimum and carefully documented and archived.

Careful and continuous documentation of network operation parameters in a logbook, log file, or in the seismic database itself, is essential. This historical information should contain all information about data acquisition parameters and their changes, a documentation of all station calibrations, a precise record of each station's downtime, descriptions of technical problems and solutions, and descriptions of maintenance and service work. The exact times of parameter changes must be thoroughly recorded. This time-dependent information must become an integral part of the seismic data archive because without it the data can not be properly interpreted.

Usually a seismic network team is divided into a seismological and a technical group. This is fine as it relates to every day network operation activities and responsibilities. However, as much as possible, the basic technical as well as basic seismological knowledge should be 'evenly' distributed among the members of both groups. This favorably influences the general quality of the work of a seismic observatory. It also helps very much in many of critical situations, such as following a severe, unexpected technical problem, following a large earthquake, during the rapid deployment of portable stations following a main shock, or when any other situation dramatically increases the amount of work for a limited period of time.

The technical group must accept that no matter how modern and sophisticated the seismic network is that they operate; their customers are the seismologists. Therefore the seismologists must define the goals of seismic network operation and its working parameters.

8.8 Establishment and running a new physical seismic network

Frequently personal frictions may appear if this issue is not clearly defined by the management.

Many seismological observatories in high seismic risk regions must have people on duty at the central-recording site 24 hours per day. This may be a more or less explicit government requirement in order to be able to quickly notify public and civil defense authorities in the case of a strong, potentially damaging earthquake. No matter how understandable such desire may be, however, this working regime is really feasible only in a very large seismological institution. Only they have enough seismologists capable of quickly and competently interpreting seismic data. Even a fully-automated central recording and processing facility requires verification and confirmation of automatically determined earthquake parameters by trained personnel. The interpretation of automatically determined earthquake parameters in terms of the expected intensities in a given region and the probability of potential fatalities and damage is still a matter of experience and is not yet a matter of automatic calculations.

In practice, the around-the-clock human presence at the observatory is often achieved using all of the available, but mostly untrained, personnel in order to formally fulfill higher authorities' requirements. Of course, the actual value of such a 'solution' is questionable. If the alarms are of primary importance for a new network, one should consider a system of electronic pagers that will automatically alarm the institution's seismologists in the event of a strong earthquake. The seismologist will then need to be able to access the database remotely unless he/she is living very close to the observatory. This is the system used at the USGS National Earthquake Information Center.

8.8.6.3 System maintenance

Maintaining a seismic network's hardware and software is a continuous activity that inevitably requires well-trained personnel. Nowadays, many vital operational parameters and equipment health at seismic stations can be remotely monitored by modern, high-end seismic systems with duplex data transmission links. Such parameters are for example: backup battery voltage, presence of charging voltage, potential software and communication problems, absolute time keeping, remote station vault and/or equipment temperature, potential water intrusion, etc. These utilities significantly reduce the need for field service work and therefore lower the cost of network operation. However, regular visits to the stations are still necessary, though far less frequently than in the past. Once per year seems a minimum.

Note that it is a mistake to simply put off visits of remote seismic stations until something goes wrong. Periodic visual checks of cables and equipment, of potential corrosion problems on equipment and grounding and lightning system, and for intrusion of water and small animals are important. Batteries, burned lightning protection elements, and desiccant must be changed regularly, and cleaning the vaults and solar panels will also help to eliminate technical problems before they occur.

When something does go wrong, the technical staff must be certain that they can respond immediately with the right personnel, action, and spare parts. One should always maintain a good stockpile of the most common spare parts and have a well-trained technician with a pager on duty around the clock. Having technical personnel, in addition to seismologists, on call 24 hours a day for potential action is a good practice in the observatory seismology business.

8. Seismic Networks

However, operators of large networks may not have the manpower or budget resources to visit all of their stations annually. The major differences in maintenance procedures for small networks versus large regional or national networks are response time to site outages, site sensor-calibrations, and preventive maintenance (PM) visits. A large, dense seismic network lessens the need for 100% uptime for all sites; maintenance visits for site outages can be scheduled with PM visits in an area, something that a small, local network of 10 to 20 sites can not afford. This eliminates the need for immediate technician response and a 'beeper' for field repairs. For example: The U.S. Geological Survey's Northern California Seismic Network (NCSN), a large, dense regional network (352 analog and 93 digital stations), visits their telephone telemetered sites every 20 months and solar-powered sites every 4 years for site electronic equipment exchanges. These maintenance intervals are possible due to the robustness and reliability of their electronic amplifier/telemetry packages and associated equipments.

Be aware that batteries require special attention. If the lightning damages are the most frequent source of technical failures during normal operation conditions of a network, then battery failures will be the number one reason for failures during main power failures and unusually high-periods of seismicity. It should be noted that the output voltage alone of a battery provides little information about its overall health and capacity. Many types of batteries may still have adequate output voltage while at the same time their charge capacity is reduced to a small fraction of its original strength. Batteries in this condition will not do the job in case of a long-duration power failure, as may occur after a damaging earthquake.

Ideally, all of the batteries in the seismic system should be laboratory tested once a year for their remaining charge capacity. The batteries should be fully discharged, then fully charged, and again discharged in a controlled manner and their true charge capacity determined. Once the measured charge capacity is less than 60% - 70% of their nominal capacity, they should be replaced with new ones. Relying solely on measurements of battery voltage will certainly lead to technical failures in the long run. The most important moment in the lifetime of the seismic network may happen only once a decade or less. One certainly does not want to miss it because of old batteries with insufficient charge capacity!

However, large networks may again not be able to laboratory test each battery once per year. The NCSN exchanges batteries using an operational window system for battery life (based upon the quality and the replacement cost of the batteries used, and their long-term experience with battery lifetimes) rather than with annual testing and rejuvenation. Their operational window for solar-panel batteries is 4 years (Tom Burdette, personal communication, 2002).

Non-chargeable batteries, particularly the lithium type, should be replaced regularly, in accordance with the manufacturer's instructions, regardless of their output voltage at the moment of lifetime expiration.

8.8.6.4 Sensor calibration

Seismological observatories should calibrate all of the sensors in their seismic system regularly - ideally, once a year. Strictly speaking, only the seismic signals recorded between two successive sensor calibrations that show no significant change in the sensor frequency response function are completely reliable. Sensor and sensor calibration issues are also different for a dense network equipped with modern sensors. Modern sensors are very robust,

and many broadband sensors have automatic self-leveling, self-correcting features that eliminate the need for annual calibrations. In addition, site electronics can be installed to provide regular, telemetered sensor tests for response and operation. These features, along with a dense network sensor configuration allow for sensors to be replaced and recalibrated on a regular schedule. For NCSN, the short-period sensors are replaced at 10-year intervals, unless a sensor fails beforehand. NCSN short-period sites have built-in calibrators that perform daily mass releases to test sensor operation and response (Tom Burdette, personal communication, 2002).

Seismic sensor calibration requires knowledge that often is not available locally. In digital seismology, the sensor transfer function representation in the 's' or 'z' plane is most commonly used. Both issues are discussed in detail in Chapter 5 and the annexed Exercises and Program Descriptions. A comprehensive description of basics is also given in Scherbaum (1996 and 2001). A description of a popular seismometer calibration program UNICAL is given in Plešinger et al. (1995).

8.8.6.5 Archiving seismic data

After several decades, or even years, of operating a seismic network, the scientific and financial value of the recorded data is extremely high. Therefore, full attention must be paid to data archiving and a failsafe backup of the data. Seismology is a typical non-experimental science and lost or corrupted seismic data can never be regenerated. It is therefore an absolute must to provide a complete and reliable backup archive. The backups should be kept in a different physical location, no matter whether they are on paper, tape, disk, CD or other memory medium. Whenever possible, one copy (or the originals) should be stored in fire-resistant cabinets or safes. It is important to note that microfiche, film, and computer media require more protection than paper records. Paper records can withstand temperatures to 177°C (350°F), but computer media is damaged beyond use by temperatures above 52°C (125°F) and 80% humidity.

When one first sets up a seismic network, one needs to think thoroughly about organizing the data that is recorded in light of the fact that eventually the network will have many, many years of accumulated records. Often, this crucial aspect of seismic system organization is overlooked or left to on-the-spot decisions by whoever is in charge of the initial network operation. This may work fine for a while, but eventually everybody will run into serious problems if the archiving system chosen is inappropriate. It is necessary to carefully think through the archiving organization at the outset and to keep the long-term future in mind.

In a small, weak-motion network in a region of low seismicity that generates only a small number of records each year, or in a small or medium size strong motion network, one can probably get by with a directory tree organization for the data archive. Nevertheless, filename coding of events must be thoroughly thought out to avoid confusion and/or file name duplications. File names also should reflect complete date and time of each event. This doesn't present any problems for operating systems such as UNIX, Windows XP, Windows 98, Windows 2000, or NT. Larger networks in moderate to high seismicity regions require a better-organized, true- relational database for archiving purposes. One should carefully consider the various options used by other seismological observatories and those available on the market before the network starts recording data. It is very painful to change the data

8. Seismic Networks

coding or archiving method after several years of network operation, once thousands upon thousands of records are already stored.

Very powerful professional databases may not be the most suitable choice for seismology, primarily due to their high initial and annual maintenance cost, and secondly, due to too many expensive build-in utilities which will never be used in seismology. Special databases which have been developed by the seismological community for the needs of seismology, thoroughly tested in several existing applications, and accepted by many, seem to be the best choice at the moment. Unfortunately, only commercial products guarantee database maintenance and long-term support.

Always keep the raw, unprocessed seismic data (raw event files, or sequences of continuous data) in the archive along with the full documentation about the recording conditions (data acquisition parameters and accompanying information). Processing and seismic analysis methods will change and evolve as time passes. Future generations will appreciate having unprocessed seismic data available to further their research and knowledge.

8.8.6 Dissemination of seismic data

International cooperation in the dissemination of seismic data is another prerequisite for the high-quality operation of any new seismic network. Broad-minded data sharing is the best way for a less experienced institution to get feedback about the quality of its own work and is also a widely accepted international obligation. Data formats for parameter and waveform data exchange are dealt with in Chapter 10.

Everyone can greatly improve their own work by observing and comparing their phase readings, event locations, magnitude determinations and source mechanism results with the results of others published in national or international seismological bulletins. Any seismic study should also include as much seismic information as possible from the neighboring regions and countries. Not only one's own data, but also all available pertinent data from others should be used in seismic research work. Disseminating one's own data will, in turn, facilitate easy and fast accessibility of data from others. It's very important to establish a generous data sharing relationship with other seismological institutions.

The U.S. Geological Survey National Earthquake Information Center (<http://neic.usgs.gov>) compiles data contributed from networks located around the globe in order to determine, as rapidly and as accurately as possible, the location and size of all destructive earthquakes that occur worldwide. This information is disseminated immediately to concerned national and international agencies, scientists, and the general public. The NEIC collects and provides to scientists and to the public an extensive seismic database that serves as a solid foundation for scientific research, principally through the operation of modern digital national and global seismograph networks and through cooperative international agreements.

Data from the NEIC is transferred to the International Seismological Centre (ISC) (<http://www.isc.ac.uk/>) for final bulletin creation about two years behind real time. The International Seismological Centre is a non-governmental organization charged with the final collection, analysis and publication of standard earthquake information from all over the world. Earthquake readings are received from almost 3,000 seismograph stations representing every part of the globe. The Center's main task is to re-determine earthquake locations making

use of all available information, and to search for new earthquakes, previously unidentified by individual agencies.

Besides these global data centers there are many national or regional centers that maintain web sites through which one can get direct or linked on-line access to seismological waveform data acquired by globally (such as IRIS/GSN, GEOFON or GEOSCOPE), regionally (e.g. MEDNET) or nationally operating networks (e.g. SZGRF/GRSN, ICC etc.). Suitable starting links are provided, e.g., from the web sites of the US Advanced National Seismic System (<http://www.anss.org/>) and of the Observatories and Research Facilities for European Seismology (ORFEUS) (<http://orfeus.knmi.nl>).

Traditionally, seismic observatories of national seismic networks or larger regional networks regularly publish preliminary seismological bulletins (weekly, biweekly, or monthly), final seismological bulletins (yearly), and earthquake catalogs of the country or region (yearly, but with a few years delay so that the data from all other external sources can be included in the analysis). These catalogs are one of the bases for earthquake hazard assessment and for risk mitigation studies.

Immediate dissemination of data from strong events is another international obligation. The Internet, fax, and phone are familiar forms of seismic data exchange in such cases. The Internet is used more and more often for sharing not only parameter data for strong events but also other publications such as seismic bulletins and earthquake waveform data. Many institutions already publish their bulletins as Internet documents only. In the very near future the Internet will replace all other seismic information exchange channels. In any country without good Internet access, seismological institutions need to undertake every possible effort to change the situation as soon as possible. One should also understand that one E-mail address per institution, although better than nothing, doesn't provide full Internet benefits. It is the nature of the Internet that it becomes fully efficient only if every professional staff member has his own Internet access and E-mail address.

Some of the currently most relevant and often used Internet addresses of global, regional and national seismological data centers can also be found and directly linked via <http://www.szgrf.bgr.de> or <http://seismo.ethz.ch/seismosurf/seismobig.html>.

Acknowledgments

The authors and the Editor are very thankful to John Lahr and Kent Fogleman of the USGS for their careful English prove-readings and complementary remarks that have helped to improve the original draft. Thanks go also to Sadaki Hori for providing Fig. 8.14 and a short draft on the Japanese seismic networks and to Peter Bormann who added the information about the German Regional Seismic Network as well as two paragraphs on site selection and network optimization in section 8.8.2.

Recommended overview readings (see References, under Miscellaneous in Volume 2)

Barrientos et al. (2001)
Havskov and Alguacil (2004)
Hardt and Scherbaum (1994)

8. Seismic Networks

Hutt et al. (2002)

Kradolfer (1996)

Lee and Steward (1981).

Rabinovitz and Steinberg (1990).

Uhrhammer et al. (1998).

Willmore (Ed.) (1979).

9

Seismic Arrays

Johannes Schweitzer, Jan Fyen, Svein Mykkeltveit
and Tormod Kværna

9.1 Outline

When Willmore (1979) published his *Manual of Seismological Observatory Practice*, only a small number of seismic arrays were in operation. The whole section on array seismology in that issue of the *Manual* was no longer than two pages, including one figure; array seismology being at that time more a matter of some specialists rather than a commonly applied technique. During the last two decades, new seismic arrays were installed all over the globe and, due to digital data acquisition systems and digital signal processing, it has become easier to handle the large amount of data from seismic arrays. Therefore, array observations have become more commonly used. This requires a separate Chapter on array seismology in the *New Manual of Seismological Observatory Practice*, which explains the principles of seismic arrays and how their data can be used to analyze seismic observations.

In the following sections we define first the term “seismic array” and show examples of seismic arrays installed around the world. We then describe the theoretical basics of the processing of seismic data observed with an array, continue with the explanation of helpful tools for automatic analysis of array data and explain how local and regional events are located at the NORSAR Data Processing Center by using single array observations. Finally, we describe some helpful rules and procedures to find the best configuration for a seismic array and present a table of operational and planned seismic arrays.

9.2 Introduction

“The Conference of Experts to study the methods of detecting violations of a possible agreement on the suspension of nuclear tests” held in 1958 in Geneva under the auspices of the United Nations, was followed by several initiatives for improving the quality of seismic stations worldwide. At the same time, the idea of installing arrays of sensors to improve the signal-to-noise ratio was adopted from radio astronomy, radar, acoustics, and sonar. In the 1960s, it was demonstrated that seismic arrays are superior to single three-component stations for detecting and characterizing signals from earthquakes and explosions. A seismic array differs from a local network of seismic stations mainly by the techniques used for data analysis. Thus, in principle, a network of seismic stations can be used as an array, and data from an array can be analyzed as from a network. However, most array processing techniques require high signal coherency across the array, and this puts important constraints on the array geometry, spatial extent, and data quality. Furthermore, proper analysis of array data is

9. Seismic Arrays

dependent on a stable, high precision relative timing of all array elements. This is required because the measurement of (usually very small) time differences of the arrival of seismic signals between the different sensors plays an important role in all array-processing techniques.

The superior signal detection capability of arrays is obtained by applying “beamforming” techniques, which suppress the noise while preserving the signal, thus enhancing the signal-to-noise ratio (SNR).

Arrays can also provide estimates of the station-to-event azimuth (backazimuth), and of the apparent velocity of different types of signals. These estimates are important both for event location purposes and for classification of signals, e.g., P, S, local, regional, or teleseismic.

In this chapter we describe procedures for estimating the apparent wavefront velocity (inverse of the slowness or ray parameter), the angles of approach (backazimuth and incidence angle) of a seismic signal as well as basic processing algorithms for signal detection, one-array regional phase association, and the preparation of an automatic event bulletin.

At the NORSAR Data Processing Center (NDPC) at Kjeller, Norway, data have been acquired for many years from different types of arrays: e.g., the large aperture NORSAR array, the small aperture arrays NORES and ARCES and the very small aperture arrays at Spitsbergen and in Apatity, Kola peninsula. The processing algorithms for a large array are different from the processing techniques used for the smaller arrays. The processing techniques for both types of arrays are described below.

We aim also at describing the general array processing techniques for training purposes and for use as a reference for analysts new to the field of seismic array processing. Some algorithms are described in detail, whereas others have references to available literature. It is assumed that the reader has basic knowledge about time-series analysis like bandpass filtering and Fourier transforms (e.g., Scherbaum, 2001).

The amount of data arising from use of an array of seismometers and digital signal processing techniques is enormous. Low-threshold detection processing leads to numerous triggers, which have to be analyzed. It is therefore of great importance to use techniques that are robust and easy to operate in an automatic, uninterrupted mode. The automatic processing steps used at NDPC are divided into three separate cases:

- Detection Processing (DP), which uses beamforming, filtering and STA/LTA detectors to define signal triggers;
- Signal Attribute Processing (SAP), which uses techniques like frequency-wavenumber (f-k) analysis to estimate the slowness vector, and other techniques to estimate parameters like onset time, period, amplitude and polarization attributes for every trigger; and
- Event Processing (EP), which analyzes the attributes and sequence of triggers to associate seismic phase arrivals to define events.

In Mykkeltveit and Bungum (1984), documentation of this method can be found with results from the first program (called RONAPP) for detecting and associating seismic signals from regional events using data from the regional array NORES.

Later, the automatic processing was re-coded to adapt to any array, several data formats and machine architectures. The programs are packaged into DP for continuous detection processing, and EP for automatic signal attribute processing, event processing, and interactive special processing (Fyen, 1989, 2001). These programs have been used for all examples herein. Section 9.8.2 shows the output of this automatic data processing for some signals observed on the ARCES array as an example of routine data analysis.

It is difficult to find publications that give details about basic array processing. There are numerous papers about advanced techniques and results from observations, but the basics of beamforming and STA/LTA detection processing are mostly assumed to be known. The type of processing used is similar to what is done in many types of signal-processing applications and time-series analysis. The algorithms are used in radar technology and in seismic prospecting. In seismic prospecting “beamforming” is called “stacking”.

The first large seismic array, LASA, was built in Montana, USA, in the mid-1960s (Frosch and Green, 1966). The *Seismic Array Design Handbook*, August 1972 by IBM, describes the processing algorithms for LASA and NORSAR. References therein are mostly to reports prepared by J. Capon and R. T. Lacoss, Lincoln Laboratories. These basic processing techniques developed in the 1960s have survived, and are still in use.

The description for many array methods and early array installations can be found in a proceeding volume (Beauchamp, 1975) of a NATO Advanced Study Institute conference in 1974 in Sandefjord, Norway. Also several NORSAR Scientific Reports describe array-processing techniques. For example, Kværna and Doornbos (1986) report on f-k analysis techniques using the integration over a wider frequency band (so-called “broadband f-k analysis”) rather than the single frequency-wavenumber analysis (e.g., Capon, 1969) as applied by many authors.

In 1990, a special issue of the *Bulletin of the Seismological Society of America* was published (Volume 80, Number 6B) with contributions from a symposium entitled “Regional Seismic Arrays and Nuclear Test Ban Verification”. This issue contains many papers on theoretical and applied array seismology. A more recent review on array applications in seismology can be found in Douglas (2002) and in Rost and Thomas (2002).

9.3 Examples of seismic arrays

Throughout the text, we use examples from the processing of data from the large array NORSAR in southern Norway, from the “regional” arrays NORES in southern Norway and ARCES in northern Norway, and from the GERES array in southern Germany.

Fig. 9.1 shows the configuration of the ARCES array and Fig. 9.2 shows the layout of the seismometer sites for the NORSAR and NORES arrays. The NORES and ARCES-type array design of sites located on concentric rings (each consists of an odd number of sites) spaced at log-periodic intervals is now used for most of the modern small aperture arrays; only the number of rings and the aperture differ from installation to installation. The Spitsbergen array has only nine sites, e.g., and corresponds to the center site plus the A and the B rings of a NORES-type array; the FINES array consists of three rings with 15 sites altogether. These regional, relatively small arrays have been developed in the last 10 to 20 years.

9. Seismic Arrays

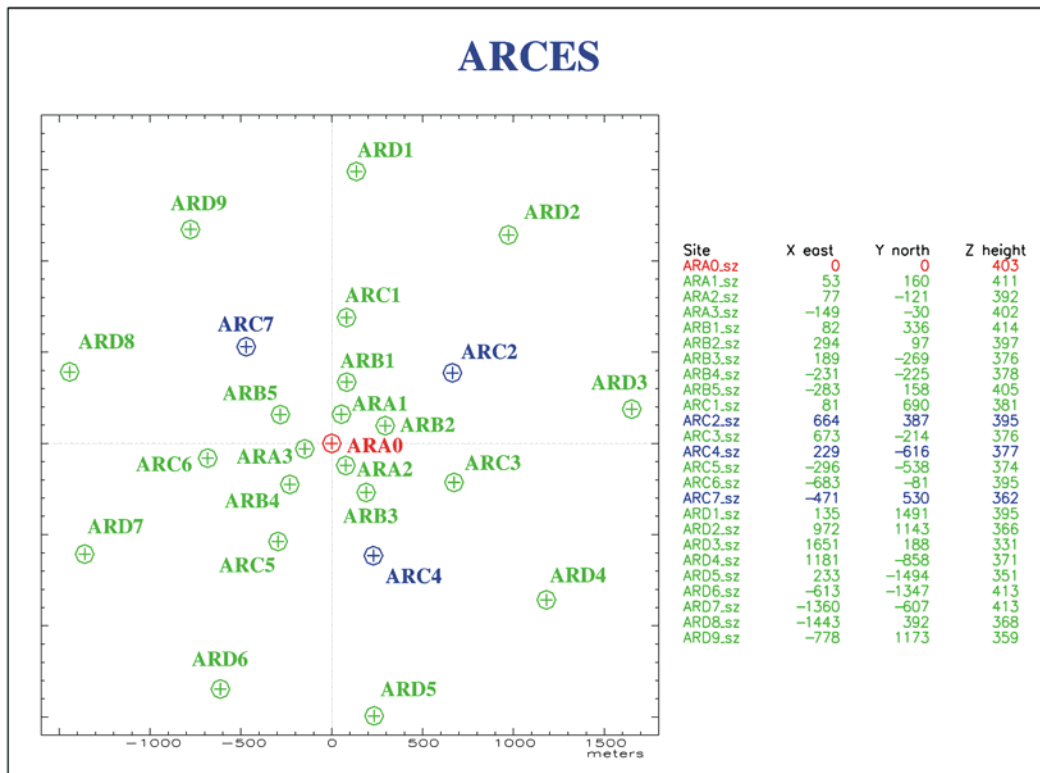


Fig. 9.1 Configuration of the regional array ARCEN, which is identical to the NORES array. Each vertical seismometer site is marked with a circle and a cross. The ARCEN array has 25 sites with vertical seismometers. Four of these sites have in addition short-period horizontal seismometers. The short-period three-component sites are marked in blue or red. At the center site (red) a broadband three-component seismometer is collocated. The array has one center instrument – ARA0 – and four rings: the A-ring with three sites and a radius of about 150 m, the B-ring with five sites and a radius of about 325 m, the C-ring with seven sites and a radius of about 700 m, and finally, the D-ring with nine sites and a radius of about 1500 m. The center seismometer of ARCEN has the geographic coordinates 69.53486°N, 25.50578°E. The table gives the relative coordinates between the single sites and the center site ARA0, and the elevation of all sites above sea level in meters.

To our knowledge, the first experimental seismic array with more than four elements was established in February 1961 by the United Kingdom Atomic Energy Agency (UKAEA) on Salisbury Plain (UK), followed in December 1961 by Pole Mountain (PMA, Wyoming, USA), in June 1962 by Eskdalemuir (EKA, Scotland, UK), and in December 1963 by Yellowknife (YKA, Canada), all with openly available data. These types of arrays (the so-called UK-arrays) are orthogonal linear or L-shaped. Later, arrays of the same type were built in Australia (Warramunga), Brasilia, and India (Gauribidanur). A detailed description of this type of arrays can be found in Keen et al. (1965), Birtill and Whiteway (1965), and Whiteway (1965, 1966). Fig. 9.3 shows the configuration of the Yellowknife array (Somers and Manchee, 1966, Manchee & Weichert, 1968, Weichert, 1975) as one example of this kind of medium-sized array, which is still in operation. The size of an array is defined by its aperture given by the largest (horizontal) distance between the single sensors. The apertures of the UKAEA arrays vary between 10 and 25 km.

In the 1960s, arrays were tested with very different aperture and geometry, from small circular arrays with apertures of some kilometers to huge arrays with apertures of up to 200 km. The largest arrays were the LASA array in Montana (USA), dedicated in 1965, with 525 seismometer sites (Frosch and Green, 1966) and the original NORSAR array in southern Norway consisting of 132 sites over an aperture of approximately 100 km with altogether 198 seismometers, which became fully operational in the spring of 1971 (Bungum et al., 1971).

NORSAR and NORES

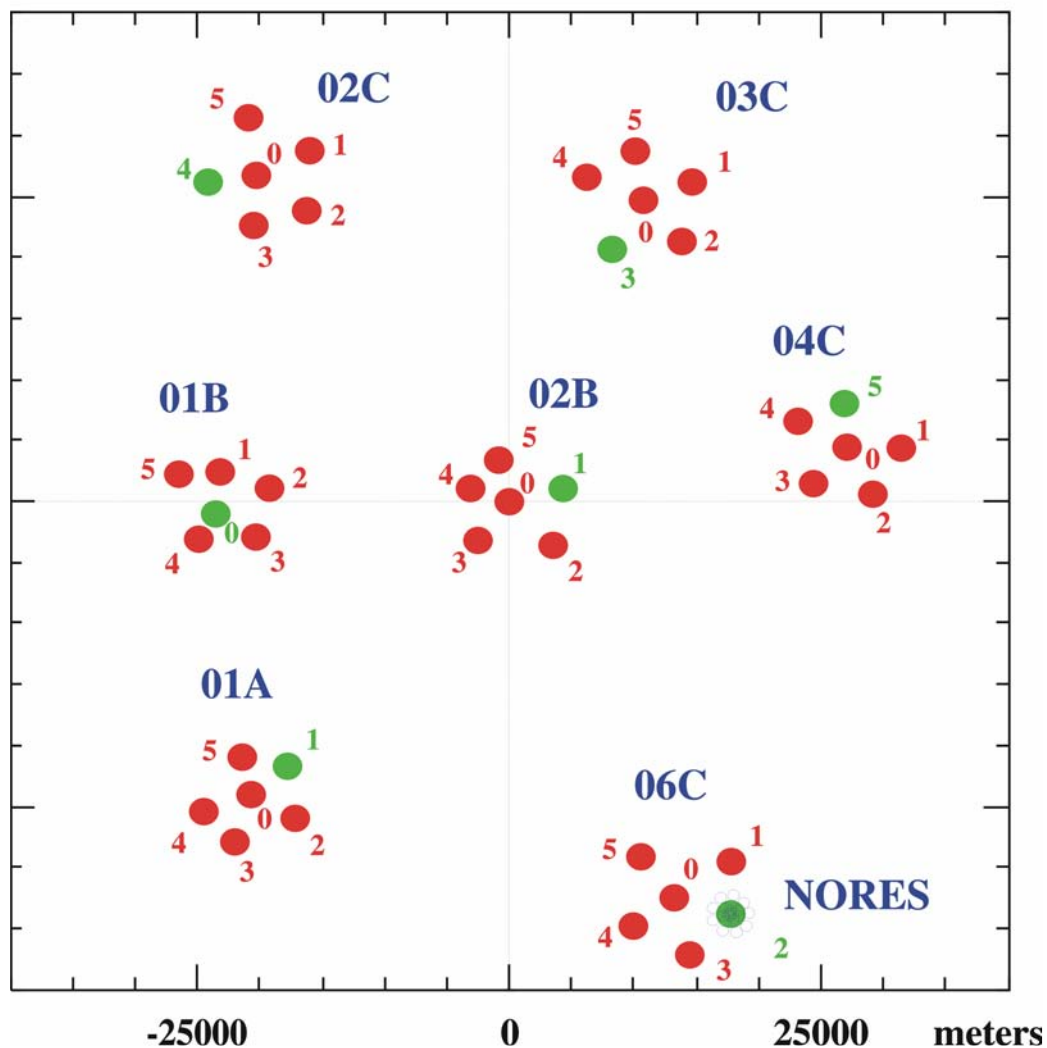


Fig. 9.2 Configuration of the large aperture array NORSAR and the small aperture array NORES. The NORES array is co-located with the NORSAR subarray 06C. The diameter of NORSAR is about 60 km and the diameter of NORES is about 3 km. Each seismometer site is marked with a circle. The present NORSAR array has 42 sites, whereas the NORES array has 25 sites. The NORSAR array has logically seven subarrays, each with six vertical seismometers. In addition, one site in each subarray (marked in green) has one three-component broadband seismometer. The geometry of NORES is identical to the geometry of ARCES shown in Fig. 9.1. The center seismometer of the NORSAR subarray 02B has the geographic coordinates 61.03972°N , 11.21475°E . The center seismometer of NORES has the geographic coordinates 60.73527°N , 11.54143°E .

9. Seismic Arrays

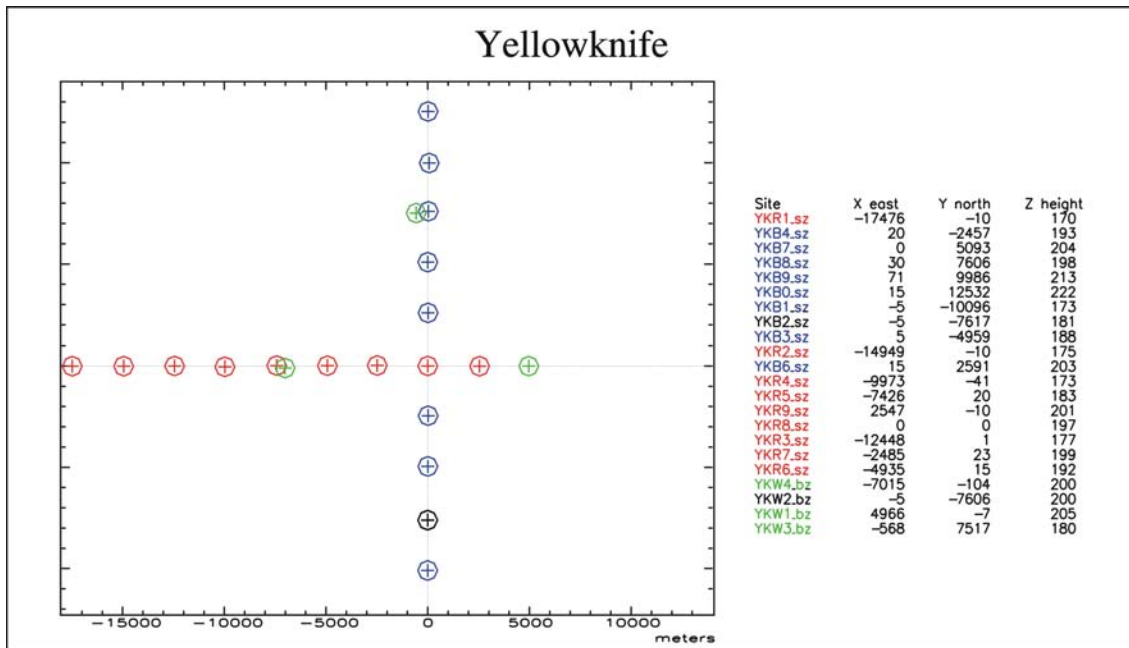


Fig. 9.3 Configuration of the United Kingdom Atomic Energy Agency - type Yellowknife array (YKA). The blue and the red sites have vertical short-period instruments, and at the green sites, three-component, broadband seismometers are installed.

The large LASA and NORSAR arrays and the UKAEA arrays have narrow band short-period seismometers and additional long-period seismometers in their original configuration, whereas the Gräfenberg Array (GRF) was planned and installed in the early 1970s as an array of broadband sensors. It has an aperture of about 100 km (Harjes and Seidl, 1978; Buttkus, 1986) and an irregular shape (Fig. 9.4), which follows the limestone plateau of the Franconian Jura.

However, the geometry and the number of seismometer sites of an array are determined by economy and purpose. Details about array configurations can be found in Haubrich (1968), Harjes and Henger (1973), or in Mykkeltveit et al. (1983, 1988).

Tab. 9.3 in 9.10 contains a list of operational and planned arrays as of September 2002, and Fig. 9.42 shows a map of these array locations.

Spudich and Bostwick (1987) used the principle of reciprocity and used a cluster of earthquakes as a source array to analyze coherent signals in the seismic coda. This idea was consequently expanded by Krüger et al. (1993) who analyzed data from well-known source locations (i.e., mostly explosion sources) with the so-called “double beam method”. Here the principle of reciprocity for source and receiver arrays is used to further increase the resolution by combining both arrays in one analysis.

Another approach to arrays with high resolution was developed in recent years. In Japan and in California the network of seismometer stations is so dense that data from all stations can be combined in the so-called J-array and the Californian array. All known array techniques can be applied to analyze data from these networks (J-array Group, 1993, Benz et al., 1994).

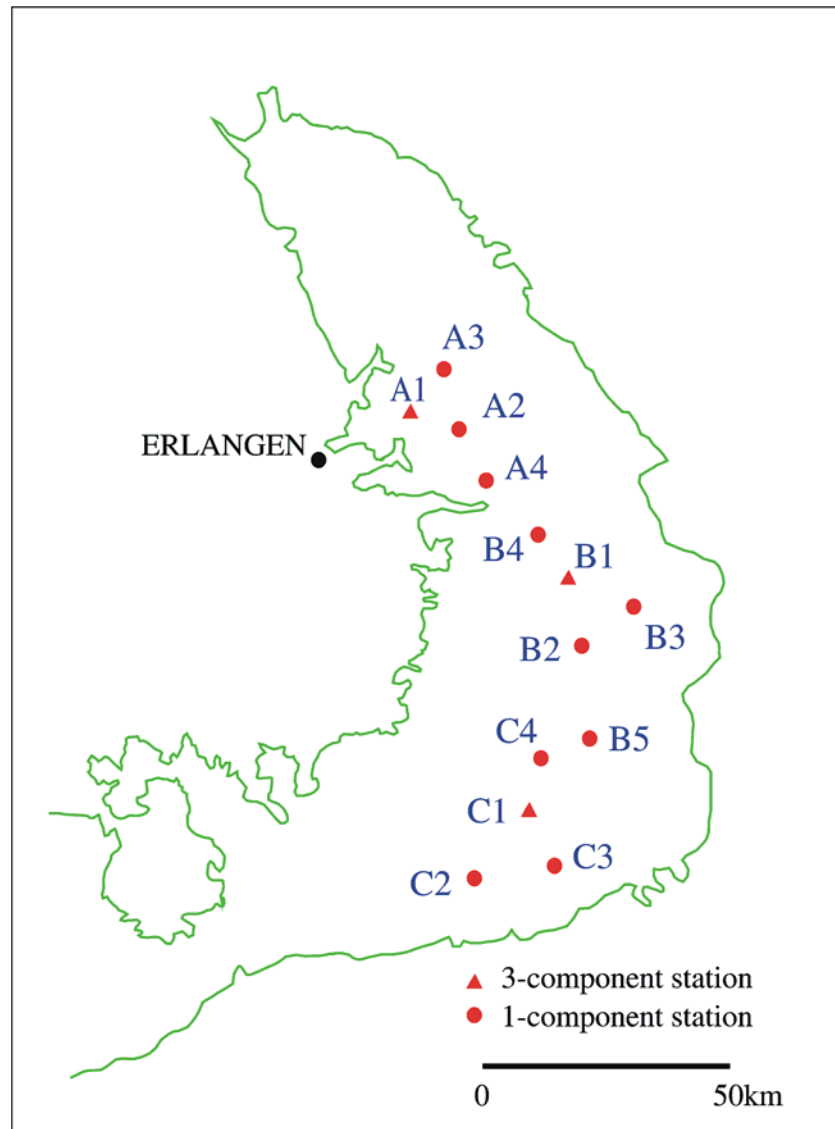


Fig. 9.4 Configuration of the irregularly shaped Gräfenberg array (GRF). At all sites vertical broadband seismometers are installed. In addition, three sites (A1, B1, and C1) contain horizontal broadband seismometers. The contour line follows the boundary of the geological unit of the Franconian Jura, on which the array is located. The reference station GRA1 (at position A1 on the map) is sited at latitude 49.69197°N and longitude 11.22200°E .

9.4 Array beamforming

With an array we can improve the signal-to-noise ratio (SNR) of a seismic signal by summing the coherent signals from the single array sites. Figs. 9.5 and 9.6 show P onsets of a regional event observed at the ARCES sites and, in addition, the summation trace (on top) of all single observations. In Fig. 9.5 the data were summed without taking any delay times into account, consequently the P onset is suppressed by destructive interference. In Fig. 9.6 all traces were time-adjusted to provide alignment of the first P pulse before summation. Note the sharp and short P pulse of the beam and the suppression of incoherent energy in the P coda.

9. Seismic Arrays

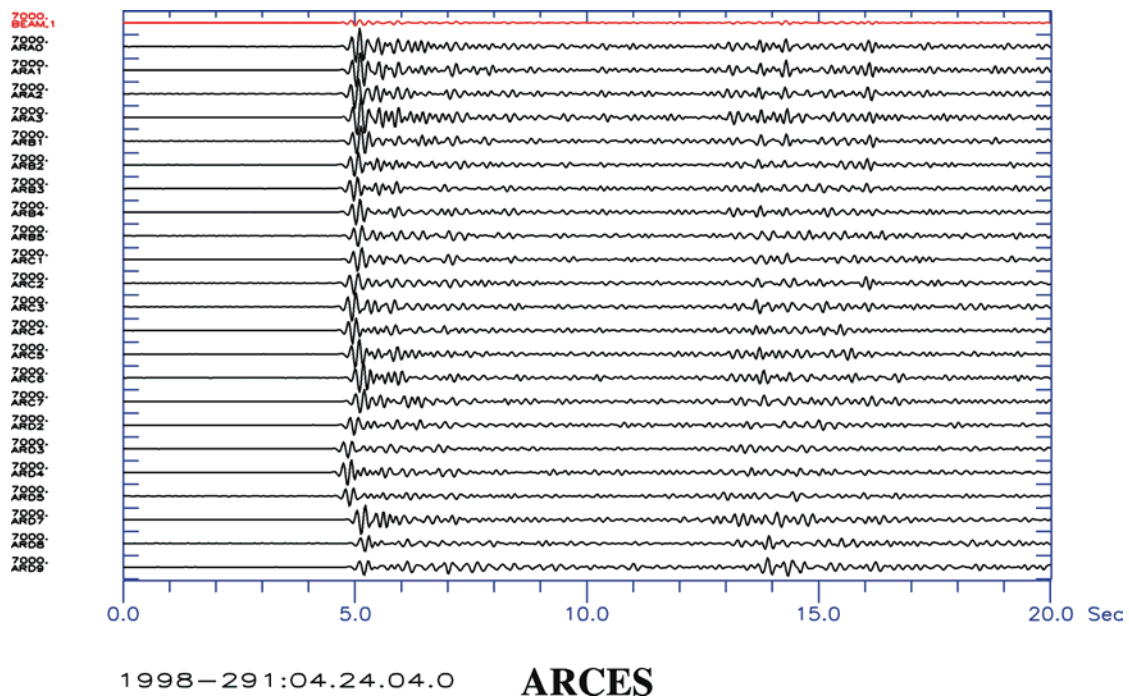


Fig. 9.5 The figure shows P-phase onsets of a regional event observed with the vertical short-period seismometers of ARCES. The top trace is an array beam, and the remaining traces are single vertical short-period seismograms. All data were filtered with a Butterworth band pass filter between 4 and 8 Hz and are shown with a common amplification. All traces were summed to create a beam (red trace) without any delay-time application.

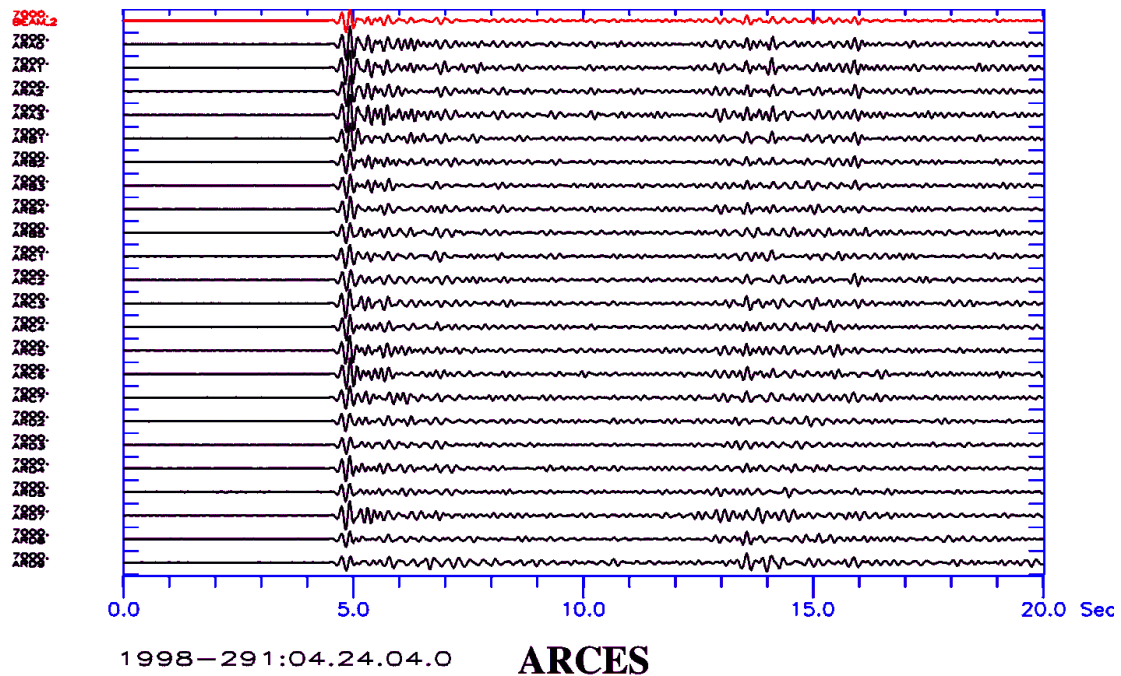


Fig. 9.6 This figure shows P-phase onsets of a regional event observed with the vertical short-period seismometers of ARCES as in Fig. 9.5 but the single traces were first aligned and then summed (beam trace in red). Note for this case the sharp and short pulse form of the first P onset of the beam and the suppression of incoherent energy in the P coda.

This shows that the most important point during the summation (or beamforming) process is to find the best delay times, with which the single traces must be shifted before summation (“delay and sum”) in order to get the largest amplitudes due to coherent interference of the signals. The simplest way is just to pick the onset times of the signal on each trace and shift the traces with respect to the onset time at the reference site of the array. But most onsets from weaker events have a much smaller SNR than in the example shown, and therefore onset times are often difficult to pick. With hundreds of onsets each day, this is not practical during routine operation of an array. Therefore, many different predefined beams are automatically calculated, and a detector then searches for interesting onsets in these beams.

Below, we explain how delay times can be theoretically calculated for known seismic signals, using some basic equations and parameter definitions, and give the formulas for a seismic beam.

9.4.1 Geometrical parameters

An array is defined by a set of seismometers with one seismometer being assigned the role of a reference site. The relative distances from this reference point to all other array sites are used later in all array specific analysis algorithms (Fig. 9.7).

\mathbf{r}_j Position vector of instrument j with a distance (absolute value) r_j from a defined origin. We use bold characters for vectors and normal characters for scalars. The position is normally given relative to a central instrument at site O , $\mathbf{r}_j = f(x, y, z)$, where (x, y, z) are the Cartesian coordinates in [km] with positive axes towards east (x), towards north (y), and vertically above sea level (z).

For distances from the source much larger than the array aperture (i.e., more than about 10 wavelengths) a seismic wave approaches an array with a **wavefront** close to a **plane**. The case of a non-plane wavefront is discussed in Almendros et al. (1999). The directions of approach and propagation of the wavefront projected on to the horizontal plane are defined by the angles Φ and Θ (Fig. 9.8).

Φ Backazimuth (often abbreviated as BAZ or for short, called azimuth) = angle of wavefront approach, measured clockwise between the north and the direction towards the epicenter in [$^\circ$].

Θ Direction in which the wavefront propagates, also measured in [$^\circ$] from the north with $\Theta = \Phi \pm 180^\circ$.

9. Seismic Arrays

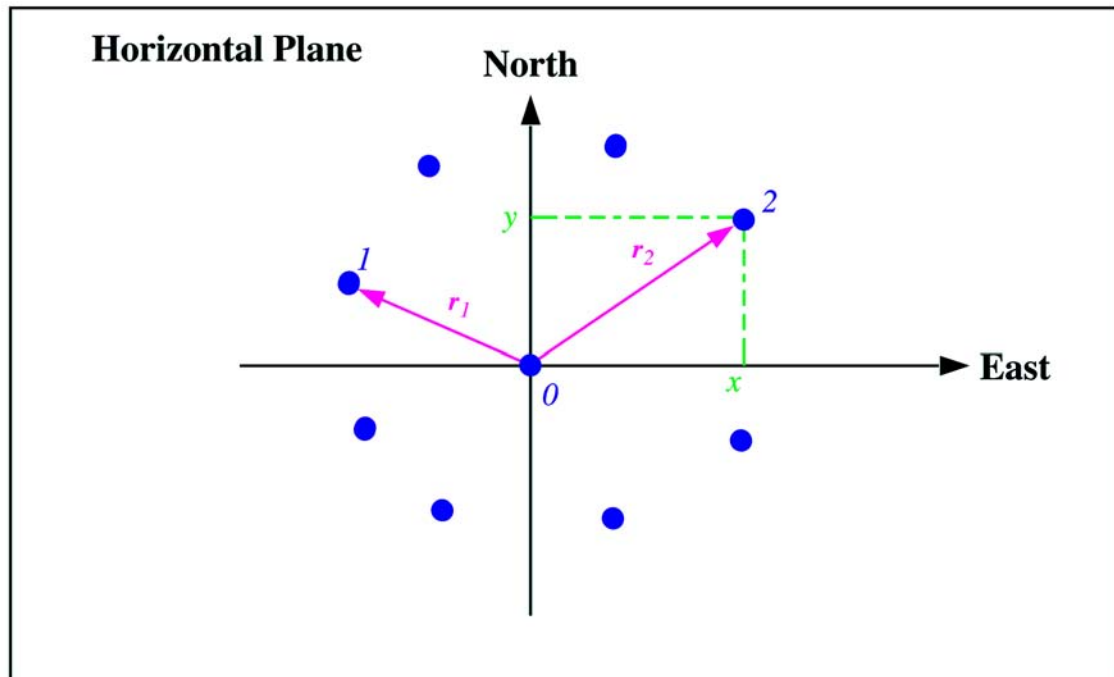


Fig. 9.7 Illustration (horizontal plane) of an array of instruments (filled circles). The center instrument 0 is used as reference and origin for the relative coordinates x, y (see also Fig. 9.1 for an example of an actual array).

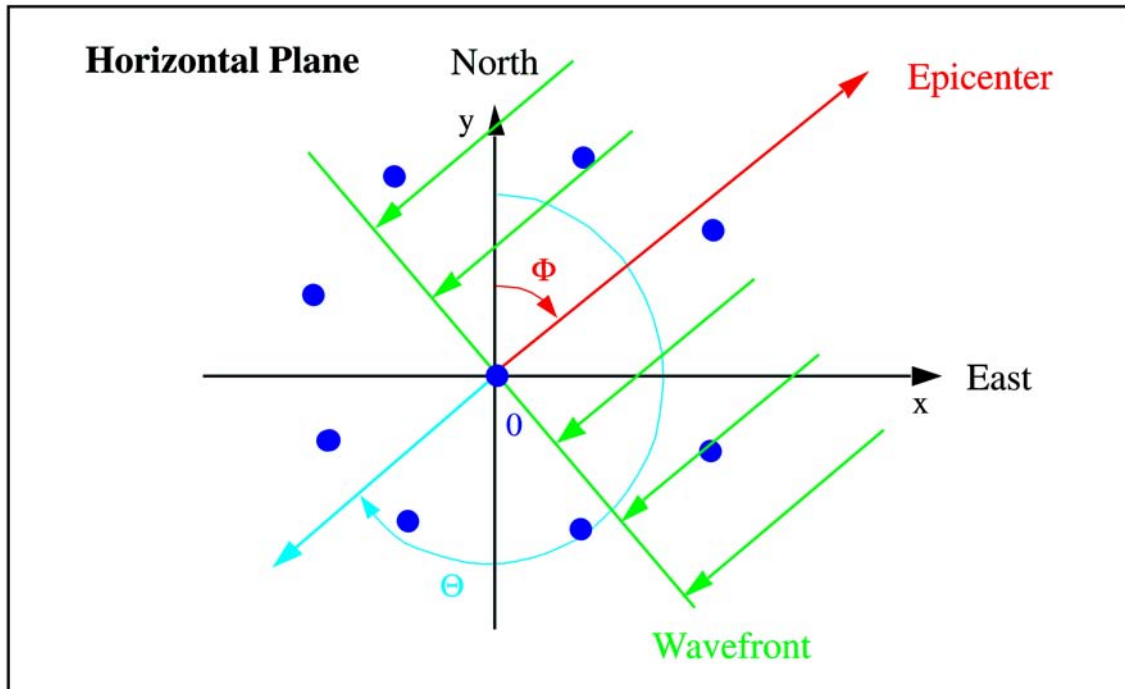


Fig. 9.8 Definition of the angles Θ (direction of wavefront propagation) and Φ (direction to the epicenter = backazimuth); here e.g., for a wavefront coming from north-east and crossing the array in a south-westerly direction.

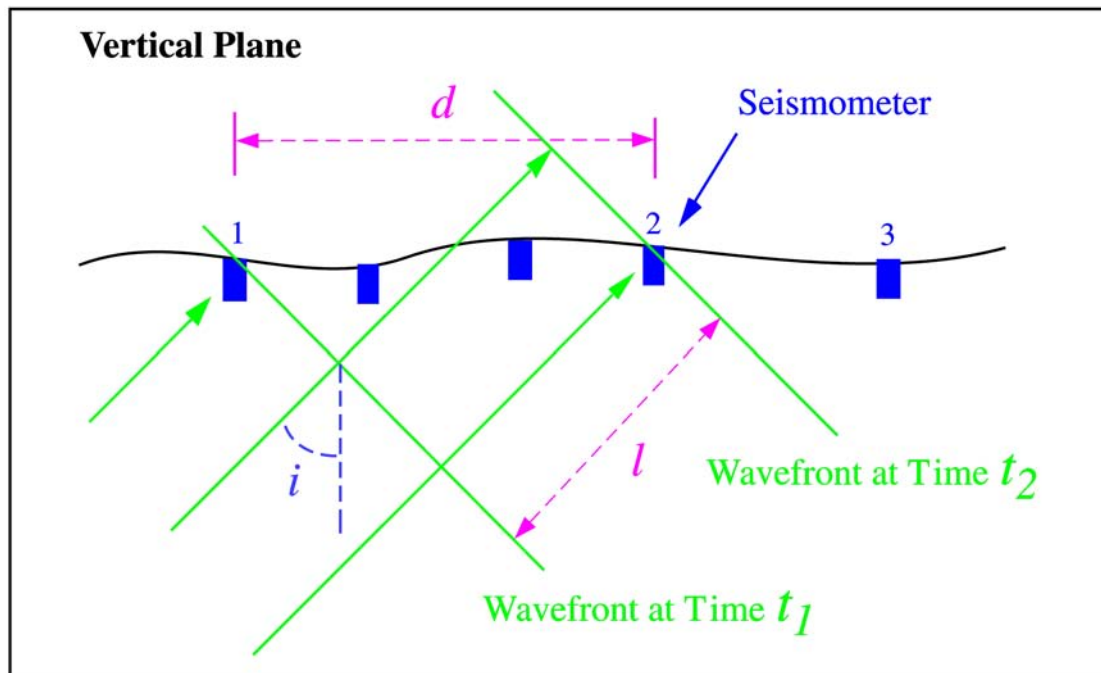


Fig. 9.9 Illustration (vertical plane) of a seismic plane wave crossing an array at an angle of incidence i .

In the vertical plane, the angle measured between the direction of approach and the vertical is called the angle of incidence i with $i \leq 90^\circ$ (see Fig. 9.9). The seismic velocity below the array in the uppermost crust and the angle of incidence define the apparent propagation speed of the wavefront crossing the array.

9.4.2 Apparent velocity and slowness

The upper crustal velocity together with the angle of incidence defines the apparent propagation speed of the wavefront at the observing instruments. This is **not** the physical propagation speed of the wavefront and is therefore called an apparent velocity. We start our consideration by defining the quantities used in following:

- d horizontal distances;
- v_c crustal velocity (P or S wave, depending on the seismic phase) immediately below the array in [km/s];
- i angle of incidence (see also Fig. 9.9);
- v_{app} absolute value of the apparent velocity vector in [km/s] of a plane wave crossing an array. Using Snell's law it can easily be proven that the apparent velocity is a constant for a specific seismic ray traveling through a horizontally layered Earth model (see Fig. 9.10);
- \mathbf{v}_{app} apparent velocity vector with its absolute value $v_{app} = 1/s$. $\mathbf{v}_{app} = (v_{app,x}, v_{app,y}, v_{app,z})$, where $(v_{app,x}, v_{app,y}, v_{app,z})$ are the single, apparent velocity components in [km/s] of the wavefront crossing an array.

9. Seismic Arrays

The inverse of the apparent velocity v is called slowness s , which is a constant for a specific ray. For local or regional applications the unit of slowness is [s/km]. For global applications it is more appropriate to use the unit [s/°] and the slowness is then called the ray parameter. The ray parameter of major seismic phases is usually tabulated for standard Earth models together with the travel times as a function of distance from the source. The following symbols are used:

- \mathbf{s} slowness vector with its absolute value $s = 1/v_{app}$. $\mathbf{s} = (s_x, s_y, s_z)$, where (s_x, s_y, s_z) are the single, inverse apparent velocity (= slowness) components in [s/km]. Note, because the vector \mathbf{s} is oriented in the propagation direction (in direction of Θ , see Fig. 9.8), a plane wave with backazimuth 45° would have negative values for both horizontal components;
- s absolute value of the slowness vector in [s/km] of a plane wave crossing an array;
- p ray parameter $p = s \cdot g$, measured in [s/°], with $g = \frac{\pi \cdot 6371 \text{ km}}{180^\circ} \cong 111.19 \text{ [km/°]}$.

The relation between the parameters of a plane wave and the actual seismic signal is given by the wavenumber vector \mathbf{k} :

- \mathbf{k} wavenumber vector defined as $\mathbf{k} = \omega \cdot \mathbf{s}$ with the angular frequency $\omega = 2 \cdot \pi \cdot f = 2 \cdot \pi / T$ measured in [1/s]. T is the period and f the frequency of the seismic signal;
- k absolute value of the wavenumber vector \mathbf{k} defined as $k = \omega \cdot u = 2 \cdot \pi \cdot f \cdot s = 2 \cdot \pi / \lambda$, measured in [1/km]. λ is the wavelength of the signal and because of the analogy between ω and k , k is also called a spatial frequency.

A time delay τ_j is the arrival time difference of the wavefront between the seismometer at site j and the seismometer at the reference site. The unit of measurement is seconds with a positive delay meaning a later arrival with respect to the reference site in the direction of the wave propagation Θ .

Assume a wavefront is propagating the distance l between time t_1 and time t_2 (Fig. 9.9). Then, if d is used for the horizontal distance between instrument 1 and 2 in [km], and if both instruments are assumed to be at the same elevation, we have:

$\tau_2 = (t_2 - t_1) = \frac{l}{v_c}$, and the apparent velocity v_{app} is then defined as a function of the incidence angle i (Fig. 9.10):

$$v_{app} = \frac{d}{(t_2 - t_1)} = \frac{v_c}{\sin i} \quad (9.1)$$

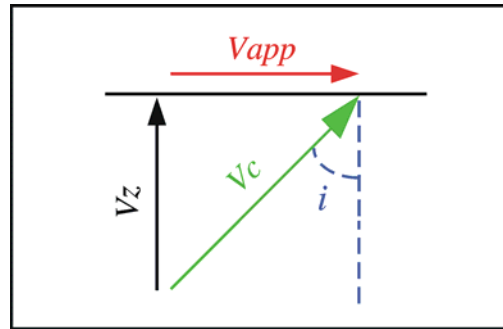


Fig. 9.10 A plane wave propagating with the velocity v_c reaches the Earth's surface. The splitting of this velocity in a vertical component v_z and a horizontal component v_{app} is directly dependent on the incidence angle i . The horizontal velocity component is only equal to the propagation velocity v_c for waves propagating parallel to the surface; in all other cases v_{app} is higher than v_c . It is called the apparent velocity v_{app} of the seismic wave.

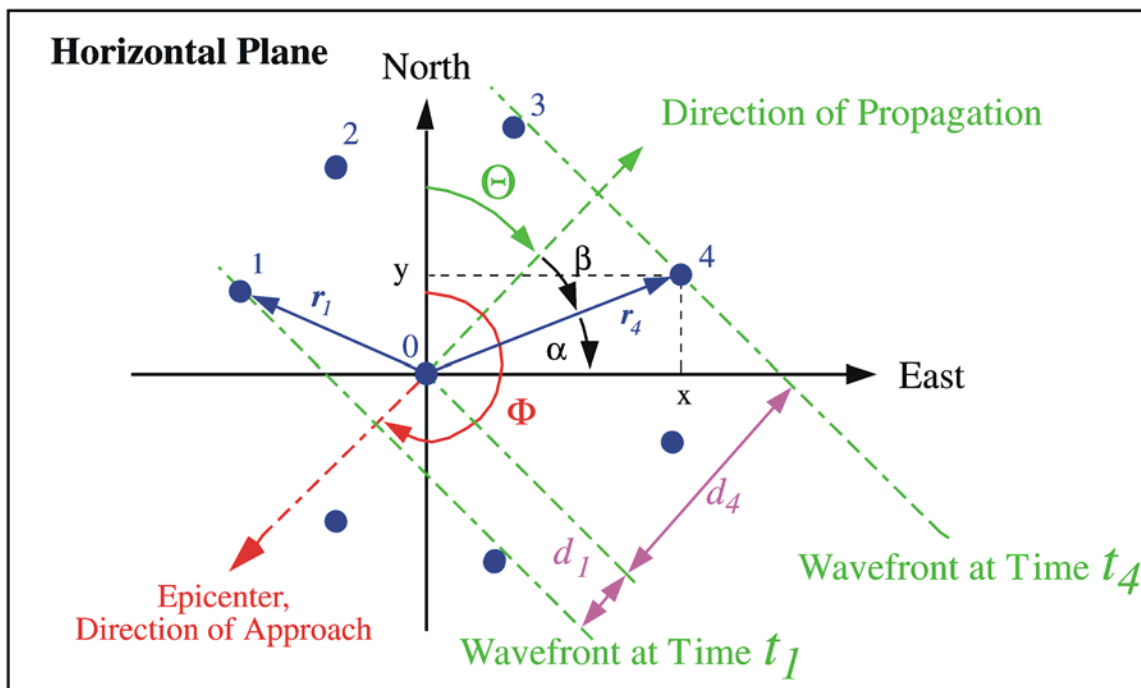


Fig. 9.11 Illustration (horizontal plane) of a plane wave, coming from south-west (backazimuth Φ), crossing an array and propagating in a north-easterly direction Θ .

9.4.3 Plane-wave time delays for sites in the same horizontal plane

In most cases, the elevation differences between the single array sites are so small that travel-time differences due to elevation differences are negligible (Fig. 9.9). We can assume, therefore, that all sites are in the same horizontal plane. In this case, we can not measure the vertical component of the wavefront propagation. The vertical apparent velocity component can then be defined as $v_{app,z} = \textit{infinite}$, and the corresponding slowness component becomes $s_z = 0$. From Fig. 9.11 we see that the time delay τ_4 [s] between the center site 0 and site 4 with the relative coordinates (x_4, y_4) is

9. Seismic Arrays

$$\tau_4 = \frac{d_4}{v_{app}} = \frac{r_4 \cdot \cos \beta}{v_{app}}, \text{ with } r_4 = |\mathbf{r}_4|.$$

Now let us omit the subscript 4, and evaluate further:

$$\alpha + \beta + \Theta = 90^\circ, \quad r \cdot \cos \beta = d, \quad r \cdot \cos \alpha = x, \quad d = \frac{x \cdot \cos \beta}{\cos \alpha}$$

$$d = \frac{x \cdot \cos(90^\circ - \alpha - \Theta)}{\cos \alpha} = \frac{x \cdot (\sin \alpha \cdot \cos \Theta + \cos \alpha \cdot \sin \Theta)}{\cos \alpha} = x \cdot \frac{\sin \alpha}{\cos \alpha} \cdot \cos \Theta + x \cdot \sin \Theta$$

$$d = x \cdot \frac{y}{x} \cdot \cos \Theta + x \cdot \sin \Theta = y \cdot \cos \Theta + x \cdot \sin \Theta$$

With $\Theta = \Phi \pm 180^\circ$ (Fig. 9.8), we get for the horizontal distance traveled by the plane wave $d = -x \cdot \sin \Phi - y \cdot \cos \Phi$.

Then, for any site j with the horizontal coordinates (x, y) , but without an elevation difference relative to the reference (center) site, we get the time delay τ_j :

$$\tau_j = \frac{d_j}{v_{app}} = \frac{-x_j \cdot \sin \Phi - y_j \cdot \cos \Phi}{v_{app}} \quad (9.2)$$

These delay times can also be written in the often-used formal vector syntax with the position vector \mathbf{r}_j and the slowness vector \mathbf{s} as parameters. In this notation the delay times are defined as projection of the position vector onto the slowness vector:

$$\tau_j = \mathbf{r}_j \cdot \mathbf{s} \quad (9.3)$$

9.4.4 Plane-wave time delays when including the elevation of sites

In some cases, not all array sites are located in one plane. Then the calculation of the time delays becomes slightly more complicated. Site 2 has the relative coordinates (x_2, y_2, z_2) . From Fig. 9.12 we see that $i + \gamma + \varphi = 90^\circ$, $z_2 = r_2 \cdot \sin \varphi$, $d_2 = r_2 \cdot \cos \varphi$, $l = r_2 \cdot \cos \gamma$, and

$$\tau_2 = \frac{l}{v_c}.$$

$$l = \frac{z_2}{\sin \varphi} \cdot \cos \gamma = \frac{z_2}{\sin \varphi} \cdot \cos(90^\circ - i - \varphi) = \frac{z_2 \cdot (\sin i \cdot \cos \varphi + \cos i \cdot \sin \varphi)}{\sin \varphi}$$

Omitting again the site number, we get:

$$l = z \cdot \frac{\cos \Phi}{\sin \Phi} \cdot \sin i + z \cdot \cos i = d \cdot \sin i + z \cdot \cos i$$

Using Eq. (9.1) and Eq. (9.2), we get for the total time delay at site j

$$\tau_j = \frac{-x_j \cdot \sin i \cdot \sin \Phi - y_j \cdot \sin i \cdot \cos \Phi + z_j \cdot \cos i}{v_c} = \frac{-x_j \cdot \sin \Phi - y_j \cdot \cos \Phi}{v_{app}} + \frac{z_j \cdot \cos i}{v_c} \quad (9.4)$$

The time delays τ_j now also depend on the local crustal velocities below the given site j and not just on the parameters of the wavefront (Φ, v_{app}) . This is a clear disadvantage of an array for which single sites are not located in one horizontal plane and should be taken into account during planning of an array installation. Writing these time delays in vector notation will again result in Eq. (9.3), but note, the vectors are now three-dimensional.

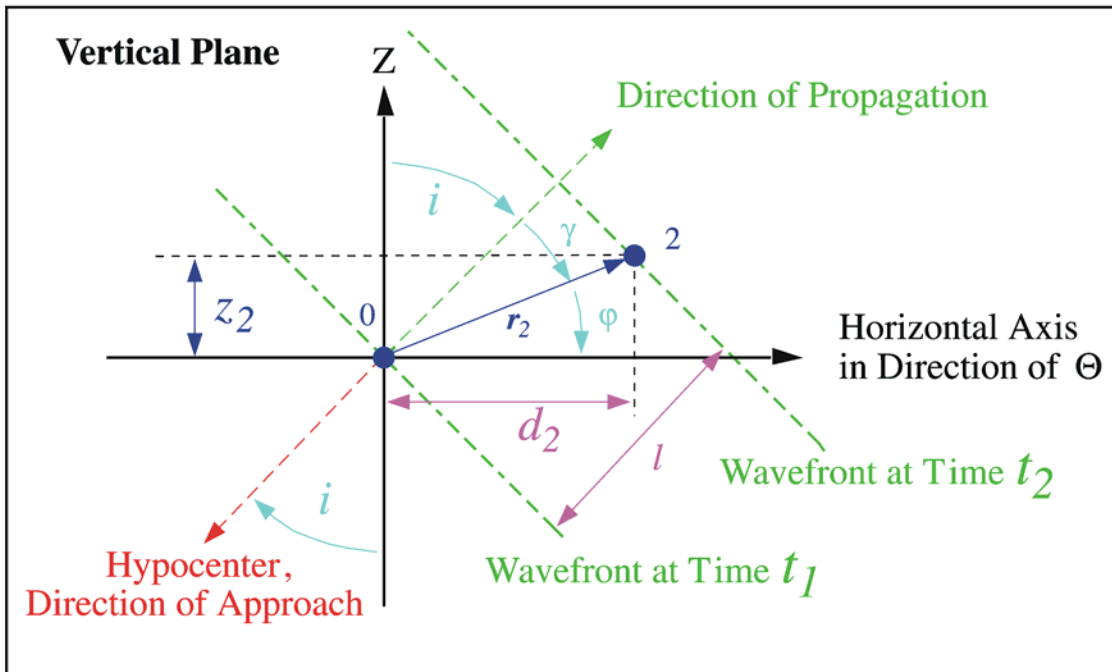


Fig. 9.12 Illustration (vertical plane) of a plane wave crossing an array at the angle of incidence i .

9.4.5 Beamforming

After deriving the delay times τ_j for each station by solving Eq. (9.2) or Eq. (9.4) for a specific backazimuth and apparent velocity combination, we can define a “delay and sum” process to calculate an array beam. In the following we will use the shorter vector syntax of Eq. (9.3) to calculate time delays. The calculated delay times can be negative or positive. This is depending on the relative position of the single sites with respect to the array’s reference point and to the backazimuth of the seismic signal. Negative delay times correspond to a delay and positive delay times correspond to an advance of the signal.

9. Seismic Arrays

Let $w_j(\mathbf{r}_j, t)$ be the digital sample of the seismogram from site j at time t , then the beam of the whole array is defined as

$$b(t) = \frac{1}{M} \sum_{j=1}^M w_j(t + \mathbf{r}_j \cdot \mathbf{s}) = \frac{1}{M} \sum_{j=1}^M w_j(t + \tau_j). \quad (9.5)$$

This operation of summing the recordings of the M instruments by applying the time delays $\mathbf{r} \cdot \mathbf{s}$ is called beamforming.

Because we are using digitized data, sampled with a defined sampling rate, we will always need an integer number of samples in programming Eq. (9.5), that is, the term $t + \mathbf{r}_j \cdot \mathbf{s} = t + \tau_j$ needs to be converted to an integer sample number. However, to avoid alias effects by following the rules of digital signal processing, it is sufficient for beamforming to use the nearest integer sample, as long as the dominating frequency is less than 25% of the sampling rate.

If seismic waves were harmonic waves $S(t)$ without noise, with identical site responses, and without attenuation, then a “delay and sum” with Eq. (9.5) would reproduce the signal $S(t)$ accurately. The attenuation of seismic waves within an array is usually negligible, but large amplitude differences can sometimes be observed between data from different array sites due to differences in the crust directly below the sites (see Fig. 4.34). In such cases, it can be helpful to normalize the amplitudes before beamforming.

Our observations $w(t)$ are, of course, the sum of background noise $n(t)$ plus signal $S(t)$, i.e., $w(t) = S(t) + n(t)$.

The actual noise conditions and signal amplitude differences will influence the quality of a beam. However, because the noise is usually more incoherent than the signal, we can try to estimate the improvement of the signal-to-noise ratio (SNR) due to the beamforming process.

Calculating the beam trace for M observations including noise we get for the sum B of all traces with Eq. (9.5):

$$B(t) = \sum_{j=1}^M w_j(t + \mathbf{r}_j \cdot \mathbf{s}) = \sum_{j=1}^M (S_j(t + \mathbf{r}_j \cdot \mathbf{s}) + n_j(t + \mathbf{r}_j \cdot \mathbf{s})).$$

Assuming that the signal is coherent and not attenuated, this sum can be split and we get:

$$B(t) = M \cdot S(t) + \sum_{j=1}^M n_j(t + \mathbf{r}_j \cdot \mathbf{s}). \quad (9.6)$$

Now we assume that the noise $n_j(\mathbf{r}_j, t)$ has a normal amplitude distribution, a zero mean value, and the same variance σ^2 at all M sites. Then, for the variance of the noise after summation, we get $\sigma_s^2 = M \cdot \sigma^2$ and the standard deviation of the noise in the beam trace will become $\sqrt{M} \cdot \sigma$. That means that the standard deviation of the noise will be multiplied only with a factor of \sqrt{M} , but the coherent signal with the factor M (Eq. (9.6)). So, the

improvement of the signal-to-noise ratio by the “delay and sum” process will be \sqrt{M} for an array containing M sites. The gain improvement G of an M -sensor array can then be written as

$$G^2 = M . \quad (9.7)$$

9.4.6 Examples of beamforming

In Fig. 9.13 (top trace), we display a beam calculated by using the known apparent velocity ($v_{app} = 10.0$ km/s and backazimuth 158°) for the P-onset of an event in Greece recorded at NORES at an epicentral distance of 21.5° . All 25 vertical sensors of the array have been used, but only a few of the sensors in the NORES D-ring have been displayed. Note that the signal on the beam is very similar to the individual signals, but the noise changes both in frequency content and amplitude level. The beam is made by calculating time delays for the given slowness using Eq. (9.2), and in the summation of the traces, the individual traces have been shifted with these delays.

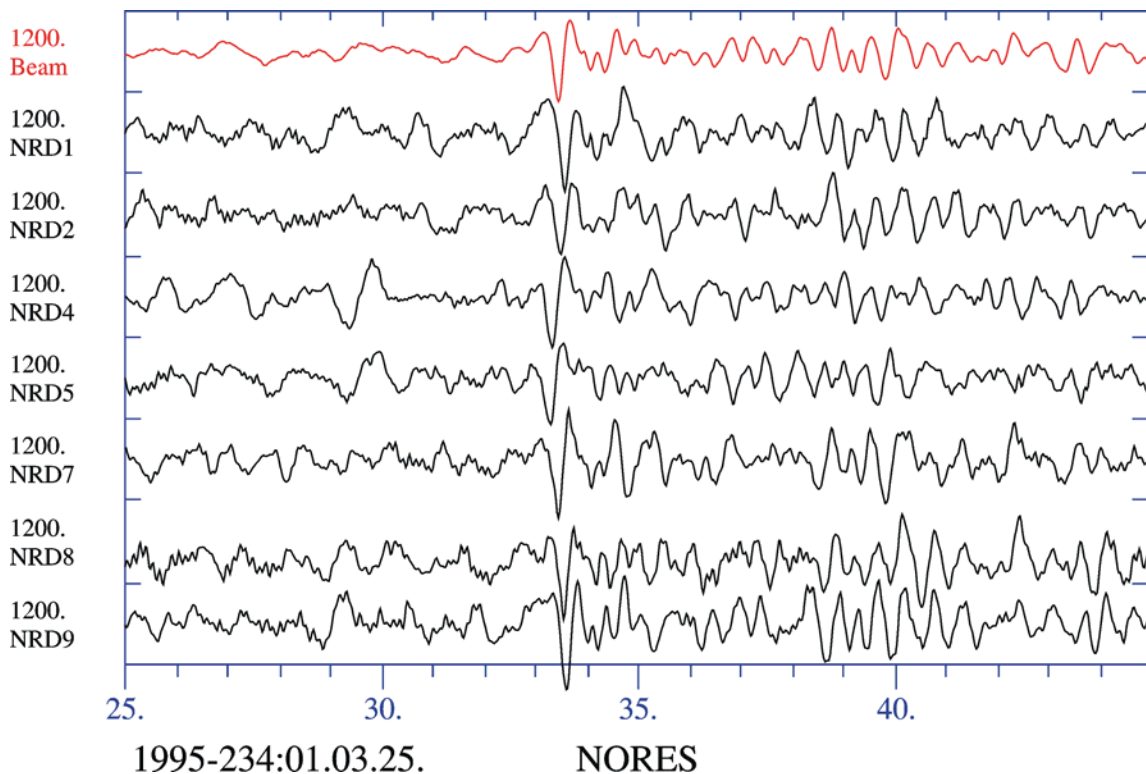


Fig. 9.13 Selected NORES channels from an event in Greece, with the beam displayed as the top trace (in red). All traces have equal amplitude scale.

The next example in Fig. 9.14 shows the ability of arrays to detect small signals that are difficult to detect with single stations. It shows the tiny onset of a PcP phase recorded at the GERES array from a deep focus event in the Tyrrhenian Sea ($h = 275$ km) at an epicentral distance of 9.6° . Note that although the signal coherence is low, the noise suppression on the beam is clearly visible and the onset can be analyzed. For the “delay and sum” process, data from 20 sites of the GERES array were used, but only a subset of the single traces is shown.

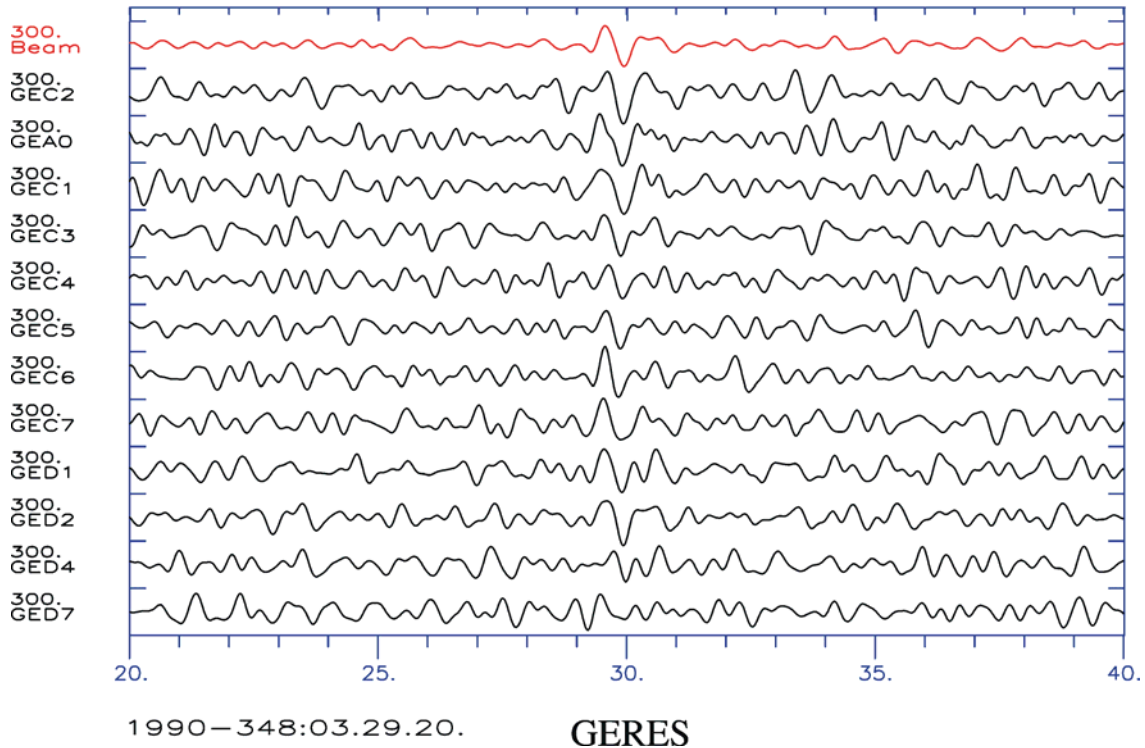


Fig. 9.14 GERES beam (top trace in red) for a PcP onset observed at an epicentral distance of 9.6° from a deep focus event in the Tyrrhenian Sea.

9.5 Beamforming and detection processing

A major task in processing seismic data is that of detecting possible signals in the data samples collected from the seismometers. A “signal” is defined to be distinct from the background noise due to its amplitudes, different shape, and/or frequency contents; in other words, the variance of the time series is increased when a signal is present. Statistically, we can form two hypotheses: the observation is noise or the observation is a signal plus noise. The signal of a plane wave observed at different sites of an array should be more coherent than random noise. If we assume that the time series recorded are independent measurements of a zero-mean Gaussian random variable, then it can be shown that the hypothesis of the recording being noise can be tested by measuring the power within a time window. If this power exceeds a preset threshold, then the hypothesis is false, i.e., the recording is signal plus noise. In practice, the threshold can not be calculated precisely and may vary with time as is true for the background noise. But an approximation to this detector in seismology is to estimate the power over a long time interval (LTA), and over a short time interval (STA). Then the ratio STA/LTA, which is usually called signal-to-noise ratio (SNR), is compared with a preset threshold. If the SNR is larger than this threshold, the status of detection is set to “true” and we are speaking about a detected seismic signal.

This kind of an STA/LTA detector was proposed by Freiberger (1963), installed and tested for the first time at LASA (van der Kulk et al., 1965), and later installed at Yellowknife (Weichert et al., 1967) and at NORSAR (Bungum et al., 1971). For complementary details on STA/LTA trigger algorithm and parameter setting in general see IS 8.1.

At NORSAR we use a sum of the absolute values rather than squared values due to computational efficiency; the difference in performance is minimal and the results are slightly more robust. The definition of the short-term average (STA) of a seismic trace $w(t)$ is:

$$STA(t) = \frac{1}{L} \cdot \sum_{j=0}^{L-1} |w(t-j)| \quad L = \text{sampling rate} \cdot \text{STA length}, \quad (9.8)$$

the recursive definition of the long-term average (LTA) is:

$$LTA(t) = 2^{-\zeta} \cdot STA(t-\epsilon) + (1-2^{-\zeta}) \cdot LTA(t-1), \quad (9.9)$$

where ϵ is a time delay, typically a few seconds, and ζ is a steering parameter for the LTA update rate. The parameter ϵ is needed to prevent a too early influence of the often-emergent signals on the LTA. In the case of a larger signal, the LTA may stay too long at a relatively high level and we will therefore have problems detecting smaller phases shortly after this large signal. Therefore the LTA update is forced to lower the LTA values again by the exponent ζ .

The signal-to-noise ratio (SNR) is defined as:

$$SNR(t) = STA(t)/LTA(t). \quad (9.10)$$

The STA/LTA operator may be used on any type of seismic signals or computed traces. That means, the input time series $w(t)$ may be raw data, a beam, filtered data or a filtered beam. L is the number of points of the time series $w(t)$ to be integrated. The recursive formula for the LTA means that the linear power estimate of the noise is based mainly on the last minute's noise situation, which is a very stable estimate. The influence of older noise conditions on the actual LTA value and a weighting of the newest STA value can be defined by the factor ζ , for which, e.g. at NORSAR, a value of 6.0 is used. It is also advisable to implement a delay of $\epsilon = 3$ to 5 seconds for updating the LTA as compared to STA. A simpler implementation is to estimate the LTA according to Eq. (9.8), but using an integration length that is 100 or 200 times longer for the LTA than for the STA. However, when detecting signals with frequencies above 1 Hz, it is also recommended that the LTA should not be updated during the SNR is above the detection threshold. This feature is easier to implement by using Eq. (9.9).

Fig. 9.15 and Fig. 9.16 demonstrate how the STA/LTA detector works for a single seismogram. The direct P onset of this regional event is sharp and clearly detected. However, the P coda increases the background noise for later phases and the SNR of these phases becomes very small. In this case, the advantages of using an array to detect seismic signals can be easily shown. The apparent velocities of the P onsets and the S onsets are so different that calculating the corresponding S beam will decrease the P-phase energy and amplify the S-phase energy (Fig. 9.17).

In Fig. 9.18, we display again the Greek event from Fig. 9.13 with the “best” beam ($v_{app} = 10.0$ km/s, backazimuth 158°) on top, together with beams using the same apparent velocity of 10.0 km/s but different backazimuths (0.0° , 90.0° , 180.0° and 270.0°). Note the difference in amplitudes of the beams for signal and noise. Because the “best” backazimuth of 158° is close to 180.0° , the top trace and the second trace from the bottom differ only slightly.

9. Seismic Arrays

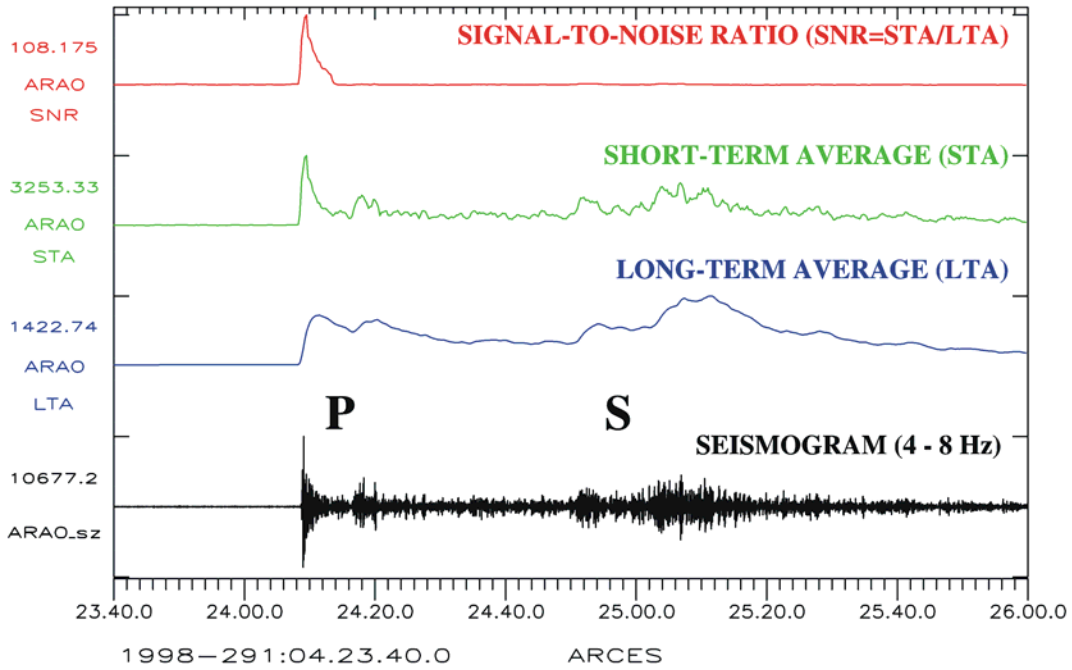


Fig. 9.15 The figure shows the LTA, STA and STA/LTA (= SNR) traces for a seismogram of a regional event observed at the ARCES reference site ARA0 (bottom). The seismogram was bandpass filtered between 4 and 8 Hz. Note the sharp onset for the P phase with an SNR of 108.175.

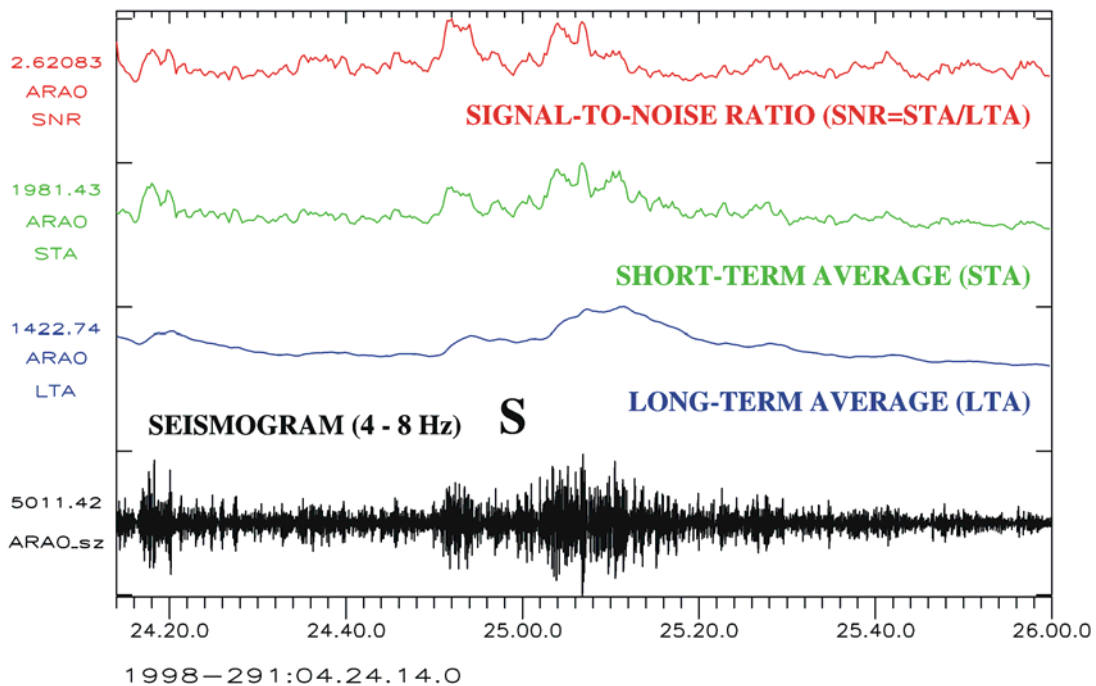


Fig. 9.16 As Fig. 9.15, but only for the time window after the direct P onset. Note that due to the P coda the noise and consequently the LTA is increased. Therefore the SNR of the S-phase onsets becomes relatively small on this single vertical trace.

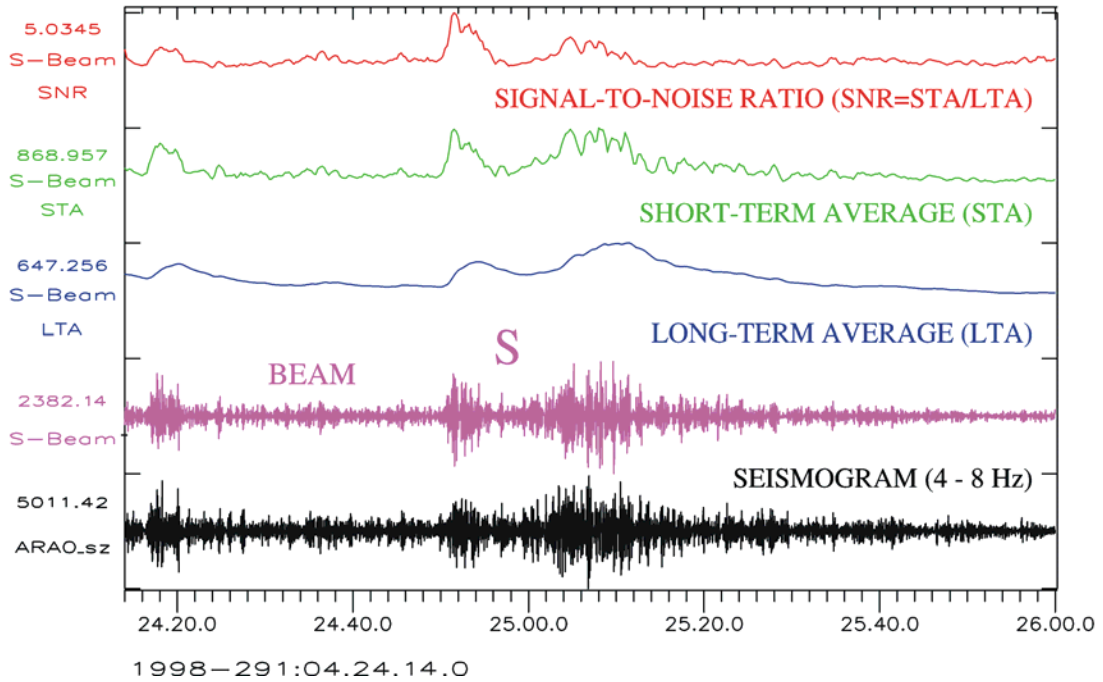


Fig. 9.17 As Fig. 9.16, but with LTA, STA and SNR calculated for a beam optimized for the first S onset. The beam is shown as the second trace from the bottom. Compare the relative amplitudes of the P-coda on the array beam and on the single station seismogram at ARA0, which is shown at the bottom.

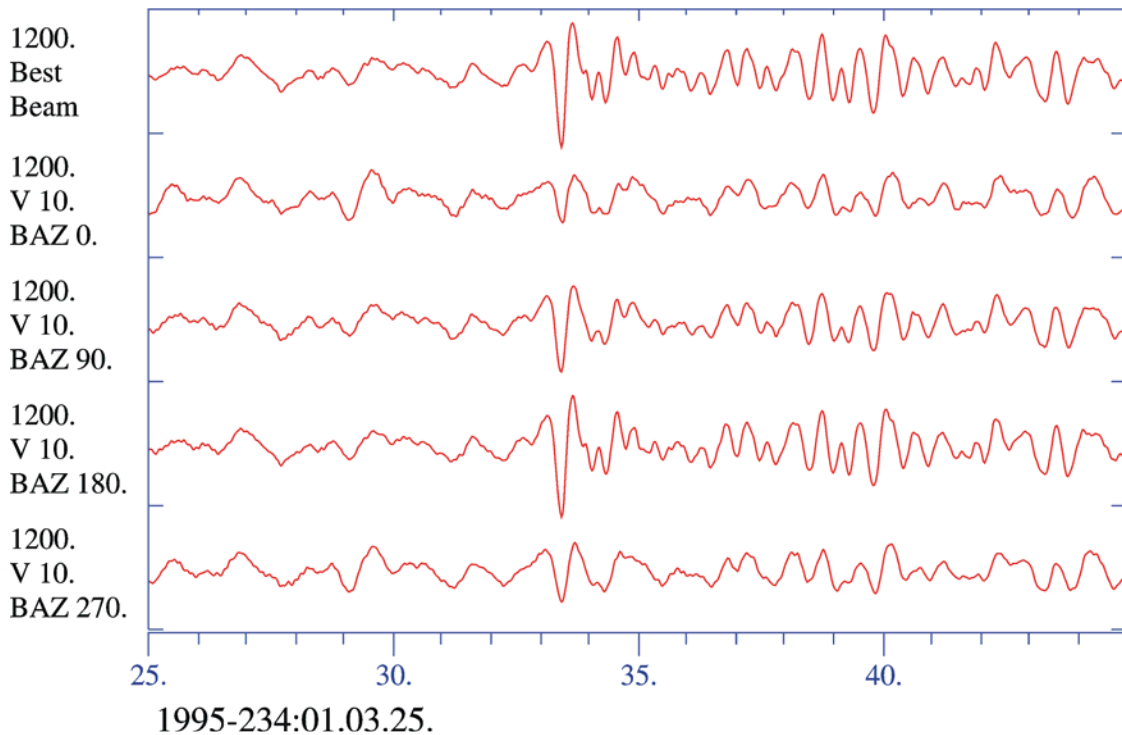


Fig. 9.18 NORES beams for the same event as in Fig. 9.13 with different slownesses. All traces have an equal amplitude scale and show unfiltered short-period data.

9. Seismic Arrays

Thus, Fig. 9.18 demonstrates the **limits of the slowness resolution** for small aperture arrays like NORES. To find the “best” beam is, in principle, a matter of forming beams with different slowness vectors and comparing the amplitudes or the power of the beams, and then finding which v_{app} -backazimuth combination gives the highest energy on the beam.

In Fig. 9.19, the same beams as in Fig. 9.18 are shown, but now filtered using a Butterworth 3rd order bandpass filter 2.0 – 4.0 Hz. When beamforming using Eq. (9.5), we can either filter all the individual traces first and then beamform, or we can beamform first, and then filter the beam, which is faster by a factor given by the number of sites minus one. Both procedures should theoretically give the same result because for both beamforming and filtering the superposition theorem of algebra is true. However, local noise conditions at single sites can make it useful to filter the single traces first. In the array detection process, several beams are formed, and several different filters are used (see Tab. 9.2). An STA/LTA detector is used on each such beam, and as seen from Fig. 9.19, we will get a trigger on several beams. The detector will compare the maximum STA/LTA (SNR) for every beam within a (narrow) time window, and usually report only the trigger with the highest SNR. The influence of different filters on the detectability of seismic signals is also demonstrated in Fig. 9.35.

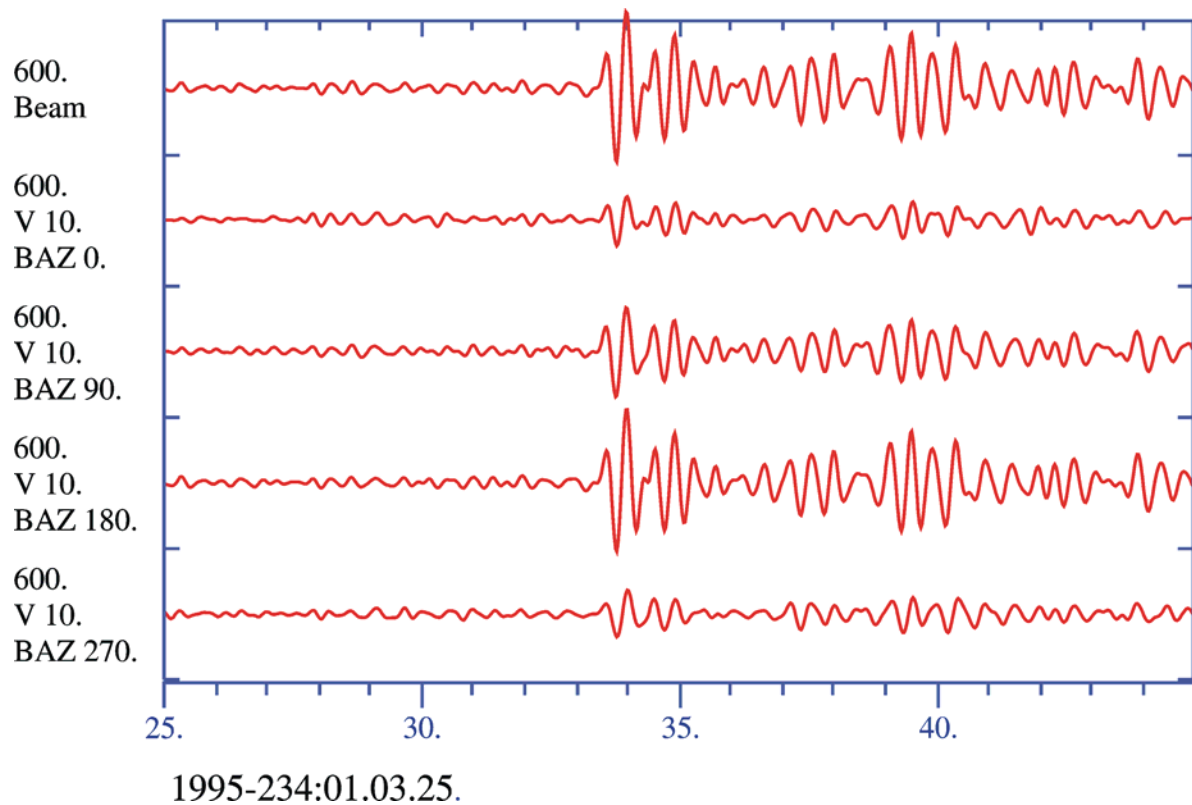


Fig. 9.19 This figure shows the same beams as in Fig. 9.18 but filtered with a Butterworth bandpass filter 2.0 – 4.0 Hz. All traces have an equal amplitude scale.

Fig. 9.20 (top trace) shows an incoherent beam, made by first filtering the raw data, then making STA time series of each trace and afterwards, summing up the STA traces. The STA traces can be time shifted using time delays for a given slowness vector, but for detection purposes when using a small aperture array, this is not necessary since the time shifts will be very small compared to the time length of the signal. An incoherent beam will reduce the

noise variance and can be used to detect signals that are incoherent across an array. Such signals are typically of high frequency.

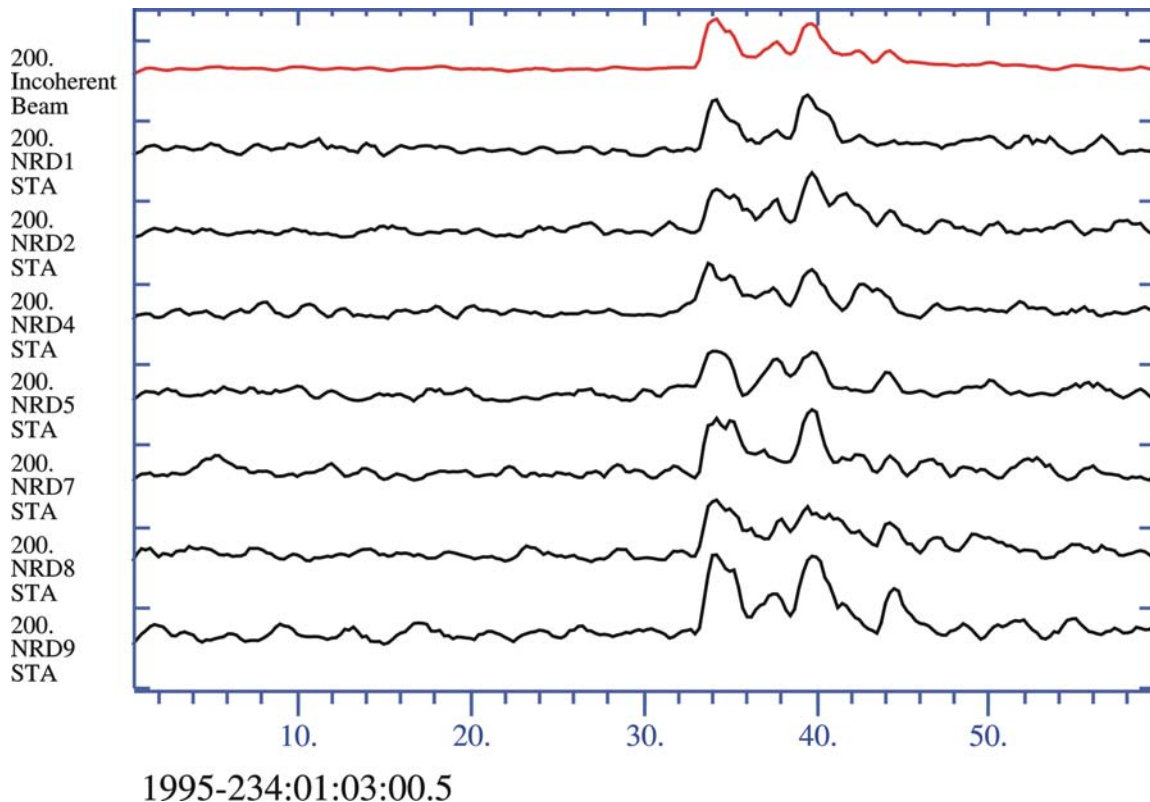


Fig. 9.20 Illustration of an incoherent beam (see text) which is shown on top (in red). The other traces are STA time series. The selected NORES channels have been prefiltered with a Butterworth bandpass filter 2.0 – 4.0 Hz. All traces have an equal amplitude scale.

9.6 Array transfer function

The array transfer function describes sensitivity and resolution of an array for seismic signals with different frequency contents and slownesses. When digitizing the output from a seismometer, we are sampling the wavefront of a seismic signal in the time domain, and to avoid aliasing effects, we need to apply an anti-aliasing filter. Similarly, when observing a seismic signal using an array, we obtain a spatial sampling of the ground movement. With an array, or a dense network, we are able to observe the wavenumber $k = 2\pi/\lambda = 2\pi \cdot f \cdot s$ of this wave defined by its wavelength λ (or frequency f) and its slowness s . While analog to digital conversion may give aliasing effects in the time domain, the spatial sampling may give aliasing effects in the wavenumber domain. Therefore the wavelength range of seismic signals, which can be investigated, and the sensitivity at different wavelengths must be estimated for a given array.

A large volume of literature exists on the theory of array characteristics, e.g., Somers and Manchee (1966), Haubrich (1968), Doornbos and Husebye (1972), Harjes and Henger (1973), Harjes and Seidl (1978), Mykkeltveit et al. (1983, 1988), and Harjes (1990). How the array transfer function can be estimated will be shown in the following.

9. Seismic Arrays

Assuming a noise and attenuation free signal, the difference between a signal w at the reference site A and the signal w_n at any other sensor A_n , is only the onset time at which this plane wave arrives at the sensors. As we know from sub-chapter 9.4, a plane wave is defined by its propagation direction and its apparent velocity, or in short by its slowness vector s_o . Thus we can write:

$$w_n(t) = w(t - \mathbf{r}_n \cdot \mathbf{s}).$$

Following Eq. (9.5) the beam of an array with M sensors for a seismic signal with the specific slowness s_o is defined as

$$b(t) = \frac{1}{M} \sum_{j=1}^M w_j(t + \mathbf{r}_j \cdot \mathbf{s}_o) = w(t). \quad (9.11)$$

The seismic signal at sensor A_n of a plane wave for any other slowness s can be written as $w_n(t) = w(t - \mathbf{r}_n \cdot \mathbf{s})$ and the beam is given by

$$b(t) = \frac{1}{M} \sum_{j=1}^M w_j(t + \mathbf{r}_j \cdot \mathbf{s}). \quad (9.12)$$

If we calculate all time shifts for a signal with the (correct) slowness s_o (Eq. (9.11)) with the (wrong) slowness s (Eq. (9.12)), we get the difference for the signal at site A_n $w(t + \mathbf{r}_n \cdot \mathbf{s}_o - \mathbf{r}_n \cdot \mathbf{s}) = w(t + \mathbf{r}_n \cdot (\mathbf{s}_o - \mathbf{s}))$ and the calculated beam can be written as

$$b(t) = \frac{1}{M} \sum_{j=1}^M w_j(t + \mathbf{r}_j \cdot (\mathbf{s}_o - \mathbf{s})). \quad (9.13)$$

This beam is now a function of the difference between the two slowness values $(s_o - s)$ and the geometry of the array \mathbf{r}_j . If the correct slowness is used, the beam calculated with Eq. (9.13) will be identical to the original signal $w(t)$. The seismic energy of this beam can be calculated by integrating over the squared amplitudes:

$$E(t) = \int_{-\infty}^{\infty} b^2(t) dt = \int_{-\infty}^{\infty} \left[\frac{1}{M} \sum_{j=1}^M w_j(t + \mathbf{r}_j \cdot (\mathbf{s}_o - \mathbf{s})) \right]^2 dt. \quad (9.14)$$

This equation can be written in the frequency domain by using Parseval's theorem and the shifting theorem:

$$E(\omega, s_o - s) = \frac{1}{2\pi} \int_{-\infty}^{\infty} |\bar{w}(\omega)|^2 \cdot \left| \frac{1}{M} \sum_{j=1}^M e^{i\omega \mathbf{r}_j \cdot (\mathbf{s}_o - \mathbf{s})} \right|^2 d\omega \quad (9.15)$$

with $\bar{w}(\omega)$ being the Fourier transform of the seismogram $w(t)$. Using the definition of the wavenumber vector $\mathbf{k} = \omega \cdot \mathbf{s}$, we can also write $\mathbf{k}_o = \omega \cdot \mathbf{s}_o$:

$$E(\omega, \mathbf{k}_o - \mathbf{k}) = \frac{1}{2\pi} \int_{-\infty}^{\infty} |\bar{w}(\omega)|^2 \cdot |C(\mathbf{k}_o - \mathbf{k})|^2 d\omega, \text{ where} \quad (9.16)$$

$$|C(\mathbf{k}_o - \mathbf{k})|^2 = \left| \frac{1}{M} \sum_{j=1}^M e^{i\omega \mathbf{r}_n \cdot (\mathbf{k}_o - \mathbf{k})} \right|^2 \quad (9.17)$$

Eq. (9.15) or Eq. (9.16) defines the energy of an array beam for a plane wave with the slowness s_o but calculating the applied time shifts for a slowness s . If the difference between s_o and s changes, the resulting beam has different amplitudes. However, this dependency is not a function of the actual signals observed at the single sites but a function of the array geometry weighted with the slowness difference $\mathbf{r}_n \cdot (\mathbf{k}_o - \mathbf{k})$. If the slowness difference is zero, the factor $|C(\mathbf{k}_o - \mathbf{k})|^2$ becomes 1.0 and the array is optimally tuned for this slowness. All other energy propagating with a different slowness will be (partly) suppressed. Therefore Eq. (9.17) is called the transfer function of an array. This function is not only dependent on the slowness of the seismic phase observed with this array, but is also a function of the wavenumber k (i.e., wavelength or frequency) of the observed signal, and of the array geometry.

Some general rules about transfer characteristics of arrays can be formulated as follows:

- 1) The aperture of an array defines the resolution of the array for small wavenumbers. The larger the aperture is, the smaller the wavenumbers (or slownesses) is that can be measured with the array. The upper limit for the longest wavelength λ that can meaningfully be analyzed by array techniques is about the aperture a of the array. The array responds like a single station for signals with $\lambda \gg a$.
- 2) The number of sites controls the quality of the array as a wavenumber filter, i.e., its ability to suppress energy crossing the array at the same time with a different slowness.
- 3) The distances between the seismometers define the position of the side lobes in the array transfer function and the largest resolvable wavenumber: the smaller the mean distance, the smaller the wavelength of a resolvable seismic phase will be (for a given seismic velocity).
- 4) The geometry of the array defines the azimuth dependence of points 1 – 3.

Some of these points can be seen in the following two examples of array transfer functions. Fig. 9.21 shows the transfer function of the cross-shaped Yellowknife array (YKA). Fig. 9.22 shows as another example the array transfer function of the circular, small aperture array ARCES. The geometry of this array (see Fig. 9.1) gives a perfect azimuthal resolution, and side lobes of the transfer function are far away from the main lobe. However, because of the small aperture, this array can not distinguish between waves with small wavenumber differences, as can be seen in the relatively wide main lobe of the transfer function. In contrast, in the case of Yellowknife, the main lobe is very narrow because of the larger aperture of the array. This results in a higher resolution in measuring apparent velocities. But the array shows resolution differences in different azimuths, which are caused by its geometry. The many side lobes of the transfer function are the effect of the larger distances between the single array sites.

9. Seismic Arrays

Details on array design for the purpose of maximizing the gain achievable by beamforming can be found in 9.8.1.

In the next sections we will introduce “f-k analysis” and “beampacking” methods. In principle, it is all a matter of forming beams with different slowness vectors and comparing the amplitudes or the power of the beams, and then finding out which v_{app} -backazimuth combination gives the highest energy on the beam, i.e., to find out which beam is the “best” beam. In f-k analysis the process is done in the frequency domain rather than in the time domain.

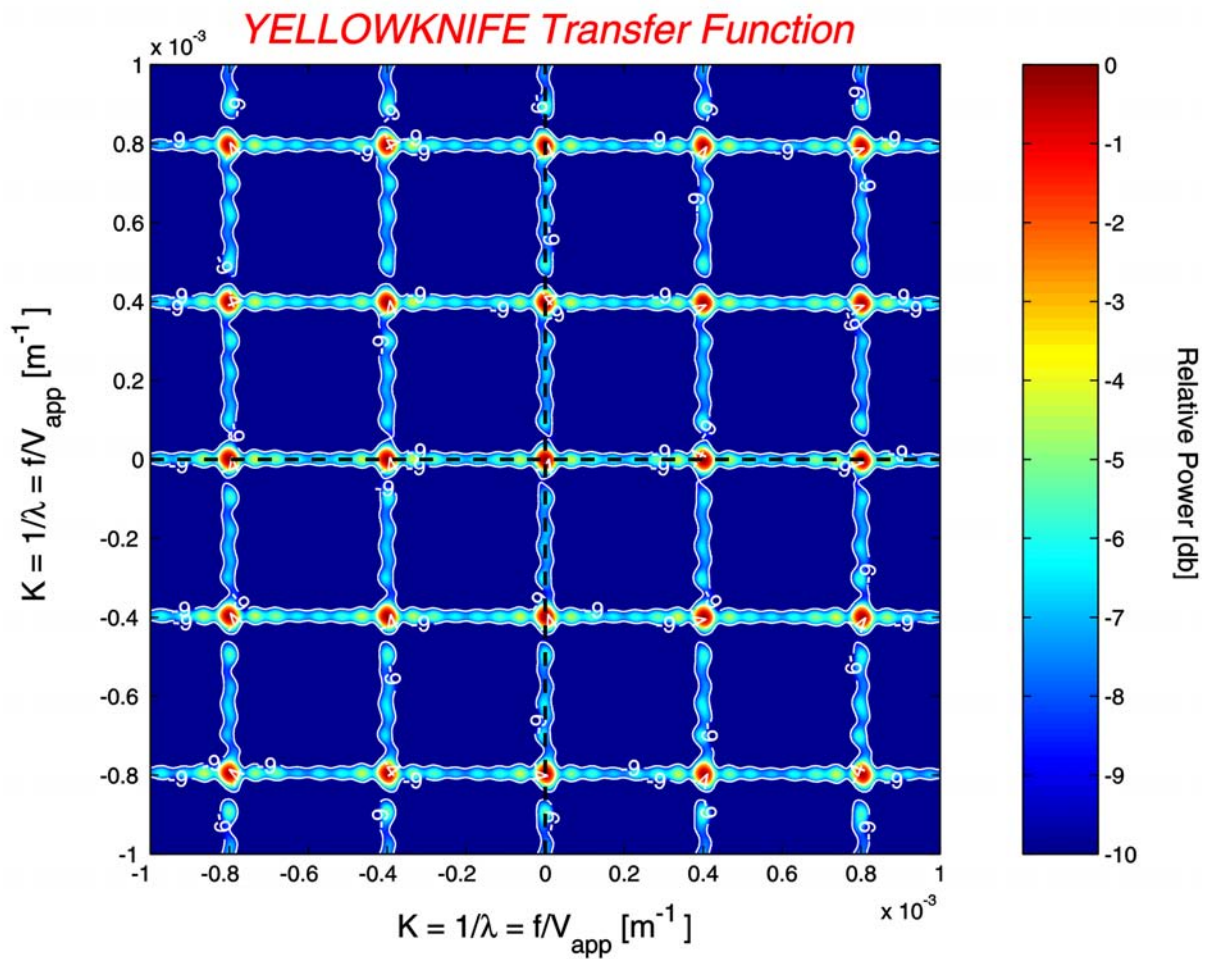


Fig. 9.21 This figure shows the array transfer function of the cross-shaped Yellowknife array (see Fig. 9.3). Plotted is the relative power of the array response normalized with its maximum.

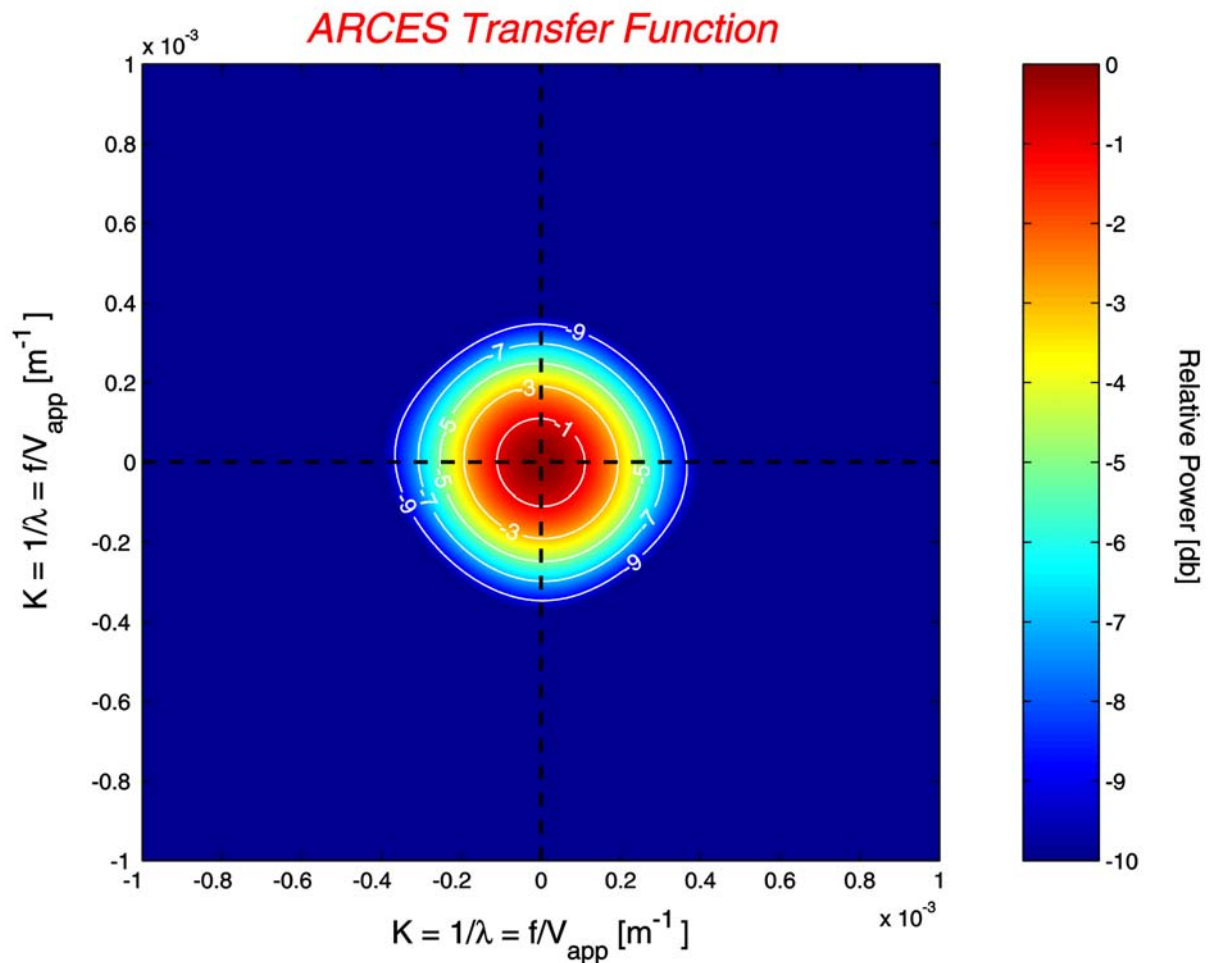


Fig. 9.22 This figure illustrates the array transfer function of the circular ARCES array (see Fig. 9.1). Shown is the relative power of the array response normalized with its maximum. White isolines were plotted at -1 , -3 , -5 , -7 , and -9 db below the maximum of the array response.

9.7 Slowness estimation using seismic arrays

9.7.1 Slowness estimate by f-k analysis

A description of frequency-wavenumber analysis – “f-k analysis” – may be found in Capon (1969). This method has been further developed to include wide-band analysis, maximum-likelihood estimation techniques, and three-component data (Kværna and Doornbos, 1986; Kværna and Ringdal, 1986; Ødegaard et al., 1990).

The f-k analysis is used as a reference tool for estimating slowness; f-k analysis is done in the frequency domain, and a time shift in the time domain is equivalent to a phase shift in the frequency domain. The principle is beamforming in the frequency domain for a number of different slowness values. Normally we use slownesses from -0.4 to 0.4 s/km equally spaced over 51 by 51 points. For every one of the 2601 points the beam power is evaluated, giving an equally spaced grid of 2601 power points.

9. Seismic Arrays

Such a power grid is displayed in Fig. 9.24 with the slowness ranging from -0.2 to 0.2 s/km; the unfiltered data used are shown in Fig. 9.23. The power is displayed by isolines of dB down from the maximum power. A process is used which will find the maximum power in the grid, and the corresponding slowness vector is the resulting estimated slowness.

The f-k plot in Fig. 9.24 also represents the color-coded relative power of the multichannel signal for 51 by 51 points in slowness space. Because the f-k analysis is a frequency-domain method, one has to define an interesting frequency range. In our case the data were analyzed in the frequency range between 1.2 and 3.2 Hz. The peak level is found at an apparent velocity 20.3 km/s, backazimuth 83.4°. The normalized relative peak power is 0.96. This measure tells us how coherent the signal is between the different sites and that a beam formed with the corresponding slowness will give a signal power that is 0.96 times the average power of the individual sensors. This means that the estimated beam signal will have practically no signal loss for this slowness and in this filter band as compared to individual sensors. The isolines tell us that using any different slowness will give a signal loss of maximum 10 dB. The equivalent beam total power is 84.22 dB.

An uncertainty of the estimated apparent velocity and backazimuth can be derived from the size of the observed power maximum in the f-k plot at a given db level below the maximum, the SNR of the signal, and the power difference between the maximum and an eventually existing secondary maximum in the plot.

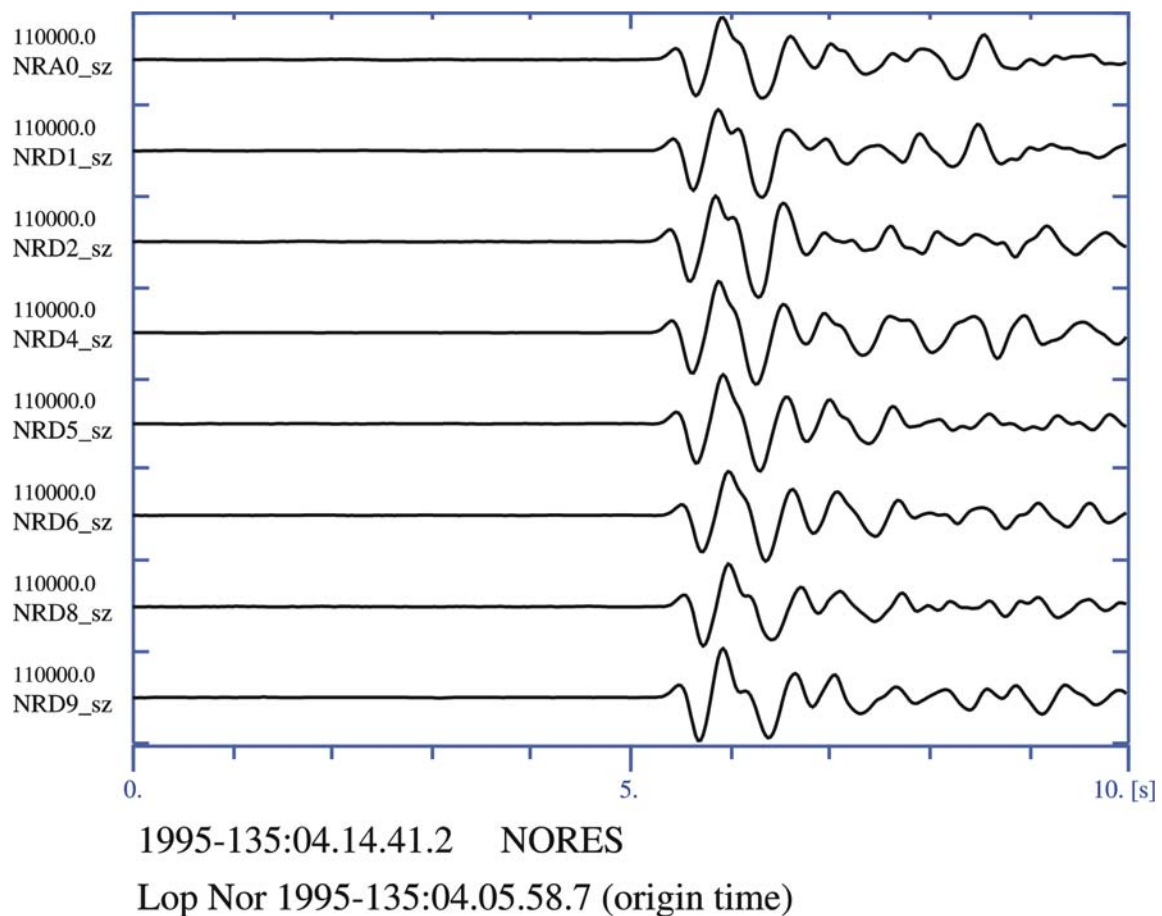


Fig. 9.23 NORES recordings (raw data) of a Lop Nor explosion on May 15, 1995. Traces from the center site A0 and the D-ring instruments are shown at the same scale.

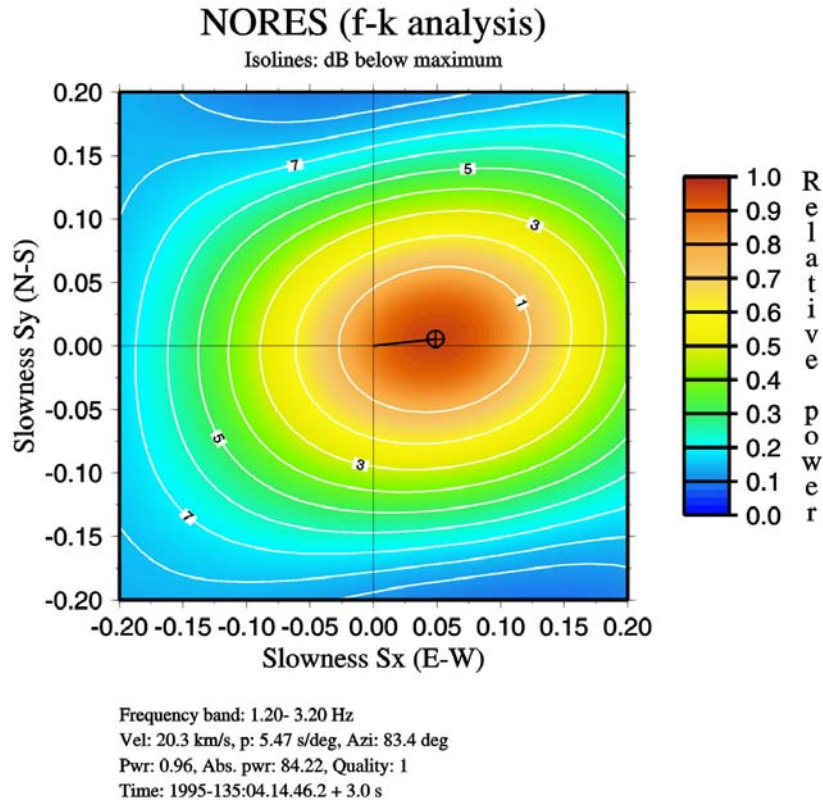


Fig. 9.24 Result from wide-band f-k analysis of NORES data from a 3 second window around the signal shown in Fig. 9.23. The isolines are in dB from maximum peak and the color-coded relative power is a measure of signal coherence.

9.7.2 Beampacking (time domain wavenumber analysis)

An alternative to the technique described above is the beampacking scheme, i.e., to beamform over a predefined grid of slowness points and measure the power. As an example see Fig. 9.25, where we used the same NORES data as for the f-k analysis in Fig. 9.24. All data were prefiltered with a Butterworth 1.2 – 3.2 Hz bandpass filter to make the results comparable with the f-k result in Fig. 9.24. To obtain a similar resolution as for the f-k analysis, the time domain wavenumber analysis requires a relatively high sample rate of the data. Therefore, we oversampled the data in this example 5 times by interpolation, i.e., we changed the sample rate from 40 to 200 Hz.

One can see from the beamforming process that we get practically the same slowness estimate as for the f-k analysis in the frequency domain (Fig. 9.24). In the time domain case, the relative power is the signal power of the beam for the peak slowness divided by the average sensor power in the same time window. The total power of 91.45 dB in Fig. 9.25 is the maximum beam power.

Compared to the f-k process used, the resulting total power is now 6 dB higher, which is due to the measurement method, and not a real gain. However, the beamforming process results in a slightly (about 10%) narrower peak for the maximum power as compared to f-k analysis.

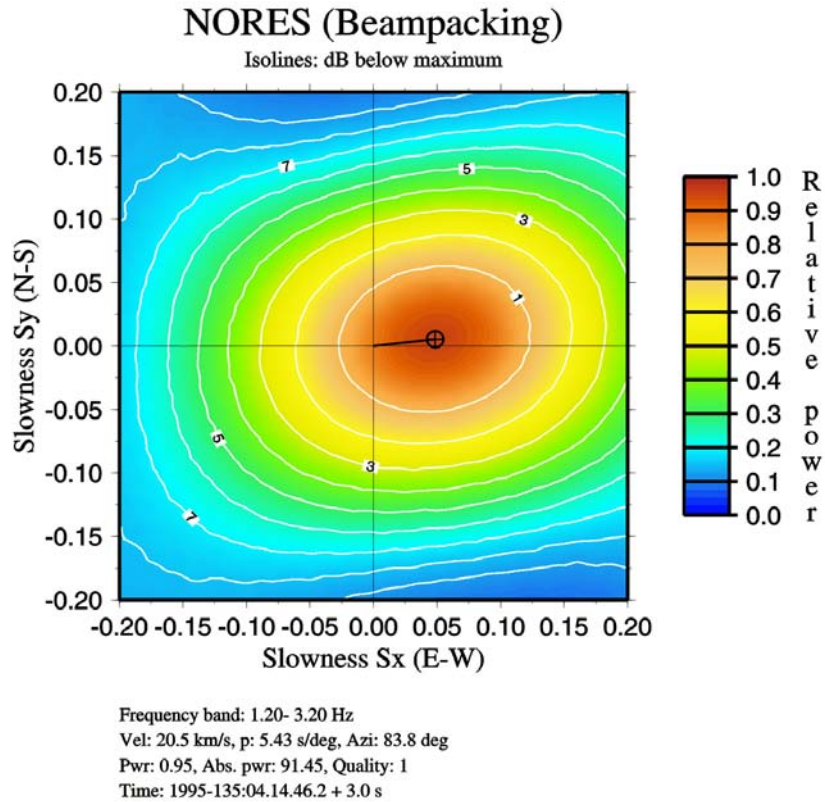


Fig. 9.25 Result from beampacking of the NORES data in Fig. 9.24 in an equispaced slowness grid. The data were prefiltered in the band 1.2 – 3.2 Hz and were resampled to 200 Hz. The isolines represent power of each beam within the 3-second window analyzed.

9.7.3 Slowness estimate by time picks

Yet another way of estimating slowness is to carefully pick times of the first onset or any other common distinguishable part of the same phase (same cycle) for all instruments in an array. Assuming again that the wavefront is plane, we may use Eq. (9.18) to estimate the slowness vector s by least squares fit to the observations.

Let t_i be the arrival time picked at site i , and t_{ref} be the arrival time at the reference site, then $\tau_i = t_i - t_{ref}$ is the observed time delay at site i . We observe the plane wave at M sites. With $M \geq 3$, we can estimate the horizontal components (s_x, s_y) of the slowness vector s by using least squares techniques. If $M \geq 4$, the vertical component of the slowness vector (s_z) can also be resolved. The uncertainties of the estimated parameters can be calculated in parallel with solving the equation system of Eq. (9.18).

$$\sum_{i=1}^M (\tau_i - \mathbf{r}_i \cdot \mathbf{s})^2 = \min \quad (9.18)$$

This method requires interactive analyst work. However, to obtain automatic time picks and thereby provide a slowness estimate automatically, techniques like cross-correlation (matched filtering) or just picking of peak amplitude within a time window (for phases that have an impulsive onset and last two or three cycles) may be used.

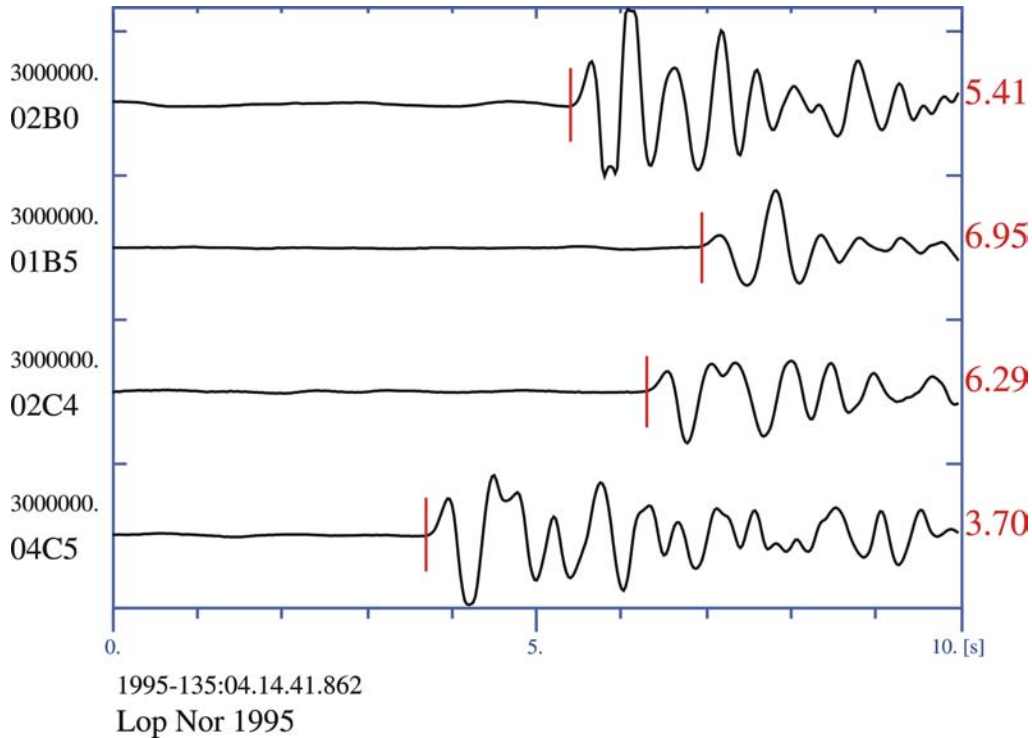


Fig. 9.26 NORARSAR recording of the Lop Nor explosion of May 15, 1995. Vertical traces (sz) from the sites 02B0, 01B5, 02C4, and 04C5 of the NORARSAR array (see also Fig. 9.2) are shown at the same amplitude scale. Note the large time delays as compared to the smaller NORES array in Fig. 9.23. The figure illustrates a simple time pick procedure of the individual onsets. A plane wave fit to these 4 onset time measurements gives an apparent velocity of 16.3 km/s and a backazimuth of 77.5°.

9.7.4 Time delay corrections

Calculating time delays using $\tau_i = \mathbf{r}_i \cdot \mathbf{s}$ is a simplification, ignoring both elevation of instruments and the fact that seismic waves are not plane waves over an array of diameter of e.g., 60 km. We have to introduce a correction $\Delta\tau_i$. The deviation from plane-wave time delays is caused by instrument elevation differences and inhomogeneities in the Earth.

Including elevation when calculating time delays as done in section 9.4.4 may compensate for the deviation due to elevation differences. Historically, and for convenience, elevation corrections have not been used for NORARSAR array beamforming. Instead, time delays have been calculated as plane-wave time delays plus a correction:

$$\tau_i = \mathbf{r}_i \cdot \mathbf{s} + \Delta\tau_i. \quad (9.19)$$

A database with time delay corrections was established that corrected for both elevation differences and inhomogeneities, and this database is still in use (Berteussen, 1974). So, for all beamforming, including each point in the beampacking process, the delays are corrected according to Eq. (9.19). The corrections depend on \mathbf{s} .

9. Seismic Arrays

A method to determine velocity heterogeneities by inverting such deviations of observed onset times from the theoretical plane wave was developed at NORSAR, the so-called ACH method (Aki, Christofferson, and Husebye, 1977).

9.7.5 Slowness corrections

When observing the backazimuth of an approaching wave, we find deviations from the expected backazimuth. In addition, the observed ray parameter will also be different from the theoretical one. This observation is valid for any seismic station. If the deviation is systematic and consistent for a given source location (or small region), we can correct for this deviation. If the predicted slowness is s_c and the observed slowness is s_o (Fig. 9.27), then the slowness deviation is

$$\Delta s = s_o - s_c . \quad (9.20)$$

It is also common to use the ray parameter p [s°] and the backazimuth BAZ [$^\circ$] as slowness vector components and to express the residuals as:

$$\Delta p = p_o - p_c \text{ and } \Delta BAZ = BAZ_o - BAZ_c . \quad (9.21)$$

However, every array has to be calibrated with its own corrections. Numerous studies have been performed to obtain slowness corrections for different seismic arrays (see e.g., Berteussen, 1976 and for the reference lists in Krüger and Weber, 1992 or in Schweitzer, 2001b). Usually the derivation of slowness corrections for the whole slowness range observable with one array needs a large amount of corresponding data and therefore some time.

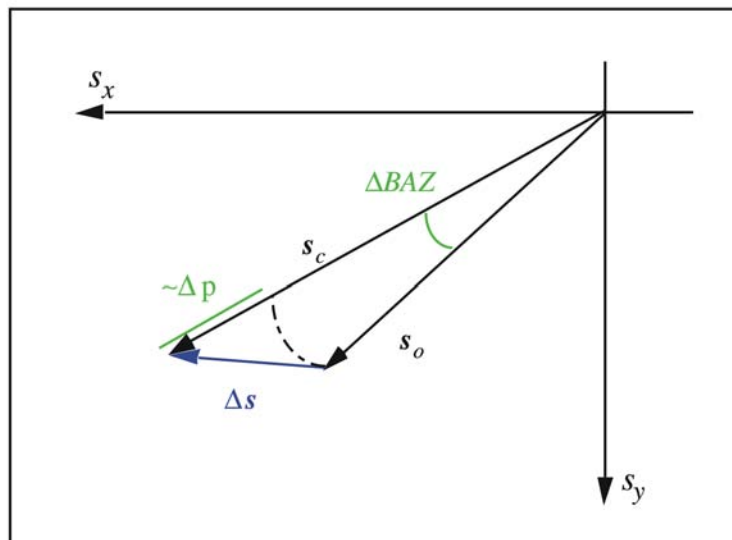


Fig. 9.27 Slowness vector deviation in the horizontal plane. The vector s_c denotes theoretical slowness. The vector s_o denotes observed slowness. The vector Δs denotes the slowness residual, also referred to as mislocation vector. The length of the slowness vector measured in [s°] is the ray parameter p , and the angle between North and the slowness vector, measured clockwise, is the backazimuth BAZ.

9.7.6 The correlation method used at the UKAEA arrays

As discussed in 9.6, the array transfer function of the UKAEA array YKA shows strong side lobes along a rectangular grid (see Fig. 9.21). This effect can be observed at all orthogonal linear or L-shaped arrays (Birtill and Whiteway, 1965). To improve the lower resolution along these principal axes, a correlation method has been introduced. In a first step, theoretical beams are separately calculated for each of the two seismometer lines; the geometrical crossing point of the two linear subarrays is used as the common reference point for both beams. If the actual signal has the same slowness as the slowness used to calculate the two beams, the signal must be in phase on both beams. In a second step calculating the cross-correlation between the two beams tests this condition. The correlator trace is calculated for a short, moving time window. This non-linear process is very sensitive to small phase differences and improves the resolution of such arrays especially along the principal axes of their transfer functions (for further details see Whiteway, 1965; Birtill and Whiteway, 1965; Weichert et al., 1967).

9.7.7 The VESPA process

A method to separate signals propagating with different apparent velocities is the VELOCITY SPectrum Analysis (VESPA) process. The principal idea of this method is to estimate the seismic energy reaching an array with different slownesses and to plot the beam energy along the time axis. The usual way to display a vespagram is to calculate the observed energy for specific beams and to construct an isoline plot of the observed energy for the different slowness values. The original VESPA process was defined for plotting the observed energy from a specific azimuth for different apparent velocities versus time (Davies et al., 1971). Fig. 9.28 shows as an example the vespagram for a mine blast in the Khibiny Massif (Kola Peninsula) observed with the ARCES array. The underground blasting of about 190 tons of explosives occurred on December 21, 1992 at 07:10 (latitude 67.67° , longitude 33.73°) at about 3.55° epicentral distance from ARCES. All beams were calculated with the theoretical backazimuth of 118° , and the seismograms were bandpass filtered between 2 and 8 Hz. Fig. 9.28 shows two of the filtered seismograms used to calculate the vespagram. The energy for the different slowness values was calculated for 3 seconds-long sliding windows moved forward in 0.5 s steps. The observed energy was normalized with the maximum value and the isolines were plotted as contour lines in [db] below this maximum. Note that the first two P onsets both have a slowness of about 0.125 s/km equivalent to an apparent velocity of 8 km/s: P_n and a superposition of onsets from several crustal phases. The S phases are clearly separated from the P phases in slowness; S_n with a slowness of about 0.225 s/km (apparent velocity of about 4.44 km/s) and the dominating L_g phase with a slowness of about 0.28 s/km or an apparent velocity of about 3.57 km/s.

9. Seismic Arrays

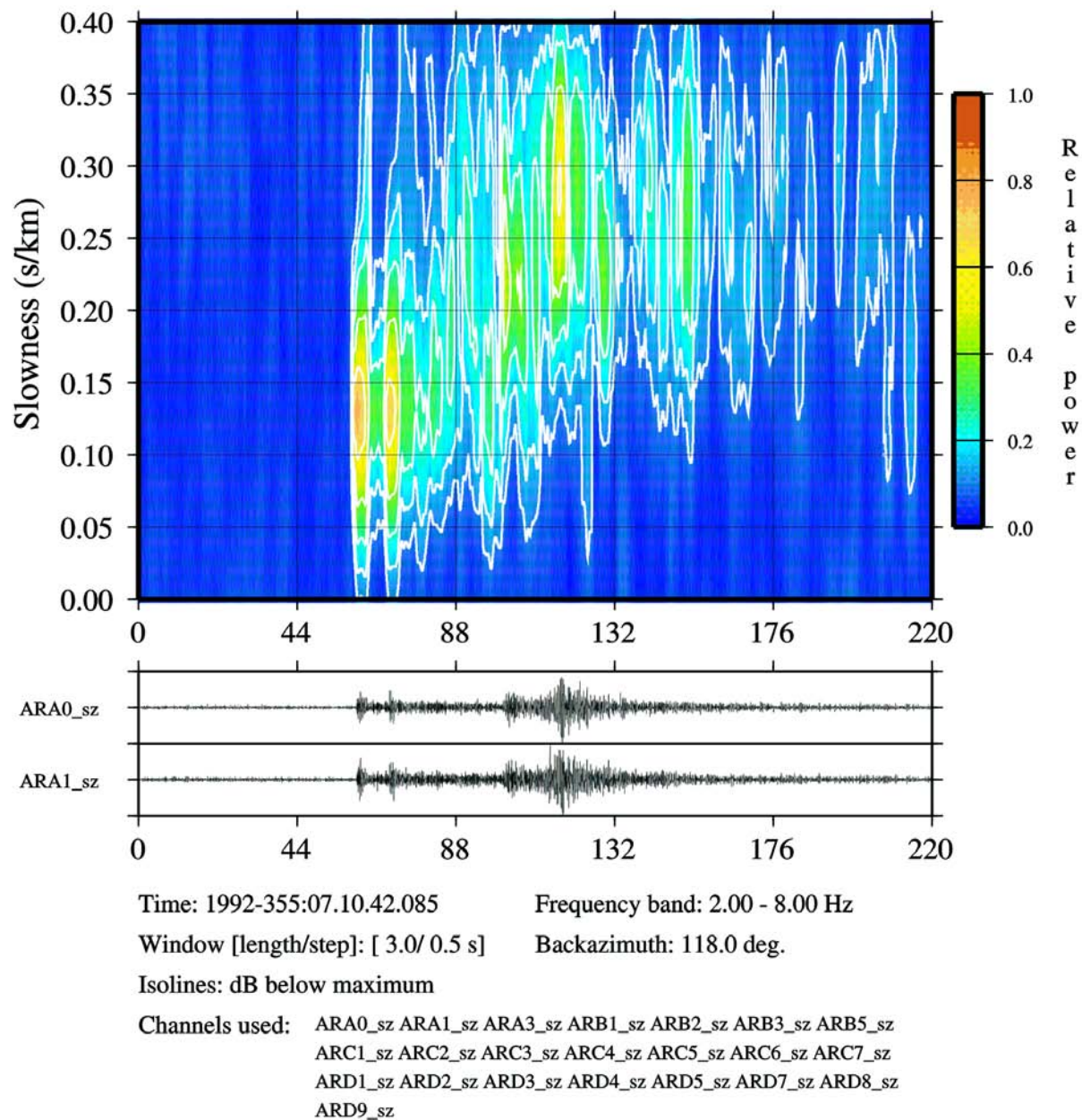


Fig. 9.28 Vespagram for a mining explosion (December 21, 1992; 07:10; lat. 67.67° , lon. 33.73°) in the Khibiny Massif observed at ARCES. Shown is the observed seismic energy for different apparent velocities (slownesses) and a constant backazimuth of 118° . For further details see text.

Later the concept vespagram was expanded by plotting the observed energy from different azimuths using a specific apparent velocity. Fig. 9.29 shows an example for such a plot for the same event in the Khibiny Massif as for Fig. 9.28. Instead of a constant backazimuth, a constant apparent velocity of 8 km/s was used to calculate the beam energy from all azimuth directions. Note also that the noise contains energy with apparent velocities around 8 km/s, but this noise approaches the array from a different backazimuth (310°), and the crustal P phases show a slight shift in the backazimuth direction relative to the first mantle P phase (P_n).

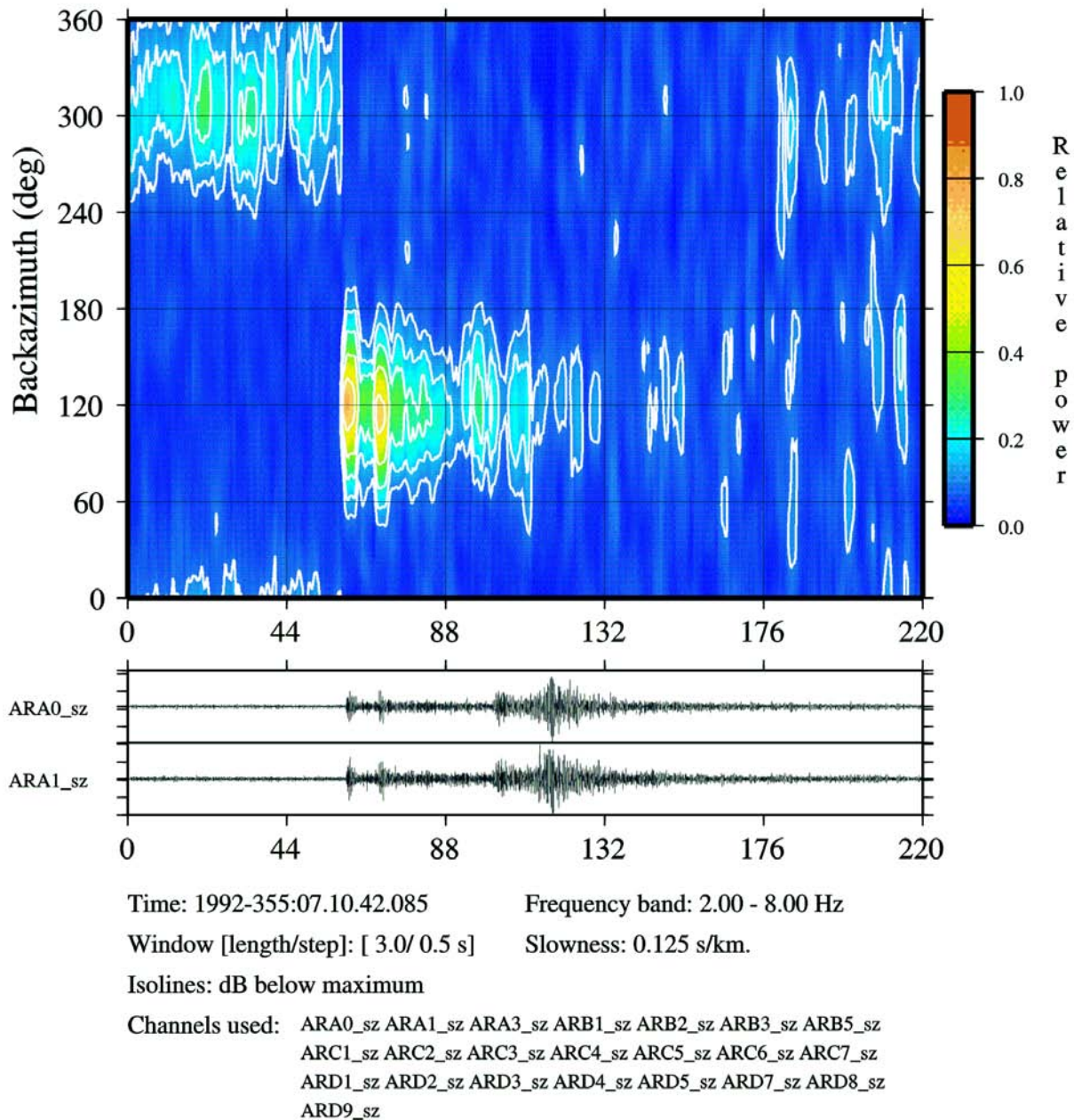


Fig. 9.29 As Fig. 9.28 but the energy is now calculated for a constant apparent velocity of 8 km/s (i.e., a slowness of 0.125 s/km) and different backazimuths.

9.7.8 The n-th root process and weighted stack methods

A non-linear method to enhance the SNR during the beamforming is the so-called n-th root process (Muirhead, 1968; Kanasewich et al., 1973; Muirhead and Datt, 1976). Before summing up the single seismic traces, the n-th root is calculated for each trace by retaining the sign information; Eq. (9.5) then becomes:

$$B_N(t) = \frac{1}{M} \sum_{j=1}^M |w_j(t + \tau_j)|^{1/N} \cdot \text{signum}\{w_j(t)\}, \quad (9.22)$$

9. Seismic Arrays

where the value of the function $\text{signum}\{w_j(t)\}$ is defined as -1 or +1, depending on the sign of the actual sample $w_j(t)$. After this summation, the beam has to be raised to the power of N , again retaining the sign information:

$$b_N(t) = |B_N(t)|^N \cdot \text{signum}\{B_N(t)\} \quad (9.23)$$

N is an integer ($N = 2, 3, 4, \dots$) that has to be chosen by the analyst. The n -th root process weights the coherence of a signal higher than the amplitudes, which results in a distortion of the waveforms: the larger N , the less the original waveform of the signal is preserved. However, the suppression of uncorrelated noise is better than with linear beamforming.

Schimmel and Paulssen (1997) introduced another non-linear stacking technique to enhance signals through reduction of incoherent noise, which shows a smaller waveform distortion than the n -th root process. In their method, the linear beam is weighted with the mean value of the so-called instantaneous phase of the actual signal. The phase term itself follows a power law, which can be defined by the analyst. With this phase-weighted stack all phase-incoherent signals will be suppressed and small coherent signals will be relatively enhanced.

Instead of the instantaneous phase, Kennett (2000) proposed the usage of the semblance of the signal as weighting function. He applied this approach not only on one (vertical) component of the observed wave field but also jointly on all three components. For this, he could also take into account the cross-semblance between the three components of ground movement. He achieved a similar resolution to the method of Schimmel and Paulssen (1997).

An easy implementable weighted stack method would be to weight the amplitudes of the single sites of an array with the SNR of the signal at this site before beamforming, but this does not directly exploit the coherence of the signals across the array. All described stacking methods can increase the slowness resolution of vespagrams (see 9.7.7).

9.8 Array design for the purpose of maximizing the SNR gain

Signal detection at array stations is governed by the gain that can be achieved in the signal-to-noise ratio (SNR) through the process of beamforming. This subsection provides some guidance as to how an array can be designed to maximize this gain. Other aspects of array design have been dealt with elsewhere in this chapter.

9.8.1 The gain formula

The SNR gain G by beamforming achievable from seismic array data can be expressed by

$$G^2 = \frac{\sum_{ij} C_{ij}}{\sum_{ij} \rho_{ij}} \quad (9.24)$$

9.8 Array design for the purpose of maximizing the SNR gain

where C_{ij} is the signal cross-correlation between sensors i and j of an array and ρ_{ij} is the noise cross-correlation between sensors i and j (see 9.4.5). For an N -sensor array, this formula collapses to the well-known relation of $G^2 = N$ for perfectly correlating signals ($C_{ij} = 1$ for all i and j) and uncorrelated noise ($\rho_{ij} = 0$ for $i \neq j$ and $\rho_{ij} = 1$ for $i = j$).

For any array geometry it is thus possible to predict the array gain if the signal and noise cross-correlations are known for all pairs of sensors of the array layout. The remainder of this subsection describes how to design an array based on the availability of such correlation data.

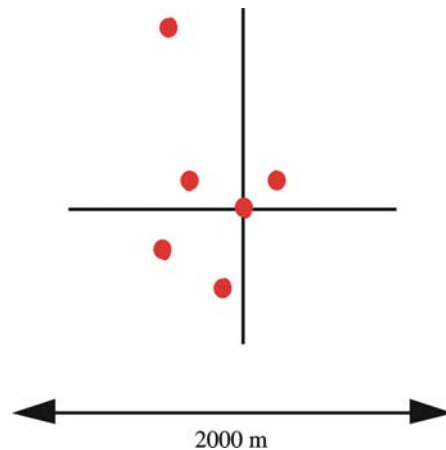


Fig. 9.30 The figure shows the first layout for the experiments eventually leading to the 25-element NORES array in Norway in 1984.

9.8.2 Collection of correlation data during site surveys

Correlation data for use in the design phase should be collected in a carefully planned site survey. The sensor layout during the survey should be planned so to represent as many intersensor distances as possible. The first layout for the experiments eventually leading to the deployment in 1984 of the 25-element NORES array in Norway utilized only 6 sensors, in a rather irregular geometry, as shown in Fig. 9.30.

The deployment for the collection of the correlation data should be done in as simple a way as possible and should take advantage of outcropping bedrock where possible. The layout should preferably comprise ten sensors or more. If, however, for example only six sensors are available for the site survey, one could start out with a configuration something like that of Fig. 9.30 and record data continuously for about one week. At the end of this one-week period, one could redeploy four of the sensors and record data for another week. Two of the sensors would then occupy the same locations for the entire two-week recording period and would provide evidence (or lack thereof) of consistency in the results between the two one-week periods. The largest intersensor separation represented in these data should be, if possible, of the order of 3 km.

The experience from the design of the NORES array showed that the signal and noise correlation curves obtained from the early experiments (with six, and later twelve sensors) possessed most of the characteristic features and thus qualitatively resembled the curves derived later on from configurations comprising many more sensors (up to 25).

9.8.3 Correlation curves derived from experimental data

In the processing of the data from the site survey, cross-correlation values must be computed for all combinations of sensor pairs of the experimental layout. Consider, for example, a geometry of six sensors. This geometry comprises 15 unique pairs of sensors. Consider also a short interval of say 30 seconds of noise data (make sure no signal is contained in this time window) and compute the cross-correlation values for each of the 15 unique pairs of sensors (no time shifts are to be introduced for this computation). The time series are first bandpass filtered so as to derive the correlation values of one particular frequency (or frequency band). The 15 correlation values are then plotted in an x-y diagram, where the x-axis represents the intersensor separation and the y-axis the correlation value (a figure between -1.0 and +1.0), resulting in a plot as shown in Fig. 9.31.

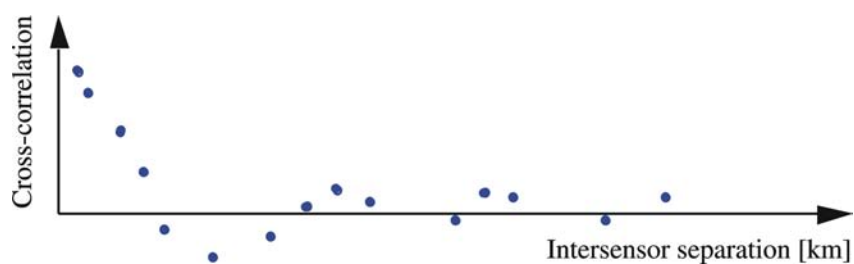


Fig. 9.31 Noise cross-correlation values for a test layout of 6 sensors.

When plotting the cross-correlation values as a function of sensor separation only and thus disregarding possible directional dependencies, an implicit assumption is made of azimuthal symmetry in wavenumber space, over a longer time interval. This assumption is justified by the NORES experience, which shows that only a relatively small scatter is exhibited in the correlation data.

Computations of the kind described above should also be done for signals, which for the purpose of this section will be assumed to be P waves (although design strategies for the detection of S-type phases will be similar to those described here). A recording period of 14 days or so during the site survey hopefully should be sufficient to record a reasonable number of representative P-wave arrivals. The time windows for these computations should be relatively short (5 seconds or so) to capture the coherent part of the signal arrival. Signal time series must be aligned in accordance with the signal slowness (phase velocity and direction of approach) before the cross-correlation is computed. Again, the time series must be filtered in a relatively narrow band around the peak frequency of the signal being considered. A plot like the one shown in Fig. 9.32 would result from this, again assuming a six-sensor layout with 15 unique combinations of sensor pairs.

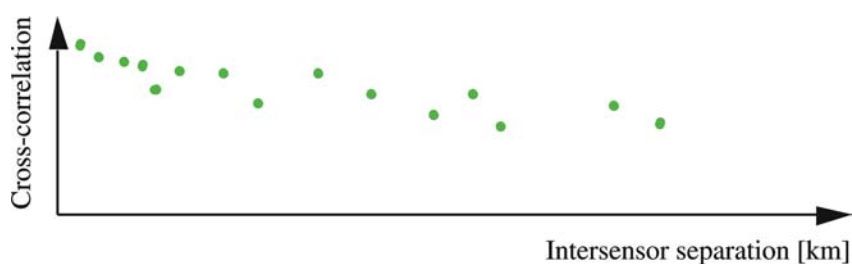


Fig. 9.32 P-wave cross-correlation values for a test layout of 6 sensors.

Computations as described above should be repeated for various time intervals for the noise, and for various P arrivals recorded during the site survey. Then, for each frequency interval of interest, all data (both noise and signal correlation data) should be combined in one diagram for the purpose of deriving curves (based on interpolation) that are representative of that frequency interval, and that would provide correlation values for all intersensor separations. These diagrams might then appear as shown in Fig. 9.33, in which the upper curve represents the signal correlation and the lower curve the noise correlation.

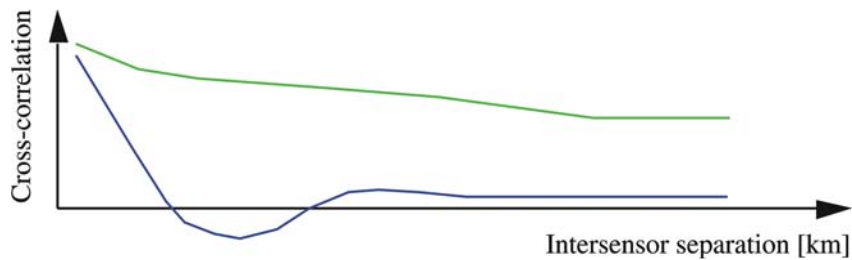


Fig. 9.33 Signal (upper) and noise (lower) correlation curves representing experimental data collected for a test array.

For the noise correlation curve in Fig. 9.33 to be representative for 2 Hz, for example, the noise data should be filtered in a band where 2 Hz is close to the lower limit of the passband, due to the spectral fall-off of the noise. A passband of 1.8 – 2.8 Hz might be appropriate for the noise, but actual noise spectra for the site in question should be computed and studied before this passband is decided on. To generate a signal correlation curve representative for 2 Hz, signals should be used that have their spectral peaks close to this frequency, and some narrow passbands centered on 2 Hz should be applied to the data. These curves would then be used to predict gains for various array designs as detailed below.

It should be noted that the rather pronounced negative minima for the noise correlation curves (as schematically represented in Fig. 9.33) are consistently observed for the NORES array. It is the exploitation of this feature that provides for gains in excess of \sqrt{N} , commonly observed at the NORES array (or subgeometries thereof). It should also be noted that this feature of negative noise correlation values is not a universal one; e.g., Harjes (1990) did not find consistently such pronounced negative minima for the GERES test array in Germany.

9.8.4 Example: A possible design strategy for a 9-element array

As an example of application of the design ideas outlined above, let us consider practical aspects of the design of a 9-element array. Several new arrays to be built for the International Monitoring System (IMS) for CTBT monitoring will comprise 9 elements. A useful design for a new 9-element array would be one for which there are 3 and 5 elements equidistantly placed on each of two concentric rings, respectively, plus one element at the center of the geometry, as shown in Fig. 9.34.

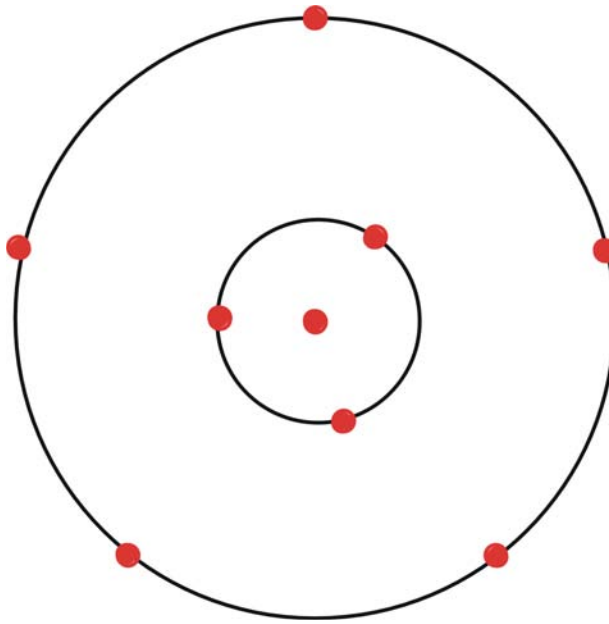


Fig. 9.34 The figure shows a possible design for a 9-element array.

The elements on the two rings should be placed so as to avoid radial alignment. If the five elements of the outer ring are placed at 0, 72, 144, 216 and 288 degrees from due north, the elements of the inner ring might be placed at 36, 156 and 276 degrees, as shown in Fig. 9.34. Within this class of design, the problem at hand is thus to find the radii of the two rings that for a given site would provide the best overall array gain. To constrain the design options even further, one might consider adopting the NORES design idea, limited to these two rings. The radii of the four NORES rings are given by the formula:

$$R = R_{\min} \cdot 2.15^n, (n = 0, 1, 2, 3) \quad (9.25)$$

For NORES, $R_{\min} = 150$ m. For the design problem at hand, only R_{\min} , the radius of the inner ring, remains to be determined from the correlation data, whereas the radius of the outer ring would then be 2.15 times the radius of the inner ring.

The final step in the procedure outlined here is to compute expected gains for various array designs within this class of geometries. To this end, one must determine which signal frequencies are of the largest importance with regard to the detection capability of the array at the site under study. Assuming that three P-wave signal frequencies, f_1 , f_2 and f_3 , (e.g., 1.8, 2.5 and 3.5 Hz) have been identified, these should be taken into account in the computations to derive the optimum array geometry. We would then have available from the site survey empirically-based correlation curves in analytical or tabular form that would provide correlation values for **all** intersensor separations of interest. The gains as a function of frequency for various values of the parameter R_{\min} could then be computed using the formula for the array gain and the correlation values derived from the correlation curves, for the relevant intersensor separations. The results of these computations could be tabulated as indicated in Tab. 9.1.

Tab. 9.1 The table provides the gains by beamforming achievable by different values of the parameter R_{min} .

R_{min} [m]	Gain (f_1) [dB]	Gain (f_2) [dB]	Gain (f_3) [dB]
200	3	6	8
300	4	8	9
400	5	9	7
...
1000	9	7	4
...

Note that for the lowest frequency considered (f_1), it might pay in terms of array gain to exclude the elements of the inner ring from the gain computations (since noise correlation values for low frequencies may be high for many sensor pairs involving sensors of the inner ring).

The optimum geometry would correspond to the value of R_{min} that gives the best overall gain in Tab. 9.1. This judgment would be based on some appropriate weighting scheme for the frequencies considered.

The procedure outlined here could be generalized to a class of designs for which the radii of the two rings are varied independently. Gain values would then be tabulated as shown in Tab. 9.1, but there would now be a sequence of tables (each table would represent a fixed radius of one of the two rings). The search for the optimum geometry would then be performed across all these tables.

9.9 Routine processing of small-aperture array data at NORSAR

9.9.1 Introduction

By way of example we will explain now the main features of the automatic routine processing of data from the regional arrays at NORSAR (Fyen 1989, 2001).

The array processing is divided into three steps:

- Detection Processing (DP), i.e., perform STA/LTA triggering on a number of predefined beams;
- Signal Attribute Processing (SAP), i.e., perform signal feature extraction of detected signals; and
- Event Processing (EP), i.e., perform phase association, location processing and event plotting.

We have earlier pointed out the importance of beamforming and filtering for signal enhancement. Fig. 9.35 shows ARCES data with one of the seismometer outputs filtered in different filter bands. An important feature seen from this figure is that the regional seismic phases Pn and Lg have their best SNR in different frequency bands. So to be sure to detect both phases, we should use several filter bands in the detector recipe. Fig. 9.18 showed

9. Seismic Arrays

different beams for the same P-wave signal. The other important lesson is that we need beams for various slowness vectors to detect the signal. In Mykkeltveit et al. (1988) and in Kväerna (1989), it is shown that different combinations of sensors, for example, within the NORES array give different noise reduction for various frequency bands. The lesson is that it is not always optimal to use all seismometers of the array to form a beam; rather one should in general use different sub-configurations, tailored to the signal frequencies.

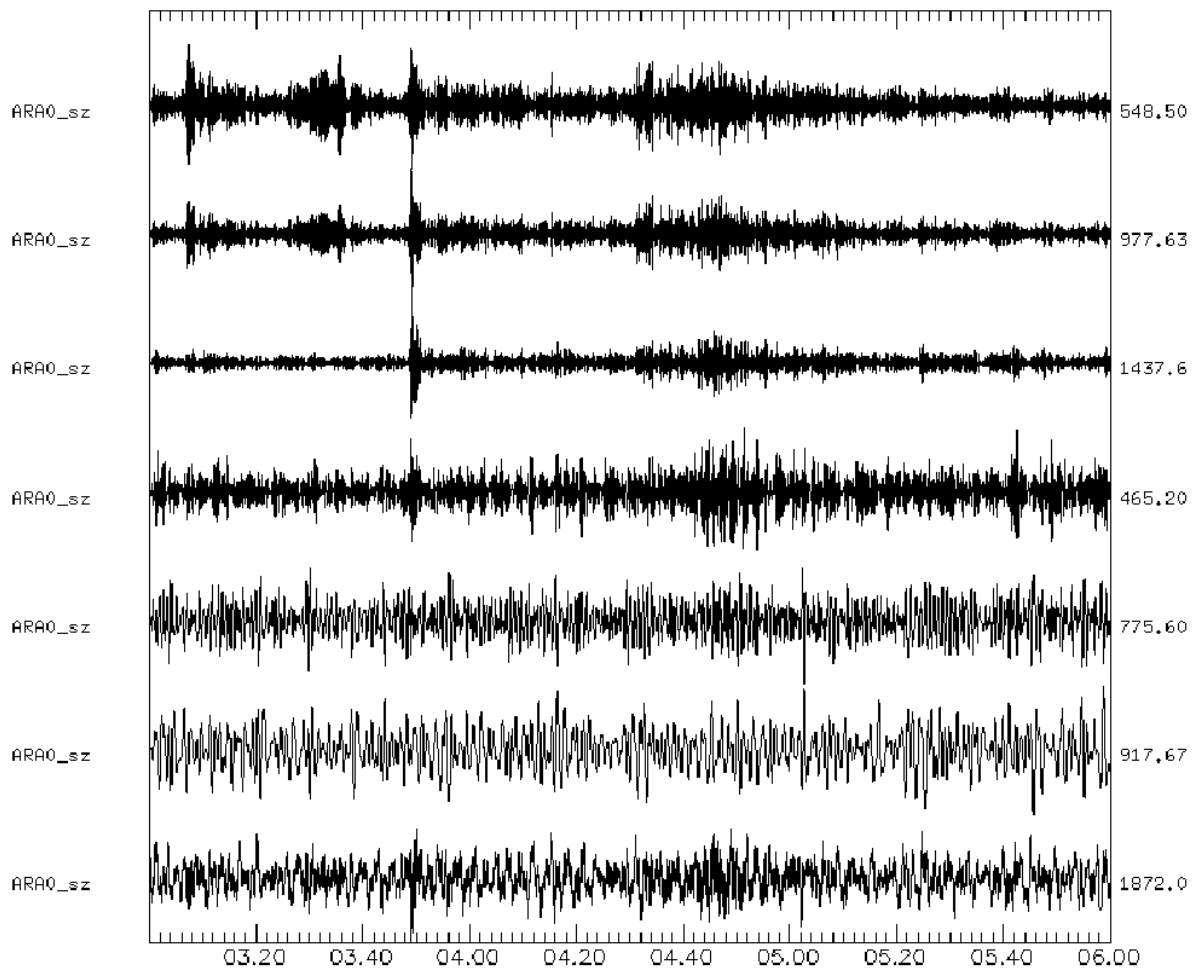


Fig. 9.35 The bottom trace of the figure shows raw data from instrument A0 at the center of the ARCES array. The next traces from bottom to top are data from the same instrument filtered with 3rd order Butterworth bandpass filters using frequency bands 0.5 – 1.5 Hz, 1.0 – 3.0 Hz, 2.0 – 4.0 Hz, 4.0 – 8.0 Hz, 6.0 – 12.0 Hz, and 8.0 – 16.0 Hz, respectively.

Now we have three parameter sets that make up the input for the STA/LTA detector: the specific array configuration to use for the beam, the slowness vector to use for the beam, and the filter band to use for the beam. Note that one could also use just a single seismometer instead of a beam. Based on experiments, a list of these parameters has been compiled at NORSAR that constitute a “detector recipe” with, e.g., numerous beams using different slownesses, different configurations, and different filter bands. For a large signal, the detector

9.9 Routine processing of small-aperture array data at NORSAR

program will trigger on many beams, and the program will use a detection reduction process to report only one detection for each signal.

As an example, a detector recipe listing the entire beam set composed of 254 beams for the online processing of data from the SPITS array, as it is in use at NORSAR, is included in Tab. 9.2. The complete process is illustrated by using a data example from the ARCES array.

Tab. 9.2 The detection beamset for the SPITS array as used at NORSAR. THR is the SNR threshold used to define a detection and “all” means that the whole SPITS array (SPA0, SPA1, SPA2, SPB1, SPB2, SPB3, SPB4, and SPB5) is used to form this beam (from Schweitzer, 1998).

BEAM NAMES	VELOCITY [km/s]	BACKAZIMUTH [deg]	FILTER		THR	SITES (verticals only)
			bandpass [Hz]	order		
S001	99999.9	0.0	0.8 – 2.0	4	4.5	SPA0 SPB1 SPB2 SPB3 SPB4 SPB5
S002	99999.9	0.0	0.8 – 2.0	4	4.5	all
S003	99999.9	0.0	1.0 – 3.0	3	4.5	SPA0 SPB1 SPB2 SPB3 SPB4 SPB5
S004	99999.9	0.0	1.0 – 3.0	3	4.5	all
S005	99999.9	0.0	2.0 – 4.0	3	4.0	SPA0 SPB1 SPB2 SPB3 SPB4 SPB5
S006	99999.9	0.0	2.0 – 4.0	3	4.0	all
S007	99999.9	0.0	3.0 – 5.0	3	4.0	SPA0 SPB1 SPB2 SPB3 SPB4 SPB5
S008	99999.9	0.0	3.0 – 5.0	3	4.0	all
S009	99999.9	0.0	0.9 – 3.5	4	4.5	SPA0 SPB1 SPB2 SPB3 SPB4 SPB5
S010	99999.9	0.0	0.9 – 3.5	4	4.5	all
S011	99999.9	0.0	1.0 – 4.0	3	4.5	SPA0 SPB1 SPB2 SPB3 SPB4 SPB5
S012	99999.9	0.0	1.0 – 4.0	3	4.5	all
SA01 – SA04	10.0	0 90 180 270	1.0 – 3.0	3	4.5	SPA0 SPB1 SPB2 SPB3 SPB4 SPB5
SA05 – SA08	10.0	45 135 225 315	1.0 – 3.0	3	4.5	all
SA09 – SA12	10.0	0 90 180 270	2.5 – 4.5	3	4.0	SPA0 SPB1 SPB2 SPB3 SPB4 SPB5
SA13 – SA16	10.0	45 135 225 315	2.5 – 4.5	3	4.0	all
SA17 – SA20	10.0	0 90 180 270	4.0 – 8.0	3	4.0	SPA0 SPB1 SPB2 SPB3 SPB4 SPB5
SA21 – SA24	10.0	45 135 225 315	4.0 – 8.0	3	4.0	all
SA25 – SA28	10.0	0 90 180 270	3.0 – 6.0	3	4.0	SPA0 SPB1 SPB2 SPB3 SPB4 SPB5
SA29 – SA32	10.0	45 135 225 315	3.0 – 6.0	3	4.0	all
SB01 – SB04	7.0	0 90 180 270	1.0 – 4.0	3	4.5	SPA0 SPB1 SPB2 SPB3 SPB4 SPB5
SB05 – SB08	7.0	45 135 225 315	1.0 – 4.0	3	4.5	all
SB09 – SB12	7.0	0 90 180 270	3.0 – 6.0	3	4.0	SPA0 SPB1 SPB2 SPB3 SPB4 SPB5
SB13 – SB16	7.0	45 135 225 315	3.0 – 6.0	3	4.0	all
SB17 – SB20	7.0	0 90 180 270	5.0 – 10.0	3	4.0	SPA0 SPB1 SPB2 SPB3 SPB4 SPB5
SB21 – SB24	7.0	45 135 225 315	5.0 – 10.0	3	4.0	all
SC01 – SC04	5.0	0 90 180 270	1.0 – 4.0	3	4.5	SPA0 SPB1 SPB2 SPB3 SPB4 SPB5
SC05 – SC08	5.0	45 135 225 315	1.0 – 4.0	3	4.5	all
SC09 – SC12	5.0	0 90 180 270	3.5 – 5.5	3	4.0	SPA0 SPB1 SPB2 SPB3 SPB4 SPB5
SC13 – SC16	5.0	45 135 225 315	3.5 – 5.5	3	4.0	all
SC17 – SC20	5.0	0 90 180 270	5.0 – 10.0	3	4.0	SPA0 SPB1 SPB2 SPB3 SPB4 SPB5
SC21 – SC24	5.0	45 135 225 315	5.0 – 10.0	3	4.0	all
SC25 – SC28	5.0	0 90 180 270	8.0 – 16.0	3	4.0	SPA0 SPB1 SPB2 SPB3 SPB4 SPB5
SC29 – SC32	5.0	45 135 225 315	8.0 – 16.0	3	4.0	all
SD01 – SD08	4.0	0 45 90 135 180 225 270 315	0.9 – 3.5	4	4.5	all
SD09 – SD16	4.0	0 45 90 135 180 225 270 315	3.0 – 6.0	3	4.0	all
SD17 – SD24	4.0	0 45 90 135 180 225 270 315	4.0 – 8.0	3	4.0	all
SE01 – SE08	3.3	0 45 90 135 180 225 270 315	1.5 – 3.5	3	4.5	all
SE09 – SE16	3.3	0 45 90 135 180 225 270 315	3.0 – 6.0	3	4.0	all
SE17 – SE24	3.3	0 45 90 135 180 225 270 315	5.0 – 10.0	3	4.0	all
SF01 – SF08	2.5	0 45 90 135 180 225 270 315	1.0 – 4.0	3	4.5	all
SF09 – SF16	2.5	0 45 90 135 180 225 270 315	2.0 – 4.0	3	4.0	all
SF17 – SF24	2.5	0 45 90 135 180 225 270 315	3.0 – 5.0	3	4.0	all
SN01	8.4	97.6	2.0 – 4.0	3	3.7	all
SN02	8.4	97.6	3.0 – 5.0	3	3.7	all
SN03	8.4	97.6	4.0 – 8.0	3	3.7	all
SN04	8.4	97.6	6.0 – 12.0	3	3.7	all
SN05	8.4	97.6	8.0 – 16.0	3	3.7	all
SN06	4.7	97.6	2.0 – 4.0	3	3.7	all
SN07	4.7	97.6	3.0 – 5.0	3	3.7	all
SN08	4.7	97.6	4.0 – 8.0	3	3.7	all
SN09	4.7	97.6	6.0 – 12.0	3	3.7	all
SN10	4.7	97.6	8.0 – 16.0	3	3.7	all
SG01 – SG12	2.0	0 30 60 90 120 150 180 210 240 270 300 330	1.5 – 3.5	3	4.5	all
SG13 – SG24	2.0	0 30 60 90 120 150 180 210 240 270 300 330	2.5 – 4.5	3	4.0	all
SG25 – SG36	2.0	0 30 60 90 120 150 180 210 240 270 300 330	3.5 – 5.5	3	4.0	all
SM01 – SM12	1.7	0 30 60 90 120 150 180 210 240 270 300 330	1.0 – 3.0	3	4.5	all
SM13 – SM24	1.7	0 30 60 90 120 150 180 210 240 270 300 330	2.0 – 4.0	3	4.0	all
SM25 – SM36	1.7	0 30 60 90 120 150 180 210 240 270 300 330	3.0 – 6.0	3	4.0	all

9. Seismic Arrays

9.9.2 Detection Processing – DP

The DP process continuously reads data off a disk loop or any other continuous database and uses beamforming, filtering, and the STA/LTA detector to obtain detections (triggers). The DP program produces, e.g., for the array ARCES (ARC) and for the day of the year (DOY) 199, 1996, the file ARC96199.DPX.

The following list gives some example lines from this file. The file contains the name of the detecting beam (e.g., F074), the time of detection (199:16.03.49.3), the end of the detection state (199:16.03.53.1), the maximum STA (242.4), the LTA at the time of detection (10.27), the SNR (STA/LTA = SNR = 23.601), and the number of beams detecting (37). The detecting beam reported (here F074) is the one beam, normally out of many beams, that detected this signal with the highest SNR.

```
FH04 199:16.02.18.6 - 02.19.9 106.52 32.15 3.313 1
FH04 199:16.02.39.1 - 02.39.6 116.09 43.91 2.644 1
FH04 199:16.02.44.4 - 02.48.6 296.52 56.63 5.236 5
F101 199:16.02.55.5 - 02.56.3 175.40 33.59 5.221 3
F074 199:16.03.49.3 - 03.53.1 242.40 10.27 23.601 37
FH03 199:16.04.32.9 - 04.35.9 291.46 73.01 3.992 5
FH02 199:16.04.46.4 - 04.50.9 297.87 75.23 3.960 24
FH04 199:16.09.57.6 - 09.58.9 80.86 24.07 3.359 2
```

The key parameters reported are the beam code, the trigger time, and the SNR = STA/LTA. The beam code points to a file (see Fig. 9.36) containing information on beam configuration, slowness and filter used. The format of a detection output is not important. The important thing is to create a list of detections that can be used for further analysis.

```
THR = 4.000
BF1 = 3.500
BF2 = 5.500
BMVEL = 11.100
BMAZI = 150.000
REFLAT = 69.535
REFLON = 25.506
REFELE = 403.000
REFSIT = ARA0_sz
SELECTED CHANNELS : ARA0_sz ARB1_sz ARB2_sz ARB3_sz ARB4_sz ARB5_sz
ARC1_sz ARC2_sz ARC3_sz ARC4_sz ARC5_sz ARC6_sz ARC7_sz
```

Fig. 9.36 Example of the contents of a file with the parameters that characterize beam F074. THR is the SNR detection threshold, BF1 and BF2 are the lower and the upper limits of the bandpass filter applied, BMVEL and BMAZI are the apparent velocity and the backazimuth for this beam, REFLAT, REFLON, and REFSIT define the reference site of the beam, and SELECTED CHANNELS lists the site configuration.

9.9.3 Signal Attribute Processing – SAP

This process sequentially reads detections from the .DPX file and performs for every detection an f-k analysis to estimate apparent velocity and backazimuth. The estimated

9.9 Routine processing of small-aperture array data at NORSAR

velocity and backazimuth is referred to as “observed slowness”. Waveform segments for the analysis are again read from a disk loop or any other database.

A special version of the EP program is used and produces, e.g., for array ARC, DOY 199, 1996 the file ARC96199.FKX. The key parameters reported in the .FKX files are the signal onset time, the beam code, the SNR, the estimated slowness, the signal amplitude and frequency, and the phase identification based on the slowness estimate.

Some lines from ARC96199.FKX are listed below. The entries are the arrival id number (e.g., 25), the estimated onset time (199:16.03.48.409), the difference between trigger and onset time (0.89), the beam name (F074), the SNR (23.6), the apparent velocity from f-k analysis (7.4), the preliminary phase name by automatically considering apparent velocity and three-component polarization analysis (Pgn, which means either Pg or Pn), the estimated backazimuth from f-k analysis (122.5°), the relative power from f-k analysis (0.72, a number between 0.0 (no coherence) and 1.0 (perfect coherence, correlation)), the f-k analysis quality indicator (2, 1=best, 4=poor), the estimated dominant frequency in Hz (4.85), the maximum amplitude in counts (476.9), the maximum STA of the detection (242.4), the polarization analysis IP, IS (0 and -3, respectively), the polarization analysis rectilinearity (0.69), the horizontal/vertical ratio (0.49), the inclination 1 (41.26°), and the polarization inclination 3 (73.94°).

█	199:16.02.18.314	0.29	FH04	3.3	2.4	nois	256.5	0.33	4	9.22	336.2	106.5	1	-3	0.77	0.68	22.88	83.77
10	199:16.02.36.964	2.14	FH04	2.6	2.4	nois	247.8	0.38	3	9.93	439.5	116.1	1	-3	0.79	0.25	4.92	83.30
15	199:16.02.43.039	1.36	FH04	5.2	2.4	nois	243.3	0.59	3	9.80	931.2	296.5	1	-3	0.55	0.49	14.66	88.32
20	199:16.02.54.915	0.58	F101	5.2	2.4	nois	236.7	0.61	3	9.85	1019.8	175.4	0	0	-1.00	-1.00	-1.00	-1.00
25	199:16.03.48.409	0.89	F074	23.6	7.4	Pgn	122.5	0.72	2	4.85	476.9	242.4	0	-3	0.69	0.49	41.26	73.94
30	199:16.04.32.160	0.74	FH03	4.0	5.4	Lg	117.7	0.32	3	6.38	596.6	291.5	D4_sz		0.57	1.07	61.00	74.64
35	199:16.04.45.785	0.61	FH02	4.0	4.1	Lg	127.4	0.27	3	5.07	531.9	297.9	D4_sz		0.48	1.36	58.36	54.76
40	199:16.09.55.770	1.83	FH04	3.4	2.4	nois	197.7	0.44	4	9.33	227.5	80.9	-1	-2	0.70	1.23	85.50	72.81
45	199:16.10.38.771	1.73	F106	4.8	2.5	nois	222.0	0.52	3	8.38	230.4	59.7	0	2	0.88	2.38	81.32	28.00

Fig. 9.37 shows raw data for the detection reported at time 199:16.03.49.3 (see detection list). The signal attribute process will use this detection time to select a 3 second wide time window starting 0.5 second before the detection time. The data from all vertical seismometers within this time window will then be used for f-k analysis to obtain the true apparent velocity of the signal. The result from the f-k analysis is shown in Fig. 9.38. This process is repeated for all detections and Fig. 9.39 shows the data interval selected for the Lg detection. The corresponding f-k analysis results are shown in Fig. 9.40. In automatic mode, of course, the EP program will not display any graphics. The figures are only produced for illustration purposes. However, the capability of displaying results graphically at any step of a process is essential to be able to develop optimum recipes and parameters. The EP program may output results into flat files or a database.

For a large array like NORSAR we can, on the basis of the phase identification and measured slowness, get a distance by screening a slowness table and thereby a location using distance and backazimuth. This is a relatively minor operation in terms of CPU power, so with every detection a corresponding location is provided in the case of NORSAR processing.

For the large array NORSAR, we may choose between beamform f-k analysis and the beampacking process. The benefit of using beampacking rather than frequency domain f-k analysis is that for every point in slowness space, we can use time delay corrections and obtain a calibrated slowness.

9. Seismic Arrays

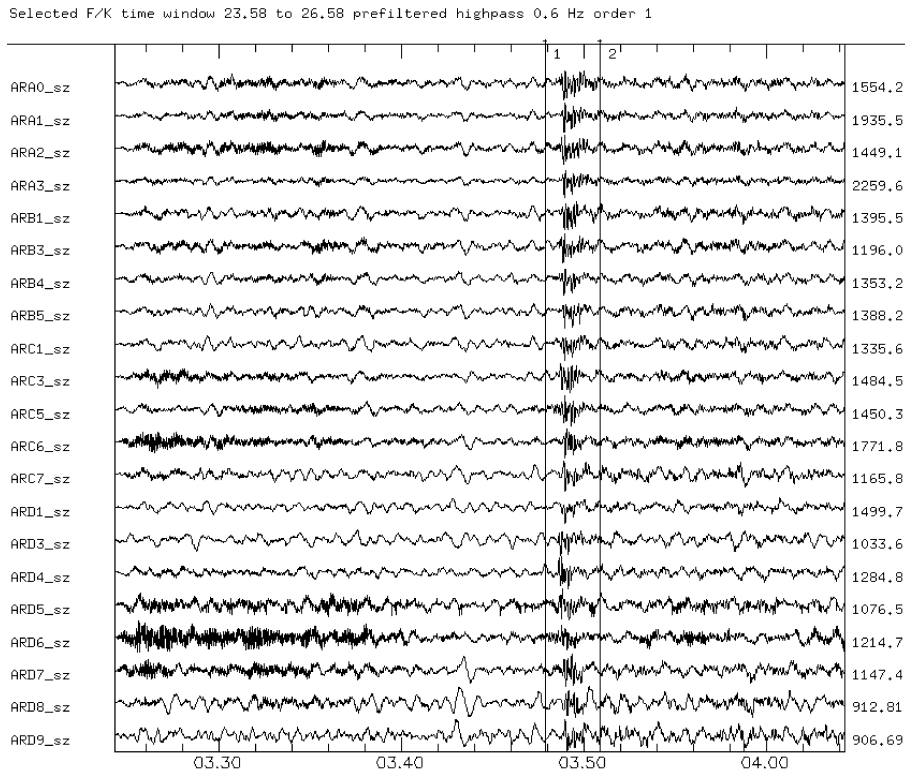


Fig. 9.37 The figure shows raw data from all the vertical seismometers of the ARCES array. The time interval contains the Pn phase of a regional event. The vertical bars define a 2 second time window that is used for the f-k analysis.

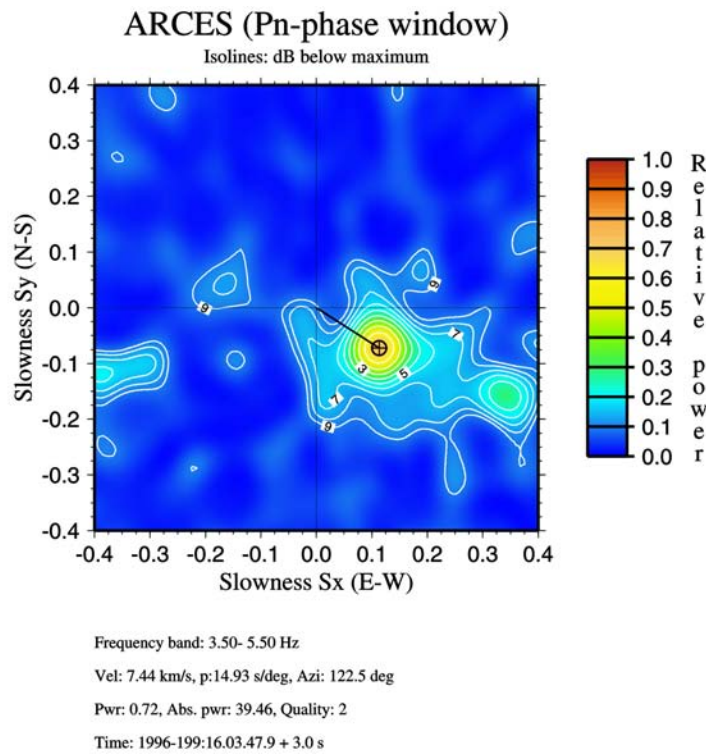


Fig. 9.38 Result of the broadband f-k analysis from the data in Fig. 9.37, pertaining to the Pn-phase interval.

9.9 Routine processing of small-aperture array data at NORSAR

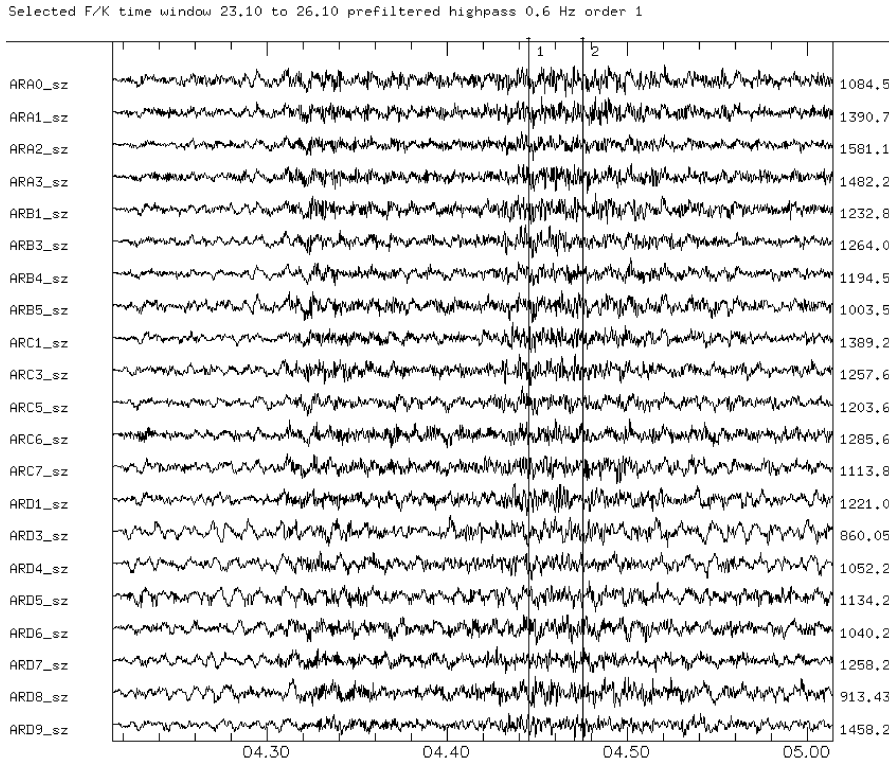


Fig. 9.39 The figure shows raw data from all the vertical seismometers of the ARCES array. The time interval contains the Lg phase of a regional event. The vertical bars define a 3 second time window that is used for the f-k analysis.

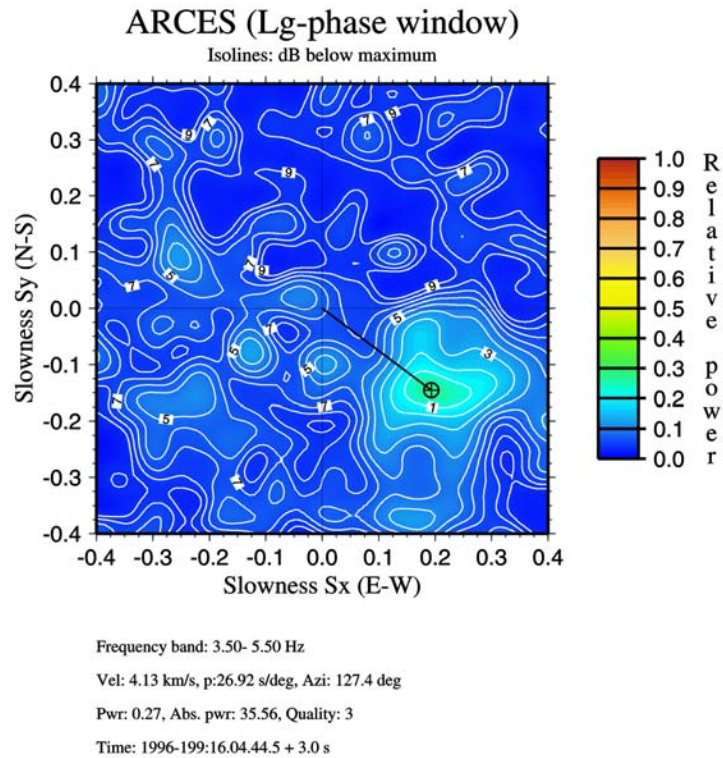


Fig. 9.40 Result of the broadband f-k analysis from the data in Fig. 9.39, pertaining to the Lg-phase interval.

9.9.4 Event Processing – EP

This process sequentially reads all detections from the .FKX file. Whenever a detection with an apparent velocity greater than, e.g., 6.0 km/s is found, it is treated as P. Additional detections are searched for, and if additional detections are found with backazimuth estimates not more than, e.g., 30° from the first detection and a detection time not more than 4 minutes from the first detection, they are used as associated detections. If detections with an apparent velocity less than 6.0 km/s are found, then they are treated as S (Sn, Lg). If phases within 4 minutes and backazimuth deviation of less than 30° with a first P and an S later are found, then they are treated as observations from a regional event. A location routine, which uses the backazimuth information, is used to locate the regional event. More details on these topics here are given in Mykkeltveit and Bungum (1984).

The result is written in the file ARC96199.EPX for array ARC, DOY 199, 1996. The key parameters reported are the origin time, the hypocenter, and the magnitude for each located event, and onset time, amplitude and frequency, SNR, beam code, and apparent velocity for all associated detections. For each declared event, an event plot may be created (see Fig. 9.41).

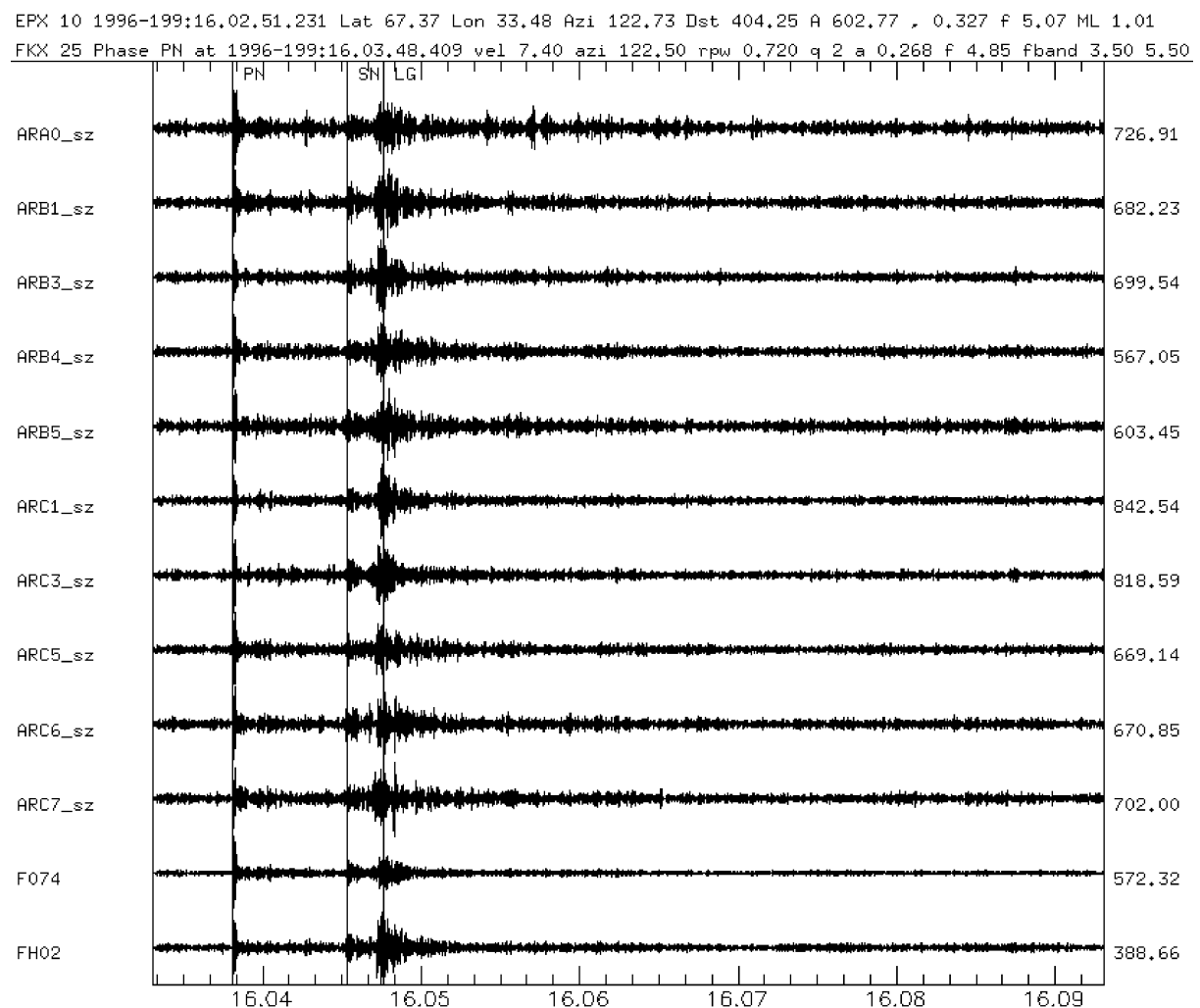


Fig. 9.41 Regional event plot for final documentation.

Some lines from ARC96199.EPX are listed below. Whenever an event is declared, a location is performed and reported with two lines (HYP and EPX) that contain event number (10), origin time (199:16.02.51.2), latitude (67.369°), longitude (33.479°), ML (1.01), distance in [km] (404.3), backazimuth (122.7°), fixed depth (0F). The associated phases are listed thereafter, and for the Pn phase we have the id number (25), the arrival time (199:16.03.48.4), the station name (here FRS, the old NORSAR internal code for ARCES), the phase name (PN), the maximum amplitude in [nm] (0.268), the corresponding dominant frequency in [Hz] (4.8), the SNR (23.6), the beam name (F074), the apparent velocity (7.4), the backazimuth (122.5°), and an explanatory code from the location process. LOCATE means that this phase was used for location, ASSOC means that this onset was associated but not used in location, Tele means that this phase is interpreted as a teleseismic onset, Noplot3ci means that this phase was not used for any event definition. The “beam-name” aVG means that the corresponding arrival time is used for measuring the amplitude for ML, and the apparent velocity is the group velocity in that case.

```

 5 199:16.02.18.3 FRS nois      0.145  9.2      3.3 FH04   2.4 256.5 Noplot3ci
10 199:16.02.37.0 FRS nois      0.194  9.9      2.6 FH04   2.4 247.8 Noplot3ci
15 199:16.02.43.0 FRS nois      0.409  9.8      5.2 FH04   2.4 243.3 Noplot3ci
20 199:16.02.54.9 FRS nois      0.448  9.9      5.2 F101   2.4 236.7 Noplot3ci
10                               HYP 724 EUROPEAN USSR
10 199:16.02.51.2 EPX                67.369  33.479  1.01      404.3 122.7  0F
25 199:16.03.48.4 FRS PN          0.268  4.8      23.6 F074   7.4 122.5 LOCATE
30 199:16.04.32.2 FRS SN          0.278  6.4       4.0 FH03   5.4 117.7 LOCATE
10 199:16.04.44.6 MAG ML          0.327  5.1     602.8 aVG   3.6 122.7 LOCATE
35 199:16.04.45.8 FRS LG          0.288  5.1       4.0 FH02   4.1 127.4 LOCATE

```

The above example identifies one group of phases with backazimuth around 123° that are within 4 minutes. The first phase within the group has regional P-wave apparent velocity, and it is followed by a phase with regional S apparent velocity. Those are the criteria for defining an event.

9.10 Operational or planned seismic arrays

Tab. 9.3 below lists operational or planned seismic arrays as of September 2002. The following symbols have been used:

- ⊕ array, which is part of the International Monitoring System (IMS) to monitor the Comprehensive Nuclear-Test-Ban Treaty (CTBT) for nuclear tests as a primary or auxiliary station;
- * circular array of NORES type design;
- ** array of UKAEA type design.

Free fields in Tab. 9.3 indicate that values are yet to be determined or are unknown to the authors of Chapter 9. Fig. 9.42 shows a map with all arrays listed in the table.

9. Seismic Arrays

Tab. 9.3 List of operational or planned seismic arrays (as of September 2002)

CODE	LAT [°]	LON [°]	HEIGHT [km]	NUMBER OF ELEMENTS	APERTURE [km]	NAME
ABKT	37.9304	58.1189	0.678			Alibek ⊕
AKASG	50.4	29.1		26		Malin ⊕
ALAR	65.0653	-147.5639	0.626	6		Alaska Long-Period
APAES	67.6061	32.9931	0.200	9	1	Apatity *
ARCES	69.5349	25.5058	0.403	25	3	ARCESS ⊕ *
ASAR	-23.6664	133.9044	0.607	20	10	Alice Springs ⊕
BAO	-15.6349	-47.9915	1.211	12		Brasilia **
BCAR	63.0656	-141.785	0.847	5		Beaver Creek
BMAR	67.4289	-144.5807	0.756	5		Burnt Mountain
BMO	44.8489	-117.3056	1.189			Blue Mountains
BRLAR	39.7	33.6	1.4	8		Keskin Long-Period
BRSAR	39.7250	33.6389	1.440	7		Keskin ⊕
BRVK	53.0581	70.2828	0.315			Borovoye ⊕
CBAR	69.1266	-105.1120	0.040	23		Cambridge Bay
CM1	45.9337	-93.3527	0.324	6		Central Minnesota
CMAR	18.4575	98.9429	0.307	24	56	Chiang Mai ⊕
EKA	55.3317	-3.1592	0.263	20	9	Eskdalemuir ⊕ **
ESDC	39.6755	-3.9617	0.753	26	40	Sonsecu ⊕
FINES	61.4436	26.0771	0.150	16	2	FINESS ⊕ *
FLAR	54.7188	-101.9958	0.229	19		Flin Flon
GBA	13.6042	77.4361	0.686			Gauribidanur **
GERES	48.8451	13.7016	1.132	25	4	GERESS ⊕ *
GRF	49.6900	11.2200	0.500	13	100	Gräfenberg
HFA0	60.1420	13.6850	0.275	10	1	Hagfors ⊕
HILR	49.5440	119.7450	0.6	9	4	Hailar ⊕
HLBN						Haleban
ILAR	64.7714	-146.8866	0.419	20		Eielson ⊕ *
IMAR	65.9835	-153.7491	0.372	5		Indian Mountain
IR1	35.4164	50.6888	1.347	7		Iran Long-Period
JAVM	48.0	106.8				Javhlant ⊕
KSAR	37.4211	127.8844	0.109	37		Wonju ⊕
KURK	50.7153	78.6203	0.184	21		Kurchatov ⊕
KVAR	43.9557	42.6952	1.196	4	0.3	Kislovodsk ⊕
LSU1	30.0733	-91.9821	-0.023	5	-0.023	Parcperdue
LUXOR	26.0	33.0				Luxor ⊕
LZDM	36.091	103.84	1.6	9	4	Lanzhou ⊕
MKAR	46.7937	82.2904	0.615	10	4	Makanchi ⊕
MJAR	36.5417	138.2088	0.422	7	10	Matsushiro ⊕
MMAI	33.0	35.4	0.4			Mount Meron (Parod) ⊕ *
NSD	65.1944	18.8185	.2	5	1	Näsudden (Malå)
NOA	61.0397	11.2148	0.717	42	60	NORSAR ⊕
NORES	60.7353	11.5414	0.302	25	3	NORESS *
NTA	37.2783	-116.4367	1.996			Nevada Test Site
NVAR	38.4296	-118.3036	2.042	14		Mina ⊕
PARI	33.65	73.252				Pari ⊕
PDAR	42.7667	-109.5579	2.214	14	4	Pinedale (Boulder) ⊕
PDYAR	59.6553	112.4408	0.489			Peleduy ⊕
PETKA	53.02	158.65	0.15			Petropavlovsk ⊕
PKF	35.8818	-120.4135	0.469			Parkfield
RC01	61.0894	-149.7367	0.374			Rabbit Creek

9.10 Operational or planned seismic arrays

SB1	31.21	-105.4378	1.570			Sierra Blanca
SONM	47.8083	106.4167				Songong
SPITS	78.1777	16.3700	0.323	9	1	Spitsbergen ⊕ *
TXAR	29.3338	-103.6670	1.013	9	4	Lajitas ⊕ *
USK	44.28	132.08	0.3			Ussuryisk ⊕
VNA2	-70.9252	-7.39267	0.350	16	2	Neumayer-Watzmann ⊕
WRA	-19.9426	134.3394	0.419	24	25	Warramunga ⊕ **
YKA	62.4932	-114.6053	0.197	20	25	Yellowknife ⊕ **
ZAL	53.94	84.80	0.2			Zalesovo ⊕
						(Niger) ⊕
						(Saudi Arabia) ⊕

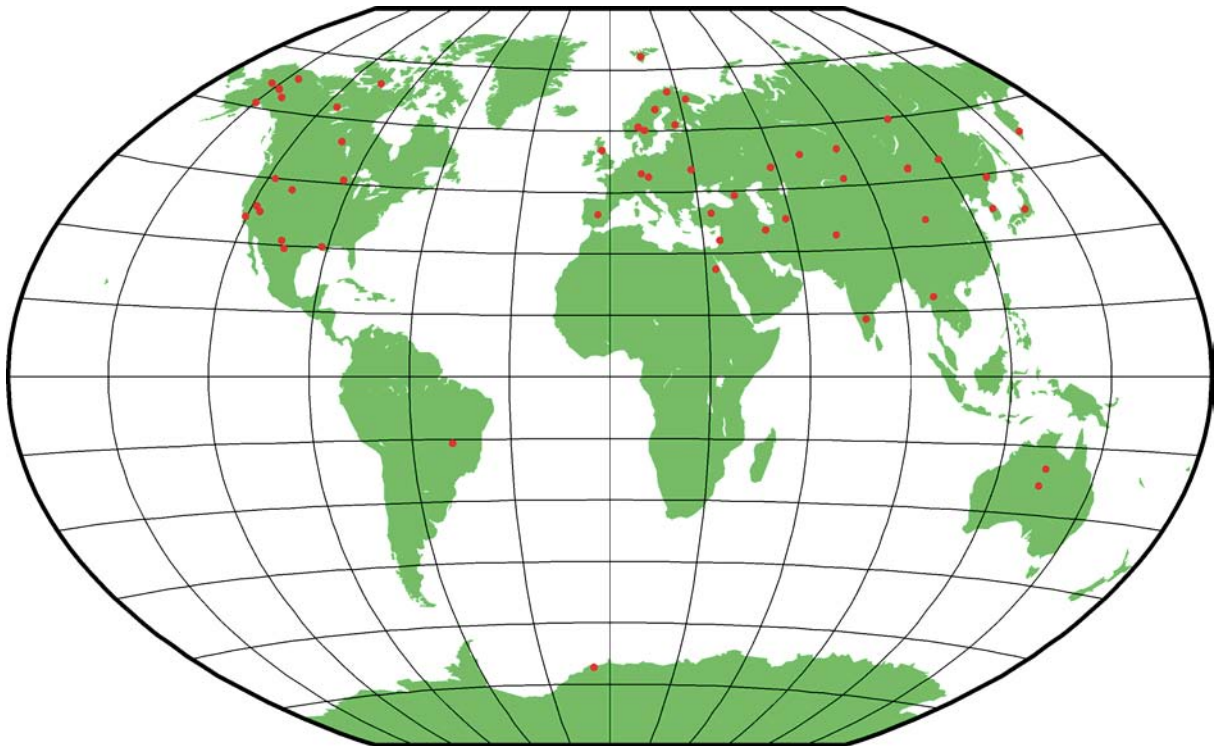


Fig. 9.42 The map shows locations of operational and planned seismic arrays (as of September 2002).

Acknowledgments

The authors thank John B. Young (Blacknest) for reprints of contributions from the old days of array seismology in Great Britain, and Peter Bormann, Brian Kennett, Frank Scherbaum, and Lyla Taylor for critical reviews of the manuscript. This is NORSAR contribution No. 685.

10

Seismic Data Formats, Archival and Exchange

Bernard Dost, Jan Zednik, Jens Havskov, Raymond Willemann and
Peter Bormann

10.1 Introduction

Seismology entirely depends on international co-operation. Only the accumulation of large sets of compatible high quality data in standardized formats from many stations and networks around the globe and over long periods of time will yield sufficiently reliable long-term results in event localization, seismicity rate and hazard assessment, investigations into the structure and rheology of the Earth's interior and other priority tasks in seismological research and applications.

For almost a century, only parameter readings taken from seismograms were exchanged with other stations and regularly transferred to national or international data centers for further processing. Because of the uniqueness of traditional paper seismograms and lacking opportunities for producing high-quality copies at low cost, original analog waveform data, cumbersome to handle and prone to damage or even loss, were rarely exchanged. The procedures for carefully processing, handling, annotating and storing such records have been extensively described in the 1979 edition of the Manual of Seismological Observatory Practice (Willmore, 1979) in the chapter *Station operation*. They are not repeated here. Also the traditional way of reporting parameter readings from seismograms to international data centers such as the U.S. Geological Survey National Earthquake Information Center (NEIC), the International Seismological Centre (ISC) or the European Mediterranean Seismological Centre (EMSC) are outlined in the old Manual in detail in the section *Reporting output*. They have not changed essentially since then. On the other hand, respective working groups on parameter formats of the IASPEI and of its regional European Seismological Commission (ESC) have meanwhile debated for many years how to make these formats more homogeneous, consistent and flexible so as to better accommodate also other seismologically relevant parameter information.

Any data report, of course, must follow a format known to the recipient in order to be successfully parsed. Some of the goals for any format are:

- *concise* avoiding unnecessary expense in transmission and storage;
- *complete* providing all of the information required to use the data;
- *transparent* easily read by a person, perhaps without documentation; and
- *simple* straightforward to write and parse with computer programs.

10. Seismic Data Formats, Archival and Exchange

Traditional formats for reporting parameter data sacrificed simplicity, transparency and even sometimes completeness in favor of the other goals. With the falling cost of data storage and exchange, modern formats more often sacrifice conciseness in favor of transparency and simplicity.

In addition, modern formats are usually extensible and include “metadata”. An extensible format includes some way for new types of data to be introduced without either collecting all the new information into unformatted comment strings or making messages with the new data types unreadable by old parsers. “Metadata” are information about the data, such as how and by whom the data were prepared.

The Telegraphic Format (TF), as documented in the Manual of Seismic Observatory Practice (Willmore, 1979), is an extreme example of a traditional format for reporting and exchanging parameter data. Since telex was very expensive compared with modern communication costs, conciseness was the paramount goal even to the point of occasional ambiguity. The year of the data, for example, might be excluded if the recipient could probably infer it. The format was intended for use in an era when many stations were isolated and could report little more than their own phase readings, so event parameters such as hypocenter and magnitude were relegated to a secondary role. The TF incorporated further restrictions due to the special limitations of telex messages, such as no lower-case letters and sometimes no control over line breaks.

A seismic network with modern, calibrated instruments can provide far more information than telegraphic format allows, while low-cost e-mail has eliminated the restrictions and high costs of telex messages. Consequently, since at least 1990 most seismic parameter data have been stored and exchanged in modern formats that are more complete, simpler and usually more transparent than the Telegraphic Format. Until recently, however, there was no generally accepted standard modern format. A major step forward in this direction was made by the Group of Scientific Experts (GSE) organized by the United Nations Conference on Disarmament. It developed GSE/IMS formats (see 10.2.4) for exchanging parametric seismological data in tests of monitoring the Comprehensive Nuclear-Test-Ban Treaty (CTBT) (see 10.2.4) which became popular also with other user groups. Seismological research, however, has a broader scope than the International Monitoring System (IMS) for the CTBT. Therefore, a new *IASPEI Seismic Format* (ISF), compatible with the IMS format but with essential extensions, has been developed and adopted by the Commission on Seismological Observation and Interpretation of the International Association of Seismology and Physics of the Earth’s Interior at its meeting in Hanoi, August 2001. It is the conclusion of a 16-year process seeking consensus on a new format and fully exploits the much greater flexibility and potential of E-mail and Internet information exchange as compared to the older telegraphic reports (see 10.2.5).

Digital waveform data, however, are nowadays by far the largest volume of seismic data stored and exchanged world-wide. The number of formats in existence and their complexity far exceeds the variability for parameter data. With the wide availability of continuous digital waveform data and unique communication technologies for world-wide transfer of such complete original data, their reliable exchange and archival has gained tremendous importance. Several standards for exchange and archival have been proposed, yet a much larger number of formats are in daily use. The purpose of the section on digital waveform data is to describe the international standards and to summarize the most often used formats. In addition, there will be a description of some of the more common conversion programs.

Beforehand, however, a short description of the most common parameter formats is given below.

10.2 Parameter formats

Parameter formats deal with all earthquake parameters like hypocenters, magnitudes, phase arrivals etc. Until recently, there were no real standards, except the Telegraphic Format (TF) used for many years to report phase arrival data to international agencies (Willmore, 1979; Chapter “Reporting output”). The format is not used for processing. There have been attempts to modernize TF for many years through the IASPEI Commission of Practice (now the Commission on Seismological Observation and Interpretation) and as mentioned in the introduction, the IASPEI Seismic Format (ISF) was approved as a standard in 2001. In practice, many different formats are used and the most dominant ones have come from popular processing systems. In the following, some of the most well known formats will be briefly described. For complete description of the formats, the reader is referred to original Manuals or publications.

10.2.1 HYPO71

The very popular location program HYPO71 (Lee and Lahr, 1975) has been around for many years and has been the most used program for local earthquakes. The format was therefore limited to work with only a few of the important parameters. Tab. 10.1 gives an example.

Tab. 10.1 Example of an input file in HYPO71 format. Each line contains, from left to right: Station code (max 4 characters), E (emergent) or I (impulsive) for onset clarity, polarity (C – compression; D – dilatation), year, month, day, and time (hours, minutes, seconds, hundredth of seconds) for P-phase onset, second for S-phase onset (seconds and hundredth of seconds only), and, in the last column, record duration. The blank space between ES and duration has been used for different purposes like amplitude. The last line is a separator line between events and contains control information.

FOO	EPC	96	6	6	64848.47	62.67ES	136
MOL	EPC	96	6	6	64849.97	65.87ES	144
HYA	EP	96	6	6	64856.78	78.07ES	135
ASK	EP	96	6	6	649 2.94	34.72ES	183
BER	EPC	96	6	6	649 7.56	36.61ES	
EGD	EPD	96	6	6	649 5.76	40.53ES	
					10 5.0		

The format is rather limited since only P- or S-phase names can be used and the S phase is referenced to the same hour-minute as the P phase; also, the format can not be used with teleseismic data. However, it is probably one of the most popular formats ever for local earthquakes. The HYPO71 program has seen many modifications and the format exists in many forms with small changes.

10.2.2 HYPOINVERSE

Following the popularity of HYPO71, several other popular location programs followed like Hypoinverse (Klein, 1978) and Hypoellipse (Lahr, 1989). Tab. 10.2 gives an example of the input format for Hypoinverse.

Tab. 10.2 Example of the Hypoinverse input format. Note that year, month, day, hour, min is only given in the header and only one phase is given per line.

```
96 6 60648
FOO EPC 48.5 136
FOO ES 62.7
MOL EPC 50.0 144
MOL EPC 50.9
MOL ES 65.9
```

10.2.3 Nordic format

In the 1980's, there was one of the first attempts to create a more complete format for data exchange and processing. The initiative came from the need to exchange and store data in Nordic countries and the so-called Nordic format was agreed upon among the 5 Nordic countries. The format later became the standard format used in the SEISAN data base and processing system and is now widely used. The format tried to address some of the shortcomings in HYPO71 format by being able to store nearly all parameters used, having space for extensions and useful for both input and output. An example is given in Tab. 10.3.

Tab. 10.3 Example of Nordic format. The data is the same as seen in Tabs. 10.1 and 10.2. The format starts with a series of header lines with type of line indicated in the last column (80) and the phase lines are following the header lines with no line type indicator. There can be any number of header lines including comment lines. The first line gives among other things, origin time, location and magnitudes, the second line is the error estimate, the third line is the name of the corresponding waveform file and the fourth line is the explanation line for the phases (type 7). The abbreviations are: STAT: Station code, SP: component, I: I or E, PHAS. Phase, W: Weight, D: polarity, HRMM SECON: time, CODA: Duration, AMPLIT: Amplitude, PERI: Period, AZIMU: Azimuth at station, VELO: Apparent velocity, SNR: Signal-to-noise ratio, AR: Azimuth residual of location, TRES: Travel-time residual, W: Weight in location, DIS: Epicentral distance in km and CAZ: Azimuth from event to station.

```
1996 6 6 0648 30.4 L 62.635 5.047 15.0 TES 13 1.4 3.0CTES 2.9LTES 3.0LNAO1
GAP=267 5.92 18.8 43.0 31.8 -0.5630E+03 0.8720E+03 -0.3916E+03E
1996-06-06-0647-46S.TEST__011 6
STAT SP IPHASW D HRMM SECON CODA AMPLIT PERI AZIMU VELO SNR AR TRES W DIS CAZ7
FOO SZ EP C 648 48.47 136 -0.110 116 180
FOO SZ ESG 649 2.67 0.710 116 180
FOO SZ E 649 2.89 426.4 0.3 116 180
MOL SZ EP C 648 49.97 144 -0.310 129 92
MOL SZ EPG C 648 50.90 0.410 129 92
MOL AZ E 649 5.86 129 92
MOL SZ ESG 649 5.87 0.410 129 92
MOL SZ E 649 6.98 328.6 0.6 129 92
HYA SZ EP 648 56.78 135 0.810 174 159
HYA SZ IP D 648 56.78 0.810 174 159
HYA SZ EPG D 648 57.56 0.110 174 159
```

```

HYA SZ ESG          649 18.07                                0.610 174 159
NRA0 SZ Pn         0649 24.03                                309.6  8.5 139  5 -0.410 403 119
NRA0 SZ Pg         0649 32.60                                305.6  7.285.2  1  0.410 403 119
NRA0 SZ Lg         0650 22.05                                302.0  4.016.0 -1 -0.410 403 119

```

10.2.4 The GSE/IMS formats

The GSE format (versions GSE1.0 and GSE2.0) was originally developed by the Group of Scientific Experts (GSE) of the Conference on Disarmament in Geneva and was used for the global technical test GSETT-3 organized by the GSE. With the establishment of the International Monitoring System (IMS) for the Comprehensive Nuclear-Test-Ban Treaty (CTBT) monitoring a significantly revised version of this format, termed GSE 2.1, was renamed to IMS1.0. This format has been widely used by many institutions around the globe, particularly in AutoDRM data exchanges (<http://seismo.ethz.ch/autodrm>) and for data transmission to international data centers, however less as a processing format than HYPO71 or the Nordic format. IMS1.0 is similar in structure to the Nordic format but more complete in some respects and lacking features in other. A major difference is that the line length can be more than 80 characters long, which is not the case for any of the previously described formats. After SEISAN, IMS1.0 is the first major format for which completeness or readability has been recognized as a more important design goal than conciseness.

The official custodian of the IMS format is the Comprehensive Nuclear-Test-Ban Treaty Organisation (CTBTO). As of December 2002, 166 States signed the CTBT and are participating in the development of the IMS system. The WEB page of CTBTO is <http://www.ctbto.org>. The IMS1.0 data format description can be obtained through National Data Centres (NDC) for CTBT which have been established in many countries on all continents. It is also available from the web site of the former Prototype International Data Centre (PIDC) under the heading "3.4.1 Rev3 Formats and Protocols for Messages" via <http://www.cmr.gov/pidc/librarybox/idcdocs/idcdocs.html>. It can be expected that in future CTBTO will post on its WEB page updates of its data formats, including the IMS format.

Tab. 10.4 Example of the IMS1.0 parameter format which contains the same data as given in Tabs. 10.1 to 10.3. The first lines are message information etc. The remaining lines are more or less self-explanatory. Note that more information, with a higher accuracy, can be given for each phase (like magnitude) than in the Nordic format. On the other hand, information like component and event duration is missing. These are added in the new ISF format.

```

BEGIN GSE2.0
MSG_TYPE DATA
MSG_ID 1900/10/19_1711 ISR_NDC
DATA_TYPE ORIGIN GSE2.0
EVENT 00000001

```

Date	Time	Latitude	Longitude	Depth	Ndef	Nsta	Gap	Mag1	N	Mag2	N	
1996/06/06	06:48:30.4	62.6350	5.0470	15.0	25	13	267			ML 2.9	8	
1.40	+- 5.92	0.0	0.0	0	+- 31.8	1.04	4.84			+-0.3		
Sta	Dist	EvAz	Phase	Date	Time	TRes	Azim	AzRes	Slow	SRes	Def	SNR
FOO	1.04	180.0	mc P	1996/06/06	06:48:48.5	-0.1					T	
FOO	1.04	180.0	m SG	1996/06/06	06:49:02.7	0.7					T	
FOO	1.04	180.0	m	1996/06/06	06:49:02.9							
426.4	0.30	ML 3.2		00000003	(from previous line)							
MOL	1.16	92.0	mc P	1996/06/06	06:48:50.0	-0.3					T	
MOL	1.16	92.0	mc PG	1996/06/06	06:48:50.9	0.4					T	

10. Seismic Data Formats, Archival and Exchange

```
MOL      1.16  92.0 m           1996/06/06 06:49:05.9
MOL      1.16  92.0 m   SG     1996/06/06 06:49:05.9   0.4                T
MOL      1.16  92.0 m           1996/06/06 06:49:07.0
NRA0    3.62 119.0 m   Pn     1996/06/06 06:49:24.0  -0.4 309.6    5.0  8.5    TAS 13.9
(from previous line)
NRA0    3.62 119.0 m   Pg     1996/06/06 06:49:32.6  0.4 305.6    1.0  7.2    TAS 85.2
NRA0    3.62 119.0 m   Lg     1996/06/06 06:50:22.0  -0.4 302.0   -1.0  4.0    TAS 16.0
(from previous line)
STOP
```

10.2.5 The IASPEI Seismic Format (ISF)

The need for an agreed-upon parameter format for comprehensive seismological data exchange has led to the IASPEI Seismic Format (ISF), adopted as standard in August 2001. ISF conforms to the IMS.1.0 standard but has essential extensions for reporting additional types of data. This allows the contributor to include complementary data considered to be important for seismological research and applications by the IASPEI Commission on Seismological Observation and Interpretation. The format looks almost like the IMS1.0 example in Tab. 10.4 above, except for the extensions. The ISF has been comprehensively tested at the ISC and NEIC and incompatibilities have been eliminated. The definite detailed description of the ISF is available from the ISC home page and kept up-to-date there (see <http://www.isc.ac.uk/Documents/isf.pdf>). Therefore, it is not reproduced in this Manual.

Consensus on the ISF was reached partly by including many optional items, so the format is not as simple as some alternatives. Despite this, the completeness, transparency, extensibility and metadata of ISF are expected to make it very widely used. Wide use of ISF will bring back the advantages of a generally accepted standard so that it becomes easier to exchange data, re-use data collected for past projects, and employ programs developed elsewhere.

In Volume 2, IS 10.1 and IS 10.2, examples are given of how event parameter data and unassociated parameter readings by seismic stations are reported according to the IMS format with ISF extensions.

10.3 Digital waveform data

Many different formats for digital data are used today in seismology. For a summary and the abbreviations used, see the following sections. Most formats can be grouped into one of the following five classes:

- 1) local formats in use at individual stations, networks or used by a particular seismic recorder (e.g., ESSTF, PDR-2, BDSN, GDSN);
- 2) formats used in standard analysis software (e.g., SEISAN, SAC, AH, BDSN);
- 3) formats designed for data exchange and archiving (SEED, GSE);
- 4) formats designed for database systems (CSS, SUDS);
- 5) formats for real time data transmission (IDC/IMS, Earthworm).

Use of the term "designed" in describing Class 3 and 4 formats is intentional. It is usually only at this level that very much thought has been given to the subtleties of format structure which result in efficiency, flexibility and extensibility.

The four classes (1-4) show a hierarchical structure. Class 4 forms a superset of the others, meaning that classes 1-3 can be deduced from it. The same argument applies to class 3 with respect to classes 1 and 2. Nearly all format conversions performed at seismological data centers are done to move upwards in the hierarchy for the purpose of data archiving and exchange with other data centers. Software tools are widely available to convert from one format to another and particularly upwards in the hierarchy.

This hierarchy also explains why there are so many formats. The design of class 1 formats depends on the manufacturer of the data acquisition system. In the early days of digital seismometry, display and analysis software was often proprietary and marketed specifically for a certain manufacturer's equipment and data format. There was no real need for manufacturers to adhere to a standard recording format, until users began to realize the advantages of exchanging data with other seismologists and discovered that this was quite difficult unless the other party was using the same hardware and/or software.

Station operators, who were not satisfied with the proprietary analysis software supplied with the procured data acquisition systems, started to convert data from Class 1 formats into the Class 2 formats which were used by more powerful and widely available analysis packages such as SAC. These programs usually provide subroutines that make conversion from local formats fairly easy. New analysis packages (e.g., SeisGram) which are developed around a Class 1 format (BDSN in this case) implicitly offer their format preference as a candidate for a new standard in Class 2, but it hardly matters as long as the necessary software tools are available to convert to and from the data exchange formats.

The GDSN (Global Digital Seismic Network) format began as a Class 1 format, but because it was used by an important global seismograph network (DWWSSN, SRO), it became accepted as a de facto standard for data exchange (Class 3). The beginning of widespread international data exchange within the FDSN (Federation of Digital Seismic networks) and GSE (Group of Scientific Experts) groups in the late 1980s revealed the GDSN format's weaknesses in this role and put in motion the process of defining more capable exchange formats.

The volume of commonly available digital seismic data continues to increase dramatically. It increased from 600 MB annually in 1980 to 300 GB in 1992 and today we are talking about many terabytes. Database systems, which are specially designed to handle these large datasets, have therefore begun to appear as a superset of the standard data exchange formats. The SUDS system is an example of this type of format.

In the 1990s, several activities (e.g., the GSETT-3 experiment and the U.S. National Seismograph Network (USNSN) have emerged which feature real-time exchange of seismological data, and interest has focused on formats which are suitable for such applications. In the late 1990s, this idea was carried farther by systems such as Earthworm, which implement format-independent protocols. Earthworm also is designed to exchange data across a peer network of multiple, independent nodes, as well as in a traditional network of dependent nodes with a centralized collection and distribution center.

Following is a brief description of some of the classes of formats as defined above.

10.3.1 Data archival

Data archival requires the storage of complete information on station, channel(s) and the structure of the data. Most existing formats are designed to provide part of the information. Most archival formats presently in use do include information on station and channel, but are not always complete in the description of the data. What we envisage is demonstrated through several features in the Standard for the Exchange of Earthquake Data (SEED) format:

- Data Description Language (DDL)
- reference to byte order;
- response information

The DDL is defined to enable the data itself to be stored in any data format (integer, binary, compressed). The language consists of a number of keys defining, for example, the applied compression scheme, number of bytes per sample, mantissa and gain length in bits and the use of the sign convention. The reader interprets the DDL and knows exactly how to deal with the data. The advantage of the DDL is that the original data structure can be maintained and is known. A disadvantage is that readers will have to interpret the DDL and have less performance in reading. However, the decoding information is available directly with the data and this is extremely important, since data are collected on platforms having different byte orders. In SEED the byte order of the original data is defined in the header, so the reader will be able to decide whether the data should be swapped.

In most archival formats, response information can be supplied in terms of poles and zeroes. Fewer efforts are undertaken to give the FIR filter coefficients in the header, although they are accounted for in the definition of SEED and GSE2.X. A problem occurs when a description of the instrument response is given only in measured amplitude and phase data as a function of frequency, as is the case in the GSE1.0 format. Also, the GSE2.X does not specify what is a minimum requirement. The main purpose of the response information is to correct for instrument response and thus the user will have to find the best fitting poles and zeroes to the given response. Although tools are available to calculate poles and zeroes from frequency, amplitude and phase data (e.g., in Preproc), results from the multiple inversion of the discrete frequency, amplitude and phase data will be different from the original data.

The deployment of large mobile arrays consisting of heterogeneous instrumentation is an important research tool. Data archival of these data is important. Although there is a tendency to store the data in a common format, the responses of sensors and data acquisition systems are often poorly known. It is recommended to pay attention to this issue before the experiment starts!

Finally, an issue in data archival is the responsibility of the data quality and the mechanism of reporting data errors. The network/station operator is responsible for the quality of the original data. However, the data may be subjected to format conversion at a remote data center. This last stage could introduce errors and it is the originator of the data, which must be responsible for data quality and should agree on the final conversion, if such a conversion is done externally.

10.3.2 Data exchange formats

The data exchange formats are closely related to the way data is exchanged. Therefore, these formats are described separately. Essentially, any format can be used for exchange, however the idea of an exchange format is to make it easy to send electronically, have a minimum standard of content and be readable on all computer platforms.

At present, there are many different techniques in use to exchange data, either between data users and data centers or between data centers. An overview of existing techniques is given below.

	Technique	Advantage	Disadvantage
Indirect on-line	autoDRM, NetDC	email based (no connection time)	small volume or download through ftp
Direct on-line	ftp, WWW, DRM (Spyder/Wilber/FARM)	direct access, enables easy data selection	slow for large data volumes
Off-line	CD-ROM (DVD)	direct access	no real-time data

Indirect on-line data exchange is arranged through (automated) *Data Request Managers* (DRMs) where the request mechanism is based on email traffic. There is work towards standardization on AutoDRM (<http://seismo.ethz.ch/autodrm>) to prevent a situation where users will have to learn a multitude of data request mechanisms with each having its own specific request format. One step further is the implementation of a communication protocol for exchange between data centers in such a way that a user only has to send one request to a nearby data center node. His/her request is then automatically routed through the data centers that may contribute to the requested data set. Such a protocol is under development and is known as the NetDC initiative (Casey and Ahern, 1996).

One basic problem in using email as the transport mechanism is the restricted data volume that can be exchanged. Also, the format sometimes will have to be ASCII. The format issue is taken care of in the GSE format, although in the description of the AutoDRM protocol it is mentioned that also a format like SEED can be used. The only difference is that the user is requested to get the data through anonymous ftp (pull) or the data is pushed into an anonymous ftp area defined by the user. The AutoDRM system at the Orfeus Data Centre (ODC) supports the SEED format in data exchange.

Direct on-line access to data is arranged at the ODC, for example, mainly through a website (<http://orfeus.knmi.nl>). A distinction is made between near real-time data collection (Spyder) and complete data volumes (ODC-volumes, FARM). Spyder data are available within a few hours after a major event, while ODC volumes lag behind real-time. At this moment there is a delay of approximately 3-4 years.

Internet speed is presently still limiting the usefulness of this direct on-line data exchange, especially since the volumes that are to be transferred may be large. One major advantage of direct on-line availability of the data is the capability to make a selection out of the vast amount of digital data. Procedures are presently under development to increase the power of these selection tools.

10. Seismic Data Formats, Archival and Exchange

Off-line data access provides complete, quality controlled data that are locally available at each institute in the form of CD-ROMs. The completeness and quality control takes time and CD-ROMs have a limited data volume. Digital Versatile Disks (DVDs) will probably replace CDs in the near future.

10.3.3 Formats for data base systems

Formats for data base systems are specially designed and no details will be given here. Examples of such formats are CSS and the derived “IDC Database Schema” (see IS 10.3 and <http://www.cmr.gov/pidc/librarybox/idcdocs/idcdocs.html>) and SUDS.

10.3.4 Continuous data protocols and formats

With better communication systems, real time transmission of digital data becomes more common. There is no internationally agreed upon format for this and equipment manufacturers use their own formats. The most widely used standard format is at present the CD-1.0 protocol used by the International Data Centre (IDC) for the International Monitoring System (IMS) as described under 10.2.4. Complete documentation can be found on the secure website <https://www2.ctbto.org> (authorized users only) and openly on <http://www.cmr.gov/pidc/librarybox/idcdocs/idcdocs.html>.

Up to 100 channels from a station or array of stations can be transmitted in near-real time using a single connection. Digital data are provided in compressed or uncompressed format and with or without authentication signatures. The protocol uses units of information called frames to establish or alter a connection and to exchange data between the sender and the receiver. Only one frame is being transmitted or received at any instance. A time-out is used in case of lost connection.

Establishing connections. The sender initiates the connection with the receiver to a pre-designated IP address and port by sending a Connection Request Frame. The receiver validates the authenticity of the sender and provides a new port and Internet Protocol (IP) address in a Port Assignment Frame. The sender drops the original connection and connects to the assigned IP address and port that is subsequently used for all data transfer.

Transmitting data. After the connection is established, the sender sends a Data Format Frame, which describes the format of the subsequent Data Frames. The sender can then send Data Frames data. The Data Format Frame provides information about itself and about Data Frames that will follow. The Data Frame contains the raw time series data. Each Data Frame has a single Data Frame Header and multiple channel sub-frames.

Altering connections. Either the sender or the receiver can alter the connection through the exchange of Alert Frames. The receiver sends the Alert Frame to notify the sender to use a different port. The sender uses Alert Frames to notify the receiver that the communication will cease or that a new data format is about to be used.

Terminating connections. Typically, an established connection remains active and in use until the sender or receiver terminates it for maintenance or reconfiguration. The connection can be intentionally terminated by sending an Alert Frame. Unintentional termination due to a slow or failed communications system is detected after the time-out period.

The CD-1.0 protocol is being replaced by the CD-1.1 protocol for transmission of IMS data; a description can be found on <https://www2.ctbto.org> and <http://www.cmr.gov/pidc/librarybox/idcdocs/idcdocs.html>.

Another real time data protocol is Earthworm, which is being used in North America. Documentation for this protocol can be found on the USGS website <http://gldbrick.cr.usgs.gov>.

10.4 Some commonly encountered digital data formats

Following is an alphabetical list of formats in use. For each format some description is given. The list of formats, of course, is not be complete, particularly for formats in little use, however, the most important formats in use today (2000) are included. In a later section, a list of popular analysis software systems is mentioned as well as a brief description of some conversion programs.

Only those formats are listed which can be converted by at least one of these analysis software systems. It is of particular importance to know on which computer platform the binary file has been written since only a few analysis programs work on more than one platform. Therefore, the data file should usually be written on the same platform as the one on which the analysis program is run. Accordingly, we will mention below, for each format, the respective computer platform.

AH

Class: 2 Platform: Unix

The Ad Hoc (AH) format is used in the AH waveform analysis software package developed at Lamont Doherty Geological Observatory, N.Y., USA. This package also supports a number of conversion tools.

CSS

Class: 2,4 Platform: Unix

The Center for Seismic Studies (CSS) Database Management System (DBMS) was designed to facilitate storage and retrieval of seismic data for seismic monitoring of test ban treaties [CSS]. The seismic data separate into two categories: waveform data and parametric data.

For the parametric data, the design utilizes a commercial relational database management system. Information is stored in relations that resemble flat, two-dimensional tables as in the ISF format (see annexed IS 10.1). The description of waveform data is physically separated from the waveform data itself. The index to the waveform archive is maintained within the relational database. Data are stored in plain files, called non-DBMS files. Each non-DBMS file is indexed by a relation that contains information describing the data and the physical location of the data in the file system. Each waveform segment contains digital samples from only one station and one channel. The time of the first sample, the number of samples and the sample rate of the segment are noted in an index record. The index also defines in which file

10. Seismic Data Formats, Archival and Exchange

and where in the file the segment begins, and it identifies the station and channel names. A calibration value at a specified frequency is noted. The index records are maintained in the **wfdisc** relation. Each **wfdisc** record describes a specific waveform segment and contains an id number to designate detailed information on the station and instrumentation of the trace.

GeoSig

Class: 1 Platform: PC

Binary format used by GeoSig recorders. The format consists of a header and multiplexed data.

Güralp format

Class: 1 Platform: PC

Format used by Güralp recorders.

ESSTF binary

Class: 1 Platform: All

The European Standard Seismic Tape Format (ESSTF) grew out of a major corporate effort by Lennartz Electronic GmbH [LEN]. ESSTF has been used as the framework for the file system in the SAS-58000 data acquisition system. ESSTF combines header information in ASCII format with seismic data in binary format.

The event header block is a single block preceding the data blocks, containing information on event start time. Each data block contains a 48-character header block (channel number, time, etc.) in ASCII. All channels are stored in a multiplexed form in one file. Data are organized in frames, each containing 500 data points. The most efficient access to the binary data is by unformatted, buffered reading with the capability of decoding the ASCII data directly out of a memory buffer.

GSE

Class 3 Platform: All

The format proposed by the Group of Scientific Experts (GSE format) has been extensively used with the GSETT projects on disarmament. The GSE2.1, now renamed IMS1.0, is the most recent version. The manual can be downloaded from (http://orfeus.knmi.nl/manuals/provisional_GSE2.1.ps) or the web pages of the Center for Monitoring Research in Arlington (http://www.cmr.gov/web-gsett3/CRP-243/www/FmtProt/FmtProt_5.html#HEADING113; <http://www.cmr.gov/pidc/librarybox/idcdocs/idcdocs.html>).

A GSE2.1 waveform data file consists of a waveform identification line (WID2) followed by the station line (STA2), the waveform information itself (DAT2), and a checksum of the data (CHK2) for each DAT2 section (Provisional GSE 2.1 Message Formats & Protocols, 1997). The default line length is 132 bytes. No line may be longer than 1024 bytes. The response data type allows the complete response to be given as a series of response groups that can be cascaded. Response description is made up of the CAL2 identification line plus one or more of the PAZ2, FAP2, GEN2, DIG2 and FIR2 response sections in any order.

Waveform identification line WID2 gives the date and time of the first data sample; the station, channel and auxiliary codes; the sub-format of the data, the number of samples and sample rate; the calibration of the instrument represented as the number of nanometers per digital count at the calibration period; the type of the instrument, and the horizontal and vertical orientation.

Line STA2 contains the network identifier, latitude and longitude of the station, reference coordinate system, elevation and emplacement depth.

Data section after DAT2 may be in any of six different sub-formats recognized in the GSE2.1 waveform format: INT, CM6, CM8, AUT, AU6, and AU8. INT is a simple ASCII sub-format, "CM" sub-formats are for compressed data and "AU" sub-formats are for authentication data. All represent the numbers as integers and therefore can be sent by email.

A checksum CHK2 must be provided in the GSE2.1 format. The checksum is computed from integer data values prior to converting them to any of the sub-formats.

IRIS dial-up expanded ASCII

Class: 1 Platform: All

The IRIS dial-up data retrieval system can be used to search for, display, and write data from IRIS GSN stations which are equipped with dial-up capabilities. Digital waveforms can be written in ASCII using the various on-line commands, e.g., "V" variable- and "F" fixed-record-length, expanded ASCII. These files contain two types of records: header records (one per file) and data records. The header record contains station and instrument information, the start time of the data record, and the number of samples. The data record contains the record number, 8 sample values and a checksum. This format uses a separate file for each component of each station.

ISAM-PITSA

Class: 2,4 Platform: Unix

Indexed Sequential Access Method (ISAM) is a commercial database file system designed for easy access. PITSA bases its internal file structure for digital waveform data on ISAM. This structure is often referred to as the ISAM format, but it should not be confused with the underlying database engine. An ISAM-PITSA file system consists of two database files containing the headers and the indexing information for all traces, and at least one trace file per channel. The trace file is a binary image of the floating-point data that can in principle be accessed independently. All files in an ISAM-PITSA file system have the same file name base. The extensions are ".nx0" and ".dt" for the database files, and ".001", ".002", etc. for the trace files.

Ismes

Class:1 Platform: PC

Format used by Italian Ismes recorders.

Kinematics formats

Class:1 Platform: PC

Kinematics have several binary formats although the two main formats are for the DataSeis recorders and the K2 class recorders.

Lennartz

Class: 1 Platform: PC

10. Seismic Data Formats, Archival and Exchange

Format for Lennartz recorders. The most common is the Mars88 format although there is also a format used with the older tape recorders.

Nanometrics

Class: 1 Platform: PC

Format used by Nanometrics recorders. The most common format is the Y-format.

NEIC ORFEUS

Class: 2 Platform: PC

The NEIC ORFEUS program SONIC1 can be used to search, display, and write data from the NEIC Earthquake Digital Data CD-ROMs (NEIC Waveform Catalog, 1991). Digital waveform data in ASCII contain two types of records: header records and data records. A header record contains station information, the start time of the data, sample rate, and the parameters of the transfer function. Data records contain the actual data retrieved from CD-ROM. Each data record is preceded by the number of data points contained in the data record. For more information, see the documentation on the NEIC ORFEUS SONIC Program Disk .

PDAS

Class: 1 Platform: PC

The format used by the Geotech PDAS recorders. This format has seen more use than just for the recorder output and there are examples of whole data sets converted to PDAS format.

PITSA BINARY

Class 2,3 Platform: PC and UNIX

In order to facilitate portability and to permit every user to write their own conversion routines without having to purchase commercial 3rd party software, a new format called BINARY has been added to PITSA's I/O. It is simply a binary image of the internal representation of data in PITSA, without the database overhead of the ISAM format. Another advantage to BINARY format is that it makes exchange of data files across platforms fairly easy. It is only necessary for the user to provide a code to do any required byte swapping. For a transitional period, fully equivalent I/O for both ISAM and BINARY routines have been implemented in both the PC and the Sun versions of PITSA, but the ISAM format will disappear eventually.

Each file consists of a short file header followed by as many data blocks as there are traces. Everything is binary. The file header consists of:

1. NCHANNELS: a long integer containing the number of channels in the file.
2. SIZE[]: An array of long integers of dimension NCHANNELS. Each element SIZE[i] contains the block size for block i, in bytes. In this context, block size of the i-th block means the size of the i-th trace header plus the size of the i-th trace.
3. BLOCK[i], for i = 1 to NCHANNELS: One block per trace. Each block consists of a binary image of the data header (as described in file data.h) followed by the binary image of the trace data.

Public Seismic Networks

Class: 1,2 Platform: PC

This format is used both as a recording and analysis format by Public Seismic Networks

SAC

Class 2 Platform: Unix

Seismic Analysis Code (SAC) is a general-purpose interactive program designed for the study of time sequential signals [SAC]. Emphasis has been placed on analysis tools used by research seismologists. A SAC data file contains a single data component recorded at a single seismic station. Each data file also contains a header record that describes the contents of that file. Certain header entries must be present (e.g., the number of data points, the file type, etc.). Others are always present for certain file types (e.g., sampling interval, start time, etc. for evenly spaced time series). Other header variables are simply informational and are not used directly by the program. Although the SAC analysis software only runs on Unix platforms and the general format is binary, there is also an ASCII version that can be used on any platform.

SEED

Class 3 Platform: All

The Standard for the Exchange of Earthquake Data (SEED) format was developed within the FDSN. The first set-up was designed at the U.S. Geological Survey's National Earthquake Information Center (NEIC) and Albuquerque Seismic Laboratory (ASL), primarily for the exchange of unprocessed waveform data. SEED was adopted by the Federation of Digital Seismographic Networks (FDSN) in 1987 as its standard. IRIS has also adopted SEED, and uses it as the principal format for its datasets. SEED uses four types of control headers:

- volume identifier headers;
- abbreviation dictionary headers;
- station headers;
- time-span headers.

Each header can use several blockettes - individual portions of information that are header specific - that conform to the organization rules of their volume type. Some blockettes vary in length and can be longer than the logical record length. Data fields in control headers are formatted in ASCII, but data fields (in data records) are primarily formatted in binary. The full description can be found in the SEED reference Manual [SEED].

It is worth pointing out that formats (such as SEED) designed to handle the requirements of international data exchange are seldom suited to the needs of individual researchers. Thus, the wide availability of software tools to convert between SEED and a full suite of Class 2 formats is crucial for its success.

A number of the present generation data acquisition systems (e.g., Quanterra, Nanometrics) produce data in SEED volumes only (miniSEED), without any of the associated control header information. Software packages have been developed to produce full SEED volumes from miniSEED volumes (e.g., SeedStuff). At the ODC, a package has recently been developed and will be distributed as a general tool.

10. Seismic Data Formats, Archival and Exchange

SEISAN

Class 2 Platform: All

The SEISAN binary format is used in the seismic analysis program SEISAN (<http://www.ifj.uib.no/seismo/software/seisan.html>). This program was developed at the Institute of Solid Earth Physics at the University of Bergen, Norway. The format consists of a main header describing all channels. Each channel then follows with a channel header with basic information including response. SEISAN can read the binary SEISAN files written on any platform. The SEISAN analysis system can also use GSE as a processing format.

SeisGram ASCII and binary

Class: 2 Platform: PC

Time series are contained in sequential, formatted ASCII files or sequential binary files. The SeisGram software (Lee, 1995) also reads fixed-record-length files using the BDSN Direct Access format. The following header information is included in both the ASCII and the binary data files:

File type, Data format, Network, Station and instrument identifier, Type of recording, Date, Event number, Orientation of the Y component, Time unit per sample, Sample rate, Amplitude units, Amplitude units per digital count, Start time, Number of samples, Comment on event and data, Time series processing history.

The ASCII files should be opened with "sequential access, formatted" format options. All header entries except start time are written with a single value on each line. The binary files are designed for compactness and fast access. Binary files should be opened with "sequential access, binary" format options. SeisGram's Direct Access data files are designed to store large sets of binary, direct access data from the BDSN (the network, not the format). The data in the file is identical to the data stream from the telemetry system, except for the addition of an eight-record header to identify uniquely the recording source, start time, and format. The Direct Access files should be opened with the "direct access, binary" format options.

Sismalp

Class: 1 Platform: PC

Sismalp is a widespread French data seismic recording system.

Sprengnether

Class: 1 Platform: PC

Format used by Sprengnether recorders.

SUDS

Class: 1,2,4 Platform: PC

SUDS stands for "The Seismic Unified Data System". The SUDS format was launched to be a more well thought out format useful for both recording and analysis and independent of any particular equipment manufacturer. The format has seen widespread use, but has lost some momentum, partly because it is not made platform-independent.

10.5 Format conversions

10.5.1 Why convert?

Ideally, we should all use the same format. Unfortunately, as the previous descriptions have shown, there are a large number of formats in use. With respect to parameter formats, one can get a long way with HYPO71, Nordic and GSE/ISF formats for which converters are available, such as in the SEISAN system. For waveform formats, the situation is much more difficult. First of all, there are many different formats and, since most are binary, there is the added complication that some will work on some computer platforms and not on others. This is a particular problem with binary files containing real numbers as for example, the SeisGram format. Additional problems are that: some formats have seen slight changes and exist in different versions; different formats have different contents so not all parameters can be transferred from one format to another; and conversion programs might not be fully tested for different combinations of data.

Many processing systems require a higher level format than the often primitive recording formats which is probably the most common reason for conversion; a similar reason is to move from one processing system to another. The SEED format has become a success for archival and data exchange, but it is not very useful for processing purposes, and almost unreadable on PCs. So it is also important to be able to move down in the hierarchy. Therefore, the main reasons for format conversion are to move:

- upwards in the hierarchy of formats for the purpose of data archiving and exchange;
- downward from the archive and exchange formats for analysis purposes;
- across the hierarchy for analysis purposes;
- from one computer platform to another.

10.5.2 Ways to convert

There are essentially two ways of converting. The first is to request data from a data center in a particular format or to log into a data center and use one of their conversion programs. The other more common way is to use a conversion program on the local computer. Such conversion programs are available both as free standing software and as part of processing systems. Equipment manufactures will often supply at least a program to convert recorder data to some ASCII format and often also to some more standard format as SUDS.

10.5.3 Conversion programs

Since conversion programs are often related to analysis programs, Tab. 10.5 lists some of the better-known analysis systems and the format they use directly.

Tab. 10.5 Examples of popular analysis programs.

Program	Author(s)	Input format(s)	Output format(s)
CDLOOK	R.Sleeman	SEED	SAC, GSE
Geotool	J.Coyne	CSS, SAC, GSE	CSS, SAC, GSE
PITSA	F.Scherbaum, J.Johnson	ISAM, SEED, Pitsa binary,	ISAM, ASCII

10. Seismic Data Formats, Archival and Exchange

		GSE, SUDS	
SAC	LLNL	SAC	SAC
SEISAN	J.Havskov, L. Ottemöller	SEISAN, GSE	SEISAN, GSE, SAC
SeismicHandler	K.Stammler	q, miniSEED, GSE, AH, ESSTF	q, GSE, miniSEED
SNAP	M.Baer	SED, GSE	SED, GSE
SUDS	P.Ward	SUDS	SUDS
Event	M.Musil	ESSTF, ASCII	ESSTF, ASCII
SeisBase	T.Fischer	ESSTF, Mars88, GSE	GSE

An overview of available format conversion programs can be found on the ORFEUS Web pages under ORFEUS Seismological Software Library (<http://orfeus.knmi.nl/wirjung.groups/wg4/index.html>). Here we present just a few packages in alphabetical order. Only those programs are mentioned which are able to read at least one of the formats mentioned in sub-Chapter 10.4.

Codeco

Program **codeco** was written by U. Kradolfer and modified by K. Stammler and K. Koch. Input files can be in SAC binary or ASCII, or GSE formats. Output formats are: integer or compressed GSE1.0 or GSE2.0, SAC binary or ASCII, and miniSEED. **Codeco** is available through the SZGRF software library (<ftp://ftp.szgrf.bgr.de/pub/software>).

Convseis

Converts 14 data formats on PCs like GSE1.0 and GSE2.0 INT, PCEQ, SEG Y and SUDS. **Convseis** has been written by L. Oncescu and M. Rizescu.

isam2gse

Data in ISAM format can be converted to GSE format by using the program **isam2gse**. The code is available through the SZGRF software library (<ftp://ftp.szgrf.bgr.de/pub/software>).

ESSTF to GSE

Program **len2gse2**, written by B. Ruzek (Geophysical Institute, Prague) converts multiplexed ESSTF binary format, Mars88 binary format or ASL ASCII format in *data_file* to the GSE2.0 CM6 compression format. The user can select the time window and mask channels and streams. The code is written in C++.

GSE to SEED

Program **gse2seed**, developed by R. Sleeman (Orfeus Data Centre, de Bilt), converts a GSE2.X file to the SEED2.3 format. Multiple traces are handled. For each WID2 section, the GSE file must contain corresponding data types STATION, CHANNEL and RESPONSE.

PASSCAL package

The PASSCAL package was written by P. Friberg, S. Hellman, and J. Webber, developed on SUN under SunOs4.1.4, compiled under Solaris 2.4 and higher and also under LINUX. It converts RefTek to SEGY and miniSEED. Program **pql** provides a quick and easy way to view SEGY, SAC, miniSEED or AH seismic data. **pql** operates in the X11 window environment. The package is available from the PASSCAL instrument center (<http://www.passcal.nmt.edu>) at New Mexico Tech., Socorro.

Preproc

Preproc has been designed to assist the seismologist who wishes to analyze large sets of raw digital data that need to be preprocessed in some standard way prior to the analysis. Preproc was written by Miroslav Zmeskal for the ISOP project in the period 1991-1993. It was rewritten recently in the object-oriented form. As a by-product, **preproc** can perform data conversion from GSE / PITSA ISAM to GSE / PITSA ISAM. In the near future new input/output formats will be implemented (ESSTF, miniSEED). **preproc** was successfully compiled on HP, SUN, Linux and DOS. Program package **preproc** and a detailed Manual are available through the ORFEUS Seismological Software Library

Rdseed

Rdseed reads from the input tape or file in the SEED format. According to the command line function option specified by the user, **rdseed** will read the volume and recover the volume table of contents (-c), the set of abbreviation dictionaries (-a), or station and channel information and instrument response table (-s). In order to extract data from the SEED volume for analysis by other packages, the user must run **rdseed** in user prompt mode (without any command line options). As data is extracted from the SEED volume, **rdseed** looks at the orientation and sensitivity of each channel and corrects the header information on request. Implemented output formats are (option d): SAC, AH, CSS 3.0, miniSEED and SEED. A Java version of rdseed is to be released in 2001. **Rdseed** was developed by Dennis O'Neill and Allen Nance, IRIS DMC.

SeedStuff

SeedStuff is a set of basic programs provided by the GEOFON DMS software library in Potsdam (<ftp://ftp.gfz-potsdam.de/pub/home/st/GEOFON/software>) to process and compile raw data from Quanterra, Comserv and RefTek data loggers. The goal is to check and extract data from station files/tapes to miniSEED files and to assemble miniSEED files to full SEED volumes. The SeedStuff package was written by Winfried Hanka and compiled on the SUN, HP and Linux. The following tools are available:

- extr_qic:** extracts multiplexed raw Quanterra station tapes to demultiplexed miniSEED files containing only one station / stream / component;
- extr_file:** like extr_qic for multiplexed miniSEED, RefTec files;
- extr_fseed:** disassemble full SEED tapes. SEED headers are skipped, data are stored into station / stream / component files;
- check_seed:** checks the contents of miniSEED data files or tapes ;

10. Seismic Data Formats, Archival and Exchange

check_gic: analysis the contents of a Quanterra data tape;

copy_seed: assembles a full SEED volumes from miniSEED files for a given set of station / stream / component defined in the copy_seed.cfg configuration file

make_dlsv: generates a dataless (header only) SEED volume for a set of station/stream/component defined in copy_seed.cfg.

SEED to GSE

There is no special program developed for converting either full SEED volumes or miniSEED files to the GSE format. Such a package would be strongly needed for providing data in the GSE format by the AutoDRM services.

On the SUN platform, program CDLOOK (see 11.5.2.2) can read full SEED volumes and write traces in the GSE format. This program can be downloaded from <ftp://orfeus.knmi.nl/pub/software>.

SEISAN

The SEISAN analysis system has about 40 conversion programs, mostly from some binary format to SEISAN. The SEISAN format can then be converted to any standard format like SEED, SAC or GSE. SEISAN has format converters for most recorders on the market including Kinometrics, Nanometrics, Teledyne, GeoSig, Reftek, Lennartz, Güralp and Sprengnether.

Acknowledgments

The authors acknowledge with thanks the careful review by Bruce Presgrave of the US Geological Survey. It has improved both the language of the original draft and provided useful references to the Earthworm system. Thanks go also to Xiaoping Yang who kindly provided the links to the data bases of the Center for Monitoring Research and the CTBTO.

Special references

- [CSS] Anderson, J., W. Farrell, K. Garcia, J. Given, and H. Swanger, Center for Seismic Studies Version 3 Database: Schema Reference Manual, SAIC Technical Report C90-01, 1990.
- [IDC3.4.1] Formats and Protocols for Messages, Rev. 3, 2001.
- [GSE] Provisional GSE2.1 Message Formats & Protocols, 1997. Operations Annex 3, GSETT-3.
- [LEN] SAS-58000 User's Guide and Reference Manual, 1986. Lennartz electronic GmbH
- [SAC] W.C. Tapley & J.E. Tull, 1992. SAC - Seismic Analysis Code. LLNL, Regents of the University of California
- [SEED] Standard for the Exchange of Earthquake Data, 1992. Reference Manual, SEEDFormat v2.3, FDSN, IRIS, USGS

11

Data Analysis and Seismogram Interpretation

Peter Bormann, Klaus Klinge and Siegfried Wendt

11.1 Introduction

This Chapter deals with seismogram analysis and extraction of seismic parameter values for data exchange with national and international data centers, for use in research and last, but not least, with writing bulletins and informing the public about seismic events. It is written for training purposes and for use as a reference source for seismologists at observatories. It describes the basic requirements in analog and digital routine observatory practice i.e., to:

- recognize the occurrence of an earthquake in a record;
- identify and annotate the seismic phases;
- determine onset time and polarity correctly;
- measure the maximum ground amplitude and related period;
- calculate slowness and azimuth;
- determine source parameters such as the hypocenter, origin time, magnitude, source mechanism, etc..

In modern digital observatory practice these procedures are implemented in computer programs. Experience, a basic knowledge of elastic wave propagation (see Chapter 2), and the available software can guide a seismologist to analyze large amounts of data and interpret seismograms correctly. The aim of this Chapter is to introduce the basic knowledge, data, procedures and tools required for proper seismogram analysis and phase interpretation and to present selected seismogram examples.

Seismograms are the basic information about earthquakes, chemical and nuclear explosions, mining-induced earthquakes, rock bursts and other events generating seismic waves. Seismograms reflect the combined influence of the seismic source (see Chapter 3), the propagation path (see Chapter 2), the frequency response of the recording instrument (see 4.2 and 5.2), and the ambient noise at the recording site (e.g., Fig. 7.32). Fig. 11.1 summarizes these effects and their scientific usefulness. Accordingly, our knowledge of seismicity, Earth's structure, and the various types of seismic sources is mainly the result of analysis and interpretation of seismograms. The more completely we quantify and interpret the seismograms, the more fully we understand the Earth's structure, seismic sources and the underlying causing processes.

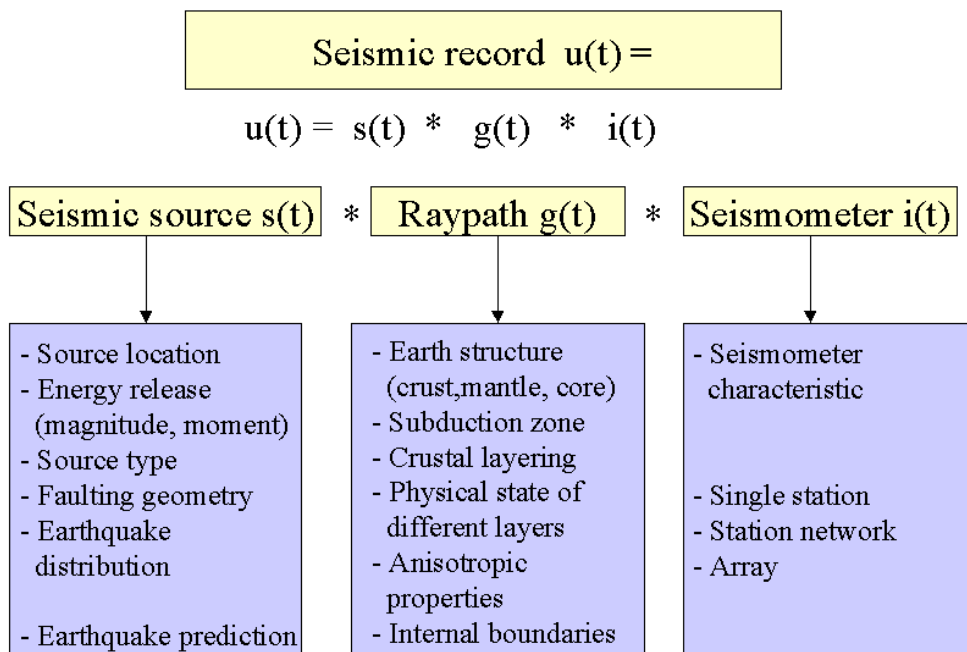


Fig. 11.1 Different factors/sub-systems (without seismic noise) which influence a seismic record (yellow boxes) and the information that can be derived from record analysis (blue boxes).

Seismological data analysis for single stations is nowadays increasingly replaced by network (see Chapter 8) and array analysis (see Chapter 9). Array-processing techniques have been developed for more than 20 years. Networks and arrays, in contrast to single stations, enable better signal detection and source location. Also, arrays can be used to estimate slowness and azimuth, which allow better phase identification. Further, more accurate magnitude values can be expected by averaging single station magnitudes and for distant sources the signal coherency can be used to determine onset times more reliably. Tab. 11.1 summarizes basic characteristics of single stations, station networks and arrays. In principle, an array can be used as a network and in special cases a network can be used as an array. The most important differences between networks and arrays are in the degree of signal coherence and the data analysis techniques used.

Like single stations, band-limited seismometer systems are now out-of-date and have a limited distribution and local importance only. Band-limited systems filter the ground motion. They distort the signal and may shift the onset time and reverse polarity (see 4.2). Most seismological observatories, and especially regional networks, are now equipped with broadband seismometers that are able to record signal frequencies between about 0.001 Hz and 50 Hz. The frequency and dynamic range covered by broadband recordings are shown in Fig. 11.2 and in Fig. 7.48 of Chapter 7 in comparison with classical band-limited analog recordings of the Worldwide Standard Seismograph Network (WWSSN).

Tab. 11.1 Short characteristic of single stations, station networks and arrays.

Single station	Classical type of seismic station with its own data processing. Event location only possible by means of three-component records.
Station network	Local, regional or global distribution of stations that are as identical as possible with a common data center (see Chapter 8). Event location is one of the main tasks.
Seismic array	Cluster of seismic stations with a common time reference and uniform instrumentation. The stations are located close enough to each other in space for the signal waveforms to be correlated between adjacent sensors (see Chapter 9). Benefits are: <ul style="list-style-type: none"> • extraction of coherent signals from random noise; • determination of directional information of approaching wavefronts (determination of backazimuth of the source); • determination of local slowness and thus of epicentral distance of the source.

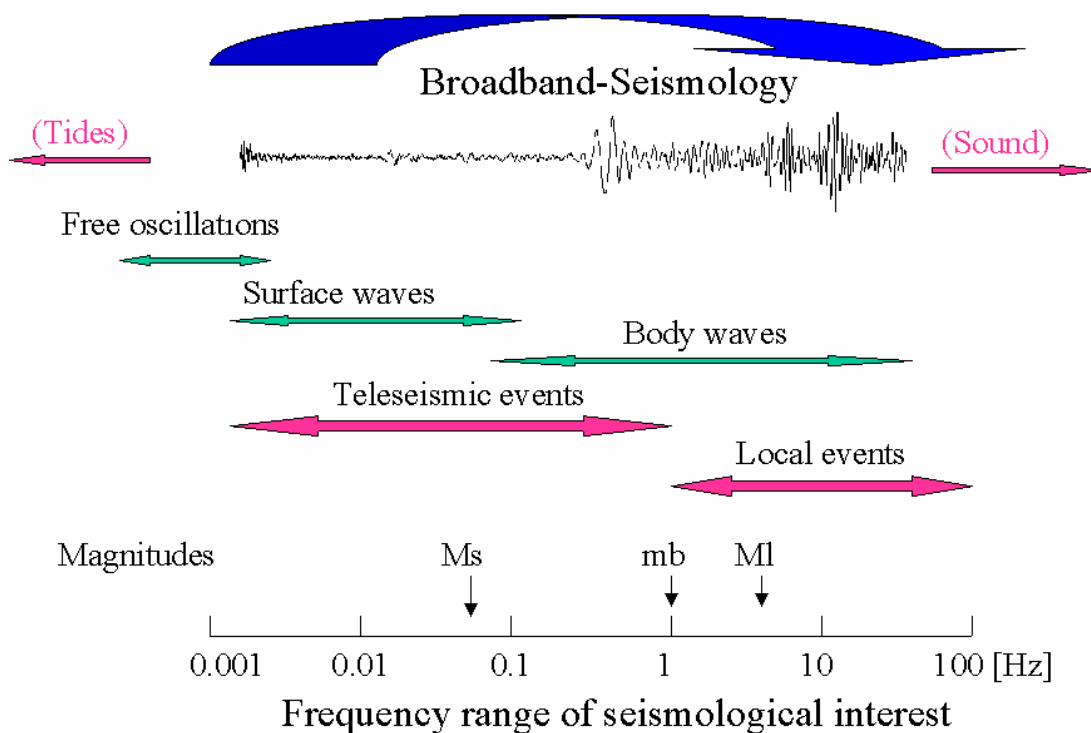


Fig. 11.2 Frequency range of seismological interest.

A number of these classical seismograph systems are still in operation at autonomous single stations in many developing countries and in the former Soviet Union. Also, archives are filled with analog recordings of these systems, which were collected over many decades.

These data constitute a wealth of information most of which has yet to be fully analyzed and scientifically exploited. Although digital data are superior in many respects, both for advanced routine analysis and even more for scientific research, it will be many years or even decades of digital data acquisition before one may consider the bulk of these old data as no longer needed. However, for the rare big and thus unique earthquakes, and for earthquakes in areas with low seismicity rates but significant seismic risk, the preservation and comprehensive analysis of these classical and historic seismograms will remain of the utmost importance for many years.

More and more old analog data will be reanalyzed only after being digitized and by using similar procedures and analysis programs as for recent original digital data. Nevertheless, station operators and analysts should still be in a position to handle, understand and properly analyze analog seismograms or plotted digital recordings without computer support and with only modest auxiliary means. Digital seismograms are analyzed in much the same way as classical seismograms (although with better and more flexible time and amplitude resolution) except that the digital analysis uses interactive software which makes the analysis quicker and easier, and their correct interpretation requires the same knowledge of the appearance of seismic records and individual seismic phases as for analog data. The analyst needs to know the typical features in seismic records as a function of distance, depth and source process of the seismic event, their dependence on the polarization of the different types of seismic waves and thus of the azimuth of the source and the orientation of sensor components with respect to it. He/she also needs to be aware of the influence of the seismograph response on the appearance of the record. Without this solid background knowledge, phase identifications and parameter readings may be rather incomplete, systematically biased or even wrong, no matter what kind of sophisticated computer programs for seismogram analysis are used.

Therefore, in this Chapter we will deal first with an introduction to the fundamentals of seismogram analysis at single stations and station networks, based on analog data and procedures. Even if there is now less and less operational need for this kind of instruction and training, from an educational point of view its importance can not be overemphasized. An analyst trained in comprehensive and competent analysis of traditional analog seismic recordings, when given access to advanced tools of computer-assisted analysis, will by far outperform any computer specialist without the required seismological background knowledge.

Automated phase identification and parameter determination is still inferior to the results achievable by well-trained man-power. Therefore, automated procedures are not discussed in this Manual although they are being used more and more at advanced seismological observatories as well as at station networks (see Chapter 8) and array centers (see Chapter 9). The Manual chiefly aims at providing competent guidance and advice to station operators and seismologists with limited experience and to those working in countries which lack many specialists in the fields which have to be covered by observatory personnel. On the other hand, specialists in program development and automation algorithms sometimes lack the required seismological knowledge or the practical experience to produce effective software for observatory applications. Such knowledge and experience, however, is an indispensable requirement for further improvement of computer procedures for automatic data analysis, parameter determination and source location in tune also with older data and established standards. In this sense, the Manual also addresses the needs of this advanced user community.

Accordingly, we first give a general introduction to routine seismogram interpretation of analog recordings at single stations and small seismic networks. Then we discuss both the similarities and the principal differences when processing digital data. The basic requirements for parameter extraction, bulletin production as well as parameter and waveform data exchange are also outlined. In the sub-Chapter on digital seismogram analysis we discuss in more detail problems of signal coherence, the related different procedures of data processing and analysis as well as available software for it. The majority of record examples from Germany has been processed with the program Seismic Handler (SHM) developed by K. Stammler which is used for seismic waveform retrieval and data analysis. This program and descriptions are available via <http://www.szgrf.bgr.de/sh-doc/index.html>. Reference is made, however, to other analysis software that is widely used internationally (see 11.4).

Typical examples of seismic records from different single stations, networks and arrays in different distance ranges (local, regional and teleseismic) and at different source depth are presented, mostly broadband data or filtered records derived therefrom. A special section is dedicated to the interpretation of seismic core phases (see 11.5.2.4 and 11.5.3). Since all Chapter authors come from Germany, the majority of records shown has unavoidably been collected at stations of the German Regional Seismic Network (GRSN) and of the Gräfenberg array (GRF). Since all these stations record originally only velocity-broadband (BB-velocity) data, all examples shown from GRSN/GRF stations of short-period (SP), long-period (LP) or BB-displacement seismograms corresponding to Wood-Anderson, WWSSN-SP, WWSSN-LP, SRO-LP or Kirnos SKD response characteristics, are **simulated records**. Since their appearance is identical with respective recordings of these classical analog seismographs this fact is not repeatedly stated throughout this Chapter and its annexes. The location and distribution of the GRSN and GRF stations is depicted in Fig. 11.3a. while Fig. 11.3b shows the location of the events for which records from these stations are presented. Users of this Chapter may feel that the seismograms presented by the authors are too biased towards Europe. Indeed, we may have overlooked some important aspects or typical seismic phases which are well observed in other parts of the world. Therefore, we invite anybody who can present valuable complementary data and explanations to submit them to the Editor of the Manual so that they can be integrated into future editions of the Manual.

For routine analysis and international data exchange a standard nomenclature of seismic phases is required. The newly elaborated draft of a IASPEI Standard Seismic Phase List is given in IS 2.1, together with ray diagrams for most phases. This new nomenclature partially modifies and completes the earlier one published in the last edition of the Manual of Seismological Observatory Practice (Willmore, 1979) and each issue of the seismic Bulletins of the International Seismological Centre (ISC). It is more in tune than the earlier versions with the phase definitions of modern Earth and travel-time models (see 2.7) and takes full advantage of the newly adopted, more flexible and versatile IASPEI Seismic Format (ISF; see 10.2.5) for data transmission, handling and archiving.

The scientific fundamentals of some of the essential subroutines in any analysis software are separately treated in Volume 2, Annexes (e.g., IS 11.1 or PD 11.1). More related Information Sheets and Program Descriptions may be added in the course of further development of this Manual.

a)

GRSN/GRF stations

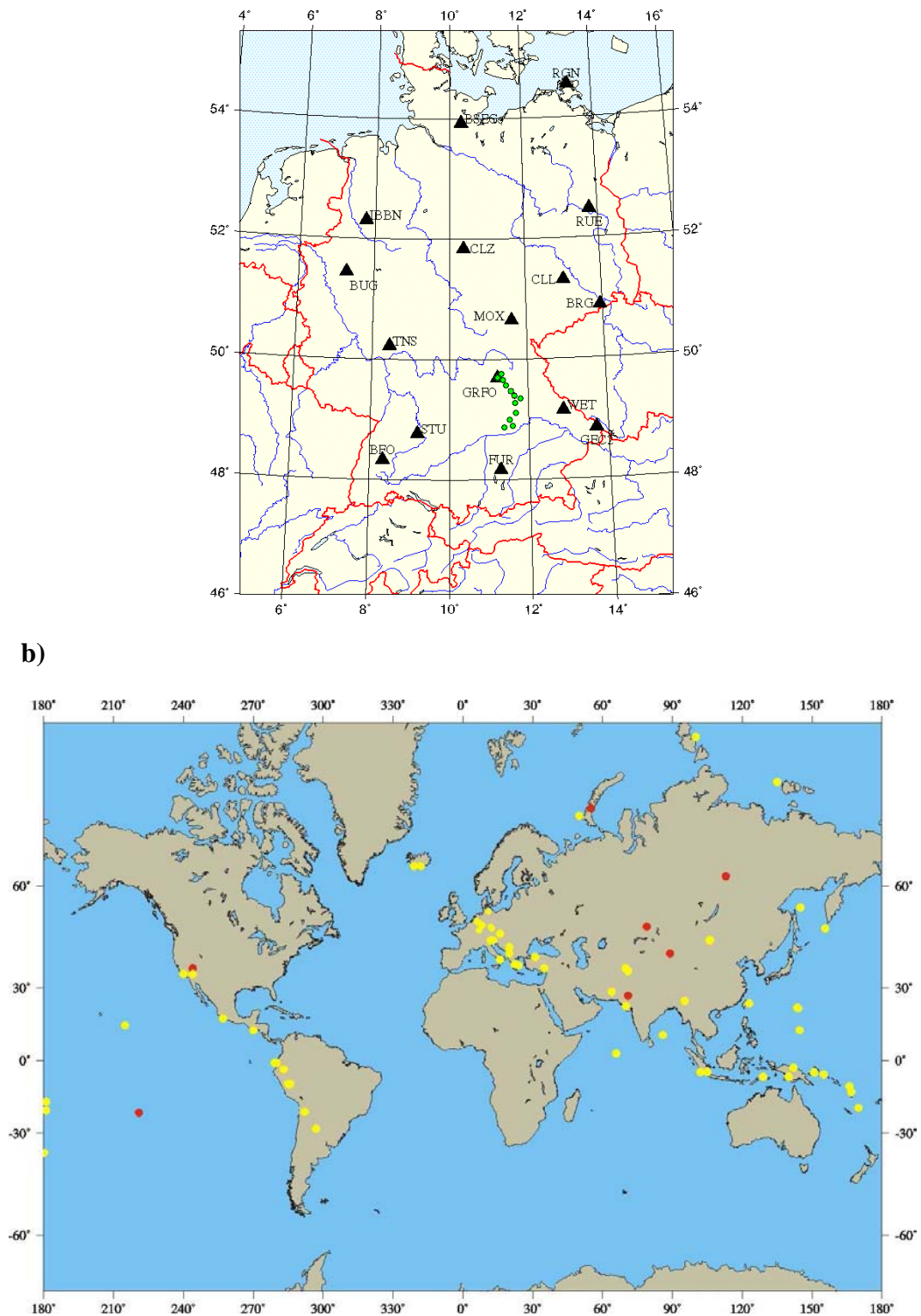


Fig. 11.3 a) Stations of the German Regional Seismological Network (GRSN, black triangles) and the Graefenberg-Array (GRF, green dots); b) global distribution of epicenters of seismic events (red dots: underground nuclear explosions; yellow dots: earthquakes) for which records from the above stations will be presented in Chapter 11 and DS 11.1-11.4.

11.2 Criteria and parameters for routine seismogram analysis

11.2.1 Record duration and dispersion

The first thing one has to look for when assessing a seismic record is the duration of the signal. Due to the different nature and propagation velocity of seismic waves and the different propagation paths taken by them to a station, travel-time differences between the main wave groups usually grow with distance. Accordingly, the record spreads out in time. The various body-wave groups show no dispersion, so their individual duration remains more or less constant, only the time-difference between them changes with distance (see Fig. 2.48). The time difference between the main body-wave onsets is roughly < 3 minutes for events at distances $D < 10^\circ$, < 16 min for $D < 60^\circ$, < 30 min for $D < 100^\circ$ and < 45 min for $D < 180^\circ$ (see Fig. 1.2).

In contrast to body waves, velocity of surface waves is frequency dependent and thus surface waves are dispersed. Accordingly, depending on the crustal/mantle structure along the propagation path, the duration of Love- and Rayleigh-wave trains increases with distance. At $D > 100^\circ$ surface wave seismograms may last for an hour or more (see Fig. 1.2), and for really strong events, when surface waves may circle the Earth several times, their oscillations on sensitive long-period (LP) or broadband (BB) records may be recognizable over 6 to 12 hours (see Fig. 2.19). Even for reasonably strong regional earthquakes, e.g., $M_s \approx 6$ and $D \approx 10^\circ$, the oscillations may last for about an hour although the time difference between the P and S onset is only about 2 min and between P and the maximum amplitude in the surface wave group only 5-6 min.

Finally, besides proper dispersion, scattering may also spread wave energy. This is particularly true for the more high-frequency waves traveling in the usually heterogeneous crust. This gives rise to signal-generated noise and coda waves. Coda waves follow the main generating phases with exponentially decaying amplitudes. The coda duration depends mainly on the event magnitude (see Figure 1b in DS 11.1) and only weakly on epicentral distance (see Figure 2 in EX 11.1). Thus, duration can be used for calculating magnitudes M_d (see 3.2.4.3).

In summary, signal duration, the time difference between the Rayleigh-wave maximum and the first body-wave arrival (see Table 5 in DS 3.1) and in particular the time span between the first and the last recognized body-wave onsets before the arrival of surface waves allow a first rough estimate, whether the earthquake is a local, regional or teleseismic one. This rough classification is a great help in choosing the proper approach, criteria and tools for further more detailed seismogram analysis, source location, and magnitude determination.

11.2.2 Key parameters: Onset time, amplitude, period and polarity

Onset times of seismic wave groups, first and foremost of the P-wave first arrival, when determined at many seismic stations at different azimuth and at different distance, are the key input parameter for the location of seismic events (see IS 11.1). Travel times published in travel-time tables (such as Jeffreys and Bullen, 1940; Kennett, 1991) and travel-time curves, such as those shown in Figs. 2.40 and 2.50 or in the overlays to Figs. 2.47 and 2.48, have been derived either from observations or Earth models. They give, as a function of epicentral distance D and hypocentral depth h , the differences between *onset times* t_{ox} of the respective seismic phases x and the *origin time* OT of the seismic source. Onset times mark the first

energy arrival of a seismic wave group. The process of recognizing and marking a wave onset and of measuring its onset time is termed *onset time picking*. The recognition of a wave onset largely depends on the spectral signal-to-noise-ratio (SNR) for the given waveform as a whole and the steepness and amplitude of its leading edge. Both are controlled by the shape and bandwidth of the recording seismograph or filter (see Figs. 4.9 to 4.13). It is a classical convention in seismological practice to classify onsets, as a qualitative measure for the reliability of their time-picking, as either impulsive (i) or emergent (e). These lower case letters i or e are put in front of the phase symbol. Generally, it is easier to recognize and precisely pick the very first arrival (usually a P wave) on a seismogram than later phases that arrive within the signal-generated noise coda of earlier waves.

The relative precision with which an onset can be picked largely depends on the factors discussed above, but the absolute accuracy of onset-time measurement is controlled by the available time reference. Seismic body-wave phases travel rather fast. Their apparent velocities at the surface typically range between about 3 km/s and nearly 100 km/s (at the antipode the apparent velocity is effectively infinite). Therefore, an absolute accuracy of onset-time picking of less than a second and ideally less than 0.1 s is needed for estimating reliable epicenters (see IS 11.1) and determining good Earth models from travel-time data. This was difficult to achieve in earlier decades when only mechanical pendulum clocks or marine chronometers were available at most stations. They have unavoidable drifts and could rarely be checked by comparison with radio time signals more frequently than twice a day. Also, the time resolution of classical paper or film records is usually between 0.25 to 2 mm per second, thus hardly permitting an accuracy of time-picking better than a second. In combination with the limited timing accuracy, the reading errors at many stations of the classical world-wide network, depending also on distance and region, were often two to three seconds (Hwang and Clayton, 1991). However, this improved since the late 1970s with the availability of very-low frequency and widely received time signals, e.g., from the DCF and Omega time services, and recorders driven with exactly 50 Hz stabilized alternating current.

Yet, onset-time reading by human eye from analog records with minute marks led to sometimes even larger errors, a common one being the ± 1 min for the P-wave first arrival. This is clearly seen in Fig. 2.46 (left), which shows the travel-time picks collected by the ISC from the world-wide seismic station reports between 1964 and 1987. Nowadays, atomic clock time from the satellite-borne Global Positioning System (GPS) is readily available in nearly every corner of the globe. Low-cost GPS receivers are easy to install at both permanent and temporary seismic stations and generally affordable. Therefore the problem of unreliable absolute timing should no longer exist. Nevertheless, also with high resolution digital data and exact timing now being available it is difficult to decide on the real signal onset, even for sharp P from explosions. Douglas et al. (1997) showed that the reading errors have at best a standard deviation between 0.1 and 0.2 s. However, human reading errors no longer play a role when digital data are evaluated by means of seismogram analysis software which automatically records the time at the positions where onsets have been marked with a cursor. Moreover, the recognizability of onsets and the precision of time picks can be modified easily within the limits which are set by the sampling rate and the dynamic range of recording. Both the time and amplitude scales of a record can be compressed or expanded as needed, and task-dependent optimal filters for best phase recognition can be easily applied.

Fig. 11.4 shows such a digital record with the time scale expanded to 12 mm/s. The onset time can be reliably picked with an accuracy of a few tenths of a second. This P-wave first arrival has been classified as an impulsive (i) onset, although it looks emergent in this particular plot.

11.2 Criteria and parameters for routine seismogram analysis

But by expanding the amplitude scale also, the leading edge of the wave arrival becomes steeper and so the onset appears impulsive. This ease with which digital records can be manipulated largely eliminates the value of qualitative characterization of onset sharpness by either *i* or *e*. Therefore, in the framework of the planned but not yet realized International Seismological Observing Period (ISOP), it is proposed instead to quantify the onset-time reliability. This could be done by reporting, besides the most probable or interpreter-preferred onset time, the estimated range of uncertainty by picking the earliest (t_{ox-}) and latest possible onset time (t_{ox+}) for each reported phase *x*, and of the first arrival in particular (see Fig. 11.6).

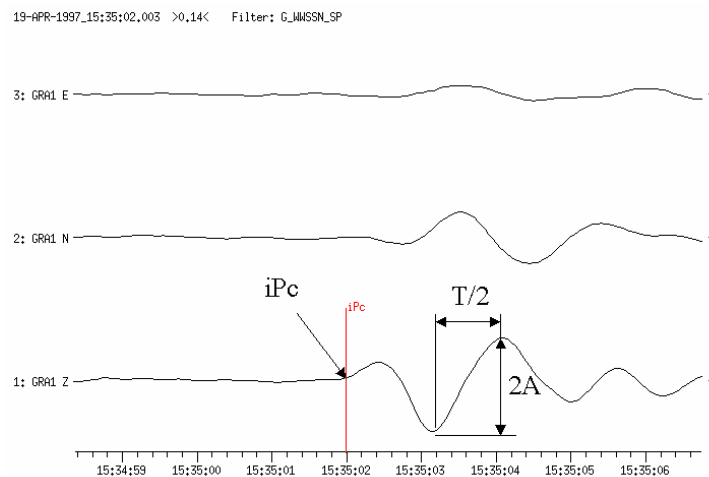


Fig. 11.4 First motion onset times, phase and polarity readings (c – compression; d – dilatation), maximum amplitude *A* and period *T* measurements for a sharp (*i* - impulsive) onset of a P wave from a Severnaya Zemlya event of April 19, 1997, recorded by a broadband three-component single station of the Gräfenberg Array, Germany.

Whereas the quality, quantity and spatial distribution of reported time picks largely controls the precision of source locations (see IS 11.1), the quality and quantity of amplitude readings for identified specific seismic phases determine the representativeness of classical event *magnitudes*. The latter are usually based on readings of maximum ground-displacement and related periods for body- and surface-wave groups (see 3.2). For symmetric oscillations amplitudes should be given as half peak-to-trough (double) amplitudes. The related periods should be measured as the time between neighboring peaks (or troughs) of the amplitude maximum or by doubling the time difference between the maximum peak and trough (see Fig. 11.4 and Fig. 3.9). Only for highly asymmetric wavelets should the measurement be made from the center line to the maximum peak or trough (see Fig. 3.9b). Some computer programs mark the record cycle from which the maximum amplitude *A* and the related *T* have been measured (see Figures 3 and 4 in EX 3.1).

Note that the measured maximum trace amplitudes in a seismic record have to be corrected for the frequency-dependent magnification of the seismograph to find the “true” ground-motion amplitude, usually given in nanometers ($1 \text{ nm} = 10^{-9} \text{ m}$) or micrometers ($1 \text{ } \mu\text{m} = 10^{-6} \text{ m}$), at the given period. Fig. 3.11 shows a few typical displacement amplification curves of standard seismographs used with paper or film records. For digital seismographs, instead of displacement magnification, the frequency dependent *resolution* is usually given in units of nm/counts, or in $\text{nm s}^{-1}/\text{count}$ for ground velocity measurements. Note that both record amplitudes and related dominating periods do not only depend on the spectrum of the arriving

waves but are mainly controlled by the shape, center frequency and bandwidth of the seismograph or record filter response (see Fig. 4.13). Also, the magnifications given in the seismograph response curves are strictly valid only for steady-state harmonic oscillations without any transient response. The latter, however, might be significant when narrow-band seismographs record short wavelets of body waves. Signal shape, amplitudes and signal duration are then heavily distorted (see Figs. 4.10 and 4.17). Therefore, we have written “true” ground motion in quotation marks. Scherbaum (2001) gives a detailed discussion of signal distortion which is not taken into account in standard magnitude determinations from band-limited records. However, signal distortion must be corrected for in more advanced digital signal analysis for source parameter estimation. The distortions are largest for the very first oscillation(s) and they are stronger and longer lasting the narrower the recording bandwidth (see 4.2.1 and 4.2.2). The transient response decays with time, depending also on the damping of the seismometer. It is usually negligible for amplitude measurements on dispersed teleseismic surface wave trains.

To calculate ground motion amplitudes from record amplitudes, the frequency-dependent seismometer response and magnification have to be known from careful calibration (see 5.8). Analog seismograms should be clearly annotated and relate each record to a seismometer with known displacement magnification. For digital data, the instrument response is usually included in the header information of each seismogram file or given in a separate file that is automatically linked when analyzing data files. As soon as amplitudes and associated periods are picked in digital records, most software tools for seismogram analysis calculate instantaneously the ground displacement or ground velocity amplitudes and write them in related parameter files.

Another parameter which has to be determined (if the signal-to-noise-ratio permits) and reported routinely is the polarity of the P-wave first motion in vertical component records. Reliable observations of the first motion polarity at stations surrounding the seismic source in different directions allows the derivation of seismic fault-plane solutions (see 3.4 and EX 3.2). The wiring of seismometer components has to be carefully checked to assure that compressional first arrivals (c) appear on vertical-component records as an upward motion (+) while dilatational first arrivals (d) are recorded as a downward first half-cycle (-). The conventions for horizontal component recordings are + (up) for first motions towards N and E, and - (down) for motions towards S and W. These need to be taken into account when determining the backazimuth of the seismic source from amplitude and polarity readings on 3-component records (see EX 11.2, Figure 1). However, horizontal component polarities are not considered in polarity-based fault-plane solutions and therefore not routinely reported to data centers. Fig. 11.4 shows a compressional first arrival.

One should be aware, however, that narrow-band signal filtering may reduce the first-motion amplitude by such a degree that its polarity may no longer be reliably recognized or may even become lost completely in the noise (see Figs. 4.10 and 4.13). This may result in the wrong polarity being reported and hence erroneous fault-plane solutions. Since short-period (SP) records usually have a narrower bandwidth than medium- to long-period or even broadband records, one should differentiate between first-motion polarity readings from SP and LP/BB records. Also, long-period waves integrate over much of the detailed rupture process and so should show more clearly the overall direction of motion which may not be the same as the first-motion arrival in SP records which may be very small. Therefore, when reporting polarities to international data centers one should, according to recommendations in 1985 of the WG on Telegraphic Formats of the IASPEI Commission on Practice, unambiguously differentiate between such readings on SP (c and d) and those on LP and BB records,

11.2 Criteria and parameters for routine seismogram analysis

respectively (u for “up” = compression and r for “rarefaction” = dilatation). Note, however, that reliable polarity readings are only possible on BB records!

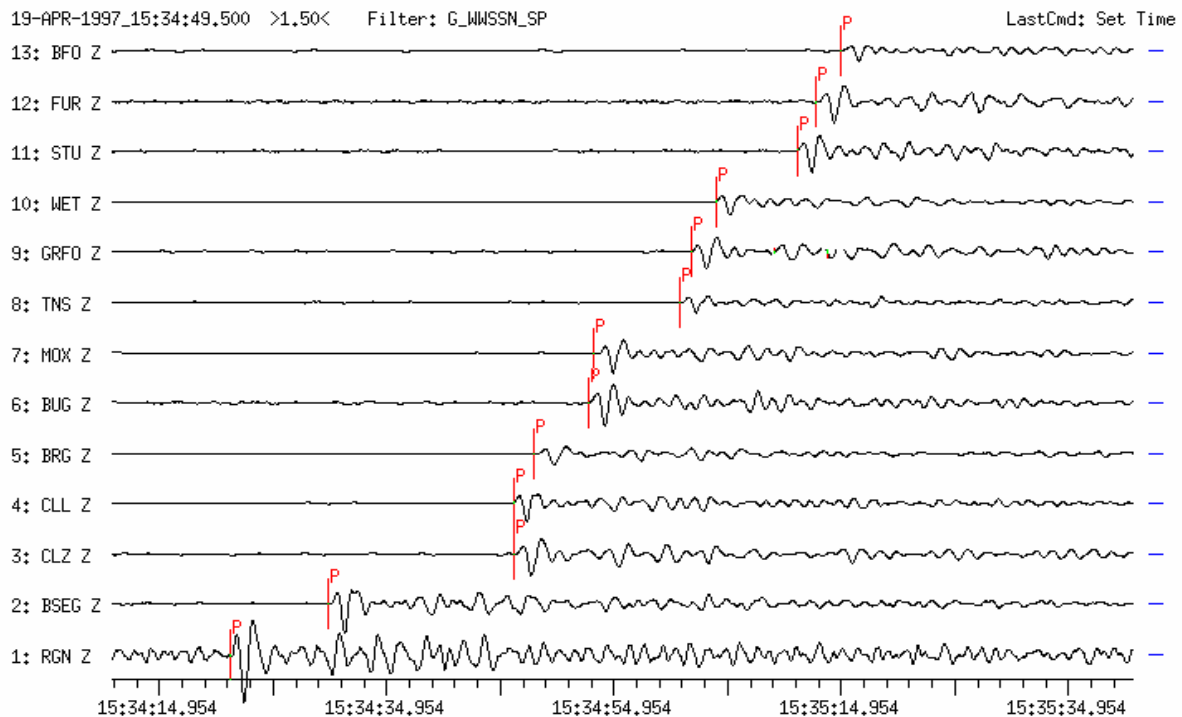


Fig. 11.5 WWSSN-SP vertical-component records of GRSN stations for the same event as in Fig. 11.4. While the P-wave amplitudes vary significantly within the network, the first-motion polarity remains the same.

11.2.3 Advanced wavelet parameter reporting from digital records

The parameters discussed in 11.2.1 have been routinely reported over the decades of analog recording. Digital records, however, allow versatile signal processing so that additional wavelet parameters can be measured routinely. Such parameters may provide a much deeper insight into the seismic source processes and the seismic moment release. Not only can onset times be picked but their range of uncertainty can also be marked. Further, for a given wave group, several amplitudes and related times may be quickly measured and these allow inferences to be drawn on how the rupture process may have developed in space and time. Moreover, the duration of a true ground displacement pulse t_w and the rise time t_r to its maximum amplitude contain information about size of the source, the stress drop and the attenuation of the pulse while propagating through the Earth. Integrating over the area underneath a displacement pulse allows to determine its signal moment m_s which is, depending on the bandwidth and corner period of the recording, related to the seismic moment M_0 (Seidl and Hellweg, 1988). Finally, inferences on the attenuation and scattering properties along the wave path can be drawn from the analysis of wavelet envelopes.

Fig. 11.6 depicts various parameters in relation to different seismic waveforms. One has to be aware, however, that each of these parameters can be severely affected by the properties of the seismic recording system (see Fig. 4.17 and Scherbaum, 1995 and 2001). Additionally, one may analyze the signal-to-noise ratio (SNR) and report it as a quantitative parameter for

characterizing signal strength and thus of the reliability of phase and parameter readings. This is routinely done when producing the Reviewed Event bulletin (RED) of the International Data Centre (IDC) in the framework of the CTBTO. The SNR may be either given as the ratio between the maximum amplitude of a considered seismic phase to that of the preceding ambient or signal-generated noise, or more comprehensively by determining the spectral SNR (see Fig. 11.47).

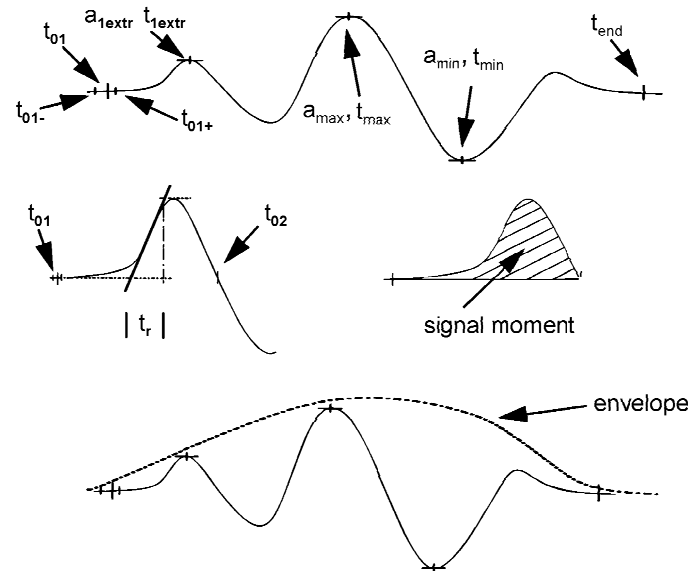


Fig. 11.6 Complementary signal parameters such as multiple wavelet amplitudes and related times, rise-time t_r of the displacement pulse, signal moment m_s and wavelet envelope (with modification from Scherbaum, Of Poles and Zeros, Fig. 1.9, p. 10, © 2001; with permission of Kluwer Academic Publishers).

Although these complementary signal parameters could be determined rather easily and quickly by using appropriate software for signal processing and seismogram analysis, their measurement and reporting to data centers is not yet common practice. It is expected, however, that the recently introduced more flexible formats for parameter reporting and storage (see ISF, 10.2.5), in conjunction with e-mail and internet data transfer, will pave the way for their routine reporting.

11.2.4 Criteria to be used for phase identification

11.2.4.1 Travel time and slowness

As outlined in Chapter 2, travel times of identified seismic waves are not only the key information for event location but also for the identification of seismic wave arrivals and the determination of the structure of the Earth along the paths which these waves have traveled. The same applies to the horizontal component s_x of the slowness vector s . The following relations hold:

$$s_x = dt/dD = p = 1/v_{app}$$

11.2 Criteria and parameters for routine seismogram analysis

were v_{app} is the apparent horizontal velocity of wave propagation, dt/dD the gradient of the travel-time curve $t(D)$ in the point of observation at distance D , and p is the ray parameter. Due to the given structure of the Earth, the travel-time differences between various types of seismic waves vary with distance in a systematic way. Therefore, differential travel-time curves with respect to the P-wave first arrival (see Figure 4 in EX 11.2) or absolute travel-time curves with respect to the origin time OT (see Figure 4 in EX 11.1 or overlay to Fig. 2.48) are the best tools to identify seismic waves on single station records. This is done by matching as many of the recognizable wave onsets in the record as possible with travel-time curves for various theoretically expected phases at epicentral distance D .

Make sure that the plotted $t(D)$ -curves have the same time-resolution as your record and investigate the match at different distances. Relative travel-time curves thus allow not only the identification of best matching phases but also the distance of the station from the epicenter of the source to be estimated. Note, however, that from certain distance ranges the travel-time curves of different types of seismic waves (see Figure 4 in EX 11.2) are close to each other, or even overlap, for example for PP and PcP between about 40° and 50° (see Figure 6a in DS 11.2) and for S, SKS and ScS between 75° and 90° (see Fig. 11.7 and 11.54). Proper phase identification then requires additional criteria besides travel-time differences to be taken into account (see 11.2.4.2 to 11.2.4.4). Select the most probable distance by taking these additional criteria into account. Absolute travel-time curves allow also the origin time to be estimated (see exercises EX 11.1 and EX 11.2).

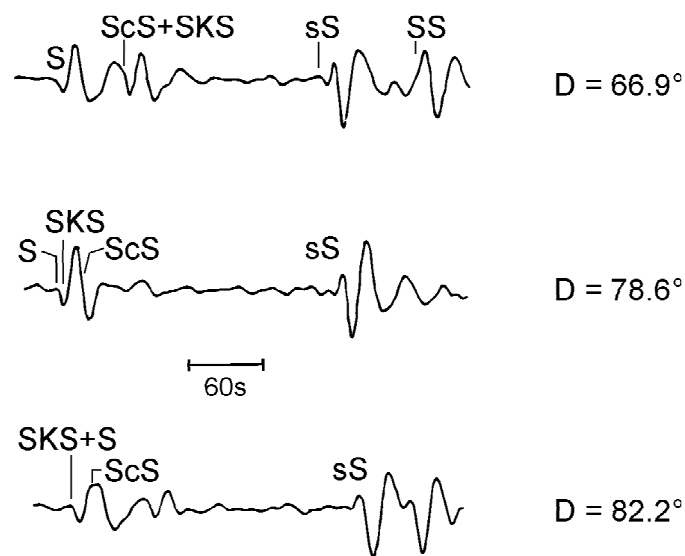


Fig. 11.7 Example of long-period horizontal component seismogram sections from a deep-focus earthquake in the Sea of Okhotsk (20.04.1984, $m_b = 5.9$, $h = 588$ km), recorded at the stations RSSD, RSNY, and RSCP, respectively, in the critical distance range of overlapping travel-time branches of S, SKS and ScS. Because of the large focal depth the depth phase sS is clearly separated in time.

Note, however, that the travel-time curves shown in the overlays to Figs. 2.47 and 2.48, or those given in EX 11.1 and EX 11.2, are valid for near-surface sources only. Both absolute and (to a lesser extent) relative travel times change with source depth (see IASPEI 1991 Seismological Tables, Kennett, 1991) and, in addition, depth phases may appear (see Fig. 2.43 and Table 1 in EX 11.2). Note also that teleseismic travel-time curves ($D > (17)20^\circ$) vary little from region to region. Typically, the theoretical travel times of the main seismic phases

deviate by less than 2 s from those observed (see Fig. 2.52). In contrast, local/regional travel-time curves for crustal and uppermost mantle phases may vary strongly from region to region. This is due to the pronounced lateral variations of crustal thickness and structure (see Fig. 2.10), age, and seismic wave velocities in continental and oceanic areas. This means local/regional travel-time curves have to be derived for each region in order to improve phase identification and estimates of source distance and depth.

Often, rapid epicentre and/or source depth estimates are already available from data centers prior to detailed record analysis at a given station. Then modern seismogram analysis software such as SEISAN (Havskov, 1996; Havskov and Ottemöller, 1999), SEIS89 (Baumbach, 1999), GIANT (Rietbrock and Scherbaum, 1998) or Seismic Handler (SH and SHM) (Stammler, <http://www.szgrf.bgr.de/sh-doc/index.html>) allow the theoretically expected travel times for all main seismic phases to be marked on the record. This eases phase identification. An example is shown in Fig. 11.13 for a record analyzed with Seismic Handler.

However, **theoretically calculated onset-times based on a global average model should only guide the phase identification but not the picking of onsets!** Be aware that one of the major challenges for modern global seismology is 3-D tomography of the Earth. What are required are the location and the size of anomalies in wave velocity with respect to the global 1-D reference model. Only then will material flows in the mantle and core (which drive plate tectonics, the generation of the Earth's magnetic field and other processes) be better understood. Station analysts should never trust the computer generated theoretical onset times more than the ones that they can recognize in the record itself. For Hilbert transformed phases (see 2.5.4.3) onset times are best read after filtering to correct for the transforming. Without unbiased analyst readings we will never be able to derive improved models of the inhomogeneous Earth. Moreover, the first rapid epicenters, depths and origin-times published by the data centers are only preliminary estimates and are usually based on first arrivals only. Their improvement, especially with respect to source depth, requires more reliable onset-time picks, and the identification of secondary (later) arrivals (see Figure 7 in IS 11.1).

At a local array or regional seismic network center both the task of phase identification and of source location is easier than at a single station because local or regional slowness can be measured from the time differences of the respective wave arrivals at the various stations (see 9.4, 9.5, 11.3.4 and 11.3.5). But even then, determining D from travel-time differences between P or PKP and later arrivals can significantly improve the location accuracy. This is best done by using three-component broadband recordings from at least one station in the array or network. The reason this is recommended is that travel-time differences between first and later arrivals vary much more rapidly with distance than the slowness of first arrivals. On the other hand, arrays and regional networks usually give better control of the backazimuth of the source than 3-component recordings (see 11.2.4.3), especially for low-magnitude events.

11.2.4.2 Amplitudes, dominating periods and waveforms

Amplitudes of seismic waves vary with distance due to geometric spreading, focusing and defocusing caused by variations in wave speed and attenuation. To correctly identify body-wave phases one has first to be able to differentiate between body- and surface-wave groups and then estimate at least roughly, whether the source is at shallow, intermediate or rather large depth. At long range, surface waves are only seen on LP and BB seismograms. Because of their 2D propagation, geometrical spreading for surface waves is less than for body waves

11.2 Criteria and parameters for routine seismogram analysis

that propagate 3-D. Also, because of their usually longer wavelength, surface waves are less attenuated and affected less by small-scale structural inhomogeneities than body waves. Therefore, on records of shallow seismic events, surface-wave amplitudes dominate over body-wave amplitudes (see Figs. 11.8 and 11.9) and show less variability with distance (see Fig. 3.13). This is also obvious when comparing the magnitude calibration functions for body and surface waves (see figures and tables in DS 3.1).

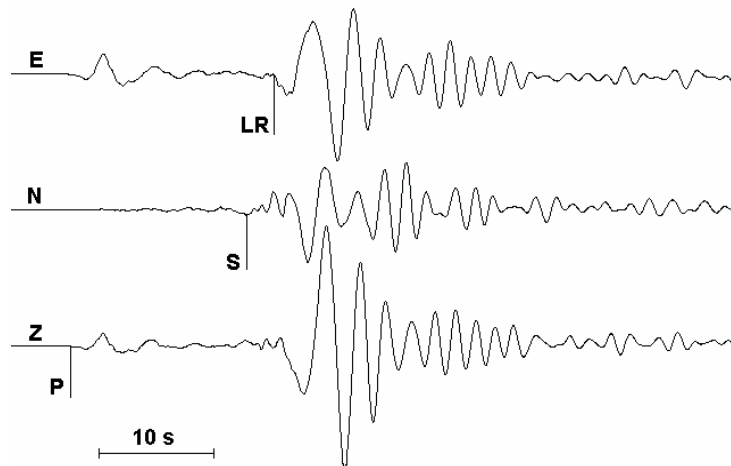


Fig. 11.8 Three-component BB-velocity record at station MOX of a mine collapse in Germany; (13 March 1989; $M_I = 5.5$) at a distance of 112 km and with a backazimuth of 273° . Note the Rayleigh surface-wave arrival LR with subsequent normal dispersion.

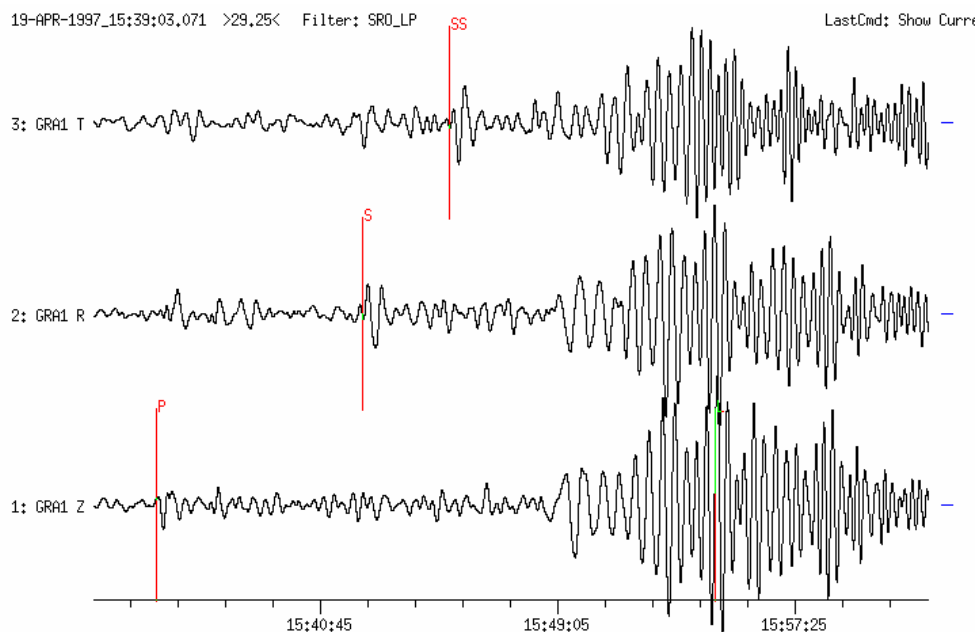


Fig. 11.9 T-R-Z rotated three-component seismogram (SRO-LP filter) from an earthquake east of Severnaya Zemlya (19 April 1997, $D = 46.4^\circ$, $m_b = 5.8$, $M_s = 5.0$). The record shows P, S, SS and strong Rayleigh surface waves with clear normal dispersion. The surface wave maximum has periods of about 20 s. It is called an Airy-phase and corresponds to a minimum in the dispersion curve for continental Rayleigh waves (see Fig. 2.9).

However, as source depth increases, surface-wave amplitudes decrease relative to those of body waves, the decrease being strongest for shorter wavelengths. Thus, the surface waves from earthquakes at intermediate (> 70 km) or great depth (> 300 km) may have amplitudes smaller than those of body waves or may not even be detected on seismic records (see Figure 2 in EX 11.2). This should alert seismogram analysts to look for depth phases, which are then usually well separated from their primary waves and so are easily recognized (see Fig. 11.7 above and Figure 6a and b in DS 11.2).

Another feature that helps in phase identification is the waveform. Most striking is the difference in waveforms between body and surface waves. Dispersion in surface waves results in long wave trains of slowly increasing and then decreasing amplitudes, whereas non-dispersive body waves form short duration wavelets. Usually, the longer period waves arrive first (“normal” or “positive” dispersion) (see Figs. 11.8 and 11.9). However, the very long-period waves ($T > 60$ s), that penetrate into the mantle down to the asthenosphere (a zone of low wave speeds), may show inverse dispersion. The longest waves then arrive later in the wave train (see Fig. 2.18).

For an earthquake of a given seismic moment, the maximum amplitude of the S wave is about five-times larger at source than that of the P waves (see Figs. 2.3, 2.23, and 2.41). This is a consequence of the different propagation velocities of P and S waves (see Eq. (3.2)). Also the spectrum is different for each wave type. Thus, P-wave source spectra have corner frequencies about $\sqrt{3}$ times higher than those of S. In high-frequency filtered records this may increase P-wave amplitudes with respect to S-wave amplitudes (see Fig. 11.10 right). Additionally, the frequency-dependent attenuation of S waves is significantly larger than for P waves.

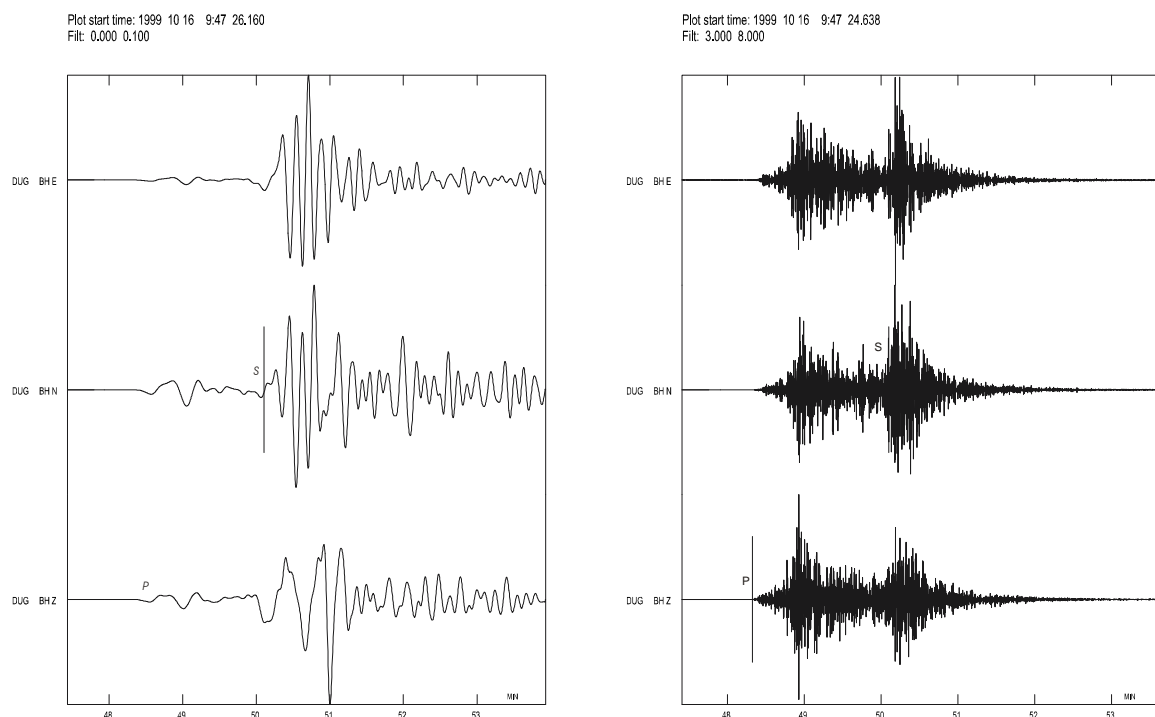


Fig. 11.10 Left: Low-pass filtered (< 0.1 Hz) and right: band-pass filtered (3.0-8.0 Hz) seismograms of the Oct. 16, 1999, earthquake in California ($m_b = 6.6$, $M_s = 7.9$) as recorded at the broadband station DUG at $D = 6^\circ$ (courtesy of L. Ottemöller).

11.2 Criteria and parameters for routine seismogram analysis

Due to both effects, S waves and their multiple reflections and conversions are – within the teleseismic distance range – mainly observed on LP or BB records. On the other hand, the different P-wave phases, such as P, PcP, PKP, and PKKP, are well recorded, up to the largest epicentral distances, by SP seismographs with maximum magnification typically around 1 Hz.

Generally, the rupture duration of earthquakes is longer than the source process of explosions. It ranges from less than a second for small microearthquakes up to several minutes for the largest shallow crustal shocks with a source which is usually a complex multiple rupture process (see Fig. 11.11, Fig. 3.7 and Figure 5b in DS 11.2).

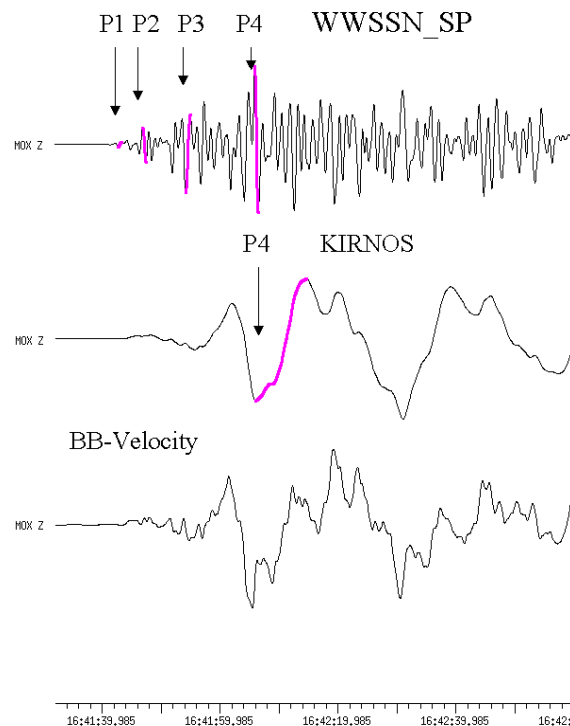


Fig. 11.11 Vertical component records of the P-wave group from a crustal earthquake in Sumatra (04 June 2000; $m_b = 6.8$, $M_s = 8.0$) at the GRSN station MOX at $D = 93.8^\circ$. **Top:** WWSSN-SP (type A); **middle:** medium-period Kirnos SKD BB-displacement record (type C), and **bottom:** original BB-velocity record. Clearly recognizable is the multiple rupture process with $P_4 = P_{\max}$ arriving 25 s after the first arrival P1. The short-period magnitude m_b determined from P1 would be only 5.4, $m_b = 6.3$ from P2 and $m_b = 6.9$ when calculated from P4. When determining the medium-period body-wave magnitude from P4 on the Kirnos record then $m_B = 7.4$.

As compared to shallow crustal earthquakes, deep earthquakes of comparable magnitude are often associated with higher stress drop and smaller source dimension. This results in the strong excitation of higher frequencies and thus simple and impulse-like waveforms (see Fig. 4.13 and Figures 6a and b in DS 11.2). Therefore S waves from deep earthquakes may be recognizable in short-period records even at teleseismic distances. The same applies to waveforms from explosions. As compared to shallow earthquakes, when scaled to the same magnitude, their source dimension is usually smaller, their source process simpler and their source duration much shorter (typically in the range of milliseconds). Accordingly, explosions generate significantly more high-frequency energy than earthquakes and usually produce shorter and simpler waveforms. Examples are given in Figures 1 to 5 of DS 11.4. Note,

however, that production explosions in large quarries or open cast mines, with yields ranging from several hundred to more than one kiloton TNT, are usually fired in sequences of time-delayed sub-explosions, which are spread out over a large area. Such explosions may generate rather complex wave fields, waveforms and unusual spectra, sometimes further complicated by the local geology and topography, and thus not easy to discriminate from local earthquakes.

At some particular distances, body waves may have relatively large amplitudes, especially near caustics (see Fig. 2.29 for P waves in the distance range between 15° and 30° ; or around $D = 145^\circ$ for PKP phases). In contrast, amplitudes decay rapidly in shadow zones (such as for P waves beyond 100° ; see Fig. 11.63). The double triplication of the P-wave travel-time curve between 15° and 30° results in closely spaced successive onsets and consequently rather complex waveforms (Fig. 11.49). At distances between about 30° and 100° , however, waveforms of P may be simple (see Figs. 11.52 and 11.53). Beyond the PKP caustic, between $145^\circ < D < 160^\circ$, longitudinal core phases split into three travel-time branches with typical amplitude-distance patterns. This, together with their systematic relative travel-time differences, permits rather reliable phase identification and distance estimates, often better than 1° (see Figs. 11.62 and 11.63 as well as exercise EX 11.3).

Fig. 11.12 is a simplified diagram showing the relative frequency of later body-wave arrivals with respect to the first arrival P or the number n of analyzed earthquakes, as a function of epicentral distance D between 36° and 166° . They are based on observations in standard records (see Fig. 3.11) of types A4 (SP - short-period, < 1.5 s), B3 (LP - long-period, between 20 s and 80 s) and C (BB - broadband displacement between 0.1 s and 20 s) at station MOX in Germany (Bormann, 1972a). These diagrams show that in the teleseismic distance range one can mainly expect to observe in SP records the following longitudinal phases: P, PcP, ScP, PP, PKP (of branches ab, bc and df), P'P' (= PKPPKP), PKKP, PcPPKP, SKP and the depth phases of P, PP and PKP. In LP and BB records, however, additionally S, ScS, SS, SSS, SKS, SKSP, SKKS, SKKP, SKKKS, PS, PPS, SSP and their depth phases are frequently recorded. This early finding based on the visual analysis of traditional analog film recordings has recently been confirmed by stacking SP and LP filtered broadband records of the Global Digital Seismic Network (GDSN) (Astiz et al., 1996; see Figs. 2.47 and 2.48 with overlays).

Since these diagrams and stacked seismogram sections reflect, in a condensed form, some systematic differences in waveforms, amplitudes, dominating periods and relative frequency of occurrence of seismic waves in different distance ranges, they may, when used in addition to travel-time curves, give some guidance to seismogram analysts as to what kind of phases they may expect at which epicentral distances and in which kind of seismic records. Note, however, that the appearance of these phases is not "obligatory", rather, it may vary from region to region, depending also on the source mechanisms and the radiation pattern with respect to the recording station, the source depth, the area of reflection (e.g., underneath oceans, continental shield regions, young mountain ranges), and the distance of the given station from zones with frequent deep earthquakes. Therefore, no rigid rules for phase identification can be given. Also, Fig. 11.12 considers only teleseismic earthquakes. Local and regional earthquakes, however, are mainly recorded by SP short-period seismographs of type A or with Wood-Anderson response. There are several reasons for this. Firstly, SP seismographs have usually the largest amplification and so are able to record (at distances smaller than a few hundred kilometers) sources with magnitudes of zero or even less. Secondly, as follows from Fig. 3.5, the corner frequency of source displacement spectra for

11.2 Criteria and parameters for routine seismogram analysis

events with magnitudes < 4 is usually > 1 Hz, i.e., small events radiate relatively more high-frequency energy. Thirdly, in the near range the high frequencies have not yet been reduced so much by attenuation and scattering, as they usually are for $f > 1$ Hz in the teleseismic range. Therefore, most local recordings show no waves with periods longer than 2 s. However, as M_L increases above 4, more and more long-period waves with large amplitudes are generated and these dominate in BB records of local events, as illustrated with the records in Figs. 11.8 and 11.10.

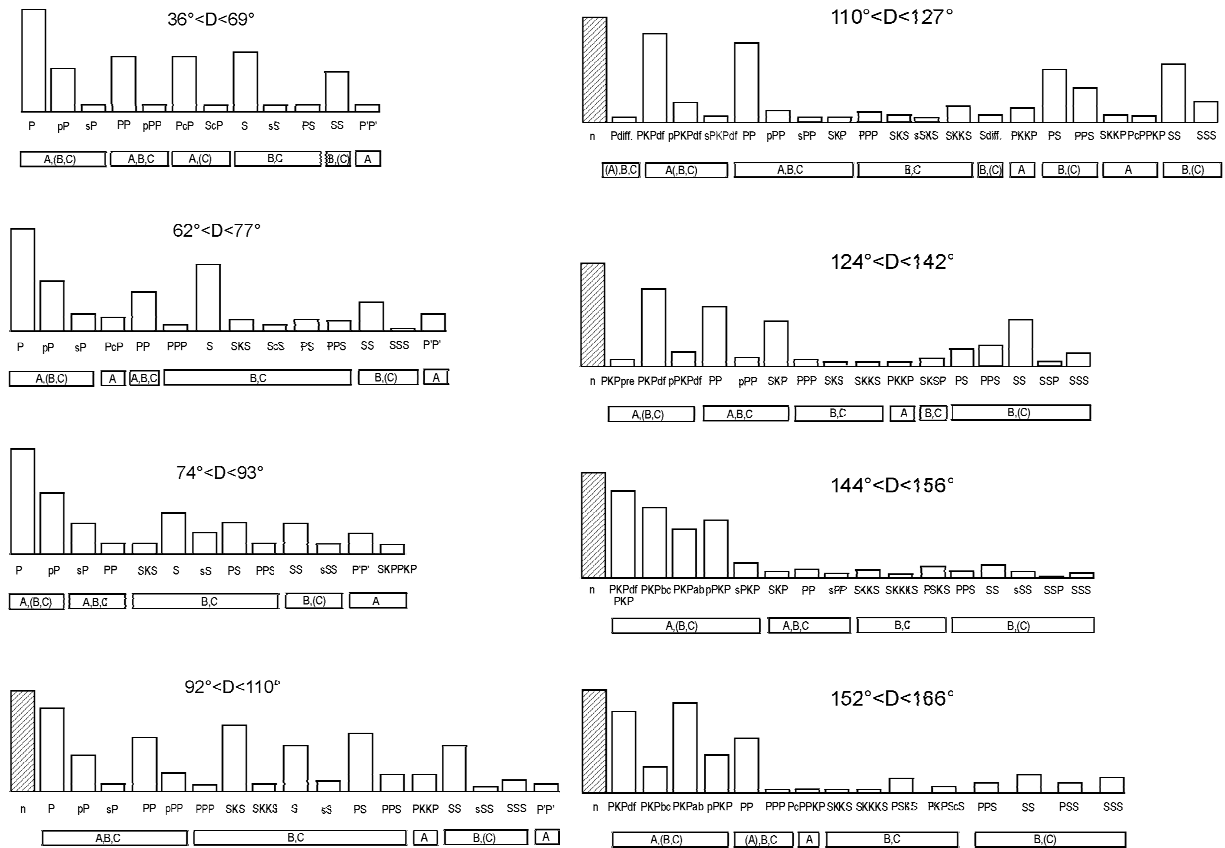


Fig. 11.12 Relative frequency of occurrence of secondary phases in standard analog records at station MOX, Germany, within the teleseismic distance range 36° to 166° . The first column relates to 100% of analyzed P-wave first arrivals or of analyzed events (hatched column), respectively. In the boxes beneath the phase columns the type of standard records is indicated in which these phases have been observed best or less frequently/clear (then record symbols in brackets). A – short-period; B – long-period LP, C – Kirnos SKD BB-displacement.

11.2.4.3 Polarization

As outlined in 2.2 and 2.3, P and S waves are linearly polarized, with slight deviations from this ideal in the inhomogeneous and partially anisotropic real Earth (see Figs. 2.6 and 2.7). In contrast, surface waves may either be linearly polarized in the horizontal plane perpendicular to the direction of wave propagation (transverse polarization; T direction; e.g., Love waves) or elliptically polarized in the vertical plane oriented in the radial (R) direction of wave propagation (see Figs. 2.8, 2.13 and 2.14). P-wave particle motion is dominantly back and forth, parallel to the seismic ray, whereas S-wave motion is perpendicular to the ray direction.

Accordingly, a P-wave motion can be split into two main components, one vertical (Z) and one horizontal (R) component. The same applies to Rayleigh waves, but with a 90° phase shift between the Z and R components of motion. S waves, on the other hand, may show purely transverse motion, oscillating in the horizontal plane (SH; i.e., pure T component, as Love waves) or motion in the vertical propagation plane, at right angles to the ray direction (SV), or in any other combination of SH and SV. In the latter case S-wave particle motion has Z, R and T components, with SV wave split into a Z and an R component.

Thus, when 3-component records are available, the particle motion of seismic waves in space can be reconstructed and used for the identification of seismic wave types. However, usually the horizontal seismometers are oriented in geographic east (E) and north (N) direction. Then, first the backazimuth of the source has to be computed (see EX 11.2) and then the horizontal components have to be rotated into the horizontal R direction and the perpendicular T direction, respectively. This *axis rotation* is easily performed when digital 3-component data and suitable analysis software are available. It may even be carried one step further by rotating the R component once more into the direction of the incident seismic ray (longitudinal L direction). The T component then remains unchanged but the Z component is rotated into the Q direction of the SV component. Such a *ray-oriented co-ordinate system* separates and plots P, SH and SV waves in 3 different components L, T and Q, respectively. These axes transformations are easily made given digital data from arbitrarily oriented orthogonal 3-component sensors such as the widely used triaxial sensors STS2 (see Fig. 5.13 and DS 5.1). However, the principle types of polarization can often be quickly assessed with manual measurement and elementary calculation from analog 3-component records and the backazimuth from the station to the source be estimated (see EX 11.2).

Note that all direct, reflected and refracted P waves and their multiples, as well as conversions from P to S and vice versa, have their dominant motion confined to the Z and R (or L and Q) plane. This applies to all core phases, also to SKS and its multiples, because K stands for a P-wave leg in the outer core. In contrast, S waves may have both SV and SH energy, depending on the source type and rupture orientation. However, discontinuities along the propagation path of S waves act as selective SV/SH filters. Therefore, when an S wave arrives at the free surface, part of its SV energy may be converted into P, thus forming an SP phase. Consequently, the energy reflected as S has a larger SH component as compared to the incoming S. So the more often a mixed SH/SV type of S wave is reflected at the surface, the more it becomes of SH type. Accordingly, SSS, SSSS etc. will show up most clearly or even exclusively on the T component (e.g., Fig. 11.37) unless the primary S wave is dominantly of SV-type (e.g., Fig. 11.13). As a matter of fact, Love waves are formed through constructive interference of repeated reflections of SH at the free surface. Similarly, when an S wave hits the core-mantle boundary, part of its SV energy is converted into P which is either refracted into the core (as K) or reflected back into the mantle as P, thus forming the ScP phase. Consequently, multiple ScS is also usually best developed on the T component.

Fig. 11.13 shows an example of the good separation of several main seismic phases on an Z-R-T-component plot. At such a large epicentral distance ($D = 86.5^\circ$) the incidence angle of P is small (about 15°; see EX 3.3). Therefore, the P-wave amplitude is largest on the Z component whereas for PP, which has a significantly larger incidence angle, the amplitude on the R component is almost as large as Z. For both P and PP no T component is recognizable above the noise. SKS is strong in R and has only a small T component (effect of anisotropy, see Fig. 2.7). The phase SP has both a strong Z and R component. Love waves (LQ) appear as the first surface waves in T with very small amplitudes in R and Z. In contrast, Rayleigh

11.2 Criteria and parameters for routine seismogram analysis

waves (LR) are strongest in R and Z. SS in this example is also largest in R. From this one can conclude, that the S waves generated by this earthquake are almost purely of SV type. In other cases, however, it is only the difference in the R-T polarization which allows S to be distinguished from SKS in this distance range of around 80° where these two phases arrive closely to each other (see Fig. 11.14 and Figure 13e in DS 11.2).

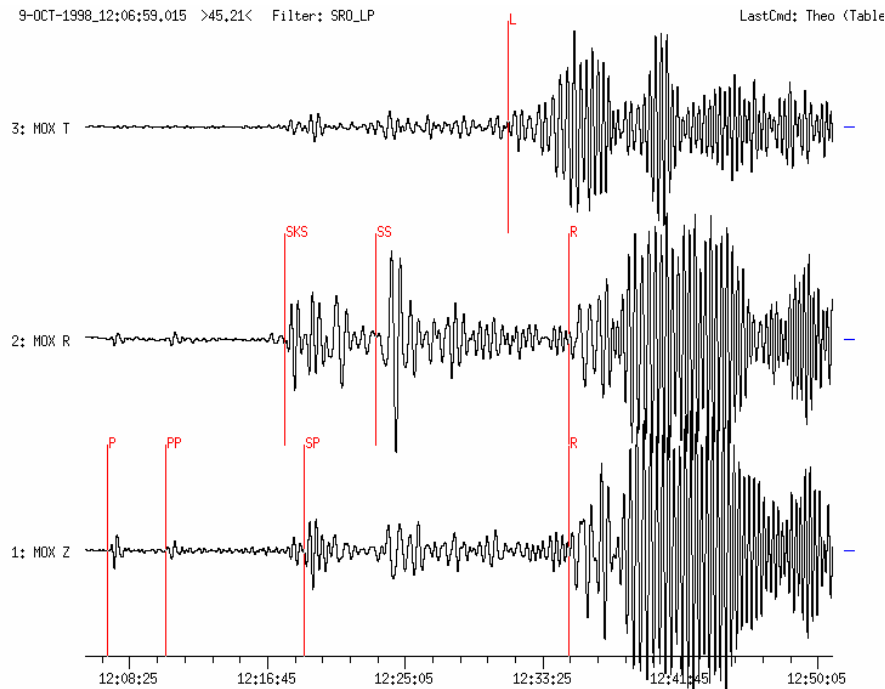


Fig. 11.13 Time-compressed long-period filtered three-component seismogram (SRO-LP simulation filter) of the Nicaragua earthquake recorded at station MOX ($D = 86.5^\circ$). Horizontal components have been rotated (ZRT) with R (radial component) in source direction. The seismogram shows long-period phases P, PP, SKS, SP, SS and surface waves L (or LQ for Love wave) and R (or LR for Rayleigh wave).

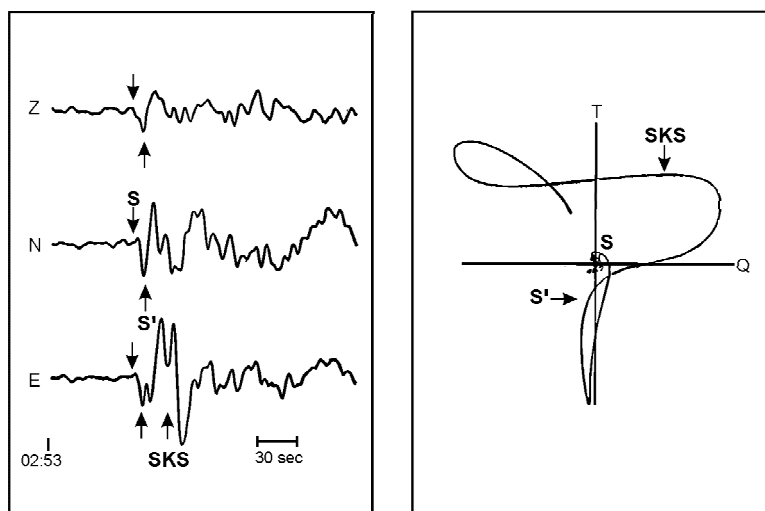


Fig. 11.14 Ray-oriented broadband records (left: Z-N-E components; right: particle motion in the Q-T plane) of the S and SKS wave group from a Hokkaido $M_s = 6.5$ earthquake on 21 March 1982, at station Kasperske Hory (KHC) at an epicentral distance of $D = 78.5^\circ$.

The empirical travel-time curves in Fig. 2.49 (from Astiz et al., 1996) summarize rather well, which phases (according to the overlay of Fig. 2.48) are expected to dominate the vertical, radial or transverse ground motion in rotated three-component records.

If we supplement the use of travel-time curves with seismic recordings in different frequency bands, and take into account systematic differences in amplitude, frequency content and polarization for P, S and surface waves, and when we know the distances, where caustics and shadow zones occur, then the identification of later seismic wave arrivals is entertaining and like a detective inquiry into the seismic record.

11.2.4.4 Example for documenting and reporting of seismogram parameter readings

Fig. 11.15 shows a plot of the early part of a teleseismic earthquake recorded at stations of the GRSN. At all stations the first arriving P wave is clearly recognizable although the P-wave amplitudes vary strongly throughout the network. This is not a distance effect (the network aperture is less than 10% of the epicentral distance) but rather an effect of different local site conditions related to underground geology and crustal heterogeneity. As demonstrated with Figs. 4.35 and 4.36, the effect is not a constant for each station but depends both on azimuth and distance of the source. It is important to document this. Also, Fig. 11.15 shows for most stations a clear later arrival about 12 s after P. For the given epicentral distance, no other main phase such as PP, PPP or PcP can occur at such a time (see differential travel-time curves in Figure 4 of EX 11.2). It is important to pick such later (so-called secondary) onsets which might be “depth phases” (see 11.2.5.1) as these allow a much better determination of source depth than from P-wave first arrivals alone (see Figure 7 in IS 11.1).

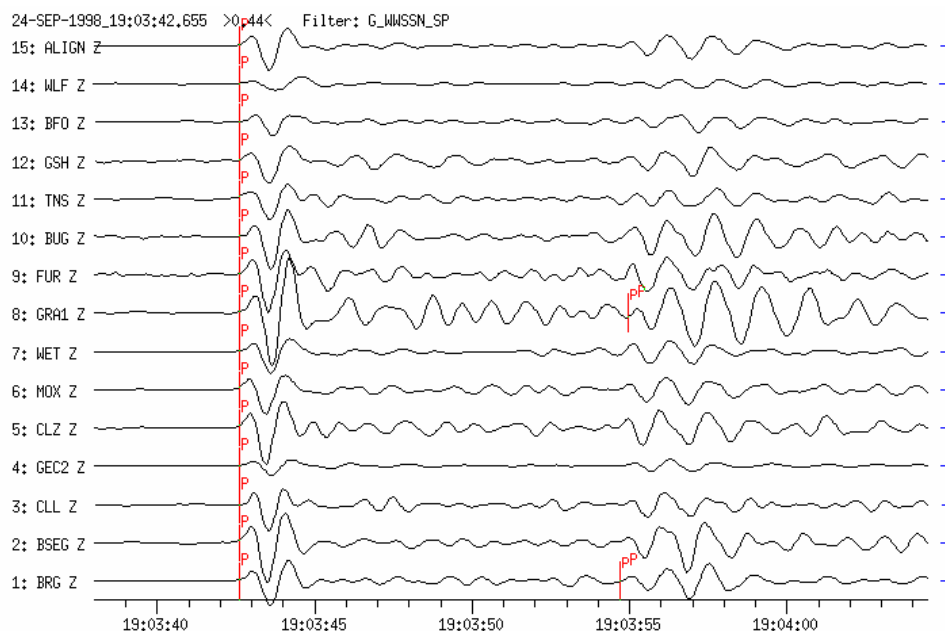


Fig. 11.15 WWSSN-SP filtered seismograms at 14 GRSN, GRF, GERESS and GEOFON stations from an earthquake in Mongolia (24 Sept. 1998; depth (NEIC-QED) = 33 km; mb = 5.3, Ms = 5.4). Coherent traces have been time-shifted, aligned and sorted according to epicentral distance ($D = 58.3^\circ$ to BRG, 60.4° to GRA1 and 63.0° to WLF). Note the strong variation in P-wave signal amplitudes and clear depth phases pP arriving about 12 s after P.

11.2 Criteria and parameters for routine seismogram analysis

Tab. 11.2 gives for the Mongolia earthquake shown in Fig. 11.15 the whole set of parameter readings made at the analysis center of the Central Seismological Observatory Gräfenberg (SZGRF) in Erlangen, Germany:

- first line: date, event identifier, analyst;
- second and following lines: station, onset time, onset character (e or i), phase name (P, S, etc.), direction of first particle motion (c or d), analyzed component, period [s], amplitude [nm], magnitude (mb or Ms), epicentral distance [°]; and
- last two lines: source parameters as determined by the SZGRF (origin time OT, epicentre, average values of mb and Ms, source depth and name of Flinn-Engdahl-region).

Generally, these parameters are stored in a database, used for data exchange and published in lists, bulletins and the Internet (see IS 11.2). The onset characters i (impulsive) should be used only if the time accuracy is better than a few tens of a second, otherwise the onset will be described as e (emergent). Also, when the signal-to-noise-ratio (SNR) of onsets is small and especially, when narrow-band filters are used, the first particle motion should not be given because it might be distorted or lost in the noise. Broadband records are better suited for polarity readings (see Fig. 4.10). Their polarities, however, should be reported as u (for “up” = compression) and r (for “rarefaction” = dilatation) so as to differentiate them from short-period polarity readings (c and d, respectively).

Tab. 11.2 Parameter readings at the SZGRF analysis center for the Mongolia earthquake shown in Fig. 11.15 from records of the GRSN.

						ev_id 980924007		KLI	
1998-09-24									
BRG	19:03:27.2	e P	Z T	1.2	A 135.5	mb 5.9	D	58.3	
ALIGN	19:03:27.2	e P	Z T	1.1	A 124.1	mb 5.8			
BSEG	19:03:28.2	e P	Z T	1.1	A 198.3	mb 6.0	D	58.4	
CLL	19:03:28.6	e P	Z T	0.9	A 98.9	mb 5.8	D	58.5	
GEC2	19:03:36.3	i P	c Z T	1.2	A 46.9	mb 5.4	D	59.6	
CLZ	19:03:36.6	e P	Z T	1.1	A 177.7	mb 6.0	D	59.6	
MOX	19:03:36.9	e P	Z T	1.2	A 122.4	mb 5.8	D	59.6	
WET	19:03:38.5	e P	Z T	1.2	A 107.2	mb 5.7	D	59.9	
BRG	19:03:39.3	e pP	Z						
GRA1	19:03:42.6	i P	c Z T	1.1	A 286.5	mb 6.2	D	60.4	
					b_slo 6.8	b_az 54			
BUG	19:03:48.5	e P	Z T	1.1	A 162.4	mb 5.8	D	61.4	
FUR	19:03:48.6	e P	Z T	1.1	A 174.3	mb 5.8	D	61.3	
TNS	19:03:49.9	e P	Z T	1.1	A 103.0	mb 6.0	D	61.5	
GSH	19:03:54.5	e P	Z T	1.3	A 132.3	mb 6.0	D	62.3	
GRA1	19:03:55.0	e pP	Z						
BFO	19:03:57.4	e P	Z T	1.1	A 55.2	mb 5.6	D	62.8	
WLF	19:04:00.1	e P	Z T	1.7	A 80.3	mb 5.6	D	63.0	
GRA1	19:11:52.2	e S	E				D	60.4	
GEC2	19:30:36.0	e L	Z T	19.9	A 3895.8	MS 5.5			
GRA1	19:31:03.6	e L	Z T	20.6	A 3398.7	MS 5.5			
SZGRF OT 18:53:39.3 45.30N 106.84E mb_av 5.8 MS_av 5.5									
DEP 44km ▲ MONGOLIA									

Note that for this event the international data center NEIC had “set” the source depth to 33 km because of the absence of reported depth phases. The depth-phase picks at the GRSN, however, with an average time difference of pP-P of about 12 s, give a focal depth of 44 km. Also note in Tab. 11.2 the large differences in amplitudes (A) determined from the records of individual stations. The resulting magnitudes mb vary between 5.4 (GEC2) and 6.2 (GRA1)!

11.2.5 Criteria to be used in event identification and discrimination

11.2.5.1 Discrimination between shallow and deep earthquakes

Earthquakes are often classified on depth as: shallow focus (depth between 0 and 70 km), intermediate focus (depth between 70 and 300 km) and deep focus (depth between 300 and 700 km). However, the term "deep-focus earthquakes" is also often applied to all sub-crustal earthquakes deeper than 70 km. They are generally located in slabs of the lithosphere which are subducted into the mantle. As noted above, the most obvious indication on a seismogram that a large earthquake has a deep focus is the small amplitude of the surface waves with respect to the body-wave amplitudes and the rather simple character of the P and S waveforms, which often have impulsive onsets (see Fig. 4.13). In contrast to shallow-focus earthquakes, S phases from deep earthquakes may sometimes be recognizable even in teleseismic short-period records. The body-wave/surface-wave ratio and the type of generated surface waves are also key criteria for discriminating between natural earthquakes, which mostly occur at depth larger than 5 km, and quarry blasts, underground explosions or rockbursts in mines, which occur at shallower depth (see 11.2.5.2).

A more precise determination of the depth h of a seismic source, however, requires either the availability of a seismic network with at least one station being very near to the source, e.g., at an epicentral distance $D < h$ (because only in the near range the travel time $t(D, h)$ of the direct P wave varies strongly with source depth h), or the identification of seismic *depth phases* on the seismic record. The most accurate method of determining the focal depth of an earthquake in routine seismogram analysis, particularly when only single station or network records at teleseismic distances are available, is to identify and read the onset times of depth phases. A depth phase is a characteristic phase of a wave reflected from the surface of the Earth at a point relatively near the hypocenter (see Fig. 2.43). At distant seismograph stations, the depth phases pP or sP follow the direct P wave by a time interval that changes only slowly with distance but rapidly with depth. The time difference between P and other primary seismic phases, however, such as PcP , PP , S , SS etc. changes much more with distance. When records of stations at different distances are available, the different travel-time behavior of primary and depth phases makes it easier to recognize and identify such phases. Because of the more or less fixed ratio between the velocities of P and S waves with $v_p/v_s \approx \sqrt{3}$, pP and sP follow P with a more or less fixed ratio of travel-time difference $t(sP-P) \approx 1.5 t(pP-P)$ (see Figs. 11.16 and 11.17). Animations of seismic ray propagation and phase recordings from deep earthquakes are given in files 3 and 5 of IS 11.3 and related CD-ROM.

The time difference between pP and sP and other direct or multiple reflected P waves such as pPP , sPP , $pPKP$, $sPKP$, $pPdif$, $sPdif$, etc. are all roughly the same. S waves also generate depth phases, e.g., sS , $sSKS$, sSP etc. The time difference $sS-S$ is only slightly larger than $sP-P$ (see Figs. 1.4 and 11.17). The difference grows with distance to a maximum of 1.2 times the $sP-P$ time. These additional depth phases may also be well recorded and can be used in a similar way for depth determination as pP and sP .

Given the rough distance between the epicenter and the station, the hypocenter depth (h) can be estimated within $\Delta h \approx \pm 10$ km from travel-time curves or determined by using time-difference tables for depth-phases (e.g., from $\Delta t(pP-P)$ or $\Delta t(sP-P)$; see Kennett, 1991 or Table 1 in EX 11.2) or the "rule-of-thumb" in Eq. (11.4). An example is given in Fig. 11.18. It depicts broadband records of the GRSN from a deep earthquake ($h = 119$ km) in the

11.2 Criteria and parameters for routine seismogram analysis

Volcano Islands, West Pacific. The distance range is 93° to 99° . The depth phases pP and pPP are marked. From the time difference pP-P of 31.5 s and an average distance of 96° , it follows from Table 1 in EX 11.2 that the source depth is 122 km. When using Eq. (11.4) instead, we get $h = 120$ km. This is very close to the source depth of $h = 119$ km determined by NEIC from data of the global network.

Note that on the records in Fig. 11.18 the depth phases pP and pPP have larger amplitudes than the primary P wave. This may be the case also for sP, sS etc., if the given source mechanism radiates more energy in the direction of the upgoing rays (p or s; see Fig. 2.43) than in the direction of the downgoing rays for the related primary phases P, PP or S. Also, in Fig. 11.18, pP, PP and pPP have also longer periods than P. Accordingly, they are more coherent throughout the network than the shorter P waves. Fig. 11.37 shows for the same earthquake the LP-filtered and rotated 3-component record at station RUE, Germany, with all identified major later arrivals being marked on the record traces. This figure is an example of the search for and comprehensive analysis of secondary phases.

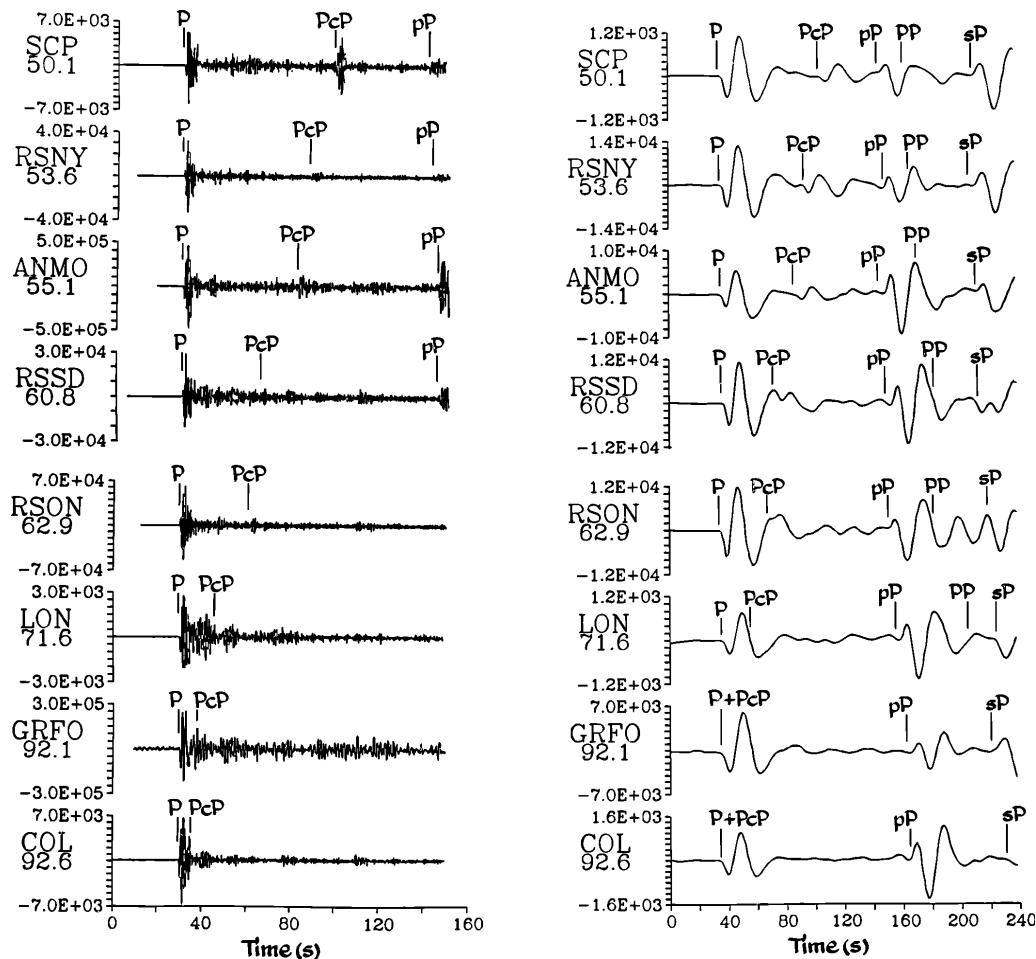


Fig. 11.16 Short-period (left) and long-period (right) seismograms from a deep-focus Peru-Brazil border region earthquake on May 1, 1986 ($m_b = 6.0$, $h = 600$ km) recorded by stations in the distance range 50.1° to 92.2° . Note that the travel-time difference between P and its depth phases pP and sP, respectively, remains nearly unchanged. In contrast PcP comes closer to P with increasing distance and after merging with P at joint grazing incidence on the core-mantle boundary form the diffracted wave Pdif (reprinted from *Anatomy of Seismograms*, Kulhánek, Plate 41, p. 139-140; © 1990; with permission from Elsevier Science).

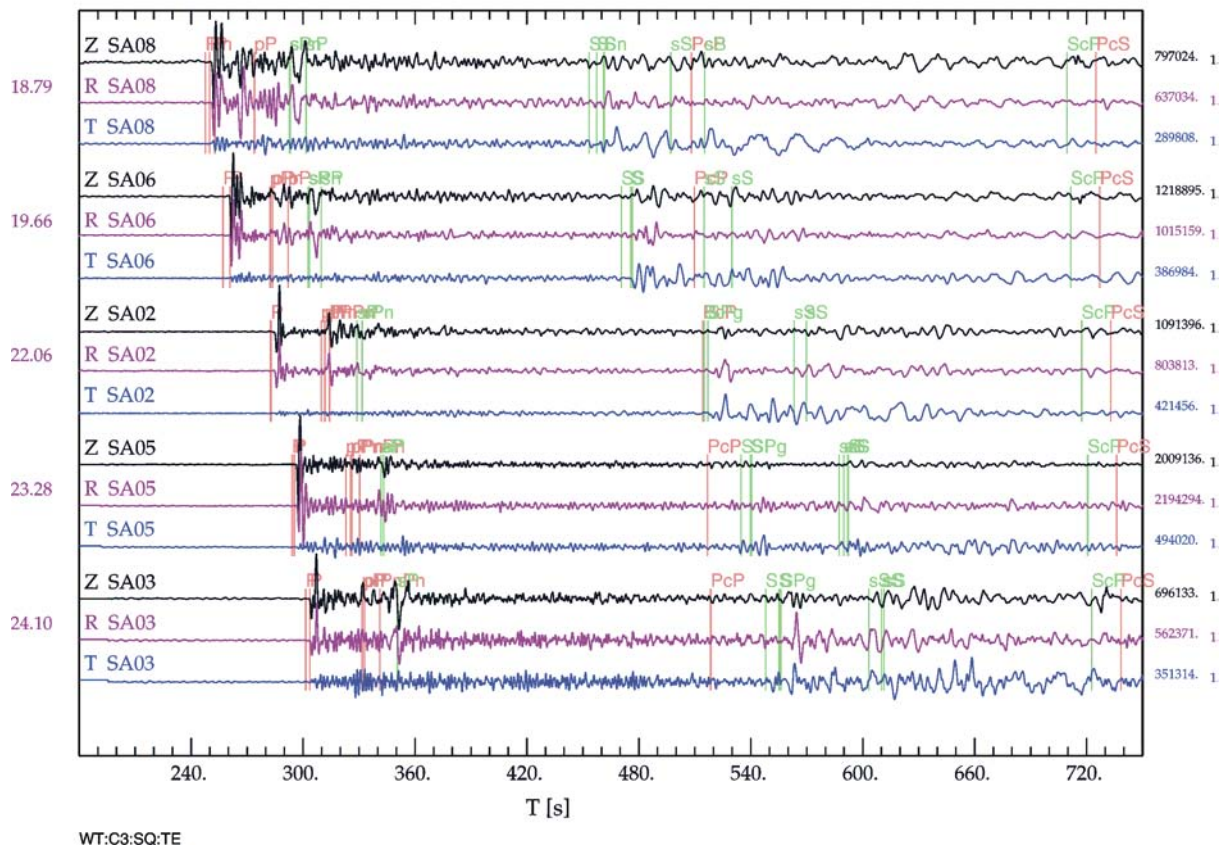


Fig. 11.17 3-component recordings in the distance range 18.8° to 24.1° from a regional network of portable BB instruments deployed in Queensland, Australia (seismometers CMG3ESP; unfiltered velocity response; see DS 5.1). The event occurred in the New Hebrides at 152 km depth. On each set of records the predicted phase arrival times for the AK135 model (see Fig. 2.53) are shown as faint lines. The depth phases pP, sP and sS are well developed but their waveforms are complex because several of the arrivals have almost the same travel time (courtesy of B. Kennett).

Crustal earthquakes usually have a source depth of less than 30 km, so the depth phases may follow their primary phases so closely that their waveforms overlap (see Fig. 11.19). Identification and onset-time picking of depth phases is then usually no longer possible by simple visual inspection of the record. Therefore, in the absence of depth phases reported by seismic stations, international data centers such as NEIC in its Monthly Listings of Preliminary (or Quick) Determination of Epicenters often fix the source depth of (presumed) crustal events at 0 km, 10 km or 33 km, as has been the case for the event shown in Fig. 11.15. This is often further specified by adding the capital letter N (for “normal depth” = 33 km) or G (for depth fixed by a geophysicist/analyst). Waveform modeling, however (see 2.8 and Figs. 2.57 to 2.59), may enable good depth estimates for shallow earthquakes to be obtained from the best fit of the observed waveforms to synthetic waveforms calculated for different source depth. Although this is not yet routine practice at individual stations, the NEIC has, since 1996, supplemented depth determinations from pP-P and sP-P by synthetic modeling of BB-seismograms. The depth determination is done simultaneously with the

11.2 Criteria and parameters for routine seismogram analysis

determination of fault-plane solutions. This has reduced significantly the number of earthquakes in the PDE listings with arbitrarily assigned source depth 10G or 33N.

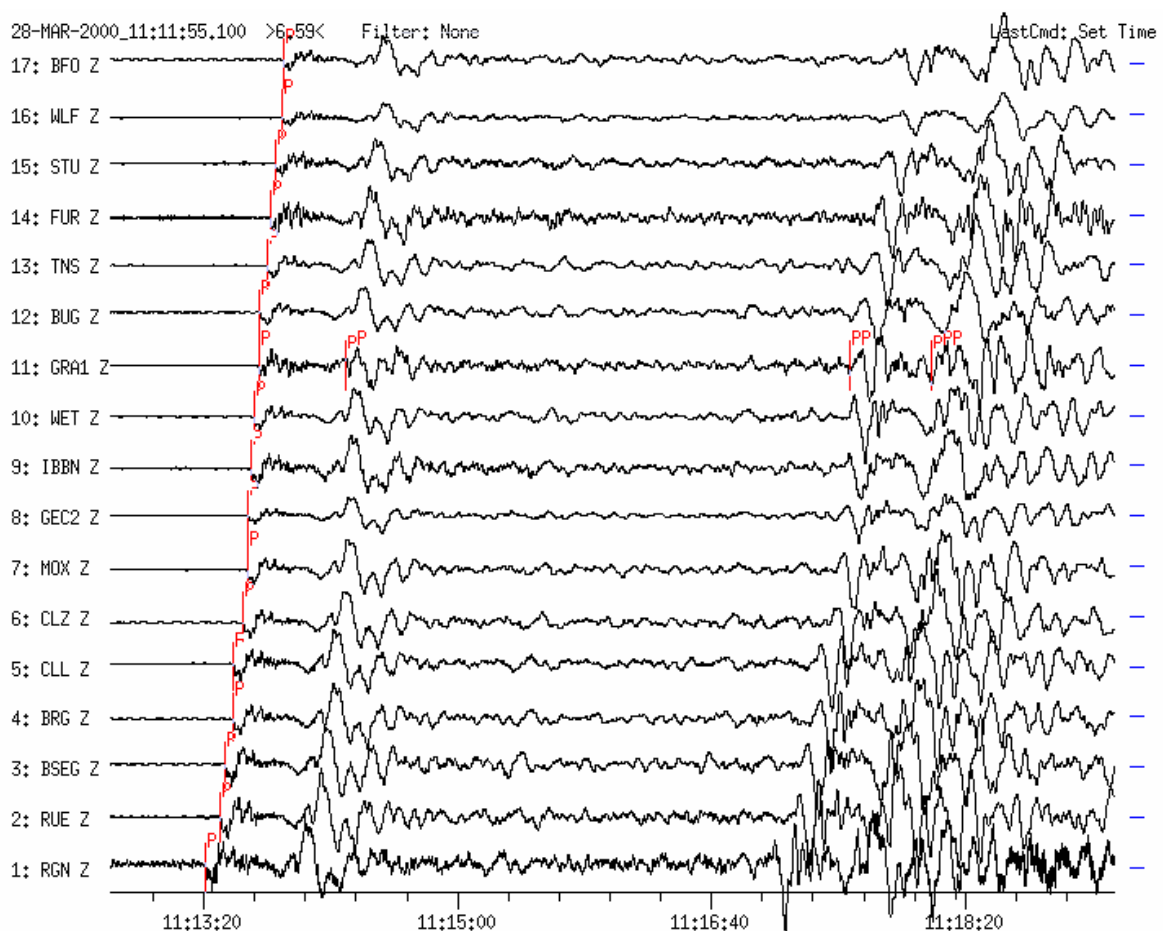


Fig. 11.18 Broadband vertical-component seismograms of a deep ($h = 119$ km) earthquake from Volcano Islands region recorded at 17 GRSN, GRF and GEOFON stations. (Source data by NEIC: 2000-03-28 OT 11:00:21.7 UT; 22.362°N , 143.680°E ; depth 119 km; mb 6.8; $D = 96.8^{\circ}$ and $BAZ = 43.5^{\circ}$ from GRA1). Traces are sorted according to distance. Amplitudes of P are smaller than pP. Phases with longer periods PP, pP and pPP are much more coherent than P.

Note, however, that often there is no clear evidence of near-source surface reflections in seismic records, or they show apparent pP and sP but with times that are inconsistent from station to station. Douglas et al. (1974 and 1984) have looked into these complexities, particularly in short-period records. Some of these difficulties are avoided in BB and LP recordings. Also, for shallow sources, surface-wave spectra may give the best indication of depth but this method is not easy to apply routinely. In summary, observational seismologists should be aware that depth phases are vital for improving source locations and making progress in understanding earthquakes in relation to the rheological properties and stress conditions in the lithosphere and upper mantle. Therefore, they should do their utmost to recognize depth phases in seismograms despite the fact that they are not always present and that it may be difficult to identify them reliably.

More examples of different kinds of depth phases are given in Figs. 11.34 and 11.35d as well as in Figure 6b of DS 11.2 and Figures 1b, 2b, 5b and 7a +b in DS 11.3.

SK1: 1993.232.05.r7

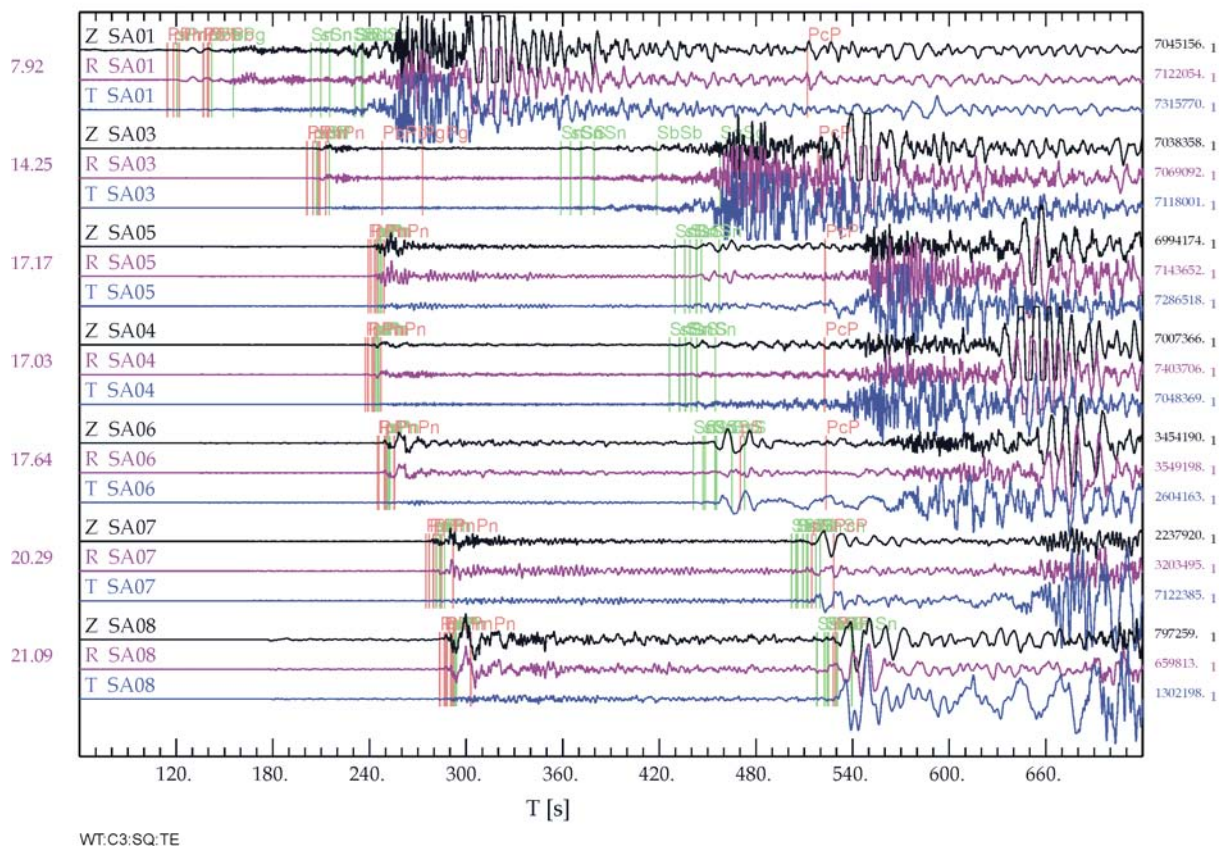


Fig. 11.19 3-component records in the distance range between 7.9° and 21.1° by a regional network of portable broadband instruments deployed in Queensland, Australia (seismometers CMG3ESP; unfiltered velocity response). The event occurred in Papua New Guinea at 15 km depth. As in Fig. 11.17 the predicted phase arrival times for the AK135 model are depicted. Primary, depth and other secondary arrivals (such as PnPn in the P-wave group and SbSb as well as SgSg in the S-wave group) superpose to complex wavelets. Also note that several of the theoretically expected phases have such weak energy that they can not be recognized on the records at the marked predicted arrival times above the noise level or the signal level of other phases (e.g., PcP at most stations) (courtesy of B. Kennett).

11.2.5.2 Discrimination between natural earthquakes and man-made seismic events

Quarry and mining blasts, besides dedicated explosion charges in controlled-sources seismology, may excite strong seismic waves. The largest of these events may have local magnitudes in the range 2 to 4 and may be recorded over distances of several hundred kilometers. Rock bursts or collapses of large open galleries in underground mines may also generate seismic waves (see Figure 3 in EX 11.1). The magnitude of these induced seismic events may range from around 2 to 5.5 and their waves may be recorded world-wide (as it was the case with the mining collapse shown in Fig. 11.8). In some countries with low to moderate natural seismicity but a lot of blasting and mining, anthropogenic (so-called “man-made” or “man-induced”) events may form a major fraction of all recorded seismic sources,

11.2 Criteria and parameters for routine seismogram analysis

3and may even outnumber recordings of earthquakes. Then a major seismological challenge is the reliable discrimination of different source types. Fig. 11. 39 shows a comparison of seismograms from: (a) a mining-induced earthquake; (b) a quarry blast; (c) a local earthquake; (d) a regional earthquake; and (e) a teleseismic earthquake. Seismograms (a) and (b) show that the high-frequency body-wave arrivals are followed, after S_g , by well developed lower-frequency and clearly dispersed Rayleigh surface waves (R_g ; strong vertical components). This is not so for the two earthquake records (c) and (d) because sources more than a few kilometers deep do not generate short-period fundamental Rayleigh waves of R_g type. For even deeper (sub-crustal) earthquakes (e.g., Fig. 2.41) only the two high-frequency P- and S-wave phases are recorded within a few hundred kilometers from the epicenter.

Based on these systematic differences in frequency content and polarization, some observatories that record many quarry blasts and mining events, such as GRFO, have developed automatic discrimination filters to separate them routinely from tectonic earthquakes. Chernobay and Gabsatarova (1999) give references to many other algorithms for (semi-) automatic source classification. These authors tested the efficiency of the spectrogram and the P_g/L_g spectral ratio method for routine discrimination between regional earthquakes with magnitudes smaller than 4.5 and chemical (quarry) explosions of comparable magnitudes based on digital records obtained by a seismic network in the Northern Caucasus area of Russia. They showed that no single method can yet assure reliable discrimination between seismic signals from earthquakes and explosions in this region. However, by applying a self-training algorithm, based on hierarchical multi-parameter cluster analysis, almost 98% of the investigated events could be correctly classified and separated into 19 groups of different sources. However, local geology and topography as well as earthquake source mechanisms and applied explosion technologies may vary significantly from region to region (see page 18 of this Chapter). Therefore, there exists no straightforward and globally applicable set of criteria for reliable discrimination between man-made and natural earthquakes.

In this context one should also discuss the discrimination between natural earthquakes (EQ) and underground nuclear explosions (UNE). The Comprehensive Nuclear-Test-Ban Treaty (CTBT) has been negotiated for decades as a matter of high political priority. A Preparatory Commission for the CTBT Organization (CTBTO) has been established with its headquarters in Vienna (<http://www.ctbto.org>) which is operating an International Monitoring System (IMS; see http://www.nemre.nn.doe.gov/nemre/introduction/ims_descript.html, Fig. 8.12 and Barrientos et al., 2001). In the framework of the CTBTO, initially a Prototype International Data Centre (PIDC; <http://www.pidc.org/>) was established in Arlington, USA, which is replaced since 2001 by the International Data Centre in Vienna. Agreement was reached only after many years of demonstrating the potential of seismic methods to discriminate underground explosions from earthquakes, down to rather small magnitudes $m_b \approx 3.5$ to 4. Thus, by complementing seismic event detection and monitoring with hydroacoustic, infrasound and radionuclide measurements it is now highly probable that test ban violations can be detected and verified.

The source process of UNEs is simpler and much shorter than for earthquake shear ruptures (see Figs. 3.3 – 3.5 and related discussions). Accordingly, P waves from explosions have higher predominant frequencies and are more like impulses than earthquakes and have compressional first motions in all directions. Also, UNEs generate lower amplitude S and surface waves than earthquakes of the same body-wave magnitude (see Fig. 11.20).

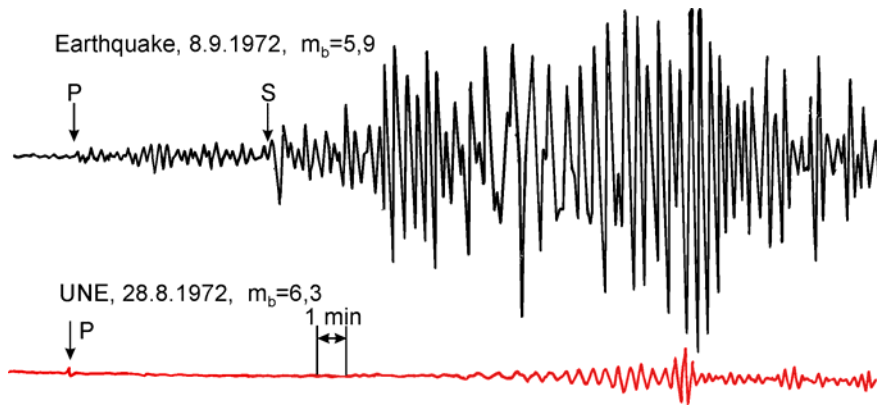


Fig. 11.20 Broadband displacement records of an earthquake and an underground nuclear explosion (UNE) of comparable magnitude and at nearly the same distance (about 40°).

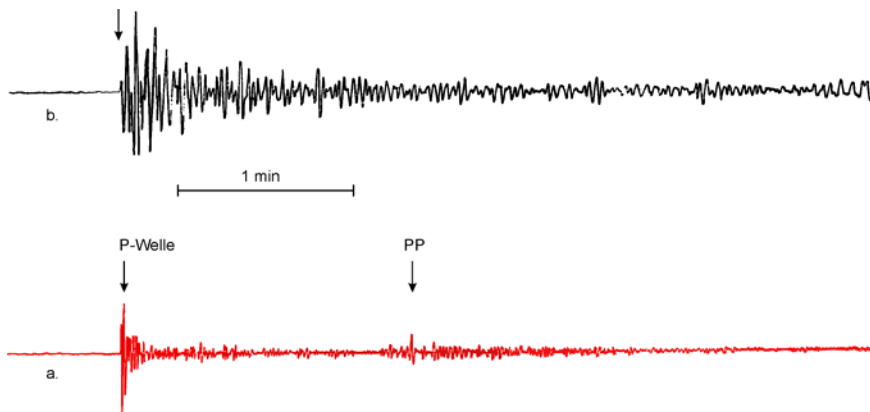


Fig. 11.21 Short-period records at station MOX a) of an underground nuclear explosion at the Semipalatinsk (SPT) test site in Kazakhstan ($D = 41^\circ$) and b) of an earthquake with comparable magnitude and at similar distance.

In short-period records of higher time resolution the difference in frequency content, complexity and duration of the P-wave group between underground nuclear explosions and earthquakes is often clear. Fig. 11.21 gives an example. As early as 1971 Weichert developed an advanced short-period spectral criterion for discriminating between earthquakes and explosions and Bormann (1972c) combined in a single complexity factor K differences in frequency content, signal complexity and duration to a powerful heuristic discriminant.

Another powerful discriminant is the ratio between short-period P-wave magnitude m_b and long-period surface-wave magnitude M_s . The former samples energy around 1 Hz while the latter samples long-period energy around 0.05 Hz. Accordingly, much smaller M_s/m_b ratios are observed for explosions than for earthquakes (see Fig. 11.20). Whereas for a global sample of EQs and UNEs the two population overlap in an M_s/m_b diagram, the separation is good when earthquakes and explosions in the same region are considered (Bormann, 1972c). Early studies have shown that with data of $m_b \geq 5$ from only one teleseismic station 100% of the observed UNEs with magnitudes from the SPT test site could be separated from 95% of the EQs in Middle Asia, whereas for the more distant test site in Nevada ($D = 81^\circ$) 95% of the UNEs could be discriminated from 90% of the EQs in the Western USA and Middle America (see Fig. 11.22).

11.2 Criteria and parameters for routine seismogram analysis

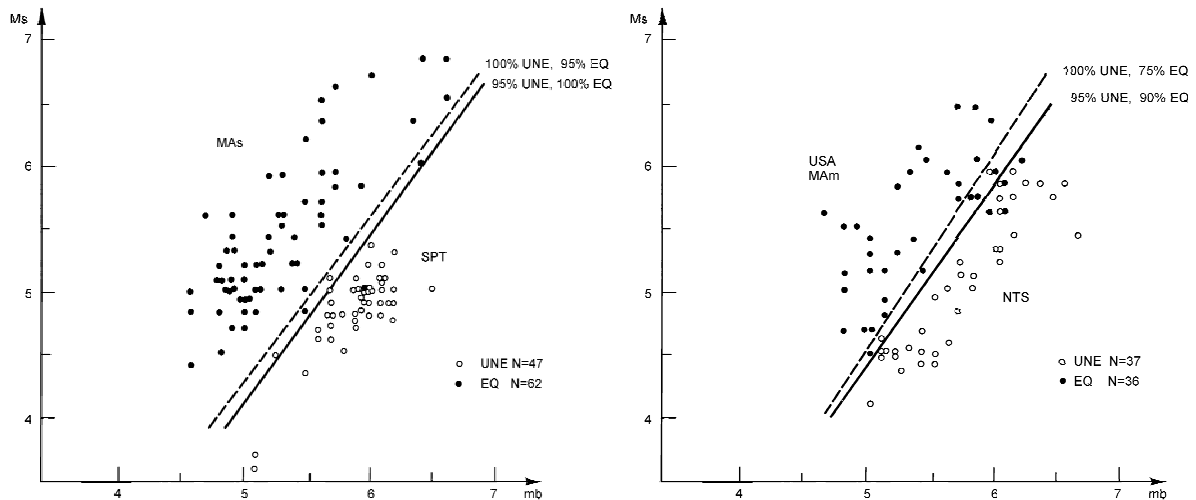


Fig. 11.22 Separation of EQs and UNEs by the M_s/m_b criterion according to data collected at station MOX, Germany. Left: for Middle Asia and the test site in Semipalatinsk (SPT), right: for USA/Middle America and the Nevada test site (NTS).

Other potential discrimination criteria, such as the different azimuthal distribution of P-wave first-motion polarities expected from UNEs (always +) and EQs (mixed + and -), have not proved to be reliable. One reason is, that due to the narrowband filtering, which is applied to reach the lowest possible detection threshold, the P waveform, and particularly the first half cycle, is often so much distorted, that the real first-motion polarity is no longer recognizable in the presence of noise (see Fig. 4.10). Detailed investigations also revealed that simplified initial model assumptions about the difference between explosion and earthquake sources do not hold true. Surprisingly, the explosion source is poorly understood and source dimensions around magnitude mb seem to be the same for earthquakes and explosions. Also, many explosions do not approximate to a point-like expansion source in a half-space: significant Love waves are generated (e.g., by Novaya Zemlya tests) and many P seismograms show arrivals that can not be explained (see, e.g., Douglas and Rivers, 1988). Further, it has become clear that much of the differences observed between records of UNEs and EQs are not due to source differences but rather to differences in the geology, topography and seismotectonics of the wider area around the test sites, and that this necessitates the calibration of individual regions (e.g., Douglas et al., 1974).

In summary, one can say that the key criteria to separate EQs and explosions usually work well for large events, however, difficulties come with trying to identify every EQ down to magnitudes around $m_b = 4$ with about 8000 earthquakes of this size per year. It is beyond the scope of this section to go into more detail on this issue. Rather, the Editor has invited experts from the CTBTO community to write for Volume 2 of the Manual a complementary information sheet on advanced event detection and discrimination routines. This still forthcoming information sheet will catalog the most important criteria, which have been developed so far for discrimination and show more examples about their application to and efficiency in different regions.

11.2.6 Quick event identification and location by means of single-station three-component recordings

11.2.6.1 What is the best way of analyzing three-component seismograms?

Increasingly seismograms are being analyzed at laboratories that receive the data in (near) real time from networks or arrays of seismometers (see Chapters 8 and 9). The seismograms can then be analyzed jointly. Nevertheless, there remain many single, autonomous stations operating around the world, in countries of the former Soviet Union and developing countries in particular. Some of these single stations still record only with analog techniques. Yet much can be done even under these “old-fashioned” conditions by the station personnel, provided that at least some form of 3-component recording, either BB or both SP and LP, is available. With such recordings it will be possible to assess quickly the source type, estimate its rough location and magnitude, and identify in some detail later seismic phases, without waiting for rapid epicenter determinations by international data centers before record analysis can begin. Rather, there would be advantages if, in future, readings of secondary phases, particularly depth phases, were reported as early as possible to regional and global data centers. Such readings are indispensable for more accurate hypocenter location (see Figure 7 in IS 11.1). Only recently both NEIC and the ISC began considering the introduction of more flexible and sophisticated algorithms that can best make use of secondary phase readings for more reliable (and rapid) hypocenter locations.

It has also been realized that accurate epicentral distances estimated from three-component broadband readings of secondary phases can significantly improve location estimates by array stations based purely on measurements of the P-wave vector slowness (originally by using solely vertical-component SP sensors). Now, since modern software for digital seismogram analysis has made it much simpler and faster than in the “analog past” to evaluate three-component broadband data, we focus on such data here. Other procedures of modern multi-station (but usually single-component) data analysis are dealt with later *en passant*. Array analysis is discussed in detail in Chapter 9.

How then to proceed best in analyzing analog presentations of seismograms? The most important rules, taking the discussion under 11.2.4 and 11.2.5 into account, are:

Take interest! Be curious! Ask questions!
to your seismic record

- 1.** Are you **NEAR** ($D < 20^\circ$) **or** **TELESEISMIC** ($D > 20^\circ$)?
- Criteria:**
- **Frequencies** on SP records **$f \geq 1$ Hz** **$f \leq 1$ Hz**
 - **Amplitudes** on LP records **not or weaker** **large, also for later phases**
 - **Record duration** **< 20 min** **> 20 min**
(for magnitudes < 5 ; may be longer for strong earthquakes; see Fig. 1.2)
- 2.** Is your **D < 100°** **or** **D > 100°** ?
- Criteria:**
- **Surface wave max.** after P arrival **$< 45 \pm 5$ min** **or** **$> 45 \pm 5$ min** (Table 5 in DS 3.1)
 - **Record duration** on LP records **< 1.5 hours** **or** **> 1.5 hours**
(may be larger for very strong earthquakes; see Fig. 1.2)

11.2 Criteria and parameters for routine seismogram analysis

3. Are you SHALLOW or DEEP (> 70 km)?

Criteria:

- **Surface waves** on LP records **strong** **weak or none**
- **Depth phases** usually **not clear** **well separated and often clear**
- **Waveforms** usually **more complex** **more impulsive**

4. Is the first strong horizontal arrival S or SKS ?

Criteria:

- **Time difference to P** **< 10 ± 0.5 min** **≈ 10 ± 0.5 min**
- **Polarization** large horiz. A **in R and/or T** **in R only**

Warning ! If the first strong horizontal arrival follows P after $\approx 10 \pm 0.5$ min it may be SKS. Check polarization! (see Fig. 11.14). Misinterpreting SKS as S may yield D estimates up to 20° too short. Look also for later multiple S arrivals (SP, SS, SSS) with better D control.

5. What are the first longitudinal and transverse onsets for $D > 100^\circ$?

Beyond 100° epicentral distance first arrivals may still be P, which may be seen particularly in LP records of large earthquakes up to about almost 150° (see Fig. 11.63). This P, however, has been diffracted around the core-mantle boundary and is termed Pdif (old Pdiff; see Figs. 11.59 and 11.63). First onsets in SP records are usually PKiKP and PKPdf (see Fig. 11.59), or, somewhat later PP, which is often the first strong longitudinal Z-component arrival in both SP, LP and BB records (see Figs. 11.60 and 11.63). The first strong arrivals on horizontal (R) components are PKS or SKS. Misinterpretation of the first P-wave and S-wave arrivals as direct P and S, respectively, may result in epicentral distance estimates up to more than 70° too short! This can be avoided by taking the criteria under 2. into account. Also note, that the travel-time difference between PKPdf and PKS or SKS is (almost) independent of distance. The first arriving P and S waves do not then allow distance to be estimated. Therefore look for later arriving multiple reflected S waves such as SS, SSS, etc., which are usually well developed in this distance range on horizontal LP records and so allow D to be estimated with an error of usually $< 2^\circ$.

Additionally, one might look for criteria discussed in sub-section 11.2.5.2 for discriminating between explosions and earthquakes.

If only very broadband digital records are available, which are usually proportional to ground velocity, it is best to filter them to produce standard analog WWSSN-SP and -LP seismograms before starting a reconnaissance analysis. One may also simulate Kirnos SKD BB-displacement and Wood-Anderson (WA) SP-displacement seismograms (for response characteristics see Fig. 3.11), because all these responses are required for proper magnitude estimation according to established standards. Only after these seismograms have been produced should one begin with the detailed analysis. The analysis might include phase identification, picking of onset times, amplitudes and periods, and the application, if required, of special filters, such as the ones for inverse Hilbert transformation of phases, which have been distorted by traveling through internal caustics (see 2.5.4.3), or for separating phases on their polarization to improve phase discrimination.

Of course, in countries with many seismic sources recorded every day it will not be possible, particularly for untrained interpreters, to apply all these criteria to every seismic signal. On the other hand, this kind of checking takes only a few seconds, minutes at most, for an experienced interpreter who has already trained himself/herself in recognizing immediately

the different record patterns on seismograms from systems with standard responses. In addition, many data centers specialize in analyzing only seismograms from local, regional or teleseismic sources. Accordingly, either the number of questions to be asked to the record or the number of signals to be analyzed will be reduced significantly. Also, the task might be significantly eased at observatories or analysis centers which have advanced routines available for digital seismogram analysis such as SEISAN or Seismic Handler. Provided that first hypocenter estimates are already available from international data centers or from analysis of array or network recordings, these computer programs allow the theoretical onset times of expected seismic phases to be displayed on the seismogram. However, these theoretical times should not be followed blindly but considered only as assistance. The additional information on amplitudes, frequency content, and polarization has to be taken into account before giving a name to a recognizable onset! (see 11.2.4 and 11.2.5).

On the other hand, it is meaningless to list more detailed and strict criteria and rules about the appearance and identification of seismic phases in different distance ranges, because they vary from event to event and from source region to source region. They also depend on the specific conditions of the given propagation paths and the local environment at the receiving station. Therefore, every station operator or network analyst has to develop, through experience and systematic data analysis, his/her own criteria for improved seismogram analysis, source identification, and location. In any event, however, the general approach to record analysis given above should be followed to avoid the analysis becoming thoughtless, boring and routine, which will inevitably result in the reporting of inhomogeneous and incomplete low-quality data of little value for research or to the general user.

11.2.6.2 Hypocenter location

If well calibrated 3-component broadband and/or long-period recordings are available then it is possible to locate sufficiently strong local events ($M_l > 3$) and teleseismic sources ($m_b > 5$) with an accuracy comparable to or even better than those for un-calibrated arrays or station networks. This was demonstrated more than 30 years ago (Bormann, 1971a and b) by using standard film records of type A, B and C (responses see Fig. 3.11). Amplitudes and onset times were at that time still measured by using an ordinary ruler or a sub-millimeter scaled magnification lens. Nevertheless, the mean square error of epicenters thus located within the distance range $20^\circ < D < 145^\circ$ was less than 300 km when compared with the epicenter coordinates published by the seismological World Data Centers A and B. Fig. 11.23 shows the statistical distribution of errors in azimuth and distance based on several hundred 3-component event locations.

Note that the errors in distance estimated from readings of P and later secondary phases within the distance range $80^\circ < D < 120^\circ$ are mostly less than about $\pm 1^\circ$ and rarely greater than $\pm 2^\circ$. The mean errors seldom differ significantly from zero, and where they do it is usually for specific regions (distance/azimuth ranges). Taking such systematic errors into account, the location accuracy can be improved. Many seismic arrays and networks now use routinely multi-phase epicentral distance determinations for improving their slowness-based source locations. Some advanced software for seismogram analysis like SHM (see 11.4.1) includes this complementary interactive analysis feature.

Backazimuth derived from SP 3-component recordings may have large systematic errors up to several tens of degrees. This is not so if LP or BB records are used. Whereas individual

11.2 Criteria and parameters for routine seismogram analysis

determinations of backazimuth from SP records might deviate up to about 40° from the true source azimuth, the errors are rarely (except at low SNR) larger than 10° when BAZ is determined from BB records (provided that the magnification of the horizontal components is known with high accuracy or identical!). The reason for this is obvious from Fig. 2.6 and the related discussion. The particle motion in SP records is complicated and random due to wave scattering and diffraction by small-scale heterogeneities in the crust and by rough surface topography at or near the station site (see Buchbinder and Haddon, 1990). In contrast, LP or BB records, which are dominated by longer wavelength signals, usually show simpler P waveforms with clearer first-motion polarity than do SP records. In addition, later phase arrivals, which are crucial for accurate distance determination from single station records, stand out more clearly or are recognizable only in BB or LP records (see Fig. 11.24).

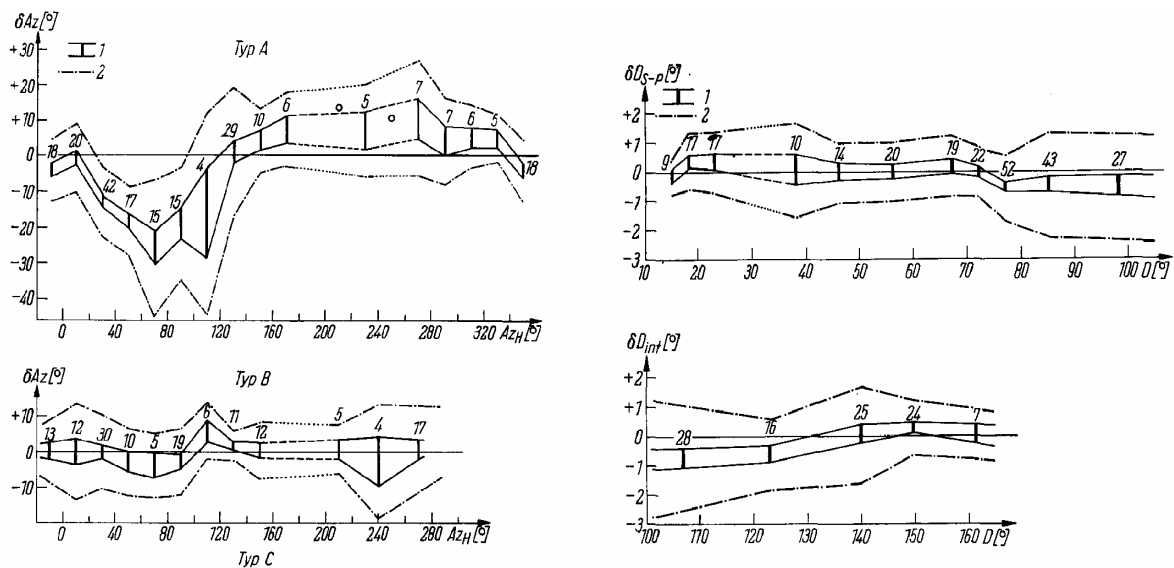


Fig. 11.23 Left: Errors in backazimuth Az (or BAZ) at station MOX estimated using 3-component records of type A (SP) and of type C (Kirnos SKD BB-displacement). Right: Errors in estimating the epicentral distance D at station MOX from records of type C using travel-time difference $S-P$ in the distance range $10^\circ < D < 100^\circ$ or travel-time differences between other seismic phases for $D > 100^\circ$. The solid lines give the 90% confidence interval for the mean error with number of the observations; the dash-dot lines are the 90% confidence interval for a single observation.

Simple 3-component event locations based solely on readings of onset times of identified phases, polarity of P-wave first motions and horizontal component amplitude ratio should proceed as follows:

- general event classification (near/far; shallow/deep; $D < 100^\circ / > 100^\circ$ etc.);
- picking and identifying the most pronounced phases by comparing the 3-component record traces and related polarization characteristics (Fig. 11.24);
- determination of D by a) matching the identified body-wave phases with either overlays of differential travel-time curves of equal time scale (see Figures 2 to 4 in EX 11.2), b) by measuring their onset-time differences and comparing them with respective distance-dependent differential travel-time tables or c) by computer calculation of D based on digital time picks for identified phases and local, regional and/or global travel-time models integrated into the analysis program;

- determination of source depth h on the basis of identified depth phases (see 11.2.5.1) and following correction of D , again by using either travel-time curves, differential t - D tables or computer assisted time-picks and comparison with travel-time models;
- determination of the backazimuth (against North) from the station to the source from the first-motion directions in the original Z , N and E component records and from the amplitude ratio A_E/A_N . For details see Figure 1 and explanations given in EX 11.2;
- determination of the epicenter location and coordinates by using appropriate map projections with isolines of equal azimuth and distance from the station (see Figure 5 in EX 11.2) or by means of suitable computer map projections.

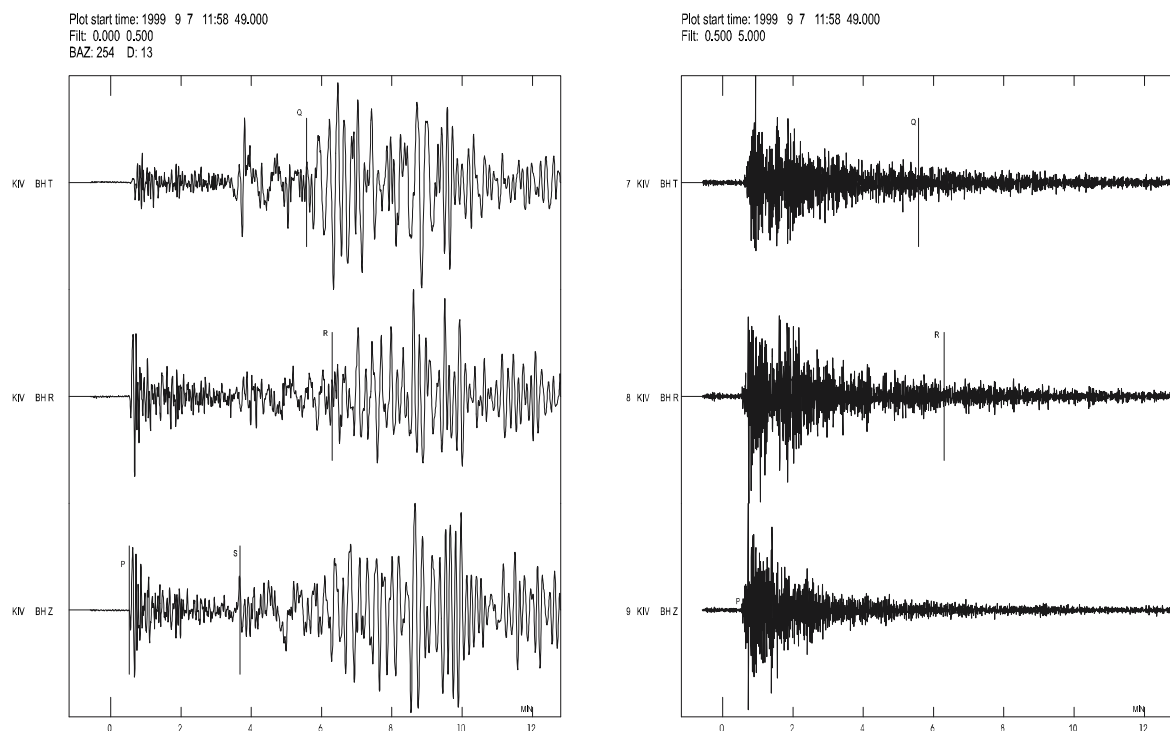


Fig. 11.24 Left: Low-pass filtered digital broadband record of the Global Seismograph Network (GSN) station KIV from the shallow ($h = 10$ km) Greece earthquake of 07 Sept. 1999 ($m_b = 5.8$) at a distance of $D = 13^\circ$. Note the clearly recognizable polarity of the first P-wave half-cycle! The record components have been rotated into the directions Z , R and T after determination of the backazimuth from first-motion polarities in Z , N and E ($BAZ = 134^\circ$). Accordingly, P and Rayleigh waves are strongest in Z and R while S and Love wave are strongest in T . **Right:** The recordings after SP bandpass filtering (0.5 - 5.0 Hz). The SNR for the P -wave first-motion amplitude is much smaller and their polarity less clear. Also later arrivals required for distance determination are no longer recognizable (signal processing done with SEISAN; courtesy of L. Ottemöller).

Rough estimates of D may be made - in the absence of travel-time tables or curves or related computer programs - using the following “rules-of-thumb”:

$$\text{hypocenter distance } d \text{ [in km]} \approx \Delta t(\text{Sg-Pg}) \text{ [in s]} \times 8 \text{ (near range only)} \quad (11.1)$$

11.2 Criteria and parameters for routine seismogram analysis

$$\text{epicentral distance } D \text{ [in km]} \approx \Delta t(\text{Sn-Pn}) \text{ [in s]} \times 10 \text{ (in Pn-Sn range } < 15^\circ) \quad (11.2)$$

$$\text{epicentral distance } D \text{ [in } ^\circ] \approx \{\Delta t(\text{S-P}) \text{ [in min]} - 2\} \times 10 \text{ (for } 20^\circ < D < 100^\circ) \quad (11.3)$$

In the absence of travel-time curves or tables for depth phases one may use another “rule-of-thumb” for a rough estimate of source depth from the travel-time difference $\Delta t(\text{pP-P})$:

$$\begin{aligned} \text{source depth } h \text{ [in km]} \approx & \Delta t(\text{pP-P})/2 \text{ [in s]} \times 7 \text{ (for } h < 100 \text{ km)} \\ & \text{or } \times 8 \text{ (for } 100 \text{ km} < h < 300 \text{ km)} \\ & \text{or } \times 9 \text{ (for } h > 300 \text{ km)} \end{aligned} \quad (11.4)$$

Bormann (1971a) showed that in the absence of a sufficiently strong P-wave arrival, the backazimuth can be determined from horizontal components of any later seismic phase which is polarized in the vertical propagation plane, such as PP, PS, PKP or SKS. These phases are often much stronger in BB or LP records than P. However, because of phase shifts on internal caustics (PP, PS, SP, PKPab) for most of these phases the 180° ambiguity in azimuth determined from the ratio A_E/A_N can not be resolved as it can for P by taking into account the first-motion polarity in the Z component. However, by considering the inhomogeneous global distribution of earthquake belts, this problem can usually be solved.

Modern computer programs for seismogram analysis include subroutines that allow quick determination of both azimuth and incidence angle from particle motion analysis over the whole waveform of P or other appropriate phases. This is done by determining the direction of the principal components of the particle motion, using, as a measure of reliability of the calculated azimuth and incidence angle, the degree of particle motion linearity/ellipticity. Such algorithms are available in the SEIS89 software (Baumbach, 1999). Christoffersson et al. (1988) describe a maximum-likelihood estimator for analyzing the covariance matrix for a single three-component seismogram (see also Roberts and Christoffersson, 1990). The procedure allows joint estimation of the azimuth of approach, and for P and SV waves the apparent angle of incidence and, hence, information on apparent surface velocity and thus on epicentral distance. This was been implemented in the SEISAN software (Havskov and Ottemöller, 1999). Fig. 11.25 shows an example of the application of the software to a portion of the BB recording at Kongsberg (KONO) in Norway for the 12 November 1999, Turkey earthquake ($M_w = 7.1$). The program finds a high correlation (0.9) between the particle motions in the three components, gives the estimate of the backazimuth as 134° , an apparent velocity of 9.6 km/s and the corresponding location of this earthquake at 40.54°N and 30.86°E . This was only about 50 km off the true epicenter.

Applying similar algorithms to digital 3-component data from short-period P waves recorded at regional distances, Walck and Chael (1991) show that more than 75% of the records yielded backazimuth within 20° of the correct values. They found, however, a strong dependence on the geological structure. Whereas stations located on Precambrian terranes produced accurate backazimuth for $\text{SNR} > 5$ dB, stations on sedimentary rocks with complicated structure had much larger errors. Excluding these stations, the RMS backazimuth error is only about 6° for recordings with $\text{SNR} > 10$ dB.

Ruud et al. (1988) found that three-component locations for epicenters at distances up to about 1000 km seldom deviated more than 50 km from network solutions, such deviations being mainly due to errors in azimuth estimates. For short-period teleseismic P waves, however, location errors occasionally exceeded 800 km, mainly because of poor distance

estimates derived from incidence angles (slowness) alone. For stronger sources, where BB records can be used, distance can be determined using travel-time differences. The location errors are then reduced to about 1° . Thus, three-component digital broadband data allow reliable epicenters to be determined quickly with just single station records, and even data from stations that still use analog recording may provide rapid and reliable epicenter estimates. For combined single station and network location see Cassidy et al. (1990).

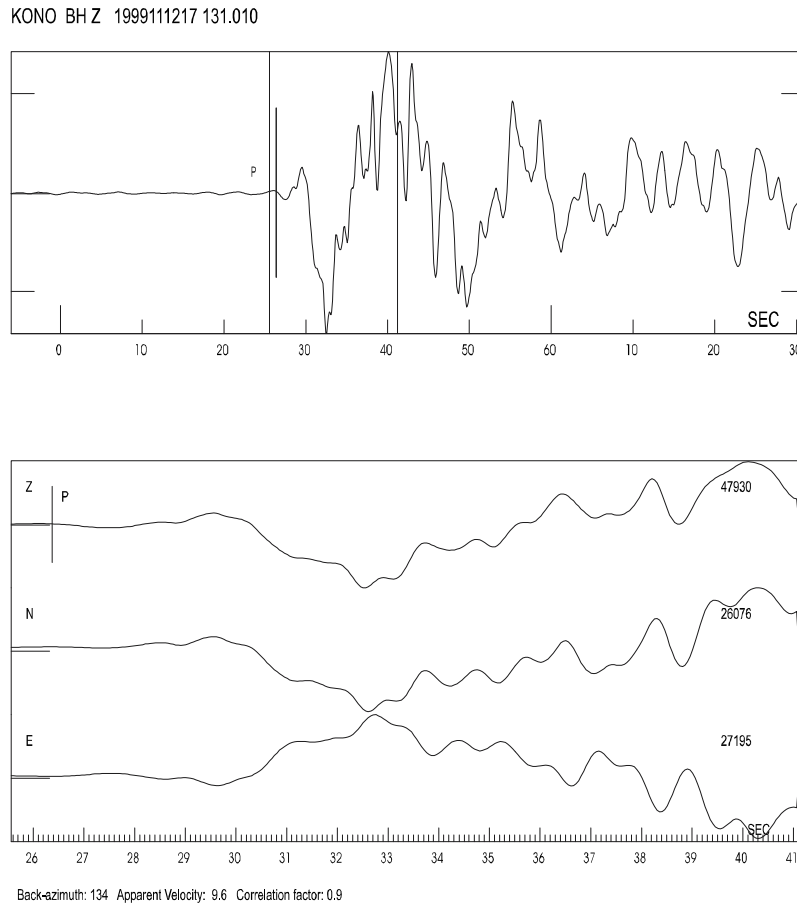


Fig. 11.25 Example of azimuth determination and epicenter location of the 12 Nov. 1999 Turkey earthquake by correlation analysis of three-component digital BB records at station KONO, Norway. Backazimuth, apparent velocity, and correlation factor are determined from the P-wave record section marked in the upper figure. For more details see text (signal processing done with SEISAN; courtesy of L. Ottemöller).

11.2.7 Magnitude determination

When epicentral distance and depth of a seismic source are (at least roughly) known the magnitude of the event can be estimated. The general procedures to be followed in magnitude determination (and the measurement of amplitudes, periods or record duration) as well as the specifics of different magnitude scales to be used for local, regional or teleseismic recordings are dealt with in detail in section 3.2. DS 3.1 gives the magnitude calibration functions, both for the teleseismic standard magnitudes (m_b and M_s) and several other magnitude scales for local, regional and teleseismic magnitudes. The various procedures can be learnt from an exercise given in EX 3.1, which also gives solutions for the different tasks.

11.2.8 Hypocenter location by means of network and array recordings

Hypocenter location is simplified if records from at least 3 stations are available. The more uniformly the stations are distributed around the source in azimuth and distance (with distances ranging from close-in to long range) and the more seismic phases are used for location, the lower the uncertainty in the estimates. The procedures in both manual and computer assisted multi-station hypocenter location are outlined in IS 11.1, which gives the underlying algorithms and error calculations, as well as standard and advanced methods for both absolute and relative location. Also discussed is the influence of deviations from the assumed Earth models on the locations. The improvements in hypocenter relocation achievable with better Earth models are also demonstrated.

EX 11.1 aims at epicenter location by a simple circle and chord method using seismograms from local stations both inside and outside the network. The epicentral distances have to be determined first for each station by identifying on its records the phases Pg, Sg, Pn and/or Sn and matching them to a local travel-time curve.

With digital multi-station data and advanced seismogram analysis software, source location becomes almost a trivial task. One just picks a sufficient number of first arrival times (see Fig. 11.5), activates the relevant location program for local, regional and/or teleseismic sources and gets the result, including a map showing the epicenter if required, in an instant. The accuracy of location, particularly source depth, can be significantly improved by picking not only P-wave first arrivals but later arrivals too, which give a much better distance and depth control than slowness data alone. Examples for both local and teleseismic event locations based on seismic network and array data are given in the following sections. Location using array data is described in Chapter 9, together with the underlying theory.

11.3 Routine signal processing of digital seismograms

Standard analysis includes all data pre-processing and processing operations for the interpretation and inversion of broadband seismograms. Important time-domain processes are signal detection, signal filtering, restitution and simulation, phase picking, polarization analysis as well as beamforming and vespagram analysis for arrays. In the frequency domain the main procedures are frequency-wavenumber (f - k) and spectral analysis. Array-techniques as f - k and vespagram analysis, slowness and azimuth determination for plane waves, and beamforming are discussed in detail in Chapter 9 but a few examples are also shown below. Spectral analysis can be used for the estimation of the frequency content of a seismic wave, and of seismic noise (see 4.1 and 7.2, respectively).

11.3.1 Signal detection

The first task of routine data analysis is the detection of a seismic signal. A signal is distinguishable from the seismic background noise either on the basis of its larger amplitudes or its differences in shape and frequency. Various methods are used for signal detection. Threshold detectors and frequency-wavenumber analysis are applied to the continuous stream of data. In practice, the threshold is not constant but varies with the season and the time of the day. For this reason, the threshold detectors determine the average signal power in two

moving time windows: one long term (LTA) and one short term (STA). The ratio of the STA to LTA corresponds to the signal-to-noise-ratio (SNR). For details on the STA/LTA trigger and its optimal parameter setting see IS 8.1.

In practice, BB records are filtered before detectors are used. Useful filters are Butterworth high-pass filters with corner frequencies $f_c > 0.5$ Hz or standard band-pass types with center frequency $f = 1$ Hz for teleseismic P waves and high-pass filter with $f_c > 1$ Hz for local sources. Fig. 11.26 demonstrates detection and onset-time measurement for a weak, short-period P wave. In the lowermost 30 s segment of a BB-velocity seismogram the oceanic microseisms dominate in the period band 4-7 s. The two other traces are short-period seismograms after narrow band-pass (BP) filtering with: (1) a filter to simulate a WWSSN-SP seismogram; and (2) a two step Butterworth BP filter of 2nd-order with cut-off frequencies of 0.7 and 2 Hz, respectively. The latter filter produces, for the noise conditions at the GRF-array, the best SNR for teleseismic signals. Seismic networks designed to detect mainly local seismic events may require other filter parameters that take account of local noise conditions, for optimal detection (see IS 8.1).

Generally, a seismic signal is declared when the SNR exceeds a pre-set threshold. Various procedures, some analytical and some based on personal experience, are used to differentiate between natural earthquakes, mining-induced earthquakes and different kinds of explosions. Usually, the detected signals are analyzed for routine parameter extraction and data exchange.

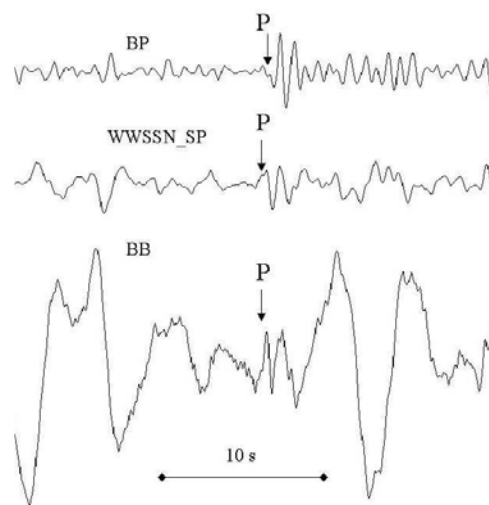


Fig 11.26 Bandwidth and SNR: A small short-period P-wave arrival which is within the noise level on a BB-velocity record (lower trace) may be detected by using a WWSSN-SP simulation filter (middle trace) or a Butterworth band-pass filter (BP; uppermost trace). The SNR is 0.2 on the original BB record, about 1 on the WWSSN-SP filter and about 2 on the BP-filtered trace. The seismogram is of an earthquake in the Kurile Islands on 25 March 2002, 6:18:13 UT, recorded at station GRA1, Germany.

11.3.2 Signal filtering, restitution and simulation

Classical broadband seismographs, such as the Russian Kirnos SKD, record ground displacement with constant magnification over a bandwidth of 2.5 decades or about 8 octaves. The IDA-system (International Deployment of Accelerometers) deployed in the 1970s, used originally LaCoste-Romberg gravimeters for recording long-period waves from strong earthquakes proportional to ground acceleration over the band from DC to about 0.1 Hz

11.3 Routine signal processing of digital seismograms

(nowadays replaced by STS1). Modern strong-motion sensors such as the Kinemetrics Inc. Episensor ES-T have a flat response to ground acceleration in an even broader frequency band from DC to 200 Hz. In contrast, feedback-controlled BB sensors for recording weak-motion usually have a response proportional to the ground velocity (see Fig. 11.27 right). Such BB recordings, however, are often not suitable for direct visual record analysis and parameter extraction in the time domain. Low-frequency signals and surface waves of weak earthquakes are not or only poorly seen. Therefore, BB data must be transformed by applying digital filters in a way that yields optimal seismograms for specific investigations and analysis.

For some research tasks and ordinary routine analysis of BB seismograms the application of high-pass, low-pass and band-pass filters is usually sufficient. However, simultaneous multi-channel data processing or the determination of source parameters according to internationally agreed standards (such as body- and surface-wave magnitudes, which are defined on the basis of former analog band-limited recordings) often require simulation of a specific response, including those of classical analog seismograph systems (Seidl, 1980). Another special problem of simulation is “restitution”. Restitution is the realization of a seismograph system whose transfer function is directly proportional to ground displacement, velocity or acceleration in the broadest possible frequency range. The restitution of the true ground displacement down to (near) zero frequencies is a precondition for seismic moment-tensor determinations both in the spectral and the time domain (e.g., signal moment; see Fig. 11.6). It is achieved by extending the lowermost corner frequency of the seismometer computationally far beyond that of the physical sensor system. Both the simulation of arbitrary band-limited seismograph systems as well as the extreme broadband “restitution” of the true ground motion is therefore a necessary step in pre-processing of digital BB data.

Simulation is the mapping of a given seismogram into the seismogram of another type of seismograph, e.g., those of classical analog recordings such as WWSSN-SP, WWSSN-LP, Kirnos SKD, SRO-LP, and Wood-Anderson (WA). Up to now, amplitudes and periods for the determination of body- and surface-wave magnitudes m_b and M_s are measured on simulated WWSSN-SP and WWSSN-LP or SRO-LP seismograms, respectively, and the maximum amplitude for the original local Richter magnitude is measured on Wood-Anderson simulated seismograms. Fig. 11.27 (left) depicts the displacement response of these seismographs.

The possibility of carrying out these simulations with high accuracy and stability defines the characteristics that have to be met by modern digital broadband seismograph:

- large bandwidth;
- large dynamic range;
- high resolution;
- low instrumental seismometer self-noise (see 5.6.2);
- low noise induced by variations in air pressure and temperature (see 5.3.4, 5.3.5, and 7.4.4);
- analytically exactly known transfer function (see 5.2).

Fig. 11.27 (right) depicts the displacement responses of a few common BB-velocity sensors such as:

- the original Wielandt-Streckeisen STS1 with a bandwidth of 2 decades between the 3-db roll-off points at frequencies of 0.05 Hz and 5 Hz (anti-aliasing filter). These seismographs are deployed in the world’s first broadband array (GRF) around Gräfenberg/Erlangen in Germany (see Fig. 11.3a);

- the advanced STS1 that is generally used at the global IRIS network of very broadband (VBB) stations (velocity bandwidth of about 3.3 decades between 5 Hz and 360 s; see also DS 5.1);
- the STS2 seismographs (see DS 5.1) that are usually operated in the frequency range between 0.00827 Hz and 40 Hz (velocity bandwidth of 3.7 decades or about 12 octaves, respectively). They are used at the stations of the GRSN (see Fig. 11.3a) but also deployed world-wide at stations of the GEOFON network and at many others.

All these seismographs can be considered to be linear systems within the range of their usual operation. The transfer function $H(s)$ of a linear system can be calculated from its poles and zeros by using the following general equation:

$$H(s) = N * \prod (s - z_i) / \prod (s - p_k) \quad (11.5)$$

where N is the gain factor, $s = j\omega$ with $\omega = 2\pi f$ and j the complex number $\sqrt{-1}$, z_i are the zeros numbering from $i = 1$ to m and p_k the poles with $k = 1$ to n . Zeros are those values for which the numerator in Eq. (11.5) becomes zero while the poles are the values for which the denominator becomes zero.

Tab. 11.3 summarizes the poles and zeros of the classical standard responses WWSSN-SP, WWSSN-LP, WA (Wood-Anderson), Kirnos SKD and SRO-LP which control the shape of the response curves. Tab. 11.4 gives the same for the three broadband responses shown in Fig. 11.27 on the right. Not given are the gain factors because they depend on the specific data acquisition system and its sensitivity.

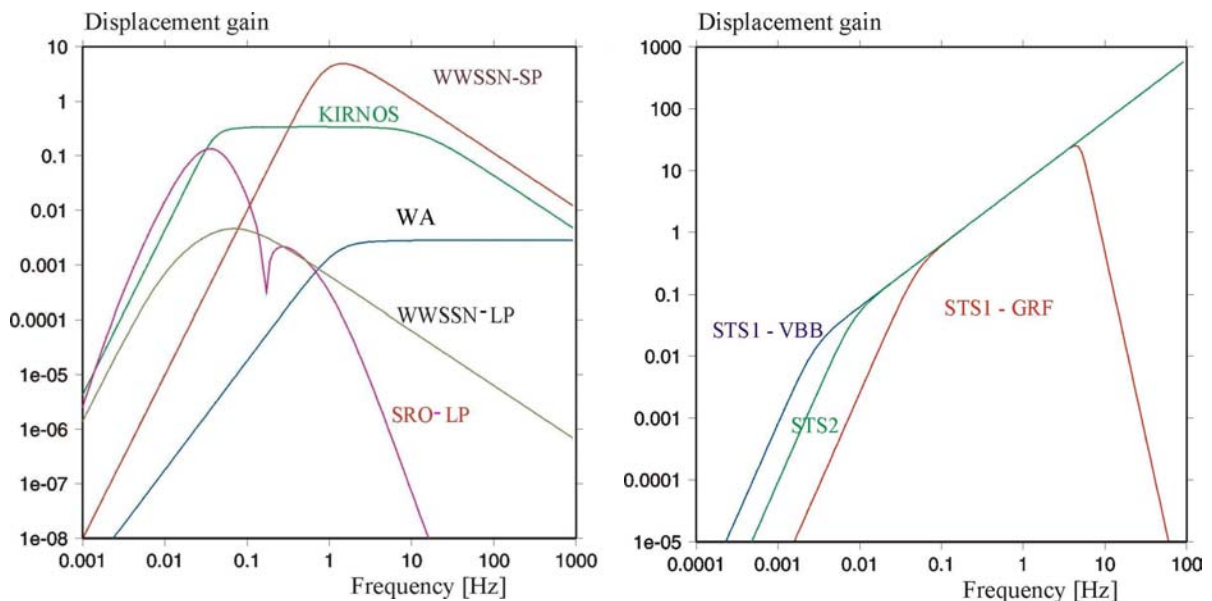


Fig. 11.27 Left: Displacement amplitude response characteristics of classical seismographs; **right:** The same for broadband seismographs STS1(GRF) (old version as used at the Gräfenberg array), STS1 (VBB) (advanced version as used in the IRIS global network) and STS2. For STS1 (VBB) and STS2 no anti-aliasing filter is shown. The classical responses shown on the left can be simulated with digital data from these broadband systems (see text).

11.3 Routine signal processing of digital seismograms

Tab. 11.3 Zeros and poles corresponding to the displacement transfer functions depicted in Fig. 11.27 left for the classical analog standard seismographs WWSSN-SP, WWSSN-LP, WA, Kirnos SKD and SRO-LP.

Seismograph	Zeros	Poles
WWSSN-SP	(0.0, 0.0) (0.0, 0.0) (0.0, 0.0)	(-3.3678, -3.7315) (=p ₁) (-3.3678, 3.7315) (=p ₂) (-7.0372, -4.5456) (=p ₃) (-7.0372, 4.5456) (=p ₄)
WWSSN-LP	(0.0, 0.0) (0.0, 0.0) (0.0, 0.0)	(-0.4189, 0.0) (-0.4189, 0.0) (-6.2832E-02, 0.0) (-6.2832E-02, 0.0)
WA	(0.0, 0.0) (0.0, 0.0)	(-6.2832, -4.7124) (-6.2832, 4.7124)
Kirnos SKD	(0.0, 0.0) (0.0, 0.0) (0.0, 0.0)	(-0.1257, -0.2177) (-0.1257, 0.2177) (-80.1093, 0.0) (-0.31540, 0.0)
SRO-LP	(0.0, 0.0) (0.0, 0.0) (0.0, 0.0) (-5.0100E+01, 0.0) (-0.0, 1.0500) (-0.0, -1.0500) (0.0, 0.0) (0.0, 0.0)	(-1.3000E-01, 0.0) (-6.0200, 0.0) (-8.6588, 0.0) (-3.5200E+01, 0.0) (-2.8200E-01, 0.0) (-3.9300, 0.0) (-2.0101E-01, 2.3999E-01) (-2.0101E-01, -2.3999E-01) (-1.3400E-01, 1.0022E-01) (-1.3400E-01, -1.0022E-01) (-2.5100E-02, 0.0) (-9.4200E-03, 0.0)

Tab. 11.4 Zeros and poles corresponding to the displacement transfer functions of the velocity-proportional broadband seismographs STS1(GRF), STS1-VBB(IRIS) and STS2 as depicted in Fig. 11.27 right. From their output data seismograms according to the classical analog standard seismographs WWSSN-SP, WWSSN-LP, WA, Kirnos SKD and SRO-LP are routinely simulated at the SZGRF in Erlangen, Germany.

Seismograph	Zeros	Poles
STS2	(0.0, 0.0) (0.0, 0.0) (0.0, 0.0)	(-3.674E-2, -3.675E-3) (-3.674E-2, 3.675E-3)
STS1(GRF)	(0.0, 0.0) (0.0, 0.0) (0.0, 0.0)	(-0.2221, -0.2222) (-0.2221, 0.2222) (-31.416, 0.0) (-19.572, 4.574) (-19.572, -24.574) (-7.006, 30.625) (-7.006, -30.625) (-28.306, 13.629) (-28.306, -13.629)
STS1(VBB))	(0.0, 0.0) (0.0, 0.0) (0.0, 0.0)	(-1.2341E-02, 1.2341E-02) (-1.2341E-02, -1.2341E-02)

Using the data given in these tables, the exact responses of the respective seismographs can be easily found. As an example, we calculate the response curve of the WWSSN-SP. According to Tab. 11.3 it has three zeros and four poles. Thus we can write Eq. (11.5) as

$$H(s) = N * s^3 / (s-p_1)(s-p_2)(s-p_3)(s-p_4) \quad (11.6)$$

with

$$\begin{aligned} p_1 &= -3.3678 - 3.7315j \\ p_2 &= -3.3678 + 3.7315j \\ p_3 &= -7.0372 - 4.5456j \\ p_4 &= -7.0372 + 4.5456j. \end{aligned}$$

Taking into account the discussions in section 5.2.7, the squared lower angular corner frequency of the response (that is in the given case the eigenfrequency of the WWSSN-SP seismometer) is $\omega_l^2 = p_1 \cdot p_2$ whereas the squared upper angular eigenfrequency (which used to be in the classical SP records that of the galvanometer) is $\omega_u^2 = p_3 \cdot p_4$. Since the product of conjugate complex numbers $(a + bj)(a - bj) = a^2 + b^2$ it follows for the poles:

$$\begin{aligned} \omega_l^2 &= 25.27 & \text{with } f_l &= 0.80 \text{ Hz} & \text{and} \\ \omega_u^2 &= 70.18 & \text{with } f_u &= 1.33 \text{ Hz}. \end{aligned}$$

When comparing these values for the corner frequencies of the displacement response of WWSSN-SP in Fig. 11.27 (left) one recognizes that the maximum displacement magnification (slope approximately zero) lies indeed between these two values. Further, as outlined in 5.2.7, a conjugate pair of poles such as p_1 and p_2 or p_3 and p_4 correspond to a second order corner of the amplitude response, i.e., to a change in the slope of the asymptote to the response curve by 2 orders. Further, the number of zeros controls the slope of the response curve at the low-frequency end, which is three in the case of the WWSSN-SP (see Eq. (11.6) and Tab. 11.3). Thus, at its low-frequency end, the WWSSN-SP response has according to its three zeros a slope of 3. This changes at the first pair of poles, i.e., at $f_l = 0.8$ Hz, by 2 orders from 3 to 1 (i.e., to velocity proportional!), and again at $f_u = 1.33$ Hz by two orders from 1 to -1 . This is clearly to be seen in Fig. 11.27. In the same manner, the general shape of all the responses given in that figure can be assessed or precisely calculated according to Eq. (11.5) by using the values for the poles and zeros given in Tabs. 11.3 and 11.4. Doing the same with the values given in Tab. 11.3 for WWSSN-LP one gets for $f_l = 0.06667$ Hz, corresponding to the 15 s seismometer and $f_u = 0.009998$ Hz corresponding to the 100 s galvanometer, used in original WWSS-LP seismographs. The aim of the exercise in EX 5.5 is to calculate and construct with the method shown above the responses of seismographs operating at several seismic stations of the global network from the data given in their SEED header information.

Note that the poles and zeros given in Tabs. 11.3 and 11.4 are valid only if the input signal to the considered seismographs is ground displacement (amplitude A_d). Consequently, the values in Tab. 11.3 are not suitable for simulating the responses of the classical seismographs if the input signal to the filter is not displacement. From the output of the STS2, any simulation filter gets as an input a signal, which is velocity-proportional within the frequency range between 0.00827 Hz and 40 Hz. Its amplitude is $A_v = \omega A_d$. Accordingly, the transfer function of the simulation filter $H_{fs}(s)$ has to be the convolution product of the inverse of the transfer function $H_r(s)$ of the recording instrument and the transfer function $H_s(s)$ of the seismograph that is to be simulated:

11.3 Routine signal processing of digital seismograms

$$H_{fs}(s) = H_r^{-1}(s) * H_s(s). \quad (11.7)$$

Thus, even for the same $H_s(s)$ to be simulated, the poles and zeros of the simulation filter differ depending on those of the recording seismograph. Tab. 11.5 gives, as an example from the SZGRF, the poles and zeros of the displacement filters for simulating the responses shown in Fig. 11.27 (left), and the poles and zeros given in Tab. 11.3, from output data of the STS2.

Tab. 11.5 Poles and zeros of the simulation filters required for simulating standard seismograms of WWSSN-SP, WWSSN-LP, WA, Kirnos SKD and SRO-LP, respectively from STS2 BB-velocity records.

Simulation-filter for	Zeros	Poles
WWSSN-SP	(-3.6743E-02, -3.6754E-02) (-3.6743E-02, 3.6754E-02)	(-3.3678, -3.7316) (-3.3678, 3.7315) (-7.0372, -4.5456) (-7.0372, 4.5456)
WWSSN-LP	(-3.6743E-02, -3.6754E-02) (-3.6743E-02, 3.6754E-02)	(-0.4189, 0.0) (-0.4189, 0.0) (-6.2832E-02, 0.0) (-6.2832E-02, 0.0)
WA	(-3.6743E-02, -3.6754E-02) (-3.6743E-02, 3.6754E-02)	(-6.2832, -4.7124) (-6.2832, 4.7124) (0.0, 0.0)
Kirnos SKD	(-3.6743E-02, -3.6754E-02) (-3.6743E-02, 3.6754E-02)	(-0.12566, -0.2177) (-0.1257, 0.2177) (-80.1094, 0.0) (-0.3154, 0.0)
SRO-LP	(-3.6744E-02, -3.6754E-02) (-3.6743E-02, 3.6754E-02) (-5.0100E+01, 0) (-0, 1.0500) (-0, -1.0500) (0.0, 0.0) (0.0, 0.0)	(-1.3000E-01, 0.0) (-6.0200, 0.0) (-8.6588, 0.0) (-3.5200E+01, 0.0) (-2.8200E-01, 0.0) (-3.9301E+00, 0.0) (-2.0101E-01, 2.3999E-01) (-2.0101E-01, -2.3999E-01) (-1.3400E-01, 1.0022E-01) (-1.3400E-01, -1.0022E-01) (-2.5100E-02, 0.0) (-9.4200E-03, 0.0)

Fig. 11.28 shows a comparison of the original three-component BB-velocity record of an STS2 at station WET from a local earthquake in Germany with the respective seismograms of a simulated Wood-Anderson (WA) seismograph. For a teleseismic earthquake Fig. 11.29 gives the STS2 BB-velocity record together with the respective simulated records for WWSSN-SP and LP. Figs. 11.30 and 11.31 give two more examples of both record simulation and the restitution of very broadband (VBB) true ground displacement. VBB restitution of ground displacement is achieved by convolving the given displacement response of the recording seismometer with its own inverse, i.e.,:

$$H_{rest}(s) = H_s^{-1}(s) * H_s(s). \quad (11.8)$$

However, Eq. (11.8) works well only for frequencies smaller than the upper corner frequency (anti-alias filter!) and for signal amplitudes that are well above the level of ambient, internal (instrumental), and digitization noise.

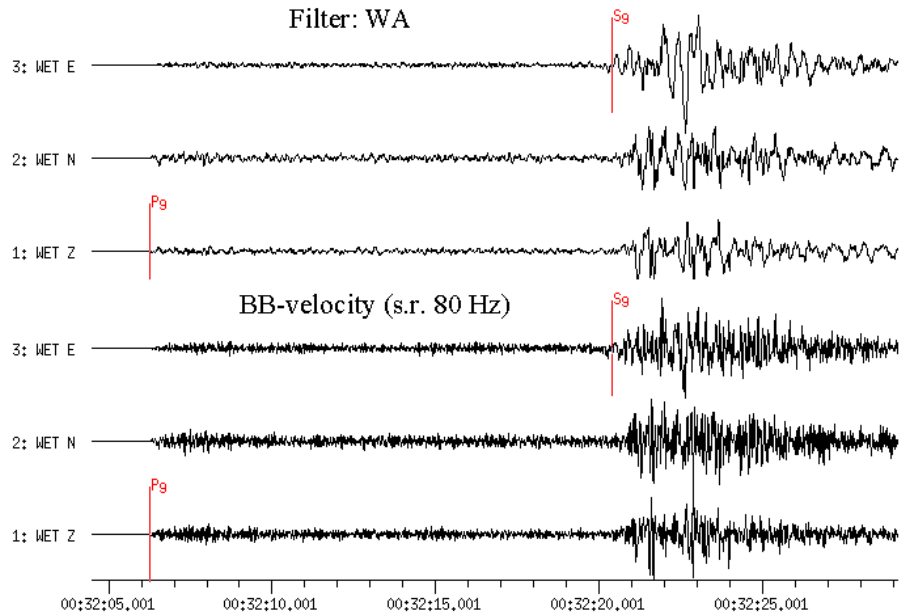


Fig. 11.28 3-component recordings at station WET (Wetzell) of a local earthquake at an epicentral distance of $D = 116$ km. Lower traces: original STS2 records with sampling rate of 80 Hz; upper traces: simulated Wood-Anderson (WA) recordings. Note that the displacement-proportional WA record contains less high frequency oscillations than the velocity-proportional STS2 record (compare responses shown in Fig. 11.27).

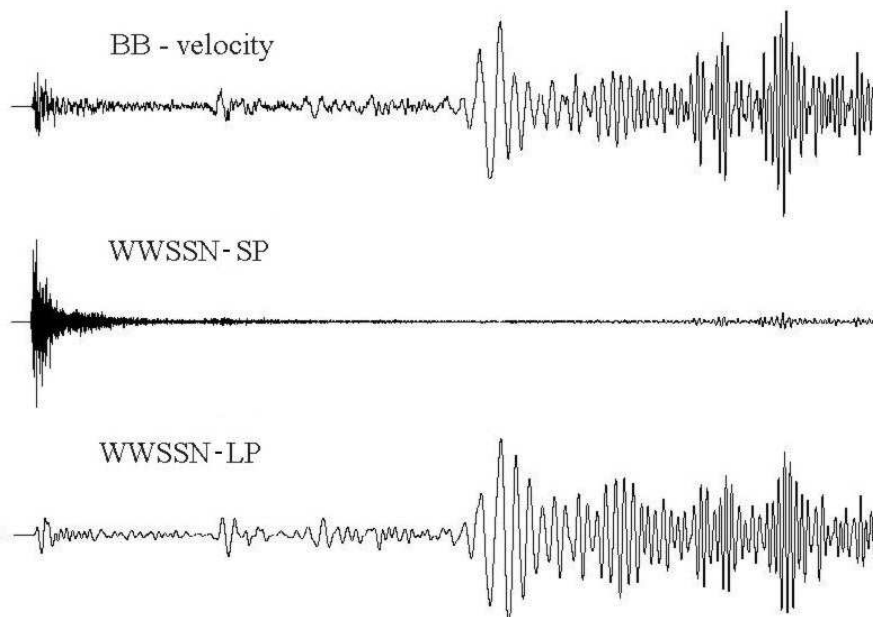


Fig. 11.29 BB-velocity seismogram (top) and simulated WWSSN-SP (middle) and WWSSN-LP seismograms (bottom). Note the strong dependence of waveforms and seismogram shape on the bandwidth of the simulated seismographs.

11.3 Routine signal processing of digital seismograms

Both Fig.11.29 and 11.30 show clearly the strong influence of differences in bandwidth and center frequencies of the seismometer responses (compare with Fig. 11.27) on both the individual waveforms and the general shape of the seismogram. This is particularly obvious in the simulated teleseismic earthquake records. Fig. 11.30 shows the recordings of the teleseismic P-wave group of an earthquake in California on 16 Sept. 1999. Shown are the restitution of a BB-displacement seismogram derived from a BB-velocity seismogram and the simulations of WWSSN-SP and SRO-LP seismograms. In the BB-velocity seismogram one recognizes clearly the superposition of a low-frequency signal and a high-frequency wave group. The latter is clearly seen in the WWSSN-SP record but is completely absent in the SRO-LP simulation. From this comparison it is obvious that both the BB-velocity and the SP seismograms enhance short-period signal amplitudes. Therefore, only the former recordings are well suited for studying the fine structure of the Earth and determining the onset time and amplitude of short-period P waves. In contrast, BB-displacement seismograms and LP-filtered seismograms suppress the high-frequencies in the signals. Generally they are more suited to routine practice for surface-wave magnitude estimation and for the identification of most (but not all!) later phases (see Figs. 11.12, 11.13, 11.37, and Fig. 2.23).

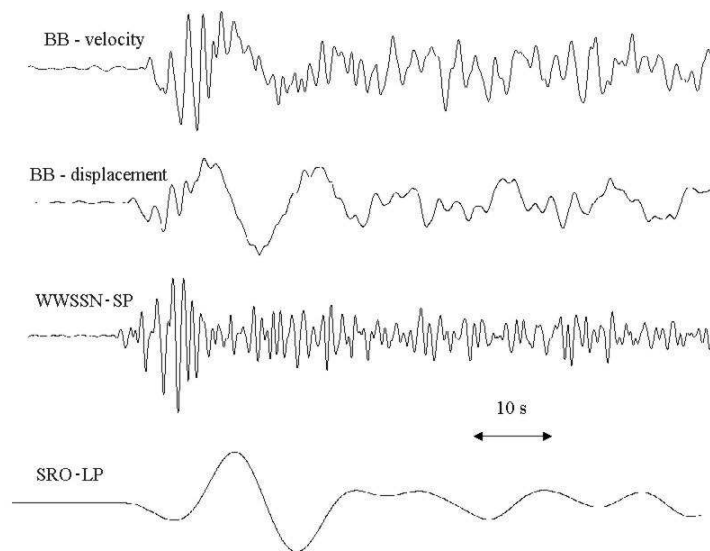


Fig. 11.30 From top to bottom: The original BB-velocity seismogram recorded at station GRFO; the BB-displacement record derived by restitution; the simulated WWSSN-SP; and the simulated SRO-LP seismograms of the P-wave group from an earthquake in California (16 Sept. 1999; $D = 84.1^\circ$; $M_s = 7.4$).

Fig. 11.31 shows 10-days of a VBB record from an STS1 vertical-component seismograph (corner period $T_c = 360$ s) at station MOX and simulated WWSSN-SP and SRO-LP seismograms for a short (40 min) time segment of this VBB record.

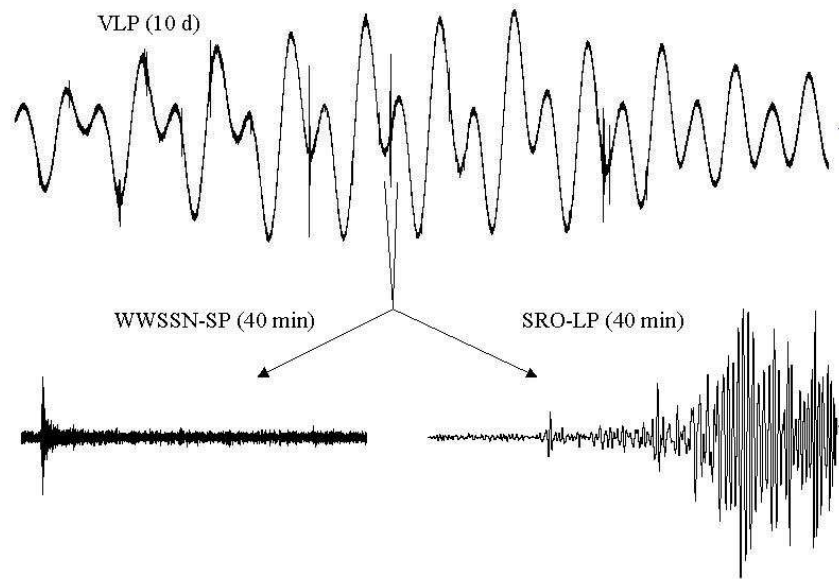


Fig. 11.31 STS1 ($T_c = 360s$) vertical-component seismogram with a length of 10 days (upper trace) as recorded at MOX station, Germany. In the seismogram we recognize Earth's tides and different earthquakes as spikes. For one of these earthquakes a WWSSN-SP and SRO-LP simulation filter was applied (lower traces). The length of the filtered records is 40 minutes.

Figs. 11.32a-d demonstrate, with examples from the GRSN and the GRF array in Germany, the restitution of (“true”) displacement signals from BB-velocity records as well as the simulation of WWSSN-SP, Kirnos BB-displacement and SRO-LP records. All traces are time-shifted for the P-wave group and summed (they are aligned on trace 16). The summation trace forms a reference seismogram for the determination of signal form variations. Generally, this trace is used for the beam (see 11.3.5 below). The different records clearly demonstrate the frequency dependence of the spatial coherence of the signal. Whereas high-frequency signals are incoherent over the dimension of this regional network (aperture about 500 to 800 km) this is not so for the long-period records which are nearly identical at all recording sites.

The following features are shown in Figs. 11.32a-d:

a) Time shifted BB-displacement (traces 16-30) and BB-velocity seismograms (traces 1-15) with a duration of 145 s of the P-wave group from an earthquake in Peru on 23 June 2001 ($M_s=8.1$) as recorded at 15 stations of the GRSN. The BB-displacement seismogram suppresses the high-frequencies, which are clearly shown on the BB-velocity record.

b) WWSSN-SP simulations for the same stations as in Figure 11.32a. The high-frequency signals are enhanced but the shape and amplitudes of the waveforms are shown to vary considerably within the network, i.e., the coherence is low.

c) Kirnos SKD BB-displacement and d) SRO-LP simulations for the same stations as in Fig.11.32a. The high-frequency signals are masked. All traces show coherent waveforms.

11.3 Routine signal processing of digital seismograms

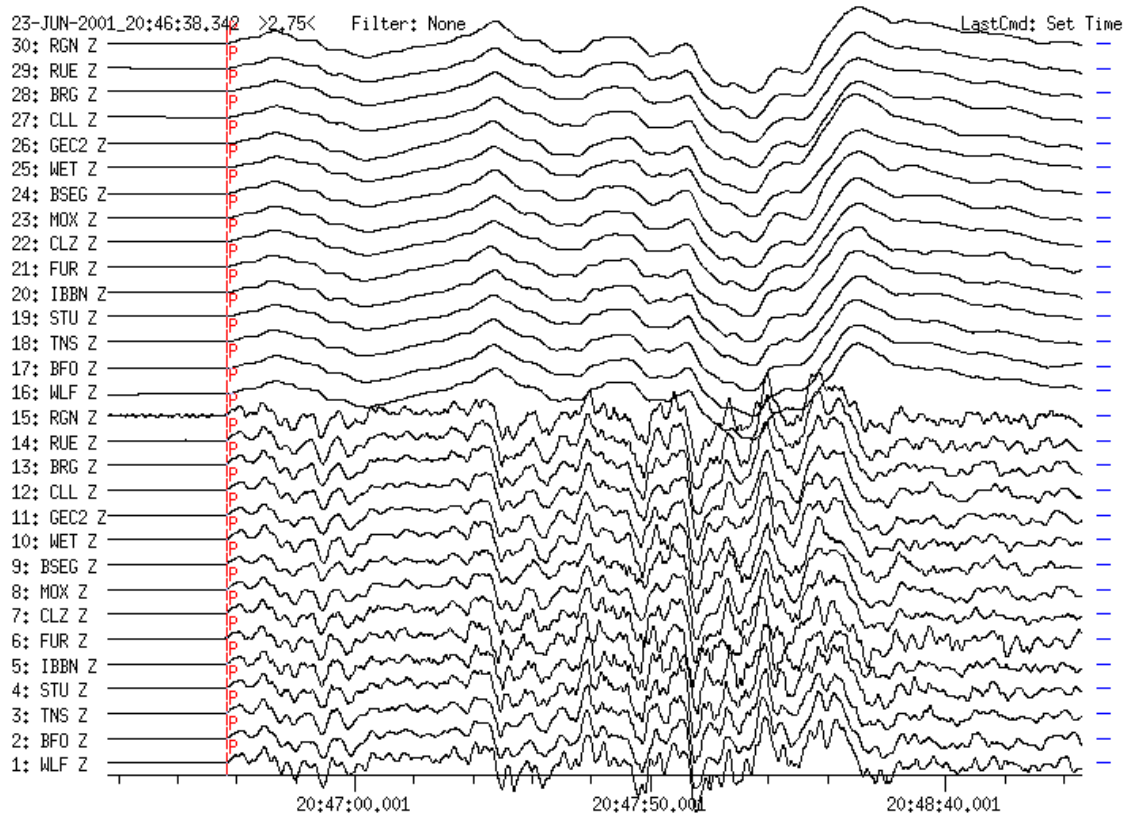


Fig. 11.32a (for explanation see text on page 48)

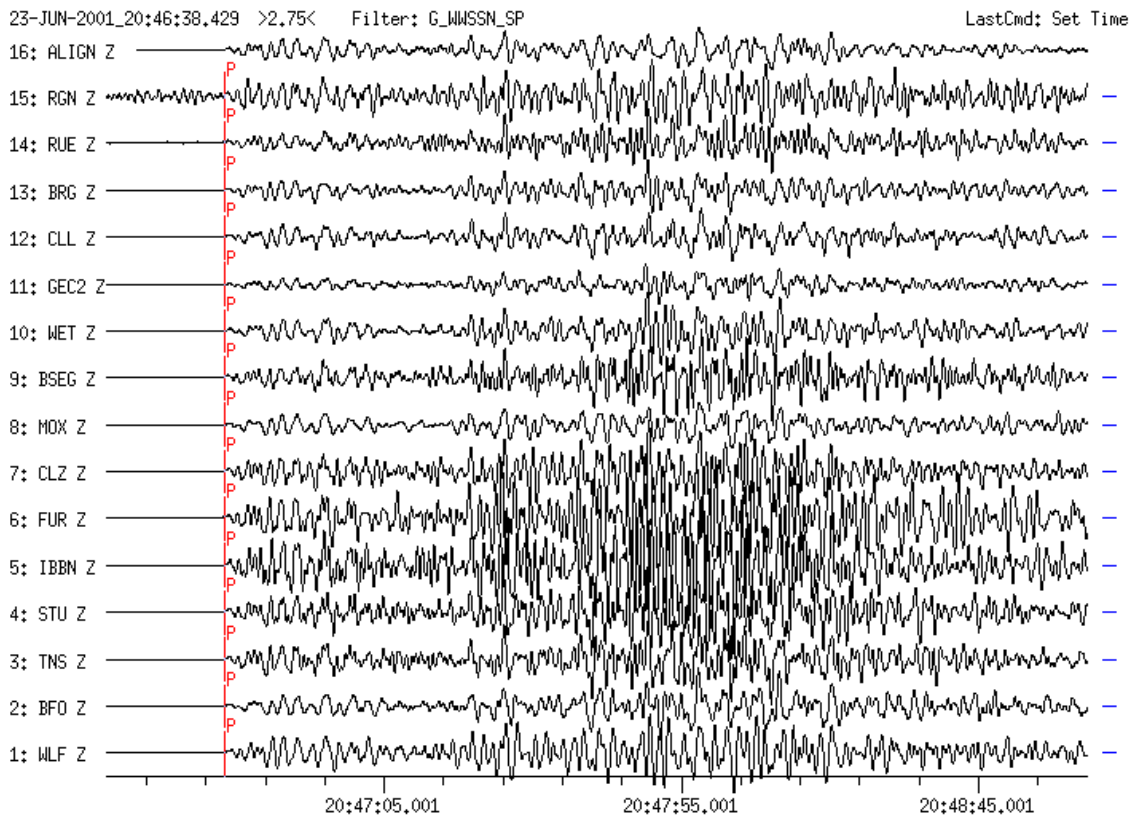


Fig. 11.32b As Fig. 11.32a however with short-period WWSSN-SP simulation.

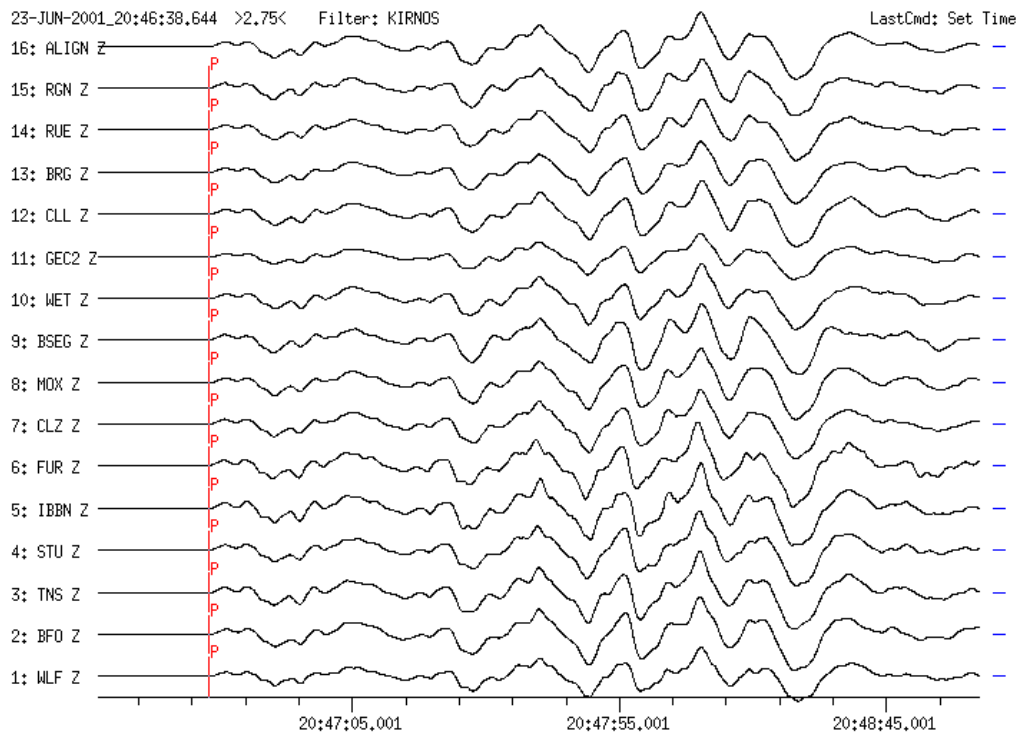


Fig 11.32c As Fig. 11.32a but for displacement-proportional Kirnos SKD simulation.

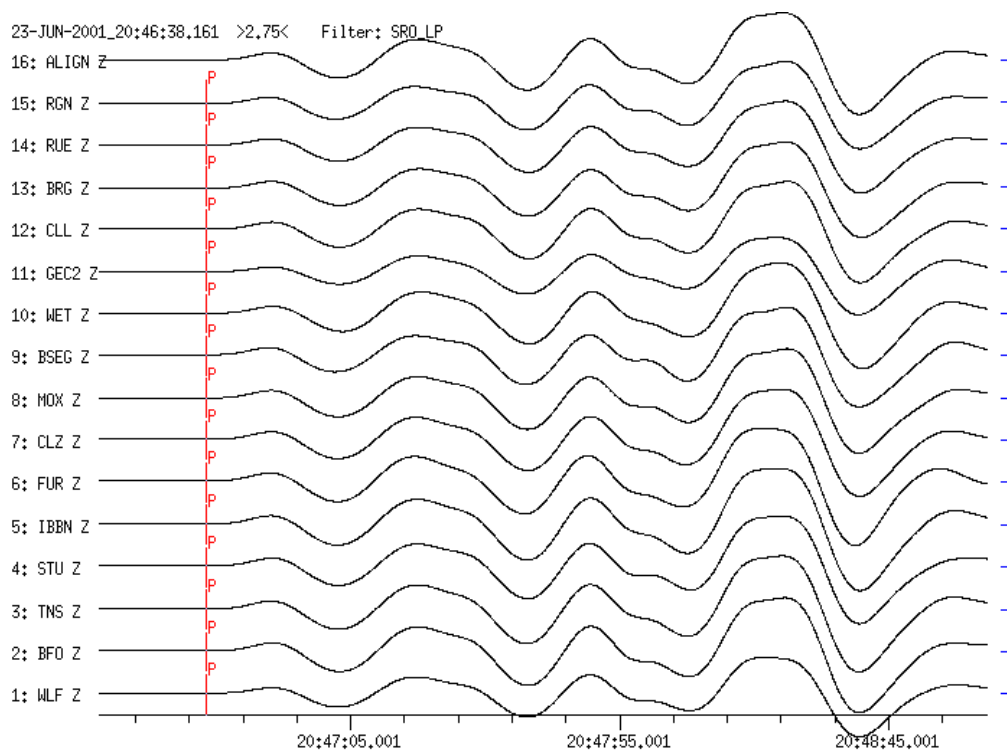


Fig. 11.32d As Fig. 11.32a but for long-period SRO-LP simulation.

Fig. 11.32a-d Restitution, simulation and coherency of seismograms demonstrated with records of the GRSN from an earthquake in Peru (23 June 2001, $M_s = 8.1$) in the epicentral distance range from 96° to 100° ; for explanation see text).

11.3.3 Signal coherency at networks and arrays

Heterogeneous crustal structure and the array aperture limit the period band of spatially coherent signals. The larger the aperture of an array the more rapidly the signal coherence falls off with frequency. At short periods the array behaves like a network of single stations whereas at long periods the array behaves like a sensitive single station. For the GRF-array (aperture about 50 to 120 km) for instance, the signals are coherent for periods between about 1 and 50 s. For the GRSN the band of coherent signals is at longer periods than for the small aperture detection arrays like GERES in Germany or NORES in Norway (aperture 4 and 3 km, respectively) where signals are coherent at periods shorter than 1 s. In the coherency band itself, waveforms vary depending on their dominant frequency, apparent horizontal velocity and azimuth of approach. For instance, coherent waveforms are observed from the GRSN for BB-displacement records, Kirnos SKD simulation and all long-period simulated seismograms (see Figs. 11.32a-d) whereas for simulated WWSSN-SP seismograms the waveforms have low coherence or are incoherent.

Figs. 11.33a and b shows a comparison of the first 14 s of the P wave of the GRSN and the GRF-array. The coherence is clearly higher in the short-period range for the recordings at the smaller GRF-array than for the GRSN. The GRSN works as an array for periods longer than about 10 s but it is a network for shorter periods where the GRF-array works as an array down to periods of about 1 s. This discussion is valid for teleseismic signals only, where the epicentral distance is larger than the aperture of the station network or array.

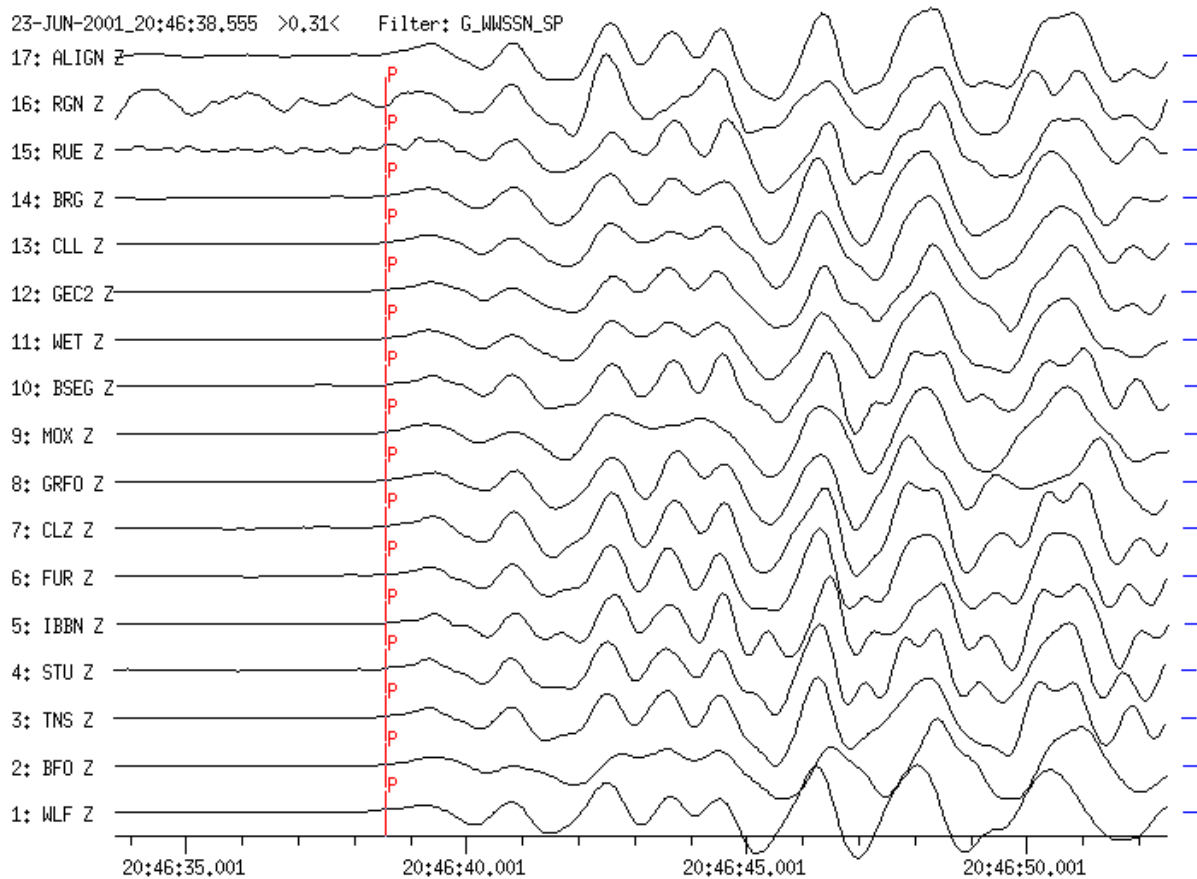


Fig. 11.33a (see figure caption below)

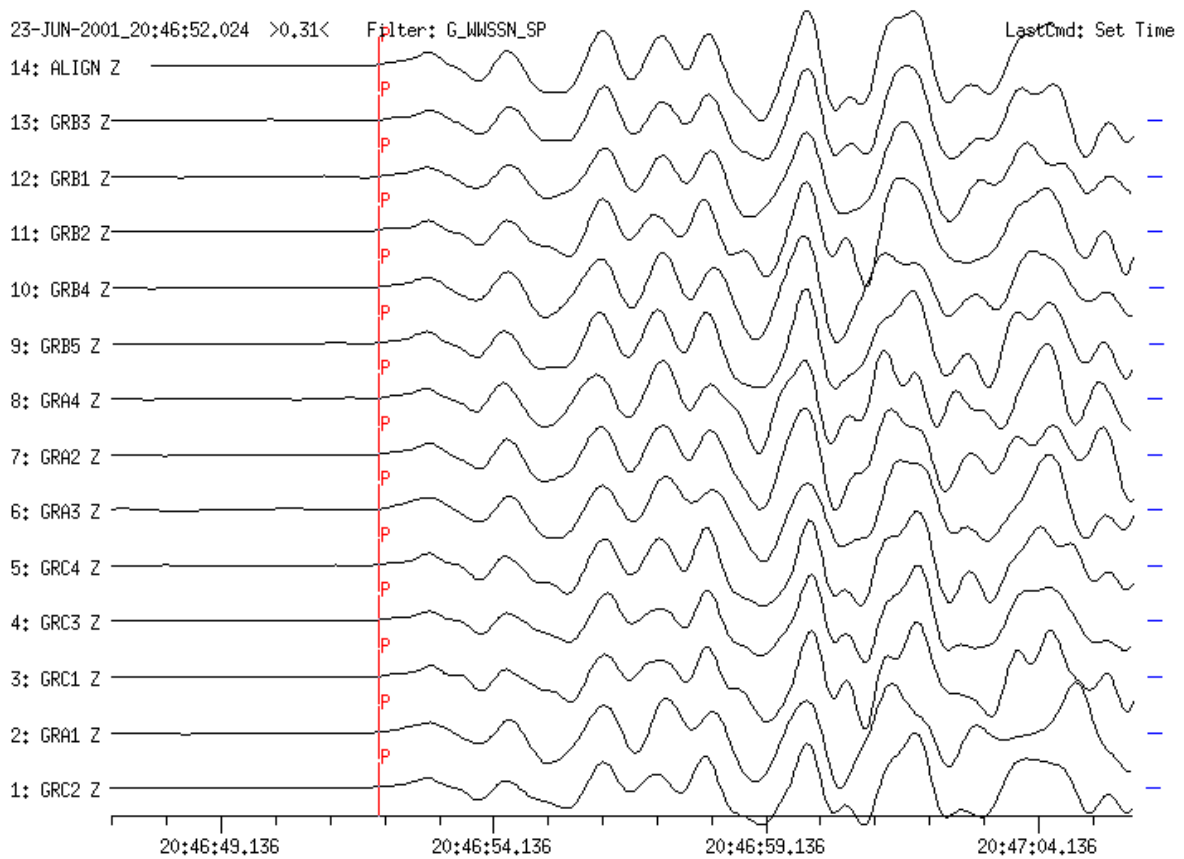


Fig. 11.33b (see figure caption below)

Fig. 11.33 WWSSN-SP simulations of the first 14 s after the P-wave onset from the same Peru earthquake as in Fig. 11.32. **a)** Recordings at the GRSN. **b)** Recordings at the GRF array. Note the lower coherence of the waveforms recorded at the stations of the regional network, which has an aperture much larger than the GRF-array (see Fig. 11.3a). The summation traces 17 and 14, respectively, are reference seismograms for the determination of signal waveform variations.

11.3.4 f-k and vespagram analysis

Array-techniques such as f-k and vespagram analysis should be applied only to records with coherent waveforms. Vespagram analysis or the velocity spectrum analysis is a method for separating signals propagating with different apparent horizontal velocities. The seismic energy reaching an array from a defined backazimuth with different slownesses is plotted along the time axis. This allows identification of later phases based on their specific slowness values. The best fitting slowness is that for which a considered phase has the largest amplitude in the vespagram. Fig. 11.34 shows the original records from the GRSN (top) and the related vespagram (bottom). More vespagrams are given in Figures 12e–g of DS 11.2.

11.3 Routine signal processing of digital seismograms

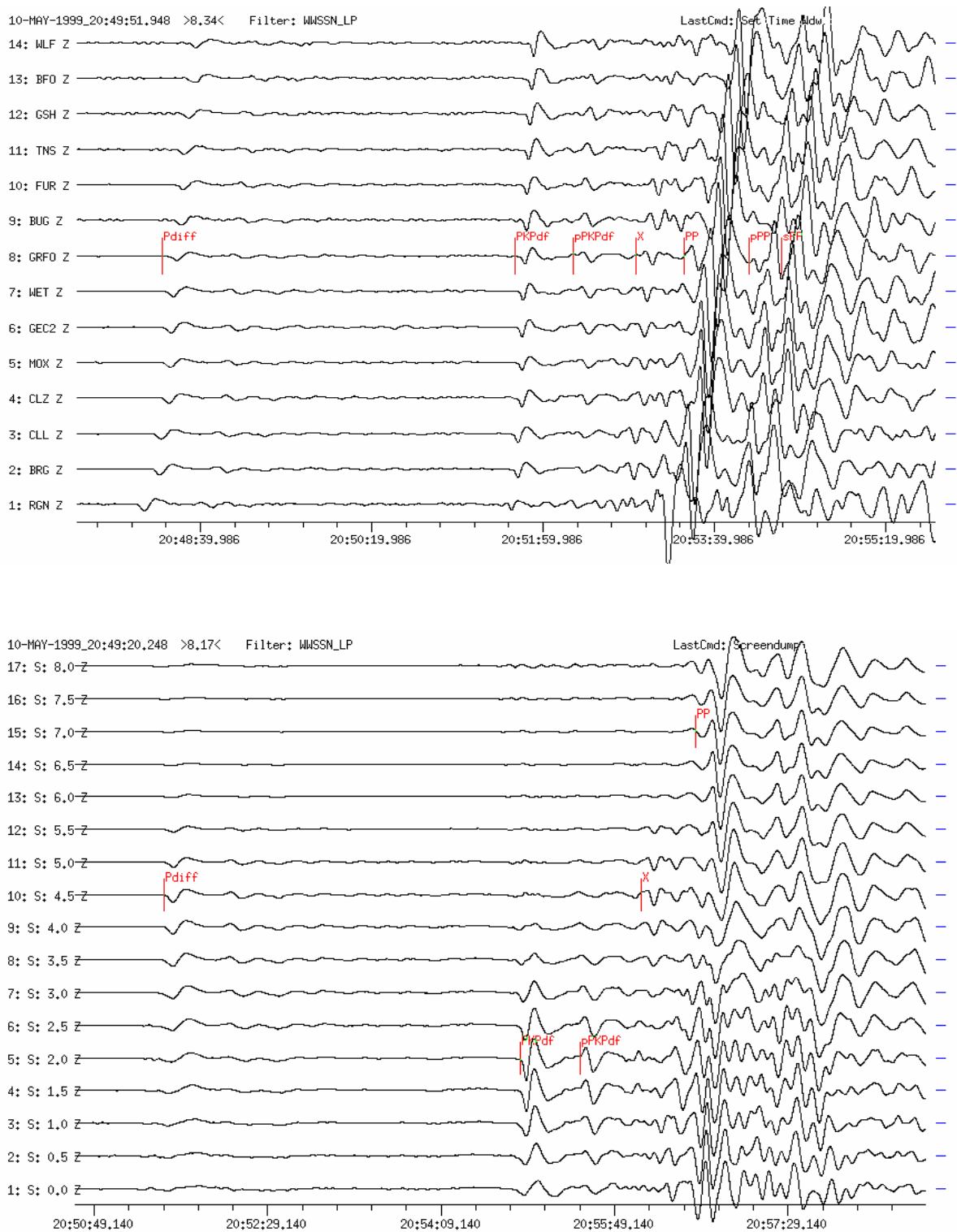


Fig. 11.34 Top: Simulated vertical-component WWSSN-LP seismograms from an earthquake in the region of Papua New Guinea. Source data NEIC-QED: 10 May 1999; depth 137 km; mb = 6.5; $D = 124^\circ$ to GRF, $BAZ = 51^\circ$. The phases Pdif (old Pdif), PKPdf, pPKPdf, PP, pPP, sPP and an unidentified phase X have been marked. **Bottom:** Vespagram of the upper record section. The analysis yields slowness values of $4.5s/^\circ$ for Pdif, $2.0s/^\circ$ for PKPdf and pPKPdf, $7.0s/^\circ$ for PP, and a value that corresponds to the slowness for Pdif for the unknown phase X.

As an example an f-k analysis is shown in Fig. 11.35. The f-k analysis is used to determine slowness and backazimuth of coherent teleseismic wave groups recorded at an array. The epicentral distance must be much larger than the aperture of the recording array. The f-k analysis transforms the combined traces within a current time window (Fig. 11.35a and b) into the frequency-wavenumber domain. The result in the f-k domain is displayed in a separate window (Fig. 11.35c) with amplitudes (corresponding to wave energy) coded in color. A good result is achieved when there is a single, prominent color in the maximum (yellow in Fig. 11.35c). This maximum denotes slowness and backazimuth of the investigated phase and is helpful for source parameter determination and phase identification. The example was recorded at the GRF-array from an earthquake in Novaya Zemlya. Slowness and backazimuth values are 7.3 s° and 11° , respectively. These values are used for producing the beam.

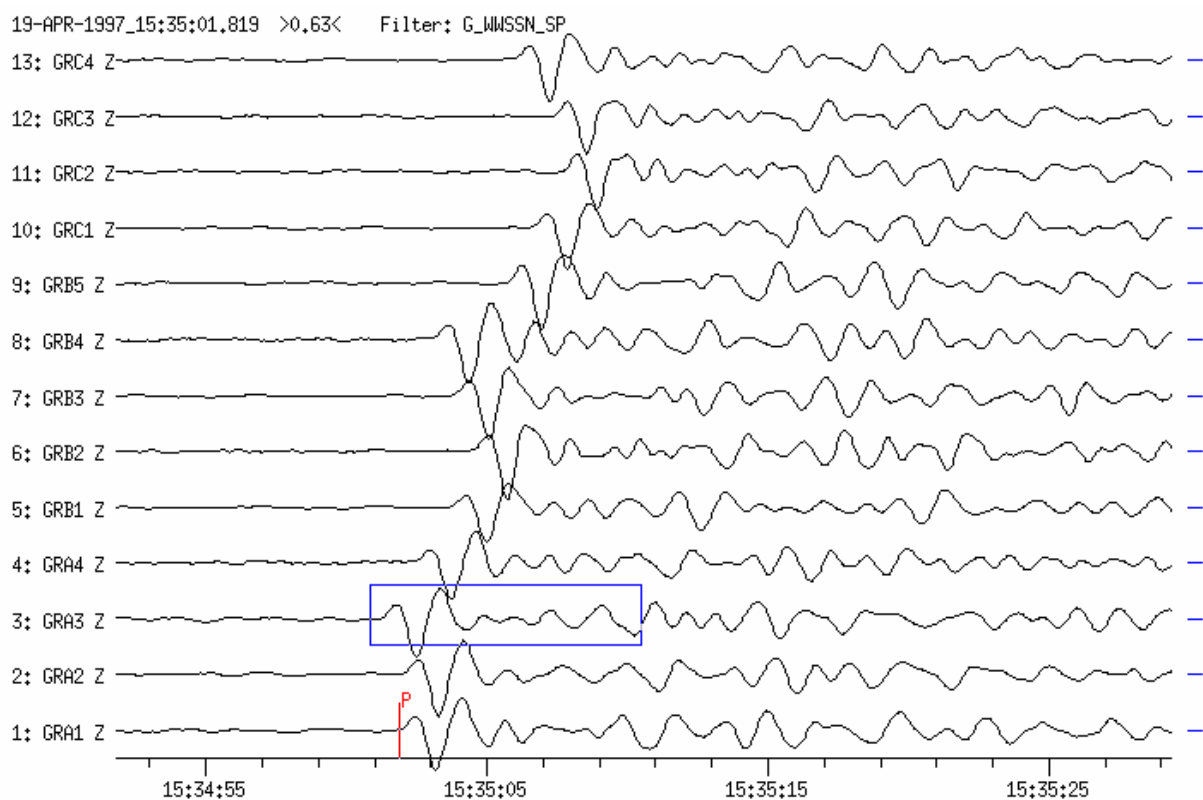


Fig. 11.35a

Figs. 11.35a-c Illustration of the procedure of frequency-wavenumber (f-k) analysis: a) coherent P-wave signals recorded at the GRF-array stations from an earthquake on 19 April 1997 (the box marks the time window selected for the f-k-analysis); b) the zoomed window used for the f-k-analysis; c) energy (coded in colors) in the frequency range 0.39-2.97 Hz as a function of wavenumber k . A good result is achieved because the single, prominent maximum (in yellow) shows the presence of a coherent signal. The estimated slowness and backazimuth values are 7.3 s° and 11° , respectively.

11.3 Routine signal processing of digital seismograms

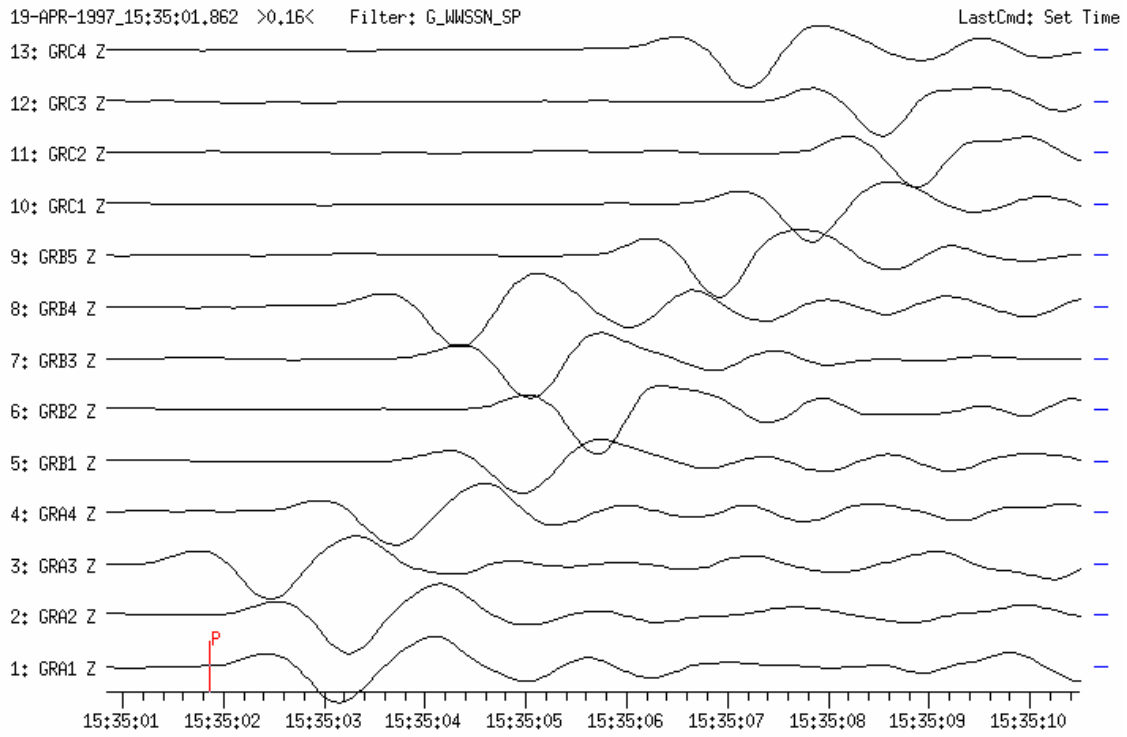


Fig. 11.35b

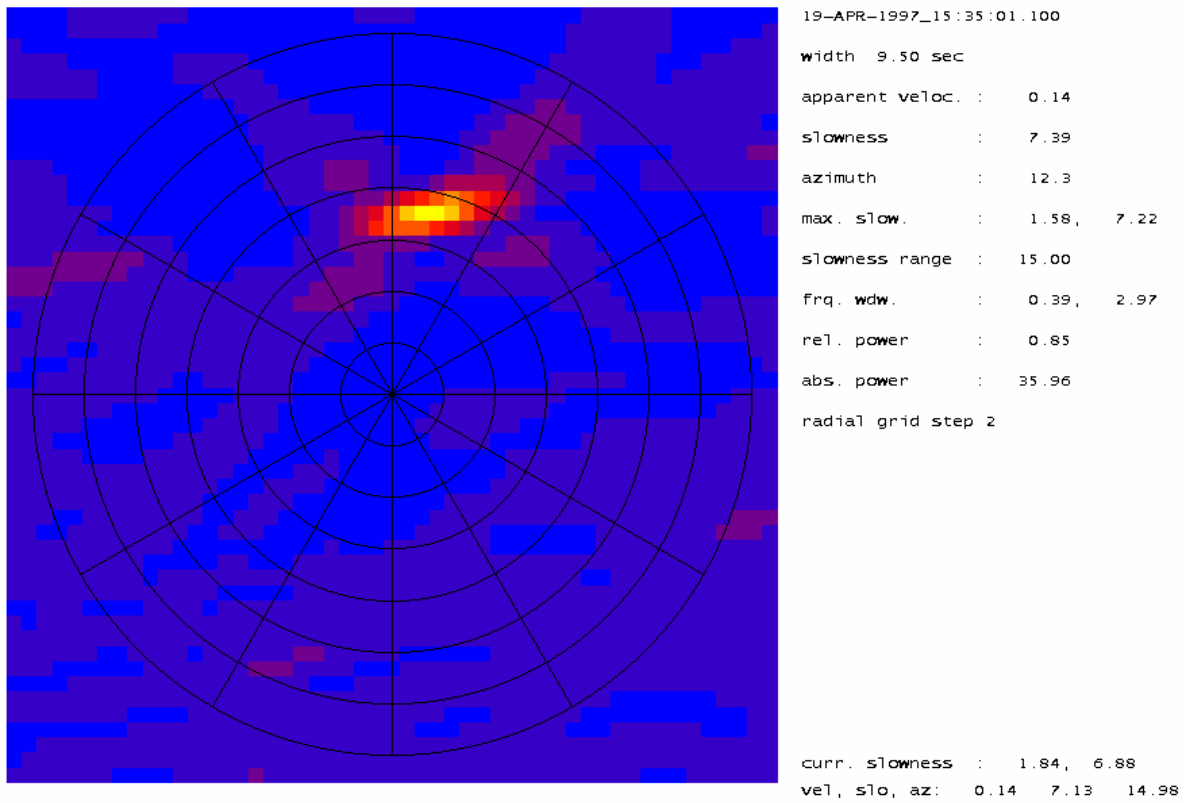


Fig. 11.35c

11.3.5 Beamforming

Beamforming improves the SNR of a seismic signal by summing the coherent signals from array stations (see 9.4.5). Signals at each station are time shifted by the delay time relative to some reference point or station. The delay time depends on ray slowness and azimuth and can be determined by trial and error or by f-k analysis. The delayed signals are summed “in phase” to produce the beam. Fig. 11.35d presents the array recordings of the signal shown in Figs. 11.35a-b time shifted, to correct for the time delay, and summed (trace 14; beam). In delay-and-sum beamforming with N stations the SNR improves by a factor \sqrt{N} if the noise is uncorrelated between the seismometers. In the summation the increase in amplitude of the coherent signal is proportional to N. For incoherent waves (random seismic noise in particular), it is only proportional to \sqrt{N} . Thus, f-k analysis and beamforming are helpful for routine analysis if very weak signals have to be detected and analyzed.

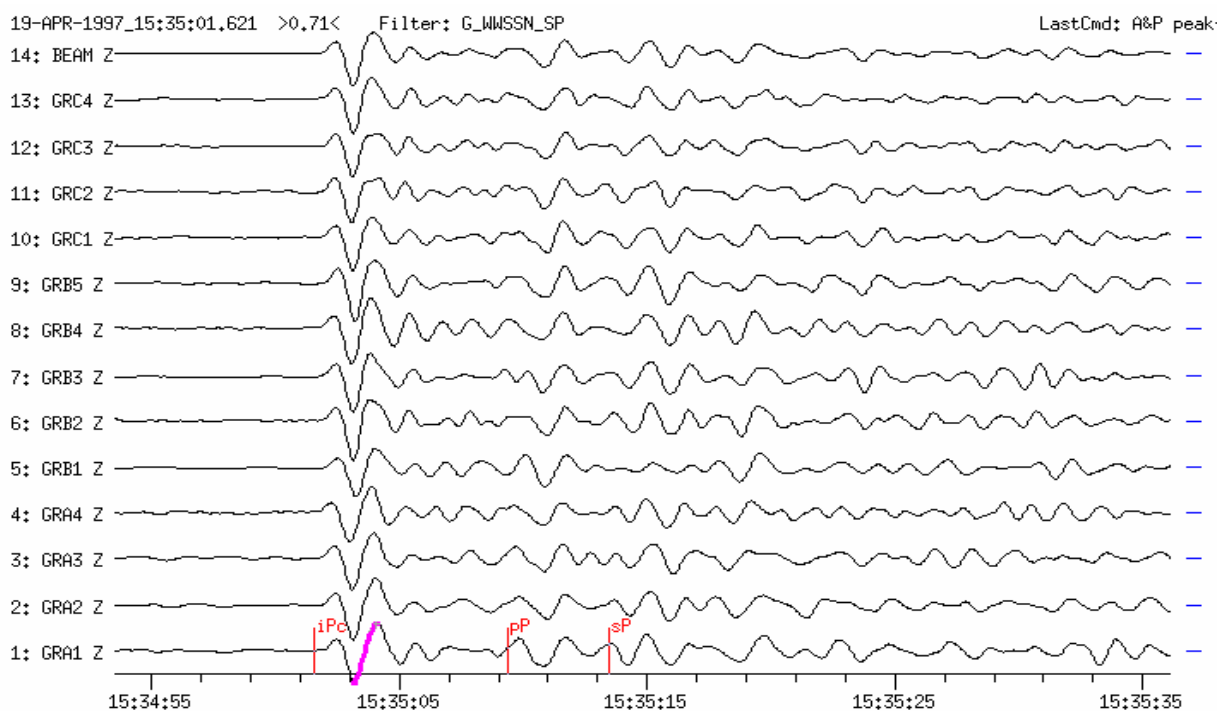


Fig. 11.35d The delay times for each of the array seismometers have been calculated from the slowness and azimuth of the signals shown in Figs. 11.35a-c. The time-shifted signals are summed “in phase” to produce the beam (top trace) which has the better signal-to-noise ratio than the recordings from the individual seismometers.

Fig. 11.36 shows another example of array processing with short-period filtered seismograms of the GRF array. The signal on the beam trace is the PKP wave of an underground nuclear explosion at Mururoa Atoll with an explosion yield equivalent of about 1 kt TNT. The onset time and signal amplitude of a weak seismic signal can only be read on the beam. The peak-to-peak amplitude is only about 2 nm with a period around 1 s.

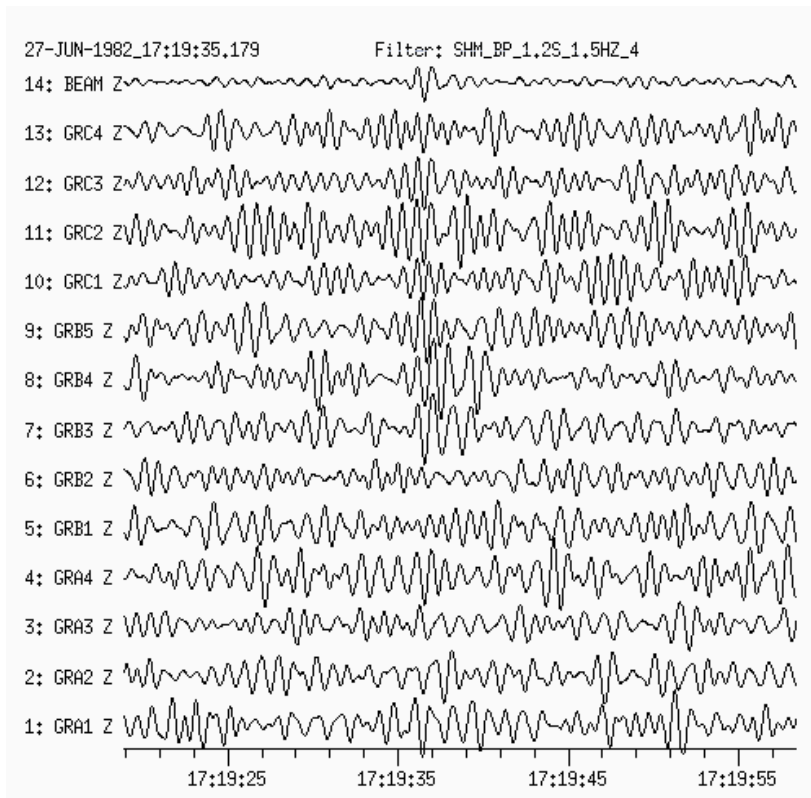


Fig. 11.36 Detection of the PKP wave of a nuclear explosion at Mururoa Atoll on 27 June 1982 at the Gräfenberg array using the delay-and-sum-method and a very narrowband Butterworth bandpass filter (BP) centered around 1 Hz. The event occurred at an epicentral distance of 146° and the explosion yield was approximately 1 kt TNT.

11.3.6 Polarization analysis

The task of polarization analysis is the transformation of recorded three component seismograms into the ray-oriented co-ordinate systems. For linearly polarized and single pulse P waves in a lateral homogeneous Earth, this task is simple, at least for signals with a high SNR; the direction of the polarization vector of the P wave clearly determines the orientation of the wave co-ordinate system. However, when propagating through heterogeneous and anisotropic media, the seismic waves have three-dimensional and frequency-dependent particle motions and the measured ray-directions scatter by ten degrees and more about the great circle path from the epicenter to the station (see Fig. 2.6).

Determination of particle motion is included in most of the analysis software. For identification of wave polarization and investigation of shear-wave splitting, the rotation of the traditional components N, E, and Z into either a ray-oriented co-ordinate systems or into the directions R (radial, i.e., towards the epicenter) and T (transverse, i.e., perpendicular to the epicenter direction) is particularly suitable for the identification of secondary later phases. An example for the comprehensive interpretation of such phases in a teleseismic record is given in Fig. 11.37.

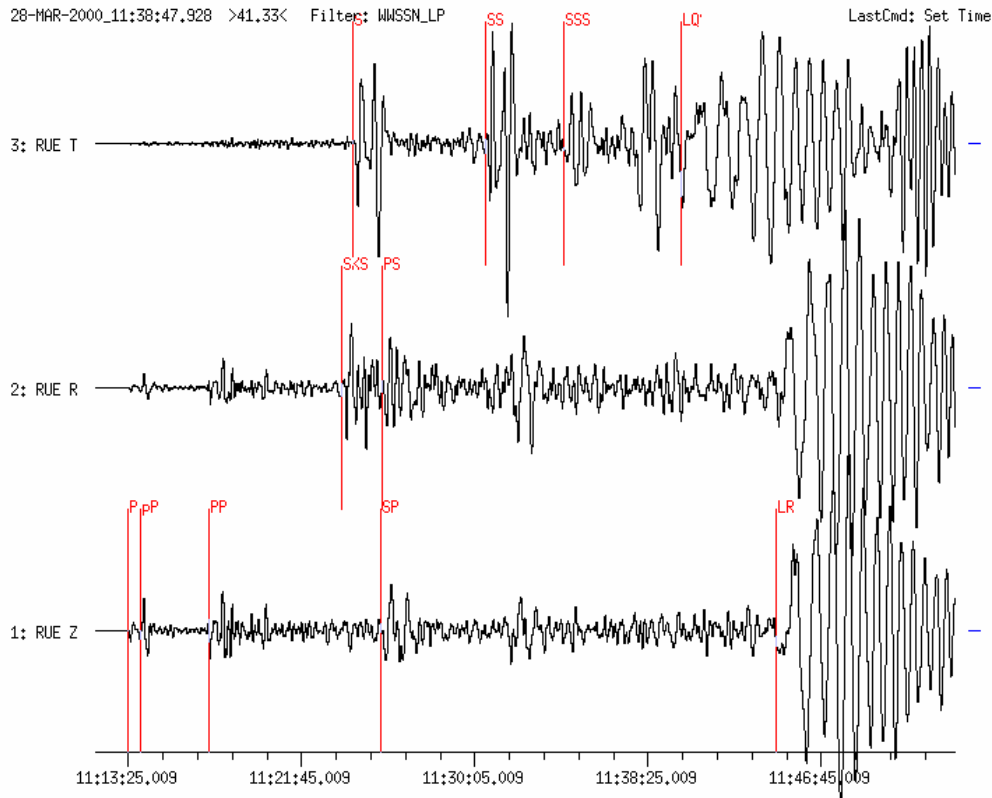


Fig. 11.37 Simulation of three-component WWSSN-LP seismograms of the Volcano Islands earthquake of 28 March 2000, recorded at station RUE in Germany ($D = 94^\circ$, $h = 119$ km). The horizontal components N and E are rotated into R and T components. The phases P, pP, SP and the beginning of the dispersed surface Rayleigh wave train LR are marked on the vertical-component seismogram, SKS, PS on the radial component (R) and S, SS, SSS and the beginning of the Love waves LQ on the transverse component (T), respectively. Not marked (but clearly recognizable) are the depth phases sS behind S, sSS behind SS, and SSSS+sSSSS before LQ. The record length is 41 min.

11.4 Software for routine analysis

11.4.1 SHM

The Seismic Handler SHM is a powerful program for analyzing local, regional and teleseismic recordings. K. Stammer of the SZGRF in Erlangen has developed it for the analysis of data from the Graefenberg (GRF) array and the German Regional Seismic Network (GRSN). The program and descriptions are available via <http://www.szgrf.bgr.de/sh-doc/index.html>.

Main features of the program are:

- application of array procedures to a set of stations (slowness- and backazimuth determination by means of beamforming and f-k analysis);
- location algorithms (teleseismic locations using travel-time tables and empirical correction vectors, local and regional locations via external programs, e.g., LocSAT).

The basic program has some (more or less) standardized options, e.g.:

- manual and automatic phase picking (see Fig. 11.5);
- trace filtering with simulation and bandpass filters (see Figs. 11.28 and 11.29);
- determination of amplitudes, periods and magnitudes (see Fig. 11.4);
- display of theoretical travel times on the traces (see Fig. 11.37).

Furthermore, the following tasks are implemented:

- rotation of horizontal components (see Figs. 11.13 and 11.37);
- particle motion diagrams (see Fig. 2.6);
- trace amplitude spectrum (see Fig. 11.47);
- vespagram trace display (see Fig. 11.34);
- determination of signal/noise ratio (see Fig. 11.47); and
- trace editing functions.

Different data formats are supported on continuous data streams of single stations, networks and/or array stations. SHM is currently supported on UNIX and Linux. A screen display of SHM is shown in Fig. 11.38.

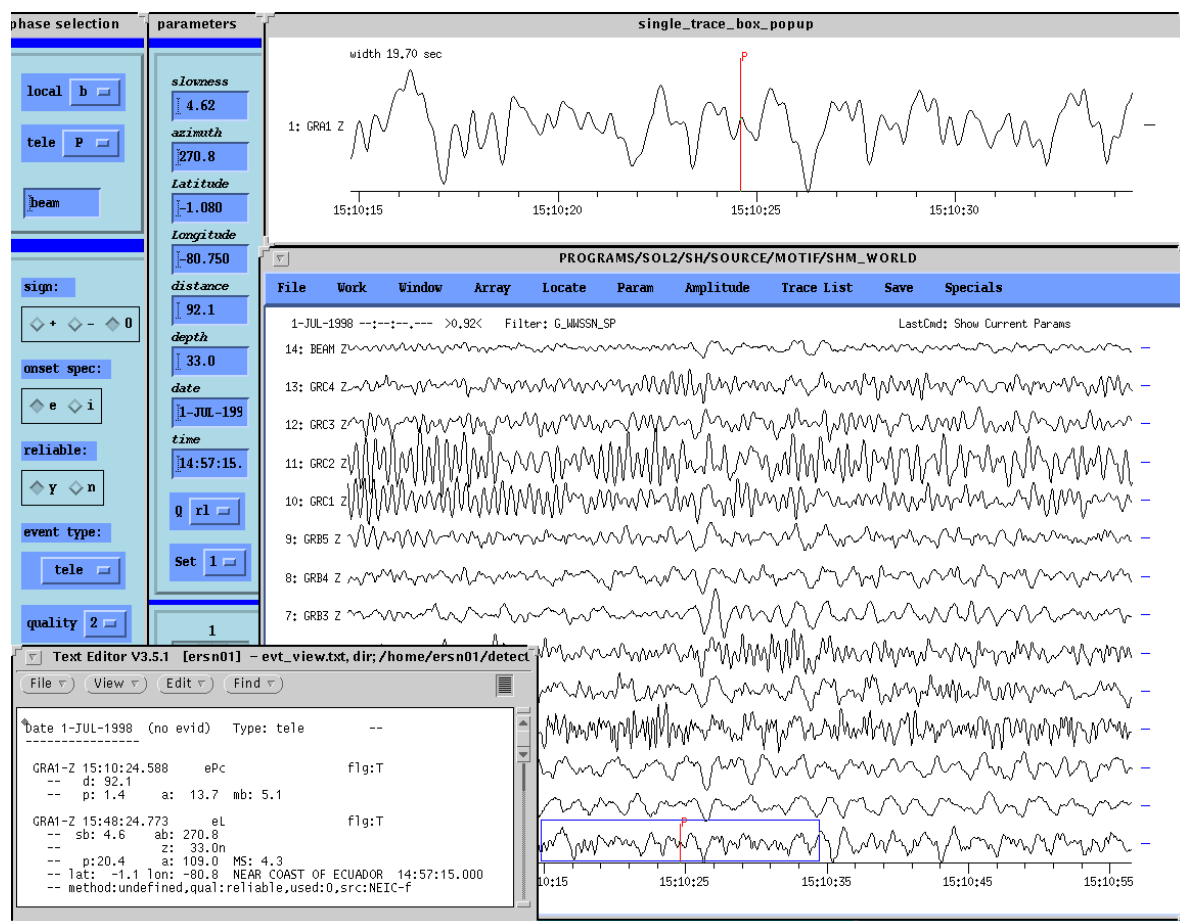


Fig. 11.38 Screen display of the seismic analysis program SHM. Different windows display a number of station recordings (large window), a zoomed single-station window, two seismogram and source parameter windows (left side) and an output window for the results of the seismogram analysis. Generally, the resulting parameters are stored in a database.

11.4.2 SEISAN

Another widely used seismic analysis system is SEISAN developed by J. Havskov and L. Ottemöller (1999). It contains a complete set of programs and a simple database for analyzing analog and digital recordings. SEISAN can be used, amongst other things, for phase picking, spectral analysis, azimuth determination, and plotting seismograms. SEISAN is supported by DOS, Windows95, SunOS, Solaris and Linux and contains conversion programs for the most common data formats. The program, together with a detailed Manual, is available via <http://www.ifjf.uib.no/seismo/software/seisan/seisan.html>.

11.4.3 PITSA

F. Scherbaum, J. Johnson and A. Rietbrock wrote the current version. It is a program for interactive analysis of seismological data and has numerous tools for digital signal processing and routine analysis. PITSA is currently supported on SunOS, Solaris and Linux and uses the X11 windowing system. It is available via <http://lbutler.geo.uni-potsdam.de/service.htm>.

11.4.4 GIANT

Andreas Rietbrock has written this program package. It is a system for consistent analysis of large, heterogeneous seismological data sets. It provides a graphical user interface (GUI) between a relational database and numerous analysis tools (such as HYPO71, FOCMEC, PREPROC, SIMUL, PITSA, etc.). The GIANT system is currently supported on SunOS, Solaris and Linux and uses the X11 windowing system and available via <http://lbutler.geo.uni-potsdam.de/service.htm>.

11.4.5 Other programs and ORFEUS software links

C. M. Valdés wrote the interactive analysis program PCEQ for IBM compatible PCs. It is widely used in conjunction with the location program HYPO71 for local events. The principal features are: picking P- and S-wave arrivals; filtering the seismogram for better P- and S-wave picks, and computing the spectra of selected seismogram sections. It is published in Volume 1 of the IASPEI Software Library (Lee, 1995).

Andrey Petrovich Akimov has written the program WSG (in English AWP: Automated workplace of seismologists), version 4.5 (in Russian). It works in an environment of Windows 95/98/NT and is used at single stations and seismic networks for estimating parameters from local, regional and teleseismic sources. The program converts different seismic data formats such as XDATA, PCC-1, CSS 2.8 and 3.0, DASS, CM6 GSE2 and can import via the TCP/IP protocol data from NRTS and LISS systems (miniSEED). The program and the program documentation in Russian is available via <http://www2.gsras.ru/engl/mainms.htm>.

ORFEUS (<http://orfeus.knmi.nl/>) presents a comprehensive list and links to available software in seismology. It concentrates on shareware. However, some relevant commercial sites are also included. Emphasis is laid on programs which run on UNIX/Linux platform.

11.5 Examples of seismogram analysis

The character of a seismogram depends on the source mechanism, the source depth, and whether the epicenter of the source is at local, regional or teleseismic distances. Seismograms of local earthquakes are characterized by short duration of the record from a few seconds to say one minute, higher frequencies, and a characteristic shape of the wave envelope, usually an exponential decay of amplitudes after the amplitude maximum, termed “coda” (see Figure 1b in DS 11.1 and Figure 2 in EX 11.1). In contrast, records at teleseismic distances show lower frequencies (because high-frequency energy has already been reduced by anelastic attenuation and scattering), and have a duration from say fifteen minutes to several hours (see Fig. 1.2). Regional events have intermediate features. The various wave groups, arriving at a station over different path, are called phases. They have to be identified and their parameters determined (onset time, amplitude, period, polarization, etc.). Phase symbols should be assigned according to the IASPEI recommended standard nomenclature of seismic phases. For phase names, their definition and ray paths see IS 2.1. Fig. 11.39 shows seismograms recorded at local, regional and teleseismic distances. They illustrate how the characteristics of seismic records vary with distance and depending on the source type. These characteristics will be discussed in more detail in the following sections.

There is no unique standard definition yet for the distance ranges termed “near” (“local” and “regional”), or “distant” (“teleseismic”; sometimes subdivided into “distant” and “very distant”). Regional variations of crustal and upper-mantle structure make it impossible to define a single distance at which propagation of local or regional phases stops and only teleseismic phases will be observed. In the following we consider a source as **local** if the direct crustal phases Pg and Sg arrive as first P- and S-wave onsets, respectively. In contrast, the phases Pn and Sn, which have their turning point in the uppermost mantle, are the first arriving P and S waves in the **regional** distance range. However, as discussed in 2.6.1 and shown in Fig. 2.40, the distance at which Pn takes over as first arrival depends on the crustal thickness, average wave speed and the dip of the crustal base. The “cross-over” distance x_{co} between Pn and Pg is - according to Eq. (6) in IS 11.1 for shallow (near surface) sources - roughly $x_{co} \approx 5 \times z_m$ where z_m is the Moho depth. Note, however, that as focal depth increases within the crust, x_{co} decreases, down to about $3 \times z_m$. Accordingly, the local distance range may vary from region to regions and range between about 100 km and 250 km. The CTBTO Technical Instructions (see IDC Documentation, 1998) considers epicentral distances between 0° to 2° , where Pg appears as the primary phase, as local distance range.

The old Manual (Willmore, 1979) defines as near earthquakes those which are observed up to about 1000 km (or 10°) of the epicenter, and P and S phases observed beyond 10° as usually being **teleseismic** phases. However, regional phases such as Pn, Sn and Lg, will generally propagate further in stable continental regions than in tectonic or oceanic regions. According to the Earth model IASP91, Pn may be the first arrival up to 18° . The rules published in the IDC Documentation (1998) allow a transitional region between 17° and 20° in which phases may be identified as either regional or teleseismic, depending on the frequency content and other waveform characteristics. Accordingly, one might roughly define seismic sources as local, regional and teleseismic if their epicenters are less than 2° , between 2° and 20° , or more than 20° away from the station. Sometimes, the regional range is further subdivided into 2° - 6° , where also the phase Rg may be well developed, and 6° - (17°) - 20° where only Sn and Lg are strong secondary phases. However, since we have not yet found good record examples with Pn beyond 15° , we will present and discuss our record examples for **near** (local and regional) and **teleseismic** sources in the ranges $D \leq 15^\circ$ and $D > 15^\circ$, respectively.

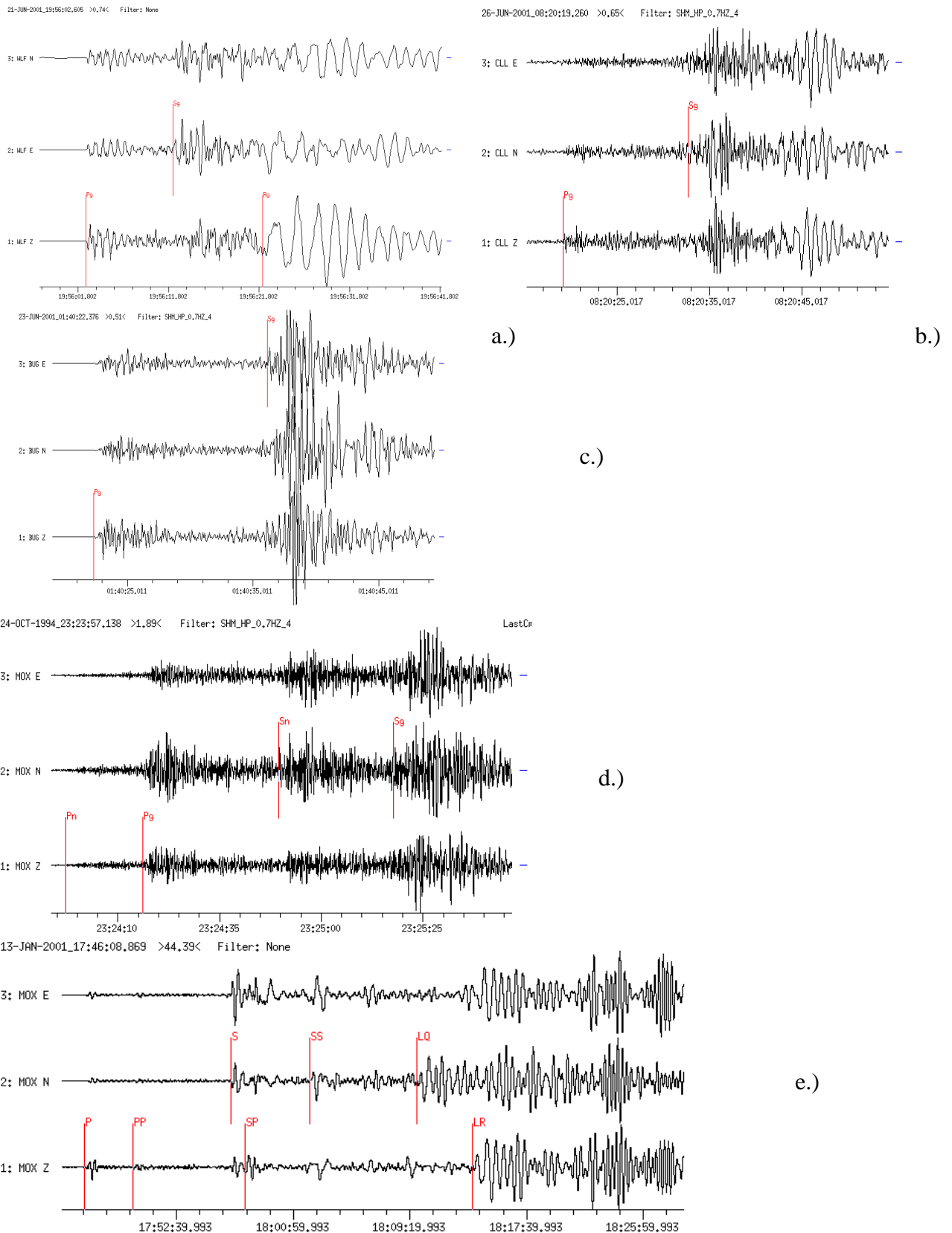


Fig. 11.39 Examples of 3-component seismograms recorded at a range of epicentral distances from one station: a) mining-induced earthquake ($D = 80$ km); b) quarry blast explosion ($D = 104$ km); c) local earthquake ($D = 110$ km); d) regional earthquake ($D = 504$ km); and e) teleseismic earthquake ($D = 86.5^\circ$). Time scales are given below the records.

The methods used to analyze seismograms and to locate seismic sources depend on how close they are to the recording station. For near events different programs (ORFEUS software library; see 11.4.5) are used for source location. Differences in arrival times of phases and slowness and azimuth estimates from the plane-wave method or frequency-wavenumber (f-k) analysis can be used to locate distant sources with either array or network data. Time differences between phases often give reliable distance estimates and, together with azimuth determination from 3-component records, allow epicenters to be estimated from single station records (see EX 11.2). If depth phases are visible and can be identified, focal depth can be determined. Amplitude and period values of different phases are used for magnitude estimation. Both body waves and surface waves can be used to estimate magnitude.

11.5.1 Seismograms from near sources ($0^\circ < D \leq 15^\circ$)

Seismograms recorded at distances $D \leq 15^\circ$ are dominated by P and S waves that have traveled along different paths through the crust and the uppermost mantle of the Earth. They are identified by special symbols for “crustal phases” (see IS 2.1). Pg and Sg, for example, travel directly from a source in the upper or middle crust to the station whereas the phases PmP and SmS have been reflected from, and the phases Pn and Sn critically refracted along (or beneath) the Moho discontinuity (see Fig. 11.40). Empirical travel-time curves are given in Exercise EX 11.1 (Figure 4) and a synthetic record section of these phases in Fig. 2.54. In some continental regions, phases are observed which have been critically refracted from a mid-crustal discontinuity or have their turning point in the lower crust. They are termed Pb (or P*) for P waves and Sb (or S*), for S waves, respectively. For shallow sources, crustal “channel-waves” Lg (for definition see IS 2.1) and surface waves Rg are observed after Sg-waves. Rg is a short-period Rayleigh wave ($T \approx 2$ s) which travels in the upper crust and is usually well developed in records of near-surface sources out to about 300 km and thus suitable for discriminating such events from local tectonic earthquakes (see Figs. 11.39a-c).

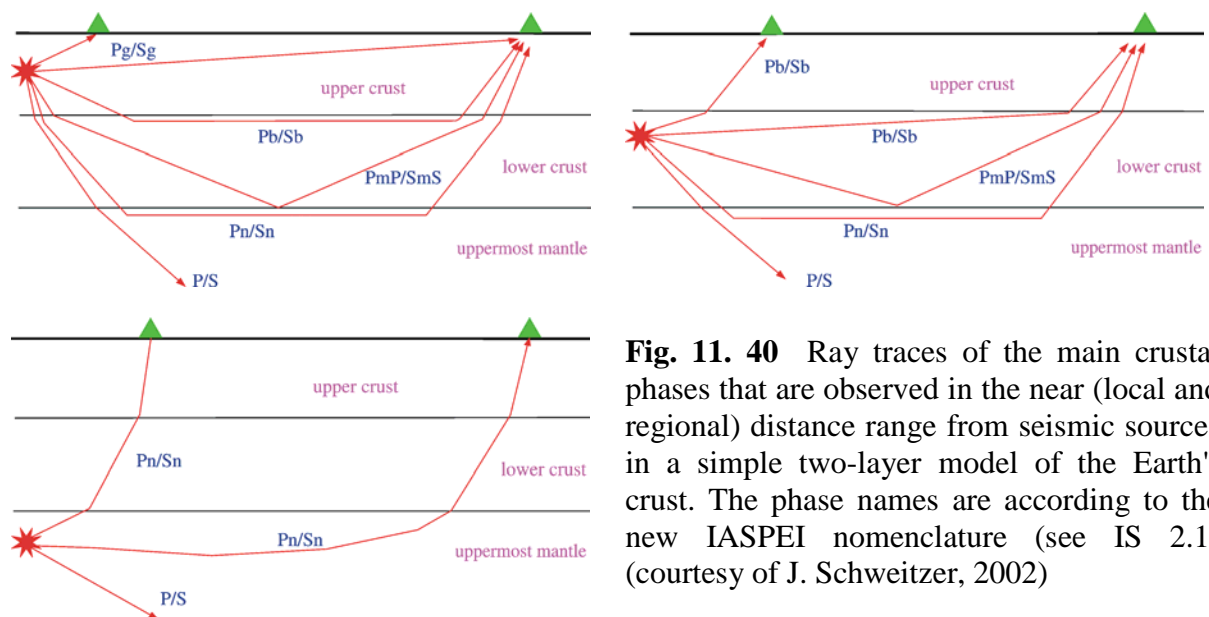


Fig. 11. 40 Ray traces of the main crustal phases that are observed in the near (local and regional) distance range from seismic sources in a simple two-layer model of the Earth's crust. The phase names are according to the new IASPEI nomenclature (see IS 2.1) (courtesy of J. Schweitzer, 2002)

Usually, Sg and SmS (the supercritical reflection, which often follows Sg closely at distances beyond the critical point; see Fig. 2.40) are the strongest body wave onsets in records of near seismic events whereas Pg and PmP (beyond the critical point) have the largest amplitudes in the early part of the seismograms, at least up to 200 – 400 km. Note that for sub-crustal earthquakes no reflected or critically refracted crustal phases exist. However, according to the new IASPEI nomenclature, P and S waves from sub-crustal earthquakes with rays traveling from there either directly or via a turning point in the uppermost mantle back to the surface are still termed Pn and Sn (see Fig. 11.40, lower left). At larger distances such rays arrive at the surface with apparent “sub-Moho” P and S velocities (see below).

Typical propagation velocities of Pg and Sg in continental areas are 5.5-6.2 km/s and 3.2-3.7 km/s, respectively. Note, that Pg and Sg are direct waves only to about 2° to 3°. At larger distances the Pg-wave group may be formed by superposition of multiple P-wave reverberations inside the whole crust (with an average group velocity around 5.8 km/s) and the Sg-wave group by superposition of S-wave reverberations and SV to P and/or P to SV conversions inside the whole crust. According to the new IASPEI phase nomenclature the definitions given for Lg waves and Sg at larger distances are identical, with the addition that the maximum energy of an Lg crustal “channel” wave travels with a group velocity around 3.5 km/s. In routine analysis, usually only the first onsets of these wave groups are picked without noting the change in character at larger distances. According to the Technical Instructions of the IDC Documentation (1998), stations of the CTBTO International Monitoring System (IMS) generally tend to name the strongest transverse arrival Lg and not Sg. A reliable discrimination is still a subject of research and not yet one of routine analysis and data reporting. Therefore, no simple and unique criteria for discrimination, which also depend on source type and propagation path, can be given here. They may be added to this Manual at a later time. Lg waves may travel in continental shield regions over large distances (see Fig. 2.15), even beyond 20° whereas Rg waves, which show clear dispersion and longer periods than Lg (see Fig. 2.16), are more strongly attenuated and generally not observed beyond 6°. The apparent velocities of Pn and Sn are controlled by the P- and S-wave velocities in the upper mantle immediately below the Moho and typically range between 7.5 - 8.3 km/s and 4.4 - 4.9 km/s, respectively.

Note: Seismograms from local and regional seismic sources are strongly influenced by the local crustal structure which differs from region to region and even between local stations. This may give rise to the appearance of other onsets (which may be strong) between the mentioned main crustal phases that can not be explained by a near-surface source in a single or two-layer crustal model. Some of these phases may relate to converted waves and/or depth phases such as sPmP (e.g., Bock et al., 1996). Also, at larger distances of up to about 30°, multiples such as PgPg, PbPb, PnPn, PmPPmP etc. and their related S waves may be well developed (see Fig. 11.19). However, usually these details can not be handled in routine data analysis and epicenter location and require specialized study. For routine purposes, as a first approximation, the IASP91 or AK135 global models (see DS 2.1) can be used for the analysis and location of near events based on the main crustal phases. However, one should be aware that crustal structure and velocities may differ significantly from region to region, and that the event location can be significantly improved when local travel-time curves or crustal models are available (see IS 11.1, Figures 11 and 12).

Fig. 11.41 shows seismograms of a shallow ($h = 8$ km) near earthquake from the Vogtland/NW Bohemia region in Central Europe, recorded at seven GRSN stations in the epicentral distance range 10 km (WERN) to 180 km (GEC2). Stations up to $D = 110$ km

11.5 Examples of seismogram analysis

(BRG) show only the direct crustal phases Pg, Sg, except GRFO, which in addition shows PmP. At GEC2 Pn arrives ahead of Pg with significantly smaller amplitude. The onset times of phases Pg, Sg and Pn were used to locate the epicenter of this event with a precision of about 2 km. If more stations close to the epicenter are included (e.g., Fig. 11.42; D = 6 – 30 km), the precision of the hypocenter location may be in the order of a few hundred meters.

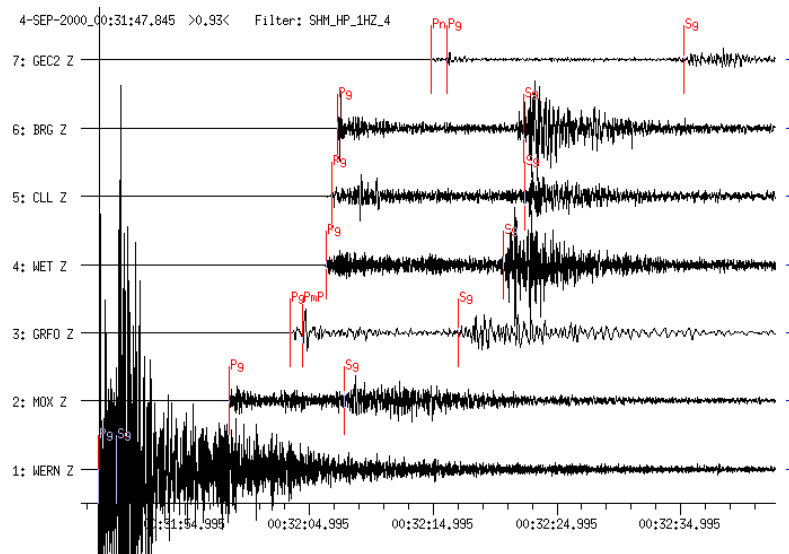


Fig. 11.41 Filtered short-period vertical component seismograms (4th order Butterworth high-pass filter, $f = 1$ Hz) from a local earthquake in the Vogtland region, 04 Sept. 2000 (50.27°N, 12.42°E; $M_l = 3.3$). Sampling rates at the stations differ: 80 Hz for MOX, WET, CLL, and BRG, 100 Hz for WERN and 20 Hz for GRFO and GEC2. Traces are sorted according to epicentral distance (from 10 to 180 km). The local phases have been marked (Pg and Sg at all stations, PmP at GRFO and Pn at the most distant station GEC2 (D = 180 km)).

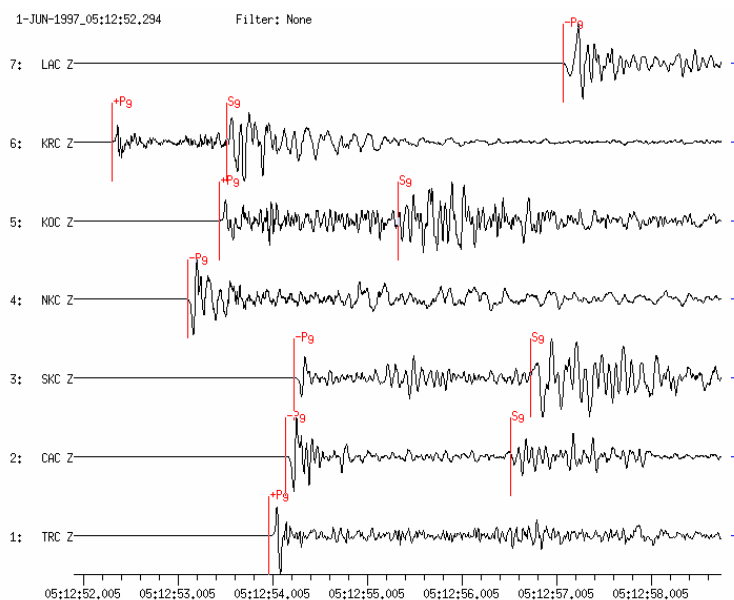


Fig. 11.42 Short-period recordings from stations of the local network of the Czech Academy in Prague from a small ($M_l = 3.3$) local earthquake in the German/Czech border region on June 1, 1997. The epicentral distance range is 6 km and 30 km. Such local networks allow hypocenters to be located to better than a few hundred meters.

Fig. 11.43 (left) shows for another Vogtland swarm earthquake, a record section with seismograms of 5 stations in the distance range 10 km to 130 km, together with the expected travel-time curves for Pg and Sg according to an average crustal model. Fig. 11.43 (right) shows some of the same seismograms on a map together with the station positions (triangles).

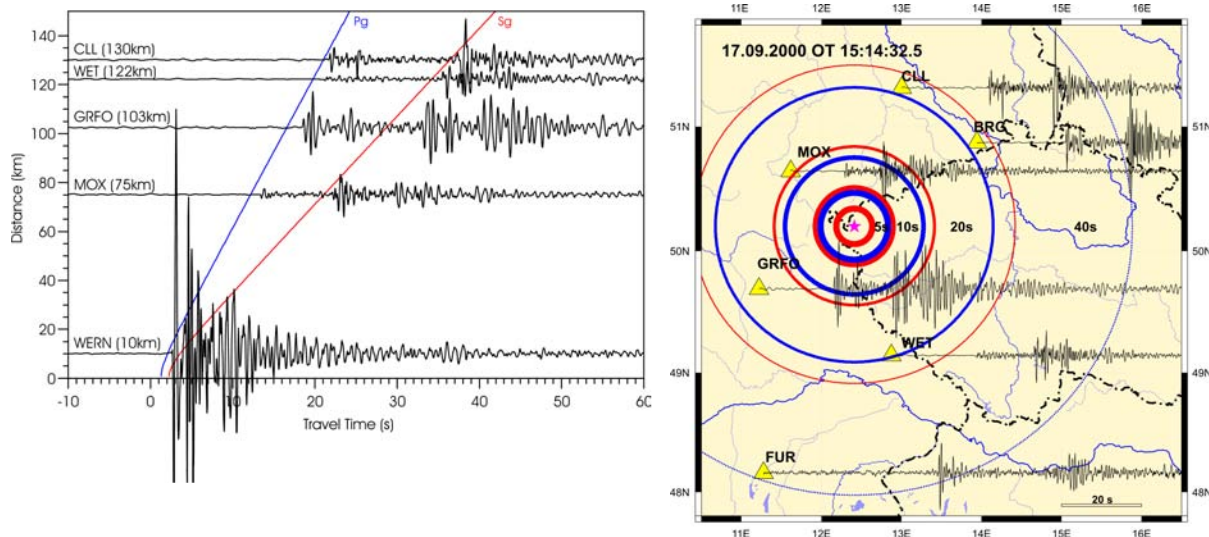


Fig. 11.43 Records of a Vogtland swarm earthquake (17 Sept. 2000; $M_I = 3.1$) at stations of a local network in Germany. Left: arranged by distance together with the expected travel times for Pg and Sg for an average crustal model; right: on a map view with station positions. The circles indicate the position of the wavefronts of Pg (blue) and Sg (red) after 5, 10, 20 and 40 s, respectively (see also file 1 in IS 11.3 and related animation on CD-ROM).

From these two figures the following conclusions can be drawn:

- at some stations the arrival times are in good agreement with the times predicted from an average crustal model, at other stations they are not, which implies crustal structure varies laterally; and
- the amplitude ratio Pg/Sg varies strongly with the azimuth because of the different radiation patterns for P and S waves. This variation can be used to derive the fault-plane solution of the earthquake (see Figs. 3.25 and 3.26 and section 3.4.4).

Other examples of local seismograms are shown in Figs. 11.44 and 11.45. Fig. 11.44 shows recordings from an earthquake in the Netherlands ($M_I = 4.0$) in the distance range 112 km to 600 km, and Fig. 11.45 those from a mining-induced earthquake in France ($M_I = 3.7$) in the range 80 km to 500 km. These records again show obvious variation in the relative amplitudes of Pn, Pg and Sg. The relative amplitudes depend on the distance and azimuth of the station relative to the radiation pattern of the source, and particularly with respect to the differences in take-off angles of the rays for the direct and the critically refracted waves (see Fig. 11.40). The source depth with respect to the major crustal discontinuities may also influence the relative amplitude ratio between these various phases.

Generally, for near-surface sources and distances smaller than about 400 km, Pn is much smaller than Pg (see also Figures 3a and 3c in Datasheet 11.1). For larger distances however, the relative amplitudes of Pn and Sn may grow so that these phases dominate the P and S

arrivals (see Fig. 2.15 and the uppermost traces in Figs. 11.44 and 11.45). This is not only because of the stronger attenuation of the direct waves that travel mostly through the uppermost heterogeneous crust but also because P and S near the critical angle of refraction at the Moho form so-called “diving” phases which are not refracted into the Moho but rather travel within the uppermost mantle with sub-Moho velocity. The recognition of these crustal body waves and the precision of onset-time picking can be significantly improved by stretching the time scale in digital records (compare Figures 3a and 3c in DS 11.1).

The great variability in the appearance of waveforms and relative amplitudes in near-earthquake recordings is also illustrated by Fig. 11.46. Even seismic records at the same station from two different sources at nearly the same distance and with similar azimuth may look very different. This may be because the waves from the two earthquakes travel along slightly different paths through the highly heterogeneous Alpine mountain range. However, the fault-plane orientation and related energy radiation with respect to the different take-off angles of Pn and Pg, may also have been different for these two earthquakes.

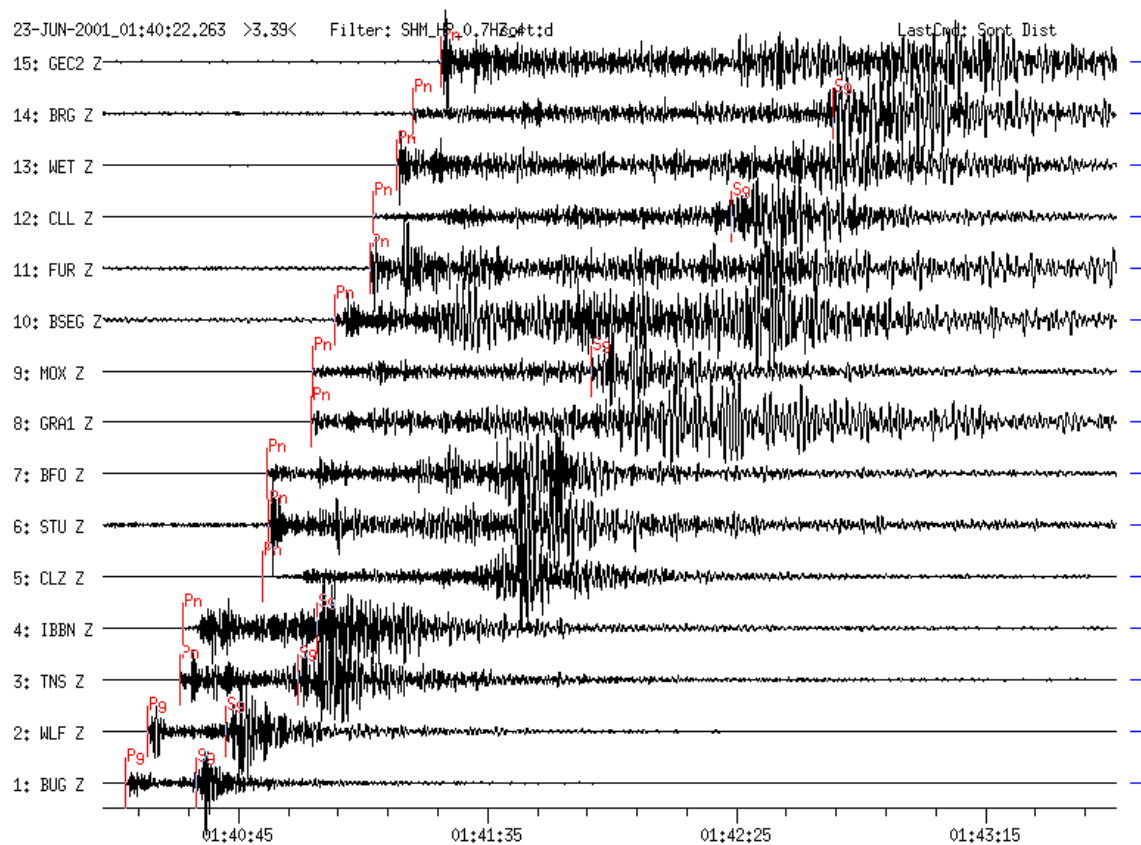


Fig. 11.44 Vertical-component short-period filtered broadband seismograms (4th order Butterworth high-pass filter, $f = 0.7$ Hz; normalized amplitudes) from a local earthquake at Kerkrade, Netherlands, recorded at 15 GRSN, GRF, GERES and GEOFON stations. $M_L = 4.0$; epicentral distances between 112 km (BUG) and 600 km (GEC2). Note the variability of waveforms and relative phase amplitudes of local/regional earthquakes in network recordings in different azimuths and epicentral distances. The suitability of filters for determination of local phase onsets has to be tested. Local magnitudes determined from a Wood-Anderson simulation.

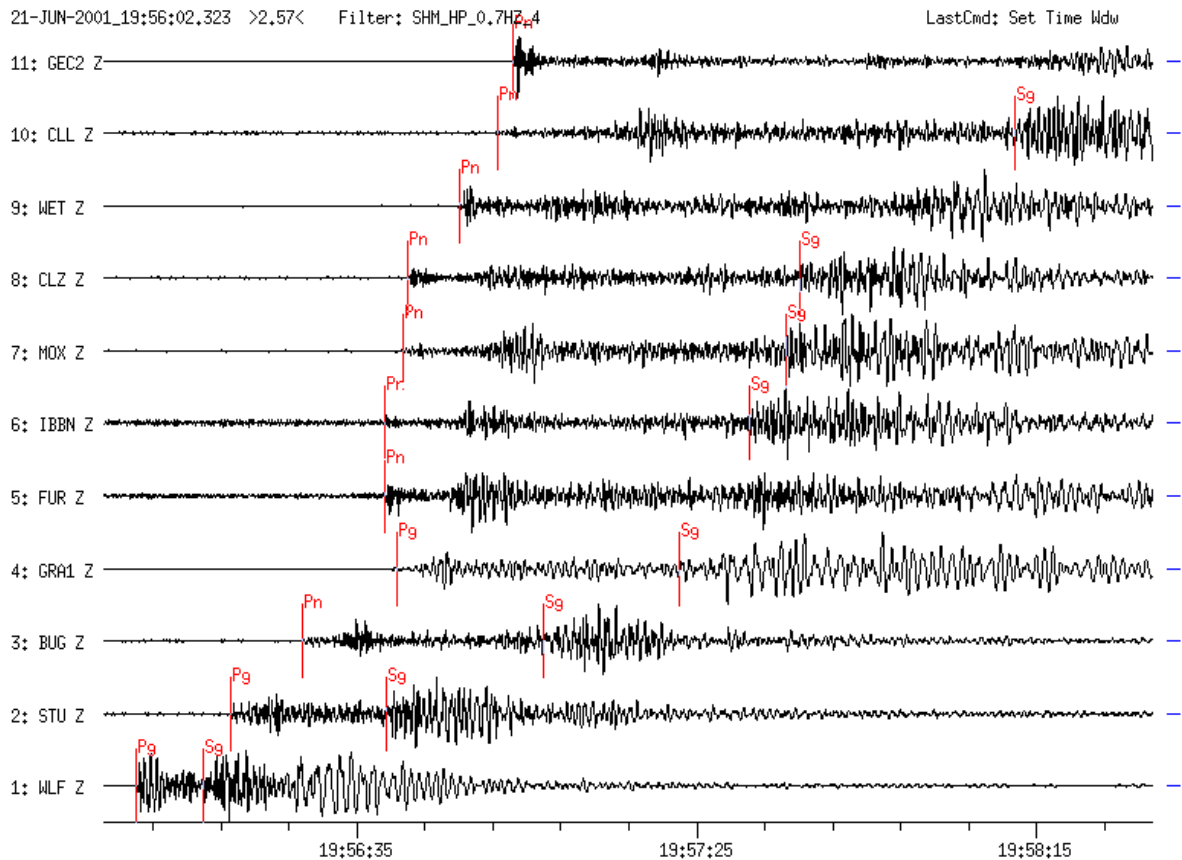


Fig. 11.45 Vertical-component short-period filtered BB seismograms (4th order Butterworth high-pass filter, $f = 0.7$ Hz, normalized amplitudes) from a local mining-induced earthquake at the French-German border recorded at 11 GRSN, GERES and GEOFON stations ($M_l = 3.7$; epicentral distances between 80 km (WLF) and 501 km (GEC2)).

Note that in Figs. 11.39a and b and Fig. 11.45 (e.g., station WLF), the longer period Rg waves, following Sg, are particularly well developed in records of near-surface quarry blasts or shallow mining-induced earthquakes but not in the natural earthquake records (as in Fig. 11.43).

As mentioned above, at distances beyond about 600 to 800 km, Pn and Sn become the dominating body-wave onsets that for shallow sources are followed by well-developed surface-wave trains. Figure 6a in DS 11.1 shows a typical 3-component BB-velocity record of such an earthquake in Italy made at station GRA1 in Germany ($D = 10.3^\circ$). Figure 6c shows the respective BB recordings of the same shock at 10 stations of the GRSN ($D = 8^\circ - 12^\circ$). Pg and Sg are no longer recognizable. In fact, Pn and Sn at these regional distances are no longer pure head waves from the Moho discontinuity but rather so-called diving phases of P and S which have penetrated into the uppermost mantle but travel also with the sub-Moho velocity of Pn of about 8 km/s. These diving phases may be of longer periods than Pn at shorter distances. One should also be aware that local and regional earthquakes do not only appear in short-period recordings. Strong near events with magnitudes above 4 usually generate also strong long-period waves (see Figs. 11.8 and 11.10).

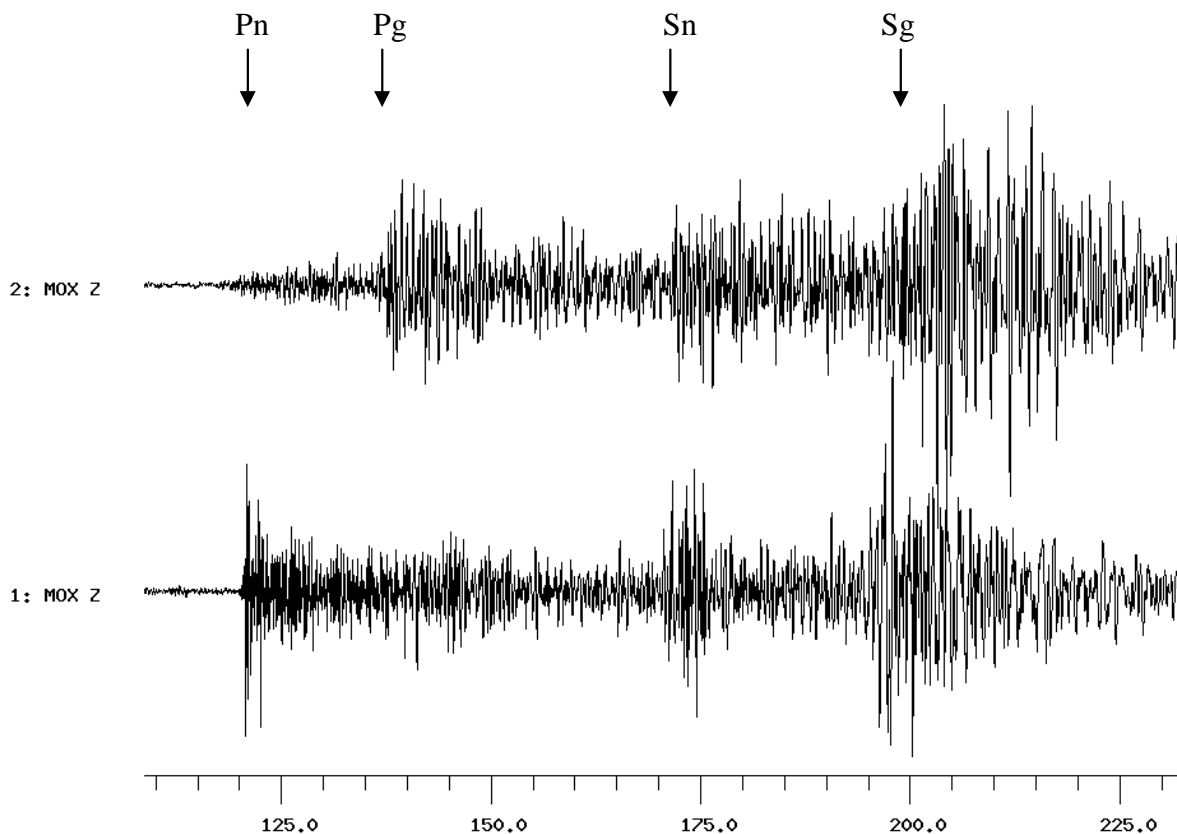


Fig. 11.46 Comparison of Z-component short-period filtered records at station MOX, Germany, of two earthquakes in Northern Italy (trace 1: 28 May 1998; trace 2: 24 Oct. 1994) at about the same epicentral distance ($D = 505$ km and 506 km, respectively) and with only slightly different backazimuth ($BAZ = 171^\circ$ and 189° , respectively). Note the very different relative amplitudes between Pn and Pg, due to either crustal heterogeneities along the ray paths or differences in rupture orientation with respect to the different take-off angles of Pn and Pg rays.

In general, regional stations and local networks complement each other in the analysis of smaller sources at local distances. Additionally, source processes and source parameters can be estimated using local station data. For this purpose, first motion polarities (compression c or +, dilatation d or -) for phases Pg, Pn, Sg and amplitude ratios (P/SV) should be measured for fault plane solution and moment tensor inversion (see 3.4 and 3.5). In regions with a poor station coverage, the mean precision of location may be several kilometers and source depths may then only be determined with teleseismic depth phases by way of waveform modeling (see 2.8).

An important aspect to consider in digital recordings and data analysis of local and regional seismograms is the sampling rate. Sampling with more than 80 s.p.s. is generally suitable for near seismic events. With lower sampling rate some of the most essential information about the seismic source process such as the corner frequency of the spectrum and its high-frequency decay, may be lost. Fig. 11.47 gives an example.

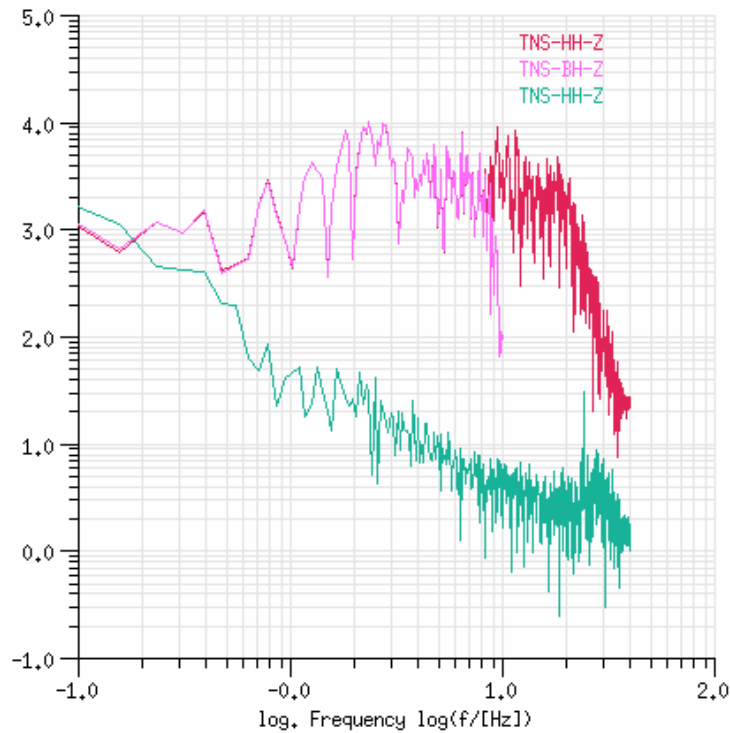
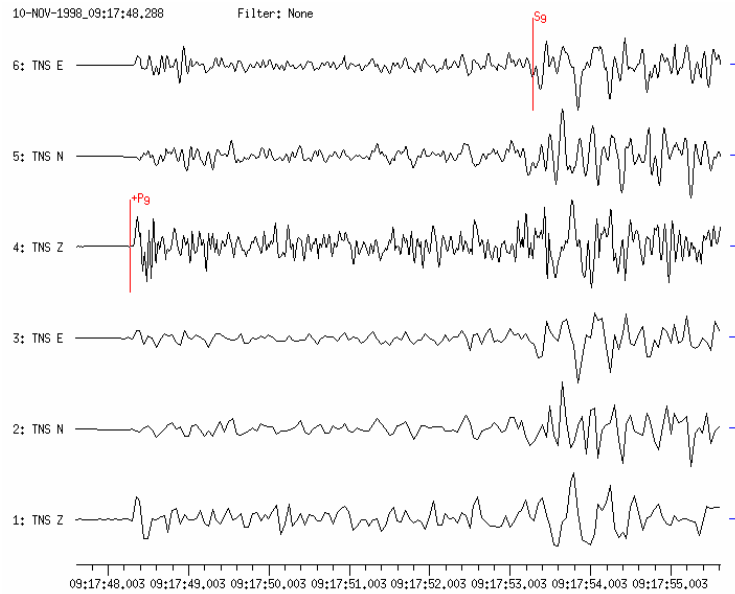


Fig. 11.47 Top: BB-velocity seismogram from a local earthquake near Bad Ems (11 Oct. 1998; $M_l = 3.2$) recorded at the GRSN station TNS ($D = 40$ km). Different sampling rates were used for data acquisition. Traces 1 – 3 were sampled at 20 Hz and traces 4 – 6 at 80 Hz. In the records with the higher sampling rate, the waveforms are much more complex and contain higher frequencies. The high frequency content is suppressed with the lower sampling rate. **Bottom:** Fourier spectrum of traces 1 (sampling rate 20 Hz – pink) and 4 (sampling rate 80 Hz – red). The lower sampling rate cuts off the high-frequency components of the seismic signal. Thus the corner frequency of the signal at about 20 Hz and the high-frequency decay could not be determined from the pink spectrum. The green spectrum represents the seismic noise.

In the example considered in Fig. 11.47 only the 80 Hz data stream with a Nyquist frequency of 40 Hz allows the corner frequency near 20 Hz to be determined. However, in some regions, or when studying very small local earthquakes, still higher frequencies have to be analyzed. This may require sampling rates between 100 and 250 Hz.

Note, that besides the regional phases Sn and Lg the teleseismic phase PcP also may be observed in the far regional distance range (6° - 20°) in short-period seismograms of strong events ($M_l > 4$). PcP, which gives a good control of source depth, can be identified in array recordings because of its very small slowness.

In Box 1 below a summary is given of essential features that can be observed in records of local and regional seismograms. For more records in this distance range see DS 11.1.

BOX 1: General rules for local and regional events

- The frequency content of local events ($D < 2^\circ$) is usually high ($f \approx 0.2 - 100$ Hz). Therefore they are best recorded on SP or SP-filtered BB instruments with sampling rates $f \geq 80$ Hz. The overall duration of short-period local and regional ($D < 20^\circ$) seismograms ranges between a few seconds and to several minutes.
- Strong local/regional sources radiate long-period energy too and are well recorded by BB and LP seismographs. In the far regional range the record duration may exceed half an hour (see Fig. 1.2).
- Important seismic phases in seismograms of local sources are Pg, Sg, Lg and Rg and in seismograms of regional sources additionally Pn and Sn, which arrive beyond 1.3° - 2° as the first P- and S-wave onsets. The P waves are usually best recorded on vertical and the S waves on horizontal components.
- Note that Pg is not generally seen in records from sources in the oceanic crust. Also, deep (sub-crustal) earthquakes lack local and regional crustal phases.
- For rough estimates of the epicentral distance D [km] of local sources, multiply the time difference Sg-Pg [s] by 8, and in the case of regional sources the time difference Sn-Pn [s] by 10. For more accurate estimates of D use local and regional travel-time curves or tables or calculations based on more appropriate local/regional crustal models.
- The largest amplitudes in records of local and regional events are usually the crustal channel waves Lg (sometimes even beyond 15°), and for near-surface sources the short-period fundamental Rayleigh mode Rg. For near-surface explosions or mining-induced earthquakes, Rg, with longer periods than Sg, may dominate the record, however usually not beyond 4° .
 - For routine analysis the following station/network readings should be made: (1) the onset time and polarity of observed first motion phases; (2) onset times of secondary local and regional phases; (3) local magnitude based either on maximum amplitude or duration. If local/regional calibration functions, properly scaled to the original magnitude definition by Richter (1935), are not available it is recommended to use the original Richter equation and calibration function, together with local station corrections.

11.5.2 Teleseismic earthquakes ($15^\circ < D < 180^\circ$)

11.5.2.1 Distance range $15^\circ < D \leq 28^\circ$

At distances beyond 15° , sometimes referred to as “far-regional”, Pn and Sn amplitudes become too small (except in some shield regions) and the first arrival phase has a travel path through deeper parts of the upper mantle. The common nomenclature for these waves with longer periods than Pn and Sn is P and S, respectively. For the next 12° , the records look rather simple in one respect, namely, that only three major wave groups are recognizable (P, S, and surface waves, see Fig. 11.48).

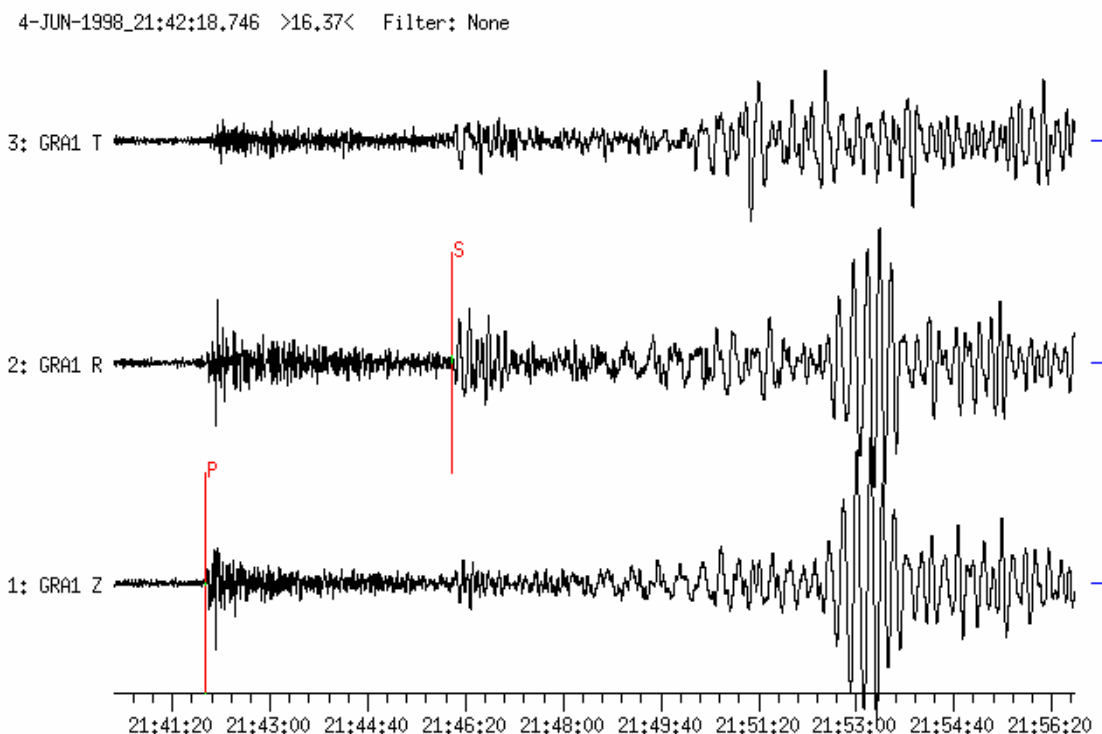


Fig. 11.48 Three-component broadband seismograms from an earthquake in Iceland on 04 June 1998, recorded at GRF-array station GRA1 ($D = 22.5^\circ$). P, S and surface waves are recognizable. Horizontal traces have been rotated (R = Radial, T = Transverse) with R showing into the source direction. The overall duration of the record is about 15 min.

The body-wave groups themselves, however, are rather complicated because of the refraction and reflection of P and S at the pronounced velocity increase at the bottom of the upper mantle (410 km discontinuity) and at the bottom of the transition zone to the lower mantle (660 km discontinuity). These strong increases/gradients in wave velocity give rise to the development of two triplications of the P-wave travel-time curve with prograde and retrograde branches which in some distance ranges follow closely each other (see Fig. 2.29), thus forming a sequence of successive P- (and S-) wave onsets (see Fig. 11.49). The largest amplitudes occur in the range of the left-side cusp of the 660 km discontinuity triplication (P660P) between about 18° and 20° (also termed “ 20° -discontinuity”) but with weaker P-wave first arrivals some 5 to 10 s earlier. Accordingly, small differences in epicentral distance

can lead to large differences in the appearance of the body-wave groups in seismic records (see Fig. 11.49). Generally, P waves are rather complex and wave onsets emergent. Surface waves of shallow earthquakes, however, are strong, clearly separated from S waves and very useful for surface wave magnitude (M_s) estimation.

Fig. 11.49 shows BB-velocity seismograms from an earthquake in Turkey recorded at stations of the GRSN in the distance range between about 14.5° and 19.5° . Note the increase of the P-wave amplitudes with distance when approaching “ 20° -discontinuity”.

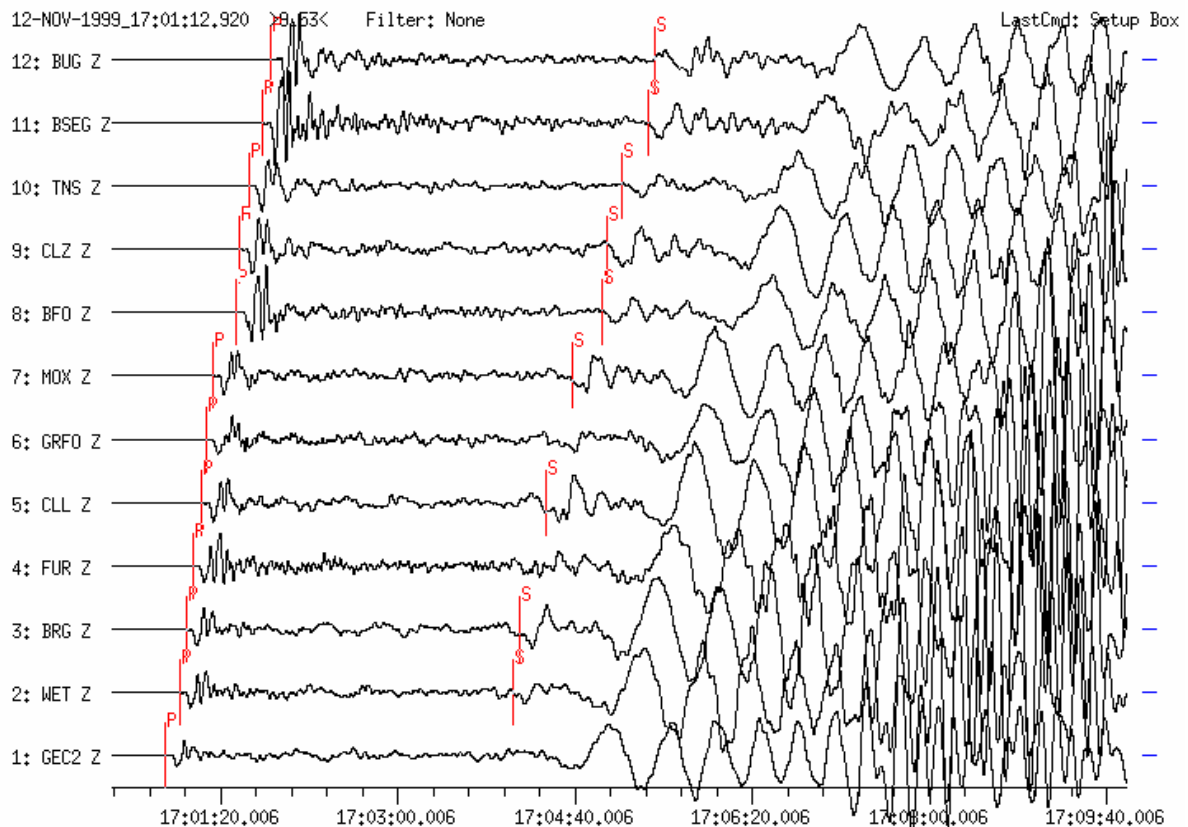


Fig. 11.49 Vertical-component BB-velocity seismograms from the damaging earthquake in Düzce, NW-Turkey, recorded at 12 GRSN-stations in the distance range 14.5° to 19.5° . (Source data from NEIC-QED: 12 Nov. 1999, OT 16:57:20; 40.79°N , 31.11°E ; $h = 10$ km; $M_w = 7.1$; $D = 16.5^\circ$ and $\text{BAZ} = 115^\circ$ from GRFO). Traces are sorted according to distance. Incoherent and complex P waves are followed by weak S waves and distinct and clearly dispersed surface waves, which have longer periods than the S waves. The body waves P and S are affected by upper mantle discontinuities. Note the increase in P-wave amplitudes with distance due to the cusp of P660P around 18° to 19° (see Fig. 2.29).

Fig. 11.50 shows 3-component records (Z, R, T) demonstrating the presence of the 20° discontinuity in another part of the world. The seismograms are from an earthquake that occurred in the southern part of the New Hebrides at 35 km depth, recorded between 16.9° and 23.6° by a regional network of portable broadband instruments deployed in Queensland, Australia (seismometers CMG3ESP; unfiltered velocity response). The complex P wavelets

appear in Z and R only. In their later parts they may contain PnPn arrivals. Similarly complex S-wave groups appear in R and T, and may include SnSn.

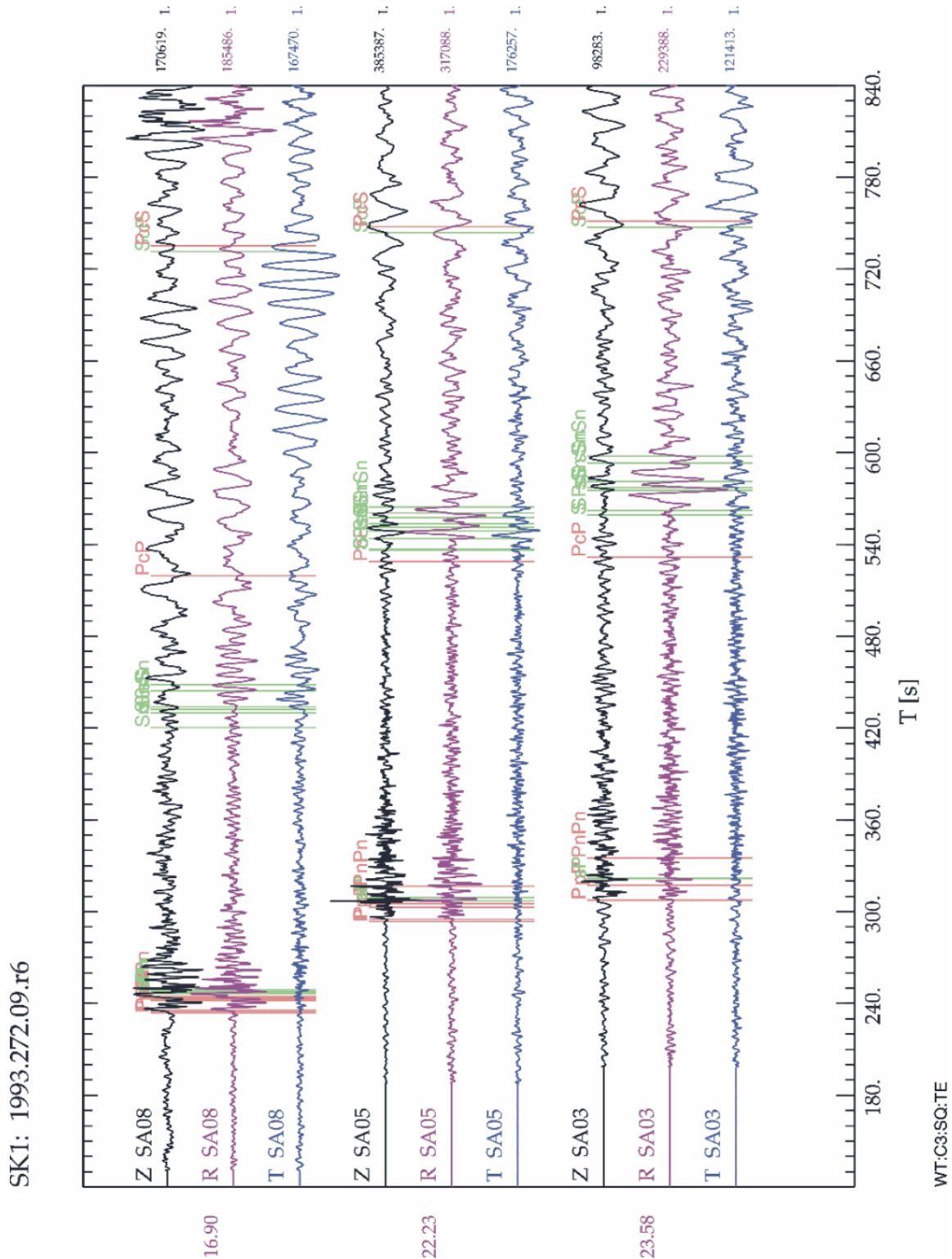


Fig. 11.50 Three-component BB records made in Queensland, Australia, from an earthquake in the New Hebrides between $D = 16.9^\circ$ and 23.6° . Note the complexity of P- and S-wave arrivals around the 20° discontinuity. On each set of records the predicted phase arrival times for the AK135 model (see Fig. 2.53) are shown as faint lines. However, there might be no

clear onset visible at these times above the noise or signal-coda level of previous phases. Never use such theoretical onset marks for picking onset times! (Courtesy of B.L.N. Kennett).

11.5.2.2 Distance range $28^\circ < D \leq 100^\circ$

The main arrivals at this distance range up to about 80° , have traveled through the lower mantle and may include reflections from the core-mantle boundary (CMB) (Fig. 11.53). The lower mantle is more homogeneous than the upper mantle (see Fig. 2.53). Accordingly, P and S waves and their multiples form rather simple long-period seismograms (Figs. 11.9 and 11.52; see also files 4 and 5 in IS 11.3 and animation on CD-ROM). Between 30° and 55° , the waves reflected from the core (e.g., PcP, ScP etc.) are also often recorded as sharp pulses on short-period records, particularly on records of deep earthquakes where depth phases appear well after the core reflections (see Fig. 11.16). At around 40° , the travel-time curve of PcP intersects those of PP and PPP (see Fig. 11.53) and in horizontal components PcS intersects S, and ScS intersects SS and SSS. This complicates proper phase separation, at least for the later phases on long-period records, where SS and SSS may be strong. ScP, however, may also be rather strong on short-period vertical components (see Fig. 11.53). Note that PP, PS, SP and SS are Hilbert-transformed (see 2.5.4.3). Their onset and amplitude picks can be improved by inverse Hilbert transformation, which is part of modern analysis software such as Seismic Handler (SH and SHM). The amplitudes of the core reflections decrease for larger distances but they may be observed up to epicentral distance of about 80° (ScP and ScS) or 90° (PcP), respectively, beyond which ScS merges with the travel-time curves of SKS and S and PcP with that of P (compare travel-time curves in Figure 4 of EX 11.2 with Figs. 11.16 and 11.55).

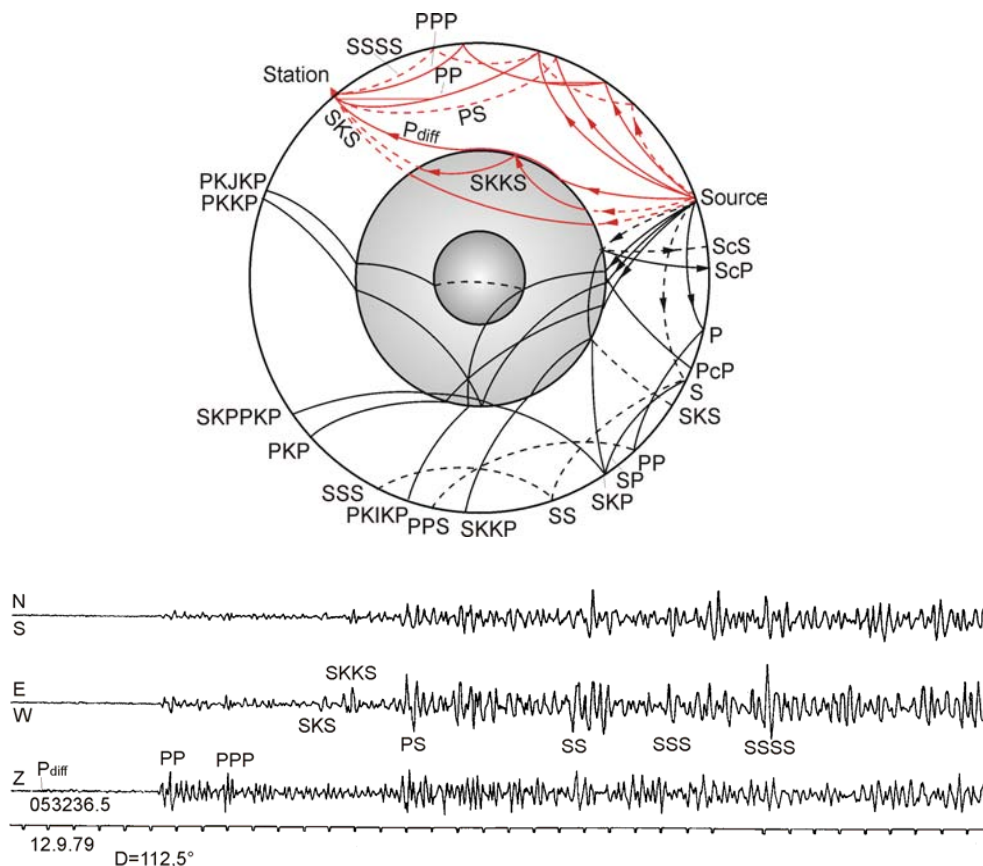


Fig. 11.51 Seismic ray paths through the mantle and core of the Earth with the respective phase names according to the international nomenclature (see Fig. 2.48 and overlay for related

travel-time curves, and IS 2.1 for phase names and their definition). The red rays relate to the 3-component analog Kirnos SKD BB-displacement record of body waves from an earthquake at $D = 112.5^\circ$ at station MOX, Germany.

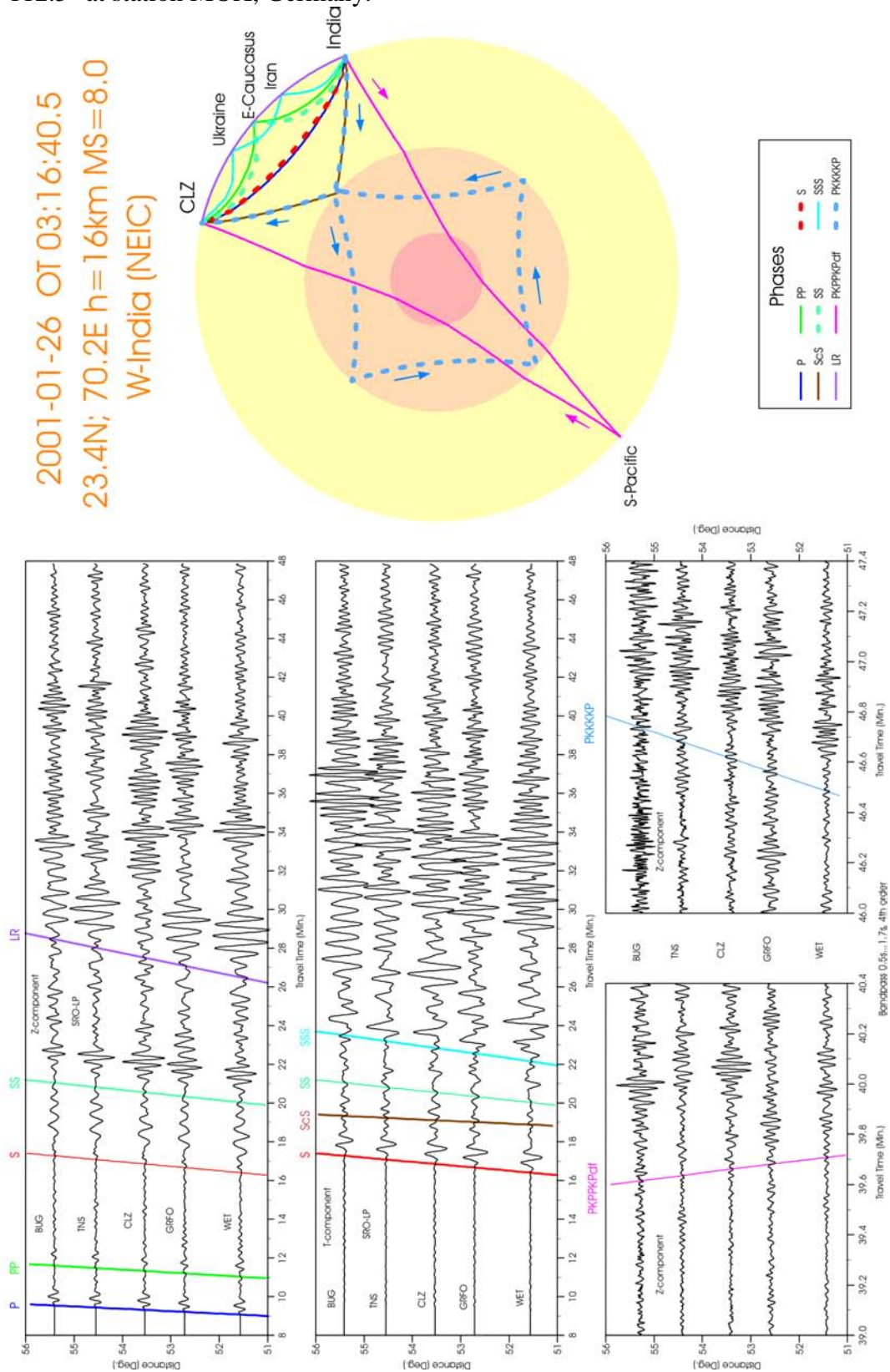


Fig. 11.52 Long-period Z- (left) and T-component seismograms (middle) of a shallow earthquake in western India recorded in the distance range 51° to 56° at stations of the GRSN.

Two cutout sections from short-period Z-component records of multiple core phases are shown on the right and the related ray paths at the top (for animation see file 4 in IS 11.3).

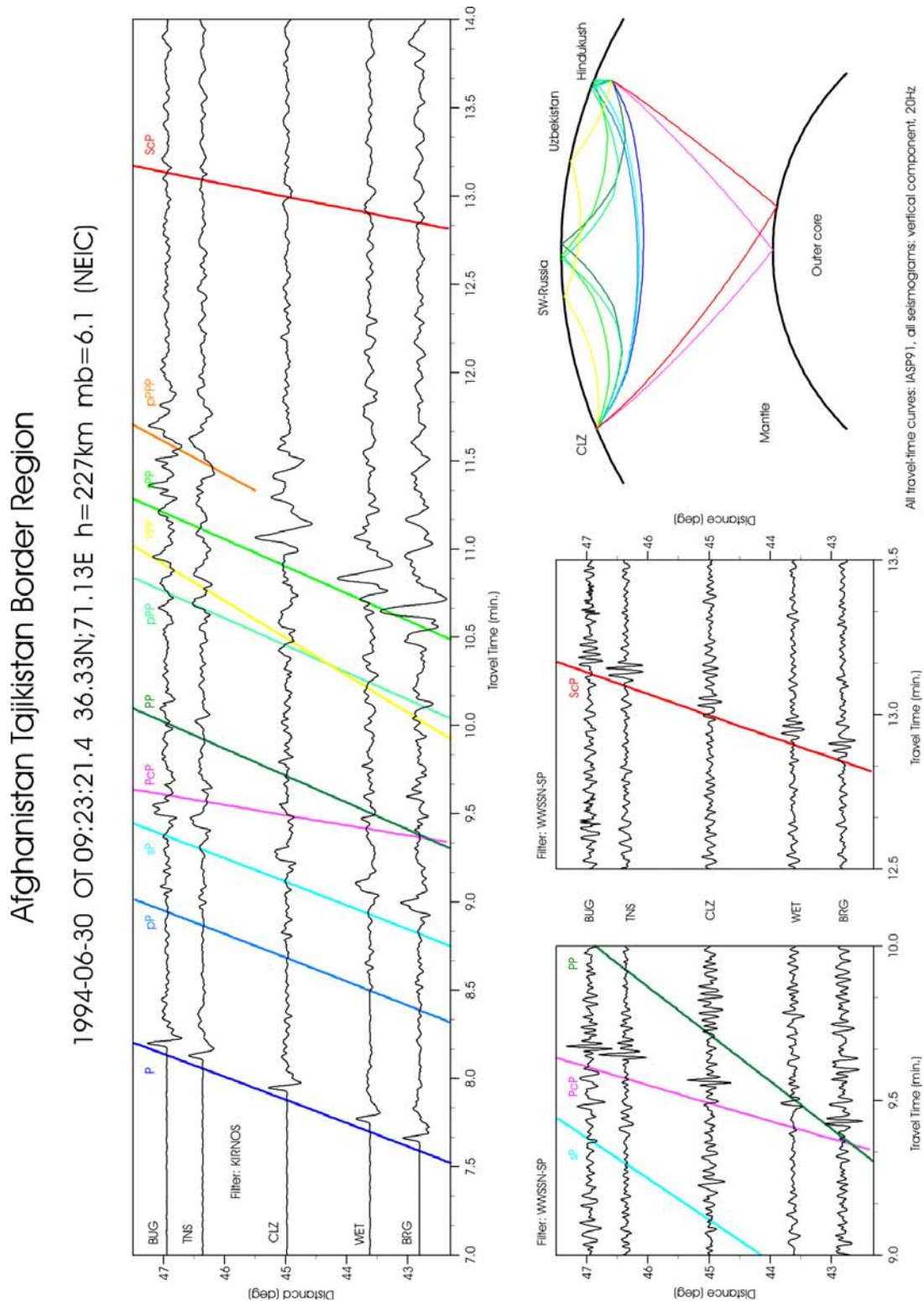


Fig. 11.53 Vertical-component Kirnos SKD BB-displacement (left) and WWSSN-SP seismograms (right) from an intermediate depth ($h = 227$ km) earthquake in the Afghanistan-Tajikistan border region recorded at stations of the GRSN. Besides P the depth phases pP, sP, pPP, sPP and pPPP and the core reflections PcP and ScP are clearly visible, particularly on

the short-period records. The ray traces of these phases are shown in the upper right corner (see also file 3 in IS 11.3 and related animation on CD-ROM).

Fig. 11.54 shows the ray paths for S, ScS and SKS and their related travel-time curves according to the IASP91 model for the whole distance range from 60° to 180° and Fig. 11.55 both short- and long-period records for these waves between 50° and 80°.

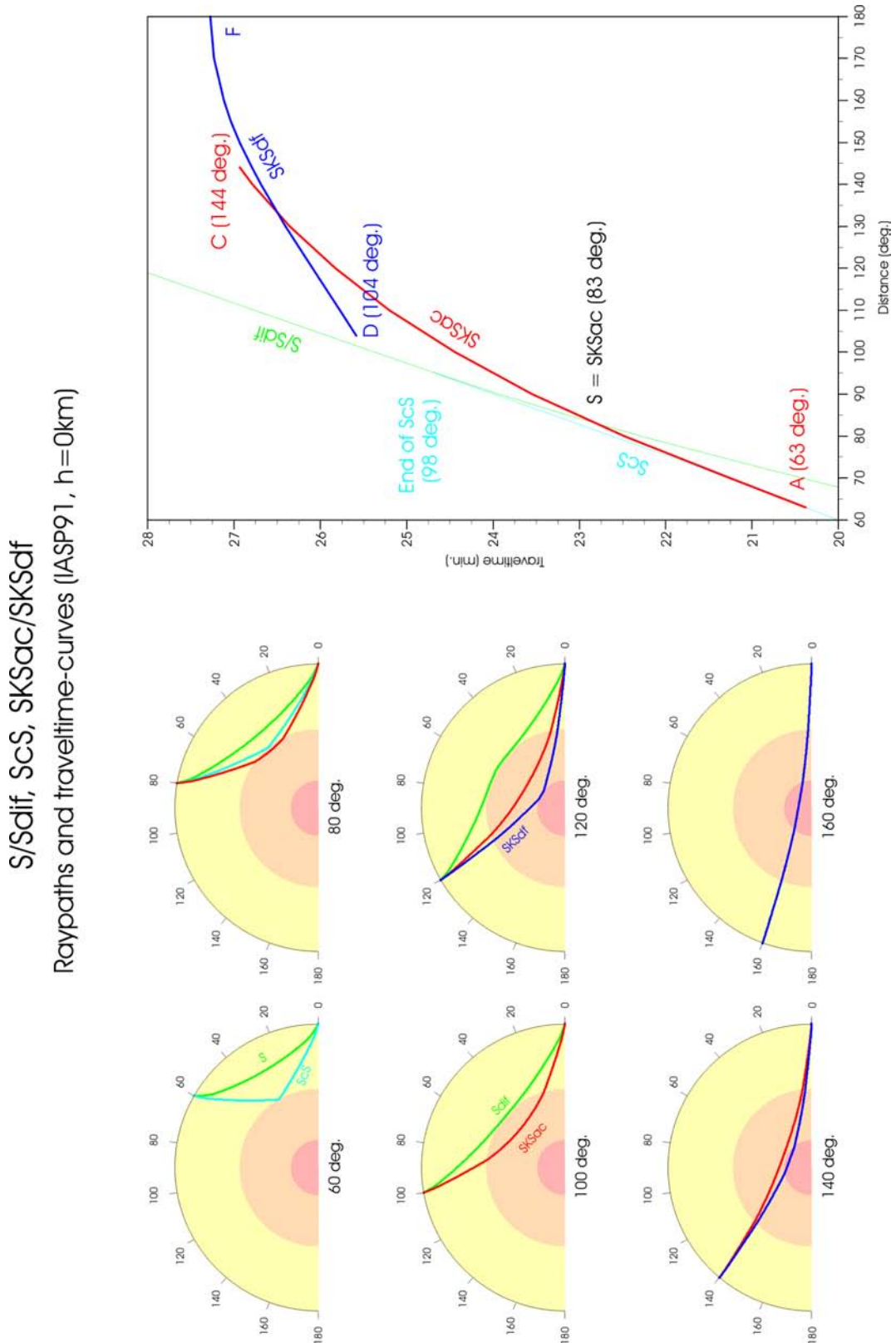


Fig. 11.54 Ray paths for S, ScS and SKS and their related travel-time curves according to the IASP91 model for the whole distance range from 60° to 180° .

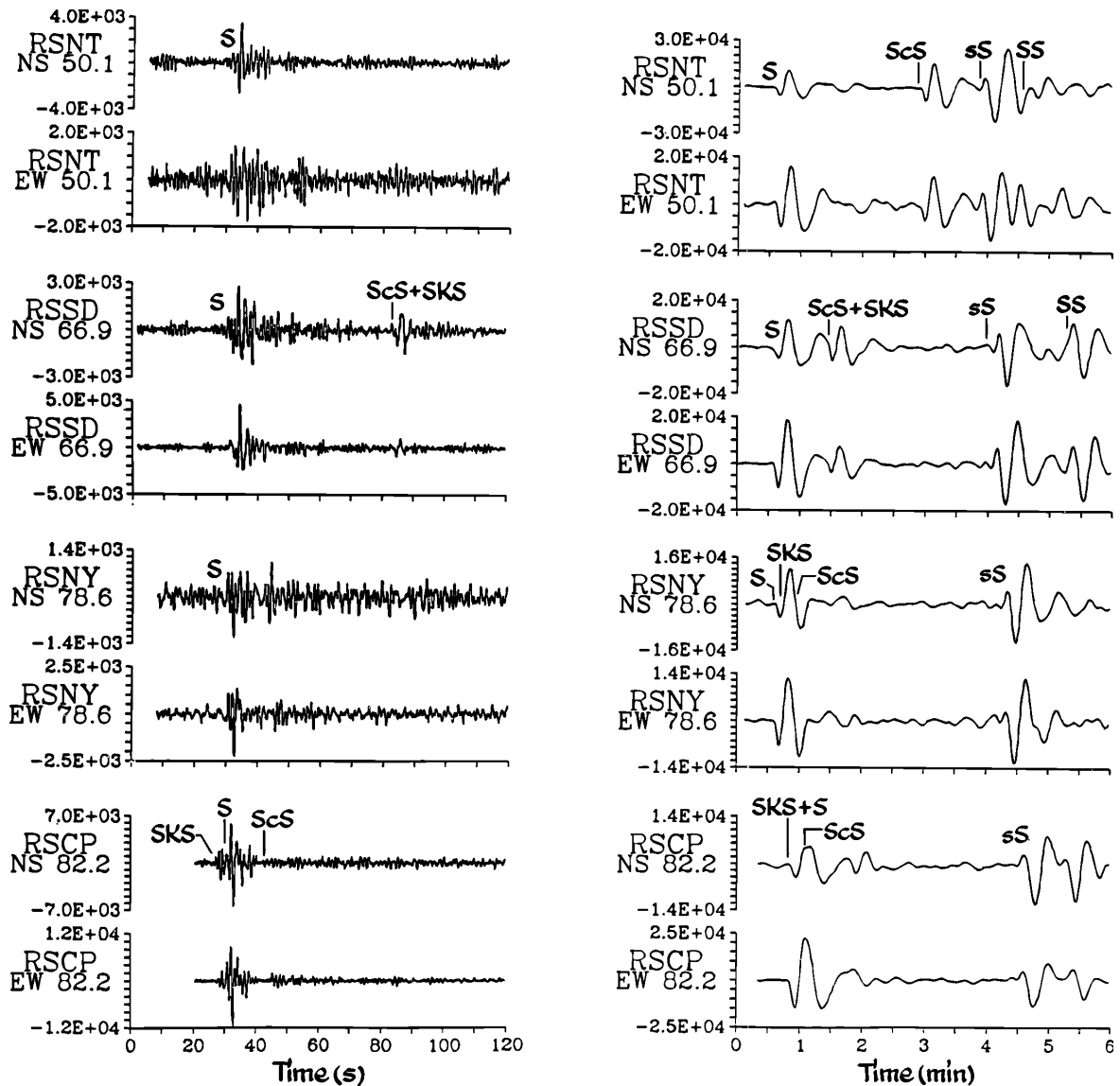


Fig. 11.55 SP (left) and LP (right) horizontal-component seismograms from a deep-focus earthquake in the Sea of Okhotsk (20 April 1984, $m_b = 5.9$, $h = 588$ km) recorded by stations in the distance range 50.1° to 82.2° . Note the different amplitude scaling. Accordingly, the amplitudes of various transverse phases are 2 to 10 times larger in long-period records when compared with short-period records. Four distinct phases are identified: S, ScS, sS and SS. SKS, which emerges at distances larger than 60° however, overlaps with ScS between about 65° and 75° . S, ScS and SKS start to coalesce as distance increases toward 82° . Beyond this distance SKS arrives before S, SKKS and ScS (reprinted from *Anatomy of Seismograms*, Kulhánek, Plate 40, p.137-138; © 1990; with permission from Elsevier Science).

Arrays and network records, which also allow f-k and vespagram analysis are very useful for identifying the core reflections PcP, ScP and ScS because their slownesses differ significantly from those of P, S and their multiple reflections (see Fig. 11.52 as well as Figures 6a and b

and 7b in DS 11.2). Surface reflections PP, PPP, SS and SSS are well developed in this distance range in long-period filtered records and converted waves PS/SP at distances above 40°. Sometimes the surface reflections are the strongest body-wave onsets at large distances (see Figures 10c and 11b in DS 11.2). Their identification can be made easier when network records are available so vespagram analysis can be used (e.g., Figure 11c in DS 11.2). In short-period filtered network records it is sometimes also possible to correlate well in this distance range multiple reflected core phases such as PKPPKP or P'P', SKPPKP and even SKPPKPPKP (see Fig. 1.4).

Beyond 83° SKS moves ahead of S and its amplitude relative to S increases with distance. Network and array analysis yields different slowness values for S and SKS because of their diverging travel-time curves (see Fig. 11.54). This helps to identify these phases correctly. Note that the differential travel time SKS-P increases only slowly with distance (see Figure 4 in EX 11.2). Misinterpretation of SKS as S may therefore result in an underestimation of D by up to 20°! Since SKS is polarized in the vertical plane it can be observed and separated well from S in radial and vertical components of rotated seismograms (see Figures 10c, 13e, 14e, and 15b in DS 11.2). The same applies for PcS and ScP, which are also polarized in the vertical plane in the direction of wave propagation.

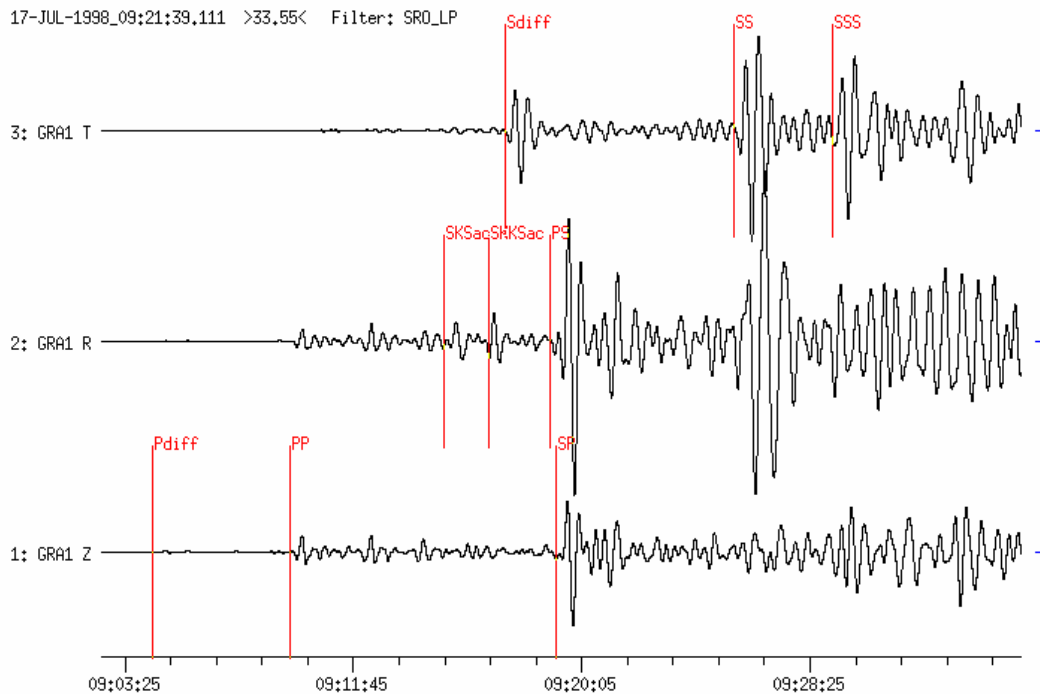
In the distance range between about 30° and 105° multiple reflected core phases P'N or between about 10° < D° < 130° the phases PNKP, with N-1 reflections either at the free surface (P'N) or from the inner side of the core-mantle boundary (PNKP) may appear in short-period records some 13 min to 80 min after P. An example for PKPPKP (P'P') and PKKKKP (P4KP) is given in Fig. 11.52. These phases are particularly strong near caustics, e.g., P'P' (see Fig. 11.69) and P'P'P' (P'3) near 70° and PKKP near 100° (see Fig. 11.71) but they are not necessarily observable at all theoretically allowed distances. Figures 9 and 10 in EX 11.3, however, document the rather wide distance range of real observations of these phases at station CLL (for P'P' between 40° and 105° and for PKKP between 80° and 126°). Note the different, sometimes negative slowness of these phases. More record examples, together with the ray paths of these waves, are presented in a special section on late core phases (11.5.3). For differential travel-time curves PKKP-P and PKPPKP-P see Figures 9 and 10 in EX 11.3. Also PKiKP, a weak core phase reflected from the surface of the inner core (ICB), may be found in short-period array recordings throughout the whole distance range, about 4.5 to 12 min after P. Its slowness is less than 2s/°. Beyond 95°, P waves show regionally variable, fluctuating amplitudes. Their short-period amplitudes decay rapidly (see Fig. 3.13) because of the influence of the core (core-shadow) while long-period P waves may be diffracted around the curved core-mantle boundary (Pdif, see Figs. 11.59 and 11.63 as well as Figures 1, 2, 4b and 6c and b in DS 11.3).

In any event, comprehensive seismogram analysis should be carried out for strong earthquakes which produce many secondary phases. Unknown phase arrivals should also be reported for further investigations into the structure of the Earth. When reporting both identified and unknown phases to international data centers the IASPEI-proposed international nomenclature should strictly be observed (see IS 2.1).

11.5.2.3 Distance range 100° < D ≤ 144°

Within this distance range, the ray paths of the P waves pass through the core of the Earth. Due to the large reduction of the P-wave velocity at the core-mantle boundary (CMB) from

about 13.7 km/s to 8.0 km/s (see Fig. 2.53) seismic rays are strongly refracted into the core (i.e., towards the normal at this discontinuity). This causes the formation of a "core shadow". This "shadow zone" commences at an epicentral distance around 100° . The shadow edge is quite sharp for short-period P waves but diffuse for long-period P and S waves that are diffracted around the curved CMB (compare Figures 6b and c as well as 7a and b in DS 11.3).



For strong earthquakes Pdif and Sdif may be observed out to distances of about 150° (see Figs. 11.56, 11.59 and 11.63).

Fig. 11.56 SRO-LP filtered 3-component seismograms at station GRA1, Germany, in $D = 117.5^\circ$ from an earthquake in Papua New Guinea (17 July 1998, $M_s = 7.0$). The N and E components have been rotated into the R and T directions. Phases Pdif, PP, PPP (not marked) and a strong SP are visible on the vertical component, whereas the phases SKS, SKKS and PS, which are polarized in the vertical propagation plane, are strong on the radial (R) component (as are PP and PPP). Sdif, SS and SSS are strong on the transverse (T) component. Note that Pdif and Sdif are still acceptable alternative phase names for Pdif and Sdif.

Fig. 11.57 shows rotated (R-T) horizontal component SRO-LP recordings at GRSN stations from two intermediate deep events in the Chile-Bolivia border region and in the Mariana Islands, respectively. The related ray paths are depicted in the upper part. The records cover the transition from the P-wave range into the P-wave core shadow. Magnified cut-outs, also of the related Z-component records, are presented for both earthquakes in Figures 1 and 2 of DS 11.3. They show more clearly the first arriving longitudinal waves and their depth phases. The following conclusions can be drawn from a comparison of these figures:

- Pdif arrives about 4 minutes (at larger distance up to 6 min; see Fig. 11.63) earlier than the stronger PP;
- The largest phases (see also Fig. 11.60) are usually PP, PPP, PS, SP, Sdif, SKS, SKKS, SS and SSS;

- SKS is the first arriving shear wave, followed by SKKS, SP or PS (and the related depth phases), all on the R component;
- S/Sdiff and SS may be strong(est) in T or R, or even in both components, depending on the SV/SH ratio of shear-wave energy radiated by the source.

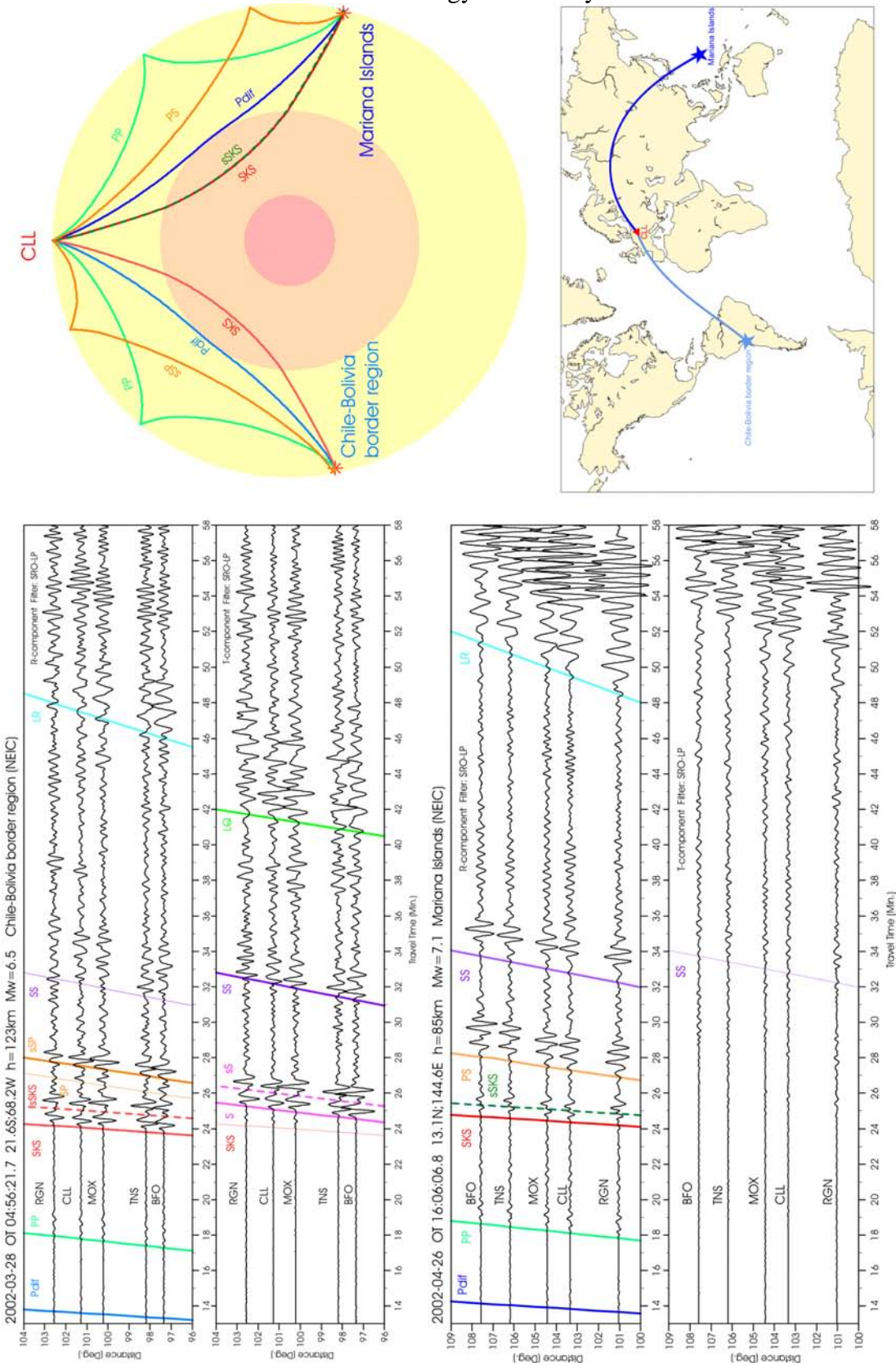


Fig. 11.57 SRO-LP filtered records of GRSN stations on R and T components in the distance range between 96° and 109° from two earthquakes on opposite backazimuth. Left: Chile-Bolivia Border region; right: Mariana Islands (source data according to the NEIC).

If no Pdif is observed, PKiKP is the first arrival in short-period records up to 113° (see Figure 3b in DS 11.3). For distances beyond 114° PKiKP follows closely after PKPdf (alternatively termed PKIKP). The latter has traveled through the outer and inner core and arrives as first onset for $D \geq 114^\circ$. PKPdf is well recorded in short-period seismograms but usually with emergent onsets and, up to about 135° distance, still with weaker amplitudes than PKiKP. Fig. 11.58 shows the amplitude-distance relationship between PKiKP, PKPdf and the other direct core phases PKPab and PKPbc, which appear with largest amplitudes beyond 143° . Fig. 11.59 depicts the ray paths and travel-time curves of Pdif, PKiKP, PKPdf, PKPab and PKPbc (for more complete ray paths see IS 2.1). Also PKKP (with its branches ab and bc) is often clearly recorded between 110° and 125° (see Figures 3c and d in DS11.3).

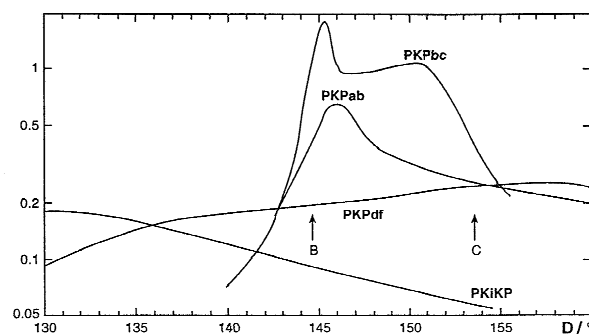


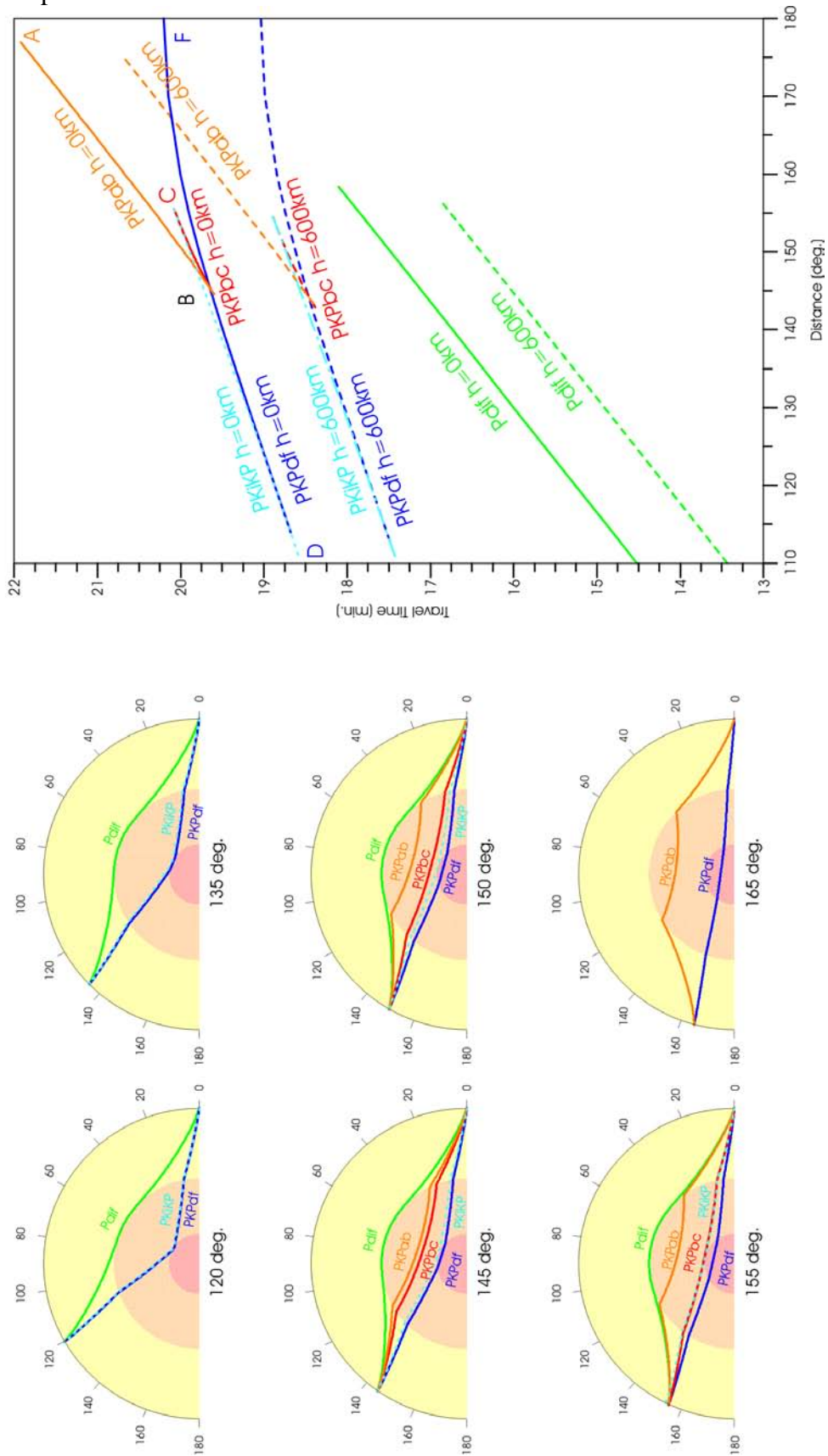
Fig. 11.58 Smoothed amplitude-distance relationships for the core phases PKiKP, PKPdf, PKPab and PKPbc as calculated for the model 1066B in the distance range 130° to 160° (modified from Houard et al., Amplitudes of core waves near the PKP caustic, ...Bull. Seism. Soc. Am., Vol. 83, No. 6, Fig. 4, p. 1840, © 1993; with permission of Seismological Society of America).

Fig. 11.60 presents records of GRSN stations in the distance range 121° to 127° from an earthquake of intermediate depth ($h = 138$ km) in the region of New Britain (see file 7 in IS 11.3 and animation CD). They show the PKPdf arrivals about 3.5 min after Pdif together with the dominant phases in this range, namely PP, PPP, PS, PPS and the Rayleigh-wave arrival LR in the Z component and the SS, SSS and the Love-wave arrival LQ in the T component. Also shown, together with the ray paths, is the core phase P4KPbc, which has been reflected 3 times at the surface of the Earth, and which is recognizable only on the short-period filtered vertical component. Between about 128° and 144° some incoherent waves, probably scattered energy from “bumps” at the CMB, may arrive as weak forerunners up to a few seconds before PKPdf. They are termed PKPpre (old PKhKP). PKPdf is followed by clear PP, after about 2 to 3 minutes, with SKP or PKS arriving about another minute later (see Fig. 11.61).

SKP/PKS have their caustics at about 132° and thus, near that distance, usually have rather large amplitudes in the early part of short-period seismograms (see Fig. 11.61). For medium-sized earthquakes these phases may even be the first ones to be recognized in the record and be mistaken for PKP. Note that for near-surface events SKP and PKS have the same travel time, but with the former having relatively larger amplitudes in the Z component whereas PKS is larger in the R component. For earthquakes at depth, PKS and SKP separate with the latter arriving earlier the deeper the source (Fig. 11.61). Beyond 135° there are usually no clear phases between SKP and SS. Misinterpretation (when Pdif is weak or missing) of PP

and SKS or PS waves as P and S may in this distance range result in strong underestimation of D (up to 70°). This can be avoided by looking for multiple S arrivals (SS, SSS) and for surface waves which follow more than 40 min later (see Table 5 in DS 3.1). For more records see DS 11.3, examples 1 to 7.

PdIf and PKiKP/PKPaIf/PKPbc/PKPab
Raypaths and travel-time curves (IASP91)



11.5 Examples of seismogram analysis

Fig. 11.59 Ray paths of Pdif, PKPdf, PKPab and PKPbc and their travel-time curves for surface focus and deep focus ($h = 600$ km) events.

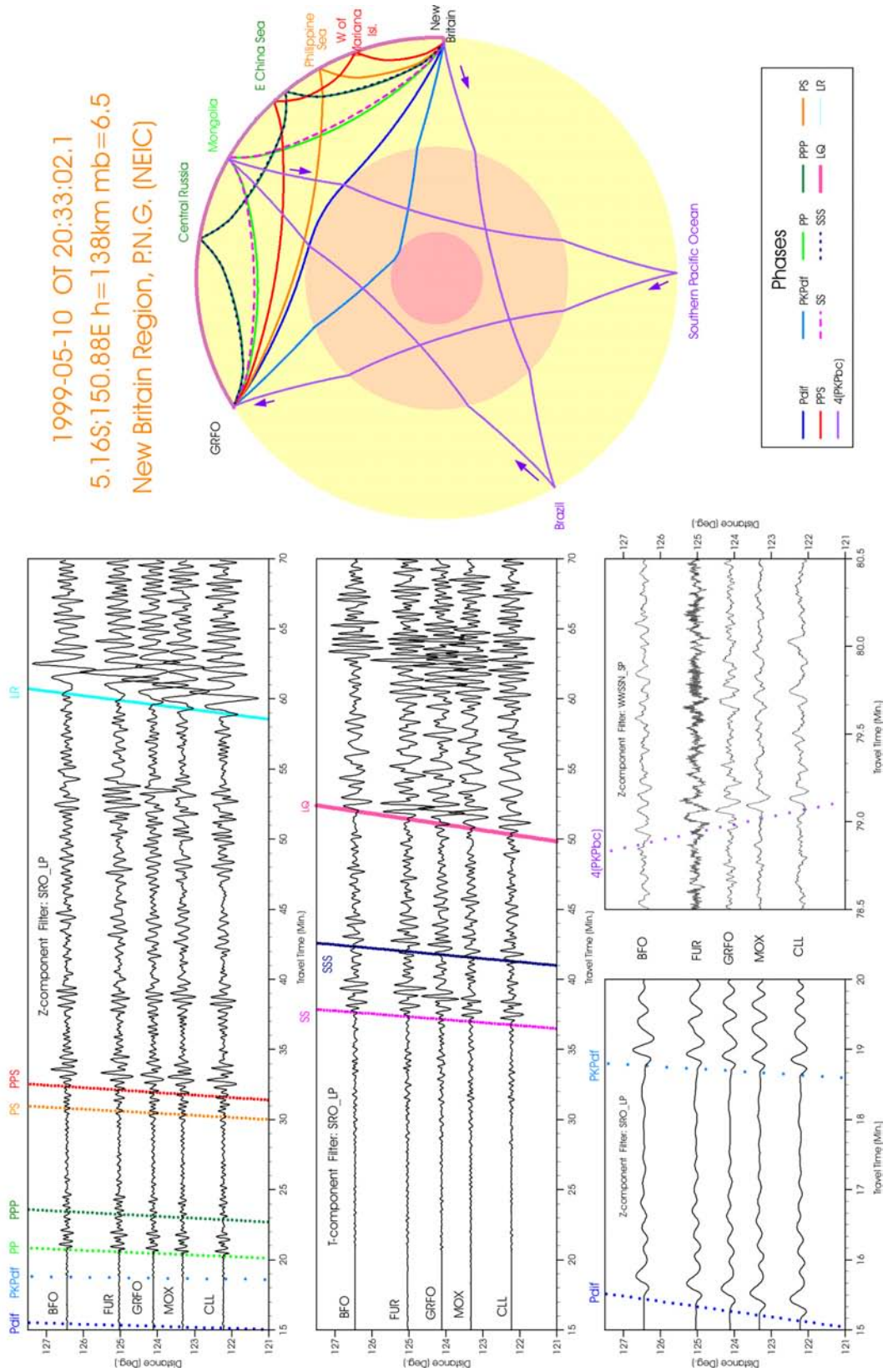


Fig. 11.60 Main seismic phases in the distance range 121° to 127° on records made at GRNS stations. Left and middle: SRO-LP filtered Z and T component, respectively. Right: SRO-LP and WWSSN-SP components. Top right: Ray traces of phases shown (see also file 7 in IS 11.3 and animation on CD-ROM).

1998-09-21 OT 12:09:39.7 13.6S;166.8E h=33km mb=6.0 Vanuatu Islands (NEIC)

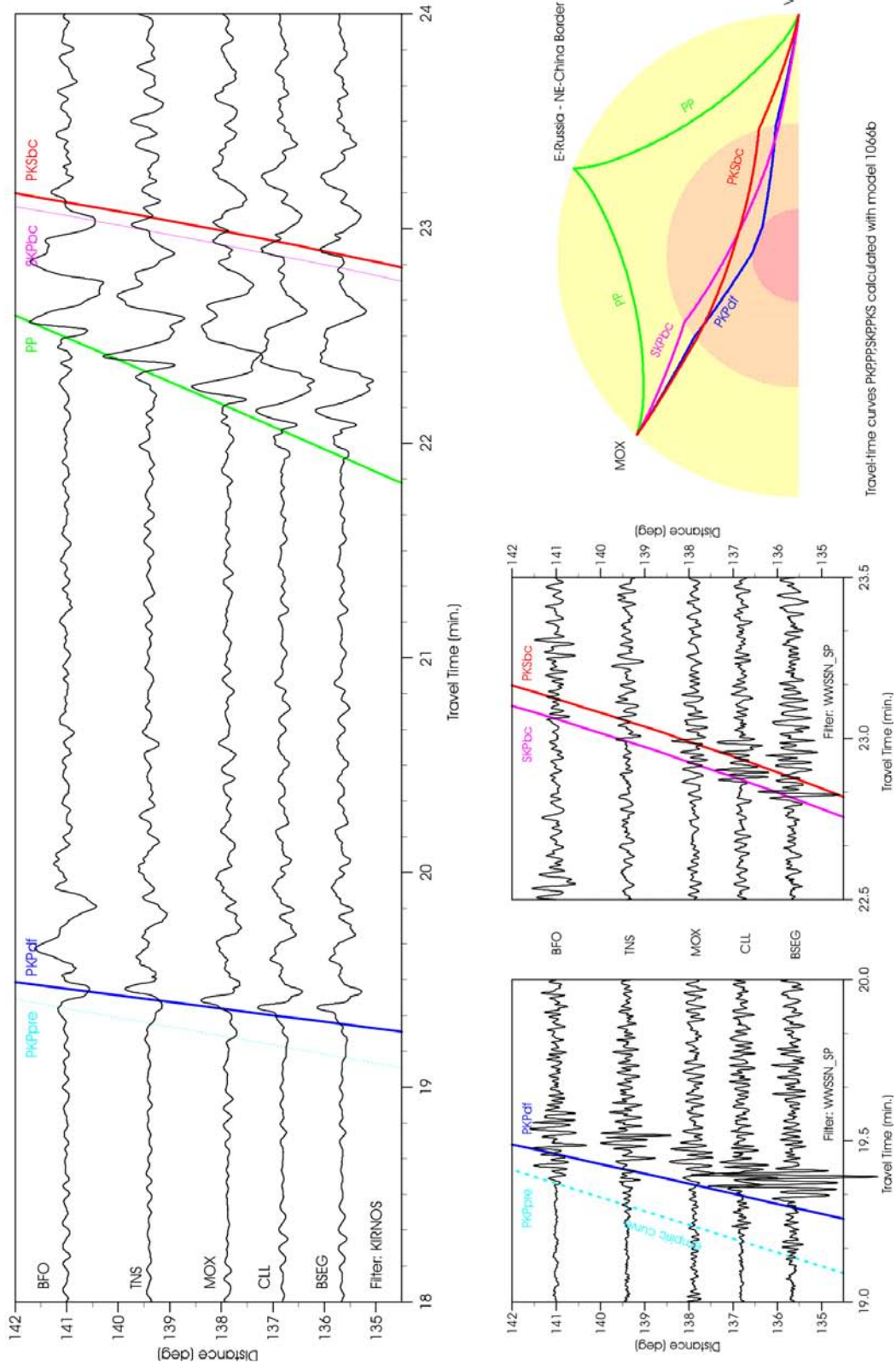


Fig. 11.61 Vertical-component seismograms at GRSN stations recorded in the distance range 135° to 141° . Left: Kirnos SKD BB-displacement; right: WWSSN-SP; top: ray paths of the phases PKPdf, PP and SKP/PKS bc. Note the precursor PKPpre.

11.5.2.4 Core distance range beyond 144°

Between 130° and 143° the first onsets of longitudinal core phases are relatively weak and complex in short-period records, but their amplitudes increase strongly towards the caustic around 144° . At this epicentral distance three PKP waves, which have traveled along different ray paths through the outer and inner core, namely PKPdf, PKPbc (old PKP1) and PKPab (old PKP2) arrive at the same time (see Fig. 11.59) so their energies superimpose to give a strong arrival with amplitudes comparable to those of direct P waves at epicentral distances around 40° (compare with Fig. 3.13). Beyond the caustic the travel-time curves of these three PKP waves split into the branches AB (or ab), BC (or bc) and DF (or df) (see Fig. 11.59). Accordingly, the various arrivals can be identified uniquely by attaching to the PKP symbol for a direct longitudinal core phase the respective branch symbol (see Figs. 11.59 and 11.62). Note that the PKPbc branch shown in Figs. 11.59 between the point B and C is ray-theoretically not defined beyond 155° . However, in real seismograms one often observes weak onsets between PKPdf and PKPab up to about 160° or even slightly beyond in the continuation of the PKPbc travel-time curve. This phase is a PKP wave diffracted around the inner core boundary (ICB) and named PKPdif (see Fig. 11.62 and 11.63).

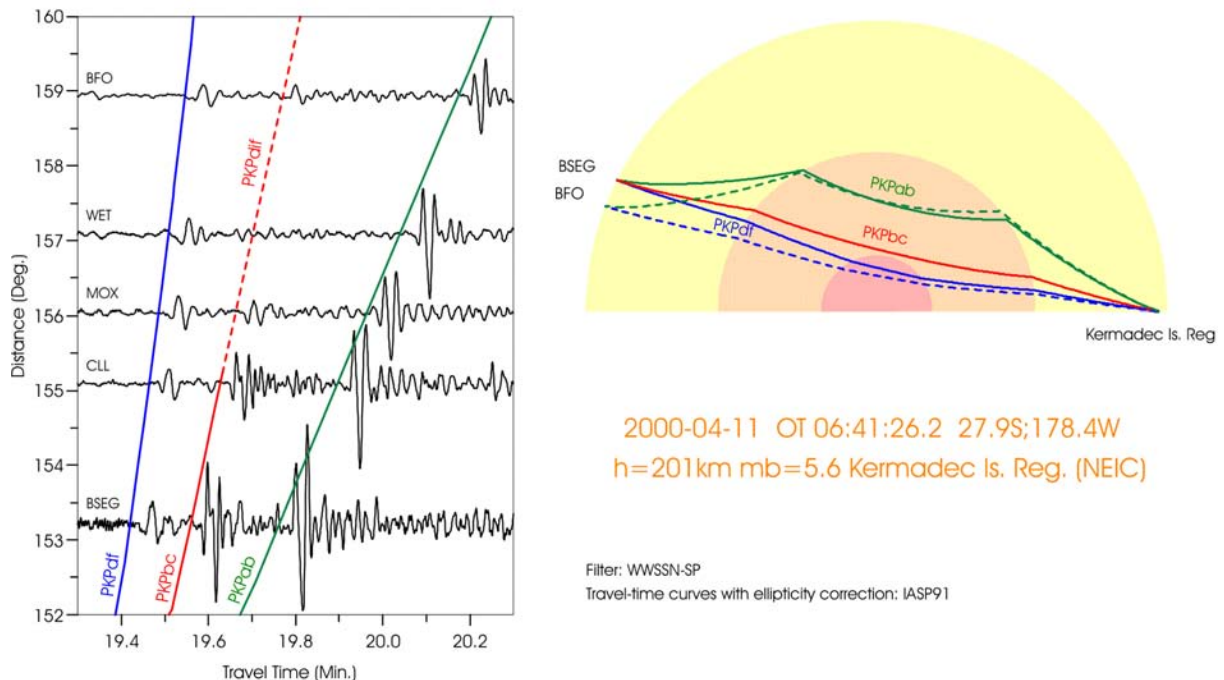


Fig. 11.62 Left: Records of the direct core phases PKPdf, PKPbc and PKPab as well as of the diffracted phase PKPdif from a Kermadec Island earthquake at stations of the GRSN in the distance range between 153° and 159° ; right: ray paths through the Earth.

The relative amplitudes between the three direct longitudinal core phases change with distance. In SP records these three phases are well separated beyond 146°, and PKPbc is the dominant one up to about 153° though the separation between these three phases is not clear within this range in LP records (Fig. 11.63 upper part and Figures 9a-c in DS 11.3).

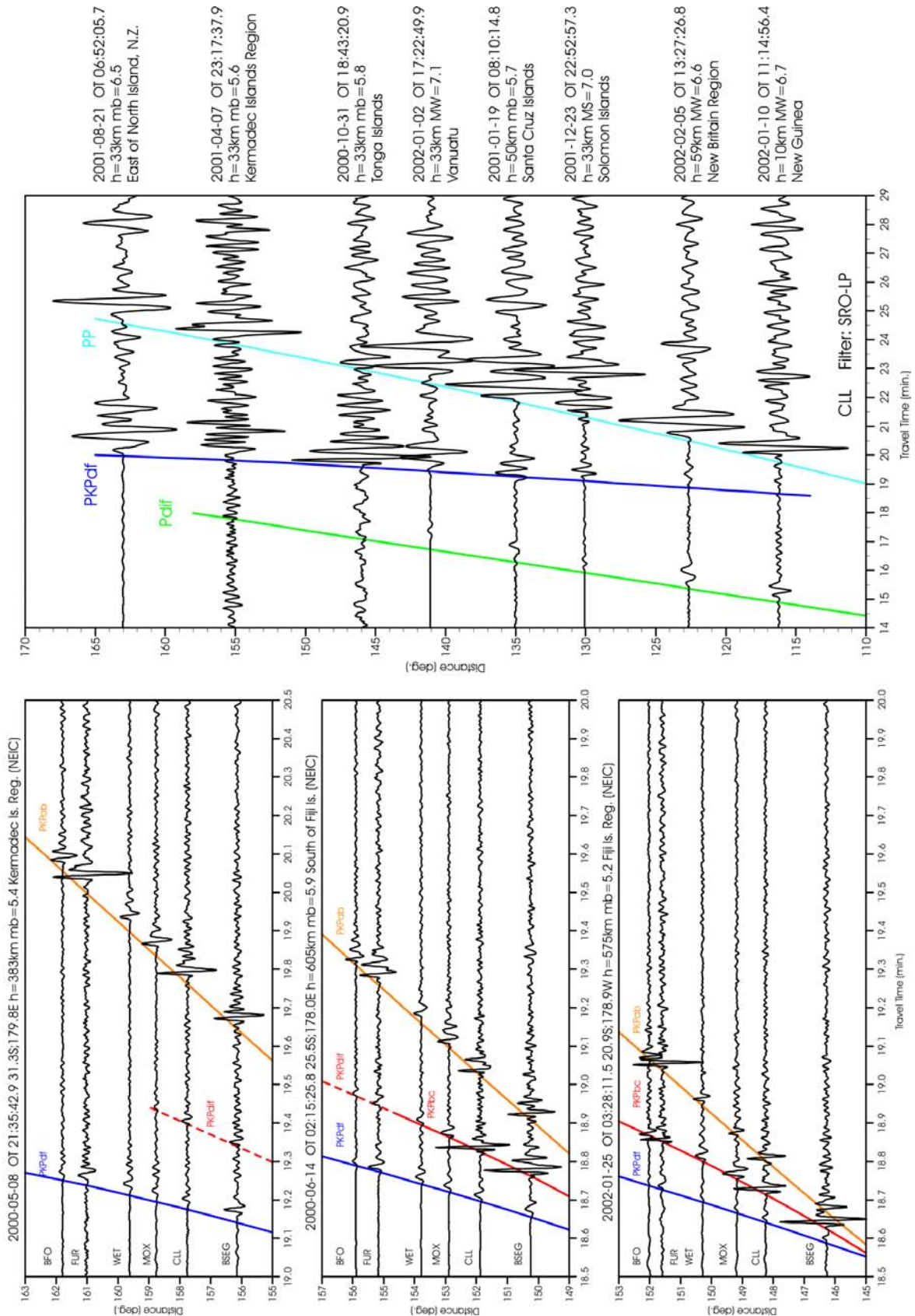


Fig. 11.63 Short-period (bottom) and long-period (SRO-LP) filtered broadband records of GRSN stations of PKP phases in the distance range 116° to 163° . In the LP records additionally the onsets of Pdif and PP have been correlated with their travel-time curves.

On short-period records the phases PKP_{df}, PKP_{bc} and PKP_{ab} are easy to identify on the basis of their typical amplitude and travel-time pattern. D can be determined with a precision better than 1.5° by using differential travel-time curves for the different PKP branches (see EX 11.3). On records of weaker sources, PKP_{bc} is often the first visible onset because the PKP_{df}, which precedes the PKP_{bc}, is then too weak to be observed above noise. On long-period records superposed different onsets may be recognizable only at distances larger than 153° . Then PKP_{ab} begins to dominate the PKP-wave group on short-period records (compare Figs. 11.63). Towards the antipode, however, PKP_{df} (PKIKP) becomes dominating again whereas PKP_{ab} disappears beyond 176° .

On LP and BB records the dominant phases on vertical and radial components are PKP, PP, PPP and PPS while on the transverse component SS and SSS are dominant. For deep sources, their depth phases sSS and sSSS may be strongest (see Fig. 11.64). Besides PP, which has traveled along the minor arc (epicentral distance D) the phase PP₂, which has taken the longer arc to the station ($360^\circ - D$), may be observable, as well as phases such as PcPPKP and others (see Fig. 11.65 as well as file 9 in IS 11.3 and related animation on CD-ROM). SKKS, SKKKS, SKSP etc. may still be well developed on radial component records (see also Figs. 2.48 and 2.49 with the related travel-time curve overlay). The whole length of BB or LP seismograms in this distance range between the first onsets and the surface wave maximum is more than an hour (see Tab. 5 in DS 3.1).

11.5.3 Late and very late core phases

For large magnitude sources, reflected core phases may be observed in addition to the direct ones, sometimes with up to 4 (or even more) repeated reflections. These phases may be observed at practically all teleseismic distances with delays behind the first arriving P or PKP onsets ranging from about 10 minutes up to about 80 minutes, depending on the number of multiple reflections. These phases are clearly discernible only in high-magnifying SP (or appropriately filtered BB) records. Most frequently observable are the single surface reflection P'P' (also termed PKPPKP), and the single reflection from the inner side of the core-mantle boundary, PKKP. As for the direct core phases, these multiple reflections develop different travel-time branches according to their different penetration depth into the outer core (see also figures in IS 2.1). Figs. 11.66 and 11.67 show the ray paths for P'P' and PKKP waves, respectively, together with their related IASP91 travel-time curves (Kennett and Engdahl, 1991) for sources at depth $h = 0$ km and $h = 600$ km. Where there is more than one reflection the respective phases are often written P'N or PNKP, respectively, with the number of reflections being N-1. Ray paths and short-period record examples for P'N with N = 2 to 4 are shown in Figs. 11.68 to 11.70 and for PNKP with N = 2 to 5 in Figs. 11.70 and 71. Fig. 11.64 shows a P5KP (PKKKKKP), which has been four times reflected from the inner side of the CMB. It is observed nearly 37 min after PKP. The phase P7KP has been found in a record at Jamestown, USA, of an underground nuclear explosion on Novaya Zemly in 1970.

All these figures show that these late arrivals may still have a significant SNR. Since they appear very late and thus isolated in short-period records, station operators may wrongly interpret them

as being P or PKP first arrivals from independent events. This may give rise to wrong phase associations and event locations, which, particularly in a region of low seismicity, may give a seriously distorted picture of its seismicity. This was demonstrated by Ambraseys and Adams (1986) for West Africa.

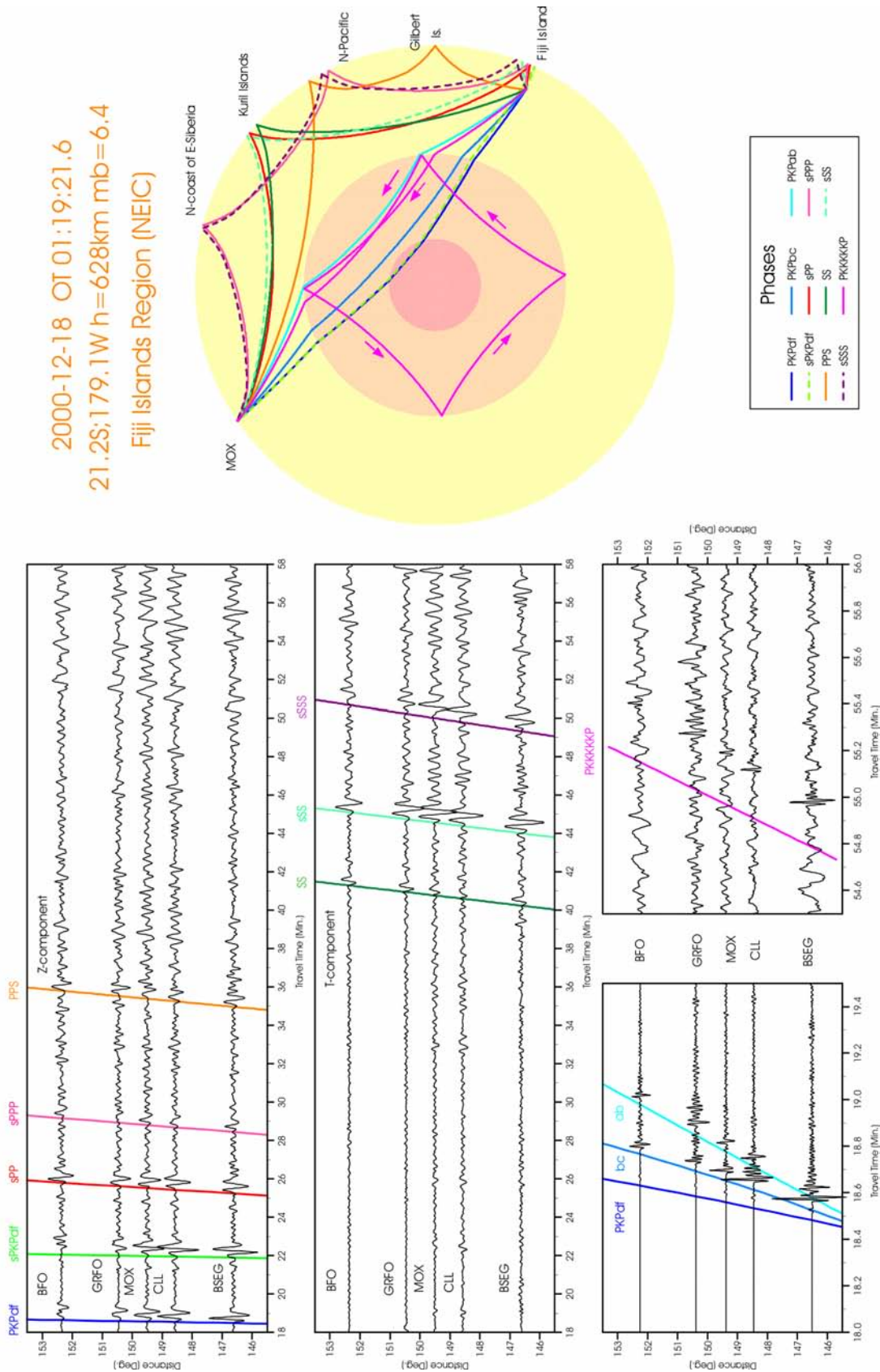


Fig. 11.64 Records of GRSN stations of a deep earthquake in the Fiji Island region. Top: ray paths and source data; bottom: records on the Z component (LP left and SP right) and T component (middle) (see also file 8 in IS 11.3 and related animation on CD-ROM).

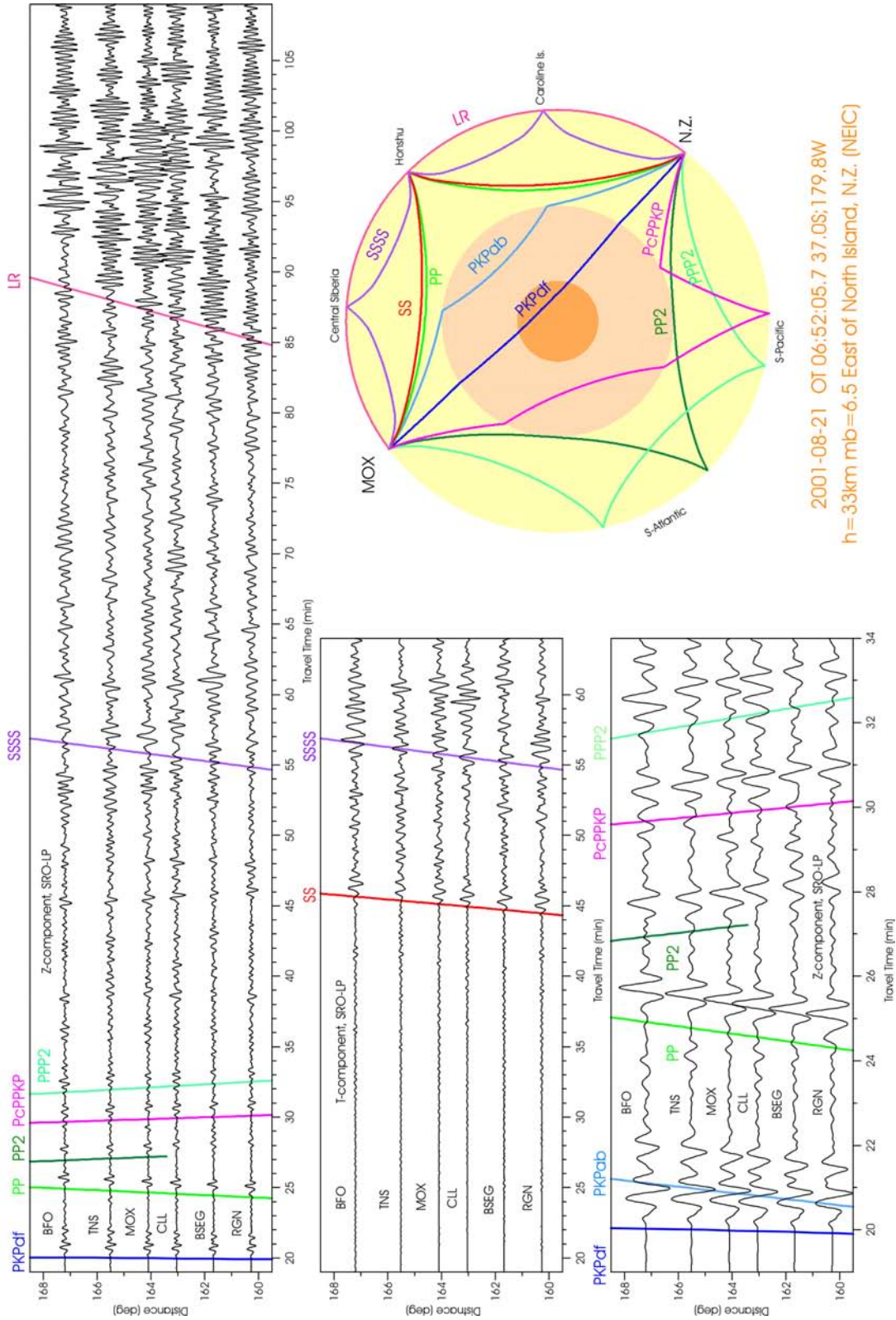


Fig. 11.65 Records of GRSN stations of a shallow (crustal) earthquake east of the North Island of New Zealand. Upper right: ray paths, source data and wavefronts of PP and PP2 arriving in Germany; bottom: records on long-period components (Z left and right; T middle). An animation has been produced that shows the ray propagation and seismogram formation for this earthquake (see file 9 in IS 11.3 and related CD-ROM).

P and P'P'df/P'P'bc/P'P'ab

Raypaths and travel-time curves (IASP91)

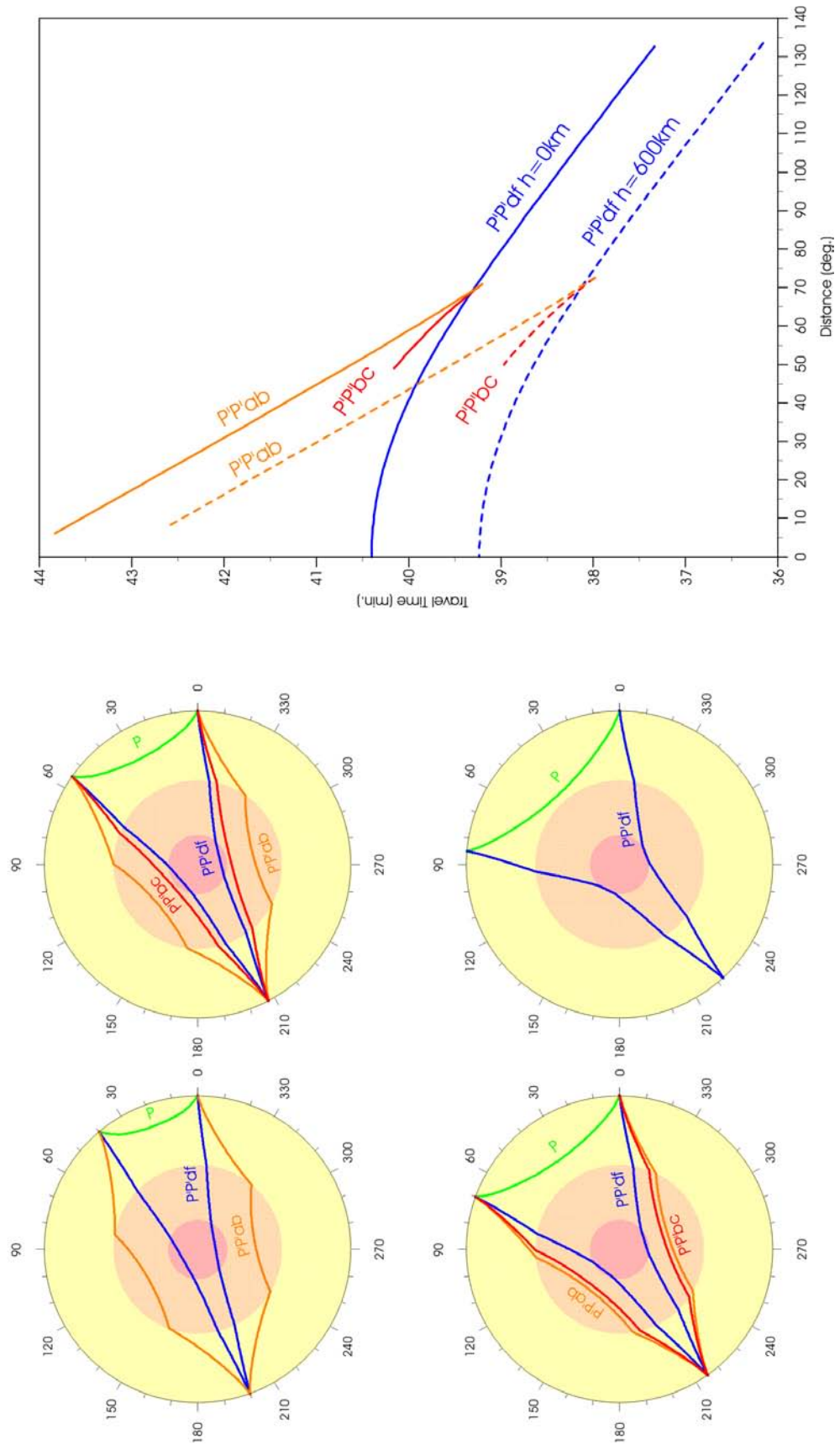


Fig. 11.66 Ray paths and travel-time curves for P'P' according to the Earth model IASP91 (Kennett and Engdahl, 1991).

PKKPdf, PKKPbc, PKKPab: Raypaths and travel-time curves

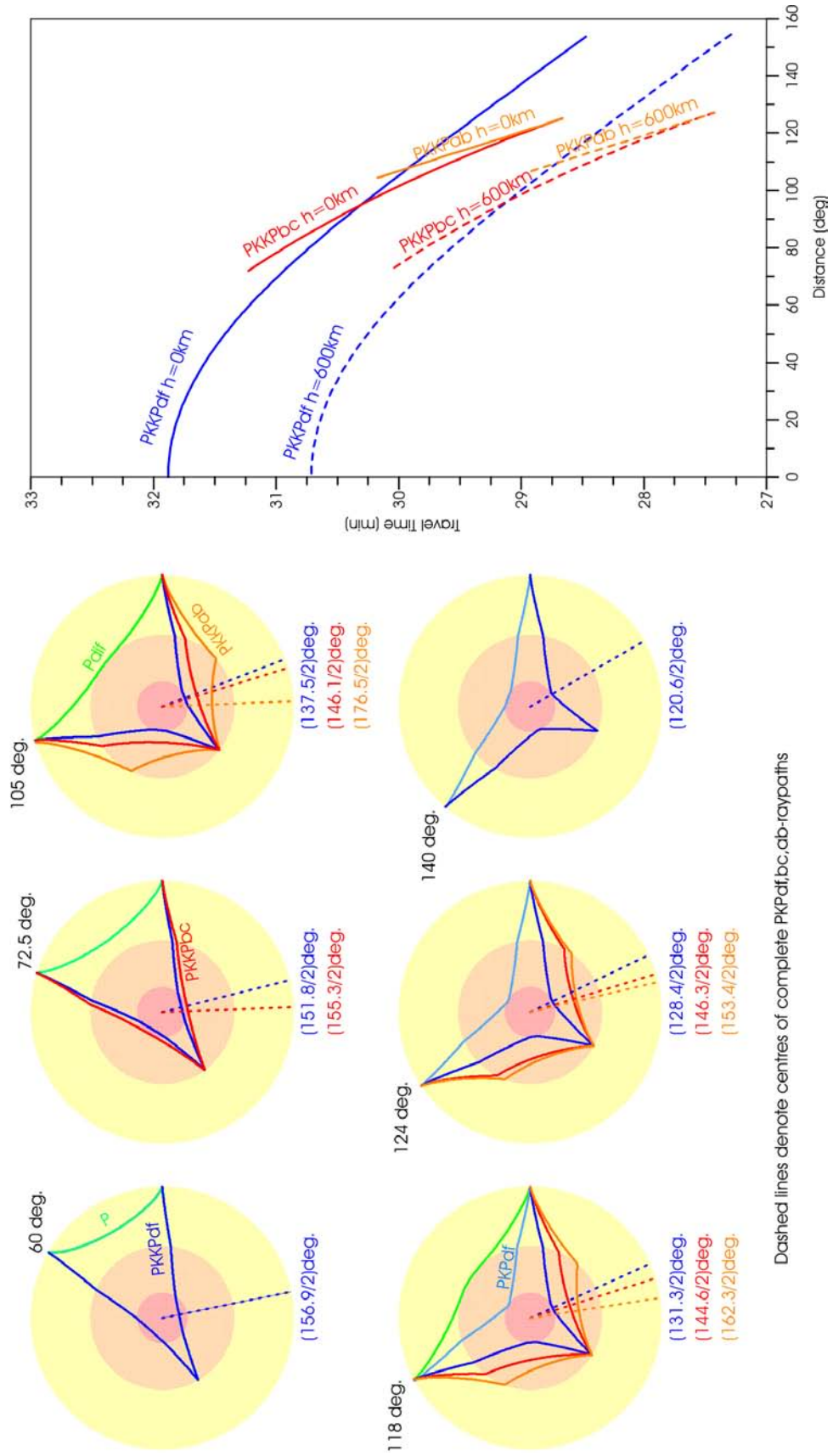


Fig. 11.67 Ray path and travel-time curves for PKKP according to the Earth model IASP91 for epicentral distances of the source between 60° and 140° .

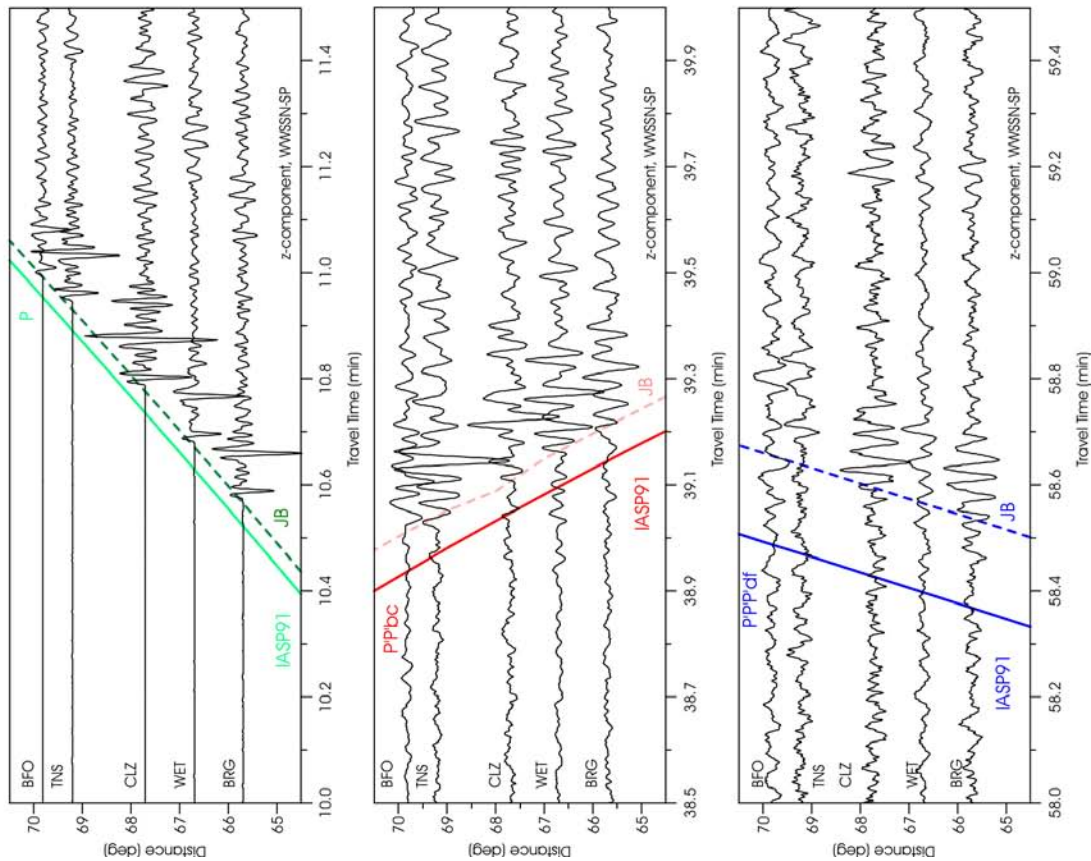
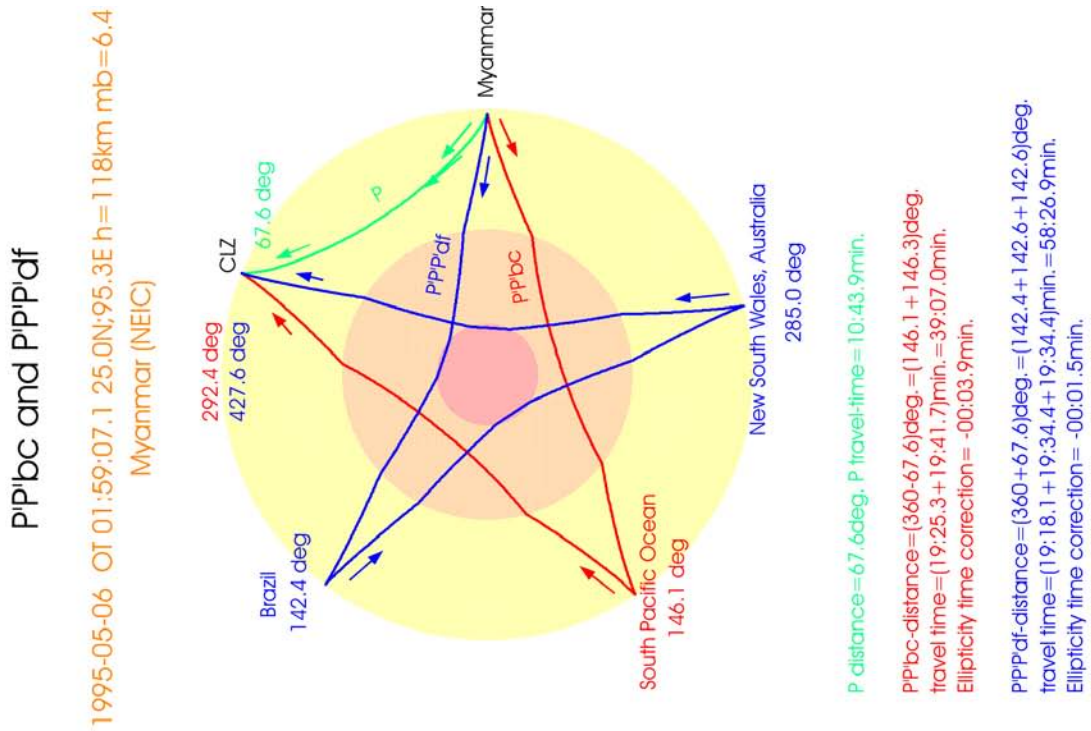


Fig. 11.68 Ray path (top) and short-period Z-component records at stations of the GRSN (bottom) of P, PP' and P'3 together with their theoretically expected arrival times according to the IASP91 and JB tables. Earthquake in Myanmar; distance range $65^\circ < D < 70^\circ$.

PP', PPP', and P'PP'P'

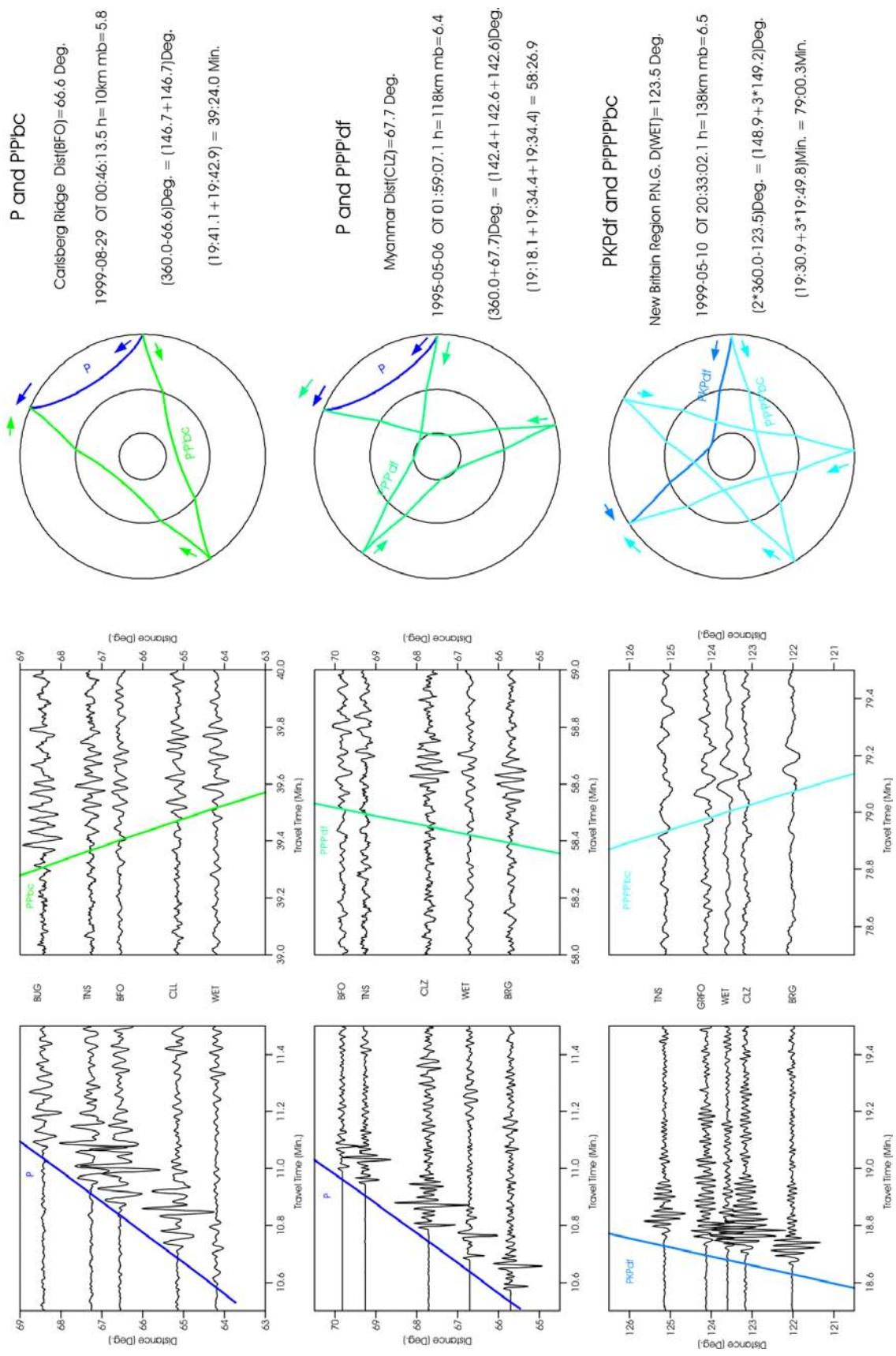


Fig. 11.69 Short-period record segments showing P and PKPdf (bottom) together with P'2, P'3 and P'4 (middle) at GRSN stations. Top: Related ray paths and source data. Note the negative slowness for P'2 and P'4. The theoretical travel-time curves relate to IASP91. Record length is one minute.

Late and very late core phases

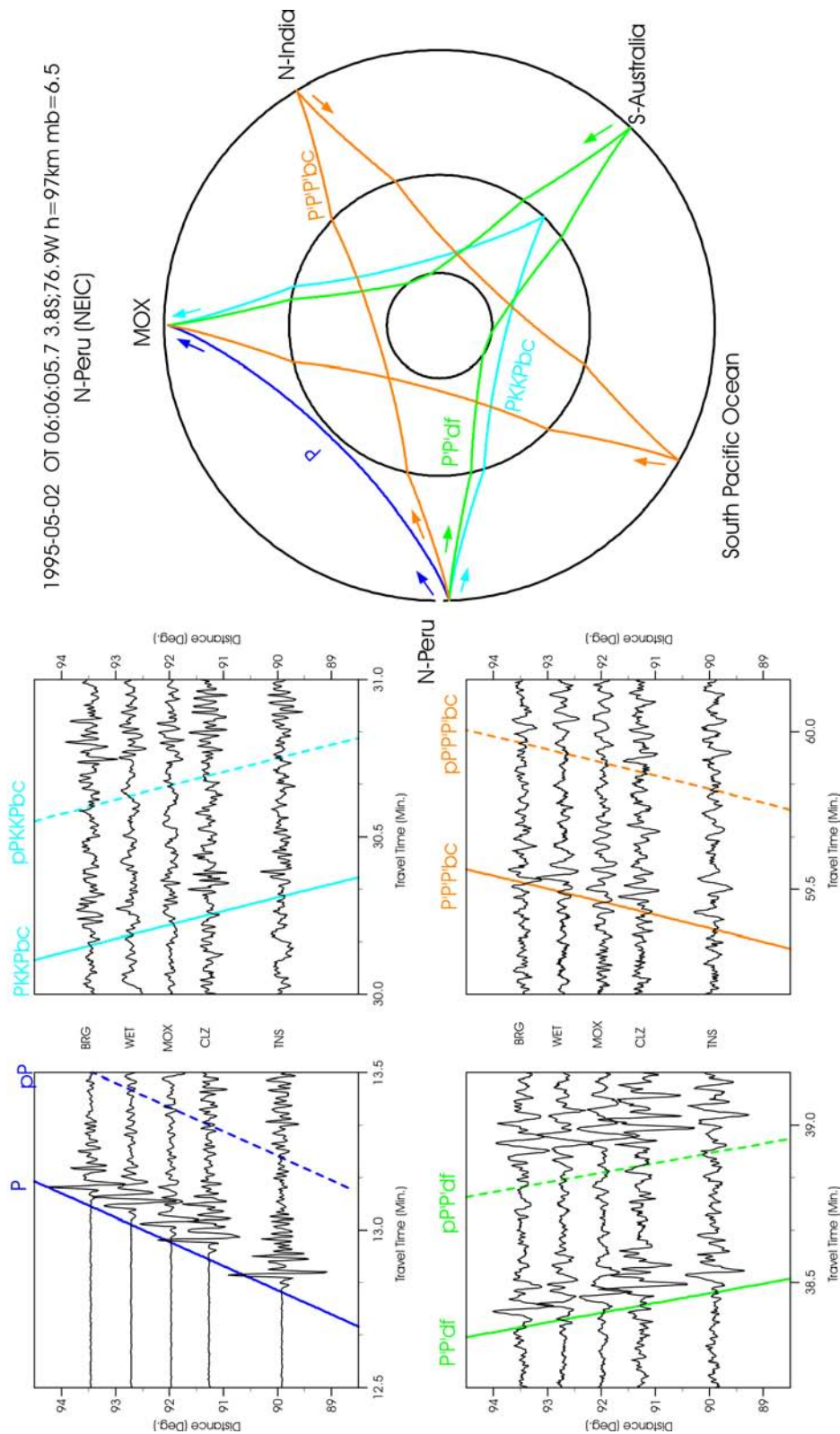


Fig. 11.70 Late and very late multiple core phases PKKP, P'2 and P'3, respectively, together with their depth phases in short-period filtered record segments of GRSN stations from an earthquake in Northern Peru at an epicentral distance around 92°. For an animation of ray propagation and seismogram formation from this source see file 6 in IS 11.3 and related CD.

PKKP, P3KP, and P5KP

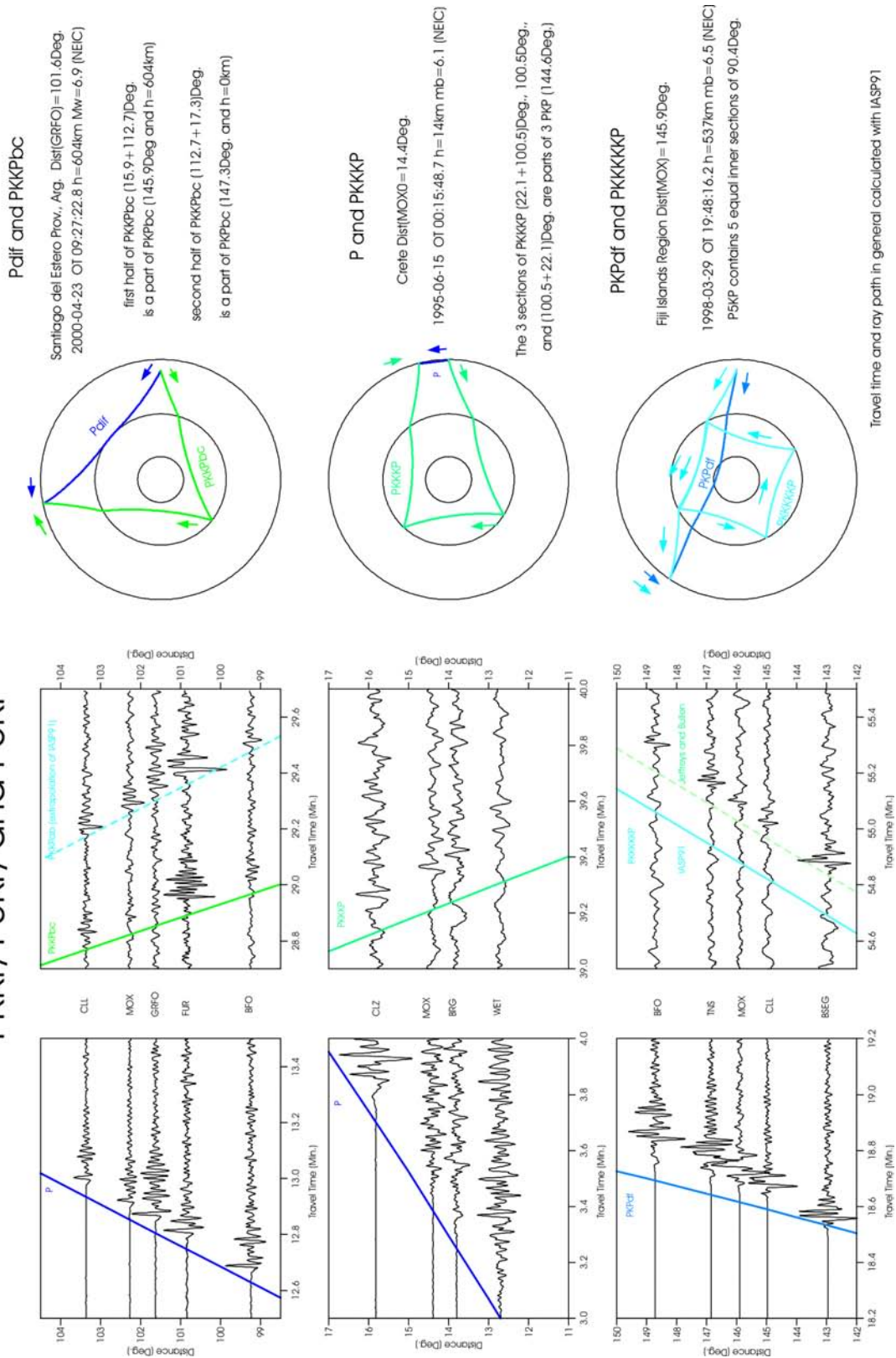


Fig. 11.71 Short-period record segments of P and PKPdf (bottom) together with those of PKKP, P3KP and P5KP (middle) at GRSN stations. Top: Related ray paths and source data. Note the negative slowness for PKKP and P3KP. The theoretical travel-time curves relate to IASP91. Record length is one minute.

In Figs. 11.62 to 11.71 the theoretical travel-time curves for core phases have been shown. For consistency, they are based on the travel-time model IASP91 (Kennett and Engdahl, 1991), as in all earlier record sections shown for the teleseismic distance range. An exception is Fig. 11.68, which shows additionally the theoretical travel-time curve for the JB model (Jeffreys and Bullen, 1940). One recognizes, that the model IASP91 yields onset times for core phases that tend to be earlier than the real onsets in the seismograms. This applies to both direct and multiple reflected core phases. The agreement between real and theoretical onsets of core phases is better when using the JB model. The JB model is still regularly used for the location of teleseismic sources at the international data centers in Boulder (NEIC), Thatcham (ISC) and Moscow whereas the IDC of the CTBTO uses IASP91. The more recent model AK135 (Kennett et al., 1995) is more appropriate than IASP91 for core phases. No recommendations have been made yet by IASPEI for using a best fitting global 1-D Earth model as standard at all international data centers. However, the NEIC is currently rewriting its processing software so that it will allow to use different Earth models, and AK135 will probably be its “default” model.

Note that the difference between the azimuth of the P wave and that of P'P' and PKKP, respectively, is 180° (see Figs. 11.66 and 11.67). The related angular difference of the surface projections of their ray paths is $360^\circ - D$ where D is the epicentral distance. Accordingly, the slowness of P'P' as well as of any even number P'N is negative, i.e. their travel time decreases with D . This also applies to PKKP and P3KP, as can be seen from Fig. 11.71. The surface projection of the travel paths of P'3 is $360^\circ + D$ and that of P'4 is $2 \times 360^\circ - D$. PKPPKP is well observed between about $40^\circ < D \leq 105^\circ$. In this range it follows the onset of P by 33 to 24 min (see Figure 10 in EX 11.3 with observed data). The existence of P'N is not limited to PKPbc. Fig. 11.68 shows an example of P'3df, recorded at a distance of about 67° . P'4 is sometimes observed in the distance range 112° to 136° . An example is given in Fig. 11.69.

Similar ray paths can be constructed for PNKP, the phase with $(N-1)$ reflections from the inner side of the core-mantle boundary (see Fig. 11.71). Figure 9 in EX 11.3 gives the differential travel-time curves for PKKP to the first arrivals P or PKP, respectively, in the distance range between 80° and 130° together with the observed data. In this range PKKP arrives 13 to 19 min behind P or 9.5 to 12 min behind PKPdf. Higher multiple reflections from the inner side of the CMB such as P3KP, P4KP and P5KP are observed, if at all, at 37 ± 1 min after the first arriving wave. The latter is true for P3KP following P at around 10° , for P4KP following P between $45^\circ < D < 75^\circ$ and for P5KP following the onset of PKPdf between about $130^\circ < D < 150^\circ$ (called “37- min” rule- of- thumb).

A particular advantage of these multiple reflected core phases is the small depth dependence of their travel-time differences to P and PKP, respectively. Consequently, their identification allows very good distance estimates to be made from single station records even when the source depth is not known. Because of the inverse differential travel-time curves of PKPPKP and PKKP with respect to P and PKP their identification can be facilitated by comparing the onset times at neighboring stations (e.g., Fig. 11.70). The polarization of both the first arrival and the possible PKKP or PKPPKP onset, determined from 3-component records, can also aid identification because their azimuths should be opposite to that of P or PKIKP, respectively. Sometimes, also converted core reflections such as SKPPKP or SKKP can be observed in short-period recordings. However, direct or reflected core phases, which have traveled along both ray segments through the mantle as S waves (such as SKS, SKKS, etc.) are mostly observed in broadband or long-period records.

11.5.4 Final remarks on the recording and analysis of teleseismic events

Box 2 below, summarizes the key criteria that should be taken into account when recording and analyzing seismograms from sources at teleseismic distances (see also 11.2.6.1).

Box 2: General rules for recording and analyzing teleseismic events

- The overall duration of teleseismic records at epicentral distances larger than 15° (or 20°) ranges from tens of minutes to several hours. It increases both with epicentral distance and the magnitude of the source.
- High frequencies, of S waves in particular, are attenuated with distance so recordings at long range are generally of lower ($f \approx 0.01 - 1$ Hz) frequency than local or regional recordings.
- Usually only longitudinal waves, both direct or multiple reflected P and PKP phases, which are much less attenuated than S waves, are well recorded by short-period, narrow-band seismographs (or their simulated equivalents) with high magnification of frequencies around 1 Hz. However, S waves from deep earthquakes may sometimes be found also in SP teleseismic records.
- Because of the specific polarization properties of teleseismic body and surface waves, polarization analysis is an important tool for identifying the different types of wave arrivals.
- According to the above, teleseismic events are best recorded by high-resolution 3-component broadband seismographs with large dynamic range and with sampling rates $f = 20$ Hz.
- The main types of seismic phases from teleseismic sources are (depending on distance range) the longitudinal waves P, Pdif, PKP, PcP, ScP, PP, and PPP and the shear waves S, Sdif, SKS, ScS, PS, SS, and SSS. The longitudinal waves are best recorded on vertical and radial components whereas the shear waves appear best on transverse and/or radial components.
- Multiple reflected core phases such as P'N and PNKP, which appear on SP records as isolated wavelets, well separated from P or PKP, may easily be misinterpreted as P or PKP arrivals from independent seismic sources if no slowness data from arrays or networks are available. Their proper identification and careful analysis helps to avoid wrong source association, improves epicenter location and provides useful data for the investigation of the deeper interior of the Earth.
- Several body wave phases such as PP, PS, SP, SS, PKPab and its depth phases, SKKSac, SKKSdf, PKPPKpab, SKSSKSab undergo phase shifts and wavelet distortions at internal caustics (see 2.5.4.3). This reduces the accuracy of their time and amplitude picks and their suitability for improving source location by waveform matching with undistorted phases. Therefore it is recommended that seismological observatories correct these phase shifts prior to parameter readings by applying the inverse Hilbert-transformation, which is available in modern software for seismogram analysis.
- Surface waves of shallow events have by far the largest amplitudes while surface wave amplitudes from deep earthquakes and large (nuclear) explosions are small at teleseismic distances.
- At seismic stations or network centers the following parameter readings should be obligatory during routine analysis: onset time and, if possible,

polarity of the first arriving phase; maximum P amplitude A [nm] and period T [s]; onset time of secondary phases; and for shallow sources additionally the maximum surface-wave amplitude A [μm] and period T [s].

- P-wave amplitudes for the determination of the short-period body-wave magnitude m_b have to be measured on standard short-period (WWSSN-SP simulated) records in the period-range $0.5 \text{ s} < T < 2 \text{ s}$ whereas the surface-wave amplitudes for the determination of the surface-wave magnitude M_s have to be measured on standard long-period filtered (SRO-LP or WWSSN-LP simulated) records, typically in the period range $17 \text{ s} < T < 23 \text{ s}$.
- For more guidance on magnitude determination, using also other phases and records/filters, consult section 3.2.1 and related annexes.
- Networks and arrays should additionally measure and report slownesses and azimuths for P waves.
- For improved determination of epicentre distance, the measurement and reporting of travel-time differences such as S–P, SS–P etc. are very important, and for improved hypocenter determination additionally the proper identification and reporting of depth phases such as pP, sP, sS and of core reflections (PcP, ScP etc.).
- Picking and reporting of onset-times, amplitudes and periods of other significant phases, including those not identified, are encouraged by IASPEI within the technical and personnel facilities available at observatories and analysis centers as being a useful contribution to global research. These extended possibilities for parameter reporting are now well supported by the recently adopted IASPEI Seismic Format (ISF), which is much more flexible and comprehensive than the traditional Telegraphic Format (see 10.2 as well as IS 10.1 and 10.2).
- For reporting of seismic phases (including onsets not identified) one should exclusively use the new IASPEI phase names. For the definition of seismic phases and their ray paths see IS 2.1.

Acknowledgments

The authors are very grateful to A. Douglas and R. D. Adams for their careful reviews which helped to significantly improve the original draft. Thanks go also to staff members of the Geophysical Survey of the Russian Academy of Science in Obninsk who shared in reviewing the various sections of this Chapter (Ye. A. Babkova, L. S. Čepkunas, I. P. Gabsatarova, M. B. Kolomiyev, S. G. Poygina and V. D. Theophylaktov). Many of their valuable suggestions and references to Russian experience in seismogram analysis were taken into account.

Recommended overview readings (see References under Miscellaneous in Volume 2)

Kennett (2002)
 Kulhanek (1990 and 2002)
 Payo (1986)
 Richards (2002)

Scherbaum (2001 and 2002)

Simon (1981)

Willmore (1979)

12

Intensity and Intensity Scales

Roger M. W. Musson*

12.1 Intensity and the history of intensity scales

Intensity can be defined as a classification of the strength of shaking at any place during an earthquake, in terms of its observed effects. The fact that it is essentially a classification, akin to the Beaufort Scale of wind speed, rather than a physical parameter, leads to some special conditions on its use. Principal among these is its being an integer quantity when assigned from observed data. Traditionally, Roman numerals have been used to represent intensity values to emphasize this point (it is hard to write "VII"). Nowadays the use of Roman numerals is largely a matter of taste, and most seismologists find Arabic numerals easier to process by computer.

The use of intensity scales is historically important because no instrumentation is necessary, and useful measurements of an earthquake can be made by an unequipped observer. The earliest recognizable use of intensity was by Egen in 1828, although simple quantifications of damage had been made in the previous century by Schiantarelli in 1783 (Sarconi, 1784), and some earlier Italian examples are said to exist. However, it was only in the last quarter of the 19th century that the use of intensity became widespread; the first scale to be used internationally was the ten-degree Rossi-Forel Scale of 1883. The early history of intensity scales can be found in Davison (1900, 1921, 1933), a later study can be found in Medvedev (1962).

The scale of Sieberg (1912,1923) became the foundation of all modern twelve-degree scales. A later version of it became known as the Mercalli-Cancani-Sieberg Scale, or MCS Scale (Sieberg 1932), still in use in Southern Europe. The 1923 version was translated into English by Wood and Neumann (1931) and became the inappropriately named Modified Mercalli Scale (MM Scale). This was completely overhauled in 1956 by Richter (1958) who refrained from adding his name to the new version in case of further confusion with "Richter Scale" magnitudes. Richter's version became instead the "Modified Mercalli Scale of 1956" (MM56) despite the fact that the link to Mercalli was now extremely remote. Local modifications of Richter's MM56 scale have been used in Australia and New Zealand. More recent attempts to modernize the MM scale further, e.g., that of Brazeo (1978) have not caught on.

In 1964 the first version of the MSK Scale was published by Medvedev, Sponheuer and Karnik (Sponheuer and Karnik, 1964). This new scale was based on MCS, MM56 and previous work by Medvedev in Russia, and greatly developed the quantitative aspect to make the scale more powerful. This scale became widely used in Europe, and received minor

* with assistance from members of the ESC WG Macroseismology

12. Intensity and Intensity Scales

modifications in the mid 1970s and in 1981 (Ad hoc group, 1981). In 1988, the European Seismological Commission agreed to initiate a thorough revision of the MSK Scale. The result of this work (undertaken by a large international Working Group under the chairmanship of Gottfried Grünthal, Potsdam) was published in draft form in 1993, with the final version released (after a period of testing and revision) in 1998 (Grünthal, 1998). Although this new scale is more or less compatible with the old MSK Scale, the organization of it is so different that it was renamed the European Macroseismic Scale (EMS). Since its publication it has been widely adopted inside and also outside Europe.

The one important intensity scale that does not have twelve degrees (now that the Rossi-Forel Scale is no longer much in use) is the seven-degree Japanese Meteorological Agency Scale (JMA Scale). This is based on the work of Omori, and is the scale generally used in Japan (but nowhere else). A recent modification to the JMA scale subdivides degrees 5 and 6 into upper and lower, and explicitly describes a degree 0, resulting in a ten-degree scale (JMA 1996).

To some extent, the middle years of the 20th century saw a decline in interest in macroseismic investigation, with the improvements in instrumental monitoring. However, since the middle 1970s there has been a revival of interest in the subject since macroseismics are essential for the revision of historical seismicity and of great importance in seismic hazard assessments. Macroseismic studies of modern earthquakes are vital for

- (i) calibrating studies of historical earthquakes;
- (ii) studying local attenuation, and
- (iii) investigations of vulnerability, seismic hazard and seismic risk.

12.1.1 European Macroseismic Scale (EMS)

The complete EMS-98 scale is too long to reproduce in its entirety, being a small book in length. This is because, while historically intensity scales have been presented simply as a list of classes and diagnostics for the user to make of what he will, the EMS-98 scale comes with extensive support material, including guidelines, illustrations and worked examples. Even the traditional "core" part of the scale contains tabular and graphical material explaining the classification of buildings and quantities used.

An essential feature of this scale is that, whereas other intensity scales such as the Modified Mercalli scale (in its 1956 incarnation, see below) have attempted to distinguish between the effects of earthquake shaking on buildings of different construction types, using type as an analog of strength, the EMS employs a series of six vulnerability classes which represent strength directly, and involve construction type, but also other factors such as workmanship and condition. These vulnerability classes allow a flexible and robust approach to assessing intensity from damage. The system is also adaptable to new or different building types, and includes consideration of engineered structures with earthquake resistant design. Damage is also handled in a new way, with discrimination between structural and non-structural damage, and the different forms damage takes in buildings of different types. A system of five damage grades is used: negligible to slight; moderate; substantial to heavy; very heavy, and destruction. These are not only defined but also illustrated pictorially.

12.1 Intensity and the history of intensity scales

The probabilistic nature of intensity is stressed by the use of numerically-defined expressions of quantity. For any intensity degree, it is expected that for buildings of equivalent strength there will be a modal level of damage that will be most frequently encountered, and that decreasing proportions of the building stock of equivalent strength will show lesser or greater degrees of damage. This relates closely to real experience from damage surveys.

Although natural phenomena such as landslips, rockfalls, cracks in ground, etc., have been used in intensity scales for a long time, more recent experience has shown that the occurrence of these is very strongly influenced by other factors than the severity of earthquake shaking - especially pre-existing hydrological conditions. In the EMS, although these effects are not deleted entirely, they are relegated to an annexe rather than being included in the core scale; they are treated in a graphical table which shows the ranges of intensities over which such phenomena are commonly (and exceptionally) encountered.

The full scale is published as Grünthal (1998). It also contains examples of intensity assignment and can be obtained in full at the following web address:

<http://seismohazard.gfz-potsdam.de/projects/ems/index.html>.

Despite the name of the scale (which reflects the fact that it was developed at the instigation of the European Seismological Commission), the scale is equally suitable for use outside Europe, and has been used successfully for assessing modern earthquakes in many parts of the world.

Here the short form (section 8 of the published scale) is reproduced. This is not suitable for, and not intended for, use in assigning intensities. It gives the character of each degree in a very simplified and generalized form for educational purposes.

EMS intensity	Definition (Description of typical observed effects (abstracted))
I Not felt	Not felt.
II Scarcely felt	Felt only by very few individual people at rest in houses.
III Weak	Felt indoors by a few people. People at rest feel a swaying or light trembling.
IV Largely observed	Felt indoors by many people, outdoors by very few. A few people are awakened. Windows, doors and dishes rattle.
V Strong	Felt indoors by most, outdoors by few. Many sleeping people awake. A few are frightened. Buildings tremble throughout. Hanging objects swing considerably. Small objects are shifted. Doors and windows swing open or shut.
VI Slightly damaging	Many people are frightened and run outdoors. Some objects fall. Some houses suffer slight non-structural damage like hair-line cracks and fall of small pieces of plaster.
VII Damaging	Most people are frightened and run outdoors. Furniture is shifted and objects fall from shelves in large numbers. Many well built ordinary buildings suffer moderate damage: small cracks in walls, fall of plaster, parts of chimneys fall down; older buildings may show large cracks in walls and failure of fill-in walls.

12. Intensity and Intensity Scales

VIII Heavily damaging	Many people find it difficult to stand. Many houses have large cracks in walls. A few well built ordinary buildings show serious failure of walls, while weak older structures may collapse.
IX Destructive	General panic. Many weak constructions collapse. Even well built ordinary buildings show very heavy damage: serious failure of walls and partial structural failure.
X Very destructive	Many ordinary well built buildings collapse.
XI Devastating	Most ordinary well built buildings collapse, even some with good earthquake resistant design are destroyed.
XII Completely devastating	Almost all buildings are destroyed.

12.1.2 Modified Mercalli (MM) Scale

Since none of the more recent versions of the MM Scale have found wide acceptance, the version that follows is Richter's 1956 draft, which is probably the most used version at the time of writing (some seismologists still use the 1931 version, however).

- I** Not felt. Marginal and long period effects of large earthquakes.
- II** Felt by persons at rest, on upper floors, or favorably placed.
- III** Felt indoors. Hanging objects swing. Vibration like passing light trucks. Duration estimated. May not be recognized as an earthquake.
- IV** Hanging objects swing. Vibration like passing of heavy trucks; or sensation of a jolt like a heavy ball striking the walls. Standing motor cars rock. Windows, dishes, doors rattle. Glasses clink. Crockery clashes. In the upper range of IV, wooden walls and frame creak.
- V** Felt outdoors; direction estimated. Sleepers wakened. Liquids disturbed, some spilled. Small unstable objects displaced or upset. Doors swing, close, open. Shutters, pictures move. Pendulum clocks stop, start, change rate.
- VI** Felt by all. Many frightened and run outdoors. Persons walk unsteadily. Windows, dishes, glassware broken. Knickknacks, books, etc., off shelves. Pictures off walls. Furniture moved or overturned. Weak plaster and masonry D cracked. Small bells ring (church, school). Trees, bushes shaken (visibly, or heard to rustle).
- VII** Difficult to stand. Noticed by drivers of motor cars. Hanging objects quiver. Furniture broken. Damage to masonry D, including cracks. Weak chimneys broken at roof line. Fall of plaster, loose bricks, stones, tiles, cornices (also unbraced parapets and architectural ornaments). Some cracks in masonry C. Waves on ponds; water turbid with mud. Small slides and caving in along sand or gravel banks. Large bells ring. Concrete irrigation ditches damaged.
- VIII** Steering of motor cars affected. Damage to masonry C; partial collapse. Some damage to masonry B; none to masonry A. Fall of stucco and some masonry walls. Twisting, fall of chimneys, factory stacks, monuments, towers, elevated tanks. Frame houses

12.1 Intensity and the history of intensity scales

moved on foundations if not bolted down; loose panel walls thrown out. Decayed piling broken off. Branches broken from trees. Changes in flow or temperature of springs and wells. Cracks in wet ground and on steep slopes.

- IX** General panic. Masonry D destroyed; masonry C heavily damaged, sometimes with complete collapse; masonry B seriously damaged. (General damage to foundations.) Frame structures, if not bolted, shifted off foundations. Frames racked. Serious damage to reservoirs. Underground pipes broken. Conspicuous cracks in ground. In alluvial areas sand and mud ejected, earthquake fountains, sand craters.
- X** Most masonry and frame structures destroyed with their foundations. Some well-built wooden structures and bridges destroyed. Serious damage to dams, dikes, embankments. Large landslides. Water thrown on banks of canals, rivers, lakes, etc. Sand and mud shifted horizontally on beaches and flat land. Rails bent slightly.
- XI** Rails bent greatly. Underground pipelines completely out of service.
- XII** Damage nearly total. Large rock masses displaced. Lines of sight and level distorted. Objects thrown into the air.

Masonry A: Good workmanship, mortar, and design; reinforced, especially laterally, and bound together by using steel, concrete, etc.; designed to resist lateral forces.

Masonry B: Good workmanship and mortar; reinforced, but not designed in detail to resist lateral forces.

Masonry C: Ordinary workmanship and mortar; no extreme weaknesses like failing to tie in at corners, but neither reinforced nor designed against horizontal forces.

Masonry D: Weak materials, such as adobe; poor mortar; low standards of workmanship; weak horizontally.

(From Richter, 1958).

12.1.3 Accuracy of assessment

Given a certain strength of shaking, it is to be expected that buildings of equivalent strength will not respond in a completely uniform way. Rather, there should be a modal level of damage observed, with some buildings suffering less and others more. The net effect approximates to a normal distribution (as has often been seen in damage surveys). Thus, for any particular level of shaking, it is expected to be found that different percentages of the building stock of a given strength will suffer different degrees of damage. In assessing intensity (and this is true of the lower degrees as well as the damaging ones) one is usually dealing with a sample or estimate of the percentages that were observed, and attempting to match these to the expected ranges for one of the intensity degrees. In most cases, given a degree of robustness, an adequate fit can be found without much problem.

Difficulties can occasionally arise when this task is compounded, as it sometimes is, by one or other of two factors: (i) that the effects of an earthquake vary considerably over very short

12. Intensity and Intensity Scales

distances, due to a combination of local conditions and the complexity of earthquake ground motion; and (ii) information is often not complete. These two factors can have an effect on the level of accuracy that can be expected in intensity assessments. The variability of earthquake effects is well-known, as in cases where, of two identical houses side-by-side, one is heavily damaged and the other nearly intact. This may give a misleading impression of difficulty in assessing intensity which might actually disappear once a larger sample of houses was assessed. The difficulty with respect to information is that one is often working from an uncontrolled, possibly unrepresentative, sample of available information (particularly when not working with data derived from a field investigation), and there may also be uncertainty about the condition of buildings before the earthquake. This can cause problems where the real percentage distribution of effects is obscured by the limited data. Also, even when the amount of data is good, there can be cases where the reported effects do not match unambiguously any of the "pen pictures" presented by the classes in the intensity scale.

Intensity scales are therefore designed to include the necessary degree of robustness to make identification of the different degrees as practical as possible. The number of degrees in a scale is controlled by the number of different levels that can be distinguished in normal use without too much difficulty. Experience shows that it is very unlikely that one could ever meaningfully discriminate intensities to a resolution of less than one degree of a twelve-degree scale. If one could state accurately in some case that the intensity was, for example, 6, this would imply that a 23 degree intensity scale could be written, which is doubtful. In cases where one can not determine intensities to a resolution of one degree, two degrees can be bracketed together to show the probable range. This can be particularly the case for lower intensity degrees; there are often cases where it is hard to be sure between intensity 2 or 3, or between 3 or 4, or between 4 and 5. In such cases one may write 4-5, meaning either intensity 4 or intensity 5.

A suggested guideline in EMS is that the description of each degree should be considered the minimum case. For example, in a case in which the data satisfy the requirements for intensity 4, but do not adequately satisfy the criteria for intensity 5, then the correct assessment is 4, even if the effects seem stronger than the basic intensity 4 description.

12.1.4 Equivalence between scales

It has often been the practice to attempt to express the equivalence between different intensity scales by way of a chart that compares different degrees of a scale either by a straight equivalence of grades or by a series of rectangles overlapping to a smaller or larger extent. Such charts should be avoided if possible, as their results are not wholly reliable. It is much preferable to revisit the original data and make a fresh intensity assignment with the desired intensity scale. The same is true with respect to empirical equations which have occasionally been suggested in the past to relate one scale to another.

For the various twelve-degree scales, it is likely the case that differences in the way that different seismologists have used intensity scales in practice can substantially outweigh any actual differences in the scales themselves. In general the equivalence between MM56, MSK and EMS is roughly one to one. The principal difference between EMS and earlier scales is that it is more clearly written, and structured in such a way as to make it easier for different investigators to obtain consistent results.

A rough equivalence for the original JMA Scale is given in the Tab. 12.1 below.

Tab. 12.1 Equivalence between JMA and EMS scale.

JMA	EMS
1	2
2	3
3	5
4	6
5	8
6	10
7	11

12.2 Collection of macroseismic data

Collection of macroseismic data from current earthquakes is derived principally from two sources - questionnaire surveys and field investigations, either or both of which may be required for a particular earthquake. As a general rule, questionnaire surveys are used for assessing intensities in the range of 2 to 6, while for 7 and above field investigations are necessary.

There is a third source - documentary material - which is the principal source of macroseismic data for historical earthquakes. The treatment of this is a separate subject involving the techniques of the professional historian as well as the seismologist, and is not dealt with here.

One thing in common with both questionnaire surveys and field investigations is the desirability of rapid response - evidence of earthquake damage is patched up within days or even hours, and human memory of details (and interest in the subject) also wanes rapidly.

12.2.1 Macroseismic questionnaires

The request has often been made for someone to produce a standard macroseismic questionnaire that could be used by everyone and ensure compatibility of results from one investigation to the next. The reason that such a thing has never been achieved is simply because social and practical considerations vary from case to case and make a unified approach impossible. To some extent, different cultures require different questionnaires simply because of the different fabric of everyday surroundings upon which the effects of an earthquake will become manifest. But more fundamental are the practical considerations facing the seismologist who wishes to distribute questionnaires - to whom will he give them?

There are two basic types of macroseismic questionnaire, dependant on the intended recipient. The first is the questionnaire to be answered by an individual citizen recounting his personal experiences of the earthquake. The second is the questionnaire designed to be answered by someone with knowledge of the experiences of the entire community. Which of these two approaches is used will shape the macroseismic investigation as a whole; the choice may well be forced on the investigator by circumstances. For example, in some countries there will be found an official in each town or rural community whose job includes completing such requests for data, and who can be relied on to fill in any questionnaire submitted. In some other countries such officials are not to be found, and this means of investigation is therefore

12. Intensity and Intensity Scales

not possible. Some institutes may have the resources to post out thousands of questionnaires as mailing shots; others may not be able to afford such a technique.

One may discern four basic types of person who may fill in a macroseismic questionnaire, two in each of the classes outlined above.

(i) The unselected individual: questionnaires may be distributed haphazardly and in great bulk by publication in newspapers, dissemination at libraries, etc. This guarantees a large response, but probably biases the results in favor of positive responses. Online Internet questionnaires have already been used with success in California (Wald et al., 1999) and this means of dissemination will become more important in the future as the proportion of the population with Internet access increases.

(ii) The randomly selected individual: there exists a methodology, highly developed in the social sciences, for disseminating questionnaires in such a way as to maximize the statistical validity of the results, using random selection procedures based on electoral rolls and direct mailing, often with some incentive to return the questionnaire (such as a prize draw). This is the best method in terms of the reliability of the results, since a random sample enables one to make statistically valid estimations of the characteristics of the whole population. The drawbacks are that such a response may be difficult to organize rapidly after an earthquake, and is likely to be relatively expensive. It should not be forgotten, that the art of questionnaire design and methodology has been studied in detail by social scientists for many years, and the expertise accumulated should not be ignored by seismologists whose background usually lies in the physical sciences.

(iii) The public official: it is very convenient to be able to send a single questionnaire to the local burgomaster/post officer/police superintendent's officer and have it filled in with the details of the effects of the earthquake in the whole of the community under the official's jurisdiction. What the seismologist can not be certain of is how conscientiously the questionnaire is filled in. Does the official make detailed enquiries, or does he jot down the first thing that comes into his head?

(iv) The volunteer: some seismological institutes have arranged networks of local volunteers with some standing in the community (schoolteachers, clergymen) and enthusiasm for the task of supplying useful data. Such volunteers can be given a stack of blank questionnaires in advance and can be relied upon to fill one in after an earthquake occurs with dependable data on the effects in the locality. Such a system is very effective, but can be laborious to set up and maintain.

A further division of questionnaire design is that between the free-form questionnaire and the multiple choice style. The first style gives open-ended questions to which the respondent can answer in his/her own words ("What sort of shaking did you experience?") while the second gives a series of boxes to tick ("The shaking was A - weak; B - moderate; C - strong"). The second style is easier to process, but runs the risk of losing information that doesn't easily fit the predefined categories. A combination of both styles is also possible.

Length of questionnaire is also important. Too long or difficult a questionnaire will discourage people from filling it in, as will asking questions that are too hard for most people to answer - for example, how many people can accurately describe their local geology? One should guard against asking questions that are not strictly necessary (such as personal details).

From the above discussion it will be seen that questionnaire design is somewhat of an art, and that what will work for one country won't work for another. A sample questionnaire, which is a synthesis of several in active use, is shown below.

EARTHQUAKE QUESTIONNAIRE

The following questionnaire is part of a study of the effects of the _____ (name) earthquake, which occurred on _____ (date) at _____ (time). You are invited to use it to record what you experienced. If you did NOT feel the earthquake, or notice it at all, please tick here [] and complete questions 1, 2 and 5, below. This information will still be useful for our study. Please send completed questionnaires to this address:

SECTION A - WHERE YOU WERE

1. At the time of the earthquake, where were you?
Address (including post code).....
- Outdoors [] Ground floor [] Upper floor [] ; if so, which floor?
- Stationary vehicle [] Moving vehicle [] Other
- If indoors, please describe the type of building:
Function (house, school, church, etc)
- Height (number of stories)
- Construction (brick, stone, wood, etc)
2. What were you doing?
Walking [] Standing [] Sitting [] Kneeling []
Lying down [] Sleeping []

SECTION B - EARTHQUAKE SHAKING AND SOUND

3. What best describes the shaking you felt?
No shaking [] Trembling [] Swaying [] Jerky motion []
Impact [] Rolling motion [] Other []
- It was ... Weak [] Moderate [] Severe []
4. What best describes any sound you heard?
No sound [] Rumbling [] Roaring [] Explosion []
Other []
- It was ... Faint [] Moderate [] Loud []

SECTION C - EFFECTS ON PEOPLE AND ANIMALS

5. Which best describes what happened where you were (your house, neighbours)?
Nobody noticed it [] Only one or two people noticed it []
Some people noticed it, but not many [] Many people noticed it []
Most people noticed it [] Everyone noticed it []
People indoors noticed it, but not those outside []
People upstairs noticed it, but not those on the ground floor []
I don't know whether other people noticed it or not []
6. (Only for earthquakes that happened at night) Did the earthquake wake you?
No [] Yes [] I wasn't asleep []
Were other people where you were woken up?
No [] Yes, a few [] Yes, many [] Yes, most/all [] Don't know []
7. Were you frightened?
No [] Yes []
Where you were, did anybody run outdoors in fright?
No [] Yes, a few [] Yes, many [] Yes, most/all [] Don't know []
8. Were any animals nearby frightened?
No [] Yes, pets [] Yes, farm animals [] No animals nearby/don't know []

SECTION D - EFFECTS ON OBJECTS, BUILDINGS, ETC

9. Did any of the following things happen?

	Yes	No	Don't know
Windows/doors rattled	[]	[]	[]
Crockery, etc rattled	[]	[]	[]
Hanging objects swung	[]	[]	[]
Pictures moved askew	[]	[]	[]
Small objects shifted or fell	[]	[]	[]
Books or similar shifted or fell	[]	[]	[]
Furniture shook visibly	[]	[]	[]
Furniture shifted out of place	[]	[]	[]
Furniture toppled over	[]	[]	[]
Pendulum clocks stopped	[]	[]	[]
Plants shook	[]	[]	[]
Liquids splashed or spilled	[]	[]	[]

10. Was there any damage to buildings where you were?
No [] Yes [] Don't know []
If yes, please describe the damage
11. Were there any effects on natural surroundings where you were, for example, landslips, cracks in ground, effects on ponds or streams, etc?
No [] Yes [] Don't know []
If yes, please describe the effects
12. Have you any other comments about the effects of the earthquake that might be useful?
.....

12. Intensity and Intensity Scales

12.2.2 Field investigations

Following a high intensity earthquake, a field investigation needs to be made as soon as possible. It is advisable to plan such investigations as much as possible before an earthquake even occurs, so that the investigation team (typically two to six people) can be assembled, together with necessary equipment, and leave for the affected area at very short notice. Team members should include people who have experience in earthquake engineering and geotechnical engineering as well as seismology. The following paragraphs draw largely on EEFIT (1993).

In the field, it is necessary to combine both detailed and general surveys of structural behavior. Structures need to be surveyed in terms of: the distribution of different types; the overall vulnerability (resistance or lack of resistance to earthquake shaking) of typical structures while noting deviations in terms of good or bad examples; and the distribution of different grades of damage within each building type. Care should be taken over making accurate records of the location of all structures studied or photographed. Data should be gathered as written notes and photographs.

For engineered structures, a detailed study should be carried out to identify both good and bad performance in a sample of both damaged and undamaged structures. External and internal damage should both be recorded, identifying typical modes of failure. In order to be able to relate the damage to the intensity scale, information on the strength of the building is required: strengths and weaknesses in the construction techniques, special points of poor vulnerability or high resistance, irregularity or symmetry in the building design, the quality of the materials used, and so on. It is a good idea to collect information on what earthquake-resistant design regulations were in force before the earthquake, and also, where possible, to investigate to what extent these regulations were followed in the buildings examined.

The case is similar for non-engineered structures; these are likely to be less individual, so the task becomes one of identifying the main characteristic structural forms, their age and condition. Again, the extent and types of damage, both interior and exterior, need to be recorded.

Detailed photographic surveys can be made of individual streets or districts to record the percentages of various types of buildings that were damaged to a lesser or greater degree. These surveys should be supplemented with internal records from at least a sample of the buildings examined.

The overall spatial distribution of damage can be recorded over a large area by the use of general surveys employing proper sampling techniques to generate statistically consistent data. Distinctions between different construction types, usage, height and age and quality of construction should always be made wherever possible.

Geotechnical aspects should also be investigated. Any relationship between local geology and damage distribution should be investigated. (This does not entail "correcting" intensities for local conditions, but does explain local variations in observed intensity). Data should be gathered on groundwater and hydrological conditions before the earthquake. The following topics also need to be considered: types of foundation and their performance; effects on embankments, cuttings and river banks; liquefaction and other ground effects like cracking; landslides and rockfalls. Negative data as well as positive data should be collected.

Special studies may be needed of individual industrial or civil facilities. Effects on factories can include damage to pipework and ducting, pumps and valves, cabling systems, tanks, machinery, electrical controls, computers and cranes. The effects on dams, bridges, port facilities, tunnels and irrigation systems should be recorded. The effects on lifelines (services, transport) also merit attention: underground provision of water, gas, electricity and telecommunications; railways, roads etc. These sorts of data are not generally suitable for intensity assessment per se, but are important to record, particularly when making an assessment of the economic impact of the earthquake, or looking at lessons to be learnt from an engineering perspective.

12.3 Processing of macroseismic data

12.3.1 Assessing intensity from data

Although the conversion of descriptive information to numerical intensity data by use of an intensity scale is fundamental to macroseismic studies, the process has in general been rather poorly documented. This has led to considerable variations in practice from worker to worker, resulting in serious inconsistencies in results. It is widely recognized that assessing intensity is to some extent a subjective exercise, and that some variations between workers will always occur, but it is better if these are minimized through common methodology as much as possible.

The following points apply to most common intensity scales:

Data should be grouped by place prior to assessing intensity. By "place" is meant a village or town or part of a city. Places should not be too big (like a county) or too small (like a single house). When assessing intensity for a place, all the data relating to that place should be considered together. If there are fifteen reports from one village, a single intensity should be assigned to those fifteen jointly, rather than making fifteen assessments and combining them.

Make sure there are sufficient data for a reasonable assessment. If there are too few reports, or the reports are too lacking in detail, it is better to record merely that the earthquake was felt rather than forcing an intensity value on inadequate data. In some cases it will be possible to make a range assessment, e.g., 4-5, >6, (4 or 5, more than 6) etc.

For each place, compare the picture of earthquake effects provided by the data with the idealized pictures provided by each description of an intensity degree in the intensity scale, in order to look for the best overall fit. The match will seldom be perfect, so it is necessary to look for the most coherent, general comparison. It should be remembered that, given the very variable nature of intensity, in any place individual effects may be observed that are higher or lower than those to be expected from the general (modal) intensity level. It is important not to give these too much attention. For example, if most of the data for a place are suggesting intensity 4, but there is a single exceptional report that a chimney fell, this chimney does not invalidate an assessment of intensity 4 for the place.

When using a quantitative intensity scale (MSK, EMS) then the comparison of the data with the scale will usually be a question of making a best fit of the percentages of a particular observation that were recorded and the percentage ranges expected for each degree of the

12. Intensity and Intensity Scales

scale. For EMS, the procedures for assessing intensity are discussed in detail in the scale support material (Grünthal, 1998).

The absence of reports of a particular phenomenon may or may not be evidence that it did not occur, depending on the nature and quality of the data. It can not automatically be inferred that, for instance, an absence of reports of damage indicates no damage occurred, although this will often be the case. A positive statement along the lines of "there was no damage" is more reliable.

To make inferences from a particular source of data requires an understanding of the nature and limitations of that data source. For instance, newspapers often pluralize things for effect, so a newspaper report that says "pictures fell from walls" may mean only one picture fell from a wall. Where the sources are historical documents, the advice of a professional historian in understanding the nature of the documents should be taken.

Effects on nature (landslides, ground water changes, etc.) should only be used with caution, since their frequency is strongly influenced by local hydrological conditions and other factors not related to intensity. It is therefore very difficult to arrive at reliable intensity values for remote, largely uninhabited, rural areas (this point has been found unpalatable by some, but unfortunately is realistic).

The use of automatic algorithms to assess intensity by computer has been experimented with since at least the mid 1980s (e.g., Zsiros, 1989). This has the advantage of removing any possible subjectivity or bias from the procedure. Such algorithms require careful calibration, and a certain amount of checking is still required. However, this is a developing field. Wald et al. (1999) demonstrate that the combination of algorithms for intensity assessment with on-line questionnaires allows the possibility of producing intensity maps extremely rapidly in the wake of a felt earthquake in areas where a very high proportion of residents have Internet connections.

12.3.2 Isoseismal maps

The presentation of intensity data is usually done in the form of a map. As well as plotting intensity points, it is usually useful to be able to draw contour lines of equal intensity, called isoseismals. An isoseismal can be defined as a line bounding the area within which the intensity is predominantly equal to, or greater than, a given value.

No precise instructions can be given for drawing isoseismals as no definitive method has ever been agreed. Some workers adopt a practice of overlaying a grid on the data and taking the modal value in each grid square prior to contouring, others prefer to work directly on the plotted intensity values. Workers have differing preferences for the amount of smoothing, extrapolation, etc., that is to be employed. Thus, at present, the drawing of isoseismals is to some degree subjective.

However, some guidelines can be given. The degree of smoothing employed should reflect the purposes to which the resulting map will be put. If the map is intended for microzonation work, i.e., to point up areas where seismic hazard may be enhanced owing to local soil conditions, then smoothing will be at a minimum, and isoseismals will be as convoluted as the data. If the map is intended for other purposes (calculation of earthquake parameters,

attenuation studies, tectonic studies, etc.) then the curves will normally be smoothed so that only major re-entrants and outliers are shown. In practice, smoothed isoseismals are much more common. It can be argued that highly detailed isoseismals present too many practical problems, and that microzonation is better served by damage maps.

As a general rule, re-entrants and outliers should not be drawn unless suggested by a grouping of at least three data points. If isoseismals have to be interpolated or extrapolated across areas of water, or areas without data points, these sections of the lines should be shown as dashed. In cases where, for example, an epicenter is offshore, and only (say) a 120 degree arc of each isoseismal would fall onshore, it is not correct to project the whole of the remaining 240 degrees of each isoseismal on a map, even as a dotted line. Only the onshore section should be drawn, with each line tailing off with a short dotted section offshore if desired. Plotting isoseismals that are completely offshore and merely projections of an intensity attenuation curve should not be done. For onshore earthquakes with few data, it is not good practice to attempt to draw isoseismals conjectured from one or two points only; at least three mutually supporting data points for one intensity value should exist before one attempts to draw even a partial isoseismal for that value.

In a case where one has data for intensity 5 and intensity 8, and data points assessed at 6-7, it is possible to have isoseismals labeled 5, 6-7 and 8. For analytical purposes it is best to treat the 6-7 isoseismal as the 6 isoseismal, and conclude that the data are insufficient to draw the 7 isoseismal. In cases where it is possible to draw isoseismals for intensities 6 and 7, one should definitely not attempt to draw a 6-7 isoseismal between them.

Computer contouring programs usually do not give good results with macroseismic data. This is because local variations in intensity can easily upset contouring algorithms by suggesting a gradient that doesn't exist.

In plotting the intensity data points on a map, the most common practice is to use Arabic numerals for each data point. Roman numerals can become very confusing when data are close together. A set of international symbols (first introduced by the Commission of the Academies of Sciences of Socialist Countries for Planetary Geophysical Research (KAPG)) based on coloring in different proportions of small circles (Fig. 12.1) is a clear alternative; as is the use of colored dots. It is strongly recommended that isoseismal maps should always have the data points displayed on them.

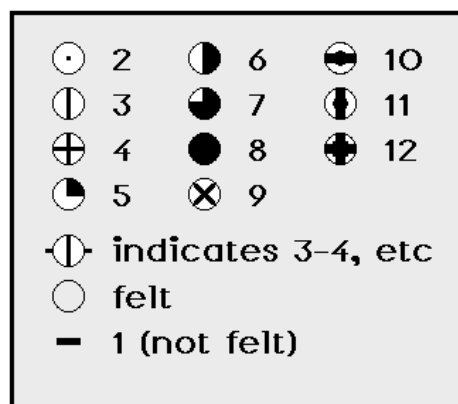


Fig. 12.1 Symbols for plotting intensity values. Those for intensities 2-9 are standard. There do not appear to be any recognized standard symbols for intensities 10-12, felt or not felt; the ones above are offered as suggestions.

12. Intensity and Intensity Scales

The use of modern software, databases, GIS and Internet applications, combine to aid the display, analysis and communication of intensity data. Two examples are given in Fig. 12.2. These both show data from the 23 January 1980 Modica (Sicily) earthquake. The first (above) shows the data from the web-enabled DOM4.1 macroseismic database (<http://emidius.mi.ingv.it/DOM/>) displayed in both text and graphical formats. The second (below) shows the same data displayed using the Wizmap II seismological display program, with the KAPG symbol set as shown in Figure 12.1, and estimated isoseismals drawn purely from a standard Italian intensity attenuation formula (see 12.3.4). The Wizmap program can be downloaded from <http://www.gsrq.nmh.ac.uk/hazard/wizmap.htm>.

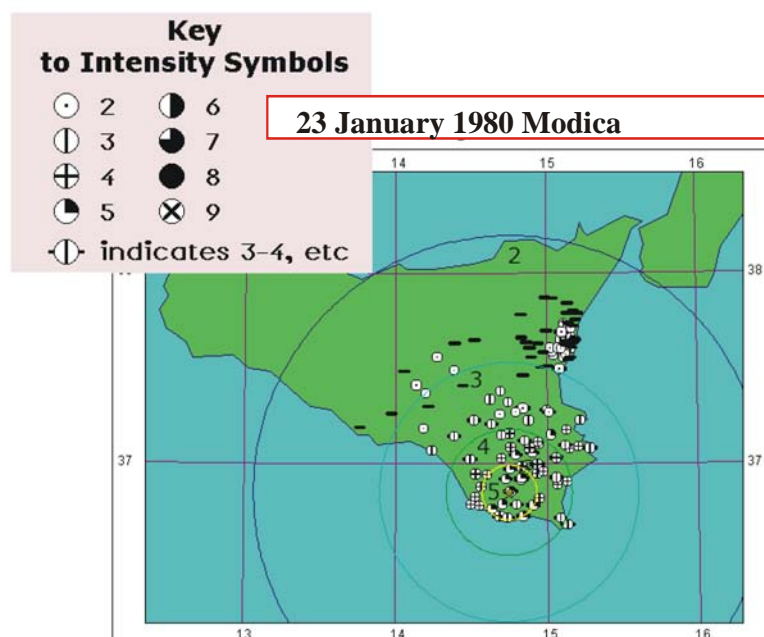
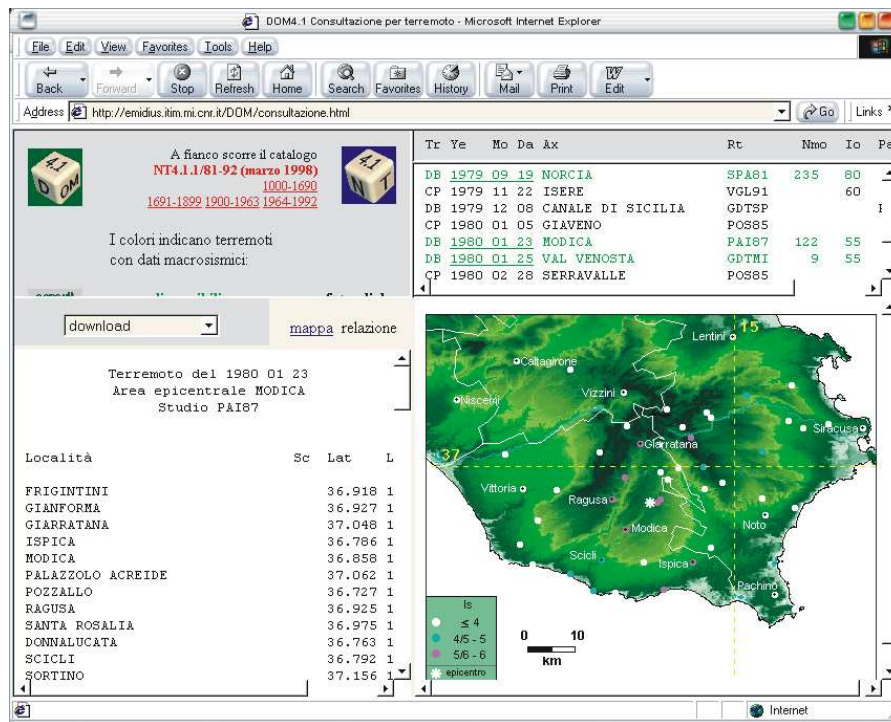


Fig. 12.2 Display of intensity data points using a web-enabled database (above), and a PC-based data exploration program (below).

It is recommended that seismologists preserve and publish tables of intensity data (place, geographical co-ordinates, intensity) whenever possible.

12.3.2.1 Example of an isoseismal map

In Fig. 12.3 a sample intensity/isoseismal map is shown. The earthquake in question is the small Lagrangeville (NY) earthquake of 26 February 1983 in the Eastern USA. This earthquake was chosen as one representing a fairly typical case for a small earthquake; since it doesn't have a very large number of data points, the whole intensity field can be seen clearly in just the one figure. The data were taken from the NOAA Earthquake Intensity Database, plotted using the KAPG symbol set, and the isoseismals added. Notice that the symbols are well mixed; between the isoseismals 4 and 5 are some data points for intensity 2, 3 and 5. This is quite normal and to be expected especially where data points represent only one or two questionnaires. It is not hard to see in this case that standard automatic contouring algorithms would have difficulty with this data set. However, the hand-drawn smoothed isoseismals in Fig. 12.3 represent quite well the general pattern of diminution of intensity with distance observed in this earthquake. It is not appropriate to try and draw an isoseismal 6 for only two data points. Nor can elaborate re-entrants be justified with the given data. The degree of smoothing is appropriate to the resolving power of the original data, and the contours are true to the expected underlying pattern of approximately elliptical areas of equal intensity.

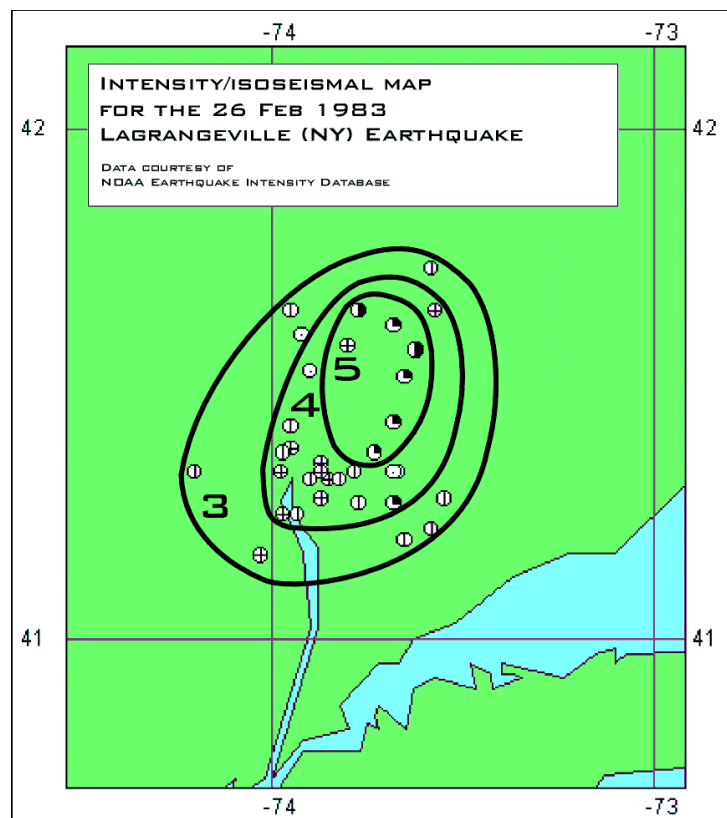


Fig. 12.3 Sample intensity/isoseismal map: the Lagrangeville (NY) earthquake of 26 February 1983.

12.3.3 Determination of earthquake parameters from macroseismic data

12.3.3.1 Macroseismic epicenter

This is an expression which has been used in the past to convey different concepts, never properly defined. The following usage is proposed for the future:

Macroseismic epicenter: The best estimate made of the position of the epicenter (i.e., the point on the Earth's surface above the focus of the earthquake) without using instrumental data. This may be derived from any or all of the following as circumstances dictate: position of highest intensities, shape of isoseismals, location of reports of foreshocks or aftershocks, calculations based on distribution of intensity points, local geological knowledge, analogical comparisons with other earthquakes, and so on. This is a rather judgmental process with some subjectivity, and does not lend itself to simple guidelines that can be applied uniformly in all cases.

Barycenter: The point on the Earth's surface from which the macroseismic field appears to radiate. This is usually the center of the highest isoseismal or the weighted center of the two highest isoseismals. Advanced computational methods have also been demonstrated for calculating the barycenter from the whole macroseismic data set. (The terms macrocenter and macroseismic center have also been proposed.)

These two points are often the same, but need not be. As an example: In the case of the 1989 Loma Prieta earthquake the apparent point of origin of the macroseismic field, for various geological reasons, was well to the north of the actual instrumental epicenter. If one were to attempt to locate a similar event from macroseismic data alone (for example, a historical Californian earthquake), one might be inclined to compensate for this effect by choosing epicentral co-ordinates to the south of the highest isoseismal. This would not affect the location of the barycenter.

Both these concepts have their uses. For any study of the tectonics of an area, the macroseismic epicenter is more useful. For studies of seismic hazard, especially those using a technique like extreme value statistics, the barycenter gives a better indication of the hazard potential of an earthquake.

12.3.3.2 Epicentral intensity

Epicentral intensity, usually abbreviated I_0 , is a parameter commonly used in earthquake catalogs but rarely defined, and it is clear that different usages exist in practice (Cecić et al., 1996). The meaning of the term is clearly the intensity at the epicenter of the earthquake, but since it is likely that there will not be observations exactly at the epicenter itself, some way of deriving this value is necessary. The two main techniques that have been used in the past are:

1) extrapolation from the nearest observed data to the epicenter without changing the value, or use of the value of the highest isoseismal. Thus, if there are a few data points of intensity 9 near the epicenter, the I_0 value is also 9. If the epicenter is significantly offshore, I_0 can not be determined;

2) calculating a fractional intensity at the epicenter from the attenuation over the macroseismic field, using a formula such as that by Blake (1941) or Kövesligethy (1906) - see 12.3.3.4 below. In this case, because this is not an observed value (and not a "true" intensity) it may be expressed as a decimal fraction without contravening the rule that intensity values are integer. This value can be determined for earthquakes with sufficient data to draw at least two (preferably three) isoseismals. This is only possible if one is using the concept of the barycenter (see 12.3.2.1 above), since the true epicenter may not be central to the macroseismic field. The term "barycentral intensity" may be preferable.

It is recommended that these two methods be discriminated between by the notation used. Thus an integer number (9 or IX) indicates method (1) and a decimal number (9.0 or 9.3) indicates method (2). It is recommended that one should not add arbitrary values to the maximum observed intensity when deriving an I_o value; the arbitrary amount is too subjective.

As well as epicentral intensity, a useful parameter is maximum intensity, abbreviated I_{max} . This is simply the highest observed intensity value anywhere in the macroseismic field. For onshore earthquakes, I_o and I_{max} may be equal. For offshore earthquakes it is often not possible to estimate I_o (never if method 1 is used), but I_{max} can be given.

12.3.3.3 Macroseismic magnitude

The use of macroseismic data can give surprisingly robust measures of earthquake magnitude. This is an extremely important part of macroseismic studies, as in this way earthquake catalogs can be extended into historical times with consistent magnitude values. Such extended earthquake catalogs are of great benefit to seismic hazard studies.

Early studies attempted to correlate epicentral intensity with magnitude; however, epicentral intensity is strongly affected by focal depth, so such correlation's perform poorly unless either (a) depths are known and taken into consideration, or (b) one is working in an area where seismogenic depth is narrowly constrained.

The total felt area (A) of an earthquake, or the area enclosed by one of the outer isoseismals (usually 3 or 4), is a much better indicator of magnitude, being not much affected by depth except in the case of truly deep earthquakes. For earthquakes below a threshold magnitude (about 5.5 Mw), the magnitude and log felt area scale more or less linearly, and so equations of the form

$$M = a \log A + b \tag{12.1}$$

can be established regionally by examination of data for earthquakes for which macroseismic data and instrumental magnitude are both available. For larger earthquakes, differences in spectral content may affect the way in which earthquake vibration is perceived, and a different scaling appears to apply. In Frankel (1994) the form

$$M = n \log \left(\frac{A}{\pi} \right) + \frac{2m}{2.3\sqrt{\pi}} \sqrt{A} + a \tag{12.2}$$

12. Intensity and Intensity Scales

is used to represent the full magnitude range, where n is the exponent of geometrical spreading and $m = (\pi f)/(Q \beta)$ where f is the predominant frequency of earthquake motion at the limit of the felt area (probably 2-4 Hz), Q is shear-wave attenuation and β is shear-wave velocity (3.5 km/sec). Using this functional form and comparing world-wide intraplate earthquakes with interplate earthquakes from one region (California), Frankel found the difference in magnitude for the same felt area to be on average 1.1 units greater for California.

Other forms that have been proposed include

$$M = a I_0 + b \ln r + c \quad (12.3)$$

where r is the radius, rather than the area, of the total macroseismic field, and

$$M = a I_0 + \sum b_i \ln r_i + c \quad (12.4)$$

in which all isoseismals (values for each i) are used as well as the epicentral intensity (see Albarello et al., 1995).

In the above equations, M has been used for generic magnitude; for any particular magnitude equation it is important to specify what magnitude type the derived values are compatible with (M_s , M_L , M_w etc.). It is also useful to determine the standard error, which will give a measure of the uncertainty attached to estimated magnitude values.

12.3.3.4 Estimation of focal depth

The estimation of focal depth from macroseismic data was first developed by Radó Kövesligethy. His first paper on the subject presented the formula

$$I - I_0 = 3 \log \sin e - 3 \alpha (r/R) (1 - \sin e) \quad (12.5)$$

where $\sin e = h / r$ and R is the radius of the earth, and α is a constant representing anelastic attenuation (Kövesligethy, 1906). A second paper, (Kövesligethy, 1907) contains a different equation:

$$I - I_0 = 3 \log \sin \varphi \quad (12.6)$$

where φ is the angle of emergence. Why the absorption term was dropped in this publication is unclear. Eq. (12.5) was subsequently rewritten and modified slightly by Jánosi (1907) to reach the now well-known formula

$$I_0 - I_i = 3 \log (r / h) + 3 \alpha M (r - h) \quad (12.7)$$

where r is the radius of the isoseismal of intensity I_i and $M = \log e$. This work was developed further by Blake (1941) whose contribution was essentially a reduction and simplification of Eq. (12.7); Blake's version is still used by some workers today, but Kövesligethy's original equation (in Jánosi's version) is more commonly encountered. Kövesligethy's equation became more widely known, in the form of Eq. (12.7), through the work of Sponheuer (1960). However, although Sponheuer references Kövesligethy (1906) in his text, he cited Kövesligethy (1907) in the reference list, and the relative inaccessibility of these papers, and

this misreference, has caused some confusion which it has only now been possible to unravel. A further confusion is that Jánosi (1907) attributes Eq. (12.7) to Cancani, transmitted by Kövesligethy; it seems that Kövesligethy named another of his equations in honour of Cancani and that Jánosi transferred this title to Eq. (12.7) (Zsiros, 1999, personal communication).

The constant value of 3 used in Eqs. (12.5) to (12.7) represents an equivalence value between the degrees of the intensity scale and ground motion amplitudes. Some workers accept it, others prefer to find their own values by fitting to data (Levret et al., 1996). In this case the formula could be written with a further variable in place of the constant 3. The attenuation parameter a is generally considered to be a regional value, reflecting the absorption of seismic energy by the crust; therefore, normally it should be determined regionally by group optimization on an appropriate data set - not for individual earthquakes.

I_0 here is properly the barycentral intensity, which has to be solved for as well as solving for h . This is usually done graphically - one can fit the isoseismal data to all possible values of h and I_0 and find a minimum error value consistent with the observed maximum intensity (e.g., Burton et al., 1985; Musson, 1996).

12.3.4 Intensity attenuation

Intensity attenuation, the rate of decay of shaking with distance from the epicenter, can be expressed in two ways. Firstly, there is the drop in intensity with respect to the epicentral intensity. This is shown by the Kövesligethy (1906) formula in Eq. (12.7); this form of intensity attenuation and depth determination from intensity are closely linked.

One can also express intensity attenuation as a function of magnitude and distance. Such formulae usually have the functional form

$$I = a M + b \log R + c R + d \quad (12.8)$$

where R is hypocentral (slant) distance, and a , b , c and d are constants. (The third term is sometimes dropped, especially in intraplate areas). Since most earthquake catalogs include magnitude as a parameter, this form of intensity attenuation is extremely useful in seismic hazard studies. Intensity is a good parameter to use for expressing seismic hazard, since it relates directly to damage. It yields hazard values which are more relevant to planners and insurers than physical ground motion parameters. Some typical values are:

$$\text{Interplate (New Zealand): } I = 1.41 M_s - 1.18 \ln R - 0.0044 R + 2.18$$

$$\text{Intraplate (SE Australia): } I = 1.64 M_s - 1.70 \ln R + 4.00$$

Such formulae also link magnitude with epicentral intensity; when epicentral distance = 0, then $R = h$. Since depth is now taken into account, much better results can be obtained than from simple I_0/M relationships.

More sophisticated models of attenuation, taking into account factors such as directionality, have been developed for seismic hazard work but are beyond the scope of this Manual.

12.3.5 Relationship with ground motion parameters

Attempts to equate intensity with physical parameters of ground motion, especially peak ground acceleration (PGA), are nothing new. One early scale (that of Cancani) amounted to little more than a table of intensity numbers and equivalent PGA values, and such tables are still often encountered in the literature. However, they can not be relied on; work in the 1970s (e.g., Trifunac and Brady, 1975) demonstrated that intensity and peak ground acceleration correlate very poorly, and any attempt to relate the two suffers from such severe scattering as to be practically useless.

There are a number of reasons for this. One is that other parameters of ground motion, such as peak ground velocity, may be just as important, if not more so, than acceleration. Another is that the duration of strong ground motion is obviously important; a high acceleration for a fraction of a second is not as damaging as a lower acceleration applied over a longer period. Thirdly, peak ground acceleration values often represent single spikes in an accelerogram record which are unrepresentative of the earthquake ground motion as a whole. Where accelerations have been recorded in excess of 1g, these have not been accompanied by any remarkably high intensity values.

Recent research has therefore turned to looking at other ways of relating intensity to physical ground motion parameters, including spectral accelerations and Arias intensity. A review of this subject is beyond the scope of this Manual.

Acknowledgments

The author would like to thank the numerous people who made comments on the text and suggested improvements; particularly Gottfried Grünthal of GeoForschungsZentrum Potsdam for many detailed comments on the text, and also Tibor Zsiros of the Seismological Observatory, Geodetic and Geophysical Research Institute of the Hungarian Academy of Sciences, without whose help it would have been impossible to sort out the historical problems addressed in sub-section 12.3.3.4. This contribution to the New Manual of Seismological Observatory Practice is published with the permission of the Director of the British Geological Survey (NERC).

Recommended overview readings (see References, under Miscellaneous in Volume 2)

- Burton, P. W. et al. (1985).
- Cecić, I. et al. (1996).
- Grünthal, G., ed. (1998).
- Musson, R. M. W. (1996).
- Richter, C. F. (1958).
- Wood, H. O. and Neumann, F. (1931).

13

Volcano Seismology

Joachim Wassermann

13.1 Introduction

Volcanic eruptions and their impact on human society, following earthquakes and meteorological disasters, are the most severe natural hazards. Since the pioneering works of Omori (1911), Sassa (1936) and Imbo (1954), much attention was focused on the seismic signals preceding or accompanying a volcanic eruption. Soon after the start of more extensive seismic monitoring it became clear that volcanoes show a variety of different seismic signals which often differ from those produced by common tectonic earthquake sources, i.e., double-couple type sources.

Starting with the availability of small portable seismographs in the late 1960s to early 1970s, a tremendous number of observations were made at different volcanoes and during different stages of activity. At the same time, first attempts were made to explain some of the seismic signals recorded and to classify the different signals by their proposed (but still mostly unknown) source mechanisms. Following this very enthusiastic period, the progress in the study of accelerated magma transport to the surface stagnated. Too many open questions remained unsolved, such as the mostly unknown source mechanisms of volcanic signals, the influence of the topography of volcanoes, the problem of proper hypocenter determination, the relationship between the occurrence of seismic signals of different type, and the associated surface activity of a volcano. Since the late 1980s to early 1990s the use of portable and robust broadband seismometers and newly developed low power consuming 24bit A/D converters, as well as the extensive use of seismic array techniques, opened new horizons and different views on the source mechanisms and the importance of volcano-seismic signals in the framework of early warning.

This Chapter should be seen as a guideline for establishing a seismic monitoring network or at least a temporary experiment at an active volcano. Because of the large number of different volcanoes and many different kinds of source mechanisms which may produce seismic signals, a description of all aspects is not possible. Also, a comprehensive review of case studies, including the variety of volcanic earthquake sequences, is beyond the scope of this paper. Relevant references include the excellent text books *Encyclopedia of Volcanoes* (Sigurdsson, 2000) and *Monitoring and Mitigation of Volcano Hazards* (Scarpa and Tilling, 1996). Most of the relevant topics dealt with in these text books are summarized below.

13.1.1 Why a different Chapter?

Volcano seismology uses many terms and methods known in earthquake seismology. This is no surprise as the same instruments and the same mechanism of elastic wave propagation through the Earth are used to investigate the subsurface structure and the activity state of a volcano. However, there are some deviations from conventional earthquake seismology, both in the physics of the signals and the methods of analyzing them. As outlined below, the signals vary from “earthquake-like” transients to long-lasting and continuous “tremor” signals. The most striking differences between earthquake and volcano seismology are the proposed source mechanisms and the related analysis techniques. In 13.2 and 13.4 we will discuss some of these aspects.

When setting up an earthquake monitoring network an optimal station coverage is needed in order to locate the events precisely. Depending on the tasks of the network, at least some stations should be located as close as possible to the active volcanic area in order to model the related seismic source with sufficient accuracy and determine the source depth. Hence, we are looking for a site-distribution which optimizes the station coverage and minimizes the influence of shallow structure and topography of the Earth. In contrast, in volcano-seismology we are left with sometimes very rough topography and nearly unknown propagation and site properties of the medium. Some of these aspects will be discussed in 13.3.

13.1.2 Why use seismology when forecasting volcanic eruptions?

The use of seismological observations in the monitoring and forecasting of volcanic eruptions is justified because nearly all seismically monitored volcanic eruptions have been accompanied by some sort of seismic anomaly. The Pinatubo 1991 (Pinatubo Volcano Observatory Team, 1991) or the Hekla 2000 eruption (<http://hraun.vedur.is/ja/englishweb/heklanews.html#strain>) are two recent examples of successful long- and short-term eruption forecasts made by mainly seismic observations. For further case studies on volcanic “early warning” see the comprehensive articles by McNutt (1996, 2000a, 2000b).

While most of these “early warnings” were simply deduced by counting the number and type of volcanic events per hour or day or even better by monitoring their hypocenter distributions, the physical meaning of the different seismic events and their relationship to the fast ascending magma are not well understood. To give an example: increasing volcanic tremor is always a sign of high volcanic activity, but although the occurrence of tremor will increase the alert level, its role for short-term prediction is still not known precisely enough because we do not know the related physical process of this signal (fluid flow; movement of magma, water and/or gas; crack extension etc.). Further: how can we distinguish between an intrusion and a developing eruption, both of which generate a large number of seismic signals?

The extensive use of seismic methods during the last decades has shown that using them alone will not help the improvement of our knowledge about the internal processes of rapid magma ascent. This will be discussed in more detail in 13.5. Planning a new monitoring network or a short-term seismic experiment, we must also keep in mind that every volcano has its own characteristics, both with respect to seismic signal generation and wave propagation effects.

13.2 Classification and source models of volcano-seismic signals

Most of the confusion in volcano seismology is caused by the huge number of different terms for classifying volcano-seismic events. While this is mainly caused by the imperfect knowledge about the source mechanisms, we will focus on the basic nomenclature widely used in the literature. Most of these terms simply describe the appearance and frequency content of the signal, while others imply a certain source mechanism. However, one should be aware in both cases that the sources are still unknown and the propagation medium may alter the shape and the spectral content of the signals significantly.

While pioneering work in classifying volcano-seismic signals was made by Shimozuru (1972) and Minakami (1974), most of the following discussion follows the work of McNutt (1996, 2000a) and Chouet (1996a). We will divide the known signals mainly into transient and continuous signals. We will also discuss, where appropriate, differences in the signal generation related to different types of magma (i.e., low/high viscous, gas rich/ poor).

13.2.1 Transient volcano-seismic signals

13.2.1.1 Volcanic-Tectonic events (deep and shallow)

Deep (below about 2 km) *Volcanic-Tectonic* events (VT-A) manifest themselves by the clear onsets of P- and S-wave arrivals and their high frequency content ($> 5\text{Hz}$). This leads also to the class name *high-frequency* event (HF) (Fig. 13.1).

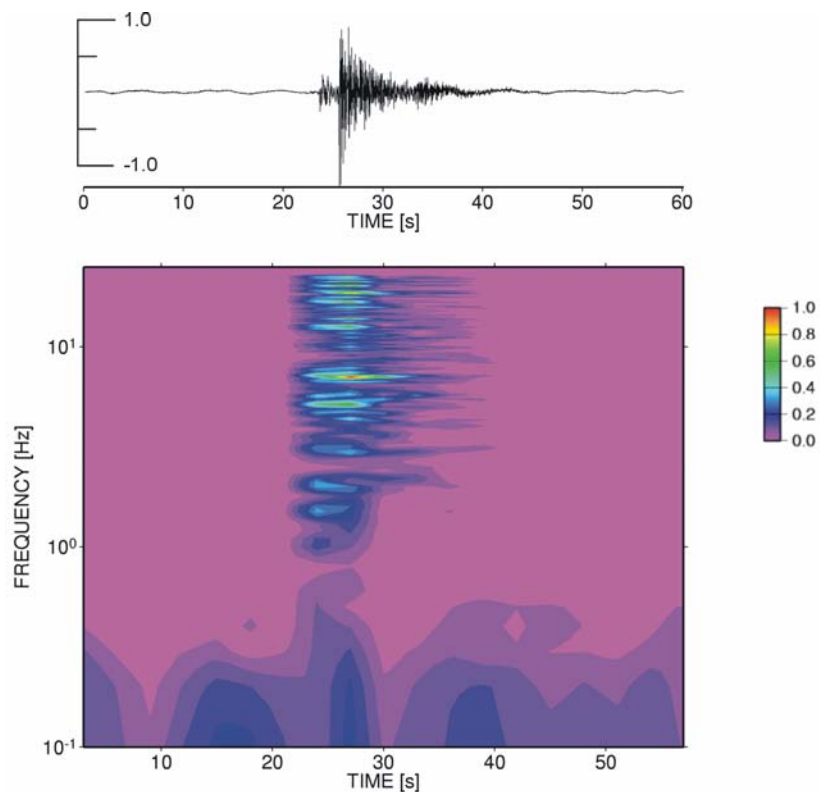


Fig. 13.1 VT-A type event recorded at Mt. Merapi, Indonesia. The impulsive P- and S-wave arrivals are clearly visible in this signal, as well as their high-frequency content and short signal duration. The given color coding, representing normalized amplitude spectral density, is valid for all following figures.

13. Volcano Seismology

The name of this event type implies a well known source mechanism, namely a common shear failure caused by stress buildup and resulting in slip on a fault plane similar to a tectonic earthquake source. The only difference from the latter is the frequent occurrence of swarms of VT events which do not follow the usual main-after-shock distribution (McNutt, 2000a). An earthquake swarm is a sequence where the largest events are similar in size and not necessarily at the beginning of the sequence. The high frequencies and the impulsiveness of the P- and S-wave arrivals seem to be caused by low scattering due to the short travel path through high scattering regions and low attenuation.

In contrast, *shallow* (above about 1-2 km) *Volcanic-Tectonic* events (VT-B) show much more emergent P-wave onsets and sometimes it is even impossible to detect any clear S-wave arrival (see Fig. 13.2). The spectral bands are shifted to lower frequencies (1-5 Hz). Both observations are thought to be caused by a more shallow hypocenter location and therefore a larger amount of scattering during wave propagation, especially of higher frequencies. While the depth distribution deviates significantly from that of VT-A events, the source mechanism may still consist mainly of a simple double-couple source.

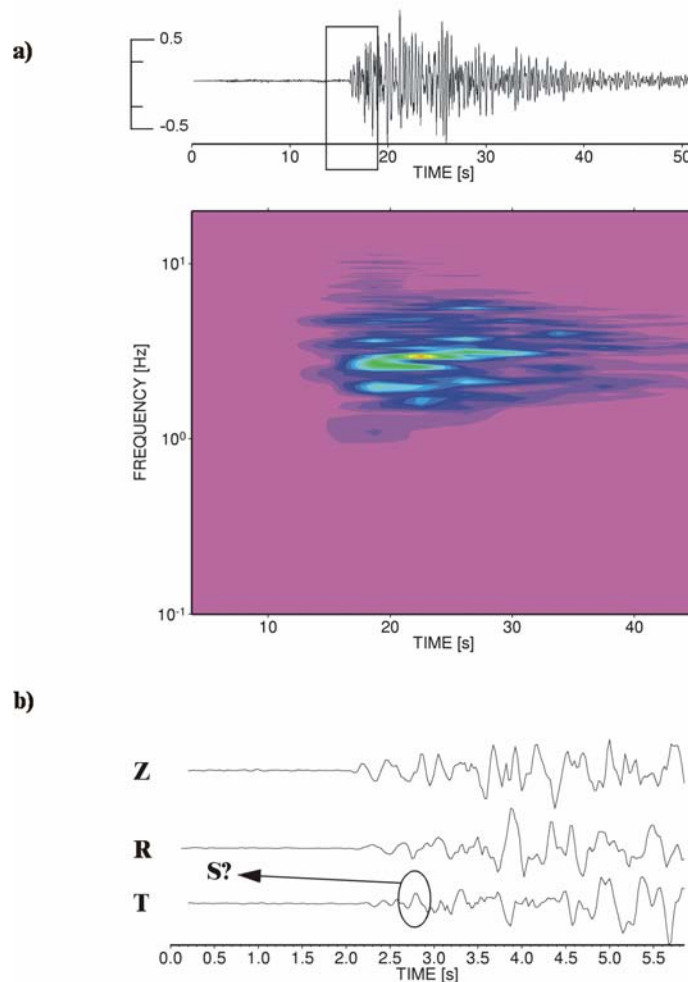


Fig. 13.2 a) typical example of a VT-B type event recorded during a high activity phase at Mt. Merapi. Note that the overall frequency content is mainly between 1 – 10 Hz with a dominant frequency at roughly 3 Hz. b) zoomed out version of the same event in its three components. Whereas the P-wave arrival is clearly visible, no clear S-wave arrival can be seen. The circle marks the wavelet that has the approximate S-wave travel time for the estimated source location.

Recently, detailed studies showed that the sources of some VT events deviate significantly from that of a pure shear failure, but show some similarities with the later described *Low-Frequency* events. Several papers on the inversion of the seismic moment tensor showed a significant contribution of non double-couple parts (Dahm and Brandsdottir, 1997; Saraò et al., 2001).

13.2.1.2 Low-Frequency events

Low-Frequency events (LF or Long Period - LP) show no S-wave arrivals and a very emergent signal onset (see Fig. 13.3). The frequency content is mostly restricted in a narrow band between 1-3 Hz. The LF sources are often situated in the shallow part of the volcano (< 2 km). Locations are deduced mainly by amplitude distance curves, from the rare hypocentral determinations using clear first onset recordings, and recently by semblance location techniques from particle motions recorded on a broad-band seismometer network (Kawakatsu et al., 2000). Some volcanoes (e.g., Kilauea) are known to produce deep (30-40 km) LF events (Aki and Koyanagi, 1981; Shaw and Chouet, 1991).

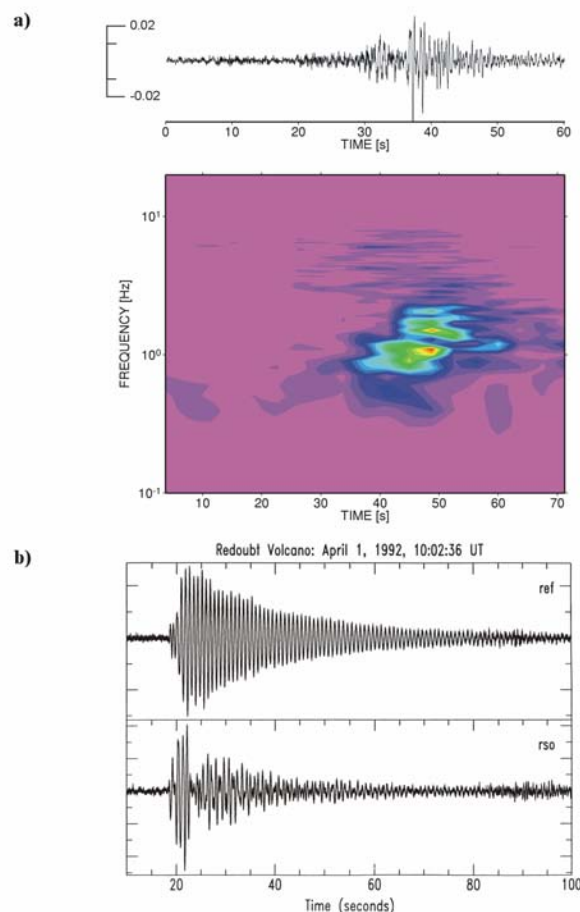


Fig. 13.3 a) example of a LF-wave group recorded at Mt. Merapi. Clearly the dominant frequency is around 1 Hz. b) shows an example of a LF event recorded at two different sites located at Redoubt volcano, Alaska (courtesy of S. McNutt, Alaska Volcano Observatory; AVO). The spindle shaped signal is also known as Tornillo.

13. Volcano Seismology

The associated source models range from an opening and resonating crack when the magma is ascending towards the surface (Chouet, 1996a) to existence of pressure transients within the fluid-gas mixture causing resonance phenomena within the magma itself (Seidl et al., 1981). Both models are able to explain a large part of the observed features in the spectral domain. Recently a pure crack model was developed which also considers the influence of the fluid properties. Recent numerical simulations show that the resonance effect and the overall shape of the seismograms and their frequency content may also be explained by fluid-solid contact and the excitation of multiple reflected borehole waves (Neuberg et al., 2000).

13.2.1.3 Hybrid events, Multi-Phases events

Some volcano-seismic signals share the signal and frequency characteristics of both LF and VT-(A,B) events. Signals of this class are usually labeled as *Hybrid events*, which may reflect a possible mixture of source mechanisms from both event types (see Fig. 13.4). For example, a VT microearthquake may trigger a nearby LP event. Lahr et al. (1994) and Miller et al. (1998) detected swarms of *Hybrid events* during the high activity phase of Redoubt (Alaska) and Soufriere Hills volcano (Montserrat, West Indies), respectively. Miller et al. (1998) concluded that such events reflect very shallow activity associated with a growing dome.

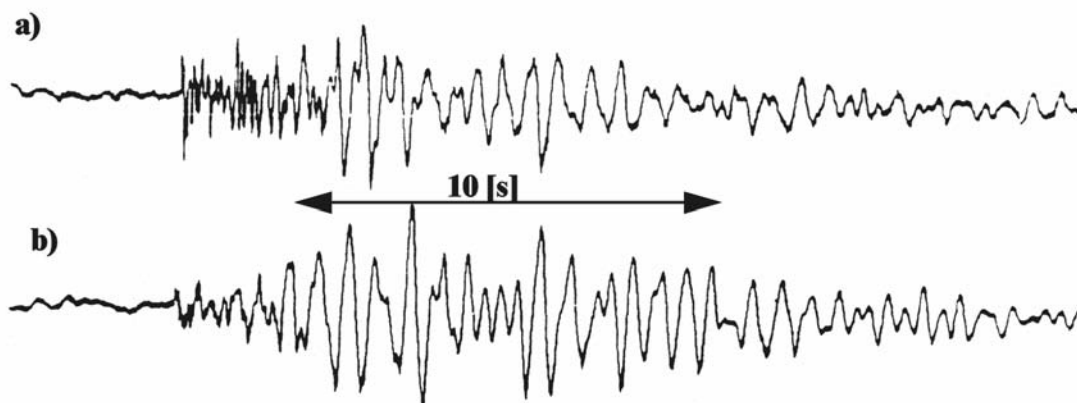


Fig. 13.4 a) shows a Hybrid event and b) a VT-B event for comparison. The higher frequencies at the beginning of the Hybrid event are an obvious feature, while the later part shows the similarity with the VT-B event (courtesy S. McNutt, AVO).

Multi-Phase events (MP also *Many-Phases* event; see Fig. 13.5; Shimosuru, 1972) are somewhat higher in their frequency content (3 to 8 Hz) than *Hybrid* events but are related as well to energetic dome growth at a very shallow level. Both types of signals and their associated mechanisms are still a topic of research as their occurrence might be a good indicator for the instability of high viscous lava domes.

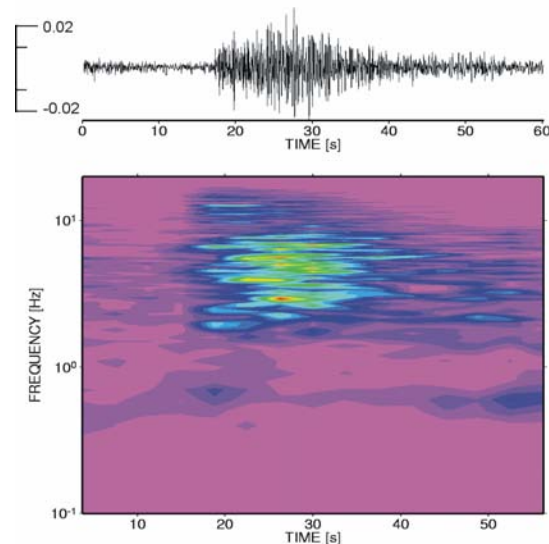


Fig. 13.5 MP-event recorded at Mt. Merapi during strong dome formation. The frequency is restricted between 3 - 10 Hz and resembles that of a VT-B type event at this volcano. Note the long duration of this event whilst its amplitude is much smaller than for the VT-B event shown in Fig. 13.2.

13.2.1.4 Explosion quakes, very-low-frequency events, ultra-low-frequency events

A very pronounced ULP and *very low frequency* (VLF; $f \sim 0.1 - 0.01$ Hz) signals were made at several volcanoes in Japan and on Hawaii (e.g., Aso: Kawakatsu et al., 2000; Iwate: Nishimura et al., 2000; Kilauea: Ohminato et al., 1998) using several broadband seismometers located in the near-field to intermediate-field distance from the source. Some of class with clear signal characteristics are the *explosion quakes*. This signal class accompanies Strombolian or other (larger) explosive eruptions. Most of these signals can be identified by the occurrence of an air wave which is caused by the sonic boost during an explosion, when the expanding gas is accelerated at the vent exit (see Fig. 13.6). This wave mainly travels through the air with the typical speed of sound (330 m/s). While we do not discuss the explosive mechanism, the source which causes this explosion is not yet clear. Some LF events show the same frequency-time behavior as the explosion quakes but lack an air phase (McNutt, 1986). This might reflect a common source mechanism of deeper situated LF-events and shallow produced explosion quakes.

Portable broadband seismometers with corner frequencies as low as 0.00833 Hz shed new light on this open question (see Fig. 13.7). It could be verified that at Stromboli volcano (Italy) an “ultra-low frequency” (ULF; ultra-long period ULP, $f < 0.01$ Hz) pressure buildup takes place several minutes before the onset of a Strombolian eruption (Dreier et al., 1994; Neuberg et al., 1994; Wassermann, 1997; Kirchdörfer, 1999). As this is only visible in the near-field of the seismic sources with a geometrical spreading factor proportional to r^{-2} , the seismic stations must be located close to the active vent of the volcano (see Fig. 13.7). A model which fits the visual and seismological observation very well consists of a shallow magma chamber and a tiny feeder system to the surface. The accumulation of a gas pocket and the ascent of this pocket as a gas slug may explain the observed pressure buildup (Vergnolle and Jaupart, 1990). However, some of the Strombolian eruptions at Stromboli show no or very small over-pressure (long-period displacement signals) without any visible difference in the associated surface activity.

13. Volcano Seismology

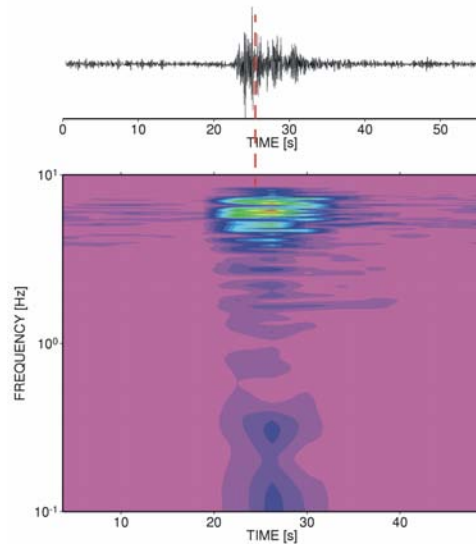


Fig. 13.6 An explosion signal recorded at Stromboli volcano, Italy. The seismic station was located just 400 m from the active vent. The dashed line gives a rough estimate of the onset of a sonic wave also visible as high (red) amplitudes in the time-frequency plot around 5 Hz.

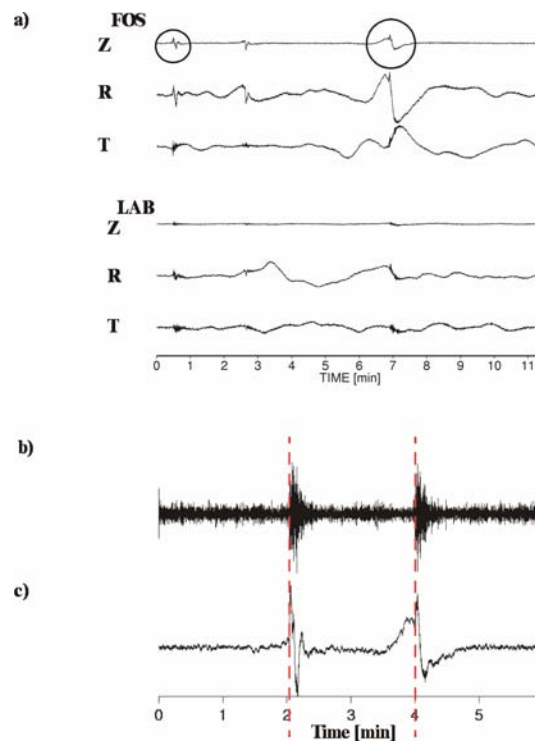


Fig. 13.7 a) ULP signal recorded with a Streckeisen STS2 broadband seismometer (DS 5.1) at Stromboli volcano. We removed the instrument response down to 300 s and the resulting traces are integrated to reflect ground displacement. The three uppermost traces show the three-component seismograms of a station located 400 m from the vent, whereas the lower three traces show the same but at a site located 1800 m from the active vent indicating a large signal only visible in the near-field. b) shows the seismogram of a 1 Hz seismometer during two different explosion quakes, the dashed lines mark the onset of strombolian eruptions. c) shows the displacement signal of two different explosion quakes also visible in a). Note, not all explosion signals are producing the same amount of long-period displacement signals.

13.2 Classification and source models of volcano-seismic signals

Since the late 1980s many of these observations were interpreted as shallow situated ($z < 1.5$ km) phreatic eruptions with a strong low frequency pressure pulse ($f \sim 0.01$ Hz; see Fig. 13.8). At the same volcano, Kawakatsu et al. (2000) also detected a second signal with dominant frequencies roughly at 0.06 Hz in the same depth range than the phreatic source. The authors classified this signal as *long period tremor* (LPT) which reflect the merging of isolated pulses into a nearly continuous signal (see Figs. 13.9 and 13.14). Kawakatsu et al. (2000) interpreted the signals as caused by the interaction of hot magma/fluid with an aquifer situated in 1 - 1.5 km depth below the craters of Aso volcano.

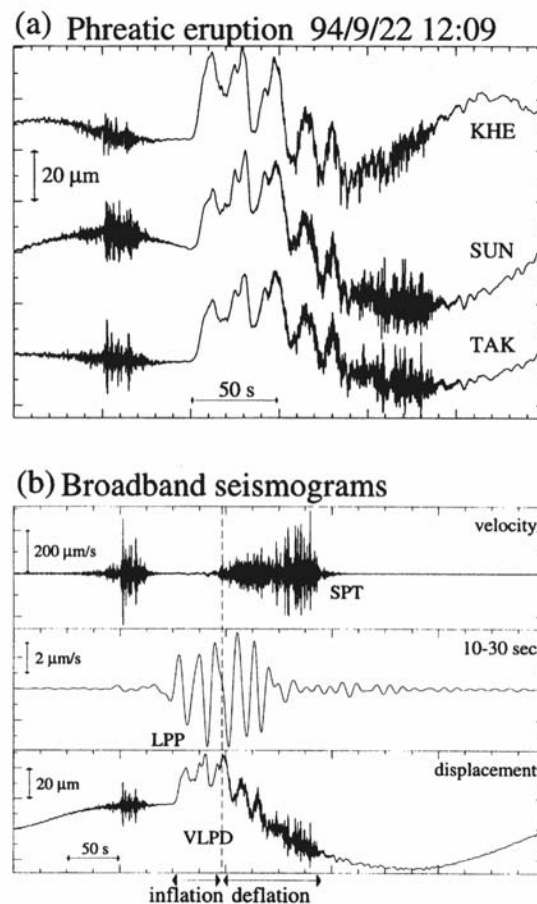


Fig. 13.8 a) ULP (or very long-period displacement) signal observed at three broadband stations during a phreatic eruption of Aso volcano. b) original velocity, band-pass filtered velocity and displacement seismogram of the same event observed at station TAK. The vertical line in b) indicates the onset of the eruption (Kawakatsu et al., 2000).

ULF and VLF events are still unknown at most andesitic and rhyolitic volcanoes, which possibly implies that slug flow (low viscous; Vergnolle and Jaupart, 1990) may be operative. In contrast, the work of Hidayat et al. (2000) showed that there exists a moderate (0.25 Hz) VLF signal in the near-field of some MP events recorded at Mt. Merapi (Indonesia).

In recent years, various approaches were made to investigate the dynamics of the different sources of the VLF and ULF signals using moment tensor analysis. While the estimation of the centroid moment tensor became a standard technique in earthquake seismology (e.g., NEIC and Harvard rapid moment-tensor solutions), the application of this technique in

13. Volcano Seismology

volcano seismology is restricted to specific applications. The difficulties are manifold. First of all the influence of topography is neglected in the standard approaches, which results in large misfits of the computed synthetic Green's functions. Moreover, Ohminato et al. (1998) showed that even when assuming a horizontal layered medium, the knowledge of the source location and the velocity model with a high confidence is needed in order to apply this technique. Compensated linear vector dipole solutions (CLVD) are often biased by the uncertainty of the assumed simplified velocity structure. However, there are some applications of moment-tensor estimations with VLF and ULF signals which give reliable results, indicating source mechanisms which deviate significantly from a pure double-couple solution commonly known of tectonic earthquake mechanisms (e.g., Fig. 3.10 from Legrand et al., 2000; Ohminato et al., 1998; Aoyama and Takeo, 2001). A further example and more references concerning seismic moment tensor inversion and non double-couple mechanisms of volcanic seismic signals are given in Sarà et al. (2001).

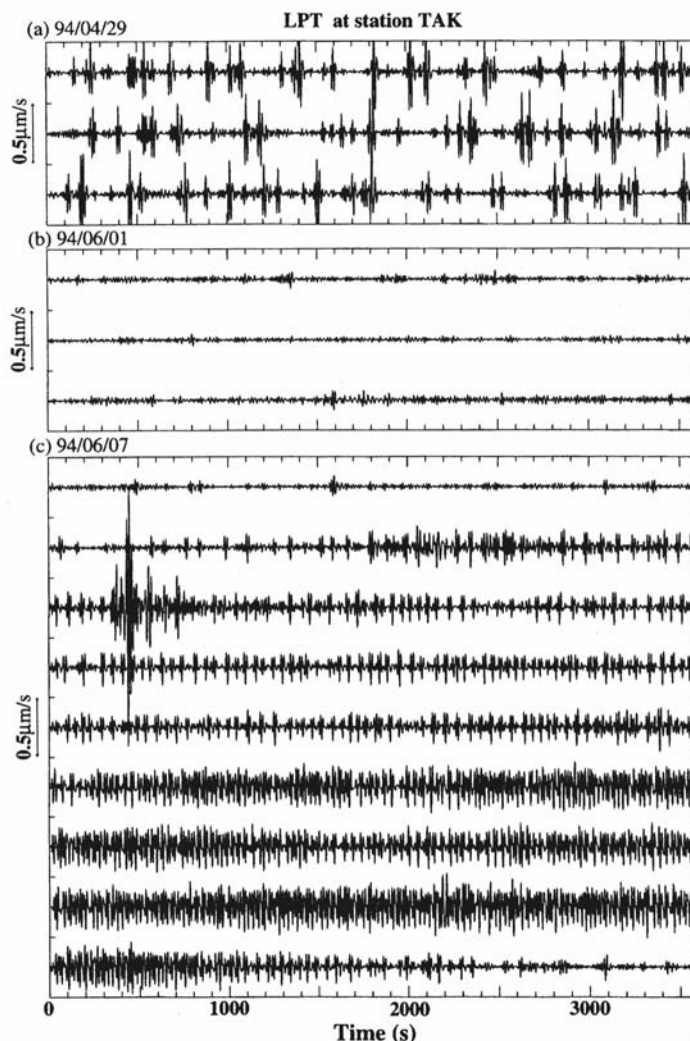


Fig. 13.9 Vertical component broadband seismograms band-pass filtered at 0.033 to 0.1 Hz at Aso volcano during three different days in 1994. The isolated ULF pulses visible in a) and b) were merged together in c) forming the continuous signal of *long period tremor* (Kawakatsu et al., 2000).

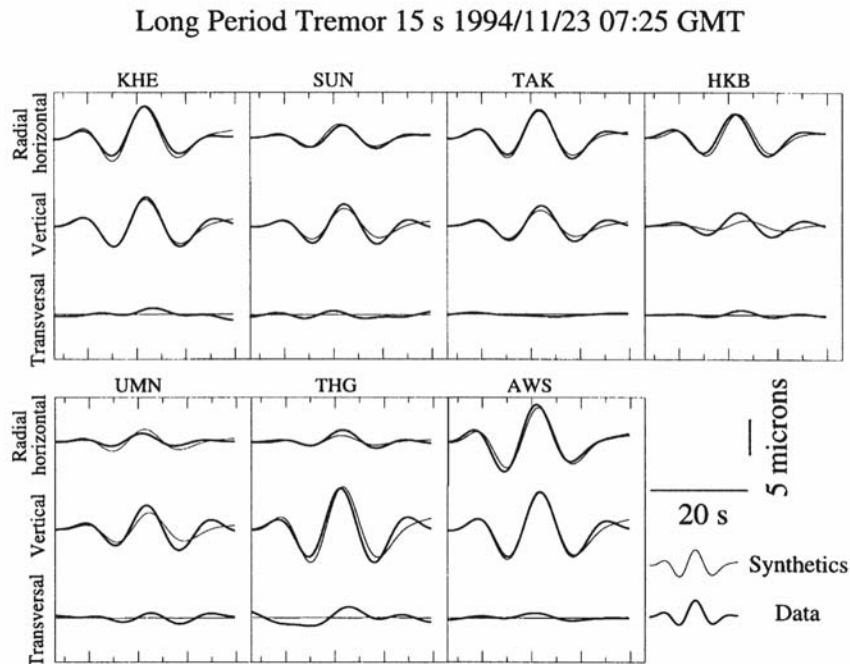


Fig. 13.10 Data (thick) and synthetic (thin) seismograms calculated from an inversion of the seismic moment tensor for a single pulse of *long period tremor* at Aso volcano. The corresponding source mechanism consists of a large isotropic component (97%) in addition to a small deviatoric part (Legrand et al., 2000).

13.2.2 Continuous volcanic-seismic signals

The appearance of continuous seismic signals at active volcanoes demonstrates the most profound difference between tectonic earthquake and volcano seismology. The suspected mechanisms range from obvious surface effects such as rockfalls, landslides or pyroclastic density flows to internal ones such as volcanic tremor. Nearly every volcano world-wide shows the signal of volcanic tremor during different activity stages. Volcanic tremor is the most favored parameter in volcano early eruption warnings. Because of possibly differing source mechanisms, we discuss tremor separately for the two flow regimes: high and low viscosity.

13.2.2.1 Volcanic tremor (low-viscous two-phase flow and eruption tremor)

Most of the monitored basaltic volcanoes show some kind of cyclic appearance of *volcanic tremor*. The tremor signals can last between minutes and months in duration and, in most of the cases, their spectra are very narrow-band (1-5 Hz; Fig. 13.11). Some tremor signals show strong and short-pulsed amplitude variations (termed *beating tremor*), while others are nearly stationary over several days or even months. The common similarities in the spectra of volcanic tremor and LF and even explosion quake events is another important observation which has to be explained when looking for the source mechanisms. At Mt. Etna volcano (Italy), strong fluctuations of volcanic tremor amplitude are associated with lava fountaining at one of its summit craters or after the opening of a flank fissure (Cosentino et al., 1989).

13. Volcano Seismology

Gottschämmer (1999) described a tremor cycle at Bromo volcano (Indonesia) where the tremor amplitude fluctuation could be correlated with heavy ash plume (large amplitude - *eruption tremor*) or white steam (small tremor amplitude) episodes (see Fig. 13.11).

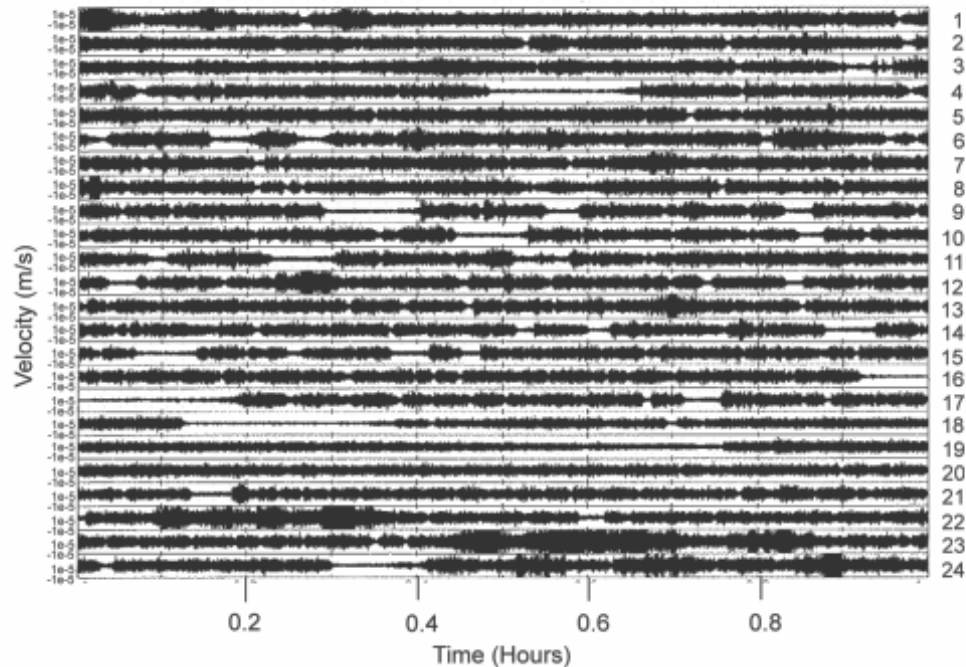


Fig. 13.11 Volcanic tremor at Bromo volcano (Indonesia) during a high activity phase at the end of 1995 (courtesy of E. Gottschämmer, University of Karlsruhe). Large tremor amplitudes correlate with the eruption of heavy ash plumes while small tremor amplitudes appear during quiet steam emissions (Gottschämmer, 1999).

These observations made at different volcanoes with either low viscosity magma or a huge amount of volatiles (free or after the fragmentation of high viscosity magma; steam) suggest the involvement of gas/fluid interaction in generation of volcanic tremor. The similarities in the overall spectral content of LF events and volcanic tremor is reflected in similarities of the proposed source mechanism or of the source region (resonating fluid). Flow instability is thought to play an important role in the excitation of volcanic tremor in multiple phase flow pattern (Seidl et al., 1981; Schick, 1988) and the associated LF events are seen as a transient within the same physical system. On the other hand, Chouet (1986) and Chouet (1987) state that a repeated excitation of a connected crack system could cause a harmonic and long-lasting signal, where the fluid is only passively reacting to the crack oscillations.

The spectral content observations support both the low viscosity magma and volatile interpretations. Explosions at Stromboli volcano excite the same frequency band as does volcanic tremor, which supports the idea of a common resonating system (see Fig. 13.12). However, care must be taken when interpreting the frequency spectra of volcanic tremor. Detailed studies on the spatial frequency distributions at Stromboli showed that single frequency peaks are possibly influenced, to an unknown amount, by the propagation medium (Mohnen and Schick, 1996).

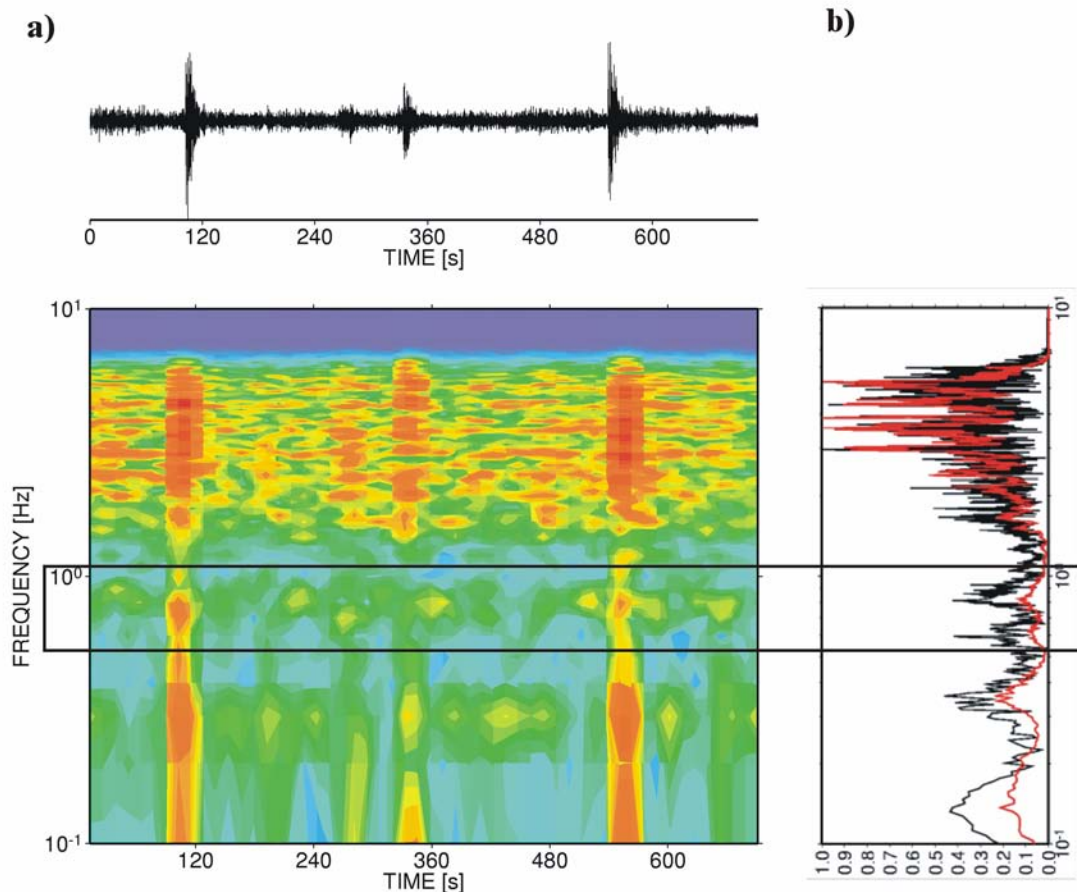


Fig. 13.12 a) explosion signals superimposed on the continuous signal of volcanic tremor at Stromboli volcano. The box marks the frequency band of weak but typical volcanic tremor band at Stromboli volcano. Note that the explosion quake also excites the same frequency band whereas below this frequency band the spectral amplitude of the explosion quake type signals are somewhat smaller. The tremor band with frequencies above 2.0 Hz is partially distorted by the ejected volcanic debris falling back to the surface and tumbling down the slope of the volcanic edifice (see 13.2.2.3). b) the normalized Fourier transform of an explosion quake type signal (black) and of a normalized power spectrum of six hour continuous recording (red). While the first reflects the typical spectrum of all explosion quakes, the overall behavior of the second spectrum is mainly due to volcanic tremor. The overall similarity between the explosion quake and tremor signal types is obvious.

13.2.2.2 Volcanic tremor (high-viscous - resonating gas phase)

During the last decade, many observations were made of the occurrence and characteristics of volcanic tremor at volcanoes with high-viscosity lava. At Semeru volcano (Indonesia) the spectra of volcanic tremor contained up to 12 overtones. This supports the assumption of a resonating medium with a high quality factor (Q) as well as a precisely working feedback mechanism (Hellweg et al., 1994; Schlindwein et al., 1995) (see Fig. 13.13). Similar observations were also made at Lascar volcano (Chile), where up to 30 overtones could be identified in the seismic signals (Hellweg, 1999).

13. Volcano Seismology

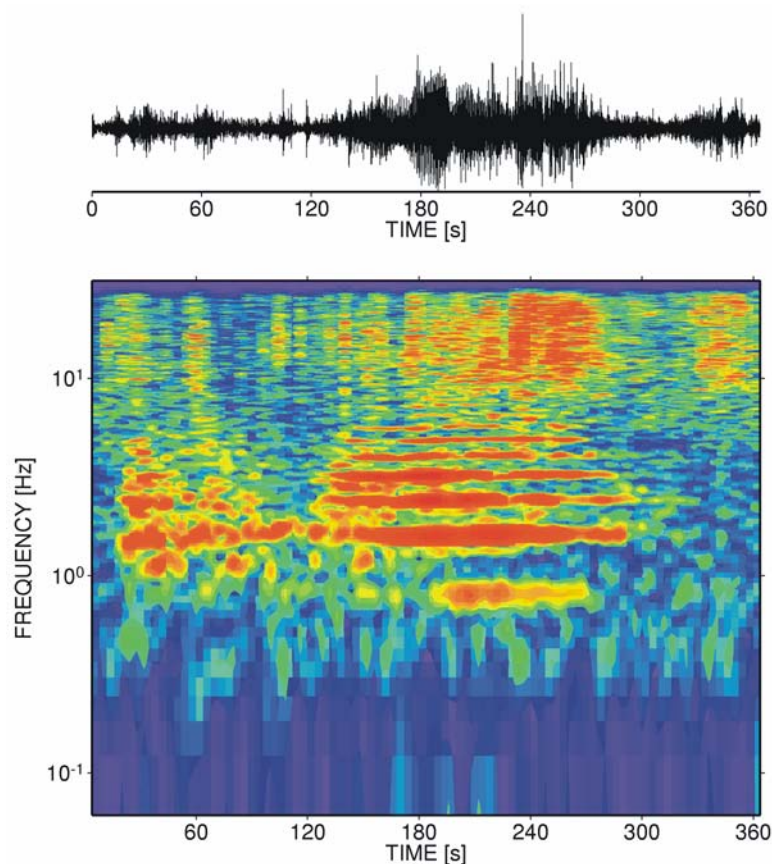


Fig. 13.13 Harmonic tremor signal recorded at Mt. Semeru, Indonesia. Up to six overtones can be recognized starting with a fundamental mode located at roughly 0.8 Hz.

Schindwein et al. (1995) proposed a feedback mechanism similar to that of sound generation in a recorder, and also discussed a repeating source with precise repetition time as a possible mechanism. This model was refined by Johnson and Lees (2000) and Neuberg et al. (2000). In the feedback mechanism case, the resonating body must consist of a pure gas phase, but the lava at Mt. Semeru is too viscous for resonating at the observed frequencies. The second mechanism requires a very precise timing mechanism for producing the highly stable overtones.

Recent observations at Montserrat volcano (Neuberg et al., 2000) and Mt. Merapi volcano (Indonesia) support the hypothesis of a repeating source (see Fig. 13.14). During several cycles of increased volcano-seismic activity we recognized the transition from closely timed MP/Hybrid events into the continuous signal of volcanic tremor and vice versa. As the source mechanisms of both types of signals are still unknown, the driving force behind these mechanisms is not known. Also the type of feedback mechanism which must be involved in this system could not yet be identified.

Volcanic tremor, as previously noted, is always a sign of high activity. However, since the exact mechanisms are still unknown, the importance and timing between the first appearance of tremor and possible eruptive activity is still a matter of discussion (McNutt, 2000a).

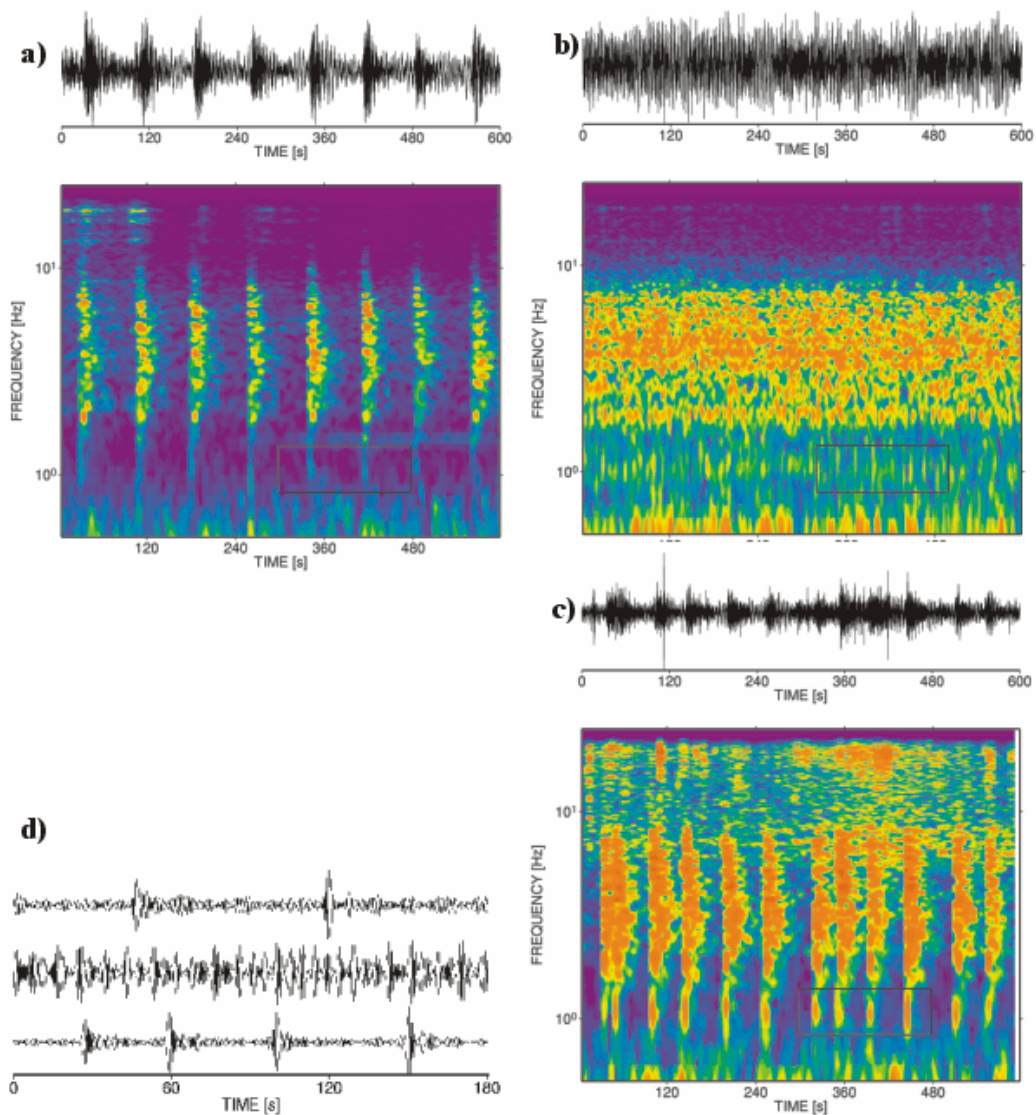


Fig. 13.14 Sequence of repeated seismic signals at Mt. Merapi volcano in 1996: a) very regularly timed MP-events before they merge together to form volcanic tremor (see b); c) after some hours the tremor is replaced by a sequence of discrete events with slightly higher amplitudes than before. Note: in contrast to the classification given in Fig. 13.5, the frequency content of these signals is lower (0.7 - 10 Hz) and might not resemble “pure” MP-events. In d) the time-frequency region of plots a)-c) are plotted in time domain. A band-pass between 0.8 - 1.3 Hz was applied before zooming. The individual wavegroups seen in the filtered continuous signal also supports the idea of the merged events causing the volcanic tremor.

13.2.2.3 Surface processes

Substantial release of seismic energy at active volcanoes is related to surface processes acting directly on the volcanoes edifice. For example, pyroclastic flows, lahars (volcanic debris flows) and rockfalls from unstable domes or crater walls can generate seismic signals with

13. Volcano Seismology

amplitudes exceeding several times those of the typical volcano-seismic signals. The most important signals for monitoring purposes are those associated with pyroclastic flows and lahars. The monitoring of lahars, which includes also acoustic and visual monitoring, is especially important when monitoring a volcano which is capped by a glacier or which is located in a tropical area. Melting of the snow during an eruption or heavy rainfall during rainy season will occasionally mobilize a huge amount of volcanic debris. The signals of all this activity are mostly high-frequency (>5 Hz) and show spindle (cigar) shaped seismogram envelopes that can last several minutes (see Fig. 13.15). The complex waveforms of pyroclastic flows are caused by a mixture of initial collapse of big lava-blocks onto the surface and ongoing fragmentations when traveling down the slope of the volcano (Uhira et al., 1994). During the January/February 2001 eruption of Mt. Merapi, it was also possible to recognize that the very first part of the signal was somewhat lower in frequency (1 - 2 Hz), indicating a possible explosion at the start of the pyroclastic flow (Ratdomopurbo, pers. communication; see also Fig. 13.12). An important monitoring question is: which signal is caused by a rockfall and which by a pyroclastic flow? The low frequency start (1 - 2 Hz at Mt. Merapi) of the latter might be crucial for discriminating between both types of events. This observation made at Mt. Merapi and also Unzen volcano (Uhira et al., 1994) might be used at other volcanoes with an active lava dome as the mechanism of flow generation seems to be the same.

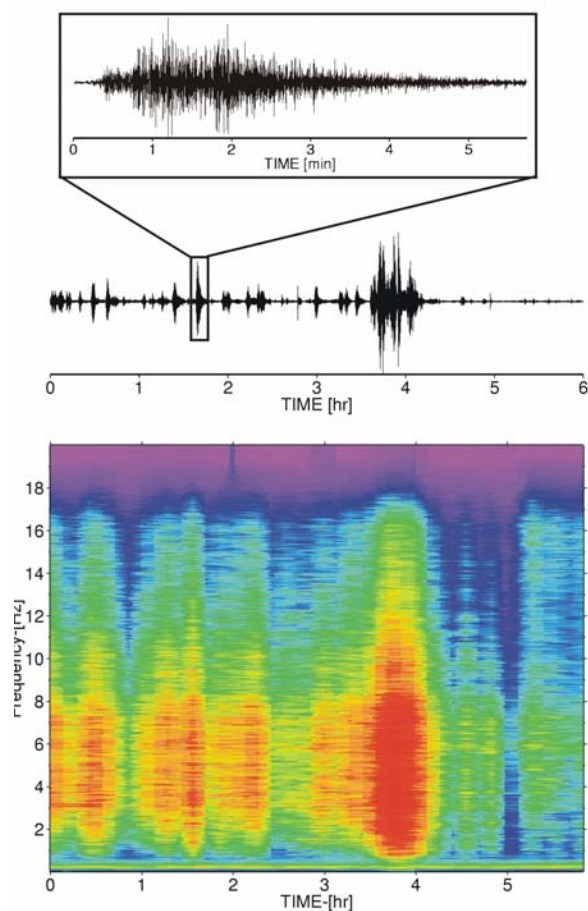


Fig. 13.15 Sequence of medium to larger pyroclastic flows recorded at Mt. Merapi volcano during the 1998 dome collapse. Note the 6-hour time scale and that individual events last many minutes longer than the seismograms of typical earthquakes. Just before 4 hours the largest pyroclastic flow in the whole eruption sequence takes place and lasts for about 30 minutes.

13.2.3 Special note on noise

Most of the extensively monitored volcanoes lie in densely populated areas with much human activity (that is why they are monitored). Hence, care must be taken when interpreting signals usually classified as volcanic tremor. In some cases, human activity excites signals occupying the narrow spectral band between 1-4 Hz (big machines etc.). Also a distinct 24 h rhythm is very likely caused by increasing human activity during daylight time and should therefore be analyzed with special care (see Fig. 13.16). Even when using three-component seismometers it is not easy to discriminate for sure between volcano-seismic and man-made noise. The topography at active volcanoes is very often radially shaped and the propagation paths to the seismic stations are shared by ambient seismic noise and volcanic signals.

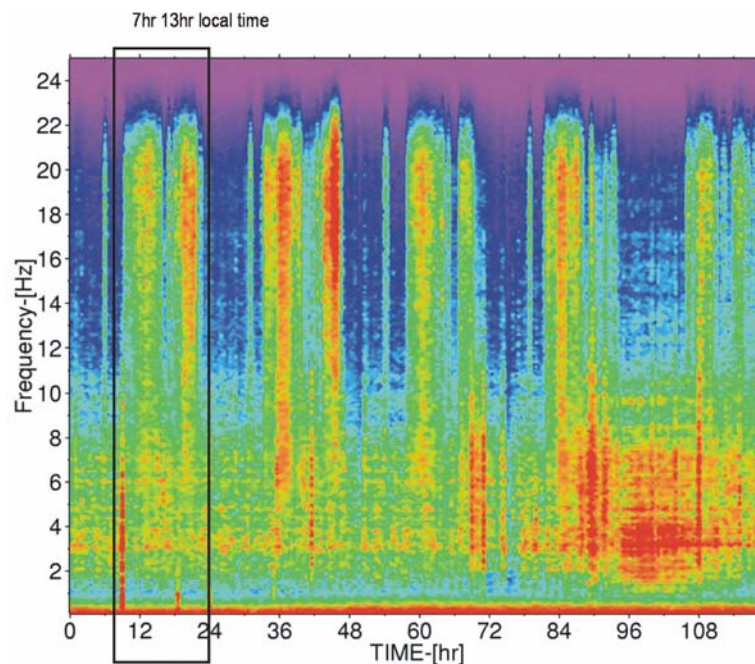


Fig. 13.16 Spectrogram of background noise recorded at a seismic station at Mt. Merapi. As the station is located in farming area, the human daylight activity can be clearly recognized by its distinct 24 hour periodicity. Furthermore, it is possible to see that there are two main working hours during daytime (marked by a box). Large spectral amplitudes are visible around 7 hours local time and a second peak is located around 15 hours hours after a time of quiescence during noon.

In conclusion, we note that most of the above classifications and proposed source mechanisms are deduced from simple observations of spectral content and overall shape of the associated seismograms rather than by physically verified constraints. Care must be taken when interpreting the occurrence of one of these signals during increasing volcanic activity. There are many examples of increasing numbers of VT events and increasing volcanic tremor amplitude without any surface activity at volcanoes. Thus, to be truly effective and diagnostic, seismic monitoring should be complemented, to the extent possible, by other instrumental monitoring techniques (e.g., geodetic, geochemical) and visual observations made regularly of the volcanoes being monitored remotely (see 13.5).

13.3 Design of a monitoring network

One of the most important decisions to be made, when establishing a seismic monitoring network, is the design of the station distribution. In most cases, volcanoes are monitored with at least four to six seismic stations which are distributed around the volcanic center. Newer deployments try to set up arrays of sensors or, even better, a network of different arrays. However, some of the design criteria deviate from the usual earthquake monitoring networks and are discussed in the following sections.

13.3.1 Station site selection

Considering a location as a possible site for a seismic station is always a compromise between noise considerations and accessibility. Of course, it would be best to place the seismic station far away from any human activity (see Fig. 13.16), away from big trees or sharp cliffs and ridges. However, the accessibility is very important, especially at the beginning of a surveillance campaign at a volcano. Also, the rough and harsh environment typical of many volcanoes usually requires frequent station visits for maintenance. Valleys, which generally are accessible places for seismic stations rather than ridges or cliffs, are often flooded during winter or the rainy season (not to mention the higher exposure to possible pyroclastic flows).

A second important decision must be made when choosing on “what” the station should be placed. Usually, seismologists prefer hard rock to unconsolidated sediments. At many active volcanoes, hard-rock sites are rare and, even if they exist, they are not necessarily good choices. Hard-rock sites often are small lava tongues or big blocks of lava buried in ash or soil, causing waveguide effects or even block rotation to an unknown degree. This is especially important when installing broadband seismic stations, which are very sensitive to tilt (see Chapter 5). A network-wide homogeneous installation with good temperature isolation is preferable to apparent “hard-rock” installations (see 13.6 for a more detailed description). Sites near singular obstacles should be avoided such as high trees, cliffs, big towers etc., as they are likely sources of wind-generated noise. While wind noise is usually high in a frequency range > 5 Hz, wind pressure is a very strong source of tilt-noise in the low frequency part (< 0.1 Hz). Hence, special care must be taken when installing a broadband seismic instrument.

13.3.2 Station distribution

Good station coverage is crucial for nearly all monitoring efforts as well as for successful scientific research. A good choice is to install a network at two scales - one large scale network extending into non volcanic regions ($\Delta < 20$ km) and one network with stations concentrated on the flanks and on the top of the volcano ($\Delta \sim 0 - 2$ km). The large-scale seismic networks are very useful to distinguish between volcano-seismic signals and regional or local earthquake activity. Also, the larger dimension improves the localization accuracy for deep-seated sources of magmatic activity. On the other hand, most of the seismic signals at active volcanoes are very shallow and usually small in amplitude. For detailed studies of the volcano-induced seismic signals, most of the stations must be placed close to the activity center(s). One or two stations should be placed as near as possible (without danger to

researchers and instruments) to the active volcanic region. Other stations should be placed so as to ensure a good overall azimuthal coverage. If possible, the station spacing should be comparable to the source depth to insure good depth control. It is good to have all parts of the focal sphere surrounding a source to be sampled by seismic stations. Best results are expected when the source is located within the station network, both lateral and vertical.

If a broadband seismometer is available, best results are achieved if it is installed as close as possible to the active area, provided that the safety of operating personnel is assured. Most of the recorded ULF signals at volcanoes are detectable only in the near-field distance range (see Fig. 13.7). If an on-line radio link is desired, the station site must be chosen so as to guarantee an undisturbed direct line-of-sight to repeaters or receivers (see 13.6 and 7.3).

13.3.3 Seismic arrays in volcano monitoring

Modern approaches to volcano seismology are based on deploying seismic antennas (arrays) at active volcanic areas. Stations in an array should be spaced close enough to sample a wavefield several times in a wavelength, often requiring a spacing of about 100 m. The main advantage of such antennas and the application of array techniques is the improvement in evaluating the radiated wavefield properties, velocity structure and the source location (see Chapter 9). A comprehensive review paper dealing with standard seismic array techniques at volcanoes has been published by Chouet (1996b).

Most of the problems in operating a seismic array at an active volcano are of a technical nature. The requirements on array site conditions are demanding, the cost of array components are rather high, and the installation and maintenance of an array during different activity stages and weather conditions require significant economic and human resources. Such requirements generally preclude the long-term use of arrays in volcano monitoring. Therefore, most of the work done so far in using array techniques at active volcanoes were short-term deployments of occasionally large arrays. Despite the mostly short duration of deployment, however, much information was gathered during these experiments. The results range from a more comprehensive description of the wavefield properties (Saccorotti et al., 1998; Chouet et al., 1997) to tracking the source volume of volcanic tremor signals (Almendros et al., 1997; Furumoto et al., 1990).

13.3.4 Network of seismic arrays

In attempting to achieve both monitoring and research objectives, a good compromise is to establish a network of small-aperture seismic arrays. The advantage compared to single (dense) array applications is the better spatial evaluation of the wavefield properties as well as the better azimuthal coverage when focusing on the location of the different seismic signals. In any event one has to compromise between aperture, number of instruments, spatial sampling and station accessibility. In 1997, a network of small-aperture arrays was established at the Merapi volcano, Indonesia (see Fig. 13.17). This network consists of three different array sites distributed around the volcano. The main objective of this array configuration is to attempt the automatic classification of the volcano-seismic events on the basis of the wavefield properties and an automatic hypocenter determination of the classified volcano-seismic events (Wassermann and Ohrnberger, 2001).

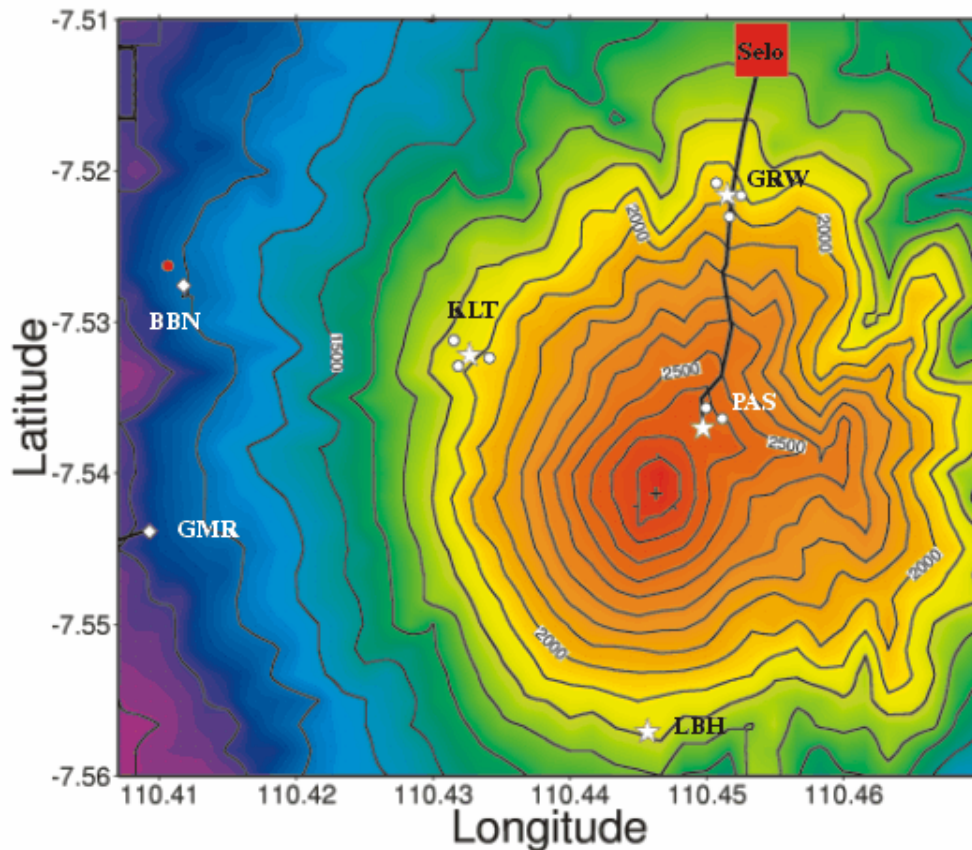


Fig. 13.17 Example of a combined seismic array/network approach at Mt. Merapi volcano. The stars show the location of broadband seismometers, whereas the circles mark the position of three-component short-period seismometers, in total forming three small-aperture arrays. The diamond symbols show the location of seismic acoustic stations (short-period sensors with a microphone array). *LBH* station is not yet installed.

Before installing a network of arrays, a detailed plan should be made of features to be investigated and criteria to be met, e.g., required spatial coverage and resolution, accuracy of hypocenter determination, shallow and/or deep seismicity, broadband signals etc. A good choice will be a network with at least four different array sites. Each array should consist of one three-component broadband seismometer as central station surrounded by three to six short-period, vertical-component seismometers deployed in a configuration which best fits to the number of seismic stations (see Chapter 9). The most suitable distance between related seismometers must be carefully evaluated during the initial stage of the setup. Decisions must be made between the peak values in the spectral domain and the desired coherence band of the signals recorded. Ideally, the stations should be roughly 100 to 200 m apart from each other (see Fig. 13.18). Reducing the inter-station distances with the same number of seismometers will cause an undesired loss of resolution in slowness due to the smaller aperture and also increase the noise coherence (see Fig. 13.18).

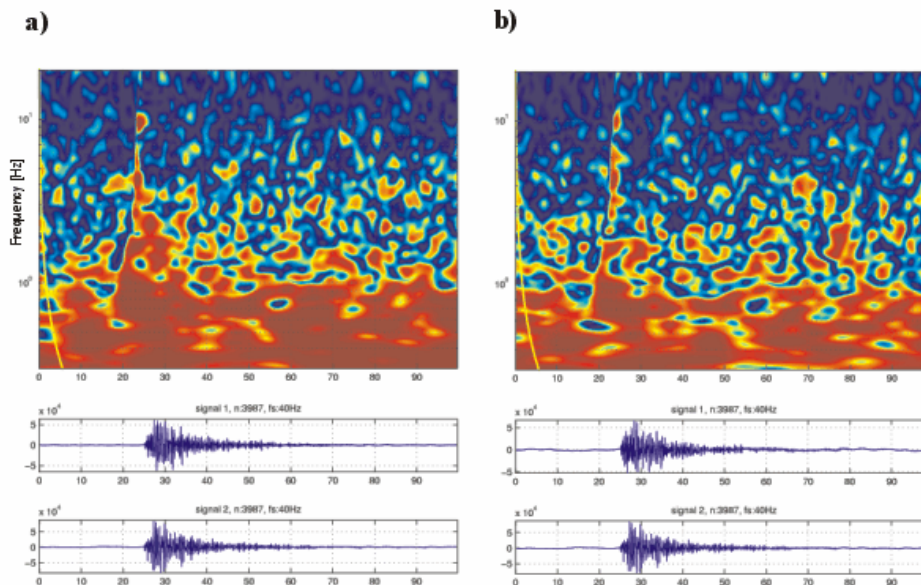


Fig. 13.18 Time-frequency coherence plot of: a) the station combinations GRW0- GRW1; and b) GRW1-GRW2 (see Fig. 13.17). The seismometers in a) are deployed in 170 m distance from each other, whereas in b) GRW1 and GRW2 are separated by roughly 300 m. Note: the signal coherence is computed in a sliding window with the time axis centered at the middle of the sliding window. High coherence above 2 Hz is only visible in the very beginning of a seismic event, indicating an array wide coherent phase arrival. It is also obvious that the overall coherence is somewhat lower in b) than in a) indicating the reduced signal coherence at more separated stations. On the other hand, the noise coherence is also reduced in b) which improves the signal-to-noise ratio of the semblance estimation significantly.

13.4 Analysis and interpretation

Here, we will briefly review the basic techniques of analyzing volcano-seismic signals. Most of the described concepts are based simply on visual pattern recognition abilities of the responsible interpreter. More recent and objective approaches that attempt to automate these tasks are discussed at the end.

13.4.1 One-component single station

Most of the observations made in the 1960s and 1970s were obtained by using only a few instruments located at the most active volcanoes. Since then, nearly all well-monitored volcanoes are equipped with at least four to six instruments and, for a number of volcanoes, dozens of instruments. However, the basics of the classification scheme discussed in 13.2 is deduced by the single station approach and even today the statement “better one than nothing” holds as regards the number of instruments. This is especially true when initiating short-term projects or monitoring very remote volcanoes.

13. Volcano Seismology

13.4.1.1 Spectral analysis

With the advent of inexpensive, portable and efficient computers, spectral analysis has become an increasingly important tool for monitoring the activity of an active volcano. As mentioned already in 13.2, most of the classification is based on the time-frequency characteristics of seismic signals. Volcanic tremor episodes are distinguished by their spectral shape and appearance. There are many different techniques for computing the spectral seismic amplitude such as *Seismic Spectral Amplitude Measurement* (SSAM; Rogers and Stephens, 1991), short-term Fourier transform or power spectral density estimates, which provide the observer with signal information in the spectral domain (e.g., Qian and Chen, 1996). An important feature of volcano-seismic signals are their narrow-band spectra. In particular, volcanic tremor sometimes shows just one dominant spectral band with a bandwidth as small as 0.2 Hz. This is the reason why it is often called “harmonic tremor”. Monitoring the changes of spectral properties is a useful tool not only for signal discrimination but also for characterizing the state of volcanic activity. An example is given in Fig. 13.19. In Fig. 13.19a the total power in the frequency range between 0.6 and 3.0 Hz is plotted as a function of time. This frequency range has been chosen because of its importance in discriminating between rockfall and pyroclastic flow signals (see 13.2.2.3). Three pronounced peaks are obvious with amplitudes well above the average value. The peaks at day 9 and day 18 are associated also with significant increase of the power density between 2 to 10 Hz (Fig. 13.19b). On the other hand, the sharp peak in day 14 in Fig. 13.19a seems to be of a different nature and might be caused by a regional or teleseismic earthquake. The remaining times with high power density amplitudes in b) might be due to small pyroclastic flows or rockfalls.

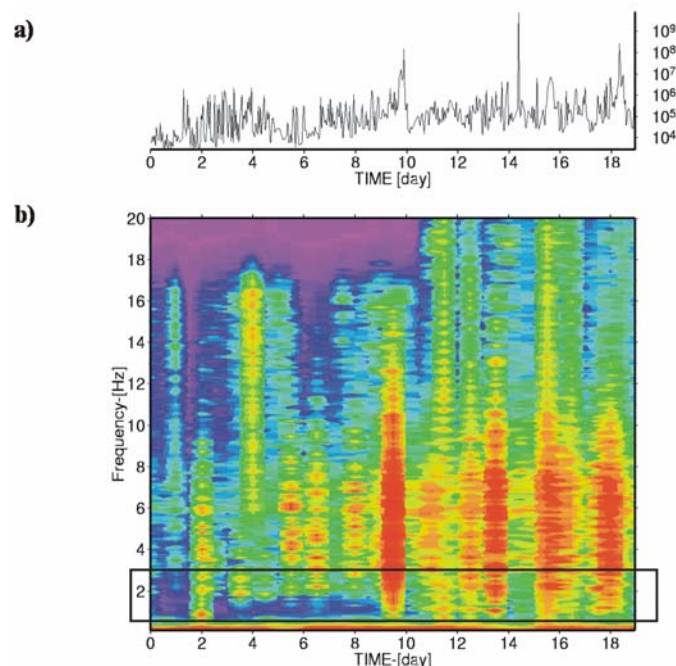


Fig. 13.19 a) shows the the total power (per 60 minutes) calculated in the frequency band between 0.6 - 3.0 Hz from 01 - 19th July 1998 at Mt. Merapi, displayed on a logarithmic scale. Two of the visible peaks (i.e., day 9 and day 18) are associated with pyroclastic flows, while the sharp peak visible at day 14 is caused by a regional earthquake; b) the power spectral density vs. time in the same time range, where the box shows the frequencies used for total power plotted in a).

At Mt. Etna (Italy), Cosentino et al. (1989) reported a significant frequency shift in the volcanic tremor spectra prior to a flank fissure eruption. The authors detected a significant shift to lower frequency values of the dominant spectral peaks of volcanic tremor just several hours before the opening of flank fissures.

Because the efficiency of today's computers is rapidly increasing, a good choice would be to calculate complete spectrograms (or periodograms) first and decimate the amount of data only in a later step (e.g., to SSAM). This would allow the extraction of any hidden information in a later "off-line" step of the analysis without any redundant work load. Crucial in this context is a good knowledge of the possible features of different signals and their relationship to the state of volcanic activity at a specific site. It must be emphasized that stations of monitoring networks at volcanoes should be maintained for years (even decades) without any changes in the system (gain, position etc.). When upgrading an old station with "up-to-date" technology, a sufficient overlap of both systems should be guaranteed. This precaution can not be overemphasized.

13.4.1.2 Envelope, RSAM and cumulative amplitude measurements

An added important source of information which can be deduced by small networks is the overall appearance of the signal shape in the time domain. This is important both for event classification (e.g., volcanic tremor, rockfall etc.) as well as for monitoring changes in the seismic activity of a volcano. A very efficient tool for visualizing increasing seismic activity is the *Real-Time Seismic Amplitude Measurement* (RSAM) technique proposed by Endo and Murray (1991). In its original form, RSAM was designed for analog telemetry and consisted of an A/D converter, averaging of the seismic signal in 1 min or 10 min intervals and storing of the reduced data on the computer:

$$RSAM(iT) = \frac{1}{T} \sum_{t=iT-\frac{T}{2}}^{iT+\frac{T}{2}} |s(t)|$$

With T as the averaging interval (originally 1 or 10 min) and $s(t)$ the sampled seismic trace. Various examples for successful applications of this technique are given by McNutt (2000b).

Some applications try to normalize the records from several seismic sensors located in different distances from the volcanic center by correcting the measured seismic amplitude for the assumed source distance (McNutt, 2000b):

$$D^b_R = \frac{Ar}{2\sqrt{2}G}, \text{ and } D^s_R = \frac{A\sqrt{\lambda}r}{2\sqrt{2}G}$$

where D^b and D^s are the reduced amplitude for body and surface waves, respectively. A is the peak to peak amplitude in centimeters, r the distance to the source, λ the seismic wavelength in cm and G the gain factor (magnification) of the seismic sensor. The only difference between these two equations are the different correction terms for the geometrical spreading. The reduced amplitude measurements should be considered as a pure observation parameter without any physical meaning. It should definitely not be used for the physical interpretation

13. Volcano Seismology

of an ongoing eruption. The reduction of the seismic amplitude assumes specific modes of wave propagation, i.e., body waves and surface waves, respectively. As there is no reliable estimation of the wavefield properties, it is possible with just one or a few seismometers that the assumption of the degree of geometrical spreading is highly speculative. Also, the effect of site amplification and the strong scattering observed frequently at volcanoes (Wegler and Lühr, 2001), which depend in general on the source location, structure and topography of the volcano, may alter the amplitude-distance relationship significantly. They are neglected in this approach.

Another way of displaying changes in the radiated seismic wavefield is based on the computation of the de-trended cumulative radiated power of the seismograms at a single station (see Fig. 13.20):

$$P_{cum}(f_{1-2}, t) = \sum_t \left(\sum_{f=f_1}^{f_2} P_t(f) - trend \right)$$

with $P_t(t)$ being the power spectral density during time interval t and f_1, f_2 the upper and lower frequency for computing the cumulative power. *trend* is the slope of the cumulative power, calculated during a quiet, i.e., baseline activity of the volcano (see Fig. 13.20).

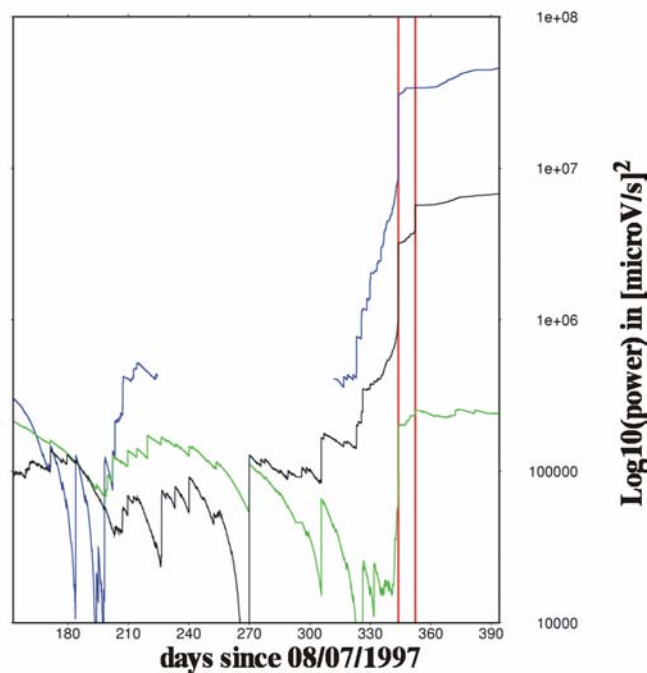


Fig. 13.20 De-trended cumulative power of the vertical components of all broadband seismometers at Mt. Merapi during 1998 activity. The red lines mark the occurrence of two pyroclastic flows. A steep increase of the total cumulative power 10 days before the onset of the first pyroclastic flow is visible, following a period with very low seismicity. Also the second eruption is preceded by an increase of cumulative power at two stations, while one station (blue) was out of operation. The background trend was estimated during a low activity phase in 1997.

To avoid a fast saturation of the cumulative power values, a good way is to estimate the slope of the cumulative power when the activity of the volcano is on its baseline. This estimated trend can be removed for each time step resulting in a de-trended cumulative power plot, which shows strong deviation from the “normal” background seismicity. Furthermore, cumulative power can analyze certain frequency bands (see Fig. 13.19a), unlike the power change in time which resembles the method of RSAM. In Fig. 13.20, the de-trended cumulative power of three broadband stations at Mt. Merapi is shown. Note the steep increase of seismic power roughly ten days prior to the first eruption. A further increase in cumulative power is obvious for two stations preceding the second large pyroclastic flow. The third station was out of operation caused by ash fall on the solar panels.

A common way to display information on the current status of a volcano is to count the different seismic event types in a hourly or daily manner (see Fig. 13.21). While the interpretation of the type of an event is sometimes impossible or an intuitive judgment when using only one station, such event/time plots are an excellent tool for displaying all information (objective and subjective) within one single plot. There are many papers which rely strongly on this kind of activity measurements. Most of the observations are summarized by McNutt (1996, 2000b). Also in this case, we must emphasize that, without a complementary detailed seismological study, this is just a visualization of observed patterns with, strictly speaking, unknown physical meaning.

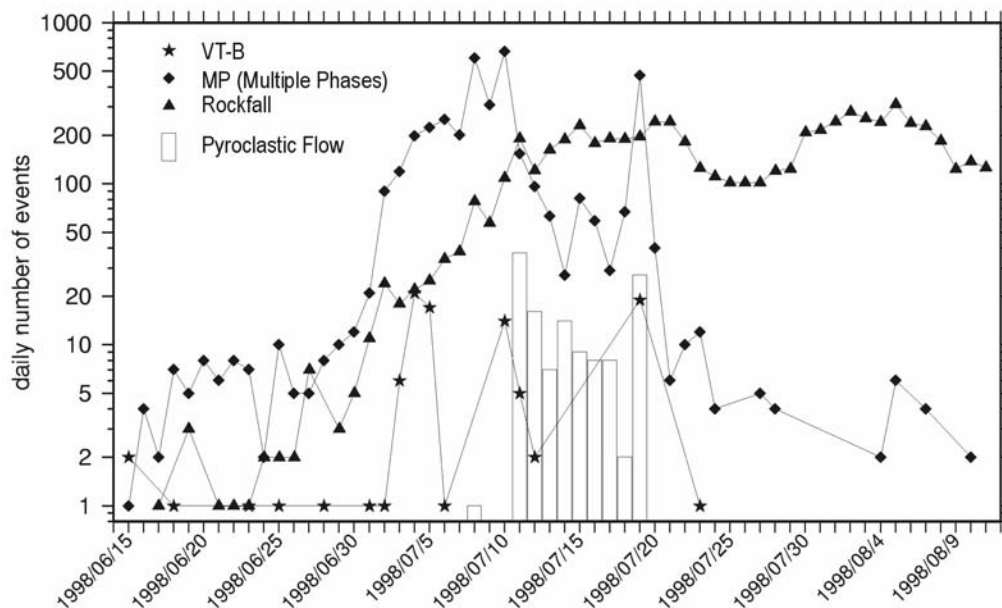


Fig. 13.21 Event-type per day plot during the high activity of Mt. Merapi during July 1998. Note the increase of the three event classes before the onset of the first pyroclastic flow. Also note the similarity of the VT-B type event curve to the occurrence of pyroclastic flows (courtesy of VSI- BPPTK, Yogyakarta).

On the other hand if knowledge about the hypocenters (see 13.4.3.1) and even source mechanism is available these event-time plots are very valuable in order to evaluate the activity state of a volcano. At Soufriere Hills volcano (Montserrat Island) it was possible to distinguish different activity phases with the help of these seismicity plots (Miller et al., 1998). Just before the surface activity starts to develop, a swarm of VT-A earthquakes

13. Volcano Seismology

appeared. During cycles of inflation in the upper part of the growing dome a large number of Hybrid and LP events were detected. Finally, a large number of surface events, mainly rockfall signals, were recorded when the dome was getting more and more unstable. While these patterns of seismic signals are very important during a high activity phase of a volcano, it must be emphasized that every volcano and every eruption has its own unique pattern.

13.4.2 Three-component single station

Most modern seismometers are three-component sensors which record the vector of ground motion produced by seismic waves. Observation of the particle motion will not help to precisely determine source locations and their variations without a detailed knowledge of the wavefield properties (e.g., Rayleigh waves, Love waves, P or SH and SV waves). Changing patterns of particle motion may help estimate the activity changes of a volcanic system in a qualitative way, however.

13.4.2.1 Polarization

Seidl and Hellweg (1991) showed results from analyzing the 3D-trajectories of a single seismic broadband station at the Mt. Etna volcano (Italy) using very narrow bandpass filters. They argued that the occasional strong variations in the azimuth and incidence angles of the trajectories might reflect sudden changes of the active source location. Recent experiments using array techniques, however, showed that the wavefield radiated from a volcanic source is a combination of complex source mechanisms and strong path influences (e.g., Chouet et al., 1997). Hence, the wavefield consists of a mixture of many wave types and care must be taken when only polarization information is available. On the other hand, carefully extracted information and the associated changes of polarization pattern during different cycles of volcanic activity may help to identify changes in the state of the volcanic system (see Fig. 13.22 below).

The use of a broadband seismic station located close to an active vent, i.e., in the near-field, improves the quality of source estimations based on simple polarization analysis. This is because of the small influence of the propagation path in the near-field. Unfortunately, complicated source mechanisms, i.e., when the usual assumption of a point source is no longer valid, will complicate the interpretation of the observed polarization pattern to an unknown degree (Neuberg and Pointer, 2000). Also, the nearly unknown influence of the topography of the volcano on signals with a wavelength comparable to the topographic obstacle will make interpretation difficult. Recent near-field measurements at Stromboli volcano (Italy) showed that, in some cases, a fairly good estimation of the source region could be made using just a single three-component broadband station (Kirchdörfer, 1999; Hidayat et al., 2000) under the assumption of a simple source mechanism.

13.4.2.2 Polarization filters

When evaluating the polarization properties of volcano-seismic signals as part of a monitoring system, an automatic estimation of parameters is needed. Best results will be obtained when focusing on the basic parameters, i.e., the azimuth, incidence angle and a measure of the rectilinearity of the signals. Various approaches will extract this information from a

continuous data stream. Most of them are based on a least-square fit of the 3D-trajectory of the seismic vector to a 3D-ellipsoid. Typical algorithms consist of solving the eigenequation and simultaneously searching for the orientation of the eigenvector corresponding to the largest eigenvalue (e.g., Flinn, 1965, Montalbetti and Kanasewich, 1970):

$$\begin{bmatrix} x_i \\ y_i \\ z_i \end{bmatrix} [\underline{C} - \lambda_i \underline{I}] = 0$$

where x_i, y_i, z_i represent the components of the i -th eigenvector, \underline{I} is the identity matrix and λ_i is the eigenvalue according to the i -th eigenvector. \underline{C} represents the covariance matrix of the 3D signal recorded:

$$C_{ij} = \sum (u_i - \bar{u}_i)(u_j - \bar{u}_j)$$

where u_i, u_j are the i -th and j -th component of the seismic sensor and \bar{u}_i, \bar{u}_j represent the mean values of the data traces within the analyzed time window. A possible way to display the polarization properties vs. time is to plot the orientation of the eigenvector associated with the largest eigenvalue (corresponding to the major axis of the ellipsoid) in the coordinate system of the sensor, i.e., its azimuth Φ_{az} and incidence angle Θ_{inc} :

$$\Phi_{az}(t) = \text{atan}\left(\frac{y_1(t)}{x_1(t)}\right), \text{ and } \Theta_{inc}(t) = \text{atan}\left(\frac{z_1(t)}{\sqrt{x_1^2(t) + y_1^2(t)}}\right)$$

with x_1, y_1, z_1 representing the eigenvector components of the largest eigenvalue $\lambda_1 (> \lambda_2 > \lambda_3)$. Note: without any further assumption of the analyzed wave-type, i.e., P, SH or SV wave etc., the computed azimuth has an ambiguity of 180 degrees, whereas the incidence angle varies between 0 - 90 degrees. Typically, a measure of the rectilinearity of the signal's polarization (i.e., the relative elongation of the ellipsoid in one direction) is computed (e.g., Vidale, 1986):

$$L(t) = 1 - \left(\frac{\lambda_2(t) + \lambda_3(t)}{\lambda_1(t)}\right)$$

$L(t)$ is only larger than 0 if λ_1 is bigger than the combination of the other two. Fig. 13.22 gives an example of the variation of the parameters Φ_{az} and Θ_{inc} over a long time range at Stromboli volcano.

Because we have no knowledge of the wave type represented by the computed polarization parameters, they must be seen as varying activity parameters rather than interpreting them as part of a technique for hypocenter determination.

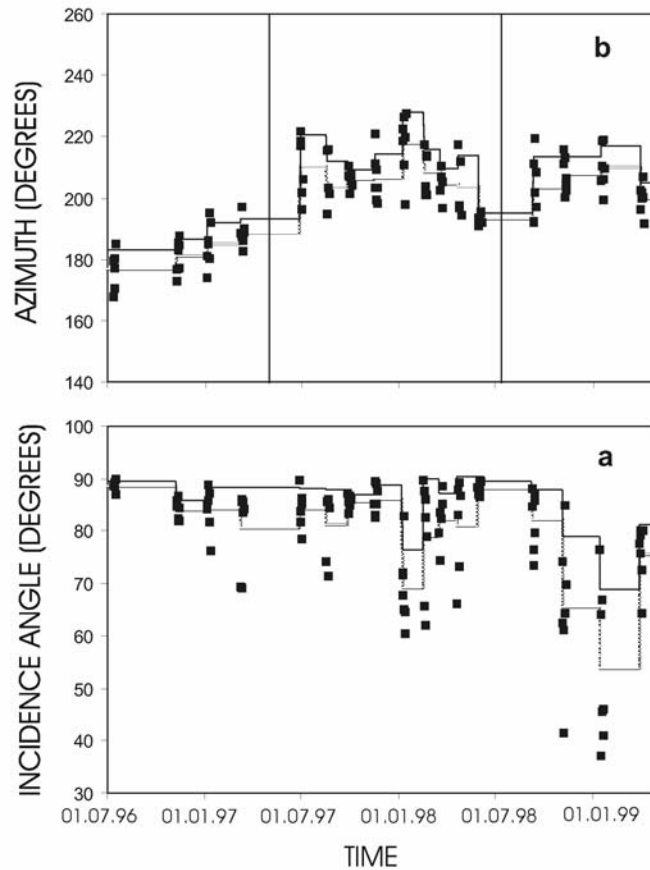


Fig. 13.22 Long-term variations of incidence angle (a) and azimuth (b) in the 115 time windows selected from July 1996 to April 1999 at Stromboli volcano. In both panels, solid and dotted lines depict mean value and standard deviation, respectively, computed over 5 to 7 consecutive days in the 17 time windows selected from July 1996 to April 1999. The polarization parameters were estimated using the technique of Montalbetti and Kanasewich (1970). The variation of this waveform information seems to match changes in the activity states of the volcano (courtesy of S. Falsaperla, Istituto Nazionale di Geofisica e Vulcanologia).

13.4.3 Network

13.4.3.1 Hypocenter determination by travel-time differences

Modern seismic monitoring networks at active volcanoes usually consist of at least four to six seismic sensors distributed in various azimuths and distances from the volcanic center. While continuous signals, such as volcanic tremor or transients like LF-events, often lack any clear phase arrival, some signals (VT, explosion quake) with clear onsets can be located using standard seismological techniques.

Usually, events with clear P- and/or S-wave onsets are selected visually and the first breaks are picked interactively. The inversion for the source location is frequently done using algorithms such as HYPO71 (Lee and Lahr, 1975) or HYPOELLIPSE (Lahr, 1989). Note, however, that most of the standard hypocenter determination programs are based on the assumption of a horizontally layered half-space and/or models with linear gradients with no

topography. Also new approaches exist, which are not restricted to 1D or 2D velocity models and which try to locate the sources in a non-linear, probability based manner (e.g., Lomax et al., 2000). However, in most cases no good velocity models for the monitored volcanoes exist, and the computed source coordinates, especially when focusing on shallow events, must be seen just as an approximation of the true hypocenter. Relative earthquake locations of multiplets with similar waveforms can greatly improve the resolution of volcanic structures (Rubin et al, 1998; Waldhauser and Ellsworth, 2000; Ratomopurbo and Poupinet, 1995).

There are many papers on the topic of imaging the hypocenter distribution during or before a volcanic eruption (e.g., Newhall and Punongbayan, 1996; Power et al., 1994; Chouet et al., 1994). Very useful information about the geometry of the plumbing system as well as the physical properties of the host rocks can be deduced by analyzing the time-space pattern of frequently occurring swarms of deeper earthquakes (Power et al., 1994).

Also the migration of hypocenters during a high activity phase of a volcano is important in forecasting the following volcanic eruption. In Fig. 13.23, an example of the 1991 Mt. Pinatubo eruption is shown. The migration of the seismic events from a cluster at 5 km depth north-west of the volcano in A) to a very shallow location directly underneath the erupting vent in B) is very obvious and possibly marks the ascending magma.

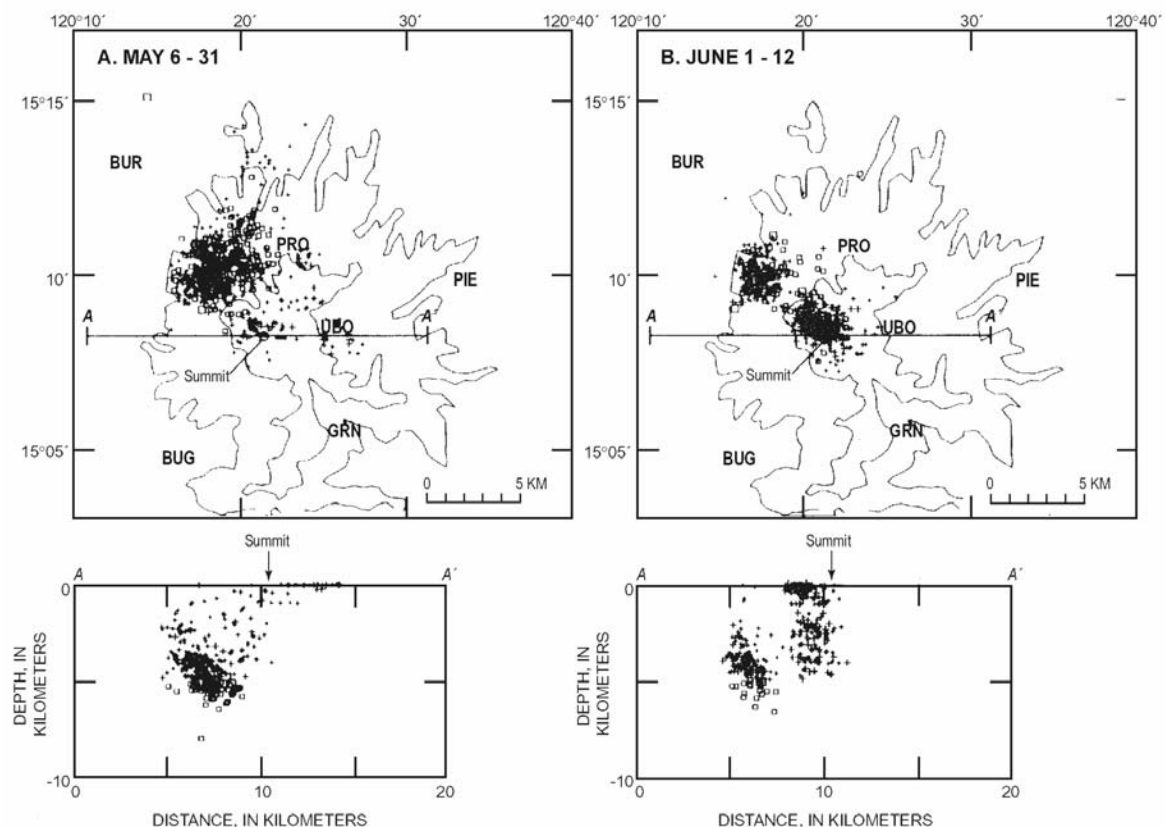


Fig. 13.23 A) Mt. Pinatubo seismicity during May 6 to May 31. The seismic events are clearly clustering northwest of the volcanic center. B) shows the seismicity between June 1 to June 12 indicating a shift of the hypocenters to shallow depths and closer to the summit of Mt. Pinatubo (courtesy of Pinatubo Observatory Team (1991), EOS Trans. Am. Geophys Union, 72, 545, 552-553, 555).

13.4.3.2 Amplitude - distance curves

Even in the case of no clear P- or S-wave arrival, it is sometimes possible to estimate an approximate source area. Assuming a certain wave type (body or surface wave), neglecting an uneven radiation pattern of the source, and assuming a simplified propagation path, it is possible to compute amplitude-distance curves and model the source region. This can be seen as an iterative approach of fitting or contouring the amplitudes or radiated energy measured in the whole network. Successful applications of this technique were reported for locating volcanic tremor at Bromo volcano, Indonesia (Gottschämmer and Suroño, 2000) and Mt. Etna, Italy (Cosentino et al., 1984). However, care must be taken in the *a priori* assumption of the wave-type, i.e., body or surface waves. Wegler and Lühr (2001) showed that the largest amplitudes visible in the seismograms recorded at the Mt. Merapi volcano are fitted best by assuming a strong scattering regime, which also alters the amplitude-distance relationship. Also the influence of near-field effects may influence the amplitude-distance curve significantly (see Fig. 13.24).

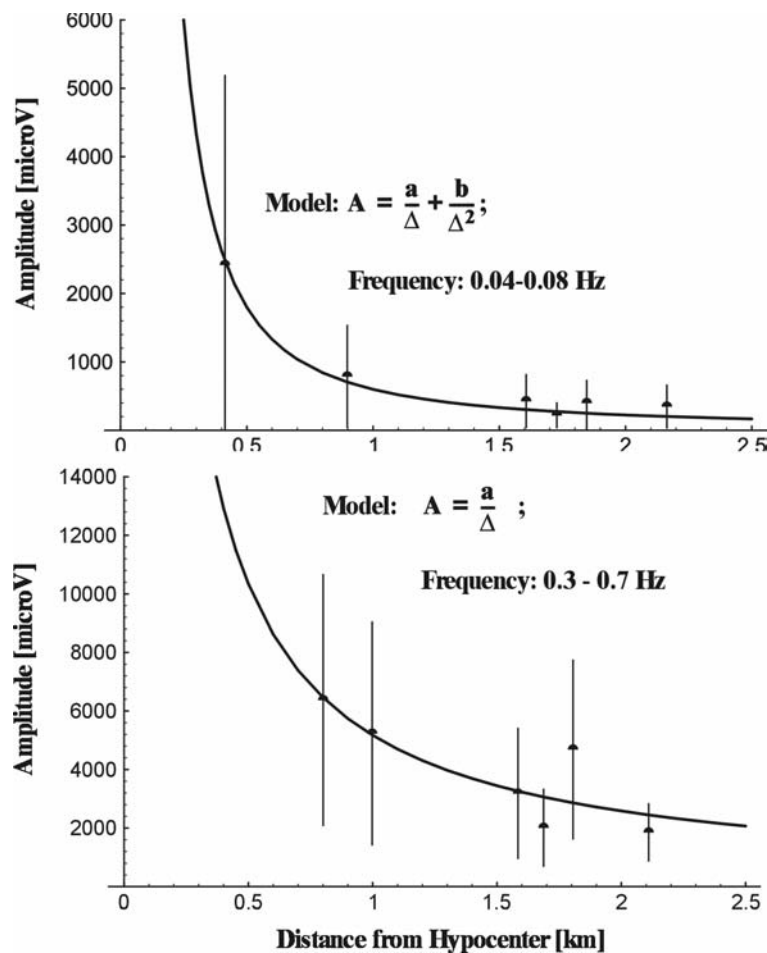


Fig. 13.24 Upper diagram: amplitude-distance relationship at Stromboli volcano; the amplitudes were measured in the frequency range 0.04 - 0.08 Hz. The best fit of the amplitudes at different distances from the active vent was obtained when an additional near-field term was added ($A \sim 1/\Delta^2$). Lower diagram: same as above but in the frequency range 0.3 - 0.7 Hz. In this case, the best fitting curve follows the usual factor of geometrical spreading $1/\Delta$ for body waves. It is also obvious that in b) site effects are more pronounced than in a).

13.4.4 Seismic arrays

The analysis of seismic signals using array techniques is seen as the most prominent and emerging modern tool for locating volcano-seismic signals and evaluating the seismic wavefield properties (e.g., Chouet, 1996b). While most of the array-techniques are discussed in Chapter 9, we will focus on some results obtained when applying them in volcano monitoring and signal analysis.

The main deviation from typical array techniques in earthquake seismology is that the height differences between the array stations can not be neglected when the array is deployed on the flanks of a volcano. The effect of a 3D-distribution of stations can be minimized by fitting a plane to the station locations, which is possibly dipping according to the topography. One then transforms all auxiliary information (i.e., station coordinates) and refers all estimated parameters (incidence, azimuth and horizontal slowness) to this “best fitting plane”.

13.4.4.1 f-k beamforming

One of the most useful properties of a seismic array is its capability for suppressing undesired signals by filtering the incoming wavefield in the spatial as well as in the frequency domain. Thus, we can estimate the coherence, the signal power, the azimuth and the apparent velocity of an incoming wave. Because most seismic signals map into different regions of the frequency-wave number plane (see, e.g., Figs. 9.28, 9.38 and 9.40), f-k beamforming is an excellent tool to distinguish between the different wave-types. Beamforming can be thought of as delaying each seismic trace in time such that waves will add constructively when summed. The delay times necessary to obtain maximum “beam-power” are used to determine the direction of wave propagation through the array. Beams “aimed” in a direction far from a source will add destructively and produce a low signal. If the seismic array is located some wavelength apart from the assumed source area, and the spatial extend of the array is small compared to the distance towards the source, we can also assume plane-wave propagation. Under these assumptions it is possible to estimate the backazimuth towards the source and, if the velocity model directly below the array is known, we can also estimate the incidence of the incoming plane wave. We can then invert for the source area of the signal (see 9.4.2 - 9.4.4).

Fig. 13.25 gives an example of a broadband f-k analysis with data recorded at Mt. Merapi. Obviously, only the very first part of the signal shows a phase with high coherence b), which additionally shows a small slowness c) (high apparent velocity). In contrast, later arrivals have randomly fluctuating backazimuth and slowness values. A possible interpretation of this pattern is that the recorded event consists of an array-wide coherent body phase (indicated by the high coherence and red color coding), which could be used for locating the event combining the backazimuth information and, if the velocity model just beneath the array is known, the incidence angle estimated from the slowness. This coherent phase is followed by randomly incident waves.

Thus, the potential of a seismic array to discriminate between various types of incoming seismic waves and to quantify their properties makes the f-k beamforming perhaps the most powerful tool for investigation of continuous signals (i.e., volcanic tremor). Furumoto et al. (1990) and Almendros et al. (1997) showed the results of tracking a volcanic tremor source in space and time using seismic array beamforming. Other applications of large seismic arrays

13. Volcano Seismology

have been reported by Saccorotti et al. (1998), Chouet et al. (1997) and La Rocca et al. (2000), to name a few.

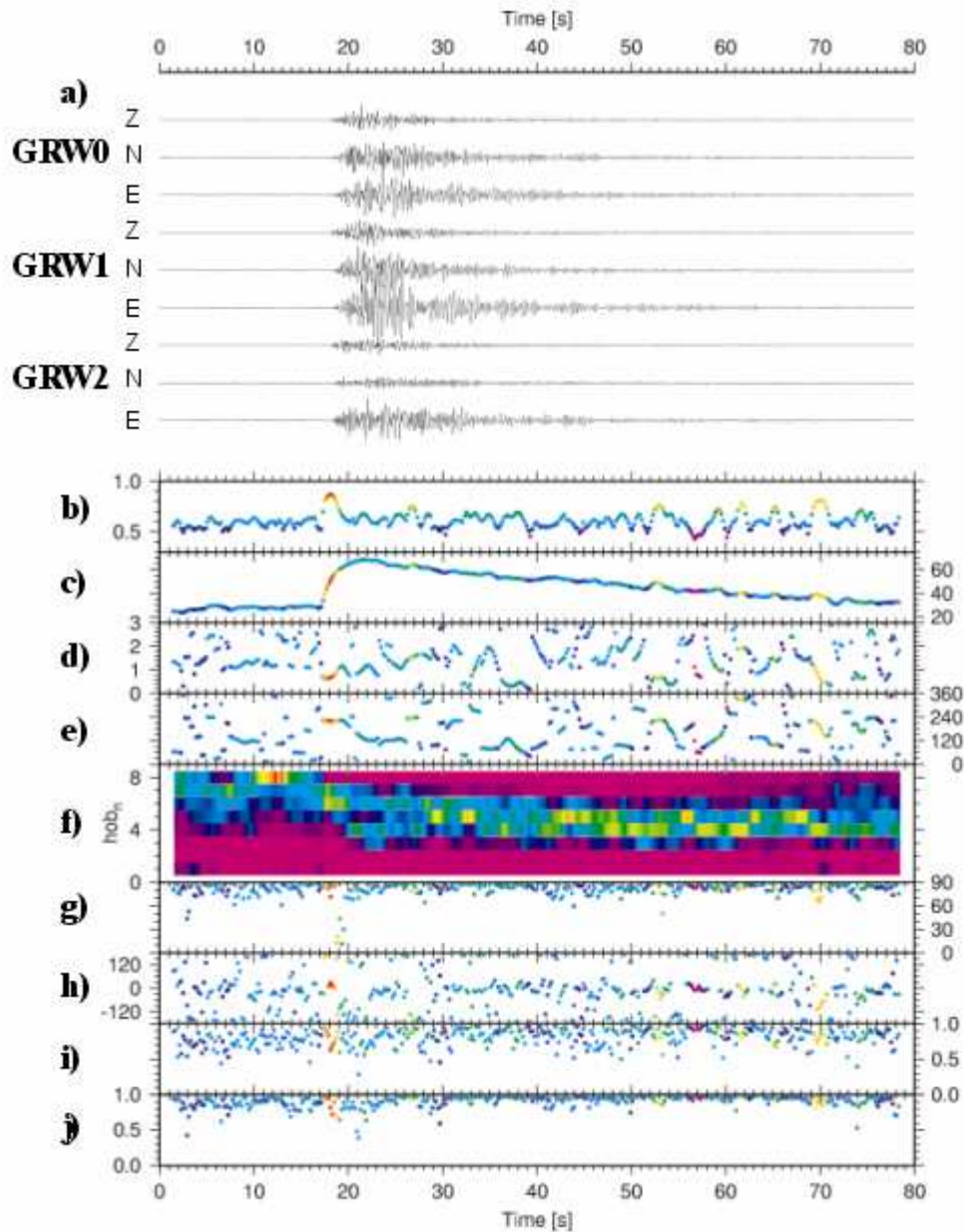


Fig. 13.25 Output of a continuous array analysis of a small seismic array with three component seismometers: a) shows the waveforms of a VT-B type event at the different seismometers; b) is the relative power (semblance) obtained by the f-k analysis; c) shows the overall power in the array in a dB scale while d) and e) give the slowness in s/km and the backazimuth in degree of the incoming waves, respectively. f) shows the array-wide averaged time-frequency pattern in 8 half octave bands; g) and h) show the incidence and azimuth of the array wide averaged polarization pattern (in degree), while i) is a measure of rectilinearity and j) is the planarity of the analyzed signal. The color coding of b) to e) and g) to j) is proportional to the highest semblance value obtained in this signal. The high coherent phase at the beginning of the signal can be used for beam steering towards the source location (courtesy of M. Ohrnberger, University of Potsdam).

However, the application of beamforming techniques in volcano monitoring requires high computer power, rarely available during a volcanic crisis. In order to reduce it, one can use the spatial filter properties of seismic arrays and apply the f-k beamforming to steer in one or several directions of special interest (similar to beamsteering used to detect underground nuclear explosions; see 9.6 and 9.7.7). Another way to reduce computational processing includes optimization of searching the maximum of the beam in the f-k plane (i.e., highest coherence value) by using simulated annealing and/or simplex techniques (Ohrnberger, 2001).

13.4.4.2 Array polarization

As three-component seismometers are becoming the standard instrument nowadays and seismic arrays consist frequently of large numbers of three axial sensors, it is also possible to evaluate the polarization properties of the whole array. While there is no straight-forward method to include the polarization properties directly into the f-k-algorithm, it is possible to estimate array-averaged parameters of the 3D-trajectories. Jurkevics (1988) showed that array-wide averaging of the covariance matrices (see 13.4.2.2) results in a more stable estimate of the seismic wave vector (see Fig. 13.22). Jurkevics (1988) also demonstrated the insensitivity of this estimate to alignment problems within the array. With this algorithm it is also possible to average the polarization properties over certain frequency bands which is a further link to the averaging properties of the broadband f-k-analysis (see 9.7).

A further method to incorporate three-component seismic recordings of an array is to compute the “waveform” semblance (e.g., Ohminato et al., 1998; Kawakatsu et al., 2000). This approach consists of a grid search over possible source locations and the simultaneous rotation of the 3D ground motion vector towards these hypothetical sources. The semblance value of the L direction is computed. The L-Q-T system is defined by the direction from the source to the station L, the plane Q perpendicular to L including the source and receiver, and the plane T perpendicular to Q. Assuming a source which generates solely a compressional wave in L direction, the energy-density on the orthogonal components should be zero. Finally the “waveform” semblance should be 1 if the signal is coherent on all array stations and no energy is left on the two directions perpendicular to L. On the other hand, the “waveform” semblance should be zero if there exists only incoherent wave-groups and/or there is still a signal on the components different to L. It must be emphasized that this approach is restricted to cases where path effects and the influence of the free surface have no, or vanishing, influence on the orientation of the particle motion, i.e., low-frequency near-field observations.

13.4.4.3 Hypocenter determination using seismic arrays

As described in the 13.4.4.1, it is possible to track seismic sources in space and time using seismic arrays. Unfortunately, the exact seismic velocity distribution of a volcano is not known. This results in large uncertainties in estimating the location of volcanic-seismic sources. One possible solution is to use not only one array but a network of arrays distributed around the volcano to compute the backazimuth of the coherent arrivals for each array separately and to invert them for the epicenter of the signal. Applications of this technique can be found in La Rocca et al. (2000).

Another difficulty arises when the seismic array is located close to the source and/or the height differences between the array stations are not negligible. Then, the usually assumed plane-wave propagation is no longer a good approximation and therefore the results are biased to an unknown extent, because neither the influence of the topography nor the deviation of the wavefront from a plane wave is exactly known. In this case, a better way to localize the seismic source is to apply a more complicated approach, which first uses f-k beamforming to detect coherent phases within the continuous seismic data records, and then to apply two-station generalized cross-correlation techniques in order to estimate the time difference of arrivals between the two stations. Wassermann and Ohrnberger (2001) successfully applied this technique to localize VT and strong MP events recorded at Mt. Merapi without the need of interactively determined onsets.

While this algorithm is only applicable to coherent and transient signals, algorithms exist which are based on the migration of coherent phases back to the source region (Almendros et al., 1999; Ohminato et al., 1998; Wassermann, 1997). Unfortunately, the computational load of these algorithms is high and their application is restricted to the “off-line” analysis of selected signals of special interest.

13.4.4.4 Classification problem using seismic arrays

When establishing a seismic array at an active volcano it is also possible to revise the classification scheme used. Besides the usually applied time-frequency analysis (see 13.4.1.1), we can also use wavefield properties obtained from the array analysis to enhance significantly our discrimination quality. Most recently Ohrnberger (2001) applied speech recognition techniques on parameters deduced from a continuous array analysis using data recorded at the Mt. Merapi volcano. Fig. 13.25 from Ohrnberger (2001) gives an example of the output of the continuous parameterization using seismic array techniques. The key point in this approach is the assumption that different signal types will show different wavefield properties (e.g., coherence, time-frequency behavior, polarization properties and absolute time-amplitude behavior).

13.4.5 Automatic analysis

During a seismic crisis or in the framework of a long-term seismic surveillance, it is not possible to apply all the analysis tools described above in a visually controlled, interactive manner. During the October 1996 volcanic crisis at Mt. Merapi, nearly 5000 events per day occurred. This large number of events obviously precludes any on-line, interactive analysis of the seismic data.

There are various approaches to automate at least some parts of the routine analysis in a volcanic observatory (e.g., Patanè and Ferrari, 1999). The most prominent software package is called Earthworm (Johnson et al., 1995), developed mainly under the auspices of the U.S.G.S. Many of the techniques described above are implemented in this “real-time” environment, e.g., continuous spectral analysis, RSAM, SSAM, automatic event associations, hypocenter location and magnitude. Mainly designed for monitoring local earthquakes, the widespread use at volcano observatories has led to the development of new, volcano related modules and promises new tools in the future. The Earthworm system appears to be very flexible and

capable of being adapted to special requirements at different volcanoes. However, the great flexibility of this software package entails rather complex and unwieldy setup procedures when establishing the system the first time.

The software for array analysis and some of the new tools for spectral analysis used in this Chapter were implemented into the Earthworm system and will be released after some beta-testing done through this year (2001).

13.5 Other monitoring techniques

As described at the beginning of this Chapter, seismology is generally seen as the most reliable and diagnostic tool for monitoring a restless or erupting volcano. However, data from seismological surveillance alone are inadequate to understand and forecast eruptions. Modern approaches to monitoring systems will therefore combine seismology with other geophysical, geochemical, geodetic and geological techniques. Below we focus on just a few of the various ground-based monitoring techniques that are closely related to seismology. We will not discuss the wide and fast-developing field of remote sensing in the volcanological context. For this we refer, as a good starting point, to Scarpa and Tilling (1996).

13.5.1 Ground deformation

Closely related to seismology is the monitoring of the deformation field caused by a magma injection and/or hydrothermal pressurization within the volcano's shallow or deep edifice. Deformation can be considered as an extension of seismology to lower, quasi-static frequencies. Modern techniques of monitoring the deformation signals of a restless volcano include borehole tiltmeters and/or strainmeters, *electronic distance meter* (EDM) networks and *Global Positioning System* (GPS) networks. Due to the increasing amount of GPS satellites and accuracy, GPS will play an important role in the field of ground deformation monitoring during the next decades.

The key point of this monitoring technique is the assumption that shallow or deep injection of large volumes of magma below a volcano will cause significant deformation of its surface. There were several successful approaches to forecast the 1980 eruption of Mt. St. Helens using deformation information (Murray et al., 2000) and at Hekla volcano, Iceland (Linde et al., 1993). The most recent 2000 eruption of the Hekla volcano was accompanied by significant signals recorded by a cluster of strain meters located around the volcano (<http://hraun.vedur.is/ja/englishweb/heklanews.html#strain>). In addition, shortly before the eruption, increasing seismicity and volcanic tremor led to a precise forecast of the following eruption (see Fig. 13.26). This can be seen as a perfect example of the interaction of two different monitoring techniques. In addition, there are many papers dealing with correlation between seismic signals and ground deformation at Kilauea volcano (Hawaii; e.g., Tilling et al., 1987).

A further example of a good correlation between measurable deformation and the appearance of seismic signals is known from Suffriere Hill volcano, Montserrat Island, West Indies, where Voight et al. (1998) observed a coincidence between several swarms of Hybrid events with cyclic changes in the deformation signals. This coincidence is very important regarding the inversion of source mechanisms of this class of signals. This kind of deformation signal,

13. Volcano Seismology

in conjunction with magma intrusion into the volcanic edifice, is known to be very small and mainly related to the active part of the volcanic dome. At Mt. Merapi, several clusters of borehole tiltmeters are installed at the flanks, but only very weak signals have been recorded until now (Rebscher et al., 2000). In contrast, strong deformation signals are visible at the volcano's summit stations (Voight et al., 2000). This might indicate that at Mt. Merapi no large-sized and shallow-situated magma chamber exists and that the volume of ascending magma during typical eruptive phases is small. However, tilt stations at the flanks of Mt. Merapi and other volcanoes with apparent small magmatic activity are very useful for discrimination between the usual small magma intrusions and possible larger ascending volumes of magma, which should then produce a much more pronounced tilt signal.

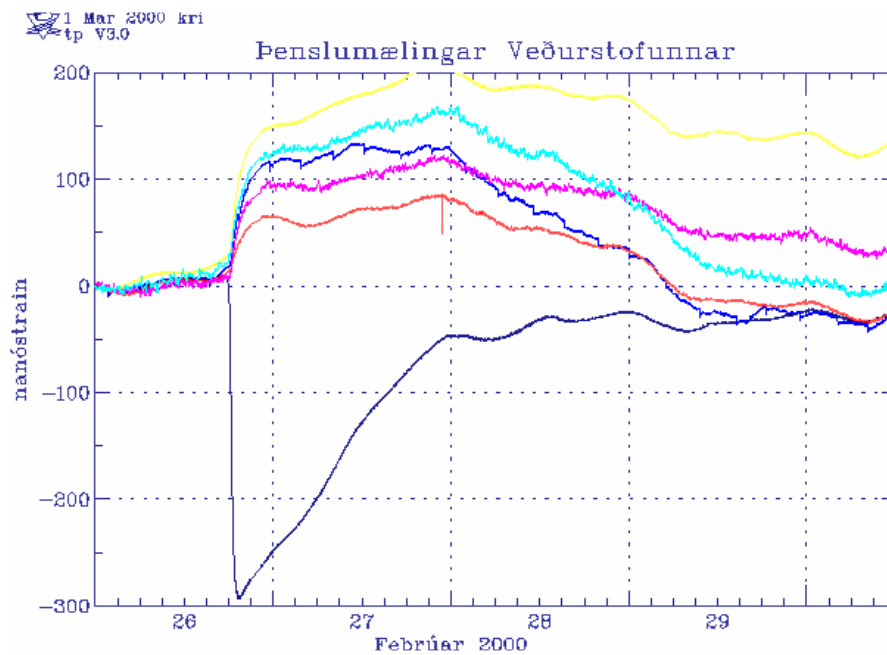


Fig. 13.26 The strainmeter data preceding the Hekla 2000 eruption are shown. As a result, three different phases could be defined. Firstly, a conduit was opened between 17:45 to 18:17. Secondly, a reduced rate of expansion of the same conduit at 19:20 could be detected and finally all stations showed an increase when the conduit was fully opened and magma was flowing directly beneath the volcano (courtesy of Icelandic Meteorological Office, <http://hraun.vedur.is/ja/englishweb/heklanews.html#strain>).

13.5.2 Micro-Gravimetry

The appearance of gravity changes at an active volcano also reflect possible inflation/deflation cycles of magmatic material. There is a complicated interaction between physical and geometric properties (i.e., density, volume, location) of the moving material and height changes caused by the deformation of the surface of a volcano. Therefore, the monitoring of gravity changes is a challenging task that should be carried out with great care. As height changes are generally the reason for gravity changes, gravity monitoring should always be combined with high precision leveling (e.g., EDM or GPS measurements). For a reliable and less ambiguous inversion of the gravity data, a good knowledge of the velocity structure of the volcano is needed. Models of the magmatic system from gravity data should be regarded with caution, unless the conclusions are also supported by other independent observations.

13.5.3 Gas monitoring

Another important parameter preceding a volcanic eruption is the volume, velocity, temperature and composition of the emitted gas from a volcanic vent or fumarole. Volatiles and released gases are seen as the most important driving forces for both an eruption and the source of volcanic signals (e.g., explosion quakes, LF, MP, volcanic tremor) (Schick, 1988; Vergnolle and Jaupart, 1990). Different techniques of gas sampling are in use, ranging from routinely collected gas samples in a weekly or monthly manner to a continuous analysis (every 20 - 30 min) of the emitted gas using a gas-chromatograph (Zimmer and Erzinger, 2001). The high sampling rate in continuous analysis at Mt. Merapi revealed surprisingly short period pulsations (with a duration of 5 hours to 3 hours; see Fig. 13.27) in the water to carbon-dioxide ratio as well as in the temperature of a fumarole (Zimmer and Erzinger, 2001). However, no significant correlation between this pulsation and the related seismicity could be found. Only the rhythms in this pulsating gas source were changed when the number of very shallow MP-events also increased. This lack of correlation of fast sampled gas data and seismic signals at Mt. Merapi might be caused by our imperfect knowledge of how to parameterize the seismicity and the gas composition, respectively. Several case studies of changes in the chemical composition of fumarolic gases, including descriptions of the accompanying seismicity and ground deformation, is given by Martini (1996).

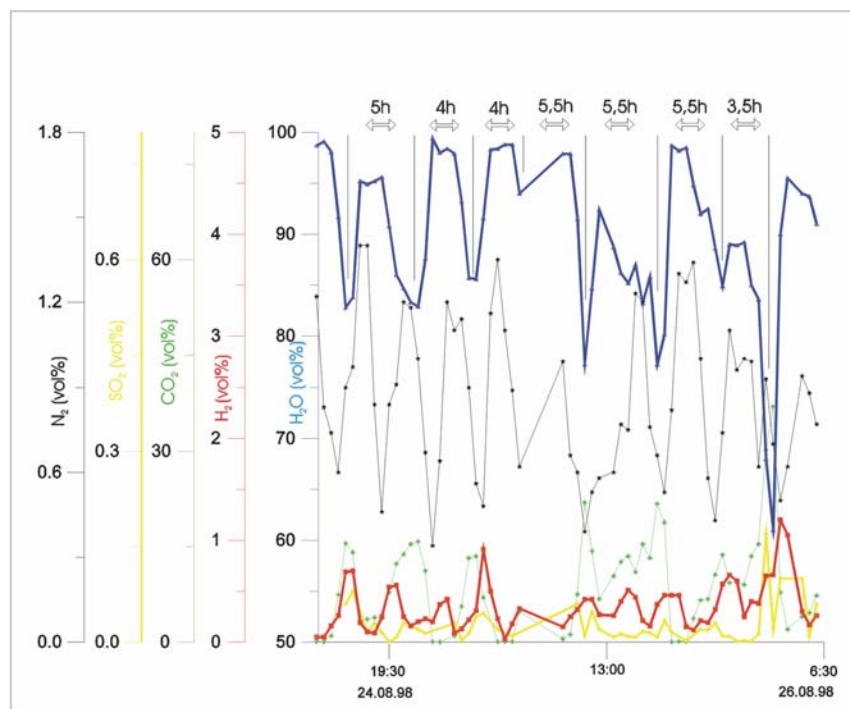


Fig. 13.27 Variation of the gas composition at one of Mt. Merapi's fumaroles. The gas is automatically analyzed approximately every 30 min using a gas-chromatograph. The analysis shows a fast changing composition of the gas with a period of roughly 5 hrs (courtesy of M. Zimmer, GeoForschungsZentrum Potsdam).

Many other papers deal with the long term variations of gas prior to a volcanic eruption, which makes this technique a useful tool for long term monitoring (e.g., Stix and Gaonac'h, 2000).

13.5.4 Meteorological parameters

While not directly linked to the eruptive behavior of a volcano, monitoring meteorological conditions is important for the proper interpretation of observed parameters as well as for the anticipation of possible triggering of volcanic activity. Lahars, i.e., volcanic debris flow, are often triggered by heavy rainfall which additionally weakens the unconsolidated volcanic material. At Mt. Merapi, small-size gravitational dome collapses take place more frequently during the tropical rainy season.

The influence of meteorological conditions on the installed monitoring equipment is manifold. Barometric pressure and temperature changes could cause severe disturbances on installed broadband seismometers and tiltmeters, respectively. While these influences can be reduced by proper installation of the sensors (see 13.6), they are never completely removed. Spectral analysis of both meteorological and surveillance parameters may help to identify possible disturbances of the installed sensors. As mentioned before, rainfall may trigger volcanic as well as seismic activity. A good monitoring station will therefore also have a continuously recording rain gauge.

In order to better judge the influence of meteorological (and also tidal) effects on the sensors and/or the volcanic activity, continuous long-term meteorological recordings are needed. Frankly speaking, this is a difficult and sometimes impossible task because of the harsh environments at many active volcanoes. However, the continuity of such measurements are among the most important functions of a volcano observatory.

13.6 Technical considerations

13.6.1 Site

After selecting a possible site (see 3.1) for a seismic station or a seismic array, much care should be taken to protect the sensor from meteorological and other external effects. In Fig. 13.28a, a sketch of a possible installation scheme is shown. If a broadband sensor is to be deployed, extra care must be taken to protect this sensitive sensor from temperature and barometric pressure influences (see 5.5 and 7.4).

The weather conditions at volcanoes at even moderate altitudes can be very rough and may change rapidly. Protection against rain and lightning is the most important task when constructing a seismic station. All equipment should be placed in water tight casings. Lightning protection is the most important and, unfortunately, the most difficult problem to solve (see 7.4.2.5). Usually, volcanoes have high resistivity surface layers (ash, lapilli etc.), making a proper grounding of the instruments nearly impossible. One of the optimal techniques to protect the equipment against lightning damage is to install a tower in the vicinity of the station with a mounted copper spire on top. The tower should be grounded as much as possible and connected entirely with the ground of the power-sensitive equipment.

Furthermore, lightning protectors should be placed in front of any equipment to reduce the effect of high-voltage bursts (see Fig. 13.28b-c). Long cable runs should be avoided or changed to fibre optics. Using fibre optic cables for signal transmission also has the advantage of being insensitive to electro-magnetic effects, which sometimes cause spike bursts on the

transmitted signals.

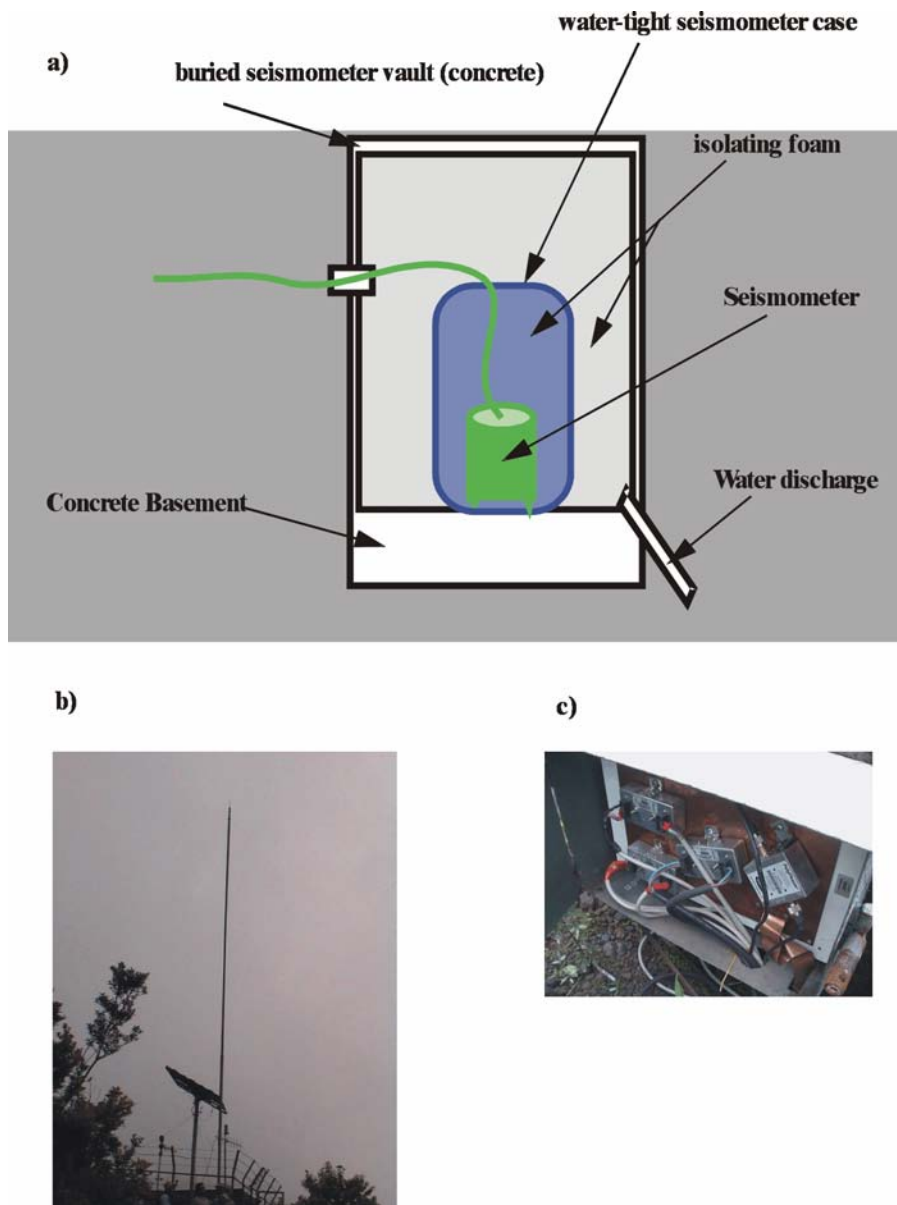


Fig. 13.28 a) Sketch of a seismometer vault: the sensor should be placed in a water tight casing which is placed firmly on a concrete basement. In order to isolate the sensor against temperature and pressure changes due to air turbulences, the void space should be completely filled with insulating rubber foam or similar (see 7.4.2); b) shows a lightning tower installed at Mt. Merapi, while c) shows additional lightning protectors for all sensitive equipment. The copper plate and all external devices (photo-voltaic modules) should be connected to the lightning tower.

13.6.2 Sensors and digitizers

Because the seismic signals produced by an active volcano cover a wide dynamic range, the choice of the digitizer, i.e., the needed dynamic range, should be carefully evaluated. Modern digitizers will sample the analog seismometer output with 24 bit resolution which results in a

13. Volcano Seismology

dynamic range of roughly 136 dB (depending on the sampling rate). A 16 bit A/D converter would usually be sufficient, but eruptive phases with various large amplitude signals will then saturate the digitizers' dynamic range (e.g., pyroclastic density flows, big explosions etc.). So called "gain-ranging" (i.e., the pre-amplification will be lowered if the signal is getting stronger) should be avoided because it will result in lower resolution and might mask small but important signals. Best suited are digitizers which sample with 24 bit resolution but store the data depending on the recorded peak amplitude (i.e., 8 bits are stored if the signals are small and the activity is low, 16 bits when the activity is increasing and 32 bits if high activity occurs and the full 24 bit range is used).

If a network of seismic sensors is planned, several three-component short-period instruments (i.e., with 1 Hz corner frequency) will be sufficient (see 13.3.2). If the near-crater range is accessible, installing one or two broadband stations (i.e., 0.00833 to 0.05 Hz corner frequency) will be a good choice. If large ($M > 4$) earthquakes from an active volcano flank or nearby fault or subduction zone are possible, some broadband stations are preferred.

If an array or a network of arrays is to be installed, a mixture of three-component broadband and short-period one-component seismometers will be sufficient (especially when realizing that there is no straight-forward technique available which includes directly 3D seismic array data).

13.6.3 Analog versus digital telemetry

Most of today's established monitoring networks at volcanoes are designed for transmitting the data "on-line" to a central data center, generally the local volcano observatory. This might be the main technical difference between a short-term seismological experiment and the long-term monitoring of a volcano. From worldwide experience, establishing a reliable radio line is a difficult and time-consuming task, which is also subject to change when new telecommunication facilities are constructed nearby and possibly worsen the data communication.

There are large differences between analog and digital radio transmission regarding data rate, dynamic range and sites to be selected and distance ranges to be covered. If a high resolution is required (e.g., using a 24 or 16 bit A/D converter at the sensor), the only way to exploit the full bandwidth of data is to transmit the signals with a digital radio modem. Meanwhile, several companies offer spread-spectrum modems which transmit in the frequency range of roughly 1 GHz and 2 GHz, respectively. The big advantage of these digital modems is the high data throughput (115,200 baud) and the low power consumption (transmitting power roughly 1 Watt). On the other hand, the high transmission frequency is the main drawback of the digital radios. As a rule, the station and the data center must be in direct line of sight, with no hills, trees or other obstacles between them. This limitation should also be kept in mind when selecting a suitable seismic station site. The problem of obstacles can be circumvented when installing several repeaters on the way to the data center. Even so, the network design depends on intended radio lines (see also 7.3 and Information Sheet IS 8.2).

A disadvantage of analog radio communication is the limited dynamic range and data throughput (usually below 38,400 baud). Most of the installed analog radio systems are barely able to transmit 12 bits and, therefore, the signals must be bandpass filtered (e.g., 1 - 20 Hz) before transmitting. This is not acceptable when installing a broadband sensor. On the other

hand, radios are cheap and the typical frequency bands (100 MHz or 400 MHz) will enable a solid radio link even when the stations are slightly “out of sight”.

13.6.4 Power considerations

Most of the stations will be remote and no access to a power network will exist. Therefore, the first step is to calculate the expected power consumption of the seismic station. This will strongly depend on the kind of digitizer and sensor used, whether the data are transmitted by radio or not and which options for local data storage are desired. Therefore the power consumption of the field equipment should be extensively tested in the lab before constructing the power supply at the site and deploying the instruments. Never trust the optimistic specifications given by the manufacturer!

Most likely the power will be delivered by photo-voltaic (PV) modules where a variety of different systems is available. All components of a monitoring installation must fit together, including the capacity of batteries and solar charger. Care must be taken when estimating the amount of solar-modules needed to supply the stations. As a rule of thumb, 10% of the nominal maximum voltage will be supplied by the panels on average (i.e., using a 50 Watt module just 5 W are available on average). Voltage will typically decrease when the panels are installed high up in the mountains. Clouds, snow or ashfall may further reduce the effective power output (i.e., 5% or even less). This significantly increases the number of PV-modules required. To give an example: if the station consumes at least 20 W (including radio, some digitizers, SCSI disks for local storage etc.), you will need 400 W panel power which in the worst case is 8 x 50 W panels at this station!

Also the capacity of the battery must be adequate in case no solar power is produced. On the other hand, the battery should not be too big in capacity as the PV-modules must be able to recharge the battery in sufficient time. Whenever possible, alternative power sources should be used, such as robust wind generators. In case the station is located near running water, a small hydro-power engine could be a good alternative.

13.6.5 Data center

All data streams, including those from monitoring techniques in addition to seismic, should be collected, stored and archived in a central facility. In the age of high-performance low-cost PC's, few standard computers will be sufficient to satisfy all needs of data collection, backup systems, automatic and visual analysis. Because continuous recording of all relevant signals is preferred over triggered data, a good backup strategy is crucial for getting complete and long-term data. Continuous recording is indispensable for improving our knowledge about volcanic activity, the underlying physical mechanisms and the relevant parameters to be observed when aiming at improving eruption forecasting. With the advent of DVD disks and CD-ROMS a good solution would be to write images of data sets onto one of these media in a daily or regular manner. CD-ROMS in particular assure a good data safety to price ratio.

Much public domain software is available for either automatic (e.g., Earthworm; Johnson et al., 1995) or interactive analysis (SeismicHandler, SAC, IASPEI-Software, PITSA/GIANT). The Orfeus homepage is a good starting point when looking for suitable software and for further contacts (see <http://orfeus.knmi.nl/>).

13. Volcano Seismology

A special requirement of the data center is the availability of an “uninterruptable power supply” (UPS) to guarantee a loss-less data collection even if the power line of the observatory is broken. Depending on the quality of the power network, a generator could be a good solution to bypass blackouts which may last several hours.

Establishing a “quick-response” volcano observatory during a volcanic crisis of a long-dormant volcano needs additional equipment and design criteria of the monitoring network to be deployed. All equipment, including the data center facilities, should be lightweight, robust and low power consuming. This demands possible down-grades in resolution and data throughput. A comprehensive description of one realization of mobile monitoring networks is given in the *Mobile Volcano-Monitoring System* by Murray et al. (1996).

Acknowledgments

I am grateful to the reviewers F. Klein, R. Scarpa and R. Tilling for their helpful comments and corrections which improved the text significantly. I also thank P. Bormann for additional editing of this Chapter. Furthermore, figures and seismograms provided by E. Gottschämmer, S. Falsaperla, S. McNutt and M. Ohrnberger, are highly appreciated.

Recommended overview readings (see References, under Miscellaneous in Volume 2)

- Civetta, L., Gasparini, P., Luongo, G., and Rapolla, A. (Eds.) (1974).
- McNutt (2002)
- Newhall, C. G., and Punongbayan, R. S. (Eds.) (1996).
- Scarpa, R. and Tilling, R. (Eds.) (1996).
- Sigurdsson, H. (Ed. in Chief) (2000).

Topic	Global 1-D Earth models
Compiled by	Peter Bormann (formerly GeoForschungsZentrum Potsdam, Telegrafenberg, D-14473 Potsdam, Germany); E-mail: pb65@gmx.net
Version	March 2002

Below, data and background information on the most frequently used 1-D Earth reference models in global seismology have been compiled by using Appendix 1 of Shearer (1999), Kennett (1991) and personal information received from B. Kennett (2002).

1 PREM Model

For many years the most widely used 1-D model of seismic velocities in the Earth has been the Preliminary Reference Earth Model (PREM) of Dziewonski and Anderson (1981). This model was designed to fit a variety of different data sets, including free oscillation center frequency measurements, surface-wave dispersion observations, travel-time data for a number of body-wave phases, and basic astronomical data (Earth's radius, mass, and moment of inertia). Table 1 summarizes, as functions of depth and Earth's radius, the PREM velocities v_p and v_s for P and S waves, the density ρ , the shear and bulk quality factors, Q_μ and Q_κ , and the pressure P . Note, that density and attenuation ($\sim 1/Q$) are known less precisely than the seismic velocities but these parameters are required for computing synthetic seismograms. In order to simultaneously fit Love- and Rayleigh-wave observations, PREM is transversely isotropic between 80 and 220 km depth in the upper mantle. Transverse isotropy is a spherically symmetric form of anisotropy in which SH and SV waves travel at different speeds. Table 1, however, lists only values from an isotropic version of PREM. The true PREM model is also specified in terms of polynomials between node points. Linear interpolation between the values given in Table 1 will produce only approximate results. All current Earth models have values that are reasonably close to PREM. The largest differences are in the upper mantle where PREM shows a discontinuity at 220 km which is not found in most other models. Fig. 2.53 in Chapter 2 depicts PREM together with the more recent model AK135 (see Table 3 below).

Table 1 Preliminary Reference Earth Model (isotropic version)

Depth (km)	Radius (km)	v_p (km/s)	v_s (km/s)	ρ (g/cm ³)	Q_μ	Q_κ	P (GPa)
0.0	6371.0	1.45	0.00	1.02	0.0	57823.0	0.0
3.0	6368.0	1.45	0.00	1.02	0.0	57823.0	0.0
3.0	6368.0	5.80	3.20	2.60	600.0	57823.0	0.0
15.0	6356.0	5.80	3.20	2.60	600.0	57823.0	0.3
15.0	6356.0	6.80	3.90	2.90	600.0	57823.0	0.3
24.4	6346.6	6.80	3.90	2.90	600.0	57823.0	0.6
24.4	6346.6	8.11	4.49	3.38	600.0	57823.0	0.6
71.0	6300.0	8.08	4.47	3.38	600.0	57823.0	2.2
80.0	6291.9	8.08	4.47	3.37	600.0	57823.0	2.5
80.0	6291.0	8.08	4.47	3.37	80.0	57823.0	2.5
171.0	6200.0	8.02	4.44	3.36	80.0	57823.0	5.5
220.0	6151.0	7.99	4.42	3.36	80.0	57823.0	7.1
220.0	6151.0	8.56	4.62	3.44	143.0	57823.0	7.1
271.0	6100.0	8.66	4.68	3.47	143.0	57823.0	8.9

Table 1 (continued)

Depth (km)	Radius (km)	v_p (km/s)	v_s (km/s)	ρ (g/cm ³)	Q_μ	Q_κ	P (GPa)
371.0	6000.0	8.85	4.75	3.53	143.0	57823.0	12.3
400.0	5971.0	8.91	4.77	3.54	143.0	57823.0	13.4
400.0	5971.0	9.13	4.93	3.72	143.0	57823.0	13.4
471.0	5900.0	9.50	5.14	3.81	143.0	57823.0	16.0
571.0	5800.0	10.01	5.43	3.94	143.0	57823.0	19.9
600.0	5771.0	10.16	5.52	3.98	143.0	57823.0	21.0
600.0	5771.0	10.16	5.52	3.98	143.0	57823.0	21.0
670.0	5701.0	10.27	5.57	3.99	143.0	57823.0	23.8
670.0	5701.0	10.75	5.95	4.38	312.0	57823.0	23.8
771.0	5600.0	11.07	6.24	4.44	312.0	57823.0	28.3
871.0	5500.0	11.24	6.31	4.50	312.0	57823.0	32.8
971.0	5400.0	11.42	6.38	4.56	312.0	57823.0	37.3
1071.0	5300.0	11.58	6.44	4.62	312.0	57823.0	41.9
1171.0	5200.0	11.78	6.50	4.68	312.0	57823.0	46.5
1271.0	5100.0	11.88	6.56	4.73	312.0	57823.0	51.2
1371.0	5000.0	12.02	6.62	4.79	312.0	57823.0	55.9
1471.0	4900.0	12.16	6.67	4.84	312.0	57823.0	60.7
1571.0	4800.0	12.29	6.73	4.90	312.0	57823.0	65.5
1671.0	4700.0	12.42	6.78	4.95	312.0	57823.0	70.4
1771.0	4600.0	12.54	6.83	5.00	312.0	57823.0	75.4
1871.0	4500.0	12.67	6.87	5.05	312.0	57823.0	80.4
1971.0	4400.0	12.78	6.92	5.11	312.0	57823.0	85.5
2071.0	4300.0	12.90	6.97	5.16	312.0	57823.0	90.6
2171.0	4200.0	13.02	7.01	5.21	312.0	57823.0	95.8
2271.0	4100.0	13.13	7.06	5.26	312.0	57823.0	101.1
2371.0	4000.0	13.25	7.10	5.31	312.0	57823.0	106.4
2471.0	3900.0	13.36	7.14	5.36	312.0	57823.0	111.9
2571.0	3800.0	13.48	7.19	5.41	312.0	57823.0	117.4
2671.0	3700.0	13.60	7.23	5.46	312.0	57823.0	123.0
2741.0	3630.0	13.68	7.27	5.49	312.0	57823.0	127.0
2771.0	3600.0	13.69	7.27	5.51	312.0	57823.0	128.8
2871.0	3500.0	13.71	7.26	5.56	312.0	57823.0	134.6
2891.0	3480.0	13.72	7.26	5.57	312.0	57823.0	135.8
2891.0	3480.0	8.06	0.00	9.90	0.0	57823.0	135.8
2971.0	3400.0	8.20	0.00	10.03	0.0	57823.0	144.2
3071.0	3300.0	8.36	0.00	10.18	0.0	57823.0	154.8
3171.0	3200.0	8.51	0.00	10.33	0.0	57823.0	165.2
3271.0	3100.0	8.66	0.00	10.47	0.0	57823.0	175.5
3371.0	3000.0	8.80	0.00	10.60	0.0	57823.0	185.7
3471.0	2900.0	8.93	0.00	10.73	0.0	57823.0	195.8
3571.0	2800.0	9.05	0.00	10.85	0.0	57823.0	205.7
3671.0	2700.0	9.17	0.00	10.97	0.0	57823.0	215.4
3771.0	2600.0	9.28	0.00	11.08	0.0	57823.0	224.9
3871.0	2500.0	9.38	0.00	11.19	0.0	57823.0	234.2
3971.0	2400.0	9.48	0.00	11.29	0.0	57823.0	243.3
4071.0	2300.0	9.58	0.00	11.39	0.0	57823.0	252.2

Table 1 (continued)

Depth (km)	Radius (km)	v_p (km/s)	v_s (km/s)	ρ (g/cm ³)	Q_μ	Q_κ	P (GPa)
4171.0	2200.0	9.67	0.00	11.48	0.0	57823.0	260.8
4271.0	2100.0	9.75	0.00	11.57	0.0	57823.0	269.1
4371.0	2000.0	9.84	0.00	11.65	0.0	57823.0	277.1
4471.0	1900.0	9.91	0.00	11.73	0.0	57823.0	284.9
4571.0	1800.0	9.99	0.00	11.81	0.0	57823.0	292.3
4671.0	1700.0	10.06	0.00	11.88	0.0	57823.0	299.5
4771.0	1600.0	10.12	0.00	11.95	0.0	57823.0	306.2
4871.0	1500.0	10.19	0.00	12.01	0.0	57823.0	312.7
4971.0	1400.0	10.25	0.00	12.07	0.0	57823.0	318.9
5071.0	1300.0	10.31	0.00	12.12	0.0	57823.0	324.7
5149.5	1221.5	10.36	0.00	12.17	0.0	57823.0	329.0
5149.5	1221.5	11.03	3.50	12.76	84.6	57823.0	329.0
5171.0	1200.0	11.04	3.51	12.77	84.6	57823.0	330.2
5271.0	1100.0	11.07	3.54	12.82	84.6	57823.0	335.5
5371.0	1000.0	11.11	3.56	12.87	84.6	57823.0	340.4
5471.0	900.0	11.14	3.58	12.91	84.6	57823.0	344.8
5571.0	800.0	11.16	3.60	12.95	84.6	57823.0	348.8
5671.0	700.0	11.19	3.61	12.98	84.6	57823.0	352.2
5771.0	600.0	11.21	3.63	13.01	84.6	57823.0	355.4
5871.0	500.0	11.22	3.64	13.03	84.6	57823.0	358.0
5971.0	400.0	11.24	3.65	13.05	84.6	57823.0	360.2
6071.0	300.0	11.25	3.66	13.07	84.6	57823.0	361.8
6171.0	200.0	11.26	3.66	13.08	84.6	57823.0	363.0
6271.0	100.0	11.26	3.67	13.09	84.6	57823.0	363.7
6371.0	0.0	11.26	3.67	13.09	84.6	57823.0	364.0

2 IASP91 velocity model

According to Kennett (1991) and Kennett and Engdahl (1991), the IASP91 model is a parameterized velocity model, in terms of normalized radius. It has been constructed to be a summary of the travel-time characteristics of the main seismic phases.

The crust consists of two uniform layers with discontinuities at 20 and 35 km. Between 35 and 760 km the velocities in each layer are represented by a linear gradient in radius. The major mantle discontinuities are set at 410 km and 660 km. The upper mantle model is designed for the specific purpose of representing the 'average' observed times for P and S waves out to 30° as well as providing a tie to teleseismic times. Since the distribution of seismic sources and recording stations is far from uniform, the IASP91 model will include geographical bias as well as the constraints imposed by the specific parameterization.

The distribution of P- and S-wave velocities, v_p and v_s , in the lower mantle is represented by a cubic radius between 760 km and 2740 km. The velocities in the lowermost mantle are taken as a linear gradient in radius down to the core-mantle boundary at 3482 km. In the core and inner core the velocity functions are specified as quadratic polynomials in radius.

Table 2.1 presents the parameterized form and Table 2.2 the tabulated form of the IASP91.

Table 2.1 Parameterized form of the IASP91 model

($x =$ normalised radius r/a where $a = 6371$ km)

Depth (z km)	Radius (r km)	v_p (km/s)	v_s (km/s)
6371-5153.9	0-1217.1	11.24094	3.56454
		$-4.09689 x^2$	$-3.45241 x^2$
5153.9-2889	1217.1-3482	10.03904	0
		$3.75665 x$	
		$-13.67046 x^2$	
2889-2740	3482-3631	14.49470	816616
		$-1.47089 x$	$-1.58206 x$
2740-760	3631-5611	25.1486	12.9303
		$-41.1538 x$	$-21.2590 x$
		$+51.9932 x^2$	$+27.8988 x^2$
		$-26.6083 x^3$	$-14.1080 x^3$
760-660	5611-5711	25.96984	20.76890
		$-16.93412 x$	$-16.53147 x$
660-410	5711-5961	29.38896	17.70732
		$-21.40656 x$	-13.50652
410-210	5961-6161	30.78765	15.24213
		$-23.25415 x$	-11.08552
210-120	6161-6251	25.41389	5.75020
		$-17.69722 x$	-1.27420
120-35	6251-6336	8.78541	6.706231
		$-0.74953 x$	-2.248585
35-20	6336-6351	6.50	3.75
20-0	6351-6371	5.80	3.36

Table 2.2 The IASP91 velocity model

Depth (km)	Radius (km)	v_p (km/s)	v_s (km/s)
6371.00	0.	11.2409	3.5645
6271.00	100.000	11.2399	3.5637
6171.00	200.000	11.2369	3.5611
6071.00	300.000	11.2319	3.5569
5971.00	400.000	11.2248	3.5509
5871.00	500.000	11.2157	3.5433
5771.00	600.000	11.2046	3.5339
5671.00	700.000	11.1915	3.5229
5571.00	800.000	11.1763	3.5101
5471.00	900.000	11.1592	3.4956
5371.00	1000.00	11.1400	3.4795
5271.00	1100.00	11.1188	3.4616
5171.00	1200.00	11.0956	3.4421
5153.90	1217.10	11.0914	3.4385
5153.90	1217.10	10.2578	0.
5071.00	1300.00	10.2364	0.
4971.00	1400.00	10.2044	0.
4871.00	1500.00	10.1657	0.
4771.00	1600.00	10.1203	0.
4671.00	1700.00	10.0681	0.
4571.00	1800.00	10.0092	0.
4471.00	1900.00	9.9435	0.
4371.00	2000.00	9.8711	0.
4271.00	2100.00	9.7920	0.
4171.00	2200.00	9.7062	0.
4071.00	2300.00	9.6136	0.
3971.00	2400.00	9.5142	0.
3871.00	2500.00	9.4082	0.
3771.00	2600.00	9.2954	0.
3671.00	2700.00	9.1758	0.
3571.00	2800.00	9.0496	0.
3471.00	2900.00	8.9166	0.
3371.00	3000.00	8.7768	0.
3271.00	3100.00	8.6303	0.
3171.00	3200.00	8.4771	0.
3071.00	3300.00	8.3171	0.
2971.00	3400.00	8.1504	0.
2889.00	3482.00	8.0087	0.
2889.00	3482.00	13.6908	7.3015
2871.00	3500.00	13.6866	7.2970
2771.00	3600.00	13.6636	7.2722
2740.00	3631.00	13.6564	7.2645
2740.00	3631.00	13.6564	7.2645
2671.00	3700.00	13.5725	7.2302
2571.00	3800.00	13.4531	7.1819
2471.00	3900.00	13.3359	7.1348

Table 2.2 (continued)

Depth (km)	Radius (km)	v_p (km/s)	v_s (km/s)
2371.00	4000.00	13.2203	7.0888
2271.00	4100.00	13.1055	7.0434
2171.00	4200.00	12.9911	6.9983
2071.00	4300.00	12.8764	6.9532
1971.00	4400.00	12.7607	6.9078
1871.00	4500.00	12.6435	6.8617
1771.00	4600.00	12.5241	6.8147
1671.00	4700.00	12.4020	6.7663
1571.00	4800.00	12.2764	6.7163
1471.00	4900.00	12.1469	6.6643
1371.00	5000.00	12.0127	6.6101
1271.00	5100.00	11.8732	6.5532
1171.00	5200.00	11.7279	6.4933
1071.00	5300.00	11.5761	6.4302
971.00	5400.00	11.4172	6.3635
871.00	5500.00	11.2506	6.2929
771.00	5600.00	11.0756	6.2180
760.00	5611.00	11.0558	6.2095
760.00	5611.00	11.0558	6.2095
671.00	5700.00	10.8192	5.9785
660.00	5711.00	10.7900	5.9500
660.00	5711.00	10.2000	5.6000
571.00	5800.00	9.9010	5.4113
471.00	5900.00	9.5650	5.1993
410.00	5961.00	9.3600	5.0700
410.00	5961.00	9.0300	4.8700
371.00	6000.00	8.8877	4.8021
271.00	6100.00	8.5227	4.6281
210.00	6161.00	8.3000	4.5220
210.00	6161.00	8.3000	4.5180
171.00	6200.00	8.1917	4.5102
120.00	6251.00	8.0500	4.5000
120.00	6251.00	8.0500	4.5000
71.00	6300.00	8.0442	4.4827
35.00	6336.00	8.0400	4.4700
35.00	6336.00	6.5000	3.7500
20.00	6351.00	6.5000	3.7500
20.00	6351.00	5.8000	3.3600
0.	6371.00	5.8000	3.3600

3 Model AK135

The AK135 velocity model has been augmented with a density and Q model by combining the study of travel times with those of free oscillations. This velocity and density model is the product of two pieces of work.

(1) The velocity model below 120 km depth comes from the work of Kennett et al. (1995). The original continental structure for the uppermost layering is given in Tab. 3.1 below. This model probably gives a reasonable representation of spherically averaged structure below 760 km depth. The upper mantle, as in IASP91, is an artificial construct which gives a good fit to the ensemble of observed travel times out to 30 degrees. The structure in D" should also be regarded as representative.

The representation of the velocity model is via point-wise values in velocity and linear interpolation in radius is used as the basis of the travel-time calculations. Note that AK135, unlike IASP91, is not a parameterized model. Any suitable interpolation scheme may be used where appropriate. A software conversion is available for reading velocity models into the IASP travel-time software and ellipticity corrections have been constructed for all the phases represented by that software. The software can be obtained from <http://rses.anu.edu.au/seismology/ttsoft.html>.

(2) Modified density and Q models come from a study by Montagner and Kennett (1996). This study introduces a density model and Q to the velocity distribution from the travel-time work to try to fit observations of free oscillation frequencies. An averaged uppermost structure is imposed on the AK135 velocities. The version of the model represented here is isotropic, even though the paper investigates the inclusion of anisotropy as well.

The complex density structure in the upper mantle with a density inversion reflects the absence of a low velocity zone in the wave-speed model. For a spherical average either a low shear-wave zone or a low density zone is needed to match the free oscillation frequencies. The Q values are those needed to bring the 1 Hz travel-time velocities into a match with the free oscillations and also give a good fit to observed Q values for the normal modes.

NB: The upper mantle density model should be treated with caution and may well change with further work.

Table 3 AK135 velocity model for travel times

3.1 Continental structure

Depth (km)	v_p (km/s)	v_s (km/s)
0.000	5.8000	3.4600
20.000	5.8000	3.4600
20.000	6.5000	3.8500
35.000	6.5000	3.8500
35.000	8.0400	4.4800
77.500	8.0450	4.4900
120.000	8.0500	4.5000

3.2 Average structure

Depth (km)	Density (g/cm ³)	v _p (km/s)	v _s (km/s)	Q _α	Q _μ
0.00	1.0200	1.4500	0.0000	57822.00	0.00
3.00	1.0200	1.4500	0.0000	57822.00	0.00
3.00	2.0000	1.6500	1.0000	163.35	80.00
3.30	2.0000	1.6500	1.0000	163.35	80.00
3.30	2.6000	5.8000	3.2000	1478.30	599.99
10.00	2.6000	5.8000	3.2000	1478.30	599.99
10.00	2.9200	6.8000	3.9000	1368.02	599.99
18.00	2.9200	6.8000	3.9000	1368.02	599.99
18.00	3.6410	8.0355	4.4839	950.50	394.62
43.00	3.5801	8.0379	4.4856	972.77	403.93
80.00	3.5020	8.0400	4.4800	1008.71	417.59
80.00	3.5020	8.0450	4.4900	182.03	75.60
120.00	3.4268	8.0505	4.5000	182.57	76.06
165.00	3.3711	8.1750	4.5090	188.72	76.55
210.00	3.3243	8.3007	4.5184	200.97	79.40
210.00	3.3243	8.3007	4.5184	338.47	133.72
260.00	3.3663	8.4822	4.6094	346.37	136.38
310.00	3.4110	8.6650	4.6964	355.85	139.38
360.00	3.4577	8.8476	4.7832	366.34	142.76
410.00	3.5068	9.0302	4.8702	377.93	146.57
410.00	3.9317	9.3601	5.0806	413.66	162.50
460.00	3.9273	9.5280	5.1864	417.32	164.87
510.00	3.9233	9.6962	5.2922	419.94	166.80
560.00	3.9218	9.8640	5.3989	422.55	168.78
610.00	3.9206	10.0320	5.5047	425.51	170.82
660.00	3.9201	10.2000	5.6104	428.69	172.93
660.00	4.2387	10.7909	5.9607	1350.54	549.45
710.00	4.2986	10.9222	6.0898	1311.17	543.48
760.00	4.3565	11.0553	6.2100	1277.93	537.63
809.50	4.4118	11.1355	6.2424	1269.44	531.91
859.00	4.4650	11.2228	6.2799	1260.68	526.32
908.50	4.5162	11.3068	6.3164	1251.69	520.83
958.00	4.5654	11.3897	6.3519	1243.02	515.46
1007.50	4.5926	11.4704	6.3860	1234.54	510.20
1057.00	4.6198	11.5493	6.4182	1226.52	505.05
1106.50	4.6467	11.6265	6.4514	1217.91	500.00
1156.00	4.6735	11.7020	6.4822	1210.02	495.05
1205.50	4.7001	11.7768	6.5131	1202.04	490.20
1255.00	4.7266	11.8491	6.5431	1193.99	485.44
1304.50	4.7528	11.9208	6.5728	1186.06	480.77
1354.00	4.7790	11.9891	6.6009	1178.19	476.19
1403.50	4.8050	12.0571	6.6285	1170.53	471.70
1453.00	4.8307	12.1247	6.6554	1163.16	467.29
1502.50	4.8562	12.1912	6.6813	1156.04	462.96
1552.00	4.8817	12.2558	6.7070	1148.76	458.72
1601.50	4.9069	12.3181	6.7323	1141.32	454.55
1651.00	4.9321	12.3813	6.7579	1134.01	450.45

Table 3.2 (continued)

Depth (km)	Density (g/cm ³)	v _p (km/s)	v _s (km/s)	Q _α	Q _μ
1700.50	4.9570	12.4427	6.7820	1127.02	446.43
1750.00	4.9817	12.5030	6.8056	1120.09	442.48
1799.50	5.0062	12.5638	6.8289	1108.58	436.68
1849.00	5.0306	12.6226	6.8517	1097.16	431.03
1898.50	5.0548	12.6807	6.8743	1085.97	425.53
1948.00	5.0789	12.7384	6.8972	1070.38	418.41
1997.50	5.1027	12.7956	6.9194	1064.23	414.94
2047.00	5.1264	12.8524	6.9416	1058.03	411.52
2096.50	5.1499	12.9093	6.9625	1048.09	406.50
2146.00	5.1732	12.9663	6.9852	1042.07	403.23
2195.50	5.1963	13.0226	7.0069	1032.14	398.41
2245.00	5.2192	13.0786	7.0286	1018.38	392.16
2294.50	5.2420	13.1337	7.0504	1008.79	387.60
2344.00	5.2646	13.1895	7.0722	999.44	383.14
2393.50	5.2870	13.2465	7.0932	990.77	378.79
2443.00	5.3092	13.3017	7.1144	985.63	375.94
2492.50	5.3313	13.3584	7.1368	976.81	371.75
2542.00	5.3531	13.4156	7.1584	968.46	367.65
2591.50	5.3748	13.4741	7.1804	960.36	363.64
2640.00	5.3962	13.5311	7.2031	952.00	359.71
2690.00	5.4176	13.5899	7.2253	940.88	354.61
2740.00	5.4387	13.6498	7.2485	933.21	350.88
2740.00	5.6934	13.6498	7.2485	722.73	271.74
2789.67	5.7196	13.6533	7.2593	726.87	273.97
2839.33	5.7458	13.6570	7.2700	725.11	273.97
2891.50	5.7721	13.6601	7.2817	723.12	273.97
2891.50	9.9145	8.0000	0.0000	57822.00	0.00
2939.33	9.9942	8.0382	0.0000	57822.00	0.00
2989.66	10.0722	8.1283	0.0000	57822.00	0.00
3039.99	10.1485	8.2213	0.0000	57822.00	0.00
3090.32	10.2233	8.3122	0.0000	57822.00	0.00
3140.66	10.2964	8.4001	0.0000	57822.00	0.00
3190.99	10.3679	8.4861	0.0000	57822.00	0.00
3241.32	10.4378	8.5692	0.0000	57822.00	0.00
3291.65	10.5062	8.6496	0.0000	57822.00	0.00
3341.98	10.5731	8.7283	0.0000	57822.00	0.00
3392.31	10.6385	8.8036	0.0000	57822.00	0.00
3442.64	10.7023	8.8761	0.0000	57822.00	0.00
3492.97	10.7647	8.9461	0.0000	57822.00	0.00
3543.30	10.8257	9.0138	0.0000	57822.00	0.00
3593.64	10.8852	9.0792	0.0000	57822.00	0.00
3643.97	10.9434	9.1426	0.0000	57822.00	0.00
3694.30	11.0001	9.2042	0.0000	57822.00	0.00
3744.63	11.0555	9.2634	0.0000	57822.00	0.00
3794.96	11.1095	9.3205	0.0000	57822.00	0.00
3845.29	11.1623	9.3760	0.0000	57822.00	0.00
3895.62	11.2137	9.4297	0.0000	57822.00	0.00

Table 3.2 (continued)

Depth (km)	Density (g/cm ³)	v _p (km/s)	v _s (km/s)	Q _α	Q _μ
3945.95	11.2639	9.4814	0.0000	57822.00	0.00
3996.28	11.3127	9.5306	0.0000	57822.00	0.00
4046.62	11.3604	9.5777	0.0000	57822.00	0.00
4096.95	11.4069	9.6232	0.0000	57822.00	0.00
4147.28	11.4521	9.6673	0.0000	57822.00	0.00
4197.61	11.4962	9.7100	0.0000	57822.00	0.00
4247.94	11.5391	9.7513	0.0000	57822.00	0.00
4298.27	11.5809	9.7914	0.0000	57822.00	0.00
4348.60	11.6216	9.8304	0.0000	57822.00	0.00
4398.93	11.6612	9.8682	0.0000	57822.00	0.00
4449.26	11.6998	9.9051	0.0000	57822.00	0.00
4499.60	11.7373	9.9410	0.0000	57822.00	0.00
4549.93	11.7737	9.9761	0.0000	57822.00	0.00
4600.26	11.8092	10.0103	0.0000	57822.00	0.00
4650.59	11.8437	10.0439	0.0000	57822.00	0.00
4700.92	11.8772	10.0768	0.0000	57822.00	0.00
4751.25	11.9098	10.1095	0.0000	57822.00	0.00
4801.58	11.9414	10.1415	0.0000	57822.00	0.00
4851.91	11.9722	10.1739	0.0000	57822.00	0.00
4902.24	12.0001	10.2049	0.0000	57822.00	0.00
4952.58	12.0311	10.2329	0.0000	57822.00	0.00
5002.91	12.0593	10.2565	0.0000	57822.00	0.00
5053.24	12.0867	10.2745	0.0000	57822.00	0.00
5103.57	12.1133	10.2854	0.0000	57822.00	0.00
5153.50	12.1391	10.2890	0.0000	57822.00	0.00
5153.50	12.7037	11.0427	3.5043	633.26	85.03
5204.61	12.7289	11.0585	3.5187	629.89	85.03
5255.32	12.7530	11.0718	3.5314	626.87	85.03
5306.04	12.7760	11.0850	3.5435	624.08	85.03
5356.75	12.7980	11.0983	3.5551	621.50	85.03
5407.46	12.8188	11.1166	3.5661	619.71	85.03
5458.17	12.8387	11.1316	3.5765	617.78	85.03
5508.89	12.8574	11.1457	3.5864	615.93	85.03
5559.60	12.8751	11.1590	3.5957	614.21	85.03
5610.31	12.8917	11.1715	3.6044	612.62	85.03
5661.02	12.9072	11.1832	3.6126	611.12	85.03
5711.74	12.9217	11.1941	3.6202	609.74	85.03
5762.45	12.9351	11.2041	3.6272	608.48	85.03
5813.16	12.9474	11.2134	3.6337	607.31	85.03
5863.87	12.9586	11.2219	3.6396	606.26	85.03
5914.59	12.9688	11.2295	3.6450	605.28	85.03
5965.30	12.9779	11.2364	3.6498	604.44	85.03
6016.01	12.9859	11.2424	3.6540	603.69	85.03
6066.72	12.9929	11.2477	3.6577	603.04	85.03
6117.44	12.9988	11.2521	3.6608	602.49	85.03
6168.15	13.0036	11.2557	3.6633	602.05	85.03
6218.86	13.0074	11.2586	3.6653	601.70	85.03

Table 3.2 (continued)

Depth (km)	Density (g/cm ³)	v _p (km/s)	v _s (km/s)	Q _α	Q _μ
6269.57	13.0100	11.2606	3.6667	601.46	85.03
6320.29	13.0117	11.2618	3.6675	601.32	85.03
6371.00	13.0122	11.2622	3.6678	601.27	85.03

Note: The bulk Q_κ given in Table 1 differs from the Q_α for P waves given in Table 3.2. The following relationship holds:

$$1/Q_{\alpha} = 4(\beta/\alpha)^2/3Q_{\mu} + [1 - 4(\beta/\alpha)^2/3]/Q_{\kappa}$$

where α is the P-wave velocity v_p and β the S-wave velocity v_s. However, Q_μ = Q_β for S waves.

References (see References under Miscellaneous in Volume 2)

Topic	Magnitude calibration functions and complementary data
Compiled by	Peter Bormann (formerly GeoforschungsZentrum Potsdam, Telegrafenberg, D-14473 Potsdam, Germany); E-mail: pb65@gmx.net
Version	May 2001

1 Local magnitude MI

Table 1 Calibration function $\sigma_L(\Delta) = -\log A_0$ for local magnitudes MI according to Richter (1958). A_0 are the trace amplitudes in mm recorded by a Wood-Anderson Standard Torsion Seismometer from an earthquake of MI = 0. Δ - epicentral distance in km.

Δ (km)	$\sigma_L(\Delta)$	Δ (km)	$\sigma_L(\Delta)$	Δ (km)	$\sigma_L(\Delta)$	Δ (km)	$\sigma_L(\Delta)$
0	1.4	90	3.0	260	3.8	440	4.6
10	1.5	100	3.0	280	3.9	460	4.6
20	1.7	120	3.1	300	4.0	480	4.7
30	2.1	140	3.2	320	4.1	500	4.7
40	2.4	160	3.3	340	4.2	520	4.8
50	2.6	180	3.4	360	4.3	540	4.8
60	2.8	200	3.5	380	4.4	560	4.9
70	2.8	220	3.65	400	4.5	580	4.9
80	2.9	240	3.7	420	4.5	600	4.9

Table 2 Regional calibration functions $\sigma_L(\Delta) = -\log A_0$ for MI determinations. Δ - epicentral distance and R - hypocentral ("slant") distance with $R = \sqrt{(\Delta^2 + h^2)}$, both in km ; h - hypocentral depth in km, T - period in s; Com. - recording component.

Region	$\sigma_L(\Delta) = -\log A_0$	Com.	Range (km)	Reference
Southern California	$1.110 \log (R/100) + 0.00189(R - 100) + 3.0$	horiz.	$10 \leq R \leq 700$	Hutton&Boore (1987)
Central California	$1.000 \log (R/100) + 0.00301(R - 100) + 3.0$	horiz.	$0 \leq \Delta \leq 400$	Bakun&Joyner (1984)
Great Basin, Western USA	$1.00 \cdot \log (R/100) + 0.0069(R - 100) + 3.0$	horiz.	$0 \leq \Delta \leq 90$	Chávez&Priestley (1985)
	$0.83 \log (R/100) + 0.0026(R - 100) + 3.0$	horiz.	$90 \leq \Delta \leq 600$	
Eastern N-America	$1.55 \log \Delta - 0.22$	horiz.	$100 \leq \Delta \leq 800$	Kim (1998)
	$1.45 \log \Delta + 0.11$	vertic.	$100 \leq \Delta \leq 800$	
Greece	$1.58 \log (R/100) + 3.0$; for $ML \leq 3.7$ $2.00 \log (R/100) + 3.0$; for $ML > 3.7$	horiz.	$100 \leq \Delta \leq 800$	Kiratzi&Papazachos (1984)
Albania	$1.6627 \log \Delta + 0.0008 \Delta - 0.433$	horiz.	$10 \leq \Delta \leq 600$	Muco&Minga (1991)
Central Europe	$0.83 \log R + (0.0017/T) (R - 100) + 1.41$	vertic.	$100 \leq \Delta \leq 650$	Wahlström&Strauch (1984)
CentralEurope	$1.11 \lg R + 0.95 R/1000 + 0.69$	vertic.	$10 < R < 1000$	Stange (2001)
Norway/Fennoskan.	$0.91 \log R + 0.00087 R + 1.010$	vertic.	$0 < R \leq 1500$	Alsaker et al. (1991)
Tanzania	$0.776 \log(R/17) + 0.000902 (R - 17) + 2.0$	horiz.	$0 < R \leq 1000$	Langston et al. (1998)
South Australia	$1.10 \log \Delta + 0.0013 \Delta + 0.7$	vertic.	$40 < \Delta < 700$	Greenhalgh&Singh (1986)

2 Teleseismic surface wave magnitude Ms

Table 3 Tabulated magnitude calibration values $\sigma_S(\Delta)$ as published in Richter (1958) for M_S determinations according to equation $M_S = \log A_{H_{\max}}(\Delta) + \sigma_S(\Delta)$. $A_{H_{\max}}$ is the (vectorially combined) maximum horizontal surface-waves displacement amplitude in μm for periods around 20 ± 2 s. Between 20° and 120° the values correspond (rounded to the nearest tenth magnitude unit), to the values calculated according to the Gutenberg (1945a) relation for the surface-wave magnitude: $M_S = \log A + 1.656 \log \Delta + 1.818$. However, for larger distances this formula yields between 0.05 to 0.55 m.u. larger magnitudes than the tabulated values.

Δ (degrees)	$\sigma_S(\Delta)$	Δ (degrees)	$\sigma_S(\Delta)$	Δ (degrees)	$\sigma_S(\Delta)$
20	4.0	60	4.8	120	5.3
25	4.1	70	4.9	140	5.3
30	4.3	80	5.0	160	5.35
40	4.5	90	5.05	170	5.3
45	4.6	100	5.1	180	5.0
50	4.6	110	5.2		

Table 4 M_S magnitude calibration values $\sigma_S(\Delta)$ for vectorially combined maximum horizontal surface-waves displacement amplitude (in μm) from shallow earthquakes ($h \leq 60$ km) as derived by the Prague-Moscow group (Vaněk et al. (1962)). The IASPEI recommended **standard magnitude formula** $M_S = \log (A_H/T)_{\max} + 1.66 \log \Delta + 3.3$ fits these tabulated values between 1° and 140° with deviations < 0.05 magnitude units. For larger distances the formula overestimates the magnitude between 0.05 and 0.55 (at 180°) m.u.. **Note:** For periods $T = 20$ s the IASPEI standard formula for M_S yields magnitude values that are 0.18 m.u. larger than those derived from the Gutenberg formula for M_S (see Tab. 3). Since - in average - maximum horizontal and vertical component surface-wave amplitudes agree well, Tab. 4 and (up to $\Delta = 160^\circ$) also the standard M_S calibration function are nowadays commonly used for M_S determination from vertical component surface-wave records.

Δ°	0°	1°	2°	3°	4°	5°	6°	7°	8°	9°
0°		3.30	3.80	4.09	4.30	4.46	4.59	4.70	4.80	4.88
10°	4.96	5.03	5.09	5.15	5.20	5.25	5.29	5.34	5.38	5.42
20°	5.46	5.50	5.53	5.56	5.59	5.62	5.65	5.68	5.71	5.73
30°	5.75	5.78	5.80	5.82	5.84	5.86	5.88	5.90	5.92	5.94
40°	5.96	5.98	5.99	6.01	6.03	6.04	6.06	6.07	6.09	6.10
50°	6.12	6.13	6.14	6.16	6.17	6.18	6.20	6.21	6.22	6.24
60°	6.25	6.26	6.27	6.28	6.30	6.31	6.32	6.33	6.34	6.35
70°	6.36	6.37	6.38	6.39	6.40	6.41	6.42	6.43	6.44	6.45
80°	6.46	6.47	6.48	6.49	6.49	6.50	6.51	6.52	6.53	6.54
90°	6.55	6.55	6.56	6.57	6.58	6.58	6.59	6.60	6.61	6.61
100°	6.62	6.63	6.64	6.64	6.65	6.66	6.66	6.67	6.68	6.69
110°	6.69	6.70	6.70	6.71	6.72	6.72	6.73	6.74	6.74	6.75
120°	6.75	6.76	6.76	6.76	6.77	6.77	6.78	6.78	6.78	6.79
130°	6.79	6.79	6.80	6.80	6.80	6.81	6.81	6.81	6.81	6.81
140°	6.82	6.82	6.82	6.82	6.83	6.83	6.83	6.83	6.83	6.83
150°	6.84	6.84	6.84	6.84	6.84	6.84	6.84	6.84	6.84	6.84
160°	6.84	6.84	6.83	6.83	6.83	6.82	6.82	6.82	6.82	6.82
170°	6.81	6.81	6.80	6.79	6.77	6.74	6.71	6.69	6.64	6.59
180°	6.49									

Surface-wave magnitudes are determined from the maximum amplitude or A/T ratio measured in the surface-wave train. This is usually the Airy phase of Rayleigh waves (R_{\max} , see 2.3 in Chapter 2). It is well developed for shallow earthquakes (depth $h < 70$ km). Table 5 gives the time difference between the R_{\max} and the P wave as a function of distance.

Table 5 Time interval ($t_{Rmax} - t_p$) between the arrival of the maximum phase of the Rayleigh wave and the first onset of P waves as a function of Δ according to Archangelskaya (1959) and Gorbunova and Kondorskaya (1977) (From Willmore, 1979).

Δ°	$t_{Rmax} - t_p$ (min)	Δ°	$t_{Rmax} - t_p$ (min)	Δ°	$t_{Rmax} - t_p$ (min)
10	4-5	55	26	100	45-46
15	6-8	60	28-29	105	47-48
20	9-10	65	31	110	48-50
25	10-12	70	33	115	53
30	13-14	75	35	120	55
35	15-16	80	37	125	57
40	18-19	85	39-40	130	60
45	21	90	42	140	64
50	24	95	43	150	70

3 Teleseismic body-wave magnitudes mB

Gutenberg (1945) developed a magnitude relationship for teleseismic body waves such as P, PP and S in the period range 0.5 s to 12 s (i.e., mostly based on medium-period readings):

$$mB = \log (A/T)_{max} + Q(\Delta, h).$$

Gutenberg and Richter (1956a) published a table with $Q(\Delta)$ values for P, PP and S waves in vertical (V=Z) and horizontal (H) components for shallow events (Table 6) as well as diagrams giving for all these waves Q values as a function of Δ and source depth h (Figs. 1a-c). These Q values are valid only when A is given in μm .

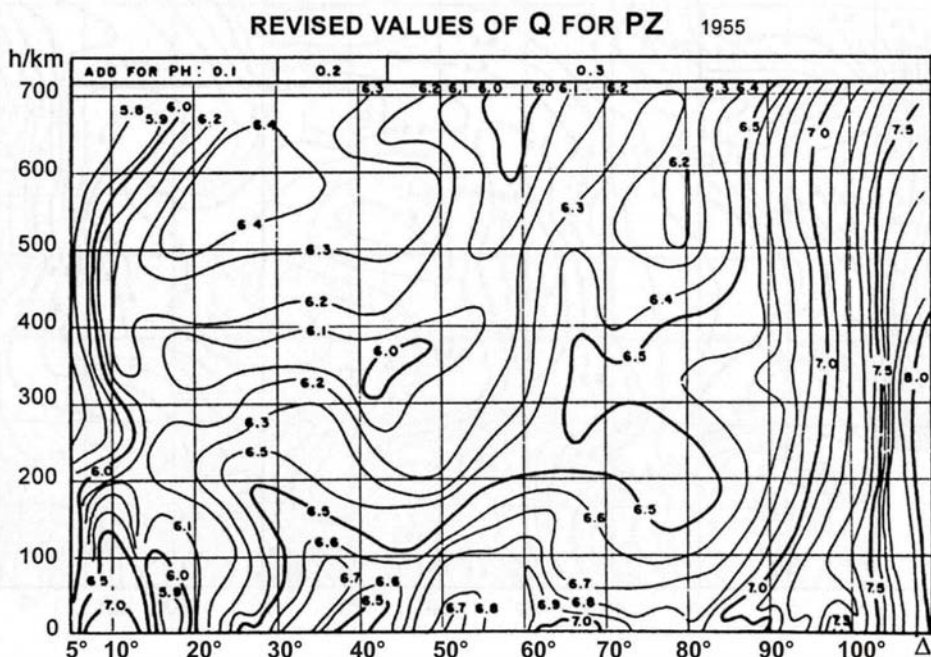


Figure 1a

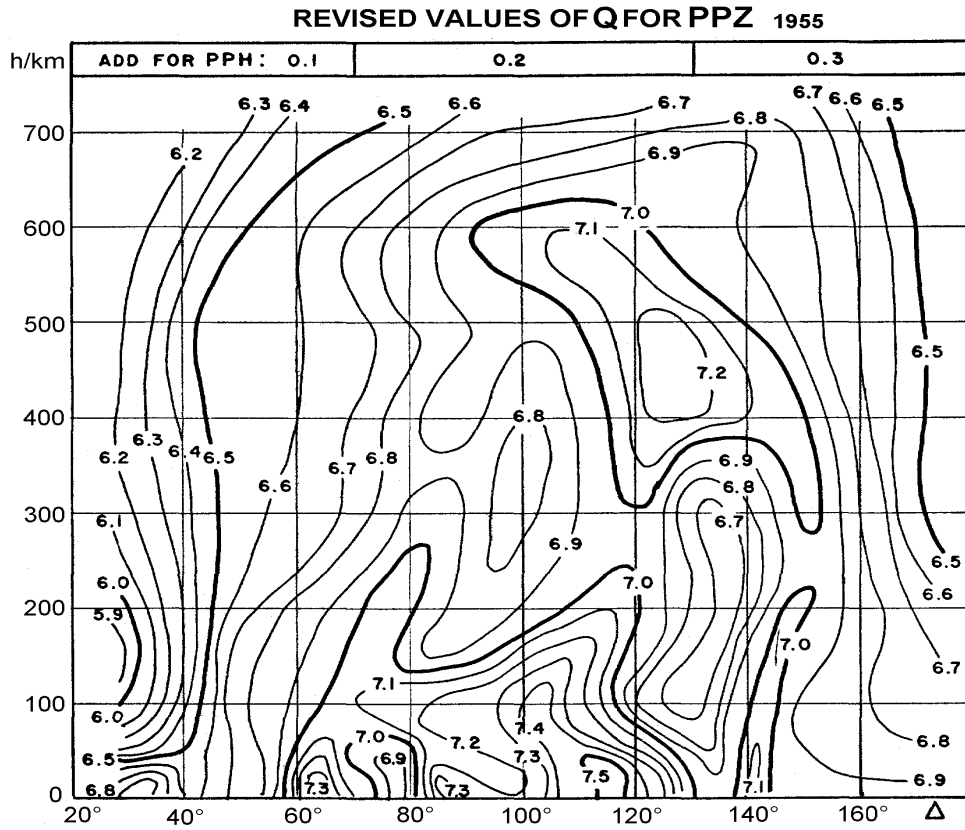


Figure 1b

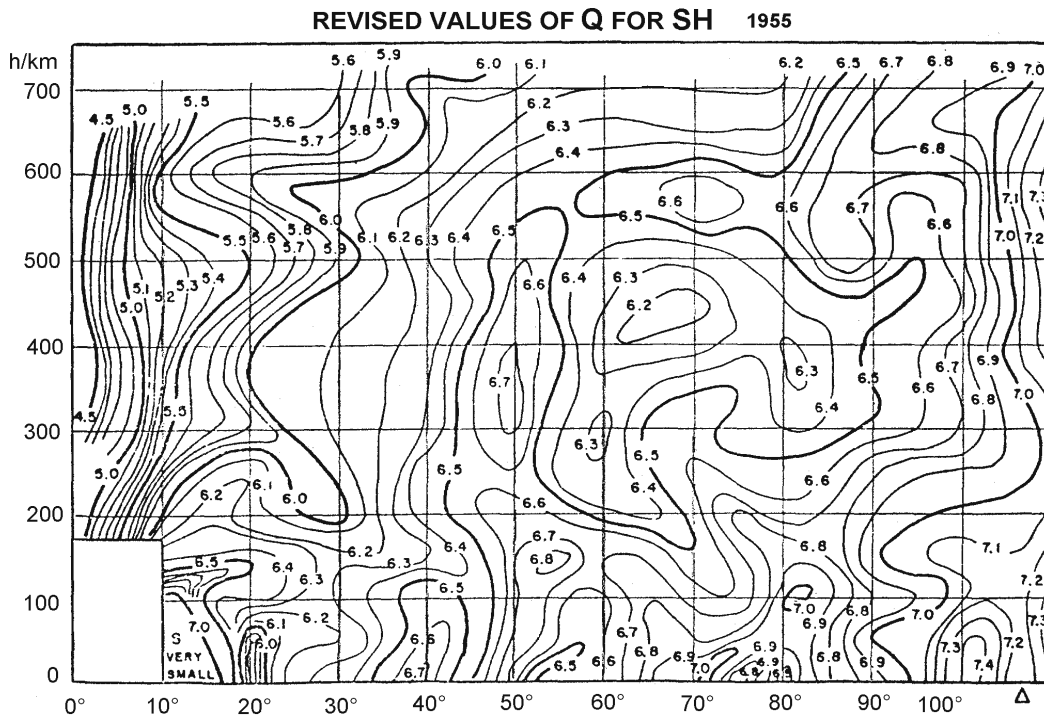


Figure 1c

Table 6 Values of $Q(\Delta)$ for P, PP and S waves for shallow shocks ($h < 70$ km) according to Gutenberg and Richter (1956a) if the ground amplitude is given in μm .

Δ°	PV	PH	PPV	PPH	SH	Δ°	PV	PH	PPV	PPH	SH	Δ°	PV	PH	PPV	PPH	SH
16	5.9	6.0			7.2	56	6.8	7.1	6.9	7.0	6.6	96	7.3	7.6	7.2	7.4	7.1
17	5.9	6.0			6.8	57	6.8	7.1	6.9	7.0	6.6	97	7.4	7.8	7.2	7.4	7.2
18	5.9	6.0			6.2	58	6.8	7.1	7.0	7.1	6.6	98	7.5	7.8	7.2	7.4	7.3
19	6.0	6.1			5.8	59	6.8	7.1	7.0	7.2	6.6	99	7.5	7.8	7.2	7.4	7.3
20	6.0	6.1			5.8	60	6.8	7.1	7.1	7.3	6.6	100	7.4	7.7	7.2	7.4	7.4
21	6.1	6.2			6.0	61	6.9	7.2	7.2	7.4	6.7	101	7.3	7.6	7.2	7.4	7.4
22	6.2	6.3			6.2	62	7.0	7.3	7.3	7.4	6.7	102	7.4	7.7	7.2	7.4	7.4
23	6.3	6.4			6.2	63	6.9	7.3	7.3	7.4	6.7	103	7.5	7.9	7.2	7.4	7.3
24	6.3	6.5			6.2	64	7.0	7.3	7.3	7.5	6.8	104	7.6	7.9	7.3	7.5	7.3
25	6.5	6.6			6.2	65	7.0	7.4	7.3	7.5	6.9	105	7.7	8.1	7.3	7.5	7.2
26	6.4	6.6			6.2	66	7.0	7.4	7.3	7.4	6.9	106	7.8	8.2	7.4	7.6	7.2
27	6.5	6.7			6.3	67	7.0	7.4	7.2	7.4	6.9	107	7.9	8.3	7.4	7.6	7.2
28	6.6	6.7			6.3	68	7.0	7.4	7.1	7.3	6.9	108	7.9	8.3	7.4	7.6	7.2
29	6.6	6.7			6.3	69	7.0	7.4	7.0	7.2	6.9	109	8.0	8.4	7.4	7.6	7.2
30	6.6	6.8	6.7	6.8	6.3	70	6.9	7.3	7.0	7.2	6.9	110	8.1	8.5	7.4	7.6	7.2
31	6.7	6.9	6.7	6.8	6.3	71	6.9	7.3	7.1	7.3	7.0	112	8.2	8.6	7.4	7.6	
32	6.7	6.9	6.8	6.9	6.4	72	6.9	7.3	7.1	7.3	7.0	114	8.6	9.0	7.5	7.7	
33	6.7	6.9	6.8	6.9	6.4	73	6.9	7.2	7.1	7.3	6.9	116	8.8		7.5	7.7	
34	6.7	6.9	6.8	6.9	6.5	74	6.8	7.1	7.0	7.2	6.8	118	9.0		7.5	7.7	
35	6.7	6.9	6.8	6.9	6.6	75	6.8	7.1	6.9	7.1	6.8	120			7.5	7.7	
36	6.6	6.9	6.7	6.8	6.6	76	6.9	7.2	6.9	7.1	6.8	122			7.4	7.6	
37	6.5	6.7	6.7	6.8	6.6	77	6.9	7.2	6.9	7.1	6.8	124			7.3	7.5	
38	6.5	6.7	6.7	6.8	6.6	78	6.9	7.3	6.9	7.1	6.9	126			7.2	7.4	
39	6.4	6.6	6.6	6.7	6.7	79	6.8	7.2	6.9	7.1	6.8	128			7.1	7.4	
40	6.4	6.6	6.6	6.7	6.7	80	6.7	7.1	6.9	7.1	6.7	130			7.0	7.3	
41	6.5	6.7	6.5	6.6	6.6	81	6.8	7.2	7.0	7.2	6.8	132			7.0	7.3	
42	6.5	6.7	6.5	6.6	6.5	82	6.9	7.2	7.1	7.3	6.9	134			6.9	7.2	
43	6.5	6.7	6.6	6.7	6.5	83	7.0	7.4	7.2	7.4	6.9	136			6.9	7.2	
44	6.5	6.7	6.7	6.8	6.5	84	7.0	7.4	7.3	7.5	6.9	138			7.0	7.3	
45	6.7	6.9	6.7	6.8	6.5	85	7.0	7.4	7.3	7.5	6.8	140			7.1	7.4	
46	6.8	7.1	6.7	6.8	6.6	86	6.9	7.3	7.3	7.5	6.7	142			7.1	7.4	
47	6.9	7.2	6.7	6.8	6.6	87	7.0	7.3	7.2	7.4	6.8	144			7.0	7.3	
48	6.9	7.2	6.7	6.8	6.7	88	7.1	7.5	7.2	7.4	6.8	146			6.9	7.2	
49	6.8	7.1	6.7	6.8	6.7	89	7.0	7.4	7.2	7.4	6.8	148			6.9	7.2	
50	6.7	7.0	6.7	6.8	6.6	90	7.0	7.3	7.2	7.4	6.8	150			6.9	7.2	
51	6.7	7.0	6.7	6.8	6.5	91	7.1	7.5	7.2	7.4	6.9	152			6.9	7.2	
52	6.7	7.0	6.7	6.8	6.5	92	7.1	7.4	7.2	7.4	6.9	154			6.9	7.2	
53	6.7	7.0	6.7	6.8	6.6	93	7.2	7.5	7.2	7.4	6.9	156			6.9	7.2	
54	6.8	7.1	6.8	6.9	6.6	94	7.1	7.4	7.2	7.4	7.0	158			6.9	7.2	
55	6.8	7.1	6.9	7.0	6.6	95	7.2	7.6	7.2	7.4	7.0	160			6.9	7.2	
												170			6.9	7.2	

At the IASPEI General Assembly in Zürich (1967) the Committee on Magnitudes recommended stations to report the magnitude for all waves for which calibration functions are available, as well as to publish amplitude and period values separately. $Q(\Delta, h)_{PZ}$ is now the accepted standard calibration function for mb magnitude determinations at international data centers based on short-period vertical component P-wave readings. This is not fully correct because the Q values have been derived mainly from intermediate-period seismic recordings.

4 Complementary short-period body-wave magnitude scales

Another calibration function $P(\Delta, h)$ for mb determination has been elaborated by Veith and Clawson (1972). It is based on large sets of short-period vertical-component P-wave amplitudes from large explosions at 19 different sites. Although specifically derived from short-period data it is not yet accepted as IASPEI standard for mb. It looks much smoother than $Q(\Delta, h)_{PZ}$ and resembles better an inverse $A-\Delta$ relationship for short-period P as shown in Fig. 3.13. It is currently used by the preliminary International Data Center established for the monitoring of the Comprehensive Test-Ban Treaty (CTBT) however with a non-standard instrument response.

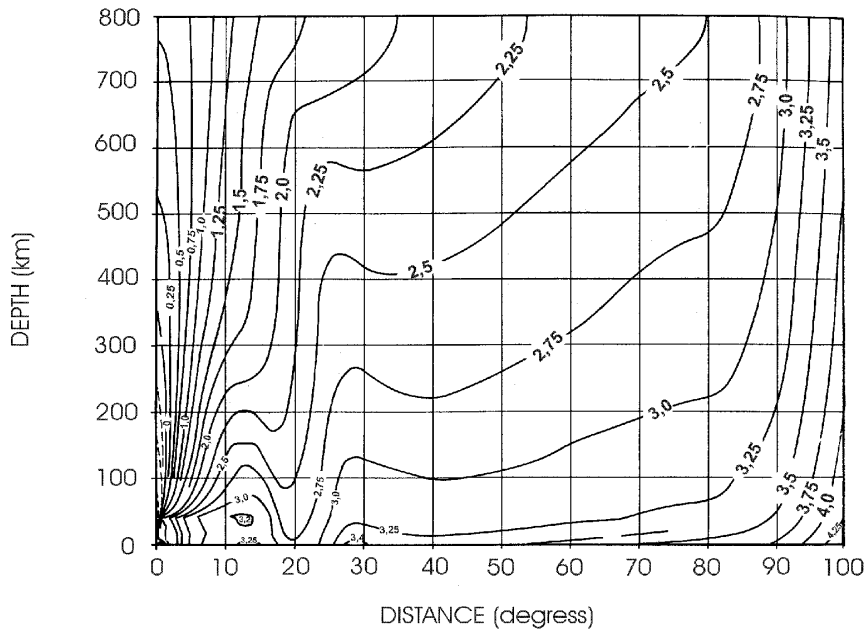


Figure 2 Calibration functions $P(\Delta, h)$ for mb determination from narrow-band short-period vertical-component records with peak displacement magnification around 1 Hz (WWSSN-SP characteristic) according to Veith and Clawson (1972). **Note:** P values have to be used in conjunction with maximum P-wave peak-to-trough ($2A!$) amplitudes in units of nanometers ($1 \text{ nm} = 10^{-9} \text{ m}$) (modified from Veith and Clawson, Magnitude from short-period P-wave data, BSSA, 62, 2, p. 446, © Seismological Society of America).

An experimental calibration function for magnitude determinations based on short-period vertical-component readings of various PKP phases in the distance range 145° to 164° has been developed by Wendt (Bormann and Wendt, 1999). The following relationship is used:

$$mb(\text{PKP}) = \log_{10} (A/T) + Q(\Delta, h)_{\text{PKPab, bc, df}}$$

with amplitude A in μm (10^{-6} m) (see Figure 3). Extensive use of this relationship at station CLL proved that mb determinations from core phases are possible with a standard deviation of less than ± 0.2 magnitude units as compared to P-wave mb determinations by NEIC and ISC. If more than one PKP phase can be identified and A and T been measured then the average value from all individual magnitude determinations provides a more stable estimate. The applicability of these calibration functions should be tested with data from other stations of the world-wide network.

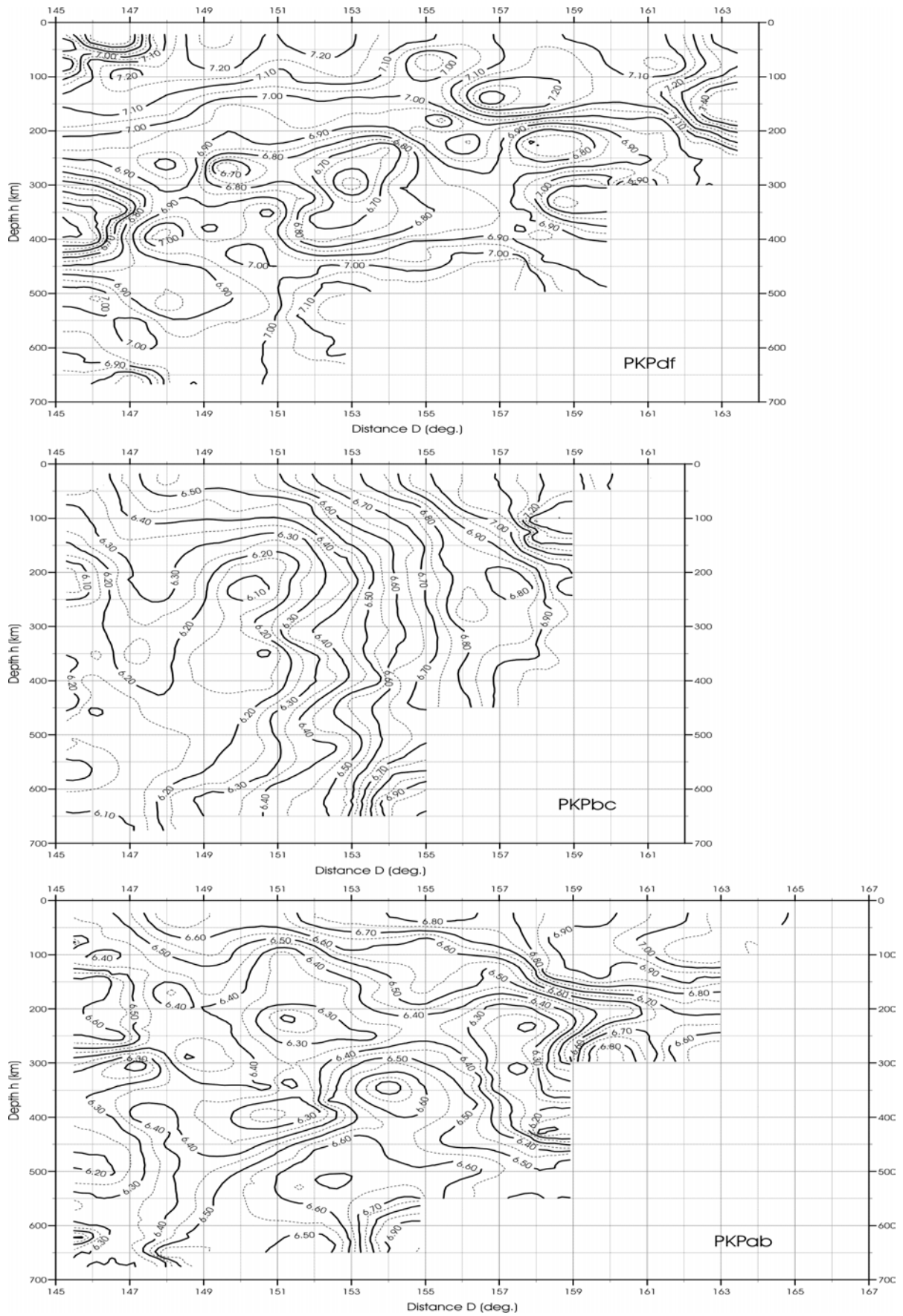


Figure 3 Calibration functions according to S. Wendt for the determination of mb(PKP) for PKPdf, PKPbc and PKPab (see Bormann and Wendt, 1999).

References (see References under Miscellaneous in Volume 2)

Topic	Common seismic sensors
Compiled by	Erhard Wielandt (formerly Institute of Geophysics, University of Stuttgart, D-70184 Stuttgart); E-mail: e.wielandt@t-online.de
Version	May 2002

Introduction

These data sheets describe some widely used broadband seismic sensors, and a few other sensors that are new or have an interesting principle of operation. We present them as examples of a format in which seismic sensors might be uniformly described; our choice does not imply any recommendation for or against a specific instrument. The reader is urged to check current versions of the data sheets on the website of the author (http://www.geophys.uni-stuttgart.de/seismometry/man_html/index.html).

A few comments to the specifications are necessary. Manufacturers' specifications, especially for complex characteristics such as sensitivity and dynamic range, are sometimes realistic, sometimes optimistic, and sometimes useless. Whenever possible, we have used data from independent tests. But independent information is not always available, and then the information from the manufacturer's data sheet must somehow be translated into our scheme. We have done this to the best of our knowledge, but errors and even a subjective bias cannot be ruled out.

Noise specifications are among the most important for the seismologist and among the most difficult for the manufacturer. Seismometers are typically produced in a noisy industrial environment, so the manufacturer cannot easily test his sensors. New instruments often show transient disturbances which may disappear within a few months in a permanent installation but interfere with noise tests immediately after production. In order to ascertain the noise specifications, lengthy tests of each instrument at a remote quiet site would be required, and a substantial portion of the production might have to go to scrap. Customers are not willing to pay for this, and consequently manufacturers do not guarantee the noise specifications. Nevertheless, depending on details of the production process and on the time allocated to testing, some manufacturers turn out a higher proportion of faultless instruments than others. The user should be aware of this problem, but we cannot extrapolate it from the past into the future, and cannot quantify it in our data sheets.

The "category" information in the data sheets may require some explanation. The term "broadband" is commonly used for instruments that have a flat response from short periods to at least 30 seconds. The nominal bandwidth however is not what really matters. Instruments should be named after the frequency band in which they deliver useful signals. We will therefore use the term "broadband" for instruments that can be used throughout the classical short-period and long-period bands, and "very broadband" or VBB for broadband instruments sensitive enough to record free oscillations of the Earth. "Symmetric triaxial" are three-component instruments with three equal inclined mechanical sensors, such as the STS2 and the Trillium.

Below, the sensor data sheets are alphabetically ordered. They may be complemented or corrected from time to time.

Type	CMG-3T
Manufacturer	Guralp Systems Limited
Address	3 Midas House, Calleva Park, Aldermaston, Reading RG7 8EA, UK
Phone	++44 118 9819 056
Fax	++44 118 9819 943
E-mail	sales@guralp.com
Homepage	www.guralp.com
Category	Force-balance VBB, three-component
Flat response	Velocity 10 mHz (100 s) to 50 Hz (others available)
Resolution: NLNM	30 mHz to 18 Hz
within 10 dB of NLNM	5 mHz to 30 Hz
within 20 dB of NLNM	3 mHz to 50 Hz
within 40 dB of NLNM	
Operating range	± 13 mm/s
Generator constant	2*750 V s / m
Adequate digitizer resol.	24 bits
Adequate digitizer range	± 20 V differential
Weight	14 kg
Size	17 cm dia., 37 cm high
Power	10 to 30 volts, 0.75 watts
Calibration coils	feedback coils used, over relays
Mass lock	remote
Mass centering	remote
Fast-settling mode	no
Accessories	control and breakout box
Typical application	Stationary, temporary, and field use
Remarks	Tight thermal shielding recommended. The CMG3 is presently (2002) one of the two most widely used broadband instruments (the other one being the STS2).

Type	Episensor ES-T
Manufacturer	Kinematics Inc.
Address	222 Vista Avenue, Pasadena, CA 91107, USA
Phone	++1 626 795 2220
Fax	++1 626 795 0868
E-mail	sales@kmi.com
Homepage	www.kinematics.com
Category	Force-balance broadband accelerometer
Flat response	acceleration DC to 200 Hz
Resolution: NLNM	not applicable (this is a strong-motion instrument)
within 10 dB of NLNM	
within 20 dB of NLNM	
within 40 dB of NLNM	
Operating range	user selectable, ± 0.25 g to ± 4 g
Generator constant	user selectable, order of $1 \text{ V s}^2 / \text{m}$
Adequate digitizer resol.	24 bits
Adequate digitizer range	± 2.5 volt single-ended to ± 20 volt differential
Weight	2 kg
Size	13 cm dia., 6 cm high
Power	± 12 V or single 12 V, 0.15 to 0.4 W (depending on option)
Calibration coils	yes
Mass lock	no
Mass centering	screwdriver
Fast-settling mode	inherent
Accessories	
Typical application	Strong-motion seismic recording
Remarks	This is a modern and popular strong-motion sensor. Its large dynamic range overlaps considerably with that of high-sensitivity seismometers, making it possible to record microearthquakes and teleseisms with this instrument.

Type	Le-3d
Manufacturer	Lennartz Electronic
Address	Bismarckstrasse 136, D-72072 Tuebingen, Germany
Phone	++49 7071 93550
Fax	++49 7071 935530
E-mail	info@lennartz-electronic.de
Homepage	www.lennartz-electronic.de
Category	Active short-period, three-component
Flat response	Velocity 1 to 80 Hz
Resolution: NLNM	---
within 10 dB of NLNM	0.2 to 0.5 Hz (microseismic peak)
within 20 dB of NLNM	0.15 to 20 Hz
within 40 dB of NLNM	0.1 to 40 Hz
Operating range	± 13 mm/s below 4.5 Hz, decreasing at higher freq.
Generator constant	400 V s / m
Adequate digitizer resol.	20 bits (or less with selectable gain)
Adequate digitizer range	± 5 volts single-ended
Weight	1.8 kg
Size	95 mm dia., 65 mm high
Power	12 V, 0.1 W
Calibration coils	No, but an electronic test pulse can be released.
Mass lock	Not required
Mass centering	Not required
Fast-settling mode	
Accessories	
Typical application	field work
Remarks	A very small and rugged three-component, short-period, active seismometer. The sensor is a commercial 4.5 Hz geophone whose response is electronically extended by a negative damping resistance (a form of negative feedback). Not as sensitive as larger seismometers but good enough where ground noise is not extremely low. A single-component version Le-1d is also available. Higher performance is offered by the Le-3d/5s and Le-3d/20s.

Type	Mark L4-3D (L-4C-3D)
Manufacturer	Mark Products
Address	10502 Fallstone Road, Houston, Texas 77099, U.S.A.
Phone	+1-713-498-0600
Fax	+1-713-498-8707???
E-mail	
Homepage	not present in the web, but try http://www.geoinstruments.com.au/
Category	Electromagnetic short-period seismometer, three-component
Flat response	1 Hz to about 100 Hz
Resolution: NLNM	0.12 Hz to 10 Hz
within 10 dB of NLNM	to 30 Hz
within 20 dB of NLNM	to 100 Hz
within 40 dB of NLNM	
Operating range	large, limited by preamplifier
Generator constant	270 Vs / m (170 Vs / m when damped to 0.7 of critical)
Adequate digitizer resol.	sub-microvolt, normally used with preamplifier
Adequate digitizer range	any
Weight	12 kg
Size	Approx. 20 cm diameter , 24 cm high
Power	passive
Calibration coils	yes
Mass lock	not required. Sensor should be tilted and coils shorted for transportation.
Mass centering	not required
Fast-settling mode	
Accessories	
Typical application	temporary installations, field work
Remarks	A popular short-period seismometer for field work. See publications by Riedesel et al. (BSSA 80 ,6) and by Rodgers (BSSA 83 ,2 and 84 ,1) for information on preamplifier design and noise.

Type	PMD 113
Manufacturer	Precision Measurement Devices
Address	105F W. Dudleytown Rd., Bloomfield, CT 06002, USA
Phone	++1 860 242 8177
Fax	++1 860 242 7812
E-mail	pmdsci@worldnet.att.net
Homepage	pmdsci.home.att.net
Category	Broadband molecular-electronic, three-component
Flat response	velocity 16.7 mHz (60 s) to 50 Hz
Resolution: NLNM	unspecified; probably 0.1 to 0.5 Hz (microseismic peak)
within 10 dB of NLNM	unspecified
within 20 dB of NLNM	unspecified
within 40 dB of NLNM	unspecified
Operating range	± 10 mm/s at low frequencies
Generator constant	2000 V s / m (other values optional)
Adequate digitizer resol.	16 bits (less for low-power version)
Adequate digitizer range	± 20 V p-p differential (less for low-power version)
Weight	5 kg
Size	18 cm dia., 14 cm high
Power	9 – 13 volt, 0.2 watt; low-power version (<100 mW) with reduced operating range available
Calibration coils	none; sensors are calibrated on a shake table
Mass lock	not required
Mass centering	not required
Fast-settling mode	no
Accessories	
Typical application	ocean-bottom seismographs, school seismographs
Remarks	An unconventional sensor. It is essentially a water-level tiltmeter where the flow velocity of the water through a platinum mesh is measured using the MET effect (molecular-electronic transfer, also used in the “solion” transducer). The vertical sensor supports the water column in a vertical tube with a membrane and a spring. These sensors have extremely low power consumption, are very rugged, need not be locked or levelled; they simply start working after power-on. Their performance is however inferior to force-balance sensors.

Type	S-13
Manufacturer	Geotech Instruments LLC
Address	10755 Sanden Drive, Dallas, Texas 75238-1336, USA
Phone	(001) 214 221 0000
Fax	(001) 214 343 4400
E-mail	mailto:info@geoinstr.com
Homepage	http://www.geoinstr.com/
Category	Electromagnetic single-component, short-period seismometer , convertible between horizontal and vertical
Flat response	1 Hz (adjustable) to about 100 Hz
Resolution: NLNM	0.06 Hz to 30 Hz with matched low-noise preamplifier
within 10 dB of NLNM	to 100 Hz
within 20 dB of NLNM	
within 40 dB of NLNM	
Operating range	large, limited by preamplifier
Generator constant	630 Vs / m, others optional
Adequate digitizer resol.	sub-microvolt. Normally used with preamplifier.
Adequate digitizer range	any
Weight	14 kg
Size	17 cm dia., 38 cm high
Power	passive
Calibration coil	yes
Mass lock	manual
Mass centering	manual; has an optical mass-position indicator
Fast-settling mode	
Accessories	
Typical application	Observatory
Remarks	A widely used high-performance, short-period seismometer. For sites with extremely low noise, Model GS-13 with a stronger magnet and a generator constant of 2180 Vs / m is available. See publications by Riedesel et al. (BSSA 80 ,6) and by Rodgers (BSSA 83 ,2 and 84 ,1) for information on preamplifier design and noise.

Type	STS1-VBB (out of production)
Manufacturer	Streckeisen AG
Address	Dättlikoner Str. 5, CH-8422 Pfungen, Switzerland
Phone	++41 52 315 2161
Fax	++41 52 315 2710
E-mail	none
Homepage	none
Category	Force-balance VBB, separate Z and H components
Flat response	velocity 2.67 mHz (360 sec) to 10 Hz
Resolution: NLNM	<0.3 mHz to 3 Hz
within 10 dB of NLNM	to 10 Hz
within 20 dB of NLNM	to 20 Hz
within 40 dB of NLNM	
Operating range	± 8 mm/s
Generator constant	2*1200 V s / m
Adequate digitizer resol.	24 bits
Adequate digitizer range	± 20 V p-p differential
Weight	4 kg (vert.); 5.5 kg (hor.)
Size	12 * 17 * 18 cm (vert.); 20 cm dia. and 16 cm high (hor.) Shields require a space of 50 * 50 cm, 60 cm high.
Power	± 15 volts, 3.5 watts per component
Calibration coils	activated over built-in relays
Mass lock	pins and screws inserted by hand
Mass centering	remote
Fast-settling mode	yes
Accessories	Feedback electronics are separate. Magnetic shield (for vert. Comp. only), aluminum shield, glass base plate, vacuum glass bell included. Monitor (breakout) box optional.
Typical application	Observatory.
Remarks	Operated under partial vacuum; no electronics inside the sensor. This seismometer made the very broadband velocity response popular, and is the only seismometer to resolve ground noise throughout the long-period seismic band. Its sensitivity is matched or slightly exceeded by some tidal gravimeters.

Type	STS2
Manufacturer	Streckeisen AG
Address	Dättlikoner Str. 5, CH-8422 Pfungen, Switzerland
Phone	++41 52 315 2161
Fax	++41 52 315 2710
E-mail	none
Homepage	none
Category	Force-balance VBB, symmetric-triaxial
Flat response	velocity 8.33 mHz (120 sec) to 50 Hz
Resolution: NLNM	30 mHz to 8 Hz
within 10 dB of NLNM	3 mHz to 20 Hz
within 20 dB of NLNM	0.1 mHz to 50 Hz
within 40 dB of NLNM	
Operating range	± 13 mm/s
Generator constant	2*750 V s / m
Adequate digitizer resol.	24 bits
Adequate digitizer range	± 20 V p-p differential
Weight	13 kg
Size	23 cm dia., 26 cm high
Power	9 to 28 volts, older models 1.5 watts, new 0.8 watts
Calibration coils	activated over built-in relays
Mass lock	by screwdriver
Mass centering	remote
Fast-settling mode	yes
Accessories	Host box with power conditioning and two parallel signal connectors included; monitor (breakout) box optional
Typical application	Stationary or temporary. Field use requires extra housing.
Remarks	Tightly-fitting thermal isolation required for optimum performance. The STS2 is presently (2002) one of the two most widely used VBB instruments (the other one being the CMG3). For global very-low-frequency seismology, the STS1 is still unrivalled.

Type	Trillium
Manufacturer	Nanometrics Inc.
Address	250 Herzberg Road, Kanata, Ontario, Canada K2K 2A1
Phone	++1 613 592 6776
Fax	++1 613 592 5929
E-mail	info@nanometrics.ca
Homepage	www.nanometrics.ca
Category	Force-balance BB, symmetric-triaxial
Flat response	velocity 33 mHz to 50 Hz
Resolution: NLNM	67 mHz to 4 Hz
within 10 dB of NLNM	50 mHz to 10 Hz
within 20 dB of NLNM	40 mHz to 30 Hz
within 40 dB of NLNM	10 mHz to 50 Hz
Operating range	± 5 mm/s
Generator constant	1500 V s / m
Adequate digitizer resol.	18 to 20 bits
Adequate digitizer range	20 V p-p differential
Weight	11 kg
Size	22 cm dia., 18 cm high
Power	9 to 36 volt, 0.4 watt
Calibration coils	yes
Mass lock	no (manufacturer says no lock is required)
Mass centering	remote
Fast-settling mode	
Accessories	
Typical application	Temporary installation and field work
Remarks	The recent mechanical design combines features of the STS2 and CMG3 seismometers. The feedback circuit has however been optimized for maximum temperature range without recentering rather than for maximum resolution.

References (see References under Miscellaneous in Volume 2)

Topic	Additional local and regional seismogram examples
compiled by	Klaus Klinge, Federal Institute for Geosciences and Natural Resources, Seismological Central Observatory, Gräfenberg (SZGRF), Mozartstrasse 57, 91052 Erlangen, Germany, Fax: +49 9131 8104 099, E-mail: klinge@szgrf.bgr.de
Version	October, 2001

Note: “G” after the depth information means that the given figure (in km) is based on the estimate by a geophysicist, “N” means that the depth was assumed to be “normal” and fixed to 33 km. If the depth is given in km it has been calculated based on (depth) phase data. D – epicentral distance in degree, BAZ – backazimuth in degree, h – source depth in km.

Example 1: Local earthquake south of Limburg/Lahn - Germany

SZGRF-data: 2000-07-26 OT 12:19:23 50.25N 8.04E h = 10G MI = 3.5

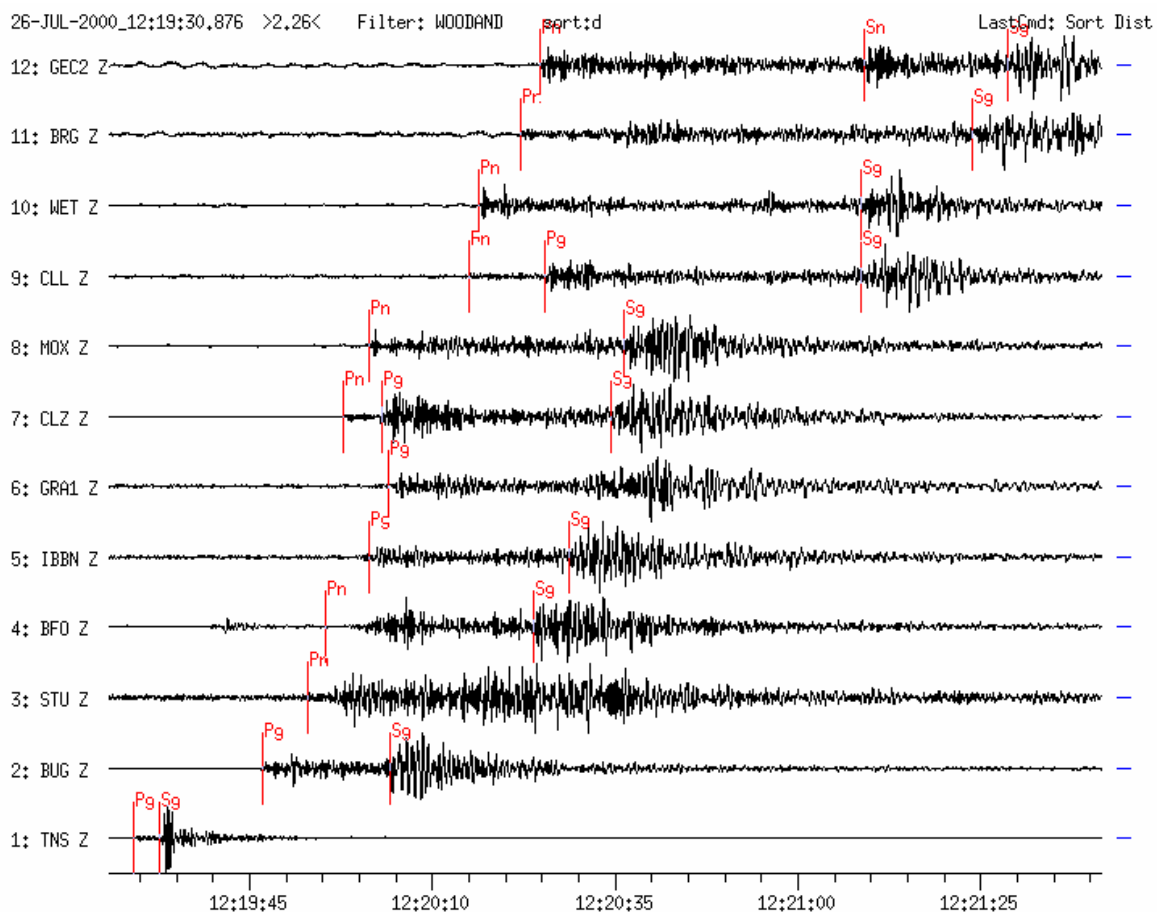


Figure 1a Short-period (Wood-Anderson = WA) filtered Z-component seismograms recorded at 12 GRSN/GRF stations (for network position and outlay see Fig. 11.3). Trace amplitudes are normalized and traces are sorted according to increasing epicentral distance from 29 km (TNS) to 447 km (GEC2).

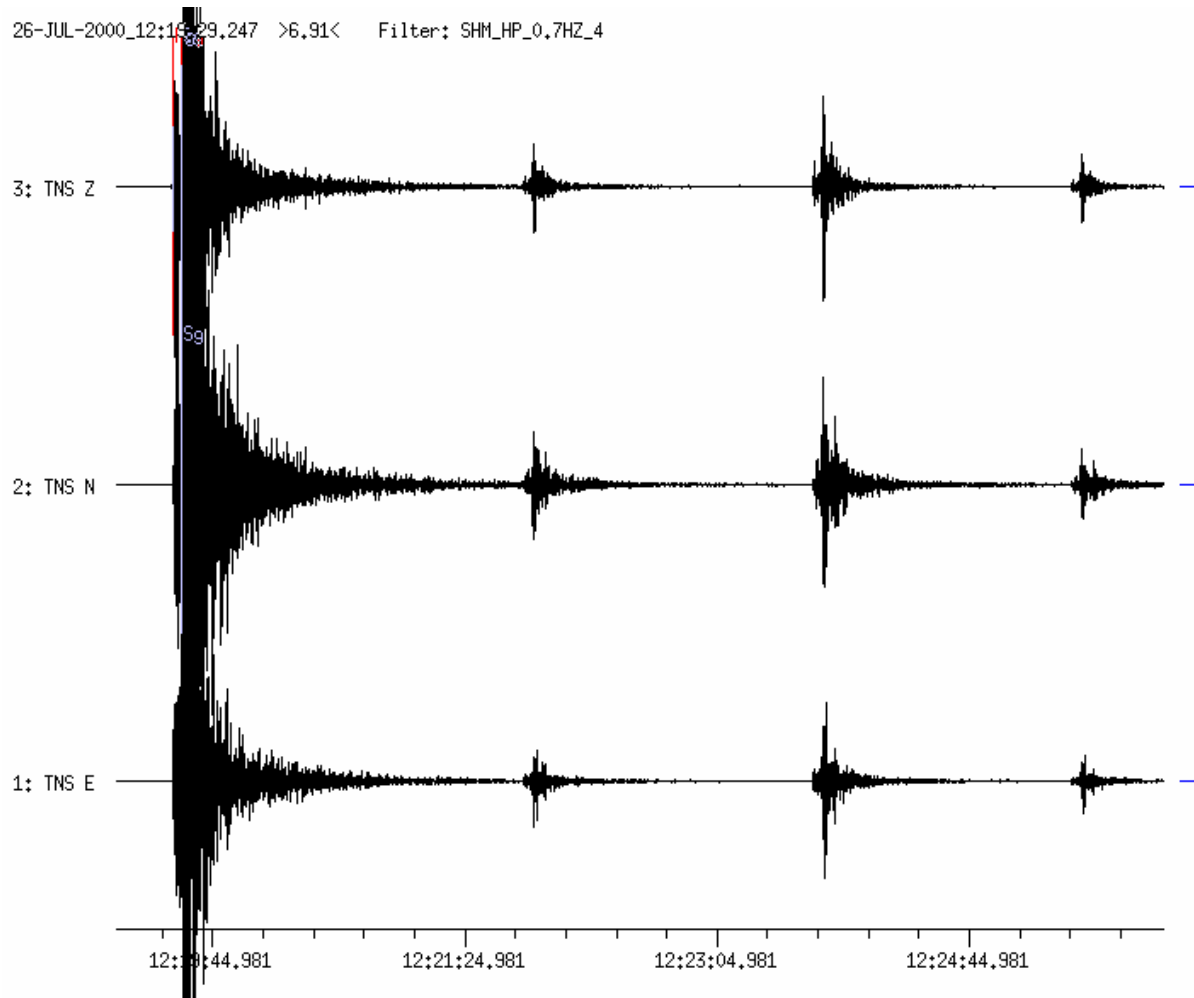


Figure 1b High-pass filtered (0.7 to 4 Hz) 3-component record of the local station TNS (D = 29 km). A few minutes after the main shock 3 smaller aftershocks occur.

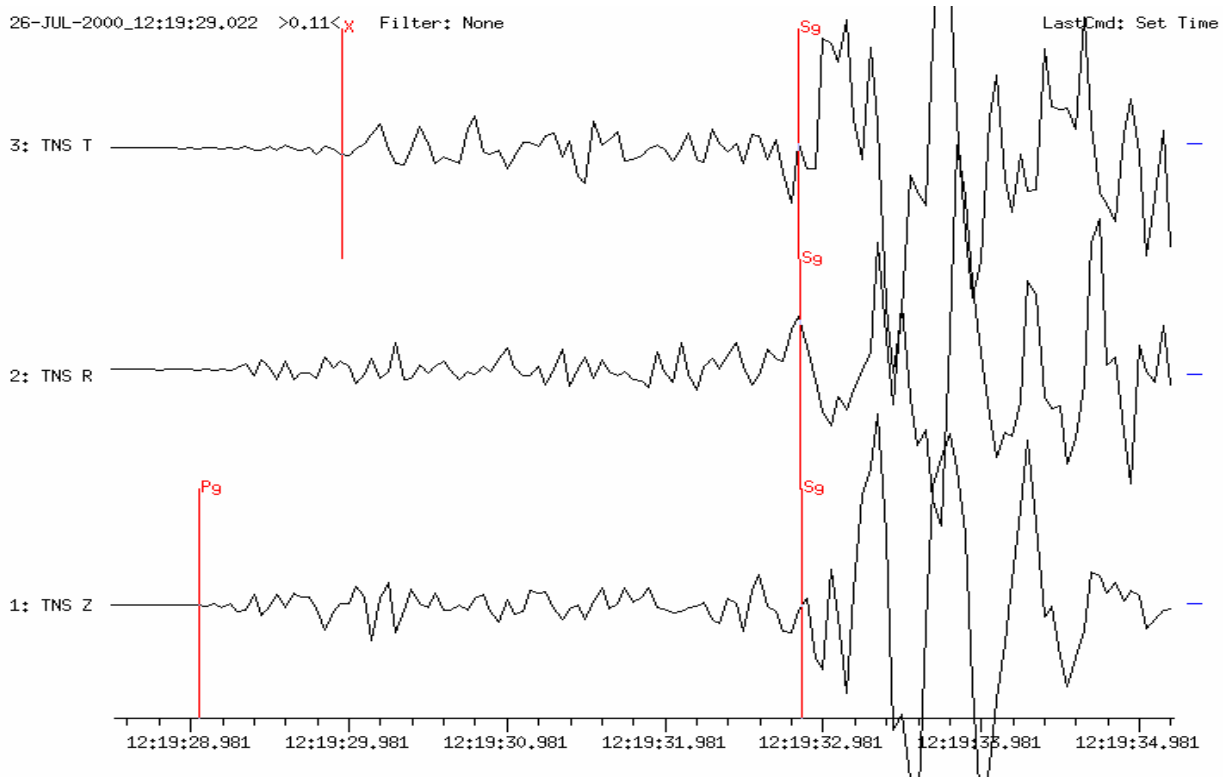


Figure 1c Three-component BB record of station TNS at $D = 29$ km. Horizontal components are rotated in the R (radial) and T (transverse) directions. One second after P_g a converted P to S wave occurs on the T component (mark X). The sampling rate is 20Hz. Note: “Filter: None” in the uppermost line always means velocity broadband record.

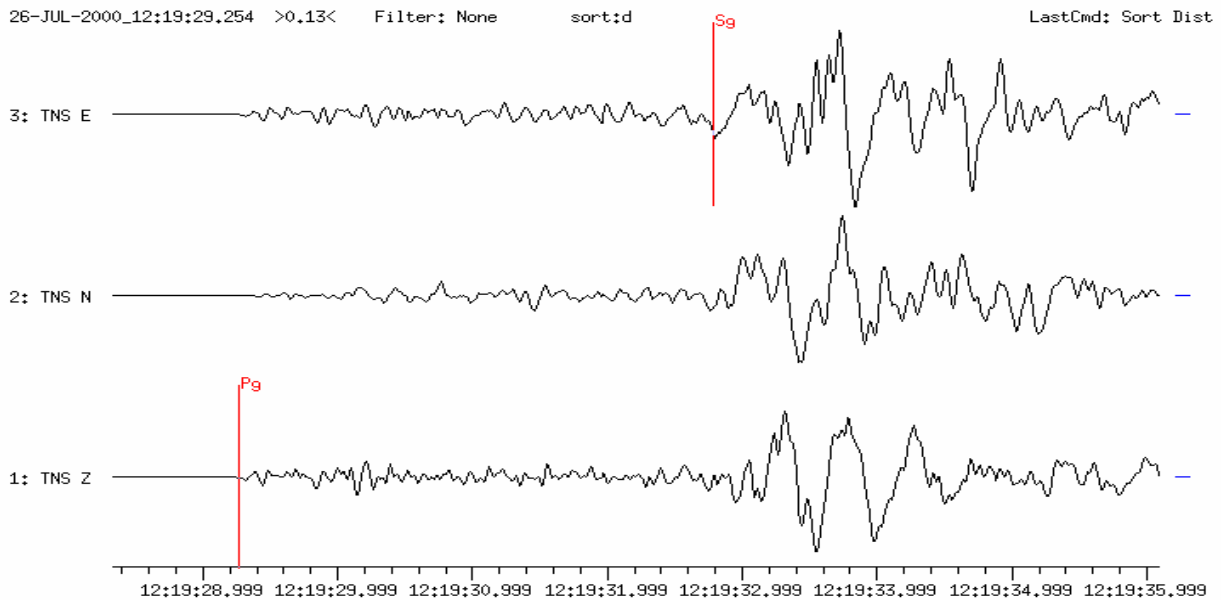


Figure 1d Three-component BB record of station TNS. The sampling rate is 80 Hz.

Example 2: Local earthquake in Northern Germany. Generally, this region is regarded as aseismic.

SZGRF-Daten: 2000-05-19 OT 19:22:40.8(UTC) 53.47N 11.10E MI = 3.4

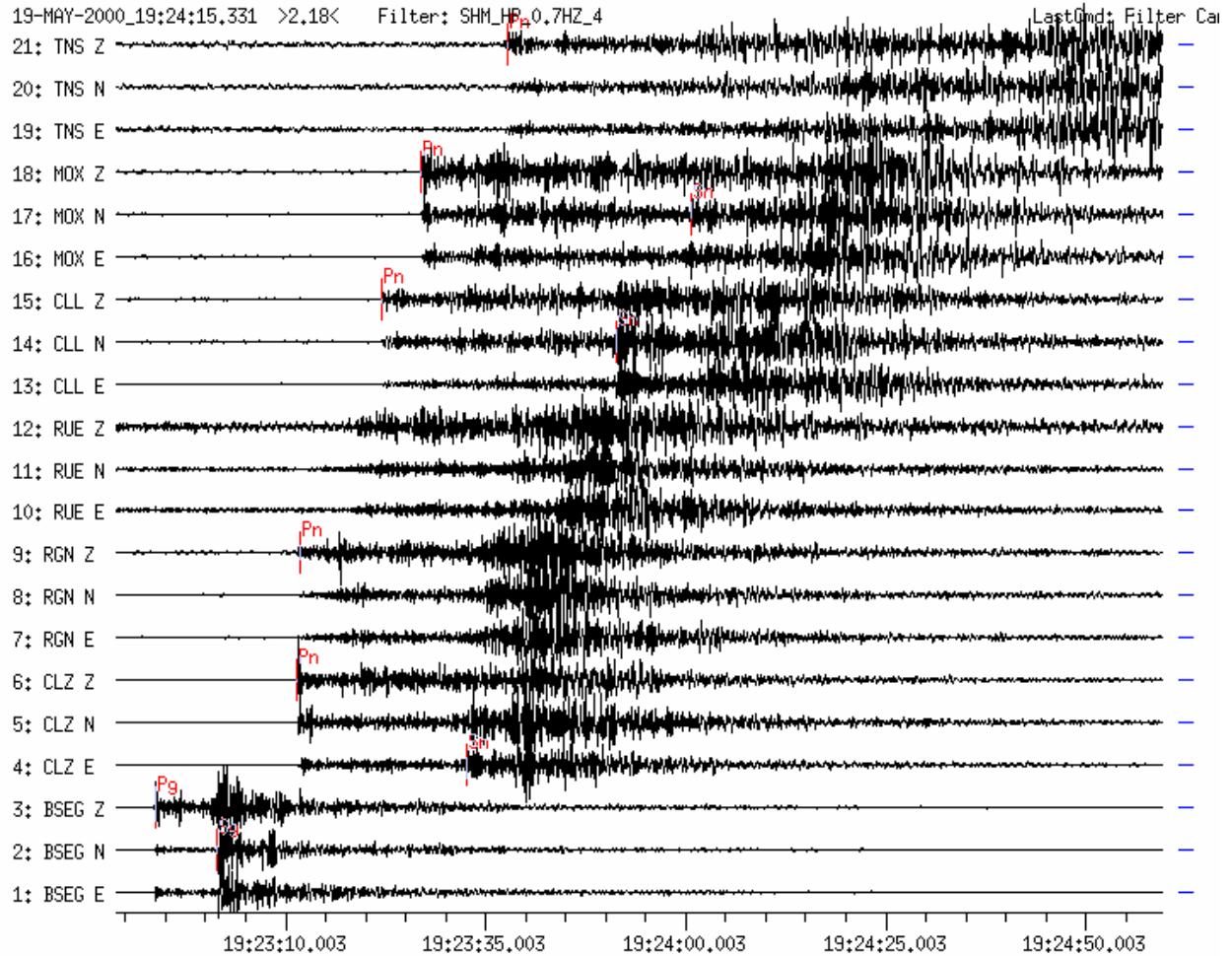


Figure 2a High-pass filtered (0.7 to 4 Hz) 3-component records of 7 GRSN stations. The traces have been sorted according to increasing distance ranging from $D = 73$ km (BSEG) to 405 km (TNS).

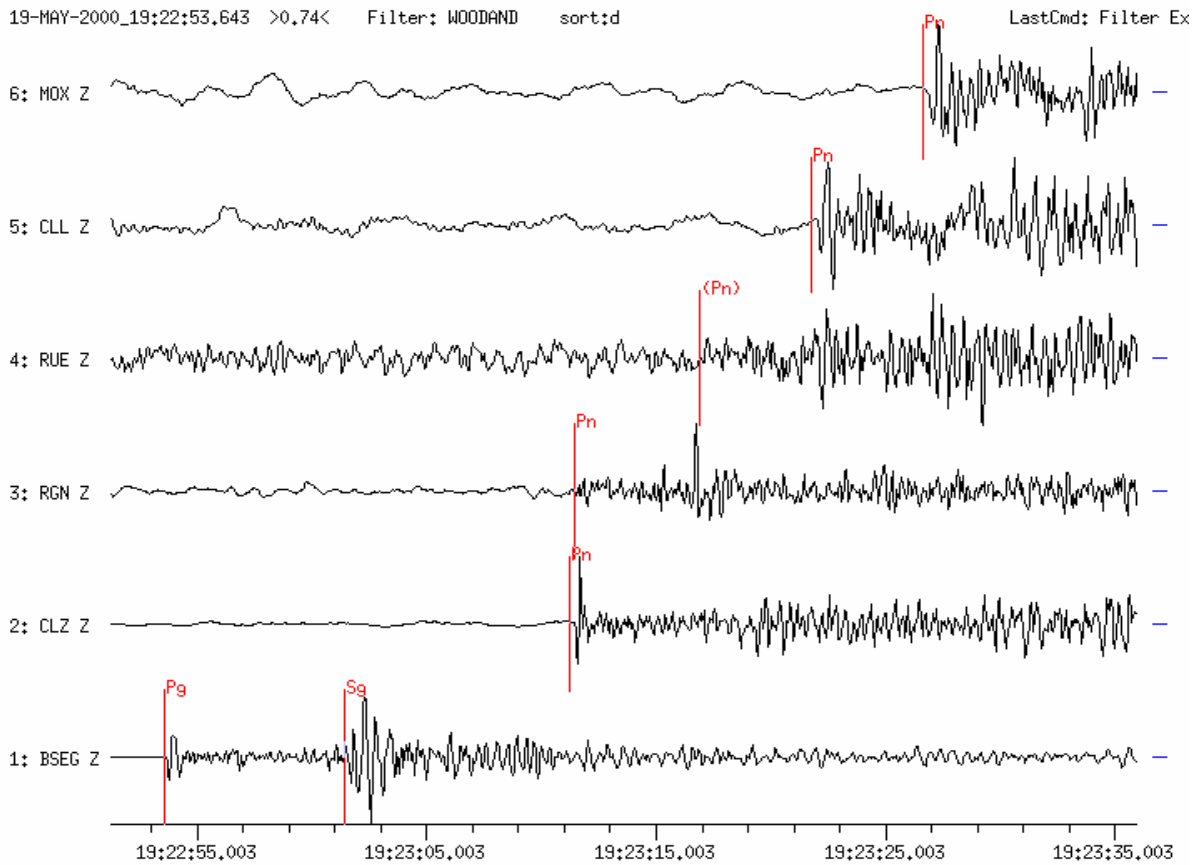


Figure 2b Short-period (WA) filtered Z-component seismograms of the same earthquake as in Figure 2a. First motion polarities can be read from traces 1, 2, 5 and 6, only.

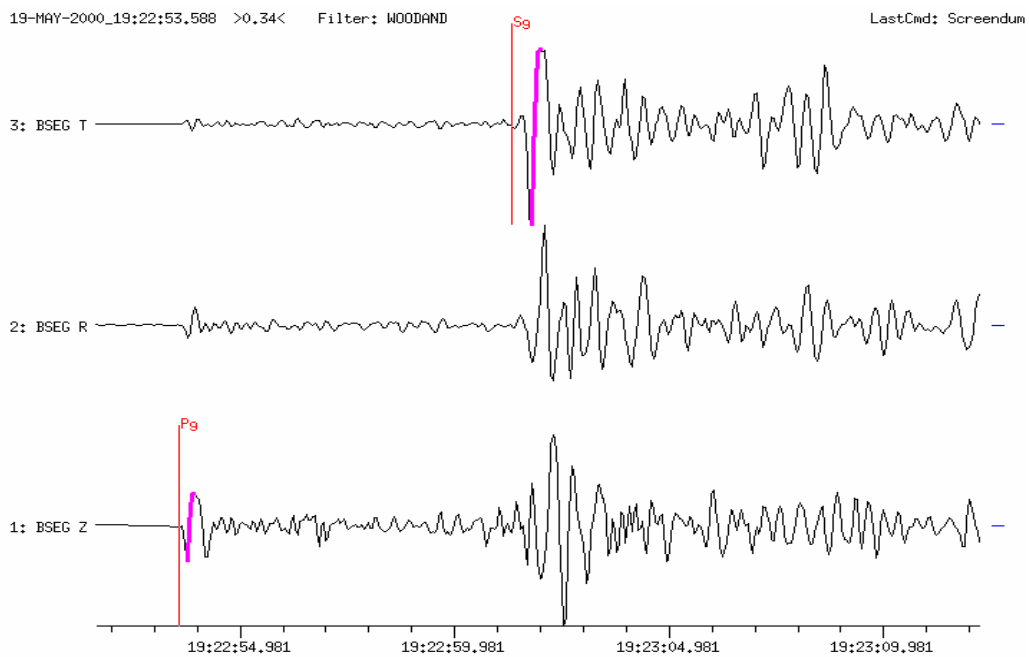


Figure 2c Three-component WA record at station BSEG at $D = 73$ km and $BAZ = 135^\circ$. The radial component R shows in the direction of wave propagation, the transversal component T is perpendicular to R.

Example 3: Regional earthquake south of Wien

SZGRF-data: 2000-07-11 OT 02:49:51(UTC) 48.10N 16.40E MI = 5.2

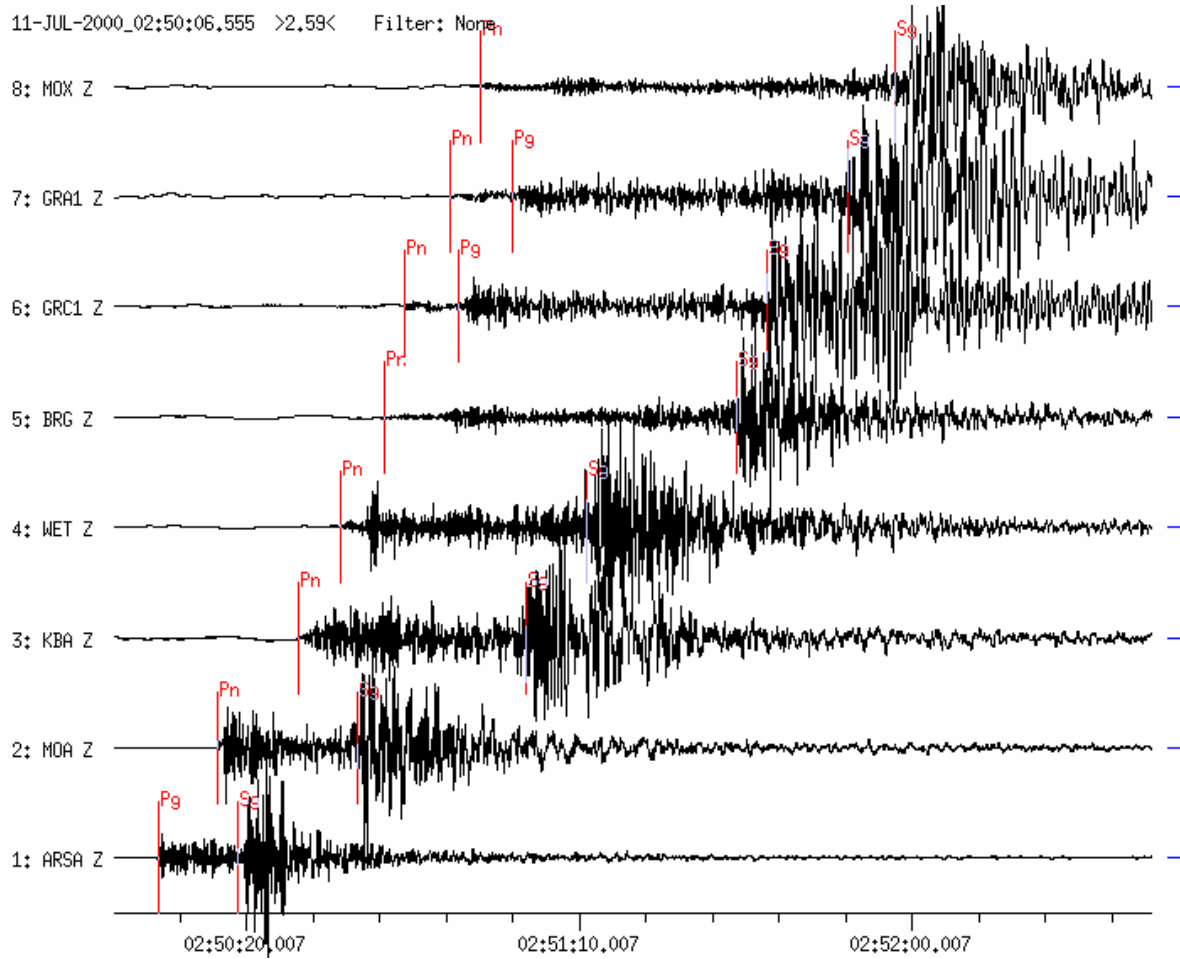


Figure 3a Vertical-component BB records of 5 GRSN/GRF stations and 3 Austrian stations (ARSA, MOA, KBA). Seismogram trace amplitudes have been normalized and the traces sorted according to increasing distance (D = 100 km to ARSA is 100 km and 490 km to MOX).

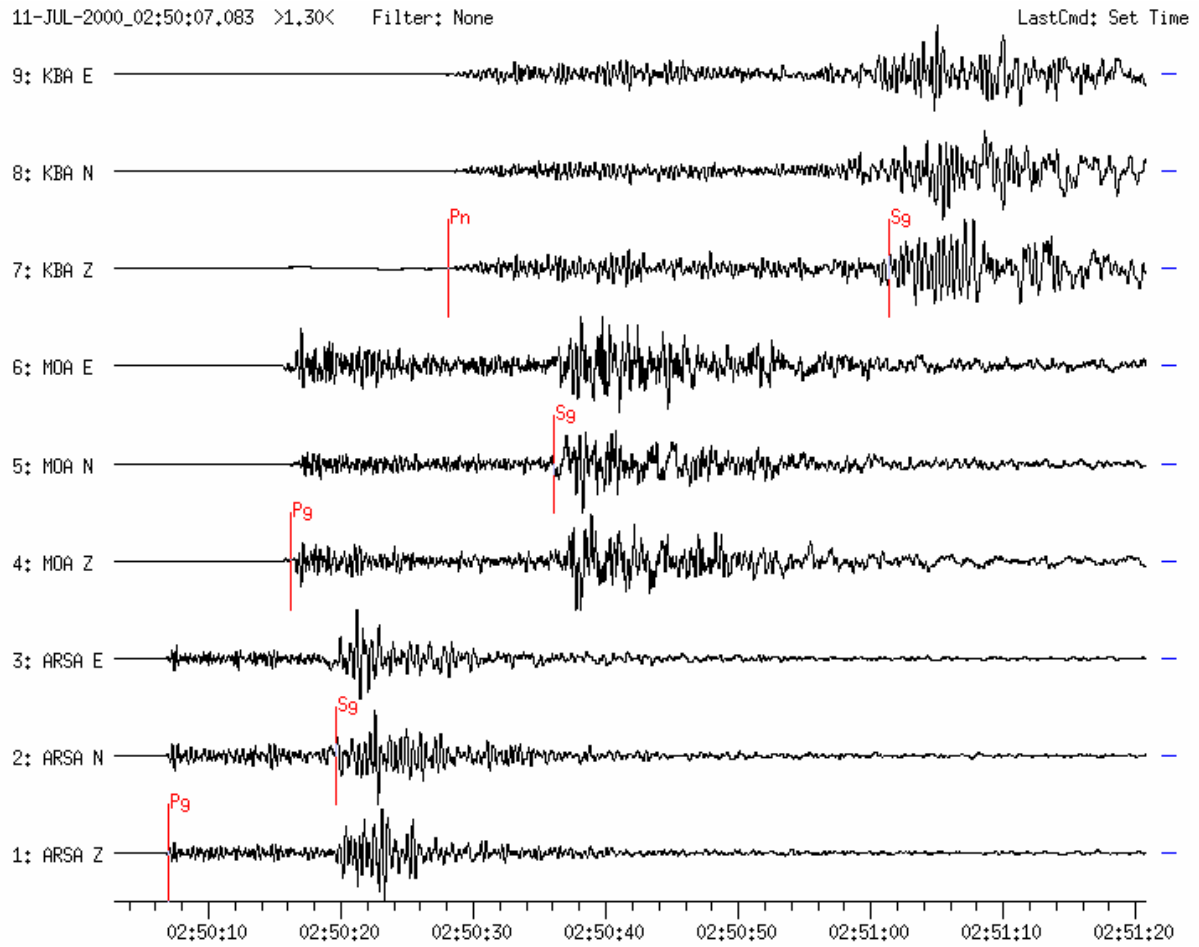


Figure 3b Three-component BB records of the stations ARSA ($D = 100$ km), MOA ($D = 160$ km) and KBA ($D = 250$ km) of the Austrian network (ZAMG Wien).

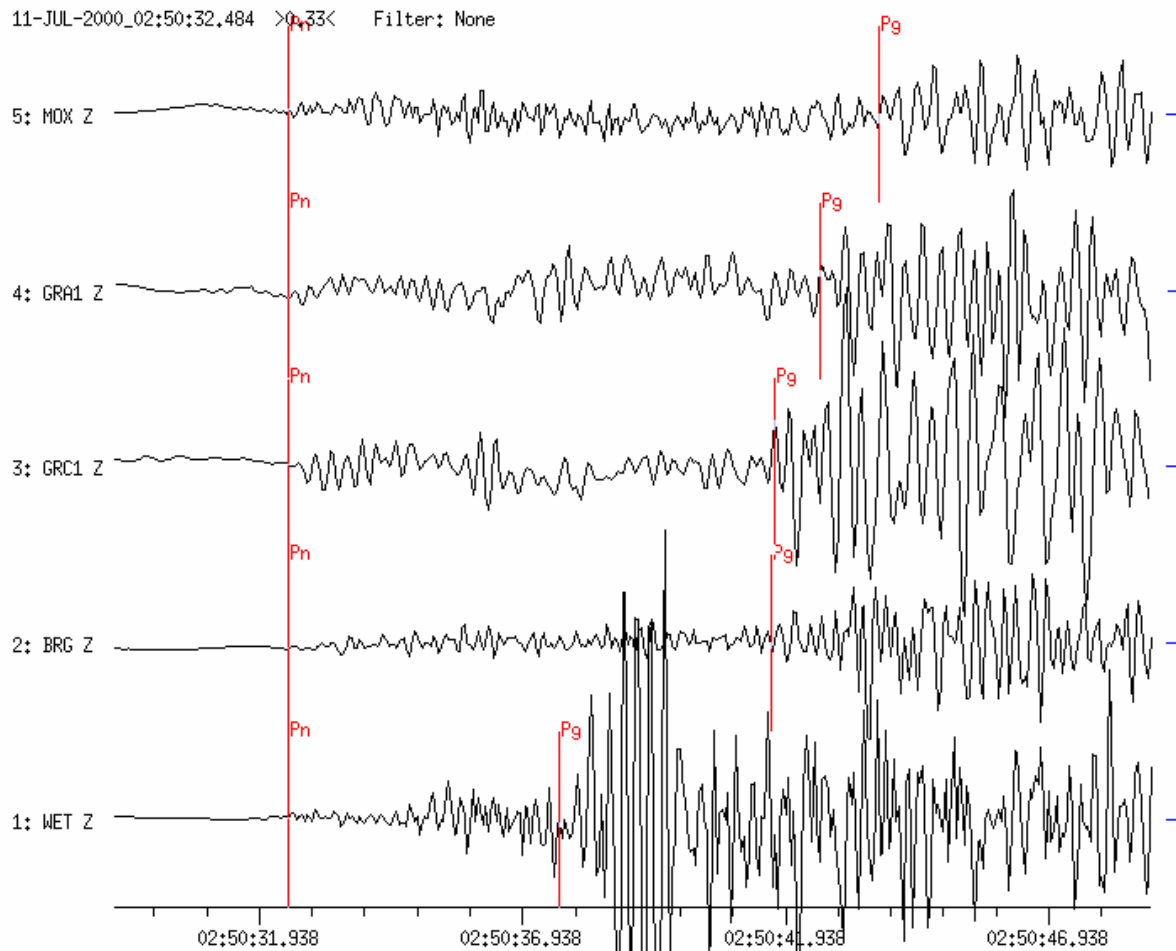


Figure 3c Vertical-component BB records of 5 GRSN stations with phases Pn and Pg. Traces are shifted and aligned for Pn according to a reference station (WET) at $D = 284$ km. Recorded Pn-onsets are weak and polarity readings are impossible

Aftershock: 2000-07-11 OT 10:56:04.5 (UTC) 48.01N 16.48E MI = 4.7

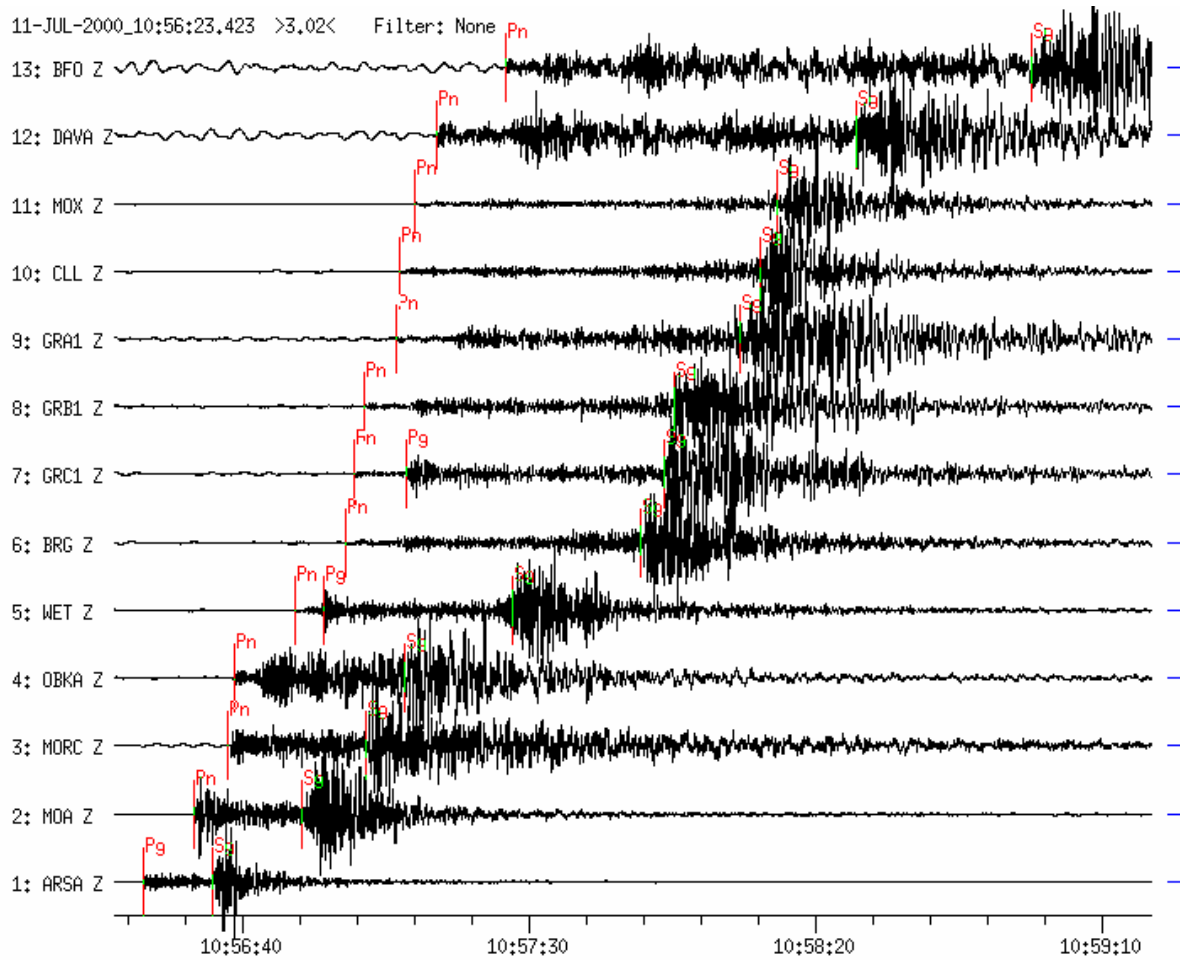


Figure 3d Vertical-component BB records of 8 German GRSN/GRF-stations (WET, BRG, GRC1, GRB1, GRA1, CLL, MOX, BFO), 4 Austrian ZAMG-stations (ARSA, MOA, OBKA, DAVA) and 1 Czech GEOFON-station (MORC). Trace amplitudes have been normalized and the stations sorted according to increasing distance ($D = 96$ km to ARSA and 920 km to BFO).

Example 4: Earthquake in Yugoslavia

NEIC-data: 1998-09-29 OT 22:14:50 44.11N 20.04E h = 10km mb = 5.2
 (D = 8.2° and BAZ = 130° from GRA1)

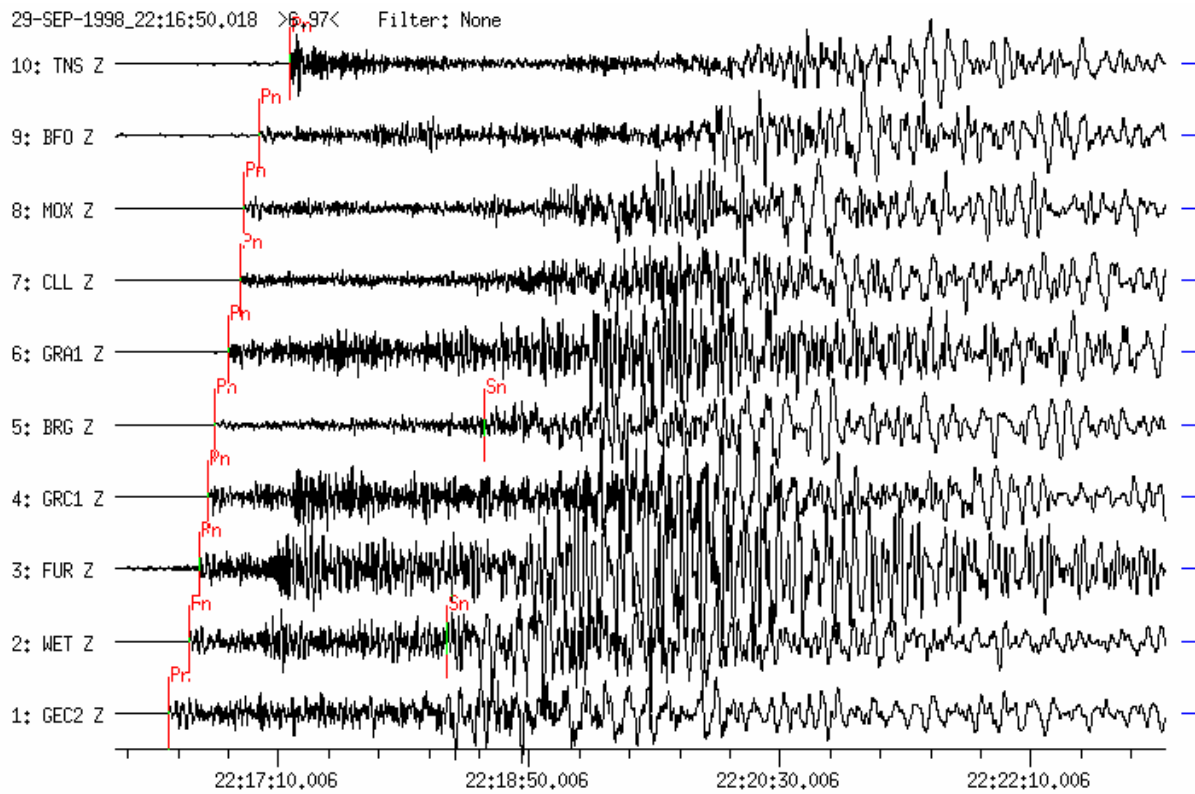


Figure 4a Vertical-component BB records of 10 GRSN/GRF-stations sorted according to increasing distance (D = 6.45° to GEC2 and 10.0° to TNS).

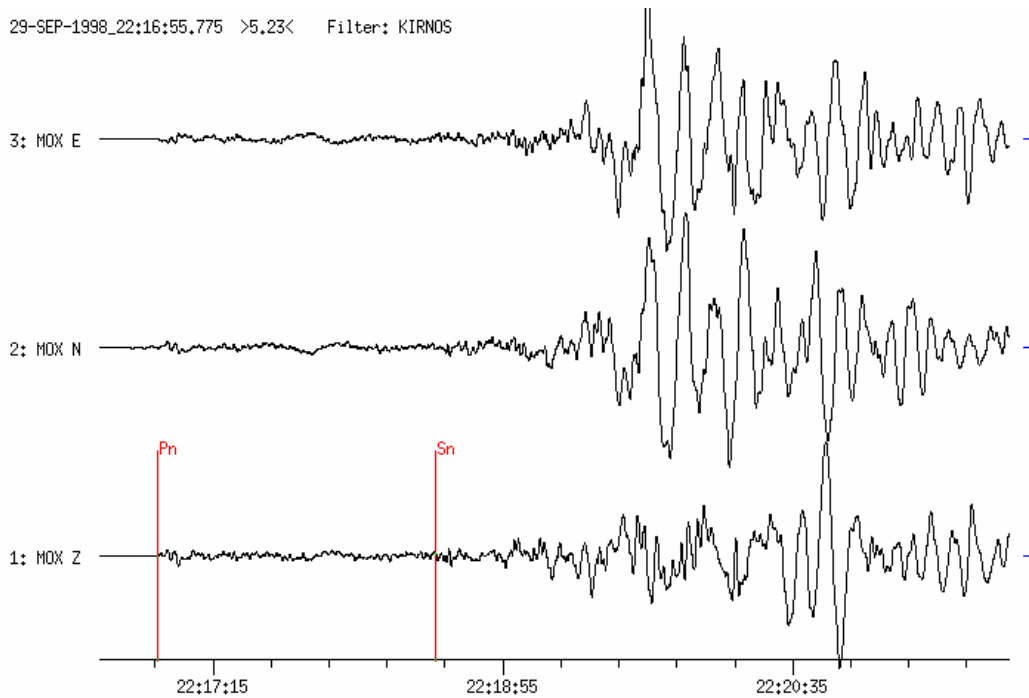


Figure 4b Three-component BB-displacement (Kirnos filtered) record of station MOX ($D = 8.7^\circ$, $BAZ = 136^\circ$) with phases Pn, weak Sn and strong dispersed surface waves (LQ onset in N-E around 22:19:10 and LR_{max} in Z at 22:20:45; note onset-like Lg phases arriving between Sn and LQ).

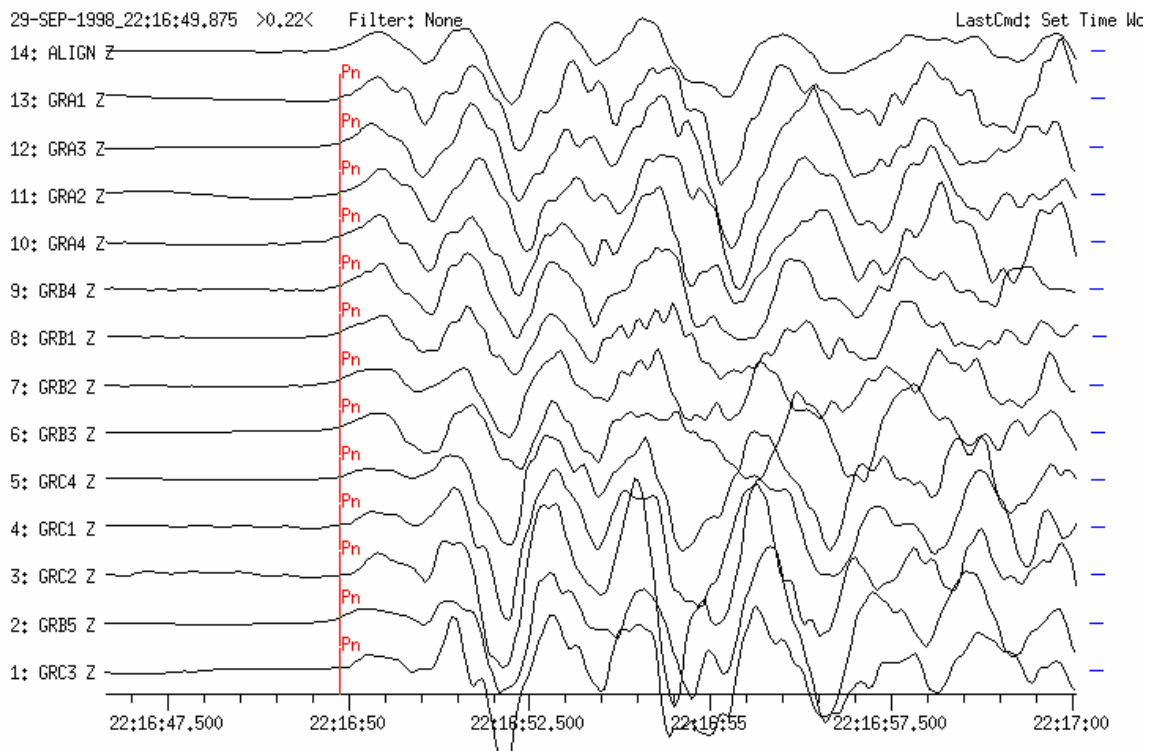


Figure 4c Time-shifted and aligned vertical components BB records of the 13 GRF-array stations (see Fig. 11.3a for array position and outline). Traces are sorted according to increasing distance.

Example 5: Earthquake in Albania

NEIC-data: 1998-09-30 OT 23:42:54 41.95N 20.39E h = 10km Ms = 5.1
 (D = 10.0° and BAZ = 137° from GRA1).

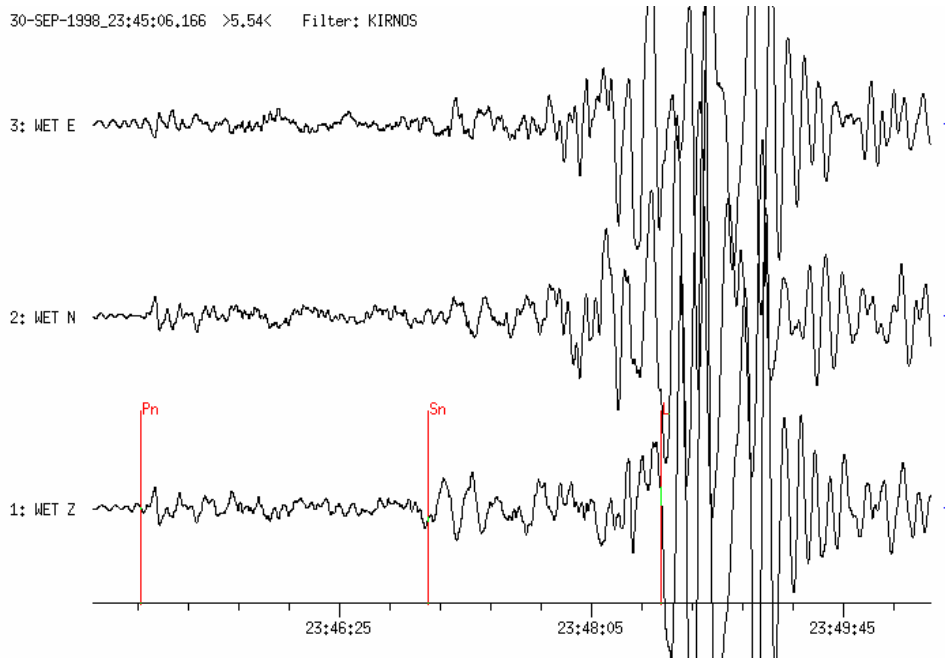


Figure 5 Three-component BB-displacement (KirnOS filtered) record at the GRSN station WET at D = 8.9° (BAZ = 136°). Note the clear onset of Pn, a very pronounced long-period Sn (as compared to the very weak Sn in the record of the Yugoslavia earthquake in Figure 4b above) and well dispersed surface waves of dominantly Rayleigh (LR) type (because of the strong vertical component).

Example 6: Earthquake in SOUTHERN ITALY

USGS NEIC-data: 1998-09-09 OT 11:27:58.6 39.964N 15.948E h = 10km
 mb = 5.3 Ms = 5.2

SZGRF-data: 1998-09-09 OT 11:28:01.8 40.1N 16.4E Ms = 5.2

Distance (GRA1) D = 10.3 deg, BAZ = 157 deg

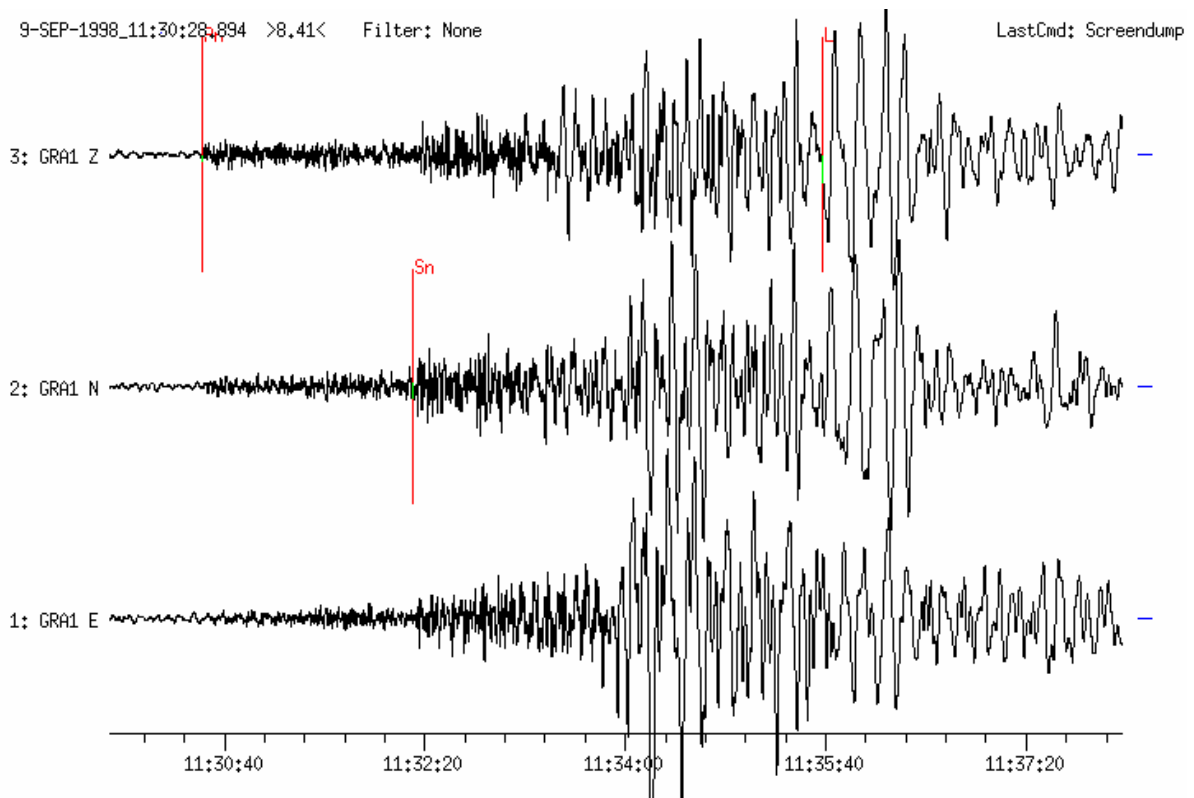


Figure 6a Three-component BB record at the GRF-station GRA1 ($D = 10.3^\circ$, $BAZ = 159^\circ$) with clear phases Pn, Sn and surface waves (Lg arriving around 11:34:00 and Rg around 11:35.40).

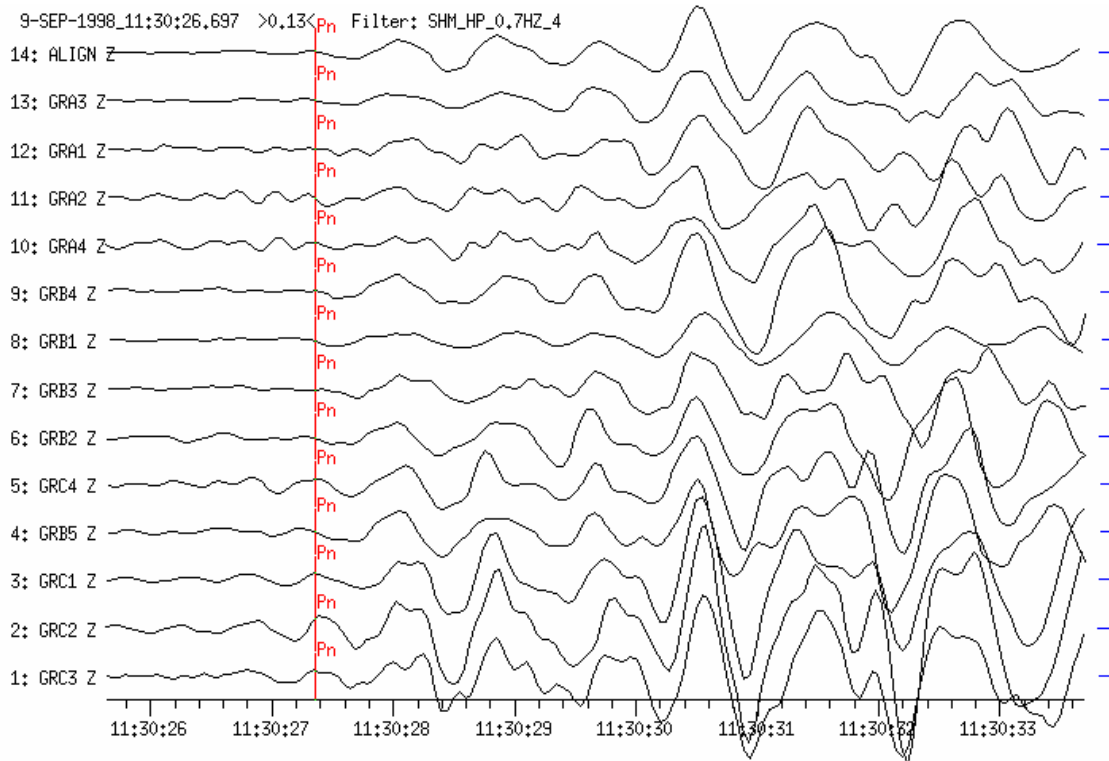


Figure 6b Highpass-filtered (0.7 to 4 Hz) Z-component records with Pn onsets at 13 GRF-array stations. Traces are aligned and sorted according to increasing distance ($D = 9.45^\circ$ to GRC3 and $D = 10.33^\circ$ to GRA3). The coherency of Pn is poor at this distance range.

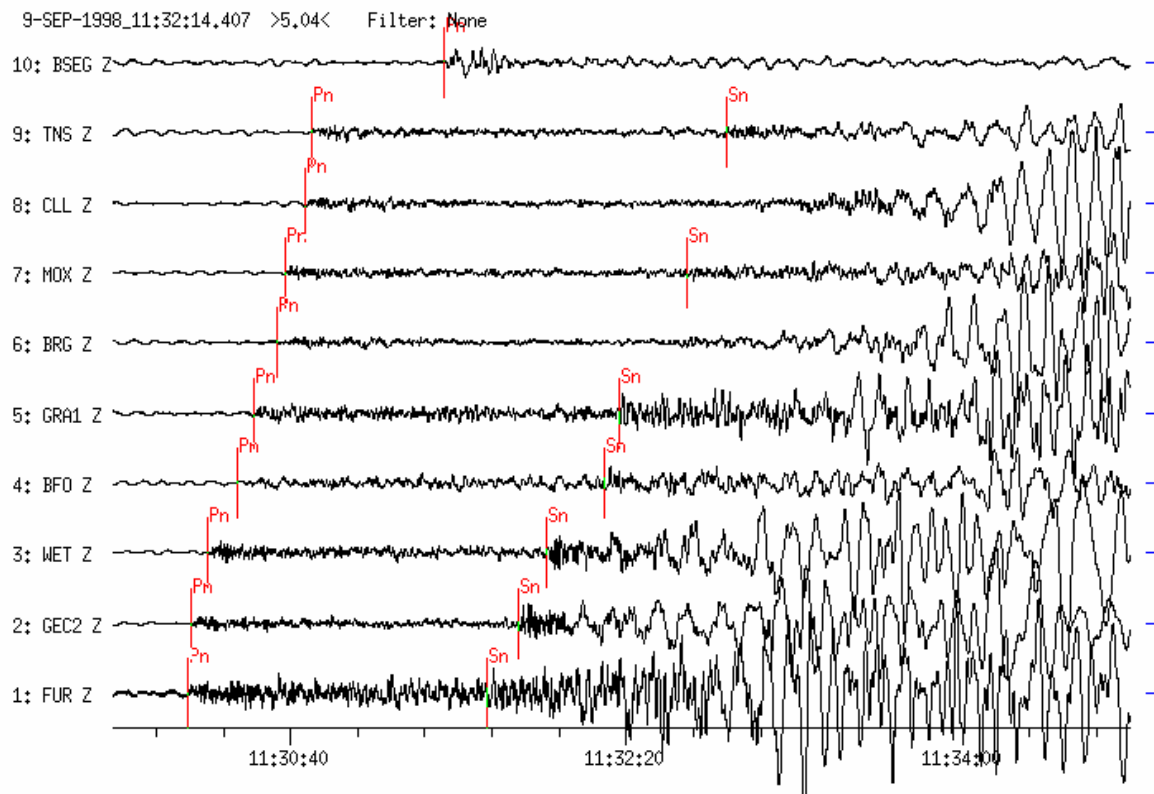


Figure 6c Vertical-component BB records with Pn and Sn waves from 10 GRSN-stations. The traces have been sorted according to increasing distance between $D = 8.86^\circ$ (FUR) and 14.5° (BSEG). Except for stations CLL, BRG and BSEG clear Sn arrivals are visible.

Topic	Additional seismogram examples within the distance range 13° - 100°
compiled by	Klaus Klinge, Federal Institute for Geosciences and Natural Resources, Seismological Central Observatory, Gräfenberg (SZGRF), Mozartstrasse 57, 91052 Erlangen, Germany, Fax: +49 9131 8104 099, E-mail: klinge@szgrf.bgr.de
Version	October, 2001

Note: Most of the examples given below show either records of the German Regional Seismic Network (GRSN; aperture about 500 x 800 km) or of the Gräfenberg broadband array (GRF; aperture 45 x 110 km; see Figs. 8.14 and 9.4 in the manual Chapters 8 and 9). The following abbreviations have been used: D – epicentral distance in degree, BAZ – backazimuth in degree, h – focal depth in kilometer. Complementary comments have been added by the Editor.

Example 1: Earthquake in Greece

USGS NEIC-data:1999-09-07 OT 11:56:50 38.13N 23.55E h = 10km mb = 5.8

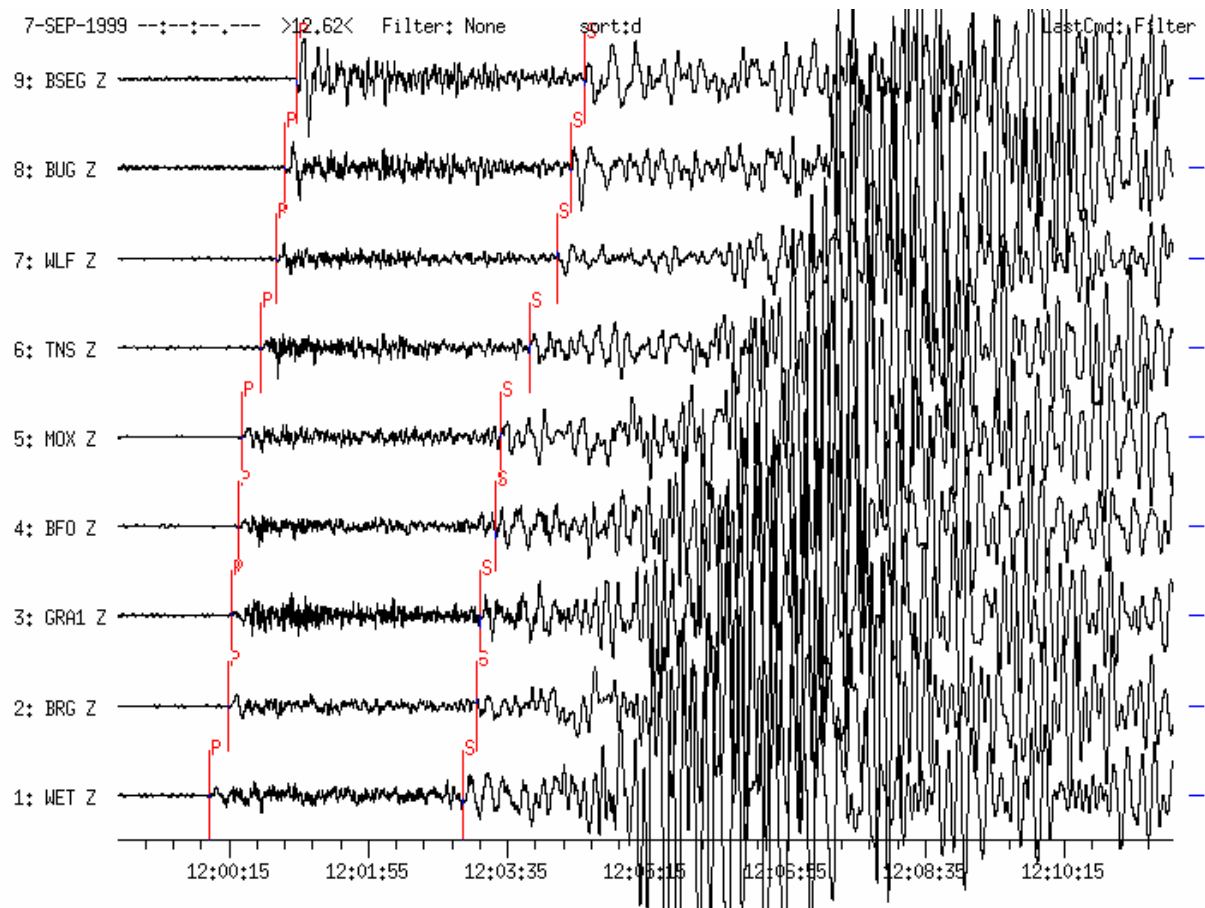


Figure 1a Broadband vertical-component seismograms recorded at 9 GRF/GRSN stations within the distance range $D = 13.4^\circ$ (WET) to 18.2° (BSEG). Traces have been sorted according to increasing distance. A complex P wave is followed by S and surface waves with longer-periods than P. Both body waves are influenced by upper mantle discontinuities. Note the large P-wave amplitude at the most distant station BSEG because amplitudes increase rapidly towards the “20° discontinuity” (see Fig. 3.13 in Chapter 3).

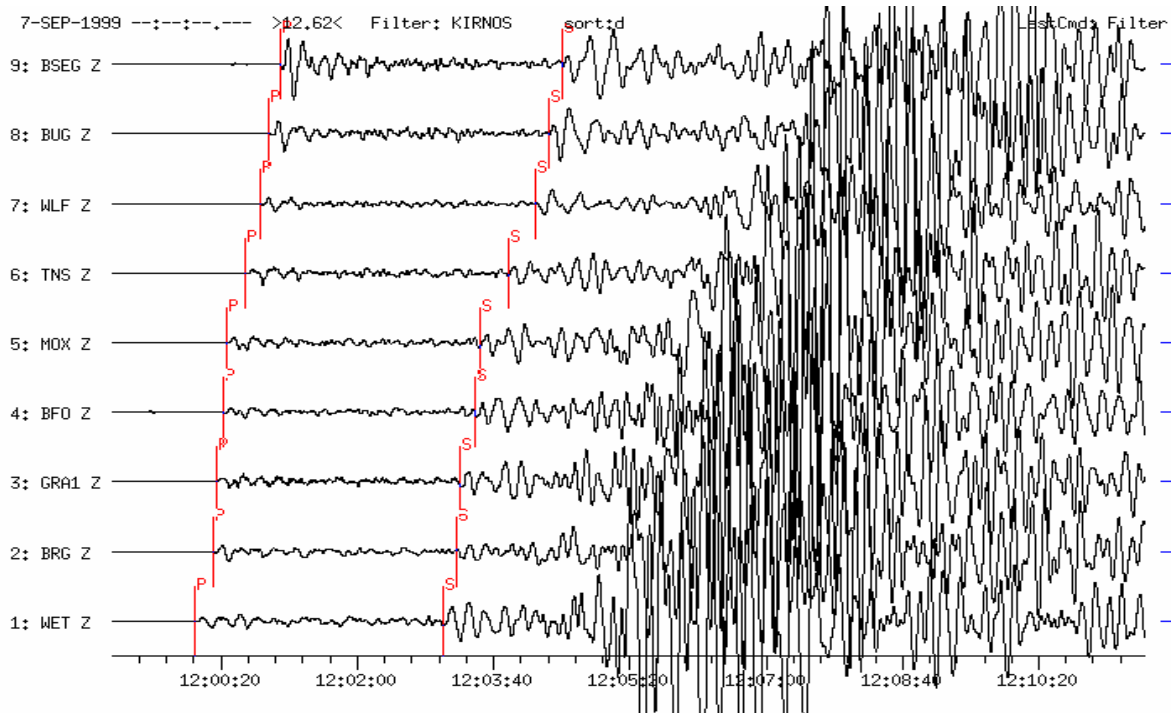


Figure 1b The same record as above, however a displacement proportional KIRNOS-filter was applied. Especially S waves are displayed better by using this filter. The network traces are not coherent.

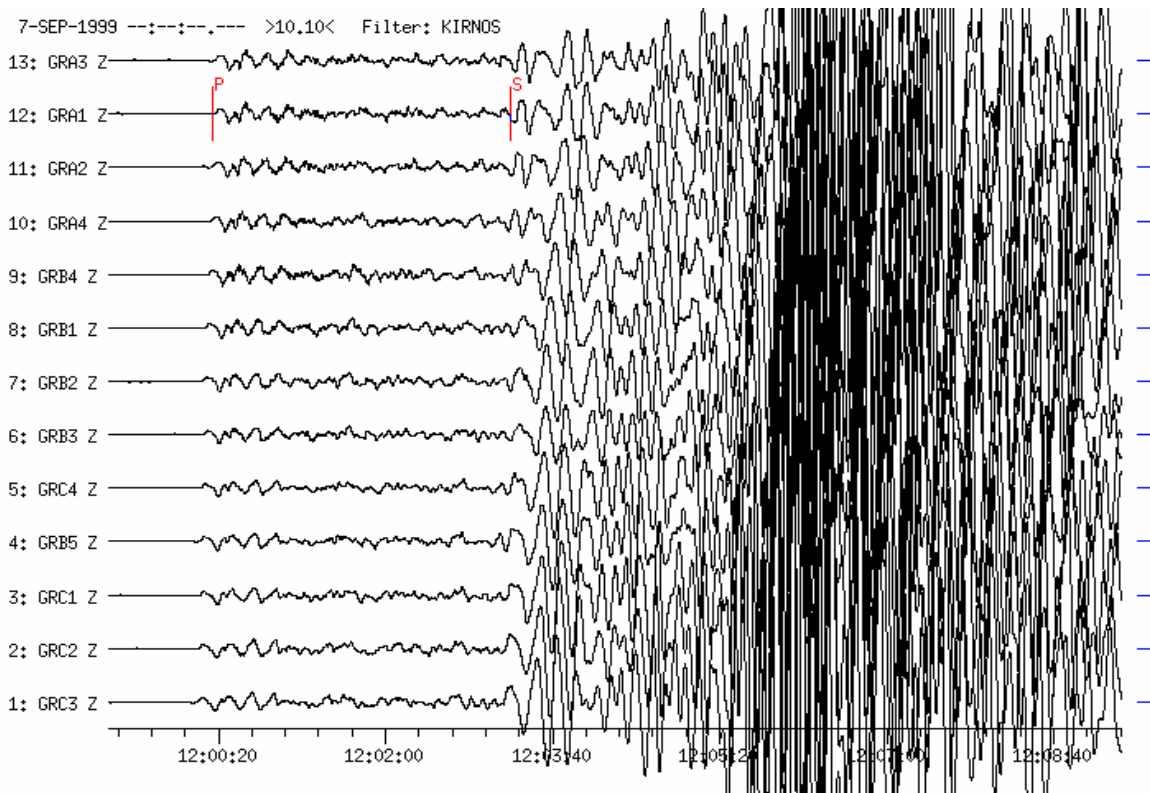


Figure 1c KIRNOS-filtered seismograms of vertical-component records at the GRF-array stations sorted according to increasing epicentral distance ($D = 13.8^\circ$ to GRC3 and 14.6° to GRA3). Note the variability of waveforms within the S-wave group.

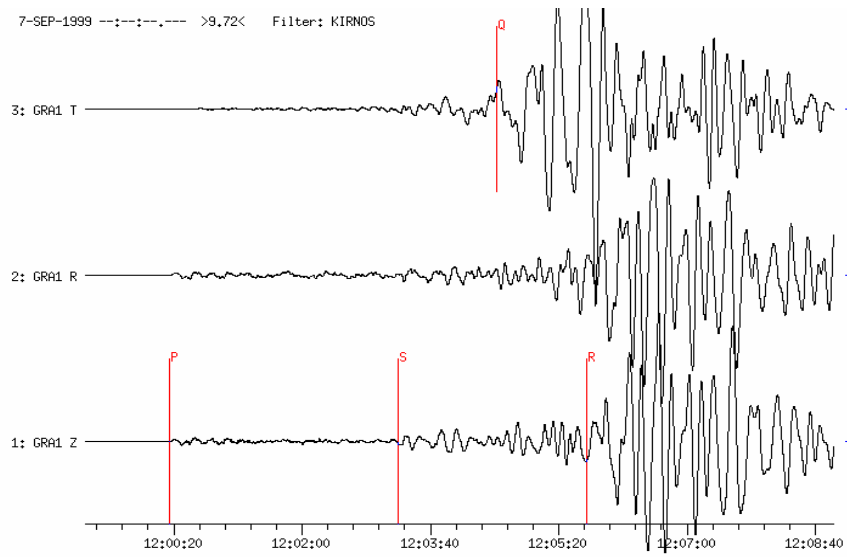


Figure 1d KIRNOS-filtered three-component seismogram from the GRF-array station GRA1 ($D = 14.55^\circ$, $BAZ = 138^\circ$). The horizontal components N and E have been rotated into the radial (R) and transverse (T) direction. The onsets of the body waves P and S and of the long-period surface waves LQ (Q) and LR (R) have been marked.

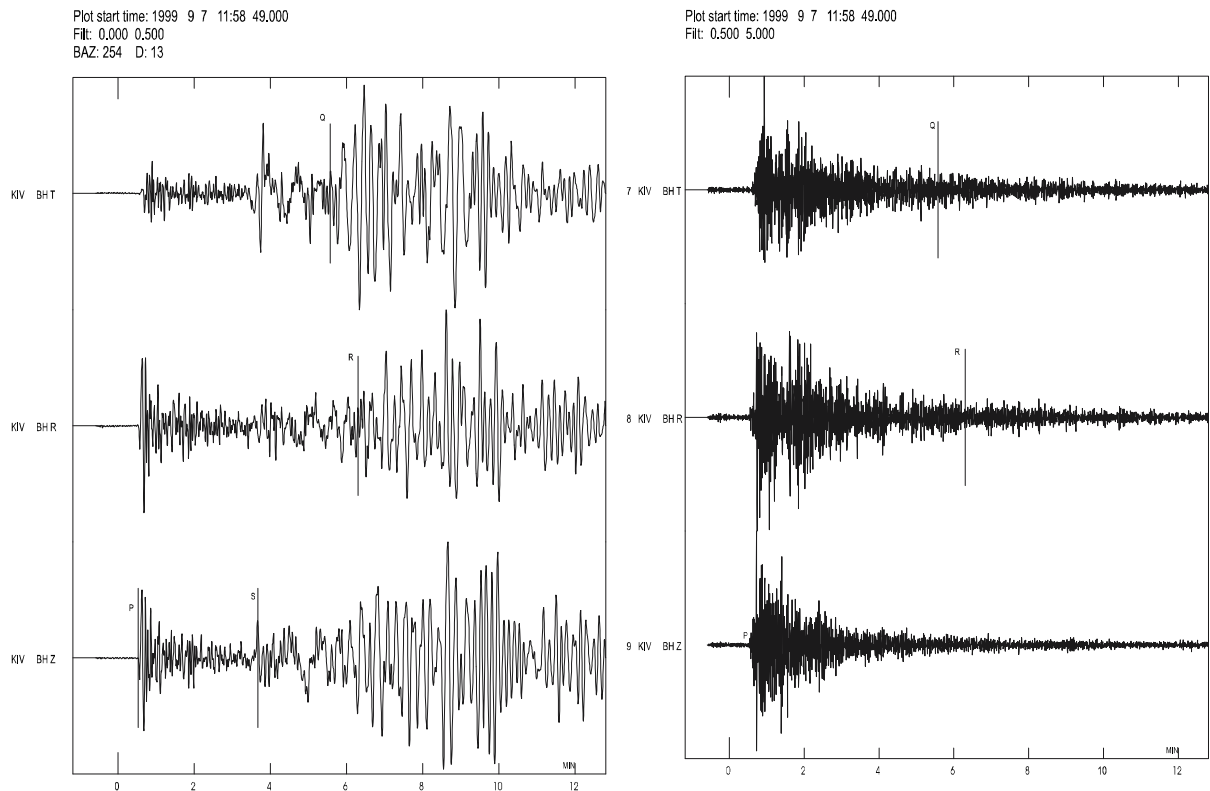
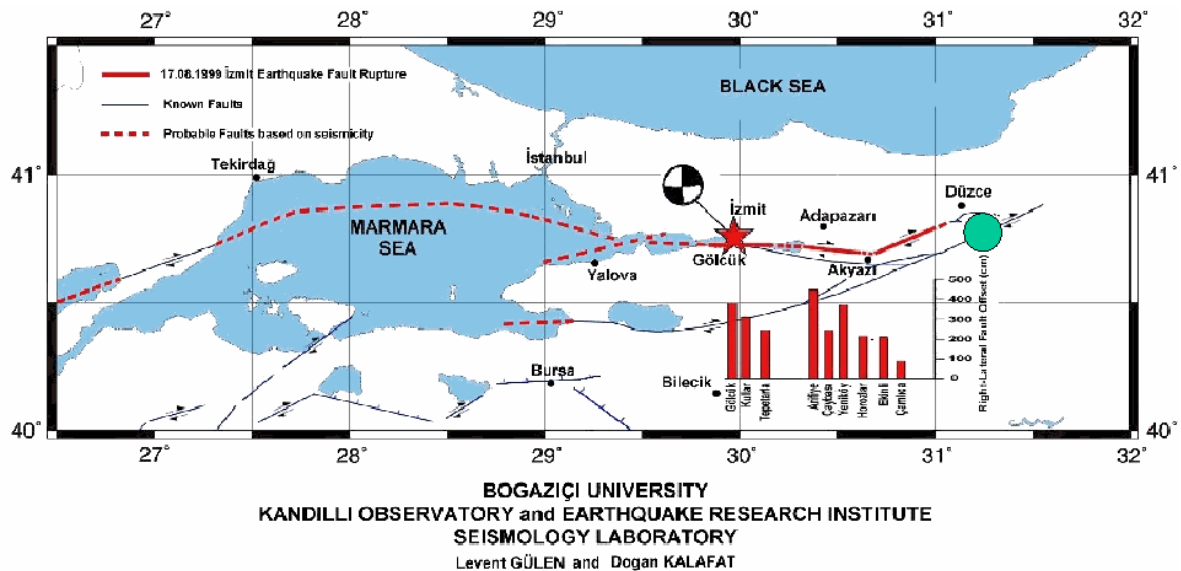


Figure 1e Low-pass (left) and high-frequency band-pass filtered (0.5-5 Hz) seismograms of the same earthquake recorded at station KIV (Kislovodsk; Russia) at the distance $D = 15.2^\circ$. The horizontal components N and E have been rotated into the R and T direction. No long-period waves are visible in the high-frequency record (courtesy of Lars Ottemöller, 2002).

Example 2: Earthquake in NW-TURKEY

USGS NEIC-data:1999-11-12 OT 16:57:20 40.79N 31.11E h = 10km Mw = 7.1
(D = 16.5° to GRF, BAZ = 115°)




 12.11.1999 Mw 7.1 (NEIC)

Figure 2a The Düzce earthquake of November 12, 1999 occurred about 110 km east of the earlier Izmit earthquake of August 17, 1999. The map shows the epicenter regions of both earthquakes together with one moment-tensor solution (for the Izmit event) and the right lateral surface displacement values (in cm) observed after the first shock.

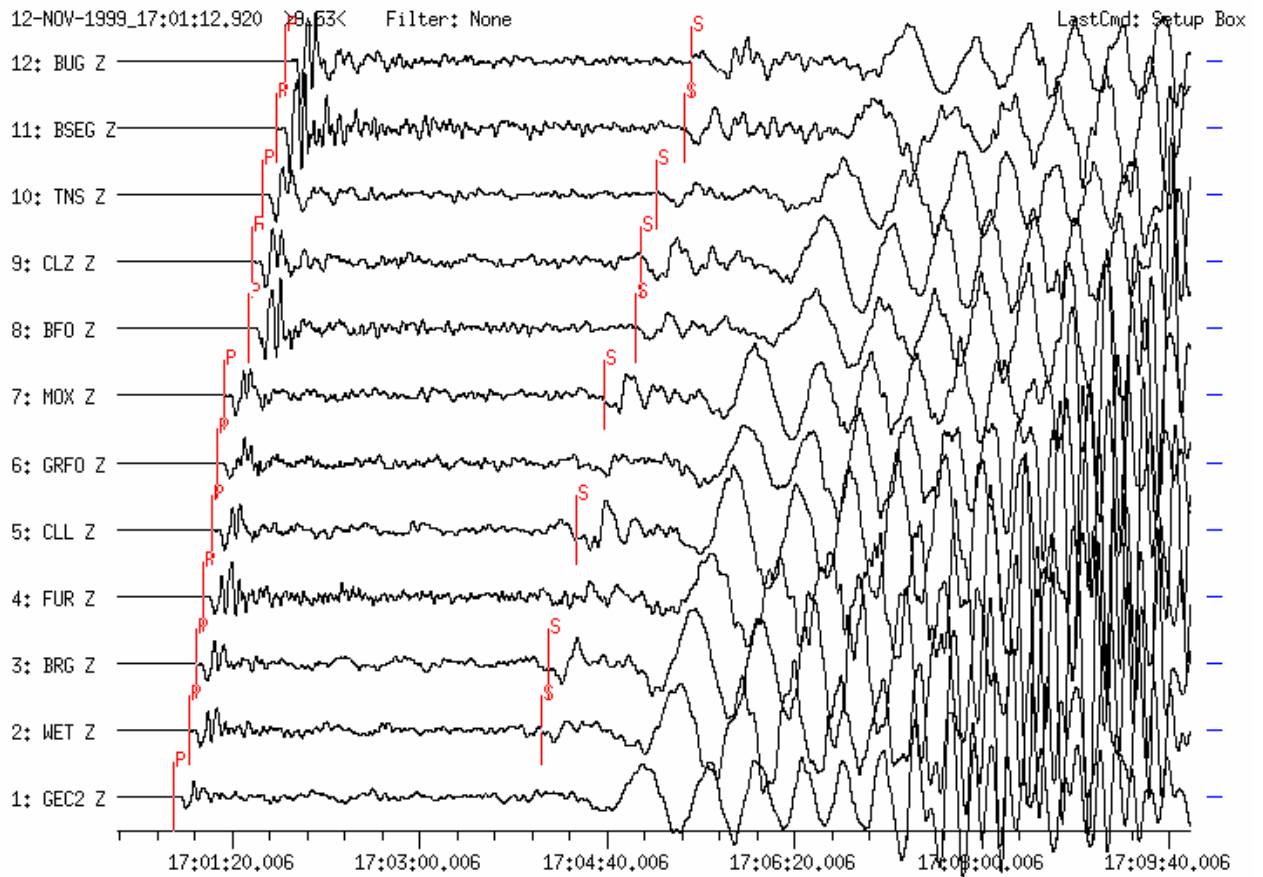


Figure 2b Broadband vertical-component seismograms recorded at 12 GRSN stations. Traces are sorted according to increasing distance ($D = 14.7^\circ$ from GEC2 and 19.6° from BUG). A clear P wave is followed by a relatively weak S and strong dispersed surface waves with much longer-periods than P. The P and S waveforms, influenced by upper mantle discontinuities, show a complicated structure. Note the growing P-wave complexity and amplitudes with increasing distance towards the “20° discontinuity” (see Fig. 2.29 in Chapter 2 and Fig. 3.13 in Chapter 3).

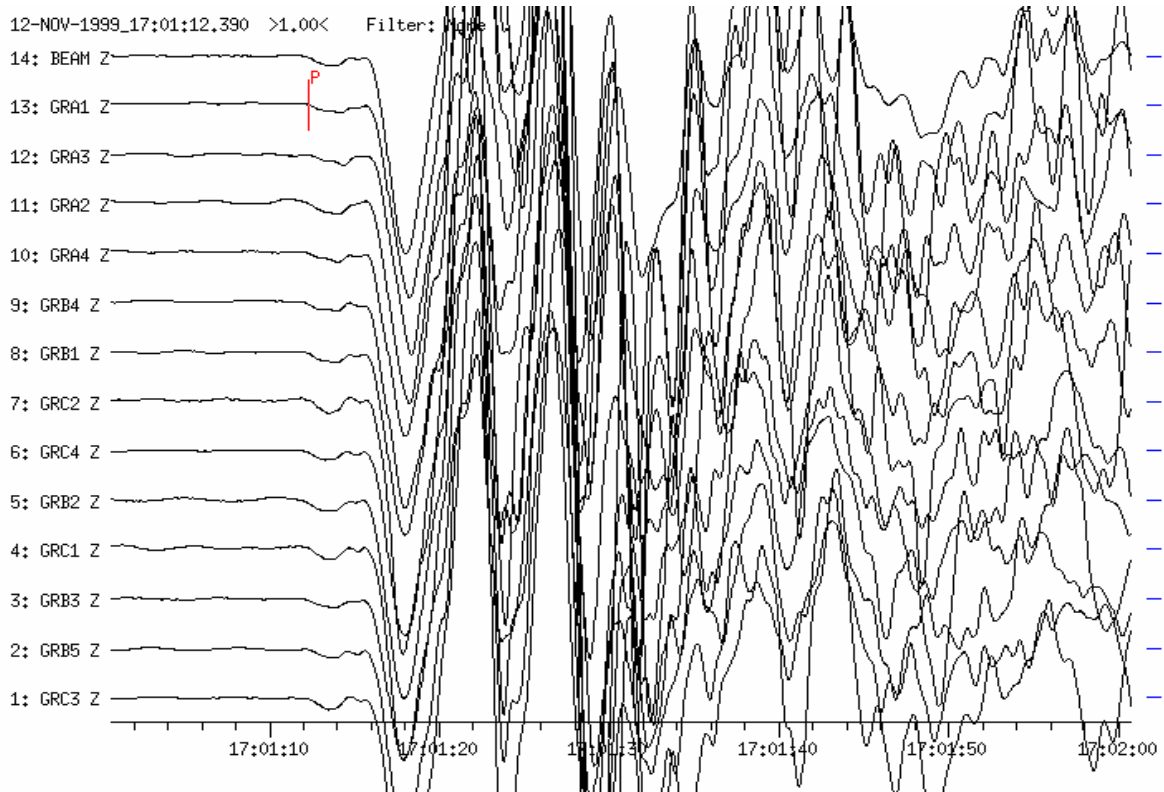


Figure 2c Broadband vertical-component seismogram with P-wave onsets recorded at all GRF-array stations. Traces are sorted according to increasing distance ($D = 12.86^\circ$ from GRC3 and 13.03° from GRA1) and shifted in time according to a reference station (beamforming). All signal onsets are coherent. The weak first arrival of the P-wave onset is marked on the GRF-station GRA1.

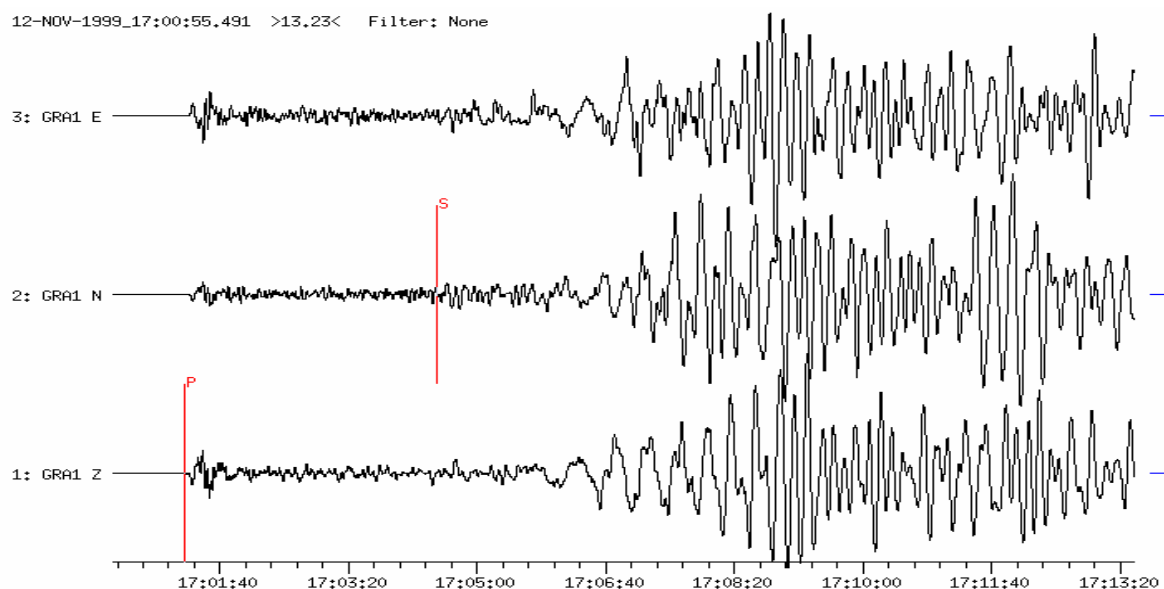


Figure 2d Broadband seismogram with P, weak S and long-period surface waves from station GRA1 (at $D = 13.0^\circ$).

Example 3: Earthquake in Southern TURKEY

USGS QED-data: 1998-06-27 OT 13:55:49 36.95N 35.31E h = 10G Ms = 6.2
(D = 21.6° to GRF)

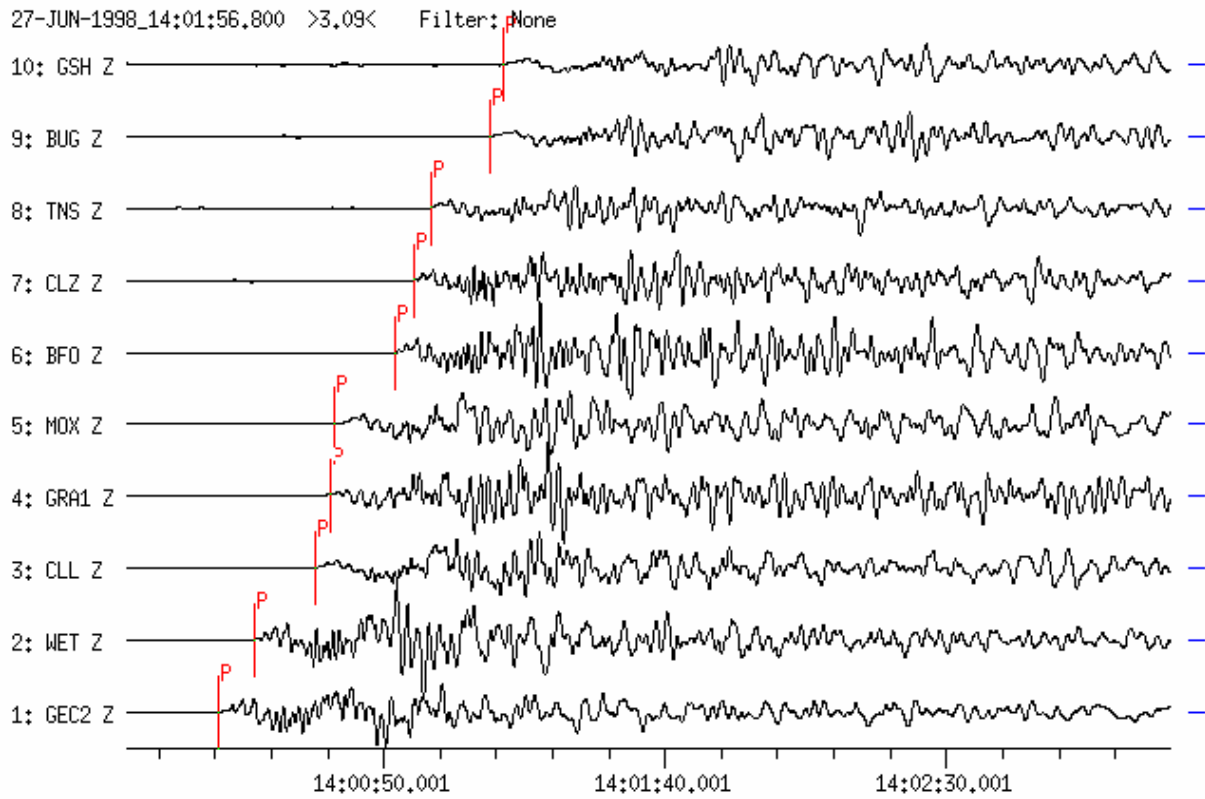


Figure 3a Broadband seismograms with high time resolution showing the complex P-wave groups. Records were made on vertical components of 10 GRSN stations at epicentral distances between $D = 19.7^\circ$ (GEC2) and 24.8° (GSH). Traces are sorted according to increasing distance. P waves on the individual traces are influenced by upper mantle discontinuities and signals are not coherent.

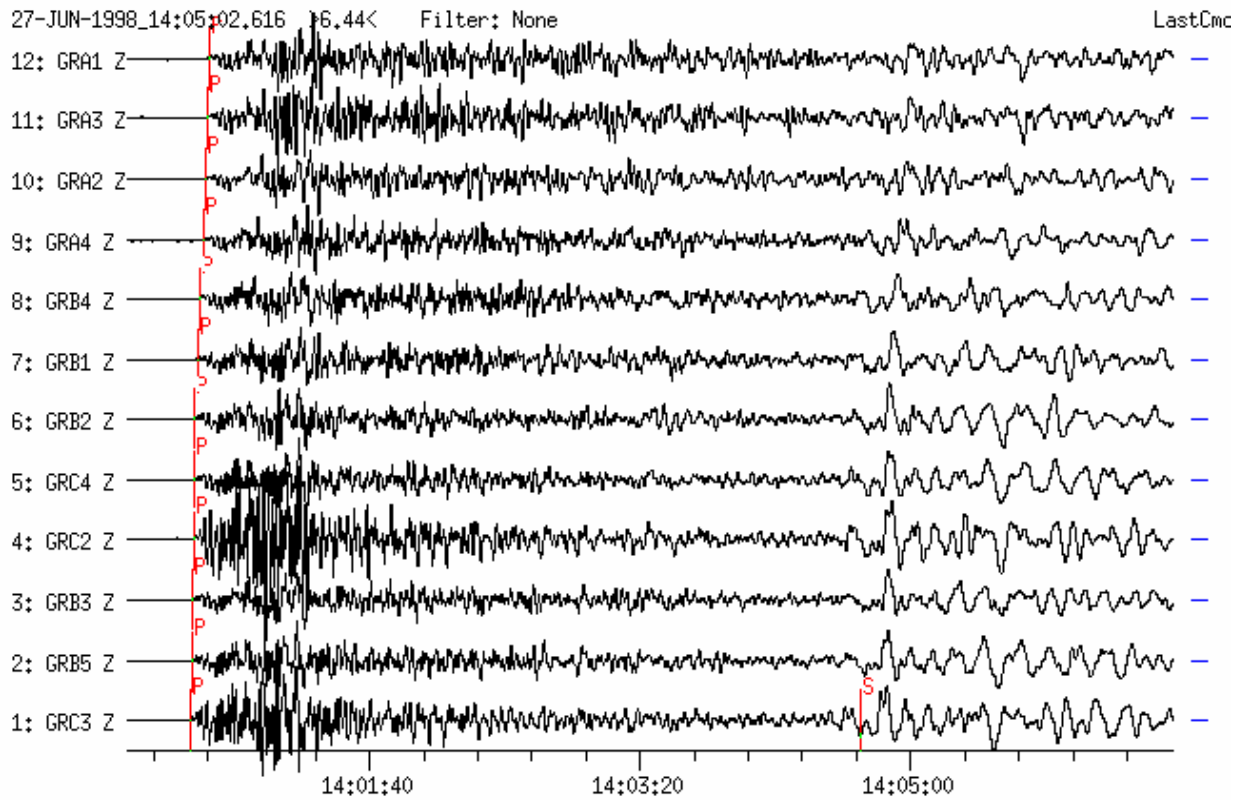


Figure 3b Broadband seismogram with P- and S-wave onsets recorded at 12 GRF-array stations. Traces are sorted according to increasing distance. P and S waves on the individual traces are influenced by upper mantle discontinuities and signals are also not coherent.

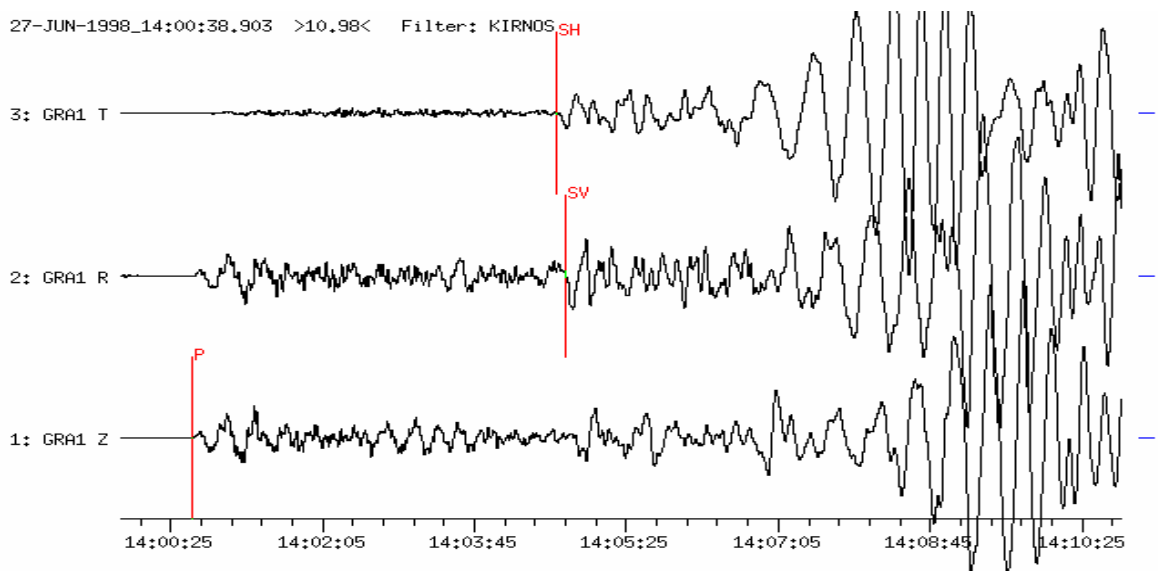


Figure 3c Three-component displacement-proportional KIRNOS-filtered seismogram recorded at the GRF-main-station GRA1 ($D = 21.6^\circ$). The original N- and E- horizontal components have been rotated with R showing into the source direction. The time difference between the onsets SH (horizontal polarized S wave) and SV (vertical polarized S wave) is about 4 sec. The reason for this difference may be the anisotropy of upper mantle layers.

Example 4: Earthquake in ICELAND REGION

USGS QED-data: 1998-06-04 OT 21:36:54.2 64.009N 21.294W h = 10G
 mb = 5.1 Ms = 5.1 (D = 22.5° to GRF)

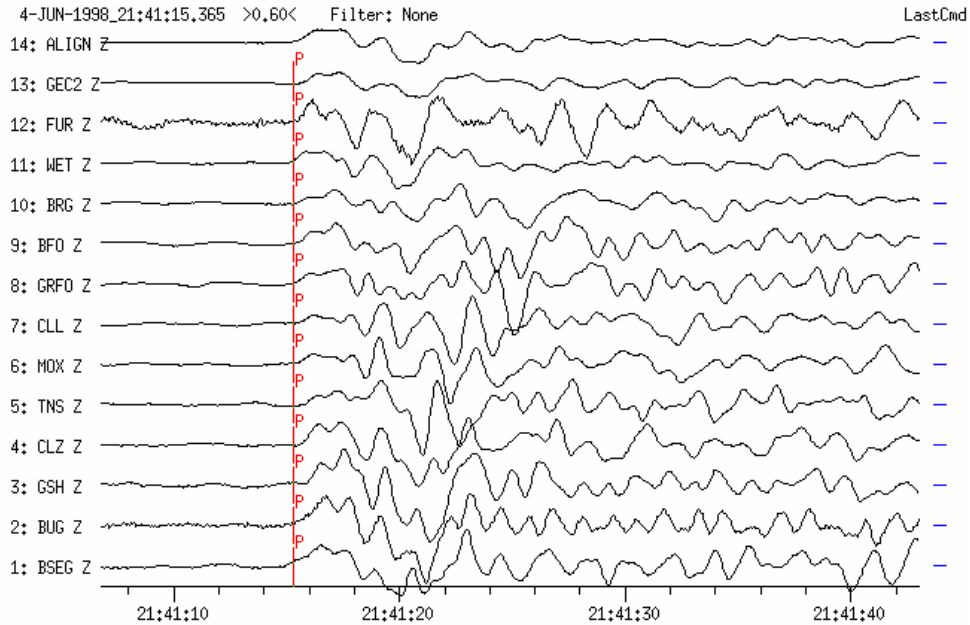


Figure 4a Broadband vertical-component seismograms recorded at 13 GRSN stations. Traces are sorted according to increasing epicentral distance (D = 18.9° to BSEG and 24.2° to GEC2), shifted in time and aligned for better signal comparison. All signals are incoherent and influenced by upper mantle discontinuities.

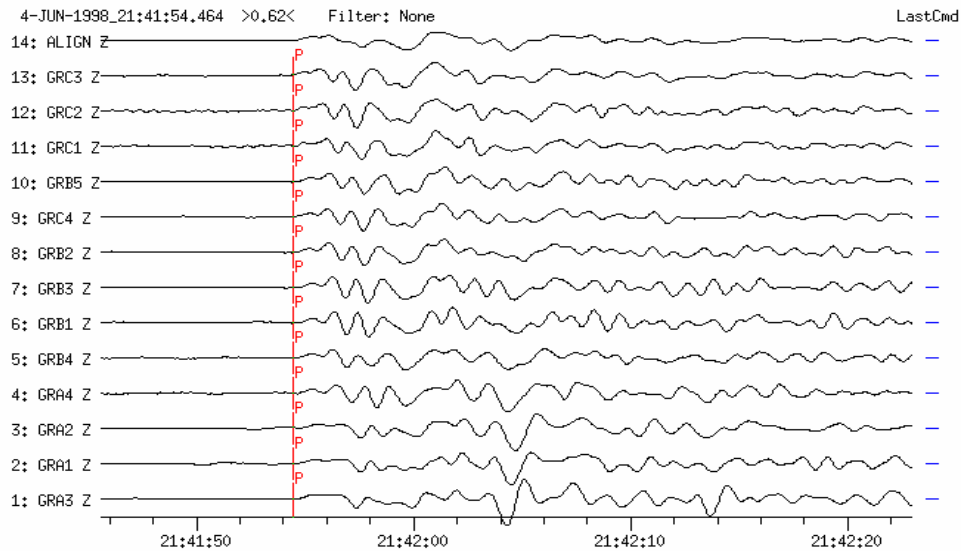


Figure 4b Broadband vertical-component seismograms recorded at the GRF-array stations. Traces are sorted according to increasing distance (D = 22.48° to GRA3 and 23.27° to GRC3), shifted in time and aligned for better signal comparison. Because of the smaller aperture of the array as compared to the GRSN network signals are more similar. At the nearest stations (GRA3 up to GRA4) a second onset appears about 10 s after P.

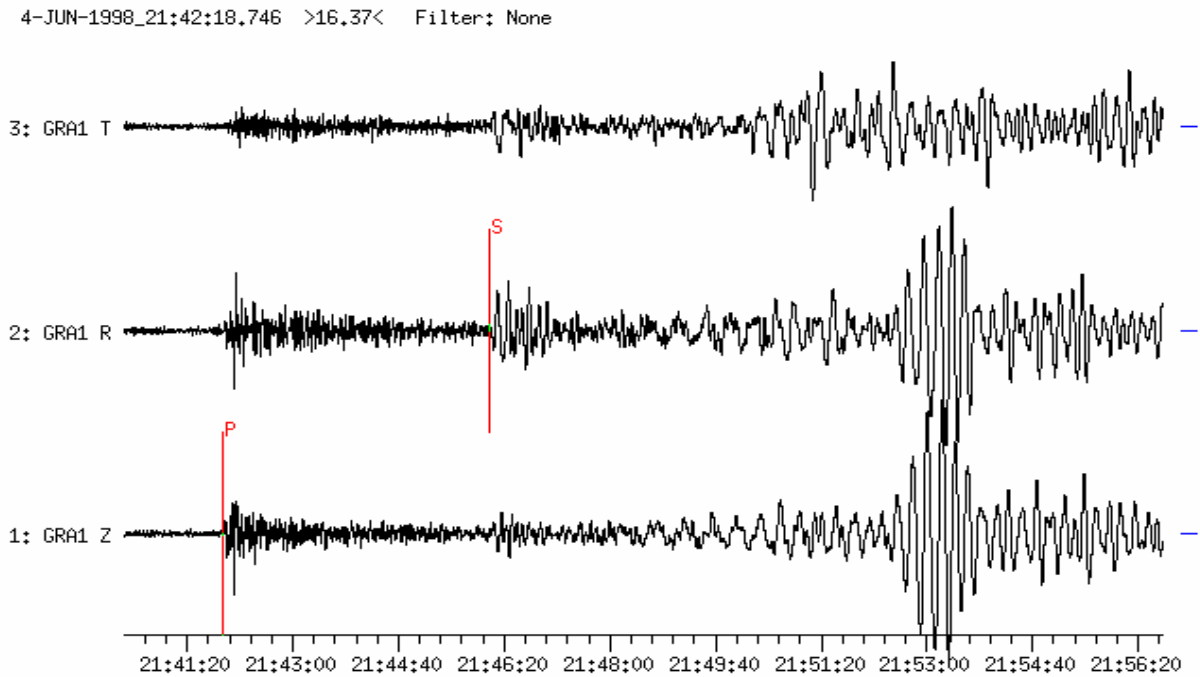


Figure 4c Simple three-component broadband seismogram at station GRA1 ($D = 22.5^\circ$) with clear P, S and surface waves. Horizontal components have been rotated (ZRT) with R into source direction.

Example 5: Earthquake at the Afghanistan -Tajikistan border region

USGS QED-data: 1998-05-30 OT 06:22:28.7 37.050N 70.086E h = 33N
 mb = 5.8 Ms = 6.9 ($D = 43.5^\circ$ and $BAZ = 83.7^\circ$ from GRF)

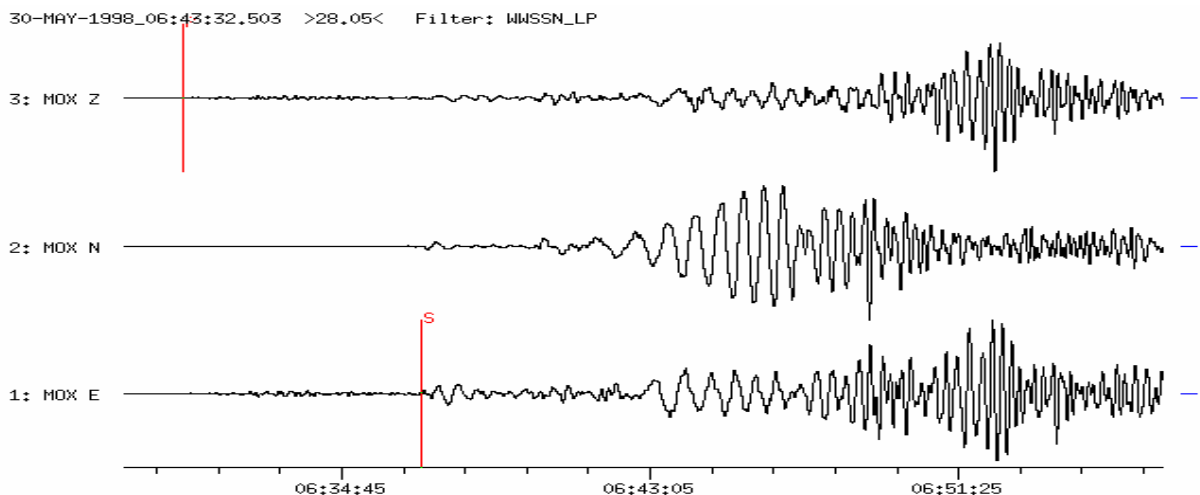


Figure 5a Three-component long-period seismogram (WWSSN-LP simulation filter) recorded at station MOX ($D = 43.2^\circ$, $BAZ = 85^\circ$) with P, S and dispersed surface waves. The nuclear explosion in Pakistan (see Figure 6.2) was recorded within the coda of this strong earthquake. As compared with the earthquake no surface waves has been recorded from the nuclear explosion.

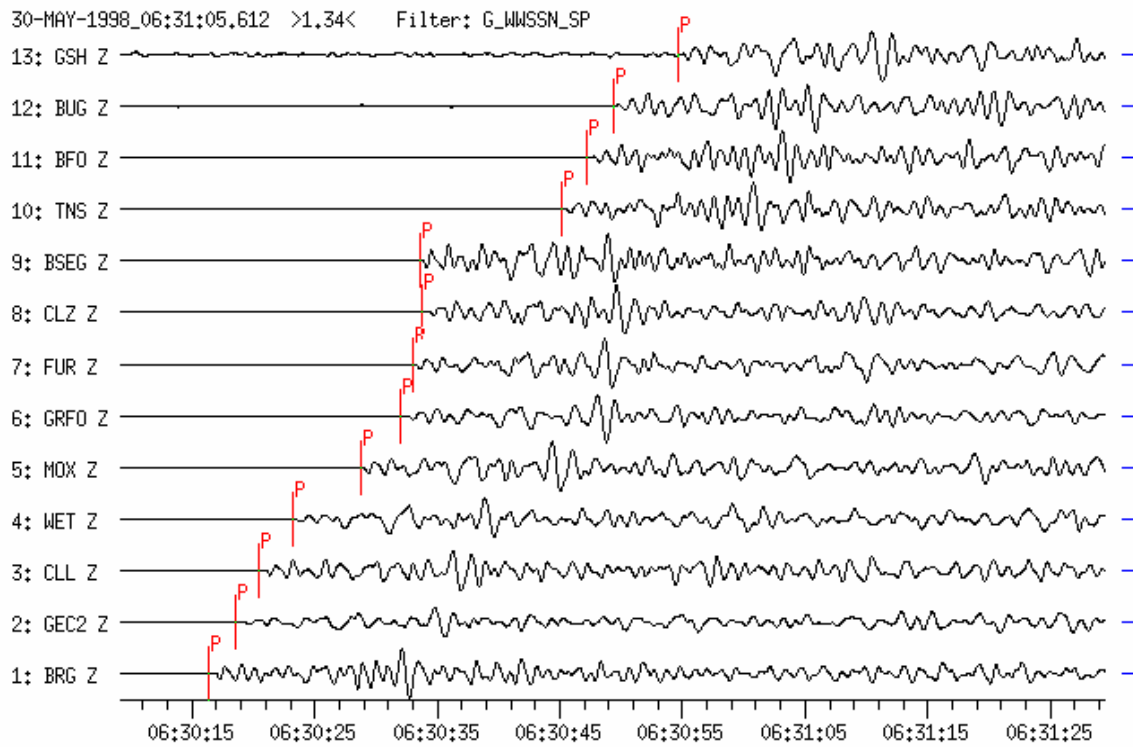


Figure 5b Short-period filtered P-wave onsets (WWSSN-SP simulation) recorded at 13 GRSN stations within the distance range between $D = 41.7^\circ$ (BRG) and 46.5° (GSH). P-wave trains are rather complex as compared with the records of the nearby underground nuclear explosions (see DS 11.4, Figures 2 and 3).

Example 6: Deep-focus earthquake in the HINDUKUSH REGION

USGS NEIC-data:1999-06-21 OT 17:37:29 36.40N 70.63E h = 249km
 mb = 5.7 (D = 44.3° to GRF, BAZ = 84.1 deg)

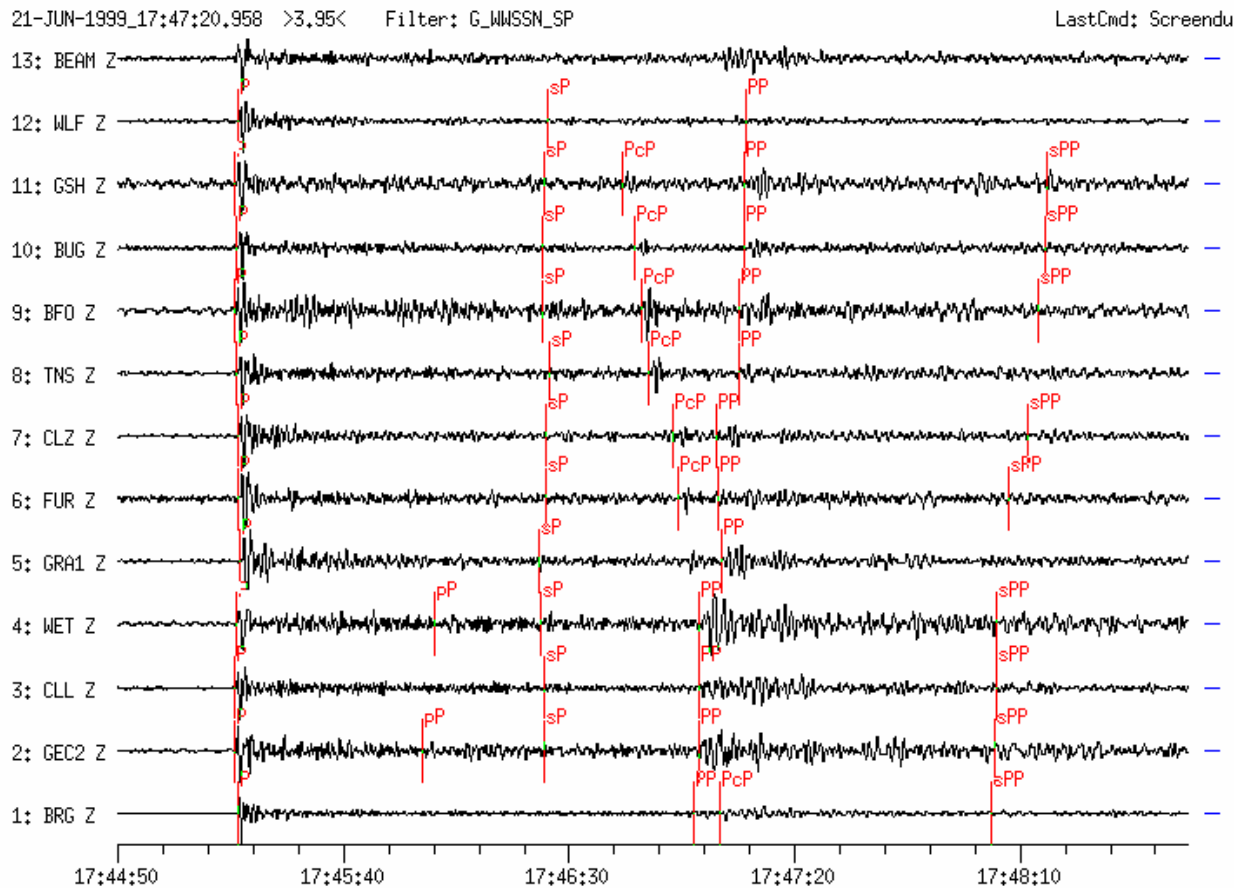


Figure 6a Short-period filtered seismogram (WWSSN-SP simulation) recorded at 12 GRSN, GRF(GRA1), GERESS and GEOFON stations. Traces are sorted according to distance (D = 42.4° to BRG and 47.6° to WLF), shifted and aligned for P onsets. Note that the travel-time curves for PcP and PP intersect in this distance range. Depth phases pP and sP (see the marked theoretically expected arrival times) are not visible on this short-period filtered record.

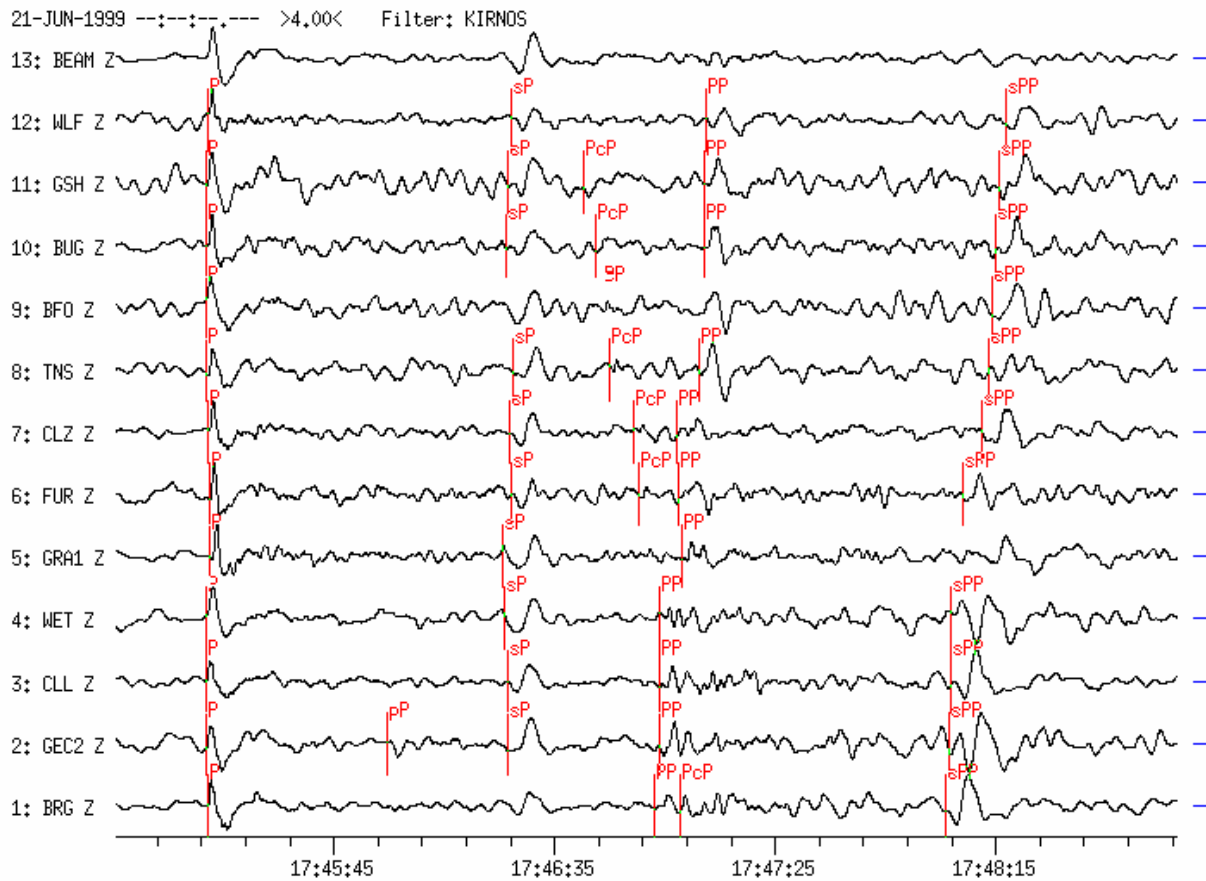


Figure 6b Stations and source parameter as in Figure 6a, however records of displacement-proportional Kirnos-simulation. Phases P, PP and the depth phases sP, sPP are clearly visible on these records while the phase pP is recognizable only at GEC2.

Example 7: Earthquake in the Laptev Sea Region

USGS NEIC-data: 1996-06-22 OT 16:47:13.1 75.812 N 134.710 E h = 10G
 mb = 5.6 Ms = 5.5

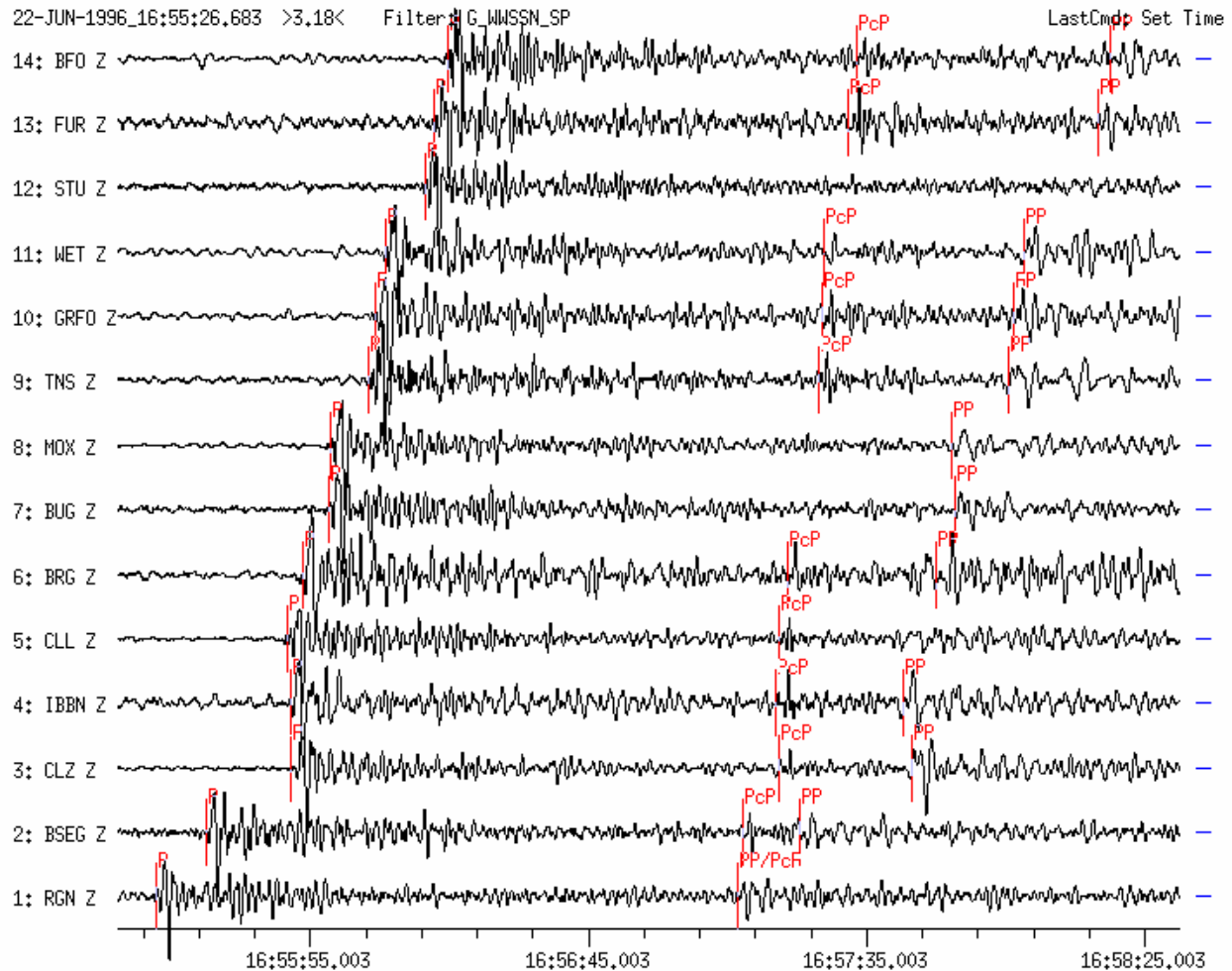


Figure 7a Vertical (Z) component short-period seismograms (WWSSN-SP simulation filter) recorded at 14 GRSN stations. Traces are sorted according to increasing epicentral distance which ranges between $D = 44.5^\circ$ for RGN (with $BAZ = 17.5^\circ$) and 51.4° for BFO (with $BAZ = 14.7^\circ$). P, PcP and PP are clearly visible. Note the decreasing travel-time difference (PcP - P) with increasing epicentral distance and the related small slowness values ($sl < 4$ s/deg) for the core-reflected wave PcP. At a distance of about 45° (see record of station RGN) the travel-time curves of PcP and PP intersect. Generally, PcP is well recorded on short-period filtered records, however no PcP onset is recognizable above the noise level in the records of stations STU, MOX and BUG.

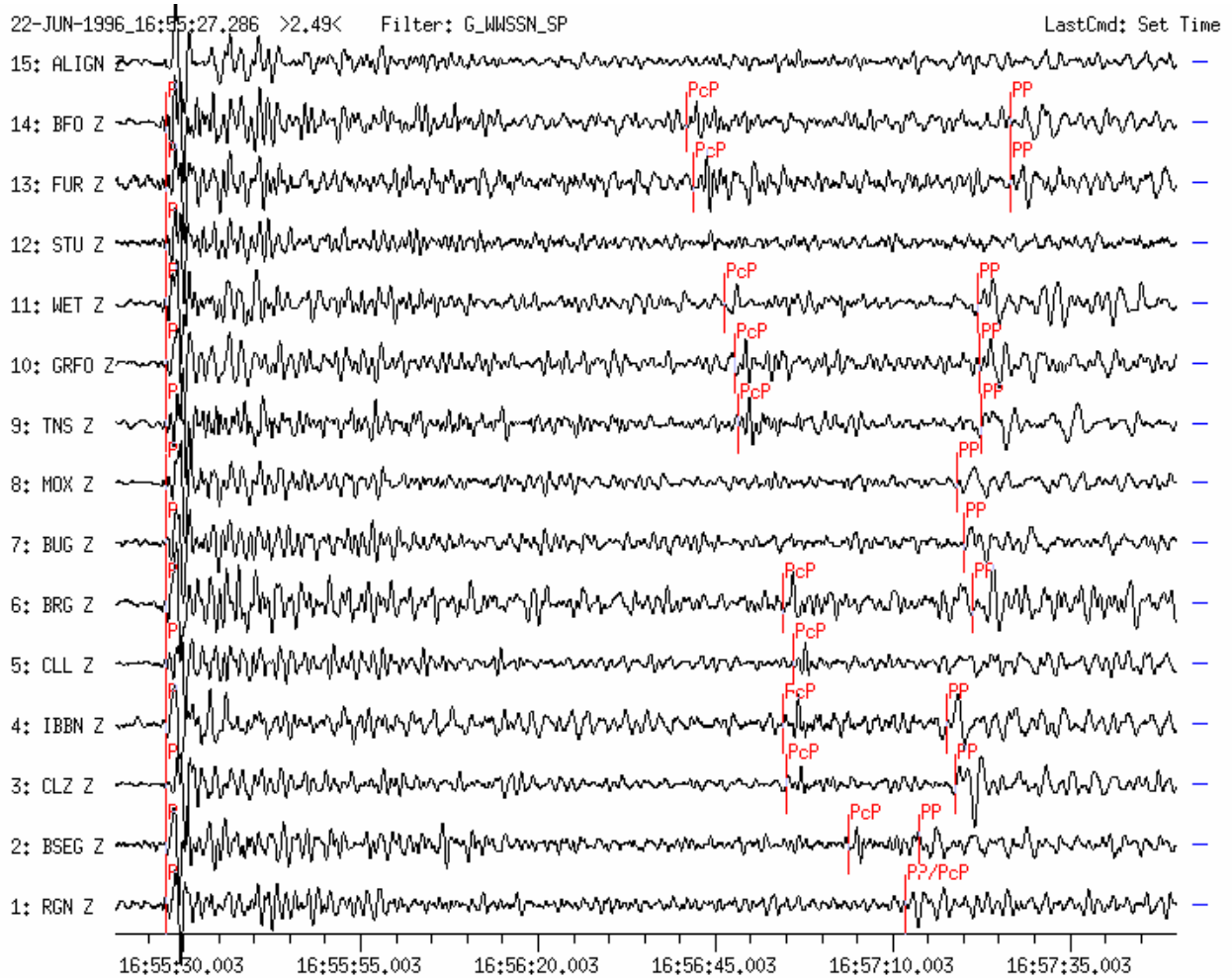


Figure 7b The same records as in Figure 7a, however, traces have been time-shifted and aligned for the P onsets. This figure shows more clearly the decreasing travel-time difference (PcP - P) with increasing distance from the epicenter.

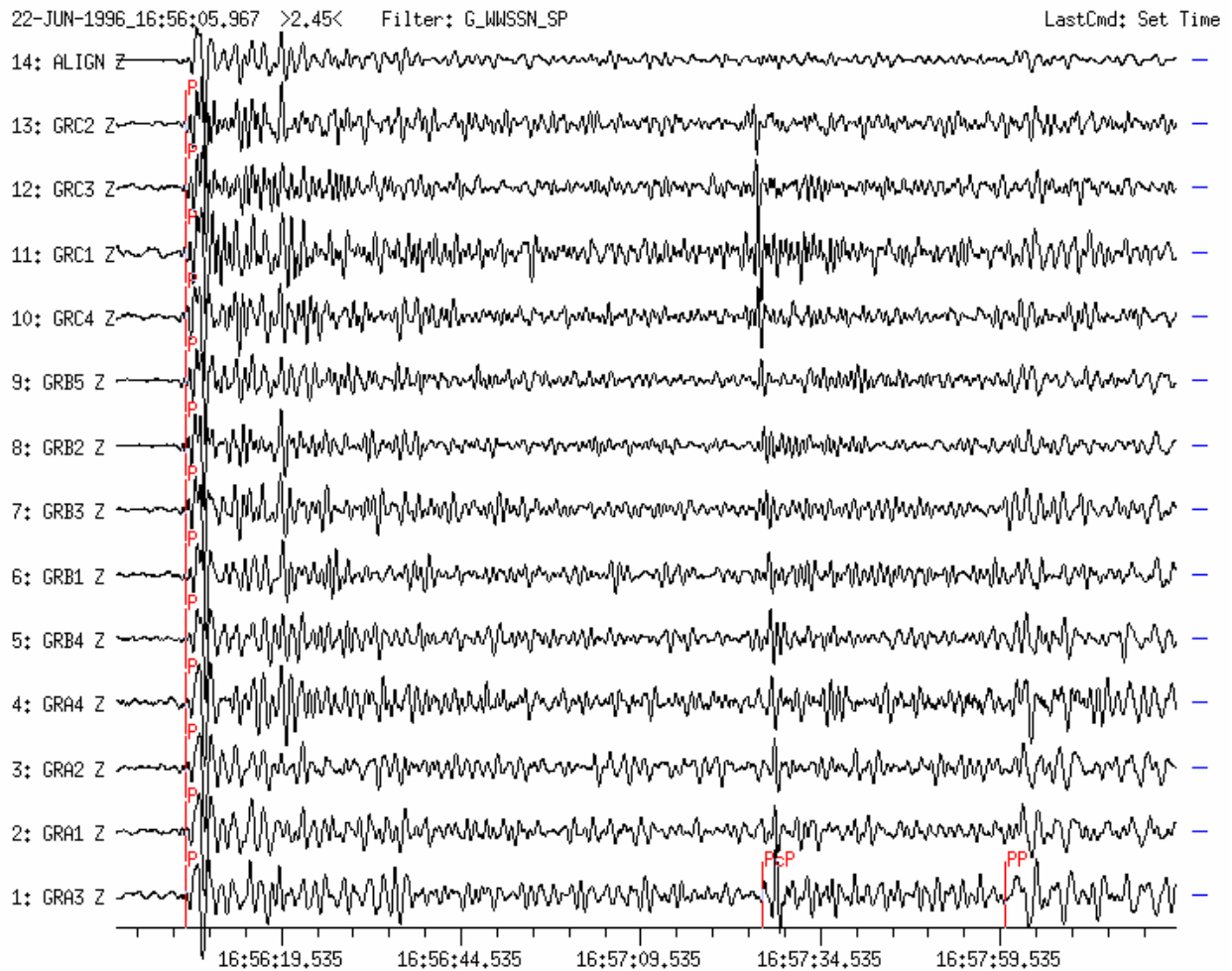


Figure 7c Short-period filtered seismograms recorded at the GRF-array. Traces are sorted according to increasing distance ($D = 49.48^\circ$ to GRA3 and 50.33° to GRC2), shifted in time and aligned for P onsets. Phases P, PcP and PP have been marked. Because of the smaller spacing of the array-stations as compared with the GRSN stations, the decrease of the travel-time difference PcP-P is less obvious.

Example 8: Record of an earthquake in Mongolia

USGS-QED-data: 1998-09-24 OT 18:53:40.2 46.274 N 106.237 E h = 33km
 mb = 5.3 Ms = 5.4, (D = 59.4° and BAZ = 54° from GRF(GRA1))

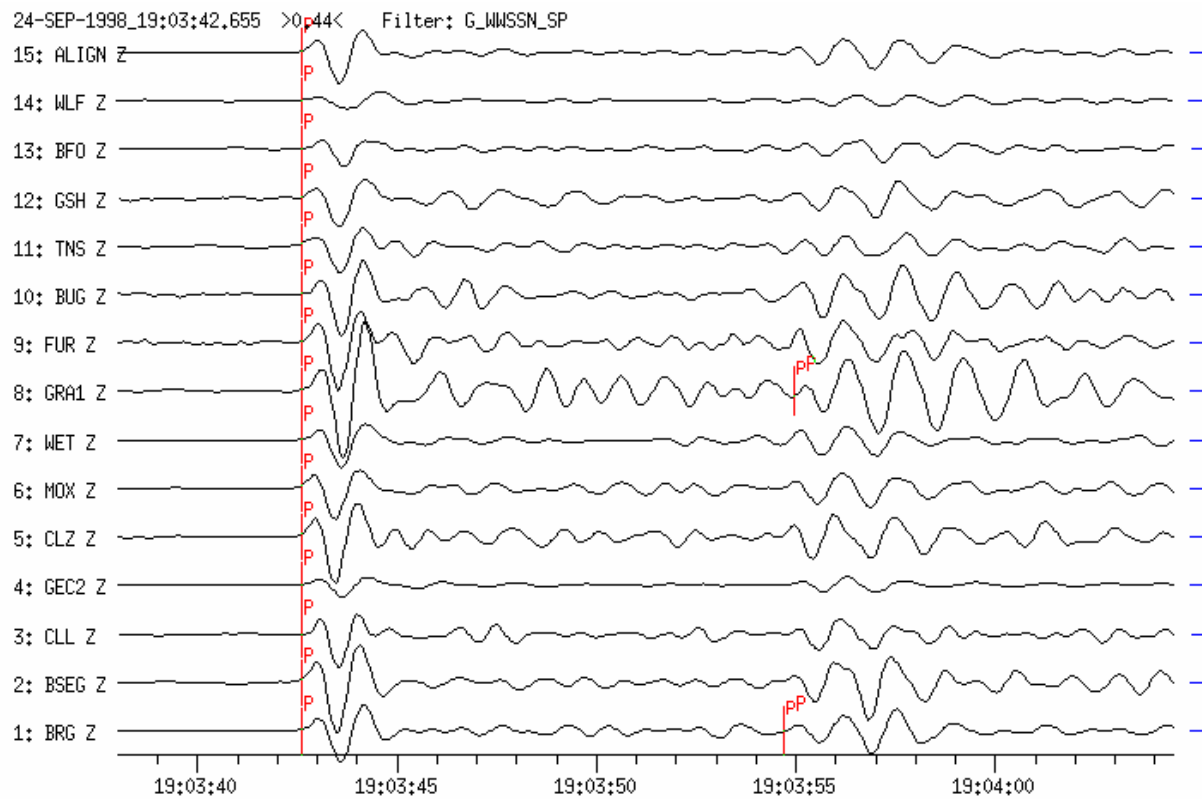


Figure 8a This is an example for an event with coherent short-period P waves within the GRSN (WWSSN-SP simulation filter). Additionally, the record of the GEOFON-station WLF in Luxembourg is shown on trace No.14. The traces are sorted according to increasing distance (D = 57.3° to BRG and 62.1° to WLF), shifted and aligned for P onsets. The most remarkable feature is the strong variability of the P-wave signal-amplitudes within this regional network. The table below gives the measured amplitudes together with the calculated magnitudes. Body-wave magnitudes mb vary between 5.4 (GEC2) and 6.2 (GRA1). The depth phase pP was used to estimate a better source depth (h = 44 km) than the value given in the QED (h = 33 km).

Table 8a Result of the seismogram analysis shown in Figure 8a. The table was printed from the GRSN databank and contains in the uppermost line source parameters like date, an event identification number (ev_id) and the name of the analyst (KLI for Klinge). The following lines give the analyzed stations, onset times, phases, polarities, components, periods T, maximum amplitudes A, body- and/or surface-wave magnitudes mb/MS, epicentral distances D, beam-slowness b_slo, beam_azimuths b_az. The lowermost part of the table contains source parameters like analysis center (SZGRF), origin time OT, latitude, longitude, average magnitude values for mb and MS, depth of the source and source region. Note the significant differences between the magnitude estimates mb from records of different network stations.

						ev_id 980924007		KLI	
1998-09-24									
BRG	19:03:27.2	e P	Z	T 1.2	A 135.5	mb 5.9	D 58.3		
ALIGN	19:03:27.2	e P	Z	T 1.1	A 124.1	mb 5.8			
BSEG	19:03:28.2	e P	Z	T 1.1	A 198.3	mb 6.0	D 58.4		
CLL	19:03:28.6	e P	Z	T 0.9	A 98.9	mb 5.8	D 58.5		
GEC2	19:03:36.3	i P	c Z	T 1.2	A 46.9	mb 5.4	D 59.6		
CLZ	19:03:36.6	e P	Z	T 1.1	A 177.7	mb 6.0	D 59.6		
MOX	19:03:36.9	e P	Z	T 1.2	A 122.4	mb 5.8	D 59.6		
WET	19:03:38.5	e P	Z	T 1.2	A 107.2	mb 5.7	D 59.9		
BRG	19:03:39.3	e pP	Z						
GRA1	19:03:42.6	i P	c Z	T 1.1	A 286.5	mb 6.2	D 60.4		
						b_slo 6.8	b_az 54		
BUG	19:03:48.5	e P	Z	T 1.1	A 162.4	mb 5.8	D 61.4		
FUR	19:03:48.6	e P	Z	T 1.1	A 174.3	mb 5.8	D 61.3		
TNS	19:03:49.9	e P	Z	T 1.1	A 103.0	mb 6.0	D 61.5		
GSH	19:03:54.5	e P	Z	T 1.3	A 132.3	mb 6.0	D 62.3		
GRA1	19:03:55.0	e pP	Z						
BFO	19:03:57.4	e P	Z	T 1.1	A 55.2	mb 5.6	D 62.8		
WLF	19:04:00.1	e P	Z	T 1.7	A 80.3	mb 5.6	D 63.0		
GRA1	19:11:52.2	e S	E						
							D 60.4		
GEC2	19:30:36.0	e L	Z	T 19.9	A 3895.8	MS 5.5			
GRA1	19:31:03.6	e L	Z	T 20.6	A 3398.7	MS 5.5			
SZGRF	OT 18:53:39.3	45.30N	106.84E	mb_av 5.8	MS_av 5.5				
DEP	44km	▲ MONGOLIA							

Example 9: Earthquake in California

SZGRF-data:1999-10-16 OT 09:46:55 34.9N 115.9 W mb = 6.6 Ms = 7.9
 The event happened east of Los Angeles (D = 83.6° BAZ = 319° from GRF) .

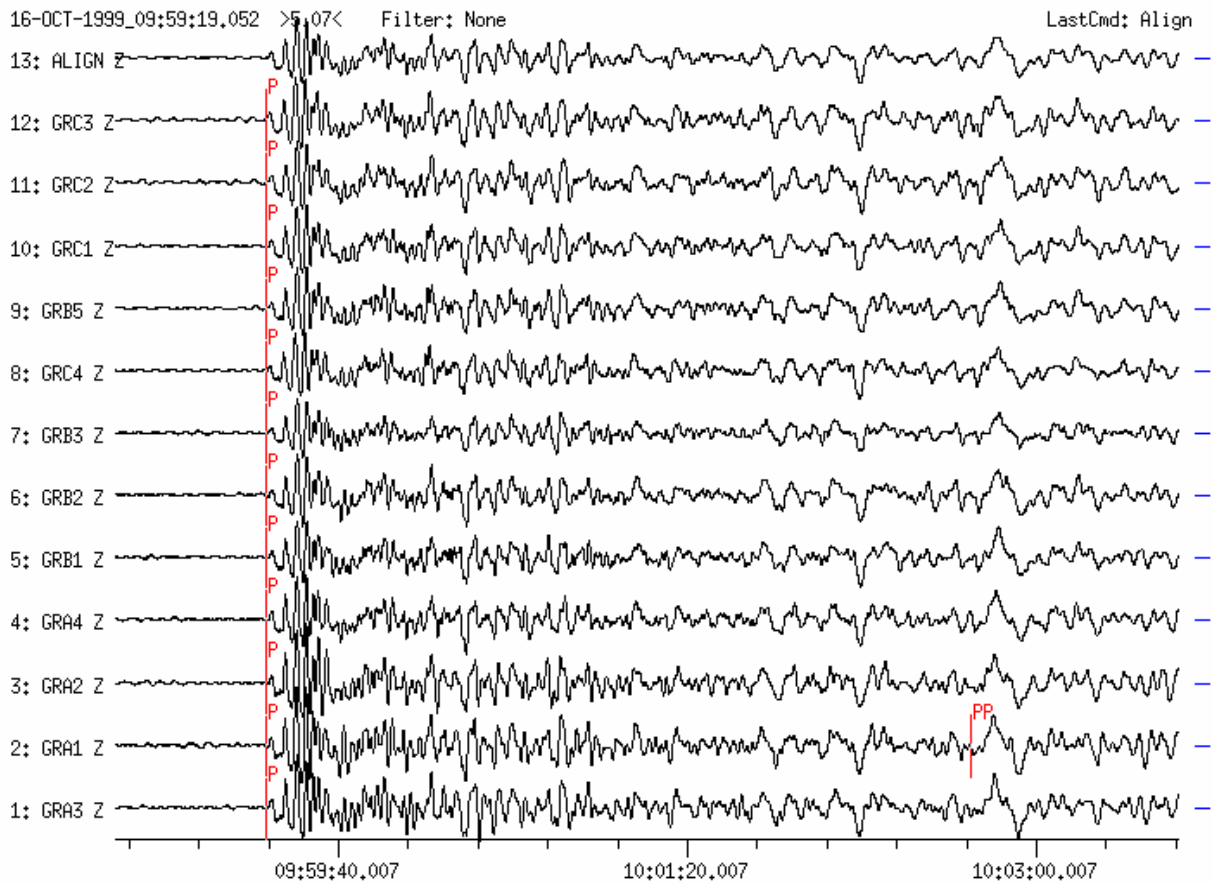


Figure 9a Broadband vertical-component seismograms recorded at 12 GRF-array stations. Traces are sorted according to increasing distance (D = 83.6° to GRA3 and 84.4° to GRC3), shifted in time and aligned for P onsets. The coherent phases P and PP are marked, however some more onsets appear ahead of PP.

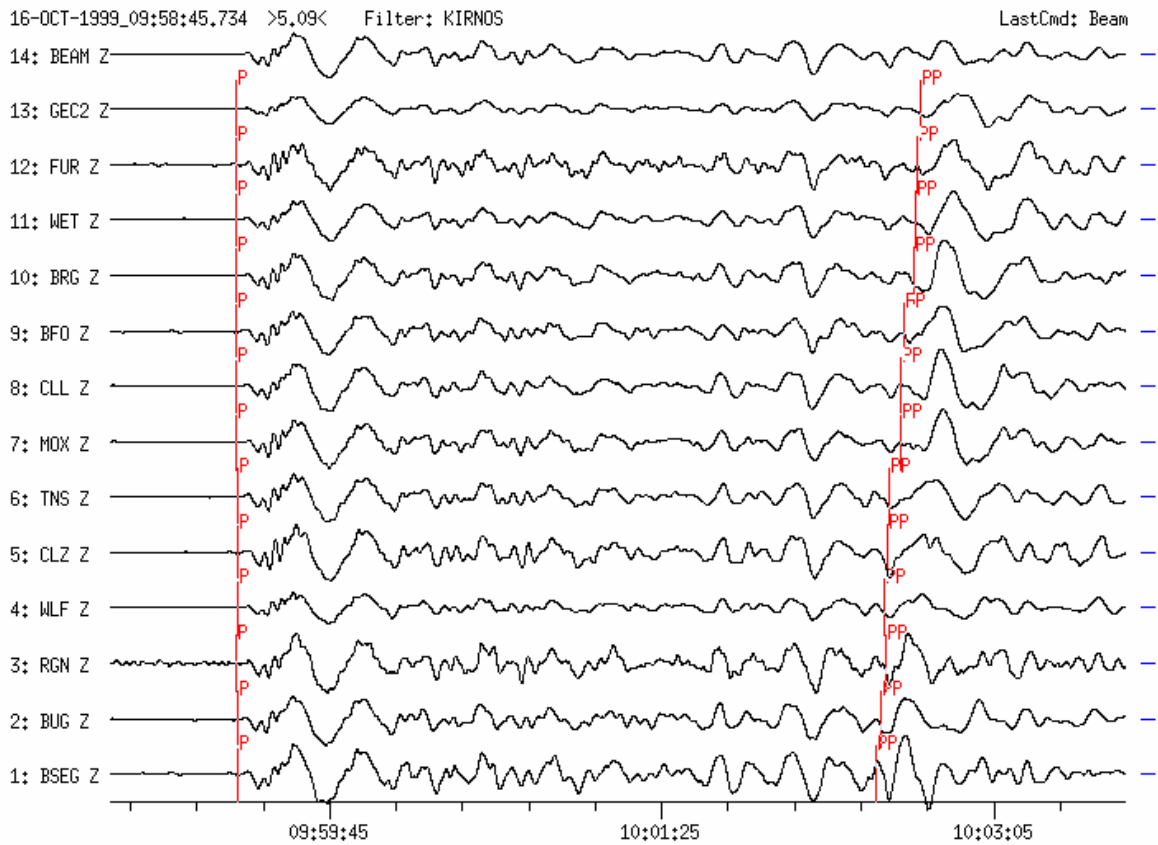


Figure 9b Broadband vertical-component seismograms recorded at 13 GRSN-stations. Traces are filtered (Kirnos-simulation), sorted according to increasing distance (80.1° to BSEG and 85.3° to GEC2), shifted in time and aligned for P onsets. The used displacement proportional broad-band filter displays clearly the coherent part of the wave train from the network. As in Figure 9a, coherent phases appear ahead of PP that have slowness values as P.

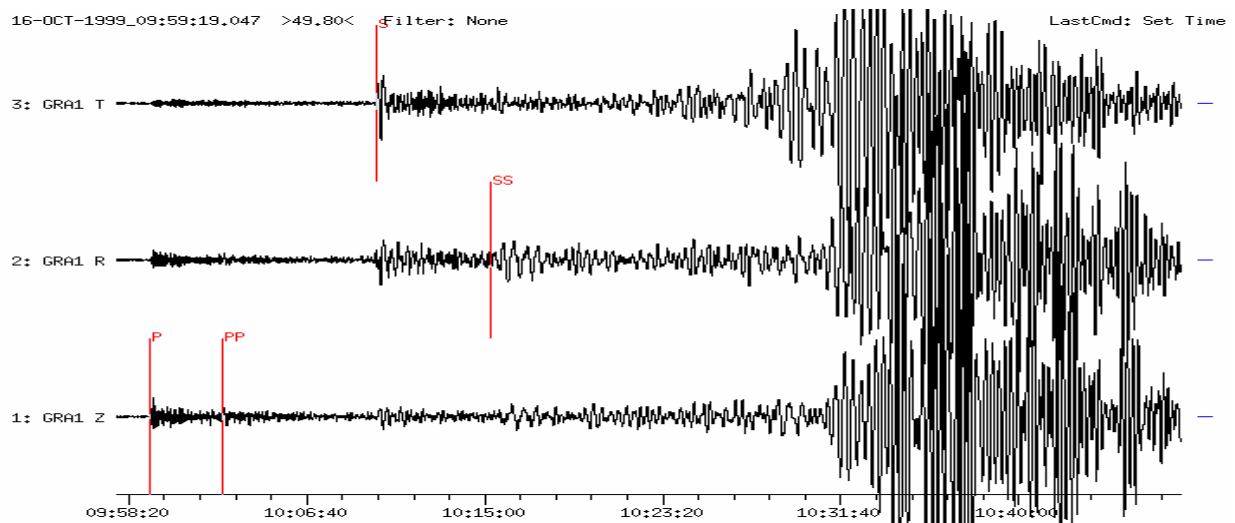


Figure 9c Broadband three-component seismogram recorded at GRA1 ($D = 83.6^\circ$). The horizontal components are rotated into the R and T direction. Phases P, PP, S, SS and surface waves are displayed. Rayleigh waves recorded on radial and vertical components appear later than Love waves recorded on the transversal component only.

Example 10: Earthquake near the coast of NICARAGUA

USGS NEIC-data: 1998-10-09 OT 11:54:29.0 11.337N 86.429W h = 10km
 mb = 5.6 Ms = 5.6 (D = 86.3° and BAZ = 282° from GRF(GRA1))

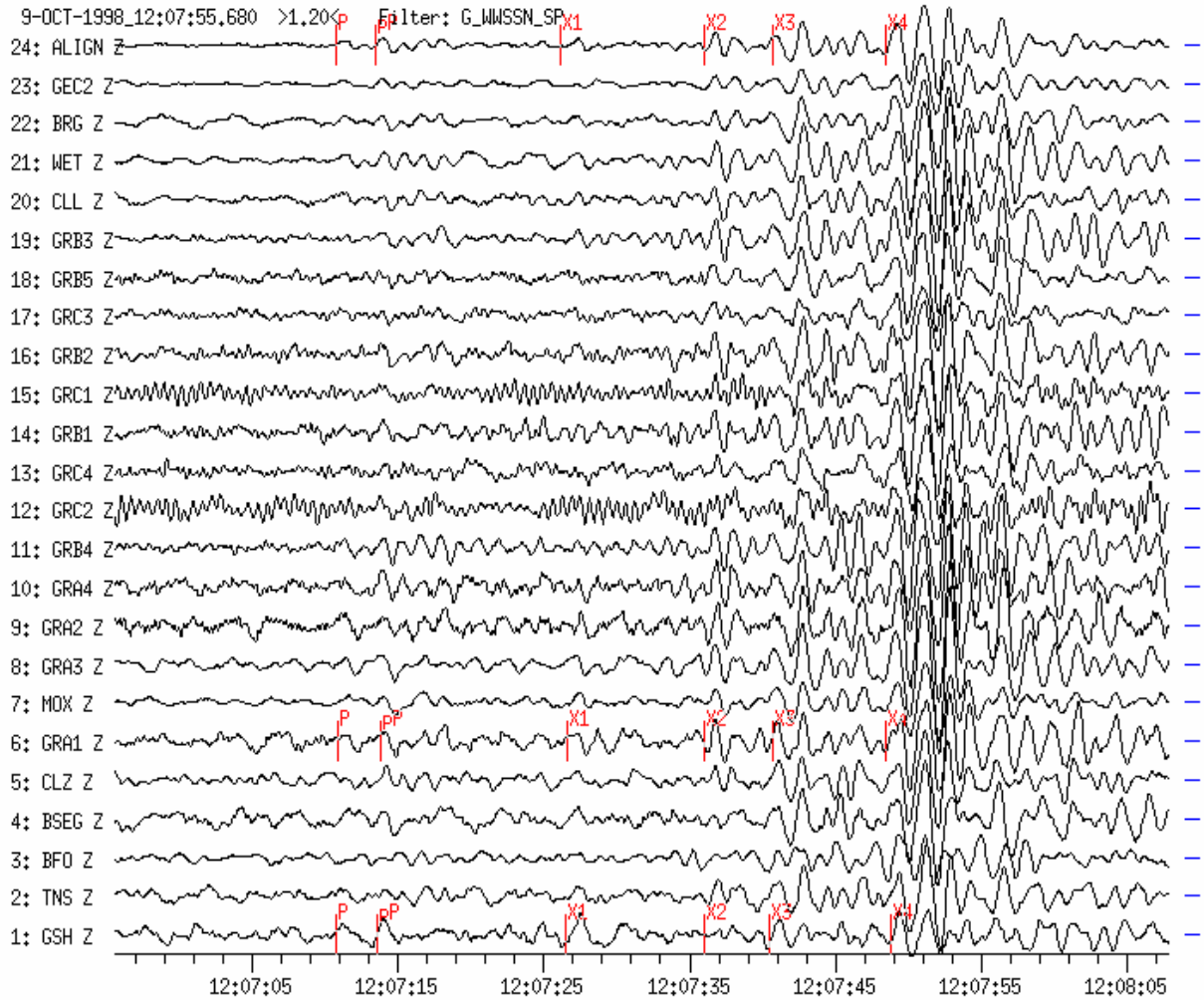


Figure 10a Short-period seismograms (WWSSN-SP simulation filter) from 23 broadband stations of the GRF-array, the GRSN network and the GERESS array (GEC2). Traces are time-shifted, aligned for P and sorted according to increasing distance (D = 83.1° to GSH and 88.1° to GEC2). Note the large number of onsets within the first 40 sec of the P-wave group (P, pP, X1, X2, X3, X4). The reason for these multiple onsets may be a multiple rupture process or (in some cases) reflections from the nearby subduction zone.

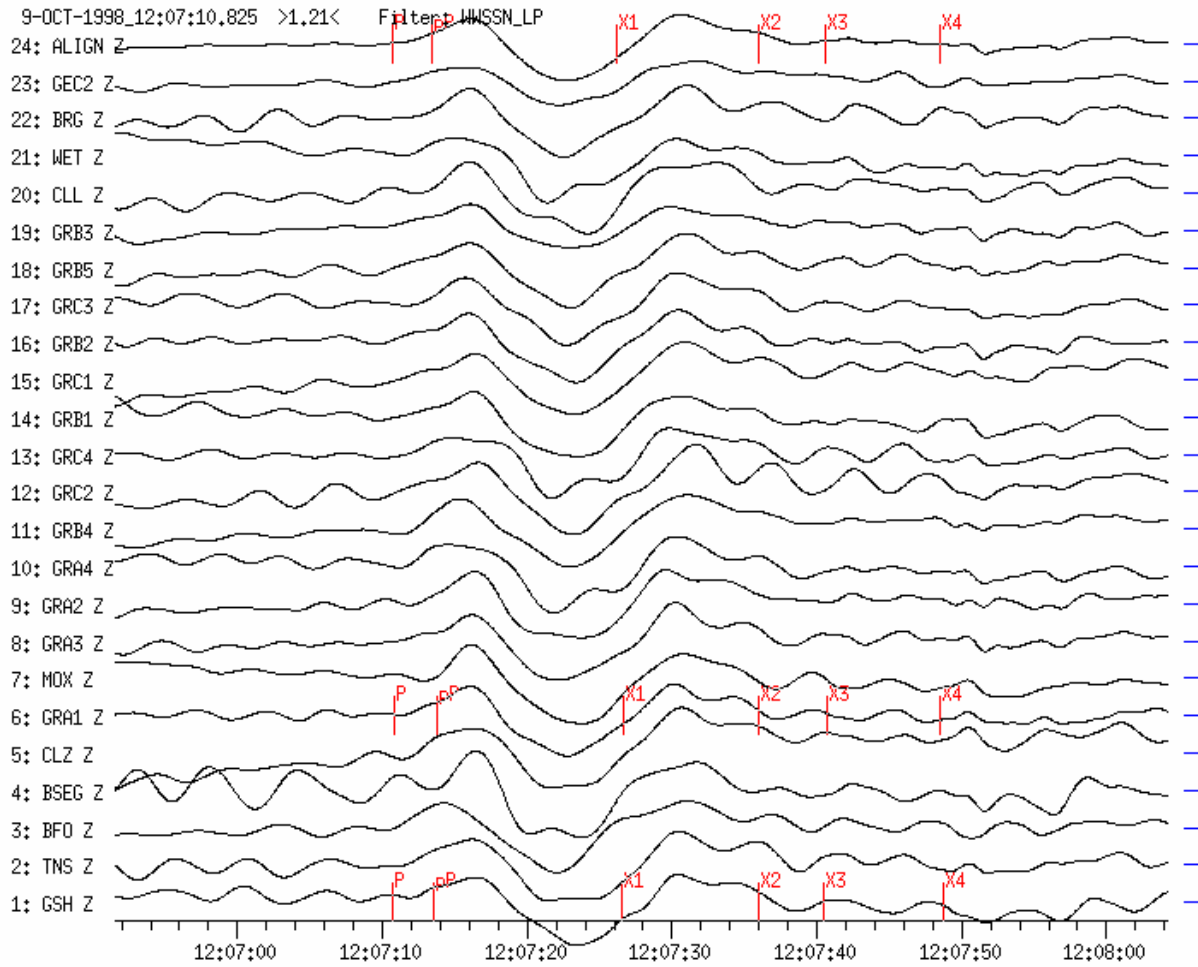


Figure 10b Long-period seismograms (WWSSN-LP simulation filter) of the same stations as in Figure 10a, depicted with high time-resolution. Traces are aligned and sorted according to increasing distance. Note the very long-period P-wave onset ($T \approx 14$ s) in the time window between P and X2 where the P-wave amplitudes are relatively small in the short-period filtered records whereas at X4, which is by far the largest onset in Figure 10a, no long-period wave onset is to be seen. This seems to speak of an initially “slow” earthquake rupture which then escalated into a faster rupture or the break of a “harder” asperity which generated more short-period energy.

9-OCT-1998_12:06:59.015 >45.21< Filter: SRO_LP

LastCmd: Theo <Table

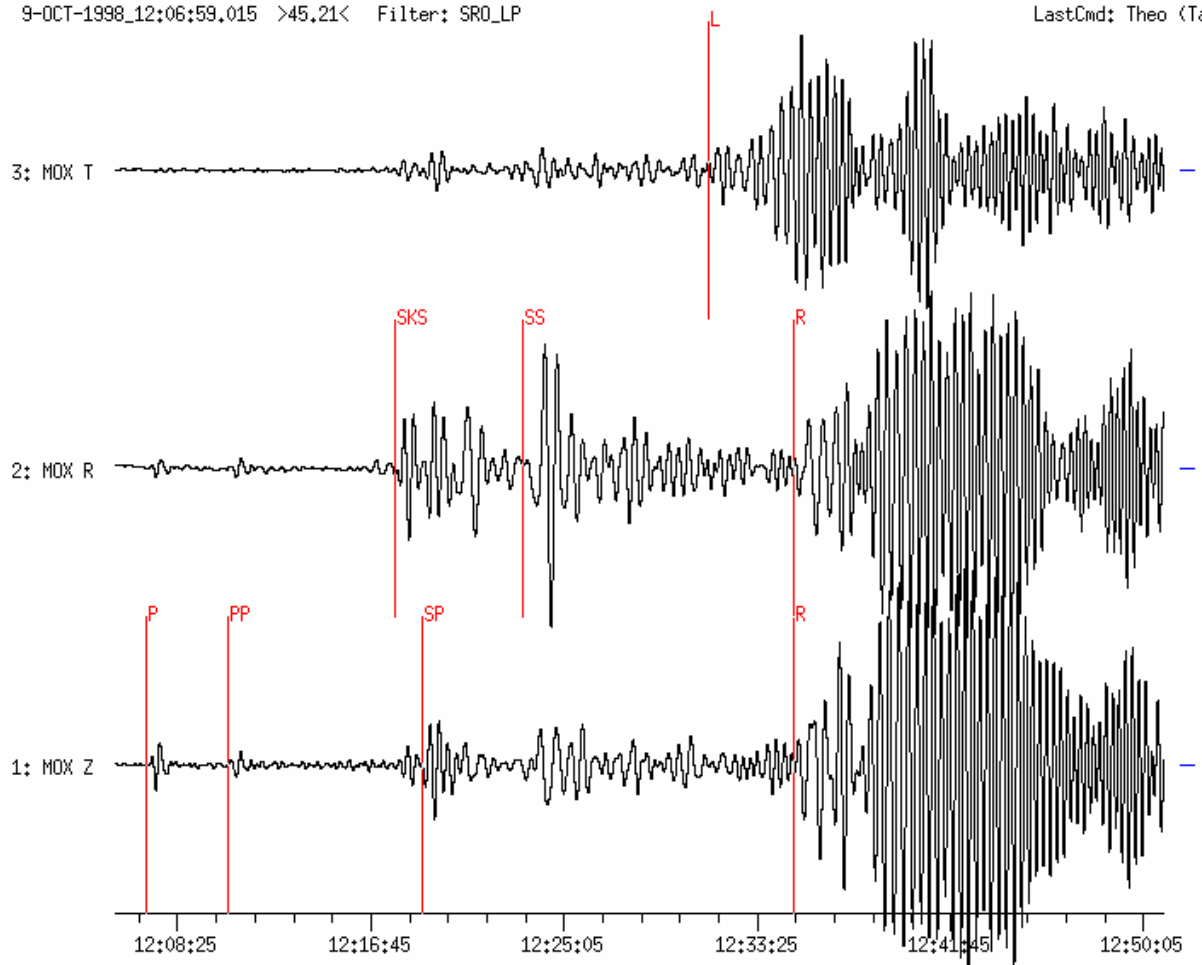


Figure 10c Time-compressed long-period filtered three-component seismogram (SRO-LP simulation filter) of the Nicaragua earthquake recorded at station MOX ($D = 86.4^\circ$, $BAZ = 283^\circ$). Horizontal components have been rotated into the R (radial) and T (transverse) direction. The seismogram shows long-period phases P, PP, SKS, SP, SS and surface waves L (or LQ for Love wave) and R (or LR for Rayleigh wave). Note the remarkably simple waveforms of P and PP as compared with the complicated structure in the short-period P-wave group in Figure 10a.

Example 11: Earthquake in Taiwan Region

USGS NEIC-data: 1996-08-10 OT 06:23:08 24.032 N 122.550 E h = 46G
 mb = 5.2 Ms = 5.2 (D = 87.1° and BAZ = 56.6° from BFO)

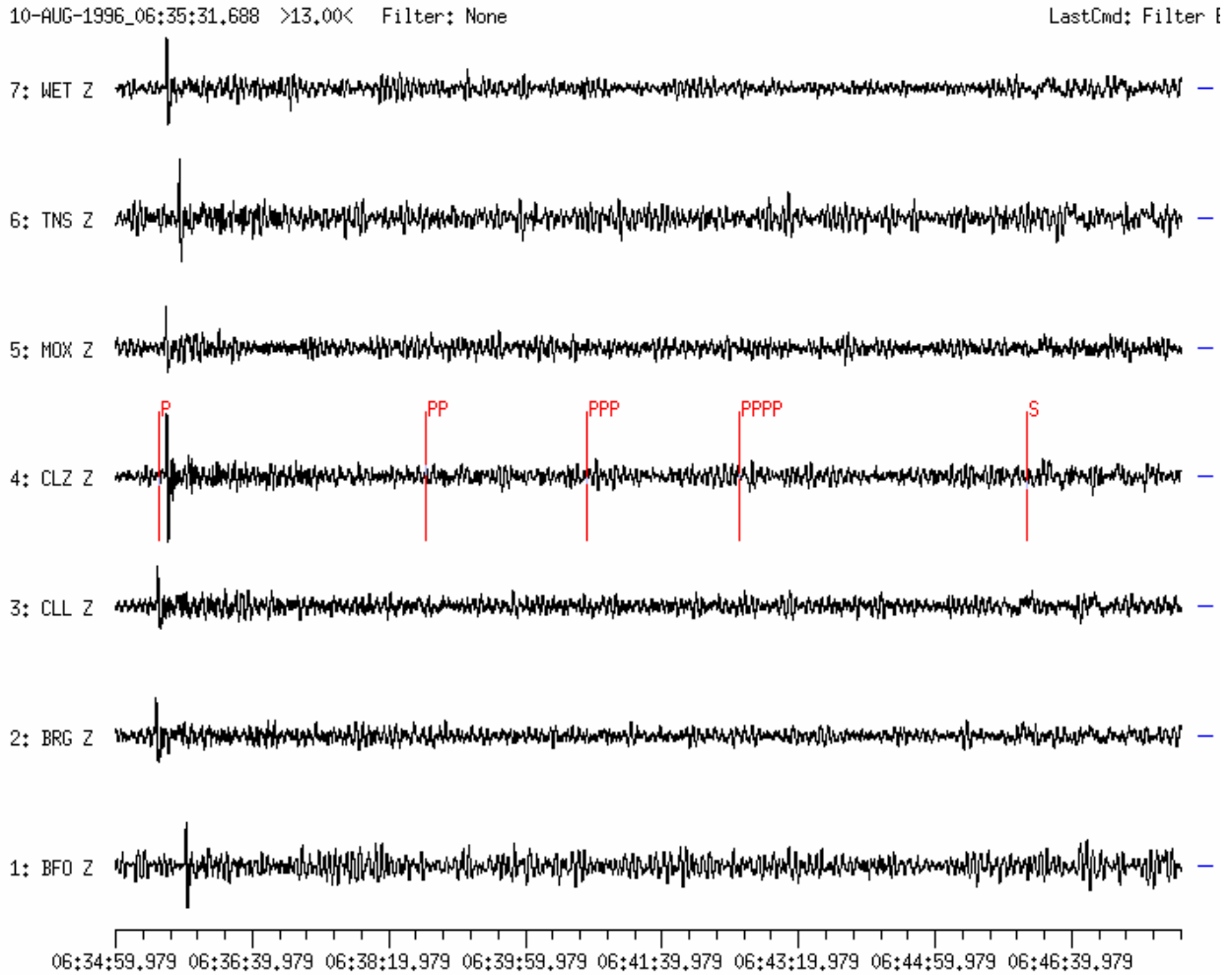


Figure 11a Broadband vertical-component seismograms of the Taiwan earthquake recorded at 7 GRSN-stations within the distance range $D = 82.9^\circ$ and 87.1° . Only the P-wave onset is recognizable on the records. Secondary onsets such as surface reflections of the P and S wave (theoretical onset times marked on the CLZ trace) are not to be seen above the noise level.

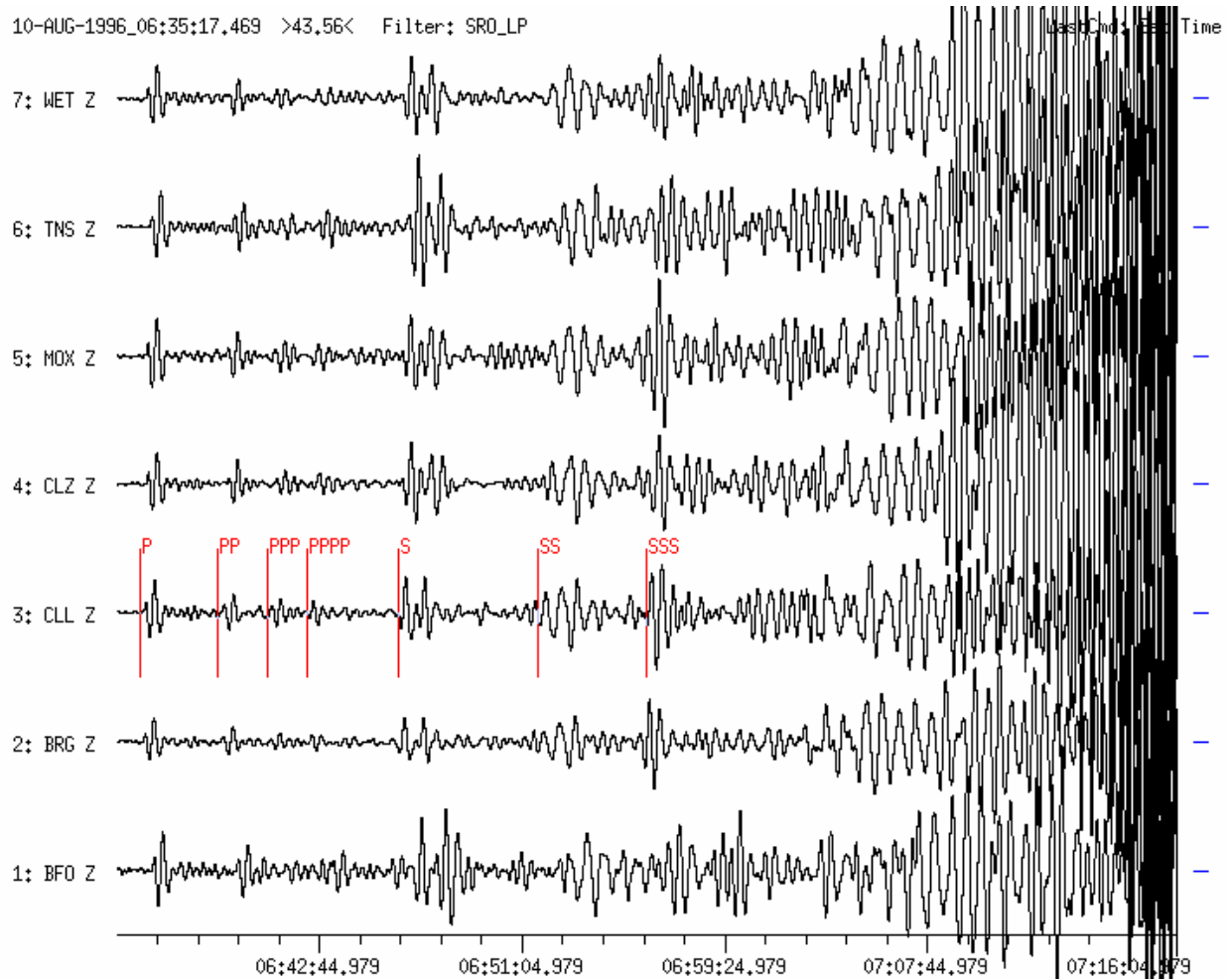


Figure 11b The same event as in Figure 11a after long-period filtering (SRO-LP simulation filter). Note the pronounced onsets of PP, PPP, PPPP as well as S, SS and SSS which are marked at the record trace of station CLL ($D = 82.9^\circ$). Phase identification is eased by using absolute (see overlay to Fig. 2.48) or differential theoretical travel-time curves (see Figure 4 in Exercise EX 11.2). This is essential when interpreting single station recordings. Modern seismogram analysis program can automatically mark the theoretically expected onset times of the various phases when the epicentral distance to the station and the source depth are known or assumed. When a network of stations or array is available, phase identification is supported by *vespagram* analysis as shown in the following figure.

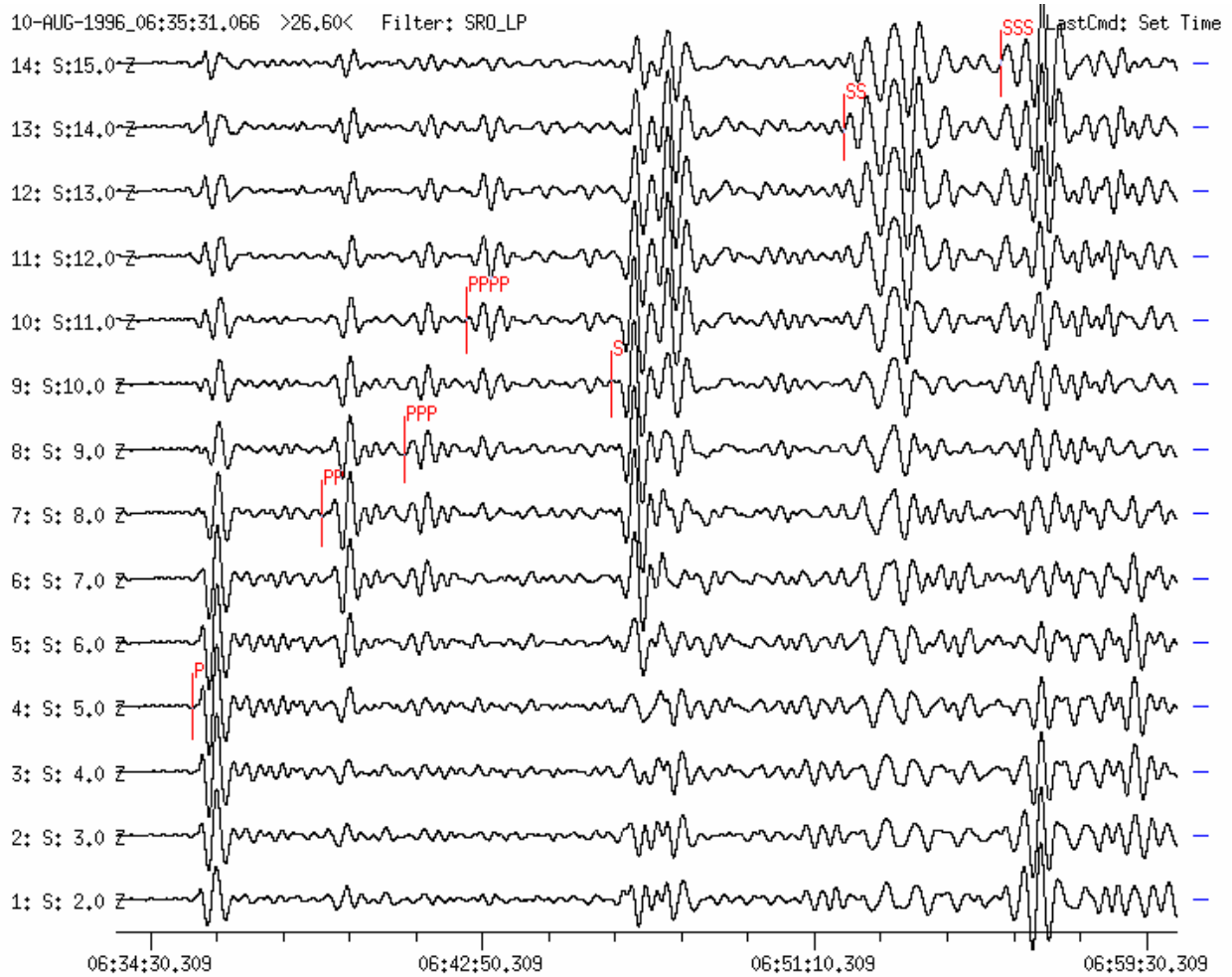


Figure 11c For better phase identification a [vespagram analysis](#) (see 9.7.7 in Chapter 9) of the long-period filtered traces was made. Identified phases have been marked on their respective slowness trace S (e.g., P on trace 4 with slowness $S = 5.0 \text{ s}^\circ$ and PP on trace 7 with $S = 8.0 \text{ s}^\circ$). In the vespagram traces the respective phases have the largest amplitudes at their proper slowness value.

Example 12: Earthquake in the region of Michoacan, Mexico

USGS NEIC-data: 1997-01-11 OT 20:28:26.0 18.193 N 102.800 W h = 33G
 mb = 6.5 Ms = 6.9 (D = 90.9° and BAZ = 299.7° from GRFO site)

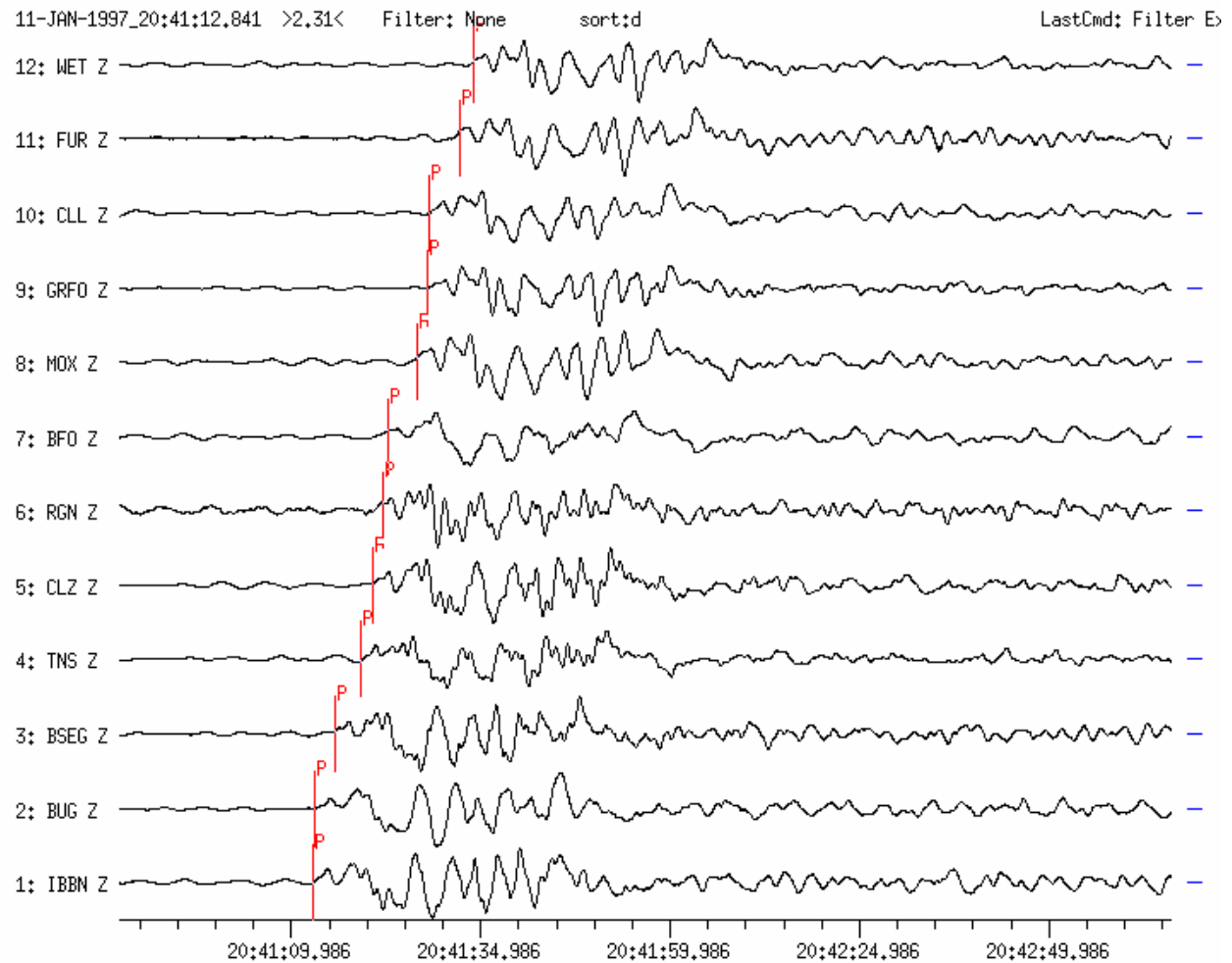


Figure 12a Broadband vertical-component seismograms recorded at 12 GRSN-stations are shown. Traces are sorted according to increasing distance of the stations (D = 87.7° to IBBN and 92.1° to WET). P-wave onsets are marked.

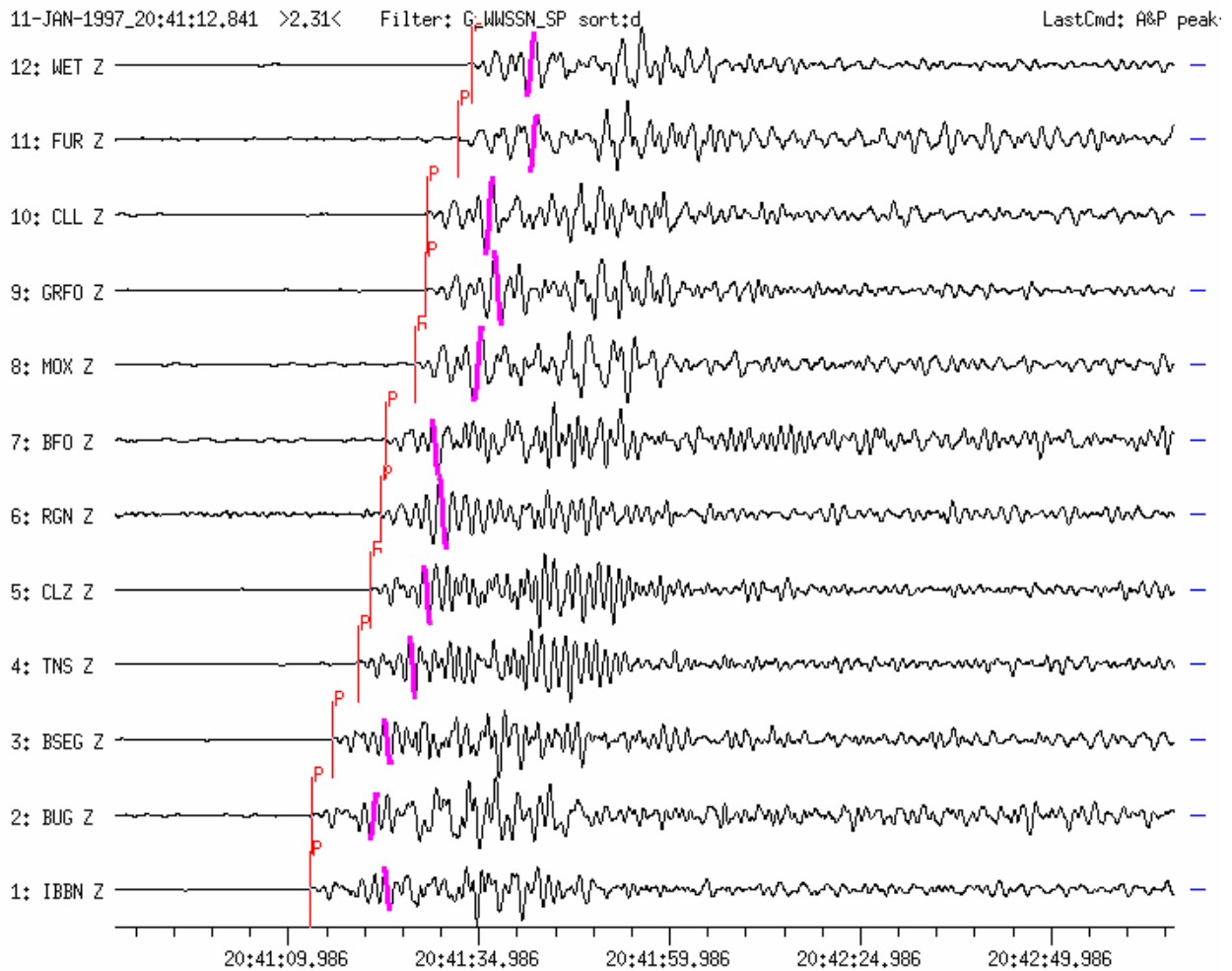


Figure 12b Records at the same stations as in Figure 12a, however after application of a short-period WWSSN-LP simulation filter. This is necessary for amplitude and period measurements required for standardized mb body-wave magnitude determinations. Maximum double-amplitudes ($2A$) and half-periods ($T/2$) are marked for the first wave group. Later onsets may belong to secondary or depth phases.

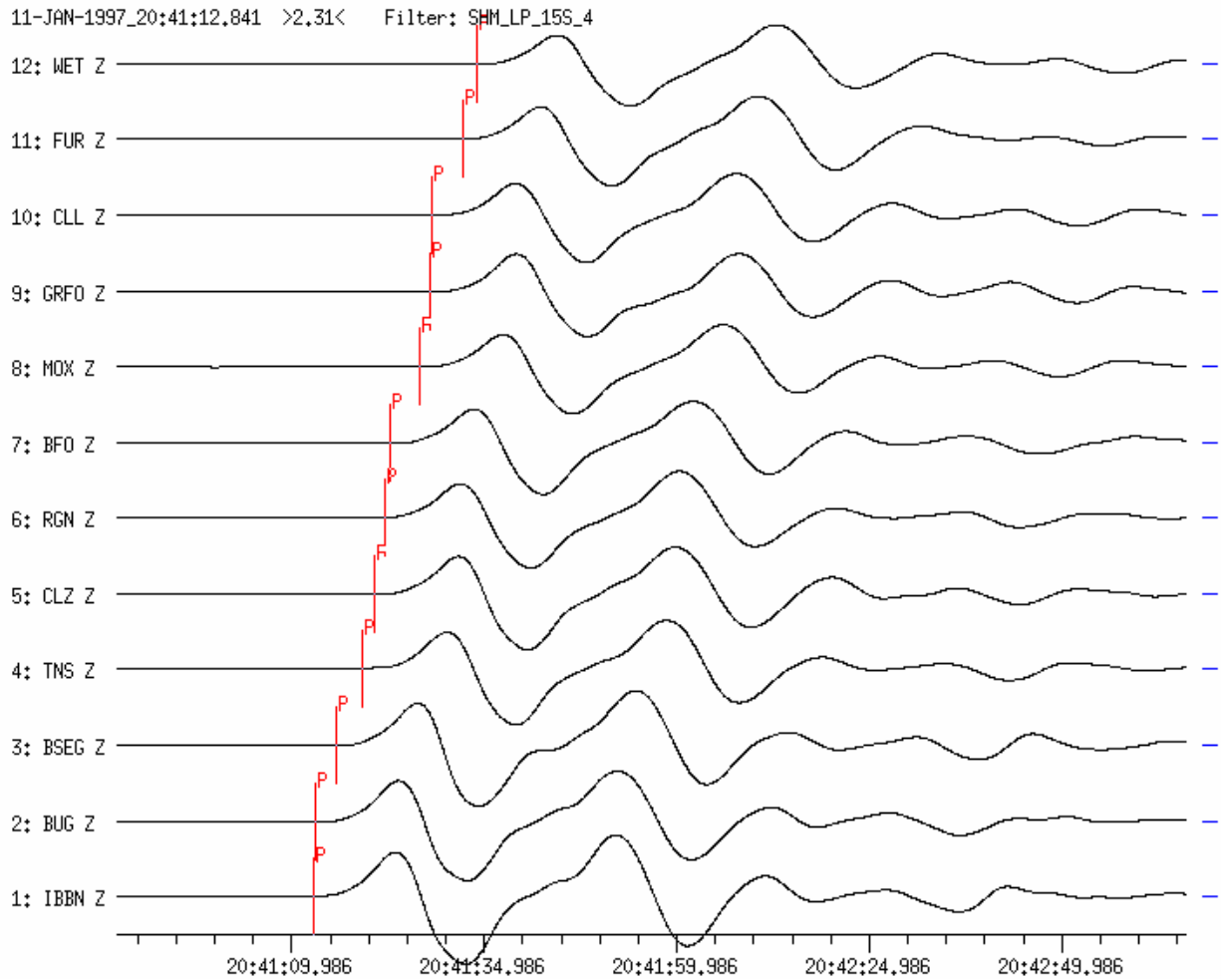


Figure 12c Records at the same stations as in Figure 12a, however after application of a 4th-order Butterworth low-pass filter ($f_c = 15$ s). They show the long-period energy content of the earthquake with P-wave periods of about 20s! All long-period network traces are coherent. In this case the network can be used as an array.

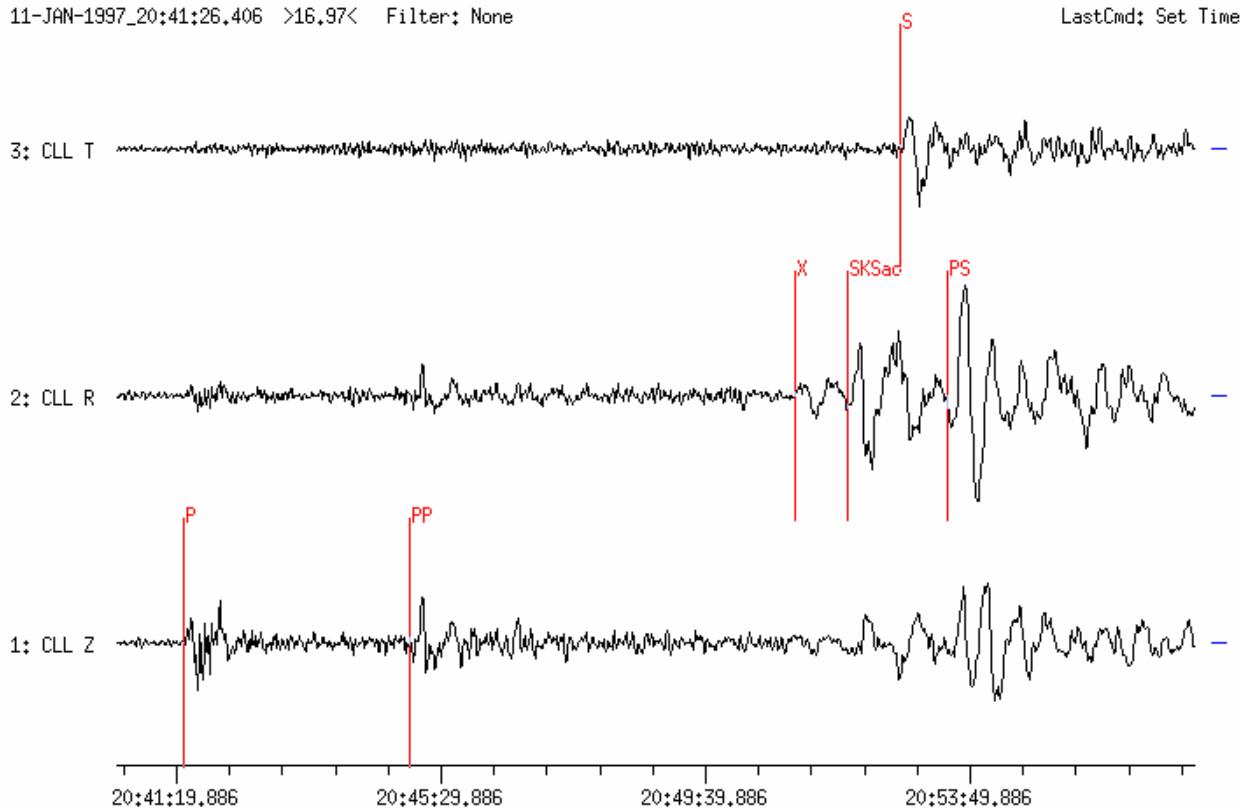


Figure 12d Broadband three-component seismogram recorded at station CLL ($D = 91.0^\circ$, $BAZ = 301^\circ$). Note that at teleseismic distances P waves and their multiples show up most clearly in the Z component because of the small incidence angle, decreasing with distance, and the oscillation of P waves in ray direction. The horizontal components are rotated, with R into the source direction. The radial component shows most clearly the direction of wave propagation (or toward the source; i.e., with a 180° ambiguity which can be resolved by taking the direction of P-wave first-motion – up or down – into account; see EX 11.2). Accordingly, in the R component all waves show up clearly which are polarized in the Z-R plane. These are, besides the primary and multiple P waves also all waves which have been converted during their propagation at discontinuities from P into S and vice versa such as PS, PPS, SP, SSP etc. but also SKP, PKS, SKS, SKKS etc. The latter had to travel at least one segment along their travel path through the Earth’s outer core (K) which is liquid and transmits no S waves. S waves, however, which have been generated by mode conversion from P waves, can oscillate only in the same Z-R plane as P itself. And when a mantle S waves hits the core-mantle boundary, only their vertically polarized SV energy can partially be converted into a P wave and penetrate into the outer core while any SH energy will be totally reflected back into the mantle. This also explains, why multiple S-wave reflections such as SS, SSS, SSSS contain an increasing part of SH energy. The primary S waves, as originating from the earthquake rupture process, may contain both SV and SH energy in variable proportions, depending on the rupture orientation in space. The SH part shows up in records of the transversal (T) component. When comparing energy arrivals in the S-wave time window in the T and R components one can discriminate between S and SKS (see figure above). Note that SKS and PS are recorded also in Z, however with smaller amplitudes because of their oscillating perpendicular to the ray orientation. An unknown phase, denoted X, appears ahead of SKS in R. Surface waves are not visible because they arrive outside of the displayed time window.

For single station analysis phases can be determined with the help of (differential) travel-time curves (see Figure 2 in Exercise EX 11.2). For a station network vespagram analysis (see also Chapter 9, section 9.7.7) proves to be a much better analysis method because of the additional slowness determination. The following three figures (12e - 12g) show vespagrams of the vertical (Z), radial (R) and transverse (T) components recorded at 12 GRSN-stations. To get a better signal coherency, all traces were filtered with a 4th- order long-period low-pass filter ($f_c = 15$ s).

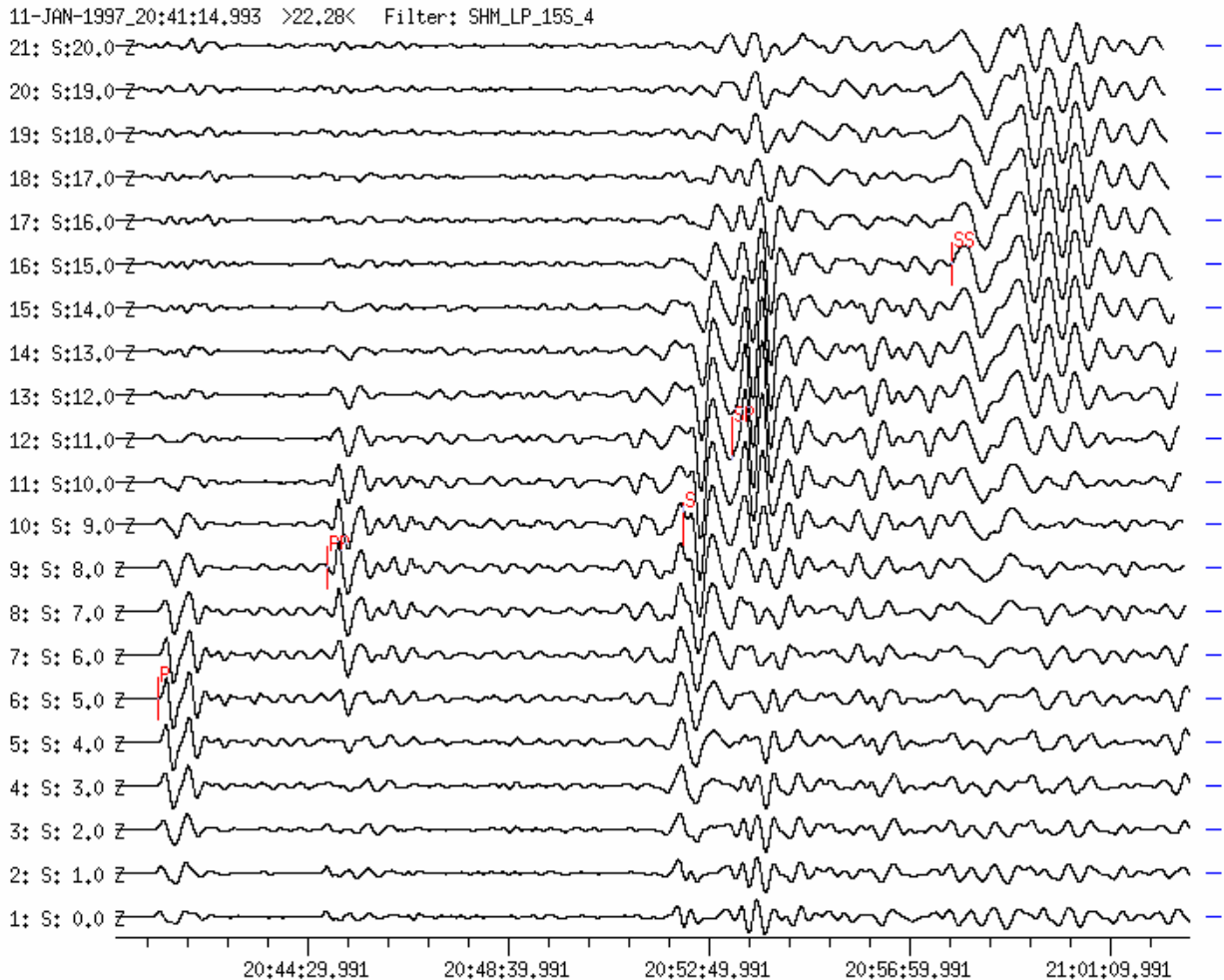


Figure 12e The identified phases from the vertical-component vespagram are marked on the respective slowness traces where they have their largest amplitudes (e.g. P on trace 6: belonging to a slowness $S = 5$ s/°, PP on trace 9 with $S = 8$ s/°, SP on trace 12 with $S = 11$ s/° and SS on trace 16 with $S = 15$ s/°).

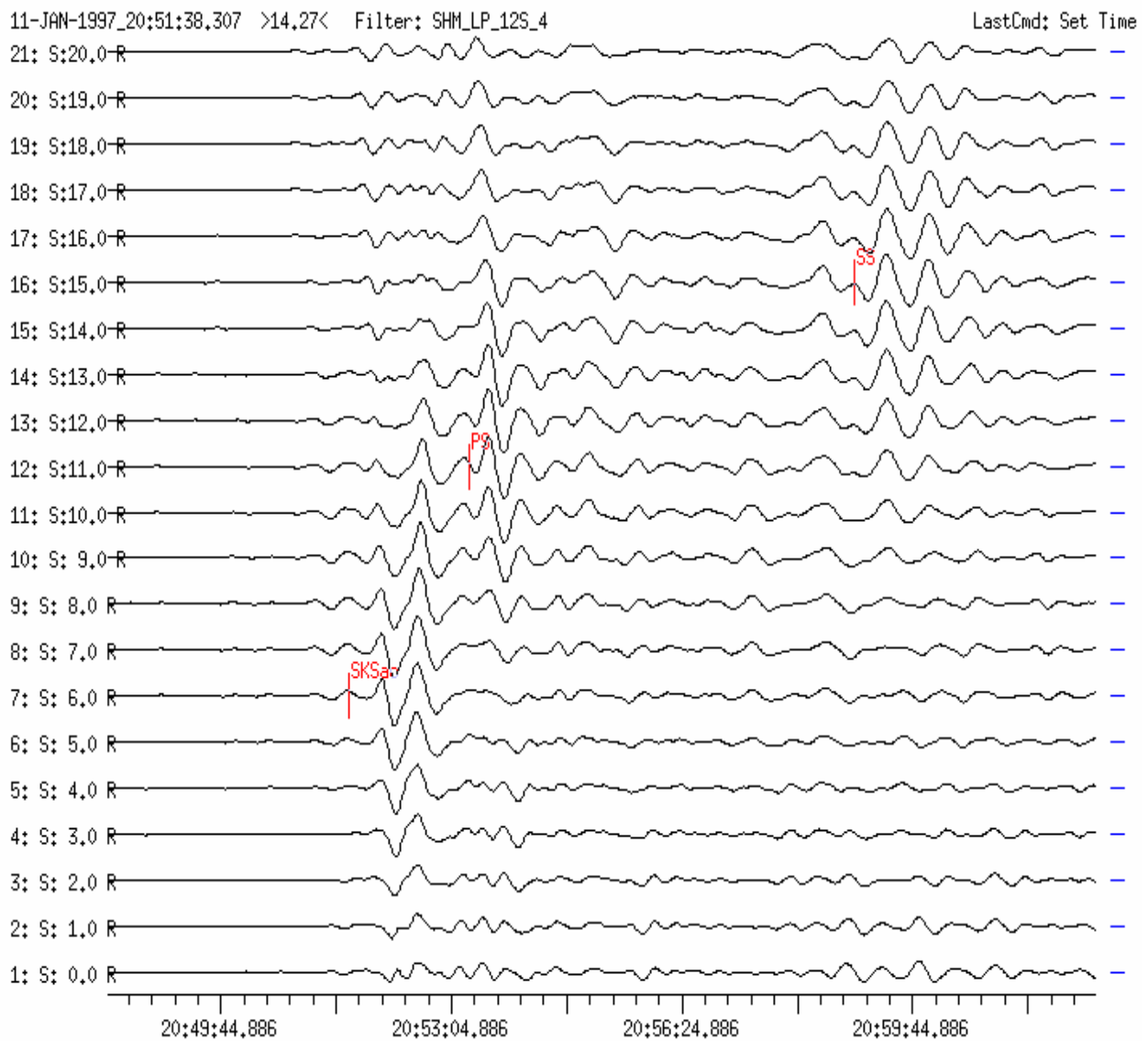


Figure 12f The identified phases from the radial-component vespagram are marked on slowness the respective slowness traces (SKSs on trace 7 with a slowness $S = 6 \text{ s}^\circ$, PS on trace 12 with $S = 11 \text{ s}^\circ$ and SS on trace 16 with $S = 15 \text{ s}^\circ$).

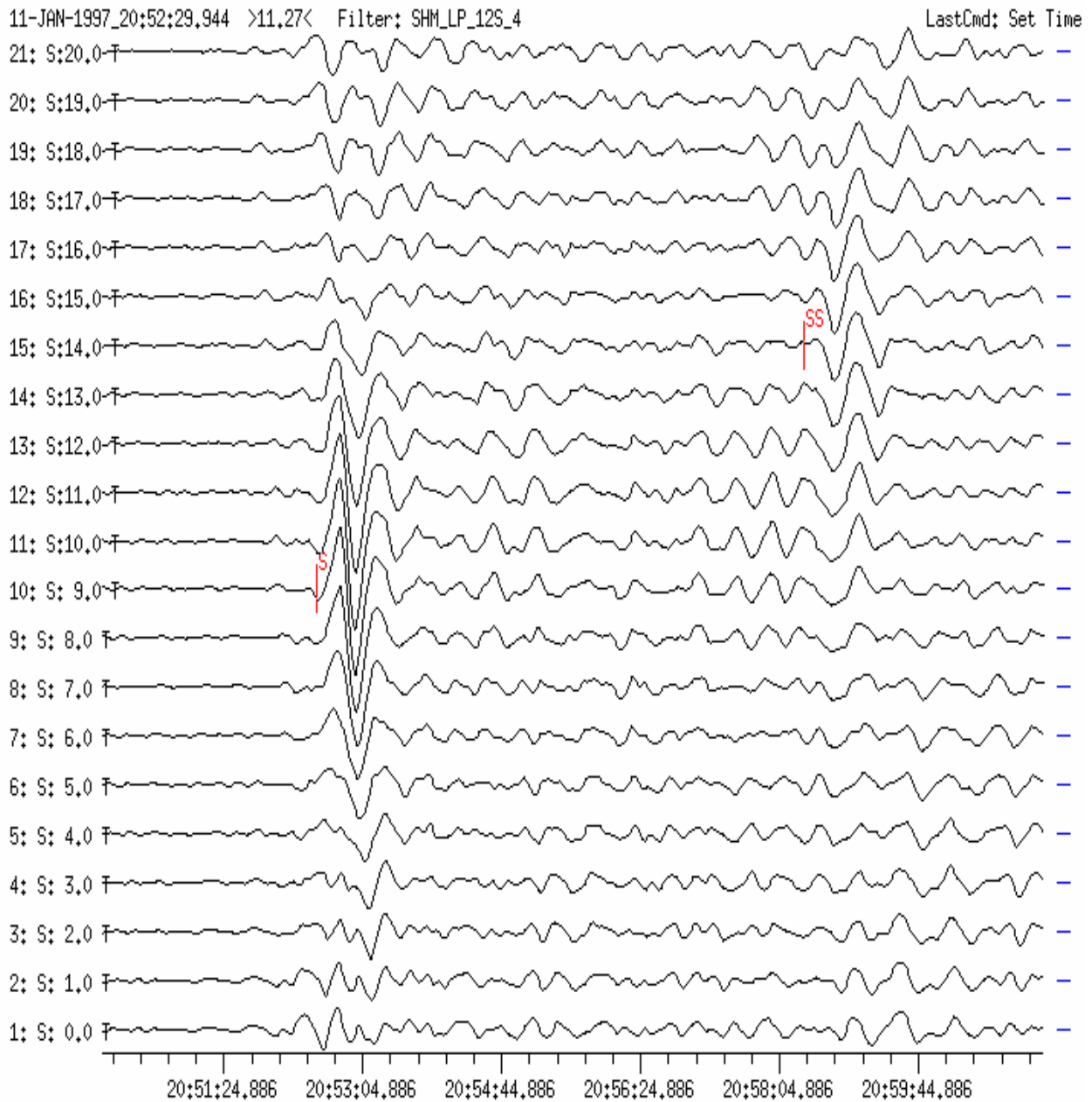


Figure 12g The identified phases from the transverse-component vespagram are marked on their respective slowness traces (S on trace 10 corresponding to a slowness $S = 9 \text{ s}^\circ$, SS on trace 15 with $S = 14 \text{ s}^\circ$). Note, by comparing the identifications in Figs. 12e to 12g that the associated slowness values might somewhat differ because the maximum amplitudes vary only slightly when changing the slowness for about ± 1 or 2 s° .

Example 13: Earthquake near the coast of Ecuador

USGS NEIC-data: 1998-08-04 OT 18:59:18.2 0.551S 80.411W h = 19G
 mb = 6.2 Ms = 7.1 (D = 91.5° and BAZ = 270.9° from GRF(GRA1))

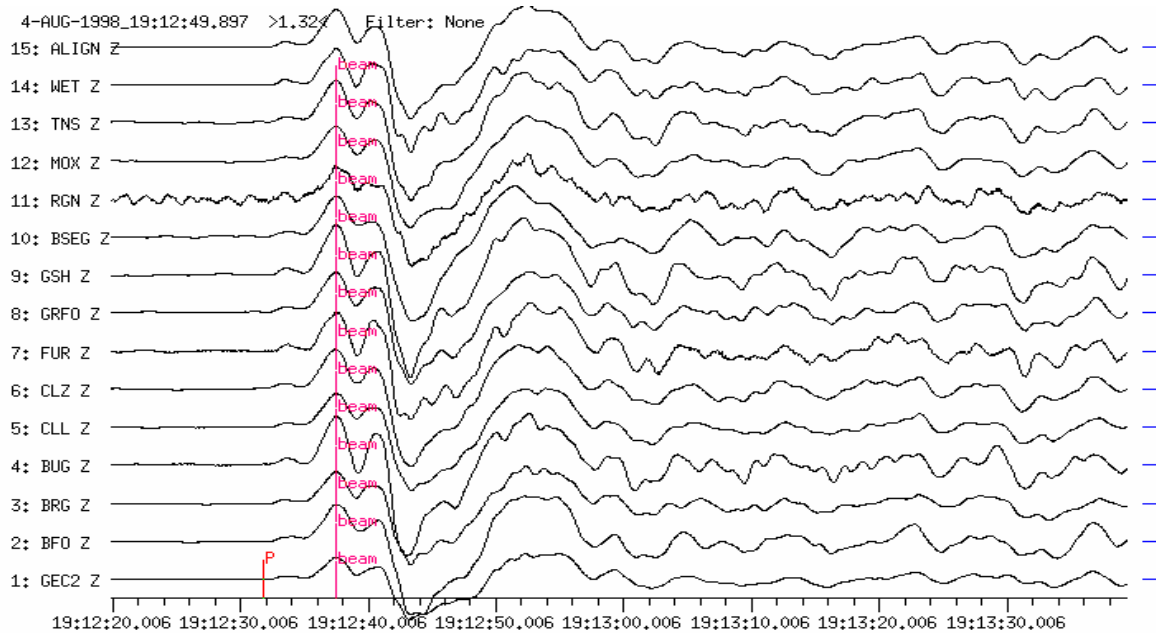


Figure 13a Broadband vertical-component seismograms recorded at 14 GRSN stations (D = 88.4° to 93.2°). Traces are time-shifted and aligned. The different waveforms observed at different network stations are coherent in the long-period range.

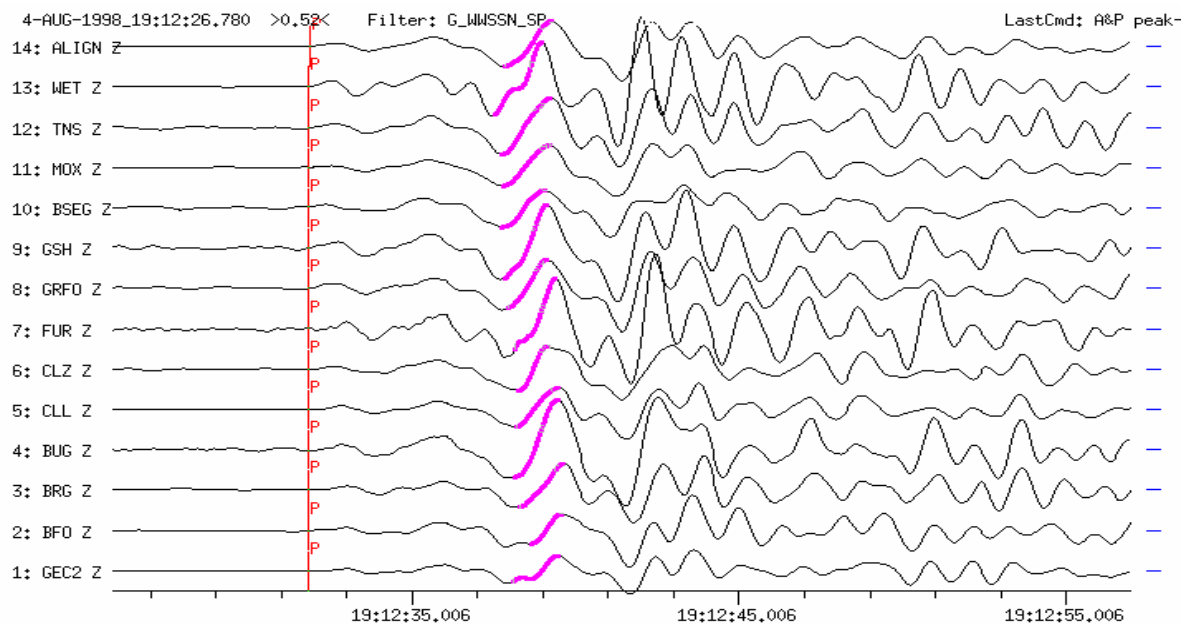


Figure 13b: After short-period filtering (WWSSN-SP simulation) the coherency of the different station-waveforms is bad. The maximum double P-amplitudes used for mb-estimation are emphasized. Because of the variability of station amplitudes within the network individual mb-values vary between 6.0 for BFO and GEC2 and 6.7 for other stations.

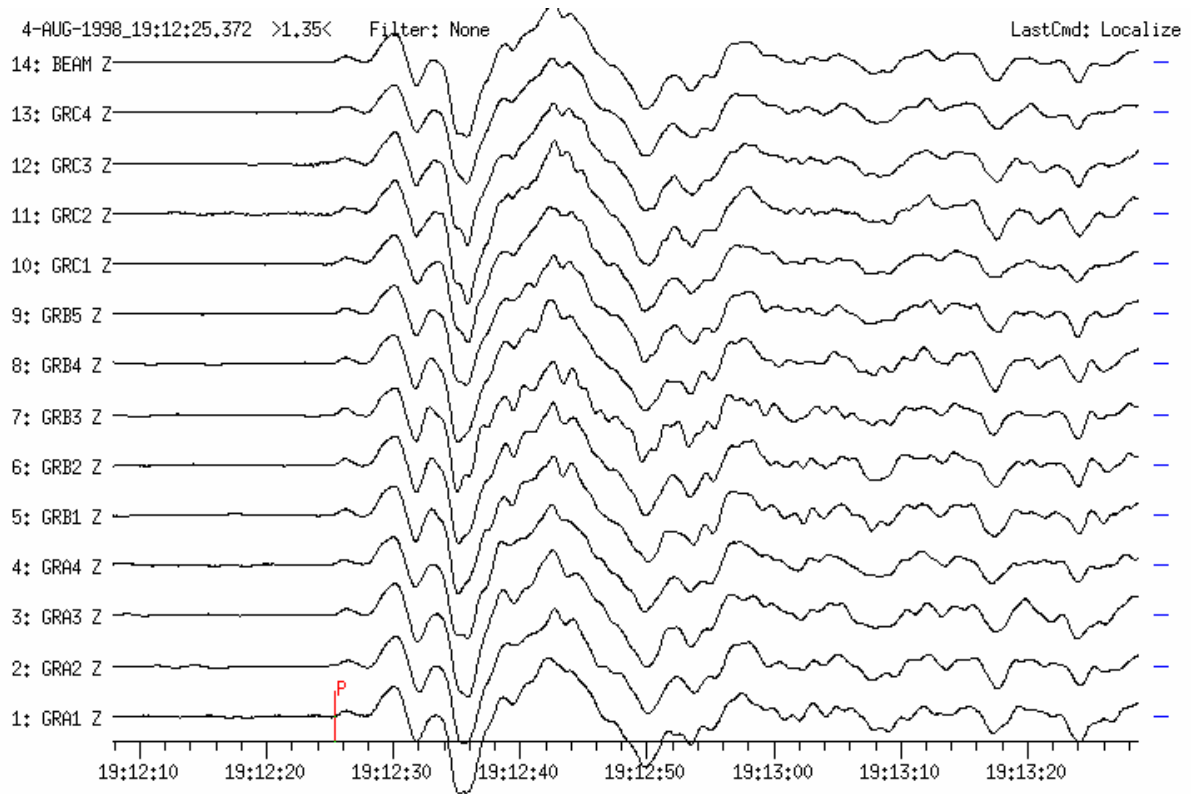


Figure 13c Broadband records of the vertical-components at 13 GRF-array stations ($D = 91.5^\circ$ to 91.7°). Because of the much smaller aperture of the array as compared to the GRSN the signal coherence is good for all array-traces.

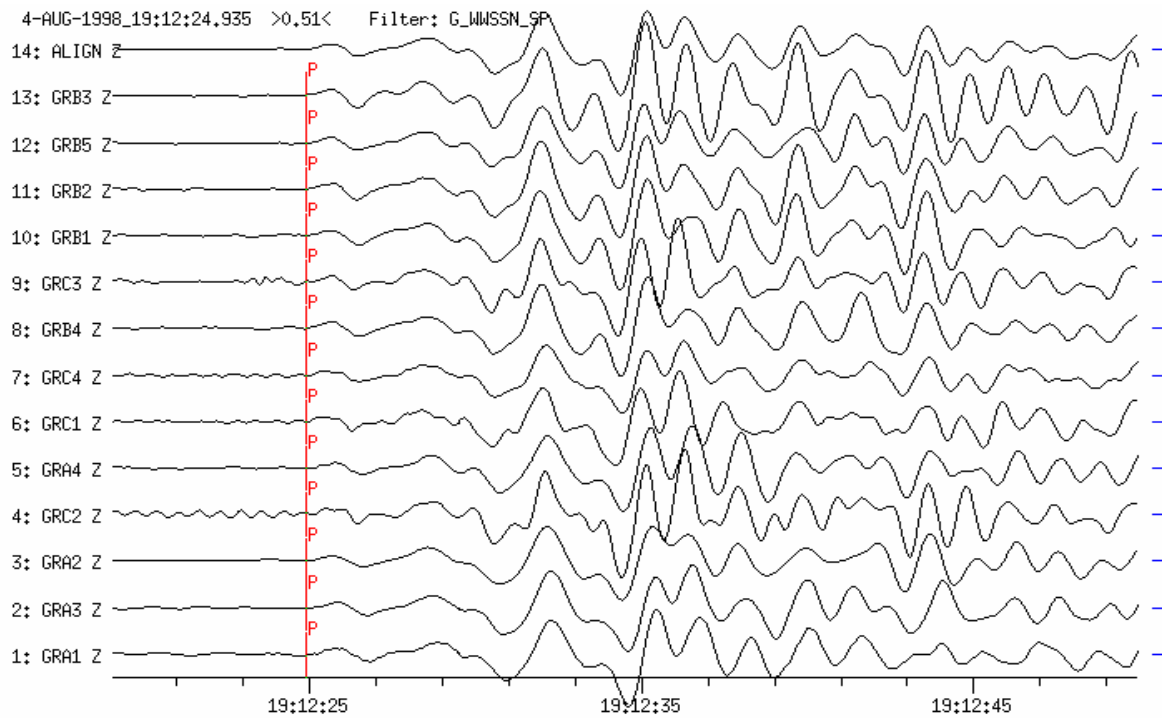


Figure 13d Even for the short-period filtered records of the GRF-array stations (WWSSN-SP simulation) the signal coherence is still good.

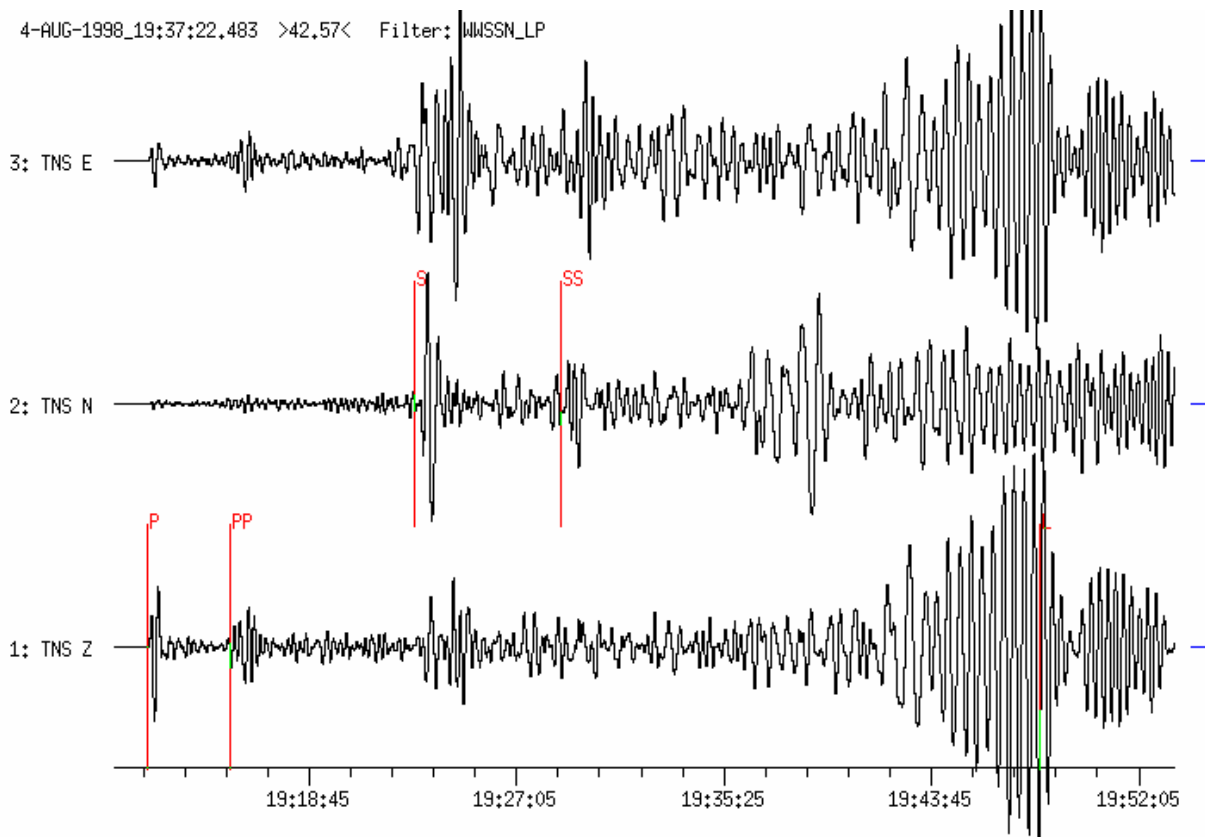


Figure 13e Three-component long-period filtered (WWSSN-LP simulation) seismogram recorded at station TNS ($D = 89.7^\circ$, $BAZ = 269^\circ$). Note the much larger P-wave amplitude in the E-W component as compared to the N-S component because of the source location in the west. Also note the strong secondary phases PP, S and SS. The maximum surface-wave amplitude on the vertical component is marked (L). The estimated magnitude is $M_s = 7.2$. This is very close to the average value determined by the USGS NEIC from data of the global seismic network ($M_s = 7.1$).

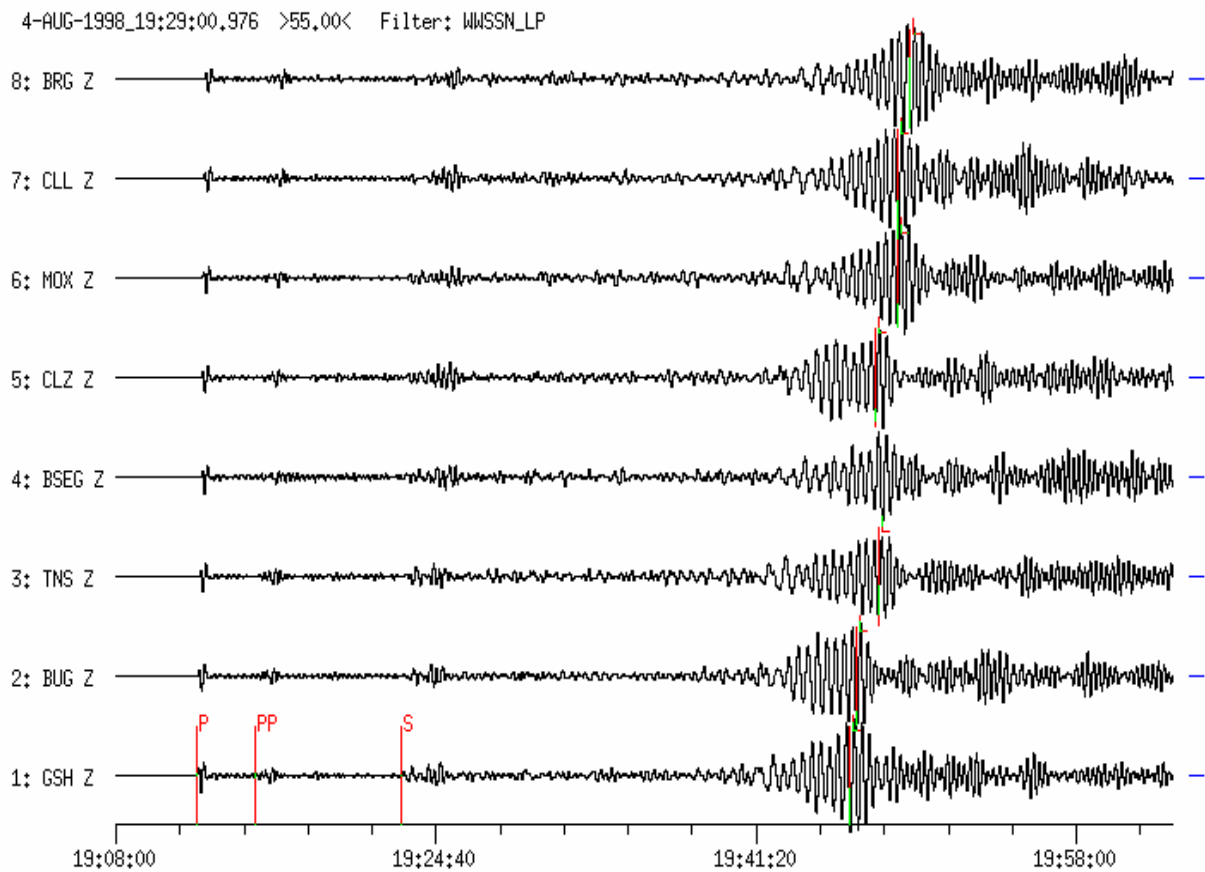


Figure 13f Long-period filtered (WWSSN-LP simulation) vertical-component records of the Ecuador earthquake at 8 GRSN stations within the distance range $D = 88.4^\circ$ (GSH) to 93.2° (BRG). The variability of the maximum surface-wave amplitudes throughout the network is less than that of short-period body-wave amplitudes (compare with Figure 13b). Accordingly, M_s estimates from individual stations are more reliable than respective m_b estimates.

Example 14: Earthquake in Southern Sumatra Region

USGS NEIC-data: 2000-06-04 OT 16:28:25.8 4.773 S 102.050 E h = 33G
 mb = 6.8 Ms = 8.0 (D = 94.1° and BAZ = 92.5° from GRF)

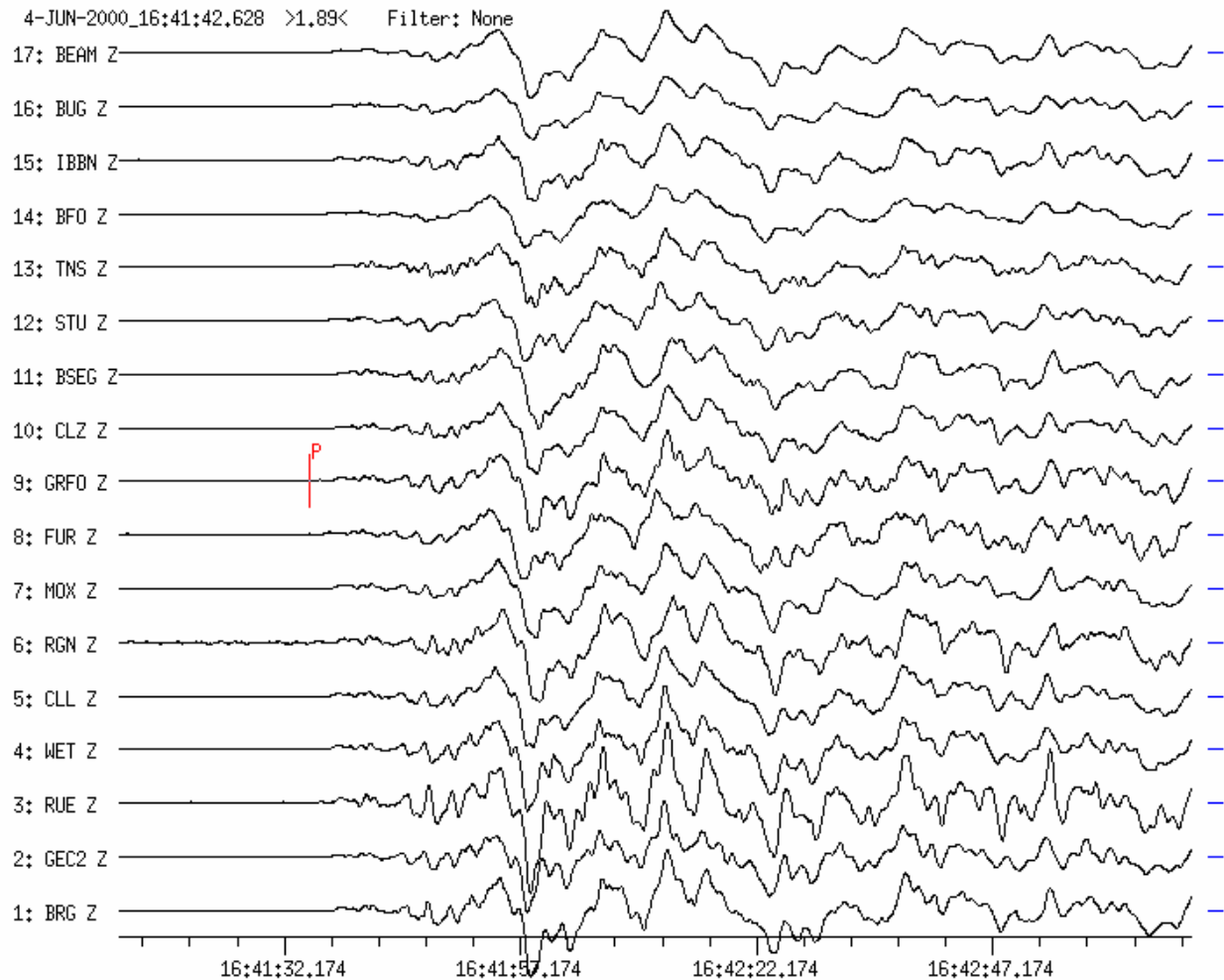


Figure 14a Broadband vertical-component seismograms recorded at 16 GRSN-stations within the distance range $D = 92.5^\circ$ to 96.7° . Traces are time-shifted and aligned for better comparison of the individual records. Note the good coherency of all traces. For these broadband records the network works like an array. The weak P-wave first arrival is marked on the record of station GRFO. Maximum P-wave amplitudes were recorded about half a minute later (multiple rupture event with successively larger energy release?).

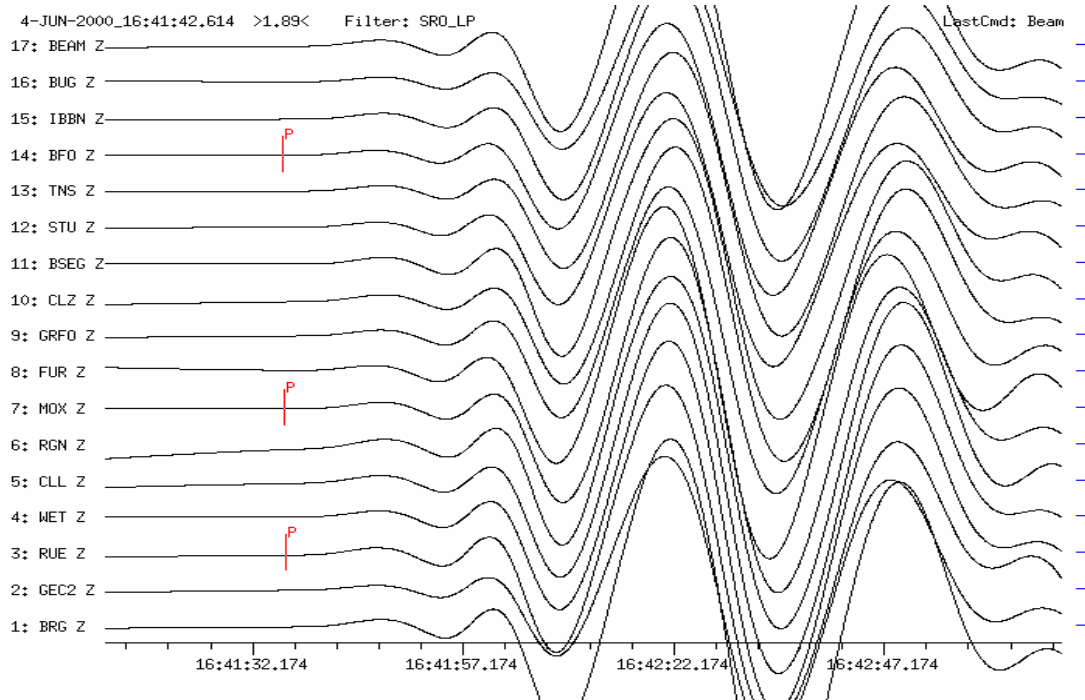


Figure 14b Seismograms of the same earthquake recorded at the same stations as in Figure 14a after applying a long-period filter (SRO-LP simulation). Note the very high signal coherence of the long-period P-waves with periods $T \approx 25$ s. Also the amplitudes are comparable at all stations.

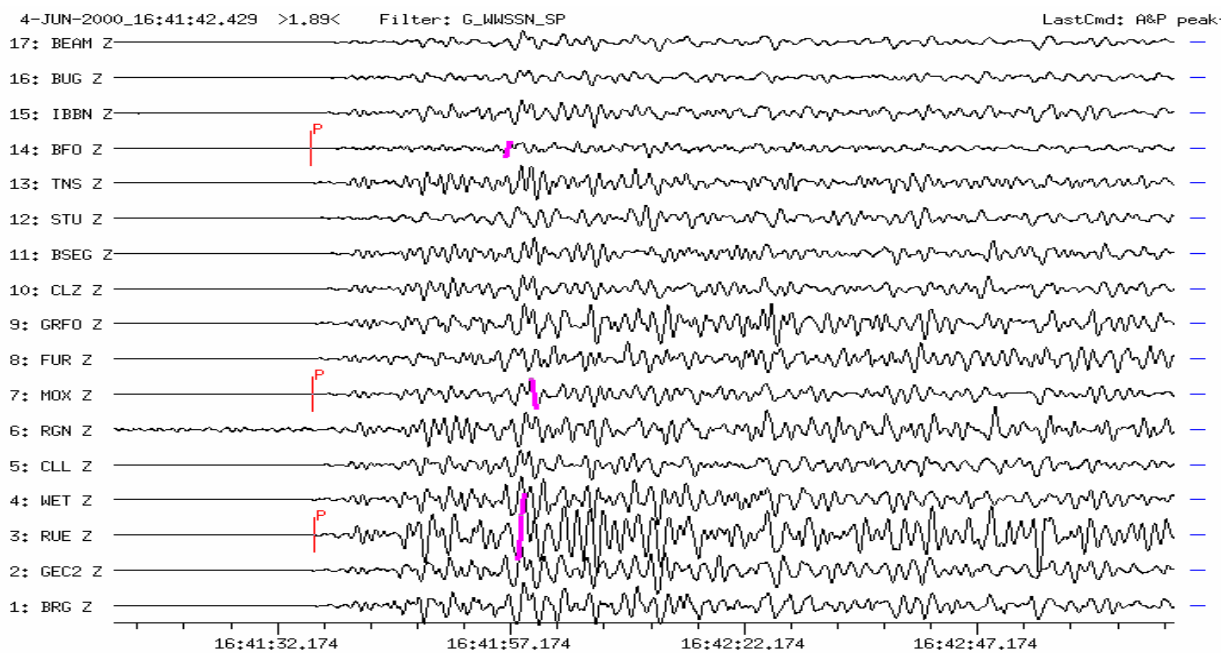


Figure 14c For mb estimates short-period records (WWSSN-SP simulation) have to be used to measure the maximum amplitudes with periods near 1 s. The respective filtered traces for the same earthquake and stations as in Figure 14a are shown. For three stations the P wave arrivals and their maximum double-amplitudes $2A$ have been marked. The latter differ by a factor of five for this event. This corresponds to a difference of 0.7 magnitude units!

4-JUN-2000_16:41:41.368 >1.10< Filter: G_WWSSN_SP

LastCmd: A&P peak

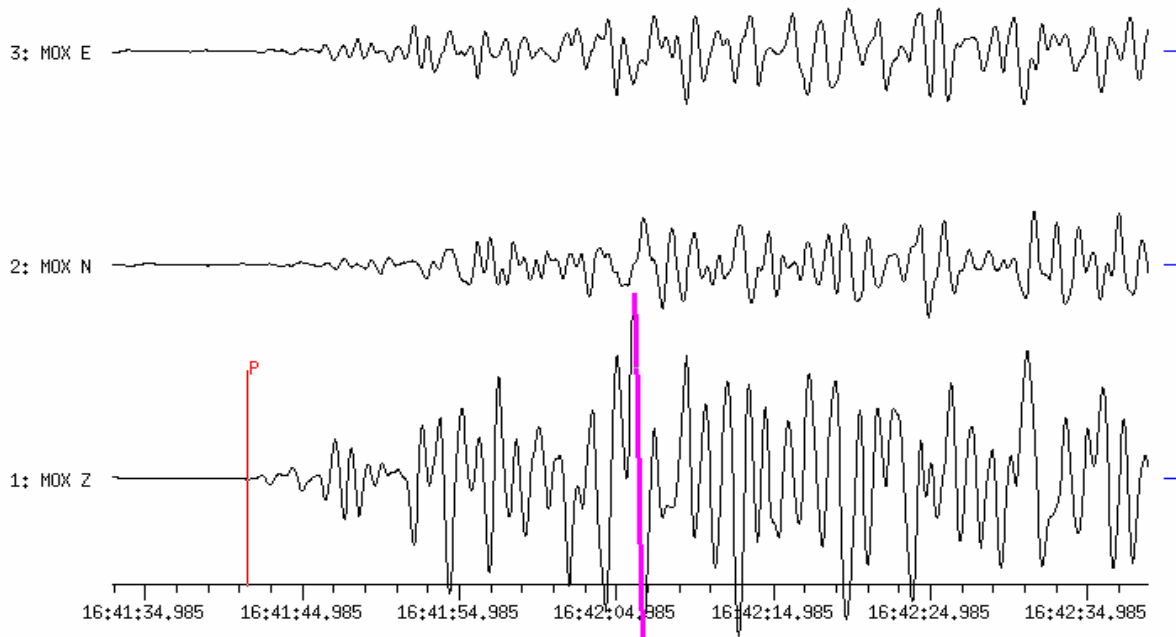


Figure 14d Three-component single station record of the Sumatra earthquake at station MOX ($D = 93.9^\circ$, $BAZ = 93^\circ$). The short-period filtered P-wave group is shown and the maximum peak-to-peak amplitude $2A$ is marked as in the Z component. In this display with high time resolution the complicated rupture process of this event, consisting of a series of sub-events with successively increasing energy release within the first 25 s is very obvious. This is a very important information also for more detailed research work on source processes. Therefore, also for routine data analysis a detailed reporting of the onset times, amplitudes and periods of these sub-events is strongly recommended. An example for such an analysis is given in Tab. 3.1 of Chapter 3. In the given case, the amplitude of the P-wave maximum around 16:42:06 is about 40 times larger than that of the first arrival. This corresponds to a difference of 1.6 magnitude units between the initial and the largest sub-event of this earthquake. Accordingly, instructions for mb measurements within the first five half-cycles (NOAA in the 1960s) or within the first 5 s (IMS nowadays) might dramatically underestimate not only the energy release of earthquake in general (stronger ones in particular, because mb will always saturate at values around 6.5; see Figs. 3.5 and 3.16 and related discussions in sections 3.1.2.3, 3.2.5.2, and 3.2.7 of Chapter 3). Even worse, they will particularly underestimate the high-frequency energy release which is most relevant for potential damage assessments and for these mb is principally more suited than M_s or M_w provided, that mb is determined really from the maximum amplitudes in short-period P-wave train.

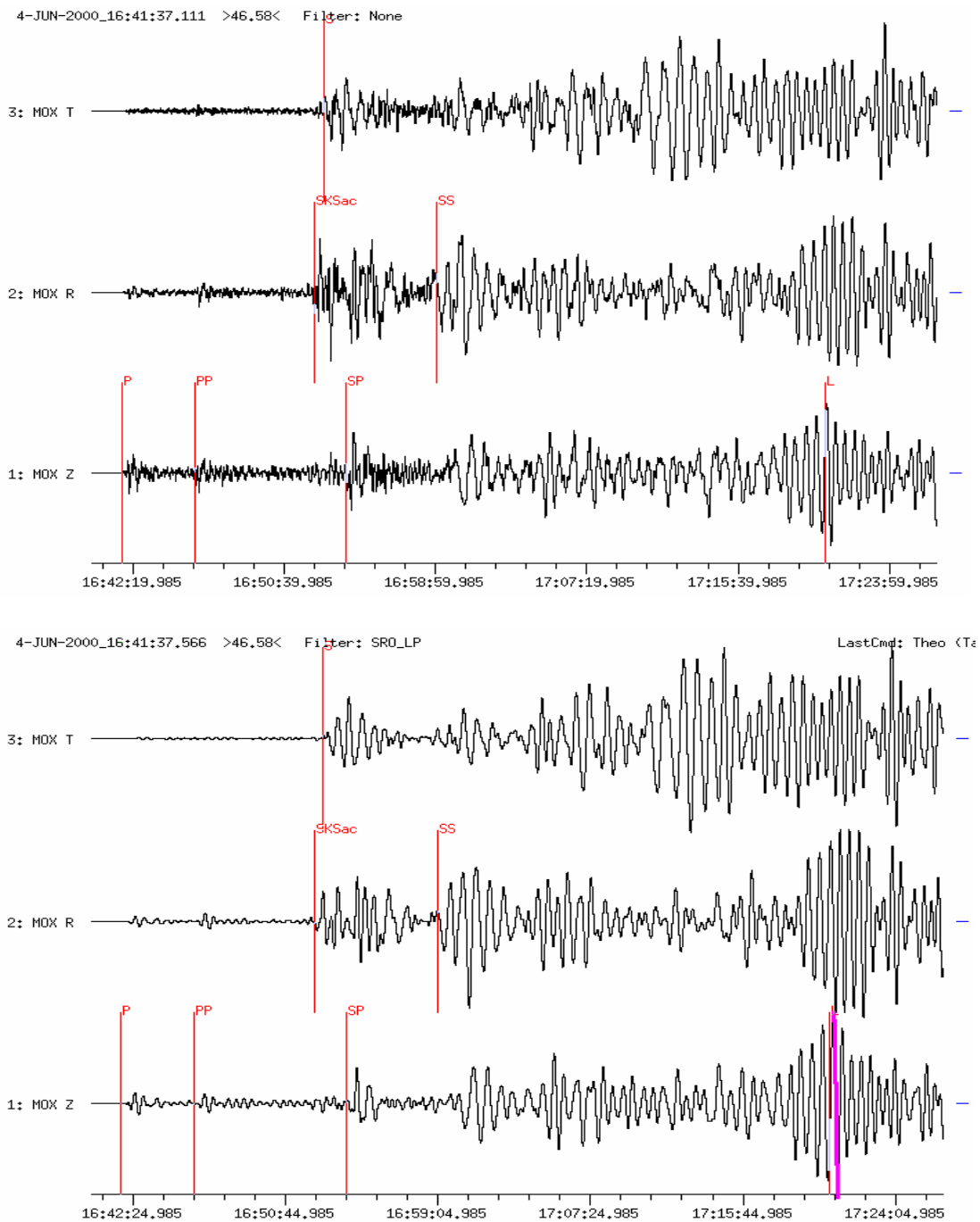


Figure 14e Broadband (top) and long-period filtered 3-component seismograms (SRO-LP simulation; below) of the Sumatra earthquake at station MOX ($D = 93.9^\circ$). The phases P, PP, S, SKSac, SP, SS and the maximum surface wave L have been marked. For better phase identification the horizontal components N and E have been rotated into the R and T directions. The S wave is seen best on the transversal component T and P, PP, SKS and SP on Z and on the radial horizontal component R, respectively. For surface-wave magnitude estimation the maximum ground displacement with a period between 18 and 22 s was measured at the marked position L from the SRO-LP filtered vertical component. Additionally, amplitudes from the horizontal components can be used for a horizontal surface-wave magnitude value.

Example 15: VOLCANO ISLANDS REGION

USGS NEIC-Daten: 2000-03-28 OT 11:00:21.7 22.362N 143.680E h = 119D
 mb = 6.8 (D = 96.8° BAZ = 43.5° from GRF(GRA1))

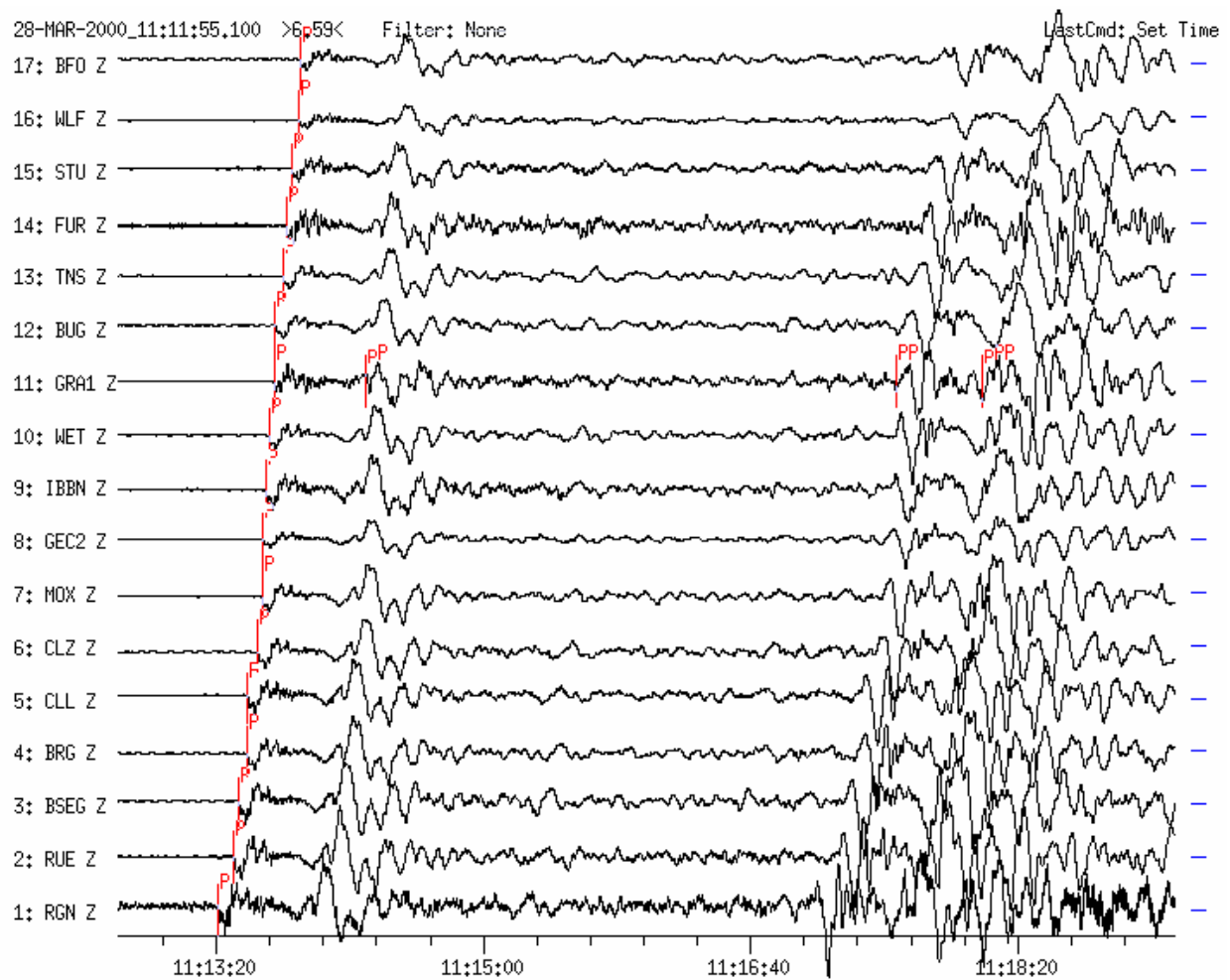


Figure 15a Broadband vertical-component seismograms recorded at 17 GRSN-, GRF- and GEOFON-stations. Traces are sorted according to increasing distance (D = 92.4° to RGN and 99.1° BFO). The phases P, PP and the depth phases pP and pPP are recorded very well.

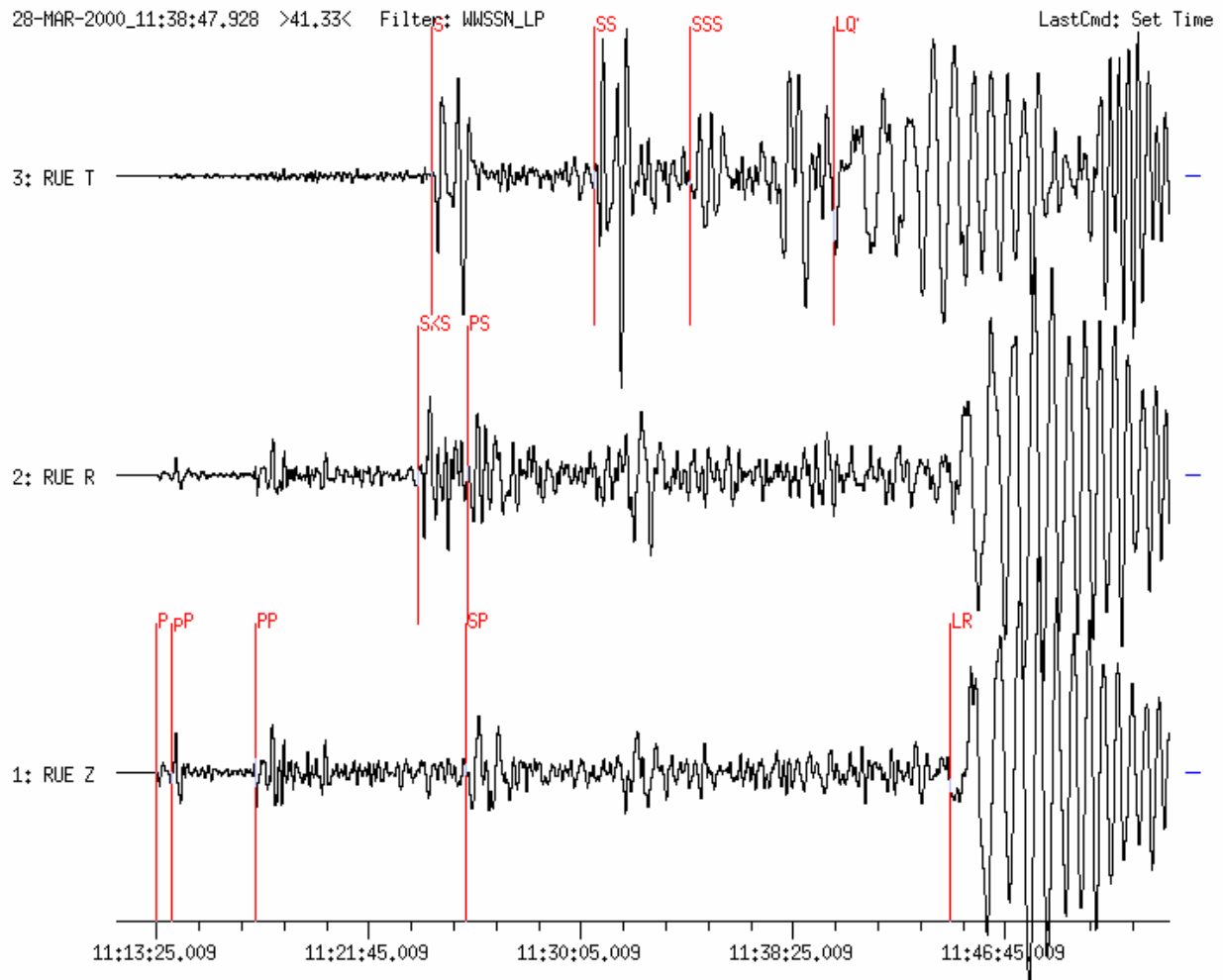


Figure 15b Long-period filtered (WWSSN-LP simulation) three-component seismogram of the Volcano Island earthquake recorded at station RUE near Berlin ($D = 93.7^\circ$, $BAZ = 45^\circ$). The horizontal components are rotated, with R in source direction. Phases P, pP, SP and the onset of the Rayleigh waves LR are marked on the vertical component, SKS and PS on the radial component and S, SS, SSS as well as the Love waves onset LQ on the transversal component, respectively.

Topic	Additional seismogram examples at distances beyond 100°
Authors	Klaus Klinge, Federal Institute for Geosciences and Natural Resources, Seismological Central Observatory, Gräfenberg (SZGRF), Mozartstrasse 57, 91052 Erlangen, Germany, Fax: +49 9131 8104 099, E-mail: klinge@szgrf.bgr.de Siegfried Wendt, Geophysical Observatory Collm, University of Leipzig, D-04779 Wernsdorf, Germany, E-mail: wendt@rz.uni-leipzig.de Peter Bormann (formerly GeoForschungsZentrum Potsdam, Telegrafenberg, 14473 Potsdam, Germany); E-mail: pb65@gmx.net
Version	October, 2002

Note: Most of the examples given below show either records of the German Regional Seismic Network (GRSN; aperture about 500 x 800 km) or of the Gräfenberg broadband array (GRF; aperture 45 x 110 km; see Figs. 8.14 and 9.4 in the manual Chapters 8 and 9, respectively). The following abbreviations have been used: OT – origin time in UT (universal time), D – epicentral distance in degrees, BAZ – backazimuth in degrees, h – focal depth in kilometer.

Example 1: Earthquake in the Chile-Bolivia border region (intermediate source depth)

USGS NEIC-data: 2002-03-08 OT 04:56:21.7 21.6S 68.2W h = 123 km Mw = 6.5; The epicentral distances of the GRSN stations range between 97° < D < 103°.

Figures 1 a and b show enlarged sections of the recordings made of this intermediate depth earthquake at stations of the GRSN around the beginning of the shadow zone of the Earth's core (for the full records see Fig. 11.57 left). Figure 1a depicts the first 24 minutes of the long-period recordings (SRO-LP simulation) of the horizontal R and T components whereas Figure 1 b shows the related Z-component recordings of the first 8 min (lower part) and 17 min (upper part), respectively. The following diagnostic features can be recognized:

- Pdif is by far the smallest body-wave arrival, even in the vertical component, however, its SNR is still large enough for this medium-size earthquake in LP recordings;
- SKS (here also with its depth phase sSKS) forms the first strong shear-wave arrival, necessarily in the radial (R) horizontal component, whereas S (also with its depth phase sS) is a comparably strong later shear-wave arrival, here (however not always!) with large amplitudes in the transverse (T)-component records;
- SP (and its depth phase) is also (necessarily!) strongest in the R component whereas SS is frequently (not always! see Figure 2) strongest in the long-period T component;
- SKS and SP have also well developed onsets in Z-component LP records with amplitudes comparably strong or even larger than for Pdif and PP;
- Pdif and PP may also have well developed depth phases (here sPdif and sPP, respectively) in Z-component LP records;
- the missing of the depth phases pPdif and pPP in Figure 1b is due to the different P- and S-wave radiation pattern from a shear source (see Figs. 3.25 and 3.26) and the specific rupture orientation with respect to the seismic station in the considered case; this is not a general feature, rather pP, pPP etc. are often stronger;
- PP has, when compared with Pdif, a larger R component because of its larger incidence angle; and SP a larger Z component than PS.

2002-03-28 OT 04:56:21.7 h = 123 km Chile Bolivia border region

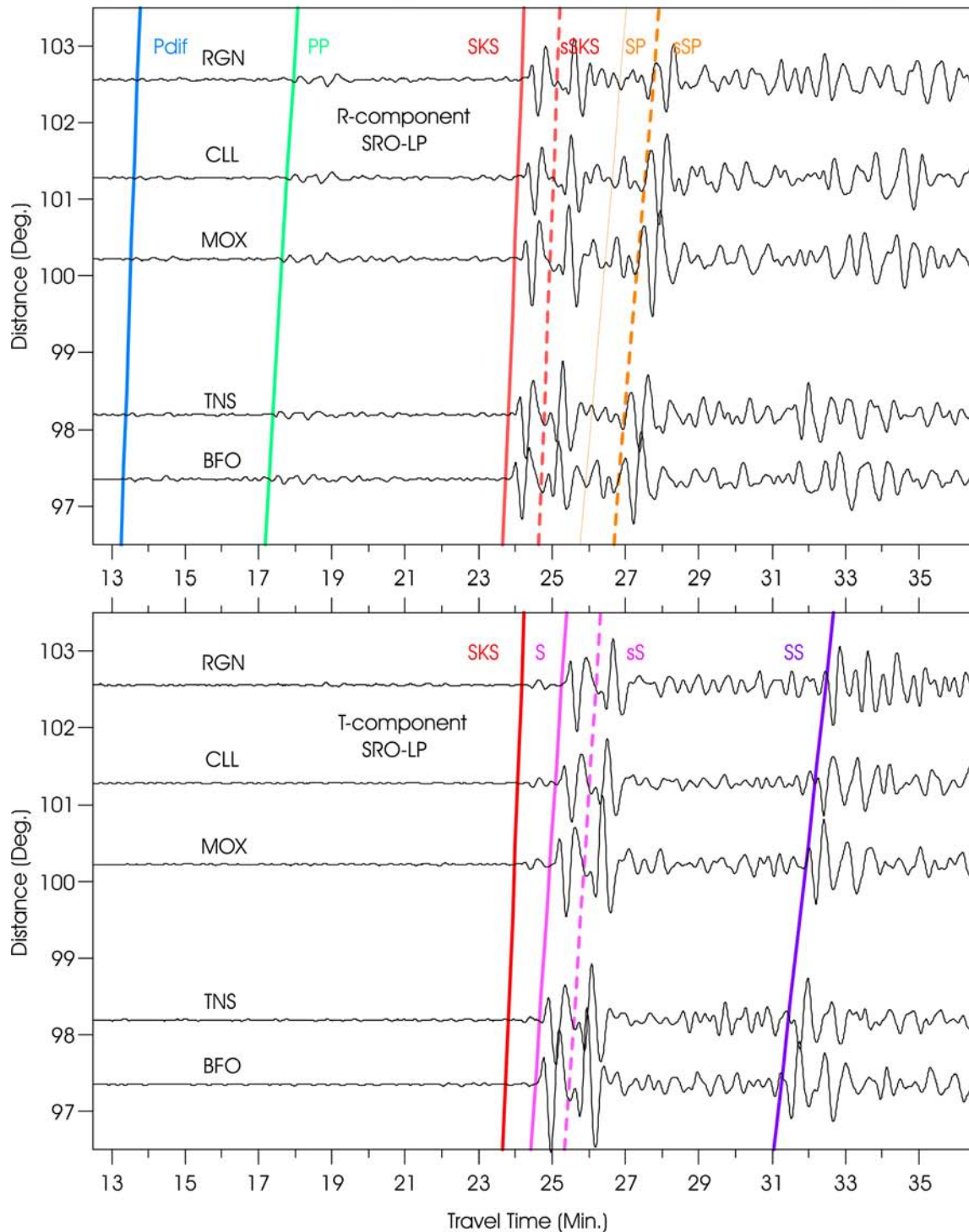


Figure 1a SRO-LP filtered BB records of GRSN stations. Upper traces: R component; lower traces: T component. Note that the phases SKS and SP, as well as their depth phases, have necessarily their largest horizontal amplitudes in the R component, as the longitudinal waves Pdif and PP. In contrast, S and SS may have their largest amplitudes in the T component, depending on the primary ratio of SV/SH energy radiated by the earthquake source.

2002-03-28 OT 04:56:21.7 h = 123 km Chile Bolivia border region

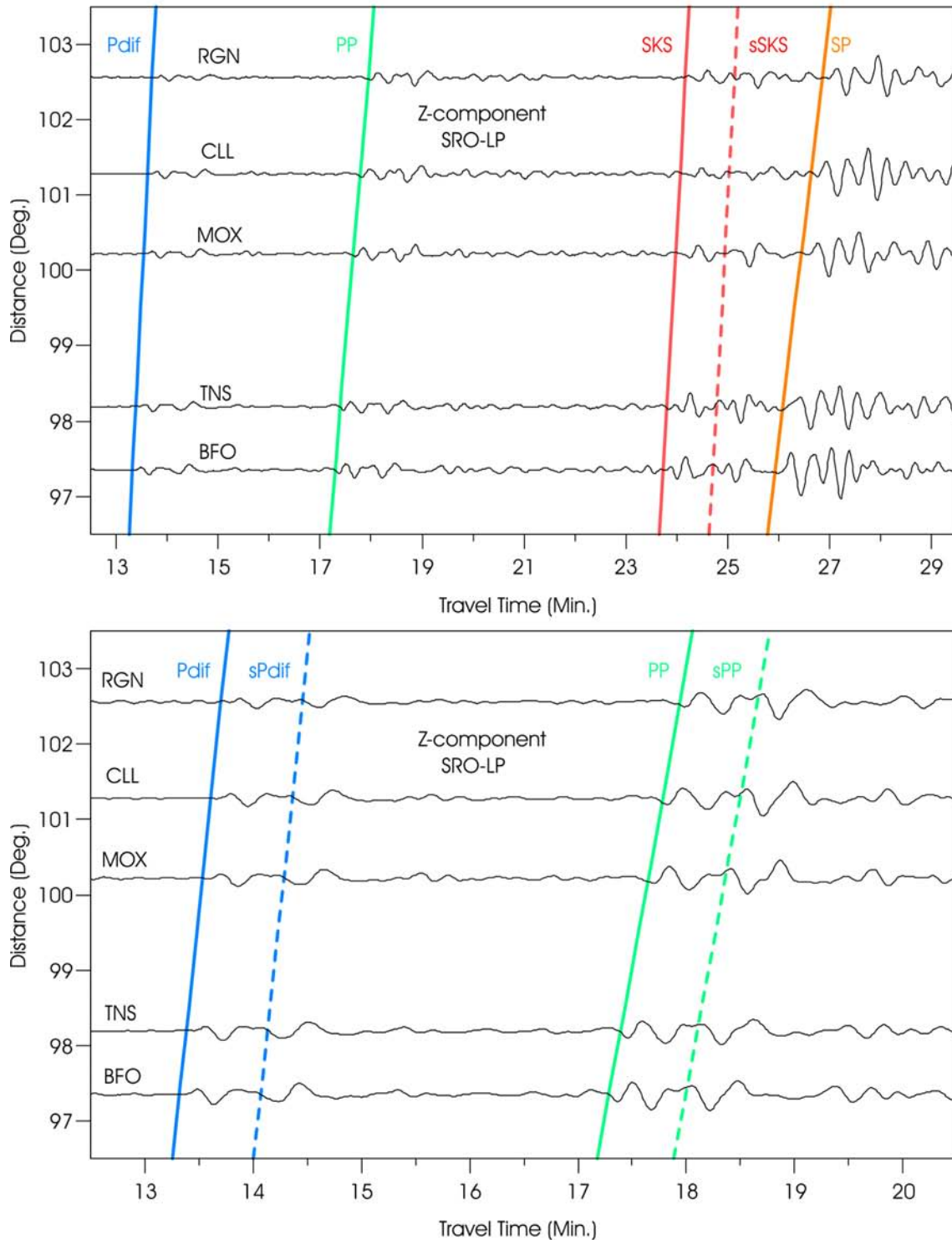


Figure 1b Enlarged vertical (Z)-component SRO-LP filtered BB records of GRSN stations shown in Figure 1a. Upper traces: Body-wave phases up to SP; lower traces: cut-out of the first 8 minutes of the record with longitudinal phases only. Note the well developed depth phases sPdif and sPP. The theoretically expected arrival times according to the IASP91 model (Kennett and Engdahl, 1991) have been inserted in both Figure 1a and b.

Example 2: Earthquake in the Mariana Islands region (intermediate source depth)

**USGS NEIC-data: 2002-04-26 OT 16:06:06.8 13.1N 144.6E h = 85 km Mw = 7.1;
The epicentral distances of the GRSN stations range between $101^\circ < D < 108^\circ$.**

The waves from this source at nearly the same distance as for the Chile-Bolivia earthquake approach the GRSN stations from nearly the opposite backazimuth (see Fig. 11.57), however, the general wave types and waveform features in different record components are nearly the same as Figure 1, with one exception: SS is best developed in the R component and there is no S wave visible in the T component, i.e., the shear-wave energy generated by this source was almost exclusively of SV type.

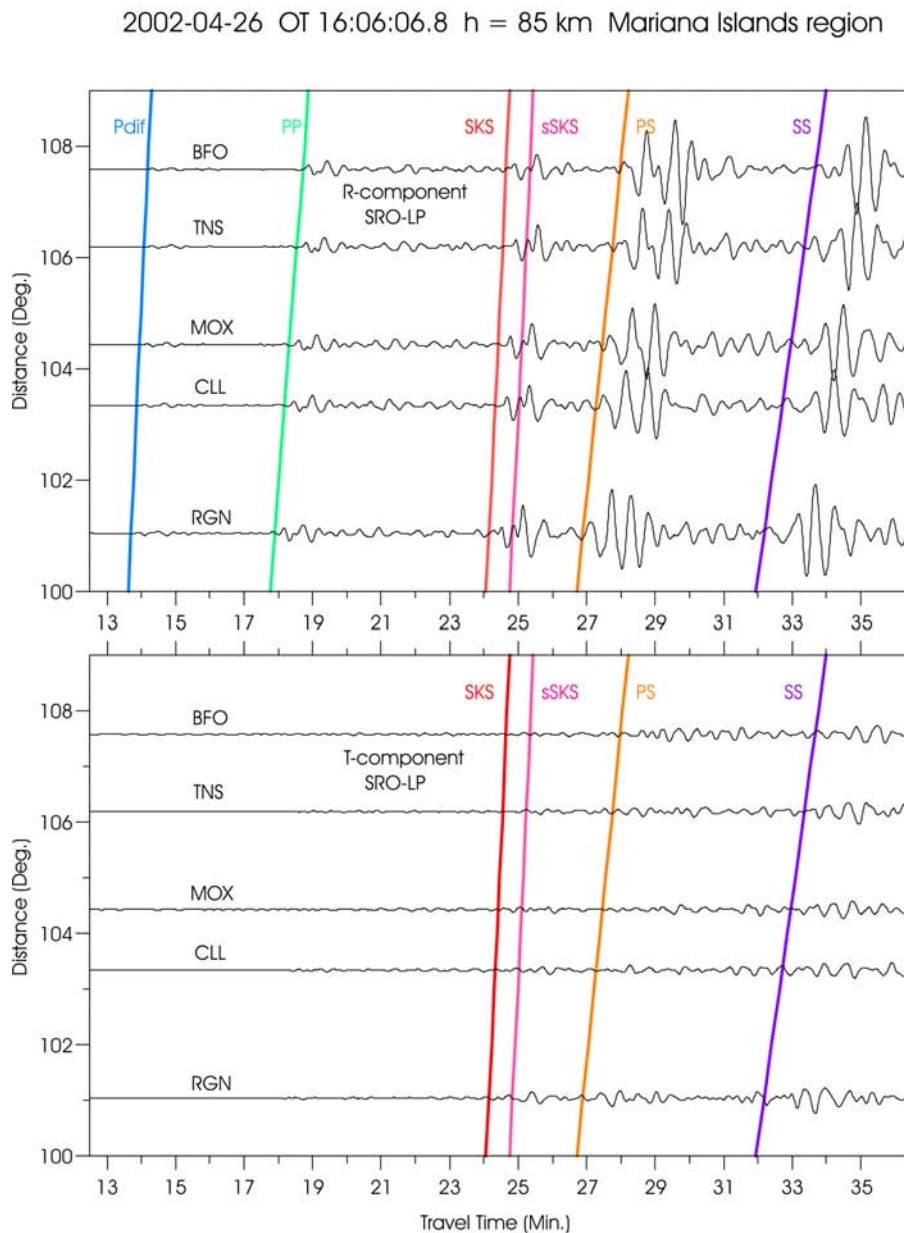


Figure 2a SRO-LP filtered BB records of GRSN stations. Upper traces: R component; lower traces: T component. Note that in these records PS has about four times larger amplitudes than SKS and all phases are not visible or rather weak in the T component.

2002-04-26 OT 16:06:06.8 h = 85 km Mariana Islands region

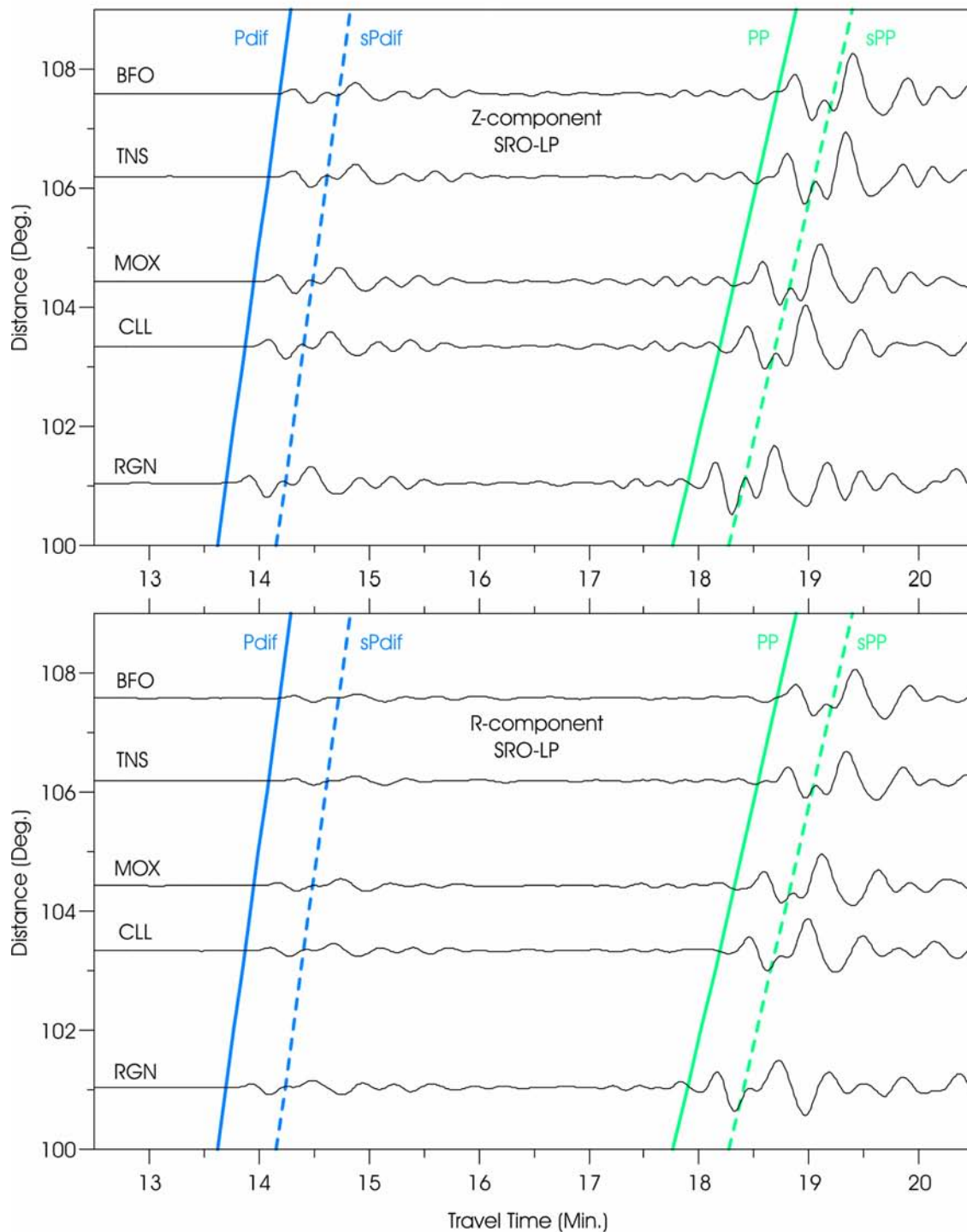


Figure 2b Enlarged cut-out of the SRO-LP filtered BB records of GRN stations shown in Figure 2a. Upper traces: Z component; lower traces: R component. Note the well developed depth phases sPdif and sPP. The theoretically expected arrival times according to the IASP91 model (Kennett and Engdahl, 1991) have been inserted in both Figure 2a and b. Note that the amplitude ratio Z/R is larger than for Pdif than for PP because of the smaller (steeper) incidence angle of Pdif.

Example 3: Earthquake in the Banda Sea region (intermediate source depth) with phases PKPdif, PKKPab and PKKPbc

USGS NEIC-data: 2000-03-03 OT 22:09:13.5 7.313S 128.642E h = 148 km mb = 6.4; (D =113° and BAZ =73.9° from GRF, h = 140 km)

Shown are various short-period filtered seismograms (WWSSN-SP simulation) recorded at GRSN-, GRF- and GEOFON-stations. All traces are sorted according to increasing epicentral distance within the range D = 110.8° (RUE) and 116.2° (WLF). Phases Pdif, PKiKP, PP, SP, PKKPbc and PKKPab are shown. Additionally, ray-paths and travel-time curves are presented.

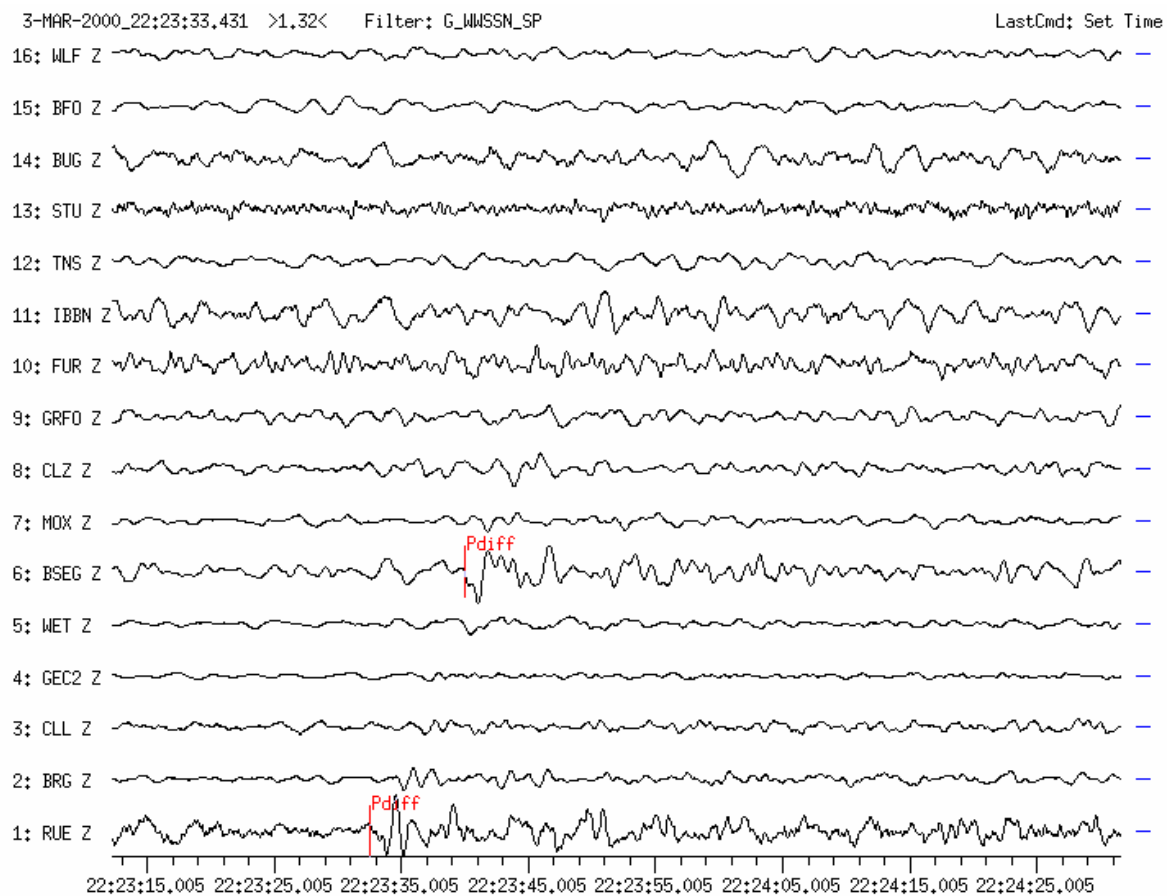


Figure 3a Pdif (old name Pdif) is the first arrival, however, as a diffracted wave, rather small, particularly in short-period records. Only a few GRSN stations have recorded it from this event. For more clear long-period records of Pdif see Figures 4b, 6c and 7b in the next examples.

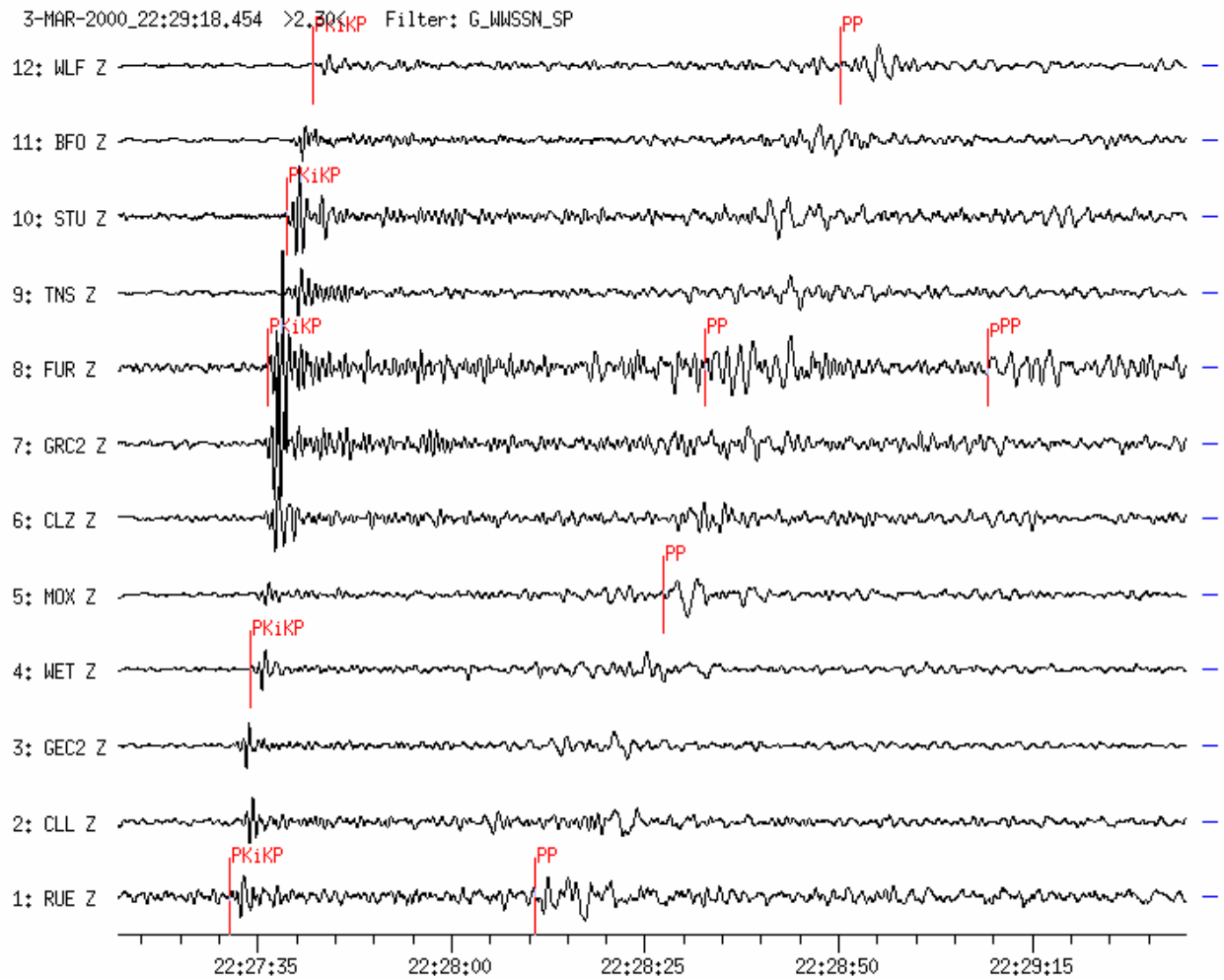


Figure 3b Phases PkiKP, PP and (pPP) are shown on this seismogram. PkiKP arrives about 4 min after Pdif shown in Figure 3a. Note the strong variation at PkiKP-amplitudes within the network by a factor of about 10. The onset-time of PP can not be determined exactly. The reflection point of PP is below the complex crustal structure of Tibet.

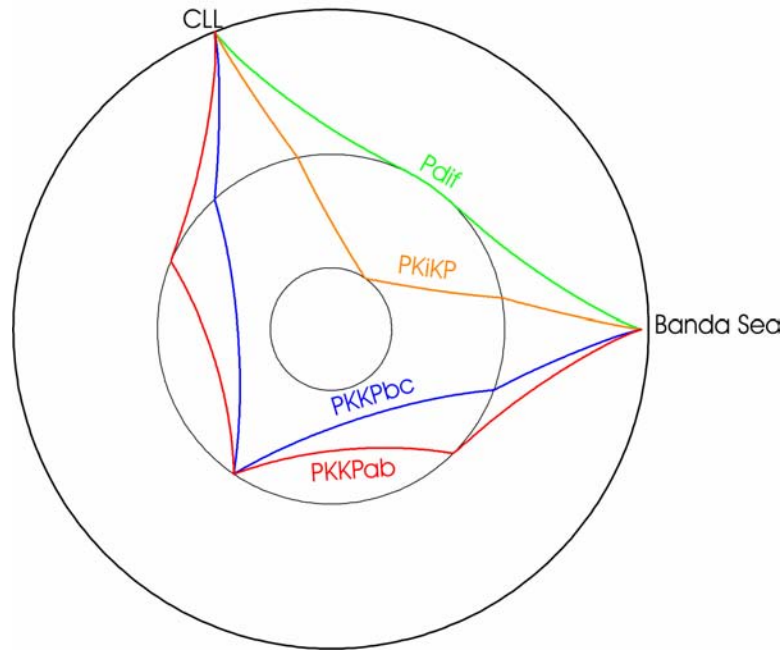


Figure 3c Ray paths for Pdif, PKiKP, PKKPbc and PKKPab for the considered event at a focal depth of 148 km and with an epicentral distance to station CLL of $D = 111^\circ$.

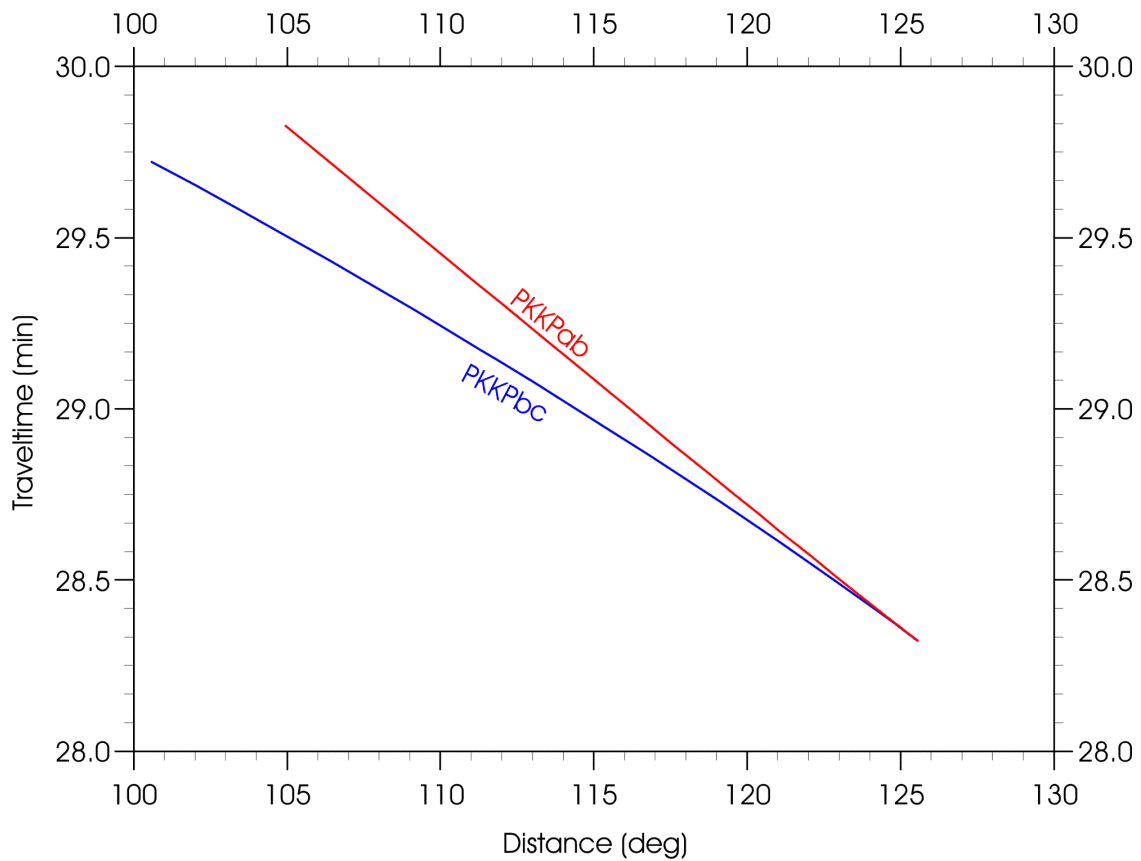


Figure 3d Travel-time curves for PKKPbc and PKKPab for a focal depth of 148 km.

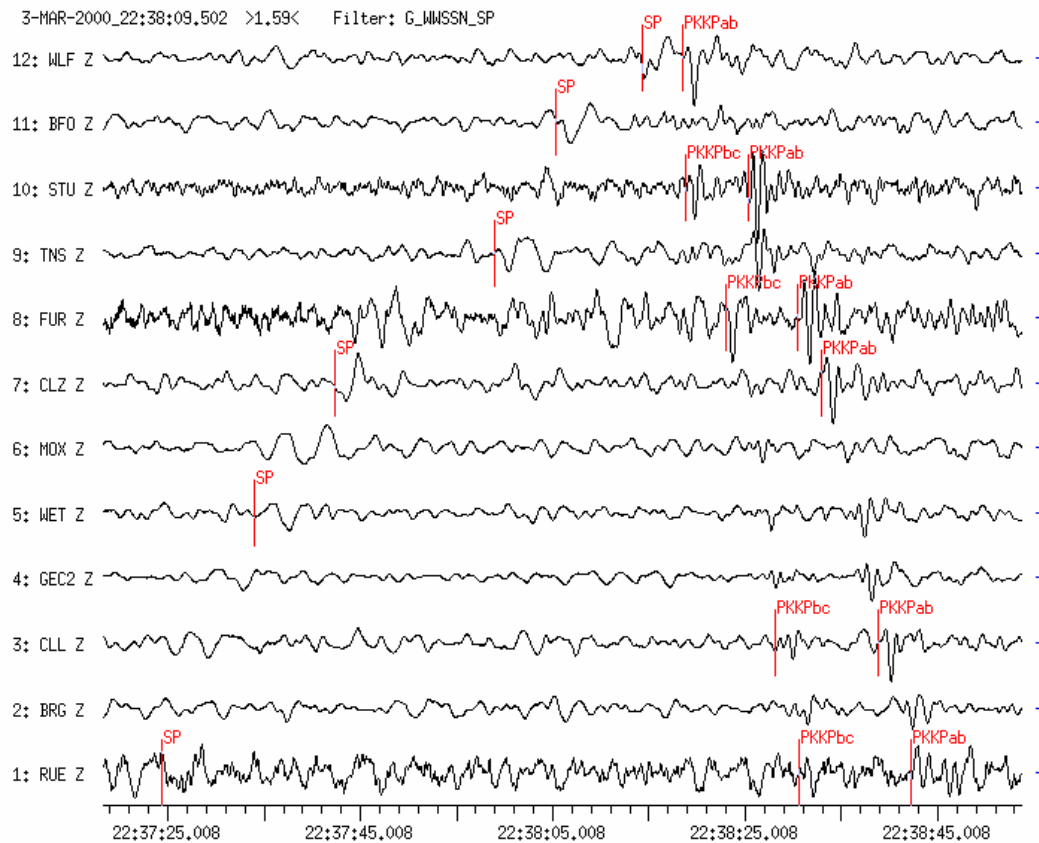


Figure 3e Vertical component short-period seismograms starting about 10 min after the PKiKP arrival in Figure 3b. Marked are the onset times of the phases SP, PKKPbc and PKKPab. For the branching of PKKP between about 90° and 125° see Figure 9 in EX 11.3. These late secondary phases appear in short-period records only. Their ray paths are shown in Figure 3c and their travel-time curves in Figure 3d above.

Example 4: Earthquake in Papua New Guinea

USGS NEIC-data: 1998-07-17 OT 08:49:15 3.08S 141.76E h = 33G Ms = 7.0; (D = 117.5° and BAZ = 58.8° from GRA1)

This earthquake occurred near the coast of Papua New Guinea. Tsunami waves with a height of 10 m flooded the coast and killed about 3000 people.

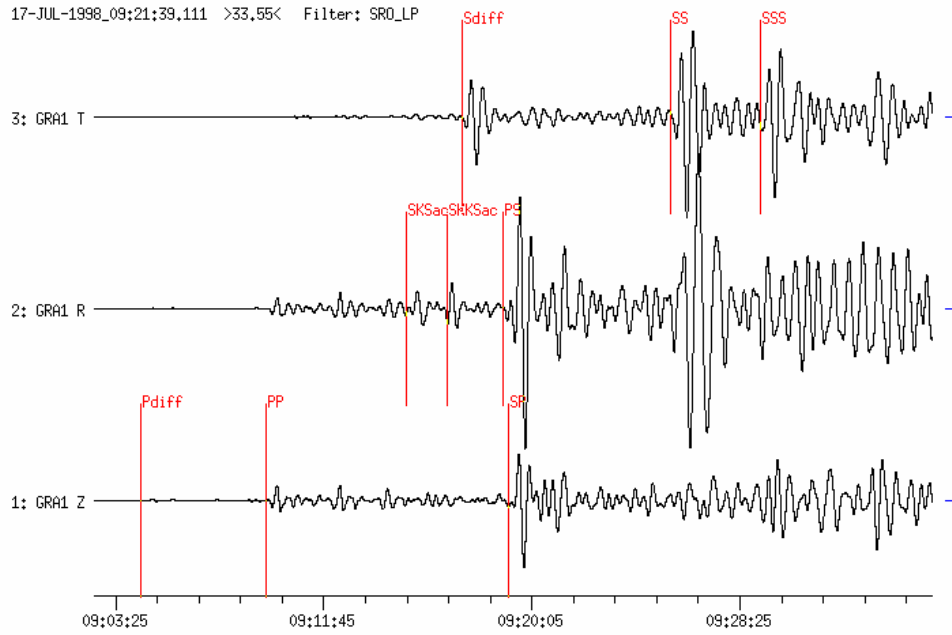


Figure 4a Long-period filtered three-component seismogram (SRO-LP simulation) recorded at station GRA1 ($D = 117.5^\circ$). The horizontal components (RT) are rotated with R into the epicentral direction. Phases Pdif, PP and a strong SP are visible on the vertical component. While the phases SKS, SKKS and PS, polarized in the vertical propagation plane, are strong on the radial (R) component Sdif, SS and SSS are strong on the transverse (T) component.

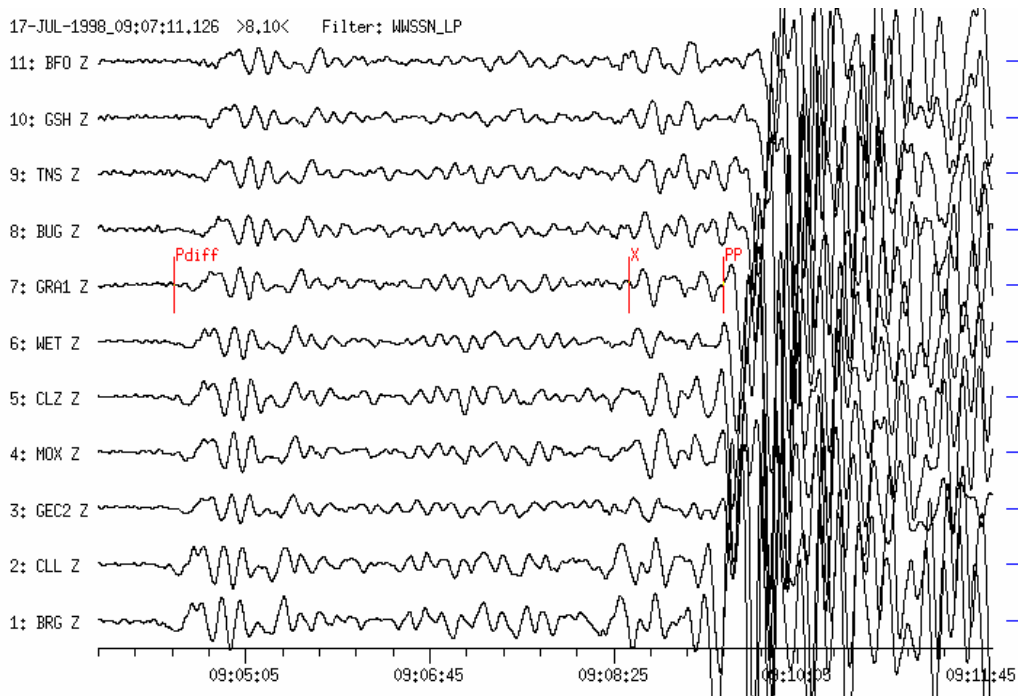


Figure 4b Long-period filtered vertical-component seismograms (WWSSN-LP simulation) recorded at 11 GRSN- and GRF-stations. Traces are sorted according to increasing distance ($D = 115.4^\circ$ to BRG and 119.9° to BFO). Long-period onsets of Pdif and PP are very clear as well as an unidentified phase X ahead of PP. The time differences between X and PP differ from station to station. Probably X results from interfering waves PKPdf and PKiKP. An answer is given in Figure 4c.

Three minutes before the Pdif onset from the earthquake in Papua New Guinea, a small P-wave onset was recorded in the seismograms of GRSN stations from an earthquake in Costa Rica. Its source parameters were:

**USGS NEIC-data: 1998-07-17 OT 08:49:01 8.59N 83.07W h = 33G mb = 5.9;
(D = 86.3° and BAZ = 278.8° from or GRA1)**

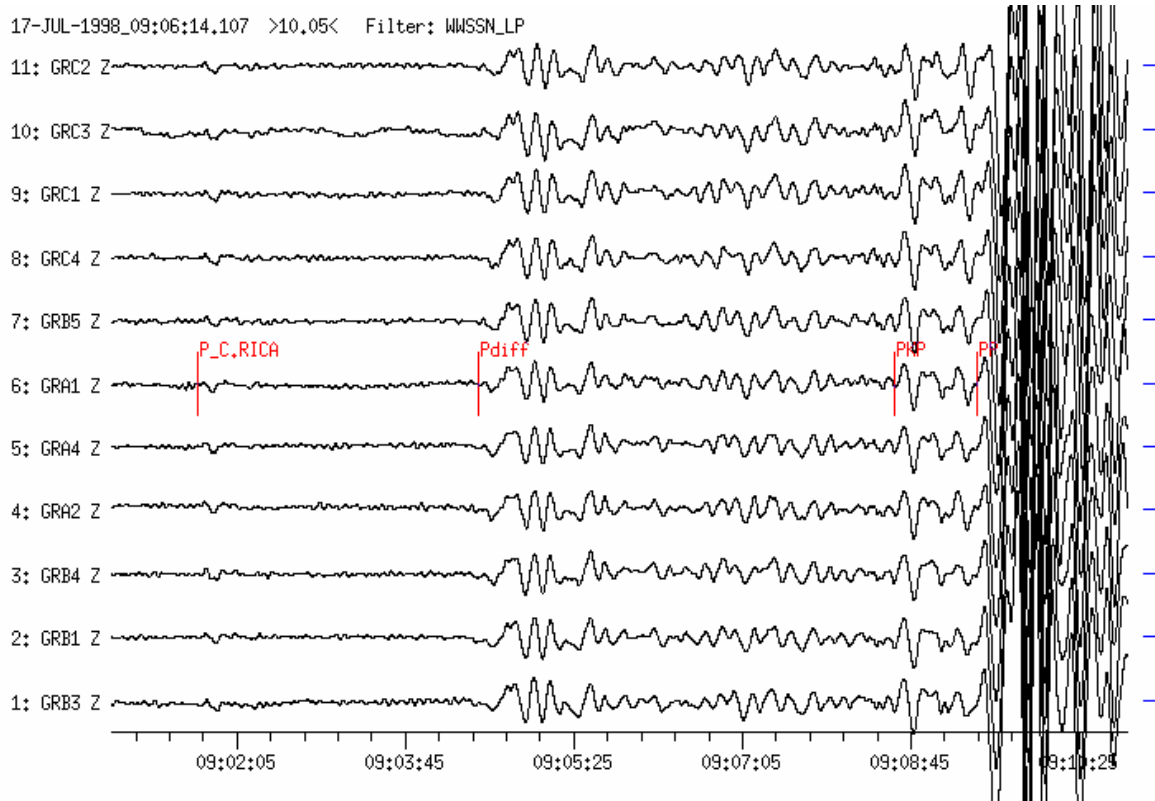


Figure 4c Long-period filtered vertical-component seismograms (WWSSN-LP simulation) recorded at 11 GRF-array stations within the distance range $D = 86.3^\circ$ to 86.7° . Long-period onsets of the P wave from the Costa Rica event appear first, followed by Pdif, PKP and PP from the earthquake in Papua New Guinea. The phase X from Figure 4b could be identified from the GRF-array records as being PKPdif from the Papua New Guinea earthquake with a slowness of about 2.0 s° .

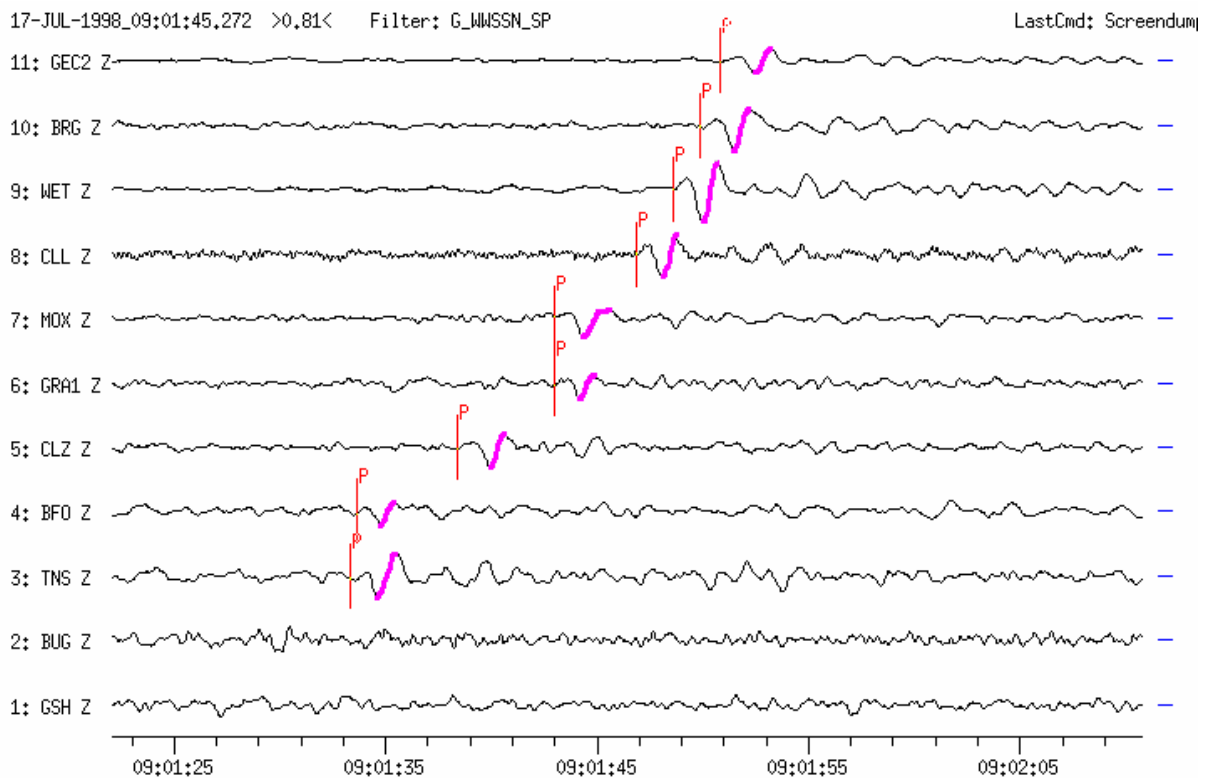


Figure 4d Short-period filtered seismograms (WWSSN-SP simulation) recorded from the Costa Rica earthquake at 11 GRSN-stations. Traces are sorted according to increasing epicentral distance ($D = 83.1^\circ$ to GSH and 88.0° to GEC2). The station-network allows to separate both events by way of slowness and azimuth determination. The estimated body-wave magnitudes m_b vary for the GRSN-stations between values below 5.0 (BUG, GSH) and 5.4 for station WET.

Example 5: Earthquake in the region of New Britain, P.N.G.

**USGS NEIC-data: 1999-05-10 20:33:02.1 5.173S 150.915E h = 137D $m_b = 6.5$;
($D = 124^\circ$ and $BAZ = 51^\circ$ from GRFO)**

This magnitude 6.5 earthquake, recorded at GRFO and at the GRSN-network, shows the phases Pdif, PKP, PP, Sdif, PS, SS, depth phases and – because of a focal depth of 137 km – weak surface waves. A rare example is the well recorded phase P'P'P' = PKPPKPPKPPK in Figure 3e below. The ray paths for the identified phases of this event are shown in Fig. 11.60. For animation of ray propagation and seismogram formation see CD-ROM attached to Volume 2 and complementary explanations given in IS 11.3.

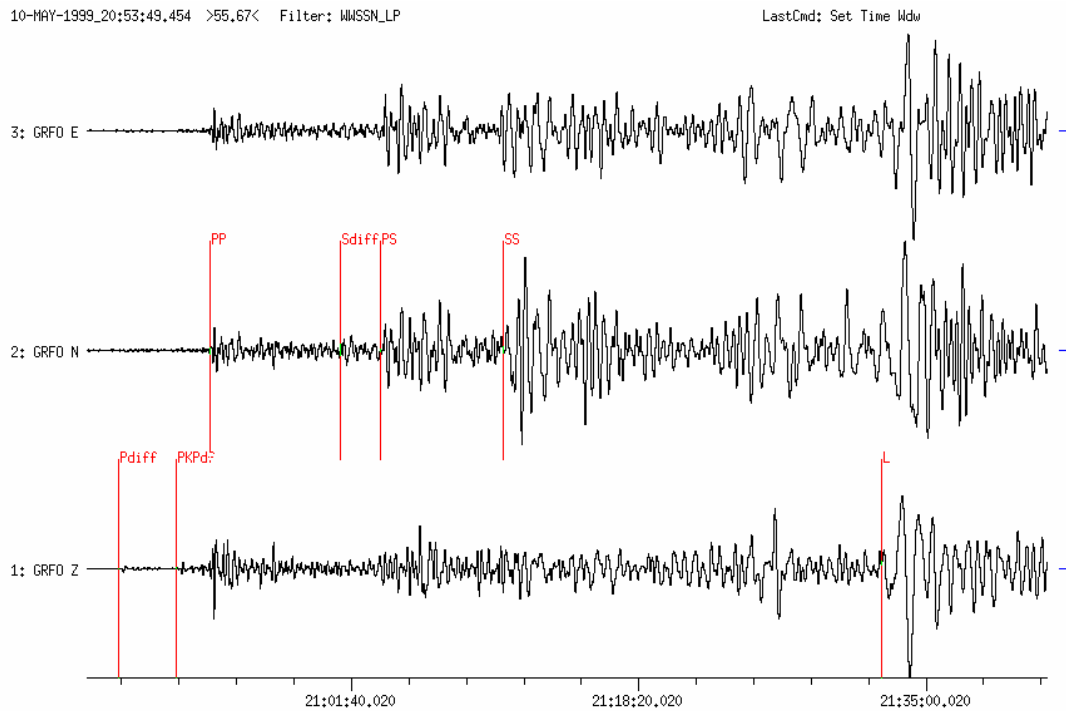


Figure 5a Long-period filtered three-component seismogram (WWSSN-LP simulation) recorded at station GRFO ($D = 124^\circ$). The length of the record is about 1 hour. Phases Pdif, PKP, strong PP, Sdif, strong PS, strong SS and – according to the large focal depth of the earthquake ($h = 137$ km) – relatively weak surface waves are recorded.

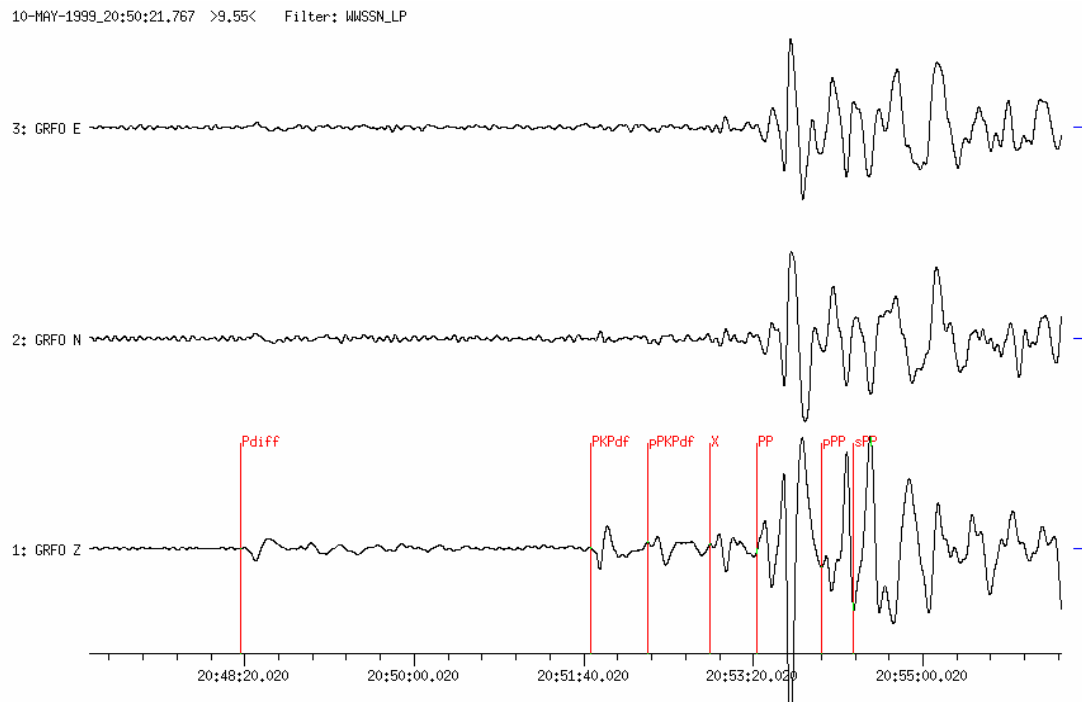


Figure 5b Shown are the first 10 minutes from the seismogram in Figure 5a. The higher time resolution separates well the phases Pdif, PKPdf, pPKPdf, an unidentified phase X (25s ahead of PP), PP and the depth phases pPP and sPP.

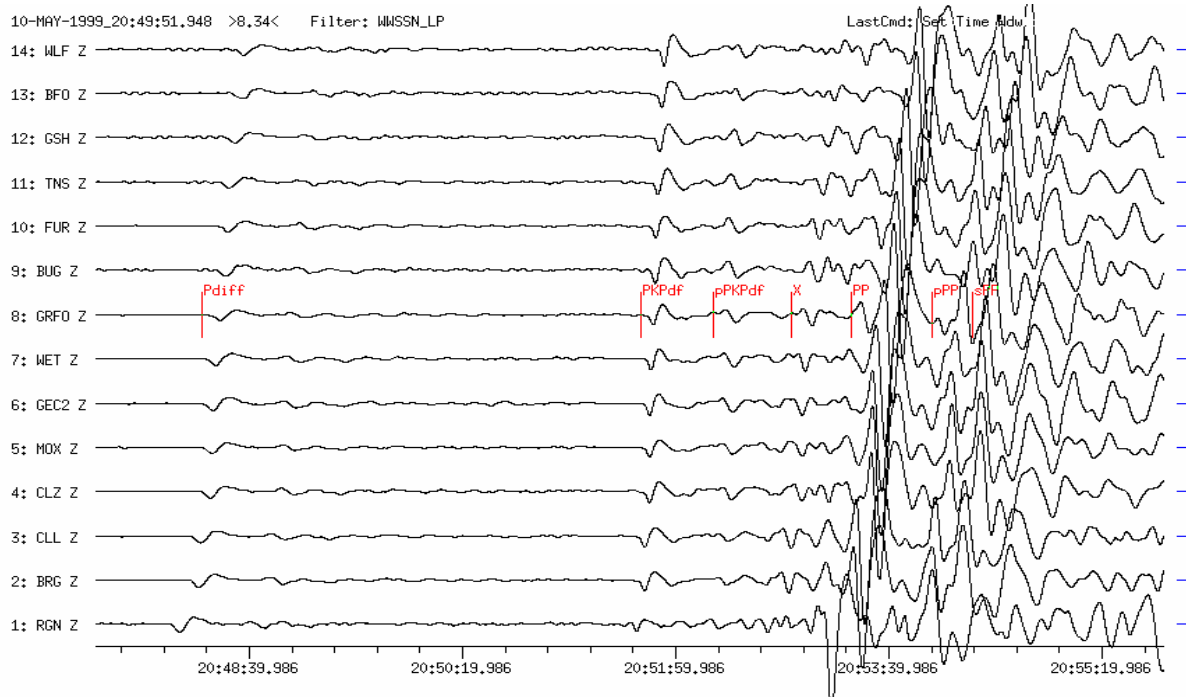


Figure 5c Long-period Z-component records (WWSSN-LP simulation) at 14 GRSN-, GEOFON- and GERESS-stations within the distance range $D = 120.1^\circ$ (RGN) to 126.6° (WLF). This record section was used to perform the vespagram analysis (see Figure5d).

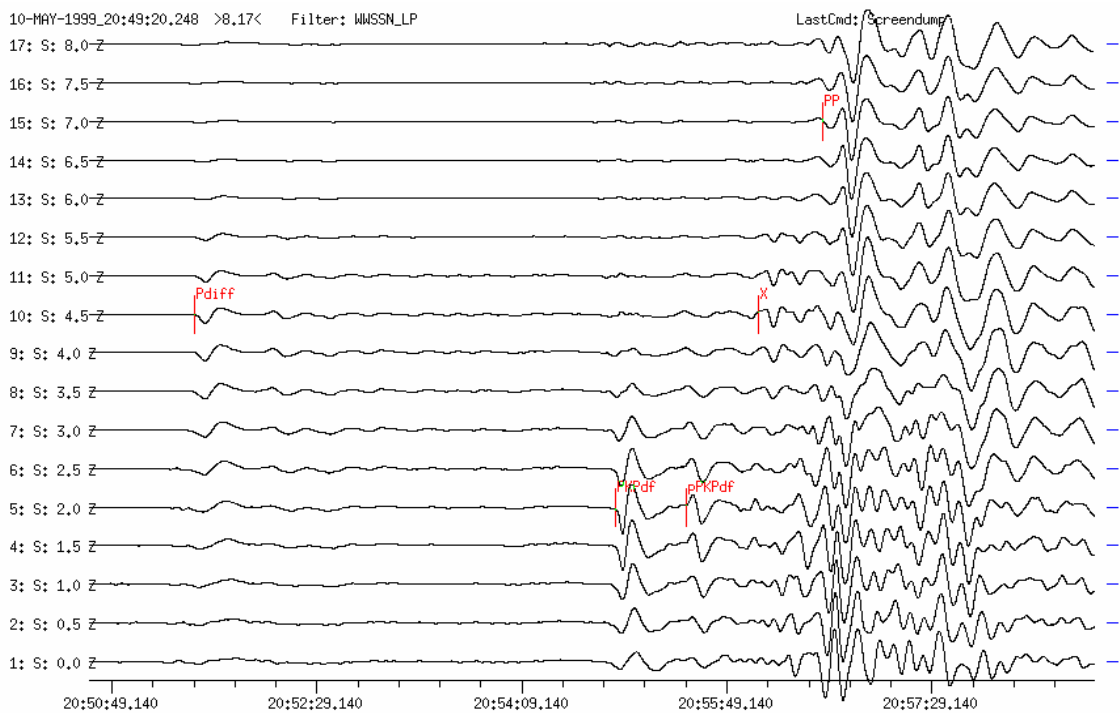


Figure 5d Vespagram analysis for vertical-components was used for slowness determination and phase identification. Phases were identified according to slowness values and travel times. The seismogram analysis program SHM allows to choose slowness steps (here in increments of 0.5 s°). The analysis yields slowness values of 4.5 s° for Pdif, 2.0 s° for PKPdf and pPKPdf, 7.0 s° for PP and for the phase X a value that would correspond to Pdif. The ray path could not be identified.

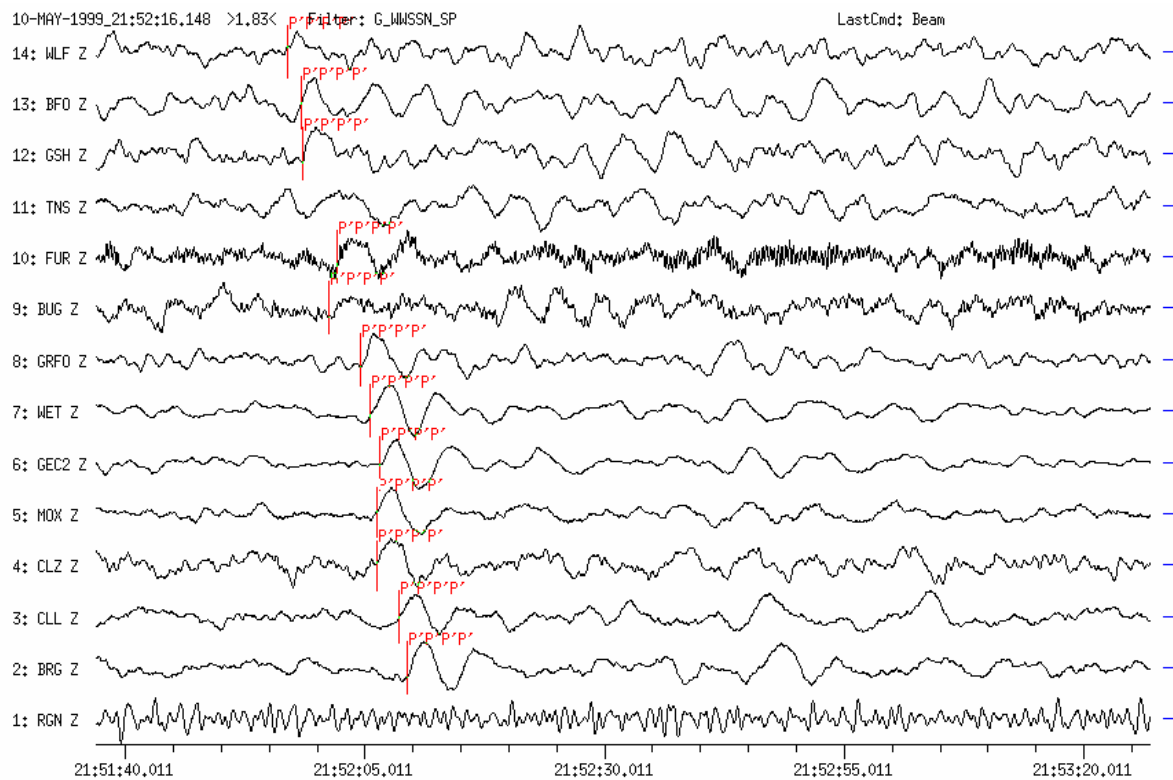


Figure 5e The network records show the rare phase 4P' (PKPPKPPKPPKP) with slowness $S = 2.5 \text{ s}^\circ$. It arrives 79 minutes after the origin time from the opposite azimuth direction (BAZ = 239°).

Example 6: Earthquake in the region of Salomon Islands

**USGS NEIC-data: 1996-04-29 OT 14:40:41.2 6.516S 155.037E h = 44G
 mb = 6.3 Ms = 7.5;
 (D = 127.3 ° and BAZ = 47.5° from GRA1)**

The example below presents clear Pdif onsets on long-period filtered seismograms as well as an excellent phase 4P' = P'P'P'P' = PKPPKPPKPPKP arriving about 63 min after the first onset. All records were made at the GRF-array (see Fig. 11.3).

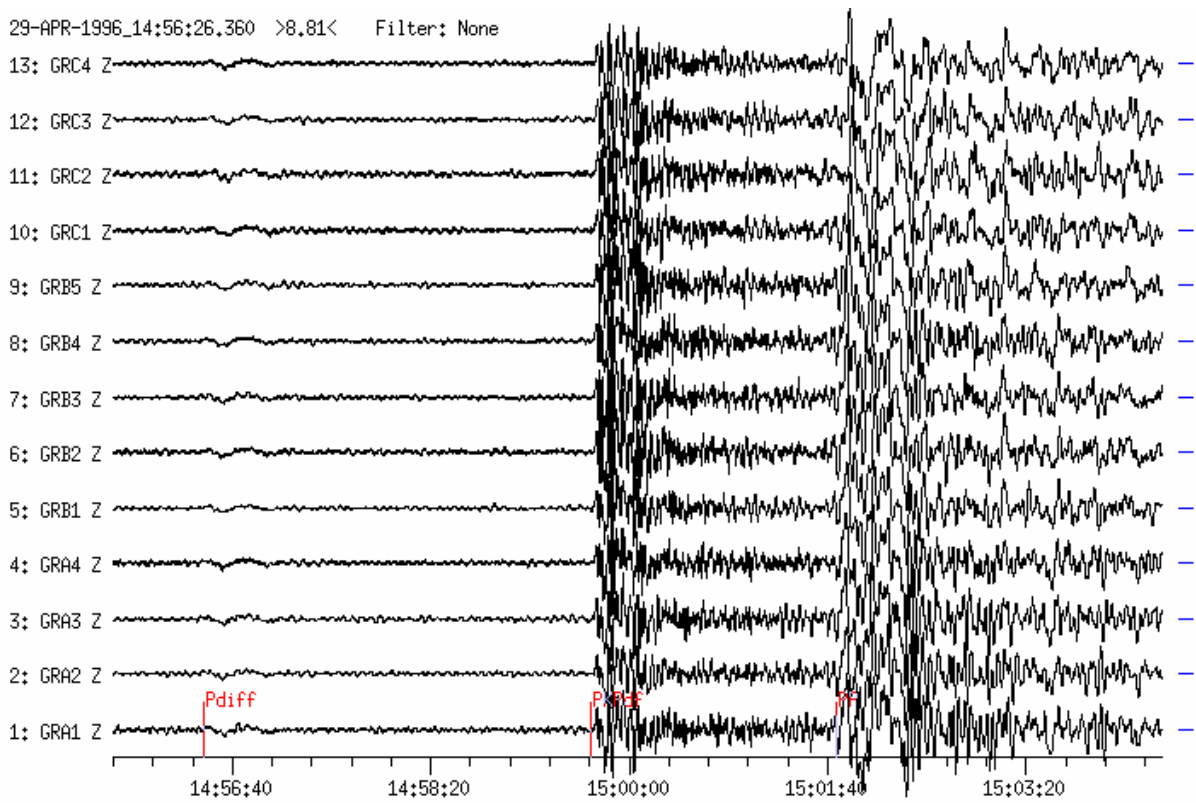


Figure 6a Broadband Z-component records at the GRF array within the distance range $D = 127.2^\circ$ to 127.8° which show, besides the rather long-period Pdif, also PKPdf and PP.

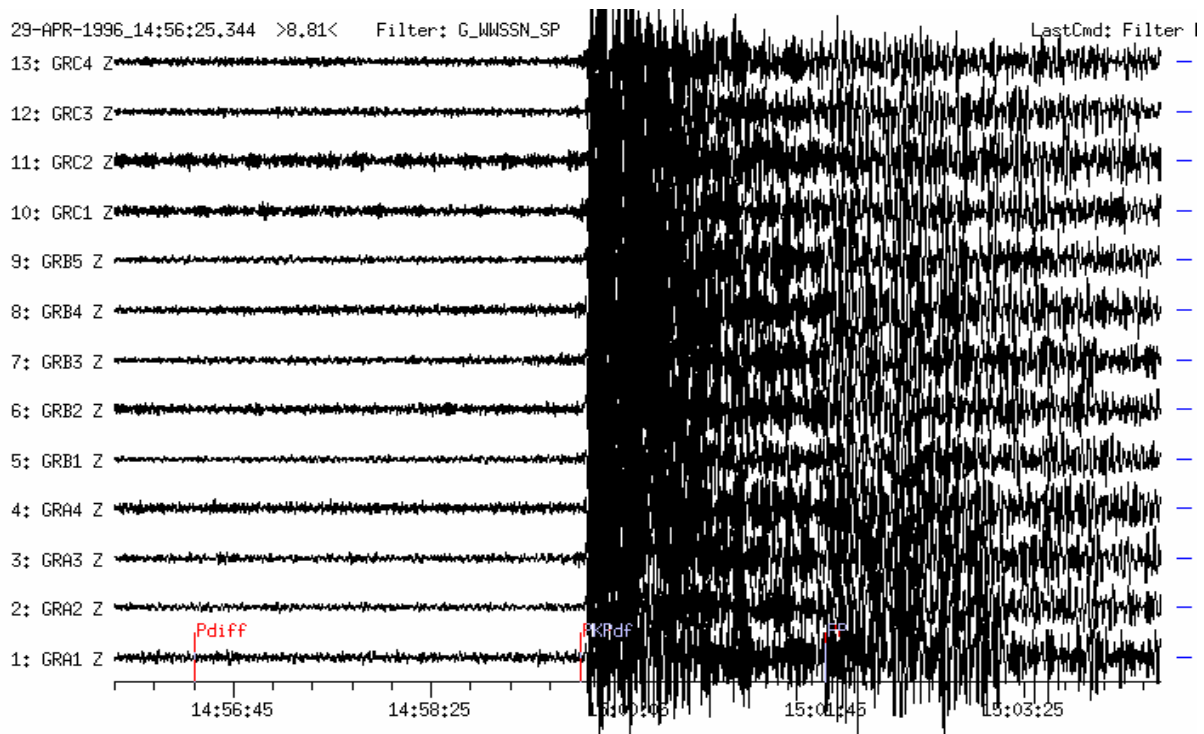


Figure 6b The same record as Figure 6a, however, a short-period filter was applied (WWSSN-SP simulation). Pdif is no longer visible above the noise level.

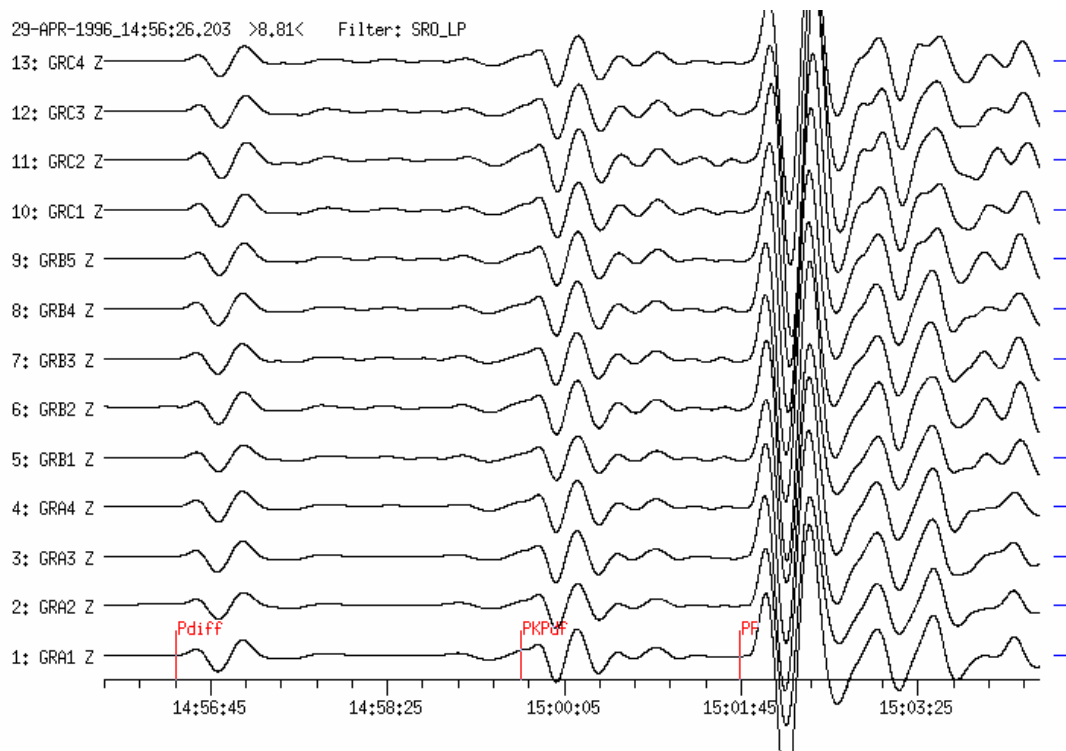


Figure 6c The same records as in Figures 6a and b, however, after applying a long-period filter (SRO-LP simulation). A distinct Pdiff appears on the record.

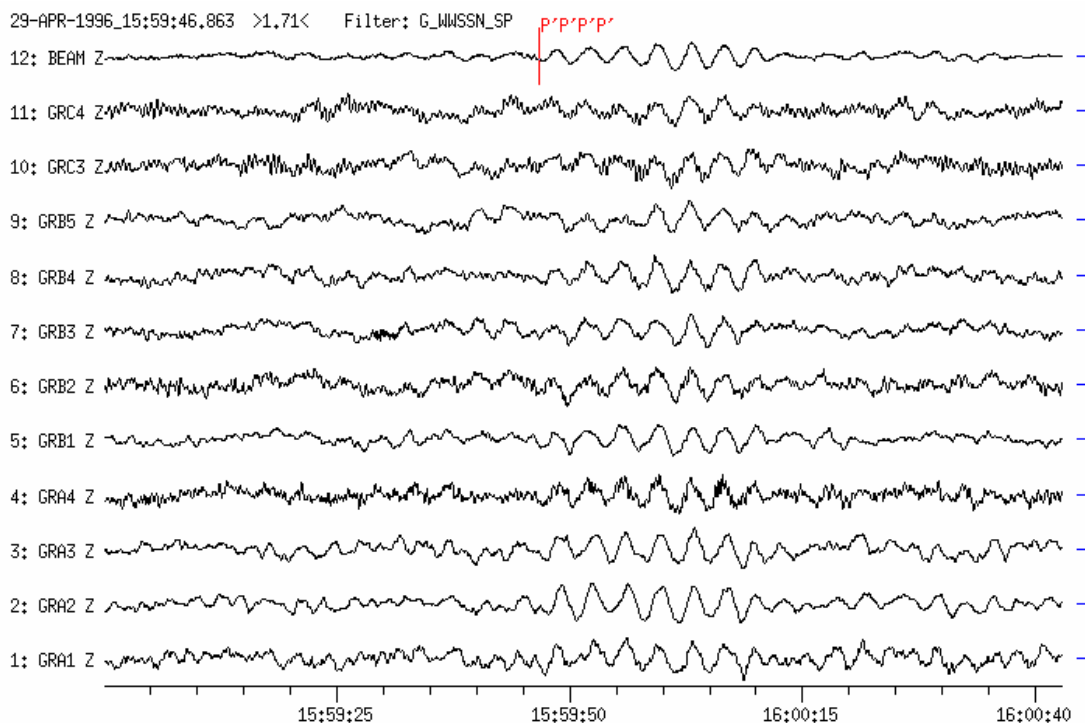


Figure 6d Short-period filtered (WWSSN-SP simulation) seismogram. The rare phase 4P' = P'P'P'P' (PKPPKPPKPPKP) was clearly recorded at the GRF-array coming from opposite direction (BAZ = 226 and S = 2.56 s/°) about 63 min after the first P onset. Trace No.12 (the sum of all traces = BEAM) shows the best signal-noise-ratio.

Example 7: Earthquake in Santa Cruz Island

USGS NEIC-data: 1998-07-16 OT 11:56:36 11.1S 165.9E h = 110G;
 (D = 136.2° and BAZ = 37.3° from GRA1).

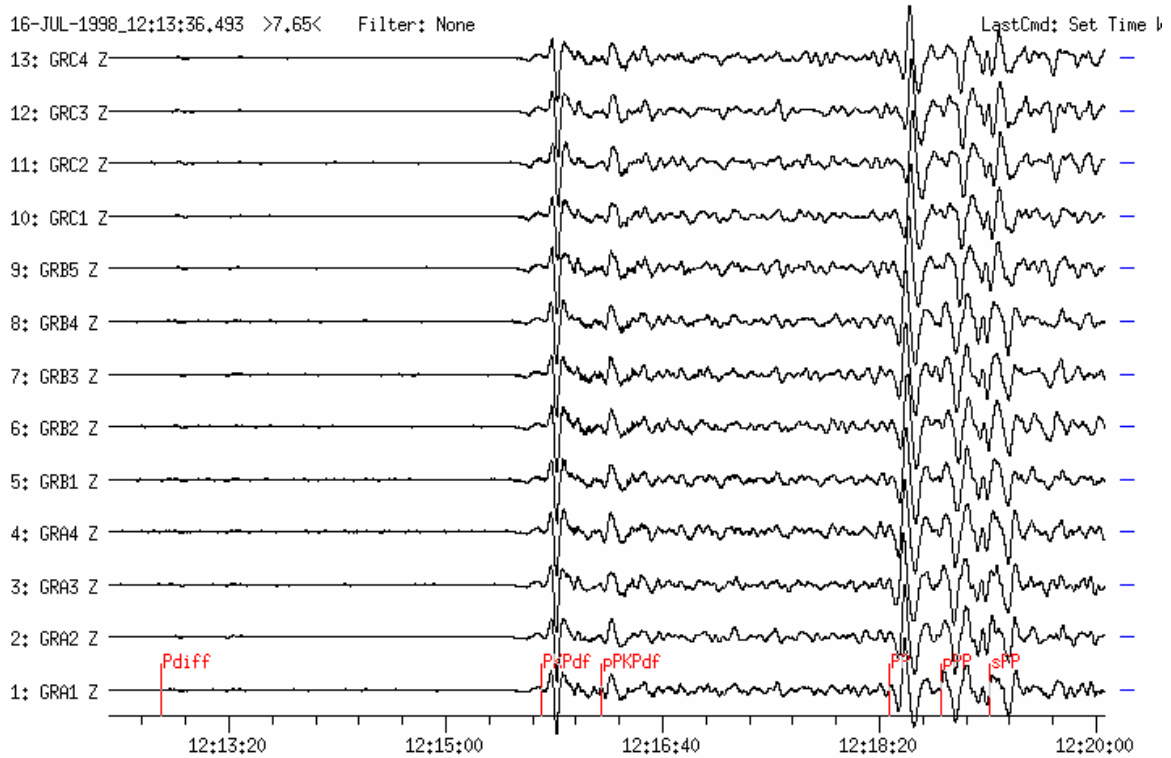


Figure 7a Vertical-component velocity BB seismograms recorded at the GRF-array (distance range between 136.1 and 136.8°). Note the very weak Pdif. The depth phases of PKPdf and PP correspond to a depth of 110 km.

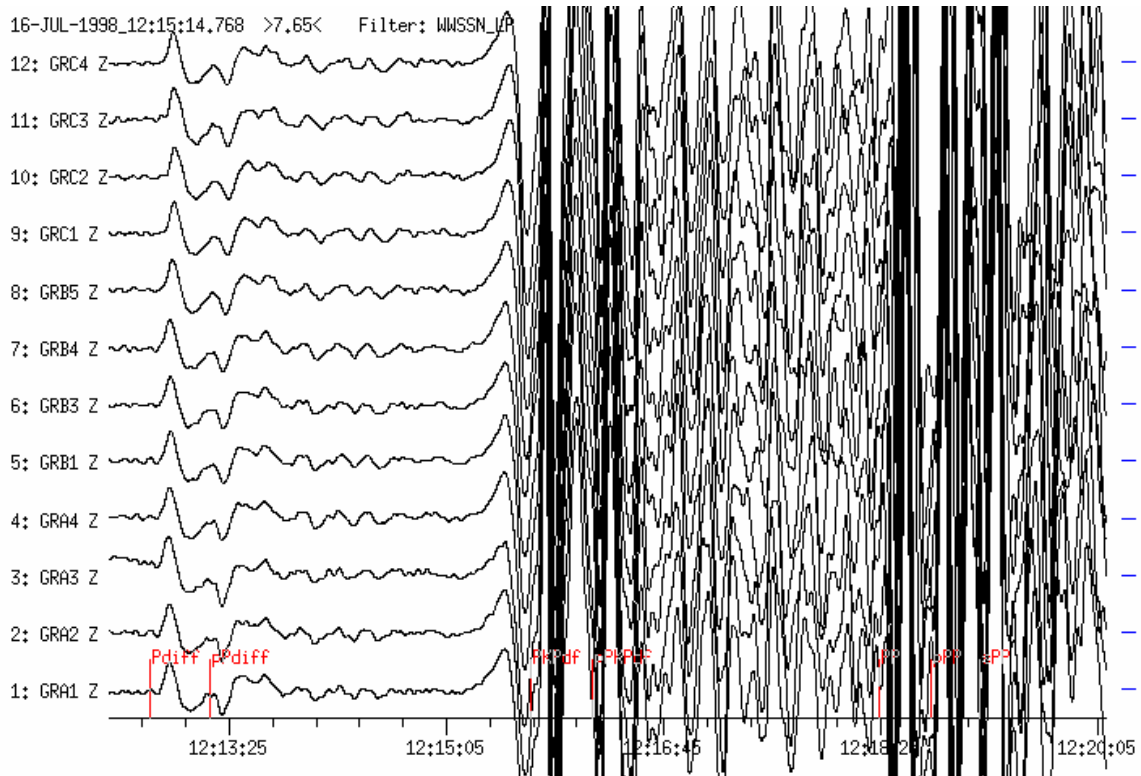


Figure 7b The same record as in Figure 7a, however, after long-period filtering (WWSSN-LP simulation). Note the pronounced onsets Pdif and pPdif. Also remarkable is the long-period and slowly emerging onset 24 sec before PKP.

Example 8: Earthquake in the region of Fiji Islands

USGS-QED-data: 1994-09-30 OT 19:30:06.9 21.102S 179.204W h = 500km(G), mb = 5.1;

The example shows pronounced core phases in the distance range 148°-152°. Short-period P waves reappear in this distance range but with discontinuous travel-time branches. In the region of the caustic, i.e. around 144°, the whole energy of direct longitudinal core phases is concentrated thus forming a strong PKP onset. Its amplitudes are comparable with that of P waves at much shorter distances (D around 50°). At distances beyond the caustic point PKP onsets are separated into individual PKP branches. The energy distribution changes with increasing distance. PKPbc (or PKP1) is the dominant branch just beyond the caustic, up to about 153°. In records of weaker events, PKPbc is often the first visible onset since PKPdf (or PKIKP), preceding PKPbc, is too weak to be observed. With increasing distance near 160° PKPbc vanishes from the record and PKPab (or PKP2) dominates the seismogram. For more details see sub-section 11.5.2.4.

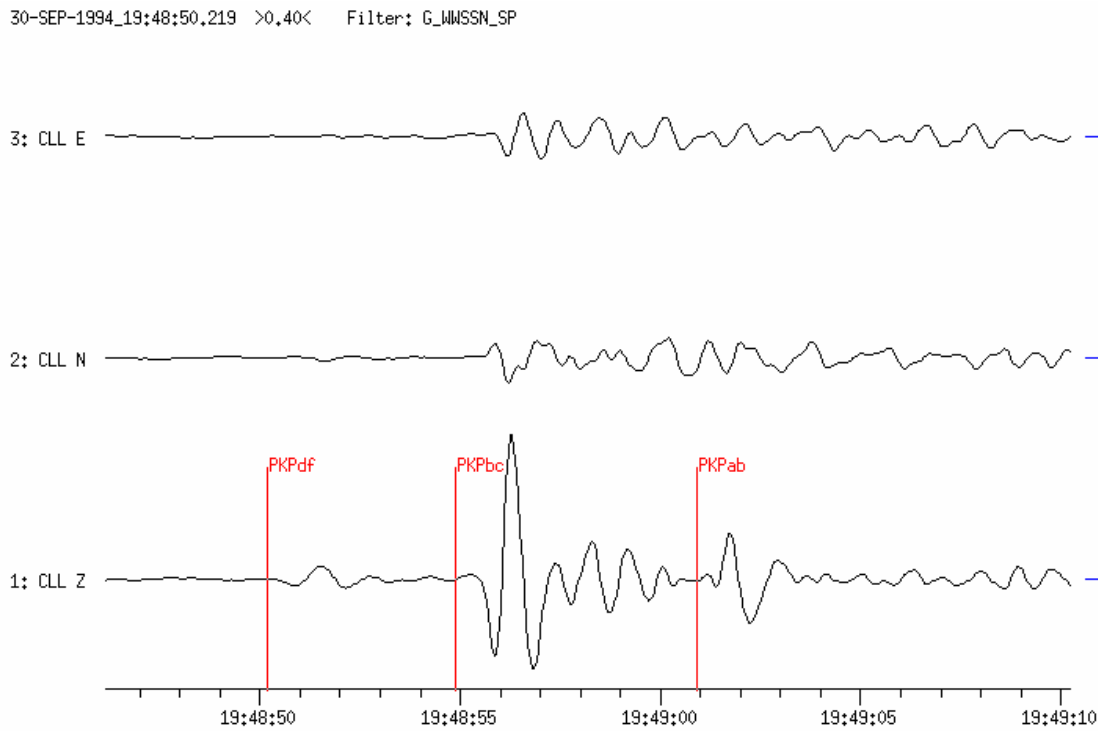


Figure 8a Short-period filtered three-component seismogram (WWSSN-SP simulation) recorded at the broadband station CLL at an epicentral distance of $D = 148.4^\circ$ ($BAZ = 22^\circ$). Phases PKPdf, PKPbc and PKPab are easy to analyse in this distance range. Travel-time curves for the different branches of these core phases allow to determine the epicentral distance from records of a single station only with an error less than 2° . Note the relatively very small amplitudes on the horizontal components because of the very small (steep) incidence angle at this large distance.

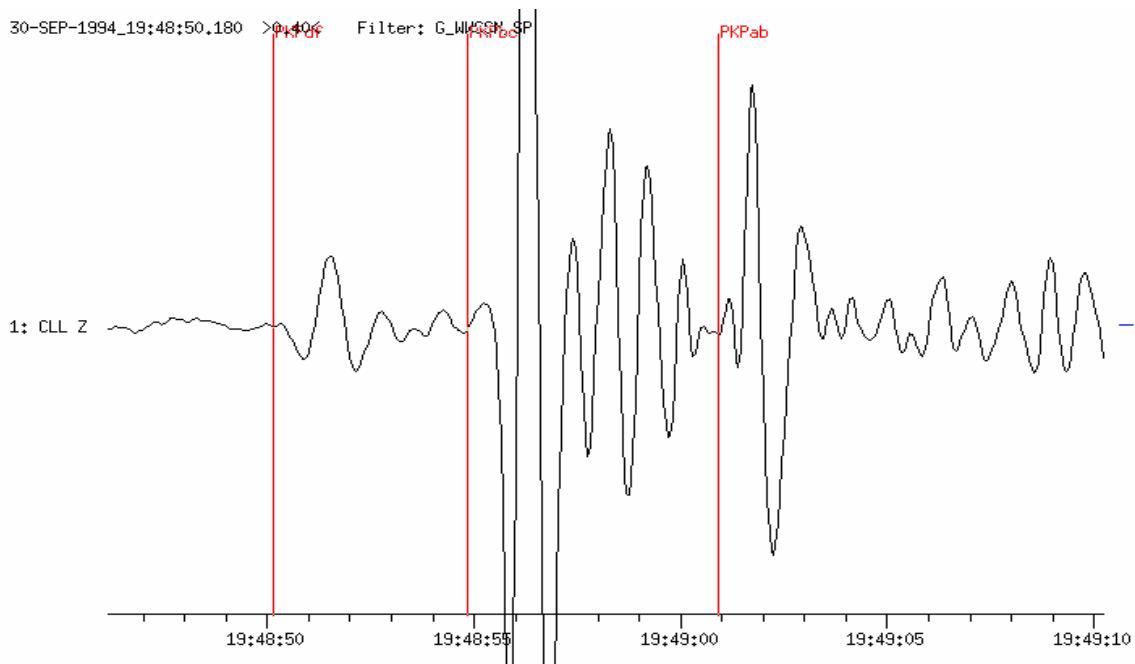


Figure 8b Vertical-component record of station CLL, displayed with higher magnification.

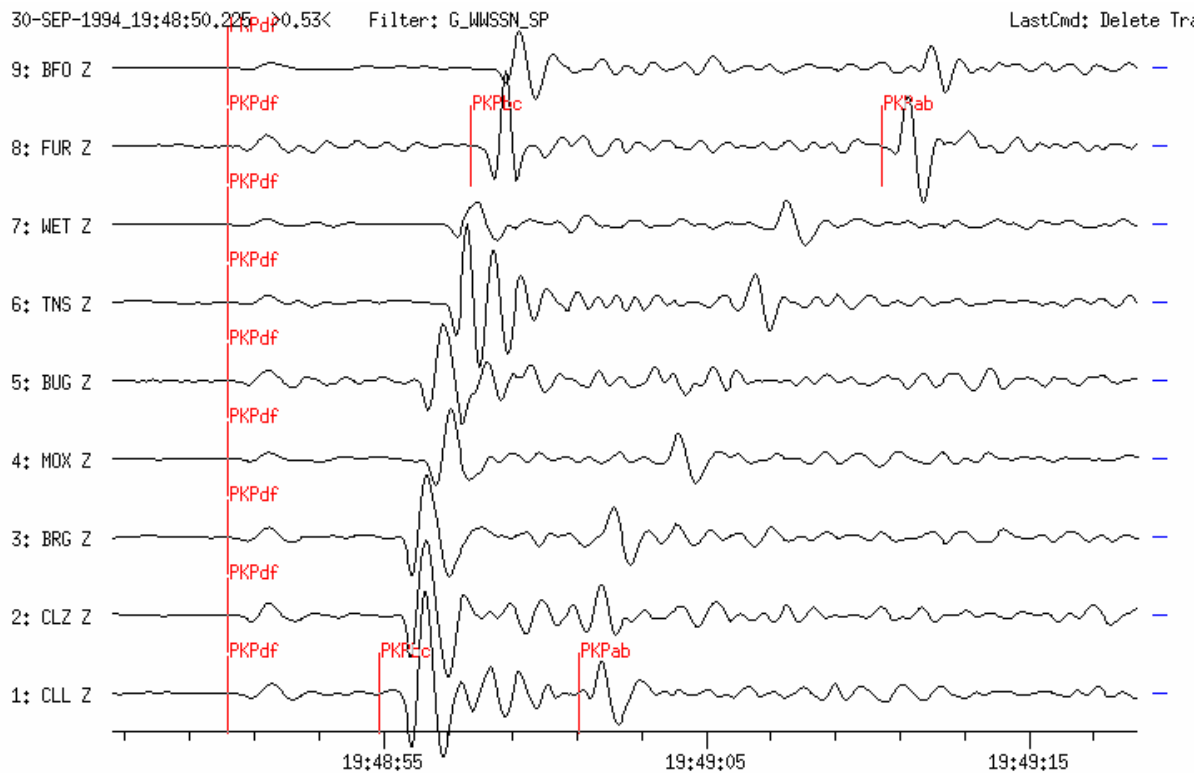


Figure 8c Short-period filtered seismograms (WWSSN-SP simulation) recorded at 9 GRSN-stations. All traces are time-shifted and aligned for PKPdf and sorted according to increasing distance. The epicentral distance for CLL is 148.4° and for the most distant station BFO 152.2° .

Example 9: Deep earthquake in the region of Fiji Islands

USGS NEIC-data: 2000-12-18 OT 01:19:21.6 21.18S 179.12W h = 628 km mb = 6.4; The epicentral distances of the GRSN stations range between $146^\circ < D < 153^\circ$.

Shown are enlarged cut-outs of the the PKP-wave group from the seismograms presented in Fig. 11.64. The PKP-wave group consists between $146^\circ < D < 156^\circ(160^\circ)$ of three distinct wave arrivals PKPab, bc and df. Fig. 11.59 shows the respective travel-time curves. The figures below demonstrate the effect of the record filter on the discrimination of these closely spaced wave arrivals and the possibility to pick their onset times. The longer the center period of applied narrowband band-pass filters, the worse is the discrimination and onset-time picking for these three core-phase arrivals. Therefore, PKP phases are best picked in SP records, however, the later phases PP and PPP from so distant earthquakes are usually recognizable only in LP or BB records.

2000-12-18 OT 01:19:21.6 h = 628 km Fiji Islands region

Z-component, SRO-LP

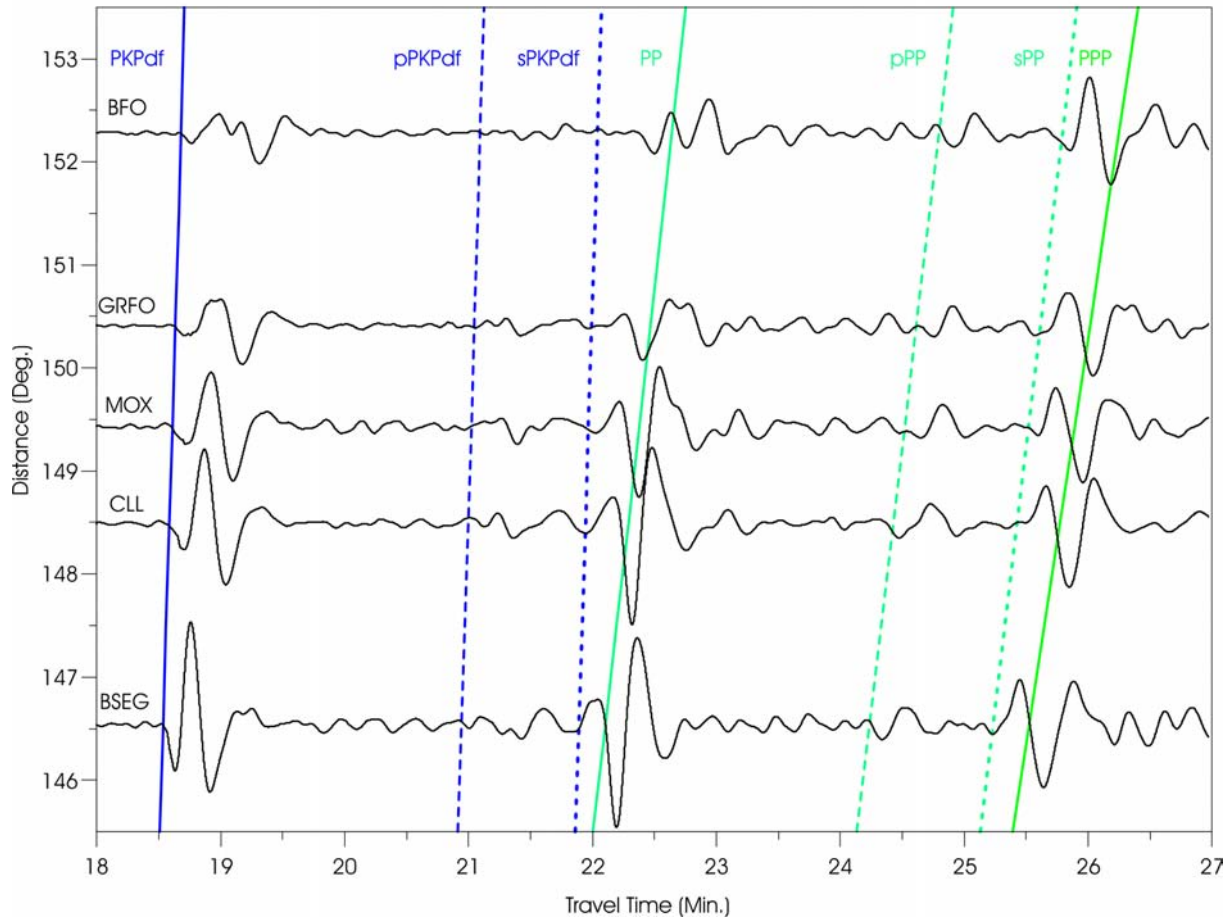


Figure 9a Z component long-period (SRO-LP simulated) records of longitudinal wave groups from a deep (h = 628 km) Fiji Islands earthquake at stations of the GRSN. Note the strong onsets of the depth phases sPKPdf and sPP prior to onsets PP and PPP, respectively, which follow closely.

2000-12-18 OT 01:19:21.6 h = 628 km Fiji Islands region

Model: IASP91 with ellipt. corr.

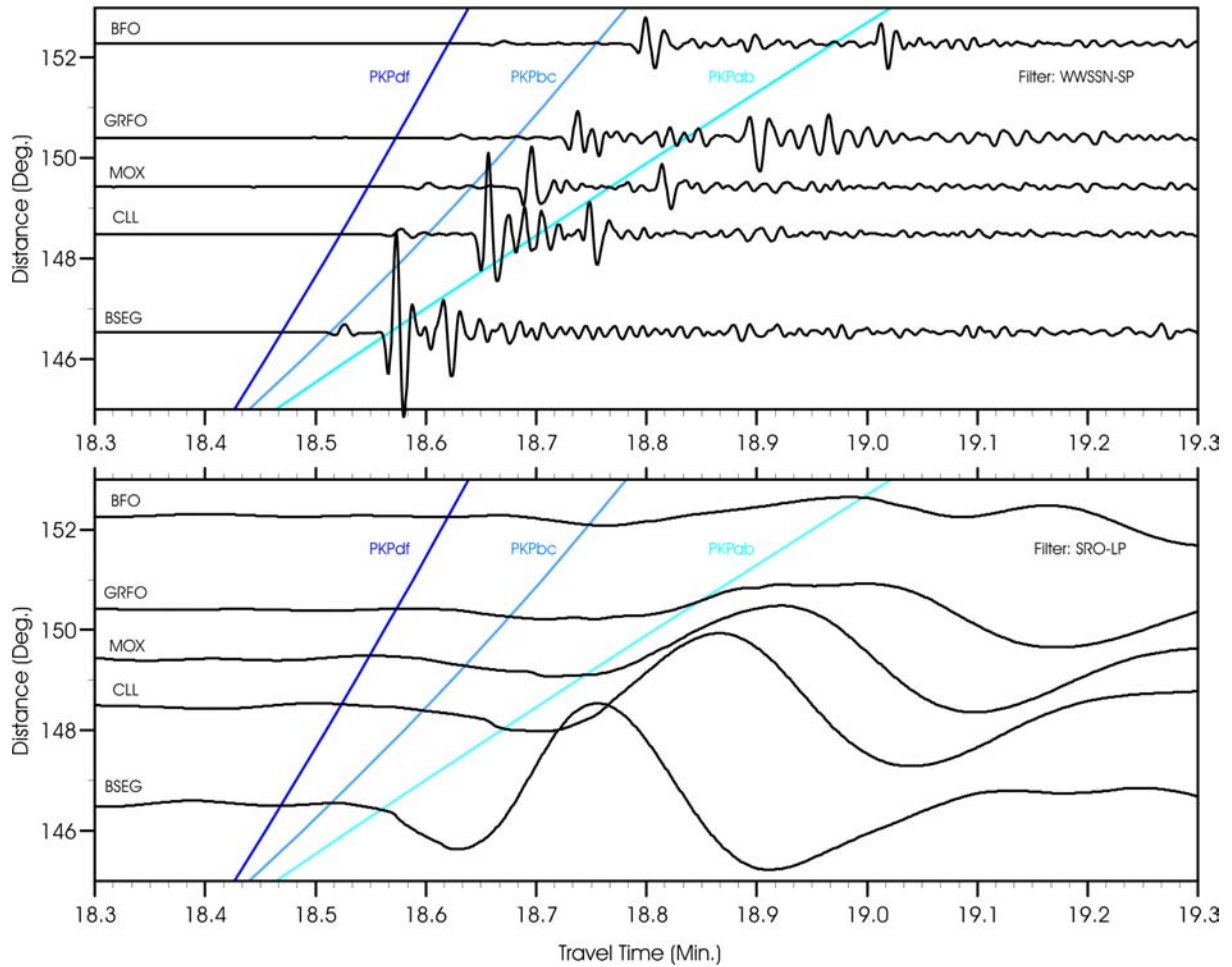


Figure 9b Enlarged cut-outs of the PKP-wave group as recorded in WWSSN-SP (upper traces) and SRO-LP filtered seismograms of the GRSN stations. Note that for all three core phases the theoretically expected onset times according to the IASP91 travel-time model are about 2 s too early.

2000-12-18 OT 01:19:21.6 h = 628 km Fiji Islands region

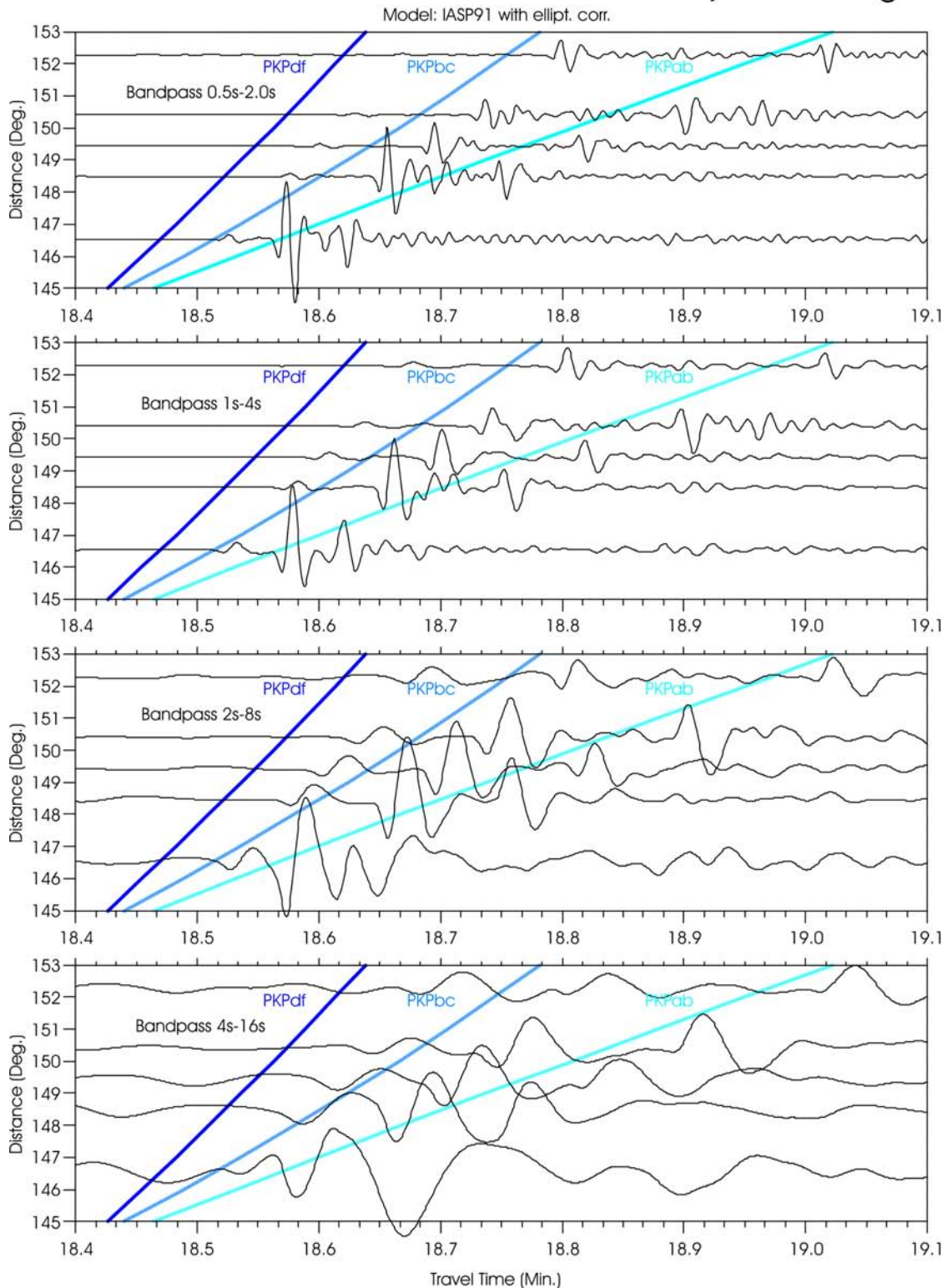


Figure 9c Enlarged cut-outs of the PKP-wave group of the deep Fiji Islands earthquake of 18 December 2000 recorded at stations of the GRSN. Shown are, from top to bottom, the bandpass filtered BB records of two octaves bandwidth with center periods around 1s, 2s, 4s and 8 s. For center periods larger than 3s the separation of the different PKP-wave arrivals and recognition of their onset times becomes less and less clear. Note that according to the IASP91 travel-time model the three core phases should arrive about three seconds earlier.

Topic	Record examples of underground nuclear explosions
compiled by	Klaus Klinge, Federal Institute for Geosciences and Natural Resources, Seismological Central Observatory, Gräfenberg (SZGRF), Mozartstrasse 57, D-91052 Erlangen, Germany, Fax: +49-9131 8104 099, E-mail: klinge@szgrf.bgr.de Johannes Schweitzer, NORSAR, P.O.Box 53, N-2027 Kjeller, Norway, Fax: +47-63818719, E-mail: johannes.schweitzer@norsar.no Peter Bormann (formerly GeoForschungsZentrum Potsdam, Telegrafenberg, D-14473 Potsdam, Germany); E-mail: pb65@gmx.net
Version	June, 2002

1 Record examples of underground nuclear explosions between 1978 and 1993 within the teleseismic distance range

Below, seismic records of underground nuclear explosions (UNEs) at 5 weapon test sites and from a peaceful nuclear explosion (PNE) are shown. All records were made in the distance range $D > 30^\circ$ by vertical-component seismographs at station GRA1 of the Gräfenberg broadband array in Germany. The original BB records were filtered in the short-period range (WWSSN-SP simulation filter). The time scale is given in the records. The amplitudes have been normalized and the records are presented in Figure 1 in the following order:

No.	Date	Time	Latitude [deg]	Longitude [deg]	Depth [km]	m_b	Location (Code Name)	D [deg]	Reference
1	1988-12-17	04:18:09.2	49.879	78.924	0	5.9	Semipalatinsk	42.34	UK AWE (1990)
2	1993-10-05	01:59:56.68	41.6322	88.6886	0	5.9	Lop Nor	52.49	ISC (2001)
3	1988-12-04	05:19:53.3	73.3660	55.0010	0	5.9	Novaya Zemlya	30.32	Richards (2000)
4	1988-10-13	14:00:00.08	37.0890	-116.0493	0	5.9	Nevada Test Site (Dalhart)	81.83	ISC (2001)
5	1987-11-19	16:31:00.2	-21.845	-138.941	0	5.7	Mururoa	143.58	UK AWE (1993)
6	1978-10-08	00:00:00.0	61.55	112.85	1.545	5.2	PNE, USSR / Siberia (Vyatka)	52.78	Sultanov et al. (1999)

D is the distance to the reference site of the Gräfenberg Array GRA1. The estimated yields for these explosions range between approximately 20 and 150 kt TNT for the weapon tests and is about 15 kt TNT for the PNE (No. 6).

With the exception of the Mururoa test all other records show a clear positive (compressional) first arrival. This should be expected from explosions at all distances and azimuths. For the Mururoa the waveform is influenced by the caustic in the core distance range near $D = 145^\circ$ and therefore the onset polarity can not be read reliably. Note the remarkable differences in P waveforms, which are rather short and simple for events No. 1, 2, 5 and 6 but much more complex and longer for events No. 3 and 4. This is mainly due to the specific geology and/or complex topography at the test sites in Nevada and on Novaya Zemlya. However, for event No. 3 we observe later P energy in an epicentral distance of about 30° due to the upper mantle triplications and for event No. 5 the distinguished onsets are later PKP-type onsets (see

Schlittenhardt, 1996). More waveform data from UNEs can be retrieved from the PIDC Nuclear Explosion Database (see IS 10.3).

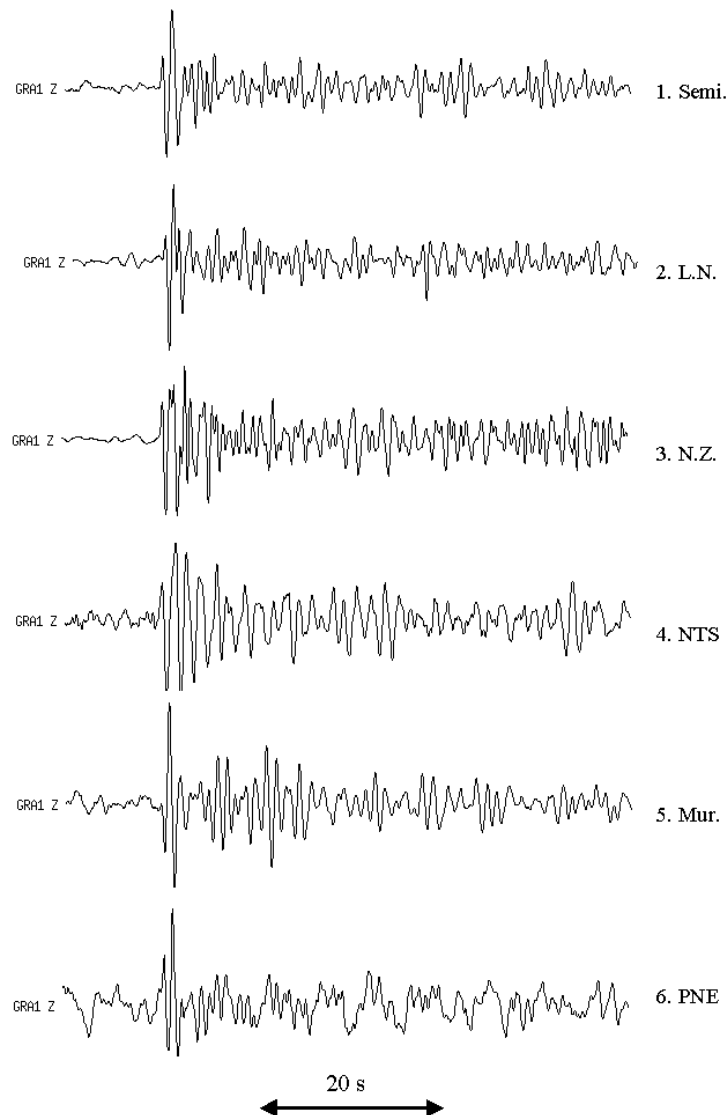


Figure 1 Short-period filtered seismograms (WWSSN-SP simulation filter) recorded at station GRA1 of the Gräfenberg broadband array in Germany from underground nuclear explosions in six different areas. For source parameters and distances to GRA1 see list above.

2 Records of the nuclear-weapon tests of India and Pakistan

Figures 2 and 3 show vertical component records of broadband stations of the German Regional Seismography Network (GRSN) from the underground nuclear weapons tests of India and Pakistan in 1998. All records were filtered narrowband in the short-period range around 1 Hz and sorted according to the epicentral distance. The source parameters are:

India: 1998-11-05, 10:13:44.2, 27.0780°N, 71.7190°E, depth 0 km, mb 5.2 (Barker et al., 1999) with epicentral distance and backazimuth from GRFO: $D = 50.99^\circ$ and $BAZ = 92.94^\circ$.

Pakistan: 1998-05-30, 06:54:54.87, 28.4434°N, 63.7375°E, depth 0 km; mb 4.7 (ISC, 2001) with epicentral distance and backazimuth from GRFO: $D = 44.91^\circ$ and $BAZ = 98.12^\circ$.

The P-wave onsets are generally simple. However, they are masked by noise at the more noisy stations. Surface-wave amplitudes were very weak and could not be analyzed at this large distance.

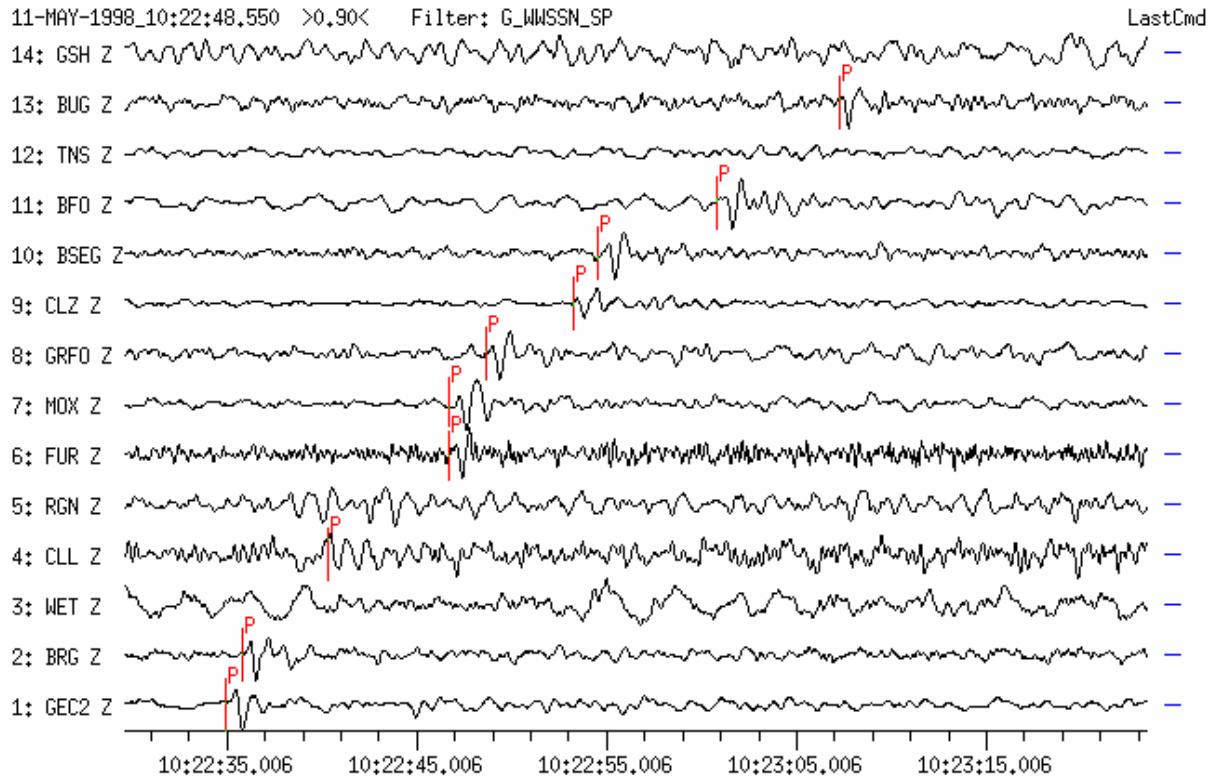


Figure 2 Records of the Indian underground nuclear test on 11 May 1998. For source parameters see above. The broadband records were filtered with the WWSSN-SP response. Typical for explosions are the compressional first onset polarities at stations with high SNR.

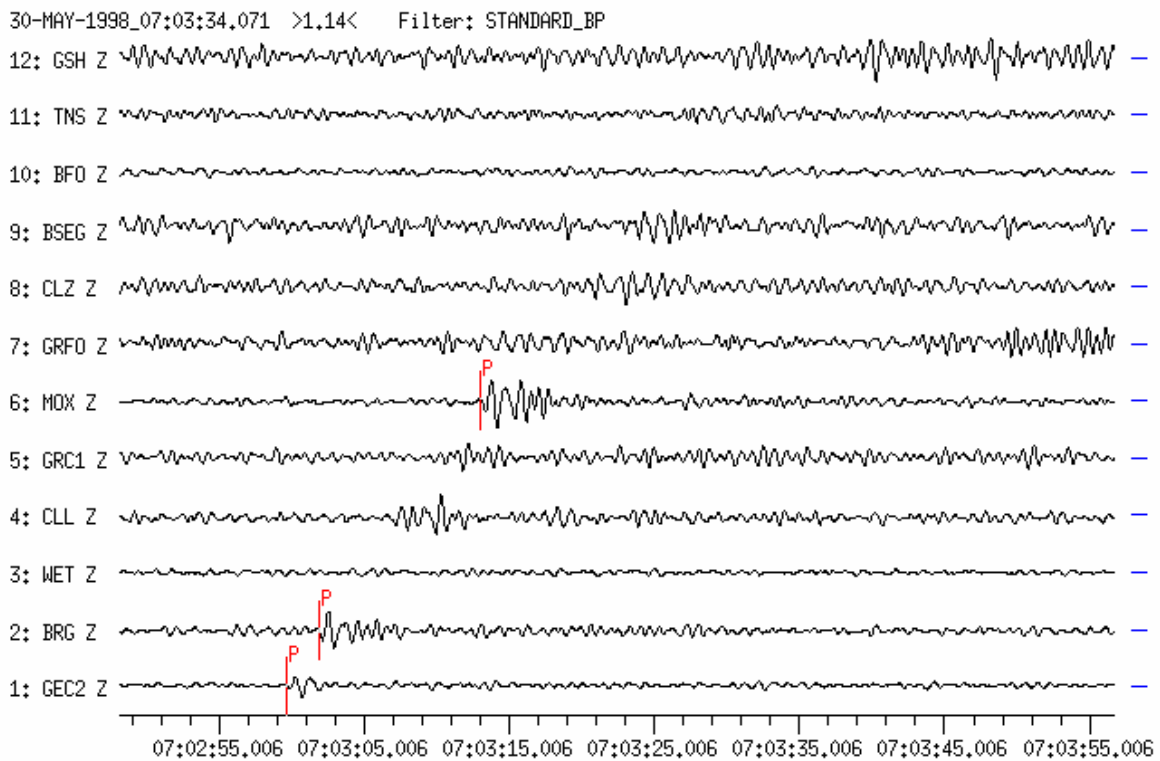


Figure 3 Records of the Pakistani underground nuclear test of 30 May 1998. For source parameters see above. The broadband records were filtered with a short-period band-pass filter (0.8 to 1.2 Hz), which has a smaller (about 0.5 octaves) bandwidth than the WWSSN-SP filter (about 1 octave). It results in a better SNR, however it is not possible to read reliable first motion polarities. In addition, the seismograms are disturbed by energy of an aftershock sequence of an earthquake in the Afghanistan-Tajikistan border region (see, e.g., Kväerna et al., 2002). Note the apparently negative first onsets at stations BRG and MOX! For related discussions see 4.2 in Chapter 4 of this Manual.

3 Records of underground nuclear explosions in the regional distance range ($7^\circ < D \leq 30^\circ$)

At shorter distances ($D \leq 30^\circ$) records from underground nuclear explosions (UNE) still contain a rather large amount of high-frequency energy. This is mainly due to the difference in the source process as compared to earthquakes (see Fig. 3.5 and the related discussions in 3.1.1.3). Two examples are shown below.

3.1 UNE at the Northern Novaya Zemlya Test Site

Source data: 1990-10-24, 14:57:58.5, 73.3310°N , 54.7570°E , depth 0 km, mb 5.7 (Richards, 2000)

The distances to the recording stations shown in Fig. 4 are: $D = 9.99^\circ$ (ARCES), 15.98° (FINES), 20.41° (NORES) and 30.40° (GERES).

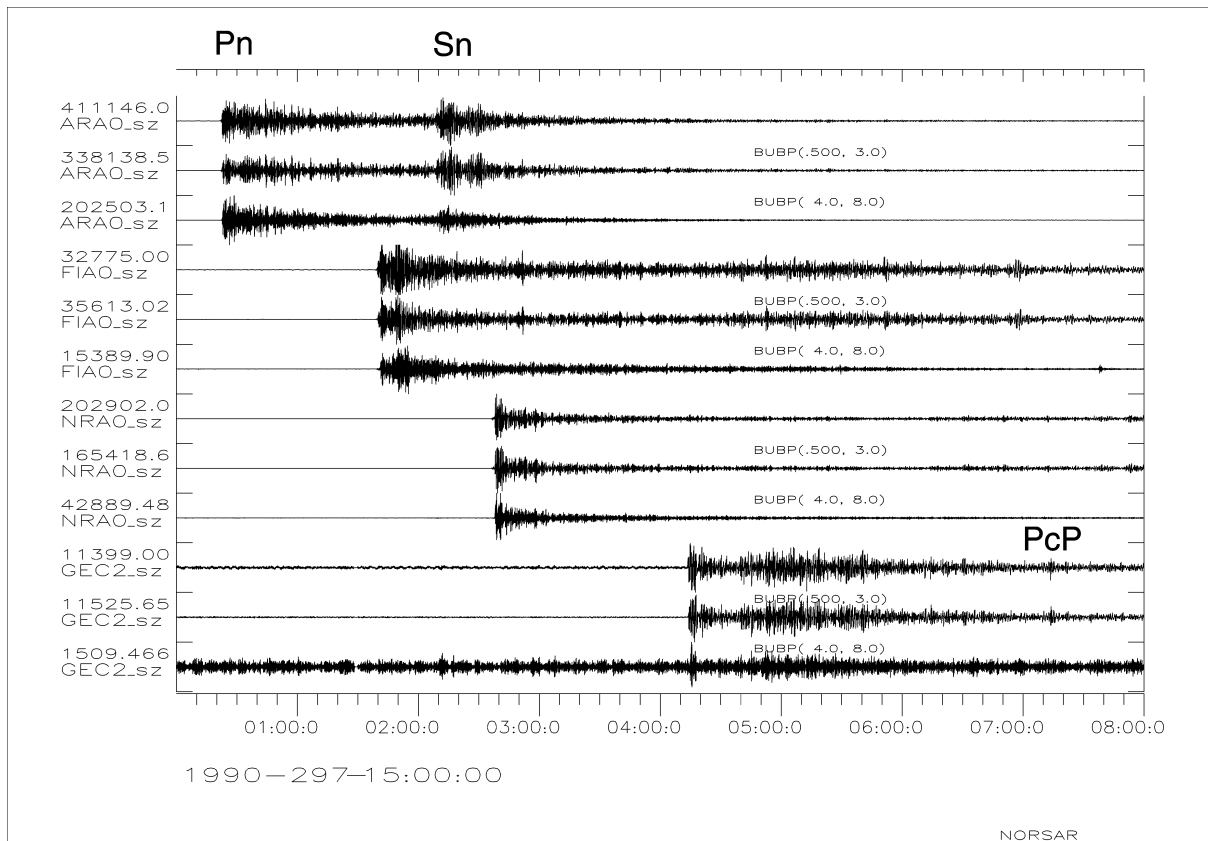


Figure 4 Records of the key stations ARA0, FIA0, NRA0 and GEC2 of the small aperture short-period arrays ARCES, FINES, NORES and GERES from the Novaya Zemlya test of 24 October 1990. These arrays are specialized for regional signals and ARCES, FINES and GERES are part of the International Monitoring System (IMS) under the Comprehensive Nuclear-Test-Ban Treaty Organization (CTBTO) in Vienna. Shown are the vertical component records a) unfiltered, b) band-pass filtered between 0.5 and 3 Hz, c) band-pass filtered between 4 and 8 Hz. Note the relatively strong high-frequency energy that is well developed in the P-wave group up to 30° distance but no longer visible above the level of signal coda for S waves beyond 10° distance. S waves are stronger attenuated than P waves. At GEC2 the core reflection PcP is nicely visible and the P-wave coda is dominated by energy scattered in the uppermost mantle. Each trace is normalized by its maximum amplitude, which is given in digital counts together with the channel name. The time axis is labeled at each minute after 15:00:00 with 10 s between two ticks.

3.2 UNE of India in 1998

In Figure 2 we showed data of the Indian UNE of 5 May 1998 as observed in Europe. This event could also be observed at a regional distance at the Pakistani station NIL (Figure 5).

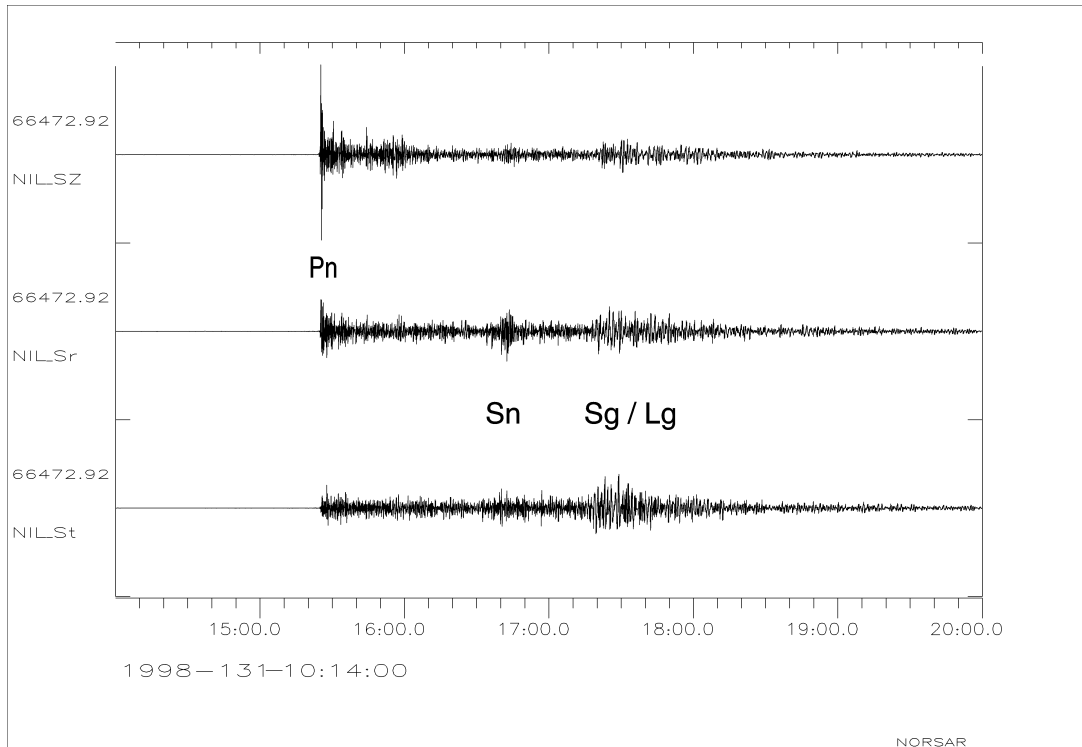


Figure 5 Z-R-T rotated three-component record at the IRIS/IDA station NIL, Pakistan. The epicentral distance to the Indian test site is about 740 km; the amplitudes are normalized by the largest signal, which is given in counts at each channel name; shown are unfiltered data. Note the strong P- but weak S-wave arrivals. The time axis is labelled for each minute after 10:14:00 with 10 s between two ticks.

References (see References under Miscellaneous in Volume 2)

Topic	Magnitude determinations
Author	Peter Bormann (formerly GeoForschungsZentrum Potsdam, Telegrafenberg, D-14473 Potsdam, Germany); E-mail: pb65@gmx.net
Version	July 2001

1 Aim

The exercises aim at making you familiar with the measurement of seismic amplitudes and periods in analog and digital records and the determination of related magnitude values for local and teleseismic events by using the procedures and relationships outlined in 3.2, and the magnitude calibration functions given in DS 3.1.

2 Procedures

The general relationship

$$M = \log (A/T) + \sigma(\Delta, h) \quad (1)$$

is used for magnitude determination, with A – maximum “ground motion” amplitude in μm (10^{-6} m) or nm (10^{-9} m), respectively, measured for the considered wave group, T – period of that maximum amplitude in seconds. Examples, how to measure the related trace amplitudes B and period T in seismic records are depicted in Fig. 3.9. Trace amplitudes B have to be divided by the respective magnification $\text{Mag}(T)$ of the seismograph at the considered period T in order to get the “ground motion” amplitude in either μm or nm , i.e., $A = B/\text{Mag}(T)$.

$\sigma(\Delta, h) = -\log A_0$ is the magnitude calibration function, for teleseismic body waves also called $Q(\Delta, h)$ or $P(\Delta, h)$. Δ - epicentral distance, for *teleseismic events* (> 1000 km) generally given in degree ($1^\circ = 111.19$ km), for *local events* (< 1000 km) usually given in km. For local events often the “slant range” or hypocentral distance R (in km) is used instead of Δ . All calibration functions used in the exercise are given in DS 3.1.

Note: According to the original definition of the local magnitude scale M_L by Richter (1935) only the *maximum trace amplitude* B in mm as recorded in standard records of a Wood-Anderson seismometer is measured (see Fig. 3.11 and section 3.2.4), i.e.,

$$M_L = \log B(\text{WA}) - \log A_0(\Delta). \quad (2)$$

Accordingly, no period T is measured, and no conversion to “ground motion” amplitude is made. However, when applying M_L calibration functions to trace amplitudes B measured (in mm too) in records of another seismograph (SM) with a frequency-magnification curve $\text{Mag}(T)$ different from that of the Wood-Anderson seismograph (WA) then this frequency-dependent difference in magnification has to be corrected. Equation (2) then becomes

$$M_L = \log B(\text{SM}) + \log \text{Mag}(\text{WA}) - \log \text{Mag}(\text{SM}) - \log A_0. \quad (3)$$

3 Data

The data used in the exercise are given in the following figures and tables.

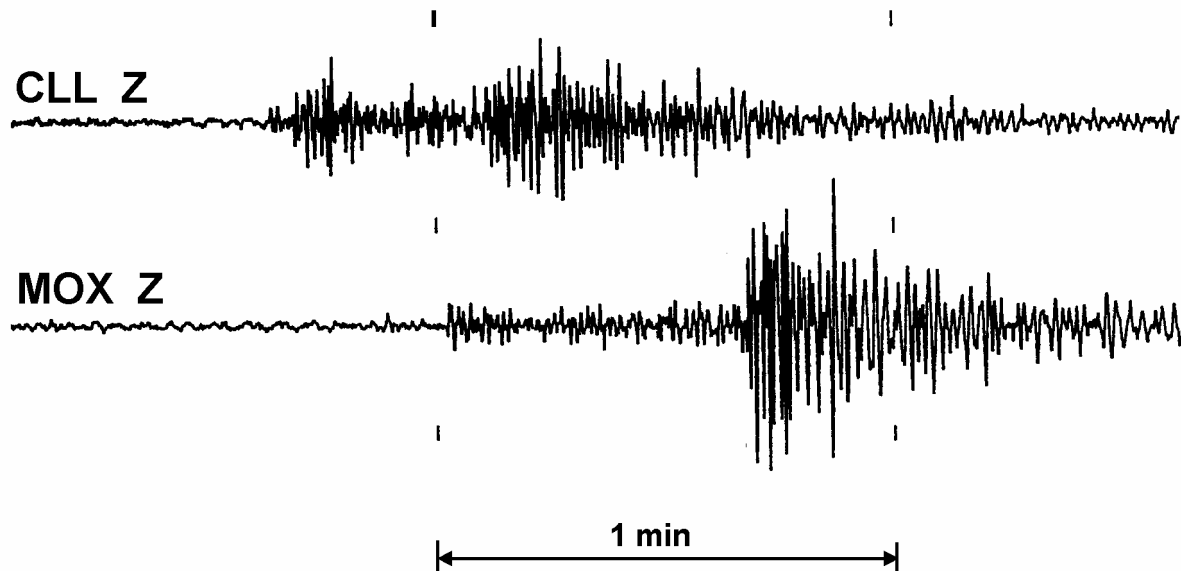


Figure 1 Vertical component records of a local seismic event in Poland at the stations CLL and MOX in Germany at scale 1:1. The magnification values $\text{Mag}(\text{SM})$ as a function of period T for this short-period seismograph are given in Table 1 below.

Table 1 Magnification values $\text{Mag}(\text{SM})$ as a function of period T in s for the short-period seismograph used for the records in Figure 1 together with the respective values $\text{Mag}(\text{WA})$ for the Wood-Anderson standard seismograph for M_I determinations.

T (in s)	$\text{Mag}(\text{SM})$	$\text{Mag}(\text{WA})$	T (in s)	$\text{Mag}(\text{SM})$	$\text{Mag}(\text{WA})$
0.1	35,000	2,800	1.1	190,000	1,100
0.2	92,000	2,700	1.2	180,000	950
0.3	125,000	2,600	1.3	170,000	850
0.4	150,000	2,400	1.4	155,000	750
0.5	170,000	2,200	1.5	140,000	700
0.6	190,000	2,000	1.6	120,000	
0.7	200,000	1,800	1.7	90,000	
0.8	201,000	1,600	1.8	80,000	
0.9	201,000	1,400	1.9	70,000	
1.0	200,000	1,200	2.0	60,000	

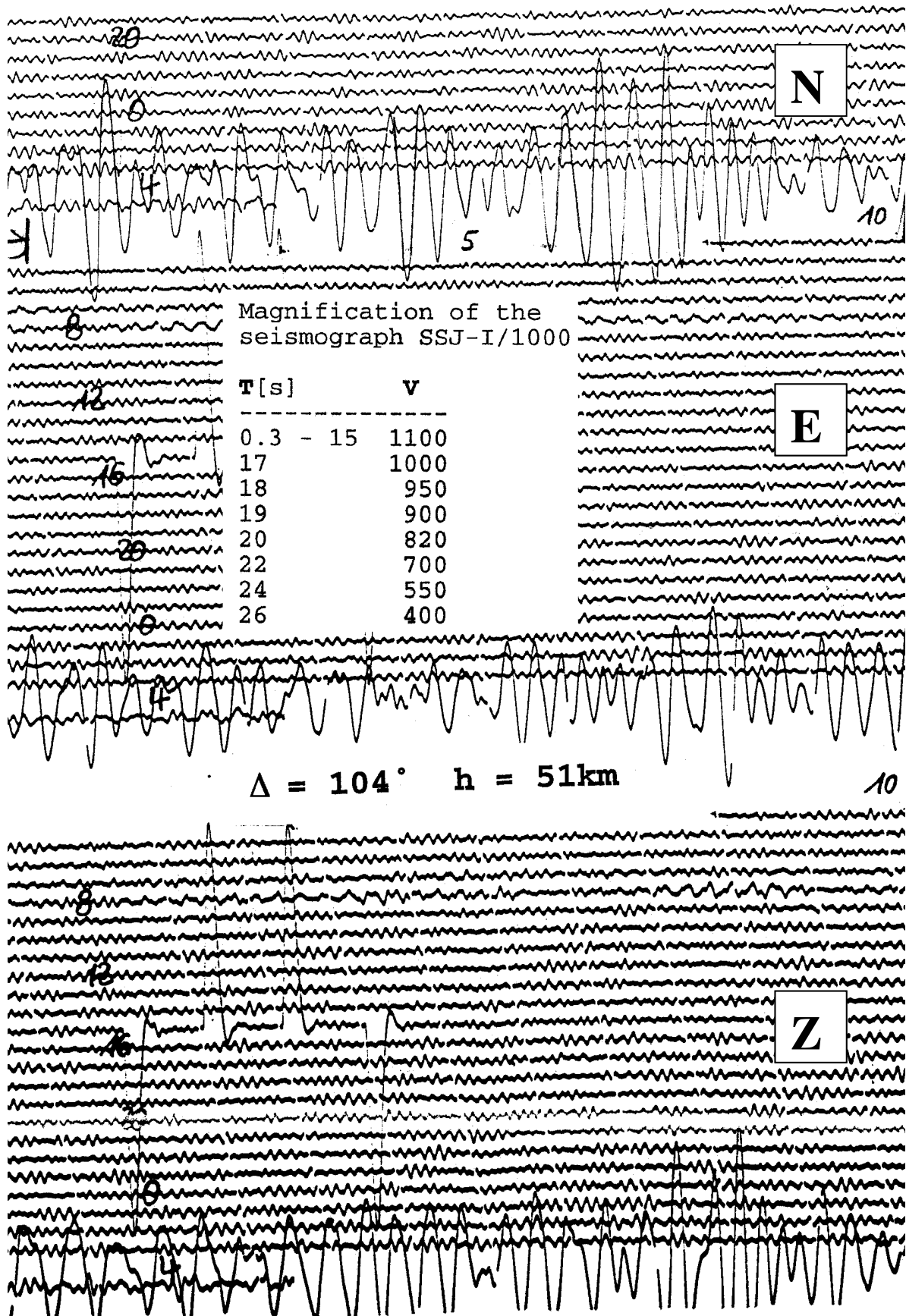


Figure 2 Analog record at scale 1:1 of a Kirnos-type seismograph from a surface-wave group of a teleseismic event. Scale: 1 mm = 4 s; for displacement Mag = V see inserted table.

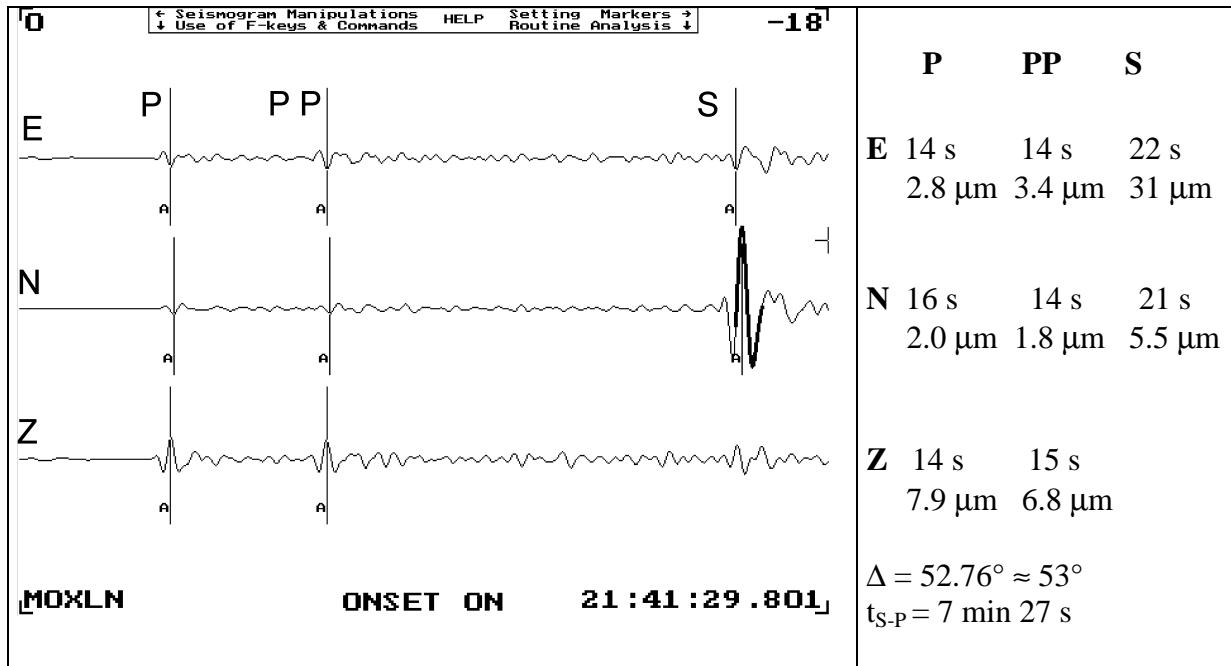


Figure 3 Display of the long-period (10 to 30 s) filtered section of a broadband 3-component record of the Uttarkasi earthquake in India (19 Oct. 1991; $h = 10 \text{ km}$) at station MOX in Germany. The record traces are, from top to bottom: E, N, Z. Marked are the positions, from where the computer program has determined automatically the ground displacement amplitudes A and related periods T for the onsets (from left to right) of P, PP and S. For S the respective cycle is shown as a bold trace. The respective values of A and T for all these phases are saved component-wise in the data-pick file. They are reproduced in the box on the right together with the computer picked onset-time difference $S - P$ and the epicentral distance Δ as published for station MOX by the ISC.

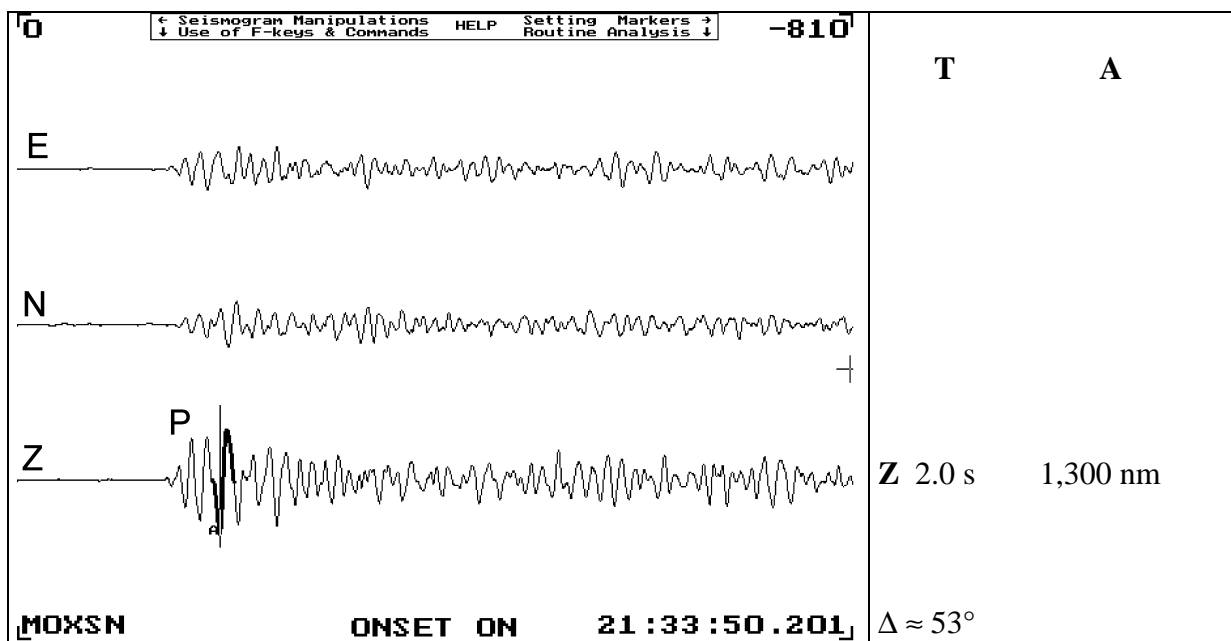


Figure 4 As for Figure 3, however short-period (0.5 to 3 Hz) filtered record section of the P-wave group only. Note that the amplitudes are given here in nm (10^{-9} m).

4 Tasks

Task 1:

- 1.1 Identify and mark in the records of Figure 1 the onsets Pn, Pg and Sg. Note that Pn amplitudes are for distances < 400 km usually smaller than that of Pg! Then determine the hypocentral (“slant”) distance R in km from the rule of thumb $t(Sg-Pg)[s] \times 8 = R$ [km] for both station CLL and MOX. Note, that for this shallow event the epicentral distance Δ and the hypocentral distance R are practically the same.
- 1.2 Determine for the stations CLL and MOX the max. trace amplitude $B(SM)$ and related period T and then, according to Equation (3), the equivalent log trace amplitude when recorded with a Wood-Anderson seismometer, i.e., $\log B(WA) = \log B(SM) + \log \text{Mag}(WA) - \log \text{Mag}(SM)$.
- 1.3 Use Equation (2) above, and the values determined under task 1.2, for determination of the local magnitude M_L for the event in Figure 1 for both station CLL and MOX using the calibration functions $-\log A_0$:
 - a) by Richter (1958) for California (see Table 1 in DS 3.1);
 - b) by Kim (1998) for Eastern North America (vertical comp.; see Table 2 in DS 3.1);
 - c) by Alsaker et al. (1991) for Norway (vertical comp., see Table 2 in DS 3.1).
- 1.4 Discuss the differences in terms of:
 - a) differences in regional attenuation in the three regions from which M_L calibrations functions were used;
 - b) amplitude differences within a seismic network;
 - c) uncertainties of period reading in analog records with low time resolution and thus uncertainties in the calculation of the equivalent Wood-Anderson trace amplitude $B(WA)$.

Task 2:

- 2.1 Measure the *maximum* horizontal and vertical trace amplitudes B in mm and related periods in s from the 3-component surface-wave records in Figure 2. Note, that the maximum horizontal component has to be calculated by combining vectorially B_N and B_E , measured at the same record time, i.e., $B_H = \sqrt{(B_N^2 + B_E^2)}$.
- 2.2 Calculate the respective maximum ground amplitudes A_H and A_V (in μm ; vertical $V = Z$) by taking into account the period-dependent magnification of the seismograph (see table inserted in Figure 2)
- 2.3 Calculate the respective surface-wave magnitudes M_s according to the calibration function
 - a) $\sigma(\Delta)$ as published by Richter (1958) (see Table 3 in DS 3.1, for horizontal component H only);
 - b) $\sigma(\Delta)$ as given for H and V by the Prague-Moscow –Sofia group in Table 4 of DS 3.1;
 - c) $\sigma(\Delta)$ as given by the Prague-Moscow formula $M_s = \log(A/T)_{\max} + 1.66 \log \Delta + 3.3$ which has been accepted by IASPEI as the standard formula for surface-wave magnitude determinations.

Note: Differentiate between surface-wave magnitudes from horizontal and vertical component records by annotating them unambiguously MLH and MLV, respectively.

Task 3:

Use the computer determined periods and amplitudes given in the right boxes of Figures 3 and 4 for the body-wave phases P, PP and S recorded from the shallow ($h = 10$ km) teleseismic earthquake in India in order to determine the respective body-wave magnitudes according to the general relationship (1):

3.1 Compare the epicentral distance calculated by the ISC for MOX ($\Delta = 52.76$) with your own quick determination of Δ using the “rule of thumb” Δ (in $^\circ$) = $[t_{S-P}(\text{in min}) - 2] \times 10$.

3.2 Compare the differences in $Q(\Delta)$ according to Table 6 in DS 3.1 when using the “exact” distance given by the ISC with your quick “rule of thumb” estimation of Δ . Assess the influence of the distance error on the magnitude estimate and draw conclusions.

3.3 Calculate MPV, MPH; MPPV, MPPH and MSH using the calibration functions $Q(\Delta)$ given in Table 6 of DS 3.1, the amplitude-period values given in Figure 3 and $\Delta = 53^\circ$. Discuss the degree of agreement/disagreement and possible reasons.

3.4 Calculate m_b for the short-period P-wave recording in Figure 4 using

- $Q(\Delta, h)$ as depicted in Figure 1a of DS 3.1 for the vertical component of P and
- $P(\Delta, h)$ as depicted in Figure 2 of DS 3.1.
- Discuss the difference between a) and b).

5 Solutions

Note: Your individual readings of times, periods and amplitudes should not deviate more than 10 % and your magnitude estimates should be within about ± 0.2 units of the values given below.

Task 1:

1.1 CLL $t(\text{Sg-Pg}) = 26$ s $R = 208$ km
 MOX $t(\text{Sg-Pg}) = 40$ s $R = 320$ km

1.2 CLL: $B(\text{MS}) = 10$ mm $T = (0.5\text{s}?)$ $\log B(\text{WA}) = -0.888$
 MOX: $B(\text{MS}) = 18$ mm $T = 1$ s $\log B(\text{WA}) = -0.967$

1.3 CLL: $M(\text{Richter}) = 2.7$ $M(\text{Kim}) = 2.6$ $M(\text{Alsaker}) = 2.4$
 MOX: $M(\text{Richter}) = 3.1$ $M(\text{Kim}) = 2.8$ $M(\text{Alsaker}) = 2.6$

1.5 California is a tectonically younger region and with higher heat flow than Eastern North America and Scandinavia. Accordingly, seismic waves are more strongly attenuated with distance. This has to be compensated by larger magnitude calibration values – $\log A_0$ for California. But even within a seismic network amplitude variations may be, depending on different conditions in local underground and azimuth dependent wave propagation, in the order of a factor 2 to 3 in amplitude, thus accounting for magnitude differences in the order of up to about ± 0.5 magnitude units between the various stations. This scatter can be reduced by determining station corrections for different source regions. Note also, that

the period reading is rather uncertain for CLL. If we assume, as for MOX, also $T = 1$ s then $\log B(\text{WA}) = -1.222$, i.e., the magnitudes values for CLL would be even smaller by 0.3 units.

Task 2:

$$2.1 \quad B_N = 20.5 \text{ mm}, T_N = 22 \text{ s}; B_E = 12 \text{ mm}, T_N = 20 \text{ s} \rightarrow B_H = 23.8 \text{ mm}, \bar{T} = 21 \text{ s} \\ B_Z = 23 \text{ mm}, T_Z = 18 \text{ s}$$

$$2.2 \quad A_H = 31.3 \mu\text{m for } T = 21 \text{ s} \quad A_Z = A_V = 24.2 \mu\text{m for } T = 18 \text{ s}$$

$$2.3.1 \quad \text{a) } \text{MLH(Richter)} = \log A_{H\text{max}} + \sigma(\Delta)_{\text{Richter}} = 1.5 + 5.15 = 6.65$$

$$\text{b) } \text{MLH(IASPEI)} = \log(A/T)_{\text{max}} + \sigma(\Delta)_{\text{Prague}} \rightarrow \text{MLH} = 6.82 \text{ and } \text{MLV} = 6.78 \approx 6.8$$

$$\text{c) } \text{Ms} = \log(A/T)_{\text{max}} + 1.66 \log \Delta + 3.3 \rightarrow \text{MLH} = 6.82 \text{ and } \text{MLV} = 6.78 \approx 6.8$$

Task 3:

3.1 The “rule of thumb” yields $\Delta = 54,5^\circ$. This is only 1.7° off the ISC determination. Generally, the rule-of-thumbs allows to estimate Δ in the range $25^\circ < \Delta < 100^\circ$ with an error not larger than $\pm 2.5^\circ$.

3.2 The deviations in $Q(\Delta)$ and thus between magnitude estimates based on either Δ values from NEIC/ISC calculations or quick S-P determinations at the individual stations and using the “rule of thumb” are generally less than 0.2 units. They are even smaller, when correct travel-time (difference) curves are available. This permits sufficiently accurate quick teleseismic magnitude estimates at individual stations even with very modest tools and without the need to wait for the event locations and distance determinations of the world data centers.


$$3.3 \quad \text{MPV} = 6.45, \text{MPH} = 6.36, \text{MPPV} = 6.36, \text{MPPH} = 6.24; \text{MSH} = 6.75$$

The magnitude values for P and PP, horizontal and vertical components, agree within 0.1 magnitude units. This speaks of a good scaling of the respective $Q(\Delta)$ calibration functions. MSH is significantly larger. This is obviously related to the different azimuthal radiation pattern for P and S waves and was one of the reasons, why Gutenberg strongly recommended the determination of the body-wave magnitudes for all these phases and averaging them to the unified magnitude value m . The latter provides more stable and less azimuth dependent individual magnitude estimates.

$$3.4 \quad \text{a) } Q_{PZ}(53^\circ, 10 \text{ km}) = 7.0, \log(A/T) = -0.19 \text{ (with } A \text{ in } \mu\text{m!)} \rightarrow \text{MPV} = \text{mb} = 6.8$$

$$\text{b) } P_Z(53^\circ; 10 \text{ km}) = 3.4, \log(A/T) = 3.1 \text{ (with } 2A \text{ in nm!)} \rightarrow \text{MPV} = \text{mb} = 6.5$$

c) $P_Z(\Delta, h)$ yields, for the same ratio $\log(A/T)$, slightly lower magnitude values as compared to $Q_{PZ}(\Delta, h)$, for deep events, in particular. This also applies for other distance ranges (see Figures 1a and 2 in DS 3.1). Note that P_Z , although specifically developed for the calibration of short-period P-wave amplitudes, is not yet a recommended standard calibration functions.

Topic	Determination of fault-plane solutions
Authors	Michael Baumbach  , and Peter Bormann (formerly GeoForschungsZentrum Potsdam, Department 2: Physics of the Earth, Telegrafenberg, D-14473 Potsdam, Germany); E-mail: pb65@gmx.net
Version	September 1999

1 Aim

The exercise aims at:

- understanding how fault slip affects the polarities of P waves;
- understanding the presentation of P-wave polarities in an equal angle (Wulff net) or equal area projection (Lambert-Schmidt net) of the focal sphere;
- constructing a fault-plane solution and determining the related parameters (**P** and **T** axes, displacement vector) for a real earthquake;
- relating the directions of the fault-plane solutions to the tectonic setting.

2 Data and procedures

Before a fault-plane solution for a teleseismic event can be constructed, the following steps must be completed:

- Interpretation of P-wave first-motion polarities from seismograms at several stations;
- Calculation of epicentral distances and source-to-station azimuths for these stations;
- Calculation of the take-off angles for the seismic P-wave rays leaving the hypocenter towards these stations. This requires the knowledge of the focal depth and of the P-wave velocity at this depth (see EX 3.3).

For the calculations b) and c) standard Earth velocity models are used (e.g., Kennett, 1991).

In the case of local events it is necessary to determine which branch of the travel-time curve is arriving first. The events should be located, if possible, with a special layered crustal velocity model for that region. Most such programs provide both the source-station azimuths and take-off angles in their output files.

The exercise below is based on the definitions, relationships and diagrams (Figs. 3.27 – 3.33) given in the NMSOP, Chapter 3, section 3.4.2 “Manual determination of fault-plane solutions.”. As an example consider the data in Table 1 that was determined following steps a)-c), by using the program HYPO71, for a locally recorded aftershock of the Erzincan earthquake in Turkey (Date: 12.04.1992, $M_l = 2.8$, latitude = 39.519° N, longitude = 39.874° E, source depth $h = 3$ km; station distance up to 50 km).

Note: The take-off angles, AIN, calculated for a ray arriving at a given seismic station may vary significantly depending on the assumed velocity model in the source region. Also, for an average single layer crustal model of 30 to 40 km thickness, all P-wave first arrivals within a distance of about 120 - < 200 km are Pg and up-going. That is, they emerge only from the upper half of the focal hemisphere. Also, when using HYPO71 with the average global two-layer crust according to the velocity model IASP91 (Kenneth 1991) only upper hemisphere take-off angles would have been calculated for the first P-wave arrivals up to distances of 50 km. But in the epicentral area under consideration a significant velocity increase in the upper

crust was already found at 4 km depth (increase of $v_p = 5.3$ km/s to 6.0 km/s). Accordingly, stations up to 50 km distance were reached by upper or lower focal sphere rays (see Fig. 3.29). Since only lower hemisphere projections will be used in the exercise values, for upper hemisphere rays ($AIN > 90^\circ$) must be corrected according to Fig. 3.28. **Conclusion:** AIN calculations based on strongly biased velocity models might result in inconsistent fault-plane solutions or not permit a proper separation of polarity readings into quadrants at all!

Table 1 gives the needed primary data. They were taken from the output file of the program HYPO71 with which the event was located. The first five columns of this file contain, as an example for the two stations ALI and ESK in Tab. 1, the following data:

STN	DIST	AZM	AIN	PRMK
ALI	3.7	40	130	IPD0
ESK	22.7	312	62	IPU1

with STN - station code; DIST - epicentral distance in km; AZM - azimuth towards the station clockwise in degree from north; AIN - take-off angle of the ray towards the station, measured as in Fig. 3.28, and calculated for the given structure-velocity model; PRMK - P-wave reading remarks. In the column PRMK P stands for P-wave onset, I for impulsive (sharp) or E for emergent (less clear) onset, D for clear (or - for poor) dilatational (downward) first motion, U for clear (or + for poor) compressional (upward) first motion as read at the station. The last character may range between 0 and 4 and is a measure of the quality (clarity) of the onset and thus of the weight given to the reading in the calculation procedure, e.g., 4 for zero and 0 for full weight. In case of the above two stations the values for ALI would need to be corrected to get the respective values for the equivalent lower hemisphere ray, i.e., $AINc = 180^\circ - 130^\circ = 50^\circ$ and $AZMc = 180^\circ + 40^\circ = 220^\circ$ while the values for ESK can be taken unchanged from the HYPO71 output file.

3 Tasks

Task 1:

If in Table 1 $AIN > 90^\circ$, then correct take-off angles and azimuths for lower hemisphere projection: $AINc = 180^\circ - AIN$, $AZMc = AZM(<180^\circ) + 180^\circ$ or $AZM(\geq 180^\circ) - 180^\circ$. In case of $AIN < 90^\circ$ the original values remain unchanged.

Task 2:

Place tracing paper or a transparency sheet over the Wulff or Lambert-Schmidt net projection (see Fig. 3.27a or b in 3.4.2). Mark on it the center and perimeter of the net as well as the N, E, S and W directions. Pin the marked sheet center with a needle to the center of the net.

Task 3:

Mark the azimuth of the station on the perimeter of the transparency and rotate the latter until the tick mark is aligned along an azimuth of 0° , 90° , 180° or 270° . Measure the take-off angle from the center of the net along this azimuth. This gives the intersection point of the particular P-wave ray with the lower hemisphere. Mark on this position the P-wave polarity with a neat + for compression or o for dilatation (U or D in Tab. 1) using *different colors* for better distinction of closely spaced polarities of different sign. **Note:** The proper distance (d) of the polarity entry from the center of the net corresponds to $d = r \times \tan(AIN / 2)$ for the Wulff net and $d = r \times \sin(AIN / 2)$ for the Lambert-Schmidt net with r the radius of the given net. In

case that rays left the source through the upper hemisphere ($AIN > 90^\circ$) $AINc$ for lower hemisphere projection has to be calculated and used!

Table 1 Original and corrected values of ray azimuth (AZM and AZMc) and take-off angles (AIN and AINc) towards stations of a temporary network which recorded the Erzincan aftershock of April 12, 1994. POL - polarity of P-wave first motions.

STA	AZM (degree)	AIN (degree)	POL	AZMc (degree)	AINc (degree)
ALI	40	130	D		
ME2	134	114	D		
KAN	197	112	D		
YAR	48	111	D		
ERD	313	103	D		
DEM	330	102	D		
GIR	301	102	U		
UNK	336	101	D		
SAN	76	62	U		
PEL	327	62	D		
GUN	290	62	U		
ESK	312	62	U		
SOT	318	62	D		
BA2	79	62	U		
MOL	297	62	U		
YUL	67	62	U		
ALT	59	62	D		
GUM	320	62	U		
GU2	320	62	D		
BAS	308	62	D		
BIN	295	62	U		
HAR	24	62	D		
KIZ	311	62	U		
AKS	284	62	D		
SUT	295	62	U		

Task 4:

By rotating the transparent sheet with the plotted data over the net try to find a great circle which separates as good as possible the expected quadrants with different first motion signs. This great circle represents the intersection trace of one of the possible fault (or nodal) planes (FP1) with the lower half of the focal sphere. **Note 1:** All N-S connecting lines on both nets are great circles! **Note 2:** Inconsistent polarities that are close to each other may be due to uncertainty in reading relatively small P-wave amplitudes. The phenomenon occurs

particularly for take-off angles near nodal (fault) planes. Thus, clusters of inconsistent polarities may guide you in finding the best separating great circle. However, be aware that isolated inconsistent polarities might be due to false polarity switching or erroneous first motion polarity reading at the seismic station.

Task 5:

Mark point A at the middle of FP1 and find, on the great circle perpendicular to it, the pole P1 of FP1, 90° apart (see Fig. 3.31). All great circles, passing this pole are perpendicular to the FP1. Since the second possible fault plane (FP2) must be perpendicular to the FP1, it has to pass P1. Find, accordingly, FP2 which again has to separate areas of different polarity.

Task 6:

Find the pole P2 for FP2 (which is on FP1!) and delineate the equatorial plane EP. The latter is perpendicular to both FP1 and FP2, i.e., a great circle through the poles P1 and P2. The intersection point of FP1 and FP2 is the pole of the equatorial plane (P3).

Task 7:

Mark the position of the poles of the pressure (**P**) and tension axes (**T**) on the equatorial plane and determine the direction of these axes towards (for **P**) and away from the center (for **T**) of the used net (see Fig. 3.31). The poles for **P** and **T** lie on the equatorial plane in the center of the respective quadrants of dilatational (-) and compressional (+) P-wave first motions, i.e., 45° away from the intersection points of the two fault planes with the equatorial plane. **Note:**

All angles in the net projections have to be measured along great circles!

Task 8:

Mark the slip vectors, connecting the intersection points of the fault planes with the equatorial plane, with the center of the considered net. If the center lies in a tension quadrant, then the slip vectors point to the net center (see Fig. 3.31). If it lies in a pressure quadrant, then the slip vector points in the opposite direction. The slip vector shows the direction of displacement of the hanging wall.

Task 9:

Determine the azimuth (strike direction ϕ) of both FP1 and FP2. It is the angle measured clockwise against North between the directional vector connecting the center of the net with the end point of the respective projected fault trace lying towards the right of the net center (i.e., with the fault plane dipping towards the right; see Fig. 3.31).

Task 10:

Determine the dip angle δ (measured from horizontal) for both FP1 and FP2 by putting their projected traces on a great circle. Measure δ as the difference angle from the outermost great circle towards the considered fault-plane trace.

Task 11:

Determine the slip direction (i.e., the sense of motion along the two possible fault planes. It is obtained by drawing one vector each from the center of the net to the poles P1 and P2 of the nodal planes (or vice versa from the poles to the center depending on the sign of the rake

angle λ). The vector from (or to) the center to (or from) P1 (P2) shows the slip direction along FP2 (FP1). The rake angle λ is positive in case the center of the net lies in the tension (+) quadrant (i.e., an event with a thrust component) and negative when it lies in the pressure (-) quadrant (event with a normal faulting component). In the first case λ is $180^\circ - \lambda^*$. λ^* has to be measured on the great circle of the respective fault plane between its crossing point with the equatorial plain and the respective azimuth direction of the considered fault plane (see Fig. 3.31). In the second case $\lambda = -\lambda^*$. For a pure strike slip motion ($\delta = 90^\circ$) $\lambda = 0$ defines a left lateral strike-slip and $\lambda = 180^\circ$ defines a right-lateral strike-slip.

Task 12:

The azimuth of the pressure and the tension axes, respectively, is equal to the azimuth of the line connecting the center of the net through the poles of **P** and **T** with the perimeter of the net. Their plunge is the dip angle of these vectors against the horizontal (to be measured as for δ).

Task 13:

Estimate the parameters of the fault planes and of the pressure and tension axes for the Erzincan aftershock and insert your results into Table 2 below:

Table 2

	strike	dip	rake
Fault plane 1			
Fault plane 2			

	azimuth	plunge
Pressure axis		
Tension axis		

Note: The angles may range between:

- $0^\circ < \text{strike} < 360^\circ$
- $0^\circ < \text{azimuth} < 360^\circ$
- $0^\circ < \text{dip} < 90^\circ$
- $0^\circ < \text{plunge} < 90^\circ$
- $-180^\circ < \text{rake} < 180^\circ$

Task 14:

The question of which of the nodal planes was the active fault plane, and hence the other was the auxiliary plane, cannot be answered on the basis of the fault-plane solution alone.

Considering the event in its seismotectonic context may give an answer. Therefore, we have marked the epicenter of the event in Figure 1 with an open star at the secondary fault F2.

- a) Decide which was the likely fault plane (FP1 or FP2)?
- b) What was the type of faulting?
- c) What was the direction of slip? and

- d) Is your solution compatible with the general sense of plate motion in the area as well with the orientation of the acting fault and the orientation of stress/deformation in the area?

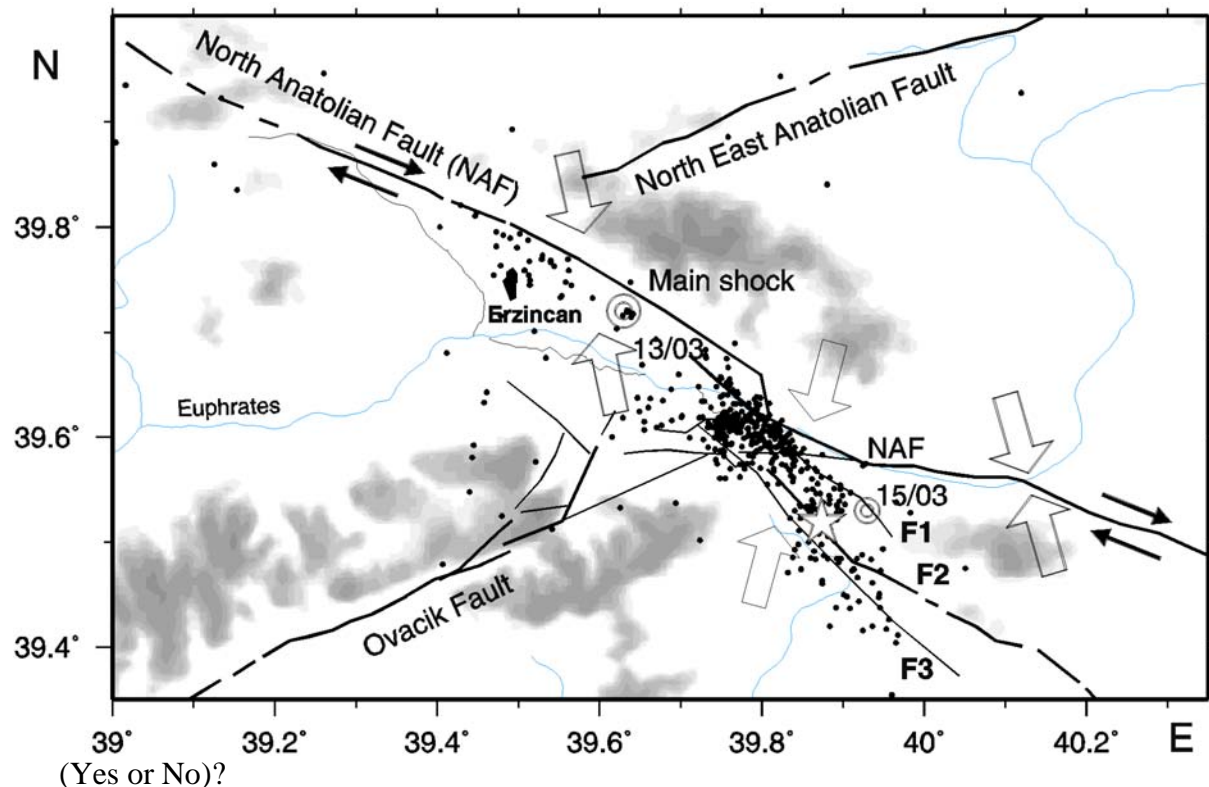


Figure 1 Epicenters of aftershocks between March 21 and June 16, 1992 of the March 13, 1992 Erzincan earthquake, Turkey. The open circles represent the main shock and its strongest aftershock on March 15, and the open star the analyzed aftershock. **F1**, **F2** and **F3** are secondary faults to the North Anatolian Fault (NAF). Black arrows - directions of relative plate motion, open arrows - direction of maximum horizontal compression as derived from centroid moment-tensor solutions of stronger earthquakes (courtesy of H. Grosser).

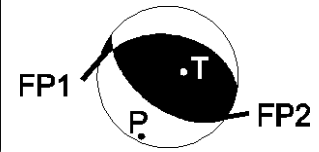
4 Solutions

In the Table 3 below the authors have given the data for their own freehand fits together with the values for the best PC fit to the data (in brackets). If your manually determined results differ by more than about 20° or even show a different type of faulting mechanism, you should critically check your data entries and/or fault-plane fits again.

Table 3

	strike	dip	rake
Fault plane 1 (FP1)	280° (278.5°)	40° (39.9°)	68° (67.4°)
Fault plane 2 (FP2)	130° (127.0°)	54° (53.7°)	108° (107.8°)

	azimuth	plunge
Pressure axis	205° (204.4°)	7° (7.1°)
Tension axis	90° (88.6°)	73° (74.0°)



The answers to the questions in Task 14 are:

- FP2 was more likely the active fault.
- The aftershock was a thrust event with a very small right-lateral strike-slip component.
- The slip direction is here strike - rake azimuth, i.e., for FP2 $130^\circ - 108^\circ = 12^\circ$ from north. This is close to the direction of maximum horizontal compression (15°) in the nearby area as derived from centroid moment-tensor solutions of stronger events.
- The strike of FP2 for this event agrees with the general direction of mapped surface fault strike and is consistent with the tendency of plate motion direction in the area under study. Therefore, it is highly probable that FP2 was the acting fault.

Topic	Take-off angle calculations for fault-plane solutions and reconstruction of nodal planes from the parameters of fault-plane solutions
Author	Peter Bormann (formerly GeoForschungsZentrum Potsdam, Telegrafenberg, D-14473 Potsdam, Germany); E-mail: pb65@gmx.net
Version	September 1999

1 Aim

The exercise aims at making familiar with the calculation of the take-off angles AIN of seismic P-wave rays leaving the seismic source towards the seismic station. These angles are required for determining fault-plane solutions (FPS) from first-motion polarity readings (see EX 3.2). Take-off angles depend on the velocity model of the Earth, the source depth h and the epicentral distance Δ , at which the considered rays arrive at the Earth's surface. The AIN calculated in this exercise for a given event and a number of seismic stations at different Δ will then be checked whether they are consistent with the reported polarity readings and FPS calculated for this event by international agencies. For this you will reconstruct on a Lambert-Schmidt net projection the fault-plane traces from the reported nodal-plane parameters.

2 Data, models and procedure

When localizing near events by using HYPO71 or similar programs the values for both the azimuth (AZM) and for the take-off angles (AIN) of the rays leaving the source towards the considered stations are given in the localization output file. One can use them, together with the first motion polarity readings, straight forward for the determination of fault-plane solutions (see EX 3.2). When one intends to determine the fault-plane solution for seismic events published in the bulletins of the International Seismological Centre (ISC) one finds therein, besides data for polarity readings from the reporting stations (\uparrow or c for up and \downarrow or d for down in short- or long-period instruments, respectively), only values for the azimuth (AZM) but not for the respective take-off angle (AIN). Figure 1 shows a typical portion of event-stations report from the ISC. Its header also gives the seismic moment tensor and fault-plane solutions calculated by various international data centers or agencies using different (sometimes automated) procedures. Values for AIN can be calculated by using the relationship

$$\sin \text{AIN} = (180/\pi) \times (v_p/r_h) \times p(\Delta, h). \quad (1)$$

$v_p(h)$ is the P-wave velocity at the depth h (in km/s), $r_o = 6371$ km is the Earth's radius and $r_h = r_o - h$. $p(\Delta, h) = dT/d\Delta$ is the ray parameter; it corresponds to the gradient of the travel-time curve at the point of observation on the Earth's surface (both in units s/deg) at the epicentral distance Δ (in degree) (see Fig. 2.27) and is a function of the hypocentral depth h (in km). The value of the ray parameter is identical with that of the horizontal component of the of the slowness vector. Tables 1 and 2 give the respective values $v_p(h)$ and $p(\Delta, h)$ for P waves.

Table 1 $v_p(h)$ according to the IASPEI91 velocity model (Kennett, 1991).

h (km)	v_P (km/s)	h (km)	v_P (km/s)	h (km)	v_P (km/s)
0	5.8000	120	8.0500	471	9.5650
20	5.8000	171	8.1917	571	9.9010
20	6.5000	210	8.3000	660	10.2000
35	6.5000	271	8.5227	660	10.7900
35	8.0400	371	8.8877	671	10.8192
71	8.0442	410	9.0300	760	11.0558
120	8.0500	410	9.3600		

Table 2 Ray parameter $p = dT/d\Delta$ (= horizontal slowness component) of Pn, P and PKP_{df} first arrivals at the Earth's surface as a function of hypocentral depth h according to IASPEI 1991 Seismological Tables (Kennett, 1991)

		p (in s/deg)			
Phase	Δ (in deg)	h = 0 km	h = 100 km	h = 300 km	h = 600 km
Pn (P)	2	13.75	12.90	7.91	4.01
	4	13.75	13.49	10.96	6.91
	6	13.74	13.58	11.95	8.60
	8	13.72	13.60	12.25	9.48
	10	13.70	13.59	12.26	9.90
	12	13.67	13.29	12.12	10.05
	14	13.64	12.91	11.03	10.06
	16	12.92	12.43	10.91	9.17
	18	12.33	10.97	10.73	9.10
	P	20	10.90	10.81	10.50
22		10.70	10.58	9.12	8.90
24		9.14	9.11	9.03	8.83
26		9.06	9.02	8.91	8.76
28		8.93	8.90	8.83	8.66
30		8.85	8.82	8.75	8.56
32		8.77	8.74	8.65	8.45
34		8.67	8.64	8.54	8.33
36		8.56	8.52	8.42	8.21
38		8.44	8.40	8.29	8.08
40		8.30	8.26	8.16	7.95
42		8.17	8.13	8.03	7.82
44		8.03	7.99	7.89	7.69
46		7.89	7.85	7.75	7.56
48	7.55	7.71	7.61	7.42	
50	7.60	7.56	7.47	7.29	
52	7.46	7.42	7.33	7.15	
54	7.31	7.28	7.19	7.02	
56	7.17	7.13	7.05	6.88	
58	7.02	6.99	6.90	6.74	
60	6.88	6.84	6.76	6.61	
62	6.73	6.70	6.62	6.47	

Table 2: cont.

Phase	Δ (in deg)	p (in s/deg)			
		h = 0 km	h = 100 km	h = 300 km	h = 600 km
P	64	6.59	6.55	6.48	6.33
	66	6.44	6.41	6.33	6.19
	68	6.30	6.27	6.19	6.05
	70	6.15	6.12	6.05	5.91
	72	6.00	5.97	5.90	5.77
	74	5.86	5.83	5.76	5.63
	76	5.71	5.68	5.61	5.49
	78	5.56	5.53	5.46	5.34
	80	5.40	5.38	5.31	5.20
	82	5.25	5.22	5.16	5.04
	84	5.09	5.07	5.01	4.90
	86	4.94	4.92	4.85	4.72
	88	4.74	4.72	4.69	4.65
	90	4.66	4.65	4.64	4.61
	92	4.61	4.61	4.60	4.57
	94	4.58	4.57	4.55	4.51
	96	4.52	4.51	4.49	4.44
	98	4.45	4.44	4.44	4.44
P _{diff}	100-144	4.44	4.44	4.44	4.44
PKP _{df}	114	1.92	1.92	1.92	1.92
	116-122	1.91	1.91	1.91	1.91
	124-126	1.90	1.90	1.90	1.90
	130	1.88	1.88	1.88	1.88
	136	1.84	1.84	1.84	1.83
	140	1.80	1.79	1.79	1.78
	142	1.76	1.76	1.76	1.75
	144	1.73	(1.72)	(1.72)	(1.71)
	146	1.68	1.68	1.67	1.66
	148	1.63	1.62	1.62	1.60
	150	1.57	1.56	1.55	1.54
	152	1.49	1.49	1.48	1.47
	154	1.42	1.41	1.40	1.39
	156	1.33	1.33	1.32	1.30
	158	1.24	1.23	1.23	1.21
	160	1.14	1.14	1.13	1.11
	162	1.04	1.03	1.03	1.01
	164	0.93	0.93	0.92	0.91
	166	0.82	0.82	0.81	0.80
	168	0.71	0.70	0.70	0.69
	170	0.59	0.59	0.58	0.58
172	0.47	0.47	0.47	0.47	
174	0.36	0.36	0.35	0.35	
176	0.24	0.24	0.24	0.23	
178	0.12	0.12	0.12	0.12	
180	0.00	0.00	0.00	0.00	

NEIC Moment-tensor solution: $s23$, scale 10^{17} Nm; $M_{rr}-3.05$;
 $M_{\theta\theta}0.97$; $M_{\phi\phi}4.03$; $M_{r\theta}2.51$; $M_{r\phi}1.95$; $M_{\theta\phi}2.71$. Depth
 272km; Principal axes: T 6.09, Plg17°, Azm117°; N -136,
 Plg27°, Azm216°; P -4.73, Plg57°, Azm358°; Best double
 couple: $M_o5.4 \times 10^{17}$ Nm; NP1: ϕ_s172° , $\delta36^\circ$, $\lambda-140^\circ$. NP2:
 ϕ_s48° , $\delta68^\circ$, $\lambda-60^\circ$.

HRVD 05^d 13^h 24^m 15^s 7 ± 0.2 , $39^\circ.10N \pm 0.02 \times 15^\circ.39E \pm 0.02$,
 $h295^{km} \pm 8^{km}$, Centroid moment-tensor solution. Data used:
 GDSN; LP body waves: $s50$, c^{**} ; Half duration: 1^s.9.
 Moment tensor: Scale 10^{17} Nm; $M_{rr}-2.17 \pm 06$;
 $M_{\theta\theta}1.97 \pm 10$; $M_{\phi\phi}4.14 \pm 09$; $M_{r\theta}3.51 \pm 09$; $M_{r\phi}-3.29 \pm 09$;
 $M_{\theta\phi}0.01 \pm 09$. Principal Axes: T 5.83, Plg27°, Azm103°;
 N 0.32, Plg30°, Azm210°; P -6.15, Plg48°, Azm339°. Best
 Double couple: $M_o6.0 \times 10^{17}$ Nm, NP1: ϕ_s146° , $\delta33^\circ$, $\lambda-157^\circ$.
 NP2: ϕ_s37° , $\delta78^\circ$, $\lambda-60^\circ$.

ISC 05^d13^h24^m11^s 4 ± 0.13 , $39.16 \pm 0.16 \times 15^\circ.18E \pm 0.014$,
 $h290^{km} \pm 1.3^{km}$, ($h286^{km} \pm 2.7^{km}$:pP-P), $n757$, $\sigma1^s.04/729$,
Mb5.7/107, 119C-155D, Southern Italy.

OVO Vesuviano	1.77	340	$\uparrow iP$	13 24 57.2	+1.5
MCT Mte Cammarata	1.95	219	P	13 24 57.7	+0.6
FG4 Candela	1.99	8	P	13 24 58.2	+0.9
MEU Monte Lauro	2.07	186	dP	13 24 56.8	-1.3
PZI Palazzolo	2.14	186	eP	13 24 57	-1.7
FAI Favara	2.21	213	dP	13 24 59.5	+0.1
MSC Monte Massico	2.23	336	$\uparrow iP$	13 25 01.1	+1.6
SGG Gregorio Matese	2.30	345	$\uparrow iP$	13 25 01.9	+1.8

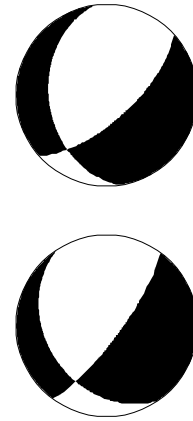


Figure 1 Typical section of an ISC bulletin (left) with NEIC (National Earthquake Information Center) and Harvard University (HRVD) moment-tensor fault-plane solutions (right) for the Italy deep earthquake ($h = 286$ km) of Jan. 05, 1994. Columns 3 to 5 of the bulletin give the following data: 3 - epicentral distance in degrees, 4 - azimuth AZM in degrees, 5 - phase code and polarity.

Table 3 gives respective selected data from the ISC bulletin for five seismic stations at different epicentral distances (Δ) and azimuth (AZM) for the Italy earthquake shown in Figure 1. The polarity readings correspond to the first P ($\Delta < 100^\circ$) or PKP ($\Delta > 110^\circ$) onsets.

Table 3

STA	Δ (deg)	AZM (deg)	POL	$v_P(h)$ km/s	v_P/Γ_h (s ⁻¹)	$p(\Delta, h)$ (s/deg)	AIN (deg)	AZMc (deg)	AINc (deg)
SGG	2.30	345	+						
KHC	10.03	354	-						
BTH	12.25	294	+						
ZAK	60.02	48	-						
PAE	154.8	324	-						

3 Tasks

Task 1:

For the data given in Table 3, calculate the missing values in the blank columns for $v_P(h)$, v_P/r_h , $p(\Delta, h)$ and AIN using Table 1 and 2 and assuming an approximate focal depth for the recorded event of $h = 300$ km. Interpolate linearly as a first approximation.

Task 2:

Decide whether your ray has left the upper or lower half of the focal sphere and whether or not you need to calculate AINc and/or AZMc according to Figs. 3.28 and 3.29 in Chapter 3. Complete Table 3 accordingly.

Task 3:

Use the values given in Figure 1 for ϕ and δ for the nodal planes NP1 and NP2 of the NEIC fault-plane solution. Reconstruct both nodal (fault) planes using the *Lambert-Schmidt net* (Fig. 3.27b) by applying the procedure inverse to the one described in the Exercise : Determination of fault-plane solutions (EX 3.2). Compare your nodal-plane pattern with that of the NEIC "beach-ball" solution (Figure 1 upper right).

Task 4:

Find the corresponding equatorial plane to your NP1 and NP2 and mark the locations of the P and T axes on the focal sphere. Draw the P and T vectors towards and from the center of the net, determine their azimuth (Azm) and plunge (Plg) [equivalent to dip, measured from the horizontal]. Compare your respective values with those given by NEIC in Figure 1.

Task 5:

Use the values that you calculated for the P-wave take-off angle AINc and ray azimuth AZMc to all 5 stations in Table 3 and mark the point where the ray penetrates the focal sphere and indicate the respective polarity. Check whether they fall into the proper T and P quadrants and whether the short-period polarity readings given in Table 3 are consistent with the fault-plane solution published by the NEIC which is based on long-period waveform data.

4 Solutions and discussions

Table 4 Solutions for **Task 1**.

STA	Δ (deg)	AZM (deg)	POL	$v_P(h)$ km/s	v_P/r_h (s ⁻¹)	$p(\Delta, h)$ (s/deg)	AIN (deg)	AZMc (deg)	AINc (deg)
SGG	2.30	345	+	8.6286	1.4213×	8.368	(137.0)	165	43.0
KHC	10.03	354	-		10 ⁻³	12.258	86.5		
BTH	12.25	294	+			11.984	77.4.1		
ZAK	60.02	48	-			6.759	33.4		
PAE	154.8	324	-			1.368	6.4		

Task 2:

Note: In the case of deep earthquakes the values of the ray parameter (and thus slowness) may increase with Δ , e.g., in Table 2 for $h = 300$ km up to $\Delta = 10^\circ$. This corresponds to seismic rays that leave the source upwards! Consequently, the value $A_{IN} = 43.0^\circ$ calculated with Equation (1) for station SGG corresponds, according to the definition given in Fig. 3.28, in fact to an angle of $180^\circ - A_{IN} = 137.0^\circ$. Accordingly, A_{ZMc} and A_{INc} for the equivalent lower hemisphere projection of this ray are $345^\circ - 180^\circ = 165^\circ$ and 43.0° , respectively.

Task 3:

Your manually drawn fault-plane solutions should look very similar to that of the NEIC solution in Figure 1 upper right.

Task 4:

Your manually re-constructed values for A_{zm} and P_{lg} of the P and T axes should agree with the NEIC solution within a few degrees ($<10^\circ$). If not, check your drawing of the three planes, of the related P and T axis and the measured angles.

Task 5:

The short-period polarity data used in this exercise are consistent with the fault-plane solution published by the NEIC which is based on long-period waveform data. All your polarities should fall properly into quadrants of either observed compressional or dilatational P-wave first motions.

References (see References under Miscellaneous in Volume 2)

Topic	Bandwidth-dependent transformation of noise data from frequency into time domain and vice versa
Authors	Peter Bormann (formerly GeoForschungsZentrum Potsdam, Telegrafenberg, D-14473 Potsdam, Germany), E-mail: pb65@gmx.net Erhard Wielandt (formerly Institute of Geophysics, University of Stuttgart, D-70184 Stuttgart, Germany), E-mail: e.wielandt@t-online.de
Version	April 2001

1 Aim

The exercise aims at:

- deepening the understanding and developing manual skills in using the related equations presented in 4.1 of Chapter 4;
- application of the conversion program NOISECON (see PD 4.1);
- demonstrating that the various data presentations given in this Exercise and in Chapter 4 on signal and noise spectra or amplitudes in different kinematic units are in fact all compatible or – if not – that reasons for it can be given.

2 Fundamentals

The underlying fundamentals have been outlined in detail in the introduction to Chapter 4. In summary, the following should be remembered:

When a broadband signal is split up into narrower frequency bands with ideal band-pass filters, then

- the instantaneous amplitudes in the individual bands add up to the instantaneous amplitude of the broadband signal,
- the signal powers (or energies in case of *transient* signals) in the individual bands add up to the power (or energy) of the broadband signal,
- the RMS amplitudes in the individual bands DO NOT add up to the RMS amplitude of the broadband signal.

A specification of noise amplitudes without a definition of the bandwidth is meaningless!

Also: Signal energy is the time-integral of power. Accordingly, transient signals have a finite energy while stationary (noise) signals have an infinite energy but a finite and, in the time average, constant power. Transient signals and stationary signals must therefore be treated differently. The spectrum of a transient signal cannot be expressed in the same units as the spectrum of a stationary signal. Earthquake spectra and noise spectra can, therefore, not be represented in the same plot, unless the conversion between the units is explained. Also, band-pass filtered amplitudes in different spectral ranges are comparable only when having been filtered with the same relative bandwidth (RBW). Note that in signal analysis the "power" of a signal is understood to be the mean square of its instantaneous amplitude.

Physical power is proportional but not identical to what is called "power" in signal analysis - for example, the electric power is $W = U^2 / R$, not $W = U^2$.

3 Data, relationships and programs

The exercises are based on data presented in Figs. 4.5 to 4.8 and the Figures 1 to 3 below.

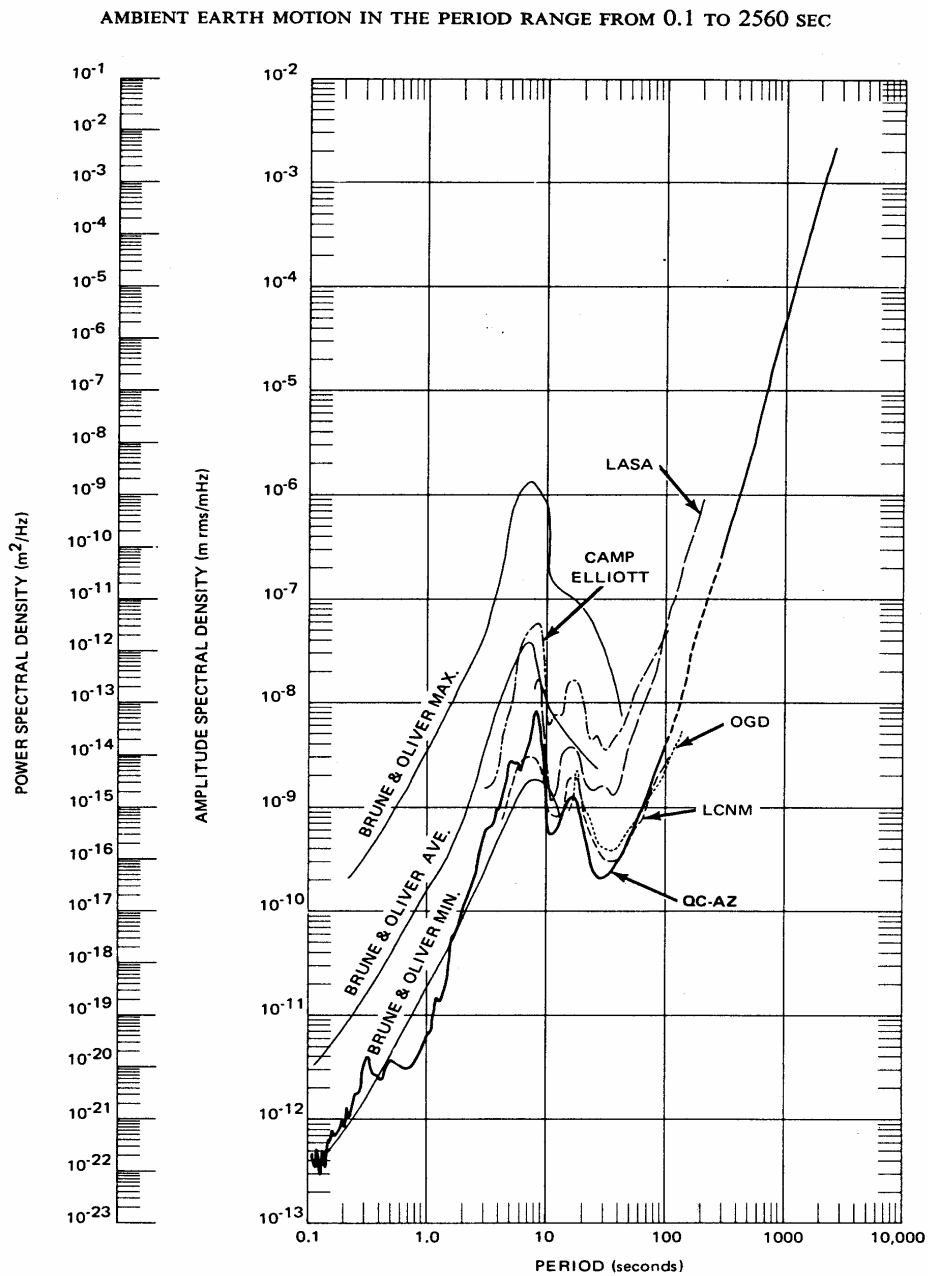


FIG. 1. Vertical Earth motion amplitude spectral density.

Figure 1 Compilation of various noise amplitude and power spectral densities at various stations and according to the Brune and Oliver (1959) noise model as published by Fix (1972).

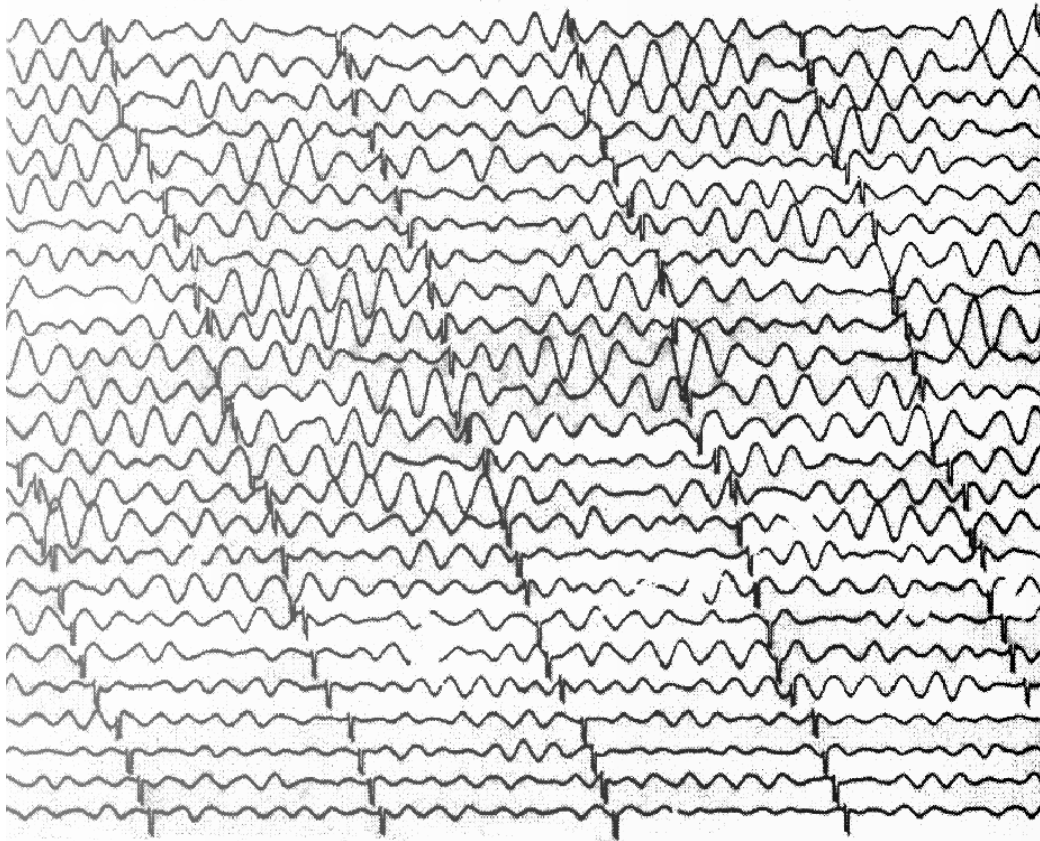


Figure 2 Cut-out section of a record of the WWSSN-LP seismograph of strong secondary ocean microseisms caused by a winter storm over the Atlantic ocean, reproduced at original scale (30 mm = 1 minute). The magnification at the dominant period is about 400 times.

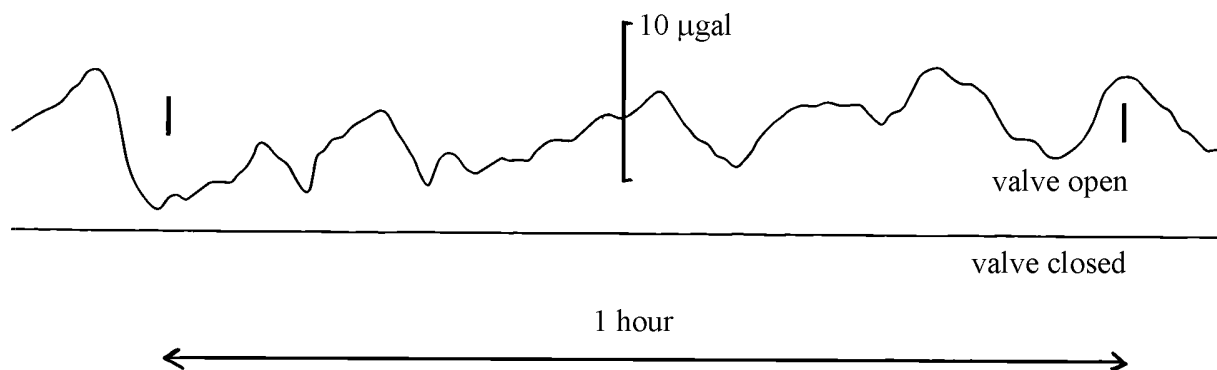


Figure 3 Output signal of an STS1 seismometer with the vacuum bell valve open (upper trace) and closed (lower trace), respectively. The noise in the top trace is caused by changes in barometric pressure.

For manual solutions use the respective relationships given in Eqs. (4.4) to (4.17) of Chapter 4 and a pocket calculator with the required basic functions. Alternatively, you may use the program NOISECON (see program description PD 4.1).

4 Tasks

Task 1: Determine the relative bandwidth (RBW) of an

- a) 2-octave filter
- b) 2/3-octave filter
- c) 1/3-octave filter
- d) 1/6-decade filter

by using Eq. (4.15) in Chapter 4 and

- e) express the bandwidth of an 1/3-decade filter in terms of octaves

by using Eq. (4.17).

Task 2: Calculate for the noise maximum of the upper curve in Fig. 4.5 the corresponding RMS ground motion (velocity and displacement).

- a) Estimate the velocity power maximum from Fig. 4.5 (Note the logarithmic scale!).
- b) Give this value also in units of $(\text{m/s})^2/\text{Hz}$.
- c) Estimate the frequency f_0 related to this maximum.
- d) Calculate the RMS-velocity amplitude $a_{v\text{RMS}}$ by considering Eqs. (4.15) and (4.16) and a relative bandwidth of 2/3 octaves.
- e) Transform this RMS velocity amplitude determined under d) into the corresponding RMS displacement amplitude $a_{d\text{RMS}}$ considering Eq. (4.4).

Task 3: Transform the displacement power values of Fig. 4.6 at $f = 1 \text{ Hz}$ and $f = 10 \text{ Hz}$ in

- a) units of m^2/Hz ,
- b) acceleration power values with units $(\text{m/s}^2)^2/\text{Hz}$ using Eq. (4.5),
- c) the values determined under b) in units of dB referred to $1 (\text{m/s}^2)^2/\text{Hz}$ according to Eq. 4.6) and
- d) compare the result with the respective values in Fig. 4.7 for the New Low Noise Model (NLNM).

Task 4: Determine from Fig. 4.7 the respective ground acceleration power spectral density values of the NLNM in units of $(\text{nm/s}^2)^2/\text{Hz}$ for

a) $f = 1 \text{ Hz}$,

b) $f = 0.1 \text{ Hz}$.

using Eq. (4.6)

Task 5: Select any period between 0.01 and 10,000 sec (e.g., $T = 100\text{s}$) and confirm that the presentations in Figs. 4.7 and 4.8 in Chapter 4 are equivalent when assuming a relative bandwidth of 1/6 decades as used in Fig. 4.8.

Task 6: Transform selected velocity PSD values given in the lower curve of Fig. 4.23 into acceleration PSD $\mathbf{P}_a[\text{dB}] = 10 \log (\mathbf{P}_a / 1 \text{ (m/s}^2\text{)}^2/\text{Hz})$ via Eq. (4.5) and compare them with the NLNM at

a) 1.5 Hz and

b) 10 Hz.

Task 7: Figure 1 has two parallel vertical scales one of which is obviously incorrect. Which one? Using the correct scale and the lowermost curve:

a) compare the noise at 100 s and 1000 s period to the respective values given for the NLNM in Fig. 4.7

b) discuss the difference.

Task 8: Assess the noise level of the microseism storm in Figure 2 with respect to the NLNM

a) Determine the range of periods of the microseisms.

b) Estimate the bandwidth of the microseisms, their center frequency f_0 and RBW.

c) Estimate the displacement a_{RMS} from the *average peak amplitudes* (which are about $1.25a_{\text{RMS}}$). The magnification of the record is about 400 at f_0 .

d) Transform the displacement a_{RMS} into acceleration a_{RMS} and \mathbf{P}_a [dB].

e) Compare with Fig. 4.7 and discuss possible differences.

Taks 9: Compare the noise level for the acceleration records of an STS1 seismometer shown in Figure 3 and compare it with the NLNM. Note that $1 \text{ gal} = 10^{-2} \text{ m/s}^2$.

a) Estimate a_{RMS} from the *average peak amplitudes* in Figure 3, upper trace.

- b) Estimate the upper limit of a_{RMS} for the lower trace in Figure 3.
- c) Estimate the periods and bandwidth of the noise in Figure 3.
- d) Compare the a_{RMS} for the upper and the lower trace with the NLNM presentation in Fig. 4.8.
- e) Discuss the differences.

5 Solutions

Note: The errors in eye readings of the required parameters from the diagrams may be 10 to 30 %. Therefore, it is acceptable if your solutions differ from the ones given below in the same order or by about 1 to 3 dB in power. In case of larger deviations check your readings and calculations. Also: all power values given below in dB relate to the respective units in Fig. 4.7.

- Task 1:**
- a) 1.5
 - b) 0.466
 - c) 0.231
 - d) 0.386
 - e) 1.1 octaves

- Task 2:**
- a) $7 \times 10^{-8} \text{ (cm/s)}^2/\text{Hz}$
 - b) $7 \times 10^{-12} \text{ (m/s)}^2/\text{Hz}$
 - c) 0.16 Hz
 - d) $a_{\text{vRMS}} \approx 7 \times 10^{-7} \text{ m/s}$
 - e) $a_{\text{dRMS}} \approx 7 \times 10^{-7} \text{ m}$

- Task 3:**
- a) $2 \times 10^{-18} \text{ m}^2/\text{Hz}$ at 1 Hz and $1.5 \times 10^{-22} \text{ m}^2/\text{Hz}$ at 10 Hz
 - b) $3.12 \times 10^{-15} \text{ (m/s}^2)^2/\text{Hz}$ at 1 Hz and $2.3 \times 10^{-15} \text{ (m/s}^2)^2/\text{Hz}$ at 10 Hz
 - c) - 145 dB for 1 Hz and -146 dB for 10 Hz
 - d) The noise power at this site is for the considered frequencies about 20 dB higher than for the NLNM.

Task 4: a) and b) ≈ -117 dB, i.e., $\approx 2 \times 10^6$ (nm/s²)²/Hz ;

Task 5: For $T = 100$ s we get from Fig. 4.7 \mathbf{P}_a [dB] = -185 dB. With $\text{RBW} = 0.3861$ for 1/6 octave bandwidth and $f = 0.01$ Hz we calculate with Eq. (4.16) $a_{\text{RMS}}^2 = 1.1 \times 10^{-21}$ (m/s²)² which is about -210 dB, in agreement with Fig. 4.8.

Task 6: a) $\mathbf{P}_a \approx -153$ db, 16 dB above the NLNM

b) $\mathbf{P}_a \approx -153$ db, 15 dB above the NLNM

Task 7: The amplitude-density scale in Figure 1 is inapplicable to noise and cannot be related to the power-density scale, which is correct.

a) at 0.01 Hz $P_d = 2 \times 10^{-14}$ corresponds to $\mathbf{P}_d = -137$ dB

at 0.001 Hz $P_d = 2 \times 10^{-6}$ corresponds to $\mathbf{P}_d = -57$ dB

b) The NLNM gives, according to Fig. 4.7, $\mathbf{P}_d \approx -137$ dB for $T = 100$ s (see also Tab. 4.2) and $\mathbf{P}_d \approx -90$ dB for $T = 1000$ s, i.e., the agreement with the Fix (1972) noise spectra is perfect for a) but for b) the noise level of NLNM at $T = 1000$ s is -33 dB lower.

Task 8: a) The periods of the microseisms in Figure 2 vary between $T = 7$ s (for the smaller amplitudes) and $T = 10$ s (for the largest amplitudes).

b) From this upper and lower period follows with Eq. (4.13) $n \approx 0.5$ octaves or $m \approx 1/6$ decade, a center frequency of $f_0 \approx 0.119$ Hz ($T_0 \approx 8.4$ s) and an RBW of ≈ 0.36

c) Maximum double trace amplitudes of the microseisms range between about 6 and 3 mm, average about 4.5 mm, corresponding to a “true” *average peak ground amplitude* of about 5.6×10^{-6} m and thus to a displacement $a_{\text{RMS}} \approx 4.5 \times 10^{-6}$ m.

d) The acceleration $a_{\text{RMS}} \approx 2.5 \times 10^{-6}$ m for $f_0 \approx 0.119$ Hz and $\mathbf{P}_a \approx -98$ dB.

e) $\mathbf{P}_a \approx -98$ dB for this microseismic storm is close to the power at the NHHM peak around $T = 5$ s (-96.5 dB) but about 15 dB higher than the NHHM values at $T \approx 8$ s. Thus, the record corresponds to a really strong microseism storm.

- Task 9:**
- a) From Figure 3, upper trace, the estimated *average peak amplitude* is about $2.5 \mu\text{gal}$ and thus a_{RMS} about $2 \times 10^{-8} \text{ m/s}^2$.
 - b) The related upper limit of about $1/100^{\text{th}}$ of a), i.e., $a_{\text{RMS}} < 2 \times 10^{-10} \text{ m/s}^2$.
 - c) The periods of the noise in Figure 3 range between roughly 180 s and 750 s. This corresponds to a bandwidth of about 2 octaves or an RBW of 1.5.
 - d) The a_{RMS} for the open valve corresponds to -154 dB , that for the closed valve to $< -194 \text{ dB}$.
 - e) Taking into account that Fig. 4.8 was calculated for $1/6$ decade bandwidth only but the bandwidth of the considered noise signals being about 3 times larger we have to assume an about 5 dB higher noise level in Fig. 4.8. Therefore, for periods $< 30 \text{ s}$ the barometric pressure noise is surely well below the NLNM when the sensor operates in a vacuum. A higher resolution of the record with the vacuum bell valve closed would be required in order to determine the noise level distance to the NLNM for $T > 30 \text{ s}$.

Title	Plotting seismograph response (BODE-diagram)
Author	Jens Bribach, GeoForschungsZentrum Potsdam, Deptment 2: Physics of the Earth, Telegrafenberg, D-14473 Potsdam, Germany; Fax: +49 331 288 1266; E-mail: brib@gfz-potsdam.de
Version	May 2001

1 Aim

The exercise aims at making you familiar with the easy way of construction of a BODE-diagram which displays the transfer function of a given device as a plot of logarithmic amplitude A and of linear phase shift ϕ versus logarithmic frequency f (or period $1/f$). Its advantage is that response curves are approximated by straight lines (see IS 5.2). The main features are:

- any Pole in the transfer function generates an amplitude decay proportional to frequency f (20 dB per decade or 6 dB per octave) and a phase shift ϕ of -90° ;
- any Zero causes a slope of 1:1 too and a phase shift of $+90^\circ$;
- corner frequencies (e.g., of filters) correspond to the point of intersection of two straight lines.

All stages of a signal-transfer chain can thus be constructed component-wise, one after the other. It is recommended to decompose all functions into parts of 1st or 2nd order. One gets the complete transfer function by multiplying these individual functions. In both the logarithmic amplitude scale and the linear phase scale this means adding the related individual curves.

2 Tasks

Task 1: Plot the BODE-diagrams (amplitude only) of the following seismograph components:

Seismometer

Transducer Constant	$G_S = 15.915 \text{ Vs/m}$
Natural Period	$T_S = 5 \text{ s}$
Attenuation	$D_S = 0.707$

HIGH Pass HP1 (1st order)

Magnification	$A_{H1} = 3$
Corner Frequency	$f_{H1} = 0.01 \text{ Hz}$

LOW Pass LP1 (1st order)

Magnification	$A_{L1} = 5$
Corner Frequency	$f_{L1} = 0.2 \text{ Hz}$

LOW Pass LP2 (2nd order)

Magnification	$A_{L2} = 2$
Corner Frequency	$f_{L2} = 10 \text{ Hz}$
Attenuation	$D_{L2} = 0.707$

Task 2: Plot the overall amplitude response of the system approximated by straight lines on double logarithmic paper (see Figure 1).

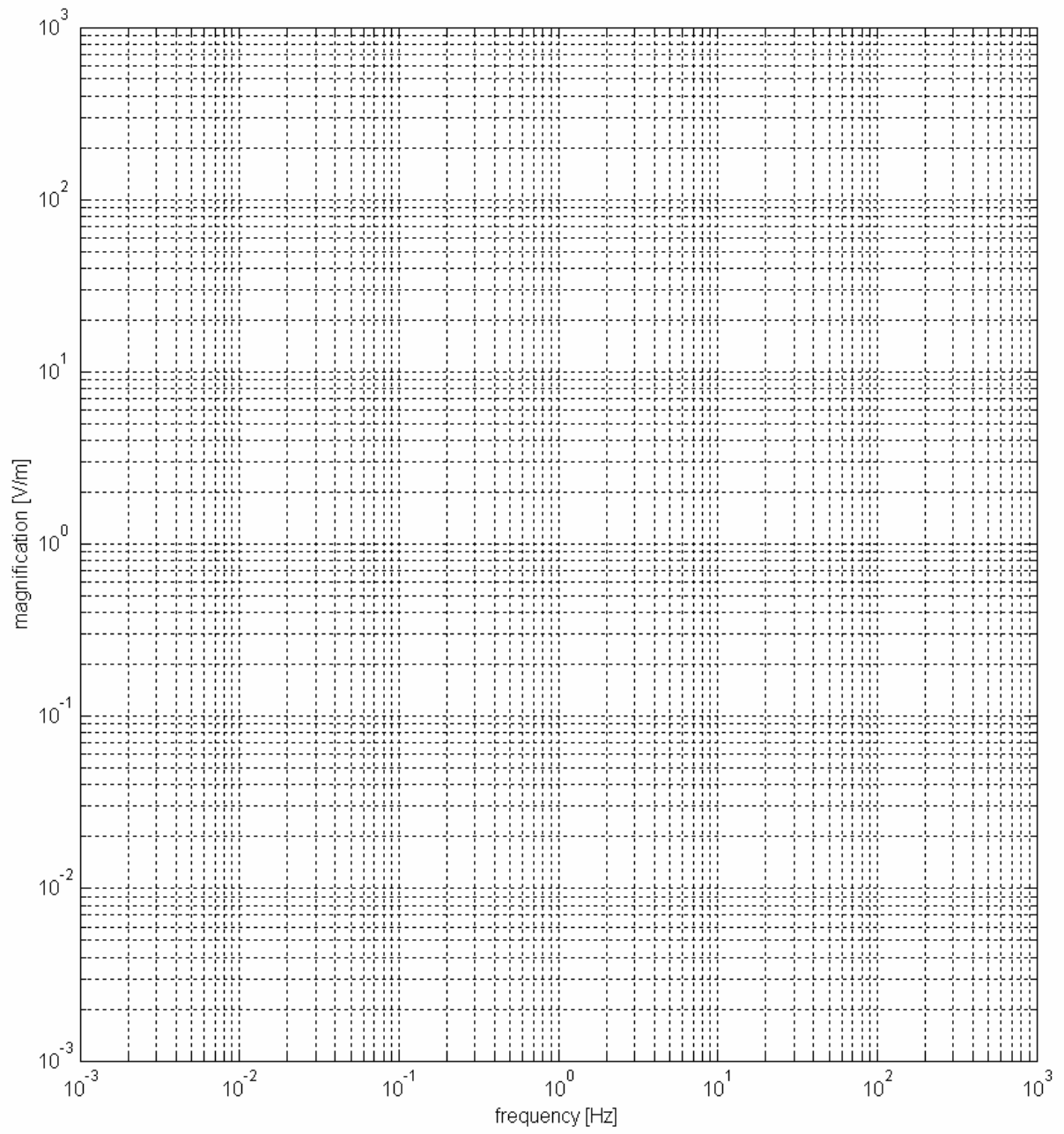


Figure 1

3 Solution

The solution to this exercise is given in Figure 2 below.

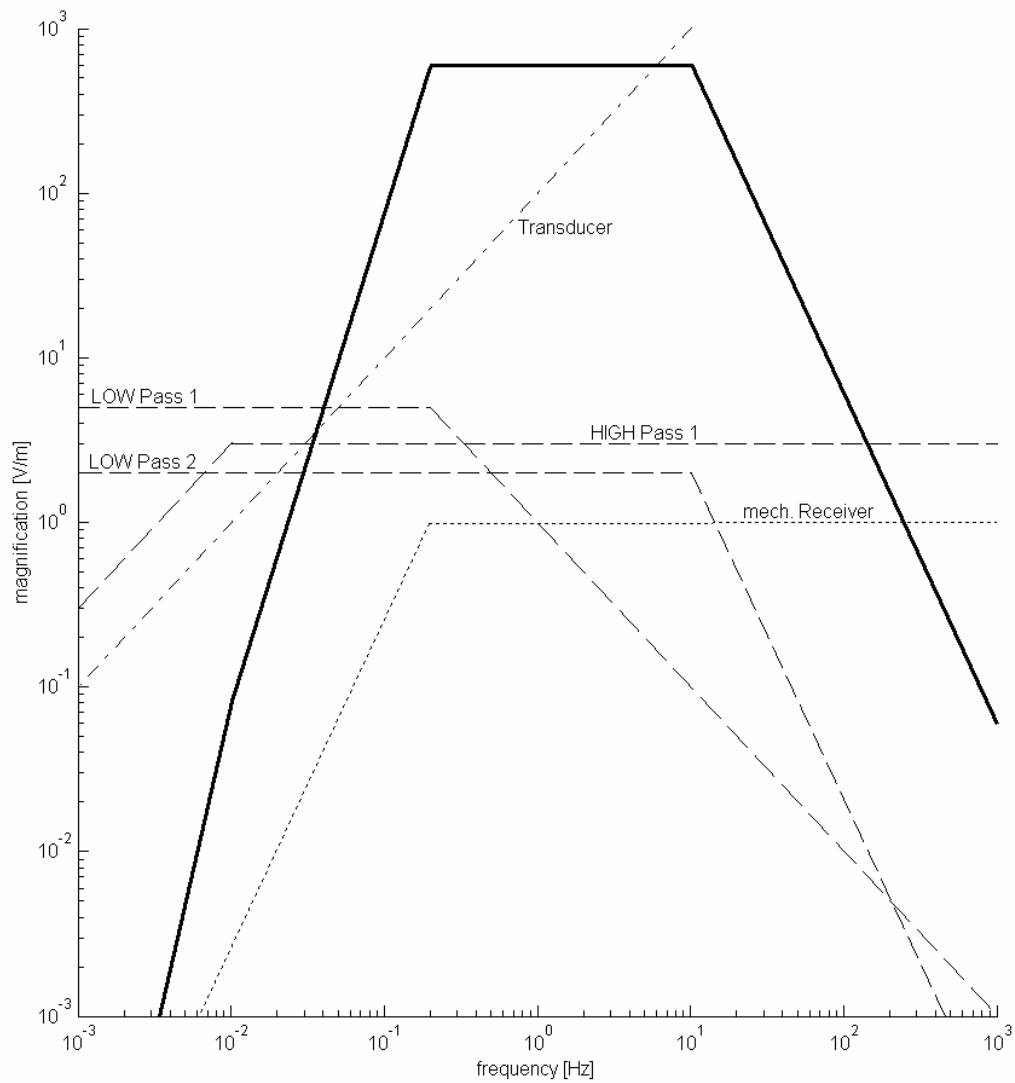


Figure 2 Overall BODE-diagram (solid curve) for the seismograph amplitude response. It results from the logarithmic addition of the BODE-diagrams of all individual components given in Task 1.

Title	Estimating seismometer parameters by step function (STEP)
Author	Jens Bribach, GeoForschungsZentrum Potsdam, Department 2: Physics of the Earth, Telegrafenberg, D-14473 Potsdam, Germany; Fax: +49 331 288 1266; E-mail: brib@gfz-potsdam.de
Version	May 2001

1 Aim

To determine the response of a seismometer system in the time domain to a *STEP function* input. Applying a step impulse to a seismometer allows to derive the main seismometer parameters by analysing the generated time series. In the absence of expensive calibration equipment (e.g., shake table) or in the case of sealed seismometers this simple method is very suitable and can also be used under field conditions.

2 Procedures and relationships

2.1 Applying STEPs to the seismometer

Applying steps is the oldest calibration method in seismology. Teupser (1962) describes three main types:

- a) pulling a thin block (thickness max. 0.01 mm) off the seismometer bottom;
- b) applying a heavy weight upon the seismometer platform;
- c) applying a constant current to the coil of an electrodynamical system (if available; for driving current see EX 5.3: Seismometer calibration by harmonic drive).

Because a) is the roughest method one should use it for field or for portable seismometers only and never for sensitive station sensors. In case a) and b) the seismometer mass will return to the former position after deflection, in case c) the seismometer mass will move to an offset position which will depend on the applied current. To ensure linearity the mass deflection - or the seismometer displacement - should not exceed several 100 micrometers.

2.2 Evaluating STEP-transition time series

2.2.1 All types of seismometers ($D_S < 0.5$)

Figure 1 shows the time series of a low-damped seismometer ($D_S = 0.1$). The time section A represents the time from the moment of step input up to the transition to a real harmonic movement of the mass. The moment of step causes odd signals. Mechanical application of a step impulse generates additional vibrations because of hitting effects. An electrical step can induce an electrical pulse if the calibration coil and the signal coil are mounted to the same core (the so-called transformer effect). Therefore the analysis of the generated time series should start only beyond section A with:

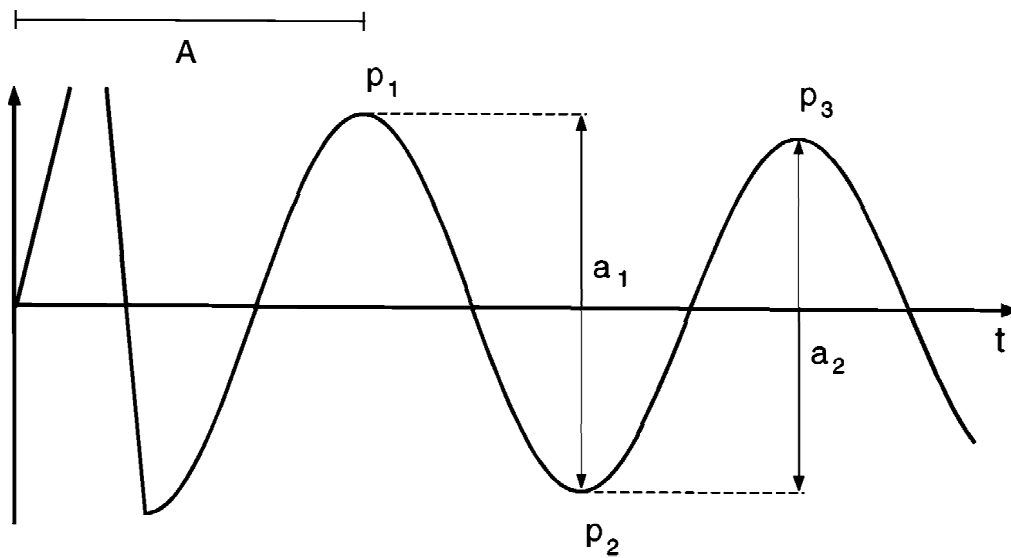


Figure 1 Response of a low-damped seismometer to a step pulse.

First step: Measuring of the period and damping of the time series.

The period T should be measured by averaging over as many cycles as possible (10 or more) to get an accuracy better than 99%.

Note! The measured period is larger than the natural period because of the seismometer damping.

The damping D is calculated from the equation

$$D = \frac{1}{\sqrt{\left(\frac{(N-1)\pi}{\ln(a_1/a_N)}\right)^2 + 1}} \quad (1)$$

with a_1 as the double amplitude between the first two oscillation peaks (p_1 and p_2) and a_N as the double amplitude between the peaks (p_N and p_{N+1}). N should be selected so as to get an $a_N \approx 0.2 \dots 0.4 a_1$.

Second step: Estimation of the natural period T_S of the seismometer.

If possible switch off all external attenuators (e.g., resistors) to decrease the measuring error. For example: with a damping $D = 0.2$ the measured period is $T = 1.02 T_S$.

The natural period of the seismometer is

$$T_S = T\sqrt{1-D^2} . \quad (2)$$

This constant can also be used when calibrating a system by harmonic drive.

Note! For pendulum seismometers there are different notations for this constant:

- 1) force/current [N/A] = [Vs/m] and
- 2) torque/current [Nm/A] = [Vs]

They are related via the reduced pendulum length l_0 as follows:

$$G_{S_1} [V_s] = G_{S_2} [V_s / m] \cdot l_0 [m]. \quad (7)$$

3 Data: Application to a specific seismometer

Below a typical seismometer parameter list is given.

Mechanical constants:

Natural period	T_S s
Open damping (Attenuation)	D_{S0}
Reduced pendulum length	l_0	0.0785 m
Inertial moment	K_S	0.0201 kg m ²
Seismic mass	m_S kg

Transducer constants 1 (signal coil):

Coil resistance	R_{S1}	6030 Ω
Electrodynamical constant	G_{S1} Vs/m

Transducer constants 2 (calibration coil):

Coil resistance	R_{S2}	835 Ω
Electrodynamical constant	G_{S2} Vs/m

4 Tasks

Task 1:

Mark those seismometer parameters which are absolutely necessary for calculating the seismometer response curve (BODE-diagram).

Task 2:

Complete the list above by analysing the related time series plots in Figure 2a - c.

Task 3:

Calculate the current I_C through the calibration coil which is necessary to deflect the seismometer mass by 1 μm at a frequency $f = 1$ Hz (see EX 5.3: Seismometer calibration by harmonic drive).



Figure 2a Seismometer step response: open circuit.

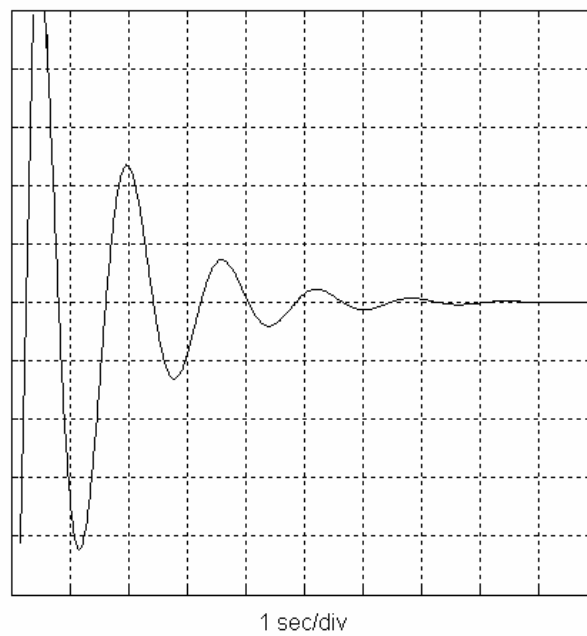


Figure 2b Seismometer step response: signal coil with external resistor $R_a = 67 \text{ k}\Omega$.

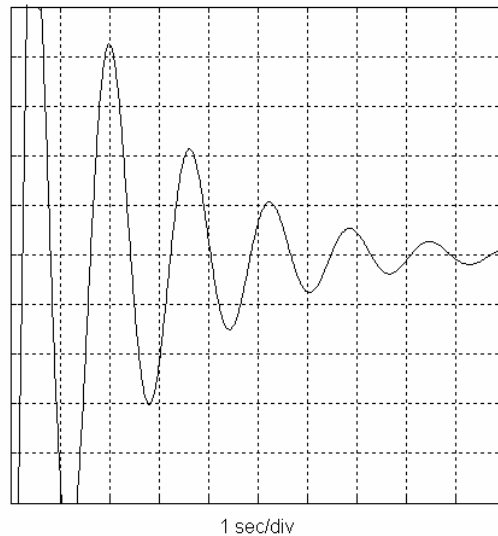


Figure 2c Seismometer step response: calibration coil with external resistor $R_a = 1 \text{ k}\Omega$.

5 Solutions

Task 1:

Seismometer parameters absolutely necessary for calculating the seismometer response curve are marked by an asterisk (*) in the listing below (see Task 2). Additionally required are the *seismometer damping*, consisting of the *open damping* plus the *external* (here: *electrodynamical*) *damping*.

Task 2:

Completed list of seismometer parameter:

Mechanical constant:

Natural Period	T_{S0}	=	1.617 s	(*)
Open damping (attenuation)	D_{S0}	=	0.0102	
Reduced Pendulum Length	l_0	=	0.0785 m	
Inertial Moment	K_S	=	0.0201 kg m ²	
Seismic Mass	m_S	=	3.262 kg	

Transducer constants 1 (signal coil):

Coil Resistance	R_{S1}	=	6030 Ω	
Electrodynamical Constant	G_{S1}	=	571.1 Vs/m	(*)

Transducer constants 2 (calibration coil):

Coil Resistance	R_{S2}	=	835 Ω	
Electrodynamical Constant	G_{S2}	=	67.97 Vs/m	

Task 3:

In order to deflect the seismometer mass for 1 μm , a current of $I_C = 0.12 \text{ mA}$ has to be driven through the calibration coil.

Title	Seismometer calibration by harmonic drive
Author	Jens Bribach (after a manuscript by Christian Teupser \ddagger) Helmholtz Centre Potsdam, GFZ German Research Centre for Geosciences, Department 2: Physics of the Earth, Telegrafenberg, D-14473 Potsdam, Germany; Fax: +49 331 288 1266; E-mail: brib@gfz-potsdam.de
Version	October 2008

If the seismometer possesses an auxiliary magnet and coil assembly, the calibration can be carried out with the aid of an electric current. According to Eq. (5.25) in Chapter 5 and related discussion a current i_s acts in the same way as a ground acceleration

$$\frac{d^2 x_e}{dt^2} = \frac{G_{S2} l_0^2}{K_S} i_s . \quad (1)$$

where G_{S2} is the electrodynamic constant of the auxiliary coil (given in [Vs/m]). For other constants see EX 5.2 *Estimating seismometer parameters by STEP function*. It corresponds to a harmonic drive of frequency f with an equivalent ground displacement

$$x_e = \frac{G_{S2} l_0^2}{4\pi^2 f^2 K_S} i_s . \quad (2)$$

For a translational seismometer, for example a geophone, with seismic mass m_s , the equivalent seismic displacement is

$$x_e = \frac{G_{S2}}{4\pi^2 f^2 m_s} i_s . \quad (3)$$

Since the output voltage of a geophone with an electromagnetic transducer is

$$E_S = G_{S1} \frac{dz}{dt} , \quad (4)$$

where z is the displacement of the seismic mass, G_{S1} is the electrodynamic constant of the signal coil and f_s the natural frequency, one obtains for a harmonic excitation

$$E_S = \frac{G_{S1} G_{S2} f}{2\pi m_s \sqrt{(f^2 - f_s^2)^2 + 4D_S^2 f^2 f_s^2}} . \quad (5)$$

Changing the frequency of the exciting current the output voltage attains a maximum at $f = f_s$. This can be used to determine the natural frequency and the damping using an oscilloscope.

Title	Seismometer calibration with program CALEX
Author	Erhard Wielandt (formerly Institute of Geophysics, University of Stuttgart, D - 70184 Stuttgart); E-mail: e.wielandt@t-online.de
Version	October 2001

1 Data

Two pairs of input ("eing") and output ("ausg") signals (which are included with the software as files eing1, ausg1, eing2, ausg2) are shown in Figures 1 and 2. They are used for calibration of a broadband seismometer and a short-period geophone, respectively.

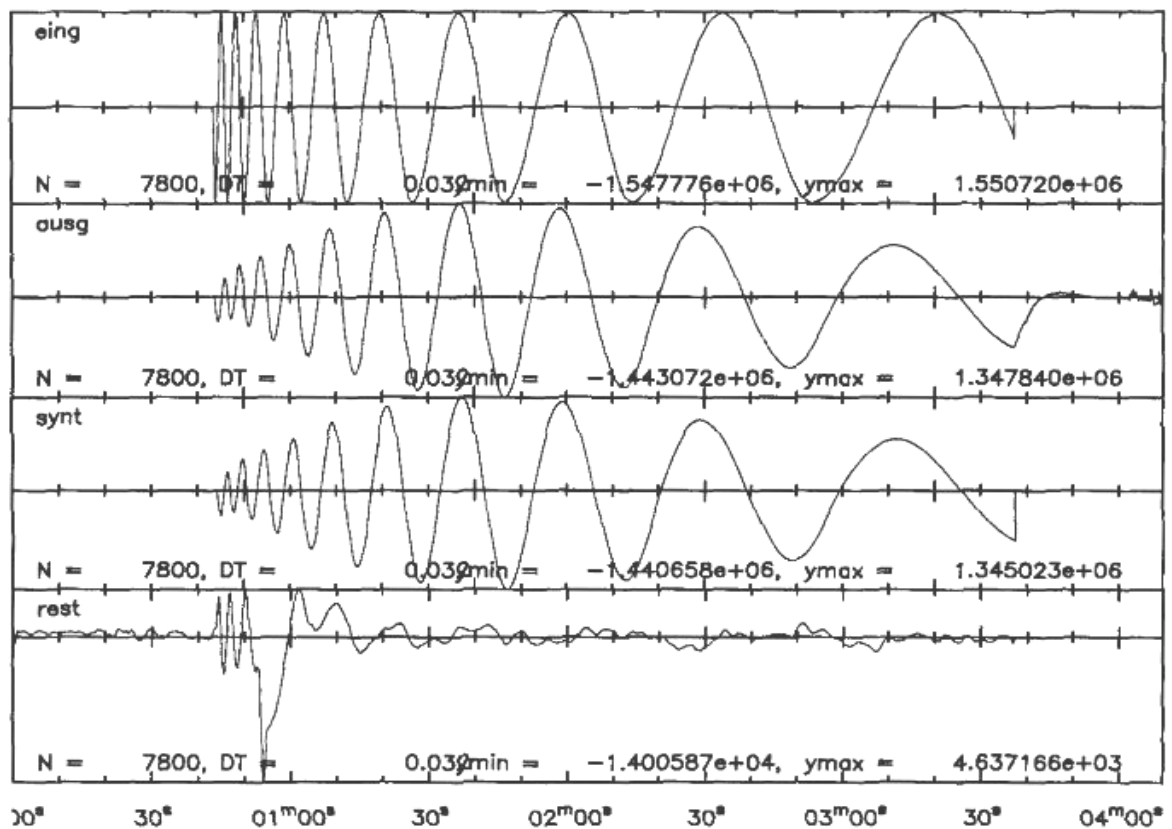


Figure 1 The input signal into the calibration coil (eing) is a "sweep", a sine-wave whose frequency is automatically tuned from about 2 s to 50 s. It is used for calibration of a 20-sec STS1 seismometer. The second and third traces show the output (ausg) signal and the best fitting synthetics (synt), respectively. The lowermost trace is the residual signal (ausg - synt = rest).

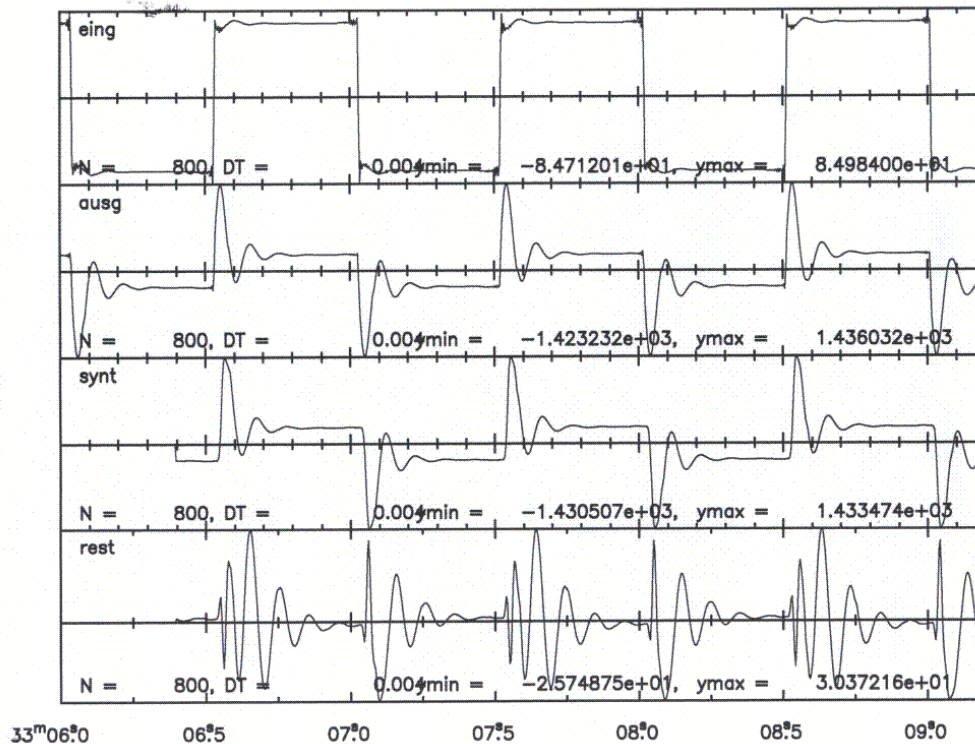


Figure 2 The input signal is a square wave. It is used for calibration of an undamped 10 Hz geophone in a half-bridge. Note that the input signal appears in the output by coupling through the coil resistance. This would not be the case for a seismic input signal and therefore must not be interpreted as part of the transfer function.

2 Tasks

- 1 - Plot the signals on the screen and get an idea of the time scale, of the free period and damping of the sensor, and of the type of response (high-pass, band-pass, low-pass?). You will also need an estimate of polarity and gain between input and output. Compare what you see in the plot to your knowledge of the general properties of seismometer transfer functions.
- 2 - Set up the calex.par file for each experiment, as specified in the program description. A sample file is listed there.
- 3 - Run CALEX to determine the exact instrumental constants. Inspect the residual signal and determine its magnitude relative to the output signal (the misfit). Is the misfit caused by improper parametrization of the transfer function, by seismic or environmental noise, or by nonlinear behavior of the sensor? In the latter case, can you guess what the problem might be?
- 4 - Run CALEX again with deliberately offset start parameters, to see if their choice (within a reasonable range) is critical. You may also restrict the analysis to a smaller time window within the record and see if you get different results.

3 Solutions

Please read the Program Description for the Calex routine (PD5.2) before continuing.
Copy 'eing1' onto 'eing' (input signal) and 'ausg1' onto 'ausg' (output signal).

Tasks 1 and 2, first signal: On a Windows PC, you may use the 'winplot' routine or one of its variants ('seipl', 'seipl02') for plotting the seismograms. To display the two signals, you have to prepare a small parameter file named 'plop' or 'plop.txt' (depending on the program version) containing parameters and file names (see program description PD5.9):

```
1,2,30,20,0,0.7
eing
ausg
```

An electromagnetic seismometer, or a broadband-velocity sensor, acts as a band-pass filter for ground accelerations or calibration signals. It gives a maximum response when the signal period equals the free period of the system. By inspecting of the ausg signal, you will recognize that this is in fact a band-pass response, and the free period is around 20 s. The damping is more difficult to estimate, but since the resonance is not sharp, damping must be considerable. Knowing that $1/\sqrt{2}$ or about 0.7 is a standard value for seismometers, you should start the inversion with this value. A more accurate value could be obtained from Fig. 5.25 of the NMSOP.

The gain between eing and ausg is around unity and the signals have the same phase at the resonance, so the gain parameter in calex.par may be set to 1.

Second signal: first copy the data files as above, and inspect the 'ausg' file. Use the "sub" parameter in place of "del" (see program description). The free period is obviously around 0.1 s. The damping may be estimated using formula 5.39 of the NMSOP; it is similar to the previous case. The gain between eing and ausg is again near unity and positive.

Task 3, first signal: you should approximately get 19.7 s for the free period, 0.72 for the damping, 1.36 for the gain, 10 ms for the delay, and a rms residual below 0.003. Change the second parameter in 'plop' to 4 and add the file names 'synt' and 'rest'. Note the transient disturbance in the 'rest' signal at the end of the first minute, which was caused by a person entering the room. Its effect on the result is quite small.

Second signal: the period is 0.102 s, the damping 0.65, the gain is 1.17, and about 48% of the input signal are present in the output signal. The rms residual is again below 0.003. Note the asymmetry in the residual between upgoing and downgoing steps. What you see is mass-position dependent, nonlinear behaviour of the geophone; this is not a bad geophone, but it's no force-balance sensor. You may also notice the small wiggles before and after each step of the input and output signals. (Zoom into a time window with 'seipl02' for better resolution.) The wiggles are not present in the analog signals but are generated by the decimation filters of the digital recorder. Since these filters affect both signals, they don't appear in the transfer function.

Task 4: the results should be nearly independent of the start parameters and of the data window as long as the essential information is preserved in the window.

Title	Determination of seismograph response from poles and zeros
Author	Erhard Wielandt (formerly Institute of Geophysics, University of Stuttgart, D - 70184 Stuttgart); E-mail: e.wielandt@t-online.de
Version	October 2001

1 Aim

The complex transfer function (or the related complex frequency response) of the analog part of a seismograph is a rational function of frequency. Such functions can be specified by corner frequencies and damping constants, by polynomial coefficients, or by their poles and zeros. The latter method is chosen in the IRIS SEED data volumes. For each data channel of each station, the data header contains a list of poles and zeros of the transfer function together with some auxiliary information. IRIS supplies a software library 'evalresp' for extracting and interpreting these parameters. The exercise aims at making you familiar with interpreting poles and zeros in terms of the amplitude response versus frequency.

2 Task

Interpret one or more of the annexed SEED headers with respect to the analog part of the seismograph. Sketch the amplitude response for one of the stations as a Bode-diagram on double logarithmic paper. (The digital part is usually of minor interest since it is supposed to have a flat amplitude response and zero phase delay.) Does the header describe a very broadband, broadband or narrowband system? Note that the answer does not only depend on the mathematical form of the response but also on the definition of the input signal - displacement, velocity or acceleration. A broadband seismograph is supposed to have a broadband response to velocity but a broadband accelerometer has a broadband response to acceleration. Be careful with the units - some headers refer to Hertz rather than radians/sec. Check also whether the poles and zeros refer to the Laplace transform or Fourier transform. Can you guess which type of sensor is used? Are the constants nominal or were they determined from an individual calibration?

A little computer program POL_ZERO in BASIC will be made available to you to do the numerical conversions and to plot the amplitude response (see PD_5.8). Use this program to analyze some more of the SEED headers. The stations are:

KIP (Kipapa, Hawaii)
 KONO (Kongsberg, Norway)
 KMI (Kunming, China)
 PFO (Pinion Flat Observatory, California)
 XAN (Xi'an, China)

3 Annex

SEED headers for stations KIP, KONO, KMI, PFO and XAN

KIP

```

:.....:
RESP.G.KIP..LHE
:.....:
#          << IRIS SEED Reader, Release 4.16 >>
#
#          ===== CHANNEL RESPONSE DATA =====
B050F03    Station:      KIP
B050F16    Network:      G
B052F03    Location:     ??
B052F04    Channel:      LHE
B052F22    Start date:   1988,147
B052F23    End date:     No Ending Time
#          =====
#          +-----+-----+-----+-----+
#          +-----+-----+-----+-----+
#          |               Response (Poles & Zeros),   KIP ch LHE               |
#          +-----+-----+-----+-----+
#
B053F03    Transfer function type:         B [Analog (Hz)]
B053F04    Stage sequence number:         1
B053F05    Response in units lookup:      M/S - Velocity
B053F06    Response out units lookup:     V - Volts
B053F07    A0 normalization factor:      25.0743
B053F08    Normalization frequency:      0.01
B053F09    Number of zeroes:             2
B053F14    Number of poles:              4
#          Complex zeroes:
#          i real      imag      real_error   imag_error
B053F10-13 0 0.000000E+00 0.000000E+00 0.000000E+00 0.000000E+00
B053F10-13 1 0.000000E+00 0.000000E+00 0.000000E+00 0.000000E+00
#          Complex poles:
#          i real      imag      real_error   imag_error
B053F15-18 0 -1.964190E-03 1.964190E-03 0.000000E+00 0.000000E+00
B053F15-18 1 -1.964190E-03 -1.964190E-03 0.000000E+00 0.000000E+00
B053F15-18 2 -3.117500E+00 3.909120E+00 0.000000E+00 0.000000E+00
B053F15-18 3 -3.117500E+00 -3.909120E+00 0.000000E+00 0.000000E+00
#          +-----+-----+-----+-----+
#          +-----+-----+-----+-----+
#          |               Channel Gain,   KIP ch LHE               |
#          +-----+-----+-----+-----+
#
B058F03    Stage sequence number:         1
B058F04    Gain:                       2.398000E+03
B058F05    Frequency of gain:            1.000000E-02 HZ
B058F06    Number of calibrations:       0
#          +-----+-----+-----+-----+
#          +-----+-----+-----+-----+
#          |               Response (Poles & Zeros),   KIP ch LHE               |
#          +-----+-----+-----+-----+
#
B053F03    Transfer function type:         B [Analog (Hz)]
B053F04    Stage sequence number:         2
B053F05    Response in units lookup:      V - Volts
B053F06    Response out units lookup:     V - Volts
B053F07    A0 normalization factor:      15593.8
B053F08    Normalization frequency:      0.01
B053F09    Number of zeroes:             0
B053F14    Number of poles:              6
#          Complex zeroes:
#          i real      imag      real_error   imag_error
#          Complex poles:
#          i real      imag      real_error   imag_error
B053F15-18 0 -4.832580E+00 1.273240E+00 0.000000E+00 0.000000E+00
B053F15-18 1 -4.832580E+00 -1.273240E+00 0.000000E+00 0.000000E+00
B053F15-18 2 -3.538230E+00 3.529300E+00 0.000000E+00 0.000000E+00
B053F15-18 3 -3.538230E+00 -3.529300E+00 0.000000E+00 0.000000E+00
B053F15-18 4 -1.295000E+00 4.829390E+00 0.000000E+00 0.000000E+00
B053F15-18 5 -1.295000E+00 -4.829390E+00 0.000000E+00 0.000000E+00
#

```

KONO

```

:.....:
RESP.IU.KONO.10.LHE
:.....:
#      << IRIS SEED Reader, Release 4.16 >>
#
#      ===== CHANNEL RESPONSE DATA =====
B050F03  Station:      KONO
B050F16  Network:      IU
B052F03  Location:      10
B052F04  Channel:      LHE
B052F22  Start date:    1999,040,13
B052F23  End date:      No Ending Time
#
#      -----
#      +-----+-----+-----+-----+
#      +               | Response (Poles & Zeros), KONO ch LHE |
#      +-----+-----+-----+-----+
#
B053F03  Transfer function type:      A [Laplace Transform (Rad/sec)]
B053F04  Stage sequence number:      1
B053F05  Response in units lookup:     M/S - Velocity in Meters Per Second
B053F06  Response out units lookup:    V - Volts
B053F07  A0 normalization factor:     7.1367E+07
B053F08  Normalization frequency:     0.1
B053F09  Number of zeroes:            2
B053F14  Number of poles:             5
#
#      Complex zeroes:
#      i real      imag      real_error  imag_error
B053F10-13  0  0.000000E+00  0.000000E+00  0.000000E+00  0.000000E+00
B053F10-13  1  0.000000E+00  0.000000E+00  0.000000E+00  0.000000E+00
#
#      Complex poles:
#      i real      imag      real_error  imag_error
B053F15-18  0 -3.701000E-02  3.701000E-02  0.000000E+00  0.000000E+00
B053F15-18  1 -3.701000E-02 -3.701000E-02  0.000000E+00  0.000000E+00
B053F15-18  2 -1.979000E+02  1.979000E+02  0.000000E+00  0.000000E+00
B053F15-18  3 -1.979000E+02 -1.979000E+02  0.000000E+00  0.000000E+00
B053F15-18  4 -9.111000E+02  0.000000E+00  0.000000E+00  0.000000E+00
#
#      +-----+-----+-----+-----+
#      +               | Channel Gain, KONO ch LHE |
#      +-----+-----+-----+-----+
#
B058F03  Stage sequence number:      1
B058F04  Gain:                      2.026400E+04
B058F05  Frequency of gain:         2.000000E-02 HZ
B058F06  Number of calibrations:    0
#
#      +-----+-----+-----+-----+
#      +               | Response (Coefficients), KONO ch LHE |
#      +-----+-----+-----+-----+
#
B054F03  Transfer function type:      D
B054F04  Stage sequence number:      2
B054F05  Response in units lookup:     V - Volts
B054F06  Response out units lookup:    COUNTS - Digital Counts
B054F07  Number of numerators:        0
B054F10  Number of denominators:      0
#
#      +-----+-----+-----+-----+
#      +               | Decimation, KONO ch LHE |
#      +-----+-----+-----+-----+
#
B057F03  Stage sequence number:      2
B057F04  Input sample rate:          5.120000E+03
B057F05  Decimation factor:          1
B057F06  Decimation offset:          0
B057F07  Estimated delay (seconds):   0.000000E+00

```


PFO

```

.....
RESP.TS.PFO.LHZ
.....
#          << IRIS SEED Reader, Release 4.16 >>
#
#          ===== CHANNEL RESPONSE DATA =====
B050F03   Station:      PFO
B050F16   Network:      TS
B052F03   Location:     ??
B052F04   Channel:      LHZ
B052F22   Start date:  1990,304
B052F23   End date:    No Ending Time
#
#          =====
#          +-----+
#          | Response (Poles & Zeros),   PFO ch LHZ |
#          +-----+
#
B053F03   Transfer function type:      A [Laplace Transform (Rad/sec)]
B053F04   Stage sequence number:       1
B053F05   Response in units lookup:    M/S - Velocity in Meters Per Second
B053F06   Response out units lookup:   V - Volts
B053F07   A0 normalization factor:    3948.58
B053F08   Normalization frequency:    0.02
B053F09   Number of zeroes:           2
B053F14   Number of poles:            4
#          Complex zeroes:
#          i real      imag      real_error  imag_error
B053F10-13 0 0.000000E+00 0.000000E+00 0.000000E+00 0.000000E+00
B053F10-13 1 0.000000E+00 0.000000E+00 0.000000E+00 0.000000E+00
#          Complex poles:
#          i real      imag      real_error  imag_error
B053F15-18 0 -1.234000E-02 1.234000E-02 0.000000E+00 0.000000E+00
B053F15-18 1 -1.234000E-02 -1.234000E-02 0.000000E+00 0.000000E+00
B053F15-18 2 -3.918000E+01 4.912000E+01 0.000000E+00 0.000000E+00
B053F15-18 3 -3.918000E+01 -4.912000E+01 0.000000E+00 0.000000E+00
#
#          +-----+
#          | Channel Gain,   PFO ch LHZ |
#          +-----+
#
B058F03   Stage sequence number:      1
B058F04   Gain:                      2.122720E+03
B058F05   Frequency of gain:          2.000000E-02 HZ
B058F06   Number of calibrations:     0
#
#          +-----+
#          | Response (Coefficients),   PFO ch LHZ |
#          +-----+
#
B054F03   Transfer function type:      D
B054F04   Stage sequence number:       2
B054F05   Response in units lookup:    V - Volts
B054F06   Response out units lookup:   COUNTS - Digital Counts
B054F07   Number of numerators:        43
B054F10   Number of denominators:     0
#          Numerator coefficients:
#          i, coefficient, error
B054F08-09 0 -3.557280E-09 -7.114550E-11
B054F08-09 1 3.273000E-06 6.546030E-08
B054F08-09 2 -3.791030E-04 -7.582060E-06
B054F08-09 3 -2.870530E-03 -5.741070E-05
B054F08-09 4 -2.949110E-03 -5.898210E-05
B054F08-09 5 3.191820E-03 6.383630E-05
B054F08-09 6 -2.121360E-03 -4.242730E-05
B054F08-09 7 -5.931070E-04 -1.186210E-05
B054F08-09 8 4.816940E-03 9.633870E-05

```

XAN

```

:.....:
RESP.IC.XAN..LHE
:.....:
#
# << IRIS SEED Reader, Release 4.16 >>
#
# ===== CHANNEL RESPONSE DATA =====
B050F03 Station: XAN
B050F16 Network: IC
B052F03 Location: ??
B052F04 Channel: LHE
B052F22 Start date: 1992,334
B052F23 End date: 1995,149
#
# -----
# +-----+
# + | Response (Poles & Zeros), XAN ch LHE |
# +-----+
#
B053F03 Transfer function type: A [Laplace Transform (Rad/sec)]
B053F04 Stage sequence number: 1
B053F05 Response in units lookup: M/S - Velocity in Meters Per Second
B053F06 Response out units lookup: V - Volts
B053F07 A0 normalization factor: 5.96806E+07
B053F08 Normalization frequency: 0.02
B053F09 Number of zeroes: 2
B053F14 Number of poles: 5
#
# Complex zeroes:
# i real imag real_error imag_error
B053F10-13 0 0.000000E+00 0.000000E+00 0.000000E+00 0.000000E+00
B053F10-13 1 0.000000E+00 0.000000E+00 0.000000E+00 0.000000E+00
#
# Complex poles:
# i real imag real_error imag_error
B053F15-18 0 -3.564700E-02 -3.687900E-02 0.000000E+00 0.000000E+00
B053F15-18 1 -3.564700E-02 3.687900E-02 0.000000E+00 0.000000E+00
B053F15-18 2 -2.513300E+02 0.000000E+00 0.000000E+00 0.000000E+00
B053F15-18 3 -1.310400E+02 -4.672900E+02 0.000000E+00 0.000000E+00
B053F15-18 4 -1.310400E+02 4.672900E+02 0.000000E+00 0.000000E+00
#
# +-----+
# + | Channel Gain, XAN ch LHE |
# +-----+
#
B058F03 Stage sequence number: 1
B058F04 Gain: 1.500000E+03
B058F05 Frequency of gain: 2.000000E-02 HZ
B058F06 Number of calibrations: 0
#
# +-----+
# + | Response (Coefficients), XAN ch LHE |
# +-----+

```

3 Solutions

- KIP** velocity very broadband, lower corner 360 s, upper corner 0.2 s
Obviously an older STS1-VBB seismometer. No extra filters.
Nominal parameters.
- KONO** velocity broadband, lower corner 120 s, upper corner 44.5 Hz
Must be an STS2 or a CMG3-T. Nominal parameters. Additional
low-pass Filter at 145 Hz.
- KMI** narrowband LP as a displacement sensor, but better characterized as
a long-period acceleration sensor. Response is flat to acceleration
from 30 s to 600 s. The sensor must be an old STS1 (20 s). A 6th-order
Butterworth low-pass filter limits the bandwidth at 30 s; this would
today be done with digital filters in the recorder. Parameters are nominal.
- PFO** velocity very broadband, lower corner 360 s, upper corner 0.1 s.
A modern STS1-VBB. No extra filters. Nominal parameters.
- XAN** velocity broadband, lower corner 120 s, upper corner 44 Hz.
Probably an STS2 or a CMG3-T seismometer. Additional low-pass
filter at 77 Hz. Parameters were probably measured.

Topic	Estimating the epicenters of local and regional seismic sources by hand, using the circle and chord method
Author	Peter Bormann, and K. Wylegalla (formerly GeoForschungsZentrum Potsdam, Telegrafenberg, D-14473 Potsdam, Germany); E-mail: pb65@gmx.net
Version	October 2001

1 Aim

The exercise aims at making you familiar with the basic “circle and chord” method for determining the epicenter of a seismic source. It is applied both to sources inside and outside of the recording networks.

2 Data

- Available are two sections of vertical component short-period records of stations of the former Potsdam seismic network from a local earthquake inside the network (see Figure 2) and a strong rock-burst in a mine located outside of the network (see Figure 3).
- Travel-time curves of the main crustal phases Pn, Pg, Sn, Sg and Lg from a near surface source up to an epicentral distance of 400 km (see Figure 4). These curves are reasonably good average curves for Central Europe. For any stations in this exercise at distances beyond 400 km, you may linearly extrapolate the curve without much error.
- Map with the positions of the recording stations and a distance scale (see Figure 5).

3 Procedure

- Identify the seismic phases in short-period records of near seismic sources.
- By means of local travel-time curves determine the source distance **d** from the best fit with the identified seismic phases.
- If no local travel-time curves are available, a first rough estimate of the hypocenter distance **d** or of the epicentral distance **D** (both in km) may be found using the following “rules-of-thumb”:

$$\mathbf{d} \approx \mathbf{t}(\mathbf{Sg} - \mathbf{Pg}) \times \mathbf{8} \quad \text{or} \quad (1)$$

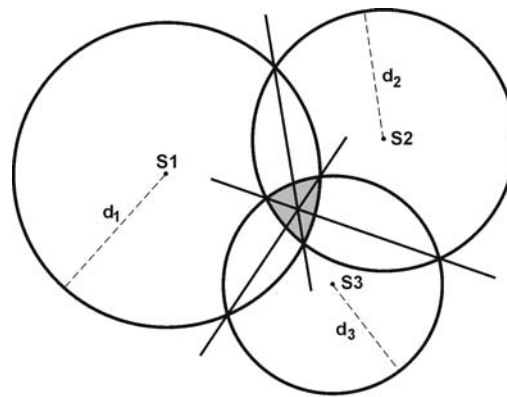
$$\mathbf{D} \approx \mathbf{t}(\mathbf{Sn} - \mathbf{Pn}) \times \mathbf{10} \quad (2)$$

with **t** as the travel-time difference in seconds between the respective seismic phases. These rules are approximations for a single layer crust with an average Pg-wave velocity of 5.9 km/s and a sub-Moho velocity of 8 km/s and a velocity ratio $v_s/v_p = \sqrt{3}$. If in your area of study the respective average P- and S-wave crustal velocities

v_p and v_s deviate significantly from these assumptions you may calculate d more accurately from the relationship:

$$\mathbf{d} = t(\mathbf{S}_g - \mathbf{P}_g) (v_p v_s)/(v_p - v_s). \quad (3)$$

- Draw circles with a compass around each station \mathbf{S}_i , which is marked on a distance-true map projection, with the radius \mathbf{d}_i determined from the records of each station.
- The circles will usually cross at two points, not one point (the thought epicenter) thus forming an area of overlap (see Figure 1, shaded area) within which the epicenter most probably lies.
- Usually, it is assumed, that the best estimate of the epicenter position is the “center of gravity” of this shaded area of overlap. The best estimate of the epicenter is found by drawing so-called “chords”, i.e., straight lines connecting the two crossing points of each pair of circles. The crossing point (or smaller area of overlap) of the chords should be the best estimate of the epicenter (see Figure 1).



$$d = t(\mathbf{S}_g - \mathbf{P}_g) \times 8$$

$$\text{or } d = t(\mathbf{S}_n - \mathbf{P}_n) \times 10$$

Figure 1 Principle of epicenter estimation by using the “circle and chord” method. S – station sites, d – distance of the event determined for each station according to travel-time curves (or “rules-of-thumb” as given in the figure).

Notes:

- 1) In the absence of independent information on the source depth and depth-dependent travel-times the distance d determined as outlined above is not the epicenter but the *hypocenter distance*. Therefore, for sources at depth the circles will necessarily overshoot, the more so the deeper the focus.
- 2) Also, an ideal crossing of circles at a point for a surface source requires that all phases are properly identified, their onset times picked without error and the travel-time curves/model for the given area (including the effects of lateral variations) exactly known. This, however, will never be so. Therefore, do not expect your circles to cross all at one point.
- 3) Despite note 2, the circles should at least come close to each other in some area, overlapping or not, within about 10 to 20 km at least, if the epicenter is expected to lie within the network and the hypocenter within the crust. If not, one should check again the phase interpretation and resulting distance estimate and also compare for all

stations the consistency of related estimates of origin time (see tasks below). Any obvious outliers should be re-evaluated.

- 4) For seismic sources outside the network the circle crossing will be worse, the error in epicenter estimation larger, particularly in the direction perpendicular to the azimuth between the network center and source; the distance control, based on travel-time differences S-P, is better than the azimuth control. Azimuth estimates are more reliable, if the source is surrounded by stations on three sides, i.e., with a maximum azimuthal gap less than 180° .
- 5) With only two stations one gets two possible solutions for the three unknowns (epicenter coordinates λ and φ and origin time OT) unless the source direction can be independently determined from polarity readings in three-component records of each station (see EX 11.2). If more than 3 stations are available, the estimates of both epi- and hypocenter will improve.

4 Tasks

4.1 Phase identification and travel-time fit

- Identify the main local phases Pn, Pg, Sn and/or Sg/Lg in the records of the Potsdam seismic network (Figures 2 and 3) by using the travel-time curves given in Figure 4.
- If possible use for it a 1:1 transparent sheet of the travel-time curve with the same time-scale resolution as the records (1 mm/s) and overlay it on the records. Take care that the distance abscissa D of the travel-time curves is strictly perpendicular to the record traces!
- Move the travel-time curves up and down until you find the best fit for the first arrival and the onsets of several later wave groups characterized by significant changes/increases in amplitude. Mark these best fitting onset times with a dot in the record together with the phase name.

Notes:

- 1) When searching for the best fit remember that the beginning of the later wave group with the largest amplitudes in the record is usually the onset of Sg, whereas in the early parts of the record it is Pg that is the largest wave. For distances < 400 km Pn is usually much smaller than Pg, although deeper crustal earthquakes with appropriate rupture orientation may be recorded with strong Pn too (see Figs. 11.44 to 11.46).
- 2) From the onset-time differences Sg-Pg or Sn-Pn you may roughly estimate the hypocenter distance d of the event by using the “rules-of-thumb” (see Equations (1) to (3) above). If your rough estimate is $d < 150$ km then the first arrival should never be interpreted as Pn but rather as Pg (unless it is a deeper crustal event or the crust is less than 30 km thick). If $d > 150$ km, try to get the best fit to the onsets by assuming that the first arrival is Pn, however remember that its amplitude is usually smaller than that of the following stronger Pg for $d < 400$ km.
- 3) The above said is true for near-surface events in a single-layer crust with average P-wave velocity of 6 km/s and sub-Moho velocity of 8 km/s. The **cross-over distance** x_{co} beyond which Pn becomes the first arrival is then approximately $x_{co} \approx 5 z_m$ with z_m as the Moho depth. In case of different average crustal and sub-Moho P-wave velocities, \bar{v}_c and v_m , you may use the relation $x_{co} = 2 z_m \{ (v_m + \bar{v}_c) / (v_m - \bar{v}_c) \}^{1/2}$ to

calculate the cross-over distance of Pn. However, be aware that for deeper crustal events Pn may over-take already at smaller distances!

4.2 Estimation of distance and origin time

- Write down for each station the distance corresponding to your phase interpretation and best travel-time fit. Mark on each record the estimated origin time which is the time of the abscissa position on the record time scale for your best phase-travel-time fit.
- Check, whether your marks for the estimated origin times are roughly the same (in vertical line) for all stations. This is a good check of the accuracy and reproducibility of your phase identifications and estimated distances. For any “outliers” check the phase identification and distance estimate again until you get agreement between the origin times within about ± 3 s.
- Compare your best estimate of origin time OT (average of all your individual origin times determined from the records of each station) with the OT computer solution given in the head lines of Figures 2 and 3.
- If your average OT deviates by more than about 3 s from the computer solution reconsider your interpretation.

4.3 Epicenter location

- Take a compass and draw circles around each station position (see Figure 5) with the radius d_i in km as determined for the distance of the source from the station S_i . Use the distance scale given on the station map.
- Connect the crossing points of each pair of circles by chords. Estimate the coordinates λ and φ (in decimal units of degree) from the chord crossings.
- Compare your coordinates with the ones given in the headlines of Figures 2 and 3. If your solutions deviate by more than 0.2° for the earthquake within the network and by more than 0.4° for the mining rock-burst outside, reconsider your phase interpretation, distance estimates and circle-drawings.

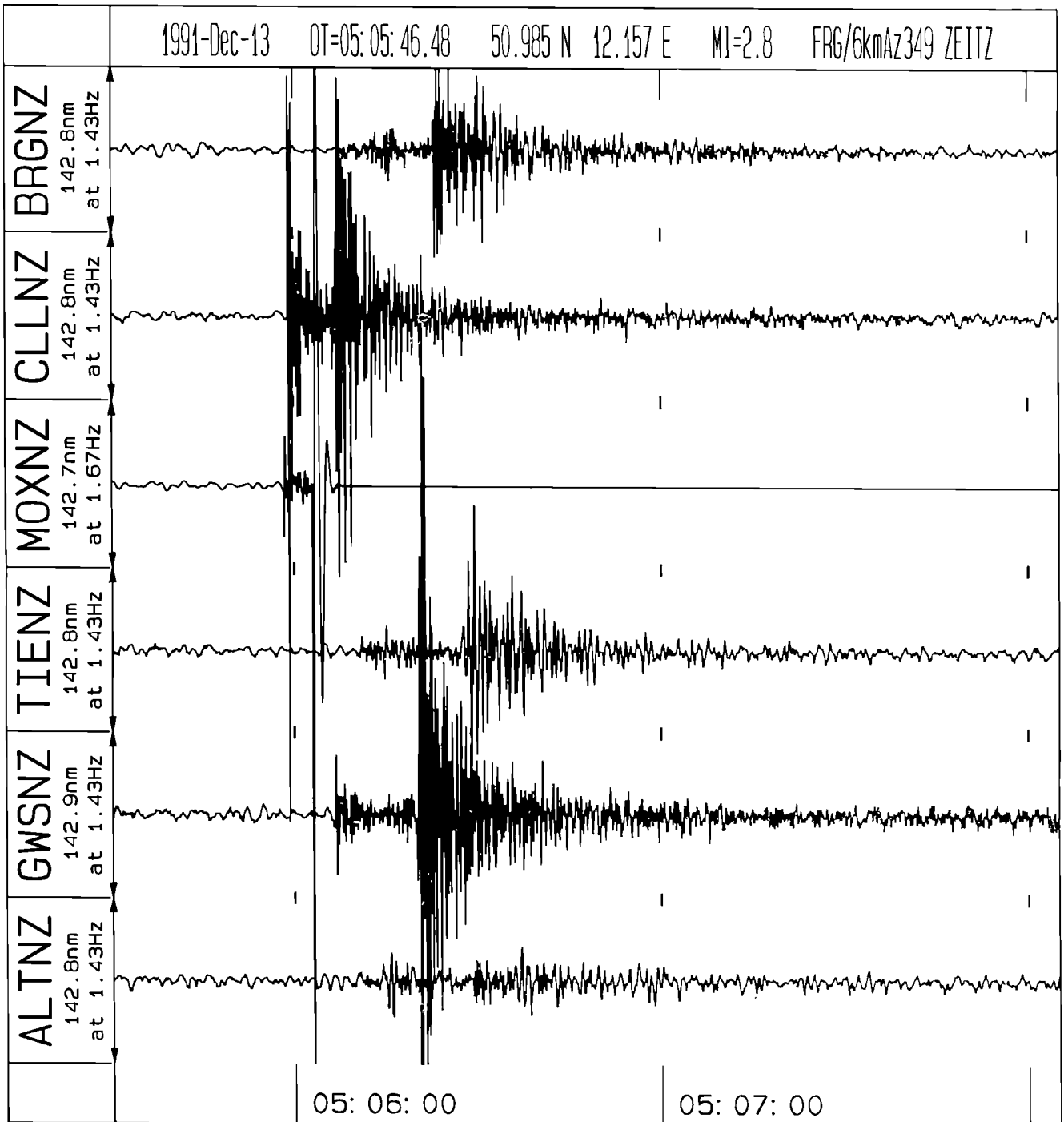


Figure 2 Recordings of a near earthquake situated within the seismic network of stations shown in Figure 5. The time scale is 1 mm/s. Note the second strong onset in the record of station MOX has a very different form and frequency than in any other record. It is not a natural wave onset but a malfunction of the seismograph, which responds to the impulse of the strong Sg with its own impulse response.

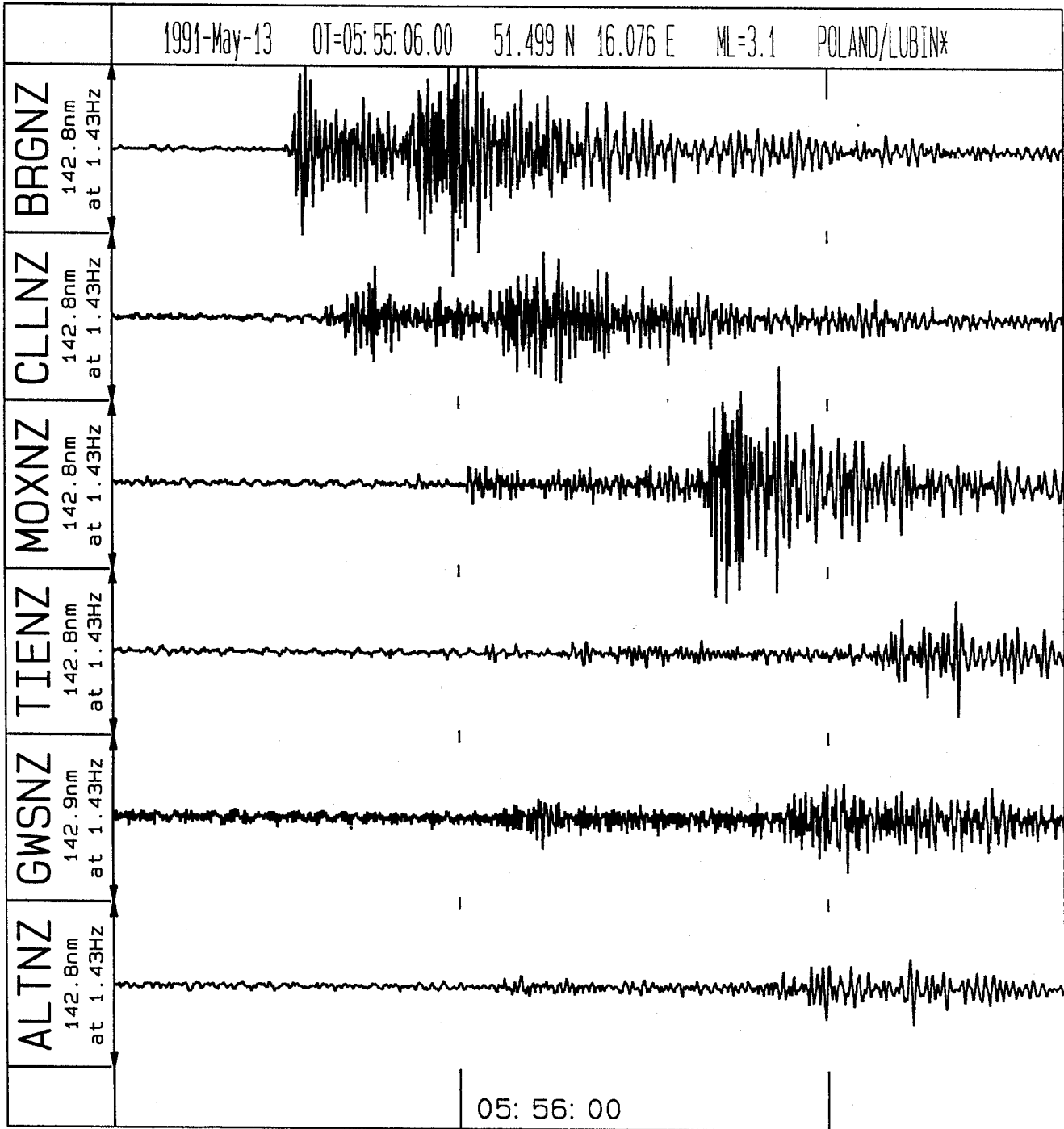


Figure 3 Recordings at regional distances from a strong mining rock-burst situated outside the seismic network of stations shown in Figure 5. The time scale is 1 mm/s.

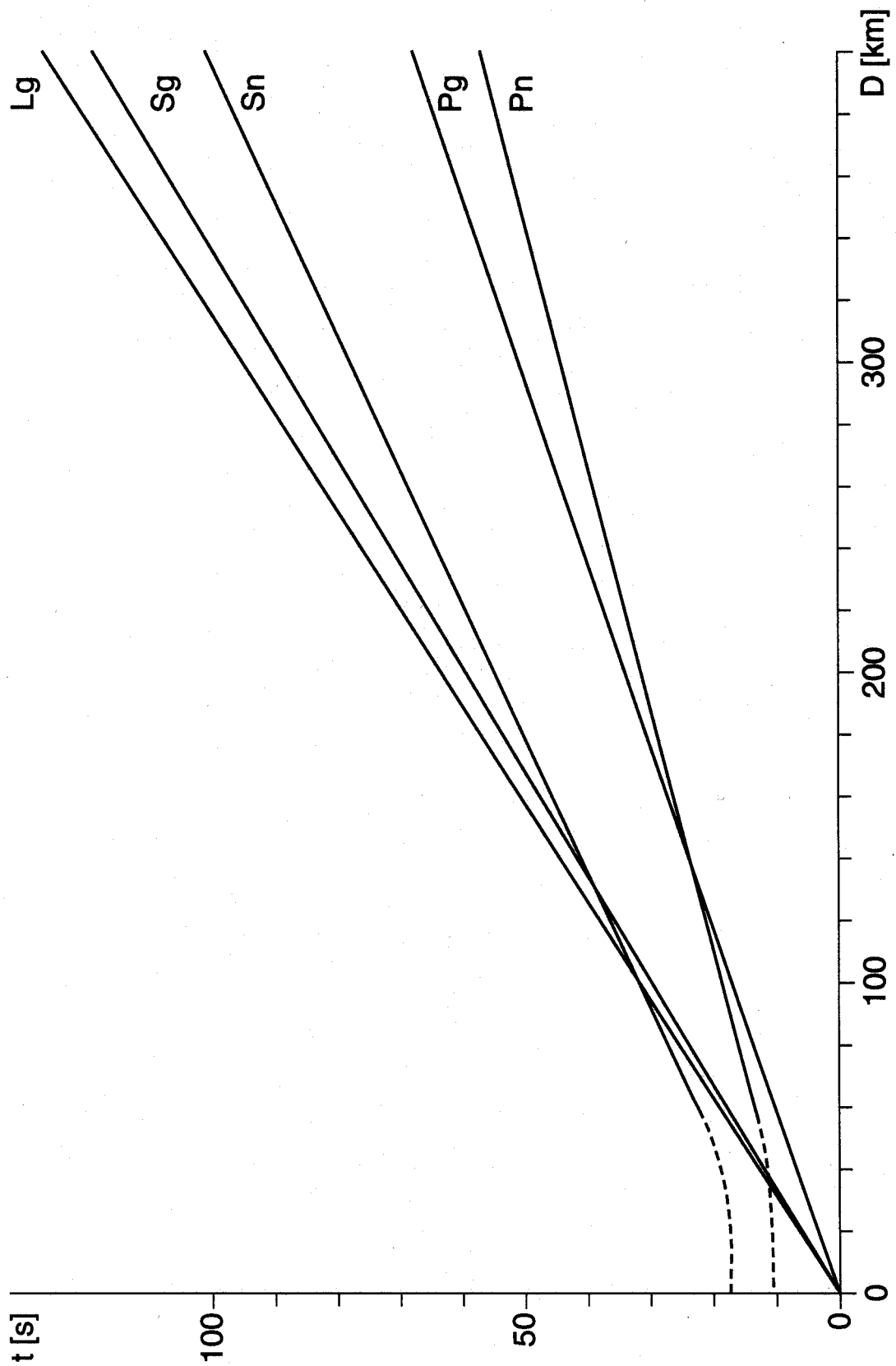


Figure 4 Travel-time curves for the main phases in seismic records of near-surface sources. They are good average curves for Central Europe with a crustal thickness of about 30 km.

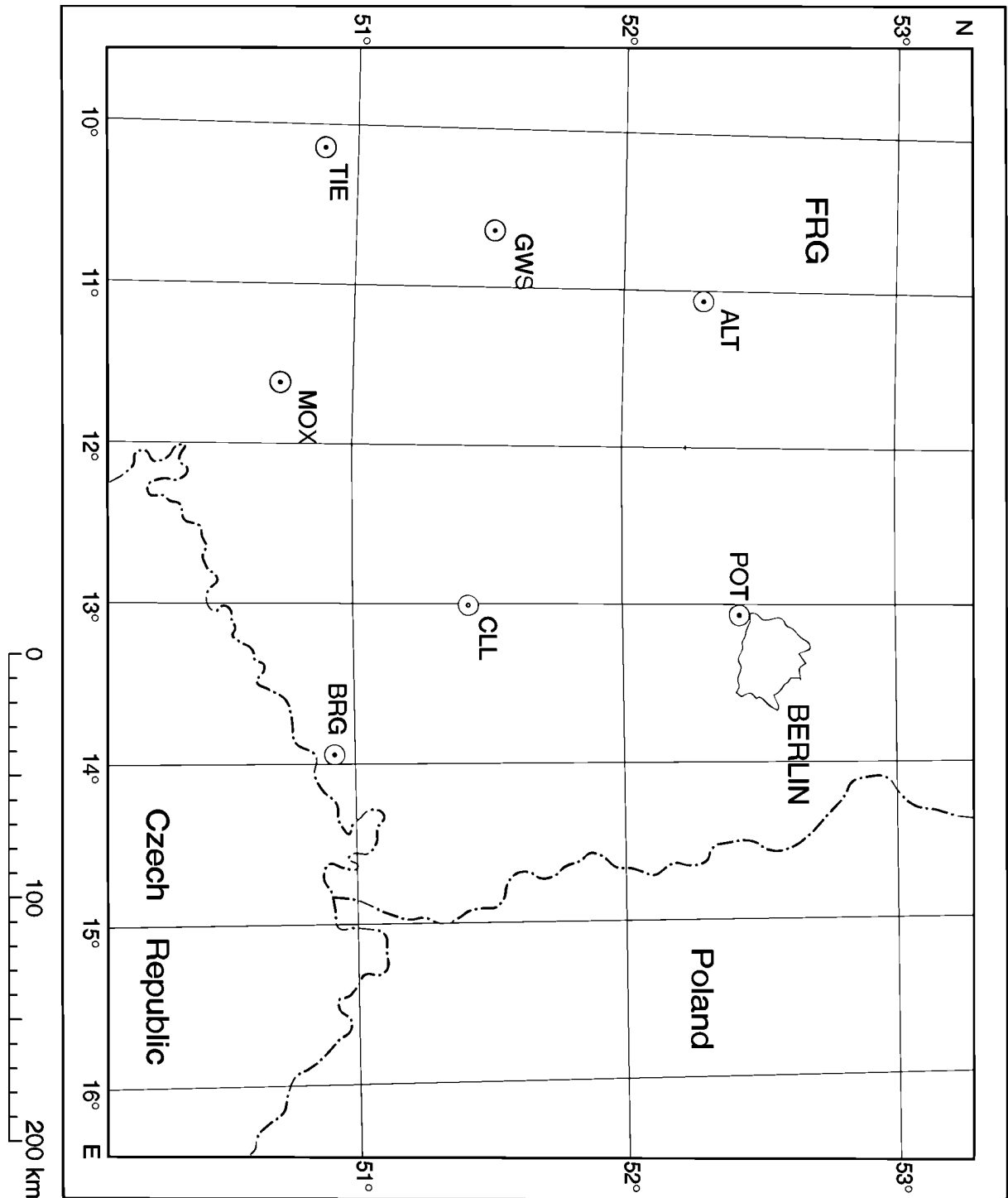


Figure 5 Map of parts of Central Europe with codes and positions (circles) of the seismic stations that recorded the seismograms shown in Figures 2 and 3 (on the map projection all distances are true).

Topic	Earthquake location at teleseismic distances by hand from 3-component records
Author	Peter Bormann, and Kurt Wylegalla (formerly GeoForschungsZentrum Potsdam, Telegrafenberg, D-14473 Potsdam, Germany); E-mail: pb65@gmx.net
Version	October 2002

1 Aim

The exercise aims at making you familiar with the basic concept of locating seismic events by means of teleseismic records from single 3-component stations. Often the results are comparably good or even better than for uncalibrated single seismic arrays.

The exercise uses teleseismic events only although the procedure outlined below is the same for local seismic events. In the latter case local travel-time curves as in Exercise EX 11.1 have to be used for phase identification and distance determination. Note however that azimuth determinations for local events are less reliable when short-period records are used. They are much more influenced by local heterogeneities in the crust than teleseismic long-period or broadband records. Accordingly, particle motion might deviate significantly from linear polarization (see Fig. 2.6) and the azimuth of wave approach for local events sometimes deviates more than 20° ($+ 180^\circ$) from the backazimuth AZI towards the source (Fig. 11.23).

2 Data

The following data are used in the exercise:

- two 3-component earthquake records: a) Kirnos BB-displacement seismogram (Figure 2) and b) long-period (WWSSN-LP) seismogram (Figure 3);
- differential body-wave travel-time curve (with respect to the P-wave first arrival) for the distance range $0^\circ < D \leq 100^\circ$ (Figure 4);
- IASP91 table of travel-time differences pP-P and sP-P, respectively, as a function of epicentral distance D (in degree) and source depth h (in km) (see Table 1);
- global map of epicenter distribution with isolines of epicentral distance D (in $^\circ$) and principal directions of backazimuth AZI from station CLL (Germany).

3 Procedure

3.1 Estimation of epicentral distance D and depth h

- Identification of first as well as later secondary arrivals from teleseismic events in broadband or long-period filtered records. At least P and S have to be identified. P is the first arrival (up to about 100°) and for teleseismic events strongest in the vertical component. S is the first arriving shear wave up to about 83° and has its largest amplitudes in horizontal components. For larger distances SKS becomes the first arriving shear wave (see Figure 4). Misinterpreting it as S might result in significant underestimation of the epicentral distance.

- Determination of epicentral distance D by using the travel-time difference $t(S-P)$ according to travel-time tables (e.g., IASPEI 1991; Kennett 1991) or by fitting best a set of differential travel-time curves as in Figure 4 with the identified phases in the record. Note that the records and the $t-D$ -curves must have the same time scale. In the distance range $20^\circ < D < 85^\circ$ the following **rule-of-thumb** allows to determine D with an error $< 3^\circ$: $D [^\circ] = [t(S-P)_{\text{min}} - 2] \times 10$.
- Note, that the travel-time difference $t(S-P)$ but also the time difference between P or PKP (beyond 105°) with other secondary phases is influenced by the source depth h . Unrecognized significant source depth might result in underestimating D by several degrees. Accordingly, it is important to assess from the outset whether an event was deep or shallow (i.e., probably within the crust).
- For a first rough discrimination between deep and shallow earthquakes one should compare the amplitudes of body waves with that of (dispersed !) surface waves. If the latter are well developed and significantly larger in amplitude than the earlier body waves, then the event can be considered a crustal earthquake. Since for shallow events it is difficult to identify any depth phases, which follow closely to the P or S onset, one may use travel-time curves or tables for surface focus ($h = 0$ km) or “normal depth” events ($h = 33$ km).
- In case of relatively weak or absent surface waves one should look for depth phases! Examples for depth phases are given in DS 11.2, Figures 7b, 9a, 16b and in DS 11.3 Figures 3b-d and 5a. See also the discussion in section 11.5.4. If depth phases such as pP and/or sP have been identified h can be calculated, when the epicentral distance is roughly known, by using differential travel-time $pP-P$ or $sP-P$ (see Table 1). If no such tables are available, one may also use another rule-of-thumb for a rough estimate, namely $h \text{ [km]} \approx 0.5 t(pP-P) \text{ [s]} \times 7$ (for $h < 100$ km),... $\times 8$ (for $h = 100 - 300$ km) or... $\times 9$ (for $h > 300$ km).

3.2 Estimation of backazimuth AZI

- Identify the proper direction of P -wave first motion in the three components Z , N , E . Make sure by exact time correlation that you really compare the same first half cycles in all three records! This is particularly important, if in one of the horizontal components the first onset is very weak or near to zero. Then one might be misled and associate the stronger amplitude of a later half cycle with the first motion in the other components and get a wrong backazimuth.
- Determine the direction of particle motion from the amplitudes of first motions in the horizontal component records according to the formula $AZI = \text{arc tan} (A_E/A_N)$. If seismograph components have been calibrated properly and avail of identical frequency responses (which is the case in these exercises) then one just calculates the ratio between measured trace amplitudes. However, as demonstrated in Figure 1, this direction may either show **towards the epicenter**, in case the first motion in Z is down (-, dilatational; see blue record traces), or away from the epicenter if the first motion in Z is up (+, compressional; see red record trace). In the latter case, the backazimuth to the epicenter is $AZI + 180^\circ$.
 - If this 180° ambiguity has been resolved, one may also calculate the azimuth from horizontal component records of either later cycles of P with larger

amplitudes or even by using the amplitude ratio in E/N from other later phases which are polarized in the vertical propagation plane such as PP, SKS, SP etc.

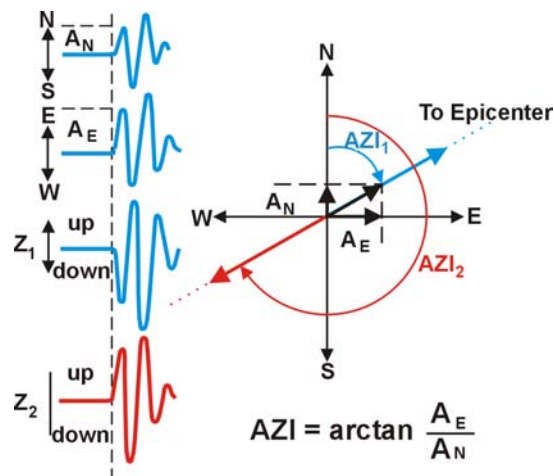


Figure 1 Principle of (back)azimuth determination from P-wave first-motion amplitudes.

3.3 Event location using the estimated epicentral distance D and backazimuth AZI

- You may use a sufficiently large globe (diameter about 0.5 to 1 m), mark there the position of your station and then use a bendable ruler with the same scale in degree as your globe and an azimuth dial to find your event location on the globe.
- Another possibility is that you get a regional (Figure 5) or global map projection (Figure 6) which shows isolines of equal azimuth and distance from your station. Such maps can nowadays easily be calculated and plotted for any station with known co-ordinates together with the the seismicity pattern.

4 Tasks

4.1 Event No. 1 (record Figure 2)

4.1.1 Assess, whether the source was shallow (< 70 km) or deep (Look for surface waves!)

- Shallow source?
- Deep source?

4.1.2 Look for possible depth phases. Are there any clear depth phases?

- Yes?
- No?
- Comments on the possible depth range of the EQ if you suspect pP and/or sP to arrive in the complex wave group after P?

4.1.3 If you do not find any clear depth phases use the differential travel-time curve in Figure 4 (which is for surface foci), and try to identify the principal phases in the vertical and horizontal component record.

- Which phases have you identified?
- Give reasons for your interpretation?

4.1.4 Match your differential travel-time curve with your identified phases. Read the distance D for your best fit and write it down:

- $D = \dots\dots^\circ$

4.1.5 Determine the backazimuth AZI from the amplitude ratio A_E/A_N using the equation given in Figure 1 and taking into account the related explanations given in 3.2.

- $AZI = \dots\dots^\circ$

4.1.6 Locate the epicenter on the map given in Figure 5.

- Source region?
- Discussion?

4.2. Event No. 2 (record Figure 3)

4.2.1 Assess, whether the event was shallow (< 70 km) or deep by looking for possible surface waves in the full record, which is inserted at strongly compressed time scale.

- Shallow event?
- Deep event?

4.2.2 Look for possible depth phases. Are there any clear depth phases?

- Yes?
- No?
- Comments?

4.2.3 Measure the time difference (in min) between the P-wave first arrival and the five marked onsets of stronger secondary wave arrivals in the records. Note that 1 cm = 1 min. Write down the time differences X_i -P (in min) in the order of their appearance.

- $X1$ -P = , $X2$ -P = , $X3$ -P = , $X4$ -P = , $X5$ -P = ?

4.2.4 In order to match these travel-time differences with the differential travel-time curve presented in Figure 4 (time scale: 1.5 cm = 1 min!), multiply these differences with 1.5. Mark the respective distances to the P-wave onset on the edge of a sheet of paper, place the P-wave onset mark on the ordinate (distance scale) and try to match the later onset marks with the differential travel-time curves given in Figure 4. Read the distance D (in $^\circ$) for your best match of travel-time curves with as many as possible of your onset marks and identify the phases related to the later onsets (give phase names):

- D (CLL) = $\dots\dots^\circ$,
- $X1 = \dots\dots$, $X2 = \dots\dots$, $X3 = \dots\dots$, $X4 = \dots\dots$, $X5 = \dots\dots$
- Comments, which support your phase interpretations ?

4.2.5 Determine the backazimuth AZI as in task 4.1.5.

- AZI (CLL) = $\dots\dots^\circ$

4.2.6 Locate the event as in task 4.1.6 by using Figure 6

- Name of source region/country?

5 Solutions

Note: Your estimates for the travel-time differences should be within about 0.2 min, for D within 2° and for the backazimuth AZI within about 5° of the solutions given below.

Event No. 1:

- 4.1.1 The earthquake is deeper than 70 km because no surface waves have been recorded.
- 4.1.2 No clear depth phases recognizable. They might however arrive within the complex wave group, which follows within about 40 s after the P onset. The ISC gives a hypocenter depth $h = 111$ km and an epicentral distance $D = 20.24^\circ$ for station MOX. According to Table 1 pP should then arrive about 21 s and sP about 35 s after P. Therefore, the first two sharp recognizable onsets after P on the Z component record are most likely the depth phases pP and sP, not PP and PPP as shown in the simplified J-B-differential travel-time curve of Figure 4. According to more recent travel-time models such as IASP91 (see DS 2.1) PP and PPP proper appear only for $D \geq 30^\circ$.
- 4.1.3 You should have identified at least P (and probably PP and PPP or depth phases) on the Z component, the S wave as the largest onset on the E component, and SS (with longer period than S) on the N component.
- 4.1.4 $D \approx 20^\circ$ (the ISC gives for station MOX $D = 20.24^\circ$)
- 4.1.5 $AZI \approx 125^\circ$ (from P-wave first motion amplitudes)
 $AZI \approx 132^\circ$ (from P-wave maximum peak-to-trough amplitudes).
- 4.1.6 Using our results from 4.1.5 and the map in Figure 5 we locate the earthquake in the coastal area of **southern Turkey**. ISC gives the coordinated 36.46°N and 31.72°E . This is near the coast of southern Turkey. Locating a sub-crustal earthquake there makes sense, because the African Plate is sub-ducted underneath southern Turkey.

Event No. 2:

- 4.2.1 Shallow earthquake with strong surface waves in the insert, with A_{\max} after about 37 min.
- 4.2.2 No depth phases recognizable in the LP records (NEIC reported for this earthquake a hypocenter depth of $h = 19$ km).
- 4.2.3 $X1\text{-P} \approx 3.65$ min, $X2\text{-P} \approx 10.5$ min, $X3\text{-P} \approx 11$ min, $X4\text{-P} \approx 12.2$ min, $X5\text{-P} \approx 17$ min
- 4.2.4 • D (CLL) $\approx 93^\circ \pm 1^\circ$ for the best match of the travel-time differences given under 4.2.3 with the with the travel-time curve shown in Figure 4. NEIC-PDE gives for station CLL 92.6° .
- The identified phases are: $X1 = \text{PP}$, $X2 = \text{SKS}$, $X3 = \text{S}$, $X4 = \text{PS/SP}$, $X5 = \text{SS}$
 - Both SKS and PS are strongest in the horizontal component E where also P has its largest horizontal amplitude. At about the time of PS in N there appears also in Z a clear energy arrival (SP!). S arrives later than SKS and is strong in the N component only.
- 4.2.5 $AZI(\text{CLL}) \approx 270^\circ$ (first motion in N not visible! Recognizable P-wave first motion in the N component begins more than 6 s later than in the Z component!). NEIC-PDE gives for CLL $AZI = 272.3^\circ$.
- 4.2.6 Using the map in Figure 6 for station CLL gives the **source area** as **Ecuador**. NEIC-PDE gives as epicenter coordinates 0.59°S and 80.39°W , i.e., near coast of Ecuador. This is very close to our location.

Figure 2 (next page) 3-component record of a Kirnos BB-displacement seismograph at station MOX, Germany. The time scale is 15 mm/minute. All seismograph components have properly been calibrated and identical magnification.

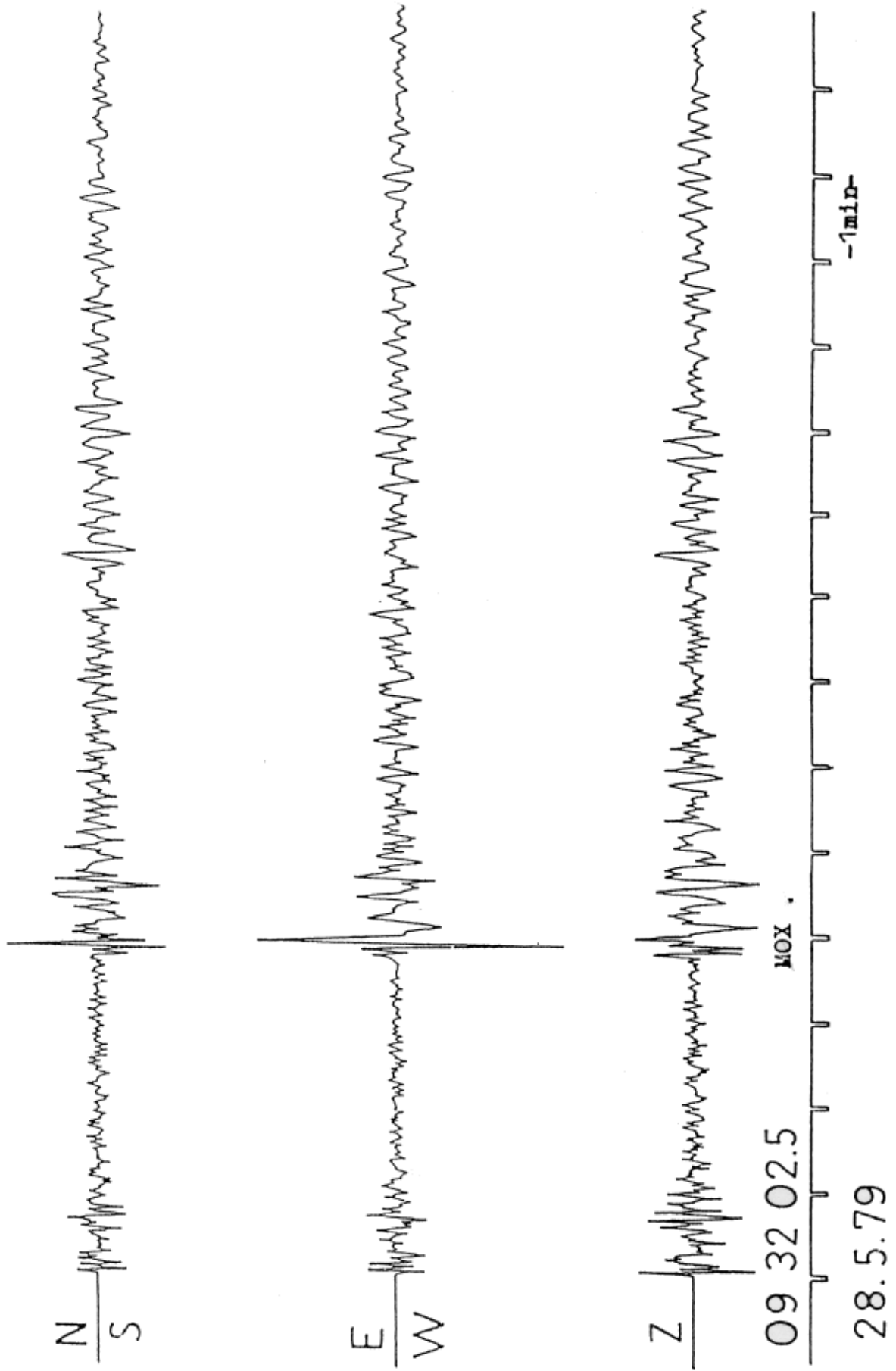


Figure 2

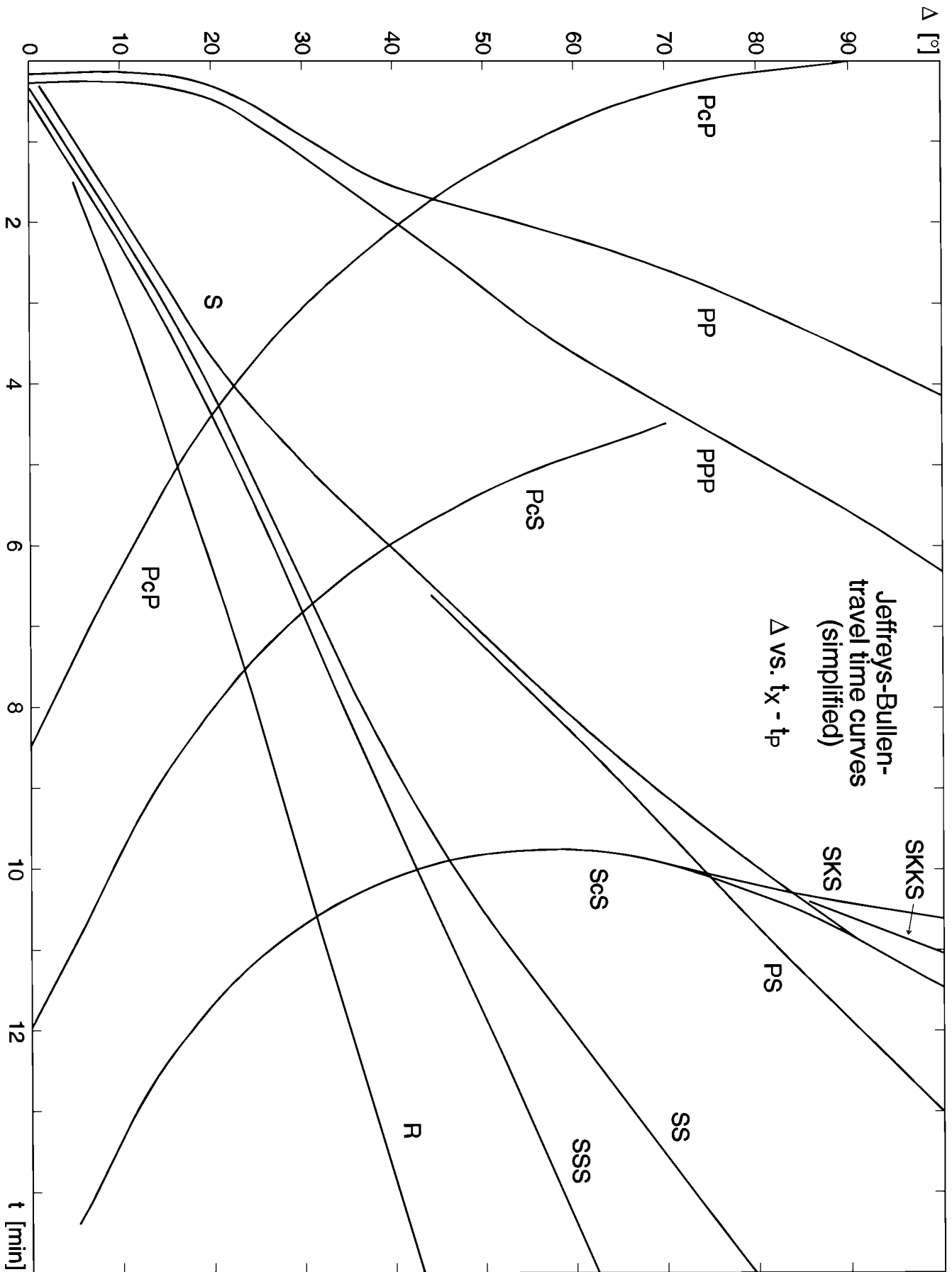


Figure 4 Simplified Jeffreys-Bullen differential travel-time curve in the distance range $0^\circ < D \leq 100^\circ$. Time scale: 15 mm = 1 min.

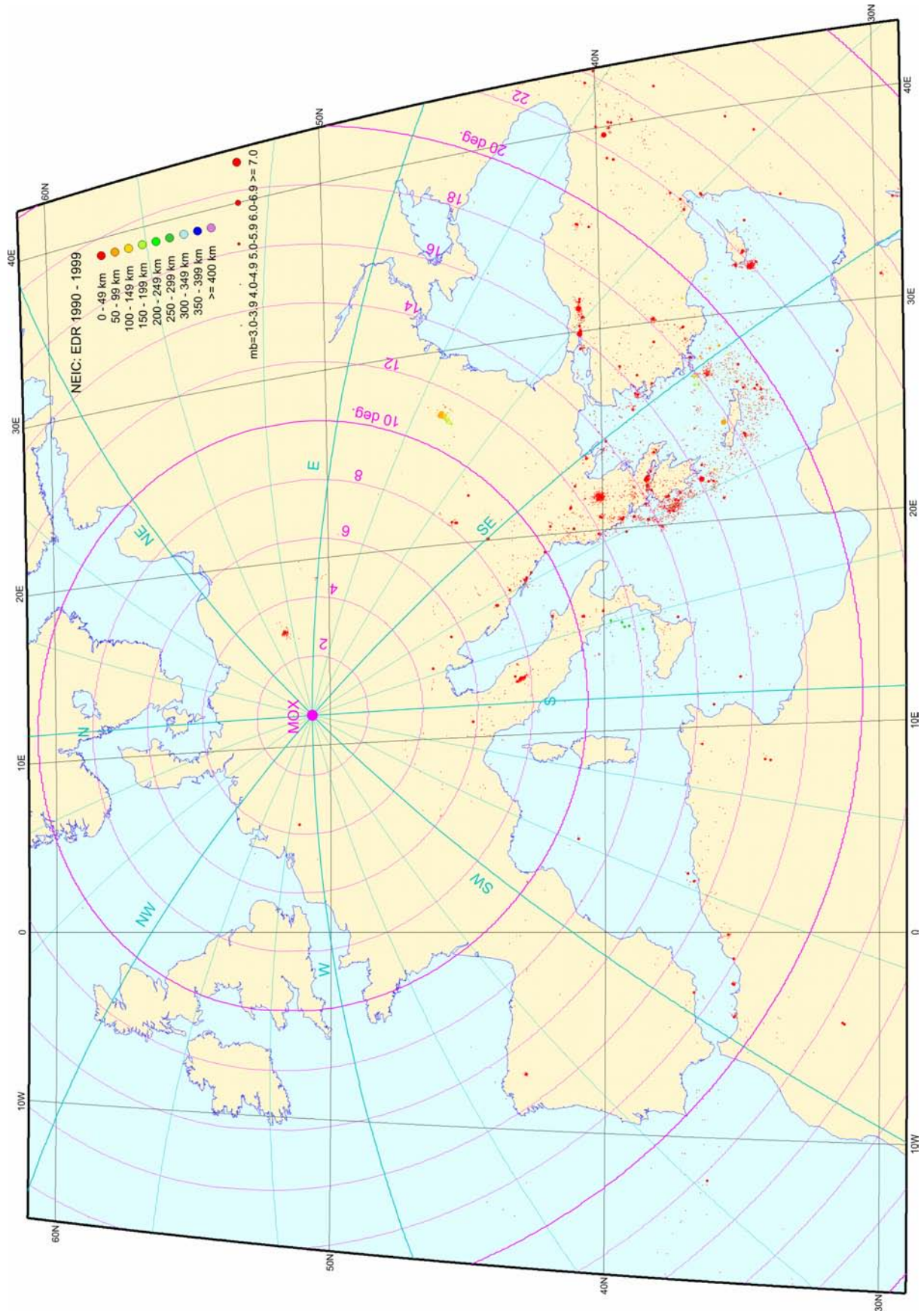


Figure 5 Regional map for Europe and the Mediterranean with earthquake epicenters and isolines of D and AZI with respect to station MOX.

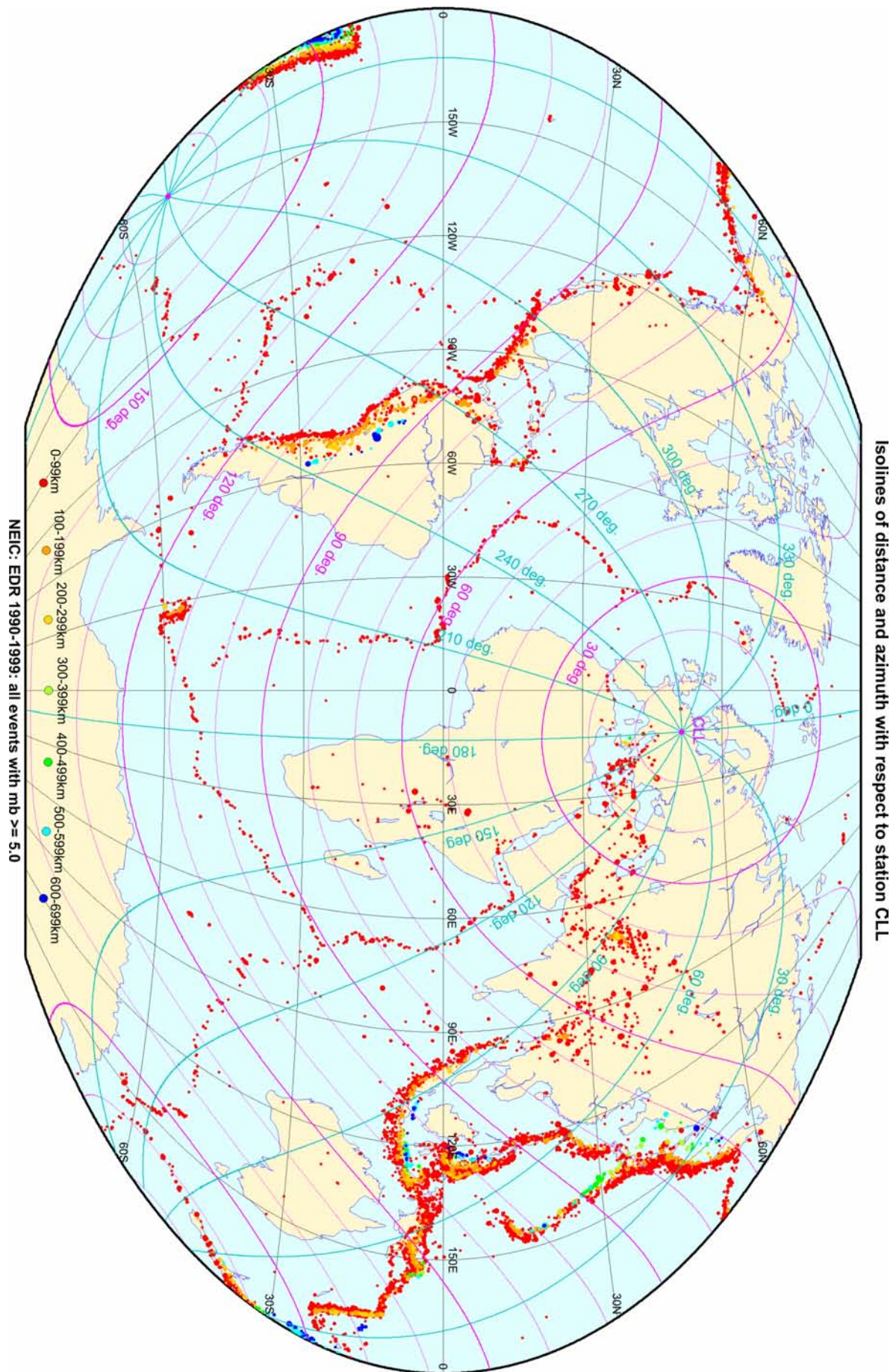


Figure 6 World map with epicenters and isolines of D and AZI with respect to station CLL.

Topic	Identification and analysis of short-period core phases
Authors	Peter Bormann (formerly GeoForschungsZentrum Potsdam, Telegrafenberg, D-14473 Potsdam, Germany); E-mail: pb65@gmx.net Siegfried Wendt, Universität of Leipzig, Institut für Geophysik und Geologie, Geophysikalisches Observatorium Collm, D-04779 Wermsdorf, Germany, E-mail: wendt@rz.uni-leipzig.de
Version	June 2002

1 Aim

This manual exercise aims at making you familiar with the identification of both direct and multiple-reflected longitudinal core phases and their use in location and magnitude determination. Clear short-period vertical component PKP seismograms of a single station contain all information needed to determine *source depth* h , *epicentral distance* D and *magnitude* m_b with an accuracy of ± 30 km, better $\pm 1.5^\circ$ and ± 0.3 magnitude units, respectively. In case of strong seismic sources and the availability of identically calibrated horizontal components with good signal-to-noise ratio, additionally the backazimuth to the source can be determined with an accuracy of about $\pm 5^\circ$ - 10° and thus the approximate location. Additionally, the identification of late reflected core phases and their use in distance determination is practiced. These phases are very suitable for calculating the epicentral distance since their relative travel-time difference to the related first arrival P or PKP is nearly independent of source depth.

2 Data

- Figure 1: Compilation of typical analog short-period recordings at station MOX, Germany, of the different direct core phases from earthquakes between $135^\circ < D < 160^\circ$;
- Figure 2: Plots of digital broadband records of the German Regional Seismograph Network (GRSN), filtered according to a WWSSN-SP response, from a Fiji-Island earthquake within the distance range 148.4° (CLL) to 152.2° (BFO);
- Figure 3: Three record examples with PKPab, bc and df phases to be analyzed;
- Figure 4: Four records with later longitudinal core phases to be evaluated;
- Figure 5: Travel times and paths of the direct longitudinal core phases and their relationship to the P-wave velocity model of the Earth;
- Figure 6: Ray path of the reflected core phases $P'P'$ (or PKPPKP) and PKKP;
- Figure 7: Differential travel-time curves pPKP-PKP for $D = 150^\circ$;
- Figure 8: Differential travel-time curves PKPbc-PKPdf (PKP1-PKIKP) and PKPab-PKPdf (PKP2-PKIKP);
- Figure 9: Differential travel-time curves PKKP-P and PKKP-PKP, respectively;
- Figure 10: Differential travel-time curves PKPPKP-P.
- Figure 11: Record with identified onsets.
- Figure 12: Magnitude calibration functions for PKPdf (old PKIKP), PKPbc (old PKP1) and PKPab (old PKP2).

Note 1: All differential travel-time curves given in this exercise have been calculated according to the earth model IASP91 (Kennett and Engdahl, 1991). The more recent model AK135 (Kennett et al., 1995) yields still better travel-times for core phases. The difference, however, is more significant for absolute and usually negligible for differential travel times.

Note 2: The first record example in Figure 1 illustrates that at $D < 145^\circ$ small amplitude precursors PKPpre of waves scattered from the core-mantle boundary (CMB) may occur. In the case of crustal earthquakes PKPdf may additionally be followed closely by depth phases. Together this may mimic a core phase triplication typical for $D > 146^\circ$. Yet, in the case of deep earthquakes with sharp onsets and no or small signal coda, the triple group of phases is usually rather distinct and its typical pattern easily recognizable.

Note 3: The typical three-phase pattern PKPdf (alternative name PKIKP), PKPbc (old name PKP1) and PKPab (old name PKP2) is however well developed between $146^\circ < D < 155^\circ$ only. Around 145° all three phases arrive at the same time and thus superpose to a rather strong impulsive onset.

Note 4: Beyond 154° still a weak intermediate phase between PKPdf and PKPab may be observed up to about 160° along the extrapolation of the PKPbc travel-time branch. It is, however, not PKPbc proper but rather the phase PKPdif which is diffracted around the inner-core boundary (see last record example in Figure 1).

Note 5: In the last record example of Figure 1 the well developed depth phase obviously relates to the strongest direct phase PKPab (old PKP2). The depth phases pPKP may, in the case of maximum possible source depth around 700 km, follow the related direct phases after up to about 2.5 minutes. When the primary core phases are rather strong, two or three related depth phases may be discernable.

Note 6: More examples based on plots from digital seismic records are given in DS 11.3.

Additionally, for the magnitude determinations, measured trace amplitudes have to be converted into ground motion amplitudes. For this the frequency dependent amplitude-magnification of the seismograph has to be known. It is given in Table 1.

Table 1 Magnification MAG of ground displacement in the seismic records of earthquakes No. 1, 2 and 3 in Figure 3 when these are reproduced with a time scale of 1 mm/s.

Period (in s)	0.9	1.0	1.1	1.2	1.3	1.4	1.6	1.8	2.0	2.4
MAG Event 1		52,440		49,210		44,090	37,550	30,660	24,420	14,000
MAG Event 2		26,220		24,600		22,040	18,770	15,330	12,210	7,000
MAG Event 3	62,020	56,000	49,980	43,960	37,940					

3 Procedure

All steps of determining h , D , AZI and mb will be practiced.

Source depth and **epicentral distance** are determined by reading the relative onset-time difference in seconds or minutes, respectively, between identified phases and using the corresponding differential travel-time curves. Note that these curves in Figures 7 and 8 have been presented with the same time-resolution as the analog records in Figure 3, i.e. with 1

mm/s. If a transparent overlay is produced from these curves, the source depth and the epicentral distance, respectively, from the records depicted in Figure 3 can be directly determined by matching the related curves with the identified onsets. Make sure that the depth and distance axes, respectively, are kept perpendicular to the center line of the record trace when matching. When reading the time differences PKKP-P and P'P'-P in Figure 4 be aware, that the time difference between subsequent traces from top to bottom is 15 minutes. Full minutes start at the left side of the 2 second long gaps or „faintings“ on the record traces.

The **backazimuth** is determined according to the instructions given under 3.2 in EX 11.2.

For epicenter **location** based on the estimated epicentral distance D and the backazimuth AZI one may use either a sufficiently large globe (diameter about 0.5 to 1 m), mark there the position of the considered station and then use a bendable ruler with the same scale in degree as your globe and an azimuth dial to find the source location on the globe. Another possibility is to use a global map projection which shows isolines of equal backazimuth and distance from your station (as Figure 5 in EX 11.2). Such maps can nowadays easily be calculated and plotted by means of computers.

The **magnitude mb(PKP)** is determined according to an experimental calibration function for magnitude determinations based on short-period readings of various PKP phases in the distance range 145° to 164° . It has been developed by S. Wendt (Bormann and Wendt, 1999). Its world-wide testing is recommended. The following relationship is used:

$$mb(\text{PKP}) = \log_{10} (A/T) + Q(\Delta, h)_{\text{PKP}} \quad (1)$$

with amplitude A in μm (10^{-6} m). If more than one PKP phase PKPab, PKPbc and/or PKPdf can be identified and A and T been measured then the individual phase magnitudes should be determined first and then the average magnitude be calculated. The latter provides a more stable estimate.

4 Tasks

- 4.1 Train yourself first by matching the travel-time curve overlay of Figure 8 with the onsets marked in Figure 1, taking into account the distance and focal depth given for each earthquake. Also consult Figure 2 and the related notes 1 to 6 in section Data above. Then mark on the records in Figure 3 for all three earthquakes the onset times of recognizable phases and give them names, both for the early and the late arrivals (depth phases).
- 4.2 Measure the time difference pPKP-PKP for the strongest PKP arrival and its respective depth phase and determine the source depth for all three earthquakes by using the differential travel-time curves given in Figure 7. Note: If the pPKP group is less distinct and its different onsets can not be well separated then relate the depth phase to the strongest direct PKP arrival.
- 4.3 Determine the epicentral distance D (in $^\circ$) of the three earthquakes shown in Figure 3 by using the differential travel-time curves shown in Figure 8 taking into account for each event the source depth determined under 4.2.
- 4.4 Measure the time difference between the P-wave first arrivals and the PKKP or P'P'phases marked in the four records presented and determine the epicentral distance D

for these earthquakes by using the differential travel-time curves shown in Figures 9 and 10, respectively.

- 4.5 Estimate from the three-component record in Figure 3 (event No. 3) for the strongest phase the backazimuth AZI according to relationship and instructions given under 3.2 of EX 11.2.
- 4.6 Try to find for event No. 3, which had been recorded at the station CLL in Germany, the source location on the map shown in Figure 5 of EX 11.2. Give the name of the source area.
- 4.7 Measure the trace amplitudes B (in mm) and related periods T for all identified phases of direct PKP in Figure 3 and convert them into “true ground motion” amplitudes A (in nm) by means of Table 1 given above in section Data.
- 4.8 Determine $\log(A/T)$ and estimate the related values for $\sigma(D, h)$ from Figure 12. Note that these values are valid for amplitudes in μm only! Correct them for nm.
- 4.9 Give the individual magnitude estimates for PKPab, PKPbc and PKPdc,
- 4.10 Calculate the average $\bar{m}_b(\text{PKP})$.
- 4.11 Compare your results with the respective solutions given by the NEIC for these three earthquakes and assess the achievable accuracy of respective individual source parameter calculations at single stations, even when based on analog recordings only and simple analysis tools.

5 Solutions

5.1 See Figure 11.

5.2 NEIC gave for the three earthquakes the following hypocentral depths:

- | | |
|-------|----------------------|
| No. 1 | $h = 435 \text{ km}$ |
| No. 2 | $h = 235 \text{ km}$ |
| No. 3 | $h = 540 \text{ km}$ |

Your own depth estimates should be within about $\pm 30 \text{ km}$ of these values. But this does not mean that your value is worse than that given by NEIC. It may be even better, because NEIC mostly does not use depth phases to constrain its solutions from direct P-wave readings.

5.3 NEIC calculated for the stations which recorded the three earthquakes in Figure 3 the following epicentral distances $\Delta = D$ (in $^\circ$):

- | | |
|-------|-------------------|
| No. 1 | $D = 148.5^\circ$ |
| No. 2 | $D = 159.5^\circ$ |
| No. 3 | $D = 150.3^\circ$ |

Using the recommended travel-time curves, your estimates should be within $\pm 1.5^\circ$ of these values.

5.4 NEIC calculated for the station CLL which had recorded the earthquakes shown in Figure 4 the following epicentral distances:

- | | |
|-------|------------------|
| No. 1 | $D = 98.5^\circ$ |
|-------|------------------|

- No. 2 $D = 111.2^\circ$
 No. 3 $D = 66.3^\circ$
 No. 4 $D = 55.3^\circ$

Using the recommended travel-time curves, your estimates should be within $\pm 1.5^\circ$ to NEIC.

5.5 $AZI \approx 22^\circ$. Your own estimate should be within $\pm 5^\circ$ of this value.

5.6 Fiji Islands

5.7 Event No. 1: PKPdf	$B = 0.5 \text{ mm}, T = 1.5 \text{ s} \rightarrow A = 12.2 \text{ nm}$
PKPbc	$B = 3.9 \text{ mm}, T = 1.0 \text{ s} \rightarrow A = 74.4 \text{ nm}$
PKPab	$B = 3.0 \text{ mm}, T = 1.0 \text{ s} \rightarrow A = 57.2 \text{ nm}$

Event No. 2: PKPdf	$B = 2.9 \text{ mm}, T = 2.4 \text{ s} \rightarrow A = 414.3 \text{ nm}$
PKPab	$B = 8.2 \text{ mm}, T = 2.0 \text{ s} \rightarrow A = 671.6 \text{ nm}$

Event No. 3: PKPdf	$B = 0.95 \text{ mm}, T = 1.3 \text{ s} \rightarrow A = 21.6 \text{ nm}$
PKPbc	$B = 20.4 \text{ mm}, T = 1.0 \text{ s} \rightarrow A = 329.0 \text{ nm}$
PKPab	$B = 6.5 \text{ mm}, T = 1.0 \text{ s} \rightarrow A = 116.1 \text{ nm}$

5.8 Event No. 1: PKPdf	$\log(A/T) = 0.9$	$\sigma_{\text{PKPdf}}(\Delta, h) = 3.95$
PKPbc	$\log(A/T) = 1.89$	$\sigma_{\text{PKPbc}}(\Delta, h) = 3.15$
PKPab	$\log(A/T) = 1.76$	$\sigma_{\text{PKPab}}(\Delta, h) = 3.39$

Event No. 2: PKPdf	$\log(A/T) = 2.24$	$\sigma_{\text{PKPdf}}(\Delta, h) = 3.8$
PKPab	$\log(A/T) = 2.53$	$\sigma_{\text{PKPab}}(\Delta, h) = 3.55$

Event No. 3: PKPdf	$\log(A/T) = 1.22$	$\sigma_{\text{PKPdf}}(\Delta, h) = 3.94$
PKPbc	$\log(A/T) = 2.52$	$\sigma_{\text{PKPbc}}(\Delta, h) = 3.23$
PKPab	$\log(A/T) = 2.06$	$\sigma_{\text{PKPab}}(\Delta, h) = 3.55$

5.9 Event No. 1: $mb(\text{PKPdf}) = 4.85$; $mb(\text{PKPbc}) = 5.04$; $mb(\text{PKPab}) = 5.15 \rightarrow \overline{mb(\text{PKP})} = 5.0$
Event No. 2: $mb(\text{PKPdf}) = 6.0$; $mb(\text{PKPab}) = 6.1 \rightarrow \overline{mb(\text{PKP})} = 6.0$
Event No. 3: $mb(\text{PKPdf}) = 5.19$; $mb(\text{PKPbc}) = 5.75$, $mb(\text{PKPab}) = 5.61 \rightarrow \overline{mb(\text{PKP})} = 5.5$

5.10 NEIC gave for these three events, based on teleseismic P-wave readings only:

- Event No. 1: $mb = 5.0$,
 Event No. 2: $mb = 5.5$,
 Event No. 3: $mb = 5.3$

5.11 Using the calibration curves for PKP waves one can get quick mb estimates from readings of PKP amplitudes at individual stations with simple analysis tools which are within about ± 0.5 magnitudes units to the mb estimates of global seismological services. Your distance estimates should also be within $\pm 1.5^\circ$ even when using only low-resolution analog data and visual time picks. The general source area can be determined properly, even for very distant events, on the basis of properly mutually calibrated 3-component recordings of single seismic stations.

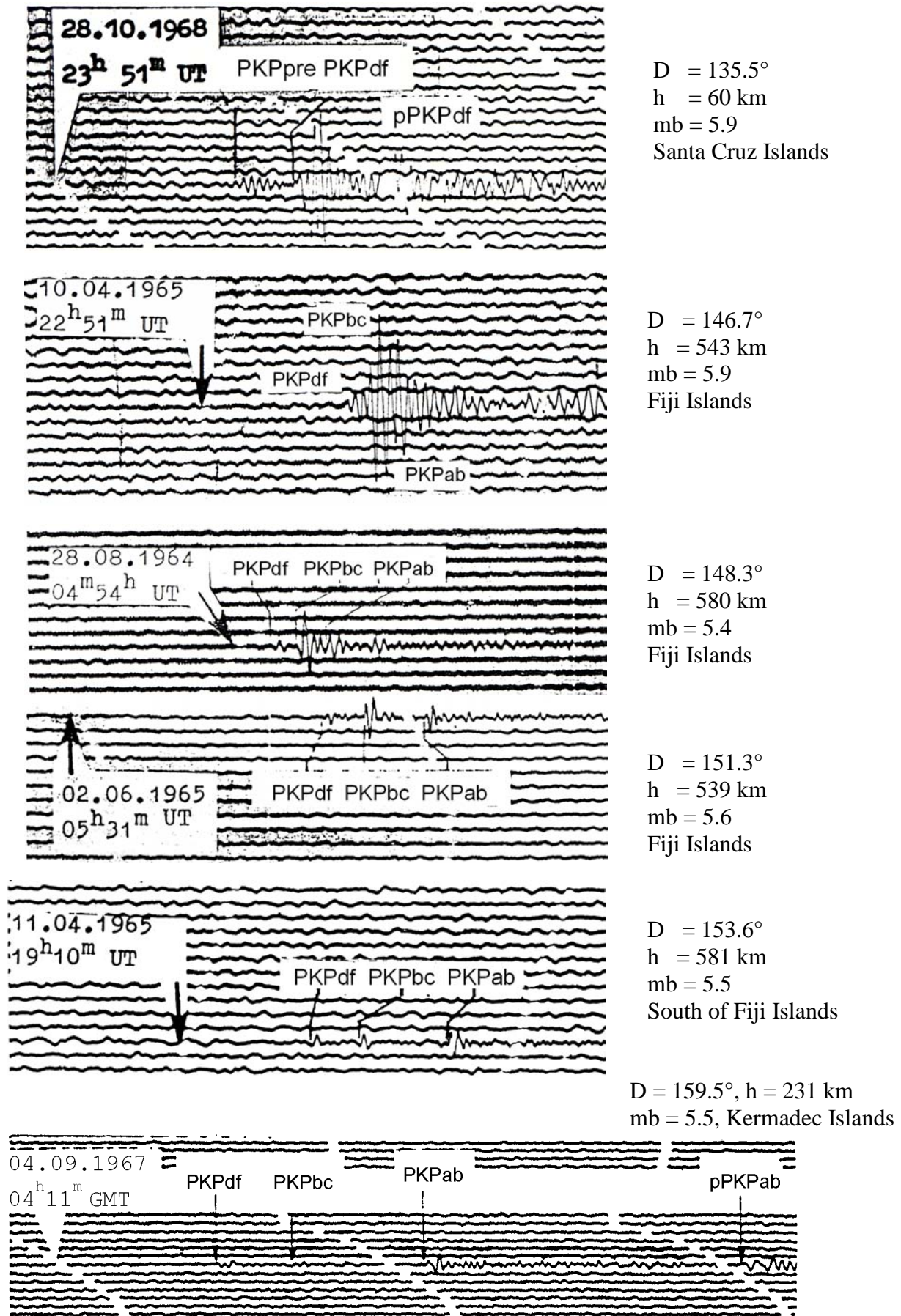


Figure 1 Examples of short-period analog records of stations CLL and MOX of longitudinal core phases in the distance range $135^\circ < D < 160^\circ$. Time scale: 1 mm/s on all records.

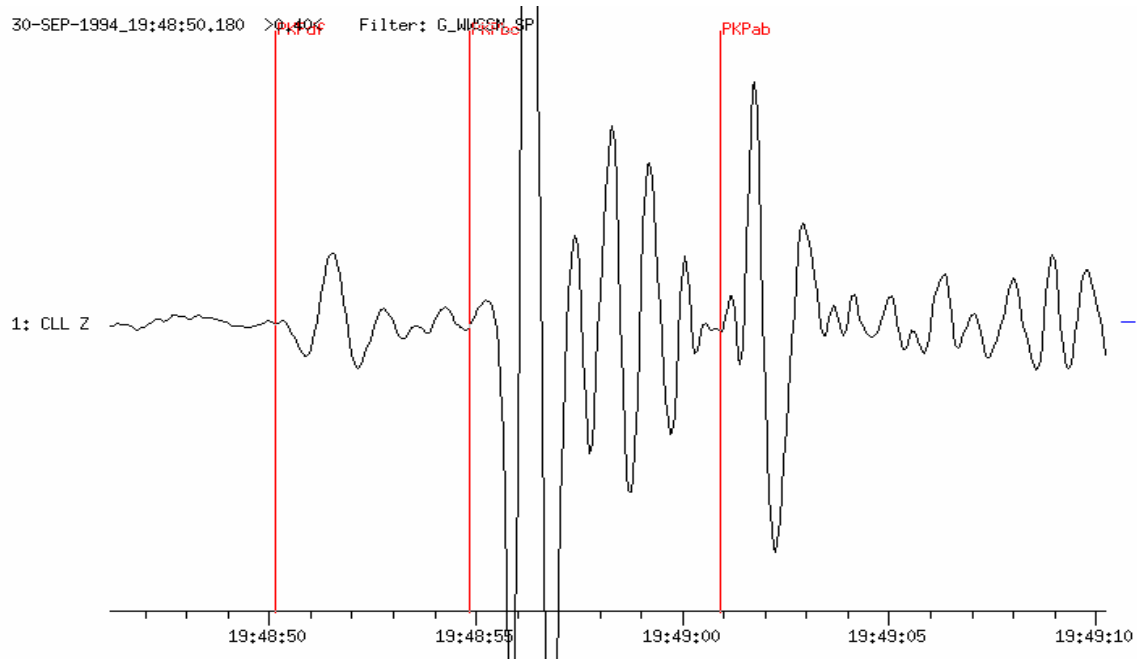
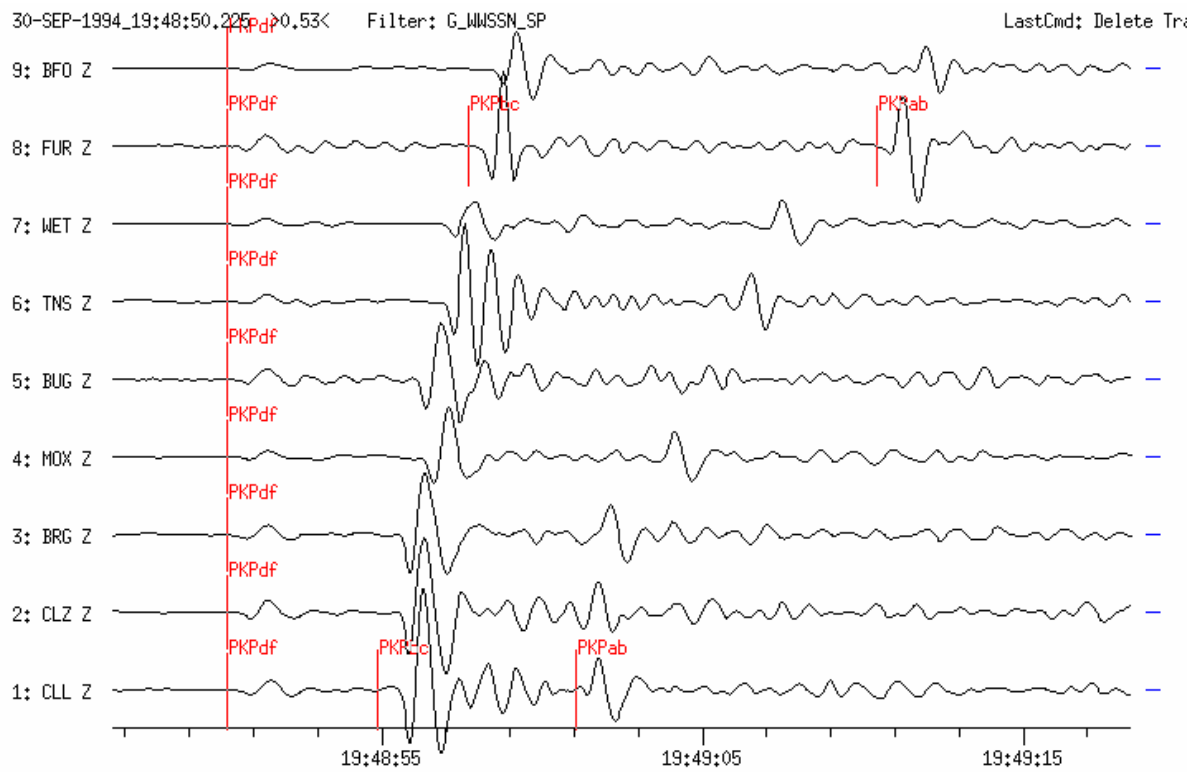


Figure 2 Top: Short-period filtered seismograms (WSSN_SP simulation) recorded at 9 GRSN stations from a deep earthquake in the Fiji Islands (Sept. 30, 1994, $m_b = 5.1$, $h = 643$ km). All traces are time-shifted and aligned with respect to PKPdf and sorted according to epicentral distance D which is 148.4° for CLL and 152.2° for the most distant station BFO. **Bottom:** The same trace of station CLL as above but with enlarged amplitude and time resolution.

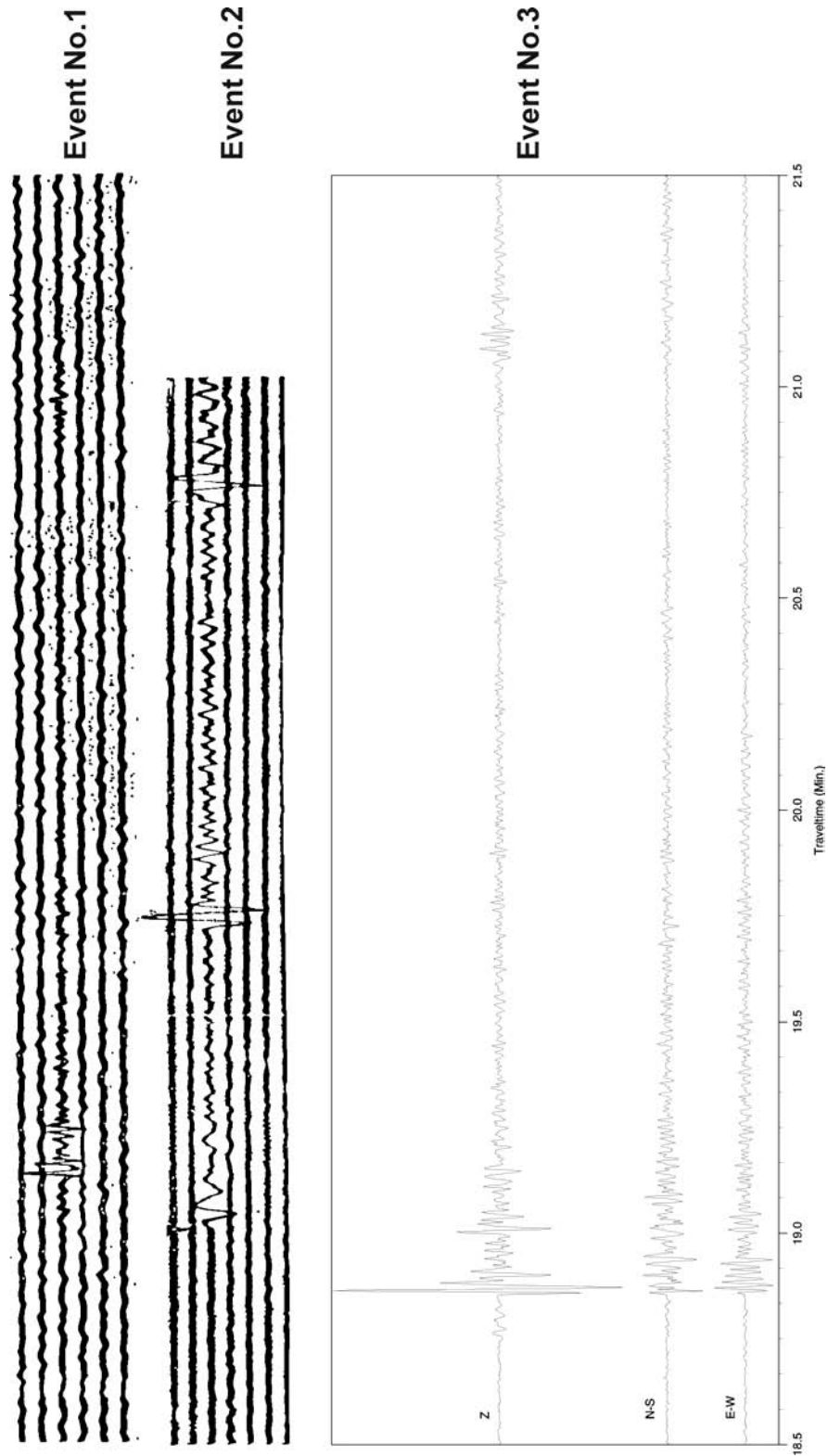
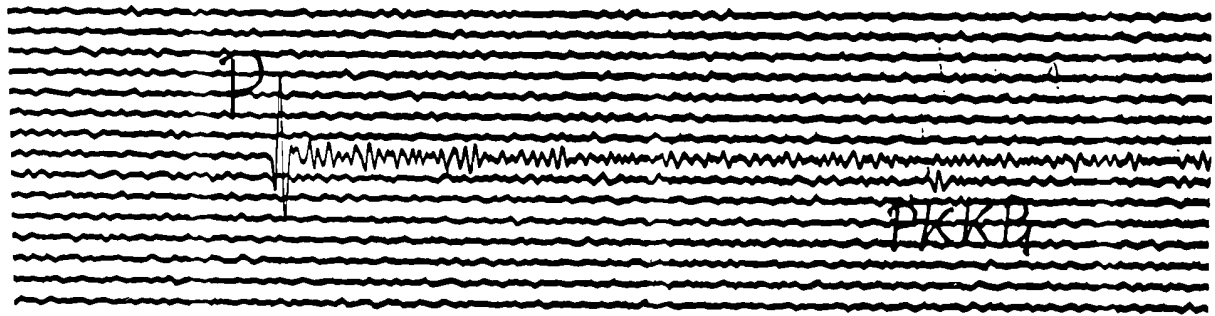
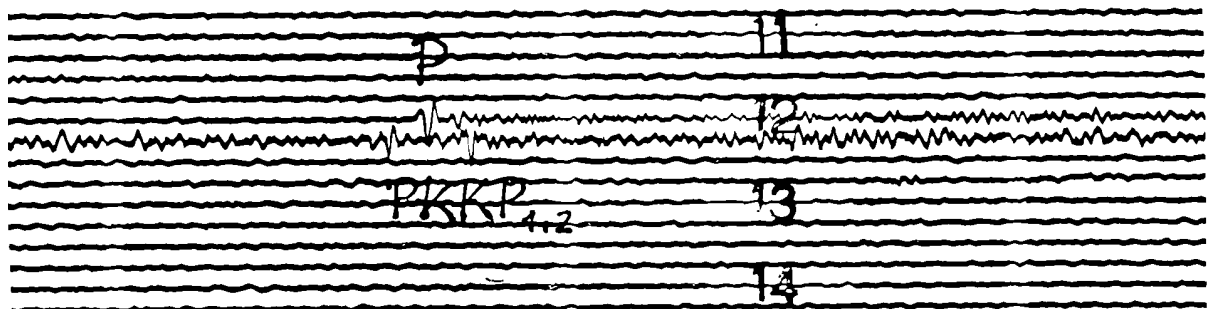


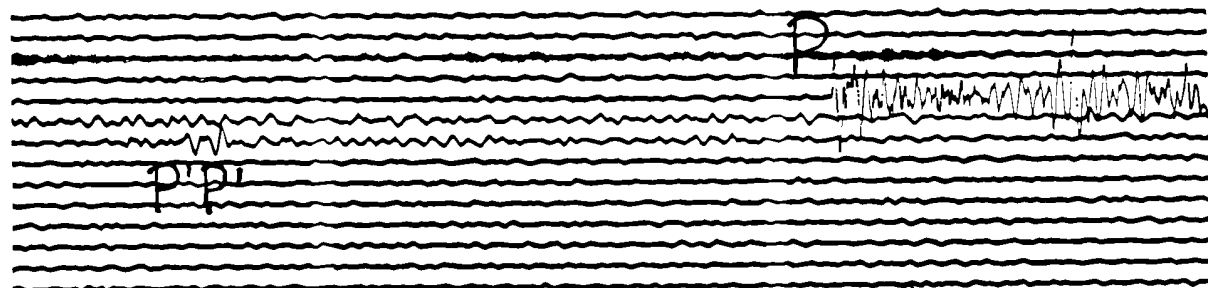
Figure 3 Short-period records of direct longitudinal core phases from three earthquakes. Time scale: 1 mm/s.



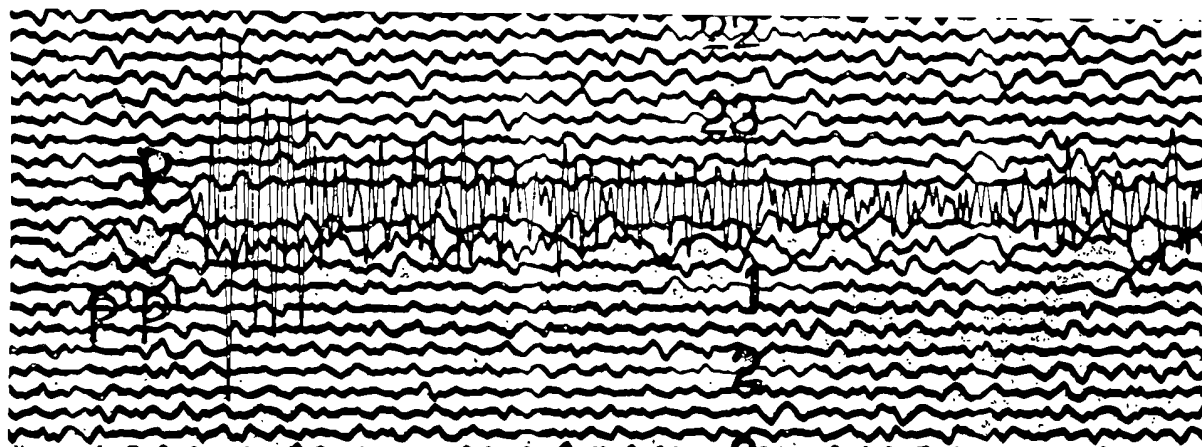
24.08.1995 Mariana Islands: H = 01:55:34.4, D(CLL) = ° ?, h = 588 km, m_b = 6.0



13.07.1994 Banda Sea: H = 11:45:23.4, D(CLL) = ° ?, h = 159 km, m_b = 6.5



08.08.1994 Myanmar: H = 21:08:31.7, D(CLL) = ° ?, h = 122 km, m_b = 6.1



18.02.1996 North of Ascension Island: H = 23:49:27.8, D(CLL) = ° ?, h = 10 km, m_b = 6.3

Figure 4 Records of station CLL of later reflected longitudinal core phases (PKKP and P'P').

Ray paths and travel-time curves of core phases PKIKP, PKP1, PKP2

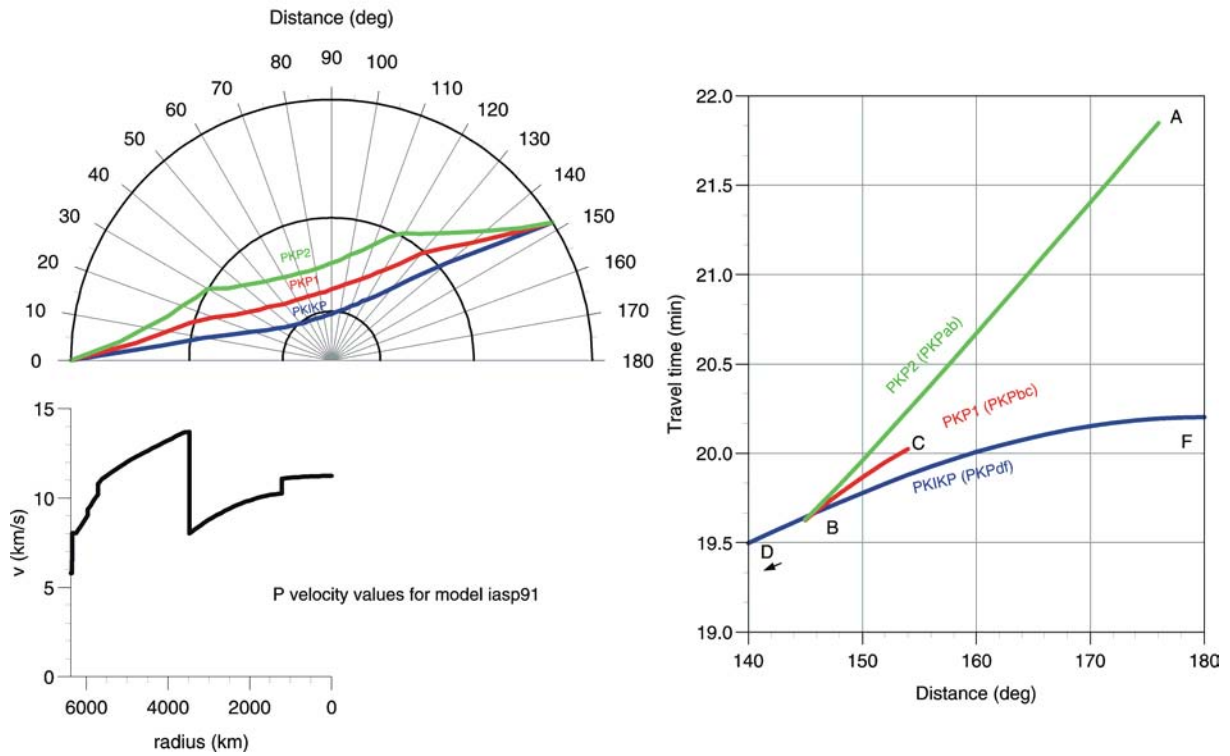


Figure 5 Ray paths and travel-time curves of direct longitudinal core phases for $D > 140^\circ$ according to the velocity model IASP91 (Kennett, 1991).

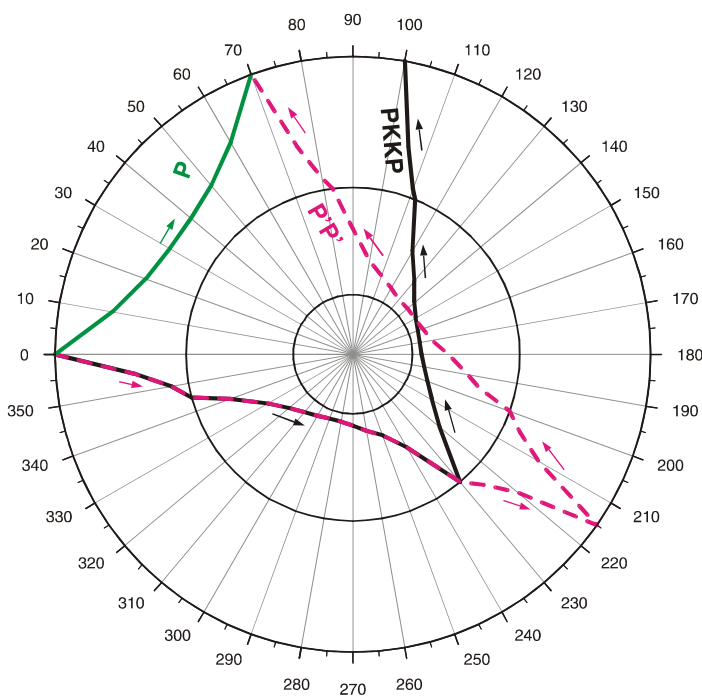


Figure 6 Ray paths of the reflected core phases $P'P'$ (or $PKPPKP$) and $PKKP$, respectively.

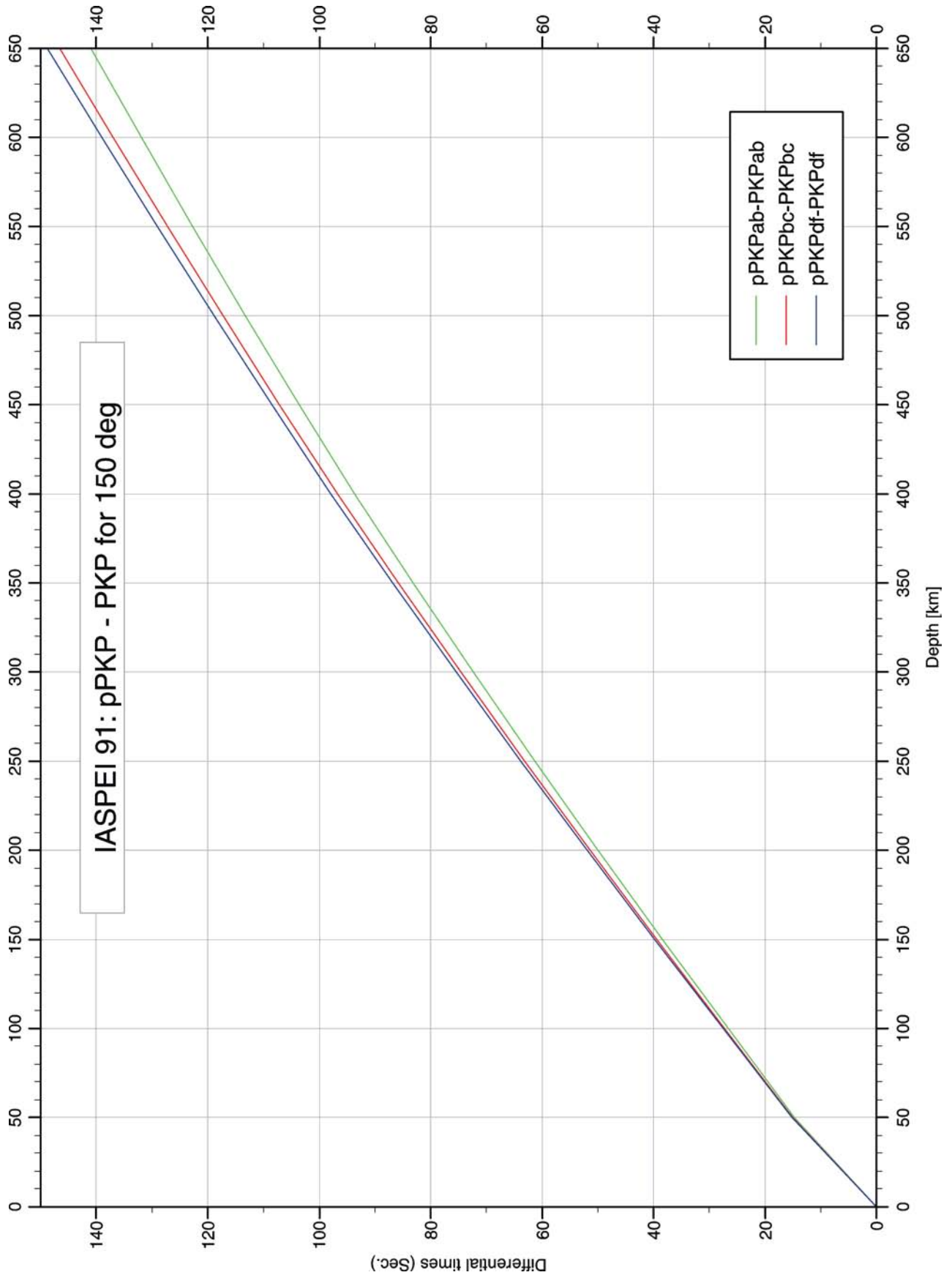


Figure 7 Travel-time differences between the PKP arrivals for the branches ab, bc and df, respectively, and their related depth phases at an epicentral distance of $D = 150^\circ$.

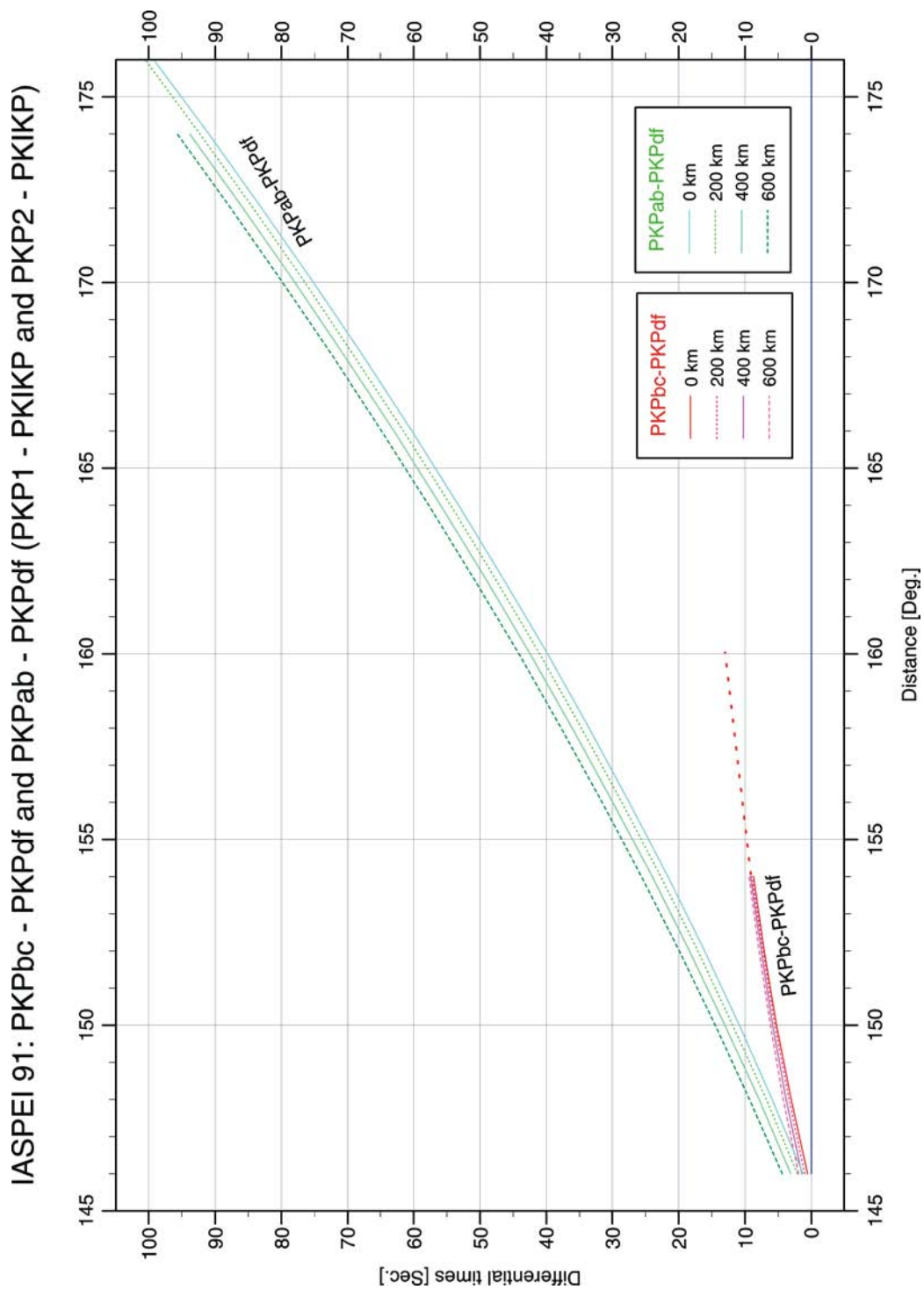


Figure 8 Travel-time differences between the PKPdf first arrival and the later arrivals PKPbc and PKPab, respectively, for different source depths. The dotted continuation of the branch PKPbc-PKPdf relates to the approximate differential arrival time of the weak phase PKPdif (PKP diffracted around the inner-core boundary).

PKKP - P and PKKP - PKP

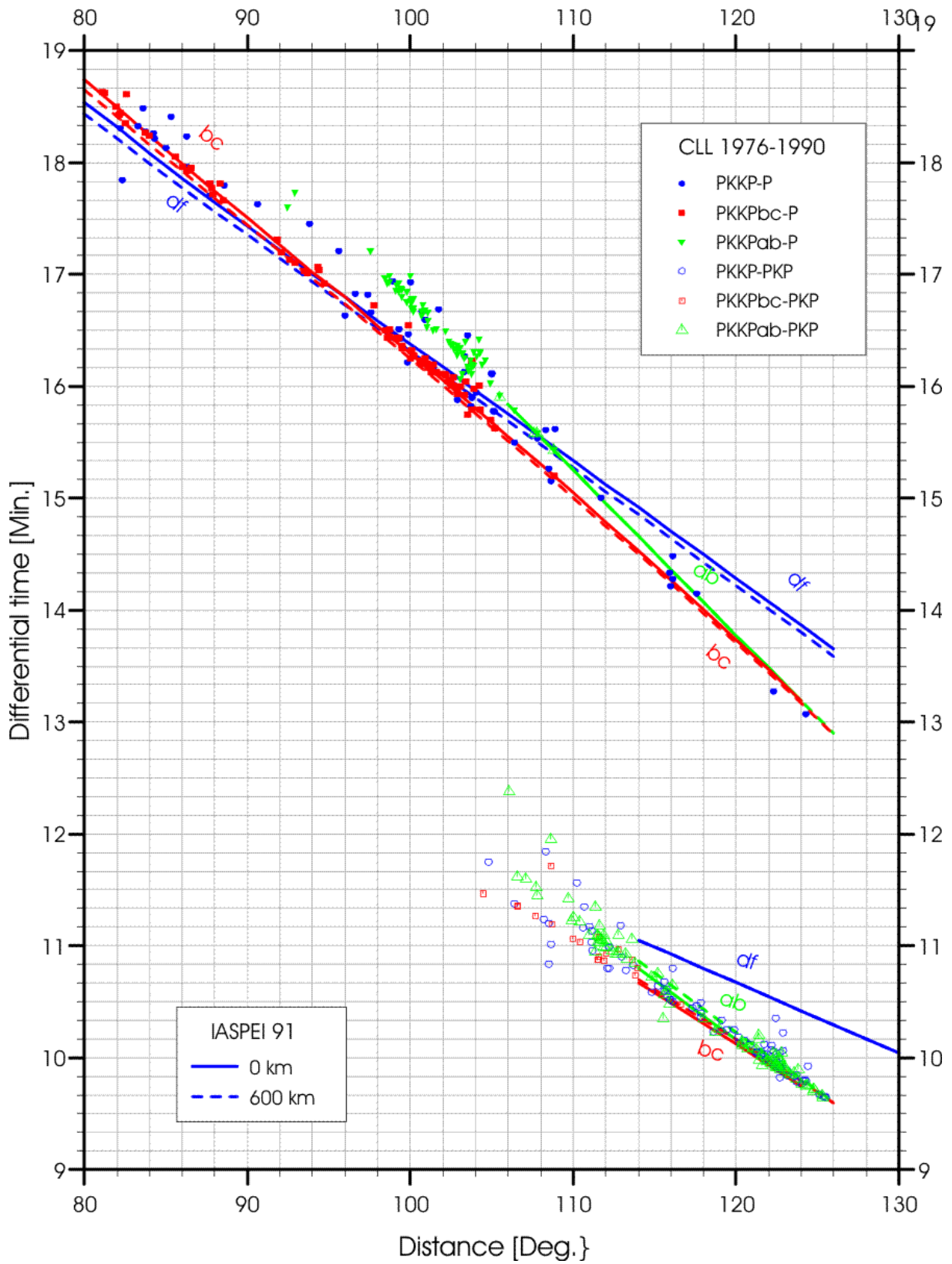


Figure 9 Comparison between theoretical (IASPEI 91) and observed travel-time differences for PKKP-P and PKKP-PKP at station CLL as a function of epicentral distance and source depth.

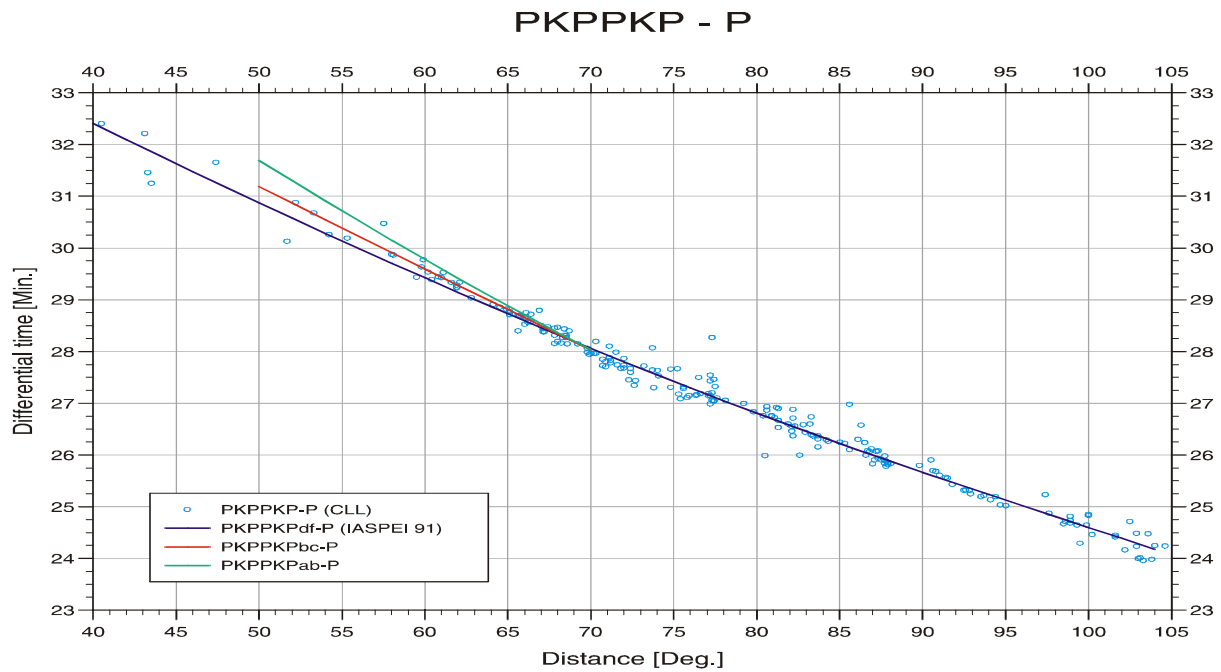


Figure 10 Comparison between theoretical (IASP91) and observed travel-time differences PKPPKP - P at station CLL depending on epicentral distance.

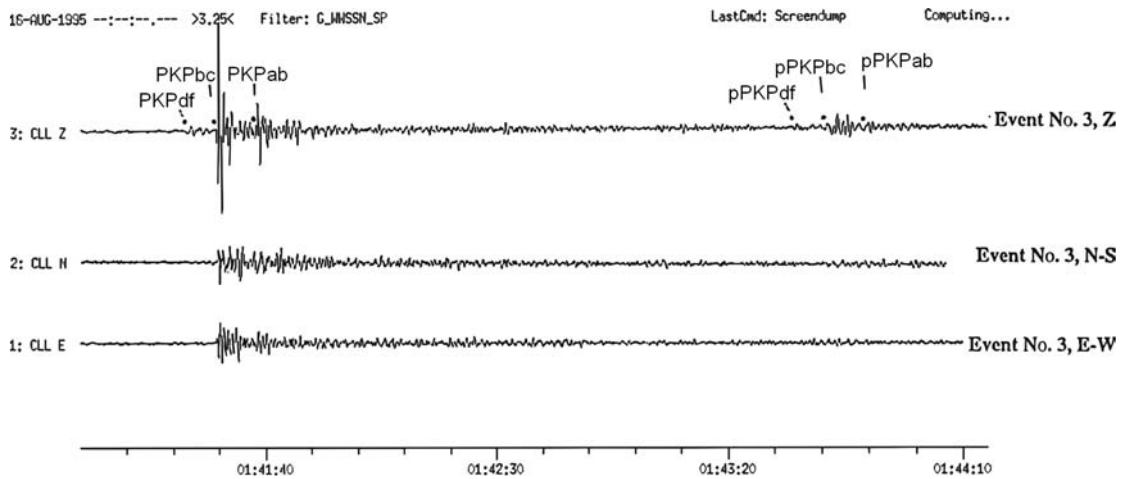


Figure 11 Reproduction of the records of event No. 3 with onsets (dots) marked and names of identified phases given on the vertical component. Only the onset of the depth phase PKPbc can be picked without any doubt. However, when taking the time differences between the three direct phases from the beginning of the record into account one recognizes prior and after pPKPbc changes in the waveforms just at the same time differences as for the primary phases. In the records of earthquakes No. 1 and No. 2 in Figure 3 only the depth phases pPKPbc and pPKPab can be picked at about 119 s and 60 s after PKPbc and PKPab, respectively.

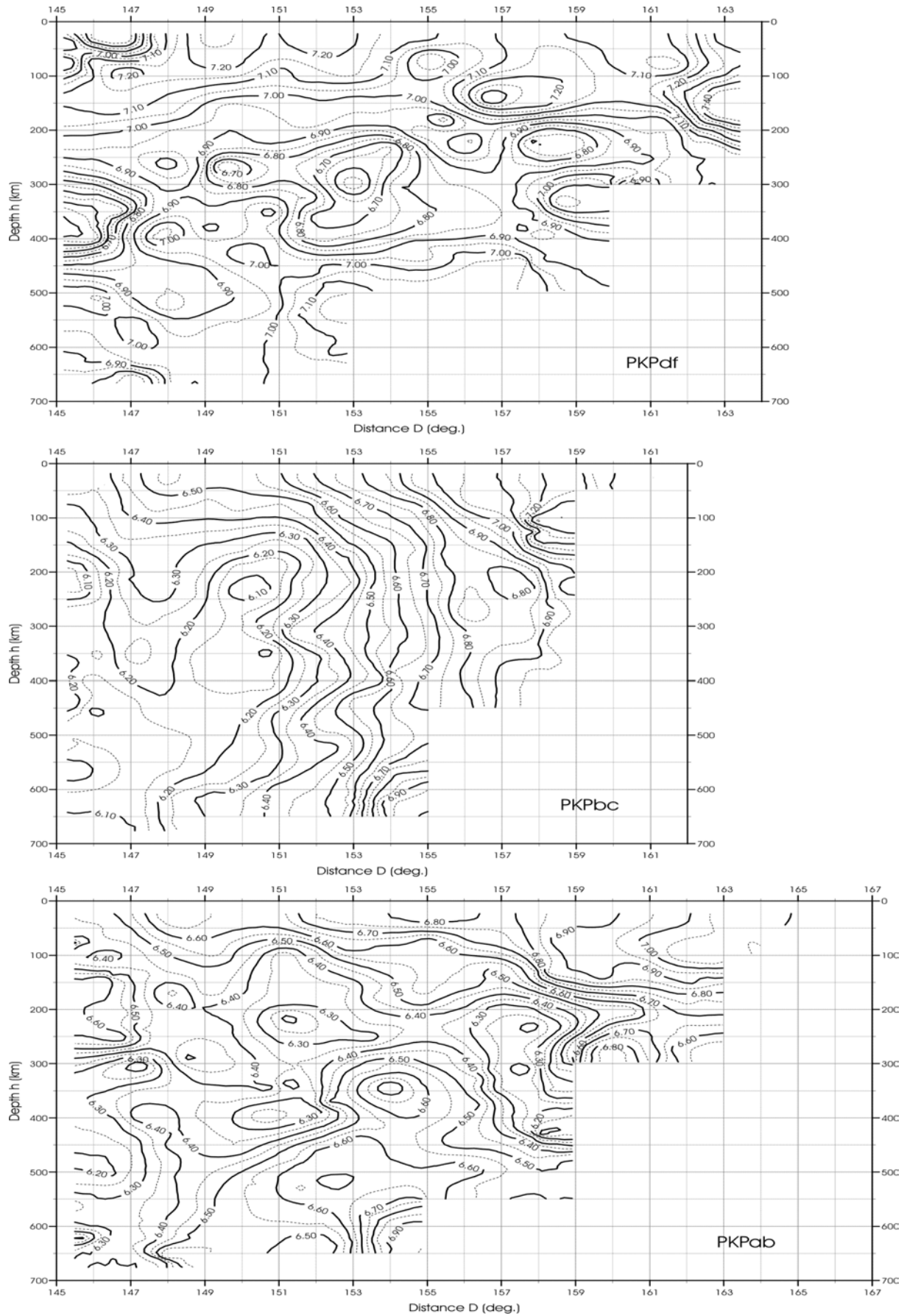


Figure 12 Calibration functions according to S. Wendt for the determination of mb(PKP) for PKIKP = PKPdf, PKP1 = PKPbc and PKP2 = PKPab (cf. Bormann and Wendt, 1999).

Topic	Standard nomenclature of seismic phases
Authors	Dmitry A. Storchak, International Seismological Centre, Pipers Lane, Thatcham, Berkshire RG19 4NS, UK, England, E-mail: dmitry@isc.ac.uk Peter Bormann (formerly GeoForschungsZentrum Potsdam, Telegrafenberg, D-14473 Potsdam, Germany); E-mail: pb65@gmx.net Johannes Schweitzer, NOR SAR, P.O. Box 53, N-2027, Kjeller, Norway, E-mail: johannes@norsar.no
Version	October 2002

1 Introduction

At its meeting in Hanoi, August 23, 2001, the IASPEI Commission on Seismological Observation and Interpretation decided to set up a Working Group on Standard Phase Names, chaired by D. A. Storchak of the ISC. Members of the group were R. D. Adams, P. Bormann, R. E. Engdahl, J. Havskov, B. L. N. Kennett and J. Schweitzer. The working group has put together a modified standard nomenclature of seismic phases, which was meant to be concise, consistent and self-explanatory on the basis of agreed rules. We did not try to create a complete list of all phases. The list is open for further development. The list is not meant to satisfy specific requirements of seismologists to name various phases used in a particular type of research. Instead, the new phase list aims at inviting data analysts and other users to ensure an expanded standardized data reporting and exchange. This will result in a broader and unambiguous database for research and practical applications. At the same time the attached list and its principles outlined below may be a useful guidance when proposing names to previously unknown seismic phases.

The new nomenclature partially modifies and complements the earlier one published in the last edition of the Manual of Seismological Observatory Practice (Willmore, 1979) and every year in the January issue of the seismic bulletins published by the ISC. It is more in tune with phase definitions according to modern Earth and travel-time models (see 2.7) and the definition of pronounced travel-time branches, of core phases in particular (see manual sections 11.5.2.4 and 11.5.3). As opposed to former practice, the WG tried to make sure that the phase name generally reflects the type of the wave and the path it has traveled. Accordingly, symbols for characterizing onset quality, polarity etc. will no longer be part of the phase name. Also, the WG acknowledges that there exist several kinds of seismic phases, crustal phases in particular, which are common in some regions but are not or only rarely found in other regions, such as e.g., Pb (P*), PnPn, PbPb, etc.. The names and definitions of acoustic and amplitude measurement phases are likely to be reviewed based on the results of recent developments in the data centers and new analysis practices being established.

The extended list of phase names as presented below in section 4 accounts for significantly increased detection capabilities of modern seismic sensors and sensor arrays, even of rather weak phases, which were rarely found on the classical analog records. It also accounts for improved possibilities of proper phase identification by means of digital multi-channel data processing such as frequency-wavenumber (f-k) analysis and polarization filtering, by modeling the observations with synthetic seismograms or by showing on the records the

theoretically predicted onset times of phases. Furthermore, limitation of classical formats for wave parameter reporting to international data centers, such as the Telegraphic Format (TF), which allowed only the use of capital letters and numbers, are no longer relevant in times of data exchange via the Internet. Finally, the newly adopted IASPEI Seismic Format (ISF; see 10.2.5 and IS 10.2) is much more flexible than the old formats accepted by the NEIC, ISC and other data centers. It also allows the reporting, computer parsing and archiving of phases with longer or up to now uncommon names. ISF also accepts complementary parameters such as onset quality, measured backazimuth and slowness, amplitudes and periods of other phases in addition to P and surface waves, for components other than vertical ones, and for non-standard response characteristics.

This increased flexibility of the parameter-reporting format requires improved standardization, which limits an uncontrolled growth of incompatible and ambiguous parameter data. Therefore, the WG agreed on certain rules. They are outlined below prior to the listing of standardized phase names. In order to ease the understanding of verbal definitions of the phase names, ray diagrams are presented in the last section. They have been calculated for local seismic sources on the basis of an average one-dimensional two-layer crustal model and for regional and teleseismic sources by using the global 1D-Earth model AK135 (Kennett et al., 1995; see also Fig. 2.53). Further examples of ray paths of typical seismic phases are presented in Fig. 2.42 and in various figures of Chapter 11. For polarization and amplitude features, phase and group velocities etc. of the various phases see Chapter 2.

Before elaborating short-cut seismic phase names one should agree first on the *language* to be used and its rules. As in any other language we need a suitable alphabet (here Latin letters), numbers (here Arabic numbers and + and - signs), an *orthography*, which regulates, e.g., the use of capital and lower case letters, and a *syntax*, i.e., rules of correct order and mutual relationship of the language elements. One should be aware, however, that the seismological nomenclature will inevitably develop exceptions to the rules, as any historically developed language, and depending on the context in which it is used. Although not fully documented below, some exceptions will be mentioned. Note that our efforts are mainly aimed at standardized names to be used in international data exchange so as to build up unique, unambiguous global databases for research. Many of the exceptions to the rules are related to specialized, mostly local research applications. The identification of related seismic phases often requires specialized procedures of data acquisition and processing, which are not part of seismological routine data analysis. Also, many of these *exceptional* phases are rarely or never used in seismic event location, magnitude determination, source mechanism calculations etc., which are the main tasks of international data centers. Below, we focus therefore on phases, which are particularly important for seismological data centers as well as for the refinement of regional and global Earth models on the basis of widely exchanged and accumulated parameter readings from such phases. In addition, we added for some phase definitions references to which the particular phase names can be traced back. For better illustration of the verbal definition of phase names, ray diagrams for the most important phases are presented in section 5.

2 Standard letters, signs and syntax used for describing seismic phases

Capital letters:

Individual capital letters that stand for primary types of seismic *body waves* such as:

- P: longitudinal wave which has traveled through Earth crust and mantle, from *undae primae* (Latin) = first waves (Borne, 1904);
- K: longitudinal wave which has traveled through the Earth's outer core, for Kern (German) = core (Sohon, 1932; Bastings, 1934);
- I: longitudinal wave which has traveled through the Earth's inner core (Jeffreys and Bullen, 1940);
- S: transverse wave which has traveled through Earth crust and mantle, from *undae secundae* (Latin) = second waves (Borne, 1904);
- T: a wave, which has partly traveled as sound wave in the sea, from *undae tertiae* = third waves (Linehan, 1940);
- J: transverse wave which has traveled through the Earth's inner core (Bullen, 1946).

Exceptions:

- A **capital letter N** used in the nomenclature does not stand for a phase name but rather for the number of legs traveled (or N-1 reflections made) before reaching the station. N should usually follow the phase symbol to which it applies. For examples see syntax below.
- The **lower case letters p** and **s** may stand, in the case of seismic events below the Earth's surface, for the relatively short **upgoing leg** of P or S waves, which continue, after reflection and possible conversion at the free surface, as downgoing P or S wave. Thus seismic *depth phases* (e.g., pP, sP, sS, pPP, sPP, pPKP, etc.) are uniquely defined. The identification and reporting of such phases is of utmost importance for a better event location, and improved source depth in particular (Scrase, 1931; Stechschulte, 1932).
- Another exception is, that many researchers working on detailed investigations of crustal and upper mantle discontinuities, e.g., by using the receiver function method, write both the up- and down-going short legs of converted or multiply reflected P and S phases as lower case letters p and s, respectively.

Individual or double capital letters that stand for *surface waves* such as:

- L: (relatively) long-period surface wave, unspecified, from *undae longae* (Latin) = long waves (Borne, 1904);
- R: Rayleigh waves (short-period up to very long-period, mantle waves) (Angenheister, 1921);
- Q: Love waves, from Querwellen (German) = transverse waves (Angenheister, 1921);
- G: (very long-period) global (mantle) Love waves, firstly observed and reported by Gutenberg and Richter (1934); Byerly proposed the usage of G for Gutenberg, as reported by Richter (1958);

- LR: long-period Rayleigh waves, usually relating to the Airy-phase maximum in the surface wave train;
- LQ: long-period Love waves.

Lower case letters and signs

Single lower case letters generally specify in which part of Earth crust or upper mantle a phase has its *turning point* or at which discontinuity it has been *reflected and eventually converted*:

- g: after the phase name characterizes waves “bottoming” (i.e., having their turning point in case of P-or S-body waves) or just travel (surface waves) within the upper (“granitic”) Earth crust (e.g., Pg, Sg; Rg), (Jeffreys, 1926);
- b: after the phase name characterizes body waves “bottoming” (i.e., having their turning point) in the lower (“basaltic”) Earth crust (Jeffreys, 1926) (e.g., Pb, Sb; alternative names for these phases are P*, S*, (Conrad, 1925));
- n: after the phase name characterizes a P or S wave which is bottoming (i.e., has its turning point) or is traveling as head wave in the Earth’s uppermost mantle (e.g., Pn, Sn), introduced after Andrija Mohorovičić discovered the Earth crust and separated the crustal travel-time curve from the (n =) normal mantle phase (Mohorovičić, 1910);
- m: stands for (upward) reflections from the outer side of the Mohorovičić (Moho) discontinuity (e.g., PmP, SmS);
- c: stands for reflections from the *outer side* of the core-mantle boundary (CMB), usage proposed by James B. Macelwane (see Gutenberg, 1925);
- i: stands for reflections from the *outer side* of the inner core boundary (ICB);
- z: stands for reflections from a discontinuity at depth z (measured in km) (any other than free surface, CMB or ICB!). Upward reflections from the *outer side* of the discontinuity *may* additionally be complemented by a + sign (e.g., P410+P; this, however, is not compulsory!) while downward reflections from the *inner side* of the discontinuity *must* be complemented by a – sign (e.g., P660-P).

Double lower case letters following a capital letter phase name indicate the travel-time branch to which this phase belongs. Due to the geometry and velocity structure of the Earth the same type of seismic wave may develop a triplication of its travel-time curve with different, in some parts well separated branches (see Fig. 2.29). Thus it is customary to differentiate between different branches of core phases and their multiple reflections at the free surface or the CMB. Examples are PKPab, PKPbc, PKPdf, SKSac, SKKSac, etc. (for definitions see the list below). The separation of the different PKP branches with letters ab, bc and df was introduced by Jeffreys and Bullen (1940).

Three lower case letters may follow a capital letter phase name in order to specify its character, e.g., as a forerunner (pre) to the main phase, caused by scattering (e.g., PKPpre) or as a diffracted wave extending the travel-time branch of the main phase into the outer core shadow (e.g., Pdif in the outer core shadow for P).

Syntax of generating complex phase names

Due to refraction, reflection and conversion in the Earth the majority of phases have a complex path history before they reach the station. Accordingly, most phases cannot be described by a single capital letter code in a self-explanatory way. By combining, however, the capital and lower case letters as mentioned above one can describe the character of even rather complex refracted, reflected or converted phases. The order of symbols (syntax) regulates the sequence of phase legs due to refraction, reflection and conversion events in time (from left to right) and in space.

3 Examples for creating complex standard phase names

Refracted and converted refracted waves:

- PKP is a pure refracted longitudinal wave. It has traveled the first part of its path as P through crust and mantle, the second through the outer core and the third again as P through mantle and crust. The alternative name for PKP is P' (Angenheister, 1921).
- PKIKP (alternative to PKP_{df}) is a pure refracted longitudinal wave too. It has traveled the first part of its path as P through crust and mantle, the second through the outer core, the third through the inner core, and the fourth and fifth parts back again through outer core and mantle/crust.
- SKS is a converted refracted wave. It has traveled as a shear wave through crust and mantle, being converted into a longitudinal wave K when refracted into the outer core and being converted back again into an S wave when entering the mantle.
- SKP or PKS are converted refracted waves in an analogous way with only one conversion from S to K when entering the core or from K to S when leaving the core, respectively.

Pure reflected waves:

- In the case of (downward only) reflections at the free surface or from the inner side of the CMB the phase symbol is just repeated, e.g., PP, PPP, KK, KKK etc.
- In the case of (upward) reflections from the outer side of the Moho, the CMB or the ICB this is indicated by inserting between the phase symbols m, c or i, respectively: e.g., PmP, PcP, ScS; PKiKP;
- In the case of reflections from any other discontinuity in mantle or crust at depth z these may be from the inner side (-; i.e., downward back into the mantle) or from the outer side (+; i.e., back towards the surface). In order to differentiate between these two possibilities, the sign has to follow z (or the respective number in km), e.g., P410+P or P660-P;
- To abbreviate names of multi-leg phases due to repeated reflections one can also write Phasename_N. This kind of abbreviation, is rather customary in case of multiple phases with long phase names such as PmP₂ for PmPPmP (surface reflection of PmP), SKS₂ for SKSSKS (which is the alternative name for S'₂, the free surface reflection of SKS), PKP₃ for PKPPKPPKP (double surface reflection of PKP; alternative name to P'₃) or P4KP for PKKKKP (triple reflection of K at the inner side of the CMB).

Note 1: PKP2 = PKPPKP are now alternative names for P'2 or P'P', respectively. This should not be mistaken for the *old* name PKP2 for PKPab!

Note 2: In the case of multiple reflections from the inner side of the CMB the WG followed the established tradition to place the number N not after but *in front* of the related phase symbol K.

Reflected waves with conversion at the reflection point:

In the case that a phase changes its character from P to S, or vice versa, one writes:

- PS (first leg P, second leg S) or SP (first leg P, second leg S) in the case of reflection from the free surface downward into the mantle;
- PmS or SmP, respectively, for reflections/conversions from the outer side of the Moho;
- PcS or ScP for reflections/conversions from the outer side of the CMB;
- Pz+S or Sz-P for reflection/conversion from the outer side or inner side, respectively, of a discontinuity at depth z. Note that the - is compulsory, the + not!

In this context it is worth mentioning, that mode conversion is impossible for reflections from K from the inner side of the CMB back into the outer core because the liquid outer core does not allow the propagation of S waves.

Along these lines and rules the new IASPEI standard phase names have been agreed. Where these deviate from other traditionally used names the latter are given as well. Either, they are still acceptable *alternative names* (alt) where the latter have been created in consistence with the above mentioned rules (e.g., PKIKP instead of PKPdf) or they are now *old names* (old), which should no longer be used.

4 IASPEI Standard Seismic Phase List (Draft)

This draft was agreed in May 2002 by the IASPEI Working Group on Phase Names, chaired by D. A. Storchak. Other members of the WG were R. D. Adams, P. Bormann, R. E. Engdahl, J. Havskov, B. Kennett and J. Schweitzer. The draft requires adoption by the IASPEI Commission on Seismological Observation and Interpretation (CoSOI) at its forthcoming meeting in Sapporo, 2003.

----- CRUSTAL PHASES -----

Pg	At short distances, either an upgoing P wave from a source in the upper crust or a P wave bottoming in the upper crust. At larger distances also arrivals caused by multiple P-wave reverberations inside the whole crust with a group velocity around 5.8 km/s.
Pb	(alt:P*) Either an upgoing P wave from a source in the lower crust or a P wave bottoming in the lower crust
Pn	Any P wave bottoming in the uppermost mantle or an upgoing P wave from a source in the uppermost mantle
PnPn	Pn free surface reflection
PgPg	Pg free surface reflection
PmP	P reflection from the outer side of the Moho
PmPN	PmP multiple free surface reflection; N is a positive integer. For example, PmP2 is PmPPmP
PmS	P to S reflection from the outer side of the Moho
Sg	At short distances, either an upgoing S wave from a source in the upper crust or an S wave bottoming in the upper crust. At larger distances also arrivals caused by superposition of multiple S-wave reverberations and SV to P and/or P to SV conversions inside the whole crust.
Sb	(alt:S*) Either an upgoing S wave from a source in the lower crust or an S wave bottoming in the lower crust
Sn	Any S wave bottoming in the uppermost mantle or an upgoing S wave from a source in the uppermost mantle
SnSn	Sn free surface reflection
SgSg	Sg free surface reflection
SmS	S reflection from the outer side of the Moho
SmSN	SmS multiple free surface reflection; N is a positive integer. For example, SmS2 is SmSSmS
SmP	S to P reflection from the outer side of the Moho
Lg	A wave group observed at larger regional distances and caused by superposition of multiple S-wave reverberations and SV to P and/or P to SV conversions inside the whole crust. The maximum energy travels with a group velocity around 3.5 km/s
Rg	Short period crustal Rayleigh wave

MANTLE PHASES

P	A longitudinal wave, bottoming below the uppermost mantle; also an upgoing longitudinal wave from a source below the uppermost mantle
PP	Free surface reflection of P wave leaving a source downwards
PS	P, leaving a source downwards, reflected as an S at the free surface. At shorter distances the first leg is represented by a crustal P wave.
PPP	analogous to PP
PPS	PP to S converted reflection at the free surface; travel time matches that of PSP
PSS	PS reflected at the free surface
PcP	P reflection from the core-mantle boundary (CMB)
PcS	P to S converted reflection from the CMB
PcPN	PcP multiple free surface reflection; N is a positive integer. For example PcP2 is PcPPcP
Pz+P	(alt:PzP) P reflection from outer side of a discontinuity at depth z; z may be a positive numerical value in km. For example P660+P is a P reflection from the top of the 660 km discontinuity.
Pz-P	P reflection from inner side of discontinuity at depth z. For example, P660-P is a P reflection from below the 660 km discontinuity, which means it is precursory to PP.
Pz+S	(alt:PzS) P to S converted reflection from outer side of discontinuity at depth z.
Pz-S	P to S converted reflection from inner side of discontinuity at depth z
PScS	P (leaving a source downwards) to ScS reflection at the free surface
Pdif	(old:Pdiff) P diffracted along the CMB in the mantle
S	shear wave, bottoming below the uppermost mantle; also an upgoing shear wave from a source below the uppermost mantle
SS	free surface reflection of an S wave leaving a source downwards
SP	S, leaving source downwards, reflected as P at the free surface. At shorter distances the second leg is represented by a crustal P wave.
SSS	analogous to SS
SSP	SS to P converted reflection at the free surface; travel time matches that of SPS.
SPP	SP reflected at the free surface
ScS	S reflection from the CMB
ScP	S to P converted reflection from the CMB
ScSN	ScS multiple free surface reflection; N is a positive integer. For example ScS2 is ScSScS
Sz+S	(alt:SzS) S reflection from outer side of a discontinuity at depth z; z may be a positive numerical value in km. For example S660+S is an S reflection from the top of the 660 km discontinuity.
Sz-S	S reflection from inner side of discontinuity at depth z. For example, S660-S is an S reflection from below the 660 km discontinuity, which means it is precursory to SS.
Sz+P	(alt:SzP) S to P converted reflection from outer side of discontinuity at depth z
Sz-P	S to P converted reflection from inner side of discontinuity at depth z
ScSP	ScS to P reflection at the free surface
Sdif	(old:Sdiff) S diffracted along the CMB in the mantle

CORE PHASES

PKP	(alt:P') unspecified P wave bottoming in the core
PKPab	(old:PKP2) P wave bottoming in the upper outer core; ab indicates the retrograde branch of the PKP caustic
PKPbc	(old:PKP1) P wave bottoming in the lower outer core; bc indicates the prograde branch of the PKP caustic
PKPdf	(alt:PKIKP) P wave bottoming in the inner core
PKPpre	(old:PKhKP) a precursor to PKPdf due to scattering near or at the CMB
PKPdif	P wave diffracted at the inner core boundary (ICB) in the outer core
PKS	Unspecified P wave bottoming in the core and converting to S at the CMB
PKSab	PKS bottoming in the upper outer core
PKSbc	PKS bottoming in the lower outer core
PKSdf	PKS bottoming in the inner core
P'P'	(alt:PKPPKP) Free surface reflection of PKP
P'N	(alt:PKPN) PKP reflected at the free surface N-1 times; N is a positive integer. For example P'3 is P'P'P'
P'z-P'	PKP reflected from inner side of a discontinuity at depth z outside the core, which means it is precursory to P'P'; z may be a positive numerical value in km
P'S'	(alt:PKPSKS) PKP to SKS converted reflection at the free surface; other examples are P'PKS, P'SKP
PS'	(alt:PSKS) P (leaving a source downwards) to SKS reflection at the free surface
PKKP	Unspecified P wave reflected once from the inner side of the CMB
PKKPab	PKKP bottoming in the upper outer core
PKKPbc	PKKP bottoming in the lower outer core
PKKPdf	PKKP bottoming in the inner core
PNKP	P wave reflected N-1 times from inner side of the CMB; N is a positive integer
PKKPpre	a precursor to PKKP due to scattering near the CMB
PKiKP	P wave reflected from the inner core boundary (ICB)
PKNIKP	P wave reflected N-1 times from the inner side of the ICB
PKJKP	P wave traversing the outer core as P and the inner core as S
PKKS	P wave reflected once from inner side of the CMB and converted to S at the CMB
PKKSab	PKKS bottoming in the upper outer core
PKKSbc	PKKS bottoming in the lower outer core
PKKSdf	PKKS bottoming in the inner core
PcPP'	(alt:PcPPKP) PcP to PKP reflection at the free surface; other examples are PcPS', PcSP', PcSS', PcPSKP, PcSSKP
SKS	(alt:S') unspecified S wave traversing the core as P
SKSac	SKS bottoming in the outer core
SKSdf	(alt:SKIKS) SKS bottoming in the inner core

SPdifKS	(alt:SKPdifS) SKS wave with a segment of mantle-side Pdif at the source and/or the receiver side of the raypath
SKP	Unspecified S wave traversing the core and then the mantle as P
SKPab	SKP bottoming in the upper outer core
SKPbc	SKP bottoming in the lower outer core
SKPdf	SKP bottoming in the inner core
S'S'	(alt:SKSSKS) Free surface reflection of SKS
S'N	SKS reflected at the free surface N-1 times; N is a positive integer
S'z-S'	SKS reflected from inner side of discontinuity at depth z outside the core, which means it is precursory to S'S'; z may be a positive numerical value in km
S'P'	(alt:SKSPKP) SKS to PKP converted reflection at the free surface; other examples are S'SKP, S'PKS
S'P	(alt:SKSP) SKS to P reflection at the free surface
SKKS	Unspecified S wave reflected once from inner side of the CMB
SKKSac	SKKS bottoming in the outer core
SKKSdf	SKKS bottoming in the inner core
SNKS	S wave reflected N-1 times from inner side of the CMB; N is a positive integer
SKiKS	S wave traversing the outer core as P and reflected from the ICB
SKJKS	S wave traversing the outer core as P and the inner core as S
SKKP	S wave traversing the core as P with one reflection from the inner side of the CMB and then continuing as P in the mantle
SKKPab	SKKP bottoming in the upper outer core
SKKPbc	SKKP bottoming in the lower outer core
SKKPdf	SKKP bottoming in the inner core
ScSS'	(alt:ScSSKS) ScS to SKS reflection at the free surface; other examples are: ScPS', ScSP', ScPP', ScSSKP, ScPSKP

NEAR SOURCE SURFACE REFLECTIONS (Depth phases)

pPy	All P-type onsets (Py) as defined above, which resulted from reflection of an upgoing P wave at the free surface or an ocean bottom; WARNING: The character "y" is only a wild card for any seismic phase, which could be generated at the free surface. Examples are: pP, pPKP, pPP, pPcP etc
sPy	All Py resulting from reflection of an upgoing S wave at the free surface or an ocean bottom; For example: sP, sPKP, sPP, sPcP etc
pSy	All S-type onsets (Sy) as defined above, which resulted from reflection of an upgoing P wave at the free surface or an ocean bottom. For example: pS, pSKS, pSS, pScP etc
sSy	All Sy resulting from reflection of an upgoing S wave at the free surface or an ocean bottom. For example: sSn, sSS, sScS, sSdif etc
pwPy	All Py resulting from reflection of an upgoing P wave at the ocean's free surface

pmPy All Py resulting from reflection of an upgoing P wave from the inner side of the Moho

SURFACE WAVES

L Unspecified long period surface wave
 LQ Love wave
 LR Rayleigh wave
 G Mantle wave of Love type
 GN Mantle wave of Love type; N is integer and indicates wave packets traveling along the minor arcs (odd numbers) or major arc (even numbers) of the great circle
 R Mantle wave of Rayleigh type
 RN Mantle wave of Rayleigh type; N is integer and indicates wave packets traveling along the minor arcs (odd numbers) or major arc (even numbers) of the great circle
 PL Fundamental leaking mode following P onsets generated by coupling of P energy into the waveguide formed by the crust and upper mantle
 SPL S wave coupling into the PL waveguide; other examples are SSPL, SSSPL

ACOUSTIC PHASES

H A hydroacoustic wave from a source in the water, which couples in the ground
 HPg H phase converted to Pg at the receiver side
 HSg H phase converted to Sg at the receiver side
 HRg H phase converted to Rg at the receiver side
 I An atmospheric sound arrival, which couples in the ground
 IPg I phase converted to Pg at the receiver side
 ISg I phase converted to Sg at the receiver side
 IRg I phase converted to Rg at the receiver side
 T A tertiary wave. This is an acoustic wave from a source in the solid earth, usually trapped in a low velocity oceanic water layer called the SOFAR channel (SOund Fixing And Ranging)
 TPg T phase converted to Pg at the receiver side
 TSg T phase converted to Sg at the receiver side
 TRg T phase converted to Rg at the receiver side

AMPLITUDE MEASUREMENT PHASES

A Unspecified amplitude measurement

AML	Amplitude measurement for local magnitude
AMB	Amplitude measurement for body wave magnitude
AMS	Amplitude measurement for surface wave magnitude
END	Time of visible end of record for duration magnitude

UNIDENTIFIED ARRIVALS

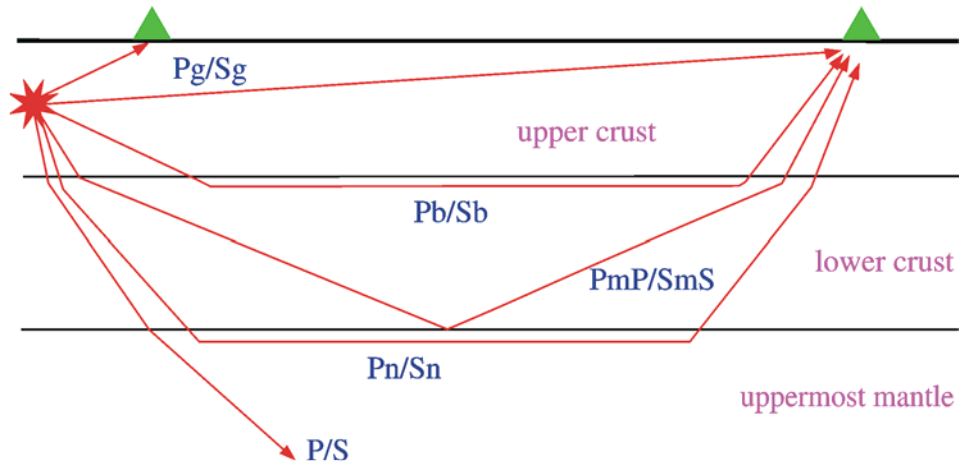
x	(old: i, e, NULL) unidentified arrival
rx	(old: i, e, NULL) unidentified regional arrival
tx	(old: i, e, NULL) unidentified teleseismic arrival
Px	(old: i, e, NULL, (P), P?) unidentified arrival of P-type
Sx	(old: i, e, NULL, (S), S?) unidentified arrival of S-type

5 Ray-paths diagrams for some of the IASPEI standard phases

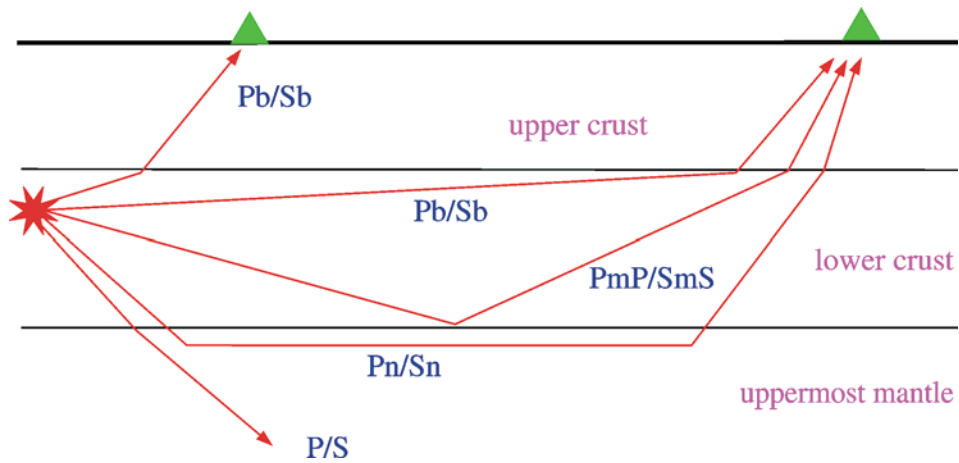
In this section we show ray paths through the Earth for most of the mentioned phases. The three figures for crustal phases are just sketches showing the principal ray paths in a two-layer crust. The rays in all other figures were calculated by using the ray picture part of the WKB3 code (Chapman, 1978; Dey-Sarkar and Chapman, 1978); as velocity model we chose the standard Earth model AK135 (Kennett et al., 1995). For some types of P and S phases the ray paths through the Earth are very similar because the velocity ratio v_P/v_S does not change enough to give very different ray pictures. In these cases, we calculated only the ray paths for the P-type ray (i.e., P, Pdif, pP, PP, P3, PcP, PcP2, P660P and P660-P) and assume that the corresponding ray paths of the respective S-type phases are very similar. To show the different ray paths for phases with similar phase names, we show on many figures rays leaving the source once to the left and once to the right in different colors. The three most important discontinuities inside the Earth are indicated as black circles (i.e., the border between upper and lower mantle, the core-mantle boundary, and the inner core boundary).

5.1 Seismic rays of crustal phases

a)



b)



c)

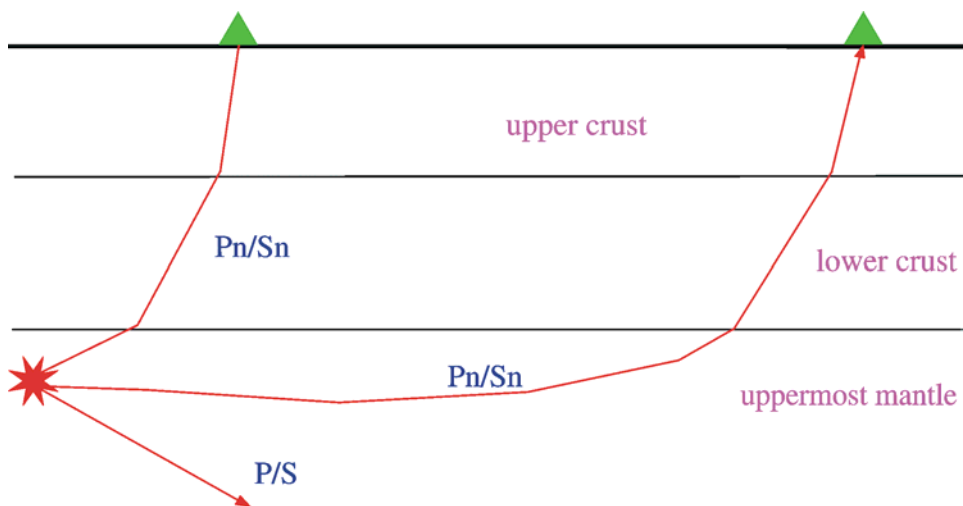


Figure 1 Seismic „crustal phases“ observed in the case of a two-layer crust in local and regional distance ranges ($0^\circ < D < \text{about } 20^\circ$) from the seismic source in the: a) upper crust; b) lower crust; and c) uppermost mantle.

5.2 Seismic rays of mantle phases

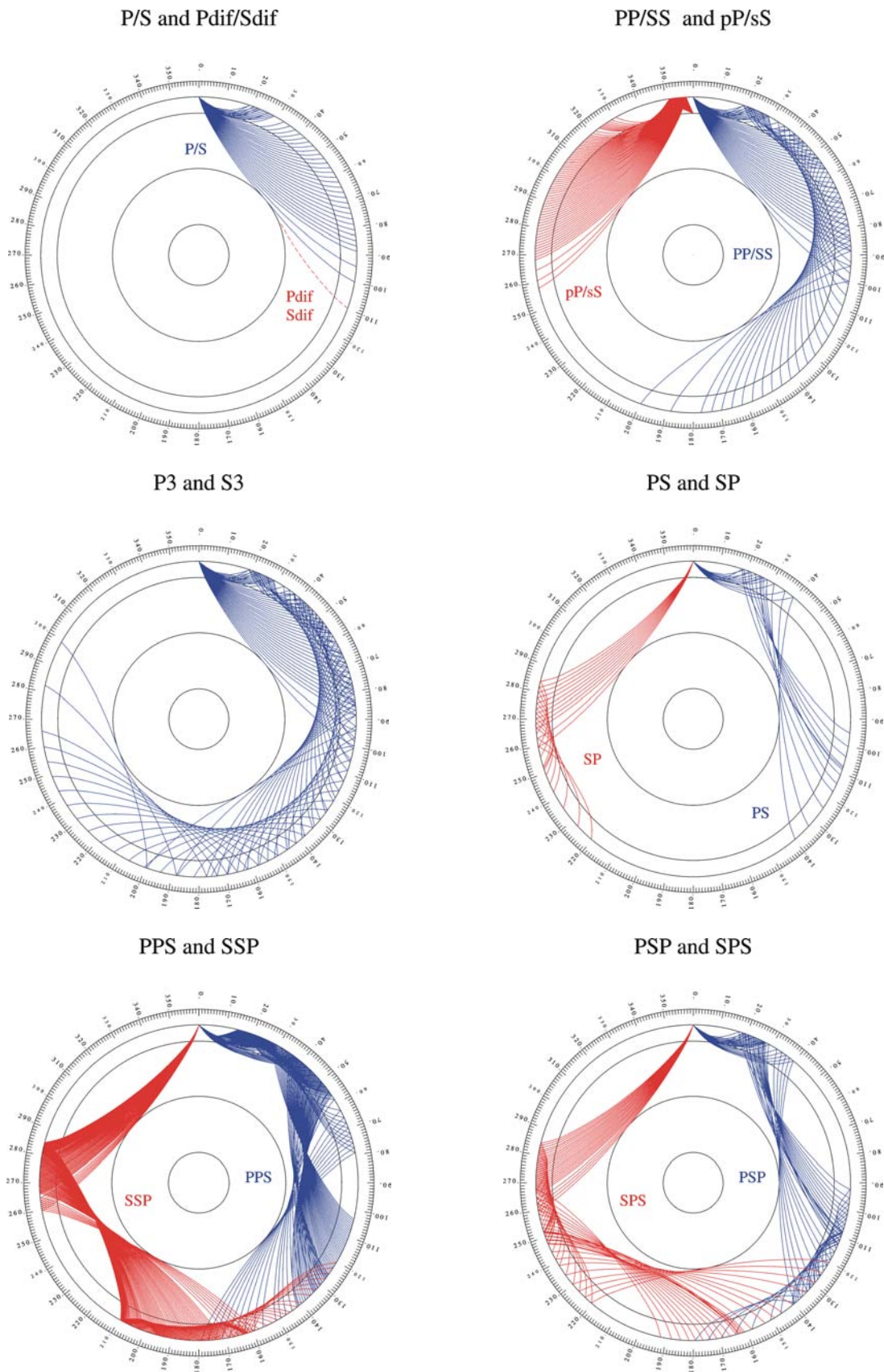


Figure 2a Mantle phases observed at the teleseismic distance range $D >$ about 20° .

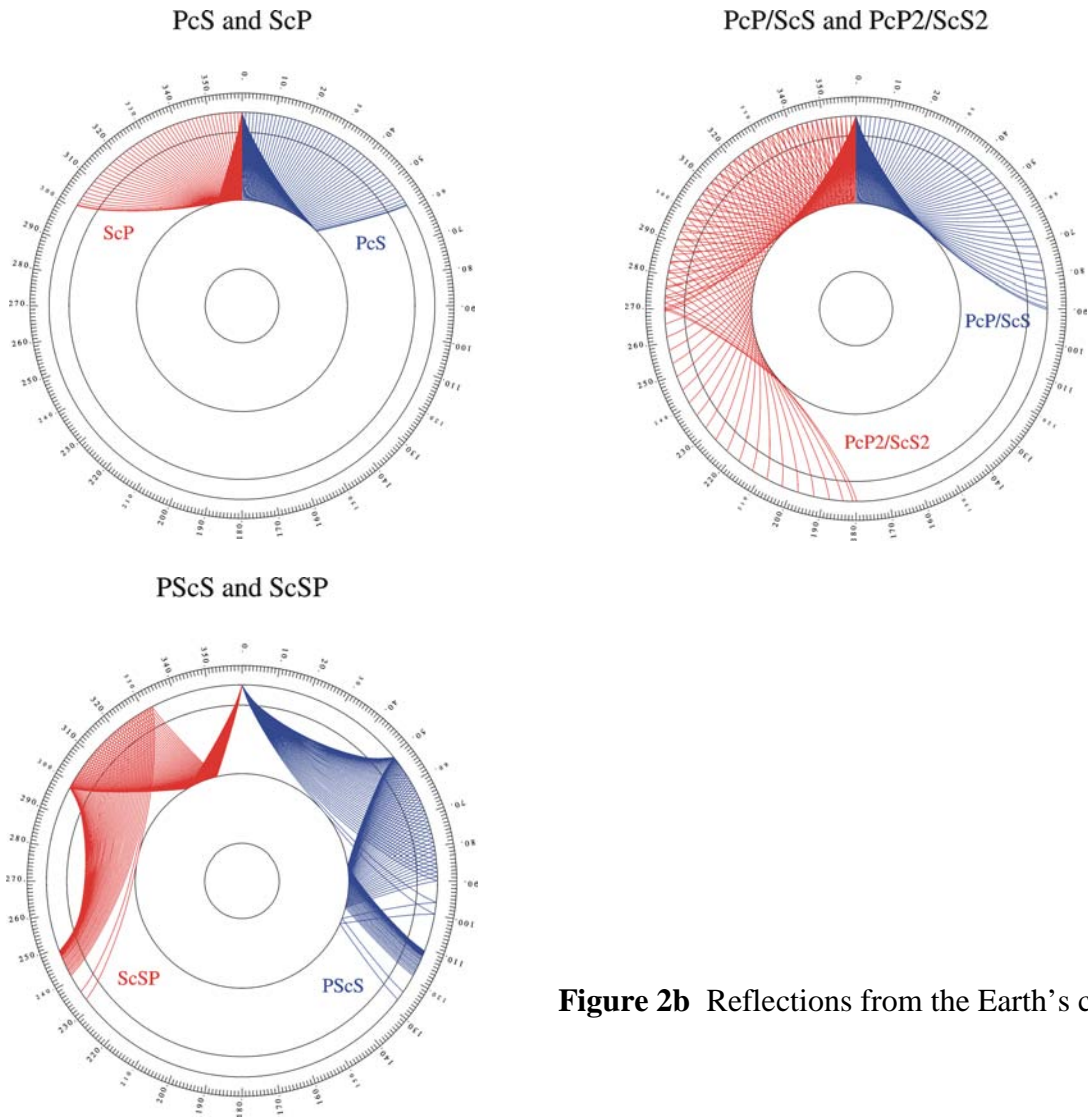


Figure 2b Reflections from the Earth's core.

5.3 Seismic rays through the Earth's core phases

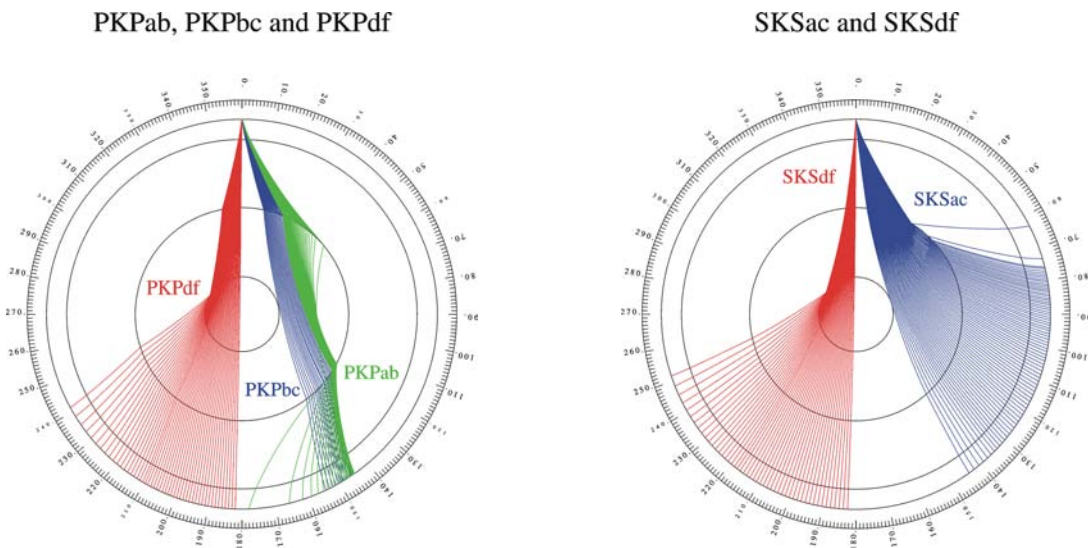
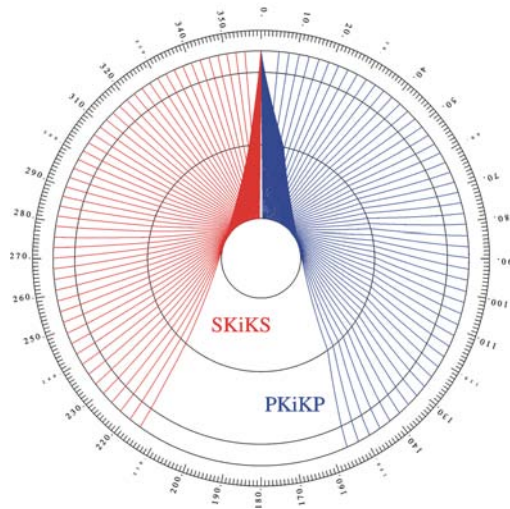
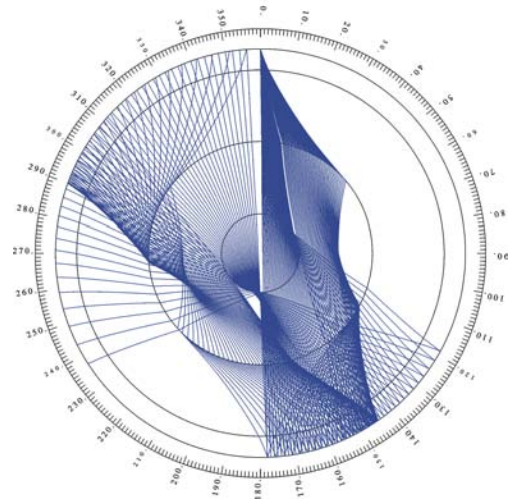


Figure 3a Seismic rays of direct core phases.

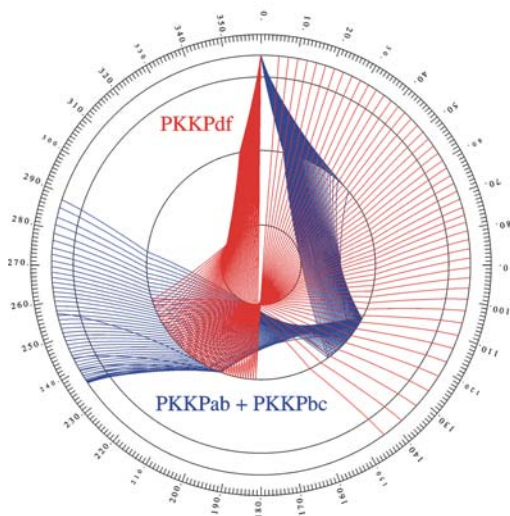
PKiKP and SKiKS



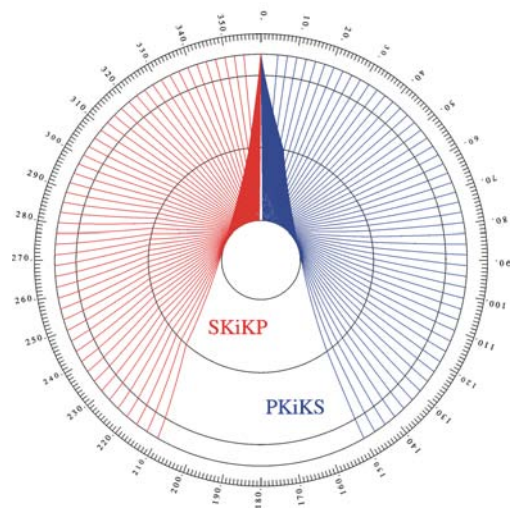
P'P'



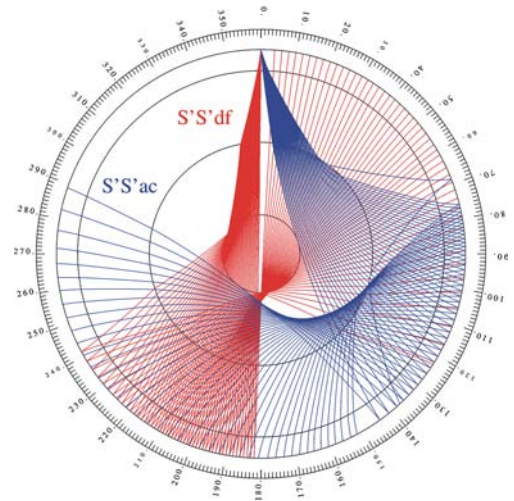
PKKP



PKiKS and SKiKP



S'S'ac and S'S'df



SKKSac

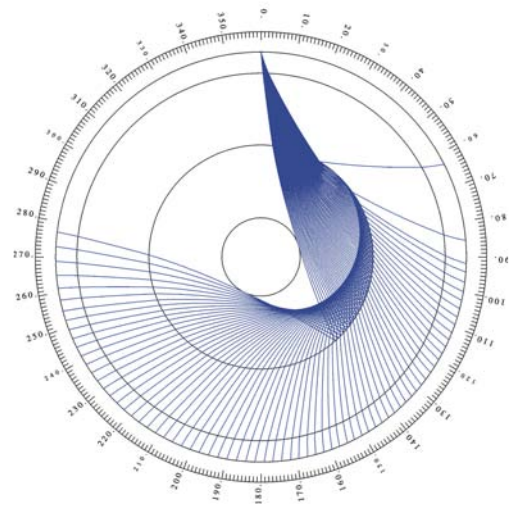
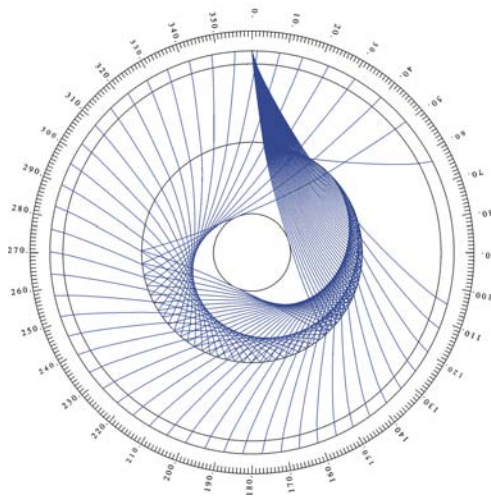
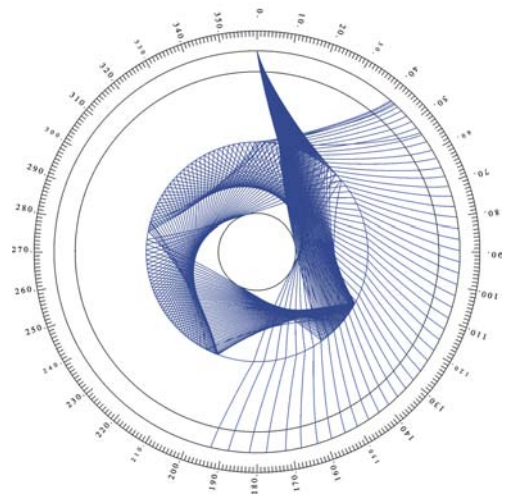


Figure 3b Seismic rays of single-reflected core phases .

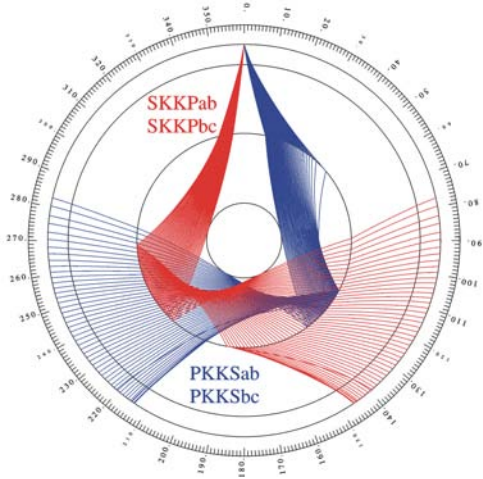
S3KSac



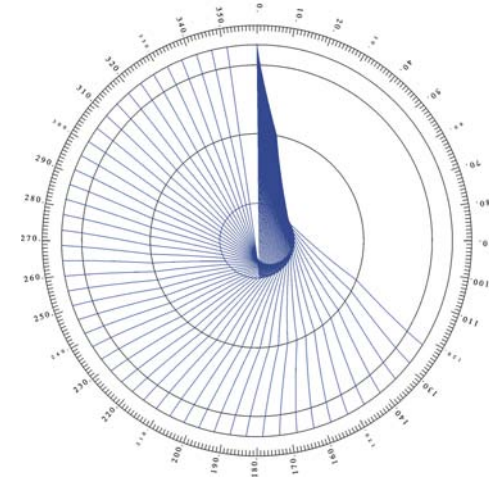
P4KPab and P4KPbc



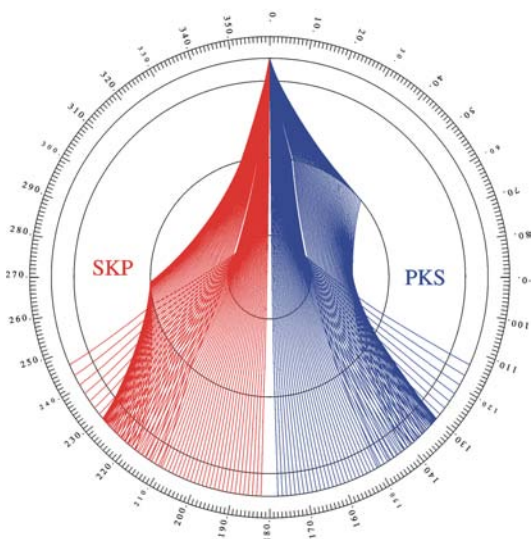
PKKSab / PKKSbc and SKKPab / SKKPbc



PK2IKP



PKS and SKP



PKJKP and SKJKS

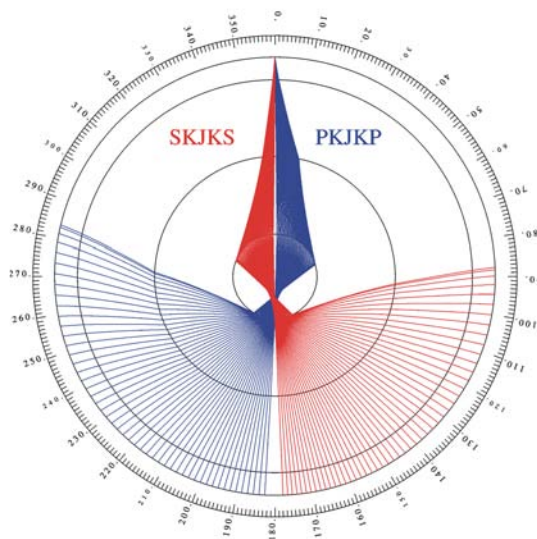


Figure 3c Seismic rays of multiple-reflected and converted core phases.

Topic	Theoretical source representation
Author	Helmut Grosser, and Peter Bormann, GeoForschungsZentrum Potsdam, Telegrafenberg, D-14473 Potsdam, Germany; E-mail: gros@gfz-potsdam.de Agustin Udias, Universidad Complutense de Madrid, Departamento de Geofísica y Meteorología, 28040 Madrid, Spain, E-mail: figeo12@emducmsl.sis.ucm.es
Version	July 2001

1 Introduction

In seismology the problem of understanding and describing the seismic source consists in relating observed seismic waves (i.e., seismograms) generated by this source to suitably conceived geometric, kinematic and dynamic parameters of a mechanical source model that represents the physical phenomenon of a brittle fracture in the Earth's lithosphere. Representations of the source are defined by parameters whose number depends on the complexity of the source models (e.g., Aki and Richards, 1980; Ben-Menahem and Singh, 1981; Das and Kostrov, 1988; Lay and Wallace, 1995; Udías, 1999). In the direct problem, theoretical seismic wave displacements are determined from source models and in the inverse problem parameters of source models are derived from observed wave displacements. In the following we will consider only source models related to earthquakes and explosions (see Chapter 3), volcanic tremors (see Chapter 13) and rock bursts. Here we will not discuss sources of seismic noise (see Chapter 4).

Strong non-linear and non-elastic processes take place in a seismic source volume. Parts of it may crack, phase transitions may take place, the temperature may increase, and so on. These kinds of processes are not described by most seismic source theories; however, there are special theories to model such processes, e.g., the time-dependent pressure within an explosion cavity, the rupture propagation on an earthquake fault, and the material behavior on a crack tip (crack criteria). We limit ourselves to the phenomenological description of a seismic source. The aforementioned complicated processes need not to be considered when looking only for their integral effect on a surface surrounding the seismic source, i.e., by replacing a volume integral by a surface integral (see, e.g., Aki and Richards, 1980).

2 Continuum mechanics

The description of the source mechanism is based on the solution of the equation of motion. In a deformable solid medium this equation is derived from classical Newtonian mechanics. The linearized equation of motion (i.e., by neglecting density changes and other second order effects) is

$$\rho \ddot{u}_i(x_s, t) - \sigma_{ij,j}(x_s, t) = f_i^b(x_s, t) . \quad (1)$$

In this equation ρ is the density of the solid body, u_i are the components ($i = 1, 2, 3$) of the displacement field that describe the deformation of the body, σ_{ik} is the stress tensor, f_i^b is the body force density acting per unit volume, \ddot{u}_i is the second time derivative $\partial^2/\partial t^2$ of the

displacement and the comma between two subscripts, e.g., in $\sigma_{ik,k}$ indicates the spatial derivative of the considered quantity. We generally use the *summation convention* which requires that one has to sum when a subscript appears twice, e.g.,

$$\sigma_{ik,k} = \frac{\partial}{\partial x_1} \sigma_{i1} + \frac{\partial}{\partial x_2} \sigma_{i2} + \frac{\partial}{\partial x_3} \sigma_{i3}.$$

The displacement is a function of the spatial co-ordinates x_i and the infinitesimal deformation is defined as

$$du_i = u_{i,k} dx_k \tag{2}$$

with

$$u_{i,k} = \beta_{ik} \tag{3}$$

as the distortion tensor. We now consider the location of a particle before and after it is deformed, described by the vectors a_i and x_i , respectively. Accordingly, an infinitesimal vector da_i at the point a_i is moved (i.e., deformed) to the vector dx_i , as shown in Figure 1.

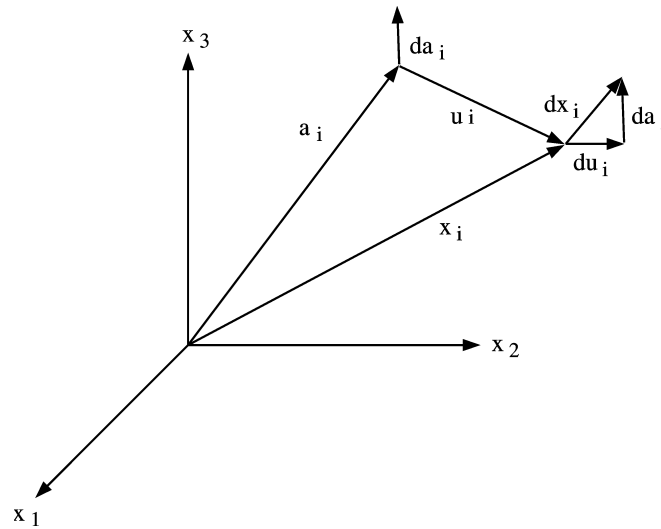


Figure 1 Coordinates and vectors describing the displacement field (see text).

Introducing ds^2 , which is the difference between the square of the length of the vectors dx_i and da_i , and, thus, a measure of the deformation of the body, i.e., $ds^2 = dx_i dx_i - (dx_i - du_i) (dx_i - du_i)$, we get with (2) and (3)

$$ds^2 = (\beta_{ij} + \beta_{ji} - \beta_{ki} \beta_{kj}) dx_i dx_j = 2\varepsilon_{ij} dx_i dx_j. \tag{4}$$

Equation (4) is the definition of the *strain tensor* ε_{ij} . It is a symmetric tensor. For small deformations it can be approximated by its linear terms

$$\varepsilon_{ij} = \frac{1}{2} (\beta_{ij} + \beta_{ji}) = \frac{1}{2} (u_{i,j} + u_{j,i}). \tag{5}$$

Thus, the strain tensor ε_{ij} is the symmetric part of β_{ij} . Any symmetric tensor can be transformed into a co-ordinate system such that

$$\varepsilon_{ij} = \varepsilon^{(i)} \delta_{ij} \quad (6)$$

where δ_{ij} is the dimensionless *Kronecker symbol*, defined by

$$\delta_{ij} = \begin{cases} 1 & \text{if } i = j \\ 0 & \text{if } i \neq j \end{cases} \quad (7)$$

and $\varepsilon^{(i)}$ are the eigenvalues of the strain tensor. The co-ordinate system where ε_{ij} is of the form (6) is called system of principle axes. The three eigenvalues describe the relative deformation in direction of the principle axes.

In continuum mechanics one distinguishes between body forces and surface forces. The body forces are sometimes also termed volume forces because they act on volume elements dV of the body. In Equation (1) we consider infinitesimal masses ρdV where dV is the infinitesimal volume of the mass element. Accordingly, an infinitesimal body force (Aki and Richards, 1980) can be written as $dF_i = f_i^b(x_s, t) dV$. Typical examples of body forces are the gravity field and the centrifugal force.

In contrast, surface forces such as cohesion, the sliding friction, or the internal stress during the deformation of the body, act on surface elements dS of the volume dV . The stress is a tensor of second order, i.e., it has two subscripts, because it is characterized both by the orientation of the force and by the orientation of the surface on which the force acts. A second-order tensor has generally 9 independent components which can be written explicitly as

$$\sigma_{ij} = \begin{pmatrix} \sigma_{11} & \sigma_{12} & \sigma_{13} \\ \sigma_{21} & \sigma_{22} & \sigma_{23} \\ \sigma_{31} & \sigma_{32} & \sigma_{33} \end{pmatrix}.$$

In general, σ_{ij} depends on position and time. It acts only between adjacent particles. Because of the conservation law of angular momentum this tensor has to be symmetric, i.e.,

$$\sigma_{ij} = \sigma_{ji}. \quad (8)$$

The relation between the incremental body force density df_i^s which acts on an internal surface element dS and the stress is

$$df_i^s = \sigma_{ij} n_j dS \quad (9)$$

where n_j is the normal vector of the surface elements (see Figure 2). $\sigma_{ij} n_j$ is called the *traction* of the stress tensor. The pressure and the surface tension in fluids are special examples of internal surface forces. Figure 3 shows the different components of σ_{ij} which act on the surfaces of an infinitesimal cube.

In the linear theory of elasticity, the strain and the stress tensor are linearly coupled. A relatively simple stress-strain relation is the generalized *Hook's law*

$$\sigma_{ij} = c_{ijkl} \varepsilon_{kl}. \quad (10)$$

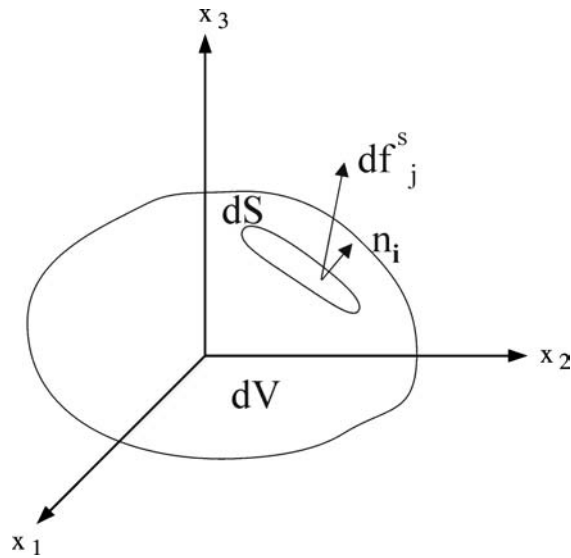


Figure 2 Schematic depiction of the considered source volume dV , a surface element dS (with its normal vector n_i) on which the force df_j^s acts.

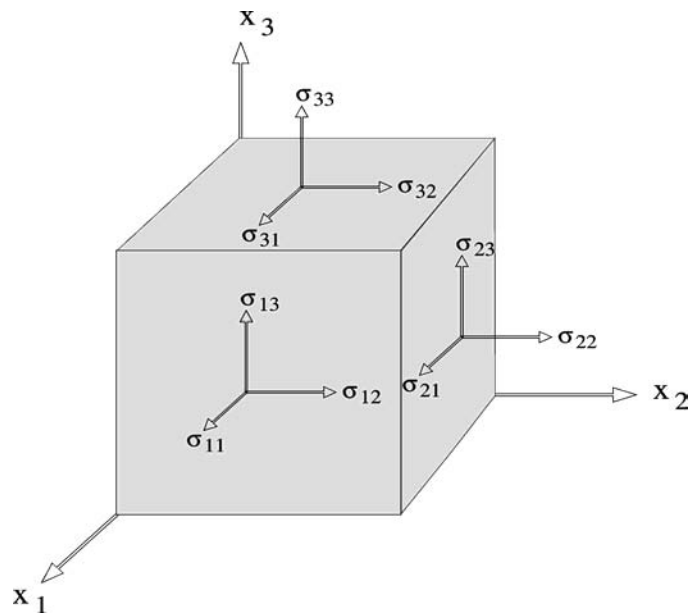


Figure 3 The nine components of the stress tensor. σ_{ij} are the components of the stress tensor parallel to x_j on planes having n_i as their normals.

The body that obeys the relation (10) is said to be *linearly elastic*. The c_{ijkl} are called *elastic constants* because they are independent of strain, however, in the case of an inhomogeneous medium, they depend on the position in the body. Due to the symmetry of strain (see Equation (5)) and stress tensor (see Equation (8)) and because of the energy balance in the body, the fourth-order tensor c_{ijkl} has the following three symmetries:

$$c_{ijkl} = c_{jikl}, \quad c_{ijkl} = c_{ijlk}, \quad \text{and} \quad c_{ijkl} = c_{klij}. \quad (11)$$

These symmetries reduce the independent components in c_{ijkl} from 81 to 21. In the case of an *isotropic medium*, i.e., when the elastic properties are independent of the orientation in the body, the elastic constants reduce to just two. Then c_{ijkl} has the form

$$c_{ijkl} = \lambda \delta_{ij} \delta_{kl} + \mu (\delta_{ik} \delta_{jl} + \delta_{il} \delta_{jk}). \quad (12)$$

The two parameter λ and μ are known as the *Lamé constants*.

If attenuation has to be included the relatively general *Boltzmann law*

$$\sigma_{ij}(t) = \int_{-\infty}^t b_{ijkl}(t-\tau) \varepsilon_{kl}(\tau) d\tau \quad (13)$$

can be used.

It is advantageous to introduce now the *Fourier transform* $f(\omega)$ of a time dependent function $f(t)$. Here, ω is the angular frequency $2\pi f$, where f is frequency in units of Hz.. We use the definitions

$$f(\omega) = \int_{-\infty}^{\infty} f(t) e^{-i\omega t} dt \quad \text{and} \quad f(t) = \frac{1}{2\pi} \int_{-\infty}^{\infty} f(\omega) e^{i\omega t} d\omega \quad (14)$$

where $i = \sqrt{-1}$ is the imaginary unit, and $f(\omega)$ is a complex function, called the complex spectrum of $f(t)$. It can be represented by

$$f(\omega) = a(\omega) + i b(\omega) = A(\omega) e^{i\Phi(\omega)}$$

where $A(\omega)$ is the amplitude spectrum and $\Phi(\omega)$ the phase spectrum. $a(\omega)$ and $b(\omega)$ are the real and the imaginary parts of $f(\omega)$, respectively. When applying the Fourier transformation to Equation (13) the integral is replaced by the product of $b_{ijkl}(\omega)$ and $\varepsilon_{kl}(\omega)$. The imaginary part of b_{ijkl} describes a linear attenuation for a propagating displacement field.

With Eqs. (5), (10), and (14) the equation of motion (1) becomes (Udías, 1999)

$$\rho \omega^2 u_i(x_s, \omega) + \sigma_{ij,j}(x_s, \omega) = -f_i^b(x_s, \omega) \quad (15)$$

and in a linear elastic but inhomogeneous medium

$$\rho \omega^2 u_i(x_s, \omega) + (c_{ijkl} u_{k,l}(x_s, \omega))_j = -f_i^b(x_s, \omega). \quad (16)$$

The second term on the left side is the stress due to the displacement u_k . In order to specify u_i in a unique way, the initial conditions have to be fixed for the displacement u_i and the related velocity \dot{u}_i as well as the boundary conditions for the displacement or the traction. The homogeneous initial condition, that both u_i and \dot{u}_i are zero before the beginning of the seismic event, is the precondition for the existence of the related Fourier transform $u_i(x_s, \omega)$. Boundary conditions can be specified for the displacement u_i or the traction $\sigma_{ij} n_j$ on internal surfaces S (or *external surfaces* such as the Earth's free surface) (see Figure 4), namely

$$u_i(\xi_s, \omega) \quad \text{or} \quad \sigma_{ij}(\xi_s, \omega) n_j \quad \text{on the internal surface } S(\xi_s) \quad (17)$$

where $S(\xi_s)$ may consist of several unconnected surfaces. The Greek letter ξ_s used as coordinates should indicate that the quantities u_i and σ_{ij} are lying on the surface $S(\xi_s)$ which is generally curved. These boundary conditions are indispensable for modeling seismic sources and computing the wave propagation through a layered medium.

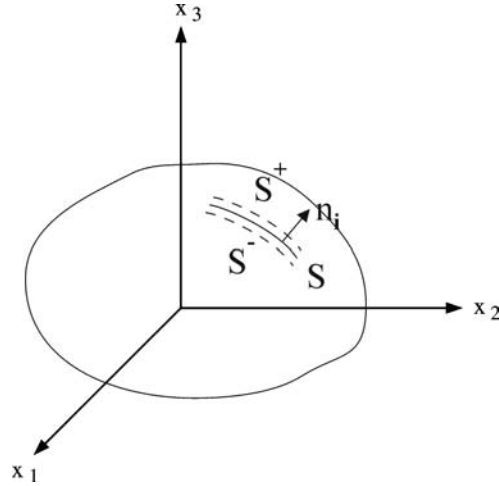


Figure 4 Illustrating the definition of boundary conditions for seismic faults representation.

3 Kinematic source models

The first mathematical formulation of the mechanism of earthquakes used the representation of the processes at the source by a distribution of the body force density $f_i^b(\xi_s, t)$ acting inside the source volume V_0 . Since these forces must represent the phenomenon of fracture, they are called equivalent forces. If it is assumed that no other body forces are present (gravity, etc.), and that on its surface S displacements and tractions are zero, we can use the representation theorem in terms of the *Green's function* to write the elastic displacements in an infinite medium in the time domain as

$$u_i(x_s, t) = \int_{-\infty}^{\infty} d\tau \int_{V_0} f_k^b(\xi_s, t) G_{ik}(x_s, t, \xi_s, \tau) dV \quad (18)$$

or in the frequency domain by

$$u_i(x_s, \omega) = \int_{V_0} f_k^b(\xi_s, \omega) G_{ik}(x_s, \xi_s, \omega) dV. \quad (19)$$

The Green's function G_{ki} is the solution of the equation of motion (16) for special impulsive single point forces, termed *Dirac* or *needle impulses*, which act inside the body. The spectrum of the Dirac impulse is 1 for all frequencies and, thus, does not appear in Equation (20) below. According to Ben-Menahem and Singh (1981) and Udías (1999), the following equation holds for the Green's function

$$\rho \omega^2 G_{in}(x_r, \xi_r, \omega) + (c_{ijkl} G_{kn,l}(x_r, \xi_r, \omega))_{,j} = -\delta_{in} \delta(x_r - \xi_r) \quad (20)$$

where $\delta(x_r - \xi_r)$ is the three-dimensional Dirac delta function which is the product of three one-dimensional Dirac delta functions, i.e., $\delta(x_r - \xi_r) = \delta(x_1 - \xi_1) \delta(x_2 - \xi_2) \delta(x_3 - \xi_3)$. Note that $\delta(x_r - \xi_r)$ has the dimension of 1/(unit volume). The three one-dimensional Dirac functions define the point in space where the three perpendicular point forces, as described by the Kronecker symbol in Equation (7), act.

The Green's function acts as a "propagator" of the effects of forces f_i^b , from the points where they are acting (ξ_i inside V_0) to points x_i outside V_0 , where the elastic displacement u_i produces the seismogram. A simplification, often used in the practice, is made by applying the point source approximation. It is valid if the source dimension is much smaller than the considered wavelength and the distance of the observation point from the source. For a point source at x_s^o we develop the Green's function in Equation(19) in a Taylor series at this point:

$$u_i(x_s, \omega) = \int_{V_0} \left[f_k^b(x_s^o + s_s, \omega) G_{ik}(x_s, x_s^o, \omega) + s_j f_k^b(x_s^o + s_s, \omega) \frac{\partial}{\partial x_j^o} G_{ik}(x_s, x_s^o, \omega) + \dots \right] dV(s_s)$$

$$= F_k(x_s^o, \omega) G_{ik}(x_s, x_s^o, \omega) + M_{jk}^f(x_s^o, \omega) G_{ik,j}(x_s, x_s^o, \omega) + \dots \quad (21)$$

If the source volume is small the Taylor series can be finished after the second term with the first derivative to the source co-ordinates x_i^o . Then (21) defines the force F_k and a seismic moment tensor M_{kl}^f for which the following relations hold:

$$F_k(x_s^o, \omega) = \int_{V_0} f_k^b(x_s^o + s_s, \omega) dV(s_s) \quad (22)$$

and

$$M_{jk}^f(x_s^o, \omega) = \int_{V_0} s_j f_k^b(x_s^o + s_s, \omega) dV(s_s). \quad (23)$$

If f_k^b is a single point force then M_{kl}^f as a whole describes a force couple (see Figure 5).

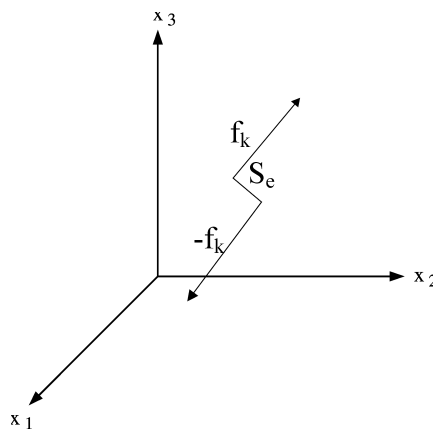


Figure 5 Schematic presentation of a general force couple $f_i s_j$

Equation (21) contains the partial spatial derivatives of the Green's function. In a homogeneous infinite body they can be written as

$$G_{ki,j} = \frac{1}{r^4 \omega^2} \sum_{n=0}^3 A_{ijk}^{(n)P} \left(\frac{\omega r}{v_P} \right)^n + \frac{1}{r^4 \omega^2} \sum_{n=0}^3 A_{ijk}^{(n)S} \left(\frac{\omega r}{v_S} \right)^n \quad (24)$$

where the $A_{ijk}^{(n)}$ are complex coefficients proportional to the amplitudes and phases of the P and S waves (see 2.2). The term of $G_{ij,k}$ with $n = 3$ is called the *far-field term* because it can still be observed at rather large distances r between the point source and the point of observation (seismic recording). In contrast, the terms with $n = 0, 1$ and 2 are called the *near field terms* because they decay with distance more rapidly than the far-field term, namely proportional to r^{-2} , r^{-3} , and r^{-4} , respectively.

Elastic displacements are given now by the time convolution of the forces acting at the focus with the Green's function for the medium. The simplest Green's function is that corresponding to an homogeneous infinite medium (full space). Internal sources must be in equilibrium, thus satisfying the condition that their resulting total force and moment are zero. Therefore, we consider as a seismic source only the symmetric part of M_{kl}^f as a seismic moment tensor, i.e.,

$$M_{jk} = M_{jk}^f + M_{kj}^f. \quad (25)$$

Fig. 3.34 shows all possible 6 couples and three dipoles of the seismic moment tensor M_{jk} .

If we want to represent the shear motion on a fault, the equivalent system of forces is that of two couples with no resulting moment, called a double-couple model (DC) (see Figure 8). If the couples are oriented in the direction of the two perpendicular unit vectors e_i and l_i , respectively, with $e_i l_i = 0$, and if their scalar seismic moment is $M_0(\omega) = \lim_{|s_i| \rightarrow 0} |s_i| |F_k|$, where $|s_i|$ is the length of the arm of the couple and $|F_k|$ the amount of the force, the displacement caused by the double-couple source is given by

$$u_i^{DC}(x_s, \omega) = M_0(\omega)(e_k l_j + e_j l_k) G_{ik,j}(x_s, x_s^o, \omega). \quad (26)$$

Note that in the given case the comma in the subscripts of G represents the partial derivative with respect to the source co-ordinates.

If an earthquake is produced by a fault in the Earth's crust, a mechanical representation of its source can be given in terms of fractures or dislocations in an elastic medium. A displacement dislocation consists of an internal surface S with two sides (S^+ and S^-) inside of the elastic medium (see Figure 5) across which there exists a discontinuity of displacement; however, stress is continuous. Thus, S is a model of a seismic fault. Coordinates on this surface are ξ_k and the normal at each point is n_i . From one side to the other of this surface there is a discontinuity in displacement D_i , which is termed the slip or dislocation on the fault:

$$D_i(\xi_k, \omega) = u_i^+(\xi_k, \omega) - u_i^-(\xi_k, \omega). \quad (27)$$

The plus and minus signs refer to the displacement at each side of the surface S . If there are no body forces ($F_i = 0$), and the stresses are continuous through S , then, for an infinite medium, the equation relating the displacement to the dislocation D_i , results in

$$u_n(x_s, \omega) = \int_S D_i(\xi_s, \omega) c_{ijkl} n_j(\xi_s) G_{nk,l}(x_s, \xi_s, \omega) dS(\xi_s). \quad (28)$$

Equation (27) corresponds to a kinematic model of the source, that is a model in which elastic displacements u_i are derived from slip vector D_i . The latter represents a non-elastic displacement of the two sides of a fault (i.e., of the model surface S). In a kinematic model slip is assumed to be known. It is not derived from stress conditions in the focal region as it is in dynamic models. Equation (28) contains the Green's function discussed in conjunction with Equation (24). When seismic waves, generated by the source, are observed in the far-field, i.e., at distances r much larger than the wavelength and the linear source dimension, than the Green's function is proportional to ω . Accordingly, the dominant term of the integrant in Equation (28) is ωD_i which is, in the time domain, proportional to the slip velocity. Thus, the elastic displacement observed in the far-field does not depend on the slip in the source but on the slip velocity and, similarly, on the seismic moment rate $\partial M_{ik}(t)/\partial t = \dot{M}_{ik}$ (see Fig. 2.4). Or, in the frequency domain, the displacement is proportional to $i\omega M_{kl}(\omega)$. This means that the source radiates elastic energy only while it is moving; when motion at the source stops it ceases to radiate energy.

The most common model for the source of an earthquake is a shear fracture, that is, a fracture in which the slip D_i is perpendicular to the normal of the fault. For a fault plane S of area A and normal n_i , the slip $D_i(\xi_s, t)$ is in the direction of the unit vector l_i contained in the plane. Accordingly, l_i and n_i are perpendicular and the scalar product $n_i l_i = 0$. For an infinite, homogeneous isotropic medium, displacement according to Equation (28) is given by

$$u_i(x_s, \omega) = \int_S \mu |D_l(\xi_s, \omega)| (l_k n_j + l_j n_k) G_{ik,j}(x_s, \xi_s, \omega) dS(\xi_s) \quad (29)$$

For modeling a shear dislocation source, the parameters on the right-hand side of Equation (29) have to be known. Implicitly these parameters include information about the rupture propagation, i.e., on the shape of the crack front, its propagation direction and propagation velocity (crack velocity), and shape of the final ruptured surface S .

The circular fault and the rectangular fault are the most important approximations. In the first case the rupture begins at the center and the crack front is described by an outward propagating circle. However, the direction of the dislocation is not necessarily radially symmetric. This circular model, described by Brune (1970) and Madariaga (1976), should be valid for small earthquakes with magnitudes smaller than about 4 to 5. Another approximation, for large earthquakes in the Earth's crust in particular, is a rectangular fault model, also called Haskell-model (Haskell, 1964). The length of the fault, generally assumed to be horizontal, is larger than its width (depth) by a factor of 2 to 10 or even more for very large earthquakes. This is due to the limited thickness of the seismogenic zone of the upper lithosphere, usually ranging between about 10 and 25 km, where brittle fracturing is possible. On the other hand, large crustal earthquakes may have a rupture length of 200 km or even more, e.g., about 450 km for the Alaska earthquake of 1964 and about 1000 km for the Chile earthquake of 1960. This rectangular model is also useful for describing deeper earthquakes in subduction zones.

When the Haskell-model is used the behavior of the rupture front must be known. The first approximation is that the rupture starts along a line and propagates unilaterally or bilaterally over the rectangular fault plane (see Figure 6). This approximation is useful for long ruptures with small width (the line-source approximation). It is also suitable for distinguishing between an in-plane and an anti-plane fault geometry. In the case of an in-plane fault the rupture moves into the direction of the slip whereas in the anti-plane case the direction of slip is parallel to the rupture front (see Figure 6).

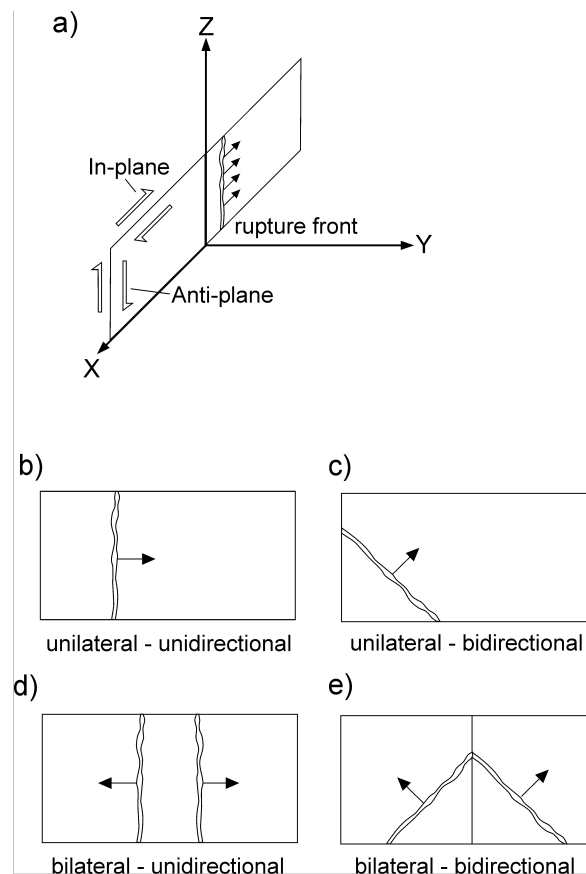


Figure 6 Several models of rupture propagation

For describing the rupture propagation in the case of a rectangular fault the following four terms and definitions, shown in Figure 6, are important:

- unilateral rupture propagation – one rupture front propagates over the entire fault plane;
- bilateral rupture propagation – two rupture fronts with different directions propagate over the rupture plane;
- unidirectional rupture propagation – the direction of rupture propagation is parallel to the length of the fault plane; and
- bidirectional rupture propagation – the rupture starts at a point and propagates across the fault plane.

Other models for describing the shape of the fault plane, the shape of the rupture front, and the mode of the rupture propagation are possible.

With respect to the velocity of rupture propagation the most common models assume values between about 0.6 to 0.9 of the shear-wave velocity v_s (see 2.2) in the source region; however, detailed field and laboratory investigations have shown that both slower (so-called “silent earthquakes”) and supersonic ($> v_s$) rupture propagation velocities are possible (e.g., Tibi et al., 2001). Rupture velocity depends on the material properties, the internal friction of the unbroken material, the frictional conditions along the fractured surface and the stress conditions (ambient and on the crack tip) in the given case.

For the point source approximation Equation (29) takes the simpler form

$$u_i(\omega) = \mu A |D_l(\omega)| (l_k n_j + l_j n_k) G_{ik,j}(\omega) \quad (30)$$

or, in the time domain,

$$u_i(t) = \mu A (l_k n_j + l_j n_k) \int_{-\infty}^{\infty} |D_l(\tau)| G_{ik,j}(t - \tau) d\tau. \quad (31)$$

Displacements are given by temporal convolution of slip with the derivatives of the Green’s function. The geometry of the source is now defined by the orientation of the two unit vectors n_i and l_i . These two vectors, which refer to the geophysical co-ordinate system of axes (North, East, Nadir), define the orientation of the source, namely n_i the orientation of the fault plane and l_i the direction of slip. These two vectors can be written in terms of the three angles that define the motion on a fault, namely, azimuth ϕ , dip δ and rake λ . The shear fracture itself is equivalent to a DC source in terms of forces (see Figure 7).

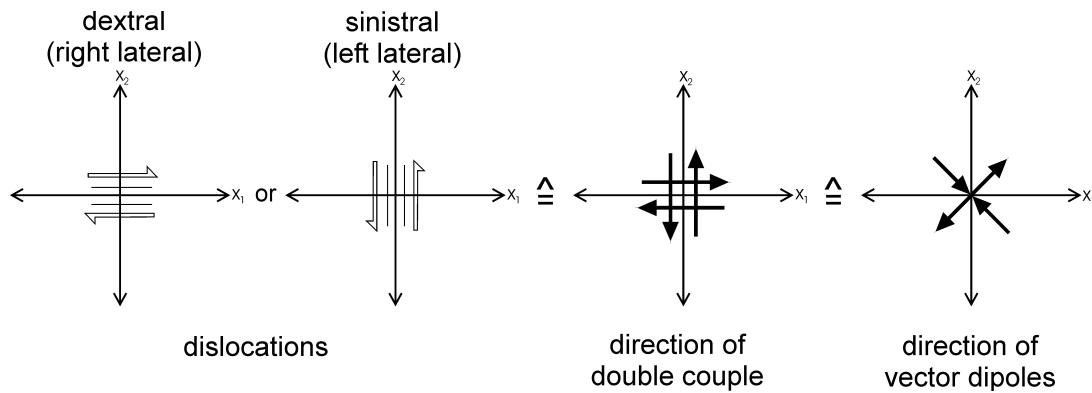


Figure 7 Depiction of the equivalence of a shear dislocation with the force double couple and the vector dipole models.

In the case that l_i and n_i are not perpendicular, Equation (29) has to be replaced by

$$u_k(x_s, \omega) = \int_S [\lambda \delta_{jk} n_l l_l + \mu (l_k n_j + l_j n_k) G_{ik,j}(x_s, \xi_s, \omega)] |D_n(\xi_s, \omega)| dS(\xi_s). \quad (32)$$

The special case when l_i and n_i are parallel is often used to model tensional volcanic earthquakes (Figure 8).

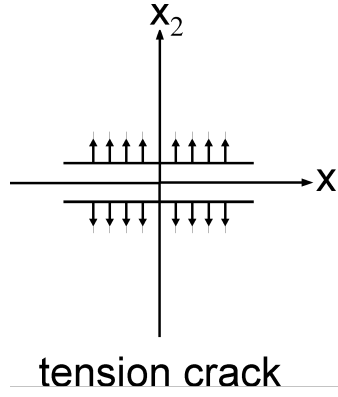


Figure 8 Illustration of a tension crack which is often used in modeling volcanic earthquakes.

Another more general representation of seismic source is given by the seismic moment tensor density m_{ij} . The moment tensor density represents that part of the internal strain drop which is dissipated in non-elastic deformations at the source. So far we have modeled the seismic source by means of the forces in the equation of motion (see Equation (1)) or by boundary conditions for the displacement (see Eqs. (17) and (28)). Now we take another approach and divide the true strain tensor ϵ_{ij}^{true} into an elastic and inelastic part, i.e.,

$$\epsilon_{ij}^{true} = \epsilon_{ij}^{ek} - \epsilon_{ij}^{inel}. \quad (33)$$

With this we define the true stress

$$\sigma_{ij}^{true} = \sigma_{ij} - m_{ij}^V \quad (34)$$

where σ_{ij} is the elastic stress related to the strain by Equation (10) or (13) and m_{ij}^V is given by

$$m_{ij}^V = c_{ijkl} \epsilon_{kl}^{inel}. \quad (35)$$

Equation (35) defines the seismic moment tensor density m_{ij}^V . The superscript V indicates that it is a volumetric density. Rice (1980) and Madariaga (1983) denote ϵ_{ij}^{inel} as the stress-free strain or transformation strain, and m_{ij}^V as the stress glut. The seismic moment tensor M_{ij} is, thus, defined by

$$M_{ij}(\omega) = \int_{V_o} m_{ij}^V(x_k, \omega) dV(x_k). \quad (36)$$

The quantities m_{ij}^V and M_{ij} play a fundamental role in the theory of seismic sources. The relations between the different kinds of stress are shown in Figure 9. When σ_{ij} in (15) is substituted by σ_{ij}^{true} an additional force term appears on the right side. It can be interpreted as an equivalent force density f_i^{eq} or as an equivalent force F_i^{eq}

$$f_i^{eq}(x_k, \omega) = -m_{ij,j}^V(x_k, \omega) \quad \text{and} \quad F_i^{eq} = -\int_{V_o} m_{ij,j}^V(x_k, \omega) dV(x_k). \quad (37)$$

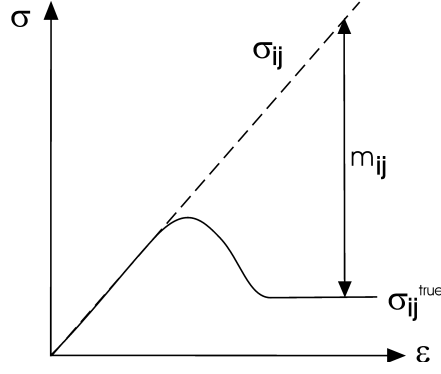


Figure 9 Relationship between the elastic stress σ_{ij} , related to the strain ε , the true stress σ_{ij}^{true} and the seismic moment density tensor m_{ij}^V .

In replacing the body force in Equation (19) by the equivalent force density in Equation (37) an additional volume integral $-\int_{V_o} G_{ij} m_{jk,k}^V dV$ appear. After an integration by parts and assuming that m_{jk}^V vanishes on S , i.e., the inelastic volume is bordered by S , the displacement produced by m_{ij}^V is

$$u_i(x_i, \omega) = \int_{V_o} G_{ik,j}(x_s, \xi_s, \omega) m_{jk}^V(\xi_s, \omega) dV(\xi_s). \quad (38)$$

When comparing Eqs. (38) and (28) one realizes that the integrands have the same form but the integration in (38) is over a volume while it is over a surface in Equation (28). Accordingly, the stress glut m_{ij}^V is equivalent to a dislocation when the inelastic volume can be approximated by an inelastic internal surface. Naming this stress glut by m_{ij}^S from Equation (28) we see that

$$m_{kl}^S = c_{ijkl} D_i n_j \quad (39)$$

for the general linear elastic case and for the shear crack in an isotropic medium holds

$$m_{ij}^S = \mu(D_i n_j + D_j n_i). \quad (40)$$

For the spatially averaged dislocation $\overline{D}_i(\omega)$, the seismic moment tensors M_{ij} in these two cases become

$$M_{ij}(\omega) = c_{ijkl} \overline{D}_k(\omega) n_l A \quad \text{and} \quad M_{ij}(\omega) = \mu[\overline{D}_i(\omega) n_j + \overline{D}_j(\omega) n_i] A, \quad (41)$$

respectively. In the latter case, when \overline{D}_i and n_j are perpendicular, the scalar seismic moment is

$$M_0(\omega) = \mu |\overline{D}_i(\omega)| A. \quad (42)$$

In the general case of an arbitrary moment tensor the scalar seismic moment is defined by

$$M_0 = \sqrt{\frac{1}{2} M_{ik} M_{ik}} . \quad (43)$$

4 Dynamic Source Models

Dynamic source models, or crack models, use a given stress on an internal surface (fault) to describe a seismic source. In this case Equation (19) is not valid. In general, two terms must be added to the right side of Equation (19). These terms include boundary conditions for the displacement and the stress. Note that only one of these conditions can be freely chosen while the other one has to be calculated. The computation of the Green's function requires boundary conditions as well, either for the Green's function itself or for the stress produced by it. These boundary conditions do not influence the result of the computation of the displacement $u_i(x_s, \omega)$. Therefore, we can freely select any suitable boundary conditions. When selecting a Green's function which produces a vanishing stress on the internal surface S this Green's function is called G_{ij}^{free} because the related internal surface behaves like a free surface. The advantage is, that this kind of source representation does not require a knowledge of the displacement produced by the given stress on the internal surface. When no body force acts it holds that

$$u_i(x_i, \omega) = \int_S G_{ik}^{free}(x_s, \xi_s, \omega) n_j \sigma_{kj}(\xi_s, \omega) dS(\xi_s) . \quad (44)$$

Equation (44) simplifies the computation of the displacement or the dislocation on the fault when the stress on the fault is given. When using other kinds of representations an inhomogeneous integral equation for $u_i(\xi_s, \omega)$ on the fault has to be solved.

In the dynamic models the static stress drop $\Delta\sigma_{ij}$ plays an important role. It is defined as the difference between the stress distribution σ_{ij}^o on the fault plane before the occurrence of the earthquake and the stress σ_{ij}^1 after the earthquake. This static stress drop is

$$\Delta\sigma_{ij}(\xi_s) = \sigma_{ij}^o(\xi_s) - \sigma_{ij}^1(\xi_s) \quad (45)$$

with $\sigma_{ij}^1(\xi_s) = \lim_{t \rightarrow \infty} \sigma_{ij}(\xi_s, t) = \lim_{\omega \rightarrow 0} i\omega \sigma_{ij}(\xi_s, \omega)$. A more general time dependent stress on the fault is shown in Figure 10 (Yamashita, 1976).

A case of practical importance is that of a circular shear fault. It is probably a good approximation for small earthquakes in the Earth's crust with magnitudes smaller than 4 as long as only frequencies $< 5-10$ Hz are considered. If a homogeneous shear stress drop $\Delta\sigma_{12}$ in the x_1-x_2 plane is assumed, the static dislocation on the fault is

$$D_1 = \frac{8}{\mu\pi} \frac{\lambda + 2\mu}{3\lambda + 4\mu} \Delta\sigma_{12} (R_0^2 - r^2)^{1/2} \quad (46)$$

where R_0 is the final radius of the broken fault and r the radial co-ordinate. If $r > R_0$ the dislocation in Equation (46) is zero. By inserting Equation (46) in (41) we get for the static seismic moment

$$M_0 = \frac{16}{3} \frac{\lambda + 2\mu}{3\lambda + 4\mu} \Delta\sigma_{12} R_0^3 \quad (47)$$

and for $\lambda = \mu$ the well known result derived by Keilis-Borok (1959) is given by

$$M_0 = \frac{16}{7} \Delta\sigma_{12} R_0^3. \quad (48)$$

Similar relations hold for rectangular shear cracks of the length L and a width W :

$$M_0 = C L^2 W \Delta\sigma_{12} \quad (49)$$

where C is a model-dependent constant in the order of **1** and $\Delta\sigma_{12}$ is uniform over the fault. In the case of a buried in-plane shear crack holds

$$C = \frac{\pi}{8} \frac{\lambda + 2\mu}{\lambda + \mu} \quad (50)$$

and for a buried anti-plane case

$$C = \frac{\pi}{4}. \quad (51)$$

When the fault is perpendicular to the Earth's surface and outcropping then C in the Eqs. (50) and (51) is twice as large.

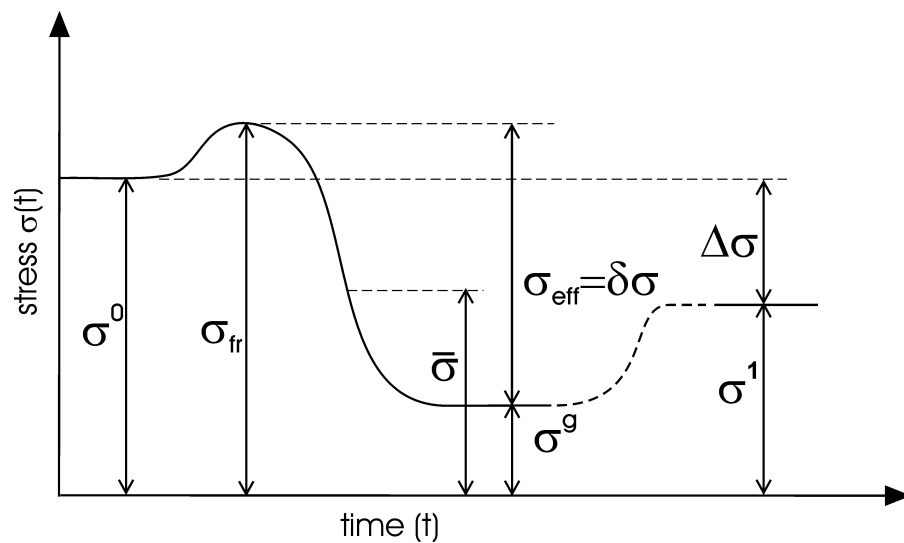


Figure 10 Time dependence of stress at a point on the fault surface during an earthquake. σ^0 and σ^1 – stress before and after the earthquake, σ_{fr} – fracture strength, $\bar{\sigma}$ - mean stress,

σ^g – friction stress, σ_{eff} – effective stress = dynamical stress drop $\delta\sigma$ and $\Delta\sigma$ - static stress drop.

The dynamic relation between the shear stress drop $\Delta\sigma$ and the dislocation can be calculated numerically. An example is shown in Figure 11. The rupture starts at $t=0$ and $r=0$ and expands with constant velocity. The time t and the dislocation $|D_i(r,t)|$ are normalized to R_0/V_p and $\Delta\sigma R_0/\mu$ where V_p is the velocity of the P wave ($V_p^2 = (\lambda + 2\mu)/\rho$ with ρ as the density of the medium).

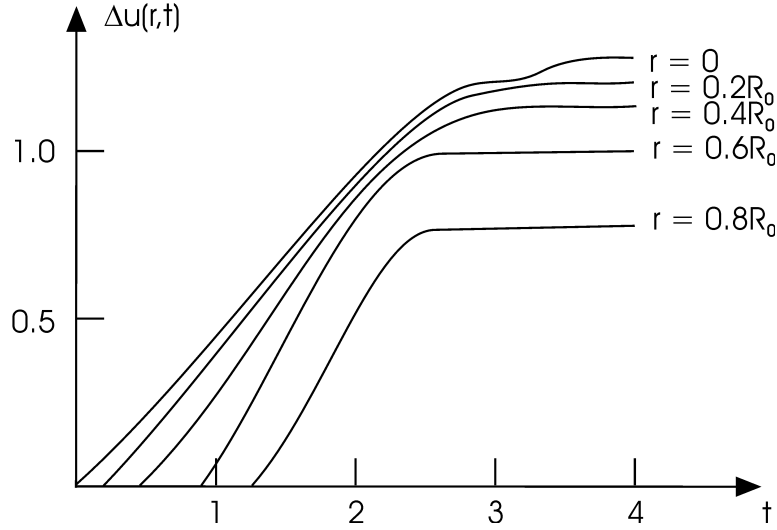


Figure 11 Dislocation function $D(r, t)$ at several distances from the center on the circular crack plotted against the normalized time t . For explanation of symbols see text (according to Madariaga, 1976; modified from Aki and Richards, 1980).

5 Energy, Moment, Dislocation and Stress drop

The radiated energy of an earthquake can be computed assuming a specific source model and its source parameters. We describe the earthquake as a shear rupture on a surface. In a relatively general form Kostrov (1975) writes for the radiated seismic energy E_S

$$E_S = \int_0^{t_{max}} dt \int_{S(t)} dS(\xi_k) (\sigma_{ij}^0 - \sigma_{ij}) \dot{D}_i n_j - \frac{1}{2} \int_A dS \Delta\sigma_{ij} D_i^0 n_j - \int_A g dS \quad (52)$$

where t_{max} is the maximum duration of the motion on the fault plane, $S(t)$ the rupture plane developing during the rupture, A the final rupture plane with $A = \lim_{t \rightarrow \infty} S(t)$, $\sigma_{ij}^0(\xi_s)$ the stress before the earthquake occurred, $\sigma_{ij}(\xi, t)$ the stress on the broken fault surface, $\dot{D}_i(\xi_s, t) = \partial/\partial t D_i(\xi_s, t)$ the dislocation velocity, $\Delta\sigma_{ij}(\xi)$ the static stress drop (see Figure 10), n_j the normal vector of the fault surface, $D_i^0(\xi_s)$ the static dislocation, and g the specific energy required to generate a new surface. Equivalent to Equation (52) is the often used form

$$E_S = \int_0^{t_{max}} dt \int_{S(t)} dS \dot{D}_j n_j (\bar{\sigma}_{ij} - \sigma_{ij}) - \int_A g dS \quad (53)$$

where $\bar{\sigma}_{ij} = (\sigma_{ij}^0 + \sigma_{ij}^1)/2$ denotes the mean stress, σ_{ij}^0 is the stress before the earthquake, and σ_{ij}^1 is the final stress, which may be equal to the frictional stress. When taking into account the grow of the rupture area during the earthquake in the formulation of the dislocation (source time) function $D_i(t)$, Equation (53) becomes

$$E_s = \int_A dS \int_0^{D_i^f} dD_i n_j [\bar{\sigma}_{ij} - \sigma_{ij}(D_k)] - \int_A g dS \quad (54)$$

where $\sigma_{ij}(D_k)$ is the stress-dislocation relation on the fault plane and D_i^f the final dislocation.. In the Eqs. (52) to (54) the seismic energy E_s is composed of released deformation energy E_{tot} , frictional energy E_f , and rupture (crack) energy E_r

$$E_s = E_{tot} - E_f - E_r \quad (55)$$

with

$$\begin{aligned} E_{tot} &= \int dS \bar{\sigma}_{ij} D_i n_j \\ E_f &= \int dS \int dD_i n_j \\ E_r &= \int g dS \end{aligned} \quad (56)$$

With this we define the seismic efficiency η

$$\eta = \frac{E_s}{E_{tot}} \quad (57)$$

and the apparent stress σ_{app}

$$\sigma_{app} = \frac{1}{A \overline{|D_i|}} \int e dS \quad (58)$$

where $\overline{|D_i|}$ is the spatial averaged absolute value of the dislocation. The energy density e is identical with the integrant of the surface integral. Therefore the following relation between the seismic energy and the scalar seismic moment holds:

$$E_s = \sigma_{app} M_0 / \mu \quad (59)$$

Further special cases are:

a)

σ_{ij}^0 , σ_{ij} , σ_{ij}^1 are homogeneous and σ_{ij} equal to the time-independent friction stress σ_{ij}^g Eqs. (3), (6) and (7) yield

$$E_s = (\bar{\sigma}_{ij} - \sigma_{ij}^g) D_i^f n_j S_0 - E_r \quad (60)$$

$$\eta = \frac{(\sigma_{ij}^0 + \sigma_{ij}^1 - 2\sigma_{ij}^g) e_i n_j - 2\bar{g}}{(\sigma_i^0 + \sigma_{ij}^1) e_i n_j} \quad (61)$$

$$\sigma_{app} = \frac{1}{2} (\sigma_{ij}^0 + \sigma_{ij}^1 - 2\sigma_{ij}^g) e_i n_j - \frac{\bar{g}}{|\bar{D}_i|} \quad (62)$$

where \bar{g} is the averaged specific rupture energy and e_i a unit vector in the direction of the dislocation. With this we get

$$\sigma_{app} = \eta \bar{\sigma}_{ij} e_i n_j. \quad (63)$$

b)

For a shear fracture, and $\sigma_{ij}^g = \sigma_{ij}^l$ with $g \approx 0$ as an approximation or $g = 0$ in the case of an *anti-plane* brittle rupture propagating with shear-wave velocity or of an *in-plane* brittle rupture propagating with Rayleigh-wave velocity, respectively, we get

$$E_s = \frac{1}{2} D_i^f n_j \Delta\sigma_{ij} S_o = \frac{1}{2\mu} \Delta\sigma_{ij} M_{ij} \quad (64)$$

with
$$\Delta\sigma_{ij} = \sigma_{ij}^0 - \sigma_{ij}^l. \quad (65)$$

Ohnaka (1978) gives the following relationship for the seismic energy of a circular shear fracture propagating with the crack velocity $v_c = 0.8 v_s$:

$$E_s = \frac{M_o \bar{D}_0}{2R} \quad (66)$$

with M_o – scalar seismic moment, \bar{D}_0 - static averaged dislocation and R – source radius. For rectangular shear fractures of length L and with unilateral fracture propagation a similar approximate relationship holds:

$$E_s \approx \frac{M_o \bar{D}_0}{3L} \quad (67)$$

and in case of partial incoherence

$$E_s \approx \frac{M_o \bar{D}}{L}. \quad (68)$$

Further, E_s can be determined directly by integrating over the displacement field. It holds

$$E_s = \sum_k \int_{-\infty}^{\infty} dt \int_S dS \rho v^{(k)} \dot{u}_i^{(k)} \dot{u}_i^{(k)} \quad (69)$$

with S – a surface surrounding the source, ρ – density distribution on this surface, $\dot{u}_i^{(k)}$ – velocity of ground motion. The sum is over all kinds of waves which leave the volume enclosed by the surface S with the velocity $v^{(k)}$. However, one has to take into account that on the way from the source to S part of the energy has already been transformed into heat by inelastic effects of wave propagation.

Equation (69) forms the theoretical background for the simple relationship between seismic energy and magnitude M

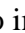
$$\log E_s = a M + b \quad (70)$$

which is based on rather simple assumptions. Nevertheless, the corresponding relationship given by Gutenberg and Richter (1956) is

$$\log E_s[\text{J}] = 1.5 M_s + 4.8 \quad (71)$$

with M_s – surface wave magnitude (see 3.2.5.1). Equation (71) has proven to yield rather good estimates of E_s . More details on direct energy determination based on digital broadband recordings is outlined in 3.3.

Acknowledgments

The authors acknowledge with thanks the fruitful discussions with Rongjiang Wang and Dietrich Stromeyer of the GFZ Potsdam and careful reviews by George Choy and Günter Bock . Their suggestions have helped to improve the first draft of this information.

References (see References under Miscellaneous in Volume 2)

Title	Proposal for unique magnitude nomenclature
Compiled by	Peter Bormann (formerly GeoForschungsZentrum Potsdam,Telegrafenberg, D-14473 Potsdam, Germany); E-mail: pb65@gmx.net
Version	June 2002

Current practice at the international seismological data centers is to determine the following “generic” magnitudes (alternative names given in brackets) from amplitude and period or signal duration readings and reports of seismological stations or networks:

mb – (m_b , Mb) short-period teleseismic P-wave magnitude from vertical component records
 Ms – (M_s , MS) surface-wave magnitude from vertical and/or horizontal component records
 Ml – (M_L , ML) local magnitude from horizontal and/or vertical component records as derived from original or simulated Wood-Anderson seismograph records
 Md – (M_D , MD) local duration magnitude using different types of records

Besides these classical magnitudes, which have been determined already for decades, mostly from analog records, others, such as the moment magnitude Mw and the energy magnitude Me, require digital broadband recordings and their spectral analysis or integration in the time-domain. Up to now they have been regularly determined only by a few specialized data centers. However, the broader use of these modern magnitude concepts is rapidly growing.

Short-comings of the current procedures to determine and annotate classical magnitudes are:

- body-wave magnitudes are determined from *vertical component* P-waves only although Gutenberg-Richter published body-wave calibration functions $Q(\Delta, h)$ for both vertical and horizontal component readings of P and PP as well as for horizontal component readings of S;
- mb is determined from *short-period* recordings only, although the body-wave Q-functions have been derived mainly from medium-period, more or less broadband recordings;
- earlier recommendations made by respective IASPEI Commissions and published in the old Manual of Seismological Practice (Willmore, 1979) have not been put into practice yet, namely to determine magnitudes for all seismic waves and from all components for which calibration functions are available and to indicate the type of instruments on which the parameter readings (amplitudes, periods and/or duration) for a given magnitude value were made;
- the currently used “generic” nomenclature does not describe unambiguously which type of seismic wave, response characteristic and record component has been used for deriving the magnitude values. This has resulted in averaging incompatible non-standard magnitude readings and sometimes uncontrolled shifts in baselines (see 1.1 and 3.2).

Data providers should be aware that earlier limitations in seismological parameter reporting to World Data Centers based on the old Telegraphic Format no longer exist. The IASPEI Seismic Format (ISF) adopted at the IASPEI meeting in 2001 (see Chapter 10, section 10.2.5) is much more flexible and permits detailed parameter reports with unambiguous flagging.

An IASPEI Working Group on magnitude measurements, established in 2001, is at present critically screening the procedures of amplitude measurement and magnitude determination practiced at seismic stations and various data centers. Its members are: J. Dewey (chairman), P. Bormann, P. Firbas, S. Gregersen, A. Gusev, K. Klinge, B. Presgrave, L. Ruifeng, K. Veith, and W.-Y. Kim. This group came to the following preliminary conclusions:

“Recently identified significant differences, e.g., in mb values determined by the IDC and NEIC, are due in part to differences in signal filtering and measurement procedures at the two centers. Therefore, the WG has been charged by IASPEI to propose by mid 2003 specific filter parameters and amplitude and period measurement procedures to be authorized by IASPEI as "standard." The WG is also to propose a unique standard nomenclature for parameter reporting. The group has agreed to elaborate such recommendation for the following "generic" magnitudes: Ml, Ms, mB, mb, Mw and Me. The first three magnitudes are based on band-limited recordings of typically 0.5 to 1, maximum of 2 decades bandwidth. They are in good agreement with the original definitions for local magnitudes by Richter (1935) and for teleseismic body-wave and surface-wave magnitudes by Gutenberg and Richter (1945a and b) and other authors. Deviating from this, the more recent mb is a short-period (1Hz) narrowband (about 0.3 decade) version of the body-wave magnitude mB for P-waves only. Its main advantage is related to the fact that this frequency band is nearly optimal for remote monitoring of even weak seismic events in any area of the Earth. Thus the number of earthquakes with known teleseismic mb is much larger than that for any other teleseismic magnitude. In contrast, Mw and Me are based on (very) broadband (typically 3 to 4 decade) digital displacement or velocity recordings and their computer-assisted analysis. These modern magnitude concepts have a clear physical basis and gain rapidly more and more importance with the current availability of low-noise high-resolution broadband sensors and digital recordings with large dynamic range. Nonetheless, both Mw and Me are scaled to Ms and the classical Gutenberg-Richter logEs-Ms relationship. Moreover, these classical magnitudes still form the majority of available magnitude data and have, besides their recognized limitations (such as saturation), well established merits, e.g. the relevance of Ml and mb, for engineering seismology, their reasonable scaling with seismic intensity and thus their relevance for seismic hazard assessment. Therefore, to assure the long-term continuity of classical standard magnitudes is a matter of high priority. This requires a proper scaling of modern magnitudes based on digital data with their forerunners that were based on analog data. Jumps in detection thresholds and catalog completeness due to unknown or not properly documented changes in measurement procedures may result in wrongly inferred changes of the relative frequency of occurrence of weaker and stronger earthquakes and be misinterpreted as changes in the seismic regime and the time-dependent seismic hazard. This is not acceptable. On the other hand one should also recognize, that no one of the above mentioned standard magnitudes can fully substitute for the others. None of them allows a comprehensive and unique quantification of the "size" of an earthquake. Rather, these scales complement each other, and - when used in combination - allow better to understand the specifics of the seismic source process. Therefore, the magnitude WG intends, after authorization by IASPEI, to publish before the end of 2003 recommended standard procedures to determine these basic magnitudes with modern data and procedures in a unique or equivalent way and assure proper scaling to their original definition. These recommendations will then become an Annex to this manual.”

By May 2002, the WG had also reached the following general understanding that:

- the “generic” magnitudes M_l , m_b and M_s (see 3.2) are most common, and related data for their determination are regularly reported by seismic stations and networks/arrays to international data centers;
- these “generic” magnitudes are widely accepted and applied by a diversity of user groups. Therefore, their names should be kept when reporting magnitude data to a broader public.
- this nomenclature is also considered to be adequate for many scientific communications, on the understanding that these magnitudes have been determined according to well established rules and procedures;
- the WG realized, however, that different data producers make their related measurements for determining these magnitudes on records with different response characteristics and bandwidths, on different components and types of seismic waves and sometimes also use different period and time windows. This increases data scatter, may produce baseline shifts and prevents long-term stable, unique and reproducible magnitude estimates that are in tune with original definitions and earlier practices;
- this situation is no longer acceptable, therefore, the WG felt a need to introduce an obligatory more “specific” nomenclature for reporting amplitude (and period) measurement data for databases and for use in scientific correspondence in which the ambiguity inherent in the “generic” nomenclature might cause misunderstanding;
- the WG notes that the recently accepted IASPEI Seismic Format (ISF, see 10.2.5) and the flexibility of internet data communication allow such specifications in nomenclature and even complementary remarks to be reported to international data centers, and to store and retrieve such data from modern relational databases.

In order to assure future IASPEI-authorized standards annotation and reporting of measurements for amplitude-based seismic magnitudes, the WG agreed therefore along these lines of understanding on the following preliminary recommendations pending future specification and approval by IASPEI:

“Amplitude measurements for identified seismic phases are to be specified and reported to data centers in the following general format:

AXY(F)

with	A	amplitude
	X	phase name according to the new IASPEI nomenclature (see IS 2.1)
	Y	component of measurement (Z = V – vertical; N – north-south; E – east-west; H – horizontal, i.e., vectorially-combined N and E; R – radial or T – transversal)
	F	one of several standard filter/seismograph responses

An IASPEI Working Group is currently elaborating standardized filter/seismograph responses (F) for making amplitude measurements for the estimation of standard generic magnitudes M_l , M_s , m_b and m_B .”

Below a starting proposal is made for further discussion on unambiguous nomenclature for “specific” magnitude names to be used in international data reporting and exchange with databases as well as in more specific scientific literature and communications. It is based on

the following established procedures, reference data such as calibration functions, earlier recommendations by former IASPEI WGs and standard seismograph response classes (A, B, C and D) as presented in Fig. 1.1 of the old Manual of Seismological Observatory Practice (Willmore, 1979).

The following abbreviations are used in Table 1 below:

- A records of type A (short-period and more or less narrowband, centered between about 1 and 2 Hz such as the WWSSN-SP);
- B records of type B (long-period band-limited as WWSSN-LP with peak magnification around 15 s);
- C displacement-proportional broadband in the period range 0.1 s to 20 s such as the Kirnos SKD seismographs;
- D velocity-proportional broadband seismographs in the period range of about 1s to 100s
- WA displacement-proportional Wood-Anderson horizontal seismographs in the period range 0.1 to 0.8 s;
- IDC response characteristic used at the International Data Center of the CTBO in Vienna, and formerly used at the Prototype International Data Center in the U.S., for filtering beam data prior to magnitude determination. The response is velocity-proportional between about 1 and 5 Hz; i.e., its displacement magnification peaks at 5 Hz;

Note 1: These symbols for standard responses might be replaced in the final recommendations by specified filters (F) for simulated responses of either classical or specific modern seismographs.

- M general symbol for magnitude. When used alone, M stands for the unified Magnitude according to Gutenberg and Richter (1956a and b). When followed by a phase symbol, the magnitude has been determined from amplitude/period readings of this phase;
- Δ epicentral distance as commonly used in calibration functions;
- h hypocentral depth;
- Q(Δ , h) body-wave calibration functions according to Gutenberg and Richter (1956a and b). They are available for PZ, PH, PPZ, PPH, SH (see Figures 1a-c and Table 6 in DS 3.1). The use of Q(Δ , h)_{PZ} for mb determination is the current practice at the NEIC and the ISC although this is not fully correct (see 3.2.5.2);
- $\sigma(\Delta)$ Prague-Moscow (Karnik et al., 1962) calibration function for surface-wave readings of both LZ and LH; recommended as standard by IASPEI and used at both the NEIC and the ISC (see Table 4 in DS 3.1)
- P(Δ , h) body-wave calibration functions according to Veith and Clawson (1972) for vertical component displacement records with peak magnification centered around 1 Hz (see Figure 2 in DS 3.1). P(Δ , h) is currently used at the IDC for mb determination although the IDC response is centered around 5 Hz. This results in an underestimation of attenuation and thus systematically lowers mb values.
- CF Stands for any other specific calibration function.

Note 2: For magnitudes that have been determined from records of seismographs with other response characteristics than the standards A to D or WA and/or by using calibration functions other than $\sigma(\Delta)$, Q(Δ , h) or local scales properly linked to the original Richter MI (ML) scale, this has to be specified by giving F and CF in brackets, i.e., M(F; CF), or by adding a complementary comment line with the name of the relevant author/institution or with a link to proper reference and documentation.

Table 1 Preliminary proposal for “specific” and “generic” magnitude names and related descriptions.

Specific	Generic	Description
MPV(A)	mb	P-wave magnitude from short-period narrowband vertical component recordings of type A calibrated with $Q(\Delta, h)$ for PZ.
MPV(IDC)	mb	P-wave magnitude from short-period vertical component recordings with the IDC narrowband velocity band-pass filter and calibrated with $P(\Delta, h)$.
MPV(C)	mB	P-wave magnitude from medium-period (more broadband) recordings calibrated with $Q(\Delta, h)$ for PZ (= PV).
MPH(C)	mB	P-wave magnitude from medium-period (more broadband) recordings calibrated with $Q(\Delta, h)$ for PH.
MPPV(C)	mB	PP-wave magnitude from medium-period (more broadband) recordings calibrated with $Q(\Delta, h)$ for PPZ (= PPV).
MPPH(C)	mB	PP-wave magnitude from medium-period (more broadband) recordings calibrated with $Q(\Delta, h)$ for PPH.
MSH(C)	mB	S-wave magnitude from medium-period (more broadband) recordings calibrated with $Q(\Delta, h)$ for SH.
MLV(B or C)	Ms	Surface-wave magnitude from L readings in vertical component records of type B or C, respectively, calibrated with the IASPEI standard “Prague-Moscow” function $\sigma(\Delta)$ (cf. Eq. 3.10 in Chapter 3).
MLH(B or C)	Ms	Surface-wave magnitude from L readings in horizontal component records of type B or C, respectively, calibrated with $\sigma(\Delta)$.
MLRV(B or C)	Ms	Surface-wave magnitude from the maximum of the Rayleigh-wave train, vertical component in records of type B or C, respectively. MLRV is identical with MLV when calibrated with $\sigma(\Delta)$. If special calibration functions are used this has to be flagged accordingly.
MLRH(B,C)	Ms	Surface-wave magnitude from the maximum of the Rayleigh-wave train in the horizontal components of records of type B or C, respectively. MLRH may be identical with MLH when calibrated with $\sigma(\Delta)$. If special calibration functions are used this has to be flagged accordingly.
MLQH(B or C)	Ms	Surface-wave magnitude from the maximum of the Love-wave train in the horizontal component only of records of type B or C. MLQH may be identical with MLH when calibrated with $\sigma(\Delta)$. If special calibration functions Love waves are used this has to be flagged accordingly.
MH(WA; CF)	MI=ML	Local magnitude from Wood-Anderson seismographs (or synthesized WA response; here for horizontal components only), as defined by Richter (1935). For M(WA) magnitudes in other regions local/regional calibration functions CF may be used which should, however, be calibrated according to the original Richter scale.

MV(WA; CF)	Ml=ML	Local magnitude from Wood-Anderson seismographs (or synthesized WA response; here for vertical component records), as defined by Richter (1935). For M(WA) magnitudes in other regions local/regional calibration function may be used which should, however, be calibrated according to the original Richter scale.
MLgH(Author)	Ml=ML	Magnitude from Lg horizontal-component amplitude or spectral readings based on records, filters, procedures/methodology and calibration functions as defined/derived by specified author(s) or institutions.
MLgV(Author; MI)	Ml=ML	Magnitude from Lg vertical-component amplitude or spectral readings based on records, filters, procedures/methodology and calibration functions as defined/derived by specified author(s) or institutions and calibrated with respect to Ml.
MLgV(Author; mb)	mbLg = Mn	Magnitude from Lg vertical-component amplitude or spectral readings based on records, filters, procedures/methodology and calibration functions as defined/derived by specified author(s) or institutions and calibrated with respect to mb.
MPnZ(Author)	mb or Ml	Magnitude from Pn vertical-component amplitude or spectral readings based on records, filters, procedures/methodology and calibration functions as defined/derived by specified author(s) or institutions.
Md(Author)	Md	Magnitude from readings of signal duration based on records, filters, procedures/methodology and calibration functions as defined/derived by specified author(s) or institutions.
Mw(Author; Year)	Mw	Non-saturating moment magnitude based on the zero-frequency plateau of the displacement spectrum or other related estimates such as signal-moment in the time domain from digital broadband records as defined/derived by specified author(s) or institutions.
Me(Author; Year)		Energy magnitude as defined/derived by specific author(s) or institutions.
Mt(Author)	Mt	Tsunami magnitude as defined/derived by specific author(s) or institutions.

Note 3: Sometimes, even the same authors or institutions change their procedures or input parameters for magnitude computation. It is then recommended, to additionally specify the year of publication of documentation for a particular procedure.

Note 4: Amplitude readings on which magnitude determinations are based have to be flagged accordingly, e.g.: APV(A), APV(PIDC), ALgV(A), ASH(C), ALH(B), APn(PIDC) etc.

When comparing the first and second column in Table 1 one recognizes immediately the ambiguity of generic magnitudes. The differences between related specific magnitudes may be larger than 0.5 magnitude units. Such systematic differences would not be acceptable in many seismological studies.

References (see References under Miscellaneous in Volume 2)

Topic	Strainmeters
Author	Walter Zürn, Black Forest Observatory, Universities Karlsruhe/Stuttgart, Heubach 206, D - 77709 Wolfach; E-mail: walter.zuern@gpi.uni-karlsruhe.de
Version	October 2001

1 Introduction

In contrast to inertial seismometers, which respond to ground acceleration and thus to the second derivative of the displacement with respect to time, strain-seismometers, commonly termed extensometers or strainmeters, respond to the spatial derivatives of the displacement field of the incoming seismic wave or in other words, to a combination of the components of the wave's strain tensor. For this reason, strainmeters are inherently instruments which are sensitive to phenomena with "zero" (i.e., very low) frequency and thus particularly suitable for studying crustal deformations due to solid Earth tides and normal mode oscillations of the Earth. More precisely, linear strainmeters record the changes of the distance between the two points at which the instrument is fixed to the ground, while volumetric strainmeters (dilatometers) record the changes of a volume standard which is imbedded in the ground. An excellent, thorough and comprehensive review of strainmeters with an extensive bibliography was written by Agnew (1986) and is still up to date. Strainmeters were introduced into seismology already by Milne (1888).

2 Types of strainmeters

2.1 Linear strainmeters

This is the most frequently deployed type of strainmeter. The changes $dL(t)$ with time t of a fixed distance L between two points of the Earth are measured with the help of some length standard. Only a handful of strainmeters ever measured non-horizontal strains and all these were vertical, by far the majority was measuring horizontal strain. Agnew (1986) distinguishes rod strainmeters, wire strainmeters and laser strainmeters (see Figure 1). The length standard should be very stable against all kinds of environmental variables, especially temperature, air pressure and humidity. Because of these requirements, rods are mostly made of quartz, invar or superinvar and wires from invar or carbon fiber. Long rods somehow must be supported without friction, while wires must be tensioned. The length changes are detected by displacement or velocity transducers very similar to the ones used in modern inertial seismometers (see 5.3.7 and 5.3.8). One example of an Invar-rod strainmeter and its installation is described by Fix and Sherwin (1970). A frequently used type of wire strainmeter is described by King and Bilham (1976) and an installation in Widmer et al. (1992). Very short rod strainmeters can be placed in borehole packages, which then must be cemented to the borehole wall. An instrument of this type is described by Gladwin (1984). Laser strainmeters use the wavelength of light as a length standard and an unequal-arm Michelson interferometer for detection of strains. The interference fringes between the light beams along the long arm (the measuring distance L) and a short reference arm are observed with different methods, details of which can be found in the references given by Agnew (1986). It is clear that simple fringe counting necessitates L to be very large to obtain high

enough sensitivity: the wavelength of light is of the order of 500 nm, which is 10 times the amplitude of the Earth tide if L equals 1 m. Therefore the fringe counting laser strainmeters at Pinion Flat Observatory in California are more than 700 m long (Agnew, 1986; Wyatt et al., 1982, Agnew et al. 1989). Two other laser strainmeters with refined methods to determine the length changes using the fringes are described by Levine and Hall (1972) and by Gouly et al. (1974). The smallness of the expected signals with respect to the local noise from changes in the environmental conditions necessitates either installation deep underground in mines or boreholes or possibilities for anchoring the mounts to points deep in the ground (Wyatt et al., 1982). A typical installation depth with hope for success is larger than about 30 m below surface. Shielding the instruments is also mandatory and not as easy as for the much smaller inertial seismometers.

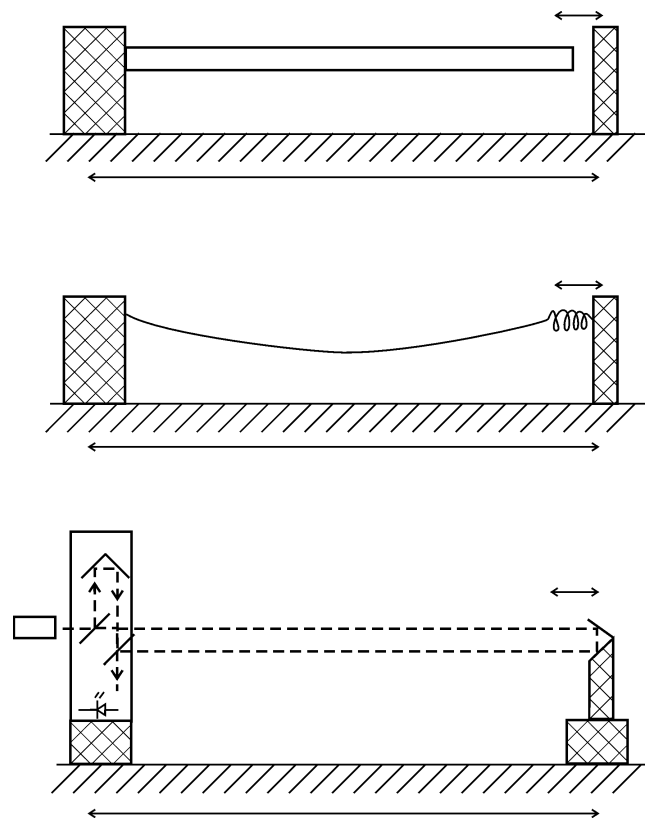


Figure 1 Schematics of the most frequent strainmeter designs. From top to bottom: rod-, (tensioned) wire- and laser strainmeters. The top two must be equipped with displacement transducers at the right. The bottom sketch indicates the laser, two beam splitters, one corner cube reflector and some sensor (symbol of photodiode) able to detect the change in the interference fringes due to the relative motion of the corner cube reflector on the pedestal to the right.

2.2 Volumetric strainmeters

Volumetric strainmeters or dilatometers measure the change $dV(t)$ of a certain volume V . A borehole instrument of this kind was constructed by Sacks et al. (1971) and widely deployed, especially in Japan. The volume changes are sensed by a liquid-filled tube which is cemented into the borehole. The deformation of the volume causes the liquid to expand or contract bellows, the movement of which is transmitted by a lever arm to displacement transducers.

In passing it should be mentioned that water wells drilled into confined aquifers act as sensors for the strain tensor in their vicinity, because applied strains force water in and out of the well, if it is open to the aquifer. Either the level of the water surface or water pressure at a constant depth are measured (e.g. Kämpel, 1992).

3 Properties

3.1 Sensitivity

A typical strain amplitude dL/L (no dimension!) of the solid Earth tide is 50 nano ($50 \cdot 10^{-9}$), while Widmer et al. (1992) reported 10 pico (10^{-11}) for the fundamental toroidal mode ${}_0T_2$ of the Earth (see Fig. 2.22) excited by the 1989 Macquarie-Ridge event with a moment magnitude of 8.2. Note that these numbers correspond to one wavelength of (red) light in 10 m and 50 km, respectively. It is obvious that the necessary resolution of the transducer depends critically on the dimension of the strainmeter, i. e. the longer L , the less resolution is needed to achieve a certain resolution in strain. Agnew (1986) shows a power spectrum of Earth's strain noise (Figure 2) and describes the sources of the noise as follows: above 0.5 Hz body wave energy, machinery and wind-blown vegetation, between 0.05 and 0.5 Hz marine microseisms with high temporal variability and from 1 mHz to 0.05 Hz atmospheric pressure changes deforming the ground (wind turbulence, infrasound) (see 4.3). Below 1 mHz the sources are hard to identify, possibilities being thermoelastic deformations, pore pressure and groundwater changes (Evans and Wyatt, 1984), or air pressure changes. Instrumental effects play an important role at the lowest frequencies (drift) and are not easily ruled out (Zadro and Braitenberg, 1999).

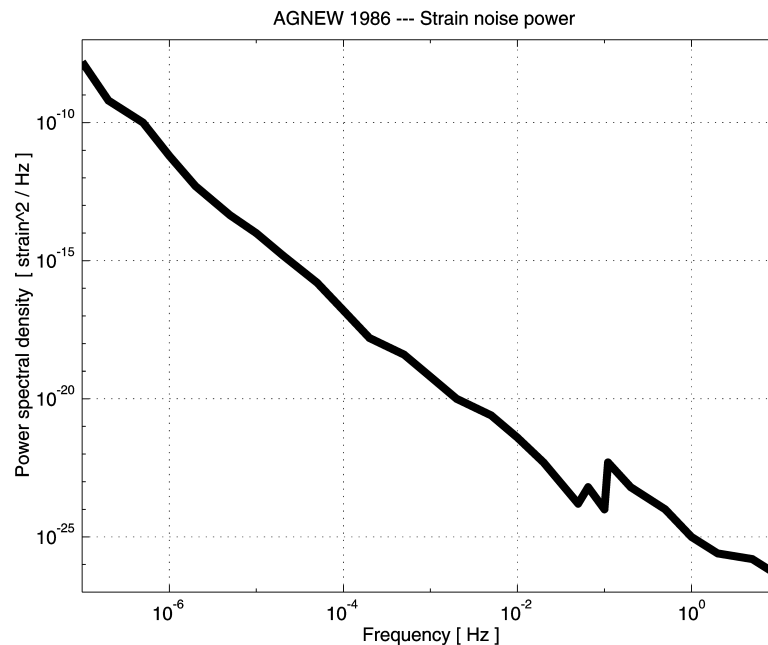


Figure 2 Power spectral density in (strain squared)/Hz as published by Agnew (1986). This is from the 730 m-NW laser horizontal strainmeter at Pinion Flat, California. This instrument is installed at the surface, but referenced with "optical anchors" to a depth of 30 m (Wyatt et al. 1982). See discussion of noise sources in text.

3.2 Frequency response

Lomnitz (1997) discusses the amplification of strainmeters for the case, when the seismic wavelength becomes comparable to the length L . However, the wavelengths of seismic waves are normally much larger than L , therefore the dependence of the amplification on the wavelength can be neglected in all but a few exceptional cases. So, basically strainmeters are extremely broadband instruments whose range extends from zero frequency to frequencies of 1 Hz and higher. However, the upper limit of this range depends very critically on the design of the individual instrument since all devices possess parasitic resonances at high frequencies.

3.3 Calibration

The method for absolute calibration of a strainmeter depends on the individual instrument. In-situ calibration is highly recommended, that is calibration of the installed device is preferable to calibration calculation from components calibrated in the laboratory. Small displacements of that end of a linear strainmeter, which is fixed to the rock simulates ground motion. Uncertainties arise from the definition of the effective length L , because basically the piers are part of the instruments and have some extent in length. Greater difficulties arise for instruments which have to be cemented into a borehole (Sacks-Evertson dilatometers, tensor strainmeters), because the strains in the ground are transferred to the actual sensor through the borehole wall, the casing and the cement. In these cases a very rough calibration can be obtained with the help of Earth tide strains, which are theoretically at least known to the order of magnitude. However, very local heterogeneities may complicate this method (King et al., 1976).

3.4 Direction sensitivity

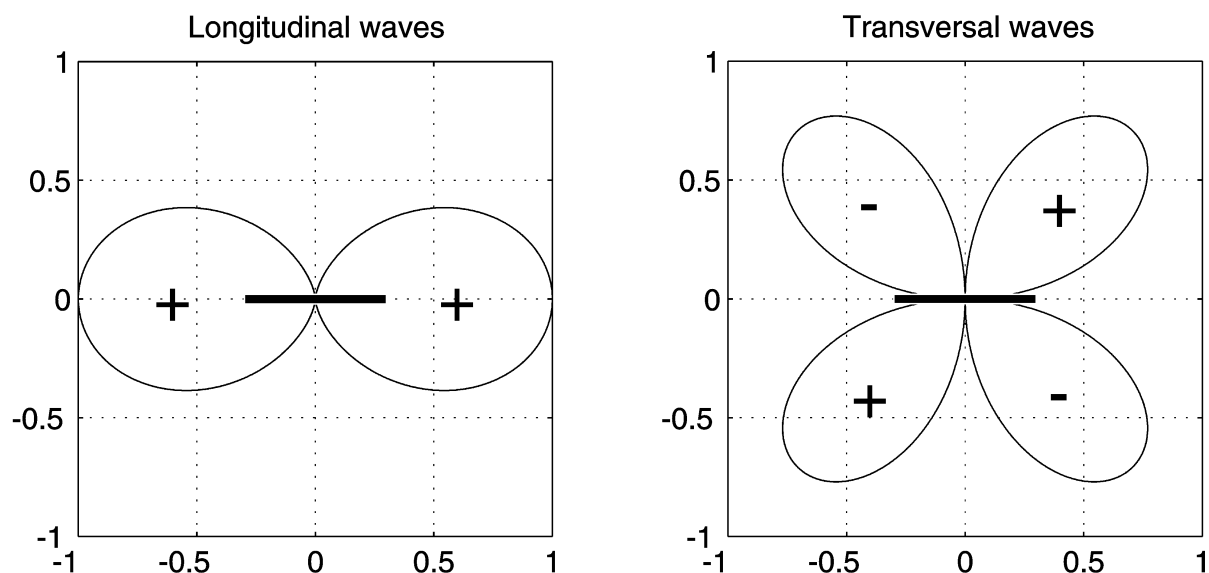


Figure 3 Relative direction sensitivity of linear strainmeters to apparent longitudinal (left) and apparent transversal (right) elastic waves. The strainmeter is indicated by the thick horizontal bar in the center of diagrams. Note that in both cases the strainmeter response is identical for opposite arrival directions.

Dilatometers naturally have isotropic direction sensitivity, the signal does not depend on the direction of arrival of the seismic wave. Figure 3 shows the directional sensitivity patterns of a horizontal strainmeter for longitudinal (left panel) and transversal (right panel) elastic waves. The thick solid bar in the center of each panel indicates the strainmeter. If p is the angle between the arrival direction of the wave and the direction L , these functions are described by $\cos(p) \cdot \cos(p)$ for longitudinal, by $\sin(2p)$ for transversal waves. This means, that when looking into a certain arrival direction, the sign of the output does not depend on whether the wave comes from the front or from behind. Near the free horizontal surface, vertical strain is proportional to the areal strain (also direction independent), therefore vertical strainmeters provide less information than horizontal strainmeters.

3.5 Local arrays of linear strainmeters

If three (or more) horizontal linear strainmeters with different azimuth are deployed at one site, any horizontal component of the strain tensor associated with the incoming wave can be determined from a particular combination of the calibrated signals. Widmer et al. (1992) use this property to demonstrate, that toroidal free oscillation peaks in shear strain spectra do not exist in the areal strain spectrum, a theoretically required result.

3.6 Local phase velocity

Assuming a plane elastic wave is recorded by a linear strainmeter and an inertial seismometer at the same station, then one can in principle derive the phase velocity of the wave at this location. This is due to the fact that the inertial seismometer's output amplitude is proportional to the second derivative of displacement with time (frequency squared), while the strainmeter output is proportional to the spatial derivative (wavenumber).

Depending on the components one can derive equations which relate the frequency-dependent phase velocity with the amplitude spectra of both instruments (Mikumo and Aki, 1964). However, this attractive method has not found many applications, because of local deviations of the deformation field from a simple plane wave (Sacks et al., 1976; King et al., 1976).

3.7 Effects of local heterogeneity

It has been already mentioned twice that the interpretation of results from strainmeters is plagued by the distortion of the strainfield of the arriving seismic waves by local heterogeneities. In tidal research this effect is well known to affect amplitudes and phases and in that field the terms: cavity, topographical and geological effects are used. Arrival times and frequencies are not affected, but the local displacement field could differ appreciably from that of a theoretical plane wave even if the approaching wave was plane (see also Wielandt 1993). The scale of these effects is of the order of magnitude of the signal and with purposeful installation one can obtain apparent mechanical amplification up to a factor of 50. Beavan et al. (1979) have shown this with a 1 m-invar wire strainmeter at BFO for earthquakes and tides. Those local effects can be minimized by installing strainmeters far from any local heterogeneities in the long direction, in an area without topography and in/on large homogeneous rock units. However, even with a lot of care these effects cannot be avoided completely. The ground around the instrument and its heterogeneities must be considered a

part of the instrument (largely unknown) if amplitudes, phases and waveforms are interpreted and these unknown properties could be a function of time. King et al. (1976) and Sacks et al. (1976) deal with this problem for seismological applications. Beaumont and Berger (1974) suggest using the geological effect on tides for earthquake prediction (see below). For inertial seismometers these effects play a role only at periods much longer than ten seconds, because at higher frequencies the inertial effect (proportional to squared frequency) overwhelms the other contributions to the extent that they are negligible (King et al. 1976). One example, where the locally produced tilts were needed to explain the observations with broadband inertial seismometers was encountered in the near-field of explosions at Stromboli, Italy by Wielandt and Forbriger (1999). Strainseismometers are subject to these effects at all frequencies because they measure in fact differences in the displacement fields. The longer the baseline length L of a strainmeter, the more one can hope that local effects are averaged out, at least small scale effects. Gomberg and Agnew (1996) discuss some results from PFO in this context.

4 Some results

The following list is not meant to be comprehensive. It should simply present the spectrum of research possibilities involving strainmeters.

- Strainmeters were successful in recording the Earth's free vibrations and long period surface waves from the beginning. One famous example is the record of the Isabella, California, quartz-rod strainmeter of the Great Chilean quake 1960 (Ben-Menahem and Singh, 1981, Fig. 5.29). Widmer et al. (1992) and Zürn et al. (2000) show shear strain spectra from 10 m Invar wire strainmeters at BFO where the fundamental toroidal mode of the Earth, oT_2 with a period of 44 minutes, stands clearly above the noise floor for the Macquarie 1989 and Balleny Island 1998 events, respectively.
- Coseismic steps consistent with source theory were repeatedly observed with the laser strainmeters at PFO for earthquakes in California (Wyatt, 1988; Agnew and Wyatt, 1989).
- Very clear postseismic strain signals lasting many days were recorded at PFO, California by the laser strainmeters, the borehole tensor strainmeter (Gladwin, 1984) and several tiltmeters (Wyatt et al. 1994) for the 1992 Landers earthquake sequence. The authors conclude that possibly different processes contribute to the observed signals and discuss those.
- Linde et al. (1993) were able to derive a detailed picture of the mechanism of an eruption of Hekla volcano, Iceland from the records of several Sacks-Evertson borehole dilatometers installed between 14 and 45 km away from the summit.
- Slow and silent earthquakes have repeatedly been reported from records by borehole dilatometers in California and Japan (e. g. Linde et al. 1996).
- Earth tides are continuously probing the Earth with periods of 12 and 24 hours. They can be used to study the response of the rocks. Agnew (1981) tried to find out about nonlinear behaviour of the rocks using data from the laser strainmeters at PFO. He concludes, that in the absence of evidence for nonlinearity from the tides,

seismologists are justified in treating the Earth as a linear system. This kind of study is limited by the strain effects of nonlinear ocean tides.

- Beaumont and Berger (1976) suggested from experiments with Finite-Element models, that the earthquake preparation process should modify rock properties near the fault (i.e., by dilatancy) and thus the amplitudes of the tidal strains observed near the fault. Several groups made attempts to make such observations with no success up to date: Linde et al. (1992) looked at borehole dilatometer and tensor strainmeter records in the vicinity of the Loma Prieta, California, quake in 1992 and Omura et al. (2001) investigated super-invar bar-strainmeter data around the 1995 Kobe earthquake from a mine at a distance of 25 km from the epicenter (see also Westerhaus and Zschau, 2001, for a short summary of other attempts). Latynina and Rizaeva (1976) report tidal strain amplitude variations observed with quartz rod strainmeters before an earthquake, but are not certain about the significance of this result.
- Secular crustal deformation rates have been always a major observation goal for strainmeters. Basically they are able to see this signal, but because of the high and non-stationary noise at ultra-low frequencies, the interpretation in this spectral band is extremely difficult. The work with the very long laser strainmeters at Pinion Flat (PFO), in combination with other instruments and methods, is the most careful one (see articles by Agnew, Wyatt and colleagues) ever performed in this direction. PFO is located between the San Andreas and San Jacinto faults in Southern California and only 10 to 15 km away from both.

5 Strain- vs. inertial seismometers

In practice inertial seismometers by far outnumber strainmeters. It is also a fact that experimental seismological research is based mainly on the records from inertial seismometers with very few contributions from the few strainmeters. There are several reasons for this high imbalance:

- Inertial seismometers, short-period and broadband, are commercially available, while highly sensitive strainmeters are not. The costs to produce a competitive laser strainmeter are very high, but a Cambridge type wire strainmeter can be produced very cheaply, compared to the cost of a modern broadband seismometer.
- Short-period and most broadband seismometers are very easy to set up. STS-1 seismometers need more care if highest quality is requested. Strainseismometers require much more work for their installation. Borehole seismometer and borehole strainmeter installation probably is comparable.
- By far the most seismological routine work, especially at the regional scale with local networks, is performed analyzing body waves with periods of a few seconds to frequencies of several tens of Hz. At these frequencies most strainmeters, due to their relatively large dimension, suffer from parasitic resonances of some kind depending on the individual design. Possible exceptions are the Sacks-Evertson dilatometer and the borehole tensor strainmeters because they are more compact.

- Strainmeters, in contrast to short-period seismometers, are extremely noisy if installed near the surface of the Earth due to environmental variations of temperature and air pressure and their effects on the instrument itself and the ground around it. Therefore high quality can only be obtained in boreholes, mines and tunnels or by anchoring them to points at depth. This leads to added installation costs, especially if boreholes have to be drilled for the installation. Basically the cost of the borehole has to be added to the cost of the instrument.

It is noted here that the users of global digital broadband data know the differences in quality between vertical and horizontal components as a function of the depth of installation. At long periods the horizontals are very sensitive to tilts (see 5.3.3). Both tilt and strain are local spatial derivatives of the displacement field and show similar local effects in terms of noise and distortions. Therefore the fairest comparison for strainmeters would be to the long-period horizontal inertial seismometers.

For a given input wave amplitude, the amplitude of the output signal is proportional to $1/\lambda = f/c$ for a strainmeter and $\sim f^2$ for an inertial seismometer (with λ - wavelength, f - frequency, c - phase velocity). Accordingly, when considering waves with equal c , strainmeters have more and more advantage the lower the frequency gets (for both types of sensors the noise power (see Figure 2) rises strongly with decreasing frequency). Most of the research cited above belongs to "zero-frequency seismology". Low-frequency research work makes sense especially in the near-fields of earthquake faults and active volcanoes (creep events, slow and silent earthquakes, pre-, co- and postseismic strain transients, de- and inflation periods, etc.) . However, it is prudent not to rely on a single instrument because noise at very long periods is non-stationary and any changes in the coupling of the instrument to the ground or in the materials of the instrument itself will appear as a signal.

References (see References under Miscellaneous in Volume 2)

Topic	Constructing response curves: Introduction to the BODE-diagram
Author	Jens Bribach, GeoForschungsZentrum Potsdam, Department 2: Physics of the Earth, Telegrafenberg, D-14473 Potsdam, Germany; E-mail: brib@gfz-potsdam.de
Version	May 2001

1 The BODE diagram

True ground motion is of major interest in seismology. On the other hand any measuring device will alter the incoming signal as well as any amplifier and any output device. Working in the frequency domain, the quotient of input signal and output signal is called the *response*. This response is complex, and to get a more meaningful result it can be split into two terms: amplitude response and phase response (see 5.2.3). Amplitude response means the output amplitude divided by the input amplitude at a given frequency. Phase response is the difference between output phase and input phase, or the phase shift. A graphical expression of this splitting is known as the BODE-diagram. One part shows the logarithm of amplitude A versus the logarithm of frequency f (or angular frequency ω , or period T , see Figure 1a). The other part depicts the (linear) phase ϕ versus the logarithm of frequency f (or $\omega = 2\pi f$, or $T = 1/f$, see Figure 1b). For A the terms *amplification* or *magnification* are also used.

1.1 The signal chain

The signal passes a chain of devices. Any single element of this chain can be described by its response. It is useful to split any response into elements of first or second order. At the end the overall amplitude response of the complete chain can be constructed by multiplying all single amplitude responses, and the overall phase response by adding all single phase shifts.

1.2 First and second order elements

For the amplitude response the double logarithmic scale of the amplitude diagram facilitates an easy and fast construction. Any element can be approximated by two straight lines. One horizontal line leads to the element corner frequency, and one line drops from that point with a slope depending on the order of the element.

A first order element is completely described by its amplification A and corner frequency f_c . The slope beyond f_c is one decade in amplitude per decade in frequency. The real amplitude value at f_c is dropped to 0.707 of the maximum amplitude (see Figure 2, full line). However, for our fast construction, we consider only a linear approximation to it (dash-dot lines).

A second order element exhibits a slope of two decades in amplitude per decade in frequency. Additionally it needs another parameter called damping D , describing the amplitude behaviour at frequencies near f_c (compare Figure 3).

2 The seismological signal chain

The seismological signal passes the chain

- mechanical receiver
- transducer
- preamplifier
- filter
- recording unit (to be recognized separately)

Note! Below we discuss in sections 2.1 and 2.2 amplitude responses related to ground displacement. Therefore, the ordinate axis of the BODE-diagram (amplitude A) for the mechanical receiver has no unit (or the unit [m/m]), and for the transducer the unit is [V/m]. Changes to other types of movement, being proportional to ground velocity or to ground acceleration, will be described in section 3.

2.1 The mechanical receiver

The mechanical receiver is a second order system. It describes the relative movement of the pendulum (i.e., a seismic mass attached to a frame by a spring) with respect to the frame. Damping D is set mostly to 0.707. Only at this damping value is the amplitude value at f_c also 0.707 (Figure 3, full curve). For higher values of damping one obtains a more flat curve (dashed). For lower values of D the dash-dot curve strongly exceeds the amplification level at f_c , indicating low-damped resonance oscillations of the pendulum, which can be stimulated by any signal.

The amplification of the mechanical receiver is $A = 1$. This means that for frequencies $f > f_c$ the amplitude of the pendulum movement with respect to the frame is similar to the ground amplitude. For the phase shift see Figure 7b (HIGH Pass 2).

2.2 The transducer

The transducer transforms the relative movement of the pendulum into an electrical signal, i.e., in a voltage. The transducer constant G gives the value of the output voltage U depending on the relative pendulum movement z . There are three main types of transducers, distinguished by their proportionality to ground motion and its derivatives:

- Displacement $U \sim z$ $G_d[\text{V/m}]$ (capacitance or inductance bridges)
- Velocity $U \sim dz/dt$ $G_v[\text{Vs/m}]$ (magnet-coil systems)
- Acceleration $U \sim d^2z/dt^2$ $G_a[\text{Vs}^2/\text{m}]$ (piezo-electric systems, $U \sim F = m a$)

The above proportionality of the transducer voltage to ground motion (i.e., to displacement, velocity or acceleration, respectively) is, of course, only given for frequencies $f > f_c$, i.e., for the horizontal part of the mechanical receiver response (see Figure 3).

All transducer amplitude responses can be drawn as straight lines over the full considered frequency range (Figure 4). They differ only in their slope.

The phase responses have a constant phase shift over the whole frequency range with values of 0° (displacement), 90° (velocity), or 180° (acceleration).

2.3 The preamplifier

The preamplifier is a first order LOW Pass. Its corner frequency is beyond the signal range of seismology - up to several 10 kHz. Thus, only the amplification is of interest (Figure 5). The response is a horizontal line drawn at the amplification level A .

The phase shift is $\phi = 0^\circ$, but one should keep in mind that, if using the inverted input, the phase shift will be $\phi = -180^\circ$ over the whole frequency range.

2.4 First and second order LOW Passes

LOW Passes have constant amplifications A for frequencies lower than their corner frequencies f_c . For frequencies higher than f_c the amplification drops with a slope depending on the order of the filter (Figure 6a). LOW Passes cut the high frequencies, therefore, also the term High Cut is used. The phase shift for $f < f_c$ is about 0° and for $f > f_c$ it turns to -90° (first order, LP1) or -180° (second order, LP2; see Figure 6b), passing half of the phase shift exactly at f_c .

Of course, the given amplitude and phase values are approximations. In reality we would obtain $\phi = 0^\circ$ only if inserting a frequency of 0 Hz, and $\phi = -90^\circ$ (-180°) for infinite frequency values. However, the accuracy is sufficient for our fast construction.

2.5 First and second order HIGH Passes

HIGH Passes have constant amplifications A for all frequencies higher than their corner frequency f_c . For frequencies lower than f_c the amplification drops with a slope depending on their order (Figure 7a). They cut the low frequencies, so one can also find the term Low Cut.

The phase shift for $f > f_c$ is about 0° , and for $f < f_c$ it turns to $+90^\circ$ (first order, HP1) or $+180^\circ$ (second order, HP2; see Figure 7b), passing half of the phase shift exactly at f_c .

Comparable to the description of LOW Passes the given amplitude and phase values are approximations.

2.6 Second order BAND Pass

The second order BAND Pass (BP2) can be explained as a combination of a first order LOW Pass and a first order HIGH Pass. It suppresses all frequencies, except f_c , with a slope of one decade in amplitude per decade in frequency (Figure 8a). The peak at f_c can be turned into a horizontal line (symmetrical to f_c) by increasing the damping to values $D > 1$. Thus it is possible to construct a BAND Pass by combining a HIGH Pass with a LOW Pass.

The phase shift for $f < f_c$ is about $+90^\circ$, and for $f > f_c$ it turns to -90° (see Figure 8b), passing half of the phase shift at f_c .

3 The overall response

The construction of the overall response should be divided into two steps:

- from mechanical receiver to the final filter stage; and
- adding the recorder response.

The first result, the electrical output, is useful for fitting the signal to the recorder input. It has to be fixed, meaning that changes in magnification (or signal resolution) should be done by setting up the recorder only.

3.1 From the mechanical receiver to the final filter

As defined in section 2, the amplitude response is constructed related to ground displacement. Multiplying all the units of our signal chain, we get the unit [V/m] for the ordinate axis. All elements, including mechanical receiver, transducer, and filter stages can be implemented in the same sheet with a double logarithmic grid, each element with its magnification and its corner frequency. Then the resulting amplitude response has to be constructed point by point at certain frequencies. This can be done either by multiplying the amplitudes of all elements at these frequencies, which is the more secure method, or, alternatively, by adding the distances (e.g., in millimetres) of all element amplitudes to the amplitude level line $A = 1$, with positive distances if above this line and negative ones if below. This method is faster. A linear addition is, in this logarithmic scale, a multiplication of the amplitude values. The final amplitude response curve can be drawn on the same sheet, together with the single elements.

3.2 Adding the recorder

In reality, at the end of our signal chain we will find a commercially available recorder, transforming the obtained voltage back into movement (drum recorder) or into computable digital values (Analogue-to-Digital Converter = ADC). Its main parameter is the input sensitivity H . In the case of a drum recorder, H is the pen deflection per Volt (in units [m/V]). For an ADC, H is the digital count per Volt (in units [digit/V]).

Thus the overall amplitude response needs a separate BODE-diagram for each recorder type. Multiplying the units we obtain the units [m/m] for the drum recorder, and [digit/m] for the ADC. You will also find derivatives of this unit, like [digit/nm] or [counts/nm].

3.3 Introducing ground velocity and ground acceleration

If the amplitude response curve has to be constructed related to ground velocity (or ground acceleration), it is sufficient to redraw either the response of the mechanical receiver or the transducer. The simpler method is to change the transducer response. Each slope will change by one order if going from displacement to velocity, or from velocity to acceleration. The unit of the ordinate changes from [V/m] (displacement) via [Vs/m] (velocity) to [Vs²/m] (acceleration). These units will also be the units of the amplitude response from the mechanical receiver to the final filter stage. Beyond this the construction of the overall amplitude response is similar to section 3.1. The units of the recorder amplitude response will alter to [m·s/m] (velocity) or [m·s²/m] (acceleration) for the drum recorder. For the ADC we obtain [digit·s/m] (velocity) or [digit·s²/m] (acceleration).

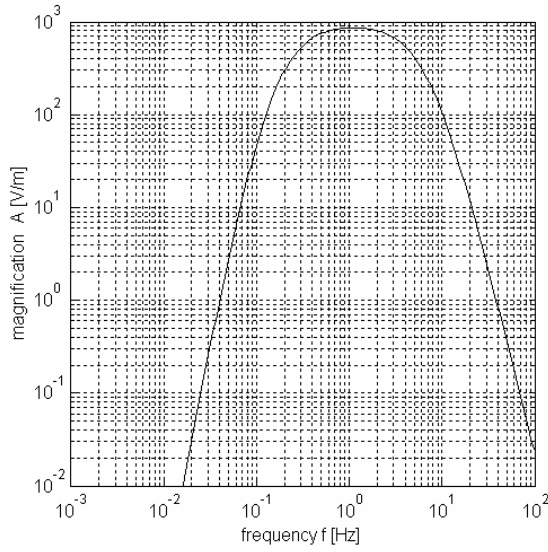


Figure 1a Amplitude Response.

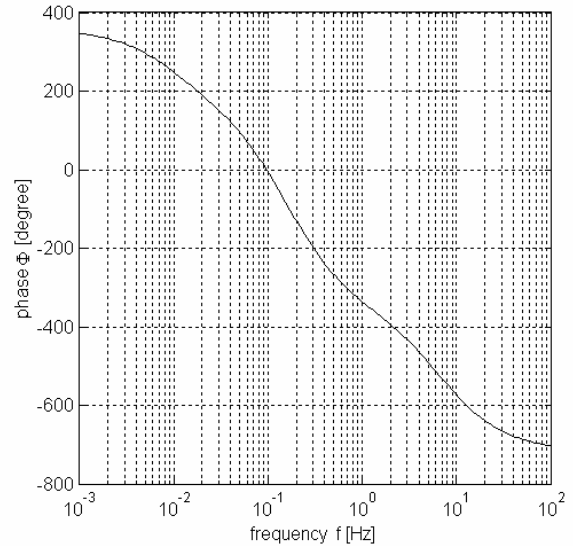


Figure 1b Phase Response.

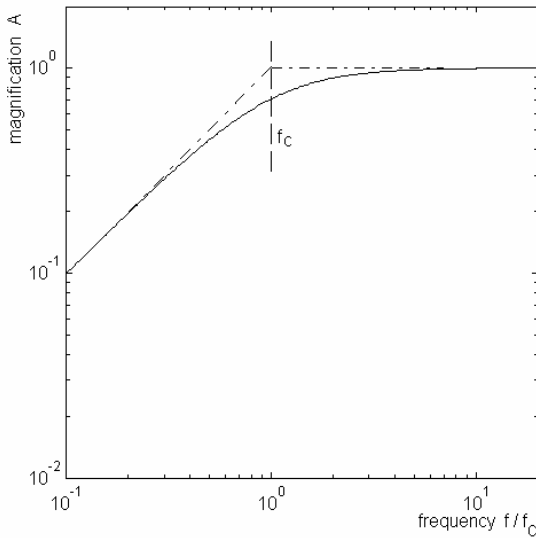


Figure 2 First Order HIGH Pass (HP1).

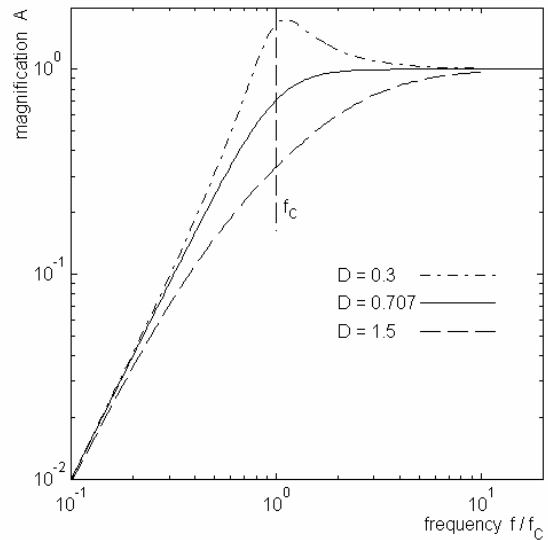


Figure 3 Second Order HIGH Pass (HP2) or Mechanical Receiver.

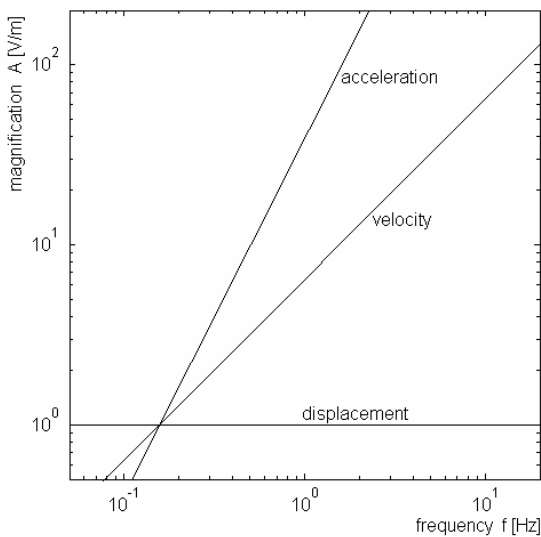


Figure 4 Transducer Amplitude Response.

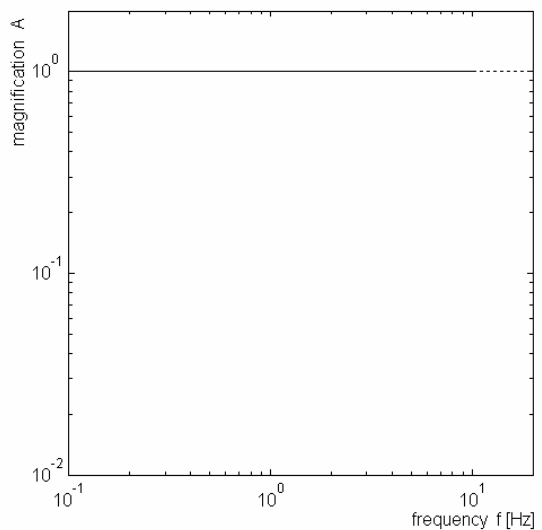


Figure 5 Preamplifier Amplitude Response.

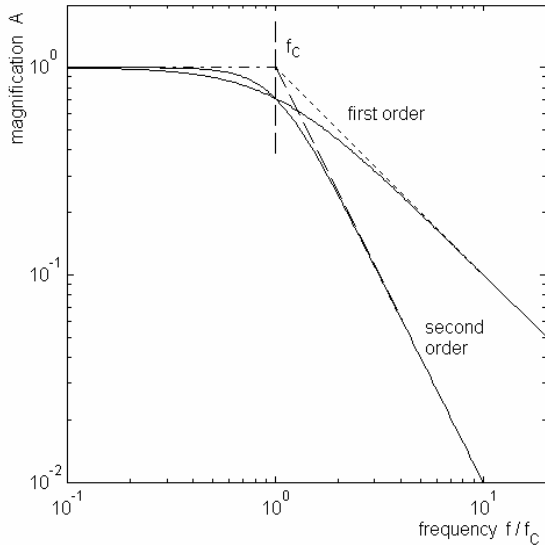


Figure 6a LOW Pass Amplitude Response.

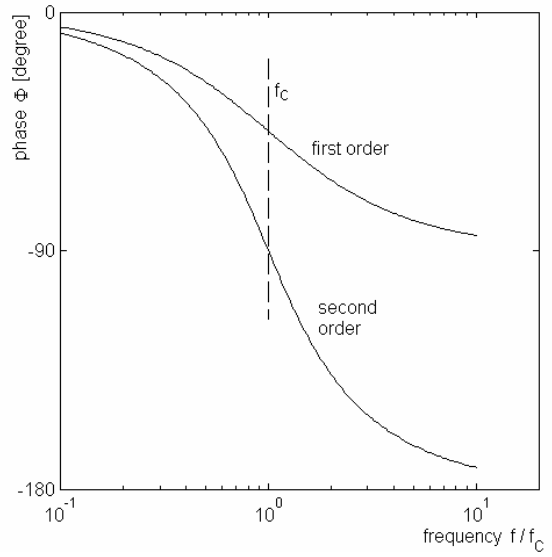


Figure 6b LOW Pass Phase Response.

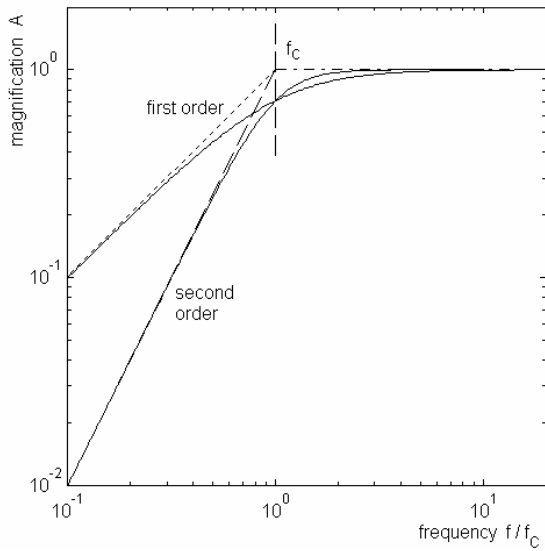


Figure 7a HIGH Pass Amplitude Response.

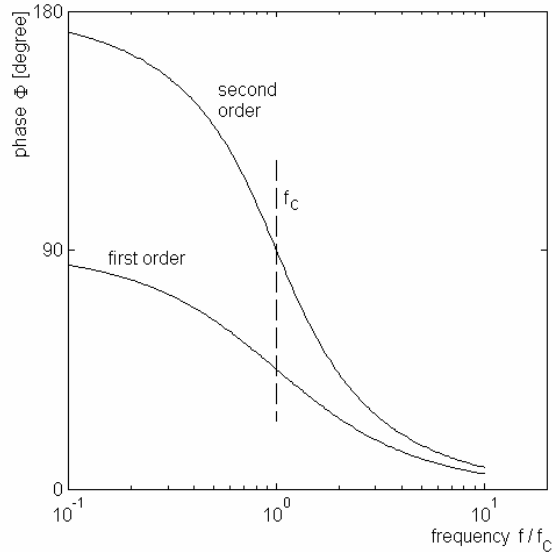


Figure 7b HIGH Pass Phase Response.

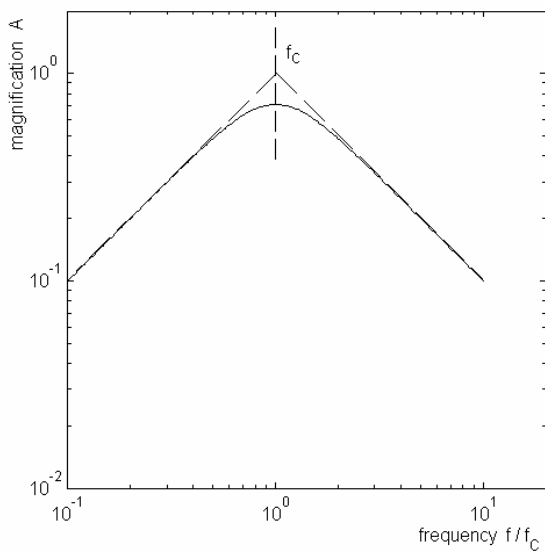


Figure 8a BAND Pass Amplitude Response.

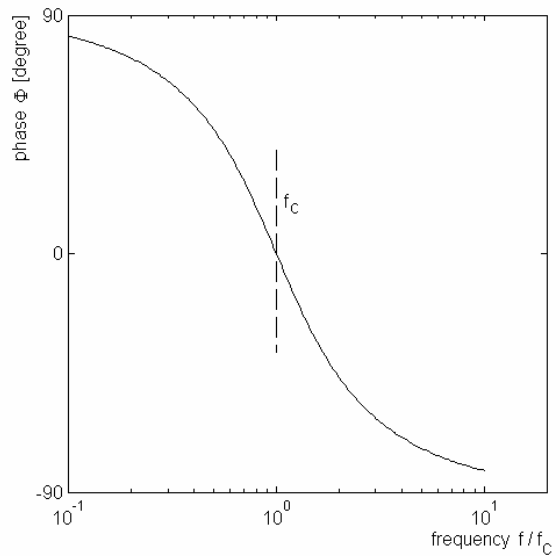


Figure 8b BAND Pass Phase Response.

Topic	What to prepare and provide if seismic site selection is purchased?
Author	Amadej Trnkoczy (formerly Kinemetrics SA); E-mail: amadej.trnkoczy@siol.net
Version	Sept. 1999

If seismic station site selection procedure is purchased as a part of services along with the seismic network equipment, the purchaser should prepare several logistic things to assure efficient work of the manufacturer's experts. Note that these services are usually paid by the time the experts work on site selection for a new seismic network and that site selection is a 'stretchable' process. The more time (read "money") one spends on it, or the more efficiently one works during a given time period, the better the station sites and, consequently, the network performances will result. Therefore, it is of direct benefit to the customer to consider carefully all the required issues and to get together all the necessary information and working material, as complete as possible under the given conditions in the particular country. The seismic network purchaser should prepare the following:

- a preliminary and approximate proposal of seismic network layout based on the goals of the network;
- a general-purpose "high school type" topographical map of the whole region of the future network with color representation of terrain altitude (basic topographical display of the region);
- regional (and local, if available) geological maps covering the region of the network;
- map of past seismic activity in and around the region where the network is planned, with instrumental (if any) and historic data be included;
- seismo-tectonic map of the region (if available);
- 1:50.000 or 1:25.000 scale topographic maps covering the entire network region for RF profiling purposes for telemetry seismic systems (1:50.000 scale maps are the best; 1:25.000 maps are better for fieldwork if there is no RF telemetry planned in the network). Get permission to export such maps if they are under export restriction, as these will be needed by the site selection provider for initial studies before fieldwork starts, particularly if the network is an RF telemetry system;
- a state-of-the-art roadmap of the country for finding easy access to potential sites during fieldwork. Try to find the latest edition of such map. Road infrastructure changes fast in many developing countries;
- 1:5.000 scale maps (or at least 1:25.000 if 1:5.000 are not available) of the area surrounding the sites in case shallow seismic profiling of potential seismic sites is planned;

- climatic data in the form of maps or tables published in annual or decade reports from the country's meteorological survey (data should include precipitation, wind, insolation - if seismic stations will be powered by solar panels -, and lightning threat information such as isokeraunic maps or number of storm days per year).
- knowledgeable staff members from the institution that will operate the network as well as well informed local people acquainted with local conditions at each potential station site. The member(s) of the responsible institution working in the field, together with manufacturer's experts, should have full competency to make 'on the spot' decisions regarding acceptability of access difficulties, land ownership issues, and other issues that may have financial consequences during network establishment and future network operation. This person should be full time and continuously with the manufacturer's experts until the site selection procedure is finished. If the region of the network is large, several local people may be needed. They can be members of local authorities (municipalities, land-use planning authorities, etc.) and should be familiar with local development conditions and present and future land use;
- one or two four-wheel-drive vehicles in technically perfect condition, one of which should be big enough to comfortably transport four people together with measuring equipment its original packing (two PC notebooks, seismometer, seismic recorder, cables and, in case of telemetry system, RF spectrum analyzer, provisory antenna mast, and Yagi antennae). Two or three customer's staff members (plus driver and enough cash, coupons or whatever documents are required to purchase gasoline) are the best size team to work with usually two manufacturer's experts;
- air-conditioned working room with three tables, main power, and safe storage place for measuring equipment. If the network is an RF telemetry system, one of the tables must be large enough, minimum 1.5 x 3 m (5 x 10 feet), to allow working with several topographical maps stuck together while taking topographical profiles; and
- permits to enter restricted areas (army camps and training land, private land, natural reserves, state border regions, etc.) for local staff and foreign experts.

The maps sent to the site selection provider and used in the field are working copies. They are normally not returned to the customer. The maps are used when preparing the final report. If color maps are code protected against copying, two copies are needed (one for fieldwork and one for the final report).

Expect from one to three days of work for each station site of the network. Any extra time needed will depend on the dimensions of the network, infrastructure in the country, and general site accessibility. An efficient day of fieldwork usually lasts from sunrise to sunset.

Hint: Print this form and put check marks in appropriate bullets while preparing on-site selection procedure.

Topic	Using existing communication tower sites as seismic sites
Author	Amadej Trnkoczy (formerly Kinometrics SA); E-mail: amadej.trnkoczy@siol.net
Version	Sept. 1999

Very often less experienced newcomers in seismometry consider mountain peaks with existing communication towers as potential seismic station sites, particularly if they are building an radio frequency (RF) telemetry seismic network. Such places appear to be an easy and inexpensive solution. Access problem is solved, RF communication paths to the central recording site, which is usually situated in the capital or another big city, is supposedly free, main power lines, and even phone lines are readily available.

Unfortunately, such sites also have several serious drawbacks and are in fact rarely suitable for seismic stations. The most important reasons are that:

- existing high towers that sway during windy periods cause high-amplitude, low-frequency seismic noise and may cause large numbers of false triggers with triggered seismic systems and deteriorate low frequency seismic signals. Consequently, a diminished seismic station gain is used resulting in a low detectability of the station;
- there is usually a very high probability of RF interference between seismic RF telemetry system and other users. RF interference may easily impair seismic data transmission and consequently seismic system reliability. Several 'high power' parties (compared to one watt or less of RF power used in seismic telemetry) are potentially polluting the RF space at such places. In addition, if other users do not maintain their RF equipment properly, the RF energy radiated within uncontrolled side lobes worsens this danger (this happens quite frequently in developing countries.
- if such sites are inhabited, it is likely there will be too high man-made seismic noise due to human activities);
- the topography of such mountain peaks is rarely suitable for a seismic station. Communication antennae towers usually try to cover an area as large as possible, therefore, as a rule, they are placed on the highest mountains in a country or region;
- nearly all such sites have powerful diesel generators to support communication equipment during power outages. When in operation, these generators are a major source of man-made, high frequency seismic noise. Of course, these generators will surely be running after a strong earthquake because that is precisely when it is most likely that the main power lines will fail. Since the periods during strong earthquakes and following aftershock sequence are the most important for the seismic network, the existing communication towers definitely are not at all suitable for seismic sites.

Topic	Recommended minimal distances of seismic sites from sources of seismic noise
Author	Amadej Trnkoczy (formerly Kinometrics SA); E-mail: amadej.trnkoczy@siol.net
Version	Sept. 1999

Recommended minimal distances from sources of seismic noise to a seismic site (according to Willmore, 1979) are:

STATION SITE NAME: _____ _____		SITE #: _____			DATE OF ANALYSIS: ___/___/___			ACTUAL DISTANCE
COORDINATES: N 0 ' ___." " W 0 ' ___." "		HARD MASSIVE ROCK, GRANITE, QUARTZITE, ETC.			HARDPAN HARD CLAY, ETC.			
		RECOMMENDED MINIMAL DISTANCES [km]						
		A	B	C	A	B	C	[km]
1. Oceans, with coastal mountains system		300	50	1	300	50	1	
2. Oceans, with broad coastal plains		1000	200	10	1000	200	20	
3. Inland seas, bays, very large lakes, with coastal mountain system		150	25	1	150	25	1	
4. Inland seas, bays, very large lakes, with broad coastal plains		500	100	5	500	100	5	
5. Large dams, high waterfalls, large cataracts		a	40	10	1	50	15	5
		b	60	15	5	150	25	10
6. Large oil or gas pipelines		a	20	10	5	30	15	5
		b	100	30	10	100	30	10
7. Small lakes		a	20	10	1	20	10	1
		b	50	15	1	50	15	1
8. Heavy reciprocating machinery, machinery		a	15	3	1	20	5	2
		b	25	5	2	40	15	3
9. Low waterfalls, rapids of a large river, intermittent flow over large dams		a	5	2	0.5	15	5	1
		b	15	3	1	25	8	2
10. Railway, frequent operation		a	6	3	1	10	5	1
		b	15	5	1	20	10	1
11. Airport, air ways heavy traffic			6	3	1	6	3	1
12. Non-reciprocating power plant machinery, balanced industrial machinery		a	2	0.5	0.1	10	4	1
		b	4	1	0.2	15	6	1
13. Busy highway, mechanized farms			1	0.3	0.1	6	1	0.5
14. Country roads, high buildings			0.3	0.2	0.05	2	1	0.5
15. Low buildings, high trees and masts			0.1	0.03	0.01	0.3	0.1	0.05
16. High fences, low trees, high bushes, large rocks			0.05	0.03	5 m	0.06	0.03	0.01

LEGEND:

- A SP seismic station with a gain of about 200,000 or more at 1 Hz
- B SP seismic station with a gain from 50,000 to 150,000 at 1 Hz
- C SP seismic station with a gain of approximately 25,000 or less at 1 Hz
- a Source and seismometer on widely different geological formations or that mountain ranges or valleys intervene
- b Source and seismometer on the same geological formation and with no intervening alluvial valley or mountain range

Instructions for use of the form:

1. Get the information about all potential sources of seismic noise around the site and write the distances to them in the extreme right column of the table.
2. From geological maps and by visiting the site decide on the quality of the bedrock at the site. Decide either for 'good' rock (left three columns A, B, and C with minimal recommended distances) or for 'less suitable' ground (right three columns A, B, and C with the minimal recommended distances).
3. For each seismic noise source (where applicable) decide about seismic coupling between seismic site and the noise source. Select the appropriate horizontal line a) or b) with minimal recommended distance.
4. Mark appropriate cells in the table based on the steps #2 and #3 and compare their content with the actual distances in the extreme right column.
5. Shade all cells of the selected A, B, and C columns where the recommended minimal distances to a noise source is bigger than the actual distance in the extreme right column. Find that of the columns A, B, or C where no shaded cells appear. If this is the column A, the site is appropriate for a sensitive SP station having gain 200,000 or more, if this is column B the site is appropriate for a medium sensitive station having the gain somewhere in between 50.000 and 150.000, if it is column C, only a moderately sensitive station with gain around 25.000 or less can be established.
6. Make such a table for all potential seismic sites studied and compare the results among alternatives.

Topic	Detectability and earthquake location accuracy modeling of seismic networks
Authors	Mladen Živčič, Geophysical Survey of Slovenia, Dunajska 47/VI SI-1000 Ljubljana, Slovenia, Tel: +386 1 4787270; Fax: +386 1 4787295, E-mail: mladen.zivcic@gov.si Jure Ravnik, Ecological Engineering Institute, Ltd., Ljubljanska 9, SI-2000 Maribor, Slovenia, Tel: +386 2 300 48 27, Fax: +386 2 300 48 35, E-mail: jure.ravnik@iei.si
Version	July 2001

This information sheet focuses on the accuracy of determination of earthquake hypocenter location with respect to the locations of seismic stations in a local network and the estimation of network detection thresholds.

Contemporary methods of determination of hypocenter location and earthquake origin time are based on modeling the travel time, which is needed for seismic waves to travel from the hypocenter to the station of a seismic network. For this we need to know:

- location and height above sea level of the seismic stations;
- accurate time on all seismic stations;
- velocity structure of the Earth, through which the seismic waves propagate.

If these parameters are known, we can calculate by means of numerical methods the theoretical travel time of seismic waves from an arbitrary hypocenter to the seismic station. The calculated travel times are then applied to the actual arrival times which were picked from seismograms on all available seismic stations and thus the hypocenter location and earthquake origin time is calculated.

The accuracy of such earthquake locations depends on the three points listed above and on the accuracy of phase picking. Additionally, the theoretical accuracy of hypocenter locations is also controlled by the spatial distribution of seismic stations. Nowadays, with GPS receivers being readily available at reasonable cost, it is not difficult to know the station location and the correct time exactly. The velocity structure of the Earth is fixed, however, and often enough not well known. By studying it, the accuracy of location can be improved. Unfortunately, the determination of the velocity structure requires either extensive specialized deep seismic refraction surveys or an already operating and sufficiently dense seismic network.

Therefore, in the phase of seismic network planning, we can improve its accuracy of event location only by reasonable distribution of the stations.

A computer program LOK has been developed which estimates the accuracy of hypocenter location based on a given spatial distribution of stations. The following assumptions are made:

- station co-ordinates are known exactly;
- for locations of seismic stations an RMS value of noise in the frequency band within which the STA/LTA trigger algorithm will operate (for digital stations) or for the frequency band of the recording equipment (for analogue stations) is known;

- for both digital and analogue stations the frequency response of the seismographs is flat and proportional to ground velocity in the frequency band of interest for modeling the station and network capabilities. This bandwidth depends on the task but also on the network geometry and sensitivity. For local networks it is usually in the range between 1 and 10 Hz;
- P and S arrival times are picked with a known a priori uncertainty (e.g., 0.1 s);
- P and S velocities within the layers and the positions of layer boundaries are known with some known uncertainty;
- travel times are computed for a flat Earth model consisting of homogeneous layers;
- the size of the network area is such that flat Earth approximation can be used.

The results obtained with LOK crucially depend on these assumptions. However, even with poor choice of input parameters (e.g. velocity model) one can get relative performance of different network geometry.

In developing the program LOK we followed mainly the method described in Peters and Crosson (1972). It uses the fact, that the errors of the travel time solution depend on partial derivatives of the travel time function by the unknowns we are looking for. These unknowns are the hypocenter location and the earthquake origin time. The derivatives can be calculated for every point within the seismic network. The area is divided into squares in terms of longitude and latitude. When LOK is run, a hypocenter error ellipsoid is constructed for every grid point. The largest semi-axis of the error ellipsoid is named the hypocenter determination error while the largest of the projections of the ellipsoid semi-axes on the horizontal plane is named the epicentre determination error.

For the computation of the error ellipsoid one should include only stations on which the expected signal is above the noise threshold as defined in the station file (amplification for analogue stations and RMS noise values and STA/LTA trigger ratio for digital stations). Thus the program also gives some information on the differences in expected detectability of events for different geometries of the network. Absolute level of detectability is impossible to predict without detailed knowledge of the attenuation in the region.

Figure 1 below shows the results of respective model calculation for the Stareslo network in Slovenia. The input and output files for this example are included in the distributed version of LOK (see below). An area of 3.5 x 1.75 degree was modeled. An earthquake of $M_l = 1.0$ was assumed to occur at 15 km hypocentral depth. The network consists of 7 stations, denoted by red triangles in the figure. The border of Slovenia is shown in thick blue. The thin black lines, which are the actual result of the modeling, are isolines of constant hypocenter location error. The numbers in the labels are in kilometers.

As one can see, the error increases outside the network, and the network also has a few blind spots within, where the hypocenter determination error is rather large. The detectability of the network for earthquakes of $M_l = 1.0$ (at least 4 stations must record the event to obtain the earthquake location) can also be seen. Other examples of magnitude threshold as well as epicenter and hypocenter error calculations using an earlier version of LOK, are shown in Figs. 7.6 to 7.8.

The software enables calculation with different hypocenter depths and earthquake magnitudes. It also includes a routine that determines the stations that recorded a particular event. LOK was written in FORTAN 77 and tested under Linux. The source code of LOK is made available on

request by the editor of the NMSOP, Peter Bormann (E-mail: course@gfz-potsdam.de). It includes instructions on how to prepare the input files (file readme in the compressed archive). Mladen Živčić is willing to answer any question of interested users and plans to arrange for an anonymous FTP server, from which the program file can be downloaded.

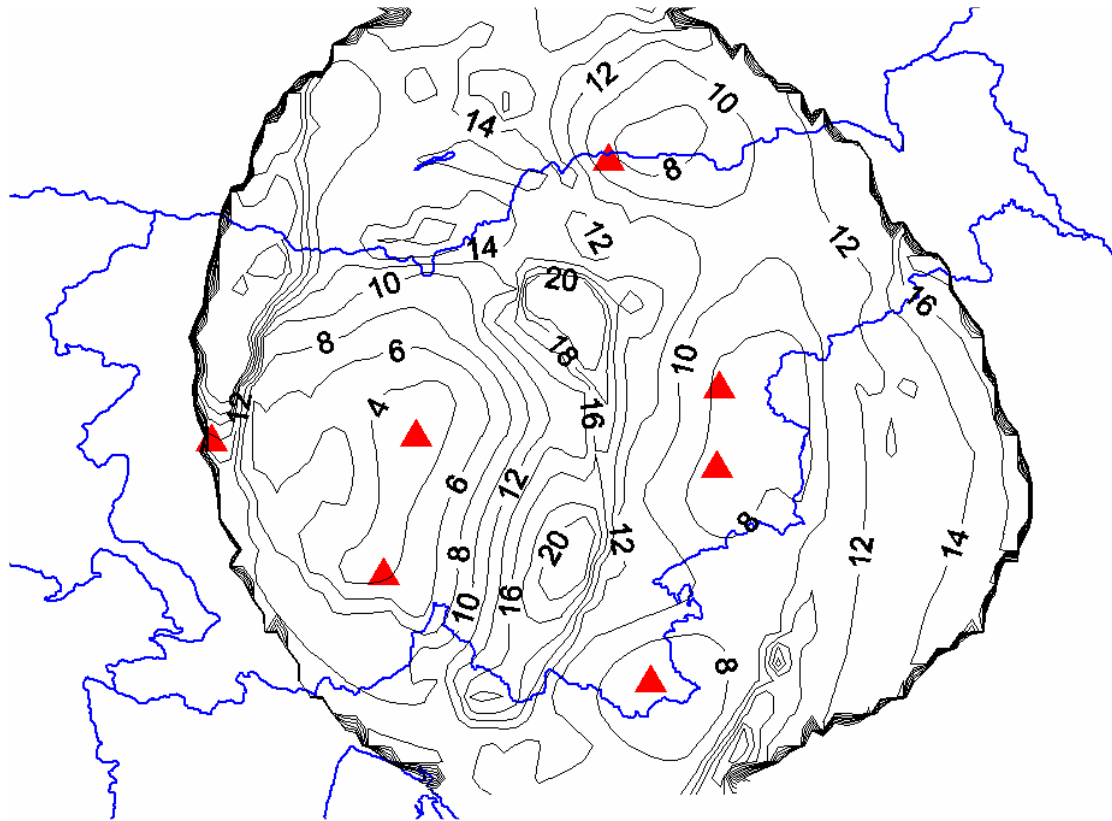


Figure 1 Result of model calculations for the Stareslo network in Slovenia for $M_I = 1.0$ earthquake. Red triangles: station positions, blue lines: borders of Slovenia, thin black lines: isolines of hypocenter location error in km; thick black outer boundary: outer limit of the network's location capability for earthquakes of $M_I = 1.0$.

References (see References under Miscellaneous in Volume 2)

Topic	Understanding and parameter setting of STA/LTA trigger algorithm
Author	Amadej Trnkoczy (formerly Kinometrics SA); E-mail: amadej.trnkoczy@siol.net
Version	September 1999

1 Introduction

By introducing digital seismic data acquisition, long-term continuous recording and archiving of seismic signals has become a demanding technical problem. A seismic network or even a single seismic station operating continuously at high sampling frequency produces an enormous amount of data, which is often difficult to store (and analyze) locally or even at the recording center of a network. This situation has forced seismologists to invent triggered seismic data acquisition. In a triggered mode, a seismic station or a seismic network still process all incoming seismic signals in real time (or in near-real-time) but incoming data is not stored continuously and permanently. Processing software - a trigger algorithm - serves for the detection of typical seismic signals (earthquakes, controlled source seismic signals, underground nuclear explosion signals, etc.) in the constantly present seismic noise signal. Once an assumed seismic event is detected, recording and storing of all incoming signals starts. It stops after trigger algorithm 'declares' the end of the seismic signal.

Automatic trigger algorithms are relatively ineffective when compared to a seismologist's pattern recognition ability during reading of seismograms, which is based on years of experience and on the enormous capability of the human brain. There are few exceptions, where the most complex detectors, mostly dedicated to a given type of seismic signals, approach to human ability. In all practical cases, automatic trigger loose some data on one side and generate falsely triggered records, which are not seismic signals, on the other. Small amplitude seismic signals are often not resolved from seismic noise and are therefore lost for ever, and, if the trigger algorithm is set sensitively, false triggers are recorded due to irregularities and occasionally excessive amplitude of seismic noise. False triggers burden off-line data analysis later and unnecessarily occupy data memory of a seismic recording system. As a result, any triggered mode data acquisition impairs the completeness of the recorded seismic data and produces some additional work to delete false records.

Several trigger algorithms are presently known and used - from a very simple amplitude threshold type to the sophisticated pattern recognition, adaptive methods and neural network based approaches. They are based on the amplitude, the envelope, or the power of the signal(s) in time domain, or on the frequency or sequency domain content of seismic signal. Among the more sophisticated ones, Allan's (1978; 1982) and Murdock and Hutt's (1983) trigger algorithms are probably the most commonly known. Many of these algorithms function in association with the seismic phase time picking task. Seismic array detection algorithms fall into a special field of research, which will not be discussed here. For more advanced algorithms see, e.g., Joswig (1990; 1993; 1995). However, in practice, only relatively simple trigger algorithms have been really broadly accepted. and can be found in seismic data recorders in the market and in most network's real time processing packages.

The simplest trigger algorithm is the amplitude threshold trigger. It simply detects any amplitude of seismic signal exceeding a pre-set threshold. The recording starts whenever this threshold is

reached. This algorithm is rarely used in weak-motion seismology but it is a standard in strong motion seismic instruments, that is in systems where high sensitivity is mostly not an issue, and where consequently man-made and natural seismic noise amplitudes are much smaller than the signals which are supposed to trigger the instrument.

The root-mean-square (RMS) threshold trigger is similar to the amplitude threshold algorithm, except that the RMS values of the amplitude in a short time window are used instead of 'instant' signal amplitude. It is less sensitive to spike-like man-made seismic noise, however it is rarely used in practice.

Today, the 'short-time-average through long-time-average trigger' (STA/LTA) is the most broadly used algorithm in weak-motion seismology. It continuously calculates the average values of the absolute amplitude of a seismic signal in two consecutive moving-time windows. The short time window (STA) is sensitive to seismic events while the long time window (LTA) provides information about the temporal amplitude of seismic noise at the site. When the ratio of both exceeds a pre-set value, an event is 'declared' and data starts being recorded in a file.

Several more sophisticated trigger algorithms are known from literature (e.g., Joswig 1990; 1993; 1995) but they are rarely used in the seismic data loggers currently in the market. Only some of them are employed in the network's real time software packages available. When in the hands of an expert, they can improve the events/false-triggers ratio significantly, particularly for a given type of seismic events. However, the sophisticated adjustments of operational parameters to actual signals and seismic noise conditions at each seismic site that these triggers require, has proven unwieldy and subject to error in practice. This is probably the main reason why the STA/LTA trigger algorithm still remains the most popular.

Successful capturing of seismic events depends on proper settings of the trigger parameters. To help with this task, this Information Sheet explains the STA/LTA trigger functioning and gives general instructions on selecting its parameters. Technical instructions on setting the trigger parameters depend on particular hardware and software and are not given here. Refer to the corresponding manuals for details.

2 Purpose

The short-time-average/long-time-average STA/LTA trigger is usually used in weak-motion applications that try to record as many seismic events as possible. These are the applications where the STA/LTA algorithm is most useful. It is nearly a standard trigger algorithm in portable seismic recorders, as well as in many real time processing software packages of the weak-motion seismic networks. However, it may also be useful in many strong motion applications, except when interest is limited to the strongest earthquakes.

The (STA/LTA) trigger significantly improves the recording of weak earthquakes in comparison with amplitude threshold trigger algorithms. At the same time it decreases the number of false records triggered by natural and man-made seismic noise. To some extent it also allows discrimination among different types of earthquakes.

The STA/LTA trigger parameter settings are always a tradeoff among several seismological and instrumental considerations. The goal of searching for optimal parameter settings is the highest possible seismic station sensitivity for a given type of seismic signal (which may also include the target 'all earthquakes') at a still tolerable number of false triggers.

The STA/LTA trigger is most beneficial at seismically quiet sites where natural seismic noise (marine noise) is the dominant type of seismic noise. It is also effective in case of changes of 'continuous' man-made seismic noise. Such changes, for example, occur due to day/night variation of human activity nearby or in urban areas. The STA/LTA algorithm is less effective in the presence of irregular, high amplitude man-made seismic noise which is often of burst and/or spike type.

3 How it works - basics

The STA/LTA algorithm continuously keeps track of the always-present changes in the seismic noise amplitude at the station site and automatically adjusts the seismic station's sensitivity to the actual seismic noise level. As a result, a significantly higher sensitivity of the system during seismically quiet periods is achieved and an excessive number of falsely triggered records is prevented, or at least mitigated, during seismically noisy periods. Calculations are repeatedly performed in real time. This process is usually taking place independently in all seismic channels of a seismic recorder or of a seismic network.

The STA/LTA algorithm processes filter seismic signals (see section 5.1 'Selection of trigger filters' in this Information Sheet) in two moving time windows – a short-time average window (STA) and a long-time average window (LTA). The STA measures the 'instant' amplitude of the seismic signal and watches for earthquakes. The LTA takes care of the current average seismic noise amplitude.

First, the absolute amplitude of each data sample of an incoming signal is calculated. Next, the average of absolute amplitudes in both windows is calculated. In a further step, a ratio of both values — STA/LTA ratio—is calculated. This ratio is continuously compared to a user selected threshold value - STA/LTA trigger threshold level. If the ratio exceeds this threshold, a channel trigger is declared. A channel trigger does not necessarily mean that a multi-channel data logger or a network actually starts to record seismic signals. All seismic networks and most seismic recorders have a 'trigger voting' mechanism built in that defines how many and which channels have to be in a triggered state before the instrument or the network actually starts to record data (see section 5.4 below - 'Selection of voting scheme parameters'). To simplify the explanation, we shall observe only one signal channel. We will assume that a channel trigger is equivalent to a network or a recorder trigger.

After the seismic signal gradually terminates, the channel detriggers. This happens when the current STA/LTA ratio falls below another user-selected parameter - STA/LTA detrigger threshold level. Obviously, the STA/LTA detrigger threshold level should be lower (or rarely equal) than the STA/LTA trigger threshold level.

In addition to the data acquired during the 'trigger active' time, seismic networks and seismic recorders add a certain amount of seismic data to the event file before triggering – pre-event-time (PEM) data. After the trigger active state terminates, they also add post-event-time (PET) data.

For better understanding, Figure 1 shows a typical local event and the trigger variables (simplified) during STA/LTA triggering. Graph a) shows an incoming continuous seismic signal (filtered); graph b) shows an averaged absolute signal in the STA and LTA windows, respectively, as they move in time toward the right side of the graph; and graph c) shows the ratio of both. In addition, the trigger active state (solid line rectangle), the post-event time (PET), and the pre-event time (PEM) (dotted line rectangles) are shown. In this example, the

trigger threshold level parameter was set to 10 and the dettrigger threshold level to 2 (two short horizontal dotted lines). One can see that the trigger became active when the STA/LTA ratio value exceeded 10. It was deactivated when the STA/LTA ratio value fell below 2. On graph d) the actually recorded data file is shown. It includes all event phases of significance and a portion of the seismic noise at the beginning.

In reality, the STA/LTA triggers are usually slightly more complicated, however, the details are not essential for the understanding and proper setting of trigger parameters.

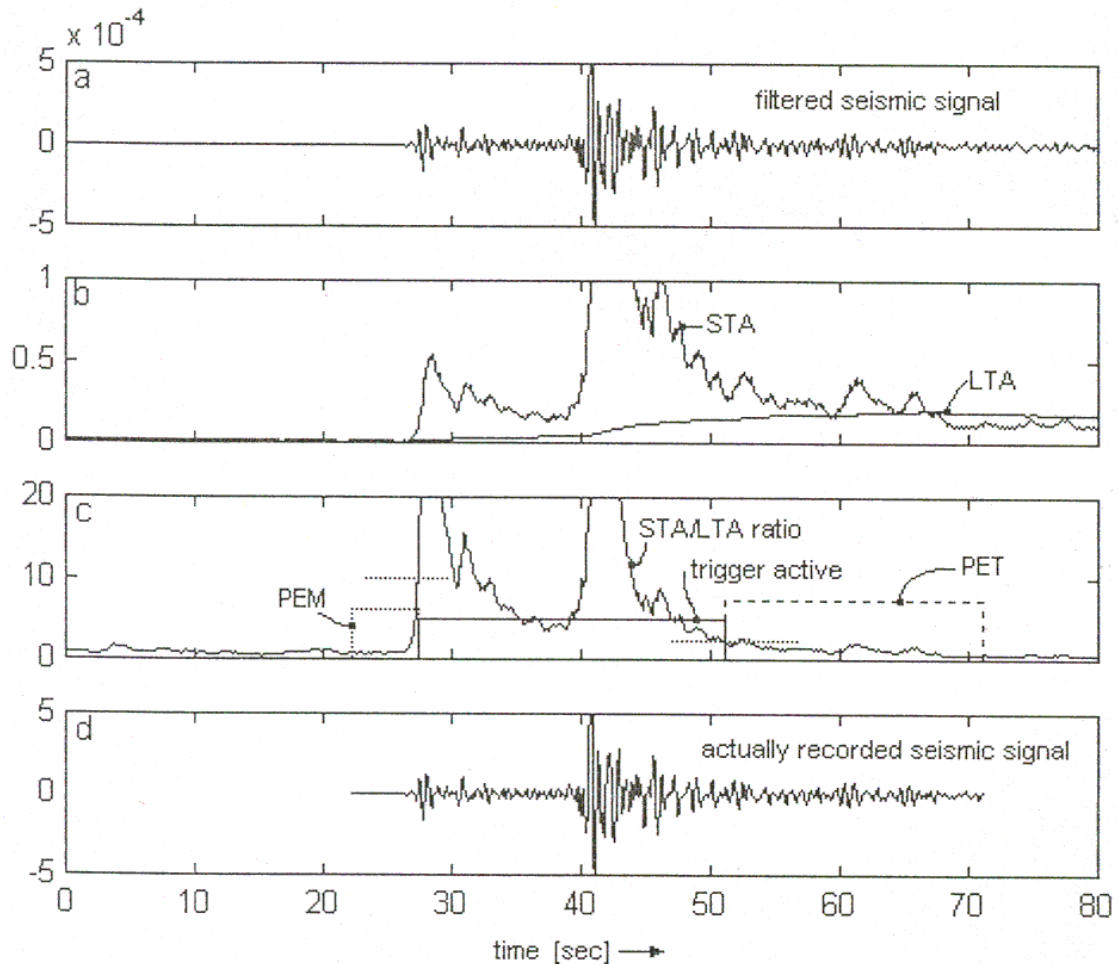


Figure 1 Function and variables of STA/LTA trigger calculations (see text for explanations).

4 How to adjust STA/LTA trigger parameters

To set the basic STA/LTA trigger algorithm parameters one has to select the following:

- STA window duration
- LTA window duration
- STA/LTA trigger threshold level
- STA/LTA dettrigger threshold level.

However, optimal triggering of a seismic recorder or a seismic network does not depend only on these parameters. There are usually four additional associated parameters which, only if well tuned with the trigger parameters, guarantee optimal data recording. These parameters are:

- trigger filters
- pre-event time (PEM)
- post-event time (PET)
- trigger voting scheme.

Although not directly related to the STA/LTA trigger algorithm, these additional parameters are also be discussed below in order to provide a complete information.

The STA/LTA trigger parameter and associated parameters' settings depend on the goal of the application, on the seismic noise condition at the site, on the properties of seismic signals at a given location, and on the type of sensor used. All these issues vary broadly among applications and among seismic sites. Obviously, there is no general, single rule on setting them. Each application and every seismic site requires some study, since only practical experience enables the determination of really optimal trigger settings.

Note that seismic recorders and network software packages come with a set of default (factory set) trigger and trigger associated parameter values. They are rarely optimal and must therefore be adjusted to become efficient in a particular application. For best results, changing these parameters and gradually finding the best settings is a process which requires a certain amount of effort and time.

4.1 Selection of short-time average window (STA) duration

Short-time average window measures the 'instant' value of a seismic signal or its envelope. Generally, STA duration must be longer than a few periods of a typically expected seismic signal. If the STA is too short, the averaging of the seismic signal will not function properly. The STA is no longer a measure of the average signal (signal envelope) but becomes influenced by individual periods of the seismic signal. On the other hand, STA duration must be shorter than the shortest events we expect to capture.

To some extent the STA functions as a signal filter. The shorter the duration selected, the higher the trigger's sensitivity to short lasting local earthquakes compared to long lasting and lower frequency distant earthquakes. The longer the STA duration selected, the less sensitive it is for short local earthquakes. Therefore, by changing the STA duration one can, to some extent, prioritize capturing of distant or local events.

The STA duration is also important with respect to false triggers. By decreasing the duration of the STA window, triggering gets more sensitive to spike-type man-made seismic noise, and vice versa. Although such noise is usually of instrumental nature, it can also be seismic. At the sites highly polluted with spike-type noise, one will be frequently forced to make the STA duration significantly longer than these spikes, if false triggers are too numerous. Unfortunately, this will also decrease the sensitivity of the recording to very local events of short duration. Figure 2 explains the effect of STA duration on local events and spike-type noise.

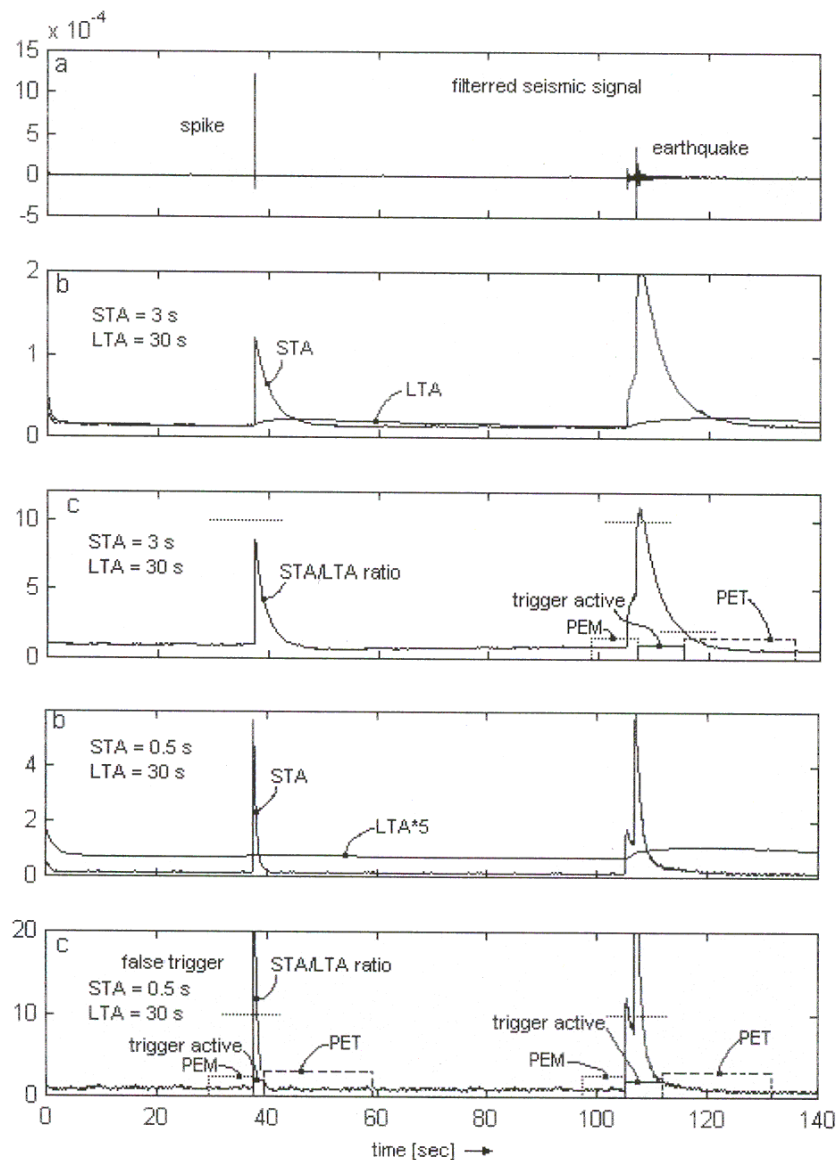


Figure 2 Influence of STA duration on trigger sensitivity to short local events and 'spiky' noise in seismic signals.

On graph a) a signal with an instrumental spike on the left and with a short, very local earthquake on the right side is shown. Graphs b) and c) show STA, LTA, STA/LTA ratio, and trigger active states along with PEM and PET. The STA/LTA trigger threshold was set to 10 and dettrigger threshold to 2. One can see that when using a relatively long STA of 3 sec, the earthquake did trigger the system, but only barely. However, a much bigger amplitude (but shorter) instrumental spike did not trigger it. The STA/LTA ratio did not exceed the STA/LTA threshold and there was no falsely triggered record due to the spike. The lower two graphs show the same variables but for a shorter STA of 0.5 sec. The spike clearly triggered the system and caused a false record. Of course, the earthquake triggered the system as well.

For regional events, a typical value of STA duration is between 1 and 2 sec. For local earthquakes shorter values around 0.5 to 0.3 s are commonly used in practice.

4.2 Selection of long-time average window (LTA) duration

The LTA window measures average amplitude seismic noise. It should last longer than a few 'periods' of typically irregular seismic noise fluctuations. By changing the LTA window duration, one can make the recording more or less sensitive to regional events in the 'Pn'-wave range from about 200 to 1500 km epicentral distance. These events typically have the low-amplitude emergent Pn- waves as the first onset. A short LTA duration allows the LTA value more or less to adjust to the slowly increasing amplitude of emergent seismic waves. Thus the STA/LTA ratio remains low in spite of increasing STA (nominator and denominator of the ratio increase). This effectively diminishes trigger sensitivity to such events. In the opposite case, using a long LTA window duration, trigger sensitivity to the emergent earthquakes is increased because the LTA value is not so rapidly influenced by the emergent seismic signal, allowing Sg/Lg waves to trigger the recording.

Figure 3 explains the described situation. In graph a) an event with emergent P waves is shown. Graphs b) and c) show the time course of trigger parameters for a relatively long LTA of 60 sec. The LTA does not change fast, allowing the STA/LTA ratio to exceed the STA/LTA trigger threshold (short horizontal dotted line) and a normal record results. Graphs d) and e) show the same situation with a shorter LTA of 30 s. The LTA value increases much faster during the initial phase of the event, thus decreasing the STA/LTA ratio value which does not exceed the STA/LTA trigger threshold. No triggering occurs and the event is missed.

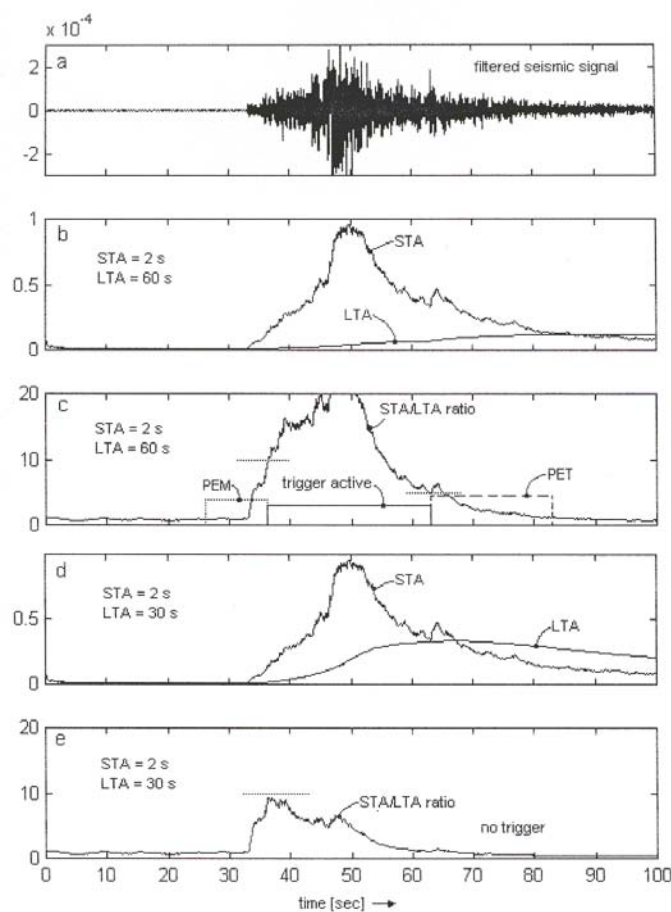


Figure 3 Influence of LTA duration on trigger algorithm sensitivity to earthquakes with emergent seismic signals.

Similarly, efficient triggering of recording of events with weak P waves compared to S waves requires a longer LTA for two reasons. First, if P waves do not trigger, they 'contaminate' true information about seismic noise prior to the event measured by LTA, since their amplitude exceeds the amplitude of seismic noise before the event. This results in diminished trigger sensitivity at the moment when S waves arrive. This 'contamination' is decreased if a longer LTA duration is selected. Second, longer LTA makes the trigger more sensitive to P waves as well, if they are not strictly of impact type.

Figure 4 represents such a case. Graph a) shows a typical event with significantly bigger later phase waves than P waves. Graphs b) and c) show trigger parameters for a long LTA of 100 s. P wave packet as well as S wave packet trigger the recorder. Appropriate PEM and PET assure that the event is recorded as a whole in a single file with all its phases and a portion of seismic noise before them. Graphs d) and e) show the same situation but for a shorter LTA of 45 sec. One can see that the P waves did not trigger at all, while the S waves barely triggered. The STA/LTA ratio hardly exceeds the STA/LTA trigger threshold. As the result, the recorded data file is much too short. P waves and information about seismic noise before them are missing in this record. A slightly smaller event would not trigger at all.

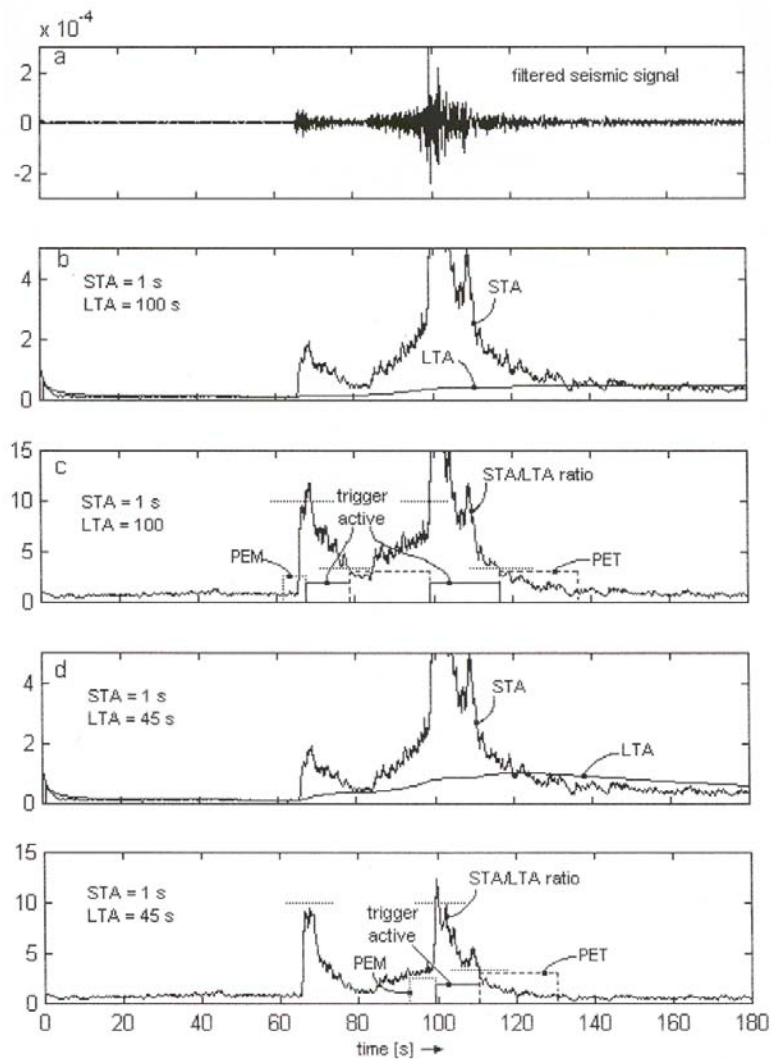


Figure 4 Influence of LTA duration on trigger algorithm sensitivity to earthquakes containing weak P waves.

On the other hand, a short LTA will successfully accommodate recorder sensitivity to gradual changes of 'continuous' man-made seismic noise. Such 'transition' of man-made seismic noise from low to high is typical for night-to-day transition of human activity in urban areas. Sometimes, using a short LTA can mitigate false triggers due to traffic. Examples of such cases could be a single heavy vehicle approaching and passing close to the seismic station on a local road, or trains on a nearby railway. A short LTA can 'accommodate' itself fast enough to such emerging disturbances and prevent false triggers.

Figure 5 shows an example of the LTA response to increased seismic noise. Graph a) shows seismic noise, which gradually increased in the middle of the record. Note that the change of its amplitude is not sudden but lasts about 20 to 30 sec. Graphs b) and c) show the situation at a short LTA of 30 sec. One can see that the LTA value more or less keeps track of the increased noise amplitude. The STA/LTA ratio remains well below the STA/LTA trigger threshold and there is no false trigger in spite of significantly increased seismic noise at the site. Graphs d) and e) show the situation with a longer LTA of 60 s. In this case, the LTA does not change so rapidly, allowing a higher STA/LTA ratio during noise increase. As the result, a false trigger occurs and a false record is generated which unnecessarily occupies data memory.

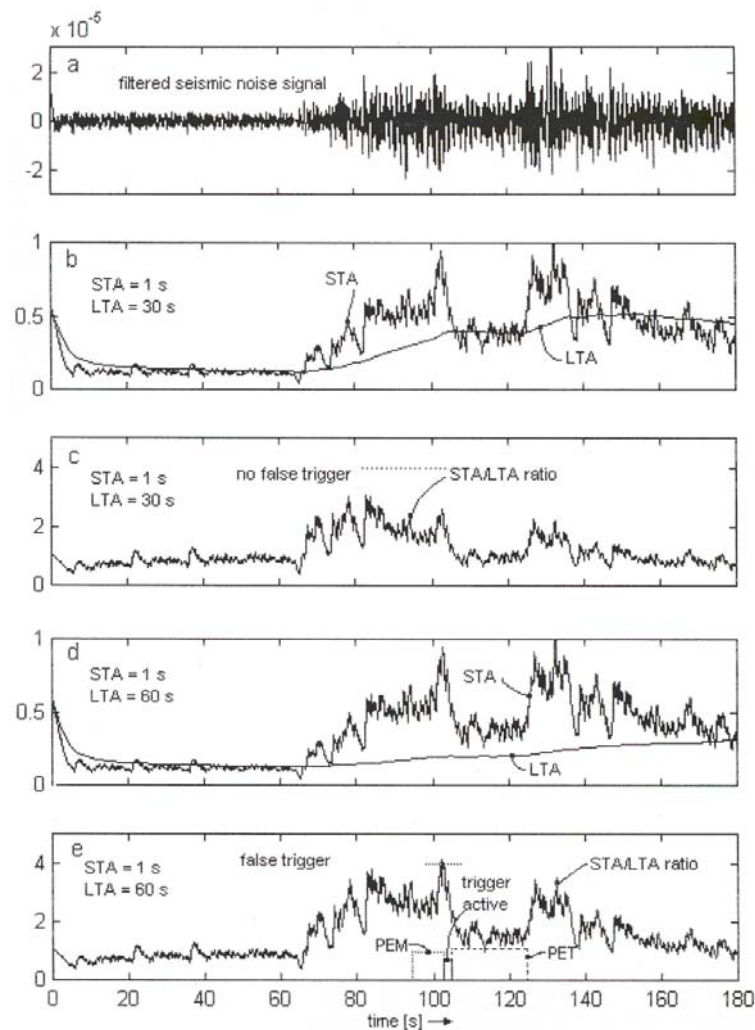


Figure 5 Influence of LTA duration on false triggering when seismic noise conditions change.

Natural seismic noise (marine noise) can change its amplitude by a factor exceeding the value of twenty. However, these changes are slow. Significant changes can occur only during a few hours period, or at worst, in several tens of minutes. Therefore even the longest LTA duration is short enough to allow LTA to accommodate completely to marine noise amplitude variations.

The LTA duration of 60 seconds is a common initial value. A shorter LTA duration is needed to exclude emergent regional events from triggering, if desired, or if quickly changing man-made noise is typical for the site. A longer LTA can be used for distant regional events with very long S-P times and potentially emergent P waves.

4.3 Frozen versus continuously updated LTA during events

Calculations of the LTA value during an event, that is after a channel trigger is declared, can be performed in the first approximation in two different ways.

Either the LTA value is continuously updated and calculated during the event as usual, or the LTA value is kept frozen at the moment when channel trigger is declared. In this case the LTA is not allowed to change (increase) during an event at all. Most of seismic recorders available in the market have both frozen or continuously updated LTA user-selectable options. However, each approach has its good and bad points.

The 'frozen' LTA window (the word 'clamped' is also used in literature) can force the unit into a permanently triggered state in case of a sudden increase of man-made seismic noise at the site. The situation is illustrated in Figure 6.

Graph a) shows an earthquake during which seismic noise increases and remains high even after the termination of the event. Such a situation can happen if, for example, a machinery is switched on in the vicinity of the recorder. In such a case, a completely frozen LTA (graph b) would never again allow the STA/LTA ratio to fall below the STA/LTA detripping threshold level (graph c) and a continuous record would result. The result is that the seismic recorder's memory soon gets full and blocks further data recording.

A continuously updated LTA (the word 'unclamped' is also used in literature), on the other hand, frequently terminates records too early. Graphs d) and e) of Figure 6 explain this situation. Very often records with truncated coda waves result because the LTA increases rapidly if the beginning portion of a large earthquake signal is included in its calculation. Thus the STA/LTA ratio decreases too rapidly and terminates recording prematurely. Coda waves of the event are then lost, as shown in the Figure 6. This undesired result could be even much more distracting for records of regional events with longer duration.

Some seismic recorders work with a special calculation of LTA. The LTA value is, to the first approximation, 'frozen' after a trigger. However, this 'freezing' is not made complete. Some 'bleeding' of event signal into the LTA calculation is allowed. Such an algorithm tries to solve both problems: it does not cause endlessly triggered records in the case of a rapid permanent increase of seismic noise and, at the same time, it does not cut coda waves too early.

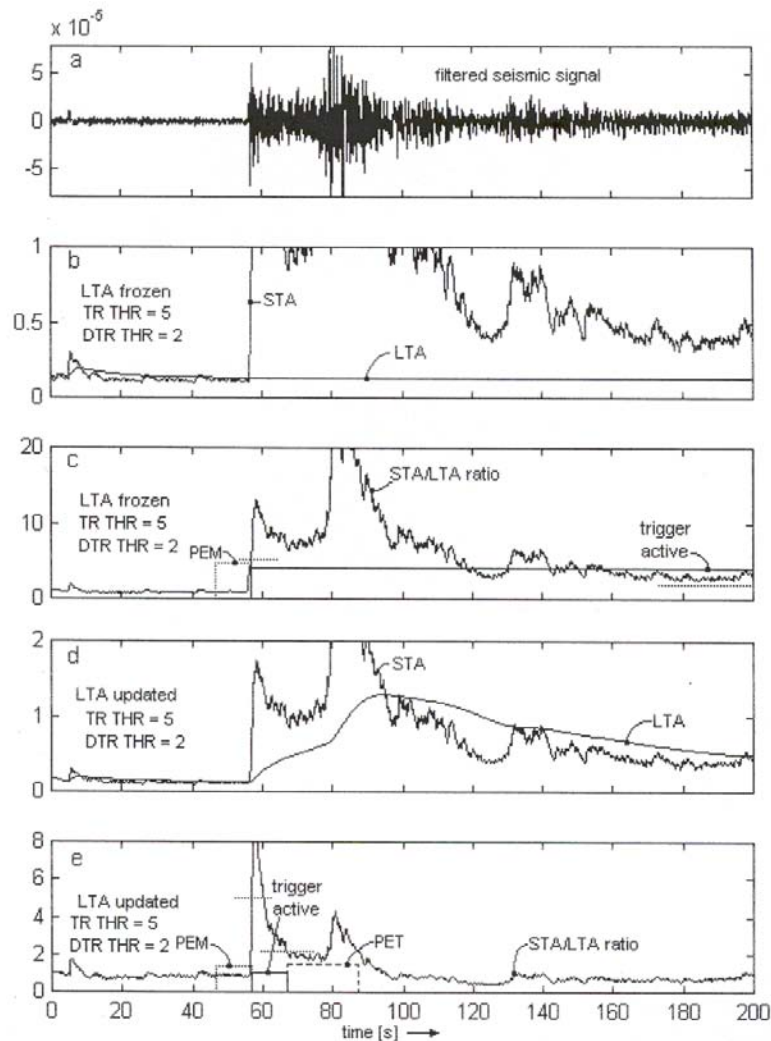


Figure 6 Potential problems with two conventional ways of calculating the LTA: an endless record with a completely frozen LTA and cut coda waves with updated LTA calculations.

4.4 Selection of STA/LTA trigger threshold level

The STA/LTA trigger threshold level to the greatest extent determines which events will be recorded and which will not. The higher value one sets, the more earthquakes will not be recorded, but the fewer false-triggers will result. The lower the STA/LTA trigger threshold level is selected, the more sensitive the seismic station will be and the more events will be recorded. However, more frequent false triggers also will occupy data memory and burden the analyst. An optimal STA/LTA trigger threshold level depends on seismic noise conditions at the site and on one's tolerance to falsely triggered records. Not only the amplitude but also the type of seismic noise influence the setting of the optimal STA/LTA trigger threshold level. A statistically stationary seismic noise (with less irregular fluctuations) allows a lower STA/LTA trigger threshold level; completely irregular behavior of seismic noise demands higher values.

Note that some false triggers and some missed earthquakes are an inevitable reality whenever recording seismic signals in an event-triggered mode. Only a continuous seismic recording, if affordable, completely solves the problem of false triggers and incompleteness of seismic data.

It is a dangerous trap to select a very high STA/LTA trigger threshold level and a high channel gain simultaneously. Many recorders in the market allow this setting without any warning messages. This situation is particularly dangerous in extremely noisy environments, where, due to too many false triggers, the instruments are usually set to record only the strongest events.

Suppose one has set the STA/LTA trigger threshold level to 20. Suppose also that one has set the gain of the channel in such a way that it has about 150 mV of average seismic noise signal at the input of the recorder and the input full scale voltage of the channel is ± 2.5 V. Obviously, this setting would require a $0.15 \text{ V} \times 20 = 3 \text{ V}$ signal amplitude to trigger the channel. Since its maximum input amplitude is limited to 2.5 V, it can never trigger, no matter how strong an earthquake occurs. Note that this error is not so obvious, especially in low seismicity regions with rare events. One can operate an instrument for a very long time without records and forever wait for a first recorded earthquake.

With certain products in the market, this potential danger of an erroneous setting is solved in the following way: whenever one uses the STA/LTA algorithm, an additional threshold trigger algorithm remains active in the 'background'. Because of it, the channel triggers whenever its input amplitude exceeds 50% of channel input voltage range, for example, in no relation to the STA/LTA trigger setting. In this way, the strongest and therefore the most important events are still recorded, no matter how carelessly the STA/LTA trigger algorithm parameters are set.

An initial setting for the STA/LTA trigger threshold level of 4 is common for an average quiet seismic site. Much lower values can be used only at the very best station sites with no man-made seismic noise. Higher values about 8 and above are required at less favorable sites with significant man-made seismic noise. In strong-motion applications, higher values are more common due to the usually noisier seismic environment and generally smaller interest in weak events.

4.5 Selection of STA/LTA detrigger threshold level

The STA/LTA detrigger threshold level determines the termination of data recording (along with the PET parameter – for more information see 5.3 below on “Selection of post-event time (PET) parameter”).

The STA/LTA detrigger threshold level determines how well the coda waves of recorded earthquakes will be captured in data records. To include as much of the coda waves as possible, a low value is required. If one uses coda duration for magnitude determinations, such setting is obvious. However, a too low STA/LTA detrigger threshold level is occasionally dangerous. It may cause very long or even endless records, for example, if a sudden increase in seismic noise does not allow the STA/LTA ratio to fall below the STA/LTA detrigger threshold level. On the other hand, if one is not interested in coda waves, a higher value of STA/LTA detrigger threshold level enables significant savings in data memory and/or data transmission time. Note that coda waves of distant earthquakes can be very long.

In general, the noisier the seismic site, the higher the value of the STA/LTA detrigger threshold level should be used to prevent too long or continuous records. This danger is high only at sites heavily polluted by man-made seismic noise.

A typical initial value of the STA/LTA detrigger threshold level is 2 to 3 for seismically quiet sites and weak motion applications. For noisier sites higher values must be set. For strong-motion applications, where coda waves are not of the highest importance, higher values are frequently used.

5 How to adjust associated parameters for proper triggering and data recording

5.1 Selection of trigger filters

Nearly all seismic recorders and networks have adjustable band-pass trigger filters. They continuously filter the incoming seismic signals prior to the trigger algorithm calculations. Selection of these filters is important for a proper functioning of the STA/LTA trigger algorithm (as well as for amplitude threshold trigger algorithm). The purpose of these filters is three-fold:

- they remove DC component from incoming seismic signals, namely, all active seismic sensors have some DC offset voltage at the output which, if too high, deteriorates the STA/LTA ratio calculation. The calculation of the absolute value of the signal becomes meaningless if the DC component is higher than the seismic noise amplitude. This results in malfunction of the STA/LTA trigger algorithm and drastic reduction of trigger sensitivity for weak seismic events;
- their frequency band-pass can prioritize frequencies corresponding to the dominant frequencies of seismic events one wants to record; and
- their stop-band can attenuate dominant frequencies of the most distracting seismic noise at a given site.

The trigger filter pass-band should generally accommodate the frequencies of the maximum energy of expected seismic events. At the same time it should have a band-pass that does not coincide with peak frequency components of typical seismic noise at the site. If this is possible, a significant improvement of the event-trigger/false-trigger ratio results. Obviously, one can understand that if the peak amplitudes of seismic noise and the dominant frequencies of the events of most interest coincide, the trigger filter becomes inefficient.

One should not forget that the frequency response function of the seismic sensor used with a recorder or in a network channel also modifies the frequency content of events and noise signals at the input of trigger algorithm. Therefore the sensor used is an important factor in the choice of a trigger filter. The type of sensor output - proportional to either ground displacement, velocity or the acceleration - has a similar effect. Sensors with ground acceleration proportional output - accelerometers - emphasize high frequencies. They usually require a filter protection against excessive high-frequency man-made seismic noise. Ordinary seismometers have typically an output proportional to ground velocity, sometimes also to ground displacement and they are less influenced by high-frequency man-made seismic noise.

The adjustment flexibility of high- and low-corners of these filters varies among different products. The same is true for the steepness of the filter flanks. Generally, one does not need very steep (high order) filters and a lot of flexibility, because events, similar to the seismic noise, are highly variable. It is generally impossible to determine very precisely where exactly to set the frequency limits of these filters.

5.2 Selection of pre-event time (PEM) parameter

Ideally, the triggered earthquake records should include all seismic phases of an event and, in addition, a portion of the seismic noise signal prior to it. Selection of an appropriate pre-event time (PEM) assures that the earthquake records are complete. For the majority of weak events, the trigger algorithm usually does not trigger at the beginning of the event but sometimes during the event, when the waves with the maximum amplitude of ground velocity reach the station. This happens very often with the earthquakes that have emergent onset waves, and with most of the weak local and regional events where the S phase amplitudes can be much bigger than the P phase. In practice, triggering on the S waves of the weak local and the regional earthquakes is actually more frequent than triggering on the P waves. But for seismological reasons, the P onset waves, plus some seismic noise prior to them, should be included in the record. A proper PEM should take care of this.

Technically this is solved in the following way. In seismic recorders and in a network's central recording computer, a portion of seismic signal prior to the instrument trigger time is temporarily stored in a pre-event ring buffer (abbreviation PEM denotes 'pre-event-memory') and added to the data recorded.

PEM must surmount the following periods of time:

- the desired record duration of seismic noise prior to the event;
- the maximal expected S-P time of earthquake records; and
- time needed to calculate the STA/LTA ratio, which, in the worst case, equals one STA window duration.

Add these three time periods and the result is the appropriate PEM value.

The effect of a too short PEM is shown in Figure 7. Graph a) shows an event approximately 400 km away from the station with weak P waves partly buried in the seismic noise. On graph b) the STA and the LTA values are shown. Graph c) shows the STA/LTA ratio and the trigger and detrigger thresholds (short horizontal dotted lines). The trigger threshold is set to 6.

One can see that the channel triggers on the S waves. However, a PEM of 10 seconds is much too short to catch the P waves. Graph d) shows the actually 'recorded' event. It starts much too late and contains no seismic noise record. Graphs e) and f) show the same event but with a properly set PEM parameter. Seismic noise as well as the P waves are properly recorded.

The maximum expected S-P time depends on the maximal distance of relevant earthquakes from the station and on seismic wave velocity in the region. For practice and for local and regional events, accurate enough results can be gained by dividing the maximum station-to-epicenter distance of interest by 5 (distance in miles) or by 8 (distance in km) to get the required maximum S-P time in seconds.

The application dictates the choice of the desired pre-event noise record duration. At least a few seconds are usually required. Note that if one wants to study spectral properties of weak events, seismic noise spectra are usually required to calculate signal-to-noise ratio as a function of frequency. This, however, requires a significant length of noise records depending on the lowest frequency of interest. The PEM must be set accordingly.

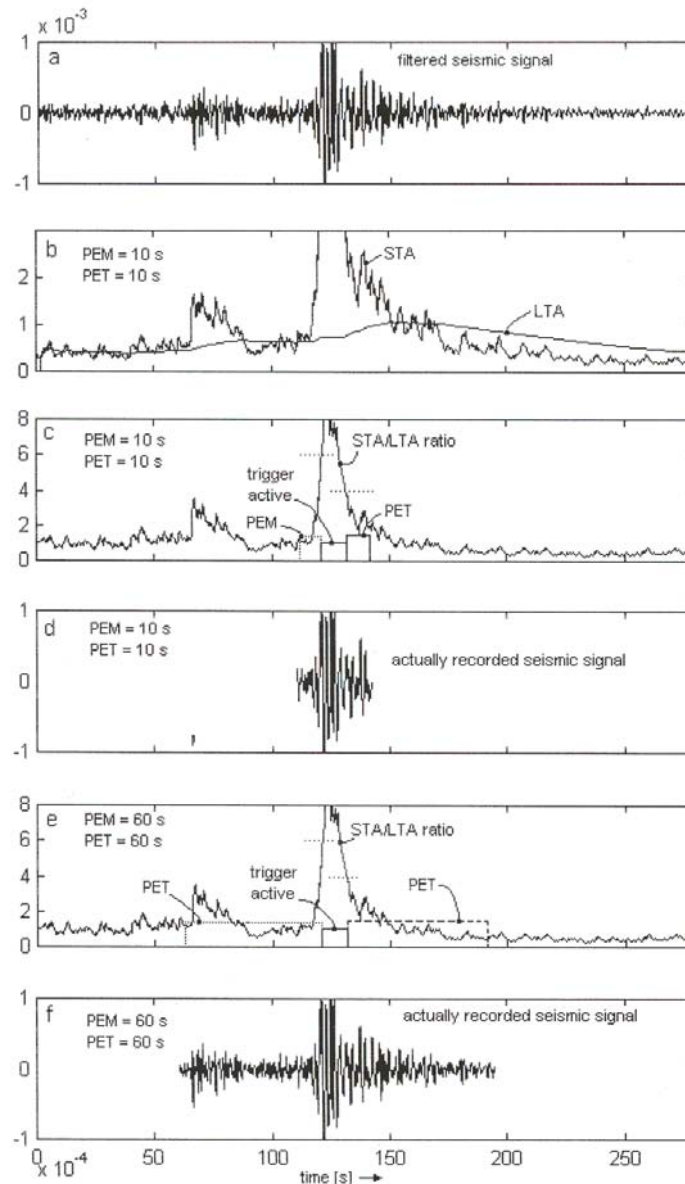


Figure 7 Proper and improper setting of the pre-event time (PEM) and the post-event time (PET)

As an example, let us calculate a required PEM parameter value for a temporary local seismic network with 50 km aperture, where 0.5 sec is set for the STA duration. Suppose that no coincidence trigger exists and all stations run independent trigger algorithms. The operator of the network is interested in the seismicity 200 km around the center of the network. He would also like to have a 10 sec long record of seismic noise before the P waves. We need 0.5 sec for STA calculation, 10 sec for seismic noise, and $\approx (200 \text{ km} + 50/2\text{km})/8 \approx 28$ sec to cover the maximum expected S-P time. Note that the most distant station from the epicenter in the network still has to record P waves — that is why we added one half of the network aperture to the maximum epicentral distance of interest. The PEM should therefore be set to $0.5 + 10 + 28 \sim 40$ sec. Obviously, smaller networks and shorter ranges of interest require shorter PEM and vice versa.

5.3 Selection of post-event time (PET) parameter

The post-event time parameter assures complete recording of seismic events after a detriquer. The main purpose of PET is catching the remaining earthquake coda waves that are smaller in amplitude than the STA/LTA detriquer threshold level. Functionally PET is simply a fixed recording time added to the event file after an instrument or a network (not individual channels!) detriquer. It has a similar effect on coda waves as the STA/LTA detriquer threshold level parameter. However, its effect is event-size independent. This makes it a less effective coda wave 'catcher' than a low STA/LTA detriquer threshold level. It is most suitable for local events. Practical values of PET are usually too short to be of any help for large distant earthquakes with very long coda waves. Contrary to a very low STA/LTA detriquer threshold level that may cause re-triggering problems, a long PET is safe in this respect (see 4.5 above on "Selection of STA/LTA detriquer threshold level").

Optimal PET duration depends mostly on the application. If coda waves are important, a long PET should be selected. If coda waves have no significance, use a short PET. Obviously, the short local events require only a short PET, regional and teleseismic events, on the other hand, would require much longer PET.

A reasonable value for local seismology would be 30 sec, and 60 to 90 sec for regional seismology, assuming one wants the coda waves well recorded. To find optimal value, observe coda waves of your records and adjust the PET accordingly.

There are usually no practical instrumental limitations on selection of the longest PET. However, note that very long PETs use up the recorder's data memory easily. So, do not exaggerate, particularly in seismically very active areas or if a high rate of false triggers is accepted.

5.4 Selection of voting-scheme parameters

The coincidence trigger algorithm, available either in seismic networks or within a multi-channel stand-alone seismic recorder, or in a group of interconnected seismic recorders, uses voting scheme for triggering. The voting-scheme parameters are actually not directly related to the STA/LTA trigger algorithm. However, inappropriate setting of voting scheme prohibits efficient functioning of overall triggering of a network or a recorder. For that reason we also deal with the voting scheme parameters in this section.

In section 4 'How to adjust STA/LTA trigger parameters', we described how each individual channel would trigger if it were the only one in an instrument or in a network. In the following section we describe how the individual channel triggers are combined to cause the system to trigger in a multi-channel recorder or in a seismic network. We call this 'voting', as a number of votes or weights can be assigned to each seismic channel so that they may cause the system to trigger. Only if the total number of votes exceeds a given pre-set value, does the system actually trigger, a new data file opens, and data acquisition begins.

How this voting system is set up depends on the nature of the signals that one is trying to record and on the seismic noise conditions at sensor sites. The noisy channels, which would frequently falsely trigger, will obviously have less 'votes' or assigned weights than the quiet, 'reliable' channels. One will need some first-hand experience of the conditions at the sites before optimizing this voting scheme. The voting mechanism and the terminology differ to

some extent among products. However, there are usually four basic terms associated with the voting scheme parameters, namely:

- Channel weights (votes)

A channel weight defines the number of votes the channel contributes to the total when it is triggered. If the channel has a good signal/noise ratio, assign it a positive number of votes. The more 'reliable' the channel in terms of the event trigger/false trigger ratio is, the higher the number should be selected. If a channel is noisy and frequently falsely triggers, give it lesser or even zero weight. In case you want a channel to inhibit triggering (a rare case indeed), give it negative weights.

- Trigger weight

This is the total number of weights required to get the seismic recorder or the network to trigger.

- Detrigger weight

The Detrigger weight is a value below which the total trigger weights (sum of all individual weights) must fall in order to cause a recorder or a network to detrigger. The Detrigger weight of 1 usually means that all voting channels must be detriggered before the recorder will detrigger. However, other definitions are also possible.

- External channel trigger weight

This value represents the number of weights one assigns to the 'external trigger channel' source. This parameter is most useful in networks of interconnected stand-alone seismic recorders. In this configuration every triggered recorder 'informs' all other units in the network that it triggered. If one wants to ensure that all recorders in the network trigger when one unit triggers, the external trigger channel should have the same weight as the Trigger weight. If one wants to use a combination of an external trigger with other internal criteria, one should set the weights accordingly.

Understanding of the voting scheme parameters is best gained through examples. The following section gives a few examples of various voting schemes.

- A classic strong-motion seismic recorder set at a free-field site has no interconnected units and normally has a three-component internal FBA accelerometer. One would set all three Channel weights to 1 and also set the Trigger weight to 1. Consequently any channel could trigger the system. At noisier sites a Trigger weight set to 2 would be more appropriate. In the latter case, two channels must be in a triggered mode simultaneously (or within a time period usually named aperture propagation window (APW) time, which is an additional parameter available with seismic networks) for the beginning of data recording.
- A small weak motion seismic network around a mine is designed for monitoring local micro-earthquakes. It consists of 5 surface seismic stations with vertical component short-period seismometers and one three-component down-hole accelerometer. An 8-channel data logger is used at the network's center. One of the surface stations is extremely noisy due to nearby construction works. All others have approximately the same seismic noise amplitudes. One can temporally set a Channel weight 0 to the noisy station to exclude its contribution to triggering and channel weights of 1 to all other surface stations. The down-hole accelerometer is very quiet but

less sensitive than surface stations (accelerometers). Select Channel weight 2 for each of its components. For this network a trigger weight of 3 would be an adequate initial selection. The system triggers either if at least three surface stations trigger, or two components of the accelerometer trigger, or one surface station and one component of the accelerometer trigger. Suppose also that there are frequent blasts in the mine. If one wishes, one can use an External trigger channel weight set to -8 and manually (with a switch) prevent seismic network recording of these blasts (down-hole: 3x2 channel votes + surface stations: 4x1 channel vote - 8 External votes < 3 Trigger votes).

- Let us suppose that an interconnected strong motion network of two seismic recorders with the internal three-component FBA accelerometers is installed in a building, one in the basement and one on the roof. Initially one can set the Channel weights to 1 for each signal channel, as well as for the External trigger channel. Suppose the Trigger weight is set to 1 as well. As a result each channel of the system can trigger both units in the system.

After a while one discovers that the seismic recorder on the roof triggers the system much too frequently, due to the swaying of the building in the wind. Changing the voting scheme of the roof unit so that Trigger weight is 3, its channels have 1 weight, while the External trigger channel has 3 weights, can compensate for this action. Now, the recorder installed on the roof triggers only if all its three channels trigger simultaneously or if the 'quiet' recorder in the basement triggers. The number of falsely triggered records will be drastically reduced.

- A small regional radio-frequency (RF) FM modulated telemetry seismic network, with a coincidence trigger algorithm at the central recording site, has 7 short period three-component seismic stations. The three stations, #1 west of the center and #2 and #3 east, not far from the center, have a low seismic noise and are connected to the center via three independent reliable RF links. The two stations north to the center, #4 and #5, are linked with the center via a joined RF repeater. The link between this repeater and the center is, unfortunately, frequently influenced by RF interference, resulting in frequent and simultaneous spikes and glitches in all six transmitted seismic signals. Due to unfavorable geology these two stations have a relatively high seismic noise. The two stations south of the center, #6 and #7, are also connected to the center via another common RF repeater. The station #6 is very quiet and the station #7 is influenced by traffic on a nearby new busy freeway. The RF link from this repeater to the center is less RF interference prone.

In such a situation (apart from trying to technically solve the RF link problem with the northern stations and repositioning of the station #7) an appropriate initial voting scheme would be as follows. A Trigger weight set to 7 (to disable otherwise much too frequent false triggering of the system due to RF interference on all 6 channels of the two northern seismic stations) and a Channel weight 1 to all channels of the northern stations (their total Channel weight should not exceed the Trigger weight), a channel weight 3 to all three channels of the station #1 (to allow independent triggering of the system if all three channels of this good station are triggered), a channel weight 2 to all channels of the stations #2 and #3 (to allow triggering of the whole system if at least four channels of these two closely situated stations are activated), a channel weight 2 to all channels of the station #6 (to accentuate its low seismic noise characteristics but to prevent independent triggering of the system due to occasional RF interference), and a weight 0 to all channels of the station #7 (to exclude its partition in triggering due to excessive man-made seismic noise).

These examples should give enough insight into the flexibility of the coincidence triggering options and about some of the ways in which this flexibility can be used for a particular application. Note also that any initial voting scheme can be significantly improved after more experience is gained with seismic noise conditions at the sites.

6 Practical recommendations for finding optimal triggering parameters

A systematic approach is required for successful adjustment of the optimal triggering and the associated parameters. First, the goals of the seismic installation must be carefully considered and *a priori* knowledge about seismic noise (if any) at the site(s) must be taken into account. Based on this information, the initial parameters are set. Information about them must be saved for documentation purpose. Start with rather low trigger threshold level settings than with a too high setting. Otherwise one can waste too much time in getting a sufficient number of records for a meaningful analysis required for further adjustment steps.

Then the instrument or the network is left to operate for a given period of time. The required length of operation without changing recording parameters depends strongly on the seismic activity in the region. At least several earthquakes and/or falsely triggered records must be recorded before the first readjustment of parameters is feasible. Judgments based on a single or a few records rarely lead to improvements. Such work simply doesn't arrive at any meaningful adjustment.

Afterwards, all records, including those falsely triggered, must be inspected. The completeness of the event records is checked (seismic noise, the P arrivals, the coda waves), and the causes of the false triggers are analyzed. The ratio of event-records/false-records is calculated and compared to the target level. If the number of false triggers does not reach the accepted level, increase the trigger sensitivity by lowering the STA/LTA trigger threshold level(s). Basically, one will acquire more seismic information for nearly the same price and effort. If the number of false triggers is too high, find the reasons why and try to mitigate them by changing STA/LTA and/or voting scheme parameters. Only if this doesn't help, must one decrease trigger sensitivities.

After the analysis is finished, the parameters are changed according to its findings and the new settings archived for documentation purposes. Again the instrument or the network is left active for a certain period of time, the new records are analyzed, and other changes made if needed. By repeating this process one will gradually find the best parameter setting.

References (see References under Miscellaneous in Volume 2)

Topic	Seismic data transmission links used in seismology in brief
Author	Amadej Trnkoczy (formerly Kinemetrics SA); E-mail: amadej.trnkoczy@siol.net
Version	September 1999

The following issues are discussed:

- cost of data transmission equipment and its installation;
- cost of operation of data transmission lines,;
- required maintaining of the data transmission links;
- data throughput;
- reliability of data transmission;
- continuous versus event file data transmission capability;
- applicability in respect to high/low seismicity regions and strong/weak motion networks;
- remote seismic station-to-recording center distance capability;
- robustness against strong earthquakes; and
- special issues.

Type of links	Description
Wire lines	<ul style="list-style-type: none"> ▪ inexpensive establishment if not too long ▪ inexpensive operation ▪ little in-house maintenance ▪ relatively high throughput with modern modems ▪ high reliability of data transmission links ▪ continuous and event file data transmission possible ▪ appropriate for high and low seismicity regions and weak and strong motion seismology ▪ useful for very short distances only (a few km maximum) ▪ robust against damaging earthquakes
Leased phone lines	<ul style="list-style-type: none"> ▪ inexpensive establishment (unless high installation taxes required) ▪ very expensive operation in the long-run, operation cost usually proportional to the total length of the lines ▪ no in-house maintenance ▪ relatively high throughput with modern modems ▪ reliable data transmission ▪ capability to transmit data continuously but less efficient in event files ▪ appropriate for high and low seismicity regions and weak motion networks, rarely used in strong motion networks ▪ appropriate for short and long distances ▪ medium robust against damaging earthquakes
Dial-up phone lines	<ul style="list-style-type: none"> ▪ inexpensive establishment ▪ medium expensive operation, cost of data transmission is proportional to the amount of data transmitted, that is to the seismicity in the region ▪ no in-house maintenance ▪ usually low effective throughput despite of modern high-throughput modems

	<ul style="list-style-type: none"> ▪ medium data transmission reliability ▪ only event file data transmission feasible ▪ applicable for strong motion networks and weak motion networks but in low seismicity regions only ▪ applicable from short to very long distances ▪ not robust against damaging earthquakes, temporarily fail to work after stronger earthquakes with macroseismic effects due to overloading or even break-down of public phone system (exceptions are seismic systems with several input phone lines and with the remote equipment which grabs the lines automatically at the moment of triggering to large events) ▪ reliability of data transmission highly depends on the overall quality of public phone systems in a country; in many developing countries this is a serious obstacle for dial-up phone line systems ▪ incapable of serving alarm and civil defense purposes
<p>Radio-frequency links on VHF or UHF RF band</p>	<ul style="list-style-type: none"> ▪ medium expensive establishment ▪ inexpensive operation ▪ require in-house maintenance ▪ moderate but mostly sufficient throughput for digital data transmission on standard 3.5 kHz bandwidth ‘voice’ channels ▪ medium reliable ▪ continuous and event data transmission possible ▪ applicable for high and low seismicity regions ▪ used mostly in weak motion networks, rarely used in strong motion applications ▪ applicable for distances up to 150 km (100 miles) with direct point-to-point connection and about three times that much using repeaters ▪ robust to strong damaging events ▪ have limited low-dynamic-range of data acquisition for analog FM telemetry ▪ free frequencies are often difficult to obtain ▪ frequently subject to RF interference in developing countries ▪ RF survey required
<p>RF spread spectrum links</p>	<ul style="list-style-type: none"> ▪ medium expensive establishment ▪ inexpensive operation ▪ require in-house maintenance ▪ medium high data throughput ▪ medium reliability of data transmission ▪ continuous and event file data transmission possible ▪ useful in high and low seismicity regions and for weak and strong motion networks ▪ useful for relative short point to point distances from 20 to 100 km maximum ▪ robust to damaging earthquakes ▪ insensitive to RF interference; implies the reduction of multi-path effects compared to VHF and UHF telemetry ▪ permission to operate is easy to obtain or not required at all ▪ maximum point-to-point distances depend on regulations limiting the maximum transmitter output power in a particular country ▪ RF survey required
<p>Microwave RF links</p>	<ul style="list-style-type: none"> ▪ expensive establishment ▪ expensive operation ▪ maintaining usually beyond the scope of seismological institutions ▪ high throughput ▪ high reliability

	<ul style="list-style-type: none"> ▪ continuous and event file data transmission possible ▪ used in high and low seismicity regions and weak motion networks ▪ appropriate for long distances ▪ medium robust against earthquakes ▪ usually these lines are hired from a second party communication company they are often a part of public phone system in the country
<p>Computer networks</p>	<ul style="list-style-type: none"> ▪ medium expensive establishment (if connection points readily available) ▪ medium expensive operation ▪ no in-house maintenance ▪ high data throughput ▪ reliable ▪ semi-continuous and event file data transmission possible ▪ used in high and low seismicity regions and strong and weak motion networks ▪ convenient for medium to very long (even global) distances ▪ allow reduced ownership cost ▪ allow 'portable' central recording site anywhere in the network ▪ frequently unavailable computer 'tabs' at remote seismic station sites (so called 'last mile problem') ▪ different protocols can be used, Internet with TCP/IP protocol is increasingly gaining popularity
<p>Satellite links</p>	<ul style="list-style-type: none"> ▪ very expensive establishment ▪ expensive operation ▪ maintaining usually above the scope of most seismological institutions ▪ high data throughput ▪ reliable ▪ continuous and event file data transmission possible ▪ appropriate for high and low seismicity regions and weak and strong motion networks ▪ medium to very large distances can be covered ▪ robust to damaging earthquakes ▪ convenient for extremely remote sites and large regional and national seismic networks ▪ rarely used at present due to high cost, however satellite data transmission cost is constantly decreasing ▪ for shared satellite hubs additional links from the hub to the seismological center required ▪ high cost of the hub in systems with 'private' local hub ▪ high power consumption of remote stations poses problem to solar panel powered stations

Topic	Retrieving data from IRIS/USGS stations
Author	Caryl Peterson, USGS Albuquerque Seismological Laboratory, 801 University SE, Suite 300, Albuquerque, NM 87106, USA, E-mail: caryl@asl.cr.usgs.gov
Version	January 2001

1 Overview

A current map showing the location of stations of the IRIS/USGS Global Seismic Network is available on the LISS website (www.liss.org) . A phone line or internet connection enables many of these stations to provide users with data recorded within minutes of a data request.. For information regarding accounts and passwords for data retrieval from stations one should contact the GSN maintenance group, gsnmaint@asl.cr.usgs.gov or call (01-505) - 462-3200.

Data can be retrieved from the IRIS/USGS stations in either decompressed ASCII format or in compressed binary (SEED) format.

1.1 Data Formats

- ASCII Format

Choices of ASCII format data include:

- a. "Expanded variable record length ascii"
- b. "Expanded fixed record length ascii"
- c. "SAC ascii digital counts"

There is a limit of 10,000 samples per request (8.3 minutes of 20 sample/second data).

- SEED Format

SEED data format is a much more efficient way to transfer and store data than ASCII data but requires a program that will decode the data (such as DIMAS or RDSEED). The limit per request varies from hours to days of data depending on the sample rate of the data.

1.2 Type of Connection

The method of data retrieval depends both on the desired data format and the type of connection available between the analysis computer and the IRIS/UGSG station computer. To access the IRIS/USGS computer at the user's station, the user can set up the following types of connections:

1. Direct Serial Connection:

This requires that a cable be connected from a serial port on the analysis computer to a serial port that is configured as a spare terminal on the IRIS/USGS computer.

2. LAN (Local Area Network) connection:

The LAN connection requires that network software (including TCP/IP programs telnet and ftp) be running on the analysis computer and that the appropriate ethernet cable and transceiver are available.

3. Dial up connection:

Most IRIS/USGS stations can be accessed by dial-up (telephone) connection. The dial-up connection requires that the analysis computer be connected via a modem to a phone line.

4. Internet Connection:

The website of the Albuquerque Seismic Lab <http://aslwww.cr.usgs.gov/> provides information about the stations, their co-ordinates and sensors as well as a tutorial and notes regarding data retrieval from the stations. The Internet connection requires that both the IRIS/USGS station and the analysis computer have access to the internet and that the analysis computer has the programs telnet and ftp. Users wishing access to the data of a particular station should send an E-mail to gsmaint@asl.cr.usgs.gov, call +1-505-462-3200 or send a request in writing to

USGS Albuquerque Seismological Laboratory
801 University SE, Suite 300
Albuquerque, NM 87106

2 Retrieving decompressed ASCII data

The basic method for retrieving ASCII format data is to capture/log a retrieve session to a file on the analysis computer. A retrieve session entails connecting to the IRIS/USGS station and logging in as user=seed and password=data. This starts a program called "Retrieve" which allows the user to select and transmit the requested data.

The method used to log the retrieve session and connect to the station computer will depend on the type of analysis computer and the software running on the computer.

2.1 Serial Connection (Direct Serial connection or dial-up connection)

For a PC running Windows95, the program Hyperterminal will allow the user to connect to the station computer through a direct serial connection or by dial-up connection. The Transfer menu option "Capture Text" will allow the user to log the retrieve session.

2.2 Internet connection or LAN connection

The Windows95 program Telnet will allow the user to make a network connection to the station. The Terminal menu option "Start Logging" will allow the user to log the retrieve session.

2.3 Examples

Once the user is connected to the station computer, the retrieve session will be the same no matter what method was used to connect to the computer.

The following is an example of a retrieve session:

```
OS-9/68K V2.4   Motorola VME147 - 68030   99/08/26 22:11:51
```

```
User name?: seed   (Enter seed for the User Name)
Password:   (Enter data - the Password will not be displayed)
Process #39 logged on   99/08/26 22:11:59
Welcome!
```

```
IRIS/GSN Seismic Network Station: GUMO
MultiSHEAR acquisition system - Copyright (C) 1998 Quanterra, Inc.
```

...please wait

```
MultiShear -***LOCATION CODES REQUIRED!!*** IRIS/GSN Seismic Network -
STATION:
GUMO
```

Please type your name and organization - up to 50 characters:

```
*****
```

```
Caryl Peterson - asl   (Enter your name and organization)
```

```
MultiShear -**LOCATION CODES REQUIRED!!** IRIS/GSN Seismic Network -
STATION:GUMO
Copyright 1986-1998 by Joseph M. Steim & Quanterra, Inc.
Retrieve (C) 1986-1998 - MSHEAR Release 36/09-0531- 68020- FPU
```

type ? for help

```
Command? ?   (Enter ? to display the help menu shown below)
```

```
Retrieve (C) 1986-1997 Quanterra, Inc. - Release 36/09-0531- 68020- FPU
"C <C/E>" = Change buffer from/to continuous/event data
"T <V/F/C/CS/S/P>" = Select Transmission file format
"F <W/S/L/V...>" = Select optional Filters
"E [ALL]/<DATE> <DATE> [<SEEDNAMES>]" = Examine available data or logs
"S <SEEDNAME> <DATE>" = Setup single data channel to retrieve
"G" = Start or resume sending selected segment
"G P[LOT]" = Plot selected segment on 4014 terminal
"G <S/B>" = Store selected segment to local/backup file
The following 3 methods are available for SEED binary transfer:
"X <SEEDNAMES> <DATE> <DATE> [MAXREC] [TIMETOL]" = Via STP
"V <SEEDNAMES> <DATE> <DATE> [MAXREC] [TIMETOL]" = Archive local file
"I <SEEDNAMES> <DATE> <DATE> [MAXREC] [TIMETOL]" = Via uuencode
"R" = Send station description
"L[|B|C|M] [ALL]" = View entries in event, caliB, Clock, or Msg Log
```

"P" = Display active Processes
 "U <N>" = View User log <N> entries backward
 "Y[T] [*|!<prog>] [<N> [<M>]]" = View <M> activity log <N> entries backward
 "M <message text>" = Send Message to station operator
 "Q" = Quit on-line session. CTL-"C" is ABORT key.
 <SEEDNAMES> supports wildcards (BH?,?LZ,???) and DET|CAL|TIM|MSG|BLK
 Command? **t** (Enter **t** to select the transmission format)

Possible transmission formats are:

"C" - Compressed hexadecimal ascii
 "CS" - Compressed hexadecimal ascii SEED
 "V" - Expanded variable record length ascii
 "F" - Expanded fixed record length ascii
 "S" - SAC ascii digital counts
 "X" - Exit to main command menu

At this point, the user can decide which type of data to transfer. To choose SAC ASCII digital counts, use option **S**.

Transfer mode? **s** (Enter **s** to select SAC ASCII digital counts)

Current transmission mode is SAC ascii

Transmit card numbers with each line of data? (y/n): **n** (no Card numbers)

Command? **s 00-bhz 99/8/26 1:00:00**
 (Select the **channel** and **start time** for data retrieval)

Search requested starting at 1999/08/26 01:00:00

Time window begins in segment 71 at buffer record 2419

Maximum number of samples to transfer? **25**
 (**number** of samples Limit = 10000 samples)

Buffer server is processing your request

skipping first 5165 samples...
 transmission will begin at requested starting time within 0.014161 sec

Use the "G" command to begin transmission
 or to re-transmit data received incorrectly.

Command? **g** (Enter **g** to transmit the data)

Start (31) and end (35) cards to transmit?<CR> (Enter <CR> for all cards)

```

0.0500000 -12345.0000000 -12345.0000000 -12345.0000000 -12345.0000000
0.0141610 1.2141610 0.0000000 0.0000000 2.0000000
-12345.0000000 -12345.0000000 -12345.0000000 -12345.0000000 -12345.0000000
-12345.0000000 -12345.0000000 -12345.0000000 -12345.0000000 -12345.0000000
-12345.0000000 -12345.0000000 -12345.0000000 -12345.0000000 -12345.0000000
-12345.0000000 -12345.0000000 -12345.0000000 -12345.0000000 -12345.0000000
-12345.0000000 13.5878000 144.8663025 14.0000000 -12345.0000000
-12345.0000000 -12345.0000000 -12345.0000000 -12345.0000000 -12345.0000000
-12345.0000000 -12345.0000000 -12345.0000000 -12345.0000000 -12345.0000000
-12345.0000000 -12345.0000000 -12345.0000000 -12345.0000000 -12345.0000000

```



```

-12345.0000000 -12345.0000000 -12345.0000000 -12345.0000000 -12345.0000000
-12345.0000000 -12345.0000000 0.0000000 0.0000000 -12345.0000000
-12345.0000000 -12345.0000000 -12345.0000000 -12345.0000000 -12345.0000000
-12345.0000000 -12345.0000000 -12345.0000000 -12345.0000000 -12345.0000000
 1999      238      1      0      0
  0      6      0      0      25
-12345    -12345    -12345    -12345    -12345
  1      1      11     -12345    -12345
-12345    -12345      40     -12345    -12345
-12345    -12345    -12345    -12345    -12345
-12345    -12345    -12345    -12345    -12345
  1      1      1      1      0
GUMO  H9923801000-BHZ
-12345  -12345  -12345
-12345  -12345  -12345
-12345  -12345  -12345
-12345  -12345  -12345
-12345  -12345  -12345
-12345  -1234500-BHZ
IU      -12345  -12345
      1565.0      1565.0      1565.0      1565.0      1565.0
      1565.0      1565.0      1565.0      1566.0      1565.0
      1565.0      1565.0      1565.0      1566.0      1566.0
      1565.0      1566.0      1565.0      1565.0      1565.0
      1565.0      1565.0      1565.0      1565.0      1565.0

```

Command? **q** (*Enter q to quit the retrieve session*)
 (Always remember to QUIT the retrieve session before exiting!)

...normal termination

...vbb data retrieval system logged out

If the user had selected the "V" option (Expanded Variable Length ASCII format data) for the transmission format: the data would have looked like the following:

```

GUMO.00-BHZ 1999/08/26 01:00:00 +0.014161 SEC 20.00 SPS UNFILTERED 25

1565 1565 1565 1565 1565 1565 1565 1565 12520
1566 1565 1565 1565 1565 1566 1566 1565 12523
1566 1565 1565 1565 1565 1565 1565 1565 12521
1565 0 0 0 0 0 0 0 1565

```

Option F for Expanded Fixed Length ASCII format data:

```

GUMO.00-BHZ 1999/08/26 01:00:00 +0.014161 SEC 20.00 SPS UNFILTERED 25

      1565      1565      1565      1565      1565      7825
      1565      1565      1565      1566      1565      7826
      1565      1565      1565      1566      1566      7827
      1565      1566      1565      1565      1565      7826
      1565      1565      1565      1565      1565      7825

```

IMPORTANT NOTE: Do not close the Hyperterminal or Telnet window before entering "q" to quit the retrieve session.

Once disconnected from the computer, the user should close the log session file. Depending on the analysis application, the file will probably need to be edited to remove all extraneous command lines (non-data).

3 Retrieving SEED data

Since SEED data is in binary rather than ASCII format, the procedure to log a retrieve session will not work. Two of the available procedures entail making a file on the IRIS/USGS computer and then transferring the file.

3.1 Serial Connection: Hyperterminal

For data requests using a direct serial connection or dial-up connection, the Windows95 program Hyperterminal will allow the user to connect to the station computer. The retrieve program option “K” is used to generate a file which is then transferred to the analysis computer using Kermit protocol. See the “Procedure to retrieve data using Kermit” in the DIMAS (Display, Interactive Manipulation and Analysis of Seismograms) operations manual for the details.

3.2 Internet Connection or LAN Connection:

For data requests using a network connection, the telnet program will allow the user to connect to the station computer. The retrieve program option “V” is used to create an archive local file. The program ftp (on the analysis computer) is used to transfer the file to the analysis computer and delete the file from the IRIS/USGS computer. See the “Procedure to create and copy a SEED data file via the network” in the DIMAS manual for details.

If the user is running the DIMAS software on the analysis computer, the DIMAS program NETRD will also allow the user to retrieve SEED data using a network connection. This is the preferred method as it does not create files on the IRIS/USGS computer disk.

4 How to ftp DIMAS Software from ASL

The following are current instructions to download the DIMAS software from the anonymous FTP site at ASL. These instructions may change with future updates of the software, so you should read the **READ.ME** files.

On your PC, make a directory called DIMAS and change to that directory. Ftp to **aslftp.cr.usgs.gov** or 136.177.123.21. At the login prompt, enter **anonymous**. At the password prompt, enter **your_email_address**. Note that your email address will not be displayed. Change to the directory **pub/data_analysis/dimas**. Get all of the files in the **DISK1** and **DISK2** directories. Quit from the ftp session and start **unarj.bat**. Move the RESPONSE.INI and STATION.INI files in the SEEDWGSN/WINDOWS directory to the Main Windows directory.

Title	Data-Type Bulletin IMS1.0: Short
Author	Raymond J. Willemann , IRIS, 1200 New York Ave, NW, Suite 800, Washington DC 20005, U.S.A.; E-mail: ray@iris.edu
Version	September 2001

Below an example is given of an ISF Bulletin which is in accordance with the IMS1.0 format of the International Monitoring System (see http://www.ctbt.rnd.doe.gov/nemre/introduction/ims_descript.html) and the current version of the document defining ISF extensions of IMS1.0 (see ISC home page <http://www.isc.ac.uk/Documents/isf.pdf>).

The example includes two events because an example of only one event would fail to show how consecutive events are to follow each other. The first event is small; with only a few data. This makes it possible to realize the typical way of data presentation at a glance. The second event is larger and this examples shows better how multiple magnitudes and event parameters are to be included.

An example can not, of course, explain which elements are required and which are optional, nor give the units in which each parameter is required to be given. Thus, it is essential for an agency intending to write ISF bulletins to read the format description as well as look at an example. The format description in this case includes the IMS1.0 (a.k.a. GSE2.1) documentation, which is available from the web site of the Vienna Prototype International Data Centre (pIDC; <http://www.pidc.org/librarybox/idcdocs/idcdocs.html>) under "3.4.1 Rev3 Formats and Protocols for Messages", as well as the extensions of IMS1.0 that constitute the ISF (see IS 10.2). The final ISF description of the extensions document will be posted to the ISC web site (<http://www.isc.ac.uk>) as a PDF document.

In the ISC Bulletin for the time period 01-09-1999 06:00:00 to 01-09-1999 06:45:00 the following 2 events were found:

Event 1847567 Turkey

```

Date           Time           Err           RMS Latitude Longitude Smaj Smin Az Depth  Err NDef Nsta Gap mdist Mdist Qual Author  OrigID
1999/09/01 06:03:51.10 3.88 0.58 40.7170 30.7580 41.2 13.6 0 5.0 23.4 5 5 0.47 1.80 m i ISK 2576986
1999/09/01 06:03:50.70 3.88 0.58 40.7830 30.7590 41.2 13.6 0 5.0 23.4 5 5 0.47 1.80 m i ISC 3325719
    
```

```

Magnitude Err Nsta Author  OrigID
MD 2.6 ISK 2576986
    
```

```

Sta Dist EVAz Phase Time TRes Azim AzRes Slow SRes Def SNR Amp Per Qual Magnitude ArrID
MDU 0.47 132.3 Pg 06:04:00.100 -0.0 3.0000 -34.0000 4.3 152 10.0F 125 125 64 25.28 157.07 40036747
EYL 0.51 244.9 Pg 06:04:01.200 0.4 4.3726 -32.2802 18.7 9.3 133 33.0 31 27.20 82.59 40036748
EYL 0.51 244.9 SG 06:04:07.700 0.4 4.7536 -32.7216 28.4 23.0 50 18.8 19 11 171 43.40 157.20 40036749
YLV 1.08 258.9 Pg 06:04:11.800 -0.4 5.1800 -32.7000 11.1 11.1 -1 15.0F 137 177 25.30 157.06 m i 40036750
IZI 1.08 246.0 PN 06:04:12.100 -0.2 0.650 1.330 0.840 0.430 17 ) 40036751
CTT 1.80 282.4 PN 06:04:22.800 0.2 0.650 1.330 0.840 0.430 17 ) 40036752
    
```

Event 1717835 Central Mid-Atlantic Ridge

```

Date           Time           Err           RMS Latitude Longitude Smaj Smin Az Depth  Err NDef Nsta Gap mdist Mdist Qual Author  OrigID
1999/09/01 06:42:34 3.0000 -34.0000 4.3 152 10.0F 125 125 64 25.28 157.07 40036747
1999/09/01 06:42:41.63 0.21 0.85 4.6760 -32.6130 6.7 4.3 152 10.0F 125 125 64 25.28 157.07 40036748
(#PARAM SCALAR_MOMENT=2.1E16)
1999/09/01 06:42:44.00 0.25 4.3726 -32.2802 18.7 9.3 133 33.0 31 27.20 82.59 40036749
1999/09/01 06:42:45.23 1.14 0.80 4.7536 -32.7216 28.4 23.0 50 18.8 19 11 171 43.40 157.20 40036750
1999/09/01 06:42:49.00 0.80 5.1800 -32.7000 11.1 11.1 -1 15.0F 137 177 25.30 157.06 m i 40036751
(#CENTROID)
(#MOMTENS sc MO fCLVD MRR MTT MPP MRT MTP ePP eRT eTP ePR NCO duration)
(# EMO eCLVD eRR eTT ePP eRT eTP ePR NCO duration)
(# 16 4.40 -5.010 2.560 2.450 0.000 1.220 0.000 12 HRVD )
(# 0.650 1.330 0.840 0.430 17 )
(+ Data Used: GSN.)
(#FAULT_PLANE Typ Strike Dip Rake NP NS Plane Author )
(# BDC 226.00 45.00 -90.00 HRVD )
(+ BDC 46.00 45.00 -90.00 HRVD )
(#PRINAX sc T_val T_azim T_pl B_val B_azim B_pl P_val P_azim P_pl Author )
(# 16 3.72 136.00 0.00 1.29 46.00 0.00 -5.01 180.00 90.00 HRVD )
1999/09/01 06:42:41.81 0.28 0.89 4.6780 -32.5870 6.1 4.9 0 10.0F 137 177 25.30 157.06 m i ISC 3325720
(#PARAM PP_DEPTH=13.30+0.80)
    
```

```

Magnitude Err Nsta Author  OrigID
mb 4.9 48 NEIC 2932984
MSZ 4.6 59 NEIC 2932984
Mw 5.1 HRVD 2932985
Mb 4.8 0.2 25 LDG 3015245
Ms 4.1 0.2 7 LDG 3015245
Mb 5.0 NAO 3125978
mb 4.4 0.1 10 EIDC 3004603
msmle 4.1 0.1 6 EIDC 3004603
    
```

MS	4.2 0.1	4 EIDC	3004603	Sta	Dist	EvAz	Phase	Time	TRes	Azim	AzRes	Slow	SRes	Def	SNR	Amp	Per	Qual	Magnitude	Arrid	
mb	4.8	63 ISC	3325720	BAO	25.30	216.8	P	06:48:08.970	-1.2				T			6.9	0.90	_e	4.4	40722779	
MS	4.6	60 ISC	3325720	BDFB	25.32	216.8	P	06:48:09.360	-1.0				T			900.0	21.00	_e	4.3	40722780	
				BDFB	25.32	216.8	LR						T			21.5	1.20	_e	4.8	40722891	
				LIC	27.48	85.5	P	06:48:30.260	-0.1				T								40722973
				TIC	27.50	84.6	P	06:48:29.180	-1.4				T								40722876
				KIC	27.77	85.3	P	06:48:30.940	-2.1				T								40722814
				CPUP	39.05	216.6	P	06:50:10.010	-0.7				T			3.5	0.80	_e	4.0	40722814	
				CPUP	39.05	216.6	LR						T			500.0	20.00	_e	4.3	40722815	
				LPAZ	40.86	238.6	P	06:50:26.160	0.4				T			6.7	0.90	_e	4.4	40722896	
				LPAZ	40.86	238.6	LR						T			470.0	19.00	_e	4.4	40722897	
				ESDC	43.38	32.6	P	06:50:47.700	1.5	231.2		8.8	T			3.5	0.79	_e	4.2	42115734	
				ESDC	43.38	32.6	SP	06:50:53.200	2.4	228.6		8.9	T			7.5	1.11	_e		42115735	
				ESDC	43.38	32.6	LR	07:06:35.307	215.0			33.0	T			168.1	18.40	_e	4.0	42115736	
				NNA	47.02	249.0	P	06:51:19.165	3.7	171.6		5.0	T			8.2	0.89	_e	4.9	42115744	
				NNA	47.02	249.0	PFAKE	06:51:20.000	4.5				T								40722923
				NNA	47.02	249.0	LR						T			520.0	19.00	_e	4.5	40722924	
				ETSF	47.48	31.9	P	06:51:19.700	0.9				T			18.9	1.21	_e	5.1	42250513	
				EPF	48.05	32.4	P	06:51:24.100	0.8				T			13.4	1.06	_e	5.0	42250514	
				MTLF	49.27	33.3	P	06:51:32.600	-0.1				T			19.7	1.02	_e	5.1	42250515	
				RJF	50.22	31.0	P	06:51:39.500	-0.5				T								42250516
				RJF	50.22	31.0	R		0.0				T			217.9	19.00	_e		42250517	
				MFF	50.31	28.7	P	06:51:40.000	-0.6				T			24.1	1.22	_e	5.0	42250518	
				SGMF	50.43	25.7	P	06:51:41.100	-0.5				T			32.6	1.18	_e	5.1	42250519	
				LASF	50.65	33.6	P	06:51:43.400	0.1				T			15.1	1.03	_e	4.9	42250520	
				BGCA	50.81	87.1	P	06:51:45.500	0.6				T			19.7	1.10	_e	5.0	40722783	
				BGCA	50.81	87.1	LR						T			330.0	20.00	_e	4.3	40722784	
				LBL	51.08	32.1	P	06:51:47.500	1.0				T								45443017
				TCF	51.25	30.5	P	06:51:47.400	-0.4				T				2.4	0.64	_e	4.3	42250521
				GRR	51.28	26.7	P	06:51:47.400	-0.6				T			11.8	1.11	_e	4.7	42250522	
				PYM	51.29	31.5	P	06:51:49.300	1.2				T								45443018
				VIVF	51.60	33.3	P	06:51:50.600	0.2				T			11.4	0.93	_e	4.8	42250523	
				LSCT	51.66	321.5	PFAKE	06:52:00.000	9.0				T								40722902
				LSCT	51.66	321.5	LR						T			330.0	19.00	_e	4.4	40722903	
				GWDE	51.71	317.2	PFAKE	06:52:00.000	8.6				T								40722853
				GWDE	51.71	317.2	LR						T			1130.0	20.00	_e	4.9	40722854	
				BGF	51.75	30.6	P	06:51:51.300	-0.3				T			7.7	0.68	_e	4.8	42250524	
				PLDF	51.76	31.6	P	06:51:52.500	0.9				T								45443019
				LDF	51.77	27.0	P	06:51:50.800	-0.9				T				5.0	0.70	_e	4.6	42250525
				AVF	52.17	30.7	P	06:51:54.100	-0.6				T				5.7	0.87	_e	4.5	42250526
				CALN	52.17	35.7	P	06:51:55.600	0.8				T								45443020
				ORIF	52.30	34.0	P	06:51:56.200	0.4				T								42250527
				ORIF	52.30	34.0	R		0.0				T			6.2	0.88	_e	4.5	42250528	
				SMF	52.32	31.1	P	06:51:55.400	-0.5				T			170.0	22.25	_e		42250529	
				MVIF	52.41	35.7	P	06:51:57.200	0.6				T								45443021

Sta	Dist	EvAz	Phase	Time	TRes	Azim	AzRes	Slow	SRes	Def	SNR	Amp	Per	Qual	Magnitude	ArrID
SCHQ	57.13	337.2	P	06:52:29.600	-1.2	123.7		8.3	T		13.7	15.4	0.79	mb	5.1	42115750
SCHQ	57.13	337.2	SP	06:52:35.675	0.5	139.5		8.8	T		7.1	15.0	0.92			42115751
PTCC	57.45	36.2	P	06:52:33.100	-0.1				T							42839620
VOY	57.57	36.8	P	06:52:34.200	0.1				T							42808147
GRF	58.08	32.0	P	06:52:37.600	0.0				T			38.7	1.30	mb	5.3	40722849
GRF	58.08	32.0	SP	06:52:43.200	1.1				T							40722850
GRF	58.08	32.0	LR	06:52:41.190	-1.1				T			300.0	18.50	MS	4.4	40722851
AAM	58.74	317.5	P	06:52:39	-3.4				T							40722765
AAM	58.74	317.5	LR	06:52:42	-1.0				T							40722766
PTU	58.85	31.2	P	07:15:53					T							36882044
MOX	58.85	31.2	L	06:52:41.800	-1.8				T							45438984
MOX	58.85	31.2	L	06:52:42.125	-1.5	246.4		4.2	T		25.5	2.4	1.00	mb	4.2	40722841
GEC2	58.95	33.9	P	06:52:48.825	0.7	228.7		5.1	T		13.4	4.5	0.95	mb	4.5	42115739
GERES	58.95	33.9	P	06:52:48.825	0.7	228.7			T			9.4	1.10			42115740
GERES	58.95	33.9	SP	06:52:50.000	5.6				T							40722992
WCI	59.03	312.2	PFAKE	06:52:44.000	-0.2				T			480.0	22.00	MS	4.6	40722993
WCI	59.03	312.2	LR	06:52:45.930	-1.7				T							44689671
KHC	59.03	33.5	P	06:52:50.600	-0.5				T			10.9	1.00	mb	4.8	40722999
KHC	59.03	33.5	P	06:52:56.200	0.6				T			530.0	19.00	MS	4.7	40723000
WVT	59.50	309.5	P	06:52:57.800	1.2				T							45569564
WVT	59.50	309.5	LR	06:52:50.600	-0.5				T							40722943
CLI	59.94	31.2	P	06:52:52.700	0.5				T			13.0	1.20	mb	4.8	40722944
PRU	60.03	33.1	P	06:52:52.700	0.5				T							40722793
PRU	60.03	33.1	SP	06:52:57.800	1.2				T			18.0	1.40	mb	4.9	40722794
BRG	60.19	32.0	P	06:53:00.000	7.1				T							40722795
BRG	60.19	32.0	SP	06:52:55.800	-0.6				T			160.0	24.00	MS	4.1	40722796
BRG	60.19	32.0	LR	06:53:00.500	1.5				T			170.0	24.00	MS	4.2	40722797
BRG	60.19	32.0	LR	06:53:01.500	-0.1				T			130.0	24.00	MS	4.2	40722933
BRG	60.19	32.0	LR	06:53:03.800	-0.4				T			970.0	21.00	MS	4.9	40722934
BRG	60.19	32.0	LR	06:53:09.940	1.0				T							41194520
BRG	60.19	32.0	LR	06:53:07.230	-1.9				T							40722986
BRG	60.19	32.0	LR	06:53:06.830	-2.3				T							41194519
OXF	60.26	307.2	PFAKE	06:52:55.800	-0.6				T							44689672
OXF	60.26	307.2	LR	06:53:00.500	1.5				T							42115752
VRAC	60.81	34.6	P	06:53:03.800	-0.4				T		3.7	9.9	0.97	mb	4.9	40722983
VRAC	60.81	34.6	P	06:53:09.940	1.0			8.8	T							40722802
VAY	61.17	44.9	P	06:53:07.230	-1.9				T			10.4	0.70	mb	5.1	40722803
VAY	61.17	44.9	P	06:53:06.830	-2.3				T			380.0	21.00	MS	4.5	40722803
MORC	61.58	34.5	P	06:53:12.300	0.8				T							36778884
MORC	61.58	34.5	P	06:53:20.000	5.7				T							40722872
OKC	61.95	34.6	P	06:53:30.000	15.2				T			440.0	19.00	MS	4.7	40722873
OKC	61.95	34.6	P	06:53:16.1	LR				T							40722880
SUR	62.63	130.1	P	06:53:16.570	0.2				T			200.0	19.00	MS	4.3	40722881
SUR	62.63	130.1	P	06:53:30.000	8.3				T							40722889
UALR	62.66	306.8	P	06:53:16.570	0.2				T			390.0	22.00	MS	4.5	40722861
UALR	62.66	306.8	P	06:53:30.000	8.3				T			12.2	0.90	mb	5.1	40722862
CCM	62.68	310.6	P	06:53:21.600	-0.8				T			540.0	22.00	MS	4.7	40722792
CCM	62.68	310.6	P						T							
CCM	62.68	310.6	LR						T							
OJC	63.07	34.8	P						T							
OJC	63.07	34.8	P						T							
JFWS	63.47	316.1	PFAKE						T							
JFWS	63.47	316.1	LR						T							
JFWS	63.47	316.1	LR						T							
KONO	63.59	22.4	LR						T							
KONO	63.59	22.4	LR						T							
KONO	63.59	22.4	LR						T							
LFTB	63.73	120.7	P						T							
LFTB	63.73	120.7	P						T							
HKT	64.55	300.9	PFAKE						T							
HKT	64.55	300.9	LR						T							
HKT	64.55	300.9	LR						T							
BOSA	64.67	124.6	P						T							
BOSA	64.67	124.6	P						T							
BOSA	64.67	124.6	LR						T							

Sta	Dist	EvAz	Phase	Time	TRes	Azim	AzRes	Slow	SRes	Def	SNR	Amp	Per	Qual	Magnitude	ArrID
NOA	65.11	21.8	P	06:53:24.150	-0.6	230.9		6.3	T		6.4	5.4	1.01	mb	4.7	42115745
NOA	65.11	21.8	SP	06:53:30.243	1.2	224.9		7.1			6.3	6.0	1.16			42115746
NOA	65.11	21.8	LR	07:20:09.114		235.0		34.5				164.1	18.14	MS	4.3	42115747
CBKS	69.33	309.7	PFAKE	06:54:00.000	8.3							540.0	22.00	MS	4.8	40722800
CBKS	69.33	309.7	LR	07:20:46.063		152.0		32.9				170.6	18.34			42115753
ULM	69.53	322.3	LR	06:54:10.000	6.5							290.0	21.00	MS	4.5	40722904
LTX	71.23	299.3	PFAKE									3.1	0.81	MS	4.5	40722905
LTX	71.23	299.3	LR									15.2	1.27			42115737
FINES	71.33	25.7	P	06:54:03.775	0.3	284.5		7.4	T		7.5					42115738
FINES	71.33	25.7	SP	06:54:10.200	2.5	260.8		6.8								40722840
GDL2	72.11	302.2	P	06:54:08.200	-0.4				T							40722840
GDL2	72.11	302.2	P	06:54:30.000	12.2											40722845
GLD	73.68	309.9	PFAKE									420.0	20.00	MS	4.7	40722846
GLD	73.68	309.9	LR	06:54:20.520	0.1				T			24.8	1.60	e mb	5.0	40722768
ANMO	74.12	304.9	P									760.0	19.00	MS	5.0	40722769
ANMO	74.12	304.9	LR													40722900
LPM	74.20	304.2	P	06:54:21.110	0.2				T							40722928
OBN	74.36	33.8	P	06:54:21.500	0.1				T							40722887
LAZ	74.63	304.3	P	06:54:23.740	0.4				T							40722951
RW3	75.42	308.2	P	06:54:28.440	0.6				T							45302922
KEV	75.43	18.1	P	06:54:26.200	-1.1				T			192.0	1.50	e mb	6.0	40722877
KIV	76.17	46.0	P	06:54:33.060	1.1				T			4.2	0.77	mb	4.6	42115741
KVAR	76.18	46.0	P	06:54:33.975	2.0	135.0		2.4	T		12.3					42115742
KVAR	76.18	46.0	SP	06:54:40.125	3.6	148.0		4.5	T		6.2	34.7	1.27			40722945
PV10	76.49	308.2	P	06:54:34.300	0.4				T			45.8	1.60	e mb	5.4	40722847
GNI	77.29	50.1	P	06:54:40.120	1.8				T			160.0	21.00	MS	4.3	40722848
GNI	77.29	50.1	LR													40722981
TUC	77.54	301.9	PFAKE	06:54:50.000	10.1							250.0	20.00	MS	4.5	40722982
TUC	77.54	301.9	LR									11.4	0.90	e mb	5.0	40722995
WUAZ	78.17	305.2	P	06:54:44.110	0.9				T			520.0	22.00	MS	4.8	40722996
WUAZ	78.17	305.2	LR													40722966
STEW	78.22	313.9	P	06:54:43.330	0.0				T							40722818
DAU	78.36	310.1	P	06:54:44.780	0.6				T							42017674
SNAA	78.64	170.8	P	06:54:44.900	-0.2				T							40722868
HWUT	78.67	311.3	P	06:54:45.500	-0.3				T			15.1	0.70	e mb	5.1	40722868
HWUT	78.67	311.3	LR									310.0	22.00	MS	4.6	40722869
QLMT	78.80	314.6	P	06:54:47.350	0.8				T							40722947
MSU	78.96	308.2	P	06:54:48.190	0.7				T							40722917
TMI	79.04	313.1	P	06:54:47.830	-0.0				T							40722975
HRV	79.23	316.5	P	06:54:48.520	-0.3				T							40722867
KNB	79.41	306.6	P	06:54:50.810	0.8				T			2.5	0.80	e mb	4.3	40722878
KNB	79.41	306.6	LR									500.0	21.00	MS	4.8	40722879
DUG	79.53	309.9	P	06:54:50.910	0.3				T			29.4	1.40	e mb	5.0	40722823
DUG	79.53	309.9	LR									320.0	20.00	MS	4.7	40722824
LRM	79.60	315.6	P	06:54:51.400	0.6				T							40722901
MCMT	79.81	314.6	P	06:54:52.390	0.4				T							40722909
HLID	80.87	313.2	P	06:54:57.900	0.3				T			12.3	1.30	e mb	4.8	40722863
HLID	80.87	313.2	LR									420.0	19.00	MS	4.8	40722864
ELK	81.40	310.3	P	06:55:00.560	0.1				T			21.2	1.50	e mb	5.0	40722828

Sta	Dist	EVaz	Phase	Time	TRes	Azim	AzRes	Slow	SRes	Def	SNR	Amp	Per	Qual	Magnitude	ArrID	
YKA	82.18	332.3	P	06:55:08.200	4.1	94.0	5.3		T		4.2	2.4	1.00	_e	mb	4.3	40723005
PFO	82.33	303.1	P	06:55:08.615	3.2	308.7	2.3		T			2.0	0.97	_	mb	4.2	42115748
NEW	82.89	317.9	P	06:55:08.560	0.5				T								40722920
NEW	82.89	317.9	PcP	06:55:20.000	6.5												40722921
NEW	82.89	317.9	LR									380.0	21.00		MS	4.7	40722922
BMN	82.91	310.0	PFAKE	06:55:20.000	11.7												40722788
BMN	82.91	310.0	LR									240.0	20.00		MS	4.6	40722789
TPH	82.92	307.6	P	06:55:09.030	0.6				T			17.6	1.10	_e	mb	5.2	40722979
TPH	82.92	307.6	LR									320.0	22.00		MS	4.7	40722980
VTV	83.05	304.1	PFAKE	06:55:20.000	10.8							560.0	20.00		MS	4.9	40722991
VTV	83.05	304.1	LR									320.0	22.00		MS	4.7	40722816
DAC	83.23	305.8	PFAKE	06:55:20.000	9.9							300.0	20.00		MS	4.7	40722817
DAC	83.23	305.8	LR									530.0	19.00		MS	4.9	40722914
MNV	83.65	308.0	PFAKE	06:55:20.000	7.8							310.0	19.00		MS	4.7	40722915
MNV	83.65	308.0	LR									530.0	19.00		MS	4.9	40722935
PAS	83.75	303.7	PFAKE	06:55:20.000	7.2							30.6	1.80	_e	mb	5.2	40722936
PAS	83.75	303.7	LR						T			310.0	19.00		MS	4.7	40722997
WVOR	83.96	312.0	P	06:55:14.520	0.9							110.0	21.00		MS	4.2	40722998
WVOR	83.96	312.0	LR									220.0	20.00		MS	4.5	40722870
ISA	83.96	305.2	PFAKE	06:55:20.000	6.2							110.0	21.00		MS	4.2	40722871
ISA	83.96	305.2	LR									220.0	20.00		MS	4.5	40722872
HAWA	84.53	316.0	PFAKE	06:55:30.000	13.5							380.0	20.00		MS	4.8	40722856
HAWA	84.53	316.0	LR									380.0	20.00		MS	4.8	40722857
BEKR	85.32	309.5	P	06:55:21.030	0.5				T			65.5	1.30	_e	mb	5.7	40722877
BEKR	85.32	309.5	LR									290.0	22.00		MS	4.6	40722878
VIPM	85.35	314.2	P	06:55:22.180	1.6				T			90.0	20.00		MS	4.2	40722882
VIPM	85.35	314.2	LR									380.0	20.00		MS	4.8	40722883
CMB	85.42	307.7	PFAKE	06:55:30.000	8.9							380.0	20.00		MS	4.8	40722808
CMB	85.42	307.7	LR									380.0	20.00		MS	4.8	40722809
LON	86.09	316.4	P	06:55:24.480	0.2				T			65.5	1.30	_e	mb	5.7	40722893
LON	86.09	316.4	LR									290.0	22.00		MS	4.6	40722894
ARU	86.78	33.8	P	06:55:28.450	1.1				T			90.0	20.00		MS	4.2	40722812
ARU	86.78	33.8	LR									90.0	20.00		MS	4.2	40722813
YBH	87.01	311.5	PFAKE	06:55:40.000	11.1							470.0	19.00		MS	4.9	40722929
YBH	87.01	311.5	LR									470.0	19.00		MS	4.9	40722930
BMW	87.08	316.2	P	06:55:29.710	0.6				T			35484913					35484913
BMW	87.08	316.2	LR									41194522					41194522
COR	87.26	314.3	PFAKE	06:55:40.000	10.0							230.0	20.00		MS	4.7	40722810
COR	87.26	314.3	LR									230.0	20.00		MS	4.7	40722811
OCWA	87.64	317.5	PFAKE	06:55:40.000	8.3							900.0	20.00		MS	5.3	40722954
OCWA	87.64	317.5	LR									900.0	20.00		MS	5.3	40722955
OCWA	87.64	317.5	LR									90.0	19.00		MS	4.4	40723001
SYO	88.03	159.9	P	06:55:34.400	1.3				T			90.0	19.00		MS	4.4	40723002
SYO	88.03	159.9	LR									90.0	19.00		MS	4.4	40723003
MALO	88.92	53.8	P	06:55:38.000	-0.2				T			90.0	19.00		MS	4.4	40722906
MALO	88.92	53.8	LR									90.0	19.00		MS	4.4	40722907
COLA	96.22	337.1	PFAKE	06:56:20.000	8.9							130.0	21.00		MS	4.5	40722984
COLA	96.22	337.1	LR									130.0	21.00		MS	4.5	40722985
SBA	106.16	184.2	PP	07:01:20.000	-1.9												
SBA	106.16	184.2	LR														
YAK	112.11	8.9	PFAKE	07:01:30.000	12.8												
YAK	112.11	8.9	LR														
MA2	115.89	358.1	PFAKE	07:01:40.000	15.3												
MA2	115.89	358.1	LR														
ULN	116.84	29.3	PFAKE	07:01:40.000	13.2												
ULN	116.84	29.3	LR														

Sta	Dist	EvAz	Phase	Time	TRes	Azim	AzRes	Slow	SRes	Def	SNR	Amp	Per	Qual	Magnitude	ArrID
SMY	118.51	341.9	LR									1090.0	21.30	MS	5.5	40722963
HON	120.61	298.0	PFAKE	07:01:50.000	15.2							1230.0	21.30	MS	5.5	40722865
HON	120.61	298.0	LR									100.0	22.00	MS	4.4	40722858
HIA	121.13	20.8	PFAKE	07:01:50.000	14.9							100.0	22.00	MS	4.4	40722859
HIA	121.13	20.8	LR									100.0	22.00	MS	4.4	40722937
PET	121.74	352.0	PFAKE	07:01:50.000	13.8							150.0	19.00	MS	4.7	40722786
PET	121.74	352.0	LR									130.0	21.00	MS	4.7	40722970
BJT	127.05	29.9	PFAKE	07:02:00.000	13.2							8.2	1.20	MS	4.7	40722971
BJT	127.05	29.9	LR									7.5	1.00	MS	4.7	40722977
TATO	141.22	39.3	PFAKE	07:02:30.000	16.4							8.7	1.20	MS	4.7	40722974
TATO	141.22	39.3	LR									2.5	0.98	MS	4.7	42115729
TOO	147.22	177.2	PKP	07:02:24.100	0.6							1.5	0.78	MS	4.7	42115730
STKA	152.40	169.3	PKP	07:02:37.500	5.8							3.1	1.12	MS	4.7	42115731
ASPA	157.06	146.7	PKP	07:02:39.700	1.4											
ASAR	157.06	146.7	PKP	07:02:41.200	2.9	203.1		1.4			12.8					
ASAR	157.06	146.7	PKP2	07:03:09.850	-1.3	200.0		4.4			7.7					
ASAR	157.06	146.7	SPKP2	07:03:16.950	1.5	209.2		4.1			4.5					

STOP

Title	Example of station parameter reports grouped according IMS1.0 with ISF1.0 extensions
Author	Raymond J. Willemann , IRIS, 1200 New York Ave, NW, Suite 800, Washington DC 20005, U.S.A; E-mail: ray@iris.edu
Version	September 2001

1 Introduction

On the following pages a sample is shown of parameter readings of seismic stations from unassociated arrivals as they were grouped by the National Earthquake Information Center (NEIC) of the USGS in Denver, USA, and reported to the International Data Center (ISC) in Thatcham, UK.

ASCII characters are used as part of the Group and Arrival IDs. According to the IMS1.0 documentation about their data-type "Grouped Arrivals" these characters should help the agency to recognize that several phase arrivals come from the same event but that the reporting station can not locate the event, so they are assigned to the same "group". Note that NEIC uses the groups more restrictively: they only let arrivals share the same group ID if they are at the same station and likely come from the same event. This is within the rules. Examples are, e.g., on page 2 for stations VRAC, TXAR and SLR.

The simple example given below fails to show an important ISF extension, namely the phase information sub-block which allows to give, e.g., for every phase reading, information about what filter was used to do the reading, and so on. This kind of information can now be put, in accordance with the ISF format (see IS10.1) into a "sub-block" that would follow the one shown below and share the same values of arrival ID (column heading ArrID).

The abbreviations used for the different columns are more or less self-explanatory. Column Sta contains the three or four letter station codes and in column Chan the components may be given, in which the parameter reading (time, amplitude, period etc.) was made (Z – vertical, H – horizontal; N – north and E – east). The column for characterizing the arrival quality (Qual) gives either e (for emergent) or i (for impulsive) onsets and may additionally give the polarity of the first motion (c for compression and d for dilatation). Note that (regrettably) in most cases no channel information is provided by the stations and also amplitudes (Amp) and period readings (Per) are rarely given. Azimuth (Azim) and slowness (Slow) readings are usually reported from seismic arrays only (see, e.g., YKA – Yellowknife Array on page 2). In the column SNR measurements of the signal-to-noise ratio could be reported, which, however, would make sense only with accompanying information in the phase information sub-block about the filter bandwidth. Note, that in some cases the column Author (reporting station or network/array) may also be blank (see page 6).

Net	Sta	Chan	Aux	Date	Time	Phase	Azim	Slow	SNR	Amp	Per	Qual	Group	C	Author	ArrID
	VRAC	???		2000/09/01	00:05:41.30	Pn							00IAAAA		VRAC	AIAAAAA
	VRAC	???		2000/09/01	00:06:04.30	Sg							00IAAAA		VRAC	AIAAAAA
	CGP	???		2000/09/01	00:09:52.50	P						e	00IAAAB		PIVS	AIAAAAA
	ITM	???		2000/09/01	00:20:22.50	Pb						e	00IAAAC		ATH	AIAAAAA
	VLI	???		2000/09/01	00:20:41.00	Pg						e	00IAAAC		ATH	AIAAAAA
	EVR	???		2000/09/01	00:20:43.00	Pb						e	00IAAAC		ATH	AIAAAAA
	BKM	???		2000/09/01	00:21:28.50	P						i	00IAAAD		NOU	AIAAAAA
	NDI	???		2000/09/01	00:36:17.00	P						e	00IAAAE		NDI	AIAAAAA
	EZN	???		2000/09/01	00:56:01.00	Pg						e	00IAAAF		ISK	AIAAAAA
	EZN	???		2000/09/01	00:56:07.50	Sg						e	00IAAAF		ISK	AIAAAAA
	PGP	???		2000/09/01	01:00:09.80	P						e	00IAAAG		PIVS	AIAAAAA
	CMAR	???		2000/09/01	01:03:39.90	P				9.1	0.50		00IAAAH		IDC	AIAAAAA
	FITZ	???		2000/09/01	01:04:04.80	P							00IAAAI		AUST	AIAAAAA
	ASAR	???		2000/09/01	01:05:27.30	P							00IAAAJ		IDC	AIAAAAA
	ASAR	???		2000/09/01	01:05:37.30	Pp							00IAAAJ		IDC	AIAAAAA
	ASPA	???		2000/09/01	01:05:27.30	P						e	00IAAAK		AUST	AIAAAAA
	STKA	???		2000/09/01	01:06:47.35	P							00IAAAL		IDC	AIAAAAA
	STKA	???		2000/09/01	01:06:57.10	Pp							00IAAAL		IDC	AIAAAAA
	STKA	???		2000/09/01	01:25:44.13	LR							00IAAAL		IDC	AIAAAAA
	MAT	???		2000/09/01	01:16:52.00	P						e	00IAAAM		JMA	AIAAAAA
	MAT	???		2000/09/01	01:17:26.00	S				12.4	0.45		00IAAAM		JMA	AIAAAAA
	GURN	???		2000/09/01	01:17:32.36	P							00IAAAN		DMN	AIAAAAA
	GHAN	???		2000/09/01	01:17:34.02	P							00IAAAN		DMN	AIAAAAA
	HARN	???		2000/09/01	01:17:48.04	P							00IAAAN		DMN	AIAAAAA
	TXAR	???		2000/09/01	01:18:06.75	PKPbc							00IAAAP		IDC	AIAAAAA
	TXAR	???		2000/09/01	01:18:17.63	Pp'bc							00IAAAP		IDC	AIAAAAA
	TXAR	???		2000/09/01	01:18:23.25	sp'bc							00IAAAP		IDC	AIAAAAA
	MAT	???		2000/09/01	01:24:12.00	P						e	00IAAAQ		JMA	AIAAAAA
	MAT	???		2000/09/01	01:24:21.00	S						e	00IAAAQ		JMA	AIAAAAA
	NB2	???		2000/09/01	01:26:59.50	P				2.1	0.80		00IAAAAR		NAO	AIAAAAA
	SLR	???		2000/09/01	01:43:25.90	P				155.0	1.00		00IAAAAS		PRE	AIAAAAA
	SLR	???		2000/09/01	01:43:40.10	S						e	00IAAAAS		PRE	AIAAAAA
	KSR	???		2000/09/01	01:43:47.90	P						e	00IAAAAS		PRE	AIAAAAA
	KSR	???		2000/09/01	01:43:54.90	S						e	00IAAAAS		PRE	AIAAAAA
	BLF	???		2000/09/01	01:44:21.30	P						e	00IAAAAT		PRE	AIAAAAA
	BLF	???		2000/09/01	01:44:55.90	S				33.0	0.70		00IAAAAT		PRE	AIAAAAA
	BOSA	PHZ		2000/09/01	01:44:21.90	P						e	00IAAAAT		NEIC	AIAAAAA
	BOSA	PHZ		2000/09/01	01:44:56.10	S						e	00IAAAAT		NEIC	AIAAAAA
	YKA	???		2000/09/01	01:50:20.60	P	274.	1.7				e	00IAAAAU		OTT	AIAAAAA
	KYTH	???		2000/09/01	01:56:56.50	Pb						e	00IAAAAV		ATH	AIAAAAA
	ITM	???		2000/09/01	01:57:02.70	Pb						e	00IAAAAV		ATH	AIAAAAA

Net	Sta	Chan	Aux	Date	Time	Phase	Azim	Slow	SNR	Amp	Per	Qual	Group	C	Author	ArrID
	PCI	???		2000/09/01	02:00:32.50	P						_ce	00IAAAW		DJA	AIAAAA^A
	VNA1	???		2000/09/01	02:06:18.90	P						_ci	00IAAAW		AWI	AIAAAA_A
	VNA3	???		2000/09/01	02:06:20.20	P						_di	00IAAAW		AWI	AIAAAA_A
	VNA2	???		2000/09/01	02:06:24.10	P						___	00IAAAW		AWI	AIAAAAaA
	PLP	???		2000/09/01	02:11:39.50	P						_i	00IAAAW		PIVS	AIAAAAaB
	EZN	???		2000/09/01	02:11:47.00	S						_e	00IAAAW		PIVS	AIAAAAbB
	EZN	???		2000/09/01	02:33:28.00	Pg						_e	00IAAAW		ISK	AIAAAAcA
	FINC	???		2000/09/01	02:33:35.00	Sg						_e	00IAAAW		ISK	AIAAAAcB
	ILAR	???		2000/09/01	02:39:19.70	P						_e	00IAAAB		PMG	AIAAAAdA
	INK	???		2000/09/01	03:20:59.90	P						___	00IAAAB		IDC	AIAAAAeA
	NVAR	???		2000/09/01	03:21:38.55	P						___	00IAAAB		IDC	AIAAAAfA
	FINES	???		2000/09/01	03:24:27.38	P						___	00IAAAB		IDC	AIAAAAgA
	TXAR	???		2000/09/01	03:24:30.20	P						___	00IAAAB		IDC	AIAAAAhA
	YKA	???		2000/09/01	03:26:00.03	P	296.	13.8				_e	00IAAAB		OTT	AIAAAAiA
	VRAC	???		2000/09/01	03:48:38.60	P						___	00IAAAB		VRAC	AIAAAAkA
	VRAC	???		2000/09/01	03:56:19.80	Pg						___	00IAAAB		VRAC	AIAAAAkA
	YKA	???		2000/09/01	03:56:38.20	Sg						___	00IAAAB		VRAC	AIAAAAkA
	GSPH	???		2000/09/01	04:29:11.40	P	272.	6.6		1.5	0.80	_e	00IAAAB		OTT	AIAAAAlA
	BIPH	???		2000/09/01	04:32:34.00	P						_ci	00IAAAB		PIVS	AIAAAAmA
	BIPH	???		2000/09/01	04:32:59.00	P						_i	00IAAAB		PIVS	AIAAAAnA
	ASAR	???		2000/09/01	04:33:27.50	S						_i	00IAAAB		PIVS	AIAAAAnB
	STKA	???		2000/09/01	04:35:05.25	P						___	00IAAAB		IDC	AIAAAAoA
	TXAR	???		2000/09/01	04:36:29.25	P						___	00IAAAB		IDC	AIAAAApA
	MAIO	???		2000/09/01	04:48:19.77	PKP						___	00IAAAB		IDC	AIAAAAqA
	MAIO	???		2000/09/01	05:05:29.00	P						___	00IAAAB		IDC	AIAAAArA
	KER	???		2000/09/01	05:06:04.00	S						_di	00IAAAB		TEH	AIAAAArB
	BILL	???		2000/09/01	05:07:04.00	P						_e	00IAAAB		TEH	AIAAAArB
	BILL	???		2000/09/01	05:08:42.10	P						_e	00IAAAB		TEH	AIAAAArB
	BILL	???		2000/09/01	05:11:57.80	S						_ci	00IAAAB		TEH	AIAAAArB
	YKA	???		2000/09/01	05:08:56.10	P	297.	12.8				_e	00IAAAB		TEH	AIAAAArB
	ISP	???		2000/09/01	05:09:23.60	Pn						_e	00IAAAB		TEH	AIAAAArB
	YKA	???		2000/09/01	05:09:40.10	P	288.	8.7		6.6	0.80	_e	00IAAAB		TEH	AIAAAArB
	ELL	???		2000/09/01	05:09:42.00	P						_e	00IAAAB		TEH	AIAAAArB
	WMQ	???		2000/09/01	05:09:57.00	P						_e	00IAAAB		TEH	AIAAAArB
	MA2	???		2000/09/01	05:10:13.40	P						_e	00IAAAB		TEH	AIAAAArB
	MA2	???		2000/09/01	05:10:43.20	Pp						_e	00IAAAB		TEH	AIAAAArB
	MA2	???		2000/09/01	05:14:42.50	S						_e	00IAAAB		TEH	AIAAAArB
	KAF	???		2000/09/01	05:10:46.10	P						_e	00IAAAB		TEH	AIAAAArB
	YAK	???		2000/09/01	05:11:14.40	P						_e	00IAAAB		TEH	AIAAAArB
	MOX	???		2000/09/01	05:11:37.40	P						_e	00IAAAB		TEH	AIAAAArB
	DAC	?HZ		2000/09/01	05:11:40.30	P						_e	00IAAAB		TEH	AIAAAArB

Net	Sta	Chan	Aux	Date	Time	Phase	Azim	Slow	SNR	Amp	Per	Qual	Group	C	Author	ArrID
	NB2	???		2000/09/01	05:11:52.70	P				2.8	0.80	__	00IAAABZ		NAO	AI4AAAB!A
	YSS	???		2000/09/01	05:11:56.70	P				50.0	1.00	_ci	00IAAACA		OBN	AI4AAAB"A
	CLNS	???		2000/09/01	05:12:00.00	P						__	00IAAACB	YARS	YARS	AI4AAAB#A
	CLNS	???		2000/09/01	05:12:31.00	sP						__	00IAAACB	YARS	YARS	AI4AAAB#B
	NRIS	???		2000/09/01	05:12:15.00	P						__	00IAAACB	OBN	OBN	AI4AAAB\$A
	KLR	???		2000/09/01	05:12:22.00	P						_e	00IAAACB	OBN	OBN	AI4AAAB%A
	TIY	??Z		2000/09/01	05:12:45.60	P						__	00IAAACD	BJI	BJI	AI4AAAB&A
	TIY	??Z				Lr				540.0	20.00	__	00IAAACD	BJI	BJI	AI4AAAB&B
	TIY	??N				Lr				470.0	15.00	__	00IAAACD	BJI	BJI	AI4AAAB&C
	TRO	???		2000/09/01	05:13:00.12	P						_e	00IAAAACE	BER	BER	AI4AAAB'A
	KTK1	???		2000/09/01	05:13:06.12	P						_e	00IAAAACE	BER	BER	AI4AAAB(A
	LVZ	???		2000/09/01	05:13:13.70	P						_e	00IAAACF	OBN	OBN	AI4AAAB)A
	APA	???		2000/09/01	05:13:15.90	P						_ci	00IAAACF	OBN	OBN	AI4AAAB*A
	TLY	???		2000/09/01	05:13:33.30	P						_ci	00IAAACF	OBN	OBN	AI4AAAB+A
	MOY	???		2000/09/01	05:13:41.00	P				32.0	1.20	__	00IAAACF	OBN	OBN	AI4AAAB+A
	NVS	???		2000/09/01	05:13:56.00	P				54.0	0.70	_i	00IAAACG	ASRS	ASRS	AI4AAAB-A
	NVS	???		2000/09/01	05:13:56.00	P						__	00IAAACG	ASRS	ASRS	AI4AAAB-B
	NB2	???		2000/09/01	05:13:58.90	P						_e	00IAAACG	BER	BER	AI4AAAB-A
	BJI	??Z		2000/09/01	05:14:06.00	P				10.0	1.00	__	00IAAAACH	BJI	BJI	AI4AAAB.A
	BJI	??Z				Lr				590.0	18.00	__	00IAAAACI	BJI	BJI	AI4AAAB/A
	HHC	???		2000/09/01	05:14:17.20	P				30.0	1.20	__	00IAAAACI	BJI	BJI	AI4AAAB/B
	HHC	???				Lr				760.0	10.00	_e	00IAAAACI	BJI	BJI	AI4AAAB0A
	HHC	??N				Lr				900.0	18.00	__	00IAAAACI	BJI	BJI	AI4AAAB0B
	HHC	??E				Lr				880.0	14.00	__	00IAAAACI	BJI	BJI	AI4AAAB0C
	ARU	???		2000/09/01	05:14:22.60	P				58.0	0.70	__	00IAAAACJ	OBN	OBN	AI4AAAB0D
	OBN	???		2000/09/01	05:14:45.10	P						_ci	00IAAAACJ	OBN	OBN	AI4AAAB1A
	OBN	???		2000/09/01	05:15:19.40	pP						_e	00IAAAACJ	OBN	OBN	AI4AAAB2A
	NJ2	???		2000/09/01	05:14:46.80	P				25.0	1.00	__	00IAAAACK	BJI	BJI	AI4AAAB2B
	NJ2	??Z				Lr				660.0	13.00	__	00IAAAACK	BJI	BJI	AI4AAAB3A
	GTA	???		2000/09/01	05:14:56.50	P				17.0	1.00	__	00IAAAACK	BJI	BJI	AI4AAAB3B
	GTA	??Z				Lr				440.0	14.00	__	00IAAAACK	BJI	BJI	AI4AAAB4A
	GTA	??N				Lr				710.0	16.00	__	00IAAAACK	BJI	BJI	AI4AAAB4B
	XAN	???		2000/09/01	05:15:03.00	P				9.4	0.80	__	00IAAAACK	BJI	BJI	AI4AAAB4C
	XAN	???				Lr				610.0	20.00	__	00IAAAACK	BJI	BJI	AI4AAAB5A
	XAN	??E				Lr				600.0	20.00	__	00IAAAACK	BJI	BJI	AI4AAAB5B
	XAN	???		2000/09/01	05:15:05.50	P				67.0	1.00	_c	00IAAAACK	BJI	BJI	AI4AAAB5C
	LZH	???		2000/09/01	05:15:32.50	pP						__	00IAAAACK	BJI	BJI	AI4AAAB6A
	LZH	???		2000/09/01	05:15:32.50	pP						__	00IAAAACK	BJI	BJI	AI4AAAB6B
	LZH	???		2000/09/01	05:15:54.00	sP				630.0	16.00	__	00IAAAACK	BJI	BJI	AI4AAAB6C
	LZH	??Z				Lr				3870.0	22.00	__	00IAAAACK	BJI	BJI	AI4AAAB6D
	LZH	??N				Lr						__	00IAAAACK	BJI	BJI	AI4AAAB6E
	WHN	???		2000/09/01	05:15:08.00	P						_e	00IAAAACK	BJI	BJI	AI4AAAB7A

Net	Sta	Chan	Aux	Date	Time	Phase	Azim	Slow	SNR	Amp	Per	Qual	Group	C	Author	ArrID
	CD2	???		2000/09/01	05:15:33.80	P				19.0	1.00	_c_	00IAAACK		BJI	AIAAAB8A
	GVA	???		2000/09/01	05:15:51.60	P				40.0	1.00	_d_	00IAAAK		BJI	AIAAAB9A
	KIV	???		2000/09/01	05:15:53.20	P				46.0	1.00	_di	00IAAAKL		OBN	AIAAAB:A
	KIV	???		2000/09/01	05:16:05.80	S						_i	00IAAAKL		OBN	AIAAAB:B
	KIV	???		2000/09/01	05:25:05.50	P						_g	00IAAAKL		OBN	AIAAAB:C
	ZEI	???		2000/09/01	05:16:02.00	P						_e	00IAAAKL		OBN	AIAAAB:A
	ZEI	???		2000/09/01	05:16:48.00	P						_e	00IAAAKL		OBN	AIAAAB;B
	LSA	???		2000/09/01	05:16:10.60	P						_e	00IAAACM		BJI	AIAAAB<A
	YKA	???		2000/09/01	05:16:12.80	P	237.	4.8		1.3	0.70	_e	00IAAACN		OTT	AIAAAB=A
	MAIO	???		2000/09/01	05:16:24.00	P						_e	00IAAACQ		TEH	AIAAAB>A
	MAIO	???		2000/09/01	05:17:44.00	P						_e	00IAAACQ		TEH	AIAAAB?A
	MAIO	???		2000/09/01	05:18:21.00	S						_e	00IAAACQ		TEH	AIAAAB?B
	KONO	???		2000/09/01	05:30:14.03	P						_e	00IAAACR		BER	AIAAAB@A
	MAT	???		2000/09/01	05:34:07.00	P						_e	00IAAACR		JMA	AIAAABAA
	MAT	???		2000/09/01	05:34:45.00	S						_e	00IAAACR		JMA	AIAAABAB
	KBS	???		2000/09/01	05:35:24.93	P						_e	00IAAACT		BER	AIAAABBA
	KSAR	???		2000/09/01	05:46:16.30	P						_e	00IAAACT		BER	AIAAABBA
	ASAR	???		2000/09/01	05:50:01.50	P						_e	00IAAACT		BER	AIAAABBA
	STKA	???		2000/09/01	05:50:55.20	P						_e	00IAAACT		BER	AIAAABBA
	FINES	???		2000/09/01	05:53:55.05	P						_e	00IAAACT		BER	AIAAABBA
	NVAR	???		2000/09/01	05:53:55.20	P						_e	00IAAACT		BER	AIAAABBA
	BKM	???		2000/09/01	06:00:48.00	P						_e	00IAAACT		BER	AIAAABBA
	PLCA	???		2000/09/01	06:01:10.06	P						_e	00IAAACT		BER	AIAAABBA
	LPZ	???		2000/09/01	06:01:21.84	P						_e	00IAAACT		BER	AIAAABBA
	STKA	???		2000/09/01	06:05:54.00	P						_e	00IAAACT		BER	AIAAABBA
	MAIO	???		2000/09/01	06:06:05.00	P						_e	00IAAACT		BER	AIAAABBA
	MAIO	???		2000/09/01	06:06:42.00	S						_e	00IAAACT		BER	AIAAABBA
	ASAR	???		2000/09/01	06:06:35.45	P						_e	00IAAACT		BER	AIAAABBA
	VNDA	???		2000/09/01	06:10:04.74	P						_e	00IAAACT		BER	AIAAABBA
	ILAR	???		2000/09/01	06:12:53.90	P						_e	00IAAACT		BER	AIAAABBA
	MRA	???		2000/09/01	06:20:20.50	P						_e	00IAAACT		BER	AIAAABBA
	MRA	???		2000/09/01	06:20:23.00	S						_e	00IAAACT		BER	AIAAABBA
	WATA	???		2000/09/01	06:20:43.60	Pg				39.6	0.10	_ci	00IAAAD		SJA	AIAAABPA
	WATA	???		2000/09/01	06:20:45.70	Pg						_ci	00IAAAD		SJA	AIAAABPB
	WATA	???		2000/09/01	06:20:43.70	Pg						_ci	00IAAAD		SJA	AIAAABPB
	WTTA	???		2000/09/01	06:20:43.70	Pg				18.2	0.20	_ci	00IAAAD		VIE	AIAAABQA
	WTTA	???		2000/09/01	06:20:46.00	Pg						_ci	00IAAAD		VIE	AIAAABQB
	SQTA	???		2000/09/01	06:20:45.10	Pg						_ci	00IAAAD		VIE	AIAAABRA
	SQTA	???		2000/09/01	06:20:48.60	Pg				5.4	0.10	_ci	00IAAAD		VIE	AIAAABRB
	MOTA	???		2000/09/01	06:20:46.30	Pg						_ci	00IAAAD		VIE	AIAAABSA
	MOTA	???		2000/09/01	06:20:46.30	Pg				6.0	0.20	_di	00IAAAD		VIE	AIAAABTB
	MOTA	???		2000/09/01	06:20:50.70	Pg						_di	00IAAAD		VIE	AIAAABTB
	DPC	???		2000/09/01	06:23:55.30	Pg						_e	00IAAADG		PRU	AIAAABUA

Net	Sta	Chan	Aux	Date	Time	Phase	Azim	Slow	SNR	Amp	Per	Qual	Group	C	Author	ArrID
	DPC	???		2000/09/01	06:24:10.60	Sg						__e	00IAAADG		PRU	AIAAABUB
	BRG	???		2000/09/01	06:23:59.90	Pg						__i	00IAAADH			AIAAABVA
	BRG	???		2000/09/01	06:24:19.30	Sg						__i	00IAAADH			AIAAABVB
	IZI	???		2000/09/01	06:52:39.00	Pn						__e	00IAADI		ISK	AIAAABWA
	BAG	???		2000/09/01	06:54:02.00	P						__i	00IAADJ		QCP	AIAAABXA
	BCPH	???		2000/09/01	06:54:06.60	P						__ci	00IAADK		PIVS	AIAAABYA
	RIY	???		2000/09/01	06:57:23.40	Pg						__i	00IAADL		ZAG	AIAAABZA
	RIY	???		2000/09/01	06:57:27.60	Sg						__i	00IAADL		ZAG	AIAAABZB
	ASAR	???		2000/09/01	06:58:23.80	P						__	00IAADM		ZAG	AIAAAB[A
	PHNC	???		2000/09/01	06:59:58.10	P						__	00IAADN		IDC	AIAAAB\A
	PHNC	???		2000/09/01	07:00:05.20	S						__	00IAADN		NIC	AIAAAB\B
	CSS	???		2000/09/01	07:00:01.00	P				2.7	0.24	__	00IAADN		NIC	AIAAABJA
	CSS	???		2000/09/01	07:00:09.50	S						__	00IAADN		NIC	AIAAABJB
	ALFC	???		2000/09/01	07:00:09.80	P						__	00IAADN		NIC	AIAAAB^A
	ALFC	???		2000/09/01	07:00:25.80	S						__	00IAADN		NIC	AIAAAB^B
	AKMC	???		2000/09/01	07:00:12.90	P						__	00IAADN		NIC	AIAAAB_A
	AKMC	???		2000/09/01	07:00:30.30	S						__	00IAADN		NIC	AIAAAB`A
	NVAR	???		2000/09/01	07:01:32.28	P						__	00IAADP		IDC	AIAAAB`B
	TXAR	???		2000/09/01	07:02:01.23	P						__	00IAADP		IDC	AIAAABBa
	ILAR	???		2000/09/01	07:02:18.50	P						__	00IAADP		IDC	AIAAABBa
	YKA	???		2000/09/01	07:02:54.60	P						__e	00IAADQ		IDC	AIAAABCA
	YLV	???		2000/09/01	07:23:09.20	Pg	29.	12.7				__e	00IAADR		OTT	AIAAABdA
	YLV	???		2000/09/01	07:23:12.30	Sg						__e	00IAADR		ISK	AIAAABdB
	IZI	???		2000/09/01	07:23:13.00	Pg						__e	00IAADR		ISK	AIAAABeA
	ISK	???		2000/09/01	07:23:13.70	Pg						__e	00IAADR		ISK	AIAAABfA
	HRT	???		2000/09/01	07:23:14.00	Pg						__e	00IAADR		ISK	AIAAABgA
	KCT	???		2000/09/01	07:23:18.60	Pg						__e	00IAADR		ISK	AIAAABhA
	EYL	???		2000/09/01	07:23:19.50	Pg						__e	00IAADR		ISK	AIAAABiA
	EYL	???		2000/09/01	07:23:31.00	Sg						__e	00IAADR		ISK	AIAAABiB
	EDC	???		2000/09/01	07:23:23.00	Pg						__e	00IAADR		ISK	AIAAABjA
	EDC	???		2000/09/01	07:23:37.00	Sg						__e	00IAADR		ISK	AIAAABjB
	DST	???		2000/09/01	07:23:26.00	Pg						__i	00IAADR		ISK	AIAAABkA
	DST	???		2000/09/01	07:23:41.00	Sg						__e	00IAADR		ISK	AIAAABkB
	MDU	???		2000/09/01	07:23:34.00	Pn						__e	00IAADR		ISK	AIAAABlA
	FIA0	???		2000/09/01	07:28:41.35	Pn						__	00IAADS		HEL	AIAAABmA
	FIA0	???		2000/09/01	07:29:09.70	Lg						__	00IAADS		HEL	AIAAABmB
	HFS	???		2000/09/01	07:29:05.45	Pn						__	00IAADT		HFS	AIAAABnA
	HFS	???		2000/09/01	07:29:51.05	Sn						__	00IAADT		HFS	AIAAABnB
	HFS	???		2000/09/01	07:30:05.78	Lg						__	00IAADT		HFS	AIAAABnC
	OBKA	???		2000/09/01	07:29:09.50	Pg						__ci	00IAADU		VIE	AIAAABoA
	OBKA	???		2000/09/01	07:29:16.10	Sg						__i	00IAADU		VIE	AIAAABoB

Topic	Access to the CMR seismic/hydroacoustic/infrasonic data
Author	Xiaoping Yang and Robert North, Center for Monitoring Research, 1300 N. 17 th Street, Arlington, VA 22209; E-mail: xiaoping@cmr.gov
Version	August 2002

1 Introduction

After the signature of the Comprehensive Nuclear-Test-Ban- Treaty (CTBT) in New York in 1996, the International Data Centre (IDC) was established within the Comprehensive Nuclear-Test-Ban Treaty Organization (CTBTO) in Vienna, Austria. The procedures developed through international co-operation during GSETT-3 (Group of Scientific Experts Technical Test 3) and originally implemented at the Prototype IDC (PIDC) in Arlington, USA, are now used and further developed at the IDC in Vienna. However, although it can be expected that more information on the IDC will be posted in future on www.ctbto.org, IDC data products are not yet openly available. In contrast, the Center for Monitoring Research (CMR; <http://www.cmr.gov>), an offspring of the PIDC, makes seismic, hydroacoustic, infrasonic (SHI) data products accessible. These data come from two sources, the PIDC and the RDSS (Research and Development Support System). The PIDC data products consist of continuous waveforms and bulletins accumulated during PIDC operations from January 1995 to September 2001 whereas collecting and archiving both historical and current data are ongoing for the RDSS data products and metadata. The RDSS data also include a subset of the PIDC data that are of interest. This document summarizes the CMR SHI data products and provides information on their open access.

The data products are managed through various Oracle databases (see <http://www.oracle.com>) using the CSS3.0/IMS1.0 schema (e.g., IDC Documentation 5.1.1, 2001). The RDSS databases are also documented individually. Waveform data are stored in a mass store system or disks, with indexes in the databases. For public access data are retrieved from inside the firewall based on user requests. For data exchange, GSE2.0/IMS1.0 formats (IDC Documentation 3.4.1, 2001) are used, and flat files of CSS (Center for Seismic Studies) tables facilitate easy integrations with Oracle databases. Many tools for data analysis and conversions are available at CMR and in other domains.

One type of data products is bulletin and metadata information. These can be openly accessed through web interfaces and/or AutoDRM (for PIDC data). Bulletins can be retrieved (both calendar retrieval and custom retrieval) at the CMR web site at <http://www.cmr.gov>. AutoDRM is a message system to which data requests may be sent in formatted messages. A front-end web interface is also available at the CMR web site for AutoDRM (event-based). The other type of data products is waveform data and related station/instrumentation information. Waveform data can be retrieved using AutoDRM (for PIDC data), web, or FTP. Related station/network information can be accessed via the CMR web.

In this document we describe each of the bulletin and waveform data products from the PIDC (Section 2) and the RDSS (Section 3), and their retrieval methods (Section 4). Tools available for data analysis are listed (Section 5). We also summarize the time lines of configuration changes that affect the data products (Section 6). More information on CMR data products and data access is described in the user's guide to the CMR data products (Yang et al., 2000b; http://www.cmr.gov/rdss/documents/user_guide/index.html).

Further documentation can be found at <http://www.cmr.gov/pidc/librarybox/ccb.html>, including IDC Documentation and the Configuration Control Board memos that document changes to the PIDC system. Users may also contact user_services@cmr.gov for questions/requests concerning CMR data products. As the success of data collection relies on cooperation among a wide range of sources, we strongly encourage users to contribute information to CMR.

2 PIDC Data Product

2.1 PIDC Bulletins

There are seven PIDC event bulletins generated from Oracle databases (Table 1). Each bulletin is a list of events and event parameters (origin and associated arrival information).

Table 1 PIDC event bulletins

Acronym	Description
REB	Reviewed Event Bulletin
SEB	Standard Event Bulletin
SSEB	Standard Screening Event Bulletin
SEL1	Standard Event List1
SEL2	Standard Event List2
SEL3	Standard Event List3
GAMMA	Supplementary Bulletin

2.1.1 Reviewed Event Bulletin (REB)

The Reviewed Event Bulletin (REB) is the analyst-reviewed final PIDC SHI bulletin. It includes only prototype and final International Monitoring System (IMS) stations, and only events formed using at least three primary stations (IDC Documentation 5.2.1, 1999).

The REB event locations were computed using PIDC software that allows for a hierarchy of corrections relevant to location improvement (Nagy, 1996). From the beginning of the PIDC operations on January 1, 1995, the IASPEI91 model (Kennett, 1991) has been used as the reference travel time set. Ellipticity and elevation corrections are made for each arrival. Slowness and azimuth are very critical when locating events with only a few stations. Tabulated Slowness and Azimuth Station Corrections (SASCs) for each station and array were used from January 1998 (Bondar, 1998) and updated in July 2000 (Wang and McLaughlin, 2000). Separate regional (distance less than 20°) travel time curves may be designated for Pn, Pg, Sn, and Lg for each IMS station. Regional 1-D travel-time tables were used in locating REB events in Fennoscandia between September 1997 and March 1999 (Bondar and Ryaboy, 1997). Since then these 1-D travel times have been only used in PIDC operations when producing the automatic bulletins (SEBs). In the hierarchy of location calibration the PIDC software may also use tabulated path corrections, or Source Specific Station Corrections (SSSCs), to apply corrections relative to IASPEI91 as a function of source location for any station and phase. Regional SSSCs were used for Fennoscandian and high latitude IMS stations from April 1999 (Yang and McLaughlin, 1999). SSSCs for North

America were used from March 2000 (Yang and McLaughlin, 2000), and some were updated in April 2001 (Ryaboy et al., 2001). The SSSCs are model-based and SASCs were developed based on the REB data; the corrections are relative to the default IASPEI91 model.

Location uncertainties are represented by error ellipses at 90% confidence level. The *a priori* errors are separated as measurement and modeling errors, starting in September 1997 (Israelsson et al., 1997). The former represents errors in arrival time picks as a function of signal-to-noise ratio. Modeling errors, as a function of distance for each type of seismic phase, specify uncertainties in the model when representing the real Earth. The location software extracts the modeling errors from the travel-time tables (and SSSCs) for a given phase (and station), and extracts the measurement errors from the arrival table for given phase picks. The measurement errors were not retro-updated in the PIDC databases for data prior to the implementation, but were updated in the RDSS databases as described in their individual documentation.

The hierarchical corrections, for example, SASCs and SSSCs, and the measurement/modeling errors were developed and implemented incrementally. They have a considerable impact on event locations, error ellipses, and residuals. When using the CMR data products covering an extensive time period, users should be aware of when such files are were implemented/updated in the PIDC system, therefore affecting the bulletins (see Section 6). If users relocate events using the PIDC software/procedures, applying the latest corrections/errors is important.

Several magnitudes are computed for REB events, including mb, ML, Ms, mb_mle, ms_mle, mb1, mb1_mle, ms1, and ms1_mle (IDC Documentation 5.2.1, 1999; Israelsson et al., 2000). They may be different from those given by other organizations such as the NEIC or ISC. Also note that amplitudes are measured by the automatic system, and are not revised by the analysts.

The mb magnitude is calculated using the Veith-Clawson (1972) attenuation correction as a function of distance and depth over the distance range of 20°-90°:

$$mb = \log_{10}(\text{amp}/\text{per}) + Q(\text{distance}, \text{depth})$$

where the amplitude amp is peak-peak in nm and per is dominant period in seconds.

The calculation of the local magnitude ML (elsewhere in the Manual termed MI) is more complicated as attenuation curves tailored to each station are being used. ML magnitudes are calculated from short term average amplitudes in the passband 2-4 Hz for Pn or P phase, if the distance is less than 20° and the estimated depth - depth error < 40 km.

The attenuation correction for ML is calculated from the formula:

$$a + b * r + c * \log_{10}(r)$$

where r is the epicentral distance (in km) and the coefficients a, b, c have been tailored for each station that contributes to the REB to maximize agreement between ML and mb. Each station has its own a, b, and c values, and the values of these coefficients may change from time to time as part of tuning work to make more consistent magnitudes. The REB ML magnitude is obtained from:

$$ML = \log_{10}(AMP/PER) + a + b * r + c * \log_{10}(r)$$

where AMP is the short term average amplitude as it appears in the REB in nm (0-peak). It has been transformed from a short-term average value, corrected for long-term noise and measured in a 2-4 Hz bandpass. PER, period in the formula above, is always 1/3 sec (0.33 in the REB) for ML, as the amplitude is measured from a band pass filtered channel (between 2-4 Hz) with a center frequency of 3 Hz. Note that for stations with instrument calibration periods different from 1 sec, the instrument calibration period will enter the formula.

The Ms magnitude is computed for surface waves only at primary seismic stations. The amplitudes and periods are measured for Rayleigh waves (LR) on a beam for arrays or vertical channel at single stations. The Ms formula is:

$$Ms = \log(\text{amp/per}) + B(r)$$

where r is distance and B(r) is the attenuation correction.

The Maximum Likelihood Estimates of mb (mb_mle) and Ms (ms_mle) magnitudes are quite different from the standard average magnitudes. For a given event, these magnitude estimates are based not only on the amplitude/period ratios of P/LR (mb/ms) waves at detecting stations, but also on noise amplitudes at stations that did not detect the event. They are calculated using the maximum likelihood algorithm of Ringdal (1976). The reason for calculating mle type magnitudes is to reduce bias for event magnitudes based on a small number of stations.

The generalized mb (mb1, mb1_mle) and Ms (ms1, ms1_mle) are calculated to improve consistencies and robustness of IDC mb and Ms magnitude. Empirical *a priori* station corrections are applied, when available, in calculating these magnitudes. On average mb1 is about 0.2 magnitude higher than mb_ave (Israelsson et al., 2000).

(Note of caution for data users outside of the CTBTO community: (P)IDC magnitudes differ from IASPEI recommended standards for magnitude determination from body and surface waves (see IS 3.2). Their main aim is to use magnitude definitions that could be automated and also extend down to lower source sizes than traditional definitions. Earthquake seismology has to assure long-term continuity and stability of standard earthquake magnitudes according to their original definitions and thus to guarantee homogeneous earthquake catalogues for seismic hazard assessment, proper estimates of time-variable seismic energy release and other seismological and engineering applications up to the strongest seismic events possible (Mw up to about 10). Note that the catalogs commonly used for hazard assessments etc., such as NEIC and ISC, also do not yet fully conform to earlier IASPEI recommendations, and in fact combine individual magnitudes calculated according to myriad, largely undocumented, definitions whose mix has changed with time. The (p)IDC methods are documented and consistent, and the results may over time provide the most complete and stable catalogs for some purposes.

2.1.2 Standard Event Bulletin (SEB)

The Standard Event Bulletin (SEB) is similar in content and format to the REB, but also includes “event characterization” parameters and “event screening” results for each event.

2.1.3 Standard Screened Event Bulletin (SSEB)

The Standard Screened Event Bulletin (SSEB) is similar in content and format to the Standard Event Bulletin (SEB), but does not include events that were screened out by a standard set of event screening criteria.

2.1.4 Standard Event List 1 (SEL1)

The Standard Event List 1 (SEL1) is the initial automatic event list generated one hour after real time. Data from auxiliary stations were requested by the automatic system based on SEL1 locations in order to improve event locations in further processing (SEL2 and SEL3). SEL1, SEL2, and SEL3 are automatic processing results of IMS seismic/hydroacoustic/infrasonic data available at the PIDC. These events are generated using algorithms similar to those of the REB. Citation or research use of the automatic event lists is strongly discouraged.

2.1.5 Standard Event List 2 (SEL2)

The Standard Event List 2 (SEL2) is the second automated event list generated six hours after real time. Data requested from auxiliary stations are used in locating events. SEL2 results are generally improved compared to SEL1.

2.1.6 Standard Event List 3 (SEL3)

The Standard Event List 3 (SEL3) is the final automated event list generated 12 hours after real time. Data requested from auxiliary stations are used in locating events. SEL3 results are further improved compared to SEL1 and SEL2 since some late data may arrive after the first two bulletins are generated.

2.1.7 Supplementary (GAMMA) Bulletin

The Supplementary (also known as GAMMA) Bulletin contains supplementary event information during the PIDC operations. These events were located by national networks and contributed to the PIDC by National Data Centers (NDCs). About 30 NDCs have provided events to the Gamma Bulletin.

The GAMMA events are compared with the REB for event correlations (origin time within 60 seconds and epicenter within 3 degrees). Events are also grouped across the NDC bulletins, but no preferred origin is chosen from multiple solutions for an event. There are no arrivals or waveforms in the GAMMA Bulletin, but PIDC arrival and waveform data are available at CMR for a GAMMA event when it is also in the REB.

The GAMMA Bulletin represents a potential source of well-located events that might be usable as ground truth events. Comparisons between the GAMMA Bulletin and the REB for common events can reveal systematic biases in the IMS network solutions and lead to concentrated regional calibration effort. However, the quality of the GAMMA Bulletin varies

from region to region. Many NDCs provide locations far outside their networks. Very often the events are provided without quality information so that it is impossible to assess the accuracy of the event parameters.

2.2 PIDC waveform and related data

PIDC waveform data include those from the waveform archive and segment archive. They were processed by PIDC Operations, and stored in a mass store system for stations whose data were received by the PIDC since 1995.

2.2.1 Waveform archive

The waveform archive consists of four hours segments of data. Pointers to the waveform data (wfdisc records) as well as derived parameters are stored in the operational database.

2.2.2 Segment waveform archive

The segment archive consists of segments of a few minutes around the arrivals, resulting in much smaller data volumes. The following rules apply for selecting data segments to all stations with at least one phase associated in the REB, all primary stations within 30 degrees of the REB event, or all auxiliary stations with waveform data available (Coyne, 1996):

- For three-component station or reference stations of arrays at regional distance, raw waveforms for all components from one minute to a group velocity of 2.5 km/s plus one minute.
- For arrays at regional distance, incoherent beams over the same time window, as well as a five minute segment of the beam to the theoretical P-wave slowness and azimuth beginning one minute before the first arrival.
- For three-component stations or reference stations of arrays at teleseismic distance, three broadband or short period channels beginning one minute before the first arrival to a total of five minutes. To include surface waves three broadband or long-period channels are filtered and decimated to 1 sample/s from one minute prior to the first arrival through a group velocity of 2.5 km/s plus one minute.
- For arrays at teleseismic distance, a five minute segment of the beam to the theoretical P-wave slowness and azimuth beginning one minute before the first sample, from a group velocity of 4.5 to 2.8 km/s.
- For hydroacoustic stations, all channels two minutes before the T phase to four minutes after.

2.2.3 Related data

Other related data are useful in requesting/analyzing waveform data. Related data include station/network/threshold monitoring status, instrument response files, and station information. Station information and instrument response are important in processing the waveform data. The station/network/threshold monitoring status provides station availability information for a given time period.

3 RDSS data product

3.1 RDSS bulletins

RDSS bulletins are not direct results from PIDC operations; they are ground truth, supplementary, and/or calibration information useful to researchers. The event bulletins are generated from a number of database accounts given in Table 2. Related metadata, e.g., data sources, are also stored and available in these databases.

Table 2 RDSS databases

Acronym	Account
REDB	Reference Event Database
EXPLOSION	Nuclear Explosion Database
SPECIAL_EVENT	Special Event Database
INFRASOUND	Infrasound Database
HYDROACOUSTIC	Hydroacoustic Database
GT	Ground Truth Database
LOPNOR	Lop Nor ACD Database
NOISE	Noise Database

3.1.1 Reference Event Database (former Calibration Event Bulletin)

The Reference Event Database (REDB, former Calibration Event Bulletin, CEB) contains selected REB events that are small to medium sized, well-located, and globally uniformly distributed during the PIDC Operations in 1995-2001. These events are potentially useful to produce global and region-dependent corrections for IMS stations, to verify regional travel-time curves proposed on the basis of tectonic structure, to test location procedures, and to refine error estimates.

REDB (former CEB) events were selected from the REB ('PIDC_REB'). Additional steps are undertaken after a REDB event is selected:

- All auxiliary data were requested and archived by the PIDC Operations. However, due to the limited life span of the station disk loops, many REDB events do not have additional waveforms because of delays in requesting auxiliary data.
- The REDB event was re-analyzed and relocated by analysts using additional waveforms if analyst resources were available ('PIDC_REV').
- NDC bulletin data were requested for events within or near their national territories. These bulletins were merged into the REDB database ('XXX_NDC').
- The REDB events were relocated using all arrivals, including those from NDCs and/or those from analysts' re-analysis ('PIDC_REDB').

The hierarchy for preferred solutions is as follows: PIDC_REB, PIDC_REV, PIDC_REDB, with increasing preference. A detailed description of the database is given in Yang et al. (2000e). The quality of REDB events is non-uniform due to limitations on obtaining NDC bulletins for all regions, on requesting auxiliary waveforms, and on human resources for re-analysis. Event locations have generally been improved in North and South America, Australia, Europe, and parts of Asia, but not in Africa and many other regions in Asia.

3.1.2 Nuclear Explosion Database

The Nuclear Explosion Database includes information (e.g., origin time, location, yield, seismic magnitude, and burial depth) on nuclear explosions worldwide in history. In the database there are 2041 events conducted by the United States, France, China, India, United Kingdom, the Soviet Union, and Pakistan during 1945-1998. Waveform data are available for about 1/3 of the events. Instrument responses and arrival picks are also collected. A detailed description of the database is given in Yang et al. (2000d). This database and related information are updated as corrections are made and as new information becomes available.

3.1.3 Special Event Database

The Special Event Database contains information on event parameters and waveform data for non-nuclear events of special interest. It consists of selected chemical explosions and earthquakes that occurred near former test sites and/or regions of interest. This also includes in- or near-water events and events of unknown character. Waveforms are obtained from the PIDC/CMR archive system, IRIS, NORSAR, and researchers. A detailed description of the database is given in Yang et al. (1998).

3.1.4 Infrasound Database

The Infrasound Database contains comprehensive information on infrasonic source locations, recorded waveforms, and related metadata. It includes Ground Truth (GT) events and waveforms, recordings of Soviet nuclear explosions in 1961, waveforms for events in the Antarctic and Alaska collected by the University of Alaska/ENSCO, synthetic waveform data for IMS stations, and other infrasound signals.

3.1.5 Hydroacoustic Database

The Hydroacoustic Database contains selected events of hydroacoustic interest, including earthquakes, nuclear explosions, and chemical explosions from various experiments. It also includes ground truth phase picks for training the neural networks that are used in hydroacoustic phase identification in the automatic processing. A detailed description of the database is given in Yang et al. (2000a).

3.1.6 Ground Truth Database (GT)

The Ground Truth (GT) database consists of explosions and earthquakes with known or estimated location accuracy, classified into separate categories. A GTX category includes events with location accuracy better than X km. The GT database contains subsets of events taken from the REB, REDB, Nuclear Explosion, Special Event, Hydroacoustic, and Infrasound databases. Other events are unique to the GT database. A description of the GT events is given in Yang et al. (2000c).

3.1.7 Lop Nor ACD Database

The Lop Nor Event Database contains the parameters, waveforms, and metadata developed during the CMR Lop Nor Advanced Concept Demonstration (ACD) project. It includes nuclear explosions and earthquakes, as well as some scaled/embedded events. There are 421 events between 5 May 1964 and 9 April 2002 in the Lop Nor ACD Box, 39°-44°N and 86°-92°E, with ~43,000 arrivals. For each event there are multiple data sources and a preferred origin is chosen based on the location accuracy. Data sources for bulletins include the ACD analysis results, IDC/PIDC REB, CMR Nuclear Explosion Database, CMR Ground Truth Database, International Seismological Centre, and the Annual Bulletin of Chinese Earthquakes. GT information is available for most of nuclear explosions and for the scaled/embedded events. A total of 205 events were thoroughly analyzed during the ACD work, including 25 out of all 45 nuclear explosions. Waveform data were obtained for these 205 events from the PIDC/CMR archive system, CMR Nuclear Explosion Database, IRIS, and Blacknest. There are also 10-day continuous waveforms in August 2-12, 2001.

3.1.8 Noise Database

The Noise Database contains background noise spectra for IMS stations since June 1997, except for a few day gaps (Bahavar and North, 2002). On average there are more than 600 background noise spectra available for each data day. The collection of noise samples is a routine automated process that requires limited human intervention. In the early days the calculation of spectra is based on 40-second and 10-second Hamming windows for the primary and auxiliary stations, respectively, with 10% tapering and 67% overlaps. Since January 1998 the windows have been changed to 100-second and 20-second for the primary and auxiliary IMS stations, respectively.

3.2 RDSS waveform and related data

RDSS waveform data are collections of historical waveform segments (as early as 1961) from various organizations. Some PIDC data are also included for events of interest. Data are stored on external disks with indexes in the RDSS databases. Related data include those such as instrument response files, noise spectra, ground truth phase picks, and station information.

3.3 Metadata

Metadata are data about data. They are useful in understanding and utilizing the information on bulletins and waveforms. Typical metadata in the RDSS databases include descriptions of data source, explosion type, and test site, and waveform and other plots.

4 CMR data retrieval

Both types of PIDC and RDSS data products (bulletins and waveforms) can be obtained from CMR. Bulletins may be obtained by calendar web retrieval, by custom web retrieval, by AutoDRM, and by FTP. Waveforms may be obtained by web, by AutoDRM, and by FTP. A

detailed summary of the databases and their retrieval methods is given in Table 3. In general users can retrieve PIDC data using AutoDRM and RDSS data using FTP. AutoDRM requires formatted messages for direct requests to obtain bulletin and waveform data. A web interface is available at CMR to form and submit event-based requests for waveform data. In both cases AutoDRM users receive information and data through E-mail/FTP.

The CMR web site is <http://www.cmr.gov>. The direct AutoDRM address is messages@cmr.gov and the web interface is available at the CMR web site. The CMR FTP site is <ftp.cmr.gov> or <ftp://ftp.cmr.gov>.

4.1 Calendar web retrieval (Bulletin)

Calendar web retrieval provides easy access to database information for a given event occurrence date. All the events in the REB, SEB, SSEB, SEL1, SEL2, SEL3, GAMMA (<http://www.cmr.gov/pidc/dataprodbox/prodavail.html>), and REDB (former CEB; <http://www.cmr.gov/rdss/resources/index.html>) since January 1995 can be accessed by calendar retrieval.

4.2 Custom web retrieval (bulletin/waveform)

Custom web retrieval allows users to specify selection criteria for events of interest. This function is provided for a group of the PIDC bulletins together (REB, SEL1, SEL2, SEL3, SEB, SSEB; <http://www.cmr.gov/pidc/dataprodbox/cust.html>) and for other PIDC/RDSS bulletins on their individual web pages (<http://www.cmr.gov/pidc/dataprodbox/prodavail.html> and <http://www.cmr.gov/rdss/resources/index.html>). Results may be sorted by such parameters as time and region.

4.3 Retrieval by AutoDRM (bulletin/waveform)

Data or subscription request for the REB, SEL1, SEL2, SEL3, and SEB can be made using AutoDRM. The available information includes bulletin, event, origin, arrival, detection, waveform, station, channel, and response. The retrieving results or error messages are sent back to users by E-mail and data can be picked up at the CMR FTP site.

4.4 Retrieval by FTP

Information on some RDSS databases can be retrieved by FTP at <ftp.cmr.gov> or <ftp://ftp.cmr.gov>.

Table 3 Retrieval methods for SHI bulletins and waveforms

Bulletin	Calendar retrieval	Custom retrieval	AutoDRM	FTP	Source
REB	bulletin	bulletin	both		PIDC data product
SEB	bulletin	bulletin	both		PIDC data product
SSEB	bulletin	bulletin	both		PIDC data product

SEL1	bulletin	bulletin	both		PIDC data product
SEL2	bulletin	bulletin	both		PIDC data product
SEL3	bulletin	bulletin	both		PIDC data product
GAMMA	bulletin	bulletin			PIDC data product
REDB (former CEB)	bulletin	bulletin			RDSS data product
EXPLOSION		both		both	RDSS data product
SPECIAL EVENT		both			RDSS data product
INFRASOUND		both			RDSS data product
HYDROACOUSTIC		both			RDSS data product
GT		both			RDSS data product
LOPNOR		both			RDSS data product
NOISE				both	RDSS data product

4.5 Format/Tools for data exchange/conversion

Bulletins are generally in the IMS1.0 format, except that GAMMA is in the GSE2.0 format. Waveform information is stored in a CSS3.0 table (wfdisc table) for indexes and in binary data files (.w files). These files can be read directly by waveform analysis tools, e.g., SAC, and Matseis. They can also be converted from CSS to other formats using some tools (see 5).

Flat files of CSS database tables other than wfdisc and Oracle export may also be used for data exchange for advanced users with direct access to Oracle databases. Table 4 lists the major relevant database tables and their brief descriptions. Schema for most of the tables are given in the IDC Documentation 5.1.1 (2001). New RDSS tables, particularly for metadata, are described in individual RDSS database documentation.

Table 4 CSS3.0/IMS1.0 and RDSS database tables

Table name	Description	Schema
affiliation	Network station information	IDC
amplitude	Arrival- and origin-based amplitude measurements	IDC
arrival	Summary information on an arrival	IDC
assoc	Data associating arrivals with origins	IDC
ceppks	Cepstral analysis results	IDC
complexity	Complexity event characterization parameter	IDC
detection	Summary information about detections	IDC
event	Event origin connection	IDC
explo	Event yield, medium, test site, explosion type	Adopted by IDC
glossary	Abbreviation descriptions	Adopted by IDC
hydro_features	Hydroacoustic signal features	IDC
infra_features	Infrasonic signal features	IDC
instrument	Calibration information for stations	IDC
location	Mine/test site information	Adopted by IDC
metadata	Metadata local residence	RDSS
netmag	Network magnitude	IDC
network	Network descriptions and identification	IDC
origaux	Additional information on origin	IDC
origerr	Errors in origin estimations	IDC

origin	Summary of hypocenter parameters	IDC
origintag	Origin-based metadata	RDSS
parrival	Predicted arrivals and associations for origin-based amplitude measurements	IDC
reference	Reference information	RDSS
remark	Comments on data	IDC
sensor	Calibration information for channels	IDC
site	Station location information	IDC
sitechan	Station-channel information	IDC
splp	Event characterization parameters for short-period/long-period energy ratios	IDC
spvar	Variance of detrended log spectrum	IDC
stamag	Station magnitude estimates	IDC
thridmom	Third moment of frequency	IDC
timefre	Time-frequency measurements for event characterization	IDC
wfdisc	Waveform index	IDC
wftag	Waveform mapping to event	IDC

5 Data analysis/conversion tools

A number of tools that aid data conversion and analysis are available at CMR or from other domains. Some most frequently used tools are summarized in Table 5.

Table 5 Tools available at CMR or other domains

Name	Description	Access
LocSAT	Off-line location program using flat files for inputs/outputs	ftp://ftp.cmr.gov/pub/rdtb/software/LocSAT
HLS	Hypocenter location server	Direct use at http://www.cmr.gov
SAC	Waveform data analysis	http://www-ep.es.llnl.gov/www-ep/esd/seismic/sac.html
MatSeis	Waveform data analysis	http://www.ctbt.rnd.doe.gov/ctbt/data/matseis/matseis.html
GMT	Graphic maps	http://www.soest.hawaii.edu/gmt
AutoDRM	Extract database data via internet	Direct use at http://www.cmr.gov
css2sac	Waveform data format conversion from CSS to SAC	http://orfeus.knmi.nl/other.services/conversion.shtml
sac2css	Waveform data format conversion from SAC to CSS	http://orfeus.knmi.nl/other.services/conversion.shtml
codeco3	Conversion between IMS1.0, SAC, and CSS formats	http://www.cmr.gov/rdss/resources/index.html

5.1 Event locations and magnitudes (LocSAT, HLS)

The event locations in the CMR bulletins are produced using application programs based on the “libloc” library. The program Global Association (GA) is used to generate locations for

automatic bulletins, SEL1, SEL2, and SEL3 (IDC Documentation 5.2.1, 1999). The program Analyst Review Station (ARS) is used to generate locations and magnitudes for the REB. Program EvLoc is used to generate the final locations and magnitudes in the REDB (former CEB).

A program, LocSAT, is similar to EvLoc except that it interfaces with flat files instead of databases, and it does not compute magnitudes. As an official release by the CMR R&D Test Bed, LocSAT is available for reproducing the REB/REDB locations.

A Hypocenter Location Server (HLS) has been developed to provide an interface for users to access EvLoc directly. HLS supports the full capabilities of EvLoc, including magnitude calculation. HLS uses the platform-independent XML format as the data exchange format (see <http://www.fdsn.org/FDSNwgII.htm>).

5.2 Seismic Analysis Code (SAC)

SAC (Seismic Analysis Code) is a general purpose interactive program designed for the study of sequential signals, especially time series data. Analysis capabilities include general arithmetic operations, Fourier transforms, three spectral estimation techniques, IIR and FIR filtering, signal stacking, decimation, interpolation, correlation, and seismic phase picking. SAC also contains an extensive graphics capability.

5.3 Matseis

Matseis is a MatLab-based data analysis tool with strong signal processing and graphic functions. It integrates origin, waveform, travel-time, and arrival data information, and provides graphical plot controls, data manipulation, and signal processing functions. Three data types are recognized, including CSS3.0 Oracle database accessed by SQL, CSS3.0 flat files, and local databases.

5.4 Generic Mapping Tools (GMT)

GMT (the Generic Mapping Tool) is a collection of UNIX tools that allow users to manipulate 2-D or 3-D data sets (including filtering, trend fitting, gridding, projecting, etc.) and produce plots ranging from simple x-y plots through contour maps to artificially illuminated surfaces and 3-D perspective views. GMT supports 25 common map projections plus linear, log, and power scaling, and comes with support data such as coastlines, rivers, and political boundaries.

5.5 Database access tools (AutoDRM)

AutoDRM provides automated E-mail message responses to requests for data in the databases. An AutoDRM web interface is available via the CMR web site. Users can select data request criteria, which are automatically translated into standard request messages. Data

requests are handled by the automated system at the PIDC and the results are sent back to the users by E-mail.

5.6 Data conversions (css2sac, sac2css, codeco3)

Programs css2sac and sac2css convert waveform data between the CSS3.0 format and the SAC formats. SAC can also read the CSS3.0 format directly, so the conversion is not necessary.

Program codeco3 converts many formats including IMS/GSE waveform (from AutoDRM) data to SAC or CSS.

6 Time lines of configuration changes

Configuration changes that affect the uniformity of the CMR products occurred very often during the PIDC Operations due to development and calibration efforts towards a better system. It is important to note the dates of configuration changes given in Table 6 when using the CMR data products. In general, the affected parameters include arrival picks, phase types, event locations, error ellipses, and magnitudes.

Table 6 Dates of configuration changes that affect CMR data products

Date	Changes to the system	Affected database/table/parameter	CCB Memo
New releases:			
12/1995	GA in SEL1	SEL1	CCB-PRO-95/29
12/1995	DFX	All	CCB-PRO-95/30
06/1996	new version of GA (128.1)	assoc, origin, origerr in SEL1, SEL2, SEL3	CCB-PRO-96/25
07/1996	new version of DFX (111.1)	arrival, assoc, detection in SEL1, SEL2, SEL3	CCB-PRO-96/28
08/1996	new release (PIDC4.0)	All	CCB-PRO-96/32
06/1997	new release (PIDC5.0)	All	CCB-PRO-97/19
03/1998	new release (PIDC6.0)	All	CCB-PRO-98/06
07/1999	new release (PIDC6.2)	All	CCB-PRO-99/13
07/2000	new release (PIDC7.0)	All	CCB-PRO-00/07
Surface waves/magnitudes:			
03/1995	ML	netmag, stamag in SEL1, SEL2, SEL3	CCB-PRO-95/05
07/1995	new maxsurf (1.2)	LP and LR phases in REB	CCB-PRO-95/14
10/1995	ML	netmag, stamag in SEL1, SEL2, SEL3	CCB-PRO-95/18

04/1996	improved dispersion curves	LP and LR phases in REB	CCB-PRO-96/13
11/1996	new maxsurf (2.2)	LP and LR phases in REB	CCB-PRO-96/40
06/1997	MS-mle	netmag, stamag in REB	CCB-PRO-97/18
04/1999	new station correction curves for ML	netmag, stamag in REB, SEL1, SEL2, SEL3	CCB-PRO-99/04
07/2000	mb1, Ms1	netmag, stamag in SEL1, SEL2, SEL3	CCB-PRO-00/06
Hydroacoustic/Infrasonic system:			
05/1996	Hydroacoustic stations included	PSUR and WAKE in REB, SEL1, SEL2, and SEL3	CCB-PRO-96/10 CCB-PRO-96/14
09/1997	StaPro for hydroacoustic stations	Arrivals in SEL1, SEL2, and SEL3	CCB-PRO-97/26
07/2000	Station specific 2D travel time tables	Assoc, origin, origerr in REB,	CCB-PRO-00/19
Event characterization:			
07/1996	routine estimation of event characterization parameters	originamp, splp in REB	CCB-PRO-96/27
08/1996	routine estimation of event characterization parameters	ceppks, complexity, and spvar in REB	CCB-PRO-96/30
07/2000	revised routine estimation of event characterization parameters	amplitude in REB, SEL1, SEL2, SEL3	CCB-PRO-00/08
Event location:			
09/1997	new measurement errors	arrival in REB, SEL1, SEL2, SEL3	CCB-PRO-97/18
09/1997	1D regional travel time tables for Fennoscandian stations	assoc, origin, origerr in REB, SEL1, SEL2, SEL3	CCB-PRO-97/22
01/1998	SASCs	assoc, origin, origerr in REB, SEL1, SEL2, SEL3	CCB-PRO-98/01
04/1999	SSSCs for Fennoscandian stations	assoc, origin, origerr in REB	CCB-PRO-99/03
03/2000	SSSCs for North American IMS stations	assoc, origin, origerr in REB	CCB-PRO-00/01
07/2000	updated SASCs	assoc, origin, origerr in REB, SEL1, SEL2, SEL3	CCB-PRO-00/20
04/2001	3D SSSCs for North American IMS stations	assoc, origin, origerr in REB	CCB-PRO-01/01

References

Here only those references are given which have been published in CCB memos and IDC Documentation. They are available from the website <http://www.cmr.gov/pidc/gi.html>. For references to publications in international journals see References under Miscellaneous in Volume 2.

- Bondar, I., and V. Ryaboy, Regional travel-time table for Fennoscandia, CCB Memo CCB-PRO-97/22, 1997.
- Bondar, I., Teleseismic slowness-azimuth station corrections (SASC) for the IMS network, CCB Memo CCB-PRO-98/01, 1998.
- Coyne, J., Waveform segment archive, CCB Memo CCB-PRO-96/19, 1996.
- IDC Documentation 3.4.1, Formats and Protocols for Messages, Rev. 3, 2001.
- IDC Documentation 5.1.1, Database schema, Rev. 3, 2001.
- IDC Documentation 5.2.1, IDC Processing of Seismic, Hydroacoustic, and Infrasonic Data, 1999.
- Israelsson, H., H. Swanger, and G. Beall, Independent modeling of time measurement and model errors, CCB Memo CCB-PRO-97/24, 1997.
- Israelsson, H., J. Wang, K. McLaughlin, J. Murphy, J. Stevens, D. Brumbaugh, and W. Nagy, Generalized mb magnitudes and station corrected Ms magnitudes, CCB Memo CCB-PRO-00/06, 2000.
- Nagy, W., New region-dependent travel-time handling facilities at the IDC; functionality, testing and implementation details, CCB Memo CCB-PRO-96/33, 1996.
- Ryaboy, V., D. Baumgardt, D. Bobrov, A. Dainty, SSSCs based on 3-D modeling for Pn, Sn, and Pg phases at IMS stations in North America, CCB Memo, CCB-PRO-01/01, 2001.
- Wang, J., K. McLaughlin, and W. Nagy, Updated Slowness-Azimuth Seismic Station Corrections for the CTBT International Monitoring System, CCB Memo CCB-PRO-00/20, 2000.
- Yang, X., K. McLaughlin, R. North, and C. Romney, CMR Special Event Database, CMR Technical Report CMR-98/30, 1998.
- Yang, X., and K. McLaughlin, SSSCs for regional phases at Fennoscandian and other stations, CCB memo, CCB-PRO-99/03, 1999.
- Yang, X., and K. McLaughlin, SSSCs for regional phases at North America IMS stations, CCB Memo, CCB-PRO-00/01, 2000.
- Yang, X., A. Gault, and R. North, CMR Hydroacoustic Database, CMR Technical Report CMR-00/09, 2000a.
- Yang, X., K. McLaughlin, and R. North, User's guide to the CMR seismic/hydroacoustic/infrasonic data products, CMR Technical Report CMR-00/14 Rev. 1, 2000b.
- Yang, X., I. Bondar, and C. Romney, PIDC Ground Truth Database (Revision 1), CMR Technical Report CMR-00/15, 2000c.
- Yang, X., R. North, and C. Romney, CMR Nuclear Explosion Database (Revision 3), CMR Technical Report CMR-00/16, 2000d.
- Yang, X., I. Bondar, and K. McLaughlin, PIDC Reference Event Database (REDB), CMR Technical Report CMR-00/17, 2000e.

Topic	Earthquake location
compiled by	Jens Havskov, University of Bergen, Department of Earth Science, Allégaten 41, N-5007 Bergen, Norway, Fax: +47 55 583660, E-mail: jens@geo.uib.no Peter Bormann, GeoForschungszentrum Potsdam, Telegrafenberg, D-14473 Potsdam, Germany; Fax: +49 331 288 1204; E-mail: pb65@gmx.net Johannes Schweitzer, NOR SAR, P.O.Box 53, N-2027 Kjeller, Norway, Fax: +47 63818719, E-mail: johannes@norsar.no
Version	October, 2002

1 Introduction

The exact location of a source, radiating seismic energy, is one of most important tasks in practical seismology and from time to time most seismologists have been involved in this task. The intention here is to describe the most common location methods without going into the mathematical details, which have been described in numerous textbooks and scientific papers but to give some practical advice on earthquake location.

The earthquake location is defined by the earthquake hypocenter (x_0, y_0, z_0) and the origin time t_0 . The hypocenter is the physical location, usually given in longitude (x_0), latitude (y_0), and depth below the surface (z_0 [km]). For simplicity, the hypocenter will be labeled x_0, y_0, z_0 with the understanding that it can be either measured in geographical or Cartesian coordinates, i.e., in [deg] or [km], respectively. The origin time is the start time of the earthquake rupture. The epicenter is the projection of the earthquake location on the Earth's surface (x_0, y_0) . When the earthquake is large, the physical dimension can be several hundred kilometers and the hypocenter can in principle be located anywhere on the rupture surface. Since the hypocenter and origin time are determined by arrival times of seismic phases initiated by the first rupture, the computed location will correspond to the point where the rupture initiated and the origin time to the time of the initial rupture. This is also true using any P or S phases since the rupture velocity is smaller than the S-wave velocity so that P- or S-wave energy emitted from the end of a long rupture will always arrive later than energy radiated from the beginning of the rupture. Standard earthquake catalogs (such as from the International Seismological Center, ISC) report location based primarily on arrival times of high frequency P waves. This location can be quite different from the centroid time and location obtained by moment-tensor inversion of long-period waves. The centroid location represents the average time and location for the entire energy radiation of the event.

2 Single station location

In general, epicenters are determined using many arrival times from different seismic stations and phases. However, it is also possible to locate an earthquake using a single 3-component station. Since the P waves are vertically and radially polarized, the vector of P-wave motion can be used to calculate the backazimuth to the epicenter (see Figure 1). The radial component of P will be recorded on the 2 horizontal seismometers **N**(orth) and **S**(outh) and the ratio of the amplitudes A_E/A_N on the horizontal components can be used to calculate the backazimuth of arrival **AZI** (elsewhere in the Manual abbreviated as **BAZ**):

$$AZI = \arctan A_E/A_N \quad (1)$$

There is then an ambiguity of 180° since the first polarity can be up or down so the polarity must also be used in order to get the correct backazimuth. If the first motion on vertical component of the P is upward, (which corresponds by definition to a compressional first motion (FM) arriving at the station related to an outward directed motion at the source) then the radial component of P is directed away from the hypocenter. The opposite is true if the P polarity is negative (see also Figure 1 in Exercise EX 11.2).

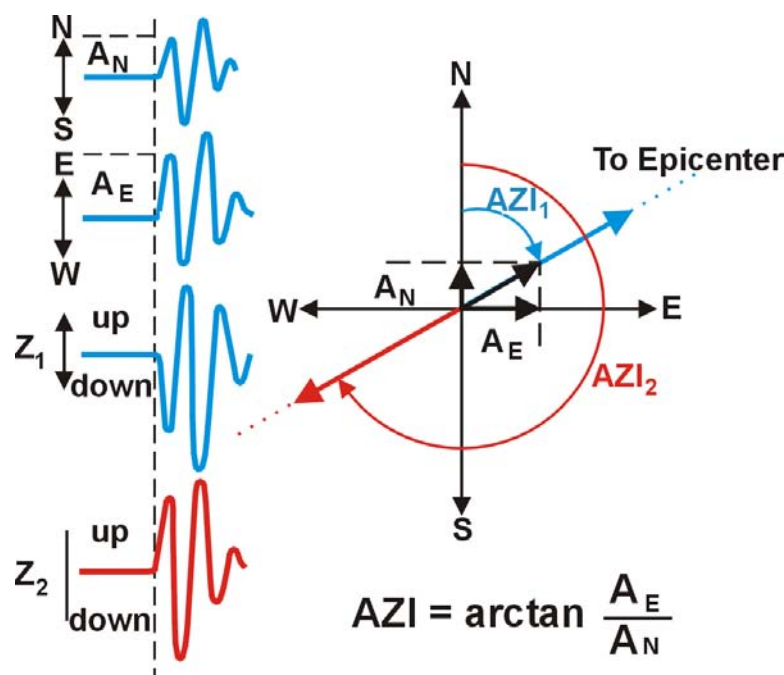


Figure 1 Example of P-wave first motions in 3-component records (left) from which the backazimuth **AZI** and incidence angle i can be derived according to Eqs. (1) and (2) (middle).

The amplitude A_Z of the Z component can, together with the amplitude $A_R = \sqrt{(A_E^2 + A_N^2)}$ on the radial components, also be used to calculate the *apparent angle of incidence* $i_{app} = \arctan A_R / A_Z$ of a P wave. However, according already to Wiechert (1907) the true incidence angle i_{true} of a P wave is

$$i_{\text{true}} = \arcsin \left(\frac{v_p}{v_s} \times \sin 0.5i_{\text{app}} \right), \quad (2)$$

with the difference accounting for the amplitude distortion due to the reflection at the free surface. Knowing the incidence angle i and the local seismic velocity v_c below the observing station, we can calculate the apparent velocity v_{app} of this seismic phase with

$$v_{\text{app}} = \frac{v_c}{\sin i} \quad (3)$$

With high frequency data it might be difficult to manually read the amplitudes of the first break or sometimes the first P swings are emergent. Since the amplitude ratio between the components should remain constant not only for the first swing of the P phase but also for the following oscillations of the same phase, we can, with digital data, use the predicted coherence method (Roberts et al., 1989) to automatically calculate backazimuth as well as the angle of incidence. Since this is much more reliable and faster than using the manually readings of the first amplitudes, calculation of backazimuth from 3-component records of single stations has again become a routine practice (e.g., Saari, 1991). In case of seismic arrays, apparent velocity and backazimuth can be directly measured by observing the propagation of the seismic wavefront with array methods (see Chapter 9). As we shall see later, backazimuth observations are useful in restricting epicenter locations and in associating observations to a seismic event. Knowing the incidence angle and implicitly the ray parameter of an onset helps to identify the seismic phase and to calculate the epicentral distance.

With a single station we have now the direction to the seismic source. The distance can be obtained from the difference in arrival time of two phases, usually P and S. If we assume a constant velocity, and origin time t_0 , the P- and S-arrival times can then be written as

$$t_p = t_0 + D/v_p \quad t_s = t_0 + D/v_s \quad (4)$$

where t_p and t_s are the P- and S-arrival times respectively, v_p and v_s are the P and S velocities respectively and D is the epicentral distance for surface sources; or the hypocentral distance d for deeper sources. By eliminating t_0 from Equation (4), the distance can be calculated as

$$D = (t_s - t_p) \frac{v_p \cdot v_s}{v_p - v_s} \quad (5)$$

with D in km and $t_s - t_p$ in seconds. But Equation (5) is applicable only for the travel-time difference between S_g and P_g , i.e., the direct crustal phases of S and P, respectively. They are first onsets of the P- and S-wave groups of local events only for distances up to about 100 – 250 km, depending on crustal thickness and source depth within the crust. Beyond these distances the P_n and S_n , either head waves critically refracted at the Mohorovičić discontinuity or waves diving as body waves in the uppermost part of the upper mantle become the first onsets (see Fig. 2.32 and 11.40). The “cross-over” distance x_{co} between P_n and P_g (or P_b) can be approximately calculated for a (near) surface focus from the relationship

$$x_{\text{co}} = 2 z_m \left\{ (v_m - \bar{v}_p) (v_m + \bar{v}_p) \right\}^{-1/2}, \quad (6)$$

with \bar{v}_p – average crustal P velocity, v_m – sub-Moho P velocity, and z_m – crustal thickness. Inserting the rough average values of $v_c = 6$ km/s and $v_m = 8$ km/s we get, as a “rule of thumb”, $x_{co} \approx 5 z_m$. At smaller distances we can be rather sure that the observed first arrival is Pg. Note, however, that this “rule of thumb” is valid for surface focus only. As demonstrated with Fig. 2.40, the crossover distance is only about half as large for near Moho earthquakes and also the dip of the Moho and the direction of observation (up- or downdip) does play a role. However, in continental (intraplate) environment, lower crustal earthquakes are rare. Mostly they occur in the upper crust.

Examples for calculating the epicentral distance D and the origin time OT of near seismic events by means of a set of local travel-time curves for Pn, Pg, Sn, Sg and Lg are given in exercise EX 11.1. In the absence of local travel-time curves for the area under consideration one can use Equation (5) for deriving a “**rule of thumb**” for approximate distance determinations from travel-time differences Sg-Pg. For an ideal Poisson solid $v_s = v_p/\sqrt{3}$. This is a good approximation for the average conditions in the crust. With this follows from Equation (5) : $D = (t_{Sg} - t_{Pg}) \times 8.0$ for “normal, medium age” crustal conditions with $\bar{v}_p = 5.9$ km/s, and $D = (t_{Sg} - t_{Pg}) \times 9.0$ for old Precambrian continental shields with rather large $\bar{v}_p = 6.6$ km/s. However, if known, the locally correct v_p/v_s ratio should be used to improve this “rule of thumb”. If the distance is calculated from the travel-time difference between Sn and Pn another good rule of thumb is $D = (t_{Sn} - t_{Pn}) \times 10$. It may be applicable up to about 1000 km distance.

For distances between about $20^\circ < \Delta < 100^\circ$ the relationship $\Delta^\circ = \{(t_s - t_p)_{\min} - 2\} \times 10$ still yields reasonably good results with errors $< 3^\circ$, however, beyond $D = 10^\circ$ the use of readily available global travel-time tables such as IASP91 (Kennett and Engdahl, 1991; Kennett, 1991), SP6 (Morelli and Dziewonski, 1993), or AK135 (Kennett et al., 1995) is strongly recommended for calculating the distance.

With both backazimuth and distance, the epicenter can be obtained by measuring off the distance along the backazimuth of approach. Finally, knowing the distance, we can calculate the P-travel time and thereby get the origin time using the P-arrival time (see EX 11.2 for location of teleseismic events by means of 3-component records).

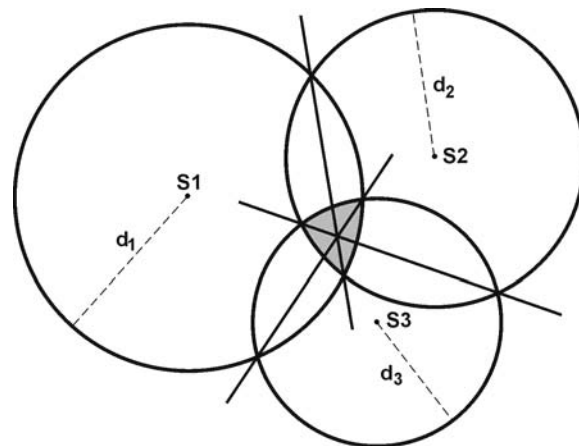
3 Multiple station location

3.1 Manual location

When at least 3 stations are available, a simple manual location can be made from drawing circles (the circle method) with the center at the station locations and the radii equal to the epicentral distances calculated from the S-P times (see Figure 2).

These circles will rarely cross in one point which indicates errors in the observations and/or that we have wrongly assumed a surface focus. In fact, $t_s - t_p$ is the travel-time difference for the hypocentral distance d which is for earthquakes with $z > 0$ km generally larger than the epicentral distance Δ (or D). Therefore, the circles drawn around the stations with radius d will normally not be crossing at a single point at the epicenter but rather “overshooting”. One should therefore fix the epicenter either in the “center of gravity” of the overlapping area (shaded area in Figure 2) or draw “chords”, i.e., straight lines passing through the crossing

point between two neighboring circles. These chord lines intersect in the epicenter (see Figure 1 in EX 11.1). Still other methods exist (e.g., Båth, 1979) to deal with this depth problem (e.g., the hyperbola method which uses P-wave first arrivals only and assumes a constant P-wave velocity), however since they are rarely used, they will not be discussed here.



$$d \approx t(Sg - Pg) \times 8$$

$$\text{or } d \approx t(Sn - Pn) \times 10$$

Figure 2 Location by the “circle and chord” method. The stations are located in S1, S2 and S3. The epicenter is found within the shaded area where the circles overlap. The best estimate is the crossing of the chords, which connect the crossing points of the different pairs of circles.

With several stations available from a local earthquake, the origin time can be determined by a very simple technique called a Wadati diagram (Wadati, 1933). Using Equation (7) and eliminating Δ , the S-P travel-time difference can be calculated as

$$t_s - t_p = (v_p/v_s - 1) \times (t_p - t_0) \quad (7)$$

The S-P times are plotted against the absolute P time. Since $t_s - t_p$ goes to zero at the hypocenter, a straight line fit on the Wadati diagram (Figure 3) gives the origin time at the intercept with the P-arrival axis and from the slope of the curve, we get v_p/v_s . Note that it is thus possible to get a determination of both the origin time and a mean v_p/v_s ratio without any prior knowledge of the crustal structure, the only assumption being that v_p/v_s is constant and that the P and S phases are of the same type like Pg and Sg or Pn and Sn. Such an independent determination of these parameters can be very useful when using other methods of earthquake location.

The Wadati diagram can also be very useful in making independent checks of the observed arrival times. Any points not fitting the linear relationship might be badly identified, either by not being of the same phase type or by misreading.

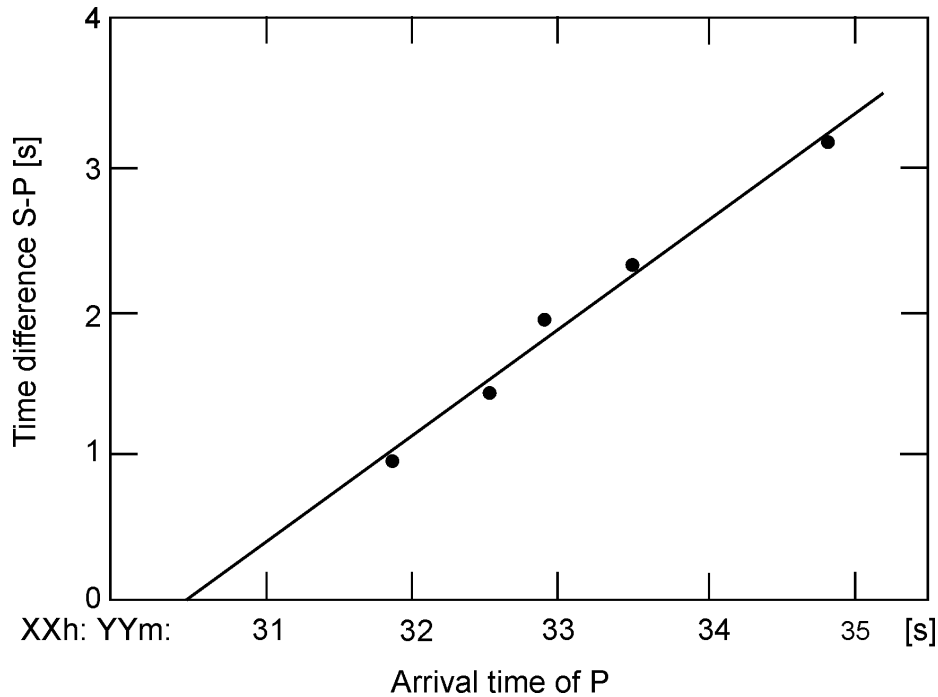


Figure 3 An arbitrary example of a Wadati diagram. The intercept of the best fitting line through the data with the x-axis gives the origin time OT. In the given case, the slope of the line is 0.72 so the v_p/v_s ratio is 1.72. This misfit of the data with a straight line indicates model and/or data reading errors.

3.2 Computer location

Manual location methods provide insight into the location problems, however in practice we use computer methods. In the following, the most common ways of calculating hypocenter and origin time by computer will be discussed.

The calculated arrival time t_i^c at station i can be written as

$$t_i^c = T(x_i, y_i, z_i, x_0, y_0, z_0) + t_0 \quad (8)$$

where T is the travel time as a function of the location of the station (x_i, y_i, z_i) and the hypocenter. This equation has 4 unknowns, so in principle 4 arrival-time observations from at least 3 stations are needed in order to determine the hypocenter and origin time. If we have n observations, there will be n equations of the above type and the system is over determined and has to be solved in such a way that the misfit or residual r_i at each station is minimized. r_i is defined as the difference between the observed and calculated travel times which is the same as the difference between the observed and calculated arrival times

$$r_i = t_i^o - t_i^c \quad (9)$$

where t_i^o is the observed arrival time. In principle, the problem seems quite simple. However, since the travel-time function T is a nonlinear function of the model parameters, it is not

possible to solve Equation (8) with any analytical methods. So even though T can be quite simply calculated, particularly when using a 1-D Earth model or pre-calculated travel-time tables, the non-linearity of T greatly complicates the task of inverting for the best hypocentral parameters. The non-linearity is evident even in a simple 2-D epicenter determination where the travel time t_i from the point (x, y) to a station (x_i, y_i) can be calculated as

$$t_i = \frac{\sqrt{(x - x_i)^2 + (y - y_i)^2}}{v}, \quad (10)$$

where v is the velocity. It is obvious that t_i does not scale linearly with either x or y so it is not possible to use any set of linear equations to solve the problem and standard linear methods cannot be used. This means that given a set of arrival times, there is no simple way of finding the best solution. In the following, some of the methods of solving this problem will be discussed.

3.2.1 Grid search

Since it is so simple to calculate the travel times of all seismic phases to any point in the model, given enough computer power, a very simple method is to perform a grid search over all possible locations and origin times and compute the arrival time at each station (e.g., Sambridge and Kennett, 1986). The hypocentral location and origin time would then be the point with the best agreement between the observed and calculated times. This means that some measure of best agreement is needed, particularly if many observations are used. The most common approach is to use the least squares solution, which is to find the minimum of the sum of the squared residuals e from the n observations:

$$e = \sum_{i=1}^n (r_i)^2 \quad (11)$$

The root mean squared residual RMS, is defined as $\sqrt{e/n}$. RMS is given in almost all location programs and commonly used as a guide to location precision. If the residuals are of similar size, the RMS gives the approximate average residual. As will be seen later, RMS only gives an indication of the fit of the data, and a low RMS does not automatically mean an accurate hypocenter determination. Generally, the precision of the computational solution, which is based on various model assumptions, should not be mistaken as real accuracy of the location and origin time. This point will be discussed later under section 7.

The average squared residual e/n is called the variance of the data. Formally, n should here be the number of degrees of freedom ndf , which is the number of observations minus the number of parameters in fit (here 4). Since n usually is large, it can be considered equal to the number of degrees of freedom. This also means that \mathbf{RMS}^2 is approximately the same as the variance. The least squares approach is the most common measure of misfit since it leads to simple forms of the equations in the minimization problems (see later). It also works quite well if the residuals are caused by uncorrelated Gaussian noise. However in real problems this is often not the case. A particularly nasty problem is the existence of outliers, i.e., individual large residuals. A residual of 4 will contribute 16 times more to the misfit e , than a residual of 1. Using the sum of the absolute residuals as a norm for the misfit can partly solve this problem:

$$e1 = \sum_{i=1}^n |r_i|. \quad (12)$$

This is called the L1 norm and is considered more robust when there are large outliers in the data. It is not much used in standard location programs since the absolute sign creates complications in the equations. This is of course not the case for grid search. Therefore, most location programs will have some scheme for weighting out or truncating large residuals (see later), which can partly solve the problem.

Once the misfits (e.g., RMS) have been calculated at all grid points, one could assign the point with the lowest RMS as the ‘solution’. For well-behaved data, this would obviously be the case, but with real data, there might be several points, even far apart, with similar RMS and the next step is therefore to estimate the probable uncertainties of the solution. The simplest way to get an indication of the uncertainty, is to contour the RMS as a function of x and y (2-D case) in the vicinity of the point with the lowest RMS (see Figure 4).

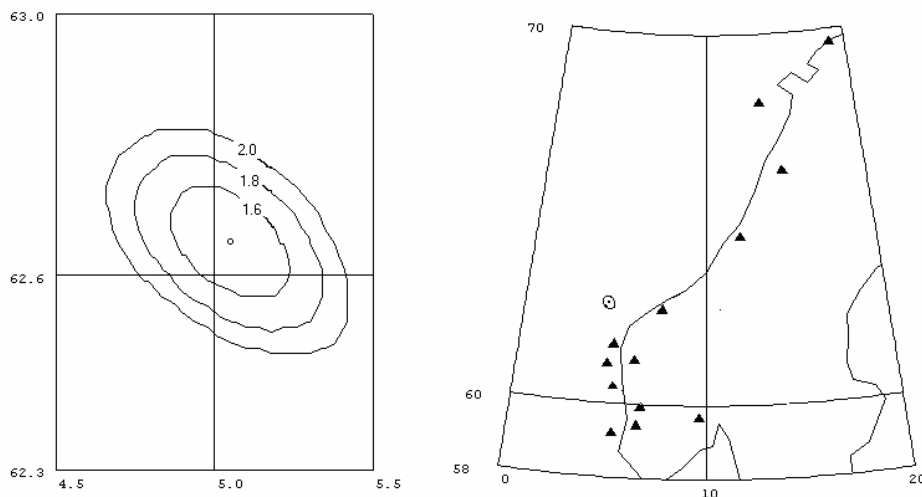


Figure 4 Left: RMS contours (in seconds) from a grid search location of an earthquake off western Norway (left). The grid size is 2 km. The circle in the middle indicates the point with the lowest RMS (1.4 s). Right: The location of the earthquake and the stations used. Note the elongated geometry of the station distribution. Its effect on the error distribution will be discussed in section 4.1 below. The RMS ellipse from the figure on the left is shown as a small ellipse in the figure at right. Latitudes are degrees North and longitudes degrees East.

Clearly, if RMS is growing rapidly when moving away from the minimum, a better solution has been obtained than if RMS grows slowly. If RMS is contoured in the whole search area, other minima of similar size might be found indicating not only large errors but also a serious ambiguity in the solution. Also note in Figure 4 that networks with irregular aperture have reduced distance control in the direction of their smallest aperture but good azimuth control in the direction of their largest aperture.

An important point in all grid-search routines is the method of how to search through the possible model space. In particular for events observed at teleseismic distances the model

space can be very large. Sambridge and Kennett (2001) published a fast neighborhood algorithm to use for global grid search.

3.2.2 Location by iterative methods

Despite increasing computer power, earthquake locations are done mainly by other methods than grid search. These methods are based on linearizing the problem. The first step is to make a guess of hypocenter and origin time (x_0, y_0, z_0, t_0) . In its simplest form, e.g., in case of events near or within a station network, this can be done by using a location near the station with the first arrival time and using that arrival time as t_0 . Other methods also exist (see below). In order to linearize the problem, it is now assumed that the true hypocenter is close enough to the guessed value so that travel-time residuals at the trial hypocenter are a linear function of the correction we have to make in hypocentral distance.

The calculated arrival times at station i , t_i^c from the trial location are, as given in Equation (8), $t_i^c = T(x_0, y_0, z_0, x_i, y_i, z_i) + t_0$ and the travel-time residuals r_i are $r_i = t_i^o - t_i^c$. We now assume that these residuals are due to the error in the trial solution and the corrections needed to make them zero are Δx , Δy , Δz , and Δt . If the corrections are small, we can calculate the corresponding corrections in travel times by approximating the travel time function by a Taylor series and using only the first term. The residual can now be written:

$$r_i = (\partial T / \partial x_i) * \Delta x + (\partial T / \partial y_i) * \Delta y + (\partial T / \partial z_i) * \Delta z + \Delta t \quad (13)$$

In matrix form we can write this as

$$\mathbf{r} = \mathbf{G} * \mathbf{X}, \quad (14)$$

where \mathbf{r} is the residual vector, \mathbf{G} the matrix of partial derivatives (with 1 in the last column corresponding to the source time correction term) and \mathbf{X} is the unknown correction vector in location and origin time.

This is a set of linear equations with 4 unknowns (corrections to hypocenter and origin time), and there is one equation for each observed phase time. Normally there would be many more equations than unknowns (e.g., 4 stations with 3 phases each would give 12 equations). The best solution to Equation (13) or Equation (14) is usually obtained with standard least squares techniques. The original trial solution is then corrected with the results of Equation (13) or Equation (14) and this new solution can then be used as trial solution for a next iteration. This iteration process can be continued until a predefined breakpoint is reached. Breakpoint conditions can be either a minimum residuum r , or a last iteration giving smaller hypocentral parameter changes than a predefined limit, or just the total number of iterations. This inversion method was first invented and applied by Geiger (1910) and is called the ‘Geiger method’ of earthquake location. The iterative process usually converges rapidly unless the data are badly configured or the initial guess is very far away from the mathematically best solution (see later). However, it also happens that the solution converges to a local minimum and this would be hard to detect in the output unless the residuals are very bad. A test with a grid search program could tell if the minimum is local, or tests could be made with several start locations.

So far we have only dealt with observations in terms of arrival times. Many 3-component stations and arrays now routinely report backazimuth of arrival ϕ . It is then possible to locate

events with only one station and P and S times (see Figure 1). However, the depth must be fixed. If one or several backazimuth observations are available, they can be used together with the arrival time observations in the inversion and the additional equations for the backazimuth residual are

$$r_i^\phi = (\partial\phi/\partial x_i) * \Delta x + (\partial\phi/\partial y_i) * \Delta y \quad (15)$$

Equations of this type are then added to the Equations (13) or (14). The Δx and Δy in Equation (15) are the same as for Equation (13), however the residuals are now in degrees. In order to make an overall RMS, the degrees must be ‘converted to seconds’ in terms of scaling. For example, in the location program Hypocenter (Lienert and Havskov, 1995), a 10 deg backazimuth residual was optionally made equivalent to 1 s travel time residual. Using e.g., 20 deg as equivalent to 1 s would lower the weight of the backazimuth observations. Schweitzer (2001a) used in the location program HYPOSAT a different approach. In this program the measured (or assumed) observation errors of the input parameters are used to weight individually the different lines of the equation system (13) or (14) before inverting it. Thereby, more uncertain observations will contribute much less to the solution than well-constrained ones and all equations become non-dimensional.

Arrays (see Chapter 9) or single stations (see Equation (3)) cannot only measure the backazimuth of a seismic phase but also its ray parameter (or apparent velocity). Consequently, the equation system (13) or (14) to be solved for locating an event, can also be extended by utilizing such observed ray parameters p (or apparent velocities) as defining data. In this case we can write

$$r_i^p = (\partial p/\partial x_i) * \Delta x + (\partial p/\partial y_i) * \Delta y + (\partial p/\partial z_i) * \Delta z \quad (16)$$

Equation (16) is independent of the source time and the partial derivatives are often very small. However, in some cases, in particular if an event is observed with only one seismic array, the observed ray parameter will give additional constraint for the event location.

Equations (13) and (14) are written without discussing whether working with a flat Earth or a spherical Earth. However, the principle is exactly the same, and using a flat-Earth transformation (e.g., Müller, 1977) any radially symmetric Earth model can be transformed into a flat model. The travel times and partial derivatives are often calculated by interpolating in tables and in principle it is possible to use any Earth model including 2-D and 3-D models to calculate theoretical travel times. In practice, 1-D models are mostly used, since 2-D and 3-D models are normally not well enough known and the travel-time computations are much more time consuming. For local seismology, it is a common practice to specify a 1-D crustal model and calculate arrival times for each ray while for global models, an interpolation in travel-time tables such as IASP91 is the most common. However, as Kennett and Engdahl (1991) pointed out, the preferred and much more precise method for obtaining travel times from the IASP91 model or other 1-D global Earth models (see DS 2.1) is to apply the tau-p method developed by Buland and Chapman (1983). To calculate your own travel-time tables for local or global Earth models, the computer program LAUFZE (see PD 11.2) can be downloaded from <ftp://ftp.norsar.no/pub/outgoing/johannes/lauf/>, a description of the program is annexed in PD 11.2. It allows calculating travel times for many different seismic phases and an arbitrary horizontally layered model with any combination of layers with constant velocities, gradients, or first-order discontinuities.

3.2.3 Example of location in a homogeneous model

The simplest case for earthquake location is a homogeneous medium. The arrival times can be calculated as

$$T_i = \frac{\sqrt{(x - x_i)^2 + (y - y_i)^2 + (z - z_i)^2}}{v} + t_0, \quad (17)$$

where v is the velocity. The partial derivatives can be estimated from Equation (17) and e.g., for x , the derivative is

$$\frac{\partial T_i}{\partial x} = \frac{(x - x_i)}{v} * \frac{1}{\sqrt{(x - x_i)^2 + (y - y_i)^2 + z^2}}. \quad (18)$$

Similar expressions can be made for y and z . Table 1 gives an example of locating an earthquake with 10 stations in a model with constant velocity (from Stein, 1991). The stations are from 11 to 50 km from the hypocenter. The earthquake has an origin time of 0 s at the point (0, 0, 10) km. The starting location is at (3, 4, 20) km at 2 s. The exact travel times were calculated using a velocity of 5 km/s and the iterations were done as indicated above. At the initial guess, the sum of the squared residuals was 92.4 s², after the first iteration it was reduced to 0.6 s² and already at the second iteration, the ‘correct’ solution was obtained. This is hardly surprising, since the data had no errors. We shall later see how this works in the presence of errors.

Table 1 Inversion of error free data. Hypocenter is the correct location, Start is the start location, and the location is shown for the two following iterations. Units for x , y and z are [km], for t_0 [s] and for the misfit e according to Equation (11) [in s²].

	Hypocenter	Start	1. Iteration	2. Iteration
X	0.0	3.0	-0.5	0.0
Y	0.0	4.0	-0.6	0.0
Z	10.0	20.0	10.1	10.0
t_0	0.0	2.0	0.2	0.0
e		94.2	0.6	0.0
RMS		3.1	0.25	0.0

3.2.4 Advanced methods

The problem of locating seismic events has recently experienced a lot of attention and new procedures have been developed such as the double-difference earthquake location algorithm (Waldhauser and Ellsworth, 2000), a novel global differential evolution algorithm (Ružek and Kvasnička (2001), a probabilistic approach to earthquake location in 3-D and layered models by Lomax et al. (2000) as well as advanced grid search procedures to be applied in highly heterogeneous media (Lomax et al., 2001). Recent advances in travel-time calculations for three-dimensional structures complements this method (e.g., Thurber and Kissling, 2000). Several of these and other more recent developments are summarized in a monograph edited by Thurber and Rabinowitz (2000), which includes also advances in global seismic event location (Thurber and Engdahl, 2000); and in a special volume about event location in context

with the special requirements for monitoring the CTBT (Ringdal and Kennett, 2001). Figure 5 shows how much the accuracy of location within earthquake clusters can be improved by applying the above mentioned double-difference earthquake location algorithm.

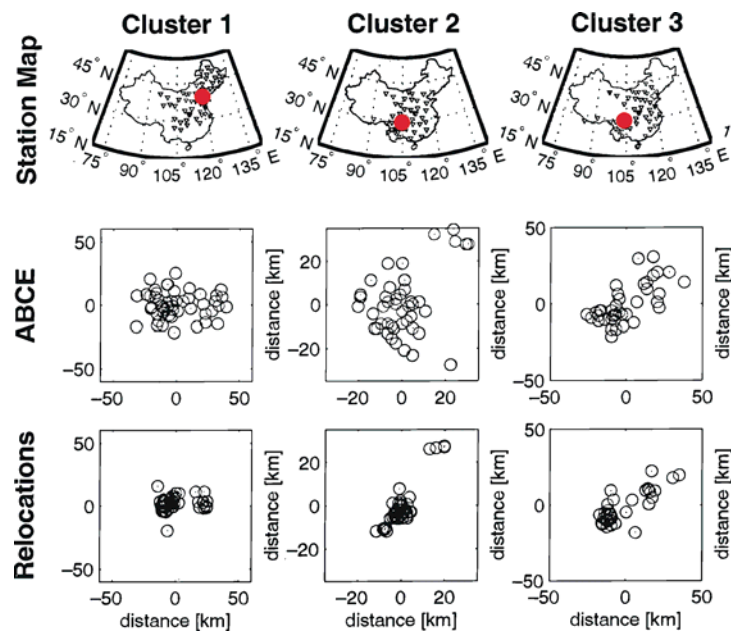


Figure 5 Examples of improving the ABCE locations for earthquake clusters (red dots) from regional networks of seismic stations (triangles) in China by relocating the events with the double-difference location algorithm (courtesy of Paul G. Richards).

4 Location errors

4.1 Error quantification and statistics

Since earthquakes are located with arrival times that contain observational errors and the travel times are calculated assuming we know the model, all hypocenters will have errors. Contouring the grid search RMS (Figure 4) gives an indication of the uncertainty of the epicenter. Likewise it would be possible to make 3-D contours to get an indication of the 3-D uncertainty. The question is now how to quantify this measure. The RMS of the final solution is very often used as a criterion for ‘goodness of fit’. Although it can be an indication, RMS depends on the number of stations and does not in itself give any indication of errors and RMS is not reported by e.g., PDE and ISC.

From Figure 4 it is seen that the contours of equal RMS are not circles. We can calculate contours within which there is a 67 % probability (or any other desired probability) of finding the epicenter (see below). We call this the error ellipse. This is the way hypocenter errors normally are represented. It is therefore not sufficient to give one number for the hypocenter error since it varies spatially. Standard catalogs from PDE and ISC give the errors in latitude, longitude and depth, however, that can also be very misleading unless the error ellipse has the minor and major axis NS or EW. In the example in Figure 4, this is not the case. Thus the only proper way to report error is to give the full specification of the error ellipsoid.

Before going into a slightly more formal discussion of errors, let us try to get a feeling for which elements affect the shape and size of the epicentral error ellipse. If we have no arrival time errors, there are no epicenter errors so the magnitude of the error (size of error ellipse) must be related to the arrival time uncertainties. If we assume that all arrival time reading errors are equal, only the size and not the shape of the error ellipse can be affected. So what would we expect to give the shape of the error ellipse? Figure 4 is an example of an elongated network with the epicenter off to one side. It is clear that in the NE direction, there is a good control of the epicenter since S-P times control the distances in this direction due to the elongation of the network. In the NW direction, the control is poor because of the small aperture of the network in this direction. We would therefore expect an error ellipse with the major axis NW as observed. Another way of understanding why the error is larger in NW than in NE direction is to look at Equation (12). The partial derivatives $\partial T/\partial x$ will be much smaller than $\partial T/\partial y$ so the Δy -terms will have a larger weight than the Δx -terms in the equations (strictly speaking the partial derivatives with respect to NW and NE). Consequently, errors in arrival times will affect Δx more than Δy . Note that if backazimuth observations were available for any of the stations far North or South of the event, this would drastically reduce the error estimate in the EW direction since $\partial\phi/\partial x$ is large while $\partial\phi/\partial y$ is nearly zero.

Another geometry of the stations would give another shape of the error ellipse. It is thus possible for any network to predict the shape and orientation of the error ellipses, and given an arrival error, also the size of the ellipse for any desired epicenter location. This could e.g., be used to predict how a change in network configuration would affect earthquake locations at a given site.

In all these discussions, it has been assumed that the errors have Gaussian distribution and that there are no systematic errors like clock error. It is also assumed that there are no errors in the theoretical travel times, backazimuths, or ray parameter calculations due to unknown structures. This is of course not true in real life, however error calculations become too difficult if we do not assume a simple error distribution and that all stations have the same arrival time error.

The previous discussion gave a qualitative description of the errors. We will now show how to calculate the actual hypocentral errors from the errors in the arrival times and the network configuration. The most common approach to earthquake location is based on the least squares inversion and a Gaussian distribution of the arrival time errors, in which case the statistics is well understood and we can use the Chi-Square probability density distribution to calculate errors. For a particular earthquake location, χ^2 can be calculated as:

$$\chi^2 = \frac{1}{\sigma^2} \sum_{i=1}^n r_i^2, \quad (19)$$

where σ is the assumed same standard deviation of any one of the residuals and n is the number of observations. We can now look at the standard statistical tables (extract in Table 2) to find the expected value of χ^2 within a given probability. As can be seen from the table, within 5% probability, χ^2 is approximately the number of degrees of freedom (*ndf*), which in our case is $n-4$.

Table 2 The percentage points of the χ^2 distribution for different numbers of degrees of freedom (*ndf*)

<i>ndf</i>	χ^2 (95%)	χ^2 (50%)	χ^2 (5%)
5	1.1	4.4	11.1
10	3.9	9.3	18.3
20	10.9	19.3	31.4
50	34.8	49.3	67.5
100	77.9	99.3	124.3

If e.g., an event is located with 24 stations (*ndf*=20), there is only a 5% chance that χ^2 will exceed 31.4. The value of χ^2 will grow as we move away from the best fitting epicenter and in the example above, the contour within which χ^2 is less than 31.4 will show the error ellipse within which there is a 95 % chance of finding the epicenter. In practice, errors are mostly reported within 67 % probability.

The errors in the hypocenter and origin time can also formally be defined with the variance – covariance matrix σ_X^2 of the hypocentral parameters. This matrix is defined as

$$\sigma_X^2 = \begin{Bmatrix} \sigma_{xx}^2 & \sigma_{xy}^2 & \sigma_{xz}^2 & \sigma_{xt}^2 \\ \sigma_{yx}^2 & \sigma_{yy}^2 & \sigma_{yz}^2 & \sigma_{yt}^2 \\ \sigma_{zx}^2 & \sigma_{zy}^2 & \sigma_{zz}^2 & \sigma_{zt}^2 \\ \sigma_{tx}^2 & \sigma_{ty}^2 & \sigma_{tz}^2 & \sigma_{tt}^2 \end{Bmatrix}. \quad (20)$$

The diagonal elements are variances of the location parameters x , y , z and t_0 while the off diagonal elements give the coupling between the errors in the different hypocentral parameters. For more details, see e.g., Stein (1991). The nice property about σ_X^2 is that it is simple to calculate:

$$\sigma_X^2 = \sigma^2 * (G^T G)^{-1}, \quad (21)$$

where σ^2 is the variance of the arrival times multiplied by the identity matrix and G^T is G transposed. The standard deviations of the hypocentral parameters are thus given by the square root of the diagonal elements and these are the usual errors reported. So how can we use the off diagonal elements? Since σ_X^2 is a symmetric matrix, a diagonal matrix in a coordinate system, which is rotated relatively to the reference system, can represent it. We now only have the errors in the hypocentral parameters, and the error ellipse simply have semi axes σ_{xx} , σ_{yy} , and σ_{zz} . The main interpretation of the off diagonal elements is thus that they define the orientation and shape of the error ellipse. A complete definition therefore requires 6 elements. Eqs. (20) and (21) also show, as stated intuitively earlier, that the shape and orientation of the error ellipse depends only on the geometry of the network and the crustal structure whereas the standard deviation of the observations is a scaling factor.

The critical variable in the error analysis is therefore the arrival-time variance σ^2 . This value is usually larger than would be expected from timing and picking errors alone, however it might vary from case to case. Setting a fixed value for a given data set could result in

unrealistic error calculations. Most location programs will therefore estimate σ from the residuals of the best fitting hypocenter:

$$\sigma^2 = \frac{1}{ndf} \sum_{i=1}^n r_i^2. \quad (22)$$

Division by ndf rather than by n compensates for the improvement in fit resulting from the use of the arrival times from the data. However, this only partly works and some programs allow setting an a priori value which is used only if the number of observations is small. For small networks this can be a critical parameter.

Recently, some studies (e.g., Di Giovambattista and Barba, 1997; Parolai et al., 2001) showed, both for regional and local seismic networks, that the error estimates ERH (in horizontal) and ERZ (in vertical direction), as given by routine location programs (e.g., in Hypoellipse) can not be considered as a conservative estimate of the true location error and might lead investigators to unjustified tectonic conclusions (see also Figures 11 and 12).

4.2 Example of error calculation

We can use the previous error free example (see Table 1) and add some errors (from Stein, 1991). We add Gaussian errors with a mean of zero and a standard deviation of 0.1 s to the arrival times. Now the data are inconsistent and cannot fit exactly. As it can be seen from the results in Table 3, the inversion now requires 3 iterations (2 before) before the locations stop changing. The final location is not exactly the location used to generate the arrival times and the deviation from the correct solution is 0.2, 0.4, and 2.2 km for x, y, and z respectively, and 0.2 s for the origin time. This gives an indication of the location errors.

Table 3 Inversion of arrival times with a 0.1 s standard error. Hypocenter is the correct location, Start is the start location, and the locations are shown after the three following iterations. e is the misfit according to Equation (11).

	Hypocenter	Start	1. Iteration	2. Iteration	3. Iteration
x [km]	0.0	3.0	-0.2	0.2	0.2
y [km]	0.0	4.0	-0.9	-0.4	-0.4
z [km]	10.0	20.0	12.2	12.2	12.2
t_0 [s]	0.0	2.0	0.0	-0.2	-0.2
e [s ²]		93.7	0.33	0.04	0.04
RMS [s]		3.1	0.25	0.06	0.06

It is now interesting to compare what is obtained with the formal error calculation. Table 4 gives the variance – covariance matrix. Taking the square root of the diagonal elements we get the standard deviations of x , y , z and t_0 as 0.3, 0.3 and 1.1 km and 0.1 s, respectively. This is close to the ‘true’ error so the solution is quite acceptable. Also note that the RMS is close to the standard error.

Table 4 Variance – covariance matrix for the example in Table 3.

	x	Y	Z	t
x	0.06	0.01	0.01	0.00
y	0.01	0.08	-0.13	0.01
z	0.01	-0.13	1.16	-0.08
t	0.00	0.01	-0.08	0.0

The variance – covariance matrix shows some interesting features. As seen from the diagonal elements of the variance – covariance matrix, the error is much larger in the depth estimate than in x and y. This clearly reflects that the depth is less well constrained than the epicenter which is quite common unless there are stations very close to the epicenter and thus $|(d-\Delta)| / \Delta \gg 1$. For simplicity, we have calculated the standard deviations from the diagonal terms, however since the off diagonal terms are not zero, the true errors are larger. In this example it can be shown that the semi-major and semi-minor axis of the error ellipse have lengths of 0.29 and 0.24 km respectively, and the semi-major axis trends N22°E, so the difference from the original diagonal terms is small.

The *zt* term, the covariance between depth and origin time, is negative, indicating a negative trade-off between the focal depth and the origin time; an earlier source time can be compensated by a larger source depth and vice versa. This is commonly observed in practice and is more prone to happen if only first P-phase arrivals are used such that there is no strong limitation of the source depth by P times in different distances.

Error calculation is a fine art, there are endless variations on how it is done and different location programs will usually give different results.

5 Relative location methods

5.1 Master event technique

The relative location between events within a certain region can often be made with a much greater accuracy than the absolute location of any of the events. This is the case when velocity variations outside the local region are the major cause of the travel-time residuals such that residuals measured at distant stations will be very similar for all of the local events. Usually, the events in the local area are relocated relative to one particularly well-located event, which is then called the **master event**. It should be clear that the Master Event Technique can only be used when the distance to the stations is much larger than the distance between the events.

Most location programs can be used for a master event location. For this travel-time anomalies outside the source region are assumed to cause all individual station residuals after the location of the master event. By using these station residuals as station corrections, the location of the remaining events will be made relative to the master event since all relative changes in arrival times are now entirely due to changes in location within the source region. It is obvious that only stations and phases for which observations are available for the master event can be used for the remaining events. Ideally, the same stations and phases should be used for all events.

5.2 Joint hypocenter location

In the Master Event Technique, it was assumed that true structure dependent residuals could be obtained absolutely correct from the master event, however other errors could be present in the readings for the master event itself. A better way is to determine the most precise station residuals using the whole data set. This is what Joint Hypocenter Determination (JHD) is about. Instead of determining one hypocenter and origin time, we will jointly determine m hypocenters and origin times, and n station corrections. This is done by adding the station residuals Δt_i^s to Equation (13) and writing the equations for all m earthquakes (index j):

$$r_{ij} = (\partial T / \partial x_{ij}) * \Delta x + (\partial T / \partial y_{ij}) * \Delta y + (\partial T / \partial z_{ij}) * \Delta z + \Delta t_i^s + \Delta t_j. \quad (23)$$

The first to propose the JHD method was Douglas (1967). Since the matrix G of Equation (14) is now much larger than the 4×4 matrix for a single event location, efficient inversion schemes must be used. If we use e.g., 20 stations with 2 phases each for 10 events, there will be $20 * 10 * 2 = 400$ equations and 80 unknowns (10 hypocenters and origin times, and 20 station residuals).

The relative locations obtained by the Master Event Technique or the JHD are usually more reliable than individually estimated relative locations. However, only if we have the absolute location of one of the events (e.g., a known explosion), will we be able to convert the relative locations of a Master Event algorithm into absolute locations, whereas for the JHD “absolute” locations are obtained for all events if the assumed velocity model is correct. Accurate relative locations are useful to study, e.g., the structure of a subduction zone or the geometry of an aftershocks area, which might indicate the orientation and geometry of the fault. Recently, Pujol (2000) has given a very detailed outline of the method and its application to data from local seismic networks. Figure 6 shows an example for increased location accuracy after applying JHD.

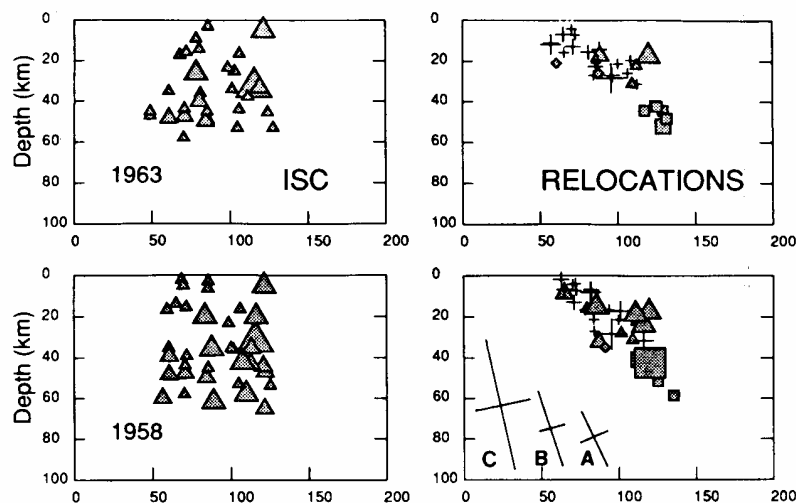


Figure 6 Comparison of earthquake locations using the normal procedure at ISC (left) and JHD relocations (right). The events are located in the Kurile subduction zone along the rupture zones of large thrust events in 1963 and 1958. The vertical cross sections shown traverse the thrust zone from left to right. Note that the JHD solutions reduce the scatter and make it possible to define a dipping plane (from Schwartz et al., 1989).

6 Practical consideration in earthquake locations

This section is intended to give some practical hints on earthquake location. The section does not refer to any particular location program, but most of the parameters discussed can be used with the Hypocenter program (Lienert and Havskov, 1995) or with HYPOSAT (Schweitzer, 2001a).

6.1 Phases

The most unambiguous phase to pick is usually P and P is the main phase used in most teleseismic locations. For local earthquakes, usually S phases are also used. Using phases with different velocities and slowness has the effect of better constraining the distances and there is then less trade-off between depth and origin time or epicenter location and origin time if the epicenter is outside the network. The focal depth is best controlled (with no trade-off between depth and origin time) when phases are included in the location procedure which have a different sign of the partial derivative $\partial T/\partial z$ in Equation (13) such as for very locally observed direct up-going Pg (positive) and Pn (negative) (see section 6.3 Hypocentral depth and Figure 9). In general, it is thus an advantage to use as many different phases as possible under the assumption that they are correctly identified. Recently Schöffel and Das (1999) gave a striking example (see Figure 7). But one very wrong phase can throw off an otherwise well constrained solution. This highlights the crucial importance of the capability of the observatory personnel to recognize and report such phases during their routine seismogram analysis.

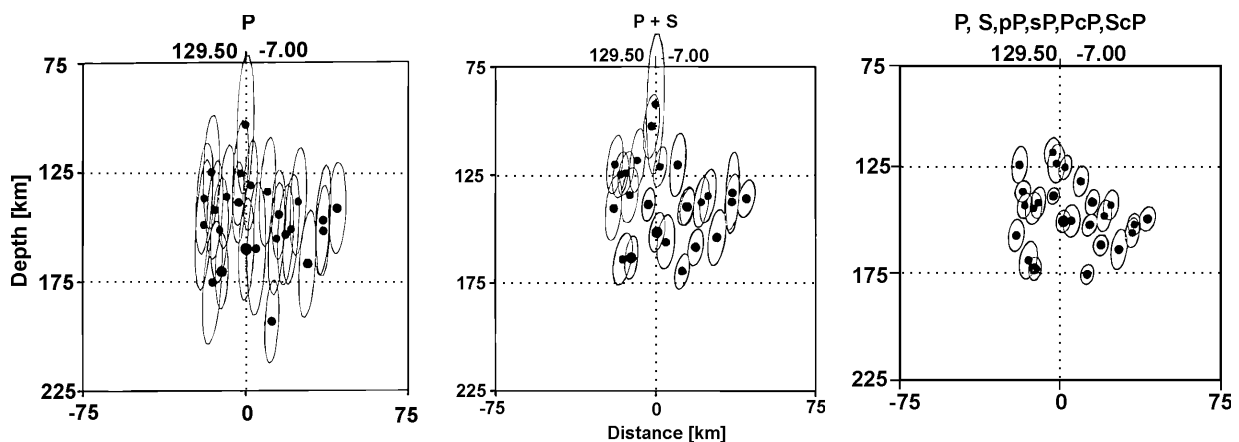


Figure 7 Examples of significant improvement of hypocenter location for teleseismic events by including secondary phases. Left: hypocenter locations using only P phases; middle: by including S phases; right: by including also depth phases and core reflections with a different sign of $\partial T/\partial z$ (modified from Schöffel and Das, *J. Geophys. Res.*, Vol. 104, No. B6, page 13,104, Figure 2; © 1999, by permission of American Geophysical Union).

Engdahl et al. (1998) used the entire ISC database to relocate more than 100,000 seismic events. They used not only a new scheme to associate correctly secondary phases, they also systematically searched for pWP onsets in the case of subduction-zone events to get better depth estimates, and they used a modern global Earth model (AK135) to avoid the known problems with the Jeffreys-Bullen tables. With all these changes the authors reached a far

more consistent distribution (in particular for subduction zones) and sharper picture of global seismicity.

The majority of location programs for local earthquakes use only first arrivals (e.g., HYPO71, Lee and Lahr, 1975). This is good enough for many cases. In some distance ranges, Pn is the first arrival, and it usually has small amplitudes. This means that the corresponding Sn phase, which is then automatically used by the program, might have also very small amplitudes and is not recognized, while actually the phase read is Sg or Lg instead. Since the program automatically assumes a first arrival, a wrong travel-time curve is used for the observed phase, resulting in a systematic location error. This error is amplified by the fact that the S phase, due to its low velocity, has a larger influence on the location than the P phase. It is therefore important to use location programs where all crustal phases can be specified.

Schweitzer (2001a) developed an enhanced routine to locate both local/regional and teleseismic events, called HYPOSAT. The program runs with global Earth models and user defined horizontally layered local or regional models. It provides the best possible hypocenter estimates of seismic sources by using travel-time differences between the various observed phases besides the usual input parameters such as arrival times of first and later onsets (complemented by backazimuth and ray parameters in the case of array data or polarization analyses). If S observations are also available, preliminary origin times are estimated by using the Wadati approach (see Figure 3) and a starting epicenter with a priori uncertainties by calculating the intersection of all backazimuth observations. By relocating events with real data Schweitzer could show that HYPOSAT solutions have the smallest errors when, besides the absolute onset times the travel-time differences of all available primary and secondary phase readings are also taken into account. The most advanced version of HYPOSAT can be found at <ftp://ftp.norsar.no/pub/outgoing/johannes/hyposat/> and a program description is given in PD 11.1.

6.2 Starting location

Iterative location programs commonly start at a point near the station recording the first arrival. This is good enough for most cases, particularly when the station coverage is good and the epicenter is near or within the network. However, this can also lead to problems when using least squares techniques, which converge slowly or sometimes not at all for events outside the limits of a regional network (Buland, 1976). Another possibility is that the solution converges to a local minimum, which might be far from the correct solution. For small-elongated networks, two potential solutions may exist at equal distances from the long axis. A starting location close to the first arrival station can then bias the final solution to the corresponding side of such a network. Although this bias usually is on the correct side, any systematic error in the first-arrival station's time can have a disproportionately strong effect on the final location. Thus in many cases, it is desirable to use a better start location than the nearest station. There are several possibilities:

- a) in many cases the analyst knows by experience the approximate location and can then manually give a start location; most programs have this option;
- b) similar phases at different stations can be used to determine the apparent velocity and backazimuth of a plane wave using linear regression on the arrival times with respect to the horizontal station coordinates. With the apparent velocity and/or S-P times, an

- estimate of the start location can be made. This method is particularly useful when locating events far away from the network (regionally or globally);
- Backazimuth information is frequently available from 3-component stations or seismic arrays and can be used as under b;
 - if backazimuth observations are available from different stations, a starting epicenter can be determined by calculating the intersection of all backazimuth observations;
 - S-P and the circle method can be used with pairs of stations to get an initial location;
 - the Wadati approach can be used to determine a starting source time.

The starting depth is usually a fixed parameter and set to the most likely depth for the region. For local earthquakes usually the depth range 10-20 km is used, while for distant events, the starting depth is often set to 33 km. If depth phases, e.g., pP are available for distant events, these phases can be used to set or fix the depth (see next section).

6.3 Hypocentral depth

The hypocentral depth is the most difficult parameter to determine due to the fact that the travel-time derivative with respect to depth changes very slowly as function of depth (see Figure 8) unless the station is very close to the epicenter. In other words, the depth can be moved up and down without changing the travel time much. Figure 8 shows a shallow (ray 1) and a deeper event (ray 2). It is clear that the travel-time derivative with respect to depth is nearly zero for ray 1 but not for ray 2. In this example, it would thus be possible to get an accurate depth estimate for the deeper event but not for the shallower one. Unfortunately, at larger distances from the source, most rays are more like ray 1 than ray 2 and locations are therefore often made with a fixed ‘normal’ start depth. Only after a reliable epicenter is obtained will the program try to iterate for the depth. Another possibility is to locate the event with several starting depths and then use the depth that gives the best fit to the data. Although one depth will give a best fit to all data, the depth estimate might still be very uncertain and the error estimate must be checked.

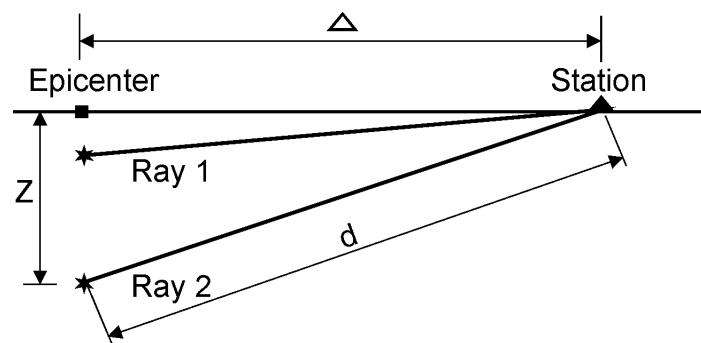


Figure 8 The depth – distance trade off in the determination of focal depth.

For teleseismic events, the best way to improve the depth determination is to include readings from the so-called depth phases (e.g., Gutenberg and Richter, 1936b and 1937; Engdahl et al., 1998) such as pP, pwP (reflection from the ocean free surface), sP, sS or similar but also reflections from the Earth's core like PcP, ScP or ScS (see Figure 7). The travel-time differences (i.e., depth phase-direct phase) as pP-P, sP-P, sS-S and pS-S are quite constant over a large range of epicentral distances for a given depth so that the depth can be

determined nearly independently of the epicenter distance. Another way of getting a reliable depth estimate for teleseismic locations is to have both near and far stations available. In particular, event observations from local and regional stations together with PKP observations have been used together for this purpose. However, this is unfortunately not possible for many source regions.

For local events, a rule of thumb is that at least several near stations should not be further away than 2 times the depth in order to get a reliable estimate (Figure 8). This is very often not possible, particularly for regional events. At a distance of more than $2 \times \text{depth}$, the depth depending partial derivative changes very little with depth if the first arriving phase is the more or less horizontally propagating Pg. But at distances where the critically refracted (so-called head-waves) Pb or Pn arrive, there is again some sensitivity to depth due to the steeply down going rays of Pb or Pn (Figure 9) and because of the different sign of the partial derivatives of their travel times with depth, which is negative, as compared to Pg, which is positive. So, if stations are available at distances with both direct and refracted rays as first arrivals, reasonably reliable solutions might be obtained. An even better solution is when both Pg and Pn are available at the same station and the location capability could be similar to using P and pP for teleseismic events. The problem is that it might be difficult to identify correctly secondary P phases and a wrong identification might make matters worse.

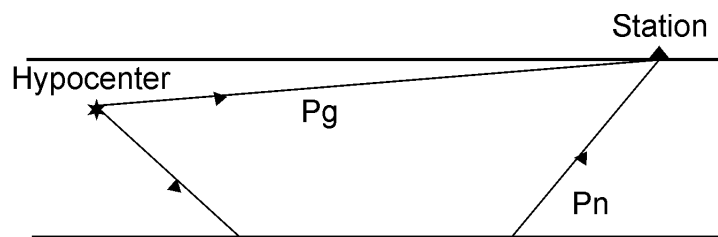


Figure 9 Example of both Pg and Pn rays in the a single layer crustal model.

The depth estimate using a layered crustal model remains problematic even with a mix of phases. In checking catalogs with local earthquakes, it will often be noted that there is a clustering of hypocenters at layer boundaries. This is caused by the discontinuities in the travel-time curves of the direct phase Pg as a function of depth at layer boundaries (see Figure 10 for an example). The Pg travel time suddenly decreases when the hypocenter crosses a boundary (here Moho) since a larger part of the ray suddenly is in a higher velocity layer, while the Pn travel time continuously decreases as the depth increases as long as the event is still within the crust. This gives rise to the discontinuities in the Pg-Pn travel-time curve. So one Pn-Pg travel-time difference is not enough to ensure a reliable depth estimate, several such phase arrivals must be available.

Many location programs give the RMS of the travel-time residuals in a grid around the calculated hypocenter. In addition to the error estimates, this gives an idea about the accuracy and thus a local minimum might be found. A more direct way of estimating the quality of the depth estimate is to calculate the RMS as a function of depth in order to check if a local minimum has been reached. This is particularly relevant for crustal earthquakes at shallow depth and can also be used as a complementary tool for discriminating better between quarry blasts and earthquakes.

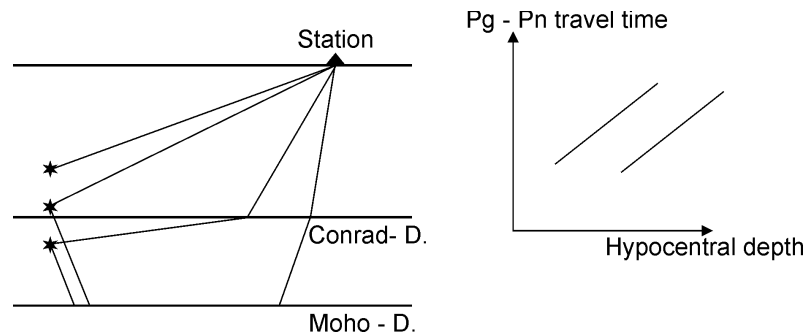


Figure 10 Ray paths of Pg and Pn phases in a two-layer crustal model (left). On the right side the travel-time curve of Pg-Pn as a function of depth is sketched.

Even when several Pg and Pn phases are available, depth estimates still remain a problem at regional distances due to the uncertainty in the crustal models. Since the depth estimates are critically dependent on the accurate calculation of Pg and Pn travel times, small uncertainties in the model can quickly throw off the depth estimate.

6.4 Outliers and weighting schemes

The largest residuals have a disproportionately large influence on the fit of the arrival times due to the commonly used least squares fit. Most location programs will have some kind of residual weighting scheme in which observations with large residuals are given lower or even no weight. Bisquare weighting is often used for teleseismic events (Anderson, 1982). The residual weighting works very well if the residuals are not extreme since the residual weighting can only be used after a few iterations when the residuals are already close to the final ones. Individual large residuals can often lead to completely wrong solutions, even when 90% of the data are good; residual weighting will not help in these cases. Some programs will try to scan the data for gross errors (like minute errors) before starting the iterative procedure. If an event has large residuals, try to look for obvious outliers. A Wadati diagram can often help in spotting bad readings for local earthquakes (see Figure 3).

The arrival-time observations by default will always have different weights in the inversion. A simple case is that S waves may have larger weights than P waves due to their lower velocities. An extreme case is the T wave (a guided wave in the ocean), which with its low velocity (1.5 km/s) can completely dominate the solution. Considering that the accuracy of the picks is probably best for the P waves, it should be natural that P arrivals have more importance than S arrivals in the location. However, the default parameter setting in most location programs is to leave the original weights unless the user actively changes them. It is normally possible to give *a priori* for all S phases a lower weight and in addition, all phases can be given individual weights, including being totally weighted out.

When working with local earthquakes, the nearest stations will usually provide the most accurate information due to the clarity of the phases. In addition, uncertainty in the local model has less influence on the results at short distances than at large distances; this is particularly true for the depth estimate. It is therefore desirable to put more weight on data from near stations than on those from distant stations and this is usually done by using a distance weighting function of

$$w_d = \frac{x_{far} - \Delta}{x_{far} - x_{near}}, \quad (24)$$

where Δ is the epicentral distance, x_{near} is the distance to which full weight is used and x_{far} is the distance where the weight is set to zero (or reduced). The constants x_{near} and x_{far} are adjusted to fit the size of the network; x_{near} should be about the diameter of the network, and x_{far} about twice x_{near} . For a dense network, x_{near} and x_{far} might be made even smaller for more accurate solutions.

6.5 Ellipticity of the Earth

Until now we only assumed that the model used for calculating distances or travel times is either a flat model for local or regional events or a standard spherical model of the Earth for teleseismic events. However, the Earth is neither a sphere nor a flat disk but an ellipsoid symmetrical to its rotation axis. It was Gutenberg and Richter (1933) who first pointed out that the difference between a sphere and an ellipsoid must be taken into account when calculating epicentral distances and consequently also the travel times of seismic phases. Therefore, they proposed the usage of geocentric coordinates instead of geographic coordinates to calculate distances and angles on the Earth. Because of the axially symmetrical figure of the Earth, the geocentric longitude is identical to the geographic longitude. To convert a geographic latitude lat_g into a geocentric latitude lat_c one can use the following formula:

$$lat_c = \arctan((1 - (6378.136 - 6356.751)/6378.136)^2 * \tan lat_g). \quad (25)$$

With this formula all station latitudes have to be converted before an event location and after the inversion, the resulting geocentric event latitude has to be converted back by applying the inverse equation

$$lat_g = \arctan(\tan lat_c / (1 - (6378.136 - 6356.751)/6378.136)^2). \quad (26)$$

With this procedure all angle calculations related to an event location are done for a sphere. The calculated distances are measured in degrees and to convert them into km, one has to use the local Earth radius R_{loc} :

$$R_{loc} = \sqrt{(6378.136 * \cos lat_c)^2 + (6356.751 * \sin lat_c)^2}. \quad (27)$$

This value has then to be applied for converting a distance D measured in degrees into a distance measured in km, or vice versa:

$$D[km] = \frac{2\pi * R_{loc}}{360} * D[deg] \quad \text{or} \quad D[deg] = \frac{360}{2\pi * R_{loc}} * D[km] \quad (28)$$

All standard Earth models are spherically symmetrical Earth with a mean radius of 6371 km. Therefore the standard tables also contain travel times calculated for a sphere. Bullen (1937, 1938, 1939) was the first to calculate latitude-depending travel-time corrections (ellipticity corrections) to be used together with travel-time tables for a spherical Earth. Later work on

this topic was done by Dziewonski and Gilbert (1976) and Dornboos (1988b). Kennett and Gudmundsson (1996) published the most recent set of ellipticity corrections for a large number of seismic phases.

In conclusion: to get the theoretical travel time for an event in teleseismic or regional distance, one has first to calculate the geocentric epicentral distance, then use travel-time tables as calculated for a spherical Earth model, and finally apply the latitude (event and station!) dependent ellipticity correction. Most location routines automatically apply the described methods and formulas but it is important to check this in detail and eventually to change a location program.

6.6 Importance of the model

In this context the importance of the model assumptions underlying the location procedure has to be emphasized. Many studies have shown (e.g., Kissling, 1988) that accuracy of locating hypocenters can be improved by using a well-constrained minimum 1-D velocity model with station corrections and is better than using a regional 1-D model. However, Spallarossa et al. (2001) recently showed that in strongly heterogeneous local areas even a 1-D model with station corrections does not significantly improve the accuracy of the location parameters. High-precision location in such cases can be achieved only by using a 3-D model. This is particularly true for locating earthquakes in volcanic areas (see Lomax et al., 2001).

Smith and Ekström (1996) investigated the improvement of teleseismic event locations by using a recent three-dimensional three-dimensional Earth model. They came to the conclusion that it "... offers improvement in event locations over all three 1-D models with, or without, station corrections." For the explosion events, the average mislocation distance is reduced by approximately 40 %; for the earthquakes, the improvements are smaller. Corrections for crustal thickness beneath source and receiver are found to be of similar magnitude to the mantle corrections, but use of station corrections together with the 3-D mantle model provide the best locations. Also Chen and Willemann (2001) carried out a global test of seismic event locations using 3-D Earth models. Although a tighter clustering of earthquakes in subduction zones was achieved by using a 3-D model rather than using depth from the ISC Bulletin based on 1-D model calculations, they concluded that the clustering was not as tight as for depths computed by Engdahl et al. (1998) who used depth phases as well as direct phases. Thus, even using the best available global 3-D models can not compensate for the non-use of depth phases and core reflections in teleseismic hypocenter location (see Figure 7).

A case example for improved location of local events is given in Figures 11 and 12. The upper panel in Figure 11 shows the initial epicenter locations of aftershocks of the Cariaco earthquake ($M_s = 6.8$) on July 9, 1997 in NE Venezuela based on an averaged 1-D crustal velocity model. The mean location error (i.e., the calculated precision with respect to the assumed model) was about 900 m. On average, the aftershocks occurred about 2 to 3 km north of the surface fault trace. A detailed tomographic study revealed lateral velocity contrasts of up to 20 % with higher velocities towards the north of the El Pilar fault. Relocating the events with the 3-D velocity the epicenters were systematically shifted southward by about 2 km and now their majority aligns rather well with fault traces mapped before the earthquake as well as with newly ruptured fault traces. Also in the cross sections the data scatter was clearly reduced so that closely spaced outcropping surface faults could be traced down to a depth of more than 10 km. These results point to the fact that in the presence

of lateral velocity inhomogeneities epicenter locations are systematically displaced in the direction of higher velocities. We will look into this problem more closely in section 7.

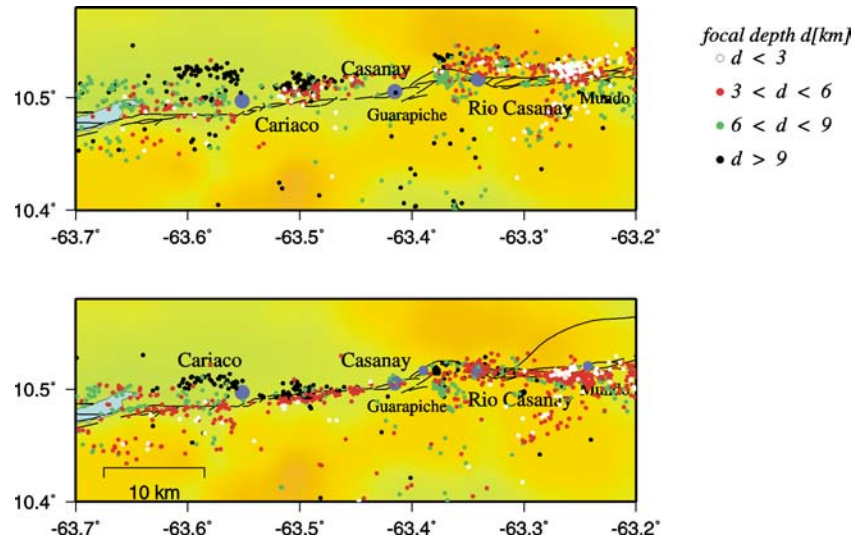


Figure 11 Epicentral distribution of aftershocks of the Cariaco earthquake ($M_s=6.8$) on July 9, 1997 in NE Venezuela. Top: results from HYPO71 based on a one-dimensional velocity-depth distribution. Bottom: Relocation of the aftershocks on the basis of a 3-D model derived from a tomographic study of the aftershock region (courtesy of M. Baumbach, H. Grosser and A. Rietbrock).

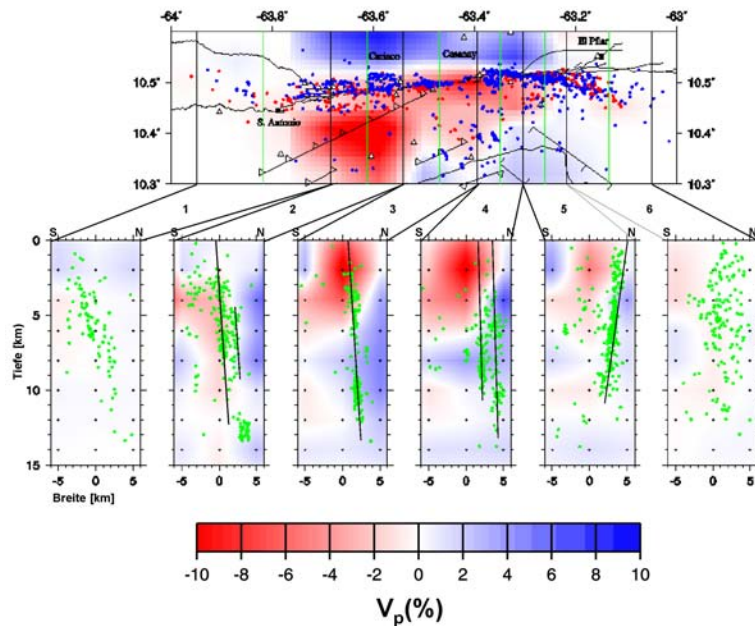


Figure 12 3-D distribution of the P-wave velocity in the focal region of the 1997 Cariaco earthquake as derived from a tomographic study. The horizontal section shows the velocity distribution in the layer between 2 km and 4 km depth. Red and blue dots mark the epicenters of the aftershocks. The red ones were chosen because of their suitability for the tomography. The six vertical cross sections show the depths' distribution of the aftershocks (green dots) together with the deviations of the P-wave velocity from the average reference model. The depth range and the lateral changes of fault dip are obvious (courtesy of M. Baumbach, H. Grosser and A. Rietbrock).

7 Internal and external (real) accuracy of locations

For decades the international data centers have located earthquakes world-wide by means of the 1-D Jeffreys and Bullen (1940, 1948, 1958, 1967, and 1970) travel-time tables without external control of the accuracy of such solutions by independently checking them with similarly strong events of exactly known position and origin time. Therefore, the question has remained open for a long time as to whether these calculated location errors were real or just the minimized average errors for the best fitting solutions to the observed data based on model assumptions with respect to the validity of the velocity model, the non-correlation of the various parameters to be determined and the Gaussian distribution of both the model errors and the data reading errors. If the latter is the case then the calculated errors are no measure of the real accuracy of the calculated location and origin time but rather a measure of the internal precision of fitting the data to the model assumptions.

In order to investigate this in more detail, Bormann (1972a and b) looked into the travel-time errors reported by the international data centers for the German seismological observatory Moxa (MOX) for earthquakes in different regions of the world. As an example, he got for the same data set of events from the Kurile Islands the mean residual $\bar{\delta t}_p = + 0.16$ s and a standard deviation $\sigma = \pm 0.65$ s when referring the MOX onset-time readings to the locations published by the U.S. Coastal and Geodetic Survey (USCGS, World Data Center A, WDC A) and $\bar{\delta t}_p = + 0.35$ s with $\sigma = \pm 1.1$ s when referring to the locations published by the Academy of Sciences of the Soviet Union (ANUSSR, World Data Center B, WDC B) which used the same J-B travel-time model as USCGS. Thus, the travel-time (or onset-time reading) errors calculated by the data centers for seismic stations are not real errors of these stations or their readings but depend on the number and distribution of stations used by these centers in their location procedure. And these were rather different for WDC A and WDC B. While the USCGS used the data of a worldwide station network, ANUSSR based its locations on the station network of the former Soviet Union and East European countries and these “looked at” events outside Eurasia from a much narrower azimuth and distance range. But this is equivalent to the discussion related to Figure 4. The mean residuals calculated by these two centers for the considered region were not significantly different and not far from zero. Therefore, the question remained as to whether there were systematic biases in these solutions and if so, of what kind and how big.

From the 1960s onwards testing of strong underground nuclear explosions (UNE) provided for the first time independent strong sources with precisely known coordinates and origin time to allow checking the accuracy of calculated seismic source locations from global seismic observations. During recent years such information has been released for many UNEs. However, for the LONGSHOT explosion on the Amchitka Islands, Aleutians, the source parameters were known for many years. For this event the residual of MOX was $\delta t_p = -4.6$ s. This contrasted sharply with calculated residuals for the Aleutian earthquakes. From 53 analyzed earthquakes in that region, no negative residual at MOX was larger than -0.8 s! Interestingly, the USGS had calculated for LONGSHOT a location 25 km NW of the true place (which explains -1 s travel-time error at MOX) and an origin time which was 3.5 s earlier than the real one (which accounts for the remaining -3.5 s) (Sykes, 1966). The too early source time is a well-understood artifact of the Jeffreys-Bullen tables, which generally give too long P-wave travel times. According to Fedotov and Slavina (1968) epicenters calculated by the WDC B from events in the Aleutians are generally displaced towards NW with respect to those of the WDC A. Consequently, with the same systematic tendency of shift, they deviate still more from the true locations of events in that area.

The ISC waits for about two years before running its final earthquake location procedure. This allows to collect as many seismogram readings as possible from worldwide distributed seismological observatories and thus assures the best geographic coverage for each seismic event.

What is the reason for this systematic mislocation, which usually remains unrecognized unless one locates strong independently controlled sources of exactly known source parameters and origin time? Figure 13 shows some hypothetical earthquakes at different depth on a vertically dipping fault. It separates two half-spaces with different wave propagation velocity $v_2 > v_1$. This is a realistic model for parts of the San Andreas Fault. The lateral velocity difference across the fault may be as large as 5 to 7 %. S1 and S2 may be two stations at the same hypocentral distances from the events. But because of $v_2 > v_1$ the onset time t_2 at S2 is earlier (travel-time shorter) than for t_1 at S1. Running the location procedure with the common residual minimization on the assumption of a laterally homogeneous velocity model will result in hypocentral distances $d_2(h) < d_1(h)$. Since the difference increases with depth, the hypocenters are not only offset from the real fault but seem to mark even a slightly inclined fault, which is not the case.

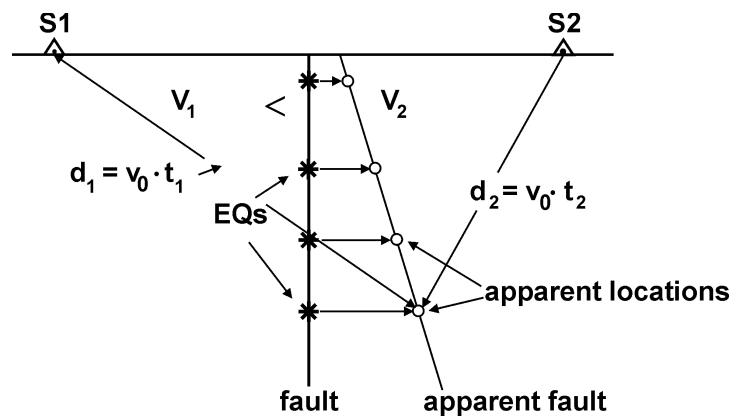


Figure 13 Illustration of the systematic mislocation of earthquakes along a fault with strong lateral velocity contrast. v_0 is the assumed model velocity with $v_2 > v_0 > v_1$.

From this hypothetical example we learn that locations based on 1-D velocity models in the presence of 2-D or 3-D velocity inhomogeneities will be systematically shifted in the direction of increasing velocities (or velocity gradients), the more so, the less the station distribution controls the event from all azimuths. This is precisely the cause for the above mentioned larger systematic mislocation of WDC B as compared to WDC A. While the latter localizes events using data from a global network, the former used solely data from the former Soviet and East European territory, i.e., stations which view the Aleutian Islands from only a narrow azimuth range. The direction of systematic mislocation of both centers to the NW agrees with the NW directed subduction of the Pacific plate underneath the Aleutians. According to Jacob (1972) this cold lithospheric plate has 7 to 10% higher P-wave velocities than the surrounding mantle. A recent study by Lienert (1997) also addresses this problem of assessing the reliability of earthquake locations by using known nuclear tests. The Prototype International Data Center (PIDC) in Arlington separated in its Reviewed Event Bulletins (REBs) the *a priori* location errors as measurement and modeling errors. The latter specify, as a function of distance for each type of seismic phases, the uncertainties in the model when representing the real Earth (see IS 10.3).

Acknowledgments

Some of the preceding text has followed a similar description in Shearer (1999). Some figures and ideas have also been taken from Stein (1991), Lay and Wallace (1995), Schöffel and Das (1999). Thanks go to M. Baumbach, H. Grosser and A. Rietbrock for making Figures 11 and 12 available and to R. E. Engdahl for critical proof reading and valuable suggestions which helped to improve the text and to complement the references.

References (see References under Miscellaneous in Volume 2)

Topic	Reports and bulletins
Author	Gernot Hartmann, Bundesanstalt für Geowissenschaften und Rohstoffe, Stilleweg 2, 30655 Hannover, Phone: +49 (511) 643 3227, E-mail: g.hartmann@bgr.de
Version	October, 2001

1 General information

The results of seismogram analyses are published in reports, event lists, bulletins and data catalogues (called "products"), which are the basis of data exchange between seismological institutions, data centers and for informing the public. The parameter data, primarily source and/or phase parameter values, should be stored in a digital database and presented in a clear and uniform manner. The predefinition of an appropriate format depends on the requirements for the major usage of the product, for example whether a product is intended for further applications on a computer or for human readability. A description of the individual used format should be given as a reference or directly attached to the product.

The products contain source and/or phase parameters. Products which include source parameters represent the seismicity within a given time period for a pre-defined area and above a reliable magnitude threshold. These limitations have to be taken into account, in order to provide a high quality product which claims to be of a high degree of completeness and accuracy.

Comprehensive products based on networks of stations distributed world-wide are published by the World Data Centre for Seismology (WDC) (operated by NEIC, Golden, Colorado, USA) (<http://neic.usgs.gov>), the International Seismological Centre (ISC) (Newbury, England) (<http://www.isc.ac.uk>), and the International Data Centre of the Comprehensive Nuclear-Test-Ban Treaty Organisation (Vienna, Austria) (<http://www.ctbto.org>). The precision of these products is $0.001^\circ < \Delta D < 1^\circ$.

In general, the products of national data centers and observatories provide data for events within an area that is well covered by the station network used for the data analysis. How complete these products are depends on the spacing between the stations, which has a major influence on the magnitude threshold. An example of such products is given by the German local bulletin at the following internet addresses: <http://www.szgrf.bgr.de/bulletins.html> and http://www.seismologie.bgr.de/catalog/catalogue_ger.html. The precision of this product is $0.001^\circ < \Delta D < 0.1^\circ$.

Publication of teleseismic epicenter data from a regional network is useful only if the precision of the data is known or reliable calibration values for the correction of systematic location errors are available. Such a calibration for the GRF array/GRSN is used by the SZGRF for determinations of epicenters world-wide in its teleseismic bulletin (<http://www.szgrf.bgr.de/bulletins.html>). The precision in the distance range $D = 13^\circ - 100^\circ$ is $\Delta D < \pm 3^\circ$.

However, if only phase parameters are available, it is also important for these to be reported to the international data centers, because these values are indispensable to improvement in the accuracy and comprehensiveness of their products. ISC, for example, compiles a data catalog

based on reported phase parameter values received from a number of observatories (<http://www.isc.ac.uk/collection.html>).

The information provided by a product also depends on how long after the event the product is to be published. For example:

2 Fast determination of epicenters of strong earthquakes

Information is provided for a single event immediately after it is detected and recognised as a strong earthquake or an earthquake which could cause substantial damage. The parameter values are obtained by automatic processing or manual analysis. They are published within minutes or hours after the event and are distributed mainly by e-mail or made available on the WWW. WDC publishes an event list with about 20 recent earthquakes, which is updated immediately after each new major event is determined (<http://neic.usgs.gov/neis/bulletin/bulletin.html>). This information is also available with the 'finger'-command: >finger quake@gldfs.cr.usgs.gov. For local and/or regional purposes in Central Europe, fast epicenter determinations are also provided by the European Mediterranean Seismological Centre (EMSC) (http://www.emsc-csem.org/Html/ALERT_main.html) and the “Schweizerischer Erdbebendienst” (SED) (<http://seismo.ethz.ch/>).

3 Preliminary products

Information is provided for all routinely analysed events at regular time intervals, typically daily, weekly or monthly. This information may be subject to modification if phase readings from additional stations or arrival times of later phases are identified at a later stage of the analysis. NEIC publishes, for example, their preliminary products on a daily basis (<ftp://ghftp.cr.usgs.gov/pub/weekly/qedevents.txt>). Events within 7 days of real time are still being revised and republished as new data are received from contributing observatories. The SZGRF produces a preliminary event list of local, regional and world-wide seismic events with a time delay of 1 – 3 days. It is published on the WWW (<http://www.szgrf.bgr.de/seisevents.html>). Revised German products are the monthly distributed German local bulletin and the regional and teleseismic bulletin (<http://www.szgrf.bgr.de/bulletins.html>). All German products are based on the GRF array, GRSN, GEOFON and, for local events, on local station data.

4 Final products

The most complete and precise data on seismic events is published when all of the available data has been analysed. These products are published up to several years after the events. ISC, for example, distributes their final products (<http://www.isc.ac.uk/Products/>) on compact disc. These products are used for scientific studies at universities and research facilities. As a local example, in Germany, the “Data Catalogue of Earthquakes in Germany and Adjacent Areas” is published by the “Bundesanstalt für Geowissenschaften und Rohstoffe” (BGR).

Additional references

USGS/NEIC, <http://neic.usgs.gov/neis/bulletin/bulletin.html>
ORFEUS software library, <http://orfeus.knmi.nl/>

Topic	Animation of seismic ray propagation and seismogram formation
Authors	Siegfried Wendt, Geophysical Observatory Collm, University of Leipzig, 04779 Wermsdorf, Germany; E-mail: wendt@rz.uni-leipzig.de Ute Starke, Computer Center, University of Leipzig, Augustusplatz 10-11, 04109 Leipzig; E-mail: starke@rz.uni-leipzig.de Peter Bormann (formerly GeoForschungsZentrum Potsdam, Telegrafenberg, 14473 Potsdam, Germany); E-mail: pb65@gmx.net
Version	October, 2002

1 Introduction

Volume 2 of the NMSOP is accompanied by a CD-ROM which contains, besides the pdf file of the whole Manual, a directory “Filme_uniLeipzig”. This directory comprises 9 movie files with animations of seismic ray propagation and the formation of seismic recordings in the distance range from 0.1° to 167° . These animations complement the illustrations provided in the Manual Chapters 2 and 11. IS 11.3 gives the necessary background information for proper handling of the CD-ROM and understanding of the record examples presented in the animations. More examples are in preparation and can be consulted by logging into the website of the digital library of the University of Leipzig (<http://www.leilib.dl.uni-leipzig.de>).

The development of such movies began at the University of Leipzig more than 10 years ago. Dr. Bernd Tittel of the University’s Geophysical Observatory Collm is an expert in identifying late and very late core phases. Therefore, the idea was born to produce an animation of the propagation of the seismic rays for such very late phases through a simple standard 1-D Earth model. The related seismic recordings of station Collm (CLL) were later added as standing pictures at the end of the movie. Several years ago one of us (S. Wendt) revived these earlier efforts by extending these animations to crustal, mantle and core phases in the local, regional and teleseismic distance range and to the “writing” of the records at several seismic stations at once, in the sequence as the rays arrive.

All ray paths and travel-time curves are calculated with the program TauP of H.P.Crotwell (1998) on the basis of the IASP91 Earth model (Kennett and Engdahl, 1991).

2 Software requirements and handling

The animations run on a Windows-PC with QuickTime Player 4 or 5, which can be downloaded from www.apple.com. After the installation of QuickTime Player start the program by opening the files on the CD-ROM you wish to see via the ikon “Filme_uniLeipzig”. Then the cover page of the respective movie file appears in a frame. You can start the movie by pressing the start-button in the middle of the lower frame ridge. Is the button not visible then you have to reduce the frame size slightly. This is possible in the QuickTimePlayer menue line which appears above the movie cover frame. There click “Movie” and then “Display Size” in order to adopt the movie frame to the size of your screen and then start the movie.

If lines, letters and numbers in the movie appear broken or blurred, the screen resolution has to be increased before starting QuickTime. Tab “Start” in the desktop area, then “Settings”, and then “Display” on the appearing “Control Panel”. When “Display Properties” appears tab “Settings” and there you may change the pixel number in the desktop area. Usually, a resolution of 1280x1024 pixels should be sufficient to resolve all details. Then return to the desk top and start the movie, either by pressing the ikon “QuickTime Player” or by directly loading the files from the disk drive via “My Computer”.

3 General structure and contents of the movies

Each movie file shows first a cover page in the start-frame, which gives the data, origin time, source co-ordinates and name of the source region of the earthquake. After starting the movie you will see, for all teleseismic earthquakes, the propagation of seismic rays of different phases, coded in different color, through a simplified cross section of the Earth. Shown are only those rays which will reach stations of the German Regional Seismic Network (GRSN). As soon as the different rays arrive at these stations, the onsets and associated waveforms will be “written” according to the original seismograms recorded at these stations from the considered earthquake. The response filters used for these records are given in the record frames, the station codes and the epicentral distances to the stations at the ordinates and the travel times are marked at the abscissa of the recording frame. For all depicted phases, the theoretical travel-time curves according to the IASP91 Earth and travel-time model are also inserted into these record frames.

An exception are the two local earthquake recordings. Here the propagation of the Pg and Sg wavefronts and the formation of the related records at stations of the GRSN in different azimuths from the source are shown in a map projection; and in one of these movies also the formation of the local travel-time curves is depicted.

4 Movie files and peculiarities of the recordings shown

Below the following information is given for each animation:

- file name;
- geographical region of epicenter;
- source parameters date, origin time OT, co-ordinates, source depth h;
- magnitude and data center which has provided these source data;
- storage requirement for this animation in megabyte (MB);
- interval of epicentral distances D of the used recording stations;
- remarks about the depicted seismic phases and recording frames;
- complementary remarks about the peculiarities of the records shown.

For the definition of seismic phase names and complementary ray diagrams see IS 2.1. The response characteristics of the standard seismographs of type Kirnos SKD, SRO-LP, WWSSN-SP and WWSSN-LP are shown in 11.3.2 together with complementary record examples.

File 1: Wendt_Vogtland_20000917_QT2.movNW- Bohemia, Czech Republic, Novy Kostel

17.09.2000 OT=15:14:33.5 50.22N 12.47E h=10km Ml=3.1 (SZGRF)

23.0 MB

D=10–130km

Pg and Sg

Left: propagating wave fronts of Pg (blue) and Sg (red); **right:** records of some stations of the GRSN. Traces are sorted according to distance. At the moment of wave-front arrival at a station the onset and related waveform of this arrival is written in the record of the seismic station.

Note that the depicted travel-time curves for an average 1-D local crustal model match well with the onsets at the stations WERN, MOX and CLL but the onsets recorded at the stations GFRO and WET are about 2 to 4 s later than the onset times expected according to this model. This illustrates the need for improved local travel-time curves which may also be azimuth-dependent.

File 2: Wendt_Vogtland_20000904_QT.movNW-Bohemia, Czech Republic, Novy Kostel

04.09.2000 OT=00:31:45.2 50.21N;12.44E h=10km Ml=3.2 (BGR)

28.3 MB

D = 10–240km

Phases: Pg and Sg

Left: developing records at several GRSN-stations; **right:** propagating wave fronts of Pg (blue) and Sg (red).

When a wave front arrives at a station the respective onset and original waveform recorded at this station is written in the seismogram. The amplitude ratio Pg/Sg strongly varies with azimuth due to the different source radiation pattern for P and S waves with respect to the station azimuth (see Figs. 3.25 and 3.26).

File 3: Wendt_Hindukush_2_19940630_.movAfghanistan-Tajikistan border region

30.06.1994 OT=09:23:21.4 36.3N;71.1E h=227km mb=6.1 (NEIC)

54.0 MB

D=43° - 47°

Phases: P, pP, sP, PcP, PP, pPP, PPP, sPP, ScP

Strong phases P, sP and sPP on KIRNOS displacement BB Z-component records (top traces) of a deep Hindukush earthquake, whereas the reflections at the core-mantle boundary PcP and ScP are more clear in WWSSN-SP-filtered traces (bottom traces). The travel-time curves of PcP and PP intersect near 43° epicentral distance. This overlap distance is depth-dependent. Also note the simple impulsive P-wave onset from this deep source as well as the different amplitudes of the depths phases pP and pPP on the one hand and the much stronger depth phases sP and sPP on the other hand. This is due to the different P- and S-wave radiation pattern in the direction of the short up-going rays p and s, respectively (see Fig. 2.43). Stations situated in another azimuth from the same source may observe a different amplitude ratio of these depth phases.

File 4: Wendt_India_20010126_QT.movW- India

26.01.2001 OT=03:16:40.7 23.3N;70.3E h=22km Ms=7.9 (NEIC)

63.5 MB

D=51.5°-55.5°

Phases: P, PP, S, ScS, SS, PKPPKpdf, and PKKKKP (P4KP)

Top: vertical (Z) component records; and middle: transverse (T) component records; both SRO-LP filtered; **bottom:** zoomed windows with Z-component short-period filtered records (4th order band-pass, 0.5 – 1.7 Hz) of the multiple reflected core phases PKPPKpdf (P'P') and PKKKKP (P4KP), which have travel times of more than 39 min and 46 min, respectively. Note that PKPPKP arrives from the opposite azimuth as compared to the direct P wave and has a negative slowness (i.e., the travel-time to stations at larger D is shorter).

File 5: Wendt_Russl_China_20020628_Q.movE-Russia-NE-China border region

28.06.2002 OT=17:19:30.2 43.8N;130.7E h=564km Mw=7.3 (NEIC)

90.1 MB

D=68.5°-75.5°

Phases: P, pP, PP, pPP, S, sS, ScS, SS, SSS

Vertical (Z)- and transverse (T)- component records with SRO-LP-simulation. This deep earthquake produced strong body waves with simple waveforms, including clear depth phases and strong, transversely polarized S waves. Surface waves are absent. The clear records of very late core phases PKPPKP, SKPPKP, and SKPPKPPKP in WWSSN-SP filtered records have not been depicted in this animation.

File 6: Wendt_Peru_19950205_QT.movN- Peru

02.05.1995 OT=06:06:05.7 3.8S;76.9W h=97km mb=6.5 (NEIC)

27.8 MB

D=90°-93°

Phases: P, PKKPbc, PKPPKpdf (P'P'df), PKPPKPPKPbc (3P'bc)

Shown are four short record windows, each one minute long, for P and pP as well as the multiple core phases PKKPbc, PKPPKpdf, and PKPPKPPKPbc with their respective depth phases. These late and very late core phases have travel-times of about 30, 38, and 59 min, respectively. Despite their long travel paths through the Earth, these late core phases still have an astonishingly good signal-to-noise ratio at most stations. They may easily be misinterpreted at individual stations as P-wave onsets from other independent events. Note the negative slowness of the phases PKKP and P'P'.

File 7: Wendt_NewBritain19990510_QT.movNew Britain region

10.05.1999 OT=20:33:02.1 5.2S;150.9E h=138km mb=6.5 (NEIC)

25.6 MB

D=122°-126°

Phases: Pdiff, PKPpdf, PP, PPP, PS, PPS, SS, SSS, LQ, LR, 4PKPbc

The rarely observed phase 4PKPbc with a travel time of about 79 min is recorded with good SNR in the WWSSN-SP filtered traces (sampling rate of 20Hz). The projection of its path on the surface is $(2 \times 360 - 124) \text{ deg} = 596 \text{ deg}$. The long-period diffracted P-wave arrival Pdif (old name Pdiff) is well developed and arrives about 3.5 min ahead of PKPdf in the SRO-LP filtered Z-component record (see record window in the lower left corner; sampling rate 1 Hz). The SRO-LP filtered Z-component (top left window) and T-component records (middle left window) show several mantle phases, a sharp onset of Love waves (LQ) in T and the onset of the Rayleigh wave LR in Z. The latter shows clear normal dispersion with rather long-period waves ($T \approx 1 \text{ min}$) and large amplitudes at the beginning whereas shorter periods have much smaller amplitudes due to the intermediate source depth of this earthquake.

File 8: Wendt_Fiji_20001218_QT.mov

Fiji Islands region

18.12.2000 OT=01:19:18.6 21.3S;179.2W h=600km mb=6.4 (NEIC)

35.9 MB

D=147°-152°

Phases: PKPdf, PKPbc, PKPab, PP, PPP, PPS, SS, sSS, sSSS, PKKKKKP (P5KP)

Shown are SRO-LP filtered vertical (Z)- and transverse (T)- component records (upper and middle record window) as well as zoomed record windows in the lower left and middle with WWSSN-SP filtered Z-component records of the beginning (PKP-wave group) and the very late part of the seismogram with the rare phase.

Note the good match of the actual and theoretically expected travel-time onsets according to the IASP91 Earth model for mantle phases in the upper and middle record window. In contrast, this model does not predict well the onsets of the core phases which arrive about 5 to 15 seconds later than expected by this model.

File 9: Wendt_NZ_200108221_QT.mov

East of North Island, New Zealand

21.08.2001 OT=06:52:06.7 37.0S;179.8W h=33km mb=6.5 (NEIC)

52.0 MB

D=160°-167°

Phases: PKPdf, PKPab, PP, PP2, PcPPKP, PPP2, SS, SSSS

The SRO-LP-filtered seismograms of this very distant event show remarkably strong PP2 and PPP2 onsets, which arrived at the stations from the opposite backazimuth over the long ray paths ($360^\circ - D$). On the inserted map of Central Europe, which also shows the position of the stations of the GRSN, the passing of these wave fronts can be watched: The phases PKP, PP, PPP, SS and SSSS approach from the NE whereas the phases PcPPKP, PP2 and PPP2 approach from the SW. Also note that the wave fronts of the first arriving waves with rather small (steep) incidence angles have a very high apparent horizontal speed of wave propagation whereas the wave fronts of the later phases with large (shallow) incidence angles travel much slower through the network of seismic stations. Also note the well developed and very long surface-wave train from this shallow (crustal) earthquake. The surface waves arrive for this very distant earthquake more than one hour after the PKP first arrival.

AC	Alternating Current
ACH method	Aki-Christofferson-Husebye method
ADC	Analog-to-Digital Converter; a device that converts data from analog to digital form (see Chapter 6)
AFTAC	United States Air Force Technical Applications Center (http://www.aftac.gov/)
AH	Ad Hoc format
ANSS	Advanced National Seismic System (USA) (http://www.anss.org/)
APA	Average Peak Amplitude
ARCES	Originally: ARCESS – Arctic Experimental Seismic System; now: Arctic regional seismic array (http://www.norsar.no/NDC/stations/ARC/)
ASL	Albuquerque Seismological Laboratory (http://aslwww.cr.usgs.gov/)
ASP	Analog Signal Preparation
ASTM	American Society for Testing and Materials (http://www.astm.org/)
AutoDRM	Automatic Data Request Manager (http://seismo.ethz.ch/autodrm/)
AZI	Azimuth
AZM	Azimuth
BAZ	Backazimuth
BB	broadband
BDSN	Local format in standard analysis software; in use at individual stations and networks (Chapter 10)
BER	Bit Error Rate
BGR	Federal Institute for Geosciences and Natural Resources (Hannover, Germany) (http://www.bgr.de/)
BP	band pass
BSSA	Bulletin of the Seismological Society of America (http://www.seismosoc.org/publications/bssa.html)
CANDIS	CANadian Digital Seismograph Network
CD-ROM	Compact Disk-Read Only Memory
CDSN	China Digital Seismograph Network
CEB	Calibration Event Bulletin (of the PIDC)
CSEM	Centre Sismologique Euro-Méditerranéen (see EMSC)
CLVD	Compensated Linear Vector Dipole
CMB	Core-Mantle Boundary
CMR	Center for Monitoring Research (USA) (http://www.cmr.com)
CMT	Centroid Moment Tensor
COSMOS	Consortium of Organizations for Strong Motion Observation Systems (http://www.cosmos-eq.org/)
CoP	former IASPEI Commission on Practice
CoSOI	Current IASPEI Commission on Seismological Observations and Interpretation (http://www.iaspei.org/commissions/CSOI.html)
CPU	Central Processing Unit
CRC	Cyclic Redundancy Check
CSS	Center for Seismic Studies (of the IMS)
CSS 3.0	A tabulated CSS waveform format

Acronyms

CTBT	Comprehensive Nuclear-Test-Ban Treaty
CTBTO	Comprehensive Nuclear-Test-Ban Treaty Organization (headquarters in Vienna) (http://www.ctbto.org/)
DAC	Digital-to-Analog Converter; a device which takes a digital value and outputs a voltage which is proportional to the input value
dB	decibel
DBMS	Database Management System
DC	Direct Current
DDL	Data Description Language
DLESE	Digital Libraries for Earth Science Education (USA)
DMC	Data Management Center
DOY	day of the year
DP	Detection Processing
DRM	Data Request Manager
DS	Datasheets (in Volume 2 of the NMSOP)
DSP	Digital Signal Processor (see Chapter 6 and Glossary 6.7)
DVD	Digital Versatile Disc
DWWSSN	Digital World-Wide Standard Seismograph Network
ECOSOC	Economic and Social Council of the United Nations (http://www.un.org/esa/coordination/ecosoc/)
EDM	Electronic Distance Meter
EEFIT	Earthquake Engineering Field Investigation Team (http://www.cen.bris.ac.uk/civil/research/eerc/links/eeffit.htm)
EERI	Earthquake Engineering Research Institute (http://www.eeri.org)
EDUSEIS	EDUcational SEISMological European Network (http://www.eduseis.com)
EMI	Electromagnetic Interference
EMS	Electromagnetic Seismograph
EMS98	European Macroseismic Scale 1998 http://seismohazard.gfz-potsdam.de/projects/ems/index.html
EMSC	European-Mediterranean Seismological Centre (http://www.emsc-csem.org/)
EOS	Earth Observing System (centerpiece of ESE) (http://eosps0.gsfc.nasa.gov/)
EP	Event Processing
EQ	Earthquake
ESC	European Seismological Commission (http://www.esc.bgs.ac.uk/)
ESE	Earth's Science Enterprise (of NASA) (http://www.earth.nasa.gov/)
ESSTF	European Standard Seismic Tape Format
EX	Exercises (in Volume 2 of the NMSOP)
FARM	Technique for data exchange
FBA	Force-Balance Accelerometer
FDSN	Federation of Digital Broad-Band Seismograph Networks (http://www.fdsn.org/)
FEC	Forward Error-Correction
FEMA	Federal Emergency Management Agency (USA) (http://www.fema.gov)
FFT	Fast Fourier Transformation

FINES	Originally: FINESA: Finnish Experimental Seismic Array; later: FINESS – Finnish Experimental Seismic System
FIR	Finite Impulse Response filter (see Chapter 6; Glossary 6.7)
f-k	frequency-wavenumber
FM	Frequency Modulated
FOCMEC	Program for the determination of focal mechanisms (Chapter 3)
PPFIT	Program for the determination of fault-plane solutions (Chapter 3)
FRF	Frequency Response Function
GCF	Guralp Compressed Format
GDSN	Global Digital Seismographic Network (see GSN)
GEOFON	GeoForschungsNetz (of broadband seismographs; run by the GFZ) (http://www.gfz-potsdam.de/geofon/)
GEOSCOPE	French program and station network for global seismological investigations (http://geoscope.ipgp.jussieu.fr/)
GERES	Originally: GERESS - German Experimental Seismic System (http://sdac.hannover.bgr.de/web/sdac/sta_eng/geress.html)
GFZ	GeoForschungsZentrum Potsdam (Germany) (http://www.gfz-potsdam.de/)
GIANT	Graphical Interactive Analysis Network Tool (http://lbutler.geo.uni-potsdam.de/service.htm)
GPS	Global Positioning System (http://www.colorado.edu/geography/gcraft/notes/gps/gps_f.html)
GRF	Station code for the digital broadband array near Gräfenberg, Germany
GRFO	Gräfenberg Observatory (http://www.szgrf.bgr.de/)
GRSN	German Regional Seismic Network (http://www.szgrf.bgr.de/)
GSE	Group of Scientific Experts of the Conference on Disarmament in Geneva
GSE (format)	formats designed for global seismic data exchange and archiving by the GSE in the framework of the IMS of the CTBTO (e.g., GSE1.0 GSE2.1, GSE2.X)
GSETT	Technical Test (recommended by the GSE)
GSETT-3	Group of Scientific Experts Third Technical Test in 1995
GSN	Global Seismographic Network (of IRIS and the FDSN) (http://www.iris.washington.edu/GSN/)
GT	Ground Truth
GUI	Graphical User Interface
HF	High-Frequency
HGLP	High Gain Long Period System
HP	High Pass
HRVD	Harvard University, USA (http://www.harvard.edu/)
IAGA	International Association of Geomagnetism and Aeronomy (http://www.ngdc.noaa.gov/IAGA/iagahome.html)
IASP91	Standard Earth and seismic travel-time model (see DS 2.1)
IASPEI	International Association of Seismology and Physics of the Earth's Interior (of the IUGG) (http://www.iaspei.org/)
ICB	Inner Core Boundary
IDA	International Deployment of Accelerometers (http://quakeinfo.ucsd.edu/idaweb/)

Acronyms

IDC	International Data Center (specifically that of the CTBTO)
IDE	Integrated Drive Electronics (see Glossary 6.7)
IIR	Infinite Impulse Response filter (see Glossary 6.7)
IMS	International Monitoring System (in the framework of the CTBTO) (http://www.nemre.nn.doe.gov/nemre/introduction/ims_descript.html)
IMS1.0	Format for the exchange of parameter data adopted by the IMS
IP	Internet Protocol; combination of numbers which is associated with a computer in the Internet, for explicit identification of a computer
IRIS	Incorporated Research Institutions for Seismology (USA) (http://www.iris.edu/)
ISAM	Indexed Sequential Access Method
ISC	International Seismological Centre (in Newbury, UK) (http://www.isc.ac.uk/)
ISDN	Integrated Services Digital Network
ISF	IASPEI Seismic Format (Chapter 10)
ISOP	International Seismic Observing Period
IUGG	International Union of Geodesy and Geophysics (http://www.iugg.org/)
JMA	Japanese Meteorological Agency (http://www.jma.go.jp/JMA_HP/jma/indexe.html)
KAPG	former Commission of the Academies of Sciences of Socialistic Countries for Planetary Geophysical Research
KNMI	The Royal Netherlands Meteorological Institute (http://www.knmi.nl/indexeng.html)
LASA	Large Aperture Seismic Network (USA)
LF	Low-Frequency
LP	Stands for either low pass (filter) or long-period (seismographs)
LTA	Long-Term Average (of noise or signal amplitudes)
LTI	Linear Time-Invariant
LVZ	Low-Velocity Zone
Ma	Megannum; an abbreviation for million years ago
M_0	Scalar seismic moment
mb	Seismic body-wave magnitude; determined from short-period P waves
mB	Seismic body-wave magnitude; determined from medium-period or broadband records of P, PP and S waves
MCS	Mercalli-Cancani-Sieberg seismic intensity scale
Me	Energy magnitude
MEDNET	MEDiterranean NETwork (http://www.mednet.ingrm.it/)
miniSEED	SEED format without any of the associated control header information
Ml or ML	Local magnitude (according to the original definition by Richter (1935))
Mm	Magnitude derived from observation of mantle surface waves
MM56	Modified Mercalli Scale of 1956
M_{ms}	Magnitude derived from macroseismic intensity observation
MOHO	Abbreviation for Mohorovičić-discontinuity (lower boundary of the Earth's crust)
MP events	Multi Phase events (observed at volcanoes)
Ms	Surface-wave magnitude

MSB	Most significant Bit
MSEED	Mini-SEED (data format)
MSK	Macroseismic intensity scale according to Medvedev, Sponheuer and Karnik
MSOP	Manual of Seismological Observatory Practice (http://www.seismo.com/msop/msopintro.html)
M_t	Tsunami magnitude
M_w	Seismic moment magnitude according to Kanamori (1977)
NASA	National Aeronautics and Space Administration (USA) (http://www.nasa.gov/)
NCSN	Northern California Seismic Network (USA) (http://quake.geo.berkeley.edu/ncsn/ncsn.overview.html)
NDC	National Data Centers (in the framework of the CTBTO/IMS)
NDPC	NORSAR Data Processing Center
NEIC	National Earthquake Information Center of the USGS; acts as WDC for earthquake data (http://neic.usgs.gov/)
NEIS	U.S. Geological Survey National Earthquake Information Service
NERC	Natural Environment Research Council (USA) (http://www.nerc.ac.uk/)
NetDC	Networked Data Center Protocol (http://www.iris.washington.edu/manuals/netdc/netdcuser.htm)
	Chapter 10
NGNM	New Global Noise Model (see section 4.1.2)
NHNM	New High-Noise Model (see section 4.1.2)
NLNM	New Low-Noise Model (see section 4.1.2)
NMSOP	New Manual of Seismological Observatory Practice (http://www.seismo.com/msop/nmsop/nmsop.html)
NNSN	Norwegian National Seismic Network (http://www.ifjf.uib.no/Seismologi/nnsn/nnsn.html)
NOAA	National Oceanic and Atmospheric Administration (USA) (http://www.noaa.gov/)
NORESS	Norwegian Experimental Seismic Station (http://www.norsar.no/NDC/stations/NRS/)
NORSAR	Norwegian Seismic Array (http://www.norsar.no/)
NPEF	Noise Prediction-Error Filter
NTS	Nevada Test Site (http://www.nv.doe.gov/nts/default.htm)
OBS	Ocean-Bottom Seismograph
ODC	ORFEUS Data Center (De Bilt, Netherlands)
ORFEUS	Observatories and Research Facilities for European Seismology (De Bilt, Netherlands) (http://orfeus.knmi.nl/)
OT	Origin Time
PASSCAL	Program for Array Seismic Studies of the Continental Lithosphere (http://www.passcal.nmt.edu/iris/passcal/passcal.htm)
PCEQ	Pulse-Coded Earthquake data format (Chapter 10)
PDAS	Portable Data Acquisition System (see Chapter 6 and Glossary 6.7)
PD	Program Descriptions (in Volume 2 of the NMSOP)
PDE	Preliminary Determination of Epicenters (NEIC event data reports)
PDR-2	Local format in use at individual stations and networks

Acronyms

PGA	Peak Ground Acceleration
PIDC	Prototype International Data Center (USA) (see IS 10.3) (http://www.pidc.org/)
PITSA	Programmable Interactive Toolbox for Seismological Analysis (http://lbutler.geo.uni-potsdam.de/service.htm)
POSEIDON	Pacific Orient SEIsmic Digital Observation Network (Japanese seismic network for global seismological studies which includes many OBS sites)
PREM	Preliminary Reference Earth Model (see DS 2.1)
PREPROC	Program for preprocessing of digital seismic data
PSRV	Pseudo Relative Velocity response spectrum.
PSD	Power Spectral Density
PVC	Poly-Vinyl-Chloride
QED	Quick Epicenter Determination (NEIC event data reports)
QLIB2	Software library (see Glossary 6.7)
Q	Quality factor; Q is inverse proportional to the attenuation of seismic waves, i.e., to the relative loss of energy per wave cycle
RBW	Relative Bandwidth
RC	Resistivity- Capacity (electric circuit, filter, element etc.)
rdseed	SEED-reading program
RDSS	Research and Development Support System (at the CMR, USA) (www.pidc.org/rdss/sitemapbox/)
REB	Reviewed Event Bulletin (of the PIDC)
REDB	Reference Event Data Base (of the PIDC)
RF	Radio Frequency
RMS or rms	Root Mean Square
ROSINE	Resolution of Site Response Issues in the Northridge Earthquake
RSAM	Real-time Seismic Amplitude Measurement
RSTN	Remote Seismic Telemetered Network
SA	Spectral Acceleration
SAC	Seismic Analysis Code (format used in standard analysis software)
SAP	Signal Attribute Processing
SAR	Successive Approximation Register
SAR-ADC	Successive Approximation Analog to Digital Converter
SASCs	Slowness and Azimuth Station Corrections (see IS 10.3)
SCRs	Stable Continental Regions
SCSI	Small Computer System Interface (see Glossary 6.7)
SCSN	Southern California Seismic Network (http://www.trinet.org/scsn/scsn.html)
SEB	Standard Event Bulletin (of the PIDC)
SEED	Standard for the Exchange of Earthquake Data (format designed for data exchange and archiving) (http://devo.liss.org/AboutSEED.shtml)
SEGY	Data format
SEISAN	Seismogram Analysis Software
SEL3	Standard Event List 3; the future name at the IDC of the CTBTO for the former REB (Reviewed Event Bulletin).
SH	Seismic Handler (data analysis program)
SHI	Seismic Hydroacoustic and Infrasonic (data products see IS 10.3)

SHM	Latest version of the Seismic Handler data analysis program.
SKD	Long-period (in Russian: Dlinnoperiodnij) seismograph constructed by D. P. Kirnos, operated as displacement-proportional broadband sensor
SNR	Signal-to-Noise-Ratio (see sub-chapter 4.4)
SP	Short-Period
SPT	Split-Barrel Sampling; also Semipalatink Test Site (Kazachstan)
SRO	Seismic Research Observatory (used in a global USA network) with a very specifically filtered long-period seismograph response
SS-1/SSR-1	Kinematics “Ranger”-Seismometer and data logger, respectively
SSAM	Spectral Seismic Amplitude Measurement
SSSCs	Source Specific Station Corrections (see IS 10.3)
STA	Short-Term Average (in a trigger algorithm) (see IS 8.1)
STA/LTA	Ratio of short-term to long-term average (trigger algorithm) (see 8.1)
STA2	station line in parameter data format (Chapter 10)
STEIM1 or 2	Algorithms proposed by J. M. Steim for data compression
STS1 or STS2	Streckeisen Triaxial Seismometers, type 1 and 2, resp. (see DS 5.1)
SUDS	Seismic Unified Data System (format designed for database systems)
TCP	Transmission Control Protocol
TCP/IP	Transmission Control Protocol over Internet Protocol (see Glossary 6.7)
TERRAScope	A very broadband seismographic network in Southern California (http://www.gps.caltech.edu/terrascope/)
TF	Telegraphic Format
THR	The SNR threshold used to define a detection
TR	Transient Response
UHF	Ultra-High Frequency range (around 450 MHz)
UKAEA	United Kingdom Atomic Energy Agency (http://www.ukaea.org.uk/)
ULF	Ultra-Low Frequency
ULP	Ultra-Long Period
UNE	Underground Nuclear Explosion
UNESCO	United Nations Educational, Scientific and Cultural Organization (http://www.unesco.org/)
UPS	Unbreakable Power Supply
USESN	United States Educational Seismology Network (http://www.indiana.edu)
USGS	United States Geological Survey (http://www.usgs.gov/)
USNSN	United States National Seismograph Network (http://neic.usgs.gov/neis/usnsn/usnsn_home.html)
UT	Universal Time
VBB	Very Broadband
VESPA	Velocity Spectrum Analysis
VHF	Very-High Frequency range (160-200 MHz)
VLP	Very Long Period
v_p	P-wave velocity
v_s	S-wave velocity
VSAT	Very Small Aperture Terminals
VT-A	Deep Volcanic-Tectonic events
VT-B	Shallow Volcanic-Tectonic events

Acronyms

WA	Wood-Anderson torsion seismometer
WAN	Wide Area Network
WDC	World Data Center
wfdisc	waveform disc; the disk loop hard drive that stores waveform data.
WIDC	Waveform IDentifiCation line
WWSSN	World-Wide Standard Seismograph Network
WWSSN-LP	Long-period seismographs of the WWSSN
WWSSN-SP	Short-period seismographs of the WWSSN
YBP	Years Before Present
YKA	Yellowknife Array (Canada)

The glossary of terms, which are frequently used in seismology and observatory practice, has been compiled by using, complementing and sometimes correcting glossaries published by the US Geological Survey (<http://www.usgs.gov/>), the Montana Bureau of Mines and Geology (<http://www.mbm.mtech.edu/>) and the International Data Center of the CTBTO (<http://www.ctbto.org>). Thanks go to Christian Nerger and Johannes Schweitzer, who assisted the Editor in compiling and editing this glossary. Note that words which are written in *italics* in the explanatory text refer to other key words for which more explanation is given elsewhere in the glossary.

acceleration	When an object, e.g., a car, changes its speed from one speed to another, it is accelerating (moving faster) or decelerating (moving slower). This change in velocity is called acceleration. When the ground is shaking during an earthquake or another kind of seismic source process, it also experiences acceleration. The peak acceleration is the largest acceleration recorded by a particular station during an earthquake. In strong-motion seismology the ground acceleration is commonly expressed as a fraction or percentage of the acceleration due to gravity (g) where $g = 981 \text{ cm/s}^2$. For the strongest earthquakes ground accelerations of more than 1.5 g have been recorded. Since the weight of an object, e.g., of a building, is equal to its mass multiplied by the gravity g the additional acceleration due to <i>ground shaking</i> causes an extra load. This extra load may exceed the strength of the building and may cause damage or even a collapse.
accelerogram	The recording of ground acceleration as a function of time during a seismic event.
accelerograph	A compact, rugged, and relatively inexpensive instrument that records the signal from an <i>accelerometer</i> . Film used to be the most common recording medium, modern accelerographs, however, record digitally with much larger dynamic range.
accelerometer	A sensor whose output is almost directly proportional to ground <i>acceleration</i> . The conventional strong-motion accelerometer is a simple, nearly critically damped oscillator having a natural frequency of about 20 Hz.
accretionary wedge	Sediments that accumulate and deform where oceanic and continental plates collide. These sediments are scraped off the top of the downgoing oceanic crustal plate and are added to the leading edge of the continental plate (see <i>subduction</i> and <i>tectonic plate</i>).
active fault	A fault that is considered likely to undergo renewed movement within a period of concern to humans. Faults are commonly considered to be active if they have moved one or more times in the last 10,000 years, but they may also be considered active when assessing the hazard for very critical installations such as nuclear power plants even if movement has occurred in the last 500,000 years. Usually, the fault movements are (at least partially) ruptural, i.e., connected with earthquakes, however slow (creeping) movements are possible as well.

Glossary

aftershocks	Earthquakes that follow the largest shock of an earthquake sequence. They are smaller than the mainshock and within 1-2 fault lengths distance from the mainshock fault. Aftershocks can continue over a period of weeks, months, or years, decreasing in frequency with time. In general, the larger the mainshock, the larger and more numerous the aftershocks, and the longer they will continue.
alluvium	Loose gravel, sand, silt, or clay deposited by streams after the last ice age (see <i>holocene</i>).
Alpide belt	Mountain belt with frequent earthquakes that extends from the Mediterranean region, eastward through Turkey, Iran and northern India.
amplification	Most earthquakes are relatively small, in fact, so small that no one feels them. In order for seismologists to see the recording of the ground movement from smaller earthquakes, the recording has to be made larger. It's like looking at the recording through a magnifying glass, and the amount that it is magnified is the amplification. Modern seismographs are able to magnify the <i>ground motion</i> 10^6 times or even more, i.e., they are able to resolve ground motion amplitudes as small as the diameter of molecules or even atoms. Shaking levels at a site may also be increased (or decreased) by focusing (or defocusing) of seismic energy caused by the geometry and the <i>velocity structure</i> of sediments, such as basin subsurface topography, or by surface topography. Both the amplification of seismographs and of the subsoil structure is usually dependent on the <i>frequency</i> of the <i>seismic signal</i> .
amplitude	The size of the wiggles on an earthquake recording; more general the height of a wave-like disturbance (called <i>waveform</i>) from the medium (zero) level to its peak. In seismology <i>ground motion</i> amplitudes are usually measured in nanometers (10^{-9} m) or micrometers (10^{-6} m). Often the double amplitude (called peak-to-peak or peak-to-trough) is measured.
anisotropic	A medium is anisotropic when its physical properties, e.g., the velocity of seismic waves or the hardness of rocks, depend on the direction considered.
array	An ordered arrangement of <i>seismometers</i> or <i>geophones</i> , the data from which feeds into a central <i>data acquisition</i> and <i>data processing</i> unit.
arc (volcanic)	A chain of volcanoes (volcanic arc) that sometimes forms on land or as volcanic islands in the sea, when an oceanic plate collides with a continental plate and then slides down underneath it (<i>subduction</i>).
arias intensity	A ground-motion parameter derived from an accelerogram and proportional to the integral over time of the acceleration squared. Expressed in units of <i>velocity</i> (m/s or cm/s).
arrival	The appearance of seismic energy on a seismic record.
arrival time	The time at which a particular wave phase arrives at a station.

aseismic	This term describes a fault (an area) on which (where) no earthquakes have been observed and are not likely to occur. Aseismic behavior may be due to lack of shear stress across the fault, a locked fault condition with or without shear stress, or release of stress by fault creep.
association (of arrivals)	To assign a seismic wave <i>arrival</i> to a specific seismic event.
asperity	A region on a <i>fault</i> of high strength produced by one or more of the following conditions: increased normal stress, high friction, low pore pressure, or geometric changes in the fault such as fault bends, offsets, or roughness. This term is used in two contexts: it may refer to sections of a fault that radiate uncommon seismic energy or it may refer to locked sections of the fault that cause fault segmentation.
asthenosphere	The ductile part of the Earth, just below the brittle <i>lithosphere</i> , in the upper <i>mantle</i> . The lithosphere/asthenosphere reaches down to about 200 km.
attenuation	When you throw a pebble in a pond, it makes waves on the surface that move out from the place where the pebble entered the water. The waves are largest where they are formed and gradually get smaller as they move away. This decrease in wave amplitude is caused by <i>geometrical spreading</i> and by attenuation of seismic wave energy. The latter is due to two different processes: 1) absorption (termed anelastic attenuation) in different Earth materials and b) scattering of seismic energy at heterogeneities in the Earth (e.g., faults or small-scale anomalous geological bodies). Q and kappa are attenuation parameters used in modeling the attenuation of <i>ground motions</i> .
attribute (of an arrival)	A quantitative measure of a seismic <i>arrival</i> such as <i>onset</i> time, (<i>back-</i>) <i>azimuth</i> , <i>slowness</i> , <i>period</i> and <i>amplitude</i> .
azimuth	In general a direction measured clock-wise in degrees against north. In seismology used to measure the direction from a seismic source to a seismic station recording this event..
backarc	The region landward of the chain of volcanoes (<i>volcanic arc</i>), in a <i>subduction</i> system.
backazimuth	The direction from the seismic station towards a seismic source, measured in degrees clock-wise against north; in short, sometimes also just called azimuth.
background noise	Permanent movements of the Earth as seen on seismic records caused by ocean waves, wind, rushing waters, turbulences in air-pressure, etc. (ambient natural noise), and/or by traffic, hammering or rotating machinery, etc. (man-made noise).
backstop	Continental rocks in the <i>backarc</i> that are landward from the trace of the subduction thrust fault and that are strong enough to support stress accumulation. These rocks are both igneous and dewatered, lithified, consolidated sediments that probably were part of the <i>accretionary-wedge</i> . The softer accretionary-wedge rocks are strongly deformed as they accumulate against the backstop. The exact position and dip direction of the backstop is not well determined, and more than one backstop may exist.

Glossary

basement	Igneous and metamorphic rocks that underlie the sedimentary-rock sequences and extend downward to the base of the crust.
beam	A waveform created from <i>array</i> station elements that are specifically summed up for the direction of a specified <i>backazimuth</i> and apparent velocity (<i>slowness</i>).
bedrock	Relatively hard, solid rock that commonly underlies softer rock, or soil, a subset of the basement.
Benioff zone	see <i>Wadati-Benioff zone</i>
blind fault	A fault that does not rupture all the way up to the surface so there is no evidence of it on the ground. It is "buried" under the uppermost layers of sediments or rock in the crust.
body wave	A seismic wave that propagates through the interior of the Earth, as opposed to <i>surface waves</i> that propagate near the Earth's surface. <i>P</i> and <i>S waves</i> , which shake the ground in different ways, are examples.
branch (of travel-time curve)	Term used in seismology for "branching" <i>travel-time curves</i> that are related to discrete ray paths of the same type of wave and due to strong velocity <i>gradients</i> and/or <i>low-velocity layers</i> in the Earth's interior, e.g., the P-wave branches due to the upper mantle discontinuities at 410 km and 660 km depth or the travel-time branches of the core phases PKPab, PKPbc and PKPdf.
brittle-ductile boundary	The depth in the crust across which the thermo-mechanical properties of the crust change from brittle behavior (tending to break) to ductile behavior (tending to bend). Most earthquakes initiate at or above this depth on steep (high-angle) faults, below this depth, fault slips may be <i>aseismic</i> and may grade from high angle to low angle.
bulk density	The mass of a material divided by its volume, including the volume of its pore spaces.
¹⁴ C age date	An absolute age obtained for geologic materials containing bits or pieces of carbon using measurements of the proportion between the radioactive carbon (¹⁴ C) and the non-radioactive carbon (¹² C). These dates are independently calibrated with calendar dates. The method is used to determine when past earthquakes occurred on a fault.
calibration	The process of determining the <i>response function</i> and sensitivity of an instrument or its derived channel.
calibration pulse channel (of a record)	An electronic signal used to calibrate seismic instruments. Usually the signal output of a one-component <i>seismic sensor</i> . Modern seismic recorders (see <i>data logger</i>) are usually able to record simultaneously the signals from many <i>seismic sensor components</i> .
Circum-Pacific belt	The zone surrounding the Pacific Ocean that is characterized by frequent and strong earthquakes and many volcanoes as well as high tsunami hazard. Also called the <i>Ring of Fire</i> .
coda	The tail of a <i>seismic signal</i> , usually with exponentially decaying <i>amplitudes</i> , which follow a strong wave <i>arrival</i> . Coda waves are due to scattering and superposition of multi-path arrivals.
coda phase	A detection of a single phase of unknown path found within the coda signal envelope, designated as tx, Px or Sx.

coherent	<i>Seismic signals</i> detected on various <i>seismic sensors</i> of an <i>array</i> or network of <i>seismic stations</i> are said to be coherent if they are related to each other in time, <i>amplitude</i> and/or <i>waveform</i> because they come from the same seismic source.
cohesionless	Referring to the condition of a sediment whose shear strength depends only on friction because there is no bonding between the grains. This condition is typical of clay-free sandy deposits.
colluvium	Loose <i>soil</i> or rock fragments on or at the base of gentle slopes or hillsides. Deposited by or moving under the influence of rain wash or downhill creep.
component	(1) One dimension of a three-dimensional signal, (2) The vertically- or horizontally-oriented (north or east) sensor of a seismic station.
compressional stress	The stress that squeezes something. It is the stress component perpendicular to a given surface, such as a fault plane, that results from forces applied perpendicular to the surface or from remote forces transmitted through the surrounding rock.
compressional wave convolution	See <i>P wave</i> A mathematically equivalent operation that describes the action of a linear (mechanical and/or electronic) system on a signal, such as that of a filter on a <i>seismic signal</i> .
core	The innermost part of the Earth. The outer core extends from about 2900 to about 5120 km below the Earth's surface and consists in its main components of a mixture of liquid iron and nickel. The inner core is the central sphere of the Earth with a diameter of 1250 km and consists of solid metal.
corner frequency	The frequency at which the curve representing the <i>Fourier amplitude spectrum</i> of a recorded seismic signal abruptly changes its slope. For earthquakes, this frequency is a property of the source and related to fault size, rupture velocity, source duration and stress drop in the source. Also the frequency at which the <i>transfer function / magnification curve</i> of a recording system changes its slope.
creep	Slow, more or less continuous movement occurring on faults due to ongoing tectonic deformation. Also applied to slow movement of landslide masses down a slope because of gravitational forces. Faults that are creeping do not tend to have large earthquakes. This fault condition is commonly referred to as unlocked.
critical facilities	Structures whose ongoing performance during an emergency is required or whose failure could threaten many lives. May include (1) structures such as nuclear-power reactors or large dams whose failure might be catastrophic, (2) major communication, utility, and transportation systems, (3) involuntary- or high-occupancy buildings such as schools or prisons, and (4) emergency facilities such as hospitals, police and fire stations, and disaster-response centers.
crossover	The distance from an event where two different <i>phases</i> arrive at the same time, allowing constructive interference that sometimes enhances the signal amplitudes.

Glossary

crust	The outermost major layer of the Earth, ranging from about 10 to 70 km in thickness worldwide. The oceanic crust is thinner (about 10 to 15 km) than the continental crust (about 25 to 70 km). The uppermost 15-35 km of the crust is brittle enough to produce earthquakes. The seismogenic crust is separated from the lower crust by the <i>brittle-ductile boundary</i> . The crust is usually characterized by P-wave velocities below 8 km/s (average velocity of about 6 km/s).
damping	The reduction in amplitude of a seismic wave or oscillator due to friction and (or) the internal absorption of energy by matter.
data	Series of observations, measurements or facts.
data acquisition	Process of acquiring and storing data.
database	Systemized collection of data that can be manipulated by data processing systems for specific purposes.
data logger	Digital data acquisition unit, usually for multi-channel recordings.
data processing	Handling and manipulating of data by computer.
defining (of an arrival)	An arrival <i>attribute</i> , such as <i>arrival time</i> , <i>azimuth</i> , <i>slowness</i> , or <i>amplitude</i> and <i>period</i> , which is used in the calculation of location or magnitude of the <i>seismic source</i> .
deformation	A change in the original shape of a material. When we are talking about earthquakes, deformation is due to stress and strain.
design earthquake	The postulated earthquake (commonly including a specification of the <i>ground motion</i> at a site) that is used for evaluating the earthquake resistance of a particular structure.
detection	Identification of an <i>arrival</i> of a <i>seismic signal</i> with <i>amplitudes</i> above and/or signal shape (waveform) different from seismic <i>noise</i> .
deterministic methods	Refers to methods of calculating <i>ground motions</i> for hypothetical earthquakes based on earthquake-source models and wave-propagation methods that exclude random effects.
dip	Inclination of a planar geologic surface (for example, a <i>fault</i>) from the horizontal (measured in degrees).
dip slip	See <i>fault</i> .
directivity	An effect of a propagating fault rupture whereby the amplitudes of the generated <i>ground motions</i> depend on the direction of wave propagation with respect to fault orientation and slip direction (radiation pattern). The directivity and thus the radiation pattern is different for P and S waves.
discriminant	A characteristic feature of a <i>seismic signal</i> that can be used to categorize its <i>source</i> , classifying it as originating from an <i>earthquake</i> , mining blast or collapse, nuclear detonation, or any other type of event.
disk loop	A storage device that continuously stores new waveform data while simultaneously deleting the oldest data on the device.

displacement	The difference between the initial position of a reference point and any later position. (1) In <i>seismology</i> , displacement is the <i>ground motion</i> commonly inferred from a <i>seismogram</i> . For example it may be calculated by integrating an accelerogram twice or a velocity proportional recording once with respect to time and is expressed in units of length, such as nanometer, micrometer or millimeter. (2) In geology, displacement is the permanent offset of a geological or man-made reference point along a fault or a landslide.
earthquake	<i>Ground shaking</i> and radiated seismic energy caused most commonly by sudden slip on a fault, volcanic or magmatic activity, or any other sudden stress changes in the Earth. An earthquake of magnitude 7 or larger is termed a great earthquake.
earthquake hazard	Any physical phenomenon associated with an earthquake that may produce adverse effects on human activities. This includes <i>surface faulting, ground shaking, landslides, liquefaction, tectonic deformation, tsunami, and seiche</i> and their effects on land use, man-made structures, and socio-economic systems. A commonly used restricted definition of earthquake hazard is the probability of occurrence of a specified level of <i>ground shaking</i> in a specified period of time.
earthquake risk	The expected (or probable) life loss, injury, or building damage in the case of an earthquake or in relation to the given <i>earthquake</i> hazard of an area. In common language, earthquake risk and earthquake hazard are occasionally used interchangeably.
earthquake swarm	A series of minor <i>earthquakes</i> , none of which may be identified as the main shock, occurring in a limited area and time period.
elastic dislocation theory	In <i>seismology</i> , the theoretical description of how the elastic Earth responds to fault slip, as represented by a distribution of displacement discontinuities.
elastic wave	A wave that is propagated by some kind of elastic deformation, that is, a deformation that disappears when the deforming forces are removed. A seismic wave is a type of an elastic wave.
epicenter	The point on the Earth's surface vertically above the point where a seismic rupture begins.
event (seismic)	General term used for a localized disturbance (earthquake, explosion, rock burst, mining collapse, volcanic event) which generates seismic waves.
f_{\max}	The frequency above which little seismic energy is observed at most strong-motion stations. This frequency cutoff may be produced by attenuation of the shaking by unconsolidated sediments underlying the recording site or may be a property of the source function.

Glossary

fault	<p>A fracture along which the two sides have been significantly <i>displaced</i> relative to each other in parallel to the fracture. Strike-slip faults are vertical (or nearly vertical) fractures along which rock masses have mostly shifted horizontally. If the block opposite an observer looking across the fault moves to the right, the slip style is termed right lateral, if the block moves to the left, the motion is termed left lateral. Dip-slip faults are inclined fractures along which rock masses have mostly shifted vertically. If the rock mass above an inclined fault moves down (due to lateral extension) the fault is termed normal, whereas if the rock above the fault moves up (due to lateral compression), the fault is termed reverse (or thrust). Oblique-slip faults have significant components of both slip styles (i.e., strike slip and dip slip).</p>
fault creep	See <i>creep</i> .
fault gouge	Crushed and ground-up rock produced by friction between the two sides when a fault moves.
fault plane	The planar (flat) surface along which there is slip during an earthquake.
fault movement	Sense of motion along a fault which separates two adjacent crustal blocks. One speaks of normal faulting, if the block overlaying the other block along an inclined fault plane is downthrown, and of reverse or thrust faulting, if the overlaying block is overriding the block underneath or the underlying block is thrust/subducted underneath the overriding block, respectively (see <i>subduction thrust fault</i>). In the case of a steeply dipping fault plane and more or less horizontal, i.e., strike-slip block movement, one discriminates between left-lateral and right-lateral strike-slip movements. Left-lateral means that if you were to stand on the fault and look along its length, that the left block moves towards you, whereas in the case of right-lateral movement the block on your right side moves towards you.
fault-plane solution	A way of showing the <i>fault</i> and the direction of slip on it from an <i>earthquake</i> , using circles with two intersecting curves that look like beach balls. A fault-plane solution is found by an analysis using stereographic projection or its mathematical equivalent to determine the attitude of the causative fault and its direction of slip from the <i>radiation pattern</i> of seismic waves using earthquake records at many stations. The most common analysis uses the direction of <i>first motion</i> of <i>P-wave</i> onsets and yields two possible orientations for the fault rupture and the direction of seismic slip. Another technique is to use the polarization of teleseismic <i>S waves</i> and/or to measure amplitude ratios between different phase types. From these data, inferences can be made concerning the principal axes of stress in the region of the earthquake. The principal stress axes determined in this method are the <i>compressional</i> axis (also called the P-axis, i.e. the axis of greatest compression, or s_1), the <i>tensional</i> axis (also known as the T-axis, i.e., the axis of least compression, or s_3), and the intermediate axis (s_2).

fault scarp	Step-like linear landform coincident with a fault trace and caused by geologically recent slip on the fault.
fault trace	Intersection of a <i>fault</i> with the ground surface, also, the line commonly plotted on geologic maps to represent a fault.
Fennoscandia	The northern European region comprising the Caledonids and the Baltic shield of Finland, Scandinavia, and the Kola Peninsula of northwestern Russia.
filter(ing)	<i>Attenuation</i> of certain frequency components of a (<i>seismic</i>) <i>signal</i> and the amplification of others. For a recorded signal, the process can be accomplished electronically or numerically in a computer. Filtering also occurs naturally as seismic energy passes through the Earth.
first arrival	The first recorded <i>seismic signal</i> attributable to a known <i>seismic source</i> .
first motion	On a seismogram, the first discernible displacement of the record trace caused by the arrival of a P wave at the seismometer. Upward motion of the ground at the seismometer indicates an expansion in the source region, downward motion indicates a contraction. When the <i>seismic signal</i> arrives in the presence of seismic <i>noise</i> the proper polarity of the first motion may be difficult to recognize.
f-k	Frequency (f) versus wavenumber (k) analysis that maps the power seismic waves observed at an <i>array</i> as function of <i>azimuth</i> and <i>slowness</i> .
focal depth	A term that refers to the depth of an earthquake hypocenter, i.e., the point where a seismic rupture begins (<i>focus</i>).
focal mechanism	See <i>fault-plane solution</i> .
focal zone	The rupture zone of an earthquake. In the case of a great earthquake, the focal zone may extend several hundred kilometers in length and several ten kilometers in width.
focus	That point within the Earth from which originates the first displacement of an earthquake and radiation of its elastic waves.
forearc	The region between the trace of the subduction thrust fault and the volcanic chain (<i>volcanic arc</i>).
foreshocks	Foreshocks are relatively smaller earthquakes that precede the largest earthquake in a series, which is termed the mainshock. Foreshocks may precede the mainshock by seconds to weeks and usually originate at or near the focus of the larger earthquake. Not all mainshocks have foreshocks.
Fourier spectrum	The relative amplitudes (and phase angles) at different frequencies that are derived from a time history by <i>Fourier analysis</i> .
Fourier analysis	The mathematical operation that resolves a time series (for example, a recording of <i>ground motion</i>) into a series of numbers that characterize the relative amplitude and phase components of the signal as a function of <i>frequency</i> .
frequency	The number of times something happens in a certain <i>period</i> of time, such as the <i>ground shaking</i> up and down or back and forth during of a seismic wave. The common unit of frequency is Hertz (Hz).

Glossary

frequency domain	A <i>seismic signal</i> that has been recorded in the <i>time domain</i> (as a <i>seismogram</i>) can be decomposed by means of <i>Fourier analysis</i> into its amplitude and phase components as a function of frequency (see <i>spectrum</i>). The representations of a seismic signal in the time and in the frequency domain are equivalent in a mathematical sense. For some procedures of data analysis the time-domain representation of a seismic records is more suitable while for others the frequency-domain approach is more appropriate and efficient.
fundamental period	The longest <i>period</i> for which an object, e.g., a <i>seismometer</i> , a structure, the sub-surface underground or the whole planet Earth shows a maximum response. The reciprocal of <i>natural frequency</i> .
G or g	G or g is the force of gravity of the Earth (an acceleration of 9.78 m/s ²). When there is an <i>earthquake</i> , the forces caused by the shaking can be measured as a fraction or percentage of the force of <i>gravity</i> (% g).
Gaussian noise spectrum	The spectrum of a time history whose sample values are generated by random selection from a statistical population that has a specified mean and a standard deviation. The values (ordinates) have a bell-shaped distribution about the mean. In earthquake studies, this type of spectrum is commonly multiplied by a theoretical <i>earthquake source spectrum</i> to obtain predicted ground-motion spectra for hypothetical earthquakes.
geodesy	The science of determining the size and shape of the Earth and the precise location of points on its surface.
geodetic	Referring to the determination of the size and shape of the Earth and the precise location of points on its surface.
geology	The study of the planet Earth - the materials it is made of, the processes that act on those materials, the products formed, and the history of the planet and its life forms since its origin.
geometrical spreading	The component of reduction in <i>wave amplitude</i> due to the radial spreading of seismic energy with distance from a given source.
geomorphology	The study of the character and origin of landforms, such as mountains, valleys, etc.
geophone	A simple <i>seismometer</i> , usually a mass-spring system with electrodynamic <i>transducer</i> , which has a relative high natural <i>frequency</i> (typically between about 5 and 25 Hz) and which is small in size and weight; commonly used in exploration <i>geophysics</i> .
geophysics	The study of the Earth and its sub-systems by physical methods.
geotechnical	Referring to the use of scientific methods and engineering principles to acquire, interpret, and apply knowledge of Earth materials for solving engineering problems.
graben	A down-dropped block of the Earth's crust resulting from extension, or pulling, of the <i>crust</i> . See also <i>horst</i> .
gradient	The rate of change, e.g., of the seismic velocity with depth in the Earth.

gravity	The attraction between two masses, such as the Earth and an object on its surface. Commonly referred to as the acceleration of gravity g . Changes in the gravity field can be used to infer information about the structure of the Earth's lithosphere and upper mantle. Interpretations of changes in the gravity field are generally applied to gravity values corrected for extraneous effects. The corrected values are referred to by various terms, such as free-air gravity, Bouguer gravity, and isostatic gravity, depending on the number and kind of corrections made.
Green's function	A mathematical representation that, in reference to earthquake shaking, is used to represent the <i>ground motion</i> caused by instantaneous slip on a small part of a fault. Green's function can be summed over a large fault surface to compute the <i>ground shaking</i> for a large earthquake rupturing a fault of finite size. The fractional fault-slip events that are summed can be records from small earthquakes on the fault or they can be theoretically computed small-earthquake records.
ground failure	A general reference to landslides, liquefaction, lateral spreads, and any other consequence of shaking that affects the stability of the ground.
ground motion /shaking	The movement of the Earth's surface from earthquakes, explosions or other seismic <i>sources</i> . Ground motion is produced by waves that are generated by sudden <i>slip</i> on a <i>fault</i> , the collapse of sub-surface cavities or sudden pressure at the explosive source and travel through the Earth and along its surface.
Gutenberg discontinuity	The seismic velocity discontinuity marking the <i>core-mantle</i> boundary (CMB) at which the velocity of P waves drops from about 13.7 km/s to about 8.0 km/s and that of S waves from about 7.3 km/s to 0 km/s. The CMB reflects the change from the solid <i>mantle</i> material to the fluid outer <i>core</i> .
halfspace	A mathematical model bounded by a planar surface but otherwise infinite. Properties within the model are commonly assumed to be homogeneous and isotropic, unlike the Earth itself, which is heterogeneous and anisotropic. Nevertheless, the half space model is frequently used to perform some theoretical calculations (forward modeling) in seismology.
harmonic tremor	Continuous rhythmic ground vibrations that can be detected by seismographs. Harmonic tremors often precede or accompany volcanic eruptions.
hazard	See <i>earthquake hazard</i> .
Hertz (Hz)	The unit of frequency; expressed in cycles per second.
Holocene	Refers to a period of time between present and 10,000 years before present. Applied to rocks or faults, this term indicates the period of rock formation or the time of most recent fault slip. Faults of this age are commonly considered active, based on the observation of historical or <i>palaeoseismic</i> activity on faults of this age in other locales.

Glossary

homogeneous	Being uniform, of the same nature; the opposite of inhomogeneous. Although the real Earth as a whole is largely inhomogeneous and weakly <i>anisotropic</i> ; the Earth can be considered for <i>seismic modeling</i> in a first approximation, at least in parts, as being homogeneous and isotropic.
horst	An upthrown block lying between two steep-angled fault blocks.
hydroacoustic	Pertaining to compressional (sound) waves in water, in particular in the ocean. Hydroacoustic waves may be generated by submarine explosions, volcanic eruptions or earthquakes.
hypocenter	The calculated location of the focus of an earthquake, i.e., of the point within the Earth where an earthquake rupture starts. Also commonly termed the <i>focus</i> .
infrasonic	Pertaining to low-frequency (sub-audible) compressional (sound) waves in the atmosphere.
inhomogeneous	The opposite of (see) <i>homogeneous</i> .
instrumental noise	See <i>noise</i> .
intensity	A measure of the effects of an earthquake at a particular place at the Earth's surface on humans and (or) structures. The intensity at a point depends not only upon the strength of the <i>earthquake</i> (magnitude) but also upon the distance from the earthquake to the epicenter, the depth of the hypocenter and the local geology at that point. Several scales exist, most of them giving the intensity in 12 degrees, usually written as Roman numerals. Most frequently used are at present the European Macroseismic Scale (EMS-98), and in the United States the Modified Mercalli scale and the Rossi-Forel scale. There are many different intensity values for one earthquake, depending on how far you are away from the epicenter; this is unlike the magnitude value, which is one number for each earthquake as a measure of the amount of seismic wave energy released by it.
Internet	World-wide network of computers linked by means of the Internet protocol (IP).
interplate / intraplate	Intraplate pertains to processes within the Earth's crustal plates. Interplate pertains to processes between the plates.
interplate coupling	The qualitative ability of a subduction thrust fault to lock and accumulate stress. Strong interplate coupling implies that the fault is locked and capable of accumulation <i>stress</i> whereas weak coupling implies that the <i>fault</i> is unlocked or only capable of accumulating low stress. A fault with weak interplate coupling could be <i>aseismic</i> or could slip by <i>creep</i> . See <i>locked fault</i> .
isoseismal	Referring to a line on a map bounding points of equal intensity for a particular earthquake.
isoseismal line	A line connecting points on the Earth's surface at which earthquake intensity is the same. It is usually a closed curve around the epicenter.
isotropic	In an isotropic medium the physical properties, e.g., the propagation velocity of seismic waves or the hardness of rock, are independent on the direction considered.
kinematic	Referring to the general movement patterns and directions, usually expressed in physical units of displacement (m) , velocity (m/s) or acceleration (m/s ²).

kinematic units	See <i>kinematic</i> .
landslide	The downslope movement of <i>soil</i> and/or rock.
Late Quaternary	The age between the present and 500,000 years before the present. Faults of this age are sometimes considered active based on the observation of historical or <i>palaeoseismic</i> activity on faults of this age in some locales.
lateral spread and flow	Terms referring to landslides that commonly form on gentle slopes and that have rapid fluid-like flow movement, like water.
least-squares fit	An approximation of a set of data with a curve such that the sum of the squares of the differences between the observed points and the assumed curve is a minimum.
left-lateral movement	See <i>fault movement</i> .
lifelines	Structures that are important or critical for a community to function, such as roadways, pipelines, power lines, sewers, communications, and port facilities.
liquefaction	Process by which water-saturated sediment temporarily loses strength and acts as a fluid. This effect can be caused by earthquake shaking and be associated with <i>sand boil</i> .
lithology	The description of rock composition (what it is made of) and texture.
lithosphere	The outer solid part of the Earth , including crust and uppermost mantle. The lithosphere is about 100 km thick, although its thickness is age-dependent (older lithosphere is thicker). The lithosphere below the crust is brittle enough at some locations to produce earthquakes by faulting, such as within a subducted oceanic plate.
locked fault	A fault that is not slipping because frictional resistance on the fault is greater than the shear stress across the fault. Such faults may store strain for extended periods that is eventually released in an earthquake when frictional resistance is overcome.
Love wave	A major type of <i>surface waves</i> having a horizontal motion that is transverse (or perpendicular) to the direction of propagation. It is named after A. E. H. Love, the English mathematician who discovered it.
leaking mode	A surface seismic wave which is imperfectly trapped, e.g., within a <i>low-velocity layer</i> or a sequence of layers so that its energy leaks or escapes across a layer boundary causing some attenuation.
low-velocity layer/zone)	Any layer in the Earth in which seismic wave velocities are lower than in the layers above and below.
Ma	An abbreviation for one million years ago (Megannum).
major earthquake	An earthquake having a magnitude of 7 or greater on the Richter scale.

Glossary

magnetic reversal	A change of the Earth's magnetic field to the opposite polarity that has occurred at irregular intervals during geologic time. Polarity reversals can be preserved in sequences of magnetized rocks and compared with standard polarity-change time scales to estimate geologic ages of the rocks. Rocks created along the oceanic spreading ridges commonly preserve this pattern of polarity reversals as they cool, and this pattern can be used to determine the rate of ocean-ridge spreading. The reversal patterns recorded in the rocks are termed sea-floor magnetic lineaments.
magnification curve	A diagram showing the dependence of <i>amplification</i> , e.g. of the seismic <i>ground motion</i> by a <i>seismograph</i> , as a function of <i>frequency</i> .
magnitude	A number that characterizes the relative size of an <i>earthquake</i> . Magnitude is based on measurement of the maximum motion recorded by a seismograph (sometimes for waves of a particular frequency), corrected for the attenuation with distance. Several scales have been defined, but the most commonly used are (1) local magnitude (Ml or ML), commonly referred to as "Richter magnitude", (2) surface-wave magnitude (Ms), (3) body-wave magnitude (mb), and (4) moment magnitude (Mw). The magnitude scales 1 – 3 have limited range and applicability and do not satisfactorily measure the size of the largest earthquakes. The moment magnitude (Mw) scale, based on the concept of seismic moment, is uniformly applicable to all earthquake sizes but is more difficult to compute than the other types. In principal, all magnitude scales could be cross calibrated to yield the same value for any given earthquake, but this expectation has proven to be only approximately true, thus the need to specify the magnitude type as well as its value.
mainshock	The largest earthquake in a sequence, sometimes preceded by one or more <i>foreshocks</i> , and almost always followed by many <i>aftershocks</i> .
mantle	The part of the Earth's interior between the <i>core</i> and the <i>crust</i> .
microearthquake	An <i>earthquake</i> that is not perceptible by man and can be recorded by seismographs only. Typically, a microearthquake has a magnitude of 2 or less on the Richter scale.
microseism	A more or less continuous motion in the Earth in a wide <i>frequency</i> range that is unrelated to any earthquake and caused by a variety of usually uncorrelated (incoherent) natural and artificial (man-made) sources. More specifically that part of seismic <i>noise</i> that is generated by wave motions on lakes and oceans and their action on shores, typically with periods between about 2 to 9 (the stronger secondary microseisms), and 11 to 18 seconds (the weaker primary microseisms).
microzonation	The identification and mapping at local or site scales of areas having different potentials for hazardous earthquake effects, such as <i>ground shaking intensity</i> , <i>liquefaction</i> or <i>landslide potential</i> .
MM scale	Mercalli intensity scale modified for North American conditions.

Moho	The abridged name for the <i>Mohorovičić discontinuity</i> .
Mohorovičić discont.	A discontinuity in seismic velocities that defines the boundary between crust and mantle of the Earth. Named after the Croatia seismologist Andrija Mohorovičić (1857-1936) who discovered it. The boundary is between 20 and 60 km deep beneath the continents and between 5 and 10 km deep beneath the ocean floor.
moment magnitude monitoring system	See <i>magnitude</i> A system for monitoring earthquakes, volcanic eruptions, tsunami, and/or other phenomena, usually consisting of a network of <i>seismic stations</i> and/or <i>arrays</i> , sometimes complemented by other types of sensors.
moveout	The time difference between like <i>arrivals</i> (such as P) at different stations, or between different arrivals at the same stations (like P and pP), which is also known as step-out.
natural frequency	The discrete frequency at which a particular elastic object or system vibrates when it is set in motion by a single impulse and not influenced by other external forces or damping. The reciprocal of <i>fundamental period</i> .
Newmark analysis	A numerical technique that models a potential landslide as a rigid block resting on a frictional slope, describing dynamic forces on the block from assumed <i>ground shaking</i> records in order to calculate the expected displacement of the block.
noise	Incoherent natural or artificial perturbations caused by a diversity of agents and distributed sources. One usually differentiates between ambient background noise and instrumental noise. The former is due to natural (ocean waves, wind, rushing waters, animal migration, ice movement, etc) and/or man-made sources (traffic, machinery, etc.), whereas instrumental (internal) noise may be due to the “flicker” noise of electronic components and/or even Brownian molecular motions in mechanical components. Digital data acquisition systems may add digitization noise due to their finite discrete resolution (least significant digit). Very sensitive seismic recordings may contain all these different noise components, however, usually their resolution is chosen so that only <i>seismic signals</i> and to a certain degree also the ambient <i>noise</i> are resolved. Disturbing noise can be reduced by selecting recording sites remote from noise sources, installation of seismic sensors underground (e.g., in boreholes, tunnels or abandoned mines) or by suitable filter procedures (improvement of the <i>signal-to-noise ratio</i>).
normal stress	That stress component that acts perpendicular to a given plane.
Nyquist frequency	Half of the digital sampling rate. It is the minimum number of counts per second needed to define unambiguously a particular frequency. If the <i>seismic signal</i> contains energy in a frequency range above the Nyquist frequency the signal distortions are called aliasing.
oceanic spreading ridge	A fracture zone along the ocean bottom that accommodates upwelling of mantle material to the surface, thus creating new crust. A line of ridges, formed as molten rock reaches the ocean bottom and solidifies, topographically mark this fracture.

Glossary

oceanic trench	A linear depression of the sea floor caused by and approximately coincident with a subduction thrust fault.
octave (filtering)	In music, the eighth full tone above (or below) a given tone having twice (or half) as many vibrations per second, e.g., the “concert pitch” a^1 has a <i>frequency</i> of 440 Hz, while the tone a^2 , which is one octave higher, has a frequency of 880 Hz. <i>Seismographs</i> typically record (filter) <i>ground motion</i> oscillations within a range of one (narrow-band) to 12 octaves (very broadband).
oscillator	A mass that moves with oscillating motion under the influence of external forces and one or more forces that restore the mass to its stable at-rest position. In earthquake engineering, an oscillator is an idealized damped mass-spring system used as a model of the response of a structure to earthquake <i>ground motion</i> . A seismograph is also an oscillator of this type.
onset	The first appearance of an acoustic or <i>seismic signal</i> on a record.
origin time	Time of a seismic, hydroacoustic, or infrasonic <i>event</i> .
outer arc ridge	A zone landward from the trace of the subduction thrust fault of elevated sea floor probably related to the compression of the rocks in the <i>accretionary wedge</i> . Also referred to as the outer arc high.
palaeoseismic	Referring to the prehistoric seismic record as inferred from ruptural displacements in young geologic sediments in combination with ^{14}C age dating.
parameter (data)	A quantitative attribute of a seismic <i>arrival</i> , such as <i>onset</i> or <i>arrival time</i> , <i>azimuth</i> , <i>slowness</i> , <i>period</i> , and <i>amplitude</i> .
Peak ground acceleration	The PGA relates to the maximum <i>acceleration amplitude</i> measured (or expected) in a strong-motion <i>accelerometer</i> record of an <i>earthquake</i> .
pedogenic	Pertaining to processes that add, transfer, transform, or remove <i>soil</i> .
period	The average duration of one cycle of a periodic motion, in seconds per cycle.
phase	(1) A stage in periodic motion, such as wave motion or the motion of an oscillator, measured with respect to a given initial point and expressed in angular measure. (2) A pulse of seismic energy arriving at a definite time, which passed the Earth on a specific path. (3) Stages in the physical properties of rocks or minerals under differing conditions of pressure, temperature, and water content.
Pleistocene	The time period between about 10,000 years before present and about 1,650,000 years before present. As a descriptive term applied to rocks or <i>faults</i> , it marks the period of rock formation or the time of most recent fault slip, respectively. Faults of Pleistocene age may be considered active though their activity rates are commonly lower than for younger faults.
Poisson distribution	A probability distribution that characterizes discrete events occurring independently of one another in time.
polarity	In <i>seismology</i> the direction of <i>first motion</i> on a <i>seismogram</i> , either up (compression) or down (dilatation or relaxation).

polarity reversal	The occurrence of <i>waveforms</i> that are mirror images of their related initial phases, e.g., the waveforms of depth phases with respect to their primary P- or S-type phases.
polarization	The shape and orientation in space of the ground-motion particle trajectory. It differs for different types of seismic waves such as P, S and <i>surface waves</i> and may be \pm linear or elliptical, prograde or retrograde. It is also influenced by heterogeneities and <i>anisotropy</i> of the medium in which the seismic waves propagate and depends on their <i>frequency</i> or <i>wavelength</i> , respectively. The polarization of <i>ground motion</i> may be reconstructed by analyzing three-component seismic recordings.
primary seismic station	IMS seismic station or array that is part of the detection network to monitor the CTBT.
P wave	A seismic body wave that involves particle motion (alternating compression and extension) in the direction of propagation. P waves travel faster than <i>S waves</i> and, therefore, arrive earlier in the record of a seismic event (P stands for “unda prima” = primary wave).
Quaternary	The geologic time period comprising about the last 1.65 million years.
radiation pattern	Dependence of the <i>amplitudes</i> of seismic <i>P</i> and <i>S waves</i> on the direction and take-off angle under which their <i>seismic rays</i> have left the <i>seismic source</i> . It is controlled by the type of source mechanism, e.g., the orientation of the earthquake <i>fault plane</i> and <i>slip</i> direction in space.
radiometric	Pertaining to the measurement of geologic time by the analysis of certain radioisotopes in rocks and their known rates of decay (see <i>¹⁴C age date</i>).
Rayleigh wave	A seismic surface wave causing a retrograde, elliptical motion of a particle at the free surface, with no transverse motion. It is named after Lord Rayleigh (1842-1919), who predicted its existence.
ray theory	Theoretical approach, which treats wave propagation as the propagation of <i>seismic rays</i> . It is an approximation, which yields good results for short wave length (high-frequency approximation) and allows easy calculations of travel times.
ray-tracing method	Computational method of calculating ground-shaking estimates that assumes that the <i>ground motion</i> is composed of multiple arrivals of <i>seismic rays</i> and related energy bundles (Gauss beams) that leave the source and are reflected or refracted at velocity boundaries according to Snell’s Law. The amplitudes of reflected and refracted waves at each boundary are recalculated according to the Law of Conservation of Energy.
recurrence interval	The average time span between large earthquakes at a particular site. Also termed “return period”.
reference channel	The array element to which the station’s timing is referenced with respect to its other elements, and thereby reflecting the timing of the array as a whole. It is typically either the element at the center of a circular <i>array</i> , or the element at the intersection of a cross-shaped array.

Glossary

reflection	The energy or wave from a <i>seismic source</i> that has been returned (reflected) from an interface between materials of different elastic properties within the Earth, just as a mirror reflects light.
reflector	An interface between materials of different elastic properties that reflects seismic waves.
refraction	(1) The deflection, or bending, of the ray path of a seismic wave caused by its passage from one material to another having different elastic properties. (2) Bending of a tsunami wave front owing to variations in the water depth along a coastline.
regression analysis	A statistical technique applied to data to determine, for predictive purposes, the degree of correlation of a dependent variable with one or more independent variables, in other words, to see if there is a strong or weak cause-and-effect relationship between two or more parameters.
relaxation theory	A concept in which radiated seismic energy is released from stored strain energy during the slip along a fault until the adjacent fault blocks reach a new state of equilibrium.
return period	See <i>recurrence interval</i> .
residual	The difference between the measured and predicted values of some quantity.
resonance	Strong increase in the amplitude of vibration in an elastic body or system when the frequency of the shaking force is close to one or more times of the natural frequencies of a shaking body.
response	The motion in a system resulting from shaking under specified conditions.
response spectrum	A curve showing the computed maximum response of a set of simple damped harmonic oscillators of different natural frequency to a particular record of ground acceleration. Response spectra, commonly plotted on tripartite logarithmic graph paper, show the oscillator's maximum acceleration, velocity, and displacement as a function of oscillator frequency for various levels of oscillator's damping. A computational approximation to the response spectrum is referred to as the pseudo-relative velocity response spectrum (PSRV). These curves are used by engineers to estimate the maximum response of simple structures to complex <i>ground motions</i> .
reverse movement	See <i>fault movement</i> .
rheological properties	The properties of rocks that describe their ability to deform and flow as a function of temperature, pressure, and chemical conditions.
right-lateral movement	See <i>fault movement</i> .
Ring of Fire	The zone of volcanoes and earthquakes surrounding the Pacific Ocean which is called the <i>Circum-Pacific belt</i> ; about 90% of the world's earthquakes occur there. The next most seismic region (5 – 6 % of earthquakes) is the <i>Alpide belt</i> .
root mean square	Square root of the mean value of a set of squared values.
run-up height	The maximum height of a tsunami wave when running into shallow waters near the coast; see <i>tsunami</i> .

rupture front	The instantaneous boundary between the slipping and locked parts of a fault during an earthquake. Rupture in one direction on the fault is referred to as unilateral. Rupture may radiate outward in a circular manner or it may radiate toward the two ends of the fault from an interior point, behavior referred to as bilateral.
rupture velocity	The speed at which a rupture front moves across the surface of the fault during an earthquake.
S wave	A seismic body wave that involves a shearing motion in the direction perpendicular to the direction of wave propagation. When it is resolved into two orthogonal components in the plane perpendicular to the direction of propagation, SH denotes the horizontal component and SV denotes the vertical component.
sand boil	Sand and water ejected to the ground surface during strong earthquake shaking as a result of <i>liquefaction</i> at shallow depth; the conical sediment deposit remains as evidence of liquefaction.
sea-floor spreading secular	See <i>magnetic polarity reversals</i> . Referring to long-term changes that take place slowly and imperceptibly. Commonly used to describe changes in elevation, tilt, and stress or strain rates that are related to long-term tectonic deformation. For example, a mountain that is growing is getting taller so slowly that we cannot see it happen, but if we measure the elevation in one year and then after, e.g., another time ten years later, we could see that it has grown taller.
segmentation	The breaking up of a fault along its length into several smaller faults. This can happen as a result of other faults crossing it, topography changes, or bends in the strike of the faults. Segmentation can limit the length of faulting in a single earthquake to some fraction of the total fault length, thus also limiting the maximum possible size of an earthquake on that fault.
seiche	Oscillation of the surface of an enclosed body of water owing to earthquake shaking. Lakes and swimming pools often have seiches during strong earthquakes.
seismic belt	An elongate earthquake zone, for example, the Circum-Pacific, Mediterranean, Rocky Mountains earthquake belt.
seismic constant	In building codes dealing with <i>earthquake hazard</i> , an arbitrarily set quantity of steady acceleration (in units of gravity g) that a building must withstand.
seismic event	General term for localized sources of different type which generate <i>seismic waves</i> .
seismic gap	A section of fault that has produced earthquakes in the past but is now quiet. For some seismic gaps, no earthquakes have been observed historically, but it is believed (on some other basis, such as plate-motion information or strain measurements) that the fault segment is capable of producing earthquakes. A long-term seismic gap may give hint to the most probable location of another strong earthquake in the future.
seismic hazard	See <i>earthquake hazard</i> .
seismic impedance	Seismic wave velocity multiplied by density of the medium.

Glossary

seismicity	The geographic and historical distribution of earthquakes.
seismic moment	A measure of the size of an earthquake based on the area of fault rupture, the average amount of slip, and the force that was required to overcome the friction sticking the rocks together that were offset by faulting. Seismic moment can also be calculated from the amplitude spectra of seismic waves.
seismic ray	Vector perpendicular to the wave front pointing into the direction of wave propagation and marking behind it the “ray trace”. The propagation of <i>seismic waves</i> can be easily modeled as the propagation of seismic rays following Snell’s Law. This assumption is a reasonable approximation for high frequency waves.
seismic line	A set of seismographs usually lined up along the Earth’s surface to record seismic waves generated by an explosion or by vibrators for the purpose of recording reflections and/or refractions of these waves from velocity discontinuities within the Earth. The data collected can be used to infer the internal structure of the Earth.
seismic risk	The probability of social or economic consequences of an earthquake.
seismic recorder	Device for recording seismic <i>ground motions</i> in analog or digital form (see <i>seismogram</i>), usually as a frequency-filtered and amplified equivalent electronic signal (see <i>transducer</i> and <i>data logger</i>).
seismic signal	A <i>coherent</i> transient <i>waveform</i> radiated from a definite, localized <i>seismic source</i> that is usually considered as an useful signal for the location of the source, the analysis of the source process and/or of the propagation medium (in contrast to <i>noise</i>)..
seismic sensor	There are two basic types of seismic sensors: inertial <i>seismometers</i> which measure ground motion relative to an inertial reference (a suspended mass), and <i>strainmeters</i> or extensometers which measure the motion of one point of the ground relative to another. Inertial seismometers are generally more sensitive to earthquake signals whereas strainmeters may outperform inertial seismometers when observing very long-period free oscillations of the Earth, tidal motions, and quasi-static deformations when it becomes increasingly difficult to maintain an inertial reference.
seismic source	A localized area or volume generating <i>coherent</i> , usually <i>transient</i> seismic <i>waveforms</i> , such as an <i>earthquake</i> , <i>explosion</i> , vibrator etc.
seismic station	See <i>station</i> .
seismic wave	An elastic wave generated by an impulse such as an earthquake or an explosion. Seismic waves may travel either along or near the Earth’s surface (<i>Rayleigh</i> and <i>Love waves</i>) or through the Earth’s interior (P and S <i>body waves</i>).
seismic zonation	Geographic delineation of areas having different potentials for hazardous effects from future earthquakes. Seismic zonation can be done at any scale - national, regional, local or site, the latter two often referred to as <i>microzonation</i> .
seismic zone	An area of seismicity probably sharing a common cause.

seismogenic	Capable of generating earthquakes.
seismogram	A record written by a seismograph in response to <i>ground motions</i> produced by an earthquake, explosion, or other sources that generate oscillating ground motions. Such a record may analog or digital.
seismograph	See <i>seismometer</i> .
seismology	The study of earthquakes and the structure of the Earth, by both naturally and artificially generated seismic waves.
seismometer	A seismometer is usually a damped oscillating mass that is connected with a fixed base and frame via a suspension, e.g., a spring. Such a damped mass-spring system is used to detect and measure seismic <i>ground motion</i> relative to the suspended mass which serves as an inertial reference. The motion of the base, which is fixed to the ground, with respect to the suspended mass is commonly transformed into an electrical voltage (see <i>transducer</i>). The electrical voltage is recorded on paper, magnetic tape, or another recording medium. This record, which may be analog or digital, is proportional to the relative motion, the velocity or the <i>acceleration</i> of the seismometer mass with respect to the ground on which the seismometer is installed, but it can be mathematically converted to a record of the absolute motion of the ground. Another type of seismometers are <i>strainmeters</i> . Seismograph is a term that refers to the seismometer as the <i>sensor</i> of the motion together with its recording device as a unit.
separation	The distance between any two parts of a reference plane (for example, a sedimentary bed or a geomorphic surface) offset by a fault, measured in any plane. Separation is the apparent amount of fault displacement and is nearly always less than the actual slip.
shear modulus	The ratio of shear stress to shear strain of a material during simple shear.
shear stress	The stress component parallel to a given surface, such as a fault plane, that results from forces applied parallel to the surface or from remote forces transmitted through the surrounding rock.
shear wave	See <i>S wave</i> .
signal	See <i>seismic signal</i> .
signal-to-noise ratio	The comparison between the <i>amplitude</i> of the <i>seismic signal</i> and the amplitude of the <i>noise</i> ; abbreviated as SNR.
signature	The appearance of a seismic signal that is more or less unique to the kind of <i>seismic source</i> .
slab	In the context of the Manual the oceanic crustal plate that underthrusts the continental plate in a subduction zone and is consumed by the Earth's <i>mantle</i> .
slab pull	The force of gravity causing the cooler and denser oceanic slab to sink into the hotter and less dense mantle material. The downdip component of this force leads to downdip extensional stress in the slab and may produce earthquakes within the subducted slab. Slab pull may also contribute to stress on the subduction thrust fault if the fault is locked.

Glossary

slickensides	Polished striated rock surfaces caused by one rock mass moving across another one on a fault.
slip	The relative <i>displacement</i> of formerly adjacent points on opposite sides of a fault.
slip model	A <i>kinematic</i> model that describes the amount, distribution, and timing of a slip associated with an earthquake.
slip rate	How fast the two sides of a fault are slipping relative to one another, as derived from seismic records in case of an earthquake or determined, as a long-term average, from geodetic measurements, from offset man-made structures, or from offset geologic features whose age can be estimated. It is measured parallel to the predominant slip direction or estimated from the vertical or horizontal offset of geologic markers.
slowness	The inverse of velocity, given in the unit seconds/degree or s/km; a large slowness corresponds to a low velocity.
soil	(1) In engineering, all unconsolidable material above the <i>bedrock</i> . (2) In soil science, naturally occurring layers of mineral and (or) organic constituents that differ from the underlying parent material in their physical, chemical, mineralogical, and morphological character because of <i>pedogenic</i> processes.
soil profile	Vertical arrangement of soil horizons down to the parent material or to <i>bedrock</i> . Commonly subdivided into A, B and C horizons.
source	See <i>seismic source</i> .
source depth	Depth of an earthquake <i>hypocenter</i> (see <i>focal depth</i>) or of a buried explosion, mining collapse, or any other type of <i>source</i> that generates seismic waves.
source function	The <i>ground motion</i> generated at the <i>fault</i> during rupture, usually as predicted by a theoretical model and represented by a time history or <i>spectrum</i> . The terms Brune spectrum, Aki spectrum, and Haskel model refer to varying representations of the source function, each based on different assumptions, as devised by the scientist for which the model is named.
spectral acceleration	Commonly refers to either the <i>Fourier amplitude spectrum</i> of ground <i>acceleration</i> or the <i>PSRV</i> ; abbreviated as SA.
spectral amplification	A measure of the relative shaking response of different geologic materials depending on the frequency of excitation; the ratio of the <i>Fourier amplitude spectrum</i> of a <i>seismogram</i> recorded on one material to that computed from a seismogram recorded on another material for the same <i>earthquake</i> or explosion.
spectrum	Curves showing <i>amplitude</i> and <i>phase</i> of a <i>time-history</i> as a function of <i>frequency</i> or <i>period</i> .
spread	The layout of <i>seismometer/geophone</i> groups from which data from a single shot (the explosive charge) or vibrator sweep are recorded simultaneously.
standard deviation	A measure of how much a set of data is different from the curve it should make when plotted on a graph. Or, the square root of the average of the squares of deviations about the mean of a set of data. Standard deviation is a statistical measure of spread or variability.

station	The site where geophysical instruments, e.g., <i>seismographs</i> , have been installed for observations. Stations can either be single sites or <i>arrays</i> .
Step-out	The time between two seismic <i>phases</i> , such as pP and P, at a specific epicentral distance of a <i>station</i> . The step-out, if it increases or decreases as the distance increases, can be a characteristic determinant for phase identification.
stick-slip	The rapid displacement that occurs between two sides of a <i>fault</i> when the shear <i>stress</i> on the fault exceeds the frictional stress. Also a jerky, sliding type of motion associated with <i>fault movement</i> in laboratory experiments. It may be a mechanism in shallow <i>earthquakes</i> . Stick -slip displacement on a fault radiates energy in the form of <i>seismic waves</i> .
stochastic strain	Applied to processes that have random characteristics. Small changes in length, volume or shape associated with deformation of the Earth by tectonic stresses or by the passage of seismic waves.
strainmeter	Strainmeters or extensometers are another basic type of <i>seismic sensors</i> . They measure the motion of one point of the ground relative to another, in contrast to inertial <i>seismometers</i> which measure the <i>ground motion</i> relative to an inertial reference such as a suspended mass.
strain rate	Strain measurements are computed from observed changes in length on the Earth's surface, commonly along multiple paths. Because the changes in length are observed over varying time periods and path lengths, they are expressed as the change in length divided by the measurement distance divided by the time period of measurement. This number, which is expressed as the change in length per unit length per unit time, is termed the strain rate. These measurements are used to infer the directions of principal strain and stress rates near the Earth's surface.
stratigraphy	The study of the character, form, and sequence of layered rocks.
stress	Force per unit area acting on a plane within a body. Six values are required to characterize completely the stress at a point in a <i>homogeneous, isotropic</i> medium: three normal components and three shear components.
stress drop	The difference between the stress on a fault before and after an earthquake. A parameter in many models of the earthquake source that has a bearing on the level of high-frequency shaking radiated by the earthquake. Commonly stated in units termed bars or megapascals (1 megapascal (MPa) = 10^6 N/m ² = 10 bars).
strike	Trend or bearing, relative to north, of the line defined by the intersection of a planar geologic surface (for example, a fault or a bed) and a horizontal surface such as the ground.
strike-slip	See <i>fault movement</i> .
strong motion	<i>Ground motion</i> of sufficient <i>amplitude</i> and duration to be potentially damaging to a building's structural components or architectural features.

Glossary

subduction	A plate tectonics term for the process whereby the oceanic lithosphere collides with and descends beneath the continental lithosphere.
subduction thrust fault	The fault that accommodates the differential motion between the downgoing oceanic crustal plate and the continental plate. This <i>fault</i> is the contact between the top of the oceanic plate and the bottom of the newly formed continental <i>accretionary wedge</i> . Also alternately referred to as the plate-boundary thrust fault, the thrust interface fault, or the megathrust fault.
subduction zone	An elongate region along which a block of crust descends relative to another crustal block, for example, the descend of the Pacific plate beneath the Andean plate along the Andean trench.
surface faulting	Displacement that reaches the Earth's surface during slip along a fault. Commonly accompanies moderate and large earthquakes having focal depths less than 20 km. Surface faulting also may accompany <i>aseismic</i> tectonic creep or natural or man-induced subsidence.
surface wave	Seismic wave that travels along or near to the Earth's surface. <i>Love</i> and <i>Rayleigh waves</i> are the most common.
S wave	A seismic <i>body wave</i> that involves a shearing <i>ground motion</i> (without volume change) perpendicular (transverse) to the direction of wave propagation. S waves travel slower than <i>P waves</i> . Accordingly, they arrive later in the <i>seismic record</i> of a <i>seismic event</i> (S stands for "unda secunda" = secondary wave).
tectonic	Refers to rock-deforming processes and resulting structures such as folds or faults that occur over large sections of the lithosphere.
tectonic plates	Large, relatively rigid plates of the <i>lithosphere</i> that move relative to one another on the outer surface of the Earth.
teleseism	A <i>seismic source</i> that is distant (more than about 2000 km away) from the recording station.
teleseismic	Pertaining to a seismic source at distances greater than about 2000 km from the measurement site.
tensional stress	The stress that tends to pull something apart. It is the stress component perpendicular to a given surface, such as a fault plane, that results from forces applied perpendicular to the surface or from remote forces transmitted through the surrounding rock.
theoretical onset	The point where an <i>arrival</i> is expected to appear on a <i>seismic record</i> , based on the known location and depth of the <i>seismic source</i> .
thrust fault	See <i>fault</i> .
tilt	An observed change in the slope of the Earth's surface.
time domain	A seismic record is usually presented in the time domain, i.e., as a display of varying amplitudes of (filtered) <i>ground motion</i> as a function of time (in contrast to the equivalent representation in the <i>frequency domain</i>) (see also <i>Fourier analysis</i>).
time history	The sequence of values of any time-varying quantity (such as a <i>ground motion</i> measurement) measured at a set of fixed times. Also termed time series.
timing error	A deviation from absolute time, as measured from a station.

transducer	Any of various devices that transmit energy from one system to another, sometimes one that converts the energy in form. For recording seismic <i>ground motion</i> the motion of the <i>seismometer</i> mass has to be transmitted either via a mechanical or optical lever system to the recorder (used in old classical <i>seismographs</i>) or to be converted into an equivalent electronic signal (as used in all modern seismometers). Transducers use different physical principles and devices such as coil-magnet systems, inductive bridges, capacity half-bridges, piezo-electric effects, interferometric-optical devices, etc. Accordingly, the output signal of the transducer may be proportional to ground <i>displacement</i> , <i>velocity</i> or <i>acceleration</i> .
transfer function	The transfer function of a seismic sensor-recorder system (or of the Earth medium through which seismic waves propagate) describes the frequency-dependent amplification, damping and phase distortion of seismic signals by a specific sensor-recorder (or medium). The modulus (real term = absolute value) of the transfer function is termed the frequency response function or <i>magnification curve</i> , e.g. of a <i>seismograph</i> .
transform fault	A special variety of strike-slip fault that accommodates relative horizontal slip between other tectonic elements, such as oceanic crustal plates. Often extend from oceanic ridges.
travel time	The time required for a wave traveling from its source to a point of observation.
travel-time curve	A graph of arrival times, commonly of direct as well as multiply reflected and converted P or S waves, recorded at different points as a function of distance from the <i>seismic source</i> . Seismic velocities within the Earth can be computed from the slopes of the resulting curves.
tsunami	An impulsively generated sea wave of local or distant origin that results from large-scale seafloor displacements associated with large earthquakes, major submarine slides, or exploding volcanic islands. When running into shallow waters near the coast the tsunami wave front, the “bore”, sometimes piles up the waters 30 m or higher and sweeps up to several km into shallow land. The run-up height strongly depends on coastal profile and shape. Bays and cone-shaped river mouths increase run-up heights.
tsunamigenic	Referring to those earthquake sources, commonly along major subduction-zone plate boundaries such as those bordering the Pacific Ocean, that can generate tsunamis.
tsunami magnitude	A number used to compare sizes of tsunamis generated by different <i>earthquakes</i> ; calculated from the logarithm of the maximum amplitude of the tsunami wave measured by a tide gauge distant from the tsunami source.
turbidite	Sea-bottom deposit formed by massive slope failures of large sedimentary deposits. These slopes fail in response to, e.g., earthquake shaking or excessive sedimentation load.
UNIX	A widely used operating system installed on many different workstations.
universal time (UT)	The absolute time using Greenwich Mean Time as reference.

Glossary

velocity	In reference to earthquake shaking, velocity is the time rate of change of ground displacement of a reference point during the passage of earthquake seismic waves, commonly expressed in nanometer or micrometer per second. However, velocity may also refer to the speed of propagation of seismic waves through the Earth, commonly expressed in kilometers per second.
velocity structure	A generalized local, regional or global model of the Earth that represents its structure in terms of the velocities of propagation of <i>P</i> and/or <i>S</i> waves.
Wadati-Benioff zone	A dipping planar (flat) zone of earthquakes that is produced by the interaction of a downgoing oceanic crustal plate with a continental plate. These earthquakes can be produced by slip along the <i>subduction</i> thrust fault (thrust interface between the continental and the oceanic plate) or by slip on faults within the downgoing plate as a result of bending and extension as the plate is pulled into the <i>mantle</i> . Slip may also initiate between adjacent segments of downgoing plates. Wadati-Benioff zones are usually well developed along the trenches of the Circum-Pacific belt, dipping towards the continents.
water table	The upper surface of a body of unconfined ground water at which the water pressure is equal to the atmospheric pressure.
waveform (data)	The complete analog or sufficiently dense sampled digital representation of a continuous wave group (e.g., of a seismic <i>phase</i>) or of a whole wave train (<i>seismogram</i>). Accordingly, waveform data allow to reconstruct and analyse the whole seismic phase or earthquake record both in the <i>time</i> and <i>frequency domain</i> whereas <i>parameter data</i> describe the signal only by a very limited number of more or less representative measurements such as <i>onset time</i> , maximum signal <i>amplitude</i> and related <i>period</i> .
wave front	The surface formed by all elements of a propagating wave, which swing “in phase”; the wave front is perpendicular to the <i>seismic rays</i> , which are oriented in direction of wave propagation.
wavelength	The distance between successive points of equal amplitude and phase on a wave (for example, crest to crest or trough to trough).

References

- Abe, K. (1975). Reliable estimation of the seismic moment of large earthquakes. *J. Phys. Earth*, **23**, 381-390.
- Abe, K. (1981). Magnitudes of large shallow earthquakes from 1904 to 1980. *Phys. Earth Planet. Interiors*, **27**, 72-92.
- Abe, K. (1989). Quantification of tsunamigenic earthquakes by the M_t scale. *Tectonophysics*, **166**, 27-34.
- Abe, K., and Kanamori, H. (1980). Magnitudes of great shallow earthquakes from 1953 to 1977. *Tectonophysics*, **62**, 191-203.
- Abercrombie, R. E. (1994). Regional bias in estimates of earthquake M_s due to surface-wave path effects. *Bull. Seism. Soc. Am.*, **84**, 2, 377-382.
- Ad Hoc Group of Scientific Experts to Consider International Cooperative Measures to Detect and Identify Seismic Events, 1991. Sourcebook for International Seismic Data Exchange. Conference Room Paper/167/Rev.2, Geneva, April 1991.
- Ad-hoc Panel (1981). Report on the Ad-hoc Panel meeting of experts on up-dating of the MSK-64 intensity scale, 10-14 March 1980, *Gerl. Beitr. Geophys.*, **90**, 261-268.
- Agnew, D. C. (1981). Nonlinearity in rock: evidence from Earth tides. *J. Geophys. Res.*, **86**, B5, 3969 - 3978.
- Agnew, D. C. (1986). Strainmeters and tiltmeters. *Rev. Geophys.*, **24**, 579 - 624.
- Agnew, D. C., Wyatt, F. K. (1989). The 1987 superstition hills earthquake sequence: strains and tilts at Pinion Flat Observatory. *Bull. Seism. Soc. Am.*, **79**, 2, 480 - 492.
- Aki, K. (1967). Scaling law of seismic spectrum. *J. Geophys. Res.*, **72**, 1217-1231.
- Aki, K., and Chouet, B. (1975). Origin of coda waves: Source, attenuation and scattering effects. *J. Geophys. Res.*, **80**, 3322.
- Aki, K., Christofferson, A., and Husebye, E. S. (1977). Determination of the three dimensional seismic structure of the lithosphere. *J. Geophys. Res.*, **82**, 277-296.
- Aki, K., and Richards, P. G. (1980). *Quantitative seismology*. Freeman, San Francisco, Vol. I and II, 932 pp.
- Aki, K., and Koyanagi, R. Y. (1981). Deep volcanic tremor and magma ascent mechanism under Kilauea, Hawaii. *J. Geophys. Res.*, **86**, 7095-7109.
- Aki, K., and Richards, P. G. (2002). *Quantitative seismology*. Second Edition, ISBN 0-935702-96-2, University Science Books, xvii + 700 pp.
- Albarelo, D., Berardi, A., Margottini, C., and Mucciarelli, M. (1995). Macroseismic estimates of magnitude in Italy. *Pure Appl. Geophys.*, **145**, 2, 297-312.
- Allen, R. V. (1978). Automatic earthquake recognition and timing from single traces. *Bull. Seism. Soc. Am.*, **68**, 1521-1532.
- Allen, R. V. (1982). Automatic phase pickers: Their present and future prospects. *Bull. Seism. Soc. Am.*, **72**, 225-242.
- Almendros, J., Ibàñez, J. M., Alguacil, G., Del Pezzo, E., and Ortiz, R. (1997). Array tracking of the volcanic tremor source at Deception Island, Antarctica. *Geophys. Res. Lett.*, **24**, 3069-3072.
- Almendros, J., Ibàñez, J. M., Alguacil, G., and Del Pezzo, E. (1999). Array analysis using circular-wave-front geometry: an application to locate the nearby seismo-volcanic source. *Geophys. J. Int.*, **136**, 159-170.
- Alsaker, A., Kvamme, L. B., Hansen, R. A., Dahle, A., and Bungum, H. (1991). The M_L scale in Norway. *Bull. Seism. Soc. Am.*, **81**, 2, 379-389.
- Ambraseys, N. N. (1975). The correlation of intensity with ground motion. Proc. XIV General Ass. ESC 1974 in Trieste, Published by Nationalkomitee für Geodäsie und Geophysik, Akademie der Wissenschaften der DDR, Berlin, 335-341.

References

- Ambraseys, N. N. (1985). Magnitude assessment of northwestern European earthquakes. *Earthquake Engineering and Structural Dynamics*, **13**, 307-320.
- Ambraseys, N. N. (1988). Magnitude-fault length relationships for earthquakes in the middle east. In: *Historical seismograms and earthquakes of the world*. Academic Press, 309-310.
- Ambraseys, N. N. (1990). Uniform magnitude re-evaluation of European earthquakes associated with strong-motion records. *Earthquake Engineering and Structural Dynamics*, **19**, 1-20.
- Ambraseys, N. N., and Adams, R. D. (1986). Seismicity of West Africa. *Annales Geophysicae*, **86**, 6, 679-702.
- Ambraseys, N. N., and Bommer, J. J. (1990). Uniform magnitude re-evaluation for the strong motion database of Europe and adjacent areas. *European Earthquake Engineering*, **2**, 3-16.
- Ambraseys; N. N., Simpson, K. A., and Bommer, J. J. (1996). Prediction of horizontal response spectra in Europe. *Earthquake Engineering and Structural Dynamics*, **25**, 371-400.
- Anderson, E. M. (1951). *The dynamics of faulting and dyke formation with applications to Britain*. 2nd ed. rev., Oliver & Boyd Publishers, Edinburgh.
- Anderson, K. R. (1982). Robust earthquake location using M-estimates, *Phys. Earth. Plan. Inter.*, **30**, 119-130.
- Anderson, D. L., and Given, J. W. (1982). Absorption band Q model for the Earth. *J. Geophys. Res.*, **87**, 3893-3904.
- Angenheister, G. H. (1921). Beobachtungen an pazifischen Beben. *Nachrichten von der Königlichen Gesellschaft der Wissenschaften zu Göttingen, Mathematisch-physikalische Klasse*, 113-146.
- Aoyama, H., and Takeo, M. (2001). Wave properties and focal mechanisms of N-type earthquakes at Asama volcano, *J. Volcanol. Geotherm. Res.*, **105**, 163-182.
- Archangelskaya, V. M. (1959). The dispersion of surface waves in the earth's crust. *Izv. Akad. Nauk SSSR, Seriya Geofiz.*, **9** (in Russian).
- Aster, R. C., and Shearer, P. (1991). High-frequency borehole seismograms recorded in the San Jacinto fault zone, Southern California. Part 1. Polarizations, *Bull. Seism. Soc. Am.*, **81**, 1057-1080.
- Astiz, L., Earle, P., and Shearer, P. (1996). Global stacking of broadband seismograms. *Seism. Res. Lett.*, **67**, 8-18.
- Atkinson, G. M., and Hanks, Th. (1995). A high-frequency magnitude scale. *Bull. Seism. Soc. Am.*, **85**, 3, 825-833.
- Bahavar, M., and North, R. (2002). Estimation of background noise for International Monitoring System seismic stations, *Pure Appl. Geophys.*, **159**, 911-944.
- Bakun, W. H., and Joyner, W. (1984). The M_L scale in Central California. *Bull. Seism. Soc. Am.*, **74**, 5, 1827-1843.
- Bard, P.-Y. (1999). Microtremor measurements: A tool for site effect estimation? In: Irikura, K., Kudo, K., Okada, H., and Sasatani, T. (Eds.) (1999). *The effects of surface geology on seismic motion*. Proc. 2nd International Symposium in Yokohama, Japan, 1-3 Dec. 1998, A. A. Balkema, Rotterdam, ISBN 90 5809 030 2, 1251-1279.
- Barker, B., Clark, M., Davis, P., Fisk, M., Hedlin, M., Israelsson, H., Khalturin, V., Kim, W.-Y., McLaughlin, K., Meade, C., Murphy, J., North, R., Orcutt, J., Powell, C., Richards, P., Stead, R., Stevens, J., Vernon, F., and Wallace, T. (1999). *Monitoring nuclear tests*. Science, **281**, 1967-1968.
- Barrientos, S., Haslinger, F., and IMS Seismic Section (2001). *Seismological monitoring of the Comprehensive Nuclear-Test-Ban Treaty*. Carl Hanser Verlag, München, Kerntechnik, **66**, 3, 82-89.

- Bartal, Y., Somer, Z., Leonhard, G., Steinberg, D. M., and Horin, Y. B. (2000). Optimal seismic networks in Israel in the context of the Comprehensive Test Ban Treaty. *Bull. Seism. Soc. Am.*, **90**, 1, p 151-165.
- Basham, P., and Kind, R. (1986). GRF-broadband array analysis of the 1982 Minamichi, New Brunswick earthquake sequence. *J. Geophys.*, **60**, 120-128.
- Bastings, L. (1934). Shear waves through the Earth's core. *Nature*, **134**, 216-217.
- Båth, M. (1979). *Introduction to seismology*, 428 pp., Birkhauser Verlag. Basel.
- Båth, M. (1981). Earthquake magnitude - recent research and current trends. *Earth Science Reviews*, **17**, 315-398.
- Båth, M. (1984). Earthquake magnitudes based on PKP and SKP waves. In: *The O.G.S. Silver Anniversary Volume*, O.G.S. Trieste, p. 93-108
- Båth, M. (1985). Surface-wave magnitude corrections for intermediate and deep earthquakes. *Physics Earth Planet. Interiors*, **37**, 228-234.
- Båth, M., Kulhánek, O., van Eck, T., and Wahlstroem, R. (1976). Engineering analysis of ground motion in Sweden. *Seismological Institute of Uppsala, University Report no. 5-76*.
- Baumbach, M. (1999). SEIS89 - A PC tool for seismogram analysis. In: Bormann (Ed.) *International Training Course 1999 on Seismology, Seismic Hazard Assessment and Risk Mitigation, Lecture and exercise notes, Vol. 1*, GeoForschungsZentrum Potsdam, Scientific Technical Reports STR99/13, 423-452.
- Beauchamp (ed.) (1975): *Exploitation of seismograph networks*, NATO Advanced Study Institutes Series E 111, Nordhoff Leiden, XII + 647 pp.
- Beauduin, R., Lognonné, P., Montagner, J. P., Cacho, S., Karczewski, J. F., and Morand, M. (1996). The effects of the atmospheric pressure changes on seismic signals or How to improve the quality of a station. *Bull. Seism. Soc. Am.*, **86**, 6, 1760-1769.
- Beaumont, C., Berger, J. (1976). Earthquake prediction: modification of Earth tide tilts and strains by dilatancy. *Geophys. J.R. astr. Soc.*, **39**, 111 - 118.
- Beavan, J., Bilham, R., Emter, D., King, G. C. P. (1979). Observation of strain enhancement across a fissure. *Dt. Geod. Komm., Reihe B*, **231**, 47 - 58.
- Ben-Menahem, A., and Singh, S. J. (1981). *Seismic waves and sources*. Springer-Verlag, New York, Heidelberg, Berlin, 1108 pp.
- Benz, H. M., Vidale, J. E., and Mori, J. (1994). Using regional seismic networks to study the Earth's deep interior. *EOS, Trans. Am. Geophys. Un.* **75**, 225, 229.
- Berckhemer, H. (1962). Die Ausdehnung der Bruchfläche im Erdbebenherd und ihr Einfluss auf das seismische Wellenspektrum. *Gerl. Beitr. Geophys.*, **71**, 5-26.
- Berckhemer, H., and Lindenfeld, M. (1986). Determination of source energy from broadband seismograms. In: Buttkus, B. (Ed.) (1986). *Ten years of the Gräfenberg Array: Defining the frontiers of broadband seismology*. *Geologisches Jahrbuch Reihe E, Heft 35*, 79-83.
- Bergman, E. A. (1991). *International Seismological Observing Period; Preliminary Science Plan. Appendix A: Global Network Phase Data Reported to the ISC*. USGS Working Document, 13 figs., 3 pp.
- Bergman, E. A. (1994). ISOP circular letter with attachments, April 10, 1994, 14 pp.
- Bergmann, E. A., and Sipkin, S. A. (1994). Measurement protocols for routine analysis of digital seismic data. January 11, 1994, 8 pp.
- Berlage Jr., H. P. (1932). *Seismometer*, *Handbuch der Geophysik* (Ed. Gutenberg, B.) Gebrüder Borntraeger Verlag, Berlin, Vol. 4, Chapter 4, 299-526.
- Berteussen, K. A. (1974). NORSAR location calibrations and time delay corrections. In: *NORSAR Semiannual Technical Summary. 1 October 1973 – 31 March 1974*. Scientific Report **2-73/74**, Kjeller, Norway, 41 pp.
- Berteussen, K. A. (1976). The origin of slowness and azimuth anomalies at large arrays. *Bull. Seism. Soc. Am.*, **66**, 719-741.

References

- Bijwaard, H., Spakman, W., and Engdahl, E. R. (1998). Closing the gap between regional and global travel time tomography. *J. Geophys. Res.*, **103**, 30055-30078.
- Birtill, J. W., and Whiteway, F. E. (1965). The application of phased arrays to the analysis of seismic body waves. *Phil. Trans. R. Soc. of London, Math. and Phys. Sciences A-258*, No. 1091, 421-493.
- Blackman, E. K., Orcutt, J. A., and Forsyth, D. W. (1995). Recording teleseismic earthquakes using ocean-bottom seismographs at mid-ocean ridges. *Bull. Seism. Soc. Am.*, **85**, 6, 1648-1664.
- Blake, A. (1941). On the estimation of focal depth from macroseismic data. *Bull. Seism. Soc. Am.*, **31**, 225-231.
- Boatwright, J., and Fletcher, J. B. (1984) The partition of radiated energy between P and S waves, *Bull. Seism. Soc. Am.*, **74**, 361-376.
- Boatwright, J., and Choy, G. (1986). Teleseismic estimates of the energy radiated by shallow earthquakes. *J. Geophys. Res.*, **91**, B2, 2095-2112.
- Bock, G., Grünthal, G., and Wylegalla, K. (1996). The 1985/86 Western Bohemia earthquakes: Modelling source parameters with synthetic seismograms. *Tectonophysics*, **261**, 139-146.
- Bolt, B. A. (1982). *Inside the Earth: Evidence from earthquakes*. Freeman, San Francisco.
- Bolt, B. A. (1993). *Earthquakes and geological discovery*. The Scientific American Library, W. H. Freeman and Company, New York, 220 pp.
- Bolt, B. A. (1999). *Earthquakes*. 4th edition, W. H. Freeman NY, 366 pp.
- Boore, D. M. (1977). The motion of the ground in earthquakes. *Scientific American*, December 1977, W. H. Freeman and Company, San Francisco, 1-19.
- Boore, D. M. (1989). The Richter scale: its development and use for determining earthquake source parameter. *Tectonophysics*, **166**, 1-14.
- Borcherdt, R. D. and Healy, J. H. (1968). A method for estimating the uncertainty of seismic velocities measured by refraction techniques. *Bull. Seism. Soc. Am.*, **58**, 1769-1790.
- Bormann, P. (1966). Recording and interpretation of seismic events (principles, present state and tendencies of development) (in German). Publications of the Institut für Geodynamik, Jena, Akademie Verlag, Berlin, Vol. 1, 158 pp.
- Bormann, P. (1971a). Statistische Untersuchungen zur Ortung teleseismischer Ereignisse aus Raumwellenregistrierungen der Station Moxa. Veröff. Zentralinstitut für Physik der Erde 9(1971), 103 pp.
- Bormann, P. (1971b). Location of teleseismic events by means of body-wave records at station Moxa (in German: Ortung teleseismischer Ereignisse aus Raumwellenregistrierungen der Station Moxa), *Monatsberichte der ADW*, **13**, 10-12, 847-852.
- Bormann, P. (1972a). A study of travel-time residuals with respect to the location of teleseismic events from body-wave records at Moxa station. *Gerl. Beitr. Geophys.*, **81**, 117-124.
- Bormann, P. (1972b). A study of relative frequencies of body-wave onsets in seismic registrations of the station Moxa. In: *Seismological Bulletin 1967, Station Moxa (MOX)*. Akademie-Verlag, Berlin 1972, 379-397
- Bormann, P. (1972c). Identification of teleseismic events in the records of Moxa station. *Gerl. Beitr. Geophys.*, **81**, 1/2, 105-116.
- Bormann, P. (1973). Standardization and optimization of frequency-characteristics at Moxa station (GDR). *Proceed. XII Assembly of ESC, Bukarest, Technical and Economic Studies, D-Series, No. 10*, 133-145.
- Bormann, P. (Ed.) (1989). *Monitoring and analysis of the earthquake swarm 1985/86 in the region Vogtland / Western Bohemia*. Akademie der Wissenschaften der DDR, Veröffentlichung Nr. 110 des Zentralinstituts für Physik der Erde, Potsdam, 419 pp.

- Bormann, P. (1994). Concept for a new "Manual of Seismological Observatory Practice". European Seismological Commission, XXIV General Assembly 1994, Sept. 19-24, Proceedings and Activity Report 1992-1994, Vol. II, Athens, Greece, Univ. of Athens, Faculty of Sciences, Dept. of Geophysics and Geothermy, Athens (1994), 698-707.
- Bormann, P. (1998). Conversion and comparability of data presentations on seismic background noise. *J. Seism.*, **2**, 37-45.
- Bormann, P. (1999). Regional International Training Course 1999 on Seismology, Seismic Hazard Assessment and Risk Mitigation. Lecture and exercise notes. Vol. I and II, GeoForschungsZentrum Potsdam, Scientific Technical Report STR99/13, 675 pp.
- Bormann, P. (2000). International Training Courses on Seismology and Seismic Risk Assessment. *Seism. Res. Lett.*, **71**, 5, 499-509.
- Bormann, P. and Stelzner, J. (1972). Seismological Bulletin 1967, Station Moxa (MOX), Zentralinstitut Physik der Erde (ZIPE), Akademie-Verlag Berlin, 396 pp.
- Bormann, P., and Khalturin, V. I. (1975). Relations between different kinds of magnitude determinations and their regional variations. Proceed. XIVth General Assembly of the European Seismological Commission, Trieste, 16-22 September 1974. Nationalkomitee für Geodäsie und Geophysik, AdW der DDR, Berlin, 27-39.
- Bormann, P., and Wylegalla, K. (1975). Investigation of the correlation relationships between various kinds of magnitude determination at station Moxa depending on the type of instrument and on the source area (in German). *Public. Inst. Geophys. Polish Acad. Sci.*, **93**, 160-175.
- Bormann, P., Wylegalla, K., and Grosser, H. (1992a). The strong mining event of March 13, 1989: Analysis of the multiple event. Proc. of the XXII. General Assembly of the European Seismological Commission (ESC), Barcelona, 17-22 Sept. 1990, Proceedings and Activity Report 1988-1990, Servei Geològic de Catalunya, 153-158.
- Bormann, P., Wylegalla, K., Strauch, W., and Baumbach, M. (1992b). Potsdam seismological station network: processing facilities, noise conditions, detection threshold and localization accuracy. *Phys. Earth Planet. Int.*, **69**, 311-321.
- Bormann, P., Burghardt, P.-T., Makeyeva, L. I., and Vinnik, L. P. (1993). Teleseismic shear wave splitting and deformations in Central Europe. *Physics Earth Planet. Int.*, **78**, 157-166.
- Bormann, P., Wylegally, K., and Klinge, K. (1997). Analysis of broadband seismic noise at the German Regional Seismic Network and search for improved alternative station sites. *J. Seism.*, **1**, 357-381.
- Bormann, P., and Wendt, S. (1999). Identification and analysis of longitudinal core phases: Requirements and guidelines. In: Bormann (1999), 346-366.
- Borne, G. von dem (1904). Seismische Registrierungen in Göttingen, Juli bis Dezember 1903. *Nachrichten von der Königlichen Gesellschaft der Wissenschaften zu Göttingen, Mathematisch-physikalische Klasse*, 440-464.
- Bracewell, R. N. (1978). *The Fourier transformation and its applications*. McGraw-Hill, New York, 2nd edn.
- Braddner, H., and Dodds, I. G. (1964). Comparative seismic noise on the ocean bottom and on land. *J. Geophys. Res.*, **69**, 20, 4339-4348.
- Braze, R. J. (1978). Reevaluation of Modified Mercalli intensity scale for earthquakes using distance as determinant, NOAA Tech. Mem EDS NGSDC-4.
- Brillinger, D. R., Udias, A., and Bolt, B. A. (1980). A probability model for regional focal mechanism solutions. *Bull. Seism. Soc. Am.*, **70**, 149-170.
- Broding, R. A., Bentley-Llewellyn, N. J., and Hearn, D. P. (1964). A study of three dimensional seismic detection system. *Geophysics*, **29**, 2, 221-249.
- Brune, J. N. (1970). Tectonic stress and the spectra of shear waves from earthquakes. *J. Geophys. Res.*, **75**, 4997-5009.

References

- Brune, J. N., and Oliver, J. (1959). The seismic noise of the Earth's surface. *Bull. Seism. Soc. Am.*, **49**, 349-353.
- Brune, J. N., and Engen, G. R. (1969). Excitation of mantle Love waves and definition of mantle wave magnitude. *Bull. Seism. Soc. Am.*, **59**, 923-933.
- Buchbinder, G. R., and Haddon, R. A. W. (1990). Azimuthal anomalies of short-period P-wave arrivals from Nahanni aftershocks, Northwest territories, Canada, and effects of surface topography. *Bull. Seism. Soc. Am.*, **80**, 5, 1272-1283.
- Bufo, E., and Udias, A. (1984). An algorithm for focal mechanism determination using signs of first motion of P, SV, SH waves. *Rev. Geofisica*, **40**, 11-26.
- Buland, R. (1976). The mechanics of locating earthquakes, *Bull. Seism. Soc. Am.*, **66**, 173-187.
- Buland, R., and Chapman, C. (1983). The computation of seismic travel times. *Bull. Seism. Soc. Am.*, **73**, 1271-1302.
- Bullen, K. E. (1937, 1938, 1939). The ellipticity correction to travel-times of P and S earthquake waves. *Montl. Not. R. Astr. Soc., Geophys. Suppl.*, **4**, 143-157, 158-164, 317-331, 332-337, 469-471.
- Bullen, K. E. (1946). A hypothesis on compressibility at pressures of the order of a million atmospheres. *Nature*, **157**, 405.
- Bullen, K. E., and Bolt, B. A. (1985). *An introduction to the theory of seismology*. Fourth Edition, Cambridge University Press, 499.
- Bulletin of the Seismological Society Special Symposia Issue (1990). Regional seismic arrays and nuclear test ban verification. *Bull. Seism. Soc. Am.*, **80**, No. 6, Part B, 1775-2281.
- Bune, V. J., Vvedenskaya, N. A., Gorbunova, J. V., Kondorskaya, N. V., Landyрева, N. S., and Fedorova, J. V. (1970). Correlation of M_{LH} and M_{PV} by data of the network of seismic stations of USSR. *Geophys. J. R. astr. Soc.*, **19**, 533-542.
- Bungum, H., Husebye, E. S., and Ringdal, F. (1971). The NORSAR array and preliminary results of data analysis. *Geophys. J. R. astr. Soc.*, **25**, 115-126.
- Burton, P. W., McGonigle, R., Neilson, G., and Musson, R. M. W. (1985). Macroseismic focal depth and intensity attenuation for British earthquakes, in: *Earthquake engineering in Britain*, Telford, London, 91-110.
- Buttkus, B. (Ed.) (1986). Ten years of the Gräfenberg array: defining the frontiers of broadband seismology. *Geologisches Jahrbuch E-35*, Hannover, 135 pp.
- Buttkus, B. (1991). *Spektralanalyse und Filtertheorie in der angewandten Geophysik*, Springer Verlag, Berlin Heidelberg New York, ISBN 3-540-54498-4, 1991.
- Bycroft, G. N. (1978). The effect of soil-structure interaction on seismometer readings, *Bull. Seism. Soc. Am.*, **68**, 823.
- Capon, J. (1969). High-resolution frequency-wavenumber spectrum analysis. *Proc. IEEE* **57**, 1408-1418.
- Casey, R., and Ahern, T. (1996). Technical manual for Networked Data Centers (NETDC) protocol (IRIS, internal report) or <http://www.iris.washington.edu/manuals/netdc/>
- Cassidy, F., Christoffersson, A., Husebye, E. S., and Ruud, B. O. (1990). Robust and reliable techniques for epicentre location using time and slowness observations. *Bull. Seism. Soc. Am.*, **80**, 1, 140-149.
- Cecić, I., Musson, R. M. W., and Stucchi, M. (1996). Do seismologists agree upon epicentre determination from macroseismic data? A survey of ESC Working Group "Macroseismology", *Annali di Geofisica*, **39**, 5, 1013-1027.
- Červený, V. (2001). *Seismic ray theory*. ISBN 0-521-36671-2, Cambridge University Press, New York, VII + 713 pp.
- Červený, V., Molotkov, I. A., and Pšenčík, I. (1977). *Ray methods in seismology*. Univerzita Karlova, Prague, 214 pp.

- Cessaro, R. K. (1994). Sources of primary and secondary microseisms. *Bull. Seism. Soc. Am.*, **84**, 1, 142-148.
- Chapman, C. H. (1978). A new method for computing synthetic seismograms. *Geophys. J. R. astr. Soc.*, **54**, 481-518.
- Chapman, C. H. (2002). Seismic ray theory and finite frequency extensions. In: Lee et al.(2002), Part A, 103-123.
- Chávez, E., and Priestley, K. F. (1985). M_L observations in the great basin and M_o versus M_L relationships for the 1980 Mammoth Lakes, California, earthquake sequence. *Bull. Seism. Soc. Am.*, **75**, 6, 1583-1598.
- Chen, P., and Chen, H. (1989). Scaling law and its applications to earthquake statistical relations. *Tectonophysics*, **166**, 53-72.
- Chen, Q. F., and Willemann, R. J. (2001). Global test of seismic event locations using three dimensional Earth models. *Bull. Seism. Soc. Am.*, **91**, 6, 1704-1716.
- Chernobay, I. P., and Gabsatarova, I. P. (1999). Source classification in the Northern Caucasus. *Phys. Earth Planet. Int.*, **113**, 183-201.
- Chinnery, M. A. (1969). Earthquake magnitude and source parameters. *Bull. Seism. Soc. Am.*, **59**, 5, 1969-1982.
- Chouet, B. (1982). Free surface displacements in the near field of a tensile crack expanding in three dimensions. *J. Geophys. Res.*, **87**, 3868-3872.
- Chouet, B. (1986). Dynamics of a fluid-driven crack in three dimensions by the Finite Difference Method, *J. Geophys. Res.*, **91**, 13, 967-13,992.
- Chouet, B. (1987). Resonance of a fluid-driven crack: radiation properties and implications for the source of long-period events and harmonic tremor. *J. Geophys. Res.*, **93**, 4375-4400.
- Chouet, B. (1996a). Long-period volcano seismicity: its source and use in eruption Forecasting. *Nature*, **380**, 309-316.
- Chouet, B. (1996b). New methods and future trends in seismological volcano monitoring. In: Scarpa, R., and Tilling, R. (1996), 23-97.
- Chouet, B. A., Page, R. A., Stephens, C. D., Lahr, J. C., and Power, J. A. (1994). Precursory swarms of long period events at Redoubt Volcano (1989-1990), Alaska: their origin and use as a forecasting tool. *J. Volcanol. Geotherm. Res.*, **62**, 95-135.
- Chouet, B., Saccorotti, G., Martini, M., Dawson, P., De Luca, G., Milana, G., and Scarpa, R. (1997). Source and path effects in the wavefields of tremor and explosions at Stromboli Volcano, Italy. *J. Geophys. Res.*, **102**, 15129-15150.
- Choy, G. L., and Richards, P. G. (1975). Pulse distortion and Hilbert transformation in multiply reflected and refracted body waves. *Bull. Seism. Soc. Am.*, **65**, 1, 55-70.
- Choy, G. L., and Cormier, V. F. (1986). Direct measurement of the mantle attenuation operator from broadband P and S Waveforms. *J. Geophys. Res.*, **91**, 7326-7342
- Choy, G. L., and Boatwright, J. L. (1995). Global patterns of radiated seismic energy and apparent stress. *J. Geophys. Res.*, **100**, B9, 18,205-18,228.
- Choy, G. L., Boatwright, J., and Kirby, S. (2001). The radiated seismic energy and apparent stress of interplate and intraslab earthquakes at subduction zone environments: Implications for seismic hazard estimation. U.S. Geological Survey Open-File Report 01-0005, 18 pp.
- Christoffersson, A., Husebye, E. S., and Ingate, S. F. (1988). Wavefield decomposition using ML-probabilities in modeling single-site 3-component records. *Geophys. Journal*, **93**, 197-213.
- Christoskov, L., Kondorskaya, N. V., and Vanek, J. (1978). Homogeneous magnitude system of the Eurasian continent. *Tectonophysics*, **49**, 131-138.

References

- Christoskov, L., Kondorskaya, N. V., and Vanek, J. (1983). Homogeneous magnitude system of the Eurasian continent: S and L waves. Report SE-34, World Data Center A for Solid Earth, Boulder.
- Christoskov, L., Kondorskaya, N. V., and Vanek, J. (1985). Magnitude calibration functions for a multidimensional homogeneous system of reference stations. *Tectonophysics*, **118**, 213-226.
- Civetta, L., Gasparini, P., Luongo, G., and Rapolla, A. (Eds.) (1974) *Physical volcanology*. Elsevier Publishers, Amsterdam, 333 pp.
- Claerbout, J. F. (1964), Detection of P-wave from weak sources at great distances. *Geophys.* **29**, 197-211.
- Conrad, V. (1925). Laufzeitkurven des Tauernbebens vom 28. November, 1923. *Mitteilungen der Erdbeben-Kommission der Akademie der Wissenschaften in Wien, Neue Folge* **59**.
- Cooley, J. S., and Tukey, J. W. (1965). An algorithm for the calculation of complex Fourier Series. *Math. Comp.*, **19**, 297-301.
- Cormier, V. F. (1982). The effect of attenuation on seismic body waves. *Bull. Seism. Soc. Am.*, **72**, 1, 169-200.
- Cosentino, M., Gresta, S., Lombardo, G., Pantane, G., Riuscetti, M., Schick, R., and Vigliani, A. (1984). Features of volcanic tremors at Mt. Etna (Sicily) during the March-August 1983 eruption. *Bull. Volcanol.*, **47**, 929-939.
- Cosentino, M., Lombardo, G., and Privitera, E. (1989). A model for internal dynamical processes on Mt. Etna. *Geophys. J. Int.*, **97**, 367-379.
- Crotwell, H. P., Owens, T. J.; Ritsema, J. (1999). The TauP toolkit: Flexible seismic travel-time and ray-path. *Seism. Res. Lett.* **70**, 154-160
- Dahlen, F. A., and Tromp, J. (1998). *Theoretical global seismology*. Princeton University Press.
- Dahlman, O., and Israelson, H. (1977). *Monitoring underground nuclear explosions*. Elsevier Scientific Publishing Company, Amsterdam-Oxford-New York, 440 pp.
- Dahm, T. (1996). Relative moment tensor inversion based on ray theory: theory and synthetic tests. *Geophys. J. Int.*, **124**, 245-257.
- Dahm, T., and Brandsdottir, B. (1997). Moment tensors of micro-earthquakes from the Eyjafjalajokull volcano in South Iceland, *Geophys. J. Int.*, **130**, 183-192.
- Das, S., and Kostrov, B. V. (1988). *Principles of earthquake source mechanics*. Cambridge University Press.
- Davies, D., Kelly, E. J., and Filson, J. R. (1971). The VESPA process for the analysis of seismic signals. *Nature* **232**, 8-13.
- Davison, C. (1900). Scales of seismic intensity, *Philosophical Magazine*, 5th Series, **50**, 44-53.
- Davison, C. (1921). On scales of seismic intensity and on the construction of isoseismal lines, *Bull. Seism. Soc. Am.*, **11**, 2, 95-129.
- Davison, C. (1933). Scales of seismic intensity: Supplementary paper, *Bull. Seism. Soc. Am.*, **23**, 158-166.
- Dawers, N. H., Anders, M. H., and Scholz, C. H. (1993). Growth of normal faults: Displacement-length scaling. *Geology*, **21**, 1107-1110.
- Deubel, K., Gaertner, H., Wolff, H., and Pröhl, S., (1996). Seismische Datenakquisition und Oberflächeneinfluß. In: Teßmer, G. (Ed.) *Lithologieerkundung für den Tiefenaufschluß mit seismischen Methoden (ILITASEIS)*", Abschlußbericht Band 1, Hamburg, 5-54.
- Dey-Sarkar, S. K. and Chapman, C. H. (1978). A simple method for the computation of body wave seismograms. *Bull. Seism. Soc. Amer.*, **68**, 1577-1593.
- Di Giovambattista, R., and Barba, S. (1997). An estimate of hypocenter location accuracy in a large network, possible implication for tectonic studies in Italy. *Geophys. J. Int.* **129**, 124-132.

- Doornbos, D. J. (Ed.) (1988a). Seismological algorithms, Computational methods and computer programs. Academic Press, New York, xvii + 469 pp.
- Doornbos, D. J. (1988b). Asphericity and ellipticity corrections. In: Doornbos (1988), 75-85.
- Doornbos, D. J., and Husebye, E. S. (1972). Array analysis of PKP phases and their precursors. *Phys. Earth Planet. Inter.*, **6**, 387-399.
- Doornbos, D. J., Engdahl, E. R., Jordan, T. H., and Bergman, E. A. (1991). International Seismological Observing Period; Preliminary Science Plan. Revised version. USGS Working Document, 11 figs., 21 pp.
- Douglas, A. (1967). Joint hypocenter determination. *Nature*, **215**, 47-48.
- Douglas, A. (2002). Seismometer arrays – their use in earthquake and test ban seismology. In: Lee et al. (2002), Part A, 357-367.
- Douglas, A., Hudson, J. A., Marshall, P. D., and Young, J. B. (1974). Earthquakes that look like explosions. *Geophys. J. R. astr. Soc.*, **36**, 227-233.
- Douglas, A., Stewart, R. C., and Richardson, L. (1984). Comments on “Analysis of broadband seismograms from the Chile-Peru area” by R. Kind, and D. Seidl. *Bull. Seism. Soc. Am.*, **74**, 2, 773-777.
- Douglas, A., and Rivers, D. W. (1988). An explosion that looks like an earthquake. *Bull. Seism. Soc. Am.*, **78**, 2, 1011-1019.
- Douglas, A., Bowers, D., and Young, J. B. (1997). On the onset of P seismograms. *Geophys. J. Int.*, **129**, 681-690.
- Douze, E. J. (1964). Signal and noise in deep wells. *Geophysics*, **29**, 5, 721-732.
- Dreier, R., Widmer, R., Schick, R., and Zürn, W. (1994). Stacking of broad-band seismograms of shocks at Stromboli. *Acta Vulcanol.*, **5**, 165-172.
- Driscoll, F. G. (1986). Groundwater and wells, Second Ed., published by Johnson Filtration Systems, Inc., St. Paul, MN, ISBN 0-9616456-0-1.
- Duda, S. J. (1986). The spectra and magnitudes of earthquakes. In: Buttkus, B. (Ed.). Ten years of the Gräfenberg Array: Defining the frontiers of broadband seismology. *Geologisches Jahrbuch Reihe E, Heft 35*, 71-79.
- Duda, S. J. (1989). Earthquakes: Magnitude, energy, and intensity. In: James, D. E. (Ed.). *The Encyclopedia of Solid Earth Geophysics*. Van Nostrand Reinhold Company, New York, 272-288.
- Duda, S. J., and Kaiser, D. (1989). Spectral magnitudes, magnitude spectra, and earthquake quantification: the stability issue of the corner period and of the maximum magnitude for a given earthquake. *Tectonophysics*, **166**, 205-219.
- Duda, S. J., and Yanovskaya, T. B. (1993). Spectral amplitude-distance curves for P-waves: effects of velocity and Q-distribution. *Tectonophysics*, **217**, 255-265.
- Dufumier, H. (1996). On the limits of linear tensor inversion of teleseismic body wave spectra. *Pageoph*, **147**, 467-482.
- Dziewonski, A. M., and Gilbert, F. (1976). The effect of small, aspherical perturbations on travel times and a re-examination of the corrections for ellipticity. *Geophys. J. R. astr. Soc.* **44**, 7-17.
- Dziewonski, A. M., Chou, T.-A., and Woodhouse, J. H. (1981). Determination of earthquake source parameters from waveform data for studies of global and regional seismicity. *J. Geophys. Res.*, **86**, 2825-2852.
- Dziewonski, A. M., and Anderson, D. L. (1981). Preliminary reference Earth model. *Physics of the Earth and Planetary Interiors*, **25**, 297-356.
- Dziewonski, A. M., and Anderson, D. L. (1983). Travel times and station corrections for P waves at teleseismic distances, *J. of Geophys. Res.*, **88**, 3295-3314.
- Eaton, J. P. (1992). Determination of amplitude and duration magnitudes and site residuals from short-period seismographs in Northern California. *Bull. Seism. Soc. Am.*, **82**, 2, 533-579.

References

- Ebel, J. E. (1982). M_L measurements for northeastern United States earthquakes. *Bull. Seism. Soc. Am.*, **72**, 1367-1378.
- Ebel, J. E. (1994). The $M_{Lg}(f)$ magnitude scale: A proposal for its use for northeastern North America. *Seism. Res. Lett.*, **65**, 2, 157-166.
- EEFIT (1993). EEFIT field investigations: objectives and methods. Earthquake Field Investigation Team, London, 2pp.
- Egen, P. N. C. (1828). Über das Erdbeben in den Rhein- und Niederlanden von 23 Feb. 1828, *Ann. Phys. Chem.*, **13**, 153-163.
- Ekström, G., and Dziewonski, A. M. (1988). Evidence of bias in estimations of earthquake size. *Nature*, **332**, 319-323.
- Endo, E. T., and Murray, T. L. (1991). Real-time seismic amplitude measurement (RSAM): a volcano monitoring and prediction tool. *Bull. Volcanol.*, **53**, 533-545.
- Engdahl, E. R., Van der Hilst, R. D., and Buland, R. P. (1998). Global teleseismic earthquake relocation with improved travel times and procedures for depth determination. *Bull. Seism. Soc. Am.*, **88**, 722-743.
- Evans, K., and Wyatt, F. (1984). Water table effects on the measurement of Earth strain. *Tectonophysics*, **108**, 323 - 337
- Evernden, J. F. (1971). Variation of Rayleigh-wave amplitude with distance. *Bull. Seism. Soc. Am.*, **61**, 231-240.
- Ewing, W. M., Jardetzky, W. W., and Press, F. (1957). *Elastic waves in layered media*. McGraw-Hill, New York.
- Fedotov, S. A., and Slavina, L. B. (1968). Estimate of the velocity of longitudinal waves in the upper mantle under the northwestern part of the Pacific Ocean and Kamchatka (in Russian). *Izv. Akad. Nauk SSSR, Fizika Zemli*, **2**, 8-31.
- Ferber, R.-G. (1989). Recursive deconvolution filters for seismograph systems. *Bull. Seism. Soc. Am.*, **79**, 5, 1629-1641.
- Fields, E., and Jacob, K. (1993). The theoretical response of sedimentary layers to ambient seismic noise. *Geophys. Res. Lett.*, **20**, 24, 2925-2928.
- Fix, J. E. (1972). Ambient Earth motion in the period range from 0.1 to 2560 sec. *Bull. Seism. Soc. Am.*, **62**, 1753-1760.
- Fix, J. E., and Sherwin, J. R. (1970). A high-sensitivity strain-inertial seismograph installation. *Bull. Seism. Soc. Am.*, **60**, 1803 - 1822.
- Flinn, E. (1965). Signal analysis using rectilinearity and direction of particle motion. *Proc. IEEE*, **53**, 1874-1876.
- Francis, T. J. G., Porter, I. T., and Lilwall, R. C. (1978). Microearthquakes near the eastern end of St. Paul's Fracture Zone, *Geophys. J. R. astr. Soc.*, **53**, 201-217.
- Frankel, A. (1994). Implications of felt area-magnitude relations for earthquake scaling and the average frequency of perceptible ground motion. *Bull. Seism. Soc. Am.*, **84**, 2, 462-465.
- Freiberger, W. F. (1963). An approximation method in signal detection. *Quart. J. App. Math.* **20**, 373-378.
- Friedrich, A. (1996). Untersuchung der breitbandigen seismischen Bodenunruhe an GRF- und GRSN-Stationen. Diploma Thesis, Department of Physics, University of Erlangen-Nürnberg.
- Friedrich, A., Klinge, K., and Krüger, F. (1998). Ocean-generated microseismic noise located with the Gräfenberg array. *J. Seism.*, **2**, 47-64.
- Frohlich, C. (1995). Characteristics of well-determined non-double-couple earthquakes in the Harvard CMT catalog, *Phys. Earth Planet. Inter.*, **91**, 213-228.
- Frosch, R. A., and Green Jr., P. E. (1966). The concept of a large aperture seismic array. *Proc. R. Soc. A* **290**, 368-384.
- Fuchs, K., and Müller, G. (1971). Computation of synthetic seismograms with the reflectivity method and comparison to observations. *Geophys. J. R. astr. Soc.*, **23**, 417-433.

- Fukushima, Y. (1996). Scaling relations for strong ground motion prediction models with M^2 terms. *Bull. Seism. Soc. Am.*, **86**, 2, 329-336.
- Furumoto, M., Kunitomo, T., Inoue, H., Yamada, I., Yamaoka, K., Ikami, A., and Fukao, Y. (1990). Twin Sources of High-Frequency Volcanic Tremor of Izu-Oshima Volcano. *Japan. Geophys. Res. Lett.*, **17**, 25-27.
- Fyen, J. (1989). Event processor program package. In: *NORSAR Semiannual Technical Summary*. 1 Oct 1988 – 31 Mar 1989. Scientific Report **2-88/89**, Kjeller, Norway.
- Fyen, J. (2001). *NORSAR seismic data processing – user guide and command reference*. NORSAR (contribution 731) Kjeller, Norway.
- Galanopolous, A. G. (1961). On magnitude determination by using macroseismic data. *Ann. Geofis.*, **14**, 225-253.
- Galitzin, B. B. (1914). *Vorlesungen über Seismometrie*. Verlag Teubner, Berlin 1914, VIII + 538 pp.
- Gal'perin, E. I. (1955). *Azimutal'nij metod sejsmiceskich nabludenij*. Gostoptechizdat, 80 pp.
- Gal'perin, E. I. (1977). *Polyarizationnyi metod seismicheskikh isledovanii* Nedra Press, Moskow.
- Geiger, L. (1910). Herdbestimmung bei Erdbeben aus den Ankunftszeiten. *Nachrichten von der Königlichen Gesellschaft der Wissenschaften zu Göttingen, Mathematisch-Physikalische Klasse*, 331-349. (1912 translated to English by F.W.L. Peebles and A.H. Corey: Probability method for the determination of earthquake epicenters from the arrival time only. *Bulletin St. Louis University* **8**, 60-71).
- Geller, R. J. (1976). Scaling relations for earthquake source parameters and magnitudes. *Bull. Seism. Soc. Am.*, **66**, 1501-1523.
- Gephart, J. W., and Forsyth, D. W. (1984). An improved method for determining the regional stress tensor using earthquake focal mechanism data: application to the San Fernando earthquake sequence. *J. Geophys. Res.*, **89**, 9305-9320.
- Gilbert, F., and Dziewonski, A. M. (1975). An application of normal mode theory to the retrieval of structural parameters and source mechanisms from seismic spectra. *Philos. Trans. R. Soc. London, Ser. A* **278**, 187-269.
- Gilpin, R. (1962). *American scientists and nuclear weapons policy*. Princeton Univ. Press.
- Gladwin, M. T. (1984). High precision multi-component borehole deformation monitoring. *Rev. Sci. Instrum.*, **55**, 2011 - 2016.
- Goforth, T., and Herrin, E. (1981). An automatic seismic signal detection algorithm based on the Walsh transform. *BSSA*, **71**, 1351-1360.
- Goldman, D. E., and Gierke, H. E. (1961). Effects of shock and vibration on man. Chapter 44, In: Harris, C. M., and Crede, C. E. (Eds.): *Shock and Vibration Handbook*. McGraw-Hill, New York.
- Gomberg, J. S., Shedlock, K. M., and Roecker, W. W. (1990). The effect of S-wave arrival times on the accuracy of hypocenter estimation. *Bull. Seism. Soc. Am.*, **80**, 6, 1605-1628.
- Gomberg, J., Agnew, D. C. (1996). The Accuracy of Seismic Estimates of Dynamic Strains: An Evaluation Using Strainmeter and Seismometer Data from Pinion Flat Observatory, California. *Bull. Seism. Soc. Am.*, **86**, 212 - 220.
- Gorbunova, I. V., and Kondorskaya, N. V. (1977). Magnitudes in the seismological practice of the USSR. *Izv. Akad. Nauk SSSR, ser Fizika Zemli*, No. 2, Moscow (in Russian).
- Gordon, D. W. (1971). Surface-wave versus body-wave magnitude. *Earthquake Notes*, **42**, 3/4, 20-28.
- Gottschämmer, E. (1999). Volcanic tremor associated with eruptive activity at Bromo Volcano. *Ann. Geofis.*, **43**, 465-481.
- Gottschämmer, E., and Surono, I. (2000). Locating tremor and shock sources recorded at Bromo Volcano. *J. Volcanol. Geotherm. Res.*, **101**, 199-209.

References

- Gouly, N. R., King, G. C. P., and Wallard, A. J. (1974). Iodine stabilized laser strainmeter. *Geophys. J. R. astr. Soc.*, **39**, 269 - 282.
- Granville, J. P., Kim, W.-Y., and Richards, P. G. (2002). An assessment of seismic body-wave magnitudes published by the Prototype International Data Centre. Pre-print, submitted to *Seism. Res. Lett.* on April 10.
- Greenhalgh, S. A., and Singh, R. (1986). A revised magnitude scale for South Australian earthquakes. *Bull. Seism. Soc. Am.*, **76**, 3, 757-769.
- Greenhalgh, S. A., Denham, D., McDougall, R., and Rynn, J. M. (1989). Intensity relations for Australian earthquakes. *Tectonophysics*, **166**, 255-267.
- Griggs, D., and Press, F. (1961). Probing the earth with nuclear explosions. *J. Geophys. Res.*, **66**, 1, 237-258.
- Grünthal, G. (Ed.) (1998). European Macroseismic Scale 1998, *Cahiers du Centre Européen de Géodynamique et de Seismologie*, 15, Conseil de l'Europe, Luxembourg, 99 pp.
- Gurwitsch, I. I., 1970. *Seismische Erkundung*. Akademische Verlagsgesellschaft Geest & Portig K.-G., Leipzig, 699 pp.
- Gusev, A. A. (1991). Intermagnitude relationships and asperity statistics. *Pure Appl. Geophys.*, **136**, 515-527.
- Gutenberg, B. (1925). *Bearbeitung von Aufzeichnungen einiger Weltbeben*. *Abhandlungen der Senckenbergischen Naturforschenden Gesellschaft*, **40**, 57-88.
- Gutenberg, B. (1945a). Amplitudes of surface waves and magnitudes of shallow earthquakes. *Bull. Seism. Soc. Am.*, **35**, 3-12.
- Gutenberg, B. (1945b). Amplitudes of P, PP, and S and magnitude of shallow earthquakes. *Bull. Seism. Soc. Am.*, **35**, 57-69.
- Gutenberg, B. (1945c). Magnitude determination of deep-focus earthquakes. *Bull. Seism. Soc. Am.*, **35**, 117-130.
- Gutenberg, B., and Richter, C. F. (1933). Advantages of using geocentric latitude in calculating distances. *Gerl. Beitr. Geophysik* **40**, 380-389.
- Gutenberg, B., and Richter, C. F. (1934). On seismic waves (first paper). *Gerl. Beitr. Geophysik* **43**, 56 – 133.
- Gutenberg, B., and Richter, C. F. (1936a). On seismic waves (third paper). *Gerl. Beitr. Geophysik*, **47**, 73-131.
- Gutenberg, B., and Richter, C. F. (1936b). Materials for the study of deep-focus earthquakes. *Bull. Seism. Soc. Am.* **26**, 341 – 390 (edition in French: *Données relatives a l'étude des tremblements de terre a foyer profond*. Publications du Bureau Central Séismologique International, Série A, *Travaux Scientifiques* **15**, 1 - 70, 1937).
- Gutenberg, B., and Richter, C. F. (1937). Materials for the study of deep-focus earthquakes (second paper). *Bull. Seism. Soc. Am.* **27**, 157 – 184 (partly edited in French: *Données relatives a l'étude des tremblements de terre a foyer profond*. Publications du Bureau Central Séismologique International, Série A, *Travaux Scientifiques* **15**, 1 - 70, 1937).
- Gutenberg, B., and Richter, C. F. (1942). Earthquake magnitude, intensity, energy and acceleration. *Bull. Seism. Soc. Am.*, **32**, 163-191.
- Gutenberg, B., and Richter, C. F. (1954). *Seismicity of the Earth*. Princeton University Press, 2nd ed., 310 pp.
- Gutenberg, B., and Richter, C. F. (1956a). Magnitude and energy of earthquakes. *Annali di Geofisica*, **9**, 1-15.
- Gutenberg, B., and Richter, C. F. (1956b). Earthquake magnitude, intensity, energy and acceleration. *Bull. Seism. Soc. Am.*, **46**, 105-145.
- Gutenberg, B., and Richter, C. F. (1956c). The energy of earthquakes. *Q. J. Geol. Soc. London*, **112**, 1-14.
- Habermann, R. E. (1995). Opinion. *Seism. Res. Lett.*, **66**, 5, 3.

- Hanka, W., and Kind, R. (1994). The GEOFON Program. *Annali di Geofisica*, **37**, 5, 1060-1065.
- Hanks, T. C. (1977). Earthquake stress drops, ambient tectonic stress, and the stresses that drive plate motion. *Pure Appl. Geophys.*, **115**, 441-458.
- Hanks, T. C., Hileman, J. A., and Thatcher, W. (1975). Seismic moments of the larger earthquakes of the southern California region. *Soc. Bull. Geol.*, **86**, 1131-1139.
- Hanks, T. C., and Johnston, A. C. (1992). Common features of the excitation and propagation of strong ground motion for North American earthquakes. *Bull. Seism. Soc. Am.*, **82**, 1-23.
- Hardt, M., and Scherbaum, F. (1994). The design of optimum networks for aftershock recordings. *Geophys. J. Int.*, **117**, 716-726.
- Harjes, H.-P. (1990). Design and siting of a new regional seismic array in Central Europe. *Bull. Seism. Soc. Am.*, **80**, 1801-1817.
- Harjes, H.-P., and Henger, M. (1973). Array-Seismologie, *Z. Geophys.*, **39**, 865-905 (in German).
- Harjes, H.-P., and Seidl, D. (1978). Digital recording and analysis of broad-band seismic data at the Gräfenberg (GRF-) array. *J. Geophys.*, **44**, 511-523.
- Haskell, N. A. (1953). The dispersion of surface waves on multilayered media. *Bull. Seism. Soc. Am.*, **43**, 17-43.
- Haskell, N. A. (1964). Total energy and energy spectral density of elastic wave radiation from propagating faults. *Bull. Seism. Soc. Am.*, **54**, 1811-1841.
- Haskell, N. A. (1966). Total energy and energy spectral density of elastic wave radiation from propagating faults. Part II. A statistical fault model. *Bull. Seism. Soc. Am.*, **56**, 125-140.
- Hatzidimitriou, P., Papazachos, C., Kiratzi, A., and Theodulidis, N. (1993). Estimation of attenuation structure and local earthquake magnitude based on acceleration records in Greece. *Tectonophysics*, **217**, 243-253.
- Haubrich, R. A. (1968). Array design. *Bull. Seism. Soc. Am.*, **58**, 977-991.
- Haubrich, R. A., Munk, W. H., and Snodgrass, F. E. (1963). Comparative spectra of microseisms and swell. *Bull. Seism. Soc. Am.*, **53**, 27-37.
- Havskov, J. (Ed.) (1996). The SEISAN earthquake analysis software for the IBM PC and SUN, Version 5.2. Institute of Solid Earth Physics, Univ. of Bergen, August 1996.
- Havskov, J., and Ottemöller, L. (1999 a). SeisNet: A general purpose virtual seismic network. *Seism. Res. Lett.*, **70**, 522-528.
- Havskov, J., and Ottemöller, L. (1999 b). Electronic Seismologist - SeisAn Earthquake Analysis Software. *Seism. Res. Lett.*, **70**, 532-534.
- Havskov, J., and Alguacil, G. . (2004). Instrumentation in earthquake seismology. *Modern Approaches in Geophysics*, Vol. 22, Springer, 358 pp. plus CD.
- Hellweg, M., Seidl, D., Kirbani, S. B., and Brüstle, W. (1994). Team investigates activity at Mt. Semeru, Java, volcano, *EOS*, **75**, 313-317.
- Hellweg, M. (1999). Listening carefully: unique observations of harmonic tremor at Lascar volcano, Chile. *Ann. Geofisica*, **42**, 451-464.
- Hellwege, K.-H. (Ed) (1982). *Landolt-Börnstein: Numerical Data and functional relationships in science and technology*. Vol. 1, Physical properties of rocks, subvolume b, Elasticity of rocks and minerals. Springer-Verlag Berlin-Heidelberg-New Yorks, 41-74.
- Henger, M. (1981). Noise measurements in a borehole near Gorleben (personal communication).
- Henger, M. (Reporter) (1995). Abschlussbericht Breitbandfassung seismischen Wellenfeldes im Bereich der Bundesrepublik Deutschland. Phase A: Errichtung und Betrieb der seismischen Stationen und des Datezentrums. DFG- Forschungsvorhaben Du 36/9-1,2 und Ba 1276/1-1, BGR Archiv Nr. 113 510.

References

- Henger, M., Stork, B., and Leydecker, G. (1981). Entwicklung und Aufbau eines seismischen Stationsnetzes im Raum Gorleben. Bericht der Bundesanstalt für Geowissenschaften und Rohstoffe, Hannover.
- Herak, M., and Herak, D. (1993). Distance dependence of M_S and calibrating function for 20 s Rayleigh waves. *Bull. Seism. Soc. Am.*, **83**, 6, 1881-1892.
- Herrmann, R. B. (1975). The use of duration as a measure of seismic moment and magnitude. *Bull. Seism. Soc. Am.*, **65**, 899-913.
- Herrmann, R. B., and Nuttli, O. W. (1982). Magnitude: The relation between M_L and m_{bLg} . *Bull. Seism. Soc. Am.*, **72**, 389-397.
- Herrmann, R. B., and Kijko, A. (1983). Modeling some empirical L_g relations. *Bull. Seism. Soc. Am.*, **73**, 1835-1850.
- Hidayat, D., Voight, B., Langston, C., Ratdomopurbo, A., and Ebeling, C. (2000). Broadband seismic experiment at Merapi Volcano, Java, Indonesia: very-long-period pulses embedded in multiphase earthquake. *J. Volcanol. Geotherm. Res.*, **100**, 215-231.
- Holcomb, G. L. (1989). A direct method for calculating instrument noise levels in side-by-side seismometer evaluations. Open-file report 89-214, U. S. Geological Survey.
- Holcomb, G. L. (1990). A numerical study of some potential sources of error in side-by-side seismometer evaluations. Open-file report 90-406, U. S. Geological Survey.
- Holcomb, G. L., and Hutt, C. R. (1992). An evaluation of installation methods for STS-1 seismometers. Open File Report 92-302, U. S. Geological Survey, Albuquerque, NM.
- Horst, W., and Küstermann, W. (1995). Ergebnisse reflexionsseismischer Messungen im Bereich der Struktur Rüdersdorf. In: Schroeder, J. H. (Ed.). Fortschritte in der Geologie von Rüdersdorf. Berliner Geowissenschaftliche Abhandlungen, Reihe A, Band 168, FU Berlin, 135-146.
- Hutton, L. K., and Boore, D. M. (1987). The M_L scale in Southern California. *Bull. Seism. Soc. Am.*, **77**, 6, 2074-2094.
- Houard, S., Plantet, J. L., Massot, J. P., and Nataf, H. C. (1993). Amplitudes of core waves near the PKP caustic, from nuclear explosions in the South Pacific recorded at the "Laboratoire de Detection et Geophysique" network in France. *Bull. Seism. Soc. Am.*, **83**, 6, 1835-1854.
- Houston, H., and Kanamori, H. (1986). Source spectra of great earthquakes: teleseismic constraints on rupture process and strong motion. *Bull. Seism. Soc., Am.*, **76**, 1, 19-42.
- Hutt, C. R., Bolton, H. F., and Holcomb, L. G. (2002). U.S. contribution to digital global seismograph networks. In: Lee et al. (2002), Part A, 319-332.
- Hutton, L. K., and Boore, D. M. (1987). The M_L scale in Southern California. *Bull. Seism. Soc. Am.*, **77**, 6, 2074-2094.
- Hutton, L. K., and Jones, L. M. (1993). Local magnitudes and apparent variations in seismicity rates in Southern California. *Bull. Seism. Soc. Am.*, **83**, 2, 313-329.
- Hwang, L. J., and Clayton, R. W. (1991). A station catalog of ISC arrivals: Seismic station histories and station residuals. U.S. Geological Service Open-File Report 91-295.
- Hyvernaud, O., Reymond, D., Talandier, J., and Okal, E. A. (1993). Four years of automated measurement of seismic moments at Papeete using the mantle magnitude M_m : 1987-1991. *Tectonophysics*, **217**, 175-193.
- IDC Documentation (May 1998). Technical Instructions: Analyst instructions for seismic, hydroacoustic, and infrozonic data, 103pp.
- Iida, K. (1959). Earthquake energy and earthquake fault length. *J. Earth Sci., Nagoya Univ.*, **7**, 98-107.
- Iida, K. (1959). *J. Earth Sci. Nagoya Univ.*, **7**, 2, 98-107.
- Imbo, G. (1954). Sismicita del parossismo vesuviano del marzo 1944. *Annali del Oss. Vesuviano, Sesta Serie*, **1**, 1-211.

- ISC (2001). International Seismological Centre, On-line Bulletin, <http://www.isc.ac.uk/Bull>, Internatl. Seism. Cent., Thatcham, United Kingdom.
- Ishihara, K. (1996). Soil Behaviour in Earthquake Geotechnics. Oxford Engineering Science Series, No 46, Clarendon Press, ISBN: 0198562241.
- Jacob, K. H. (1972). Global tectonic implications of anomalous seismic P travel-times from the nuclear explosion Longshot. *J. Geophys. Res.* **77**, 14.
- Jánosi, I. (1907). Makroszeizmikus rengések feldolgozása a Cancani-féle egyenlet alapján, in Réthly, A., (Ed.) Az 1906 évi Magyarországi Földrengések, A. M. Kir. Orsz. Met. Föld. Int., Budapest, 77-82.
- Japanese Meteorological Agency (1996). Explanation Table of JMA Seismic Intensity Scale (February 1996), 4pp.
- J-Array Group (1993). The J-array program: system and present status. *J. Geomag. Geoelectr.*, **45**, 1265-1274.
- Jeffreys, H. (1926). On near earthquakes. *Month. Not. Roy. Astr. Soc., Geophys. Suppl.* **1**, 385-402.
- Jeffreys, H., and Bullen, K. E. (1940, 1948, 1958, 1967, and 1970). *Seismological Tables*. British Association for the Advancement of Science, Gray Milne Trust, London, 50 pp.
- Jennings, P. C., and Kanamori, H. (1983). Effect of distance on local magnitudes found from strong motion records, *Bull. Seism. Soc. Am.*, **73**, 265-280.
- Johnson, C. E., Bittenbinder, A., Bogaert, B., Dietz, L., and Kohler, W. (1995). Earthworm: A Flexible Approach to Seismic Network Processing. *IRIS Newsletter*, **14**, 2, 1-4.
- Johnson, J. B., and Lees, J. M. (2000). Plugs and chugs - seismic and acoustic observations of degassing explosions at Karymsky, Russia and Sangay, Ecuador. *J. Volcanol. Geotherm. Res.*, **101**, 67-82.
- Johnston, A. C. (1993). The stable continental region data base. In: *The earthquakes of stable continental regions: Assessment of large earthquake potential*. EPRI report TR-102261, Electric Power Research Institute, Palo Alto, California.
- Jones, R. V., and Richards, J. C. S. (1973). The design and some applications of sensitive capacitance micrometers. *J. Physics E: Scientific Instruments*, **6**, 589-600.
- Jost, M. L., and Herrmann, R. B. (1989). A student's guide to and review of moment tensors. *Seism. Res. Lett.*, **60**, 37-57.
- Joswig, M. (1990). Pattern recognition for earthquake detection. *Bull. Seism. Soc. Am.*, **80**, 170-186.
- Joswig, M. (1993). Single-trace detection and array-wide coincidence association of local earthquakes and explosions. *Computers and Geosciences*, **19**, 207-221.
- Joswig, M. (1995). Artificial intelligence techniques applied to seismic signal analysis. *Conseil de Léurope, Cahiers du Centre Européen de Géodynamique et de Séismologie*, Vol. 9, Proceedings of the Workshop: Dynamic systems and artificial intelligence applied to data banks in geophysics, 5-15.
- Jurkevics, A. (1988). Polarization analysis of three-component array data. *Bull. Seism. Soc. Am.*, **78**, 1725-1743.
- Kanamori, H. (1977). The energy release in great earthquakes. *J. Geophys. Res.* **82**, 2981-2987.
- Kanamori, H., and Cipar, J. J. (1974). Focal process of the great Chilean earthquake May 22, 1960. *Phys. Earth Planet. Inter.*, **9**, 128-136.
- Kanamori, H. (1980). The size of earthquakes. *Earthquake information bulletin*, **12**, 1, 10-15.
- Kanamori, H. (1983). Magnitude scale and quantification of earthquakes. *Tectonophysics*, **93**, 185-199.
- Kanamori, H., and Anderson, D. L. (1975). Theoretical basis of some empirical relations in seismology. *Bull. Seism. Soc. Am.*, **65**, 1073-1095.

References

- Kanamori, H., and Jennings, P. C. (1978). Determination of local magnitude, M_L , from strong motion accelerograms. *Bull. Seism. Soc. Am.*, **68**, 471-485.
- Kanamori, H., Mori, J., Hauksson, E., Heaton, Th. H., Hutton, L. K., and Jones, L. M. (1993). Determination of earthquake energy release and M_L using TERRASCOPE. *Bull. Seism. Soc. Am.*, **83**, 2, 330-346.
- Kanasewich, E. R., Hemmings, C. D., and Alpaslan, T. (1973). N-th root stack nonlinear multichannel filter. *Geophysics*, **38**, 327-338.
- Karnik, V. (1969). *Seismicity of the European area. Part I.* Reidel Publishing Company, Dordrecht, 364 pp.
- Karnik, V. (1972). Differences in magnitudes. *Vorträge des Soproner Symposiums der 4. Subkommission von KAPG 1970, Budapest*, 69-80.
- Karnik, V., Kondorskaya, N. V., Riznichenko, Yu. V., Savarensky, Ye. F., Soloviev, S. L., Shebalin, N. V., Vanek, J., and Zatopek, A. (1962). Standardisation of the earthquake magnitude scales. *Studia Geophysica et Geodaetica*, **6**, 41-48.
- Kawakatsu, H., Kaneshima, S., Matsubayashi, H., Ohminato, T., Sudo, Y., Tsutsui, T., Uhira, K., Yamasato, H., Ito, H., and Legrand, D. (2000). Aso94: Aso seismic observation with broadband instruments. *J. Volcanol. Geotherm. Res.*, **101**, 129-154.
- Kawasumi, H. (1951). Measures of earthquake danger and expectancy of maximum intensity throughout Japan as inferred from the seismic activity in historical times. *Bull. Earthq. Res. Inst.*, **29**, 469-482.
- Keen, C. G., Montgomery, J., Mowat, W. M. H., and Platt, D. C. (1965). British seismometer array recording systems. *The Radio and Electronic Engineer*, **30**, 297-306.
- Keilis-Borok, V. I., (1959). On the estimation of displacement in an earthquake source and of source dimension. *Ann. Geofis.*, **12**, 205-214.
- Kennett, B. L. N. (1983). *Seismic wave propagation in stratified media.* ISBN 0-521-23933-8 Cambridge University Press, Cambridge, viii + 242 pp.
- Kennett, B. L. N. (1988). Systematic approximations to the seismic wavefields, In: Doornbos (1988a), 237-259.
- Kennett, B. L. N. (Ed.) (1991). *IASPEI 1991 Seismological Tables.* Research School of Earth Sciences, Australian National University. 167 pp.
- Kennett, B. L. N. (1992). Locating oceanic earthquakes - the influence of regional models and location criteria, *Geophys. J. Int.*, **108**, 848-854.
- Kennett, B. L. N. (2000). Stacking three-component seismograms. *Geophys. J. Int.*, **141**, 263-269.
- Kennett, B. L. N. (2001). *The seismic wavefield. Volume I: Introduction and theoretical development.* Cambridge University Press, Cambridge, x + 370 pp.
- Kennett, B. L. N. (2002). *The seismic wavefield. Volume II: Interpretation of seismograms on regional and global scales.* Cambridge University Press, Cambridge, x + 534 pp.
- Kennett, B. L. N., and Engdahl, E. R. (1991). Traveltimes for global earthquake location and phase identification. *Geophys. J. Int.*, **105**, 429-465.
- Kennett, B. L. N., Engdahl, E. R., and Buland, R. (1995). Constraints on seismic velocities in the Earth from traveltimes. *Geophys. J. Int.*, **122**, 108-124.
- Kennett, B. L. N., and Gudmundsson, O. (1996). Ellipticity corrections for seismic phases, *Geophys. J. Int.*, **127**, 40-48.
- Khromovskikh, V. S. (1989). Determination of magnitudes of ancient earthquakes from dimensions of observed seismodislocations. *Tectonophysics*, **166**, 269-280.
- Kijko, A. (1977). An algorithm for the optimum distribution of a regional seismic network - I. *Pageoph*, **115**, 999-1009.
- Kikuchi, M., and Fukao, Y. (1987). Inversion of long-period P-waves from great earthquakes along subduction zones. *Tectonophysics*, **144**, 231-247.

- Kikuchi, M., and Fukao, Y. (1988). Seismic wave energy inferred from long-period body wave inversion. *Bull. Seism. Soc. Am.*, **78**, 5, 1707-1724.
- Kikuchi, M., and Kanamori, H. (1991). Inversion of complex body waves - III, *Bull. Seism. Soc. Am.*, **81**, 2335-2350.
- Kikuchi, M., and Ishida, M. (1993). Source retrieval for deep local earthquakes with broadband records. *Bull. Seism. Soc. Am.*, **83**, 6, 1855-1870.
- Kim, W.-Y. (1998). The M_L scale in Eastern North America. *Bull. Seism. Soc. Am.*, **88**, 4, 935-951.
- Kim, W.-Y., Wahlström, R., and Uski, M. (1989). Regional spectral scaling relations of source parameters for earthquakes in the Baltic Shield. *Tectonophysics*, **166**, 151-161.
- Kind, R., (1978). The reflectivity method for a buried source. *J. Geophys.*, **44**, 603-612.
- Kind, R., (1985). The reflectivity method for different source and receiver structures and comparison with GRF data. *J. Geophys.* **58**, 146-152.
- King, G. C. P, and Bilham, R. G. (1976). A geophysical wire strainmeter. *Bull. Seism. Soc. Am.*, **66**, 2039-2047.
- King, G. C. P., Zürn, W., Evans, R., and Emter, D. (1976). Site corrections for long period seismometers, tiltmeters and strainmeters. *Geophys. J. R. astr. Soc.*, **44**, 405 - 411.
- Kiratzi, A. A., and Papazachos, B. C. (1984). Magnitude scales for earthquakes in Greece. *Bull. Seism. Soc. Am.*, **74**, 3, 969-985.
- Kiratzi, A. A., and Papazachos, B. C. (1985). Local Richter magnitude and total signal duration in Greece. *Ann. Geophys.*, **3**, 4, 531-537.
- Kirchdörfer, M. (1999). Analysis and quasistatic FE modeling of long period impulsive events associated with explosions at Stromboli volcano (Italy). *Ann. Geofisica*, **42**, 379-390.
- Kissling, E. (1988). Geotomography with local earthquake data. *Rev. Geophys.*, **26**, 659-698.
- Klein, F. W. (1978). Hypocenter location program HYPOINVERSE. U.S. Geol. Surv. Open-File Report. 78-694.
- Klein, F. W. (1985). HYPOINVERSE, a program for VAX and professional 350 computers to solve the earthquake locations. U.S. Geological Survey Open-File Report 85-515, 53 pp.
- Klinge, K. (1989). Duration magnitude. In: Bormann (1989), 109-115.
- Knothe, Ch. (1963). Verbesserte Auswertung tiefenseismischer Beobachtungen durch Verwendung von Mehrkomponenten-Stationen. *Freiberger Forschungshefte*, D149, 53 pp.
- Konno, K., Ohmachi, T., Endoh, T., and Toshinawa, T. (1994). Refinement and application of an estimation procedure for site natural periods using microtremor (abstract), 27th Gen. Assem. of IASPEI, Wellington, New Zealand, 10-21 January.
- Kostrov, B. (1974). Seismic moment and energy of earthquakes, and seismic flow of rock. *Izv. Acad. Sci., USSR, Phys. Solid Earth (Engl. Transl.)*, **1**, 23-40.
- Kostrov, B. V. (1975). *Mechanika otschaga tektonitscheskogo semletrjasenija*. Isdatelstwo Nauka, Moskva.
- Kövesligethy, R. (1906). A makroszeizmikus rengések feldolgozása, *Math. És Természettudományi Értesítő*, **24**, 349-368.
- Kövesligethy, R. (1907). Seismischer Stärkegrad und Intensität der Beben, *Beitr. zur Geoph.*, **8**, 363-366.
- Kowalle, G., Tittel, B., and Bormann, P. (1983). Determination of a magnitude calibration function using short-period readings of PKP. *Tectonophysics*, **93**, 289-294.
- Koyama, J., and Zheng, S.-H. (1985). Excitation of short-period body-waves by great earthquakes. *Physics Earth Planet. Int.*, **37**, 108-123.
- Kradolfer, U. (1996). AutoDRM - The first five years. *Seism. Res. Lett.*, **67**, 4, 30-33.
- Kravanja, S., Panza, G. F., and Sileny, J. (1999). Robust retrieval of a seismic point-source function. *Geophys. J. Int.*, **136**, 385-394.

References

- Krüger, F., and Weber, M. (1992). The effect of low velocity sediments on the mislocation vectors of the GRF array. *Geophys. J. Int.*, **105**, 387-393.
- Krüger, F., Weber, M., Scherbaum, F., and Schlittenhardt, J. (1993). Double beam analysis of anomalies in the core-mantle boundary region. *Geophys. Res. Lett.*, **20**, 1475-1478.
- Kuge, K., and Kawakatsu, H. (1990). Analysis of a deep “non double couple” earthquake using very broadband data, *Geophys. Res. Lett.*, **17**, 227-230.
- Kulhánek, O. (1990). Anatomy of seismograms. *Developments in Solid Earth Geophysics* **18**, Elsevier, Amsterdam, 78 pp.
- Kulhánek, O. (2002). The structure and interpretation of seismograms. In: Lee et al. (2002), Part A, 333-348.
- Kümpel, H.-J. (1992). About the potential of wells to reflect stress variations within the inhomogeneous crust. *Tectonophysics*, **211**, 317 - 336.
- Kværna, T. (1989). On exploitation of small-aperture NORESS type arrays for enhanced P-wave detectability. *Bull. Seism. Soc. Am.*, **79**, 888-900.
- Kværna, T., and Doornbos, D. J. (1986). An integrated approach to slowness analysis with arrays and three-component stations. In: *NORSAR Semiannual Technical Summary*, 1 October 1985 – 31 March 1986, Scientific Report **2-85/86**, NORSAR, Kjeller, Norway, 60-69.
- Kværna, T., and Ringdal, F. (1986). Stability of various f-k estimation techniques. In: *NORSAR Semiannual Technical Summary*, 1 April 1986 – 30 September 1986, Scientific Report **1-86/87**, NORSAR, Kjeller, Norway, 29-40.
- Kværna, K., Ringdal, F., Schweitzer, J., and Taylor, L. (2002). Optimized seismic threshold monitoring — part 2: teleseismic processing. *Pure Appl. Geophys.*, **159**, 989–1004.
- Lachet, C., and Bard, P.-Y. (1994). Numerical and theoretical investigations on the possibilities and limitations of the "Nakamura's" technique. *J. Physics of the Earth*, **42**, 377-397.
- LaCoste, L. J. B. (1934). A new type long period seismograph, *Physics*, **5**, 178-180.
- Lahr, J. C. (1989). *HYPOELLIPSE/Version 2.0: A computer program for determining local earthquakes hypocentral parameters, magnitude, and first motion pattern*. U.S. Geological Survey Open-File Report 89-116, 92 pp.
- Lahr, J. C., Chouet, B. A., Stephens, C. D., Power, J. A., and Page, R. A. (1994). Earthquake classification, location and error analysis in a volcanic environment: implications for the magmatic system of the 1989-1990 eruptions at Redoubt Volcano, Alaska. In: Miller, T. P., and Chouet, B. A. (Eds.), *The 1989 - 1990 eruptions of Redoubt Volcano, Alaska*, *J. Volcanol. Geotherm. Res.*, **62**, 137-151.
- Langston, C. A., and Helmberger, D. V. (1975). A procedure for modeling shallow dislocation sources. *Geophys. J. R. astr. Soc.*, **42**, 117-130.
- Langston, C. A., Brazier, R., Nyblade, A. A., and Owens, T. J. (1998). Local magnitude scale and seismicity rate for Tanzania, East Africa. *Bull. Seism. Soc. Am.*, **88**, 3, 712-721.
- Lapwood, E. R., and Usami, T. (1981). *Free oscillations of the Earth*. Cambridge University Press, Cambridge, UK.
- La Rocca, M., Petrosino, S., Saccorotti, G., Simini, M., Ibanez, J., Almendros, J., and Del Pezzo, E. (2000). Location of the source and shallow velocity model deduced from the explosion quakes recorded by two seismic antennas at Stromboli volcano. *Phys. Chem. Earth. Part A*, **25**, 731-735.
- Latynina, L. A., and Rizaeva, S. D. (1976). On tidal-strain variations before earthquakes. *Tectonophysics*, **31**, 121 - 127
- Lay, T., and Wallace, T. C. (1995). *Modern global seismology*. ISBN 0-12-732870-X, Academic Press, 521 pp.
- Lazareva, A. P., and Yanovskaya, T. B. (1975). The effect of the lateral velocity on the surface wave amplitudes. *Proc. Intern. Symp. Seismology and Solid-Earth Physics*, Jena, April 1-6, 1974. *Veröff. Zentralinstitut für Physik d. Erde*, No. 31, Vol. 2, 433-440.

- Lee, W. H. K. (1995). Realtime seismic data acquisition and processing. IASPEI Software Vol.1, 2nd Edition.
- Lee, W. H. K., Bennet, R., and Meagher, K. (1972). A method of estimating magnitude of local earthquakes from signal duration. U.S. Geol. Surv. Open-File Rep., 28 pp.
- Lee, W. H. K., and Lahr, J. C. (1975). HYPO71 (revised): A computer program for determining hypocenter, magnitude and first motion pattern of local earthquakes. U.S. Geological Survey Open-File Report 75-311, 116 pp.
- Lee, W. H. K., and Steward, S. W. (1981). Principles and applications of micro-earthquake networks, Advances in Geophysics, Supplement 2, Academic Press, New York.
- Lee, V., Trifunac, M., Herak, M., Živčić, M., and Herak, D. (1990). M_L^{SM} computed from strong motion accelerograms recorded in Yugoslavia. Earthquake Engineering and structural dynamics, **19**, 1167-1179.
- Lee, W. H. K., Kanamori, H., Jennings, P. C., and Kisslinger, C. (Editors) (2002). International Handbook of Earthquake and Engineering Seismology. Part A, Academic Press, ISBN 0-12-440652-1, xxiii+933 pp.
- Legrand, D., Kaneshima, S., and Kawakatsu, H. (2000). Moment tensor analysis of near-field broadband waveforms observed at Aso Volcano, Japan. J. Volcanol. Geotherm. Res., **101**, 155-169.
- Lemzikov, V. K., and Gusev, A. A. (1989). Coda-based energy classification of near Kamchatka earthquakes. Volcanology and Seismology (English translation), **11**, 558-579.
- Lermo, J. F., Francisco, S., and Chavez-Garcia, J. (1992). Site effect evaluation using microtremors: a review (abstract), EOS, **73**, 352.
- Levine, J., and Hall, J. L. (1972). Design and operation of a methane absorption stabilized laser strainmeter. J. Geophys. Res., **77**, 2595 - 2609.
- Levret, A., Cushing, M., and Peyridieu, G. (1996). Etude des caractéristiques de séismes historique en France: Atlas de 140 cartes macroseismiques, IPSN, Fontenay-Aux-Roses.
- Lienert, B. R. E. (1991). Report on modifications made to Hypocenter. Institute of Solid Earth Physics, University of Bergen.
- Lienert, B. R. E. (1997). Assessment of earthquake location accuracy and confidence region estimate using known nuclear tests. Bull. Seism. Soc. Am., **87**, 5, 1150-1157.
- Lienert, B. R. E., Berg, E., and Frazer, L. N. (1988). HYPOCENTER: An earthquake location method using centered, scaled, and adaptively least squares. Bull. Seism. Soc. Am., **76**, 771-783.
- Lienert, B. R. E., and Havskov, J. (1995). A computer program for locating earthquakes both locally and globally. Seism. Res. Lett., **66**, 26-36.
- Lillie, R. J. (1999). Whole Earth Geophysics. Prentice-Hall Inc., New Jersey, ISBN 0-13 4990517-2, 361 pp.
- Linde, A. T., Gladwin, M. T., and Johnston, M. J. S. (1992). The Loma Prieta Earthquake, 1989 and the Earth strain tidal amplitudes: an unsuccessful search for associated changes. Geophys. Res. Lett., **19**, 317 - 320.
- Linde, A. T., Agustsson, K., Sacks, I. S., and Stefansson, R. (1993). Mechanism of the 1991 eruption of Hekla from continuous borehole strain monitoring. Nature, **365**, 737-740.
- Linde, A. T., Gladwin, M., Johnston, M. J. S., Gwyther, R. L., and Bilham, R. (1996). A slow earthquake sequence on the San Andreas fault. Nature, **383**, 65 - 68.
- Linehan, D. (1940). Earthquakes in the West Indian region. Trans. Am. Geophys. Union, **30**, 229-232.
- Liu, H.-P., Anderson, D. L., and Kanamori, H. (1976). Velocity dispersion due to anelasticity; implications for seismology and mantle composition. Geophys. J. R. astr. Soc., **47**, 41-45.
- Lognonné, P., and Clévéde, E. (2002). Normal modes of the Earth and planets. In: Lee et al. (2002), Part A, 125-147.

References

- Lomax, A., Virieux, J., Volant, P., and Berge, C. (2000). Probabilistic earthquake location in 3D and layered models: Introduction of a Metropolis-Gibbs method and comparison with linear locations. In: Thurber and Rabinowitz (2000), 101-134.
- Lomax, A., Zollo, A., Capuano, P., and Virieux, J. (2001). Precise, absolute earthquake locations under Somma-Vesuvius volcano using a new three-dimensional velocity model. *Geophys. J. Int.* **146**, 313-331.
- Lomnitz, C. (1997). Frequency response of a strainmeter. *Bull. Seism. Soc. Am.*, **87**, 1078 - 1080.
- Lorraine, J., Hwang, and Clayton, R. W. (1991). A station catalog of ISC arrivals: Seismic station histories and station residuals. Open-File Report 91-295, U.S. Geological Survey.
- Longuet-Higgins, M. D. (1950). A theory on the origin of microseisms. *Philos. Trans. R. Soc. Lond.*, **A 243**, 1-35.
- Luco, J. E., Anderson, J. G., and Georgevich, M. (1990). Soil-structure interaction effects on strong motion accelerograms recorded on instrument shelters. *Earth. Eng. & Struct. Dyn.*, **19**, p 119.
- Madariaga, R. (1976). Dynamics of an expanding circular fault. *Bull. Seism. Soc. Am.*, **66**, 639-666.
- Madariaga, R. (1983). Earthquake source theory: a review. In: *Earthquakes: Observation, Theory and Interpretation* (Ed. Kanamori, H., Boschi, E.). Proceedings of the International School of Physics "Enrico Fermi". North-Holland Publishing Comp., Amsterdam, New York, Oxford, 1-44.
- Malischewsky, P. (1987). *Surface waves and discontinuities*. Elsevier, Amsterdam, ISBN 0-444-98959-5, 229 pp.
- Manchee, E. B., and Weichert, D. H. (1968). Epicentral uncertainties and detection probabilities from the Yellowstone seismic array data. *Bull. Seism. Soc. Am.*, **58**, 1359-1377.
- Marquering, H., Dahlen, F. A., and Nolet, G. (1999). Three-dimensional sensitivity kernels for finite-frequency traveltimes: the banana-doughnut paradox. *Geophys. J. Int.*, **137**, 805-815.
- Marrett, R. (1994). Scaling of intraplate earthquake recurrence interval with fault length and implications for seismic hazard assessment. *Geophys. Res. Lett.*, **21**, 24, 2637-2640.
- Marshall, P. D., and Basham, P. W. (1973). Rayleigh wave magnitude scale M_S . *Pure and Appl. Geophys.*, **103**, 406-414.
- Martini, M. (1996). Chemical characters of the gaseous phase in different stages of volcanism: Precursors and volcanic activity. In: Scarpa and Tilling (1996), 199-219.
- Mason, D. B. (1996). Earthquake magnitude potential of the intermountain seismic belt, USA, from surface-parameter scaling of Late Quaternary faults. *Bull. Seism. Soc. Am.*, **86**, 5, 1487-1506.
- Mayeda, K. (1993). $M_b(LgCoda)$: A stable single station estimator of magnitude. *Bull. Seism. Soc. Am.*, **83**, 3, 851-861.
- McLaren, J. P., and Frohlich, C. (1985). Model calculations of regional network locations for earthquakes in subduction zones. *Bull. Seism. Soc. Am.*, **75**, 2, 397-413.
- McNutt, S. R. (1986). Observations and analysis of b-type earthquakes, explosions, and volcanic tremor at Pavlof volcano. Alaska. *Bull. Seism. Soc. Am.*, **76**, 153-175.
- McNutt, S. R. (1996). Seismic monitoring and eruption forecasting of volcanoes: a review of the state-of-the-art and case history. In: Scarpa Tilling (1996), 99-146.
- McNutt, S. R. (2000a). Volcanic seismicity. In: Sigurdsson H. (2000), 1015-1033.
- McNutt, S. R. (2000b). Seismic Monitoring. In: Sigurdsson (2000), 1095-1119.
- McNutt, S. R. (2002). Volcano seismology and monitoring for eruptions. In: Lee et al. (2002), Part A, 383-406.

- Medvedev, S. V. (1962). Engineering seismology (in Russian). Academy of Sciences, Inst. of Physics of the Earth, Publ. house for literature on Civil Engineering, Architecture and Building Materials, Moscow.
- Meier, T., Malischewsky, P. G., and Neunhöfer, H. (1997). Reflection and transmission of surface waves at a vertical discontinuity and imaging of lateral heterogeneity using reflected fundamental Rayleigh waves. *Bull. Seism. Soc. Am.*, **87**, 1648-1661.
- Meissner, R., and Wever, Th. (1988). Lithosphere rheology: Continental versus oceanic unit. *J. Petrology*, Oxford University Press, Special Lithosphere Issue, 53-61.
- Melton, B. S. (1978). The sensitivity and dynamic range of inertial seismographs. *Rev. Geophys. Space Phys.*, **14**, 393-116
- Melton, B. S., and Kirkpatrick, B. M. (1970). The symmetric triaxial seismometer - its design for application in long-period seismometry, *Bull. Seism. Soc. Am.*, **60**, 3, 717-739.
- Mendez, A. J., and Anderson, J. G. (1991). The temporal and spatial evolution of the 19 September 1985 Michoacan earthquake as inferred from near-source ground-motion records. *Bull. Seism. Soc. Am.*, **81**, 3, 1655-1673.
- Michaelson, C. A. (1990). Coda duration magnitudes in central California: an empirical approach. *Bull. Seism. Soc. Am.*, **80**, 1190-1204.
- Mikumo, T., and Aki, K. (1964). Determination of local phase velocity by intercomparison of seismograms from strain and pendulum instruments. *J. Geophys. Res.*, **69**, 721-731.
- Miller, A. D., Stewart, R. C., White, R. A., Luckett, R., Baptie, B. J., Aspinall, W. P., Latchman, J. L., Lynch, L. L., and Voight, B. (1998). Seismicity associated with dome growth and collapse at the Soufriere Hills Volcano, Montserrat. *Geophys. Res. Lett.*, **25**, 3401-3404.
- Milne, J. (1888). The relative motion of neighbouring points of ground. *Trans. Seism. Soc. Jap.*, **12**, 63 - 66.
- Minakami, T. (1974). Seismology of volcanoes in Japan. In: Civetta et al. (Eds.). *Physical volcanology. Developments in solid earth geophysics*, **6**, Elsevier Amsterdam, 1 - 27.
- Mitronovas, W., and Wielandt, E. (1975). High-precision phase calibration of long-period electromagnetic seismographs. *Bull. Seism. Soc. Am.*, **65**, 2, 441-424.
- Mohnen, J.-U., and Schick, R. (1996). The spatial amplitude distribution of volcanic tremor at Stromboli volcano (Italy). *Ann. Geofisica*, **39**, 361-375.
- Mohorovičić, A. (1910). Potres od 8. X 1909. *God. Izvješće Zagr. met. Ops. Zag. 1909*, Zagreb (Das Beben vom 8. X 1909. *Jahrbuch des meteorologischen Observatoriums in Zagreb für das Jahr 1909*), **9**, Part 4, 1-63.
- Montagner, J.-P., and Kennett, B. L. N. (1996). How to reconcile body-wave and normal-mode reference Earth models?. *Geophys. J. Int.*, **125**, 229-248.
- Montalbetti, J. F., and Kanasewich, E. R. (1970). Enhancement of teleseismic body phases with a polarization filter. *Geophys. J. R. astr. Soc.*, **21**, 119-129.
- Mooney, W. D., Laske, G., and Masters, T. G. (1998), CRUST 5.1: a global crustal model at 5° x 5°, *J. Geophys. Res.*, **103**, 727-747.
- Morelli, A., and Dziewonski, A. M. (1993). Body wave traveltimes and a spherically symmetric P- and S-wave velocity model, *Geophys. J. Int.*, **112**, 178-194.
- Muco, B., and Minga, P. (1991). Magnitude determination of near earthquakes for the Albanian network. *Bolletino di Geofisica Teorica ed Applicata.*, **XXXIII**, 129, 17-24.
- Muirhead, K. J. (1968). Eliminating false alarms when detecting seismic events automatically. *Nature*, **217**, 553-554.
- Muirhead, K. J., and Ran Datt (1976). The N-th root process applied to seismic array data. *Geophys. J. R. astr. Soc.*, **47**, 197-210.
- Muir-Wood, R. (1993). From global seismotectonics to global seismic hazard. *Annali di Geofisica*, **36**, 3-4, 153-168.

References

- Müller, G. (1977). Earth flattening approximation for body waves derived from geometric ray theory - improvements, corrections and range of applicability. *J. Geophys.*, **44**, 429-436.
- Müller, G. (1985). The reflectivity method: A tutorial. *J. Geophys.*, **58**, 153-174.
- Murdock, J. N., and Hutt, C. R. (1983). A new event detector designed for the seismic research observatories. USGS, Open File Report 83-7851
- Murray, J. B., Rymer, H., and Locke, C. A., 2000. Ground deformation, gravity, and magnetics. In: Sigurdsson H. (2000), 1121-1140.
- Musson, R. M. W. (1996). Determination of parameters for historical British earthquakes, *Annali di Geofisica*, **39**, 5, 1041-1048.
- Mykkeltveit, S., Åstebøl, K., Doornbos, D. J., and Husebye, E. S. (1983). Seismic array configuration optimization. *Bull. Seism. Soc. Am.*, **73**, 173-186.
- Mykkeltveit, S., and Bungum, H. (1984). Processing of regional seismic events using data from small-aperture arrays. *Bull. Seism. Soc. Am.*, **74**, 2313-2333.
- Mykkeltveit, S., Fyen, J., Ringdal, F., and Kværna, T. (1988). Spatial characteristics of the NORESS noise field and implications for array detection processing. *Phys. Earth Planet. Inter.*, **63**, 277-283.
- Nabelek, J. L. (1984). Determination of earthquake source parameters from inversion of body waves, Phd thesis, MIT, Cambridge University, MA.
- Nakamura, Y. (1989). A method for dynamic characteristics estimation of subsurface using microtremor on the ground surface. *Q. Rep. Railway Tech. Res. Inst.*, **30**, 1.
- Neuberg J., Luckett, R., Ripepe, M., and Braun, T. (1994). Highlights from a seismic broad-band array on Stromboli volcano. *Geophys. Res. Lett.*, **21**, 749-752.
- Neuberg, J., and Pointer, T. (2000). Effects of volcano topography on seismic broad-band waveforms. *Geophys. J. Int.*, **143**, 239-248.
- Neuberg, J., Luckett, R., Baptie, B., and Olsen, K. (2000). Models of tremor and low-frequency earthquake swarms on Montserrat. *J. Volcanol. Geotherm. Res.*, **101**, 83-104.
- Neumann, W., Jacobs, F., and Tittel, B. (1989). Erdbeben (in German). B.G. Teubner Verlagsgesellschaft, 212 pp.
- Neunhöfer, H. (1985). Primary and secondary effects of surface wave propagation and their geophysical causes (in German). Veröff. Zentralinstitut Phys. Erde No. 85, AdW der DDR, Potsdam, 111 pp.
- Newhall, C. G., and Punongbayan, R. S. (Eds.) (1996). Fire and Mud: Eruptions and Lahars of Mount Pinatubo, Philippines: PHIVOLCS, Quezon City, and Univ. of Washington Press, Seattle, 1126 pp.
- Nishimura, T., Nakamichi, H., Tanaka, S., Sato, M., Kobayashi, T., Ueki, S., Hamaguchi, H., Ohtake, M., and Sato, H. (2000). Source process of very long period seismic events associated with the 1998 activity of Iwate Volcano, northeastern Japan. *J. Geophys. Res.*, **105**, 19135-19147.
- Nolet, G., Krueger, S., and Clouser, R. M. (1998). Empirical determination of depth-distance corrections for m_b and M_w from Global Seismograph Network stations. *Geophys. Res. Lett.*, **25**, 9, 1451-1454.
- Nowroozi, A. (1985). Empirical relations between magnitudes and fault parameters for earthquakes in Iran. *Bull. Seism. Soc. Am.*, **75**, 1327-1338.
- Nuttli, O. W. (1973). Seismic wave attenuation and magnitude relations for eastern North America. *J. Geophys. Res.*, **78**, 876-885.
- Nuttli, O. W. (1985). Average seismic source-parameter relations for plate-margin earthquakes. *Tectonophysics*, **118**, 161-174.
- Nuttli, O. W., and Zollweg, J. E. (1974). Relation between felt area and magnitude for central United States earthquakes. *Bull. Seism. Soc. Am.*, **64**, 1, 73-85.

- Ochozinskaya, M. V. (1974). Relationship between m_{PV} and M_{LH} depending on the source depth of earthquakes. In: Magnitude and energetic classification of earthquakes (II), (in Russian), Institut Fiziki Zemli, Akademii Nauk, Moskva, 203-207.
- Ødegaard, E., Doornbos, D. J., and Kväerna, T. (1990). Surface Topographic effects at arrays and three-component stations. *Bull. Seism. Soc. Am.*, **80**, 2214-2226.
- Ohnaka, M. (1978). Application of some dynamic properties of stick-slip to earthquakes. *Geophys. J. R. Astr. Soc.*, **53**, 311-318.
- Ohminato T., Chouet, B. A., Dawson, P., and Kedar, S. (1998). Waveform inversion of very long period impulsive signals associated with magmatic injection beneath Kilauea Volcano, Hawaii. *J. Geophys. Res.*, **103**, 23839-23862.
- Ohrnberger, M. (2001). Continuous automatic classification of seismic signals of volcanic origin at Mt. Merapi, Java, Indonesia. Dissertation, Institute of Geosciences, University of Potsdam, in English.
- Omori, F. (1911). The Usu-san eruption, earthquake and elevation, phenomena. *Bull. Imp. Earthq. Invest. Comm.*, **5**, 1-38.
- Omura, M., Otsuka, S., Fujimori, K., and Yamamoto, T. (2001). Tidal strains observed at a station crossing the Otsuki Fault, Kobe, Japan, before the 1995 Hyogoken-Nanbu earthquake. *J. Geodetic Soc. Japan*, **47**, 441 - 447.
- Oncescu, M. C. (1986). Relative seismic moment tensor determination for Vrancea intermediate depth earthquakes, *Pageoph*, **124**, 931-940.
- Okal, E. A. (1992a). Use of the mantle magnitude M_m for the reassessment of the moment of historical earthquakes. I: Shallow events. *Pageoph*, **139**, 1, 17-57.
- Okal, E. A. (1992b). Use of the mantle magnitude M_m for the reassessment of the moment of historical earthquakes. II: Intermediate and deep events. *Pageoph*, **139**, 1, 59-85.
- Okal, E. A., and Talandier, J. (1989). M_m : A variable-period mantle magnitude. *J. Geophys. Res.*, **94**, 4169-4193.
- Okal, E. A., and Talandier, J. (1990). M_m : Extension to Love waves of the concept of a variable-period mantle magnitude. *Pure and Appl. Geophys.*, **134**, 355-384.
- Omori, F. (1911). The Usu-san eruption, earthquake and elevation, phenomena. *Bull. Imp. Earthq. Invest. Comm.*, **5**, 1-38.
- Oppenheim, A. V., and Schaffer, R. V. (1975) *Digital signal processing*. Prentice Hall, New Jersey, USA.
- Oppenheim, A. V., and Willsky, A. S. (1983). *Signals and Systems*. Prentice Hall, New Jersey, USA.
- Ottmøller, L., and Havskov, J. (1999). SeisNet: A general purpose virtual seismic network. *Seism. Res. Lett.*, **70**, 5, 522-528.
- Panza, J. F., Duda, S. J., Cernobori, L., and Herak, M. (1989). Gutenberg's surface-wave magnitude calibrating function: theoretical basis from synthetic seismograms. *Tectonophysics*, **166**, 35-43.
- Parolai, S., Trojani, L., Monachesi, G., Frapiccini, M., Cattaneo, M., and Augliera, P. (2001). Hypocenter location accuracy and seismicity distribution in the Central Apennines (Italy). *J. Seism.*, **5**, 243-261.
- Patanè, D., and Ferrari, F. (1999). ASDP: a PC-based program using a multi-algorithm approach for automatic detection and location of local earthquakes. *Phys. Earth Planet. Int.*, **113**, 57-74.
- Pavlis, G. L. (1988). Vector and matrix manipulation, In: Doornbos (1988a), 403-426.
- Pavlis, G. L., and Vernon, F. L. (1994). Calibration of seismometers using ground noise. *Bull. Seism. Soc. Am.*, **84**, 4, 1243-1255.
- Payo, G. (1986). *Introducción al análisis de sismogramas*. Instituto Geográfico Nacional, Madrid, 125 pp.

References

- Pegeler, G., and Das, S. (1996). Analysis of the relationship between seismic moment and fault length for large crustal strike-slip earthquakes between 1977-92. *Geophys. Res. Lett.*, **23**, 905-908.
- Peters, D. C. and Crosson, R. S. (1972). Application of prediction analysis to hypocentre determination using local array. *Bull. Seism. Soc. Am.*, **62**, 3, 775-788.
- Peterson, J. (1993). Observations and modeling of seismic background noise. U.S. Geol. Survey Open-File Report **93-322**, 95 pp.
- Pinatubo Volcano Observatory Team (1991). *Eos Trans. Am. Geophys. Union*, **72**, 545, 552-553, 555.
- Plešinger, A. (1998). Determination of seismograph system transfer functions by inversion of transient and steady-state calibration responses. *Studia geoph. et geod.*, **42**, 472-499.
- Plešinger, A., Zmeškal, M., and Zednik, J. (1995). PREPROC - Software for automated preprocessing of digital data. Ver.2.1, Ed. Bergman, E., NEIC Golden/FI, Prague.
- Plešinger, A., Zmeškal, M., and Zednik, J. (1996). Automated preprocessing of digital seismograms: Principles and software. Version 2.2, Bergman, E. (Ed.), Prague & Golden.
- Pomeroy, P. W., and Oliver, J. (1960). Seismic waves from high altitudes nuclear explosions. *J. Geophys. Res.*, **65**, 10, 3445-3457.
- Power, J. A., Lahr, J. C., Page, R. A., Chouet B. A., Stephens C. D., Harlow, D. H., Murray, T. L., and Davies, J. N. (1994). Seismic evolution of the 1989-1990 eruption sequence of Redoubt volcano, Alaska. *J. Volcanol Geotherm. Res.*, **62**, 69-94.
- Proposal 1991-1995 to The National Science Foundation, (1990), IRIS Consortium
- Pujol, J. (2000). Joint event location – the JHD technique and applications to data from local networks. In: Thurber Rabinowitz(2000), 163-204.
- Purcaru, G., and Berckhemer, H. (1978). A magnitude scale for very large earthquakes. *Tectonophysics*, **49**, 189-198.
- Purcaru, G., and Berckhemer, H. (1982). Quantitative relations of seismic source parameters and a classification of earthquakes. *Tectonophysics*, **84**, 57-128.
- Quanterra, INC. FAQ Lett., June 1994.
- Qian, S., and Chen, D. (1996). Joint time-frequency analysis, Prentice Hall PTR, New Jersey, 302 pp.
- Rabinowitz, N., and Steinberg, D. M. (1990). Optimal configuration of a seismographic network: A statistical approach. *Bull. Seism. Soc. Am.*, **80**, 1, 187-196.
- Ranalli, G., and Murphy, D. C. (1987). Rheological stratification of the lithosphere. *Tectonophysics*, **132**, 281-295.
- Randall, M. J. (1973). The spectral theory of seismic sources. *Bull. Seism. Soc. Am.*, **63**, 1133-1144.
- Ratdomopurbo, A., and Poupinet, G. (1995). Monitoring a temporal change of seismic velocity in a volcano: application to the 1992 eruption of Mt. Merapi (Indonesia). *Geophys. Res. Lett.*, **22**, 775 - 778.
- Rautian, T. G. (1960). In: Methods of the detailed study of seismicity (in Russian). Moscow, Izd. AN SSSR, **176**, 75-114.
- Rautian, T. G., Khalturin, V. I., and Zakirov, M. S. (1981). Experimental studies of seismic coda (in Russian). Nauka, Moscow, 144 pp.
- Rautian, T. G., Khalturin, V. I., Dotsev, N. T., and Sarkisyan, N. M. (1989). Macroseismic magnitude. In: *Voprosy inzheneroy seismologii*, iss. 30, 98-109.
- Real, C. R., and Teng, T. L. (1973). Local Richter magnitude and total signal duration in Southern California. *Bull. Seism. Soc. Am.*, **63**, 1809.
- Reasenber, P. A., and Oppenheimer, D. (1985). FPFIT, FPLOT and FPPAGE: Fortran computer programs for calculating and displaying earthquake fault-plane solutions. U.S. Geological Survey Open-File Report 85-739, 109 pp.

- Rebscher, D., Westerhaus, M., Welle, W., and Nandaka, G. M. (2000). Monitoring ground deformation at the Decade Volcano Gunung Merapi, Indonesia. *Phys. Chem. Earth*, **25**, 755-757.
- Reches, Z. (1987). Determination of the tectonic stress tensor from slip along faults that obey the Coulomb yield condition. *Tectonics*, **6**, 849-861.
- Reinhardt, H. G. (1977). Regionale Geschwindigkeitsansätze der DDR. Report of the VEB Geophysik Leipzig.
- Rezapour, M., and Pearce, R. G. (1998). Bias in surface-wave magnitude M_S due to inadequate distance corrections. *Bull. Seism. Soc. Am.*, **88**, 1, 43-61.
- Rice, J. R. (1980). The mechanics of earthquake rupture. In: *Physics of the Earth's interior* (Ed. Dziewonski A. A., Boschi, E.). North Holl. Publ. Co., Amsterdam, 555-649.
- Richards, P. G. (2000). Accurate estimates of the absolute location of underground nuclear tests at the northern Novaya Zemlya Test Site, Proceedings of Second Workshop on IMS Location Calibration, 10-24 March 2000, Oslo, Norway.
- Richards, P. G. (2002). Seismological methods of monitoring compliance with the Comprehensive Nuclear Test-Ban Treaty. In: Lee et al. (2002), Part A, 369-382.
- Richter, C. F. (1935). An instrumental earthquake magnitude scale. *Bull. Seism. Soc. Am.*, **25**, 1-32.
- Richter, C. F. (1958). *Elementary seismology*. W. H. Freeman and Company, San Francisco and London, viii + 768 pp.
- Riedesel, M. A., Moore, R. D., and Orcutt, J. A. (1990). Limits of sensitivity of inertial seismometers with velocity transducers and electronic amplifiers, *Bull. Seism. Soc. Am*, **80**, 6, 1725 - 1752.
- Rietbrock, A., and Scherbaum, F. (1998). The GIANT analysis system (Graphical Interactive Aftershock Network Toolbox). *Seism. Res. Lett.*, **69**, 1, 40-45.
- Ringdal, F. (1976). Maximum-likelihood estimation of seismic magnitude, *Bull. Seism. Soc. Am.*, **66**, 789 - 802, 1976.
- Ringdal, F., and Kennett, B. L. N (Eds.) (2001). Special issue: Monitoring the Comprehensive Nuclear-Test-Ban Treaty: Source location. *Pure appl. Geophys.*, **158**, Number 1/2, 1-419.
- Riznichenko, Yu. V. (1960). About the magnitude of underground nuclear explosions (in Russian). *Trudy Inst. Fiziki Zemli*, **182**, 15, 53-87.
- Riznichenko, Yu. V. (1992). *Problems of seismology*. Mir and Springer Publishers, Moscow and Berlin-Heidelberg-New York, 445 pp. (English translation of the original Russian publication of 1985).
- Rivera, L. (1989). Inversion du tenseur des contraintes et des mécanismes au foyer à partir des données de polarité pour une population de séismes. Thèse de doctorat, Université Louis.Pasteur de Stasbourg.
- Roberts, R. G., Christofferson, A., and Cassidy, F. (1989). Real time event detection, phase identification and source location using single station 3 component seismic data and a small PC. *Geophys. J.*, **97**, 471-480.
- Roberts, R. G., and Christoffersson, A. (1990). Decomposition of complex single-station three-component seismograms. *Geophys. J. Int.*, **103**, 55-74.
- Rodgers, P. W. (1968). The response of the horizontal pendulum seismometer to Rayleigh and Love waves, tilt, and free oscillations of the Earth. *Bull. Seism. Soc. Am.*, **58**, 1384-1406.
- Rodgers, P. W. (1969). A note on the response of the pendulum seismometer to plane wave rotation. *Bull. Seism. Soc. Am.*, **59**, 2101-2102.
- Rodgers, P. W. (1992). Frequency limits for seismometers as determined from signal-to-noise ratios. Part 1: The electromagnetic seismometer. *Bull. Seism. Soc. Am.*, **82**, 1071-1098.

References

- Rodgers, P. W. (1993). Maximizing the signal-to-noise ratio of the electromagnetic seismometer: The optimum coil resistance, amplifier characteristics, and circuit. *Bull. Seism. Soc. Am.*, **83**, 2, 561-582.
- Rodgers, P. W. (1994). Self-noise spectra for 34 common electromagnetic seismometer/pre-amplifier pairs. *Bull. Seism. Soc. Am.*, **84**, 1, 222-229.
- Rodgers, P. W., Martin, A. J., Robertson, M. C., Hsu, M. M., and Harris, D. B. (1995). Signal-coil calibration of electromagnetic seismometers, *Bull. Seism. Soc. Am.*, **85**, 3, 845-850.
- Rogers, J. A., and Stephens, C. D. (1991). SSAM: a PC-based seismic spectral amplitude measurement system for volcano monitoring. *Seism. Res. Lett.*, **62**, 22.
- Romanowicz, B. (1992). Strike-slip earthquakes on quasi-vertical transcurrent faults: inferences for general scaling relations. *Geophys. Res. Lett.*, **19**, 481-484.
- Romanowicz, B. (1994). *Comment and Reply*: Comment on "A reappraisal of large earthquake scaling" by C. Scholz. *Bull. Seism. Soc. Am.*, **84**, 5, 1675-1676.
- Romanowicz, B., and Rundle, J. B. (1993). On scaling relations for large earthquakes. *Bull. Seism. Soc. Am.*, **83**, 1294-1297.
- Romanowicz, B., and Rundle, J. B. (1994). Reply to comment on "On scaling relations for large earthquakes by Romanowicz and Rundle" from the perspective of a recent non-linear diffusion equation linking short-time deformation to long-time tectonics. *Bull. Seism. Soc. Am.*, **84**, 5, 1684.
- Rost, S., and Thomas, C. (2002). Array Seismology: Methods and applications. *Rev. Geophys.*, **40** (3), 1008, doi: 10.1029/20000RG000100.
- Rubin, A. M., Gillard, D., and Got, J.-L. (1998). A reinterpretation of seismicity associated with the January 1983 dike intrusion at Kilauea volcano, Hawaii. *J. Geophys. Res.*, **103**, 10003-10015.
- Ruud, B. O., Husebye, E. S., Ingate, S. F., and Christoffersson, A. (1988). Event location at any distance using seismic data from a single, three-component station. *Bull. Seism. Soc. Am.*, **78**, 308-325.
- Ružek, B., and Kvasnička, M. (2001). Differential evolution algorithm in earthquake hypocenter location. *Pure appl. geophys.*, **158**, 667-693.
- Saari, J. (1991). Automated phase picker and source location algorithm for local distances using a single three-component seismic station. *Tectonophysics*, **189**, 307-315.
- Saccorotti, G., Chouet, B., Martini, M., and Scarpa, R. (1998). Bayesian statistics applied to the location of the source of explosions at Stromboli volcano, Italy. *Bull. Seism. Soc. Am.*, **88**, 1099-1111.
- Sacks, I. S., Suyehiro, S., Evertson, D. W., and Yamagishi, Y. (1971). Sacks-Evertson strain-meter, its installation in Japan and some preliminary results concerning strain steps. *papers in meteorology and geophysics*, **22**, 195 - 208.
- Sacks, I. S., Snoke, J. A., Evans, R., King, G., and Beavan, J. (1976). Single-site phase velocity measurement. *Geophys. J. R. astr. Soc.*, **46**, 253 - 258.
- Sadovsky, M. A., Kedrov, O. K., and Pasechnik, I. P. (1986). On the question of energetic classification of earthquakes (in Russian). *Fizika Zemli, Moscow*, 2, 3-10.
- Sambridge, M. S., and Kennett, B. L. N. (1986). A novel method of hypocentre location. *Geophys. J. R. astr. Soc.*, **87**, 679-697.
- Sambridge, M. S., and Kennett, B. L. N. (2001). Seismic event location: nonlinear inversion using a neighbourhood algorithm. *Pure appl. Geophys.*, **158**, 241-257.
- Sandmeier, K.-J., (1990). Untersuchung der Ausbreitungseigenschaften seismischer Wellen in geschichteten und streuenden Medien. PhD Thesis, University of Karlsruhe
- Saraó, A., Panza, G. F., Privitera, E., and Cocina, O. (2001). Non-double-couple mechanisms in the seismicity preceding the 1991-1993 Etna volcano eruption. *Geophys. J. Int.*, **145**, 319-335.

- Sarconi, M. (1784). *Istoria dei fenomeni del tremoto avvenuto nelle Calabrie, e nel Valdemone nell'anno 1783*, Luce dalla Reale Accademia della Scienze, e delle Belle Lettere di Napoli, Naples.
- Sassa, K. (1936). Micro-seismometric study on eruptions of the volcano Aso. *Mem. Coll. Sci. Kyoto Imp. Univ., Ser. A* 19, 11-56.
- Savage, M. K., and Anderson, J. G. (1995). A local-magnitude scale for the Western Great Basin-Eastern Sierra Nevada from Wood-Anderson seismograms. *Bull. Seism. Soc. Am.*, **85**, 4, 1236-1243.
- Scarpa, R., and Tilling, R. (1996). *Monitoring and Mitigation of Volcano Hazards*. Springer, Berlin Heidelberg New York, 841 pp.
- Scherbaum, F., and Johnson, J. (1992). Programmable Interactive Toolbox for Seismological Analysis (PITSA). IASPEI Software Library Volume 5, Seismological Society of America, El Cerrito.
- Scherbaum, F. (1996). *Of poles and zeros; Fundamentals of Digital Seismometry*, Kluwer Academic Publisher, Boston, 256 pp.
- Scherbaum, F. (1997). Zero phase digital anti-alias filters: Problems and cures (http://butler.geo.uni-potsdam.de/FIR/fir_daaf.htm), Version 1.0.
- Scherbaum, F. (2001). *Of poles and zeros: Fundamentals of digital seismology. Modern Approaches in Geophysics* Kluwer Academic Publishers, 2nd edition, 265 pp. (including an CD-ROM by Schmidtke, E., and Scherbaum, F. with examples written in Java).
- Scherbaum, F. (2002). Analysis of digital earthquake signals. In: Lee et al. (2002), Part A, 349-355.
- Schick, R. (1988). Volcanic tremor - source mechanisms and correlation with eruptive activity. *Natural Hazards*, **1**, 2, 125-144.
- Schick, R. (1991). Volcanic activity parameters, in: *Volcanic tremor and magma flow. Scientific Series of the International Bureau*, **4**., 183-188.
- Schimmel, M., and Paulssen, H. (1997). Noise reduction and detection of weak, coherent signals through phase-weighted stacks. *Geophys. J. Int.*, **130**, 497-505.
- Schlindwein, V., Wassermann, J., and Scherbaum, F. (1995). Spectral Analysis of Harmonic Tremor Signals at Mt. Semeru Volcano, Indonesia. *Geophys. Res. Lett.*, **22**, 1685-1688.
- Schlittenhardt, J. (1996). Array analysis of core-phase caustic signals from underground nuclear explosions: Discrimination of closely spaced explosions. *Bull. Seism. Soc. Am.*, **86**, 1A, 159-171.
- Schmidtke, E., and Scherbaum, F. (2001). *Digital Seismology Tutor*. CD-ROM program package accompanying Scherbaum (2001).
- Schöffel, H.-J. and Das, S. (1999). Fine details of the Wadati-Benioff zone under Indonesia and its geodynamic implications. *J. Geophys. Res.*, **104**, 13101-13114.
- Scholz, C. H. (1982). Scaling laws for large earthquakes: consequences for physical models. *Bull. Seism. Soc. Am.*, **72**, 1-14.
- Scholz, C. H. (1990). *The mechanics of earthquakes and faulting*. Cambridge University Press, Cambridge, 439 pp.
- Scholz, C. H. (1994). Reply to comment on "A reappraisal of large earthquake scaling" by C. Scholz. *Bull. Seism. Soc. Am.*, **84**, 5, 1677-1678.
- Scholz, C. H. (1997). Size distributions for large and small earthquakes. *Bull. Seism. Soc. Am.*, **87**, 4, 1074-1077.
- Scholz, C. H., Aviles, C. A., and Wesnousky, S. G. (1986). Scaling differences between large interplate and intraplate earthquakes. *Bull. Seism. Soc. Am.*, **76**, 1, 65-70.
- Schuessler, H. W. (1981). A signal processing approach to simulation, *Frequenz*, **35**, 174-184.
- Schwartz, S. Y., Dewey, J. W., and Lay, T. (1989). Influence of fault plane heterogeneity on the seismic behavior in southern Kurile Islands arc. *J. Geophys. Res.*, **94**, 5637-5649.

References

- Schweitzer, J. (1997): HYPOSAT – a new routine to locate seismic events, NOR SAR Scientific Report **1-97/98**, 94-102, NOR SAR, Kjeller, Norway, November 1997.
- Schweitzer, J. (1998). Tuning the automatic data processing for the Spitsbergen array (SPITS). In: NOR SAR Semiannual Technical Summary 1 April – 30 September 1998, NOR SAR Scientific Report **1-98/99**, Kjeller, Norway, 110-125.
- Schweitzer, J. (2001a). HYPOSAT – An enhanced routine to locate seismic events. *Pure and Appl. Geophys.*, **158**, 277-289.
- Schweitzer, J. (2001b). Slowness corrections – one way to improve IDC products. *Pure Appl. Geophys.*, **158**, 375-396.
- Schweitzer, J., and Kväerna, T. (1999). Influence of source radiation pattern on globally observed short-period magnitude estimates (m_b). *Bull. Seism. Soc. Amer.*, **89**, 342-347.
- Scrase, F. J. (1931). The reflected waves from deep focus earthquakes. *Proc. Roy. Soc. Of London A*-**132**, 213-235.
- Seidl, D. (1980). The simulation problem for broad-band seismograms. *J. Geophys.*, **48**, 84-93.
- Seidl, D., Schick, R., and Riuscetti, M. (1981). Volcanic tremors at Etna: a model for hydraulic origin. *Bull. Volcanol.*, **44**, 43-56.
- Seidl, D., and Berckhemer, H. (1982). Determination of source moment and radiated seismic energy from broadband recordings. *Phys. Earth Planet. Inter.*, **30**, 209-213.
- Seidl, D., and Stammer, W. (1984). Restoration of broad-band seismograms (part I). *J. Geophys.*, **54**, 114-122.
- Seidl, D., and Hellweg, M. (1988). Restoration of broad-band seismograms (part II): Signal moment determination. *J. Geophysics*, **62**, 158-162.
- Seidl, D., and Hellweg, M. (1991). Volcanic tremor recordings: polarization analysis. In: *Volcanic tremor and magma flow. Scientific Series of the International Bureau*, **4**, 31-46.
- Senatskommission für Geowissenschaftliche Gemeinschaftsforschung (Ed.) (2002). *Ten Years of German Regional Seismic Network (GRSN)*. Deutsche Forschungsgemeinschaft, Mitteilung No. 25, Wiley-VCH Verlag Weinheim.
- Shannon, C. E. (1949). Communication in presence of noise, *Proceedings of the IRE*.
- Shaw, H. R., and Chouet, B. A. (1991). Fractal hierarchies of magma transport in Hawaii and critical self-organization of tremor. *J. Geophys. Res.*, **96**, 10191-10207.
- Shearer, P. M. (1999). *Introduction to seismology*. Cambridge University Press, 260 pp.
- Sheriff, R. E., and Geldart, L. P. (1995). *Exploration seismology*. Cambridge University Press, Second Edition, 592 pp.
- Shimozuru, D. (1972). A seismological approach to the prediction of volcanic eruptions. In: *The surveillance and prediction of volcanic activity*. UNESCO Earth Sci. Monograph, **8**, 19-45.
- Shimshoni, M., and Smith, S. W. (1964). Seismic signal enhancement with three-component detectors. *Geophysics*, **29**, 5, 664-671.
- Sieberg, A. (1912). Über die makroseismische Bestimmung der Erdbebenstärke, *Gerl. Beitr. Geophys.*, **11**, 227-239.
- Sieberg, A. (1923). *Geologische, physikalische und angewandte Erdbebenkunde*. Verlag von Gustav Fischer, Jena, 572 pp.
- Sieberg, A. (1932). *Geologie der Erdbeben*. Handbuch der Geophysik, Gebr. Bornträger, Berlin, Vol 2 pt 4, 550-555.
- Sigurdsson, H. (Ed. in Chief) (2000). *Encyclopedia of Volcanoes*. Academic Press, San Diego London Sydney Tokyo, 1417 pp.
- Šilený, J., Panza, G. F., and Campus, P. (1992). Waveform inversion for point source moment retrieval with variable hypocentral depth and structural model. *Geophys. J. Int.*, **109**, 259-274.

- Šilený, J., and Pšenčík, I. (1995). Mechanisms of local earthquakes in 3-D inhomogeneous media determined by waveform inversion. *Geophys. J. Int.*, **121**, 459-474.
- Šilený, J., Campus, P., and Panza, G. F. (1996). Seismic moment tensor resolution by waveform inversion of a few local noisy records - I. Synthetic tests. *Geophys. J. Int.*, **126**, 605-619.
- Simon, R. B. (1981). *Earthquake interpretations: A manual of reading seismograms*. William Kaufmann, Inc., Los Alto, CA, 150 pp.
- Sipkin, S. A. (1982). Estimation of earthquake source parameters by the inversion of waveform data: synthetic waveforms. *Physics of the Earth and Planetary Interiors*, **30**, 242-259.
- Smith, G. P., and Ekström, G. (1996). Improving teleseismic event locations using a three-dimensional Earth model. *Bull. Seism. Soc. Am.*, **86**, 3, 788-796.
- Snoke, J. A., Munsey, J. W., Teague, A. G., and Bollinger, G. A. (1984). A program for focal mechanism determination by combined use of polarity and SV-P amplitude data. *Earthquake Notes*, **55**, 3, p. 15.
- Sohon, F. W. (1932). *Seismometry*. Part II of Macelwane, J.B., and F.W. Sohon: Introduction to theoretical seismology, New York 1932, 9+149 pp.
- Soloviev, S. L. (1955). Classification of earthquakes in order of energy (in Russian). *Trudy Geofiz. Inst. AN SSSR*, **39**, 157, 3-31.
- Somers, H., and Manchee, E. B. (1966). Selectivity of the Yellowknife seismic array. *Geophys. J. R. astr. Soc.*, **10**, 401-412.
- Sommerfeld, A. (1970). *Mechanik der deformierbaren Medien*. 6. Auflage, Akademische Verlagsgesellschaft Geest & Portig K.-G., Leipzig.
- Sornette, D., and Sornette, A. (1994). Comment on "On scaling relations for large earthquakes by Romanowicz and Rundle" from the perspective of a recent non-linear diffusion equation linking short-time deformation to long-time tectonics. *Bull. Seism. Soc. Am.*, **84**, 5, 1679-1683.
- Spallarossa, D., Ferretti, G., Augliera, P., Bindi, D., and Cattaneo, M. (2001). Reliability of earthquake location procedures in heterogeneous areas: synthetic tests in the South Western Alps, Italy. *Phys. Earth Planet. Int.*, **123**, 247-266.
- Spence, W. (1977). Measuring the size of an earthquake. *Earthquake Information Bulletin*, **9**, 4, 21-23.
- Sponheuer, W. (1960). *Methoden zur Herdtiefenbestimmung in der Makroseismik*, Freiburger Forschungshefte C88, Akademie Verlag, Berlin.
- Sponheuer, W., and Karnik, V. (1964). Neue seismische Skala, In: Sponheuer, W., (Ed.), *Proc. 7th Symposium of the ESC, Jena, 24-30 Sept. 1962*, Veröff. Inst. f. Bodendyn. u. Erdbebenforsch. Jena d. Deutschen Akad. d. Wiss., No 77, 69-76.
- Spudich, P., and Bostwick, T. (1987). Studies of the seismic coda using an earthquake cluster as deeply buried seismograph array. *J. Geophys. Res.*, **92**, 10526-10546.
- Stange, S. (2001). ML determination for local and regional events with a sparse network in Southwestern Germany. *J. Seism.* (submitted).
- Steichschulte, V. C. (1932). The Japanese earthquake of March 29, 1928. *Bull. Seism. Soc. Am.*, **22**, 81-137.
- Steim, J. M. (1986). *The very-broad-band seismograph*. Doctoral thesis, Department of Geological Sciences, Harvard University, Cambridge, Massachusetts. 184 pp.
- Stein, S. (1991). *Introduction to seismology, earthquakes and Earth structure*. Lecture notes, Department of Geological sciences, Northwestern University, USA.
- Steinberg, D. M., Rabinowitz, N., Shimshoni, Y., and Mizrachi, D. (1995). Configuring a seismograph network for optimal monitoring of fault lines and multiple sources. *Bull. Seism. Soc. Am.*, **85**, 6, 1847-1857.

References

- Stix, J., and Gaonac'h, H. (2000). Gas, plume, and thermal monitoring. In: Sigurdsson (2000), 1141-1163.
- Street, R. L. (1976). Scaling northeastern United States/southeastern Canadian earthquakes by their Lg waves. *Bull. Seism. Soc. Am.*, **66**, 1525-1537.
- stuadmin@geophys.uni-stuttgart.de, 1998. Station STU: a picture tour to the seismometer. <http://www.geophys.uni-stuttgart.de>.
- Sultanov, D. D., Murphy, J. R., and Rubinstein, Kh. D. (1999). A seismic source summary for Soviet Peaceful Nuclear Explosions. *Bull. Seism. Soc. Am.*, **89**, 3, 640-647.
- Sykes, L. R. (1966). The seismicity and the deep structure of island arcs. *J. Geophys. Res.*, **27**, 2981-3006.
- Tabulevich, V. (1992). *Microseismic and infrasound waves*. Springer-Verlag Berlin, 150 pp.
- Thomson, S. T. (1950). Transmission of elastic waves through a stratified solid medium. *J. Appl. Phys.*, **21**, 89-93.
- Thurber, C. H., Quin, H. R., and Richards, P. G. (1993). Accurate locations of nuclear explosions in Balapan, Kazakhstan, 1987 to 1989. *Geophys. Res. Lett.*, **20**, 399-402.
- Thurber, C. H., and Rabinovitz, N. (Eds.) (2000). *Advances in seismic event location*. Kluwer Academic Publishers, 266 pp.
- Thurber, C. H., and Engdahl, E. R. (2000). Advances in global seismic event location. In: in Thurber and Rabinowitz (2000), 3-22.
- Thurber, C. H., and Kissling, E. (2000). Advances in travel-time calculations for three-dimensional structures. In: Thurber and Rabinowitz (2000), 71-100.
- Tibi, R., Estabrook, C. H., and Bock, G. (1999). The 1996 June 17 Flores Sea and 1994 March 9 Fiji-Tonga earthquakes: Source processes and deep earthquake mechanisms, *Geophys. J. Int.*, **138**, 625-642.
- Tibi, R., Bock, G., Xia, Y., Baumbach, M., Grosser, H., Milkereit, C., Karakisa, S., Zünbül, S., Kind, R., and Zschau, J. (2001). Rupture processes of the 1999 August 17 Izmit, and November 12 Düzce (Turkey) earthquakes. *Geophys. J. Int.*, **144**, F1-F7.
- Tilling, R., Heliker, C., and Wright, T. L. (1987). *Eruptions of Hawaiian volcanoes: Past, present, and future*. U.S. Geol. Surv. General-Interest Publication Series, 54 pp.
- Tinti, S., Vittori, T., and Mulargia, F. (1987). On the macroseismic magnitudes of the largest Italian earthquakes. *Tectonophysics*, **138**, 159-178.
- Tittel, B. (1977). Zur Bestimmung von Erdbebenmagnituden aus longitudinalen Kernwellen. *Gerl. Beitr. Geophys.*, **86**, 79-85.
- Teupser, Ch. (1962). Die Eichung und Prüfung von elektromagnetischen Seismographen, *Freiberger Forschungshefte C130*, 103 pp.
- Texas Instruments (1998). *Oversampling techniques using the TMS320C24x Family*. 1-6, Literature Number: SPRA461.
- Tietze, U., and Schenk, Ch. (1990). *Halbleiter-Schaltungstechnik Neunte, neu bearbeitete und erweiterte Auflage*. Springer-Verlag Berlin Heidelberg NewYork London Paris Tokyo Barcelona, 771 pp.
- Tocher, D. (1958). Earthquake energy and ground breakage. *Bull. Seism. Soc. Am.*, **48**, 147-153.
- Topozada, T. R. (1975). Earthquake magnitude as a function of intensity data in California and Western Nevada. *Bull. Seism. Soc. Am.*, **65**, 5, 1223-1238.
- Trifunac, M. D., and Brady, A. G. (1975). On the correlation of seismic intensity scales with the peaks of recorded strong motion, *Bull. Seism. Soc. Am.*, **65**, 139-162.
- Trifunac, M. C. (1990). M_L^{SM} . Computational Mechanics Publications, 17-25.
- Trnkoczy, A. (1998). *Guidelines for civil engineering works at remote seismic stations*. Application Note 42, Kinometrics Inc., 222 Vista Av., Pasadena, Ca. 91107.

- Trnkoczy, A., and Živčić, M. (1992). Design of Local Seismic Network for Nuclear Power Plant Krsko, Cahiers du Centre Europeen de Geodynamique et de Seismologie, Luxembourg, **5**, 31-41.
- Tronrud, L. B. (Ed.)(1983a). Semiannual Technical Summary 1 October 1982 – 31 March 1983. NORSAR Scientific Report No. 1-82/83, 72 pp.
- Tronrud, L. B. (Ed.)(1983b). Semiannual Technical Summary 1 April 1983 - 30 September 1983. NORSAR Scientific Report No. 2-82/83, 88 pp.
- Tsuboi, C. (1954). Determination of the Gutenberg-Richter's magnitude of earthquakes occurring in and near Japan. Zisin. (J. Seism. Soc. Japan), Ser. II, **7**, 185-193.
- Tsuboi, S., Abe, K., Takano, K., and Yamanaka, Y. (1995). Rapid determination of M_w from broadband P waveforms. Bull. Seism. Soc. Am., **85**, 2, 606-613.
- Tsumura, K. (1967). Determination of earthquake magnitude from total duration of oscillation. Bull. Earthq. Res. Inst., Tokyo, **45**, 7-18.
- Tumarkin, A. G., Archuleta, R. J., and Madariaga, R. (1994). Scaling relations for composite earthquake models. Bull. Seism. Soc. Am., **84**, 4, 1279-1283.
- Udías, A. (1999). Principles of Seismology. Cambridge University Press, United Kingdom, 475 pp.
- Udías, A., and Buforn, E. (1988). Single and joint fault-plane solutions from first-motion data. In: Doornbos (1988a).
- Uhira, K., Yamasato, H., and Takeo, M. (1994). Source mechanism of seismic waves excited by pyroclastic flows at Unzen volcano, Japan. J. Geophys. Res., **99**, 17757-17773.
- Uhrhammer, R. A. (1980). Analysis of small seismographic station networks. Bull. Seism. Soc. Am., **70**, 1369-1379.
- Uhrhammer, R. A., and Collins, E. R. (1990). Synthesis of Wood-Anderson seismograms from broadband digital records. Bull. Seism. Soc. Am., **80**, 702-716.
- Uhrhammer, R. A., Loper, S. J., and Romanovicz, B. (1996). Determination of local magnitude using BDSN broadband records. Bull. Seism. Soc. Am., **86**, 1314-1330.
- Uhrhammer, R. A., Karavas, W., and Romanovicz, B. (1998). Broadband Seismic Station Installation Guidelines, Seism. Res. Lett., **69**, 15-26.
- UK AWE (1990). U.K. Atomic Weapons Establishment AWE Report No. O 12/90 (Semipalatinsk).
- UK AWE (1993). U.K. Atomic Weapons Establishment AWE Report No. O 11/93 (France).
- Utsu, T. (1982). Relationships between magnitude scales. Bull. Earthq. Res. Inst., **57**, 465-497.
- van der Kulk, W., Rosen, F., and Lorenz, S. (1965). Large aperture array signal processing study. IBM Final Report, ARPA Contract SD-296, Rockville.
- Vassiliou, M. S., and Kanamori, H. (1982). The energy release in earthquakes. Bull. Seism. Soc. Am., **72**, 371-387.
- Veith, K. F. (1977). A digital event detector. EOS, **58**, 1190
- Veith, K. F. (2001). Magnitude estimation from short-period body waves. Paper circulated on Oct. 9, 2002, amongst the members of the IASPEI WG on Magnitude Measurements, 7 pp.
- Veith, K. F., and Clawson, G. E. (1972). Magnitude from short-period P-wave data. Bull. Seism. Soc. Am., **62**, 435-452.
- Vergnolle, S., and Jaupart, C. (1990). Dynamics of degassing at Kilauea Volcano, Hawaii. J. Geophys. Res., **95**, 2793-2809.
- Vidale, J. E. (1986). Complex polarization analysis of particle motion. Bull. Seism. Soc. Am., **76**, 1393-1405.
- Voight, B., Hoblitt, R. P., Clarke, A. B., Lockhart, A. B., Miller, A. D., Lynch, L., and McMahon, J. (1998). Remarkable cyclic ground deformation monitored in real time on Montserrat and its use in eruption forecasting. Geophys. Res. Lett., **25**, 3405.

References

- Voight, B., Young, K. D., and Hidayat, D. (2000). Deformation and seismic precursors to dome-collapse and fountain-collapse nuées ardentes at Merapi volcano, Java, Indonesia. 1994-1998. *J. Volcanol. Geotherm. Res.*, **100**, 261-287.
- von Seggern, D. (1977). Amplitude-distance relation for 20-second Rayleigh waves. *Bull. Seism. Soc. Am.*, **67**, 405-411.
- Wadati, K. (1933). On the travel time of earthquake waves. Part. II, *Geophys. Mag. (Tokyo)* **7**, 101-111.
- Wahlström, R., and Strauch, W. (1984). A regional magnitude scale for Central Europe based on crustal wave attenuation. *Seismological Dep. Univ. of Uppsala, Report No. 3-84*, 16 pp.
- Walck, M. C., and Chael, E. P. (1991). Optimal backazimuth estimation for three-component recordings of regional seismic events. *Bull. Seism. Soc. Am.*, **81**, 2, 643-666.
- Wald, D. J., Quitoriano, V., Dengler, L. A., and Dewey, J. W. (1999). Utilisation of the Internet for rapid community intensity maps, *Seism. Res. Let.*, **70**, 680-697.
- Waldhauser, F., and Ellsworth, W. L. (2000). A double-difference earthquake location algorithm: method and application to the northern Hayward fault, California, *Bull. Seism. Soc. Am.*, **90**, 1353-1368.
- Wallace, T. C., Velasco, A., Zhang, J., and Lay, T. (1991). A broadband seismological investigation of the 1989 Loma Prieta, California, earthquake: Evidence for deep slow slip? *Bull. Seism. Soc. Am.*, **81**, 1622-1646.
- Wang, J.-H., and Ou, S.-S. (1998). On scaling earthquake faults. *Bull. Seism. Soc. Am.*, **88**, 3, 758-766.
- Wang, R. (1999). A simple orthonormalization method for stable and efficient computation of Green's functions. *Bull. Seism. Soc. Am.*, **89**, 3, 733-741.
- Warburton, R. J., and Goodkind, J. M. (1977). The influence of barometric pressure variations on gravity *Geophys. J. R. astr. Soc.* **48**, 281-292.
- Ward, P. L. (1992). SUDS. The Seismic Unified Data System. *EOS, Trans. Amer. Geophys. Un.*, **73**, 35, 380 pp.
- Wassermann, J. (1997). Locating the Sources of Volcanic Explosions and Volcanic Tremor at Stromboli Volcano (Italy) Using Beam-Forming on Diffraction Hyperboloids. *Phys. Earth Planet. Int.*, **10**, 271 - 281.
- Wassermann, J., and Ohrnberger, M. (2001). Automatic hypocenter determination of volcano induced seismic transients based on wave field coherence - an application to the 1998 eruption of Mt. Merapi, Indonesia. *J. Volcanol. Geotherm. Res.*, **110**, 57-77.
- Webb, S. C. (2002). Seismic noise on land and on the seafloor. In: Lee et al. (2002), Part A, 305-318.
- Wegler, U., and Lühr, B.-G. (2001). Scattering behaviour at Merapi volcano (Java) revealed from an active seismic experiment. *Geophys. J. Int.*, **145**, 579-592.
- Weichert, D. H. (1971). Short-period spectral discriminant for earthquake and explosion differentiation. *Z. Geophys.*, **37**, 147-152.
- Weichert, D. H., Manchee, E. B., and Whitham, K. (1967). Digital experiments at twice real-time speed on the capabilities of the Yellowstone Seismic Array. *Geophys. J. R. astr. Soc.*, **13**, 277-295.
- Wells, D. L., and Coppersmith, K. J. (1994). New empirical relationships among magnitude, rupture length, rupture width, rupture area, and surface displacement. *Bull. Seism. Soc. Am.*, **84**, 4, 974-1002.
- Westerhaus, M., and Zschau, J. (2001). No clear evidence for temporal variations of tidal tilt prior to the 1999 Izmit and Düzce earthquakes in NW-Anatolia. *J. Geodetic Soc. Japan*, **47**, 448 - 455.
- Wever, Th., Trappe, H., and Meissner, R. (1987). Possible relations between crustal reflectivity, crustal age, heat flow, and viscosity of the continents. *Annales Geophysicae*, **87**, 03 B, 255-266.

- Whiteway, F. E. (1965). The recording and analysis of seismic body waves using linear cross arrays. *The Radio and Electronic Engineer*, **29**, 33-46.
- Whiteway, F. E. (1966). The use of arrays for earthquake seismology. *Proc. R. Soc. A*, **290**, 328-342.
- Widmer, R., Zürn, W., and Masters, G. (1992). Observation of low-order toroidal modes from the 1989 Macquarie Rise event. *Geophys. J. Int.*, **111**, 226 - 236.
- Wiechert, E. (1904). *Verhandlungen der zweiten internationalen Seismologischen Konferenz. Beitr. Geophys., Ergänzungsband II*, 41-43.
- Wiechert, E. (1907). Über Erdbebenwellen. Theoretisches über die Ausbreitung der Erdbebenwellen. *Nachrichten von der Königlichen Gesellschaft der Wissenschaften zu Göttingen, Mathematisch-physikalische Klasse*, 413-529.
- Wielandt, E. (1975). Ein astasiertes Vertikalpendel mit tragender Blattfeder. *J. Geophys.*, **41**, 5, 545-547.
- Wielandt, E. (1990). Very- broad-band seismometry. In: Boschi, E., Giardini, D., Morelli, A. (Eds.), *Proceed. 1st Workshop on MEDNET, Sept. 10-14, 1990, CCSEM, Erice, Il Cigno Galileo Galilei, Roma*, 222-234.
- Wielandt, E. (1993). Propagation and structural interpretation of non-plane waves. *Geophys. J. Int.*, **113**, 45 - 53.
- Wielandt, E. (2002). Seismometry. In: Lee et al. (2002), Part A, 283-304.
- Wielandt, E., and Streckeisen, G. (1972). The leaf-spring seismometer and performance. *Bull. Seism. Soc. Am.*, **71**, 2349-2367.
- Wielandt, E., and Streckeisen, G. (1982). The leaf-spring seismometer: Design and performance. *Bull. Seism. Soc. Am.*, **72**, 2349-2367.
- Wielandt, E., and Steim, J. M. (1986). A digital very-broad-band seismograph. *Annales Geophysicae*, **4**, 227-232.
- Wielandt, E., and Zürn, W. (1991). Messungen der kurzperiodischen Bodenunruhe in Schiltach (BFO). In: Henger (1995).
- Wielandt, E., and Forbriger, T. (1999). Near-field seismic displacement and tilt associated with the explosive activity at Stromboli. *Annali Geofisica*, **42**, 407 - 416.
- Willmore, P. L. (1959). The application of the Maxwell impedance bridge to the calibration of electromagnetic seismographs, *Bull. Seism. Soc. Am.*, **49**, 99-114.
- Willmore, P. L. (Ed.) (1979). *Manual of Seismological Observatory Practice*. World Data Center A for Solid Earth Geophysics, Report **SE-20**, September 1979, Boulder, Colorado, 165 pp.
- Withers, M. M., Aster, R. C., Young, Ch. J., and Chael, E. P. (1996). High-frequency analysis of seismic background noise as a function of wind speed and shallow depth. *Bull. Seism. Soc. Am.*, **86**, 5, 1507-1515.
- Wolberg, J. R. (1967). *Prediction Analysis*. D. Van Nostrand Co. Inc., Princeton, N. J.
- Wood, H. O., and Neumann, F. (1931). Modified Mercalli intensity scale of 1931, *Bull. Seism. Soc. Am.*, **21**, 277-283.
- Wyatt, F. (1988). Measurements of coseismic deformation in Southern California. *J. Geophys. Res.*, **93**, 7923 - 7942.
- Wyatt, F., Beckstrom, K., and Berger, J. (1982). The optical anchor - a geophysical strainmeter. *Bull. Seism. Soc. Am.*, **72**, 1707 - 1716
- Wyatt, F., Agnew, D. C., and Gladwin, M. (1994). Continuous measurements of crustal deformation for the 1992 Landers Earthquake Sequence. *Bull. Seism. Soc. Am.*, **84**, 768 - 779.
- Yacoub, N. K. (1998). Maximum spectral energy for seismic magnitude estimation. Part I: Rayleigh-wave magnitude. *Bull. Seism. Soc. Am.*, **88**, 4, 952-962.
- Yamashita, T. (1976). On the dynamic process of the fault motion in the presence of friction and inhomogeneous initial stress. Part 1., Rupture propagation. *J. Phys. Earth*, **24**, 417-444.

References

- Yomogida, K., and Nakata, T. (1994). Large slip velocity of the surface rupture associated with the 1990 Luzon earthquake. *Geophys. Res. Lett.*, **21**, 1799-1802.
- Young, Ch. J., Chael, E. P., Withers, M. W., and Aster, R. C. (1996). A comparison of the high- frequency (>1Hz) surface and subsurface noise environment at three sites in the United States. *Bull. Seism. Soc. Am.*, **86**, 5, 1516-1528.
- Zadro, M., and Braitenberg, C. (1999). Measurements and interpretations of tilt-strain gauges in seismically active areas. *Earth Science Reviews*, **47**, 151 - 187.
- Zimmer, M., and Erzinger, J. (2001). Continuous gas monitoring by chromatograph and Alpha Scintillation counter on Merapi Volcano, Indonesia. submitted to *Bulletin of Volcanology*.
- Zoback, M. L. (1992). First- and second-order patterns of stress in the lithosphere: The World Stress Map Project. *J. Geophys. Res.*, **97**, 11703-11728.
- Zoeppritz, K. (1907). Über Erdbebenwellen. II. Laufzeitkurven. *Nachrichten von der Königlichen Gesellschaft der Wissenschaften zu Göttingen, Mathematisch-physikalische Klasse*, 529-549.
- Zonno, G., and Kind, R. (1984). Depth determinations of north Italian earthquakes using Graefenberg data. *Bull. Seism. Soc. Am.* **74**, 1645-1659.
- Zsiros, T. (1989). Macroseismic practice in Hungary, *Proc. 1st AB Workshop on Macroseismic Methods, Seis. Surv. Slov., Ljubljana*, 12 pp.
- Zürn, W., Laske, G., Widmer-Schmidrig, R., and Gilbert, F. (2000). Observation of Coriolis coupled modes below 1 mHz. *Geophys. J. Int.*, **143**, 113 - 118.

In the index reference is made to the **chapters** and related **annexes** in **bold** numbers or **letters**, respectively, followed by the page numbers where the key word appears. Numbers underlined refer to pages where definitions or main explanations of the terms are given. If an annexed paper is specifically dealing with the key word issue, no pages numbers are given.

- acceleration (see Glossary) **3:** 7, 15, 45, 86-87; **4:** 4-8; **5:** 2, 13-18, 20-21, 24-28, 34, 37, 40-41, 44; **6:** 4-5; **7:** 7, 15, 45, 86-87; **11:** 41; **12:** 20; **EX 4.1:** 4-6
- accelerometer **5:** 24-25, 44; **7:** 48-49, 61, 86-90, 92-93, 96-97, 100-102, 105-107; **8:** 3-7, 18, 30, 33, 38; **11:** 40; **EX 5.5:** 1
- aftershock **2:** 6, 68-68; **3:** 53, 80, 87; **7:** 61; **8:** 9, 20, 27, 42; **12:** 16; **IS 11.1:** 17, 24-25
- aliasing **6:** 5; **7:** 17; **9:** 23
- alias spectrum **6:** 5-6; **7:** 17
 - anti-alias(ing) filter **5:** 13; **6:** 3, 5-6, 9, 13, 19; **9:** 23; **11:** 41-42
- amplifier **5:** 27, 31-33, 45; **6:** 2, 10-11, 19; **7:** 64, 106; **8:** 17, 56; **IS 5.2:** 2-3
- amplitude
- amplitude-distance relations **2:** 1, 39; **3:** 29, 38, 40; **13:** 30
 - amplitude response (see response)
 - amplitude spectral density **4:** 2, 8; **13:** 3
 - average peak amplitude **4:** 10; **EX 4.1:** 5, 7-8
 - effective filter amplitude **4:** 8
 - instantaneous peak amplitude **4:** 10; **EX 4.1:** 1-2
 - RMS amplitude **4:** 8-10; **EX 4.1:** 1, 3-4; 6-8
- analog-to-digital converter see converter
- anisotropic see medium
- anisotropy **2:** 4, 11, 15, 17, 60; **3:** 2; **7:** 93; **11:** 20
- angle
- dip angle **2:** 35; **3:** 10, 65, 67; **EX 3.2:** 4-6; **EX 3.5:** 1-3
 - incidence angle **2:** 9-10, 26-28, 33, 40, 44, 57; **3:** 64; **9:** 2, 12-13; **11:** 20, 37-38; **13:** 26-28, 31
 - plunge angle **3:** 11, 81; **EX 3.2:** 5, 7; **EX 3.3:** 5-6
 - rake angle **3:** 10-11, 65, 67, 73; **EX 3.2:** 1-4; **EX 3.3:** 1, 4-6; **EX 3.5:** 1-2
 - slip angle see rake angle
 - strike angle (direction) **3:** 10, 65-66; **EX 3.2:** 4-6; **EX 3.5:** 1-3
 - take-off angle **3:** 33, 62-64, 69; **EX 3.3**
- ANTELOPE **8:** 13-14
- anti-plane (rupture propagation; fault geometry) **IS 3.1:** 10, 15, 18
- archiving (of data) **6:** 18; **8:** 13, 15, 54, 57-58; **10:** 6-8, 17; **11:** 5
- array (seismic) **1:** 6, 8, 13, 15-16; **2:** 1, 8, 18, 67; **3:** 51, 83; **4:** 20-22, 26-28, 31; **7:** 75, 86-91, 97, 102, 105-107; **8:** 13, 31; **9:** all Chapter; **10:** 8, 10; **11:** 2-6, 9, 14, 31-35, 38-39, 41-42, 48, 51-52, 54, 56-59, 71, 79, 98; **13:** 1, 18-21, 26, 31-35, 38, 40; **EX 11.2:** 1; **IS 5.1:** 5
- array analysis **9:** 9; **11:** 2, 80; **13:** 32, 34-35

- array aperture **9: 9; 11: 51**
- array beamforming **9: 2-3, 7-9, 15-18, 22, 26-27, 29, 31, 35-36, 41, 44; 11: 39, 56, 58; 13: 31**
- array beampacking **9: 26, 29-31, 45**
- array design **9: 3, 26, 36, 39-41**
- array examples **9: 3-7**
- array gain **9: 26, 36-37, 39-41**
- array installation **7: 88-91; 8: 3; 9: 3, 15**
- array planning **7: 87, 89-93**
- array polarization **13: 33**
- array processing **8: 13; 9: 1-3, 41; 11: 2, 56**
- array response (transfer function) **9: 27**
- strong-motion array **7: 86-89; 8: 3**
- asthenosphere **2: 13, 32; 11: 16**
- atmosphere **3: 4; 5: 29**
- attenuation **1: 12; 2: 7, 13, 20-21, 23, 37-38, 44, 62-65; 3: 8-9, 19, 23-26, 29-30, 33-35, 38-41, 44, 49, 51-52, 57, 70; 4: 1, 19-20; 7: 15, 23, 42, 45, 76-77; 8: 52; 9: 16, 24; 11: 11, 14, 16, 19, 61, 67; 12: 2, 13, 17-18, 19; 13: 4; EX 5.1: 1**
- attenuation law **3: 24, 40; 7: 15**
- attenuation (Q-) model **3: 34-35, 39-41, 70**
- attenuator **EX 5.2: 2**
- intensity attenuation **12: 2, 13-14, 17-19**
- intrinsic attenuation **2: 13, 37-38**
- noise attenuation **7: 76-77**
- scattering attenuation **2: 37**
- automatic analysis **9: 1; 13: 34**
- auxiliary plane **see plane**
- azimuth **2: 69; 3: 5, 11, 19, 22, 28, 58-60, 63-64, 66, 69, 78-79, 81; 4: 21-22, 31-32; 7: 25, 64, 81-82; 8: 42; 9: 2, 9, 25, 33-34, 38; 10: 4; 11: 1-2, 4, 7, 10, 22, 31, 34-39, 51, 56, 60, 63, 66-67, 99-100; 13: 19, 26-28, 31-32; EX 3.2: 1-3, 5, 7; EX 3.3: 1, 4-6; EX 11.1 11: 37-39, 58, 60, 63; EX 11.2: 1, 3-4; EX 11.3: 3, 5**
- (back) azimuth determination **11: 37-39, 58, 60, 63; EX 11.2: 1, 3-4; EX 11.3: 3, 5**
- backazimuth **2: 10-11, 16-17, 57; 4: 21, 31; 9: 2, 9-10, 12-13, 15, 17, 19, 22, 26, 28, 31-35, 43-45, 48-49; 11: 3, 10, 14-15, 20, 34-38, 52, 54, 58, 69, 82; 13: 31-33; EX 11.2: 1-5**
- bandwidth **1: 2, 8-9; 2: 13, 64; 3: 17, 39, 49-53, 80; 4: 3, 8-16; 5: 1, 3, 7, 9, 13, 25, 27-28, 34, 39; 6: 6, 13-14, 19; 7: 39-40, 65; 8: 21-22, 26; 11: 8, 10-11, 40-42, 46-47; 13: 22, 40; EX 4.1: 1, 3-8**
- absolute bandwidth **4: 9**
- relative bandwidth **4: 9-10; EX 4.1: 2, 3-8**
- bandwidth extension **5: 27**
- band pass **see filter**

- barometric pressure see pressure
- barycenter see macroseismic data
- beamforming see array
- beampacking see array
- bidding process **8: 47**
- blast (quarry b., mine b.) **2: 18; 9: 33; 11: 24, 28-29, 62, 68**
- Bode-diagram **EX 5.1: 1, 3; EX 5.2: 4; EX 5.5: 1; IS 5.2**
- borehole **2: 22; 4: 22-23, 29-31; 5: 28-29, 41; 7: 13, 26, 28, 39, 46-47, 58, 64, 70-71, 75-107; 8: 3, 29-30, 34, 37; 13: 6, 35-3**
- bore accelerometer **7: 89-90, 92-93, 100-102, 107**
 - borehole core **7: 98-99**
 - borehole drilling **7: 94, 102**
 - borehole installation **4: 30-31; 7: 39, 58, 64, 75-78, 80-83, 92-93; 8: 37**
 - borehole instrument(ation) **7: 77, 83-84, 93**
 - borehole location **7: 89-90, 93, 95-96, 102**
 - borehole tiltmeter **13: 35-36**
 - borehole seismometer **7: 79-80, 83-84**
 - borehole specification **7: 78**
 - borehole wave **13: 6**
- boundary **2: 25-26, 31-35, 41, 47-48, 59-60; 3: 30, 64, 88; 8: 6; 11: 20, 25, 33, 75, 82, 89, 98**
- core-mantle boundary (CMB) **2: 25, 32, 41, 47-48, 59-60, 62; 3: 30; 11: 20, 25, 33, 75, 88-89, 98; EX 11.3: 2; IS 2.1: 4, 8, 12**
 - crust-mantle boundary (Moho discontinuity) **2: 12, 14, 17, 25, 44-45, 47-48, 67; 11: 61, 63-64, 67-68; EX 11.1: 1, 3; IS 2.1: 4-7, 11**
 - inner-core boundary (ICB) **2: 25, 32, 62; 11: 80, 87; EX 11.3: 2, 12; IS 2.1: 4, 12**
- bulk modulus **2: 3-4, 8, 13, 32**
- bulletin **1: 16; 2: 58; 7: 8; 8: 58-59; 9: 2-3; 11: 1, 5, 23; IS 2.1: 1; IS 10.1; IS 10.2; IS 11.2**
- CALEX (program) **5: 38-40, 42, 45; EX 5.4: 1-3; PD 5.2**
- CALIBRAT (program) **5: 45; PD 5.1**
- calibration (of seismometers and geophones) **1: 12, 14, 16; 5: 1-3, 13, 26, 34-45; 7: 107; 8: 3, 53-54, 56-57; 10: 11-12; 11: 10; 12: 12; EX 5.2-5.4; PD 5.1-5.5; IS 5.1: 4**
- calibration by harmonic drive **EX 5.2: 4; EX 5.3**
 - calibration coil **5: 2, 34-37, 40, 45; EX 5.2: 1, 4, 6; EX 5.3: 1; DS 5.1: 2-10**
 - calibration current **5: 13, 35, 40; EX 5.2: 1, 4, 6; EX 5.3: 1**
 - calibration signal **EX 5.4: 2-3**
 - calibration of regions **11: 31**
 - calibration by stepwise motion (impulse calibration) **5: 42, 45; EX 5.2**
 - mechanical calibration **5: 34-35, 41-44**
- calibration function see magnitude

Index

- caustic **2:** 26, 29-33, 37, 39-40, 49, 67; **3:** 35; **11:** 18, 22, 33, 37, 80, 83, 87, 99; **IS 2.1:** 9
- centroid moment tensor (CMT) **3:** 79; **EX 3.2:** 6-7; **EX 3.3:** 4; **IS 11.1:** 28
- circle and chord method **11:** 39; **EX 11.1**
- coda (waves) **2:** 38, 42, 44, 65; **3:** 28, 43, 53; **9:** 6-8, 19-21; **11:** 7-8, 61, 74; **DS 11.1:** 2
- coda Q (Q_c) **EX 3.4:** 1
- coil
- calibration c. (see calibration)
 - coil resistance **5:** 32; **EX 5.2:** 3-6; **EX 5.3:** 3
 - signal coil **5:** 35, 37; **EX 5.2:** 1, 4-6; **EX 5.3:** 1
- compression(al) (signal; first motion)
- compression of data **2:** 2, 5, 7, 9, 21; **3:** 2, 5, 58-59, 63, 74, 77; **10:** 3; **11:** 9-11, 23, 29, 69; **EX 3.2:** 6-7
 - compression (P) quadrant **6:** 16-18; **8:** 25; **10:** 8, 18
- conversion
- analog-to-digital conversion **6:** 3, 6, 9-10, 13, 19; **9:** 23; **10:** 2, 7-8, 11, 14 17; **11:** 17, 20, 60, 64; **12:** 11; **EX 5.5:** 1
 - conversion factor of seismographs **6:** 3, 6, 9-10, 13, 19; **9:** 23
 - conversion of data formats and related programs **5:** 2, 25
 - conversion of units **10:** 2, 7-8, 11, 14, 17-20; **11:** 60
 - conversion of wave modes **4:** 1, 3, 6, 8; **PD 4.1**
- converter
- analog-to-digital converter (ADC) **2:** 12, 17, 24, 32-33, 42, 48, 57; **11:** 17, 20, 64
 - digital-to-analog converter (DAC) **3:** 27; **4:** 7; **6:** 2-3, 6, 9-11, 14, 18-20; **7:** 73; **8:** 8, 16-17; **10:** 17, 20; **13:** 1, 23, 40
- couple
- double couple (mechanism, source, solution) **6:** 2, 9-11, 19-20; **7:** 73; **8:** 16; **13:** 1, 23, 40
 - force couple **6:** 11, 19;
 - single couple **2:** 7; **3:** 51, 59-61, 69-71, 73-74, 77-79, 81; **13:** 1, 4-5, 10; **EX 3.5:** 2; **IS 3.1:** 11
- core (Earth's core)
- double couple (mechanism, source, solution) **3:** 72; **IS 3.1:** 7
 - force couple **3:** 73
 - single couple **2:** 7, 25, 32, 35, 38, 41, 47-52, 59-60, 62, 67; **3:** 30, 35, 42; **8:** 6; **11:** 5, 14, 18, 20, 25, 33, 75-77, 79-81, 83, 87, 89, 95, 96, 98-99
 - core phases see phases
 - core-mantle boundary see boundary
 - inner core **2:** 7, 21, 25, 32, 38, 47, 60, 62; **11:** 80, 83, 87; **IS 2.1:** 3-5, 9-10
 - inner-core boundary see boundary
 - outer core **2:** 32, 38, 47, 49, 60, 62, 67; **3:** 30
- corner frequency see frequency
- cost (of seismic sensors, systems etc.) **7:** 8, 13, 15, 25, 39-41, 43, 45, 57, 63-64, 68, 74-79, 81, 83-84, 87, 90-92, 95, 97, 102, 107; **8:** 3-5, 7, 10-11, 14-17, 20-22, 27, 33-34, 36-39, 42, 45-46, 48, 55-56, 58; **10:** 1-2; **13:** 19

- crack
- circular crack **3:** 6, 9, 11, 93
 - crack criteria **IS 3.1:** 16
 - crack energy **IS 3.1:** 1
 - crack front **IS 3.1:** 17
 - crack models **IS 3.1:** 9
 - crack propagation **IS 3.1:** 14
 - crack tip **3:**6, 9, 93; **IS 3.1:** 9
 - crack velocity **IS 3.1:** 1, 9
 - shear crack **3:**6, 9, 93; **IS 3.1:** 9, 17
 - tension crack **IS 3.1:** 13, 15
 - tension crack **EX 3.5:** 2; **IS 3.1:** 12
 - tension crack **EX 3.5:** 2; **IS 3.1:** 12
 - tension crack **EX 3.5:** 2; **IS 3.1:** 12
 - tension crack **EX 3.5:** 2; **IS 3.1:** 12
- cross-over distance **2:** 34; **11:** 61; **EX 11.1:** 3-4
- crust (Earth's crust) **2:** 1, 4, 6, 12-15, 17-18, 20, 25, 29, 31-32, 38, 42-46, 48, 62, 65, 67-68; **3:** 2, 4, 19, 23-24, 28-29, 31, 36, 42, 87-88, 91; **4:** 22; **8:** 6; **9:** 11, 15-16, 33-34; **11:** 14, 17, 22, 24, 26-29, 35, 51, 61, 63-67, 71; **12:** 19; **EX 11.1:** 3; **IS 2.1:** 3-5, 7-8, 11-12
- crustal model **2:** 44-46, 65; **11:** 64, 66, 71; **IS 2.1:** 2, 13
 - lower crust **2:** 12, 44-45; **11:** 63; **IS 2.1:** 13
 - upper crust **2:** 14, 29, 44-45; **9:** 11; **11:** 63; **IS 2.1:** 13
- crustal phases see phases
- crust-mantle boundary see boundary
- crystal chip **6:** 13
- CTBT/CTBTO **1:** 6, 8; **2:** 60; **8:** 28; **9:** 39, 49; **10:** 2, 5, 10-11, 20; **11:** 12, 29, 31, 61, 64, 98
- damping **3:** 24; **4:** 16-18; **5:** 9-10, 13, 15, 23, 26-28, 32, 35-38, 45; **7:** 101, 103; **11:** 10; **EX 5.2:** 1-6; **EX 5.3:** 1; **EX 5.4:** 3; **EX 5.5:** 1; **IS 5.2:** 1-2
- data
- data access **10:** 10; **IS 8.3;** **IS 10.3**
 - data acquisition **1:** 6, 9, 15-16; **3:** 78; **4:** 1; **6:** 10, 15-17, 19; **7:** 17, 47, 50; **8:** 1, 4, 13, 15-18, 22, 27, 40-41, 53-54, 58; **9:** 1; **10:** 7-8, 12, 15; **11:** 4, 42, 70
 - data analysis **1:** 4, 12, 16; **2:** 1, 22-23, 43; **3:** 22; **8:** 49; **9:** 1, 3; **11:** 1-2, 5, 14, 32, 39, 63, 68
 - data archival **10:** 8
 - database **9:** 31, 44-45; **10:** 6-7, 10-11, 13; **11:** 23, 59-60; **12:** 14-15; **IS 2.1:** 1-2
 - data bulletin see bulletin
 - data center (centre) **1:** 8, 15; **2:** 43, 50, 64; **3:** 19, 33, 35, 46, 48; **7:** 25-26; **8:** 9, 28, 59; **10:** 1, 5, 7-10, 17-18; **11:** 1, 3, 10, 12, 14, 23, 26, 32, 34, 80, 98; **13:** 40-42
 - data compression **6:** 16-17; **8:** 25
 - data exchange **1:** 2, 9, 13; **8:** 58-59; **10:** 4-7, 9, 15, 17, 20; **11:** 1, 5, 23, 40; **IS 2.1:** 1-2
 - data flow **7:** 41; **8:** 12, 22

- data format see format
- data logger **4:** 13; **6:** 13, 15, 18, 20; **7:** 18, 20, 26, 32, 49, 73; **8:** 3, 10-11, 17, 19, 26, 40, 49; **10:** 19
- data management **3:** 79; **6:** 16; **8:** 12
- data model **6:** 17-18
- data processing **1:** 6, 15; **2:** 4, 64; **5:** 4, 27; **6:** 1; **7:** 85; **8:** 1, 13, 36; **9:** 1-3; **11:** 3, 5, 41
- data protocols **10:** 10
- data rate **1:** 8; **8:** 25; **13:** 40
- data retrieval **10:** 3; **IS 8.3**
- data storage **6:** 1; **8:** 13, 25; **10:** 1-2, 8, 11; **13:** 41
- data transfer **8:** 1-2, 10, 12, 14, 21; **10:** 1-2, 9-10, 17; **11:** 12
- data transmission **7:** 2, 8-9, 12, 39-42, 44, 60; **8:** 4, 8-10, 15-16, 20-22, 25-28, 36, 40, 44-46, 55; **10:** 6; **11:** 5; **IS 8.2**
- hydroacoustic data **IS 10.3**
- infrasonic data **IS 10.3**
- macroseismic data **3:** 15; **12:** 6-8, 10-19
- metadata **6:** 16, 18
- seismic data **1:** 1, 6; **2:** 61; **3:** 50; **5:** 6; **6:** 19; **7:** 8, 39-41, 47-48, 75, 78, 84; **8:** 4, 10, 13, 15-17, 19-22, 24-27, 39, 49, 54-55, 57-59; **9:** 1, 18; **10:** 1-3, 7, 11-12, 19; **12:** 7, 11, 13-14, 16-18; **13:** 34
- decomposition **3:** 73, 77, 79; **5:** 9
- decomposition of moment tensor **3:** 79
- deformation **2:** 2-3, 5; **3:** 1-2, 7-9, 18, 46, 83; **7:** 46-47, 53, 61, 69; **13:** 35-37
- Delta-Sigma Modulator (DSM) **6:** 11
- density (of the medium) **2:** 4-8; **DS 2.1:** 1-3, 7-11; **EX 3.4:** 3-4
- detection **1:** 8; **4:** 27; **7:** 16, 25, 31, 38, 40, 44; **8:** 8, 10-13, 19-20, 22, 26, 28, 34, 43; **9:** 2-3, 18-19, 22, 36, 38, 40-45, 48; **11:** 2, 29, 31, 39-40, 51, 57
- detection threshold **7:** 25, 31; **8:** 19-20, 43; **9:** 19, 44; **11:** 31; **IS 8.1:** 11
- detection processing **9:** 2-3, 18, 41, 44
- detectability **7:** 1, 13, 15; **8:** 18, 43; **9:** 22; **IS 7.4**
- detrigger see trigger
- diffraction **2:** 41; **3:** 53; **4:** 1; **7:** 42; **8:** 6, 45; **11:** 35
- dilatation(al) **2:** 5, 9; **3:** 5, 58-59, 63; **11:** 9-11, 23, 69
- Dirac impulse (needle impulse) **4:** 14; **5:** 7-8; **6:** 4; **EX 3.5:** 1
- direction
 - slip direction **3:** 59, 66; **EX 3.2:** 5
 - strike direction **3:** 14, 58, 65
- directivity **3:** 19, 66, 80
- discontinuity **2:** 12, 25-26, 28, 30-31, 33-34, 37, 40-41, 44-45, 59; **7:** 38; **11:** 62, 67, 71-73, 79
- Conrad discontinuity **2:** 44-45
- first-order discontinuity **2:** 26, 29, 33
- Mohorovičić discontinuity **2:** 12, 14, 17, 25, 44-45, 47-48, 67; **11:** 61, 63-64, 67-68; **IS 2.1:** 4-7, 11

- second-order discontinuity
- discrimination **2: 28**
1: 8; 3: 10, 35, 41; 7: 25; 11: 24, 28-29, 31, 33, 64; 12: 2; 13: 22, 34, 36
- dislocation **3: 45, 58, 60-61, 73, 82, 89, 91-93; 4: 16; EX 3.4: 3-6; ES 3.5: 2; IS 3.1: 8-9, 11, 13-18; IS 3.1: 16-17**
IS 3.1: 16
5: 42-43, 45; PD 5.3
- dislocation function
 - dislocation velocity
- DISPCAL (program) **5: 45; PD 5.4**
- DISPCAL1 (program) **2: 13, 15, 17, 19, 42; 3: 30; 7: 42; 8: 6, 39, 45; 11: 7, 15-16, 64**
- dispersion **2: 13, 15, 17; 3: 30; 11: 15**
2: 19
2: 13, 17; 11: 15
- dispersion curve
 - inverse dispersion
 - normal dispersion
- displacement (of ground motion, sensor mass; response, seismogram) **1: 8; 2: 3, 5-9, 12, 21; 3: 8-9, 16, 19-20, 23-24, 27, 30-31, 33, 36, 40-41, 47, 49, 71-72, 74-75, 79, 81, 87; 4: 1, 4-8, 11, 14-16, 18, 24; 5: 1-2, 10, 13-16, 18, 23-25, 27, 41-44; 7: 7, 18-19, 26, 28-30, 33; 11: 5, 9-12, 18-19, 30, 33, 40-48, 50-51, 75, 77, 86; 13: 7-9; EX 5.2: 1, 4; EX 5.3: 1**
3: 5-10, 13, 18, 36, 38, 49, 56-58, 60-61, 65, 73-74, 82, 86-89, 92-93; EX 3.5: 1
3: 15, 73; IS 3.1: 2
3: 75; IS 3.1: 16
3: 8-10, 56-57, 85
2: 5; 3: 62; EX 3.2: 1
5: 24, 27, 42; IS 5.2: 2
3: 59, 66
- displacement (at a fault; see also dislocation) **7: 55-57, 91**
- displacement field
 - displacement function
 - displacement spectrum
 - displacement vector
 - displacement transducer
- Doppler effect **4: 31; 7: 12, 57, 76-78, 80, 83, 86, 93-98, 100-103**
- double-couple source (see couple)
- drainage **1: 2, 9; 2: 20; 3: 21, 27; 4: 6-7, 10, 13; 5: 2; 6: 13, 19; 7: 6, 13, 40, 47, 64-65, 74, 93, 97; 8: 1, 3-5, 7, 15-17, 30, 34, 40-41, 43, 49; 11: 2, 8, 41; 13: 39-40**
- drilling
- dynamic range
- Earth
 - Earth models **1: 10, 14-16; 2: 1-2, 15, 27, 36, 38, 57-64; 3: 79; 8: 53; 9: 11-12; 11: 7, 8, 39, 61, 92-93, 98; DS 2.1; IS 2.1: 2**
 - Earth's tides **2: 20; 7: 64**
 - Earth's core see core
 - Earth's crust see crust
 - Earth's mantle see mantle
 - flat Earth **2: 26**
 - spherical Earth **2: 26-27, 41; 3: 30**
- earthquake **11: 62**
 - anthropogenic/ man-made earthquake **2: 17, 45-46, 48, 68; 3: 87; 11: 17, 24, 26, 64; EX 11.1: 3-4;**
 - crustal earthquake/event

Index

- deep earthquake **2:** 15, 17, 19, 42, 48; **3:** 2, 30, 33, 37, 41, 54, 78; **11:** 17-18, 24-27, 75, 90, 99; **EX 11.2:** 2-4; **DS 11.2:** 12-13; **DS 11.3:** 1-3, 4-5, 12-14, 21-22
 - earthquake catalog **1:** 7; **3:** 15, 25, 50; **7:** 2-3, 25; **12:** 16-17, 19
 - earthquake parameters **1:** 14; **8:** 55; **10:** 3; **12:** 12, 16
 - induced earthquake **3:** 5; **8:** 2, 6, 35; **11:** 1, 29, 40, 62, 68, 71
/seismicity
 - local earthquake (records) **2:** 38, 45-46; **3:** 13, 21, 25, 28, 69; **11:** 61-71; **DS 11.1**
 - microearthquake **8:** 18-19
 - mining-induced earthquake **2:** 10; **11:** 1, 29, 40, 62, 68, 71
 - near earthquake **11:** 61, 64
 - shallow earthquake **11:** 76; **EX 11.2:** 2-4
 - slow earthquake **3:** 46, 92
 - tectonic earthquake **3:** 2-7, 17, 71; **11:** 29, 66; **13:** 1, 4, 10-11
 - teleseismic earthquake **2:** 15, 61; **3:** 51; **11:** 72-100; **DS 11.2**; **DS 11.3**
 - regional earthquake **2:** 46; **3:** 32; **11:** 61-71; **DS 11.1**
 - volcanic earthquake **3:** 4; **13:** 1
- EARTHWORM **8:** 13
- elastic moduli **2:** 2-4, 7
- electrical grounding **7:** 59
- electrodynamical constant **EX 5.2:** 3; **EX 5.3:** 1;
- electromagnetic interference (EMI) **7:** 48
- ellipticity (of the Earth) **IS 11.1:** 23-24
- energy **1:** 5, 8; **2:** 7, 12, 15, 17, 19, 24-25, 29, 32-33, 36-38, 40-41, 45, 49, 57, 64; **3:** 1, 3-4, 7, 9, 15-19, 22, 30-31, 36-39, 46, 49-57, 71, 75, 80, 82-84, 86-87, 92; **4:** 18; **5:** 5, 7, 23; **6:** 4, 6; **7:** 3, 43, 45, 93, 102, 104-105; **8:** 6; **9:** 7-8, 19, 22, 24-26, 33-35; **11:** 7-8, 17, 19-20, 25, 28, 30, 52, 54, 61, 64, 71, 81, 83; **12:** 19; **13:** 15, 30, 33
- energy magnitude (Me) **3:** 7, 18, 37-38, 50, 54, 56-57, 83
 - seismic energy (E_s) **2:** 7, 25, 33, 37; **3:** 3-4, 7, 15-19, 31, 37-39, 46, 49-51, 57, 80, 82-84, 87, 92; **4:** 18; **7:** 3; **9:** 24, 33-34; **11:** 52; **12:** 19; **13:** 15
- epicenter **3:** 3, 41, 53, 56; **8:** 2-3, 12, 41-43; **9:** 9-10; **11:** 6, 8, 13-14, 24, 26, 29, 32, 34, 36-39, 57, 61, 63-65, 99; **12:** 13, 16-19; **13:** 13, 16-17, 19; **EX 11.1:** 1-4; **EX 11.2:** 1, 5, 9
- epicenter (estimation/
determination/location) **EX 11.1**; **EX 11.2**; **IS 11.1**
- equation of motion **2:** 4-5; **5:** 17
- equatorial plane see plane
- equipment selection **8:** 49
- event
- event discrimination/
identification **11:** 24, 28-29, 31-32, 34; **13:** 36
 - event location (see location)
 - local event/seismic source **2:** 6, 42-43, 65; **3:** 21, 23-24, 29, 69-70, 80; **7:** 1,

- low-frequency events 31; **11:** 19, 34, 60, 71; **EX 3.1:** 2; **EX 11.1**
 - hybrid events **13:** 5, 7
 - multi-phases events **13:** 6, 14, 35
 - regional event/seismic source **13:** 6
 - teleseismic events **2:** 17, 67; **7:** 64, 74, 93; **9:** 1-2, 7-8, 19-20, 46-48; **EX 11.1**
 - ultra-low-frequency events **1:** 8; **2:** 46, 61, 63-64; **3:** 36, 70; **4:** 30-31; **7:** 10, 16, 37; **11:** 39, 99; **EX 3.2**
 - very-low-frequency events **13:** 7
 - volcanic-tectonic event **13:** 3-4
- explosion **1:** 8; **2:** 1-2, 17, 59-60, 66; **3:** 4-10, 12, 17, 32, 34, 40-43, 50, 73, 75, 83, 87; **4:** 1, 11-12, 15, 26-28, 32; **8:** 2, 35; **9:** 1, 6, 28, 31, 34; **11:** 1, 6, 8, 17-18, 24, 29-31, 33, 40, 56-57, 62, 71, 89, 99; **13:** 7-8, 11-13, 16, 28, 33, 37, 40; **DS 11.4**
 - explosion quakes **13:** 7-8
 - explosion yield **11:** 56-57
 - explosion source **3:** 73; **9:** 6
 - underground nuclear explosion **1:** 8; **2:** 17; **3:** 4, 8-9, 17, 32, 34, 40, 42-43, 50; **4:** 12, 26-28, 32; **8:** 2; **11:** 6, 29-31, 56-57, 89; **13:** 33; **EX 3.5:** 2; **DS 11.4**
- far-field **2:** 6-7, 38; **3:** 9, 15; **4:** 15
- fault(ing) **1:** 14, 16; **2:** 2, 43-44, 69; **3:** 2-3, 5-6, 9-15, 18, 45, 48, 53, 56-60, 62-63, 65-68, 69-75, 80-82, 85-93; **4:** 11; **7:** 2, 31; **8:** 29, 44; **13:** 4, 40
 - circular fault **IS 3.1:** 9
 - fault displacement see displacement and dislocation
 - fault length **3:** 88-91
 - fault plane (solutions) **1:** 17; **3:** 11, 15, 58-70, 80-81; **11:** 10, 27, 66-67; **EX 3.2:** 1-6 ; **EX 3.3:** 4-6; **EX 3.5:** 2-3
 - (types of) faulting **3:** 66-68; **EX 3.5:** 2-3
 - rectangular fault **IS 3.1:** 9-10
- feasibility study **8:** 35-36, 39
- feedback (system, sensor) **5:** 19-28, 31; **7:** 49, 66, 83; **8:** 7
- Fermat's principle **2:** 25-26
- Federation of Digital Broad-Band Seismograph Networks (FDSN) **4:** 25; **8:** 14, 28; **10:** 7, 15, 20
- filter(ing) **1:** 5, 8, 11-12; **2:** 10, 18-19, 22, 30, 38, 52, 64; **3:** 17, 18-20, 35, 38-39, 41, 79, 81; **4:** 1, 3, 8-10, 11-18, 25-30; **5:** 1-2, 9-10, 12-13, 15-16, 23, 27, 28, 38-39, 44-45; **6:** 3, 5-11, 13-16, 19-20; **7:** 17, 27-28, 33-38, 41, 55, 66; **8:** 6-7, 16, 19, 52; **9:** 2, 8, 19-23, 25, 28-33, 38-39, 41-44; **10:** 8; **11:** 2, 5, 8, 10, 14-16, 18, 23, 25-26, 28-29, 31, 33, 36, 40-48, 56-57, 59-60, 65, 67-69, 71, 73, 79-83, 85, 88-89, 96, 99-100; **13:** 9-10, 15, 26, 31, 33, 40; **EX 5.4:** 3; **EX 5.5:** 7
 - analog filter **6:** 3, 8, 20

- anti-alias filter see aliasing
- band-pass filter(ed) **4:** 25, 28; **5:** 12, 15, 16, 38; **7:** 34-35, 37-38; **8:** 19, 52; **11:** 16, 40-41; **13:** 9-10; **DS 11.3:** 24; **DS 11.4:** 4-5; **EX 4.1:** 1; **EX 5.4:** 2; **IS 5.2:** 3, 6
- Butterworth filter **5:** 23, 38; **6:** 5; **DS 11.2:** 29; **EX 5.5:** 7
- decade filter(ing) **EX 4.1:** 4
- decimation filter **6:** 8, 13-16; **EX 5.4:** 3
- digital filter **6:** 7-8, 11, 13, 19-20; **11:** 41; **EX 5.5:** 7
- finite impulse response filter (FIR) **6:** 8, 13-14, 19; **10:** 8
- frequency filter **4:** 25-26, 28; **11:** 16
- frequency-wavenumber (f-k) filtering see f-k analysis
- high-pass filter(ed) **4:** 1; **5:** 1, 9, 15-16, 38; **6:** 3; **7:** 27; **11:** 16, 40, 65, 67-68; **DS 11.1:** 2, 4; **EX 5.1:** 1, 3; **EX 5.4:** 2; **IS 5.2:** 3, 6
- infinite impulse response filter (IIR) **5:** 2; **6:** 8, 20
- low-pass filter **3:** 79; **4:** 1; **5:** 9-10, 13, 15-16, 38-39; **6:** 3, 5-7, 10-11; **7:** 17, 34, 37; **11:** 16, 36; **EX 5.4:** 2; **EX 5.5:** 7
- noise prediction error filter **4:** 27-28
- octave filter **4:** 9-10; **EX 4.1:** 4
- polarization filter(ing) **4:** 28-29; **11:** 33; **13:** 26; **IS 2.1:** 1
- recursive filter **5:** 39, 45
- first motion **3:** 5, 11, 58-60; **4:** 11-12, 32; **8:** 7; **11:** 9-10, 29, 35, 69, 71; **EX 3.2:** 1-3
- f-k analysis **4:** 21; **9:** 3, 25-29, 44-47; **11:** 54, 56, 58; **13:** 31-32; **IS 2.1:** 1
- focal depth see source depth
- focal mechanism **2:** 25, 69; **3:** 37, 59, 69, 81; **8:** 42; **EX 3.5:** 2
- focal sphere **3:** 59-61; 63-64; 66, 69-70; **EX:** **3.2:** 1
- force-balance accelerometer/sensor **5:** 24-25, 27-28, 33, 44; **EX 5.4:** 3
- format
 - data exchange formats **10:** 7, 9-10
 - data format **1:** 1, 16; **5:** 9, 45; **6:** 16-18; **8:** 12, 22, 58; **9:** 3; **10:** 1-20; **11:** 59-60
 - format conversion **10:** 7-8, 17-18
 - formats for database systems **10:** 10
 - GSE/IMS format **10:** 2, 5
 - IASPEI Seismic Format (ISF) **3:** 33; **10:** 2-3, 6, 11; **11:** 5, 12, 99
 - input/output formats **10:** 4, 14, 17-19
 - Nordic format **10:** 4
- free oscillations see normal modes
- free-surface reflection **EX 3.4:** 3, 5-6
- frequency
 - center frequency **4:** 9; **EX 4.1:** 5, 7
 - corner frequency **3:** 3-9, 17-18, 39, 41, 49-50, 52-53, 93; **4:** 9; **5:** 15-16; 25-27, 33; **6:** 5; **7:** 17, 23; **8:** 5, 7; **11:** 18, 41,

- frequency band
 - frequency domain
 - frequency response
 - frequency spectrum
 - gain
 - gain ranging
 - gas monitoring
 - generator constant
(see also electrodynamic constant)
 - German Regional Seismic Network (GRSN)
 - Global Digital Seismic Network
 - Global Positioning System (GPS)
 - Global Seismic Network (GSN)
 - geometric spreading
 - geophon
 - Geotech Instruments (seismometers)
 - geotechnical studies (data, sampling)
 - gradient
 - gradient zone
 - strong gradient
 - weak gradient
 - Gräfenberg array
 - Gräfenberg Observatory (GRFO)
 - great circle
 - grid search
 - ground
 - ground acceleration
 - ground deformation
 - ground displacement
 - ground velocity
 - grouting
 - Guralp (seismometer)
 - half-bridge
 - harmonic analysis
 - harmonic drive
- 44, 46, 69-70; **13**: 40; **EX 3.4**: 1, 4-6; **EX 3.4**: 4-6;
EX 5.1: 1; **EX 5.5**: 1; **IS 5.2**: 1-3; 5-6
1: 9; **3**: 17, 34, 45; **5**: 29, 41; **6**: 7; **7**: 16, 25, 39-40;
8: 11; **EX 4.1**: 1
3: 10, 51, 57, 72, 74-75, 79; **4**: 1-2, 15; **6**: 6; **9**: 45,
 24, 26-27, 29; **11**: 39; **13**: 31; **EX 4.1**
3: 17, 20, 27; **4**: 3, 16; **5**: 29, 41; **6**: 7; **7**: 17; **8**: 5, 7,
 56; **IS 5.1**: 4
4: 15; 24-25, 28
5: 2-3, 9-11, 13, 25-27, 32-33, 41-42; **6**: 19; **7**: 4, 6-
 7, 13, 15, 17, 30, 40, 42-43, 45, 90, 106; **8**: 15, 17,
 34, 44, 52; **9**: 17, 26, 29, 36-37, 39-41; **11**: 42;
13: 23; **EX 5.4**: 3
6: 12, 19; **8**: 17; **13**: 40
13: 37
DS 5.1: 2-10
1: 11; **2**: 11; **5**: 30; **7**: 12, 26-27, 67; **8**: 31; **11**: 5,
 11, 24, 41, 58, 67
3: 85
1: 9; **6**: 19; **11**: 8; **13**: 35
8: 12, 14, 25, 37
2: 38; **3**: 19, 30, 33, 38; **4**: 1; **11**: 14
5: 15-16, 23, 26-27, 31, 35-36, 42, 45; **6**: 12;
7: 104; **8**: 4-6; **EX 5.1**: 1; **EX 5.3**: 3; **EX 5.4**: 1-3
6: 20; **7**: 83-86; **DS 5.1**: 7
7: 87, 91, 95, 97, 1001, 103, 107
2: 5, 11-12, 25, 27-30, 33-34, 39-40, 45-48, 59-60,
 64; **3**: 69; **7**: 42-43, 48, 56, 69; **8**: 33, 45; **11**: 12,
 27; **12**: 13; **13**: 28
2: 5, 29-30, 33
2: 29, 39
2: 29
2: 67-68; **3**: 83; **4**: 21, 27; **8**: 11; **9**: 7
4: 14; **8**: 31
2: 19, 21; **3**: 62-63; **EX 3.2**: 3-4
IS 11.1: 7-9, 11-12
3: 7, 86; **4**: 5, 7-8, 10; **5**: 14, 18, 24-26, 28, 34, 40;
7: 53; **8**: 5; **EX 4.1**: 4-6; **EX 5.4**: 3
13: 35, 37
2: 6; **3**: 8, 19-20, 23, 31, 33, 49, 71, 74-75; **4**: 14,
 16; **5**: 1, 14, 42; **7**: 7, 18-19; **EX 4.1**: 4-5, 7
2: 6; **3**: 8, 20, 39, 49-51, 53, 57; **5**: 20, 26; **7**: 11;
8: 5, 34; **EX 4.1**: 4-6
7: 92, 94, 96-97, 100-101
6: 19; **7**: 80, 83-84, 86; **8**: 5; **DS 5.1**: 2
5: 23-24; 35; **EX 5.4**: 2
 see Fourier transform
 see calibration

- header (information, structure) **6:** 16-18; **EX 5.5**
- hemisphere (upper/lower of focal sphere, hemisphere projection) **3:** 63-64; 68, 70; **EX 3.2:** 1-3; **EX 3.3:** 6
- heterogeneity **2:** 17, 42, 59; **11:** 22; **EX 11.2:** 1; **IS 5.1:** 5
- higher mode
see mode
- high-frequency decay **3:** 10, 39; **11:** 69-70; **EX 3.4:** 5-6
- high-frequency magnitude **3:** 45
- high pass
see filter
- Hilbert transform
see transform(ation)
- Hooke's law **2:** 4; **IS 3.1:** 3
- Huygen's principle **2:** 25, 41
- hypocenter **2:** 48, 60-61, 68; **3:** 14, 45, 59, 70, 78, 80; **4:** 13; **7:** 13-14; **9:** 48; **10:** 2-3; **11:** 1, 24, 32, 34, 39, 65, 100; **13:** 1-2, 4, 19-20, 25, 27-29, 33-34; **EX 11.1:** 1-3; **7:** 13-14; **11:** 34-38, 99; **13:** 1, 19-20, 27-28, 33; **IS 11.1:** 7, 17-18, 24
EX 11.1: 1-2; **IS 11.1:** 27
see source depth
- hypocenter determination/location
 - hypocenter distance
 - hypocenter depth
- HYPO71 **3:** 28, 69-70; **10:** 3-5, 17; **11:** 60; **13:** 28
- HYPOELLIPSE **3:** 69-70; **10:** 4; **13:** 28
- HYPOINVERSE **3:** 69-70; **10:** 4
- HYPOMOD **PD 11.1**
- HYPOSAT **IS 11.1:** 10, 18-19, 30; **PD 11.1**
- identification (of seismic events) **11:** 24-34
- identification (of seismic phases) **1:** 5-6, 10-12, 14; **2:** 24, 30, 43, 47-57; **3:** 34; **11:** 2, 4, 12-22, 24-26, 32-34, 52, 57, 61-100; **1:** 5; **11:** 28-31
- identification (of underground nuclear explosions)
- impedance (acoustic) **2:** 33, 37, 41, 44, 47; **7:** 4, 12, 20, 23, 38-39; **8:** 44
- impedance (electrical) **5:** 27, 31, 33-35; **7:** 54, 59-61; **8:** 33
- in-plane (rupture propagation; fault geometry) **IS 3.1:** 10, 15, 18
- installation **1:** 6, 14-15, 16-18; **2:** 22; **4:** 20, 24, 29-31; **5:** 28-30, 34; **6:** 12, 15; **7:** 1, 4-5, 9, 15-16, 18-19, 33-35, 39, 46-49, 54, 58, 61-71, 73-78, 80-84, 86-87, 89-93, 96-97, 99-102, 105-107; **8:** 3-4, 7-8, 13, 33-34, 36-38, 50-51, 53; **9:** 3, 15; **13:** 18-19, 38, 41
4: 29-31; **7:** 39, 58, 64, 75-86, 88-90, 92-93
4: 29; **7:** 26, 28, 31-32, 47, 63, 75
7: 26, 32, 47, 58, 63, 66, 69-70, 75
7: 67-68, 71
7: 90-93

7: 75-86

7: 17-20, 47-57
- installation in boreholes
 - installation in mines
 - installation in tunnels
 - installation of an STS2
 - installation of borehole accelerometers
 - installation of borehole broadband seismometers
 - installation of seismic sensors
- intensity
see macroseismic data and observations
- intensity attenuation
see macroseismic data and observations
- intensity scales
see macroseismic data and observations

- International Data Centre (IDC) **1:** 8; **2:** 60; **3:** 34; **8:** 28; **10:** 1, 5, 10; **11:** 12, 29
- International Monitoring System (IMS) **1:** 6, 8; **8:** 28; **9:** 39, 49; **10:** 2, 5, 10; **11:** 29, 64
- International Seismological Centre (ICS) **1:** 1, 5; **2:** 50-51, 57-58; **3:** 32, 34, 49, 70; **8:** 58; **10:** 1; **11:** 5
- inversion **2:** 13, 36, 63, 65, 71; **3:** 8, 13, 69, 71, 74-76, 78-81, 93; **5:** 39; **10:** 8; **11:** 39, 69; **13:** 5, 10-11, 28, 35-36
see macroseismic data
- isoseismal map
- isotropic
see isotropy
- isotropy **2:** 4; **11:** 21
- Japanese Seismic Networks **8:** 29-30, 59
- Kinematics (seismometers and data acquisition systems) **6:** 8, 15; **7:** 18, 87, 92-93, 99, 105; **8:** 5, 13; **DS 5.1:** 3
- Kirnos (seismograph, response, record, filter) **1:** 8; **2:** 47; **3:** 23, 47; **4:** 11-12, 14; 16-17; **11:** 5, 17, 19, 33, 35, 40-43, 45, 48, 50-51, 75, 77, 86; **DS 11.1:** 11-12; **DS 11.2:** 2-3, 8, 13, 20; **DS 11.1:** 11-12; **DS 11.2:** 2-3, 8, 13, 20; **EX 11.2:** 5-6
3: 11, 62-63; **EX 3.2:** 1-3; **EX 3.3:** 5
- Lambert-Schmidt net (projection)
- Lamé parameters
- layers (Earth's layers) **2:** 1, 5, 11-13, 17, 26-28, 33-35, 37, 40, 44-45, 59-60, 62, 64-65, 67-68; **3:** 30, 66, 69, 93; **4:** 22, 29; **5:** 28-30; **6:** 17, 20; **7:** 7, 71, 81, 83, 87, 102-103; **9:** 11; **11:** 63-64; **13:** 10, 28, 38
2: 59, 62
- D" layer **2:** 27-28, 33-34, 49, 64; **IS 2.1:** 13; **13:** 10
 - horizontal layer model **2:** 13, 29, 31-32, 59; **3:** 30; **4:** 29
 - low-velocity layer/zone **2:** 28
 - multi-layer model **2:** 35, 44; **EX 11.1:** 1
 - one (single)-layer model/crust **2:** 35, 46
 - tilted layer model **2:** 33-34, 44; **11:** 63-64; **IS 2.1:** 13
 - two-layer model **7:** 15, 46, 48, 57
- layers (of insulation/shielding material)
- leaking mode see mode
- Lennartz (seismometers and data acquisition systems) **5:** 28; **6:** 20; **8:** 6; **DS 5.1:** 4
- lightning protection **7:** 48, 54-55, 59-61, 90, 93, 108; **8:** 33, 55; **13:** 38
- location (of seismic sources) **1:** 10, 12, 14, 16; **2:** 1, 5, 24, 41, 43, 45, 57-58, 63; **3:** 4, 15, 28, 69-70, 79-80; **4:** 20-21; **7:** 1, 13, 15-16, 25, 38; **8:** 1-2, 12-14, 28, 34-35, 38, 40-43, 53, 58; **11:** 2-3, 5, 7-9, 12, 14, 27, 32-39, 58, 60, 63-65, 69, 89, 98-99; **12:** 16; **EX 11.1;** **EX 11.2;** **IS 7.4;** **IS 11.1;** **PD 11.1**
IS 11.1: 1
- centroid location **7:** 13, 15, 25; **8:** 41-43; **11:** 14, 34, 39; **IS 11.1:** 7, 12, 16-17, 22, 24, 26; **IS 7.4**
 - location accuracy **IS 11.1:** 12, 15, 19, 24, 26-27
 - location errors **IS 11.1:** 7-8, 10-16, 18-19, 22, 24 and the programs given above from HYPO71 to HYPOSAT
 - location programs **IS 11.1:** 24, 27
 - mislocation
- low-frequency level (of spectrum) see spectral plateau
- low-pass filter see filter

- low-velocity layer/zone see layer
- macroseismic data and observations **1:** 2, 15; **3:** 7, 15, 39, 41, 81; **12:** 1-20
- barycenter **12:** 16-17
 - European Macroseismic Scale (EMS) **12:** 2
 - intensity attenuation **12:** 13-14, 19
 - isoseismal map **12:** 12-13
 - JMA scale **12:** 2, 7
 - macroseismic data **3:** 15; **12:** 7, 11, 13-14, 16-18
 - macroseismic effects **3:** 56
 - macroseismic epicenter **12:** 16
 - macroseismic focal depth **12:** 17-19
 - macroseismic intensity **1:** 18; **3:** 6-7, 15-16, 18, 43-45, 50, 82, 86; **12:** 1-7, 10-20
 - macroseismic intensity scales **1:** 18; **3:** 7; **12:** 1-7, 10-11, 19
 - macroseismic magnitude (see magnitudes)
 - macroseismic questionnaire **12:** 7-8
 - Modified Mercalli Scale **12:** 1-2
 - MSK scale **12:** 1-2
- magnetic core **5:** 23
- magnification (amplitude response of seismographs) **2:** 19, **3:** 17, 19-20, 23-24, 28, 41; **4:** 11, 17-18; **5:** 2, 10, 12, 28; **11:** 9, 10, 17, 34-35, 40, 42, 44, 99; **13:** 23; **EX 4.1:** 3, 5; **EX 5.1:** 1, 3; **EX 11.3:** 3; **IS 5.2:** 5-6
- magnitude **1:** 7-8, 12, 14, 16; **2:** 1, 15, 17, 20, 24, 37, 39, 45; **3:** 1, 3-7, 9, 15-50, 48-49, 51-52, 74-82, 84-87; **4:** 3, 11-12, 21, 31; **7:** 13, 18, 25, 28, 41, 67, 80; **8:** 14, 41, 53, 58; **9:** 48; **10:** 2-5; **11:** 1-2, 7, 9-10, 14-15, 17-19, 23, 28-33, 38, 41, 47, 59, 63, 67-68, 71, 73, 89, 99-100; **12:** 1, 17-19; **13:** 34; **EX 3.1:** **DS 3.1**
- body-wave magnitude **3:** 4-5, 7, 9, 33-36, 39, 42, 45-46, 49, 79, 85; **11:** 29, 100; **DS 3.1:** 3-7; **EX 3.1:** 6-7
 - broadband (medium-period) magnitude mB **3:** 38, 46-50; **DS 3.1:** 3; **EX 3.1:** 6-7
 - duration magnitude Md **3:** 27-29
 - energy magnitude Me **3:** 7, 18, 37-38, 50, 54-57, 83
 - high-frequency magnitude **3:** 45
 - Lg magnitude **3:** 42-43
 - local magnitude MI(ML) **2:** 45; **3:** 22-27, 83; **11:** 28, 67, 71; **DS 3.1:** 1; **EX 3.1:** 1-2, 5-6;
 - macroseismic magnitude **3:** 43-45; **12:** 17
 - magnitude calibration functions **1:** 8, 14, 16; **2:** 1, 17, 45; **3:** 17, 19, 22-27, 30-35, 38-42, 47-50, 83; **11:** 15, 38; **DS 3.1:** 3-6; **EX 11.3:** 1, 3, 15
 - magnitude determination **1:** 10, 14, 16; **2:** 24; **3:** 17-19, 21-23, 25, 27, 30, 33, 35, 42, 48; **4:** 12; **8:** 58; **11:** 7, 10, 38, 100; **EX 3.1**
 - magnitude nomenclature **IS 3.2**

- magnitude relationships **3:** 32, 46-49, 85
- magnitude saturation **3:** 9, 25, 34-35, 37, 39, 46, 48, 85-86, 91, 93
- magnitude scales **1:** 8; **3:** 16, 18-19, 23-50; **4:** 3; **11:** 38; **DS 3.1:** 1-7
- mantle magnitude M_m **3:** 36-37
- moment magnitude M_w **3:** 7, 9, 17-18, 31, 36, 44-45, 50, 56, 82-83, 87, 91
- PKP-wave magnitude **3:** 42; **DS 3.1:** 6-7; **EX 11.3:** 3-5, 15
- short-period P-wave magnitude mb **3:** 33-36; 40-42; 46-49; **DS 3.1:** 5-6
- spectral magnitude **3:** 17, 32, 38-40
- surface-wave magnitude M_s **2:** 15; **3:** 30-33, 43, 46-47, 49, 85; **11:** 30, 41, 47, 100; **DS 3.1:** 2; **EX 3.1:** 5, 7
- teleseismic magnitude **3:** 29;
- tsunami magnitude **3:** 46
- mantle **1:** 11; **2:** 2, 12-13, 15, 19-20, 25, 31-32, 38, 43-44, 47-49, 58-60, 62-63; **3:** 2, 20, 30-31, 36, 79; **9:** 34; **11:** 7, 13-14, 16, 20, 24-25, 27, 33, 61, 63-64, 67-68, 72-73, 75, 80, 89, 98
- Earth's mantle **2:** 2, 47, 62; **3:** 2; 20, 30-31, 36-37, 40; **11:** 24, 74; **IS 2.1:** 3-8, 10-14
- mantle transition zone **2:** 13, 30-31, 47, 62-63; **3:** 40; **11:** 72
- lower mantle **2:** 31, 39, 48-49, 51, 59, 60, 62-63; **11:** 72, 75
- upper mantle **2:** 12-13, 25, 31-32, 38, 44-45, 48, 59-62, 63; **3:** 2, 31, 36, 40; **11:** 27, 64, 72-73, 75
- Mark (seismometers) **7:** 19; **8:** 5; **DS 5.1:** 5
- medium (Earth's medium) **2:** 4-5, 9, 11, 13, 25-27, 33, 36, 39-42, 63-64; **3:** 5, 7, 11, 15-16, 18-19, 38, 69, 71, 87; **4:** 1; **7:** 38, 42; **13:** 2-3, 10, 12-13,
- anisotropic (Earth's) medium **2:** 4, 11; **11:** 19
- elastic medium **2:** 4-5
- homogeneous medium **2:** 5, 37; **EX 3.5:** 2; **IS 3.1:** 4-5, 8-9
- inhomogeneous medium **2:** 5, 25, 36
- isotropic medium **2:** 4, 9, 11, 37; **3:** 5, 11, 69; **EX 3.5:** 1-2; **IS 3.1:** 5, 9, 13
- methods
 - ACH method **9:** 32
 - beampacking method **9:** 26
 - check-sum method **8:** 26
 - CMT method **3:** 79
 - circle method **8:** 2; **EX 11.1;** **IS 11.1:** 4-5
 - compression method **6:** 17
 - correlation method **9:** 33
 - CRC method **8:** 22
 - delay-and-sum method **11:** 57
 - double-beam method **9:** 6
 - EMSC method **3:** 80
 - error-correction method **8:** 26
 - FEC method **8:** 22, 26
 - f-k method **9:** 27-29; **11:** 52-55

- gain-ranging method **6:** 19
- Herglotz-Wiechert method **2:** 57
- Nakamura method **4:** 22
- plane-wave method **11:** 63
- random signal method **5:** 2, 38-40
- ray-theoretical method **2:** 38
- reflectivity method **2:** 5, 64-65
- spectral-ratio method **11:** 29
- steady-state method **5:** 2, 36
- transient (impulse) method **5:** 2, 37-38
- vespagram method **9:** 33; **11:** 52-53
- weighted-stack method **9:** 35-36
- micro-barometric recording **2:** 22
- microseism see noise
- mislocation see location
- mode
 - higher mode **2:** 12, 17, 21, 42
 - leaking mode **IS 2.1:** 11
 - mode conversion **2:** 12, 24, 42
- models **1:** 3, 7-8, 11-12, 14, 16-18; **2:** 1-2, 4, 15, 23, 25, 27-31, 33-36, 38, 41, 44-46, 57-63; **3:** 29, 59, 69, 78-79; **5:** 17; **7:** 15; **8:** 2, 41-42, 53; **9:** 11-12; **11:** 7-8, 14, 26, 28, 31, 35-36, 39, 61, 63-64, 66, 71, 74, 78, 83, 92-93, 98; **12:** 19; **13:** 2-3
 - ABM model **3:** 40
 - AK135 model **2:** 60-63; **11:** 26, 28, 64, 74, 98; **DS 2.1:** 7-11
 - IASP91 model **2:** 44-45, 50-52, 55, 58-60; **3:** 38, 40; **11:** 61, 64, 78, 92-93, 98; **DS 2.1:** 4-6
 - Jeffreys-Bullen (J-B) model **2:** 57, 60; **11:** 98
 - PREM model **2:** 13, 15, 23, 32, 38, 57, 59, 62-63; **3:** 34, 38, 40-41; **DS 2.1:** 1-3
 - SP6 model **2:** 58-60
- model for attenuation see attenuation
- model for data see data
- model for noise see noise
- model for seismic source see source
- modeling **1:** 12; **2:** 5, 28, 38, 45, 48, 57, 63-65, 67-69; **3:** 15, 18; **5:** 36; **7:** 13-15; 43, 91, 101; **8:** 43, 45; **11:** 26, 69
- modes **2:** 2, 12-13, 17, 21-23, 29, 43, 64; **3:** 75, 77; **6:** 15; **7:** 16, 35; **8:** 20; **12:** 10; **13:** 24
 - free-oscillation modes **2:** 2
 - fundamental modes **2:** 11, 13; **3:** 75
 - higher modes **2:** 12, 21, 43; **7:** 35
 - normal modes **2:** 21-23, 64; **7:** 35
 - spherical modes **2:** 21, 23
 - toroidal modes **2:** 21, 23
- Mohorovičić discontinuity (MOHO) see crust-mantle boundary
- moment (seismic) **2:** 6, 64, 69; **3:** 4, 7-11, 13, 15-18, 22, 31-32, 36-38,

- 45-46, 49-50, 55-57, 71-80, 82-89, 91-93; **4**: 16;
6: 8, 17; **8**: 56, 58; **10**: 9, 16; **11**: 11-12, 16, 41, 68;
13: 5, 9-11; **IS 3.1**: 3, 7-9, 12-18
3: 79; **EX 3.2**: 6-7; **EX 3.3**: 4; **IS 11.1**: 28
- centroid moment tensor **3**: 75; **EX 3.5**: 2;
- elementary moment tensor **3**: 45
- high-frequency moment **3**: 7, 9, 17-18, 31, 36, 44-45, 50, 56, 82-83, 87, 91
- moment magnitude **3**: 32, 82-85
- moment-magnitude relation **2**: 6, 8-9, 13; **3**: 8-9; **IS 3.1**: 9
- moment rate **2**: 6; **3**: 4, 15, 67; **11**: 11
- moment release see tensor
- moment tensor **3**: 73, 77, 79; **EX 3.5**: 1
- moment tensor decomposition **3**: 71, 74, 78-81, 93; **11**: 69; **13**: 10
- moment-tensor inversion **2**: 64; **3**: 8, 11, 71-80, 93; **11**: 41, 68; **13**: 5, 9-11;
EX 3.5: 1-2
- moment tensor solution (determination) **3**: 7-9, 11, 82-89; **EX 3.4**: 1, 3-6; **EX 3.5**: 1; **IS 3.1**:
8, 13-14, 17-18
- static (scalar) seismic moment M_0 **1**: 1, 5, 7-9, 13-14; **7**: 2, 47, 87; **8**: 2-3, 13-14, 28,
31, 35, 44, 54; **9**: 39, 49; **10**: 2, 5, 10-12; **11**: 29;
12: 2; **13**: 1-2, 16-19, 21-23, 26, 28, 31, 33-38,
40-42
- monitoring **6**: 13, 20; **8**: 32; **DS 5.1**: 10
- Nanometrics (seismometer, instrument) **1**: 6, 8; **2**: 57-58, 64; **3**: 3, 14, 31-34, 38, 69, 79-81
- National Earthquake Information Center (NEIC) **3**: 24-25, 87; **EX 5.2**: 2; **EX 5.4**: 3
- natural (free) period **2**: 64; **8**: 5
- near field see Dirac impulse
- needle impulse
- network **7**: 15, 77; **8**: 8, 43, 53
- network configuration **IS 7.4**
- network detectability **8**: 28-32
- network examples **7**: 15; **8**: 42; **IS 7.4**
- network geometry **7**: 1, 13-15; **8**: 36, 43, 45-46; **IS 7.4**
- network layout **8**: 53
- network tuning **8**: 8-10, 14-15, 35, 40-41, 52-53
- physical seismic network **1**: 5-6, 10-11, 13, 16; **2**: 8, 46; **3**: 28, 42-43, 80, 85;
4: 20, 31-32; **5**: 30; **7**: 1-4, 7, 15-17, 25-27, 39-43,
45-46, 54, 64; **8**: 1-3, 8-22, 27-33, 35-43, 45-48, 50-
59; **10**: 2, 7, 14; **11**: 4-5, 11, 14, 18, 24-25, 31, 35,
39-41, 58, 67; **13**: 1-2, 5, 18-20, 23, 28, 30, 33, 35,
40-42; **EX 11.1**: 1, 5-6, 8; **IS 7.4**
- seismic network **3**: 13; **8**: 21
- strong-motion network **8**: 18, 43
- weak-motion network **8**: 8-10, 11-15, 20-21, 43
- virtual seismic network see noise
- New Low-Noise Model see noise
- New High-Noise Model **3**: 59-61
- nodal line see plane
- nodal plane

- noise **1:** 4, 15; **2:** 1, 22, 44,51, 65, 67; **3:** 6, 10, 28-29, 53, 78-79; **4:** 1-12, 12, 16, 18-32; **5:** 3-4, 20-22, 24, 26, 28-34, 40, 42, 46; **6:** 2, 6-11, 17, 19; **7:** 1-2, 4-7, 9-13,15-39, 41-42, 45-47, 53, 55, 58-59, 63-70, 72-77, 80-81, 84-85, 90, 93; **8:** 3-7, 16, 18-19, 21, 33-35, 41, 43-45, 49, 52; **9:** 1-2, 7, 16-19, 22-24, 34, 36-39, 41-42; **10:** 4; **11:** 1-2, 7-8, 10, 28, 31, 35, 39-41, 56, 59, 73, 88; **13:** 17-18, 20-21
3: 6; **4:** 3-4, 7, 18; **5:** 28, **7:** 17; **8:** 4; **11:** 1; **13:** 17
- ambient (background; environmental) noise **4:** 24; **5:** 21
 - barometric noise **5:** 31
 - Brownian noise **3:** 53
 - coda noise **5:** 24, 31-33
 - electrical (electronic) noise **5:** 27-28, 30, 31-33, 41, 46; **6:** 2, 6, 9, 11, 19; **7:** 59, 64-65, 84-85; **8:** 5, 33; **11:** 41
 - instrument(al) (self-)noise **3:** 6; **7:** 1, 5, 10-11, 16, 22, 24, 28, 31, 64; **13:** 17
 - man-made noise **4:** 19-21
 - microseismic noise **4:** 5-7, 10, 25; **5:** 4; 20, 28-29, 32, 46; **7:** 27 84-85
 - New Low Noise Model **4:** 5-8, 25; **7:** 30
 - New High Noise Model **4:** 10; **5:** 46; **EX 4.1;** 1-2; **PD 4.1**
 - NOISECON (program) **2:** 44, 51; **3:** 28, 52; **4:** 20, 23, 28; **5:** 28-29, 32, 41; **6:** 11; **7:** 7, 10, 16, 19-20, 24, 26, 28, 34, 42, 45, 69-70, 74-77, 81, 84-85; **8:** 16, 33-34, 43, 52; **EX 4.1:**8
 - noise level **4:** 29, 31; **7:** 9-10, 15-39; **8:** 44
 - noise measurements **4:** 3-8, 10, 25; **5:** 28; **7:** 17, 21, 26-27, 30. 64-65; **EX 4.1:** 2
 - noise model **4:** 28-29
 - noise polarization (filtering) **4:** 5-8, 22, 24
 - noise power **4:** 27-28
 - noise prediction filtering **4:** 22, 29-30; **6:** 7, 10; **7:** 24, 38-39, 67-68, 76; **9:** 42
 - noise reduction **7:**2, 5-7, 9-11
 - noise sources **4:** 3-6; **7:** 10-11, 17-18, 22-24, 33-34; **EX 4.1:** 1-2
 - noise spectrum **6:** 11
 - noise test **7:** 16
 - noise variability **4:** 18
 - ocean bottom noise **6:** 7, 10; **11:** 46
 - quantization noise All Chapter **4;** **IS 7.3**
 - seismic noise **2:** 22; **4:** 25-30
 - signal-to-noise improvement **3:** 10, 28, 78; **4:** 1, 16, 24-26, 30; **5:** 31, 41; **6:** 6-8, 10; **7:** 10, 16, 25, 34, 41-42; **8:** 21, 33-34, 41; **9:** 1-2, 7, 16-19, 36; **10:** 4; **11:** 23, 35, 40, 56, 70, 88
 - signal-to-noise ratio **5:** 31
 - thermal electronic noise **2:** 22, 24, 30; **4:** 24, 30; **5:** 20, 29-30; **7:** 46-47, 76, 81; **8:** 34; **13:** 18
 - tilt noise **5:** 26; **7:** 12, 23, 34
 - traffic noise **6:** 6
 - white noise **4:** 21, 23; **7:** 58; **8:** 35; **13:** 18
 - wind-generated noise **4:** 10; **EX 4.1:** 1; **PD 4.1**
- NOISECON (program) **4:** 10; **EX 4.1:** 1; **PD 4.1**

- nomenclature **1:** 11, 17-18; **2:** 23, 40, 47, 50-51; **3:** 34; **11:** 5, 61, 63,-64, 72, 75, 80; **13:** 3
 - magnitude nomenclature **IS 3.2**
 - nomenclature of seismic phases **IS 2.1**
normal modes see modes
NORSAR array **9:** 2, 5-6, 31
Northern California Seismic Network **3:** 28
Norwegian National Seismic Network **8:** 12, 32
nuclear explosion see explosion
Nyquist frequency **3:** 52; **6:** 5, 13; **7:** 17; **11:** 71
ocean-bottom seismograph (OBS) **4:** 20
octave **1:** 9; **3:** 6, 17, 38-40; **4:** 1, 3, 9-12, 14, 32; **5:** 20; **6:** 5; **7:** 65; **11:** 40, 42; **13:** 32
origin time **2:** 50, 60; **3:** 6, 14-15, 28; **8:** 41; **9:** 48-49; **10:** 4; **11:** 1, 8, 13, 23
oversampling **6:** 6-7; **8:** 17;
overtones (see also higher modes) **2:** 12-13, 17, 21, 23; **6:** 12; **13:** 13-14
particle motion **2:** 5, 8-12, 15-16; **11:** 19-21, 23, 35, 37, 57, 59; **EX 11.2:** 1
pendulum
 - pendulum clock **11:** 8; **12:** 4
 - pendulum length (reduced) **EX 5.2:** 3-4, 6
 - pendulum seismometer **4:** 18; **5:** 14-19, 25, 37
period
 - center period **3:** 39; **4:** 9
 - corner period **11:** 11, 47; **EX 5.5:** 7
 - eigen/free/natural period **1:** 12; **3:** 24-25, 87; **4:** 1, 16-18; **5:** 18; **EX 5.2:** 2; **EX 5.4:** 3
phase
 - Airy phase **2:** 15
 - body-wave phase **2:** 40, 43;
 - crustal (local) phases **2:** 18, 44, 46; **11:** 61, 63-65, 71; **DS 2.1:** 7, 13; **EX 11.1:** 1, 3; **IS 2.1:** 1, 7, 12-13
 - core phases **1:** 11; **2:** 50-51, 59-60, 62; **3:** 42; **4:** 13; **11:** 18, 20, 76, 80-99; **EX 11.3:** **DS 2.1:** 1, 9, 15-17
 - depth phases **1:** 11; **2:** 46, 48, 60, 67-68; **3:** 51; **11:** 13, 16, 18, 22-28, 32, 36-37, 58, 63-64, 69, 75, 77, 81, 89, 96, 99-100; **DS 2.1:** 10; **EX 11.2:** 2-4; **EX 11.3:** 2-4, 11, 14; **IS 2.1:** 3, 10; **IS 11.1:** 18, 20, 24
 - mantle phases **1:** 11; **2:** 44; **11:**14; **DS 2.1:** 8, 14-15
 - phase (mode) conversion **2:** 2, 17, 24, 33, 43, 49, 58
 - phase distortion **2:** 26, 34, 39; **8:** 6
 - phase identification/interpretation **2:** 24, 58, 60, 63; **11:** 1.2, 4, 12-14, 16, 18, 33, 54; **EX 11.1:** 2-4; **EX 11.2:** **EX 11.3**
 - phase names (seismic) **2:** 47, 49-50, 52 55, 67; **IS 2.1;** **DS 2.1**
 - phase response **IS 5.2:** 1, 5-6
 - phase shift/delay **2:** 7, 11-12, 26, 39-40; **4:** 3, 17-18, 23; **5:** 15; **6:** 8, 14; **9:** 27; **11:** 20, 36, 97; **EX 5.1:** 1; **EX 5.4:** 3;

- phase spectrum **EX 5.5:** 1; **IS 5.2:** 1, 5-6
 - phase velocity **4:** 2-4
 - secondary phases **2:** 12,15; **IS 5.1:** 5
- seismic phases **1:** 5-6, 10; **2:** 2, 24, 43; **3:** 47-48, 65; **11:** 19, 27, 32, 34, 39, 79, 98
 - 1:** 5-6, 10, 16; **2:** 1-2, 15, *17-20*, 24, 29-30, 32, 43-57, 59-61, 64; **3:** 16, 20, 22, 24, 29-31, 33-34, 42, 48, 51, 53, 70; **4:** 3; **9:** 2, 11-12, 25, 41; **11:** 1, 4-5, 7, 9, 13-14, 21, 25, 32-34, 36, 38, 70, 84, 98-99;
 - EX 11.1:** 1-7; **IS 2.1**
- plane
 - auxiliary plane **3:** 59-61, 66; **EX 3.2:** 5
 - equatorial plane **3:** 66; **EX 3.2:** 4-5
 - nodal plane **3:** 70; **EX 3.2:** 4-5; **EX 3.5:** 5
 - fault plane see fault
 - plane wave see wave
- plunge **3:** 11, 81; **EX 3.2:** 5, 7
- Poisson's ratio **2:** 3-4, 6, 8
- Poisson solid **2:** 4, 6, 12
- polarity **2:** 40; **3:** 5-6, 58-60, 62, 64, 66-67; 69-71, 81; **4:** 11, 28; **5:** 33, 38; **6:** 2; **8:** 7; **10:** 3-4; **11:** 1-2, 7, 9-11, 23, 31, 35-37, 71, 100; **EX 3.2:** 1-4; **EX 3.3:** 1, 4-5
- polarization **2:** 5, 9, 11-13, 43, 57-58; **4:** 19, 22-23, 28-29; **5:** 29; **7:** 46; **9:** 2, 45; **11:** 4, 19-22, 29, 33-35, 36, 39, 57, 61, 98-99; **13:** 26-28, 32-34; **EX 11.2:** 1
- polarization filter (see filter) **4:** 28-29
- pole
 - pole (of a plane) **3:** 66; **EX 3.2:** 4-5
 - poles of the pressure (P) and tension (T) axes **3:** 66, 68; **EX 3.3:** 1, 4, 5
 - poles and zeros (of a transfer function) **3:** 35; **5:** 5-7, 11-13, 45; **EX 5.1:** 1; **EX 5.5:** 1-6
- point source see source
- power
 - power spectral density **4:** 4-8; **7:** 26, 76, 85; **13:** 22, 24; **EX 4.1:** 2, 5-7
 - power spectrum (see spectrum) **3:** 38, 56-57; **4:** 4-6; **5:** 4
 - power consideration **7:** 2, 8; **13:** 41
 - power consumption **1:** 14; **6:** 2, 9, 15-16; **7:** 41, 43; **8:** 16; **13:** 40-41
 - power dissipation **6:** 13
 - power law **9:** 36
 - power supply **5:** 22; **6:** 18; **7:** 8, 47
 - quantization of noise power **6:** 7
- pre-amplifier **5:** 27, 31-32, 45; **6:** 2; **7:** 18, 106
- pressure **2:** 2-4, 8, 22, 31; **3:** 2, 6, 11, 60-61, 66, 69-70; **4:** 18-19, 21, 24; **5:** 20-22, 29-30, 33; **7:** 28, 33, 46, 48, 53, 63, 65, 66-68, 73, 75, 79-80, 92, 100-101, 103
- air/barometric pressure **2:** 22; **4:** 24; **5:** 21-22, 29-30, 33; **7:** 46; **13:** 38;

- confining pressure **EX 4.1:** 3, 8
 - fluid pressure **2:** 8
 - pressure (P) axis **7:** 100
 - pressure (P) pole **3:** 59-61, 66, 68-70; **EX 3.2:** 1, 4-5, 7; **EX 3.3:** 5-6
 - pressure quadrant **3:**66, 68, **EX 3.2:**, 7
 - pressure shielding see quadrant
 - wind pressure **5:** 30; **7:** 33, 67
- principal axes **7:** 28
- principal stress **3:** 11, 74, 77, 81
- processing see stress
- array processing **1:** 4, 6, 10, 12-13, 15-16; **2:** 2, 4, 61, 63; **3:** 50, 78;
 - detection processing **4:** 1, 16, 24, 30; **5:** 2-4, 8, 27, 45; **6:** 1, 10, 17; **7:** 11, 41-42, 45, 48, 85; **8:** 1, 3-4, 6-8, 10, 13, 15, 18, 20, 25, 36, 40, 49-50, 52-55, 58; **9:** 1-3, 16, 18, 38, 41, 43-45, 48; **10:** 1, 3-5, 16-17; **11:** 2-3, 5, 11-12, 36, 38-39, 41, 56, 60, 98; **12:** 11; **13:** 33
 - event processing see array
 - pre-processing **9:** 2-3, 18, 41, 44
 - signal-attribute processing **9:** 2-3, 41, 48
 - signal processing **3:** 78; **4:** 16; **11:** 39, 41
- Prototype International Data Center (PIDC) **9:** 2-3, 41, 44
- purchasing (of seismic systems and services) **3:** 78; **4:** 16; **11:** 39, 41
- Q (quality factor) **9:** 2-3, 41, 44
- Q (function) **3:** 78; **4:** 16; **11:** 39, 41
- quadrant **9:** 2-3, 41, 44
- compressional quadrant (of first-motion polarities) **4:** 30; **5:** 2-3, 8; **6:** 1, 10; **8:** 3, 50; **9:** 1-2, 16; **11:** 11-12, 39, 60
 - dilatational quadrant (of first-motion polarities) **10:** 5; **11:** 29; **IS 10.3:** 1-7, 9, 14
 - pressure (P) quadrant **7:** 8-9, 40, 42, 66, 84; **8:** 36-39, 47-50
 - tension (T) quadrant **2:** 37-38, 62; **3:** 40; **DS 2.1:** 1-3, 7-11; **EX 3.4:** 1
- quarry blast see magnitude calibration function
- radio-frequency interference **2:** 37-38, 62; **3:** 40; **DS 2.1:** 1-3, 7-11; **EX 3.4:** 1
- radiation pattern see magnitude calibration function
- radio-frequency (RF) interference **3:** 60; **EX 3.2:** 4; **EX 3.3:** 6
- radio-frequency (RF) survey **3:** 59-60; **EX 3.2:** 4; **EX 3.3:** 6
- radio-link data transmission **3:** 59-61, 66, 68-70; **EX 3.2:** 1, 4-5, 7; **EX 3.3:** 5-6
- ray **3:** 59-60; **EX 3.2:** 4; **EX 3.3:** 5
- ray angle see blast
 - ray defocusing **7:** 45
 - ray diagrams **3:** 8, 33, 51, 57, 59-61, 63-64; **EX 3.4:** 3
 - ray focusing **7:** 75-76; **8:** 46
 - ray parameter **7:** 39-46; **8:** 45-46

- ray path **2:** 25-28, 37, 39-41, 43, 47-49, 67-68; **3:** 34, 52, 59, 69; **11:** 6, 63, 69, 75-78, 80-82, 84-87, 90-97; **IS 2.1:** 13-17
 - ray propagation **IS 11.3 and related animation CD-ROM**
 - ray theory **2:** 5, 25, 33, 38, 40-41, 64
 - ray tracing **2:** 47, 50, 64
 - ray tube **2:** 36-37, 39, 64
 - seismic ray **2:** 7-9, 24-26, 29, 31, 33, 36, 39, 41, 44, 47; **3:** 54, 58; **9:** 11; **11:** 20, 66, 74, 79
- receiver (mechanical; see seismometer) **IS 5.2:** 2, 4
- recorder **1:** 4; **2:** 1, 63-64; **3:** 24, 27; **5:** 24-25, 27, 31, 34, 36, 38-39, 45; **6:** 1, 3, 8-9, 12, 15-17, 20; **7:** 6, 17, 64, 105; **8:** 4, 8-9, 15, 17-19, 27; **10:** 6, 12-14, 16-17, 20; **11:** 8; **13:** 14; **EX 5.4:** 3
- record examples
- reflection **2:** 11, 24, 26, 30, 32-34, 37, 40-43, 48, 57, 64, 67; **3:** 51, 71; **4:** 1, 30; **6:** 1, 15; **7:** 42, 102; **8:** 45; **11:** 17-18, 20, 27, 61, 72, 75, 77, 79-80, 89, 98, 100
- reflection coefficient **2:** 33, 40; **3:** 51
 - reflectivity method see methods
- refraction **2:** 26, 32, 43, 50, 68; **3:** 31, 69; **6:** 20; **7:** 12, 102, 107; **11:** 67, 72
- residual **2:** 61; **3:** 52; **5:** 39-40; **7:** 49, 106; **8:** 5; **9:** 32; **10:** 4
- residual signal **5:** 39-40; **EX 5.4:** 1
- resistor **EX 5.2:** 2-3; **EX 5.3:** 2
- resolution **1:** 9-10, 17; **2:** 29, 41, 61; **3:** 21, 27; **4:** 7, 13, 17; **6:** 1-2, 6-7, 9-10, 12-13, 19; **7:** 7, 17-18, 33, 35, 38, 65, 85; **9:** 6, 22-23, 25, 29, 33, 36; **11:** 4, 8-9, 13, 30, 41, 99; **12:** 6; **13:** 20, 29, 39-40, 42; **EX 11.1:** 3
- resonance (and resonance effects) **2:** 1, 37; **3:** 66, 4; 17-19; **5:** 27, 37; **13:** 6; **EX 5.4:** 3
- response
- amplitude response **4:** 13, 16, 18; **5:** 2, 6, 12-13, 15-16, 38; **11:** 42, 44; **EX 5.5:** 1; **IS 5.2:** 1, 5-6
 - frequency response **3:** 17, 20, 27; **4:** 3, 16; **5:** 1-3, 6-8, 41-42; **7:** 17, 25-26; **8:** 5, 7, 56; **11:** 1-2, 42; **EX 5.5:** 1; **IS 5.1:** 4
 - impulse (step) response **3:** 71; **5:** 1, 7, 13, 37-38, 45; **6:** 4, 8, 19-20; **EX 5.2:** 1, 5-6; **EX 11.1:** 5
 - instrument response **1:** 12; **2:** 64; **3:** 8, 50, 79; **4:** 16; **5:** 8
 - phase response **5:** 2, 6; **IS 5.2:** 1, 5-6
 - recorder response **IS 5.2:** 4
 - response function/curve **3:** 72; **5:** 15, 45; **6:** 2; **8:** 5-6, 30, 31, 56-57; **EX 5.1;** **IS 5.2;** **PD 5.8**
 - seismograph response **2:** 64; **5:** 2; **11:** 4, 10; **EX 5.1;** **EX 5.5**
 - seismometer response **2:** 63; **4:** 18; **11:** 10, 47; **EX 5.2:** 2, 4; **EX 5.5:** 7
 - site response **7:** 87, 89, 91, 97, 101, 103, 108
 - step response see impulse response
 - temperature response **7:** 106
 - transient response **3:** 17; **4:** 15, 17-18; **5:** 35; **11:** 10

- restitution (of the true signal) **1:** 6, 13; **3:** 17; **4:** 14; **5:** 42; **11:** 39-41, 45, 47-48, 50
- restoring force **2:** 36; **5:** 1, 13, 17-18, 20
- RF link **7:** 5, 9, 39-44, 59; **8:** 10, 45, 49; **IS 8.2:** 2
- RF survey **7:** 39, 42-43, 45-46; **8:** 45-46
- rigidity **2:** 3, 7, 13; **3:** 7, 55; **EX 3.4:** 3; **EX 3.5:** 1
- ring buffer **6:** 17; **8:** 11, 18, 20
- rise time **3:** 6, 9
- rock burst **2:** 18; **3:** 5; **11:** 1, 28; **EX 11.1:** 4, 6
- rupture **2:** 2, 6, 45, 64; **3:** 2, 4, 6, 9-15, 18, 20-22, 37-38, 41, 46, 53, 58-59, 66, 69, 71, 78-80, 82, 86-93
3: 10, 12; **EX 3.4:** 4-6
 - circular rupture **3:** 10, 12, 85; **EX 3.4:** 4, 6
 - rectangular rupture **3:** 10, 87-88; **IS 3.2:** 17; **EX 3.4:** 3-6
 - rupture area **IS 3.1:** 18
 - rupture energy **3:** 9-10, 37, 82, 87-93; **IS 3.1:** 9
 - rupture (fault)length **IS 3.1:** 10
 - rupture front **3:** 6; **IS 3.1:** 10-12
 - rupture model **3:** 59, 65-68; **EX 3.4:** 6; **EX 3.5:** 1; **IS 3.1:** 10, 16
 - rupture plane **3:** 9-10; **EX 3.4:** 6; **EX 3.5:** 1; **IS 3.1:** 1, 9-11
 - rupture propagation (anti-plane, bi-lateral, bi-directional in-plane, radial, unilateral) **5:** 7; **6:** 1-14, 16-17, 19;
 - rupture sampling **3:** 92
 - rupture time **3:** 10, 45, 87-89, 91; **EX 3.4:** 6
 - rupture width **3:** 87, 92-93; **IS 3.1:** 11
 - rupture velocity **5:** 45-46; **10:** 6-7, 15, 17-20; **13:** 41
- successive approximation register (SAC) **6:** 4
- sample device **6:** 9, 11
- sample & hold device **3:** 49; **6:** 1-14, 16-17, 19; **8:** 17-18
- sampling **7:** 94-95, 97-99
 - geotechnical sampling **6:** 6-7; **8:** 17
 - oversampling **6:** 1, 3-8, 11-14, 16-17; **7:** 11, 17, 26, 40; **8:** 17; **9:** 16; **11:** 8, 46, 65, 69-71; 99; **13:** 37, 40
 - sampling rate (frequency) **7:** 6, 12, 59; **8:** 45
- seismic coupling **EX 5.2:** 3-4, 6
- seismic mass see noise
- seismic noise **7:** 8, 47-48, 78; **8:** 7, 33-34, 52
- seismic shelter **IS 7.2**; **IS 7.3**
- seismic sites **7:** 45, 59, 90; **8:** 1, 9-10, 13-16, 18-20, 26, 35-36, 46-47, 49-51, 55-57, 59
- seismic system **8:** 15
 - analog seismic system **8:** 16
 - digital seismic system **8:** 15-16
 - mixed seismic system **8:** 8-10; 47, 50
 - physical seismic system **8:** 11-14
 - virtual seismic system see waves
- seismic waves **7:** 2, 4, 6, 9, 12, 31, 61
- seismo-geological conditions

- seismogram
- seismogram analysis **1:** 6, 10; **2:** 26; **3:** 70; **4:** 16; **11:** 1, 4-5, 7-8, 10, 12, 14, 24, 32, 34, 37, 39, 59, 61, 80, 99-100
 - seismogram examples **1:** 5, 11; **2:** 6, 10-11, 14, 16, 18, 20, 24, 42-43, 46-48, 50, 65-66, 68-69; **3:** 21, 39, 53; **4:** 12-14, 16-17, 22, 25-32; **7:** 21-25, 27-28, 33, 35-38, 66, 69-70, 72-74, 88; **8:** 2; **9:** 8, 1-18, 20-23, 28, 31, 34-35, 42, 46-48; **11:** 3, 9, 11-13, 15-17, 21-22, 25-28, 30, 36, 38, 40, 46-59, 62, 65-70, 72-77, 79, 81-82, 84-88, 90-91, 94-97; **13:** 3-16, 21-32; **EX 11.1:** 5-6; **EX 11.2:** 6-7; **EX 11.3:** 6-9; **DS 11.1 - DS 11.4** **2:** 2, 5, 21, 63-68; **3:** 74; **4:** 17; **IS 2.2:** 1
 - synthetic seismogram **2:** 2, 5, 21, 63-68; **3:** 74; **4:** 17; **IS 2.2:** 1
- seismometer (seismograph, seismic sensor)
- borehole seismometer **7:** 79-83
 - broadband seismometer/seismograph/sensor **1:** 5,12; **2:** 6, 47, 52, 55-56; **3:** 50; **4:** 7, 13, 17, 30; **5:** 20, 24-25, 27, 29-30, 33-34, 41-42, 44; **7:** 46-48; **8:** 5; **9:** 6-7; **11:** 2; **13:** 1, 7-8, 19-20, 24, 38; **EX 5.4:** 1, 3; **EX 5.5:** 1, 7
 - electromagnetic seismometer **EX 5.4:** 3
 - long-period (LP) seismometer **1:** 8, 12; **2:** 19; **3:** 22, 30; **4:** 16; **5:** 9, 17-18, 20, 27, 34; **7:** 81; **8:** 8; **9:** 6
 - seismometer calibration see calibration
 - short-period (SP) seismometer (records) **2:** 45, 48; **4:** 17; **5:** 32; **7:** 1, 16, 33; **8:** 29; **9:** 6, 8; **13:** 20
 - strong-motion seismometer (see also accelerometer) **7:** 61, 105; **8:** 5, 7, 18, 30
 - very broadband seismometer **8:** 5; **EX 5.5:** 7
 - weak-motion seismometer **7:** 61; **8:** 4-5
- sensor (seismic) see also seismometer, seismograph
- acceleration sensor **EX 5.5:** 7
 - active sensor **5:** 23, 28, 31, 42; **7:** 49; **8:** 6-7; 33
 - BB sensor see broadband seismometer
 - passive sensor **5:** 23-26, 31, 39, 42; **7:** 55; **8:** 6-7, 33
 - displacement sensor **3:** 49; **5:** 25; **11:** 33
 - sensor calibration **1:** 12; **5:** 34-36; **8:** 53, 56-57
 - sensor shielding see shielding
 - strong-motion sensor see accelerometer
 - weak-motion sensor **8:** 4-5
- shake table **5:** 2-3, 17, 34, 36, 41-42
- shear modulus (see rigidity)
- shielding **5:** 30; **7:** 8, 15-16, 19, 28, 33, 46-47, 55, 65-68, 71-74; **8:** 33-34; **13:** 18
- signal (definition see Glossary)
- broadband signal **5:** 2; **13:** 20; **EX 4.1:** 1
 - input/output signal **3:** 17, 27, 39, 69-70, 74, 77; **4:** 3-4, 8, 15-16, 18, 27-28; **5:** 1-3, 5,7-8, 10, 13, 24-27, 35-36, 38-40, 42-46; **6:** 1, 4-6, 8-12, 14, 19; **7:** 42-44, 48-49, 55, 81-84; **8:** 5-7, 17, 26, 33, 56; **9:** 19; **11:** 44-45;

- signal analysis **EX 5.4:** 1-3; **EX 5.5:** 1
 - signal coherence **4:** 14; **4.1:** 2
 - signal energy **9:** 17, 29; **11:** 2, 5, 51; **13:** 21
 - signal detection **EX 4.1:** 1
 - signal discrimination **9:** 2; **11:** 2, 39
 - signal filtering **13:** 22, 34
 - signal preparation **11:** 10, 39-40
 - signal processing **6:** 2
 - signal restitution see processing
 - signal-to-noise ratio **1:** 14; **3:** 17
 - signal transmission see noise
 - stationary signal **7:** 39; **13:** 39
 - transient signal (disturbance) **4:** 15; **5:** 4
- simulation **4:** 2-4, 7, 10-11, 13, 15; **5:** 6, 31, 34; **6:** 14; **EX 5.4:** 1
- SINFIT (program) **4:** 16, 18; **5:** 40; **11:** 21, 39-41, 44-45, 47-52, 58-59, 67; **13:** 6
- site effect **5:** 36, 46; **PD 5.6**
- site (and instrument) location **3:** 19; **7:** 89; **13:** 30
- site selection **7:** 1, 5, 19, 55, 63, 71, 75
- slip **1:** 13, 16; **4:** 31; **5:** 28-29; **7:** 1-2, 5, 8-9, 12, 15-17, 43, 47, 77-78, 93, 102; **8:** 7, 36, 43-47; **13:** 18; **IS 7.1**
- slip direction **3:** 2, 10-11, 12, 15, 70, 82, 88-89, 91-92
 - slip vector **3:** 10, 59-61, 65-66; **EX 3.2:** 5
 - slip velocity **3:** 11, 65; **EX 3.5:** 1; **IS 3.1:** 9
 - dip slip **3:** 13-14, 92
 - strike slip **3:** 13-14, 75
- slowness **3:** 3, 5, 11, 37, 59, 65, 67-68, 75, 88, 91
- slowness correction **2:** 26-29; **3:** 52; **9:** 2, 11-14, 17, 21-30, 32-36, 38, 42, 44-45; **11:** 1-3, 12, 14, 32, 34, 39, 52-54, 56, 63, 71, 79-80, 95, 97-100; **13:** 20, 31-32; **EX 3.3:** 1-2, 6
 - slowness estimate **9:** 32
- Snell's law **9:** 29-30, 45
- software **2:** 25-27, 33; **9:** 11
- GIANT software **1:** 9-10, 12-13, 16; **2:** 40, 63; **3:** 70; **4:** 14, 16; **5:** 38, 40, 42, 45-46; **6:** 14, 18, 20; **7:** 15, 43, 45; **8:** 4, 8, 10-13, 17, 22-23, 25-26, 36, 49-50, 53-55;
 - ORFEUS software links **10:** 6-7, 11, 14-20; **11:** 1, 4-5, 8, 10, 12, 14, 20, 32-34, 37, 39, 57-58, 60, 63, 75, 98-99; **12:** 14; **13:** 34-35, 41; **EX 5.4:** 1; **PD 4.1;** **PD5.1-5.9;** **PD 11.1-11.2**
 - PITSA software **11:** 14, 60
 - SEISAN software **11:** 60
 - SHM software **4:** 16; **5:** 45-46; **10:** 13-14, 18-19; **11:** 60; **13:** 41
- SHM software **3:** 70; **4:** 16; **10:** 4-6, 15-18, 20; **11:** 14, 33, 36-37, 60
 - SHM software **11:** 5, 14, 35, 58-59, 74

- source
- explosion source **3:** 4-6, 8-10, 67; **9:** 1, 6, 28, 31, 34
 - double-couple source model (focal mechanism) **2:** 7; **3:** 51, 59-61, 70-74, 78; **13:** 4; **EX 3.5:** 1-2; **IS 3.1:** 11
 - point source **2:** 7; **3:** 10, 43, 58-59, 71, 78-79; **IS 3.1:** 7-8, 11
 - seismic source **1:** 4, 10, 12, 15; **2:** 1-2, 17, 35, 44, 65; **3:** 1, 6-8, 10, 12, 15-18, 48, 50, 71, 74, 82, 87; **4:** 1, 15; **7:** 87; **11:** 1, 8, 10-11, 24, 28, 33, 38, 61, 63-64, 69, 99; **13:** 2, 7, 33-34; **EX 11.1:** IS 3.1
 - shear source (see also shear dislocation) **2:** 7, 39; **3:** 7-9
 - source area **3:** 3, 7, 10, 15; **EX 3.4:** 3-6
 - source depth (focal depth, hypocenter depth) **2:** 19, 43, 45, 48, 60, 64, 67-69; **3:** 7, 16, 19, 24, 31, 37, 48; **11:** 5, 13, 14, 16, 18, 22-27, 36-37, 39, 61, 66, 69, 71, 98; **EX 11.2:** 1-2, 5; **EX 11.3:** 1-3, 12-13; **IS 11.1:** 16, 18, 20-22
 - source dislocation **EX 3.4:** 3-6
 - source model **3:** 43, 69, 71, 79, 85, 91; **13:** 3, 6; **IS 3.1:** 1, 6, 14, 16
 - source parameter **1:** 15; **2:** 42, 65, 69; **3:** 1, 4, 12, 18, 25, 71, 74, 80-81, 83, 88; **11:** 1, 10, 23, 41, 54, 59, 69; **EX 3.1-3.5**
 - source process **2:** 7; **3:** 1, 4-5, 9-10, 16, 32, 38-39; **4:** 1, 20, 23; **11:** 4, 11, 17, 29, 69; **IS 3.1**
 - source radius **3:** 10; **EX 3.4:** 4-6; **IS 3.1:** 15, 18
 - source/rupture model **2:** 38; **3:** 6, 10-12, 14-15, 43, 58, 68-71, 79, 85, 87, 91; **IS 3.1:** 1, 6, 14; **4:** 16; **13:** 6
 - source pulse **2:** 2, 6; **4:** 15
 - source spectrum **2:** 39; **3:** 7-8, 17, 39, 49, 93
 - source-time function **2:** 6, 65, 68-70; **3:** 10, 73-74, 93; **EX 3.5:** 1; **IS 3.1:** 17
 - source volume **3:** 87; **IS 3.1:** 1, 4, 6-7;
- Southern California Seismic Network spectrum **8:** 29
- amplitude spectrum **2:** 13, 38; **3:** 7-8, 10, 17, 36, 38-39, 45, 49-50, 52, 82, 93; **4:** 2-5, 14-15, 19, 25, 29; **5:** 7; **6:** 5-7, 12; **7:** 64, 68, 74, 85; **9:** 33; **11:** 10, 16, 52, 59, 69-70; **13:** 13, 40
 - alias spectra **3:** 36, 45; **4:** 2, 4; **5:** 7
 - alias spectra see aliasing
 - frequency spectrum **4:** 15, 24-25, 28
 - Fourier spectrum **4:** 2; **11:** 70
 - noise spectrum see noise
 - phase spectrum **4:** 2-4
 - power spectrum **3:** 38; **4:** 4-8; **7:** 18, 21-24, 26, 30, 33-36, 68, 76, 85; **13:** 13
 - spectral analysis **4:** 4; **11:** 39, 60; **13:** 22, 34-35, 38
 - spectral density **4:** 2, 4-6, 8; **7:** 26, 76, 85; **13:** 3, 22, 24
 - spectral domain **2:** 22; **13:** 6, 20, 22
 - spectral plateau **3:** 8-10, 39 ; **EX 3.4:** 3, 5-6
 - spread spectrum **7:** 39-42, 45-46; **8:** 10
- definition see Glossary

- speed (of seismic waves) **2:** 59, 61; **DS 2.1:** 1, 7
- SRO-LP (long-period seismograph,filter) **4:** 17; **7:** 28, 82-83; **11:** 15, 21, 41-43, 45, 47-48, 50, 81-82, 85, 88, 100; **DS 11.2:** 23, 25, 39, 41; **DS 11.3:** 1-5, 10, 17, 22-23
- station (see glossary)
- seismic station **1:** 4, 12, 15-16; **2:** 9, 15, 19, 37, 43, 48, 50, 69; **3:** 8, 18, 22, 29, 33, 58; **4:** 11, 20; **7:** 1, 4-8, 10-13, 15, 27, 31-32, 40-41, 43-47, 50, 55, 58-60, 62, 75; **8:** 1, 3-4, 7-10, 12-13, 22-25, 29, 32-34, 37-38, 41-45, 51, 53, 55; **9:** 1, 32; **10:** 6, 15; **11:** 3, 7-8, 26, 30, 44, 100; **13:** 7-8, 17-20, 26, 38, 40-41; **EX 5.5:** **2:** 68; **3:** 38-39, 47, 50; **8:** 14, 36; **9:** 17, 21, 25; **11:** 2-5, 9, 13-14, 24, 32, 35, 38, 51, 59-60, 63, 98; **13:** 21, 24, 26
 - single-station (method) **7:** 5, 10; **13:** 19
 - station access(ibility) **2:** 60; **3:** 19, 22, 24, 27
 - station correction **13:** 18 (see also **IS 7.4** and network configuration)
 - station distribution see site selection
 - station site selection **7:** 61; **8:** 4, 41; **9:** 1
 - three-component station see impulse response
- step response **EX 5.2:** 1-2
- step function/impulse **2:** 2-4, 36; **3:** 2-3, 7, 32, 36, 82, 93; **7:** 101, 103; **13:** 2-3, 8, 31, 35, 77, 88; **IS 3.1:** 2-4, 12-13; **IS 5.1:** 1, 3-8
- strain **3:** 32, 36
- strain energy **3:** 82
 - strain rate **IS 3.1:** 2-3, 12; **IS 5.1:** 1, 3, 5
 - strain tensor **5:** 1; **13:** 35-36; **IS 5.1**
- strainmeter **2:** 2-5, 36, 69; **3:** 2, 4, 6, 10-11, 15-17, 22, 36-39, 45, 48, 55-57, 69, 73, 82-84, 87-88, 90, 92-93; **5:** 21; **7:** 53, 97; **13:** 4; **IS 3.1:** 1, 3-5, 8-9, 11-17
- stress **3:** 37, 55-57
- apparent stress **IS 3.1:** 17
 - frictional stress **3:** 11
 - principal stress **3:** 11
 - stress direction **3:** 4, 7, 10, 15, 17-18, 36-39, 45, 48, 55, 57, 69, 82-84, 87-88, 90, 92-93; **11:** 11, 16; **EX 3.4:** 4-6; **IS 3.1:** 14-16
 - stress drop **2:** 2, 4, 36; **IS 3.1:** 3
 - stress-strain relationship **2:** 5; **3:** 11; **IS 3.1**
 - stress tensor
- strech module (see Young's module)
- strong motion **5:** 25; **7:** 3, 9, 19, 21, 27, 38, 40; **8:** 3-4, 6, 9, 21, 27, 38, 40;
- strong-motion accelerometer **7:** 88
 - strong-motion array **7:** 86-89, 91, 97, 102, 107
 - strong-motion borehole system **7:** 92, 104
 - strong-motion data **7:** 87-88
 - strong-motion installation **7:** 86-87, 90-92

Index

- strong-motion instrumentation **7:** 50, 87, 93
- strong-motion network **8:** 3, 19, 21, 27
- strong-motion observations/
monitoring/studies **7:** 87, 92
- strong-motion sensor (see also
accelerometer) **7:** 61-62, 92, 105
- strong-motion site (response) **7:** 101, 104
- strong-motion systems **7:** 87, 92
- STS1/2 (seismometers, response) **2:** 20, 22; **4:** 10, 16.17; **5:** 19, 22, 27, 30, 40, 43;
7: 26, 27, 32, 46, 65-74, 81, 84; **8:** 5, 31, 38; **11:** 20,
41-48; **13:** 8; **DS 5.1:** 8-9; **EX 5.4:** 1; **EX 5.5:** 7
EX 3.4: 3, 5-6
- surface amplification
- synthetic seismogram **2:** 2, 5, 21, 64-66, 68; **3:** 74
- system installation **8:** 50-51
- telemetry **6:** 19; **7:** 5, 8-9, 39-42, 44-45, 59; **8:** 13, 15, 33, 38-
39, 44-45, 56; **10:** 16; **13:** 23, 40
- teleseismic distance (range) **2:** 43, 48, 65; **3:** 16, 29, 34; **4:** 20; **11:** 17-19, 24, 61,
89, 98-99; **EX 11.2:** 1
- teleseismic record **2:** 64, 67-68; **3:** 15, 66; **11:** 38, 57-58, 99; **DS 11. 2**
to **DS 11.4**; **EX 11.2:** 1, 6-7; **EX 11.3:** 6-9
- temperature **2:** 31; **3:** 2; **4:** 30; **5:** 19, 21-22, 29, 33; **6:** 3, 11,
17; **7:** 8, 32, 47-49, 51, 53, 58, 61-63, 65-70, 72-73,
75, 100, 106; **8:** 6, 33, 44, 49, 55, 57; **11:** 41; **12:** 5;
13: 18, 37-39
- temperature shielding see shielding
- tension **2:** 2-3; **3:** 2, 11, 52, 59, 66, 69-70, 74, 77
3: 59-61, 66, 68, 70; **EX 3.2:** 1, 4-5; **EX 3.3:** 5-6
- tension axis
- tension quadrant see quadrant
- tensor **2:** 4
3: 75-76; **EX 3.5:** 2
2: 64; **3:** 8, 11, 71-80; **IS 3.1:** 7-8, 12-14
2: 5; **3:** 11; **IS 3.1:** 1, 3-4
- TERRASCOPE **6:** 14, 21
- thermal
 - thermal drift **5:** 21, 26, 34; **7:** 49
 - thermal equilibrium **5:** 34
 - thermal inertia **5:** 21; **7:** 53
 - thermal insulation **5:** 21; **7:** 8, 46, 49, 53, 57, 62-63, 67, 75
 - thermal noise (see noise)
 - thermal shielding **5:** 30; **7:** 15
- tilt **2:** 22; **4:** 24, 30; **5:** 18-22, 25-26, 29-30, 34, 42, 44;
7: 15, 27-28, 46-48, 53, 61, 65, 74, 76, 79, 81;
8: 34; **13:** 18, 36
13: 35-36, 38
- tilt meter see noise
- tilt noise see noise
- tilt sensitivity **7:** 27
- TILTCAL (program) **5:** 44-45; **PD 5.5**
- time

- onset time **2:** 40, 45, 68; **3:** 22, 28; **4:** 29; **9:** 2, 9, 24, 31-32, 45, 48; **11:** 1-2, 7-9, 11, 14, 23-24, 33-35, 40, 47, 56, 61, 65, 71, 74, 98-100; **EX 11-1:** 2-3
- origin time **2:** 51, 61; **3:** 6, 14-15, 28; **8:** 41; **9:** 48-49; **10:** 4; **11:** 1, 7, 12-13, 23; **EX 11.1:** 3-4
- time accuracy **8:** 1, 27; **11:** 8, 23, 99
- time base **6:** 15, 18
- time delay **2:** 11; **8:** 9, 12, 20, 27; **9:** 12-17, 19, 22, 30-31, 45; **11:** 56
- time domain **3:** 71, 74-75, 79; **4:** 1-2, 8, 14-15; **5:** 8, 45; **6:** 8; **7:** 11, 20, 24; **9:** 23, 26-27, 29; **11:** 41; **13:** 15, 23; **EX 4.1**
- time series **3:** 72, 75; **4:** 2, 23, 27; **5:** 6, 8, 33; **6:** 3, 6, 17; **7:** 26; **9:** 18-19, 22-23, 38; **10:** 10, 15-16
- timing problem **6:** 15; **11:** 8
- transducer **5:** 10, 14-15, 17-18, 20, 23-27, 31, 34, 42, 44; **6:** 2, 20, 23-25, 27, 31, 34, 42, 44
- acceleration transducer **IS 5.2:** 2
- electromagnetic transducer **5:** 10, 23, 31; **EX 5.3:** 1
- displacement transducer **5:** 24, 27, 42; **IS 5.2:** 2
- force transducer **5:** 23-25
- transducer constant **EX 5.1:** 1; **EX 5.2:** 4, 6
- velocity transducer **IS 5.2:** 2
- transient response **3:** 17; **4:** 15, 17-18; **11:** 10
- transient signal **3:** 17; **4:** 4; **5:** 6; **6:** 14; **7:** 26; **13:** 34
- transition zone **2:** 13, 30-31, 47, 62; **3:** 40; **11:** 71
- transducer **5:** 10, 14-15, 17-18, 20, 23-25, 27, 31, 34, 42, 44; **6:** 2; **EX 5.1:** 3; **EX 5.3:** 1; **IS 5.2:** 2-3; 5
- transfer
 - data transfer/transmission **8:** 1, 10, 12, 14, 21; **10:** 10; **11:** 5, 12
 - transfer function **1:** 12; **3:** 17, 80; **4:** 1, 14; **5:** 1-2, 5-14, 27, 33-34, 36, 38-40, 42, 45; **6:** 5, 8; **8:** 57; **9:** 23-27, 33; **10:** 14; **11:** 41-44; **EX 5.1:** 1; **EX 5.4:** 2-3; **EX 5.5:** 1
- transform(ation) **2:** 39-41, 65; **3:** 4, 37, 51, 63-64, 72, 81; **4:** 1, 4-9; **5:** 4-8, 10, 15, 22; **9:** 2, 24; **11:** 14, 20, 33, 41, 54, 57, 75, 99; **13:** 13, 22, 31; **EX 4.1:** 1, 4
- fast Fourier transform (FFT) **5:** 7
- Fourier transform(ation) **3:** 72; **4:** 1, 4, 25; **5:** 5-7; **6:** 4-5; **9:** 2, 24; **13:** 13, 22; **EX 5.5:** 1
- Hilbert transform(ation) **2:** 39-40; **3:** 81; **5:** 6; **11:** 14, 33, 75, 99
- Laplace transform(ation) **5:** 4-9; **6:** 8; **EX 5.5:** 1
- of units **4:** 10; **EX 4.1**
- transformer effect **EX 5.2:** 1
- transformer generated noise **7:** 20, 23, 25, 55, 59, 64
- transmission **2:** 32-33, 37-38, 41, 65; **3:** 71; **6:** 20; **7:** 2, 8-9, 12, 39-45, 47, 50, 60; **8:** 4, 8-10, 15-16, 20-22, 25-28, 32, 36, 39-40, 44-46, 55; **10:** 1, 5-6, 10; **11:** 5; **13:** 38, 40

- data transmission see data
- transmission coefficient **2:** 37, 64
- transmission links **IS 8.2**
- travel time **2:** 1, 24-25, 27-28, 33-34, 38, 41-43, 47, 57-61; **7:** 102, 104-105; **9:** 12; **10:** 4; **11:** 12-14, 26, 59, 66, 80, 98; **13:** 4; **PD 11.2**
- reduced travel-time (curve) **2:** 29-31, 46, 58, 64-66, 68
- travel-time branch **2:** 29-32, 39-40, 68; **4:** 13; **11:** 13, 18, 89; **EX 11.3:** 2; **IS 2.1:** 1, 4
- travel-time curve **1:** 16; **2:** 1, 25, 28-36, 40-41, 43, 45-48, 51-53, 57, 65, 68; **4:** 13; **11:** 7, 13-14, 18, 22, 24, 35-37, 39, 63-64, 66, 71-72, 75, 78, 80, 83-84, 87-89, 92-93, 95, 97-98; **EX 11.1:** 7; **EX 11.2:** 8; **EX 11.3:** 10-14
- travel-time differences **4:** 31; **9:** 13; **11:** 7, 13-14, 18, 24-25, 33, 35, 37-38, 98, 100; **13:** 28; **EX 11.1:** 1-3; **EX 11.2:** 2-5, 10; **EX 11.3:** 11-13
- travel-time fit **EX 11.1:** 3-4
- travel-time model **2:** 57; 60; **11:** 5, 35-36, 98
- travel-time residual **10:** 4
- travel-time tables **2:** 49, 58-59, 64; **3:** 69; **11:** 7, 35-36, 58, 71; **EX 11.2:** 2, 10
- tremor **3:** 4; **13:** 2, 9-15, 17, 19, 22-23, 28, 30-31, 35, 37
- trigger(ed) **3:** 5-6; **4:** 11; **6:** 15; **7:** 1, 41; **8:** 9-12, 18-20, 22-23, 26-27, 29-30, 32, 40-41, 43, 52-53; **9:** 2, 18, 22, 41, 43-45; **11:** 39; **13:** 6, 38, 40-41
- coincidence trigger **8:** 10, 19-20, 27; **IS 8.1:** 15-16, 18
- detriquer threshold **IS 8.1:** 3-4; 6, 10, 12-14, 16
- false trigger **IS 8.1:** 9, 17
- STA/LTA trigger **8:** 19, 53; **9:** 18, 41; **11:** 40; **13:** 40; **IS 8.1**
- trigger algorithm **8:** 10, 18-20, 40, 53; **9:** 18; **IS 8.1:** 1-2, 4-5, 7-8, 12-16, 18
- trigger threshold **7:** 1; **8:** 19-20, 43, 53; **IS 8.1:** 6-7, 9, 11-12, 14, 19
- tsunami **3:** 36, 38, 46, 57, 92
- tsunami magnitude 46
- UKAEA array typ **9:** 6
- underground nuclear explosion (see explosion)
- UNICROP (program) **5:** 33, 46; **PD 5.7**
- vault (seismic) **4:** 24; **5:** 1, 21, 28-29; **7:** 1, 8-9, 12-13, 26, 46-64, 66, 68-76, 78; **8:** 6-7, 30, 33-35, 37, 45, 55; **13:** 39
- vault construction **7:** 61, 64, 69, 71, 73; **13:** 39
- vault-type seismic station **7:** 47-53
- vector dipoles **3:** 72-73, 77
- velocity (speed) **2:** 5-8, 12-15, 26-37, 44, 59, 62; **3:** 6, 8-9, 24, 29-31, 38, 40, 56-57, 59, 66, 69-70, 78; **4:** 22, 24, 26-27, 29; **7:** 4, 12, 37, 101-104; **8:** 42, 44, 53; **DS 2.1:** 1-11; **EX 3.2:** 1-2; **EX 3.3:** 1-2; **EX 11.1:** 1, 3
- (of seismic wave propagation) **9:** 33-36; **11:** 39, 52-53, 59, 79-80
- vespagram **13:** 2, 11-15, 17, 19, 22-23, 28, 30-31, 35, 37
- volcanic tremor **13:** 1, 3, 6, 16, 18, 21-22, 26, 31
- volcano-seismic signals

- volcano seismology
 wall (hanging wall, foot wall)
 wave (seismic)
- body wave
1: 8, 10; **2:** 2, 5-7, 21, 24-25, 41-42, 57, 63; **3:** 4-5, 7, 16, 19-20, 22, 26, 29-30, 34-35, 51-53, 71, 78-81; **4:** 10-12, 20, 22, 29; **11:** 7-8, 10, 14-18, 35, 63-64, 67-68, 72-73, 75, 99; **13:** 24, 30; **EX 11.2:** 2; **IS 2.1:** 3-4, 12
 - channel wave
11: 71
 - compressional wave
2: 7; **13:** 33
 - converted wave
2: 41; **11:** 64, 79
 - diffracted wave
2: 41; **11:** 25
 - diving wave
2: 33
 - guided wave
2: 17
 - head wave
2: 33, 35, 40-41, 44; **3:** 70
 - longitudinal wave
2: 5; **3:** 5, 30, 61; **11:** 81, 99
 - Love wave
2: 11-12, 17, 19, 43; **3:** 33, 37; **11:** 19-21, 31, 36, 58; **IS 2.1:** 3-4, 11
 - P wave
1: 8; **2:** 5-9, 14, 31-32, 38-40, 43, 45, 49-50, 58, 60, 69; **3:** 5, 9, 16-17, 19, 21, 28-30, 34-36, 38-42, 45-49, 51-53, 59-60, 69, 78-79, 81; **4:** 11, 14, 22, 26, 29, 31-32; **7:** 37-38, 57, 103-104; **8:** 19; **9:** 38; **11:** 8-9, 16, 18, 20, 22, 24-25, 29, 31, 35, 37, 40, 47, 51, 56-57, 63, 71, 73, 80-81, 87, 98, 100; **13:** 4; **IS 2.2:** 3
3: 42, 81; **7:** 38; **11:** 56-57, 87; **EX 11.3;** **IS 2.1:** 5-6, 9
 - PKP wave
2: 8-9, 25-26, 39; **9:** 11-15, 18, 24-25, 30-32; **13:** 31, 34
 - primary wave
2: 25, 44; **11:** 16
 - Rayleigh wave
2: 11-15, 17, 19, 42; **3:** 31, 33, 37, 42, 48; **4:** 19, 22; **11:** 15, 20-21, 29, 36, 58, 63; **13:** 26; **IS 2.1:** 3-4, 11
 - reflected wave
2: 12, 26, 34, 44-46; **4:** 29, 31;
 - refracted wave
2: 48; **11:** 66
 - S wave
1: 7; **2:** 5-9, 11, 17-18, 24, 32, 37-39, 41-42, 44, 46-47, 57-63; **3:** 8-10, 19-20, 33-34, 48, 51, 57-58, 60-61, 70-71, 80-81; **7:** 4, 12, 38, 103-105; **8:** 2; **11:** 16-17, 19-21, 24, 29, 33, 61, 63-65, 71, 73, 75, 81, 98-99; **IS 2.2:** 3
 - scattered wave
2: 33, 66; **3:** 28
 - secondary wave
2: 25, 47
 - shear wave
2: 7, 11, 46; **3:** 6, 52, 62; **4:** 22; **7:** 101; **11:** 81; **12:** 18
 - surface wave
1: 5-8; **2:** 5, 7, 11-17, 19-21, 24, 37, 42-43, 64, 67; **3:** 7, 9, 16, 19-22, 29-37, 46-47, 54, 71, 89; **4:** 20-

- tertiary (T) wave
 - transverse wave
 - wave attenuation
 - wave equation
 - waveform

 - waveform fitting
 - waveform modeling
 - wavefront
 - wave theory
 - wave velocity

 - Wood-Anderson (seismograph, filter, response)
 - World Data Center (Centre) (WDC)
 - Worldwide Standard Seismograph Network (WWSSN)
 - Wulff net
 - WWSSN-SP (short-period seismograph, filter, response)

 - WWSSN-LP (long-period seismograph, filter, response)

 - Young's modulus
 - zeros (see poles and zeros)
 - zero-frequency seismology
- 22; **8:** 6, 19; **11:** 7, 9-10, 14-16, 19-22, 24, 27, 29, 33, 41, 63, 68, 72-73, 83, 89, 99-100; **13:** 23-24, 30; **EX 11.2:** 2-3; **IS 2.1:** 2, 3-4, 11-12
IS 2.1: 11
2: 48; **IS 2.1:** 3
2: 37-38, 62; **3:** 8, 26; **7:** 15; **12:** 18
2: 5, 11-12
1: 9, 12, 15; **2:** 5-7, 26, 29, 39-41, 43, 47-48, 63-65, 67-69; **3:** 8, 15, 18-19, 36, 66, 71, 76, 78-80; **5:** 3, 7, 34, 36; **6:** 18; **7:** 1, 5, 25, 57-58; **8:** 11-12, 24, 41, 58-59; **9:** 36, 45; **10:** 1-2, 4, 6, 11-15, 17; **11:** 5, 8, 14, 16-18, 26, 33, 35, 37, 46-48, 51-52, 61, 67-70, 99; **13:** 16, 28-29, 32
2: 64; **11:** 26, 69, 98-99; **EX 5.4:** 1
2: 48, 63-69; **5:** 36
2: 7-9, 25-26, 36-37, 39; **9:** 9; **11:** 3, 66, 91; **13:** 34
2: 33, 40-41, 64
2: 8-9, 11, 13-14, 21, 25, 32-33, 38, 49, 59; 62-63;
3: 9, 57; **4:** 22, 29; **7:** 4, 12, 101-102, 104; **8:** 53;
11: 72, 80; **12:** 18
1: 7; **3:** 16, 20, 23-24, 26-27; 4: 16-17; **11:** 5, 18, 33, 41-42, 45-46, 67; **DS 11.1:** 1
11: 34
1: 6; **3:** 16, 23; **5:** 9, 30; **11:** 2, 5, 11, 17, 22, 33, 40-49, 51-53, 58, 77, 85-86, 100
3: 62, 68; **EX 3.2:** 1-2; **EX 3.3:** 1
1: 8; **3:** 33, 41-42, 45; **4:** 11-12, 14, 16-17; **7:** 65;
11: 11, 17, 22, 33, 40-49, 50, 52, 77, 85-86, 100;
DS 11.2: 11-12, 14, 17, 21, 34-35, 39; **DS 11.3:** 6, 12, 16-17, 20-21, 23; **DS 11.4:** 1-4
2: 5; **4:** 16-17; **5:** 9, 11-13; **7:** 65; **11:** 41-46, 53, 58, 100; **DS 11.2:** 10, 22, 28, 36-37, 43; **DS 11.3:** 10-11, 13-14, 19; **EX 11.2:** 1, 7
2: 3-4
IS 5.1: 8